Journal of the European Ceramic Society **15** (1995) 1–8
© 1995 Elsevier Science Limited
Printed in Great Britain. All rights reserved
0955-2219/95/$9.50

Control of Texture in Al_2O_3 by Gel-casting

T. Carisey, A. Laugier-Werth & D. G. Brandon

Department of Materials Engineering, Technion, Israel Institute of Technology, Haifa 32000, Israel

(Received 19 April 1994; accepted 2 May 1994)

Abstract

Small alumina platelets were distributed in an alginate-containing alumina slip and oriented by tape-casting using a water-based doctor-blade process. The tape was gelled at the exit from the doctor-blade by a cation-exchange reaction. The tape thickness could be controlled from 0·2 to 2 mm and there appeared to be no limit to the laminate thickness which could be produced by tape lay-up and filter-pressing. The platelets were aligned parallel to the green tape to better than 10°. Several cation reactions were investigated and both their gelling behaviour and their effect on the sintering characteristics were studied. The large-grained sintered products were highly textured and showed pronounced anisotropy in their crack propagation resistance.

1 Introduction

In many engineering materials microstructural or crystallographic anisotropy (texture) can be used to inhibit crack propagation. The control of crystalline texture is a frequent objective in metal working processes but is seldom applied to conventional ceramic processing technology. Nevertheless, the production of a crystallographically and microstructurally oriented monolithic ceramic could be a useful alternative to the introduction of aligned second-phase reinforcement. Within limits, the control of crystalline texture could result in a beneficial mechanical anisotropy, avoiding the aligned two-phase microstructural geometries characteristic of a composite material, many of which have problems associated with mismatch of the chemical, thermal or elastic properties of the two phases.

Reinforcement of a ceramic matrix with semi-aligned SiC platelets has already been shown to give improved mechanical properties with pronounced mechanical anisotropy. For example,[1] the addition of 30% of SiC platelets to an Si_3N_4 matrix powder prior to hot-pressing has led to significant increases in the fracture toughness, the Weibull modulus and Young's modulus. The mechanical anisotropy was also demonstrated in indented samples, for which the extent of crack propagation in the two directions parallel and perpendicular to the direction of hot-pressing was markedly different.

The tape-casting process has been used to produce ceramic tapes, 25 to 300 μm in thickness,[2] for electronic applications, and alumina is one of the commonest tape-cast materials.[3] Particle alignment during tape-casting has also been studied[4] and it was shown that, providing the pressure gradient is neglected, the orientation of the particles depends only on their concentration and shape, while the effects of slip viscosity, trolley velocity and tape thickness on the particle alignment were minor. The flow behaviour of a ceramic slip during tape-casting has been analysed based on the principles of fluid dynamics.[5] The fluid flow process can be considered a linear combination of Poisseuille pressure flow and Couette drag, so that the velocity distribution in a slip flowing between an extended 'doctor-blade' and a moving substrate carrier is given by:

$$V_z = -\rho g H(x^2 - hx)/2\mu l + V_0 x/h$$

where ρ is the density (1750 kg/m^3), g is the gravity acceleration (9·81 m/s^2); H is the height in the container (10 mm); h is the 'blade' gap (2 mm); μ is the slip viscosity (10 Pa.s); l is the length of the 'blade' (30 mm); V_0 is the trolley velocity (200 mm/s) and V_z is the slip velocity at a distance x from the 'blade' surface.

The first term in the equation is the pressure effect component and the second is the drag effect, while the dimensions given in parentheses are appropriate for the geometry used in the present work. From this equation and with these dimensions, it is obvious that pressure flow can be

neglected and the platelets should orient in the uniform shear field of the dominant drag flow.[4] The authors have previously prepared alumina/alumina platelet composites by conventional tape-casting[6] and found that the shear forces acting during tape-casting could orient the platelets to better than 15°. However, the laminate thickness which could be prepared by subsequent tape layup was limited by the long times required for burn-out if the large amount of organic plasticizer present was not to cause bloating and delamination.

Far smaller quantities of organic additives have been reported[7] for a water-based tape-casting process which uses a cellulose ether binder. The process involved a compromise between the requirements for a high green density (a high ratio of inorganic to organic components) and a high green strength (a high ratio of binder to plasticizer). The liquid to solid (sol–gel) transformations used in green moulding can be achieved by a number of routes of which solidification of a plasticizer or solvent evaporation are two of the commonest. An acrylic polymerization reaction has been shown to give a flexible gelled slip in aqueous solution at concentrations of organic additives of only 5% with up to 60% solids loading.[8] This process has been patented under the name of *gel-casting*, although irreversible polymerization is just one gel-formation process.

A sol–gel route has been developed for the production of a gelled thread containing aligned whiskers. An early report[9] described the production of a Ca alginate fibre containing aligned whiskers but gave no experimental details. More recently[10] it was shown that extrusion of a Na alginate-containing water-based Al_2O_3 or Si_3N_4 slip with SiC whisker additions could give good whisker alignment. Extruded thread was gelled to form a flexible 'spaghetti' on exiting an extrusion needle immersed in gelling solution. Whisker alignment was retained after filter-pressing and sintering, and the small amount of organic additives present (less than 2%) did not require any especial burn-out schedule.

The sol–gel reaction between water-soluble Na alginate and polyvalent cations yields an insoluble cation cross-linked alginate and is used in many food and pharmaceutical applications.[11] The reaction is based on ion exchange,[12] for example:

$$Na_n \text{ alginate} + n/2\ Ca^{2+} \longrightarrow n Na^{+} + Ca_{n/2} \text{ alginate} \quad (1)$$

Smidsrød & Haug[13,14] showed that many divalent cations could be used to obtain the gel reaction and could be ranked according to their efficacy in precipitating the alginate. In the present application, some cation will remain as a dopant in the ceramic, so that the gelling cation should be a good sintering agent rather than a deleterious impurity.

In the present contribution a process for water-based tape-casting of a platelet-containing slip by the sol–gel route, followed by tape layup and filter-pressing to yield a green body with well-oriented platelets is reported. A number of polyvalent gelling cations have been investigated.

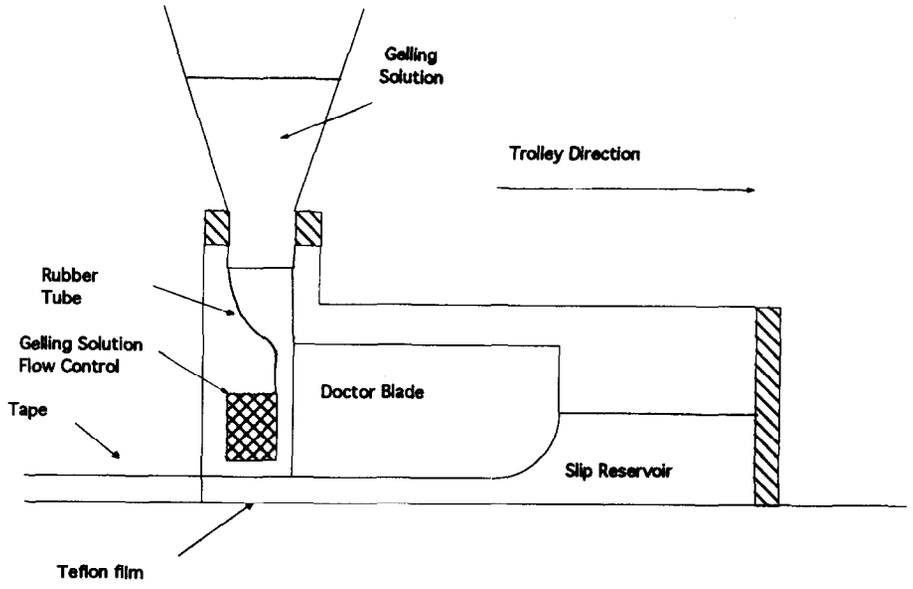
2 Experimental

2.1 Machine design

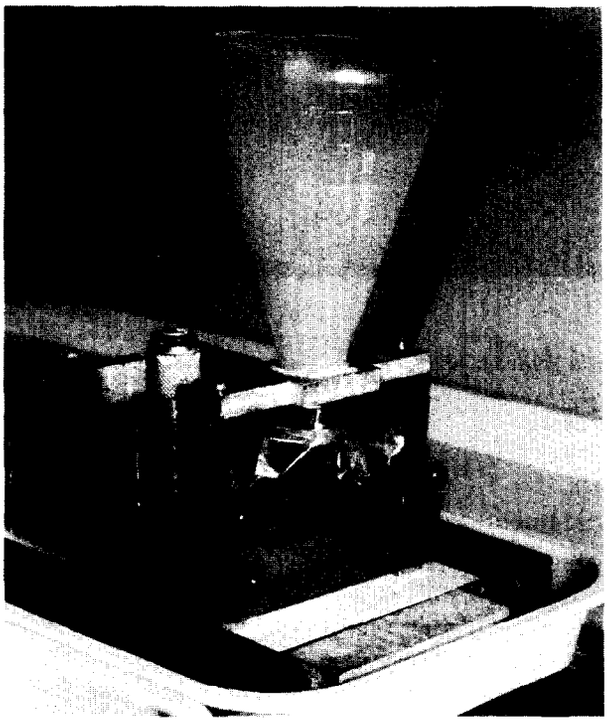
The tape-casting unit was based on a conventional design for the tape-caster trolley, but with an additional section for gelling (Fig. 1). The conventional sections comprise an extended doctor-blade, which controls both the thickness of the tape and the alignment of the platelets, and the slip reservoir. The new section consists of a flexible tube which is attached to the exit from the extended doctor-blade and controls the supply of the gelling solution from a reservoir. During casting the tape-caster trolley is pulled at a fixed speed up an inclined teflon-covered support plate, the inclination being necessary to drain away the gelling solution and prevent gelling of the slip beneath the doctor-blade (Fig. 2). As in conventional tape-casting, the blade gap (the tape thickness), the trolley velocity and the slip viscosity can be independently varied, together with, in the present case, the flow rate of the gelling solution.

2.2 Composite fabrication

The alumina powder used for the present study was Sumitomo AKP50 and the alumina platelets were supplied by Elf-Atochem in three different sizes: 3–7 μm, 10–15 μm and 15–25 μm. A solution of Na alginate was prepared with 4 wt% of alginic acid sodium salt. This solution was diluted with distilled water (2 : 3) and a dispersant was added (Dolapix PC85). After adding the platelets (typically 5 wt% in the final green body), the pH was adjusted to 10 by adding NH_4OH and ultrasonic agitation was used to break up any soft platelet agglomerates. The alumina powder was then incorporated and, after 18 to 20 h of ball-milling, the slip was tape-cast onto the teflon substrate. On inverting the substrate in a water bath, the cast tape detached from the teflon under its own weight and was then washed to remove excess cation. The tape was cut into squares (31 × 31 mm) which were stacked and compacted by filter-pressing before drying and sintering. The sintering programme comprised three stages: 600°C for 2 h, to burn out the small amount of organic



(a)



(b)

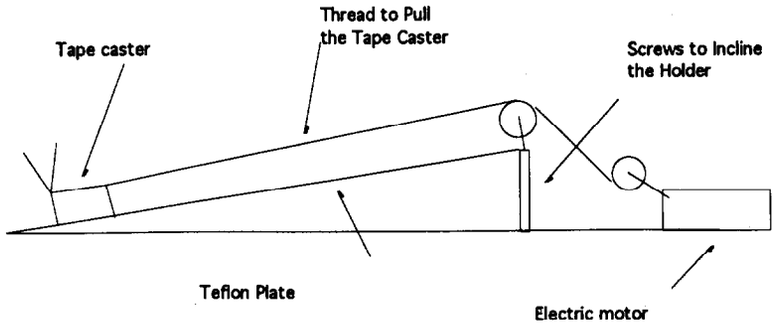
Fig. 1. (a) Schematic drawing of the gel-caster trolley, (b) photograph of the gel-caster trolley.

additives, 900°C for 17 h, to stabilize the interconnected pore structure, and a final sinter at 1475 to 1550°C for 3 to 15 h, to collapse the pore structure and reach the final sintered density. The heating rate was 2°C/min and the final cooling rate was 5°C/min.

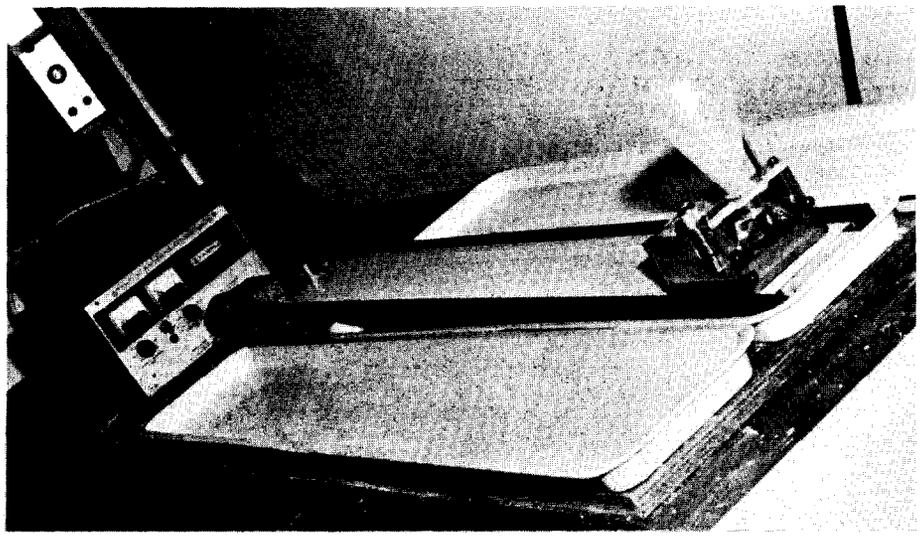
The shrinkage on sintering was markedly anisotropic, with the through thickness shrinkage appreciably greater than the lateral shrinkage. Typical sample dimensions after sintering at 1500°C for 9 h were 26 × 26 mm, with a sample thickness of 3–5 mm, depending on the number and thickness of the tape layers used in the layup. Sample densities were determined by the Archimedes method, using water as the immersion medium.

2.3 Characterization

Optical and scanning electron microscopy (SEM) were used to characterize polished and thermally etched (1450°C for 30 min) sintered samples cut parallel and perpendicular to the original tape surface. Optical microscopy was used to characterize the platelet distribution in cross-sections of the dry green body which had been vacuum impregnated with epoxy resin. Crack propagation



(a)



(b)

Fig. 2. (a) General layout of the gel-caster system, (b) photograph of the gel-caster system.

was studied by Vickers indentation on polished sections of the sintered samples.

The degree of platelet alignment was determined by X-ray diffraction using the (0006) reflection (2θ = 41·65°) wth CuK_α radiation and rotating the sample about the normal to the plane defined by the incident and diffracted beams. The integrated intensity of the (0006) peak was measured as a function of the angle of tilt of the original tape surface in the diffractometer. The range of tilt angles available with the diffractometer geometry and sample size used was −10 to +15°, and peak intensity measurements were taken at 5° intervals of sample tilt.

3 Results

Figures 3 and 4 show the (0006) integrated diffracted intensities for sintered samples containing 3–7 μm and 15–25 μm platelets respectively. These 'rocking curves' were taken from both the 'top' and 'bottom' of the samples, as well as both parallel (0°) and perpendicular (90°) to the tape casting direction (where 'top' is here the surface formed by the extended doctor-blade and 'bottom' is that in contact with the teflon substrate). In all cases the samples were strongly textured parallel to the original tape surface with most diffracting grains (full-width, half-maximum of the curves) aligned within ±5°. In these samples, and as might be expected,[4] the larger platelets gave a stronger texture than the smaller platelets, but the difference was not large. The curves are symmetrical about the 0° position and there is very little difference between the top and bottom of the samples or between the texture parallel and perpendicular to the casting direction. The largest differences were for the smallest platelets, for which the texture at the interface with the teflon substrate was significantly greater parallel to the casting direction (Fig. 3). In all cases, few grains have a *c*-axis which is tilted more than 10° to the specimen surface. It should be noted that the tape thickness in the case of Fig. 4 was 2·25 mm, which was the maximum studied.

Figure 5 shows transverse sections of the green tape, dried in alcohol (to avoid cracking) and epoxy impregnated. The first two micrographs contain 5 wt% of the small (Fig. 5(a)) and large platelets (Fig. 5(b)). In both cases the platelets are seen to be uniformly aligned and distributed

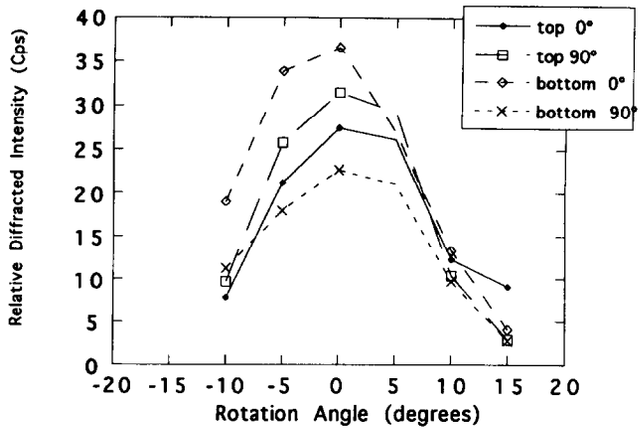


Fig. 3. Diffracted intensity versus tape surface tilt angle for a sintered sample made from 1 mm thick green tape containing 5 wt% of 3–7 μm platelets.

throughout the tape thickness. In Fig. 5(c) the sample contains 10 wt% of the small platelets, which again are uniformly aligned and distributed.

The maximum achievable tape thickness is determined both by the requirement to align the platelets in the shear stress field under the extended doctor-blade, and by the rate of diffusion of the ion-exchange cation through the tape as it exits from the doctor-blade. In general, good alignment for the small platelets was retained for tape thicknesses up to 2 mm, while the larger platelets were well-aligned at even larger tape thicknesses. The gelling reaction was always sufficiently fast to prevent further flow of the slip once it had exited from the doctor-blade, but the thicker tape had to be kept in contact with the gelling solution for several minutes in order to complete the gelling reaction through the full tape thickness. Typically, 10 layers of gelled tape could be stacked to produce a filter-pressed green sample 4–6 mm thick. Filter-pressing was accompanied by some loss of water and increase in green density.

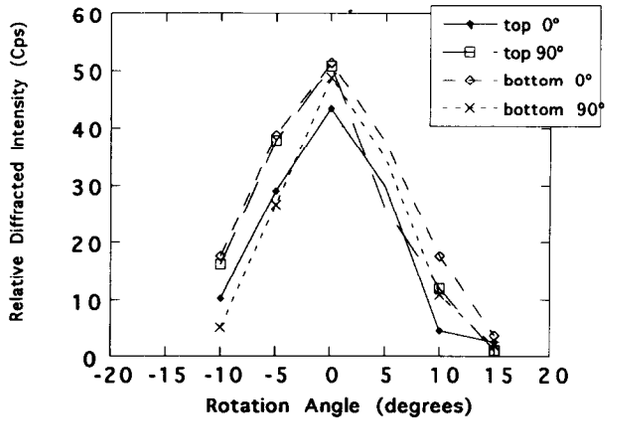
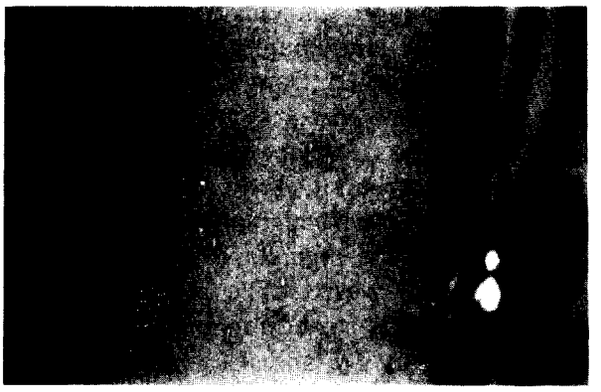


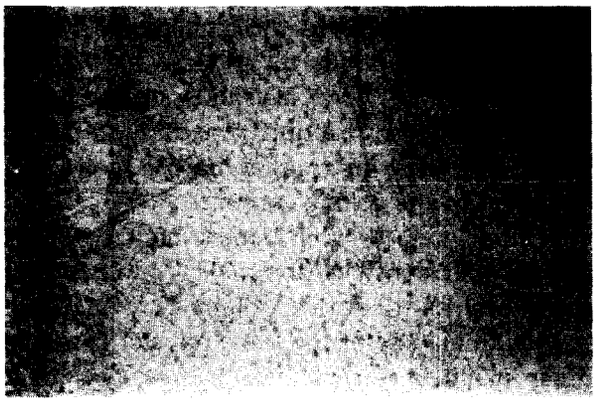
Fig. 4. Diffracted intensity versus tape surface tilt angle for a sintered sample made from 2·25 mm thick green tape containing 5 wt% of 15–25 μm platelets.



(a)



(b)



(c)

Fig. 5. Polished transverse sections of epoxy resin-impregnated green tape, showing the platelet distributions: (a) 5 wt% of 3–7 μm platelets, (b) 5 wt% of 15–25 μm platelets, (c) 10 wt% of 3–7 μm platelets.

As already noted, shrinkage on sintering was markedly anisotropic and the final sintered sample thickness was 3–5 mm.

There appeared to be no limit to the number of layers which could be bonded by filter-pressing, and no evidence for any delamination was observed either before or after sintering. Neither was there any microstructural indication of the position of the original tape surface in the polished and thermally etched cross-sections cut from the sintered product.

Six gelling cations were compared: 2+—Ca, Sr and Ba; 3+—Y and La; 4+—Ce. All these cations have an ionic radius of about 0·1 nm, which

appears to be that necessary to coordinate and ionically crosslink the negatively charged polysaccharide chains.[14] The minimum concentration of alginate and the maximum volume fraction of solids which still gave a strong, flexible tape were determined approximately for Ca and found to be 1·6 wt% of alginate with 68 wt% of powder. The strengths of the gels formed using the other cations were then compared at this same slip composition, and the following rank order was observed:

$$Ba > Sr > Ca > Ce > Y > La$$

This is completely consistent with the results of Smidsrød & Haug,[13] who investigated only divalent cations. The lanthanum gelled tapes were too weak to be detached from the teflon substrate without tearing, so that a higher alginate concentration would be necessary with this cation. The yttrium and cerium gelled tapes were easily handled at the 1·6 wt% alginate level, while in the case of calcium the alginate concentration could be reduced to 1·4 wt%. The minimum alginate concentrations for strontium and barium gelled tapes were about 1·2 and 1·0 wt% respectively. Previous work has shown that the ion-exchange reaction for calcium is complete when about 20 wt% of Ca is bonded to the alginate, so 1·4 wt% of alginate corresponds to about 0·3 wt% of Ca added to the 68 wt% of solids in the slip. It follows that the gel reaction, as used in the present process, will result in an alumina product with up to 0·5 wt% of the gelling cation.

The filter-pressed green bodies made from these tapes all had densities about 47% of theoretical, significantly less than that obtained by filter-pressing an alumina slip of the same powder containing neither platelets nor alginate (57%). The highest green density was obtained for the calcium gel—50% of theoretical. The variation of sintered density with sintering temperature (9 h, in each case) is shown in Fig. 6. The rapid sintering in the presence of calcium at only 1500°C is associated with excessive grain growth. As expected, the presence of the platelets introduces local constraints which inhibit shrinkage. Nevertheless, densities exceeding 97% are readily attainable.

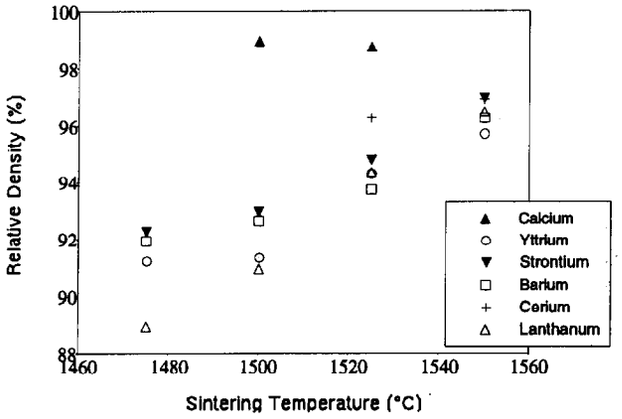
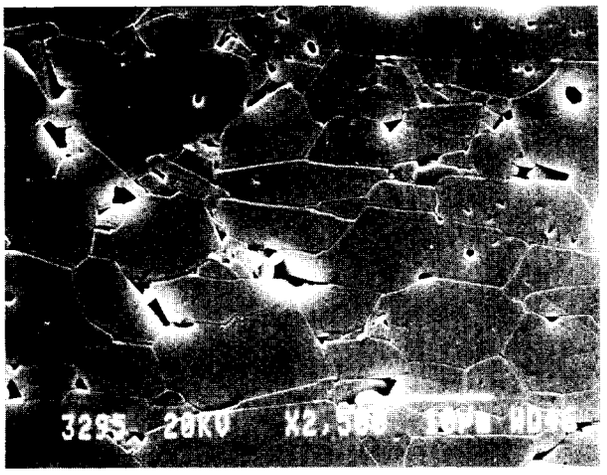
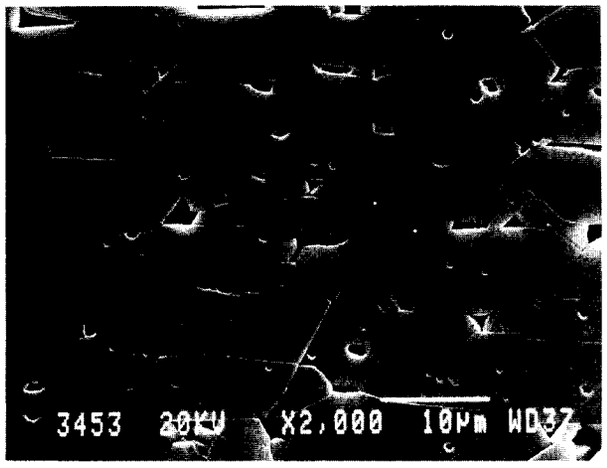


Fig. 6. Effect of sintering temperature on the relative density for different gelling cations (5 wt% of 3–7 μm platelets).



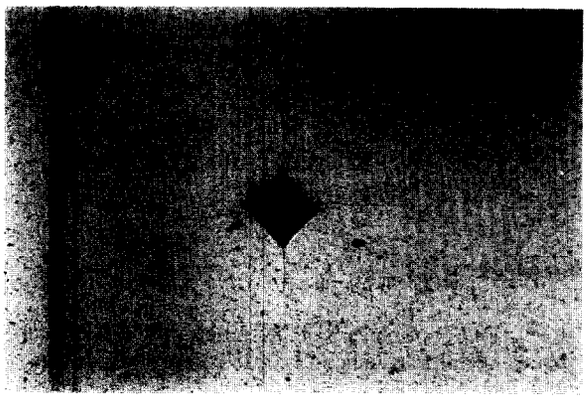
(a)



(b)

Fig. 7. SEM micrographs of thermally etched sintered samples: (a) 3–7 μm platelets at 5 wt%, (b) 10–15 μm platelets at 5 wt%.

The microstructural anisotropy of these monolithic aluminas is evident in Fig. 7. The platelets have acted as seed crystals to develop the strong (0001) crystalline texture (c-axis perpendicular to the surface) as well as significant grain-size anisotropy (flattened grains, foreshortened perpendicular to the surface). This microstructural anisotropy and texture has been found to lead to anisotropic crack propagation resistance. Figure 8 compares a 200N Vickers hardness indentation in two samples prepared by the gel-casting route. The first sample (Fig. 8(a)) contained no platelets, while the second (Fig. 8(b)) contained aligned platelets. The crack propagation resistance in the through-thickness direction is clearly superior in the platelet-containing alumina.



(a)



(b)

Fig. 8. Vickers indentation cracking at 200 N; (a) sintered gel-cast alumina containing no platelets, (b) sintered gel-cast alumina containing 5 wt% of 3–7 μm platelets.

4 Discussion

The present results have demonstrated the practical feasibility of producing gel-cast tape preforms of alumina containing aligned seed platelets. This tape can be compacted and sintered to yield a laminated and textured product. The mechanical properties of these materials, which will be reported elsewhere, reflect the microstructural anisotropy of the product and show improved through-thickness crack propagation resistance.

The gelling cation used in the ion-exchange reaction plays a critical role, since this cation is subsequently introduced into the final ceramic product as a dopant. Calcium is known to promote grain growth and for this reason is generally considered to be deleterious. The remaining cations which have been studied are considered to be either beneficial sintering aids (Y, Ce and La), or else harmless (Sr and Ba). All these additions should lead to some second-phase formation, which is generally expected to be undesirable. The gelling response of the alginate solution should depend on the pH, so that pH control of the gelling solution, independent of the pH of the slip, offers one possibility for reducing the amount of gelling cation required for the process. The addition of an alcohol derivative could also affect the gelling response favourably and will be investigated, as will the use of other organic additives aimed at modifying either the gelling reaction, or the surface reactivity of the powder, or both.

The density of the final product is a major parameter controlling the mechanical properties. The values currently achieved (better than 97% of theoretical) are insufficient for many applications and are in part related to the comparatively low green densities of the filter-pressed layup made from the wet, gelled tape. The best way of improving the green density is probably by increasing the volume fraction of solids in the slip, which can only be done by reducing the casting velocity (for a more viscous slip) or reducing the slip viscosity. More viscous slips are difficult to handle (and may contain entrained gas bubbles), while suitable additives to reduce slip viscosity have not yet been found.

The aligned alumina platelets exercise an appreciable constraint on the shrinkage during the sintering process, and result in higher through-thickness shrinkage perpendicular to the sample surface. The relative rates of shrinkage in the transverse and radial directions change during the sintering reaction: initially the rates are approximately uniform, but the rate of transverse shrinkage then slows down while the through-thickness shrinkage continues. The sintering constraints due to the aligned platelets depend not only on the aspect ratio and volume fraction of the platelets, but also on the homogeneity and isotropy of the platelet distribution in the gelled sample. In general, the oriented platelets are not randomly distributed, but are more closely spaced in the through-thickness direction. The shrinkage anisotropy is then less than would be expected on the basis of a random, isotropic distribution of the platelets, while the aspect ratio of the final grains is appreciably less than 1.

The gel-casting process for the production of a water-based tape preform could have some interesting manufacturing potential. For example, the tape could be slit and spirally wound to form tube. Tape layups to form plate or bar products should be straightforward. Tapes of different composition (for example, alumina/zirconia slips) could be laminated to any desired thickness in any desired combination, for example to form graded structures. Tape could also be cast and fired on a substrate as a coating or enamel, and in this case control of the transverse sintering shrinkage by the aligned platelets could be used to improve the coating integrity and inhibit cracking during sintering. It should also be possible to cast onto a

rotating drum or moving band from which the tape could be stripped and collected continuously.

5 Conclusions

(1) A water-based tape of alumina containing aligned alumina platelets can be formed by gelling an alginate-containing slip in a modified design of doctor-blade tape-caster.
(2) Flexible wet tapes of 0·2–2 mm thickness can be produced in which the platelets are uniformly distributed and aligned to better than ±10°.
(3) The wet, gel-cast tape can be cut, layed up and compacted by filter-pressing into a green body with no detectable processing defects in the interface regions.
(4) The filter-pressed and dried green body can be sintered to near theoretical density to yield a strongly textured product with a high degree of microstructural anisotropy.
(5) The crystalline texture and microstructural anisotropy inhibit crack propagation in the through-thickness direction, as demonstrated by a Vickers indentation test.
(6) Several polyvalent cations are suitable gelling agents for this gelling reaction, but their effect on the microstructure and properties of the sintered product have yet to be studied.

Acknowledgements

The authors would like to acknowledge the provision of research funding for this project by Elf-Atochem, as well as the encouragement and support of Dominique Cotto and Jacques Macé of Elf-Atochem. The authors would also like to acknowledge the support of the French government for one of them (T.C.) under their VSN programme, as well as the support of École Nationale Supérieure de Mines de Paris, which enabled one of them (A.L.-W.) to contribute to this work.

References

1. Baril, D., Tremblay, S. P. & Fiset, M., Silicon carbide platelet-reinforced silicon nitride composites. *J Mat. Sci.*, **28** (1993) 5486–94.
2. Runk, R. B. & Andrejco, M. J., A precision tape casting machine for fabricating thin ceramic tapes. *Am. Ceram. Soc. Bull.*, **54**(2) (1975) 199–200.
3. Mistler, R. E., High strength alumina substrates produced by a multiple-layer casting technique. *Am. Ceram. Soc. Bull.*, **52**(11) (1973) 850–4.
4. Watanabe, H., Kimura, T. & Yamaguchi, T., Particle orientation during tape casting in the fabrication of grain-oriented bismuth titanate. *J. Am. Ceram. Soc.*, **72**(2) (1989) 289–93.
5. Chou, Y. T., Ko, Y. T. & Yan, M. F., Fluid flow model for tape casting. *J. Am. Ceram. Soc.*, **70**(10) (1987) C-280–C-282.
6. Grylls, R., Investigations into the alignment of discontinuous reinforcement in alumina. Project Report, Technion Haifa, Israel, June 1993.
7. Chartier, T. & Bruneau, A., Aqueous tape casting of alumina substrates. *J. Eur. Ceram. Soc.*, **12** (1993) 243–7.
8. Young, A. C., Omatete, O. O., Janney, M. A. & Menchhofer, P. A., Gel-casting of alumina. *J. Am. Ceram. Soc.*, **74**(3) (1991) 612–18.
9. Parratt, N. J., Whisker alignment by the alginate process. *Composites*, (9) (1969) 26–7.
10. Farkash, M. & Brandon, D., Whisker alignment by slip extrusion. *Mat. Sci. Eng. A*, **177** (1994) 269.
11. Clare, K., Algin. In *Industrial Gums*, 3rd edn, Chapter 6, ed. R. L. Whistler. Academic Press, 1993, 105–143.
12. Reed, J. S., Principle of ceramics processing. Chapter 11-6. Wiley-Interscience Publication, John Wiley & Sons, 1988.
13. Smidsrød, O. & Haug, A., The effect of divalent metals on the properties of alginate solutions. 1. Calcium ions. *Acta Chem. Scand.*, **19** (1965) 329–40.
14. Smidsrød, O. & Haug, A., The effect of divalent metals on the properties of alginate solutions. 2. Comparison of different metal ions. *Acta Chem. Scand.*, **19** (1965) 341–51.

Journal of the European Ceramic Society **15** (1995) 9–16
© 1995 Elsevier Science Limited
Printed in Great Britain. All rights reserved
0955-2219/95/$9.50

Effect of Powder Granulometry and Pre-treatment on Sintering Behavior of Submicron-grained α-Alumina

Eiichi Sato* & Claude Carry‡

Laboratoire de Céramique, Ecole Polytechique Fédérale de Lausanne, MX-Ecublens, CH-1015 Lausanne, Switzerland

(Received 14 December 1993; revised version received 3 June 1994; accepted 13 June 1994)

Abstract

Two kinds of commercial, submicron-grained, non-doped α-alumina powders were cold-isostatically pressed and then sintered at a constant heating rate. Before the sintering, pre-treatments were executed at 820 or 920°C for 50 h. The effects of the pre-treatments on the densification behavior and the microstructural development are discussed.

The powders contained some nano-sized alumina particles about 10 nm in diameter as well as sub-micron-sized primary particles about 0·1 μm in diameter, which agglomerated in packs of 0·2–0·4 μm diameter. The densification rate curves showed a low temperature shoulder during sintering attributed to these nano-sized particles. After pre-treatments, the nano-particles disappeared, resulting in disappearance of the shoulder in the subsequent densification rate curves. These treatments, however, caused little change in the apparent activation energy in the intermediate stage sintering. For the weakly agglomerated powders, the bodies sintered with pre-treatments had coarser final microstructures.

1 Introduction

In order to obtain ceramics with pore-free, fine-grain structures by stress-free sintering, there is always a competition between densification and grain growth.[1] For nano-phase ceramics the competition is much more significant.[2] The main obstacles in obtaining ceramics with theoretical density have been attributed to nonuniformities in green bodies, and the particle size distribution and degree of agglomeration of the starting powder are the main origins of the nonuniformities.[3]

The packing of a powder with a bimodal particle size distribution can give a higher green density than a mono-sized powder, due to the effective interspace filling between coarse particles by fine particles.[4] In spite of the higher green density, enhanced densification in compacts prepared from powders with bimodal[5,6] or wide size distributions[7] has not been observed. This is because the shrinkage rate is primarily governed by the large grains,[8] and localized stresses developed around them prevented an enhanced densification.

A narrow size distribution, on the other hand, is thought to be important[9] because a uniform pore distribution results in sintering to high final densities.[10] It has been reported that both classification of powders[11] and controlled colloidal techniques[12] to obtain narrow-sized powders allow powder compacts to sinter more rapidly and to higher densities at lower temperatures than compacts made from conventional powders. It must be pointed out that the controlled colloidal techniques give powders not only narrow-sized but also agglomerate-free, the other factor often cited as a cause of inhomogeneities in green bodies.

Recently, Chu *et al.*[13] reported that pre-treatments of a green compact at a low temperature without densification produced a compact with a more uniform microstructure than the initial one. This kind of treatment provides an ideal stage to discuss the effect of granulometry on sintering behavior. They, however, gave neither detailed observation nor clear explanation on how the densification proceeded and the microstructure developed during the subsequent sintering. As another method of heat schedule, 'Rate-controlled sintering' (where the heating rate is decreased to avoid rapid shrinkage in the intermediate stage), has had practical success,[14] it should be fruitful to compare these two methods.

It is the purpose of the present paper to reveal the effects of powder granulometry and pretreat-

* On leave from the Institute of Space and Astronautical Science, 3-1-1 Yoshinodai, Sagamihara 229, Japan.
‡ Present address: Institut de Science des Matériaux, Université de Paris-Sud, Bâtiment 413, Centre d'Orsay, 91405 Orsay Cedex, France.

ments on sintering behavior and on microstructural development using non-doped, submicron-grained alumina powders with different particle size distributions as model materials. Adopting a constant heating rate condition allows the shrinkage behavior in the initial stage of sintering to be observed[15] and the apparent activation energy in the intermediate stage to be estimated.[16]

2 Experimental Procedure

Two kinds of commercial, submicron-grained, non-doped α-alumina powders were used: they are denoted by BO (CR15-AS1, Baikowski, France) and TA (TM-DR, Taimei Chemicals, Japan). The main impurities are Si, K, Na and Fe, for the BO powders of 57, 45, 10 and 7 mass ppm and for the TA powders of 10, 2, 2 and 8 mass ppm, respectively. Figure 1 shows the particle size distribution of the powders given by the suppliers. Both powders consist of mainly submicron-sized particles with median volume diameters of 0·2 μm (TA) and 0·4 μm (BO).

Green compacts were prepared by cold-isostatic pressing (CIP) at a pressure of 250 MPa. They were machined into cylindrical samples with 15 mm height and 10 mm diameter. Some of them were annealed in a chamber furnace in air at 820 or 920°C for 50 h; this will be referred to as a pretreatment. The treatment at 820°C caused almost no densification, and that at 920°C caused a small increase in the relative density of 0·02 for compacts of both powders.

The samples were sintered in a vertical dilatometer (DHT2050K, Setaram, France) under constant heating rate conditions at various rates from 1·0 to 10°C/min up to 1600°C under dry air atmosphere. The dimensional change was measured *in situ* using pure alumina probes with a load less than 0·02 N, which corresponds to a pressure of less than 0·25 kPa. The final density was measured by the Archimedes method. The relative density ρ and its temperature derivative $d\rho/dT$ were calculated from the final density and the continuously measured shrinkage; they are plotted as functions of temperature T. Apparent activation energies at several densities were calculated from Arrhenius plots of the densification rates at different heating rates.[16]

The morphology of the powders was observed by transmission electron microscopy (TEM). The microstructure of powder compacts at various stages of heat treatments was observed by scanning electron microscopy (SEM). Specimens with grain sizes larger than 1 μm were observed on polished and thermally etched surfaces, while those with grain sizes less than 1 μm were observed on fractured surfaces to avoid grain growth during thermal etching.

3 Results

3.1 Powder agglomeration and green bodies

Figure 2 shows the powder morphology observed by TEM. Both BO and TA powders consisted mainly of submicron-sized primary particles with diameters of 0·1 μm or less. Agglomerates of these particles had larger sizes and more irregular shapes for the BO powders than for the TA powders and this indicates that the size distribu-

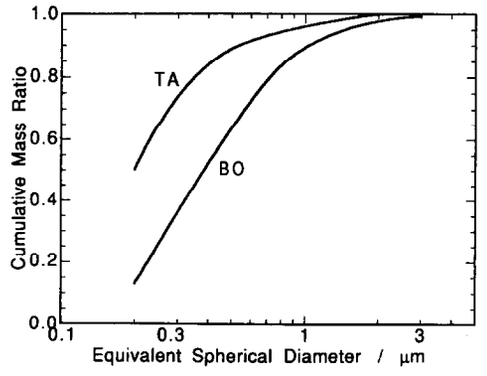


Fig. 1. Particle size distributions of BO and TA powders given by the suppliers.

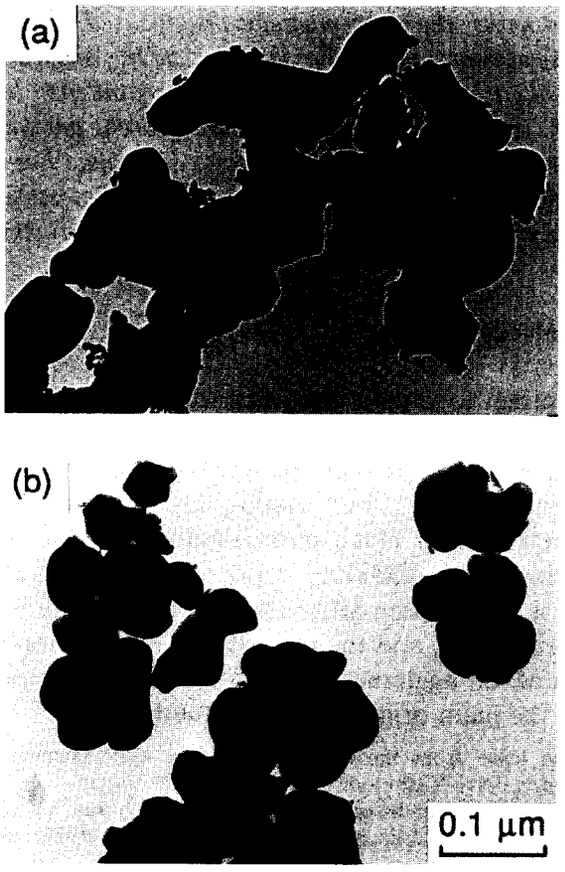


Fig. 2. Transmission electron micrographs of (a) BO and (b) TA powders.

tion shown in Fig. 1 was of agglomerates.

In addition to these primary particles, the BO powders have another kind of very fine particle with diameters of about 10 nm (they are referred to as nano-sized particles). A few nano-sized particles are also observed in the micrograph of the TA powders. These particles contained no metallic element other than aluminum based on the energy dispersion analysis of X-ray in TEM, although they were too small to determine their crystal structure. As the size is similar to the typical of γ-alumina, they might be non-transformed γ-alumina.

After CIP, the BO and TA powder compacts had relative densities of 0·481 and 0·566, respectively. This difference in green density is attributed to the difference in agglomerate size and morphology; in the BO powder compacts, the irregular shape of agglomerates made the packing more difficult.

3.2 Initial stage of sintering

General densification behavior at a constant heating rate is illustrated in Fig. 3: (a) is for the BO powders and (b) is for the TA powders. At low temperatures around 1100°C, a shoulder was observed on the densification rate curve of an as-CIPed BO powder compact (Fig. 3 (a)). The

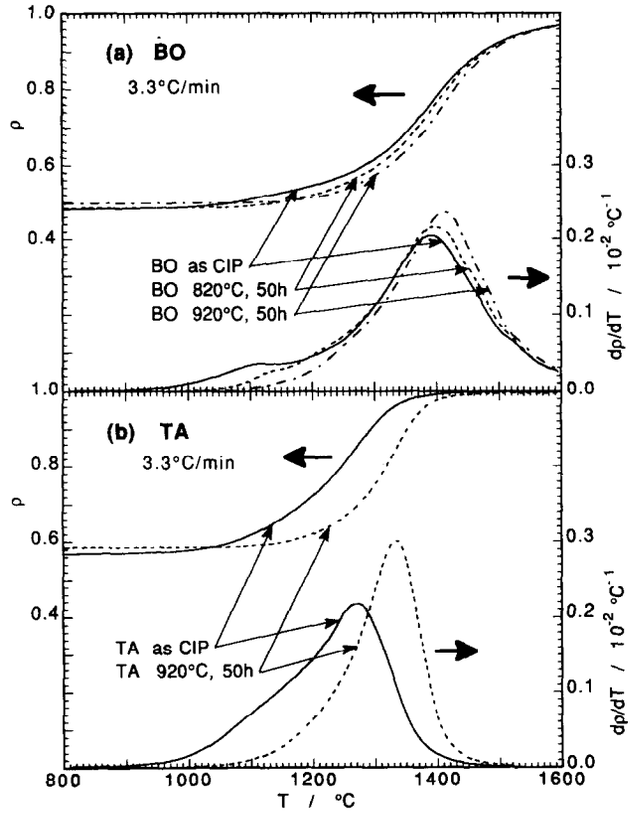


Fig. 3. Densification curves during sintering at a heating rate of 3·3°C/min for powder compacts of (a) BO and (b) RA with and without pre-treatment. The upper and lower curves in both (a) and (b) are the relative densities, ρ, and their temperature derivatives, $d\rho/dT$, respectively.

observation of such a shoulder has already been reported by the authors.[17] The shoulder became very small after the pre-treatment at 820°C for 50 h and disappeared almost completely after 50 h at 920°C. This shoulder was shifted towards lower temperatures with decreasing heating rate (not shown in Fig. 3(a)), implying a thermally activated process. For an as-CIPed TA powder compact, a much less distinct shoulder on the main peak was observed at almost the same temperature as the shoulder for the BO powder compact (Fig. 3 (b)). This shoulder also disappeared after the pre-treatment at 920°C for 50 h.

Figure 4 shows the microstructural developments during the pre-treatment and/or the initial stage sintering corresponding to the shoulder of BO powder compacts observed by SEM. The nano-sized particles observed by SEM are seen as small bright spots in the as-CIPed compact along with many large particle agglomerates of 0·1 to 0·3 μm (Fig. 4(a)). A particle network of the large agglomerates of about 0·3 μm is seen in this micrograph. After sintering up to the end of the shoulder, more than half of the nano-sized particles disappeared (Fig. 4 (b)). After the pre-treatment at 920°C for 50 h, almost all of the nano-sized particles disappeared (Fig. 4 (c)). In addition, the agglomerates of the primary particles show rather rounded morphology and seem to have a narrower size distribution. During all of these treatments the large agglomerates making up the particle network remain at a very similar size of about 0·3 μm.

Figure 5 shows the microstructural developments during the pre-treatment of the TA powder compacts. Compared to the as-CIPed TA compacts (Fig. 5(a)) the pre-treated TA compact consisted of more uniform but much larger particles (Fig. 5(b)).

In both the BO and TA powder compacts, the nano-sized particles disappear during low temperature annealing, i.e. during the shoulder in the initial stage sintering or during the pre-treatment. Their disappearance appears to be as a result of mass transport from them onto or into the submicron-sized particles which they contact. Among diffusional mechanisms considered normally, volume and grain boundary diffusions contribute to both densification and coarsening, while surface diffusion contributes only to coarsening and has the lowest values of activation energy and power index of particle size.[3] It means a process controlled by surface diffusion is more likely at lower temperatures and for finer particles. The dominant mechanism for the disappearance of the nano-sized particles could not, however, be determined clearly because the apparent activation energy

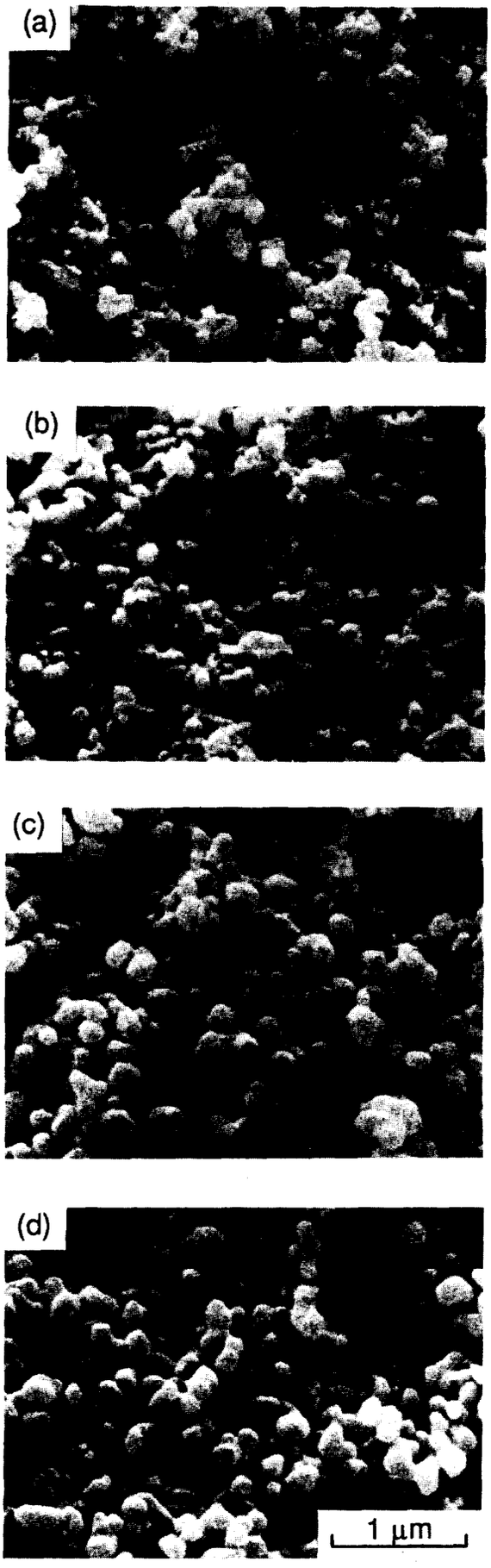


Fig. 4. Scanning electron micrographs of fracture surfaces of BO powder compacts: (a) as compacted, (b) sintered at 3·3°C/min until 1160°C, (c) pre-treated at 920°C for 50 h, and (d) sintered at 3·3°C/min until 1160°C with pre-treatment at 920°C for 50 h.

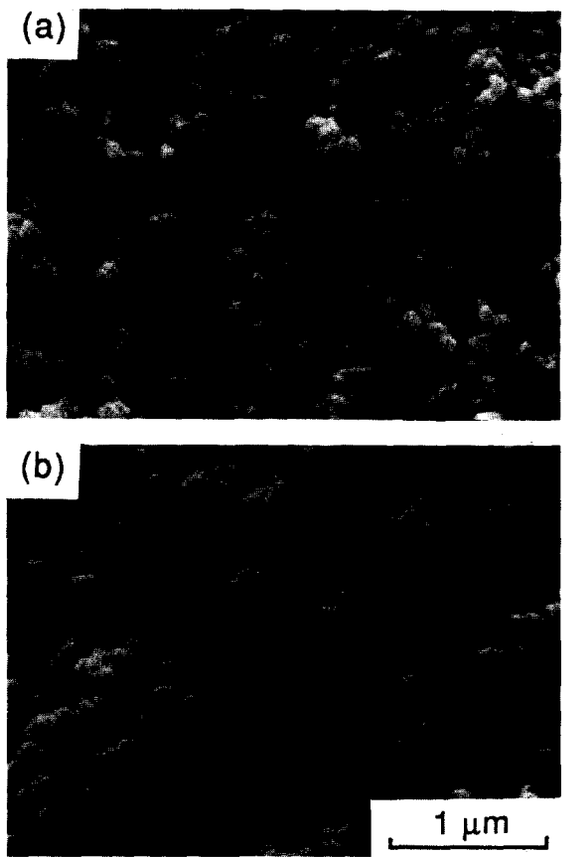


Fig. 5. Scanning electron micrographs of fracture surfaces of TA powder compacts: (a) as compacted, (b) pre-treated at 920°C for 50 h.

could not be measured, as described in the following paragraph.

Using the logarithmic plot of $T(\mathrm{d}(\Delta L/L_0)/\mathrm{d}T)$, which equals $-(T/3\rho_0)(\mathrm{d}\rho/\mathrm{d}T)$, versus $1/T$, Young & Cutler[15] obtained the apparent activation energy for the initial stage of sintering. Here $\Delta L/L_0$ is the relative change in length of the compact. Because their powder was coarser than 1 μm, there was negligible grain growth during this stage. Unfortunately, the significant grain growth of the present powder compacts does not allow a calculation of the apparent activation energy by their method.

3.3 Intermediate stage of sintering

The pre-treatment at 920°C for 50 h shifted the main densification rate peak toward higher temperatures by 60°C and raised its height by 36% in TA powder compacts (Fig. 3(b)), while it shifted the peak by only 20°C and raised the height by only 15% in BO powder compacts (Fig. 3(a)). Because the pre-treatment did not significantly coarsen the large agglomerates which made up the particle network for the as-CIPed BO powder compacts, as already mentioned, it did not cause a big change in the sintering behavior of the BO powder compacts. On the other hand, the pre-

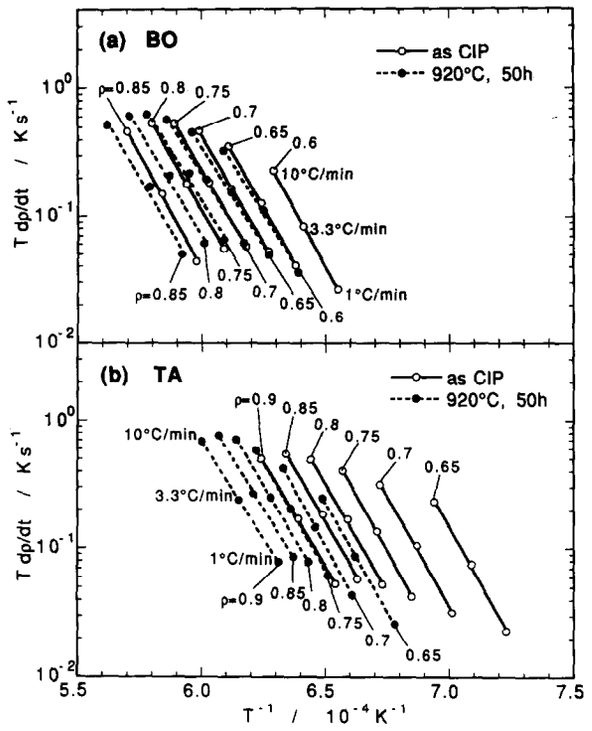


Fig. 6. Arrhenius plots of constant heating rate sintering of powder compacts (a) BO and (b) TA, with and without pre-treatment.

treatment strongly shifted the main densification peak to higher temperatures in TA powder compacts because the agglomerates coarsened very much during the treatment. The average grain size in TA powder compacts was still smaller than in BO, resulting in the lower temperature of the main densification peak.

The peaks were shifted toward lower temperatures with decreasing heating rates, as expected for a thermally activated process (not shown in Fig. 3). Figure 6 shows the Arrhenius plots of densification rates at different heating rates. In the intermediate stage of sintering, the apparent activation energies were 653 and 617 kJ/mol for the as-CIPed and pre-treated BO powder compacts, respectively, and 650, and 638 kJ/mol for those of the TA powder compacts. These values were obtained in the region of relative density from 0·65 to 0·80 for BO samples and from 0·70 to 0·85 for TA samples, where the effect of the shoulder was no longer apparent. In these regions grains did grow, but the sizes at a given density were almost identical among the compacts heated at different rates, which is indispensable for estimating the apparent activation energy. The little effect of pre-treatment on the apparent activation energy for both BO and TA powder compacts implies no change in the rate-controlling mechanism in the intermediate stage of sintering.

3.4 Final microstructure

Figure 7 shows the final microstructure of the BO materials with and without pre-treatments. The three samples shown in Fig. 7 had the same final density of 0·970 after sintering up to 1600°C at 3·3°C/min. These three had the same mean grain size of 1·9 μm; it was calculated as 1·38 times the mean intercept area on a plane section of more than 1000 grains observed in five different positions for each sample. Compared at the same sintering condition and the same density, the pre-treatment had no significant influence on the final microstructure in BO ceramics.

As already seen in Fig. 3 (b), the TA powder

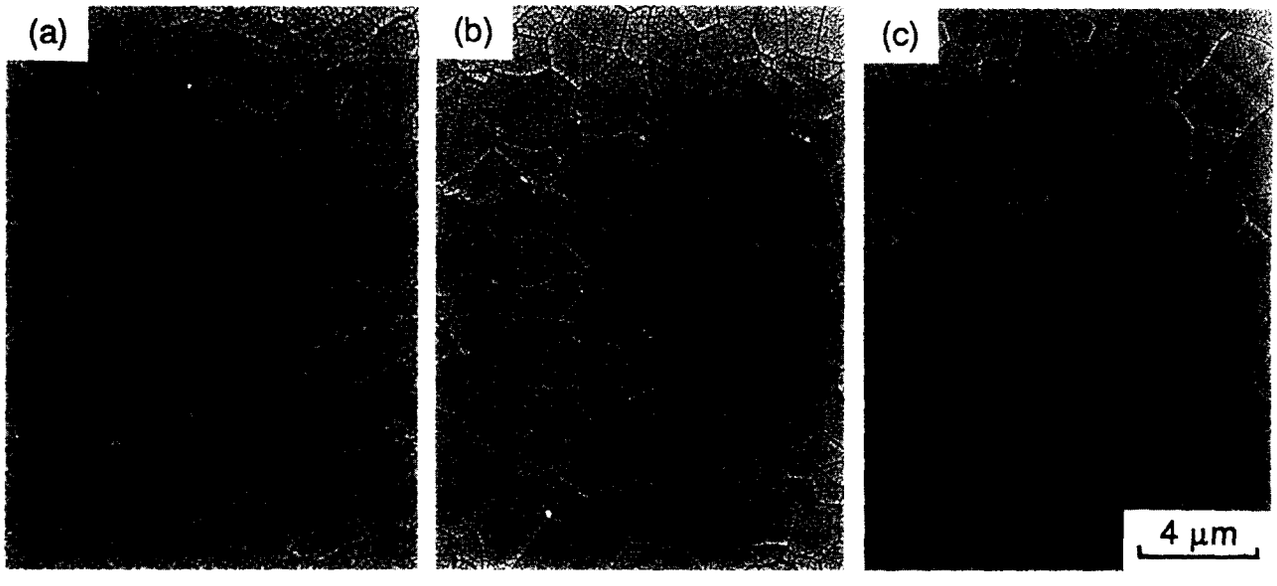


Fig. 7. Scanning electron micrographs of polished and thermally etched surfaces of BO ceramics sintered with 3·3°C/min until 1600°C: (a) without pre-treatment, (b) with pre-treatment at 820°C for 50 h, and (c) with pre-treatment at 920°C for 50 h. All of these specimens have the same final density of 0·97.

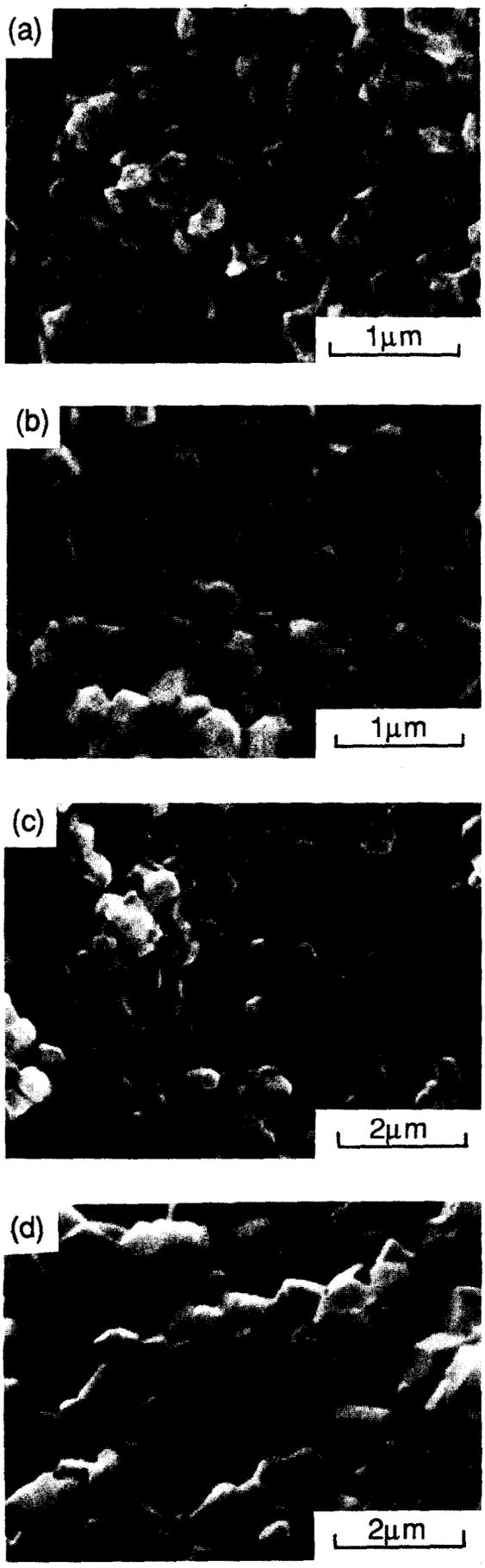


Fig. 8. Scanning electron micrographs of fracture surfaces of TA ceramics sintered at 3·3°C/min: (a) sintered up to 1290°C, (b) sintered up to 1350°C with a pre-treatment at 920°C for 50h, (c) sintered up to 1375°C, and (d) sintered up to 1430°C with the pre-treatment. Both (a) and (b) have the same final density of 0·89, and both (c) and (d) have that of 0·99.

compacts without and with pre-coarsening treatment reached the final density of 0·998 and 0·995, respectively, at about 1500°C: no more densification occurred in the sintering above this temperature. For this powder, pre-treatment decreased the highest density which a compact can achieve. The microstructures at certain densities lower than 0·995 are shown in Fig. 8, by interrupting the sintering cycle: (a) and (b) are microstructures at the density of 0·890, without and with pre-treatment, respectively, and (c) and (d) are at the density of 0·990. Here, fracture surfaces were observed because microstructures finer than 1 μm grain size easily coarsen during thermal etching. When comparing samples of the same density but different sintering temperature, the pre-treatment made the final microstructure coarser in the TA powder compacts.

4 Discussion

After pre-treatments, the nano-particles disappeared, resulting in disappearance of the initial shoulder in the densification rate curves in the subsequent sintering. For the BO powder compacts, however, the size of the large agglomerates which made up the particle network remained very similar during the pre-treatment, leading to little influence on the sintering behavior in the intermediate stage and the final microstructure. For the TA powder compacts, a coarsening of the agglomerates of the primary particles took place during the pre-treatments. The size increase influenced the sintering behavior in the intermediate stage and the final microstructure. Here we discuss these effects based on the results of TA powder compacts.

Firstly, the particle size increase in the treatment resulted in the shift of the main densification peak toward higher temperature as already mentioned. In addition to the temperature shift, the height of the main densification peak was raised by the treatment. Although the height of the densification peak has not been discussed in detail in the literature to the knowledge of the authors, it can be deduced that the narrower the size distribution, the higher the peak should be, providing all other conditions are identical. The height change in the TA powder compact data is qualitatively explained by a narrowing of the particle size distribution.

The effect of the pre-treatment, an increase in the height of the main densification rate peak, is the opposite to the policy of 'rate-controlled sintering,[14] which tries to avoid rapid shrinkage by decreasing the heating rate in the intermediate stage. Rapid shrinkage is expected to introduce

large closed pores inside the sintered body by differential densification. This explains why for TA powder compacts the sintered body with the pre-treatment could reach the final density a little lower than that achieved without the pre-treatment, and had a coarser microstructure when compared at the same density. In contrast, powders with narrow size distributions produced by colloidal techniques are not agglomerated to some extent and more regularly packed, resulting in a higher final density than powders with larger size distributions.[9,11,12]

In contrast to a coarsening effect of the pre-treatments for the final microstructure as seen for the TA powders, Chu *et al.* reported finer microstructures for conventional grade alumina and magnesia powders and high-grade alumina powders.[13] The conventional grade powder compacts revealed abnormal grain growth at the final stage (see Figs 6 and 7* of Ref. 13; Figs 7(c) and (d) must be placed in reverse order). Abnormal grain growth starts at a certain stage of annealing when some of the largest grains start to grow quickly by absorbing the surrounding grains. The more uniform the microstructure, the more strongly the onset of abnormal grain growth is retarded: this could be the microstructural fining effect found by Chu *et al.*

In the case of the high-grade powder compacts, Chu *et al.* reported that the sintered body with pre-treatment gave a finer final microstructure than without under the same sintering conditions.[13] Because the pre-treatment delays densification, an as-CIPed compact arrives at the final stage of sintering sooner (where coarsening is predominant[3]) than a pre-treated compact. For example, the TA powder compacts with and without pre-treatment showed grain sizes of 5 and 8 μm, respectively, after the sintering with 3·3°C/min up to 1600°C. This could also explain the microstructural fining effect found by Chu *et al.*

5 Conclusions

The commercial, non-doped α-alumina powders used in this study contained some nano-sized alumina particles (10 nm) as well as submicron-sized primary particles (0·1 μm), which agglomerated into diameters of 0·2–0·4 μm. The powder with many of these nano-sized particles showed a low temperature shoulder in densification rate curves of constant heating rate sintering while for the powder with fewer nano-sized particles the shoulder was less marked. The nano-sized particles disappear almost completely after a pre-treatment, resulting in the disappearance of the shoulder in the subsequent densification rate curves.

When the size of the large agglomerates which made up the particle network remained similar during the pre-treatment, the treatment had little influence on the intermediate and final stage sintering (BO powder). On the other hand when the growth of the agglomerates of the primary particles took place during the pre-treatments, the treatments shifted the main densification rate peak toward higher temperatures and raised its height (TA powder). The treatments, however, caused little change in the apparent activation energy, implying no change in the rate-controlling mechanism in the intermediate stage sintering. Because the treatments caused more rapid shrinkage in the intermediate stage, the sintered body with the treatment had coarser microstructure than the body with it when compared at the same density.

Finally, it was pointed out that pre-treatments have the possibility to retard the onset of abnormal grain growth by creating a more uniform microstructure before densification begins.

Acknowledgment

Helpful comments and discussion about powder agglomeration from Dr Paul Bowen, Laboratoire de Technologie des Poudres, EPFL, are gratefully acknowledged.

References

1. Harmer, M. P., Science of sintering as related to ceramic powder processing. In *Ceramic Transactions Vol. 1, Ceramic Powder Science II*, ed. G. L. Messing *et al.* American Ceramic Society, 1991, pp. 824–39.
2. Aeraback, R. S., Höfler, H. J., Hahn, H. & Logar, J. C., Sintering and grain growth in nanocrystalline ceramics. *Nanostructured Mater.*, **1** (1992) 173–8.
3. Shaw, N. J., Densification and coarsening during solid state sintering of ceramics: a review of models. *Powder Metallurgy Int.*, **21** (1989) 16–21.
4. Gray, W. A., *The Packing of Solid Particles*. Chapman and Hall, London, 1968.
5. Messing, G. L. & Onoda, Jr, G. Y., Sintering of inhomogeneous binary powder mixtures. *J. Am. Ceram. Soc.*, **64** (1981) 468–72.
6. Smith, P. & Messing, G. L., Sintering of bimodally distributed alumina powders. *J. Am. Ceram. Soc.*, **67** (1984) 238–42.
7. Yeh, T.-S. & Sacks, M. D., Effect of particle size distribution on the sintering of alumina. *J. Am. Ceram. Soc.*, **71** (1988) C484–7.
8. O'Hara, M. J. & Cutler, I. B., Sintering kinetics of binary mixtures of alumina powders. *Proc. Brit. Ceram. Soc.*, **12** (1969) 145–54.
9. Lange, F. F., Powder processing science and technology for increased reliability. *J. Am. Ceram. Soc.*, **72** (1989) 3–15.
10. Yan, M. F., Cannon, Jr, R. M., Bowen, H. K. & Chowdhry, U., Effect of grain size distribution on sintered

density. *Mater. Sci. Eng.*, **60** (1983) 275–81.
11. Barringer, E. A. & Bowen, H. K., Formation, packing, and sintering of monodisperse TiO_2 powders. *J. Am. Ceram. Soc.*, **65** (1982) C199–201.
12. Hay, R. A., Moffatt, W. C., & Bowen, H. K., Sintering behaviour of uniform-sized α-Al_2O_3 powder. *Mater. Sci. Eng.*, **A108** (1989) 213–19.
13. Chu, M-Y., De Jonghe, L. C., Lin, M. K. F. & Kin, F. J. T., Precoarsening to improve microstructure and sintering of powder compacts. *J. Am. Ceram. Soc.*, **74** (1991) 2902–11.
14. Palmour III, H., Rate controlled sintering for ceramics and selected powder metals. In *Science of Sintering*, ed. D. P. Uskovic *et al.* Plenum Press, 1989, pp. 337–56.
15. Young, W. S. & Cutler, I. B., Initial sintering with constant rates of heating. *J. Am. Ceram. Soc.*, **53** (1970) 659–63.
16. Wange, J. & Raj, R., Estimation of the activation energies for boundary diffusion from rate-controlled sintering of pure alumina, and alumina doped with zirconia or titania. *J. Am. Ceram. Soc.*, **73** (1990) 1172–5.
17. Sato, E. & Carry, C., Effect of yttrium doping on sintering behaviour of fine grained alumina. In *Third Euro-Ceramics*, Vol 1, ed. P. Duran & J. F. Fernandez. Faenza Editrice Ibérica, 1993, pp. 691–6.

Journal of the European Ceramic Society **15** (1995) 17–23
© 1995 Elsevier Science Limited
Printed in Great Britain. All rights reserved
0955-2219/95/$9.50

Influence of Oxygen Partial Pressure on the Metastability of Undoped Zirconia Dispersed in Alumina Matrix

Henryk Tomaszewski[a] & Krzysztof Godwod[b]

[a] Institute of Electronic Materials Technology, 01-919 Warsaw, Wólczyńska 133, Poland
[b] Institute of Physics, 02-688 Warsaw, A1. Lotników 32/46, Poland

(Received 25 February 1994; revised version received 1 June 1994; accepted 14 June 1994)

Abstract

The influence of oxygen content in the sintering atmosphere on zirconia phases in alumina–zirconia ceramics was studied. As was demonstrated, in the case of samples sintered in an atmosphere with oxygen partial pressure between $2{\cdot}80 \pm 10^{-5}$ *Pa and* $2{\cdot}80 \times 10^{-2}$ *Pa, 100% of zirconia was found to be in the cubic form. The appearance of transformable cubic zirconia is a result of oxygen vacancy concentration in zirconia. The increase of oxygen partial pressure and decrease of oxygen vacancy concentration leads to a breakdown of the cubic phase which transforms to the t- and/or m-phases. Critical values of oxygen vacancy concentration responsible for the metastability of cubic and tetragonal zirconia were estimated.*

1 Introduction

Transformation toughening in ZrO_2-containing ceramics requires the presence of metastable tetragonal (t) zirconia, so that the toughening obtainable from the stress-induced martensitic transformation to monoclinic (m) symmetry can be realized. As has been shown recently,[1–3] when this type of ceramic is sintered in oxygen-deficient conditions, transformable cubic (c) phase appears, as a result of nonstoichiometry of ZrO_2. The metastability of t- and c-ZrO_2 at low temperatures either in powder state or in compact form was proposed by different theories and hypotheses.[4–11] Unfortunately, the controlling mechanisms responsible for metastability of high-temperature phases of zirconia are still unknown.

The present work is aimed to explain the effect of oxygen content in sintering atmosphere and related oxygen vacancy concentration on c–t inversion in undoped zirconia grains dispersed in alumina matrix.

2 Experimental Methods

The starting material was a powder composition containing : 99·55 wt% Al_2O_3, 0·20 wt% MgO and 0·25 wt% Y_2O_3. Alumina powder (made by CEMAT-Skawina, Poland) was 99·99 wt% pure and the average grain size below 0·5 μm. The remaining two components were of the same purity.

The components of the composition were homogenized for 48 h in a ball mill in distilled water. Then 10 wt% zirconia—obtained from zirconyl chloride by chemical methods described earlier[12]—was added and homogenized for further 48 h. The powders were cold isostatically pressed at 140 MPa into rectangular die (41 × 65 mm). The samples were sintered at 1973 K of 90 min either in a gas furnace (air atmosphere) or in an electric furnace under eleven levels of oxygen partial pressure (p_{O_2}) in sintering atmosphere between $2{\cdot}8 \times 10^{-5}$ Pa and $1{\cdot}07 \times 10^{+4}$ Pa. The values of p_{O_2} were realized by controlled introduction (by using electronic valves) of air into the high-vacuum chamber of the furnace or earlier prepared oxygen–argon gas mixtures.

The critical stress-intensity factor, K_{Ic}, was determined after Evans[13] on notch-beam specimens of configuration described earlier[12] and an Instron TIM type testing machine. The bearing spacing was 36 mm and the rate of loading 0·1 mm min^{-1}.

The bending strength was determined by three-point bending on bars 5 × 5 × 50 mm using the same testing machine, the same rate of loading and bearing spacing. These tests were performed on 15 samples for each composition.

Table 1. Mechanical properties of alumina ceramics containing 10 wt% zirconia

Properties	*Sintering atmosphere*	
	Air	*0·133 mPa vacuum*
	Oxygen partial pressure (Pa)	
	$2{\cdot}1 \times 10^{+4}$	$2{\cdot}8 \times 10^{-5}$
Critical stress-intensity factor, K_{Ic}, MPa $m^{1/2}$	6·60 ± 0·57	8·00 ± 0·67
Bending strength, MPa	324·40 ± 58·7	397·80 ± 28·5
Grindability, mm	0·1	0·01

The measurement of grindability was carried out with a Mackensen blower using 500–630 μm SiC powder, 0·15 MPa pressure and a cell of 28 cm^3 volume. To intensify the abrasion by the grinding powder, the test was repeated three times at the same place on the samples. As a measure of grindability, the depth of the hole blown by the grinding powder in 15 samples for each composition was recorded.

The phase composition of zirconia in each of the free and fractured surfaces ceramics was determined by X-ray diffraction (Siemens diffractometer Kristalloflex 4). The measurements were carried out in the 2Θ-angle 20–160° at 293 K using monochromatized CuK_{α_1} radiation (quartz, (10$\bar{1}$1) reflection Johanson type) in steps of 1/16 deg min^{-1}. The precision of goniometer was tested using an ultrapure silicon powder standard.

The phase content was estimated using integral intensities of the strongest lines taking into account the polarization, Lorentz, structure and multiplicity factors.[14] The lattice parameters were calculated using the least-squares Cohen method.[14]

The loss of oxygen in ZrO_2 of samples sintered in atmospheres with increasing p_{O_2} was estimated by measuring the weight increasing during its reoxidation in air at 1273 K (1000 h). This allows the level of the oxygen vacancy concentration to be determined.

3 Results and Discussion

As can be seen from the data shown in Table 1, the critical stress-intensity factor, K_{Ic}, of ceramics sintered in high vacuum (0·133 mPa) is really higher than that for the air-sintered ceramics. The bending strength and Mackensen's grindability of these ceramics also differ in the same way.

Table 2. Zirconia phases in Al_2O_3–10 wt% ZrO_2 measured from free surface as a function of sintering atmosphere

Sintering atmosphere	*Phases of zirconia (%)*		
	Monoclinic	*Tetragonal*	*Cubic*
Air	16·5	83·5	—
0·133 mPa vacuum	—	—	100

Table 3. X-ray data of c-ZrO_2 in Al_2O_3–10 wt% ZrO_2 sintered in vacuum (free surface)

	2θ, degrees	I/I_0	*h*	*k*	*l*
1	30·12	100	1	1	1
2	34·96	17	2	0	0
3	50·22	32	2	2	0
4	59·74	16	3	1	1
5	62·68	2	2	2	2
6	73·94	1	4	0	0
7	81·76	2	3	3	1
8	84·40	3	4	2	0
9	94·74	1	4	2	2
10	102·68	1	3	3	3
11	125·40	1	5	3	1
12	128·64	<1	6	0	0

The observed differences can be correlated with the presence of zirconia phases in the matrix. In the case of air-sintered samples, 83·5% of zirconia is in the tetragonal form (Table 2).

X-ray analysis of samples sintered in high vacuum indicates 100% presence of the cubic form. The X-ray data of c-ZrO_2 obtained from free surface are listed in Table 3.

As can be seen from the phase diagram of the system Zr–O (Fig. 1) determined by Ruh & Garrett,[15] the presence of c-ZrO_2 at 1973 K (the tetragonal–cubic phase transformation temperature is at 2558 ± 15K) is possible under the conditions of high anion deficiency equal to $2 - x = 1{\cdot}688 - 1{\cdot}740$.

It seems that the appearance of metastable c-ZrO_2 in alumina ceramics is a result of sintering in high vacuum (under very low oxygen partial pressure) accompanied by oxygen nonstoichiometry. Furthermore, the constraint of the alumina matrix prevents the c-phase transforming during cooling from the sintering temperature to room temperature.

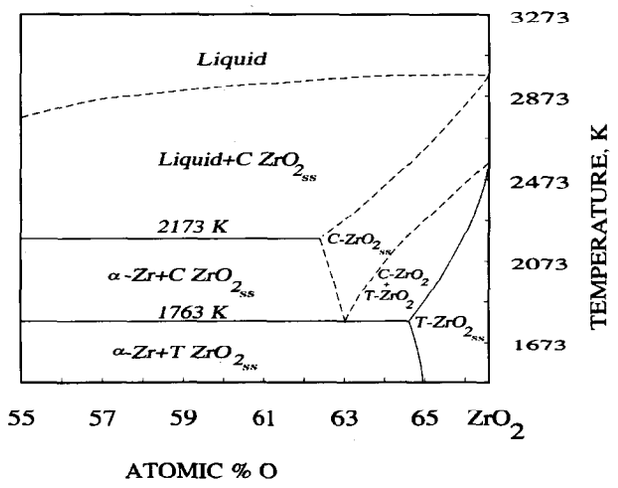


Fig. 1. Phase diagram of the Zr–O system.[15]

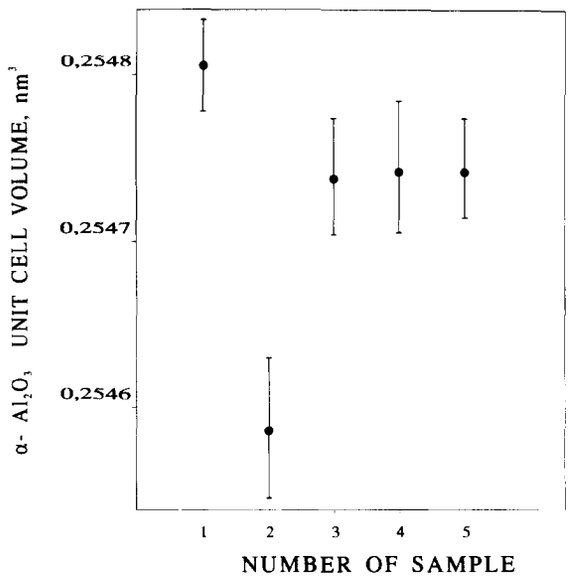


Fig. 2. Volume of α-Al_2O_3 unit cell in Al_2O_3–10 wt% ZrO_2 versus sintering and measuring conditions. The measured samples are: (1) α-Al_2O_3 matrix; (2) free surface of high vacuum-sintered alumina–zirconia ceramics; (3) free surface of air-sintered alumina–zirconia ceramics; (4) fractured surface of high vacuum-sintered alumina–zirconia ceramics; (5) fractured surface of air-sintered alumina–zirconia ceramics.

The presence of the stress field in the ceramics confirms the X-ray results for the α-Al_2O_3 unit cell volume for the alumina matrix with and without zirconia particles sintered in air and in vacuum (Fig. 2). As shown, the largest deformation of the α-Al_2O_3 unit cell is in samples where only the c-phase of ZrO_2 exists. In other samples deformations are relaxed. It should be expected that the particles of c-ZrO_2, when placed in the locally enhanced tensile stress field at the tip of an advancing crack, are freed from the constraint of the matrix and transform to the forms stable at the lower temperature range.

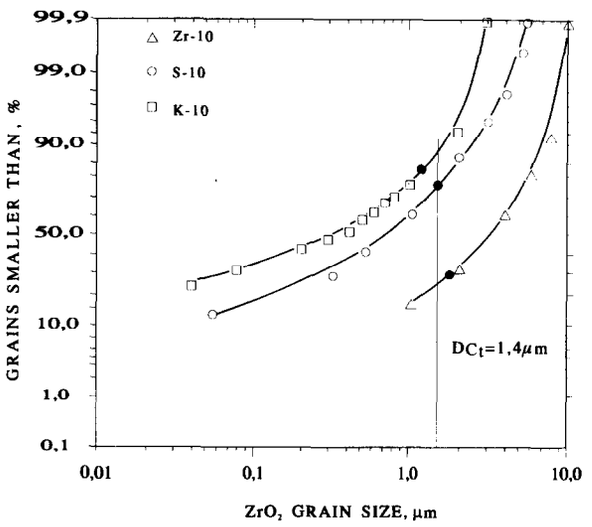


Fig. 3. Zirconia grain-size distribution of air-sintered alumina ceramics containing 10 wt% Zr-type ZrO_2, 10 wt% S-type ZrO_2 and 10 wt% K-type ZrO_2.[2] ●, Content of the finest ZrO_2 grains corresponding to the content of tetragonal form.

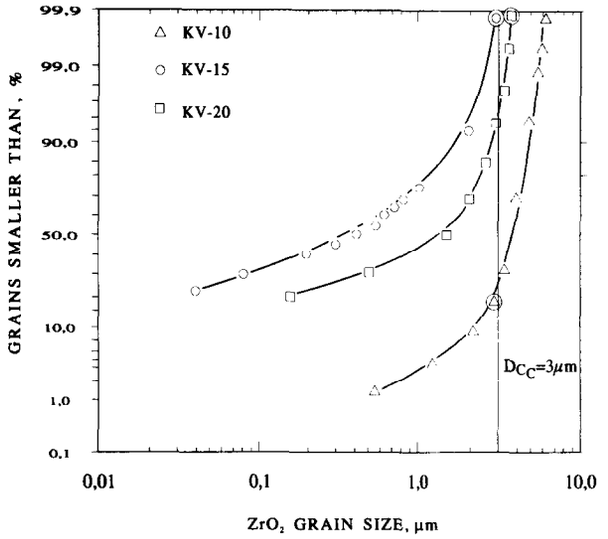


Fig. 4. Zirconia grain-size distribution of high vacuum-sintered alumina ceramics containing 10 wt%, 15 wt% and 20 wt% ZrO_2 of K-type (obtained by chemical method).[2] ○, Content of the finest ZrO_2 grains corresponding to the content of cubic form.

Tetragonal and monoclinic zirconia on fractured surfaces of vacuum-sintered ceramics show that the cubic form is the transformable phase and is responsible for enhancing the toughness of the ceramics.[3] This phase then appears to play the same role as the tetragonal form in the case of ceramics sintered in an oxidizing atmosphere.

The critical grain size of t-ZrO_2 inclusions in the case of air-sintered ceramics is d_{ct} = 1·4 μm (Fig. 3).[12] This value was estimated by comparison of ZrO_2 grain size distribution with the content of retained t-ZrO_2. A similar estimation made for samples sintered in high vacuum (Fig. 4) indicates an increase of the critical grain-size inclusion for c-ZrO_2 up to a value of d_{Cc} = 3·0 μm.[2] Obviously, the reason for the enhancement of the critical grain-size inclusion could be found in the non-stoichiometry of ZrO_2.

According to the present results, if the oxygen vacancy concentration plays a decisive role in the metastability of c-phase, it would then be possible to transform it to t- or m-phase, due to the reduction of the vacancy concentration in the ZrO_2 lattice as a result of sintering alumina–zirconia ceramics in atmospheres richer in oxygen. After Kountouros *et al.*,[11] a critical minimum and a critical maximum vacancy concentration for each ZrO_2 phase should also exist.

As can be seen from Table 4, in the p_{O_2} range between 2·80 × 10^{-5} and 2·80 × 10^{-2} Pa, the cubic form is the only phase of zirconia. However, an increase of oxygen content in the sintering atmosphere causes changes in the lattice parameters of the c-phase (see Table 5 and Fig. 5). An increase of the constant a values and the unit cell volume is observed. These results seem to be an effect of oxygen loss decrease from the zirconia structure

Table 4. Zirconia phases in Al_2O_3–10 wt% ZrO_2 measured from free surface as a function of oxygen content in sintering atmosphere

Oxygen partial pressure (Pa)	*Oxygen vacancy concentration (%)*	*Phases of ZrO_2 (%)*		
		m	*t*	*c*
$2{\cdot}80 \times 10^{-5}$	14·85	—	—	100
$2{\cdot}80 \times 10^{-4}$	13·65	—	—	100
$2{\cdot}80 \times 10^{-3}$	12·90	—	—	100
$2{\cdot}80 \times 10^{-2}$	9·13	—	—	100
$1{\cdot}40 \times 10^{-1}$	5·25	—	20·6	79·4
$1{\cdot}80 \times 10^{-1}$	3·12	Traces	100	—
$1{\cdot}07 \times 10^{0}$	0·45	5·6	94·4	—
$1{\cdot}00 \times 10^{1}$	0·145	7·0	93·0	—
$0{\cdot}85 \times 10^{2}$	0·05	8·0	92·0	—
$1{\cdot}39 \times 10^{3}$	0	8·4	91·6	—
$1{\cdot}07 \times 10^{4}$	0	10·6	89·4	—
$2{\cdot}10 \times 10^{4}$	0	16·5	83·5	—

during sintering in less oxygen-deficient atmospheres. The decrease of the X-ray mean half breadth (Fig. 6) and lattice parameter scattering from a value of 0·000 16 to 0·000 02 (see Table 5) also indicates an improvement in the c-phase structure.

When the oxygen content in the sintering atmosphere decreases below the critical p_{O_2} value for the c-phase. t-ZrO_2 appears and coexists with c-ZrO_2 (see Table 4—$p_{O_2} = 1{\cdot}40 \times 10^{-1}$Pa).

In the case of $1{\cdot}80 \times 10^{-1}$ Pa oxygen pressure t-ZrO_2 is the only form of zirconia present, but from $1{\cdot}07 \times 10^{0}$ Pa oxygen pressure is accompanied by m-ZrO_2. It indicates that the critical minimum vacancy concentration for t-phase has been exceeded. A further increase of the oxygen content (air atmosphere) leads to an increase of m–ZrO_2 up to 16·5%.

Table 5. Lattice parameters of c-ZrO_2 as a function of oxygen content in sintering atmosphere

Oxygen partial pressure (Pa)	*Lattice constants a (nm)*	*Volume of unit cell (nm^3)*
$2{\cdot}80 \times 10^{-5}$	0·512 49 ± 0·000 16	0·134 604 ± 0·000 129
$2{\cdot}80 \times 10^{-4}$	0·512 98 ± 0·000 11	0·134 989 ± 0·000 089
$2{\cdot}80 \times 10^{-3}$	0·513 19 ± 0·000 08	0·135 155 ± 0·000 063
$2{\cdot}80 \times 10^{-2}$	0·514 63 ± 0·000 02	0·136 302 ± 0·000 017
$1{\cdot}40 \times 10^{-1}$	0·514 14 ± 0·000 32	0·135 908 ± 0·000 253

In a similar way to the cubic form, an increase of the oxygen content in the sintering atmosphere influences the lattice parameters of the t- and m-phases (Tables 6 and 7). As can be seen from Fig. 7 the tetragonality (*c/a* axial ratio) of t-ZrO_2 considerably improves. An increase of the m-phase unit volume is also observed (Table 7). Figures 8 and 9 illustrate the changes of zirconia phase composition with oxygen content in a sintering atmosphere.

The presence of the stress field in samples with c-ZrO_2 is also confirmed by XRD results of the α-Al_2O_3 unit cell volume of samples sintered in p_{O_2} atmospheres between $2{\cdot}80 \times 10^{-4}$ and $2{\cdot}80 \times 10^{-2}$ Pa (see Fig. 10). Calculated deformation of α-Al_2O_3 unit cell is equal to 0·2% (see Table 8). In other samples with t-ZrO_2 the unit cell volume becomes similar to values typical for alumina ceramics without zirconia. In this way, t-ZrO_2 seems to be a factor responsible for the relaxation of stresses caused by c-ZrO_2 in the matrix.

Table 6. Lattice parameters of t-ZrO_2 as a function of oxygen content in sintering atmosphere

Oxygen partial pressure (Pa)	*Lattice constants (nm)*		*c/a*	*Volume of unit cell (nm^3)*
	a	*c*		
$1{\cdot}40 \times 10^{-1}$	0·360 661 ± 0·000 059	0·518 793 ± 0·000 087	1·438 45 ± 0·000 48	0·067 482 72 ± 0·000 033 63
$1{\cdot}80 \times 10^{-1}$	0·360 265 ± 0·000 021	0·519 391 ± 0·000 039	1·441 69 + 0·000 19	0·067 412 20 ± 0·000 012 89
$1{\cdot}07 \times 10^{0}$	0·360 275 ± 0·000 017	0·519 365 ± 0·000 039	1·441 58 ± 0·000 18	0·067 412 52 ± 0·000 011 28
$1{\cdot}00 \times 10^{1}$	0·360 271 ± 0·000 016	0·519 382 ± 0·000 041	1·441 64 ± 0·000 18	0·067 410 31 ± 0·000 011 09
$0{\cdot}85 \times 10^{2}$	0·359 981 ± 0·000 156	0·519 848 ± 0·000 038	1·444 10 ± 0·000 17	0·067 365 3 ± 0·000 010 7
$1{\cdot}39 \times 10^{3}$	0·360 409 ± 0·000 188	0·519 299 ± 0·000 049	1·440 86 ± 0·000 21	0·067 454 3 ± 0·000 013 4
$1{\cdot}07 \times 10^{4}$	0·360 409 ± 0·000 042	0·519 006 ± 0·000 070	1·440 05 ± 0·000 36	0·067 416 2 ± 0·000 024 9
$2{\cdot}10 \times 10^{4}$	0·360 159 ± 0·000 092	0·519 340 ± 0·000 016	1·441 97 ± 0·001 73	0·067 366 5 ± 0·000 055 2

Table 7. Lattice parameters of m-ZrO_2 as a function of oxygen content in sintering atmosphere

Oxygen partial pressure (Pa)	*Lattice constants (nm)*			*Volume of unit cell (nm^3)*
	a	*b*	*c*	
$1{\cdot}07 \times 10^{0}$	0·513 253 ± 0·000 408	0·517 343 ± 0·000 339	0·530 255 ± 0·000 425	0·138 998 21 ± 0·000 328 81
$1{\cdot}00 \times 10^{1}$	0·513 438 ± 0·000 795	0·516 957 ± 0·001 005	0·530 112 ± 0·000 498	0·139 011 33 ± 0·000 637 25
$0{\cdot}85 \times 10^{2}$	0·513 476 ± 0·000 277	0·518 789 ± 0·000 433	0·529 819 ± 0·000 303	0·139 437 45 ± 0·000 286 96
$1{\cdot}39 \times 10^{3}$	0·513 435 ± 0·000 565	0·517 513 ± 0·000 893	0·530 798 ± 0·000 443 8	0·139 267 98 ± 0·000 529 16
$2{\cdot}10 \times 10^{4}$	0·515 450 ± 0·000 110	0·530 900 ± 0·000 110	0·518 390 ± 0·000 110	0·140 006 12 ± 0·000 148 50

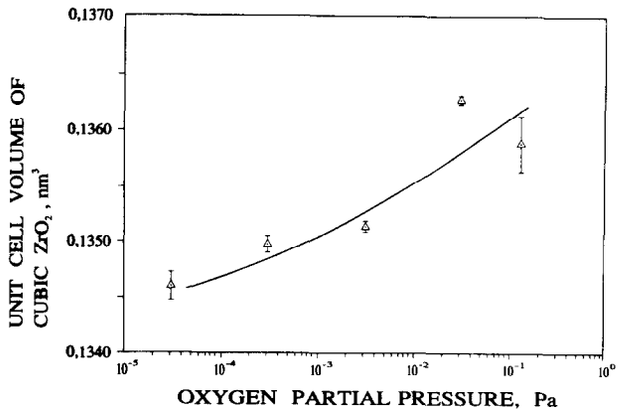


Fig. 5. Cubic zirconia unit cell volume as a function of oxygen content in sintering atmosphere.

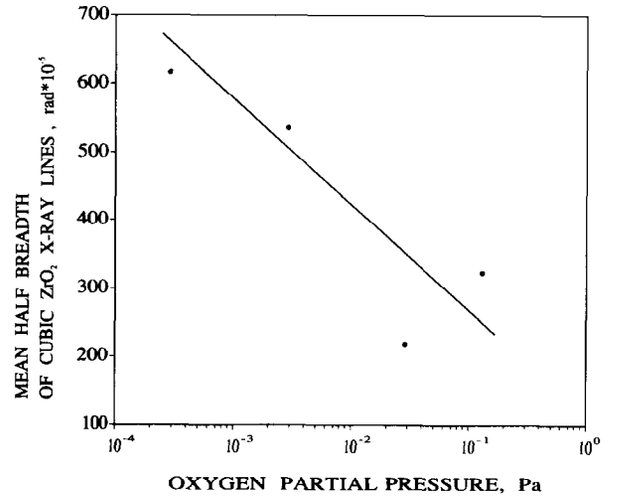


Fig. 6. Mean half breadth of X-ray lines of c-ZrO_2 as a function of oxygen content in sintering atmosphere.

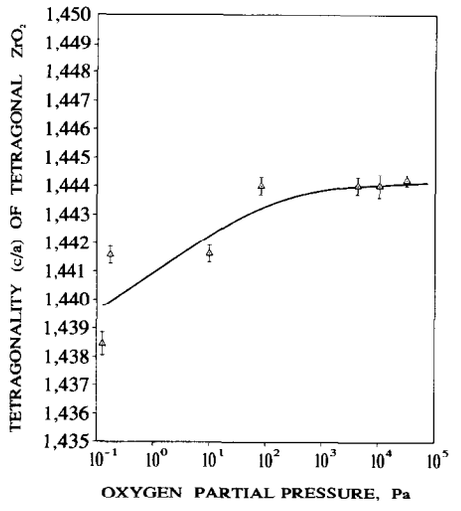


Fig. 7. Tetragonality (*c*/*a*) of t-ZrO_2 as a function of oxygen content in sintering atmosphere.

Samples sintered in p_{O_2} atmosphere equal to 1·40 $\times$ 10^{-1} Pa, where 20·6% of the tetragonal form coexists with 79·4% of the c-phase, are a good confirmation of the previously mentioned thesis.

The main conclusion concerning the influence of oxygen vacancy concentration on the meta-

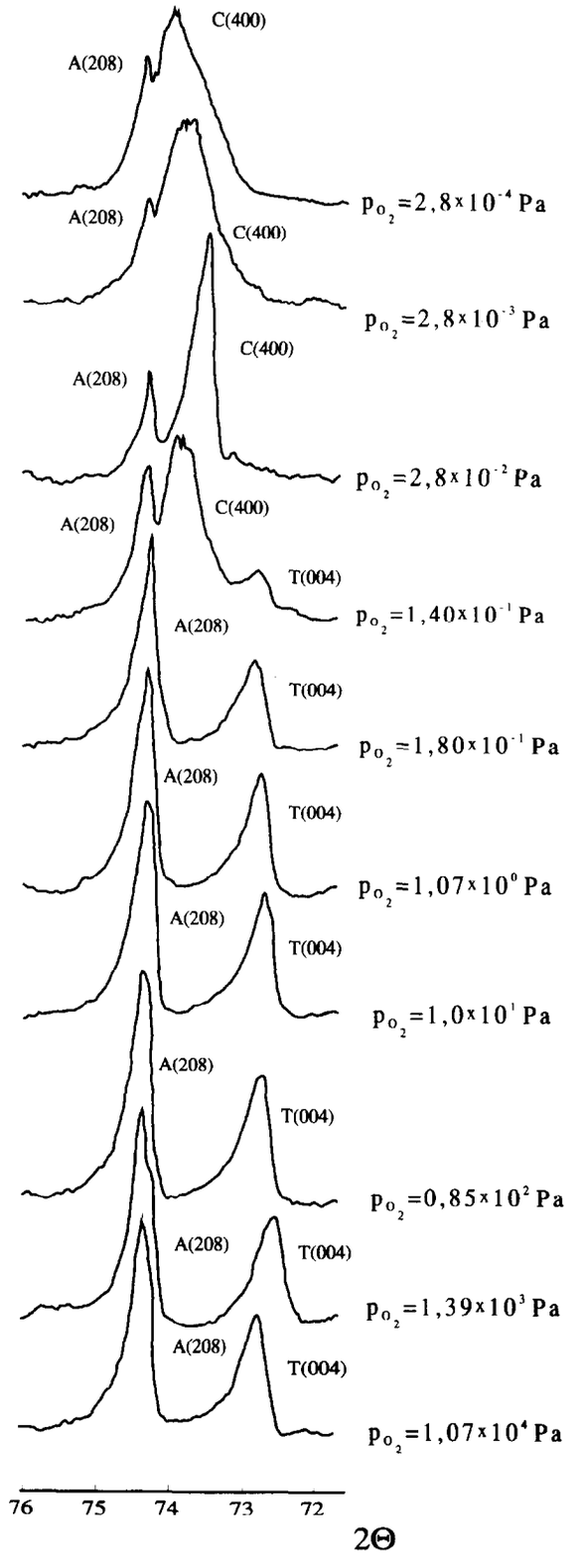


Fig. 8. Changes of XRD profiles of Al_2O_3–10 wt% ZrO_2 ceramics (2Θ = 72–76°) as a function of oxygen content in sintering atmosphere. A = α-Al_2O_3, C = cubic, T = tetragonal zirconia respectively.

stability of zirconia phases comes from thermogravimetric determinations. In this case, samples sintered in oxygen-deficient conditions were reoxidized by reheating in air at 1273 K for 1000 h and an increase of their weight was recorded. Results of oxygen vacancy concentration in zirconia are listed in Table 4.

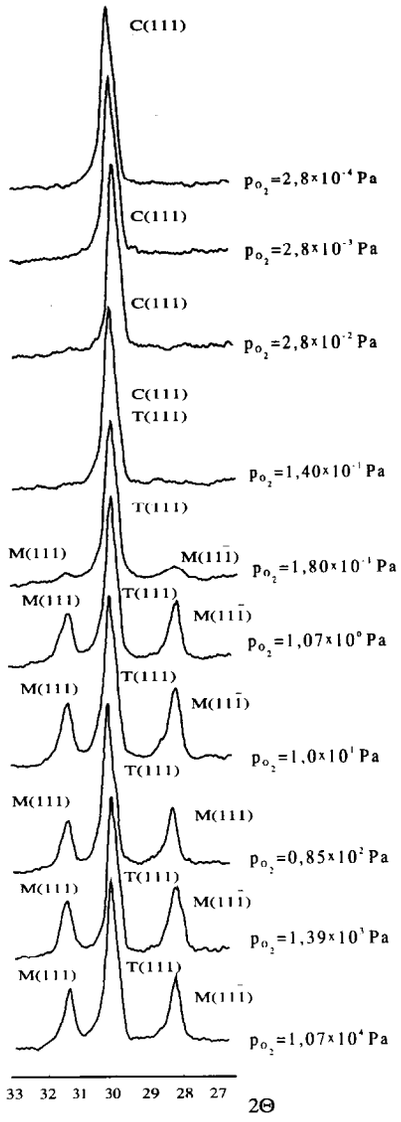


Fig. 9. Changes of XRD profiles of Al_2O_3–10 wt% ZrO_2 ceramics (2Θ = 27–33°) as a function of oxygen content in sintering atmosphere. C = Cubic, T = tetragonal and M = monoclinic zirconia respectively.

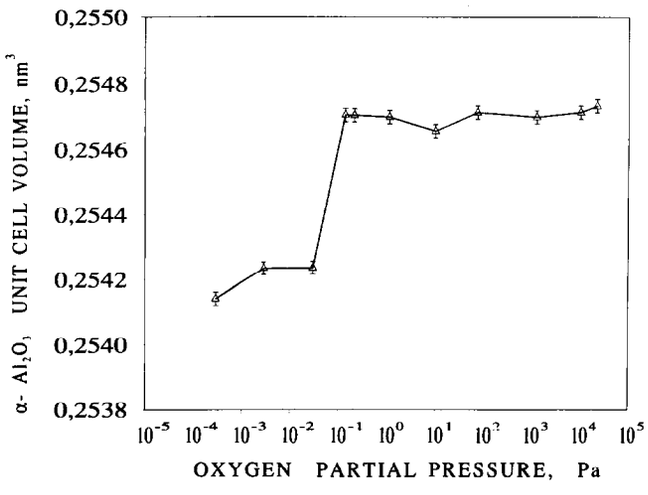


Fig. 10. Changes of α-Al_2O_3 unit cell volume in Al_2O_3–10 wt% ZrO_2 ceramics as a function of oxygen content in sintering atmosphere.

Table 8. Changes of unit cell volume and mean half breadth X-ray lines of αAl_2O_3 in Al_2O_3–10 wt% ZrO_2 as a function of oxygen content in sintering atmosphere

Oxygen partial pressure (Pa)	*Change of unit cell volume ΔV/V (%)*	*Mean half breadth (rad)*
$2{\cdot}80 \times 10^{-4}$	0·225	0·002 69
$2{\cdot}80 \times 10^{-3}$	0·182	0·002 75
$2{\cdot}80 \times 10^{-2}$	0·183	0·002 19
$1{\cdot}40 \times 10^{-1}$	0·002	0·001 35
$1{\cdot}80 \times 10^{-1}$	0·000	0·001 47
$1{\cdot}07 \times 10^{0}$	0·005	0·001 62
$1{\cdot}00 \times 10^{1}$	0·022	0·001 53
$0{\cdot}85 \times 10^{2}$	0·001	0·001 77
$1{\cdot}39 \times 10^{3}$	0·003	0·001 64

As was shown, the cubic form is the only phase of zirconia which exists in the oxygen vacancy concentration between 14·85 and 9·13%, that corresponds to a oxygen partial pressure in the sintering atmosphere in the range $2{\cdot}80 \times 10^{-5}$ Pa to $2{\cdot}80 \times 10^{-2}$ Pa. When the oxygen content increases to $1{\cdot}40 \times 10^{-1}$ Pa and the oxygen vacancy concentration decreases to a value of 5·25%, c-ZrO_2 coexists with the tetragonal form. Complete inversion to t-ZrO_2 is observed for 3·12% of oxygen vacancy content and this value seems to be a critical minimum value of oxygen vacancy concentration for this phase. Increasing the oxygen content in the sintering atmosphere the volume

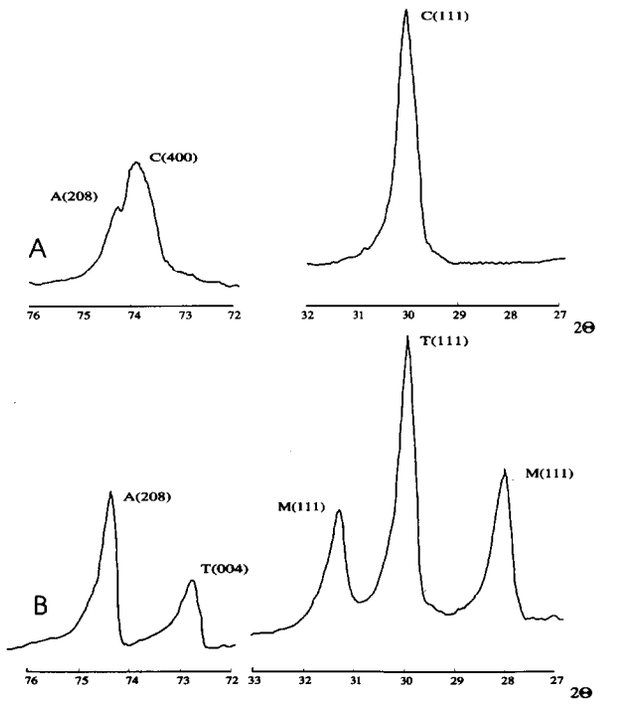


Fig. 11. Changes of zirconia phase composition as result of reoxidation heating of alumina–zirconia ceramics. A, Sample of ceramics sintered in atmosphere with oxygen partial pressure equalled $2{\cdot}80 \times 10^{-3}$ Pa; B, the same sample after reoxidation heating at 1273K for 1000 h in air. Explanation: A = α-Al_2O_3, C = cubic, T = tetragonal and M = monoclinic zirconia respectively.

of m-ZrO_2 increases also up to value of 16·5%, typical for samples sintered in oxidizing (air) atmosphere.

These results confirm the earlier thesis[11] that the oxygen vacancies in zirconia are mainly responsible for the metastability of c- and t-phases. Decreasing the oxygen vacancy concentration with an increase of the oxygen partial pressure in the sintering atmosphere below the critical minimum value leads to a breakdown of the c-phase which transforms to the t- and/or m-phase (see Fig. 11).

4 Conclusions

This study demonstrated that the oxygen content in a sintering atmosphere clearly influences the phase composition of undoped zirconia grains dispersed in alumina matrix.

In the case of ceramics sintered in atmospheres with oxygen partial pressure between $2{\cdot}80 \times 10^{-5}$ Pa and $2{\cdot}80 \times 10^{-2}$ Pa, 100% of zirconia is in the cubic form. The appearance of transformable c-ZrO_2 is a result of oxygen vacancy concentration in zirconia. The concentration of oxygen vacancy equal to 9% seems to be the critical minimum value for this phase. Decreasing the oxygen vacancy concentration, as a result of increasing the oxygen content in the sintering atmosphere, below 9%, causes an increase of the t-ZrO_2 content. The critical value of the oxygen vacancy concentration for the tetragonal form is 3%. A further increase of the oxygen content to $1{\cdot}07 \times 10^{0}$ Pa and a decrease of oxygen vacancy concentration to 0·5% lead to the appearance of m-ZrO_2.

Acknowledgement

This work was supported by the State Committee for Scientific Research under Grant No. 7.1013 91 01.

References

1. Tomaszewski, H., *et al.*, Influence of oxygen content in a sintering atmosphere on the phase composition and mechanical properties of Al_2O_3–10 wt% ZrO_2 ceramics. *J. Mat. Sci. Lett.*, **7** (1988) 778.
2. Tomaszewski, H., Effect of sintering atmosphere on thermomechanical properties of Al_2O_3–ZrO_2 ceramics. *Ceramics Int.*, **15** (1989) 141.
3. Tomaszewski, H., Effect of oxygen content in sintering atmosphere on t–c inversion of unstabilized zirconia grains dispersed in alumina matrix. In *Proceedings of Third Euro-Ceramics*, Vol. 1, *Processing of Ceramics*, ed. P. Duran & J. F. Fernandez. Faenza Editrice Iberica S.L., 1993, pp. 1005–10.
4. Livage, J. *et al.*, Nature and thermal evolution of amorphous hydrated ziconium oxide. *J. Amer. Ceram. Soc.*, **51** (1968) 349.
5. Subbarao, E. C., Zirconia—an overview. In *Advances in Ceramics*, Vol. 3, *Science and Technology of Zirconia*, ed. A. H. Heuer & L. W. Hobbs. American Ceramic Society, Columbus, OH, 1981, pp. 1–24.
6. Mitsuhashi, T. *et al.*, Characterization and stabilization of metastable tetragonal ZrO_2. *J. Amer. Ceram. Soc.*, **57** (1974) 97.
7. Heuer, A. H. *et al.*, Stability of tetragonal ZrO_2 particles in ceramic matrices. *J. Amer. Ceram. Soc.*, **65** (1982) 642.
8. Yoshimura, M., Phase stability of zirconia. *Bull. Amer. Ceram. Soc.*, **67**, (1988) 1950.
9. Morinaga, M. *et al.*, Electronic structure and phase stability of ZrO_2. *J. Phys. Chem. Solids*, **44** (1983) 301.
10. Hannink, R. H. J. *et al.*, Microstructural changes during isothermal ageing of calcia partially stabilized zirconia alloy. In *Advances in Ceramics*, Vol. 3, *Science and Technology of Zirconia*, ed. A. H. Heuer & L. W. Hobbs. American Ceramic Society, Columbus, OH, 1981, pp. 116–36.
11. Kountouros, P. *et al.*, Defect chemistry, phase stability and properties of zirconia polycrystals. In *Proceedings of the Fifth International Conference on Science and Technology of Zirconia*. Technomic Publishing Co. Inc., PA, USA, 1993, pp. 30–48.
12. Tomaszewski, H., Toughening effects in Al_2O_3–ZrO_2 system. *Ceramics Int.*, **14** (1988) 117.
13. Evans, A. G., Fracture mechanics of ceramics. Vol. 1, *Concept, Flaws and Fractography*, ed. R. C. Bradt, D. P. H. Hasselman & F. F. Lange. Plenum Press, New York, London, 1973, pp. 17–48.
14. Klug, H. R. & Alexander, L. E., X-Ray diffraction procedures for polycrystalline and amorphous materials. Wiley-Interscience, 1974, pp. 142–74 and 531–65.
15. Ruh, R. & Garrett, H. J., Nonstoichiometry of ZrO_2 and its relation to tetragonal–cubic inversion in ZrO_2. *J. Amer. Ceram. Soc.*, **50** (1967) 257.

Journal of the European Ceramic Society **15** (1995) 25–32
© 1995 Elsevier Science Limited
Printed in Great Britain. All rights reserved
0955-2219/95/$9.50

Grain Boundary Ionic Conduction in Zirconia-based Solid Electrolyte with Alumina Addition*

Xin Guo,[a]‡ Chao-Qun Tang[b] & Run-Zhang Yuan[a]

[a] State Key Laboratory for Synthesis and Processing of Advanced Materials, Wuhan University of Technology, Wuhan, Hubei Province 430070, People's Republic of China
[b] Department of Physics, Huazhong University of Science and Technology, Wuhan, Hubei Province 430074, People's Republic of China

(Received 2 February 1994; accepted 1 April 1994)

Abstract

The grain boundary resistance of 9 mol% Y_2O_3-stabilized ZrO_2 with Al_2O_3 addition was measured by the complex impedance approach. The effect of Al_2O_3 addition on the grain boundary resistance was analyzed from the aspects of microstructure and crystal defects by means of SEM, EPMA, TEM and the positron annihilation technique. The Al_2O_3 addition up to 5 mol% was found to reduce the grain boundary resistance per unit surface area of the grain boundaries and the activation energy for the grain boundary resistance. This phenomenon was explained by the scavenging of the grain boundary impurities, e.g. SiO_2, by the Al_2O_3 and the formation of the crystal grain boundary phases with very high defect concentration. By the analyses with a simplified theoretical model, the Al_2O_3 addition was considered to have no detrimental effect on the emf of the ZrO_2 oxygen sensor.

1 Introduction

In polycrystal ceramic materials, grain boundaries have a large, often controlling importance for properties. The studies on grain boundary behavior are essential for the design of ceramic materials, and the control and optimization of their performances. Thus a concept of 'grain boundary engineering' was put forward, i.e. to improve the properties of ceramics by modifying grain boundaries.[1] Now the grain boundaries of ZrO_2-based solid electrolyte have attracted much attention.

As one of the most important solid electrolytes, much research has been performed on ZrO_2. Although the research results are not totally in keeping with each other, the following points have been clarified: (1) the grain resistivity of polycrystal ZrO_2 is equivalent to that of a single crystal, and it is usually not affected by sintering temperature, atmosphere and heat treatment;[2] (2) the efforts to reduce the grain resistivity by changing composition (e.g. adding Y_2O_3, CaO, MgO, rare earth oxides, and two, three or more oxides are simultaneously added) are now nearly exhausted, the optimum stabilizer concentrations, e.g. 8–9 mol% Y_2O_3 or 13–14 mol% CaO have been generally established;[3] it is difficult to find a new stabilizer which can remarkably reduce the grain resistivity in a expectable period; (3) the property and structure of grain boundary phases are strikingly influenced by impurity, sintering temperature, atmosphere and heat treatments;[4] (4) the ZrO_2 grain boundary resistivity may be lower or higher than that of grain due to the difference of segregated elements and variation of grain boundary structure.[5,6] All these points suggest that a feasible way to further enhance the ionic conduction of ZrO_2 is to reduce the grain boundary resistivity by adding a new kind of ingredient. In order to densify ZrO_2 during sintering, certain amounts of Al_2O_3 were often added to ZrO_2.[7] After further study, it was discovered that Al_2O_3 can also reduce the resistance of ZrO_2.[8] In this paper, Al_2O_3 up to 5 mol% is added and the grain boundary resistance is studied.

2 Experimental Procedure

2.1 Preparation of specimens

The compositions of specimens are listed in Table 1. Powders used to produce the specimens were prepared from $ZrOCl_2 \cdot 8H_2O$, YCl_3 and $AlCl_3$ by

* Project supported by China Postdoctoral Science Foundation.
‡ To whom correspondence should be addressed.

Table 1. Compositions of specimens

Specimen	*Composition*
0AYZ	ZrO_2–9 mol% Y_2O_3
1·5AYZ	ZrO_2–9 mol%Y_2O_3–1·5 mol% Al_2O_3
5AYZ	ZrO_2–9 mol% Y_2O_3–5 mol% Al_2O_3

a coprecipitation method, average particle sizes measured by a centrifugal particle size analyzer (type SA-CP3) are 0·45 μm, 0·40 μm and 0·48 μm respectively. The powders were subsequently pressed into pellets (22 mm in diameter by 4 mm thick) at 200 MPa, then sintered at 1600°C for 2 h. The platinum electrodes were applied to the ZrO_2 specimens by the decomposition of chloroplatinic acid at 1000°C.

2.2 Measurements and analyses

The specimens under went the following measurements and analyses. (1) Resistances were measured by the complex impedance approach in a frequency range of 20 Hz to 1 MHz with a HP4285A precision LCR meter, the grain and grain boundary resistances were separated out by the analyses of the complex plots. (2) Al distribution information inside the specimens was examined by EPMA (type JCXA-733) on the specimens polished and coated with carbon. (3) Microstructure studies were carried out with SEM (type JSM-35C) and TEM (type H-800, Philips-CM_{12}/STEM). (4) Crystal defect changes were detected by the positron annihilation technique (CANBERRA Series 35).

3 Results

3.1 Grain boundary resistance

The complex impedance approach has been used extensively in the examination and development of solid electrolytes after the initial report by Bauerle.[9] This approach can effectively probe the grain resistance as well as the resistance across grain boundaries and electrode/electrolyte interfaces.

The grain boundary resistances R_{gb} of the specimens were measured at 440°C and 500°C; the results are listed in Table 2. In order to explain further the measured results, the grain boundary resistances per unit surface area of grain boundaries R_{gbs} were calculated from[10]

$$R_{gbs} = \rho_{gb}/D = R_{gb}(S/l)/D \qquad (1)$$

where ρ_{gb} is the grain boundary resistivity, S/l is the cross-section/length ratio of the specimen and D the grain boundary density. R_{gbs} has been used before by Miyayama and coworkers to explain intrinsic and extrinsic grain boundary phenomena,[8,10] because R_{gbs} values contain no microstructural effects. The R_{gbs} values are also listed in Table 2. For the case studied in this paper, if space charges resulting from the irregularity of lattice can account for the resistance of the grain boundary surface (intrinsic effect), the R_{gbs} should be constant, i.e. independent of Al_2O_3 content. However, for the extrinsic effects (impurity dominated), when the Al_2O_3 addition increases, the concentration of Al_2O_3 per unit surface area of grain boundaries also increases, notwithstanding the change of the grain boundary density D. Therefore, the R_{gbs} should be affected by the Al_2O_3 addition; this, in fact, is the case for the specimens used in this study. The R_{gbs} of the specimen 0AYZ is much higher than those of the specimens 1.5AYZ and 5AYZ; the specimen 5AYZ has the smallest R_{gbs} value.

Activation energies for the grain boundary resistance can be calculated from the Arrhenius equation

$$R = A \exp(E/KT) \qquad (2)$$

where K and T have their usual meanings. The values are listed in Table 2. The specimen 0AYZ has the largest grain boundary resistance activation energy E_{gb}, and E_{gb} decreases with increasing Al_2O_3 content.

3.2 Positron annihilation

The measurements of positron lifetime spectra were carried out at room temperature (21 ± 1)°C by a fast–fast coincidence lifetime spectrometer with a resolution of 230ps. A ^{22}NaCl positron source was used in the measurements. A normal specimen–source–specimen sandwich arrangement was adopted. A total of 10^6 counts in each spectrum were collected. After substracting the source and background contribution, all lifetime spectra were

Table 2. The grain boundary resistances and the activation energy of the specimens

Specimen	*Measured at 440°C*		*Measured at 500°C*		*Activation energy*
	R_{gb} (Ω)	R_{gbs} (Ω/cm²)	R_{gb} (Ω)	R_{gbs} (Ω/cm²)	E_{gb}(kJ/mol)
0AYZ	1 400	6·5	300	1·4	117·6
1·5AYZ	215	4·1	50	0·96	111·3
5AYZ	175	1·2	50	0·35	95·6

Table 3. Positron lifetime parameters

Specimen	τ_1 *(ps)*	τ_2 *(ps)*	τ_3 *(ps)*	I_1 *(%)*	I_2 *(%)*	I_3 *(%)*	$K(\mu s^{-1})$
0AYZ	239	269	1 802	90·5	8·2	1·3	38·3
1·5AYZ	205	353	1 685	90·5	7·6	1·5	155·4
5AYZ	204	375	1 806	92·0	6·9	1·2	153·7

analyzed with three components by the program POSITRONFIT EXTENDED. Lifetimes τ_1, τ_2 and τ_3 and their relative intensities I_1, I_2 and I_3 were obtained (listed in Table 3). The long lifetime component τ_3, whose intensity is about 1·4%, may arise from the positron annihilation in the positron source and associated foils, and/or interfaces that are unavoidable with the sandwich arrangement, so τ_3 will not be discussed. The short lifetime component τ_1 reflects the positron annihilation feature in perfect lattices, and τ_2 is the positron lifetime in crystal defects. According to the two-state trapping model,[11] the trapping rate of the defects to positron K can be derived,

$$K = I_2 \Big/ \left(\frac{1}{\tau_1} - \frac{1}{\tau_2}\right) \tag{3}$$

The K values are listed in Table 3. Because $K = \mu C$, where C is the concentration of defects and μ is the specific trapping rate which can be considered as a constant when the type or structure of the defects does not change; thus the change of K can roughly reflect the change of the defect concentration. The K value increases when Al_2O_3 is added to ZrO_2, this tendency is opposite to that of the grain boundary resistance per unit surface area of grain boundaries R_{gbs}; in other words, with increasing Al_2O_3 content, the defect concentration of the specimens increases, and consequently the R_{gbs} value decreases.

3.3 Microstructure

The solubility of Al_2O_3 in ZrO_2 grain is very low, only 0·5 mol% Al_2O_3 can be dissolved in Y_2O_3-stabilized ZrO_2 sintered at 1700°C and cooled at 220°C/h,[8] and the solubility of Al_2O_3 is about 0·1 mol% when sintered at 1300°C.[12] So it is obvious that the Al_2O_3 additions in the present work are far beyond the Al_2O_3 solubility.

Figure 1 shows the scanning electron micro-

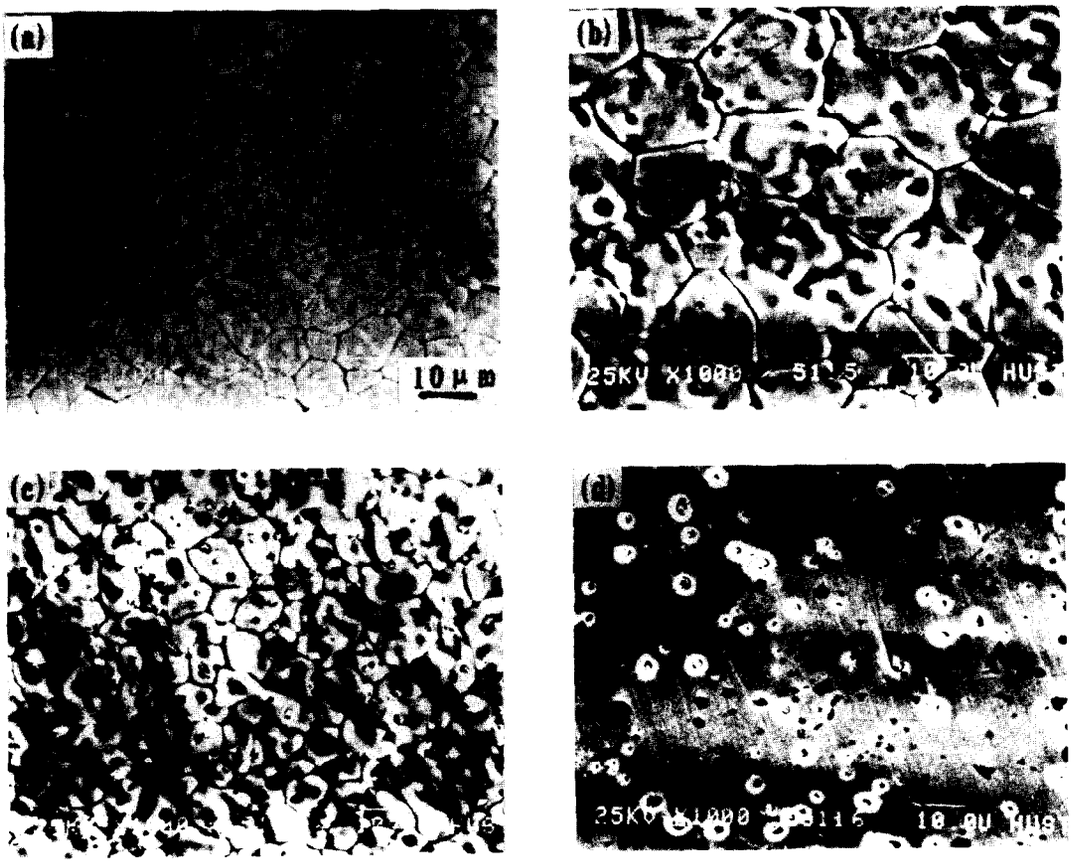


Fig. 1. Scanning electron micrographs of the surfaces of as-sintered specimens. (a) 0AYZ, (b) 1·5AYZ, (c) 5AYZ, (d) 1·5AYZ, polished surface.

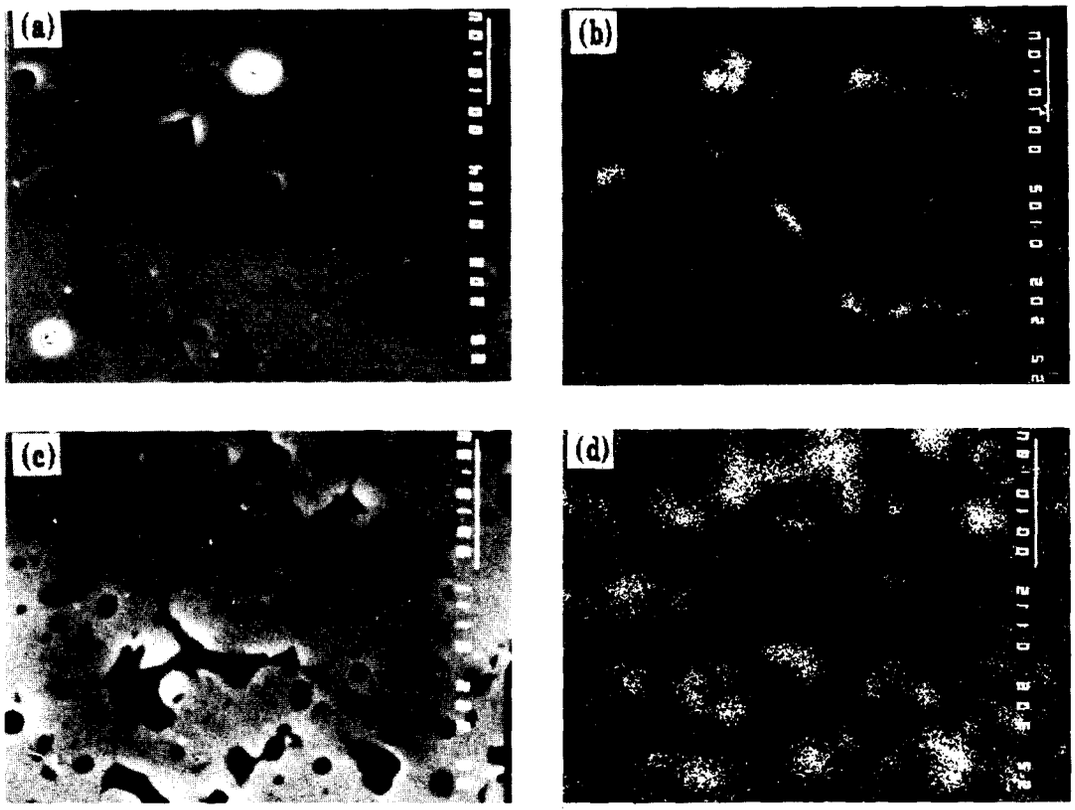


Fig. 2. EPMA photographs of the specimens with different Al_2O_3 content. (a), (b) 1·5AYZ, (c), (d) 5AYZ.

graphs of the surfaces of the as-sintered specimens 0AYZ, 1·5AYZ and 5AYZ, and the polished surface of the specimen 1·5AYZ. The specimen 0AYZ has a homogeneous mono-phase structure, while Al_2O_3 particles can be observed as bright or dark spots in the specimens 1·5AYZ and 5AYZ; the Al_2O_3 particles are situated both inter- and intragranularly. Because there are quite large differences in the elastic modulus and the thermal expansion coefficient between Al_2O_3 and ZrO_2, the intragranular Al_2O_3 particles are always accompanied by pores, which can be seen from the polished surface.

Figure 2 shows the EPMA analysis results, in which photographs (a) and (c) are scattered electron images and photographs (b) and (d) display the Al distributions. From these photographs, it can be seen that Al is mainly segregated at grain boundaries, and that the Al segregation is more serious in the specimen 5AYZ. Some small dark spots inside grains shown in the scattered electron images are Al_2O_3 particles and pores. Apparent enrichment of Si and Ca at grain boundaries was not observed.

Because of the segregation of Al_2O_3 and impurities at grain boundaries, grain boundary phases are often formed. Two types of grain boundary phases were discovered in the specimens with Al_2O_3 addition; one type is shown in Fig. 3. The small bright particle situated at the triple point of ZrO_2 grains is an Al_2O_3 particle (Fig. 3(a)), the grain boundary phases have a peculiar morphology. Figure 3(b) is the SADP of the grain boundary phases, the diffraction rings indicate that the grain boundary phases consist of large amount of crystallites. The ratio of the square radii of the diffraction rings is

$$R_1^2 : R_2^2 : R_3^2 : R_4^2 : R_5^2 : R_6^2 \approx 1 : 2 : 3 : 6 : 7 : 9 \quad (4)$$

According to the ratio and brightness distribution of the diffraction rings, these crystallites do not have crystal structure of α-Al_2O_3 or cubic ZrO_2; because of the large errors usually involved in electron diffractions, it is still difficult to determine the crystal structure of the crystallites. The composition of the grain boundary phases measured by EDAX is given in Table 4. An enrichment of Al was found and no impurities such as Si, Ca were detected. However, for the crystal grain boundary phases at different regions of the specimen, different SADP patterns are produced and different Al, Y and Zr concentrations are measured by EDAX. The phases may be con-

Table 4. Composition of the crystal grain boundary phases measured by EDAX

Element	*wt%*	*at.%*
Al	2·62	8·29
Y	15·76	15·17
Zr	81·62	76·54

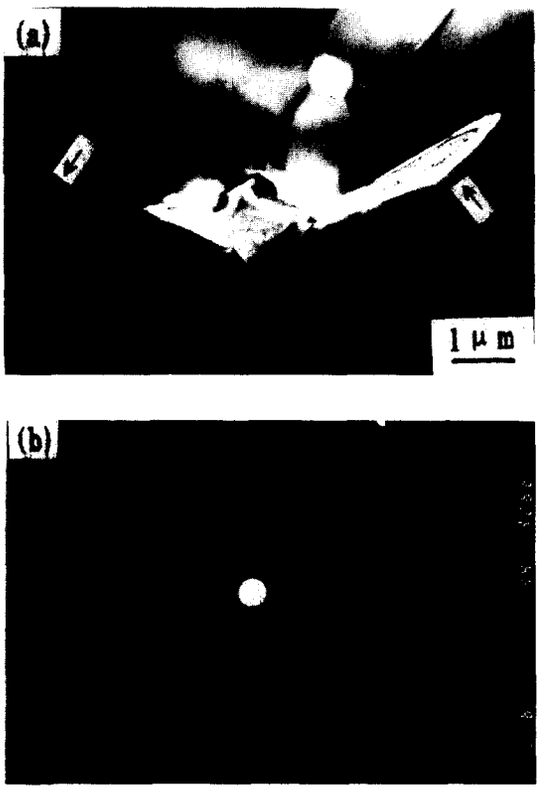


Fig. 3. Transmission electron micrographs of the crystal grain boundary phases. (a) Bright field image, (b) SADP. The arrows indicate the grain boundary phases.

cluded to be a kind of Al-rich compound with a chemical formula

$$(Al_2O_3)_x(Y_2O_3)_y(ZrO_2)_z(x + y + z = 1).$$

The amount of the crystal grain boundary phases is quite large; they are distributed at grain boundaries and Al_2O_3/ZrO_2 interfaces.

Another type of grain boundary phase is shown is Fig. 4. This type of grain boundary phase is rarely found in the specimens, they are distributed at triple points (Fig. 4(a)) and Al_2O_3/ZrO_2 interfaces (Fig. 4(b)). The SADP of the grain boundary phases (Fig. 4(c)) indicates that they are amorphous, and corresponding EDAX measurement (Table 5) discovers impurities Si and Ca, besides the enrichment of Al. The grain boundaries without amorphous phases are quite clean, no impurities such as Si and Ca are presented there.

According to these analyses, it can be concluded that there are three forms of Al_2O_3 in existence in ZrO_2. They are: (1) a very small amount of Al_2O_3 is dissolved in ZrO_2 grains; (2) the surplus Al_2O_3 then forms Al_2O_3 particles, which are extensively situated intra- and intergranularly; (3) Al_2O_3 segregates at grain boundaries, and forms the crystal and the amorphous Al-rich grain boundary phases; the amorphous one contains impurities such as Si and Ca.

Table 5. Composition of the amorphous grain boundary phases measured by EDAX

Element	*wt%*	*Oxide%*
Al	9·26	17·50
Si	29·40	62·91
Ca	8·00	11·20
Y	4·43	5·63
Zr	2·48	3·35



Fig. 4. Transmission electron micrographs of the amorphous grain boundary phases. (a), (b) Bright field images, (c) SADP. The arrows indicate the grain boundary phases.

4 Discussions

4.1 Effect of Al_2O_3 on the grain boundary resistance of ZrO_2

Al_2O_3 can reduce the ZrO_2 grain boundary resistance. Butler & Drennan suggested that this is because that Al_2O_3 acts as a scavenger for SiO_2 located at grain boundaries.[13] There are two types of grain boundary phases in ZrO_2, the crystal and the amorphous. Table 2 shows that the ZrO_2 grain boundary resistance is controlled by the Al_2O_3 addition and that Al_2O_3 reduces the R_{gbs}. This phenomenon may be explained with two mechanisms that are related to the two types of grain boundary phases.

Mechanism I: the Al_2O_3 addition scavenges SiO_2 located at grain boundaries and results in a low grain boundary resistance. This is similar to the results of Butler & Drennan. The only difference from the experiment of Butler & Drennan is that the specimens used in this paper contain CaO as well as SiO_2. According to the $CaO–Al_2O_3–SiO_2$ phase diagram,[14] CaO, Al_2O_3 and SiO_2 with a concentration relation listed in Table 5 will react with each other according to the following equation:

$$CaO + Al_2O_3 + 2SiO_2 \rightarrow CaAl_2Si_2O_3 \quad (5)$$

The impurities CaO and SiO_2 are transported by grain boundary diffusion to the triple points with high Al_2O_3 concentration and the Al_2O_3 particle surface, and by the chemical reaction (5), the grain boundary impurities are scavenged, and as a result, E_{gb} decreases.

Mechanism II: The crystal grain boundary phases contain no CaO or SiO_2, so the mechanism I can not explain all the experimental phenomena. And besides, the positron annihilation results show that Al_2O_3 increases the crystal defect concentration in ZrO_2. The defects can be roughly divided into two main parts, the defects in grains and those in the crystal grain boundary phases. The defects in grains are determined by the dopant Y_2O_3, and the Al_2O_3 solubility in grains is very low, so the effect of Al_2O_3 on the grain defects is negligible. This means that the increased crystal defect concentration is a result of the increasing of crystal defects in the crystal grain boundary phases, and consequently the resistance of the crystal grain boundary phases is very low, so the R_{gbs} subsequently decreases. Thus a new mechanism is derived as follows: the Al_2O_3 segregated at grain boundaries forms crystal grain boundary phases with very high defect concentration, so the grain boundary resistance decreases. Aono and coworkers observed a somewhat similar phenomenon in the solid electrolyte based on $LiTi_2(PO_4)_3$[15,16] in which grain boundary conductivity increases considerably by adding Li_3BO_3 or $Li_4P_2O_7$. The reason for the conductivity enhancement was attributed to the enhancement of the lithium concentration at the grain boundaries and the formation of a new conductive phase at the grain boundaries.

It should be noted that the enhancement of the ionic conductivity of some compounds by the incorporation of fine non-conduction particles seems to be quite popular,[17,18] It was usually considered to be due to the formation of conductive, defect-rich interfaces. This explanation is not quite applicable to the phenomena observed in this study, because Fig. 1(d) shows that the intragranular Al_2O_3 particles are accompanied by pores, and no such defect-rich interfaces were found for them, only for the intergranular Al_2O_3 particles, where such defect-rich interfaces were observed. So it must be stressed that the inter- and intragranular particles have different effects on the conductivity, when there are large difference in properties between the particles and the matrix, the conductive, defect-rich interfaces can only form for the intergranular particles.

4.2 Effect of grain boundaries on the emf of the ZrO_2 oxygen sensor

As an oxygen ion conductor, ZrO_2 is popularly used in oxygen sensors. By the emf output of the oxygen sensor, the oxygen partial pressure in all kinds of atmospheres can be measured. There are lots of factors affecting the emf output, the principle ones are electrode structure, electrode/electrolyte interfaces and ZrO_2 microstructure. In a practical process of an oxygen sensor, all the above factors simultaneously bring about an influence, and it is almost impossible to differentiate the individual influences by experiments, therefore, the effect of the grain boundaries on the output of the ZrO_2 oxygen sensors is analysed with a simplified model as follows.

Figure 5 is a simplified schematic representation of an oxygen sensor containing grain boundary phases. Suppose $t_i<1$ for the grain boundary phases, because the current through the grain boundary phases is also carried by oxygen ions; apart from an increase of internal resistance, the grain boundary phases do not influence the exclusively ionic nature of the conductivity of ZrO_2. The emf of the oxygen sensor can be given by eqn (6),[19] if the

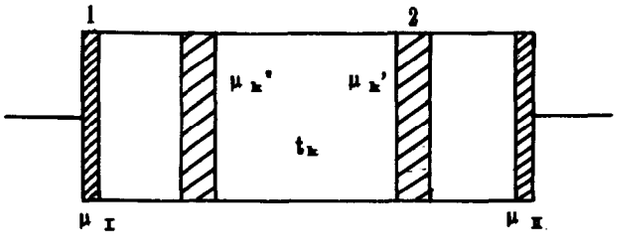


Fig. 5. Simplified schematic representation of an oxygen sensor. 1, Electrode; 2, grain boundary phases.

oxygen sensor is divided into several parts, as shown in Fig. 5. The meaning of t_k, μ_k'' and μ_k' can be seen from Fig. 5.

$$E = -\frac{1}{2ZF}\int_{\mu_I}^{\mu_{II}} t\,\mathrm{d}\mu$$

$$= -\frac{1}{2ZF}\sum t_k(\mu_k'' - \mu_k') \qquad (6)$$

When $t_k = 1$, the chemical potential of the region k can be totally transferred into the emf; when $t_k < 1$ and $\mu_k'' - \mu_k' = 0$, or $t_k = 0$ and $\mu_k'' - \mu_k' \neq 0$, the region k does not make any contribution to the emf. Under this condition, $E = E_{th}$ is held true, E_{th} being the theoretical value. When $t_k < 1$ and $\mu_k'' - \mu_k' \neq 0$, then $E < E_{th}$. When oxygen partial pressures over the electrodes are changed, during a transient situation, an appreciable oxygen potential drop may occur over the grain boundary phases, if $t_k < 1$ this yields a deviation from the E_{th} and an emf drift. Because the chemical diffusion inside ZrO_2 is very slow, the emf drift will last as long as several hours.

There are three kinds of grain boundary regions in the ZrO_2 with Al_2O_3 addition, the 'clean' grain boundaries but with Al segregation, the grain boundaries with amorphous phases and the grain boundaries with crystal phases. As Kingery has pointed out,[20] the ionic nature of ceramic oxide always leads to the formation of an electrostatic potential on grain boundaries, the sign and magnitude of the electrostatic potential depending strongly on impurity concentration. The Al segregation at the 'clean' grain boundaries certainly will change the grain boundary electrostatic potential, so the μ_k', μ_k'' values are changed, but although the nature of the 'clean' grain boundaries is unclear, $t_i = 1$ will hold true from them, thus the 'clean' grain boundaries do not have a negative effect on the emf. For the amorphous grain boundary phase, supposing $t_i = 0$ may be reasonable, and the amount of the amorphous phases is very limited, then according to this discussion the amorphous phases make no contribution to the emf. This means that the amorphous phases also do not have a negative effect on the emf. As proved by the present experiments, the crystal grain boundary phases are very conductive, and it can be seen from the Nernst–Einstein equation

$$D = \frac{\sigma KT}{CZ^2} \qquad (7)$$

where D is the charge carrier's diffusivity, C is the concentration of charge carrier, Z the charge quantity, and K and T have their usual meanings, that the oxygen ion diffusivity in the crystal grain boundary phases is very high. As long as chemical diffusivity in the grain boundary phases is very high, there will be practically no oxygen concentration drop (that is, chemical potential drop) over these phases. Therefore, for the crystal grain boundary phases $\mu_k'' - \mu_k' = 0$ might hold true, and then the phases will also possibly not have a negative effect on the emf of the oxygen sensor, notwithstanding that $t_i = 1$ or $t_i < 1$ for the crystal grain boundary phases. As the Al_2O_3 addition can scavenge the grain boundary impurities, it can be concluded that the Al_2O_3 segregation at the grain boundaries not only does not have a negative effect on the emf of the ZrO_2 oxygen sensor but also can release, even wipe out the detrimental effects of the other impurities, e.g. SiO_2.

5 Conclusion

The Al_2O_3 addition up to 5 mol% can reduce the grain boundary resistance per unit surface area of the grain boundaries and the activation energy for the grain boundary resistance of the 9 mol% Y_2O_3-stabilized ZrO_2. This is due to the scavenging of the impurities segregated at the grain boundaries, e.g. SiO_2, by Al_2O_3 and the formation of the Al-rich crystal grain boundary phases with very high defect concentration. The Al_2O_3 addition has no detrimental effect on the emf of the ZrO_2 oxygen sensor. All of this proves that the Al_2O_3-containing Y_2O_3-stabilised ZrO_2 is a kind of very good solid electrolyte and that to decrease the grain boundary resistance by adding new ingredients is a feasible way to further enhance the ionic conduction of ZrO_2. The next step that should be taken is to explore more oxides with characteristics similar to Al_2O_3.

References

1. Yen, T. S., The microstructure and properties of ceramics. 1. The development of ceramic microstructure and modern methods of investigation. *J. Chin. Ceram. Soc.*, **9** (1981) 64–79.
2. Badwal, S. P. S. & Drennan, J., Yttria–zirconia: effect of microstructure on conductivity. *J. Mat. Sci.*, **22** (1987) 3231–9.
3. Etsell, T. H. & Flengas, S. N., The electrical properties of solid oxide electrolyte. *Chem. Rev.*, **70** (1970) 339–76.
4. Badwal, S. P. S & Hughes, A. E., The effects of sintering

atmosphere on impurity phase formation and grain boundary resistivity in Y_2O_3-fully stabilized ZrO_2. *J. Eur. Ceram. Soc.*, **10** (1992) 115–22.
5. Keiger, K., Burggraaf, A. J. & De With, G., The effect of Bi_2O_3 on the electrical and mechanical properties of ZrO_2–Y_2O_3 ceramics. *J. Mat. Sci.*, **17** (1982) 1095–102.
6. Verkerk, M. J., Winnubst, A. J. A. & Burggraaf, A. J., Effect of impurities on sintering and conductivity of yttria-stabilized zirconia. *J. Mat. Sci.*, **17** (1982) 3113–22.
7. Radford, K. C. & Bratton, R. J., Zirconia electrolyte cells. Part 1. Sintering studies. *J. Mat. Sci.*, **14** (1979) 59–65.
8. Miyayama, M., Yanagida, H. & Asada, A., Effects of Al_2O_3 additions on resistivity and microstructure of yttria-stabilized zirconia. *Am Ceram. Soc. Bull.*, **65** (1985) 660–4.
9. Bauerle, J. E., Study of solid electrolyte polarization by a complex admittance method. *J. Phys. Chem. Solids*, **30** (1969) 2657–70.
10. Miyayama, M. & Yanagida, H., Dependence of grain-boundary resistivity on grain-boundary density in yttria-stabilized zirconia. *J. Am. Ceram. Soc.*, **67** (1984) C194–5.
11. Brandt, W. & Dupasquier, A., *Positron Solid State Physics*. North Holland, Amsterdam, 1983, p. 24, p. 200.
12. Bernard, H., Sintered stabilized zirconia microstructure and conductivity. Report CEA-R-5090, Commissariat à l'Energie Atomique, CEN-Saclay, France, 1981, p. 117.
13. Butler, E. P. & Drennan, J., Microstructural analysis of sintered high-conductivity zirconia with Al_2O_3 additions. *J. Am. Ceram. Soc.*, **65** (1982) 474–8.
14. Gottwald, G., Forkel, K. & Wihsmann, F. G., Computer assisted design of phase diagrams. *Silikattechnik*, **36** (1985) 49–53.
15. Aono, H. & Sugimoto, E., Ionic conductivity of solid electrolytes based on lithium titanium phosphate. *J. Electrochem. Soc.*, **137** (1990) 1023–7.
16. Aono, H., Sugimoto, E., Sadaoka, Y., Imanaka, N. & Adachi, G., Ionic conductivity of $LiTi_2(PO_4)_3$ mixed with lithium salts. *Chem. Lett.*, **219** (1991) 331–4.
17. Liang, C. C., Conduction characteristics of the lithium iodide-aluminum oxide solid electrolytes. *J. Electrochem. Soc.*, **120** (1973) 1289–92.
18. Jow, T. & Wagner, Jr, J. B., The effect of dispersed alumina particles on the electrical conductivity of cuprous chloride. *J. Electrochem. Soc.*, **126** (1979) 1963–72.
19. Beekmans, N. M & Heyne, L., Correlation between impedance microstructure and composition of calcia-stabilized zirconia. *Electrochem. Acta*, **12** (1976) 303–10.
20. Kingery, W. D., Plausible concepts necessary and sufficient for interpretation of ceramic grain-boundary phenomena: 1. Grain-boundary characteristics, structure, and electrostatic potential. *J. Am. Ceram. Soc.*, **57** (1974) 1–8.

Journal of the European Ceramic Society **15** (1995) 33–43
© 1995 Elsevier Science Limited
Printed in Great Britain. All rights reserved
0955-2219/95/$9.50

Processing, Microstructure and Mechanical Properties of SiC Platelet-reinforced 3Y-TZP Composites

A. Selçuk, C. Leach & R. D. Rawlings

Department of Materials, Imperial College of Science, Technology and Medicine, London, SW7 2BP, UK

(Received 25 March 1994; revised version received 1 June 1994; accepted 30 June 1994)

Abstract

A study has been carried out on the processing of silicon carbide platelet-reinforced yttria-stabilised zirconia ceramics, using slip casting techniques followed by cold isostatic pressing and pressureless sintering. Optimisation of the process variables, in particular the stability and homogeneity of the composite slurry and mould configuration, enabled samples with good platelet alignment and densities >96% of theoretical to be produced routinely after pressureless sintering. The pore formation and desintering phenomena in the presence of platelets are explained in relation to the microscopy and dilatometry results. The decreases in the room-temperature fracture toughness and flexural strength with increasing platelet content are attributed to the reduction in transformation hardening and the increase in porosity.

1 Introduction

Recent studies on SiC whisker-reinforced yttria-stabilised tetragonal zirconia ceramics (Y-TZP) have shown considerable improvements in fracture toughness since the stress-induced martensitic transformation toughening in the matrix is coupled with whisker toughening, which is achieved by the combination of mechanisms, including crack pinning,[1] crack deflection,[2] crack bridging, and pull-out.[3–5] The fracture toughness of SiC whisker–3Y-TZP composite can be increased up to about 12 MPa $m^{1/2}$ at the expense of a decrease in strength to about 670 MPa.[6] Whisker reinforcement leads to improvements in strength at high temperatures where the positive modulus load transfer reduces the effective stress at the crack tip.[6] The high-temperature toughness of the composite is expected to be governed by whisker toughening mechanisms, since transformation toughening becomes less effective with increased temperature, and does not operate above a critical temperature (≈700°C for Y-TZP).

Whiskers, however, due to their geometry, are a severe health hazard when inhaled.[7] Furthermore, the formation of a whisker network in the ceramic matrix introduces constraints on the sintering, leading to a considerable reduction of sintered density.[8–10] The densification to closed porosity in these composites often requires the application of pressure and a much higher sintering temperature than that for the monolithic material. One way to overcome these problems is the use of silicon carbide platelets (SiC_p), which are thought to offer similar mechanical property improvements to those of whisker-reinforced TZPs with minimal associated health hazard and at a reduced cost. The comparable effects of SiC platelets to whiskers in improving toughness have been demonstrated in SiC platelet-reinforced alumina[11] and mullite.[12]

For SiC platelets distributed randomly in a ceramic matrix at a concentration over 10 vol.%, the geometrical arrangement of platelets has been found to inhibit densification to full density under pressureless sintering conditions.[13] Hence the overall strength is expected to be reduced by the platelets, which act as Griffith flaws. When the platelets are oriented parallel to the tensile stress axis, the defect size is effectively reduced to the thickness of the platelets and the constraints on sintering are eased, due to a better sinter shrinkage being achieved in the matrix material between the parallel planes of platelets. Thus, the reduction of strength with platelet content can be minimised by the optimisation of composite processing conditions to yield denser materials through control of the platelet orientation.

The study reported here is concerned with the slip casting, cold isostatic pressing and sintering of

SiC_p–3mol%Y-TZP composites and the resultant mechanical properties microstructural characteristics, such as preferred orientation of platelets, porosity and grain boundary and SiC/matrix interface structure. The change in strength and fracture toughness with the platelet content is related to the observed microstructural features.

2 Experimental

2.1 Materials and processing

The matrix material used for the production of SiC_p–3Y-TZP composites in this study was the commercially available tetragonal zirconia powder with 3 mol% Y_2O_3 content (TZ-3YS, Tosoh Corporation, Japan), designed for slip casting operations. TZ-3Y powder of the same composition and particle size as those of TZ-3YS powder, but with a smaller primary crystallite size (25 nm) and a larger specific surface area (15·4 m^2/g), was used for the preliminary tests on slurry preparation and slip casting operations. The properties of both powders are listed in Table 1. The silicon carbide platelets (SiC_p) were of 99·9% pure stoichiometric α-phase (Third Millennium Technologies Inc., USA, -400 mesh grade) with 10 μm average diameter and 0·5–3 μm thickness.

Figure 1 shows the processing route used for the preparation of the green structures of 3Y-TZP containing 10 and 20 vol.% SiC_p. Prior to processing in the composite, the SiC platelets were subjected to acid (0·2M HNO_3 solution) and base (0·1 5M NH_4OH solution) washes for 24 h in order to remove leachable impurities and to enhance the dispensability of platelets in water. Each wash was followed by the repeated dispersion of platelets in deionised water and filtering until the suspensions reached a constant pH. The platelets were then rinsed in ethanol, which was found to minimise agglomeration on drying and the subsequent processes in aqueous solution.

Stable composite slurries of SiC_p and 3Y-TZP powder were prepared by mixing the constituents in proportion in deionised water at pH 3 using a

Table 1. Properties of TZ-3Y and TZ-3YS powders

	TZ-3Y	*TZ-3YS*
Composition, wt%		
Y_2O_3	5·13	5·06
Al_2O_3	<0·005	<0·005
SiO_2	<0·002	<0·002
Fe_2O_3	0·004	0·002
Na_2O	0·022	0·005
Particle size, μm	0·3	0·3
Crystallite size, nm	25·1	36
Specific surface area, m^2/g	15·4	6·3

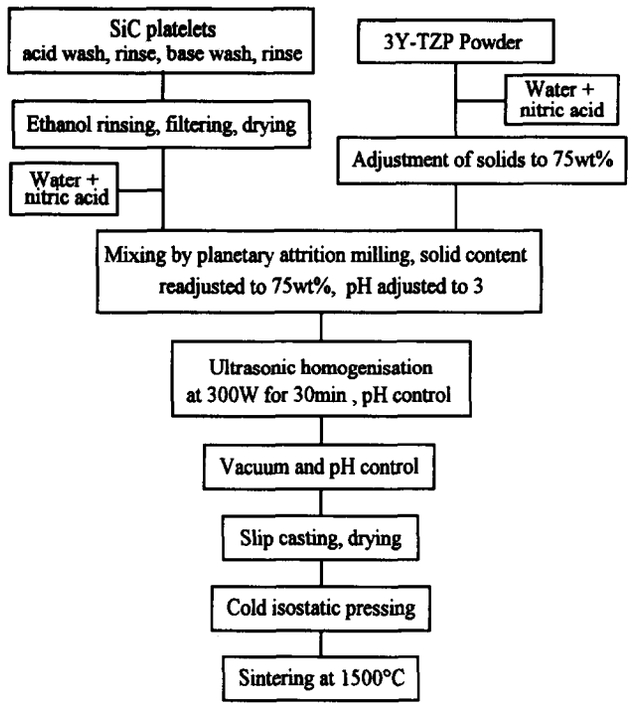


Fig. 1. Processing chart of SiC platelet–3Y-TZP ceramic composites.

planetary attrition mill with an agate container and ball. The pH was adjusted during mixing by the addition of dilute HNO_3 solution. The solid loading of the resultant slurries was always maintained at 75 wt%. Subsequent tests showed that the slurries were stable at pH 3 after planetary milling for 30 min, suggesting that sufficiently high electrostatic repulsive forces were generated to avoid flocculation. The agglomerates that were present in the as-received 3Y-TZP powder could not be broken up by the planetary milling. Ultrasonic dispersion was employed at 300W for 30 min for complete deagglomeration and homogeneous dispersion of the slurries after planetary milling. The entrapped gas in the slurry was removed under vacuum. pH 3 was maintained throughout above procedures. The final composite slurries showed very good stability and slip-casting properties.

For slip casting, samples with 0, 10 and 20 vol.% SiC platelet contents were formed into bars (48 mm × 12 mm × 10 mm) such that the SiC platelets, which orientate parallel to the mould surfaces during casting, would be parallel to the tensile stress axis of the four-point bend tests employed in the present work. Sample geometry and plaster mould configuration are shown schematically in Fig. 2. The slip-cast bars were dried at 40°C for 24 h, followed by heating at 120°C for 4 h and cold isostatic pressing at a pressure of 175 MPa. The green density was determined from the measured weight and volume of samples. Sintering behaviour of samples was

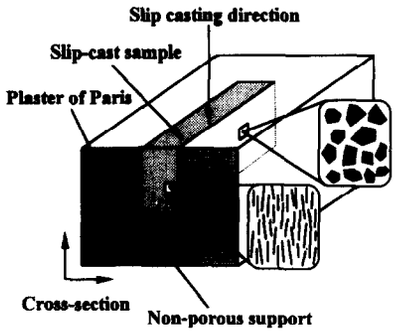


Fig. 2. Schematic configuration of a plaster mould and a sample on slip casting.

characterised by dilatometry on heating up to 1500°C at a heating rate of 4°C/min. Samples prepared for microstructural examination and mechanical testing were sintered at 1500°C for 3 h in flowing Ar atmosphere in a high-temperature graphite resistance furnace lined with impervious alumina tube to permit the control of supplied atmosphere. Heating and cooling rates of 3°C/min and 4°C/min respectively, were employed for the sintering of all samples. The sintered density and the percentage open porosity was measured by the Archimedes water-displacement technique.[14]

2.2 Specimen preparation and mechanical testing

Test pieces, containing 0, 10 and 20 vol.% SiC platelets sintered to >96% of theoretical density, were ground to produce flexural bend test specimens (38 mm × 3 mm × 3 mm) and single-edge notch beam specimens, SENB, (38 mm × 6 mm × 3 mm where $W = 2B = 6$mm) using diamond grinding wheels at 60 mm/s. For both types of specimens, the prospective tensile surfaces were kept parallel to the plane at which the platelets were aligned during slip casting so that the crack propagation direction was always perpendicular to the plane of the platelet alignment. The tensile surfaces of all flexure bars were polished through to 1 μm diamond lapping and the edges were bevelled. A straight notch, having a root radius of 80–100 μm, was introduced to each SENB specimen using a 0·15 mm thick SiC slitting disc of a sharp end profile. The relative notch depth (a/W) was in the range 0·1 to 0·12.

A four-point bend test fixture, with an inner span of 15 mm and an outer span of 20 mm, and a servo hydraulic testing machine were employed for the evaluation of fracture strength and toughness. The displacement during tests was monitored by the use of two transducers, situated at the mid-span and the outer span of each specimen. Thus, any displacement associated with the test rig was eliminated from the actual displacement of the specimen by recording the differential output from the transducers using a signal conditioning unit. At least five specimens were tested for each composition at a cross-head speed of 0·5 mm/min to determine the room-temperature strength and toughness. From the results of four-point bend tests, flexural strength, σ_b, was calculated using the equation:

$$\sigma_b = \frac{3}{BW^2}\frac{P(s-L)}{2} \tag{1}$$

where P is the applied load, s the inner span, L the outer span, B the specimen breadth and W the specimen width. The fracture toughness, K_{IC}, was determined by:

$$K_{IC} = \frac{6}{BW^2}\frac{P(s-L)}{4}Ya^{1/2} \tag{2}$$

where the geometric factor, Y, is given by:[15]

$$Y = 1{\cdot}99 - 2{\cdot}47(a/W) + 12{\cdot}97(a/W)^2 - 23{\cdot}17(a/W)^3 + 24{\cdot}8(a/W)^4 \tag{3}$$

2.3 Microstructural investigations

Phase identification after sintering was performed by X-ray diffraction using CuK_α radiation. The extent of the phase transformation from tetragonal to monoclinic structure in the matrix phase, induced by fracture toughness testing, was determined from the integrated X-ray intensity of diffraction lines, $I_{m,t}(hkl)$, of the monoclinic and tetragonal phases, using the following equations:[16]

$$X_m = \frac{I_m(111) + I_m(11\bar{1})}{I_m(111) + I_m(11\bar{1}) + I_t(111)} \tag{4}$$

where X_m is the integrated intensity ratio for monoclinic phase, which yields the volume fraction

$$V_m = \frac{PX_m}{1 + (P-1)X_m} \tag{5}$$

where $P = 1{\cdot}311$ for tetragonal–monoclinic mixtures.

The microstructures of sintered bars and the features on fracture surfaces after mechanical tests were characterised by scanning electron microscopy (SEM). The orientation distribution of platelets at different sections of slip-cast and sintered samples was determined using an optical image analysis system. For each section, at least five SEM pictures, corresponding to over 2000 platelets, were analysed.

3 Results and Discussion

3.1 Consolidation of SiC_p-reinforced zirconia structures

Slip casting followed by cold isostatic pressing is a suitable method for the production of composites where a uniform distribution and preferred orien-

tation of reinforcing agents, such as platelets, are required. High green densities, no damage to the platelets during processing, and the ease and inexpensive production of composite components are the additional advantages of the slip-casting process. However, the production of electrostatically stabilised homogeneous composite slips for the best slip casting properties depends on the simultaneous adjustment of a number of variables.

The casting characteristics are influenced primarily by the morphology, surface quality and dimensional characteristics of the starting powders. Other parameters, such as pH value, viscosity, homogeneity and solid concentration, are of particular importance to maintain the maximum colloidal stability of slurries. A commonly employed means of obtaining a well-dispersed suspension is to impart a repulsive surface charge on particles by pH adjustment. In the present case, the optimisation of the slurry variables is complicated by the presence of SiC platelets that are of different composition, size, geometry and surface quality from the matrix material. Uniform distribution and electrostatic stabilisation of both phases in the composite slurry were achieved by the acid/base surface treatment of SiC platelets, planetary mixing of the constituents in aqueous media, adjustment of solid loading, and high power ultrasonic dispersion, in sequence, accompanied by continuous pH adjustment (Fig. 1).

As observed for SiC whisker-reinforced ceramic composites,[8] the suspension stability of SiC platelets was the major factor in determining a pH that would provide codispersion of zirconia particles and platelets in dense slurries. The zeta potential, measured on dilute suspensions of platelets over a pH range of 2 to 9, showed that the moderate to high levels of surface charge necessary for the electrostatic stabilisation of the slurry occur at pH $\leq$ 3. This is in agreement with the previous electrophoresis mobility and viscosity measurements of SiC whisker suspensions.[17,18] It was further reported that the modification of whisker surface chemistry, by either surface oxidation or acid and base washing of whiskers, enhances the electrostatic stabilisation of the suspensions. Since the presence of free SiO_2 at the oxidised surfaces of SiC platelets is not desired for the zirconia matrix, the acid/base washing technique was adopted in the present processing.

Concerning the zirconia matrix phase, the recent work of Nikumbh *et al.*[19] on slip casting slurries of TZ-3YS powder has shown that the slips with $\leq$75 wt% solid content at pH $\leq$ 4 gives minimum viscosity with Newtonian flow behaviour in which the electrostatic repulsive forces at particles are large and the viscosity remains constant with the change in shear rate. They also observed that the viscosity of the slurry increases drastically when the solid loading (solid/liquid ratio) exceeds 75 wt% ($\approx$35 vol.%) ZrO_2. In the present work, the preliminary slip-casting tests on slurries of TZ-3Y and TZ-3YS powders, each containing 20 vol.% SiC platelets, revealed that stable slurries of low viscosity and with good flow behaviour can be formed at pH 3 providing solid loadings of $\leq$50 wt% for TZ-3Y powder and $\leq$75 wt% for TZ-3YS powder are used. The chemical composition and the particle size of both powders were the same and the higher solid content achieved in the slurries of TZ-3YS powder was attributed to its lower specific surface area and a higher crystallite size than those for TZ-3Y powder (Table 1). Also, slip casting times for SiC_p-TZ-3Y composite slurries to form 10 mm thick samples were as short as 1 h compared to 3 h required when TZ-3Y powder was used. Therefore, all samples for mechanical tests were prepared using TZ-3YS powder.

Although the mechanical mixing and the adjustment of pH and solid content were successful in forming stable slurries, there were always soft agglomerates of particles and platelets, inherited from the original materials. Complete deagglomeration of composite slurries were achieved using an ultrasonic probe at 300W output power for 30 min. The agitation caused by ultrasonic waves also served to increase the homogeneity of the slurry. Other workers have found similar results for the ultrasonic dispersion of SiC whisker–Al_2O_3 composites without the use of deflocculants.[8,20]

The achievement of a high green density and a strong preferred orientation of platelets was the main advantage of slip casting over other processing techniques. As shown in Fig. 3, the slip casting bar samples without SiC platelets yielded a relative green density of 55%, but this increased to 60% with increasing platelet content. The increase in green density is due to substitution of the

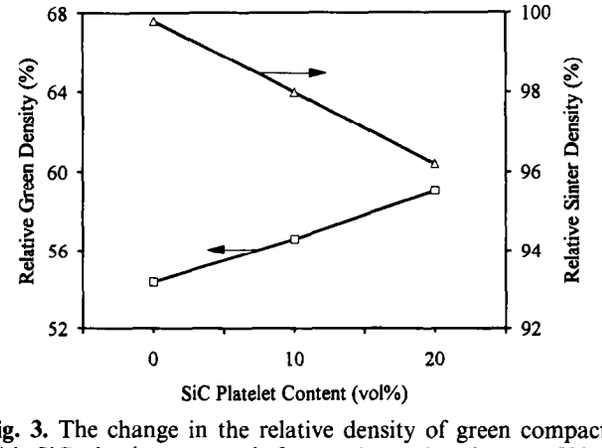


Fig. 3. The change in the relative density of green compacts with SiC platelet content before and are sintering at 1500°C for 3 h.

matrix and its porosity by fully dense SiC platelets. A further increase of the green density by around 2% was achieved by cold isostatic pressing.

3.2 Sintering characteristics

The plots of relative linear shrinkage, dL/L_o, and linear shrinkage rate, $d(dL/L_o)/dT$, as a function of temperature for a slip-cast 3Y-TZP sample and a composite containing 20 vol.% SiC_p are shown in Figs 4 (a) and (b), respectively. The dependency of the sinter shrinkage on platelet orientation was not studied in the present work and the plots for the composite sample in Fig. 4 are for data obtained in a direction perpendicular to the plane in which the basal plane of platelets are preferentially oriented. It follows that dL/L_o at a given temperature is the relative shrinkage of the matrix regions between the basal planes of platelets.

As shown in Fig. 4 (a), the shrinkage of both samples starts at around 900°C and the sintering curves are identical up to 1200°C, at which point the platelets starts inhibiting the sintering of the composite. The shrinkage of the composite up to 1200°C is referred to as the first stage sintering. This is followed by a period of negligible shrinkage until the second stage sintering commences at around 1250°C. The two stages of sintering are revealed by the presence of two successive peaks on the sintering rate plot for the composite (Fig. 4(b)) as the sintering rate approaches zero at the plateau region of the shrinkage plot and then starts increasing at ≈1250°C reaching a maximum at ≈1400°C. In contrast, the sintering rate plot for the monolithic material shows a single peak with a maximum at ≈1400°C.

Under isothermal conditions, the sintering temperature was chosen as 1500°C in order to enhance the density of the matrix, particularly in the presence of platelets. Sintering at 1500°C for 3 h yielded relative densities that depended on the SiC_p content but were >96% (Fig. 3). The relative densities obtained in the present study were superior to those of similar composites produced by other processing techniques, e.g. 91% and 94% for 20 vol.% Al_2O_3 platelet-reinforced 12Ce-TZP and 3Y-TZP composites, respectively, each pressureless sintered at 1500°C.[21] X-Ray diffraction analysis of sintered samples revealed only the presence of SiC phase and tetragonal zirconia with no detectable monoclinic phase.

As shown in Fig. 3, the sintered density reduced while the green density increased with SiC_p content. Near theoretical density (6070 kg/m^3) was easily achieved on sintering the monolithic material. However, densification in the platelet-reinforced zirconia systems depended on the flow and sintering of the matrix between platelets. An increase in platelet content resulted in partial inter-platelet bridging that hindered particle rearrangement in the matrix and thus lead to the formation of elongated crack-like pores at the platelets, as exemplified by the micrograph in Fig. 5. The number of pores increased in the regions where the platelets were

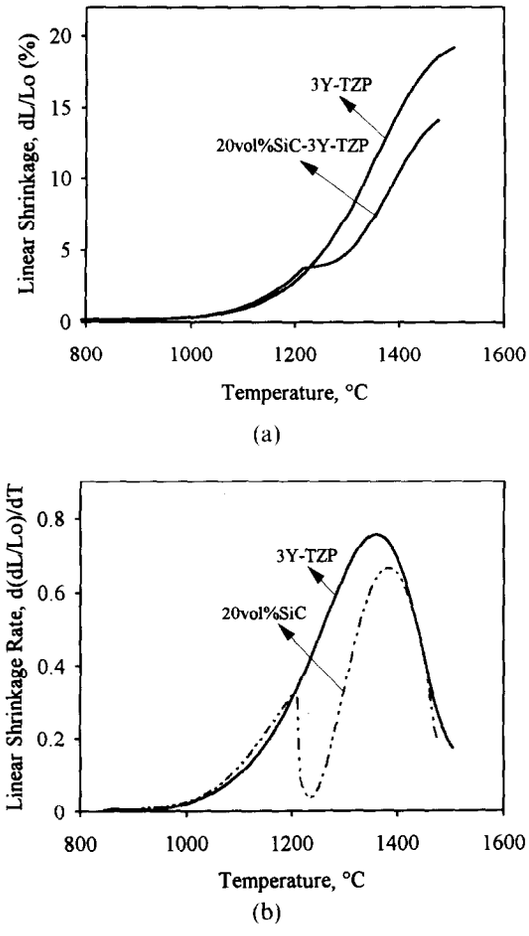


Fig. 4. (a) The relative linear shrinkage and (b) the linear shrinkage rate of 3Y-TZP and 20 vol.% SiC_p reinforced 3Y-TZP compacts on non-isothermal sintering at a heating rate of 4°C/min.



Fig. 5. An SEM micrograph from the cross-section of a 20 vol.% SiC platelet reinforced 3Y-TZP composite, revealing crack-like voids and porosity associated with platelets as shown by arrows.

bridged or the density of platelets was relatively high. The crack-like pores are unlikely to be reduced by increasing the sintering temperature but could probably be closed by applying pressure during sintering.

Previous work on the effect of inclusions on densification[22–24] has already demonstrated that the underlying phenomenon for the interruption of sintering in the presence of rigid particles is the development of localised strains in the porous matrix. The type and magnitude of the matrix strains change with the location in the matrix, inter-platelet distance and the geometrical arrangement, volume fraction and size of platelets in the surrounding volume.[23,24] Therefore the densification of the matrix is heterogeneous. A region under localised compressive stress densifies first, producing non-deformable networks where the porosity tends towards zero.[22,23] These highly dense regions are expected to constrain the shrinkage of the adjacent porous matrix by inducing hydrostatic tensile stresses, which finally leads to desintering and the formation of local porosity. Hence the overall sintering rate is reduced with increasing ratio of the hydrostatic tensile stress to the compressive sintering stress of the matrix, σ_h/Σ_m.[25,26]

In view of these observations, it is considered that the two-stage sintering process in the 20 vol.% SiC_p–3Y-TZP composite can be explained in terms of the development of compressive and tensile stresses in the matrix. That is, the first stage of sintering in the composite sample (Fig. 4) is attributed to the free sintering of the matrix until heterogeneous densification and the compressive and tensile stresses develop in the matrix. This is evident from the sinter shrinkage plots for the monolithic and the composite samples being identical at temperatures up to 1200°C. The following reduction in the sintering rate is related to a rapid densification at locations between closely spaced SiC platelets while relatively high porosity is retained in the remaining matrix.

The onset of the increase in shrinkage at the second stage of sintering may be explained by the thermal activation at temperatures >1250°C being large enough for the growth of highly dense networks at the expense of the pore growth in the adjacent porous matrix. The porous regions under the hydrostatic tensile stresses go through desintering and the formation of crack-like voids at the SiC platelet–matrix interface. This can occur provided the hydrostatic tensile stresses are large enough to induce the break up of grain bridges linking polycrystalline clusters in porous regions.

To summarise, high sintered densities were achieved in these composites by slip casting and pressureless sintering, although the formation of some voids on sintering was unavoidable. It may be that the pressureless-sintered density can be further increased to a level, possibly close to theoretical density, by the use of SiC platelets with relatively small thickness, provided that slip-cast-

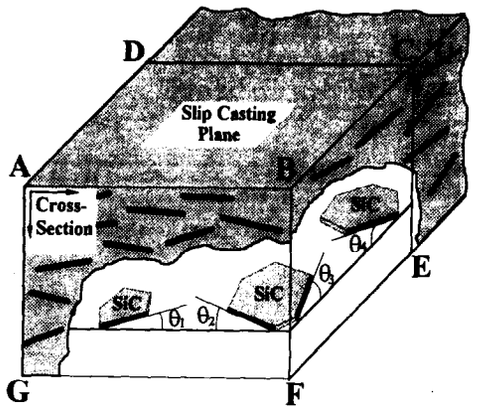
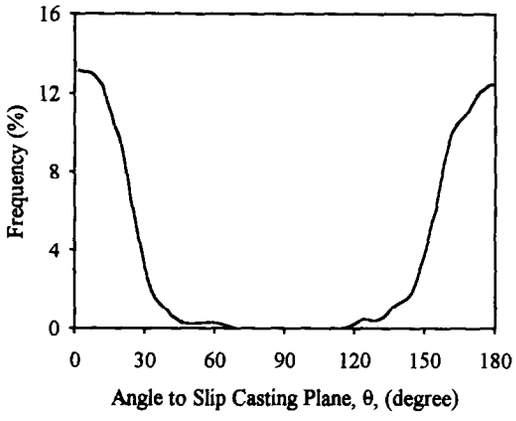
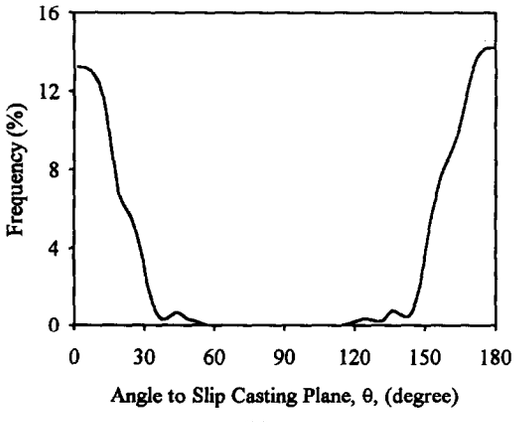


Fig. 6. Schematic of three dimensional array of platelets in a slip-cast sample, showing the edge lines of platelets observed in the ABFG and BCEF planes, in tilted positions at angles, θ_i with the slip casting plane (ABCD). The BCEF plane is perpendicular to the mould face (ABCD) and the ABFG plane is the cross-section of a bar sample.



(a)



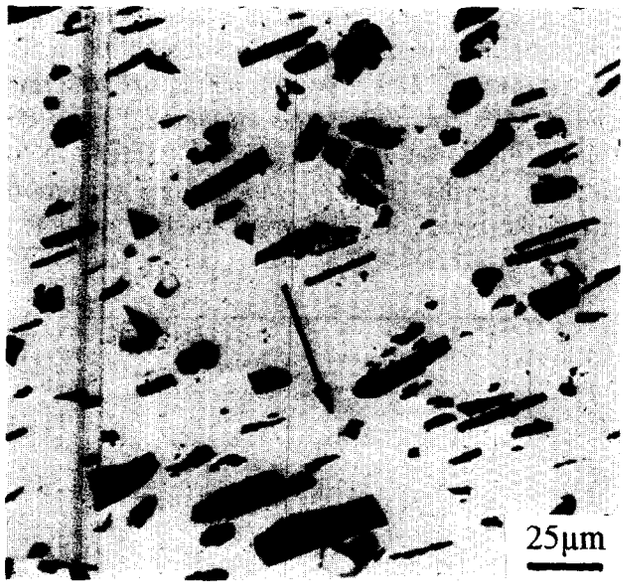
(b)

Fig. 7. The orientation distribution of SiC platelets in relation to the slip-casting plane (the mould surface) observed in the ABFG planes of bar samples (Fig. 6), containing (a) 10 vol.% and (b) 20 vol.% SiC platelets.

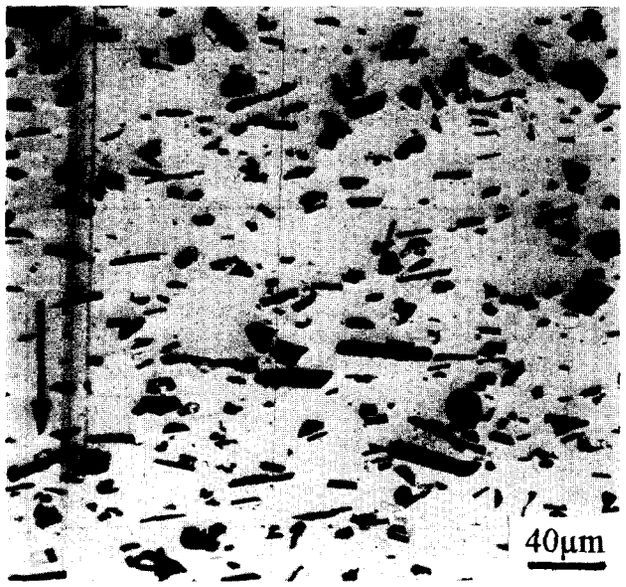
ing results in a very strong preferred orientation of platelets.

3.3 Orientation distribution of platelets after sintering

The effect of slip casting on the orientation distributions of SiC platelets was studied by determining the frequency of platelets (%), oriented with their basal planes at a given angle, θ, to the porous mould face (ABCD in Fig. 6) which is referred to as the slip-casting plane. Figures 7(a) and (b) show the plots of platelet frequency as a function of θ, taken from the sections (BCEF in Fig. 6) perpendicular to the slip-casting plane, for composite samples containing 10 and 20 vol.% SiC_p, respectively. Both plots show that θ for the majority of platelets is within $\Delta\theta = \pm 30°$. The corresponding SEM micrographs, shown in Figs 8(a) and (b), exemplify the platelet distribution and orientation presented in the frequency–angle plots; it is clear from these micrographs that there is a strong preferred orientation with the basal platelet planes, mostly in close alignment with the slip-casting plane.



(a)



(b)

Fig. 8. SEM micrographs exemplifying the platelet orientation distribution in the BCEF planes (Fig. 6) over an area near to the porous mould face in bar samples, containing (a) 10 vol.% and (b) 20 vol.% SiC platelets. Arrows are perpendicular to the porous mould face.

The platelet alignment was attributed to the flow of water towards the porous mould surface, which is believed to tilt and rotate the platelets until they reach the interface of consolidation. However, the orientation distribution of platelets, although good, was not ideal as evident from the frequency–angle plots in Figs 6(a) and (b) and the corresponding micrographs (Figs 8(a) and (b)) which show some platelets in tilted positions with their basal planes at arbitrary angles to the slip-casting plane. The misorientation of platelets may be associated with variations in their geometry; as shown in Fig. 9, some of the as-received platelets have a low aspect ratio and some are very small and irregularly shaped, resembling particulate. It was concluded that the orientation distribution of platelets is most likely to be improved by control of the SiC_p reinforcement, particularly the aspect ratio which should be large (>10), than by further optimisation of the processing conditions.

Figure 10 shows the frequency versus angle plot, obtained from averaging the data from a number of areas across the complete cross-section (ABFG in Fig. 6) of a composite bar containing 20 vol.% SiC_p. The cross-sectional orientation profile of platelets is complicated with the presence of small peaks at a tilt angle of ~25° to the slip-casting plane, superimposed on the main preferred orientation peaks. The small peaks were

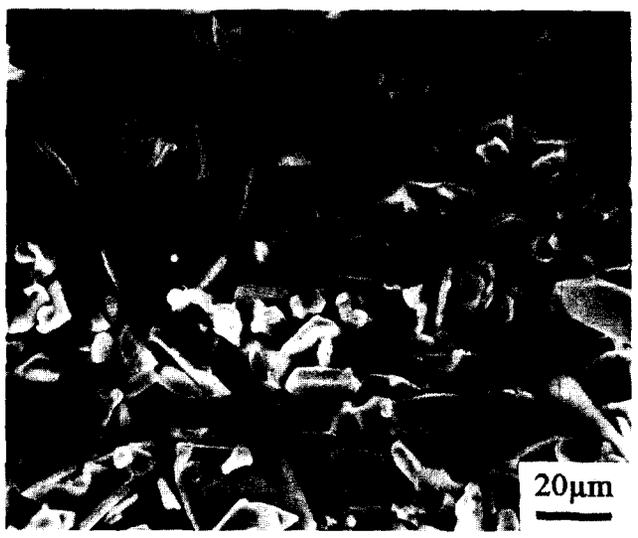


Fig. 9. SEM micrograph of as-received SiC platelets used in the production of composites.

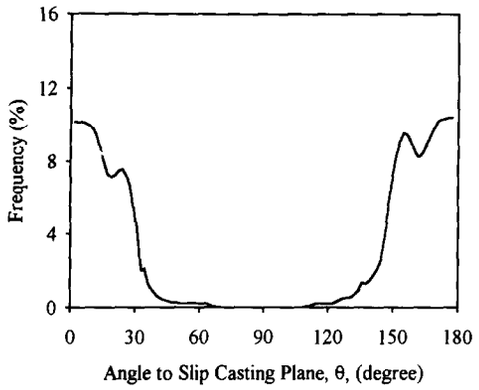


Fig. 10. The orientation distribution of SiC platelets in relation to the slip casting plane (the mould surface) observed in the ABFG planes (the cross-section in Fig. 6) of bar samples with 10 vol.% SiC platelet content.

associated with a V-shaped orientation distribution band of the platelets in the central regions of the cross-section (0·5 mm in thickness) between the porous faces of the mould (Fig. 11), whereas the rest of the cross-section has the same preferred orientation of platelets as that observed near to the porous face of the mould in section BCEF (Figs 7(b) and 8(b)).

It is known[27,28] that the capillary force of the mould, which forms the suction pressure to remove water from the slurry, becomes less effective with increasing thickness of the consolidated layer. This results in a highly reduced rate of water flow due to the pressure drop across the consolidated layer. Therefore, the central region of the cast between the faces of the mould is consolidated at a gradually reducing rate and the water flow rate is not high enough to induce a strong preferred orientation of platelets; this is partially because the SiC platelets increase the flow path of the water, as observed previously in slip casting whisker-reinforced ceramics.[10,29] Thus, the platelets are tilted under gravitational forces away from the preferred orientation, leaving them in a V-shaped configuration in central regions of the cast.

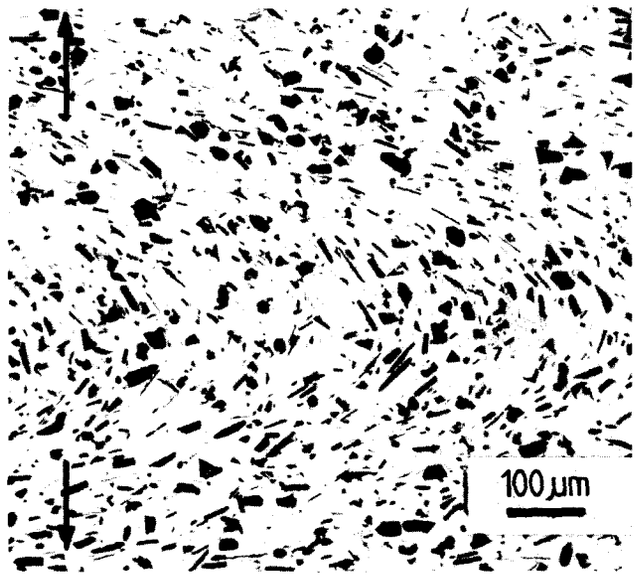


Fig. 11. SEM micrograph revealing V shaped orientation distribution of SiC platelets at the central regions of the cross-section (the ABFG plane in Fig. 6) of a composite bar, containing 20 vol.% SiC platelets. Arrows are perpendicular to the porous mould faces.

3.4 Influence of platelet content on mechanical properties

During strength and toughness testing, all composites exhibited a linear increase in stress with deflection; there was no evidence of non-linearity prior to catastrophic failure. The graphs of flexural strength and fracture toughness as a function of platelet content (Fig. 12 (a)) show that both these properties degrade with the platelet content. At 20 vol.% SiC_p content, the composite exhibits a flexure strength of 440 MPa and a fracture toughness of 6·4 MPa $m^{1/2}$. Thus the mechanical properties follow the same trend with SiC content as the sintered density (Fig. 3), which suggests that the crack-like pores, formed preferentially at some of

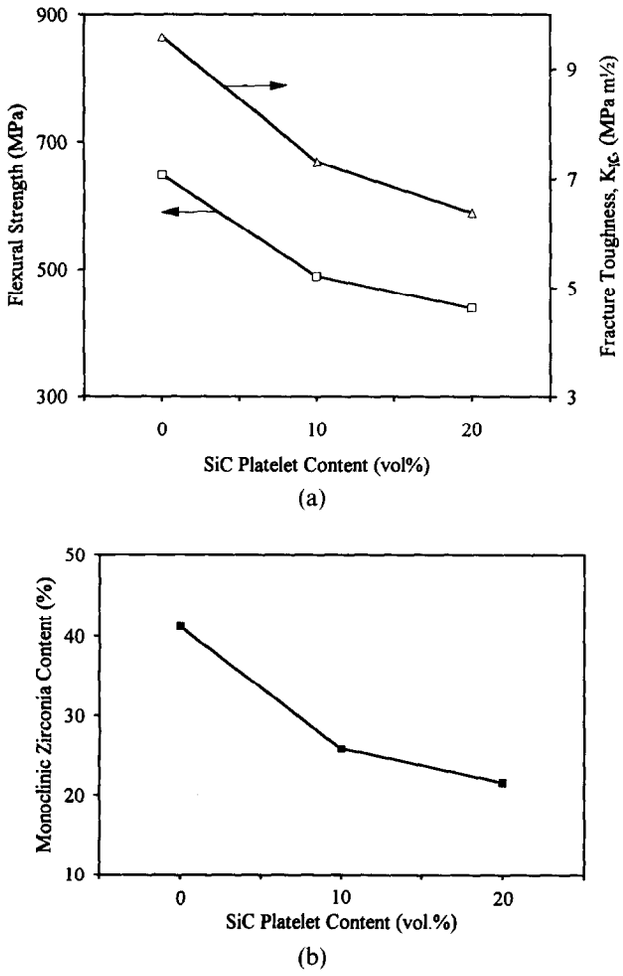


Fig. 12. (a) Flexural strength and fracture toughness of SiC_p-3Y-TZP composites as a function of volume fraction of SiC platelets and (b) the monoclinic zirconia content, determined by X-ray diffractometry at the fracture surfaces of SENB specimens, as a function of SiC platelet content.

the platelet–matrix interfaces, act as Griffith flaws on testing.

The reduced fracture toughness also suggests that the transformation-toughening mechanism in the matrix is hindered as the developing transformation zone at a crack tip is hampered by the incorporation of SiC platelets. Evidence for this type of behaviour was obtained from the determination of the monoclinic ZrO_2 content at fracture surfaces of SENB samples by X-ray diffractometry. The results plotted in Fig. 12 (b) show that the m-ZrO_2 content at fracture surfaces reduces with SiC platelet content. The decreasing fraction of transformed phase with increasing platelet content was attributed to a reduction in the transformation zone size due to platelets decreasing the stress intensity at a crack tip. Hence, the reduction in transformation toughening efficiency, together with the crack-like pores acting as flaws, lowers the strength and toughness with increasing platelet content. However, as the transformation toughening mechanism is unlikely to be significant in the monolithic material as the test temperature is raised, it is expected that the composite will exhibit relatively better, and perhaps even superior, toughness at elevated temperatures.

These explanations for the reduction in toughness with increasing SiC content requires strong interfacial bonding between the platelets and the matrix.[30] SEM observations of fracture surfaces of platelet containing specimens revealed that most of the platelets on the fracture plane had ruptured (Fig. 13 (a)), indicating that except where crack-like pores were present, the interfacial bonding was strong. As exemplified in Fig. 13 (b), the change of the crack plane from one platelet to another at the fracture surface suggests that there is some contribution of the crack deflection mechanism to toughening. Other toughening mechanisms, such as debonding and pull-out of platelets and crack bridging,[3–5] were not commonly observed due to strong interfacial bonding. Initial TEM studies of the platelet–matrix interfaces indicate the presence of amorphous films connected to sizeable pockets of glass. This will be reported in a future publication.

If the platelets are to contribute more effectively to the toughness of the composite, it is essential to eliminate porosity by applying an external pressure on sintering and to reduce the interfacial bond strength by additions of appropriate interfacial segregating species to the matrix, such as P, Si and Ti.



(a)



(b)

Fig. 13. Fracture surface of 3Y-TZP containing 20 vol.% SiC platelets, showing (a) the platelets ruptured on the fracture plane and (b) the crack deflection at platelets as indicated by arrows.

4 Conclusions

(1) Stable slurries of silicon carbide platelets (SiC_p) and yttria-stabilised tetragonal zirconia with good slip-casting properties have been produced with up to 75 wt% solid loading. Slurry processing at pH 3 by means of planetary milling, high-power ultrasonic dispersion and vacuum degassing resulted in a homogeneously dispersed composite slurry with minimal agglomeration.

(2) Slip casting of the composite slurries yielded relative green densities of 60%. A further increase in the green density of about 2% was achieved by cold isostatic pressing. Pressureless sintering at 1500°C for 3 h resulted in relative densities which fell with SiC_p content but were above 96%.

(3) There was a strong preferred orientation of the platelets with their basal planes parallel to the slip-casting plane, i.e. parallel to the porous mould faces, through the section of

the 48 mm × 12 mm × 10 mm bars. Overall misorientation of the platelets was attributed to variations in platelet geometry; the platelets with low aspect ratio and small size cannot be aligned to the preferred orientation by the force of water flow in the slurry. The misorientation of platelets in central regions of the cast was accounted for by the reduction in suction pressure across the consolidated cake and the gravitational forces tilting the platelets. The preferred orientation of platelets could be further enhanced by using SiC platelets with a larger aspect ratio.

(4) The room-temperature strength and toughness were found to reduce with platelet content. At 20 vol.% SiC_p content, the composite exhibited a flexure strength of 440 MPa and a fracture toughness of 6·4 MPa $m^{1/2}$. Analysis of fractography results indicated that crack deflection process may contribute to fracture toughness, but the crack-like voids, formed preferentially at the platelets, had an adversely predominant effect on both strength and toughness. The transformation toughening reduced with increasing platelet content and the toughening by debonding and pull-out of platelets could not occur due to strong interfacial bonding.

Acknowledgement

The authors gratefully acknowledge the funding provided by SERC award, grant number GR-F81729, and the supply of silicon carbide platelets by Third Millennium Technologies Inc., USA.

References

1. Lange, F. F., The interaction of a crack front with a second-phase dispersion. *Phil. Mag.*, **22**(179) (1970) 983–92.
2. Faber, K. T. & Evans, A. G., Crack deflection process. I. Theory. *Acta Metall.*, **31**(4) (1983) 565–76.
3. Marshall, D. B., Cox, B. N. & Evans, A. G., Mechanics of matrix cracking in brittle-matrix composites. *Acta Metall.*, **33**(11) (1985) 2013–21.
4. Homeny, J., Vaughn, W. L. & Ferber, M. K., Processing and mechanical properties of SiC-whisker–Al_2O_3-matrix composites. *Am. Ceram. Soc. Bull.*, **65**(2) (1986) 333–8.
5. Becher, P. F., Hsueh, C. H., Angelini, P. & Tiegs, T. N., Toughening behaviour in whisker-reinforced ceramic matrix composites. *J. Am. Ceram. Soc.*, **71**(12) (1988) 1050–61.
6. Claussen, N., Weisskopf, K. L. & Ruhle, M., Tetragonal zirconia polycrystals reinforced with SiC whiskers. *J. Am. Ceram. Soc.*, **69**(3) (1986) 288–92.
7. Birchall, J. D., Stanley, D. R., Mockford, M. J., Pigott, G. H. & Pinto, P. J., Toxicity of silicon carbide whiskers. *J. Mater. Sci Lett.*, **7** (1988) 350–52.
8. Sacks, M. D., Lee, H. W. & Rojas, O. E., Suspension processing of Al_2O_3/SiC whisker composites. *J. Am. Ceram. Soc.*, **71**(5) (1988) 370–9.
9. Lee, H. W. & Sacks, M. D., Pressureless sintering of SiC-whisker-reinforced Al_2O_3 composites: I. Effect of matrix powder surface area. *J. Am. Ceram Soc.*, **73**(7) (1990) 1884–93.
10. Hoffmann, M. J., Nagel, A., Greil, P. & Petzow, G., Slip casting of SiC-whisker-reinforced Si_3N_4. *J. Am. Ceram. Soc.*, **72**(5) (1989) 765–9.
11. Becher, P. F., Microstructural design of toughened ceramics. *J. Am. Ceram. Soc.*, **74**(2) (1991) 255–69.
12. Nischik, C., Seibold, M. M., Travitzky, N. A. & Claussen, N., Effect of processing on mechanical properties of platelet-reinforced mullite composites. *J. Am. Ceram. Soc.*, **74**(10) (1991) 2464–8.
13. Baril, D. & Jain, M. K., Evaluation of SiC platelets as a reinforcement for oxide matrix composites. *Ceram. Eng. Sci. Proc.*, **12** (1991) 1175–92.
14. Stewards, N. I., The influence of particle size distribution on the sintering of ceramic powder compacts. PhD Thesis, Imperial College of Science and Technology, London, 1989.
15. Brown, W. F. & Srawley, J. E., Plain strain crack toughness testing of high strength metallic materials. ASTM Special Technical Publication, No.410, American Society for Testing and Materials, 1966.
16. Toraya, H., Yoshimura, M. & Somiya, S., Calibration curve for quantitative analysis of the monoclinic–tetragonal ZrO_2 system by X-ray diffraction. *J. Am. Ceram. Soc.*, **67** (1984) C119–121.
17. Melluish, I. & Konsztowicz, K. J., The effects of surface treatment of SiC whiskers on rheological properties of their aqueous suspensions. In *Proc. Int. Symp. Advances in Processing of Ceramic and Metal Matrix Composites*, ed. S. Mostaghaci. Pergamon Press, 1989, pp. 15–26.
18. Adair, J. H., Mutsuddy, B. C. & Drauglis, E. J., Stabilisation of silicon carbide whisker suspensions: I. Influence of surface oxidation in aqueous suspensions. *Adv. Ceram. Mater.*, **3**(3) (1988) 231–4.
19. Nikumbh, A. K., Schmidt, H., Martin, K. & Porz, F., Slip casting of partially stabilised zirconia. *J. Mater. Sci.*, **26** (1991) 3649–56.
20. Konsztowicz, K. J., Ultrasonic homogenization of dense colloidal suspensions of SiC_w/Al_2O_3 composites. *Ceram. Eng. Sci. Proc.*, **11**(7–8) (1990) 695–708.
21. Heussner, K. H. & Claussen, N., Yttria- and ceria-stabilised tetragonal zirconia polycrystals (Y-TZP, Ce-TZP) reinforced with Al_2O_3 platelets. *J. Eur. Ceram. Soc.*, **5** (1989) 193–200.
22. Sudre, O. & Lange, F. F., Effect of inclusions on densification: I. Microstructural development in an Al_2O_3 matrix containing a high volume fraction of ZrO_2 inclusions. *J. Am. Ceram. Soc.*, **75**(3) (1992) 519–24.
23. Sudre, O., Bao, G., Fan, B., Lange, F. F. & Evans, A. G., Effect of inclusions on densification: II. Numerical model. *J. Am. Ceram. Soc.*, **75**(3) (1992) 525–31.
24. Lange, F. F., Constrained network model for predicting densification behaviour of composite powders. *J. Mater. Res.*, **2**(1) (1987) 59–65.
25. Tuan, W. H. & Brook, R. J., Sintering of heterogeneous ceramic compacts, Part 2. ZrO_2–Al_2O_3. *J Mater. Sci.*, **24** (1989) 1953–8.

26. De Jonghe, L. C., Rahaman, M. N. & Hsueh, C. H., Transient stresses in bimodal compacts during sintering. *Acta Metall.*, **34**(7) (1986) 1467–71.
27. Hampton, J. H. D., Savage, S. B & Drew, R. A. L., Experimental analysis and modelling of slip casting. *J. Am. Ceram. Soc.*, **71**(12) (1988) 1040–5.
28. Tiller, F. M. & Tsai, C. D., Theory of filtration of ceramics: I. Slip casting. *J. Am. Ceram. Soc.*, **69**(12) (1986) 882–7.
29. Chouh, Y. S. & Green, D. J., Silicon carbide platelet/alumina composites: I. Effect of forming technique on platelet orientation. *J. Am. Ceram. Soc.*, **75**(12) (1992) 3346–52.
30. Poorteman, M., Descamps, P., Cambier, F., Leriche, A. & Thierry, B., Hot isostatic pressing of SiC-platelets Y-TZP composites. *J. Eur. Ceram. Soc.*, **12**(2) (1993) 103–9.

Journal of the European Ceramic Society **15** (1995) 45–49
© 1995 Elsevier Science Limited
Printed in Great Britain. All rights reserved
0955-2219/95/$9.50

Nb_2O_5 and Ta_2O_5 Codoped Zirconia

G. Gritzner,[a] C. Puchner[a] & J. Dusza[b]

[a] Institut für Chemische Technologie Anorganischer Stoffe, Johannes Kepler Universität Linz, A-4045 Linz, Austria
[b] Institute of Materials Research, Slovak Academy of Sciences, SQ-043 53 Košice, Slovakia

(Received 18 August 1993; revised version received 29 June 1994; accepted 1 August 1994)

Abstract

Orthorhombic zirconia codoped with 5 mol-% Nb_2O_5 and 5, 7, 10, 12 and 15 mol-% Ta_2O_5 as well as samples with 5 mol-% Ta_2O_5 and 7, 10, 12 and 15 mol-% Nb_2O_5, respectively, were made from precursors prepared by hydrolysis of the metalalkoxide solutions in 1-propanol with water. The amorphous, coprecipitated hydroxides were converted to the oxides at 900°C. The powders were characterized by the specific surface areas, the particle size distributions and by electron microscopy. The codoped zirconia powders were attributed, isostatically compacted and sintered at temperatures ranging from 1500 to 1650°C. Three-point bend-strengths, Weibull moduli, fracture toughnesses, Vickers hardnesses, densities and phase compositions were measured for the sintered specimens. Average three-point bend-strengths ranged between 85 and 257 MPa. No phase transformations occurred during fracture. Fractography showed that the fracture origins were either surface flaws or pores near the tensile surface. Depending on the composition and the sintering conditions, fracture toughnesses between 2·1 and 3·6 MPa $m^{1/2}$, Vickers hardnesses between 6·8 and 9·9 GPa and theoretical densities between 96·8 and 99·0% were observed. Increasing dopant concentrations resulted in increases in the b- *and* c-*axes and in a decrease in the* a-*axis of the orthorhombic cell.*

1 Introduction

Single doping of zirconia with either Nb_2O_5 or Ta_2O_5 above 12 mol-% of the dopant stabilized the orthorhombic phase at room temperature.[1] In a previous publication we reviewed the literature on orthorhombic zirconia and reported the preparation and mechanical properties of zirconia doped with varying concentrations of either Nb_2O_5 or Ta_2O_5. These studies are now extended to investigations on the preparation of zirconia powders codoped with Nb_2O_5 and Ta_2O_5, on the sintering conditions, the mechanical properties and the fractography of Nb_2O_5–Ta_2O_5 codoped orthorhombic zirconia ceramics, for which such data have not been reported before.

2 Experimental

2.1 Powder preparation and sintering

The preparation of the precursor materials niobium penta-l-propoxide and tantalum penta-l-propoxide from niobium pentachloride and tantalum pentachloride respectively, has been reported.[1] Zirconium-l-propoxide was commercially available (Johnson Matthey, USA). Solutions of the alkoxides of zirconium, niobium and tantalum in l-propanol were prepared in a glove-box under the exclusion of moisture to prevent decomposition. The solutions of the metal alkoxides were then sprayed into water. The precipitated hydroxides were filtered, first washed with water and then with ethanol. The powders were dried at 70°C and 670 Pa followed by a calcination at 900°C (heating rate 5 K min^{-1}). Thermogravimetric measurements showed that conversion of the hydroxides to the oxides was completed around 700°C.[1] The calcined oxides were attrition milled in portions of 30 g with 1200 g of yttria stabilized zirconia balls (2 mm diameter, 600 min^{-1}) in 160 ml of l-propanol for 4 h in an attritor lined with polyethylene. Upon filtering off the balls through a 1 mm sieve, the solvent was evaporated under vacuum. The powders were dried at 100°C at 670 Pa and then heated to 600°C to burn out the polyethylene. The powders were isostatically compressed at 800 bar into blocks of 20 mm × 15 mm × 48 mm. These blocks were presintered at 1000°C. Specimens of 5 mm × 4 mm × 40 mm were cut from the blocks and polished. These samples were then sintered at a rate of 1 K min^{-1} up to 400°C and kept there for 1 h. The temperature was then increased at

Table 1. Properties of Nb_2O_5–Ta_2O_5 codoped zirconia

Mol.%		*Specific*	*Crystallite*	*Green bulk*	*Bulk densities after sintering*			
Nb_2O_5	*Ta_2O_5*	*surface area[a] ($m^2\ g^{-1}$)*	*size[a] (nm)*	*densities ($g\ cm^{-3}$)*	*1500°C*	*1550°C*	*1600°C*	*1650°C*
5	5	25·9 (2)	36	2·899 (4)	4·181 (3)	4·806 (2)	5·923 (2)	6·319 (10)
5	7	27·2 (2)	33	3·043 (4)	4·410 (2)	5·257 (3)	6·239 (4)	6·492 (10)
5	10	23·0 (1)	38	3·173 (8)	5·835 (6)	6·730 (9)	6·817 (2)	6·715 (10)
5	12	22·8 (1)	37	3·205 (10)	6·965 (8)	6·996 (4)	6·927 (8)	6·331 (8)
5	15	22·5 (1)	37	3·247 (2)	7·094 (4)	6·992 (6)	6·914 (2)	6·713 (8)
7	5	25·9 (1)	35	2·962 (5)	5·554 (9)	6·268 (8)	6·464 (1)	6·420 (8)
10	5	24·1 (1)	38	3·020 (9)	6·390 (10)	6·456 (5)	6·440 (1)	6·219 (9)
12	5	25·9 (3)	35	2·967 (10)	4·965 (8)	6·125 (2)	6·452 (1)	6·335 (15)
15	5	20·9 (3)	44	3·072 (2)	6·417 (4)	6·209 (2)	6·082 (2)	5·413 (2)

[a] Attrited powders.

5 K min^{-1} to 1000°C and at 3 K min^{-1} to the final sintering temperature. The final sintering temperature was maintained for 2 h. The samples were cooled at 20 K min^{-1}. The powders for the analysis of the lattice parameters were heated to 1000°C at a rate of 5 K min^{-1}, then to 1400°C at 3 K min^{-1}. The cooling rate was 20 K min^{-1}.

2.2 Apparatus and procedures

BET-surface area measurements were carried out on a Quantasorb (Quantachrome, USA) and crystallite sizes were calculated from the specific surface areas from the equation: $d = 6/\rho A_s$ where d is the crystallite diameter, ρ the density and A_s the specific surface area. The particle size distribution was analysed by means of a laser particle sizer (Coulter LS 130, USA).

X-Ray diffraction spectra were measured on a Geigerflex D/max II with Ni-filtered Cu K_α radiation (Rigaku, Japan) between 25° and 80° (40 kV, 20 mA) with Si (99·999% Balzers, Liechtenstein) as internal standard. X-Ray fluorescence analysis was performed on a Geigerflex M 3064 spectrometer with a Rh anode (Rigaku, Japan) with 35 kV and 15 mA. Electron micrographs were obtained on JSM-6400 scanning microscope (Jeol, Japan). Thermogravimetric measurements were carried out on a TG-770 (Stanton Redcraft, UK). A HT 64/17 (Naber, Germany) oven with a maximum temperature of 1750°C served for sintering. Three-point bend-strength measurements were carried out on a dead weight loaded system (Tonitech, Germany).

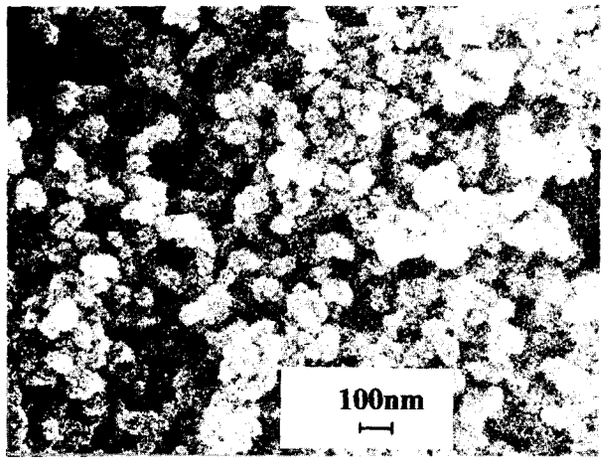


Fig. 1. SEM micrograph of zirconia powders codoped with 5 mol.% Nb_2O_5 and 10 ml.% Ta_2O_5, 50 000×.

2.3 Mechanical properties and microstructure

Three-point bend-strength tests were carried out on 4 mm × 3 mm × 40 mm samples employing a 20 mm span. The tensile surfaces of the samples were diamond-polished to a 1 μm finish and the edges chamfered prior to the bending tests. The load during the testing was increased at a rate of 12 N s^{-1}. Vickers hardnesses were measured with the load of 49 N. Fracture toughness values were obtained from the indentation fracture technique[2] with an indentation load of 49 N. The mean diagonals of the indentation sites and the indentation crack lengths were measured by optical microscopy. The fracture toughness values were calculated using the equation $K_{Ic} = 0{\cdot}0824\ P/c^{1.5}$ (K_{Ic}: in MPa $m^{1/2}$, P: indentation load in MN, c: half of the half-penny crack diameter in m). The microstructure of the samples was analysed by optical and scanning electron microscopy. Specimens were either chemically etched in 60 wt% NaOH for

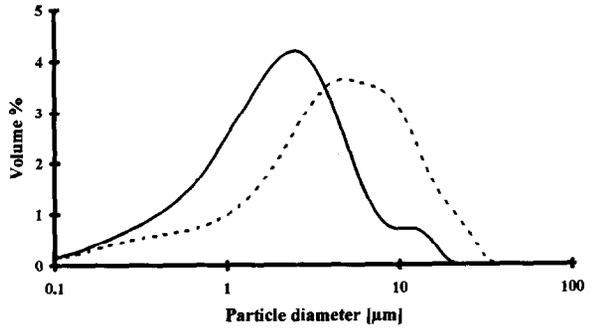


Fig. 2. Particle size distribution of calcined zirconia powders codoped with 10 mol.% Nb_2O_5 and 5 mol.% Ta_2O_5; – – – before attrition, —— after attrition.

Table 2. Mechanical properties of sintered Nb_2O_5-Ta_2O_5 codoped zirconia

Mol.% Nb_2O_5	Ta_2O_5	*Sintering temp.*	σ_{3P}[a] *(MPα) aver. max*		m[b]	HV[c] *(GPα)*	K_{Ic} *(MPa m$^{1/2}$)*	ρ[d] *(g cm^{-3})*	*Relative density (%)*	*Orthorh. phase (%)*	*Grain width*[e] *(μm)*
5	5	1650	85±34	134	2·7	6·8	3·6±0·1	6·319	96·8	100	—
5	7	1650	188±58	235	3·5	7·7	2·5±0·6	6·492	97·1	100	0·9/2·5
5	10	1600	242±39	278	6·5	8·5	3·0±0·2	6·817	98·5	100	1·0/2·4
5	12	1550	241±42	296	5·9	9·8	2·1±0·1	6·996	99·0	100	0·8/2·0
5	15	1500	193±33	241	6·4	9·9	2·5±0·1	7·094	97·5	100	1·0/2·2
7	5	1600	230±30	266	8·6	8·6	2·5±0·2	6·464	99·0	100	0·8/2·5
10	5	1600	257±58	350	4·8	9·0	2·6±0·1	6·456	98·7	100	0·4/2·0
12	5	1600	240±47	280	5·3	8·7	2·8±0·5	6·452	98·6	100	0·7/2·5
15	5	1500	215±29	227	8·5	8·7	3·4±0·5	6·417	98·0	100	0·7/2·4

[a] Three-point bend-strength; [b] Weibull modulus; [c] Vickers hardness; [d] Bulk density; [e] Two types of elongated grains with average aspect ratios ranging from 3 to 4.

2 h at 180°C or thermally etched for 2 h at 1450°C. During etching experiments we found that the Nb_2O_5–Ta_2O_5 codoped zirconia were quite corrosion resistant in both acid and basic media. Fractographic studies were carried out to learn about the fracture origins (strength degrading defects) and fracture mechanisms by means of scanning electron microscopy.

3 Results and Discussion

3.1 Powder characteristics and mechanical properties

The hydroxides obtained after hydrolysis were amorphous. The specific surface areas and the densities of the calcined, attributed powders are summarized in Table 1. The specific surface areas of the attrited Nb_2O_5–Ta_2O_5 codoped zirconia powders were very similar and ranged from 21 to 27 $m^2\ g^{-1}$. Crystallites sizes between 33 and 44 nm were calculated from the specific surface areas, in close agreement with observations made by scanning electron microscopy (Fig. 1). The particle size distribution analysis of the calcined powders showed that the prime crystallites had formed larger particles with mean diameters between 6 and 10 μm. No particles larger than 40 μm were found. Attrition milling improved the particle size distributions, yielding particles with mean diameters around 2–3 μm (Fig. 2). The largest particles observed in the attrited powders were around 20 μm.

For total concentrations of the doping oxides up to 12 mol.% an increase in the densities with increasing sintering temperatures up to 1650°C was noted. Ceramics doped with higher concentration of the doping oxides showed a slight decrease in the densities with the sintering temperatures for the temperature range studied. The temperatures for the sintering of the specimen for mechanical testing were selected according to the highest values for the densities.

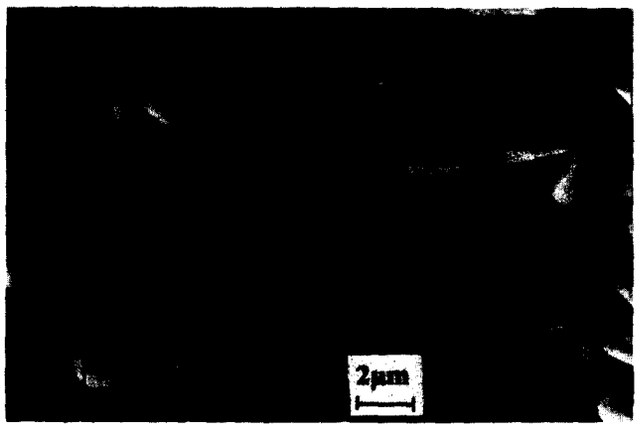


Fig. 3. SEM micrograph of zirconia codoped with 5 mol.% Nb_2O_5 and 12 mol.% Ta_2O_5 (thermally etched).

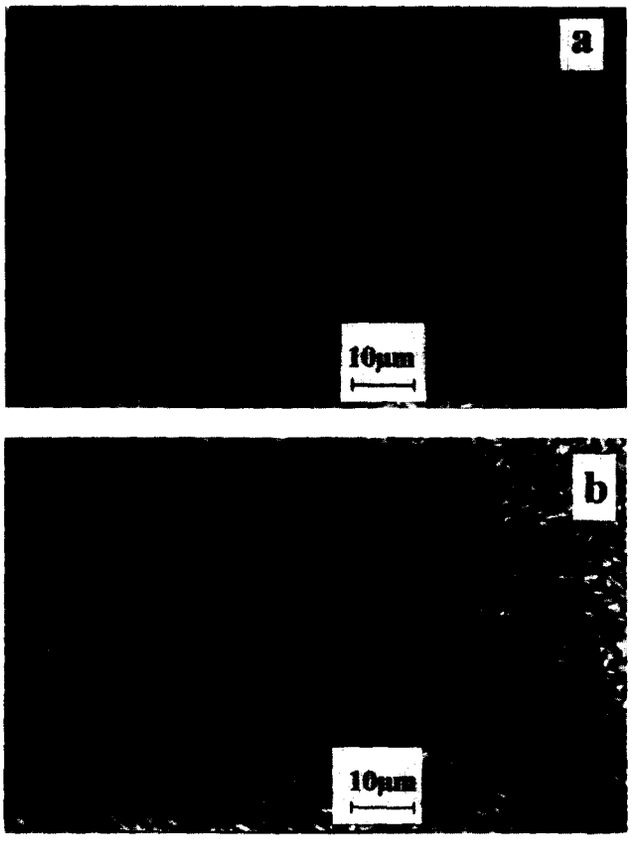


Fig. 4. Comparison of the microstructure of codoped zirconia: (a) 5 mol.% Nb_2O_5 and 10 mol.% Ta_2O_5. (b) 10 mol.% Nb_2O_5 and 5 mol.% Ta_2O_5.

Table 3. Lattice parameters and theoretical densities for Nb_2O_5–Ta_2O_5 codoped zirconia

Nb_2O_5 mol.%	Ta_2O_5 mol.%	a (nm)	b (nm)	c (nm)	Theor. density (g cm^{-3})
0[a]	0	0·5042	0·5092	0·5257	6·062
5	5	0·5003	0·5123	0·5289	6·525
5	7	0·4991	0·5130	0·5301	6·689
5	10	0·4967	0·5143	0·5300	6·920
5	12	0·4957	0·5159	0·5309	7·068
5	15	0·4948	0·5151	0·5304	7·280
7	5	0·4986	0·5128	0·5297	6·531
10	5	0·4964	0·5146	0·5304	6·539
12	5	0·4981	0·5137	0·5304	6·551
15	5	0·4948	0·5156	0·5308	6·544

[a] Ref. 4.

The mechanical properties of the sintered bodies are summarized in Table 2. The bending strengths and fracture toughnesses of the studied ceramics were rather low and showed considerable scatter. Due to the involved procedures in preparing the powders only 8 to 12 sintered specimens were available for the three-point bend-strength measurements. Table 2 therefore contains both the standard deviations and the Weibull moduli, although we realize that the number of specimens is small for reliable Weibull statistics. The maximum strength values were achieved for samples having a total dopant concentration between 15 and 17 mol.%. Maximum values from 280 to 350 MPa could be obtained for these dopant concentrations. The hardness of the samples increased with increasing Ta_2O_5-concentration in codoped samples with 5 mol.% Nb_2O_5. The fracture toughnesses varied modestly between 2·1 and 3·6 MPa $m^{1/2}$.

A comparison of the mechanical properties of the Nb_2O_5–Ta_2O_5 codoped zirconia ceramics with the Nb_2O_5 or Ta_2O_5 singly doped ceramics showed that the values for the three-point bend-strengths were higher by about 100 MPa for the codoped samples than for either the Ta_2O_5 or the Nb_2O_5 singly doped ceramic.[1] We attribute this increase in bend-strength to the improved microstructure of the codoped ceramics. The K_{Ic} values and Vickers hardness values are comparable.

The microstructures of the Nb_2O_5 and Ta_2O_5 codoped ceramics were very similar. They consisted of fine grain sized matrix with mean grain widths of 0·5–1·0 μm. The average aspect ratio was 3. The matrix formed about 70% of the material. Larger elongated grains (average width 2–2·5 μm, average aspect ratio 4) were imbedded in this matrix (Fig. 4). Pores usually ranged from 1·0 to 10·0 μm. Larger pores with pore diameters up to 150 μm were rare.

Fractographic analysis of the fracture surfaces of the samples after the bend-strength tests revealed that the main strength degrading defects were either half-penny shaped surface flaws approximately 25 μm in depth and 60 μm wide (Fig. 5) or machining damages.

Fractures occasionally also originated from

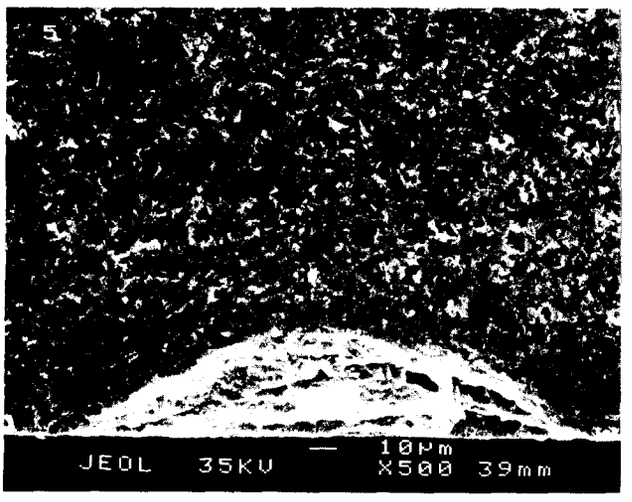


Fig. 5. Fracture origin of zirconia codoped with 12 mol.% Nb_2O_5 and 5 mol.% Ta_2O_5 (defect located at the tensile surface).

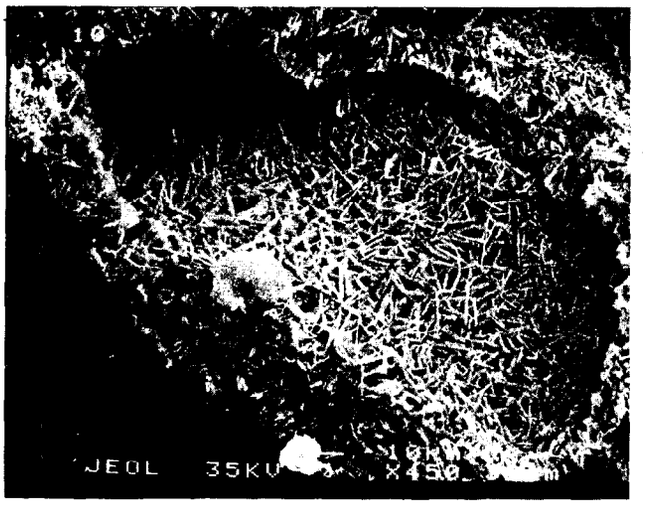


Fig. 6. Volume defect of zirconia codoped with 5 mol.% Nb_2O_5 and 15 mol.% Ta_2O_5 as fracture origin.

Table 4. Coefficients for the calculation of lattice parameters of Nb_2O_5 and Ta_2O_5 codoped zirconia from the equation: $a(b, c) = a_0(b_0, c_0) + k_a k_b, k_c)$ (X_2O_5/mol.%)

Oxide	a_0 (*nm*)	k_a $\times 10^4$	r^a	b_0 (*nm*)	k_b $\times 10^4$	r^a	c_0 (*nm*)	k_c $\times 10^4$	r^a
5 mol.% Nb_2O_5 5–15 mol.% Ta_2O_5	0.503 (7)	−6.460	0.99	0.509 (8)	4.278	0.95	0.526 (8)	3.127	0.88
5 mol.% Ta_2O_5 5–15 mol.% Nb_2O_5	0.503 (5)	−5.813	0.95	0.509 (8)	3.981	0.96	0.526 (6)	3.268	0.92

[a] Correlation coefficient.

volume defects, usually from large pores (100–150 μm) or pores filled with agglomerates of grains (Fig. 6). No marks around the fracture origins (mist, mirror, hackle) were identified. The fractures of the very brittle ceramics were transgranular in all cases without any reinforcing mechanisms such as crack deflection or crack bridging as shown in Fig. 3, on a crack initiated by Vickers indentations.

3.2 Lattice parameters

All codoped samples studied were composed of the orthorhombic phase (Fig. 7). Generally a slight decrease in the *a*-axis and an increase in the *b*- and *c*-axes were observed with increasing dopant concentrations (Table 3). The changes in the lattice parameters for codoped samples, with either 5 mol.% Nb_2O_5 and varying concentrations of Ta_2O_5 or with 5 mol.% Ta_2O_5, and varying concentrations of Nb_2O_5 can be presented by the following equation: $a(b,c) = a_0(b_0,c_0) + k_a(k_b,k_c)$ (X_2O_5/mol.%). X_2O_5 represents the oxide, the concentration of which has varied. The respective values for *a*, *b*, *c*, a_o, b_o, c_o, k_a, k_b and k_c together with the theoretical densities for Nb_2O_5 and Ta_2O_5 codoped zirconia—obtained from the lattice parameters—are summarized in Table 4. The Miller indices for the crystal planes of orthorhombic zirconia were assigned as published for $8ZrO_2 \cdot Nb_2O_5$.[3]

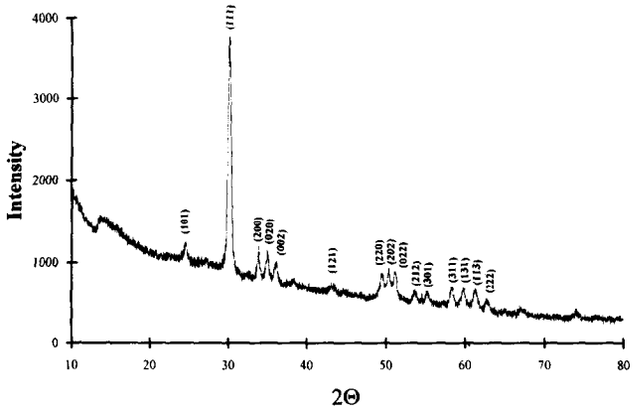


Fig. 7. X-ray diffraction of zirconia codoped with 5 mol.% Nb_2O_5 and 10 mol.% Ta_2O_5.

4 Conclusions

Zirconia ceramics codoped with Nb_2O_5–Ta_2O_5 yielded orthorhombic sintered bodies with three-point bend-strengths ranging from 140 to 260 MPa. This brittle, corrosion resistant material showed transgranular fractures originating generally from surface flaws or pores near the tensile surface. No transformation toughening, crack deflection or crack bridging occurred upon fracture. Bend-strengths for the codoped material were generally higher by 100 MPa than for Nb_2O_5 or Ta_2O_5 monodoped zirconia due to the improved microstructure in the codoped samples.

Vickers hardness values ranged between 6·8 and 9·9 GPa, relative densities between 96·8 and 99·0%, and K_{Ic}-values varied between 2·1 and 3·6 MPa $m^{1/2}$. The best values for the mechanical properties were found for a total content of doping oxides of about 15–17 mol.%.

Acknowledgement

Financial support by the Fonds zur Förderung der wissenschaftlichen Forschung (Austria) and the Jubiläumsfonds der Österreichischen Nationalbank is gratefully appreciated. The authors thank Mr K. Kellner for carrying out the XRD-measurements and Dipl.-Ing. M. Ratajski for electron micrographs.

References

1. Gritzner, G. & Puchner C., V_2O_5, Nb_2O_5 and Ta_2O_5 doped zirconia ceramics, *J. Eur. Ceram. Soc.*, **13** (1994) 387–94.
2. Anstis, G. R, Chantikul, P., Lawn, B. R. & Marshall, D. B., A critical evaluation of Indentation techniques for measuring fracture toughness: I, Direct crack measurements. *J. Am. Ceram Soc.*, **64** (1981) 522–38.
3. International Center for Diffraction Data (Swarthmore, PA, USA), powder diffraction file 23–452.
4. International Center for Diffraction Data (Swarthmore, PA, USA), powder diffraction file 37-1413.

Journal of the European Ceramic Society **15** (1995) 51–55
© 1995 Elsevier Science Limited
Printed in Great Britain. All rights reserved
0955-2219/95/$9.50

Ionic Conductivity of Fully Stabilized ZrO_2 : MgO and Blocking Effects

Eliana N. S. Muccillo[a] & M. Kleitz[b]

[a] Instituto de Pesquisas Energéticas e Nucleares, Comissão Nacional de Energia Nuclear S. P., C.P. 11049-Pinheiros, 05422-970 Sao Paulo, S.P., Brazil
[b] Laboratoire d'Ionique et d'Electrochimie du Solide de l'INP de Grenoble, Associé au CNRS, BP 75, 38402 St. Martin d'Hères Cedex, France

(Received 23 February 1994; revised version received 1 June 1994; accepted 14 June 1994)

Abstract

Ionic conductivity measurements were performed by impedance spectroscopy on ZrO_2–MgO 13·7 mol%, in the 270–700°C temperature range. The diagrams show characteristic intragrain and grain boundary semicircles. Activation energies for the intragrain conductivity and the intergrain blocking effect are 126 and 141 kJ mol^{-1}, respectively. The estimated specific conductivity is 9·8 S m^{-1} at 1000°C. The conductivity blocking effect at the grain boundaries is very similar to that of yttria-stabilized zirconia.

1 Introduction

There has been significant interest in zirconia-based ceramic materials for several applications. Some of them (SOFCs, oxygen sensors and pumps, etc.) are based on the high oxide ion conductivity of the so-called stabilized zirconias. The majority of the zirconias investigated for this property contain trivalent cations as stabilizers. They induce higher conductivities than the divalent cations.

Mg-doped zirconia solid solutions have received less attention because of an instability of the cubic phase that results in a gradual degradation of its properties. Over the last decade, it has been demonstrated that an aging treatment at 1100°C slows down the decomposition reaction and, simultaneously, improves the thermal shock resistance of partially stabilized zirconias.[1] This has prompted new investigations on this system, mostly focused on mechanical properties. So far, relatively few studies[2–6] have dealt with its electrical properties and, in most cases, the conductivities have been measured by DC techniques, with no attention given to the microstructure effects.

Muccillo[7] has examined the correlations between the phase decompositions and the electric properties of the system using impedance spectroscopy. This paper reports results on the cubic phase containing 13·7 mol% of MgO which can be regarded as a sort of reference. As in other zirconia systems, the conductivity of the ZrO_2–MgO cubic phase is predominantly ionic and oxide ions are the charge carriers. Reported conductivity values[2] at 1000°C lie between 0·82 and 4·0 S m^{-1}. The literature data[2] on the conduction activation energy present an unusually broad dispersion, ranging from 82 to 141 kJ mol^{-1}. From diffusion measurements[8] in the cubic phase, it has been found that the oxygen diffusion activation energy is 63 kJ mol^{-1}. That of the Mg–Zr interdiffusion[9] is 285 kJ mol^{-1}.

Impedance spectroscopy has been widely used for characterizing other zirconia-based materials.[3,5,10–12] It is capable of separating the specific electric response of the material, the so-called intragrain response, from that of the grain boundaries which is always characterized by an additional resistance.

2 Experimental

The starting materials were ZrO_2 (DK-2 type, Zirconia Sales) and MgO (analytical grade from Merck). The following analyses were carried out: Hf content by neutron activation, other metallic impurities by spectrographic analysis, surface area by BET, distribution of particle size by sedimentation and particle/agglomerate morphology by scanning electron microscopy.

Pellets (typically 0·95 cm in diameter and 0·16 cm high) were prepared by conventional ceramic processing involving wet mixing, pressing, sintering at 1650°C for 2 h and machining. The apparent

Table 1. Results of chemical and physical analyses performed on starting powders (S: surface area, Dp: mean particle/agglomerate size)

	Hf (%)	*Fe* (ppm)	*Si* (ppm)	*Al* (ppm)	*Surface area (S)* (m^2/g)	*Mean particle/ agglomerate size (Dp)* (μm)
ZrO_2	1·30	15	400	100	3·4	2·5
MgO	—	50	—	—	34·5	<0·2

density of the sintered specimens was determined by the hydrostatic method and their phase content by X-ray diffractometry. Microscopic examinations were done on polished and chemically etched or fractured surfaces. The Mg content was confirmed by neutron activation analysis, checking on possible MgO losses by surface evaporation.[13]

For electrical measurements, Pt and Ag electrodes were applied by painting. Silver electrodes have been found to give a much smaller interference between the material responses and the electrode characteristics, allowing a more accurate determination of the electric parameters. Impedance measurements were performed from 5 Hz to 13 MHz with a HP 4192A impedance analyzer, in the 270–700°C temperature range. Data were collected during heating and cooling cycles. The results were analyzed in the impedance mode, using a special computer program.[14]

3 Results and Discussion

The MgO content of all sintered samples was determined to be 13·7 mol%, and the diffractogram profiles only exhibited the cubic phase reflections.

Table 1 shows the results of the powder analyses. The main impurity is silicon, at a level normally found in most technical zirconia powders. The mean particle/agglomerate size (2·5 μm) obtained by sedimentation, was taken as usual as the value corresponding to 50 wt% of the particles finer than it.

The relative density of the sintered pellets was about 80%, due to a large closed porosity. Figure 1 is a typical micrograph of a fractured surface showing the extensive intragranular, intergranular and triple-point porosities. The average grain size determined from a polished and etched surface is about 18 μm.

To improve the mechanical characteristics of Mg-partially stabilized zirconias, it is common practice to sinter the material at a relatively high temperature ($T > 1800$°C) and subsequently to quench and then anneal it at a temperature slightly higher than that at which the eutectoid decomposition starts. This gives ceramics with an average grain size in the 50–100 μm range.[15] With sintering temperatures of about 1700°C, ceramics with average grain sizes of about 20 μm were obtained.[16] The present data on the fully stabilized solid solutions sintered at 1650°C agree with these last results.

A three-dimensional impedance plot obtained at 441°C is presented in Fig. 2. In the 300–600°C temperature range, all diagrams show the same features: a predominant high-frequency semicircle and a smaller low frequency semicircle (and part of the electrode response). As usual with zirconia-based solid electrolytes, the semicircle centers fall

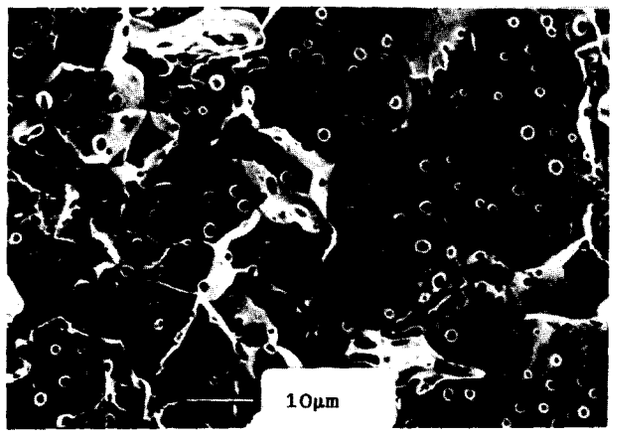


Fig. 1. Typical fracture surface of a ZrO_2–MgO 13·7 mol% sample sintered at 1650°C for 2 h.

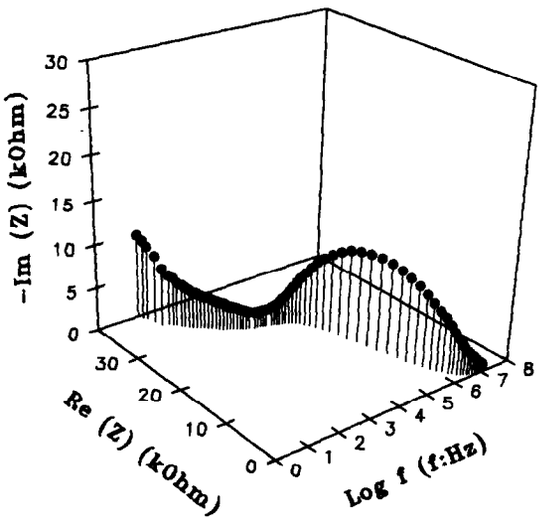


Fig. 2. Three-dimensional impedance plot recorded at 441°C (with Pt electrodes).

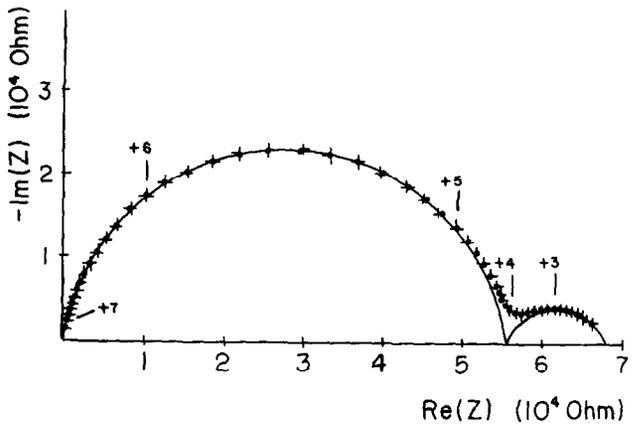


Fig. 3. Complex impedance plot recorded at 456°C (with Ag electrodes). The figures on the diagram indicate the decimal logarithms of the measuring frequencies.

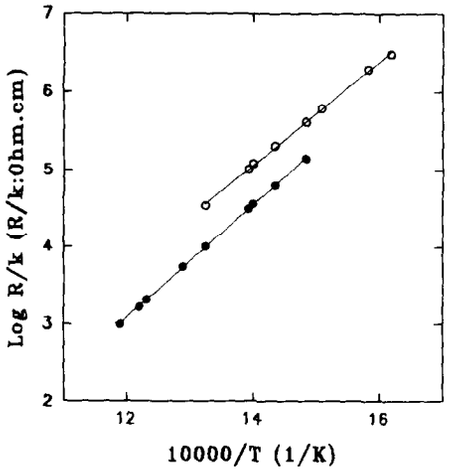


Fig. 5. Arrhenius diagram of the resistivities: (○) intragrain and (●) intergrain resistivities.

below the real axis. The off-axis angles are of the order of 12 and 18 degrees, respectively, for the high- and low-frequency semicircles. The high-frequency semicircle describes the intragrain resistance and capacitance relaxation. The low-frequency semicircle is related to conductivity blocking effects at grain boundaries. It is relatively small, because of a rather low grain boundary density (a rather high average grain size). In more conventional yttria-stabilized zirconias,[10] the relative magnitude of the grain boundary blocking effect is similar for a similar grain size. Details are given later in terms of a blocking factor.

Figure 3 presents an example of curve fitting performed on experimental data. Both intragrain and grain boundary contributions can be readily separated in this way in the temperature range 300–600°C. The data analysis was restricted to this temperature range where a reasonably good accuracy for the conductivity parameters was obtained.

Figure 4 shows the logarithms of the relaxation frequencies determined at the apex of the semi-

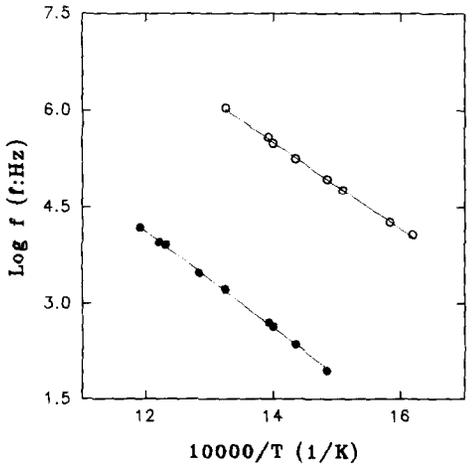


Fig. 4. Arrhenius diagram of the relaxation frequencies: (○) intragrain and (●) intergrain responses.

circles as functions of temperature. The fitted straight lines are approximately parallel. A similar observation was also made with zirconia–yttria ceramics.[11,12] At 400°C, the frequency ratio is equal to $1{\cdot}1 \times 10^{-3}$. It is very similar to the value ($0{\cdot}99 \times 10^{-3}$) quoted for an yttria-stabilized zirconia,[12] indicating similar average morphologies for the grain boundaries.

Values of the specific resistivities R/k have been determined from the intersections of the impedance arcs with the real axis, R being the resistances and k the geometrical factors of the samples. Figure 5 shows the Arrhenius plots of the intragrain and intergrain resistivities. There is no noticeable change in the slope of the intragrain resistivity in the investigated temperature range. This is in contrast with common observations on yttria-stabilized zirconias, but in agreement with results obtained by DC techniques, where no change of the Arrhenius slope has been observed, at least up to 1000°C.[6,17]

Activation energies and pre-exponential factors are given in Table 2. As is frequent in zirconia-based ionic conductors,[11] the difference between the activation energies of the intragrain and intergrain resistivities is about 15 kJ mol^{-1}. From the intragrain parameters one can estimate, by extrapolation, an intragrain conductivity of 9·8 S m^{-1} at 1000°C. At this temperature the blocking effect of charge carriers by grain boundaries is negligible, and hence intragrain and DC conductivities are the same. The conductivity value is slightly higher

Table 2. Activation energies *(E)* and pre-exponential factors *(A)* of the intragrain and intergrain resistivities

	Intragrain	*Intergrain*
E (kJ mol^{-1})	126	141
A (10^{-7} Ω m)	6·6	0·17

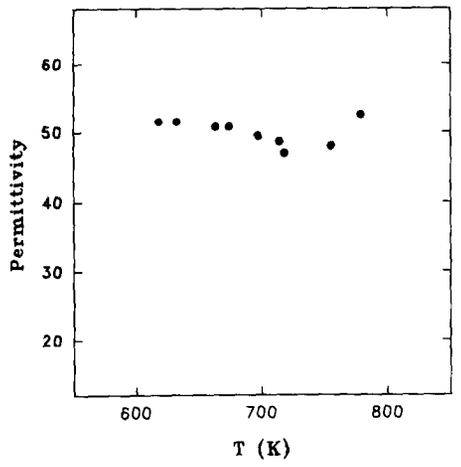


Fig. 6. Variation of the permittivity with temperature.

than reported data. This may be a consequence of different sintering conditions. It is well known that increasing the sintering temperature and sintering time greatly enhance the average grain size and modify the porosity. The grain size has no net effect on the bulk electrical characteristics, but porosity increases the intragrain resistivity.[11,18]

From the bulk semicircles a dielectric constant can also be calculated. As shown in Fig. 6, it does not vary much with temperature and is close to 50, a value similar to that (about 60) measured with yttria-stabilized zirconias under similar experimental conditions.[19]

Referring to a previous analysis by Dessemond and coworkers,[11,20] the blocking of the electric charge carriers at the grain boundaries by the blocking factor α_R can be defined by the equation:

$$\alpha_R = R_{\text{grain b.}}/(R_{\text{intrag.}} + R_{\text{grain b.}})$$

It measures the fraction of ionic carriers being blocked at grain boundaries. Over the rather narrow temperature range where it could accurately be determined, it is approximately independent of temperature (Fig. 7). Its average value is 0·24.

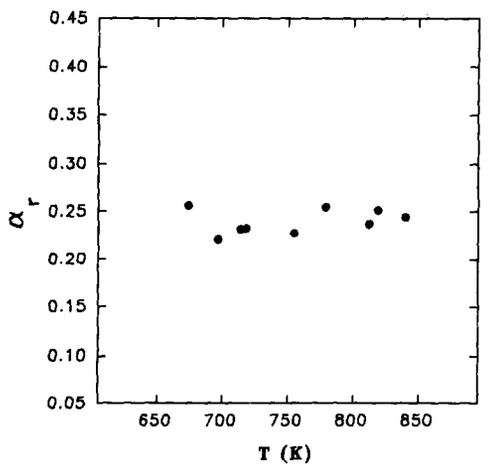


Fig. 7. Variation of the grain boundary blocking factor with temperature.

4 Conclusions

The main conclusions are:

—The impedance diagrams of fully stabilized ZrO_2–MgO ceramics prepared by solid-state synthesis present two well-resolved semicircles as for other cubic zirconia systems. The activation energies for the intragrain resistivity and the intergrain blocking effect are 126 and 141 kJ mol^{-1}, respectively.

—The estimated specific conductivity is 9·8 S m^{-1} at 1000°C.

—The specific dielectric constant and the ion-blocking parameters are very similar to the equivalent parameters of yttria-stabilized zirconias.

Acknowledgments

The authors acknowledge CNPq-RHAE for a scholarship to one of the authors (E.N.S.M.) and Zirconia Sales for providing the zirconia powder.

References

1. Hannink, R. H. J. & Garvie, R. C., Sub-eutectoid aged Mg-PSZ alloy with enhanced thermal up-shock resistance. *J. Mater Sci.*, **17** (1982) 2637–43.
2. Etsell, T. H. & Flengas, S. N., The electrical properties of solid oxide electrolytes. *Chem. Rev.*, **70** (1970) 339–52.
3. Wen, T. L., Li, N. X., Kuo, C. & Weppner, W., Conductivity of MgO-doped ZrO_2. *Solid State Ionics*, **18/19** (1986) 715–9.
4. Poulsen, F. W., Sorensen, J. B. B., Ahari, K. G., Knab, G. G. & Hartmanova, M., Oxygen ion conduction in ternary zirconia mixtures: effect of SrO on MgSZ. *Solid State Ionics*, **40/41** (1990) 947–51.
5. An, S., Wu, X., Wu, W. & Lin, Q., Effect of heat treatment on structure and properties of MgO–PSZ electrolyte. *Solid State Ionics*, **57** (1992) 31–4.
6. Badwal, S. P. S., Zirconia-based solid electrolytes: microstructure, stability and ionic conductivity. *Solid State Ionics*, **52** (1992) 23–32.
7. Muccillo, E. N. S., Impedance spectroscopy and internal friction in ZrO_2 : MgO solid electrolytes, Thesis (in Portuguese), IPEN, Universidade de São Paulo, Brazil, 1993.
8. Ando, K., Oishi, Y., Koizumi, H. & Sakka, Y., Lattice defect and oxygen self-diffusion in MgO-stabilized ZrO_2. *J. Mater. Sci. Lett.*, **4** (1985) 176–80.
9. Sakka, Y., Oishi, Y. & Ando, K., Cation interdiffusion in polycrystalline fluorite-cubic MgO–ZrO_2. *Bull. Chem. Soc. Jpn*, **55** (1982) 420–2.
10. Kleitz, M., Bernard, H., Fernandez, E. & Schouler, E., Impedance spectroscopy and electrical resistance measurements on stabilized zirconia. In *Advances in Ceramics*, Vol. 3, *Science and Technology of Zirconia I*, ed. A. H. Heuer & L. W. Hobbs. American Ceramic Society, Columbus, OH, 1981, pp. 310–36.
11. Dessemond, L., Spectrocopie d'impédance des fissures dans la zircone cubique. Thesis, Polytechnic Institut, Grenoble, France, 1992.

12. Kleitz, M., Pescher, C. & Dessemond, L., Impedance spectroscopy of microstructure defects and cracks characterization. In *Zirconia V, Science and Technology of Zirconia*, ed. S. P. S. Badwal, M. J. Bannister & R. H. J. Hanninck. Technomic, Lancaster, UK, 1993, pp. 593–608.
13. Sakka, Y., Oishi, Y. & Ando, K., Enhancement of MgO evaporation from MgO-stabilized ZrO_2 by grain-boundary diffusion. *J. Am Ceram Soc.*, **69** (1986) 111–3.
14. Kleitz, M. & Kennedy, J. H., Resolution of multi-components impedance diagrams. In *Fast Ion Transport in Solids, Electrodes and Electrolytes*, ed. P. Vashishta, J. N. Mundy & G K. Shenoy. North-Holland, Amsterdam, 1979, pp. 185–8.
15. Subbarao, E. C., Zirconia, an overview. In *Advances in Ceramics*, Vol. 3, *Science and Technology of Zirconia I*, ed. A. H. Heuer & L. W. Hobbs. American Ceramic Society, Columbus, OH, 1981 pp. 1–24.
16. Krishnamoorthy, P. R., Ramaswamy, P. & Narayana, B. H., Microstructural developments in Mg–Ti–PSZ systems. *J. Mater. Sci.*, **27** (1992) 1016–22.
17. Guillou, M., Millet, J., Asquiedge, M., Busson, N., Jacquin, M. & Palous, S., Propriétés électriques des zircones contenant de la magnésie. *C. R. Acad. Sci. Paris*, **262** (1966) 616–19.
18. Bonanos, N., Steele, B. C. H. & Butler, E. P., Applications of impedance spectroscopy. In *Impedance Spectroscopy*, ed. J. R. Macdonald. Wiley, New York, 1987, pp. 191–237.
19. Steil, M. C., Thevenot, F., Dessemond, L. & Kleitz, M., Impedance spectroscopy analysis of conduction percolation in zirconia–alumina composites. In *Proc. 3rd European Ceramic Society Conference*, ed. P. Duran & J. F. Fernandez. Faenza Editrice Iberica S. L., San Vincente, Spain, 1993, pp. 271–80.
20. Dessemond, L., Muccillo, R., Henault, M. & Kleitz, M., Electric effects of voids and second phases in stabilized zirconia. *Appl. Phys.*, **A57** (1993) 57–60.

Journal of the European Ceramic Society **15** (1995) 57–63
© 1995 Elsevier Science Limited
Printed in Great Britain. All rights reserved
0955-2219/95/$9.50

Synthesis and Sintering of PLZT Powder Made by Freeze/Alcohol Drying or Gelation of Citrate Solutions

M. A. Akbas & W. E. Lee

University of Sheffield, Department of Engineering Materials, Sheffield, UK

(Received 11 March 1994; revised version received 1 June 1994; accepted 14 June 1994)

Abstract

Citrate salts of PLZT 9/65/35 were prepared by drying (alcohol and/or freeze drying) and gelation of citrate solutions of PLZT. The decomposition of the citrate salts to form PLZT powder was studied by thermal analysis, X-ray diffraction, and scanning electron microscopy (SEM). It was found that the citrate salts of PLZT composition decompose in two separate stages; after decomposition, powder derived from alcohol dehydration, freeze drying and gelation have similar characteristics. Calcined powders in all cases consisted of 1 μm agglomerates with a surface area of approximately 11 m^2/g. Freeze drying and gelation are preferred over expensive alcohol dehydration. Dense pellets can be obtained from the citrate derived powder by a two stage pressureless sintering process.

1 Introduction

Lanthanum-doped lead zirconate titanate ceramics (PLZT), when fabricated as thin polished plates, have high optical transparency and exhibit excellent electro-optical characteristics.[1] As a result, many applications have been proposed in the field of electro-optics such as optical shutters, light modulators, memories and display devices.[2]

The production of high quality technical ceramics such as electro-optic PLZT components requires close control of powder characteristics such as purity, chemical homogeneity and particle-size distribution. By using chemical solution techniques for the preparation of multi-component powders, it is possible to produce fine, highly pure and homogeneous powders. The preparation of such PLZT powders via solution techniques has been demonstrated by several workers.[3–7] Another technique involves preparing multi-cation aqueous citrate solutions and co-precipitating PLZT citrate powder by alcohol dehydration of this solution.[8]

This method was first applied to the production of chemically homogeneous and fine $BaTiO_3$ powders[9] and later to the formation of PLZT and PZT powders.[8–10] In the alcohol dehydration process, droplets of a PLZT source solution are atomised into an alcohol bath to obtain PLZT citrate salt. The relative volumes of alcohol and source solution are critical; there must be at least 10 times greater volume of alcohol than solution to maintain the amount of water in the bath at a low level. The resulting powder can be filtered, and after drying, calcined to obtain PLZT.

Unfortunately, the alcohol dehydration technique is impractical because of the large volumes of expensive alcohol required which cannot be re-used without purification, and because of the susceptibility of the resulting salt to moisture absorption. Furthermore, the stoichiometry of the powder may be lost during co-precipitation. For instance, when co-precipitating titanium, 1% and 0.1% Ti remains in solution in ten-fold volumes of methyl and ethyl alcohol respectively.[9] This problem is prevented by using either freeze drying or gelation of the solution to yield the citrate salt.

The aim of the present study was to develop a technique which avoided the need for alcohol dehydration. PLZT citrate solutions were either (a) freeze dried, (b) alcohol dehydrated or (c) gelled. Freeze drying and alcohol dehydration yielded citrate powders while gelation led to a bulk citrate gel. All products were then calcined with the aim of forming PLZT powders.

The manufacture and decomposition of the citrate salts and the reaction mechanism to form PLZT powder is described. The properties and sinterability of powders obtained by freeze drying

and gelation are compared to those of a powder made by alcohol dehydration.

2 Experimental Procedure

Lead oxide (PbO, >99·9%), lanthanum oxide (La_2O_3, >99·99%), zirconium oxychloride octahydrate ($ZrOCl_2 . 8H_2O$, >99%), titanium butoxide ($Ti[O(CH_2)_3CH_3]_4$, >99%) and citric acid (Analar grade) were used as starting materials. Citrate solutions of each of the cations La^{2+}, Pb^{2+}, Zr^{4+} and Ti^{4+} were prepared by mixing their respective oxides and hydroxides with a citric acid solution and using ammonia gas to regulate the pH so as to obtain a clear solution.[9] The individual citrate solutions were then combined to obtain source solutions of PLZT 9/65/35 with excess Pb^{2+} in order to provide 10 wt% excess PbO to the composition after calcination. The Cl^- anions arising from $ZrOCl_2 . 8H_2O$ used in the preparation of zirconium citrate solutions were removed by repeating the precipitation of ammonium zirconyl citrate in large volumes of ethyl alcohol; washing the precipitate; and re-dissolving in distilled water until there was no reaction with photographic paper. This chloride-free zirconium solution was then used to produce PLZT source solution. Removal of chlorides (Cl^-) from the solution is critical to obtaining single-phase product after calcination.[11,12]

By holding the temperature at 60°C for 16–20 h, PLZT solutions were gelled under magnetic stirring. The starting pH of the solutions was around 7. However, the pH gradually decreased below 6 due to ammonia loss at the gelation temperature, and a white precipitate formed in the solution at these low pH values. The precipitate was re-dissolved by adjusting the solution pH between 8 and 8·5 with ammonia solution. This process yielded translucent or transparent bulk citrate gel.

Alcohol dehydration was carried out by spraying source solution at a rate of 15 cm^3/min (compressed-air sprayer, Aldrich Z12, 630-6) into an ethanol (99%) bath which had a volume 20 times that of the solution to be sprayed in order to maintain the water content in the bath at a low level. The pH of the bath was adjusted between 4 and 4·5 with formic acid during co-precipitation. The white PLZT citrate precipitate was centrifuged from the bath, washed with ethanol and dried at 40°C for 18 h.

PLZT citrate powder was also produced by freeze drying. The source solution was frozen by spraying the solution into liquid nitrogen. Water was then removed from the solid particles of salt and ice sublimation in a freeze dryer (Edwards, Freeze Dryer Modulyo) at −50°C and 133 Pa for 48 h.

The powder surface area was determined by using a Micromeritics Gemini 2360 unit; morphology was examined by secondary electron imaging in a scanning electron microscope (SEM, Camscan series 2). Energy dispersive spectroscopy (EDS) was performed using a LINK AN 10000 system with a Be-window detector.

Decomposition of the citrate salt was studied by DTA and TG (Du Pont thermal analyst 2000, Stanton Redcroft TG-770) at a heating rate of 10°C/min in air. To identify the intermediate phases formed, powders were quenched after being held for 4·5 h at various temperatures in air (10°C/min heating rate), and were analysed by X-ray diffraction using Cu K_α radiation (Philips diffractometer equipped with 1710 diffractometer control unit operated at 40 kV and 30 mA). Due to the 4·5 h isothermal treatment, direct comparison between thermal analysis results and those of quenched samples is not possible.

The citrate gel was calcined by heating in air at 10°C/min to 300°C for 1 h. The resulting homogeneous black powder was ground and re-heated to 500°C at 10°C/min in nitrogen and held for another hour. The nitrogen atmosphere was then diluted by passing oxygen through the furnace, and the powder was further calcined for another 4 h.

Both alcohol- and freeze-dried powders were calcined by direct heating to the calcination temperature (500°C) without any intermediate steps (as was used when calcining the gel) and the atmosphere and thermal treatment times were the same.

The resulting powders were energy milled in 2-propanol with yttria-stabilized zirconia balls in polyethylene jars for an hour. Green pellets of 10 mm in diameter and 1 to 2 mm in thickness were then produced by uniaxial pressing at 130 MPa. A two stage sintering technique was used to densify the green pellets. In this technique the pellets were placed in an upside-down platinum crucible with a tight lid. A small amount of identical PLZT powder was used to prevent reaction between the pellets and the platinum crucible. The platinum crucible was flushed with oxygen and the samples were held at 1180°C for 1 h in an oxygen atmosphere. The samples were then transferred in a closed alumina crucible (the so-called double crucible technique, one inside the other) and re-sintered at 1125°C for 13 h in air. Heating and cooling rates were 400°C/h during sintering. This two-stage sintering technique is a modified form of the improved atmospheric sintering method reported by Snow.[13]

Grain size measurements were made using the linear intercept method[14] on samples thermally etched at 1050°C for 1 h in closed platinum crucibles. Optical transmission was determined by using a Perkin-Elmer 330 Spectrophotometer for wavelengths of 350 to 1050 nm on 0·2 mm thick samples polished to an optical finish with 0·25 μm diamond paste.

3 Results and Discussion

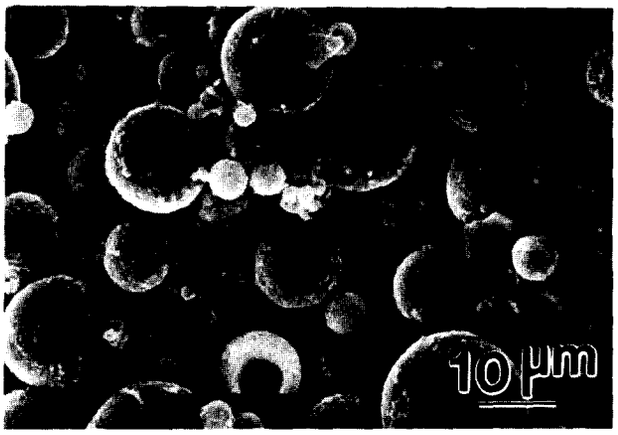
3.1 Processing and morphology of powders

3.1.1 Preparation of citrate solutions and gelation
The citrate route yielded a clear and colourless solution of each individual component of PLZT. No precipitation was observed when individual solutions were mixed together to obtain PLZT source solution of the desired composition. After gelation, the colour of the gel was cloudy white and all the solutions and gels were stable even after seven months storage in airtight plastic containers.

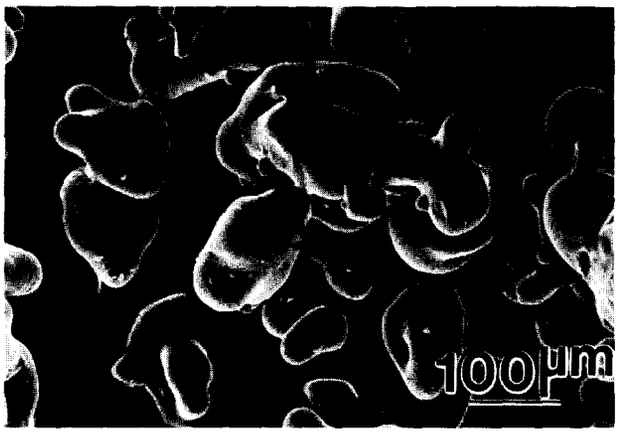
3.1.2 Alcohol- and freeze-dried powders
Both alcohol- and freeze-dried powders were white in colour and free flowing when fully dried. The alcohol-dried particles were spherical prior to calcination and 4–10 micron in size (Fig. 1(a)). While various particle shapes, such as globules and rods,[8,9] have been reported previously for alcohol-dried powders, spherical particles have not been obtained although this is simply achieved by control of the parameters when spraying the solution into the alcohol bath. TEM could not be used to resolve the fine structure of the powder due to rapid decomposition under the electron beam.

The freeze-dried powder consists of large 100-micron agglomerates which have the shape of deformed spheres (Fig. 1(b)). These agglomerates most likely formed due to partial melting upon freeze drying. This indicates that the freezing temperature of the solution (pH >7) is below −50°C at atmospheric pressure. The early stages of combination of the spherical particles to form agglomerates are indicated by the arrow (Fig. 1(b)).

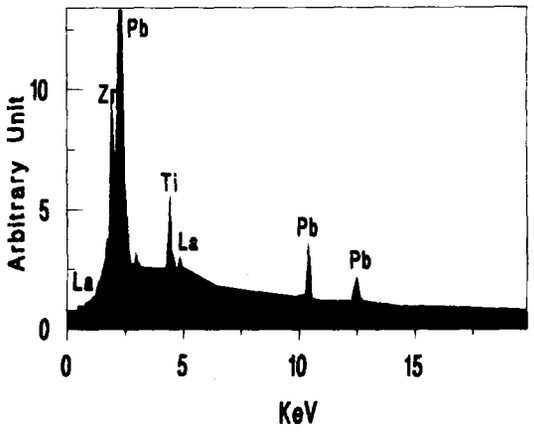
Both the freeze- and alcohol-dried powders have surface areas below 1 m^2/g as expected from the large particle size and smooth surfaces. Although particles are susceptible to electron beam damage, many EDS analyses obtained from individual particles indicate a homogeneous distribution of elements (Fig. 1(c)).



(a)



(b)



(c)

Fig. 1. Secondary electron imaging of (a) alcohol-dehydrated powder revealing its spherical morphology, (b) freeze-dried powder revealing some agglomeration and (c) EDS analysis taken from alcohol dehydrated spheres indicating a homogeneous distribution of the elements.

3.2 Decomposition of PLZT citrate salts

3.2.1 Thermal analysis
TG analysis (Fig. 2) indicates that PLZT citrate salts decompose in two separate stages. Previous work by Courty *et al.*[15] recognised the existence of two types of pyrolysis for the citrate–nitrate precursors. Type I was characterised by a con-

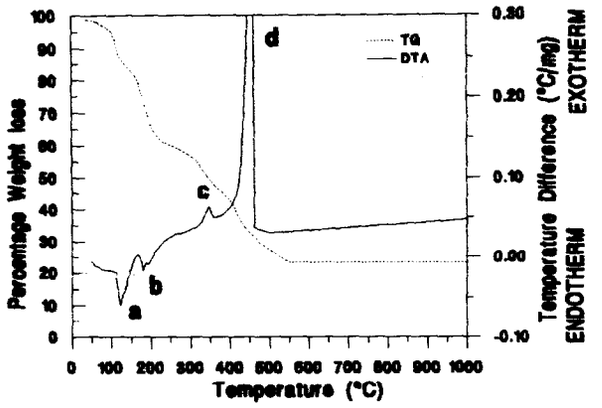


Fig. 2. DTA/TG of PLZT citrate gel. Similar curves result from alcohol-dehydrated and freeze-dried PLZT citrate salts.

tinuous and vigorous reaction which occurred with precursors containing metals with a strong catalytic activity in the oxidation process. Type I decomposition is characterised by a single-stage decomposition in TG. Type II is typified by two stages in which an intermediate decomposition step occurs as a result of the formation of a metastable semi-decomposed precursor which is thought to be a mixed citrate salt.

Citrate gel and alcohol/freeze-dried powders all showed very similar decomposition behaviour. TG and DTA (Fig. 2) indicate that the first stage of decomposition after the removal of water starts at around 120°C (endotherm a on Fig. 2), and continues until 180°C. This part of the decomposition was associated with a 20% weight loss. Samples quenched from 160°C indicated a yellow ochre intermediate phase which was amorphous (Fig. 3). Removal of ammonia and break up of some citrate chains is believed to occur at this stage.[16] The second stage of decomposition is indicated by an endothermic peak at 180°C (endotherm b on Fig. 2) and an associated loss of 25 wt% in a relatively small temperature range of 180°C to 225°C. Samples quenched from 200°C were dark brown to coffee coloured and still amorphous (Fig. 3). Most of the decomposition of the citrate chains occurs at this stage. From 225°C to 500°C, a gradual weight loss is detected due to the break up of any remaining citrate chains. Samples quenched from 300°C were black and still amorphous (Fig. 3) indicating almost complete break up of citrate chains and the presence of carbon as a decomposition product. DTA indicated an exothermic reaction at 340°C (exotherm c on Fig. 2) corresponding to the oxidation of Pb. The rate of weight loss increased after lead oxidation as indicated by TG (Fig. 2). This may imply that lead oxidation acts like a catalyst to ignite carbon oxidation. Exotherm d corresponds to vigorous oxidation of the remaining carbon. Samples quenched from 375, 505, 600, 700 and 800°C were yellow and crystalline (Fig. 3). This indicates that

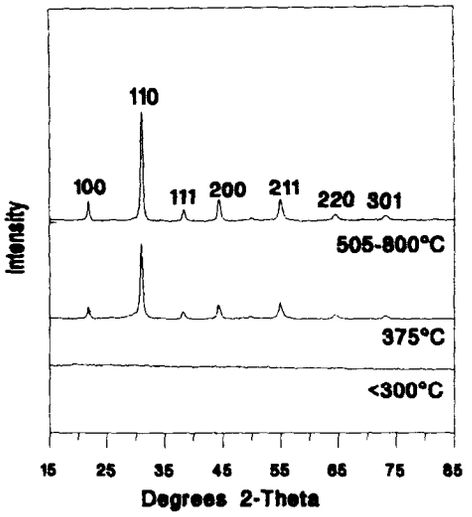


Fig. 3. X-Ray diffraction from citrate gel quenched from various temperatures after 4·5 h isothermal hold. No intermediate phases were observed during the crystallisation of PLZT.

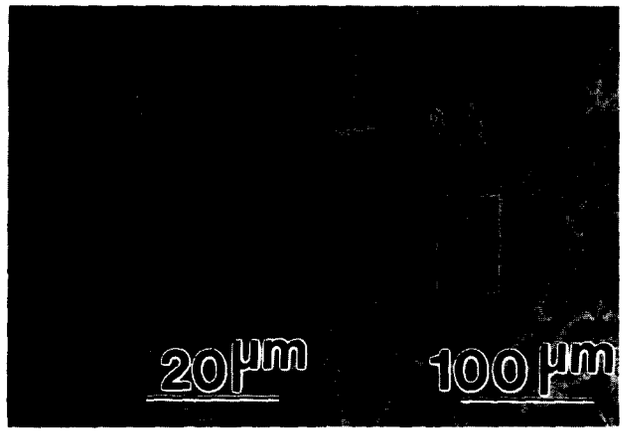
crystallisation of the powder is favoured by the heat produced by oxidation and occurred simultaneously. Although the onset temperature for this reaction was determined as 420°C by DTA, samples quenched from 375°C indicated that the reaction could start at lower temperatures if they were held isothermally for long times. No further DTA peaks were observed above 525°C and the weight remained constant from 530°C to 1000°C.

3.2.2 X-Ray diffraction, surface area and SEM analysis

Many workers have investigated the reaction mechanism of formation of PZT solid solution from oxide precursor mixtures. Although these studies reached different conclusions, invariably intermediate phase(s), such as $PbTiO_3$,[17] $PbZrO_3$,[18] and a PbO solid solution[19] were observed prior to crystallisation of PZT. Figure 3 shows a series of XRD patterns obtained from citrate gel quenched from various temperatures after 4·5 h isothermal holds. XRD was not attempted for freeze/alcohol-dried powders since thermal analysis and calcination indicated that the crystallisation mechanism was identical to that of the gel. The powder remained amorphous up to 300°C and then apparently crystallised directly to single-phase PLZT by a vigorous oxidation/ decomposition reaction after 4·5 h at a temperature of 300–375°C. Brown & Mazdiyasni,[4] Duran & Moure,[20] Thomson[5] and Yoshikawa & Tsuzuki[21] reported 600°C, 550°C (16 h), 500°C (16 h), 450°C (14 h) respectively, as the minimum temperature (and time) required to obtain crystalline PLZT phases for their chemically prepared powders. In the present work, this minimum temperature was less than 375°C (4·5 h). No intermediate phases were observed and all the diffraction peak positions and intensities match



(a)



(b)



(c)

Fig. 4. SEM micrographs of citrate gel powder quenched from (a) 160, (b) 375 and (c) 500°C after 4·5 h at temperature indicating the powder morphology at various stages of decomposition.

with those reported for PLZT.[22] With increasing temperature, the peaks get sharper and stronger indicating an increase in crystallite size and amount.

The morphology of the citrate gel powder quenched from 160°C reveals large (30 μm) platy, angular particles with smooth surfaces (Fig. 4(a)). Their smooth appearance indicates that not much citrate decomposition has occurred at this temperature. After the strong oxidation of carbon at

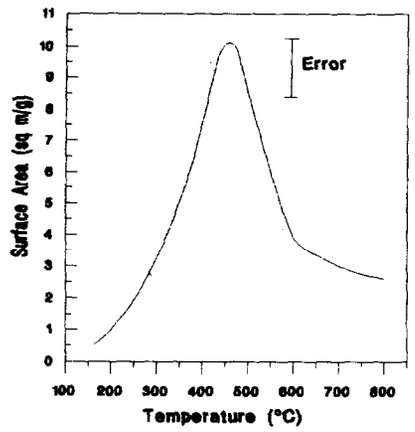


Fig. 5. Change in the surface area of powder with temperature during decomposition. Surface area was measured for powder quenched from various temperatures after 4·5 h isothermal hold of PLZT citrate gel.

375°C, the particles contain many micro-channels and pores presumably arising from decomposition of citrate chains (Fig. 4(b)). The large porous plates break up revealing many (1 μm) agglomerates after subsequent calcination at higher temperatures (Fig. 4(c)).

Figure 5 shows the variation in the surface area of the calcined gel powder with temperature. Powder surface area increases sharply with increasing temperature up to around 500°C due to the decomposition of citrate salts to porous oxide powders and the fragmentation of the larger plate-like particles (Fig. 4(a)–(c)). A maximum surface area of 10·5 m^2/g was obtained at approximately 450–500°C. Powders calcined at higher temperatures showed decreased surface area due to particle coarsening. Therefore, the optimum calcination temperature was determined to be about 500°C for citrate salts of PLZT.

3.3 Calcination and densification of resulting powder

3.3.1 Calcination of citrate salts

Mulder[9] proposed that properly dried citrate powder does not melt during calcination and hence preserves its shape. However, the morphology of the alcohol and/or freeze-dried powders (Fig. 6), calcined at 500°C in nitrogen/oxygen diluted atmosphere indicates that the spherical shape was lost during calcination. Although the alcohol/freeze-dried powder appeared fully dried and free flowing (Fig. 1(a) and (b)), it was physically observed to melt at around 90°C. The shape of the calcined alcohol/freeze dried powders and their surface areas (11 m^2/g) were similar to those obtained from gel. It was thought that the melting of alcohol/freeze-dried powders might be prevented kinetically by rapid heating of the powder above the carbon combustion temperature. Consequently, some samples were heated to 700°C in

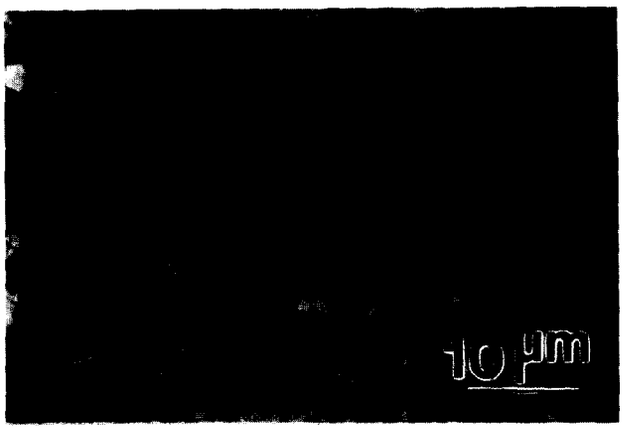


Fig. 6. SEM micrograph of calcined alcohol-dehydrated powder. A similar morphology was also observed for freeze dried powder.

less than 1 min and held for 15 min. However, the morphology of these rapidly decomposed powders was also not spherical.

3.3.2 Ceramic fabrication

After the first sintering stage, all samples were dull red, indicating the presence of excess PbO added to compensate PbO loss and to aid densification. There was no difference between the densification behaviour and final densities of the pellets prepared from alcohol/freeze dried or gel-derived powders. After the second sintering stage, pellets were pale yellow and their final densities were 97% of the theoretical density (which for this composition is 7·9 g/cm^3)[1].

Microstructures consisted of equiaxed grains (Fig. 7) with mean grain size 2·6 ± 0·2 micron. EDS analysis from various grains showed a homogeneous distribution of all elements in the microstructure. Figure 8 shows the variation of transmission percentage with wavelength. Pellets



Fig. 7. Scanning electron micrograph of thermally etched PLZT pellet made from gel-derived powder. The dense microstructure reveals equiaxed grains with mean grain size 2·6 micron. Similar densities and microstructure were observed in pellets made from powders prepared by alcohol or freeze drying.

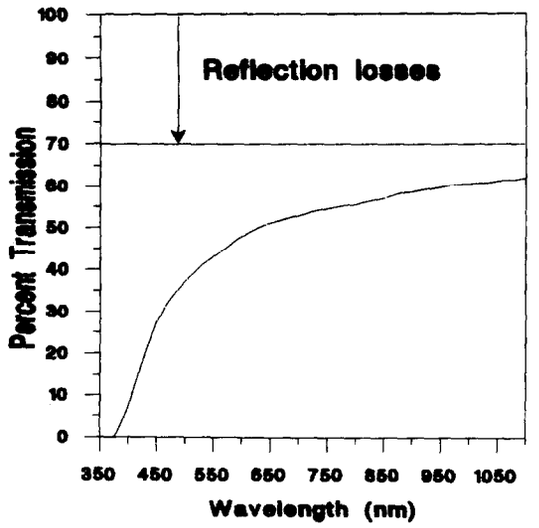


Fig. 8. Optical transmission of a 0·2 mm thick pellet. Maximum transmission was measured at 62%. This particular curve is from the gel-derived pellet with the microstructure given in Fig. 7.

prepared from precipitated or gel-derived powders had similar microstructures and the transmission reached 62% in all cases. This transmission value compares reasonably with those reported for atmosphere sintered samples.[21]

4 Conclusions

(1) PLZT composition citrate salts manufactured by freeze/alcohol drying or gelation of citrate solutions decompose in a two-step process.

(2) Crystallisation of PLZT powder is catalysed by the heat evolved on oxidation of carbon present from citrate groups, occurring at temperatures below 375°C. This is a lower temperature than comparable methods have achieved. PLZT forms directly without any intermediate phase formations.

(3) The characteristics of the PLZT powders formed in each case (alcohol/freeze-dried or gelled) are similar. Alcohol dehydrated powder, however, is expensive to produce and stoichiometry may be lost. Consequently, powders derived from citrate gel or freeze drying are preferred.

(4) Dense and fine-grained ceramics can be made from the powders and lead to high homogeneity via a two-stage sintering process.

Acknowledgements

The authors would like to thank Dr D. A. Hall (UMIST) for helpful discussions and A. Mergen for experimental assistance. This work is sponsored by the Turkish Ministry of Education in the form of a scholarship (M.A.A.).

References

1. Heartling, G. H. & Land, C. E., Hot-pressed (Pb, La) (Zr, Ti) O_3 ferroelectric ceramics for electro-optic applications. *J. Amer. Ceram. Soc.*, **54**(1) (1971) 1.
2. Heartling, G. H., Electro-optic ceramic and devices. In *Electronic ceramic, properties devices and applications*, ed. L. M. Levinson. Marcel Dekker, Inc., New York, 1988, pp. 454–81.
3. Heartling, G. H. & Land, C. E., Recent improvements in the optical and electro-optic properties of PLZT ceramics. *Ferroelectrics*, **3** (1972) 269.
4. Brown, L. M. & Mazdiyasni, K. S., Cold pressing and low temperature sintering of alkoxy-derived PLZT. *J. Amer. Ceram. Soc.*, **55** (1972) 541.
5. Thomson, J. R., Chemical preparation of PLZT powders from aqueous nitrate solutions. *Bull. Amer. Ceram. Soc.*, **53** (1974) 421.
6. Yamamura, H., Tanada, M., Haneda, H., Shiraska, S. & Mariyashi, Y., Preparation of PLZT by oxalate method in ethanol solution. *Ceramic Int.*, **11** (1985) 23.
7. Lin, W. K., Jo, M. S. & Chang, Y. H., Chemical preparation of PLZT powders by the carbonate method. *Ceramic Int.*, **14** (1988) 223.
8. Li, C. E., Ni, H. Y. & Yin, Z. W., Preparation of active powder for electronic ceramics by alcohol dehydration of citrate solutions. In *Ceramic Powders*, ed. P. Vincenzini. Elsevier Scientific Publishing Company, Amsterdam, 1983, pp. 593.
9. Mulder, B. J., Preparation of $BaTiO_3$ and other ceramic powders by co-precipitation of citrates in alcohol. *Amer. Ceram. Soc. Bull.*, **49**(11) (1970) 990.
10. Bastos, C. M. R., Jafelicci, JR. M., Varela, J. R. & Zaghette, M. A., Preparation of PZT powder from citrates. In *Ceramics Today—Tomorrow's Ceramics*, ed. P. Vincenzini. Elsevier Science Publisher B. V., 1991, pp. 1983–90.
11. Akbas, M. A. & Lee, W. E., Preparation of PLZT powder by a citrate gel technique. *Brit. Ceram. Proc.*, **52** (1994) 139.
12. Wang, H., Hall, D. A. & Sale, F. R., Phase homogeneity and segregation in PZT powders prepared by thermal decomposition of metal—EDTA complexes derived from nitrate and chloride solutions. *J. Amer. Ceram. Soc.*, **75**(1) (1992) 124.
13. Snow, G. S., Improvements in atmosphere sintering of transparent PLZT ceramics. *J. Amer. Ceram. Soc.*, **50**(9) (1973) 25.
14. Mendelson, M. I., Average grain size in polycrystalline ceramics. *J. Amer. Ceram. Soc.*, **52**(8) (1969) 443.
15. Courty, P. H., Ajot, H., Marcilly, C. & Delmon, B., Oxydes mixtes ou en solution solide sous forme tres divisee obtenus par decomposition thermique de precurseurs amorphes. *Powder Technol.*, **7** (1973) 21.
16. Anderton, D. J. & Sale, F. R., Production of conducting oxide powders by amorphous citrate process. *Pow. Metall.*, **1** (1979) 14.
17. Chandratreya, S. S., Fulrath, R. M., & Pask, J. A., Reaction mechanisms in the formation of PZT solid solutions. *J. Amer. Ceram. Soc.*, **64**(7) (1981) 422.
18. Yamaguchi, T., Cho, S. H., Hakomori, M. & Kuno, H., Effect of raw materials and mixing methods on the solid state reactions involved in fabrication of electronic ceramics. *Ceramurgia Int.*, **2**(2) (1976) 76.
19. Hiremath, B. V., Kingon, A. I. & Biggers, J. V., Reaction sequence in the formation of lead zirconate–lead titanate solid solutions: Role of raw materials. *J. Amer Ceram. Soc.*, **66** (1983) 790.
20. Duran, P. & Moure, C., High density PLZT ceramics prepared chemically from different raw materials. *Am. Ceram. Soc Bull.*, **64**(4) (1985) 575.
21. Yoshikawa, Y. & Tsuzuki, K., Fabrication of transparent lead lanthanum zirconate titanate ceramics from fine powders by two-stage sintering. *J. Amer. Ceram. Soc.*, **75**(9) (1992) 2520.
22. Keve, E. T. & Bye, K. L., Phase identification and domain structure in PLZT ceramics. *J. Appl. Phys.*, **46**(2) (1975) 810.

Journal of the European Ceramic Society **15** (1995) 65–70
© 1995 Elsevier Science Limited
Printed in Great Britain. All rights reserved
0955-2219/95/$9.50

TEM Investigation of Cordierite Crystallization from a Glass Powder with Composition $Mg_2Al_4Si_{11}O_{30}$

Wolfgang Winter,[a,*] Axel Berger,[b] Gerd Müller[b] & Wolfgang Pannhorst[c]

[a] Institut für Mineralogie, Technische Hochschule Darmstadt, Schnittspahnstr. 9, D-64287 Darmstadt, Germany
[b] Fraunhofer-Institut fur Silicatforschung, Neunerplatz 2, D-97082 Würzburg, Germany
[c] Schott Glaswerke, Hattenbergstr. 10, D-55122 Mainz, Germany

(Received 7 December 1993; revised version received 27 June 1994; accepted 29 June 1994)

Abstract

The crystallization of a glass powder with composition $Mg_2Al_4Si_{11}O_{30}$ to β-quartz$_{ss}$ and the transformation of β-quartz$_{ss}$ to α-cordierite were investigated by means of SEM and TEM. Crystallization of β-quartz$_{ss}$ starts at the surfaces of the glass grains. At first growth proceeds nearly isotropically, but due to mutual hindrance growth perpendicular to the surface is preferred when the β-quartz$_{ss}$ crystals impinge on each other. The transformation of β-quartz$_{ss}$ to cordierite starts at the surfaces of the β-quartz$_{ss}$ crystals. In a first stage the cordierite nuclei grow over long distances only along the grain boundaries of several β-quartz$_{ss}$ crystals. On prolonged annealing the cordierite rims grow dendritically into the cores of β-quartz$_{ss}$, maintaining the same crystallographic orientation.

1 Introduction

In recent years the fabrication and the properties of glass-ceramics based on cordierite ($Mg_2Al_4Si_5O_{18}$) have frequently been investigated due to the extraordinary combination of valuable properties of cordierite. The excellent electrical properties of cordierite such as high volume resistivity (≈ 3×10^{15} Ω cm) and low dielectric constant (≈ 5·3 at 1 MHz) make it a promising material, especially for integrated circuit devices.[1,2] Moreover, cordierite glass-ceramics have a low thermal expansion coefficient (1–2 × 10^{-6}/K),[3,4] matching approximately that of silicon, a high deformation temperature, high chemical durability and high mechanical strength.

The double-ring silicate MAS osumilite ($Mg_2Al_4Si_{11}O_{30}$) is another compound from the system $MgO–Al_2O_3–SiO_2$ with structural and physical properties similar to those of cordierite.[5] This phase is metastable but endures extended heat treatments up to 1150°C. The similar thermal expansion behaviour to cordierite makes MAS osumilite ($\alpha_{25-600°C}$: $1{\cdot}1 \times 10^{-6}$/K) also very interesting for glass-ceramic applications. MAS osumilite crystallizes from glasses of a narrow compositional range in the system $MgO–Al_2O_3–SiO_2$ with BaO or SrO additions. The crystallization of MAS osumilite from glass proceeds via a complex mechanism involving nucleation of precursor Ba- or Sr-containing osumilite phases and a high quartz solid solution (β-quartz$_{ss}$, $MgAl_2Si_xO_{4+2x}$) which subsequently is transformed into MAS osumilite.[6]

However, when a glass of MAS osumilite composition itself without any additions is heat treated, MAS osumilite never crystallizes under any conditions. The glass crystallizes only to β-quartz$_{ss}$ and, at higher temperatures, the thermodynamically stable phases cordierite and α-quartz or cristobalite.

Depending on the glass composition, the sintering additives, nucleating agents and the crystallization temperature the crystallization sequence of cordierite-type glass powders and the microstructural development differ considerably.[7–11] The devitrification process of TiO_2- and ZrO_2-containing cordierite glasses usually involves phase separation in the liquid state. At low temperatures β-quartz$_{ss}$ always appears as a metastable precursor which transforms into cordierite after prolonged heating. At higher temperatures above about 1000–1200°C no β-quartz$_{ss}$ appears and cordierite crystallizes directly from the glass.

The morphology of the initial β-quartz$_{ss}$ varies greatly. In a sintered glass-ceramic with greater MgO and lower Al_2O_3 than stoichiometric

* Present address: Laboratoire de Science des Matériaux Vitreux, Université Montpellier II, 34095 Montpellier, France.

cordierite with additions of P_2O_5 and B_2O_3 Bridge *et al.*[1] found roughly spherical crystals concentrating at the original boundaries of the glass particles. Rudolph *et al.*[12] examined a glass with a similar basic composition but without B_2O_3. They report a β-quartz$_{ss}$ skeleton forming along the original particle surfaces. In this thin β-quartz$_{ss}$ layer individual crystals could not be identified. Similar β-quartz$_{ss}$ boundary layers together with co-precipitated spherulitic ZrO_2 were observed by McCoy & Heuer[13] in a glass of similar composition containing 15 wt% ZrO_2. However, the ZrO_2 crystallites did not act as nucleation sites for the β-quartz$_{ss}$ crystals. In bulk glasses containing more SiO_2 and additions of ZrO_2, TiO_2 or CaF_2 Zdaniewski[8] observed spherulitic growth of β-quartz$_{ss}$.

Chaim & Heuer[14] studied the crystallization sequence of a glass with stoichiometric cordierite composition and an addition of 2 wt% BaO. In this glass the crystallizing β-quartz$_{ss}$ had a dendritic hexagonal morphology. BaO was rejected from the growing β-quartz$_{ss}$ and concentrated in an interdendritic amorphous phase. On the other hand, in the crystallization sequence of an MAS osumilite glass-ceramic from a similar BaO-containing glass but with higher SiO_2 content Winter *et al.*[6] found rounded and elongated non-dendritic β-quartz$_{ss}$ crystals nucleating at the original particle surfaces and growing perpendicular to the surfaces into the cores of the glass grains. BaO was rejected into an intergranular residual glass phase.

The microstructural evolution of a glass-ceramic during the transformation of β-quartz$_{ss}$ to cordierite and the mechanism of this process have been investigated by several authors. Watanabe *et al.*[15] described the variations in morphology of cordierite crystallizing both from β-quartz$_{ss}$ or directly from the glass as a function of crystallization temperature. Barry *et al.*[16] investigated the bulk crystallization of glasses of stoichiometric cordierite composition with various amounts of TiO_2 and ZrO_2. With increasing temperature these authors observed continuous exsolution of MgO and Al_2O_3 from β-quartz$_{ss}$ and formation of spinel and sapphirine. At temperatures above 1150°C the remaining SiO_2-rich β-quartz$_{ss}$ reacts with the exsolution products to form cordierite. Chaim & Heuer[14] showed that in BaO-containing compositions cordierite nucleates within the dendritic β-quartz$_{ss}$ grains or at the β-quartz$_{ss}$/glass interfaces. The morphology of cordierite also is dendritic and growth proceeds preferentially within the β-quartz$_{ss}$ grains.

The present paper presents a detailed study of the crystallization mechanism in a glass of composition $Mg_2Al_4Si_{11}O_{30}$ without any additives. The focus was mainly on the nucleation of cordierite and the transformation of the precursor phase β-quartz$_{ss}$ into cordierite. As already reported, the mechanisms of these processes are supposed to depend critically on the composition and the morphology of β-quartz$_{ss}$ and hence on the composition of the parent glass. In particular, an understanding of the present crystallization mechanism might also explain why MAS osumilite does not crystallize although the glass investigated is of MAS osumilite composition.

2 Experimental Details

The glass investigated has the composition of MAS osumilite ($Mg_2Al_4Si_{11}O_{30}$) (in wt%: 8·5 MgO; 21·6, Al_2O_3; 69·9 SiO_2). Stoichiometrically, this composition can be described as a mixture of 61·8% cordierite and 38·2% SiO_2.

A homogeneous glass was prepared from reagent grade Al_2O_3 and MgO from Merck AG (Darmstadt, Germany) and SiO_2 (Sipur, Bremthaler Quarzwerke, Usingen, Germany) by melting the constituents at 1550°C for 4 h in platinum crucibles and quenching the melt into cold water. After grinding the glass frit in an alumina ball mill to a grain size <63 μm samples for the crystallization process were cold-isostatically pressed. The 10 × 4 × 4 mm sized samples were put into a preheated furnace and crystallized isothermally at a temperature of 1150°C and various heating times.

The nucleation and crystallization sequence of the glass powder was studied by means of SEM and TEM.

For TEM preparation the crystallized samples were cut into thin sections which were ion thinned with a 5 kV argon beam. The TEM analyses were performed on a Philips CM12 microscope (Philips, Eindhoven, The Netherlands) equipped with an EDAX 9900 EDX device. Polished and HF-etched samples were studied with a Philips SEM500 scanning electron microscope.

3 Results

The first phase appearing in the crystallization sequence is β-quartz$_{ss}$ nucleating at the surfaces of the glass grains. Growth proceeds isotropically in a first stage, but due to mutual hindrance further growth proceeds preferentially perpendicular to the surface into the volume of the glass grains. Figure 1 shows a typical microstructure of an early growth stage with slightly elongated β-quartz$_{ss}$ crystals growing from the surface into the residual glass at the centre of the glass grain.

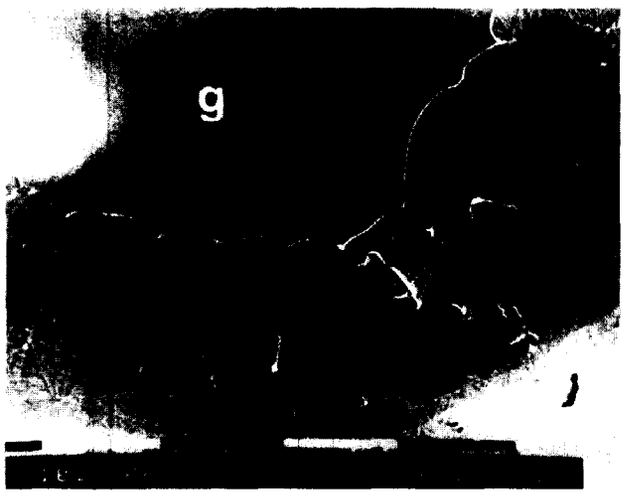


Fig. 1. SEM micrograph of several elongated β-quartz$_{ss}$ crystals growing from the surface (bottom) into the centre of a glass grain (g). Heat treatment: 1150°C, 2 min.

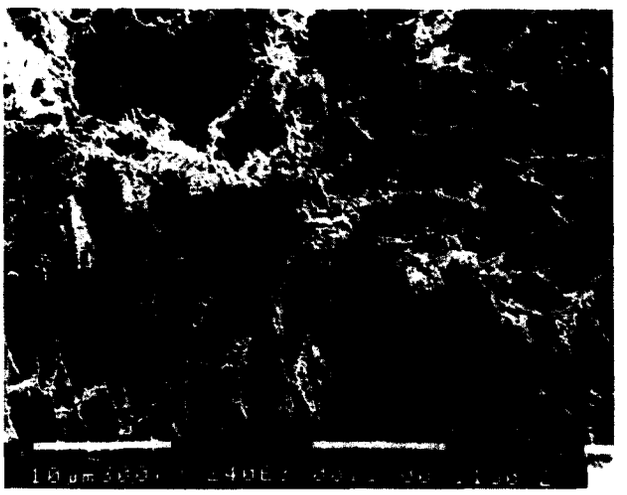


Fig. 3. SEM micrograph of the cordierite network (bright areas) around the β-quartz$_{ss}$ grains (dark areas) in the centre of a former glass grain. Heat treatment: 1150°C, 10 min.

EDX analysis confirmed that the composition of the β-quartz$_{ss}$ crystals corresponds to that of the parent glass which has the theoretical composition of the starting mixture. No residual glass phase could be found on the grain boundaries between adjacent β-quartz$_{ss}$ crystals by means of TEM (Fig. 2). EDX measurements suggest that the chemical composition is homogeneous within one β-quartz$_{ss}$ crystal and within the whole sample.

The transformation of β-quartz$_{ss}$ to α-cordierite starts at the grain boundaries of the β-quartz$_{ss}$ crystals. In a first stage the cordierite nuclei always grow along β-quartz$_{ss}$ grain boundaries. Figure 3 shows a typical cordierite network around the β-quartz$_{ss}$ crystals in the centre of a former glass grain. TEM diffraction analysis shows that this network typically consists of cordierite crystals forming rims of the same orientation over large areas and surrounding numerous β-quartz$_{ss}$ grains. Figure 4 shows an example with cordierite in an $[0\bar{2}1]$ orientation. Only a slight rotation around the $[0\bar{2}1]$ zone axis is observed during growth over about 4 μm along the grain boundaries of several adjacent β-quartz$_{ss}$ grains.

The dark field photograph of another locality of the sample shows that the cordierite rims along the β-quartz$_{ss}$ grain boundaries have a dendritic spinal-type microstructure with an interspatial amorphous phase (Fig. 5). The volume of this phase is too small for an EDX analysis but as the β-quartz$_{ss}$ crystals are much richer in SiO_2 than cordierite a second phase with a relatively high SiO_2 concentration must be formed during the β-quartz$_{ss}$ to cordierite transformation.

Starting from the β-quartz$_{ss}$ grain boundaries the cordierite rims begin to grow into adjacent β-quartz$_{ss}$ grains. Frequently, preferred growth planes of cordierite are observed. The bright and dark field photographs of Fig. 6 show a cordierite crystal with pronounced lamellar growth along (100) planes. These growth planes are preferred probably due to their high atom occupancy. It was frequently observed that starting from the same cordierite rim crystal the (100) planes grow into different β-quartz$_{ss}$ crystals without changing

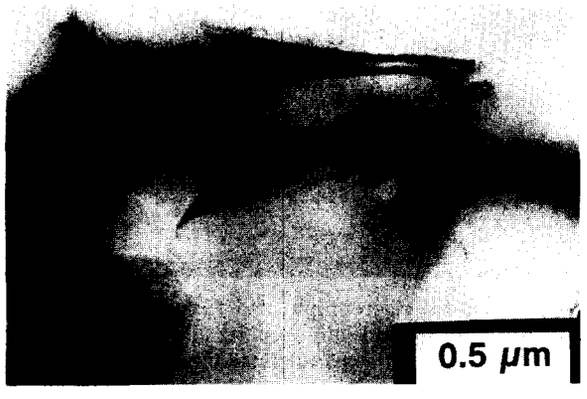


Fig. 2. TEM micrograph of grain boundaries between β-quartz$_{ss}$ crystals. Heat treatment: 1150°C, 2 min.



Fig. 4. TEM BF micrograph of the first stage of cordierite growth along grain boundaries of several β-quartz$_{ss}$ grains. Heat treatment: 1150°C, 60 min.



Fig. 5. TEM (100) DF micrograph of the spinal morphology of the cordierite rims on the β-quartz$_{ss}$ grain boundaries. Heat treatment: 1150°C, 60 min.



Fig. 7. BF micrograph of the dendritic growth of cordierite in a highly transformed β-quartz$_{ss}$ crystal. Orientation of cordierite is [001] parallel to the electron beam. {100} faces are preferentially formed. Heat treatment: 1150°C, 60 min.

their orientation. This suggests that the transformation does not proceed along distinct directions of the β-quartz$_{ss}$ structure. Hence, it is not of a topotactic nature. The orientation of cordierite growth within a β-quartz$_{ss}$ crystal depends only on the orientation of the cordierite seed crystals.

In Fig. 7 a β-quartz$_{ss}$ grain is penetrated completely by a cordierite dendrite in a more advanced stage of the transformation process. The cordierite crystal maintains its orientation over the whole former β-quartz$_{ss}$ grain with the [001] zone axis parallel to the electron beam as can be seen from electron diffraction (SAD). This orientation shows, that preferentially hexagonal prismatic {100} planes are formed. Since the transformation of β-quartz$_{ss}$ into cordierite is not an isochemical reaction again an SiO_2-rich amorphous phase develops within the cordierite dendrites.

After about 3 h at 1150°C, the amorphous SiO_2-rich phase between the cordierite dendrites has crystallized to β-quartz. The α-quartz crystals can reach the size of a former β-quartz$_{ss}$ grain, show-

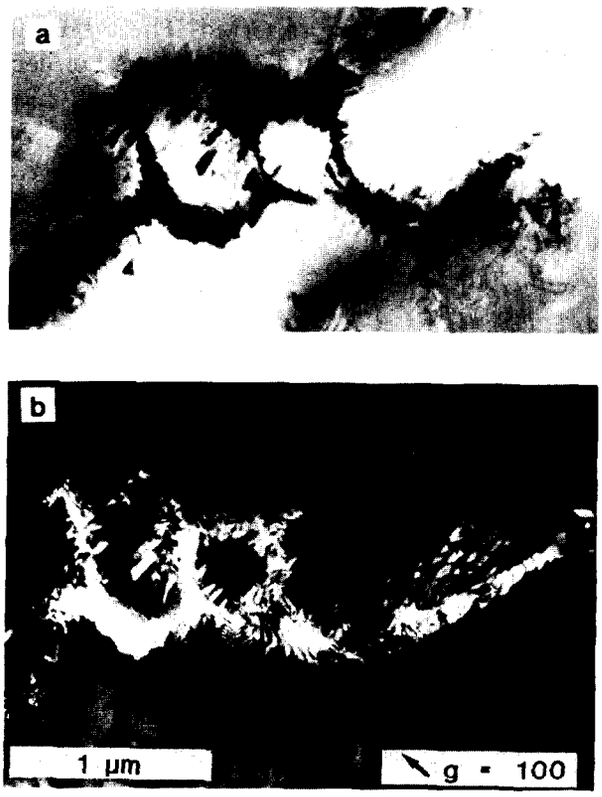


Fig. 6. (a) TEM BF micrograph, (b) TEM (100) DF micrograph of the preferred growth of cordierite along (100) planes into neighbouring β-quartz$_{ss}$ grains. Heat treatment: 1150°C, 60 min.

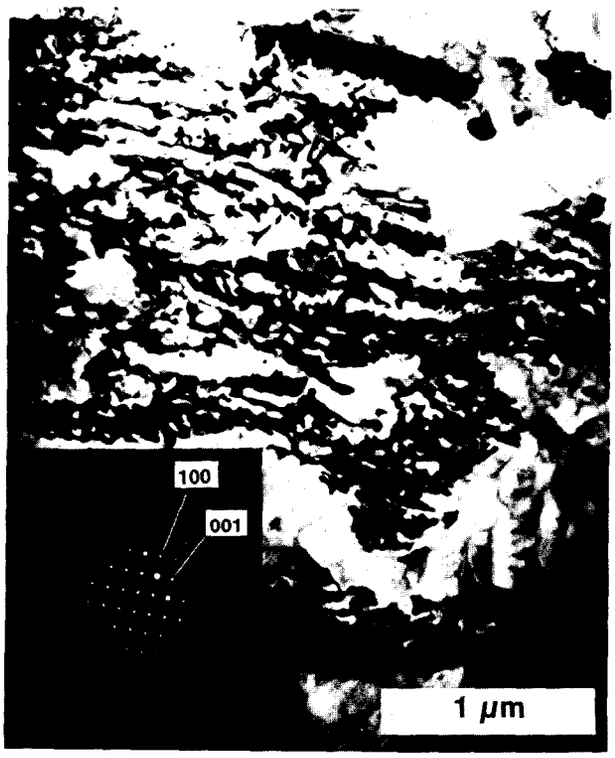


Fig. 8. TEM BF micrograph of a former β-quartz$_{ss}$ crystal completely transformed into α-quartz and cordierite. α-Quartz with orientation [0$\bar{1}$0] parallel to the electron beam. The forbidden reflections 00l with l = 3 result from dynamical interaction of h00 and h0l reflections. Heat treatment: 1150°C, 60 min.

ing a dendritic morphology that is finely interlaced with the cordierite dendrites (Fig. 8).

4 Discussion

In the crystallization sequence of the studied glass MAS osumilite did not appear, although the glass is of MAS osumilite composition ($Mg_2Al_4Si_{11}O_{30}$). This is in accordance with previous results about MAS-osumilite crystallization from BaO containing glasses[5,6] and can be explained in terms of the nucleation kinetics of the crystallizing phases. For the formation of MAS osumilite pre-crystallization of a stable osumilite-type phase such as Ba osumilite ($BaMg_2Al_6Si_9O_{30}$) is necessary on which it can nucleate epitactically. Even then MAS osumilite nucleation competes with the simultaneous epitactic nucleation of cordierite on Ba osumilite. However, the nucleation rate of MAS osumilite is higher than that of cordierite in this case. In a pure MAS osumilite glass the formation of a stable osumilite-type phase is not possible. Cordierite, on the other hand, can nucleate at the interfaces between the β-quartz$_{ss}$ crystals, but although the crystal structures are similar, cordierite does not supply suitable surfaces for epitactic nucleation of MAS osumilite. One reason for this is that the cordierite surfaces are enriched in SiO_2 and hence no longer of the MAS osumilite composition.

The second interesting observation concerns the differences in the growth morphologies between β-quartz$_{ss}$ and cordierite. The nucleation of both phases is interface induced. The interfaces of the glass grains and of the β-quartz$_{ss}$ crystals, respectively, represent the nucleation sites for β-quartz$_{ss}$ and cordierite.

Metastable β-quartz$_{ss}$ nucleates first, possibly because it has a closer relation with the glass structure than α-cordierite. In a first stage the growth of β-quartz$_{ss}$ is isotropic. When neighbouring crystals impinge on each other further growth is only possible perpendicular to the surface of the glass grains into their core and the β-quartz$_{ss}$ crystals become more elongated.

On the other hand, the first nucleating cordierite crystals show a preferred growth along the β-quartz$_{ss}$ surfaces. Thus, the β-quartz$_{ss}$ crystals are characterized by an isotropic three-dimensional growth while the first nucleating cordierite crystals show only two-dimensional growth. The differences in crystal growth morphology and orientation are supposed to depend on the transformation kinetics of the glass to β-quartz$_{ss}$ and the β-quartz$_{ss}$ to cordierite transformation, respectively. The decisive difference in the crystallization of β-quartz$_{ss}$ and cordierite in the present glass lies in the different chemical compositions. The glass to β-quartz$_{ss}$ transformation proceeds isochemically, whereas the β-quartz$_{ss}$ to cordierite transformation is of an allochemical nature. Hence, the latter process is diffusion controlled. Grain boundaries generally represent a defective crystal structure of a higher energy state than the perfect crystal. Hence, crystallization and growth of cordierite along the β-quartz$_{ss}$ grain boundaries provides both a fast reduction of stored energy and effective diffusion paths. The present results show that this leads to fast two-dimensional growth. Obviously, the growth rate of cordierite along the grain boundaries is very high in comparison to the nucleation rate. During growth into the cores of the β-quartz$_{ss}$ grains the diffusion rate probably limits the growth rate of cordierite. The necessity for the cordierite crystals to pierce through a simultaneously rejected SiO_2-rich layer during growth results in the formation of a dendritic morphology.

5 Conclusion

The present results suggest that in general the nucleation and growth kinetics and the morphology of cordierite during the β-quartz$_{ss}$ to cordierite transformation depend critically on the morphology and chemical composition of the β-quartz$_{ss}$ crystals. In the present case of diffusion-controlled cordierite crystallization from β-quartz$_{ss}$ of a different chemical composition two stages can be distinguished:

(i) fast two-dimensional growth along the β-quartz$_{ss}$ grain boundaries leads to formation of a cordierite network with relatively large areas of the same crystallographic orientation.

(ii) cordierite growth proceeds dendritically into the bulk of the β-quartz$_{ss}$ grains. Quartz crystallizes within the SiO_2-rich dendritical interspaces.

References

1. Bridge, D. R., Holland, D. & McMillan, P. W., Development of the alpha-cordierite phase in glass-ceramics for use in electronic devices. *Glass Technology*, **26**(6) (1985) 286–92.
2. Owate, I. O. & Freer, R., Electrical properties of some cordierite glass-ceramics in the system MgO–Al_2O_3–SiO_2–TiO_2. *J. Mater. Sci.*, **25**(12) (1990) 5291–7.
3. Lachman, I. M., Bagley, R. D. & Lewis, R. M., Thermal expansion of extruded cordierite ceramics. *Am. Ceram. Soc. Bull.*, **60**(2) (1981) 202–5.
4. Hirose, Y., Doi, H. & Kamigaito, O., Thermal expansion of hot-pressed cordierite glass-ceramics. *J. Mater. Sci Lett.*, **3**(2) (1984) 153–5.

5. Winter, W., Bogdanow, C., Müller, G. & Pannhorst, W., Crystallization sequence of Ba-osumilite and MAS-osumilite glass-ceramics with low thermal expansion. *Glastech. Ber.*, **66**(5) (1993) 109–17.
6. Winter, W., Berger, A., Müller, G. & Pannhorst, W., Crystallization mechanism of an MAS–osumilite with composition $Mg_2Al_4Si_{11}O_{30}$ from glass. *J. Am. Ceram. Soc.*, **76**(7) (1993) 1837–43.
7. Zdaniewski, W., Crystallization and structure of a MgO–Al_2O_3–SiO_2–TiO_2 glass-ceramic. *J. Mater. Sci.*, **8** (1973) 192–202.
8. Zdaniewski, W., Microstructure and kinetics of crystallization of MgO–Al_2O_3–SiO_2 glass-ceramics. *J. Am. Ceram. Soc.*, **61**(5–6) (1978) 199–204.
9. McCoy, M., Lee, W. E. & Heuer, A. H., Crystallization of MgO–Al_2O_3–SiO_2–ZrO_2 glasses. *J. Am. Ceram. Soc.*, **69**(3) (1986) 292–6.
10. Sue, Y. J., Shen, P., Chen, S. Y. & Lu, H. Y., Spherulitic growth from a phase-separated vitreous matrix in a cordierite-Y-stabilized zirconia glass-ceramic. *J. Am. Ceram. Soc.*, **74**(1) (1991) 85–91.
11. Lim, B. C. & Jang, H. M., Phase transformation in seeded monophasic cordierite gel. *Ceram. Trans.*, **22** (1991) 431–6.
12. Rudolph, T., Szabo, D. V., Pannhorst, W., Weisskopf, K. L. & Petzow, G., Microstructural development of a P_2O_5-modified cordierite glass ceramic during sintering. *Glastech. Ber.*, **64**(8) (1991) 218–24.
13. McCoy, M. A. & Heuer, A. H., Microstructural characterization and fracture toughness of cordierite–ZrO_2 glass-ceramics. *J. Am. Ceram. Soc.*, **71**(8) (1988) 673–7.
14. Chaim, R. & Heuer, A. H., Crystallization in a Ba-containing magnesium aluminosilicate glass-ceramic. *J. Am. Ceram. Soc.*, **75**(6) (1992) 1512–21.
15. Watanabe, K., Giess, E. A. & Shafer, M. W., The crystallization mechanism of high-cordierite glass. *J. Mater. Sci.*, **20** (1985) 508–15.
16. Barry, T. I., Cox, J. M. & Morrell, R., Cordierite glass-ceramics—effect of TiO_2 and ZrO_2 content on phase sequence during heat treatment. *J. Mater. Sci.*, **13** (1978) 594–610.

Journal of the European Ceramic Society **15** (1995) 71–80
© 1995 Elsevier Science Limited
Printed in Great Britain. All rights reserved
0955-2219/95/$9.50

Morphological Characterization of Hot-pressed α-SiC with Al-based Additives Deformed by Compression at High Temperature

M. L. Duval-Riviere,[a] M. Coster,[a] L. Chermant,[a] J. Vicens[a] & C. Carry[b]

[a] Lermat, URA CNRS 1317, ISMRA, 6 Bd du Maréchal Juin, 14050 Caen Cedex, France
[b] ISMA, Université Paris-Sud, Orsay, France

(Received 22 January 1994; revised version received 15 June 1994; accepted 28 June 1994)

Abstract

An automatic image analysis method has been used to study the microstructure evolution of polycrystalline α-SiC samples hot pressed with 0·3 wt% and 1·5 wt% Al-based additives after compression at high temperature. Microstructures have been characterized in terms of grain shape, grain size and grain orientation with respect to the macroscopic stress direction. It has been shown that grains tend to flatten perpendicularly to the external stress for the 0·3 wt% Al grade. By contrast, for the same macroscopic deformation value, grains of the 1·5 wt% Al grade do not exhibit any shape change after creep tests, suggesting that a certain amount of superplastic deformation has occurred.

1 Introduction

Among the thermomechanical ceramics, polycrystalline ceramics based on silicon carbide have been one of the primary candidate ceramic materials for use in structural applications at high temperature. Consequently many studies have been devoted to their mechanical behaviour in a wide range of stress and temperature.[1–16] However, many experiments were conducted in a temperature range not exceeding 1600–1700°C and/or with bending as the preferred mode of testing, so that overall strains of a few percent were reached.[1–7] In most cases, high-temperature creep in polycrystalline SiC has been interpreted in terms of diffusional atomic flow rather than in terms of dislocation glide even if a parallel dislocation glide mechanism can contribute to the total strain.[1–7] However, experiments conducted on SiC single crystals have shown that plastic strain was due to dislocation glide motion on the basal slip system and was controlled by a Peierls mechanism.[15,16] The same mechanism was found in CVD SiC deformed between 1400–1600°C.[10]

During the high-temperature thermomechanical treatments, a modification of the microstructure of the material can occur,depending on the experimental conditions as well as on the mechanism inducing the deformation. For example, grain shape modification is generally observed for dislocation and diffusional creep[17] but not during superplastic creep.[18] The change of the microstructure is usually investigated by means of image analysis methods. In SiC materials these methods were used in a few cases to characterize grain sizes and grain shapes before and after deformation.[11,12]

On the other hand, compressive tests of different grades of α-SiC sintered with Al-based additives were carried out by Carry & Mocellin beyond 1800°C in compression so that, in contrast to the preceding studies,[1–7] higher strain values could be reached (0·43) without cavitation.[8]

The aim of this work is to characterize by using image analysis methods the microstructural evolution of the α-SiC materials creep tested in conditions given in Ref. 8. Grain size and grain shape evolutions have been determined for the two grades containing 0·3 wt% Al and 1·5 wt% Al compressed at different stress values in a temperature range 1850–1950°C. The present study is a part of a more general microstructural investigation performed on several crept polycrystalline SiC materials taking into account creep parameters.

2 Materials and procedure

Two grades of commercial hot-pressed Al-doped α-SiC (Elektroschmelzwerk Company, Kempten,

Table 1. Annealing and creep parameters (following the data of Carry & Mocellin[8])

Sample numbers	*T(°C)*	*σ(MPa)*	*t(min)*	*$\|\varepsilon_f\|$*	*⟨L⟩ (μm) ± 0·2*	*$\sqrt{\bar{s}}$*	*e*	*d_1/d_2 (± 0·05)*	*$\langle L_\parallel\rangle/\langle L_\perp\rangle$*	*α(°)*
As-sintered (0·3 wt%)	—	—	—	—	—	2	—	—	0.83	—
1	1900	—	420	—	3·01	—	0·40	0·92	—	26
2	1900	45–55	420	0·250	2·86	—	0·68	0·73	—	4
				—	2·58	—	0·30	0·95	—	23
3	1950	—	395	—	—	2·50	—	—	0·90	—
	1950	45–55	395	0·428	3·12	—	0·79	0·61	—	1·5
					—	2·70	—	—	0·60	—
4 $\sigma_\parallel$	1950	45–55	395	0·428	2·32	—	0·44	0·90	—	68
4 $\sigma_\perp$										
As-sintered (1·5 wt%)	—	—	—	—	—	1·1	—	—	0·71	—
5	1900	—	200	—	1·71	—	0·72	0·69	—	77
6	1900	44–52	200	0·274	1·55	—	0·74	0·67	—	73
					—	1·60	—	—	0·70	—
7	1900	88–102	95	0·430	1·45	—	0·70	0·71	—	76
8	1850	—	147	—	—	1·3	—	—	0·90	—
9	1850	88–102	147	0·26	—	1·3	—	—	0·80	—

Results of global analysis for annealed and deformed samples are given. Mean intercept length $\langle L\rangle$, eccentricity e, d_1d_2 ratios and α are displayed for several samples.
Results obtained by the classical intercept method are also given. The mean grain size $\sqrt{\bar{s}}$ and $\langle L_\parallel\rangle/\langle L_\perp\rangle$ ratios are displayed for several samples and should be compared to $\langle L\rangle$ and d_1/d_2 ratios respectively when results are displayed for the two methods.

Germany) have been crept by compression between 1850–1950°C. Aluminium levels were 0·3 wt% and 1·5 wt%. Test samples for creep experiments were obtained by diamond cutting and machining from the as-received discs (75 mm diameter by 25 mm height). Relative positions and orientations of samples inside the original discs were recorded. Indeed, structural and chemical composition variations might be expected between the core and the outer surfaces. Results of the present work have been focused on samples located in the core of the original discs. Samples for creep experiments with dimensions $a \times a \times 3a$ ($8{\cdot}7 < a < 13$ mm) were used and smaller pieces were also cut to serve as reference samples. They were heated with the piece being creep tested. Annealing and creep parameters are given in Table 1, according to the data reported in Ref. 8. Moreover, metallographic sections, which were studied by image analysis methods, were chosen in the middle part of the high-temperature deformed specimens.

3 Image Analysis Method

Automatic image analysis was used to obtain quantitative information on the microstructure of SiC samples. Metallographic sections containing the compressive and/or the hot-pressing directions were etched by the Murakami solution (NaOH + $[Fe(CN)_6]K_3$). Then optical (Olympus BH2) and SEM micrographs (Jeol JSM T330 A) were analysed by using a texture analyser Nachet Microcontrole NS1500.

For this work, two types of morphological data are necessary: the grain size and the grain anisotropy characterized by orientation and shape indices. Before measurements, the video image was thresholded to obtain a binary image (using a top hat transformation). Then binary images were filtered by morphological and geodesical opening. This is followed by a skeletonization by influence zone denoted SKIZ.[19,20] In these conditions, white pixels belong to SiC grains and black pixels to grain boundaries. After SKIZ, the grain boundary thickness was reduced to a thickness of one pixel. After this image processing two types of analyses were used. In the first case, measurements were performed on the binary image itself (global analysis). In the second case, each grain totally included in the image field was separately measured (individual analysis).

For global analysis several parameters have to be chosen. Parameters corresponding to the grain size are obtained by mean intercept measurements by unit length denoted N_L. If V_v is the volumic ratio of the additive phase, the mean grain size $\langle L\rangle$ is given by $(1 - V_v)/N_L$, or $1/N_L$ when the intergranular phase content is negligible. Since a hexagonal lattice of pixels is used in our texture analyser NS1500, the modelization of the grain anisotropy is realized by using an equivalent ellipse associated with the grains. An algorithm given by Serra[20] allows the associated ellipse to be defined by means of parameters which have been indicated in Fig. 1. The minor and the major axes of the ellipse denoted d_1 and d_2 are related to the eccentricity value e of the ellipse following the

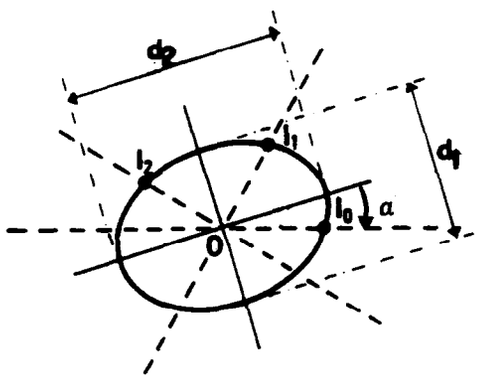


Fig. 1. Equivalent ellipse associated to the grains with its parameters.

relation:

$$e = \sqrt{1 - \frac{d_1^2}{d_2^2}} \tag{1}$$

The angle α is related to the orientation of the major axis d_2 with respect to a reference direction.

Because measurements are made in a hexagonal lattice of pixels, three intercept values N_L are determined in the three main directions (0, $\pi/3$, $2\pi/3$) (Fig. 1). Then a conic can be drawn passing through I_0, I_1 and I_2 (denoted in Fig. 1). I_0, I_1 and I_2 are expressed in a polar coordinate system. In the present case an elliptic model is always obtained.

The same type of parameters (grain size $\langle L \rangle$, eccentricity e and orientation α) have been determined by individual image analysis methods. Results are displayed either by cumulative or frequency distributions. The grain size d is given by the equivalent diameter of the surface area of each grain. The equivalent ellipse of each grain is obtained by the same algorithm as the global analysis method by using a hexagonal convex hull of each grain in order to minimize the noise of grain boundaries. By individual analysis it is possible to draw grain size and angle distributions. This information may be different from the previous one obtained by global analysis since, for example, anisotropic grains can give an isotropic texture if the grains are distributed in all directions.

This last point is illustrated in the schematic representation of Fig. 2 where anisotropic grains have been randomly orientated in Fig. 2(a). By contrast, anisotropic grains have been drawn in a preferential orientation in Fig. 2(b). In both cases (Fig. 2(a) and (b)) the individual analysis method does indicate that grains have an anisotropic shape. However, by global analysis, examples of Fig. 2(a) and (b) will be found to be isotropic and anisotropic respectively.

In parallel to this automatic method, other metallographic sections of several samples were also analysed by a classical intercept method. In this last method only average section area $\bar{s}$ and intercept values in two perpendicular directions related to the hot-pressing direction P or to the compressive stress σ are measured. Thus this method gives only two morphological parameters: the mean grain size $\sqrt{\bar{s}}$ and $\langle L_{\parallel} \rangle / \langle L_{\perp} \rangle$ ratios.

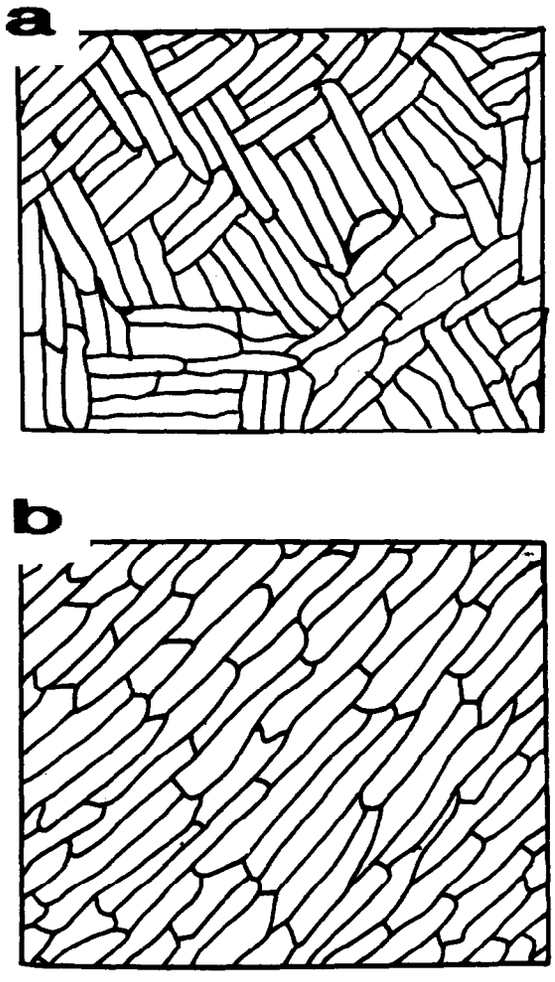


Fig. 2. Schematic representation of (a) anisotropic grains and isotropic structure; (b) anisotropic grains and anisotropic structure.

4 Results and Discussion

All specimens analysed are listed in Table 1. Two grades of SiC-Al additives samples are reported. For each grade, the as-sintered and two or three annealed samples with their deformed states have been studied. So this group is considered to be representative for the study of microstructural modifications occurring during these five creep experiments performed in a very short range of temperatures and stresses. Moreover, as shown in Table 1, results obtained from the automatic and the classical intercept methods are reported for several samples.

In Section 4.1 the main microstructural evolution is described from optical or SEM micrographs of each sample.

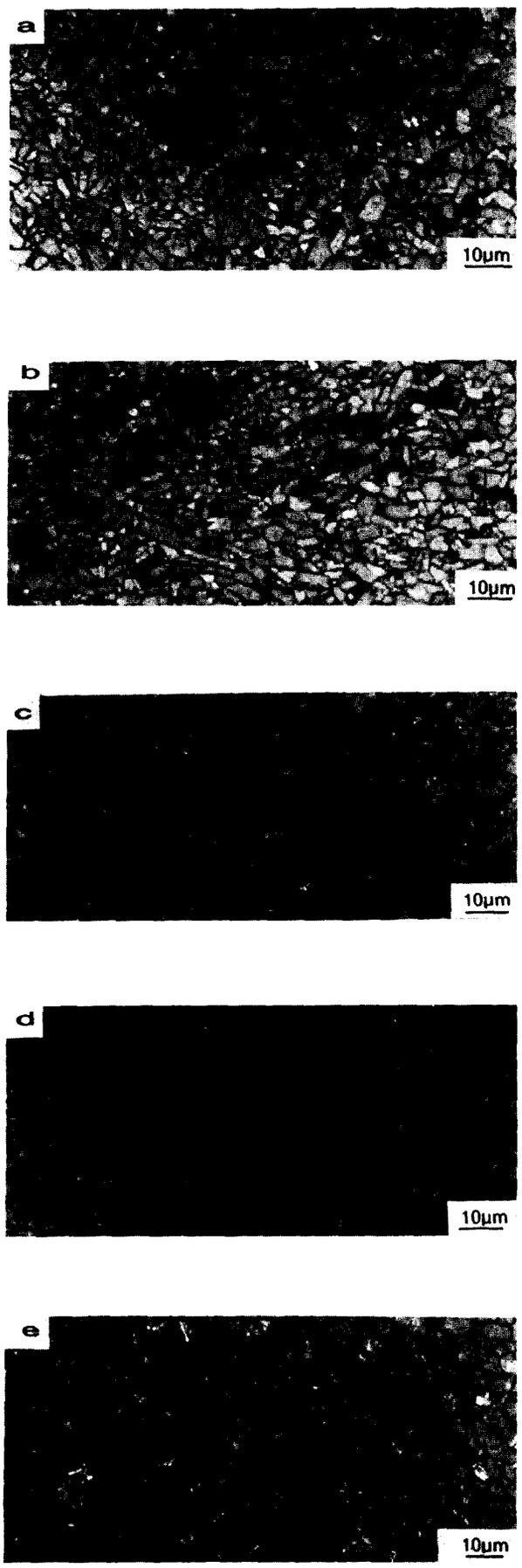


Fig. 3. Optical micrographs of the 0·3 wt% grade. (a) Sample 1 annealed at 1900°C. P is the direction of the stress acting during the sintering. (b) Sample 2 deformed with an overall strain ε_f = 0·25. The direction of the compressive stress σ is indicated. (c) Sample 3 annealed at 1950°C. (d) Sample 4 deformed with an overall strain ε_f = 0·428. (e) Same sample as in (d) but shown perpendicularly to the external stress σ.

4.1 Qualitative analyses of annealed or deformed specimens

4.1.1 Al grade (0·3 wt%)

Optical micrographs of the 0·3 wt.% Al grade are presented in Fig. 3. The two reference states (1 and 3) with their corresponding deformed specimens (2 and 4) are shown in Fig. 3(a) to (e). The hot-pressing stress direction P as well as the compressive stress direction σ have been indicated on each micrograph. Metallographic sections of deformed specimens contain the compressive stress direction σ. Moreover, a metallographic section perpendicular to σ is also given for the sample 4 (Fig. 3(e)). These optical micrographs are good enough to visualize all grain boundaries. However, in order to increase the contrast, it has been necessary to draw in dark ink all grain boundaries being acquired. The dark pockets which can be seen on these micrographs are likely to be due to the presence of the additives used during the sintering process.

In all deformed specimens, no significant grain growth could be detected by comparison with annealed samples. It appears that grains have a tendency to flatten in a direction perpendicular to the external stress σ after the compressive test (Fig. 3(b) and (d)). This is quite clear for sample 4 (Fig. 3(d)) which has the highest strain value (0·43). For the same sample the section cut perpendicularly to σ (Fig. 3(e)) shows grains with a quasi-equiaxed shape. This indicates that grains viewed in a cross-section containing σ can be probably described by an elliptic shape. Thus the large axis is located in a plane normal to σ. By contrast, no preferential orientation of the grains with respect to P is clearly visible in the reference state 3 (Fig. 3(c)). However, grains appear slightly elongated in a direction perpendicular to P (sample 1, Fig. 3(a)).

4.1.2. Al grade (1·5 wt.%)

For this grade the optical method was not suitable because the grain size is twice as small as the grain size of the 0·3 wt.% Al grade. Thus the SEM method was chosen. Micrographs of samples 5, 6 and 7 are given in Fig. 4(a)–(c). The reference state (5) is displayed in Fig. 4(a) and the two deformed samples (6 and 7) in Fig. 4(b) and (c).

Compared to the other grade (0.3 wt.%), it seems that no grain shape modification has appeared in the two deformed samples even for sample 6 which has a high strain value (0·43) and has been deformed under 88–102 MPa.

4.2 Image analysis results

Qualitative results displayed in Section 4.1 have been quantified either by global or individual image analysis.

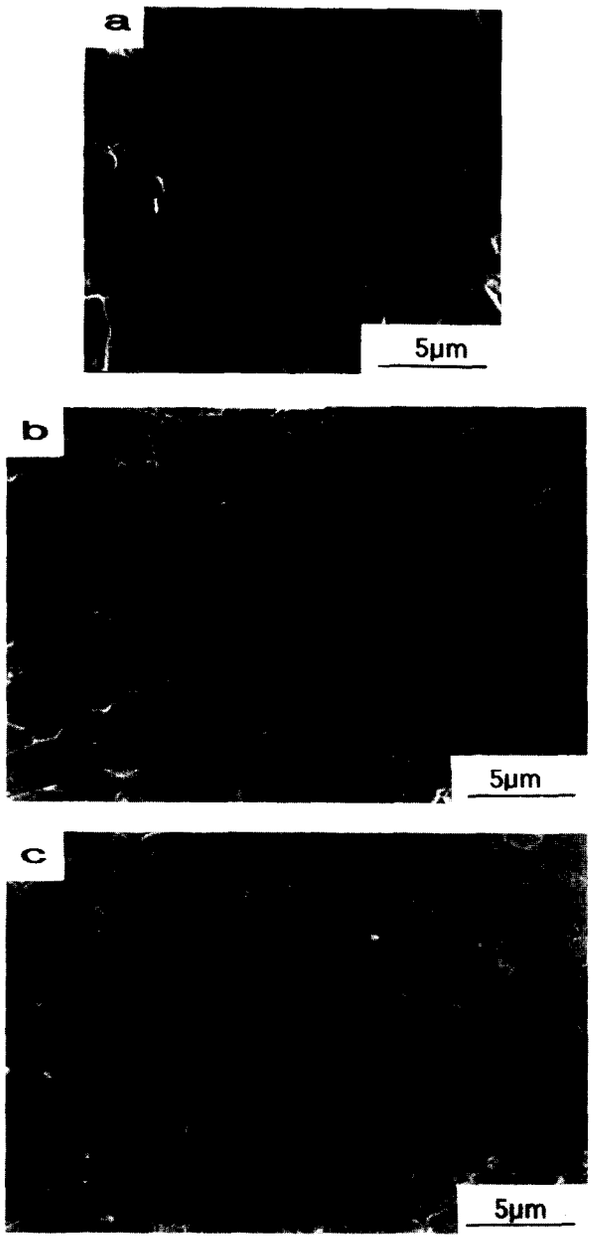


Fig. 4. SEM micrographs of the 1·5 wt% grade. (a) Sample 5 annealed at 1900°C. (b) Sample 6 deformed with an overall strain ε_f = 0·274. (c) Sample 7 deformed with an overall strain ε_f = 0·43. P and σ stress directions have been indicated on each micrograph.

4.2.1 Global analysis

Due to the two different techniques used in this work, i.e. optical and SEM, the number of analysed grains is more than 1500 for the 0·3 wt% grade and about 800 for the 1·5 wt% grade, which is enough to obtain quantitative data. Results of global and classical intercept analyses are in good agreement if $\langle L \rangle$ and d_1/d_2 ratios (global analysis) are compared with $\sqrt{s}$ and $\langle L_\parallel \rangle / \langle L_\perp \rangle$ ratios (classical intercept method) respectively (Table 1).

4.2.1.1 Al grade (0·3 wt.%). The mean grain size value is equal to ~3 μm and a very slight grain growth is observed for sample 4 (3·12 μm) compared to its reference state, sample 3 (2·58 μm).

The reference states (samples 1 and 3) are equivalent in terms of eccentricity and correspond to a quasi-equiaxed structure with d_1/d_2 ratios close to 0·9. For the two deformed specimens, d_1/d_2 ratios deduced from the eccentricity values are 0·73 (sample 2) and 0·61 (sample 4). As a comparison, a ratio d_1/d_2 equal to 0·5 corresponds to an eccentricity value of 0·86. For the reference states (samples 1 and 3) the α values do not indicate a clear preferential orientation with respect to the hot-pressing stress. By contrast, it is clearly demonstrated that, as previously suggested on the micrographs, deformed grains tend to align perpendicularly to σ (α = 1·5° (sample 4) and α = 4° (sample 2)). Consequently the minor axis of the equivalent ellipse denoted d_1 is found to be parallel to the external stress. Thus, in the following, d_1 and d_2 are denoted $d_\parallel$ and $d_\perp$ respectively.

Moreover, if grain growth is negligible, it is possible to define the grain deformation ε_g by the formula

$$\varepsilon_g = \ln (d_\parallel / d_0) \tag{2}$$

where $d_\parallel$ and d_0 are respectively the diameter parallel to the external stress and the grain diameter of the undeformed specimen.[21]

If the volume of grains remains constant before and after the grain deformation, the relation between $d_\parallel$ and $d_\perp$ and d_0 can be written $d_\parallel \cdot d_\perp^2 = d_0^3$. Then the grain deformation ε_g becomes

$$\varepsilon_g = 2/3 \ln (d_\parallel / d_\perp) \tag{3}$$

Grain, deformation is theoretically calculated from a quasi-equiaxed initial shape. Because grains are slightly elongated in the as-sintered state, the calculation underestimates the grain deformation.

Grain deformation ε_g and the total strain of the sample ε_f values are reported in Fig. 5 (samples 2 and 4). This curve shows that grains follow approximately the same shape change as the sample at the macroscopic level. Thus the slight grain growth observed for samples 2 and 4 (Table 1) does not affect the result shown in Fig. 5.

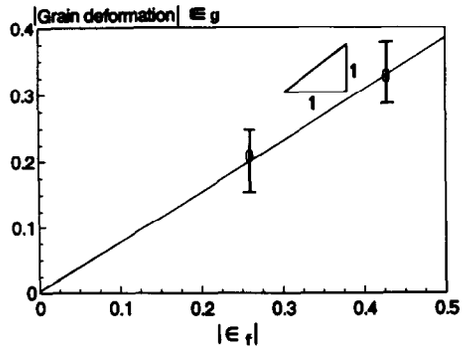
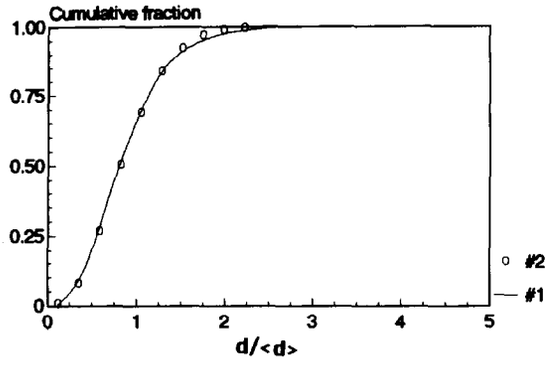
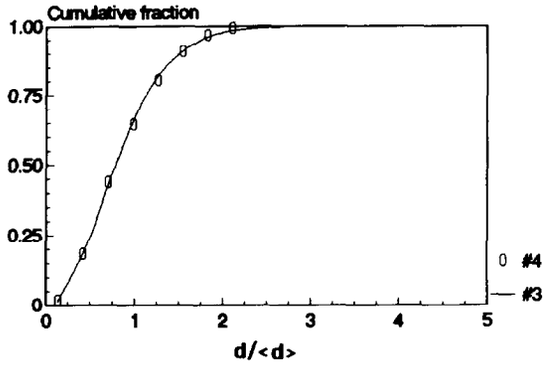


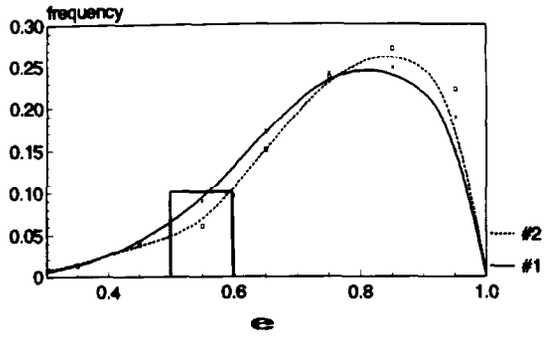
Fig. 5. Evolution of the grain deformation ε_g with the overall deformation of the sample ε_f : ε_g = 2/3 ln ($d_\parallel/d_\perp$).



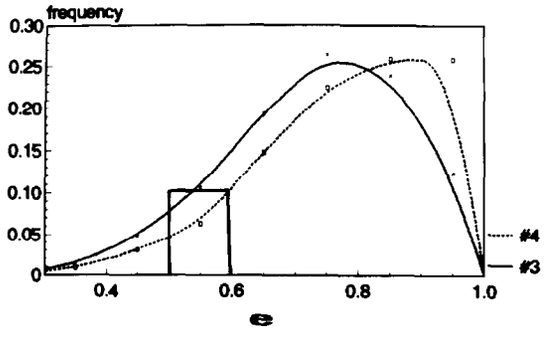
(a)



(b)



(c)



(d)

Fig. 6. Cumulative fractions of the normalised equivalent grain diameter $d/\langle d\rangle$ for (a) samples 1 and 2 and (b) for samples 3 and 4. Frequency distributions of the eccentricity e (c) for samples 1 and 2 and (d) for samples 3 and 4. The value of the class used in these frequency distributions has been drawn in (c) and (d).

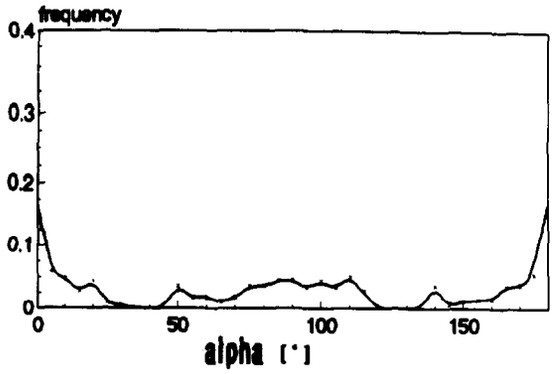
4.2.1.2 Al grade (1·5 wt%). For this grade, the grain size of annealed and deformed specimens is found to be close to 1·5 μm. The reference state (sample 5) exhibits an anisotropy of the grain shape in contrast to the preceding cases (samples 1 and 3). It can be noted that the deformed specimens, even the most deformed one (sample 7), have the same eccentricity values as the reference state (e ~ 0·7). Consequently the grain deformation cannot be correlated to the overall deformation of the sample. These results are in agreement with the α values, found to be nearly equivalent for the three samples (5, 6, 7). This indicates that no strong preferential orientation has occurred during the creep tests.

Finally the grain size $\langle L\rangle$ and d_1/d_2 ratios of the two grades in the as-sintered state have been found to be equal respectively to: $\langle L\rangle = 2$ μm, $\langle L_\parallel\rangle/\langle L_\perp\rangle = 0{\cdot}83$ (0·3% Al grade) and $\langle L\rangle = 1{\cdot}1$ μm, $\langle L_\parallel\rangle/\langle L_\perp\rangle = 0{\cdot}71$ (1·5 wt.% Al grade) (Table 1). By comparison with values concerning annealed samples (1, 3, 5, 8), it appears that a slight grain growth has occurred during the annealing treatments for the two grades.

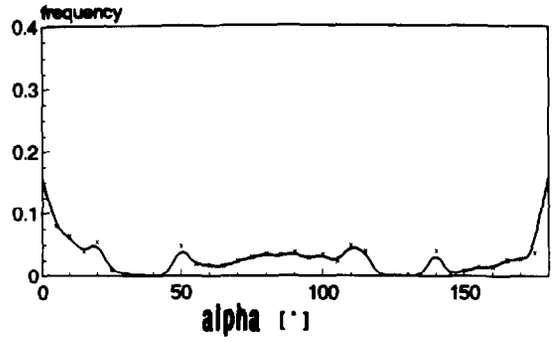
4.2.2 Individual analysis

4.2.2.1 Al grade (0·3 wt%). Results concerning the grain size and the grain shape are given in Fig. 6. Cumulative fractions of the normalized equivalent grain diameter $d/\langle d\rangle$ are given in Fig. 6(a) (samples 1 and 2) and in Fig. 6(b) (samples 3 and 4). Frequency distributions of the eccentricity e are shown in Fig. 6(c) (samples 1 and 2) and in Fig. 6(d) (samples 3 and 4). The main evolutions of these two parameters (d and e) are in agreement with the results of the global analysis. Particularly, for the two deformed samples, the eccentricity values, displayed by frequency curves, are shifted towards higher values. In fact these displacements can be evaluated by the mode values for each curve. For the most deformed specimen (sample 4, Fig. 6(d)), the mode value is found to be 0·9 compared to 0·75 in the annealed state (sample 3) which is significant, taking into account the value of the class of the distribution curve (0·1), indicated on Fig. 6(c) and (d). Therefore the slight variation of the mode found for samples 1 and 2 (0·80 to 0·85) is less significant. On the other hand, the cumulative curves of grain size distribution are close to a normal logarithmic law and seem not to be affected by thermomechanical treatments.

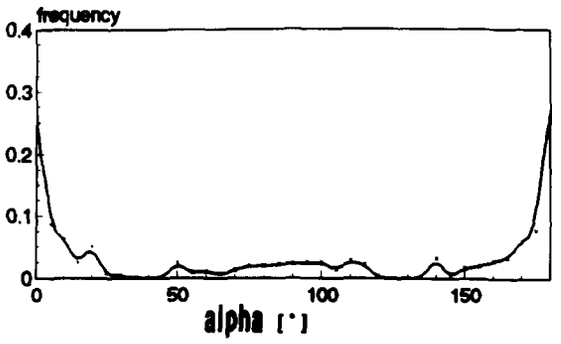
Moreover, the distribution of α values is displayed in Fig. 7 for the four samples. A difference is visible between the distribution curves of references (samples 1 and 3, Fig. 7(a) and (b)) and deformed states (samples 2 and 4, Fig. 7(c) and (d)).



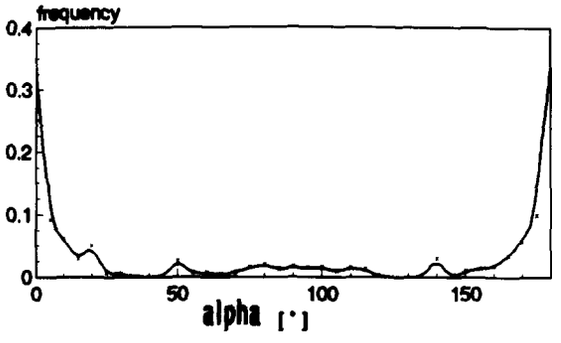
(a)



(b)

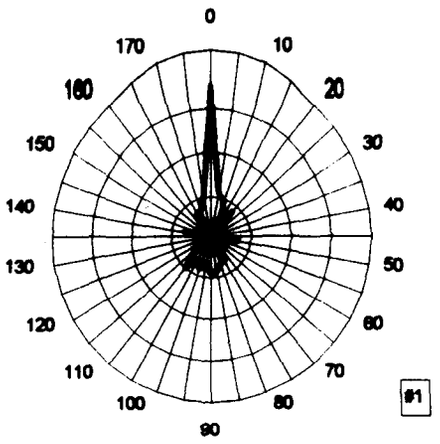


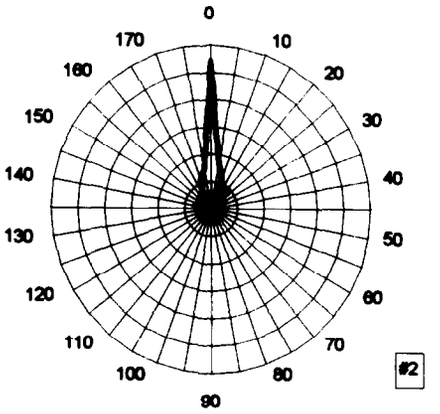
(c)

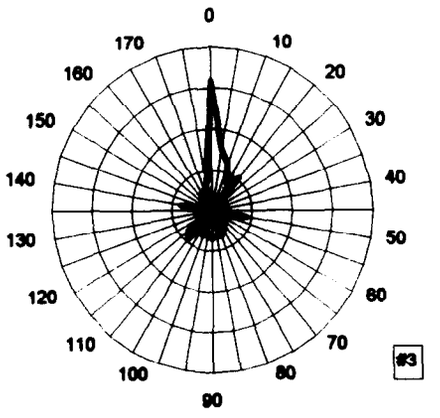


(d)

Fig. 7. Frequency distributions with respect to the angle α for the references (samples 1 and 3, (a) and (b)) and for the deformed states (samples 2 and 4, (c) and (d)).







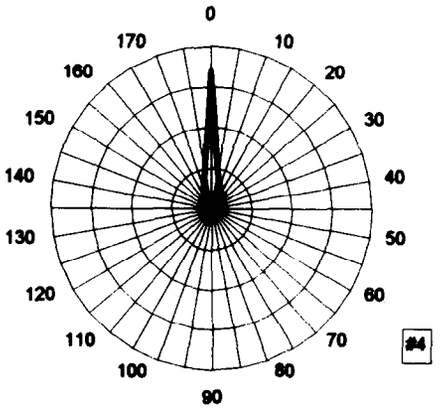


Fig. 8. Frequency distributions with respect to the angle α for the references (samples 1 and 3) and for the deformed states (samples 2 and 4) in a rose representation.

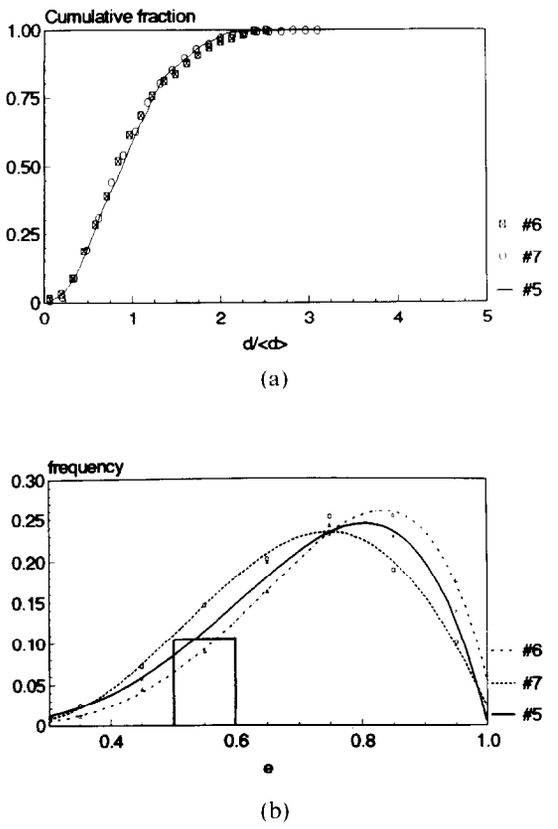


Fig. 9. Cumulative fractions with respect to the normalized equivalent grain diameter $d/\langle d\rangle$ (a) and frequency distributions with respect to the eccentricity e (b) for samples 5, 6 and 7. The value of the class has been drawn in (b).

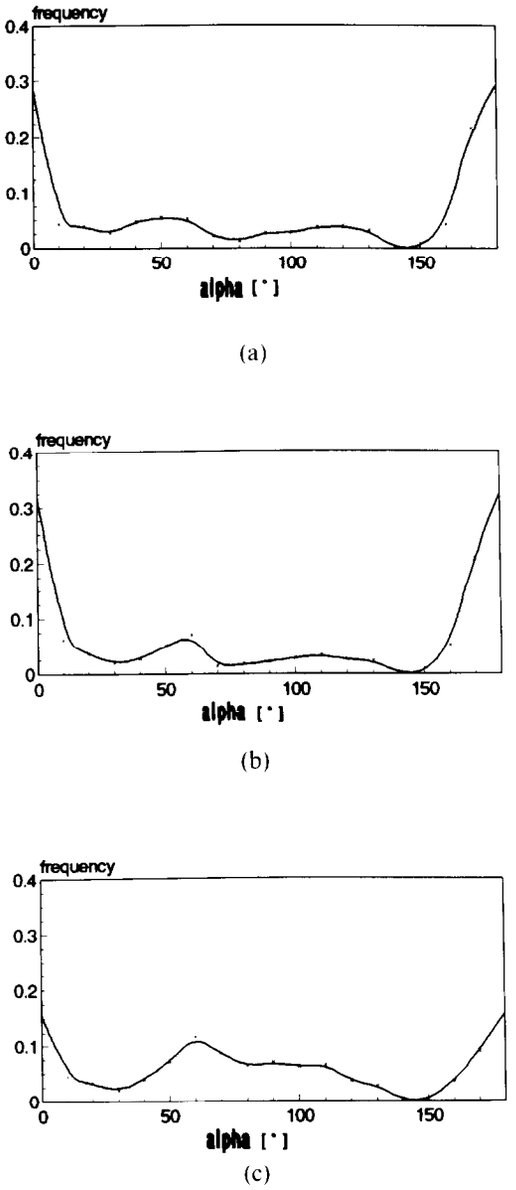


Fig. 10. Frequency distributions with respect to the angle α for samples (a) 5, (b) 6 and (c) 7.

In the curves corresponding to the two deformed states (Fig. 7(c) and (d)), it can be noticed that the number of grains for which α is close to 0° or 180° progressively increases with the deformation value, which is in agreement with the global analysis. This indicates that grains are preferentially orientated perpendicularly to the compressive stress σ.

These results are also displayed in a rose representation (Fig. 8). For the reference states (samples 1 and 3) grains are orientated in all directions. However, a maximum value of frequency is found close to 0°–180°. This indicates a slight preferential orientation of grains perpendicularly to P. This result was not clearly established by global analysis. As expected for the deformed specimens (samples 2 and 4) the majority of the grains are more preferentially orientated close to 0–180°.

4.2.2.2 Al grade (1·5 wt%). The cumulative distributions of the normalized equivalent grain diameter $d/\langle d\rangle$ (Fig. 9(a)) and the frequency curves of the eccentricity (Fig. 9(b)) (samples 6 and 7) seem not to be affected by the creep tests compared to the reference (sample 5). Taking into account the value of the class (0·1) for eccentricity, the slight shift of the modes for deformed samples is not significant compared to the reference state (Fig. 9(b)). On the other hand, if the distribution curves of α values for the three samples (5, 6 and 7, Fig. 10) are compared, sample 7 exhibits a different behaviour in terms of a decrease of the number of grains for which α is close to 0°–180°C. Consequently, grains of sample 7 (Fig. 10(c)), which is highly deformed, tend to be orientated in all directions.

The difference in distribution curves of α values for the three samples can be understood by the existence of a slight preferential orientation with respect to the stress P in the reference state (sample 5, Fig. 10(a)). Grains seem to have been reorientated with their large axes normal to the stress direction σ in sample 6 (Fig. 10(b)) while such orientated texture is not observed in sample 7 (Fig. 10(c)). These results for samples 5, 6 and 7 are also displayed in Fig. 11 in rose representations.

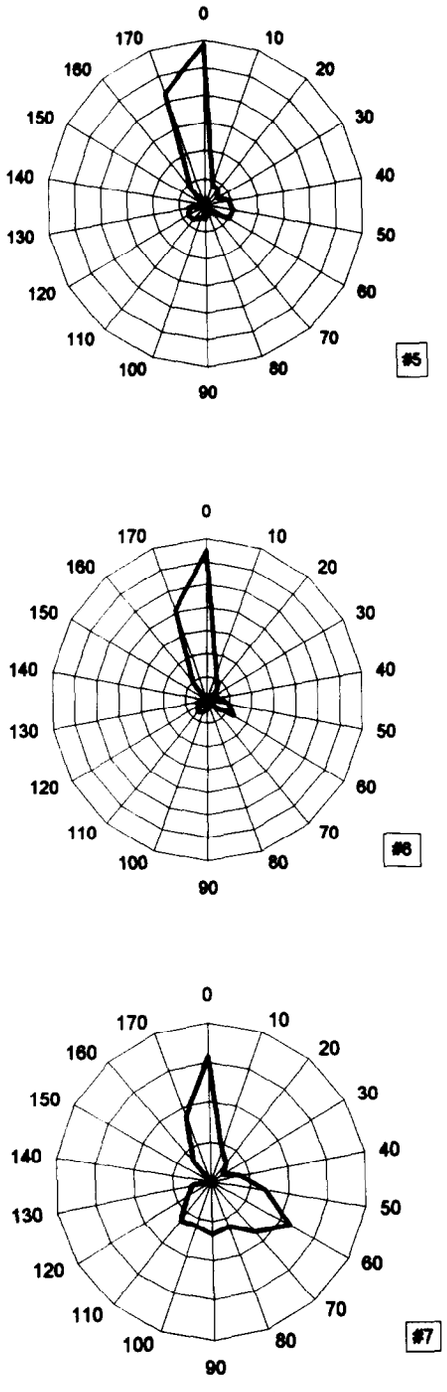


Fig. 11. Frequency distributions with respect to the angle α for samples 5, 6 and 7 in a rose representation.

5 Concluding Remarks

In this work, the microstructures of two SiC grades (0·3 and 1·5 wt% Al) have been characterized by automatic image analysis methods. Results of global and individual image analyses are in good agreement. The slight grain growth observed in annealed or deformed samples compared to the statistical scattering of the grain size does not allow a kinetic law of grain growth to be drawn in these experiments. The main results of the present work are the observation of a grain shape modification and a grain reorientation with respect to the external stresses which can be summarized as the following: grains of the deformed 0·3 wt% Al grade tend to flatten perpendicularly to the external stress. This was deduced from the eccentricity and α angle values (Table 1), showing that grains viewed in a cross-section containing σ can be described by an elliptic model. The other grade (1·5 wt%) exhibits a different microstructure evolution for a same deformation temperature range. Indeed, even for a high macroscopic deformation value, grains do not show any shape change after the creep test. Consequently, no texture formation could be found. All these results are important to understand the mechanical behaviour of these two SiC grades but further microstructural characterizations should be performed by TEM and microanalyses. Nevertheless, at this stage of the work, some hypotheses concerning the deformation mechanisms can be put forward:

(i) Al–SiC grade (0·3 wt%)
Different mechanisms could explain the fact that grain deformation follows approximately the specimen deformation as is demonstrated in this work (Fig. 3). A first mechanism is based on an important intragranular dislocation activity. SiC crystals exhibit mainly the hexagonal polytype (4H) and only one slip system (basal plane) is known to be the most activated.[13] This can induce the formation of a crystallographic texture. TEM observations[22] have effectively confirmed that grain boundaries tend to be parallel to the basal plane and normal to the stress direction. Moreover, an extended dislocation activity has also been analysed in detail in this deformed sample.[22] Consequently, an intragranular dislocation mechanism seems to be more favoured than a pure diffusion process which might also explain the grain shape change for this grade. Because no cavitation is observed, the grain boundary deformation has to be also accommodated either by an intergranular dislocation glide and/or by some diffusional matter transport via an intergranular film. Microanalyses and HREM experiments are still in progress to confirm effectively the presence of a thin intergranular film.

(ii) Al–SiC grade (1·5 wt%)
Compared to the preceding case, the mean grain size of the 1·5 wt% Al–SiC grade is now twice as small (Table 1). Because no grain shape change occurs the contribution of an intragranular dislocation activity to the overall deformation might be much lower than for the previous SiC grade. Moreover, as shown in Fig. 10, grains of the most deformed specimen (sample 7) are now dis-

tributed in all directions and have lost the slight preferential orientation observed by image analysis in the reference state (sample 5). These results suggest that an important rearrangement of grains has occurred during the deformation. All these data are in agreement with a superplastic-like behaviour for this grade as was previously suggested.[8] Because no cavitation is observed, stress accommodation could be relieved via diffusion and/or intergranular dislocation generation. Further observations in TEM should be performed to ascertain the exact mechanism.

Acknowledgement

One of the authors (M.L.D.) thanks the CNRS and the region of Basse Normandie for their financial support.

References

1. Krishnamachari, V. & Notis, M. R., Interpretation of high temperature creep of SiC by deformation mapping techniques. *Mat. Sci. Ing.*, **27** (1977) 83.
2. Wiederhorn, S. M., Ellis Roberts, D., Chuang, T. J. & Chuck, L., Damage-enhanced creep in a siliconized silicon carbide: Phenomenology. *J. Am. Ceram. Soc.*, **71** (1988) 602.
3. Moussa, R., Contribution à l'étude du comportement en fluage de matériaux SiC. Thesis, Caen, 1985.
4. Grathwohl, G., Reets, T. & Thummler, F., Creep of hot-pressed and sintered SiC with different sintering additives. *Sci. Ceram.*, **11** (1981) 425.
5. Farnsworth, P. L. & Coble, R. L., Deformation behavior of dense polycrystalline SiC. *J. Am. Ceram. Soc.*, **49** (1966) 264.
6. Francis, T. L. & Coble, R. L., Creep of polycrystalline silicon carbide. *J. Am. Ceram. Soc.*, **51** (1968) 115.
7. Djemel, A., Cadoz, J. & Philibert, J., Creep and fractures of engineering materials and structure, ed. B. Whilshire & D. R. J. Owen. Swansea Pineridge Press, 1981, p. 381.
8. Carry, C. & Mocellin, A., High temperature creep of dense fine grained silicon carbides. In *Materials Science Research, Vol 18*, eds. R. E. Tressler & R. C. Bradt. Plenum Press, New York, 1984, p. 391.
9. Carter, Jr, C. H., Davis, R. F. & Bentley, J., Kinetics and mechanisms of high-temperature creep in silicon carbide: I. Reaction-bonded. *J. Am. Ceram. Soc.*, **67** (1984) 409.
10. Carter, Jr, C. H., Davis, R. F. & Bentley, J., Kinetics and mechanisms of high-temperature creep in silicon carbide: II. Chemically vapor deposited. *J. Am. Ceram. Soc.*, **67** (1984) 732.
11. Lane, J.E., Carter, Jr, C. H. & Davis, R. F., Kinetics and mechanisms of high-temperature creep in silicon carbide: III. Sintered α-silicon carbide. *J. Am. Ceram. Soc.*, **71** (1988) 281.
12. Nixon, R. D. & Davis, R. D., Diffusion-accommodated grain boundary sliding and dislocation glide in the creep of sintered alpha silicon carbide. *J. Am. Ceram. Soc.*, **75**(7) (1992) 1786.
13. Lee, S. J. & Vicens, J., Interactions between Shockley dislocations and perfect screw dislocations with large Burgers vectors in high-temperature deformed α-SiC. *Phil. Mag. A*, **65** (1992) 551.
14. Demenet, J. L., Rabier, J. & Garem, H., Microstructure of sintered α-SiC deformed below 1000°C. In *6th M.S M. Inst. Phys. Conf. Ser. No. 100*, Section 5, Oxford, UK, 10–13 April 1989. p. 445.
15. Maeda, K., Suzuki, K., Fujita, S., Ichihara, M. & Hyodo, S., Defects in plastically deformed 6H SiC single crystals studied by transmission electron microscopy. *Phil. Mag. A*, **57** (1988) 573.
16. Fujita, S., Maeda, K. & Hyodo, S., Dislocation glide motion in 6H SiC single crystals subjected to high-temperature deformation. *J. Mater. Sci. Lett.*, **5** (1986) 450.
17. Burton, B., In *Diffusional Creep of Polycrystalline Materials*. Diffusion and Defects Monograph, Scrie Trans. Tech. Publ., 1977.
18. Kashyap, B. P. & Mukherjee, A. K., In *Superplasticity*, ed. B. Baudet & M. Suery, CNRS, Paris, 1985, p. 41.
19. Coster, M. & Chermant, J. L., *Précis d'analyse d'images*, 2nd edn. CNRS, Paris, 1989.
20. Serra, J., *Mathematical Morphology and Image Analysis*, Academic Press, New York, 1982.
21. Nauer, M., Microstructure et superplasticité de zircones yttriées. Thesis EPFL No. 996, Lausanne, Switzerland, 1992.
22. Duval-Riviere, M.L., Carry, C. & Vicens, J., Creep behaviour and microstructure evolution of hot-pressed alpha-silicon carbide deformed at high temperature. In *Third Euro-Ceramics*, Vol. 3, ed. P. Duran & J. F. Fernandez, FAENZA Editirice, Iberica S. L., 1993, p. 435.

Journal of the European Ceramic Society **15** (1995) 81–88
© 1995 Elsevier Science Limited
Printed in Great Britain. All rights reserved
0955-2219/95/$9.50

Chlorine and Oxygen Inhibition Effects in the Deposition of SiC-based Ceramics from the Si–C–H–Cl System

D. Lespiaux,[a] F. Langlais,[a] R. Naslain,[a] S. Schamm[b] & J. Sevely[b]

[a] Laboratoire des Composites Thermostructuraux, UMR 47, CNRS, SEP, UB1 Domaine Universitaire 3 allée de la Boëtie, 33600-Pessac, France
[b] Centre d'Elaboration de Matériaux et d'Etudes Structurales, Laboratoire d'Optique Electronique, UPR 8011, CNRS, BP 4347, 31055 Toulouse Cedex, France

(Received 19 November 1993; accepted 13 June 1994)

Abstract

The inhibitory role of HCl and oxygen in the chemical vapour deposition of SiC-based ceramics from the Si–C–H–Cl system, is pointed out in terms of nucleation and growth process on the basis of experimental and theoretical approaches. The addition of HCl to methyltrichlorosilane MTS–H_2 gaseous precursors (i) decreases the nucleation and growth rate, (ii) induces a transition from a diffusion to a reaction rate control of the deposition process, (iii) improves the smoothness of the films surface, (iv) results in a transition from anisotropic films with columnar microstructure and Si, C and O concentration gradients to nanocrystallized materials with quite constant Si, C and O contents. These behaviours are tentatively explained by assessments of the gas phase supersaturation and calculations of the chemisorbed layer composition. The occurrence of oxygen within the nanocrystallized films is then related to the growth inhibition effect and the presence of silicon excess shown by EELS analyses.

1 Introduction

Chemical vapour deposition (CVD) is a suitable technique to prepare silicon carbide films of high quality. Owing to its good thermal, mechanical and chemical properties, SiC is used as a ceramic matrix in fibre-reinforced ceramic–ceramic composites elaborated by chemical vapour infiltration (CVI), a technique which derives directly from CVD.[1,2]

Most of SiC-depositions involve the Si–C–H–Cl chemical system. The organometallic compound CH_3SiCl_3 (MTS) is often used as precursor partly for its ability to be decomposed at moderate temperatures (which usually favours the CVI process), and partly for economical reasons.[3–6]

A model was proposed recently to simulate and optimize the homogeneity and the rate of the infiltration in a single straight cylindrical pore.[7] This model, when applied to the CVI of SiC in the MTS–H_2 system,[8] pointed out the fundamental role of HCl in the control of the quality of the infiltration. Hydrogen chloride is successively produced by (i) the homogeneous decomposition of MTS precursor and (ii) the heterogeneous reaction of SiC deposition from carbon and silicon intermediate species.[9] The infiltration gradient along the pore is related to the HCl concentration which is found, at the pore centre, to be very similar to those of source species at the entrance.[8]

The first purpose of the present paper is to assess the influence of HCl content in the precursor gas mixture on: (i) the nucleation and growth processes and (ii) the physico-chemical nature of the deposits performed on an amorphous SiO_2 substrate. The effects resulting from a HCl excess will be discussed on the basis of supersaturation estimates and chemisorption calculations.

Under well-defined conditions, the MTS–H_2 precursor provides nanocrystalline SiC films with silicon excess and a small amount of oxygen.[10] The second purpose of this article is to correlate the silicon excess (and oxygen content) with the growth rate, through chemisorption data previously calculated.[11] Finally, a structural model will be proposed for these nanocrystalline SiC-based ceramic films, built on EELS analyses including both valence and inner-shell electron excitations.

Journal of the European Ceramic Society 0955-2219/95/$9.50 © 1995 Elsevier Science Limited, England. Printed in Great Britain

2 Experimental

The various procedures and equipments which have been used for both the nucleation/growth experiments and the physico-chemical characterization of the films, have been described in detail in Ref. 10.

The deposition experiments were performed in a vertical hot-wall CVD reactor working under reduced pressure. The initial composition of the MTS–HCl–H_2 gas precursor is given by α and δ defined as follow:

$$\alpha = \frac{P_{H_2}}{P_{MTS}} = \frac{Q_{H_2}}{Q_{MTS}} \quad (1)$$

$$\delta = \frac{P_{HCl}}{P_{MTS}} = \frac{Q_{HCl}}{Q_{MTS}} \quad (2)$$

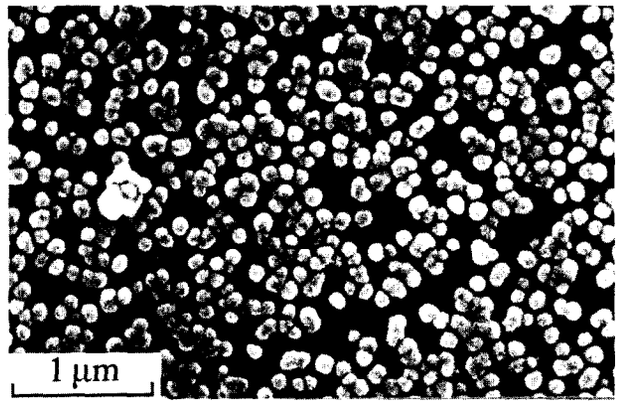
where P_i, and Q_i are the initial partial pressures and flow rates of species i. A microbalance was used to detect the transient and steady-state stages in the deposition process and to determine the various growth rates. The substrates were amorphous silica layers obtained by oxidizing silicon wafers. To investigate the nucleation process, very short experiments were carried out, followed by (i) SEM observations of the resulting nuclei and (ii) determination of the nucleation characteristics such as the saturation nucleus density N_S, the saturation nucleus size ϕ_S and the nucleation rate I.[10]

After a first microstructural approach by SEM and X-ray diffraction, transmission electron microscopy (TEM) (bright-field and dark-field observations and selected area electron diffraction) combined with local (60 or 30 nm diameter probe sizes) electron energy loss spectroscopy analysis (EELS) were used for a description of the SiC-based films at a nanometric scale. The local chemical and structural organization of the films was investigated by using core excitations (Si-L, C-K and O-K edges) and volume plasmon characteristic signals.

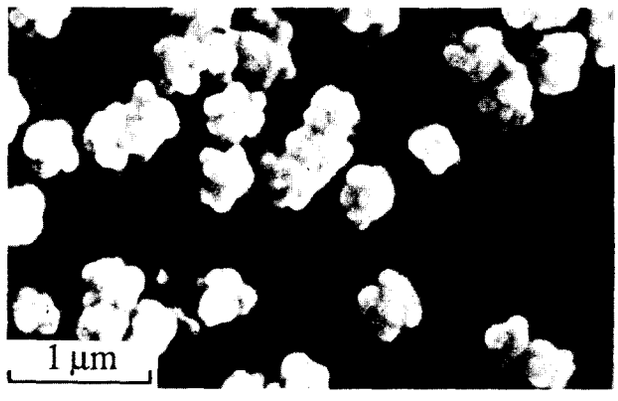
3 Influence of HCl Content on the Deposition Process of SiC-based Ceramics

3.1 Nucleation process

When the initial MTS–H_2 mixture contains HCl, the initial stages of the deposition are highly modified. As shown in Fig. 1, for T = 1100°C, P = 3 kPa and α = 30, the SiO_2 surface is not totally covered by SiC-based deposit after an exposure of 2600 s to a MTS–H_2–HCl mixture (with δ = 0·5), while the saturation is almost performed after 45 s of exposure to MTS–H_2 mixture (with δ = 0). An important decrease of the nucleation rate from $2{\cdot}5 \times 10^{12}$ to 3×10^8 is readily achieved by adding 50% HCl to the MTS source, but a further increase of HCl initial concentration does not modify the nucleation rate any longer. Moreover, when δ = 0·5, nuclei are not adjacent but form aggregates from only a few sites. This result can be correlated with an inhibition effect of HCl on a SiO_2 surface.



(a)



(b)

Fig. 1. SEM pictures of nucleus density observed on SiO_2 substrates for T = 1100°C, α = 30, P = 3 kPa and (a) δ = 0 and after an exposure time of 45 s, and (b) δ = 0·5 after an exposure time of 2600 s.

3.2 Growth kinetics

When the steady state is reached, the deposition rate can be deduced from the slope of the mass–time curves. The variations of this rate as a function of HCl partial pressure (ratio varying from 0·1 to 1) are plotted in Fig. 2 for α = 10, P = 3 kPa and two temperatures (1000 and 1100°C). The growth rate is observed to decrease when δ increases above 0·2. This result confirms the inhibition effect of HCl, previously mentioned for the nucleation process.

To identify the kinetic regime of the deposition, the growth rate was studied as a function of the temperature and the total flow rate, for two initial compositions of the gas phase ((i) α = 10 and δ = 0, (ii) α = 10 and δ = 1), the total pressure being 3 kPa, the temperature ranging from 1000 to 1125°C and the total flow rate from 200 to 550 sccm (Figs 3 and 4). When δ = 0, the deposition rate does not depend significantly on the temperature (Fig. 3) and it increases continuously with the total flow rate (Fig. 4). This behaviour is typical for a kinetic

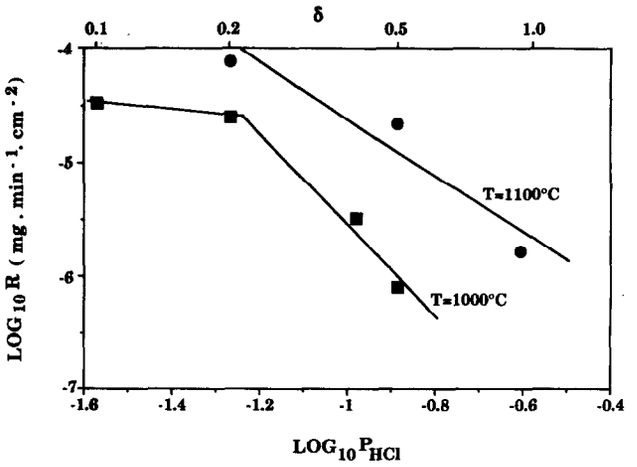


Fig. 2. Variations of the deposition rate R versus HCl partial pressure PHCl and δ ratio for α = 10, P = 3 kPa and ■, T = 1000°C; ●, T = 1100°C.

process controlled by mass transport, e.g. by diffusion through a boundary layer. When δ = 1, the growth rate decreases exponentially with the reciprocal temperature and does not depend on the total flow rate. This second behaviour, which corresponds to a kinetic control by the surface reactions, can be explained by a decrease of the heterogeneous reaction rate due to the inhibition effect of added HCl. As a consequence, the addition of HCl to the gaseous precursor results in a transition from a diffusion rate control to a reaction rate control of the deposition of SiC-based ceramics. This type of transition was already evidenced for BN deposition in the B–N–H–F system: it was induced by variations of the temperature, the total pressure and also the initial composition of the gas phase.[12,13]

3.3 Physico-chemical characteristics of the deposits

As demonstrated in a related paper, the change in the kinetic regime of SiC-based ceramic deposition has a great influence on the microstructure of the films.[10] When a diffusion-controlled kinetic process is changed to a reaction-controlled one (by

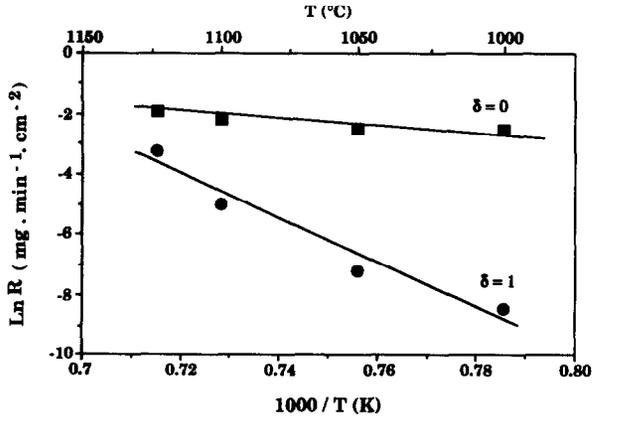


Fig. 3. Variations of the logarithm of the deposition rate R versus reciprocal temperature for α = 10, P = 3 kPa, Q = 400 sccm and ■, δ = 0, ●, δ = 1.

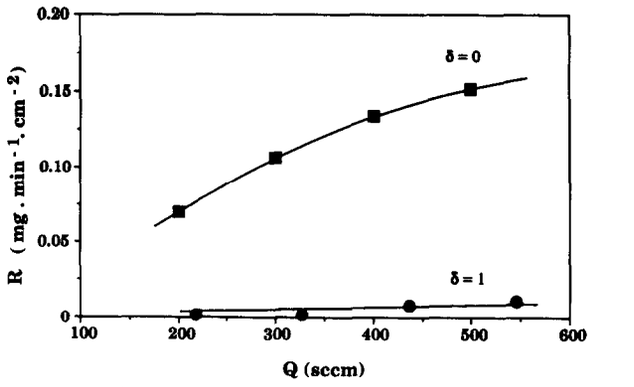
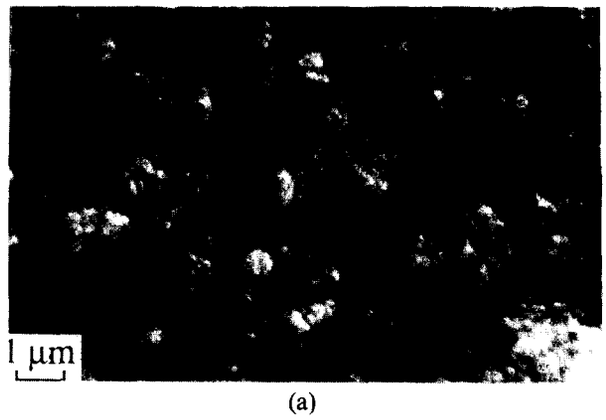


Fig. 4. Variations of the deposition rate R versus total flow rate Q for T = 1100°C, α = 10, P = 3 kPa and ■, δ = 0; ●, δ = 1.

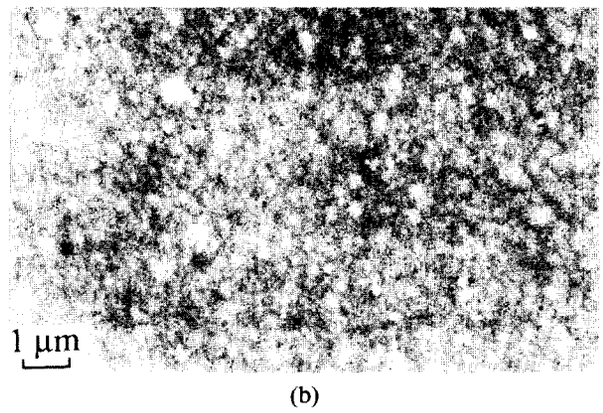
varying temperature and/or total pressure), a transition occurs from a crystallized film with columnar crystals to a nanocrystalline deposit. Thus, a detailed experimental investigation was performed in order to show whether the kinetic transition presently induced by adding HCl to the initial gas mixture results or not in similar microstructural changes.

3.3.1 Morphology and microstructure

The surface morphology of the films deposited for 1100°C, α = 10 and P = 3 kPa is influenced by the addition of HCl to the MTS–H_2 mixture (Fig. 5).



(a)



(b)

Fig. 5. SEM pictures showing the surface morphology of SiC-based deposits obtained for T = 1100°C, α = 10, P = 3 kPa and (a) δ = 0; (b) δ = 0·5.

Table 1. X-Ray (CuK_α) analyses of SiC-based deposits on SiO_2 substrates for T = 1100°C, α = 10, P = 3 kPa and various δ ratios

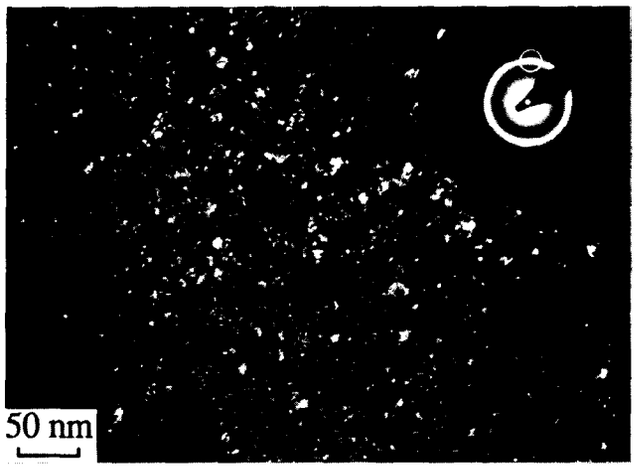
δ	0	0·2	0·5	*References from ASTM tables*
Crystallite size (nm)	14	11	7	
I^a (111) (% a.u)	100	100	100	100
I^a (220) (% a.u)	1·5	2	8	63

[a] $I_{(111)}$ and $I_{(220)}$ represent respectively the intensities of the (111) and (220) diffraction lines.

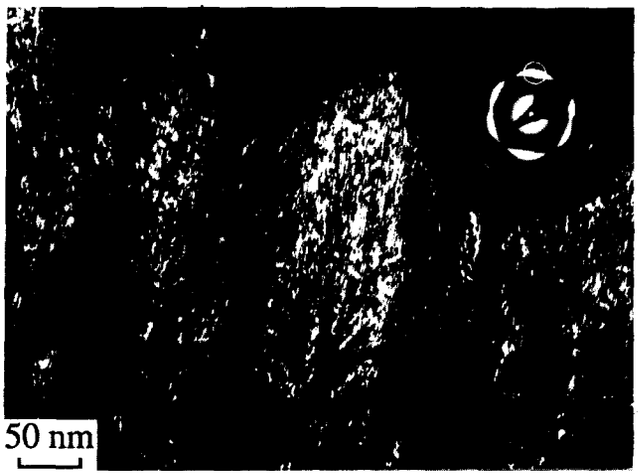
When δ is raised from 0 to 0·5, i.e. when the kinetics become controlled by the surface reactions, the roughness of the surface is decreased, a feature which is consistent with previous results reported in Ref. 10 for SiC and Ref. 12 for BN deposition.

X-Ray diffraction analyses of the films deposited under the same T, P, α conditions for δ = 0, 0·2 and 0·5 show again the preferred growth of silicon carbide along the ⟨111⟩ crystallographic direction perpendicular to the substrate surface (Table 1). Nevertheless, the increase of HCl content in the gas phase seems to weaken this textural effect. The Scherrer formula, applied to the (111) X-ray diffraction line of the diffraction patterns without taking into account the internal stress effect, leads to crystallite apparent sizes decreasing with increasing δ values.

The nanostructure of the films prepared under the same T, P, α values and without HCl in the precursor changes when moving from the interface with the substrate to the external surface, as supported by TEM observations. Figure 6 shows dark-field images obtained by selecting with the objective aperture a part of the first electron diffraction ring (mainly SiC (111)). In the observation, close to the substrate, a nanocrystalline material is shown with isotropic grains of about 5 nm in size (Fig. 6(a)). From 500 nm away from the substrate, an anisotropy is observed, giving rise to a slightly columnar microstructure (Fig. 6(b)). Conversely, when δ = 0·5, no microstructure variation is observed through the thickness of the film (Fig. 7): the whole deposited material being nanocrystalline and rather homogeneous.



(a)



(b)

Fig. 6. Dark-field images and SAD patterns (inserts) of a SiC-based deposit on a SiO_2 substrate for T = 1100°C, α = 10 and P = 3 kPa, (a) near the substrate, (b) at 1 μm from the substrate.

3.3.2 Chemical composition

The relative concentrations of Si, C and O have been assessed by local EELS analyses which were carried out as a function of d, the distance from the substrate/deposit interface, for the samples prepared under the following conditions: T = 1100°C, α = 10, P = 3 kPa and δ = 0 or 0·5.

For the MTS–H_2 precursor (δ = 0), Si and C are present near the deposit/substrate interface in proportions respectively above and below the values corresponding to stoichiometric SiC (Fig. 8(a)). Conversely, from d = 400 nm, the silicon to



Fig. 7. Dark-field image and SAD pattern (insert) of a SiC-based deposit on a SiO_2 substrate T = 1100°C, α = 10, P = 3 kPa and δ = 0·5 at 1 μm from the substrate.

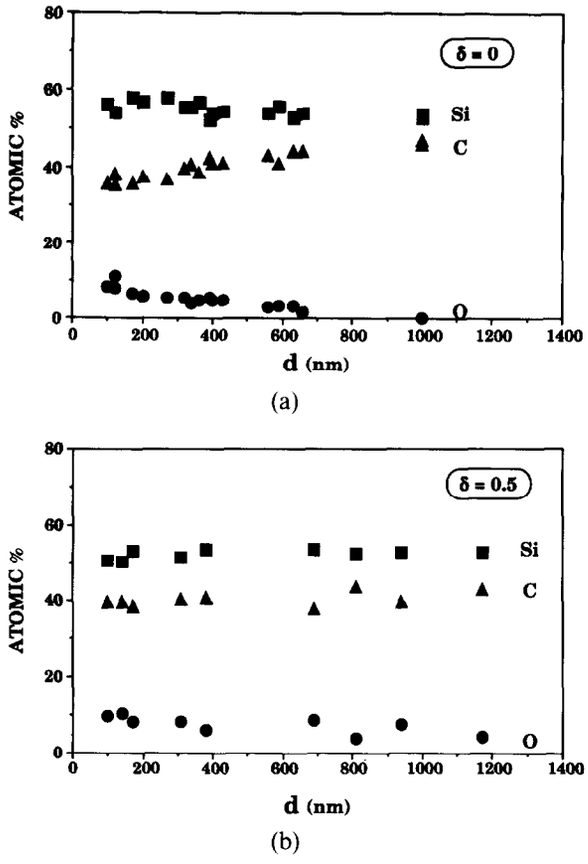


Fig. 8. Variations of Si, C and O contents with the distance d measured between the analysed area and the substrate/deposit interface, in SiC-based films obtained for T = 1100°C, α = 10, P = 3 kPa and (a) δ = 0 and (b) δ = 0·5.

carbon ratio moves towards the stoichiometric ratio. In addition a small amount of oxygen occurs in the deposit close to the substrate and decreases to zero through the thickness of the film.

Conversely, when HCl is added to the initial MTS–H_2 mixture (for δ = 0·5), the chemical composition of the film is almost constant (Fig. 8(b)), which is in accordance with the rather homogeneous nanostructure of the material. Nevertheless, a slight decrease of the oxygen content is observed from the substrate/deposit interface to the external surface of the film.

3.4 Theoretical approach: supersaturation and chemisorption

3.4.1 Assessment of gas phase supersaturation

For T = 1100°C, P = 3 kPa and α = 10, a transition from a diffusion rate control to a reaction rate control of the deposition process is induced by adding HCl to the initial MTS–H_2 mixture. Consequently, when δ is very small (δ < 0·2), the local supersaturation (which represents the departure from heterogeneous equilibrium) close to the substrate, is very low: due to the concentration gradients occurring through the boundary layer, the local gas phase composition is almost given by the heterogeneous equilibrium. Nevertheless, this low supersaturation value cannot be easily calculated under such conditions.

Conversely, when δ is increased beyond 0·2, i.e. under conditions of kinetic regime controlled by surface reactions, the gas phase becomes highly supersaturated near the substrate surface and the calculation of the supersaturation is then possible. It is based (i) on the assumption of rapid homogeneous reactions and (ii) on any heterogeneous reaction giving rise to pure SiC deposition, e.g.:

$$CH_4 + SiCl_2 \rightarrow SiC_{(S)} + H_2 + 2HCl \qquad (3)$$

As detailed in a previous study,[10] the theoretical supersaturation γ can be written as:

$$\gamma = \frac{P_{CH_4} P_{SiCl_2}}{P_{H_2} P_{HCl}^2} \cdot K_P(T) - 1 \qquad (4)$$

where $K_P(T)$ is the equilibrium constant corresponding to the reaction (3) and P_{CH_4}, P_{SiCl_2}, P_{H_2} and P_{HCl} are the partial pressures close to the solid surface calculated under the assumption of the homogeneous equilibrium. γ values were calculated for δ varying from 0·2 to 1 and for various conditions of temperature and pressure. As shown in Fig. 9, in spite of a slight decrease, calculated γ values remain very high ($\gamma > 10^4$) for the investigated range of conditions.

3.4.2 Calculation of the chemisorbed layer composition

On the basis of a previously described approach of the Langmuir chemisorption on amorphous SiO_2 or β-SiC substrates,[11] the composition of the adsorbed layer in the CVD of SiC from the Si–C–H–Cl system was calculated for various HCl contents in the precursor.

Figure 10 shows the variations of coverages θ_i on a SiO_2 surface as a function of δ ratio for the conditions used in the nucleation experiments, i.e. for T = 1100°C, P = 3 kPa and α = 30. A highly

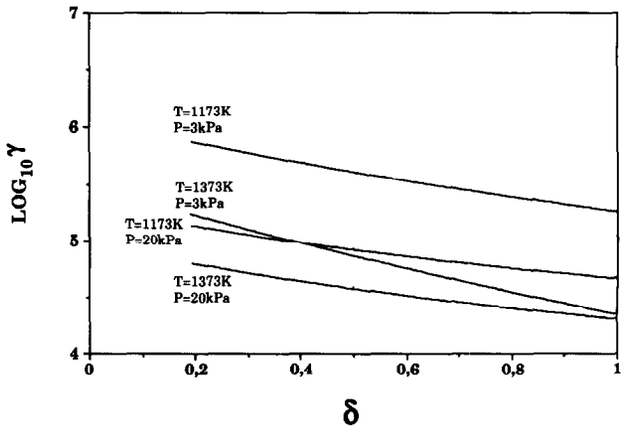


Fig. 9. Variations of the calculated supersaturation γ versus δ ratio ($[HCl]_{in}/[MTS]_{in}$) for various temperature and pressure conditions.

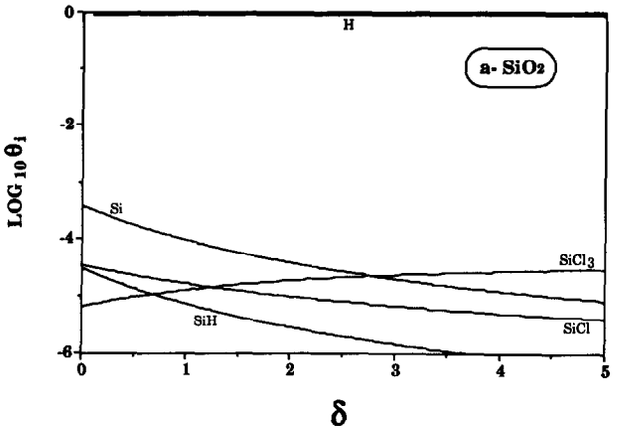
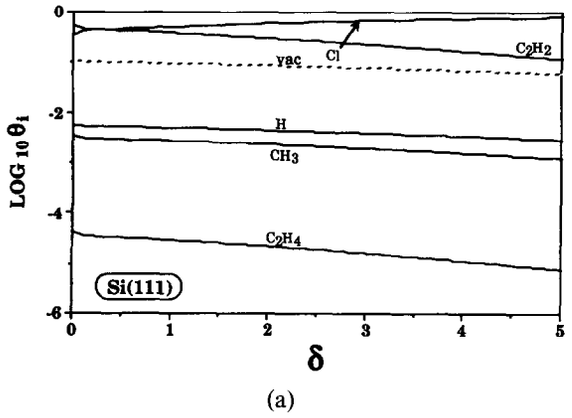


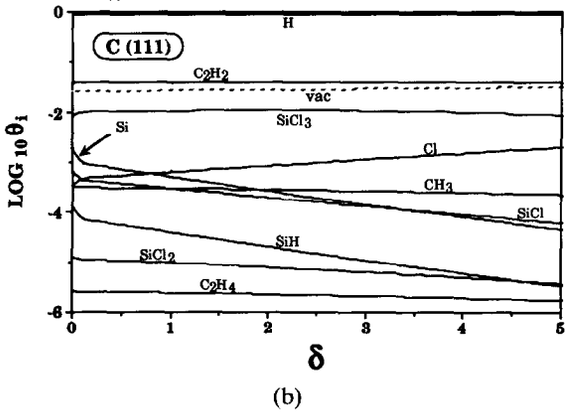
Fig. 10. Coverages of an oxygen plane of amorphous SiO_2 substrate versus δ ratio for T = 1100°C, α = 30 and P = 3 kPa.

dominant coverage is found for H radical over the whole δ range. The only source species coverages (i.e. the silicon containing species), are decreased by raising δ ratio, except for $SiCl_3$. Due to this decrease of silicon species, the addition of HCl to the gaseous precursor enhances the inhibition of the nucleation on a SiO_2 surface.

In Fig. 11, the coverages on a C(111) and a Si(111) plane of β-SiC are represented versus δ for T = 1100°C, P = 3 kPa and α = 30. For the C plane, the dominant adsorbed species are H and to a less extent C_2H_2 and $SiCl_3$ whose coverages are not influenced by δ. An increase of δ results only in the increase of Cl coverage which remains very low. For the Si plane, Cl and C_2H_2 are the main chemisorbed species. Cl coverage increases and the one of C_2H_2 decreases as δ rises. Here again, an inhibition effect of HCl, particularly on the formation of C on a Si(111) plane, is demonstrated by the chemisorption approach.



(a)



(b)

Fig. 11. Coverages of (a) a Si (111) plane of β-SiC and (b) a C (111) plane of β-SiC versus δ ratio for T = 1100°C K, α = 30 and P = 3 kPa.

3.5 Discussion

The present experimental and theoretical approach of the SiC-based ceramic deposition permits a correlation stated in a previous study between (i) the supersaturation of the gas phase close to the deposition surface, (ii) the crystallization state and (iii) the surface morphology of the deposit to be confirmed. A high increase of the local supersaturation, presently induced by the addition of HCl to the MTS–H_2 mixture, results in a transition from a deposit with a columnar microstructure and a rough surface to a rather smooth and nanocrystallized film.

The inhibitory effect of HCl is also pointed out in the present study. The nucleation process on amorphous SiO_2 surface is particularly inhibited by HCl. This effect is partly explained by a chemisorption of source species on SiO_2 unfavoured by HCl. The selectivity of the nucleation with respect to the nature of the substrate, reported in a previous paper,[11] is highly increased by introducing HCl in the initial gaseous mixture. A continuous renucleation regime is favoured on silicon carbide rather than on SiO_2, as shown in Fig. 1.

The growth process of silicon carbide itself is highly inhibited by the HCl enrichment of the precursor, a feature which confirms the assumptions proposed in previous investigations of the deposition[14] or infiltration mechanisms for the MTS–H_2

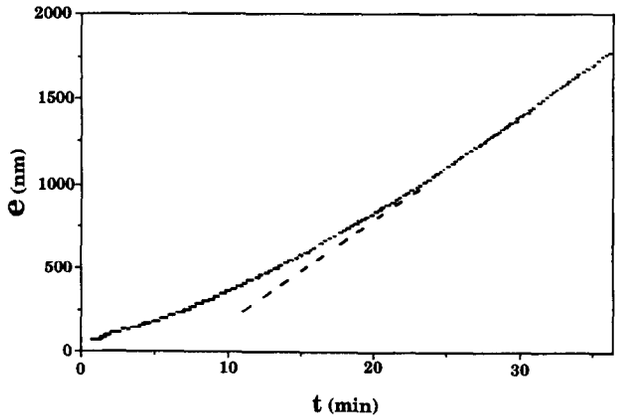
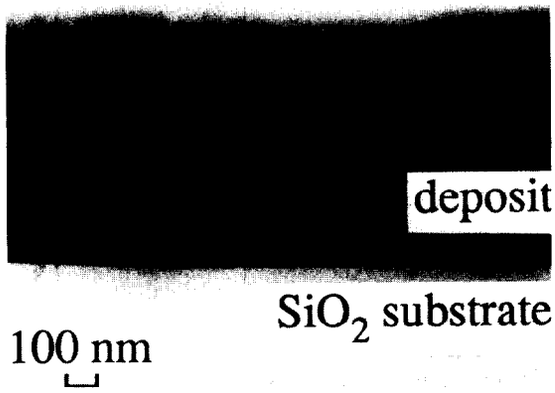


Fig. 12. Mass–time curve recorded during the deposit of a SiC-based film for T = 900°C, α = 3 and P = 3 kPa on a SiO_2 substrate.

system.[8,9] This inhibition can be explained partly by a higher coverage of Cl species on Si(111) planes of β-SiC. On the other hand, one of the main surface reaction assumed to lead to silicon formation from $SiCl_x$ intermediate, $1 \leq x \leq 3$, is probably rate-limited by the corresponding reaction:

$$SiCl_x^* + x/2\ H_2 \rightleftharpoons Si + xHCl + * \qquad (5)$$

where $SiCl_x^*$ represents the adsorbed form of $SiCl_x$ and * a free surface site. Equation (5) shows that an increase of HCl content in the gas phase can highly inhibit the growth process by favouring the reverse reaction.



(a)



(b)

Fig. 13. (a) Bright-field image and (b) SAD pattern of a SiC-based deposit on a SiO_2 substrate or T = 900°C, α = 3 and P = 3 kPa.

4 Influence of Oxygen on the CVD Kinetic Process and Related Characteristics of SiC-based Ceramics

4.1 Growth rate

In a previous work, transient stages were reported for the mass–time curves recorded under conditions of high supersaturation, i.e. when the kinetic process is controlled by the surface reactions.[10] For T = 900°C, α = 3 and P = 3 kPa, a relatively long time (of about 25 mn) is needed to reach the steady state (Fig. 12). During the transient stage, the deposition rate is increasing continuously with time up to a value of about 5 μm h^{-1}.

4.2 Structural and chemical analysis by TEM and EELS

In order to explain this kinetic behaviour, a nano-characterization of the ceramic films prepared under the present conditions was carried out from a chemical and structural point of view. The TEM bright-field image in Fig. 13(a) shows that the deposit is nanocrystallized with an about 1·5 nm mean crystal size (Fig. 13(b)). Interreticular distances calculated from the diameter of the rings do not correspond to those of cubic β-SiC silicon carbide. This is related to a study of the relative concentrations of silicon and carbon, by using core excitation signals. These elements are present in proportions above and below the values corresponding to SiC respectively (Fig. 14). In addition, a small amount of oxygen is present in the deposit, which decreases with d to a few atomic percents. All these element concentrations change slowly but monotonically with thickness.

The corresponding valence energy loss study has been carried out. A single plasmon profile has been found for each analysed zone of the deposit, whose energy falls between the energies of Si and SiC plasmons (16·7 and 22·5 eV respectively)

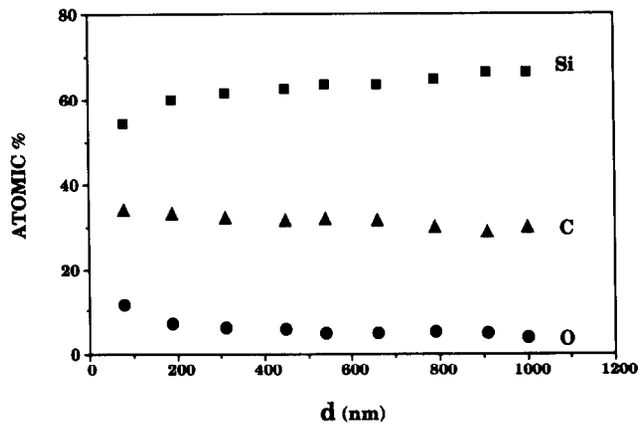


Fig. 14. Variations of Si, C and O contents with the distance d measured between the analysed area and the substrate/deposit interface, in a SiC-based film obtained at T = 900°C, α = 3, P = 3 kPa.

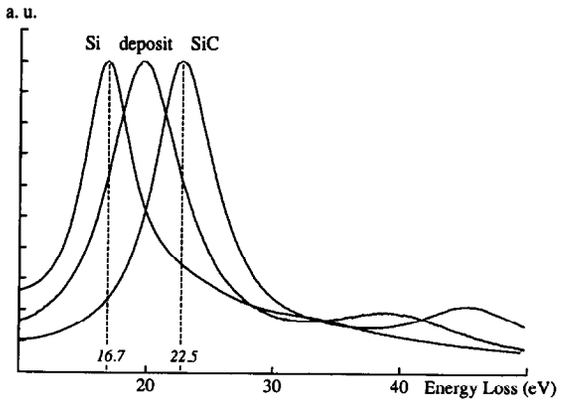


Fig. 15. Plasmon profiles of a SiC-based deposit (T = 900°C, α = 3, P = 3 kPa) and of Si and SiC reference materials.

(Fig. 15). It is also observed that this energy decreases progressively from 20·1 to 19·6 eV with d varying from 200 to 1000 nm in relation with the increase of the excess of silicon.

4.3 Discussion

The oxygen profile within the film could be correlated to the important transient stage observed in the kinetic curve: the growth rate increases when the oxygen percentage decreases and both become constant when $d > 750$ nm. This result means that oxygen might act as an inhibitor for the deposition of silicon carbide. As reported in a previous paper, the chemisorption of intermediate source species is unfavoured when the SiC substrate is replaced by an amorphous SiO_2 substrate, owing to the preferred chemisorption of the inhibitor species H (the O–H bond being very strong).[11] It has also been shown that oxygen occurs in nanocrystalline rather in columnar films.[10] The very small crystals in the former are thought to trap rather easily residual oxygen of the reactor, which results in blocking the growth sites by chemisorption of H atoms.

The above results have been used to propose a distribution of the Si, C and O elements within the deposit.[15] From thermodynamic considerations, on the one hand,[16] X-ray diffraction and Raman spectroscopy microprobe experiments, on the other hand,[9] carbon is known to be present only in silicon carbide and free silicon to be very often codeposited with silicon carbide. From the nanocrystallized structure of the deposit and the single profile of the plasmon loss which are observed, the occurrence of SiC nanocrystals including Si excess is assumed.[15]

Acknowledgements

The authors wish to thank Dr C. Bernard (LTPCM, Grenoble) for his contribution to the thermodynamic calculations, R. Fourmeaux and P. Salles (CEMES-LOE, Toulouse) for their support in electron microscopy experiments. This work has been supported by Société Européenne de Propulsion and CNRS (via a grant given to D. L.). The authors are indebted to J. Rey, C. Robin-Brosse and S. Goujard from SEP for their assistance and valuable discussions.

References

1. Hirai, T. & Sasaki, M., In *Silicon Carbide Ceramics—1*, ed. S. Somiya & Y. Inomata. Elsevier Science Publishers, London, New York, 1991, p. 77.
2. Naslain, R., Langlais, F. & Fedou, R., In *Proc. 7th Eur. Conf. on CVD*, ed. M. Ducarroir, C. Bernard L. Vandelbulcke. 1989, p. C5–191.
3. Schlichting, J., *Powder Metall. Int.*, **12**(3) (1980) 141 and **12** (4)(1980). 196.
4. Fitzer, E. & Gadow, R., *Am. Ceram. Soc. Bull.*, **65** (1986) 326.
5. Giso, M. & Chun, J., *J. Vac. Sci. Technol. A.*, **6**(1) (1988) 5.
6. Minato, K. & Fukuda, K., *J. Mater. Sci.*, **23** (1988) 699.
7. Fedou, R., Langlais, F. & Naslain, R., *J. Mater. Synth. Process*, **1**(1) (1993) 43.
8. Fedou, R., Langlais, F. & Naslain, R., *J. Mater. Synth. Process*, **1**(2) (1993) 61.
9. Langlais, F. & Prebende, C. In *Proc. 11th Int. Conf. on CVD*, ed. K. E. Spear & G. W. Cullen. The Electrochemical Society, Pennington, 1990, p. 686.
10. Lespiaux, D., Langlais, F., Naslain, R., Schamm, S. & Sevely, J., submitted to *J. Mater. Sci.*
11. Lespiaux, D. & Langlais, F., submitted to *Thin Solid Films.*
12. Prouhet, S., Langlais, F., Guette, A., Naslain, R. & Rey, J., *Eur. J. Solid State Inorg. Chem.*, **30** (1993) 953–69.
13. Prouhet, S., Vignoles, G., Langlais, F., Guette, A. & Naslain, R., *Eur. J. Solid State Inorg. Chem.*, **30** (1993) 971–89.
14. Besmann, T., Sheldon, B. W. & Kaster, M. D., *J. Am. Ceram. Soc.*, **75**(10) (1992) 2899.
15. Schamm, S., Kihn, Y., Severly, J., Lespiaux, D. & Langlais, F., *Proc. 10th Europ. Congress on Electron Microscopy*, Vol. 1. Granada, Spain, ed. A. Rios, J. M. Arias, L. Megras-Megras & A. Lopez-Galindo, 7–11 September 1992, p. 277.
16. Christin, F., Naslain, R. & Bernard, C., In *Proc. 7th Int. Conf. on CVD.* ed. T. O. Sedgwick. 1979, p. 499.

Journal of the European Ceramic Society **15** (1995) 89–94
© 1995 Elsevier Science Limited
Printed in Great Britain. All rights reserved
0955-2219/95/$9.50

Computer Simulation of β'-Sialon Synthesis

Lucia F. S. Dumitrescu* & Bo Sundman

Royal Institute of Technology, Department of Materials Science and Engineering, 100 44 Stockholm, Sweden

(Received 24 January 1994; accepted 10 May 1994)

Abstract

Thermodynamic calculations in the system Si–Al–O–N were used to assess the capabilities of SiO_2 and Al_2O_3 mixtures to synthesise β'-sialon powders by reduction–nitridation. The Thermo-Calc databank, a sophisticated computer software together with assessed thermodynamic data, has been applied to calculate not just traditional phase diagrams but also various sections, isopleths, activity plots and property diagrams such as phase fraction diagrams. By controlling the temperature, the partial pressures of oxygen and nitrogen and the Si : Al ratio in the precursor mixtures the experimental work can be reduced to a minimum, based on the calculations. β'-Sialon was found to be stable only within a small region of oxygen and nitrogen partial pressures.

1 Introduction

The good mechanical and thermal properties of sialon ceramics make them useful as structural materials. To minimize the variation of the strength values, the fabrication of materials with uniform microstructure is required. When β'-sialon ceramics are formed from mixed powders such as silicon nitride, aluminum nitride and alumina,[1] the homogeneity is reduced and the microstructural control is difficult due to the complex mechanism of the preparation. The microstructure is more uniform and the densification temperature for synthesized sialon powders is 50–100°C lower when high-purity pre-prepared β'-sialon is used instead.[2] The production of nitrogen ceramics by simultaneous reduction and nitridation of oxides is of interest both because of the versatility of the process and the current availability of potential raw materials.[3]

To determine optimal values for the parameters that are necessary for the synthesis of β'-sialon powders, and thus minimize expensive and time-consuming experimental work, thermodynamic calculations have become important. Thermodynamic calculations have been used for many years to obtain information on the possible reactions in chemical and metallurgical systems.[4,5] In recent years thermodynamic software has been used not only for traditional equilibrium and phase diagram calculations but also for material development,[6] solidification simulations,[7] etc. Heterogeneous reactions make up the most significant group of interactions of interest in ceramics. In particular, those reactions involving gases and solids are of prime importance, e.g. reduction of solid oxides and chemical vapor deposition. Above 1000°C one can often use equilibrium thermodynamics together with simple kinetic estimations to understand the possible results of an experiment even if full equilibrium will not be established in the experiment. A thermodynamical description is always needed to simulate transformations as it is otherwise impossible to know the final state the system tries to reach.

Materials processes can often be described as a sequence of steps where the system is in equilibrium 'locally'. Combining extensive thermodynamic calculations in such a local equilibria simulation of a process was first done by Eriksson & Johansson[8] in the so-called SOLGAS-reactor. In a following paper a similar method will be used for the silicon nitride powder synthesis with a generic reactor module connected to Thermo-Calc.[9]

There are two requirements for the successful application of thermodynamic calculations to understand a chemical problem. One is a flexible and general software like Thermo-Calc and the other is a carefully assessed thermodynamic database for the system of interest. Such a database does not only contain data for the compounds and gases but also descriptions of the solid solution phases using sophisticated models[10] which can take into account the various types of crystalline

* On leave from MATPUR SA, Sos. Garii Catelu nr 5, Bucharest 3, Romania.

structures of the condensed phases and how the components mix on different sublattices. Databases with thermodynamical parameters describing mixtures make it possible to predict the equilibrium state of very complex systems of non-ideal phases.

In this paper a thermodynamic database for the Si–Al–O–N system[11] was used to assess the capabilities of mixtures of SiO_2 and Al_2O_3 to produce β'-sialon by reduction–nitridation. Attention was focused on important factors in the synthesis process such as the temperature, the partial pressures of oxygen and nitrogen and the Si : Al ratio in the starting oxides mixture. The calculations are a powerful tool for planning experimental work as one may eliminate a large amount of experiments that are unlikely to give useful results.

2 The SiAlON System

A system formed by four elements can always be represented by a tetrahedron. In the SiAlON system the elements form two oxides and two nitrides, and take only one valency state in these condensed compounds. The plane generated by connecting the points representing these four compounds becomes an irregular four-cornered plane. Representing such an irregular quadrangle in atom % is not very practical. Instead Gauckler & Petzow[12] suggested a representation for the silicon nitride based systems using equivalent % of one cation and one anion, which transform the irregular quadrangle into a square. The system Si_3N_4–AlN–Al_2O_3–SiO_2 represented in this way is generally called the SiAlON system in the literature.

For the SiAlON system some isothermal experimental studies are known.[13,14] Gauckler *et al.*[13] indicate the existence of an homogeneous single-phase material with an expanded lattice, isostructural with β-Si_3N_4, which was termed β'-sialon. Solubility occurs only with a constant cation : anion ratio of 3 : 4 according to an atomic formula $Si_{6-z}Al_zO_zN_{8-z}$ within a solubility range of $0 < z < 4$. Compositional variation with this ratio does not require vacancies or interstitial atoms in the β-Si_3N_4 lattice. Other important phases in the system are the Si_2N_2O solid solution (O'), the X_1 phase and the polytypes in the AlN corner.

A database for the SiAlON system has been assessed thermodynamically by Dorner *et al.*[15] and more recently by Hillert & Jonsson.[11] In such a database each phase is described by a model giving the variation of the Gibbs energy with temperature, pressure and composition. A number of model parameters must be assessed to give a good description of the experimental information. This technique has been used successfully in many metallic systems[16] and is often referred to as the 'Calphad technique'. Due to the lack of experimental information at the time when the SiAlON system was assessed some simplifications were introduced, for example only one polytype phase, 27R, is considered and it is restricted to the AlN–Al_2O_3 quasi-binary section.

Three of the phases in the SiAlON system, β'-sialon, O' and mullite have significant variations in composition and reciprocal models with ionic constituents have been selected by Hillert & Jonsson to describe this. For the β'-sialon phase the model has Si^{+4} and Al^{+3} on one sublattice with 3 sites and N^{-3} and O^{-2} on a sublattice with 4 sites, and this can be written as $(Si^{+4}, Al^{+3})_3(N^{-3}, O^{-2})_4$. Figure 1 shows the constitutional square of this reciprocal model. It has four corners and only one of these represent a real neutral compound, $(Si^{+4})_3(N^{-3})_4$, the others have a net charge and are thus unphysical. The line in Fig. 1 represents the neutral combinations of Al^{+3} and O^{-2} additions. The line goes from the Si_3N_4 corner to a composition Al_3O_3N on the opposite side.

For the O' phase the model selected by Hillert & Jonsson is a slightly modified reciprocal model. In this case there are three sublattices and the model can be written $(Si^{+4}, Al^{+3})_2(N^{-3}, O^{-2})_2(O^{-2})_1$. In the third sublattice there is only one constituent and thus the model is actually equivalent to a reciprocal one.

The mullite phase was modeled with three sublattices and the model can be written $(Al^{+3})_2$. $(Al^{+3}, Si^{+4})_1(O^{-2}, Va)_5$. As the first sublattice has only one constituent this is also a reciprocal model.

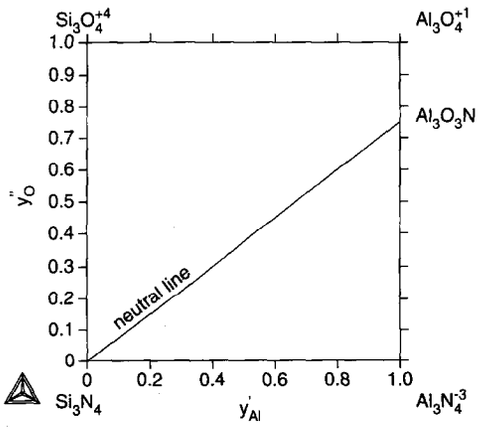


Fig. 1. The constitutional square for the β'-sialon model. The square represents a reciprocal model but only one corner is an electrically neutral compound. The axes represent the variation of Al^{+3} in sublattice 1 and O^{-2} in sublattice 2. The line drawn in the square represents the electrically neutral ratio of Al^{+3} and O^{-2} additions to Si_3N_4.

All other phases are treated as stoichiometric compounds. For X_1 the composition was selected to be $Si_{12}Al_{18}O_{39}N_8$ and $Al_9N_7O_3$ for R27.

In the development of a database it is important to be compatible with assessments of other oxide, nitride and metallic systems in order to make it possible to combine and extrapolate from different assessments. Some parameters for the spinel phase, stable at higher temperatures in the Al_2O_3 system, were thus taken from an assessment of the MgO–Al_2O_3 system by Hallstedt.[17]

Figure 2 is one example of the use of the SiAlON system assessed by Hillert & Jonsson, and shows the isothermal phase equilibrium at 1400°C without including the gas phase. Any phase or combination of phases, contained in Fig. 2, can be obtained by controlling the Si : Al ratio in the precursor and the oxygen and nitrogen partial pressures.

3 Calculated Diagrams in the SiAlON System

The database can be used to calculate any equilibrium state in the system using, for example, the Thermo-Calc software system.[18] This system uses the Gibbs energy minimization method[19] where the total free energy of the system is minimized with respect to the prescribed conditions. In Thermo-Calc a very flexible set of conditions can be used, not just the overall composition, temperature and pressure but also activities, the set of stable phases, composition of a phase, volumes, enthalpies, etc. The use of generally applicable software for thermodynamic calculations makes it possible to obtain diagrams that could not be perceived without this software. It is a useful tool for understanding how the system behaves under varying conditions and for testing the effect of different experimental techniques for controlling the system.

In this paper the calculations made to simulate the synthesis of two β'-sialon compositions, by reduction–nitridation of two silica : alumina mixture precursors with the ratio 2 : 1, composition A in Fig. 2, and 1 : 1, composition B in Fig. 2, respectively, are presented. The dotted lines into the diagram show the path of the reduction–nitridation process giving the final β'-sialon single-phase product.

Figure 3 describes the synthesis process better and shows the stable phase regions versus equivalent fraction aluminum and oxygen partial pressure in the system, at 1400°C. Reduction and nitridation of precursor mixture A shows that, as the reaction proceeds, first tridymite + mullite then tridymite + X_1, X_1 + O', β'-sialon + O' and β'-sialon are formed. For precursor mixture B first tridymite + mullite are formed as in the case of mixture A but then X_1 + mullite, X_1 + corundum, corundum + β'-sialon and β'-sialon are the phase fields through which the process progresses. The diagram was calculated at a constant activity of nitrogen equal to unity. Figure 3 emphasizes the importance of controlling the oxygen activity for the process and thus further calculations concerning that have been done.

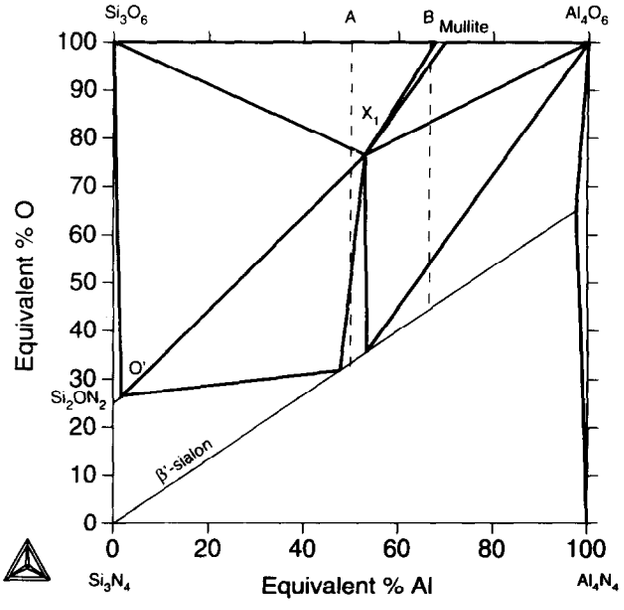


Fig. 2. Calculated isothermal section at 1400°C of the SiAlON system based on the database by Hillert & Jonsson.[11] The gas phase has been excluded. The mullite, O' and β'-sialon phases are treated with reciprocal solution models. The equivalent fraction of O and Al are used as axes. The dashed lines represent the precursor mixture A and B respectively.

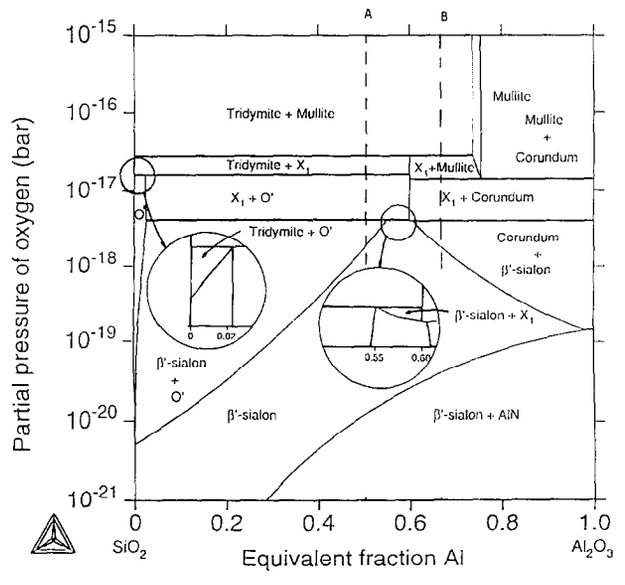
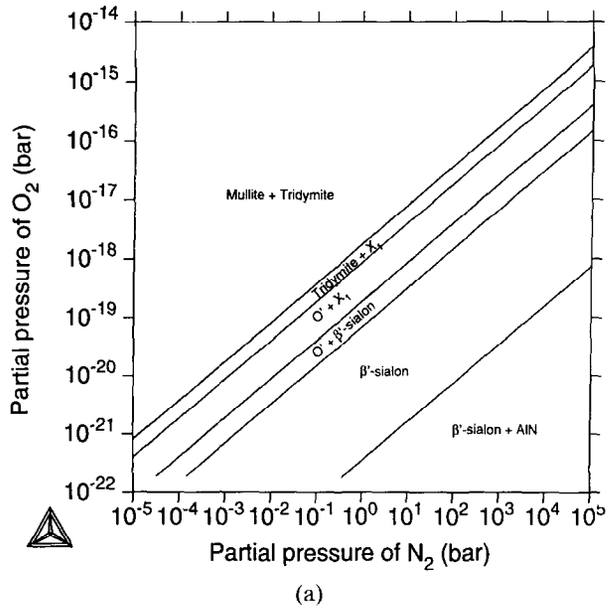


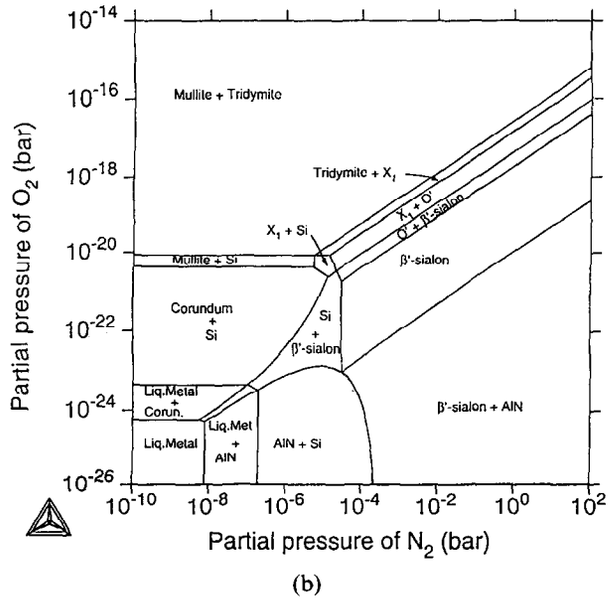
Fig. 3. The same diagram as in Fig. 2 but plotted with the variation in oxygen partial pressure instead of the equivalent % of oxygen on the vertical axis. The β'-sialon single-phase region is now an area and the three-phase regions are horizontal lines. The dashed lines represent the precursor mixture A and B respectively.

The stability regions for the phases in equilibrium at various nitrogen and oxygen partial pressures were calculated at 1250 and 1350°C for the precursor mixture A. Figure 4 shows the result. For the onset of β'-sialon formation the increase of oxygen partial pressure requires the nitrogen partial pressure to increase. This effect is more pronounced at lower temperatures. For a given nitrogen partial pressure the β'-sialon single-phase region has a width of about two orders of magnitude in oxygen partial pressure. For example at 1 bar nitrogen partial pressure Fig. 4(a) shows that the single β'-sialon region falls between 5×10^{-20} bar and 5×10^{-22} bar oxygen partial pressure. In Fig. 4(b) the phases appearing at very low oxygen and nitrogen partial pressures are shown. The left hand corner is liquid metal. Most of these phase regions are out of the experimental setup for β'-sialon synthesis.

The same tendency to displace the β'-sialon stable region toward higher nitrogen partial pressures with increasing oxygen partial pressure is also observed for precursor mixture B. Figure 5(a) and (b) show the result of calculations for this mixture at 1250 and 1350°C respectively. The difference between mixtures A and B at 1250 or 1350°C is the β'-sialon stability region which is narrower for precursor B than for A. This means that the precursor B is less suitable for preparation of β'-sialon as the oxygen partial pressure must be kept in a smaller range. Experimentally this is much more difficult.

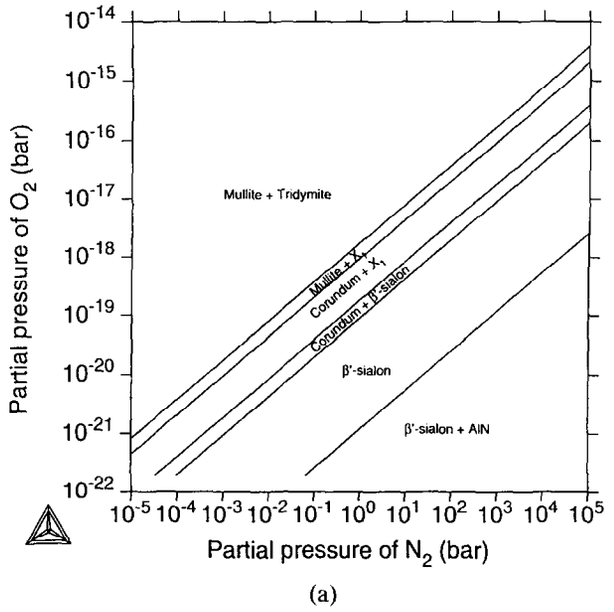


(a)

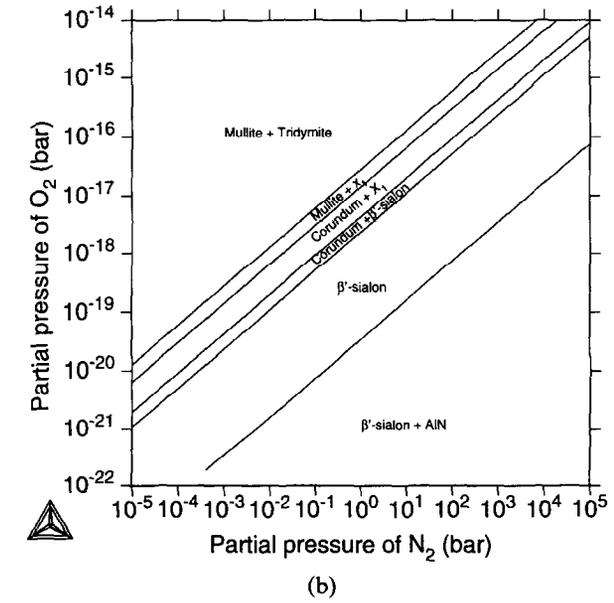


(b)

Fig. 4. The stability regions for the phases in equilibrium at various nitrogen and oxygen partial pressures. The ratio SiO_2 : Al_2O_3 is 2 : 1. (a) Calculated at 1250°C; (b) calculated at 1350°C.



(a)



(b)

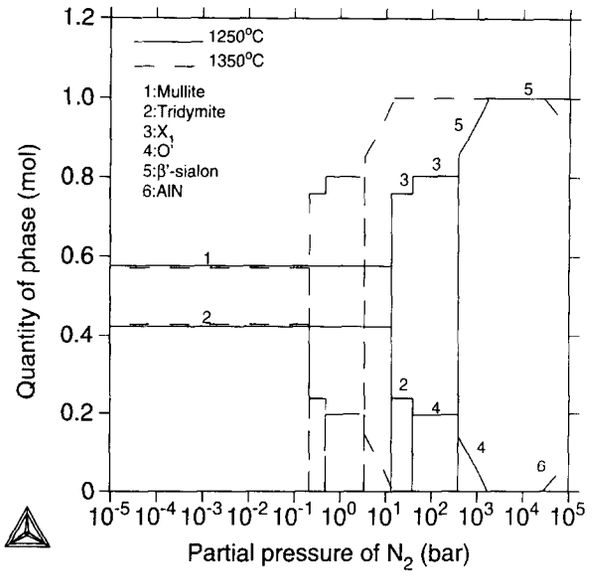
Fig. 5. The stability regions for the phases in equilibrium at various nitrogen and oxygen partial pressures. The ratio SiO_2 : Al_2O_3 is 1 : 1. (a) Calculated at 1250°C; (b) calculated at 1350°C.

A more suggestive way to present the result of the calculations and to see the influence of temperature, partial pressures of oxygen and nitrogen on the β'-sialon synthesis is to plot the quantity of phase as a function of partial pressure of nitrogen at different fixed temperatures, partial pressures of oxygen and silica : alumina ratios.

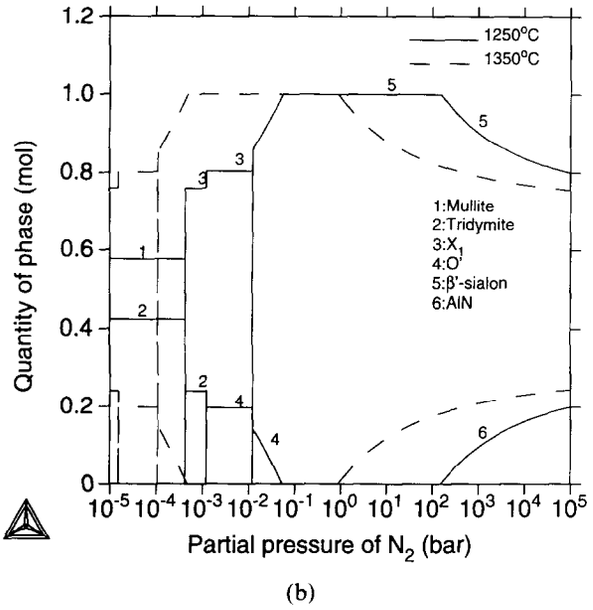
Figures 6 and 7 show the quantity of phase for a system with one mole of components, for the precursor mixture A and B respectively, as a function of partial pressure of nitrogen. The calculations were made for a partial pressure of oxygen equal to 10^{-17} bar, Figs 6(a) and 7(a), and 10^{-20} bar, Figs 6(b) and 7(b). Each figure shows calculations at two temperatures, 1250 and 1350°C, using solid and dashed lines respectively.

The experimental facilities to obtain β'-sialon powders can provide a partial pressure of nitrogen between 1 and 5 bar. The calculated diagrams, Figs 6(a) and 7(a), show that if the partial pressure of oxygen is 10^{-17} bar, it will be impossible to produce β'-sialon.

When the partial pressure of oxygen is 10^{-20} bar the synthesis of single-phase β'-sialon is experimentally possible at the lower temperature 1250°C, for both precursor mixtures A and B, Figs 6(b) and 7(b). Experiments to synthesize β'-sialon based on these thermodynamic calculations for the precursor mixture A were presented by Teoreanu *et al.*[20]

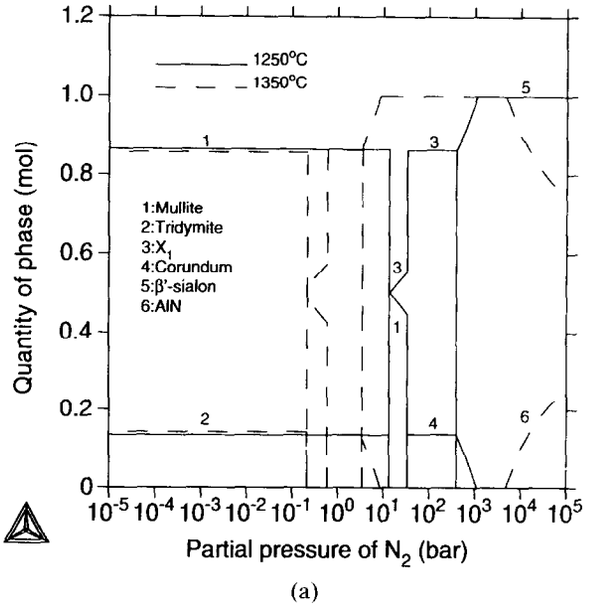


(a)

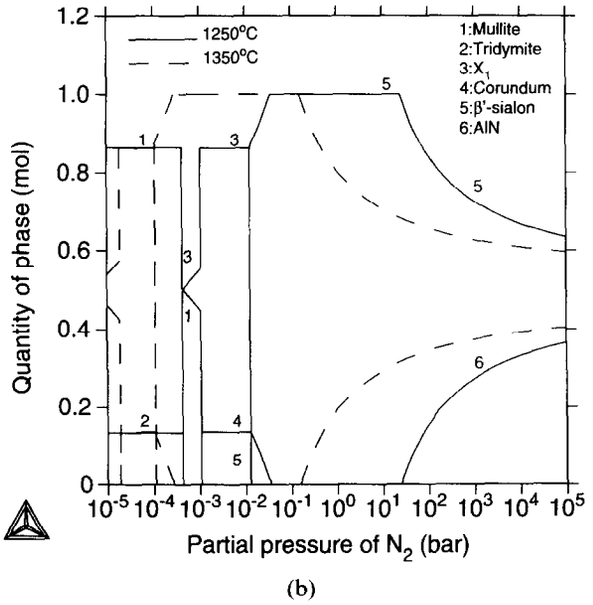


(b)

Fig. 6. Quantity of phase for a system with one mole of components as a function of nitrogen partial pressure. Calculations at 1250 and 1350°C are shown with solid and dashed lines respectively. The ratio $SiO_2 : Al_2O_3$ is 2 : 1. In (a) the oxygen partial pressure is 10^{-17} bar. In (b) the oxygen partial pressure is 10^{-20} bar.



(a)



(b)

Fig. 7. Quantity of phase for a system with one mole of components as a function of nitrogen partial pressure. Calculations at 1250 and 1350°C are shown with solid and dashed lines respectively. The ratio $SiO_2 : Al_2O_3$ is 1 : 1. In (a) the oxygen partial pressure is 10^{-17} bar. In (b) the oxygen partial pressure is 10^{-20} bar.

4 Conclusions

This paper sets out the thermodynamic basis for β'-sialon powder synthesis and describes the variables which must be controlled to obtain materials of desired phase composition, chemistry and morphology.

The most important variables in the β'-sialon synthesis are partial pressures of oxygen and nitrogen, Si : Al ratio in the precursor mixture and the temperature. The β'-sialon single-phase region exists only within a small region of oxygen and nitrogen partial pressures.

Thermodynamic calculations in the SiAlON system help to screen the most effective β'-sialon synthesis conditions and give guidelines for experimental work.

Acknowledgment

One of the authors (L. Dumitrescu) is grateful to the Swedish Institute for financial support.

References

1. Jack, K. H., Sialon and related nitrogen ceramics. *J. Mater. Sci.*, **11** (1976) 1135–58.
2. Edrees, H. J. & Hendry, A., Pressureless sintering of pre-prepared sialon powders. In *Complex Microstructures*, ed. D. P. Thompson. 1989, pp. 49–52.
3. Higgins, I. & Hendry, A., The mechanism of formation of β'-sialon from oxides. In *Novel Fabrication Processes and Applications*, ed. R. W. Davidge, 1987, pp. 163–77.
4. Barry, T. I., (ed.). *The Industrial Use of Thermochemical Data*. The Chemical Society, 1979.
5. Hayes, F. H. (ed.), *User Aspects of Phase Diagrams*. Institute of Metals, 1991.
6. Olson, G. B., Science of steel. In *Innovations in Ultrahigh-Strength Steel Technology*, ed. G. B. Olson, W. Azrin & E. S. Wright. Sagamore Army Materials Research Conf. Proc., 1987, pp. 3–66.
7. Yamada, W., Matsumiya, T. & Sundman, B., Development of a simulator of solidification path and formation of nonmetallic inclusions during solidification of stainless steels. In *Computer Aided Innovation of New Materials*, ed. M. Doyama, T. Suzuki, J. Kihara & R. Yamamoto. North Holland, 1991, pp. 587–90.
8. Eriksson, G. & Johansson, T., Chemical and thermal equilibrium calculations for a quantitative description of a non-isothermal reactor, with application to the silicon arc furnace. *Scand. J. Metall.*, **7** (1978) 264–70.
9. Jansson, B., Schalin, M., Selleby, M. & Sundman, B., The Thermo-Calc database system. In *Computer Software in Chemical and Extractive Metallurgy*, ed. C. W. Bale & G. A. Irons. CIM, 1993, pp. 57–71.
10. Sundman, B., Review of alloys modelling. *Anales de Fisica Serie B*, **86** (1991) 69–82.
11. Hillert, M. & Jonsson, S., Thermodynamic calculation of the Si–Al–O–N system. *Z. Metallkd.*, **83** (1992) 720–8.
12. Gauckler, L. J. & Petzow, G., Representation of multicomponent silicon nitride based systems. In *Nitrogen Ceramics*, ed. F. L. Riley. Noordhoff International Publishing, 1977, pp. 41–63.
13. Gauckler, L. J., Lukas, H. L. & Petzow, G., Contribution to the phase diagram Si_3N_4–AlN–Al_2O_3–SiO_2. *J. Am. Ceram. Soc.*, **58** (1975) 346–7.
14. Naik, I. K., Gauckle, L. J. & Tien, T. Y., Solid–liquid equilibria in the system Si_3N_4–AlN–SiO_2–Al_2O_3. *J. Am. Ceram. Soc.*, **61** (1978) 332–5.
15. Dörner, P., Gauckler, L. J., Krieg, H., Lukas, H. L., Petzow, G. & Weiss, J., Calculation of heterogeneous phase equilibria in the SiAlON system. *J. Mat. Sci.*, **16** (1981) 935–43.
16. Guillerment, A. F., Study of the thermodynamic properties of the Co–Fe–Ni–W–C system. PhD Thesis, Royal Institute of Technology, Stockholm, 1988.
17. Hallstedt, B., Thermodynamic assessment of the system MgO–Al_2O_3. *J. Am. Ceram. Soc.*, **75** (1992) 1497–507.
18. Sundman, B., Jansson, B. & Andersson, J.-O., The Thermo-Calc databank system. *Calphad*, **9** (1985) 153–90.
19. Jansson, B., A general method for calculating phase equilibria under different types of conditions. Trita-Mac 0233, Royal Institute of Technology, Stockholm, 1984.
20. Teoreanu, I., Andronescu, E., Dumitrescu, L. F. S. & Rowcliffe, D., Factors affecting the synthesis of sialon. In *Third Euro-Ceramics*, Vol. 1, ed. P. Duran & J. F. Fernandez. Faenza Editrice Iberica S. L., 1993, pp. 1053–8.

Journal of the European Ceramic Society **15** (1995) 95–99
© 1995 Elsevier Science Limited
Printed in Great Britain. All rights reserved
0955-2219/95/$9.50

Oxygen Enrichment at Inversion Domain Boundaries in Aluminium Nitride—Influence on Thermal Conductivity

G. Gorzawski,[a,b] M. Sternitzke,[a] W. F. Müller,[b] A. Berger[c] & G. Müller[c]

[a] Fachbereich Materialwissenschaft and [b] Institut für Mineralogie, Technische Hochschule Darmstadt, D-642 87 Darmstadt, Germany
[c] Fraunhofer Institut für Silicatforschung, D-97082 Würzburg, Germany

(Received 10 December 1993; accepted 10 May 1994)

Abstract

Inversion domains (IDs) are a common feature in the microstructure of AlN ceramics. It is shown by transmission electron microscopy (TEM) that the frequency of IDs can be influenced to a large extent by processing and sintering parameters. Evidence is presented that the presence of IDs has a favourable effect on thermal conductivity. This is explained by oxygen trapping at the inversion domain boundaries (IDBs). Direct proof for the oxygen enrichment at the IDBs is given by electron energy-loss spectroscopy (EELS) in combination with TEM.

1 Introduction

High thermal conductivity makes AlN ceramics (wurtzite-type crystal structure with space group $P6_3mc$) an attractive material for electronics. Slack[1] reported that thermal conductivity decreases linearly by dissolution of oxygen in the lattice of AlN single crystals. Oxygen can be incorporated into the AlN lattice by the following reaction:

$$Al_2O_3 \Rightarrow 2Al_{Al} + [\ ]_{Al} + 3O_N$$

($[\ ]_{Al}$ denotes an aluminium vacancy). Besides other defects inversion domains (IDs) have been frequently observed within the grains of AlN ceramics.[2–5] The character of the inversion domain boundaries (IDBs), showing Al–Al or N–N bonds, suggests an incorporation of oxygen. In fact, energy dispersive X-ray analysis (EDX) by Westwood & Notis indicates the presence of oxygen at the IDBs.[5]

Transmission electron microscopy (TEM) contrast analysis of different defect structures has led to a model for nucleation of IDs. In previous papers a description of inversion domain nucleation in combination with dislocations has been given.[6,7] The aim of this work was to investigate the oxygen enrichment at IDBs and their influence on thermal conductivity of the ceramic. For this purpose, it was necessary to control the formation and growth of IDs during processing. The oxygen distribution across IDBs has been measured by electron energy-loss spectroscopy (EELS). EELS in combination with TEM allows the quantitative determination of the oxygen content in AlN with a high spatial resolution. This method has been applied to AlN ceramics in earlier investigations.[8,9]

2 Experimental

Two different AlN starting powders were used. Powder A (Grade B, H. C. Starck, Berlin, Germany) has a medium particle size of 1·3–2 μm and a total oxygen content of 1·8 wt%. Powder B (Grade F, Tokuyama Soda, Tokyo, Japan) has a medium particle size of 1·2 μm and a total oxygen content of 1 wt%. Mixtures of both AlN powders and Y_2O_3 powder (H. C. Starck, Berlin, Germany) were attrition milled using Al_2O_3 balls in isopropanol. Y_2O_3 is a usual sintering aid for AlN ceramics. Attrition milling time was varied between 30 min and 8 h and Y_2O_3 addition between 0 and 4 wt%. Cold isostatically pressed cylinders were sintered in a gas-pressure sintering furnace with graphite heating elements under a pressure of 0·2 MPa N_2. End temperatures ranged between 1750°C and 2000°C and sintering times between 30 min and 4 h.

Hot gas extraction analysis (TC-436, LECO Co., St. Joseph, MI, USA) was carried out for selective determination of lattice-dissolved oxygen and oxide-bound oxygen of AlN ceramics.[10] Thermal conductivity was measured by a comparative method according to DIN 51908. In this measuring technique a cylindrical shaped sample (d = 18 mm, h = 20 mm) is placed in series with a reference cylinder between two heat reservoirs at constant temperatures (20 and 40°C). Thermal conductivity is derived by measuring the thermal gradient in the reference sample. The measuring range is 10 to 200 W/(mK) with an accuracy of ~3%.

Starting powders and sintered samples were investigated by TEM (Model Philips CM12, Eindhoven, The Netherlands, with 120 kV acceleration voltage). About 1000 grains of each sample were examined in order to determine the fraction of grains that contains dislocations or IDs. For TEM investigations grains of the uncrushed starting powders were transferred from a suspension in ethanol to a copper grid covered with a C-film after ultrasonic treatment. Electron transparent samples of the compact ceramics were prepared by argon ion milling.

The TEM is equipped with a parallel electron energy-loss spectrometer (PEELS, Model 666, Gatan, Pleasanton, CA, USA) and a double tilt specimen holder cooled with liquid nitrogen (Model 636, Gatan). Cooling of the specimen was necessary to prevent contamination effects. The EELS measurements were all recorded using the convergent beam mode in the TEM to provide a high spatial resolution. The illumination half-angle was 7 mrad, the collection half-angle was in the range of 10 to 20 mrad, the integration time was 25 ms for the low loss spectra and 100 s for the core-loss spectra, and the probe current density was approximately 3×10^6 e^-/nm^2. The EELS measurements allow the quantitative determination of the concentration ratio of nitrogen and oxygen ([N]/[O]) and of the sample thickness.[8] The complex data acquisition and processing in EELS is described in the literature.[11,12] Concentration profiles were measured by recording EEL spectra of a series of spots on a line across the IDB. The distance from the spots to the IDB was determined using the measuring function of the TEM. A series of micrographs with different exposure times was taken to estimate the electron spot size. A plot of the reciprocal exposure time versus the radius of the spot led to a Gaussian distribution with a full width half maximum (FWHM) of 15 nm in one case and 20 nm in another.

Spontaneous growth of an oxide layer at room temperature in air has to be taken into account for quantitative measurements of oxygen concentrations. In an earlier paper a method has been reported that enables the determination of the thickness of such oxide layers. The [N]/[O] ratios can then be corrected for the influence of the oxide layer.[8]

3 Results and Discussion

3.1 Occurrence of IDs during ceramic processing

Investigations of the starting powders show the presence of dislocations in both AlN powders. 90% of the grains in powder A contain dislocations, generally with a high dislocation density. The dislocations are connected to hexagonal networks in approximately 1% of the grains. By contrast, less than 1% of the grains in powder B have dislocations. While no IDs were found in starting powder A, 1% of the grains of powder B, contain IDs. Powder B was used to investigate the influence of attrition milling time on the amount of grains containing dislocations. The results are plotted in Fig. 1. Obviously, longer times of attrition milling increase the number of dislocations in the starting powder. Cold isostatic pressing of the mixed powders does not change the defect structures.

The defect structure of AlN ceramics after sintering was also investigated. IDs can be observed in ceramics made from both starting powders. They are often connected with dislocations. The amount of IDs in the sintered ceramics using powder B depends on the attrition milling time of the powder mixtures and therefore on the amount of dislocations. A higher amount of dislocations in the starting powder yields a higher number of IDs in the ceramic, as shown in Fig. 1. Powder A initially contains many grains with dislocations, therefore IDs were always observed in the sintered ceramic.

The fraction of grains containing IDs in ceramics of powders A and B after 8 h attrition milling depends on sintering temperature and Y_2O_3 content.

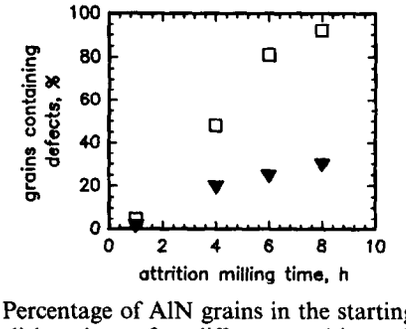


Fig. 1. □, Percentage of AlN grains in the starting powder B containing dislocations after different attrition milling times. The symbols ▼ represent the number of grains containing IDs of the sintered ceramics (1800°C).

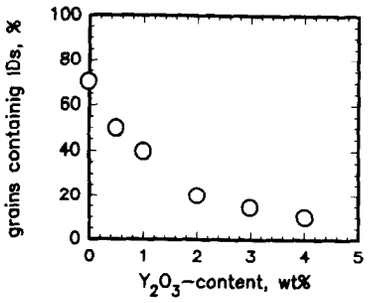


Fig. 2. Percentage of AlN grains containing IDs as a function of the Y_2O_3 content. The AlN ceramics were sintered at 1850°C for 1 h.

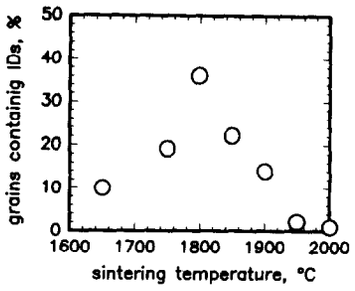


Fig. 3. Percentage of AlN grains containing IDs as a function of sintering temperature. The AlN ceramics were sintered with 2 wt% Y_2O_3 for 1 h.

Figure 2 shows the dependence of the number of IDs per 100 grains on Y_2O_3 content for a ceramic of powder A after sintering at 1850°C. As can be seen, the number of IDs decreases rapidly with an increasing Y_2O_3 content (Fig. 2). The correlation between IDs and temperature is presented in Fig. 3. A maximum of IDs is reached at 1800°C. The number of IDs drops to zero for the sintering temperature of 2000°C. Sintering time was investigated in the range between 30 and 240 min. For these sintering times no influence on the number of grains containing IDs has been found.

3.2 Thermal conductivity

Table 1 compares the oxygen content, number of IDs, and thermal conductivity of three pairs of differently sintered AlN ceramics. The difference between the two samples of each pair is that samples 1a, 2a and 3a were attrition milled for 1 h and samples 1b, 2b, and 3b, 6 h. Different dislocation densities in the powders and finally different numbers of IDs were found in each sample pair a and b (Table 1).

According to hot gas extraction analysis the powders take up oxygen during attrition milling. However, as can be seen in Table 1, milling time only increases the total oxygen concentration, not the lattice oxygen content. In the series of samples 1a to 3a and 1b to 3b thermal conductivity decreases. This is caused by an increase of the oxygen content dissolved in the AlN lattice. This in turn is a function of the Y_2O_3 content and the sintering conditions, as has been shown in several papers.[1,13]

There is no significant difference in lattice dissolved oxygen between samples a and b of each pair. However, thermal conductivity is always higher in sample a. This indicates that the presence of IDs has a favourable effect on thermal conductivity. This influence can be understood if indeed, as stated in the introduction, oxygen impurities are trapped at and dragged along with the IDBs. In this case the growth of the IDs would purify the interior of the IDs and thus increase their thermal conductivity. The IDs themselves must be supposed to be thermal conductivity barriers, but as they are very thin they probably are not very effective.[13] Oxygen segregated at the IDBs and oxygen dissolved in the AlN lattice cannot be distinguished by hot gas extraction analysis. Therefore, EELS in combination with TEM is necessary for a definite proof of the oxygen segregation at the IDBs.

The results described show the influence of IDs on thermal conductivity. Higher concentration of IDs increases the thermal conductivity. A low Y_2O_3 content is one condition to achieve a high concentration of IDs. However, a low oxygen content in the lattice resulting from high Y_2O_3 contents improve thermal conductivity. Therefore, the effect of improving thermal conductivity by IDs is contrary to the effect of high Y_2O_3 contents.

Table 1. Sintering and preparation conditions, oxygen contents, thermal conductivity and number of IDs for selected samples of powder B

Sample	*T (°C)*	*t (h)*	*Y_2O_3 (wt%)*	*Attrition milling (h)*	*$[O]_{total}$ (wt%)*	*$[O]_{lattice}$ (wt%)*	*Thermal conductivity (W/mK)*	*Number of IDs per 100 grains*
1a	1850	2	4	6	2·54 (5)	0·17 (5)	179 (6)	10
1b	1850	2	4	1	1·70 (5)	0·15 (5)	165 (6)	1
2a	1800	3	2	6	1·83 (5)	0·22 (5)	141 (6)	35
2b	1800	3	2	1	1·10 (5)	0·19 (5)	119 (6)	1
3a	1800	2	2	6	2·20 (5)	0·28 (5)	121 (6)	30
3b	1800	2	2	1	1·52 (5)	0·25 (5)	93 (6)	1

3.3 Oxygen enrichment at inversion domain boundaries

Figure 4(a) shows a TEM micrograph of an ID from sample 3a of Table 1. The end of the ID, where a planar and a curved IDB run close together, is shown. The planar IDB is oriented // (0001) in the AlN crystal. Figure 4 (b) gives the oxygen concentration profile measured by EELS across these two IDBs. Significantly increased oxygen concentrations with values of ~8 at.% at the IDBs have been found.

The width of the boundaries is small compared to the electron spot size of approximately 15 nm. The distance between the two IDBs is also 15 nm. The maximum of the profile in Fig. 4(b) therefore cannot be interpreted as the real oxygen concentration at the IDB. The measured oxygen concentration profile (Fig. 4(b)) represents the true oxygen distribution convoluted with the intensity distribution of the electron spot. A convenient method to interpret this type of profile, is the calculation of theoretical profiles and comparison to the measured one. The first step is to assume an ideal rectangular oxygen distribution. The oxygen incorporation at the IDBs can be described in terms of small oxygen layers similar to those in polytypes.[14] In the following calculations Al_2O_3 layers with an oxygen concentration of 60 at.% were assumed. High-resolution TEM investigations show that the width of an IDB is approximately 0·5–1 nm. These results agree with current studies.[15] Consequently, for the profile calculations a rectangular oxygen distribution with a width of 1·6 nm (two parallel IDBs) and a height of 60 at.% was convoluted with a Gaussian function (FWHM = 15 nm, diameter of the electron spot) and drawn in Fig. 4(b) as a solid line. The model corresponds reasonably with the measured data. However, the accuracy of the method is not sufficient to derive explicit values for the true oxygen concentration at the IDB.

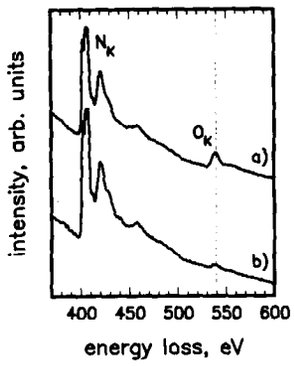


Fig. 5. EEL spectra measured (a) exactly at the IDB and (b) 35 nm beside the IDB. The EEL spectra include the characteristic N_K and O_K ionization edges.

Two typical EEL spectra are presented in Fig. 5. The range of energy loss is 370 to 600 eV including the N_K and O_K edges. The first EEL spectrum (a) was measured directly at the IDBs in Fig. 4 (x = 0). EEL spectrum (b) was recorded in a distance of 40 nm from the IDBs.

Figure 6(a) shows typical IDs of dome-like shape. A second EELS measurement (Fig. 6(b)) was obtained across one whole ID, including both the curved and planar boundary (see marks in Fig. 6(a)). The solid line in Fig. 6(b) was calcu-

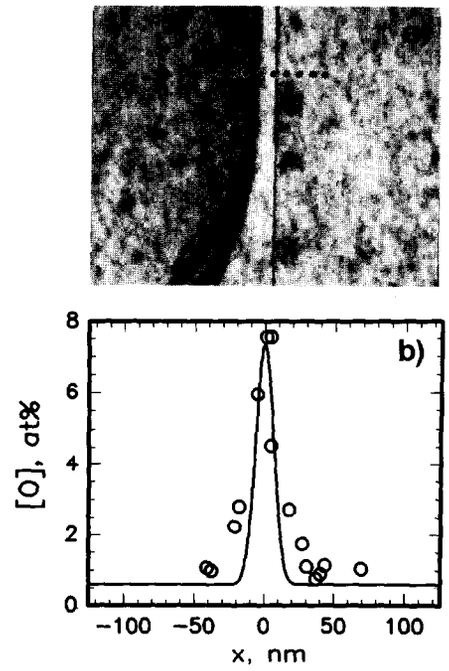


Fig. 4. (a) TEM micrograph of two IDBs. The primary beam is oriented // [$\bar{1}2\bar{1}0$]; (b) the oxygen concentration profile across the IDBs of (a) with the same scale.

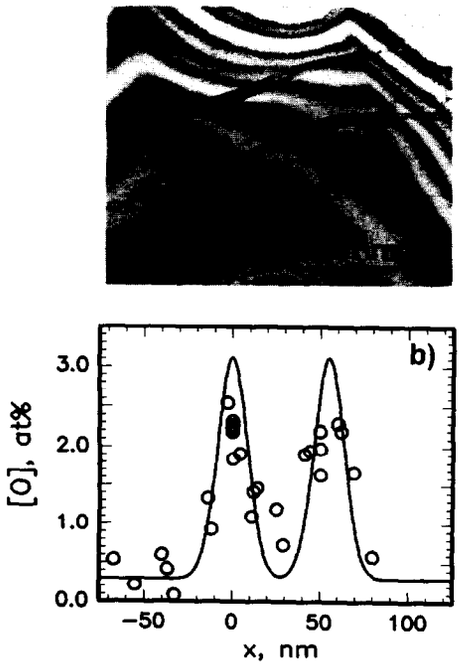


Fig. 6. (a) TEM micrograph of an AlN grain showing IDs. The primary beam is oriented // [$\bar{1}2\bar{1}0$]. (b) The oxygen concentration profile measured along the marked line.

lated using the same model as in the first example. In this case the width of each IDB amounts to 0·8 nm, the height to 60 at.% and the spatial resolution to 20 nm. The oxygen enrichment at the IDBs is again obvious.

4 Conclusions

It has been shown that the concentration of IDs in sintered AlN ceramics can be controlled by the powder processing and sintering parameters. The processing parameters chosen do not affect the total oxygen content within the AlN grains. Therefore, the influence of IDs on thermal conductivity can be evaluated directly. Evidence is presented that thermal conductivity increases with the concentration of IDs.

EELS in combination with TEM was successfully used to prove oxygen enrichment at IDBs. The improved thermal conductivity can be interpreted as an indirect result of this oxygen enrichment at the IDBs, if it is assumed that the lattice oxygen content is lowered inside the ID. This assumption has to be proved by further EELS measurements. In view of recent models[13] it seems reasonable that the positive effect on thermal conductivity resulting from the lower lattice oxygen content inside the ID overrides the negative influence of the oxygen enrichment at the narrow IDBs.

Acknowledgements

This work has been supported by the Deutsche Forschungsgemeinschaft, which is gratefully acknowledged. Thanks are also due to the Materials Research Department of Hoechst AG, Frankfurt, where the measurements of thermal conductivity have been made.

References

1. Slack, G. A., Nonmetallic crystals with high thermal conductivity. *J. Phys. Chem. Solids*, **34** (1973) 321–35.
2. Denanot, M. F. & Rabier, J., Characterisation of the microstructure of sintered AlN by transmission electron microscopy. *Mater. Sci. Engineering*, **A109** (1989) 157–160.
3. Hagege, S., Ishida, Y. & Tanaka, S., TEM analysis of impurity induced microstructures in sintered aluminium nitride ceramics. *Nippon Seramikkusu Kyokaki Gakujutsu Ronbunshi*, **92** (1988) 1119–26.
4. Berger, A., Inversion domains in aluminium nitride. *J. Am. Ceram. Soc.*, **74**(5) (1991) 1148–51.
5. Westwood, D. & Notis, M. R., Inversion domain boundaries in aluminium nitride. *J. Am. Ceram. Soc.*, **74**(6) (1991) 1226–39.
6. Berger, A., Nucleation and growth of inversion domains in AlN. Part I: Study of fundamental processes. *J. Am. Ceram. Soc.*, 1995.
7. Gorzawski, G., Weber, O., Berger, A. & Müller, W. F., Nucleation and growth of inversion domains in AlN. Part II: Study of advanced configurations. *J. Am. Ceram Soc.*, 1995.
8. Sternitzke, M., Growth of oxide layers on thin aluminum nitride samples measured by EELS. *J. Am. Ceram. Soc.*, **76**(9) (1993) 2289–94.
9. Sternitzke, M. & Müller, G., EELS study of oxygen diffusion in aluminum nitride. *J. Am. Ceram. Soc.*, **77**(3) (1994) 737–42.
10. Thomas, A. & Müller, G., Determination of the concentration of oxygen dissolved the AlN lattice by hot gas extraction from AlN ceramics. *J. Eur. Ceram. Soc.*, **8** (1991) 11–19.
11. Egerton, R. F., *Electron Energy-Loss Spectroscopy in the Electron Microscope*. Plenum Press, New York, 1986.
12. Disko, M. M., Ahn, C. C. & Fultz, B. (ed.), *Transmission Electron Energy Loss Spectrometry in Materials Science*. The Minerals, Metals and Materials Society, Warendale, PA, 1992.
13. Buhr, H. & Müller, G., Microstructure and thermal conductivity of AlN(Y_2O_3) ceramics sintered in different athmospheres. *J. Eur. Ceram. Soc.*, **12** (1993) 271–8.
14. Jack, K. H., Review—Sialons and related nitrogen ceramics. *J. Mat. Sci.*, **11** (1976) **11** 1135–58.
15. Ishida, Y., Hagege, S., Ichinose, H. & Takahashi, Y., High-resolution electron microscopy of ceramic interfaces. *J. Electr. Microsc, Techn.*, **12** (1989) 244–51.

Journal of the European Ceramic Society **15** (1995) 101–107
© 1995 Elsevier Science Limited
Printed in Great Britain. All rights reserved
0955-2219/95/$9.50

Laminar Ceramic Composites

T. Chartier, D. Merle & J. L. Besson

LMCTS, URA CNRS 320, ENSCI, 47 av. Albert Thomas, 87065 Limoges, France

(Received 18 April 1994; accepted 27 June 1994)

Abstract

The processing of laminar ceramic composites from stacking of layers obtained by tape casting is described. In the case of composites for structural applications, the reinforcement mechanisms are briefly reviewed. It is shown that both strength and toughness can be improved. The evaluation of residual stresses allows a strategy for tailoring the mechanical properties of such composites to be developed. As an example, results are given in the case of laminar composites with layers made of alumina with various zirconia contents.

1 Introduction

Designers require materials with higher and higher performances. Sometimes, materials must be corrosion resistant at elevated temperatures while retaining high mechanical properties (rupture strength and toughness). Ceramic materials, such as alumina, silicon carbide, silicon nitride or mullite seem to be potential candidates for such applications. However, these materials, like all the monolithic ceramics, are brittle, which limits their use in numerous systems.

The usual approach to improve the mechanical behaviour is to eliminate the flaws that initiate the catastrophic failure, or at least to reduce their size. Recently, new strategies have emerged that are fundamentally different from the conventional approach. These strategies involve energy dissipative mechanisms to develop 'flaw-tolerant' materials. Among them are the ceramic–ceramic composites. In the flaw tolerance approach, the microstructure is designed to promote the bridging of the cracks which leads, in the ideal case, to the strength being independent of flaw size. The process must produce a material generally with two phases, with a controlled heterogeneous microstructure. The presence of the second phase, either long fibres, whiskers or particles (zirconia, for instance) enhances the mechanical properties.

Long fibre-reinforced ceramics exhibit high mechanical and thermomechanical properties. However, the routes available to process the matrix (i.e. infiltration or impregnation across a fibre fabric) are expensive, and only parts with limited thickness can be obtained. Moreover, carbon or silicon carbide fibres, which are the most used, exhibit a limited thermal stability in oxidizing environments.

By contrast, whisker- or particle-reinforced ceramic composites can be processed following classical routes. The reinforcing phase may be dispersed quasi-isotropically in the matrix, whereas some processing techniques, such as tape casting, allow a preferential orientation of whiskers.

Special attention must be focused on laminar composites. Whereas laminar composites with organic matrix are well developed, laminar composites with ceramic matrix are relatively new. These structures provide the advantage for tailoring the properties by stacking layers of different compositions in a suitable sequence.[1–17] Then, it is possible to produce functionally gradient ceramics. Tape casting, which is extensively used for electronic ceramics, is well suited to the fabrication of ceramic sheets that can be reinforced by whiskers or particles.

In this paper, the different mechanisms that can be used to reinforce laminar composites will be briefly reviewed in the first section. Then, the next section will deal with the processing by tape casting of laminar ceramic composites. The classical laminated plate theory will be used to predict the composite behaviour in the third section and the results compared with the experimental data obtained for alumina–zirconia composites.

2 Strengthening and Toughening Mechanisms in Laminar Ceramic Composites

Laminar ceramic composites consist of alternate layers reinforced by whiskers or particles. This type of composite allows the association of two

Table 1. Strength to failure σ_f (MPa) (four-point bend test) and toughness K_c (MPa$\sqrt{m}$) (SENB)

		SiC_w (vol·%)						
Forming		*0*	*10*	*20*	*30*	*40*	*50*	*Ref.*
Tape casting	σ_f	320	470	560	670	940	805	1
	K_c	2·73	3·46	4·54	5·69	6·85	6·5	
Extrusion moulding	σ_f			407				18
	K_c			4·6				
Slip casting	σ_f			452				18
	K_c			4·44				
Slip casting	σ_f			438				20
	K_c			4·6				

reinforcing mechanisms: the first one, acting at the scale of the microstructure, inside the layers, due to the second phases, leading to flaw-tolerant materials; the second one, acting at a macroscopic scale, due to the interfaces between the layers. The aim is to improve both the toughness and the strength.

2.1 Reinforcement mechanisms inside the layers

2.1.1 Whiskers

The incorporation of whiskers allows load transfers from the matrix to the whiskers (crack bridging) and crack deflection. An optimum toughening is achieved by loading whiskers by internal compressive stresses. Hence, the matrix–whisker couple must be judiciously chosen with a thermal expansion coefficient mismatch and chemical compositions leading to an appropriate bonding.

Whisker reinforced composites have already been the subject of numerous studies.[1,6,18–23] Some results concerning SiC_w reinforced mullite are reported in Table 1.

2.1.2 Particles

Zirconia-toughened ceramics are the best example of particle-reinforced materials.[24–30] The most effective toughening mechanism in ZrO_2-containing ceramics is the stress-induced transformation of small ZrO_2 particles in their metastable tetragonal state. Both toughness and strength can be increased, although a compromise between these two effects must be accepted.[31] Other mechanisms, that is, crack deflection and microcracking around monoclinic particles, increase toughness but generally at the expense of strength.

The transformation of zirconia particles is also used to develop compressive surface stresses, increasing the modulus of rupture.

Some results obtained on zirconia-reinforced alumina are given in Table 2.

Table 2. Strength to failure σ_f (MPa) (four-point bend test) and toughness K_c (MPa$\sqrt{m}$) (SENB)

		ZrO_2 (vol.%)					
Forming		*0*	*5*	*10*	*15*	*20*	*Ref.*
Pressing	σ_f		459	412	285		30
	K_c		5·8	6·2	6·2	5·7	
Slip casting	σ_f		382	390	370		30
	K_c		5·7	5·5	4·9		
Tape casting	σ_f	335	441	444			3
	K_c	4·6	4·9	5·4			

2.2 Reinforcement mechanisms at layer interfaces

The laminar ceramic–ceramic composites must fulfill two requirements:

—improve the toughness and the work of rupture,
—improve the modulus of rupture in bending.

The first objective is obtained using mechanisms involving crack 'clamping' stresses, crack deflection or microcracking, that operate at a macroscopic scale, thanks to the laminar structure of the material, instead of operating at a local scale (microstructure).

In the laminar structure, residual stresses develop during cooling from the sintering temperature because of the difference in thermal expansions between layers of different compositions. But, contrary to the case of monoliths, these stresses built up in the whole volume of the layers. The sign and the magnitude of these stresses may be adjusted through the compositions (ZrO_2 amount in Al_2O_3–ZrO_2 composites), but also through the layer thickness. Hence, it is possible to develop high compressive stresses in thin layers whereas the tensile stresses remain low in the associated thick layers. The propagation of the crack in mode I being impeded by the compressive stresses, propagation modes I and III can occur, leading to crack deflection at the interface and to an increase of the surface of rupture. An example is given by Chartier and coworkers[3,5] for alumina–zirconia composites.

Crack deflection at the layer interface can be favoured by a weak interlayer bond. Clegg *et al.*[10] have fabricated SiC-graphite laminar composites that, although the onset of microcracking appears at 500 MPa, exhibit an ultimate strength three times higher, an apparent toughness (calculated from the ultimate strength) of 15 MPa$\sqrt{m}$ and a work of fracture of 4625 Jm^{-2}. For comparison, the modulus of rupture, the toughness and the work of fracture of monolithic SiC were 500 MPa, 3·6 MPa$\sqrt{m}$ and 25 Jm^{-2}, respectively.

Toughness can also be enhanced by deflection

of the growing crack at a porous layer in laminar composites consisting of a sequence of dense and porous layers.[9]

Folsom *et al.*[11] have developed composites with alumina and carbon fibre-reinforced epoxy resin layers in which alumina sheets provide high strength, high stiffness and abrasion resistance, whereas the fibre-reinforced sheets provide high toughness and flaw tolerance. They suggest that composites for high-temperature applications could be designed in a similar way, replacing the epoxy resin by an inorganic glass.

The second objective is reached by choosing for the outer layers a material with a thermal expansion coefficient smaller than the inner layer one. In this configuration, the outer layers sustain compressive stresses.[2,5]

3 Processing of Alumina–Zirconia Laminar Composites

Laminar composites consisting in a regularly alternate stacking of $(2n + 1)$ layers made of alumina with various zirconia content (Al_2O_3 = A; Al_2O_3 + 5 vol.% ZrO_2 = AZ5; Al_2O_3 + 10 vol.% ZrO_2 = AZ10) were fabricated by tape casting, stacking, thermocompression, pyrolysis of organic components and sintering. The sequences were chosen to put the outer layers in a compressive state. The layer thickness was adjusted by superposing a variable number of individual identical tapes. So the AZ10/AZ5/AZ10 composite with n = 2 was fabricated by stacking five layers, each consisting in three identical tapes whereas the AZ10/AZ5/AZ10 composite with n = 10 was fabricated with 21 alternate tapes.

Tape casting is the prominent process for producing homogeneous wide and thin (25–1000 μm) ceramic sheets with controlled thicknesses and smooth surfaces.[32] Tape casting, basically, consists in depositing a suspension composed of the ceramic powder and organic components on a support, either by spreading under a blade (doctor blade process) or by coating. Typical applications are substrates of Al_2O_3 (or AlN) for thick- and thin-film circuitry and $BaTiO_3$ for multilayer capacitors, which represent the two principal markets in electronic ceramics. Tape casting is now used on a larger scale to produce thin ceramic sheets and multilayer structures of various materials for different applications. The evaporation of the solvents leads to a dried green tape with sufficient strength and flexibility to be handled and cut to the proper shape. After removal of organic components, green sheets or multilayer systems made by stacking and laminating green sheets are sintered.

3.1 Slurry formulation

The composition of the slurry and the drying stage greatly affect the microstructure and hence the properties of the green tapes (density and strength). The rheological behaviour of the slurry is an important parameter for the homogeneity and the microstructure of the green tape, and for the reproducibility of the process. Tape-casting slurries are complex, multicomponent systems, which contain ceramic powders (including sintering aids), solvents, dispersants, binders and plasticizers. The control of such a system requires the knowledge of the role of each component.

3.1.1 Powder

Powders of fine particle size are used to obtain thin films, smooth surfaces, high densities and small critical flaw size. The particle size distribution greatly influences the rheology of the slurry. The starting powders are 99·7 wt% purity, 0·5 μm grain size alumina (P172SB, Péchiney, France) and 97·5 wt% purity, 0·4 μm grain size zirconia (UPH 12, Criceram, France).

3.1.2 Solvent

The solvents ensure the dissolution of all organic components (i.e. dispersant, binders and plasticizers) to give an homogeneous slurry. Interactions between the solvent and the solid surfaces influence the further adsorption of the dispersant and of the binders, and then the stability and the rheological behaviour of the slurry. Mixtures of organic solvents, and particularly binary systems, are preferred for solubility reasons: the various organic additives have their higher solubility in different solvents. The solvent used is an azeotropic mixture of methyl ethyl ketone (MEK) and ethanol (40/60).

3.1.3 Dispersant

Dispersants are necessary to obtain a good deagglomeration and dispersion of the ceramic particles in the solvent, and to stabilize the tape-casting suspensions with a high ceramic–organic ratio. A stable dispersion of deagglomerated particles leads to a dense particle packing and to a homogeneous microstructure.

The best stabilization is given by a combination of electrostatic and steric repulsion (referred as electrosteric stabilization). The steric hindrance prevents contact between particles and the double layer, which may be due to net charge on the particle surface and/or charges associated with the adsorbed polymer, providing repulsion by a potential energy barrier at larger distances.

The dispersant used is a phosphate ester (Beycostat C213, CECA, France).

3.1.4 Binder

After evaporation of the solvent, the binders provide the strength to the green tape, to enable handling and subsequent processing steps like punching. Binders are polymeric molecules which adsorb on the particle surfaces and form organic bridges between them. The slurry should exhibit a shear thinning behaviour caused by an alignment of the binder molecules at high shear rate.

The binder used is a poly(vinyl butyral) (PVB).

3.1.5 Plasticizer

Most binders require the addition of plasticizers to improve the flexibility and workability of the green tape. Plasticizers are low molecular weight species which can reduce the glass transition temperature of the binder at room temperature or below, leading to a better plasticity. The addition of plasticizers modifies the mechanical properties of the green tape, the strain to failure increases but the strength decreases.

The plasticizer used is a mixture of poly(ethylene glycol) (PEG) and dibutyl phthalate (DBP).

The slurry must be adjusted, not only for tape casting but taking into account other processing parameters such as shaping (cutting, punching, thermocompression), pyrolysis of organic components and sintering (Table 3).

3.2 Slurry preparation

The preparation of slurries is carried out in two stages, namely (i) deagglomeration and dispersion of powders in the solvent with the aid of the dispersant, and (ii) homogenization of the slurry with binders and plasticizers. The sequence of component addition is critical. The dispersant has to be added before the binders to prevent competitive adsorption. The initial adsorption of the binder on the particle surfaces would prevent the dispersant from being subsequently adsorbed, thereby decreasing its effectiveness. Furthermore, the deagglomeration is more efficient in a low viscosity system (i.e. without binders and plasticizers) and the mechanical damage of the binder molecules is minimized by this sequence of addition. The deagglomeration is done by ultrasonic treatment. The second stage of homogenization is performed by milling for 24 h. The slurry is kept rotating at a slow speed for deairing and to prevent settling.

Table 3. Composition of a tape casting slurry

Component	*Function*	*vol.%*
Alumina + zirconia	Ceramic powder	30·6
MEK/ethanol	Solvent	57·6
Phosphate ester	Dispersant	0·8
PVB	Binder	4·6
PEG 300	Plasticizer	2·9
DBP	Plasticizer	3·5

3.3 Tape casting

Tape casting is performed with a laboratory tape-casting bench (Cerlim Equipement, Limoges, France). Slurries were tape cast onto a fixed glass plate with a moving double blade device at a constant speed of 1 m min^{-1}.

4 Evaluation of Residual Stresses in Alumina-Zirconia Laminar Composites

The determination of the distribution of the residual stresses allows the appropriate choice of the layer composition and thickness and of the stacking sequence, for an optimum reinforcement. Models have previously been developed for organic composites[33] or glass-to-metal seals.[34]

During cooling, the difference in deformation, due to the different thermal expansion coefficients of the layers, is accommodated by creep, as long as the temperature is high enough. Below a certain temperature, that will be called the 'joining' temperature, the different layers become bonded together and internal stresses appear.

For laminar composites with symmetrical stacking (odd number of layers) and with a low thickness compared with the plate size, the problem is that of an in-plane stress state with the stress normal to the surface equal to zero ($\sigma_{33} = 0$) (Fig. 1).

In the case of a solid with an isotropic, linear elastic behaviour, the mechanical strains are expressed as follow:

$$\varepsilon_{ijel} = \frac{1+\nu}{E}\sigma_{ij} - \frac{\nu}{E} Tr\tilde{\sigma}\delta_{ij} \qquad (1)$$

$$\varepsilon_{11} = \frac{1}{E}(\sigma_{11} - \nu\sigma_{22})$$

$$\varepsilon_{22} = \frac{1}{E}(\sigma_{22} - \nu\sigma_{11})$$

$$\varepsilon_{12} = \frac{1+\nu}{E}\sigma_{12}$$

$$\varepsilon_{33} = -\frac{\nu}{1-\nu}(\varepsilon_{11} + \varepsilon_{22})$$

$$\varepsilon_{13} = \varepsilon_{23} = 0$$

where $\tilde{\varepsilon}$ is the strain tensor, $\tilde{\sigma}$ the stress tensor, ν the Poisson ratio and E the Young modulus.

In a loading configuration which is symmetrical in respect to directions 1 and 2, and the axes 1 and 2 are equivalent (orthotropic system), then:

$$\sigma_{11} = \sigma_{22} \qquad (2)$$

and

$$\varepsilon_{11} = \frac{1 - \nu}{E}\sigma_{11} = \varepsilon_{22}$$

$$\varepsilon_{12} = \frac{1 + \nu}{E}\sigma_{12}$$

In each layer I, the total deformation after sintering, is the sum of an elastic component and of a thermal component. In the case of a perfectly rigid bonding between the layers, the total deformation will be the same for all the layers, then:

$$\varepsilon_{11}^I = \frac{1 - \nu_I}{E_I}\sigma_{11}^I + \alpha_I \Delta T = \text{constant} \qquad (3)$$

where ΔT is the difference in temperature between the actual temperature, T_o, and the joining temperature, T_j.

The force balance requires (in normal stresses):

$$\sum_I \sigma_{11}^I d_I = 0 \qquad (4)$$

where d_I is the thickness of the Ith layer.

That gives, for a symmetrical composite with $2n + 1$ alternate layers of type 1 and 2:

$$(n + 1)\sigma_{11}^1 d_1 + n\sigma_{11}^2 d_2 = 0 \qquad (5)$$

From eqns (3) and (5), it comes:

$$\sigma_{11}^1 = \frac{nE_1E_2d_2(\alpha_2 - \alpha_1)\Delta T}{n(1 - \nu_1)E_2d_2 + (n + 1)(1 - \nu_2)E_1d_1} \qquad (6)$$

and

$$\sigma_{11}^2 = -\frac{(n + 1)E_1E_2d_1(\alpha_2 - \alpha_1)\Delta T}{n(1 - \nu_1)E_2d_2 + (n + 1)(1 - \nu_2)E_1d_1} \qquad (7)$$

The magnitude of these stresses depends on the thermal expansion coefficient mismatch (that must be small enough to avoid delamination) and on the relative thickness of the layers.

In order to limit the sensitivity to surface flaws, the composite is tailored to develop compressive residual stresses in the outer layers. In the case of a symmetrical laminate, this is obtained by choosing the layer compositions so that the thermal expansion of the odd layers is smaller than the even ones ($\alpha_1 < \alpha_2$).

For a three layer composite ($n = 1$), the change

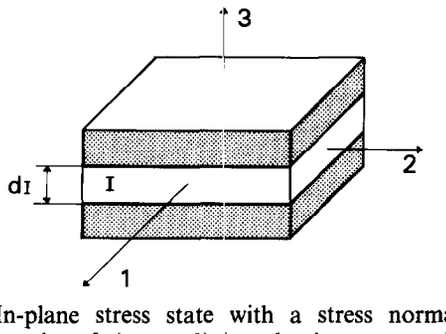


Fig. 1. In-plane stress state with a stress normal to the surface equal to 0 ($\sigma_{33} = 0$) in a laminar composite with a symmetrical stacking.

Table 4. Young modulus, Poisson ratio and thermal expansion coefficient of 'pseudo-laminar composites' consisting of 21 identical layers with a thickness of 160 μm in the green state

	E (GPa)	*ν*	*αΔT*
A/A	341	0·234	-120×10^{-4}
AZ5/AZ5	328	0·241	-125×10^{-4}
AZ10/AZ10	325	0·242	$-121{\cdot}5 \times 10^{-4}$

in compressive (σ_{11}^1) and tensile (σ_{11}^2) stresses with the thickness ratio ($x = d_2/d_1$) of the layers, taking $\nu_1 = \nu_2 = \nu$, is given by eqns (8) and (9):

$$\sigma_{11}^1(x) = \frac{E_1E_2(\alpha_2 - \alpha_1)\Delta T}{(1 - \nu)}\frac{x}{2E_1 + E_2x} \qquad (8)$$

$$\sigma_{11}^2(x) = -2\frac{\sigma_{11}^1(x)}{x} \qquad (9)$$

Figure 2 illustrates these changes for an A/AZ5 composite. The characteristics of the constitutive materials are given in Table 4.

The compressive stress increases when the d_2/d_1 ratio increases, whereas the tensile stress decreases. In the case of brittle materials, which have a high sensitivity to cracking under tensile stresses, the thickness of the layers in tension must be high enough to avoid catastrophic failure.

This result is consistent with Amateau & Messing[2] who observed a decrease in crack frequency in the inner layer (under tension) in a Al_2O_3 + y vol.% SiC_w (20/0/20) when d_2/d_1 increases from 1 to 4.

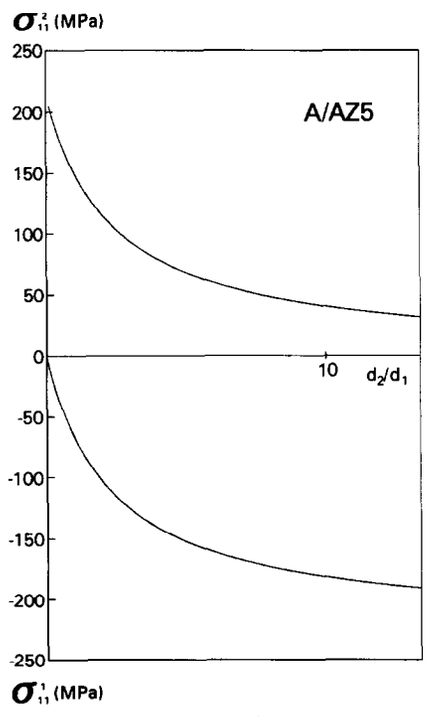


Fig. 2. Compressive stresses (σ_{11}^1) developed in alumina layers and tensile ones (σ_{11}^2) in alumina containing 5 vol.% zirconia layers versus the thickness ratio ($x = d_2/d_1$) in a A/AZ5 composite.

Table 5. Strength to failure σ_f (MPa) (three and four-point bend tests), toughness K_c (MPa$\sqrt{m}$) (SENB) and residual and calculated stresses

	K_c (MPa$\sqrt{m}$)	σ_f (three-point) (MPa)	σ_f (four-point) (MPa)	σ^1_{11} (MPa)	σ^2_{11} (MPa)	σt (calculated) (MPa)
A/A	4·6	335				
AZ5/AZ5	4·9	441	357			
AZ10/AZ10	5·4	444	351			
A/AZ5, $n = 10$	5·1	437		−114	126	449
AZ10/AZ5, $n = 2$			404	−60	90	411
AZ10/AZ5, $n = 10$	8·0	560		−118	130	562

5 Mechanical Properties of Alumina—Zirconia Laminar Composites

5.1 Characteristics of the layer materials

Young modulus and Poisson ratio of the materials were measured using a vibrating technique[35] on monoliths fabricated by stacking 21 identical layers ('pseudo-laminar composites'). The thermal expansion coefficient was measured from 20°C to 1400°C. 1400°C was taken as the joining temperature. The data are given in Table 4.

5.2 Mechanical properties

Table 5 shows the experimental results for ultimate strength in three-point and four-point bending (load normal to the layers), toughness measured by the SENB method (beam notched perpendicularly to the layer planes) together with the internal stresses and the calculated strength.

5.2.1 Flexural strength

In this sollicitation, and taking into account the fact that ceramics are more resistant in compression than in tension, the rupture is initiated in a zone in tension. It can develop either from surface flaws, or from internal defects located in the outest layer in tension.

In the first case, the rupture strength will be equal to the strength of material constituting the outer layer increased of the compressive residual stress.

In the second case, in contrast, the tensile internal stress overlaps the applied stress, leading to a strength lower than the strengths of the constitutive materials of the composite.

The experimental results in Table 5 show a good agreement with the strength calculated under the assumption of a rupture initiated from surface flaws. In fact, the processing flaws have their size limited to the thickness of the individual layer (about 135 μm after sintering) and their growth is impeded by the compressive stresses in the adjacent layers and by the deflection effects at the interfaces.

5.2.2 Toughness

The higher toughness of 'pseudo-laminar composites' AZ5/AZ5 and AZ10/AZ10 reflects the reinforcement due to the tetragonal–monoclinic transformation of zirconia particles. A slight increase of toughness is observed for A/AZ5/A composites in which the compressive stresses in the alumina layers contribute to the lowering of the stress field at the crack tip. The improvement is much higher for AZ10/AZ5/AZ10 composites in which the compressive stresses, induced by the phase transformation of the zirconia particles, are superimposed to the internal compressive stresses in the AZ10 layers, leading to a synergetic effect. Toughness increases from 4·9–5·4 to 8 MPa$\sqrt{m}$.

6 Conclusion

These results illustrate the interest of laminar ceramic–ceramic composites for structural applications. A similar concept could be used to design materials with an improved resistance to high-temperature corrosion. To achieve this goal, a corrosion-resistant material will be chosen for the outer layers and the inner layer will provide mechanical resistance.

Besides composites with layers differing by their mechanical, chemical or thermal properties, it is possible to create sequences of microstructures with different porosities or grain sizes. Hence, it could be possible to have a fluid to flaw through the composite or even to impregnate the composite with a metal (Ni, Al, etc.).

Laminar ceramic–ceramic composites afford an outstanding opportunity to create materials with functional gradients and have immense potential applications.

References

1. Wu, M., Messing, G. L. & Amateau, M. F., Laminate processing and properties of oriented SiC-whiskers reinforced composites. In *Proceedings on Composites: Processing, Microstructure and Properties*, ed. M. D. Sacks. American Ceramic Society, Westerville, OH, 1991, pp. 51–89.
2. Amateau, M. F. & Messing, G. L., Laminated ceramic composites. In *International Encyclopedia of Composites*, Vol. 3, ed. S. M. Lee. VCH, NY, 1990, pp. 11–16.

3. Charter, T., Besson, J. L. & Boch, P., Mechanical properties of ZnO_2–Al_2O_3 laminated composites. In *Advances in Ceramics, Science and Technology of Zirconia III*, Vol. 24, ed. S. Somiya, N. Yamamoto & Yanagida. American Ceramic Society, Westerville, OH, 1988, pp. 1131–8.
4. Boch, P., Chartier, T. & Huttepain, M., Tape casting of Al_2O_3/ZrO_2 laminated composites. *J. Am. Ceram. Soc.*, **69**(8) (1986) 191–2.
5. Chartier, T. & Besson, J. L., Behaviour of ZrO_2–Al_2O_3 laminated composites loaded by various mechanical arrangements. In *Science of Ceramics*, Vol. 14, ed. D. Taylor. The Institute of Ceramics, UK, 1988, pp. 639–44.
6. Kim, T., Amateau, M. F. & Messing, G. L., Residual stresses in SiC-whiskers–mullite laminated composite. In *Proceedings on Composites: Processing, Microstructure and Properties*, ed. M. D. Sacks. American Ceramic Society, Westerville, OH, 1991.
7. Russo, C. J., Harmer, M. P., Chan, H. M. & Miller, G. A., Design of laminated ceramic composite for improved strength and toughness. *J. Am. Ceram. Soc.*, **75**(12) (1992) 3396–400.
8. Harmer, M. P., Chan, H. M. & Miller, G. A., Unique opportunities for microstructural engineering with duplex and laminar ceramic composites. *J. Am. Ceram. Soc.*, **75**(7) (1992) 1715–28.
9. Takebe, H. & Morinaga, K., Fabrication and mechanical properties of lamellar Al_2O_3 ceramics. *J. Ceram. Soc. Jpn. Int.*, **96** (1988) 1122–8.
10. Clegg, W. J., Kendall, K., Alford, N. McN., Button, T. W. & Birrchall, J. D., A simple way to make tough ceramics. *Nature (London)*, **347**(6292) (1990) 455–7.
11. Folson, C. A., Zok, F. W., Lange, F. F. & Marshall, D. B., Mechanical behavior of a laminar ceramic/fiber-reinforced epoxy composite. *J. Am. Ceram. Soc.*, **75**(11) (1992) 2969–75.
12. Marshall, D. B., Ratto, J. J. & Lange, J. J., Enhanced fracture toughness in layered microcomposites of Ce–ZrO_2 and Al_2O_3. *J. Am. Ceram. Soc.*, **74**(12) (1991) 2979–87.
13. Virkar, A. V., Huang, J. L. & Cuttler, R. A., Strengthening of oxide ceramics by transformation-induced stresses. *J. Am. Ceram. Soc.*, **70**(3) (1987) 164–70.
14. Virkar, A. V., Jue, J., Hansen, J. & Cuttler, R. A., Measurement of residual stresses in oxide–ZrO_2 three-layer composites. *J. Am. Ceram. Soc.*, **71**(3) (1988) 148–51.
15. Hansen, J., Cuttler, R. A., Shetty, D. K. & Virkar, A. V., Indentation fracture response and damage resistance of Al_2O_3–ZrO_2 composites strengthened by transformation-induced residual stresses. *J. Am. Ceram. Soc.*, **71**(12) (1988) 501–5.
16. Requena, J., Moreno, R. & Moya, J. S., Alumina and alumina/zirconia multilayer composites obtained by slip casting. *J. Am. Ceram. Soc.*, **72** (1989) 1511–13.
17. Moya, J. S., Sanchez-Herencia, A. J., Requena, J. & Moreno, R., Functionally gradient ceramics by sequential slip casting, *Materials Letters*, **14** (1992) 333–5.
18. Claussen, N. & Petzow, G., Whiskers-reinforced zirconia-toughened ceramics. In *Tailoring Multiphase and Composite Ceramics*, ed. R. E. Tressler, G. L. Messing, C. G. Pantano & R. E. Newnham. Plenum Press, NY, 1985, pp. 649–62.
19. Claussen, N. & Petzow, G., Whiskers-reinforced oxide ceramics. *J. Phys. C1 Suppl. 2.*, **47** (1986) C1-693–702.
20. Wei, G. C. & Becher, P. F., Development of SiC-whiskers-reinforced ceramics. *Am. Ceram. Soc. Bull.*, **64**(2) (1985) 298–304.
21. Wei, G. C. & Becher, P. F., Toughening behaviour in SiC-whisker-reinforced alumina. *Am. Ceram. Soc.*, **67**(2) (1984) C267–9.
22. Homeney, J., Vaugh, W. L. & Ferber, M. K., Processing and mechanical properties of SiC-whiskers–Al_2O_3-matrix composites. *Am. Ceram. Soc. Bull.*, **67**(2) (1987) 333–8.
23. Buljan, T. S., Pasto, A. E. & Kim, H. J., Ceramic whisker- and particular-composites: Properties, reliability, and applications. *Am. Ceram. Soc. Bull.*, **68**(2) (1989) 387–94.
24. Evans, A. G. & Cannon, R. M., Toughening of brittle solids by martensitic transformations. *Acta Metall.*, **34**(5) (1986) 761–800.
25. Evans, A. G., Toughening Mechanisms in Zirconia Alloys. In *Advances in Ceramics, Science and Technology of Zirconia II*, Vol. 12, ed. N. Claussen, M. Rühle & A. H. Heuer. American Ceramic Society, Columbus, OH, 1983, pp. 193–212.
26. Claussen, N. & Rühle, M., Design of transformation toughened ceramics. In *Advances in Ceramics, Science and Technology of Zirconia*, Vol. 3, ed. A. H. Heuer & L. W. Hobbs. American Ceramic Society, Columbus, OH, 1981, p. 137.
27. Claussen, N., Microstructural design of zirconia toughened ceramics (ZTC). In *Advances in Ceramics, Science and Technology of Zirconia II*, Vol. 12, ed. N. Claussen, M. Rühle & A. H. Heuer, American Ceramics Society, Columbus, OH, 1983, pp. 325–51.
28. Steinbrech, R. W., Toughening mechanisms for ceramic materials. *J. Eur. Ceram. Soc.*, **10** (1992) 131–42.
29. Green, D. J., A technique for introducing surface compression into zirconia ceramics. *J. Am. Ceram. Soc.*, **66**(10) (1983) 178–9.
30. Leriche, A., Moortgat, G., Cambier, F., Homerin, P., Thevenot, F., Orange, G. & Fantozzi, G., Preparation and characterization of a dispersion toughened ceramic for thermomechanical uses (ZTA). Part II: Thermomechanical characterization. Effect of microstructure and temperature on toughening mechanisms. *J. Eur. Ceram. Soc.*, **9** (1992) 177–85.
31. Swain, M. & Rose, L. R. F., Strength limitations of transformation-toughened zirconia alloys. *J. Am. Ceram. Soc.*, **69**(7) (1986) 511–18.
32. Boch, P. & Chartier, T., Ceramic processing techniques: The case of tape casting. *Ceram. For. Int.*, **4** (1989) 55.
33. Gay, D. (ed.), Matériaux composites. *Traité des Nouvelles Technologies*. Hermes, Paris, 1991.
34. Dietzel, A., Zum Problem der Emailspannungen und ihrer Berechnung. *Mitt. Ver. deut. Emailfachl.*, **10** (1962) 35–42.
35. Glandus, J. C., Rupture fragile et résistance aux chocs thermiques de céramiques à usages mécaniques. Thesis, University of Limoges, France, 1981.

Journal of the European Ceramic Society **15** (1995) 109–116
© 1995 Elsevier Science Limited
Printed in Great Britain. All rights reserved
0955-2219/95/$9.50

Shrinkage and Particle Packing during Removal of Organic Vehicle from Ceramic Injection Mouldings

Heidi M. Shaw & Mohan J. Edirisinghe

Department of Material Technology, Brunel University, Uxbridge, Middlesex, UK, UB8 3PH

(Received 21 February 1994; revised version received 3 June 1994; accepted 30 June 1994)

Abstract

Alumina suspensions, containing 50 and 57 vol.% ceramic in isotactic polypropylene and microcrystalline wax, were prepared by high shear mixing and injection moulded. The test bars produced were heated in air at 5°C h^{-1} to four different temperatures in the range 155–225°C and up to about 25 wt% of organic vehicle was removed. Shrinkage in the bars was measured after cooling to room temperature. The difference in the coefficient of thermal expansion of the suspension during heating and cooling, the changes in the crystallinity of the polypropylene and wax compared with the as-moulded state and the mobility of the ceramic particles due to removal of the organic vehicle are contributory factors to the measured shrinkage. The anticipated dimensional changes due to the first two factors have been determined experimentally and thereby the change in particle packing in the inner regions (core) of the test bars due to the mobility of the ceramic in the suspension have been calculated. Results show that in both suspensions heating to just above the softening point caused appreciable particle packing. Subsequently, particle packing decreases substantially and the reasons for this are discussed, taking into account thermal expansion of the organic vehicle, capillary migration of the microcrystalline wax, loss of organic vehicle and development of porosity. Comparison of results with previous investigations show that particle packing is affected by the rate of heating and the atmosphere used during pyrolysis. Particle packing, during pyrolysis, in the more concentrated suspension (57 vol.% ceramic) was, as expected, smaller, except at 225°C, when the core of each test bar containing this formulation showed a steep increase in weight loss. Otherwise, both formulations show similar trends in particle packing during the initial stages of the removal of organic vehicle.

1 Introduction

A commercially attractive method of producing large numbers of dimensionally accurate complex shap engineering ceramic components is plastic forming ceramic suspensions containing an organic vehicle.[1,2] However, full-scale industrial exploitation of plastic-forming methods (e.g. injection moulding, vacuum forming, blow moulding, film blowing) has not been possible, due to difficulties in removing the organic vehicle from the ceramic prior to sintering, without creating defects.

The organic vehicle can be removed by using solvents or, more frequently, by slow pyrolysis.[3] A decade ago successful use of the latter method was thought to involve mainly careful control of the rate of heating as a function of weight loss.[4] However, as plastic-forming methods were used increasingly to produce components with larger section sizes (>10 mm), it became clear that several factors determined the outcome of the crucial pyrolysis stage. These have been reviewed recently[5] and the major factors are:

(1) The rate of heating and the atmosphere in which pyrolysis is carried out.
(2) Characteristics of the organic vehicle.
(3) Characteristics of the ceramic.
(4) A balance between degradation of the organic vehicle and the outward diffusion of the resulting products.
(5) Formation of porosity.

One important phenomenon that occurs during the removal of organic vehicle by pyrolysis but has not been investigated extensively is the movement of the ceramic particles. It is known that, at the end of the organic vehicle removal stage, shrinkage and an increase in particle packing are observed.[6] Ceramic particles can be drawn towards each other under the influence of capillary forces which arise from the curvature of inter-par-

ticle surface menisci or of internal porosity formed during pyrolysis, much like in the initial stages of liquid-phase sintering.[7] However, during the initial stages of pyrolysis the liquid organic vehicle expands[8,9] and it is suggested[9] that this can result in the development of hydraulic pressures in the suspension with the ceramic particles forming a rigid network preventing further packing. Thermal expansion coefficients of ceramic suspensions can be measured in the liquid and the solid state,[10] indicating that particles are mobile and therefore the hypothesis that they form a rigid network lacks experimental evidence.

It is well known that packing of ceramic particles depends on their characteristics,[11] in particular their shape.[12] In the case of spherical powders, particle centres approach each other and porosity decreases due to the increase in packing. However, most commercial ceramic powders are non-spherical and their motion to enhance packing requires both the approach of particle centres and particle rotation. Removal of the organic vehicle from inter-particle spaces in the suspension can give rise to the former type of movement but the latter could be difficult in a suspension having high viscosity, especially during the initial stages (low temperatures) of pyrolysis. Another factor which could retard rotation of the particles is the presence of immobile layers of adsorbed organic vehicle on the ceramic surfaces.[13]

The measured shrinkage after heating to various temperatures and subsequent cooling to room temperature during pyrolysis of the organic vehicle does not fully correspond to the particle packing that has taken place. Firstly, compared to the heating cycle, the suspension contains a different amount of organic vehicle during cooling to room temperature and this can result in a difference in the coefficient of thermal expansion, causing a dimensional change that has to be taken into account. Secondly, the crystalline polymeric components in the organic vehicle, such as isotactic polypropylene and microcrystalline wax in the present work, can have different percentage crystallinities dependent on thermal history and processing[14,15] and this causes dimensional change. Therefore, the associated dimensional change due to the difference in crystallinity of the relevant constituents in the organic vehicle after heating to various temperatures during pyrolysis and subsequent cooling to room temperature has to be estimated.

Previous investigations[16,17] led to a quantitative assessment of the development of porosity (during the initial stages of pyrolysis in air) in injection-moulded test bars containing 50 and 57 vol.% alumina, suspensions made using an organic vehicle in which isotactic polypropylene and microcrystalline wax were the major and minor constituents, respectively. In the present work, identical ceramic suspensions and test bars are used and pyrolysis has been interrupted at four different temperatures to measure shrinkage after cooling to room temperature. The corresponding dimensional changes due to thermal expansion coefficient and crystallinity already discussed have been calculated from experimental results. Thereby the measured shrinkage has been corrected to calculate the vol.% shrinkage caused by the packing of ceramic particles during the initial stages of pyrolysis when up to 25 wt% organic vehicle is removed.

2 Experimental details

2.1 Production of test bars

Two formulations A and B containing 50 and 57 vol.%, respectively, of A16.SG alumina (Alcoa Manufacturing (GB) Ltd, Worcester, UK) were prepared using an organic vehicle containing isotactic polypropylene (density 905 kg m^{-3}), microcrystalline wax (density 910 kg m^{-3}) and stearic acid in the weight ratio 6:2:1. Further details of the ceramic powder and each constituent in the organic vehicle have been published earlier.[17]

Preblends of formulations A and B were prepared by tumbling the formulations in a container and then compounding in a twin screw extruder (Model TS40, Betol Machinery, Luton, Bedfordshire, UK). Compounding conditions of these formulations have been published previously.[17] The extrudate was dried and granulated, and the ceramic loading was verified by ashing samples (by heating to 600°C).

A 6GV/50 Sandretto reciprocating screw injection-moulding machine was used to produce 3 mm thick tensile test bars (Fig. 1) according to conditions reported previously.[17] The injection pressure, nozzle temperature and mould temperature used were 127MPa, 50°C and 235°C, respectively. The test bars were X-ray radiographed to verify that there were no voids or cracks present after moulding.

2.2 Pyrolysis

Test bars were pyrolysed in a muffle furnace in static air. The rate of heating was determined by trial and error experiments such that pyrolysis does not produce voids or cracks in the mouldings. The bars were heated initially from room temperature to a few degrees below the softening points of the formulations (148°C) at 50°C h^{-1} and then soaked for 24 h at this temperature. Subsequently, heating was continued at 5°C h^{-1}. Three

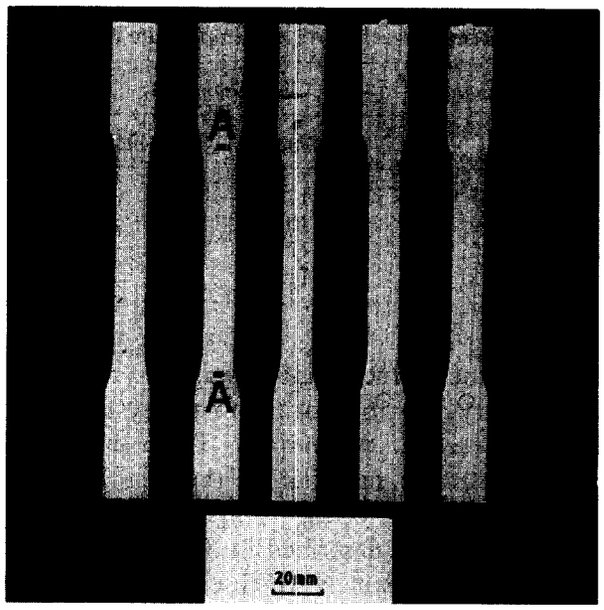


Fig. 1. Injection mouldings produced (nominal thickness 3mm). AA indicates the position and length of the test bars used for measurement of linear shrinkage.

test bars of each formulation were heated to 155, 170, 195 and 225°C (referred to as pyrolysis temperatures in the text and measured to an accuracy of ± 1°C) before cooling in the furnace to room temperature. Test bars were X-ray radiographed after pyrolysis to verify that voids and cracks were absent and subsequently were used to carry out the following experiments in triplicate.

2.3 Measured linear shrinkage

Two marks were scribed on the test bars as shown in Fig. 1 prior to pyrolysis. The distance between the two marks was measured with a travelling microscope before and after pyrolysis to the temperatures given in Section 2.2.

2.4 Loss on ignition

After pyrolysis, the test bars showed a clear contrast in colour between the core and surface regions (Fig. 2). Therefore, the material in the surface region was carefully separated from the core by scoring with a scalpel blade. The dimensions of the core were measured using Vernier callipers to calculate (separately) the vol.% of test bar that constitutes the core and the surface regions as pyrolysis progressed. Samples of both surface and core material were heated to 600°C (in triplicate) to calculate the weight loss of organic vehicle.

2.5 Dilatometry

Thermal expansion curves were obtained for 2·5 × 2·5 mm cross-section core samples (4mm thick) using a Perkin Elmer TMS1 thermomechanical analyser (TMA). Expansion was measured along the length of the test bars. A load of 3 g was used

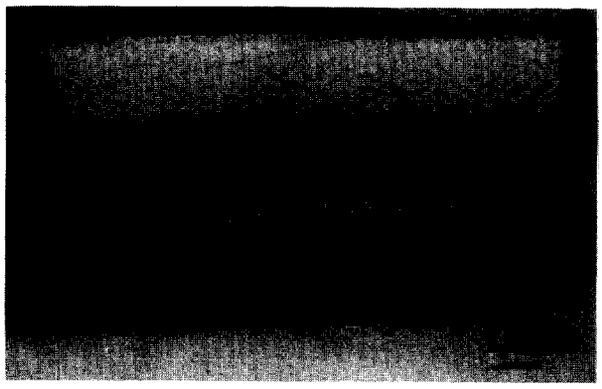


Fig. 2. Typical appearance of the cross-section of test bars after pyrolysis showing the dark surface region. Examples shown are: (a) A test bar of formulation A pyrolysed to 195°C; (b) a test bar of formulation B pyrolysed to 195°C.

on a flat-ended silica glass rod (diameter 4 mm) during heating the samples at $8°C^{-1}$ h to 120°C. These experimental conditions have been used successfully in previous work[18] to calculate the linear thermal expansion coefficient of ceramic suspensions. The TMA was calibrated using a pure sample having a linear thermal expansion coefficient of $2·3 \times 10^{-5}$ K^{-1}.

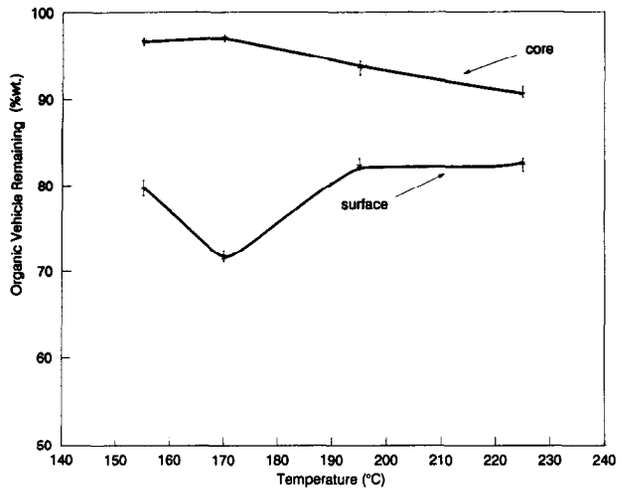
2.6 Differential scanning calorimetry (DSC)

A Perkin-Elmer DSC2 was used to measure enthalpies of fusion of samples taken from the core of pyrolysed test bars. A scan speed of 10 K min^{-1} was used during heating the samples between room temperature and 250°C.

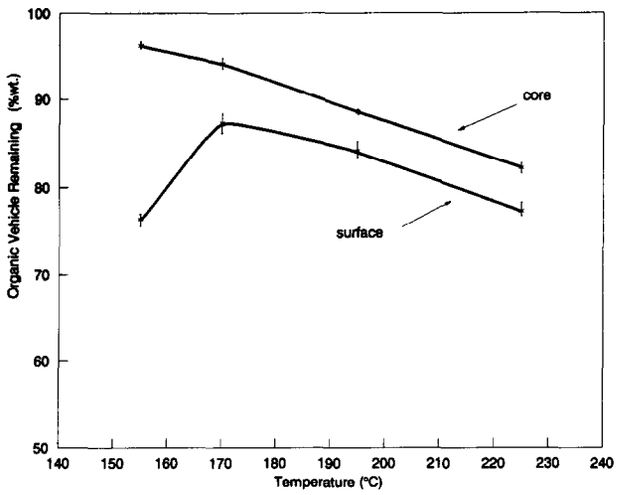
3 Results and discussion

3.1 Mechanisms of removal of the organic vehicle

The dark appearance of the surface of pyrolysed test bars of both formulations (Fig. 2) suggests that the organic vehicle present in these regions has been subjected to a greater level of degradation compared with the core. This is due to the presence of oxygen in the atmosphere in which pyrolysis is carried out. Oxidative degradation occurs in the surface regions while thermal degradation dominates in the core of the mouldings[19,20] and the former is known to give rise to a higher weight loss at a lower temperature.[21] Loss on ignition results of surface and core samples shown in Fig. 3 indicate an increase in the wt% of organic vehicle in the surface regions at 195 and 225°C in formulation A and at 170°C in formulation B. Therefore, enrichment of the organic vehicle in the surface regions occurred in both formulations (over a wider temperature range in formulation A which contained more organic vehicle) during the initial stages of pyrolysis. The organic vehicle in both surface and core regions of the test bars after



(a)



(b)

Fig. 3. Variation of weight of organic vehicle remaining (as a percentage of the initial weight of organic vehicle in the as-moulded test bars) with pyrolysis temperature in the surface region and the core of the mouldings of (a) formulation A; (b) formulation B. Formulations A and B contained 81·24 (±0·05) wt% (equivalent to 49·7 vol.%) and 85·17 (±0·14) wt% (equivalent to 56·7 vol.%) ceramic in the as-moulded state (from ashing at 600°C). Thus the green densities of formulations A and B are 2440 kg m^{-3} and 2655 kg m^{-3}, respectively.

pyrolysis has been analysed by gel permeation chromatography (GPC) and reported previously.[22] GPC results show that the polypropylene in the core of test bars of both formulations did not show any appreciable degradation but the intensity of the wax peak decreased. In contrast, at the surface, although the polypropylene present in the organic vehicle degraded to some extent (particularly at 225°C), the significant feature was the increase in the intensity of the wax peak. Therefore, in the context of the present investigation, the important mechanism of removal of organic vehicle from the core of the test bars of both formulations during the initial stages of pyrolysis is the capillary migration of the microcrystalline wax to the surface.

The rate of weight loss due to oxidative degradation in the surface regions was also affected by the capillary migration of the microcrystalline wax from the core to the surface. The vol.% of discoloured surface material in the test bars (presented in Table 1 using results from the experimental procedure described in Section 2.4) hardly varies in formulation A which contained more organic vehicle and showed capillary migration of microcrystalline wax over a wider temperature range, as already discussed. In contrast, there is a rapid increase in the vol.% of surface material in test bars of formulation B.

Table 1. Volume of test bar which contains discoloured surface material at each pyrolysis temperature investigated

Temperature (°C)	*Volume (%)*	
	Formulation A	*Formulation B*
155	12	6
170	10	13
195	10	19
225	11	22

3.2 Measured shrinkage

The linear shrinkages (S_L) measured (Table 2) were converted to volume shrinkages (S_v) by using the expression:

$$S_v = 3S_L - 3S_L^2 + S_L^3 \quad (1)$$

Figure 4 shows the variation of S_v with pyrolysis temperature. In order to understand further the behaviour of the suspensions during pyrolysis, S_L of the test bars was also measured at 150°C (just below the softening point of both formulations; dilatometric measurements give 151°C (formulation A) and 154°C (formulation B)) and the corresponding S_v values are also shown in Fig. 4. In both formulations S_v increases initially. This is expected as residual stresses are released on heating past the softening point and the ceramic particles have the opportunity to move towards each other as suspensions begin to lose organic vehicle. However, at 170°C both formulations show a decrease in S_v.

Bandyopadhyay & French[8] observed a similar effect during the interrupted pyrolysis of injection-

Table 2. Linear shrinkages (S_L) in test bars of formulations A and B at each pyrolysis temperature

Temperature (°C)	*S_L(%)*	
	Formulation A	*Formulation B*
155	1·24, 1·31, 1·33	0·56, 0·75, 0·85
170	0·68, 0·62, 0·63	0·46, 0·49, 0·46
195	0·59, 0·56, 0·54	0·40, 0·31, 0·38
225	0·20, 0·15, 0·12	0·18· 0·15, 0·18

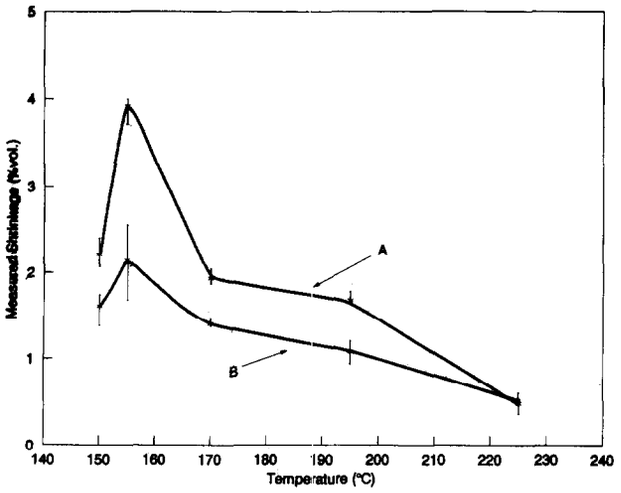


Fig. 4. Variation of measured vol.% shrinkage (S_v) with pyrolysis temperature in formulations A and B. S_v values correspond to the average S_L value of the measurements given in Table 2.

moulded test bars and spheres made using silicon nitride powder and an organic vehicle which contained microcrystalline wax and epoxy resin as the major and minor constituents, respectively. Volume expansion of the organic vehicle takes place during heating but S_L, measured at room temperature, can only show a decrease if the ceramic particles in the core of the mouldings are restrained from moving during cooling. However, S_v values can also be influenced by changes in the properties of organic vehicle during pyrolysis (see Sections 3·3 and 3·4). After off-setting the effect on S_v due to changes in the properties of the organic vehicle during pyrolysis, particle packing in the suspensions investigated is discussed in Section 3.5.

3.3 Thermal expansion

The loss of organic vehicle during pyrolysis causes the linear thermal expansion coefficient (α_L) of samples of test bars to differ from the as-moulded values during cooling and this affects the S_L values calculated. This effect can be corrected for by measuring α_L of core samples of pyrolysed test bars (Table 3) and calculating:

$$(\Delta L)_{exp} = \{(\alpha_L)_{as\text{-}moulded} - (\alpha_L)_{pyrolysed}\}\,\Delta T \quad (2)$$

where $(\Delta L)_{exp}$ is the dimensional change in the test bars due to the change in α_L and ΔT is the difference between the pyrolysis temperature and the room temperature. Since $(\alpha_L)_{as\text{-}moulded} > (\alpha_L)_{pyrolysed}$ at all the temperatures investigated (Table 3), $(\Delta L)_{exp}$ is an expansion. α_L of injection-moulded ceramic bodies shows anisotropy[23] and therefore all measurements were made along the length of the test bars, the direction in which S_L was measured. $(\Delta L)_{exp}$ values were converted to vol.%, $(\Delta V)_{exp}$, using eqn (1) and these results are also presented in Table 3. The maximum error in

Table 3. Coefficient of linear thermal expansion (α_L) of formulations A and B at each pyrolysis temperature and $(\Delta V)_{exp}$ corresponding to the average of the α_L values given

Temperature (°C)	*Formulation A*		*Formulations B*	
	$\alpha_L(MK^{-1})$	$(\Delta V)_{exp}$ *(vol.%)*	$\alpha_L(MK^{-1})$	$(\Delta V)_{exp}$ *(vol.%)*
20 (as moulded)	146, 139, 142	—	134, 147, 152	—
155	133, 110, 120	0·0114	110, 114, 93	0·0156
170	71, 73, 82	0·0303	70, 52, 74	0·0355
195	115, 114, 106	0·0160	95, 105, 107	0·0218
225	59, 51, 60	0·0526	43, 44, 46	0·0614

$(\Delta V)_{exp}$, due to the use of the average α_L values, is 36%. However, these values are of the order 10^{-2} and the actual magnitude of the error involved is extremely small. The error does not change the conclusions of this investigation. In fact, $(\Delta V)_{exp}$ has a negligible effect on particle packing, as described in Section 3.5.

3.4 Crystallinity

DSC results of each sample showed two peaks corresponding to the crystalline melting of microcrystalline wax (MCW) and isotactic polypropylene (IPP). The enthalpies of fusion of 100% crystalline MCW and IPP are 267 J g^{-1} and 165 J g^{-1}, respectively.[24] These values were compared with the measured enthalpies of fusion to calculate the percentage crystallinities of MCW and IPP in each sample (Table 4). These results show that as the test bars were cooled to room temperature, the percentage crystalinity of MCW, in particular, becomes smaller at higher pyrolysis temperatures. The vol.% shrinkage, $(\Delta V)_{crys}$, associated with the crystallinity of MCW and IPP, can be calculated separately using eqn (3):

$$(\Delta V)_{crys} = \text{specific volume change} \times \text{density of MCW (or IPP)} \times \%\ \text{crystallinity} \times \text{vol.\% of MCW (or IPP) in the organic vehicle} \quad (3)$$

The specific volume changes for MCW and IPP are 0·193 $m^3\ Mg^{-1}$ and 0·116 $m^3\ Mg^{-1}$,[24] respectively. The vol.% of MCW and IPP in the organic vehicle was estimated using the relative intensities of the gel permeation chromatograms reported previously[22] and the fact that in the as-moulded state the MCW : IPP weight ratio was 3 : 1 (as mixed proportions). Gel permeation chromatograms also show that in the pyrolysis temperature range investigated the molecular weights of MCW and IPP in the core of the test bars do not change significantly[22] and therefore their as-received densities (given in Section 2.1) were used in calculating the vol.% of the MCW and the IPP in

Table 4. Percentage crystallinity, $(\Delta V)_{crys}$ and $(\Delta V)^*_{crys}$ of formulations A and B at each pyrolysis temperature

Formulation	*Temperature (°C)*	*Percentage crystallinity*		*$(\Delta V)_{crys}$ (vol.%)*			*$(\Delta V)^*_{crys}$ (vol.%)*
		MCW	*IPP*	*MCW*	*IPP*	*Total*	
	20 (as moulded)	33, 40, 37	44, 52, 43	0·76	1·70	2·46	—
	155	31, 36, 30	55, 54, 53	0·50	2·11	2·61	0·15
A	170	23, 30, 24	50, 52, 48	0·41	1·95	2·36	−0·10
	195	22, 24, 25	52, 55, 49	0·39	1·97	2·36	−0·10
	225	13, 20, 21	48, 49, 46	0·26	1·82	2·08	−0·38
B	20 (as moulded)	40, 36, 37	44, 46, 44	0·66	1·42	2·08	—
	155	24, 26, 24	57, 59, 54	0·35	1·86	2·21	0·13
	170	12, 16, 18	48, 50, 53	0·20	1·63	1·83	−0·26
	195	26, 14, 21	50, 50, 50	0·23	1·60	1·83	−0·25
	225	21, 12, 11	43, 36, 41	0·15	1·25	1·40	−0·68

The average percentage crystallinity values were used in the calculations.
A minus sign indicates an expansion.

the organic vehicle and $(\Delta V)_{crys}$ at each pyrolysis temperature.

The organic vehicle also contains approximately 11 wt% of stearic acid which is used as a processing aid.[25] Thermogravimetry of stearic acid shows that at 150°C (approximately the softening point of the formulations) over 50 wt% of the stearic acid is removed. In addition, taking into account processing of the ceramic suspensions in the twin-screw extruder and the injection-moulding machine (Section 2.2), it can be assumed that only a very small amount of stearic acid remains in the formulations at the pyrolysis temperatures investigated and its effect has not been taken into account in the present analysis.

$(\Delta V)_{crys}$ values and the change in $(\Delta V)_{crys}$ at each pyrolysis temperature, compared with the as-moulded samples, $(\Delta V)^*_{crys}$, are also shown in Table 4. The maximum error in $(\Delta V)_{crys}$, due to the use of the average crystallinity values, is 10% and does not change the conclusions of this investigation.

3.5 Particle packing

The measured shrinkage (Table 2) is the sum of the shrinkages caused by particle packing, expansion due to the change in the coefficient of linear thermal expansion coefficient ($(\Delta V)_{exp}$ in Table 3), and the shrinkage (or expansion) due to the change in crystallinity ($(\Delta V)^*_{crys}$ in Table 4). The shrinkage due to particle packing at each pyrolysis temperature calculated on this basis is shown in Fig. 5.

In the as-moulded state of the test bars, all inter-particle space is filled with organic vehicle.[26] Removal of organic vehicle during pyrolysis results in particles moving closer together (particle packing) or the creation of porosity. Previous work[6] has shown that once pyrolysis is complete the vol.% of ceramic in the body could increase only to V^*_{max}, where $V < V^*_{max} < V_{max}$. V is the initial vol.% of ceramic in the suspension and V_{max} is the maximum volume of ceramic that can be incorporated in the suspension and this value is deduced from viscosity data.[27] V^*_{max} is approximately equal to the measured CPVC (critical powder volume concentration) value.[28] Therefore, V^*_{max} represents a situation where the particles move closer to each other and 'lock into position', preventing any further movement.

At 155°C (just above the softening point of the suspensions), when the core of the test bars of both formulations show a 3–4 wt% loss of organic vehicle, calculated particle packing shrinkages are 3·78 vol.% and 2·03 vol.% in formulations A and B, respectively (Fig. 5). However, at 150°C (just below the softening point of the suspensions) when weight loss of organic vehicle is negligible (<1%) the core of the test bars of formulations A and B show measured shrinkages of 2·2 vol.% and 1·6 vol.% respectively (Fig. 4). Relaxation of residual stresses in the test bars caused by injection moulding occurs on heating to the softening point[29] and this can influence the bulk measured shrinkage and particle packing. The more dilute

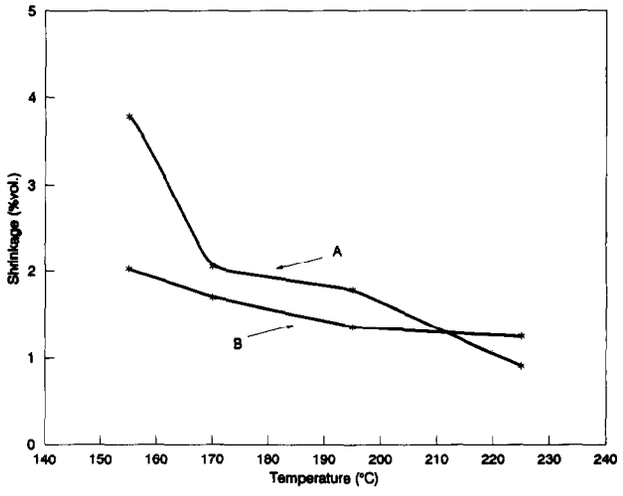


Fig. 5. Variation of shrinkage due to particle packing with pyrolysis temperature in formulations A and B.

formulation A shows a larger initial shrinkage due to particle packing. This is expected as $(V_{max}-V)$ is larger in the case of formulation A. Subsequently, at 170 and 195°C both formulations show a decrease in particle packing in the core of the test bars (Fig. 5). This shows that the volume expansion due to melting of the organic vehicle, which occurs as the temperature exceeds the softening point of the formulations, is not relaxed completely on cooling to room temperature and, in effect, particles are pulled apart. This is despite capillary migration of the MCW from the core of the test bars helping the particles to be drawn towards each other as discussed earlier (see Section 1).

This decrease in particle packing can be explained by considering the interaction between the surface region and the core of each test bar. The surface region loses a larger amount of organic vehicle (Fig. 3) and therefore will experience a greater shrinkage. Previous work[17] has shown that the surface and interconnected porosity remains virtually constant at almost 2–3 vol.% in the temperature range 155–195°C, in both formulations. V^*_{max} of formulations A and B are 51 and 58%, respectively.[6] Taking into account loss of organic vehicle from the surface region (Fig. 3) and neglecting the formation of porosity, the vol.% of ceramic in the surface increases to 54 and 61% (average for the temperature range 155–195°C), in formulations A and B, respectively. Even if the levels of porosity are accounted for completely as surface porosity, the vol.% of ceramic in the surface region is $\simeq V^*_{max}$ of each formulation. Thus, the ceramic particles in the surface region have achieved the maximum packing efficiency and are 'locked together'. This effect makes the surface regions behave like a rigid skin (which appears as a dark degraded region as shown in Fig. 2) and 'holds' the ceramic particles in the core, restraining them from further packing during cooling after being pulled apart due to the volume expansion of the organic vehicle. It can be argued that this type of restraint can lead to cracking. However, cracking was not observed in the present work. The presence of the organic vehicle (>75 wt% remaining in both formulations at 225°C) allows the suspension to behave like a plastic mass, which helps to prevent cracking.

At 225°C, this phenomenon continues to hinder particle packing in formulation A. However, in formulation B, the reduction in particle packing decreases (Fig. 5). This coincides with an increase in the development of porosity in formulation B, as discussed in previous work.[17] Figure 3 shows that in the case of formulation B, compared with formulation A, the rate of weight loss in the core of the test bars is greater and that at 225°C it has lost a higher wt% of the organic vehicle. Therefore, at this temperature, the ceramic particles in formulation B can be expected to pack to a greater extent.

This reduction in particle packing during the early stages of removal of organic vehicle was not observed in previous work.[30,31] In these instances (the same organic vehicle was used), particle packing during interrupted pyrolysis was reported as measured linear shrinkage (uncorrected) and these approached a limiting value at about 190°C. However, a variable rate of heating (much faster than the constant 5°C h^{-1} in the present work) was used to pyrolyse the test bars during the initial stages and a dark skin at the surface of the test bars was not evident. This provides additional evidence for the argument that the extent to which the surface regions form a degraded rigid skin, which seems to be related to the rate of heating during pyrolysis, is an important feature affecting the packing of the ceramic particles during the removal of the organic vehicle. It also indicates that the atmosphere in which pyrolysis takes place will affect shrinkage (and particle packing) in the artefacts. If pyrolysis was carried out in an inert atmosphere such as N_2 where oxidative degradation does not take place, a surface skin which could restrain particle packing in the core of the mouldings would not prevail and larger shrinkages will be observed, as noted by Wright *et al.*[6] Bandyopadhyay & French[8] pyrolysed mouldings in N_2 but their observation of a reduction in shrinkage during the early stages of pyrolysis, as in the present work, was most probably caused by the fact that the mouldings were packed in ceramic powders, which were used as a wicking medium, and this created a restraining effect on the surface.

4 Conclusions

The shrinkage due to the packing of ceramic particles in the core of injection-moulded test bars during the initial stages of pyrolysis in static air has been calculated by correcting measured shrinkage values for changes in the coefficient of thermal expansion and the changes in the crystallinity of the constituents of the organic vehicle. Initially, particle packing increased at a temperature just above the softening point of the formulations but it is likely that the relaxation of residual stresses caused by injection moulding would have influenced shrinkage measurements and affected particle packing. However, subsequent particle packing in the core of the test bars decreased as it was restrained by the rigid surface regions which

form due to oxidative degradation. Comparison of the results of the present work with previous investigations show that the rate of heating and the atmosphere used during pyrolysis also affect particle packing. Although shrinkage due to particle packing in the more concentrated suspension was, as expected, smaller (except at 225°C when there was a steep increase in weight loss compared to the other formulation), there were no major differences in these trends in the two formulations investigated. This indicates that the 7% difference in initial volume fraction of ceramic in the suspensions did not have a significant effect on particle packing during the initial stages of removal of the organic vehicle.

Acknowledgements

The authors wish to thank SERC for financial support given to Ms Shaw during the period 1990–1993. Mr K. K. Dutta is thanked for technical help. The help of Mrs Kathy Goddard in the preparation of this manuscript is gratefully acknowledged.

References

1. Evans, J. R. G., Plastic forming operations for ceramic suspensions. In *New Materials and their Applications*, ed. D. Holland. Institute of Physics, UK 1990, pp. 25–32.
2. Carlsson, R., Shaping of engineering ceramics. *Materials and Design*, **10** (1989) 10–14.
3. Edirisinghe, M. J. & Evans, J. R. G., Review: fabrication of engineering ceramics by injection moulding. II. Techniques. *Int. J. High Technology Ceramics*, **2** (1986) 249–78.
4. Johnson, A., Carlstroem, E., Hermansson, L. & Carlsson, R., Rate controlled thermal extraction of organic binders from injection moulded bodies. *Advances in Ceramics*, **9** (1984) 241–5.
5. Shaw, H. M. & Edirisinghe, M. J., Removal of binder from ceramic bodies fabricated using plastic forming methods. *Bull. Amer. Ceram. Soc.*, **72** (1993) 94–9.
6. Wright, J. K., Edirisinghe, M. J., Zhang, J. G. & Evans, J. R. G., Particle packing in ceramic injection moulding. *J. Am. Ceram. Soc.*, **73** (1990) 2653–8.
7. Kingery, W. D., Densification during sintering in the presence of a liquid phase I. Theory. *J. Appl. Phys.*, **30** (1959) 301–6.
8. Bandyopadhyay, G. & French, K. W., Injection-molded ceramics: Critical aspects of the binder removal process and component fabrication. *J. Eur. Ceram. Soc.*, **11** (1993) 23–34.
9. Barone, M. R. & Ulicny, J. C., Liquid-phase transport during removal of organic binders in injection-moulded ceramics. *J. Amer. Ceram. Soc.*, **73** (1990) 3323–33.
10. Zhang, T., Evans, J. R. G. & Dutta, K. K., Thermal properties of ceramic injection moulding suspensions in the liquid and solid states. *J. Eur. Ceram. Soc.*, **5** (1989) 303–9.
11. German, R. M., *Powder Injection Moulding*. Metal Powder Industries Federation, NJ, USA 1990, p. 301.
12. Shukla, V. N. & Hill, D. C., Binder evolution from powder compacts: thermal profile for injection moulded articles. *J. Amer. Ceram. Soc.*, **72** (1989) 1797–803.
13. Evans, J. R. G. & Edirisinghe, M. J., Interfacial factors affecting the incidence of defects in ceramic mouldings. *J. Mater. Sci.*, **26** (1991) 2081–8.
14. Brydson, J. A., *Plastic Materials*, 5th ed. Butterworth-Heinemann Ltd, London, UK, 1989, pp. 165–7.
15. Wright, D. G. M., Dunk, R., Bouvart, D. & Autran, M., The effect of crystallinity on the properties of injection moulded polypropylene and polyacetal. *Polymer*, **29** (1988) 793–6.
16. Shaw, H. M., Hutton, T. J. & Edirisinghe, M. J., On the formation of porosity during removal of organic vehicle from injection moulded ceramic bodies. *J. Mater. Sci. Lett.*, **11** (1992) 1075–7.
17. Shaw, H. M. & Edirisinghe, M. J., Porosity development during removal of organic vehicle from ceramic injection mouldings. *J. Eur. Ceram. Soc.*, **13** (1994) 135–42.
18. Edirisinghe, M. J. & Evans, J. R. G., Properties of ceramic injection moulding formulations. Part 2. Integrity of mouldings. *J. Mater. Sci.*, **22** (1987) 2267–73.
19. Woodthorpe, J., Edirisinghe, M. J. & Evans, J. R. G., Properties of ceramic injection moulding formulations. III. Polymer removal. *J. Mater. Sci.*, **24** (1989) 1038–48.
20. Wright, J. K., Evans, J. R. G. & Edirisinghe, M. J., Degradation of polyolefin blends used in ceramic injection moulding. *J. Amer. Ceram. Soc.*, **72** (1989) 1822–8.
21. Hansen, R. H., Thermal and oxidative degradation of polyethylene and polypropylene and related olefin polymers. In *Thermal Stability of Polymers*, Vol. 1, ed. R. T. Conley. Marcel Dekker, NY, 1970, pp. 153–87.
22. Shaw, H. M., Edirisinghe, M. J. & Holding, S., Binder degradation and redistribution during pyrolysis of ceramic injection mouldings. *J. Mater. Sci. Lett.*, **12** (1993) 1227–30.
23. Zhang, T. & Evans, J. R. G., Anomalies in the thermal expansion of ceramic injection moulded bodies. *J. Mater. Sci. Lett.*, **9** (1990) 672–4.
24. Wunderlich, B., *Macromolecular Physics*, Vol. 3, *Crystal Melting*, Academic Press Inc. (London) Ltd, 1980, pp. 46–9.
25. Edirisinghe, M. J., The effect of processing additives on the properties of a ceramic–polymer formulation. *Ceramics International*, **17** (1991) 89–96.
26. Wright, J. K. & Evans, J. R. G., Removal of organic vehicle from moulded ceramic bodies by capillary action, *Ceramics International*, **17** (1991) 79–87.
27. Edirisinghe, M. J., Shaw, H. M. & Tomkins, K. L., Flow behaviour of ceramic injection moulding suspensions. *Ceramics International*, **18** (1992) 193–200.
28. Markoff, C. J., Mutsuddy, B. C. & Lennon, J. W., Method of determining critical powder volume concentration in the plastic forming of ceramic mixes. In *Forming of Ceramics*, Vol. 9, ed. J. Mangels & G. L. Messing, American Ceramic Society, OH, USA, 1984, pp. 246–50.
29. Zhang, J. G., Edirisinghe, M. J. & Evans, J. R. G., The use of modulated pressure in ceramic injection moulding. *J. Eur. Ceram. Soc.*, **5** (1989) 63–72.
30. Pinwill, I. E., Edirisinghe, M. J. & Bevis, M. J., Shrinkage during removal of organic vehicle from injection moulded aluminium bodies. *Powder Metallurgy*, **35** (1992) 113–16.
31. Shaw, H. M. & Edirisinghe, M. J., Mobility of powder particles during debinding green ceramic bodies. In *Euro-Ceramics II*, Vol. 1, *Basic Science and Processing of Ceramics*, ed. G. Ziegler & H. Hausner. Deutsche Keramische Gesellschaft e.V., 1991, pp. 423–7.

Journal of the European Ceramic Society **15** (1995) 117–125
© 1995 Elsevier Science Limited
Printed in Great Britain. All rights reserved
0955-2219/95/$9.50

The Use of Overpressure in Thermolytic Debinding of Moulded Ceramic Bodies

P. D. Hammond & J. R. G. Evans

Department of Materials Technology, Brunel University, Uxbridge, Middlesex, UK, UB8 3PH

(Received 18 April 1994; revised version received 3 June 1994; accepted 30 June 1994)

Abstract

A furnace within a pressure vessel capable of withstanding 0–1 MPa and temperatures up to 600°C is described. The furnace allows the pyrolysis of injection moulded ceramics to take place at higher heating rates than is possible at atmospheric pressure without defects caused by bloating or cracking. The effectiveness of the method is described for a commercial injection-moulding composition pyrolysed in nitrogen. The various effects of gas pressure on the process are listed and the main beneficial effect is considered to be the increase in boiling point of the polymer-degradation product solution which forms the continuous phase. In the early stages of heat treatment, this allows more rapid mass transport both by diffusion and fluid flow.

1 Introduction

Many techniques drawn from polymer processing have been successfully applied to ceramic suspensions in order to facilitate the arrangement of particles into complex shapes before firing.[1] The most versatile of these is injection moulding, but they all have the disadvantage that organic matter initially filling the interstitial space must be removed before firing. This presents particular problems for thick sections made by injection moulding.

Capillary[2] and solvent[3] methods have been used for binder removal but the most popular method is pyrolysis either in an oxidative atmosphere,[4] an unreactive atmosphere[5] or in vacuo.[6] Frequently mouldings are packed in a powder bed during heat treatment and loss of molten organic vehicle is assisted by partitioning between the two powder assemblies. During pyrolysis, three weight loss processes can be identified, dependent on ambient atmosphere and molecular weight of the organic vehicle.[7] For low molecular weight material, evaporation proceeds without chain scission and the thermogravimetric characteristics are little affected by atmosphere. For high molecular weight organic vehicles, chain scission must precede evaporation and this can occur either by oxidative degradation, in which case it is likely to be affected by the diffusion of oxygen into the body,[8] or by thermal degradation, in which case it will occur uniformly throughout the body if the degradation reaction is irreversible.

Under oxidising atmospheres the former reaction predominates, although under conditions of prolonged heating, such as those needed for binder removal from thick sections, thermal degradation will proceed to some extent in all cases. Thermal degradation therefore deserves priority of attention because low molecular weight products of decomposition are formed throughout the body at a stage when interconnected porosity is absent.

A manufacturer often wishes to minimise the debinding time in order to reduce the number of stationary semi-finished products. Low-temperature furnace costs are modest and debinding times often compare favourably with raw material bulk storage times so that the debinding stage does not incur such a prohibitive debit as is sometimes claimed. The main benefit of shortening this stage accrues if the lead time for new products can be reduced. Another advantage of enhancing the debinding stage is that larger sections may be successfully treated in sensible time scales.

Several strategies are available under this objective. The organic vehicle can be selected to decompose steadily as temperature rises.[9,10] The process can be controlled by an external loop so that weight loss is a linear function of temperature.[11] The organic vehicle can be synthesised to have the combined properties needed to prevent the boiling of degradation products in solution.[12] Pressure can be applied to the decomposing system.[13] This work explores the latter intervention.

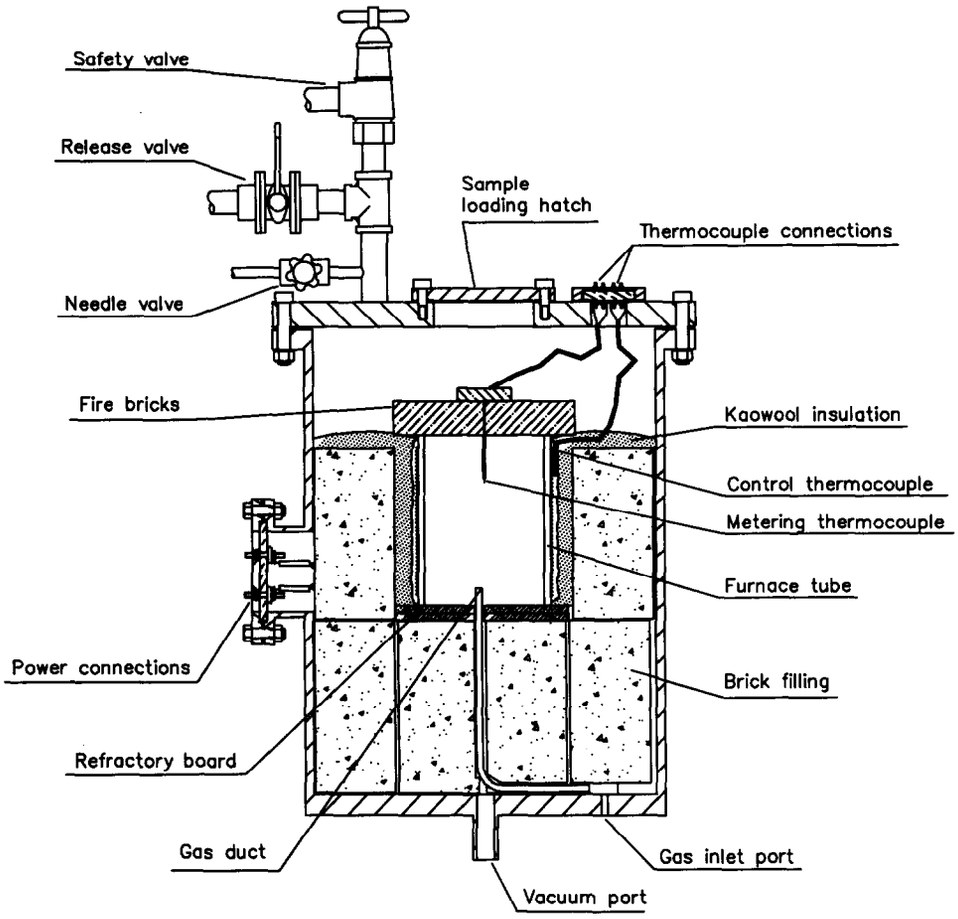


Fig. 1. Diagram of the pressure vessel and furnace.

2 Experimental Details

2.1 Furnace design

The pressure vessel was manufactured from carbon–manganese steel to the specifications of BS1500, which has recently been superseded by BS5500.[14] Its internal dimensions were 435 mm diameter × 600 mm in height. This allows a large furnace to be incorporated or alternatively a series of small furnaces. The present work was carried out with a 150 mm diameter × 200 mm furnace wound from 80/20 Ni/Cr wire on a silica glass tube. Figure 1 shows the vessel and furnace diagrammatically. The top, wall and base were water-cooled by independent circuits incorporating flow indicators. Wall temperature was monitored by three series-connected thermal switches (opening at 40°C) which latched a relay controlling electric power to the furnace. Oxygen-free nitrogen was used in all the experiments. A preset Nabic spring-operated safety valve was fitted to prevent the rated working pressure of 1·05 MPa being exceeded. Gas throughput was controlled by a needle valve venting through a flow meter into an oil indicator. Electric leadthroughs were made through 20 mm thick discs of cloth-reinforced phenol–formaldehyde resin (Tufnol, Birmingham, UK) clamped with O-ring seals. The internal and external surfaces of the vessel were treated with a two-part organic-resistant epoxy-based paint (Trimite, Uxbridge, UK). The general arrangement of the furnace vessel and its ancillary circuits are shown in Fig. 2.

A Eurotherm 818P temperature controller was used to provide linear heating rates and the controller thermocouple, mounted on the outside of the windings, was calibrated dynamically against the hot zone thermocouple at three gas pressures, 0·1, 0·6 and 1·0 MPa, and for each sample container. The procedure for filling the vessel involved evacuation to about 2·5 kPa followed by filling with oxygen-free nitrogen. A gas flow of 10^{-6} m^3 s^{-1} was maintained during experiments and the internal pipework allowed the gas to enter at the base of the furnace tube. Although the oxygen content of the nitrogen was not measured directly, the furnace was heated to 600°C with copper powder and the weight changes indicated that negligible oxidation had taken place. Significant polymer oxidation may therefore also be assumed to be absent.

2.2 Materials and mouldings

The ceramic powder was a proprietary silica (<200 μm) having a density of 2200 kgm^{-3}, used for leachable foundry cores for nickel alloy tur-



Fig. 2. The pressure vessel showing the arrangement of valving and coolant.

bine blades. The organic vehicle was a proprietory blend based on a low molecular weight polyethylene glycol diluted with waxes and a stearate as a processing aid and had a density of 1110 kgm^{-3}. Ashing showed a 22·1% weight loss indicative of a powder loading of 64 vol.%. Injection moulding of 17 mm diameter cylinders, 100 mm in length was performed at Fairey Tecramics Ltd using a Florin injection-moulding machine with a maximum barrel temperature of 60°C and a maximum injection pressure on material of 52MPa. The cylinders were contact radiographed before pyrolysis using a Hewlett Packard Faxitron camera. A Perkin Elmer TMA dilatometer with a flat-ended silica rod and a 10 g load was used to determine the dilatometric softening point of the suspension. Thermogravimetry was performed on a Perkin Elmer (Beaconsfield, Bucks, UK) model TGS2.

2.3 Pyrolysis

Three methods of sample support were used. Some samples were placed on a refractory tile with a dusting of coarse alumina (Grade LG20, Alcan Chemicals, UK). Others were fully packed in this alumina powder, either in a steel trough or a ceramic crucible. In the third series of experiments, samples were packed in coarse SiC powder (Grade C6, Besco Abrasives Ltd, Surrey, UK). Tests were done at gas pressures of 0·1, 0·6 and 1·0 MPa. After heat treatment, the samples were lightly sintered to facilitate handling, by heating to 1150°C, holding for 4 h and furnace cooling. They were then examined externally, radiographed and cut across the central lateral cross-section to establish integrity. On certain samples, measurements of the horizontal and vertical diameters were taken at the centre of the bar, to find the ovality. Positive ovality (the difference between the horizontal diameter and the vertical diameter) was taken as an indication of the degree of slumping which had occurred. Linear heating from 70°C to 500°C was used throughout, with a ramp of 60°C h^{-1} from 20°C to 70°C and from 500°C to room temperature.

3 Results and Discussion

Although it is routine practice to carry out a steady-state furnace calibration, what is required here is a dynamic calibration because the integrity of samples is assessed in terms of a critical heating rate. The hot zone temperature initially lags behind the set temperature but the hot zone rate increases as temperature rises, producing families of calibration curves such as that shown in Fig. 3.

At the low heating rates typical of thermolytic debinding at atmospheric pressure, the rates coincide over the range of temperatures of interest. The high rates of heating that are possible under overpressure conditions, however, may lead to substantial deviations. The choice of temperature at which to deduce the actual rate is fixed by the initial region of rapid thermal degradation and may be deduced from appropriate thermogravimetric curves. Since the thermogravimetric loss behaviour varies with heating rate, the problem is to decide at which temperature to convert set rate to actual rate. The procedure used here was to select the temperature at which an arbitrary 20wt% loss based on the initial weight of binder had occurred.

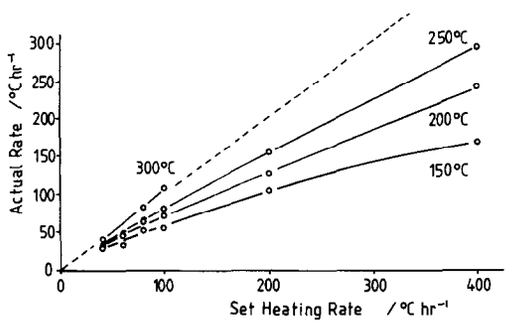


Fig. 3. An example of the dynamic calibration for heating rate at various hot zone temperatures. (0·6 MPa, setter powder LG20 alumina in stainless steel trough.) The dashed line represents set rate = actual rate.

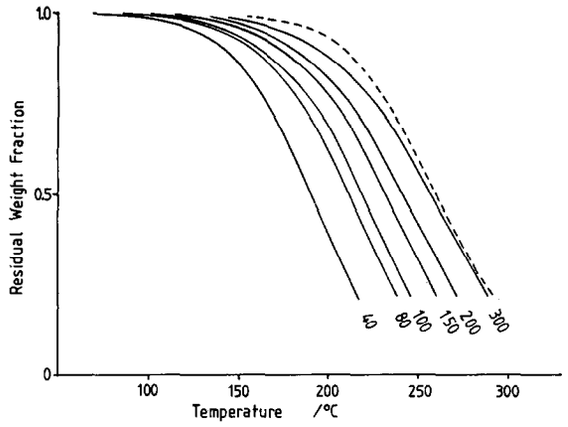


Fig. 4. Thermogravimetric curve for the organic vehicle heated in nitrogen at 300°C h^{-1} (dashed line) and calculated curves for other heating rates labelled on the curves in °Ch^{-1}.

From the thermogravimetric loss curve at a rate of 300°C h^{-1} the activation energy E and specific rate constant K_0 were obtained by the method of Wendlandt.[15] This makes the assumption that the weight loss is a first order reaction and therefore neglects the effect of evaporation of low molecular weight additives which are lost by zero order kinetics. It does not attempt to assess the loss of fluid by partitioning into the porous powder support.

The reaction is therefore treated as obeying

$$\frac{dw}{dt} = -Kw \tag{1}$$

where w is the weight fraction of binder remaining and K is the rate constant which varies with temperature as

$$K = K_0 \exp\left(\frac{-E}{RT}\right) \tag{2}$$

Once K_0 and E are known, the thermogravimetric loss curve can be constructed for any heating rate Z using

$$w = \exp\left\{-K_0 \frac{RT^2 \exp(-E/RT)}{ZE} \times \left[1 - \frac{2RT}{E} + \frac{6(RT)^2}{E^2}\right]\right\} \tag{3}$$

Figure 4 shows the experimental thermogravimetric curve at a rate of 300°C h^{-1}, together with the curve recalculated using eqn (3). This method inevitably results in some error because the activation energy plot is linear over a restricted range of temperature; in this case 212° to 276°C.

The corresponding curves for other heating rates are also shown. This is an approximate way of executing the rate calibration and the errors are most pronounced at high set rates. Both set and calculated heating rates are quoted for overpressure experiments in Tables 1—3.

The bars were radiographed to ensure that they were free from shrinkage voids or cracks caused by the injection-moulding processes which might interfere with the assessment of critical heating rate. In general the bars were free from such defects and examples of prints of radiographs are shown in Fig. 5.

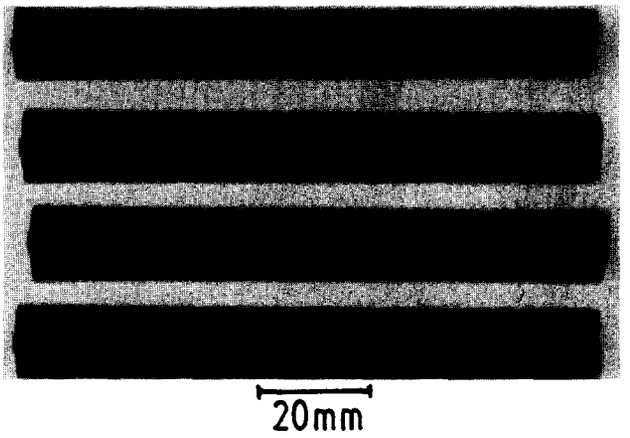


Fig. 5. Prints of radiographs of moulded bars before heat treatment.

In the first series of experiments, the samples were supported on a refractory tile with a thin layer of alumina powder. The results are summarised in Table 1. This identifies three factors influencing the quality of moulding after binder removal. The effect of heating rate is seen by comparing samples heated at set rates of 5°C h^{-1} and 15°C h^{-1}, showing that the critical heating rate at atmospheric pressure lies between these temperatures. The sample heated at a set rate of 5°C h^{-1} is shown in Fig. 6. Samples heated at a set rate of 40°C h^{-1} under 0·6 MPa pressure, although defective in cross-section, were only marginally worse than the sample heated at 15°C h^{-1} under 0·1 MPa, indicating that overpressure has a beneficial effect. Samples heated at set rates of 100 and 200°C h^{-1} showed severe deformation due to

Table. 1. Integrity of mouldings heat treated on a tile, unsupported by powder

Heating rate °Ch^{-1}		*Pressure (MPa)*	*Results*
Set	*Actual*		
5	5	0·1	No surface cracks, no visible defects in cross-section
15	13	0·1	No surface cracks, signs of slight internal cracking
20	18	0·6	Some surface cracks, signs of internal cracking
40	35	0·6	Some surface cracks, signs of internal cracking
100	83	0·6	Extensive surface cracks and parallel cracks in section, extensive slumping
200	180	0·6	Extensive surface cracks and parallel cracks in section, extensive slumping

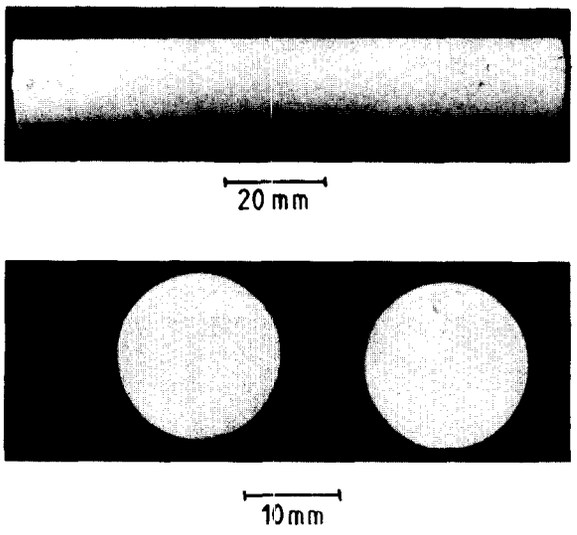


Fig. 6. Sample heated on a tile at a set rate of 5°C h^{-1} at atmospheric pressure.

slumping and the cracks in the cross-section were perpendicular to the direction of deformation. This highlights the sample support as a relevant variable; an issue that does not arise at lower heating rates (Fig. 6). It follows that the interaction of the supporting medium with the component during pyrolysis must also be assessed.

Figure 7 shows the outer appearance and cross-sections of the sample heated at 200°C h^{-1} on the refractory tile. Although the rate is well above critical for this condition, much of the damage is associated with the deformation. The extent of sagging is measured by ovality and plotted as a function of heating rate in Fig. 8 for samples resting on a shallow bed of powder (curve A) and for samples fully embedded in powder (curve B). For heating rates which could be used at atmospheric pressure, slumping does not occur. This is because the deformation of moulded ceramics is sensitive to ceramic volume loading and when sufficient

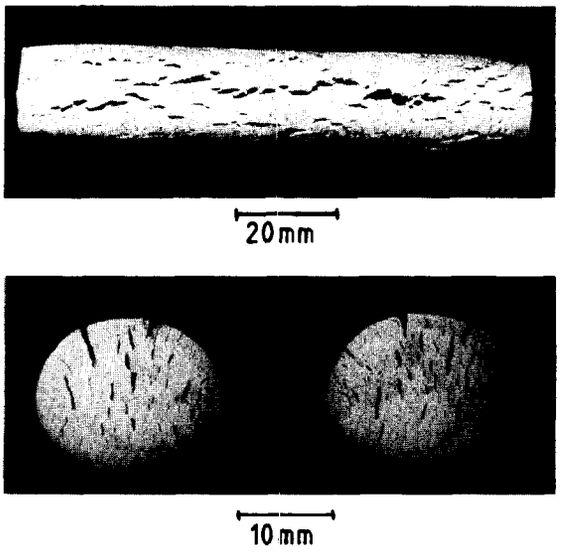


Fig. 7. Slumping caused by inadequate support during heating at a set rate of 200°C h^{-1} at 0·6 MPa.

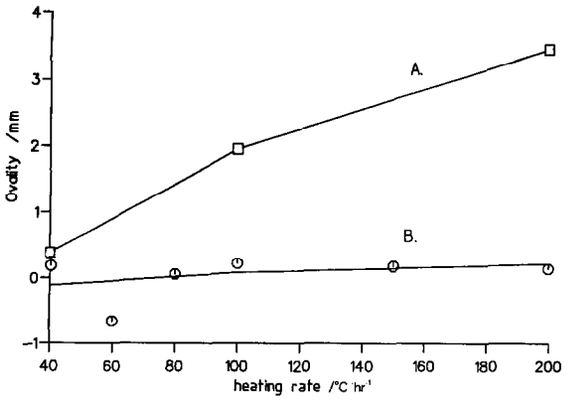


Fig. 8. The effect of sample support on deformation due to slumping. A: Samples resting on shallow powder bed. B: Samples packed inside powder bed.

binder has been displaced, the suspension acquires quasi-solid properties.[16] Under circumstances where an overpressure permits the use of higher heating rates, the thermogravimetric weight loss curve is displaced to higher temperatures.[17] The organic phase then has lower viscosity and, due to differential thermal expansion, occupies a higher volume fraction, so that flow is enhanced. Thus, when overpressure is employed, extra precautions are needed for component support.

The second series of experiments was therefore carried out with samples embedded in the alumina powder. As well as supporting the component, the powder bed may also contribute to safe debinding by capillary extraction when the organic vehicle is based on a low molecular weight system.[18,19] The amount of binder extracted in the molten state isothermally at 130°C after heating for 3 h and 19 h in the alumina powder was 21% and 69% respectively. A sample heated on an alumina tile for the same periods lost 1·4% and 6·1% respectively. Thus the alumina powder is effective in removing some of the organic vehicle by capillary extraction. However, the 19 h heat treatment considerably exceeds the time for which the binder was molten during pyrolysis under overpressure, which was typically less than 3 h at 0·6 MPa.

Figure 8 shows that shape was retained over the range of heating rates explored when a powder bed was used and this is reflected in the pattern of defects. Figure 9 shows a bar heated at a set rate of 200°C h^{-1} and 0·6 MPa, which should be compared with Fig. 7. The slumping is absent and the cracks are no longer unidirectional.

The results for samples embedded in alumina (Table 2) suggest that at 0·1 MPa the critical heating rate is not greatly increased by the presence of the powder bed. In the sample heated at a set rate of 100°C h^{-1} the effect of boiling of low molecular weight organic compounds in solution in the main polymer is clearly seen as bloating (Fig. 10). At this pressure the boiling occurs at a temperature

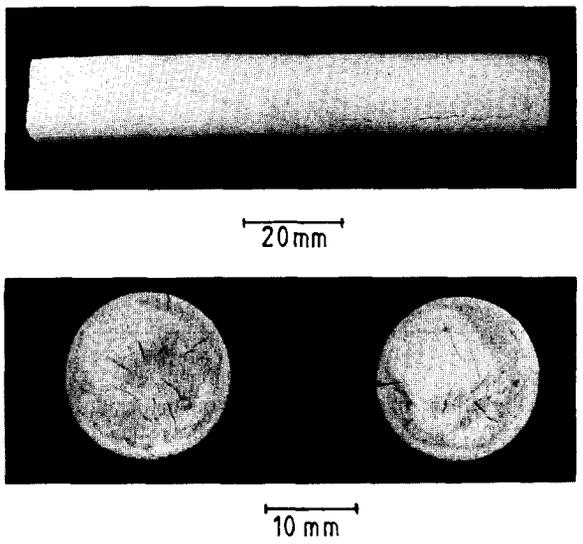


Fig. 9. Defects in a bar supported in an alumina powder bed and heated at a set rate of 200°C h^{-1} under 0·6 MPa.

where the suspension is fluid because little binder has been expelled; an effect resulting from the high heating rate. In subsequent work at higher pressures and similar heating rates the defects take the form of cracks because their initiation has been deferred to higher temperatures by the suppression of boiling and by that stage more binder has gone and the ceramic volume fraction is consequently higher.

At 0·6 MPa, the critical heating set rate is in the region 80–100°C h^{-1}. Figure 11, for example, shows the surface and sections of a bar heated at 80°C h^{-1}, which is of good quality. The use of a pressure of 1·0 MPa gave a sample free from internal defects at a set rate of 100°C h^{-1} (actual rate 63°C h^{-1}). This sample showed slight surface cracks on the top surface associated with loss of setter powder. Exposed surfaces generally presented this problem. The loss was caused by admitting nitrogen to the vessel at too high a rate. The use of 1MPa overpressure did not give an improvement over the critical rate achieved at 0·6MPa. Three reasons why the full benefit of overpressure may not be obtained in practice are discussed later.

The pressures used here do not present severe laboratory safety problems provided normal precautions are taken. The construction of the apparatus involved very modest capital expenditure.

Table 2. Integrity of moulding heat treated in an alumina powder bed

Heating rate °Ch $^{-1}$		*Pressure (MPa)*	*Results*
Set	*Actual*		
20	18	0·1	Outer surface defect-free, slight internal cracking at centre
40	30	0·1	As above
100	70	0·1	Severe surface cracking, internal bloating
15	14	0·6	Free from macro-defects
40	32	0·6	Free from macro-defects
60	44	0·6	Free from macro-defects
80	60	0·6	Free from macro-defects
100	70	0·6	Slight surface cracking, slight internal cracking
150	100	0·6	Slight cracking, internal cracks
200	130	0·6	Surface cracking, internal cracking
100	63	1·0	No internal cracks, surface cracks due to loss of powder
125	75	1·0	Surface defect-free, very slight central cracks
150	95	1·0	Surface very slightly cracked, internal cracks
200	125	1·0	Surface cracks, internal cracks

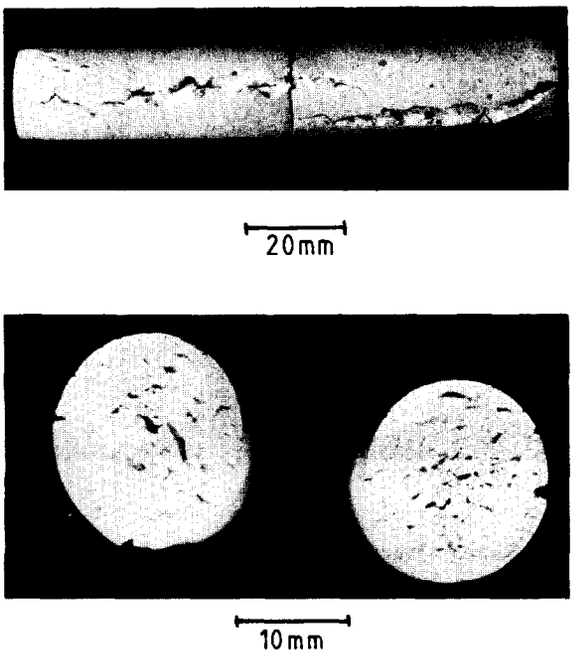


Fig. 10. Surface and sections of a bar heated at a set rate of 100°C h^{-1} under 0·1 MPa while supported in a powder bed. Defects at the centre take the form of bubbles resulting from boiling because at this heating rate the suspension retains fluidity.

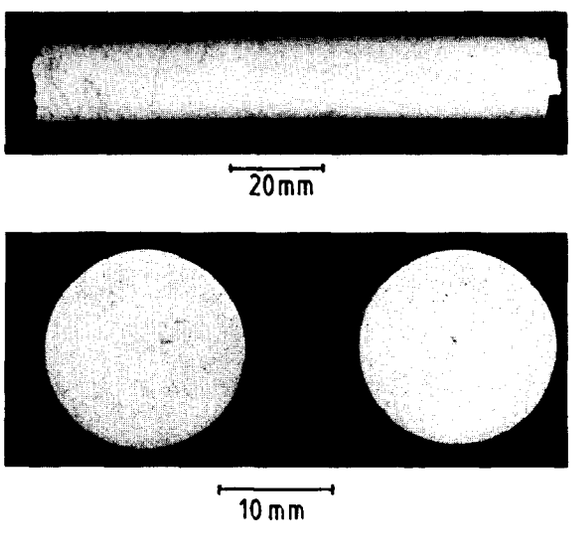


Fig. 11. Surface and sections of a bar heated at a set rate of 80°C h^{-1} under 0·6 MPa.

These factors imply that the widespread use of overpressure debinding is relatively unimpeded.

In order to understand the role of overpressure in a non-oxidising environment, one may enumerate the individual effects it may have on the system as follows:

(1) Increase in the boiling point of low molecular weight constituents of the organic vehicle and of the solution of degradation products (as solute) in molten polymer (as solvent)
(2) Decrease in diffusion coefficient of degradation product in solution caused by reduction in polymer free volume.[20]
(3) Closure of pre-existing defects when the organic vehicle is molten.
(4) Increase in vapour pressure of volatile species.
(5) Dissolution of ambient gas in the molten polymer.
(6) Increase in convective heat transfer in the furnace.
(7) Influence on gaseous diffusion of degradation products in the porous region.
(8) Changes in the distribution of degradation products.
(9) Changes in miscibility of organic liquid mixtures.

These effects are assessed individually elsewhere[21] and arguments are presented to suggest that the first contribution is overriding. Thermal degradation, which occurs throughout a moulding, liberates low molecular weight products of decomposition which dissolve in the parent polymer. When the vapour pressure over this solution at any point reaches ambience, boiling occurs. The resulting defects may take the form of round 'voids' characteristic of boiling in a liquid and examples are shown in Fig. 10 in a sample heated at 100°C h^{-1} at atmospheric pressure. If, however, some polymer has already been lost, and hence ceramic volume fraction has risen, the suspension behaves as a solid,[16] even though continuous porosity has not yet formed. Defects then take the form of a crack. When the external pressure is raised, the boiling point is elevated and the system can reach higher temperatures without defects occurring. Mass transport processes which are thermally activated are then enhanced.

The critical stage in thermolytic debinding occurs in the early stages of degradation where most pores are filled. The suppression of boiling enhances the diffusion coefficient for degradation products migrating in solution in the continuous phase both by raising the temperature and by allowing a higher diffusant concentration to prevail. In free volume theory, both effects conspire to have a pronounced influence on diffusion.[22]

Table 3. Integrity of samples heated in a coarse SiC powder bed

Heating rate °Ch^{-1}		*Pressure (MPa)*	*Results*
Set	*Actual*		
20	16	0·6	Very slight internal cracking
40	30	0·6	Outer surface defect free
150	102	0·6	Some internal cracks
200	135	0·6	Many internal cracks
400	[a]	0·6	Surface and internal cracks, no slumping.

[a] Outside the range of calibration.

Secondly, by allowing the polymer to reach a higher temperature, viscosity is reduced and capillary flow into the surrounding powder is speeded up.[19] It is beyond the scope of this work to quantify the competition between these two transport processes but an indication of their relative importance can be found by using a powder which supports the sample against slumping but has negligible ability to extract the organic vehicle by capillary flow.

This comparison is shown in the third series of experiments in which coarse silicon carbide powder was used as the setter powder. In partitioning experiments, the amount of binder based on the initial weight in the sample after 3 h and 19 h in the SiC setter powder was identical, to within 1%, to the loss experienced by companion samples heated at 130°C on a tile.

Table 3 shows the result of experiments with the silicon carbide setter. The critical heating rate at 0·6 MPa is lower than that obtained in the alumina powder, indicating that capillary extraction is a significant transport path in the alumina setter powder. At 0·6 MPa the extent of damage in samples supported in silicon carbide powder was less than that seen in samples which were unsupported or heated without overpressure for comparable heating rates.

Three reasons can be discerned for the failure to obtain the full potential benefit of overpressure. In the first place, the use of a powder bed reduces the effective surface mass transport coefficient for gaseous products leaving the body because of the static boundary layer provided by the powder. If support is mandatory, as implied by the results in Fig. 8, it will tend to provide a resistance to gaseous transport away from the surface of mouldings. A second reason is that where liquid capillary flow is a significant transport path, the capillary pressure falls with an increase in temperature due to the reduction of the surface energy of polymers with increasing temperature.[19] These factors may explain why the high values of critical

heating rate found with the alumina setter at 0·6 MPa were not further enhanced at 1 MPa.

A third reason why the full benefit of overpressure may not be achieved in practice arises from the problem of pressure transmission to the core of a moulding throughout the decomposition region. Before the open porosity stage is reached, shrinkage of the core as polymer is lost must be accompanied either by collapse of the shell or by diffusion of nitrogen to the centre. Collapse of the outer shell may be impeded if the peripheral ceramic weight fraction rises towards V_{max}, the weight fraction at which viscosity approaches infinity,[16] and this is likely to occur at an early stage and to be associated with the shrinkage due to binder removal. Pressure transmission may thus rely upon diffusion of dissolved gas in the continuous phase.

Closely related to the problem of pressure transmission is the possibility that elevated ambient pressure applied to mouldings in the molten state will cause defects to collapse. This possibility was investigated empirically for similar bars moulded with low injection pressure which contained injection-moulding voids.

Two such test bars, measuring 10 mm × 10 mm × 75 mm, were radiographed to confirm the presence of voids. They were then heated to 80°C in the pressure furnace under atmospheric pressure. The softening point of the material was determined by thermomechanical analysis to be 51°C. When that temperature had been attained, the pressure was increased as rapidly as possible to 1 MPa, and held while the samples were cooled. They were radiographed again, but showed no difference in the internal voids. It is possible that nitrogen had diffused through the material to fill the pores in the time it was being admitted to the vessel, as filling the chamber took about 90s, or that the applied pressure was insufficient to cause the necessary deformation.

Samples of the same material were heated to 130°C inside the pressure vessel and the gas pressure was raised to 1 MPa. They were then cooled to room temperature under pressure and, upon removal, promptly placed in a glass-fronted oven at 130°C. Very slight surface bloating could be detected on reheating, which did not appear on samples reheated without overpressure treatment, indicating the presence of dissolved gas in the continuous phase.

4 Conclusions

The use of modest overpressure (0–1 MPa) significantly increased the critical rate of heating of commercial injection-moulded ceramics. The main benefit is considered to result from an increase in boiling point of the binder components and their degradation products in solution. This means that higher temperatures can be reached before boiling in the continuous phase occurs. At higher temperatures, mass transport by diffusion through the continuous phase and liquid flow into a surrounding powder are both enhanced.

When the higher heating rates made possible by overpressure are used, the sample must be supported against slumping, a requirement that does not prevail at low rates of heating for the samples tested here.

Acknowledgements

The authors are grateful to the Science and Engineering Research Council for a studentship for PDH and to Fairey Tecramics for jointly supporting this work. Thanks are due to Mrs K. Goddard for typing the manuscript.

References

1. Evans, J. R. G., Plastic forming operations for ceramic suspensions. In *New Materials and their Applications*, ed. D. Holland. Institute of Physics, UK, 1990, pp. 43–52.
2. Patterson, B. R. & Aria, C. S., Debinding injection-moulded materials by melt wicking. *JOM*, **41** (1989) 22–24.
3. Johnson, K. P., Metal injection by the InjectAMAX process. In *Advances in Powder Metallurgy 1989* Vol. 3. ed. T. G. Gasbarre & W. F. Jandeska. Metal Powder Industries Federation, NJ, USA, 1989, pp. 17–24.
4. Gilissen, R. & Smolders, A., Binder removal from injection moulded ceramic bodies. *Mater. Sci. Monog., High Technology Ceramics, pt A*, **38A** (1987) 591–4.
5. Mizuno, S., Binder removal from ceramic injection moulded bodies. JP Patent 61117 116 A2, 4 June 1986.
6. Mann, D. L., Injection moulding of sinterable, silicon base non-oxide ceramics. *Air Force Laboratory Technical Report AFML-TR-78-200*, December 1978.
7. Wright, J. K., Evans, J. G. R. & Edirisinghe, M. J., Degradation of polyolefin blends used for ceramic injection moulding. *J. Amer. Ceram. Soc.*, **72** (1989) 1822–8.
8. Wright, J. K. & Evans, J. R. G., Kinetics of the oxidative degradation of ceramic injection moulding vehicle. *J. Mater. Sci.*, **26** (1991) 4897–903.
9. Saito, K., Tanaka, T. & Hibino, T., UK Patent 1426317 25 February 1976.
10. Stedman, S. J., Evans, J. R. G. & Woodthorpe, J., A method for selecting organic materials for ceramic injection moulding. *Ceramics International*, **16** (1990) 107–13.
11. Johnsson, A., Carlstrom, E., Hermansson, L. & Carlsson, R., Minimisation of the extraction time for injection moulded ceramic. *Proc. Brit. Ceram. Soc.*, **33** (1983) 139–47.
12. Matar, S. A., Evans, J. R. G., Edirisinghe, M. J. & Twizell, E. H., The influence of monomer and polymer properties on the removal of organic vehicle from ceramic and metal mouldings. To be published.
13. Katagiri, T., Dewaxing furnace for technical ceramics. *Powder Metallurgy International*, **22** (1990) 37–9.

14. BS 5500, *Unfired fusion-welded pressure vessels*. British Standards Institution, London, UK, 4th revision, 1991.
15. Wendlant, W. W., *Thermal Method of Analysis*. Wiley Interscience, NY, 1964, pp. 32–4.
16. Wright, J. K., Edirisinghe, M. J., Zhang, J. G. & Evans, J. R. G., Particle packing in ceramic injection moulding. *J. Amer. Soc.*, **73** (1990) 2653–8.
17. Coates, A. W. & Redfern, J. P., Thermogravimetric analysis. *Analyst*, **88** (1963) 906–24.
18. Wright, J. K. & Evans, J. R. G., Removal of organic vehicle from moulded ceramic bodies by capillary action. *Ceramics International*, **17** (1991) 79–87.
19. Bao, Y. & Evans, J. R. G., Kinetics of the capillary extraction of organic vehicle from ceramic bodies. II. Partitioning between porous media. *J. Eur. Ceram. Soc.*, **8** (1991) 329–38.
20. Ferry, J. D., *Viscoelastic Properties of Polymers*, Wiley, NY, 3rd edn, pp. 285–98.
21. Hammond, P. D., Thermolytic debinding of ceramic injection mouldings using overpressure. To be published.
22. Vrentas, J. S. & Duda, J. L., Diffusion. In *Encyclopedia of Polymer Science and Engineering*, Vol. 5, ed. J. I. Kroshwirtz *et al.* Wiley, NJ, 1986, pp. 36–8.

Journal of the European Ceramic Society **15** (1995) 127–133
© 1995 Elsevier Science Limited
Printed in Great Britain. All rights reserved
0955-2219/95/$9.50

Laser Ablation of Barium Titanate Ceramics Prepared by the Citric Route: The Evolution of Residual Carbon Content

C. Miot,[a] C. Proust,[a,b] E. Husson,[a,b] G. Blondiaux[c] & J. P. Coutures[a]

[a] CRPHT-CNRS, 45071 Orléans cedex 2, France
[b] LPMM, ESEM, Université d'Orléans, B.P. 6747, 45067 Orléans cedex 2, France
[c] CERI-CNRS, 45071 Orléans cedex 2, France

(Received 15 February 1994; revised version received 24 June 1994; accepted 8 July 1994)

Abstract

The laser-induced ablation mechanism of $BaTiO_3$ ceramics has been followed by SEM and EPMA analyses. The evolution of the residual carbon content has been studied by $^{12}C(d,p)^{13}C$ nuclear technique under a 10^{-9} mbar vacuum with laser powers below and above the ablation threshold. The residual carbon remains constant for laser powers below the ablation threshold and is ejected from the crater formed and partly deposited around it when ablation occurs. Immediately after the end of laser ablation, the residual carbon diffuses from the bulk to the surface of the ceramic, leading to high C concentrations in the whole ceramic surface layer. The chemical form of carbon and its mobility in such ceramics are discussed.

1 Introduction

Residual carbon remaining in ceramic materials after the sintering step, originating from the use of organic precursors during the powder fabrication, may influence the material properties. In a previous paper,[1] the residual carbon content has been evaluated in $BaTiO_3$ ceramics. It was shown that the C content is about 50 ppm by weight in the ceramic bulk and that it increases at the surface which exhibits a concentration of several hundreds or thousands of ppm. The surface layer carbon could have two origins: an atmospheric contamination carbon adsorbed at the surface of the ceramic, and material intrinsic carbon, the concentration of which depends on the shape of ceramic pieces and the sintering temperature.

Laser ablation is becoming increasingly significant in materials processing techniques with which to obtain thin films. However, in spite of the scientific and technological importance of this process, relatively little has been published about the physical and chemical mechanisms of laser-induced desorption and ablation from these materials.[2–4] Recent works on laser ablation of $BaTiO_3$[5–11] or other perovskite oxides,[12–15] performed under partial pressure of O_2, are only interested in the production of thin films with a good stoichiometry or a preferred orientation[16] and a little has been published about bulk ceramics.

It seems appropriate to (i) study the ablation mechanism by the evolution of the microstructure by scanning electron microscopy and local analyses by electron probe microanalysis as a function of the number or the power of laser shots, (ii) follow the evolution of the residual carbon content by the $^{12}C(d,p)^{13}C$ nuclear technique after laser-induced desorption and ablation, as a function of the time under an ultra-high vacuum or in air, (iii) discuss the mobility and the chemical form of the residual carbon.

2 Experimental

2.1 Samples

$BaTiO_3$ powders were obtained by a citric resin method, described in previous papers.[17–19] The mixed citrate $BaTi(C_6H_6O_7)_3\ 6H_2O$ is prepared and then dissolved in a mixture of citric acid, ethylene glycol and water with the ratio of $BaTiO_3$ mass/solution mass (R) being 1%. This mixture was calcined at 700°C in static air and gave pure $BaTiO_3$ powders after 2 h. After an ultrasonic deagglomeration step, powders were pressed to give discoidal samples, then they were sintered in

air at 1300°C or 1400°C for 2 h with a heating rate of 300°C/h up to 600°C then 70°C/h up to 1300°C or 1400°C. Sintered discs were about 1·8 cm diameter and 1 mm thick.

2.2 Laser device

The laser ablation was performed at room temperature in an ultra-high vacuum (UHV) chamber with a pressure of about 10^{-9} mbar. Samples were mounted on a micromanipulator and placed in the UHV chamber. A YAG laser with a pulse width of 7 ns and a doubled output (532 nm) was used. Average energy levels were between 20 and 70 mJ producing powers of between 1·4 and 8·6 $\times$ 10^7 W/cm^2 on the sample. The diameter of the laser spot was between about 2 and 5 mm.

2.3 EPMA analysis

Electron probe microanalysis (EPMA) semi-quantitative measurements were performed with a Cameca instrument with a voltage of 10 kV and an intensity of 30 nA under a vacuum of 10^{-5} mbar. The detectors used were PET for Ti ($K_{\alpha 1}$ radiation) LiF for Ba ($L_{\alpha 1}$ radiation) and PC2 for C (K_α radiation). The ablated ceramics were metallized with nickel. The depth analyzed was about 0·2 μm and the surface was a few μm in diameter, thus it was possible to focus the electron incident beam on a ceramic grain. The results given have been averaged over several tens of measurements.

2.4 Raman spectroscopy

Raman spectra of the ablated ceramics were performed with a Dilor Raman microprobe using the 514·5 nm wavelength of a Ar^+ laser with a power of several hundreds of mW. The area and depth analyzed were about 1 μm.

2.5 Carbon analysis

The carbon concentration analysis was carried out by $^{12}C(d,p)^{13}C$ nuclear technique using deuterons from the Van-de-Graaff accelerator of the Centre d'Etude sur les Radiations Ionisantes (CERI). The method has been described in different articles.[20–22] The measurements were performed at 950 keV and 1420 keV deuteron energy in a UHV chamber with a vacuum of about 10^{-9} mbar. The detector was a diode with an active surface of 300 mm^2 situated 64 mm from the sample position and protected by a 20 μm thick Al foil. The detection angle θ was 150°. The beam current was 10 nA. A collimator was placed at the entry of the UHV chamber and 60 mm from the target, giving a constant deuteron beam diameter of 7 mm^2. The counting time was about 20 min per data point.

For 950 keV energy incident deuterons, the carbon content (t) is given in g/cm^2 by the formula:

$$t = \frac{dA}{\Phi} * \frac{1}{\frac{d\sigma}{d\Omega}} * \frac{1}{d\Omega} * \frac{M}{N}$$

where dA = number of detected particles = reaction peak area; Φ = number of incident particles = $Q/1{\cdot}6 \times 10^{-19}$ with Q = total incident charge measured by the integrator (C); $d\sigma/d\Omega$ = differential cross-section (cm^2/sr/nucleus); $d\Omega$ = solid angle determined by the detector and the impact point of the beam on the target (sr); M = atomic mass of the studied nucleus (g/mol); and N = Avogadro number. The differential cross-section has been taken equal to 30 mbarns according to Ref. 23. The solid angle is $7{\cdot}32 \times 10^{-2}$ sr.

Taking into account the density of the ceramics and the depth of the material analyzed (0·4 μm), it is possible to deduce the carbon content in ppm (by weight) in the surface layer.

For 1420 keV energy incident deuterons, a surface carbon content (0·4 μm depth) has been evaluated taking a cross-section of 40 mbarns, then, if it is assumed that there is no gradient of concentration as a function of the depth, the carbon content of the subsurface (between 0·4 and 4·4 μm) may be evaluated taking an average cross-section of 64 mbarns.

3 Results

The sintered ceramics had densities approaching 99% of the theoretical density (d_{th} = 6·02 g/cm^3) and SEM observations showed an average grain size of about 100 μm.

3.1 Ablation mechanism

The physical phenomena that occur when a laser beam is focused onto a material surface depend mainly on (i) the power of the laser beam, (ii) the thermal properties of the material and (iii) the absorptivity of the material at the wavelength used. According to Sankur & Cheung,[24] three power density regimes can be defined: low (<10^6 W/cm^2), intermediate (>10^6 and <10^6 W/cm^2) and high (>10^8 W/cm^2). In the low power density regime, surface melting and evaporation are under quasi-equilibrium conditions. In the high power density regime a plasma is formed. In the intermediary regime, the plasma contribution is small but dissociated species are observed in the evaporation stream. The present experimental conditions, with a laser power of about 10^7 W/cm^2, correspond to this last case

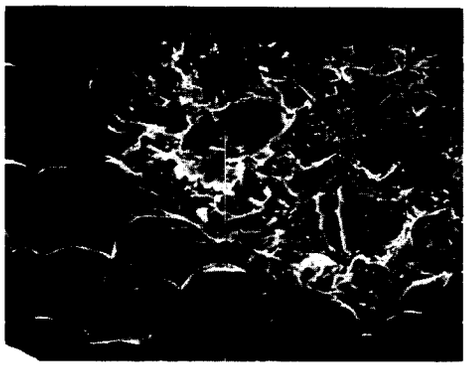


Fig. 1. SEM image of a $BaTiO_3$ ceramic damaged by 100 shots at $2{\cdot}7 \times 10^7$ W/cm^2. Grain explosion is observed without the appearance of a molten zone.



Fig. 3. SEM image of a $BaTiO_3$ ceramic damaged by 100 shots at $3{\cdot}9 \times 10^7$ W/cm^2. The first molten zones appear at triple grain boundaries and at pores, in addition to grain explosion.

The ablation phenomenon was followed by SEM by using increasing powers of the laser beam and numbers of shots.

Firstly, a series of 100 laser shots with variable powers was performed onto as-sintered ceramic surfaces. In order to avoid interactions of one series of shots with another one, a new ceramic sample was used for each series.

For a laser power of $2{\cdot}7 \times 10^7$ W/cm^2, an explosion of the grains was observed without appearance of a molten zone (Fig. 1). Thus the ablation threshold is situated at about $2{\cdot}6 \times 10^7$ W/cm^2 in these conditions. At $3{\cdot}2 \times 10^7$ W/cm^2, the same phenomenon was observed (Fig. 2) but the ceramic was ablated to 4–5 μm depth. At $3{\cdot}9 \times 10^7$ W/cm^2, the first molten zones appeared at triple grain boundaries and at pores (Fig. 3) in addition to grain explosion and an ablation depth of about 5 μm. For higher laser powers (experiments were performed at 5·1 and $7{\cdot}7 \times 10^7$ W/cm^2) only molten zones were observed with very irregular features (Fig. 4). As the laser power increases, the formation of a more and more regular crater is observed: a regular form 200–300 μm deep is obtained for laser powers of $5{\cdot}7$–$7{\cdot}1 \times 10^7$ W/cm^2. The ablation depth was roughly evaluated during SEM observations.

The influence of the number of shots at constant laser power was studied. Two values for the laser power were chosen: $2{\cdot}7$ and $5{\cdot}7 \times 10^7$ W/cm^2. A series of 500 shots at $2{\cdot}7 \times 10^7$ W/cm^2 showed, in addition to the grain explosion already mentioned for 100 shots at this laser power, a rise of grains from the surface due to the release of occluded gas (Fig. 5). Even for a number of shots greater than 500, no molten zone was observed. It seems that, below a certain laser power threshold, molten zones are never observed. Finally, for 500 shots at $5{\cdot}7 \times 10^7$ W/cm^2, the formation of a regular crater is clearly observed: Fig. 6 shows the different zones at the surface of the ceramic:

(i) The zone undamaged by the laser beam.
(ii) The circular zone around the crater, which is smooth and covered in places by more or less spherical nodules which seem to come from the crater center. Black soot-like deposits are also observed. Sometimes holes like chimneys appear that are probably due to the release of gas.
(iii) The crater bottom with a very damaged surface: the erosion seems to always originate at the pores and at the triple grain boundaries.

If the laser beam power is increased (up to $9{\cdot}3 \times$

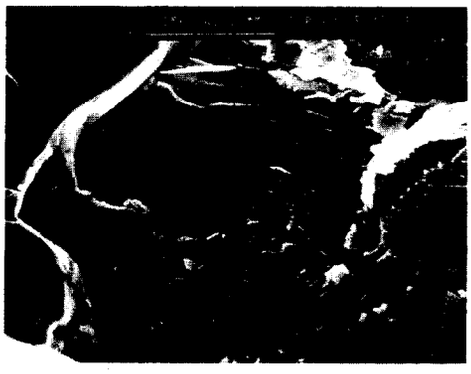


Fig. 2. SEM image of a $BaTiO_3$ ceramic damaged by 100 shots at $3{\cdot}2 \times 10^7$ W/cm^2. The ceramic is ablated to a depth of 4–5 μm.

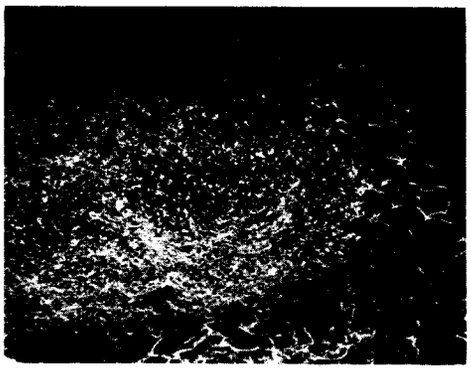


Fig. 4. SEM image of a $BaTiO_3$ ceramic damaged by 100 shots at $4{\cdot}3 \times 10^7$ W/cm^2. Very irregular molten zones are observed.

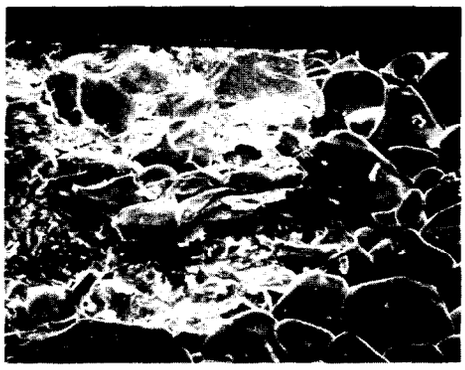


Fig. 5. SEM image of a $BaTiO_3$ ceramic damaged by 500 shots at $2{\cdot}7 \times 10^7$ W/cm^2. Grain explosion is observed as well as an upthrust of grains due to the release of occluded gas.

10^7 W/cm^2) or if the shot number is increased (up to 1500 shots) the observed phenomena are similar with the crater formed being much deeper.

3.2 Analysis of Ti and Ba compositions in ablated ceramics

Measurements of Ti and Ba contents have been performed by electron microprobe. Ceramics studied before laser treatment had a Ba/Ti ratio of $1{\cdot}03 \pm 0{\cdot}03$. The citric method used to produce the present ceramics gives, in principle, a Ba/Ti ratio equal to 1. The slightly higher value found may be explained because standards such as TiO_2 or $BaSO_4$ were not used to calibrate the measurements and because there probably exist interaction effects between Ti and Ba elements. This value is a relative value that is self-consistent and only its variation is studied.

A ceramic damaged by 500 laser shots at $5{\cdot}7 \times 10^7$ W/cm^2 was then analyzed. The crater bottom exhibits a Ba/Ti ratio of 1·25, the glossy, black circular zone around it has a ratio of 0·95 and the ejected particles a ratio of 1·08. The non-irradiated part of the ceramic exhibits a ratio of 1·03. Thus, the crater and the ejected particles are richer in Ba whereas the black circular zone is richer in Ti than the stoichiometric composition.

Measurements have also been performed by Rutherford back-scattering (RBS) technique on such a ceramic. A very slight decrease of the Ti content in the crater confirmed the electron microprobe measurements.

3.3 Analysis of the carbon content by $^{12}C(d,p)^{13}C$

Measurements performed on as-sintered ceramics at a 950 keV deuteron energy gave a carbon content of 90 ng/cm^2 in the surface layer (0·4 μm), corresponding to about 350 ppm.[1] Then, the authors tried to desorb the surface carbon by laser-beam cleaning but no change in the C content was observed until the laser power was high enough to ablate the ceramic surface.

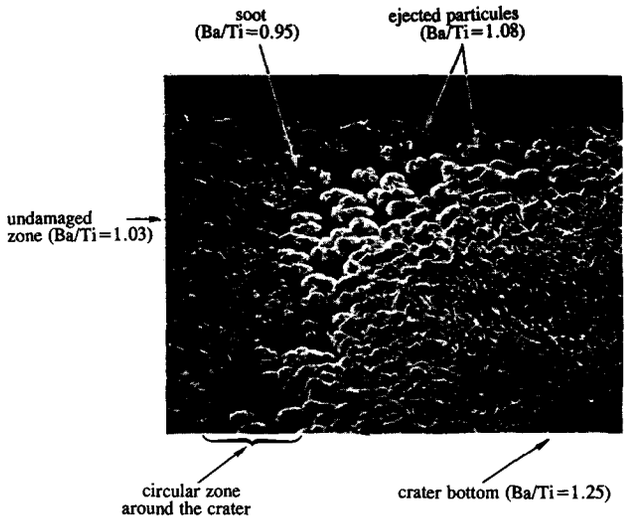


Fig. 6. SEM image of a $BaTiO_3$ ceramic damaged by 500 shots at $5{\cdot}7 \times 10^7$ W/cm^2. A regular crater is formed (200–300 μm depth) and different zones may be observed: the crater bottom, a circular zone around the crater with soot and ejected spherical particles and unperturbed surface.

Finally, ceramics damaged by 500 laser shots at $5{\cdot}7 \times 10^7$ W/cm^2 were studied. Taking into account the technical difficulties in focusing the laser and deuteron beams onto a given area, a large crater was formed by scanning the laser shots over a square of area 16 mm^2. The C content was measured in different areas of the damaged ceramics: in the crater center, around it and in unperturbed zones. The results are given in Table 1. It is observed that immediately after laser ablation, the C content is much smaller in the crater and higher in the glossy, black aureole around the crater, whereas the nonirradiated part of the ceramic exhibits a C content of about 350 ppm like the as-sintered ceramics. A measurement performed at 1420 keV energy in the crater showed also a very low carbon concentration. Thus the carbon does not migrate below the surface of the crater under the laser shots. There is, more probably, an ejection–redeposition mechanism.

The evolution of the carbon content of these ceramics left in a 10^{-9} mbar vacuum was observed, after 1·5 h, the C content had increased in all the

Table 1. Carbon content (in ppm) measured as a function of the time for areas for the ceramics with differing degrees of damage

Time	*Crater center*	*Around the crater*	*Undamaged surface*
Before laser shots[a]	350	350	350
After laser shots[a]	110	600	380
After 1·5 h[a]	180	840	560
After 72 h[a]	820	870	900
After 3 months[b]			
Surface	12000	6000	3000
Subsurface	830	100	100

[a] In UHV chamber.
[b] After an exposure to air for 3 months.

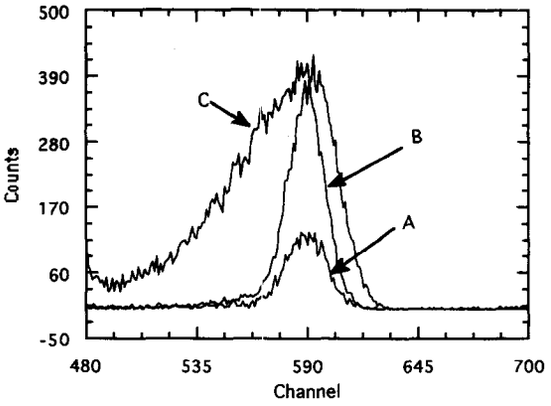


Fig. 7. The C peaks of the proton spectra of $^{12}C(d,p)^{13}C$ reaction obtained from 1420 keV incident deuteron energy: (A) far from the crater, (B) around the crater, (C) in the crater bottom. A symmetrical shape characterizes a C content much higher in the surface layer than in the bulk. The very unsymmetrical (C) peak reveals that C content is high both in the surface layer and in the bulk.

zones, particularly in the zone around the crater; after 72 h the C concentration was practically constant in the whole surface and increased by a factor close to 2·5 in comparison with the C content found in the as-sintered ceramics before laser shots. An equilibrium seemed to be established between the ceramic surface and the chamber atmosphere.

It was interesting to study the evolution of the C content with time after removing the ceramic from the UHV chamber of the apparatus. After an exposure in air for three months, $^{12}C(d,p)^{13}$ C measurements were performed in the same conditions in the UHV chamber with 950 keV energy incident deuterons. The results obtained are reported in Table 1. A strong increase of the surface carbon content was observed. The surface of the ceramic which was not damaged by the laser beam impact exhibits a C content of about 3000 ppm, whereas as-sintered ceramics of 1 mm thick generally exhibit a surface C content of about 350 ppm, a value remaining constant even after an exposure of several months in the air.[1] The surface around the crater and the crater bottom exhibit C contents of 6000 ppm and 12000 ppm respectively. These results were confirmed by EPMA analysis. In the crater bottom a large concentration of carbon was observed. $^{12}C(d,p)^{13}$ C measurements performed with 1420 keV energy incident deuterons showed that in the subsurface the C content is low (about 100 ppm) except in the crater center (830 ppm). The spectra given in Fig. 7 show the shape of the peaks: they are quasi-symmetrical for the measurements performed around the crater and further from it and very unsymmetrical for those performed in the crater center, this last profile is characteristic of a high C content both in the surface layer and in the bulk.

4 Discussion

Chan & Mazumder[2] have developed a model describing laser ablation damage. When an intense laser beam arrives at the target surface, different processes may occur. At the beginning of the laser pulse, the absorbed laser energy heats the target up to the melting point and then to the vaporization temperature. The vaporization generates a recoil pressure that pushes the vapour away from the target and expels the liquid sideways. Thus a part of the material is removed from the target both in vapor and liquid form. The absorbed laser energy should be partitioned into (i) loss into the target, (ii) latent heat of fusion and vaporization and (iii) creation of a recoil pressure to push the vapor away and expel the liquid.

In the present case, the circular zone exhibiting a glossy and black feature seems to be a consequence of the vapor ejection and lateral expulsion of the liquid. The ablation mechanism could be described as follows:

—Because of the high heating of the material, there is formation of a liquid and then vapor phases that are Ti-rich, the lightest elements being ejected first, as was observed by other workers.[14]

—The liquid phase deposited in the bottom of the crater or around it could correspond to the ultimate step before evaporation, the material not having reached a sufficient temperature to be volatilized.

—The ceramic grains which remain in the crater bottom or which have been ejected under the repeated laser shots on the surface around the crater are richer in heaviest elements, i.e. Ba in the present case.

Concerning the C content evolution after laser ablation, the same type of phenomenon is observed: the very light C element is eliminated when the ceramic is heated; thus the crater center exhibits a very low C content. One could think that C is totally evaporated when the vapor phase is formed; in fact, a relatively high C content is measured in the neighboring crater; the black color of the glossy zones could be due to the formation of carbon in a chemical form close to graphite, although this could not be confirmed by Raman microprobe. Thus carbon ejected from the crater is surely present in the vapor phase and also in the liquid phase.

The evolution of the C content with the time after laser ablation seems quite surprising. As ceramics are maintained in ultra-high vacuum conditions and the undamaged surface exhibits an increased C content, it seems more probable that

carbon comes from the bulk of the ceramic rather than from the chamber of the apparatus (although this last hypothesis could not be totally eliminated). Thus, it can be assumed that residual carbon is, in the sintered ceramic, in the form of chains; in the regions of the ceramics damaged by the laser thermal phenomenon, the C–C bonds should be broken and carbon become more mobile and diffuse to the surface of the ceramic.

After removing the ceramic from the UHV chamber and exposing it in the air for three months, the surface C content strongly increased, this phenomenon may have two origins:

(i) The observed carbon comes from the bulk of the ceramic; in this case the diffusion of carbon continues after 72 h in the UHV chamber.

(ii) The observed carbon results from the atmospheric contamination, the surface of the ceramic becoming more active under the laser bombardment. The measured C contents show in this case that this carbon is not totally desorbed when the ceramic is replaced in the UHV chamber to perform new measurements but seems quite well bonded to the ceramic.

At the present time, it is not possible to differentiate between these two points and further experiments are now in progress. In any case, the Raman microprobe spectra performed both on as-sintered and ablated ceramics showed that carbon is not present as carbonate, carbon dioxide or carbides but rather as hydrocarbon chains. XPS measurements could give more information about the chemical form of this carbon.

5 Conclusion

This work allowed the laser-induced ablation mechanism of $BaTiO_3$ ceramics to be followed and new information to be obtained about the residual carbon present in $BaTiO_3$ ceramics prepared by the citrate route. For laser powers below the ablation threshold, C is not desorbed by laser-beam cleaning, thus it seems well bounded or trapped in the material. For laser powers above the threshold ablation, C is ejected from the crater formed and deposited partly as soot around it. The laser beam–material interaction leads, after ablation, to an important diffusion of the carbon from the bulk of the ceramic to its surface. Residual carbon could be present in as-sintered ceramics in the form of hydrocarbon chains and the laser bombardment could break them and give much more mobile carbon or hydrocarbon species.

References

1. Proust, C., Husson, E., Blondiaux, G. & Coutures, J. P., Residual carbon detection in barium titanate ceramics by nuclear reaction technique. *J. Eur. Ceram. Soc.*, **14** (1994) 215–19.
2. Chan, C. L. & Mazumder, J., One-dimensional steady-state model for damage by vaporization and liquid expulsion due to laser–material interaction. *J. Appl. Phys.*, **62**, (1987) 4579–86.
3. Cheung, J. T. & Sankur, H., Growth of thin films by laser-induced evaporation. *Solid State Mater. Sci.*, **15**, (1988) 63–109.
4. Haglund, Jr, R. F., Tank, K. & Chen, C. H., Production of molecular clusters of lithium niobate by ultraviolet and visible laser abalation. *Mater. Res. Soc. Symp. Proc.*, **243** (1992) 405–10.
5. Nashimoto, K. & Fork, D. K., Epitaxial growth of MgO on GaAs(001) for growing epitaxial $BaTiO_3$ thin films by pulsed laser deposition. *Appl. Phys. Lett.*, **60**, (1992) 1199–201.
6. Davis, G. M. & Gower, M. C., Epitaxial growth of thin films of $BaTiO_3$ using excimer laser ablation. *Appl. Phys, Lett.*, **55** (1989) 112–14.
7. Roy, D. & Krupanidhi, S. B., Pulsed excimer laser ablated barium titanate thin films. *Appl. Phys. Lett.*, **61** (1992) 2057–9.
8. Gibson, U. J., Ruffner, J. A., McNally J. J. & Peterson, G., Nd: YAG laser ablation of $BaTiO_3$ thin films. *Mat. Res. Soc. Symp.*, **191** (1990) 19–24.
9. Norton, M. G. & Carter, C. B., Observation of the early stages of heteroepitactic growth of $BaTiO_3$ thin-films. *J. Mat. Res.*, **5** (1990) 2762–5.
10. Nashimoto, K., Fork, D. K., Ponce, F. A. & Tramontana, J. C., Epitaxial $BaTiO_3$/MgO structure grown on GaAs(100) by pulsed laser deposition. *Jpn. J. Appl. Phys.*, **32** (1993) 4090–102.
11. Cheng, H. F., Yeh, M. H., Liu, K. S. & Lin, I. N., Characteristics of $BaTiO_3$ films prepared by pulsed laser deposition. *Jpn. J. Appl. Phys.*, **32** (1993) 5656–60.
12. Tabata, H., Kawai, T., Kawai, S., Murata., O., Fujioka, J. & Minakata, S., Preparation of $PbTiO_3$ thin films at low temperature by an excimer laser ablation technique. *Appl. Phys. Lett.*, **59** (1991). 2354–6.
13. Hirano, T., Fujii, T., Fujino, K., Sakuta, K. & Kobayashi, T., Epitaxial $SrTiO_3$ thin films grown by ArF excimer laser deposition. *J. Appl. Phys.*, **31**, (1992) L511–14.
14. Haglund, Jr, R. F., Affatigato, M., Niehof, A. & Heiland, W., Ultraviolet laser ablation of halides and oxides. *Nucl. Inst. Methods Phys. Res. Sect. B*, (1992) 206–11.
15. Eyett, M., Bauerle, D., Wersing, W., Lubitz, K. & Thomann, H., Laser-induced chemical etching of ceramic $PbTi_{1-x}Zn_xO_3$ *Appl. Phys.*, **A40** (1986) 235–9.
16. Norton, M. G., Cracknell, K. P. B. & Carter, B., Pulsed-laser deposition of barium titanate thin films. *J. Am. Ceram. Soc.*, **75** (1992) 1999–2002.
17. Pechini, M., US Patent 3330 697, 1967.
18. Coutures, J. P., Odier, P. & Proust, C., Barium titanate formation by organic resins formed with mixed citrate. *J. Mater. Sci.*, **27**, (1992) 1849–56.
19. Proust, C., Husson, E., Odier, P. & Coutures, J. P., Sintering ability of $BaTiO_3$ powders elaborated by citric process. *J. Eur. Ceram. Soc.*, **12** (1993) 153–7.
20. Wengeler, H., Knobel, R., Kathrein, H., Freund, F., Demortier, G. & Wolff, G., Atomic carbon in magnesium oxide single crystals. Depth profiling, temperature- and time-dependent behavior. *J. Phys. Chem. Solids*, **43** (1982) 59–71.
21. Oberheuser, G., Kathrein, H., Demortier, G., Gouska, H. & Freund, F., Carbon in olivine single crystals analyzed by the $^{12}C(d,p)^{13}C$ method and by photoelectron

spectroscopy. *Geochim. Cosmochim. Acta*, **47** (1983) 1117–29.
22. Mathez, E.A., Carbon abundances in mantle minerals determined by nuclear reaction analysis. *Geophys. Res. Lett.* **11** (1984) 947–50.
23. Huez, M., Quaglia, L. & Weber, G., Fonction d'excitation de la réaction $^{12}C(d,p)^{13}C$ entre 400 et 1350 keV. Distributions angulaires. *Nucl. Instr. Methods*, **105** (1972) 197–203.
24. Sankur, H. & Cheung, J. T., Formation of dielectric and semiconductor thin films by laser-assisted evaporation. *Appl. Phys.*, (1988) **A47** 271–84.

Journal of the European Ceramic Society 15 (1995) 135–143
© 1995 Elsevier Science Limited
Printed in Great Britain. All rights reserved
0955-2219/95/$9.50

Surface Decontamination Treatments of Undoped $BaTiO_3$—Part I: Powder and Green Body Properties

Claude Hérard, Annelise Faivre & Jacques Lemaître*

École Polytechnique Fédérale de Lausanne (EPFL), Laboratoire de Technologie des Poudres, MX-Ecublens, CH-1015 Lausanne, Switzerland

(Received 3 March 1994; revised version received 17 June 1994; accepted 30 June 1994)

Abstract

Five commercial barium titanate powders were subjected to various surface decontamination treatments: calcination at 500°C, followed by leaching either in pure water or acetate buffer solution. They were then de-agglomerated by ultrasonic treatment and finally characterised by XRD, TGA, XPS, EGA, pyrolysis/FT-IR, BET specific surface area and particle size analysis. The main contaminating elements in raw powders were carbon and sulphur, present as barium carbonate (between 0·7 and 1·2wt%) and barium sulphate (about 0·5 wt%). Barium sulphate is thermally stable up to 1400°C and is not affected by the treatments. Barium carbonate decomposes in two steps, between 500 and 900°C and 1200 and 1400°C by reaction with TiO_2 and $BaTiO_3$ to release CO_2. Carbonation is slightly reduced by calcination, but subsequent water cleaning promotes re-carbonation. Acid cleaning substantially decreases the $BaCO_3$ content, down to 0·07–0·7 wt%. The remaining quantity corresponds to the most stable form which decomposes near 1200–1400°C and is still partially present at the surface of the particles. Forming of ceramics green bodies by slip casting of aqueous suspensions stabilised by ammonium poly(acrylate) was then investigated. The dispersing solution compositions have been optimised for each powder and treatment, in order to minimise the liquid/solid ratio of the slip. In all cases, the properties of the slips and of the cast specimens have been improved by the cleaning treatments: higher solid volume fractions in the slip up to 60% for the best case and higher green densities. In particular green densities as high as 70% have been obtained which is very close to the theoretical maximum packing density of log-normally polydispersed spheres. This enhancement can be ascribed to the beneficial effect of decarbonation on the de-agglomeration of the powders.

* To whom correspondence should be addressed.

1 Introduction

Over the past few years it has become evident that different commercial ceramic powders which are apparently identical according to supplier's data (in particular with respect to stoichiometry, granulometry, surface area and bulk composition) actually exhibit quite different behaviour during the processing steps to produce a final product. This variability is mainly related to the surface chemistry of the powders, which is very difficult to control during the elaboration process and is also very sensitive to handling (storage, contact with atmosphere). The surface of the particles can be contaminated with impurities, whose nature, amount and impact on subsequent processing is not completely understood.

Barium titanate, which is still the most widely used material in the electronic industry for capacitors[1] and positive temperature coefficient of resistivity (PTCR) devices,[2] is typically faced with these problems. Its surface is contaminated either with impurities present in the raw materials, or with carbonates,[3] which result from exposure to atmospheric CO_2 or are produced during the synthesis of the powders[4] (high-temperature solid state, wet chemical or hydrothermal). The presence of this impure surface layer can be detrimental to forming, in particular slip casting, because it alters the rheological properties of the slip,[5] either by enhancing frictional forces between surfaces of the particles, or by promoting the formation of agglomerates. The optimal solid volume fraction in the slip is consequently reduced and results in low green densities after drying. Also the sintering step is affected, with an increased porosity which eventually weakens the final properties (especially dielectric strength). Therefore, it would be interesting to be able to modify available commercial powders[6] by appropriate surface treatments in order to gain reproducibility from one powder

source to another and obtain the desired final ceramic properties.

The aim of this work presented in a series of two papers is to elucidate the exact influence of surface contamination in undoped barium titanate powders and investigate the possibility and consequences of its elimination. Therefore five commercial powders representative of different synthesis routes have been selected and subjected to various thermal and chemical treatments aimed at removing their surface carbonate. In Part I, decontamination treatments (calcination, cleaning in aqueous solution and in acid solution) are described. Investigation of the powders by X-ray diffraction (XRD), thermogravimetric analysis (TGA), X-ray photoelectron spectroscopy (XPS), evolved gas analysis (EGA), pyrolysis/infra-red spectroscopy (PY/FT-IR), specific surface area measurement and particle size distribution analysis are then reported. The effect of such treatments on casting green bodies from aqueous slips stabilised with ammonium poly(acrylate) is presented. Statistical design and analysis of experiments were used throughout this study, and results are discussed in terms of liquid limit of the slips and green densities. In Part II, the sintering behaviour of such surface modified powders will be described and correlated with relevant physical parameters of the initial powders.

2 Experimental procedure

Five commercial $BaTiO_3$ powders were used in this study: Criceram lot VPP20, TAM HPB lot 688, TAM HPB lot 745, Cabot BT10 lot 6243-24, and Rhône-Poulenc type Elmic BT 100 lot 7958. The three first powders were synthesised by the oxalate route, the fourth one by hydrothermal synthesis and the last one by suspending titania sols in barium nitrate aqueous solutions followed by drying, calcination and milling.[7] The supplier's main specifications are summarised in Table 1. Impurities such as Ca, Si, K, Cr, Fe, Sr, Na, Al are present in all powders, without exceeding 100 ppm, except Sr (<600 ppm).

Thermal treatment was intended to decompose surface barium carbonate and possible organic additives present in the raw powders. They were calcined at 500°C for 16 h in air. Since the treatment resulted in agglomeration of the powders, they were subjected to ultrasonic de-agglomeration just after calcination (see later).

Table 1. Suppliers' specifications of initial powders

Powder	*Ba/Ti*	*Specific surface area (m^2/g)*	*Median diameter by volume (μm)*
Criceram	0·99	2·5	1·3
Rhône-Poulenc	1·000	2·7	0·84
TAM 688	0·998	3·22	1·41
TAM 745	0·998	2·89	1·43
Cabot	1·007	7·87	0·4

Chemical treatment was performed on non de-agglomerated calcined powders in order to complete the surface decontamination treatment. 0·3M acetic acid–ammonium acetate buffer (pH of 4·5) was used: [CH_3COOH (50%) + CH_3COONH_4 (50%)]. 50g of each powder were put into 200 cm^3 of this cleaning solution. These amounts were determined from $BaCO_3$ content in raw powders, estimated from preliminary TGA measurements, and assuming the consumption of 20% of the acetic acid during the carbonate dissolution. The stirred suspensions (250 rpm) were maintained for 16 h at 30°C, the powders were then centrifuged, the supernatant was discarded and replaced by boiled demineralised water; washing was repeated until constant conductivity of the supernatant was obtained. The powders were then dried in a desicator in primary vacuum using $CaCl_2$ as a desiccant and finally ground lightly in an agate mortar. In order to ensure that the acid cleaning treatment has no secondary effects inherent to manipulations (suspension, drying), a control cleaning experiment with boiled demineralised water was performed under exactly the same conditions and used as a reference.

De-agglomeration of the powders in suspension by ultrasonic treatment was studied using a 2^4 factorial statistical design. The factors investigated were (A) sonication time (20–40 min), (B) volume of the suspension (125–250 cm^3), (C) solid weight fraction (20–40 wt%) and (D) nature of the solvent (either water or isopropanol). Optimal conditions were found to be 30 min ultrasonication with a 150W horn in boiled demineralised water (50 g of powder in 200 cm^3 water). After sedimentation, the supernatants were removed and the powders were dried in a 32% relative humidity desicator with $CaCl_2$.

XRD experiments were performed on a Siemens Kristalloflex 805 diffractometer with the Ni-filtered Cu K_α wavelength on 10 mg samples.

Thermogravimetric measurements were performed on a Setaram 92-16.18 thermobalance, under flowing oxygen atmosphere. For each run, approximately 200 mg of powder were accurately weighed in a platinum crucible, and the temperature was raised from ambient up to 1000°C at 10°C/min and then from 1000 to 1400°C at 5°C/min.

XPS analyses were made with a Perkin-Elmer Phi 5500 ESCA system spectrometer using the Mg K_α line (15 keV–350W). Several mg of powder

were placed for each run on an indium substrate. The signal curves were fitted using Gaussian peaks summation and Shirley baseline subtraction.[8]

Chemical analyses were carried out on a specific carbon + sulphur analyser from Leybold-Heraeus type CSA 2003. For each measurement 0·1 g of powder, mixed with melting agents (1 g Fe + 0·5 g W) to ensure complete decomposition, were placed in a crucible in an induction furnace with flowing oxygen. The evolved gases were first separated from H_2O and then analysed by infrared detectors specially calibrated for CO_2 and SO_2.

FT-IR analyses were conducted with a Mattson Instruments Inc. type Galaxy 4020 spectrophotometer coupled to a CDS1000 pyrolysis unit. Flash pyrolyses (heating rate: 5°C/ms then 20s at 700 or 1300°C) were done on 5 mg of powder for each run, with nitrogen as carrier gas. The measuring chamber was carefully purged before each run in order to avoid erroneous measurements due to the presence of residual atmospheric carbon dioxide.

Specific surface areas of powders were measured by N_2 adsorption according to the BET model with a Micromeritics type Gemini 2360 surface area analyser. 3 g of powder were used for each measurement.

Particle size distributions of powders were determined with a Horiba CAPA-700 cuvet photo centrifuge, using 10 mg of powder and an aqueous solution of poly(acrylic acid) (0·8 wt%) as dispersion liquid. Prior to measurement the suspensions were ultrasonicated (P = 300W, 7 litre bath) for 10 min. The reliability of the results was guaranteed by four repetitions of the same measurement.

Slip-cast specimens were prepared for each powder source and each treatment from aqueous $BaTiO_3$ suspensions stabilised with poly(acrylic acid)(PAA),[9] the acidity of the stabiliser being neutralised by NH_3. For each powder and treatment, the composition of the dispersion liquid has been optimised in two steps.[10] Firstly, the response of the liquid limit of the powders (LL, defined as the minimum liquid/solid ratio necessary to obtain a free flowing slurry, in cm^3/g) to variations in the PAA concentration ([PAA] = 0·3–0·5 %wt) and the neutralisation ratio ($[NH_3]$/[PAA] = 1·2–1·5) was investigated, using a 2^2 factorial statistical design; LL was experimentally measured by adding to 2 g of dry powder the dispersing solution by increments of 20 μlitre, with strong agitation between two additions, up to the liquid point. Second, LL was minimised for each powder and treatment by acting on the factor(s) found to have a significant effect. The effect of the slip composition (i.e. [PAA] around the optimum value for LL, and liquid/solid ratio in smaller or larger excess above LL) was investigated and optimised using the same statistical methodology. The liquid limit is a processing parameter directly related to the viscosity of the slip and is very sensitive to the degree of agglomeration of the powder. It is easily determined on small quantities of material and provides ready to use information for the casting process. The slips were then vibrated for 30 s at 30 Hz, ultrasonicated (P = 300W, 7 litre bath) for two min, and outgassed for 2 min under vacuum. The slips were cast in a silicon rubber mould, placed on a flat gypsum base; direct contact between the samples and the gypsum base was prevented by inserting a 0·2 μm cellulose membrane. Samples were prepared this way in the form of blocs (12·5 × 6·5 × 6·5 mm) for dilatometry measurements. The samples were withdrawn from the mould after 15 min and then left to dry for 24 h in a desicator containing $CaCl_2$ as a desiccant (32% relative humidity).

Green densities have been measured by Archimedes' method, using isopropanol as the immersion liquid, and assuming the value of 6·02 g/cm^3 for the theoretical density of $BaTiO_3$; the samples were first saturated with isopropanol under vacuum (0·15 bar).

3 Results

3.1 Powder properties

The presence of barium carbonate, which is thought to be the major contaminant at the surface of raw powders, has been investigated by *X-ray diffraction*. Only two crystalline phases were detected: tetragonal $BaTiO_3$ and orthorhombic $BaCO_3$. After acid cleaning the peaks corresponding to barium carbonate have disappeared, as shown in Fig. 1 for the Rhône-Poulenc powder.

Preliminary *thermogravimetric analyses* were performed in order to obtain quantitative data required for treatments of initial powders. Differential thermogravimetric curves of raw powders are shown in Fig. 2, and are similar for all

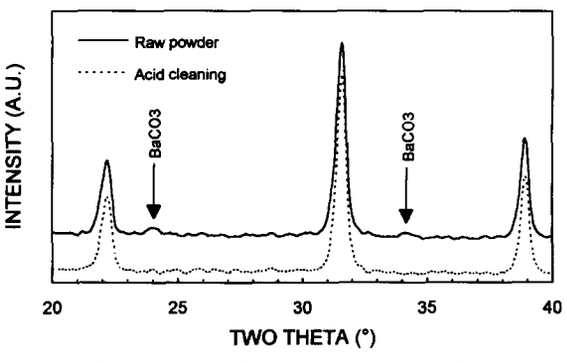


Fig. 1. XRD patterns for as-received and acid-cleaned Rhône-Poulenc powders.

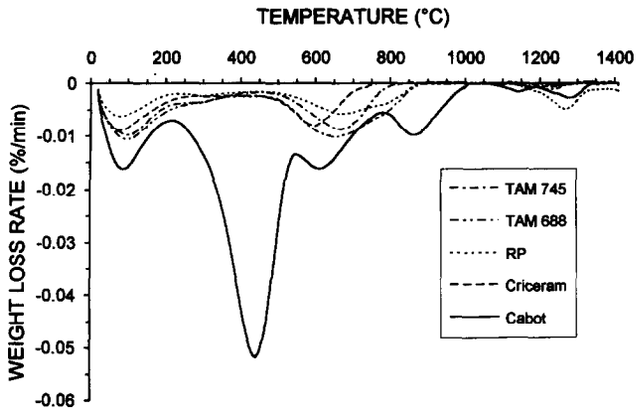


Fig. 2. DTG curves for as-received powders.

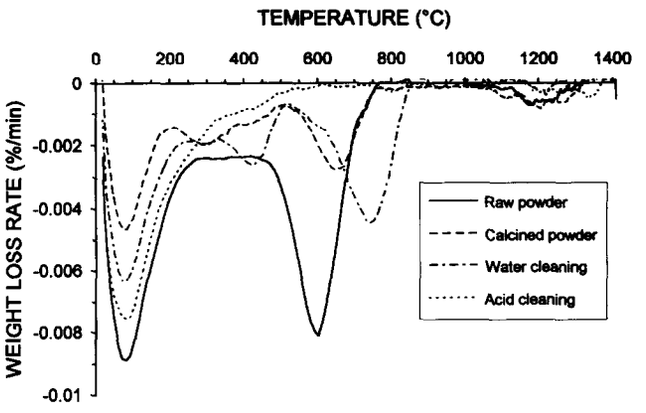


Fig. 4. DTG curves for Criceram powder.

powders: the first loss peak near 100°C results from adsorbed water removal. A second peak common to all powders between 500 and 900°C can be ascribed to the evolution of CO_2 upon $BaCO_3$ decomposition and represents 0·15–0·25% weight loss. Another diffuse peak common to all powders appears between 1200 and 1400°C: it represents only about 0·003 to 0·1 wt% and the nature of the corresponding gas release was ascertained with aid of other techniques (see later). The Cabot powder shows an extra broad peak between 200 and 600°C, due to the elimination of water incorporated in the perovskite lattice, which is typical of powders synthesised hydrothermally.[11]

The effect of the various treatments performed on the initial powders are clearly visible on DTG curves shown in Figs 3—7. In every case, calcination decreases only slightly the CO_2 losses between 500 and 900°C. Water cleaning following calcination has a negative effect with respect to $BaCO_3$ removal in that CO_2 losses increase again. Acid cleaning proves to be efficient for all powders, in that it totally eliminates the $BaCO_3$ loss peak between 500 and 900°C. The position of this peak remains unchanged after calcination and water cleaning for Cabot powder, while it is shifted to high temperatures are calcination then once again are water cleaning for the other powders. The diffuse loss peak above 1200°C is not significantly affected by the treatments, except for the Rhône-Poulenc powder, which exhibits an increase in weight loss in that temperature range after water and acid cleaning.

X-Ray photoelectron spectroscopy allowed the detection of only four elements at the surface of raw and treated powders: Ba, Ti, O and C. The ratio Ba/(Ba+Ti) calculated from the $Ba_{3d5/2}$ and Ti_{2p} transitions appears to decrease from 40 at.% for raw powders to 30 at.% after acid cleaning, meaning that Ba^{2+} ions have been dissolved and removed during this treatment. The shape of oxygen and carbon lines were not investigated in detail, because of their high sensitivity to the atmospheric contamination. The Ti_{2p} line consisted in every instance of a single narrow Gaussian peak, meaning that titanium is present only in a single chemical state, i.e. $BaTiO_3$. The $Ba_{3d5/2}$ transition could be resolved into two Gaussian components separated by 1·58 ± 0·09eV. The lower binding energy corresponds to the titanate environment, and the higher one can be ascribed to a carbonate environment.[12] After acid cleaning, this last peak is decreased by a factor of two when compared to the raw powder data, as shown in Fig. 8 for the Rhône-Poulenc powder. The fact that the peak

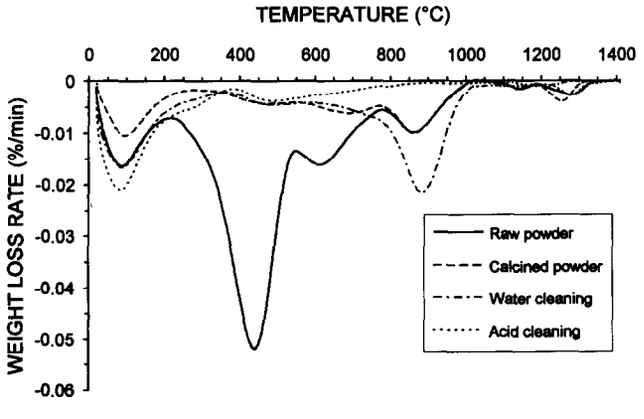


Fig. 3. DTG curves for Cabot powder.

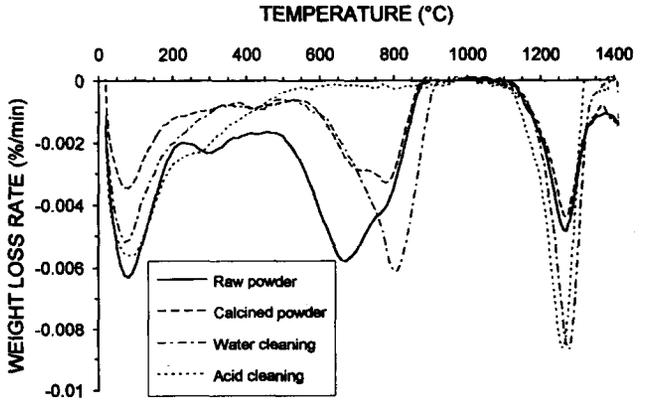


Fig. 5. DTG curves for Rhône-Poulenc powder.

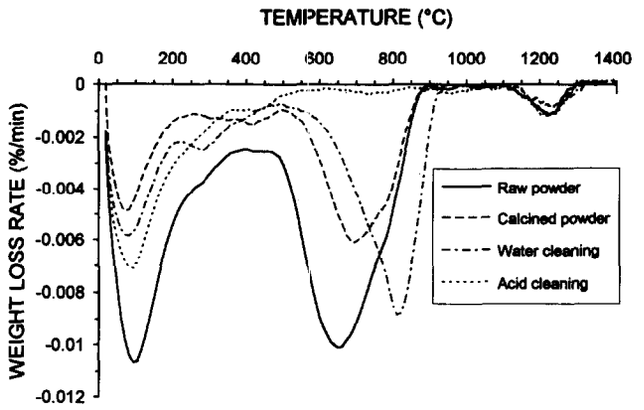


Fig. 6. DTG curves for TAM 688 powder.

has not completely disappeared after acid washing indicates that some $BaCO_3$ subsists at the surface of the particles.

Presence of elemental carbon and sulphur (which is a common contaminant in inorganic raw materials) has been investigated by *EGA* on Rhône-Poulenc calcined and acid-cleaned powders. It turns out that carbon (0·055wt%) and sulphur (0·067wt%) are both present in calcined powders, and that acid cleaning leaves the sulphur content unchanged and lowers the carbon content to 0·034wt%.

Gases released between 500 and 900°C and near 1300°C were identified on as-received powders by *FT-IR* analysis of evolving gas from a pyrolysis unit. FT-IR spectra obtained both at 600 and 1300°C on the same powder samples only reveal the presence of CO_2, as shown in Fig. 9.

Examination by *scanning electron microscopy (SEM)* of untreated, calcined water and acid-cleaned powders does not show any difference in surface roughness, nor in shape. The surface appears smooth in both cases, as shown in Fig. 10 for Rhône-Poulenc powder.

Specific areas of different powders before and after treatments are not affected by the treatments. Measured values are: 2·92 m^2/g for TAM 745 powder, 3·05 m^2/g for TAM 688 powder, 2·49 m^2/g for Rhône-Poulenc powder, 3·05 m^2/g for

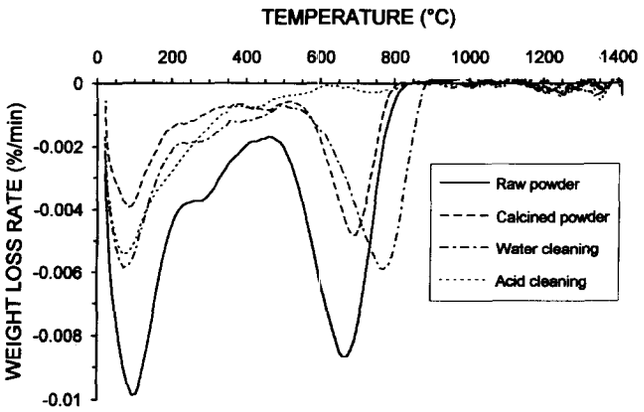


Fig. 7. DTG curves for TAM 745 powder.

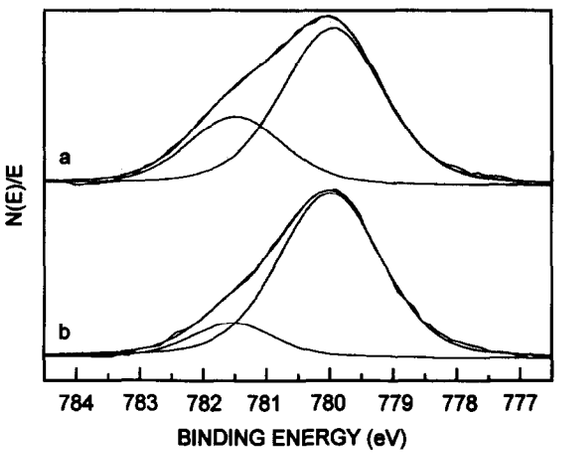


Fig. 8. $Ba_{3d5/2}$ XPS curve fit for Rhône-Poulenc powder. (a) As-received; (b) acid cleaned.

Criceram powder, and 7·79 m^2/g for Cabot powder. These values are in close agreement with the suppliers' data and confirm that the treatments have no influence on surface roughness.

Particle size distributions were determined for all powders and treatments, and are reasonably close to log-normal distributions. Calcination alone tends to slightly agglomerate the powders, which are then efficiently de-agglomerated by ultrasonication. Acid cleaning without ultrasonic de-agglomeration proved to de-agglomerate the calcined powders to the same extent as sonication alone, and subsequent ultrasonic treatment of acid-cleaned powders did not provide further improvement. Water cleaning alone did not show any significant effect. Figure 11 shows the effect of calcination–sonication and acid cleaning on Rhône-Poulenc powder particle size distribution (average of four runs): both treatments promote the removal of some agglomerates. The mean particle size remains unchanged.

3.2 Rheological properties

For all the powders, only [PAA] has been found to affect the *liquid limit* very significantly (above

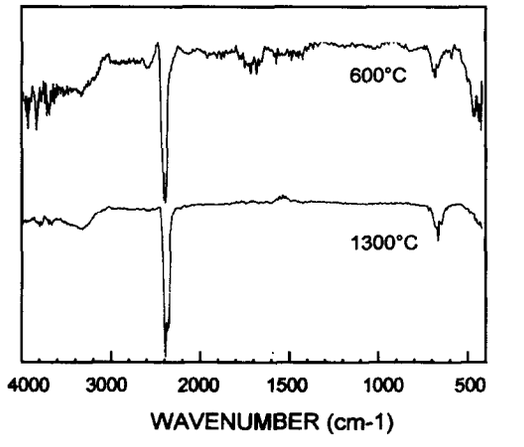


Fig. 9. Transmittance infrared spectra of gas evolved from pyrolysed Cabot raw powder at 600 and 1300°C.

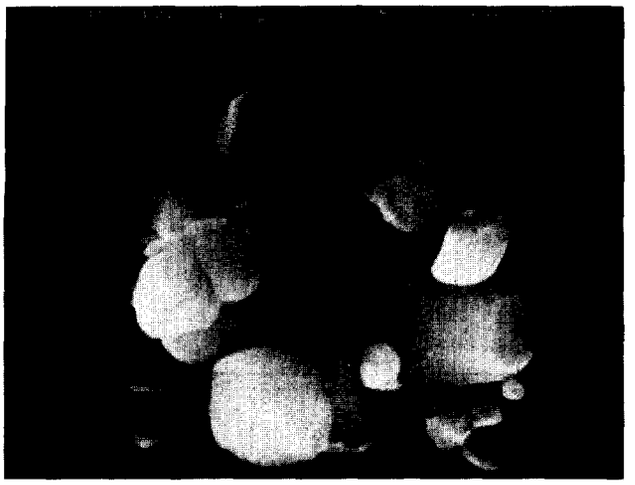


Fig. 10. SEM micrography of Rhône-Poulenc powder.

the 99·9% confidence level); within the experimental range investigated [NH_3]/[PAA] played no role, nor did it change the effect of [PAA]. The optimisation was thus conducted by varying [PAA] (0·10–1·00%wt), while keeping [NH_3]/[PAA] constant at 1·5. The effect of [PAA] on the liquid limit of raw powders is shown in Fig. 12. The lowest value for the liquid limit is reached for [PAA] = 0·6wt% for Criceram, TAM688, TAM745 and Rhône-Poulenc powders for all treatments, and between 0·8 and 1 %wt for Cabot powder depending on the treatments. The higher [PAA] level necessary for the Cabot powder is a consequence of its higher specific surface area. The corresponding optimal LL and [PAA] values are shown in Fig. 13. All the treatments have a positive effect by decreasing the liquid limit, the best improvement being for Cabot powder (−35% by acid cleaning). The best absolute value for LL is obtained for TAM 688 and Rhône-Poulenc powders after acid treatment, corresponding to a solid volume fraction in the slip higher than 60%. Acid-cleaning treatment is the most efficient in that sense except for Criceram powder, whose lowest LL is obtained on only calcined and sonicated powder. It has been observed that ultrasonic de-agglomeration of acid-cleaned powders does not improve the liquid limit.

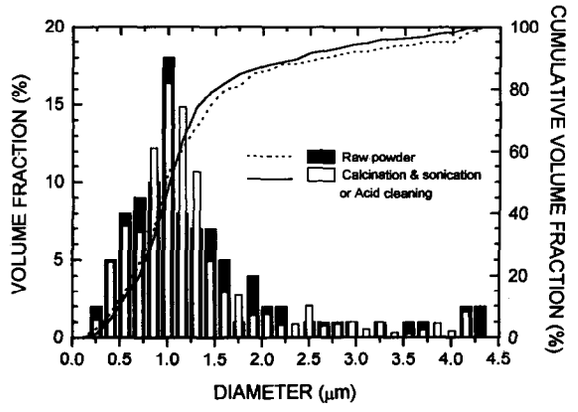


Fig. 11. Effects of treatments on particle size distribution.

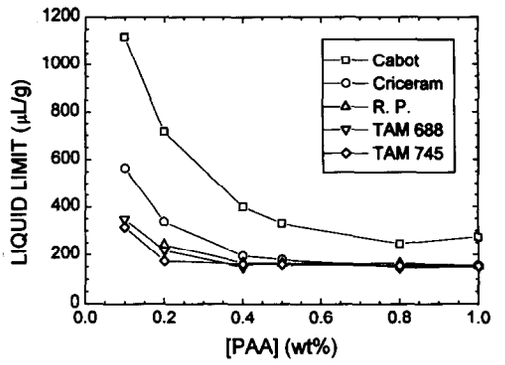


Fig. 12. [PAA] dependence of the liquid limit for raw powders ([NH_3]/[PAA] = 1·5).

3.3 Green body properties

The slip composition was then optimised in order to obtain the highest *green density*, by varying [PAA] (0·60–0·80 %wt) and the volume of dispersant added (LL + 0·025–0·050 cm^3/g). The slightly higher amount of dispersant with respect to LL is intended to compensate for evaporation during slip processing. Statistical analysis revealed a significant effect of the volume of dispersant, its lower level yielding the highest green densities for the five powders. Figure 14 shows the effect of the treatments on the green densities of cast samples, resulting from the average of four samples for each powder and treatment obtained with optimised slip compositions. Cabot raw specimens were too brittle to be manipulated and have not been considered for further studies. Large variations in relative green density can be seen with respect to the powder sources, between 57 and 70% theoretical density. Statistical analysis reveals that calcination and sonication treatment has drastically improved the green density, the most dramatic enhancement being for Rhône-Poulenc powder (+16%). However, acid or water cleaning do not significantly provide further improvement, confirming that de-agglomeration by acid cleaning is equivalent to sonication.

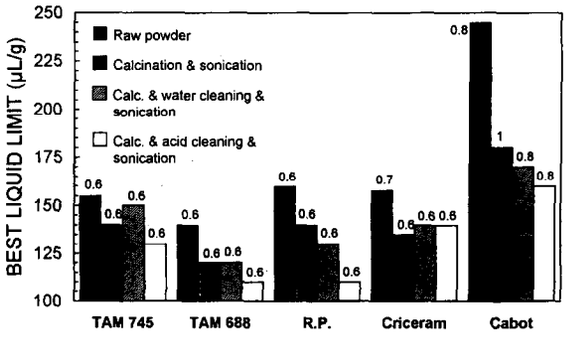


Fig. 13. Effects of treatments on the optimal liquid limit with corresponding [PAA] (in wt%).

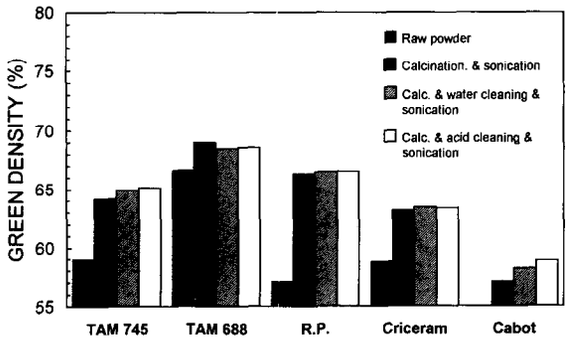


Fig. 14. Effects of treatments on green density.

4 Discussion

The major elemental contaminants in raw powders appear to be carbon and sulphur, in approximately the same weight concentration. XRD and XPS experiments show that carbon is present at the surface as barium carbonate. On the other hand, no sulphur compound was detected, neither by XRD, nor by XPS, suggesting that sulphur is distributed in the bulk of the particles, probably as $BaSO_4$, as a result of the preparation conditions of the $BaTiO_3$ powders.

FT-IR pyrolyses show that only CO_2 is released up to 1300°C; the absence of SO_2 or SO_3 release means that barium sulphate remains stable in that temperature range. The possibility of O_2 release (not detectable by infrared spectroscopy), by an exchange mechanism of oxygen between the $BaTiO_3$ lattice and the ambient atmosphere,[13] although reported for donor-doped $BaTiO_3$,[14] is not expected for undoped $BaTiO_3$ sintered in an oxidising atmosphere; TGA experiments performed in nitrogen still gave rise to similar weight losses, indicating that the origin of the gas release is not the atmosphere but the powders themselves. Therefore, weight losses observed by TGA on raw powders between 500 and 900°C, and 1200 and 1400°C, can definitely be ascribed to evolving CO_2.

Based upon this finding, three decomposition reactions for the barium carbonate contamination can be considered:[15]

$$BaCO_3 + TiO_2 \rightarrow BaTiO_3 + CO_2(g) \qquad T_d = 400{\cdot}5°C \quad (1)$$

$$BaCO_3 + BaTiO_3 \rightarrow Ba_2TiO_4 + CO_2(g) \qquad T_d = 1002°C \quad (2)$$

$$BaCO_3 \rightarrow BaO + CO_2(g) \quad T_d = 1540°C \quad (3)$$

where the decomposition temperatures T_d are computed using standard thermodynamic data[16] and assuming $p_{CO_2} = 1$ atm. Barium carbonate decomposes directly into barium oxide and carbon dioxide (reaction (3)) at a temperature higher than conventional sintering temperature for $BaTiO_3$.

Table 2. $BaCO_3$ content: Comparison of EGA and TGA estimations (Rhône-Poulenc powder)

Treatment	*Total [$BaCO_3$] (wt%) from EGA*	*Total [$BaCO_3$] (wt%) from TGA*	*Relative deviation (%)*
Calcined	0·910	0·942	3·4
Acid cleaned	0·551	0·718	23·2

The presence of $BaTiO_3$ or TiO_2 lowers its decomposition temperature; TiO_2 does not exists as a true second phase in the particles, but a compositional gradient $Ba_{1-x}TiO_{3-x}$ develops at the vicinity of the $BaCO_3/BaTiO_3$ interface. This results in a gas release in the sintering temperature range which is detrimental for obtaining high densities (see Part II).

Weight losses near 600 and 1300°C recorded on raw powders by TGA can thus be accounted for by reactions (1) and (2), respectively, the shift in temperature arising from the arbitrary value of 1 atm for p_{CO_2}. $BaCO_3$ content for all powders and treatments was then calculated from weight losses between 500 and 1400°C. Comparison with EGA measurement for Rhône-Poulenc powder showed relatively good agreement, as shown in Table 2.

For all treatments the barium sulphate content remains unchanged, due to its high decomposition temperature, low solubility and distribution in the bulk of the particles. Figure 15 shows the total barium carbonate content present for all powders and treatments, based on TGA measurements. Raw powder carbonation is not correlated with particle size; it is probably determined by a combination of synthesis conditions and ageing phenomena.

Examination of DTG curves of Figs 4, 5, 6 and 7 shows that for Criceram, Rhône-Poulenc, TAM 688 and TAM 745 powders, the calcination treatment promotes the dissociation of the most reactive part of the carbonate (low-temperature side of the 600°C loss peak), with a corresponding shift towards higher temperature of the resultant maximum loss rate. This easily decomposable carbon-

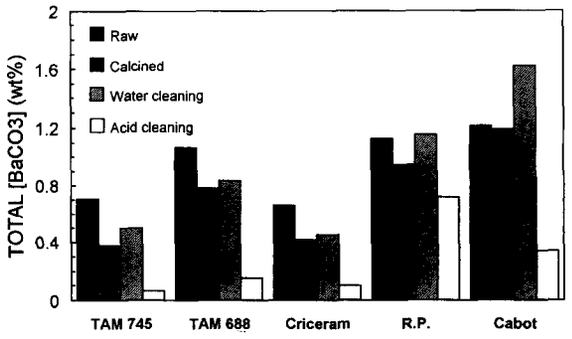


Fig. 15. Effects of treatments on total $BaCO_3$ content.

ate probably arises from atmospheric contamination. After water cleaning the 600°C loss peak is increased again, meaning that recarbonation due to CO_2 dissolved in water has occurred. This $BaCO_3$ species formed in aqueous conditions is more stable because it decomposes at a slightly higher temperature (850°C instead of 650°C). In contrast, the corresponding loss peak for Cabot powder (Fig. 3) is not affected by calcination and water-cleaning treatments, and is also centred on 850°C: The $BaCO_3$ contaminating the surface originates from the hydrothermal synthesis, resists calcination at 500°C and has the same features that those formed during water cleaning.

A substantial amount of carbonate is eliminated by acid cleaning. Recarbonation of acid washed powders does not take place because the surface is deficient in barium due to Ba^{2+} ions going into solution. TGA experiments performed six months after the treatment do not show any recarbonation.

On the other hand, $BaCO_3$ is not completely eliminated by acid cleaning (weight losses above 1100°C). Two consecutive acid cleaning treatments using the same acetate buffer (0·3M) were then performed in order to try to dissolve the remaining carbonate, but without any improvement. This suggests that barium carbonate contamination originates from different mechanisms: surface alteration, by contact with atmosphere or water, producing carbonate decomposing at low temperature (TG losses between 500 and 900°C) and easily removed by acid cleaning, and contamination during the synthesis of the powders (incomplete reactions, contaminated precursors, etc.), resulting in a more stable form of carbonate decomposing at higher temperature (TG losses between 1100 and 1400°C). This phase is still partially present at the surface after acid cleaning, as shown by XPS. Its low solubility in the cleaning solution is probably because it is more tightly bonded to the $BaTiO_3$ surface. Free carbonate grains are not likely to resist acid-cleaning treatment, but the possibility of a bulk contamination of the particles, i.e. $BaCO_3$ entrapped in $BaTiO_3$ crystals, could also be consistent with the partial removal upon acid cleaning.

The effects of the various treatments on forming can be summarised as follows: For all powders, calcination alone tends to agglomerate the powders; calcination in association with the ultrasonic de-agglomeration treatment promotes a higher green density. The same improvement results after acid cleaning of calcined powders without subsequent sonication, and a further ultrasonic treatment of acid-cleaned powders does not improve the green density, showing the efficient de-agglomerating effect of acid washing. The liquid limit of the slips is also markedly improved after calcination and sonication, and acid cleaning brings about a further improvement. Compared to calcination, water cleaning does not change significantly the green density and the liquid limit, which means that modifications by acid cleaning are definitely not due to handling artefacts (suspending, de-agglomeration and drying).

Physical characteristics of individual particles of $BaTiO_3$ such as morphology, diameter and specific surface area do not seem to be affected by the decontamination treatments. The surface carbonate distribution, either homogeneous or heterogeneous, cannot be inferred from SEM analysis, because the carbonate layer thickness is below the resolution of the apparatus. XPS analysis shows that $BaCO_3$ still subsists at the surface after acid cleaning, so that the colloidal stabilisation mechanisms involved in the slips elaboration are almost unaffected (cf. PAA content in Fig. 13). It can be concluded that the improvements of the liquid limits of the slips (i.e. decrease in viscosity) by the treatments result mainly from their de-agglomerating effects. Acid cleaning does not always improve the green density and the liquid limit to the same extent. However, a lower green density can be compensated by a larger shrinkage during drying.

The improvement due to cleaning treatments, as far as rheological and green body properties are concerned, can be interpreted according to the following scheme. In raw powders, some $BaTiO_3$ particles form soft agglomerates, $BaCO_3$ acting as a 'cement'. Calcination treatment, by its temporary decomposition of $BaCO_3$, may be sufficient to destroy these soft agglomerates. Acid cleaning is a more drastic treatment: not only does it dissolve $BaCO_3$, but it can also slightly alter the $BaTiO_3$ surface and in some instances totally dissolve the necks between partially sintered particles that form hard agglomerates (chemical de-agglomeration). The improvement of green body properties already reported can then be accounted for by a geometric argument: the surface treatments performed appear to decrease the number of agglomerates present in raw powders and consequently increase the packing efficiency by minimising bridging effects between particles. The highest green density value of 70%, obtained with calcined TAM 688 powder, is remarkably close to the theoretical maximal packing density of about 72% predicted from computer simulation[17,18] for random close packing of log-normally distributed spheres with a geometric standard deviation of 1·7, as measured for this powder.

5 Conclusions

The study presented in the first part of this series of two papers shows that commercial undoped $BaTiO_3$ powders are mainly contaminated by barium sulphate and barium carbonate. Barium sulphate is thermally stable beyond 1400°C and is unaffected by heat or washing treatments. Barium carbonate, on the other hand, thermally decomposes in two steps, near 600°C and 1300°C, to release CO_2. This carbonation originates from two sources: atmospheric or aqueous CO_2 contamination results in the formation of a surface $BaCO_3$ layer, easily decomposed, either thermally or chemically. Carbonate originating from the synthesis stage is more stable, resists acid cleaning and decomposes above 1200°C. It is thought that carbonate remaining after acid cleaning is mainly distributed at the surface of the particles, without excluding a residual bulk contamination. The decarbonating effect of the calcination or chemical treatments (acid dissolution), although not complete, proved to be substantially beneficial with respect to green body densities of ceramics samples obtained by slip casting. For all powders the liquid limits of the slips have been decreased and the green density increased, respectively as much as 35% and 16%. Advantage may be taken of the corresponding reduction of shrinkage during sintering for obtaining complex shape samples. These improvements can be seen as a consequence of the elimination of agglomerates present in raw powders, as a result of the reduction of surface barium carbonate content yielding figures very close to the theoretical optimal values of packing density. A point to note is that the range within which the processing parameters vary as a function of powder source has been substantially reduced by the treatments, which means that a better reproducibility of ceramic green samples can be achieved by controlling the surface chemistry of the raw powders.

Acknowledgements

The Swiss National Foundation is gratefully acknowledged for financial support. The authors are grateful to Dr Y. Houst for EGA measurements, to Mr N. Xanthopoulos for XPS measurements, to M. R. Mullone for SEM analysis and Dr P. Bowen for his assistance in the preparation of the manuscript.

References

1. Chiou, B. S., Lin, S. T., Duh, J. G. & Chang, P. H., Equivalent circuit model in grain boundary barrier layer capacitors. *J. Am. Ceram. Soc.*, **72**(10) (1989) 1967-75.
2. Fagan, J. G. & Amarakoon, V. R. W., Reliability and reproducibility of ceramic sensors: Part II, PTC thermistors. *Am. Ceram. Soc. Bull.*, **72**(2) (1993) 69–76.
3. Kingery, W. D., Bowen, H. K. & Uhlmann, D. R., *Introduction to Ceramics*. John Wiley and Sons, NY, 1976.
4. Jaffe, B., Cook, Jr, W. R. & Jaffe, H., *Piezoelectric Ceramics*. Academic Press, London and NY, 1971.
5. Dobias, B., *Coagulation and Flocculation. Theory and Applications*. Marcel Dekker, NY, 1993.
6. Fernandez, J. F., Duran, P. & Moure, C., Influence of surface modification on sintering of $BaTiO_3$. In *Proceedings of the 2nd European Ceramic Society Conference*, Vol. 3, ed. G. Ziegler & H. Hausner. Deutsche Keramische Gesellschaft e.V., Augsburg, 1991, pp. 1891–5.
7. Lavielle, D., Poumarat, J., Montardi, Y., Bernard, P. & Aguerre-Charriol, O., Microstructure/properties relationships in chemically processed barium titanate for X7R characteristics. In *Proceedings of the 2nd European Ceramic Society Conference*. Vol. 3, ed. G. Ziegler & H. Hausner. Deutsche Keramische Gesellschaft e.V., Augsburg, 1991, pp. 1903–7.
8. Briggs, D. & Seah, M. P., *Practical surface analysis*, 2nd edn, Vol. 1, *Auger and X-Ray Photoelectron Spectroscopy*. John Wiley & Sons, Chichester, 1990.
9. Chen, Z. C., Ring, T. A. & Lemaître, J., Stabilization and processing of aqueous $BaTiO_3$ suspension with polyacrylic acid. *J. Am. Ceram. Soc.*, **75**(12) (1992) 3201–8.
10. Lemaître, J., Hérard, C. & Vogel, D., Microstructure and piezoelectric properties of slip cast barium titanate ceramics. In *Proceedings of the 3rd European Ceramic Society Conference*, Vol. 2, ed. P. Duran & J. F. Fernandez. Faenza Editrice Iberica, Madrid, 1993, pp. 59–64.
11. Hennings, D. & Schreinemacher, S., Characterization of hydrothermal barium titanate. *J. Eur. Ceram. Soc.*, **9** (1992) 41–6.
12. Hung, C. C., Riman, R. E. & Caracciolo, R., An XPS investigation of hydrothermal and commercial barium titanate powders. In *Ceramic Powder Science III*, Vol. 12, ed. G. L. Messing, S. Hirano & H. Hausner. The American Ceramic Society, Inc., Westerville, 1990, pp. 17–25.
13. Chan, N. H., Sharma, R. K., & Smyth, D. M., Nonstoichiometry in undoped $BaTiO_3$. *J. Am. Ceram. Soc.*, **64**(9) (1981) 556–62.
14. Drofenik M., Popovic, A., Irmancnik, L., Kolar, D. & Krasevec, V., Release of oxygen during the sintering of doped $BaTiO_3$ ceramics. *J. Am. Ceram. Soc.*, **65**(12) (1982) C203–4.
15. Beauger, A., Mutin, J. C. & Niepce, J. C., Synthesis reaction of metatitanate $BaTiO_3$. Part I. Effect of the gaseous atmosphere upon the thermal evolution of the system $BaCO_3$—TiO_2. *J. Mat. Sci.*, **18** (1983) 3041–6.
16. Barin, I. & Knacke, O., *Thermochemical Properties of Inorganic Substances*. Springer, Berlin, 1973.
17. Nolan, G. T. & Kavanagh, P. E., Computer simulation of random packings of spheres with log-normal distributions. *Powder Technology*, **76** (1993) 309–16.
18. Yu, A. B. & Standish, N., An analytical-parametric theory of the random packing of particles. *Powder Technology*, **55** (1988) 171–86.

Journal of the European Ceramic Society **15** (1995) 145–153
© 1995 Elsevier Science Limited
Printed in Great Britain. All rights reserved
0955-2219/95/$9.50

Surface Decontamination Treatments of Undoped $BaTiO_3$—Part II: Influence on Sintering

Claude Hérard, Annelise Faivre & Jacques Lemaître*

École Polytechnique Fédérale de Lausanne (EPFL), Laboratoire de Technologie des Poudres, MX-Ecublens, CH-1015 Lausanne, Switzerland

(Received 3 March 1994; revised version received 17 June 1994; accepted 30 June 1994)

Abstract

Natural sintering and microstructure of undoped $BaTiO_3$ ceramics obtained by slip casting from five commercial powders subjected to various surface decarbonation treatments (calcination and cleaning in pure water or acetate buffer solution) were investigated. Two densification steps followed in certain instances by a desintering step were observed for as-received powders. At maximum density the microstructure is either coarse-grained or bimodal, with dense large grains between 20 and 100 μm in a fine-grained matrix (<1 μm). At the end of swelling a coarse intergranular and fine intragranular porosity is present and total conversion into large grains has occurred, their size remaining unchanged up to 1400°C. Calcination and water cleaning had no noticeable influence on sintering behaviour. Acid cleaning appeared to substantially modify the shape of dilatometric curves: shrinkage starts later, the onset of abnormal grain growth is delayed, the maximum fired densities are slightly increased, but the subsequent swelling of specimens above 1300°C is also enhanced.

It is suggested that abnormal grain growth in undoped barium titanate results from the presence of a liquid phase at grain boundaries. Due to the presence of trace impurities, it can form locally at a temperature below the eutectic temperature of 1317°C of the system BaO–TiO_2. Decontamination by acid cleaning raises the eutectic point, but also increase the amount of liquid phase above 1300°C, by lowering the Ba content at the surface of the particles. The plasticity of the material is then increased, promoting swelling due to internal CO_2 pressure, originating from the decomposition of $BaCO_3$ which still subsists after acid cleaning.

* To whom correspondence should be addressed.

1 Introduction

Electrical properties of structural ceramics are strongly dependent on their microstructure. This is particularly true in the case of $BaTiO_3$-based capacitors, where exaggerated final porosity drastically decreases the dielectric strength and the dielectric constant.[1] The porosity evolution during sintering is often complicated by the presence of impurities and by anomalous grain growth.[2] The possibility of obtaining fully dense sintered materials is then greatly related to the impurity content in initial powders.

This is the second part of a series of two papers dealing with surface contamination effects in undoped barium titanate. It was shown in Part I[3] by chemical analyses that an important source of contamination for $BaTiO_3$ raw powders is barium carbonate, resulting from reaction of the surface with atmospheric CO_2 or formed during the synthesis of the powders, which is distributed mainly at the surface of the particles and which thermally decomposes in two steps near 700 and 1300°C to release CO_2; thermal (calcination) or chemical (cleaning in a pH 4·5 acetate buffer) treatments of different undoped barium titanate commercial powders proved to be an efficient way to reduce the surface $BaCO_3$ content. The effects of such treatments on forming green bodies by slip casting were described, the corresponding improvement in green density being ascribed to the reduction of agglomerates in the starting slips. The work presented in the present paper is focused on the sintering stage of such thermally and chemically surface decarbonated $BaTiO_3$ powders. Sintering kinetics in air were monitored by dilatometry and optical microscopy on slip-cast green bodies obtained from five commercial powders, subjected to the decontamination treatments reported in Part I.[3] Densification and grain growth processes are discussed and interpreted in terms of internal gas

release and the presence of a liquid phase correlated with the surface chemical composition of the powders.

2 Experimental Procedure

The five commercial $BaTiO_3$ powders used in this study, Criceram lot VPP20, TAM HPB lot 688, TAM HPB lot 745, Cabot BT10 lot 6243-24, and Rhône-Poulenc type Elmic BT 100 lot 7958, are described in Part I,[3] along with the de-agglomeration and decontamination treatments performed (calcination at 500°C for 16 h, acid cleaning in a 0·3M acetate buffer with pH = 4·5 for 16 h at 30°C, and demineralised water cleaning).

For each powder source and each treatment *slip-cast specimens* were prepared from aqueous $BaTiO_3$ suspensions stabilised with poly(acrylic acid)(PAA), with [PAA] ranging from 0·6 to 1 wt%. The acidity of the stabiliser was neutralised by NH_3, with $[NH_3]/[PAA] = 1·5$. The amount of dispersing liquid was between 135 and 270 μlitre/g. The methodology used is described in Part I.[3]

Non-isothermal *sintering* of the compacts was studied in dry air in a differential dilatometer Setaram DHT; the heating cycle was 10°C/min up to 800°C, 3·3°C/min up to 1400°C, and 5°C/min down to 20°C.

Fired densities were measured by Archimedes' method, using isopropanol as immersion liquid, and assuming the value of 6·02 g/cm^3 for the theoretical density of $BaTiO_3$. Intermediate fired densities were either calculated from dilatometric curves corrected for thermal expansion and calibrated with respect to measured final densities (i.e. at the end of the thermal cycle), or measured directly on specimens whose heating cycle was interrupted at some particular temperature.

Microstructures were observed with a Olympus type BHM optical microscope on polished and thermally etched samples (heating rate: 5°C/min from 20 to 1200°C then down to 20°C in air).

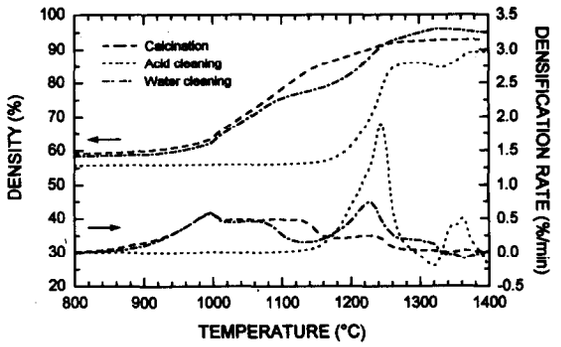


Fig. 2. Dilatometric curves for Cabot powder.

3 Results

3.1 Dilatometry

The sintering behaviour of raw powders is illustrated by dilatometric curves shown in Fig. 1. Criceram, TAM 688 and TAM 745 raw powder curves present a similar shape: shrinkage starts at 1050°C and two distinct densification peaks appear between 1240 and 1340°C. The density passes through a maximum beyond which swelling of the samples occurs, followed by a small redensification step.

The Rhône-Poulenc raw powder exhibits a quite different behaviour: shrinkage starts earlier (800°C) due to the smaller mean particle size, densification progresses continuously up to 1400°C and is not completed at this temperature. (Cabot raw powder could not be sintered because cast green bodies were too brittle).

Dilatometric curves of calcined, acid-cleaned and water-cleaned powders can be seen in Figs 2–6 along with raw powder curves for comparison. The same trend is again found for Criceram, TAM 688 and TAM 745 powders: the general shape of the densification curves is not modified, although acid cleaning slightly increases the maximum density, the corresponding temperature being slightly increased. However, the subsequent desintering step is amplified (up to 8% theoretical density for TAM 745 2nd Criceram powders) and its corresponding temperature increased. Water cleaning has no effect on calcined powders, and calcination alone only reduces the shrinkage

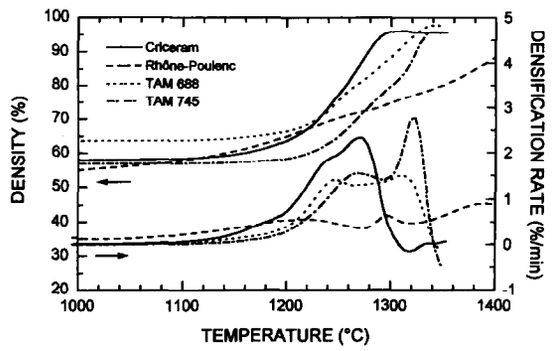


Fig. 1. Dilatometric curves for raw powders.

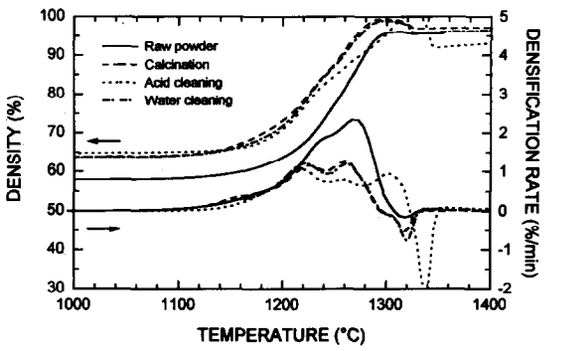


Fig. 3. Dilatometric curves for Criceram powder.

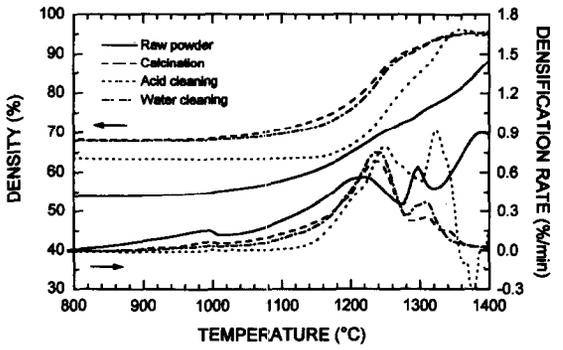


Fig. 4. Dilatometric curves for Rhône-Poulenc powder.

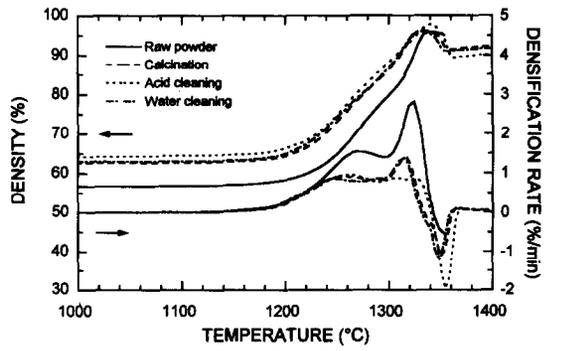


Fig. 6. Dilatometric curves for TAM 745 powder.

(because of a higher green density) to finally yield the same maximum density as raw powders. Treatments on the Rhône-Poulenc powder have drastically changed the sintering kinetics. Densification of the calcined powder is almost complete at 1400°C, maximum density has been increased and the beginning of densification is slightly delayed. Water cleaning does not affect the calcined powder, and the densification of acid cleaned powder starts later near 1100°C and then presents two peaks followed by a desintering step, as for Criceram and TAM powders. The sintering of calcined and water-cleaned Cabot powders starts at 800°C, and is continuous up to 1330°C. After acid cleaning it starts at 1100°C and a sharp densification rate peak is seen at 1240°C followed by a weak dedensification and then redensification step providing a lower density than calcined or water-cleaned powders. Figure 7 shows the maximum fired densities for all powders and treatments, which are not correlated with green densities and range between 95 and 100% except for Cabot powder. Calcination and water cleaning have no significant effect on maximum fired density, but acid cleaning slightly increases it, except for Criceram and Rhône-Poulenc powders.

3.2 Microstructures

In order to understand the mechanisms involved in the densification process the heating cycles of some specimens were interrupted at the temperature of maximum density and at the end of swelling in order to observe the corresponding microstructures. For all powders calcination and water cleaning have no noticeable effect on microstructure compared to raw powders.

At *maximum density* between 1300 and 1400°C the microstructure is bimodal for TAM 745, TAM 688 and Criceram raw powders (dense large grains of about 50–70 μm in a fine-grained matrix), while for Rhône-Poulenc raw powder it is entirely formed of large grains of about 100 μm with fine intragranular porosity. Acid cleaning decreases the proportion of large grains for the TAM and Criceram powders, and renders bimodal the microstructure of Rhône-Poulenc powder, which is now similar to that of TAM and Criceram powders. Calcined and water-cleaned Cabot powder microstructure at maximum density is formed of large grains (100 μm). Their size is reduced to 50 μm by acid cleaning, accompanied by the development of coarse inter- and intragranular porosity.

For powders presenting a dedensification step beyond the maximum density (TAM 745, TAM 688, Criceram, water and acid-cleaned Cabot and acid-cleaned Rhône-Poulenc powders) total conversion into large grains has occurred at the secondary *relative minimum density*, which is the point where the samples begin to redensify. At this point, an important porosity can be seen, both intra- and intergranular, the latter resulting from pore coalescence, and increased by acid cleaning. As the temperature goes up, some specimens slightly redensify, (TAM 745, Criceram) but grain size remains unchanged. This behaviour is

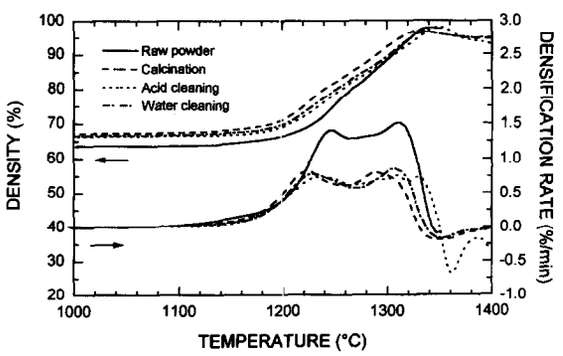


Fig. 5. Dilatometric curves for TAM 688 powder.

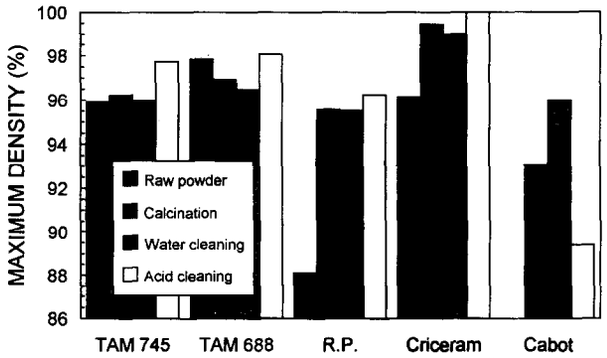


Fig. 7. Effects of treatments on maximum fired density.

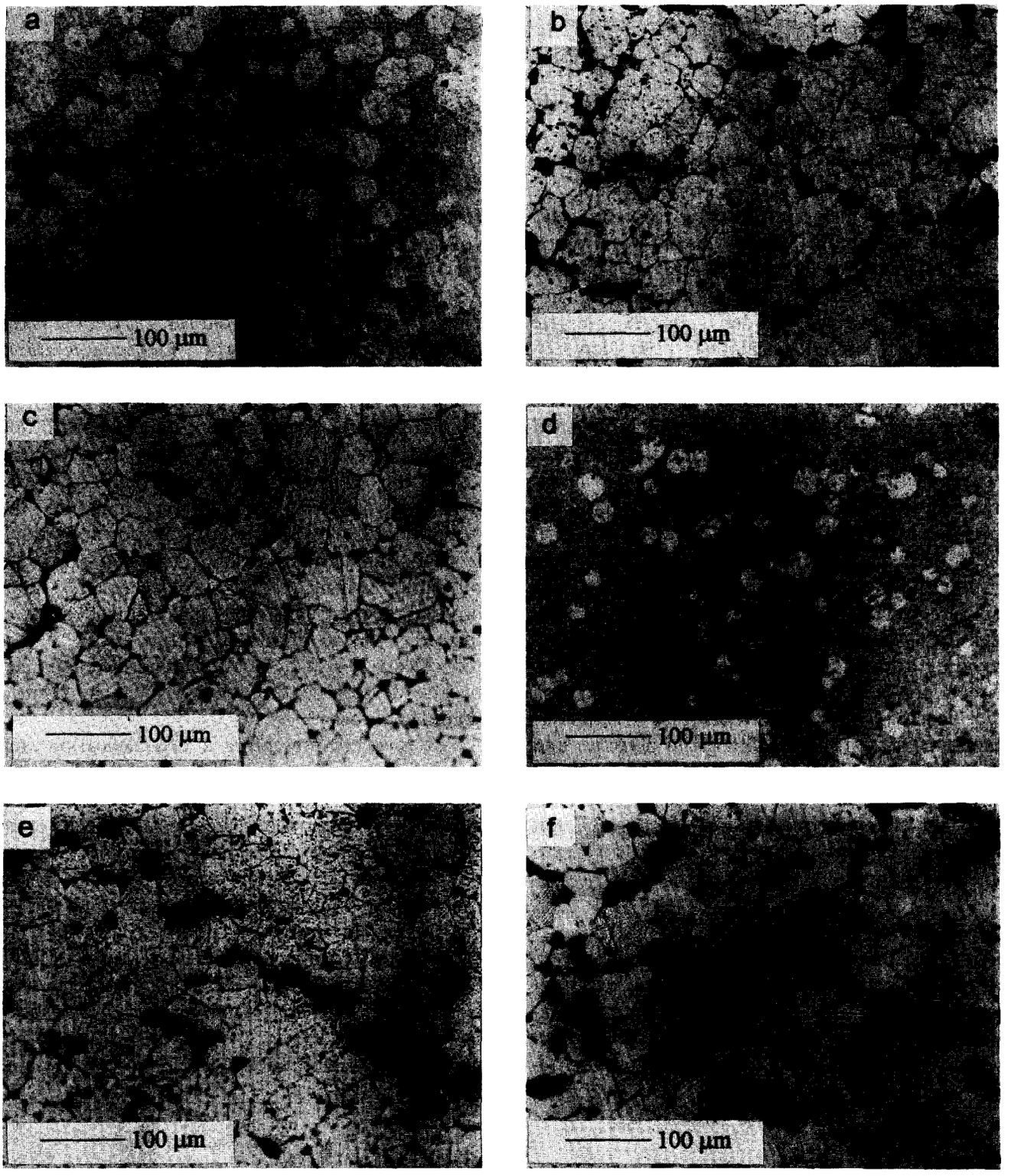


Fig. 8. Microstructure of Criceram samples: (a) Calcined powder at maximum density (1295°C); (b) calcined powder at the end of swelling (1338°C); (c) calcined power at 1400°C; (d) acid cleaned at maximum density (1324°C); (e) acid cleaned at the end of swelling (1352°C); (f) acid cleaned at 1400°C.

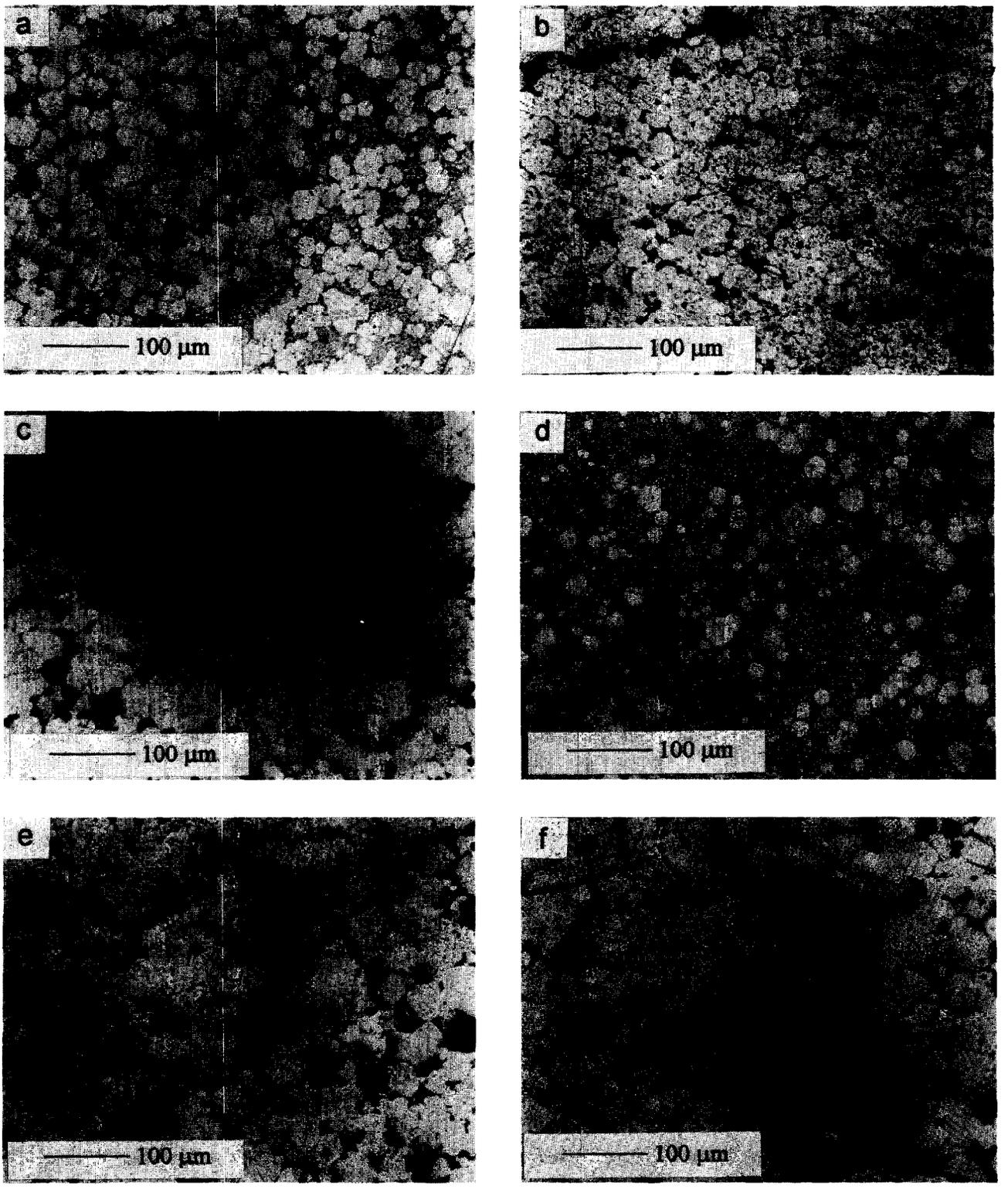


Fig. 9. Microstructure of TAM 745 samples: (a) Calcined powder at maximum density (1334°C); (b) calcined powder at the end of swelling (1363°C); (c) calcined powder at 1400°C; (d) acid cleaned at maximum density (1341°C); (e) acid cleaned at the end of swelling (1367°C); (f) acid cleaned at 1400°C.

Table 1. Density evolution during sintering.

Powder	*Treatment*	*Green density (%)*	*Maximum density (%)*	*Temperature for maximum density (°C)*	*Density after swelling (%)*	*Temperature at the end of swelling (°C)*
TAM 745	Raw	59·0	95·9	1338	—	—
	Calcined	64·0	96·2	1334	91·6	1363
	Acid cleaning	64·6	97·7	1341	89·6	1367
	Water cleaning	65·1	96·0	1331	91·1	1360
TAM 688	Raw	66·7	97·8	1342	—	—
	Calcined	69·0	96·9	1330	94·5	1400
	Acid cleaning	68·5	98·1	1351	92·7	1400
	Water cleaning	68·8	96·5	1337	94·7	1400
Criceram	Raw	58·8	96·1	1315	95·7	1334
	Calcined	63·4	99·4	1295	97·0	1338
	Acid cleaning	63·6	100·0	1324	92·1	1352
	Water cleaning	63·4	99·0	1297	95·7	1334
Rhône-Poulenc	Raw	57·1	88·1	1400	—	—
	Calcined	66·9	95·6	1400	—	—
	Acid cleaning	66·5	96·3	1355	94·8	1395
	Water cleaning	66·5	95·5	1400	—	—
Cabot	Raw	—	—	—	—	—
	Calcined	57·1	93·1	1400	—	—
	Acid cleaning	57·6	89·4	1385	84·6	1332
	Water cleaning	58·8	96·0	1328	95·1	1396

exemplified by microstructures of calcined and acid-cleaned Criceram and TAM 745 powders shown in Figs 8 and 9. The case of acid-cleaned Cabot powder is particularly interesting because it presents two consecutive desintering steps, near 1290 and then 1385°C. At the end of the heating cycle (1400°C) the microstructures are coarse-grained for all powders and treatments, with an important porosity, increased by acid cleaning. This treatment does not affect the final grain size for TAM 688, TAM 745 and Criceram powder (40 μm), but decreases it for Cabot and Rhône-Poulenc powders, from 100 to 40 μm (cf. Fig. 10).

Measured densities of specimens at the beginning of sintering, at maximum density and at the end of swelling when present are reported in Table 1, along with corresponding temperatures, for all powders and treatments.

4 Discussion

4.1 Raw powders

The apparent decrease in densification rates of treated powders compared to untreated ones is a mere consequence of the improvement of the green densities. It provides also slight but significant enhancements in the maximum fired density, except for Cabot powder, as shown in Table 1. The difference between sintering behaviour of raw powders is probably due to their particle size and specific surface contamination, resulting from both their history and their synthesis route.

Sintering of the larger particle raw powders (TAM 688, TAM 745, Criceram—d_{v50} about 1·4 μm) looks similar: during the initial stage, up to 1100°C, the compacts consolidate without densification. The first densification peak, corresponding

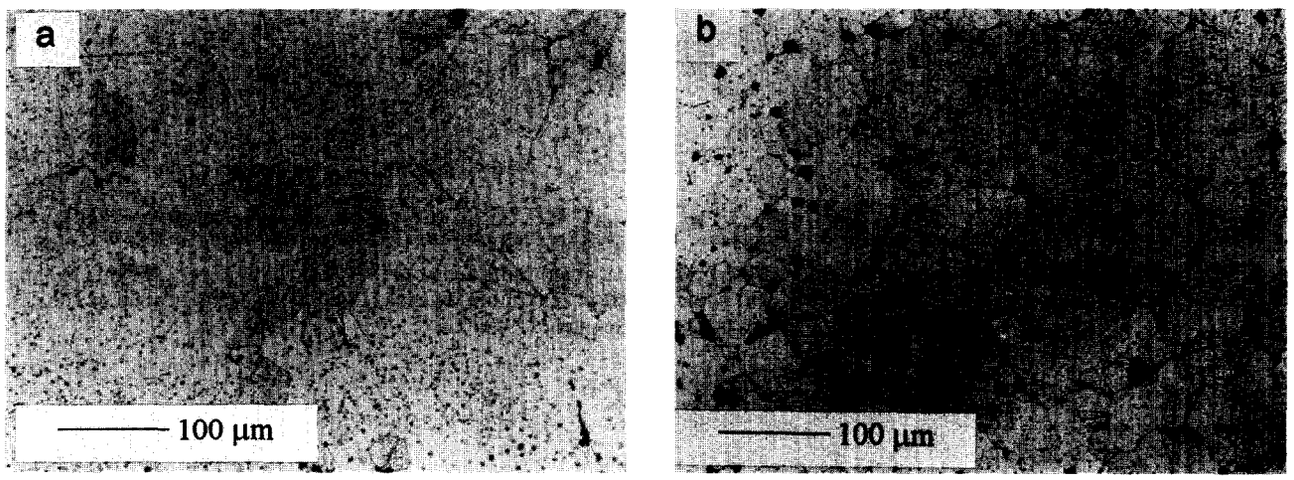


Fig. 10. Microstructure of Rhône-Poulenc samples at 1400°C: (a) Water-cleaned powder, (b) acid-cleaned powder.

to the intermediate stage, may be ascribed to normal grain growth, which progresses by bulk and boundary diffusion[4] as long as diffusion paths are not too long. At this point the most favourable mechanism to reduce surface free energy is abnormal grain growth, i.e. growth of large grains at the expense of smaller ones, which corresponds to the final stage and can account for the second densification peak. Abnormal grain growth, by reduction of the boundary areas, leads to pore coalescence. However, if this stage is too fast some pores may remain trapped inside large grains, lowering the maximum density. The temperature at which abnormal grain growth starts is correlated with the impurity content, as will be discussed later. Once total conversion into large grains has occurred, a desintering step is observed (cf. Figs 3, 5 and 6). A fine intragranular porosity is then present at the secondary minimum density which was absent at maximum density (Figs 8(a), 8(d), 9(a) and 9(d)), suggesting internal gas release. When the temperature increases, fine intragranular pores condense at the boundaries, giving rise to temporary interconnected open porosity (Figs 8(b), 8(e), 9(b) and 9(e)); at this stage evolved gas can escape from the body and further densification can occur. At 1400°C intragranular porosity has disappeared, leaving mainly intergranular porosity (Figs 8(c), 8(f), 9(c) and 9(f)).

A smaller powder such as Rhône-Poulenc (d_{v50} = 0·84 μm) is more reactive; as a result it densifies earlier, as soon as 800°C is reached (see Fig. 4). This fast shrinkage prevents the efficient removal of porosity (pore trapping), eventually yielding a low density at 1400°C. The final coarse-grained microstructure presents an homogeneously distributed intragranular porosity, which has not yet condensed at the boundaries.

4.2 Gas release

It was shown in Part I[3] by TGA and FT-IR that only CO_2 was released up to 1400°C, besides water evolution below 200°C; therefore it is suggested that CO_2 released from barium carbonate decomposition is responsible for the swelling phenomenon, because of its low solubility in $BaTiO_3$. CO_2 release in the 500–900°C range has been shown to be due to $BaCO_3$ reaction with TiO_2 to form $BaTiO_3$ (reaction (1) in Part I[3]), which does not interact with densification because porosity is still open at that temperature, so that CO_2 can escape from the compact material. The second $BaCO_3$ decomposition step near 1300°C, by reaction with $BaTiO_3$ to form Ba_2TiO_4 and CO_2 (reaction (2) in Part I[3]), undoubtedly promotes swelling at that temperature, because the porosity is then closed. The CO_2 decomposition pressure P_d for reaction (2) of Part I_3 was calculated using:

$$P_d = \exp\left(-\frac{(\Delta H^\circ - T\Delta S^\circ)}{RT}\right) \quad (1)$$

where ΔH° and ΔS° are respectively the standard enthalpy and entropy of reaction (2) of Part I[3] R the gas constant and T the absolute temperature. Thermodynamic data give ΔH° = 178 kJ/mol and ΔS°= 140·3 J/mol K at 1300°C,[5] so P_d is about 2·8 MPa; such a pressure is larger than the stress necessary to initiate plastic deformation of fine-grained $BaTiO_3$, which is 2MPa at this temperature,[6] allowing swelling and the observed bloating phenomenon. Table 2 shows measured weight losses between 1100 and 1400°C and the corresponding gas volume produced at 2 MPa and 1400°C. Based upon the lowest of these figures (0·007% weight loss between 1200 and 1400°C for TAM 745 powder) and using perfect gas law, a density decrease down to 6·2% below the maximum value can then be explained, which is consistent with the desintering magnitudes observed.

4.3 Effects of the treatments

As already mentioned, calcination and water cleaning have no noticeable effect on the sintering of TAM 688, TAM 745 and Criceram powders, while they improve the final density of Rhône-Poulenc powder, which shows the same coarse-grained porous microstructure as the untreated powder. Calcined and water-cleaned Cabot powders densify approximately the same way, which is different from the other powders. On the other hand, the sintering behaviour of all powders is substantially modified by acid cleaning, giving rise to more similar dilatograms and final microstructures. The most remarkable effect of acid cleaning is the moving from 800°C up to 1100°C of the incipient sintering temperature for the Rhône-Poulenc and Cabot powders. As mentioned before the technical data sheets indicate approximately the same level for various impurities in all powders. However, due to their smaller particle sizes, the Cabot (0·4 μm) and Rhône-Poulenc (0·84 μm) samples are likely to be decontaminated more

Table 2. Weight losses between 1100 and 1400°C (measured by TGA) and corresponding CO_2 volume produced at 2 MPa and 1300°C

Powder	*CO_2 (wt%) released between 1100 and 1400°C*	*Gas volume (%) at 2 MPa–1400°C*
TAM 745	0·007	6·2
TAM 688	0·022	17·3
Criceram	0·017	13·9
Rhône-Pulenc	0·116	52·5
Cabot	0·087	45·3

thoroughly upon acid leaching; as a consequence, one may expect that acid washing will suppress any sintering phenomena below 1100°C but surface diffusion, therefore suppressing any shrinkage below that temperature.

The delay of the onset of abnormal grain growth by acid cleaning can be explained under the assumption that this last phenomenon is triggered by the formation of a liquid phase at the boundaries, even in raw powders. Examination of Fig. 1 shows that the onset temperature of the second densification peak corresponding to abnormal grain growth may be located, for some raw powders and in particular Criceram, below the eutectic temperature of 1317°C in the BaO–TiO_2 diagram.[7] However, impurities such as Si, Al or Na are generally present in commercial undoped barium titanate: between 20 and 100 ppm according to the suppliers of the powders used in this study. Ternary diagrams of such compositions show that the eutectic point can be drastically lowered, down to 1250°C, for example, for the system $BaTiO_3$–SiO_2 or even 942°C for the system $NaSiO_3$–$BaTiO_3$.[8] Compositional fluctuation of impurities can then give rise locally to sufficiently concentrated zones to form a liquid phase at the boundaries and consequently constitute nuclei for exaggerated grain growth by a dissolution–precipitation mechanism (Ostwald ripening)[9] at temperatures far below 1317°C. Abnormal grain growth has already been reported in $BaTiO_3$ below 1322°C in the absence of a liquid phase,[10] with twinned platelike grains growing by a solid-state process. In contrast, the rounded shape of large grains found below 1317°C in the present samples strongly indicates the presence of a liquid phase. Acid cleaning, by removing such melting agent impurities from the surface of the particles, raises the eutectic point to the expected value near 1320°C for 'pure' $BaTiO_3$ and consequently retards and slows down abnormal grain growth. Dilatometric curves for TAM 688 powder (Fig. 5) reveal only a weak contamination, the position of the second densification peak and maximum density being only slightly shifted (about 10°C). Conversely, Criceram powder appears to be more contaminated (Fig. 3): the second densification peak occurs at 1270°C for raw powder and is shifted to 1301°C after acid cleaning.

Despite the fact that surface barium carbonate is greatly reduced after acid cleaning, this treatment promotes an unexpected enhancement of the desintering stage on TAM 688, TAM 745 and Criceram powders. Rhône-Poulenc and Cabot powders present a desintering stage after acid cleaning only. The same phenomenon was observed on annealing hot-pressed samples (TAM 688), compacts being obtained without organic additive (PAA): therefore it is concluded that PAA decomposition plays no role in swelling, which is only due to $BaCO_3$ decomposition. XPS, EGA and TGA investigations[3] show that barium carbonate is still found after acid cleaning; the thermogravimetric weight losses between 1200 and 1400°C after acid cleaning are the same as for the raw powders, indicating that the acid-cleaning solution used was not strong enough to dissolve the $BaCO_3$ completely. Discrete $BaCO_3$ particles are not likely to be present after acid cleaning, unless they are trapped inside $BaTiO_3$ grains. It is more probable that a layer of carbonate more strongly bonded to the surface subsists, as shown by XPS, this remaining quantity corresponding to the weight losses shown in Table 2. These weight losses, if assumed to produce CO_2, are sufficient to account for desintering amplitudes as high as those observed for TAM 745 and Criceram acid-cleaned powders (8%). The magnitude of swelling is not proportional to the residual barium carbonate content—provided it is greater than 0·03 wt%—because once the porosity opens again, CO_2 can escape freely from the material.

The *increase* in swelling after acid cleaning results from a secondary effect of this treatment. During acid cleaning some Ba^{2+} ions were dissolved from the surface of the particles, which consequently become barium deficient, as shown by XPS in Part I.[3] This means that the isocompositional line has been shifted towards the TiO_2 side: the amount of liquid phase present at grain boundaries above 1300°C is then increased. As a consequence the plasticity of the material is enhanced, hence promoting swelling upon the development of internal CO_2 pressure inside the samples.

5 Conclusions

The effect of decontamination treatments of the surface of $BaTiO_3$ powders on sintering was investigated. Calcination only improves green densities of slip-cast bodies, which then densify upon sintering in more or less the same way as raw powders. Acid cleaning has extra repercussions on the sintering stage: increases in green densities combined with a delayed abnormal grain growth improve the elimination of porosity during the first stage of sintering, yielding slightly higher maximum densities. However, swelling above 1300°C is also increased, resulting from the development of internal CO_2 pressure inside the samples at high temperature after closure of the porosity. This carbon dioxide release originates from the decomposition of residual $BaCO_3$ which still subsists after acid cleaning. It is argued that impurities com-

monly found in undoped $BaTiO_3$ can promote the formation of a liquid phase at lower temperatures, responsible for abnormal grain growth. The formation of this liquid phase, and consequently the microstructure, can be controlled by acid cleaning, by eliminating both the melting agents present as impurities, and changing the surface Ba/Ti ratio. Complete removal of surface $BaCO_3$, using more acidic cleaning solutions, could lead to fully dense specimens by suppressing gas release at high temperature, assuming no $BaCO_3$ in the bulk.

Processing of commercial $BaTiO_3$ raw powders, especially by acid cleaning, appears to be beneficial on final properties. Removal of most of the barium carbonate by this treatment and various impurities hardly quantifiable present at the surface of the particles give rise to an approximately similar sintering behaviour for all powders. A similar final microstructure less sensitive to the starting commercial powder can then be obtained, confirming the great influence of the surface chemistry of initial powders on the final properties of the ceramics made thereof.

Acknowledgements

The Swiss National Foundation is gratefully acknowledged for financial support. The authors would like to thank Dr P. Bowen for his assistance in the preparation of the manuscript and Prof C. Carry for fruitful discussions.

References

1. Gerson, R. & Marshall, T. C., Dielectric breakdown of porous ceramics. *J. Appl. Phys.*, **30**(11) (1959) 1650–3.
2. Xue, L. A. & Brook, R. J., Promotion of densification by grain growth. *J. Am. Ceram. Soc.*, **72**(2) (1989) 341–4.
3. Hérard, C., Faivre, A. & Lemaître, J., Surface decontamination treatments in undoped $BaTiO_3$. Part I: Powder and green body properties. *J. Eur. Ceram. Soc.*, (1994) (1442).
4. Kingery, W. D., Bowen, H. K. & Uhlmann, D. R., *Introduction to Ceramics*. John Wiley and Sons, NY, 1976.
5. Barin, I. & Knacke, O., *Thermochemical Properties of Inorganic Substances*. Springer, Berlin, 1973.
6. Carry, C. & Mocellin, A., Superplastic creep of fine grained $BaTiO_3$ in a reducing environment. *J. Am. Ceram. Soc.*, **69**(9) (1986) C215–16.
7. Rase, D. E. & Roy, R., Phase equilibria in the system BaO–TiO_2. *J. Am. Ceram. Soc.*, **38**(3) (1955) 102–13.
8. Levin, E. M., Robbins, C. R. & McMurdie, H. F., *Phase Diagrams for Ceramists*. American Ceramic Society, Colombus, 1964.
9. Hennings, D. F. K., Janssen, R. & Reynen, P. J. L., Control of liquid phase-enhanced discontinuous grain growth in barium titanate. *J. Am. Ceram. Soc.*, **70**(1) (1987) 23–7.
10. Schmelz, H. & Meyer, A., The evidence of anomalous grain growth below the eutectic temperature in $BaTiO_3$ ceramics. *Ber. Dtsch. Keram. Ges.*, **59**(8/9) (1982) 436–40.

Journal of the European Ceramic Society **15** (1995) 155–164
© 1995 Elsevier Science Limited
Printed in Great Britain. All rights reserved
0955-2219/95/$9.50

Characterization of Submicron Alumina Dispersions with Poly(methacrylic acid) Polyelectrolyte

Wen-Cheng J. Wei, Su Jen Lu & Bu-Kon Yu

Institute of Materials Science and Engineering, National Taiwan University, Taipei, Taiwan 106

(Received 4 December 1993; revised version received 3 June 1994; accepted 30 June 1994)

Abstract

Colloidal dispersion of two submicron alumina powders (A-16SG and APA-0·2) and their mixtures were investigated in an aqueous suspension with and without dispersant (ammonium salt of poly(methacrylic acid), PMAAN). The ζ-potential and isoelectric point (iep) of the powders in aqueous solution were determined in the presence of the dispersant and electrolyte (NaCl). The adsorption of dissociated $PMAA^-$ on alumina powders was determined via the titration technique. The dispersant was observed to exert a strong influence on the surface potential, flowing behaviors and packing densities of the aluminas. The results showed that the dispersion conditions were strongly affected by factors including the solid concentration of submicron alumina particles, the pH value and the concentration of PMAAN in the suspensions, and that these three factors were cross-influencing. A reaction model at the interface of alumina—solution was developed, based on the dissociation of PMAAN and the adsorption of surface hydrocarboxyl groups on alumina surface.

1 Introduction

Fine-grained and uniform microstructures are desirable for most structural ceramic applications in producing a strong and reliable structural part. One method which accomplishes these goals involves using submicron powder[1–3] as well as processing the ceramic powder through colloidal states.[4–8] Colloidal processing has gained considerable attention during the past decade, having proven itself as being one of the effective routes in producing high-performance ceramic components.

Ceramic particles in a solution are charged and may possibly become dispersed in a repulsive manner by the forces developed at the surface of the particles. The particles can be dispersed in an aqueous solution by three mechanisms, i.e either by electrostatic, steric, or electrosteric stabilization.[9] These stabilizations are accomplished by generating common surface charges either at the surface of particles or else on the polymer chains which are adsorbed on the surface of the particle. The force, which is formed from the repulsion of similar charges and offers this stabilization, is commonly termed a Coulombic force. In addition to these forces, the adsorbed polymeric chains can also perform a spatial repulsion. Electrosteric stabilization is active if the polymer chains are absorbed on ceramic surface and the chains are charged with dissociated functional groups. It is closely related to the conformation and dissociation of polymeric chains in various acidic–basic conditions, which have been discussed extensively in consideration of the interaction with the oxide surface.[4,5,10] The electrosteric effect produces significant repulsion forces between the polymeric chains and particles. However, the ceramic particles, especially for submicron powder and in high solid-content suspensions, are easily coagulated in a poor solution unless the suspension has favorable stabilization conditions.

The rheology of a ceramic suspension is strongly influenced by the nature of the ceramic particles, the composition and chemical nature of the solvent and dispersant, as well as the solid content.[4,10,11] Two of the important parameters that can be used to describe the state of dispersion of ceramic colloids are the ζ-potential and the isoelectric point (iep) of the colloidal surface.[12] The surface potential has been extensively employed in accounting for the electrokinetics properties of ceramic suspensions.[6,7,13] The values of the potential, although somewhat controlled by the nature of the solid particles, e.g. the crystalline phase[14] and the surface impurity,[15] are most significantly controlled by the acidity of dispersing medium and the additive (or dispersant) in the medium.

Some research effort involving ceramic composites was recently undertaken which employs the colloidal process in preparing mixtures of various dissimilar ceramic and/or metallic colloids. The use of a toughening phase, e.g. zirconia particulates for toughening alumina, or the preparation of the mixture of two similar powders to tailor the size distribution of the powder mixture, or the production of nanocomposites would require understanding of the behavior of each phase, especially the fine portion of powder mixture, in colloidal states.

Many difficulties involving colloidal processing cases are encountered in powder mixtures. Phase segregation of ceramic particles in slip-casting, size segregation during sedimentation or consolidation of suspension, and flocculation of the fine particles in a mixture have a close relationship with the stability of a suspension system. Attempting to homogeneously mix two different powders is a rather difficult task.

Segregation of a heavy particle from the powder mixture or local segregation of different charged particles has been the major concern of these research efforts.[6,13] Some useful treatments are proposed as well as some promising results being provided. Velamakanni & Lange[6] reported that the requirements for colloidal particles to achieve their best packing properties were strong interparticle forces (high surface potential) and optimization of particle size distribution. Achieving strong interparticle forces is also true for stabilization of the suspensions with powders having different surface compositions and physical properties.

The principal objectives of this research involve analyzing the effects of polymeric dispersant when adsorbed on two alumina powders and identifying the critical parameters associated with the colloidal processes, as well as revealing the relationships of dispersion conditions with the purities of alumina powders. The phenomena of surface charging and adsorption of polymeric chains on alumina are cited here as accounting for the behavior of submicron alumina particles in a highly concentrated suspension system.

2 Experimental procedure

2.1 Materials

The alumina powders used in this study were A-16SG (supplied by Aluminum Co. of America, Pittsburg, PA, USA; BET surface area = 9·0 m^2g^{-1}, purity = 99·7%) and APA-0·2 (supplied by Ceralox Co., Arizona, USA; BET surface area = 34·0 m^2g^{-1}, purity = 99·97%). The properties of these powders are listed in Table 1. A-16SG and APA-0·2 powders have a different crystalline phase and average particle size (d_{50}) of 0·41 and 0·21 μm, respectively. A polyelectrolyte dispersant used in the preparation of dispersed alumina slurries was the ammonium salt of poly(methacrylic acid) (abbreviated as PMAAN) with molecular weight (Mw) ranging from 10000 to 16000. The water for dissolving dispersant was distilled, then deionized. The pH of alumina slurries was adjusted via the titrants diluted from analytical grade HCl and NaOH. Analytical grade NaCl was used as an electrolyte in a concentration of 0·01 N to adjust the ionic strength of diluted alumina suspensions which were subjected to the measurement of ζ-potential.

Table 1. Properties of alumina powders

	APA-0·2[a]	A-16SG[b]
BET (m^2/g)[c]	34	9
Particle Size, $d_{50}(\mu m)$	0·21	0·4
Phase[d]	$\theta(+\alpha)$	α
Purity (%)	99·97	99·7
Na_2O (ppm)	<4	800
SiO_2 (ppm)	57	800
Fe_2O_3 (ppm)	126	100
MgO (ppm)	28	500
CaO (ppm)	2	—
B_2O_3 (ppm)	—	10
Density[e]	3·58	3·986

[a] APA-0·2 data sheet, Ceralox, Arizona, USA.
[b] A-16SG data sheet, Alcoa Industrial Chemicals, Pittsburgh, PA, USA.
[c] Nitrogen Adsorption Flowsorb 2300, Micromeritics, GA, USA.
[d] Verified with X-ray diffractometer, PW1729, Philips Instrument, Netherlands.
[e] Verified with Pycnometer 1305, Micromeritics, GA, USA.

2.2 Sample preparation

2.2.1 Slurry preparation

The dispersant was first dissolved in the treated water. A specific amount of alumina powder was then gradually added to the solution. Some suspensions prepared for ζ-potential measurement required dilution to the concentration 0·001 mg cm^{-3} for analysis. The suspension was transferred into a polyethylene (PE) bottle which was loaded with zirconia grinding media, then agitated by a turbomixer for 1–24 h. According to the volume ratio of A-16SG to APA-0·2, powder mixtures were also prepared and designated A80, A70 and A60. For instance, A80 represents an alumina (A) mixture of eight parts of A-16SG and two parts of APA-0·2 by volume.

2.2.2 Green compact preparation

Green alumina pieces were prepared via a pressure-casting method. The alumina slurries were

contained in an air-pressurizing mold which is constituted of two plates manufactured from 316 stainless steel and a thick-wall tube of transparent polyacrylic material. Compressed air at a pressure of 10 kg cm^{-2} was supplied, along with the slurry being driven through a plastic filter paper.

2.3 Property measurement

2.3.1 Zeta (ζ)-potential measurement
Electrophoresis measurement was conducted using a Zeta-Meter 3·0+ instrument (Zetameter Inc., USA) so as to determine the ζ-potential of the alumina particles in aqueous suspension. The instrument was carefully calibrated and tested with the standard colloids offered by the manufacturer. In this study, alumina powder was dispersed in a prepared solution in a solid concentration close to 0·001 mg cm^{-3}, The pH value of the solution with a specific amount of the dispersant was adjusted via either a dissolved acidic or a basic solution, as well as NaCl electrolyte. The suspension was ultrasonicated using a NEY ultrasonicator (2Q-100) at a power level of 30 W for at least 5 min before the measurement being taken.

2.3.2 Acid titration of dispersant
Adsorption of the dispersant on alumina powders and the pH of alumina suspension with various amounts of PMAAN were determined using an auto-titration instrument (VIT90 Video Titrator, TitraLab™ Radiometer, USA). The calibration curve of PMAAN titrated with 0·1 N HCl is shown in the Appendix. The adsorption of PMAAN on alumina was then determined in the following procedure. The mixed alumina suspension was centrifuged using a Hermle Z380 centrifuger (Berthold Hormle GMBH & Co, Germany) at 6000 rpm for 60 min to obtain a clear suspension. The clear solution was next removed from the suspension container, and titrated with 0·1 N HCl standard solution. The amount of required acid to balance the dissolved PMAAN in the clear suspension was determined by the IPT (infection point titration) method, which can be referred to in the operation manual of the VIT90 Video Titrator. As a consequence, $PMAA^-$ species adsorbed on alumina could be calculated from the equivalent point of the acid measured by the previously mentioned IPT method.

2.3.3 Viscosity measurement
The measurements were conducted with two rotary viscometers (Model DV II, Brooksfield Eng. Labs Inc., USA) which have different shear-rate ranges. These instruments were calibrated with three standard viscous fluids, which have the viscosities of 93·8, 975 and 12200 cps (or mPas), respectively. Flocculation of alumina particles in a poorly dispersed slurry would influence the rheological properties of the slurry. Therefore, the measurement steps were adjusted according to previous reports;[4,5] in addition, the apparent viscosity values were taken from the average of at least two different measurements.

2.3.4 Pore size and volume measurements
Green samples were dried at 500°C for 10 min before they were tested with a mercury porosimeter (Autopore II 9220, Micromeritics Instrument Co., USA).

2.3.5 Microstructural observation
Alumina green samples were broken, coated with a thin Au film for electric conductivity, and observed using a scanning electron microscope (JSM-T100 mini SEM, JEOL Co., Japan).

3 Results and discussion

3.1 Surface potential of alumina with and without dispersant

The effect of pH on the ζ-potentials of the two alumina powders in an aqueous solution is shown in Fig. 1. The isoelectric point (iep) of A-16SG is at pH = 8·5, for APA-0·2 alumina it is at pH = 8·9. According to the literature,[11] the iep of aluminas could vary with the sources of alumina and the varieties of measurement techniques: The alumina prepared from the precipitation with incomplete hydration has a zero point of charge (zpc) (which could be considered as iep) near pH 6·9 if measured by the electrophoresis method. For the natural product, however, alumina has a zpc at pH 8·4 if measured by the same method, or 9·5 if by the streaming potential method. Rao[13] employed two different techniques in measuring the property, reporting that the iep of alumina is at pH 9.

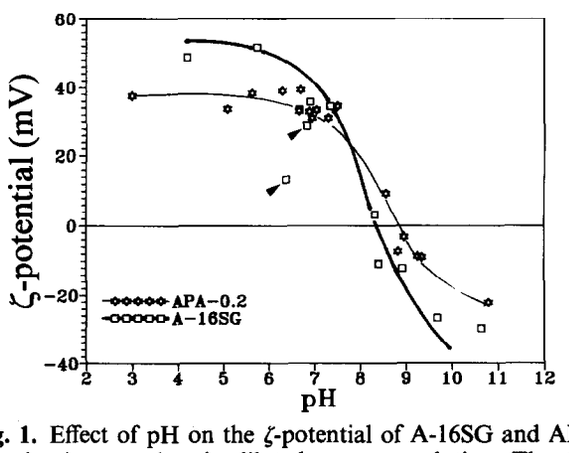


Fig. 1. Effect of pH on the ζ-potential of A-16SG and APA-0·2 alumina powders in diluted aqueous solution. The data indicated by arrows are discussed in the text.

A similar result of the iep value of the A-16SG powder, as determined by an improved measurement apparatus,[14] was reported to be at pH 8.

Kelso & Ferrazzolli[15] determined the relative acoustophoretic mobility of A-16SG alumina in water, and found a negative mobility (i.e. a negative ζ-potential on the surface) of A-16SG, as compared to a high purity alumina (XA-139SG, purity ≥99·95 wt%, supplied by Alcoa, USA) which has a positive value in deionized water (pH = 5·0). They assumed that the surface impurity Na_2O of A-16SG would possibly become ionized and for hydrated in an aqueous solution. The ζ-potential of A-16SG measured in this work was a positive value, similar to that of the high purity aluminas, XA-139SG,[14] and APA-0·2 in the present case. However, the surface potential values of A-16SG were observed in this study to be rather dependent upon the aging time of the alumina suspension. The ζ-potential values of A-16SG are relatively scattered within the range pH 5–7, and would be smaller in value if the suspension is aged more than 30 min, as shown by two data points in Fig. 1. It is due to the release of ionizable species, e.g. Na^+, Mg^{+2}, from the powder. High purity APA-0·2 powder has a consistent surface charge in an aqueous solution.

At the pH below the iep of alumina, the aqueous solution permits charge and proton transfer at the solid–solution interface, resulting in an electrically positive surface on alumina, e.g. the formation of $AlOH_2^+$. That is the reason why the alumina particles in weakly acidic water solution exhibits a positive potential. However, the observation of the pH value of freshly prepared suspensions changed from weakly acidic to neutral, or to weakly basic conditions as they aged. A similar change was reported[15] in which the pH of the water increased up to 9·6 for an alumina content in the solution of 16·7 wt%. The acidity of the suspension is dependent on the interaction of alumina in acidic suspension. However, the formation of the positive $AlOH_2^+$ species is interrupted by the presence of Na_2O and other ionizable oxide impurities. Surface Na_2O is considered here as possibly releasing Na^+ in forming a negative NaO^- so as to compensate for the positive charge ($AlOH_2^+$) on the surface of alumina. In addition, MgO, used as a grain-growth inhibitor, (as is the report indicated in by the powder supplier, Alcoa, USA), is present in A-16SG, and tends to dissolve in water to form a strongly basic solution. The contents of Na_2O and MgO are appreciable (0·08% and 0·05%, respectively) in A-16SG, but ignorable in a high purity APA-0·2 powder (Table 1). Therefore, the dissolution of Na_2O and MgO is not occurring in APA-0·2 between pH 5 to 7 in Fig. 1. The dissolved Na and Mg ions could alter the thickness of the double layer on the surface of alumina particles. As a consequence, the ζ-potential of A-16SG at the pH away from its iep is higher than that of APA-0·2 particles. The significance of surface impurities having reacted with water shows that the surface potential can be a time-dependent variable.

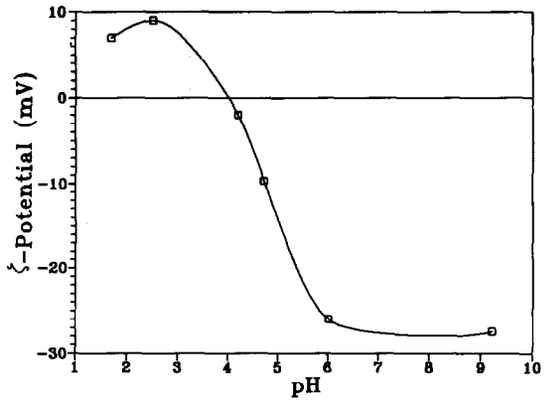


Fig. 2. Effect of pH on the ζ-potential of diluted A-16SG slurries with 0·125 wt% PMAAN (based on alumina).

Figure 2 shows the effect of pH on the ζ-potential of diluted A-16SG suspensions originally containing 30 wt% alumina and 0·125 wt% PMAAN (based on alumina). The alumina surface has reversed its electrical charging condition at pH 4·0. A similar chemical PMAA–Na salt[4] was reported as not being dissociated at the pH below 3·5, but fully dissociated at the pH values over than 8·0. If the dispersant used in this study has a similar dissociation behavior, the adsorption of dissociated $PMAA^-$ can only take place at the pH ranging from 3·5 to 8·2 (the iep of A-16SG). The surface potential of the alumina, which is positively changed, shifts to negative when the surface is covered with $PMAA^-$. As a result, the ζ-potential in the acidic conditions (pH = 3·5–8·2) is changed from a positive to a negative surface. Thus, iep of A-16SG in the presence of PMAAN is accordingly changed to pH 4·0.

A plot of the ζ-potential of A-16SG and APA-0·2 suspensions is provided in Fig. 3 which contains 0·01 N electrolyte NaCl and various amount of PMAAN. The surface potential of A-16SG alumina in diluted NaCl (0·01 N) solution is about 38 mV. However, the potential dramatically changes to negative if the amount of PMAAN is more than 0·02 wt% based on A-16SG alumina. Similarly the potential of APA-0·2 reverses as the concentration of PMAAN is greater than 0·04 wt%. That is a result of adsorption of a dispersant with an anionic-type functional group, and the amount of dispersant is surface-area dependent. The potential values, which reach a plateau, show that the adsorption on alumina becomes saturated if

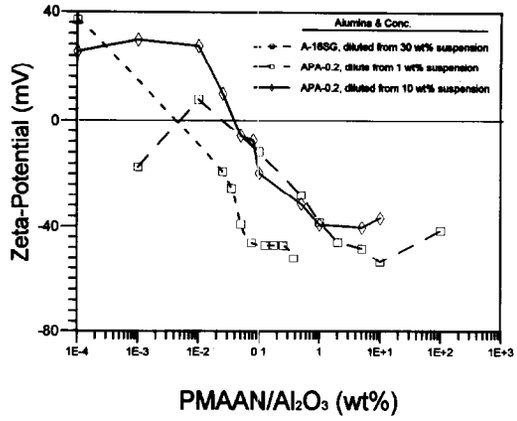


Fig. 3. Effect of PMAAN on the ζ-potential of A-16SG and APA-0·2 slurries which contain 0·01 N NaCl.

more than 0·07 wt% or 0·5 wt% PMAAN is added in the A-16SG or APA-0·2 suspensions, respectively.

The pH values of suspensions which contain various amounts of alumina are plotted in Fig. 4 against the added PMAAN. These results show that the water changes its pH value to weakly basic (pH 8·0) if PMAAN is added—even as little as 0·01 wt% (based on the solution). However, the pH becomes more basic if A-16SG powder is added at a level of more than 1·0 wt% of the deionized water. Kelso & Ferrazzolli[15] reported a similar change of the pH of pure water up to 9·6 if the addition of A-16SG alumina powder in the solution was 16·7 wt%, but up to pH 8·0 if the solution contained the same amount of high-purity alumina (XA-139SG).

First of all, the alumina surface tends to change from a neutral surface to a positively charged surface as alumina powder is steeped in deionized water. The adsorption of protons on the alumina surface causes the water to have an increasing OH^- concentration. This concentration causes the pH of the solution to be basic (pH > 7). The newly formed aluminum hydrate has an amphoteric property. The reactions of the hydrated alumina surface at various pH conditions can be expressed as follows

$$x\mathrm{H_3O^+} + [\mathrm{O{-}Al{-}}]_n(\mathrm{OH})_x \Leftrightarrow [\mathrm{O{-}Al{-}}]_n(\mathrm{OH_2^+})_x + x\mathrm{H_2O} \quad \text{at pH} \leq \text{iep} \quad (1)$$

$$[\mathrm{O{-}Al{-}}]_n(\mathrm{OH})_x + x\mathrm{OH^-} \Leftrightarrow x\mathrm{H_2O} + [\mathrm{O{-}Al{-}}]_n(\mathrm{O^-})_x \quad \text{at pH} \geq \text{iep} \quad (2)$$

However, the dissolution of PMAAN in water would interfere with the pH value of the suspension. The alumina suspension (Al_2O_3 content ≥1·0 wt% of the solution) is indicated from Fig. 4(a) to have higher pH values than the aqueous solution only with PMAAN. The difference of the pH value between the solution (with PMAAN) and alumina suspension is reducing (approaching to

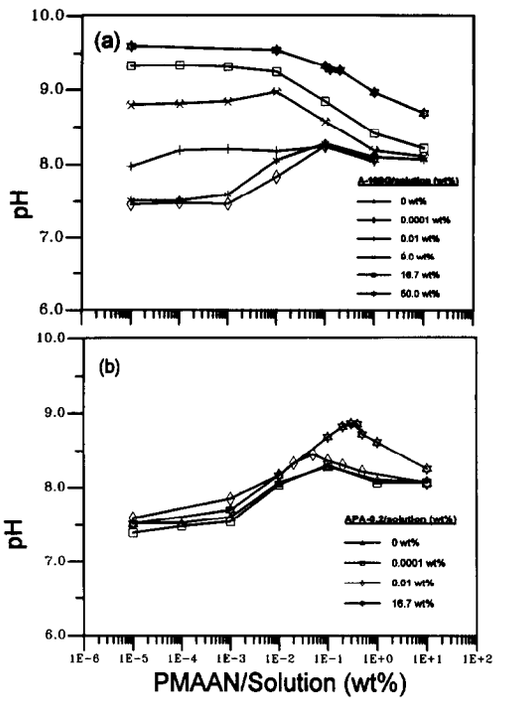


Fig. 4. Effect of PMAAN on the pH of alumina slurries for various concentrations of alumina (a) A-16SG and (b) APA-0·2.

pH 8·3) as the PMAAN concentration increases. The presence of alumina and PMAAN chemical have closely interfered with each other in aqueous solution.

Alumina is scarcely dissolved in a weakly basic solution of which the added PMAAN gives a stable pH value near 8·1. For a suspension system including a solid phase in equilibrium with the solution, the isoelectric point of the solution corresponds to the point of minimum solubility of the solid.[12] The formation of molecular $Al(OH)_3$ or AlOOH in weakly basic alumina suspension is ignorable. For the reactions of PMAAN, a combination of the dissociation of PMAAN and the adsorption of $PMAA^-$ on the alumina surface, are revealed by the pH evaluation of alumina suspensions.

The dissociation of PMAAN and the reaction with water can be expressed in the following equations:

$$\mathrm{PMAA - NH_4} \Leftrightarrow \mathrm{PMAA^- + NH_4^+} \quad (3)$$

$$\mathrm{PMAA^- + H_2O} \Leftrightarrow \mathrm{PMAA - H + OH^-} \quad (4)$$

If α is the fraction of dissociated group of PMAAN in suspension. The titration of a 33 vol.% (or 66 wt%) A-16SG suspension with 0·125 wt% PMAAN reveals that nearly 32% of $PMAA^-$ is adsorbed on the surface of APA-0·2. A high concentration (about 2/3) of the charged polymeric chains of $PMAA^-$ is available in this suspension and can be adsorbed on alumina particles, subsequently resulting in the decrease of surface potential (Fig. 3) of the alumina. However, several

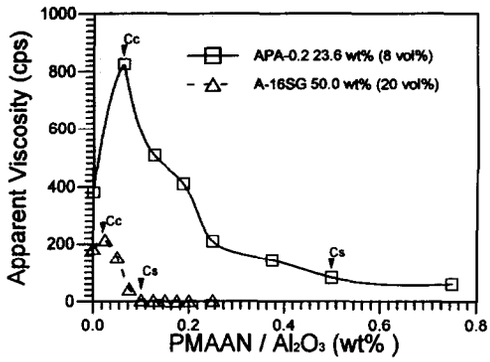


Fig. 5. Effect of PMAAN on the apparent viscosity of A-16SG and APA-0·2 slurries tested in a shear rate 18 s^{-1}.

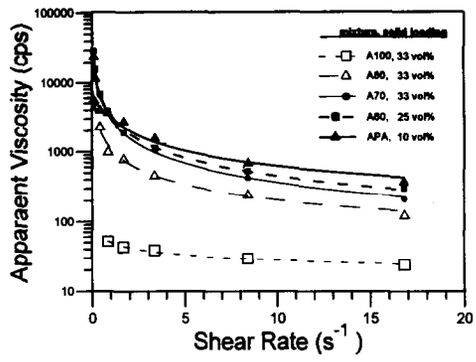


Fig. 6. Apparent viscosity of various alumina slurries with 0·5 wt% PMAAN (based on alumina) at various shear rates.

researchers[4,10] have pointed out that the conformation of $PMAA^-$ or a similar polymer, e.g. PAA^-, in weak base, influenced its adsorption phenomena near the saturation point. The stretched $PMAA^-$ prevents more $PMAA^-$ from adsorbing at the alumina particle surface. Therefore, the ζ-potential of A-16SG and APA-0·2 alumina suspensions can no longer increase their absolute values.

The adsorption of dissociated PMAAN on alumina not only alters the surface potential of alumina, but also changes the pH value of the solution if the adsorption on alumina is over the saturation point. As the concentration of PMAAN in A-16SG suspension rises over 0·01 wt%, the pH (or the acidity) of the alumina suspension changes to close to the pH of pure PMAAN with aqueous solution, but for high purity APA-0·2 it is over 0·05 wt%, as revealed in Fig. 4(a) and (b). Therefore, the pH of alumina suspension with an increase of non-adsorbed PMAAN approaches 8.1.

3.2 Slurry viscosity

The addition of dispersant $PMAA–NH_4$ can effectively reduce the viscosity of the alumina slurries if it is added into the formulation in a concentration of more than a critical amount (C_c). C_c is 0·02 wt% for A-16SG and 0·07 wt% for APA-0·2, as illustrated in Fig. 5. the electrosteric repulsion which arises from the adsorption of $PMAA^-$ polymeric chains on alumina is effective only if the added PMAAN is in an amount over C_c. This observation is consistent with the reverse of surface potential observed in Fig. 3. The interparticle forces, which are a result of surface electric potential, stabilize the colloidal particles in the concentrated suspension. Since the adsorption of the $PMAA^-$ on the alumina is near the saturation point (C_s in Fig. 5), the surface potential of A-16SG alumina is maintained at around 47 mV (Fig. 3), which is nearly the maximum potential in the suspension. A strong surface potential causes the viscosity of the A-16SG suspension to reach its lowest value. Similar behavior is found for the APA-0·2 suspension containing a lower solid content (i.e. 8 vol.%) than the A-16SG suspension.

The amount of polyelectrolyte necessary to achieve a good dispersion is surface-area dependent. The BET surface area of APA-0·2 is about four times higher than that of A-16SG powder, as indicated from Table 1. The curves provided in Fig. 5 are similar, only different in the scale of viscosity. The ratio of the critical amount (C_c) and the saturation amount (C_s) of required PMAAN implies that the specific surface area of the two powders, one of 34 $m^2\ g^{-1}$ the other of 9 $m^2\ g^{-1}$, is dominating the required amount of adsorbed $PMAA^-$.

Figure 6 illustrates the effect of PMAAN on the apparent viscosity of pure A-16SG, APA-0·2 slurries and the slurries of their mixtures, A80, A70 and A60. The rheological data in Fig. 6 were measured from the slurries with various solid concentrations. One APA-0·2 suspension can only be dispersed at the solid concentration less than 15 vol.%. All of the APA-0·2 containing slurries have a pseudo-plastic flow behavior; however, pure A-16SG slurry is nearly Newtonian. It has been demonstrated[16] by the Dougherty–Krieger equation that the rheological states are mainly affected by the solid loading (or solid/liquid ratio), particle shape and the average particle size. Interactions between the electrical double layer and/or the adsorbed polyelectrolyte have to be taken into account,[17] if the volume fraction of the particles in suspension is increased. The suspension of APA-0·2, having an average particle size two times less than that of A-16SG, was confirmed in this study as being very viscous (almost gelled) at solid concentrations over 15 vol.% if only 0·5 wt% PMAAN dispersant was used.

Rao[13] has reported that the electrophoretic mobility versus pH profiles and the position of the isoelectric point of powder mixtures are apparently governed by the powder having a large total surface area in the mixture, but not necessarily the

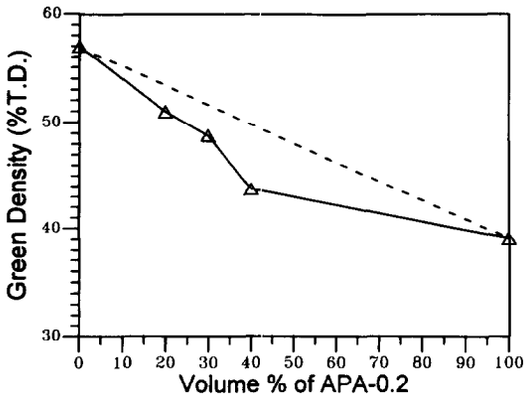


Fig. 7. Green densities of various alumina mixtures.

weight fraction. Thus, the viscosity of the mixed suspension could be controlled by the flowing behavior of fine APA-0·2 powder, as depicted in Fig. 6.

3.3 Properties of green alumina mixtures

Green densities of various alumina mixtures, which have been pressure-casted and dried, are given in Fig. 7. The green density is an index of powder packing conditions. A-16SG has a relative green density of 0·57, APA-0·2 is 0·39 only. The green pieces were prepared from the slurries with 0·125

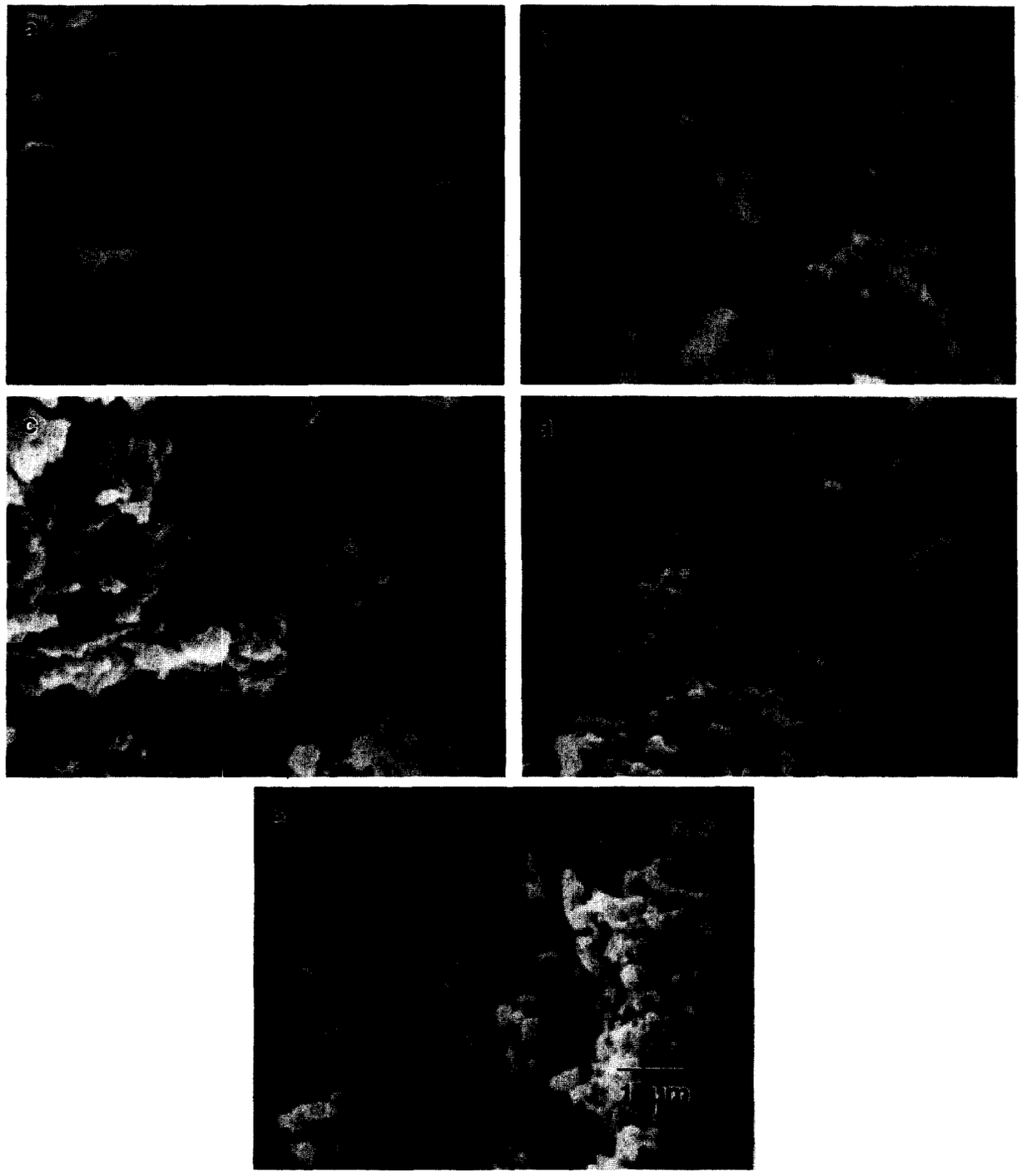


Fig. 8. SEM micrographs of the fracture surfaces of green (a) A-16SG, (b) APA-0·2, (c) A80, (d) A70 and (e) A60 powder compacts.

or 0·5 wt% PMAAN dispersant (based on alumina). The difference of green densities between two green pure materials is mainly a result of the surface forces and the dispersion conditions of powders. The slurries of the fine agglomerated APA-0·2 particles still produce the green pieces in a loose pack.

Zok *et al.*[19] developed a model of binary powder packing to illustrate the effects of large particle surface and touching of the particles on the packing density of ceramic powders. In contrast, Messing & Onoda's work[20] attempted to describe the inhomogeneity (defined by the degree of mixing) on the packing density of binary powder. Both groups pointed out that the experimental data for composite mixtures deviate from the theoretical values of ideal packing density. Particularly, packing densities of different size powder mixtures are higher than random packing densities of the mixtures. In Velamakanni & Lange's work,[6] the fine alumina, AKP-series, has a random packing density of 0·63, however the mixtures with 20 to 40% fines allow a density of 0·68 to be reached, which is far lower than the theoretical density 0·87, but those values are still larger than 0·63.

In the present case, the green densities of the mixtures (A80, A70 and A60) are even lower than those density values calculated from the volume fractions of two-ended materials, as the broken line indicates in Fig. 7. Restated, the powder mixtures have shear thickening properties. The reasons for a reduction of the packing density have been proposed by others[6] as possibly being physically a consequence of the presence of local compositional variations. In the present case, the composition variation should be treated as a packing-type structural variation in the mixtures of two alumina powders. The observation (Fig. 8(c) to (e)) of the fractured surfaces of three mixtures has confirmed that fine alumina particles (APA-0·2) are retaining some degree of agglomeration in sizes 0·6 μm or larger. The agglomerates are still retained from previous dispersion and mixing stages. Therefore, the green powder mixtures have at least two varieties of porosity. The porosity was revealed by the measurement of pore size, and the results were plotted in Fig. 9. The pore size distribution of APA-0·2 has two maxima, i.e. at 0·09 and 0·035 μm, respectively. The fine pores, which are believed to have formed between agglomerates, are one of the characteristics of partially agglomerated powder. Additionally, the pore size distributions of A80, A70 and A60 notably exhibits a fraction of pores having sizes ranging from 0·02 to 0·06 μm (Fig. 9(a)) similar to that of APA-0·2. The mixtures possess some degree of the agglomeration of pure APA-0·2 powder.

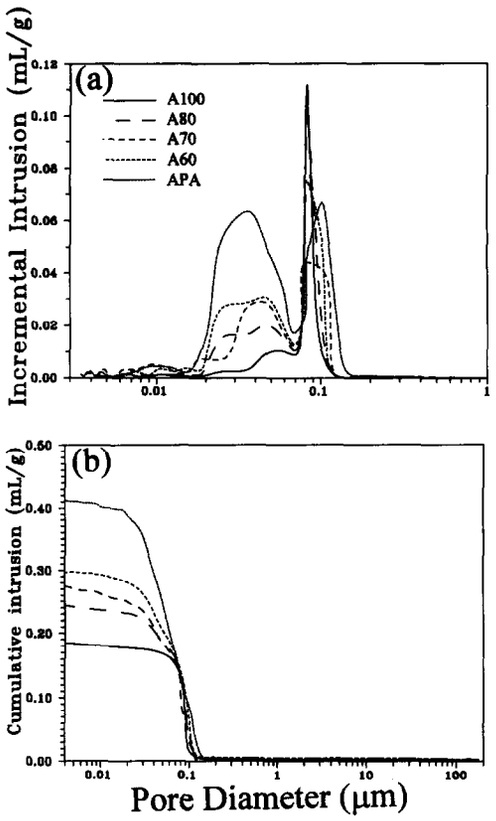


Fig. 9. (a) Pore size distribution and (b) cumulative pore volume of various alumina mixtures.

4 Conclusion

The surface potential, adsorption of dispersant, flowing behavior and green packing properties of alumina powders in additional of PMAAN dispersant were investigated in this study. The packing and mixing of ideal powder mixtures could be optimized not only from the dispersing conditions, but most importantly from the control of agglomeration—especially in fine powder. Some conclusions can be drawn, i.e.:

(1) The iep of A-16SG powder in aqueous suspension is determined to be at pH = 8·5 and that of APA-0·2 is at pH = 8·9. The iep is shifted to pH 4·0 if the anionic-type dispersant PMAAN is added to the alumina suspension;

(2) The adsorption of dispersant PMAAN changes the surface potential of A-16SG and APA-0·2 to negative values and also offers an electrosteric stabilization for alumina particles in aqueous solution;

(3) The rheological behavior of pure alumina particles in suspension is controlled by the reactions of PMAAN, the specific surface area of the powder, acidity and solid loading of the suspension. Conversely, the dissociation of PMAAN is affected by the amount of alumina powder in suspension;

(4) The flowing behavior of the alumina suspension which is the mixture of two powders is dominated by the fine powder, i.e. APA-0·2, which is still partially agglomerated in dispersed suspension; and
(5) APA-0·2 is difficult to fully disperse in an aqueous condition. Its green compacts exhibit a bimodal distribution porosity with pore sizes around 0·09 and 0·035 μm. The fine pores are retained in powder mixtures which are similar to that of pure APA-0·2.

Acknowledgment

The authors would like to acknowledge the funding from National Science Council (#NSC82-0405-E002-119) and thank Professor Dah-Tong Ray for the measurement of ζ-potential conducted in his laboratory at the National Cheng-Kung University. Helpful discussion with Professors D. S. Tsai and K. S. Chou is also acknowledged.

References

1. Yeh, T.-S. & Sacks, M. D., Low temperature sintering of aluminum oxide, *J. Am. Ceram.*, **71**(10) (1988) 841–4.
2. Yeh, T.-S. & Sacks, M. D., Effect of particle size distribution on the sintering of alumina. *Comm. Am. Ceram. Soc.*, **71**(12) (1988) C-484–C-487.
3. Tsai, D.-S. & Hsieh, C.-C., Controlled gelation and sintering of monolithic gels prepared from γ-alumina fume powder. *J. Am. Ceram. Soc.*, **74**(4) (1991) 830–6.
4. Cesarano III, J., Aksay, I. A. & Bleier, A., Stability of aqueous α-alumina suspensions with poly(methacrylic acid) polyelectrolyte. *J. Am. Ceram. Soc.*, **71**(4) (1988) 250–5.
5. Cesarano III, J. & Aksay, I. A., Processing of highly concentrated aqueous α-alumina suspensions stabilised with polyelectrolytes. *J. Am. Ceram. Soc.*, **71**(12) (1988) 1062–7.
6. Velamakanni, B. V. & Lange, F. F., Effect of interparticle potentials and sedimentation on particle packing density of bimodal particle distributions during pressure filtration. *J. Am. Ceram. Soc.*, **74**(1) (1991) 166–72.
7. Hirata, Y., Nishimoto, A. & Ishihara, Y., Effects of addition of polyacrylic ammonium on colloidal processing of α-alumina. *J. Ceram. Soc. Jpn, Int. Edn*, **100** (1992) 972.
8. Novich, B. E. & Pyatt, D. H., Consolidation behavior of high-performance ceramic suspension. *J. Am. Ceram. Soc.*, **73**(2) (1990) 207–12.
9. Napper, D. H., *Polymeric Stabilization of Colloidal Dispersions*. Academic Press, London, 1983, pp. 8–15.
10. Chen Z. C., Ring, T. A. & Lemaitre, J., Stabilization and processing of aqueous $BaTiO_3$ suspension with polyacrylic acid. *J. Am. Ceram. Soc.*, **75**(12) (1992) 3201–8.
11. Chou, K. S. & Lee, L. J., Effect of dispersants on the rheological properties and slip casting of concentrated alumina slurry. *J. Am. Ceram. Soc.*, **72**(9) (1989) 1622–7.
12. Parks, G. A., The isoelectric points of solid oxides, solid hydroxides and aqueous hydroxy complex systems. *Chem. Rev.*, **65** (1965) 177.
13. Rao, A. S., Electrophoretic mobility of alumina, titania and their mixtures in aqueous dispersion. *Ceram. Int.*, **14** (1988) 71–6.
14. Hashiba, M., Okamoto, H., Nurishi, Y. & Hiramatsu, K., The zeta-potential measurement for concentrated aqueous suspension by improved electrophoretic mass transport apparatus—application to Al_2O_3, ZrO_2 and SiC suspension. *J. Mat. Sci.*, **23** (1988) 2893–6.
15. Kelso, J. F. & Ferrazzoli, T. A., Effect of powder surface chemistry on the stability of concentrated aqueous dispersions of alumina. *J. Am. Ceram. Soc.*, **72**(4) (1989) 625–7.
16. Lee, Y. C. & Wei, W., Dispersion and high-pressure filtration of zircon/alumina composite slurry. *Chin. J. Mat. Sci.*, **24**(2) (1992) 113–22.
17. Frith, W. J., Mewis, J. & Strivens, T. A., Rheology of concentrated suspensions: experimental investigations. *Powder Tech.*, **51** (1987) 27–34.
18. Nikumbh, A. K., Schmidt, H., Martin, K., Porz, F. & Thummler, F., Influence of pH on rheological properties of alumina slips. *J. Mat. Sci.*, **25** (1990) 15–21.
19. Zok, F., Lange, F. F. & Porter, J. R., Packing density of composite powder mixtures. *J. Am. Ceram. Soc.*, **74**(8) (1991) 1880–5.
20. Messing, G. L. & Onoda, G. Y., Inhomogeneity–packing density relations in binary powders—experimental studies. *J. Am. Ceram. Soc.*, **61**(7–8) (1978) 363–6.

Appendix follows

Appendix

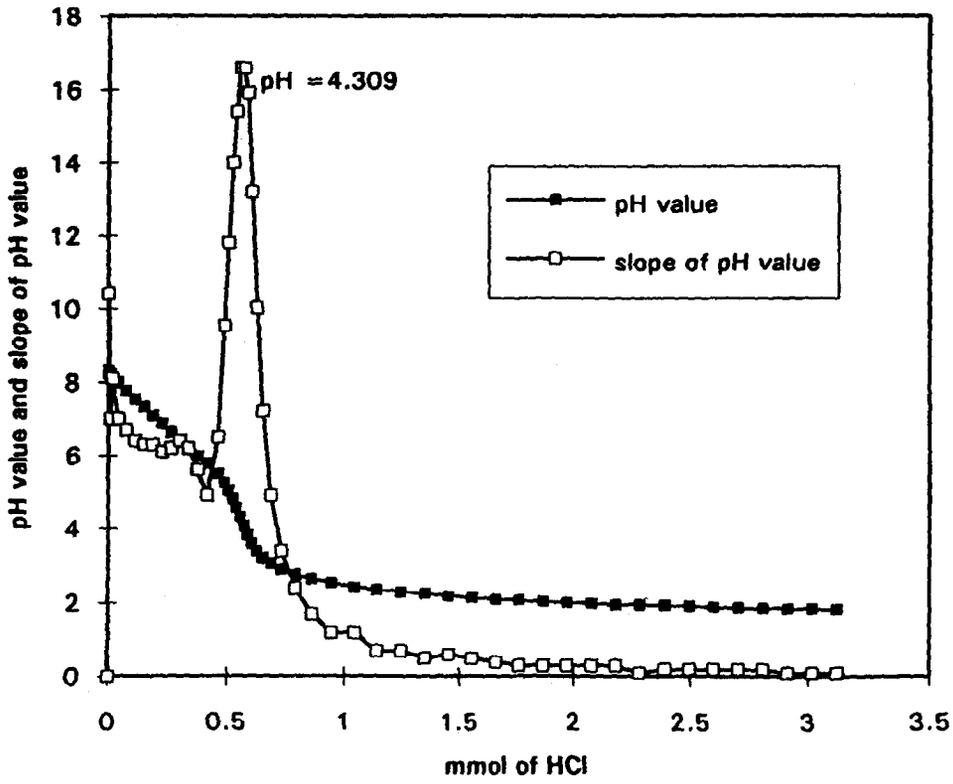


Fig. A1. The titration curve of PMAAN by 0·1 N HCl standard acid. The equivalent point of 0·25 g PMAAN is determined to be 0·268 mmol of HCl at pH 4·3.

Journal of the European Ceramic Society **15** (1995) 165–171
1995 Elsevier Science Limited
Printed in Great Britain

The Densification and Microstructural Development of Al_2O_3 with Manganese Oxide Addition

H. Erkalfa, Z. Mısırlı, M. Demirci, Ç. Toy & T. Baykara*

TUBITAK, Marmara Research Center, Materials Research Department, 41470 Gebze, Turkey

(Received 19 April 1994; accepted 5 July 1994)

Abstract

The effect of MnO_2 as an additive on the densification behaviour and microstructural evolution of α-Al_2O_3 has been investigated over a wide sintering regime. A colloidal technique was applied for the mixing of MnO_2 in order to achieve a uniform distribution and homogeneous microstructures. Sintered density, average grain size and microstructural features were elaborated along with the microhardness and mechanical strength measurements. Manganese oxide was found to promote grain growth and an intergranular second phase formation was detected for additions over 0·5 wt% MnO_2. Excessive grain growth and draining of the second phase were observed in the samples with 3 wt% MnO_2 additions sintered above 1500°C.

1 Introduction

Additives in small amounts are deliberately and commonly used in ceramic systems to influence densification processes either by reducing sintering temperature or suppressing/promoting grain growth or enhancing mechanical and physical properties. A variety of oxides such as MgO, TiO_2, SiO_2, MnO_2, Cr_2O_3, Fe_2O_3 are some of the typical additives that have been commonly used in alumina ceramics.[1–3] As examples, it is well known that small additions of MgO to Al_2O_3 reduce the grain growth rate, while Fe_2O_3 and TiO_2 additions were found to enhance sintering along with a grain growth. On the other hand, CaO and SiO_2 additions were found to be detrimental to the densification process, although they yielded finer grain size and distribution in the microstructures.[4–7]

Very few investigations have been conducted on the influence of manganese oxide additions for the initial sintering of alumina. However, examination of the microstructural features and development during the sintering and detailed analysis in the densification regime has not been reported yet. Considering the commercial importance of structural alumina components with manganese oxide addition as thread guides, o-rings, sealants and nozzles, there is a considerable lack of information and data on these compositions.

The influence of manganese oxide addition to alumina, according to the results of those earlier studies based on shrinkage data, was shown to accelerate the sintering rate and grain growth. Similar to the effect of TiO_2, the sintering rate increases to a maximum and then levels off and starts decreasing as the Mn concentration exceeds 0·3 wt%, presumably due to the formation of a second phase. However, in these studies the formation of the second phase particles was not experimentally verified.[8–13]

It was first proposed that the addition of MnO_2 in the proportion of 0·1–1·0 wt% caused a change in diffusion mechanism from a grain boundary process to a bulk diffusion process, which was also observed for the sintering of undoped alumina samples.[9] The rate-controlling mechanism for densification by both bulk and grain boundary diffusion is oxygen ion diffusion. In the case of MnO_2 addition in the sintering of Al_2O_3, Mn occupying a cation site increases the oxygen ion vacancy concentration. A gradient in Mn concentration results in a wide region of enhanced diffusion at the grain boundaries.

Earlier studies on the Al_2O_3–MnO_2 system did not examine the grain morphologies and it was claimed that there was no evidence of grain growth observed in the composition with 0·3 wt% MnO_2 sintered at 1600°C.[11,12] However, MnO_2 is known to greatly enhance grain growth. Discontinuous grain growth and the anisotropy of the grains, especially in the large grains in Al_2O_3 with addition of MnO_2, have been reported.[10] It was

* To whom correspondence should be addressed.

also argued in the earlier reports that manganese oxide forms a spinel and also goes into solid solution in the excess Al_2O_3 which brings about grain growth of alumina.[3]

The purpose of this study was to investigate the microstructural development and densification characteristics in the Al_2O_3–MnO_2 system in an extensive sintering and composition regime using varying amounts of MnO_2 addition ranging between 0, 0·1, 0·3, 0·5, 1·0, 1·5 and 3·0 wt%. This report also discusses the measured microhardness values and strength data of the samples with respect to the microstructural features which developed at different sintering temperatures.

2 Experimental

In ceramic processing, a sufficient mixing of additives and major powders is absolutely essential to obtain high quality, homogeneous mixtures. For this reason, colloidal techniques were employed in this study to prepare homogeneous batches of Al_2O_3—MnO_2 compositions. Alcoa A 16SG alumina powder with an average particle size of 0·37 microns and specific surface area of 9 m^2/g and reagent grade $Mn(CH_3COO)_2.4H_2O$ were used as the starting materials. The acetate of manganese can easily be dissolved in water to its ions to yield a homogeneous dispersion. For the preparation of alumina suspensions with addition of 0·1, 0·3, 0·5, 1·0, 1·5, and 3·0 wt% MnO_2, manganese (2) acetate was dissolved in water and its pH adjusted to 2 with formic acid and HCl. As alumina powder is gradually added into the water–acetate solution, continuous magnetic stirring and ultrasonicating were applied to the suspension to break up the agglomerates. Colloidal suspensions with 0·1, 0·3, 0·5 and 3·0 wt% MnO_2 were oven-dried at 90–110°C for 12 h and mixed regularly to prevent sedimentation. Colloidal suspensions with 0·5, 1·0 and 1·5 wt% MnO_2 additions were freeze-dried in order to obtain soft agglomerates which form due to capillary forces between the particles during the removal of frozen solvent by sublimation. Powders dried using both oven and freeze drying were calcined at 600°C for 1 h in order to obtain insoluble oxides of the additives.

Powder compacts were prepared using the dry, uniaxial pressing technique in a steel die to make pellets nominally 2–2·5 cm in diameter and 0·3 cm in height, applying a pressing stress of 100 MPa. Freeze-dried powders were pressed into a bar shape and these samples were further isostatically cold pressed at 300 MPa. For the purpose of comparison, undoped alumina powders and pellets were also prepared using the same techniques as those applied to MnO_2-added samples. Green densities of the samples were measured dimensionally. For the compositions with 0·1, 0·3 and 0·5 wt% MnO_2 the sintering regime of 1550, 1600 and 1650°C for 1 h is selected for densification, whereas in the case of 1·0 and 1·5 wt% MnO_2 additions, the sintering temperature was selected to be 1550°C for 2 h sintering hold period. For the undoped and doped samples with 3 wt% MnO_2, sintering at temperatures ranging 1250 to 1650°C for 1 h were performed. In all cases the sintering was done under normal furnace atmospheric conditions at a heating rate of 5–10°C/min and cooled at the same rate in the furnace atmosphere.

After sintering, sample densities were determined by the water immersion technique. The microstructure of the samples were studied by scanning electron microscopy (SEM) equipped with an energy dispersive X-ray spectrometer (EDS) attachment on polished and thermally etched surfaces. Vickers microhardness values were measured with a Leitz Mini Load Hardness Tester and a Shimadzu Microhardness Tester (Type M) by applied loads E of 200, 300 and 500 g. The average of 10–20 indentations per specimen was taken. The average mechanical strength of samples was calculated using the failure loads of samples determined from a ball-on-ring test and a tensile testing apparatus (Instron, model 1115) equipped with a three-point loading system.

3 Results and discussion

Compositions, the percentage of the theoretical density attained after sintering and the average grain size values which were determined using standard line intercept technique are tabulated in Table 1. As explained before, the data and micrographs for undoped alumina samples are also presented for the purpose of comparison. The sintered densities of the samples were found to be between 98–99% of the theoretical densities with insignificant differences between the sintering temperatures of 1550–1650°C.

As can be seen in the micrographs given in Fig. 1, undoped alumina can be sintered to its full density at temperatures above 1550°C, during which a relatively homogeneous grain growth occurs and only a few pores are retained between the grains. The average grain size is increased to 3·05 microns after sintering at 1650°C for 1 h. As shown in Fig. 2, 0·1 wt% MnO_2 addition led to inhomogeneous grain growth after sintering at 1600°C for 1 h, resulting in a microstructure with localized regions of finer grains around larger sized grains. Further addition of MnO_2, 0·3–1·5 wt%, caused a drastic

Table 1. The percentage of theoretical density attained and grain size measurements as a function of MnO_2 (wt%) and the sintering conditions

MnO_2 (wt%)	Sintering conditions	Percentage theoretical density attained	Grain size (μm)
0·0 (undoped)	1250°C, 1 h	68·7	0·32
	1350°C, 1 h	77·1	0·33
	1450°C, 1 h	89·9	0·84 ± 0·04
	1550°C, 1 h	97·5	1·48 ± 0·25
	1600°C, 1 h	99·5	
	1650°C, 1 h	100	3·05
0·1	1550°C, 1 h	98·0	
	1600°C, 1 h	99·0	2·74 ± 0·28
	1650°C, 1 h	99·2	
0·3	1550°C, 1 h	98·0	
	1600°C, 1 h	98·5	13·9 ± 3·73
	1650°C, 1 h	99·2	
0·5	1550°C, 1 h	98·2	7·5 ± 2·88
	1600°C, 1 h	98·0	17·2 ± 6·01
	1650°C, 1 h	98·5	25·1 ± 6·42
0·5	1550°C, 2 h	98–99	20·55 ± 4·14
1·0	1550°C, 2 h	98–99	19·29 ± 2·79
1·5	1550°C, 2 h	98–99	17·87 ± 1·69
3·0	1250°C, 1 h	73·0	0·51
	1350°C, 1 h	86·3	0·84 ± 0·03
	1450°C, 1 h	96·2	1·34 ± 0·14
	1550°C, 1 h	98·7	13·84 ± 10·23



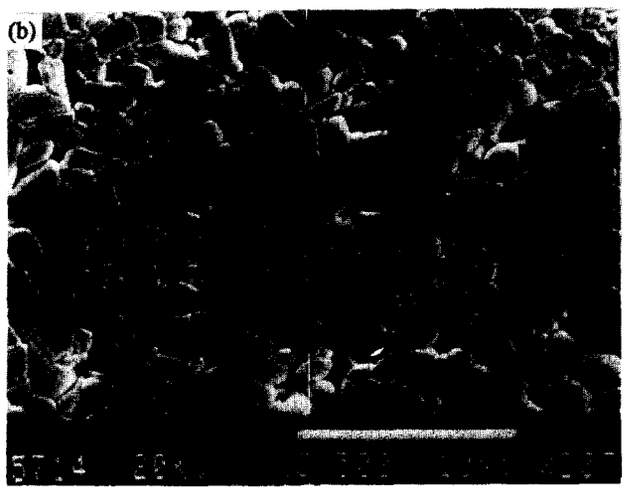


Fig. 1. SEM micrographs of undoped alumina samples after sintering (a) at 1550°C for 1 h and (b) at 1650°C for 2 h.

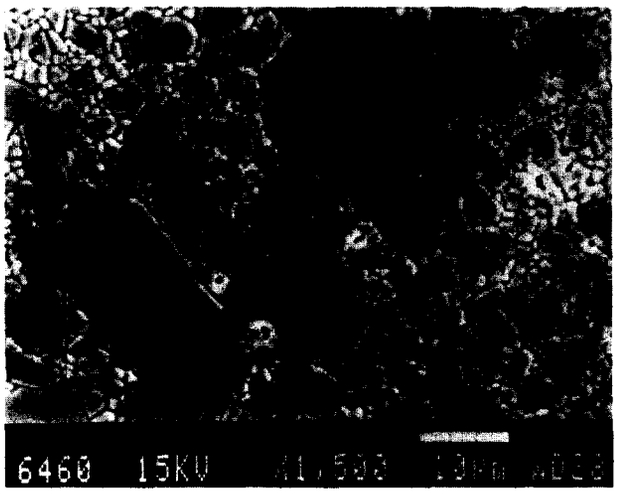


Fig. 2. SEM micrograph of 0·1 wt% manganese-doped alumina after sintering at 1600°C for 1 h.

change in the microstructures after sintering at 1550–1650°C, exhibiting exaggerated grain growth with grains as big as 25–100 microns (Figs. 3–5). A considerable amount of both inter- and intragranular pores is observed in the microstructure. At and above 0·5 wt% MnO_2 additions, less than one micron sized fine pores trapped inside the grains become more evident with sintering hold times of 2 h at 1550°C. In these micrographs (Figs. 4–6), elongated grains of up to 100 microns in length exist to yield irregular grain shapes with faceted morphologies. Furthermore, in these samples, a second phase exists as an intergranular grain boundary phase covering most of the grain boundary area, which is presumably in liquid form at the sintering temperature. It appears that this intergranular phase was distributed along the grains both as a continuous layer and in irregular forms (Fig. 7). According to the phase diagram given in Fig. 8, an eutectic composition is present in the MnO_2-rich side of the binary MnO_2–Al_2O_3 system at 1520°C. This grain boundary phase is

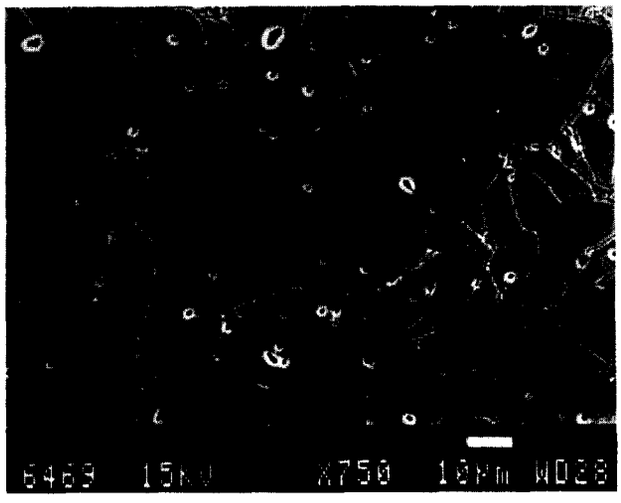


Fig. 3. SEM micrograph of 0·3 wt% manganese-doped alumina after sintering at 1600°C for 1 h.

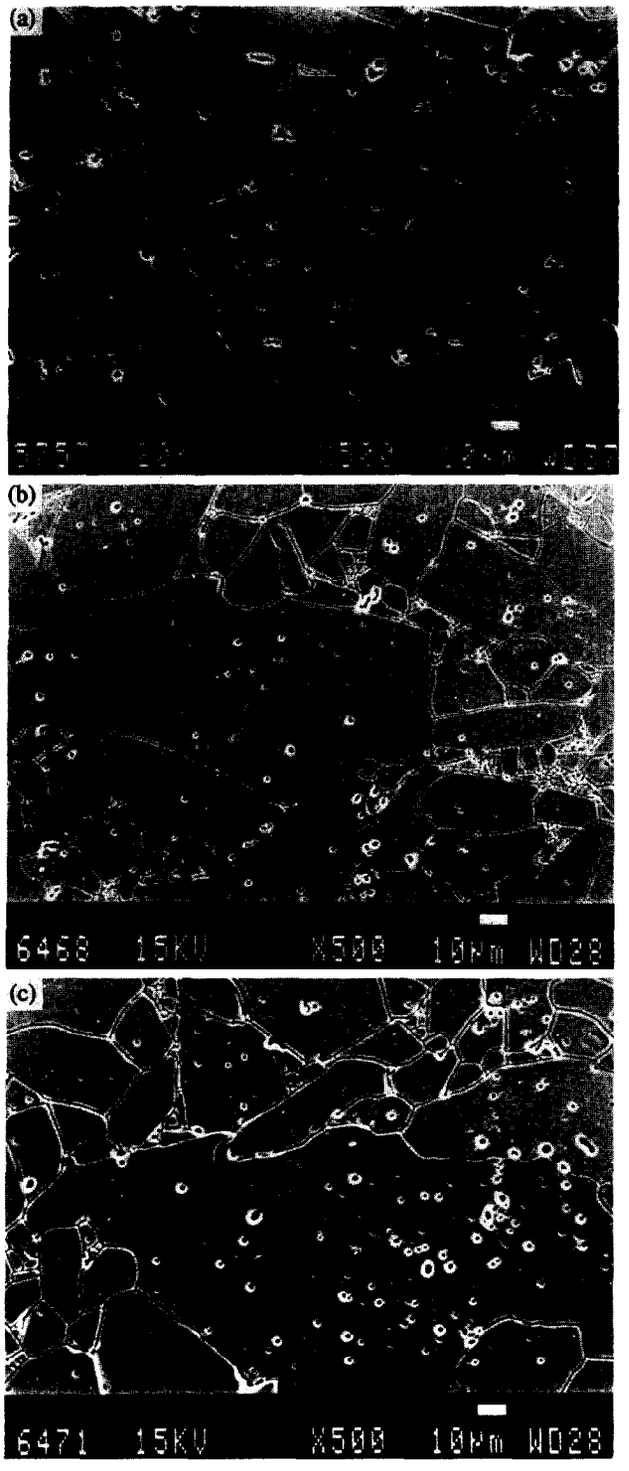


Fig. 4. SEM micrographs of 0·5 wt% manganese-doped alumina after sintering (a) at 1550°C for 2 h, (b) at 1600°C for 1 h and (c) at 1650°C for 1 h.

found to be Mn- and Ca-rich as analysed by the point analysis of energy dispersive X-ray spectroscopy (EDS) (Fig. 9).

In the earlier investigations, the shrinkage data was evaluated to show that bulk and boundary diffusion both are effective for the initial stage of sintering up to 4% shrinkage.[11,12] However, no detailed study was presented for the later stage of sintering. The micrographs shown in Figs. 2–4 for the samples with 0·1–0·5 wt% MnO_2 addition sintered at 1550–1650°C for 1 h do not indicate

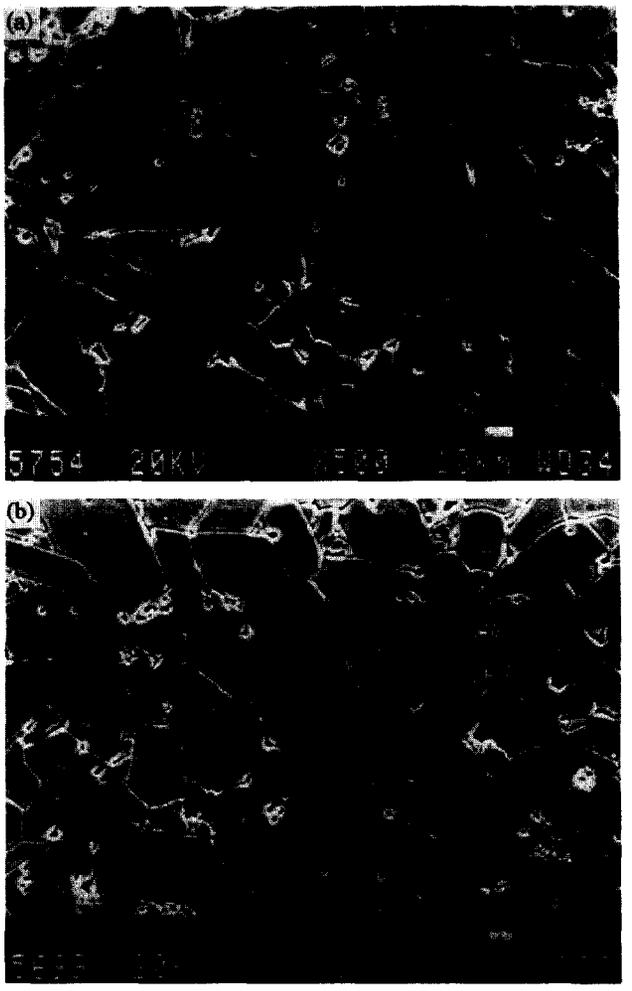


Fig. 5. SEM micrographs of manganese-doped alumina after sintering at 1550°C for 2 h; (a) 1·0 wt% and (b) 1·5 wt% manganese.

the presence of any grain boundary phase formation between the grains. Intergranular grain boundary phase was detected between the grains in those samples with 0·5–1·5 wt% MnO_2 additions sintered at 1550°C for 2 h. Based on these observations, the volume or grain boundary diffusion mechanism acts as the controlling process according to the composition and the sintering conditions during the later stages of densification.

It appears that the densification in compositions with 0·1–0·5 wt% MnO_2 additions sintered at 1550–1650°C for 1 h is enhanced via the volume diffusion process rather than the formation of an intergranular liquid phase. Manganese, like iron, displays variable valency, so that complex series of oxides and hydroxides exist. The ready valency change of manganese leads to many defect structures and non-stoichiometric compounds. Therefore, it may be suggested that different manganese cations with different valency states can substitute the Al cation sites within the crystalline structure, resulting in either vacancy formation or an extra electron. This type of phenomenon was shown to exist during sintering in the case of TiO_2 doping of alumina by activating the volume diffusion rate of

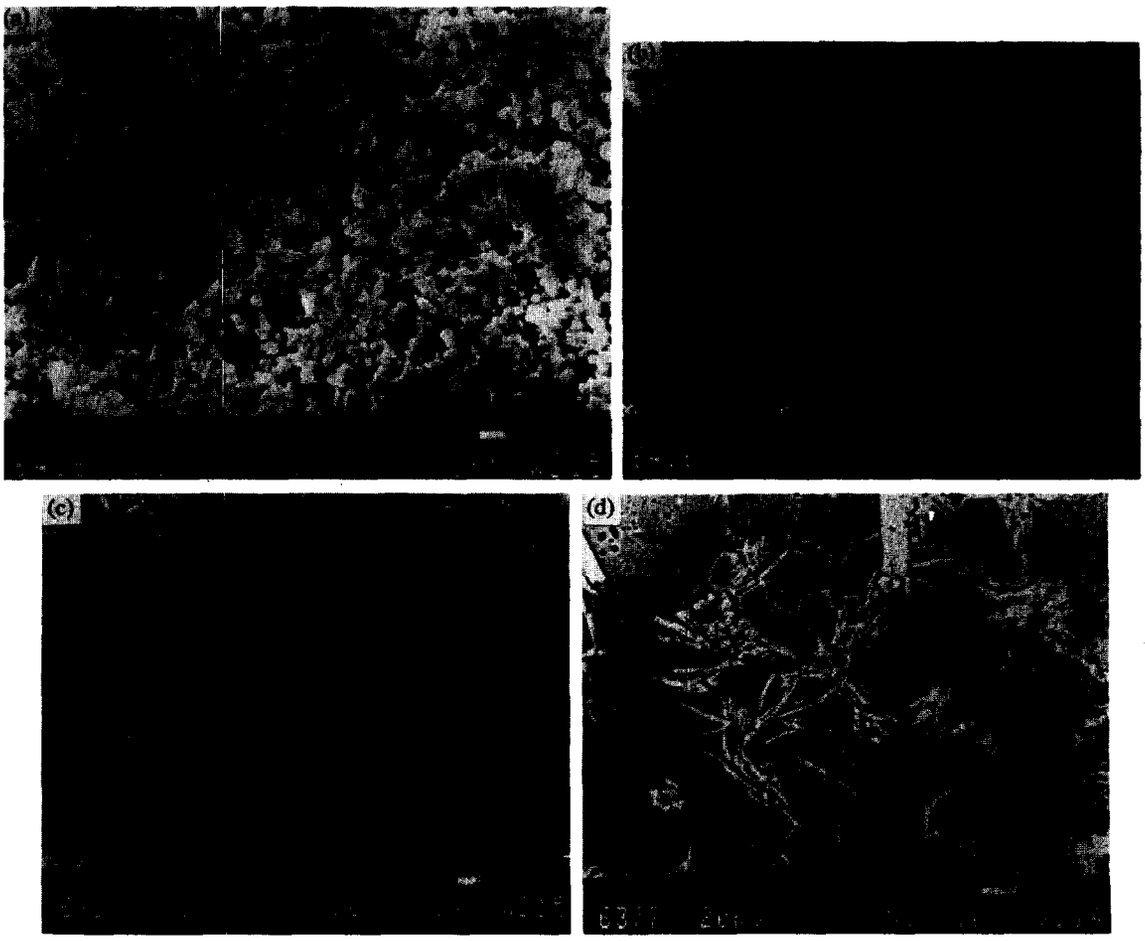


Fig. 6. SEM micrographs of 3·0% manganese-doped alumina after sintering (a) at 1250°C for 1 h, (b) at 1350°C for 1 h, (c) at 1450°C for 1 h, (d) at 1550°C for 1 h.

species[15]. The sintering rate is proportional to the vacancy concentration that forms as Ti^{+3} and Ti^{+4} enters Al_2O_3 substitutionally, and when the charge neutrality is being achieved by the presence of other divalent cations in the powder. In the earlier studies, suggested evaluation of the sintering data indicated that Mn, which substitutes Al in the alumina lattice, can be present in its Mn^{+2} and Mn^{+3} form and thus creates oxygen vacancies to increase diffusion coefficient. An energy dispersive X-ray analysis that was carried out on polished and thermally etched samples in SEM indicated that manganese was well distributed throughout the grains, and no segregation of manganese was detected at the grain boundaries (Fig. 10). Therefore, it may be elaborated that manganese cations substitute the Al sites, resulting in fast diffusion paths within the single grains during the sintering process. As a result of the faster diffusion paths formed, the process of excessive grain growth is enhanced when the amount of manganese oxide addition is between 0·1–0·5 wt% (Figs 2–4).

On the other hand, in the compositions with 1–1·5 wt% MnO_2 addition sintered at 1550°C for 2 h the presence of a secondary intergranular phase both in the form of continuous layer and irregular shapes indicates that the controlling mechanism is due to to grain boundary diffusion process (Fig. 7).

A wide range of sintering regimes, 1250–1550°C for 1 h, was studied on those samples with 3 wt% MnO_2. As shown in Fig. 6, the degree of densification can be observed in the micrographs sintered at 1250; 1350, 1450 and 1550°C for 1 h. In these samples, sintering up to 1450°C indicates a regular densification (73% to 96·2% of the theoretical density) and grain growth (0·51 to 1·34 microns) behaviour, whereas the micrographs for the samples sintered at 1550°C (Fig. 6) exhibits an abnormal and discontinious grain growth (up to 100 microns) with large number of pores trapped inside the grains. Such an abnormal and discontinious grain growth during the late stage of sintering leads to grain boundaries breaking away from the pores, resulting in excessive pore formation inside these newly formed large grains. These pores trapped inside the grains enlarge the diffusion distance to the next grain boundary to inhibit densification. Elimination of such pores is difficult. In these micrographs, the Mn-rich second phase seems to be squeezed out of the grain boundaries in needle-like shapes. Such a draining away from the grain boundaries justified the conclusion that a eutectic liquid phase formed between the grains.

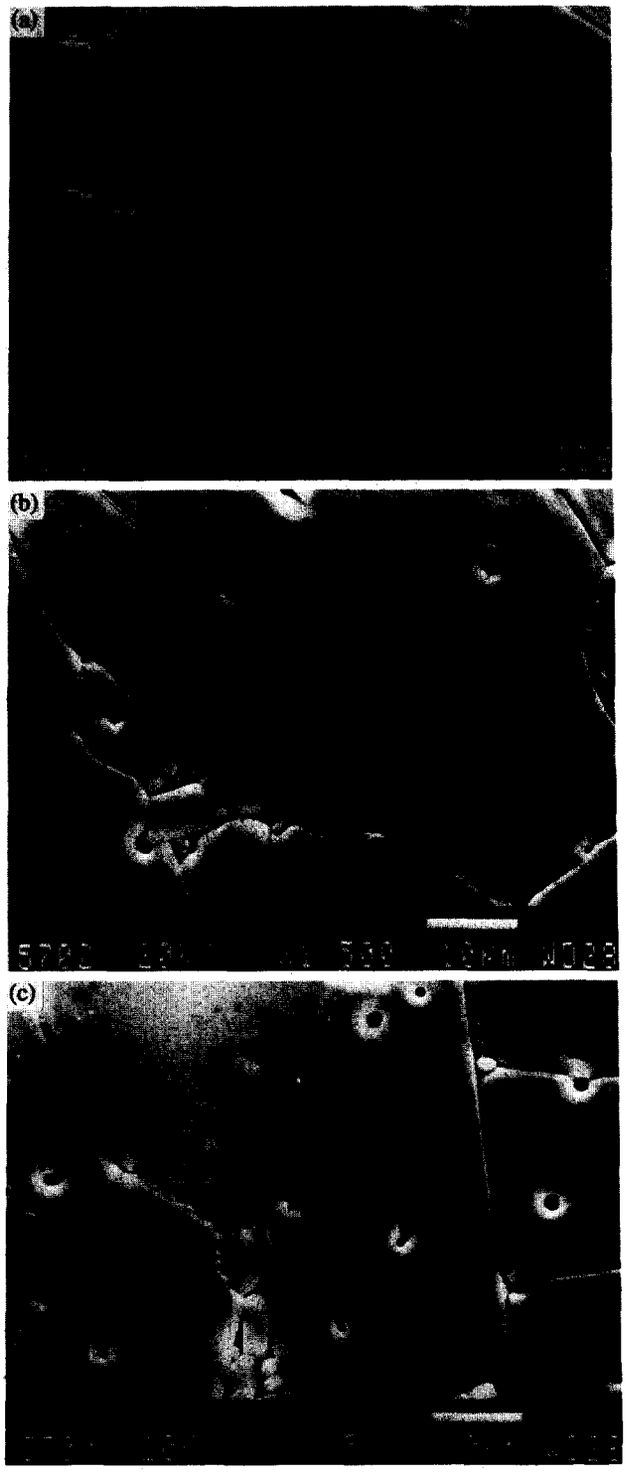


Fig. 7. Interganular second phase formation in the samples sintered at 1550°C for 2 h; (a) 0·5 wt%, (b) 1·0 wt% and (c) 1·5 wt% manganese.

Microhardness measurements and some of the strength data are presented in Table 2 as a function of sintering temperature and composition. It appears that there is an increase in microhardness values with sintering temperature and there is a slight increase with the manganese oxide additions. Microhardness measurements showed considerable variation and scatter for the compositions with 0·5 (sintered at 1550°C for 2 h, 1·0, 1·5 and 3·0 wt% MnO_2 additions, presumably due to formation of the softer second phase. It is difficult

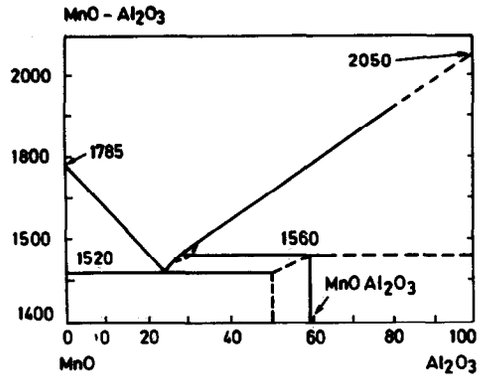


Fig. 8. The phase diagram of $MnO–Al_2O_3$ system.[14]

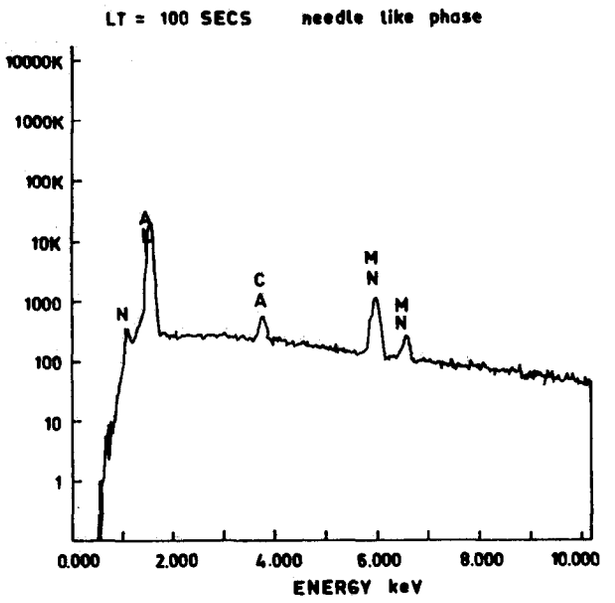


Fig. 9. Energy dispersive X-ray point analysis of the grain boundary phase.

Table 2. The microhardness measurements and strength data as a function of MnO_2 (wt%) and the sintering conditions.

MnO_2 (wt%)	Sintering conditions	Microhardness (GPa)	Strength (MPa)
0·0 (undoped)	1250°C, 1 h	—	—
	1350°C, 1 h	18·23 ± 1·56	—
	1450°C, 1 h	20·59 ± 1·27	—
	1550°C, 1 h	18·98 ± 0·64	344 ± 76·9
	1600°C, 1 h	19·41 ± 0·58	363 ± 53·2
	1650°C, 1 h	20·29 ± 0·85	334 ± 71·7
0·1	1550°C, 1 h	18·94 ± 0·44	299 ± 45·4
	1600°C, 1 h	19·36 ± 0·38	318 ± 37·6
	1650°C, 1 h	20·15 ± 0·63	296 ± 49·4
0·3	1550°C, 1 h	18·33 ± 0·72	239 ± 21·8
	1600°C, 1 h	18·86 ± 0·67	203 ± 16·7
	1650°C, 1 h	19·56 ± 0·55	380 ± 27·7
0·5	1550°C, 1 h	18·30 ± 0·79	200 ± 24
	1600°C, 1 h	18·80 ± 0·35	190 ± 20·3
	1650°C, 1 h	19·53 ± 0·42	353 ± 29·1
0·5	1550°C, 2 h	22·9 ± 1·60	439 ± 27
1·0	1550°C, 2 h	22·9 ± 0·77	453 ± 43
1·5	1550°C, 2 h	23·2 ± 1·56	465 ± 14
3·0	1250°C, 1 h	—	
	1350°C, 1 h	19·2 ± 2·03	
	1450°C, 1 h	21·4 ± 2·10	
	1550°C, 1 h	24·8 ± 2·67	

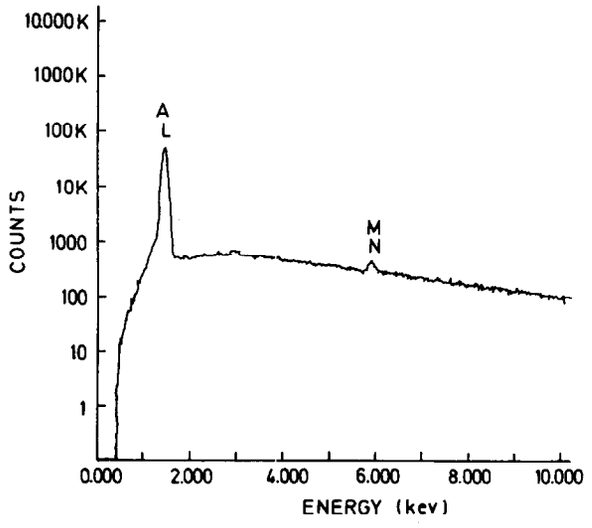


Fig. 10. Energy dispersive X-ray point analysis of the grain interior of 0·5 wt% MnO_2-doped Al_2O_3.

to derive definite information regarding the strength data given in this table; even the data shows higher strength values in the case above 0·5 wt% MnO_2 addition. It seems that further cold isostatic pressing of the samples with 0·5, 1·0 and 1·5 wt% MnO_2 sintered at 1550°C for 2 h led to such an increase in strength data. However, the scatter and variation in this set of data is at considerable level and should be interpreted cautiously.

4 Conclusion

The microstructural development of Al_2O_3 with MnO_2 addition was characterized at different sintering conditions. Grain growth was promoted with manganese oxide additions and in some cases due to prolonged sintering holds, an exaggerated grain growth behaviour was observed. It appears that the densification is controlled by a grain boundary diffusion mechanism in those samples with MnO_2 additions higher than 0·5 wt%. On the other hand, the volume diffusion mechanism is suggested to be the controlling process in the case of 0·1–0·5 wt% MnO_2 addition. Microhardness values and strength data do not reveal a definite trend; however, an increase in the microhardness values with temperature and the percentage MnO_2 were evident. Strength data also shows an increase with MnO_2 addition.

Acknowledgements

The authors acknowledge the support of NATO-SFS Programme for this study. The authors also thank Prof. Dr I. A. Aksay and F. Dogan of Princeton University for their contribution during the course of this investigation.

References

1. Rossi, G. & Burke, J. E., Influence of additives on the microstructure of sintered Al_2O_3. *J. Amer. Ceram Soc.*, **56** 1973 543–9.
2. Harmer, R. D., Roberts, E. W. & Brook, R. J., Rapid sintering of pure and doped α-Al_2O_3. *Trans. Brit. Ceram. Soc.*, **78** (1979) 22–5.
3. Smothers, W. J. & Reynolds, H. J., Sintering and grain growth of alumina. *J. Amer. Ceram. Soc.*, **37** (1954) 588–95.
4. Roy, S. K. & Coble, R. L., Solubilities of magnesia, titania, and magnesium titanate in aluminium oxide. *J Amer. Ceram. Soc.*, **51** (1968) 1–6.
5. Dorre, E. & Hubner, H., *Alumina: Processing, Properties, and Applications*. Springer-Verlag, 1984, p. 49.
6. Bagley, R. D., Cutler, I. B. & Johnson, D. L., Effect of TiO_2 on initial sintering of Al_2O_3. *J. Amer. Ceram. Soc.*, **53** (1970) 136–41.
7. Gitzen, W. H., *Alumina as a Ceramic Material*. The American Ceramic Society, OH, 1970, pp. 131–4.
8. Rabe, T., Nobst, P. & Moser, B., Phasenbestand und Sinterverhalten von Mn–Ti-dotierter Al_2O_3-Keramik in Abhängigkeit von der Sinteratmosphare. *Silikattechnik*, **34** (1983) 49–52.
9. Cahoon, H. P. & Christensen, C. J., Sintering and grain growth of alpha-alumina. *J. Amer. Ceram. Soc.*, **39** (1956) 337–44.
10. Cutler, I. B., Nucleation and nuclei growth in sintered alumina. In *Kinetics of High Temperature Processes.*, ed. W. D. Kingery. MIT Press, Cambridge, MA, 1959, pp. 120–7.
11. Keski, J. R. & Cutler, I. B., Effect of manganese oxide on sintering of alumina. *J. Amer. Ceram. Soc.*, **37** (1954) 653–4.
12. Keski, J. R. & Cutler, I. B., Initial sintering of Mn_xO–Al_2O_3. *J. Amer. Ceram. Soc.*, **51** (1968) 440–4.
13. Kostic, E., Kiss, S. J. & Boskovic, S., Sintering and microstructure development in the Al_2O_3—MnO—TiO_2 system. *Pow. Met. Int.*, **22** (1990) 29–30.
14. Leven, E. M., Robbins, C. R., McMurdie, H. F. & Reser, M. K., *Phase Diagrams for Ceramics* (ed.), 4th printing. The American Ceramic Society, 1979, p. 114.
15. Kingery, W. D., Bowen, H. K. & Uhlmann, D. R., *Introduction to Ceramics*. 2nd edn, John Wiley & Sons, 1976, p. 479.

Journal of the European Ceramic Society **15** (1995) 173–184
© 1995 Elsevier Science Limited
Printed in Great Britain. All rights reserved
0955-2219/95/$9.50

Reaction Process and Densification Process of Mixed α'/β'-Sialon Ceramics

Koji Watari, Masaki Yasuoka, Maria Cecilia Valecillos & Shuzo Kanzaki

Department of Ceramics Science, National Industrial Research Institute of Nagoya, Hirate-cho, Kita-ku, Nagoya, 462 Japan

(Received 3 May 1994; revised version received 24 June 1994; accepted 5 July 1994)

Abstract

The sintering behavior of mixed α'/β'-sialon ceramics, fabricated from α-Si_3N_4, AlN and Ln_2O_3 (Y_2O_3, Er_2O_3 and Yb_2O_3), was examined by high-temperature dilatometry, and the densification process was discussed through the consideration of chemical reactions to form α'- and β'-sialon and kinetical analysis of shrinkage. The formation of α'-sialon and melilite caused temporary retardation of the densification rate, while during the formation of β'-sialon the densification proceeded remarkably. The densification accompanied by precipitation of β'-sialon is ascribed to dissolution of residual α-Si_3N_4, α'-sialon with low solid solubility and melilite into a liquid, which may result in an increase of liquid volume and in a decrease of liquid viscosity. These phenomena are considered to induce the solution–precipitation process, particle disintegration process and cooperative flow process of the particle–liquid mixture, yielding to rapid shrinkage. The densification at the initial and middle stages and the reactions from α'-sialon and α-Si_3N_4 to β'-sialon accelerated in the order of Y_2O_3 > Er_2O_3 > Yb_2O_3 addition, because the liquidus temperature and viscosity of liquid formed decreased in the order of Y_2O_3 < Er_2O_3 < Yb_2O_3 addition.

1 Introduction

Two significant properties of silicon nitride (Si_3N_4) ceramics are mechanical strength and fracture toughness. Si_3N_4 ceramics with prismatic grains show high flexural strength at room temperature, but this strength degrades at temperatures higher than 1300°C due to the presence of an intergranular glassy phase containing impurities such as metals and halogens. As the viscosity of the glassy phase softens at temperatures higher than 1000°C, grain-boundary sliding occurs, accompanied by nucleation and growth of cavities in the intergranular glassy phase.[1] It is then important to reduce the amount of impurities concentrated at the grain boundaries, and to control the character and amount of grain-boundary phase in Si_3N_4 ceramics, in order to improve their high-temperature strength.

On the other hand, fracture toughness is strongly influenced by aspect ratio and volume fraction of the grown grains in the final products.[2,3] It has been reported that Si_3N_4 ceramics with microstructures consisting of elongated rod-like grains in the small grain matrix have fracture toughness as high as 8–11 $MPam^{0.5}$.[4] Such materials with duplex microstructures are called 'in-situ composites' or 'self-reinforced materials'. It is, therefore, desirable for the obtention of the Si_3N_4-based materials that both the reduction of glassy phase content at grain boundaries and the control of Si_3N_4 grain morphology are made compatible.

Si_3N_4 ceramics occur in two structural modifications, α and β. The solid solution in β-Si_3N_4, which is called β'-sialon, is formed by simultaneous equivalent substitution of aluminum and oxygen for silicon and nitrogen, and the reaction is commonly described by the following equations:

$$(4 - z)Si_3N_4 + 2zAlN + zSiO_2 \rightarrow 2Si_{6-z}Al_zO_zN_{8-z} \quad (1)$$

$$(6 - z)Si_3N_4 + zAlN + zAl_2O_3 \rightarrow 3Si_{6-z}Al_zO_zN_{8-z} \quad (2)$$

In the equations, z takes a value between 0 and 4·2.[5,6]

α'-sialon, which is the solid solution of α-phase structure, is obtained by a substitution of similar elements as for β'-sialon, with some metal cations accommodated in the two large interstices of the unit cell, thus giving a general formula of the type $Mx(Si,Al)_{12}(O,N)_{16}$, where M is Li, Mg, Ca or

lanthanide metals except La and Ce. When x is $0{\cdot}3 < x < 2{\cdot}0$, single-phase α'-sialons are fabricated. Reaction in the formation of single-phase α'-sialon is as follows:[7,8]

$$(4 - 1{\cdot}5x)Si_3N_4 + 0{\cdot}5x(Y_2O_3 + 9AlN) \rightarrow Yx Si_{12-4{\cdot}5x}Al_{4{\cdot}5x}O_{1{\cdot}5x}N_{16-1{\cdot}5x} \quad (3)$$

With x values less than 0·3, mixtures of α'-sialon and β'-sialon are obtained.[9]

Densification of these sialon ceramics proceeds in a reaction-sintering process involving the formation of a transient liquid phase, namely, during the middle and final stages of sintering the ingredients of the liquid are incorporated into the α and β structures.[9–11] In consequence, sialon ceramics have been expected to possess only a small amount of intergranular glassy phase and in recent years these materials have been reported to maintain the room-temperature strength at temperatures as high as 1300°C.[12] It has been, however, reported by several investigators that single-phase sialon ceramics show lower mechanical strength and lower fracture toughness than β-Si_3N_4 containing Y_2O_3 and Al_2O_3 additives. The reason is interpreted as that sialons consist of grains with low aspect ratio,[13] and furthermore they have weak pullout and absence of crack-branching effects due to the strong bonding between interfaces of grains.[14,15]

Recently, mixed α'/β'-sialon ceramics have received a great deal of attention, since the microstructure of these materials comprises prismatic β-grains and roundish fine α-grains, and presents a small amount of grain boundary phase.[16,17] It has also been demonstrated that they show higher mechanical strength at elevated temperatures and higher fracture toughness[16] as well as better creep properties, compared to the β-Si_3N_4 ceramics with oxide addition.[18] Furthermore, in the case of sintering of mixed α'/β'-sialon ceramics, their microstructure and their mechanical as well as thermal properties can be controlled by the phase composition, and it is possible to alter widely the quantity and type of elements that can be accommodated in a Si_3N_4 structure.[15,19] However, the densification mechanism, which links directly to control of the microstructural development and phase composition, has not been understood yet.

In this work, an attempt is made to investigate the reaction process in the formation of α'- and β'-sialons during sintering of mixed α'/β'-sialon ceramics with AlN and lanthanide oxides (Ln_2O_3) such as Y_2O_3, Er_2O_3 and Yb_2O_3. The shrinkage behavior of mixed α'/β'-sialon ceramics is studied by high-temperature dilatometry, and the densification process is also discussed in combination with chemical reactions to form sialons.

2 Experimental procedure

It is well known that powder characteristics strongly influence the sintering process of sialon as well as of Si_3N_4 ceramics. Especially, in the case of sintering of mixed α'/β'-sialon ceramics, accompanied by complicated reaction pathways, densification behavior and resultant amount of α'-sialon, as well as reaction sequence, are changed due to powder characteristics.[20] In a preliminary work, the authors have evaluated the influence of Si_3N_4 powder characteristics on the sintering behavior of mixed α'/β,-sialon ceramics, and on the sinterability and formation of α'- and β'-sialons. The results pertaining to sintering behavior are as indicated in the Appendix, and the raw powder A was used in this work. The raw powder A (Denki Kagaku Kogyo, K K, Japan) used in the present work had an oxygen content of 1·3wt%, total metallic impurities content of 350 ppm, fluorine content of 520 ppm, and a specific surface area of 11·3 $m^2\ g^{-1}$. This powder was composed of 94% α- and 6% β-Si_3N_4.

The AlN (Tokuyama Soda Co. Ltd, Japan), Y_2O_3, Er_2O_3 and Yb_2O_3 (Hokko Chemicals Industry Co. Ltd, Japan) powders were also employed as the starting materials to produce the mixed α'/β'-sialon. The starting AlN powder had an oxygen content of 1·05 wt% and a specific surface area of 3·2 $m^2\ g^{-1}$. Nominal composition of powder mixtures was 83·10 mol% for Si_3N_4, 1·69 mol% for AlN and 15·21 mol% for Ln_2O_3, and the atomic proportion in the overall composition is represented by the following formula: $Ln_{0{\cdot}15}Si_{11{\cdot}325}Al_{0{\cdot}675}O_{0{\cdot}225}N_{15{\cdot}775}$.

These powders were vibrationally mixed in toluene with deflocculant for 6 h using a Si_3N_4 pot and balls. After drying at 800°C for 1 h in nitrogen gas with 10% H_2 to remove the deflocculant, rectangular bars with dimensions of 10 × 10 × 45 mm and discs with 14 mm diameter × 8 mm height were made from the mixed powders using a homemade die, followed by cold isostatic pressing (CIP) at 490MPa for 60s. The green density of all the specimens was 1950 ± 20 kgm^{-3}.

In order to investigate the sintering phenomena, thermal shrinkage of bars was measured at temperatures from 1000 to 1850°C at a heating rate of 10°C min^{-1} under a N_2 gas pressure of 1 MPa using a high-temperature dilatometer (Rigaku Denki, HPHT-TMA, Japan).[21] From the results of preliminary work, a large amount of shrinkage was observed after thermal shrinkage measurement at 1850°C, when operated at a heating rate of 10°C min^{-1}. Therefore, the heating rate of 10°C min^{-1} was selected. Isothermal shrinkage measurements at 1500, 1550 and 1600°C were performed

to investigate the kinetic parameter on densification and to clarify the densification process. The heating rate for isothermal shrinkage measurements was 10°C min^{-1}. The reason for setting such a slow heating rate will be explained later. Detection errors of shrinkage and shrinkage rate were less than $1{\cdot}8 \times 10^{-2}$% and $3{\cdot}2 \times 10^{-3}$ %min^{-1}, respectively.

Simultaneously, specimens were prepared by firing at various temperatures followed by quenching, to observe the change in bulk density and microstructural development as well as the reaction sequence during sintering. The discs were embedded in a mixture of Si_3N_4/AlN/Ln_2O_3/BN in a graphite crucible, and fired in a graphite furnace at different temperatures starting from 1300 to 1850°C for 15 min and 4 h at a heating rate of 10°C min^{-1} under a N_2 gas pressure of 1 MPa, followed by quenching at a cooling rate of above 100°C min^{-1} until near 1000°C.

Density measurements were performed by the Archimedes method in distilled water. Relative density was obtained by comparing measured density to theoretical density. The theoretical density of mixed α'/β'-sialon was calculated from the amount and density of Si_3N_4, AlN and Ln_2O_3, and was estimated as 3221 kgm^{-3} for Y_2O_3 addition, 3288 kgm^{-3} for Er_2O_3 addition, and 3296 kgm^{-3} for Yb_2O_3 addition. Carbon and gold were evaporated onto the fractured surfaces and onto the polished surfaces, and scanning electron microscopy (SEM, JEOL, T-330AS, Japan) observation was conducted to examine the microstructure. Before the evaporation of carbon and gold, the surfaces of interest were chemically etched by immersing the specimens into molten NaOH and KOH in a silver crucible at 200°C.

The quenched samples were crushed in a tungsten carbide jar, and passed through a 200 mesh sieve. X-ray diffractometry (XRD, Rigaku Denki, RAD-B, Japan) measurements of the crushed powders were carried out using CuK_α radiation at 40kV and 100 mA to identify crystalline phase and to obtain phase composition. The α-Si_3N_4, α'-sialon, and β-Si_3N_4/β'-sialon contents in the sintered bodies were determined as follows: after XRD measurements, the X-ray peak areas of α-Si_3N_4 and α'-sialon for <102> and <201> planes, and of β-Si_3N_4/β'-sialon for <101> and <201> planes were calculated using the Lorents function, and the relative amount of these phases was obtained by comparing their peak areas. Lattice parameters were measured with Si as internal standard, and the solid solubility of AIN and oxide into a Si_3N_4 structure was determined by referring to the published data.[22,23]

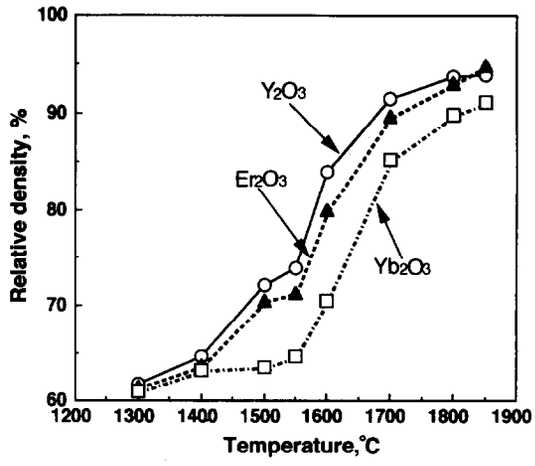


Fig. 1. Relative density of disks quenched at different temperatures for 15 min. The theoretical density of mixed α'/β'-sialon was calculated from the amount and density of Si_3N_4, AlN and Ln_2O_3, and was estimated as 3221 kgm^{-3} for Y_2O_3 addition, 3288 kgm^{-3} for Er_2O_3 addition and 3296 kgm^{-3} for Yb_2O_3 addition. After sintering at 1850°C for 4 h, bulk density of all the specimens reached theoretical values.

3 Results

3.1 Density and shrinkage

The relative densities of the discs quenched from different temperatures in the range of 1300 to 1850°C are shown in Fig. 1. For Y_2O_3 and Er_2O_3 additions, relative density increases slowly at temperatures between 1300 and 1550°C, and increases rapidly at temperatures between 1550 and 1800°C. On the other hand, the relative density of specimens obtained by Yb_2O_3 addition remains almost constant at temperatures from 1300 to 1550°C, whereas a rapid increase in the relative density was observed at temperatures higher than 1550°C. After sintering at 1850°C for 4 h, bulk density of all the specimens reached the theoretical values.

Figure 2 shows the shrinkage of rectangular bars. The shrinkage of all the compacts starts

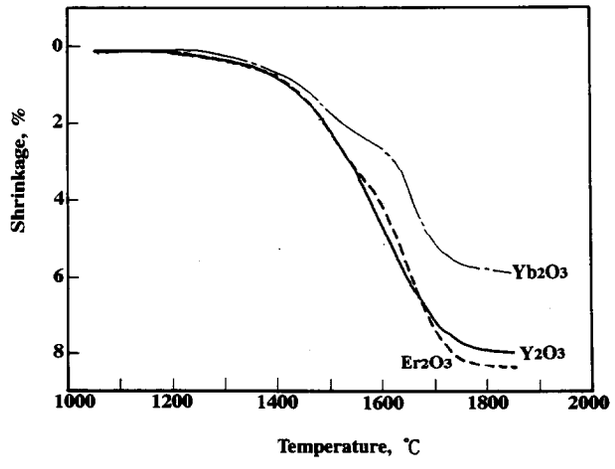


Fig. 2. Temperature dependence of shrinkage of Ln_2O_3-doped α'/β'-sialon ceramics.

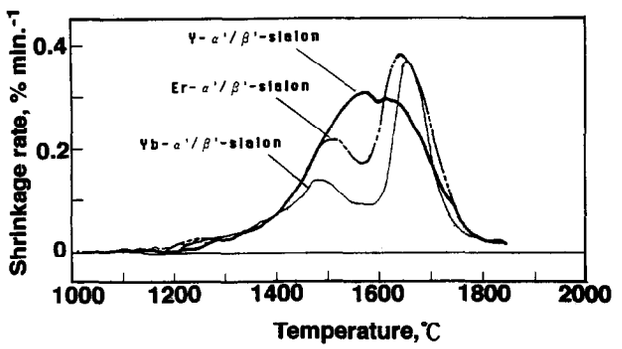


Fig. 3. Temperature dependence of shrinkage rate of Ln_2O_3-doped α'/β'-sialon.

around 1200°C, and increases with increasing the sintering temperature. The type of lanthanide oxides produces differential sintering behavior, which translates into the changes of shrinkage rate observed in the curves of Fig. 3. In the case of Y_2O_3 addition, the shrinkage rate increases gradually at temperatures higher than 1350°C, and reaches the maximum around 1570°C. Subsequently, the shrinkage rate shows a slight decrease and again an increase at temperatures between 1570 and 1620°C, decreasing rapidly at temperatures higher than 1620°C. For Er_2O_3 and Yb_2O_3 additions, the shrinkage rate shows an increase up to 1510°C for Er_2O_3 addition, and 1480°C for Yb_2O_3 addition, decreasing thereafter until reaching the vicinity of 1580°C. At temperatures over 1580°C, the shrinkage rate presents a rapid increase, showing a maximum at 1630°C for Er_2O_3 addition, and at 1650°C for Yb_2O_3 addition, decreasing thereafter with increasing sintering temperature.

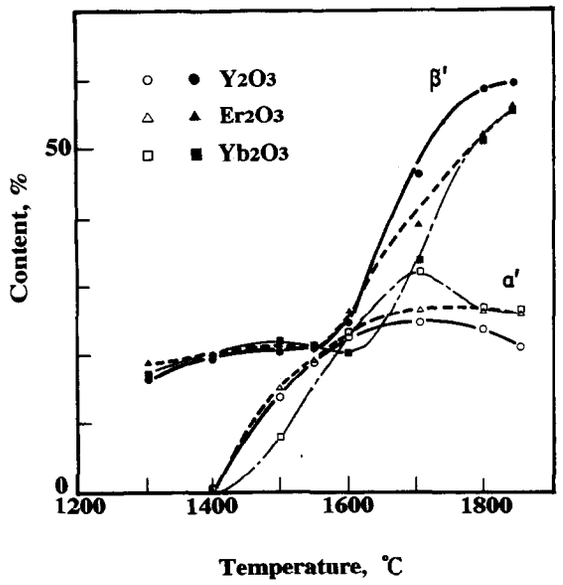


Fig. 4. Phase change during the formation of α'/β'-sialon ceramics at temperatures between 1300 and 1850°C. *J*-phase ($Ln_4Si_2O_7N_2$) and melilite ($Si_3N_4{\cdot}Ln_2O_3$) were identified as the grain boundary phase in specimens sintered at 1300–1400°C and at 1500–1700°C, respectively.

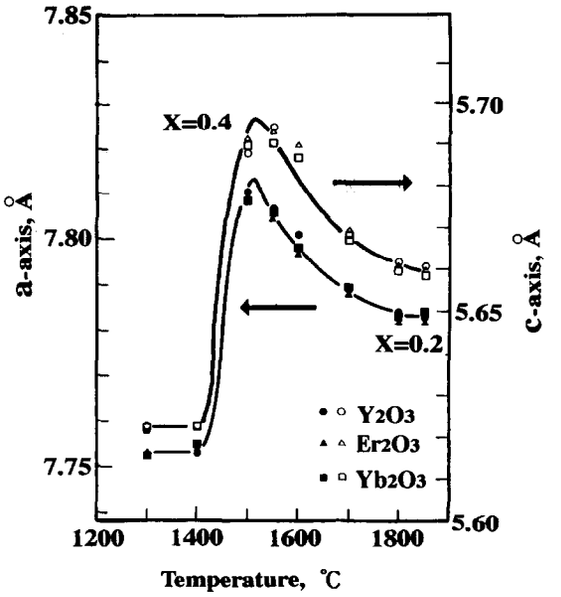


Fig. 5. Change of lattice parameters of α'-sialon. From the relationships between the x value in $Yx(Si,Al)_{12}(O,N)_{16}$ and lattice parameters,[21] the x value was 0·4 for the specimen heated at 1500°C and 0·25 for the specimen heated at 1850°C.

3.2 Phase change

Figure 4 reveals the phase change during the formation of α'- and β'-sialons at temperatures between 1300 and 1850°C. Also the variation with temperature of the lattice parameters of α'- and β'-sialons are shown in Figs 5 and 6, respectively.

α-sialon with large unit cell dimensions is initially formed at temperatures between 1400 and 1500°C, and its content increases with raising the sintering temperatures, but decreases above 1700°C . The amount of α'-sialon varies with the

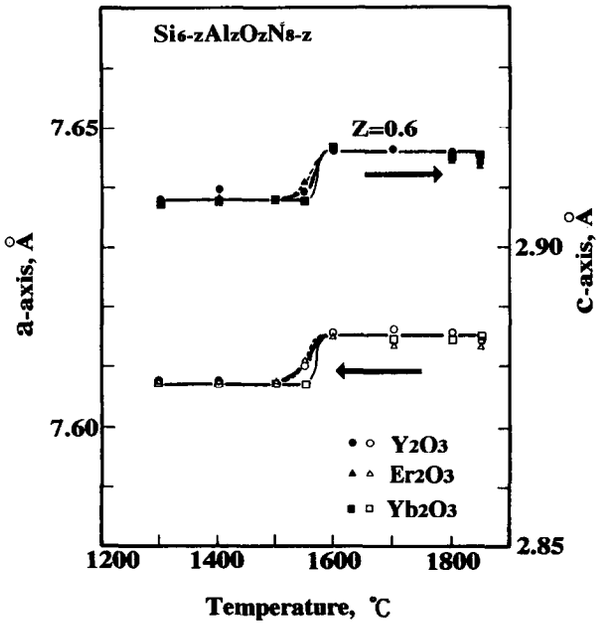


Fig. 6. Change of lattice parameters of β'-sialon. Referring to the relationships between the z value and lattice parameters,[22] the value of z in the formula, $Si_{6-z}Al_zO_zN_{8z}$, varies from 0 to 0·6 at temperatures from 1500 to 1600°C.

type of oxides. A rapid increase in the amount of α'-sialon is observed at temperatures between 1400 and 1600°C for Y_2O_3 and Er_2O_3 additions, and at temperatures between 1500 and 1700°C for Yb_2O_3 addition. Lattice parameters of α'-sialon attain a maximum at 1530°C, but thereafter decrease as the temperature is raised. The influence of the type of lanthanide oxide on the lattice parameters has not been identified in the present work. From the relationships between the x value in $Yx(Si, Al)_{12}$ $(O, N)_{16}$ and the lattice parameters,[22] the x value is 0·4 for the specimen obtained at 1500°C and 0·25 for the one at 1850°C.

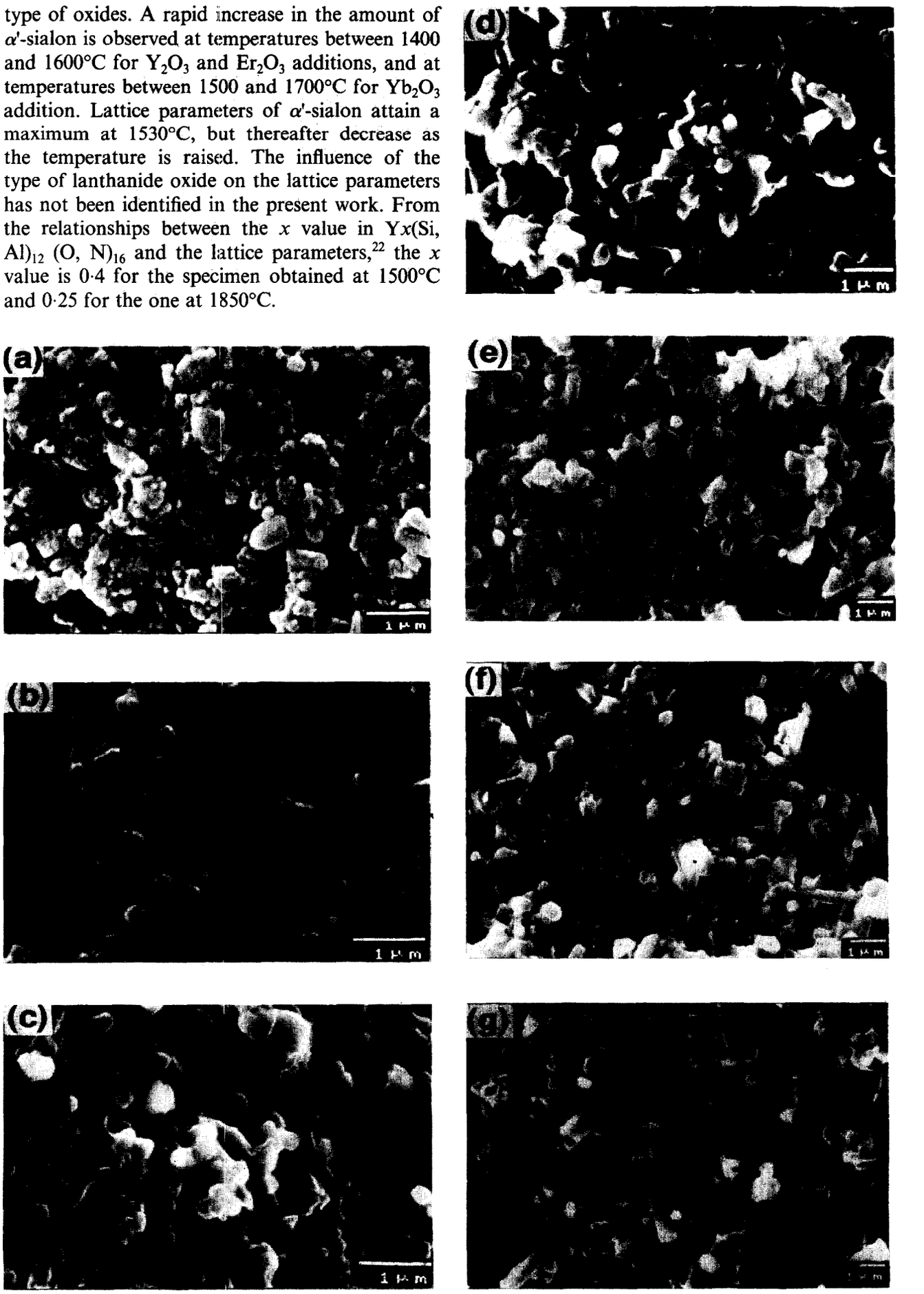


Fig. 7. Fractured surface and polished surface of a specimen with Er_2O_3 addition (a) CIPed, and quenched at (b) 1400, (c) 1500, (d) 1600, (e) 1700, (f) 1800 and (g) 1850°C for 15 min and (h) at 1850°C for 4 h. The polished surface of the specimen quenched at 1850°C for 4 h was chemically etched with molten NaOH and KOH at 200°C for 15 min.

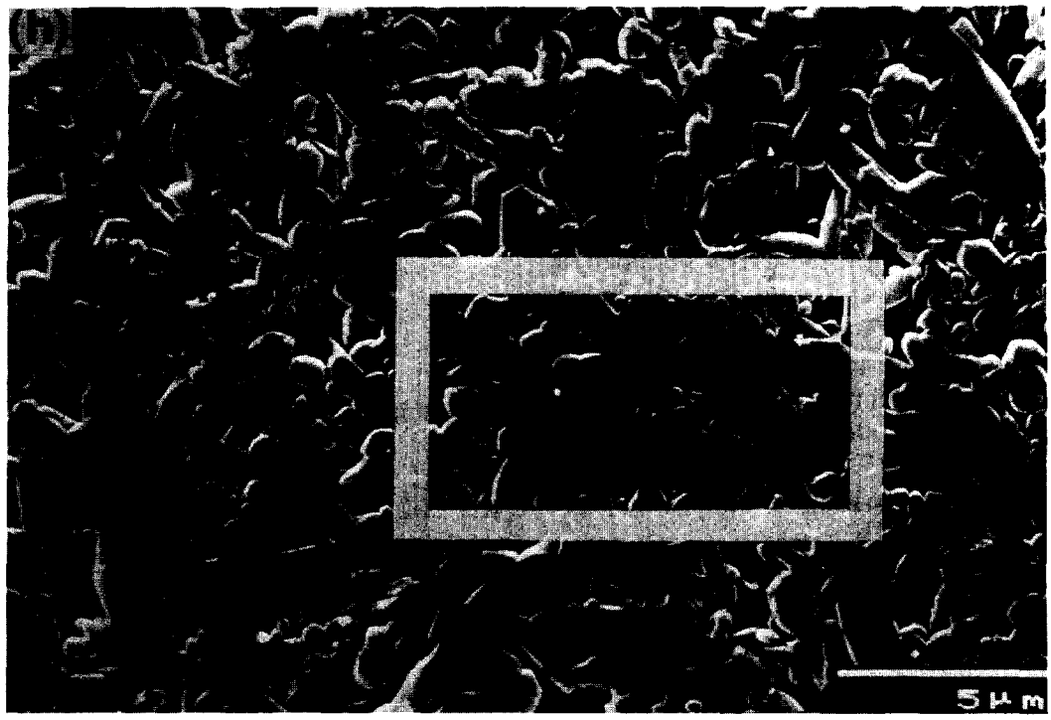


Fig. 7.—*Contd.*

A remarkable increase in the amount of β'-sialon is observed at temperatures ranging from 1600 to 1700°C for Y_2O_3 and Er_2O_3 additions, and at temperatures ranging from 1600 to 1800°C for Yb_2O_3 addition. A significant change in the lattice parameters is present at temperatures between 1500 and 1600°C, but the influence of the oxide type on lattice parameters is not detected. According to published data,[23] the value of z in the formula, $Si_{6-z}Al_zO_zN_{8-z}$, was 0·6 for the specimen sintered at temperatures higher than 1600°C.

Identification of X-ray diffraction peaks indicates, besides the formation of α'- and β'-sialons, J-phase ($Ln_4Si_2O_7N_2$) and melilite (Si_3N_4 . Ln_2O_3) in specimens quenched at temperatures between 1300 and 1400°C, and at temperatures between 1500 and 1700°C, respectively. Disappearance of X-ray diffraction peaks of raw AlN and Ln_2O_3 was recognized above 1500 and 1300°C, respectively.

3.3 Microstructure

Fractured surface of specimens with Er_2O_3 addition CIPed and sintered at temperatures between 1400 and 1850°C are shown in Fig. 7. The microstructure of CIPed specimens consists of grains with irregular shape and wide particle distribution (Fig. 7(a)). At temperatures from 1400 to 1600°C, the size and shape of particles are not well defined (Fig. 7 (b)–(d)), because the particles are covered with a material like a glassy phase. Elongated angular grains are found in specimens quenched from 1700°C (Fig. 7 (e) and (f)), and subsequent grain growth and interlocking are observed at 1850°C (Fig. 7 (g)). The microstructure of the specimens sintered at 1850°C for 4 h consists of rod-like grains with aspect ratio of around 5 : 1 and a maximum of about 8 : 1 in a small equiaxed grains matrix (Fig. 7(h)).

Figure 8 shows the fractured surface of specimens with Y_2O_3 and Yb_2O_3 addition obtained by quenching from 1400°C. In the case of Yb_2O_3 addition, roundish grains are found, but in the case of Y_2O_3 addition, identification of size and shape of particles in the fractured surface is difficult.

Table 1. Possible reactions to form the α'- and β'-sialons[a]

α'-Sialon

$SiO_2 + Al_2O_3 + Ln_2O_3 + Si_3N_4/AlN \rightarrow$ Nitrogen glass + J-Phase ($Ln_4Si_2O_7N_2$) (a)

J-Phase + Nitrogen glass + Si_3N_4/AlN $\rightarrow$ α'-Sialon^H + Melilite(Si_3N_4 . Ln_2O_3) + Nitrogen glass (b)

$Si_3N_4 + 9AlN$. $Ln_2O_3 \rightarrow \alpha'$-Sialon^H (c)

$Si_3N_4 + \alpha'$-Sialon$^H \rightarrow \alpha'$-Sialon^L (d)

β'-Sialon

Si_3N_4 + Melilite + Nitrogen glass $\rightarrow$ β'-Sialon + Nitrogen glass (e)

$Si_3N_4 + \alpha'$-Sialon^L + Nitrogen glass $\rightarrow$ β'-Sialon + Nitrogen glass (f)

[a] H and L indicate the α'-sialons with high and low solid solubility, respectively.

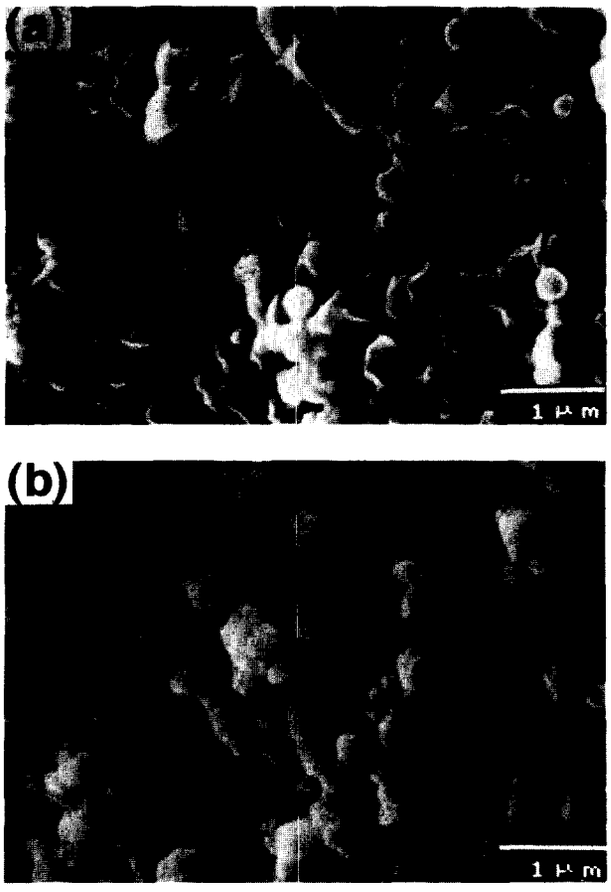


Fig. 8. SEM micrographs of fractured surface for specimens with (a) Y_2O_3 and (b) Yb_2O_3 addition quenched at 1400°C.

4 Discussion

4.1 Reaction process to form α'- and β'-sialons

From the results of the reaction sequence, change in phase composition and lattice parameters, possible reactions in the formation of α'- and β'-sialons are summarized in Table 1.

At the initial stage of liquid-phase sintering of sialon and Si_3N_4 ceramics, nitrides and oxide additives as well as impurities (oxides, metals and halogens) react to form a liquid, and subsequently, nitrogen glass and a partial crystalline phase appear at the grain boundaries. The phenomena are described by reaction (a). Here, the silica and alumina are the oxide impurities on the surface of raw Si_3N_4 and AlN particles.

α'-sialon is compatible with melilite. Furthermore, a α'-sialon with high solid solubility was observed at the initial stage. The reaction in precipitation of α'-sialon from a liquid are expressed as eqn (b). In the case of formation of α'-sialon with high solid solubility, reaction of α-Si_3N_4 with AlN and Ln_2O_3 should be considered, and eqn (c) is given. With respect to formation of α'-sialon at the initial stage, heterogeneous and homogeneous nucleation should be noted. The nucleation sites of α'-sialon formed at the initial stage were investigated by mean of TEM observation by Chatfield *et al.*[23] and Chen & Hwang.[24] Chatfield *et al.* reported that a core of unreacted α-Si_3N_4 raw material frequently remained in the α'-sialon particles, indicating that the unreacted α-Si_3N_4 raw material acts as nuclei for α'-sialon. Such a heterogeneous nucleation was also observed in sintering of β'-sialon.[23] On the other hand, the evidence of homogeneous nucleation of α'-sialon from a liquid matrix was not observed, but this event can not be discarded. The operation of heterogeneous and homogeneous nucleation of α'-sialon are thought to cause the change in solid solubility limits of the α'-sialon formed, and to greatly influence the thermal stability of α'-sialon, as will be mentioned later.

As the content of α'-sialon increases and lattice parameters decrease with raising the temperature, reaction (d) should be also considered. In the present work, it was not, however, possible to confirm the presence of α'-sialon with various solid solubilities, because the lattice parameters measured strike an average one of diverse solid solubilities.

Melilite disappeared due to precipitation of β'-sialon, and the chemical reaction in the formation of β'-sialon is expressed as eqn (e). It is also considered that precipitation of β'-sialon could proceed through reaction (f). Han *et al.*[25] investigated the phase transformation from α'-sialon to β'-sialon by liquid infiltration in the Y–Si–Al–N–O system, and they reported that during heating the glass matrix penetrated into the sintered α'-sialon specimen to induce the phase transformation of α'- into β'-sialon, and that no trace of α'-sialon existed in β'-sialon grains. Sugiyama *et al.*[26] investigated recently the thermal stability of α'-sialons with various solid solubility in mixed α'/β'-sialon. They reported that α'-sialon with a lattice parameter of the *c*-axis less than 5·65Å disappeared under heat-treatment at 1850°C for 50 h, and the amount of β'-sialon increased. On the other hand, the α'-sialon with a lattice parameter of the *c*-axis higher than 5·65Å remained after the heat-treatment, then its lattice parameters went up to nearly 5·66Å, and the amount of α'-sialon and β'-sialon decreased and increased, respectively. The former phenomena are anticipated to occur during precipitation of β'-sialon in the present work, since the increase in amount of α'-sialon is slowed by the formation of β'-sialon, and thereafter the amount of α'-sialon decreases slightly, as do, simultaneously, the lattice parameters. Consequently, reaction (f) is given.

4.2 Densification process

It is generally accepted that densification of Si_3N_4 ceramics with oxide additives and Si_3N_4 solid solu-

tions proceeds via liquid phase sintering, which consists of three stages: (I) particle rearrangement, (II) solution–precipitation and (III) coalescence of grains.[21,27] In the sintering process of sialon, several reactions to form the sialons, as described in the previous section, greatly influence the densification behavior. In the following section, the densification process of mixed α'/β'-sialon ceramics is discussed from the results of shrinkage, in connection with the reaction processes in the formation of sialons.

Shrinkage was initiated around 1200°C (Figs 1 and 2). The densification at the initial stage occurs by the rearrangement process, as the particles move to pack closer by capillary forces of the liquid.[27] It is well known that the temperature at which initial particle rearrangement occurs is related closely to the lowest eutectic temperature of oxides and impurities contained in the raw powders. Considering that SiO_2 and Al_2O_3 exist on the surface of Si_3N_4 and AlN particles, respectively, the eutectic liquid is the SiO_2–Al_2O_3–Ln_2O_3 system, whose minimum eutectic temperature is reported to be around 1450°C for Er_2O_3 addition.[28] Besides the oxide impurities, the liquidus temperature is reduced by the presence of metallic and halogen impurities. In this work, metallic impurities amounting to 350 ppm may be not high enough to reduce the liquidus temperature, but, on the other hand, a large amount of fluorine was present. In a previous work, Watari *et al.*[29] examined the effect of fluorine content (70, 440 and 670 ppm) in raw powders on the densification of Si_3N_4 ceramics with Y_2O_3 and Al_2O_3 addition by high-temperature dilatometry. They found that the temperature at which shrinkage starts decreased with increasing the fluorine content, and confirmed that shrinkage of Si_3N_4 powder with fluorine content of 670 ppm occurred at 1120°C. As the fluorine content in the raw powder used here is at the level of several hundred ppm, it must yield a reduction in the eutectic temperature.

In the case of sintering of Si_3N_4 ceramics, the influence of nitrogen ions on the liquid formation should also be considered. Hampshire & Jack[30] have pointed out that nitrogen as an additional component lowers the eutectic temperature by 100–200°C. In an experiment concerning nitrogen-glass preparation from the melting of a mixture of silica, alumina, lanthanide oxide and silicon nitride powders, the solubility of nitrogen ions in the liquid in the Si–Al–Y–O–N system is less than 15 at.%.[31] Wang *et al.*[32] have also mentioned that the solubility of nitrogen in Nd-sialon glass can reach 25 at.%, whereas in the Si–Al–Y–O–N system the highest solubility is only about 15 at.% and they also reported that the behavior of heavy rare-earth oxides is, in many aspects, similar to that of Y_2O_3. The solubility of nitrogen in a liquid is not, however, clarified in the sialon system. From the existence of impurities and nitrogen, it is, therefore, considered that reaction (a) of Table 1 occurs and that there is formation of a liquid phase around 1200°C, resulting in shrinkage due to initial particle rearrangement.

The next densification stage is due to a solution–precipitation process, which is accompanied by grain growth through the dissolution of small particles in the liquid and their reprecipitation on large particles.[27] In the fractured surface of the specimen sintered at 1400°C shown in Fig. 7 (b), the size and shape of particles are hardly distinguishable. After chemical etching for 15 min, roundish particles with a diameter of about 0·4 μm appeared, and they are different in size and shape from particles in the raw material shown in Fig. 7 (a). This microstructural change suggests that this temperature range corresponds to the solution–reprecipitation stage. Moreover, as shown in Fig. 7 (b) and (c), a large amount of glassy phase is formed, and it seems to have filled the interstice between particles. Such a phenomenon suggests that liquid flow is a significant densification mechanism at the solution–precipitation stage in sintering of Si_3N_4 ceramics.

At the solution–precipitation stage, reactions in formation of α'- and β'-sialons proceed through eqns (b), (c), (d), (e) and (f) of Table 1. The formation of α'-sialon yields reduction of the shrinkage rate at temperatures from 1510 to 1580°C for Er_2O_3 and at 1480 to 1580°C for Yb_2O_3 additions, because the ingredients in the liquid, i.e. lanthanide, aluminum and oxygen, are removed from it, causing the quantity and the viscosity of the liquid phase to decrease and to increase, respectively, interrupting then the dissolution of residual α-Si_3N_4 into the liquid. Furthermore, precipitation of melilite should be considered to hinder the densification process. As melilite formation consumes rare-earth cations, and it has a high melting point (~1900°C for yttrium-melilite[33] and >1700°C for samarium-melilite[34]), the amount of transient liquid is reduced over time. Consequently, the reduction of shrinkage rate at temperatures from 1480 to 1580°C is ascribed to formation of α'-sialon and melilite.

At temperatures higher than 1600°C, precipitation of β'-sialon and rapid increase of shrinkage rate occur concurrently, when Er_2O_3 and Yb_2O_3 were added. This increase of the shrinkage rate is associated with reactions in the formation of β'-sialon, indicated as eqns (e) and (f), which may induce the increase in liquid volume and the decrease in its viscosity, in contrast to the formation of α'-sialon, which causes the liquid volume to be

small and its viscosity high, and dissolution of residual Si_3N_4 into the liquid is difficult. As already mentioned, α'-sialon with low solid solubility is unstable thermodynamically during the sintering accompanied by formation of β'-sialon. Furthermore, disappearance of melilite occurs when β'-sialon precipitates. The acceleration of reactions (e) and (f) suggests that Ln_2O_3, which was accommodated into the α-Si_3N_4 structure or consumed by the formation of melilite, remains at the grain boundaries. In this case, it is postulated that an increase in the amount and a decrease in the viscosity of the liquid occur during precipitation of β'-sialon, and that the solution–precipitation process is, therefore, accelerated during the precipitation of β'-sialon. To date, the variations of volume and viscosity of liquid during the sintering of Si_3N_4 and sialon ceramics have not been measured in situ, and are the subject of absorbing interest when considering the liquid-phase sintering process of these materials. The authors have been considering that low-temperature specific heat and internal friction measurements can provide the information on the amount and viscosity of liquid during the heating.[35] The results concerning the character and quantity of liquid phase and grain boundary crystalline/glassy phase at various sintering temperature will be reported in the near future.

Figure 9 presents the isothermal shrinkage of compacts containing Yb_2O_3 addition with a heating rate of 10°C min^{-1}. When the heating rates of 30 and 50°C min^{-1} were used in preliminary experiments, the resultant amounts of α'-sialon and melilite formed at middle stage of sintering were small, indicating that a large amount of shrinkage took place. In this work, the heating rate was set at 10°C min^{-1} to clarify the densification process in rapid shrinkage at 1580 to 1700°C for Er_2O_3 and Yb_2O_3 additions. The kinetic parameter obtained takes values between 0·76 and 0·70, which are much larger than values predicted for the solution–precipitation process in the classical liquid-phase sintering model proposed by Kingery.[27] It is not possible here to clarify the sintering process through a mathematical analysis, and the densification can not be explained only by the solution–precipitation mechanism of the classical liquid-phase sintering model.

Since Kingery proposed a liquid-phase sintering model, a number of additional solution–precipitation mechanisms have been found, such as pore elimination due to cooperative flow of the particle–liquid mixture, Ostwald ripening with shape accommodation, and particle disintegration.[36] It is suggested that sintering of mixed α'/β'-sialon is a concurrent process involving these mechanisms. It

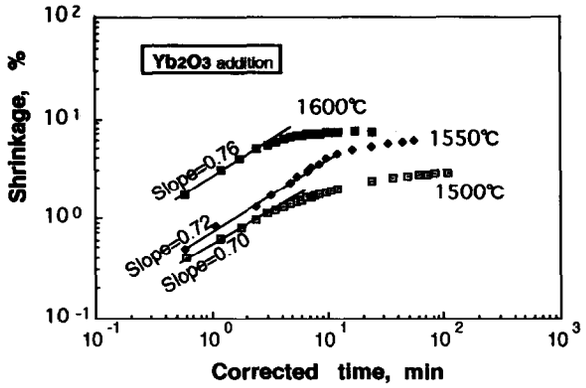


Fig. 9. Isothermal shrinkage of compacts with Yb_2O_3 addition.

is considered that the pore-elimination process due to cooperative flow of particle–liquid mixtures causes the rapid shrinkage observed at 1580 to 1700°C for Er_2O_3 and Yb_2O_3 additions and the kinetic parameters larger than any of the rate exponents predicted by Kingery' s model, since the rate of particle migration toward the interstices between particles is very fast. However, as shown in Fig. 1, the relative density at 1600°C was 80% for Er_2O_3 addition and 70% for Yb_2O_3 addition, which are much higher than a typical packing density of a monosized powder (64 vol.%). In this case, it can not be said that rapid shrinkage observed at 1580 to 1700°C for Er_2O_3 and Yb_2O_3 additions took place only by the particle migration process. It was expected from the results of Han *et al.* that in the present sintering, disintegration of α'-sialon grains occurs at temperatures higher than 1600°C, it then being easy for α'-sialon grains to migrate toward the interstice between particles, resulting in rapid shrinkage.

Besides these densification mechanisms, Ostwald ripening mechanism with shape accommodation is also anticipated to take place. In the present work, it was found that after sintering at 1850°C for 4 h, in the region containing the large grains, particles agglomerate, and large grains come into contact widely with other large ones (see Fig. 7 (h), the region surrounded with a white line). These microstructural features suggest that grain growth by Ostwald ripening occurs, grown grains contact with other ones, and subsequently the interstices between particles fill up by shape accommodation of grown grains. At the middle and final stages of sintering, this process is considered to help the densification further.

The densification process of mixed α'/β'-sialon ceramics has been discussed through the consideration of chemical reactions in formation of α'-sialon and β'-sialon and kinetical analysis of shrinkage. At the solution–precipitation stage, the formation of α'-sialon caused the retardation of densification, but during the formation of β'-

sialon, the densification proceeded rapidly. The densification at a latter stage relates to dissolution of α'-sialon formed at the early stage and of melilite into the liquid. From kinetical analysis, it was thought that dissolution of α'-sialon and melilite into the liquid and precipitation of β'-sialon induces the cooperative flow process of the particle–liquid mixture and particle disintegration process, besides the solution–precipitation process. Such an interpretation, however, may be too simplistic, and further work, such as identification of the disintegration of α'-sialon particles during heating, is necessary to understand the densification process exactly.

4.3 Effect of type of lanthanide oxide on densification and formation of sialon

The type of Ln_2O_3 added determines different sintering phenomena in mixed α'/β'-sialon ceramics and produces different amounts of α'- and β'-sialons. In Fig. 8, for Yb_2O_3 addition, the size and shape of particles can be identified, and the surface of particles is covered with a thin film of a material like a glassy-phase, which links neighboring particles. On the other hand, in the case of Y_2O_3 addition, the size and shape of particles are not well defined, because the particles seem to dissolve in the liquid. When Er_2O_3 is added, the microstructural feature (see Fig. (b)) is thought to be an intermediate microstructure between the corresponding to Yb_2O_3 and to Y_2O_3 addition. It is estimated from the microstructural features that in sintering at 1400°C for 15 min the amount and viscosity of the liquid for Y_2O_3 addition are, respectively, rather larger and lower than those for Er_2O_3 and Yb_2O_3 additions.

The resultant amounts of α'-sialon and melilite were different for each type of Ln_2O_3 addition. Recently, O'Reilly *et al.*[37] investigated the effect of diverse oxide additions on the sinterability of α'-sialon and on the resultant amounts of α'-sialon and melilite, and they summarized the correlation between the relative density and the amounts of these phases as functions of liquid volume and viscosity. Being the volume and viscosity of liquid different for diverse amounts of α'-sialon and melilite, the exact effect of the type of lanthanide oxide on densification can not be discussed. In this section, based on the reported data, the influence of the ionic radii of the lanthanide ion on the viscosity and amount of liquid is discussed without considering the effect of α'-sialon and melilite contents.

It has been reported that the eutectic temperature in the Si–O–N–M system, where M is a lanthanide, increases[38] and that the viscosity of glasses in the Si–Al–O–N–M system also increases[39] with decreasing ionic radius of the M ion. It is considered from these relations that at the initial stage of sintering, the liquidus temperature and viscosity of liquid formed decrease in the order of $Y_2O_3<Er_2O_3<Yb_2O_3$. Therefore, it is anticipated that for Y_2O_3 addition, solution–precipitation, liquid flow and cooperative flow of the particle–liquid mixture, as well as particle disintegration are accelerated, compared to Er_2O_3 and Yb_2O_3 additions.

As already mentioned, in the case of Er_2O_3 and Yb_2O_3 additions the formation of α'-sialon and melilite results in retardation of the shrinkage rate, while rapid shrinkage occurs when β'-sialon precipitates. However, as for Y_2O_3 addition, the retardation in shrinkage rate due to formation of α'-sialon and melilite was very slight. This is interpreted as dissolution of α'-sialon and melilite in the liquid and precipitation of β'-sialon occurring at an earlier stage.

5 Concluding remarks

The following conclusions can be drawn from this study:

(1) Possible reactions to form α'- and β'-sialons during the sintering of mixed α'/β' sialon ceramics were investigated from the results of reaction sequence, change in phase composition and lattice parameters. They were

$$SiO_2 + Al_2O_3 + Ln_2O_3 + Si_3N_4/AlN \rightarrow \text{Nitrogen glass} + \text{J-Phase } (Ln_4Si_2O_7N_2) \quad (a)$$

$$\text{J-Phase} + \text{Nitrogen glass} + Si_3N_4/AlN \rightarrow \alpha'\text{-Sialon}^H + \text{Melilite } (Si_3N_4 \cdot Ln_2O_3) + \text{Nitrogen glass} \quad (b)$$

$$Si_3N_4 + 9AlN \cdot Ln_2O_3 \rightarrow \alpha'\text{-Sialon}^H \quad (c)$$

$$Si_3N_4 + \alpha'\text{-Sialon}^H \rightarrow \alpha'\text{-Sialon}^L \quad (d)$$

$$Si_3N_4 + \text{Melilite} + \text{Nitrogen glass} \rightarrow \beta'\text{-Sialon} + \text{Nitrogen glass} \quad (e)$$

$$Si_3N_4 + \alpha'\text{-Sialon}^L + \text{Nitrogen glass} \rightarrow \beta'\text{-Sialon} + \text{Nitrogen glass} \quad (f)$$

where H and L indicate the α'-sialons with high and low solid solubility, respectively.

(2) As the formation of α'-sialon and melilite consumes the ingredients of the liquid, the densification is retarded over time. This phenomenon was clearly observed in sintering of mixed α'/β'-sialons containing Er_2O_3 and Yb_2O_3. On the other hand, during the formation of β'-sialon, densification was accelerated remarkably, and rapid shrinkage was observed. This is ascribed to the disso-

lution of α'-sialon with low solid solubility and melilite in the liquid and to precipitation of β'-sialon. It is, then, considered that volume and viscosity of liquid increase and decrease, respectively, resulting in acceleration of solution–precipitation, liquid flow, cooperative flow of the particle–liquid mixture, and particle disintegration.

(3) The type of lanthanide oxide strongly influences the sintering phenomena and phase composition. Densification at the initial and middle stages and reactions from α'-sialon and α-Si_3N_4 to β'-sialon accelerated in the order Y_2O_3 > Er_2O_3 > Yb_2O_3, because the liquidus temperature and viscosity of the liquid formed decrease in the order Y_2O_3 < Er_2O_3 < Yb_2O_3.

(4) The α'-sialon formed at the initial stage presented a high solid solubility in the α-structure, but thereafter lattice parameters decreased with elevating sintering temperatures. The x value in $Yx(Si, Al)_{12}(O,N)_{16}$ was 0·4 for the specimen obtained at 1500°C and 0·25 for the one at 1850°C. In the case of the β-structure, significant change in the lattice parameters were observed at temperatures between 1500 and 1600°C, and the value of z in the formula, $Si_{6-z}Al_zO_zN_{8-z}$ was 0·6 for the specimen sintered at temperatures higher than 1600°C. An influence of the type of the lanthanide oxide on lattice parameters was not apparent.

References

1. Lange, F. F., High-temperature strength behavior of hot-pressed Si_3N_4: evidence for subcritical crack growth. *J. Am. Ceram. Soc.*, **57** (1974) 84–7.
2. Becher, P. F., Microstructural design of toughened ceramics. *J. Am. Ceram. Soc.*, **74** (1991) 255–69.
3. Nagaoka, T., Watari, K., Yasuoka, M., Hirao, K. & Kanzaki, S., Interrelation between two and/or three-dimension grain morphology and fracture toughness of Si_3N_4 ceramics. *J. Ceram. Soc. Japan*, **100** (1992) 1256–60.
4. Kawashima, T., Okamoto, H., Yamamoto, H. & Kitamura, A., Grain size dependence of the fracture toughness of silicon nitride. *J. Ceram. Soc. Japan*, **99** (1991) 320–3.
5. Oyama, Y. & Kamigaito, O., Solid solubility of some oxides in Si_3N_4. *Japan. J. Appl. Phys.*, **10** (1972) 1637–42.
6. Jack, K. H. & Wilson, W. I., Ceramics based on the Si–Al–O–N and related system. *Nature*, **238** (1977) 28–9.
7. Hampshire, S., Park, K. H., Thompson, D. P. & Jack, K. H., α-sialon ceramics. *Nature*, **274** (1978) 880–2.
8. Huang, Z. K., Sun, W. Y. & Yan, D. S., Phase relations of the Si_3N_4–AlN–CaO system. *J. Mater. Sci. Lett.*, **4** (1985) 225–9.
9. Ishizawa, K., Ayuzawa, N., Shiratani, A., Takai, M., Uchida, N. & Mitomo, M., Some properties of α-sialon ceramics. In *Ceramic Materials and Components for Engines*, ed. W. Bunk & H. Hausner. German Ceramic Society, Bad Honnef., Germany, 1986, pp. 511–18.
10. Nagel, A., Greil, P. & Petzow, G., Reaction of sintering of yttrium containing α-silicon nitride solid solution. *Revue de Chemie Minerale*, **22** (1985) 437–47.
11. Slasor, S. & Thompson,. D. P., Preparation and characterization of α'-sialons. In *Non-Oxide Technical and Engineering Ceramics*, ed. S. Hampshire. Elsevier, London, 1986, pp. 223–30.
12. Mitomo, M., Hasegawa, Y., Bando, Y., Watanabe, A. & Suzuki, H., The strength of hot-pressed β-sialon. *Yogyo-Kyokai-Shi*, **88** (1980) 78–84.
13. Umebayashi, S., Kishi, K., Tani, E. & Kobayashi, K., The strength of hot-pressed β-sialons with Z = 1 in $Si_{6-z}Al_zO_zN_{8-z}$. *Yogyo-Kyokai-Shi*, **92** (1984) 35–51.
14. Tanaka, I., Pezzotti, G., Miyamoto, Y. & Okamoto, T., Fracture toughness of Si_3N_4 and its Si_3N_4 whisker composite without sintering aids. *J. Mater. Sci.*, **26** (1991) 208–10.
15. Ekstrom, T. & Nygren, M., Sialon ceramics. *J. Am. Ceram. Soc.*, **72** (1992) 259–76.
16. Ukyo, Y. & Wada, S., High strength Si_3N_4 ceramics. *J. Ceram. Soc. Japan*, **97** (1989) 872–4.
17. Cao, G. Z., Metselaar, R. & Ziegler, G., Relations between composition and microstructure of sialons. *J. Eur. Ceram. Soc.*, **11** (1992) 115–22.
18. Jack, K. H., Sialon ceramics: retrospect and prospect. In *Silicon Nitride Ceramics—Scientific and Technological Advances, Materials Research Society Proceedings*, Vol. 287, ed. I.-W. Chen, P. F. Becher, M. Mitomo, G. Petzow & T.-S. Yen. Materials Research Society, Pittsburgh, 1993, pp. 15–28.
19. Mandal, H., Thompson, D. P. & Ekstrom, T., Reversible α–β sialon transformation in heat-treated sialon ceramics. *J. Eur. Ceram. Soc.*, **12** (1993) 421–9.
20. Ekstrom, T., Ingelstrom, N., Brage, R., Hatcher, M. & Johansson, T., α–β Sialon ceramics made from different silicon nitride powders. *J. Am. Ceram. Soc.*, **71** (1988) 1164–70.
21. Abe, O., Sintering process of Y_2O_3-added Si_3N_4. *J. Mater. Sci.*, **25** (1990) 3641–8.
22. Ukyo, Y. & Wada, S., Formation and stability of Y-α'-sialon co-existing with β'-sialon. In *Euro-Ceramics*, Vol. 1., ed. G. de With. A. Terpstra & R. Metselaar. Elsevier Science, London, 1989, pp. 566–72.
23. Chatfield, C., Ekstrom, T. & Nikus, M., Microstructural investigation of alpha–beta yttrium sialon materials. *J. Mater. Sci.*, **21** (1986) 2297–307.
24. Chen, I.-W. & Hwang, S.-L., Superplastic sialon—a bird's eye view of silicon nitride ceramics. In *Silicon Nitride Ceramics—Scientific and Technological Advances—Materials Research Society Proceedings*, Vol. 287, ed. I.-W. Chen, P. F. Becher, M. Mitomo, G. Petzow & T.-S. Yen. Materials Research Society, Pittsburgh, 1993, pp. 209–22.
25. Han, S. M., Kang, S.-J. & Lee, Y.-T., Phase transformation from α' to β'-sialon by liquid infiltration in Y–Si–Al–O–N system. *J. Eur. Ceram. Soc.*, **12** (1993) 431–4.
26. Sugiyama, N., Ukyo, Y. & Wada, S., Thermal stability of phases in Si_3N_4 (–SiO_4)–AlN–Y_2O_3 system. *J. Ceram. Soc. Japan*, **102** (1994) 145–8.
27. Kingery, W. D., Densification during sintering in the presence of a liquid phase: I. *J. Appl. Phys.*, **30** (1969) 301-6.
28. Murakami, Y. & Yamamoto, H., Phase equilibria and properties of glasses in the Al_2O_3–Yb_2O_3–SiO_2 system. *J. Ceram. Soc. Japan*, **101** (1993) 1101–6.
29. Watari, K., Kanzaki, S., Asayama, M., Tsuge, A., Isozaki, K. & Hirotsuru, H., Influence of halogen impurities in raw powder on sinterability of Si_3N_4 ceramics, In *Proceedings of Annual Meeting of the Ceramics Society of Japan*. Ceramics Society of Japan, Tokyo, 1993, p. 610.
30. Hampshire, S. & Jack, K. H., The kinetics of densification and phase transformation of nitrogen ceramics. *Proc. Brit. Ceram. Soc.*, **31** (1980) 37–49.

31. Loehman, R. E., Preparation and properties of yttrium–silicon–aluminium oxygen nitride glasses. *J. Am. Ceram. Soc.*, **62** (1979) 491–4.
32. Wang, P. L., Sun, W. Y. & Yen, T. S., Formation and densification of R–α'-sialons (R = Nd, Sm, Gd Dy, Er and Yb). In *Silicon Nitride Ceramics—Scientific and Technological Advances—Materials Research Society Proceedings*, Vol. 287, ed. I.-W. Chen, P. F. Becher, M. Mitomo, G. Petzow & T.-S. Yen. Materials Research Society, Pittsburgh, 1993, pp. 387–92.
33. Jack, K. H., Silicon nitride, sialons, and related ceramics. In *Ceramics and Civilization*, Vol. III, *High-Technology Ceramics*. American Ceramics Society, Columbus, OH, 1986, pp. 259–88.
34. Cheng, Y.-B. & Thompson, D. P., Aluminium-containing nitrogen melilite phases. *J. Am. Ceram. Soc.*, **77** (1994) 143–8.
35. Watari, K., Sakaguchi, S., Kanzaki, S., Hamasaki, T. & Ishizaki, K., Quantity and character of grain boundary phase in mixed α'/β'-sialon ceramics. *J. Mater. Res.*, **9** (1994) 2741–4.
36. Petzow, G. & Kaysser, W. A., Basic mechanisms of liquid-phase sintering. In *Sintering Key Papers*, ed. S. Somiya & Y. Moriyoshi. Elsevier Applied Science, London and New York, 1990, pp. 595–614.
37. O'Reilly, K. P., Redington, M., Hampshire, S. & Leigh, M., Parameters affecting pressureless sintering of α'-sialons with lanthanide modifying cations. In *Silicon Nitride Ceramics—Scientific and Technology Advances—Materials Research Society Proceedings*, Vol. 287, ed. I.-W. Chen, P. F. Becher, M. Mitomo, G. Petzow & T.-S. Yen. Materials Research Society, Pittsburgh, 1993, pp. 393–9.
38. Gazza, G. E., *Progress in Nitrogen Ceramics (NATO ASI Series)*, ed. F. L. Riley. Martinus Nijhoff, The Hague, Netherlands, 1983, p. 273.
39. Drew, R. A. (ed.), *Nitrogen Glass*. Research Reports in Materials Science, The Parthenon Press, Castertonhall, Lancashirela, UK, 1986, Fig. VII. 9.

Appendix

As has been pointed out by many investigators, characteristics of raw Si_3N_4 powders such as the amount, type and distribution of impurities, grain size and particle distribution influences greatly the sintering behavior, sinterability, microstructural development and mechanical properties of sintered materials, as well as the amount and composition of the grain boundary crystalline/glassy phase. Experimental results of the shrinkage rate obtained by high-temperature dilatometry measurements provide some useful information to evaluate the relationships between the characteristics of raw Si_3N_4 powders and densification behavior. Figure A1 shows the temperature dependence of shrinkage rate of compacts, whereas the characteristics of raw Si_3N_4 powders are shown in Table A1. As can be observed, sintering behavior and sinterability are greatly influenced by the type of raw powder. The temporary retardation of shrinkage rate due to formation of α'-sialon and melilite can be seen at temperatures between 1500 and 1600°C in Fig. A1, irrespective of the characteristics of raw powders; however, the densities of specimens obtained from the powders C, D and E are very much lower than the densities of those from the powders A and B. The significant parameters affecting the densification are not clarified at present.

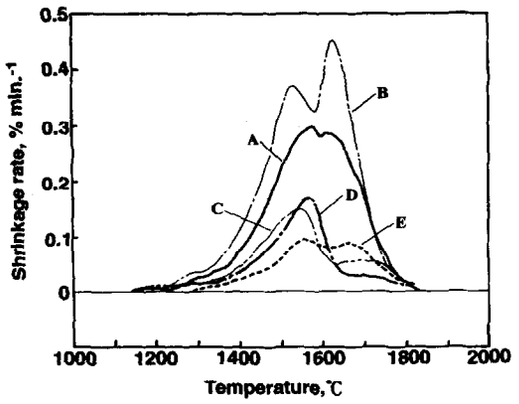


Fig. A1. Influence of powder characteristics on shrinkage rate of Si_3N_4 compacts with 1·69 mol% AlN and 15·21 mol% Y_2O_3. The characteristics of the powders used are shown in Table A1. After thermal shrinkage measurements at 1850°C for 15 min, the relative density was 85·5% for powder A, 89·2% for powder B, 63·9% for powder C, 65·2% for powder D, and 64·8% for powder E.

Table A1. Representative properties of raw Si_3N_4 powder

Raw powder	*Specific surface area* ($m^2\ g^{-1}$)	*Oxygen content* (*wt%*)	*Carbon content* (*wt%*)	*α-Phase content* (%)
A	11·3	1·30	0·11	94·0
B	10·5	1·20	0·14	90·1
C	12·4	1·00	0·04	90·2
D	11·1	0·8	0·05	90·4
E	9·9	1·2	0·02	98·0

Journal of the European Ceramic Society **15** (1995) 185–190
© 1995 Elsevier Science Limited
Printed in Great Britain. All rights reserved
0955-2219/95/$9.50

Association of the CVI Process and of the Use of Polysilazane Precursor for the Elaboration of Ceramic Matrix Composites Reinforced by Continuous Fibres

M. F. Gonon,[a] G. Fantozzi,[b] M. Murat[b] & J. P. Disson[c]

[a] Ceramic Research Unit, National Technological Park, University of Limerick, Limerick, Republic of Ireland
[b] G.E.M.P.P.M., Bt 502 I.N.S.A. de Lyon, 20 ave A. Einstein - F69621 Villeurbanne cedex, France
[c] Elf Atochem, Centre de Recherche Rhône-Alpes, rue Henri Moissan, F-69310 Pierre-Béinte, France

(Received 19 April 1994; revised version received and accepted 22 June 1994)

Abstract

A new process route for ceramic composites, associating CVI of SiC and impregnation and pyrolysis cycles with a polysilazane precursor, has been developed. The interest of this process is, firstly, a shorter time of elaboration than for CVI alone and, secondly higher mechanical properties than those resulting from a conventional use of the precursor. Composites with mechanical properties comparable to those of composites entirely obtained by CVI of SiC have been realised. The flexual strength of these materials is about 400 MPa, whereas that of composites resulting from a conventional use of the same polysilazane does not exceed 200 MPa.

1 Introduction

New materials able to operate under hostile stress–temperature–environment conditions are required for the development of high performance applications (e,.g. aeronautics).

The material used presently (e.g. SiC/C/SiC or C/SiC obtained by CVI) have high mechanical properties (e.g. flexural strength about 400–500 MPa) but their elaboration needs a very long time, and is, therefore, very expensive.[1,2] An alternative way to the CVI process is the use of organometallic precursors leading, after pyrolysis, to ceramic products. However, to date, the mechanical properties of the material obtained by this method are not able to compete with those of composites resulting from the CVI route (e.g. flexural strength lower than 200 MPa.[3–5]

The 'conventional' use of the precursor consists of a sequence of successive impregnation and pyrolysis cycles of a fabric preform with the precursor. The matrix obtained is composed of numerous ceramic blocks corresponding to the successive cycles (Fig. 1(a)). Such a structure is not as strong as the continuous one resulting from the CVI route (Fig. 1(b)). Indeed, the interfaces between the different blocks create some weak points. Moreover, when these interfaces are perpendicular to the loading direction, they lead to stress concentrations on the fibre surfaces what may cause the fracture of these fibres (Fig. 1(a)). This can explain the low mechanical properties of such composites. On the other hand, the deposition rate by CVI is very low. Therefore, the elaboration of dense composites by this process needs a very long time.

The basic idea of this study is, firstly to elaborate a high porosity composite preform by CVI of SiC on bidirectional SiC Nincalon fabrics and, secondly, to fill the porosity by successive impregnation and pyrolysis cycles with the polysilazane (Fig. 1(c)).

2 Experimental

2.1 Characteristics of Pyrofine PV Polysilazane

The precursor used is a commercial polysilazane produced by Elf Atochem: Pyrofine PV.[6] At room temperature, this product is a viscous liquid (density = 1). Its viscosity decreases with the increase of temperature up to 200°C (Table 1).

Upon heating to 300°C under introgen, the precursor becomes cross linked. the product obtained is solid unmeltable and insoluble.

Pyrolysis under a nitrogen atmosphere at a temperature between 900°C and 1400°C yields an amorphous ceramic. At 1000°C, the ceramic yield varies form 60 to 65 wt%, depending on the heating rate used during the crosslinking.[7] The typical elemental composition of the ceramic obtained is

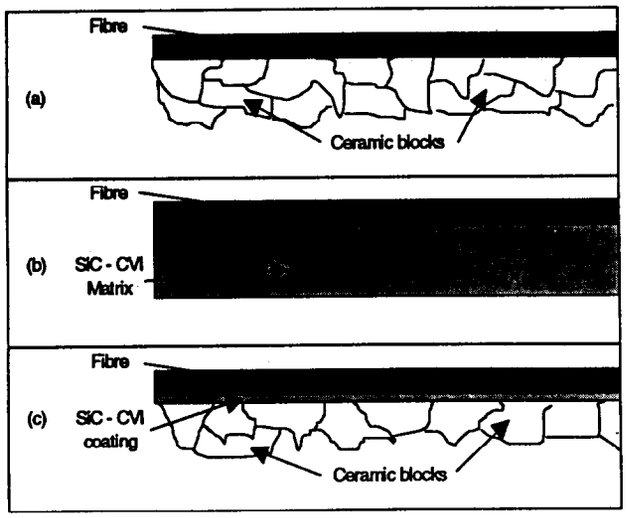


Fig. 1. Structure of the ceramics matrix obtained from (a) an organometallic precursor (b), in the case of CVI process and (c) in the present process.

given Table 2 (oxygen originates from the precursor). The density measured by He psycnometry is 2·13 g/cm^3. Thus, the volumetric yield of the transformation is about 30%.

2.2 Characteristics of the composite preforms

Starting materials are 3·0 to 3·2 mm thick plates. They are composed of eight woven layers of Nicalon NL 202 S8 fabric (from Nippon Carbon).

The fibres volume ratio is about 40 vol.%. A 0·5–1·0 μm thick graphite carbon coating of the fabric is used to limit fibres–matrix bonding and thus, to lead to the unbrittle behaviour of the materials.[8]

A 1·0–2·0 μm thick SiC coating is then realised by CVI.

The porosity determined by Archimedes' method is 36·8 ± 1% and is in agreement with the 38·6 ± 1·3% corresponding to the theoretical calculated value.

2.3 Densification process

To reduce the porosity and then to increase the mechanical properties, successive impregnation and pyrolysis cycles are realised with the polysilazane.

Table 1. Variation of the viscosity of Pyrofine PV polysilazane versus temperature

Temperature,	°C	50	100	150
Viscosity,	mPa.s	1000	100	20

Table 2. Composition of the ceramic obtained from Pyrofine PV polysilazane after pyrolysis at 1000°C

	Si	*C*	*N*	*O*
at.%	30·0	34·7	27·1	8·2
wt%	47·5	23·6	21·5	7·4

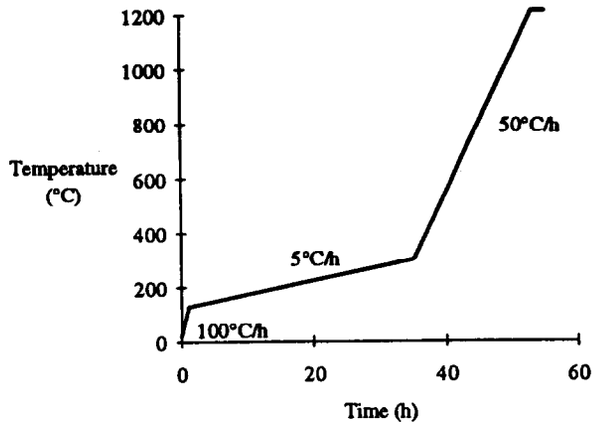


Fig. 2. Pyrolysis temperature schedule of Pyrofine PV polysilazane.

The preforms are charged into a reactor and degassed under 500 Pa at 150°C for 2 h. Thereafter, the precursor, preheated at 150°C to reduce its viscosity, is injected into the preform by means of a pressure gradient between the outside (nitrogen atmospheric pressure) and the inside of the reactor. After injection, preforms are soaked in the precursor at 150°C for 2 h under a nitrogen atmosphere before being removed and placed in the pyrolysis furnace.

Pyrolysis is operated under nitrogen according to the following temperature schedule: 100°C/h up to 130°C; 5°C/h from 130°C up to 300°C; 50°C/h from 300°C up to 1200°C + 4 h hold (Fig. 2).

A separate study has shown that pyrolysis up to 1400°C leads to the highest mechanical properties of the ceramic matrix.[7] However, the thermal resistance of Nicalon fibers limits the temperature of pyrolysis to 1200°C.

2.4 Measure of the physical and mechanical properties

The pore volumes were determined after each impregnation—pyrolysis cycle by Archimedes' method (open porosity) and from the theoretical calculation (total porosity) based on the volume ratio of the components and their absolute density.

The pore size distribution was determined by mercury porosimetry on the preform and after 1, 2 and 5 cycles.

Room-temperature flexural strengths were measured in three-point bending on a Schenck RM-T 25 kN using a support span of 50 mm and a crosshead speed of 0·5 mm/min. The average dimensions of the composite test bars are 65 × 10 × 3 mm^3.

Youngs modulus was determined from the load displacement curves.

Due to the unbrittle behaviour of the materials. The characterisation of the composite toughness requires the calculation of the resistance to crack

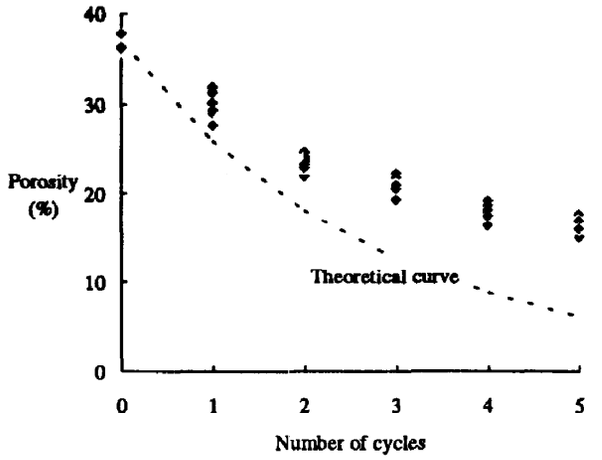


Fig. 3. Variation of the porosity of the composites according to the number of impregnation pyrolysis cycles.

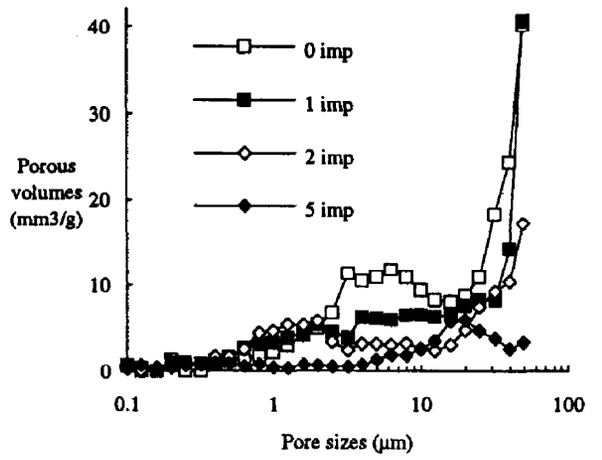


Fig. 4. Pore sizes distribution of (□) the preform and composites after (■) 1, (◇) 2 and (◆) 5 cycles.

propagation curves (*R*-curves). These curves show the stress intensity factor K versus the ratio of the crack length increase, da, to initial ligament thickness of the test bar w–a. The measures were made by the single-edge notched-beam techinque (SENB) with $a/w = 0{\cdot}5$ (a, initial crack length; w, thickness of the test bar). According to Bouquet *et al.* and R'mili,[9,10] calculations of da and K have been based on the assumption of a linear–elastic behaviour.

3 Results

3.1 Variation of the porosity with the number of cycles

Archimedes' method (open porosity) and the theoretical calculation (total porosity) lead to similar results: the porosity is essentially open.

The experimental porosity–number of cycles curve deviates for the theoretical one corresponding to a complete impregnation of the samples (Fig. 3). After five cycles, the porosity tends to an asymptotic value between 10 and 15%. The porosity being essentially open, this may be due to fine porosity which, due to the viscosity of the precursor, cannot be filled during the impregnation. However, weighing the composites after the precursor injection indicates that 96–97% of the free volume is filled.

On the other hand, after each pyrolysis, a residue of pyrolysed precursor is present at the bottom of the reactor. It is therefore concluded that the deviation between the experimental and theoretical porosity evolution curves is mainly due to the release of precursor during the early stage of pyrolysis, while its viscosity is still low (temperature range 150–200°C).

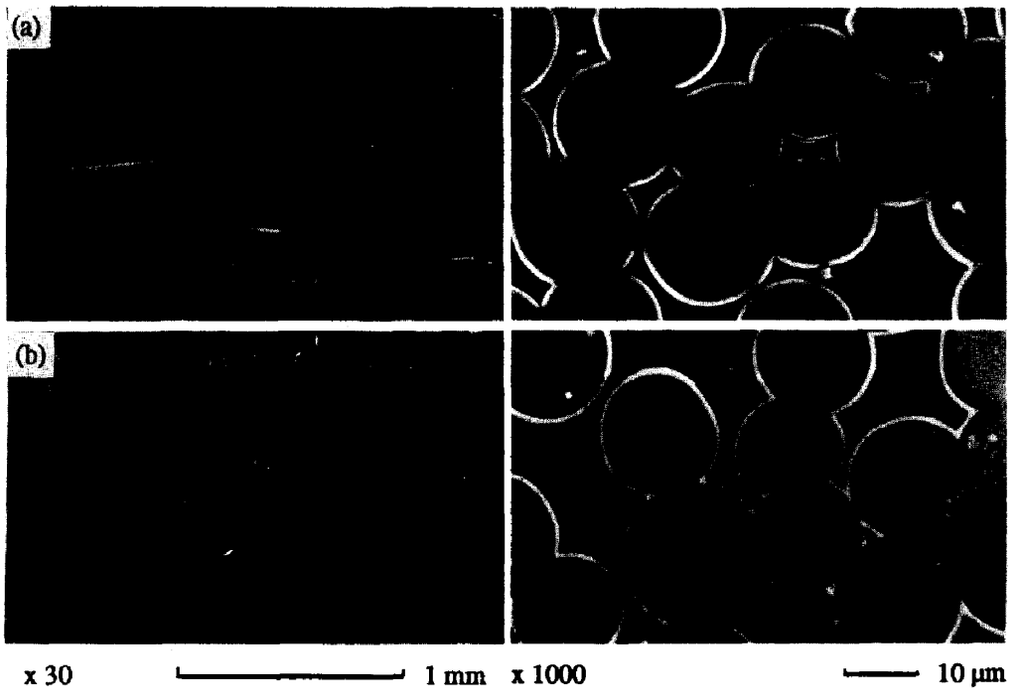


Fig. 5. SEM observation of the cross-sections of the composites (a) before the impregnation pyrolysis cycles with the polysilazane and (b) after 5 cycles.

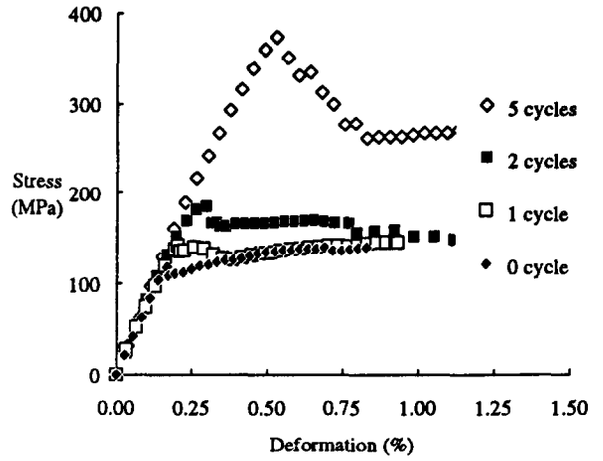


Fig. 6. Composite stress–deformation curves obtained in three-point bending.

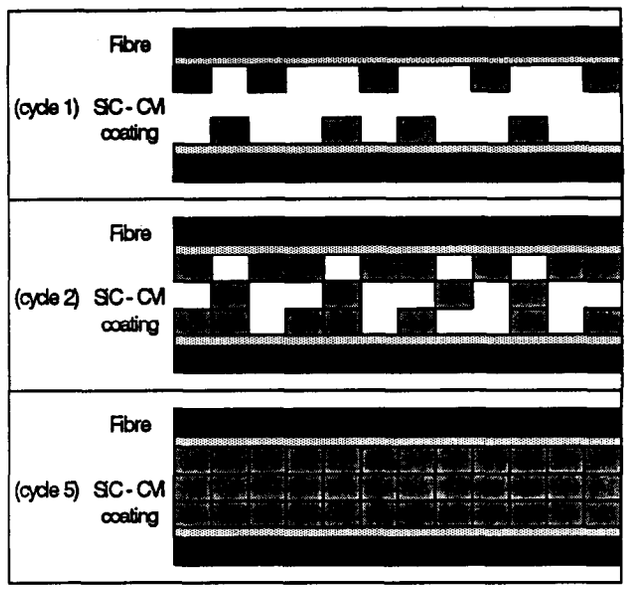


Fig. 8. Processing of the ceramic matrix during the successive impregnation and pyrolysis cycles with the polysilazane.

The pore size distribution was determined on the preform and after 1, 2 and 5 cycles. Two classes of pores are observed on the pore volume distribution graph (Fig. 4): firstly 1–10 μm radius pores corresponding to the space which separates the fibres within a same cloth; this porosity decreases readily according to the number of cycles; and secondly, pores with a radius larger than 50 μm, corresponding to the voids between two woven cloths. This porosity starts decreasing only after the second cycle. A SEM observation shows the good filling of the interfibres voids, whereas the space between cloths is only partially filled (Fig. 5(a) and (b)). This seems to confirm that the precursor could flow out of the largest process before the crosslinking.

3.2 Variation of the mechanical properties with the number of cycles

The stress–deformation curves obtained (Fig. 6) show the unbrittle behaviour of the materials. This is the result of the weak fibre–matrix interface. Samples of preform and of composites after one and two cycles fail in a shear mode by delamination between the plies. Their flexural strengths are similar, about 150 to 180 MPa, corresponding to a delamination strength of about 10 MPa.

On the other hand, the failure of the composites obtained after five cycles is perpendicular to the fabrics. The flexural strength is higher, 400 MPa, and a large amount of fibre pullout is observed on the fracture surfaces. A similar evolution of the failure mode according to the number of cycles is observed by Boisvert & Diefendorf.[3]

The Young's modulus versus porosity curves show a three-stage variation (Fig. 7).

The ceramic residues of the first cycle are too dispersed to build a continuous network (Fig. 8, 1 cycle). Their contribution to the composite elastic modulus is low. No siginficant increase is ascer-

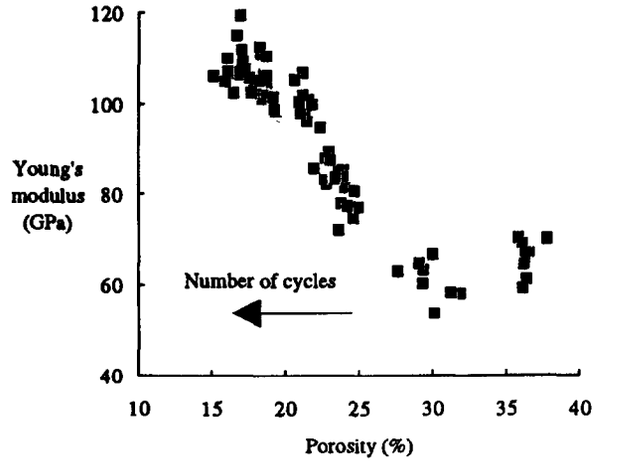


Fig. 7. Variation of the Young's modulus versus the porosity of the composites.

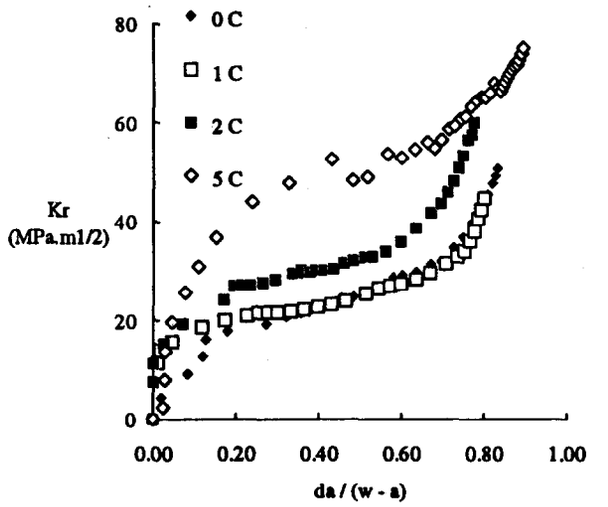


Fig. 9. R-Curves obtained on the assumption of a linear–elastic behaviour.

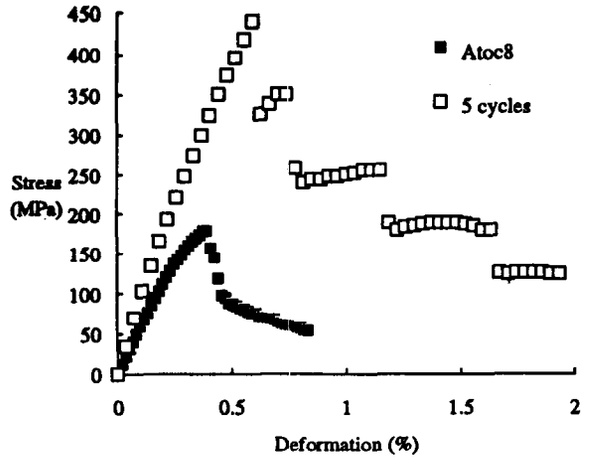


Fig. 10. Stress–deformation curves in three-point bending of composites elaborated from the new process (CVI + 5) and from the conventional one (Atoc8).

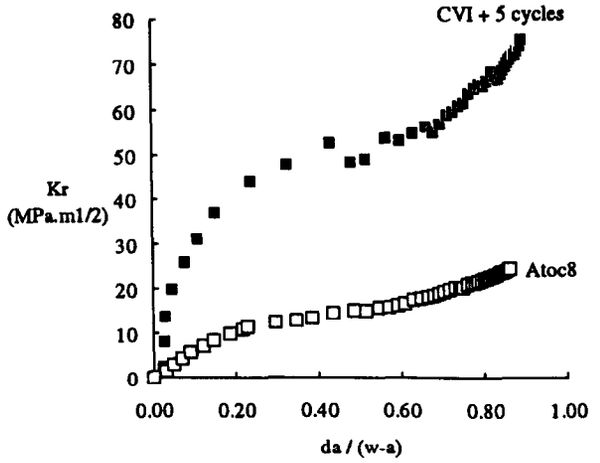


Fig. 11. *R* curves of composites elaborated from the new process (CVI+5) and from the conventional one (Atoc8).

tained. Then, the decrease in porosity from 30 to 22% leads to a large increase in the modulus. The ceramic blocks corresponding to the second and third cycles create progressively a ceramic 'framework' (Fig. 8, 2 cycles).

Thereafter, this framework is filled and strengthed (Fig. 8, 5 cycles). This corresponds to the more gradual increase in modulus when the porosity decreases below 20%, that is to say, during the fourth and fifth cycles.

As expected, the *R*-curves show that *K* increases with the crack length (Fig. 9). Indeed, in addition to the generation of new surfaces, several energy dissipative mechanisms occur during crack propagation, leading to the increase in the crack propagation resistance. The variation of these curves as a function of the number of cycles is similar to that of the flexural strength.

The curves obtained with the preforms and after one or two cycles are almost superimposed, whereas those obtained after five cycles are significantly higher. This can also be explained by the evolution of the failure mode. After the first cycles the cracks are propagated only through the matrix, the crack propagation resistance is low. On the opposite after five cycles, the crack propagation is perpendicular to the fabrics. In this case, the weak fibre matrix interface allows several energy dissipative mechanisms (e.g. fibre pull-out, interface debonding, etc.), increasing the resistance to the crack propagation.

3.3 Comparison with a conventional use of the same percursor

Another type of composite has been realised from a conventional use of the same percursor when the fibres are coated with pyrolytic carbon and placed in an injection mould. The impregnation process is similar to the one described above.

The materials have been tested in three-point bending. The values of the mechanical properties are listed in Table 3. The stress–deformation curves and the *R*-curves obtained in this case (Figs 10 and 11) are siginficantly lower than those obtained with the process CVI + precursor. The flexural strengths of the composites are lower than 200 MPa compared to 400 MPa for the first process and the elasticity modulus does not exceed 70 GPa compared to 105 GPa. Nevertheless, these results are comparable to those obtained with some other precursors used in a similar process.[3–5]

Table 3. Mechanical properties o the composites

Process route	*Ref. comp.*	*Cycle number*	*Fibre Ratio (vol.%)*	*Carbone coating (μm)*	*Porosity (%)*	*Flexural strength (sf) (MPa)*	*Young's modulus (E) (GPa)*
Conventional	Atoc6	8	49	0·50	10·4 ± 0·6	166 ± 27	81 ± 4
Conventional	Atoc7	8	49	0·25	13·6 ± 0·9	159 ± 13	62 ± 6
Conventional	Atoc7b	9	49	0·25	11·8 ± 1·1	168 ± 21	85 ± 5
Conventional	Atoc8	7	41	0·20	17·0 ± 0·7	179 ± 22	55 ± 3
New	CVI+0	0	38·5	0·5 ± 1·0	36·8 ± 1·0	156 ± 20	65 ± 10
New	CVI+1	1	38·5	0·5 ± 1·0	29·8 ± 1·1	135 ± 11	69 ± 4
New	CVI+2	2	38·5	0·5 ± 1·0	23·5 ± 1·5	185 ± 23	95 ± 6
New	CVI+5	5	38·5	0·5 ± 1·0	16·4 ± 1·3	376 ± 62	103 ± 11

4 Conclusion

This new process route leads to high mechanical property composites. Only five impregnation–pyrolysis cycles with Pyrofine PV polysilizane on the SiC/C/SiC preforms are required to increase the flexural strength form 149 to 380 MPa and the Young's modulus from 65 to 105 GPa. The toughness follows the same evolution. These results are comparable to those of composites entirely obtained by CVI and SiC and siginficantly higher than those obtained by a conventional use of the same precursor (flexural strength lower than 200 MPa). However this process is not as fast as expected. Indeed, after each cycle, the porosity decreases less than calculated from the volumetric yield of the percursor during the pyrolysis. The porosity is 15% after five cycles instead of the 7% expected. This is due to the release of the precursor from the preform during the early stage of the pyrolysis.

References

1. Veltri, R. D. & Galasso, F. S., Chemical-vapour-infiltrated silicon intride and silicon carbide matrix composites. *J. Amer. Ceram. Soc.*, **73**(7) (1990) 2137–40.
2. Cornie, J. A., Yet-ming Chiang, Uhlmann, D. R., Mortensen, A. & Collins, L. M., Processing of metal and ceramic matrix composites. *Ceram. Bull.*, **65**(2) (1986) 293–304.
3. Boisvert, R. P. & Diefendorf, R. J., Polymeric precursor SiC matrix composites. *Ceram. Eng. Sci. Proc.*, **9**(7–8) (1988) 873–80.
4. Diefendorf, R. J. & Boisvert, R. P., Processing of Polymeric Precursor, Ceramic Matrix Composites. *Mater. Res. Soc. Symp. Proc.*, **120** (1988) 157–62.
5. Boisvert, R. P., Hutter, R. K. & Diefendorf, R. J., Interface manipulation in ceramic matrix composite for improved mechanical performance. In *Proceeding 4th Japan–US Conference Composite Materials*, 1988, pp. 873–80.
6. Colombier, C., Study of new polysilazane precursors to Si–C–N–O ceramics. In *Proceeding of the 1st European Ceramic Society Conference*, 18–23 June 1989, Vol. 1, Maastricht, The Netherlands. Elsevier Science, 1989, pp. 1.43–1.52.
7. Gonon, M. F., Elaboration et Caractérisation de Composites à Fibres Longues et à Matric Céramique Obtenue par Pyrolyse d'un Précurseur organométallique de type Polysilazane. Thesis, I.N.S.A., Lyon, France, 1993.
8. Lowden, R. A., Fiber coating and the mechanical properties of a fiber-reinforced ceramic. *Composite Ceram. Trans.*, **19** (1991) 619—29.
9. Bouquet, M., Birbis, J. M. & Quenisset, J. M., Toughness Assessment of Ceramic Matrix Composites *Composite Sci. Technol.*, **37**(1–3) (1990) 223–48.
10. R'mili, M., Application de la mécanique de la rupture aux com-posites Carbone/Carbone. Thesis, I.N.S.A., Lyon, France 1990.

Journal of the European Ceramic Society **15** (1995) 191–199
Elsevier Science Limited
Printed in Great Britain
0955-2219/95/$9.50

Fractography of Fatigued and Fractured Regions in a Silicon Carbide Whisker Reinforced Alumina Composite

Ashok Kr. Ray, Swapan Kr. Das, Prabir Kr. Roy

National Metallurgical Laboratory, Jamshedpur 831007, Bihar, India

&

S. Banerjee

Research and Development Centre for Iron and Steel—SAIL, Ranchi 834002, Bihar, India

(Received 18 May 1994; revised version received 19 July 1994; accepted 1 August 1994)

Abstract

Fatigue cracked and fast fractured regions in four point bend specimens prepared from 25 wt% silicon carbide whisker reinforced alumina composites were examined by Scanning Electron Microscopy. In the fatigue cracked region, the alumina matrix failed mainly in a transgranular mode and the whiskers failed mainly with a flat fracture surface but without pullout. On the other hand, in the fast fractured region, the whiskers failed predominantly by pullout and the alumina matrix failed in a mixed mode with about half in transgranular and the other half in intergranular fracture. Thus, to improve the fracture toughness of the material, the grain boundary strength of alumina and the matrix whisker interfacial bonding should be improved. To increase the resistance to fatigue, the fracture strength of the alumina grains should be improved by using finer α-alumina particles and the fatigue strength of the whisker has to be increased by improving the uniformity in distribution of β-SiC whiskers during hot pressing.

1 Introduction

Fatigue crack growth rate (FCGR)[1,2] and fracture toughness[1–3] of 25 wt% silicon carbide whisker reinforced alumina ceramic composite have been studied and reported.[1–3] Such studies are important since these materials have potential application in the production of structural components used at elevated temperatures, in high efficiency heat engines and heat recovery systems and for making cutting tools to machine special materials. When used in such applications, these ceramic components would often encounter monotonic and cyclic loading which produce crack extension. Therefore, the fractographic features of the fatigue failed samples need to be examined to identify the likely micromechanism of crack advance under monotonic and cyclic loading in this composite. Recently, Dauskardt *et al.*[4] have made an extensive fractography of fatigue failed regions in a 15 vol% SiC whisker-reinforced alumina composite. The identification of the fractographic features at the low, medium and high Stress Intensity Range (ΔK) fatigue region as well as in the fast fracture region can give us a clue to the likely mechanisms of fracture in our material.

2 Experimental Procedure

The four point bend specimens were sliced, prepared, surface finished and randomised from a 15 mm × 50 mm × 12·5 mm preformed billet of 25 wt% silicon carbide whisker reinforced alumina composite material (Fig. 1(a)). The details of fabrication of the billet are given elsewhere.[3]

The alumina powder used was of α-type.[1] The SiC whiskers had been produced by a carburization process at 1600°C where the sources of silicon and carbon were rice husk ash and rice husk hydrocarbons.[3,5]

The particle size of the alumina powder was less than 1 μm. The average whisker diameter was 0·1–0·25 μm as revealed in the LT plane of the montage of the ceramic composite investigated here (Fig. 1(b)). The length of the whiskers varied between 10 and 30 μm.[3]

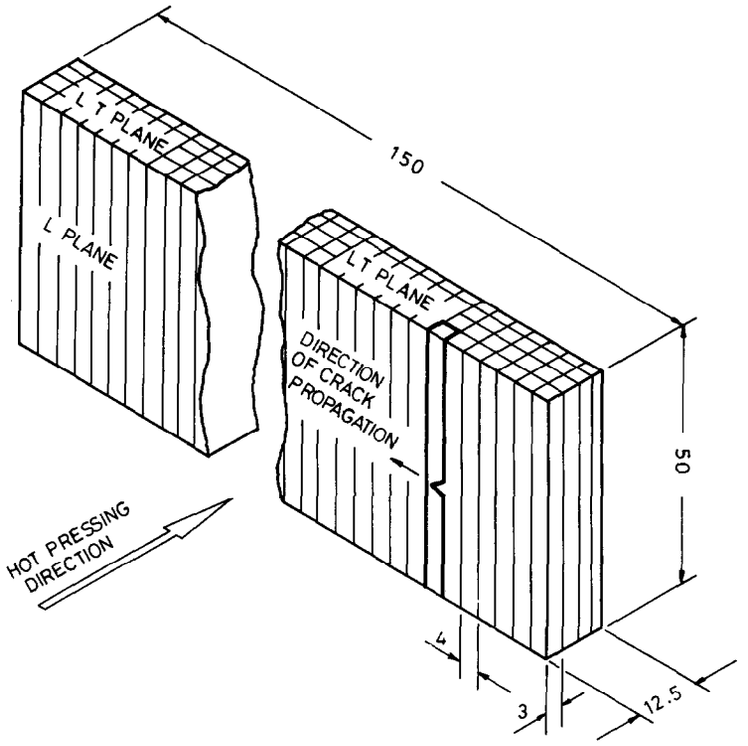


Fig. 1(a). Portion of the billet prepared from the 25 wt% silicon carbide–alumina composite. All dimensions are in mm.

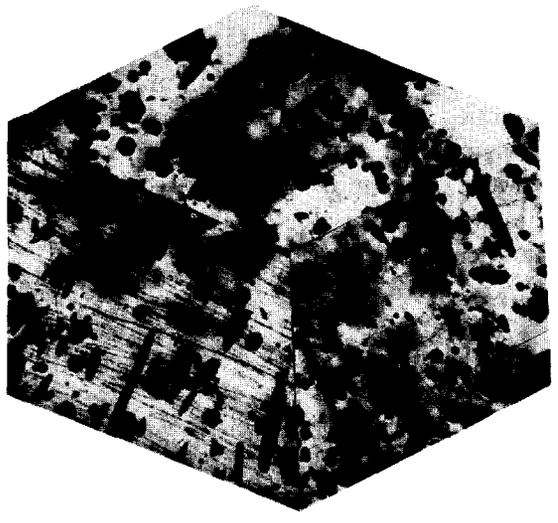


Fig. 1(b). Montage of the microstructures shows distribution of SiC_w along the three planes.



Fig. 2. Fracture surface of the composite showing the size and shape of the alumina matrix.

The SEM (Scanning Electron Microscope) examination of the fractured surface of the specimens which failed due to premature crack extension during precracking in the conventional bridge fixture,[1,3] showed that the alumina grain size after fabrication varied between 1 and 6 μm. This confirms that during hot pressing, the alumina underwent substantial grain coarsening. In areas where either whiskers were absent or there was evidence of pores (Fig. 2), the grain size was as high as 6 μm. However, in other areas, the majority of the alumina grain size was in the range of 2–4 μm.

The montage of the ceramic composite revealed the 3D-distribution pattern of the whiskers in the longitudinal (L), long transverse (LT) and short transverse (ST) planes. In the L plane, the whiskers appeared to be randomly oriented as the hot pressing direction is perpendicular to this L plane. During hot pressing, whiskers which are not normal to the L plane get further inclined thus producing the random orientation of the whiskers.[1] Since maximum material flow occurred along the LT planes during hot pressing, the whiskers tend to get oriented parallel to the L plane. In the ST plane, there was a mixture of random orientation as well as normal alignment of the whiskers.

Becher and Wei had concluded in their work[6] that whisker orientation during processing of hot pressed SiC-whisker reinforced alumina leads to anisotropy in both fracture toughness and fracture strength of the composites. In other words, their fracture strengths are limited by the nonuniformity of the distribution of the whiskers, i.e by the ability to disperse the SiC whiskers. They also found that the dispersion of the whiskers improved by using finer alumina powder and hence an increase in the fracture strength of the composite was observed. Nevertheless, they have clearly observed[6,7] that similar to our composite under investigation (Fig. 1(b)), the whiskers were preferentially aligned perpendicular to the hot pressing axis. This type of distribution of whiskers suggested that a great deal of rearrangement of whiskers and powder occurred in the initial stage of densification of the composites and/or the matrix material underwent considerable deformation or creep during hot pressing.

The dimensions of the billet and the orientation of the four point bend specimens (3 mm × 4 mm × 50 mm) in the billet is given in Fig. 1(a). The 4 mm × 50 mm faces, were normal to the hot-pressing direction so that both the direction of crack propagation (Fig. 3) and the crack plane were parallel to the LT plane (Fig. 1(a)) and normal to the hot-pressing direction.[3] The 3 mm × 50 mm faces of the specimen were parallel to the ST plane.

A Vickers indentation produced at 0·8 kN load at the centre of the 3 mm × 50 mm face of the sample acted as the crack starter on half of the four point bend specimens. On the remaining half, notches were inserted exactly at the centre of the 3 mm × 50 mm surface of the specimens with a carborundum wheel to a depth of 0·1 mm. Thereafter, the specimens were subjected to fatigue loading in a servohydraulic test machine MTS-880 (100 kN capacity) to precrack the specimen in an articulated bridge fixture,[2] till the ratio of crack length to width was 0·05 on the (4 mm × 50 mm) surface of the specimen. Precracking was conducted at a force of 4–5 kN, load ratio, R = 0·1 and frequency, f = 20 Hz. After this, the fatigue crack growth rate in the specimen was determined at increasing values of Stress Intensity Range ΔK (Fig. 4), under normal four point bend loading (see Fig. 3) until the ratio of crack length to width was about 0·45–0·5, on the 4 mm × 50 mm surface of the specimen. Thereafter, the test to determine the fatigue crack growth rate (FCGR) was terminated and the specimen was subjected to monotonic loading to determine the fracture toughness of the material[1] as per ASTM STP 410.[8] For both FCGR as well as fracture toughness (K_{IC}) tests, a 1 kN load range of the MTS-880 test machine was used. The test frequency was 1 Hz and the loading rate was 0·25 N s^{-1}. Tests were conducted in laboratory atmosphere and at ambient temperature. The fracture toughness testing produced the fast fracture. The details of fracture toughness and FCGR tests are given elsewhere.[1,2]

The fracture surfaces were coated with a thin film of gold (thickness 0·02 μm) prior to SEM (Scanning Electron Microscopic examination, in a JEOL JSM 840A microscope).

The three regions, namely low ΔK corresponding to 0·8–1·8 MPa $\sqrt{m}$; high ΔK corresponding to 2·8–3 MPa $\sqrt{m}$; and, the fast fracture region corresponding to a K_{IC} value of 5·9 MPa $\sqrt{m}$, were, at first, identified on the fracture surface at a magnification of 30 X under SEM (Fig. 5) — using the details of the crack growth rate data generated on

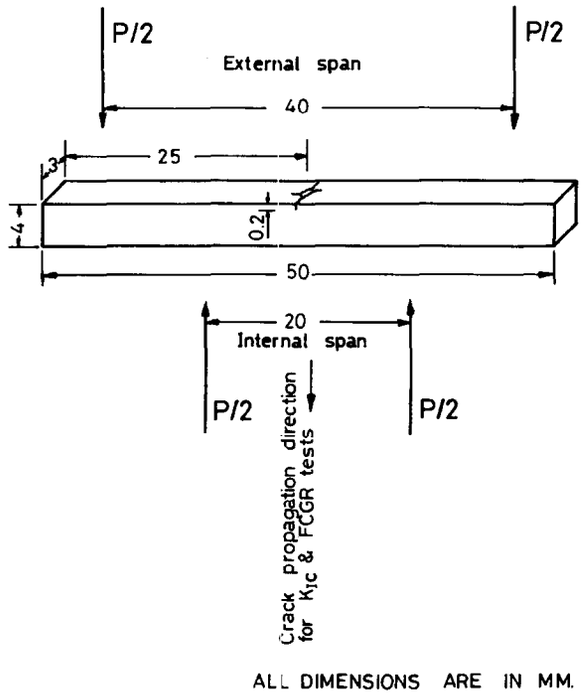


Fig. 3. Indented and precracked specimen for four point bend loading. Cracks are located at the four corners of indentation.

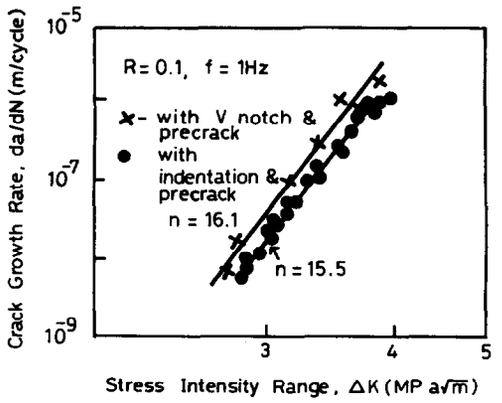


Fig. 4. Fatigue crack growth data of 25 wt% SiC reinforced Al_2O_3 composite.



Fig. 5. Entire fracture surface. Right-hand side—low ΔK region; middle—high ΔK region; left-hand side — fast fracture region (FF).



Fig. 6. At low ΔK (0·8–1·8 MPa $\sqrt{m}$) region, the majority of the whiskers failed with a square fracture without evidence of large scale pullout.



Fig. 7. At high ΔK (2·8–3 MPa $\sqrt{m}$) region the whiskers failed in a mixed mode, i.e. both with a square fracture and also by pullout.

the specimen as a guideline. The difference between the fatigue and fast fracture could, however, be discerned through observation even with the naked eye. The distinction between the low and the high ΔK fatigue regions was made from the crack length versus the number of cycles data generated during the fatigue loading of the specimen.

Each region was, at first, carefully scanned at low magnification, to identify the general and uniformly distributed features. Thereafter, it was examined at two different magnifications 4500 X and 7500 X, in order to identify the fractographic features and the mechanism of fracture in the low ΔK and the fast fracture regions.

3 Fractographic Observations

A summary of the results of the fractographic observations is reported in Table 1.

Table 1 states that, at low ΔK (0·8–1·8 MPa $\sqrt{m}$), the whiskers failed predominantly by shearing with a flat or square fracture without any visible evidence of necking; this was typical of fatigue fracture (Fig. 6). However, at high ΔK (2·8–3 MPa $\sqrt{m}$), the whisker failed in two different ways: that is about 60% of the whiskers failed with a flat fracture and the balance failed by pullout (Fig. 7). On the other hand, in the fast fracture region, the whiskers failed predominantly by pullout (Fig. 8).

Table 1. Fractographic features in the fatigue and fracture regions in a 25 wt% silicon carbide whisker reinforced alumina

Mechanism of failure		*Fatigue*		*Monotonic*
		Low ΔK 0.8–1.8 MPa√m	*High ΔK 2.8–3.0 MPa√m*	*Fracture 5.96 MPa√m*
Whisker	Pullout (%)	5	40	85
	vs. shear (%)	95	60	15
Matrix	Transgranular (%)	95	55	45
	vs. intergranular (%)	5	45	55
	o Branching	P	A	A
	o Deflection	P	A	A
Crack	o River pattern	P	A	A

P = present; A = absent.

Table 1 also reports that the matrix alumina grains failed predominantly through transgranular fracture (Fig. 9) at low ΔK (0·8–1·8 MPa$\sqrt{m}$). In the high ΔK (2·8–3 MPa$\sqrt{m}$) region, the matrix failed in a mixed mode wherein about 45% of the alumina grains failed by intergranular and the balance by the transgranular mode, as shown in Fig. 10. During monotonic loading, the alumina grains in the fast fracture region also failed in a mixed mode with a slightly increased percentage of intergranular (~55%) and the balance by transgranular mode—as shown in Fig. 11.

It is noteworthy that in the low ΔK region, the crack had frequently branched (Fig. 12) and deflected (Fig. 13) while it propagated. River pattern

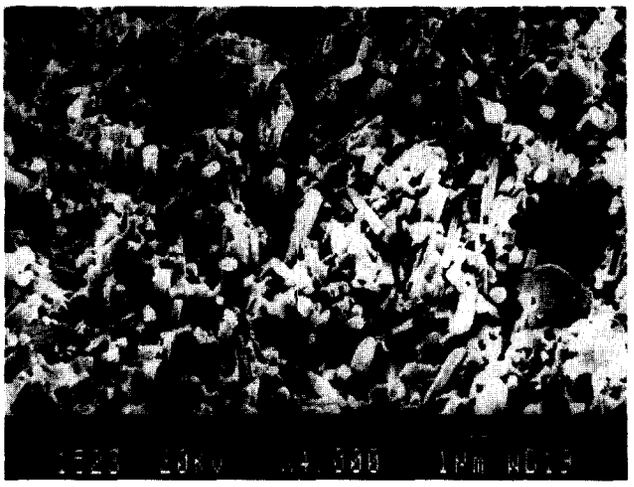


Fig. 8. In the fast fracture region (K_{IC} = 5·9 MPa$\sqrt{m}$), whiskers failed predominantly by pullout mechanism.

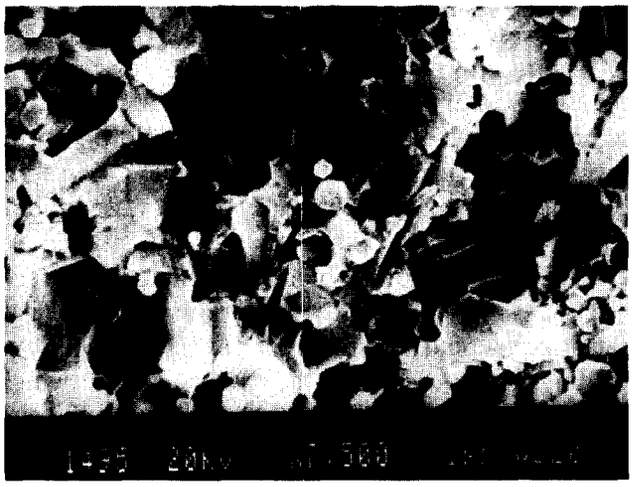


Fig. 9. At low ΔK region, the alumina matrix failed predominantly through transgranular fracture.



Fig. 10. At high ΔK region, the alumina grains failed in a mixed mode, i.e. intergranular (~45%) and transgranular (~55%).

markings with steps (Fig.14) were also present in the cleavage facets. However, in the fast fracture region, the branching and deflection of the crack were virtually absent.

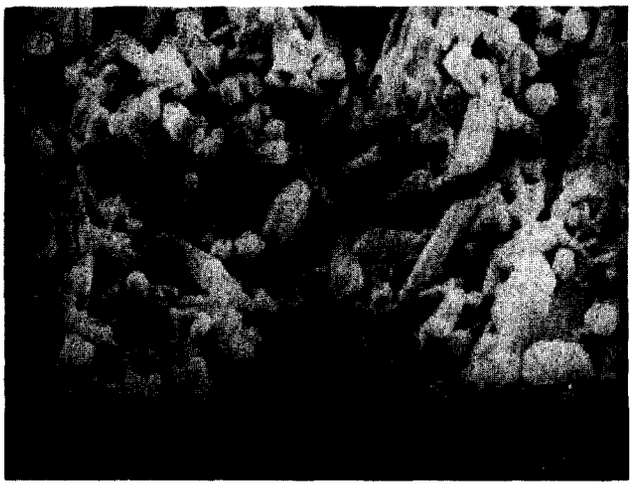


Fig. 11. In the fast fracture region (monotonic loading), the alumina grains failed in a mixed mode, i.e. intergranular (~55%) and transgranular (~45%).



Fig. 12. Crack branching in the low ΔK region.

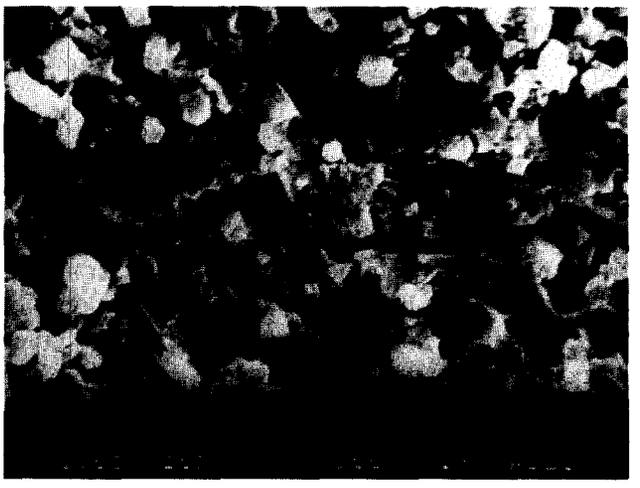


Fig. 13. Crack deflection in the low ΔK region.

4 Discussion

Twenty-five weight percent silicon carbide whisker reinforced alumina composite is susceptible to a fatigue crack growth phenomenon[1,2] (Fig. 4), which is similar to that in the case of metallic

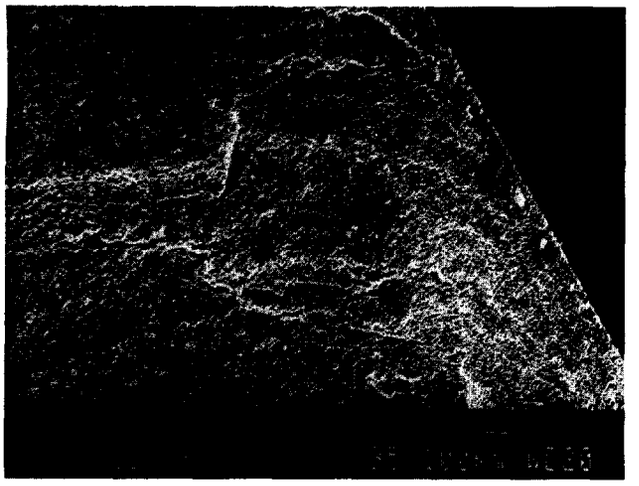


Fig. 14. River pattern marking with steps in the low ΔK region (YZ—modulation SEM image).

metals, but with a higher crack growth exponent (n = 15·5). Figure 4 shows that the FCGR data of this material fits the usual Paris equation $da/dN = A(\Delta K)^n$.

Since the manner of failure of the whiskers and the α-alumina grains were entirely different in the low ΔK fatigue and the fast fracture regions, the schemes of crack growth under these two conditions are discussed separately, to focus on their contradistinctions.

4.1 Low ΔK fatigue region

During fatigue loading at the low ΔK regions, where ΔK = 0·8–1·8 MPa $\sqrt{m}$ the alumina grains of the matrix failed mainly by transgranular cleavage with frequent crack branching and crack deflection. Also, the cleavage facets revealed river pattern and steps. At low ΔK, the K_c values and consequently the traction force ahead of the crack tip, were not adequate to promote intergranular fracture.

At low ΔK, the amount of crack extension is very low. So even though the energy dissipated per cycle is low, the number of cycles and the cumulative energy required for a given amount of crack extension is quite significant and can thus account for the higher surface area required for the various features encountered like crack branching, river pattern and steps.

At low ΔK fatigue, the whisker could fail in three different modes

- pullout,
- tensile fracture,
- fatigue.

Table 1 shows that only a few of the whiskers failed due to pullout at low ΔK fatigue. This naturally indicated that the maximum traction forces generated ahead of the crack tip during the low ΔK fatigue was not adequate to produce a pullout. Thus, it is likely that the whiskers continue to bridge the crack even after some of the surrounding alumina grains had failed by transgranular cleavage. Therefore, under these circumstances, the whisker could fail due to tensile fracture or fatigue.

One might rule out the possibility of tensile fracture if one had examined the relative values of strength and Young's modulus reported in Refs 9 and 10. The fracture strength of the whisker is about 6·5–7 times higher than that of alumina. Accordingly, the tensile fracture of the whisker was unlikely if the traction forces ahead of the crack tip were to be distributed in proportion to the relative cross sections of the whisker and alumina in the plane of the crack. Even if the whiskers were to carry the major part of the traction forces ahead of the crack tip, the high traction forces would produce failure by pullout rather than by tensile fracture, as was observed in the fast fracture region where K_{IC} values and consequently the traction forces, were high.

Since the possibility of large scale failure by pullout or tensile fracture was discounted, whiskers were most likely to fail by fatigue. At low ΔK, the whiskers which had bridged the crack after the surrounding alumina grains had failed by cleavage, would continue to experience fatigue loading, then failed with a square fracture which is typical of fatigue. The fatigue failure of the silicon carbide whisker under such circumstances, could be significantly influenced by the stacking fault such as is reported Ref. 11 in Fig. 15, since such fault could be responsible for nucleating the fatigue crack. However, this aspect needs careful study.

Since the cleavage of the α-alumina grains probably occurred before the whiskers (located mainly at the grain boundaries) had failed, it was necessary to improve the fatigue resistance of the α-alumina grains. This apart, the dislocation pile-up

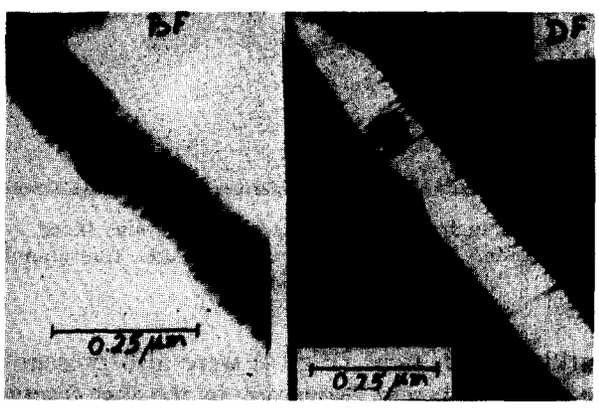


Fig. 15. TEM of β-SiC whisker showing stacking fault by dark field and bright field techniques.

model[12] would obviously indicate that the cleavage failure of α-alumina could be prevented through the refinement of alumina grains in the aggregate structure. The size of alumina grains varied between 1 and 6 μm. In this context, one should note that one could obtain higher resistance to low ΔK fatigue, if ultra-fine or nano-size alumina grains, such as that produced by the solgel technique, were to be used to fabricate this composite.

A schematic view of crack propagation mechanism is representated in Fig. 16(a). It illustrates that at low ΔK fatigue, the matrix failed predominantly by transgranular cleavage and the advancing crack frequently branched and tilted and twisted in its course of deflection. Since the whiskers were predominantly located at the grain boundaries and the crack propagation along the grain boundary at low ΔK fatigue was negligible, the possibility that the crack would encounter these whiskers as it advances would be rather low. Only a few of those whiskers which had bridged the crack with an orientation normal to the advancing crack plane, could fail by pullout. The other whiskers were likely to fail by directly experiencing fatigue loading. This could explain why

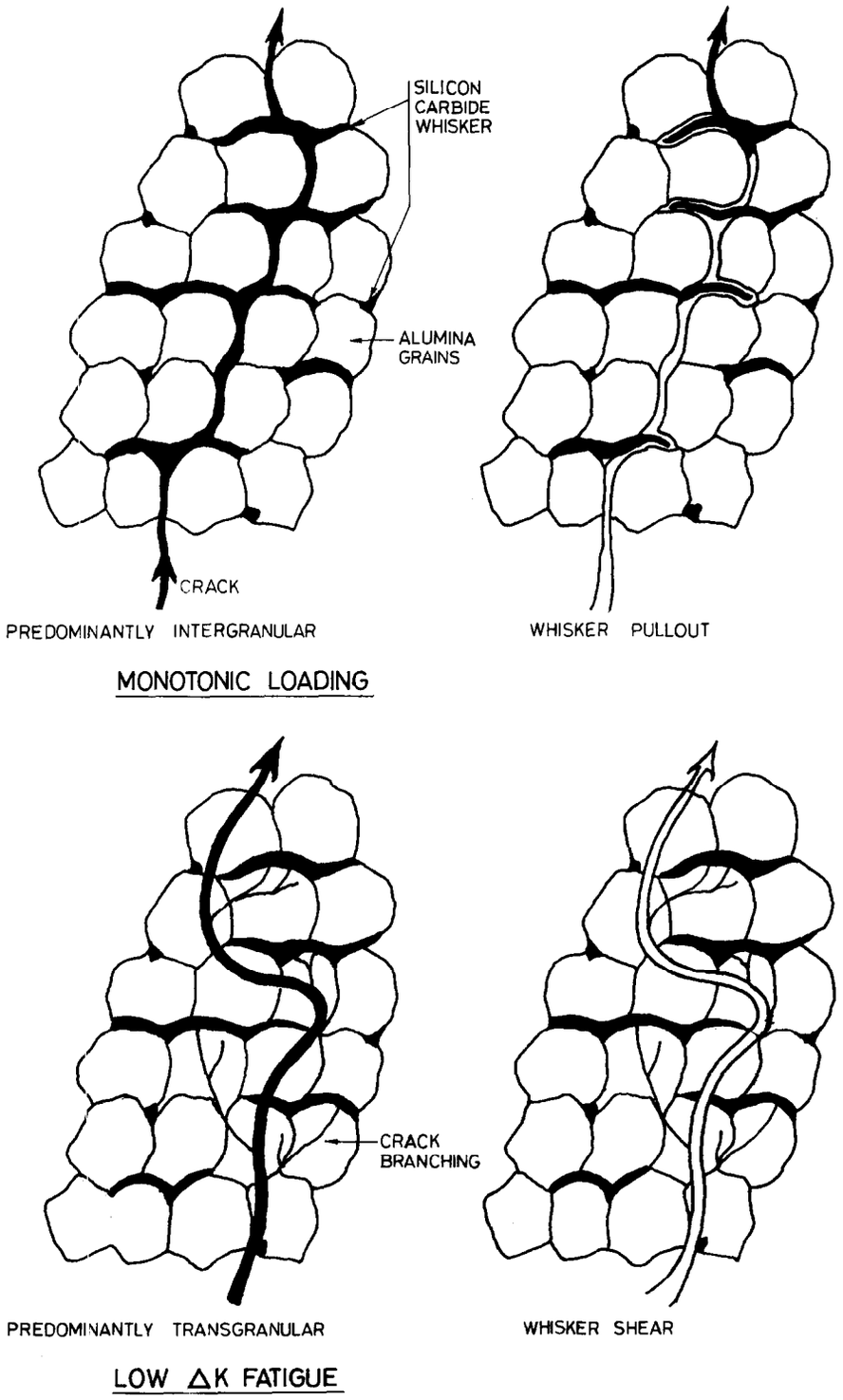


Fig. 16. Schematic of the crack propagation during monotonic and cyclic loading.

at low ΔK fatigue, the majority of the whiskers failed with a square fracture and without pullout.

4.2 Fast fracture region

During the fast fracture under monotonic loading such as during the fracture toughness testing, some of the α-alumina grains of the matrix failed by intergranular fracture; the others failed by transgranular cleavage. The value of K_{IC} during such monotonic loading was 5·9 MPa $\sqrt{m}$. At such values of K_C, the traction force generated ahead of the crack tip was adequate to produce the intergranular failure in those grains which were favourably oriented with respect to the direction of the traction force. Debonding and pullout of those whiskers at the fractured grain boundaries would therefore occur.

It is difficult to summarise from the fractographic features as to which of these, i.e. transgranular cleavage or intergranular fracture, occurred, at first, under monotonic loading.

After some of the grains had failed through the intergranular mode, the other neighbouring grains which were less favourably oriented or which were strongly anchored by the whiskers across the grain boundaries, failed through transgranular cleavage.

The pullout of the whiskers could be avoided if the whisker α-alumina interfacial strength was improved or if finer and more numerous whiskers and also finer α-alumina particles were used in fabricating the composite. Similarly, the intergranular fracture could be avoided by strengthening the boundaries.

As illustrated schematically in Fig. 16(b), the fracture due to monotonic loading showed a substantial amount of intergranular failure of the matrix and pullout of the whiskers. Crack deflection, branching and the characteristic river pattern marking with steps, were absent in this region.

The matrix failure was predominantly intergranular. Nevertheless, the whiskers were located mainly at the grain boundaries. Therefore, the probability of the advancing crack front interacting with the whiskers was extremely high. The whiskers tending to bridge the advancing crack quite frequently would therefore get debonded and pulled out—which is schematically illustrated and shown in Fig. 16(b). This justifies the fact that during the monotonic fracture, failure of whiskers by the pullout mechanism was frequently observed in the fractograph.

During fatigue loading at high ΔK, mechanism of fracture was an intermediate situation between the two extreme cases: that is between the case of monotonic fast fracture and that of the low ΔK fatigue fracture.

Since the ceramic material is often expected to survive both monotonic and fatigue loading, one could make the following general observations based on the scheme of crack growth under the two conditions as discussed above.

To prevent fracture failure of this ceramic material under monotonic loading, its microstructural features would have to be strengthened to avoid intergranular fracture of α-alumina and the pullout of the whisker. This requires that the grain boundary strength of α-alumina and the whisker—matrix interfacial strength should be increased. Similarly, to retard crack extension during low ΔK fatigue, intergranular cleavage fracture of α-alumina grains and fatigue failure resistance of the silicon carbide whiskers should be improved, possibly by using finer α-alumina powder[6,7] and by improving the uniformity of distribution of whiskers in the matrix during hot pressing.[6,7]

5 Conclusions

The micromechanism of fracture of a 25 wt% silicon carbide whisker reinforced alumina composite when loaded in fatigue was quite different from that when loaded monotonically. Consequently, the fractographic features in the two instances of loading were significantly different.

When loaded in fatigue, the alumina matrix failed in a transgranular mode and the whiskers failed by producing a flat fracture but without their pullout.

When loaded monotonically, the whiskers predominantly failed by pullout and the alumina matrix failed in a mixed mode with about 55% in intergranular and the balance in transgranular mode. Whereas the grain boundary strength of α-alumina and the whisker–matrix interfacial bonding should be increased to produce increased resistance to failure under monotonic loading. The fatigue failure resistance of the composite could be improved by improving the cleavage strength of the α-alumina grains, i.e. by using finer α-alumina particles and by increasing the fatigue strength of the whiskers by improving the uniformity in the distribution of β-SiC whiskers during hot pressing.

Acknowledgements

The authors gratefully acknowledge the help and advice of Mr N. K. Das and Professor O. N. Mohanty in the SEM work. The authors are thankful to Professor P. Ramachandrarao Director-National Metallurgical Laboratory, for allowing us

to publish this work and to NIST (National Institute of Standards and Technology) NBS-USA for supplying us the ceramic specimens.

References

1. Ray, A. K., Fuller, E. R. & Banerjee, S., Fatigue crack growth rate and fracture toughness of 25 weight percent silicon carbide whisker reinforced alumina composite with residual porosity. Submitted to *J. Eur. Ceram. Soc.* (1994).
2. Ray, A. K. & Banerjee, S., Precracking of ceramic specimen and determination of fracture crack growth rate of 25 wt% SiC reinforced Al_2O_3 composite. Accepted for publication in *J. Am. Ceram. Soc.* (1995).
3. Krause, R. F. Jr & Fuller, E. R. Jr, Fracture resistance behaviour of silicon carbide whisker-reinforced alumina composites with different porosites. *J. Am. Ceram. Soc.*, **73**(3) (1990) 559–66.
4. Dauskardt, R. H., James, M. R., Porter, J. R. & Ritchie, R. O., Cyclic fatigue crack growth in a SiC whisker—reinforced alumina ceramic composite. *J. Am. Ceram. Soc.*, **75**(5) (1992) 759–71.
5. Cook, J. L. & Rhodes, J. R., Silicon carbide whiskers. Presented at the 88th *Annual Meeting of the American Ceramic Society*, Chicago, IL, April 28, 1986 (Engineering Ceramics Division, Paper No. 18-C-86).
6. Becher, P. F. & Wei, G. C., Toughening behaviour in SiC-whisker-reinforced alumina. *J. Am. Ceram. Soc.*, **67**(12) (1984) 267–9.
7. Wei, G. C. & Becher, P. F., Development of SiC—whisker—reinforced ceramics. *J. Am. Ceram. Soc.-Bull.*, **64**(2) (1985) 298–304.
8. Brown, W. F., Jr & Srawley, J. E., *American Society for Testing and Materials STP—410*. ASTM, Philadelphia, PA, 1966.
9. Ray, A. K., Mohanty, G. & Ghose, A., Effects of catalysts and temperature on silicon carbide whiskers formation from rice husk. *J. Mater. Sci. Lett.*, **10** (1991) 227–9.
10. Fisher, E. S., Manghnani, M. H. & Routbort, J. L., Study of the elastic properties of Al_2O_3 and Si_3N_4 material composites with SiC, whisker reinforcement. *High Performance Composites for the 1990s*, ed. S. K. Das, C. P. Ballard and F. Marikar, The Minerals, Metals and Materials Society, 1991.
11. *Reinforcing Tomorrows Technology*. Ceram. Indust. April (1992).
12. Kingery, W. D., Bowen, H. K. & Uhlmann, D. R., *Introduction to Ceramics*, 2nd ed., John Wiley and Sons, Inc. New York, 1976, p. 795.

Journal of the European Ceramic Society **15** (1995) 201–207
Elsevier Science Limited
Printed in Great Britain
0955-2219/95/$9.50

Determining the Fracture Toughness of Brittle Materials by Hertzian Indentation

P. D. Warren

Department of Materials, Oxford University, Parks Road, Oxford OX1 3PH, UK

(Received 21 December 1993; revised version received 14 July 1994; accepted 1 August 1994)

Abstract

The use of Hertzian indentation as a method for determining the fracture toughness of any brittle material is described. The advantage of the method described here is that the only quantity to be measured is a fracture load. Experimental determinations of K_{IC} *for soda-lime glass and high-purity alumina give results 0·71 and 3·72 MPa* $m^{1/2}$*, respectively.*

Introduction

The fracture toughness of a brittle material is one of its most important mechanical properties. Determination of this value is frequently a complicated process involving preparation of specimens with well-defined sharp cracks of known length. A recent review article[1] has presented a summary of available techniques. However, one method was conspicuous by its absence—that of Hertzian indentation. It is the purpose of this paper to suggest that this method should be looked at afresh.

Indentation techniques in general have certain advantages compared with the more conventional methods: the experimental procedure is straightforward, involving minimal specimen preparation, and the amount of material needed is small. The Vickers indentation method[2–4] is well known. However, it is not without drawbacks. There are now a very large number of theoretical models in the literature (19 are reviewed by Ponton and Rawlings[5,6]) relating the surface crack length measured after indentation to the indenter load and material parameters—Young's modulus, hardness and fracture toughness. There is still considerable debate as to the nature of the cracks observed around a Vickers indentation—the idealised 'half-penny' characteristics of the median/radial system, as opposed to Palmqvist cracking. Cook and Pharr[7] have presented a considerable amount of evidence to suggest that *radial* cracks form almost immediately on loading in a wide variety of crystalline solids. There is also debate on how to determine the type of cracking from the surface-crack length vs applied load relation. For a spirited discussion of these matters the articles by Li *et al.*[8,9] and Srinivasan and Scattergood[10] should be consulted. It should be noted, however, that Lawn[11] asserts that Palmqvist cracks '. . . retain the essential half-penny character.'

Many attempts have been made to use Hertzian indentation—where a hard sphere is pressed into the flat surface of a brittle substrate—to determine K_{IC} for brittle materials: work by Frank and Lawn—glass,[12] by Powell and Tabor—TiC,[13] by Wilshaw—glass,[14] by Nadeau—vitreous carbon,[15] by Warren—TiC, ZrC, VC and WC,[16] by Matzke *et al.*—UO_2,[17] by Matzke—ThO_2,[18] by Inoue and Matzke—ThO_2,[19] by Matzke and Warren—ThO_2,[20] by Matzke and Politis—NbC, Nb(C,N) and NbN,[21] by Matzke *et al.*—(U,Pu)C and (U,Pu)(C,N),[22] by Laugier—TiN coatings on WC–Co,[23] Al_2O_3—ZrO_2,[24] various Al_2O_3—ZrO_2 composites and Sialons,[25] various WC–Co composites[26] and finally, by Zeng *et al.*—glass, Al_2O_3 and Al_2O_3–SiC composites.[27,28]

Broadly speaking, the early work, prior to 1978, used the theory of Frank and Lawn,[12] which strictly only applies for ring-cracks initiating exactly at the edge of the contact zone. The papers by Warren and co-workers,[16–19,21,22] (and those of Laugier[23–26]) used Warren's theory,[16] which involves measuring the radius of the ring-crack seen on the surface after fracture: Matzke and Warren[20] and the recent work by Zeng *et al.*[27,28] involved the cross-sectioning of the specimens after fracture to determine the *depth* of the cone crack. The results obtained so far have been variable. Almond *et al.*[29] point out that the values obtained by Warren[16] on various metal carbides are significantly lower than conventional values; Laugier,[26] on the other hand, for various WC—Co composites, found values considerably higher. This poor

agreement may be one reason why the test is not more commonly used. This is a pity because the Hertzian indentation test has at least one considerable advantage over Vickers indentation: until fracture occurs around the indenter the deformation of the substrate is entirely elastic (unless spheres of very small radius, <1 mm, are used). This means that the complications associated with the residual stresses in the Vickers indentation technique do not exist. Furthermore, the elastic stress field is well known.[30]

The disadvantages in the method may be due to the following factors: (i) the stress gradients in the Hertzian field are very steep so that it is difficult to obtain accurate estimates for stress-intensity factors for cracks driven by Hertzian loading; (ii) the results of the analysis are extremely sensitive to the value of Poisson's ratio of the substrate, and (iii) a number of previous experimental determinations of fracture toughness have ignored the effects of elastic mismatch (and friction at the indenter–substrate interface) when the sphere and the substrate are made of elastically dissimilar materials. Much work has been done using either steel or tungsten carbide spheres on glass substrates and there is good experimental evidence[31] that the effects of this significant elastic mismatch on the observed fracture loads are *not* negligible.

Below, we summarise the main aspects of the theory of Hertzian fracture and present a method which enables the value of K_{IC} to be found for any brittle material, as long as it is indented by a sphere made of the same material. The method described here is extremely easy to use, does not require measurement of the ring-crack size and gives reliable results.

Theory

Figure 1 shows a sphere (radius R, elastic constants ν_I, E_I) pressed by a load P into a flat substrate (with elastic constants ν, E). The load is supported over a circular area whose radius, a, is given by:[32]

$$a = \left(\frac{3RP}{4E^*}\right)^{1/3} \tag{1}$$

where:

$$\frac{1}{E^*} = \frac{1-\nu^2}{E} + \frac{1-\nu_I^2}{E_I} \tag{2}$$

The peak pressure under the sphere, p_o, is given by:

$$p_o = \frac{3P}{2\pi a^2} \tag{3}$$

The stress field outside the contact zone has a tensile radial stress near to the surface which

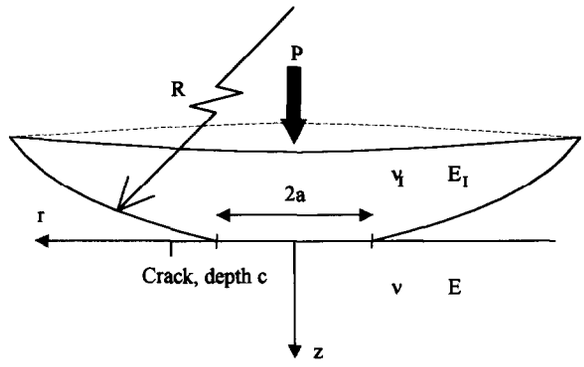


Fig. 1. The geometry of Hertzian contact.

rapidly decreases, and soon becomes compressive, with depth. Thus calculating the stress intensity factors for surface-breaking cracks is not trivial. For short cracks (i.e. those whose depth is less than $a/10$) lying perpendicular to the free surface the method of Nowell and Hills[33] (employing distributed dislocations) can be used to derive expressions for the mode I (and mode II) stress intensity factors. This approach differs from previous work[12,14,16,27,28,34] where it was assumed that the crack path initially lay along the trajectory of the minimum principal stress; here, the pre-cursor flaws are assumed to be perpendicular to the surface; this will tend to *reduce* the K_I values derived here compared to previous results. The use of the method of distributed dislocations enables the effects of the free surface to be accounted for; this will tend to *increase* the K_I values. In this method, a short plane crack of depth c, normal to the free surface, is placed close to the contact zone. The state of stress in the crack's absence is found. When the crack is inserted, unsatisfied tractions appear along the line of the crack. These may be cancelled by the application of equal and opposite tractions along the crack faces, which may be generated by installing a distribution of dislocations. (These dislocations are not real dislocations in a crystalline lattice, but a mathematical device.) The state of stress induced by one of these dislocations is known—the expressions are given explicitly in Ref. 33. By applying a distribution of dislocations, of unknown density $B_r(z)$, the requirement that the crack faces be traction-free may be ensured by writing

$$0 = \tilde{\sigma}_{ij}(z, r) + \frac{G}{\pi(\kappa+1)}\int_0^c B_r(z)K(z, r)\,dz \tag{4}$$

G is the shear modulus of the material, κ is Kolosov's constant (= $3-4\nu$ in plane strain), the coordinates r, z are as in Fig. 1; the function $K(z,r)$ is given in Ref. 33. The unknown quantity, $B_r(z)$, is defined by $B_r(z) = db_r/dz$, and $\tilde{\sigma}$ represents the state of stress induced by the contact in the crack's absence, i.e. in this case the radial

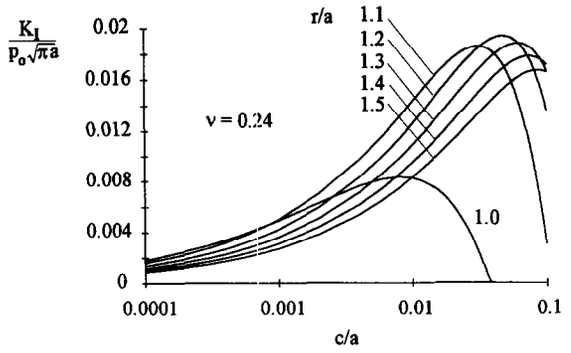


Fig. 2(a). Normalized mode I stress intensity factors as a function of normalized crack size for six normalized crack positions. Poisson's ratio = 0·24.

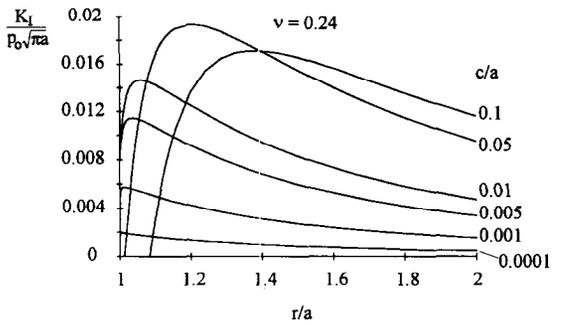


Fig. 2(b). Normalized mode I stress intensity factors as a function of normalized crack position for six normalized crack sizes. Poisson's ratio = 0·24.

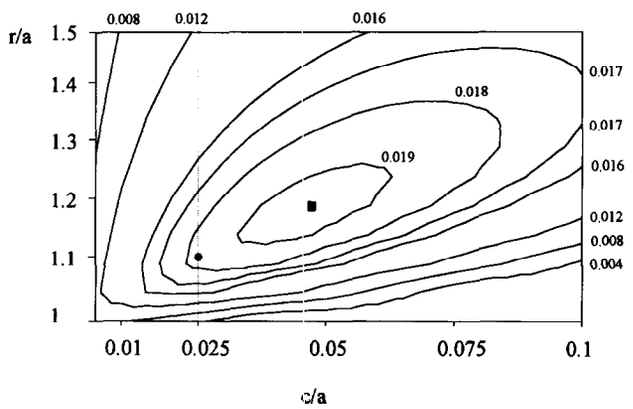


Fig. 2(c). Contours of normalized mode I stress intensity factors $K_I/(p_o\sqrt{\pi a})$ as a function of crack depth ($0{\cdot}005 < c/a < 0{\cdot}1$) and crack position ($1{\cdot}0 < r/a < 1{\cdot}5$). The filled circle shows the maximum value for $c/a = 0{\cdot}025$; at this position ($r/a \sim 1{\cdot}1$), $K_I \sim 0{\cdot}0182\, p_o\sqrt{\pi a}$. The filled square marks the position of the absolute maximum: $K_I \sim 0{\cdot}01937\, p_o\sqrt{\pi a}$ at $c/a \sim 0{\cdot}046$, $r/a \sim 1{\cdot}18$.

component of the Hertzian stress field. This integral equation is effectively represented by a set of linear algebraic equations, typically 20: the (normalized) mode I stress intensity factor can then be expressed in terms of the unknown coefficients in these linear equations. A standard computer library routine for solution of simultaneous equations is then employed. This technique is very well adapted to problems where cracks exist in a steep stress gradient. If the radial Hertzian stress (= $\tilde{\sigma}$) is expressed in terms of the peak Hertzian pressure, p_o, (eqn (3)) then the result of the calculation is a number μ which is related to the (dimensional) mode I stress intensity factor, K_I, by:

$$\mu = \frac{K_I}{p_o\sqrt{\pi c}} \quad \text{where} \quad \mu = f\left(\frac{r}{a}, \frac{c}{a}, \nu\right) \tag{5a}$$

Normalizing with respect to a (rather than c) we have:

$$\frac{K_I}{p_o\sqrt{\pi a}} = \mu\sqrt{c/a} \tag{5b}$$

The rationale for this second normalization is that the dependence of K_I on the crack size is now exclusively in the two terms on the RHS of the equation. All subsequent results presented below are in terms of this second normalization. Warren *et al.*[35] present results for the case where the sphere and the substrate are made of the same material. In this case the stress field in the substrate (and hence the values of K_I) depends on only one material parameter—Poisson's ratio of the substrate. Figures 2(a), (b) and (c) show some basic results from this analysis.

Figure 2(a) shows the normalized mode I stress intensity factor as a function of normalized crack length (c/a) for six normalized crack positions (r/a), for Poisson's ratio = 0·24. Figure 2(b) shows values for the normalized K_I as a function of r/a for six values of c/a; again $\nu = 0{\cdot}24$. Figure 2(a) shows that K_I has a maximum value as a function of c/a for each r/a; furthermore for large cracks situated close to the contact radius the implied value of K_I is negative (because the crack tip is now deep enough that it lies within the compressive region of the Hertzian radial stress). Figure 2(b) shows that for each c/a the maximum in K_I occurs for $r/a > 1$. This explains the well-known fact that ring cracks are always observed to form outside the contact zone, even though the surface radial stress has its largest value at $r/a = 1$. This point has been noted previously.[16,34,36] Figure 2(c) shows a contour plot of $K_I/(p_o\sqrt{\pi a})$ as a function of crack position and crack depth (both normalized). We note two things. For each c/a, we can mark the position of the largest normalized K_I—this is shown by the filled circle for $c/a = 0{\cdot}025$. At this position ($r/a \sim 1{\cdot}1$), $K_I \sim 0{\cdot}0182 p_o\sqrt{\pi a}$); $0{\cdot}0182/\sqrt{0{\cdot}025}$ is therefore the maximum value of μ (= μ_{max}) for this value of c/a, ($c/a = 0{\cdot}025$). μ_{max} is thus just a function of c/a and ν, $\mu_{max} = g(\frac{c}{a}, \nu)$. Secondly K_I has an absolute maximum—marked by the filled square, at $c/a \sim 0{\cdot}046$, $r/a \sim 1{\cdot}18$, $K_I \sim 0{\cdot}01937 p_o\sqrt{\pi a}$.

The above expressions are in terms of stress intensity factors; we will now re-write them in terms of loads. When K_I for one small surface flaw reaches K_{IC} (at a load $P = P_F$), it begins to grow—

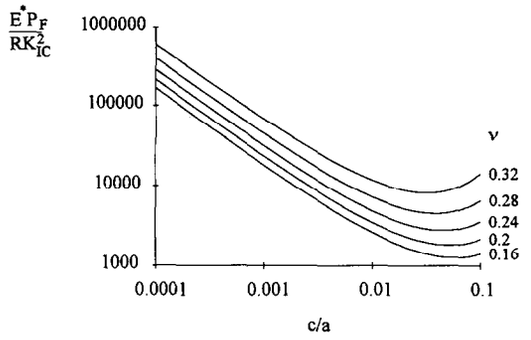


Fig. 3. Minimum normalized fracture load necessary to propagate a crack of normalized size c/a. Results for five different values of Poisson's ratio. The value of the absolute minimum for $\nu = 0{\cdot}28$ is shown.

to form either a ring crack or the well-known ring–cone system. Using eqns (1) and (3), equation (5b) becomes:

$$\frac{E^*P_F}{RK_{IC}^2} = \frac{\pi}{3\mu^2(c/a)} \tag{6}$$

We define a normalized fracture load, P_{FN}:

$$P_{FN} = \frac{E^*P_F}{RK_{IC}^2} \tag{7}$$

Assuming that the flaw distribution is dense enough so that there will always be a flaw (of size c/a) situated close to the position where the crack tip stress intensity experienced is a maximum (for this crack size) eqn (6) can be written

$$P_{FN} = \frac{\pi}{3\mu_{max}^2(c/a)} \tag{8}$$

These values of P_{FN} are therefore the minimum normalised loads necessary to propagate cracks of size c/a. Plots of P_{FN} as function of c/a (for five different values of ν) are shown in Fig. 3. For all values of Poisson's ratio there is an absolute minimum in the normalized fracture load for c/a values in the range 0·02–0·06. For a given ν, this absolute minimum in P_{FN} corresponds to the absolute maximum in $K_I/(p_o\sqrt{\pi a})$. For example, for $\nu = 0{\cdot}24$ Fig. 2(c) shows that the absolute maximum in $K_I/(p_o\sqrt{\pi a})$ is 0·01937; therefore the absolute minimum in normalized fracture load, P_{FN}^{min}, is $\pi/3/(0{\cdot}01937)^2 \sim 2790$. The values of these absolute minima and the corresponding values of c/a as a function of Poisson's ratio are shown in Fig 4 and also listed in Table 1. We emphasise that P_{FN}^{min} is a dimensionless quantity. (For all values of Poisson's ratio the absolute minimum in fracture load occurs at a relative crack position $r/a \sim 1{\cdot}20$.)

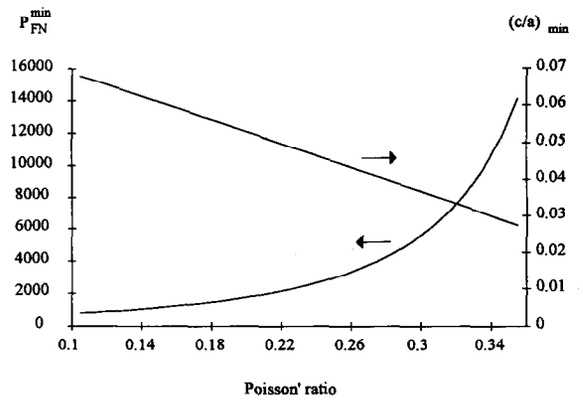


Fig. 4. Absolute minimum normalized fracture loads (P_{FN}^{min}) and the corresponding values of (c/a) as a function of Poisson's ratio.

Determination of K_{IC}

The principle of the method for determining K_{IC} is now clear. For a material with a given E^* and K_{IC} one searches for the minimum value of P_F/R. If one performs a series of Hertzian tests with a sphere of given R (25 tests should be sufficient), noting the fracture loads P_F, there exists a definite minimum load for fracture, as shown in Fig. 5. If one assumes that the crack propagated in this test (by a load P_{Fmin}) is of a size within the range where P_{FN} shows a minimum with c/a then the fracture toughness can be determined from the following equation:

$$K_{IC} = \left(\frac{E^*P_{F\,min}}{P_{FN}^{min}R}\right)^{1/2} \tag{9}$$

where the number P_{FN}^{min} can be read from Table 1 assuming that Poisson's ratio for the substrate is accurately known. Similar results, but for specific r/a values (r/a = 1·05, 1·10, 1·20) were published by Matzke *et al.*[17] Since typical Hertzian contact radii are of the order of a few hundred microns (for spheres with radii 1–5 mm), to obtain the appropriate c/a values shown in Table 1 one needs flaw sizes, $c > 10$ μm. Therefore the specimen surface should be prepared by coarse diamond polishing or abrasion with fine SiC grits. Severe grinding of the surface

Table 1. P_{FN}^{min} and the corresponding c/a values as a function of ν

ν	P_{FN}^{min}	$(c/a)_{min}$	ν	P_{FN}^{min}	$(c/a)_{min}$
0·10	789	0·0679	0·23	2490	0·0472
0·11	850	0·0664	0·24	2790	0·0456
0·12	917	0·0648	0·25	3131	0·0444
0·13	991	0·0632	0·26	3530	0·0423
0·14	1074	0·0616	0·27	4001	0·0407
0·15	1167	0·0600	0·28	4560	0·0391
0·16	1270	0·0584	0·29	5229	0·0374
0·17	1386	0·0568	0·30	6037	0·0357
0·18	1517	0·0553	0·31	7022	0·0341
0·19	1665	0·0537	0·32	8235	0·0324
0·20	1883	0·0521	0·33	9748	0·0307
0·21	2025	0·0504	0·34	11658	0·0290
0·22	2247	0·0488	0·35	14106	0·0273

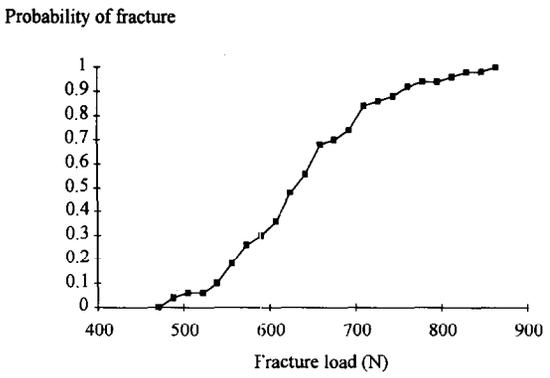


Fig. 5. Experimentally determined fracture loads, showing a minimum fracture load at P_F = 470 N. Material (substrate and sphere) — alumina; sphere radius = 2·5 mm.

may introduce flaws of suitable depth. but it is well known[37] that such treatment can introduce considerable surface residual stresses. The tests can then be repeated with spheres of different radii and the minimum value of P_{Fmin}/R found. This method requires no knowledge of the initial crack size, no measurement of the radius of the ring-crack seen on the surface after fracture, nor any measurement of the final depth of the cone-crack. It is important to note that the average fracture load found will give an overestimate of K_{IC} because not all cracks will be situated at the particular *r/a* value for which K_I, is a minimum—most cracks will be found at greater *r/a* values, since in reality the flaw density is not infinite.

It is appropriate here to discuss some of the limitations of this approach. With the sharp indentation method, part of the uncertainty in the analysis lies in the assumption of a particular crack geometry (median–radial or Palmqvist) after indentation. With the Hertzian method, the uncertainty lies in the value of the constant P_{FN}^{min}, which in turn depends on the assumed shape of the pre-cursor flaw before indentation. Warren *et al.*[35] assumed that the pre-cursor flaws were of a given depth *c*, but large in extent (with respect to the contact radius) across the surface, i.e. the sort of flaw produced by a sharp point dragged across the surface. Work is currently in progress[38] to evaluate stress intensity factors for different crack geometries, such as semi-circular or semi-elliptical flaws. The analysis presented here assumes that the sphere and the substrate are made of the same material. The method also assumes that the material does not show a substantial *T*-curve, i.e. increasing fracture resistance with crack extension. Finally, both the Vickers and the Hertzian method are affected by the presence of near-surface residual stresses. The Hertzian method may be particularly affected because the surface finish should specifically not be a fine diamond polish; the surface preparation method needs to be carefully chosen to produce 5–10 μm flaws without introducing residual stresses.

* Engineering Systems (Nottm), 1 Loach Court, Radford Bridge Road, Nottingham NG8 INB

Table 2. Material properties

Material	*ν*	*E(GPa)*	P_{FN}^{min}
Glass	0·25	70	3131
Alumina	0·24	390	2790

Experimental Technique and Results

Hertzian indentation tests were performed using a modified ET500 testing machine (Engineering Systems (Nottm)*). A wide-band acoustic emission transducer was mounted in the loading train to detect the growth of a small surface flaw into the characteristic ring— or ring–cone-crack. Two different substrate materials were used—glass, and high purity (99·99%) alumina. The assumed elastic constants and the expected minimum normalised fracture load, P_{FN}^{min}, for the materials are listed in Table 2. In each case two different sphere radii were used—2·5 and 5 mm. The spheres were made of glass and alumina. The specimens had a variety of surface treatments: the alumina was either ground with 600-grit SiC slurry on a cast iron lap, or ground and then polished with 6 μm polycrystalline diamond powder; the glass was tested in the 'as received' condition, and also after grinding with 600-grit SiC. In each case about 25 tests were performed. The results are shown in Table 3 for glass and Table 4 for alumina. The average fracture loads (± one standard deviation) are also listed.

We therefore estimate the values of K_{IC} (derived from the minimum fracture loads from the SiC-abraded surfaces) to be 0·71–0·74 MPa $m^{1/2}$ for glass and 3·72–3·80 MPa $m^{1/2}$ for alumina. These values are in good agreement with those in the literature—for example Zeng *et al.*[28] found values 0·8 and 3·77 MPa $m^{1/2}$ for glass and alumina,

Table 3. Glass results

Surface treatment	*Sphere radius (mm)*	*Average fracture load (N)*	*Minimum fracture load (N)*	K_{IC} *(MPa* $m^{1/2}$*)*
As-received	2·5	290 ± 110	127	0·78
	5·0	638 ± 135	340	0·90
SiC grit	2·5	158 ± 95	105	0·71
	5·0	348 ± 107	231	0·74

Table 4. Alumina results

Surface treatment	*Sphere radius (mm)*	*Average fracture load (N)*	*Minimum fracture load (N)*	K_{IC} *(MPa* $m^{1/2}$*)*
SiC grit	2·5	739 ± 160	470	3·72
	5·0	1600 ± 280	982	3·80
Diamond	2·5	849 ± 145	540	3·99
	5·0	1751 ± 260	1273	4·33

respectively. It can be seen that in every case the average fracture load is at least 35% bigger than the minimum load, and as expected the calculated value of K_{IC} is most accurate for the most badly damaged surface indented with the smallest sphere. This is because the more damaged the surface the larger c/a because of the increase in c; the smaller the sphere the larger c/a because of the reduction in a. In either case, the more likely it is that a crack of the appropriate size will be found.

Some of the experimental limitations are now described. (1) The crack extension must be sufficiently rapid to be detected by the acoustic emission transducer.[39] In all cases here, the detection of an acoustic signal corresponded to the appearance of a circular crack seen on the surface; in a very few cases, examination of the surface after detection of a signal revealed the presence of two ring cracks, suggesting that the first fracture event was not picked up. Because the sphere and substrate were made of identical materials, it is unlikely that cracking occurred on unloading; Johnson *et al.*[31] showed that if the substrate is more compliant than the indenter then the frictional tractions at the substrate–interface, which reduce the radial tension on loading, enhance the radial tension on unloading. (2) If an acoustic emission transducer is not available then the detection of the minimum load must be done by trial and error. (3) Obviously, the substrate must crack before the sphere does, this was not found to be a problem but the fact that it may occur suggests that tough spheres with the appropriate elastic constants (to minimise the extent of elastic mismatch between the sphere and the substrate) might be used—for instance, glass–ceramic spheres to test glass, or silicon nitride spheres to test other engineering ceramics. The effects of elastic mismatch on Hertzian fracture have been analysed,[40] the use of different indenter materials can substantially affect the value of P_{FN}^{min}.

Conclusions

Use of a refined stress intensity factor formulation for surface-breaking cracks in steep stress gradients[35] has enabled accurate estimates to be made of the minimum loads necessary to propagate cracks by Hertzian indentation. At present the analysis only applies for the case where the sphere and the substrate are made of the same material. However, the analysis is comprehensive in that it can be applied to sphere–substrate systems with any value of Poisson's ratio. By measuring this minimum load (and that is the only quantity that must be measured) an accurate estimate of K_{IC} may easily be made. The only other requirement is that the surface should be coarsely polished and a sphere of relatively small radius (<5 mm) should be used.

Two further points are worthy of note. Because the only quantity that must be measured is a fracture load, it is possible that this method of determining K_{IC} can be automated. Also, the existence of an absolute minimum fracture load, for a given sphere size, suggests that the Hertzian indentation test could find use as a localized proof-test.

Acknowledgements

The author gratefully acknowledges discussions with Professor Sir P. B. Hirsch, Dr S. G. Roberts and Dr D. A. Hills.

References

1. Sakai, M. & Bradt, R. C., Fracture toughness testing of brittle materials. *Int. Met. Rev.*, **38** (1993) 53–78.
2. Evans, A. G. & Charles, E. A., Fracture toughness determinations by indentation. *J. Am. Ceram. Soc.*, **59** (1976) 371–2.
3. Lawn, B. R., Evans, A. G. & Marshall, D. B., Elastic/plastic indentation damage in ceramics: the median/radial system. *J. Am. Ceram. Soc.*, **63** (1980) 574–81.
4. Anstis, G. R., Chantikul, P. Lawn, B. R. & Marshall, D. B., A critical evaluation of indentation techniques for measuring fracture toughness. *J. Am. Ceram. Soc.*, **64** (1981) 533–8.
5. Ponton, C. B. & Rawlings, R. D., Vickers indentation fracture toughness test—Part 1: Review of literature and formulation of standardised indentation toughness equation. *Mat. Sci. Technol.*, **5** (1989*a*) 865–72.
6. Ponton, C. B. & Rawlings, R. D., Vickers indentation fracture toughness test—Part 2: Application and critical evaluation of standardised indentation toughness equations. *Mat. Sci. Technol.*, **5** (1989*b*) 961–76.
7. Cook, R. F. & Pharr, G. M., Direct observation and analysis of indentation cracking in glasses and ceramics. *J. Am. Ceram. Soc.*, **73** (1990). 787–817.
8. Li, Z., Ghosh, A., Kobayashi, A. S. & Bradt R. C., Indentation fracture toughness of sintered silicon carbide in the Palmqvist regime. *J. Am. Ceram. Soc.*, **72** (1989) 904–11.
9. Li, Z., Ghosh, A., Kobayashi, A. S. & Bradt, R. C., Reply to Comment on Indentation fracture toughness of sintered silicon carbide in the Palmqvist regime. *J. Am. Ceram. Soc.*, **74** (1991) 889–90.
10. Srinivasan, S. & Scattergood R. O., Comment on Indentation fracture toughness of sintered silicon carbide in the Palmqvist regime. *J. Am. Ceram. Soc.*, **74** (1991) 887–8.

11. Lawn, B. R., *Fracture of Brittle Solids*, Second Edition. Cambridge University Press, Cambridge, 1993, p. 259.
12. Frank, F. C. & Lawn, B. R., On the theory of Hertzian fracture. *Proc. R. Soc. Lond.*, **A229** (1967) 291–306.
13. Powell B. D. & Tabor, D., Fracture of TiC under static and sliding contact. *J. Phys. D: Appl. Phys.*, **3** (1970) 783–8.
14. Wilshaw, T. R., The Hertzian fracture test. *J. Phys. D: Appl. Phys.*, **4** (1971) 1567–81.
15. Nadeau, J. S., Hertzian fracture of vitreous carbon. *J. Am. Ceram. Soc.*, **56** (1973) 467–72.
16. Warren, R., Measurement of the fracture properties of brittle solids by Hertzian indentation. *Acta Metall.*, **26** (1978) 1759–69.
17. Matzke Hj., Inoue, T. & Warren R., The surface energy of UO_2 as determined by Hertzian indentation. *J. Nucl. Mater.*, **91** (1980) 205–20.
18. Matzke, Hj., Hertzian indentation of thorium dioxide, ThO_2. *J. Mater. Sci.*, **15** (1980) 739–46.
19. Inoue, T. & Matzke, Hj., Temperature dependence of Hertzian indentation fracture surface energy of ThO_2. *J. Am. Ceram. Soc.*, **64** (1981) 355–9.
20. Matzke Hj. & Warren R., Hertzian crack growth in ThO_2 observed by serial sectioning. *J. Mater. Sci. Lett.*, **1**, (1982) 441–4.
21. Matzke, Hj. & Politis, C., The fracture properties of NbC, Nb(C,N) and NbN by Hertzian indentation. *Phys. Stat. Sol.*, **A69** (1982) 269–80.
22. Matzke, Hj., Meyritz, V. & Routbort, J. L., Fracture-surface energy and fracture toughness of (U,Pu)C and (U,Pu)(C,O). *J. Am. Ceram. Soc.*, **66** (1983) 183–8.
23. Laugier, M., Load bearing capacity of TiN coated WC–Co cemented carbides. *J. Mater. Sci. Lett.*, **2** (1983) 419–21.
24. Laugier, M., Hertzian indentation of sintered alumina. *J. Mater. Sci.*, **19** (1984) 254–8.
25. Laugier, M., Toughness determination of some ceramic tool materials using the method of Hertzian indentation fracture. *J. Mater. Sci. Lett.*, **4** (1985) 1542–4.
26. Laugier, M., Hertzian indentation of ultra-fine grain size WC–Co composites. *J. Mater. Sci. Lett.*, **6** (1987) 841–3.
27. Zeng, K., Breder, K. & Rowcliffe, D. J., The Hertzian stress field and formation of cone cracks—I. Theoretical approach. *Acta Metall. Mater.*, **40** (1992*a*) 2595–600.
28. Zeng, K., Breder K. & Rowcliffe D. J., The Hertzian stress field and formation of cone cracks—II. Determination of fracture toughness. *Acta Metall. Mater.*, **40** (1992*b*) 2601–05.
29. Almond, E. A., Roebuck, B. & Gee, M. G., Mechanical testing of hard materials. In *Science of Hard Materials*, Inst. Phys. Conf. Ser. Vol. 75, pp. 155–77.
30. Huber, M. T., On the theory of contacting solid elastic bodies. *Ann. Phys.*, **14** (1904) 153–63.
31. Johnson, K. L., O'Connor, J. J. & Woodward, A. C., The effect of the indenter elasticity on the Hertzian fracture of brittle materials. *Proc. R. Soc. Lond. A.*, **334** (1973) 95–117.
32. Hertz, H., On the contact of elastic solids. *Zeitschrift fur die Reine und Angewandte Mathematik*, **92** (1881) 156–71. English translation in *Miscellaneous Papers* (translated by D. E. Jones and G. A. Schott); pp. 146–62. Macmillan, London, U.K., 1896.
33. Nowell D. & Hills, D. A., Open cracks at or near free surfaces. *J. Strain Anal.*, **22** (1987) 177–84.
34. Mouginot, R. & Maugis, D., Fracture indentation beneath flat and spherical punches. *J. Mater. Sci.*, **20** (1985) 4354–76.
35. Warren, P. D., Hills, D. A. & Roberts, S. G., Surface flaw distributions and Hertzian fracture. Submitted to *J. Mater. Res.*
36. Finnie, I., Dolev, D. & Khatibloo, M., On the physical basis of Auerbach's law. *J. Engng Mater. Technol.*, **103** (1981) 183–4.
37. Marshall, D. B., Evans, A. G., Khuri-Yakub, B. T., Tien, J. W. & Kino, G. S., The nature of machining damage in brittle materials. *Proc R. Soc. Lond A.*, **385** (1982) 461–75.
38. Dai, D. N., Hills, D. A., Warren, P. D. & Nowell, D., The propulsion of surface flaws by elastic indentation testing. Accepted for publication, *Acta Metall. et. Mater.*
39. Scruby, C. B., Quantitative acoustic emission techniques. In *Research Techniques in Non-destructive Testing*, vol. 8, ed. R. S. Sharp. Academic Press, London, 1985, p. 141.
40. Warren, P. D. & Hills, D. A., The influence of elastic mismatch between indenter and substrate on Hertzian fracture. *J. Mater. Sci.*, **29** (1994) 2860–6.

Journal of the European Ceramic Society **15** (1995) 209–224
© 1995 Elsevier Science Limited
Printed in Great Britain. All rights reserved
0955-2219/95/$9.50

Mechanical Properties of C/SiC Composites as Explained from their Interfacial Features

Jean-François Després & Marc Monthioux

Laboratoire Marcel Mathieu, CNRS-UPPA, Centre Hélioparc, 2 avenue du Président Angot, F64000, Pau, France

(Received 10 March 1994; revised version received 28 June 1994; accepted 1 August 1994)

Abstract

Carbon fibre reinforced ceramic matrix composites with pyrolytic carbon interphases prepared following various conditions are compared, together with interphase-free composites. Four composite grades are thus defined, considering similarities in the ultimate tensile strength and strain values. Textural then structural investigations of the interfacial zones are performed from a centimetric to nanometric scale in an attempt to explain the specific mechanical features of the composites for each grade. Results show that the carbon interphase texture obviously controls the macroscopic behavior of the composites. Composite toughnesses are directly related to the relative strengths of the various interfaces, which depend on the covalent/Van der Waals bond ratio.

1 Introduction

Despite their high ultimate strength or elastic modulus values, monolithic ceramic materials have not been used as structural materials because of their lack of toughness. However, reinforcing them with carbon fibres, which may have both high ultimate strength and Young's modulus values, has allowed tough 2D ceramic matrix composites to be obtained,[1] making them convenient for structural uses in industrial applications.

However, composites only built with carbon fibres as reinforcement within a pure silicon carbide matrix, though reaching higher performances than the monolithic matrix, have a peculiar tensile strength/strain behavior. Considering curve 2 in Fig. 1, three different zones are seen as compared with an unreinforced bulk ceramic material (curve 1). From O to A, the composite exhibits a high elastic modulus value, which depends on the fibre/matrix volume proportions. In A, failures occur in the matrix, because of its lower ultimate strain value compared to the fibres. As failures generalize, multiple fracture of the matrix induces a high strain value, though the increase in strength remains low, resulting in the A—B plateau. In B, the multiple fracture is maximal and the slope of the curve becomes mainly influenced by the fibre modulus, assuming that, as discussed later, the fibre/matrix bonding is weak. The slope of the curve therefore increases (B—C zone). Finally, when the strain-to-failure value of the fibres is reached, fibres quickly break one after the other from C to D. D is the point of final rupture of the sample. The fact that fibres and matrix react successively instead of combining their properties does not provide a good example of the right composite. Such a behavior is specific from a two-component C/SiC composite. Fig.2 gives an example ('interphase-free' curve).

Changing the behavior becomes possible with adding a third component: the interphase (C/C/SiC composites). Fibres are therefore coated with a pyrolytic carbon interphase deposited from a chemical vapor deposition (CVD) process, prior to the densification with the silicon carbide matrix, also from a chemical vapor infiltration (CVI) process. The tensile strength/strain behavior of the resulting composites is now as shown in Fig. 2 ('Grade 3' curve for instance).

However, composites made of the same components (i.e. carbon fibres, pyrolytic carbon interphase, and SiC matrix) may have various ultimate strength and strain values, though coarsly following the same moduli (compare Grade 1, 2, and 3 curves on Fig. 2). Though useful anyway, the efficiency of the pyrocarbon interphase is therefore conditioned by factors other than the chemical nature of the components. The aim of the present paper is to determine these factors.

2 Experimental

All the composites were prepared by the Société Européenne de Propulsion (SEP), the details of

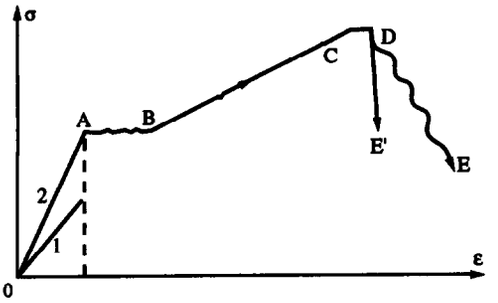


Fig. 1. Sketch of the tensile strength/strain trend for a bulk ceramic (curve 1) and a fibre-reinforced ceramic matrix composite (curve 2).

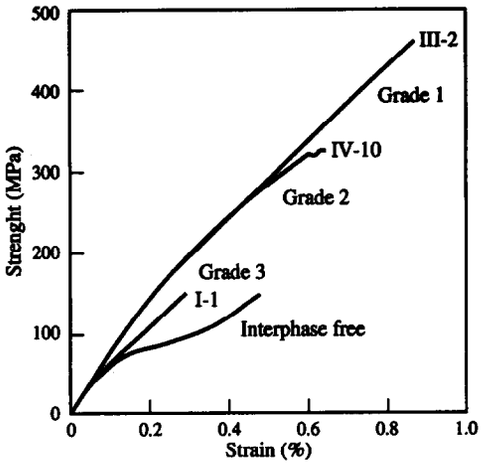


Fig. 2. Strength/strain behaviors for experimental C/C/SiC composites from the various grades and a C/SiC (interphase-free) composite.

which have to be kept confidential. They are built from about ten 2D carbon clothes (polyacrilonitrile-based fibres) which are stacked, then coated with a pyrolytic carbon interphase (from CVD) the thickness of which may vary from 80 to 800 nm, then infiltrated with a polycrystalline and pure SiC matrix (from CVI). Also, interphase-free composites were studied. Three different makes of carbon fibre have been used, including T300 from Toray (fibre A). However, no basic differences were detected in the resulting composites, though differences were observed between fibres. Discrepancies in surface topology between fibre types and the peculiar textural features of the T300 fibre (accumulation of cylindrical pores close to the surface, ring-like change in texture from isotropic to radial) were reported elsewhere from a TEM study.[2,3] As far as ultimate tensile strength, σ, and strain, ε, values coarsly evolve together (Table 1), the whole sample set (23 interphase-containing composites) is arbitrarily divided into three mechanical grades following a classification factor $F = \sigma \times \varepsilon$. Thus, composites from Grade 1 have $F > 350$, Grade 2 composites have $100 < F < 350$, and Grade 3 composites have $F < 100$. On the contrary, no relationships may be found between the grades and the interphase thickness. Tensile tests were performed by SEP according to their standard procedure (gauge length = 100 mm).

Textural and structural investigations have used a glass lens (macroscopic scale), a scanning electron microscope (SEM, micrometric scale) and a high resolution transmission electron microscope

Table 1. Description and three-grade classification of the sample set

	Code	*Fibre*	σ *(MPa)*	ε *(%)*	*Thickness (μm)*	*E (GPa)*	*F*
Grade 1	I—2	A	520	0·99	0·50	104	515
	II—1	A	450	1·00	0·30	82	450
	II—3	C	440	1·00	0·30	105	440
	V—6	A	430	0·96	0·30	89	413
	III—2	A	460	0·86	0·65	90	396
Grade 2	II—2	A	380	0·89	0·15	105	338
	II—4	C	410	0·84	0·15	88	344
	II—6	B	370	0·84	0·70	70	311
	III—1	A	400	0·86	0·40	88	344
	III—3	A	400	0·78	0·55	90	312
	III—4	A	400	0·78	0·50	85	312
	III—6	A	400	0·80	0·35	95	320
	III—7	A	250	0·50	0·80	75	125
	III—8	A	420	0·70	0·55	90	294
	IV—10	A	340	0·68	0·85	100	231
	V—1	A	240	0·49	0·50	91	118
	V—2	A	400	0·78	0·50	88	312
	V—3	A	310	0·57	0·60	76	177
	V—4	A	290	0·67	0·25	95	194
	V—5	A	360	0·74	0·25	92	266
Grade 3	I—1	A	150	0·31	0·50	76	47
	II—5	B	170	0·46	0·10	88	78
	III—5	A	140	0·18	0·08	130	25
Interphase—free	IV—12	A	160	0·50	—	133	—
	IV—13	A	120	0·25	—	80	—

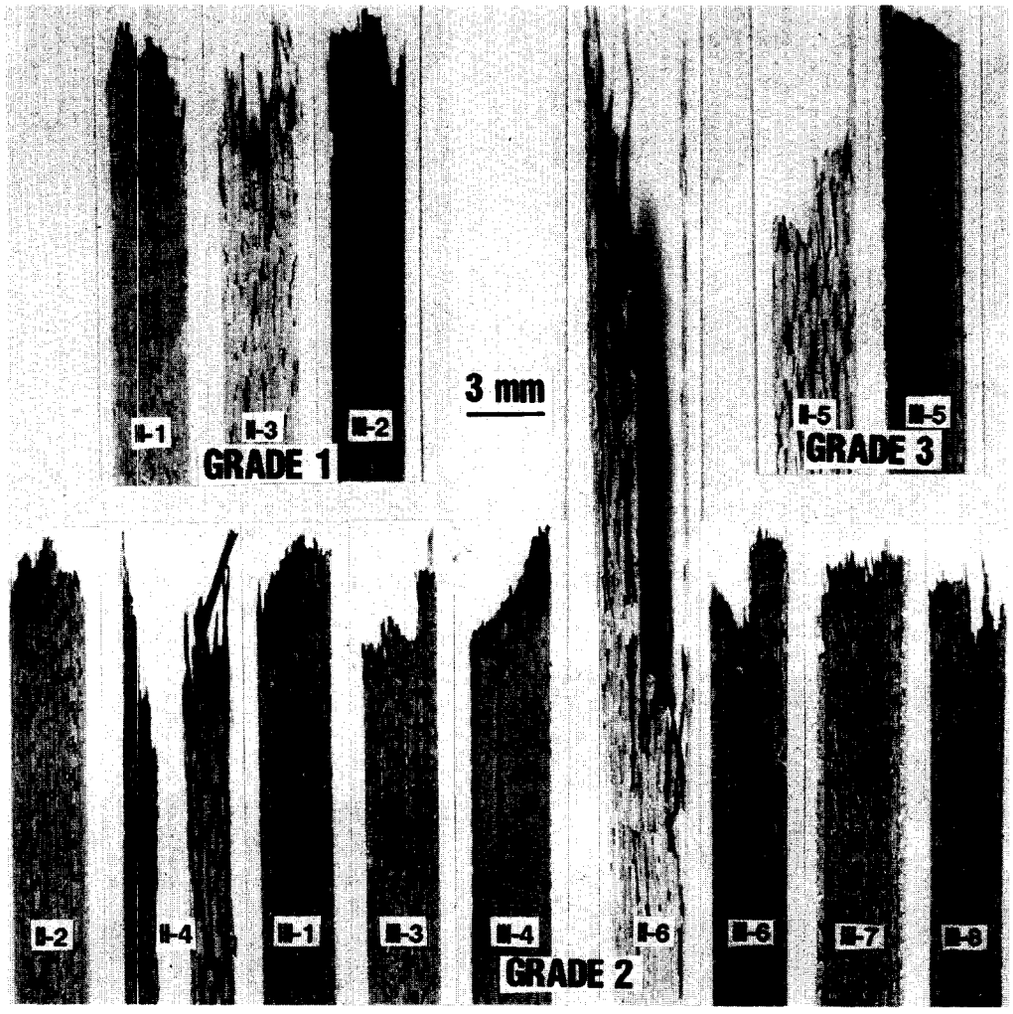


Fig. 3. Macroscopic fracture profiles of some composite samples from Grades 1, 2 and 3 (tensile test).

(TEM, nanoscopic scale). Only composite samples broken by the tensile test were examined by the glass lens and SEM (which required a Au coating to prevent charge effects). For TEM examinations, samples were taken from composites using diamond drilling performed far from the damaged zone, then prepared using a diamond saw into 3 mm disks, which were mechanically thinned (diamond powder polishing) then ion-thinned with argon ions (Gatan DUOMILL and IONTECH). TEM microscopes were Philips CM12 and Philips EM400 (120 kV). Contrasted bright field (BF), dark field (DF), lattice fringes (LF) and selected area diffraction (SAD) modes were used following conventional procedures; DF was more specifically[4] used for imaging carbon. Regarding the micrographs, DF images are mainly obtained from the 002 reflection of polyaromatic turbostratic carbon. Any graphene stack (graphene = a single polyaromatic layer) not disposed edge-on relative to the electron beam (i.e. not disposed perpendicularly to the plane of the picture) will therefore not be imaged. Because of the use of a small objective aperture, the DF images are built only with a small length of the 002 ring and therefore provide directional information. Taking two successive pictures using two orthogonal positions for the objective aperture helps any possible anisotropy to be revealed. If the two pictures appear statistically identical, (similar number and size of bright domains) the carbon material is isotropic (zone 1 in Fig. 11 for instance). If they are not, the carbon material is anisotropic (zone 2 in Fig. 11 for instance). The mean azimutal orientation is shown by the '=' sign on each picture.

Optical diffraction using a laser source has also been performed on original LF micrograph films, when lattice fringes were imaged. The diffraction patterns thus obtained act as a very local electron diffraction (scattering area is about 600 nm^2).

3 Results

3.1 Macroscopic scale

The tensile test samples were examined after mechanical testing, in order to tentatively reveal any possible correlation between the fracture profile and the mechanical behavior observed. Figure 3 illustrates the fracture profiles of the tensile test

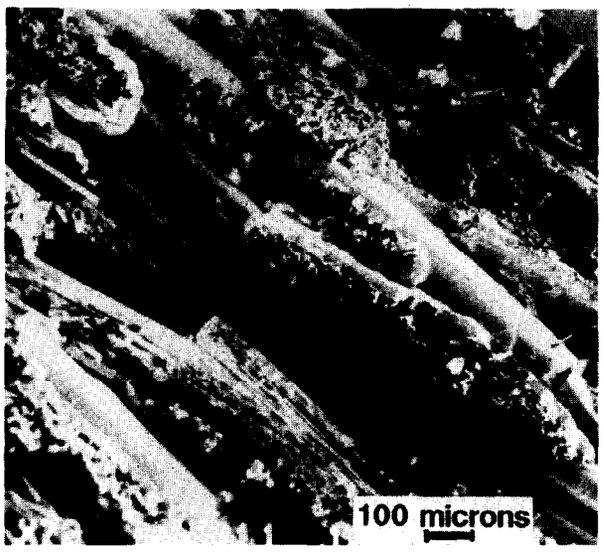


Fig. 4. Characteristic enlarged SEM view of tows within any C/C/SiC composites. Tows may often be considered as independent entities.



Fig. 5. Example of the mechanical independence of neighboring tows: one is fractured, while the transverse one is not (SEM view).

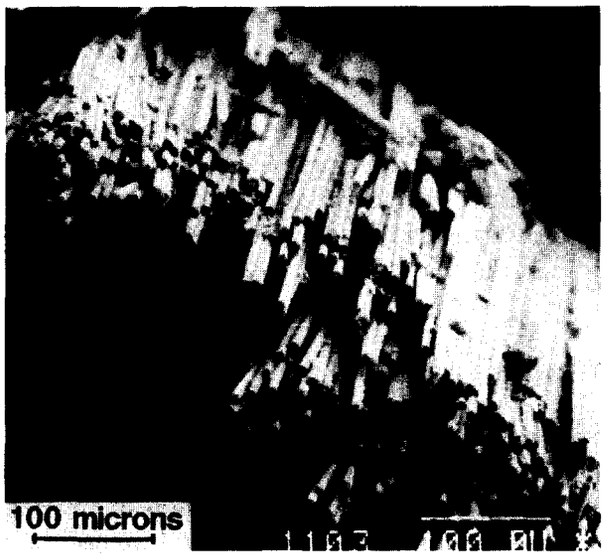


Fig. 6. Typical SEM view of the fracture surface of a tow within a Grade 1 composite.



Fig. 7. Typical SEM view of the fracture surface of a tow within a Grade 3 composite.

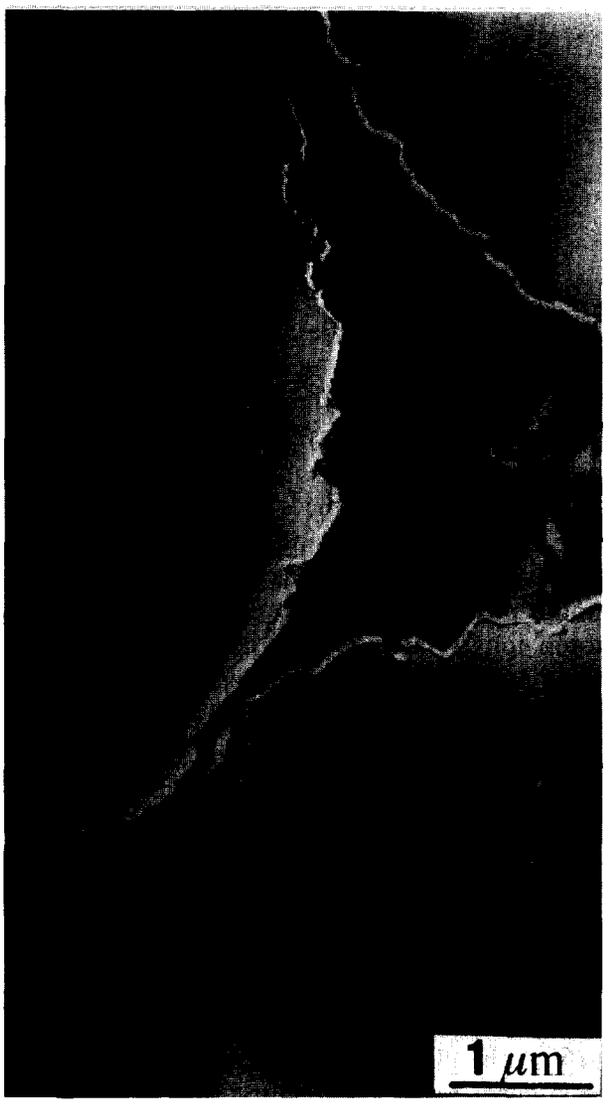


Fig. 8. Low magnification BF TEM view of a decohesion path in an interphase-free composite (C/SiC).

samples of some composites from Grades 1, 2, or 3. Obviously, a specific grade is not characterized by a specific fracture profile. For instance, samples II-5 and III-5, though both from Grade 3, exhibit very different fracture profiles. The profile amplitude is about 10 mm for the former, while only 2 mm for the latter. Likewise, samples II-6 and III-1 from Grade 2 have fracture profile amplitudes of 30 and 3 mm respectively. Therefore, no simple relationship exists between the fracture profile and the ultimate tensile strength value of the C/C/SiC composites.

3.2 Microscopic scale

A general statement is that all the C/C/SiC composites are built from an elementary entity, which is defined as a tow of pyrocarbon-coated carbon fibres, covered with a silicon carbide sheath which is more or less able to densify the tow (Fig. 4). This suggests that tows should be independent of one another regarding failure propagation, as illustrated in Fig. 5 which shows that a longitudinal entity has been damaged, while the neighboring transversal entity has not.

Starting from the statement above, simple correlations are now able to be found between the fracture profiles and the various grades, when considering the tows as 'basic mechanical units'. Indeed, any Grade 1 composite was found to mainly contain tows exhibiting fibre pull-out at the fracture surface (Fig. 6), while any Grade 3 composite was found to mainly contain tows exhibiting an almost planar fracture surface (Fig. 7). Therefore, the fracture profiles of the tows, rather than the fracture profiles of the composites, are related to the macroscopic mechanical features of the C/C/SiC composites. Obviously, this must be governed by the behavior of the pyrolytic carbon interphase within the tows.

3.3 Microscopic and nanoscopic scale

Prior to describing the pyrocarbon-containing composites, Figs 8 and 9 illustrate some specific features of the pyrocarbon-free composites. Firstly, decohesions at the fibre/matrix interface

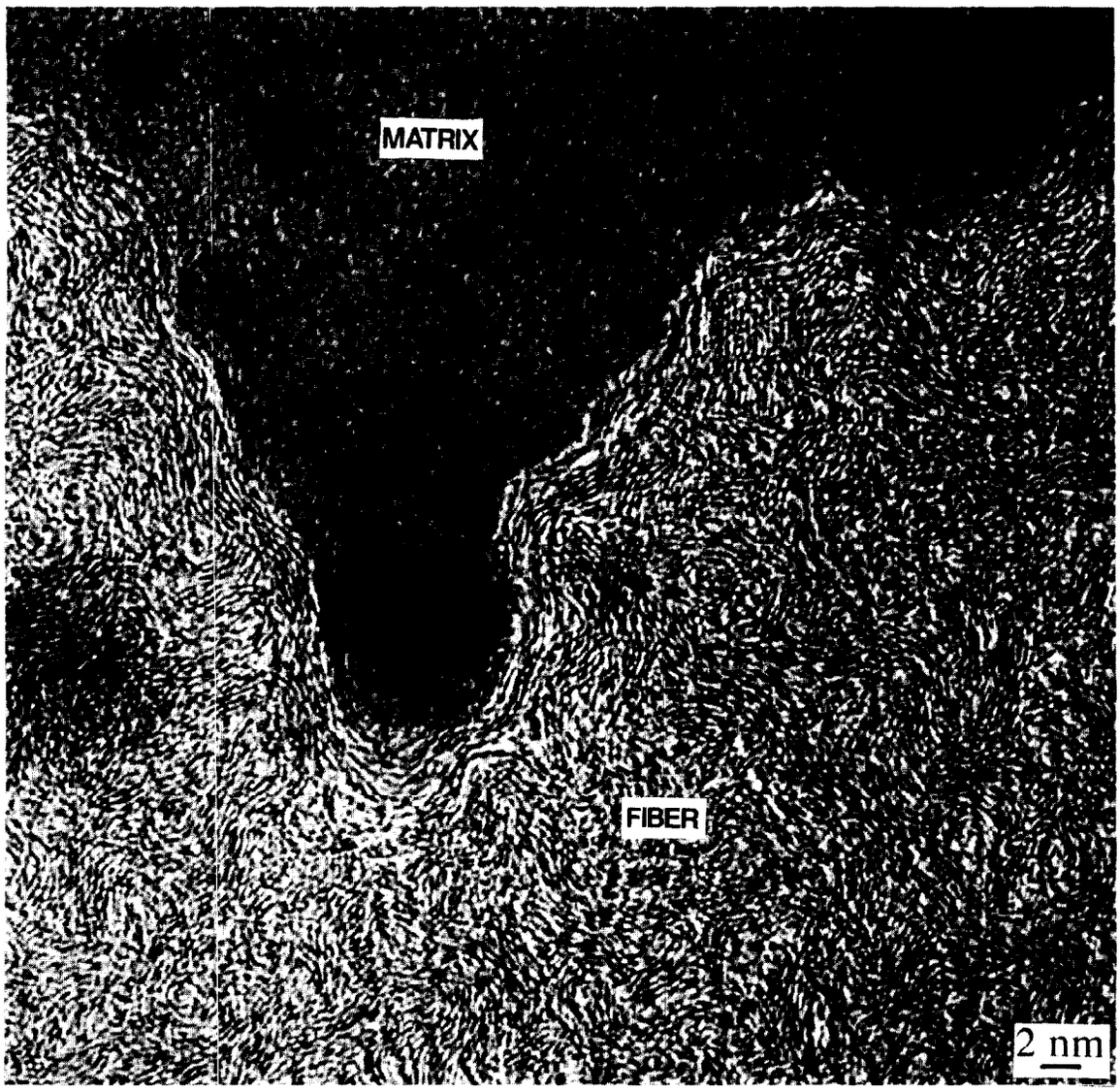


Fig. 9. LF TEM image of the fibre/matrix interface in an interphase-free composite (C/SiC).

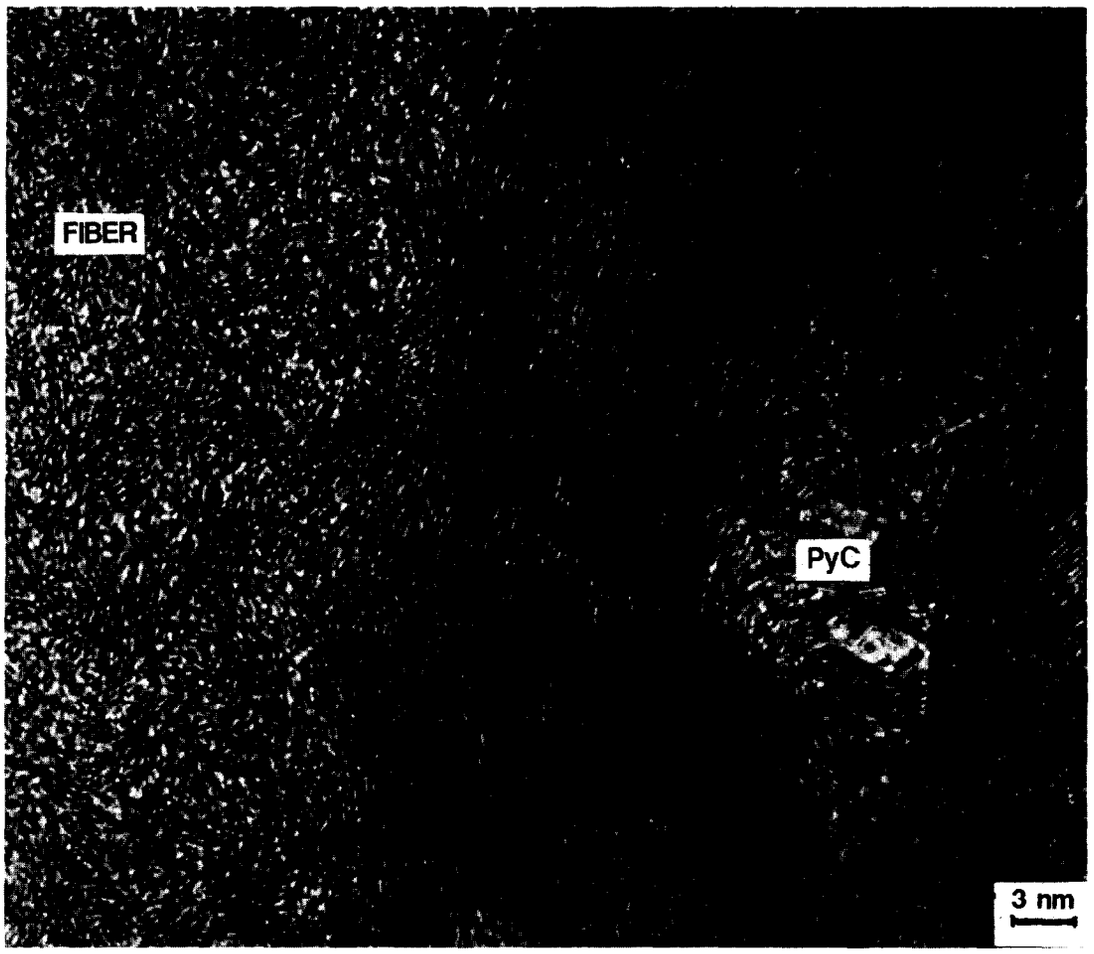


Fig. 10. LF TEM image showing how the fibre surface induces a local anisotropy of the graphene stacks at the very beginning of the pyrolytic carbon deposition.

are systematic (Fig.8), indicating that no chemical interactions occur between the carbon of the fibre and the SiC crystals. Because no pyrocarbon is covering the fibre surface, the texture of the graphene stacks at the fibre surface is clearly observable (Fig. 9). Obviously, the last 3–5 graphene layers are oriented parallel to the fibre surface (T300 fibres in that case). Such a texture does not help in promoting chemical reactions between polyaromatic carbon and SiC. Decohesions are certainly due to the difference in thermal expansion coefficients (TEC), i.e. 15–20 $\times$ 10^{-6}/K for the fibre transversally, and 4 $\times$ 10^{-6}/K for the SiC matrix, rather than to the mechanical test, and therefore are an intrinsic feature of the composites. However, because of the lack in adhesion between the fibre and the matrix, the multiple fracture of the matrix is probably not directly due to the difference in TEC but to the anisotropic stresses induced by the presence of the reinforcement during the shrinkage of the matrix when cooling. Figure 9 also illustrates the depth of the roughness of the fibre (T300) surface, which can reach about 25% of the fibre diameter for the T300, while only about 3% and 10% for fibres B and C respectively.

Investigating all the samples using TEM has allowed three interfacial pyrocarbon texture types to be described. Whatever the texture type or the grade for the C/C/SiC composites, the first ten nanometers of the pyrolytic carbon are deeply influenced by the fibre topology (Fig. 10). Graphene stacks are highly anisotropic and lie flat upon the fibre surface, despite its rather high roughness.

3.3.1 Bimorphic interphases

These are made of two parts of equal thicknesses. The pyrolytic carbon texture of the fibre-side part is identified as 'bulky oriented isotropic' (BOI-PyC), i.e. all the possible orientations are found for the graphene stacks which the pyrocarbon is made of, but a main specific orientation—parallel to the interfaces—is found (Fig. 11, zone 1). The pyrolytic carbon texture of the matrix-side part is described as 'anisotropic' (ANI-PyC), since no graphene stacks oriented perpendicularly to the main direction of orientation—again parallel to the interfaces—are found (Fig. 11, zone 2). At high magnifications (LF mode), the change in texture from zone 1 (BOI-PyC) to zone 2 (ANI-PyC) appears progressive (Fig. 12). The related optical

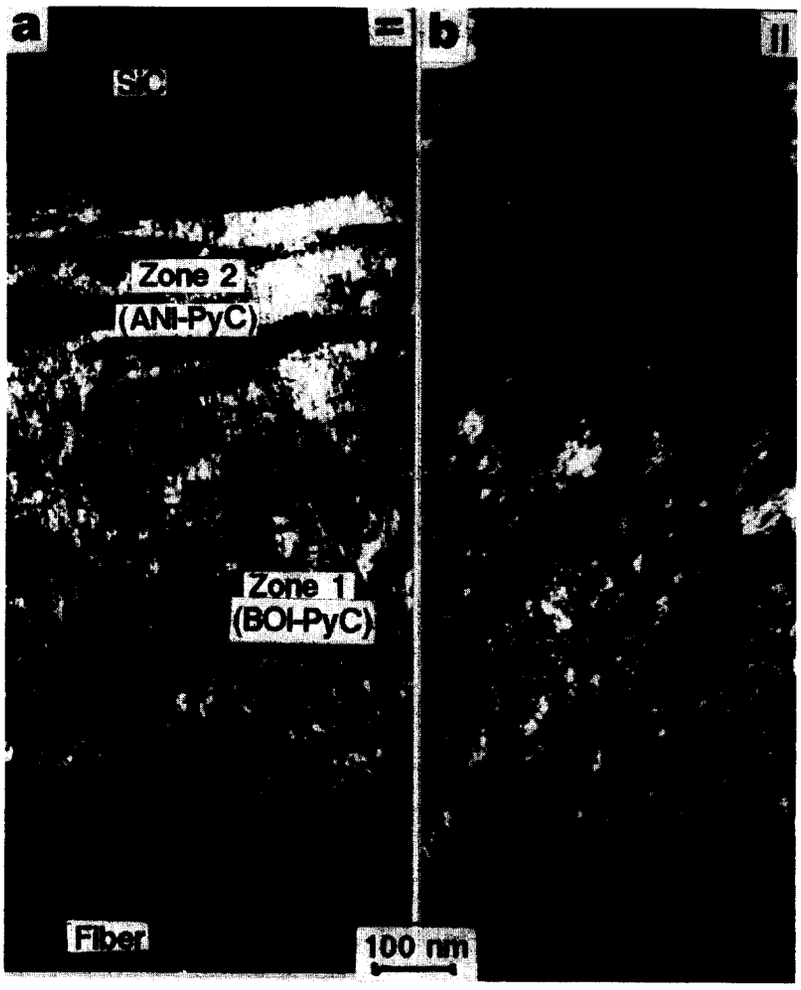


Fig. 11. C_{002} DF micrographs of a bimorphic-type interphase: two orthogonal orientations are imaged. (a) The two parts (zones 1 and 2) of the pyrocarbon interphase appear very bright. (b) Zone 1 is still lighted-on but does not appear bright, while zone 2 appears dark. Zone 1 therefore corresponds to a bulky oriented isotropic carbon (BOI-PyC) and zone 2 corresponds to an anisotropic carbon (ANI-PyC).

diffraction patterns in Fig. 12 well illustrate how the anisotropy increases from the fibre side (bottom) to the matrix side (top). The 002 ring is progressively replaced by two 002 arcs, the angular opening of which decreases as the extent of angular misorientations between graphene stacks decreases, and therefore becomes smaller. Close to the matrix (Fig. 13), the graphene stacks are very well organised, inducing a high anisotropy and a specific contrast effect as dark bands (so-called Bragg fringes) perpendicular to the direction of carbon layers.

Within the ANI-PyC texture (zone 2), slit pores are often observed, actually indicating a lenticular porosity, as far as the transverse or longitudinal views of the interphase are identical. Pore walls are made of sheets of graphene stacks locally disconnected (Fig. 14). Lateral transitions from area of high compactness to area with lenticular porosity are rather sudden, and nearly periodic (Fig. 15).

Within the bimorphic interphase type, decohesions always occur either at the pyrocarbon/matrix interface, or at the zone 1/zone 2 transition or within the ANI-PyC (Fig. 16). Obviously, the anisotropic but entangled texture is efficient in dispersing the fracture energy through a multiple fracture effect.

3.3.2 Carbon wall-ending interphases

The main part of the interphase is from the BOI-PyC type, previously described. It corresponds to the light-on part in Fig. 17(a). However, the very end part of the carbon interphase (i.e. matrix side) is made of a different texture, specifically long carbon walls preferentially oriented perpendicularly to the interfaces. They are shown in Fig. 17(b). The carbon wall zone is highly porous as seen in Fig. 18, which also illustrates the perfection of the graphene layers within the walls since they exhibit Bragg fringes, which indicate their high organisation. Important features are that the walls penetrate deeply within the SiC matrix (Figs 17(b) and 19), sometimes as far as 100 nm. The end tip of the carbon walls may exhibit an edge shape which enhances the possibility of chemical bonding with the surrounding SiC crystals (Fig. 19).

Within the carbon wall-ending interphases, decohesions are always observed at the BOI-PyC/fibre interface, or within the BOI-PyC (Fig. 20).

3.3.3 Mixed interphases

These exhibit textures combining features of both interphases. Thus, the whole pyrocarbon texture may be a mere BOI-PyC texture without being associ-

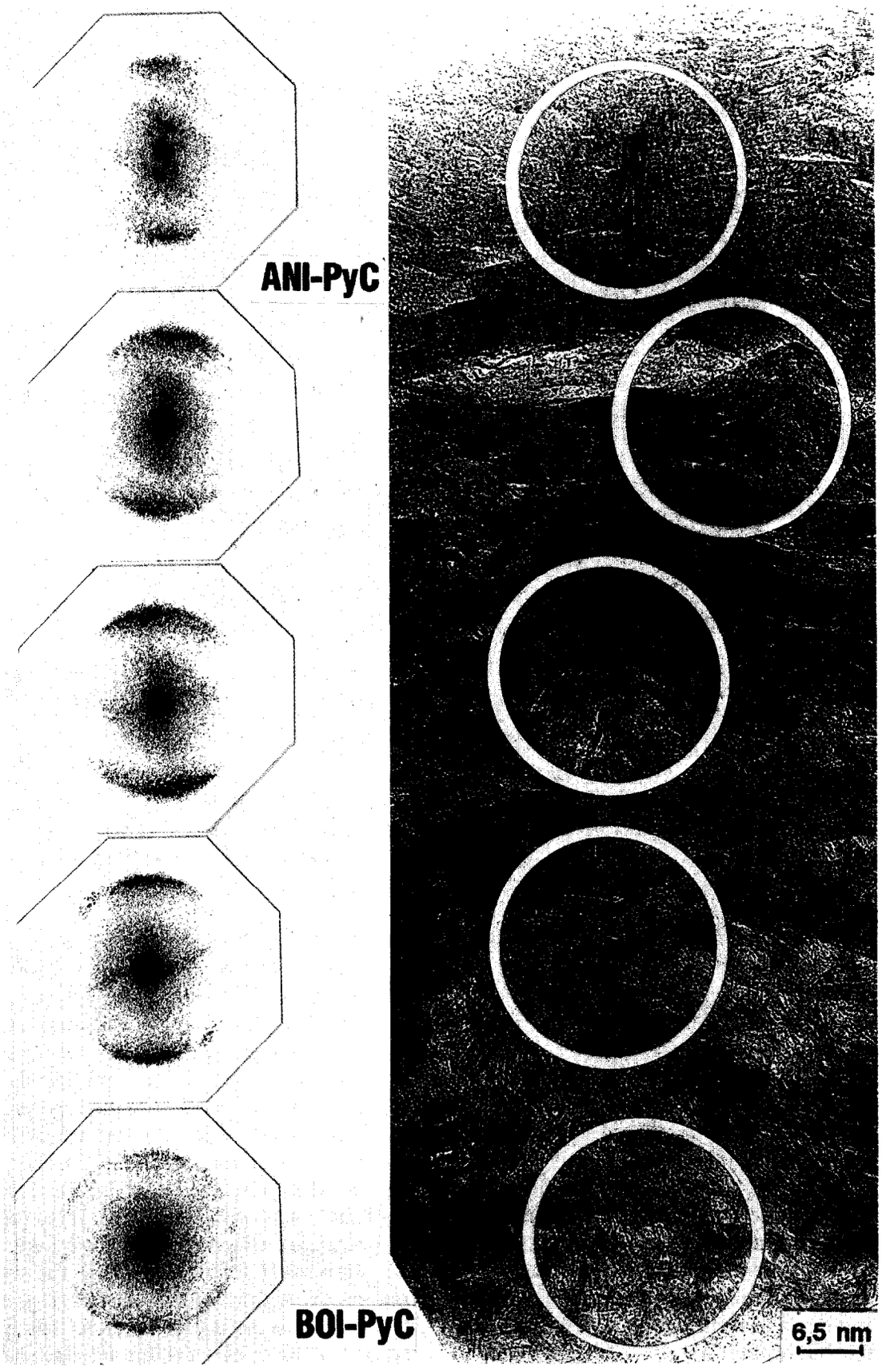


Fig. 12. LF TEM images of the zone 1/zone 2 transition within a bimorphic texture pyrocarbon interphase. Related optical diffraction patterns are inserted. Fibre side is below, matrix side is above.

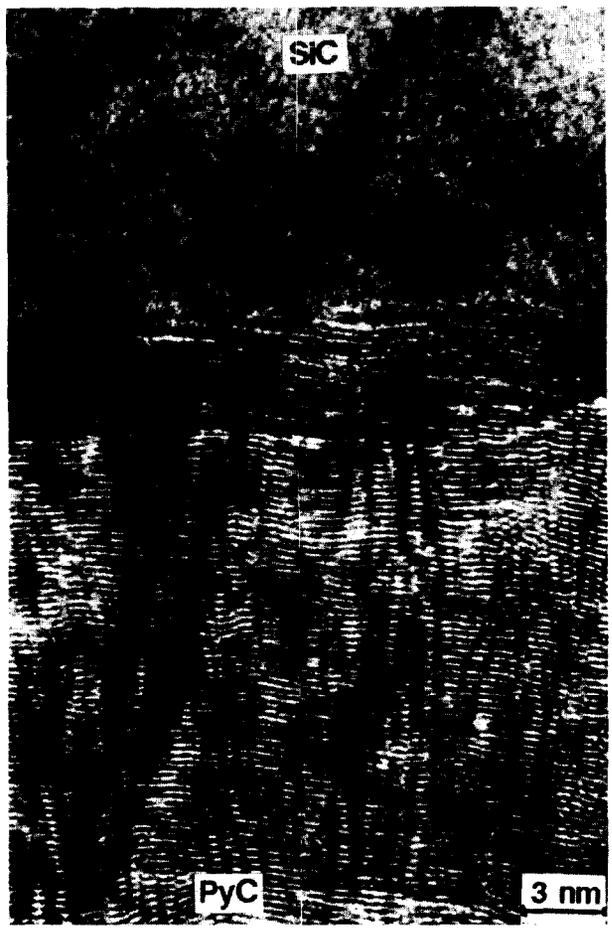


Fig. 13. LF TEM image of the pyrolytic carbon interphase (ANI-PyC) matrix interface. Note the high anisotropy parallel to the interface, and the nearly perfect organisation of the graphene sheets.

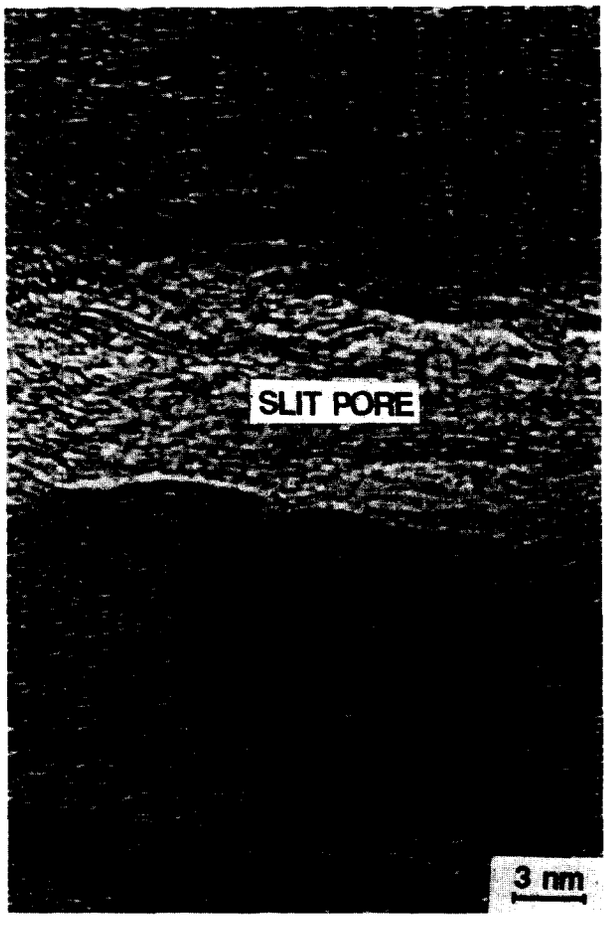


Fig. 14. LF TEM image of a slit (lenticular) pore within the ANI-PYC part of the interphase. The contrast within the pore is due to overlapping matter.

ated with any carbon-wall or ANI-PyC texture (Fig. 21, right), or may also be similar to a bimorphic type including a ANI-PyC part—but with a lower anisotropy (Fig. 21, upper left, Fig. 22). Anisotropic textures may be associated with graphene layers penetrating the SiC matrix and therefore resembling a carbon wall-ending interphase (Fig. 22).

4 Discussion

There is an exact correspondence between the three texture types of the pyrocarbon interphase described above and the three composite grades as defined in Section 2. Specifically, all the Grade 1 composites exhibit bimorphic pyrocarbon interphases. Grade 3 composites exhibit carbon wall-ending pyrocarbon interphases, and Grade 2 composites contain mixed interphases.[5] Considering the latter grade, it is worthy to note that interfacial areas may have different textures, though very close to each other (Fig. 21). On the contrary, Grades 1 and 3 are homogeneous.

Therefore, textural discrepancies in the interphases may originate from differences in deposition conditions. In addition to differences in the process, differences may also be very local, as shown by the interphase heterogeneities found in Grade 2 composites. This was rather expected, because of the 3D porous feature of the preform which is likely to induce local differences in gas flows, partial pressures, turbulences, etc. On the other hand, regarding the effect expected from a porous substrate, the interphase homogeneity of Grade 1 or 3 composites is remarkable.

4.1 Bonding strength of the various interfaces

Considering all the interface types encountered and the location of the decohesion paths in the composites (whatever the grade) allows the various interfaces to be ordered following the increasing bonding strength (Table 2). Actually, decohesions, due to either the tensile test or the preparation method for TEM examination, indicate the weak interfaces within the composites. Obviously, the weakest interface is the fibre/matrix interface in the pyrocarbon-free composite.

The ANI-PyC/matrix interface in Grade 1 composite is stronger but still weak, since no chemical bonding other than weak interactions are allowed by the planar (polyaromatic) faces of graphene

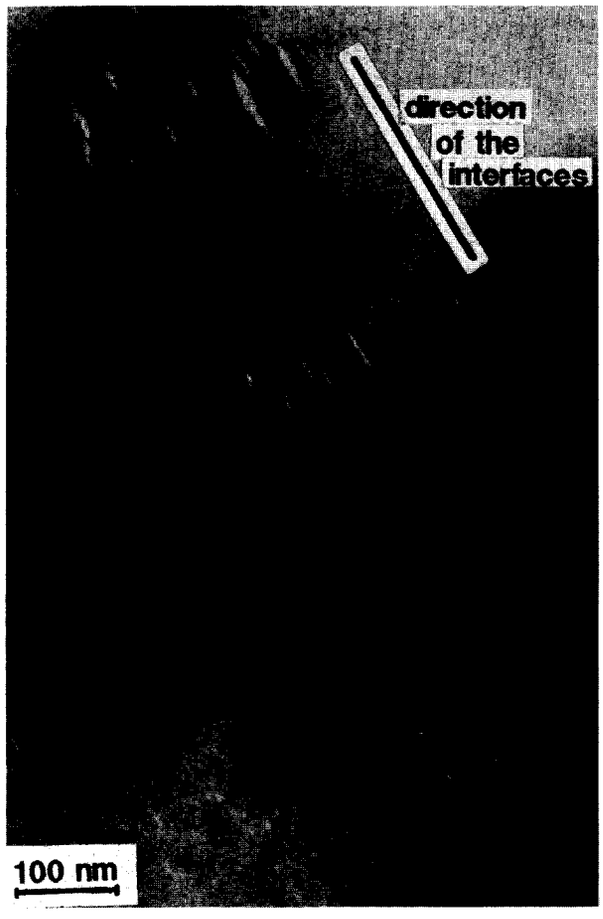


Fig. 15. BF TEM image of a carbon interphase exhibiting a nearly periodic occurrence of the lenticular porosity.

sheets. It could be wondered why the interface always exhibits a PyC/matrix contact (except when disturbed by a failure due to the mechanical test) instead of showing the same voids due to TEC differences, as in the pyrocarbon-free composite. This is probably due to a compensation effect of the pyrocarbon interphase, which is related to the presence of the lenticular porosity in the ANI-PyC part, and which will be discussed later.

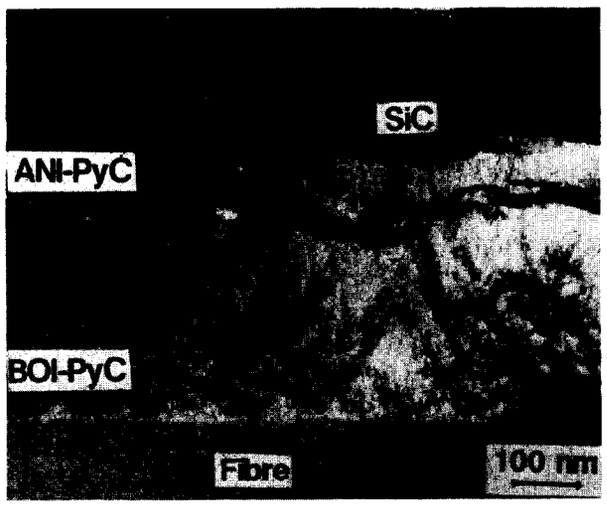


Fig. 16. Low magnification C_{002} DF image of a decohesion path within a bimorphic-type pyrocarbon interphase.

Table 2. Classification of the various interfaces in order of decreasing bonding strength

Interface	*Grade*	*Bond*
PYCX/matrix	3	σ chemical bond
Fibre/PyC	All	A majority of σ, and Van der Waals
PyC/matrix	2	Van der Waals and σ
BOI-PyC/ANI-PyC	1	Van der Waals and σ
PyC/matrix	1	Van der Waals
Fibre/matrix	Free	'Mechanical' bond

However, placing this interface type before or after the BOI-PyC/ANI-PyC interface in Table 2 is difficult since it depends on the degree of mixity.

Certainly stronger is the BOI-PyC/ANI-PyC interface in Grade 1 composites, since it allows both Van der Waals bonds—when graphene sheets are arranged face to face—and chemical (covalent) bonds—when graphene sheets are arranged edge-to-edge, or through defect sites.

The BOI-PyC/matrix interface in Grade 2 composites is stronger than the ANI-PyC/matrix interface mentioned above since it enhances the possibility of covalent bonds.

Even stronger is the fibre/BOI-PyC interface in Grade 1, 2, or 3 composites, where one failure only has been observed among about 100 interfaces investigated. Proportions of covalent bonds are higher than with the BOI-PyC/ANI-PyC interface, though also dealing with graphene/graphene interactions. It is assumed that the proportion of potential sites for covalent bonds increases as the number of defects and grain boundaries increases, with respect to the mean size of the coherent domains (i.e. the length *La* of the straight carbon layers within associated graphene stacks). Actually, it is obvious that the sizes of the coherent domains are smaller for the carbon fibre (see Fig. 9 for instance, where *La* ~2 nm) than for the pyrolytic carbon deposit (see Fig. 10 for instance, where *La* = 3–5 nm for the BOI-PyC deposit, and Fig. 13 for instance, where *La* > 10 nm for the ANI-PyC deposit). In addition, the BOI-PyC/fibre interface, because of the fibre topology, is much rougher than the ANI-PyC/BOI-PyC interface, which is not likely to promote easy delamination. Therefore, both structural and textural considerations are able to explain the difference in strength between the two graphene/graphene interfaces.

Finally, the strongest interface is the PyC/matrix interface encountered in Grade 3 composites, which is characterized by carbon walls perpendicular to the interface and deeply inserted into the matrix. This originates from the fact that the carbon walls are strongly linked on the one hand to the pyrocarbon on the other hand to the SiC

crystals by σ bonds. The high strength of the aromatic C = C bonds (the highest for solids) of the nearly perfect graphenes which the carbon walls are made of prevents any strain or shearing to occur, either perpendicular or parallel to the interface.

4.2 Mechanical behavior of the composites related to their interfacial features

Considering Table 2 explains why Grade 3 composites have the strongest fibre/matrix bonding of the sample set. Indeed, they contain the two

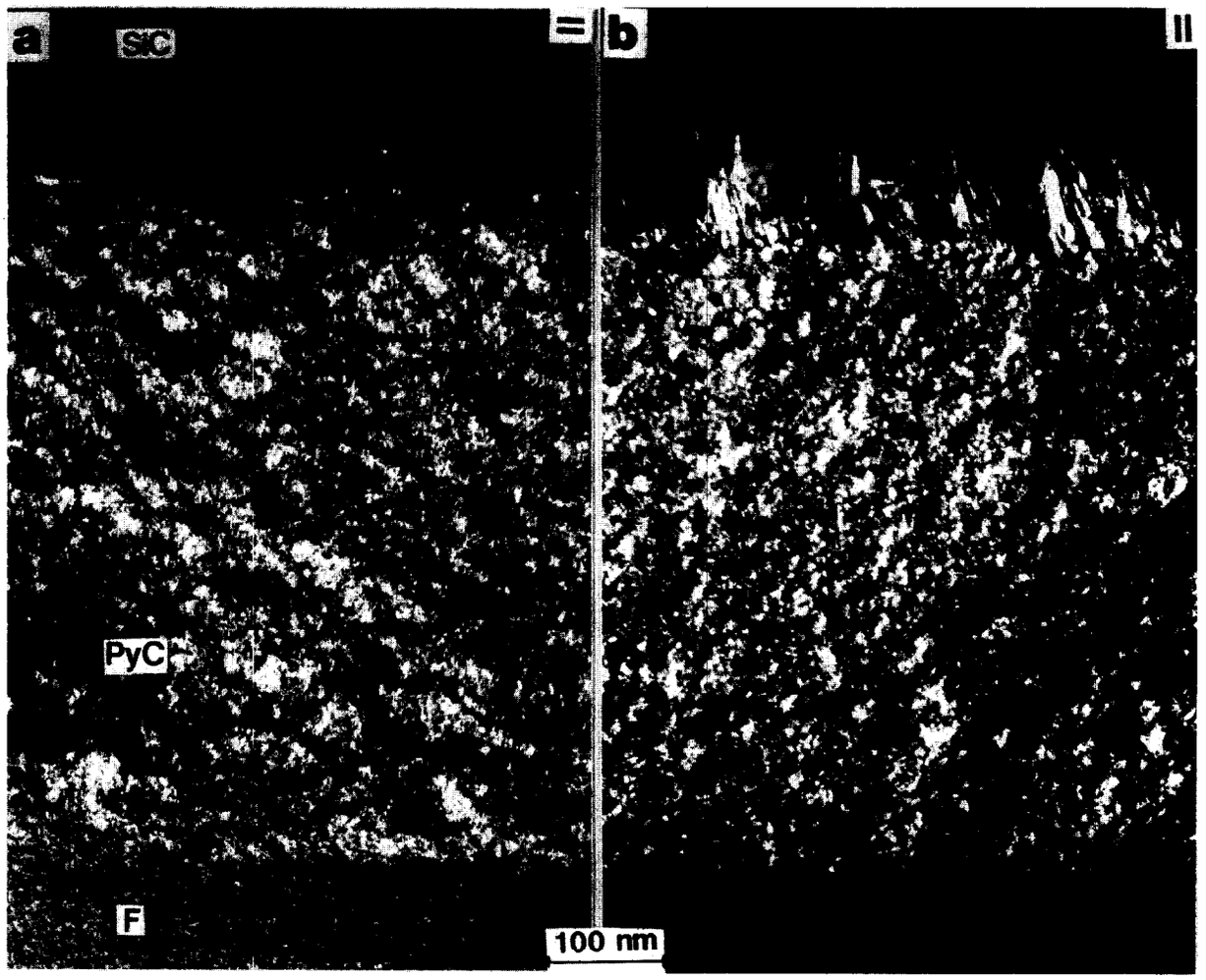


Fig. 17. Two orthogonal DF TEM images of a wall-ending type pyrocarbon interphase. Comparing (a) and (b) indicates that the whole pyrocarbon interphase is from the BOI- PyC type texture. Micrograph (b) clearly evidences the carbon walls (see text) as bright stripes oriented perpendicularly to the pyrocarbon/matrix interface.

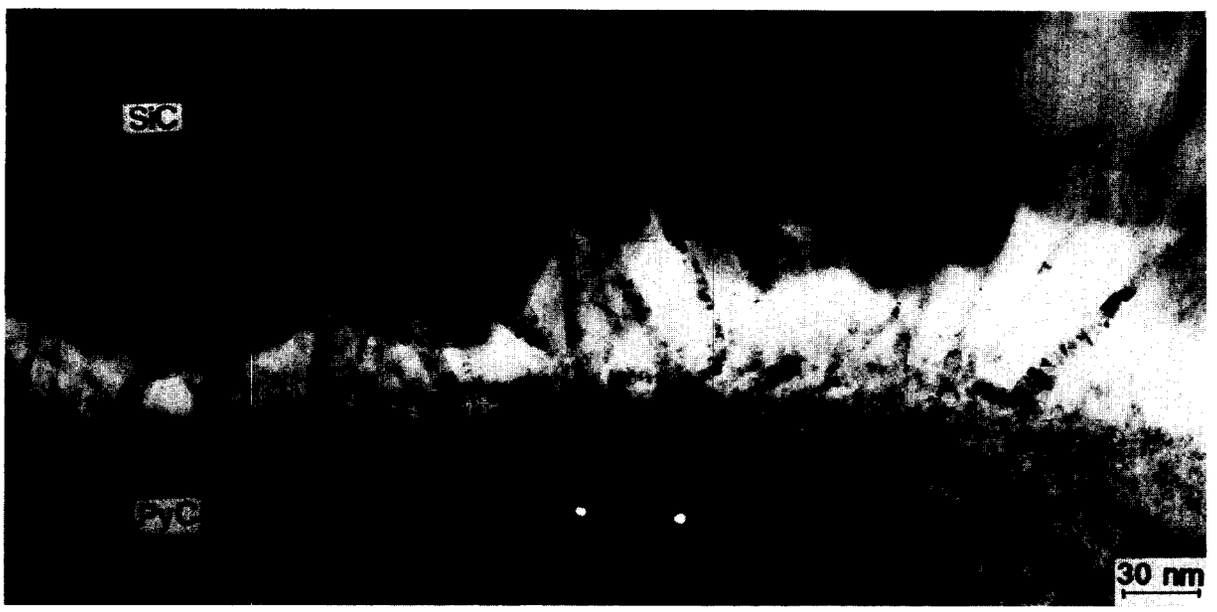


Fig. 18. BF TEM image of a carbon wall area. Note the high porosity.

strongest interfaces encountered. Therefore, a failure will progress straight from the matrix (which is the component with the lowest deformability) to the fibre through the interphase, in order to follow the strain induced by the opening of the failure edges (Fig. 23(a)). At the other extreme, Grade 1 composites have two weak interfaces, in which the

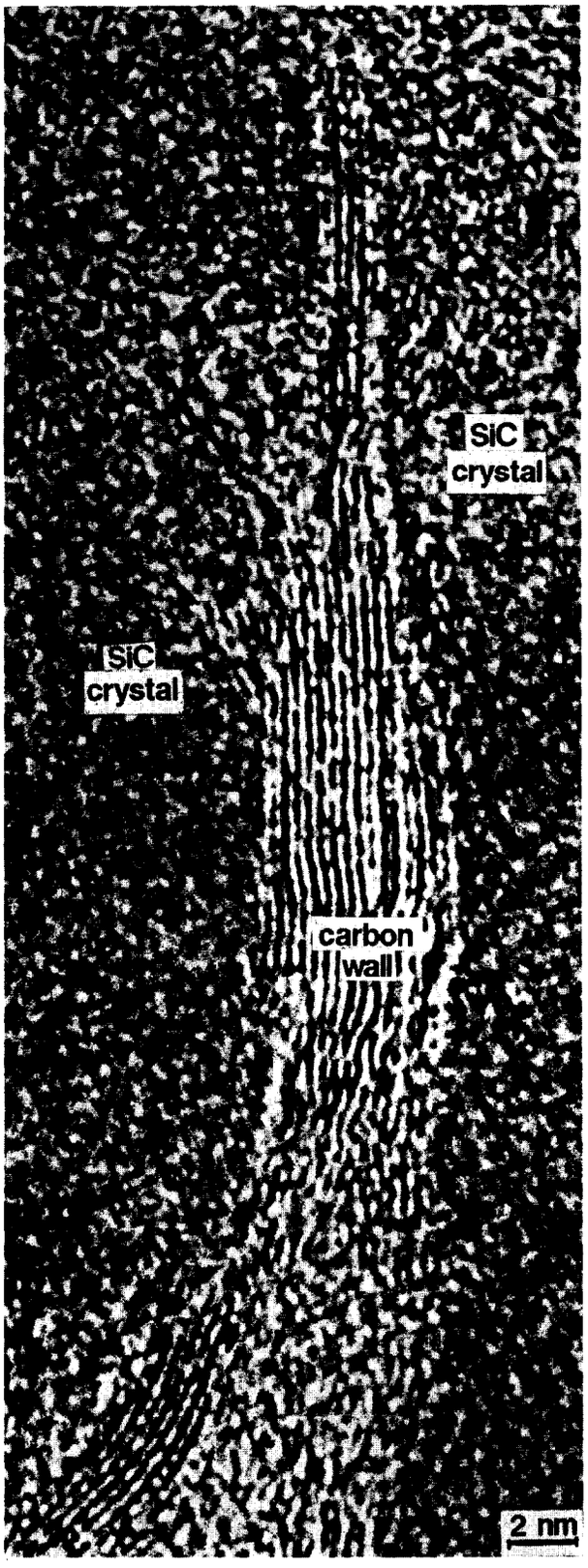


Fig. 19. LF TEM image of the end tip of a carbon wall between SiC crystals, exhibiting a peculiar edge-shape.

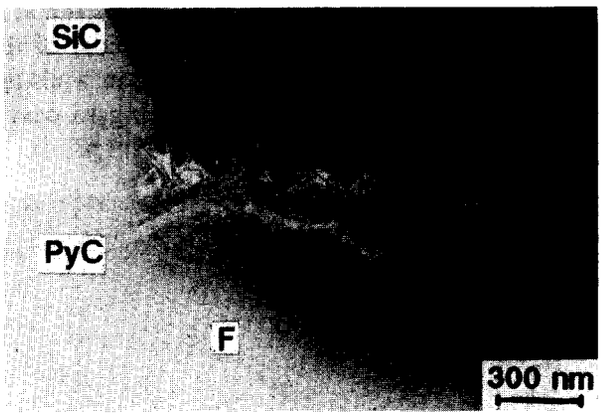


Fig. 20. Low magnification BF TEM view of a decohesion path within a carbon wall-ending type pyrocarbon interphase.

ANI-PyC part of the interphase is involved. Because the ANI-PyC is able to easily delaminate due to the anisotropic orientation of graphenes, the strain which goes with the crack propagation will not concern the fibre since it is somewhat compensated by a mode I/mode II change of the failure path (Fig. 23(b)). Successive delaminations within the ANI-PyC will help the fracture energy to disperse, and are likely to restrain the failure propagation until possibly stopping it. The fibre rupture will thus be delayed, leading to the highest ultimate strength values. Describing such an interphase as a 'fuse' is common but not appropriate, as far as the 'fuse' concept would mean that the interphase would not play any role in the mechanical behavior of the composite but once, i.e. until a critical value for the applied strength is reached

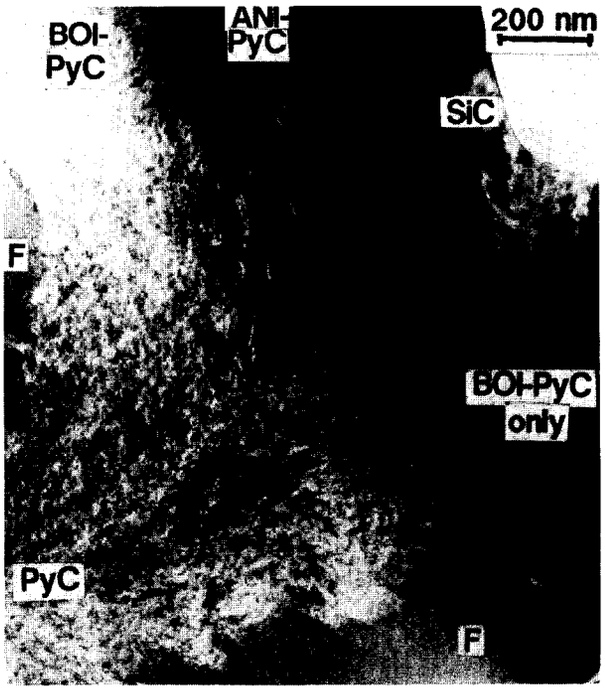


Fig. 21. BF TEM view of an example of mixed type associated interphases.

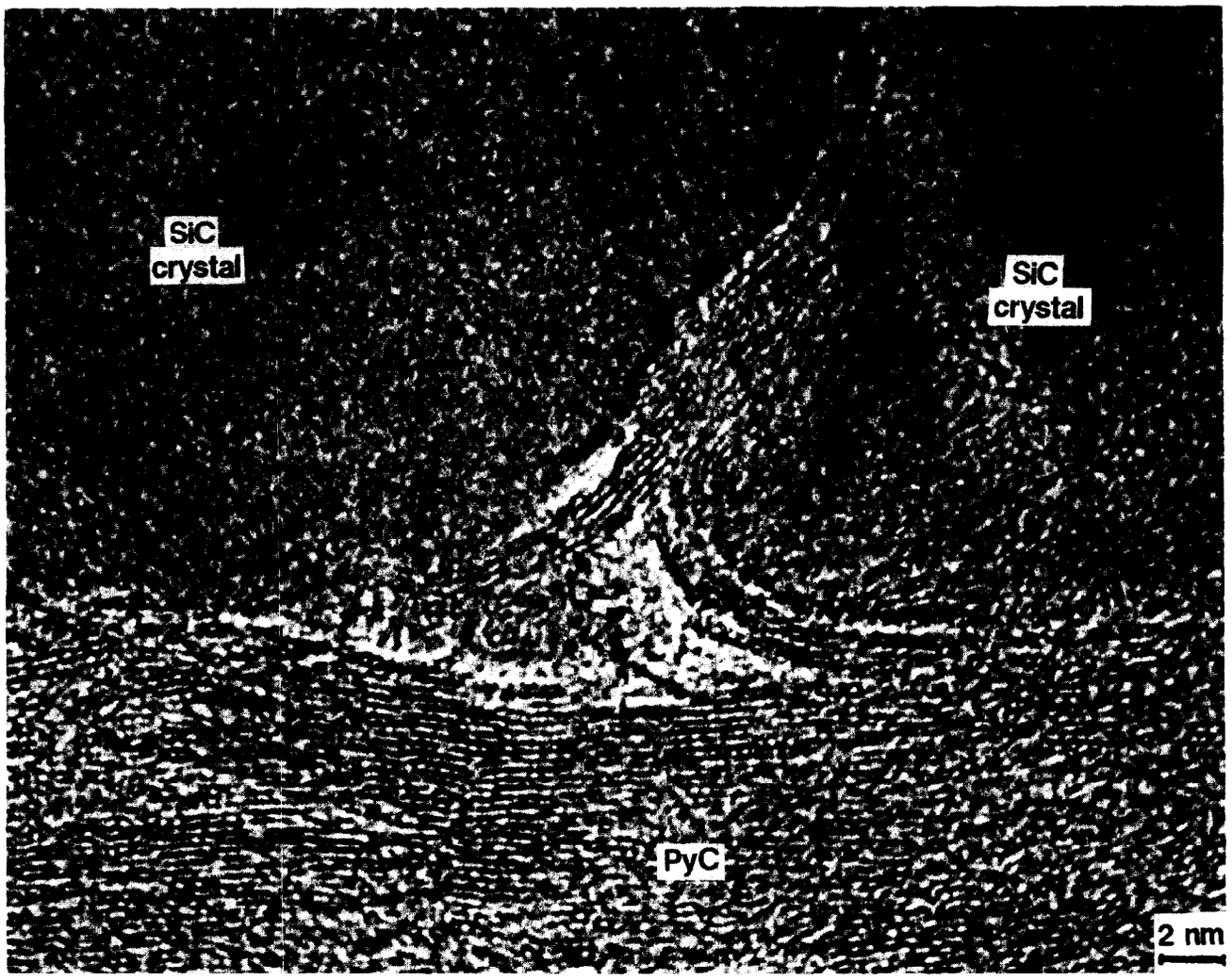


Fig. 22. LF TEM image of an example of a mixed type interphase. Note the combination of a ANI-PyC type texture with a carbon wall-ending type texture.

(corresponding to the fusing current for the electrical fuse). Obviously, the role of the interphase is not that binary, since helping in preventing the failure far before the ultimate strength is reached.

These considerations are consistent with the observations that tows exhibit mirror type fracture profiles in Grade 3 composites, while they do not exhibit planar fracture profiles in Grade 1 composites.

Due to the intermediate features of their interphases, Grade 2 composites logically behave intermediately, combining the two extreme fracture mechanisms described above in various proportions.

Finally, Table 2 indicates that the interphase-free composite has the weakest interface (PyC/fibre interface). Because differences in CET induce an interfacial void, the interface is too weak to allow the fracture energy to disperse. Even though the mode I failure propagation will again change for a mode II, the energy is fully maintained and the stress is quickly transferred to the fibre. However, the fibre will not break in front of the failure exit site within the matrix, but somewhere else along the fibre where strength is weakened by defects.

4.3 Origin of the carbon walls

Carbon walls, lying perpendicular to the interface at the pyrocarbon/matrix transition, are mainly observed in Grade 3 composites. Because they have been already observed in pyrocarbon-free SiC/SiC composites,[6–8] they have to be considered as an early step phenomenon of the SiC matrix deposition process, rather than a late step phenomenon of the pyrocarbon deposition process. They have been previously assumed to originate from the transformation of SiC crystals into C (and SiO_2, because of the presence of oxygen traces),[6] or to the decomposition into Si species and solid C of the early SiC crystals which could be abnormally unstable.[7,8] Indeed, some time is certainly required for the CVI process parameters to reach the steady-state, inducing transient and inappropriate turbulences, gas proportions, etc.[7,8] Both hypotheses are complementary, and oxygen

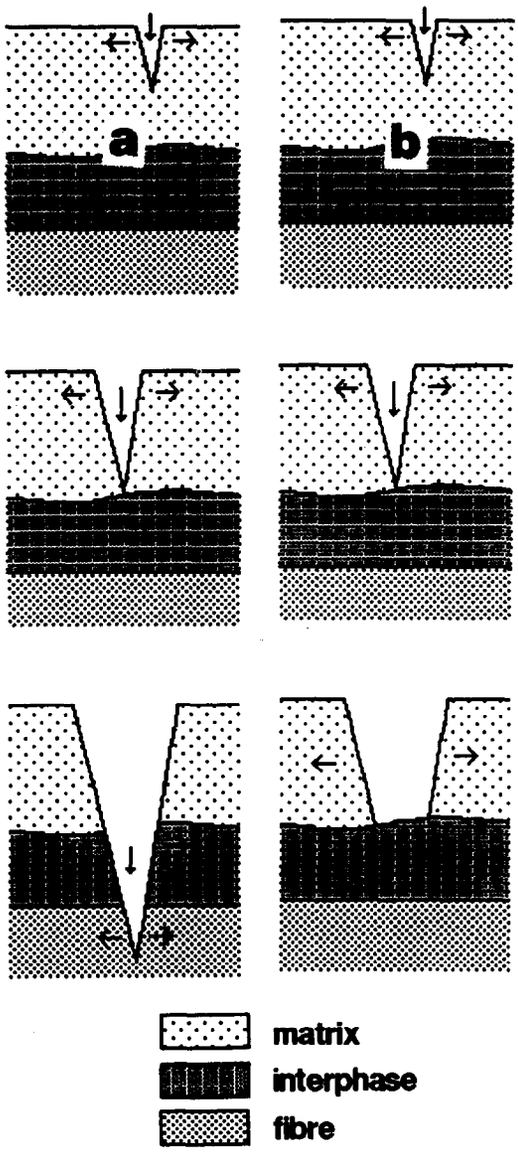


Fig. 23. Sketches of failure propagation: (a) Grade 3 composites; (b) Grade 1 composites.

traces present at the early step of the CVI process are likely to combine quickly with Si to form gaseous SiO. No silica was observed in our composites, nor those of Refs 7 and 8, but SiO_2 may be reduced to gaseous SiO as soon as gaseous hydrocarbons or hydrogen are present. Actually, such gases are used in the CVI process. Also, the presence of oxygen traces and hydrocarbons may possibly promote the direct transformations of SiC into gaseous SiO, SiH_4, SiH and solid C.[9]

4.4 Lenticular porosity

Grade 1 composites often exhibit a lenticular porosity, located within the ANI-PyC part of the bimorphic interphase. The texture suggests local decohesions between graphenes, favored by the weakness of the graphene/graphene interactions (when parallel). Such decohesions do not seem to occur spontaneously in anisotropic pyrolytic carbon films when deposited on polished alumina plates at least in the 1050–1200°C temperature range.[3,10] Therefore, we assume that they are again due to differences in TEC. Actually, the TEC for the fibre is about 20×10^{-6}/K in a transverse direction, since it is statistically isotropic. This is rather high as compared with the TEC value in the direction of the graphene sheets, which is similar to that of graphite, when considered parallel to the graphene direction (no expansion). Likewise, the TEC on the ANI-PyC part of the pyrocarbon interphase in a direction perpendicular to the graphene sheets is close to that of graphite ($28{\cdot}5 \times 10^{-6}$/K). On the opposite, the TEC for the SiC matrix is rather low (4×10^{-6}/K). Taking into account on the one hand the various TEC values above for the various phases within a Grade 1 composite, and considering on the other hand the fact that the occurrence of the lenticular porosity has appeared to be somewhat periodic, simple calculations below have allowed the lenticular porosity to be simulated (Fig. 24). The calculations mean that, while the SiC matrix does not shrink much during cooling, the fibre shrinks a lot, relatively. Because the pyrocarbon interphase is firmly bonded to the fibre, the interphase has to follow the fibre shrinkage. However, because of the low TEC along the graphene sheets, the circumference of the ANI-PyC part of the interphase all around the fibre remains unchanged. Therefore, the ANI-PyC part is led to wrinkle, that induces internal stresses strong enough to overcome the weak Van der Waals bonds between graphene and to promote decohesions (lenticular porosity).

Considering a carbon fibre 7 μm in diameter, coated with a thin pyrolytic carbon layer (thin enough for its thickness being neglected relative to the fibre diameter) partly having a ANI-PyC texture, then surrounded with a SiC matrix, both submitted to a 1000°C difference in temperature from the preparation conditions to ambient. The 'length' L_0 of the ANI-PyC around the fibre is taken equal to the circumference C_0 of the fibre and is $7 \times \pi = 22$ μm. The shrinkage of the fibre diameter during cooling is $7 \times 20 \times 10^{-6} \times 1000 = 0{\cdot}14$ μm. The circumference C imposed to the ANI-PyC by the fibre shrinkage is then $21{\cdot}56$ μm, while the real length L of the ANI-PyC remains 22 μm ($L = L_0 = C_0$). Considering a period of ~0·2 μm between the occurrence of slit pores (see Section 3 and Fig. 15), there are $21{\cdot}56/0{\cdot}2 = 107{\cdot}8$ periods around the fibre. The length x of the triangular unit of the slit pores (Fig. 24) is thus $22/(2 \times 107{\cdot}8) = 0{\cdot}102$ μm. This allows the height h of the pore to be calculated at $h \sim 20$ nm using trigonometry.

Although the calculations above are simple—even simplistic—they indicate that the porosity

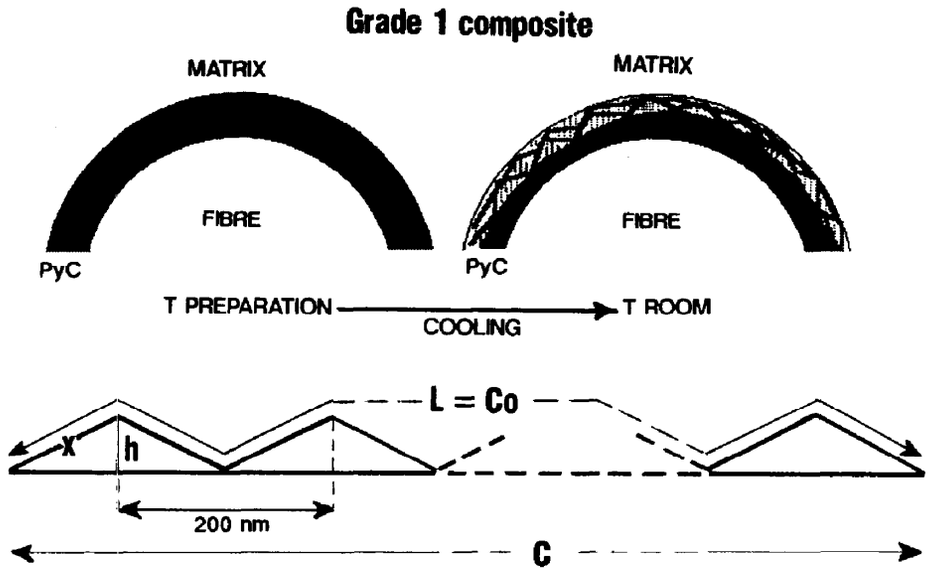


Fig. 24. Sketch of the formation mechanism of the lenticular porosity within the ANI-PyC part of the bimorphic type interphase texture, due to differences in the fibre and pyrocarbon TEC (see text).

induced by the difference in TEC is in the same range as the porosity observed. We thus believe that the lenticular porosity within Grade 1 composites is a secondary texture inherited from the cooling step rather than an intrinsic texture induced by the primary deposition step.

5 Conclusion

As previously stated for SiC/C/SiC composites, the texture of the pyrolytic carbon interphase has a major influence on the macroscopic mechanical behavior of the C/C/SiC composites. Obviously, controlling the pyrocarbon texture allows the matrix-to-fibre stress transfer to be controlled, leading to more-or-less tough composites. A common observation for tough composites is that the fibre/matrix interface has to reach a compromise: not too weak but not too strong. Whatever the texture, a pyrocarbon interphase is always efficient in dispersing the fracture energy, as compared with interphase-free C/SiC composites. Whatever the number of interfaces, the bulk behavior of the composite is mainly controlled by the weakest one. However, the efficiency is all the higher as the number of weak interfaces is high. This points out the importance of being able to order the interface strengths. For C/C/SiC composites, the interface strength may be directly related to the Van der Waals/covalent bond ratio, and increases as the ratio decreases. The 'compromise rule'—sustained by the observations—leads to the conclusion that an interface strength with a nil value is not desirable (case of the C/SiC composites), since allowing no stress transfer. In other words, some minimum strength value is necessary to get a tough composite. As compared with the interphase texture and the interface strength, other parameters such as interphase thickness or fibre topology are subordinate.

Acknowledgement

The authors thank Société Européenne de Propulsion for providing samples, results of mechanical tests, and financial support.

References

1. Christin, F., Les composites carbone–carbone–carbure de silicium: une nouvelle famille de matériaux destinés à des applications à haute température. State Thesis, Université de Bordeaux I, France, 1979.
2. Després, J.-F. & Monthioux, M., Etudes des interfaces des composites C/C/SiC. Relation avec les propriétés mécaniques. Internal Report to SEP, 1992.
3. Després, J.-F., Les interphases de carbone pyrolytique dans les composites carbone/carbure de silicium. PhD thesis, Université de Pau & des Pays de l'Adour, France, 1993.
4. Oberlin, A., Application of dark-field electron microscopy to carbon study. *Carbon*, **17** (1979) 7–20.
5. Després, J.-F. & Monthioux, M., Microtextures of interfaces related to mechanical properties in carbon fibre reinforced ceramic matrix composites. In *5th European Conference on Composite Materials Proceedings*, ed. A. R. Bunsell, J. F. Jamet & A. Massiah. EACM, Bordeaux, 1992, pp. 901–6.
6. Maniette, Y., Contribution a l'étude de phénomènes d'interphases dans des composites de carbure de silicium. PhD thesis, Université de Pau & des Pays de l'Adour, France, 1988.
7. Cojean, D., Monthioux, M. & Oberlin, A., Phénomènes interfaciaux dans des composites SiC/SiC 2D de propriétés mécaniques variées. In *Comptes-Rendus des Septièmes Journées Nationales sur les Composites*, ed. G. Fantozzi & P. Fleischmann. AMAC, Paris, 1990, pp. 103–11.

8. Cojean, D. & Monthioux, M., Microtextures of interfaces related to mechanical properties in ceramic fibre reinforced ceramic matrix composites. In *5th European Conference on Composite Materials Proceedings*, ed. A. R. Bunsell, J. F. Jamet & A. Massiah. EACM, Bordeaux, 1992, pp. 729–34.
9. Gulbransen, E. A. & Jansson, S. V. The high temperature oxidation, reduction and volatilization of silicon and silicon carbide. *Oxidation of Metals*, **4** (1972) 181–201.
10. Després, J.-F., Vahlas, C. & Oberlin, A., Chemical vapor deposition of pyrolytic carbon on polished substrates. *J. Phys. IV*, **3** (1993) 563–70.

Journal of the European Ceramic Society **15** (1995) 225–232
Elsevier Science Limited
Printed in Great Britain
0955-2219/95/$9.50

Properties and Interface Structures of Ni and Ni–Ti Alloy Toughened Al_2O_3 Ceramic Composites

X. Zhang,[a] G. Lu,[b] M. J. Hoffmann[c] & R. Metselaar[a]

[a]Centre for Technical Ceramics, Eindhoven University of Technology, Eindhoven, The Netherlands
[b]Max-Plank-Institut für Metallforschung, Institut für Physik, Stuttgart, Germany
[c]Max-Plank-Institut für Metallforschung, Institut für Werkstoffwissenschaften, Pulver-metallurgisches Laboratorium, Stuttgart, Germany

(Received 8 February 1994; revised version received 20 June 1994; accepted 1 August 1994)

Abstract

Ni/Al_2O_3 and $Ni–Ti/Al_2O_3$ composites sintered in different atmospheres are investigated. Argon as a sintering atmosphere is found to be more beneficial to the fracture toughness of the composites than CO. Ni inclusions at 12 vol.% enhance the fracture toughness up to 36%, corresponding to a fracture energy twice that of the alumina matrix, whereas titanium alloying to Ni makes a negative contribution to the mechanical behaviour. The interfacial structures of Ni/Al_2O_3 and $Ni–Ti/Al_2O_3$ are studied by using electron microscopy. The titanium distribution at the interfaces is studied and correlated to the mechanical properties.

1 Introduction

Brittle ceramic materials can be toughened by the incorporation of ductile reinforcements. The toughening mechanism has already been investigated both theoretically and experimentally.[1–4] The plastic stretching of ductile reinforcements accounts for the predominant toughening. For effective toughening the appropriate interface bonding strength is the first requirement. If the bonding strength is too weak, cracks will propagate along the interface and plastic stretching of the ductile reinforcements will not occur. This is the usual case for many metal/ceramic composites. If the bonding strength is too strong, a rare case, the plastic stretching will be only localized to a limited zone between surfaces of propagating cracks and the toughness of the reinforcements will not be utilized adequately.[5] Therefore, in a metal reinforced ceramic composite, the fracture toughness can be enhanced by optimizing the metal/ceramic interface behaviour, which depends on both the physical properties (such as morphology, elastic modulus, thermal expansion coefficient) and the chemical characters of each material.

As a model system, Ni particle toughened Al_2O_3 has been studied.[6,7] A large increase in fracture toughness has been reported for Ni/Al_2O_3 composites compared to that of the monolithic alumina matrix. However, it seems that the potential for toughening is not fully reached because the plastic stretching of the Ni particles is limited. Cracks propagate often around the Ni particles, i.e. along the Ni/Al_2O_3 interfaces, owing to the low interface bonding strength as compared to the high yielding strength of Ni. Therefore, in order to get a well-toughened composite, the interface bonding between Ni and Al_2O_3 should be strengthened.

The common practice for interface strength adjustment is to introduce a degree of interfacial chemical reaction. In preparing composite materials, this can be achieved either by controlling the sintering atmosphere or by introducing additives. As far as the atmosphere is concerned, Ni can be oxidized to form a NiO or a $NiAl_2O_4$ spinel interlayer. As to additives, titanium is widely used as a wetting agent in brazing ceramics with alloys to achieve strong joints.[8] It has been reported that the interface energy between Ni and sapphire (or sintered Al_2O_3) decreases sharply on the addition of a small amount (about 2%) of Ti in Ni because of the segregation of Ti and the formation of Ti_2O_3 at the interface.[9] According to the concept of the work of adhesion, W_{ad}, defined as:

$$W_{ad} = \gamma_{Ni} + \gamma_{Al_2O_3} - \gamma_{Ni/Al_2O_3}$$

the interface bonding between Ni/Al_2O_3 can be improved by the presence of Ti. In the present work, pure Ni and Ni–Ti alloy toughened Al_2O_3 composites are prepared by sintering in either Ar

Table 1. Properties of the Ni(Ti)/Al_2O_3 composites

Sample	*Al_2O_3 (air)*	*1 12 vol%Ni (CO)*	*2 12 vol%Ni (Ar)*	*3 12 vol%Ni–Ti (CO)*	*4 12 vol%Ni–Ti (Ar)*
Density (%TD)	99·9	99·5	99·9	99·3	99·7
Strength (MPa)[a]	326 ± 24	196 ± 14	306 ± 13	180 ± 15	188 ± 10
K_{1c} (MPa $m^{1/2}$)[a]	3·6	4·1	4·9	3·2	3·5

[a] Results of six measurements.

or CO atmospheres. The purpose is to investigate the influence of the atmospheres and of the titanium addition on the interface reactions and on the mechanical properties of the composites.

2 Experimental Procedures

The composites were prepared by a typical powder metallurgical route. Pure nickel powders (99·99 + %. ≤ 63 μm, Goodfellow) or Ni–Ti alloy powders (5 wt% or 6·06 at% Ti in Ni, prepared by an atomizer, sieved to under 63 μm) in the amount of 12 vol.% were mixed with fine Al_2O_3 powder (99·99% up, TM-DR, ultra pure sinterable alumina) in an attritor for 4 h with alumina balls and isopropanol as the milling media. The slurries were dried and sieved. Powder compacts with dimensions of about 13 × 21 × 57 mm were formed by cold isostatic pressing under a pressure of 625 MPa. The green compacts were sintered at 1400°C for 2 h in CO (generated by burning of carbon powder in a closed alumina crucible) and in Ar (static argon in an alumina tube furnace) respectively.

After sintering, the surfaces of the samples were carefully observed. The density was measured by the Archimedes method. Bending bars, 3 × 4 × 45 mm in size, were machined from the large sintered blocks. The mechanical testing was performed in the four-point-bending mode at a cross head speed of 0·1 mm/min. The strength was determined on the bending bars with inner/outer spans of 20/40 mm. The toughness was characterized on the subsequent half bars with inner/outer spans of 7/20 mm by the single-edge-notched-beam (SENB) method. The notch width was controlled to within 100 μm and the depth was about one fourth of the sample height, i.e. 1 mm.

The phases in the composites were examined by X-ray diffraction (XRD). The general morphology of the samples was studied with optical microscopy. The detailed structure of the interfaces was investigated by scanning electron microscopy (SEM) and transmission electron microscopy (TEM). The composition of the interfacial layers was determined by electron probe microanalysis (EPMA). Because of the uncertainties associated with analyzing oxygen content, quantitative analysis was only done on Ti, Ni and Al, using pure metals as the standards. To estimate the oxygen content, semi-quantitative (standardless) analysis was performed using energy dispersive spectroscopy (EDS) mode in SEM or TEM. Since the interfacial layers are generally very thin, analysis was always performed at places where the layers are relatively thick.

3 Results

3.1 Properties of the composites

The relative density, the fracture strength and toughness of the monolithic Al_2O_3 and of the composites are given in Table 1. All the samples were sintered nearly to their theoretical densities in the different atmospheres by normal sintering. The composites have lower fracture strength than monolithic Al_2O_3. The Ni/Al_2O_3 composites have improved fracture toughness with an increase of 14 and 36% over Al_2O_3 in the case of CO and Ar as the sintering atmospheres, respectively. Calculation from the toughness shows that the fracture energy ($\gamma = K_{1c}^2/2E$) of Al_2O_3 and of sample 2 are 16·8 J/m^2 and 32·9 J/m^2, namely a doubling of the fracture energy in the composite as compared with the pure matrix material. For the Ni–Ti/Al_2O_3 composites, a decrease in fracture toughness is found with either CO or Ar as the sintering atmosphere. These results suggest that the atmospheres have a large influence on the fracture properties of the composites, and that an Ar atmosphere is more beneficial than a CO atmosphere. The addition of Ti to Ni produces no improvement in toughening.

3.2 Microstructures and interfaces

The appearance of all the sintered composites is more or less yellow-green, but with one surface blue, which was in contact with the alumina crucible during sintering. XRD analyses reveal that the yellow-green surfaces contain NiO and the blue ones $NiAl_2O_4$ spinel. After removing the surface scales, which are thinner than 0·5 μm, the samples

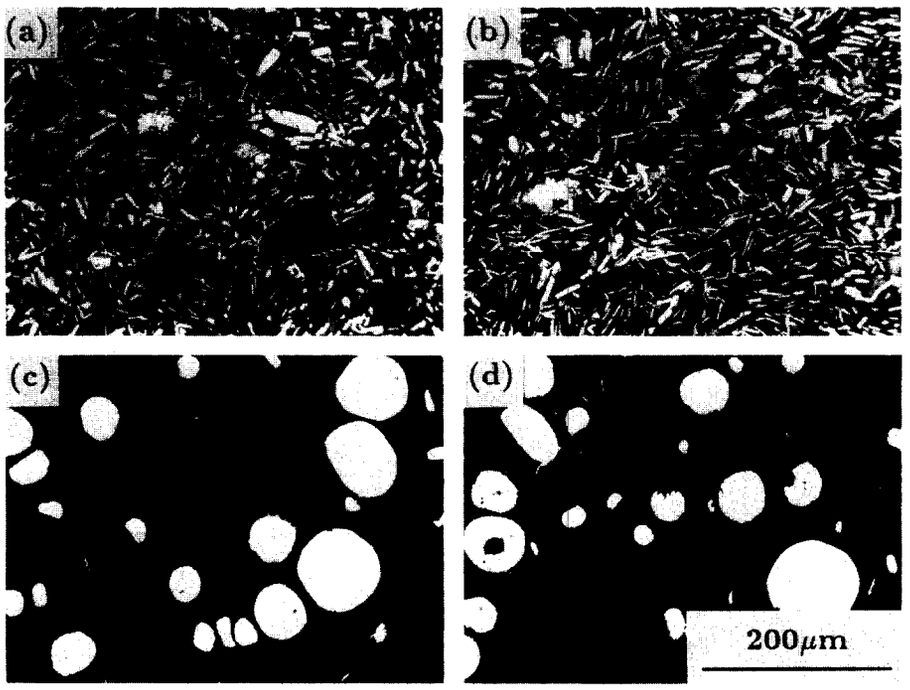


Fig. 1. Optical micrographs of the samples: (a) 1, (b) 2, (c) 3 and (d) 4.

appear dark grey for the Ni/Al_2O_3 composites and grey for the $Ni–Ti/Al_2O_3$ composites. No other phases except Ni (Ni–Ti) and Al_2O_3 can be detected by XRD. Since we are interested in the bulk properties of the composites, further analyses are based on the interiors of the materials.

Figure 1 shows the optical microstructures of the composite samples. The morphology of the Ni particles in samples 1 and 2 is very different from that of Ni–Ti particles in samples 3 and 4. The Ni particles appear to be small rods of about 20 μm long and 2–3 μm across; some particles agglomerate together. On the other hand, the Ni–Ti particles are spheres with a diameter of about 50 μm, and the particles are distributed discretely and randomly. The difference in morphology of the metal particles originates from the starting powders and from the processing. Although both powders are sieved under 63 μm, the Ni powders are originally finer and more agglomerated than the Ni–Ti powders. During attrition milling Ni particles become rod-shaped because of the plastic deformation caused by inter-particle friction, while Ni–Ti particles are very rigid and much less influenced by milling.

The regions near the interfaces between the metal particles and ceramics have been studied by SEM. In samples 1 and 2, the interface between the Ni and Al_2O_3 is sharp. In samples 3 and 4, an interfacial reaction layer between Ni–Ti and Al_2O_3 is observed. EDS analysis indicates that the interface layer is rich in Ti, as shown in Fig. 2 which is the Ti mapping in samples 3 and 4. In sample 3, Ti is mostly concentrated at the rim of each Ni–Ti particle, while in sample 4, Ti is distributed throughout the Ni–Ti particle, although it is also enriched at the particle surfaces.

To investigate the details of the structure in the

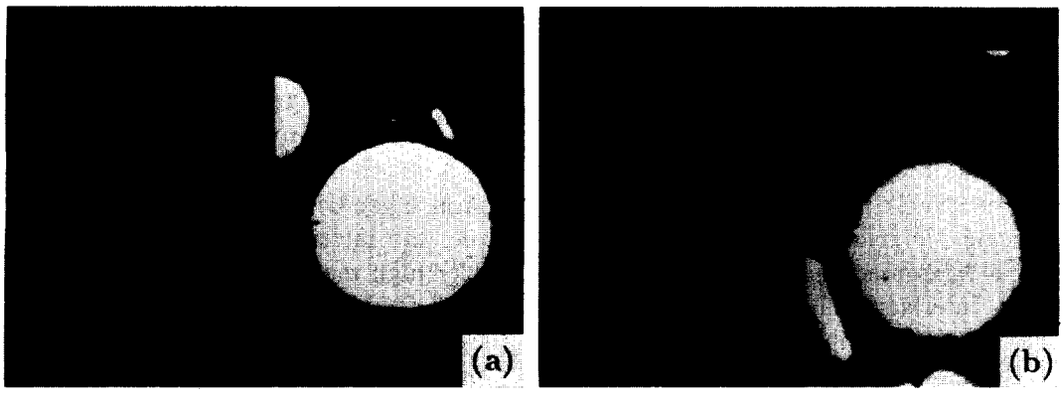


Fig. 2. Ti mapping by SEM/EDS, (a) sample 3 and (b) sample 4.

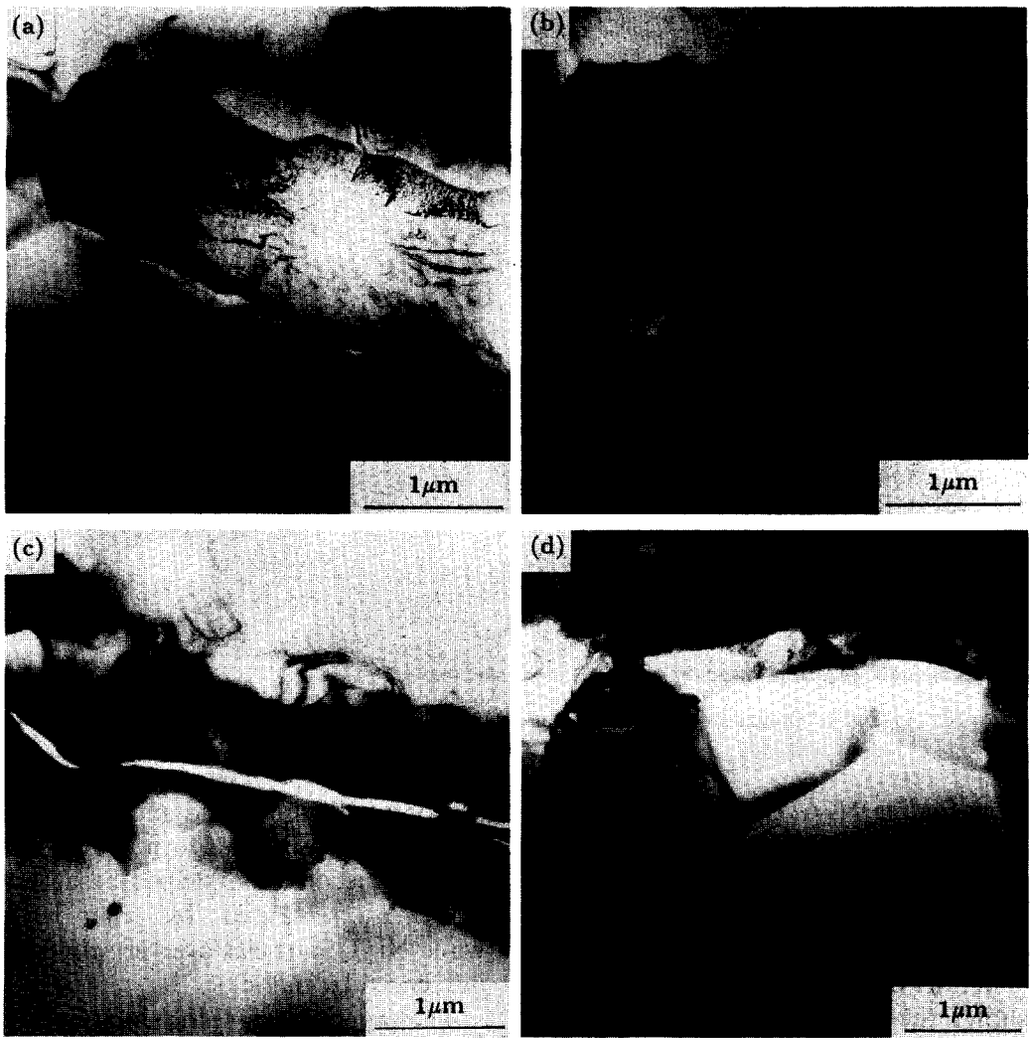


Fig. 3. TEM low magnification images which show general structures of the Ni(Ti)/Al_2O_3 interface. In (a) for sample 1 and (b) for sample 2 no interfacial layer is observed. In (c) for sample 3 and (d) for sample 4 a reaction layer can be seen.

interfacial region, TEM experiments have been carried out. Figure 3 shows the general structures around the metal particles under TEM with low magnification. In Fig. 3 (a) and (b), the bright-field images of the interfaces in samples 1 and 2, the Ni particle is surrounded by Al_2O_3 grains with an average size of about 0·6 μm, and the interface remains sharp and clear. In Fig. 3(c) and (d), an interfacial layer exists between the Ni–Ti and Al_2O_3 as also observed by SEM. On average, the layer is about 2–3 μm thick in sample 3 and about 1 μm thick in sample 4. Cracks are often observed along the interfacial regions in sample 3, within the layer as shown in Fig. 3 (c) or at the boundary between the layer and the ceramic matrix. The interfacial layer and the Ni–Ti particle are bonded very well. This indicates a relatively strong bonding between interfacial layer/metal and a relatively weak bonding between interfacial layer/ceramic. Similar interfacial behaviour is also observed by examining the details of the indentation crack path in both samples 3 and 4 under SEM.

In addition to the interfacial layer, another feature in the microstructure of the Ni–Ti/Al_2O_3 composites is the inhomogeneity of the Al_2O_3 grain size. The grains close to the interface, about 2·5 μm in sample 3 and 1·4 μm in sample 4, are much larger than the grains further away from the interface, which are, as in samples 1 and 2 (Fig. 3(a) and (b)), under 1 μm. In this study, the grain size of the monolithic Al_2O_3 is about 2·5 μm. Therefore, it can be concluded that while Ni and Ni–Ti inclusions suppress grain growth in the Al_2O_3 matrix, Ti diffusion from the Ni–Ti bulk promotes grain growth in the surrounding Al_2O_3 matrix near the interface.

To determine whether there is an interfacial reaction layer between the Ni and Al_2O_3 at a local scale, the interfaces have been analyzed by TEM under high magnification, as demonstrated in Fig. 4 (a) and (b) for a typical interface region in samples 1 and 2 respectively. Some shadowed regions along the interfaces are observed due to the projection of the interface plane which is not parallel

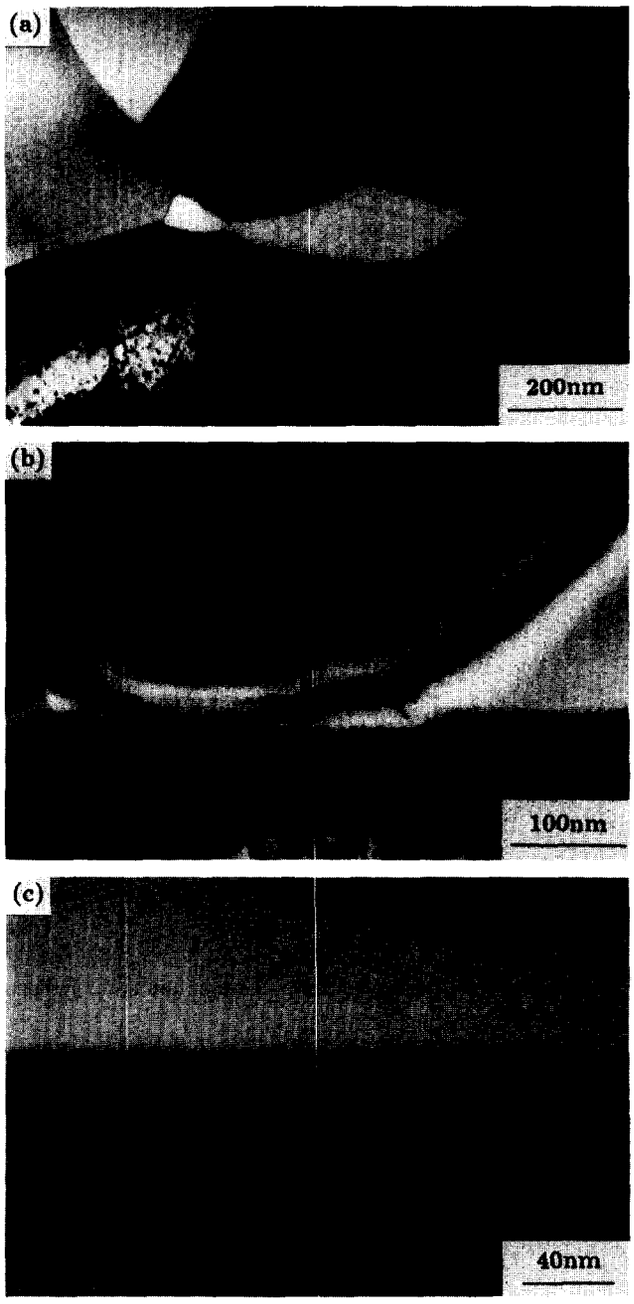


Fig. 4. High magnification TEM images of the Ni/Al_2O_3 interface, (a) sample 1, (b) sample 2; and (c) sample 1, same as (a) but at higher magnification.

to the electron beam. The interface becomes sharp and narrow when the specimen is tilted to an appropriate orientation so that the interface becomes vertical. Figure 4 (c) is a portion of the interface in sample 1 at an even higher magnification. The fringes parallel to the interface are due to the shallow interface. Apart from that there is no sign of interfacial layers or of precipitates larger than about 10 nm.

The interfacial layers in samples 3 and 4 are seen in more detail in high magnification in Fig. 5. The contrast of the interfacial layer is clearly different from that of the Ni–Ti particle and of the matrix. In Fig. 5 (a) for sample 3, some egg-shaped grains appear in the layer, and again there

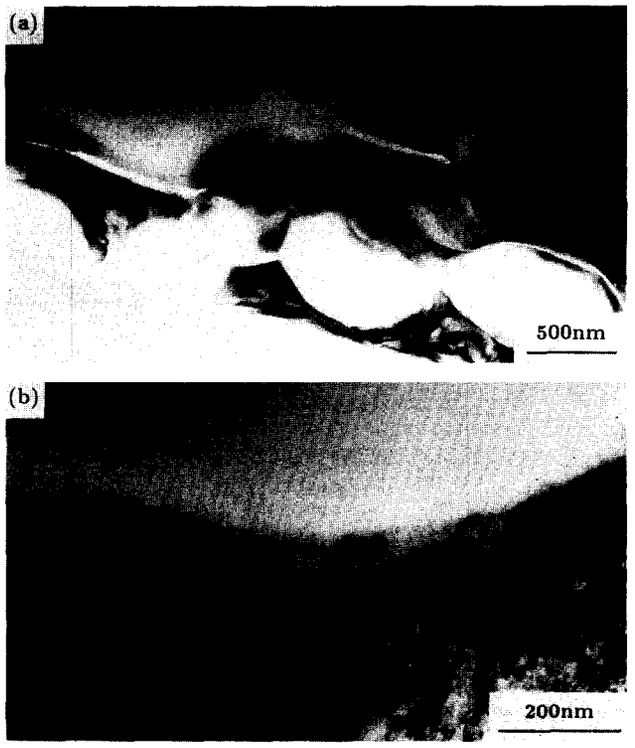


Fig. 5. High magnification TEM images of the $Ni–Ti/Al_2O_3$ interface, (a) sample 3, and (b) sample 4.

is a crack mainly along the boundary between the layer and the ceramic matrix. In Fig. 5 (b) for sample 4, the interfacial layer is thinner and less rich in structure than that in 3.

Figure 6 shows the concentration profiles of Ti, Al and Ni across an interfacial layer after a quantitative analysis by line scan from a Ni–Ti particle (left) to the Al_2O_3 matrix (right) in sample 3. In the Ni–Ti particle, Ti is almost completely depleted. In the layer, the content of Ni is very limited, and Ti is concentrated. The diffusion depth of Ti is as much as 4–5 μm into the Al_2O_3.

Semi-quantitative analysis from TEM/EDS reveals that a large amount of oxygen is present in the layers. Figure 7 (a) shows the concentration profiles after a series of analyses, and Fig. 7(b) is the corresponding TEM image with the points

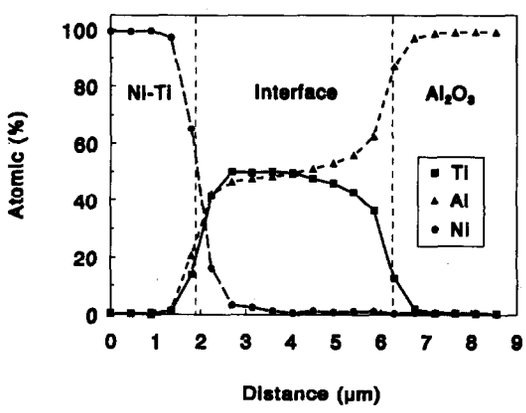
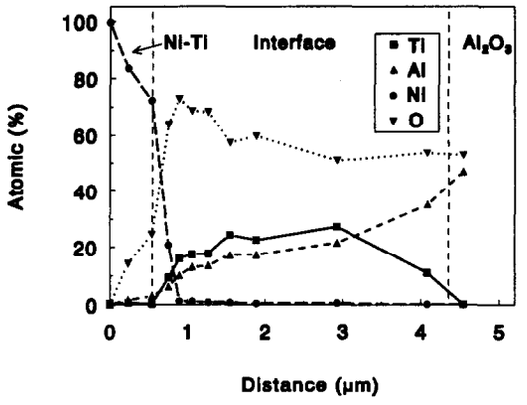


Fig. 6. Composition profile around the interface in sample 3 after a quantitative analysis by SEM/EDS with standard.



(a)



(b)

Fig. 7. (a) Composition profile in sample 3 after a semi-quantitative analysis by TEM/EDS. (b) The contamination spots indicate where the EDS analyses were taken.

where the spectra were taken indicated by the contamination spots. The high oxygen level should be treated with caution because of the nature of the semi-quantitative analysis. Some oxygen has diffused into the Ni–Ti particle to a distance of about 500 nm, associated with the diffusion of small amounts of Al. Similar to Fig. 6, Ti approaches zero in the Ni–Ti particle, but diffuses into Al_2O_3 to a distance of 4·5 μm.

The interfacial layers in sample 4 have been similarly examined. Due to the very thin thickness (only about 1 μm), the exact composition of the layer cannot be determined quantitatively. Semi-quantitative analyses by TEM/EDS indicate the presence of Ti, Al and O in the layers.

4 Analysis

4.1 Chemistry of the interface

As stated earlier, interfacial reactions play an important role in the final mechanical properties of composite materials. The probable reactions can be predicted from thermodynamic data.[10] In the Ni/Al_2O_3 system, the possible reactions are the formation of NiO or $NiAl_2O_4$ spinel. For the reaction

$$2Ni + O_2 \rightarrow 2NiO \quad (1)$$

$\Delta G = -198{\cdot}2$ kJ and the equilibrium oxygen partial pressure is 5×10^{-7} bar at 1400°C. As soon as NiO is formed, reaction with Al_2O_3 will proceed to develop $NiAl_2O_4$ spinel, because the reaction

$$NiO + Al_2O_3 \rightarrow NiAl_2O_4 \quad (2)$$

with $\Delta G = -18{\cdot}5$ kJ has a negative Gibbs energy at 1400°C.

However, direct formation of $NiAl_2O_4$ spinel between Ni and Al_2O_3 is also possible as illustrated in Ni/Al_2O_3 diffusion couples and diffusion bonding experiments.[11–13] The formation of $NiAl_2O_4$ spinel at Ni/Al_2O_3 interfaces need not proceed through a NiO intermediate, but requires a threshold activity of oxygen dissolved in Ni, which is less than the solubility limit of oxygen in Ni in equilibrium with NiO. The threshold oxygen level is 0·025 at% (250 ppm) at 1400°C from thermodynamic calculation.[13]

In the present work, the oxygen level in the CO atmosphere is estimated to be 3×10^{-17} bar in equilibrium conditions (calculated from the oxidation of C to CO at 1400°C). Comparing this value with the equilibrium oxygen partial pressure for

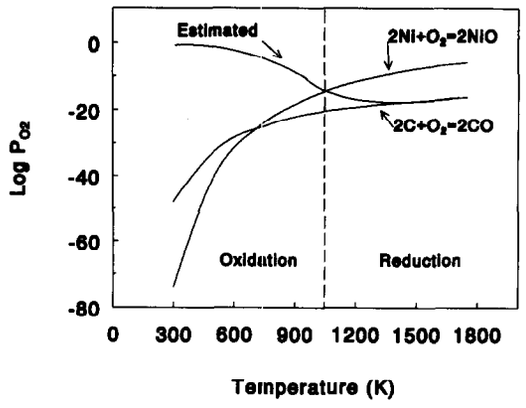


Fig. 8. Oxygen level estimated in the CO sintering atmosphere during heating.

Ni oxidation, 5×10^{-7} bar, it appears that NiO formation in the CO atmosphere is not predicted. Therefore spinel formation should not arise through a NiO precursor. On the other hand, direct spinel formation is also not predicted because the oxygen content in the Ni is very limited in the raw material (99·99 + %). In the case of Ar atmosphere, the oxygen partial pressure is expected to be 3×10^{-6} bar. Ni should then be oxidized and $NiAl_2O_3$ should be also formed subsequently. These estimations do not completely agree with the experimental observations, which show that both NiO and $NiAl_2O_4$ spinel are present on the surfaces, but not in the interiors of all the samples sintered in both atmospheres. The difference can be attributed to the real oxygen level during heating. The CO atmosphere is generated by burning C powder in a closed crucible, so that the oxygen level decreases from 0·21 bar in the initial air to as low as 3×10^{-17} bar at 1400°C under equilibrium conditions. This process is shown schematically in Fig. 8. During the initial period of heating, the oxygen level is high enough for Ni oxidation and $NiAl_2O_4$ formation. The oxide and spinel formed can be reduced again at higher temperatures when the oxygen level approaches the equilibrium one. This has been supported in our experiments by extending the holding time at 1400°C. The surface NiO and $NiAl_2O_4$ spinel layer is observed to diminish. In both atmospheres, oxygen is consumed gradually. Penetration of the oxygen into the interior of the samples is probably too limited to make Ni oxidized there. The initial oxygen enclosed in the powder compacts (green bodies) alone cannot cause prominent Ni oxidation. Provided that all the oxygen in the interior is consumed to produce NiO, a layer as thin as about 3 Å is estimated on surfaces of the Ni particles, which cannot be detected by TEM analysis. In fact, some of the oxygen may be dissolved in Ni, making the NiO layer even thinner.

In the Ni–Ti/Al_2O_3 composites, the interfacial layer contains only Ti, Al and O, and Ni is much less involved. Apparently, Ti diffuses from the interior of the Ni–Ti particles to the particle surfaces, and then the Ti at the particle surfaces reacts further with oxygen and the Al_2O_3 matrix.

From the phase diagram of the Ti–O system,[14] Ti can dissolve a large amount of oxygen and can be very easily oxidized to form a family of oxides such as TiO, Ti_2O_3, TiO_2 and so on. Considering the following reactions

$$Ti + 1/2O_2(g) \rightarrow TiO \qquad \Delta G = -382 \text{ kJ} \quad (3)$$

$$Ti + 3/4O_2(g) \rightarrow 1/2Ti_2O_3 \qquad \Delta G = -534 \text{ kJ} \quad (4)$$

$$Ti + O_2(g) \rightarrow TiO_2 \qquad \Delta G = -642 \text{ kJ} \quad (5)$$

and the activity of 6 at% Ti in Ni, estimated to be $2{\cdot}6 \times 10^{-4}$ at 1400°C,[15] the equilibrium oxygen partial pressures for the above reactions are $2{\cdot}1 \times 10^{-17}$, $3{\cdot}5 \times 10^{-18}$ and $3{\cdot}5 \times 10^{-17}$ bar, respectively. Because of the high oxygen level in both sintering atmospheres (especially high during heating in the CO atmosphere as indicated from the Ni/Al_2O_3 surface reactions), Ti can be easily oxidized. The oxide is probably in the form of TiO_2 (rutile), since experiments on the Ni–Ti powders treated in CO atmospheres similar to those of the sintering conditions show that a layer of TiO_2 (rutile) is present on the surface of each Ni–Ti particle. The titanium oxide at the Ni–Ti/Al_2O_3 interface can dissolve into the Al_2O_3 and promote Al_2O_3 grain growth.[16] The thicker reaction layer in the CO atmosphere than in the Ar atmosphere is attributed to the higher oxygen level in the former case during the heating stage. The formation of TiC is not possible from thermodynamic considerations.

4.2 Relationship between structure and properties

From the fracture surface analyses and from the indentation crack path examinations, it is found that the Ni or Ni–Ti metallic particles do not undergo substantial plastic stretching as a crack tip passes by. Cracks propagate mainly along the interface between the metal inclusions and the Al_2O_3 ceramic. The toughening mainly comes from the crack deflection instead of from the desired plastic stretching of the metal. Because crack deflection is relatively ineffective in toughening,[17] this explains the small improvement in the toughness of the composites. As to the low fracture strength of the composite compared to monolithic Al_2O_3, this is due to defects introduced by the metal inclusions (which themselves can be taken as flaws) and to the influence of the sintering atmospheres. Contamination from C due to the CO atmosphere may be responsible for the specially low strength of the composites sintered in CO. As is known, C is detrimental to the mechanical properties of alumina.[18]

For samples 1 and 2, the difference in microstructure and interface is hardly detectable. The difference in fracture toughness can be attributed to the ductility of Ni. In sample 1, the absorption of C from the atmosphere make the Ni particles more resistant to yield,[19] hence providing a lesser contribution to the toughening. For samples 3 and 4, the negative influence of the Ni–Ti inclusions on the fracture toughness is related to the weak interfacial layer and boundary between the layer and the Al_2O_3 matrix. Cracks occur at the interface resulting from the stress of thermal expansion mismatch between the large metal particles and the matrix. So the metal particles may act to some extent as pores. The weak interface debonding releases only very little energy to resist the crack propagation. Furthermore, titanium does not only modify the interface structure but also changes the yield strength of the Ni particles, which makes the plastic stretching of the metal particles even more difficult.

5 Conclusions

Ni/Al_2O_3 and $Ni–Ti/Al_2O_3$ composites have been fabricated by sintering in CO and Ar atmospheres. All the samples are well densified after sintering at 1400°C. The fracture toughness is not much improved compared with the matrix because of the very limited plastic stretching of the metal particles. Argon atmosphere is found to be beneficial to the mechanical properties relative to CO atmosphere for all the composites. In both sintering atmospheres no interfacial reaction layers are formed in the Ni/Al_2O_3 composites; in contrast there are reaction layers up to 1–3 μm in thickness in the $Ni–Ti/Al_2O_3$ composites. The reaction is due to the oxidation of Ti, and is more accelerated in CO atmosphere than in Ar. As expected, Ti diffuses from the interior of Ni–Ti alloy particles to the particle interfaces, but the weak interfacial layer and the poor bonding between the layer and the matrix result in materials which are not toughened.

Acknowledgement

The authors gratefully acknowledge the suggestions and criticism provided by Prof. R. J. Brook and Prof. F. J. J. van Loo during the experimental work and preparation of the manuscript.

References

1. Sigl, L. S., Mataga, P. A., Dalgleish, B. J., & Mcmeeking, R. M., On the toughness of brittle materials reinforced with a ductile phase. *Acta Metall.*, **36** (1988) 945–53.
2. Ashby, M. F., Blunt, F. J. & Bannister M., Flow characteristics of highly constrained metal wires. *Acta Metall.*, **37** (1989) 1847–57.
3. Flinn, B. D., Rühle, M. & Evans, A. G., Toughening in composites of Al_2O_3 reinforced with Al. *Acta Metall.*, **37** (1989) 3001–6.
4. Lu, T. C., Evans, A. G., Hecht, R. J. & Mehrabian, R., Toughening of $MoSi_2$ with a ductile (niobium) reinforcement. *Acta Metall. Mater.*, **39** (1991) 1853–62.
5. Chen Z. & Mecholsky, J. J., Jr, Control of strength and toughness of ceramic/metal laminates using interface design. *J. Mater. Res.*, **8** (1993) 2362–9.
6. Tuan, W. H. & Brook, R. J., The toughening of alumina with nickel inclusions. *J. Eur. Ceram. Soc.*, **6** (1990) 31–7.
7. Sun, X. & Yeomans, J. A., The toughening of alumina matrices by the inclusion of nickel particles. *Special Ceramics*, **9**, 1990.
8. Nicholas, M. G. & Crispin, R. M., Brazing ceramics with alloys coating titanium. *Ceram. Eng. Sci. Proc.*, **10** (1989) 1602–12.
9. Armstrong, W. M., Chaklader, A. C. D. & Clarke, J. F., Interface reactions between metals and ceramics: I. Sapphire-nickel alloys. *J. Am. Ceram. Soc.*, **45** (1962) 115–18.
10. SGTE (Scientific Group Thermodata Europe) Substance Data Files, Thermodata GmbH, Grenoble University, St martin d'heres, France, 1987.
11. Backhaus-Ricoult, M., Diffusion process and interphase boundary morphology in ternary metal–ceramic systems. *Ber. Bunsenges. Phys. Chem.*, **90** (1986) 684–90.
12. Metselaar, R. & Van Loo, F. J. J., The use of phase diagrams for the study of metal–ceramic interdiffusion. In *Ceramic Developments*, Vols. 34–36. ed. C.C. Sorrel & B. Ben-Nissan, *Materials Science Forum*, 1988, pp. 413–20.
13. Trumble, K. P. & Rühle, M., The thermodynamics of spinel interphase formation at diffusion-bonded Ni/Al_2O_3 interfaces. *Acta Metall. Mater.*, **39** (1991) 1915–24.
14. Murray, J. L. & Wriedt, H. A., The O–Ti (oxygen–titanium) system. *Phase Diagrams of Binary Titanium Alloys*, 1987.
15. Murray, J. L., The Ni–Ti (nickel–titanium) system. *Phase Diagrams of Binary Titanium Alloys*, 1987.
16. Tsui, Y.-P. & Johnson, D. L., Influence of TiO_2 and Fe_2O_3 on the densification of Al_2O_3. In *Proc. Int. Symp. of Factors in Densification and Sintering of Oxide and Non-Oxide Ceramics*, Japan, 1978.
17. Faber, K. T. & Evans, A. G., Crack deflection processes —I. Theory. *Acta Metall.*, **31** (1983) 565–76.
18. Döre, E. & Hübner, H., *Alumina, Processing, Properties, and Applications*. Springer-Verlag, Berlin, 1984.
19. Ross, R. B., *Metallic Materials Specification Handbook*, 3rd Edn. E. & F. N. Spon Ltd, London, 1980, pp. 227–8.

Journal of the European Ceramic Society **15** (1995) 233–238
© 1995 Elsevier Science Limited
Printed in Great Britain. All rights reserved
0955-2219/95/$9.50

Thermal Expansion and Adhesion of Ceramic to Metal Sealings: Case of Porcelain–Kovar Junctions

Armando Zanchetta, Pierre Lefort*

Laboratoire de Céramiques Nouvelles, LMCTS, URA CNRS 320, 123 Avenue Albert Thomas, 87060 Limoges Cedex, France

&

Emile Gabbay

General Electric Medical Systems-Europe, 52 Boulevard Gallieni, BP 45, 92133 Issy les Moulineaux, France

(Received 23 February 1994; revised version received 6 July 1994; accepted 1 August 1994)

Abstract

Glass to metal sealings necessitate a pre-oxidation of the metal, producing a thin superficial oxide layer. In the case of porcelain–kovar junctions a glassy interphase is necessary, which reacts and dissolves the oxide layer during the bonding thermal treatment. In the interfacial zone this leads to a good fitting of the thermal expansion coefficients of the phases present: in the alloy the superficial part is impoverished in iron and its thermal expansion coefficient is close to that of the FeO-rich glass which has dissolved the oxide layer. The resulting buffer zone limits the effect of strains appearing during cooling at the end of the bonding thermal treatment. Moreover, the FeO-rich glass penetrates the open porosity of the superficial alloy layer (due to its pre-oxidation) providing a good physical adherence of glass to kovar. At the porcelain–glass interface there is no problem because of the similarity of dilatometric behaviour of the two materials.

1 Introduction

Glass to metal sealings necessitate a preliminary oxidation treatment of the metal. The resulting oxide layer reacts subsequently with glass to make a strong junction between glass and metal. This bonding thermal treatment is achieved at temperatures near to that of glass softening, and during cooling the difference in thermal expansion between glass and metal may generate interfacial strains strong enough to break the junction. To prevent this, special alloys and glasses are used, their main characteristic being the similarity in their thermal expansion.

On the basis of this very simple theoretical approach, a technology has long been developed industrially, and many various pieces for a wide range of applications are currently produced. Nevertheless many questions remain unanswered, such as: why are the conditions (sealing time, temperature, etc.) of the alloy pre-oxidation so important, or why must the duration of the joining thermal treatment be so sharp? In spite of the industrial importance of these questions a limited number of papers is available in the literature,[1–6] and the know-how remains in the factories.

Some studies[1–4] have shown that a good junction depends on the degree of preoxidation, sealing time and temperature. It has been shown[5,6] that iron diffusion into the glass produces a modification in the thermal expansion behaviour of glasses. According to Ikeda and Samalima[5] the glass thermal expansion increases, while according to Mayer *et al.*[6] it decreases.

In order to shed some light on the mechanism of the glass to metal junction, we decided to study each step of the process, by working on the example of porcelain–kovar joining with a glass interphase. We have already our published results on the oxidation of kovar.[7] This material which is the one most used for glass junctions, is a Fe–Co–Ni alloy, but its oxidation layer is mainly composed of iron oxides. The underlying oxide is enriched in cobalt and nickel and presents an important porosity. During the reaction with glass, the oxide layer of the alloy is dissolved by the glass, and this improves its wetting quality and produces good junctions.[8]

*To whom correspondence should be addressed.

Table 1. Measured thermal expansion coefficients, α

Material	*Kovar*	*Glass*	*Porcelain*
α ($\times 10^7$)	50	52	52

The aim of this work was to study what the effects of these treatments are on the thermal expansion of the interfacial zone in order to understand better the origins of the bonding.

2 Materials and Methods

The materials used have very similar measured thermal expansion coefficients, as shown in Table 1.

Kovar was provided by Imphy SA (ref. 08D1006), porcelain by KPCL S.A. (ref. CM10) and glass was made from a Cerdec S.A. frit.[9]

When kovar is oxidized, the composition of the alloy near the interface is very different from that of the bulk[7] and gives the approximate compositions of the metallic phase existing in the interfacial zone. From Fig. 1, it is obvious that the thermal expansion of the interfacial zone is certainly strongly perturbed by the composition modifications due to the bonding reaction as well in the alloy[7] as in the oxide and glassy phases.[9] This induces local coefficient values very different from those given in Table 1. It was impossible for us to determine directly these values on real pieces of complex morphology, and the only feasible way was to make different samples having compositions corresponding to those followed by EDX analysis across the interface in the case of a strong and vacuum-tight junction.

Table 2. Main impurities of the metallic powders

	Iron	*Nickel*	*Cobalt*
Al	0·007	0·008	0·005
Ca	0·001	<0·001	0·005
Ni	0·02		0·05
Si	0·1	0·02	0·03
Sr	<0·001	<0·001	
Ti	0·01		
Cr		0·001	
Cu		0·005	0·04
Fe		0·001	0·01
Mg		0·001	
Mn			0·005

For the alloy, bars were prepared from metallic powders of iron, cobalt and nickel provided by Cerac Inc. mixed for 4 h in a Turbula mixer (Prolabo S.A.). Table 2 presents the main impurity contents of these powders. They were then heated in an alumina crucible at 1420°C under a flow of pure argon (L'Oxygène Liquide S.A., quality U) for 1 h in a graphite furnace. After cooling, small bars (4 × 4 × 35 mm) were cut and polished. The iron oxide–glass mixtures were made with iron monoxide (from Cerac Inc.) since it has been shown that the iron oxide scale, initially composed of Fe_3O_4 and Fe_2O_3, becomes only iron monoxide above 900°C.[9] Elemental composition is given in Table 3 and the composition of the glass frit, provided by Cerdec S.A., in Table 4.

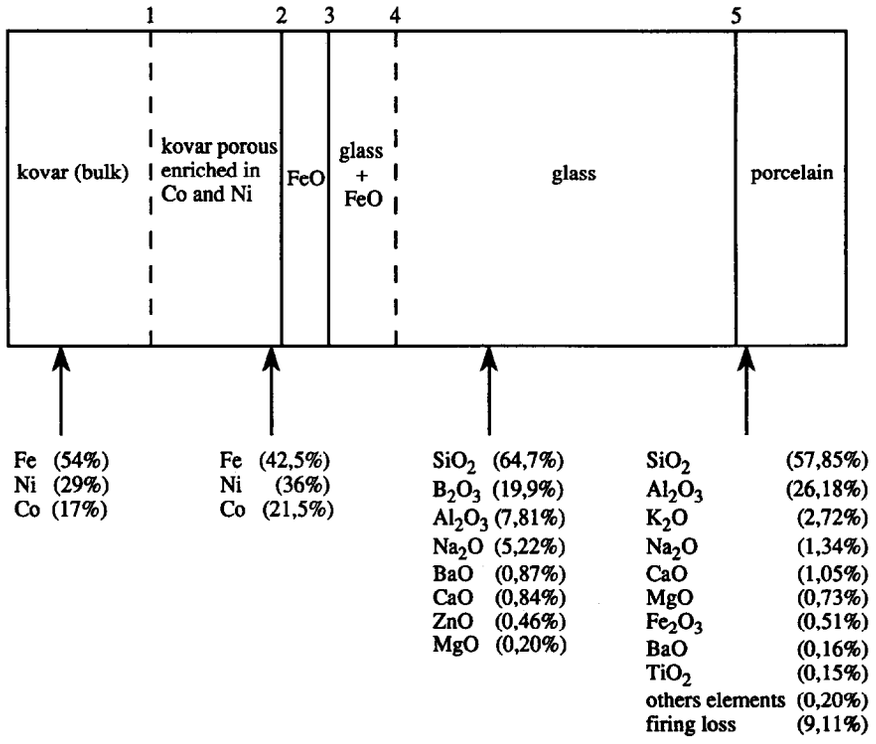


Fig. 1. Major components of the interfacial zone after bonding.

Table 3. Metallic elements content of the iron monoxide powder

Fe	*Al*	*Ca*	*Co*	*Cr*	*Cu*	*Mg*	*Ni*	*Ti*
77·28	0·02	<0·01	<0·01	<0·01	0·001	0·1	0·02	<0·02

Table 4. Composition of the glass frit

Oxide	SiO_2	Al_2O_3	B_2O_3	Na_2O	*MgO*	*CaO*	*BaO*	*ZnO*
% (pds)	64·7	7·81	19·9	5·22	0·20	0·84	0·87	0·46

Iron monoxide and glass powders were mixed in an agate mortar and then put in a silico-alumineous crucible previously covered with kaolin to avoid any bonding between glass and crucible. They were heated to over 900°C in accordance with the bonding thermal treatment.[9] After cooling, the pellets were cut with a diamond saw to obtain small bars for dilatometry. Great attention was paid to avoid the presence of kaolin traces, and finally the samples were carefully polished. The dimensions of the pieces were about 4 × 4 × 40 mm. Dilatometry measurements were carried out in a Netzsch 402E-3 differential dilatometer, coupled to a computer which processed the signal. Bars were heated under an argon flow to 1000°C at the rate of 2°C min^{-1} for the alloy bars and until the dilatometric softening point.

3 Results

In order to determine the composition of the alloy sample and that of the glass–FeO mixtures, we obtained the concentration profiles of the elements present in the interfacial zone after short thermal treatments.[9] Figure 2 shows that, in the interfacial zone from kovar to glass, there are four distinct domains:

- the original alloy with its nominal composition (part I);
- the Fe-impoverished alloy zone (part II) extending for about 8 μm where the alloy composition was of 42·5 wt% Fe, 21·5 wt% Co and 36 wt% Ni at 2 μm from the interface with oxide or glass;
- a narrow range (2 μm) containing both glass and iron oxide partially or entirely dissolved (part III);
- a large domain extending 30 μm in which iron diffuses into the glass.

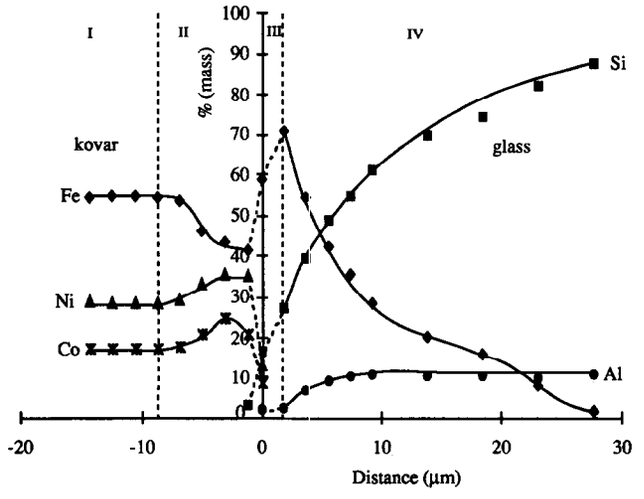


Fig. 2. Concentration profiles of the elements iron, nickel, cobalt, silicon and aluminium by EDX analysis of the kovar/glass interface after 15 min at 910°C.

Based on these observations we prepared an alloy sample with the same composition as measured near the alloy surface (Fe: 42·5 wt%; Co: 21·5 wt%; Ni: 36 wt%) and three FeO–glass mixtures with weight ratios of 20–80%, 40–60% and 60–40% respectively.

Dilatometric measurements were carried out on samples having these compositions and Fig. 3 presents their dilatometric curves between 20 and 1000°C together with those of original glass, kovar and porcelain.

One can see that the glass expansion and the softening temperature grow appreciably with increasing FeO content. The relevant values as well as the thermal expansion coefficients of kovar, prepared alloy and porcelain are given in Table 5. One can also notice, examining Fig. 3, that the increase in thermal expansion due to the glass transition becomes smaller with increasing FeO content in the glass. Concerning the prepared alloy, which contains less iron than kovar, its thermal expansion is greater than that of porcelain and of kovar.

4 Discussion

During the joining reaction, the oxide layer of the kovar reacts and is progressively dissolved into the glass.[8] As a consequence, near the interface 3 (Fig. 1)

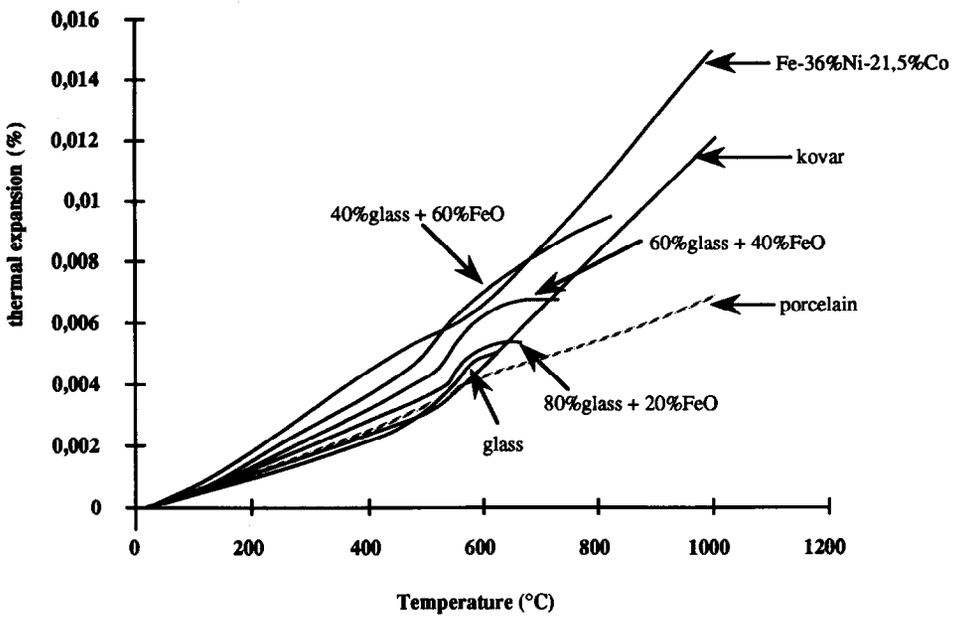


Fig. 3. Dilatometric curves of glass, prepared alloy, glass and FeO, kovar and porcelain.

the FeO content of the glassy phase increases rapidly: to a certain extent a kind of continuity may occur at this interface between the dilatometric behaviour of FeO and that of the glassy phase rich in FeO. On the dilatometric curves of Fig. 3 and considering Table 5, we actually observe that the thermal expansion of the FeO-rich glassy phases tends to approach the value[10] of pure FeO ($\alpha = 12{\cdot}2 \times 10^{-6}$ °C^{-1}), and therefore the behaviour of the glass tends towards that of a cristallized phase with the narrowing of the glass transition zone.

We have previously shown,[8] on the basis of the examination of the pseudo ternary phase diagrams of $FeO–Al_2O_3–SiO_2$[11] and $FeO–Na_2O–SiO_2$[12] (the $FeO–B_2O_3–SiO_2$ phase diagram is not available) that the effect of FeO dissolution in the glass is a lowering of the temperature of apparition of the liquid phase, the optimum being reached for FeO content of about 50 wt%, and, consequently, we have observed that FeO dissolution noticeably improves the wetting of the glassy phase. There is a double beneficial effect of the FeO dissolution in the glass which fits the dilatometric characteristics of glass and oxide layer at the interface 3 (Fig. 1) and which contributes to good wetting.

At the beginning of the dissolution process, there is a significant dilatation gap between the reaction zone and the bulk of the glass, because the diffusion area of FeO is still very restricted. For this reason this zone is very brittle and may crack when cooling. It is necessary therefore to prolong the treatment time at the joining temperature to allow the FeO dissolution gradient to attain an optimal width to avoid this problem.

In the alloy region (interface 2 of Fig. 1) the results of Fig. 3 are also very interesting. One can see that the impoverishment in iron of this zone corresponds to an increase in its thermal expansion coefficient since Table 5 shows that the Fe(42·5 wt%)–Ni(36 wt%)–Co(21·5 wt%) alloy has a thermal expansion coefficient nearly twice that of kovar and close to that[10] of FeO. Between interfaces 1 and 2 (Fig. 1) there is certainly a regular increase of the thermal expansion related to the changes of composition of the alloy in this domain. This constitutes a buffer zone which tends to fit the dilatometric behaviour of kovar and

Table 5. Thermal expansion coefficients of the different compounds present in the interfacial zone and softening temperatures of the glassy phases

	Glass	*80% glass + 20% FeO*	*60% glass + 40% FeO*	*40% glass + 60% FeO*	*Kovar*	*42·5% Fe +36% Ni +21·5% Co*	*Porcelain*
α (300°C) $\times 10^7$	52	61	78	84	50	102	52
Softening temperature (°C)	620	654	733	832			

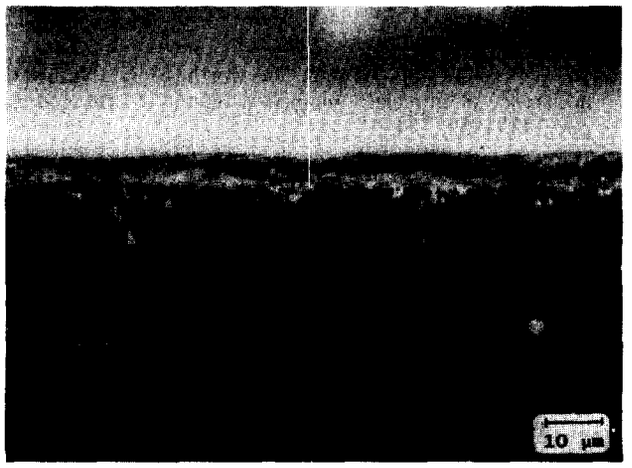


Fig. 4. Micrograph of a kovar/glass interface.

FeO-rich glass or FeO phase. It would seem improbable that the joining can be strong if the FeO phase is present, because its porosity constitutes a low resistance zone. This result has been experimentally confirmed.[9]

In these conditions a good bonding is reached when the entire iron oxide layer has reacted with the glass. At this point the interfaces 2 and 3 meet and there is a good fitting of thermal expansion coefficients on both sides. A good fitting is also found between interfaces 1 and 2 due to the smooth change of the composition of the alloy in this zone. This condition is also fulfilled in the glassy phase through the FeO diffusion space. If the thermal treatment is too long, FeO diffusion leads to a complete homogenization of the glassy phase. In this case we have a small FeO concentration in the glass and we find again a thermal expansion coefficient similar to that of the original glass resulting once again in a dilatation gap at the interface 2/3 (Fig. 1). This result is consistent with experimental results[9] and with industrial know-how, as far as it can be ascertained.

Looking at the interface 5 (Fig. 1), there is never any dilatation problem in this region because the glass quantity is sufficient to avoid any dilatometric change when FeO is dissolved, and the values of the thermal expansion coefficients do not differ from those of Table 1.

At this point, one important question arises: if the result of this precise treatment is only to obtain a good fitting of thermal expansion coefficients in the interfacial zone, why are they necessary, since the original materials (Table 1) had already very similar dilatometric behaviour? We propose two answers: first, the glass wetting improvement as previously shown,[8] and second, the achievement of a physical adhesion through the penetration of glass into the alloy. Indeed the

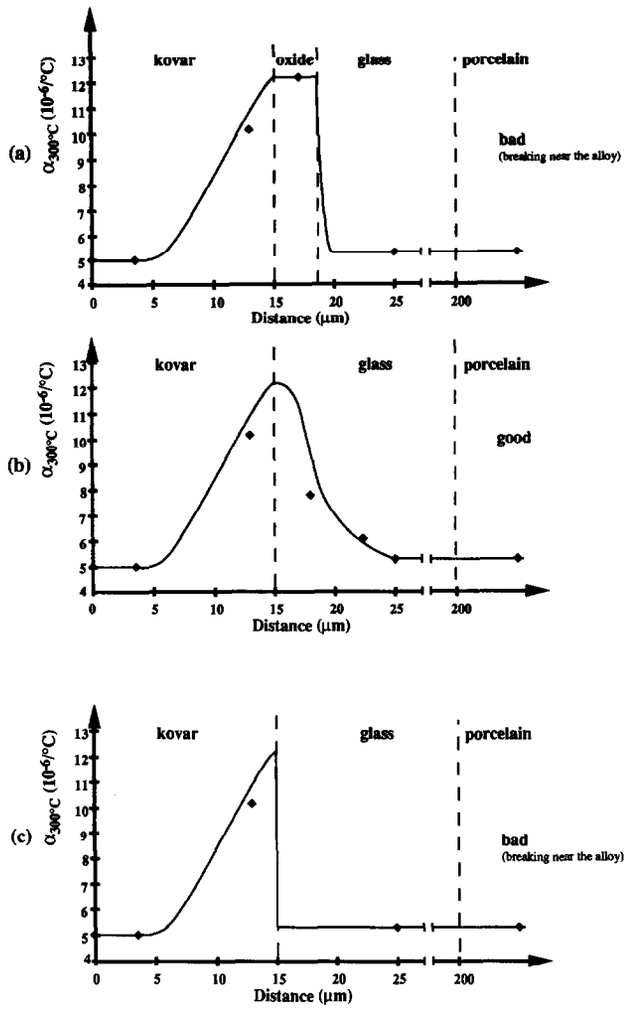


Fig. 5. Dilatometric profile of the interfacial zone: (a) oxide layer slightly dissolved; (b) oxide layer almost totally dissolved; (c) the whole oxide layer is dissolved.

pre-oxidation treatment creates some superficial open porosity in the alloy that glass invades during FeO dissolution as shown in Fig. 2. Here one may observe that there is some silicon located in the iron-impoverished alloy (part II), and otherwise it is well illustrated by the micrograph of Fig. 4 which shows the glass penetration in the open porosity of the iron-impoverished alloy. Our experiments do not allow any assertion to be made about an eventual chemical process, which is possible, but not proved.

5 Conclusion

This work sheds some light on the role of the pre-oxidation of the alloy in the glass to metal sealings. Not only does it improve the glass wetting[8] but it is also responsible for the fitting of thermal expansion coefficients in the interfacial zone. In fact the formation of the oxide layer creates an iron-impoverished zone whose thermal expansion is higher than that of underlying alloy, and the

oxide dissolution into the glass increases the thermal expansion of the glass to values approaching those of the iron-impoverished alloy. At last, the pre-oxidation creates open porosity in the alloy[7] in which FeO-rich glass penetrates during bonding treatment, so creating a strong physical adhesion.

The duration of the bonding thermal treatment is very important and its role is well summarized in Fig. 5 which presents diagrams describing the thermal expansion coefficients evolution in the interfacial zone according to the time of thermal treatment. If it is too short (Fig. 5(a)), the brittle oxide layer remains and the FeO-dissolved gradient is very strong, so that the bonding is weak. If the treatment duration corresponds to that of a complete reaction or dissolution of the FeO layer in the glass (Fig. 5(b)), it is the best case where there is a large gradient of FeO in the glass, hence a good fitting of the thermal expansion coefficients in the interfacial zone, and a sufficient penetration of the glass in the superficial porosity of the alloy. For too long times (Fig. 5(c)) homogenization of the glass leads to a significant gap of the thermal expansion coefficients at the glass to alloy interface and the bonding breaks during cooling at the end of thermal treatment.

References

1. King, B. W., Tripp, H. P. & Dukworth, N. H., Nature of adherence of porcelain enamels to metal. *J. Am. Ceram. Soc.*, **42** (1959) 504.
2. Boron, M. D. & Pask, J. A., Role of 'Adherences oxides' in the development of chemical bonding at the glass/metal interface. *J. Am. Ceram. Soc.*, **49** (1966) 1.
3. Ritchie, D., Schaeffer, H. A. & White, D., The presence of an iron oxide layer at the enamel/steel interface in one-coat porcelain enamelling. *J. Mat. Sci.*, **18** (1983) 599.
4. Paparazzo, E., Fiero, G., Ingo, G. & Sturlese, S., Microchemistry and mechanisms of adherence in steel/enamel interfaces. *J. Am. Ceram. Soc.*, **71** (1988) C-494.
5. Ikeda, I. & Samahima, Y., Interfaces of Fe–Ni–Co alloy to borosilicate glass seals. Seventh Japan Congress on Testing Materials — Non Metallic Materials, 1964, p. 127.
6. Mayer, P., Topping, J. A. & Murthy, M. K., Correlation between thermal expansion of glass and glass to metal adherence. *J. Can. Ceram. Soc.*, **43** (1974) 43.
7. Zanchetta, A. & Lefort, P., Approche de l'oxydation du kovar dans l'air. *J. Alloys and Compounds*, **210** (1994) 247.
8. Zanchetta, A., Labbe, J. C. & Lefort, P., Rôle du monoxyde de fer sur la mouillabilité du kovar par le verre. *J. Chim. Phys.*, **91** (1994) 563.
9. Zanchetta, A., Thesis, University of Limoges, 1993.
10. Petit, J. A., Liaisons céramique-métal. *Mater. & Technics*, **Mars** (1988) 13.
11. Aramaki, S. & Roy, R., Phase diagram for the system $FeO–Al_2O_3–SiO_2$. *Nature*, **184** (1959) 631.
12. Carter, P. T. & Ibrahim, M., Phase diagram for the system $Na_2O–FeO–SiO_2$. *J. Soc. Glass Technics*, **36** (1952) 156.

Journal of the European Ceramic Society **15** (1995) 239–247
Elsevier Science Limited
Printed in Great Britain
0955-2219/95/$9.50

A Thermodynamic Reassessment of the Si–Al–O–N System

Lucia Dumitrescu* & Bo Sundman

Department of Materials Science and Engineering, Royal Institute of Technology, 100 44 Stockholm, Sweden

(Received 6 June 1994; accepted 6 July 1994)

Abstract

The Si–Al–O–N system has been thermodynamically reassessed due to the new model used for liquid in the Al_2O_3–SiO_2 binary system and new experimental data in the Al_2O_3–AlN system. The β'-sialon phase is described by a new model, $(Al^{3+},Si^{4+})_3(O^{2-},N^{3-})_3(N^{3-})_1$, and a set of new parameters was found to describe better the experimental behaviour phase diagram and the β'-sialon stability in the system even at reasonably low temperatures. Phase diagrams calculated using the new assessment are presented.

1 Introduction

A thermodynamic assessment of the Al–Si–O–N system was recently presented by Hillert and Jonsson.[1] Later Hallstedt *et al.*[2] proposed changes in the model for the liquid phase in the binary subsystem Al_2O_3–SiO_2 in order to extrapolate this system into the ternary CaO–Al_2O_3–SiO_2. There is also new experimental information on the Al_2O_3–AlN system given by Willems *et al.*[3,4] This requires a revaluation of the SiO_2–Al_2O_3 and Al_2O_3–AlN systems and subsequently of the Si_3N_4–AlN–Al_2O_3-SiO_2 system. The results of this reevaluation will be presented here. A second reason for the reevaluation is that it was discovered that the parameter values presented by Hillert and Jonsson predict that the β'-sialon phase is stable in the AlN–Al_2O_3 system below a certain temperature. There is no experimental support for such a result.

2 The Al_2O_3–SiO_2 System

The amphoteric nature of Al_2O_3 causes problems when this compound is mixed with either a strong acid like SiO_2 or a strong base like CaO. Previously,[5] Al_2O_3 was treated as a basic oxide, assuming that it would easily give away its oxygen. In the ternary system Al_2O_3–CaO–SiO_2 such an assumption would give, using the ionic liquid model,[6] the following model for the liquid phase

$$(Al^{3+},Ca^{2+})_p(O^{2-},SiO_4^{4-},SiO_2)_q$$

The site ratios, p and q, are set equal to the average charge on the other sublattice in order to maintain electroneutrality:

$$p = 2y_{O^{2-}} + 4y_{SiO_4^{4-}}$$

$$q = 3y_{Al^{3+}} + 2y_{Ca^{2+}}$$

Although each binary system could be described satisfactorily with this model it was impossible to obtain a reasonable extrapolation into the ternary system. As described by Hallstedt *et al.*[2] a better extrapolation could be obtained using the neutral species $AlO_{1.5}$ which would yield the following model for the liquid phase

$$(Ca^{2+})_p(O^{2-},SiO_4^{4-},SiO_2,AlO_{1.5})_q$$

The choice of $AlO_{1.5}$ rather than Al_2O_3 may be justified by the assumption that a network of triangles of O with an Al in the middle[7] forms in the liquid. As each O is shared between two Al, the basic unit is $AlO_{1.5}$. The reason for having SiO_2 as a constituent is similar because in SiO_2, which forms tetrahedra of four O with an Si in the middle, each O is shared between two Si. For the Al_2O_3–SiO_2 system this model reduces to $(AlO_{1.5},SiO_2)$, a simple associated solution model and this system was assessed in such a way by Hillert *et al.*[8]

3 The Al_2O_3–AlN System

McCauley and Corbin[9] published a phase diagram

*On leave from Matpur SA, Sos. Garii Catelu nr. 5, Bucharest 3, Romania.

for the Al_2O_3–AlN system and they listed seven phases, AlN (with a wurtzite structure); $Al_9O_3N_7$ (with a 27R AlN polytype structure); $Al_7O_3N_5$ (with a 21R AlN polytype structure); $Al_6O_3N_4$ (with a 12H AlN polytype structure); $Al_{23}O_{27}N_5$ (with an AlON spinel structure); $Al_{22}O_{33}N_2$ (with a ϕ-spinel structure); and Al_2O_3 (with a corundum structure).

In the present work all phases, except $Al_{22}O_{33}N_2$ (ϕ-spinel structure), were taken into account. The new experimental information concerning the extention of the spinel phase in the quasibinary system Al_2O_3–AlN was also included.

The width of the homogeneity of the spinel phase varies with temperature: at 1850°C spinel is the stable phase between 66 mol% Al_2O_3 and 81 mol% Al_2O_3.[4] This region becomes smaller at lower temperatures. Below 1640°C[3] spinel is not stable.

Hillert and Jonsson[1] described the liquid phase in this quasibinary system with the model $(Al^{3+})_p(N^{3-},O^{2-})_q$. However, in line with the choice of $AlO_{1.5}$ as a species the present work will use the substitutional model ($AlO_{1.5}$,AlN).

4 The Si–Al–O–N System

The Si–Al–O–N system has four components and should be represented by a regular tetrahedron (Fig. 1). If the elements have their normal valencies (Si^{IV}, Al^{III}, O^{II}, and N^{III}) then all possible solid compounds lie on an irregular quadrilateral plane, and if the concentrations are expressed in equivalents, i.e. the corners of the tetrahedron are respectively $3Si^{12+}$, $4Al^{12+}$, 60^{12-} and $4N^{12-}$, then these solid compounds all lie on a square plane in which any point represents a combination of 12 positive and 12 negative valencies (Fig. 2). Conventionally, Si_3N_4 is placed at the bottom left-hand corner of the square diagram and distances from left to right

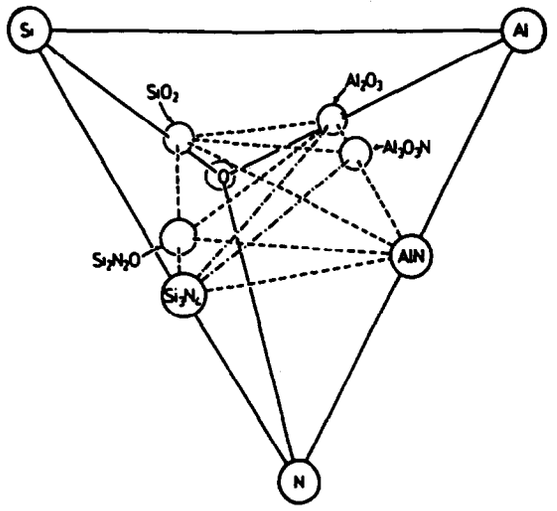


Fig. 1. The tetrahedral representation of the Si–Al–O–N system. Possible compositions are on the neutral plane indicated by the shared area.

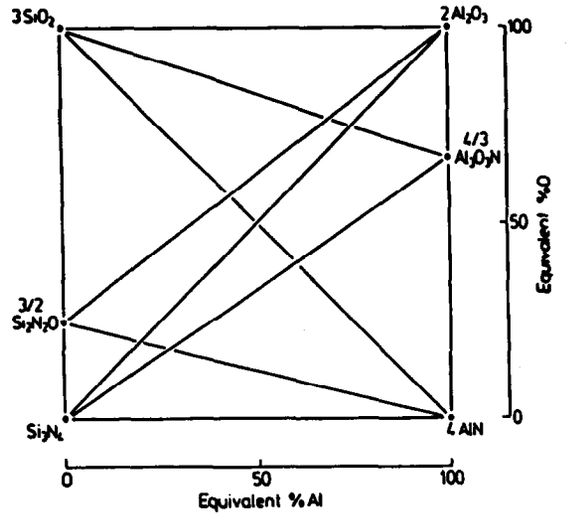


Fig. 2. The square representation of the Si–Al–O–N system using equivalent concentration.

represent replacement of silicon by its equivalent of aluminium and distances from bottom to top the replacement of nitrogen by oxygen.[10]

The experimental work on the phase relations in the quasi-ternary system Si_3N_4–AlN–Al_2O_3–SiO_2

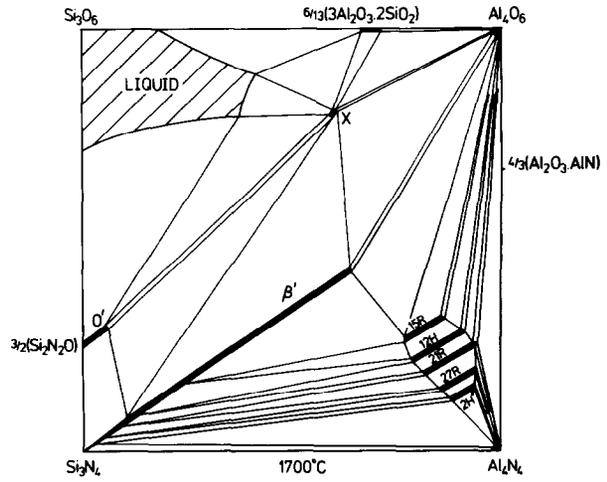


Fig. 3. The Si–Al–O–N behaviour diagram based on experimental data at 1700°C.[13]

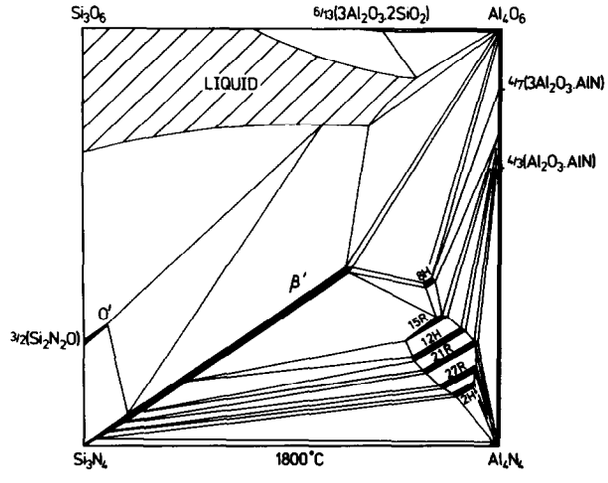


Fig. 4. The Si–Al–O–N behaviour diagram based on experimental data at 1800°C.[13]

was carried out mainly for the Si_3N_4–Al_2O_3–SiO_2 region of the diagram. The thermodynamic assessment of the SiAlON system is based on the experimental work of Naik *et al.*,[11] Bergman *et al.*[12] and on the most recent behaviour diagrams by Jack[13] for the Si_3N_4–Al_4N_4–Al_4O_6–Si_3O_6 system at 1700 and 1800°C (Figs 3 and 4). These two behaviour diagrams represent a summation of experimental observations. Jack did not claim that it is an equilibrium phase diagram in a thermodynamic sense due to the following difficulties and uncertainties of the experimental observations:

- weight losses due to evaporation, which change the overall composition;
- in the absence of liquid phase, the reaction between nitrides is very slow;
- in most experiments, the gaseous environment is ill-defined and many species are present in trace amounts (SiO(G), Si(G), Al_2O(G) etc.) and play a part depending on both thermodynamics and kinetics, and they affect the final phase assemblage.

Each phase in the system extends in a direction of constant metal:non-metal atom ratio (M:X) along which Si+N is replaced gradually by Al+O. The homogeneity ranges perpendicular to this are quite small.

The Si_3N_4 phase can dissolve a large amount of Al_2O_3 + AlN and forms β'-sialon. This phase extends essentially along the 3M:4X line with a homogeneity range described by $Si_{6-z}Al_zO_zN_{8-z}$, where z reaches a maximum of about 4 at 1700°C but decreases with decreasing temperature.

The Si_2N_2O phase can dissolve Al_2O_3 and forms O'-phase. This phase extends with a limited composition range along the 2M:3X line toward Al_2O_3.

The X-phase present in the system has a small range of homogeneity but, as in the previous assessment work by Hillert and Jonsson, it will be treated as a phase of fixed composition, $Si_{12}Al_{18}O_{39}N_8$. This composition is further supported by recent work by Anya and Hendry.[14]

Near the AlN corner of the diagram, six phases have been interpreted in terms of AlN-polytypes containing excess non-metal atoms. Their structures are directly related to their compositions M_mX_{m+1} and are described by the Ramsdell symbols 8H, 15R, 12H, 21R, 27R, and 2H.[15] In the strictest sense, polytypes are layer structures which, within very narrow limits, preserve a constant chemical composition and differ only in the way the layers are stacked together. In the sialon 'polytypes', both the composition and the unit cell dimensions show a systematic variation with structure type and the International Union of Crystallography has assigned the name 'polytypoids' to such series.[16]

For the β'-sialon phase a slightly modified model compared to that of Hillert and Jonsson will be adopted as there are two distinctly different sites for nitrogen.[17] It will be assumed that O^{2-} can enter only into one of the N^{3-} sublattices, leaving the other sublattice with one site always filled with N^{3-}. The new model would thus be

$$(Al^{3+},Si^{4+})_3(O^{2-},N^{3-})_3(N^{3-})_1$$

The maximum theoretical amount of Al to dissolve in β'-sialon would thus be Al_3O_3N.

At reasonably low temperatures the liquid phase exists mainly in the quasi-binary Al_2O_3–SiO_2 and it extends at higher temperatures considerably into the square towards the AlN corner of the diagram. It will be described with an associated solution model based on the species $SiN_{4/3}$ in addition to those already mentioned:

$$(AlN,\ AlO_{1.5},\ SiO_2,\ SiN_{4/3})$$

5 Optimization

The optimization was made using a computer program called Parrot,[18] which allows the simultaneous consideration of different types of thermodynamic and phase diagram data. First, models that depict different phases in the system were selected. A number of parameters for each phase were then optimized in order to describe the experimental information as well as possible. The program works by minimizing an error sum by varying selected model parameters. The sum of errors is calculated from the experimental information where each piece of information used is given an experimental uncertainty and also a weight according to its estimated accuracy and relative importance. In this system the available experimental information is not enough to allow the optimizing program to determine the model parameters without manual interaction.The weights were changed by trial and error and the model parameters were optimized until most of the information could be satisfactorily described. As input, selected experimental data together with known thermodynamical data for the solids and liquids were used.

The binary assessment of SiO_2–Si_3N_4 from Hillert and Jonsson[19] was accepted and together with the two new assessments of the quasibinaries, AlN–Al_2O_3 and SiO_2–Al_2O_3, a new thermodynamic assessment of the SiAlON system was attempted. There is no experimental information in the quasibinary system AlN–Si_3N_4.

The final thermodynamic description of the system, including the values of the assessed parameters, is given in Appendix 1.

The heat capacities for the crystalline phases were assumed to follow a Neuman–Kopp relation using linear combinations of the four stable compounds SiO_2, Al_2O_3, AlN and Si_3N_4.

Two interaction parameters were optimized for the liquid phase, one for the diagonal ($SiN_{4/3}$–$AlO_{1.5}$) and one for the ternary ($SiN_{4/3}$–SiO_2–$AlO_{1.5}$). Both parameters were assumed to be temperature independent.

For the β'-sialon phase two of the corner compounds were optimized, the neutral compound Al_3O_3N and for the charged compound $Al_3N_3^{4-}$. The parameter for the neutral compound was assumed to be linearly temperature dependant. In addition, the model has a reciprocal parameter, representing the simultaneous exchange of Al^{3+} with Si^{4+} and O^{2-} with N^{3-}. It was found that this parameter was necessary in order to keep the low solubility of Al_2O_3 in β'-sialon in the three-phase equilibrium liquid+O'+β'-sialon.

The solubility of Al_2O_3 in the O' phase was optimized using the fictitious corner compound $Si_2O_3^{2-}$ only. A linear temperature dependence for this parameter was required to describe the solubility for the whole temperature range. The model for the O' phase extends all the way to the composition Al_2O_3 but the parameter for this metastable compound was kept fixed to the same value as estimated by Hillert and Jonsson.

The melting temperature of the X phase was fitted to 1727°C using a single parameter representing the enthalpy of formation of X.

In the present work, the polytypes were only considered in the assessment of the AlN–Al_2O_3 system due to the very meagre information on their extension into the square diagram. They were thus treated as stoichiometric Al_2O_3–AlN phases. 21R, 27R and 12H were considered and only a single enthalpy value was fitted to describe the experimental sublimation or melting temperature. In the cases when the phases had a lower temperature limit an entropy of formation was also fitted.

6 Results

The new calculated phase diagram for the quasibinary AlN – Al_2O_3 is given in Fig. 5. Selected experimental data are included in Fig. 6 to give a comparison of the calculated diagram with the experimental data.

Figures 7–10 give a series of isothermal sections of the Si_3N_4–Al_4N_4–Al_4O_6–Si_3O_6 system. The comparison with experimental data shows good agreement. Figure 11 shows an extrapolation to higher temperature, 1900°C.

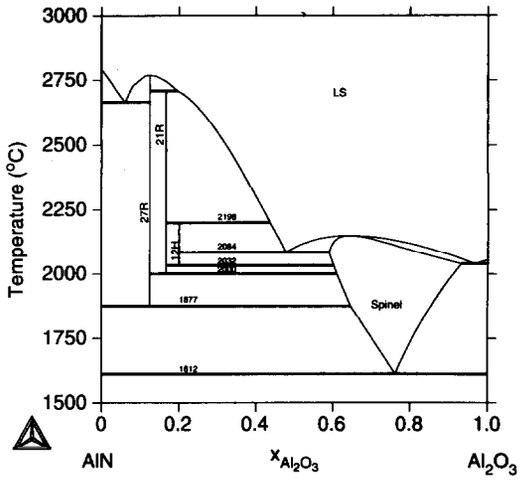


Fig. 5. The AlN–Al_2O_3 phase diagram at 1 bar, according to the present optimization, calculated without including the gas phase. The calculation includes one spinel phase and 27R, 21R, and 12H AlN-polytype phases.

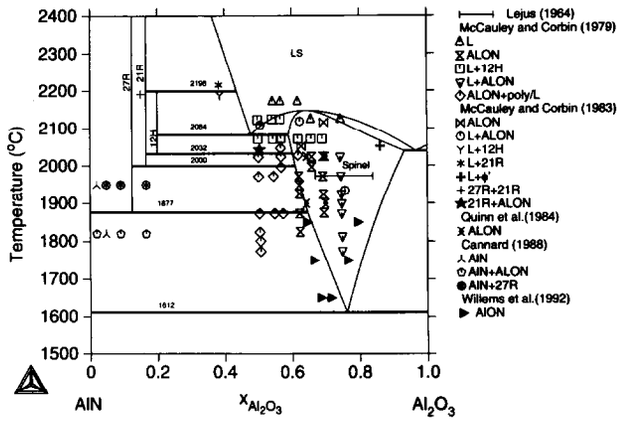


Fig. 6. Comparison of the calculated AlN–Al_2O_3 phase diagram with experimental data from several sources.

The calculated diagram at 1400°C is given in Fig. 12. Figure 13 shows an alternative presentation of this diagram using the oxygen potential as one of the axes. In this representation, the diagram is useful for determining the optimal values for the partial pressures of oxygen, an important

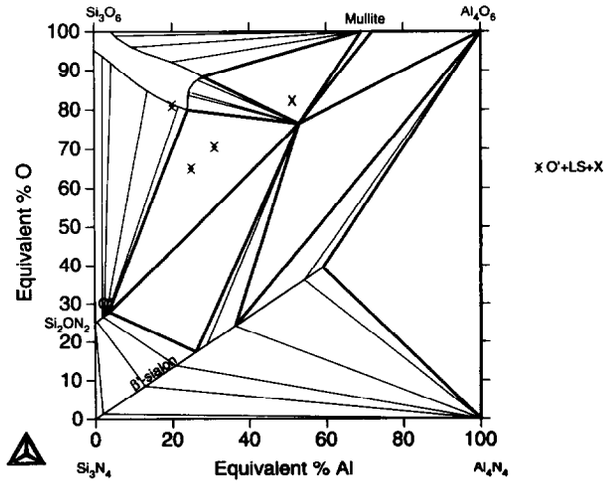


Fig. 7. Calculated section at 1600°C, in comparison with experimental data from Naik *et al.*[11]

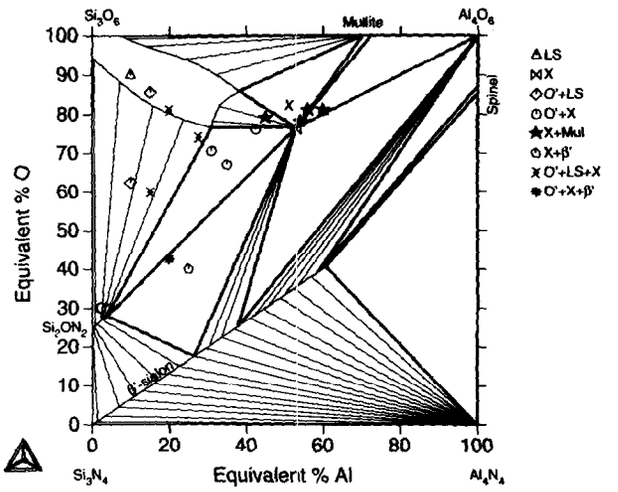


Fig. 8. Calculated section at 1650°C, in comparison with experimental data from Naik *et al.*[11]

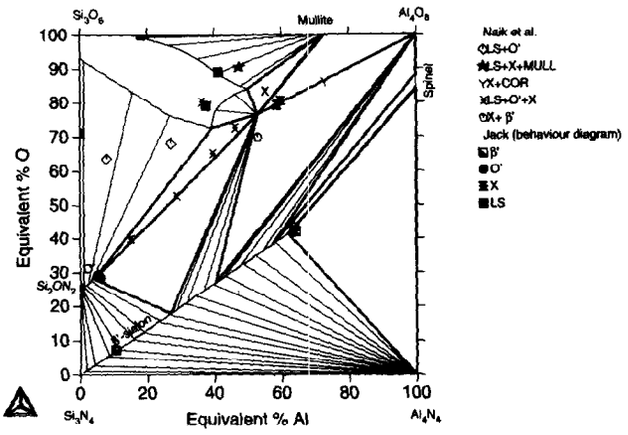


Fig. 9. Calculated section at 1700°C, in comparison with experimental data from Jack[13] and Bergman *et al.*[12]

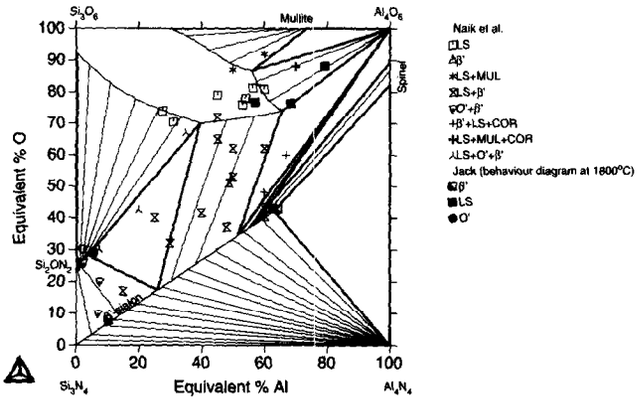


Fig. 10. Calculated section at 1750°C, in comparison with experimental data from Naik *et al.*[11] Good fit to experimental data has been obtained.

parameter for synthesis of different materials in the system, β'-sialon for example.

Generally there is good agreement between experimental and calculated data both for the AlN–Al_2O_3 and Si_3N_4–Al_4N_4–Al_4O_6–Si_3O_6 system.

In the AlN–Al_2O_3 diagram the spinel phase extends closer to the Al_2O_3 composition than

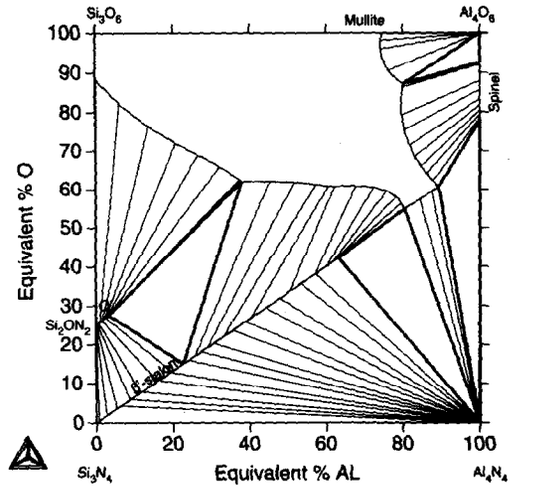


Fig. 11. Calculated section at 1900°C according to the present optimization.

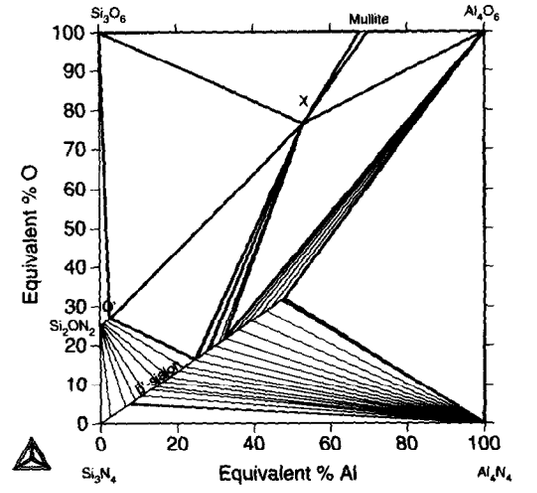


Fig. 12. Calculated section at 1400°C according to the present optimization.

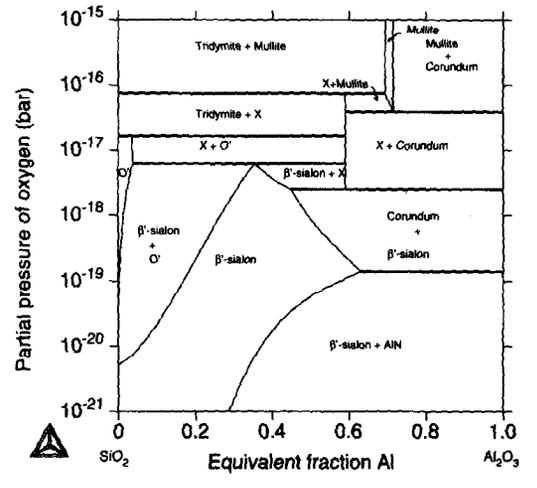


Fig. 13. The same calculation as for the diagram in Fig. 12 but using oxygen potential as an alternative presentation of the result.

experimental data can support. However, the description of the spinel phase must agree with the estimated stability of γ-alumina for pure Al_2O_3 as given by Hallstedt.[20] This restricts the possibilities to vary its composition. The experimental phase

diagram in this range has several impossible features and the current fit is acceptable until better experimental data are available. The 27R, 21R, and 12H AlN-polytypes have been considered and the assessment give a good fit of their stability temperature range. Hillert and Jonsson only considered the 27R polytype but, otherwise, the present diagram is very similar to theirs. However, it should again be emphasized that their parameter values for β'-sialon make it stable in the $AlN–Al_2O_3$ diagram, a fact which was not noticed by them. This has now been avoided by the new assessment of the β'-sialon.

Figure 14 is a reproduction of the $Si_3N_4–Al_4N_4–Al_4O_6–Si_3O_6$ system at 1750°C calculated by Hillert and Jonsson and it may be compared with Fig. 10 from the present assessment. The most striking difference is that the β'-sialon phase does not extend as close to the $AlN–Al_2O_3$ side as before. This is a result of the new model for β'-sialon and of the set of new parameters. This has also resulted in the β'-sialon corners of three-phase triangles moving closer to the Si_3N_4 corner. This has resulted in a better agreement with the experimental points for LS + β' but some of those points still fall outside the calculated two-phase field.

Another improvement can be seen in Fig. 9 where an experimental point for X+corundum falls on the calculated two-phase field. According to Hillert and Jonsson, this two-phase field only exists at considerably lower temperatures. The parameter values given by Hillert and Jonsson predict that the X phase should melt at 1721°C. This is only 1°C different from the experimental value of Naik *et al.*[11] The present assessment predicts a melting point of 1727°.

Another difference between the two assessments concerns the liquid phase field which is wider and extents deeper into the diagram according to the present assessment. This has resulted in three experimental points for O'+LS+X at 1650°C, now falling outside the calculated three-phase triangle.

It should again be emphasized that the ternary polytypes in the AlN-rich part of the diagram remain unassessed as there is no thermodynamical information available to evaluate them. Calorimetric measurements of the enthalpy of formation or the enthalpy of transformation are needed and their extension into the square diagram should be studied in more detail.

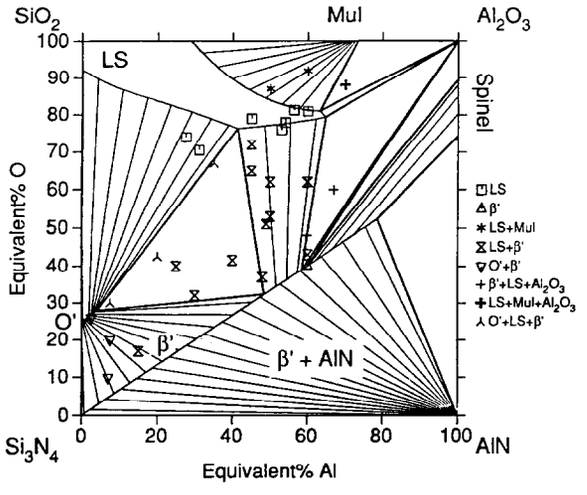


Fig. 14. Phase diagram at 1750°C calculated by Hillert and Jonsson using a different model for the liquid and β' phases.

Acknowledgements

Valuable advice from Professor Mats Hillert is gratefully acknowledged. One of the authors (L. D.) is grateful to the Swedish Institute for financial support.

References

1. Hillert, M. & Jonsson, S., Thermodynamic calculation of the Si–Al–O–N system. *Z. Metallkde.*, **83** (1992) 720–8.
2. Hallstedt, B., Hillert, M., Sellby, M. & Sundman, B., Modelling of acid and basic slags. *Calphad*, **18** (1994) 31–7.
3. Willems, H. X., Hendrix, M. M. R. M., Metselaar, R. & de With, G., Thermodynamics of AlON I: Stability at lower temperatures. *J. Europ. Ceram. Soc.*, **10** (1992) 327–37.
4. Willems, H. X., Hendrix, M. M. R. M., de With, G. & Metselaar, R., Thermodynamics of AlON II: Phase relations. *J. Europ. Ceram. Soc.*, **10** (1992) 339–45.
5. Hallstedt, B., Assessment of the $CaO–Al_2O_3$ system. *J. Am. Ceram. Soc.*, **73** (1990) 15–23.
6. Hillert, M., Jansson, B., Sundman, B. & Agren, J., *Metall. Trans. A.*, **16A** (1985) 261–6.
7. Richardson, F. D., *Physical Chemistry of Melts in Metallurgy*, Vol. 1. Academic Press, London, 1974, p. 284.
8. Hillert, M., Wang, X. & Sundman, B., An assessment of $Al_2O_3–SiO_3$, TRITA-MAC-0549, Royal Institute of Technology, Stockholm, Sweden, 1994.
9. McCauley, J. W. & Corbin, N. D., High temperature reactions and microstructures in the Al_2O_3 – AlN system. In *Progress in Nitrogen Ceramics*, Martinus Nijhoff, Boston, 1983, pp. 111–18.
10. Jack, K. J., Sialons and related nitrogen ceramics: their crystal chemistry, phase relationships, properties and industrial potential. In *High Temperature Chemistry of Inorganic and Ceramic Materials*, ed. F. P. Glasser & P. E. Potter. Burlington House, London, 1976, pp. 204–28.
11. Naik, I. K., Gauckler, L. J. & Tien, T. Y., Solid – liquid equilibria in the system $Si_3N_4–AlN–SiO_2–Al_2O_3$. *J. Am. Ceram. Soc.*, **61** (1978) 332–5.
12. Bergman, B., Ekstrom, T. & Miscki, A., The Si–Al–O–N system at temperatures of 1700–1775°C. *J. Eur. Ceram. Soc.*, **8** (1991) 141–51.
13. Jack, K. H., Silicon nitride, sialons, and related ceramics. In *Ceramic and Civilisation, Vol. III, High Technology Ceramics — Past, Present, and Future*. The American Ceramic Society, 1987, pp. 259–88.
14. Anya, C. C. & Hendry, A., Stoichiometry and crystal structure of X-phase sialon. *J. Europ. Ceram. Soc.*, **10** (1992) 65–74.
15. Jack, K. H., Review: Sialons and related nitrogen ceramics, *J. Mater. Sci.*, **11** (1976) 1135–58.

16. Thompson, D. P., Korgul, P. & Hendry, A., The structural characterisation sialon polytypoids. In *Progress in Nitrogen Ceramics*, ed. F. I. Riley, 1983, pp. 61–74.
17. Villars, P. & Calvert, L. D., *Pearson's Handbook of Crystallographic Data for Intermetallic Phases*, Vol. 4. ASM International, Materials Park, OH, 1991, pp. 4489–90.
18. Jansson, B., Evaluation of parameters in thermochemical models using different types of experimental data simultaneously, TRITA-MAC 234, Royal Institute of Technology, Stockholm, Sweden, 1984.
19. Hillert, M. & Jonsson, S., Thermodynamic calculation of the Si–N–O system. *Z. Metallkd.*, **83** (1992) 648–54.
20. Hallstedt, B., Thermodynamical assessment of $MgO–Al_2O_3$. *J. Am. Ceram Soc.*, **75** (1992) 1497–507.

Appendix 1. Thermodynamic Description of the Si–Al–O–N System

All parameter values are given in SI units (joules, moles, kelvin); R = 8.31451 J/(mol K).

Liquid slag (LS), $(AlN, AlO_{1.5}, SiN_{1.3}, SiO_2)$

$${}^0G^{LS}_{AlN} = {}^0G^{liq}_{AlN} = {}^0G_{AlN} + 70541 - 23T$$

$${}^0G^{LS}_{AlO_{1.5}} = 0.5\,{}^0G^{liq}_{Al_2O_3}$$

$${}^0G^{LS}_{SiN_{4/3}} = 1/3\,{}^0G^{liq}_{Si_3N_4} = 1/3({}^0G_{Si_3N_4} + 209300 - 80.5T$$

$${}^0G^{LS}_{SiO_2} = {}^0G^{liq}_{SiO_2}$$

$${}^0L^{LS}_{AlO_{1.5},SiO_2} = 80121 - 30T$$

$${}^1L^{LS}_{AlO_{1.5},SiO_2} = 96000 + 44T$$

$${}^0L^{LS}_{AlO_{1.5},SiN_{4/3}} = -15000$$

$${}^0L^{LS}_{AlO_{1.5},SiN_{4/3},SiO_2} = -134000$$

AlN, $(Al)_1(N)_1$

$${}^oG^{AlN}_{Al:N} - H^{SER} = {}^oG_{AlN} - H^{SER} = -345837.2 + 359.86191T - 54.308659T\ln T + 8.5550404\cdot10^{-4}T^2 + 2326379.8\,/\,T - 1.2556503\cdot10^8T^{-2}$$

β', $(Al^{3+},Si^{4+})_3(N^{3-},O^{2-})_3(N^{3-})_1$

$${}^oG^{\beta'}_{Al^{+3}:N^{-3}} - H^{SER} = {}^o4G_{AlN} - 2340925$$

$${}^oG^{\beta'}_{Si^{+4}:N^{-3}:N^{-3}} - H^{SER} = {}^oG_{Si_3N_4}$$

$${}^oG^{\beta'}_{Al^{+3}:O^{-3}:N^{-3}} - H^{SER} = {}^oG_{Al_2O_3} + {}^oG_{AlN} + 250300 - 92.3T$$

$${}^oG^{\beta'}_{Si^{+4}:O^{-2}:N^{-3}} = {}^oG_{Si_3N_4} + 100000$$

$${}^0L^{\beta'}_{Al^{+3}:Si^{+4}:N^{-3},O^{-2}:N^{-3}} = 893000$$

Al_2O_3 (corundum), $(Al)_2(O)_3$

$298 < T < 600$ K

$${}^oG^{Al_2O_3}_{Al:O} - H^{SER} = {}^oG_{Al_2O_3} - H^{SER} = -1707351.3 + 448.021092T - 67.4804T\ln T - 0.06747T^2 + 1.4205433\cdot10^{-5}T^3 + 938780\,/\,T$$

$600 < T < 1500$ K

$${}^oG^{Al_2O_3}_{Al:O} - H^{SER} = {}^oG_{Al_2O_3} - H^{SER} = -1724886.06 + 754.856573T - 116.258T\ln T - 0.0072257T^2 + 2.78532\cdot10^{-7}T^3 + 2120700\,/\,T$$

$1500 < T < 3000$ K

$${}^oG^{Al_2O_3}_{Al:O} - H^{SER} = {}^oG_{Al_2O_3} - H^{SER} = -1772163.19 + 1053.4548T - 156.058T\ln T + 0.00709105T^2 - 6.29402\cdot10^{-7}T^3 + 12366650\,/\,T$$

SiO_2 (cristobalite) $(SiO_2)_1$

$298 < T < 373$ K

$${}^oG_{SiO_2} - H^{SER} = -601467.73 - 8140.2255T + 1399.8908T\ln T - 2.8579085T^2 + 0.0010408145T^3 - 13144016\,/\,T$$

$373 < T < 453$ K

$${}^oG_{SiO_2} - H^{SER} = -1498711.3 + 13075.913T - 2178.3561T\ln T + 3.493609T^2 - 0.0010762132T^3 + 29100273\,/\,T$$

$453 < T < 543$ K

$${}^oG_{SiO_2} - H^{SER} = -3224538.7 + 47854.938T - 7860.2125T\ln T + 11.817149T^2 - 0.0033651832T^3 + 1.2750272\cdot10^8\,/\,T$$

$543 < T < 3300$ K

$${}^oG_{SiO_2} - H^{SER} = -943127.51 + 493.26056T - 77.5875T\ln T + 0.003040245T^2 - 4.63118\cdot10^{-7}T^3 + 2227125\,/\,T$$

$3300 < T < 4000$ K

$${}^oG_{SiO_2} - H^{SER} = -973891.99 + 587.05606T - 87.373T\ln T$$

Mullite, $(Al^{3+})_1(Al^{3+})_1(Al^{3+},Si^{4+})_1(O^{2-},Va)_5$

$${}^{o}G^{Mullite}_{Al^{+3}:Al^{+3}:Al^{+3}:O^{-2}} - H^{SER} = -2808415.35 + 13484407.2 / T + 1600.541T - 246.032747T\ln T + 0.0138772261T^2 - 8.37441995\cdot10^{8} / T^2$$

$${}^{o}G^{Mullite}_{Al^{+3}:Al^{+3}:Si^{+4}:O^{-2}} - H^{SER} = -2649812 + 2348905.07 / T + 1050.05906T - 165.804515T\ln T - 0.0160571905T^2$$

$${}^{o}G^{Mullite}_{Al^{+3}:Al^{+3}:Al^{+3}:VA} - H^{SER} = 0$$

$${}^{0}G^{Mullite}_{Al^{+3}:Al^{+3}:Si^{+4}:VA} - H^{SER} = 3894128.51 + 2348905.07 / T + 1050.05906T - 165.804515T\ln T - 0.0160571905T^2$$

$${}^{o}L^{Mullite}_{Al^{+3}:Al^{+3}:Al^{+3}:Si^{+4}:O^{-2}} = -498147.243 + 64.0830461\ T$$

O', $(Al^{3+},Si^{4+})_2(N^{3-},O^{2-})_2(O^{2-})_1$

$${}^{o}G^{O'}_{Al^{+3}:N^{-3}:O^{-2}} - H^{SER} = 0$$

$${}^{o}G^{O'}_{Si^{+4}:N^{-3}:O^{-2}} - H^{SER} = {}^{o}G_{Si_2N_2O} - H^{SER} - 966831.914 + 731.008345T - 111.723752T\ln T - 0.00587194833T^2 + 2184668.61 / T$$

$${}^{o}G^{O'}_{Al^{+3}:O^{-2}:O^{-2}} = 2{}^{o}G_{\gamma\text{-}Al_2O_3} - {}^{o}G_{Al_2O_3}$$

$${}^{o}G^{O'}_{Si^{+4}:O^{-2}:O^{-2}} = {}^{o}G_{Si_2N_2O} + 2{}^{o}G_{\gamma\text{-}Al_2O_3} - {}^{o}G_{Al_2O_3} + 10000 + 90T$$

27R, $(Al)_9(N)_7(O)_3$

$${}^{o}G^{27R}_{Al:N:O} = 7\ {}^{o}G_{AlN} + {}^{o}G_{Al_2O_3} + 340000 - 163T$$

21R, $(Al)_7(N)_5(O)_3$

$${}^{o}G^{21R}_{Al:N:O} = 5\ {}^{o}G_{AlN} + {}^{o}G_{Al_2O_3} + 308000 - 147T$$

12H, $(Al)_6(N)_4(O)_3$

$${}^{o}G^{12H}_{Al:N:O} = 4\ {}^{o}G_{AlN} + {}^{o}G_{Al_2O_3} + 274000 - 131T$$

Spinel, $(Al^{3+})_1(Al^{3+},Va)_2(N^{3-},O^{2-})_4$

$${}^{o}G^{Spinel}_{Al^{+3}:Al^{+3}:N^{-3}} = 4\ {}^{o}G_{AlN} + 4\ {}^{o}G_{Al_2O_3} + 617000 - 220T$$

$${}^{o}G^{Spinel}_{Al^{+3}:Va:N^{-3}} = 4\ {}^{o}G_{AlN} + 12\ {}^{o}G_{Al_2O_3} + 7632.4319 - 41.8012T$$

$${}^{o}G^{Spinel}_{Al^{+3}:Al^{+3}:O^{-2}} - H^{SER} = 0$$

$${}^{o}G^{Spinel}_{Al^{+3}:Va:O^{-2}} = 8{}^{o}G_{\gamma\text{-}Al_2O_3} + 44.9543T$$

X, $(Si)_{12}(Al)_{18}(O)_{39}(N)_8$

$${}^{o}G^{X}_{Si:Al:O:N} - H^{SER} = 2\ {}^{o}G_{Si_3N_4} + 6\ {}^{o}G_{SiO_2} + 9\ {}^{o}G_{Al_2O_3} - 350000$$

Parameters

298 < T < 600 K

$${}^{o}G^{liq}_{Al_2O_3} - H^{SER} = -1607850.8 + 405.559491T - 67.4804T\ln T - 0.06747T^2 + 1.4205433\cdot10^{-5}T^3 + 938780 / T$$

600 < T < 1500 K

$${}^{o}G^{liq}_{Al_2O_3} - H^{SER} = -1625385.57 + 712.394972T - 116.258T\ln T - 0.0072257T^2 + 2.78532\cdot10^{-7}T^3 + 2120700 / T$$

1500 < T < 1912 K

$${}^{o}G^{Liq}_{Al_2O_3} - H^{SER} = -1672662.69 + 1010.9932T - 156.058T\ln T + 0.00709105T^2 - 6.29402\cdot10^{-7}T^3 + 12366650 / T$$

1912 K < T < 2327 K

$${}^{o}G^{Liq}_{Al_2O_3} - H^{SER} = 29178041.6 - 168360.926T + 21987.1791T\ln T - 6.99552951T^2 + 4.10226192\cdot10^{-4}T^3 - 7.98843618\cdot10^{9} / T$$

2327 < T < 4000 K

$${}^{o}G^{Liq}_{Al_2O_3} - H^{SER} = -1757702.05 + 1344.84833T - 192.464T\ln T$$

298 < T < 2980 K

$${}^{o}G^{Liq}_{SiO_2} - H^{SER} = -923689.98 + 316.24766T - 52.17T\ln T - 0.012002T^2 + 6.78\cdot10^{-7}T^3 + 665550 / T$$

2980 < T < 4000 K

$${}^{o}G^{Liq}_{SiO_2} - H^{SER} = -957614.21 + 580.01419T - 87.428T\ln T$$

298 < T < 700 K

$${}^{o}G_{Al} - H^{SER} = -7976.15 + 137.071542T - 24.3671976T\ln T - 0.001884662T^2 - 8.77664\cdot10^{-7}T^3 + 74092 / T$$

700 < T < 933.6 K

$${}^{o}G_{Al} - H^{SER} = -11276.24 + 223.02695T - 38.5844296T\ln T + 0.018531982T^2 - 5.764227\cdot10^{-6}T^3 + 74092 / T$$

933.6 < T < 6000 K

$${}^{o}G_{Al} - H^{SER} = -11277.683 + 188.661987T - 31.748192T\ln T - 1.234264\cdot10^{28}T^{-9}$$

298 < T < 1687 K

$${}^{o}G_{Si} - H^{SER} = -8162.609 + 137.227259T - 22.8317533T\ln T - 0.001912904T^2 - 3.552\cdot10^{-9}T^3 + 176667 / T$$

$1687 < T < 6000$ K

$${}^{\circ}G_{Si} - H^{SER} = -9457.642 + 167.271767T - 27.196T\ln T - 4.20369\cdot10^{30}T^{-9}$$

$298 < T < 600$ K

$${}^{\circ}G_{\gamma\text{-}Al_2O_3} - H^{SER} = -1689977.34 + 469.458181T - 70.5452T\ln T - 0.070794T^2 + 1.491345\cdot10^{-5}T^3 + 981165 / T$$

$600 < T < 1500$ K

$${}^{\circ}G_{\gamma\text{-}Al_2O_3} - H^{SER} = -1708389.72 + 791.591946T - 121.754T\ln T - 0.0075467T^2 + 2.89573\cdot10^{-7}T^3 + 2222750 / T$$

$1500 < T < 3000$ K

$${}^{\circ}G_{\gamma\text{-}Al_2O_3} - H^{SER} = -1758861.75 + 1110.41976T - 164.253T\ln T + 0.00775305T^2 - 6.8247\cdot10^{-7}T^3 + 13162750 / T$$

H^{SER} represents the sum of the enthalpies of the stable forms of the elements at 298 K and 1 bar.

Journal of the European Ceramic Society **15** (1995) 249–254
© 1995 Elsevier Science Limited
Printed in Great Britain. All rights reserved
0955-2219/95/$9.50

Aluminum Magnesium Oxynitride: A New Transparent Spinel Ceramic

Arielle Granon, Patrice Goeuriot & François Thevenot

Ecole Nationale Supérieure des Mines de Saint-Etienne, 158 Cours Fauriel, 42 023 Saint-Etienne, France

(Received 13 May 1994; revised version received 27 July 1994; accepted 1 August 1994)

Abstract

A pure and dense spinel solid solution can be obtained by reaction-sintering between alumina–magnesia or aluminate of magnesium and aluminum nitride or oxynitride. The influence of post isostatic pressing on density, microstructure and transmittance (visible-IR) is studied for different starting materials. Transmittances of 65 and 80% are obtained for a 6 mm thick sample in visible and infra-red spectra, respectively.

1 Introduction

New technologies need optical materials with the best mechanical properties. Initially monocrystalline ceramics as quartz or sapphire were developed, and more recently polycrystalline ceramics like $MgAl_2O_4$[1–3] and γAlON[4–8] have been studied. Indeed these spinel solid solutions can be obtained transparent in the range 0·1–6 μm. The aluminate of magnesium is more easily sintered than γAlON (sintering temperature 1600–1700°C against 1850–1900°C for γAlON), but γAlON exhibits good mechanical properties: MOR = 500 MPa[8] instead of 400 MPa for $MgAl_2O_4$.[3]

The present paper describes the preparation of a new transparent polycrystalline oxynitride spinel phase, MgAlON (Fig. 1). A pure solid-solution containing Al–Mg–O and N could be prepared by reaction sintering between Al_2O_3–AlN–MgO or Al_2O_3–$MgAl_2O_4$–AlN. Jack[9] observed at 1800°C a large field of homogeneity of this solid-solution. Later, Weiss *et al.*[10] at 1750°C and Sun *et al.*[11] at 1600°C specified this field. Weiss *et al.*[10] remarked that the magnesium aluminate was an intermediate phase before obtaining the MgAlON phase during the Al_2O_3–AlN–MgO reaction. Laurent-Fievez[12] observed MgAlON at 1350°C and this result has been confirmed by Willems.[8] Previous papers have described the reactivity[13] and the sintering-reaction[14] of MgAlON whose main results were: (i) the control of the parasite reaction between AlN–MgO and AlN–$MgAl_2O_4$; (ii) the role of cationic vacancies of the intermediate aluminate of magnesium phase; and (iii) the morphology role of the starting materials.

2 Experiments

Six compositions (A to F) with different starting materials (Table 1) were studied: alumina (α + γ and γ crystallographic forms), magnesium oxide or aluminate of magnesium, aluminum nitride (commercial powder or obtained by nitridation of boehmite[15]), aluminum oxynitride (also obtained by nitridation of boehmite[16]) and MgAlON powder prepared in the laboratory.

Starting powders (samples A to E) were milled with highly pure alumina balls in anhydrous ethyl alcohol with phosphoric ester as dispersant agent (1·5 wt%). After drying under vacuum, the powders were sieved at 200 μm. In one case (D), polyvinyl butyral (PVB) and polyethylene glycol (PEG) were used as binder and plasticizer (1·5 wt%/dry powder). The slurry was then spray-dried.

Samples F were prepared in a different way. First, pellets with α-alumina, MgO and AlN (Starck) powders were heated at 1550°C for 6 h to perform the reaction. Then the pellets were crushed in an Aurec grinder and ball milled for 24 h with 1 wt% of MgO, 0·5 wt% PVB and 1 wt% PEG. Finally the slurry was spray-dried.

The pellets for samples A to F (about 25 × 25 × 10 mm) were obtained by isostatic pressing in plastic mold under 400 MPa; if necessary a debonding cycle was carried out to remove organic binder (samples D and F).

The reaction sintering (samples A to E), like the sintering (sample F), took place in a graphite furnace at 1675°C for 6 h in a powder bed made of 50 wt% AlN and 50 wt% MgO under a nitrogen atmosphere (0·1 MPa).

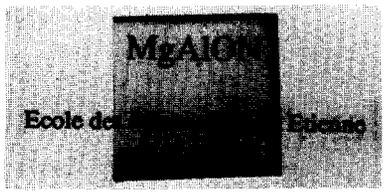


Fig. 1. MgAlON transparent piece (25 × 25 × 6 mm).

All the samples were post-hipped in the temperature range 1675–1810°C for 1 or 1·5 h under 155 MPa of nitrogen. (HIP treatments were performed by National Forge Europe (B).)

Samples were characterized by density (by the Archimede's method in water), X-ray control, microstructure analysis (SEM after thermal etching in N2 atmosphere at about 1600°C, 1 min, rate ramp: 15°C/min TEM), transmittance in visible (Perkin-Elmer Lambda 2) and infra-red (Biorad FTS40) spectra after polishing down to 1 μm diamond.

3 Results

The given compositions (Table 1) have been determined previously[13,14] to obtain pure and sintered (without open porosity) MgAlON samples at low temperature (1550°C). For each composition (A to F) the ratio between chemical elements was the same and corresponding to 21 mol% MgO, 13 mol% AlN, 66 mol% Al_2O_3.

After a treatment at 1675°C for 6 h, each sample was monophased but due to parasite reactions between AlN–MgO or AlN–$MgAl_2O_4$[13] which induce a loss of Mg and N, the spinel solid compositions differ. Each sample contained 3–3·5 wt% of nitrogen determined by complete oxidation.[13]

3.1 HIP effects on chemical composition

Monophased MgAlON samples obtained from the compositions A to F by reaction-sintering or sintering at 1675°C for 6 h, preserved the same lattice parameter after post-hipping whatever the HIP temperature was. For all the samples, lattice parameters measured after sintering were between 0·7992 and 0·8009 nm and were between 0·7994 and 0·8004 nm after HIP treatments. These values are within the accuracy of measurement (0·005 nm).

3.2 HIP effects on densification

Results are given in Table 2. As the relative accuracy of the density determination was 0·1%, HIP treatments had a significant effect at 1675°C (the same temperature as those of the sintering cycle): +3·3% for A and +0·5% for other samples (B to E). Higher HIP temperatures had no effect on the densification.

After reaction-sintering, samples A could have some very fine open porosity, not detected by measurement (in water), so HIP treatment was inefficient for these samples.

Only one HIP treatment was performed at 1810°C for 1 h, it induced an increase of densification (1·7%).

3.3 Microstructural effects of HIP treatments

Before hipping, sample microstructures could be arranged in three classes:

(i) homogeneous and fine grain size (2–3 μm) for B, C, D samples (see Fig. 2)
(ii) homogeneous and coarse grain size (about 10–15 μm) for A, E and F samples (see Fig. 3).
(iii) inhomogeneous for D with binder or D annealed above 1750°C (see Fig. 4).

A TEM observation of D with binder had shown that the fine intergranular porosity disappeared by hipping at 1675°C with a light grain growth (Fig. 5). This was also observed by SEM analysis for B and C samples up to 1810°C HIP treatment and for D up to 1765°C HIP treatment.

Table 1. Studied compositions (mol%)

Composition	Al_2O_3 (%)	AlN (%)	MgO (%)	$MgAl_2O_4$ (%)	γAlON (%)	MgAlON (%)
A	γAl_2O_3[a] 53	7[b]		40[c]		
B	αAl_2O_3[d] 46	13[f]	21[g]			
	αAl_2O_3[e] 20					
C	αAl_2O_3[d] 55	13[f]	21[g]			
	$\gamma + \alpha$ Al_2O_3[h] 11					
D	$\gamma + \alpha$ Al_2O_3[h] 66	13[b]	21[g]			
E			11[g]		89[i]	
F			1 wt%			99[j]

[a] CR125 Baïkowski Chimie.
[b] Starck grade C.
[c] S30 Baïkowski Chimie.
[d] Residue of nitridation.
[e] SM8 Baïkowski Chimie.
[f] Nitridation of boehmite.
[g] Rhône Poulenc.
[h] CR30 Baïkowski Chimie.
[i] Nitridation of boehmite.
[j] Laboratory prepared.

Table 2. Specific mass (g cm^{-3}) evolution by HIP-treatments (relative accuracy 0·1%)

	A	B	C	D	D(with binder)	E	F
Before post-hipping							
1675°C, 6 h HIP	$3{\cdot}48_5$	$3{\cdot}60_2$	$3{\cdot}58_7$	$3{\cdot}57_5$	$3{\cdot}60_0$	$3{\cdot}55_5$	$3{\cdot}50_3$
1675°C, 1 h HIP	$3{\cdot}60_5$	$3{\cdot}62_9$	$3{\cdot}60_0$	$3{\cdot}60_1$	$3{\cdot}62_5$	—	—
1720°C, 1 h 30 HIP	$3{\cdot}49_9$	$3{\cdot}63_3$	$3{\cdot}61_5$	$3{\cdot}60_3$	$3{\cdot}62_9$	—	—
1765°C, 1 h HIP	$3{\cdot}56_5$	$3{\cdot}62_8$	$3{\cdot}60_5$	$3{\cdot}60_2$	$3{\cdot}62_6$	—	—
1810°C, 1 h	—	$3{\cdot}62_7$	$3{\cdot}61_5$	$3{\cdot}60_5$	$3{\cdot}62_8$	$3{\cdot}60_2$	$3{\cdot}56_0$

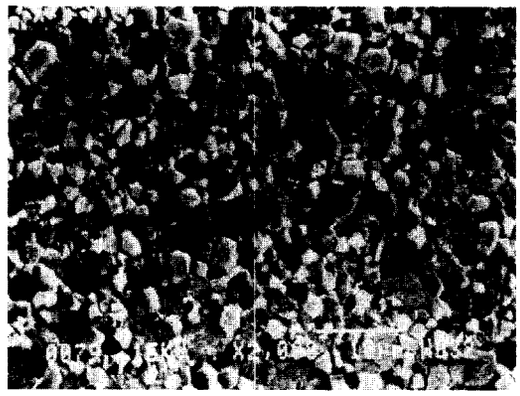


Fig. 2. Microstructures of B, C and D samples sintered at T = 1675°C, 6 h.

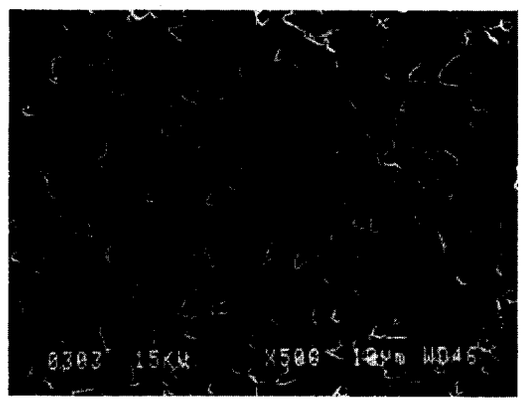


Fig. 3. Microstructure of A, F samples sintered at T = 1675°C, 6 h.

For homogeneous but coarse grain size (A,E,F samples) the grain size did not change, as shown in Fig. 6, and up to 1765°C, intergranular porosity still remained. At 1810°C, E samples presented large grains (2–300 μm) with intragranular porosity (Fig. 7) whereas F samples had a homogeneous grain size (50 μm) without porosity (Fig. 8).

When initial samples presented some heterogeneity (some large grains) as D with binder or D annealed samples, HIP treatment preserved this microstructure up to 1765°C (Fig. 9) but above this temperature the grain size became bimodal (see Fig. 10).

The post-hip treatment can be considered as an annealing treatment under pressure. To analyse the pressure effect, homogeneous samples were annealed for several hours under 0·1 MPa of N_2. Up to 1750°C a homogeneous microstructure had remained but at 1750°C the grain growth and



Fig. 4. Microstructure of D (with binder or annealed) sintered at T = 1675°C, 6 h.



(a)



(b)

Fig. 5. TEM observations (a) before HIP, (b) after HIP.

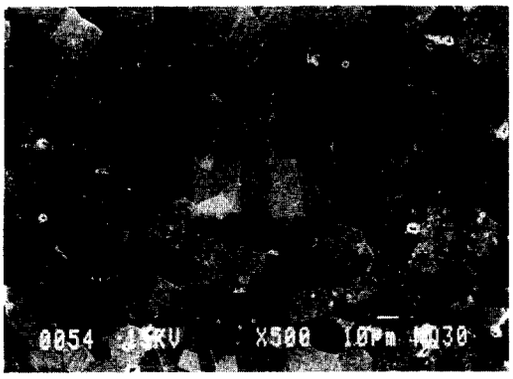


Fig. 6. Microstructures of A, E and F samples after hipping at 1765°C, 155 MPa.



Fig. 7. Microstructure of E samples after hipping at 1810°C, 155 MPa.

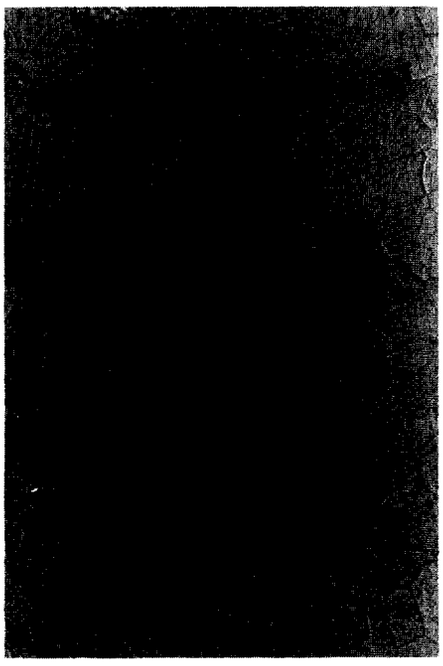


Fig. 8. Microstructure of F samples after hipping at 1810°C, 155 MPa.

porosity appeared (Fig. 11). So the pressure delays the grain growth during the HIP treatment. Nevertheless this delay depends on the HIP temperature and the initial kind of microstructure. For C and D samples grain growth occurred at 1810°C HIP treatment; conversely in samples A the microstructure remained almost identical whatever the HIP treatment (between 1675 and 1810°C).

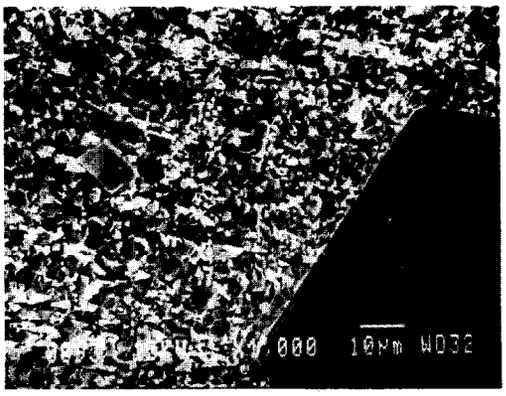


Fig. 9. Microstructure of D (with binder or annealed) after hipping up to 1765°C, 155 MPa.



Fig. 10. Microstructure of D (with binder or annealed) after hipping up to 1810°C, 155 MPa.

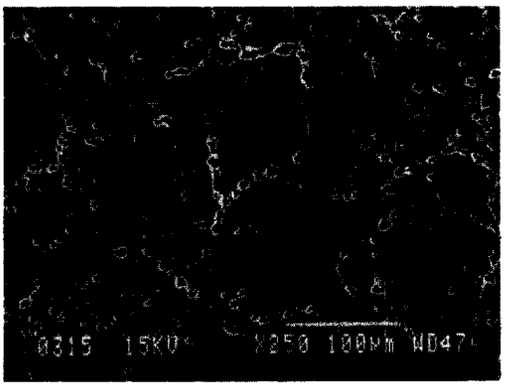


Fig. 11. Effect on grain size by annealing treatment without pressure ($T < 1750$°C).

The microstructure evolution of hipped samples was linked to the initial state of the sample and also to the HIP treatment conditions.

3.4 Optical effects of HIP treatments

Table 3 reports transmittance results (%) in visible wavelength for different HIP treatments.

Samples A and E were impervious to visible waves because of the fine intragranular porosity which has been previously observed. For B, C and D (without binder) samples, although a maximum density was reached from 1675°C, the transmit-

Table 3. Transmittance in line (%) in visible spectrum versus HIP treatments at 500 and 700 nm (thickness of the sample in mm)

	A		B		C		D (with binder)		D (without binder)		E		F	
λ (nm)	500	700	500	700	500	700	500	700	500	700	500	700	500	700
1675°C, 1 h	opaque		0	10	3	18	3	20	0	0	—	—	—	—
			(5,4)	(5,4)	(4)	(4)	(6,3)	(6,3)	(6)	(6)				
1720°C, 1·5 h	—		50	60	5	20	10	20	5	15	—	—	—	—
			(6,2)	(6,2)	(5,2)	(5,2)	(6,2)	(6,3)	(7,6)	(7,6)				
1765°C, 1 h	translucent		10	30	10	25	35	50	15	30	—	—	—	—
			(5)	(5)	(5)	(5)	(6)	(6)	(7,3)	(7,3)				
1810°C, 1·5 h	—		50	65	35	45	18	25	15	30	opaque	white	5	5
			(6)	(6)	(4)	(4)	(6)	(6)	(4,5)	(4,5)			(3)	(3)

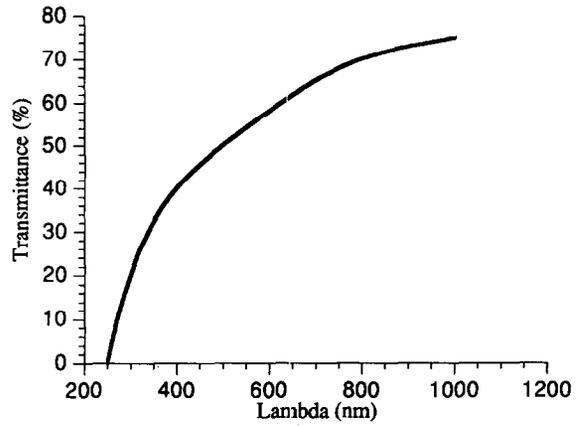


Fig. 12. Visible spectrum of B samples (thickness 6 mm).

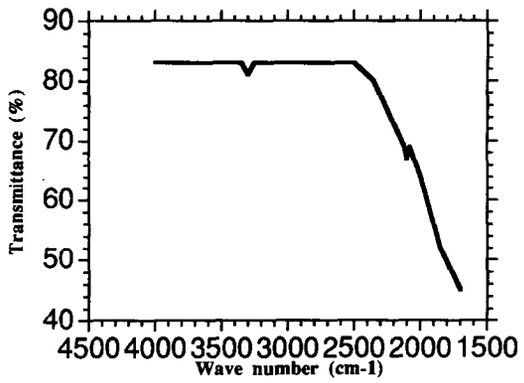


Fig. 13. Infra-red spectrum of B samples (thickness 6 mm).

tance increased above this HIP temperature (65% for B sample at 1810°C, Fig 12). For D samples the binder effect was significant on densification but when the grain size was bimodal the transmittance decreased (at 1810°C) as shown in Table 3. For F samples despite a regular grain size and no porosity, the transmittance for a thickness of about 3 mm in the visible spectrum is very poor (5%).

Unfortunately the samples were often coloured perhaps by carbon or metallic oxide pollution. Only B samples were not coloured, the nitridation could increase the purity of powders.

The I-R spectrum is shown in Fig. 13. A weak peak of OH or NH absorption can be seen. The transmittance was 80% up to 2500 cm^{-1} and the cut off appeared at 1700 cm^{-1}. This spectrum is very close to those of γAlON and $MgAl_2O_4$.

4 Conclusion

γAlON has very good mechanical properties but it is difficult to obtain it transparent with a sufficient thickness. The magnesium aluminate ($MgAl_2O_4$) is easier to sinter but its intrinsic mechanical properties are lower than those of γAlON.

It has been shown in this study that it is possible to obtain a new transparent solid solution spinel: a MgAlON spinel phase sample has been made transparent (Fig. 1) in visible (60%) and infra-red spectra (80%) for a 6 mm thickness with a very fine grain size 5–7 μm and about 3 wt% of nitrogen. The choice of the starting powders and the choice of the reaction-sintering cycle linked to a HIP temperature are the predominant parameters which allow the attainment of transparent samples with a homogeneous microstructure.

Acknowledgements

The authors would like to acknowledge the DRET who financed this study (contract no. 51–1161A) and would like to thank Prof. Y. Laurent and his team for their help during this study. This work is a part of a PhD thesis (A. Granon, Saint-Etienne, 1994).

References

1. Bratton, R. I., Translucent sintered $MgAl_2O_4$. *J. Am. Ceram. Soc.*, **57** (1974) 283–6.
2. Roy, D. W., Emerging optical materials. SPIE 297, 1981, pp. 13–18.
3. Raynal, R., Elaboration et étude des céramiques transparentes de type spinelle dans le système $MgO–Al_2O_3$. Thesis, Limoges, 1988.

4. McCauley, J. W. & Corbin, N. D., US Patent, 1980, 4, 241,000.
5. Hartnett, T. M., Maguire, E. A., Gentilman, R. L., Corbin, N. D. & McCauley, J. W., Aluminium oxynitride spinel (AlON)—A new optical and multi made window material. *Ceram. Eng. Sci. Proc.*, **3** (1982) 67–76.
6. Hartnett, T. M. & Gentilman, R. L., Optical and mechanical properties of highly transparent spinel and AlON domes. *Proc. SPIE*, Int. Soc. Opt. Eng., 1984, pp. 15–22 .
7. Ado, G., Billy, M., Guillo, P. & Lefort, P., Une céramique polycristalline transparente: l'oxynitrure d'aluminium *Indus. Ceram.*, **792** (1985) 173.
8. Willems, R., Preparation and properties of translucent γAlON. PhD Thesis, Eindhoven, 1992.
9. Jack, K. H., Review: Sialons and related nitrogen ceramics. *J. Mater. Sci.*, **11** (1976) 1135–58.
10. Weiss, J., Greil, P. & Gauckler, L. J., *J. Am. Ceram. Soc.*, **65** (1982) C68–69.
11. Sun, W., Ma, L. & Yan, D., Phase relationship in the system MgAlON. *Chinese Sc. Bull.*, **35** (1990) 1189–92.
12. Laurent-Fievez, F., Influence d'ajouts d'oxydes (Y_2O_3 ou MgO) sur le frittage et les propriétés d'une céramique composite alumine-oxynitrure d'alumininium γ. Thesis, Saint-Etienne, 1991.
13. Granon, A., Goeuriot, P., Thevenot, F., Guyader, J., L'Haridon, P. & Laurent, Y., Reactivity in Al_2O_3–AlN–MgO system: The MgAlON phase. *J. Europ. Ceram. Soc.*, **13** (1994) 365–70.
14. Granon, A., Goeuriot, P. & Thevenot, F., Reaction-sintering in Al_2O_3–AlN–MgO system. Third Euro-Ceramic V-1, ed. P. Duran & J. H. Fernandez, Iberica S. L. 1993, pp. 703–8.
15. Guyader, J., Verdier, P. & Laurent, Y., French Patent CNRS no. 8415104 — 2/10/84.
16. Goeuriot-Launay, D., Guyader, J., Laurent, Y., L'Haridon, P., Sappei, J. & Thevenot, F., French Patent no. 8901754 — 10/02/89.

Journal of the European Ceramic Society **15** (1995) 255–263
© 1995 Elsevier Science Limited
Printed in Great Britain. All rights reserved
0955-2219/95/$9.50

The Effect of $La_2Ti_3O_9$ Second Phase on the Microstructure and Dielectric Properties of $La_2Ti_2O_7$ Ceramics

Yuan Jian Zhong,* Feridoon Azough & Robert Freer‡

Materials Science Centre, University of Manchester/UMIST, Grosvenor Street, Manchester M1 7HS, UK

(Received 22 January 1994; revised version received 21 July 1994; accepted 1 August 1994)

Abstract

Lanthanum dititanate ceramics have been prepared by the mixed oxide route. Up to 6 mol% Nb_2O_5 or 10 mol% excess TiO_2 was added to the starting mixes. Sintered products exhibited densities of ≥ 95% theoretical. $La_2Ti_3O_9$ was present as a second phase in all doped samples. With the addition of increasing amounts of Nb_2O_5 or TiO_2 there was formation of $La_2Ti_3O_9$ within the $La_2Ti_3O_9$ matrix, and the average grain size decreased slightly. Dielectric properties were sensitive to the presence of the second phase: relative permittivity increased from 47 to ~56 with additions; the dielectric loss tangent was independent of the amount of excess titania but increased dramatically when > 3 mol% Nb_2O_5 was added; the temperature coefficient of capacitance (TCC) decreased monotonically from +50 ppm/°C for undoped $La_2Ti_2O_7$ ceramics to —50 ppm/°C for specimens containing ~10 mol% additions. Material with zero TCC can be achieved with the addition of ~5 mol%, Nb_2O_5 or excess TiO_2.

1 Introduction

Lanthanum dititanate, ($La_2Ti_2O_7$) is an important member of the ferroelectric family, having the general formula $A_2B_2O_7$ and a layered perovskite structure. Investigations of the electrical properties of $La_2Ti_2O_7$ ceramics commenced over 30 years ago,[1,2] but more recent studies of single crystals revealed that lanthanum dititanate has a very high Curie temperature (1500°C)[3] and exhibits strong piezoelectric and electro-optic effects.[4] The room temperature structure of $La_2Ti_2O_7$ is essentially monoclinic, although two modifications have been proposed; one with symmetry $P2_1$[5,6] and one with symmetry $Pbn2_1$.[7] The structure changes to orthorhombic ($Cmc2_1$) at approximately 780°C, and at 1500°C it transforms into the paraelectric phase.[8] The layered perovskite (or perovskite - slab) structure contains slabs of four distorted TiO_6 octahedra linked by La atoms.[5] The structural anisotropy is expected to lead to anisotropy in dielectric and electrical properties.[9]

With its unusually high Curie temperature and temperature-stable dielectric properties, $La_2Ti_2O_7$ is a candidate for high temperature piezoelectric and electro-optic devices,[9] and microwave frequency components.[10]

Ceramics of $La_2Ti_2O_7$ have mainly been prepared by the classical mixed oxide route,[1,2] although Fuierer and Newnham[9] employed Evaporative Decomposition of Solutions (EDS) and molten salt synthesis routes. Takahashi and Kageyama[11] used a coprecipitation method to prepare ceramics of mixed phases of $La_2Ti_2O_7$ and $La_2Sn_2O_7$. Most studies to date have focussed on the microstructure and properties of the end member $La_2Ti_2O_7$, or solid solutions involving this compound.[11,12] The primary objectives of the present study were to assess the effect of (i) excess TiO_2, and (ii) additions of Nb_2O_5 on the behaviour of $La_2Ti_2O_7$ prepared by the mixed oxide route. Specific attention was paid to the role and effect of second phase $La_2Ti_3O_9$.

2 Experimental

Two series of samples were prepared by the standard mixed oxide route: (A) $x\mathrm{TiO_2}.(1\text{-}x)\mathrm{La_2Ti_2O_7}$ where x = 0, 0·02, 0·04, 0·06, 0·08 and 0·10; (B) $y\mathrm{Nb_2O_5}.(1\text{-}y)\mathrm{La_2Ti_2O_7}$, where y = 0, 0·005, 0·015, 0·03 and 0·06.

Hence $x = y = 0$ represents the undoped, $La_2Ti_2O_7$ reference composition.

* Present address: Beijing Institute of Radio Measurement, P.O. Box 3923, No. 8, Beijing 100854, P. R. China.
‡ Author to whom correspondence should be addressed.

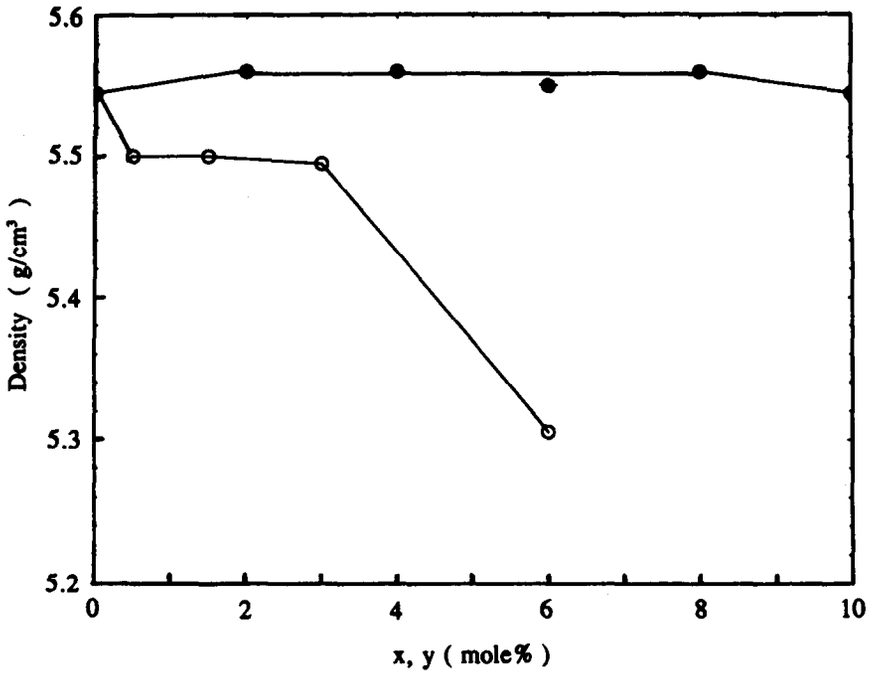


Fig. 1. Specimen densities as a function of additive content: ○ Nb_2O_5; ● TiO_2.

The starting materials were La_2O_3, TiO_2 (Fluka, purity of 99·98, and 99% respectively) and Nb_2O_5, (BDH, purity 99·5%). Prior to weighing the lanthanum oxide was dried by heating at 700°C for 4 h. Powders of La_2O_3 and TiO_2, in the molar ratio of 1 : 2, were mixed and vibration-milled in propan-2-ol with zirconia balls for 6 h. The dried mixtures were then calcined at 1100°C for 4 h. The required amounts of excess TiO_2 or Nb_2O_5 were added to batches to form compositions in the series (A) and (B). The powders were then remilled in propan-2-ol for 8 h. Pellets 16 mm in diameter and 8 mm high were pressed uniaxially at 900 kg/cm^2 without binder and then sintered at temperatures in the range 1300–1400°C for 4 h. Specimens for electrical measurements, diameter ~12·4 mm and thickness typically 1·4 mm, were cut from the sintered pellets. Specimens for microstructural studies were ground to 1200 grade SiC, polished with diamond paste down to 1/4 μm and then thermally etched at a temperature of approximately 1150°C.

X-ray diffraction analysis was carried out using Cu K_α radiation with a Philips PW1710 diffractometer and horizontal goniometer. Microstructures were studied by optical microscopy and scanning electron microscopy, Philips SEM 505 with energy

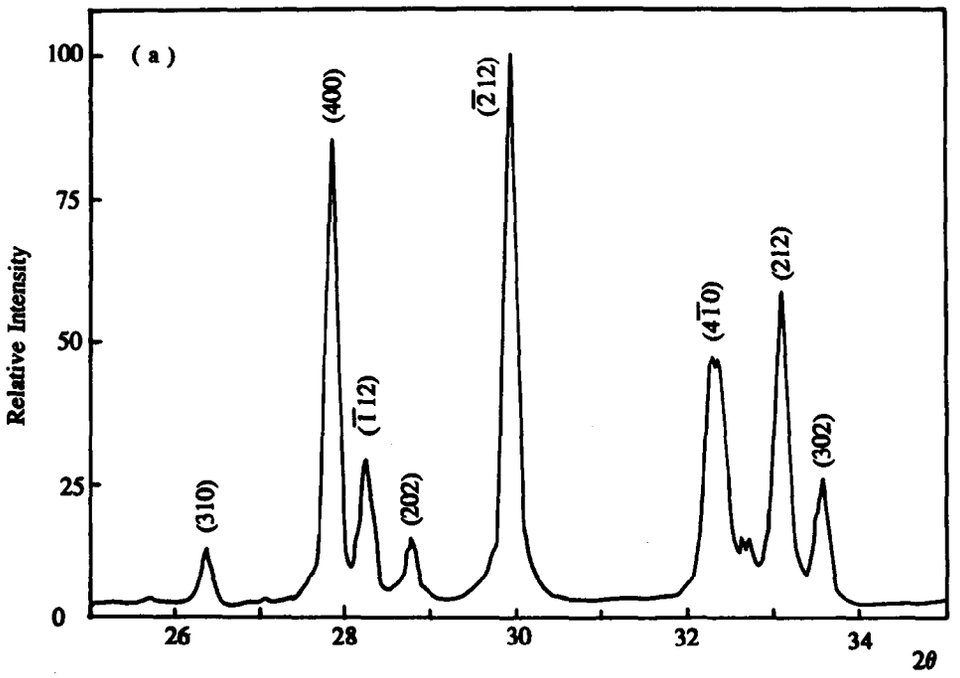


Fig. 2. X-ray diffraction spectra for ceramic specimens prepared from starting mixes $(y)Nb_2O_5.(1\text{-}y)La_2Ti_2O_7$, (a) $y = 0$; (b) $y = 0{\cdot}015$; (c) $y = 0{\cdot}06$. $LT_2 = La_2Ti_2O_7$; $LT_3 = La_2Ti_3O_9$.

dispersive X-ray analyser EDAX, model 9100. For each specimen, 5–8 grains of each type were analysed and the average composition determined. Area fractions of each phase, based upon contrast differences, were determined manually, after applying fine mesh grids to SEM micrographs for each specimen. The average grain sizes were obtained by the mean linear intercept method.

A Hewlett Packard 4284A precision LCR meter was used to determine relative permittivity (via capacitance measurements) and loss factor as a function of temperature from 15 to 120°C at frequencies up to 1 MHz. Values for the temperature coefficient of capacitance (TCC) were determined from data obtained in the range 15–85°C.

3 Results and Discussion

3.1 Specimen density

Figure 1 shows the densities for specimens of the two series as a function of composition. The theoretical density for $La_2Ti_2O_7$ is 5·782 gm cm^{-3} [13] and that of the related phase $La_2Ti_3O_9$, 5·325 gm cm^{-3}.[14] The presence of extra titania (Series A) did not have any significant effect on density. For all samples, density was approximately 96% theoretical. For the niobia-doped samples, densities were around 95% theoretical at low doping levels, but much lower in the specimens doped with 6 mol% Nb_2O_5.

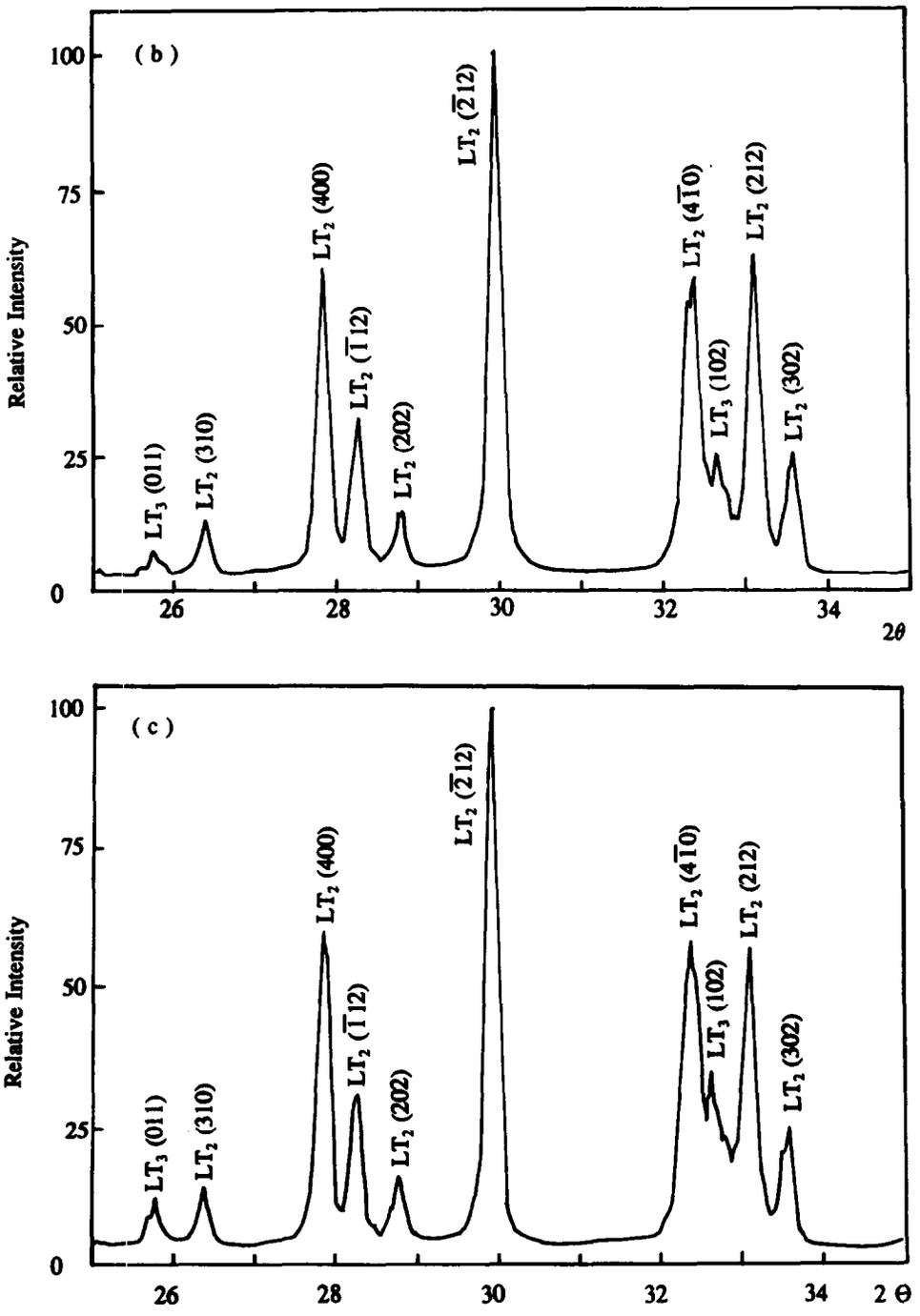


Fig. 2. — continued.

3.2 Phase analysis

Figure 2 shows parts of the X-ray diffraction spectra obtained for selected specimens. The major peaks for all the samples containing up to 6 mol% Nb_2O_5 (i.e. $y \leq 0{\cdot}06$) and up to 10 mol% excess TiO_2 (i.e. $x \leq 0{\cdot}10$) can be indexed to monoclinic $La_2Ti_2O_7$ with the space group as $P2_1$.[1] The positions and intensities of the peaks are in satisfactory agreement with published data.[13] In the X-ray diffraction spectra specimens, a number of extra reflections are present, e.g. near 25·8 and 32·7° 2θ (Figs 2(b) and (c)). None of the extra peaks could be assigned to the phase $La_4Ti_9O_{24}$, which is expected to be the nearest compound to $La_2Ti_2O_7$ on the TiO_2-excess side of $La_2Ti_2O_7$ in the phase diagram of the La_2O_3–TiO_2 system.[2] However, the positions and intensities of the extra peaks were found to represent $La_2Ti_3O_9$.[14] The peaks corresponding to the (011), (102) and (111) reflections of the $La_2Ti_3O_9$ phase grew in intensity as x and y increased. (NB: the peak for (111) occurs at 2θ angle of 40·50 which is outside the range covered by Fig. 2.)

3.3 Microstructures

Undoped $La_2Ti_2O_7$ specimens are single phase with a near homogeneous microstructure (Fig. 3). The grains, ranging in size from 10 to 30 microns, are somewhat elongated, but not to the degree reported by Fuierer[9] where the grains appeared as highly anisotropic platelets. For the specimens prepared with excess TiO_2, or Nb_2O_5 additions, a second phase is visible in SEM micrographs (e.g. Fig. 4) as clusters of grains much smaller than those of the major phase. These small grains look darker than the matrix, indicating lower average atomic number.

Quantitative EDAX analyses for the specimens prepared with excess titania gave a La:Ti ratio of approximately 50 : 50 for the large grains of the major phase (Table 1), irrespective of the level of TiO_2 added, and a La:Ti ratio of approximately 40 : 60 for the dark second phase grains (Table 2). These analyses confirm that the second phase in $La_2Ti_2O_7$ specimens prepared with excess TiO_2 is $La_2Ti_3O_9$.

For the Nb-doped materials, the elemental distribution is more complicated, because the Nb dopant atoms are incorporated into both the major and the second phases. EDAX analyses again gave a La:Ti atomic ratio of approximately

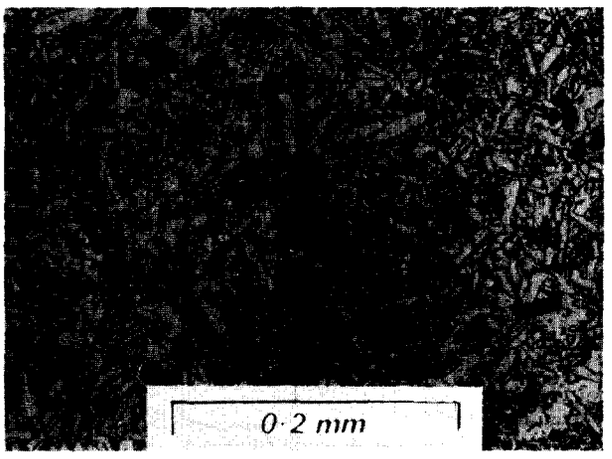
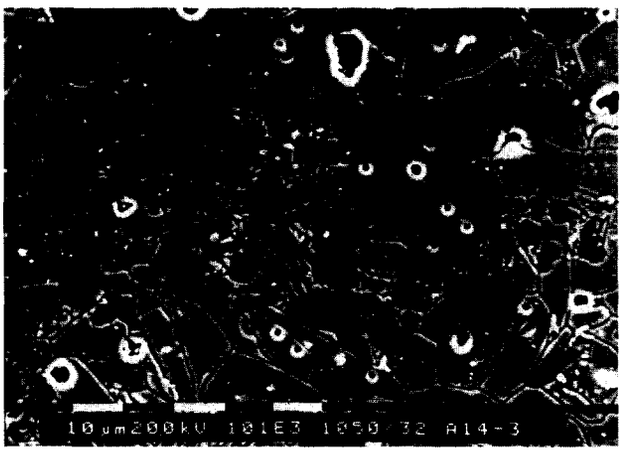
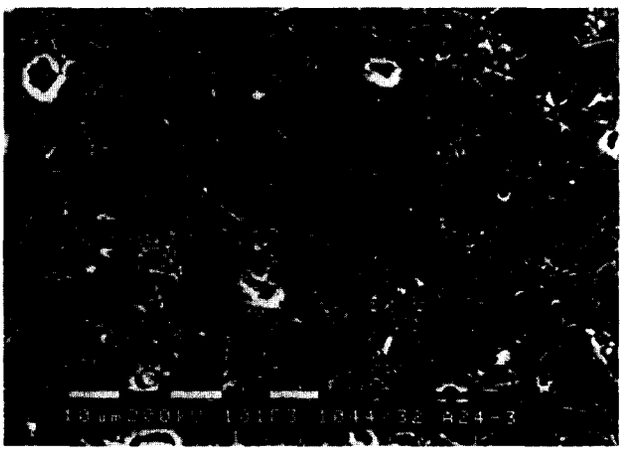


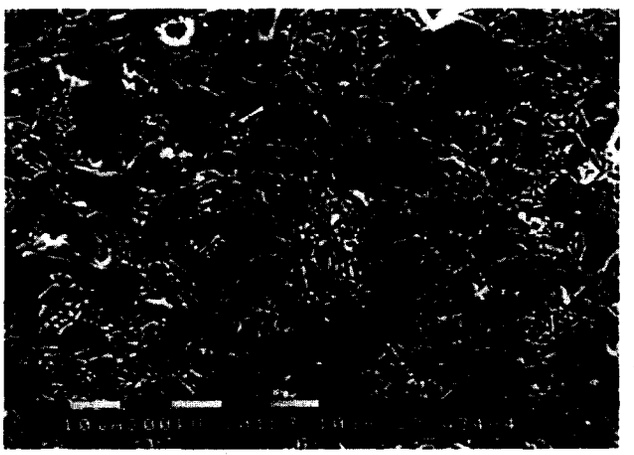
Fig. 3. Optical micrograph of polished and thermally etched $La_2Ti_2O_7$ ceramic.



(a)



(b)



(c)

Fig. 4. SEM micrographs of polished and thermally etched $La_2Ti_2O_7$-based specimens: prepared with (a) 0·5 mol% Nb_2O_5, (b) 3 mol% Nb_2O_5 and (c) 6 mol% Nb_2O_5.

Table 1. Elemental concentrations (atomic %) detected in the major phases of ceramics prepared from starting mixes $y Nb_2O_5.(1-y)La_2Ti_2O_7$ and $xTiO_2.(1-x)La_2Ti_2O_7$

	Mol% Nb_2O_5 additions (y)					*Mol% TiO_2 excess (x)*
	0	0·5	1·5	3·0	6·0	2·0,10·0
Nb	0	0·8	2·3	3·7	5·9	—
Ti	50·2	50·2	48·8	47·8	45·3	50·3
La	49·8	49·0	49·9	48·5	48·8	49·7
σ^a	0·45	0·83	0·74	0·60	0·90	1·0

[a] The maximum standard deviation for all the elements present in the specimen.

Table 2. Elemental concentrations (atomic %) detected in the minor phase of ceramics prepared from starting mixes $y Nb_2O_5.(1-y)La_2Ti_2O_7$ and $xTiO_2.(1-x)La_2Ti_2O_7$

	Mol% Nb_2O_5 additions (y)					*Mol% TiO_2 excess (x)*
	0	0·5	1·5	3·0	6·0	2·0,10·0
Nb	—	2·2	3·5	5·9	8·6	—
Ti	—	58·2	56·7	54·2	52·6	59·5
La	—	39·6	39·8	39·9	38·8	40·5
σ^a	—	0·71	0·82	0·54	0·87	0·83

[a] The maximum standard deviation for all the elements present in the specimen.

50:50 for the major phase, and approximately 40:60 for the minor phase (Tables 1 and 2). The concentrations of Nb atom in the two phases are shown as a function of the amount of dopant in Fig. 5. More niobium atoms enter the minor phase than the major phase. Since the ionic radii for Nb^{5+} and Ti^{4+} ions are very similar (0·78 and 0·745 Å respectively),[15] it is possible that Nb^{5+} ions enter the Ti^{4+} sites. The higher TiO_2 content in $La_2Ti_3O_9$ (75%) than in $La_2Ti_2O_7$ (67%), and therefore the availability for exchange with the dopant, may account for the uneven distribution of Nb between the two phases.

Kestigian and Ward[16] reported the preparation of $La_2Ti_3O_9$ in the presence of trivalent Ti^{3+} ions. Later, Marzullo and Bunting,[1] as part of a larger study concerned with TiO_2–Rare Earth Oxide compounds, reported the dielectric properties of $La_2Ti_3O_9$ produced by conventional ceramic methods. This intermediate phase was not shown in the phase diagram of the La_2O_3–TiO_2 system presented by MacChesney and Sauer.[2] Subsequently, several authors described the preparation (and some of the electric properties) of $La_2Ti_3O_9$ ceramics, e.g. prepared with a slight oxygen deficiency,[14,17] stabilized by 2+ or 1+ ions,[18–22] and prepared from coprecipitated powder.[23,24] For example, Nenasheva *et al.*[21] obtained similar results to those of MacChesney and Sauer[2] but noted that $La_2Ti_3O_9$ is unstable because there are vacancies on 1/3 of the sites in the *A* sublattice (i.e. $La_{2/3}\square_{1/3}TiO_3$, where $\square$ is a vacancy in the *A* sublattice of the perovskite structure compound $ATiO_3$); $La_2Ti_3O_9$ on its own decomposes into $La_2Ti_2O_7$ and rutile (TiO_2). Indeed, attempts by Nenasheva *et al.*[21] to synthesise $La_2Ti_3O_9$ by the mixed oxide route yielded only 80% of the desired perovskite structured phase with the remainder as $2La_2O_3.9TiO_2$. They confirmed that additions of $CaTiO_3$, $SrTiO_3$ or $PbTiO_3$ to a mixture of

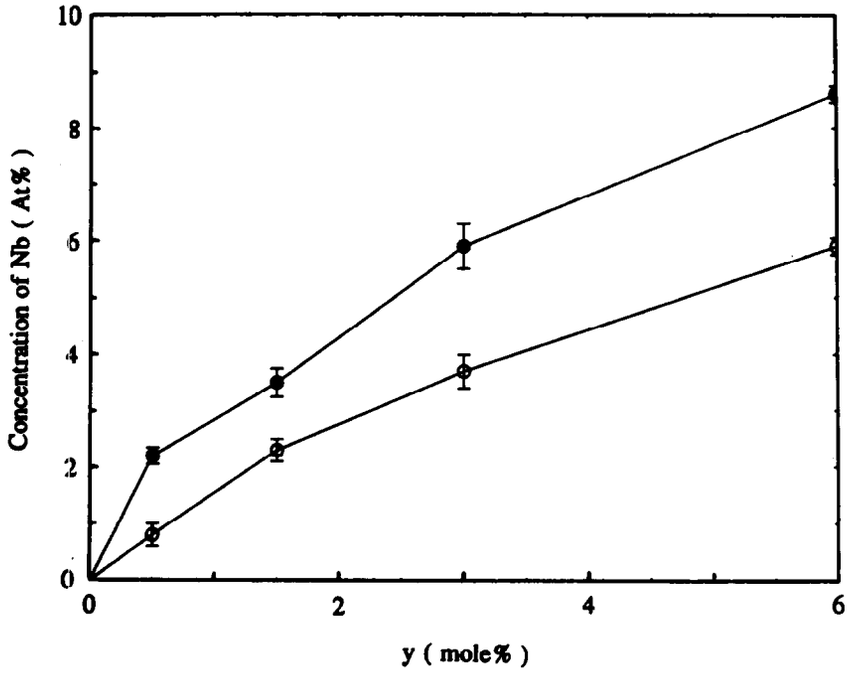


Fig. 5. Niobium (Nb) content of the major ($La_2Ti_2O_7$) phase (O) and minor ($La_2Ti_3O_9$) phase (●) of $La_2Ti_2O_7$ based-ceramics as a function of Nb_2O_5 content (y) of the starting mixture.

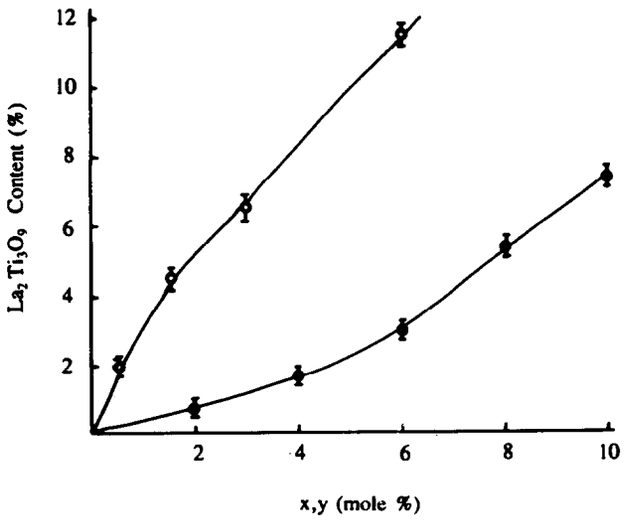


Fig. 6. Fraction of minor phase ($La_2Ti_3O_9$) in $La_2Ti_2O_7$ ceramics prepared with excess TiO_2 (●) and Nb^2O_5 (○) additions.

$La_2O_3.3TiO_2$ led to the formation of single phase perovskite-type structures ($A_{3/4}\square_{1/4}TiO_3$) although the use of lead titanate caused a tetragonal distorted structure (c/a = 1·004). In the present study, a compound of the formula $La_2Ti_3O_9$-type was formed as a second phase in ceramics in the La_2O_3-TiO_2 system prepared by means of the usual mixed oxide route when excess TiO_2 or Nb_2O_5 was present.

The formation of the phases in samples prepared with excess TiO_2 can be described by:

$$(1 - x)La_2Ti_2O_7 + xTiO_2 \rightarrow (1 - 2x)La_2Ti_2O_7 + xLa_2Ti_3O_9 \quad (1)$$

Thus in the case of specimens prepared with x mol% excess TiO_2, there should be $x/(1\text{-}x)$ mole of $La_2Ti_3O_9$ produced. For the samples doped with Nb_2O_5, the situation is more complex since the niobia enters both the primary $La_2Ti_2O_7$ and secondary $La_2Ti_3O_9$—type phases. However, if it is assumed that the Nb is located only on Ti sites, then we can envisage reactions of the form

$$(1 - y)La_2Ti_2O_7 + yNb_2O_5 \rightarrow (1 - 3y)La_2(Ti,Nb)_2O_7 + 2yLa_2(Ti,Nb)_3O_9 \quad (2)$$

Whilst accepting the approximate nature of eqns (1) and (2), it would appear that doping with niobia (eqn (2)) should generate more $La_2Ti_3O_9$ second phase than 'doping' with excess TiO_2 (eqn(1)). Figure 6, showing the $La_2Ti_3O_9$ content of the ceramics confirms that the niobia-bearing specimens contain typically 2—3 times more second phase than the samples prepared with excess titania.

The actual compositions of the products of the B series ceramics vary with doping level, but when y = 0·03 for example, typical analyses (Tables 1 and 2) indicate that the major and minor phases may be described as $La_2Ti_{1.97}Nb_{0.15}O_{7.3}$ and $La_2Ti_{2.72}Nb_{0.29}O_{9.16}$ respectively, when no allowance is made for any vacancies present.

In specimens of the Nb_2O_5-doped system, there is a tendency for the grain size to decrease as increasing amounts of dopant are employed; in addition, clusters of small grains appear, most of which are the minor phase, ($La_2Ti_3O_9$). SEM micrographs for three specimens in this series are shown in Fig. 4.

3.4 Dielectric properties

3.4.1 Relative permittivity

Figure 7 shows the relative permittivity of lanthanum dititanate ceramics as a function of added excess

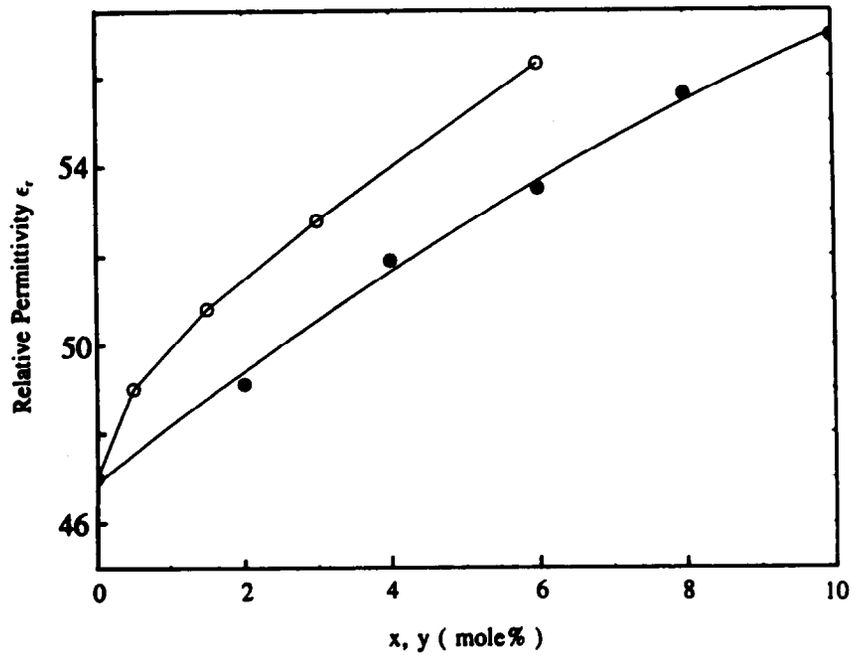


Fig. 7. Relative permittivity of $La_2Ti_2O_7$ ceramics at 1 MHz as a function of added Nb_2O_5 (○) and excess TiO_2 (●).

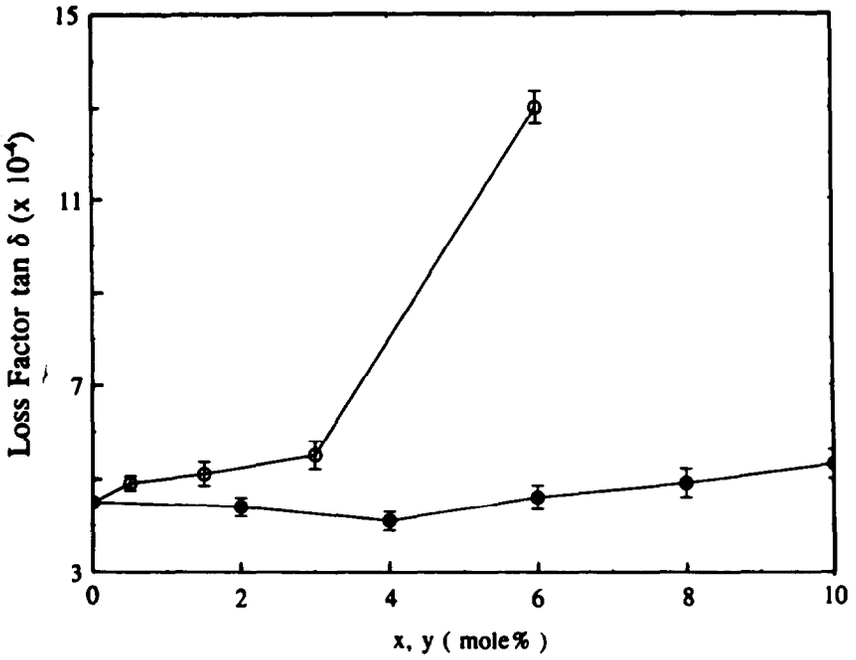


Fig. 8. Dielectric loss factor (tan δ) for $La_2Ti_2O_7$ ceramics at 1 MHz as a function of added Nb_2O_5 (○) and excess TiO_2 (●).

TiO_2 or Nb_2O_5 for the two systems. For the end-member $La_2Ti_2O_7$ the relative permittivity (at 1 MHz ~ 47) was higher than that reported by Mazullo and Bunting[1] (44) and Takahashi and Kageyama[11] (41), but close to that obtained by Fuierer and Newnham[9] for mixed oxide-prepared ceramics (48·8). The last named authors obtained marginally lower values for chemically prepared ceramics and hot forged specimens parallel to the forging direction. The increase in relative permittivity with increasing Nb_2O_5 or TiO_2 (Fig. 7) and the generation of the second phase (Fig. 6) suggests that the $La_2Ti_3O_9$ second phase has a higher relative permittivity than the primary $La_2Ti_2O_7$ phase. For the system with excess titania, extrapolation of the relationship between ε_r and composition (Fig. 7) indicates a relative permittivity of 77 for $La_2Ti_3O_9$. In spite of the long extrapolation this is clearly different from the value of 45 obtained by Marzullo and Bunting[1] (which is in fact lower than recent determinations of ε_r for the $La_2Ti_2O_7$ end member), but in excellent agreement with that reported by Nenasheva *et al.*[21] for $La_2Ti_3O_9$.

3.4.2 *Dielectric loss*

Undoped $La_2Ti_2O_7$ has a comparatively low dielectric loss with the Q value (Q ~ 1/tanδ) ranging from typically 1500 to 3500 at 100 kHz depending on the sintering and processing conditions. Winfield[12] obtained a Q value of 1250 at 1 MHz for mixed oxide prepared $La_2Ti_2O_7$ whilst Fuierer and Newnham[9] at 100 kHz obtained Q values of 900 for Evaporative Decomposition of Solution (EDS) derived material, 5300 for mixed oxide ceramics, 3500 and 4750 for molten salt synthesis products, 2600 and 2950 for hot forged samples. In general, the Q values increased with specimen density. The incorporation of excess titania does not increase the loss significantly (Fig. 8). This is predictable since, as shown in eqn (1), the addition of extra titania induces no defects which may serve as charge carriers and thereby increase conduction. However, a sharp rise in dielectric loss was observed for materials containing more than 2 mol% Nb_2O_5 (Fig. 8).

The substitution of Nb^{5+} into $La_2Ti_2O_7$ and $La_2Ti_3O_9$ requires the operation of some charge compensation mechanism to ensure charge neutrality. For the primary $La_2Ti_2O_7$ phase the situation in the undoped reference material can be described in terms of Kroger-Vink notation[25] by:

$$La_2O_3 + 2TiO_2 \rightarrow 2La_{La}^{x} + 2Ti_{Ti}^{x} + 7O_o^{x} \quad (3)$$

After doping with niobia, charge compensation could be achieved by:

(i) cation vacancies

$$5La_2O_3 + 4Nb_2O_5 \rightarrow 10La_{La}^{x} + 8Nb_{Ti}^{\bullet} + 2V_{Ti}^{''''} + 35O_o^{x} \quad (4)$$

or (ii) electronic defects

$$La_2O_3 + Nb_2O_5 \rightarrow 2La_{La}^{x} + 2Nb_{Ti}^{\bullet} + 7O_o^{x} + \tfrac{1}{2}O_2 + 2e' \quad (5)$$

Although the second phase ($La_2Ti_3O_9$) is much smaller in quantity, similar mechanisms may be envisaged for the incorporation of Nb. Starting with the undoped material:

$$La_2O_3 + 3TiO_2 \rightarrow 2La_{La}^{x} + 3Ti_{Ti}^{x} + 9O_o^{x} \quad (6)$$

After doping, charge compensation could be achieved by:

(i) cation vacancies:

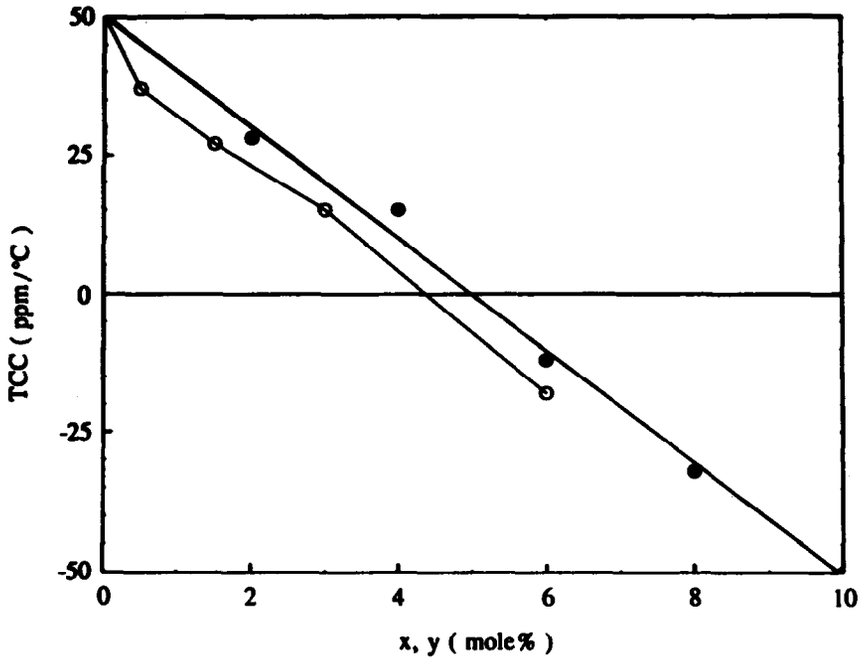


Fig. 9. Temperature coefficient of capacitance (TCC) of $La_2Ti_2O_7$-based ceramics as a function of added Nb_2O_5 (O) and excess TiO_2 (●).

$$5La_2O_3 + 6Nb_2O_5 \rightarrow 10La_{La}^{x} + 12Nb_{Ti}^{\bullet} + 3V_{Ti}'''' + 45O_o^x \quad (7)$$

or (ii) electronic defects

$$2La_2O_3 + 3Nb_2O_5 \rightarrow 4La_{La}^{x} + 6Nb_{Ti}^{\bullet} + 18O_o^x + 1\tfrac{1}{2}O_2 + 6e' \quad (8)$$

Thus, at small doping levels of Nb_2O_5, charge compensation can be achieved by cation vacancies (eqns (4) and (7)); at high doping levels there may be a transition to a compensation mechanism based on electronic defects (eqns (5) and (8)). Dielectric losses are higher in niobia-containing specimens than ceramics prepared with excess TiO_2 (Fig. 8), and losses increase rapidly above 2 mol% Nb_2O_5. It seems probable that charge compensation is by cation vacancies at the low Nb_2O_5 doping levels, but there is insufficient data to confirm whether or not there is any contribution from electronic defects at the higher doping levels.

The intrinsic losses in a material are defined by the lattice vibrational modes,[26] and these will be modified by the presence of significant numbers of defects. It is now established[27] that oxygen vacancies increase losses in $ZrTiO_4$-based dielectrics. In the lanthanum ditanate ceramics of the present study, the niobium atoms incorporated into the structure probably give rise to large numbers of cation vacancies, thereby modifying the lattice vibrational modes and increasing the dielectric losses (Fig. 8).

3.4.3 Temperature coefficient of capacitance (TCC)

It is of interest from a practical point of view to define temperature-stable ceramic compositions, particularly those which exhibit a zero value TCC. One of the standard methods to achieve this property is to prepare a solid solution from components which possess characteristics with negative and positive dependencies on temperature. Marzullo and Bunting[1] were the first to report TCC values for $La_2Ti_2O_7$ and $La_2Ti_3O_9$ of +30 and –60 ppm/°C respectively. This implies that a material with a zero TCC can be prepared if $La_2Ti_3O_9$ is introduced as a minor phase in a $La_2Ti_2O_7$ matrix. This presumption is justified by the temperature-dependence of the 'doped' materials shown in Fig. 9. With increasing Nb_2O_5 or excess titania, the TCC decreases linearly from a value of +50 ppm/°C in the undoped material to approximately –50 ppm/°C for starting compositions containing approximately 10 mol% of additions. The increasing amount of the $La_2Ti_3O_9$ phase appears to be responsible for this phenomenon.

The rate of change of TCC with additive level is greater for the niobium doped specimens than for TiO_2 excess specimens. This corresponds to the difference in the yield of the minor phases produced by equal amounts of additions. The TCC value of the sample prepared with 10 mol% excess titania is unexpectedly high in view of the previously reported value of –60 ppm/°C[1] for pure $La_2Ti_3O_9$. Due to the low level of additions, it is not possible to extrapolate the TCC data to that equivalent to the pure $La_2Ti_3O_9$ phase with any degree of reliability, but it can be anticipated that the value will be much lower than –60 ppm/°C, or even lower than the value of –170 to –200 ppm/°C

reported by Nenasheva *et al.*[21] for $La_2Ti_2O_7$–$La_4Ti_9O_{24}$ mixtures. The most interesting result, however, is that $La_2Ti_2O_7$-based compositions with zero TCC, and thus temperature stable dielectric characteristics, can be obtained by the addition of approximately 4·2 mol% Nb_2O_5 or 5 mol% excess TiO_2 to the starting mixtures. It can be seen that the presence of the second phase $La_2Ti_3O_9$ is responsible for, and therefore favourable to the improvement of the dielectric properties. However, the addition of > 3 mol% Nb_2O_5 leads to a rapid increase in dielectric losses.

4 Conclusions

(1) Good quality lanthanum dititanate ceramics have been prepared using conventional mixed oxide ceramic methods. Modification of the structure and electrical properties were achieved by the additions of up to 10 mol% Nb_2O_5 or excess titania to $La_2Ti_2O_7$.

(2) With increasing amounts of additives there was a growth of $La_2Ti_3O_9$ as a second phase within the $La_2Ti_2O_7$ matrix.

(3) Changes in the dielectric properties of the families of ceramics can be correlated with the presence of the second phase:

(a) relative permittivity increased with the additions;
(b) dielectric loss was independent of the amount of excess titania but increased dramatically when > 3 mol Nb_2O_5 was added;
(c) TCC values for the materials decreased monotonically from +50 ppm/°C for undoped-$La_2Ti_2O_7$ to approximately —50 ppm/°C for materials containing 10 mol% addition. Thus, a material with zero TCC value can easily be obtained.

Acknowledgements

During the performance of this work, Y. J. Zhong was supported by a British Council Scholarship. Helpful discussions with Dr D. A. Hall, Manchester Materials Science Centre are gratefully acknowledged.

References

1. Marzullo, S. & Bunting, E. N., Dielectric properties of titania or tin oxide containing varying proportions of rare-earth oxides. *J. Am. Ceram. Soc.*, **41** (1958) 40–1.
2. MacChesney, J .B. & Sauer, H. A., The system La_2O_3–TiO_2; phase equilibrium and electrical properties. *J. Am. Ceram. Soc.*, **45** (1962) 416–22.
3. Kimura, M., Nanamatsu, S., Doi, K., Matsushita, S. & Takahasi, M., Electro optic and piezoelectric properties of $La_2Ti_2O_7$ crystals. *Japan. J. Appl. Phys.*, **11** (1972) 904.
4. Nanamatsu, S., Kimura, M., Doi, K., Matsushita, S. & Yamada, N., A new ferroelectric $La_2Ti_2O_7$. *Ferroelectrics*, **8** (1974) 511–3.
5. Gasperin, M., Dititanate de lanthane. *Acta Crystallogr.*, **B31** (1975) 2129–30.
6. Balachandran, U. & Eror, N. G., X-ray diffractional and vibrations-spectroscopy study of the structure of $La_2Ti_2O_7$. *J. Mater. Res.*, **4** (1989) 1525–8.
7. Schuenemann, K. & Muller-Burschbaum, H. K., Zur kristallstruktur von $La_2Ti_2O_7$. *J. Inorg. Nucl. Chem.*, **37** (1975) 1878–81.
8. Ishizawa, N., Marumo, F., Iwai, S., Kimura, M. & Kawamura, T., Compounds with perovskite-type slabs, V: a high temperature modification of $La_2Ti_2O_7$. *Acta Crystallogr.*, **B38** (1982) 368–72.
9. Fuierer, P. A. & Newnham, R. E., $La_2Ti_2O_7$ ceramics. *J. Am. Ceram. Soc.*, **74** (1991) 2876–81.
10. Ouchi, H. & Kawashima, S., Dielectric ceramics for microwave applications. *Japan J. Appl. Phys. Suppl.*, **24** (1985) 60–4.
11. Takahasi, J. & Kageyama, K., Compositional and microstructural dependence of the dielectric properties of complex low-loss capacitors in the La–Sn–Ti–O system. *Ceramic Transactions 8: Ceramic Dielectrics — Composition, Processing and Properties* (Amer. Ceram. Soc., Westerville, USA, 1990). pp. 333–43.
12. Winfield, G., MSc. dissertation, University of Manchester (1992).
13. ASTM X-ray Powder Diffraction Files, Card No. 28–517.
14. Abe, M. & Uchino, K., X-ray study of the deficient perovskite $La_{2/3}TiO_3$. *Mater. Res. Bull.*, **9** (1974) 147–56.
15. Shannon, R. D., Revised ionic radii and systematic studies of interatomic distances in halides and chalcogenides. *Acta Crystallogr.*, **A32** (1976) 751–67.
16. Kestigan, M. & Ward, R., The lanthanum titanium oxygen system. *J. Am. Chem. Soc.*, **77** (1955) 6199–220.
17. Yokoyama, M., Ota, T., Yamai, I. & Takahashi, J., Flux growth of perovskite-type $La_{2/3}TiO_3$ crystals. *J. Cryst. Growth*, **96** (1989) 490–6.
18. Tien, T. Y. & Hummel, F. A., Solid solutions in the system $SrTiO_3$–(La_2O_3.3TiO_2). *Trans. Br. Ceram. Soc.*, **45** (1962) 233–45.
19. Hennings, D., *Mater. Res. Bull.*, **6** (1971) 329.
20. Sasaki, H. & Matsuo, Y., Oxidation–reduction phenomena in the $PbTiO_3$–$La_{2/3}TiO_3$ system. *Am. Ceram. Soc. Bull.*, **51** (1972) 164–6.
21. Nenasheva, E. A., Rotenberg, B. A., Gindin, E. I. & Prokhvatilov, V. G., High frequency capacitor dielectrics based on lanthanum and bivalent metal titanates. *Izv. Akad. Nauk SSSR, Neorg. Mater.*, **15** (1979) 1890–3. (English translation), **15** (1980) 1489–91.
22. Belous. A. G., Gavrilova, L. G., Polianetckaia, S. V., Ja Makarova, Z. & Chalyi, V. P., Stabilisation of perovskite lanthanum titanate structure. *Ukr. Khim. Zh.*, **50** (1984) 460–1.
23. Sych, A. M., Bilyk, D. I., Klenus, V. G. & Novik, T. V., Lanthanum, praseodymium, and neodymium metatitanates. *Russ. J. of Inorg. Chem.*, (English translation) **21** (1976) 1775–7.
24. Sych, A. M. & Novik, T. V., Investigation of interaction of coprecipated hydroxides or rare earths and titanium. *Zh. Neorg. Khim.*, **22** (1977) 68–73.
25. Kroger, F. A. & Vink, H. J., *Solid State Physics*, Vol. 3, ed. F. Seitz and D. Turnbull, Academic Press Inc., New York, 1956, p. 307.
26. Wakino, K., Murata, M. & Tamura, H., Far infrared reflection spectra of $Ba(Zn,Ta)O_3$–$BaZrO_3$ dielectric resonator material. *J. Am. Ceram. Soc.*, **69** (1985) 34–7.
27. Iddles, D. M., Bell, A. J. & Moulson, A. J., Microwave properties of ZrO_2–TiO_2–SnO_2 ceramics. *J. Mater. Sci.*, **27** (1992) 6303–10.

Journal of the European Ceramic Society **15** (1995) 265–269
© 1995 Elsevier Science Limited
Printed in Great Britain. All rights reserved
0955-2219/95/$9.50

Low Temperature Synthesis of Zinc Ferrite using Hydrazine Monohydrate

M. Ueda, S. Shimada & M. Inagaki

Department of Applied Chemistry, Faculty of Engineering, Hokkaido University, Kita-Ku, Sapporo 060, Japan

(Received 18 May 1994; revised version received 28 July 1994; accepted 1 August 1994)

Abstract

Crystalline powder of zinc ferrite was synthesized from the mixed solution of $FeCl_2$ and $ZnCl_2$ by adding hydrazine monohydrate solution and aging near room temperature from 30 to 60°C. The temperature condition for this synthesis was the same as that using aqueous ammonia reported previously. However, it was necessary to keep the concentration of metal chlorides below 1×10^{-1} mol dm^{-3} to obtain zinc ferrite, because hydrazine complexes with metal chlorides in solutions with high concentration. Zinc ferrite was also formed starting with $FeCl_3$ solution, probably because hydrazine reduces Fe^{3+} partly to Fe^{2+}.

1 Introduction

Hydrazine (N_2H_4) is known to be complexing, strongly reducing and also a basic agent. In the first case, it behaves either as a unidentate ligand as in $BF_3N_2H_4$ or a bidentate bridging ligand as in $Zn(N_2H_4)_2Cl_2$. Its complexes with transition metal salts and lanthanide metal salts have been prepared[1,2] and characterized by infra-red absorption spectroscopy.[3–5] Thermogravimetric studies and magnetic moment measurements on the complexes with nickel salts have been carried out,[6] as has a structural analysis of $Zn(N_2H_4)_2Cl_2$ crystals.[7] As a reducing agent, hydrazine has been widely used for non-electrolytic plating (chemical plating) and for precipitation of metals from solution, e.g. fixing solution of photo films.

For the purpose of ceramic synthesis, however, only a few reports using hydrazine have been presented: hydrazine prevents the formation of ferric oxide on the synthesis of magnetite (Fe_3O_4),[8] and its complexes with metal nitrates are used as a precursor for the zinc nickel mixed ferrite.[9]

In a previous paper,[10] crystalline powder of zinc ferrite was synthesized using ammonia near room temperature. It was formed in the temperature range 30–80°C via an intermeditate phase of so-called green-rust which contains both Fe^{2+}, Fe^{3+} and possibly Zn^{2+}. For this synthesis, the use of Fe^{2+} solution was essential. Only amorphous product was formed from Fe^{3+} solution because of no formation of the green-rust phase.

The development of the synthesis of ceramics at such a low temperature is believed to be important in relation to energy conservation because most ceramic materials have been prepared at high temperatures. In the present work, the synthesis of zinc ferrite powder was attempted using hydrazine monohydrate ($N_2H_4 \cdot H_2O$). The result was compared with a previous synthesis using ammonia in order to clarify the advantages and disadvantages of the present process.

2 Experimental

The experimental procedure is shown in Fig. 1, being almost the same as the one used previously,[10] except that hydrazine was used instead of ammonia. First, aqueous solutions of metal chlorides $FeCl_2$ and $ZnCl_2$ of reagent grade were prepared separately at a concentration of 5×10^{-2} mol dm^{-3}, and then mixed with each other to give a molar ratio of iron to zinc of 2. The flask containing this reaction solution was set in a temperature controlled water bath with a shaker. Hydrazine monohydrate of reagent grade diluted to a concentration of 4 mol dm^{-3} was added to the mixed solution of metal chlorides at a temperature ranging from 0 to 80°C. After aging of the solution for air oxidation and shaking at a constant speed, the precipitates were filtered, and washed with distilled water and acetone, followed by drying at room temperature.

In order to investigate the effect of the concentrations, metal chloride solutions in the range of 5×10^{-1}–5×10^{-3} mol dm^{-3} and hydrazine monohy-

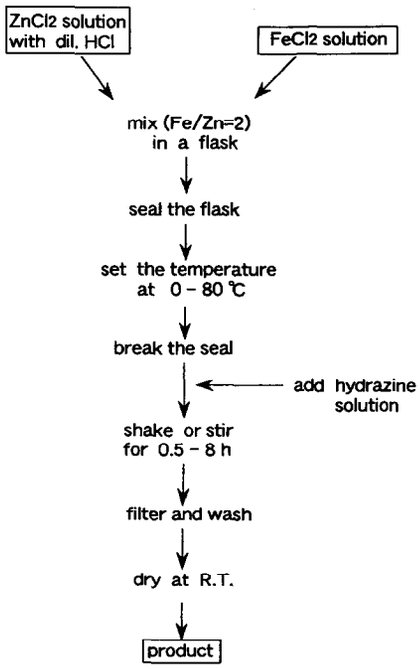


Fig. 1. Experimental procedure.

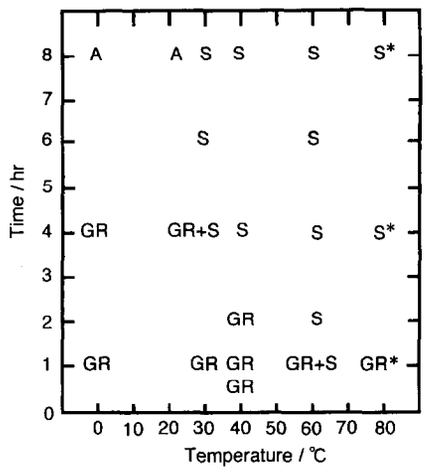


Fig. 2. Formation diagram of the phases as functions of temperature and time for aging. The symbol S stands for spinel-type $ZnFe_2O_4$, GR for green-rust and A for amorphous phase. S* and GR* indicate the coexistence of a small amount of unknown phase with S and GR, respectively. Metal chloride solutions of 5×10^{-2} mol dm^{-3} and hydrazine monohydrate solution of 4 mol dm^{-3} were used.

drate solution without dilution (20 mol dm^{-3}) were used. For the solution with high concentration, magnetic stirring was used in order to mix thick solutions.

The precipitates obtained were examined by X-ray diffraction (XRD) with Co Kα radiation, thermogravimetry coupled with differential thermal analysis (TG–DTA), infra-red spectrometry (IR) and atomic absorption spectrometry.

3 Results and Discussion

3.1 Formation of spinel phase of zinc ferrite

The phases formed in the mixed solutions of $FeCl_2$ and $ZnCl_2$ with a concentration of 5×10^{-2} mol dm^{-3} by adding hydrazine monohydrate solution with a concentration of 4 mol dm^{-3} are summarized in Fig. 2, as functions of temperature and time of aging. The resultant phases are green-rust, spinel and amorphous, as in the case where aqueous ammonia was used.[10]

At the beginning of aging, the green-rust phase is formed at all temperatures. Its XRD pattern gave broad peaks at 13·70° and 27·60° in 2θ (0·75 and 0·375 nm in d-spacing, respectively).

By further aging, the formation of zinc ferrite spinel was observed above 30°C. The line profiles of XRD patterns for the spinel phase are rather broad, as shown in Fig. 3. The crystallinity of the spinel phase was improved with increasing aging temperature. The half-maximum breadth of 311 lines for the products at 30 (Fig. 3(a)), 40 and 60°C (Fig. 3(b)) after 8 h of aging were 1·3°, 0·91° and 0·74° in 2θ, respectively. At 80°C, another phase which cannot be

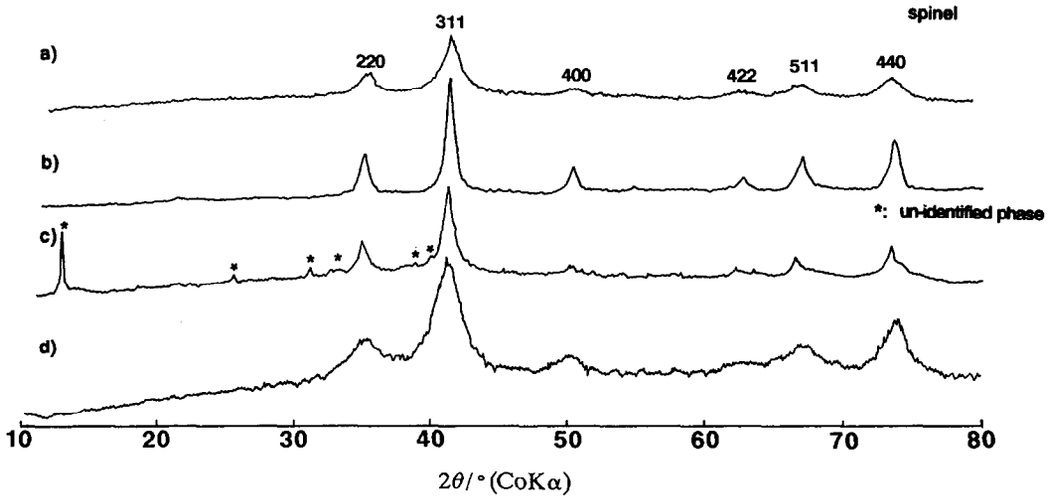


Fig. 3. X-ray powder patterns for the spinel phase synthesized from $FeCl_2$ solution at (a) 30°C, (b) 60°C, (c) 80°C and (d) that from $FeCl_3$ at 80°C.

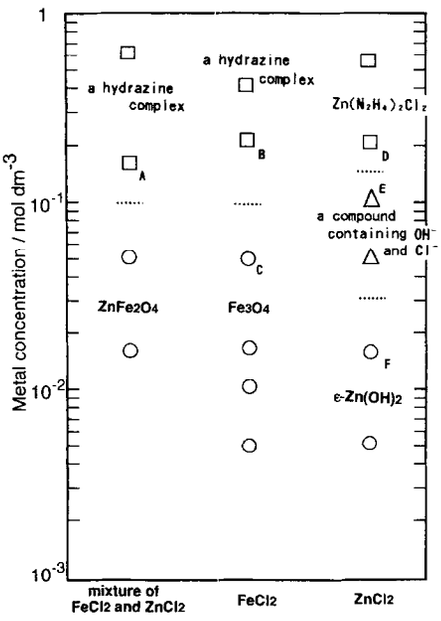


Fig. 4. The phases formed from the mixed solutions of $FeCl_2$ and $ZnCl_2$ (Fe/Zn = 2), $FeCl_2$ solutions and $ZnCl_2$ solutions with hydrazine monohydrate solution at 4 mol dm^{-3} by aging at 40°C for 4 h as a function of concentration of metal chloride solution.

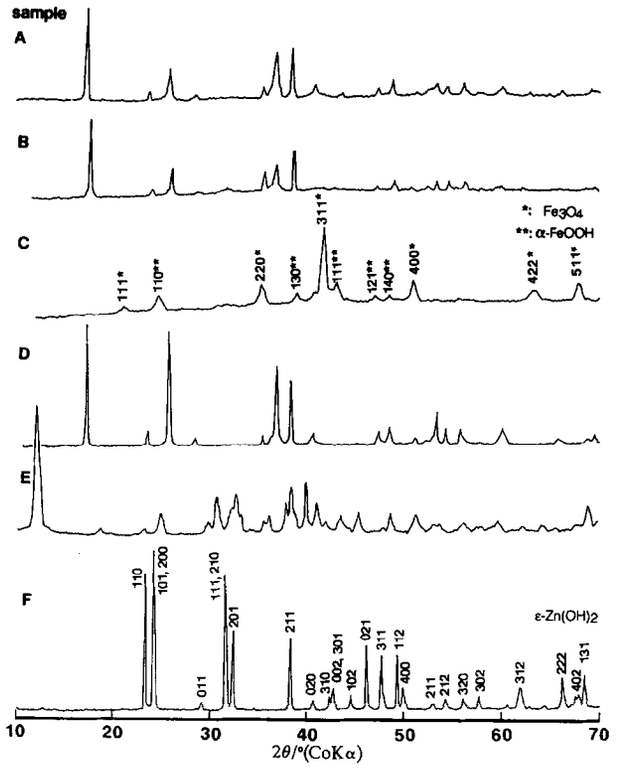


Fig. 5. X-ray powder patterns of the samples A to F of which the formation conditions are shown in Fig. 4.

identified from XRD powder patterns was formed in addition to the spinel phase (Fig. 3(c)). This seemed to be closely related to the fact that the evaporation of the reaction solution was remarkable at 80°C, suggesting that the concentration of metal ions and also anions were changed during aging, which brought considerable effect to the product phases. The relationship between the metal concentration of the solutions and products is discussed below.

The chemical analysis by atomic absorption spectrometry showed that the spinel obtained was zinc ferrite having the Fe/Zn ratio of 2·05–2·20.

Amorphous phase was formed by aging at 0°C for 8 h and it did not change to spinel phase without heating above 400°C.

3.2 Starting with $FeCl_3$

Starting with $FeCl_3$ solution, broad peaks of zinc ferrite appeared on XRD patterns by the reaction at 80°C (Fig. 3(d)). At 40°C, however, they were too broad to be detected. This result is a distinct difference from the previous one[10] where only amorphous phase was obtained by the addition of ammonia to the solution of $FeCl_3$. Using hydrazine, however, spinel phase was obtained even from $FeCl_3$ solution, probably because Fe^{2+} was produced by the strong reducing action by hydrazine.

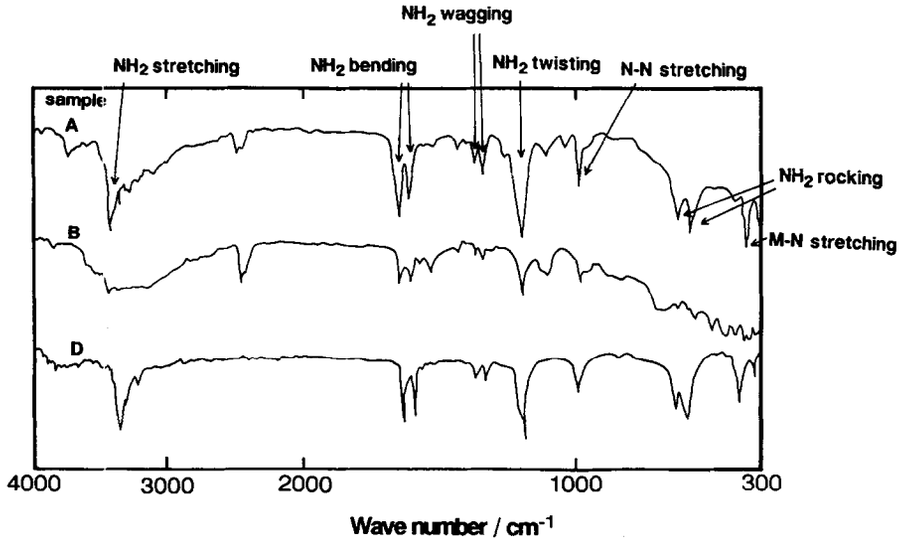


Fig. 6. IR spectra of samples A, B and D in Fig. 4.

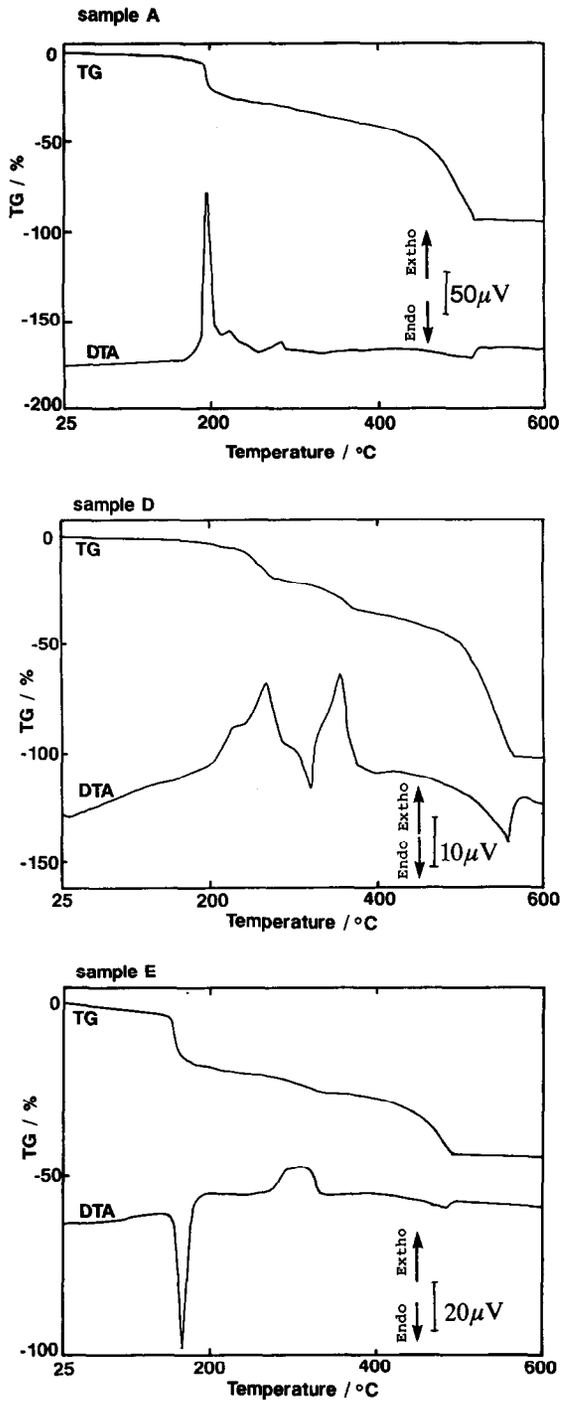


Fig. 7. TG-DTA curves for samples A, D and E in Fig. 4.

3.3 Effect of concentration

The relationship between the concentration of metal chloride solutions and the phases formed was investigated. The experimental results at 40°C after aging for 4 h are summarized as a function of metal chloride concentration in Fig. 4, by showing the concentration range for different phases which were deter mined from XRD, IR and TG–DTA studies.

It is clear that the products depend on the concentration of the starting solutions and that the borderlines are located around 1×10^{-1} mol dm^{-3} for the metal chloride solutions. Another line is present around 3×10^{-2} mol dm^{-3} for $ZnCl_2$ solution. The products shown by A to F in Fig. 4 were studied in detail in order to identify their phases.

The products formed in the solutions with low concentration are identified to be $ZnFe_2O_4$ (which has been described in Section 3.1), Fe_3O_4 (sample C) and ϵ-$Zn(OH)_2$ (sample F), respectively, from their XRD patterns (Fig. 5). The other products are not identified by XRD. Only sample D is considered to be a hydrazine complex because the d-spacings of diffraction peaks coincided with those reported for $Zn(N_2H_4)_2Cl_2$[7] though the relative intensities were different. In addition, samples A and B are also supposed to be complexes because the patterns obtained for samples A, B and D are all very similar.

For these products, IR and TG-DTA measurements were carried out and the results are shown in Figs 6 and 7, respectively.

Samples A, B and D give IR absorption peaks attributed to stretching, bending, wagging and twisting in the NH_2 group and stretching of N–N and metal–N bonds (Fig. 6), according to previous work.[6] These experimental results strongly suggest that they are the hydrazine complexes with respective metal chlorides. Characteristic sharp and strong exothermic peak, accompanying certain weight loss, observed in their TG–DTA curves also showed the existence of hydrazine in the products. TG–DTA curve of sample A is shown in Fig. 7. This exothermic peak has been considered to be due to the oxidation of liberated hydrazine to nitrogen oxides.[11] The result of sample B was very similar to that of sample A. Sample D in Fig. 7 shows slightly different behavior; the exothermic peaks are not so large and sharp. From this sample after heating above 550°C, nothing was left probably because the complexes released hydrazine to return to metal chloride which evaporated out above 500°C.

Sample E was not suggested to be a hydrazine complex, especially because of its IR spectrum which did not show any absorption peaks corresponding to the NH_2 group. On its TG–DTA curve (Fig. 7), a very strong endothermic peak, instead of an exothermic one on hydrazine complexes, is seen. This peak can be attributed to a dehydration reaction which had been observed in sample F. After heating up to 600°C, sample E gave ZnO powder, which was in contrast with sample D. As the common points among TG–DTA curves of samples D and E, a gradual weight loss above 400°C and an endothermic peak around 550°C are seen, suggesting the presence of $ZnCl_2$ component in sample E. These results suggest that the product E is the compound having both OH^- and Cl^-.

4 Concluding Remarks

Making use of a property of hydrazine as a base,

crystalline powder of zinc ferrite was obtained after aging at a temperature between 30 and 60°C though the crystallinity was rather inferior to that prepared in the same temperature range by using aqueous ammonia.[10] The concentration of starting metal chloride solutions was required to be below 1×10^{-1} mol dm^{-3} to prevent the formation of hydrazine complexes, which did not change to zinc ferrite either by aging or by heat treatment at high temperatures.

By using the strong reducing ability of hydrazine, zinc ferrite was obtained even starting with $FeCl_3$ solution, which was very advantageous compared to the use of aqueous ammonia.

Acknowledgement

This work was partly supported by a Sasagawa Scientific Research Grant from The Japan Science Society, Tokyo.

References

1. Franzen, H. & von Mayer, O., *Z. Anorg. Chem.*, **60** (1908) 247–91.
2. Aliev, R. Y., Guseinov, M. N., Kuliev, A. D. & Musaev, D. B., *Russ. J. Inorg. Chem.*, **8** (1973) 199–200.
3. Sacconi, L. & Sabatini, A., *J. Inorg. Nucl. Chem.*, **25** (1963) 1389–93.
4. Linke, K. H., Durholz, F. & Handicke, P., *Z. Anorg. Allg. Chemie.*, **356** (1968) 113–17.
5. Braibanti, A., Dallavalle, F., Pellinghelli, M. A. & Leporati, E., *Inorg. Chem.*, **7** (1968) 1430–3.
6. Tsuchiya, R., Yonemura, M., Uehara, A. & Kyuno, E., *Bull. Chem. Soc. Jpn.*, **47** (1974) 660–4.
7. Ferrari, A., Braibanti, A. & Bigliardi, G., *Acta Cryst.*, **16** (1963) 498–502.
8. Regazzoni, A. E., Urutia, G. A., Blesa, M. A. & Maroto, A. J. G., *J. Inorg. Nucl. Chem.*, **43** (1981) 1489–93.
9. Chen, C. J., Brindger, K., Winzer, S. R. & Paivernerker, V., *J. Appl. Phy.*, **63** (1988) 3786–8.
10. Ueda, M., Shimada, S. & Inagaki, M., *J. Mater. Chem.*, **3** (1993) 1199–201.
11. Cantero, M., Martinez-Lara, M., Bruque, S. & Moreno-Real, L., *Solid State Ionics*, **63–65** (1993) 501–5.

Journal of the European Ceramic Society **15** (1995) 271–281
© 1995 Elsevier Science Limited
Printed in Great Britain. All rights reserved
0955-2219/95/$9.50

Deformation and Strength of Engineering Ceramics and Single Crystals

G. A. Gogotsi & D. Yu. Ostrovoy

Institute for Problems of Strength, National Academy of Sciences of Ukraine, 2 Timiryazevskaya str., Kiev 252014, Ukraine

(Received 12 November 1993; revised version received 29 June 1994; accepted 9 August 1994)

Abstract

A comparative investigation has been performed of the laws of deformation and strength of engineering silicon nitride-, alumina, and zirconia-based ceramics, as well as zirconia crystals. The specimens were tested in four-point bending in air over a temperature range from ambient to 1400°C. The materials' mechanical behaviour was analyzed by load versus deflection diagrams (deformation diagrams). It has been found that above the brittle-to-ductile transition temperature, T_{BD}, for the ceramics studied it is possible to choose such combinations of temperature and deformation rate, which would ensure the same path of deformation diagrams, i.e. equivalent influence of those two parameters on the mechanical behaviour of ceramics is observed. The mechanism of inelastic deformation of the ceramics studied is shown to be associated with the development of two processes: viscous flow of the grain boundary phase and crack propagation to a critical size, with one of them prevailing at different load levels. In contrast to ceramics, the strength of zirconia crystals remained practically unchanged (partially-stabilized crystals) up to 1400°C or even increased (fully-stabilized crystals). For all the crystals, static elasticity moduli were independent of the number of repeated-static loading cycles at high temperatures (their values remained constant), while for ceramics a reduction was observed. Partially-stabilized zirconia crystals, as compared to other investigated materials, exhibited practically no creep up to 1400°C at loads close to limiting ones. This allows them to be considered as a promising engineering material for high-temperature application.

1 Introduction

Along with extensive investigations of engineering ceramics and their application in industry, nowadays researchers pay much attention to finding possibilities for practical application of such promising refractory materials as zirconia crystals.[1] According to some preliminary estimates[2–5] in a high-temperature loading region they can compete not only with metals but also with ceramics. One of the reasons restricting the introduction of these materials in many areas of engineering is insufficient understanding of specific features of their mechanical behaviour at high temperatures. This is associated with the fact that most studies, e.g. of zirconia crystals, are concerned with physical aspects of their deformation and fracture[6–15] and the data on their strength and fracture toughness which appear in some publications[2,4,16,17] are insufficient for the correct evaluation of their performance from the criteria used in practical engineering. This situation with both ceramics and single crystals can be explained by the use of different test methods that result in inconsistency of the results obtained. In this case, for instance, strength characteristics of such materials determined in the high-temperature region by the known standards[18] at one constant loading or deformation rate turn out to be insufficient for revealing a complete picture of their actual mechanical behaviour. This conclusion is strongly confirmed by the fact[19] known for conventional structural materials (metals, polymers), according to which appreciable changes occur in the conditions of reaching the ultimate state by them due to simultaneous temperature and loading or deformation rate variation. In this case the probability of their brittle fracture even at the temperature of viscous (plastic) flow[20] may increase. The data on this problem for ceramics[22–25] and single crystals[2,8,21] are not only limited but in most cases[21,23,25] they do not take into account such an important characteristic of the materials as their deformability. For this reason such results tell us little of possible performance of these materials under real service conditions. To eliminate this gap the present work was performed where attention was paid to the investigation of the laws of deformation and strength of zirconia crystals at different temperatures and deformation rates as compared with the

Table 1. Physico-mechanical characteristics of investigated ceramics and crystals at ambient temperature (average values)

Material (orientation of the specimen axis)	*Density (g/cm^3)*	*Ultrasonic velocity (m/s)*	*Elastic modulus (GPa)*		*Bending strength (MOR)[a] (MPa)*	*Ultimate strain[a] ($\times 10^{-4}$ m/m)*
			Dynamic	*Static[a]*		
Ceramics						
SN-1	3·21	9289	277	280	465	16·6
SN-2a	3·27	9690	307	305	510	16·7
A-1	3·70	9347	323	320	300	9·4
Y-PSZ-3	5·94	5951	210	207	908	44·0
Crystals						
Y-FSZC-10 (<101>)	5·87	5933	207	180	134	7·4
Y-FSZC-20 (<101>)	5·76	6116	215	185	140	7·6
Y-PSZC-3 (<111>)	6·04	5394	176	149	642	43·0

[a]Obtained at V_{ch} = 0·5 mm/min.

behaviour of the most widely spread types of engineering ceramics (silicon nitride, alumina, zirconia) under similar loading conditions.

2 Materials and Experimental Procedure

The materials investigated were silicon nitride-, alumina-, and zirconia-based ceramics and zirconia crystals (Table 1).

A silicon nitride-based ceramic, SN-1,[26] with an addition in the initial state of 5% Y_2O_3 and 2% Al_2O_3 was produced by hot-pressing in graphite moulds (the sintering temperature was 1750°C, pressure 50 MPa). Its main components were β-Si_3N_4 and a grain boundary phase. The latter consisted of the amorphous phase containing Si, N, Al, Y, O and yttrium oxynitrides. The SN-1 structure was a mixture of equiaxial and elongated grains of β-Si_3N_4. The average size of those grains was 3–5 μm. A silicon nitride-based ceramic, SN-2,[26] was obtained from powders: 82% Si, 2·5% Al_2O_3 and R_2O_3 (a mixture of rare-earth element oxides: 64% Nd_2O_3, 17% Pr_2O_3, 14% La_2O_3 and 1% Sm_2O_3) by the method of reaction bonding (nitriding in an atmosphere of N_2 + H_2 at 1380°C). Then it was sintered under pressure of 50 MPa at 1850°C in an atmosphere of N_2. This ceramic consisted mostly of β-Si_3N_4 and of the grain boundary phase. By varying the quantity of R_2O_3 three compositions of this ceramic were obtained: SN-2a, SN-2b and SN-2c with the content of the amorphous phase 8·5, 10·6 and 13·5%, respectively. In its structure SN-2 ceramic was close to SN-1. The cross dimension and the length of elongated grains β-Si_3N_4 of this ceramic were, on the average, 0·5 and 4 μm, respectively.

An alumina-based ceramic, A-1,[26] with an addition of MgO was produced by semi-dry pressing at a pressure of 200 MPa and sintered in air at 1600°C. Its grain size averaged between 4 μm and 5 μm.

Zirconia-based materials contained different quantities of stabilizing additive Y_2O_3. Thus Y-PSZ-3 ceramic with 3 mol% of Y_2O_3 was hot-pressed at 1750°C in an atmosphere of N_2. It contained a minute quantity of Al_2O_3. Its average grain size was less than 1 μm. Crystals[3,27] were grown by a skull melting technique using direct high-frequency heating. Their growth rate was 10 mm/h. They were then cooled down from the temperature of their crystallization at a rate of 10°C/min. The crystals contained 3(Y-PSZC-3), 10(Y-FSZC-10) and 20(Y-FSZC-20) mol% of Y_2O_3. The first of them were partially stabilized, the rest were fully stabilized. In accordance with the classification,[28] all the materials chosen for the investigation were brittle (i.e. deforming linearly-elastically at ambient temperature).

The tests in the temperature range from ambient to 1400°C were performed in air using the loading module (Fig. l) designed and manufactured for the purpose and mounted on a conventional testing machine. The test method has been evaluated elsewhere,[5,28] The test specimens were beams 3·5 × 5·0 × 50·0 mm in size cut from billets by a diamond tool and then ground along the longitudinal axis. Their sharp edges were bevelled. Crystallographic orientation of the crystal specimen longitudinal axes was defined by the Laue back-reflection X-ray technique. Prior to mechanical testing, dynamic elasticity moduli E_d were determined from measurements of the ultrasonic vibration propagation velocity along the specimen longitudinal axis.

The specimens were loaded in four-point bending under isothermal conditions with the testing machine cross-head speed, V_{ch} from 0·005 to 5·0 mm/min. As most often happens in these investi-

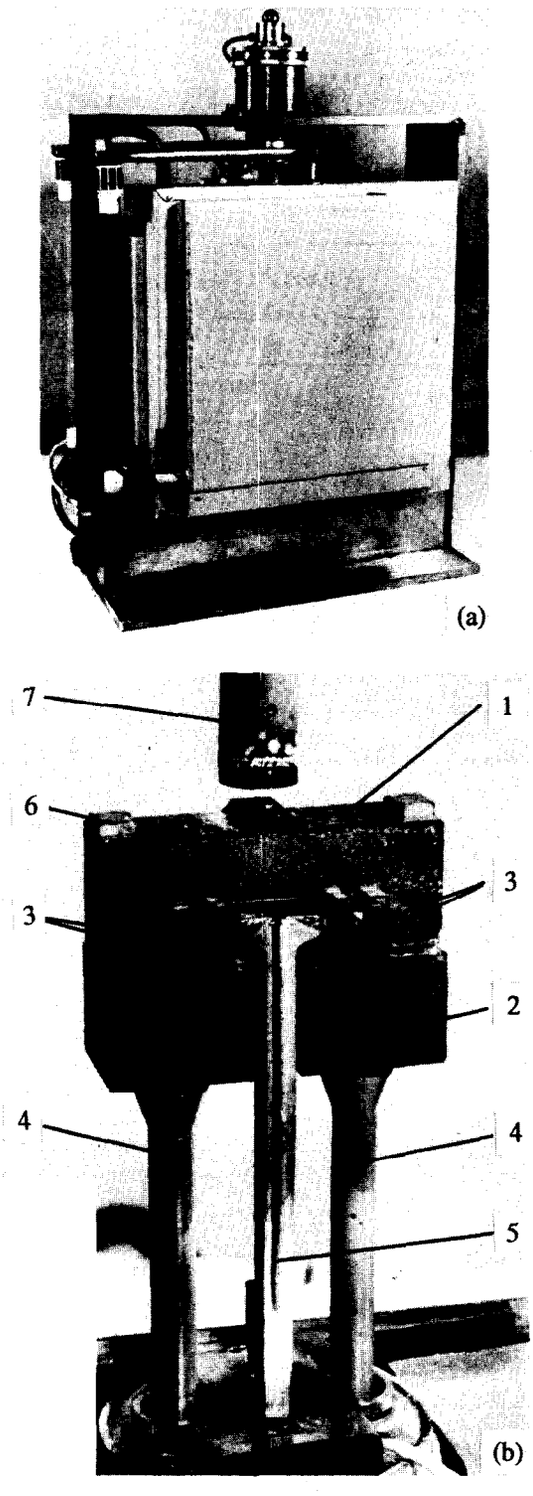


Fig. 1. General view of (a) the loading module and (b) the loading arrangement. (1) Upper prism, (2) lower prism, (3) swing roller support, (4) supporting column, (5) bending deflection measurer, (6) slide-way, (7) loading rod.

gations (Fig. 2), the cross-head speed V_{ch} equal to 0·5 mm/min was chosen as the main one. It is convenient because the time to specimen fracture in testing is less than 1 min. The distance between the inner and outer swing roller supports was 20 and 40 mm, respectively. A special feature of the experimental procedure used was recording 'applied load–specimen deflection' dependences (the deformation diagrams) using a deflection measuring

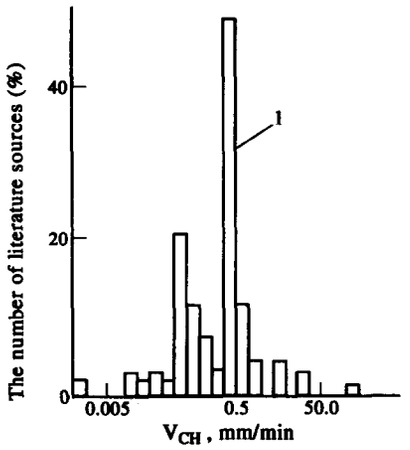


Fig. 2. Histogram of the testing machine cross-head speeds, V_{ch} (from the data from 175 literature sources): (1) the main speed.

gauge (LVDT)[29] which was hung on the specimen (5 in Fig. 1) and was in no way connected to the testing machine. In this way the influence of deformation of the loading device parts was excluded from the measurements, unlike conventional determination of specimen deflection by the testing machine cross-head displacement or by the measuring gauge connected with the testing arrangement.

Mechanical characteristics were calculated by the known relationships of applied mechanics (linear-elastic approximation), i.e. strength, for instance, was characterized by the magnitude of the modulus of rupture (MOR = $2aP/bh^2$, where P is the load, α is the length of the cantilever part of the specimen, b and h are the specimen width and height, respectively). This approach proved to be acceptable since the present work involved a comparative analysis of the mechanical behaviour of ceramics and crystals rather than precise determination of their strength characteristics. At the same time, the known Nadai formula ($\sigma = 2a/bh^2 \times (P + \delta/2 \cdot dP.d\delta)$, where σ is the mean stress in the specimen, δ is the specimen deflection) used earlier by us[3,29] and other investigators[22] turned out to be unacceptable here, since the deformation diagrams of the specimens (see below) had not only ascending but also extensive horizontal portions.

3 Results

The main investigations were performed at temperatures above some critical temperature for each of the materials at which their deformation diagrams exhibited nonlinearity, associated with the intensification of creep. At the same time, the dependence of the mechanical properties of these materials on time or strain rate was observed. The latter was defined by the cross-head speed, V_{ch}.

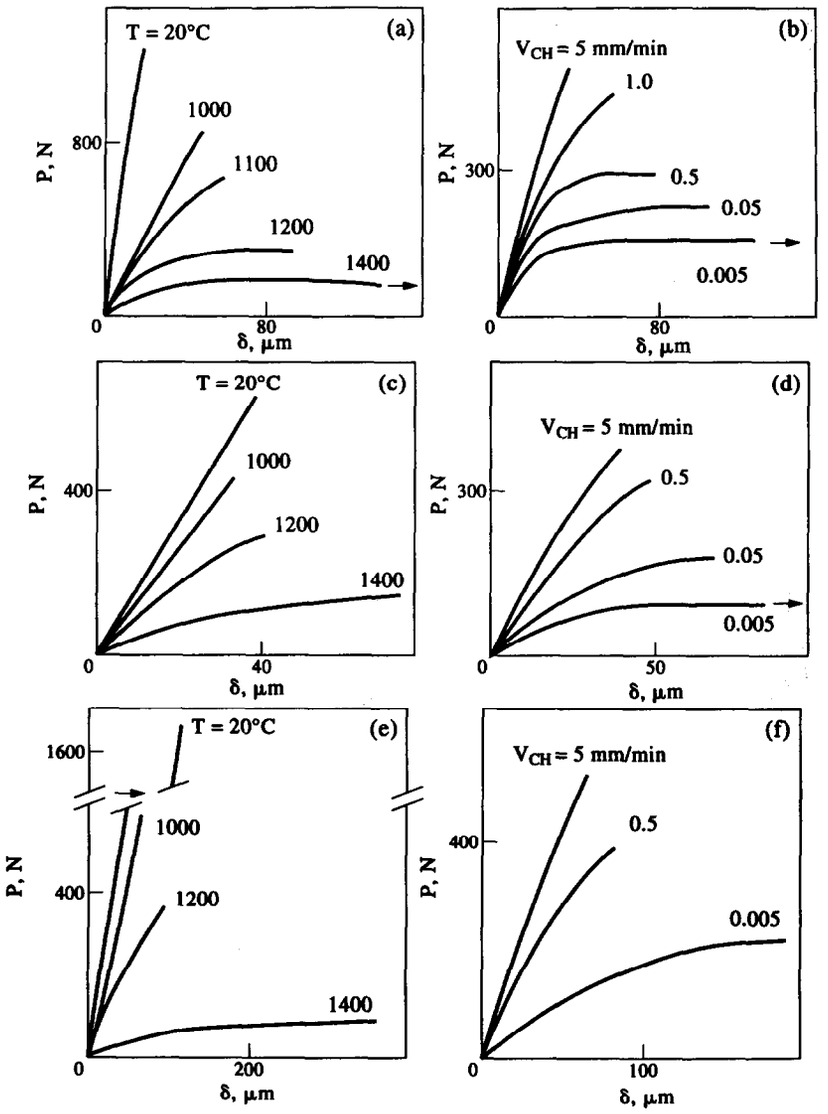


Fig. 3. The influence of the temperature, T (a,c,e) at V_{ch} = 0·5 mm/min and of the speed V_{ch} (b,d,f) at T = 1200°C on the appearance of the load (P) versus deflection (δ) diagrams: (a,b) SN-1; (c,d) A-1; (e,f) Y-PSZ-3.

This critical temperature is often called brittle-to-ductile transition temperature, T_{BD},[22,23] by analogy with the respective transition in steels. Note that the T_{BD} value is not a material constant: it depends on the strain rate, the size of the specimens, their structure, etc. In the present work, T_{BD} was determined by the deviation from linearity of the deformation diagrams for the same specimens of the materials studied, recorded while the temperature was increasing gradually and at a cross-head speed of 0·5 mm/min. For SN-1, SN-2 and A-1 ceramics the T_{BD} value was about 1100–1150°C and for Y-PSZ-3 it was about 1050°C. For zirconia crystals T_{BD} was in the range 1000–1100°C, whereas it was 500–600°C when the latter were loaded by the Vickers indenter.[30]

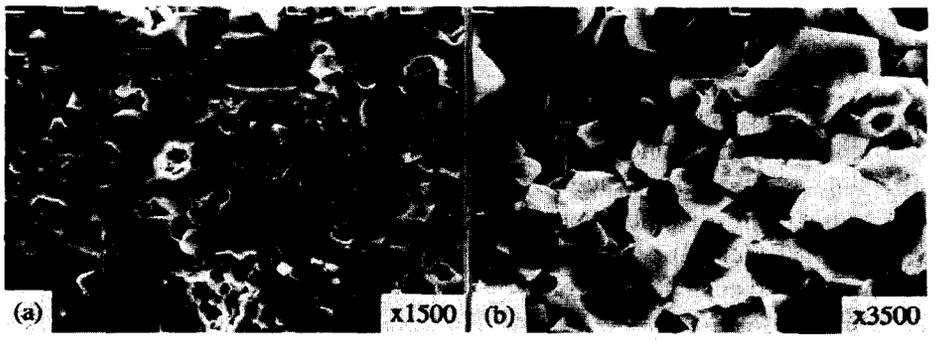


Fig. 4. Photographs of fracture surface fragments of A-1 specimens tested at T = 1200°C and (a) V_{ch} = 5·0 and (b) V_{ch} = 0·005 mm/min.

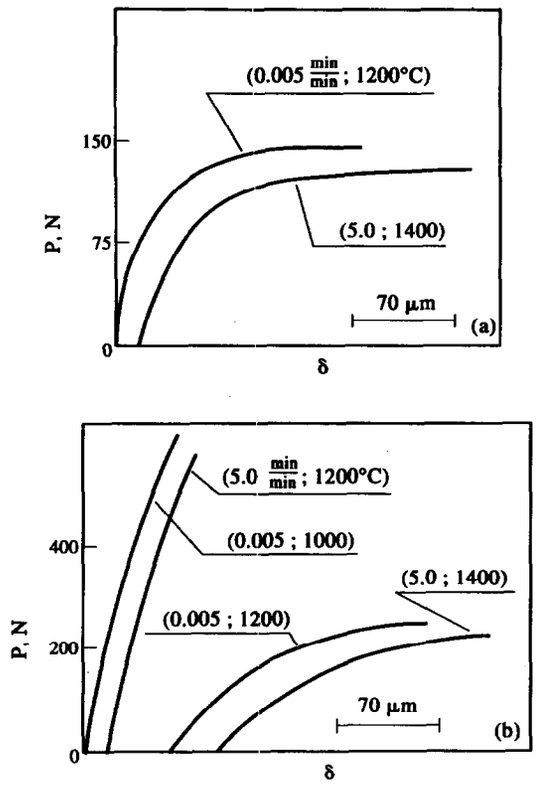


Fig. 5. Load (P) versus deflection (δ) diagrams for (a) SN-1 and (b) Y-PSZ-3 under different conditions of deformation (V_{ch} in mm/min; T in °C).

Check tests of ceramics at temperatures below T_{BD} revealed that, irrespective of the combination of temperature and cross-head speed, it exhibited linearly-elastic deformation and brittle fracture thus confirming the results obtained earlier.[22–24] In particular, the cross-head speed affected the strength of only alumina-based ceramics A-1. Such an influence is generally evaluated by the magnitude of the power parameter N in the equation[25] for the crack growth rate (V) in a corrosion-active environment: $V = M \cdot K_I^N$, where M is a parameter, K_I is the stress intensity factor at the crack tip. The higher the value of N, the greater the material resistance to the subcritical crack growth. The value of N was determined from the equation $\sigma_1/\sigma_2 = (V_{ch_1}/V_{ch_2})^{1/N+1}$, where σ_1 and σ_2 are fracture stresses (MOR) at speeds V_{ch_1} and V_{ch_2}, respectively, which was obtained from analytical relationships proposed elsewhere.[25] In the case for A-1 the magnitude of N was 20, whereas for the test of ceramic materials it exceeded 100. It should be noted that the above N values for ceramics remained almost unchanged up to the T_{BD} temperature, above which their reduction was observed.

The deformation diagrams obtained for ceramics at temperatures above T_{BD} revealed that irrespective of the production technology (see the test results for other similar materials[27,29]) their mechanical behaviour at increasing temperature, T, and constant V_{ch} (Fig. 3(a),(c),(e)) is similar to that at decreasing V_{ch} and constant T (Fig. 3(b),(d),(f)). In addition, at a certain combination of the temperature and speed, the ceramics exhibited (see Fig. 3) a transition from totally inelastic to linearly-elastic deformation and brittle fracture even at the temperatures of probable material creep. This was also evidenced by specific features of ceramic specimen fracture surfaces, where (e.g. material A-1) the transition from primarily intercrystalline (Fig. 4(b)) to mostly transcrystalline (Fig. 4(a)) crack propagation was observed with an increase in V_{ch}. This fact was also noted by other investigators.[31]

These data allow us to say that, at least in the temperature and V_{ch} ranges used, an equivalence of the influence of these two parameters on the resistance of ceramics to deformation took place, since different pairs of deformation conditions were selected (V_{chi}, T_i). This ensured similar paths of the deformation diagrams within the scatter band of the experimental data, as is shown, for instance, in Fig. 5 for SN-1 and Y-PSZ-3 materials. It should be noted that these equivalent conditions of deformation also result in similar features of micro- and macrofractures of specimens of the given ceramics.

An interesting feature of the ceramic behaviour also reported elsewhere[22] was the appearance of characteristic horizontal portions (Fig. 3) on the deformation diagrams at temperatures above T_{BD} and at low V_{ch} values, where the increase in the specimen deformation occurred at almost constant applied load. To find out the reasons for the appearance of such portions, as an example, a detailed investigation was carried out on SN-1 specimens only, since the behaviour of all the ceramics was similar. After testing, a lot of cracks (Fig. 6(a)) appeared on the specimen surface at the sites of action of the maximum tensile stresses σ_t. Their faces were mostly orthogonal to the direction of those stresses. On fracture surfaces there were ridged regions (Fig. 6(b)) corresponding to those cracks and their size grew with both a decrease in V_{ch} at constant temperature, and with an increase in temperature at constant V_{ch}. At sufficiently low temperature (below T_{BD}) and at high V_{ch} these regions on fracture surfaces were almost indistinguishable with a conventional optical microscope. We should note that all the observations for SN-1 materials were also true of A-1. With Y-PSZ-3 materials the size of these regions, as well as that of the cracks (Fig. 6(c)) was appreciably smaller than with other ceramics investigated under the same loading conditions (V_{chi}, T_i) (Fig. 5).

For this reason it could be expected that those cracks affected appreciably the mechanical properties at high temperatures. For SN-1 materials this influence was observed under repeated-static load-

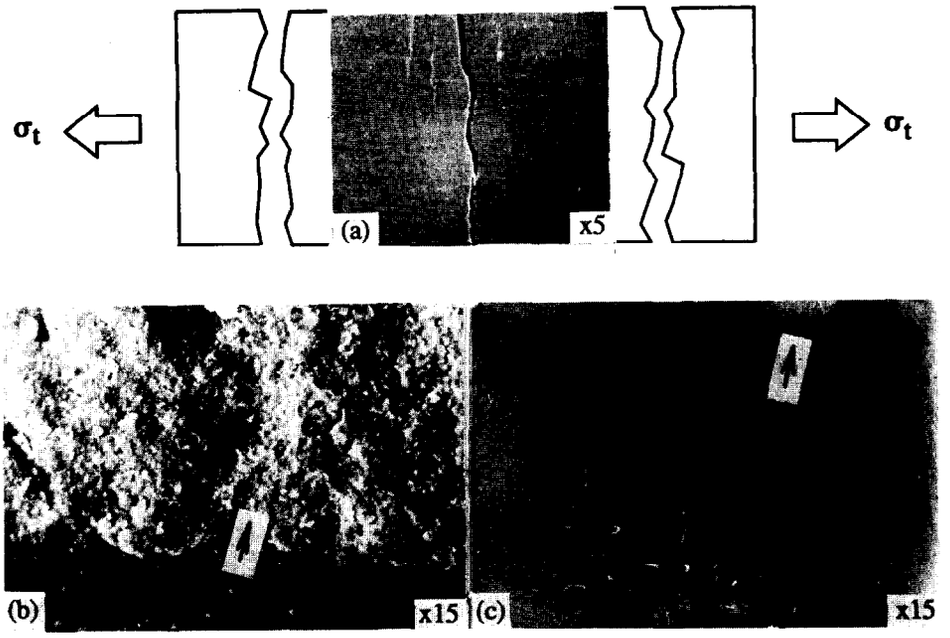


Fig. 6. Photographs of (a) tensile and (b) fracture surface of SN-1 and (c) fracture surface of Y-PSZ-3 specimens tested at T = 1200°C and V_{ch} = 0·005 mm/min. Arrows (b,c) show surface roughness.

ing (Fig. 7(a)) and in creep tests (Fig. 8(a)). Under such loading conditions the process of crack growth was strongly intensified each time when the applied load reached the magnitudes corresponding to the horizontal portions on the deformation diagrams. For this ceramic with each loading cycle the slopes (α) of the lines tangent to the diagram (Fig. 7(a)) at the origin of the coordinates decreased. The slope of the diagram is related to the elasticity modulus, E, by a simple expression $tg\alpha = Eb/2(h/a)^3 M_p/M_\delta$, where M_p and M_δ are the scales of the plot in Fig. 7(a) along the axes 'p' and 'δ', respectively. See above for other designations. The creep stage associated with such crack formation and culminating in fracture manifested itself more distinctly (Fig. 8(a)) only at loads close to the limiting ones on the deformation diagrams. At the same time, the Y-PSZ-3 material exhibited no noticeable reduction of static elasticity modulus (Fig. 7(b)) under repeated-static loading, and in creep testing no creep stage (Fig. 8(b)) characteristic of the crack propagation in SN-1 was observed due to consider-

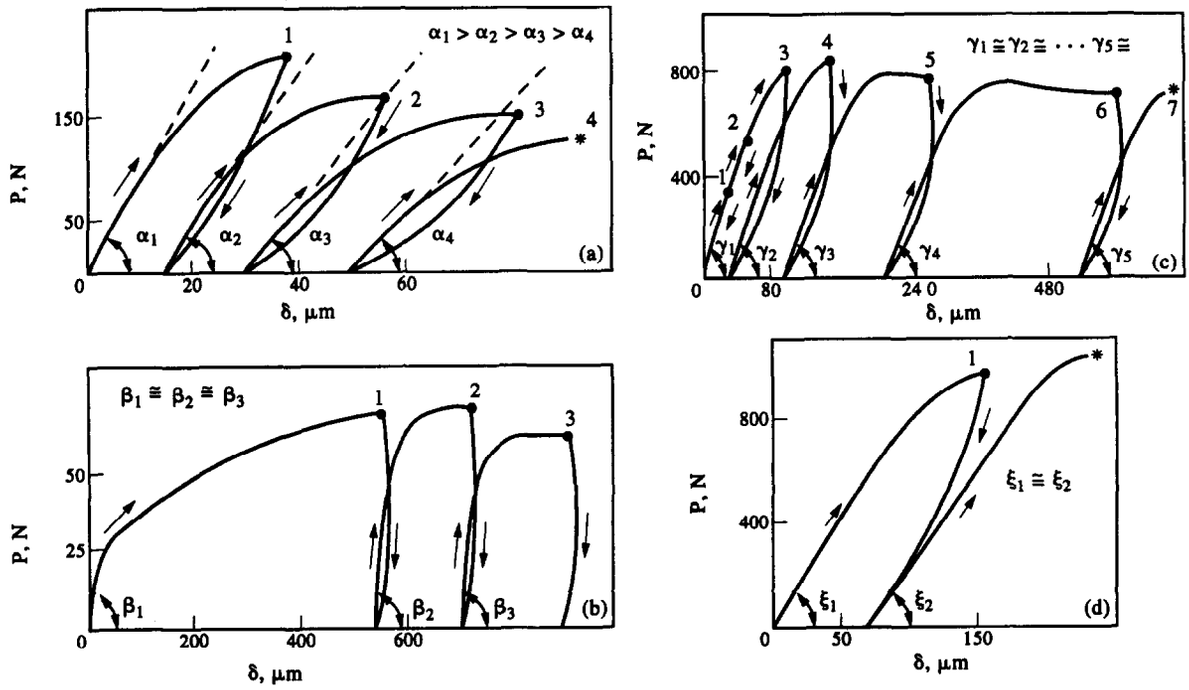


Fig. 7. Unloading and repeated loading diagrams for (a) SN-1 at V_{ch} = 0·05 mm/min and 1200°C; (b) Y-PSZ-3 at 0·5 mm/min and 1300°C; (c) Y-FSZC-10 at 0·5 mm/min and 1400°C; (d) Y-PSZC-3 at 0·005 mm/min and 1400°C. The number of repeated static load applications (1–7), the beginning of unloading (●), specimen fracture (*).

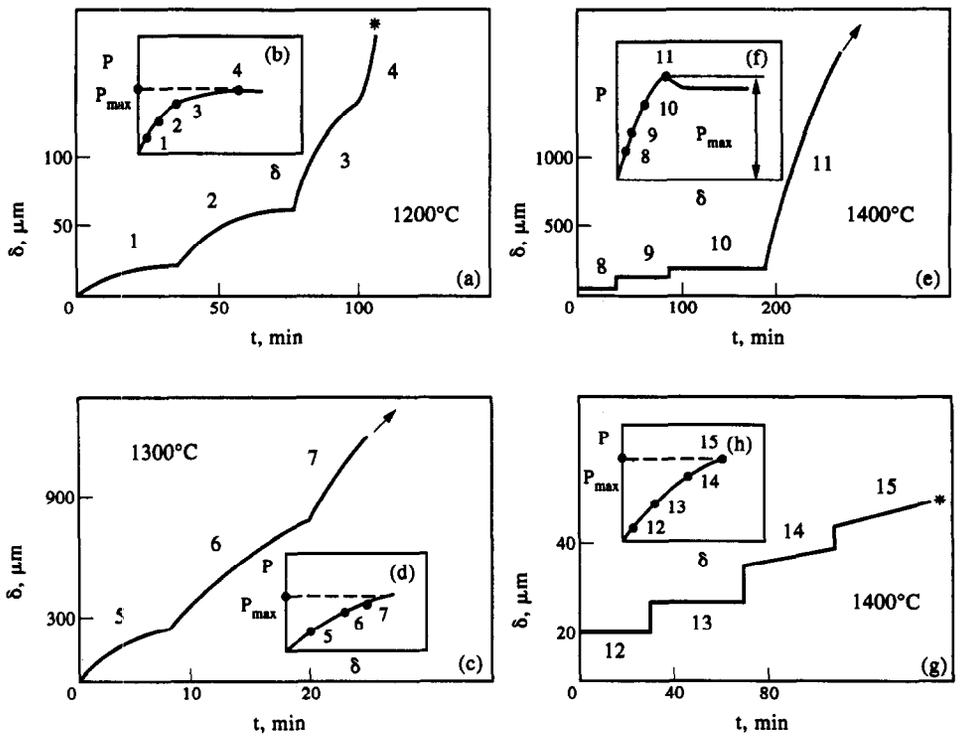


Fig. 8. Creep curves for (a) SN-1, (c) Y-PSZ-3, (e) Y-FSZC-10 and (g) Y-PSZC-3 at P = const. P_{max} = 200 (b,d), 600 (f) and 900 (h) N: 30 (1,5,8,12), 50 (2,6,9,13), 70 (3,7,10,14) and 100 (4,11,15) $\%P_{max}$. Specimen fracture (*).

able residual deformation of specimens which does not result in their fracture. Thus, crack propagation was probably one of the reasons for the increase in nonlinearity of the ceramics deformation diagrams, though with Y-PSZ-3 material, where the crack growth is less pronounced, such behaviour could be induced for other reasons as well.

Nonlinearity of the deformation diagrams and crack propagation could also occur in ceramics at high (above T_{BD}) temperatures as a result of softening of its grain boundary phase which has a lower melting temperature than the basic material. In order to confirm this an evaluation (Fig. 9) was made of the influence of the quantity of glass

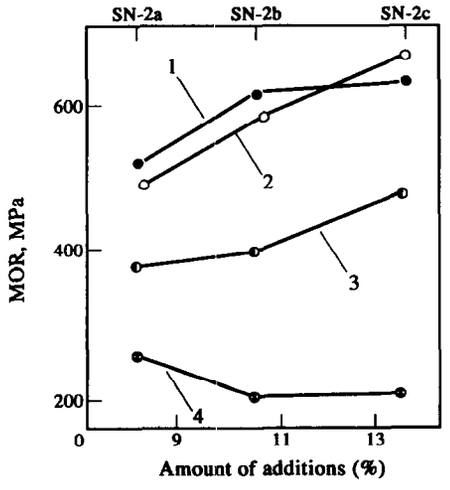


Fig. 9. The influence of the quantity of additives on the MOR (1–4) for SN-2: T = 20°C (1,2), 1200°C (3,4). V_{ch} = 0·5 (1,3) and 0·005 (2,4) mm/min.

phase upon the mechanical behaviour of the SN-2 material which is similar in its properties to SN-1 but contains different quantities of amorphous additives (composition SN-2a, S-2b and SN-2c). It was found that with such combination of the temperature and speed, which provides a near linear-elastic deformation of the SN-2 material (Fig. 10(a)), an increase in the quantity of additives resulted in the increase in its strength (1–3, in Fig. 9), while at inelastic deformation it caused a decrease in strength (4 in Fig. 9), intensification of creep (Fig. 10(b)), enhancement of the crack growth process and an increase in nonlinearity (Fig. 10(a)) of the deformation diagrams.

Zirconia crystals were studied at minimal (ambient) and maximal (1400°C) test temperatures. At ambient temperature all crystals (similarly to the ceramics studied) exhibited linear-elastic deformation (1 in Fig. 11(a) for Y-FSZC-10). At 1400°C Y-FSZC crystal exhibited an increase in strength as compared to that at ambient temperature (Table 2) at all the speeds used in the experiment (see also Refs 2 and 3).

At 1400°C, when Y-FSZC-10 crystals were tested at high V_{ch}, their deformation diagrams were linear, similar to those at ambient temperature (2 in Fig. 11(a)). At V_{ch} = 0·5 mm/min their diagrams showed horizontal portions (3 in Fig. 11(a)), at $V_{ch} \leq 0{\cdot}05$ mm/min well-pronounced upper and lower yield points were observed (4, 5 in Fig. 11(a)). Note that similar deformation behaviour at 1400°C was observed for Y-FSZC-20 crystals as

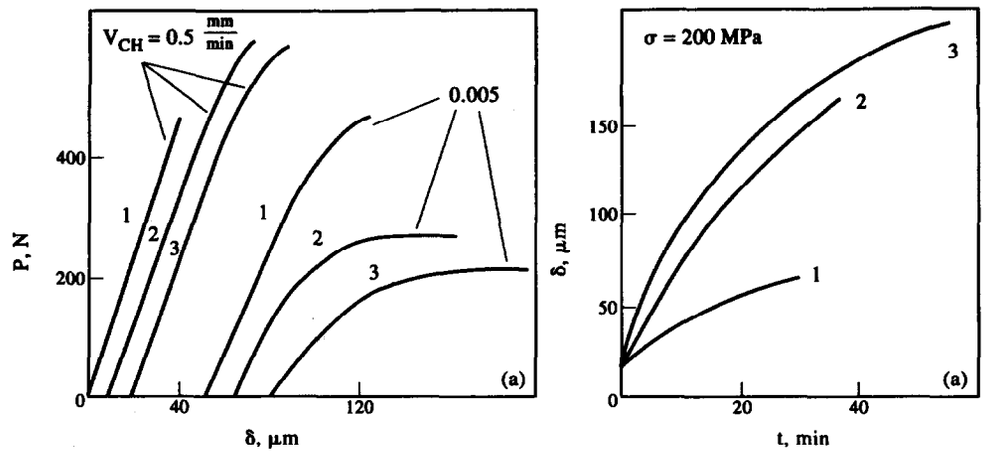


Fig. 10. The influence of the quantity of additives on (a) the load (P) versus deflection (δ) diagrams and (b) creep curves at T = 1200°C for: SN-2a (1), SN-2b (2), SN-3c (3).

well. However, the diagrams of the latter were already linear at V_{ch} = 0·5 mm/min and the ratio of the upper and lower yield points increased almost twice at V_{ch} = 0·005 mm/min as compared to those shown in Fig. 11(a). An interesting observation is that the appearance of the upper and lower yield points for all Y-FSZC crystals was preceded by characteristic maximum in strength (see 3 in Fig. 11(a)).

Y-FSZC crystal samples tested at 1400°C and at speeds equal to or above 0·5 mm/min fractured into many pieces both transverse to and along their axis (see Ref. 27 for details). In contrast, specimens tested at lower speeds (0·05 and 0·005 mm/min) were curved strongly without fracturing, the fact being also noted for similar materials.[2]

With partially stabilized Y-PSZC-3 crystals, whose strength remained practically unchanged (Table 2) up to 1400°C, there were practically no inelastic strains (Fig. 11(b)) and they appeared only at the loads close to the limiting ones irrespective of the temperature and speed regimes. In fracture the specimens of these crystals separated generally into several parts, yet no traces of residual strains were observed in them even at V_{ch} = 0·005 mm/min. We should note that ceramic specimens at all the loading regimes used fractured with only one propagating crack (Fig. 6(a)) though at high temperatures very many nuclei of other cracks could be observed next to it.

4 Discussion

The data presented above may be an indication of a noticeable difference in specific features of the mechanical behaviour of the ceramics and zirconia single crystals investigated.

A specific feature of the ceramic behaviour (as was also noted in Refs 32 and 33) is the deterioration of its strength characteristics at temperatures above T_{BD}. As has been confirmed by the results of the present investigation, this is to a great extent associated with the crack propagation in ceramics (see Fig. 6) In oxygen-free materials such defects can also originate due to oxidation.[34] The development of these defects changes appreciably the inelastic behaviour of ceramics whose specific feature is the presence of extensive horizontal portions (Fig. 3) on the deformation diagrams

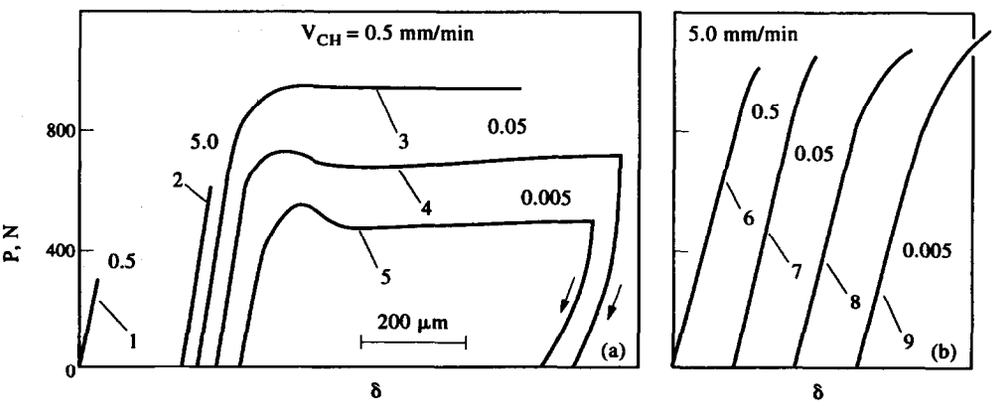


Fig. 11. Load (P) versus deflection (δ) diagrams for (a) Y-FSZC-10 and (b) Y-PSZC-3 at V_{ch} = var.: T = 20°C (1) and 1400°C (2–9). Arrows show specimen unloading.

Table 2. Average values of mechanical characteristics of investigated crystals at 1400°C

Material	V_{ch} *(mm/min)*	*Elastic limit (MPa)*	*Upper yield point*[a] *(MPa)*	*Lower yield point (MPa)*	*Strain at elastic limit* ($\times 10^{-4}$ *m/m)*	*Strain*[a] *at upper yield point (MPa)*	*Elastic modulus (GPa)*
Y-FSZC-10	5·0	274	—	—	17·5	—	157
	0·5	327	445	445	23·2	51·5	141
	0·05	269	338	318	18·7	32·2	144
	0·005	210	250	234	16·9	28·4	124
Y-FSZC-20	5·0	213	—	—	15·3	—	140
	0·5	300	—	—	21·6	—	139
	0·005	276	324	295	23·2	35·7	119
Y-PSZC-3	5·0	393	444	—	31·2	37·5	126
	0·5	403	475	—	33·0	42·5	122
	0·05	400	550	—	32·8	75·2	122
	0·005	390	556	—	35·8	74·4	109

[a]For Y-PSZC-3 crystals — ultimate stress and strain values.

recorded at a constant speed, corresponding approximately to the load (or stress) which induces a continuous increase in the strain rate at the final stage of creep (Fig. 8(a)), while, for instance in metals this effect is often associated[35] with steady-state creep stage where, as is known, the strain rate is constant.

Thus, the data obtained reveal that the general mechanism of ceramic inelastic deformation, at least for the silicon nitride- and alumina-based materials studied in this investigation, can consist of two simultaneous and competing effects: softening and viscous flow of the grain boundary phase (which has been emphasized in a number of investigations[36–38]) and the growth of cracks up to their critical size. In this case the first effect prevails at low load levels and the second becomes appreciable with the load reaching its limiting value, as can be seen in Fig. 8 from the transition, at stepwise load increase, from the stage of transient creep to that associated with cracking. If we consider zirconia-based materials, for Y-PSZ-3 ceramics the results obtained (Figs 7(b) and 8(c)) point to the existence of most likely one and the same mechanism of deformation (creep) which is not connected with noticeable upsetting of the material continuity.

For fully stabilized (cubic) zirconia crystals Y-FSZC a noticeable increase in their strength with temperature is a distinguishing feature in their behaviour compared to ceramics. One of the causes of this strength enhancement can be the annealing of specimens in the course of testing and the resulting reduction of the degree of their surface damage caused by machining. Indirect evidence for the above assumption is the fact that the ambient temperature testing of specimens annealed at 1400°C yielded the following results: the strength of specimens which were not annealed was 135 and 145 MPa and that of annealed ones 170 and 215 MPa for Y-FSZC-10 and Y-FSZC-20, respectively. A similar conclusion was also made elsewhere.[2]

An increase in the difference between the upper and lower yield points of Y-FSZC-20 crystals is probably associated with the formation of a more ordered solid solution ZrO_2–Y_2O_3[6,8] with an increase in the content of Y_2O_3 from 10 to 20%, while the appearance of two yield points in such crystals is related by some authors[6,8,11] to the involvement of additional slip systems in their deformation process. This can be evidenced by a noticeable intensification of creep in Y-FSZC crystals (Fig. 8(c)) only when the load reaches the upper yield point, whereas in ceramics it was registered at practically all load levels.

The maximum in the Y-FSZC crystal strength prior to the appearance of the upper and lower yield points has not been explained adequately in the present paper, though the effect of strength increase prior to the appearance of plasticity or creep is also known for ceramics.[23]

The deformation diagrams of Y-FSZC and Y-PSZC-3 crystals at all temperature and speed combinations used in the experiment exhibit pronounced linear portions (Fig. 11) within which the deflection disappears completely (Fig. 7(c),(d)) after removal of the applied load. With ceramics such portions on the diagrams were observed only at low temperatures (close to T_{BD} and lower) or at high speeds. It is probably owing to this fact, as well as to the absence of grain boundaries, that elastic moduli of Y-FSZC and Y-PSZC-3 crystals in contrast to ceramics were independent (Fig. 7(c),(d)) of the number of cycles of repeated loading irrespective of the limiting values of the loads reached, which correspond to the appearance of plateaus on the deformation diagrams with the former crystals and to fracture with the latter. The Y-PSZC-3 crystals under repeated loading exhibited an increase in the proportionality limit (Fig. 7(d)), though similarly for ceramics and

Y-FSZC crystals the unloading lines are indicative of their viscoelastic behaviour.

The existence in practice of equivalent ceramic deformation regimes (Fig. 5) can be probably explained by the action under such loading conditions of the same predominant deformation mechanism which is independent of the load and strain level. There was no possibility of choosing such deformation regimes for crystals, probably owing to differences in the character of their deformation (Fig. 8(e),(g)) at different loads.

As noted above, with all the ceramics and Y-FSZC crystals studied, creep intensified noticeably at the limiting loads, while with Y-PSZC-3 crystals almost complete absence of creep (Fig. 8(g)) was observed. This once again testifies to their appreciable difference from and the advantage over all other materials studied.

5 Conclusions

In the present investigation an attempt was made to obtain a general comparative picture of the mechanical behaviour of different types of ceramics and zirconia single crystals over a wide range of temperatures and deformation rates.

Specific features of the behaviour of the materials studied supplement appreciably the information about the processes which accompany their deformation and fracture and show that when making a choice among them for high temperature applications using, as most often happens in engineering practice, conventional criteria of applied mechanics, for a reliable evaluation of their load carrying capacity and, on the whole, efficiency, one should take into account their actual mechanical properties rather than idealize them using different hypotheses.

In spite of the fact that the deformation and fracture mechanisms of partially stabilized zirconia crystals have not been studied sufficiently, comparison of their mechanical properties with those of ceramics under different loading conditions reveals their higher serviceability at higher (up to 1400°C) temperatures. This makes it possible to consider them as new promising engineering materials.

Acknowledgements

This study was supported by the State Committee for Science and Technology of Ukraine. The authors are grateful to the ISF for the grant to their laboratory. The authors wish to thank Dr M. Herrmann (Fraunhofer-Einrichtung für Keramische Technologien und Sinterwerkstoffe, Germany) for cooperation in performing the test of SN-2 ceramics. Many thanks are expressed to Prof. T. Kobayashi (Toyohashi University of Technology, Japan) for supplying the Y-PSZ-3 ceramics for a joint investigation, the results of which are being prepared for publication.

References

1. Ingel, R., Lewis, D., Bender, B. A. & Rice, R. W., Physical, microstructural and thermomechanical properties of ZrO_2 single crystals. *J. Amer. Ceram. Soc.*, **26** (1984) 408–14.
2. Ingel, R., Lewis, D., Bender, B. A. & Rice, R. W., Temperature dependence of strength and fracture toughness of ZrO_2 single crystals. *J. Amer. Ceram. Soc.*, **65** (1982) 150–2.
3. Gogotsi, G. A., Lomonova, E. E. & Osiko, V. V., Studies of mechanical characteristics of zirconia single crystals for structural application. *Refractories*, **32** (1991) 14–17.
4. Gogotsi, G. A., Drozdov, A. V. & Pejchev, V. G., Mechanical behavior of zirconium dioxide crystals partially stabilized with yttrium oxide. *Strength of Materials*, **23** (1991) 86–91.
5. Gogotsi, G. A., Lomonova, E. E. & Pejchev, V. G., Strength and fracture toughness of zirconia crystals. *J. Eur. Ceram. Soc.*, **11** (1993) 123–32.
6. Dominguez-Rodriguez, A., Lagerlof, K. P. D. & Heuer, A. H., Plastic deformation and solid-solution hardening of Y_2O_3-stabilized ZrO_2 *J. Amer. Ceram. Soc.*, **69** (1986) 218–84.
7. Dominguez-Rodriguez, A., Lanteri, V. & Heuer, A. H., High-temperature precipitation hardening of two-phase Y_2O_3-partially-stabilized ZrO_2 single crystals. The first report. *J. Amer. Ceram. Soc.*, **69** (1986) 285–7.
8. Lankford, J., Page, R. A. & Rabenberg, L., Deformation mechanisms in yttria-stabilized zirconia. *J. Mater. Sci.*, **23** (1988) 4144–56.
9. Heuer, A. H., Lanteri, V. & Dominguez-Rodriguez, A., High-temperature precipitation hardening of Y_2O_3-partially-stabilized ZrO_2 (Y-PSZ) single crystals. *Acta Metall.*, **37** (1989) 559–67.
10. Martinez-Fernandez, J., Jimenez-Melendo, M., Dominguez-Rodriguez, A. & Heuer, A. H., High-temperature creep of yttria-stabilized zirconia single crystals. *J. Amer. Ceram. Soc.*, **73** (1990) 2452–56.
11. Fries, E., Guiberteau, F., Dominguez-Rodriguez, A., Cheong, D.-S. & Heuer, A. H., High-temperature plastic deformation of Y_2O_3-stabilized ZrO_2 single crystals. I. The origin of the yield drop and associated glide polygonization. *Phil. Mag. A.*, **60** (1989) 107–21.
12. Cheong, D.-S., Dominguez-Rodriguez, A. & Heuer, A. H., High-temperature plastic deformation of Y_2O_3-stabilized ZrO_2 single crystals. II. Electron microscopy studies of dislocation substructures. *Phil. Mag. A.*, **60** (1989) 123–38.
13. Cheong, D.-S., Dominguez-Rodriguez, A. & Heuer, A. H., High-temperature plastic deformation of Y_2O_3-stabilized ZrO_2 single crystals. III. Variation in work hardening between 1200 and 1500°C. *Phil. Mag. A.*, **63** (1991) 377–88.
14. Dominguez-Rodriguez, A., Cheong, D.-S. & Heuer, A. H., High-temperature plastic deformation of Y_2O_3-stabilized ZrO_2 single crystals. IV. The secondary slip systems. *Phil. Mag. A.*, **64** (1991) 923–29.
15. Michel, D., Mazerrolles, L. & Gorban, M., Fracture of metastable tetragonal zirconia crystals. *J. Mater. Sci.*, **18** (1983) 26–8.
16. Ingel, R. P. & Rice, R. W., Room-temperature strength and fracture of ZrO_2-Y_2O_3 single crystals. *J. Amer. Ceram. Soc.*, **65** (1982) 108–9.

17. Pajares, A., Guiberteau, F., Dominguez-Rodriguez, A. & Heuer, A. H., Microhardness and fracture toughness anisotropy in cubic zirconium oxide single crystals. *J. Amer. Ceram. Soc.*, **71** (1988) 332–3.
18. Quinn, G. D. & Baratta, F. I., Flexure data. Can it be used for ceramics part design? *Adv. Mater. Proc.*, **1** (1985) 31–5.
19. Sukhovarov, V. F., On the equivalence of the temperature and strain rate influence on the curves of copper and nickel plastic flow. *Izvestiya vuzov, Fizika*, **5** (1959) 164–71 (in Russian).
20. Bartenev, G. M., Strength and fracture mechanisms of polymers. Khimiya, Moscow, 1984 (in Russian).
21. Lankford, J., Inverse strain rate effects and microplasticity in zirconia crystals. *J. Mater. Sci. Lett.*, **8** (1989) 947–9.
22. Cannon, R. F., Roberts, J. T. A. & Beals, R. J., Deformation of UO_2 at high temperatures. *J. Amer. Ceram. Soc.*, **54** (1971) 105–12.
23. Knickerbocker, S. H., Zangvil, A. & Brown, S. D., Displacement rate and temperature effects in fracture of a hot-pressed silicon nitride at 1100 to 1325°C. *J. Amer. Ceram. Soc.*, **67** (1984) 365–68.
24. Govila, R. K., Statistical strength evaluation of hot-pressed Si_3N_4. *Amer. Ceram. Soc. Bull.*, **62** (1983) 1251–55, 58.
25. Evans, A. G. & Wiederhorn, S. M., Proof testing of ceramic materials – an analytical basis for failure prediction. *Int. J. Fract.*, **10** (1974) 379–92.
26. Gogotsi, G. A. & Ostrovoy, D. Yu., Deformation behaviour of ceramics in heating. *Refractories*, **33** (1992) 28–34.
27. Gogotsi, G. A., Lomonova, E. E. & Ostrovoy, D. Yu., Deformation behaviour of cubic ZrO_2 single crystals. *Refractories*, **33** (1992) 152–8.
28. Gogotsi, G. A., Deformational behaviour of ceramics. *J. Eur. Ceram. Soc.*, **7** (1991) 87–92.
29. Gogotsi, G. A., Zavada, V. P., Kutnyak, V. V. & Ostrovoy, D. Yu. A machine for determination of the mechanical properties of ceramics at high temperatures. *Strength of Materials*, **20** (1988) 558–62.
30. Gogotsi, G. A. & Swain, M. V., Comparison of strength and fracture toughness of single and polycrystalline zirconia. In *Science and Technology of Zirconia V*, ed. S. P. S. Badwal, M. J. Bannister & R. H. J. Hannink. Technomic Publishing Co., Lancaster, Basel, 1993, pp. 347–59.
31. Rawlins, M. H., Nolan, T. A., Allard, L. E. & Tennery, V. J., Dynamic and static fatigue behavior of sintered silicon nitride: II, Microstructure and failure analysis. *J. Amer. Ceram. Soc.*, **72** (1989) 1338–42.
32. Evans, A. G. & Dalgleish, B. J., Some aspects of the high temperature performance of ceramics and ceramic composites. *Ceram. Eng. Sci. Proc.*, **7** (1986) 1073–94.
33. Davidge, R. W., Briggs A. & Piller, R. C., Limitations to the performance of engineering ceramics under stress at high temperature. *Proc. Brit. Ceram. Soc.*, **39** (1987) 207–14.
34. Gogotsi, G. A., Gogotsi, Yu. G. & Ostrovoy, D. Yu., Mechanical behaviour of hot-pressed boron carbide in various atmospheres. *J. Mater. Sci. Lett.*, **7** (1988) 814–16.
35. Rabotnov, Yu. N. & Milejko, S. T., Short-term creep, Nauka, Moscow, 1970 (in Russian).
36. Belchuk, M., Watt, D. & Dryden, J., Modeling creep in materials with soft boundary phases. *Proc. Int. Symp. Adv. Struct. Mater.*, Montreal, 28–31 Aug., 1988, New York, 1989, pp. 123–9.
37. Clarke, D. R., Perspective concerning grain boundaries in ceramics. *Amer. Ceram. Soc. Bull.*, **69** (1990) 682–5.
38. Cheeseman, C. R. & Groves, G. W., The mechanism of the peak in strength and toughness at elevated temperatures in alumina containing a glass phase. *J. Mater. Sci.*, **20** (1985) 2614–22.

Journal of the European Ceramic Society **15** (1995) 283–289
© 1995 Elsevier Science Limited
Printed in Great Britain. All rights reserved
0955-2219/95/$9.50

Microstructure and Mechanical Properties of Textured Al_2O_3

T. Carisey, I. Levin & D. G. Brandon

Department of Materials Engineering, Technion — Israel Institute of Technology, Haifa 32000, Israel

(Received 19 April 1994; revised version received 5 July 1994; accepted 2 August 1994)

Abstract

The mechanical properties of a highly textured alumina have been studied and show a significant improvement in bend strength and Weibull modulus when compared to a randomly textured alumina of similar purity. The crystalline texture was due to growth of a small concentration of aligned and uniformly distributed alumina seed platelets into a fine-grained powder matrix during sintering. The (0001) texture of the sintered product gave a non-equiaxed, flattened grain structure, with the c*-axis of the hexagonal unit cell approximately normal to the plane of the specimen tiles. This highly textured microstructure drastically reduces the residual stresses which are associated with thermal contraction anisotropy in polycrystalline alumina, and inhibits crack propagation in the through-thickness direction. Two platelet sizes were investigated, the smaller of which gave the smaller final grain size and the better mechanical properties. At 5 wt% of platelet additions the properties were significantly more reproducible than at 10 wt% of the platelets, probably because of significant interference in packing the platelets at the higher loading.*

Introduction

The main limitation on the use of ceramics as structural materials is their brittleness. The production of a microstructurally and crystallographically oriented monolithic ceramic could be one route towards improving the strength and the resistance to crack propagation, since an oriented and textured monolithic ceramic should avoid some of the problems associated with reinforcement by a second phase; in particular, mismatch of the chemical, thermal or elastic properties of the reinforcing and matrix phases.

Previous work[1] on an alumina matrix reinforced with SiC whiskers has shown that the bend strength and the fracture toughness can be improved, although the whiskers need to be handled with care because of the health problems associated with possible ingestion. SiC platelet reinforcement is also effective, and reinforcement of a ceramic matrix with aligned SiC platelets has been shown to give mechanical anisotropy. For example,[2] the addition of 30% of SiC platelets to a Si_3N_4 matrix powder increased the fracture toughness, the Weibull modulus and Young's modulus of the hot-pressed product, while the mechanical anisotropy was demonstrated in indented samples, for which the extent of crack propagation parallel and perpendicular to the direction of hot- pressing was markedly different.

The bend strength of a zirconia matrix[3] with 5% of SiC platelet additions was reported to be slightly improved from room temperature to 600°C, while the toughness of the composite was about 50% higher than the matrix. The same matrix when reinforced with alumina platelets[4] gave a high toughness and bend strength with 10% of platelet additions from room temperature up to 800°C, and at 1400°C high strain rates resulted in 17% plastic deformation over 30 min, suggesting the onset of super plastic behaviour.

The effect of the shape of the reinforcement has been considered in other work on crack propagation[5,6] and whiskers and platelets were compared. The crack path was found to depend on the shape, size and volume fraction of the second phase particles. These were precipitated by heat treatment in a lithium-alumino-silicate glass ceramic. The fracture toughness was found to be invariant with the particle size.

The present work reports the mechanical properties of a crystallographically textured monolithic alumina produced by gel-casting of a slip containing aligned seed platelets.[7] The bend strength, Weibull modulus, fracture toughness and hardness are compared and correlated with the crystalline texture, the microstructural anisotropy and grain-size, and the state of internal stress. Vickers indentation cracking has been used to demonstrate the anisotropy of the crack propagation resistance.

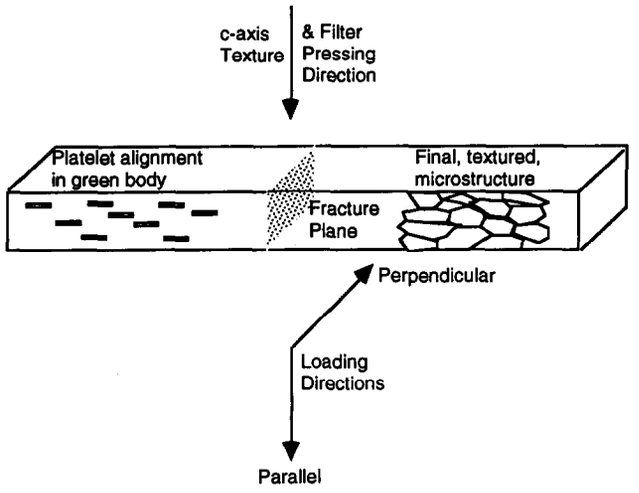


Fig. 1. Seed platelet and bend-bar geometries for textured alumina specimens.

Experimental

Composite fabrication

Highly textured monolithic alumina plate samples were prepared with the *c*-axis of the hexagonal unit cell within 10° of the normal to the plate surface. The samples were prepared by filter compaction and sintering of wet, water-based, gelled tape containing alumina seed platelets which had been aligned by a doctor-blade gel-casting process, as described previously.[7] The textured aluminas were compared with untextured (randomly oriented) samples prepared from the same powder and using the same processing route (water-based tape-casting, followed by lay-up, filter pressing and pressureless sintering), but with no seed platelet additions.

Characterization

Optical and scanning electron microscopy (SEM) were used to characterize the microstructure of polished cross-sections of the pressureless-sintered tile samples. Crack propagation was studied by varying the orientation of a Vickers indentation on polished sections cut perpendicular to the plate surface. SEM was the preferred method for evaluating the sintered microstructure, the fracture surfaces of bend specimens and the indentation crack morphology. The indentation samples were polished but unetched, while all other sintered specimen sections were polished and thermally etched at 1450°C for 30 min.

Mechanical testing

The sintered tiles were sectioned into 30 × 4 × 3 mm test bars with a 20 mm load span. The bend strength[8] was determined in 3-point bending for samples in which the tensile surface was either parallel or perpendicular to the plane defined by the original, aligned seed platelets. That is, the plane of the fracture was always the same, but the normal to the tensile surface was either parallel or perpendicular to the principal *c*-axis of the textured samples (Fig.1). The specimen span was 20 mm. About 25 samples were tested to allow for Weibull analysis of the strength data.[9,10] The fracture toughness was measured using the single edged notched beam test (SENB)[11,12] and was determined for the same fracture plane and failure directions as in the bend tests. The hardness was determined by Vickers indentation at 50 N with the loading axis either parallel or perpendicular to the normal to the original platelets (the principal *c*-axis of the textured samples), taking the average of measurements made on 10 separate indentations.

Thermal stresses

The thermal stresses present in the sintered tiles were evaluated by X-ray diffraction peak-shift measurements, as described elsewhere.[13] These measurements were taken from polished surface sections cut parallel and perpendicular to the original plane of alignment of the seed platelets. The accuracy of the measurements was limited to approximately 1 part in 10^5 by the X-ray goniometer and the positioning of the sample. The reflections used were a compromise between the requirements for reasonable signal intensity and the need to sample strains parallel and perpendicular to the *c*-axis of the textured alumina grains. The reflections chosen were 41·6 and 41·0, for which the penetration depth at 90% absorption of the incident X-ray beam is about 80 μm, much larger than the observed grain size of the samples. The average microstrain perpendicular to the sample surface for the crystallographic directions corresponding to the planes satisfying the reflecting conditions is obtained from the reflection shift with respect to a standard powder sample. For the sample section cut perpendicular to the alignment plane, the measured strains are predominantly from the textured grains, while it is the residual, randomly-oriented grains which dominates the strain measurement from the parallel section. The prediction is that thermal stresses should be absent if the material contains only ideally textured grains with the *c*-axes fully aligned, since α-Al_2O_3 has only two coefficients of thermal expansion, parallel and perpendicular to the *c*-axis, the former exceeding the latter by about 10% at all temperatures.

Results

Figures 2 (a) and (b) show the bend strengths for two seed-platelet concentrations (5 and 10 wt%)

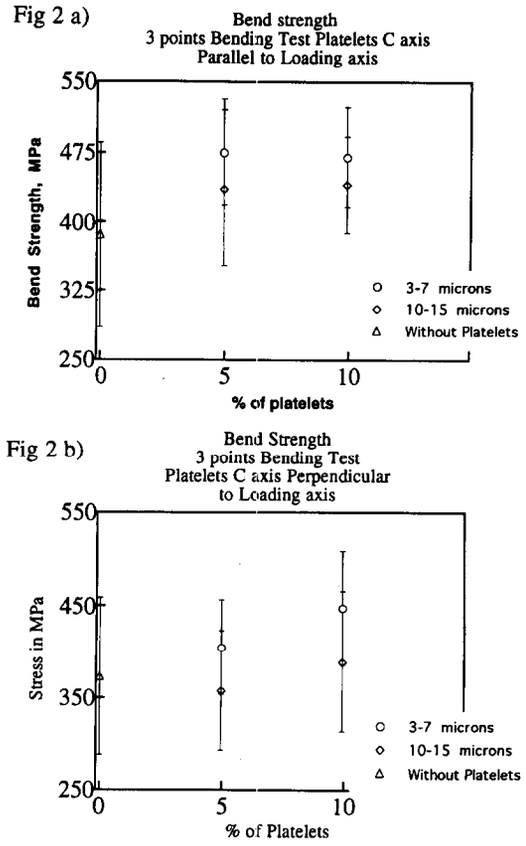


Fig. 2. Bend strength vs platelet concentration for both sizes of seed platelet additions: (a) principal *c*-axis of the textured tile parallel to the loading axis, (b) principal *c*-axis of the textured tile perpendicular to the loading axis.

and sizes (3–7 and 10–15 μm). The scatter bands shown are those calculated separately for each set of test results. In Fig. 2 (a) the tensile surface is parallel to the plane of the platelets, while in Fig. 2 (b) the plane of the tensile surface is perpendicular to the plane of the platelets. Clearly, the texture increases the bend strength when the tensile surface is parallel to the plane of the platelets, even though the grain size of the platelet-seeded and textured material is far larger than that of the unseeded alumina. The increase in bend strength after seeding with the smaller and larger platelets is 25 and 15%, respectively. In all cases the smaller seed platelets gave the smaller final grain size and were more effective than the larger ones in strengthening the product. The bend strength for crack propagation parallel to the principal *c*-axis of the texture was higher than that perpendicular to this axis. The mechanical behaviour of the specimens seeded with the larger platelets and with the tensile surface perpendicular to the original plane of the platelets was similar to that of alumina sintered without seed platelets, in spite of the much larger grain size of the seeded material, but with both sizes of seed platelets, the bend strength increased with platelet loading.

Figure 3 shows the Weibull moduli determined on 25 samples for the case of the tensile surface

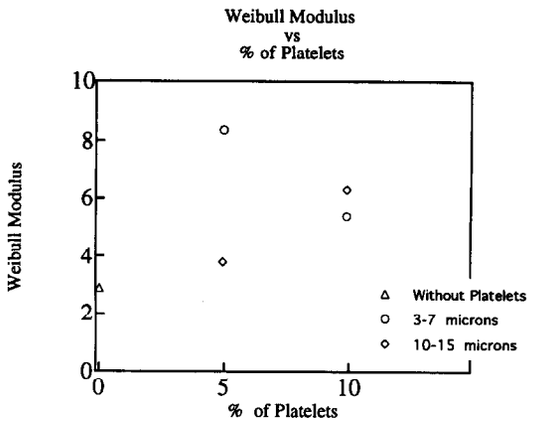


Fig. 3. Weibull modulus vs platelet concentration: principal *c*-axis of the texture parallel to the loading axis.

parallel to the original platelets. In view of the small number of samples, these values lack significance, but the small scale of the laboratory units constructed for gel-casting, tape lay-up and filter-pressing is thought to be primarily responsible for the very low value observed for the samples with no seed platelets. The improvement in Weibull modulus with the addition of seed platelets is thought to be significant. The best value of the modulus (about 8) was obtained for 5% additions of the smaller platelets. The platelet seeding appears to have improved the reliability of the sintered product, in addition to the improvement in the average mechanical strength.

The results for fracture toughness are presented in Fig.4 which again shows the two cases of the tensile surface either parallel (Fig. 4(a)) or perpendicular (Fig. 4(b)) to the platelets. The average fracture toughness calculated for the sample without platelets is questionably high for alumina, but the large standard deviation for this material puts it within the range of the other, textured samples. In Fig 4(a), the smaller seed platelets gave a better fracture toughness than the larger platelets, while in Fig. 4(b) all the values are very close together. In effect, the fracture toughness of the textured alumina is about 5 MPa $m^{-1/2}$, almost independent of the parameters examined.

Figure 5 shows the Vickers hardness results; firstly, in Fig. 5(a), as a function of the loading of the two sizes of seed platelets and, secondly, Fig. 5(b), in a comparison of the hardness measured on a cross-section of the tile (loading axis perpendicular to the principal *c*-axis of the texture) with that on the tile surface (the surface parallel to the plane of alignment of the seed platelets). The indent shape and crack propagation on the tile surface were similar for both the textured and the randomly oriented alumina. The indent shape on the cross-section will be discussed further below, but the measured hardness on this cross-section

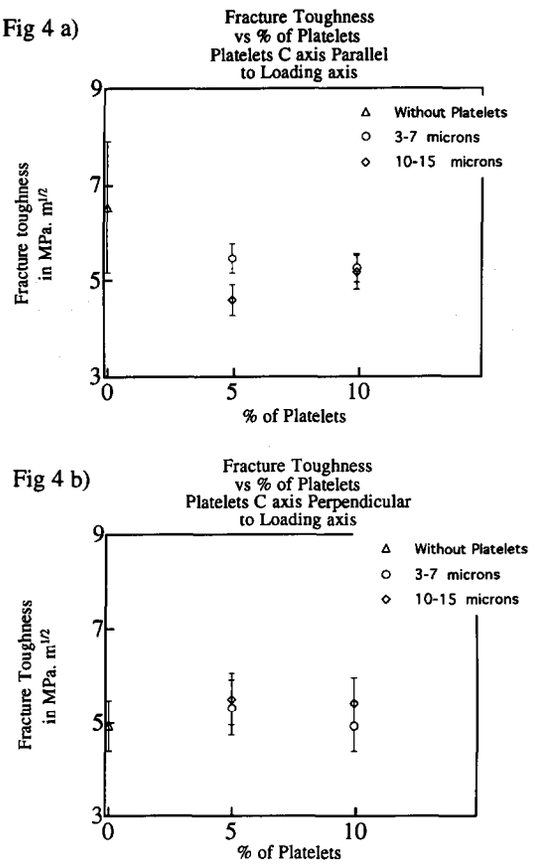


Fig. 4. Fracture toughness vs platelet concentration for both seed platelet sizes: (a) principal c-axis of the textured tile parallel to the loading axis; (b) principal c-axis of the textured tile perpendicular to the loading axis.

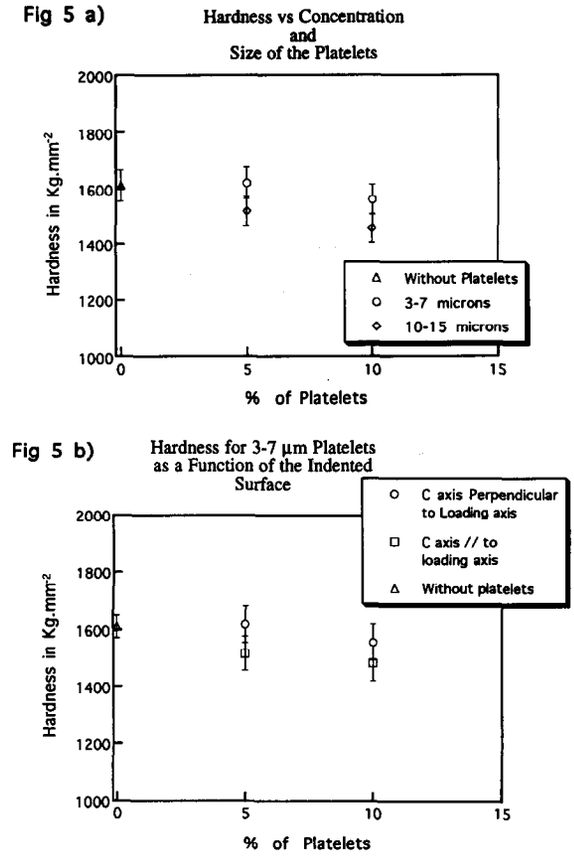


Fig. 5. Vickers hardness at 50 N vs platelet concentration: (a) for both sizes of seed platelet; (b) for two different indented surfaces: the sample cross-section and the surface parallel to plane of the original seed platelets.

was lowest for the smaller platelets (largest grain size), while the highest hardness, obtained for the sample without platelets, is associated with the small sintered grain size in the absence of the seed platelets.

The microstructure of the gel-cast alumina without platelets consisted of equiaxed grains with a grain size of about 3 μm. By contrast, the average grain size of the samples containing seed platelets was about 6 μm. The micrographs shown in Fig. 6 are taken from a tile cross-section. The non-equiaxed (oblate) grain structure is a result of the non-equiaxed distribution of the centres of gravity of the original aligned seed platelets. These have grown during sintering to consume most of the initial powder matrix. The final microstructure is highly textured and anisotropic, with a comparatively large grain size. It is the size of the original seed platelets and their volume fraction which determine the final grain size. A homogeneous distribution of the platelets[7] should give isotropic behaviour in the plane of the sample plate. In addition, grain growth has been enhanced by the presence of calcium in the green body associated with the current gel-casting process.

The mechanical anisotropy is demonstrated in Fig. 7, which shows optical micrographs of indented polished sections cut perpendicular to the tile surface. Figure 7(a) is from an indented sintered sample which contained no platelets, while Figure 7(b) shows a textured sample which contained 5 wt% of the smaller, aligned seed platelets. In the first case the cracks have the same length, while in the second case crack propagation parallel to the principal c-axis of the texture is clearly inhibited. Figure 8 shows SEM micrographs of indentation cracks, (a) propagating approximately parallel to the original direction of platelet alignment and (b) propagating approximately perpendicular to the alignment direction. In the first case, delamination has tended to generate a stepped surface, while in the second case the flattened, textured grains have inhibited crack propagation and given rise to a highly irregular crack path.

The thermal expansion coefficient α of alumina parallel to the c-axis is approximately 10% higher than that perpendicular to the c-axis, and is expected to lead to cumulative thermal strains in a random polycrystal cooled below the relaxation temperature. The total elastic mismatch at room temperature, $\Delta\alpha\Delta T$, assuming that the minimum value of ΔT is 1000°C, is about $7{\cdot}6 \times 10^{-4}$ in a random polycrystal. Assuming elastic isotropy, this will lead to a maximum c-axis compressive

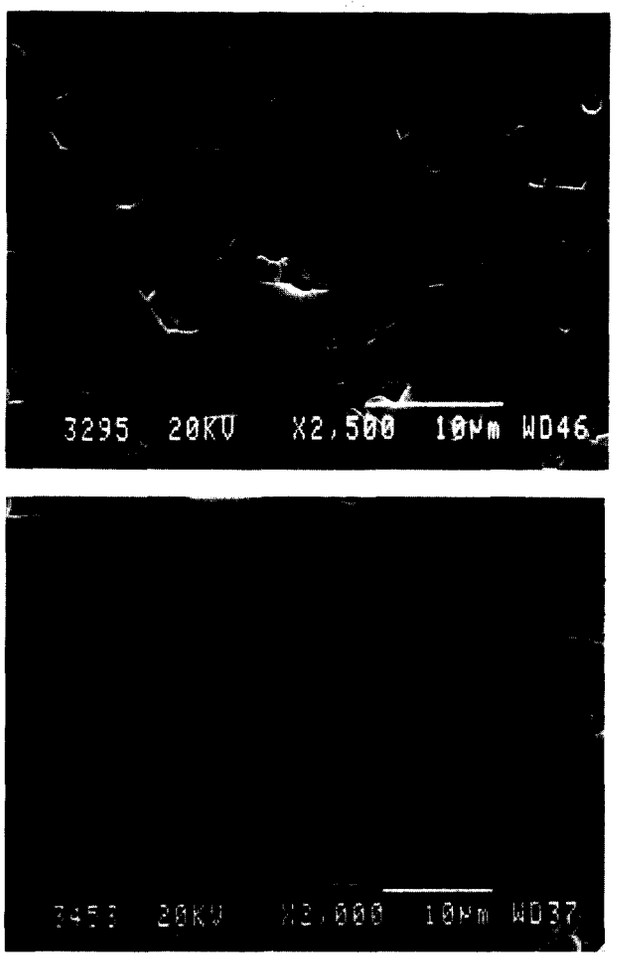


Fig. 6. SEM micrograph of thermally-etched samples: (a) sample with 5 wt% of 3–7 μm platelets; (b) sample with 5 wt% of 10–15 μm platelets.

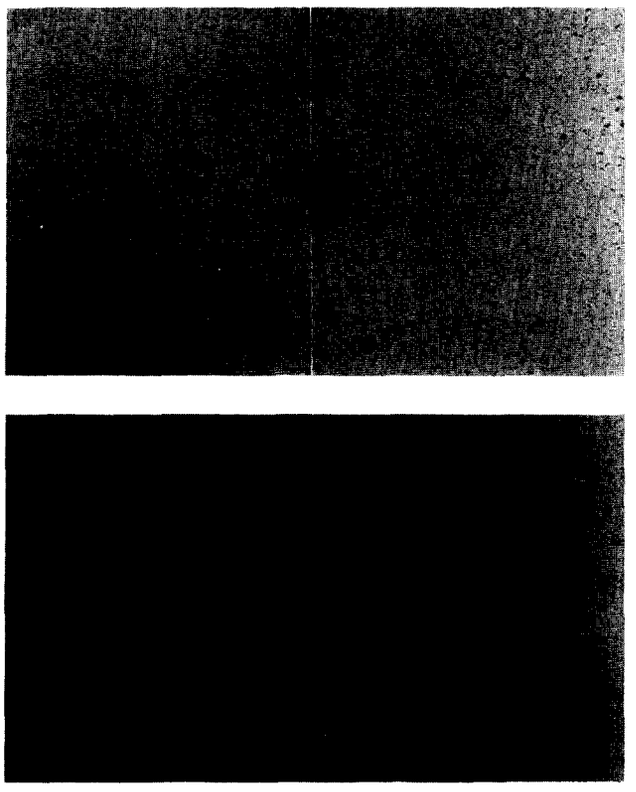


Fig. 7. Optical micrographs of Vickers indentation cracking at 200 N: (a) sample without platelets; (b) sample with 5 wt% of small platelets.

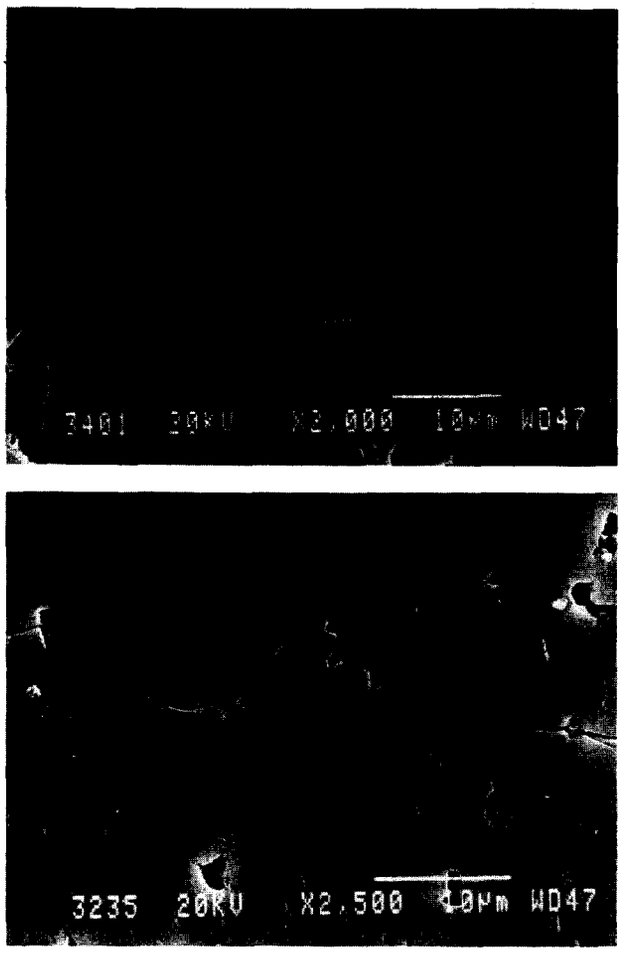


Fig. 8. SEM micrographs of Vickers indentation cracking at 200 N: (a) crack propagation parallel to the direction of original seed platelet alignment; (b) crack propagation perpendicular to the direction of original seed platelet alignment.

strain of about -5×10^{-4} and a maximum tensile strain perpendicular to the *c*-axis of about $2{\cdot}6 \times 10^{-4}$. In a *c*-axis textured alumina containing some randomly oriented material, the thermal strain in the textured material will be reduced, while that in the residual, randomly-oriented material will increase. The residual strain measurements made in the present work on a sample tile containing no seed platelets gave an average strain value for the 41·6 reflection (the only suitable high-angle, strong reflection close to the *c*-axis) of $-1{\cdot}4 \times 10^{-4}$, while that measured from the same reflection parallel and perpendicular to the *c*-axis of a strongly textured sample gave compressive strains of $-2{\cdot}4 \times 10^{-4}$ and $-0{\cdot}2 \times 10^{-4}$, respectively. The former value is associated with the strain in the small volume fraction of residual, randomly oriented grains, which are strongly constrained by the surrounding textured material, while the latter value is that associated with the dominant volume fraction of highly textured grains. The implication is that, as predicted, the textured material has a much reduced level of thermal stress.

Discussion

The present results have demonstrated a significant improvement in the mechanical properties of a textured alumina produced by gel-casting a slip containing aligned alumina seed platelets, in spite of the residual porosity and large grain size of this material. These results were obtained with high levels of calcium doping (of the order of 0·5%), due to the use of calcium as the gelling cation (the commonest cation used to promote the alginate gel reaction).

The microstructural observations on the sintered samples seeded with both sizes of alumina platelets showed that the matrix powder for the most part had been consumed during sintering to leave large, non-equiaxed, highly textured grains which had formed by the growth of the aligned seed platelets. The distribution of the seed platelets influenced both the final texture and the degree to which the grains are non-equiaxed, and the final grain size depended on both the volume fraction of the seed platelets and their initial size. The smaller platelets gave the smaller final grain size at a given loading of seed platelets and, consistent with this, the best mechanical properties. Further improvements could presumably be anticipated if the seed platelet size were to be further reduced, leading to a smaller ultimate grain size due to the greater number density of platelets at the same loading.

Calcium was selected as the gelling cation, since the calcium alginic ion-exchange reaction is well-characterized. However, calcium is known to cause abnormal grain growth which is expected to degrade the mechanical properties. Several cations have been used to gel the water-based tape used in this work[7] and satisfactory results have been achieved with alternative alumina cation dopants which are considered either beneficial (Y, Ce, La) or harmless (Sr and Ba).

The present large grain size, monolithic alumina, produced by the sintering of green bodies which contain well-aligned alumina seed platelets, is highly textured and constitutes a new class of monolithic ceramic which could have some interesting applications. These materials could be used for any wear or abrasion resistant component requiring improved crack propagation resistance normal to the surface, while the large grain size should lead to improved microstructural stability at high temperatures, and hence to improved creep resistance. The wet, gelled tape, which is produced by the gel-casting process,[7] is an intermediate product which could be wound to form tube or plastically shaped. The present results have shown that the crystalline texture reduces the thermal stresses and should also improve the thermal shock resistance, leading to potential applications as furnace tubes in electronic substrate furnaces (which are generally made only from alumina). Since only small quantities of the seed platelets are required, the increased raw material costs are minimal, while the proposed processing route is relatively uncomplicated and requires only pressureless sintering.

Conclusions

(1) A textured alumina, produced from a gel-cast slip containing aligned alumina seed platelets by tape lay-up, filter-pressing and pressureless sintering, has been found to possess good mechanical properties.
(2) Although the sintered seeded product had a far larger grain size than an equivalent, unseeded alumina, the bend strength could be enhanced by more than 20%, while the fracture toughness was unaffected.
(3) The Weibull modulus was also improved by processing with the aligned seed platelets.
(4) The Vickers hardness was only slightly reduced in the textured material, presumably due to the increased grain size.
(5) The crystalline texture and microstructural anisotropy (large, plate-like grains) inhibit crack propagation in the through-thickness direction, as demonstrated by Vickers indentation cracking.
(6) The residual thermal stresses, as determined by X-ray diffraction peak shift measurements, are significantly reduced in the textured alumina to less than one third of their value in randomly oriented alumina samples subjected to the same sintering cycle.
(7) The texture (preferred orientation) and the microstructural anisotropy (non-equiaxed grain structure) are both associated with the growth of the aligned seed platelets into the fine-grained matrix during the pressureless sintering process.

Acknowledgements

The authors would like to acknowledge the provision of research funding for this project by Elf-Atochem, as well as the encouragement and support of Dominique Cotto and Jacques Macé, of Elf-Atochem. We would also like to acknowledge the support of the French government for one of us (T.C.) under their VSN programme.

References

1. Farkash, M. & Brandon, D., Whisker alignment by slip extrusion. *Mater. Sci. Engng. A*, **177** (1994) 269–75.
2. Baril, D., Tremblay, S. P. & Fiset, M., Silicon carbide platelet-reinforced silicon nitride composites. *J. Mater. Sci.*, **28** (1993) 5486–94.
3. Poorteman, M., Descamps, P., Cambier, F., Leriche, A. & Thierry, B., Hot isostatic pressing of SiC-platelets/Y-TZP composites. *J. Eur. Ceram. Soc.*, **12** (1993) 103–9.
4. Poorteman, M., Descamps, P. & Cambier, F., Superplastic deformation of alumina platelets reinforced Y-TZP. *3rd. Euro-Ceramics*, ed. P. Duràn and J. F. Fernàndez. Faenza Editrice Ibérica S. L., 1993, Vol. 3, pp. 659–64.
5. Faber, K. T. & Evans, A. G., Crack deflection processes — I. Theory. *Acta Metall.* **31**(4) (1983) 565–76.
6. Faber, K. T. & Evans, A. G., Crack deflection processes — II. Experiment. *Acta Metall.*, **31**(4) (1983) 577–84.
7. Carisey, T., Laugier-Werth, A. & Brandon, D. G., Control of texture in Al_2O_3 by gel-casting. *J. Eur. Ceram. Soc.*, **15** (1995) 1–8.
8. Quinn, G. D., Baratta, F. I. & Conway, J. A., Commentary on U.S. Army standard test method for flexural strength of high performance ceramics at ambient temperature. Army Materials and Mechanics Research Center. (08-1985). AMMRC 85–21.
9. Fantozzi, G., Rupture des matériaux 1ère et 2 ième parties. Departement Génie Physique des Matériaux. INSA Lyon édition. (1992).
10. Creyke, W. E. C., Sainsbury, I. E. J. & Morrell, R., *Design with Non-ductile Materials*. Appl. Sci. Publ., 1982.
11. Henshall, J. L., Rowcliffe, D. J. & Edington, J. E. W., Fracture parameters in Refel silicon carbide. *J. Mater. Sci.*, **9** (1974) 1559–61.
12. Srinivasan, M. & Seshadri, S. G., Application of single edge notched beam and indentation techniques to determine fracture toughness of alpha silicon carbide. *Fracture Mechanics Methods for Ceramics, Rocks, and Concrete*, Am. Soc. Test. Matls. STP 745, ed. S. W. Freiman and E. R. Fuller, Jr. ASTM, Philadelphia, PA, 1981, pp. 46–86.
13. Levin, I., Kaplan, W. D. & Brandon, D. G., Residual stresses in alumina-SiC nanocomposites. *Acta Metal. et Mater.*, **42**, (1994) 1147.

Journal of the European Ceramic Society **15** (1995) 291–295
© 1995 Elsevier Science Limited
Printed in Great Britain. All rights reserved
0955-2219/95/$9.50

Toughening and Strengthening of Alumina with Silver Inclusions

W. B. Chou & W. H. Tuan*

Institute of Materials Science & Engineering, National Taiwan University, Taipei, Taiwan 10764

(Received 23 June 1993; received in revised form 20 June 1994; accepted 27 June 1994)

Abstract

The fracture toughness and flexural strength of Al_2O_3/Ag composites are investigated. Both the strength and toughness of alumina are enhanced as silver inclusions are added. From microstructural observation, the crack is bridged or deflected by silver inclusions. The toughness enhancement is contributed mainly by the plastic deformation of the silver inclusions. The strengthening effect is contributed both by the matrix grain refinement and by the toughness enhancement.

1 Introduction

The application of ceramics as structural components is often limited by their brittleness. A major research objective has therefore been to improve their toughness. Previous studies have demonstrated that brittle solids can be toughened by incorporating metallic inclusions into them.[1–7] Similar to the zirconia toughened ceramics (ZTC),[8] the toughness of the metal-toughened ceramics can be described as

$$K_{IC,composite} = K_{IC,matrix} + \Delta K_{IC,metal} \quad (1)$$

where $K_{IC,\ composite}$ is the toughness of the composite, $K_{IC,matrix}$ the toughness of the matrix and, $\Delta K_{IC,metal}$ the toughness increase contributed by the metallic reinforcement. The toughness enhancement for the ceramic–metal composites is believed to be contributed by the plastic deformation of metallic inclusions.[9–11]

As metallic inclusions are embedded within ceramic matrices, the metallic inclusion is constrained by the brittle and rigid matrix. The deformation behaviour of the constrained inclusion has been investigated by Ashby *et al.*[9–10] They suggested that the toughness increase, contributed by plastic deformation, $\Delta K_{IC,plastic\ deformation}$, is proportional to square root of the product of the volume fraction, F, and the inclusion size, d, as

$$\Delta K_{IC,plastic\ deformation} = C\,(F\,d)^{1/2} \quad (2)$$

where C is a constant. The constant depends on the bonding characteristics. Deve *et al.* have suggested that the toughness enhancement is increased with the increase of the ductility of metallic inclusion.[11] Among metals, silver is superior for its ductility. Furthermore, silver is chemically stable up to temperatures higher than its melting point, 960°C. Therefore, the silver containing composites can be prepared by pressureless sintering in air.[12,13]

The mechanical properties of Al_2O_3/Ag composites have been studied recently.[12,13] In these studies, the toughness is determined by the indentation technique. As we are going to show later, this technique tends to over-estimate the toughness of Al_2O_3/Ag composites. In the present study, the toughness of the Al_2O_3/Ag composites is determined by the single-edge-notched-beam (SENB) technique. Furthermore, the effect of silver inclusions on the strength of alumina is not determined in the previous studies. In this study, the strength of the Al_2O_3/Ag composites is also measured.

2 Experimental Procedures

Alumina (AKP-50, Sumitomo Chem. Co. Ltd., Japan) and various amounts of silver oxide (Ag_2O, Johnson Matthey Co., UK) were milled in ethyl alcohol for 4 h. The slurry of the powder mixtures was dried with a rotary evaporator. The dried lumps were crushed and sieved. The powder compacts were prepared by pressing uniaxially at 56 MPa. The sintering was performed in air at 1600°C or 1700°C for 1 h. The heating and cooling rates were 5°C/min. In order to determine the toughness of alumina as a function of grain size, the alumina specimens with different grain size were prepared by sintering the alumina compacts at 1400–1700°C for 1 h. These Al_2O_3 specimens

*To whom correspondence should be addressed.

were prepared with the same procedures as those for the Al_2O_3/Ag composites.

The decomposition behaviour of silver oxide was determined by a differential thermal analyzer (DTA, Netsch Co., Germany). Phase identification was performed by X-ray diffractometry (XRD). The final density was determined by the water displacement method. Before submerging the specimens in water, a wax was applied to the surface to prevent water penetration. The microstructure was observed by a scanning electron microscope (SEM) and a transmission electron microscope (TEM). Both microscopes were equipped with an energy dispersive X-ray spectrometer (EDX). Polished surfaces were prepared by grinding and polishing with diamond paste to 6 μm and subsequently with silica suspension to 0·05 μm. Since the partial pressure of liquid silver at elevated temperature is high (10 mmHg/1600°C and 23 mmHg/1700°C),[14] a silver-free surface layer is formed.[13] After removing the silver-free layer by grinding, the volume fraction of silver after sintering was recalculated by counting the point fraction on the polished surfaces. The size of silver inclusions was determined by using the linear intercept technique. The dihedral angle of the silver inclusion within alumina matrix was estimated from polished microstructures by applying a stereological counting technique.[15] The polished specimens were thermally etched at 1500°C for 1 h to reveal the grain boundaries of alumina. The size of the matrix grains was also determined by the linear intercept technique. More than 200 grains or inclusions were counted.

The sintered specimens were machined longitudinally with a 325 grit resin-bonded diamond wheel at cutting depths of 5 μm/pass. The silver-free layer was removed during the grinding procedure. The final dimensions of the samples were 3 mm × 4 mm × 36 mm. The strength of the samples was determined by the 4-point bending technique at ambient conditions. The upper and lower spans were 10 and 30 mm, respectively. The rate of loading was 0·5 mm/min. The fracture toughness was determined by the single-edge-notched-beam (SENB) technique. The notch was generated by cutting with a diamond saw. The width of the notch was around 0·5 mm. The indentation technique was also used to determine the toughness of the composites. The load applied was 50 N.

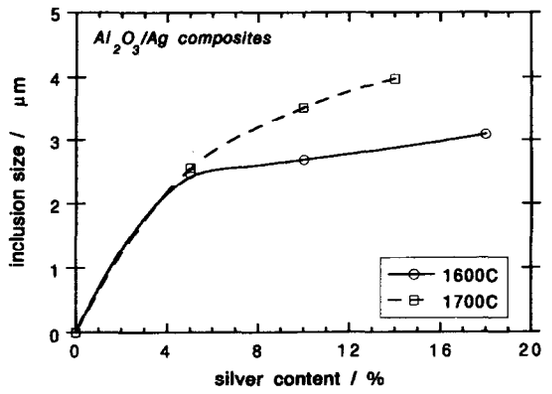


Fig. 2. The size of silver inclusions found in the composites shown in Fig. 1.

3 Results and Discussion

The DTA analysis suggests that the silver oxide starts to decompose from 410°C. The XRD patterns indicate that there is no residual silver oxide in Al_2O_3/Ag composites after sintering. The relative density of the composites is shown as a function of silver content in Fig. 1. The size of silver inclusions is shown as a function of silver content in Fig. 2. The grain size of alumina matrix is shown in Fig. 3. Typical microstructures for the composites are shown in Fig 4. The dihedral angle of the silver inclusion within the alumina matrix is 110±7·8° for the composites sintered at 1600°C and 101±5·5° for the composites sintered at

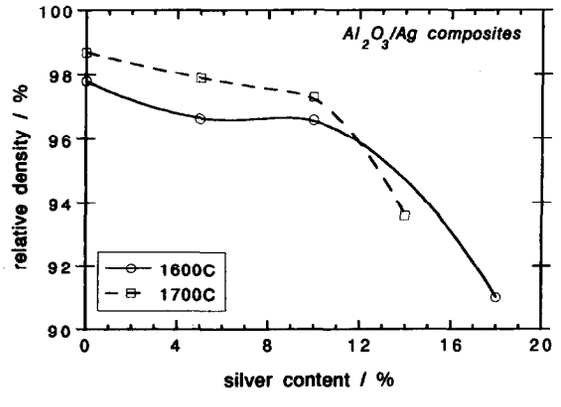


Fig. 1. The density of the composites as a function of silver content with the samples sintered at the indicated temperatures for 1 h.

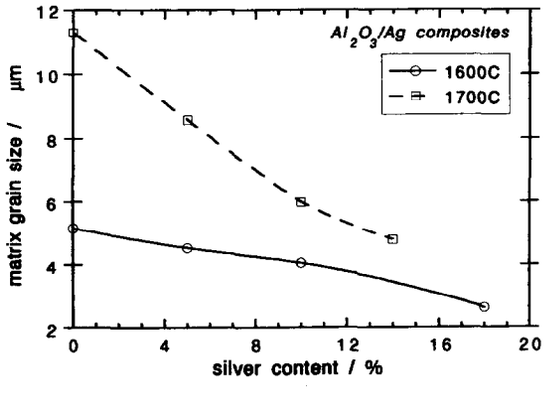


Fig. 3. The size of alumina matrix found in the composites shown in Fig 1.

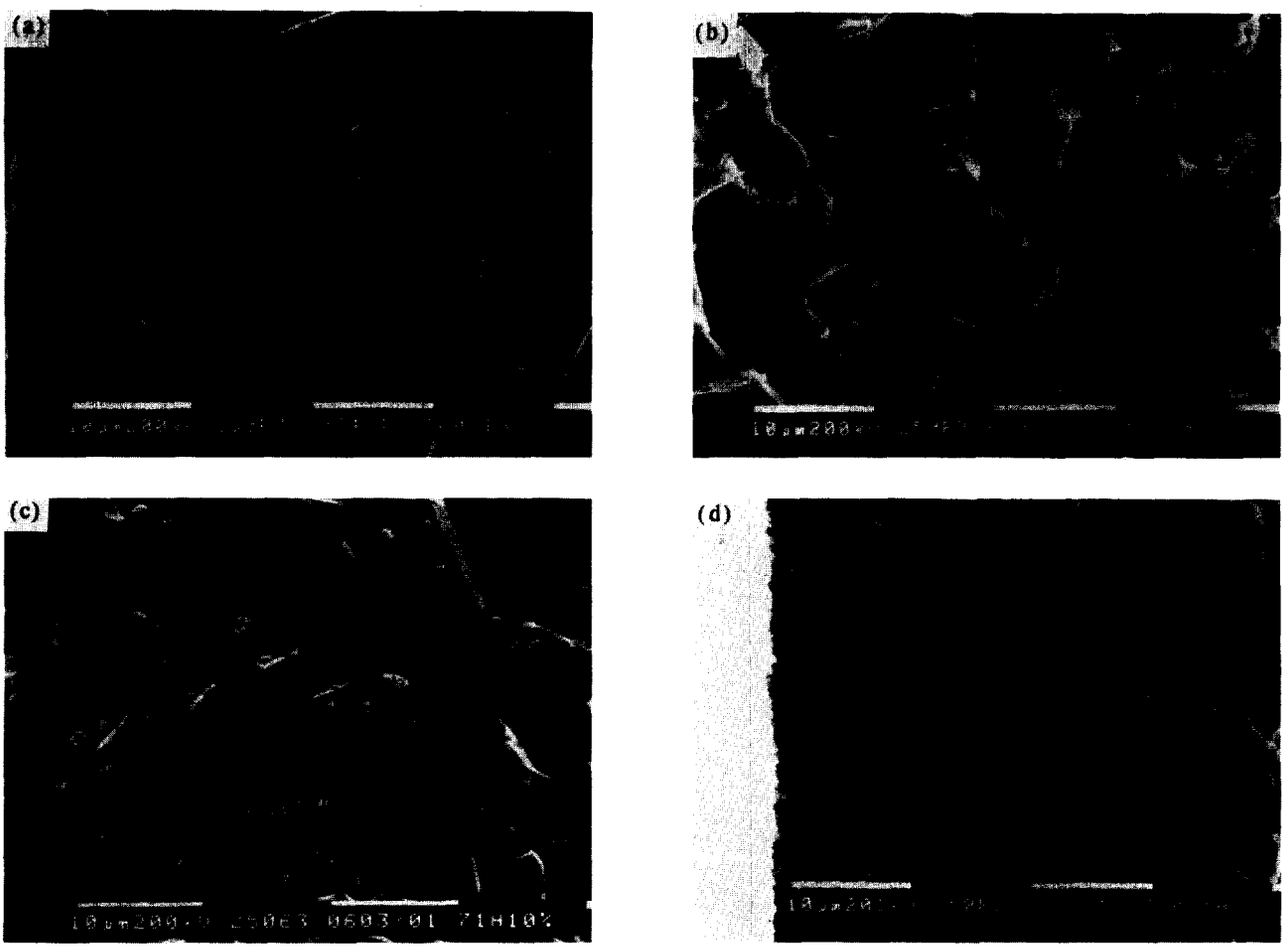


Fig. 4. Typical microstructures of Al_2O_3/Ag composites. The vol.% of silver in the composites shown is (a) 0, (b) 5, (c) 10 and (d) 14. The composites are sintered at 1700°C for 1 h.

1700°C. These values are close to the reported values determined by the sessile drop technique.[16] Since the wetting is poor, silver melt behaves as an inclusion to the alumina matrix. The densification of the alumina matrix is thus hindered. From Fig. 4, most silver inclusions are located at the grain boundaries of alumina, the grain growth of alumina matrix is slowed down due to the presence of silver inclusions.

Since the thermal expansion of silver (22/MK) is bigger than that of alumina (9/MK), thermal stress results after the cooling step. Twins can be observed within the silver inclusions, (Fig. 5). Due to the fact that the twins are lens-shaped, they are deformation twins.[17] It suggests that the silver inclusions are highly constrained due to the presence of residual stress. Occasionally, small particles can be observed near the Al_2O_3/Ag interface, (Fig. 5). The small particles analyzed by EDX are mainly composed of Cr and Fe. It may be from the contamination from the steel mold used for forming. From the TEM study, no reaction layer can be observed at the interface and no Al detected within the silver inclusions. Since the solubility of alumina in Ag is negligible, it further confirms that the silver melt can not act as an effective liquid phase to promote the densification.

The fracture toughness of the composites is shown as a function of silver content in Fig. 6. The interactions between a crack and silver inclusions are shown in Fig. 7. In the figure, the crack is bridged by, or deflected by, the silver inclusions. It suggests that the toughening mechanisms for the composites are plastic deformation and crack deflection. Both the plastic deformation[9–11] and crack deflection[18] mechanisms can contribute to the toughness enhancement. The toughness of Al_2O_3/Ag composites determined by the SENB and indentation techniques is thus higher than that of Al_2O_3 alone. However, the toughness determined by the indentation technique results in higher values. The crack opening introduced by the indentation is much smaller than the notch width produced by cutting with a diamond saw. Since the crack surfaces with a small opening are bridged by silver inclusions (Fig. 7), the propagation of the crack with a small opening is more difficult. Therefore, the toughness determined by the indentation technique is much higher than that determined by the SENB technique.

In order to determine the toughness of alumina matrix, $K_{IC,matrix}$, the toughness of the alumina

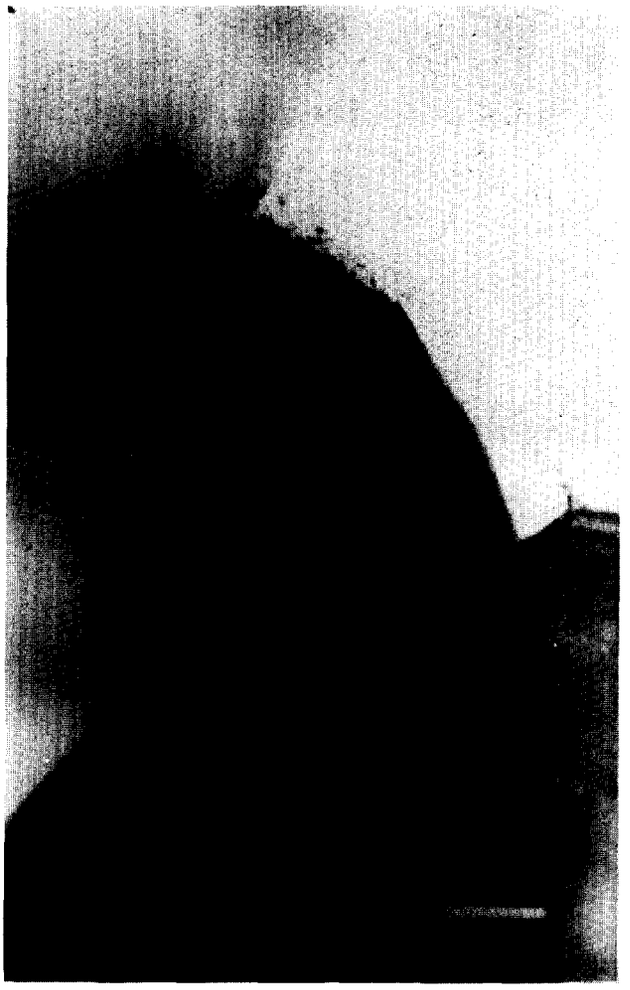


Fig. 5. A highly constrained silver inclusion found within the alumina matrix.

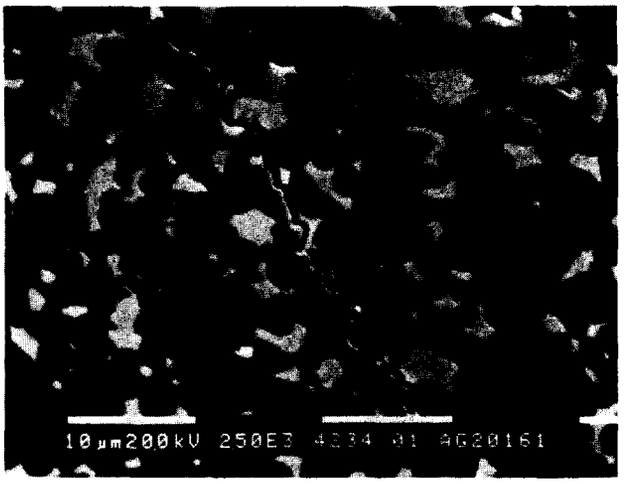


Fig. 7. The interactions between silver inclusions and a crack introduced by indentation.

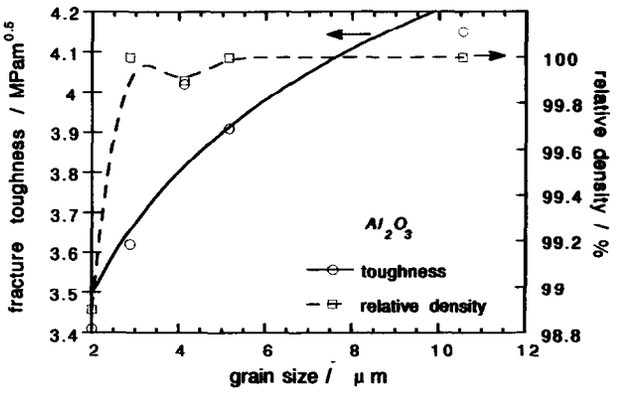


Fig. 8. The fracture toughness determined by the SENB technique and the density of Al_2O_3 specimens as a function of grain size.

specimens sintered at various temperatures is determined (Fig. 8). The toughness is determined by the SENB technique. The density of the Al_2O_3 specimens is varied from 98·9 to 99·9%; therefore, the effect of porosity on the toughness can be ignored. The toughness of alumina is increased with the increase of grain size. It is similar to the results reported by Tuan *et al.*[19] According to eqn (1), the toughness increase, $\Delta K_{IC,metal}$, contributed by the metallic inclusions which can be determined as $K_{IC,matrix}$ is known. The toughness increase of the composites is shown as a function of the square root of the product of volume fraction, F, and inclusion size, d, in Fig. 9. Since the enhancement from the deflection around spherical inclusions is limited,[18] more significance is to be given to the

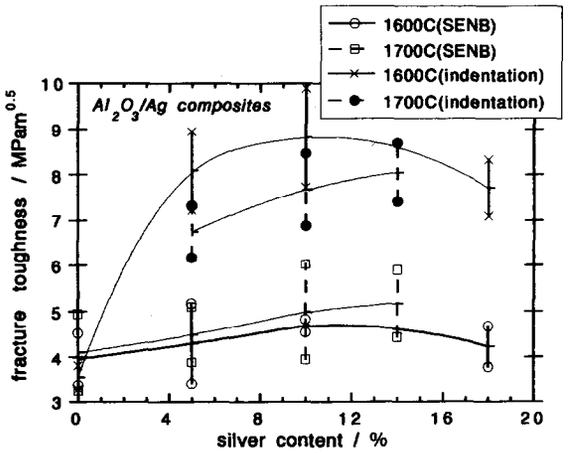


Fig. 6. The fracture toughness determined by the SENB and the indentation techniques for the composites shown in Fig. 1 as a function of silver content.

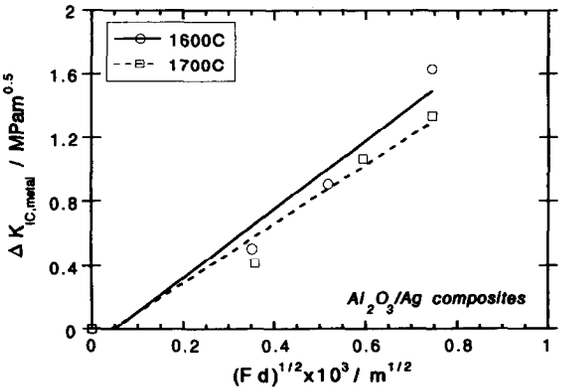


Fig. 9. The fracture toughness increase as a function of the square root of the product of volume fraction and inclusion size. The sintering temperatures are indicated.

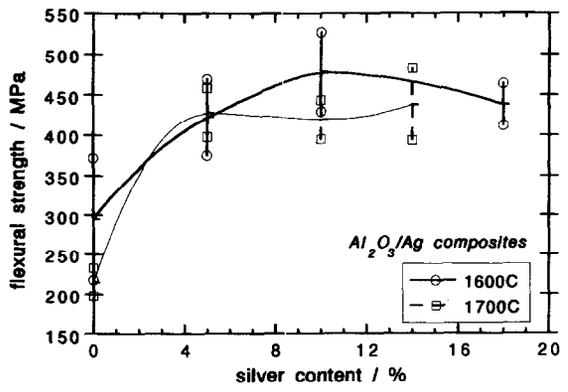


Fig. 10. The flexural strength for the composites shown in Fig. 1 as a function of silver content.

plastic deformation mechanism. This is supported by the linear relationship between the toughness increase and the square root of the product of volume fraction and inclusion size (Fig. 9).

The flexural strength of the composites is shown as a function of silver content in Fig. 10. With the enhanced toughness and the reduced grain size of alumina matrix as silver is added, the strength of alumina is improved substantially.

4 Conclusions

Dense Al_2O_3/Ag composites are prepared by pressureless sintering at 1600°C and 1700°C for 1 h. The densification behaviour, microstructure development, and mechanical properties of the composites are investigated. Even though the silver inclusions are melted during sintering, due to the fact that the wetting of silver melt on alumina is poor and the solubility of alumina in silver is limited, the presence of silver inclusions hinders the densification. The matrix alumina grains are refined due to the grain boundaries being dragged by the silver inclusions. The addition of ductile inclusions not only toughens but also strengthens the ceramic matrix. The toughening is contributed mainly by the plastic deformation of silver inclusions. Due to the increase in toughness and the refinement of matrix grain size induced by the presence of the inclusions, the strength of the alumina is also significantly increased.

Acknowledgements

The present study is supported by the National Science Council, ROC., through the contract no. NSC81-0405-E002-26. We are grateful for the valuable comments given by Prof. R. J. Brook, Oxford University.

References

1. Rankin, D. T., Stiglich, J. T., Petrak, D. R. & Ruh, R., Hot-pressing and mechanical properties of Al_2O_3 with Mo-dispersed. *J. Am. Ceram. Soc.*, **54** (1971) 277.
2. Flinn, B. D. Ruhle, M. & Evans, A. G., Toughening in composite of Al_2O_3 reinforced with Al. *Acta Metall.*, **37** (1989) 3001.
3. Baran, G., Degrange, M., Rouques-Carmes, C. & Wehbi, D. Fracture toughness of metal reinforced glass composite. *J. Mater. Sci.*, **25** (1990) 4211.
4. Aghajanian, M. K., Macmillan, N. H., Kennedy, C. R., Luszcz, S. J. & Roy, R., Properties and microstructures of Lanxide Al_2O_3–Al ceramic composite materials. *J. Mater. Sci.*, **24** (1989) 658.
5. Wu, S., Gesing, A. J., Travitzky, N. A. & Claussen, N., Fabrication and properties of Al-infiltrated RBAO-based composites. *J. European Ceram. Soc.*, **7** (1991) 277.
6. Tuan, W. H. & Brook, R. J., The toughening of alumina with nickel inclusions, *J. European Ceram. Soc.*, **6** (1990) 31.
7. Tuan, W. H. & Wu, J. M., Effect of microstructure on the hardness and toughness of $YBa_2Cu_3O_{7-x}$/Ag composites. *J. Mater. Sci.*, **28** (1993) 1415.
8. Becher, P. F. & Tiegs, T. N., Toughening behaviour involving multiple mechanisms: whisker reinforcement and zirconia toughening. *J. Am. Ceram. Soc.*, **70** (1987) 651.
9. Ashby, M. F., Blunt F. J. Bannister, M., Flow characteristics of highly constrained metal wires. *Acta Metall.*, **37** (1987) 1847.
10. Bannister, M. & Ashby, M. F., The deformation and fracture of constrained metal sheets. *Acta Metall.* **39** (1991) 2575.
11. Deve, H. E., Evans, A. G., Odette, G. R., Mehrabian, R., Emiliani, M. L. & Hecht, R. J., Ductile reinforcement toughening of γ-TiAl: effects of debonding and ductility. *Acta Metall.*, **38** (1990) 1491.
12. Tuan, W. H. & Chou, W. B., Toughening alumina with silver inclusions, *Proc. of the 2nd European Ceram. Soc., Vol. 2*, ed. by Ziegler, G. & Hausner, H., Vol. 2, Deutsche Kermische Gesellschaft e.V., Germany 1991, pp. 1703.
13. Wang, J., Ponton, C. B. & Marquis, P. M., Silver toughened alumina ceramics. *Br. Ceram. Trans.*, **92** (1993) 67.
14. Wise, E. M. & Coxe, C. D., in *Metal Handbook, Vol. 1*, Am. Soc. for Metal, Ohio, USA, 1961, pp. 1181.
15. DeHoff, R. T., Estimation of dihedral angles from stereological counting measurements. *Metallography*, **19** (1990) 209.
16. Nikolopoulos, P. & Agathopoulos, S., Interfacial phenomena in Al_2O_3-liquid metal and Al_2O_3-liquid alloy systems. *J. European Ceram. Soc.*, **10** (1992) 415.
17. Wang, J., Ponton, C. B., Marquis, P. M., The microstructure of pressureless sintered silver-toughened alumina: an in-situ TEM study. *Mater. Sci. Eng.*, **A161** (1993) 119.
18. Faber, K. T. & Evans, A. G., Crack deflection processes — I. Theory. Acta Metall., **31** (1983) 565.
19. Tuan, W. H., Lai, M. J., Lin, M. C., Chan, C. C. & Chiu, S. C., The mechanical performance of alumina as a function of grain size. *Mater. Chem. Phys.*, **36** (1994) 246.

Journal of the European Ceramic Society **15** (1995) 297–305
© 1995 Elsevier Science Limited
Printed in Great Britain. All rights reserved
0955-2219/95/$9.50

Toughening of X-Sialon with Al_2O_3 Platelets

Y. Zhou, J. Vleugels, T. Laoui & O. Van der Biest

Department of Metallurgy and Materials Engineering, Katholieke Universiteit Leuven, De Croylaan 2, B-3001 Leuven, Belgium

(Received 28 January 1994; revised version received 15 July 1994; accepted 11 August 1994)

Abstract

Toughening of an X-sialon matrix with up to 53 volume percent Al_2O_3 platelets was investigated. The effect of platelet content on both matrix phase composition and mechanical properties of the composites was evaluated. The extent of cracks introduced by Vickers hardness indentations showed a reduced length with increasing platelet content, indicating an increase in fracture toughness. The toughness has been shown to increase from 1·77 MPa · $m^{1/2}$ for pure X-sialon up to 4·16 MPa · $m^{1/2}$ for the composite containing 28 volume percent platelets. For higher platelet additions, toughness increases further but the composition of the matrix shifts to β'-sialon. The E*-modulus of the composites increases with the amount of platelets. The improvement in fracture toughness was attributed to debonding, crack bridging and crack deflection.*

1 Introduction

Sialon ceramics have been investigated extensively due to their remarkable properties which make them suitable for high temperature structural applications.[1–3] They are also being considered for cutting tools; β'-sialons for instance are already being used for machining of cast irons, but they are not suitable for most steels. Our recent research has shown that at the high cutting speeds at which ceramic cutting tools need to be used to be competitive, chemical compatibility with the workpiece material may be a more important selection criterion than other material properties such as hardness.[4,5] A recent study showed that X-sialon ceramics exhibit a much better chemical compatibility with steel at high temperatures compared to β'-sialon based ceramics.[6] The high chemical wear resistance of X-sialon may indicate that cutting tools could be an interesting potential application. However, actual turning trials[7] indicated that the poor toughness of the material caused frequent chipping of the cutting edge. An indentation fracture toughness value of about 1·77 MPa $m^{1/2}$ was measured.[6] The low fracture toughness of X-sialon will thus limit the use of this ceramic in the field of cutting tools.

To overcome this common problem encountered in the application of monolithic ceramic materials, many attempts have been made to improve their fracture toughness. For instance, the incorporation of a second phase into the monolithic ceramic matrix can result in an improved fracture toughness of the composite. Toughening of ceramics has usually focused on the introduction of whiskers into the matrix phase. A recent concern regarding the reinforcing components has shown less interest in whiskers because of several unfavourable aspects, including the high price, toxicity and difficulty in achieving a uniform dispersion during processing. Platelets could be a good alternative to whiskers as a reinforcement in monolithic ceramics because the toughening mechanisms contributing to whisker composites such as crack bridging, debonding, pullout and crack deflection could also operate in platelet ceramic composites.[8,9] Furthermore, the use of platelets in ceramic composites has some advantages over whisker reinforced ceramics, including the ease of dispersion into ceramic matrix at high loading without agglomerates, safer handling and lower cost. In this study, Al_2O_3 platelets are selected to toughen X-sialon ceramic matrix. According to the Si–Al–O–N phase diagram[1] both matrix and reinforcement should be in chemical equilibrium.

A limited number of studies have been published concerning platelet reinforced ceramics. To our knowledge, toughening of X-sialon with Al_2O_3 platelets has never been reported in the literature. In a Si_3N_4–SiC platelet system, Hanninen reported that there was a dependence of fracture toughness on platelet content and direction.[10] A maximum value of 9·9 MPa · $m^{1/2}$ was obtained at 25 vol.% platelets in the plane parallel to the hot press axis and perpendicular to the platelet basal faces, whereas a toughness of 6·8 MPa · $m^{1/2}$ was obtained for the unreinforced Si_3N_4 matrix.[10] Claussen achieved a toughness of 8 MPa · $m^{1/2}$ from approximately 4·8 MPa · $m^{1/2}$ for the matrix, in RBSN with 20 vol.% SiC platelets.[9] In both cases toughness was enhanced, but strength dropped with the

Table 1. Characteristics of starting materials given by the supplier

Si_3N_4	N:	38·36 wt%	FSSS*:	0·41 μm
grade HCST	C:	0·15 wt%	BET:	19·1 m^2/g
LC12-SX	O:	2·06 wt%	β-Si_3N_4:	97%
Starck Berlin	Fe:	70 ppm		
	Al:	46 ppm		
	Ca:	12 ppm		
Al_2O_3	Na:	40 ppm	Particle	
grade SM8	Fe:	15 ppm	size:	submicron
Bailkowski	Si:	60 ppm	α-Al_2O_3:	95%
	Ca:	10 ppm		
	K:	60 ppm		
	Others:	<5 ppm		
SiO_2	Purity:	99·8%		
fumed	Particle			
Sigma U.S.A.	size:	0·014 μm		
Al_2O_3 Platelet	Al:	51%		
grade 2	O:	47%		
Atochem France	F:	1–2%		
	Na:	1500 ppm		
	Si:	500 ppm		
	S:	250 ppm		
	Ca:	200 ppm		
	Size:	10–15 μm diameter		
		1 μm thickness		

*Mean particle size as determined by using Fisher Subsieve Sizer.

addition of platelets into a Si_3N_4 matrix. Ketchion *et al.* attempted to improve the properties of a Si_3N_4 matrix by adding SiC whiskers and platelets.[11] Their results showed that there was no drastic increase in the fracture toughness, nevertheless the platelet containing composites had slightly better values than those containing whiskers. On the other hand, strength was reported to be maintained in the whisker reinforced samples, while there was a significant drop in those containing platelets. Literature on Al_2O_3–SiC platelet composites has also shown an increase in toughness and a decrease in strength with respect to the matrix. For instance, Fischer *et al.* have reported that the toughness of the Al_2O_3-SiC platelet composite increased from the base value for alumina of 4·35 to 5·68 MPa · $m^{1/2}$ for a 30 vol.% SiC platelet loaded sample, while the strength decreased from 346·1 to 198·4 MPa.[12] Becher reported fracture toughness values for SiC platelet reinforced Al_2O_3 close to those obtained with whiskers.[13] As to Al_2O_3 platelet reinforced ceramic composites, Claussen has reported, in a study on a TZP – Al_2O_3 platelet system, an increase in toughness in a low toughness TZP matrix with increasing platelet addition, but a decrease in toughness in a high toughness TZP matrix.[9] The strength dependence was reversed, i.e. the low toughness TZP matrix showed a decrease in strength with increasing platelet content.



Fig. 1. SEM micrograph of Al_2O_3 platelets.

The objective of this study is to investigate the possibility of X-sialon matrix composites reinforced with Al_2O_3-platelets in various volume fractions. Composites with Al_2O_3 platelet loading up to 53 vol.% were fabricated. Their microstructure and mechanical properties were evaluated and compared to the unreinforced X-sialon matrix material.

2 Experimental Procedure

The composition of the composites was based on $Si_{12}Al_{18}O_{39}N_8$ as a matrix material with a wide range of Al_2O_3 platelet addition. The starting materials used in this study were Si_3N_4, Al_2O_3, SiO_2 powders and Al_2O_3 platelet. Their characteristics are summarised in Table 1. The morphology of Al_2O_3 platelets is shown in Fig. 1.

The powder–platelet mixtures were processed via a wet mixing technique. The Al_2O_3 platelet and Si_3N_4, SiO_2 and Al_2O_3 powders in a desired composition were mixed with ethanol, using high density alumina cylinders as media, for about 72 h.

The resulting slurries were then heated on a sand bath for about 1–2 days in order to evaporate the alcohol. The mixture of platelet–powders obtained after drying was in the form of granulates.

A dense product was obtained by hot-pressing using graphite dies under moderate vacuum (<1 Pa). Hot-pressing schedule followed in this study is the same as the one reported in previous work,[6] e.g. hot-pressing for 1 h at a temperature of 1650°C and a pressure of 30 MPa.

The density of the hot-pressed samples was measured using the water displacement method, recording the mass in air and then immersed in water.

Phase analysis was mainly based on X-ray diffraction patterns obtained either from the hot-pressed surface as received or from a cross-sectioned surface of the specimen. Spectra were recorded using CuKα radiation from 5 to 80° 2θ

at the scan rate of 0·02°/s. Aside from XRD, electron probe micro-analysis (EPMA) was used to assist with phase identification.

The microstructure of the hot-pressed materials and crack propagation from indentation were observed with the scanning electron microscope (JEOL 733). SEM specimens were coated with gold to reduce specimen charging under the electron beam. Secondary and backscattered electron images were recorded at an accelerating voltage of 20 kV.

Vickers hardness was measured on polished samples, using a load of 10 kg. Elastic modulus was measured by the resonance frequency method with a Grindo-sonic apparatus using a test bar of approximately 25 mm long, 4 mm wide and 2·5 mm thick.

Comparative values for the fracture toughness of the different materials were obtained by the indentation method. Examination of crack morphology was made with electron micrographs on Vickers indentations for all specimens. The fracture toughness was calculated using the following equation derived by Anstis *et al.*[14]

$$K_{Ic} = 0{\cdot}016\ (E/Hv)^{1/2}\ P/c^{3/2} \qquad (1)$$

where E is the elastic modulus (Pa); H_v is the Vickers hardness (N/m^2); P is the Vickers load (N); and c is the radius of the crack length (m).

Samples for transmission electron microscope (TEM) were prepared by mechanical thinning, dimpling and then ion milling with an argon beam. Ion milled foils were coated with carbon for the examination in a JEOL 200CX microscope operating at 200 kV.

3 Results

The different grades with the amount of platelets added, are listed in Table 2.

Typical SEM micrographs of the platelet reinforced composites are shown in Figs 2 and 3. The examination of SEM micrographs revealed a dense, crack free hot-pressed body for all the composites. The pores appearing on polished surfaces could be due in part to platelet pullout during polishing. The reinforcing platelets are uniformly dispersed throughout the X-sialon matrix, without apparent cluster formation. However, the platelets are anisotropically oriented, with their basal planes preferentially aligned normal to the hot-pressing direction. This type of orientation of platelets suggests that a considerable rearrangement of platelets occurred during the liquid phase sintering of the powder mixture. The alignment of platelets was facilitated by the uni-axial load during hot pressing.

Table 2. Platelet content of the composite materials and phases identified by XRD

Sample	*Volume percent of platelets (vol. %)*	*Phase type*		
		X-sialon	*β'-sialon*	*α-Alumina*
XA0	0	X-sialon		
XA7	7·179	X-sialon		Al_2O_3
XA13	13·39	X-sialon		Al_2O_3
XA18	18·83	X-sialon		Al_2O_3
XA23	23·63	X-sialon		Al_2O_3
XA28	27·88	X-sialon		Al_2O_3
XA43	43·61	X-sialon	β'-sialon	Al_2O_3
XA53	53·71		β'-sialon	Al_2O_3

When the volume fraction of Al_2O_3 platelets increased to 53%, platelets appeared more interlocked and locally sintered together, the microstructure obtained was free of cracks and large pores as shown in Fig. 3.

The results of the X-ray diffraction (XRD) phase analysis of the hot pressed composites are summarised in Table 2. A single X-sialon phase pattern was found in sample XA0, corresponding to an Al_2O_3-platelet free X-sialon starting composition. Both X-sialon and Al_2O_3, which are the main and secondary phases, respectively, were observed in

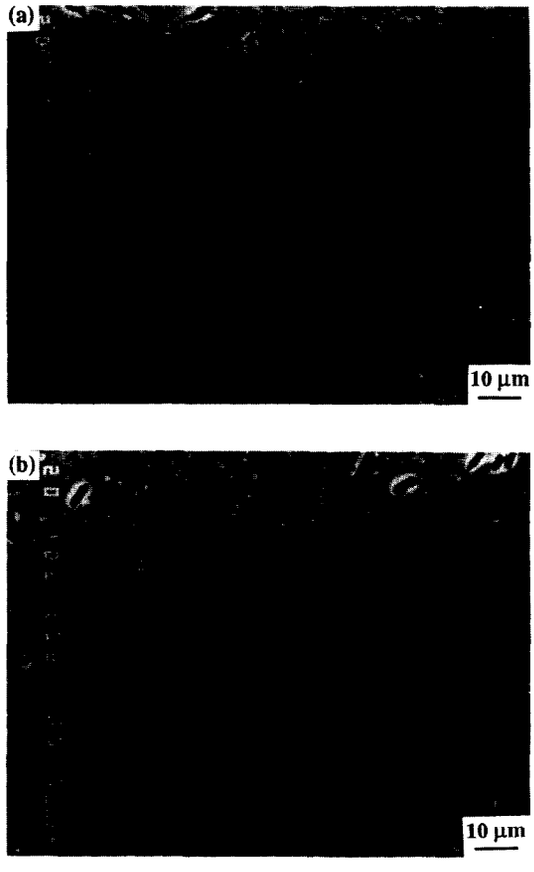


Fig. 2. SEM micrographs of the polished sections of Al_2O_3-platelet–X-sialon matrix composite containing 28 vol.% platelets. (a) Normal to the hot-pressing direction. (b) Parallel to the hot-pressing direction.

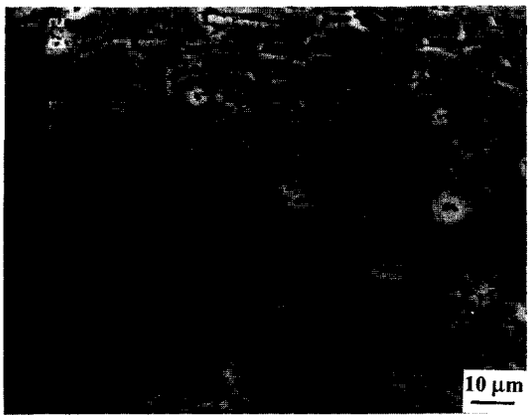


Fig. 3. SEM micrographs of the polished cross-section of sample XA53 containing 53 vol.% of the platelets.

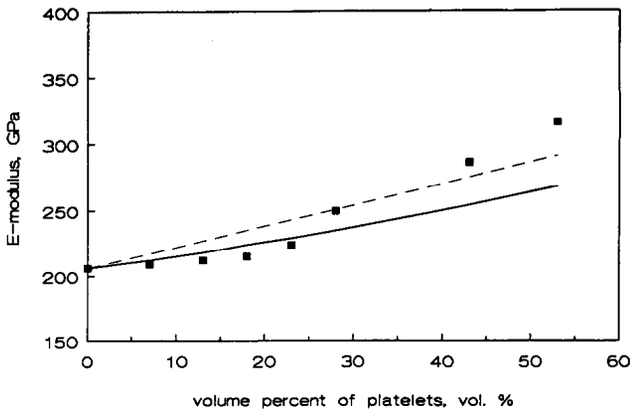


Fig. 4. E-modules vs Al_2O_3 platelet content. Calculated curves according to formula (2) and (3) are indicated.

all X-sialon composite samples with a platelet content up to 28 vol.%. If the platelet content is further increased, β'-sialon is formed in addition to X-sialon. In the composite grade XA53, containing 53 vol.% platelets, the matrix phase is β'-sialon and no X-sialon could be detected.

The measured and calculated densities of the hot-pressed sialon–Al_2O_3 platelet composites are listed in Table 3. The pure X-sialon was found to be pore-free by ceramography and was assumed to be 100% dense. The value of 3·04 g/cm^3 corresponds well with the value of 3·00 g/cm^3 reported by Zangvil *et al.*[15] The calculated density in Table 3 was estimated from nominal volume fraction of intended X-sialon matrix and reinforcing Al_2O_3 platelet, taking the constituent phase density of pure X-sialon phase as 3·04 g/cm^3 and that of Al_2O_3 as 3·93 g/cm^3.

The measured elastic modulus as a function of Al_2O_3 platelet content is shown in Fig. 4. An E-modulus of 367 GPa for a pure dense Al_2O_3 sample processed under the same experimental condition was obtained by Grindo-sonic measurement, thus slightly lower than 380 GPa given as a typical value for dense alumina.[16] The E-modulus obtained in all Al_2O_3 platelet reinforced sialon

Table 3. Measured and calculated densities and Vickers hardness (HV) of sialon–Al_2O_3 composites. The Vickers hardness was measured on a cross-section parallel to the hot-press axis, for directions perpendicular (PER) and parallel (PAR) to the hot-press axis

Sample	*Density g/cm³ (measured)*	*Density g/cm³ (calculated)*	*Percent of calculated value*	*Hardness kg/mm²*	
				$Hv10^{PER}$	$Hv10^{PAR}$
XA0	3·04			1256	1278
XA7	3·09	3·10	99·68	1304	1278
XA13	3·11	3·16	98·42	1288	1220
XA18	3·14	3·21	97·82	1272	1241
XA23	3·16	3·25	97·23	1208	1220
XA28	3·18	3·29	96·66	1270	1222
XA43	3·59	3·43	104·6	1490	1382
XA53	3·76	3·52	106·8	1306	1227

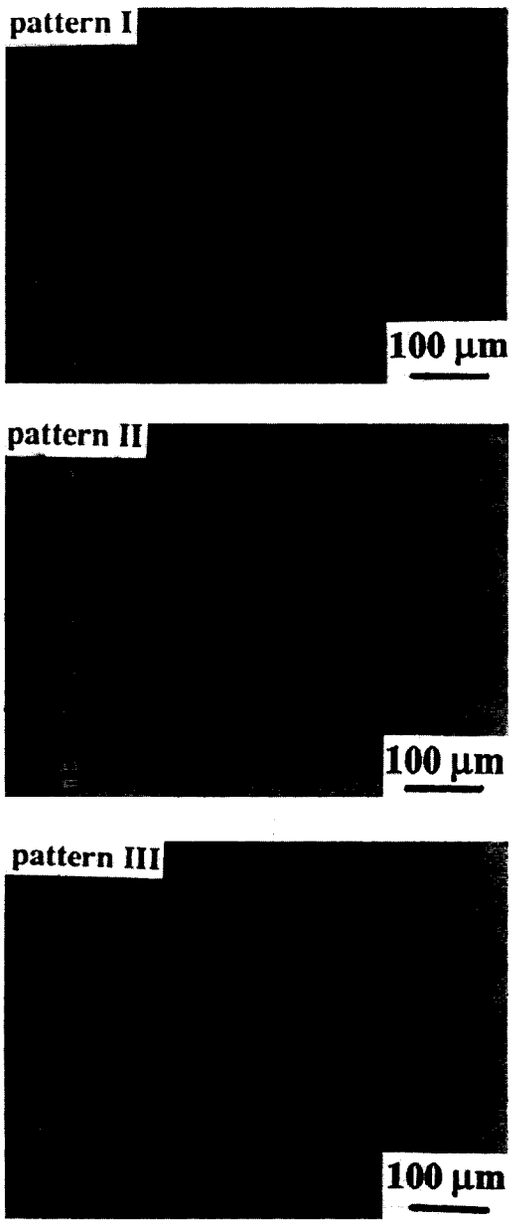


Fig. 5. Illustration of three types of indentation crack patterns. Pattern I: chipping as main feature (pure X-phase sample). Pattern II: well developed crack traces (platelet volume fraction lower than 28%), Pattern III: disruption of clearly defined cracks (platelet volume fraction higher than 28%). The hot-pressing direction is vertically oriented.

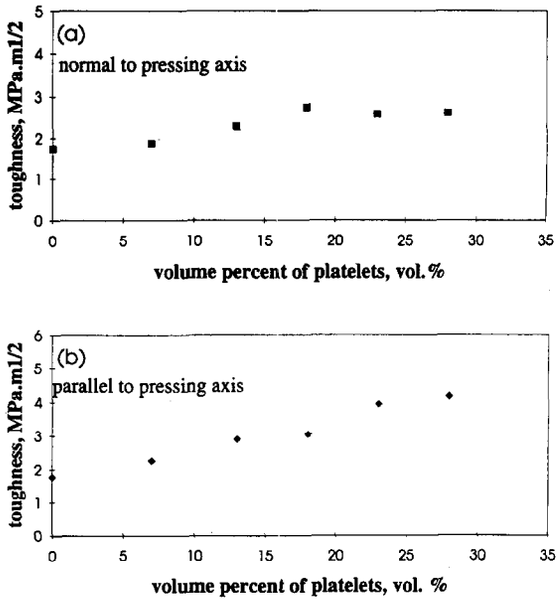


Fig. 6. Fracture toughness as a function of platelet volume fraction in two directions; (a) normal to pressing direction, and (b) parallel to pressing direction.

composites has shown an increase with respect to the platelets content.

The hardness values determined for each sample from Vickers indentation are the average data of five tests. A 10 kg load was applied on a polished cross-section parallel to the hot-press axis, taking care to align the diagonals of the impression with one normal to the hot-pressing axis and the other parallel to the hot-pressing axis in order to identify if there is any anisotropy in hardness. Indentation measurements indicated essentially similar hardness levels between 1200 and 1300 kg/mm^2 for all composite samples, except for the one with 43 vol.% platelets which showed approximately an increase in hardness by 18%, compared to an unreinforced X-sialon matrix (Table 3).

Figure 5 shows three types of indentation crack patterns observed around Vickers hardness indents. The main feature of crack pattern I is chipping around indentation. The pure X-phase sample XA0 was almost exclusively matching pattern I and measurement of crack length was difficult. The brittle nature of X-sialon is evidently illustrated by crack pattern I. Crack pattern II gives clearly defined radial cracks and the crack length was easily measured. Most reinforced X-sialon composites, e.g. XA7, XA13, XA18, XA23, XA28, showed this crack pattern, indicating an improved toughness relative to X-sialon. Crack pattern III shows multiple cracking with cracks emanating from corners as well as from the sides of the indent and is accordingly unsuitable for crack size measurement. Samples XA43 and XA53 have this type of disrupted crack pattern.

Figure 6 shows the fracture toughness of the reinforced composites as a function of direction

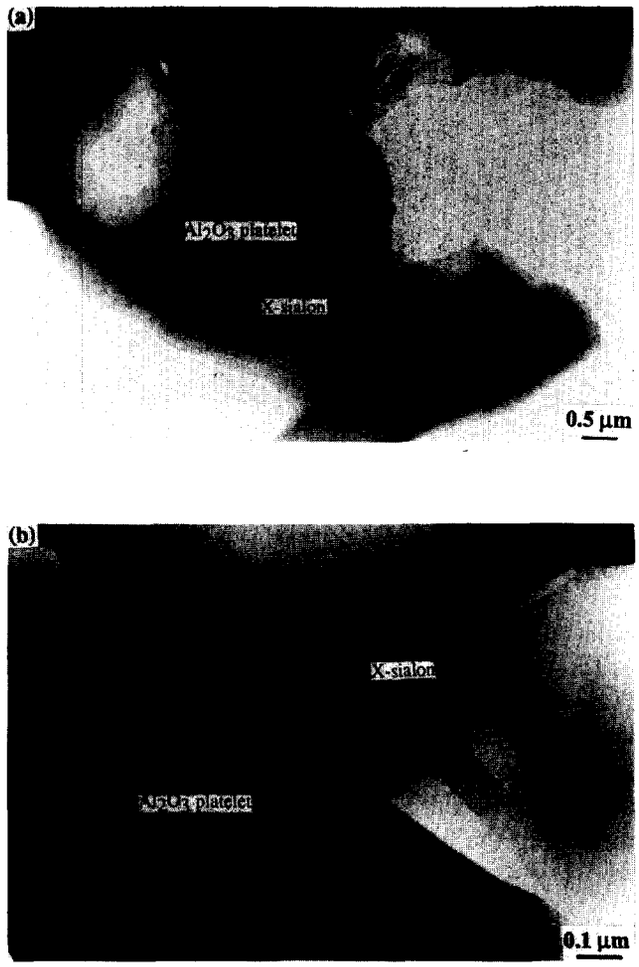


Fig. 7. TEM micrographs (a) and (b) of X-sialon matrix composite with 28 vol.% Al_2O_3 platelets showing a clean interface between X-sialon matrix and Al_2O_3 platelets.

and Al_2O_3 platelet content. There was a general increase in the fracture toughness with increasing platelet content both normal and parallel to the hot-pressing direction. However, a great deal of difference in K_{Ic} values obtained in both directions was noticeable.

For X-sialon based composites, the highest K_{Ic} value was 4·16 MPa · m$^{1/2}$ for a 28 vol.% Al_2O_3 platelet containing sample, whereas unreinforced X-sialon was only 1·77 MPa · m$^{1/2}$. When the addition of platelets exceeded 28 vol.% the value of fracture toughness could not be precisely evaluated with a Vickers indentation method due to disruption of a well defined crack propagation pattern. However, visual examination of these cracks shown in Fig. 5 reveals an apparent shortening of crack length both parallel and normal to the hot-pressing direction for higher platelet loaded sialon composites, indicating that the crack resistance is considerably enhanced. A toughness of about 7 MPa · m$^{1/2}$ could be estimated from the extent of the diagonal cracks parallel to the hot-pressing direction for a composite with nominally 53 vol.% platelets.

In TEM micrographs (Fig. 7) a clean interface between the smoothly contoured platelet and the

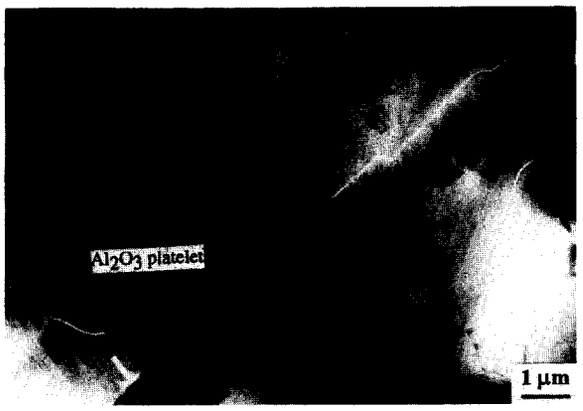


Fig. 8. TEM micrograph of X-sialon matrix composite with 28 vol.% Al_2O_3 platelets showing a crack following the X-sialon matrix–Al_2O_3 platelets interface. The arrow marks the point where the crack is deflected into the interface. Further along the interface, this crack is not always seen edge-on.

adjacent twinned X-sialon grain is observed down to the resolution at which the sample was examined. However, the existence of a very thin amorphous layer between Al_2O_3 platelets and the surrounding matrix is not excluded. As shown in Fig. 8, debonding occurs along the platelet–matrix interface indicating the weak nature of the interface.

4 Discussion

All specimens were easily fabricated to reach densities of more than 97% theoretical values by uniaxial hot-pressing. Difficulties usually experienced with processing of whisker reinforced ceramic composites such as whisker dispersion and low densities,[17] were essentially avoided. The Al_2O_3 platelets were easily dispersed into the matrix, forming highly densified X-sialon and β'-sialon composites at the hot-pressing temperature and pressure.

Analysis of densities of a series of hot-pressed products were consistent with phase analysis results as shown in Table 2. The theoretical density of Al_2O_3-platelet–X-sialon matrix composites was almost reached in samples containing up to 28 vol.% platelets, whereas the fact that measured densities of composites containing 43 and 53 vol.% platelets were higher than those predicted for the Al_2O_3-platelet–X-sialon composite can be explained by the shift from X-sialon to β'-sialon phase (density is about 3·1–3·2 g/cm^3) and the apparent growth of the platelets.

Indeed if one studies the microstructure of the composite with 53 vol.% platelets (Fig. 3) one notices that the volume fraction of platelets is much higher than the nominal value of 53 vol.%. Also the average size of the platelets appears to have increased somewhat. The composition of the

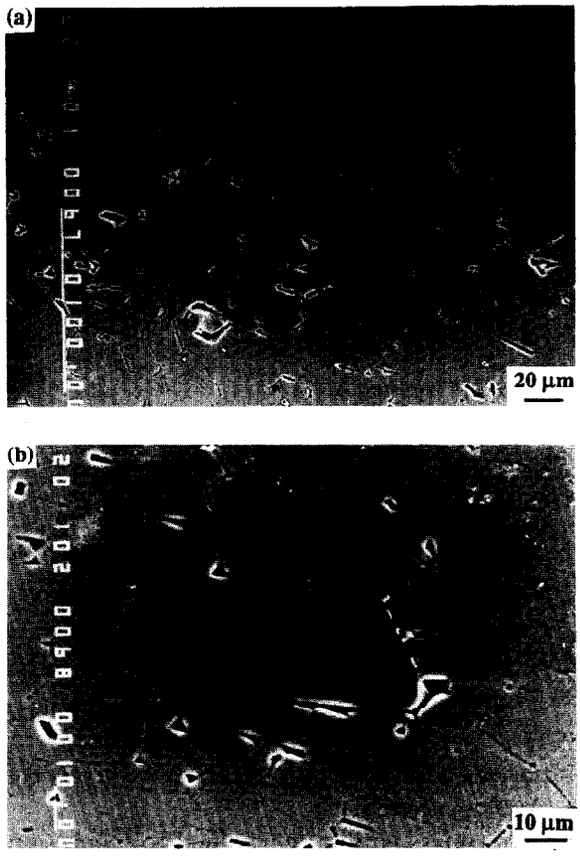


Fig. 9. SEM micrographs of the polished and etched cross section of sample with 53 vol.% Al_2O_3 platelets in Al_2O_3 matrix at two magnification; lower magnification (a) and higher magnification (b).

matrix phase of composite XA53 and pure X-sialon XA0 was compared using EPMA. An average value of 1·28 for Al–Si ratio was obtained in the pure X-sialon sample (XA0), but an average value of 0·72 was obtained in the matrix of a composite with 53 vol.% content of platelets (XA53), indicating a much lower Al content in the matrix composition. Hence it is considered that part of the Al_2O_3 powder which was intended to go to the X-sialon matrix is consumed by the growing platelets. As a consequence, the composition is shifted from the X-sialon composition towards the β'-sialon solubility region in the phase diagram.

To understand the platelet growth at high platelet volume fraction, a composite made with pure Al_2O_3 matrix containing 53 vol.% Al_2O_3 platelets was prepared under the same experimental condition as X-sialon composites. Figure 9 shows the microstructures of this sample which was polished and then etched using HF. Substantial platelet growth was clearly observed in the Al_2O_3 matrix composite with the size of the platelets increasing by a factor of about 6. The equation of the form $G^3-G_0^3 = Kt$,, where G_0 is the initial grain size, G the grain size after hot pressing, t the holding time, and K a temperature-dependent growth rate constant, has been used to

Table 4. Comparison of Al_2O_3 grain growth rate constants

Source	*k* ($\times 10^{-18}$ m^3/s)		
	1600°C	*1650°C*	*1800°C*
Al_2O_3 platelet (in this study):			
parallel to hot-pressing direction		2·24	
perpendicular to hot-pressing direction		146·68	
Pure Al_2O_3 (in Ref. 18)	0·517		
(in Ref. 19)	0·0516		
(in Ref. 20)			980

estimate platelet growth rate and allow direct comparison with Al_2O_3 grain growth rate from the literature.[18–20] The average value of G is equal to $1{\cdot}5L$, where L was the average length of 10 growing platelets in SEM micrographs of the polished cross section. Table 4 shows the results of K obtained both in this study and in the literature. Two points can be noted: first, the platelet growth rate is higher in the direction perpendicular to hot-pressing than the one parallel to hot-pressing. Second, the platelet growth rate perpendicular to the hot-pressing direction is considerably higher than growth rate reported either by Bennison *et al.*[18] or Rödel *et al.*[19] for pure Al_2O_3 at 1600°C, and close to the growth rate reported by Kaysser *et al.*[20] for pure Al_2O_3 at 1800°C. This unusually fast grain growth compared with pure alumina is attributed to the high impurity content of the platelets which includes F, Si, Na and Ca. The observation that platelet growth was much slower in the composite with the same platelet content but with a nominal X-sialon composition, indicates that the presence of silicon nitride appears to slow down the growth of the platelets. It is interesting to note here that β'-sialon can suppress grain growth of alumina.[21] At the lower volume fractions of platelets (28 vol.% and below) no platelet growth was observed. The reasons for that are presumably the higher viscosity of the melt due to the lower impurity content and higher N_2 in the composite composition which may inhibit and suppress growth of Al_2O_3 platelets.

Additional evidence that impurities are responsible for platelet growth can be derived from the following experiments: no shift of matrix composition was found when X-sialon containing 43 and 53 vol.% Al_2O_3 particles (5·5 μm, low soda alumina, grade CTB 3, 99·8%, ALCOA) was processed under the same conditions as the X-sialon–platelet composites. X-sialon matrix was formed in both samples and no β'-sialon could be detected from XRD analysis. Thus the high impurity content of the platelets which includes F, Si, Na and Ca is considered as the main reason for the shift of the matrix composition from the X-sialon into the β'-sialon.

To estimate the E-modulus of Al_2O_3-platelet–X–sialon composites, the formula given by Davidge[22] was applied here, e.g.:

$$E_{\perp HP} = E_1V_1 + E_2V_2 \tag{2}$$

$$E_{\parallel HP} = E_1E_2/(E_2V_1 + E_1V_2) \tag{3}$$

where $E_{\perp HP}$ and $E_{\parallel HP}$ are the E-modulus of the composites in the direction perpendicular and parallel to hot press, corresponding to the direction parallel and normal to the platelet basal plane respectively; E_1 and E_2 represent the E-modulus of matrix phase and reinforcing phase, taking the value of 206 GPa from Grindo-sonic measurement for the pure dense X-sialon and 367 GPa for Al_2O_3; V_1 and V_2 are the nominal volume fractions of the two phases.

As Young's modulus for alumina (367 GPa) is much higher than the one for X-sialon (206 GPa), it is expected that E-modulus of Al_2O_3-platelet–X-sialon composites will increase with increasing platelet volume fraction according to formula (2) or (3). The calculated curves are also indicated in Fig. 4 for comparison with experimental data. Note that the elastic modulus was measured on bars with the long direction normal to the hot-press direction and that these bars were loaded in flexure for the measurement of resonance frequencies. One would expect that for perfect alignment of the platelets formula (2) is applicable rather than formula (3), which indeed is the case for the composite with 28 vol.% platelets, where the platelets are well aligned. At lower volume fractions the data appear to follow formula (3) better. In these composites the alignment with respect to the hot-pressing axis is not perfect. Also the presence of some residual porosity and spontaneous microcracking would need to be taken into account and could explain why the experimental values are slightly below the line for formula (3). In other particulate reinforced composites such as SiC-platelet–Si_3N_4 composite, SiC-platelet–Al_2O_3 composite and some other materials, a decrease of the E-modulus with respect to the matrix has been reported[12,23,24] and has also been attributed to the presence of pores and spontaneous microcracking. In view of the relative magnitude of the thermal expansion coefficient of the two phases ($8{\cdot}0 \times 10^{-6}$/°C for Al_2O_3[16] and $3{\cdot}7$–$4{\cdot}5 \times 10^{-6}$/°C for X-sialon[25]) spontaneous microcracking is also possible here depending on the size of the platelets. The higher values obtained for composites with 43 and 53 vol.% are due to the platelet growth and the change in matrix to β'-sialon which has a higher E-modulus of about 240 GPa.[26]

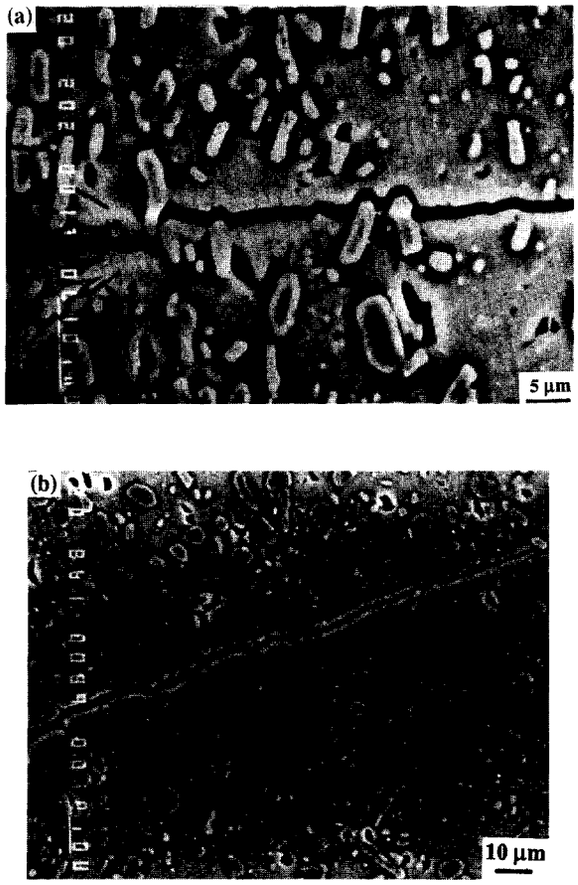


Fig. 10. SEM images of crack propagation in the composite sample with 28 vol.% Al_2O_3 platelets (XA28). (a) Plane parallel to hot-pressing direction. (b) Plane normal to hot-pressing direction.

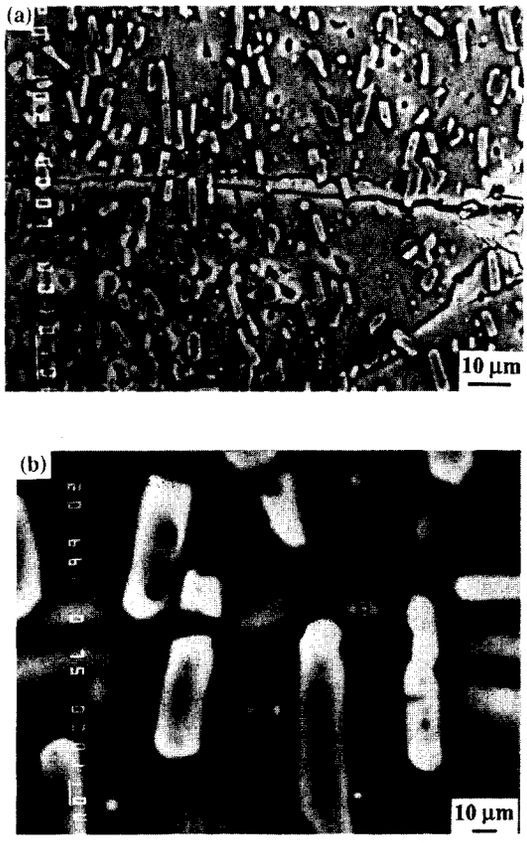


Fig. 11. SEM micrographs (a) and (b) showing crack bridging by Al_2O_3 platelets. B marks bridging sites.

The observed increase in fracture toughness for the Al_2O_3-platelet–sialon matrix composites can be attributed to a combination of crack deflection, crack debonding and crack bridging mechanisms. Figures 10 and 11 further illustrate the extent of crack–microstructure interactions. As shown in Fig. 10, cracks are frequently deflected along platelet–matrix interfaces. In Fig. 11, platelets are seen bridging across the crack wake plane, probably contributing to the greatest extent to the toughness increase over the monolithic X-sialon. A higher degree of toughening was measured when the crack plane propagated parallel to the hot-pressing direction perpendicular to Al_2O_3 platelet basal planes. The increase of fracture toughness increase normal to the hot-pressing axis was lower, because the orientation of platelets is not so favourable for crack deflection and crack bridging.

The composites displayed a much rougher fracture surface as compared to monolithic X-sialon. The fracture surface shown in Fig. 12 (a) illustrates platelet debonding and/or pullout, in contrast to the intragranular fracture exhibited by the unreinforced X-sialon as shown in Fig. 12 (b).

Thermal expansion mismatch and interfacial bonding strength between reinforcing phase and

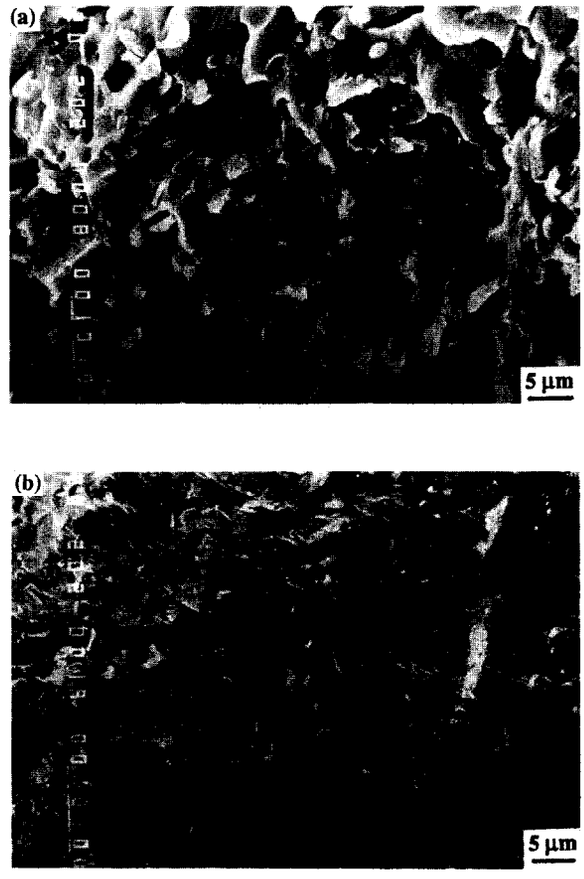


Fig. 12. SEM observation of fracture surface. (a) Al_2O_3 platelet reinforced sialon composite showing debonding. (b) Monolithic X-sialon showing intragranular fracture.

matrix are thought to be the crucial factors determining the toughening of ceramics. Since the thermal expansion coefficient of Al_2O_3 is much higher than that of X-sialon a high internal stress might be generated by this large thermal expansion mismatch in this system; circumferential compression and radial tension are created in the matrix and the platelet is in tension. In this situation cracks are deflected around the platelets. Interfacial bonding at the alumina–X-sialon interface appears to be sufficiently weak for the cracks to follow the contours of the platelets as can be seen in Fig. 8.

5 Conclusions

X-sialon phase can be toughened by Al_2O_3 platelet additions. Reinforcing Al_2O_3 platelets were not agglomerated and well distributed throughout the matrix. Due to hot-pressing, however the material shows alignment of Al_2O_3 platelets with the basal face normal to the hot-pressing direction.

The mechanical properties of hot-pressed sialon composites reinforced with Al_2O_3 platelets were investigated as a function of Al_2O_3 platelet content. The toughness has been shown to increase from 1·77 MPa · $m^{1/2}$ for pure X-sialon up to 4·16 MPa · $m^{1/2}$ for the composite containing 28 vol.% platelets. For higher platelet additions, toughness increases further but the composition of the matrix shifts to β'-sialon. A Young's modulus of 250 GPa and hardness of 1270 kg/mm^2 were achieved in the X-sialon containing 28 vol.% platelet.

SEM and TEM observations of the crack propagation behaviour, along with the fractography result revealed the evidence of debonding, crack bridging and crack deflection, all contributing to the toughening of X-sialon by Al_2O_3 platelets.

References

1. Jack, K. J., Review: sialons and related nitrogen ceramics. *J. Mater. Sci.*, **11** (1976) 1135–58.
2. Gauckler, L. J., Lukas, H. L. & Petzow, G., Contribution to the phase diagram Si_3N_4–AlN–Al_2O_3–SiO_2. *J. Am. Ceram. Soc.*, **58** (1975) 346.
3. Ekstrom, T. & Nygren, M., Sialon ceramics. *J. Am. Ceram. Soc.*, **75** (1992) 259–76.
4. Vleugels, J., Laoui, T., Vercammen, K., Celis, J. P. & Van Der Biest, O., Chemical interaction between a sialon cutting tool and iron-based alloys. Accepted for publication in *Mater. Sci. Engng.*, **A187** (1994) 177–82.
5. Laoui, T., Vleugels, J., & Van Der Biest, O., Effect of secondary phase on sialon/steel chemical interaction. Accepted for publication in *J. Mater. Sci. Engng.*, **A183** (1994) L19–L21.
6. Zhou, Y., Vleugels, J., Laoui, T. & Van Der Biest, O., Preparation and properties of x-sialon ceramics. *J. Mater. Sci.* (submitted).
7. Vleugels, J., & Van Der Biest, O., unpublished work.
8. Faber, K. T. & Evans, A. G., Crack deflection processes: I, theory. *Acta Metall.*, **31** (1983) 565–76.
9. Claussen, N., Ceramic platelet composites. In *Proc. 11th RISØ Int. Symp. Metallurgy and Materials Science 1990, Structure Ceramics Processing, Microstructure and Properties*, ed. J. J. Bentzen, J. B. Bilde-Sørensen, N. Christiansen, A. Horsewell and B. Ralph. RISØ National Laboratory, Roskide, Denmark, 1990, pp. 1–12.
10. Hanninen, M., Haber, R. A. & Niesz, D. E., Mechanical properties of silicon carbide platelet and particulate reinforced silicon nitride. *Ceram. Trans.*, **19** (1991) 749–56.
11. Ketchion, S. M., Leng-Ward, G. & Lewis, M. H., SiC dispersoid-reinforced Si_3N_4 composites. *Ceram. Trans.*, **19** (1991) 757–64.
12. Fischer III, W. F., Haber, R. A. & Anderson, R. M., Mechanical properties of alumina matrix composites reinforced with silicon carbide platelets and particulate. *Ceram. Trans.*, **19** (1991) 773–80.
13. Becher, P. F., Microstructural design of toughened ceramics. *J. Am. Ceram. Soc.*, **74** (1991) 255–69.
14. Anstis, G. R., Chantikul, P., Lawn, B. R. & Marshall, D. B., A critical evaluation of indentation techniques for measuring fracture toughness: I, direct crack measurements. *J. Am. Ceram. Soc.*, **64** (1981) 533–8.
15. Zangvil, A., Gauckler, L. J. & Ruhle, M., Indexed x-ray diffraction data for the sialon x-phase. *Mater. Sci. Lett.*, **15** (1980) 788–90.
16. Morrell, R., *Handbook of Properties of Technical & Engineering Ceramics*. Her Majestys Stationery Office, London 1985, pp. 95.
17. Hayami, R., Si_3N_4–SiC whisker composite material. *Mater. Sci. Res.*, **20** (1986) 663–74.
18. Bennison, S. J. & Harmer, M. P., Grain-growth kinetics for alumina in the absence of a liquid phase. *J. Am. Ceram. Soc.*, **68** (1985) C-22–C-24.
19. Rödel, J. & Glaeser, A. M., Anisotropy of grain growth in alumina. *J. Am. Ceram. Soc.*, **73** (1990) 3392–401.
20. Kaysser, W. A. & Sprissler, M., Effect of a liquid phase on the morphology of grain growth in alumina. *J. Am. Ceram. Soc.*, **70** (1987) 339–43.
21. Takatori, K., Pressureless sintering and mechanical properties of alumina–sialon composites. *J. Mater. Sci.*, **26** (1991) 4484–90.
22. Davidge, R. W., *Mechanical Behaviour of Ceramics*, ed. R. W. Cahn, M. W. Thompson and L. M. Ward. Cambridge Unversity Press, 1979, pp. 24.
23. Chos, Y. S. & Green, D. J., Silicon carbide platelet/alumia composites: II, mechanical properties. *J. Am. Ceram. Soc.*, (1993) 1452–8.
24. Sakai, K., Matsuhiro, K. & Furuse, Y., Mechanical properties of SiC platelet reinforced ceramic composites. *Ceram. Trans.*, **19** (1991) 765–72.
25. Yamai, I. & Ota, T., Thermal expansion of sialon. *Adv. Ceramic Mater.*, **2** (1987) 784–8.
26. Gauckler, L. J., Prietzel, S., Bodemer, G. & Petzow, G., Some properties of β-$Si_{6-x}Al_xO_xN_{8-x}$. *Nitrogen Ceramics*, ed. F. L. Riley. Noordhoff, Leyden, Netherlands, 1977, pp. 529–37.

Journal of the European Ceramic Society **15** (1995) 307–312
© 1995 Elsevier Science Limited
Printed in Great Britain. All rights reserved
0955-2219/95/$9.50

Fracture Tests for Ceramics under Mode-I, Mode-II and Mixed-Mode Loading

T. Fett, G. Gerteisen, S. Hahnenberger, G. Martin & D. Munz

Forschungszentrum Karlsruhe, Institut für Materialforschung II, and Universität Karlsruhe, Institut für Zuverlässigkeit und Schadenskunde im Maschinenbau, D 76021 Karlsruhe, Germany

(Received 26 July 1993; revised version received 2 June 1994; accepted 28 July 1994)

Abstract

In the theoretical part of this paper a wide data base of stress intensity factors is presented for three types of tests appropriate for mixed-node investigations on ceramic materials. In the experimental part the test methods are applied to determine the failure behaviour of Al_2O_3 under mixed-mode loading. In particular, the influence of the starter crack, modelled by a narrow saw-cut and a pre-crack is illustrated.

1 Introduction

Regarding ceramic material interest is increasing in the failure behaviour under mixed-mode conditions.[1-4] The aim of the investigations is:

(1) to determine the fracture toughness data K_{Ic} K_{IIc}.
(2) to check the failure criteria by which failure under mixed-mode conditions can be predicted from the fracture toughness values K_{Ic}, K_{IIc}.

In this paper stress intensity factors will be presented for three types of tests appropriate for mixed-mode investigations. Their applications to Al_2O_3 will be demonstrated.

2 Bending Tests with Bars Containing Oblique Edge Notches

Bending specimens containing edge-cracks or narrow saw-cuts are often used in the determination of fracture toughness of ceramic materials. Whilst cracks orthogonal to the specimen surfaces are applied in K_{Ic}-determination, oblique edge-cracks are appropriate for mixed-mode fracture. Figure 1 illustrates the geometrical data of a specimen loaded in a four point bending test.

The stress intensity factors are given by

$$K_I = \sigma F_I \sqrt{\pi a}\,,\ K_{II} = \sigma F_{II} \sqrt{\pi a}\,;\ \sigma = \frac{3}{2}\frac{S_1 - S_2}{BW^2}P \quad (1)$$

where B is the specimen thickness and F_I, F_{II} are the geometric functions. A literature overview of these data is given in Ref. 5.

3 Three Point Bending with Eccentric Notch

Asymmetric bending arrangements have been studied by several authors using different methods.[6-10] In Ref. 10 the weight function method was applied. The stresses in the symmetrically supported three-point bending bar (Fig. 2) have been studied by Filon[11] who derived an analytical solution for the stress state. This solution, which take into consideration the stress magnification due to the line contacts of the rollers, is given by

$$\sigma_x = -\frac{3yPL}{2W^3} - \frac{4P}{L}\sum_{n=1}^{\infty} \frac{\sinh mW/2 - mW/2 \cosh mW/2}{mW + \sinh mW} \cos mx \cosh my$$

$$- \frac{4P}{L}\sum_{n=1}^{\infty} \frac{my \sinh mW/2}{mW + \sinh mW} \cos mx \sinh my$$

$$- \frac{4P}{L}\sum_{n=0}^{\infty} \frac{\cosh MW/2 - MW/2 \sinh MW/2}{\sinh MW - MW} \cos Mx \sinh My$$

$$- \frac{4P}{L}\sum_{n=0}^{\infty} \frac{My \cosh MW/2}{\sinh MW - MW} \cos Mx \cosh My \quad (2)$$

$$\tau = \frac{4P}{L}\sum_{n=1}^{\infty}\frac{mW/2\cosh mW/2}{mW+\sinh mW}\sin mx\sinh my$$

$$-\frac{4P}{L}\sum_{n=1}^{\infty}\frac{my\sinh mW/2}{mW+\sinh mW}\sin mx\cosh my$$

$$+\frac{4P}{L}\sum_{n=0}^{\infty}\frac{MW/2\sinh MW/2}{\sinh MW-MW}\sin Mx\cosh My$$

$$-\frac{4P}{L}\sum_{n=0}^{\infty}\frac{My\cosh MW/2}{\sinh MW-MW}\sin Mx\sinh My \quad (3)$$

with $m = 4n\pi/L$, and $M = 2(2n+1)\pi/L$

In order to determine the geometric function F_I and F_{II} defined by

$$K_I = \sigma_0 F_I\sqrt{\pi a}\,,\ K_{II} = \sigma_0 F_{II}\sqrt{\pi a}\,;\ \sigma_0 = \frac{3}{2}\frac{PL}{W^2B} \quad (4)$$

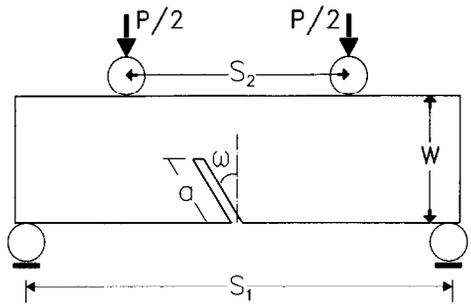


Fig. 1. The oblique edge-crack under four-point bending load.

Table 1. Geometric function for the edge-cracked plate in bending: influence of the crack length a/W and the angle ω on F_I

$\omega(°)$	$a/w = 0{\cdot}1$	0·2	0·3	0·4	0·5	0·6	0·7
0	1·049	1·058	1·126	1·26	1·495	1·915	2·71
15	0·980	1·02	1·058	1·185	1·365	1·698	2·30
22·50	0·935	0·955	0·985	1·090	1·26	1·53	2·04
30	0·874	0·883	0·91	0·985	1·12	1·32	1·74
40	0·765	0·752	0·772	0·810	0·90	1·032	1·03
45	0·699	0·68	0·695	0·710	0·794	0·89	1·09
60	0·450	0·446	0·451	0·467	0·510	0·56	0·64
90	0	0	0	0	0	0	0

Table 2. Geometric function for the edge-cracked plate bending: influence of the crack length a/W and the angle ω on F_{II}

$\omega(°)$	$a/w = 0{\cdot}1$	0·2	0·3	0·4	0·5	0·6
0	0	0	0	0	0	0
22·5	0·23	0·216	0·215	0·220	0·235	0·265
30	0·286	0·278	0·274	0·275	0·286	0·302
40	0·335	0·320	0·310	0·312	0·321	0·340
45	0·344	0·329	0·316	0·321	0·326	0·349
60	0·306	0·304	0·302	0·306	0·315	0·318
90	0	0	0	0	0	0

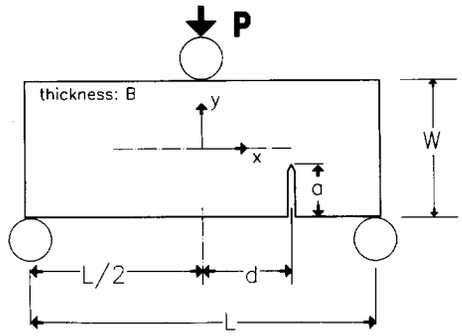


Fig. 2. Geometrical data of the asymmetric notched bending bar.

the mode-I and mode-II stress intensity factors were calculated by use of the mode-I and mode-II weight functions given in Ref. 10. The results are expressed by the normalized geometric functions $F'_I = F_I\,(1-a/W)^{3/2}$ and $F'_{II} = F_{II}\,(1-a/W)^{1/2}$, where

Table 3. Normalized geometric function for mode-I F'_I

L/W	a/W	$2d/L = 0{\cdot}2$	0·4	0·6	0·7	0·8	0·9
2	0·2	0·6145	0·5032	0·3521	0·2564	0·1345	−0·0011
	0·3	0·5240	0·4210	0·2864	0·2094	0·1274	0·0497
	0·4	0·4648	0·3664	0·2468	0·1837	0·1206	0·0601
	0·5	0·4235	0·3276	0·2194	0·1648	0·1106	0·0584
3	0·2	0·6179	0·4755	0·3252	0·2496	0·1604	0·0344
	0·3	0·5315	0·4067	0·2745	0·2070	0·1331	0·0533
	0·4	0·4720	0·3581	0·2398	0·1801	0·1187	0·0571
	0·5	0·4280	0·3220	0·2148	0·1615	0·1079	0·0547
4	0·2	0·6187	0·4625	0·3111	0·2399	0·1651	0·0607
	0·3	0·5330	0·3989	0·2673	0·2034	0·1364	0·0597
	0·4	0·4729	0·3536	0·2362	0·1785	0·1194	0·0583
	0·5	0·4278	0·3196	0·2132	0·1605	0·1075	0·0545
8	0·2	0·6101	0·4553	0·3035	0·2282	0·1551	0·0825
	0·3	0·5279	0·3945	0·2630	0·1976	0·1333	0·0682
	0·4	0·4692	0·3511	0·2341	0·1757	0·1180	0·0597
	0·5	0·4250	0·3184	0·2123	0·1593	0·1065	0·0537

Table 4. Normalized geometric function for mode-II

L/W	a/W	$2d/L = 0{\cdot}2$	0·4	0·6	0·7	0·8	0·9
2	0·2	0·0557	0·0868	0·1069	0·1359	0·2146	0·3893
	0·3	0·0743	0·1167	0·1453	0·1750	0·2315	0·3093
	0·4	0·0899	0·1378	0·1649	0·1858	0·2172	0·2522
	0·5	0·1041	0·1513	0·1709	0·1825	0·1979	0·2116
3	0·2	0·0553	0·0696	0·0638	0·0649	0·0871	0·1912
	0·3	0·0712	0·0895	0·0856	0·0895	0·1131	0·1779
	0·4	0·0827	0·1018	0·0995	0·1036	0·1206	0·1550
	0·5	0·0915	0·1081	0·1063	0·1091	0·1189	0·1358
4	0·2	0·0497	0·0543	0·0481	0·0454	0·0499	0·1049
	0·3	0·0633	0·0693	0·0632	0·0616	0·0692	0·1131
	0·4	0·0722	0·0781	0·0730	0·0723	0·0793	0·1062
	0·5	0·0777	0·0820	0·0783	0·0779	0·0827	0·0971
8	0·2	0·0276	0·0259	0·0258	0·0253	0·0236	0·0249
	0·3	0·0352	0·0333	0·0332	0·0328	0·0311	0·0345
	0·4	0·0395	0·0378	0·0377	0·0373	0·0361	0·0396
	0·5	0·0413	0·0400	0·0400	0·0397	0·0388	0·0413

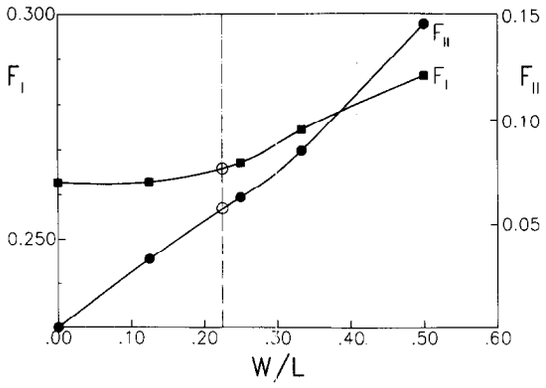


Fig. 3. Interpolations for the two geometric functions F_I and F_{II} (three-point bending with eccentric crack).

F_I, F_{II} are defined by eqn (4). Data for F'_I are entered in Table 3 and Table 4 contains values of F'_{II}.

Tables 3 and 4 allow geometric functions for a wide range of L/W ratios to be interpolated. Since additionally the values for $L/W \to \infty$ are known, namely

$$F_I\Big|_{L/W=\infty} = \left(1-2\frac{d}{L}\right) F_I\Big|_{L/W=\infty,\, d/L=0} \tag{5a}$$

$$F_{II}\Big|_{L/W=\infty} = 0 \tag{5b}$$

all L/W-values in the range $2 \le L/W < \infty$ can be evaluated. For the geometric function F_I at $d/L = 0$ the solution of Nisitani and Mori[12] may be applied.

$$F_I = 1{\cdot}122 - 1{\cdot}121\alpha + 3{\cdot}74\alpha^2 + 3{\cdot}873\alpha^3 - 19{\cdot}05\alpha^4 + 22{\cdot}55\alpha^5 \tag{5c}$$

For practical use interpolation of W/L instead of L/W is recommended as illustrated im Fig. 3 for the geometrical data (L = 20 mm, W = 4·5 mm) used in the experimental part.

4 The Asymmetric Four-point Bending Test

For the determination of the fracture toughness K_{IIc} with edge-notched (or pre-cracked) beams asymmetric bending arrangements (Fig. 4) are recommended which show a negligible mode-I contribution. Stress intensity factors have been determined for special geometrics by FE-calculations

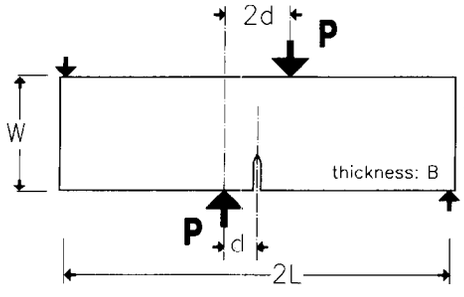


Fig. 4. Geometrical data of the asymmetrically loaded notched bending bar.

Table 5. Geometric function for mode II

a/W	$d/W = 0{\cdot}25$	0·300	0·375	0·500	0·625
0·1	0·3746	0·3428	0·3318	0·3450	0·3599
0·2	0·7881	0·7180	0·6719	0·6633	0·6741
0·3	1·0374	0·9933	0·9560	0·9399	0·9431
0·4	1·1858	1·1819	1·1753	1·1702	1·1695
0·5	1·3120	1·3380	1·3579	1·3661	1·3641
0·6	1·4674	1·5079	1·5387	1·5507	1·5472
0·7	1·6948	1·7318	1·7553	1·7600	1·7547
0·8	2·053	2·0687	2·073	2·0684	2·0635
0·9	2·7563	2·7545	2·7505	2·7467	2·7452

Table 6. Geometric function for mode I

a/W	$d/W = 0{\cdot}25$	0·300	0·375	0·500	0·625
0·1	0·2615	0·3695	0·4241	0·3841	0·2918
0·2	–0·0038	0·1129	0·2110	0·2448	0·2060
0·3	–0·0307	0·0447	0·1184	0·1580	0·1410
0·4	0·0024	0·0483	0·0904	0·1098	0·09534
0·5	0·0407	0·0672	0·0842	0·0806	0·06268
0·6	0·0716	0·0808	0·0771	0·0566	0·03706
0·7	0·0855	0·0769	0·0581	0·03198	0·0164
0·8	0·0641	0·0460	0·0271	0·0106	0·00359
0·9	–0·0048	–0·0002	0·0077	0·01406	0·0138

and energy considerations[9–14] and for a wide range of geometries by the weight function method.[15]

The stresses in this loading case were also computed by Filon[11] with formulae similar to eqns (2) and (3). The geometric functions F_I and F_{II} defined by

$$K_I = \frac{P}{WB}\left(1-\frac{d}{L}\right)\sqrt{\pi a}F_I,\; K_{II} = \frac{P}{WB}\left(1-\frac{d}{L}\right)\sqrt{\pi a}F_{II} \tag{6}$$

are given in Table 5 and 6.[15]

As can be seen from Table 6, the geometric function F_{II} is approximately independent of the value of d/W in the range $0{\cdot}375 \le d/W \le 0{\cdot}625$. An analytical approximation can be given by

$$F_{II} = 3{\cdot}9204\alpha - 5{\cdot}1295\alpha^2 + 14{\cdot}4566\alpha^3 - 26{\cdot}2916\alpha^4 + 17{\cdot}073\alpha^5,\; \alpha = a/W \tag{7}$$

5 Experiments

5.1 Failure diagram for edge-notched specimens

Mixed-mode fracture tests were performed with bending bars having the dimensions B = 3·5 mm, W = 4·5 mm and length >43 mm, made of two Al_2O_3–ceramics (material I: Al_2O_3+ 3% SiO_2, V37; material II: 99.1% Al_2O_3, B40; both materials from Feldmühle AG, Plochingen). The specimens were edge-notched with saw-cuts of 50 μm width. Several specimens were provided with oblique notches, angles ω = 0°, 22·5°, 30° and 40° and relative notch lengths in the range of $0{\cdot}1 < a/W < 0{\cdot}4$. In Fig. 5 the mode-I stress intensity factors at failure are plotted versus the mode-II stress intensity factors for material

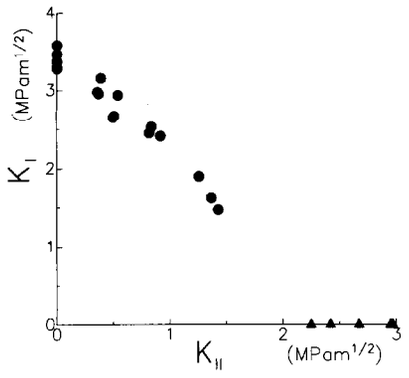


Fig. 5. K_I vs K_{II} at failure for Al_2O_3 (material I); circles: eccentric three-point bending test, triangles: asymmetric four-point bending test.

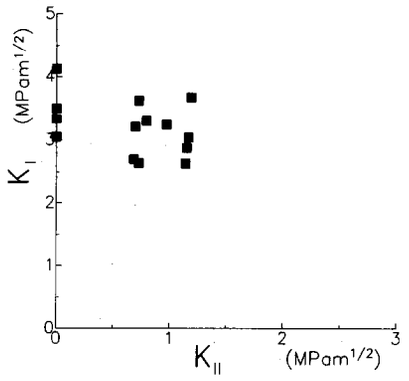


Fig. 6. K_I vs K_{II} at failure for Al_2O_3 (material II) measured with oblique edge notched specimens.

I. The circles represent fracture tests carried out in three-point bending arrangements with eccentric notch (Fig. 2), $a/W = 0{\cdot}35$–$0{\cdot}5$, $L = 20$ mm; the triangles were determined in the asymmetric four-point bending test with $a/W \simeq 0{\cdot}45$–$0{\cdot}5$, $L = 20$ mm, $d = 5$ mm. Figure 6 shows results obtained for material II. The data are obtained in tests with oblique notches. The differences in the K_I–K_{II} dependencies shown in Figs 5 and 6 seem to be caused more by the specific material properties than by the different types of measurement.

5.2 Mode-I and mode-II fracture toughness

Fracture toughness measurements were carried out in three and four-point bending tests with different starter cracks. Small saw-cuts were introduced as well as sharp pre-cracks produced with the bridging method. Some of the precracked specimens were annealed in order to remove residual stresses caused by the bridging procedure, and some pre-cracked specimens were renotched so that $\simeq$ 80–90% of the original crack was removed. The results are shown in Tables 7 and 8.

The numbers in the column heads of the tables denote the test procedure.

1 — saw-cut ($a/W = 0{\cdot}33$), four-point bending (inner roller span 20 mm, outer roller span 40 mm);

Table 7. K_{Ic}, Al_2O_3: (material I)

1	2	3	4	5
3·28	3·08	3·02	3·44	2·93
3·59	2·69	3·31	3·27	3·25
3·47	2·84	3·50	3·28	3·32
3·37	2·80	3·58	3·23	3·14
3·30	2·98	3·59	3·36	3·14
$K_{Ic} = 3{\cdot}40$	2·88	3·40	3·32	3·16

Table 8. K_{IIc}, Al_2O_3: (material I)

6	7	8
2·42	4·16	4·56
2·67	5·15	5·01
2·97	4·90	
2·25	5·19	
2·95		
$K_{Ic} = 2{\cdot}65$	4·85	4·8

2 — pre-cracked ($a/W \simeq 0{\cdot}45$), four-point bending (inner roller span 20 mm, outer roller span 40 mm);

3 — pre-cracked and annealed ($a/W \simeq 0{\cdot}45$), four-point bending (inner roller span 20 mm, outer roller span 40 mm);

4 — saw-cut ($a/W \simeq 0{\cdot}33$), three-point bending (roller span 20 mm);

5 — pre-cracked ($a/W \simeq 0{\cdot}4$–$0{\cdot}35$), three-point bending (roller span 20 mm),

6 — saw-cut ($a/W = 0{\cdot}47$), asymmetric four-point bending;

7 — pre-cracked ($a/W \simeq 0{\cdot}45$–$0{\cdot}50$), asymmetric four-point bending;

8 — pre-cracked and re-notched ($a/W \simeq 0{\cdot}47$), asymmetric four-point bending.

5.3 Influence of the starter crack on the failure diagram

Mixed-mode strength tests were carried out in eccentric three-point bending with the different crack types. Figure 7 shows the results for Al_2O_3 (material I) for specimens with saw-cuts, pre-cracks and re-notched cracks. In Fig. 7 also mode-I fracture toughness data are introduced (small solid circles) which were obtained with pre-cracked specimens annealed for 5 h at 900°C in the vacuum (third column of Table 7).

6 Discussion and Conclusions

6.1 Fracture toughness of Al_2O_3

- The mode-I fracture toughness K_{Ic} of Al_2O_3 has been found to be

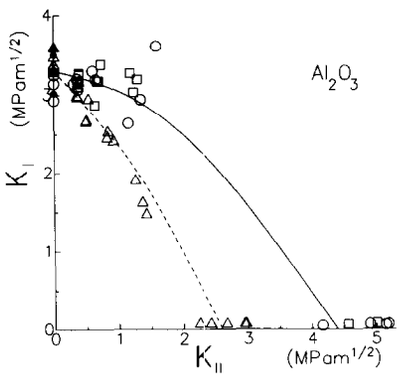


Fig. 7. K_I vs K_{II} at failure for Al_2O_3 measured in eccentric three-point bending tests and asymmetric four-point bending tests. Triangles: specimens with saw-cut, circles: pre-cracked with bridging method, squares: pre-cracked and re-notched specimens, solid circles: pre-cracked and annealed.

3·40 ± 0·13 MPa $\sqrt{m}$ for the edge-notched specimens in four-point bending;
3·32 ± 0·08 MPa $\sqrt{m}$ for the edge-notched specimens in three-point bending;
3·40 ± 0·24 MPa $\sqrt{m}$ for the specimens with an edge-precrack which has been annealed;
3·16 ± 0·14 MPa $\sqrt{m}$ for the specimens with an edge-precrack (without annealing) in three-point bending; and
2·88 ± 0·15 MPa $\sqrt{m}$ for the same specimens in four-point bending.

It is obvious that within the scatter ranges the edge-notched specimens show the same results as the pre-cracked and subsequently annealed specimens.

The precracked specimens which were not annealed show a reduced fracture toughness. One can conclude that the fracture toughness data obtained with pre-cracked specimens are reduced due to internal stresses caused by a misfit between the two crack surfaces. This effect overcompensates an expected *R*-curve effect which would yield an increase in K_{Ic} for the pre-cracked specimens.

- Under mode-II loading the pre-cracked specimens showed — in contrast to the mode-I results — significantly higher fracture toughness than the notched specimens:
  2·65 ± 0·3 MPa $\sqrt{m}$ for notched specimens;
  4·85 ± 0·3 MPa $\sqrt{m}$ for pre-cracked specimens;
  ≃4·8 MPa $\sqrt{m}$ for pre-cracked and then partially re-notched specimens.

  These results may be explained by crack surface interactions. Under mode-II loading the rough surface of the pre-crack can carry a part of the externally applied load and, therefore, the actual crack tip stress intensity factor is reduced, i.e. a crack-shielding effect occurs. Consequently, the applied load has to be increased to reach the critical crack tip stress intensity factor that is necessary for the onset of stable crack propagation followed by catastrophic failure.

From the fact that in the case of partially re-notched specimens (≃80–90% of the pre-crack were re-notched) the K_{IIc} is nearly unaffected by the re-notch procedure we conclude that the main part of mode-II crack shielding effect occurs directly in the neighbourhood of the crack tip.

- The ratio of the mode-II and mode-I fracture toughness results for the notched specimens is $K_{IIc}/K_{Ic} = 0·78$.

6.2 Conclusion

Several types of starter cracks have been used in mixed-mode fracture tests, namely

- edge-notched specimens (saw-cut of 50 μm width);
- pre-cracked specimens (bridge method);
- pre-cracked and subsequently annealed specimens;
- pre-cracked and subsequently re-notched specimens.

If a rising crack-growth resistance curve exists, the tests with specimens with a saw-cut lead to K_{Ic}-values at the onset of crack extension provided that the notch width is small enough. The results for the Al_2O_3 investigated were:

$$K_{Ic} = 3·4 \text{ MPa } \sqrt{m}\,, \quad K_{IIc} = 2·65 \text{ MPa } \sqrt{m}\,, \quad K_{IIc}/K_{Ic} = 0·78$$

As a general result of the measurements presented it is recommended to prefer edge-notched specimens for mode-I and mode-II fracture toughness measurements.

References

1. Petrovic, J. J., Mixed-mode fracture of ceramics. In *Fracture Mechanics of Ceramics*. Plenum Press, New York, Vol. 8, 1986, pp. 127–35.
2. Petrovic, J. J., Mixed-mode fracture of hot-pressed Si_3N_4. *J. Am. Ceram. Soc.*, **68** (1985) 348–55.
3. Shetty, D. K., Rosenfield, A. R. & Duckworth, W. H., Mixed-mode fracture of ceramics from surface flaws in diametral-compression. *J. Am. Ceram. Soc.*, **69** (1986) 437–43.
4. Shetty, D. K., Rosenfield, A. R. & Duckworth, W. H., Mixed-mode fracture in biaxial stress state: application of the diametral-compression (Brazilian disk) test. *Engng Fract. Mech.*, **26** (1987) 825–40.
5. Fett, T., Mixed-mode stress intensity factors for the oblique edge-crack in rectangular specimens. *Int. J. Fract.*, **61** (1993) R3–R10.
6. Jen, W. K., Lin, H. C. & Hua, K., Calculation of stress intensity factors for combined mode bend specimens. In *Fracture*, ed. D. M. R. Taplin. Pergamon Press, Oxford, 1977, Vol. 4., pp. 123–33.
7. Gao, H., Chang, S., Combined mode I–mode II fracture. *Acta Metall. Sinica*, **12** (1981) 1–15 (in Chinese).
8. Maccango, T. M. & Knott, J. F., Brittle fracture under mixed mode I/mode II loading. In *Fracture Control of Engineering Structures, European Conference on Fracture 6* ed. H. C. van Elst and A. Bakker. Engng Mater. Adv. Services, Warley, 1986.
9. Suresh, S., Shih, C. F., Morrone, A. & O'Dowd, N. P., Mixed-mode fracture toughness of ceramic materials. *J. Am. Ceram. Soc.*, **73** (1990) 1257–67.

10. Fett, T., Mixed-mode stress intensity factors for three-point bending bars. *Int. J. Fract.*, **48** (1991) R67–R74.
11. Filon, L. N. G., On an approximate solution for the bending of a beam of rectangular cross-section under any system of load, with special reference to points of concentrated or discontinuous loading. *Phil. Trans., A*, **201** (1903) 63–155.
12. Nistani, H. & Mori, K., Tech Reports of the Kyushu Univ. Vol. 58 (1985), pp. 751–5.
13. Otsuka, A., Tohgo, T., Kiba, T. & Yamada, S., Mode-II fatigue crack growth characteristics and mechanism in aluminium alloy 7N01-T4 weldments under mode-II loading. *Advances in Fracture Research, Proc. ICF 6*, 3, Pergamon, Oxford, 1984, pp. 1671–8.
14. Hem, M.Y., Cao, H. C. & Evans, A. G., Mixed-mode fracture: The four-point shear specimen. *Acta Metall. Mater.*, **38** (1990) 839–46.
15. Fett, T., Stress intensity factors for edge crack subjected to mixed mode four-point bending. *Theor. Appl. Fract. Mech.*, **15** (1991) 99–104.

Journal of the European Ceramic Society **15** (1995) 313–318
© 1995 Elsevier Science Limited
Printed in Great Britain. All rights reserved
0955-2219/95/$9.50

Determination of Oxide Thickness on an Si_2N_2O–ZrO_2 Composite by Spectroscopic Ellipsometry

M. Heim,[a] H. Arwin,[b] J. Chen[a] & R. Pompe[c]

[a] Department of Inorganic Chemistry, Chalmers University of Technology and University of Göteborg, S-412 96 Göteborg, Sweden

[b] Laboratory of Applied Physics, Department of Physics and Measurement Technology, Linköping Institute of Technology, S-581 83 Linköping, Sweden

[c] Swedish Ceramic Institute, Box 5403, S-402 29 Göteborg, Sweden

(Received 13 May 1994; accepted 20 June 1994)

Abstract

Initial oxidation behaviour of an Si_2N_2O–ZrO_2 composite material has been investigated by spectroscopic ellipsometry (SE), X-ray diffraction (XRD), and scanning electron microscopy (SEM). The material was exposed to air in the temperature range of 1000–1450°C and the oxide layer thickness was determined by SE using the Bruggeman effective medium approximation for the modelling of the oxide layer. It was shown that the oxide film on a porous Si_2N_2O–ZrO_2 material can be characterized by SE. The results provide important information about film growth in the initial stage of oxidation of this composite. The optical constants for the composite and ZrO_2 were determined.

1 Introduction

Silicon oxynitride ceramics have good oxidation, corrosion, and thermal shock resistance which makes them interesting for high temperature applications.[1] A low-cost Si_2N_2O–ZrO_2 composite, fabricated by the nitrided pressureless sintering technique (NPS) at the Swedish Ceramic Institute with $ZrSiO_4$ and Si as starting materials, according to eqn (1) was investigated.[2,3]

$$ZrSiO_4 + 3\,Si + 2\,N_2 \rightarrow 2\,Si_2N_2O + t\text{-} + m\text{-}ZrO_2 \quad (1)$$

(t tetragonal, m monoclinic)

Initial oxidation kinetics of nitride materials is expected to be important for the understanding of the entire oxidation mechanism of the material. The measurement of the oxide growth, however, is usually difficult because the oxidized layer is too thin to be detected by gravimetric methods.

To follow the initial stage of oxidation, spectroscopic ellipsometry (SE) has been anticipated to be useful for studying the growth of the oxide layer on this ceramic material. This non-contact and non-destructive optical method, has been increasingly used to study thin film materials. Several investigations on ceramic film deposited on single crystal Si wafers have been done.[4–8] However, to our knowledge, no SE measurement aiming at evaluation of the oxidation process on ceramic composite systems, such as the Si_2N_2O–ZrO_2 material, has been reported.

The advantage in use of spectroscopic ellipsometry in comparison to single wavelength ellipsometry is that by achieving a good fit of the model the probability of receiving 'true' values increases enormously.

The objective of this work has been to demonstrate that SE is a potential method to evaluate the initial oxidation kinetics, not only for monolithic ceramic materials, but also for porous ceramic composites. The kinetic data is useful for the evaluation of internal and external oxidation of the porous composite.

2 Experimental

2.1 Sample preparation

The bulk density of the as-received material was determined to be 2·55 g/cm^3 or 72·4% of the theoretical density and the open porosity of the material is 24·5%.

For the ellipsometry measurement the Si_2N_2O–ZrO_2 composite (3 × 5 × 1 mm) and ZrO_2-ceramic specimen (10 × 10 × 3 mm) were cleaned with a standardized procedure. The samples were

ground and carefully polished with diamond spray down to 0·25 μm fineness and cleaned in water, trichlorethene and acetone in an ultrasonic bath. Afterwards, the samples were cleaned in a solution of H_2O:H_2O_2:NH_3 (25%) = 5:1:1 and a solution of H_2O:H_2O_2:HCl (conc) = 6:1:1, respectively, at 80°C for 5 min and finally washed with distilled water. The samples were dried in dry nitrogen and then oxidized in an alumina tube furnace in static air at 1000, 1250 and 1450°C, respectively, and taken out periodically for the SE measurements.

2.2 Microstructural analysis

The chemical composition of the as-received and in the thermobalance oxidized material was characterized by using X-ray diffractometry (XRD, SIEMENS D5000). The micro-morphology was investigated by scanning electron microscopy (SEM, JEOL JSM-5300).

2.3 Ellipsometry

Only a brief description on SE is given here and a detailed background to ellipsometry can be found elsewhere.[9,10] The technique is based on the polarization changes that occur upon oblique reflection of polarized light. The quantity an ellipsometer measures is the so called complex reflectance ratio $\rho = \tan\psi e^{i\Delta} = R_p/R_s$, where ψ and Δ are the ellipsometric angles, and R_p and R_s are the complex reflection coefficients for light polarized parallel and perpendicular to the plane of incidence, respectively. ψ and Δ can readily be determined with a precision better than 0·01° and once ρ has been measured it can be analyzed with respect to the parameters examined. The most common parameters which are quantified by ellipsometry are film thickness and optical constants of thin films or film-free bulk materials.

In this study we have used a rotating analyser spectroscopic ellipsometer (J. A. Woollam Co.) for measuring ψ and Δ in the wavelength range 3000–8000 Å at an angle of incidence of 68°. Figure 1 shows the principle arrangement of the instrument.

Table 1. Surface phase composition at different oxidation temperatures for an Si_2N_2O–ZrO_2 material

Temperature (°C)	*Phase composition*				
	Si_2N_2O	m-ZrO_2	t-ZrO_2	$ZrSiO_4$	SiO_2
as received	s	s	m	-	-
1000	s	s	m	-	w
1300	w	w	w	m	w
1450	w	w	m	m	w
1600	w	w	w	vs	w

w-weak, m-medium, s-strong, vs-very strong

3 Results and Discussion

3.1 Elemental composition

After exposing selected samples in the thermobalance, the phase compositions were investigated by XRD. The penetration depth was calculated to be 56 μm at $2\Theta = 65°$ (which is much higher than the medium grain size), with the assumption that the material is completely converted to $ZrSiO_4$ and SiO_2. Table 1 shows the results for the exposure for 7 h at the respective temperatures.

The results obtained from XRD investigations show that the chemical reaction of the Si_2N_2O–ZrO_2 system during oxidation can be divided into two temperature areas.

(1) ≈ 1000°C

$$Si_2N_2O\text{–}ZrO_2 + 3/2\,O_2 \rightarrow 2\,SiO_2 + ZrO_2 + N_2 \quad (2)$$

At 1000°C the temperature is too low for ZrO_2 to take part in the reaction. This means that only Si_2N_2O contributes to the reaction and cristobalite (SiO_2) is formed. From other work done on this material.[11,12] it is known that at this temperature external and internal oxidation of the material takes place due to the open porosity.

(2) ≥ 1250°C

$$Si_2N_2O\text{–}ZrO_2 + 5/2\,O_2 \rightarrow ZrSiO_4 + SiO_2 + ZrO_2 + N_2 \quad (3)$$

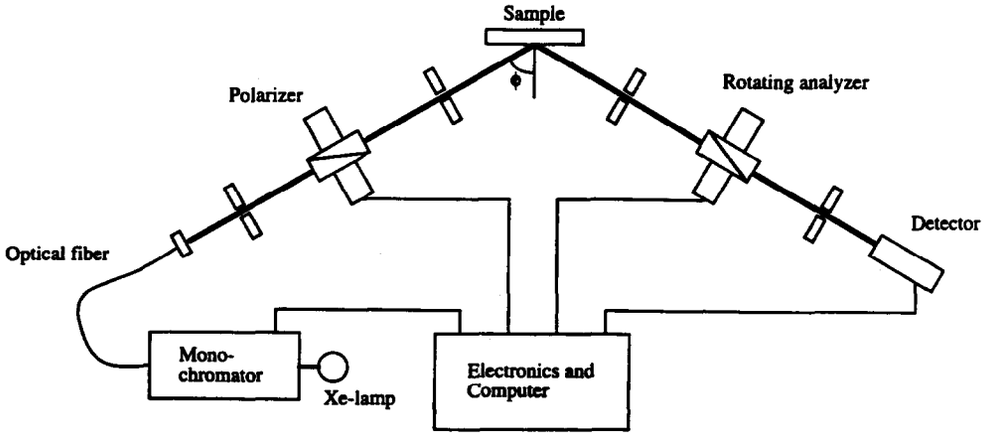


Fig. 1. Spectroscopic ellipsometer of the rotating analyzer type.

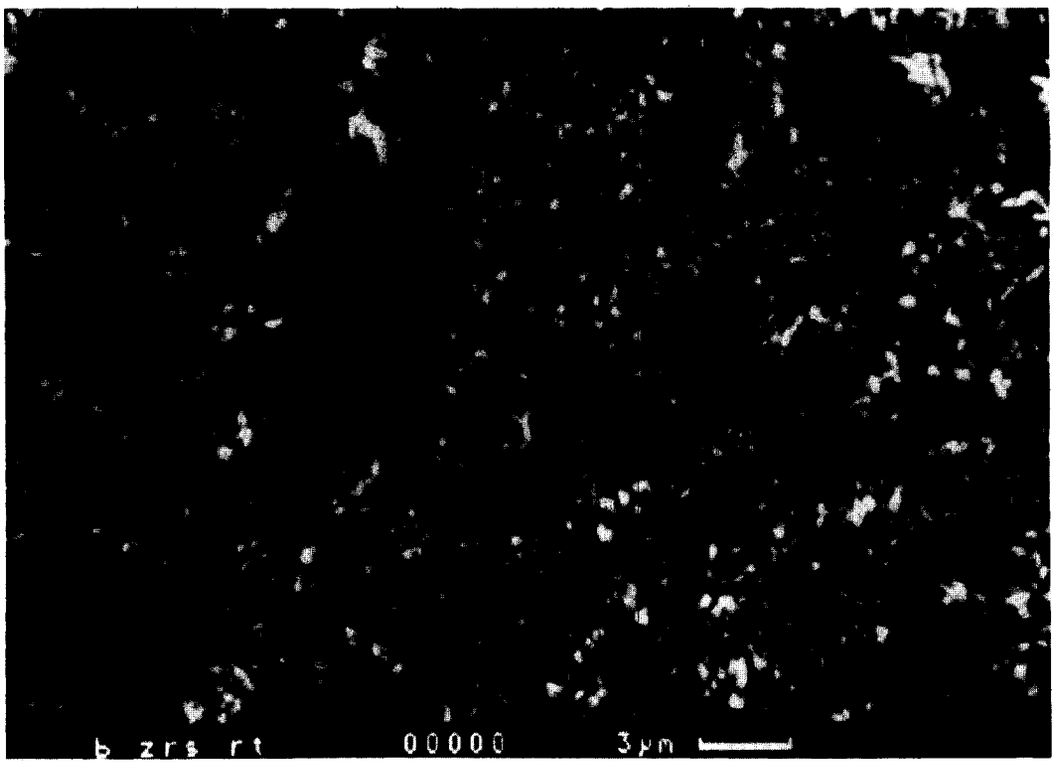


Fig. 2. Backscattered SEM image of a polished surface of an as-received Si_2N_2O–ZrO_2 material (light spots ZrO_2, dark areas Si_2N_2O and pores).

At temperatures ≥ 1250°C zircon ($ZrSiO_4$) and cristobalite are formed as the main reaction products. After initial weight gain the weight stabilizes which is thought to be caused by the formation of a dense oxide film containing $ZrSiO_4$, preventing further oxidation. The higher the temperature the less weight gain occurred.

3.2 Microstructural analysis

Figure 2 shows an SEM image of the surface of the as-received material. The porosity of the material can be clearly seen. Figure 3 shows schematic model of the as-received material, also in cross section.

3.3 Ellipsometric measurement and optical modelling

From the SEM image shown in Fig. 2 it can be seen that the surface is quite porous compared to monolithic ceramics like Si or Si_3N_4.[13] This is caused by the presence of open porosity. Because the grain size (0·5–2 µm) is larger than the selected range of wavelength of incident light, it was assumed that the surface is locally flat and the radius of curvature in a general point of the rough surface is much greater than the selected range of wavelength. The effects of surface roughness can then be neglected in the calculations.

Figure 4 shows the models of samples exposed to 1000°C, and ≤ 1250°C, respectively, which are assumed in the calculations.

At 1000°C only the thickness of the formed SiO_2 is measured. Because ZrO_2 does not react at this temperature, the index of refraction does not change and does not contribute to a change of polarization.

At all temperatures, ZrO_2 could be detected in the surface layer. Because no data for the index of refraction is available for $ZrSiO_4$ in the wavelength range needed for the modelling, the top

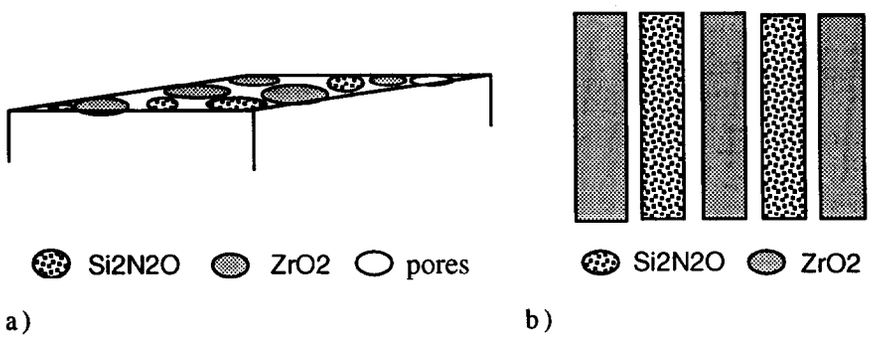


Fig. 3. Schematic illustration of the composition of as-received Si_2N_2O–ZrO_2 material. (a) Top view, (b) cross section.

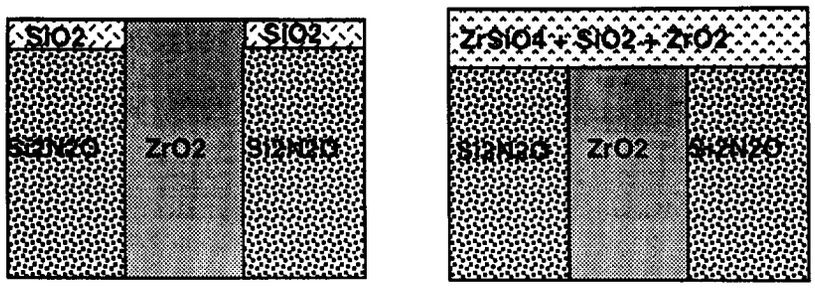


Fig. 4. Models used for oxidation of a Si_2N_2O–ZrO_2 material at (a) 1000°C and (b) ≥ 1250°C.

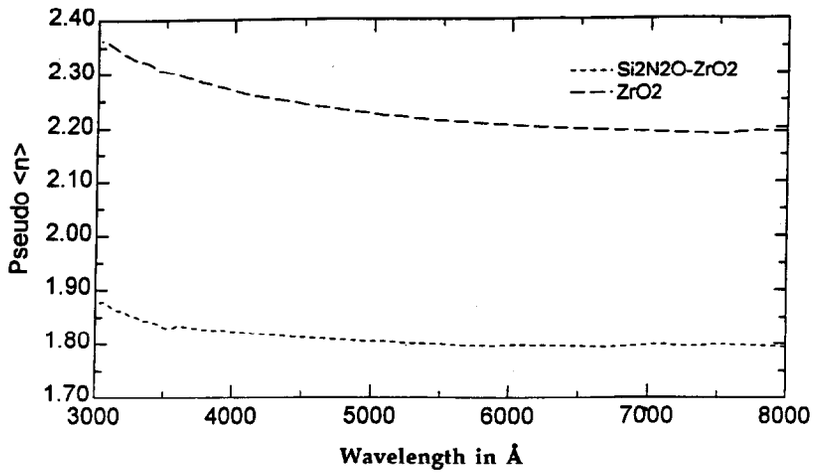


Fig. 5. Refractive indices as function of wavelength for ZrO_2 and Si_2N_2O–ZrO_2 at room temperature.

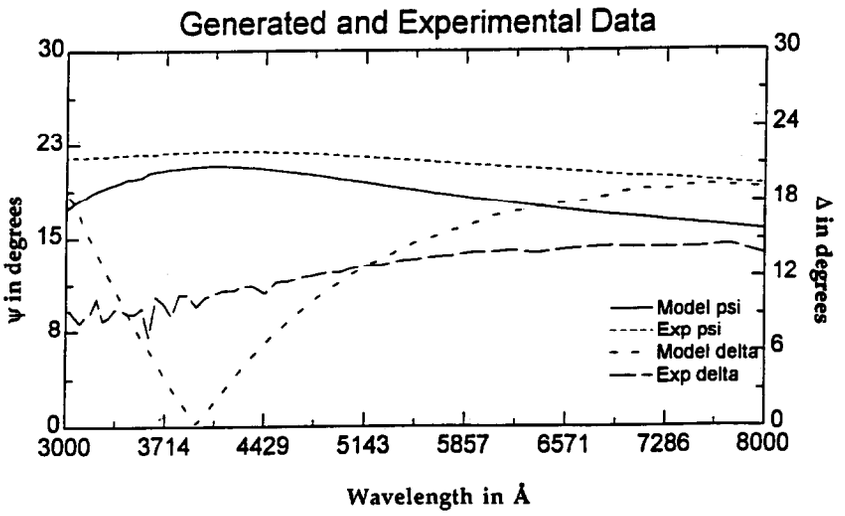


Fig. 6. An example of optical modelling for a sample of Si_2N_2O–ZrO_2 oxidized for 60 min at 1250°C.

layer was modelled on the assumption that it was a physical mixture consisting of two distinct phases, SiO_2 and ZrO_2, and modelled with the Bruggeman effective medium approximation (EMA).[14] Accordingly, the effective (macroscopic) refractive index n of $ZrSiO_4$ can be obtained from the following equations:

$$f_{SiO_2}\frac{n_{SiO_2}^2 - n^2}{n_{SiO_2}^2 + 2n} + f_{ZrO_2}\frac{n_{ZrO_2}^2 - n^2}{n_{ZrO_2}^2 + 2n} \quad (4)$$

and

$$f_{SiO_2} + f_{ZrO_2} = 1 \quad (5)$$

where f_{SiO_2} and f_{ZrO_2} are the relative volume fractions of SiO_2 and ZrO_2 in the material. The refractive index for SiO_2 is taken from the literature,[15] while the refractive index for ZrO_2 was determined experimentally.

Samples of pure ZrO_2 and unexposed Si_2N_2O–ZrO_2 were measured with SE and their

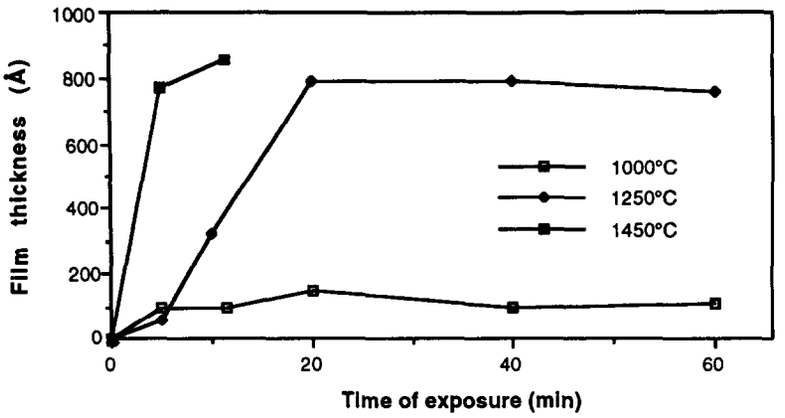


Fig. 7. Oxide film thickness as function of temperature and time of exposure for the Si_2N_2O–ZrO_2 material.

refractive indices were determined by a numeric inversion of $\rho = \tan \psi e^{i\Delta}$ in the wavelength range from 3000 to 8000 Å with results as shown in Fig. 5. Oxide thickness and film composition of Si_2N_2O–ZrO_2 samples were determined with least square regression procedures in a three-phase (Ambient-layer-substrate) model.

After oxidation of the Si_2N_2O–ZrO_2 samples, the thicknesses of the formed $ZrSiO_4/SiO_2$ surface layer were determined ellipsometrically. Figure 6 shows an example of the data fitting using the three-phase model described above. The ψ values of the model fit the experimental data closely and the Δ values show a reasonably good fit, considering the small scale given in the figure. Therefore the error of the determined thickness would be marginal, as described elsewhere.[16]

Figure 7 shows the results obtained for the external oxide scale thicknesses at different temperatures. After exposing the samples for more than 11 min at 1450°C, it was impossible to align the sample due to severe scattering of the incoming light and no results could be obtained.

The measured values of the external oxide film thickness after short exposure time are consistent with the weight gain measurements and SEM investigation.[11] At 1000°C a continuous oxidation of the pore walls occurs at a relatively low constant rate — thus the initial film thickness at the outer specimen surface does not change significantly within the time frame of 1 h. At higher temperatures (≥ 1250°C) the starting oxidation rate is much higher and thus, the thickness of the initial oxide film reaches rapidly a higher level at the outer surface. After that oxygen will diffuse into the interior and oxidize the internal pore surface. SEM observations indicate that a thicker oxide scale has been formed in the surface region of the sample.

Investigations are under way to find a quantitative correlation between the oxide film thickness values obtained through VASE and those directly observed with other methods.

4 Conclusions

(1) The refractive indices of ZrO_2 and Si_2N_2O–ZrO_2 have been determined.
(2) The film thickness of $ZrSiO_4$ formed on oxidized samples has been measured.
(3) A determination of the film thickness is possible on this rather porous ceramic material.

Acknowledgements

Thanks to Dr C. O'Meara (Department of Physics, Chalmers University of Technology) for the SEM investigations. Financial support from the Swedish National Board for Industrial and Technical Development is gratefully acknowledged (Contract No. 88-04709P)

References

1. Hoggard, D. B., Park, H. K., Morrison, R. & Slasor, S., O–Zirconia and its refractory application. *Am. Ceram. Soc. Bull.*, **69** [7] (1990) 1163–6.
2. Pompe, R., Method for producing ceramic composite materials containing silicon oxynitride and zirconium oxide. U.S. Pat. 438 416, 1 June 1987.
3. Pompe, R. & Carlsson, R., *Reaction Sintered Si_2N_2O/ZrO_2 Composite*. Abstract 90th AcerS Meeting, 83-C-88, 1988.
4. Knolle, W. R., Correlation of refractive index and silicon content of silicon oxynitride films. *Thin Solid Films*, **168** (1989) 123–32.
5. Snyder, P. G., Xiong,Y. -M., Woollam, Y. A., Al-Jumaily, G. A. & Gagliardi, F. J., Graded refractive index silicon oxynitride thin film characterized by spectroscopic ellipsometry. *J. Vac. Sci. Technol. A*, **10** (4) (1992) 1462-6.
6. Xiong, Y. -M., Snyder, P. G., Woollam, J. A., Al-Jumaily, G. A., Gagliardi, F. J. & Mizerka, L. J., Controlled index of refraction silicon oxynitride films characterized by variable angle spectroscopic ellipsometry. *Thin Solid Films*, **206** (1991) 248–53.
7. Xiong, Y. -M., Snyder, P. G., Woollam, J. A., Al-Jumaily, G. A., Gagliardi, F. J. & Mizerka, L. J., Optical characterization of silicon oxynitride thin films by variable angle spectroscopic ellipsometry. *Surface and Interface Analysis*, **18** (1992) 124–8.

8. Xiong, Y.-M., Snyder, P. G., Woollam, J. A., & Krosche, E. R., Silicon nitride/silicon oxynitride/ silicon dioxide thin film multilayer characterized by variable angle spectroscopic ellipsometry. *J. Vac. Sci Technol. A*, **10** (4) (1992) 950–4.
9. Azzam, R. M. A. & Bashara, N. M., *Ellipsometry and Polarized Light*, North-Holland, Amsterdam, 1977.
10. Azzam, R. M. A., *Selected Papers on Ellipsometry*, SPIE Optical Engineering Press, Bellingham, 1991.
11. Heim, M., Pompe, R., Arwin, H. & Chen, J., High temperature oxidation behaviour of an Si_2N_2O–ZrO_2 composite, In *Proc. of the 5th International Symposium on Ceramic Materials & Components for Engines*, Shanghai, 1994.
12. O'Meara, C., Heim, M. & Pompe, R., The oxidation behaviour of a porous Si_2N_2O–ZrO_2 composite material, submitted for publication.
13. Chen, J., Arwin, H., Heim, M. & Sjöberg, J., Oxidation of pure Si_3N_4: spectroscopic ellipsometry and glancing angle X-ray diffraction studies. In *Proc. of the International Conference on Silicon Nitride-Based Ceramics*, Stuttgart, 4–6 October, 1993, Trans Tech Publications, 1994, pp. 301–6.
14. Kuiper, E. T., Koo, S. W., & Habraken, F. H. P. M., Correlation of refractive index and silicon content of silicon oxynitride films. *J. Vac. Sci.*, **B1**, (1983) 62.
15. Maltison, I. H., Interspecimen comparison of the refractive index of fused silica. *J. Opt. Soc. Am.*, **55** (1965) 1205–9.
16. Chen, J., Arwin, H. & Lindqvist, O., Spectroscopic ellipsometry measurement of the oxide thickness on silicon nitride ceramics. In *Proc. of the 5th International Symposium on Ceramic Materials & Components for Engines*, Shanghai, 1994.

Journal of the European Ceramic Society **15** (1995) 319–328
© 1995 Elsevier Science Limited
Printed in Great Britain. All rights reserved
0955-2219/95/$9.50

The Oxidation Behaviour of a Porous Si_2N_2O–ZrO_2 Composite Material

Colette O'Meara,[a] Maiken Heim[b] & Robert Pompe[c]

[a] Department of Physics and [b]Department of Inorganic Chemistry, Chalmers University of Technology and University of Göteborg, S-412 96 Göteborg, Sweden
[c] Swedish Ceramic Institute, Box 5403, S-402 29 Göteborg, Sweden

(Received 13 May 1994; accepted 20 June 1994)

Abstract

The oxidation behaviour of a low-cost, porous Si_2N_2O–ZrO_2 composite material produced without the use of sintering aid was investigated in air between 1000 and 1520°C. The extent of internal oxidation was found to be dependant on the oxidation temperature. At temperatures ≤ 1300°C considerable internal oxidation of the material occurs with concommitant large weight gains. The material exhibits excellent oxidation resistance at high temperatures (>1300°C) and the higher the oxidation temperature the lower the weight gain. A very thin layer of oxide primarily consisting of $ZrSiO_4$ forms on the internal pore walls which, together with the surface oxide layer, protects the material from further oxidation. At 1300°C the stresses induced in the matrix by the volume expansion of the oxidation products cause severe cracking of the material on cooling from the annealing temperature. Following oxidation exposures at temperatures ≥1300°C the unstabilised ZrO_2 phase in the matrix is inhibited from undergoing the t–m *transformation. This is most probably due to the dissolution of nitrogen in ZrO_2 resulting in the stabilised, non-transformable* t'-ZrO_2 *phase.*

1 Introduction

The improvement in toughness hoped for by the inclusion of partially stabilised zirconia into a silicon nitride-based matrix has not been realised. This is mainly due to the additional stabilisation of zirconia by nitrogen which prevents the martensitic transformation from *t–m* ZrO_2 under mechanical stress.[1] In addition, the formation of oxidation prone zirconia oxynitride phases during material fabrication inhibits the use of these materials at intermediate temperatures (500–800°C) and the results from high-temperature oxidation studies are not promising.[2,3]

In this work a Si_2N_2O–ZrO_2 composite is examined which has been produced for high-temperature application. The material has been fabricated by the NPS technique without the use of sintering aid/stabiliser. Nitridation and subsequent reaction sintering via the reaction: $Si_3N_4 + ZrSiO_4 \rightarrow 2\ Si_2N_2O + ZrO_2$ results in a porous microstructure consisting of Si_2N_2O and unstabilised ZrO_2 and which avoids the formation of undesirable zirconium oxynitride phases. The high-temperature behaviour of porous silicon-based materials differs considerably from that of dense materials because of the inherent open porosity. Although the oxidation rate will be correlated to the net area available for reaction it has been found that the rate of oxidation appears to decrease at higher temperatures. This paper examines the oxidation behaviour of the porous composite in the temperature range 1000–1520°C.

2 Experimental

2.1 Material

A Si_2N_2O–ZrO_2 composite, fabricated without sintering aid by the NPS technique from Si and $ZrSiO_4$ was used in this work. The material was produced at the Swedish Ceramic Institute.[4,5] The as-received density was determined to be 2·55 g/cm^3 or 72·4% of TD with 24·5% open porosity. The stoichiometric composition of the sintered material was 64 wt% Si_2N_2O and 36 wt% ZrO_2.

2.2 Oxidation exposures

Specimens for oxidation were cut with a diamond saw into samples of dimensions 3 × 4 × 10 mm, polished with various grades of SiC paper and then ultrasonically cleaned in acetone and alcohol. Sample holders of Al_2O_3 were used. The samples were oxidized in an alumina tube furnace in the range 1000–1520°C in flowing dry air with 6 l/h

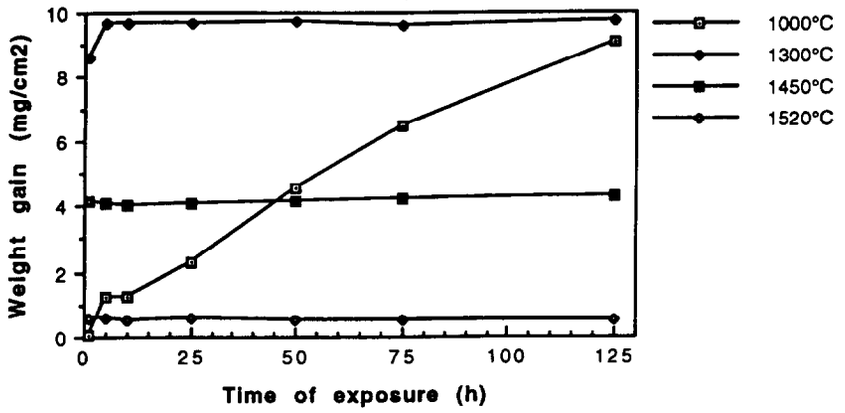


Fig. 1. Weight gain of Si_2N_2O–ZrO_2 material exposed at various oxidation temperatures.

flow rate. The samples were intermittently taken out from the furnace and weighed on an analytical balance with ±5 μg sensitivity. In so doing all the samples were rapidly cooled/reheated to the oxidation temperature. This procedure thus also reflected the effect of cycling on the stability of the oxide scale. Other samples were subjected to the same procedure for up to 250 h but when removed from the furnace were used for SEM examination and pore characteristic determinations. Additional oxidation experiments were carried out at 1450°C to examine the effect of scale removal on the weight gain. The samples were oxidized for 1 h, removed from the furnace and weighed. The oxide scale was then taken away by grinding. The samples were then exposed for another hour at the same temperature.

2.3 Microstructural analysis

Phase analysis of the as-sintered and oxidized materials was carried out by X-ray diffractometry (XRD) using a SIEMENS X-ray diffractometer (D5000). Slices of the material of dimensions *ca* 1 cm^2 were exposed in a thermobalance for 7 h at temperatures between 1000 and 1600°C. The X-ray penetration depth was calculated to be 56 μm at $2\Theta = 65°$. The microstructure of as-sintered material was characterised by analytical transmission electron microscopy (TEM/STEM/EDX) in a Jeol 2000 FX TEM/STEM instrument. The microstructure of the oxidised materials was investigated by analytical scanning electron microscopy in surface and cross-section using a CAM Scan S-4 80DV scanning electron microscope (SEM) equipped with a Link eXL EDX analysis system.

2.4 Determination of pore characteristics

All investigations have been carried out on whole unpowdered samples.

2.4.1 Determination of the surface area by nitrogen adsorption

The BET method was used to determine the internal surface area of the material. Specimens of unexposed and oxidized material were degased at 250°C in a Desorb 2300A for 100 min. The measurements were made in a Flowsorb II 2300 (Micromeritics) using N_2 as adsorbant. Around a 10% mean deviation can be expected at low surface areas (1–2 mg^2/g).

2.4.2 Determination of the density by water penetration

The bulk density was determined using Archimedes' principle. The dry weight was first measured,

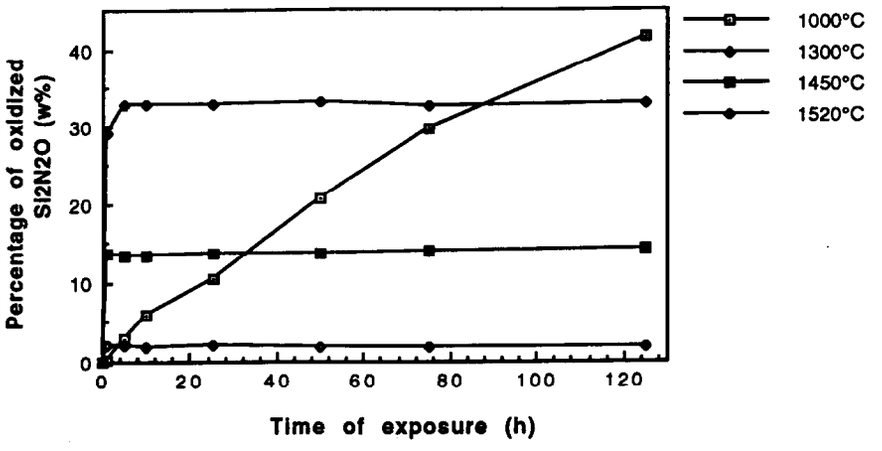


Fig. 2. The percentage of oxidized Si_2N_2O in Si_2N_2O–ZrO_2 material exposed at various oxidation temperatures.

the samples were put under vacuum (<25 mm Hg) for 30 min, then covered with distilled water (under vacuum) and left to soak for 12 h. The wet weight in air and in water was measured and the bulk density was calculated.

2.4.3 Determination of the porosity by mercury porosimetry

The open porosity and volume distribution of the porosity have been measured with the aid of mercury porosimetry using a Micromeritics Poresizer 9305 instrument. The registration of the pressure and the mercury volume intruded in the sample are related to the volume distribution of the pores.

3 Results

3.1 Weight gain versus time curves

The measured oxidation isotherms for samples cyclically oxidized at 1000, 1300, 1450 and 1520°C are shown in Fig. 1. A linear weight increase is observed for material oxidised at 1000°C. The rate of weight gain does not decrease even after long exposure times. At temperatures >1000°C the initial weight gain decreases with increasing oxidation temperature being lowest at 1520°C. At these high temperatures the isotherms show that the maximum weight gain occurs in the first 5 h of exposure after which little or no weight gain takes place.

The oxidation mass balance reaction for the composite is:

$$Si_2N_2O\text{–}ZrO_2 + 3/2O_2 \rightarrow ZrSiO_4 + SiO_2 + N_2(g) \quad (1)$$

As can be seen from eqn (1) ZrO_2 does not contribute to the mass change. Based on the weight change obtained for each measurement at a given temperature, the percentage of reacted Si_2N_2O was calculated and is shown in Fig. 2. In the case of complete oxidation the total weight gain was calculated to be 12·38 wt%. As can be seen from Fig. 1 this percentage was not reached experimentally.



Fig. 3. TEM micrograph showing the general microstructure of as-received Si_2N_2O–ZrO_2 material to consist of sub-micron size ZrO_2 grains (Z) homogeneously distributed in a matrix of sub-micron size Si_2N_2O crystals.

Table 1. Surface phase composition at different oxidation temperatures for Si_2N_2O–ZrO_2 material

Temperature (°C)	*Exposure time (h)*	*Phase composition*				
		Si_2N_2O	*m–ZrO_2*	*t(t')-ZrO_2*	*$ZrSiO_4$*	*SiO_2*
As-received	7	s	s	w	—	—
1000	7	s	s	w	w	w
1300	7	w	w	m	m	w
1450	7	w	w	m	m	w
1600	7	w	w	m	vs	w

w—weak, m—medium, s—strong, vs—very strong.

For the reoxidation experiments at 1450°C the weight increase after reoxidation was found to be approximately 10% of the original weight increase.

3.2 Microstructural analysis

3.2.1 XRD

The identification of oxidation products and phase changes at the various oxidation temperatures and times is detailed in Table 1.

XRD of the surface of the oxidized materials shows an increasing volume of oxidation products, $ZrSiO_4$ and SiO_2, to be present in the scales with increasing temperature reflecting an increasing surface scale thickness. Little amorphous material could be detected. The proportion of *t*–ZrO_2 in the matrix is seen to increase following oxidation at temperatures ≥1300 with a concommitant decrease in the amount of *m*–ZrO_2 as compared with the as-sintered material.

3.2.2 TEM

As shown in Fig. 3 the general microstructure of the as-received material consists of a matrix of sub-micron Si_2N_2O grains in which sub-micron size ZrO_2 grains are homogeneously distributed. The plate-like Si_2N_2O crystals are randomly oriented and of high aspect ratio. The zirconia grains are observed to have an irregular intergranular morphology and were identified by electron diffraction to be predominantly monoclinic (Fig. 4). Small volumes of an amorphous phase surround the matrix grains. Regions of incomplete sintering, containing small (≤ 50 nm) Si_2N_2O grains in a Si rich amorphous phase were frequently observed. A more detailed description of the microstructure can be found in Ref. 6.

3.2.3 SEM

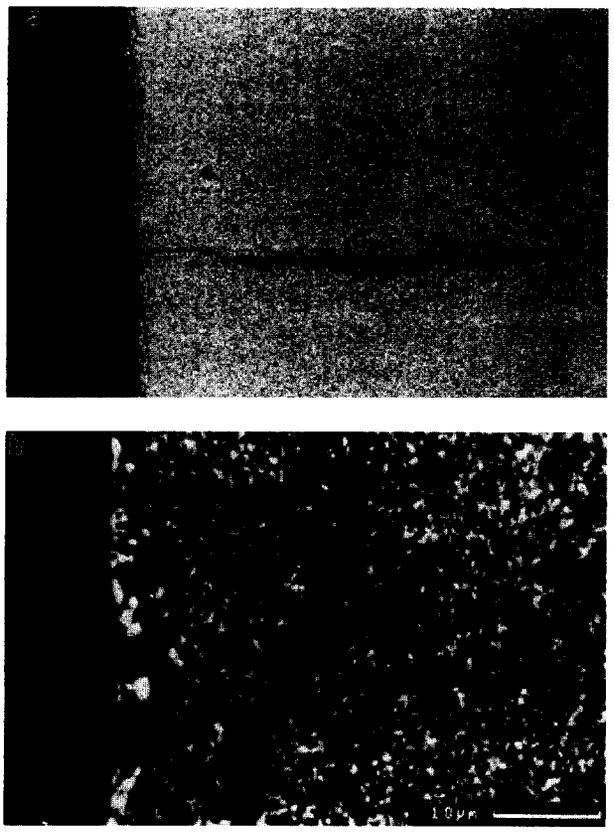
The specimens were examined in SEM in surface and cross-section using the back-scattered electron mode after 2, 10, 50, 100, 150 and 250 h exposure at each temperature. EDX analysis was carried out on cross-section specimens.



Fig. 4. TEM micrograph showing the monoclinic ZrO_2 phase (m) in as-received Si_2N_2O–ZrO_2 material: (a) bright field and (b) dark field.

(1) 1000°C

Compared with the microstructure of as-received material no unambiguous evidence or indication of external or internal oxidation could be detected in SEM. However on cutting the material for preparation for SEM it was observed visually to have 'whitened' all the way through the matrix indicating extensive internal oxidation.







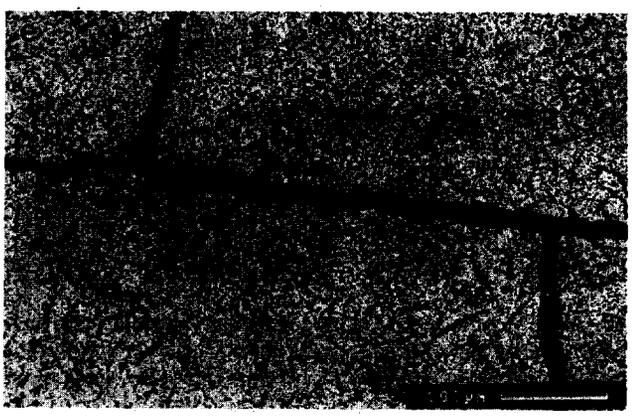


Fig. 5. SEM back-scattered images of the oxide scales of Si_2N_2O–ZrO_2 material exposed at 1300°C. (a) Cross-section showing large cracks in the matrix after 2 h oxidation. (b) Severe cracking observed in the matrix parallel with the surface after 100 h exposure. (c) Cross-section of the oxide scale after 250 h exposure showing $ZrSiO_4$ crystals (Z), crystalline SiO_2 (C) and an amorphous mixed silicate phase (A). (d) A large internal pore in the matrix showing extensive oxidation after 2 h exposure. (e) Oxide surface after 150 h oxidation showing the scale to contain large volumes of $ZrSiO_4$ crystals (Z) and a small volume of crystalline SiO_2 (C).

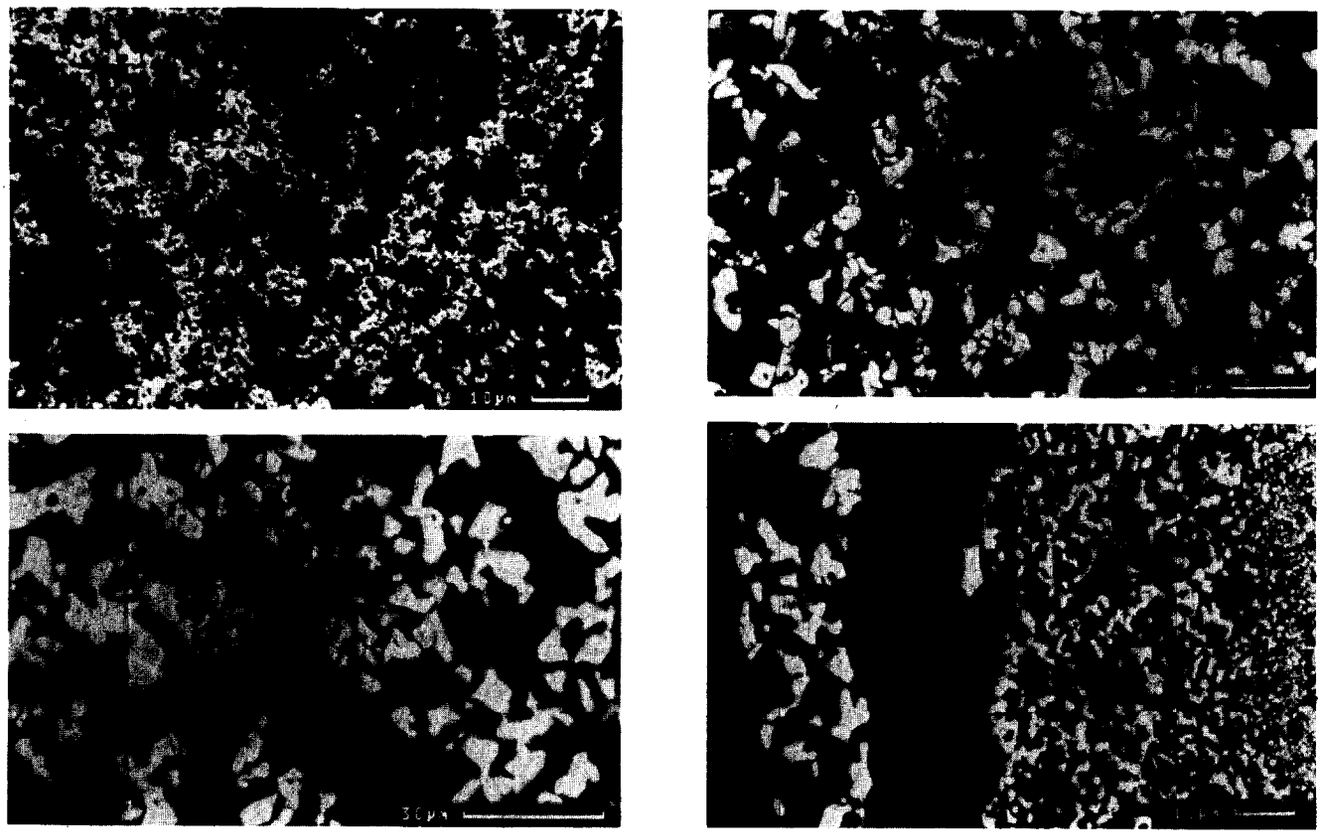


Fig. 6. Back-scattered SEM images of Si_2N_2O–ZrO_2 material exposed at 1450°C. (a) Oxide surface of material exposed for 2 h showing a rough uneven surface. (b) After 100 h extensive cracking of the surface is observed associated with the crystalline silica phase (C). (c) After 250 h the crystalline silica phase (C) assumes a long needle-like morphology. (d) In cross-section duplex scales are seen to form after 50 h exposure showing a region of extensive porosity (P) and a denser outer region with extensive cracking (O).

(2) 1300°C

As is shown in Fig. 5(a) large cracks were observed in the material following oxidation at 1300°C. The cracks frequently extended through the matrix and were of dimensions 10–30 μm in diameter. Additional severe cracking was also observed in the material parallel with and just below the surface (Fig. 5(b)). Cracking associated uniquely with the scale is observed only after longer exposures times (≥100 h). In transverse section thin discontinuous oxide scales ≤2 μm were observed for shorter exposure times. The oxide scale increased in thickness and continuity with time to reach a maximum of approximately 20 μm after 250 h exposure (Fig. 5(c)). Considerable oxidation of larger internal pores was evident in all the specimens (Fig. 5(d)).

As is shown in Fig. 5(e) the scale contained large volumes of small brightly contrasting structures, shown by EDX to contain Zr, Si and O and therefore probably crystalline $ZrSiO_4$, and small volumes of a darker contrasting phase containing Si and O, possibly cristobalite. In addition, an intermediate contrasting phase is observed which contains Si, O and small amounts Fe, Na and K and is possibly an amorphous mixed silicate. The atom number density, size and shape of the crystals increases with increasing exposure time.

(3) 1450°C

Following oxidation at 1450°C the scales have a rough, uneven topography and small cracks are observed within the scale as shown in Fig. 6(a). The cracking of the scale is more extensive after longer oxidation exposures and is observed to be associated with the crystalline silica phase (Fig. 6(b)). A continuous, thick (≤50 μm) oxide scale is observed after short exposure times. No SEM evidence of internal oxidation could be detected.

The phase content of the scales as detected by SEM consists of a large volume of crystalline $ZrSiO_4$, SiO_2 and a mixed silicate phase. After longer oxidation times the atom number density, size and morphology of the crystalline components of the scale show considerable change. The zircon crystals become larger and more particulate with increasing time at temperature as shown in Fig. 6(c). The crystalline silica phase changes in form from almost spheroidal at 100 h to long needle-like grains at 250 h. The scale structure is duplex with an outer more dense region and an inner extensively porous region (Fig. 6(d)).

(4) 1520°C.

After 2 h oxidation at this temperature considerable porosity is observed in the scales in planar section (Fig. 7(a)). With increasing time at temperature the porosity is no longer observed but

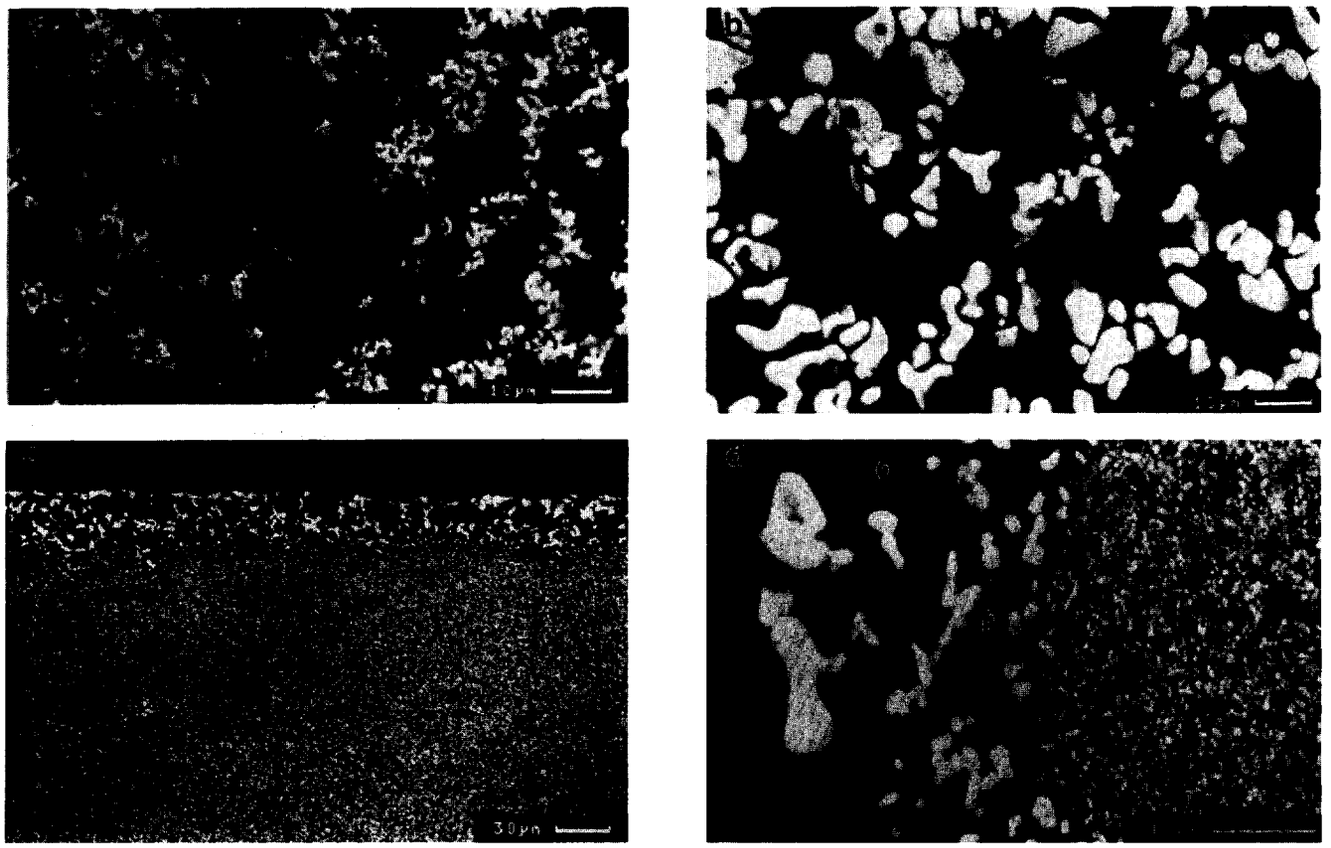


Fig. 7. SEM back-scattered images of Si_2N_2O–ZrO_2 material exposed at 1520°C. (a) Oxide surface after 2 h exposure showing considerable porosity. (b) After 150 h extensive cracking of the surface is observed associated with the crystalline silica phase. (c) Cross-section showing the oxide scale to be up to 50 μm thick after 250 h exposure. (d) Duplex scales are seen to form with a region of extensive porosity (P) and a denser outer region with extensive cracking (O) after 150 h exposure.

extensive cracking is noted associated with the crystalline silica phase (Fig. 7(b)). No evidence of matrix cracking or internal oxidation could be detected. The atom number density of the crystalline components of the scale are observed to increase with increasing time. Duplex oxide scales up to 50 μm thick are seen to develop even at short time exposures at this high temperature. The duplex scale shows extensive porosity in the lower region and extensive cracking in the outer region (Figs 7(c) and (d)).

3.3 Pore characteristics

3.3.1 Specific surface area

The specific surface area of the as-received material was 1·1 ± 0·1 m^2/g. Figure 8 shows selected specific surface area data for samples oxidized for different times at the various oxidation temperatures.

An increase in the specific surface area is observed only at 1000°C. In general the higher the temperature the less the specific surface area differs from that of the as-received material.

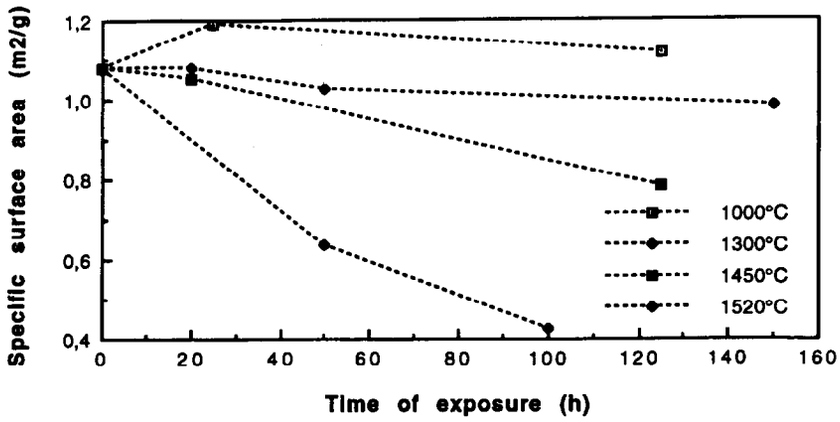


Fig. 8. Specific surface area of Si_2N_2O–ZrO_2 material exposed at various oxidation temperatures.

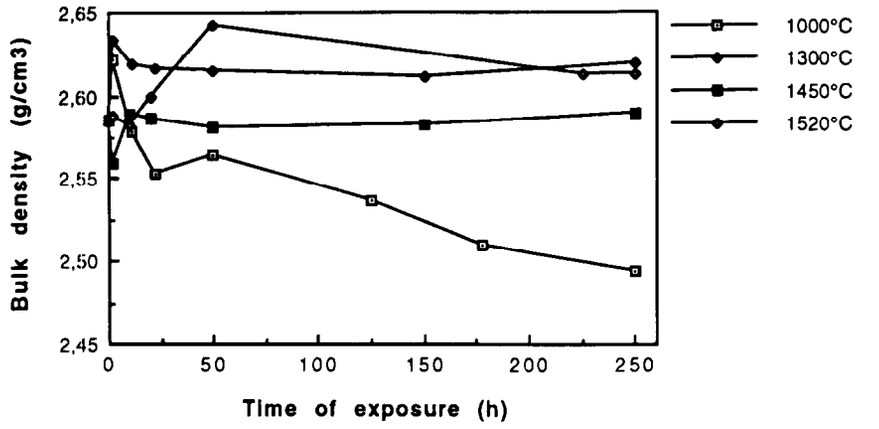


Fig. 9. Bulk density of Si_2N_2O–ZrO_2 material exposed at various oxidation temperatures.

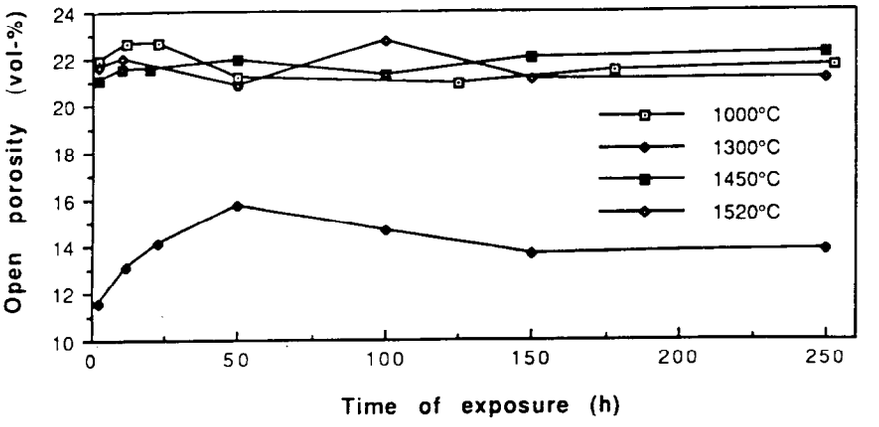


Fig. 10. Open porosity of Si_2N_2O–ZrO_2 material exposed at various oxidation temperatures.

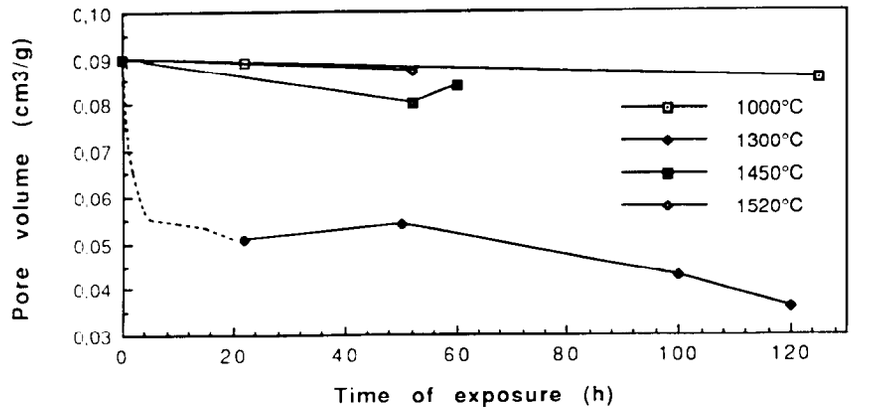


Fig. 11. Pore volume of Si_2N_2O–ZrO_2 material exposed at various oxidation temperatures.

3.3.2 Density

Figure 9 shows the results obtained for the bulk density measurements. The density of the as-received material was determined to be 2·585 g/cm^3.

A significant tendency for density to decrease with time is observed at 1000°C. At all other temperatures the density shows no significant change.

Figure 10 shows the open porosity. The open porosity of as-received material was determined to be 22·3 vol%.

The obtained results show that the open porosity only changes significantly at 1300°C showing a definite decrease.

3.3.3 Pore volume

Porosimetry measurements have been performed on as-received material as well as with oxidized specimens. Figure 11 shows the results for measurements of the pore volume. The pore volume decreases slightly on oxidation at 1000°C. At 1300°C a significant decrease in the pore volume is

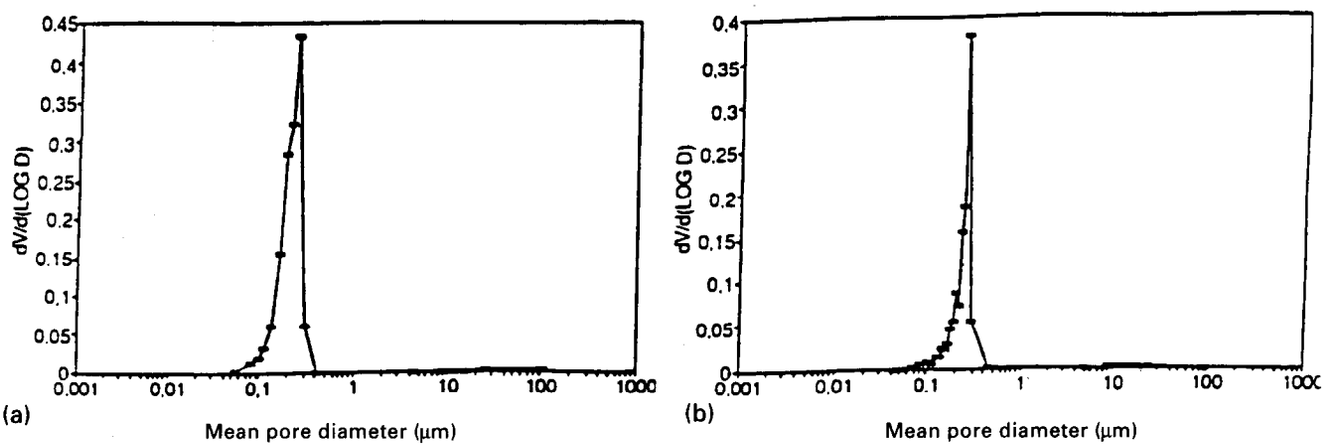


Fig. 12. Pore frequency distribution of a sample of Si_2N_2O–ZrO_2 material: (a) as-received and (b) after oxidation for 120 h at 1300°C.

observed. At higher temperatures the values do not change markedly from that of the as-received material.

Figure 12 shows the pore frequency in as-received material and in a sample exposed for 120 h at 1300°C.

The mean pore diameter is found to be around 0·2 μm. From Fig. 12 it can be seen clearly that neither the mean pore diameter nor the distribution of the pore sizes change significantly.

4 Discussion

In general the results fall into the temperature categories 1000, 1300 and >1300°C in which it is most convenient to discuss the oxidation behaviour.

(1) 1000°C

The linear weight gain curve showing a large and continuous weight increase at this temperature is not consistent with a lack of surface oxide scale formation. The calculations of the percentage of oxidized material show that approximately 40 wt% of the available matrix has reacted. This indicates that a considerable amount of internal oxidation has taken place at this temperature. SEM and XRD show that no oxidation of the ZrO_2 phase had occurred. This implies that oxidation of the Si_2N_2O phase in the pores and pore channels must account for the observed weight gain and results in a thin film of amorphous and crystalline SiO_2 throughout the specimen which could not be detected in SEM. This is reflected in the measured increase in specific surface area, decrease in pore volume and decrease in bulk density as follows:

$$\underset{2\cdot82}{\rho\ (g/cm^3)}\quad Si_2N_2O + 3/2\,O_2 \rightarrow \underset{2\cdot33}{2\,SiO_2} + N_2 \qquad (2)$$

The pores remain open as oxygen diffusion inwards is faster than the oxidation reaction which is slow at this temperature. This results in continued oxidation even after long oxidation times. This type of behaviour is similar to that observed in RBSN materials at low temperatures.

(2) 1300°C

The weight increase is observed to be highest at this temperature and to occur within the first 5 h of exposure. It was calculated that approximately 32 wt% of the Si_2N_2O had been oxidized by this time. This large initial weight increase with formation of thin (2–10 μm) oxide scales is consistent with the occurrence of both internal and external oxidation. As the XRD results show, the ZrO_2 phase is now involved in the oxidation process (eqn (1)) and zircon is formed. This is associated with a large volume increase (~8%). Cristobalite, also detected by XRD and SEM, probably forms during cooling from the oxidation temperature and its formation is also associated with a large increase in volume (~5%). SEM revealed the larger internal pores to be covered with an oxide scale containing zircon, and an Si and O containing phase. Oxidation after the first 5 h is accompanied by a significant decrease in the specific surface area, an increase in density and a decrease in pore volume implying the filling up of internal pores with oxidation products. The oxidation products are of larger volume than the original matrix material and will result in internal stresses and pore filling but will also act as a diffusion barrier to further oxidation. However, due to the volume increase significant internal stresses are built up within the material causing the severe cracking observed at this temperature and which most probably occurred on cooling from the oxidation temperature. If pore closure is responsible for the weight gain stabilisation of the samples after the first 5 h of exposure, then considering the extensive cracking that is observed in the matrix after each cycle, one would expect additional weight gain due to the oxidation of newly exposed surfaces when the samples are replaced in the furnace. However, no additional weight gain is

observed, indicating that complete pore closure does not occur.

The ZrO_2 phase, which is predominantly monoclinic in the as-received material, transforms to t–ZrO_2 at the oxidation temperature (t–m transformation ~1170°C). As it is unstabilised the t-ZrO_2 phase should transform to m-ZrO_2 on cooling. However, the XRD results show t-ZrO_2 to be the main ZrO_2 phase present in the matrix. The inhibition of the t–m transformation can arise from two sources: (i) the stresses in the matrix arising from the volume expansion during internal oxidation mechanically constrain the transformation; and (ii) a high N_2 activity during internal oxidation at these temperatures can result in the dissolution of nitrogen in ZrO_2 forming the stabilised non-transformable t'-ZrO_2 phase. It is possible that both factors contribute to stabilisation but with regard to the similar behaviour observed at higher temperatures (next section) where extensive internal oxidation does not occur, it is thought that nitrogen stabilisation is the most probable explanation and this is presently under investigation in TEM studies.[6]

(3) >1300°C

The material shows excellent oxidation resistance at high temperatures. The weight gain curves show that the higher the oxidation temperature the lower the weight gain. Calculations of the percentage of reacted Si_2N_2O indicate that only 14 and 2 wt% had oxidized at 1450 and 1520°C respectively. This weight gain occurred within the first 2 h of exposure and SEM showed it to be accompanied by the growth of thick predominantly crystalline surface oxide scales (up to 50 μm) with no evidence of internal oxidation. These oxide scales were continuous but considerable microcracking was observed associated with the formation of cristobalite on cooling. Although this implies that rapid external oxidation seals off the surface pores before internal oxidation can occur this does not seem to be the case as the specific surface does not decrease nor is any change noted in pore volume as compared to the as-received material. In addition, in the reoxidation experiments at 1450°C a weight gain of only 10% of the original weight gain (2·7%) was recorded following scale removal and reoxidation. If pore closure was entirely responsible for the low weight gains at this temperature then the weight gain upon reoxidation should be similar to the original weight gain. This indicates that pore closure may not be occurring. Instead, it is thought that the internal pores are rapidly covered with a very thin layer of oxide primarily consisting of $ZrSiO_4$ with small amounts of silica. This layer, together with the surface oxide layer, protects the material from further oxidation which should occur as a result of the surface cracks formed during the thermal cycling excursions.[6]

The XRD results show that the t-ZrO_2 is retained to room temperature as observed following oxidation at 1300°C and is presently under investigation.[6]

In general the oxidation behaviour of the porous composite is similar to that of RBSN material where the oxidation rate is also seen to decrease significantly at higher temperatures. The latter effect has been explained by Davidge who proposed a two stage oxidation process for porous ceramics, namely surface oxidation and the oxidation of the pore channel walls in the interior of the material.[7] At higher temperatures where surface oxidation is more rapid, pore closure will occur before internal oxidation is completed.[9] Although this general trend is similar for the composite as is discussed above, the results of this work indicate that pore closure may not be occurring. Instead it is thought that a very thin layer of oxide primarily consisting of $ZrSiO_4$ forms on the internal pore walls which, together with the surface oxide layer, protects the material from further oxidation. In addition, the composite consists of two highly refractory phases. Although the eutectic of the Si_2N_2O–ZrO_2–SiO_2 system is not known, the XRD results obtained for material exposed at 1600°C show no indications of amorphous material resulting from eutectic melting. This implies that the eutectic temperature lies above 1600°C. The oxidation behaviour is superior to that reported of other Si_3N_4–ZrO_2 or Si_2N_2O–ZrO_2 composites.[2,3,8] The latter have been prepared using metal oxide sintering aids/stabilisers which in general lower the eutectics of the system and decrease the viscosity and softening point of intergranular amorphous phases in the matrix with concommitant decrease in oxidation resistance.

5 Conclusions

(1) In general the trend in the oxidation behaviour of the Si_2N_2O–ZrO_2 composite is similar to that of other porous nitrogen ceramic materials where the oxidation rate is seen to decrease significantly at higher temperatures.

(2) At temperatures ≤1300°C considerable internal oxidation of the material occurs with concommitant large weight gains. At 1300°C the stresses induced in the matrix by the volume expansion of the oxidation products cause severe cracking of the material on cooling from the annealing temperature.

(3) The material exhibits excellent oxidation resistance at high temperatures (>1300°C) and the higher the oxidation temperature the lower the weight gain. Protective oxide scales form at external and internal surfaces within the first 2 h of exposure which inhibit further oxidation. It is thought that narrowing of the pore channels may take place but complete pore closure does not occur.

(4) Following oxidation exposures at temperatures ≥1300°C the unstabilised ZrO_2 phase in the matrix is inhibited from undergoing the *t–m* transformation. This is most probably due to the dissolution of nitrogen in ZrO_2 resulting in the stabilised, non-transformable *t'*-ZrO_2 phase.

Acknowledgements

We would like to thank Dr Vratislav Langer for help with the XRD investigations. Financial support from the Swedish National Board for Industrial and Technical Development (NUTEK) is gratefully acknowledged.

References

1. Cheng, Y., O'Meara, C., Slasor, S., Pompe, R. & Thompson, D. P., Some features and limitations of zirconia toughened nitrogen ceramics. In *Proc. 4th Int. Symp. Ceramic Materials and Components for Engines*, ed. R. Carlsson, T. Johansson & L. Kahlman. Elsevier Applied Science, London, 1992, pp. 657–64.
2. Falk, L. K. L. & Rundgren, K., Microstructure and short-term oxidation of hot-pressed $Si_3N_4/ZrO(+Y_2O_3)$ ceramics. *J. Am. Ceram. Soc.*, **1** (1992) 28–35.
3. O'Meara, C., The microstructure and the oxidation behaviour of Si_2N_2O/ZrO_2 composites. In *Proc. 4th Int. Symp. Ceramic Materials and Components for Engines*, ed. R. Carlsson, T. Johansson & L. Kahlman. Elsevier Applied Science, London, 1992 pp. 252–9.
4. Pompe, R., Method for producing ceramic composite materials containing silicon oxynitride and zirconium oxide. U.S. Pat. No. 438 416, SE. Pat. No. 8702268-7, 1987.
5. Pompe, R., Method for producing ceramic composite materials containing silicon oxynitride and zirconium oxide. Patent Co4B 35/48,35/58,1988.
6. O'Meara, C. & Heim, M. to be presented at ECRS4, Ricione, Italy, October, 1995.
7. Davidge, R. W., Evans, A. G., Gilling, D. & Wilyman, P. R., *Special Ceramics 5*, ed. P. Popper. British Research Association, Manchester, 1972, pp. 329–43.
8. O'Meara, C., Sjöberg, J., Dunlop, G. & Pompe, R., Oxidation of pressureless sintered Si_2N_2O materials. *J. Europ. Ceram. Soc.*, **7** (1991) 369–78.
9. Porz, F. & Thümmler, F., Oxidation mechanism of porous silicon nitride. *J. Mater. Sci.*, **19** (1984) 1283–95.

Journal of the European Ceramic Society **15** (1995) 329–335
1995 Elsevier Science Limited
Printed in Great Britain
0955-2219/95/$9.50

Corrosion Resistance of Ceramic-coated Stainless Steel in a Br_2–O_2–Ar Atmosphere

Makoto Sasaki & Toshio Hirai

Institute for Materials Research, Tohoku University, Katahira 2-1-1, Aoba-ku, Sendai 980, Japan

(Received 13 May 1994; revised version received 15 July 1994; accepted 12 August 1994)

Abstract

Coatings of SiC/TiC compositional graded film (FGM), m-HfO_2 and c-HfO_2 films on stainless steel (SUS304) plates have been investigated as candidate materials for 'UT-3' which is an effective process of hydrogen production through thermochemical decomposition of water. Changing the source gas concentration leads to composition control in TiC–SiC composite films. Cracks in the films could not be avoided in either the TiC-coated SUS304 nor the SiC–TiC double layer-coated SUS304. However the SiC/TiC FGM-coated SUS304 had no cracks. Corrosion of the TiC and SiC–20 mol%TiC double-layer-coated SUS304 in the Br_2–O_2–Ar atmosphere was mainly caused by oxidation of the TiC film and SUS304. The SiC/TiC FGM-coated SUS304 showed superior corrosion resistance in isothermal and cyclic heating conditions.

m-HfO_2 and c-HfO_2 (7·1–44·5 mol% Y_2O_3) were attained by the changing of $Y(DPM)_3$ gas concentration. XRD measurement shows the monoclinic and cubic HfO_2. Both plate-like and columnar texture in the m-HfO_2 and c-HfO_2 films were observed. m-HfO_2, in which columnar texture, coated SUS304 showed the excellent corrosion resistance in Br_2–O_2–Ar atmosphere under heat cyclic conditions. This is thought to be due to the effects of columnar texture on the thermal stress relaxation, and of the excellent corrosion resistance of the m-HfO_2.

1 Introduction

Hydrogen gas (H_2) is expected to be used as a new energy source because conventional fuels tend to destroy the natural environment. One of the methods to produce H_2 is the thermochemical decomposition of water called 'UT-3'.[1] The 'UT-3' process causes high temperature corrosion of structural materials because highly corrosive gases such as O_2, Br_2 and HBr might be used at temperatures from 500 to 1000 K. Considering practical applications, metals should be used as structural materials. However, no metal is known to resist the corrosive conditions caused by 'UT-3'. Ceramic-coated metals are expected to be candidate structural materials. Titanium carbide (TiC) films are highly adherent to metals, and silicon carbide (SiC) is resistant to corrosion. CVD is the most suitable method for the surface modification of metals, because it allows the preparation of dense and adherent films. On the other hand, Functionally Gradient Materials (FGMs) having an excellent thermal stress relaxation property are well known as thermal barrier materials.[2–7] In the present work, single-layer TiC or SiC, double-layer SiC and TiC, and SiC/TiC FGM coatings were placed on stainless steel (SUS304) using the CVD method. On the other hand, HfO_2 has a superior thermal expansion matching to the stainless steel. Thus, m-HfO_2 and c-HfO_2(Y_2O_3) coatings were also deposited on the SUS304 using the CVD method. The corrosion behaviour of these materials in Br_2–O_2–Ar atmosphere was investigated.

2 Experimental

2.1 Preparation of TiC, SiC and SiC–TiC composite films

Stainless steel (SUS304) plates (15 mm in diameter and 2 mm in thickness) were used as substrates. Source gases $TiCl_4$, CH_3SiCl_3(MTS), CH_4 and H_2 were introduced into a hot-wall type CVD reactor. Deposition temperature (T_{dep}) and total gas pressure (P_{tot}) were fixed at 1323 K and 0·1 MPa, respectively. H_2 gas flow rate was kept at $8{\cdot}3 \times 10^{-6}m^3s^{-1}$. $TiCl_4$ gas flow rate was changed from 0 to $3{\cdot}3 \times 10^{-7}m^3s^{-1}$, MTS gas flow rate from 0 to $1{\cdot}6 \times 10^{-6}m^3s^{-1}$. The ratio of CH_4 to MTS was kept at 1·7 to fabricate the TiC-containing films. The structure of CVD films was examined by XRD (Rigaku: RAD-C), the surface and the

Table 1. Preparation conditions of m-HfO_2

Substrate temperature (T_{sub}), T/K	873~1173
Total gas pressure (P_{tot}), P/kPa	1·3
Gas flow rate, $FR/10^{-6}m^3s^{-1}$	
Ar for $Hf(DPM)_4$	1·7
O_2	1·7
Temperature of $Hf(DPM)_4$ reservoir (THf), T/K	453
Deposition time (T_{dep}), t/ks	1·2~4·8

Table 2. Preparation conditions of c-HfO_2

Substrate temperature (T_{sub}), T/K	873~1073
Total gas pressure (P_{tot}), P/kPa	1·3
Gas flow rate, $FR/10^{-6}m^3s^{-1}$	
Ar for $Hf(DPM)_4$	1·7
Ar for $Y(DPM)_3$	1·7
O_2	1·7
Temperature of $Hf(DPM)_4$ reservoir (THf), T/K	433~463
$Y(DPM)_3$ reservoir (THf), T/K	403~421
Deposition time (T_{dep}), t/ks	1·2~7·2

cross-sectional texture observed by SEM spectroscopy (Akashi:ALPHA-30). SiC and TiC content in the films were determined by EPMA measurement as substitutions for the Si (Ka) and Ti (Ka) intensity.

2.2 Preparation of SiC/TiC FGM film

On the basis of the preparation conditions of SiC–TiC composite films, SiC/TiC FGM films were fabricated on SUS304 by changing the source gas concentration ('a'=MTS/($TiCl_4$+MTS)) at T_{dep}=1323 K and P_{tot}=0·1 MPa. 'a' was changed stepwise from 0 for 4 h, 0·7 for 1 h to 1·0 for 1 h. The surface and cross-sectional texture were observed by SEM.

2.3 Preparation of m- and c-HfO_2 films

(100)Si and Stainless steel (SUS304) plates (15 mm in diameter and 2 mm in thickness) were used as substrates. Source gases $Hf(DPM)_4$, $Y(DPM)_3$, O_2 and Ar were introduced into a hot-wall type CVD reactor. Tables 1 and 2 demonstrate the CVD conditions. Deposition temperature (T_{dep}) and total gas pressure (P_{tot}) were fixed at 1073 K and 13 kPa, respectively. The structure of CVD films was examined by the XRD, the surface and the cross-sectional texture observed by the SEM. Film composition was determined by ICP and XRF measurements.

2.4 Measurement of corrosion rates

Figure 1 demonstrates the experimental set-up for the evaluation of corrosion rate. The specimens were suspended by a platinum wire in an electric furnace. Weight changes during corrosion were continuously measured using an electric balance connected to a computer (NEC:PC-9801). The electric balance was kept at 298 K in a constant temperature box. Ar gas was passed through the electric balance and introduced into the quartz tube. O_2 gas containing Br_2 was introduced from the bottom of the balance box into the quartz tube. The Br_2 reservoir was maintained at 288 K. The corrosion temperature (T_{cor}) was kept at 1173 K in isothermal experiments. In the case of cyclic heating, T_{cor} was cyclically changed from 1173 to 773 K under the same gas flow rates in isothermal corrosion experiment.

3 Results and discussion

3.1 Preparation of TiC, SiC and SiC–TiC composite films

The possibility of the CVD method to control film composition was investigated. Figure 2 shows the relationship between input gas concentration and film composition. SiC content in the film increases

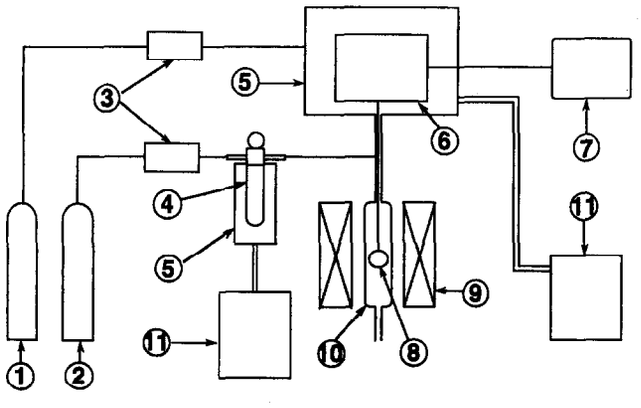


Fig. 1. Schematic diagram of corrosion rate measurement: (1) Ar gas, (2) O_2 gas, (3) mass flow meter, (4) Br_2 reservoir, (5) constant temperature bath, (6) electric balance, (7) computer, (8) specimen, (9) electric furnace, (10) quartz tube, (11) cool pump.

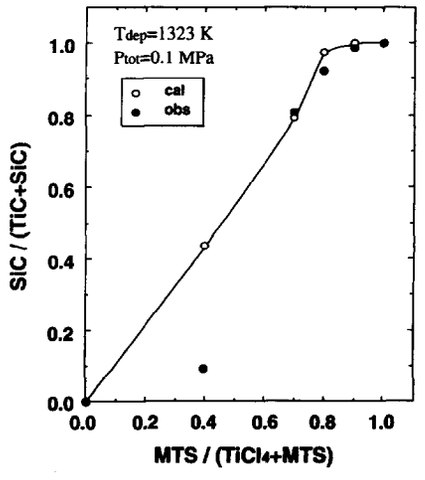


Fig. 2. Relationship between input gas concentration and film composition compared with theoretical film composition.

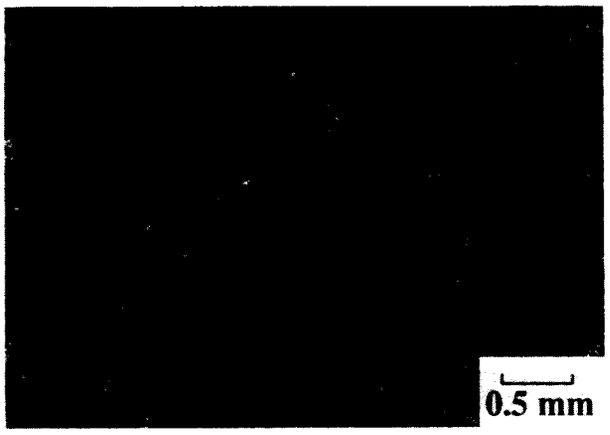


Fig. 3. SEM photograph of deposited surface of the SiC and TiC double-layer-coated SUS304.

with increasing MTS concentration. Figure 2 also demonstrates the theoretical composition of the films calculated using JANAF data[8] under the thermodynamic equilibrium conditions based on a free energy minimisation method. Experimental compositions of the films agree well with those of the calculated values except at the *a* of 0·4. The lower value is thought to be due to the kinetics of the CVD process. These data show that SiC content in the SiC–TiC composite films can be controlled.

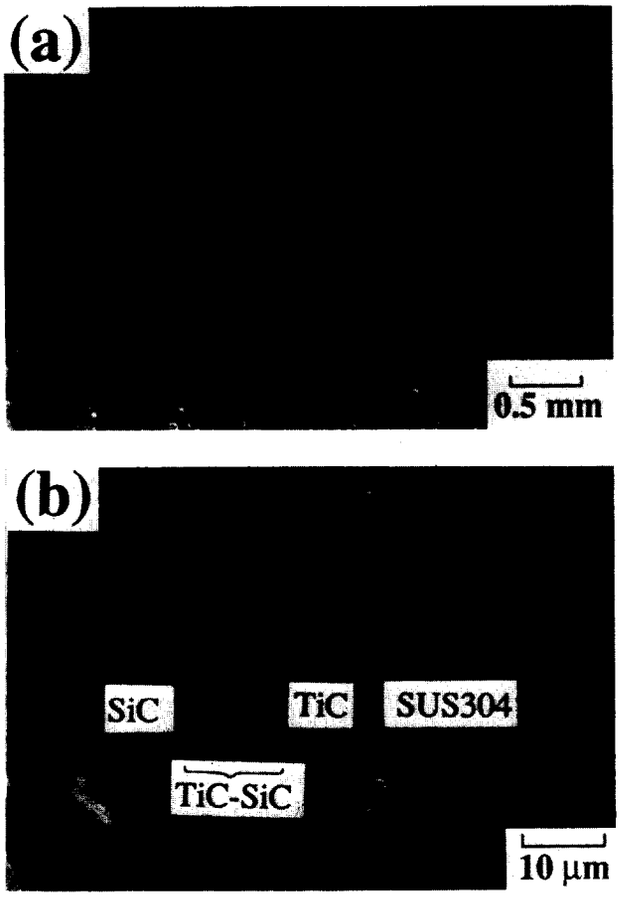


Fig. 4. SEM photographs of the SiC/TiC FGM-coated SUS304. (a) Surface of the specimen. (b) Cross-section of the specimen.

While direct coating of TiC on the SUS304 was achieved, the SiC–TiC composite film was not obtained on the SUS304 because Fe_3Si and $FeSi_2$ formed as a result of easy reaction between MTS and SUS304. This result demonstrates the impossibility of direct coating of SUS304 with SiC. Reaction protection layers such as TiC are indispensable between SiC and SUS304. An SiC coating on the TiC-coated SUS304 was attempted. Figure 3 shows the SEM photograph of the surface of the SiC/TiC double layer-coated SUS304. SiC was deposited on the TiC interlayer. Cracks were observed on the surface of the TiC-coated SUS304. Thermal expansion coefficients of TiC, SiC and SUS304 are $7{\cdot}6 \times 10^{-6}$, $4{\cdot}3 \times 10^{-6}$, $1{\cdot}73 \times 10^{-5}K^{-1}$, respectively. As shown in Fig. 4, cracking also occurred in the SiC film as a result of the mismatch between thermal expansion coefficients of SiC and SUS304. Even if the thicknesses of SiC and TiC were ranged from 2 to 20 μm, cracking could not be avoided.

3.2 Preparation of an SiC/TiC FGM film

For the purpose of residual thermal stress relaxation and the protection of crack formation, continuous change of the thermal expansion coefficients, so-called Functionally Gradient Materials (FGMs) might be useful. Figure 4 shows the SEM photographs of the surface and the cross-section of the SiC/TiC FGM-coated SUS304.

Compositional graded layer from TiC to SiC forms on the SUS304. Despite the mismatch of thermal expansion coefficients between SiC, TiC and SUS304, no cracks in the SiC/TiC FGM-coated SUS304 appear on the deposited surface, as shown in Fig. 4. The result suggests that the introduction of the compositional gradation between the SiC and TiC layers reduce the surface tensile stress of the SiC/TiC FGM-coated SUS304.

3.3 Synthesis of m-HfO_2 films

The m-HfO_2 formation was confirmed by X-ray diffraction (JCPDS card No. 34-104). The thickness increased from 0·8 to 3·2 μm with increasing T_{dep} from 873 to 1073 K, and was kept constant above 1073 K. The SEM photographs of the surface of m-HfO_2 deposited on the (100)Si substrate are shown in Fig. 5. Figure 5(a) shows a plate-like dense m-HfO_2 film deposited at a T_{dep} of 973 K and at a t_{dep} of 1·2 ks, which has cracks and detached from the substrate. On the other hand, as shown in Fig. 5(b), the film deposited at a T_{dep} of 1073 K and at a t_{dep} of 2·4 ks has a columnar texture. Figure 5(b) also shows the dense layer around the interface film-substrate with no cracks and no detachment from the substrate.

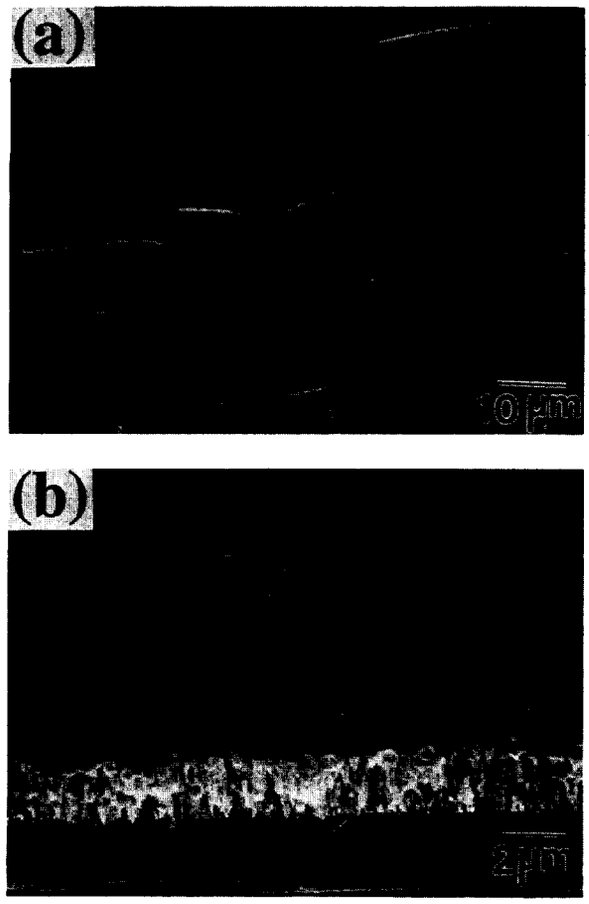


Fig. 5. SEM photographs of the plate-like (a) and columnar (b) m-HfO_2.

As shown in Fig. 5, a plate-like dense film was deposited in the T_{dep} range from 873 to 973 K. Its XRD pattern, characterised by broad peaks, demonstrated the lower degree of crystallisation. On the other hand, the film deposited in the T_{dep} range from 1023 to 1173 K has a columnar structure and showed relatively higher crystallinity.

3.4 Synthesis of c-HfO_2 films

The film deposited at a T_{dep} of 1073 K, a T_{Hf} of 453 K, a T_Y of 406 K, a t_{dep} of 2·4 ks, FA_{Ar} of 1·7 × 10^{-6} m^3s^{-1}, FR_{O_2} of 1·7 × 10^{-6} m^3s^{-1}, and at a P_{tot} of 1·3 kPa, was identified as the c-HfO_2 (JCPDS card No. 24-1406).

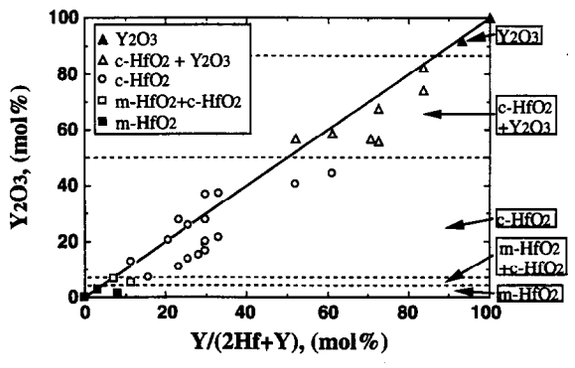


Fig. 6. Relationship between input gas concentration and film composition.

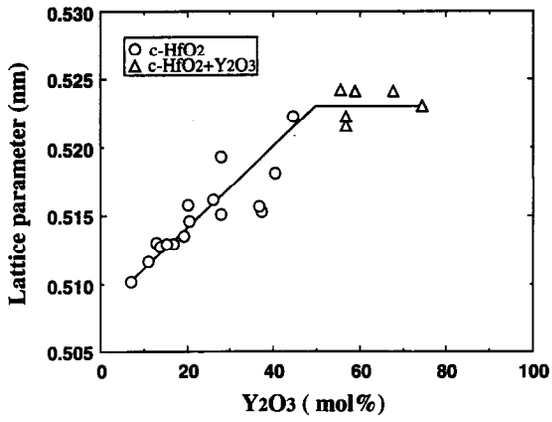


Fig. 7. Relationship between film composition and lattice parameter of c-HfO_2.

Figure 6 shows the relationship between input gas molar ratio and the Y_2O_3 content in the films. The straight line in Fig. 6 demonstrates the ideal Y_2O_3 content in the films, obtained by the following reaction:

$$x\mathrm{Hf(DPM)_4}+y\mathrm{Y(DPM)_3}+\mathrm{O_2}\rightarrow x\mathrm{HfO_2}+(y/2)\mathrm{Y_2O_3}+(\text{Volatile compounds})$$

Y_2O_3 content was determined by ICP method in which the substitution of Y content in the films. m-HfO_2+c-HfO_2) composites were deposited in the Y_2O_3 range from 5·03 to 6·52 mol%, single c-HfO_2 phase in the Y_2O_3 range from 7·1 to 44·5 mol%, c-HfO_2+Y_2O_3 composites in the Y_2O_3 range from 56·6 to 82·3 mol%.

The relationship between Y_2O_3 content and the lattice parameters measured by (400) X-ray intensity is shown in Fig. 7. The (400) peak of the substrate was used as an inner standard. The lattice parameters have a tendency to increase with increasing Y_2O_3 content.

3.5 Corrosion behaviour

(a) SiC–TiC composites and SiC/TiC FGM

Weight loss of the TiC-coated SUS304 during corrosion experiment was observed at T_{cor}=1173 K, P_{Br_2} = 4·4 kPa and P_{O_2} = 0·1 kPa. As large quantities of O_2 gas might be generated in the 'UT-3' process, corrosion experiments should be conducted at large O_2 gas concentration including Br_2 gas. Figure 8 shows the relationship between time and weight change by the corrosion at T_{cor}=1173 K, P_{Br_2} = 4·4 kPa and P_{O_2} = 46 kPa (isothermal corrosive condition). All the specimens revealed weight gain in this corrosive condition. The surfaces of the TiC-coated SUS304, TiC and SiC-20 mol% TiC double-layer-coated SUS304, and SiC and TiC double-layer-coated SUS304 after the corrosion at T_{cor}=1173 K, P_{Br_2} = 4·4 kPa and P_{O_2} = 46 kPa were observed by SEM. The surface of the TiC was extremely damaged by corrosion. In the case of the SiC-20 mol% TiC, the surface

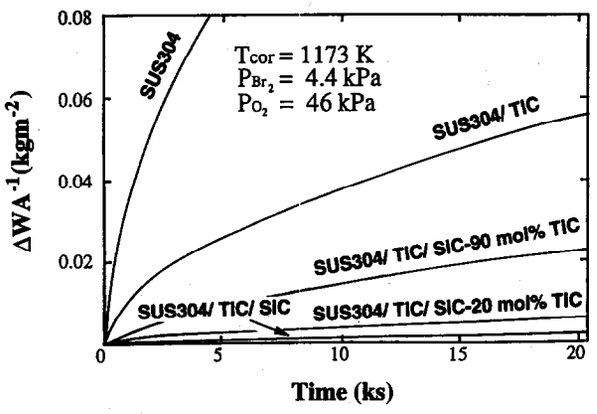


Fig. 8. Relationship between time and weight gain of the SiC–TiC composites by the corrosion at T_{cor} = 1173 K, P_{Br_2} = 4·4 kPa and P_{O_2} = 46 kPa.

texture became porous and rough. This result occurs due to the difference of corrosion rate between SiC and TiC. SiC is likely to have excellent corrosion resistance. Phases formed after corrosion were investigated by using XRD. TiO_2, Fe_2O_3 and Fe_3O_4 were observed at the surface of the TiC-coated SUS304. The SUS304 substrate was oxidised by corrosive Br_2–O_2 that diffused through the cracks of the TiC film. On the other hand, only TiO_2 was formed on the TiC/SiC-20 mol% TiC double-layer-coated SUS304.

Figure 9 shows the dependence of corrosion rate on the film composition in the SiC–TiC composite system. Clearly, the addition of SiC into the TiC film improves the corrosion resistance of TiC. SiC provide high corrosion resistance, but the TiC/SiC-20 mol% TiC can not be used as the surface material in 'UT-3', because a corrosion of TiC in the composite film is indispensable. To compare the corrosion resistance of TiC/SiC-20 mol% TiC double-layer-coated SUS304 with that of the SiC/TiC FGM-coated SUS304, a corrosion experiment with different heat cycles was attempted.

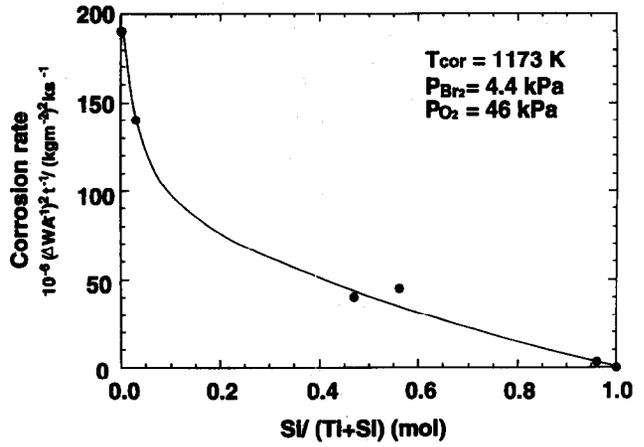


Fig. 9. Dependence of corrosion rate on the composition of SiC–TiC composite films by the corrosion at T_{cor} = 1173 K, P_{Br_2} = 4·4 kPa and P_{O_2} = 46 kPa.

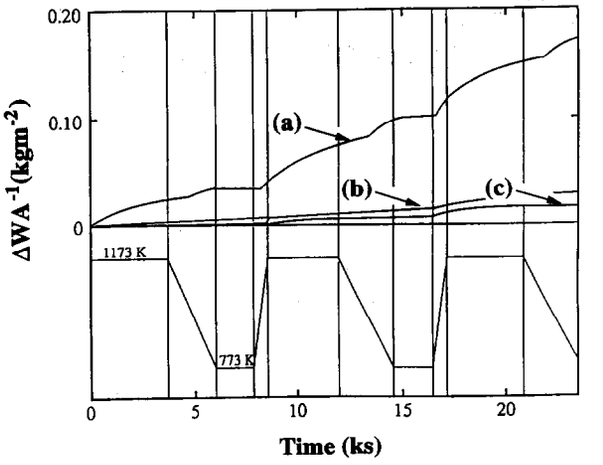


Fig. 10. Relationship between time and weight gain by the corrosion under the cyclic test between 1173 K to 773 K at P_{Br_2} = 4·4 kPa and P_{O_2} = 46 kPa. (a) TiC-coated SUS304; (b) TiC/SiC–20 mol% TiC double-layer-coated SUS304; (c) SiC/TiC FGM-coated SUS304.

Figure 10 shows the relationship between time and weight gain by the corrosion under the cyclic test between 1173 and 773 K at P_{Br_2} = 4·4 kPa and P_{O_2} = 46 kPa. TiC-coated SUS304 has less corrosion resistance. Both TiC/SiC-20 mol% TiC double-layer-coated SUS304, and the SiC/TiC FGM-coated SUS304 were covered with SiC on the surface.

Cracks in the film could not be avoided in the SiC/TiC double-layer-coated SUS304. However, the SiC/TiC FGM-coated SUS304 had no cracks (Figs 3 and 4). The result of corrosion experiments in the heat cyclic condition shows the capability of FGM coating to achieve thermal stress relaxation and corrosion resistance.

(b) m- and c-HfO_2 films

Figure 11 shows the weight change of the HfO_2-coated-SUS304 under the isothermal corrosion experiments at a T_{cor} of 1173 K, a P_{Br_2} of 4·4 kPa, a P_{O_2} of 46 kPa, a P_{tot} of 0·1 MPa, and at *a* t_{cor} of 21·6 ks. The specimens used for the corrosion experiments were the columnar m-HfO_2 with film thickness of 14 and 4 μm, the plate-like m-HfO_2 with thickness of 4 μm, the columnar c-HfO_2 with thickness of 14 μm, and bare SUS304. c-HfO_2-coated SUS304 was not corrosion resistant, while m-HfO_2-coated SUS304 showed a superior corrosion resistance.

XRD measurements of bare SUS304 and c-HfO_2-coated SUS304 showed that after the corrosion experiments, Fe_2O_3, Fe_3O_4 and Cr_2O_3 were formed. On the surface of the specimens after the corrosion experiments, the detachment of oxide scale from the SUS304, with a thickness of 0·19 μm could be observed. In the case of c-HfO_2-coated SUS304, the detachment of the film from

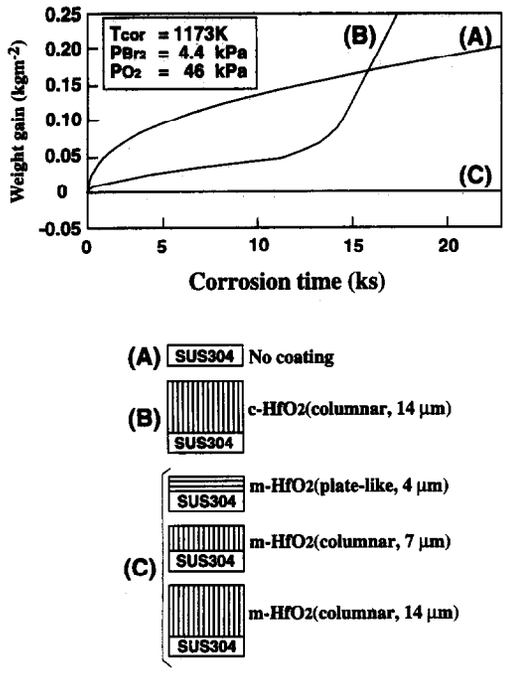


Fig. 11. Relationship between time and weight gain of m-HfO_2-coated SUS304 by the corrosion at T_{cor} = 1173 K, P_{Br_2} = 4·4 kPa and P_{O_2} = 46 kPa (isothermal condition).

the SUS304 partially occurred. The corrosion and the detachment of the film might occur around the interface of c-HfO_2 film and SUS304.

The corrosion resistance of the m-HfO_2-coated SUS304, which revealed the superior corrosion resistance under isothermal conditions, was investigated by the heat-cyclic corrosive test.

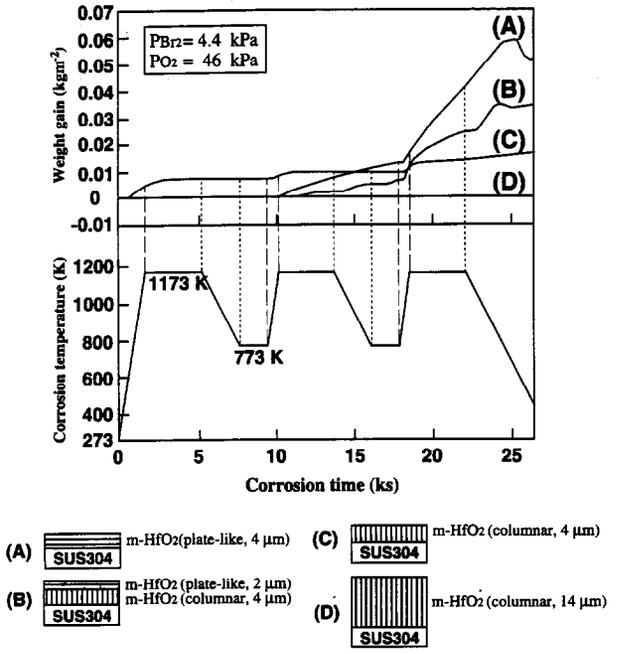


Fig. 12. Relationship between time and weight gain by the corrosion under the cyclic test between 1173 K to 773 K at P_{Br_2} = 4·4 kPa and P_{O_2} = 46 kPa. (a) m-HfO_2 (plate-like, 4 μm); (b) m-HfO_2 (columnar, 4 μm; plate-like, 2 μm); (c) m-HfO_2 (columnar, 4 μm); (d) m-HfO_2 (columnar, 14 μm).

Figure 12 shows the temperature change and the experimental results of the weight change of m-HfO_2-coated SUS304. The columnar m-HfO_2 (14 μm) coated SUS304 had superior corrosion resistance. Corrosion resistance decreased in the order: columnar m-HfO_2(4 μm), m-HfO_2 (texture changed from columnar to plate-like), plate-like m-HfO_2.

The examination of the surfaces of plate-like m-HfO_2 (4 μm in thickness) and columnar m-HfO_2 (14 μm in thickness) by SEM after the cyclic heating corrosion test, showed that the excellent corrosion resistance of the 14 μm-columnar m-HfO_2 coated SUS304, was related to the absence of cracks and detachment from the substrate. This is thought to be due to the effects of columnar texture on the thermal stress relaxation, and of the excellent corrosion resistance of the m-HfO_2.

4 Conclusions

Coatings of TiC, SiC–TiC, SiC/TiC FGM, m-HfO_2 and c-HfO_2 on stainless steel (SUS304) using CVD method were examined as possible corrosion resistant structural materials for 'UT-3.' The corrosion resistance of these materials in a Br_2–O_2–Ar corrosive atmosphere was investigated. The following results were obtained:

Changing the source gas concentration leads to composition control in the TiC–SiC composite films. The composition of TiC–SiC films prepared at a deposition temperature of 1323 K and at a total gas pressure of 0·1 MPa agreed with calculations. The SiC–20 mol% TiC composite film was prepared at a MTS/($TiCl_4$ + MTS) of 0·7. Cracks in the films after CVD could not be avoided in either the TiC-coated or the SiC, TiC double-layer-coated SUS304. However, both the TiC and SiC–20 mol% TiC double-layer-coated SUS304, and the SiC/TiC FGM-coated SUS304 had no cracks. Corrosion of the TiC and SiC–20 mol% TiC double-layer-coated SUS304 was mainly caused by oxidation of the TiC film and SUS304. SiC/TiC FGM-coated SUS304 showed superior corrosion resistance in isothermal and cyclic heating conditions.

Cracks in the m- and c-HfO_2 films after CVD could not be avoided in neither plate-like m-HfO_2 nor plate-like c-HfO_2. Columnar m-HfO_2-coated or columnar c-HfO_2-coated SUS304 had no cracks. Corrosion of the c-HfO_2-coated or plate-like-m-HfO_2-coated SUS304 was mainly caused by oxidation of the SUS304. Columnar m-HfO_2-coated SUS304 showed superior corrosion resistance in isothermal and cyclic heating conditions. This is

thought to be due to the effects of columnar texture on the thermal stress relaxation, and of the excellent corrosion resistance of the m-HfO_2.

Acknowledgement

This research was partially supported by a Grant-in-Aid for Scientific Research from the Ministry of Education, Science and Culture.

References

1. Sasaki, M., Hiratani, T. & Hirai, T., Corrosion Resistance of SiC/TiC FGM-coated Stainless Steel in Br_2–O_2–Ar Atmosphere, *Proc. 2nd Int. Symp. Functionally Gradient Materials*, 1993, pp. 369–376.
2. Niino, M., Hirai, T. & Watanabe, R., Functionally Gradient Materials as Heat-resistant Use for Space Plane, *J. Japan Soc. Composite Materials, (in Japanese)*, **13** (1987) 257–264.
3. Sasaki, M., Wang, Y., Hirano, T. & Hirai, T., Design of SiC/C Functionally Gradient Material and Its Preparation by Chemical Vapor Deposition, *J. Ceram. Soc. Jpn. Inter. Ed.*, **97** (1989) 530–534.
4. Kumakawa, A., Maeda, S., Sasaki, M., Niino, M., Sakamoto, A., Sasaki, M. & Hirai, T., Evaluation of Thermomechanical Properties of Functionally Gradient Material under High Temperature Difference, *Proc. European Space Agency Symp.*, ESA SP-303, 1990, pp. 339–344.
5. Sasaki, M. & Hirai, T., Fabrication and Thermal Barrier Characteristics of CVD SiC/C Functionally Gradient Material, Proc. *1st Int. Symp. Functionally Gradient Material*, edited by M. Yamanouchi, M. Koizumi, T. Hirai and I. Shiota, 1990, pp. 83–88.
6. Sasaki, M. & Hirai, T., Fabrication and Evaluation of SiC/C Functionally Gradient Material, *Journal de Physique IV*, **C2** (1991) 649–655.
7. Sasaki, M. & Hirai, T., Fabrication and Properties of Functionally Gradient Materials. The Centennial Memorial Issue of The Ceramic Society of Japan, *J. Ceramic Soc. Jpn.*, **99** (1991) 1002–1013.
8. JANAF Thermochemical Tables, 2nd Ed. No.NRSDS-NBS-37, edited by D. R. Stull and H. Prophet, U.S. Government Printing Office, Washington DC, 1971.

Journal of the European Ceramic Society 15 (1995) 337–342
© 1995 Elsevier Science Limited
Printed in Great Britain. All rights reserved
0955-2219/95/$9.50

Borosilicate Coatings on Mild Steel Prepared from Aqueous Amine Solutions: A Comparison with the Alkoxide Routes

N. Maliavski,[a] E. Tchekounova,[a] P. Innocenzi,[b] D. Festa,[b] M. Guglielmi[b]* & L. Mancinelli Degli Esposti[c]

[a] Department of General Chemistry, Moscow Civil Engineering University, Yaroslavskoe sh. 26, 129337 Moscow, Russia
[b] Dipartimento di Ingegneria Meccanica, Sez. Materiali, Unversità di Padova, Via Marzolo 9, 35131, Padova, Italy
[c] I.S.R.I.M., Loc. Pentima Bassa 21, 05100 Terni, Italy

(Received 12 November 1993; revised version received 24 May 1994; accepted 6 July 1994)

Abstract

Sol-gel coatings on metals, as barriers against oxidation of the substrate may be obtained by the dip-coating technique. Different alkoxide solutions have been previously used to deposit coating films on various metallic substrates. Borosilicate coatings gave a good protection against the oxidation of mild steel. The preparation of these coatings has however some disadvantages, such as the required low humidity during deposition and the high cost of precursors.

In this work we studied an alternative method based on aqueous amine solutions. The borosilicate solutions prepared by amines and by alkoxides were characterized by measuring viscosity and stability. Coatings were deposited on mild steel by both methods.

Samples were treated at 550°C and the oxidation was evaluated by glancing angle X-ray diffraction. Adhesion tests and microscopic observations were performed to compare the behavior of amine- and alkoxide-derived borosilicate coating films.

1 Introduction

In recent years several works have appeared on the deposition by dip-coating of sol-gel films on metal substrates. Inorganic coating films obtained via sol-gel were used as barriers against oxidation of metal surfaces. Particularly borosilicates,[1,2] silica,[3,4] alumina,[5] aluminosilicates,[6,7] zirconia,[8,9,10] and fluorine doped zirconia[11] were used as coating films on stainless steel and mild steel.

Alkoxides were always used as precursors. In previous work[12] an alternative sol-gel technique for the synthesis of oxide materials, based on aqueous solutions of amine-containing precursors,[13–15] was used. Silica coating films were deposited on mild steel by alkoxide and water–amine solutions. The use of the amine route shows important advantages such as reproducibility of the desired chemical compositions, great choice and low cost of raw materials.

In this work borosilicate coating films on mild steel were prepared starting from alcoholic and aqueous solutions. A comparative study of their properties and protective effect against oxidation is presented.

2 Experimental

2.1 Preparation of solutions

One alkoxide and two amine-based solutions were prepared for the deposition of borosilicate coating films.

The borosilicate alkoxide solution, indicated as SiBT, was prepared using tetraethoxysilane, $Si(OC_2H_5)_4$, (TEOS) and triethylborate, $B(OCH_3)_3$, (TEOB) as precursors. The TEOS/TEOB molar ratio was 80/20. TEOS was prehydrolized in ethanol (EtOH) with H_2O (H_2O/TEOS = 5), using HNO_3 as catalyst (HNO_3/TEOS = 0·07). After refluxing for 4 h, TEOB was added and the solution was refluxed for an additional 4 h. The SiBT solution had a concentration of about 10 wt%. Methylamine–Borosilicate solutions (SiBM) were prepared as follows: solid silicic acid was mixed with an aqueous solution of methylamine (MA) (20 wt%) and the obtained mixture was stirred for 1 h in a ball-mill and for one day in a magnetic stirrer.

*To whom correspondence should be addressed.

A methylamine–borate solution was then separately prepared by dissolving boric acid (H_3BO_3) in an aqueous solution of MA. Both solutions were mixed and diluted with water to a concentration of 8 wt% oxides. SiBM solutions with different compositions were prepared to study the effect of the content of boron.

A second type of aqueous borosilicate solution (SiBQ) was obtained using quaternary ammonium cation. A silicate of the quaternary ammonium base was prepared according to the scheme proposed by Weldes,[16] replacing ethanolamine and ethylene oxide with diethylamine (DEA) and propylene oxide (PO) respectively. A solution of diethylamine silicate was prepared by dissolving solid silicic acid in an aqueous solution of diethylamine (25 wt%), stirring the solution 1 h in a ball mill and one day in a magnetic stirrer. Then PO (2 mol per mol of DEA) was added, the solution was stirred for 4 h and heated slightly to evaporate residues of PO and to increase the SiO_2 concentration up to 7 wt%. A borate solution was prepared as previously described for SiBM and added to the silicate solution. The borosilicate solution was diluted with water to a concentration of 5·8 wt% SiO_2 and 1·6 wt% B_2O_3.

2.2 Coating films preparation

Mild steel plates were used as substrates. The steel plates were cleaned ultrasonically in acetone and rinsed with ethanol before coating. Coating films were deposited by dip-coating in a humidity controlled box. The relative humidity was less than 20% for the SiBT samples and less than 40% for the others. After deposition the samples were dried at 60°C for 15 min, heated in air at a constant rate of 5°C/min up to 500°C and immediately left to cool in the off furnace. This thermal treatment will be indicated as Procedure 1.

2.3 Characterization of solutions and coatings

The viscosity as a function of time was measured for SiBT, SiBM and SiBQ, using a rotational viscometer.

The thermal evolution of gel films was observed using a multi-plate platinum holder in a thermogravimetric apparatus (TGA). Thick layers of about 100 μm were poured onto the plates and dried for 1 h at 100°C. Then the temperature was raised up to 1000°C, at a constant rate of 5°C/min.

Coating thickness was measured at different withdrawal rates on films deposited on glass slides under the same conditions as those used for coating the mild steel substrates. The influence of the substrate was assumed to be negligible. The thickness was evaluated with a profilometer, measuring the step on the coating produced with a scratch, after drying at 60°C. Samples were observed by scanning electron microscopy (SEM) after the oxidation test.

A semiquantitative evaluation of the adhesion was done by means of a scratch test, using a microindenter. Samples were moved under the indenter, at a constant rate, using different loads. The load at which delamination was observed was considered as the critical load.

2.4 Oxidation test

The resistance against oxidation was measured on samples treated in air at 500°C (Procedure 1) and on samples reheated at 5°C/min up to 550°C and maintained at this temperature for 1 h (Procedure 2). Oxidation was evaluated by Cu K_α X-ray diffraction with a glancing angle technique. The area (A) of peaks at 2θ = 35·5 (Fe_3O_4 + α-Fe_2O_3) and 2θ = 44·6 (α-Fe) was calculated using a Pseudo-Voigt representation to fit the profiles.[17]

The area ratio of the peaks at 2θ = 35·5 and 2θ = 44·6 was evaluated for coated (R_c) and uncoated (R_u) samples. The ratio R_u/R_c was taken as a measure of the oxidation degree and indicated as the protection factor (PF):

$$PF = \frac{R_u}{R_c} = \frac{\dfrac{A_u\,(Fe_3O_4 + \alpha - Fe_2O_3)}{A_u(\alpha - Fe)}}{\dfrac{A_c\,(Fe_3O_4 + \alpha - Fe_2O_3)}{A_c(\alpha - Fe)}}$$

The kinetics of oxidation at higher temperature were also measured by evaluating the weight gain by TGA, at a constant rate of 5°C/min up to 800°C.

3 Results and Discussion

Figure 1 shows the logarithm of solution viscosity η as a function of time. In the case of SiBM and SiBQ no changes in viscosity were observed even after 60 days from the preparation. For SiBT the viscosity is stable for about 10 days and then abruptly rises.

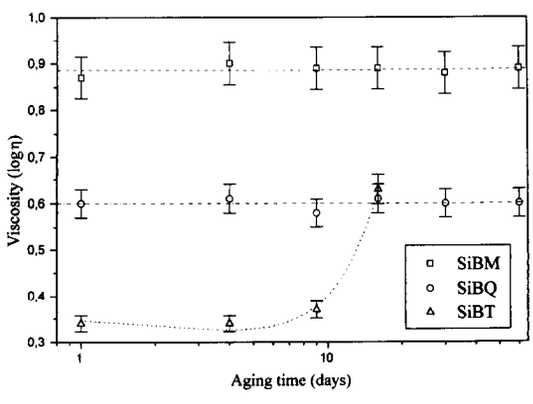


Fig. 1. Viscosity as a function of time for solutions SiBM, SiBQ and SiBT.

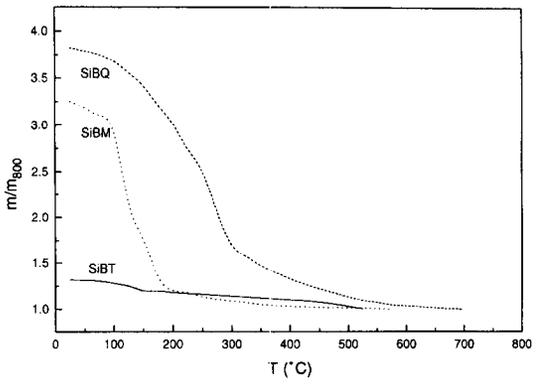


Fig. 2. TGA curves of gels obtained from solutions SiBM, SiBQ and SiBT pre-heated at 100°C for 1 h. m_{800} is referred to the mass value at 800°C.

This different behavior is ascribed to the different chemical character of alkoxide and amine solutions. SiBT, prepared from TEOS and TEOB, undergoes the sol-gel transformation by hydrolysis and condensation of alkoxides. This process continues in time giving the gelation of the solution. For alkoxide borosilicate solutions[18,19] a delaying in the gelation time proportional to the B_2O_3 content was observed and it was ascribed to the decreasing of potential condensation sites due to the trigonal coordinated boron. This can explain the stability of SiBT for about ten days, a longer time than that found with silica solutions. A much higher stability was however observed in the amine solutions, where the high pH values (11–12·5) displace the polycondensation equilibrium to low polymerized silicate and borate anions, which are stable in aqueous solutions. The viscosity of SiBM is higher than SiBQ because of the higher concentration of organic substances in the solution.

Thermogravimetric results are reported in Fig. 2. The curves relative to SiBM and SiBQ show one main effect, associated with an endothermic peak in the DTA. This effect ends at about 200°C for SiBM and 300°C for SiBQ. The weight loss is attributed to the escape of water in the case of SiBT and water

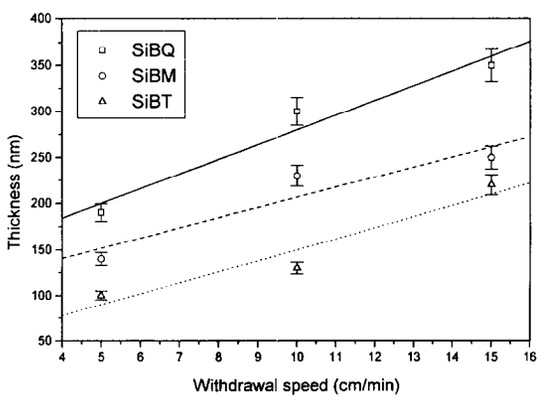


Fig. 3. Thickness as a function of withdrawal speed for coatings obtained from borosilicate solutions SiBM, SiBQ and SiBT.

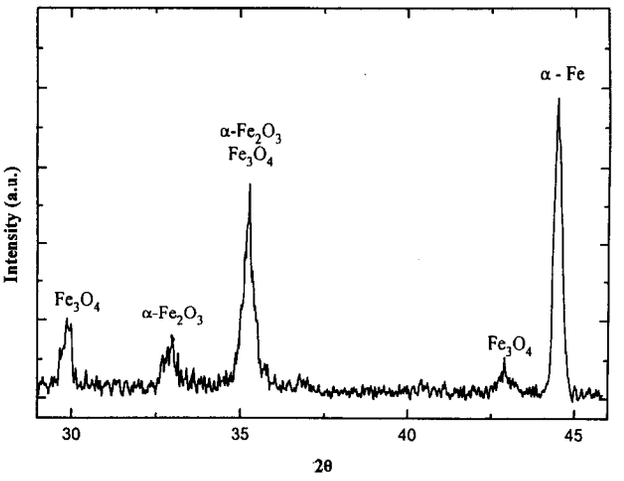


Fig. 4. Typical XRD spectra of a coated sample with partial oxidation of the substrate.

plus MA for SiBM and SiBQ. The difference in the mass loss between SiBM and SiBT may be explained by the quite strong chemical connection of MA and H_2O to the silicate network. Wet SiBT gels contain only non-bonded volatiles (ethanol and water) which are easily removed at 60°C. The mass loss over 60°C is due to the water which results from the reactions of polycondensation that continue up to higher temperatures. The SiBQ curve shows a supplementary mass loss in the range of temperature 400–600°C, accompanied by an exothermic DTA effect. This loss may be attributed to the oxidation decomposition of resin-like residuals of the quaternary ammonium silicate.

Figure 3 shows the thicknesses of the coatings deposited from solutions SiBT, SiBM and SiBQ, at three different withdrawal speeds. In the dip coating process the thickness depends on such solution properties as concentration, viscosity, density and surface tension.[20–22]

In the present case, the thickness differences are mainly due to viscosity (Fig. 1), which increases from SiBT to SiBQ.

Figure 4 shows a typical diffraction pattern obtained from X-ray glancing angle measurements on the coated samples.

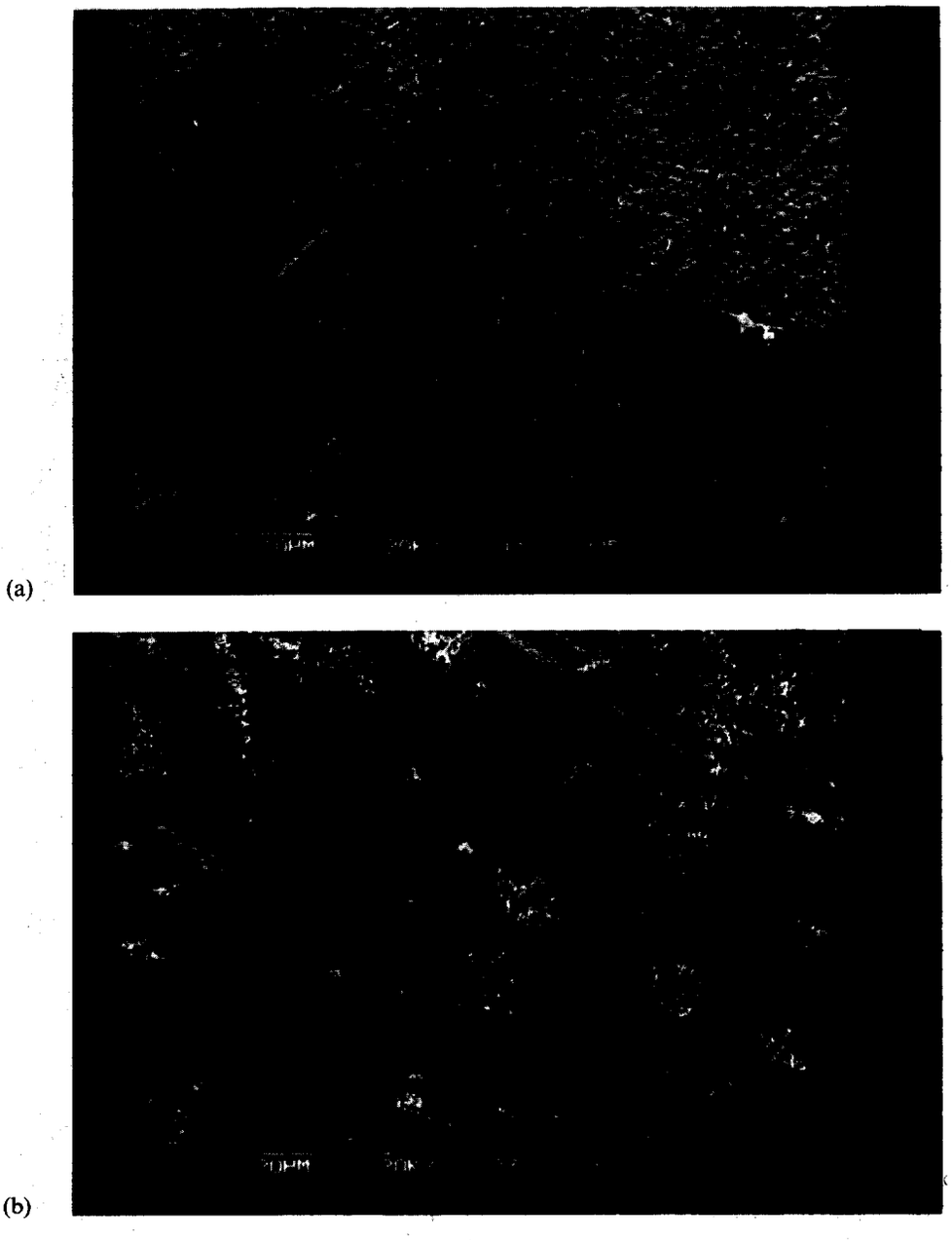
Comparative XRD data, obtained in the oxidation tests are reported in Table 1. The data in the table refer to samples after firing at 550°C (Procedure 1) and to samples re-heated at 550°C for 1 h, (Procedure 2). The thickness of the coating films was tailored to obtain almost the same thickness value for SiBT, SiBM, and SiBQ. In the table the data from previous work,[12] where silica coatings were studied, are also reported. The thickness values are quite different in this case, but the data may be useful for comparison. Coatings containing boron may, in general, give higher protection, compared with SiO_2 films. As observed previously,[1] boron probably has the effect of reducing

Table 1. Comparative XRD data relative to the oxidation tests. The reported data are referred to samples after firing at 500°C (Scheme 1) and to samples re-heated at 550°C for 1 h (Procedure 2). Data referred to silica coating films on mild steel[12] are also reported for a comparison.

	Alkoxide-derived		*QAB-derived*		*MA-derived*	
	without B_2O_3[a]	*SiBT*	*without* B_2O_3[a]	*SiBQ*	*without* B_2O_3[a]	*SiBM*
Film thickness (nm)	30	200	250	190	68	230
Protection factor (Procedure 1)	4	78	27	24	24	62
Protection factor (Procedure 2)	3	39	2·5	18	6	39

[a] Data from[12].

the intrinsic stress in the sol-gel films. As a matter of fact the critical thickness, t_c, i.e. the maximum thickness achievable free of cracks,[22] is higher. Sol-gel borosilicate coatings, prepared from fresh solutions, have a critical thickness of about 350–400 nm, while typically for silica coatings t_c is about 200–250 nm.[23] Furthermore the lower intrinsic stress may reduce the presence of microcracks in the coatings[1,3] thus increasing the protective action.



(a)

(b)

Fig. 5. SEM micrographs of a sample coated with solutions (a) SiBT 200 nm, (b) SiBM 230 nm and (c) SiBQ 190 nm. All samples were treated following Procedure 2.

(c)

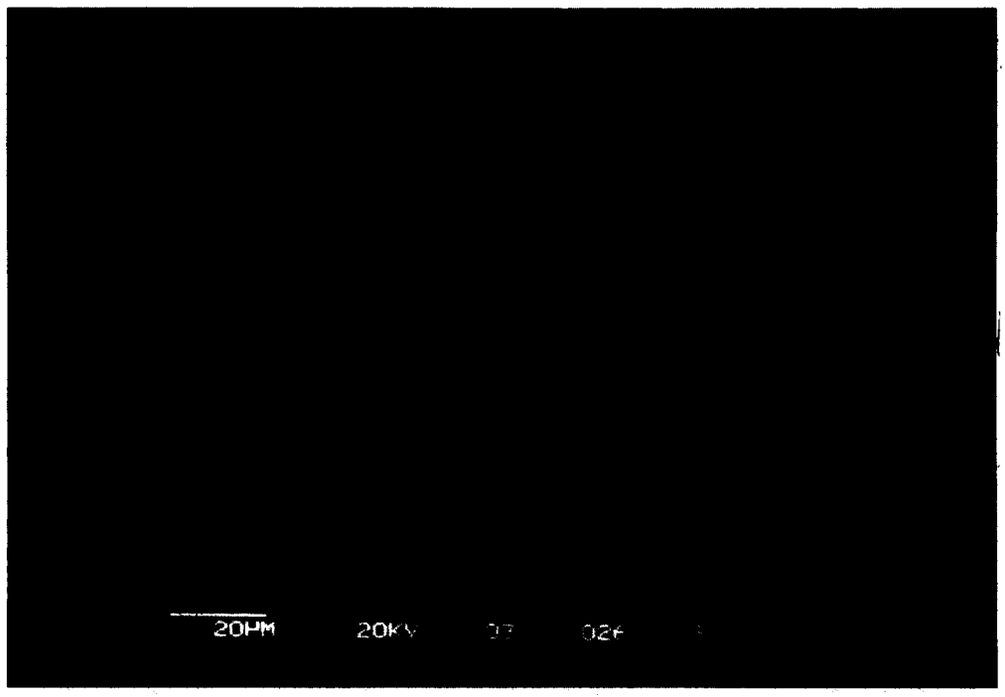


Fig. 5—*contd.*

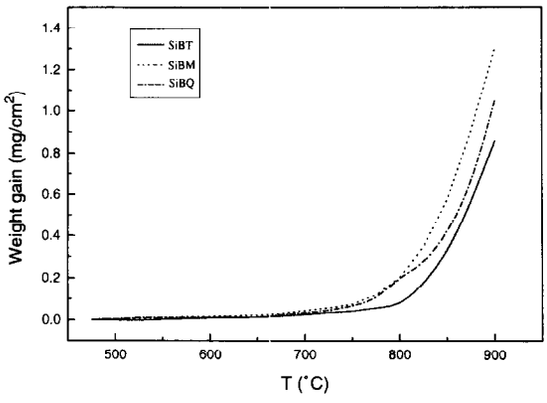


Fig. 6. Weight gain as a function of temperature for samples coated with solutions SiBT, SiBQ and SiBM.

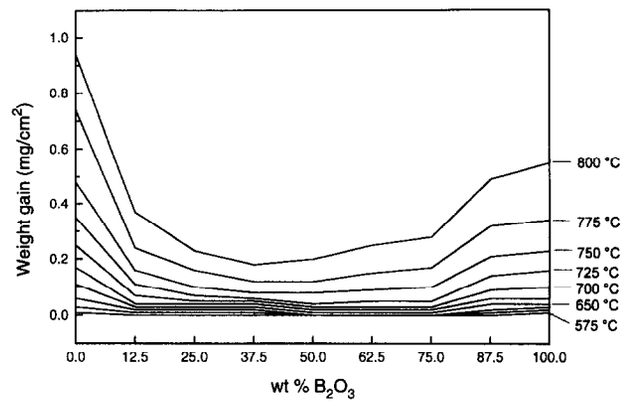


Fig. 7. Weight gain as a function of thermal treatment, for samples coated using SiBM solutions with different B_2O_3 contents.

SiBT and SiBM gave better protection against oxidation, with a quite similar PF; also SiBQ has a good protective effect, even if this is about half that of SiBM and SiBT. As the thicknesses for SiBT, SiBM and SiBQ are quite similar, the differences in the protective effect should be attributed to structural differences in the coatings.

As revealed by SEM observations, SiBT and SiBM coatings were mostly uncracked (Fig. 5(a) and (b)) differently from SiBQ (Fig. 5(c)). Also a different porosity between SiBM and SiBQ might be supposed, due to the different concentration of organic substances in the xerogels. However, due to difficulties in obtaining measures of thin film porosity, a direct proof is not available.

The kinetic results from TGA for the oxidation of samples in the high temperature region (up to 900°C) are shown in Fig. 6. Weight gain up to 750°C is negligible. At higher temperatures, the oxidation of the metallic substrate rapidly increases. In this test no significant difference between samples could be detected.

Figure 7 shows the weight gain as a function of temperature and B_2O_3 content for SiBM samples.

In Table 2, data relative to adhesion tests are reported. For every sample the adhesion was found to be good. SiBM provides the best adhesion.

Table 2. Critical load measured on samples after thermal treatment at 500°C.

Sample	$L_c(g)$
SiBQ	200
SiBT	300
SiBM	500

4 Conclusions

Borosilicate alkoxide and amine derived coatings were prepared on mild steel. Differences in the protective effect against oxidation of the metallic substrate were investigated. The anti-oxidation protective action of coatings was studied by XRD and TGA measurements up to 800°C. Amine derived films showed a protection comparable to that of coatings obtained from alkoxide solutions.

Furthermore, amine derived solutions have much higher stability, and lower costs than alkoxide ones. They are, therefore, more suitable for practical applications.

Acknowledgement

The work has been supported by the 'Progetto Finalizzato Materiali Speciali per Tecnologie Avanzate' of CNR, Rome.

References

1. Innocenzi, P., Guglielmi, M., Gobbin, M. & Colombo, P., Coating of metals by the sol-gel dip-coating method, *J. Europ. Ceram. Soc.*, **10**, (1992), 431.
2. Guglielmi, M., Festa, D., Innocenzi, P., Colombo, P. & Gobbin, M., Borosilicate coatings on mild steel, *J. Non-Cryst. Solids*, **147 & 148**, (1992) 474.
3. De Sanctis, O., Gomez, L., Pellegri, N., Parodi, C., Marajovsky, A. & Duran, A., Protective glass coatings on metallic substrates, *J. Non-Cryst. Solids*, **121**, (1990), 338.
4. Murakami, M., Izumi, K., Deguchi, T., Morita, A., Tohge, N. & Minami, T., SiO_2 coating on stainless steel sheets from $CH_3Si(OC_2H_5)_3$, *J. Ceram. Soc. Jpn. Inter. Ed.*, **97** (1989), 86.
5. Miyazawa, K., Itoi, K. & Sakuma, T., *Proceed. of Intern. Conference on Stainless Steels*, Ceramic coating on austenitic stainless steel by sol-gel process, Chiba, ISIJ, 1991, p. 992.
6. Williams, A. G. & Interrante, L. V., Design and synthesis of metal-organic precursors to aluminosilicates, *Mat. Res. Soc. Symp. Proc.*, **32**, (1984), 151.
7. Di Giampaolo Conde, A. R., Puerta, M., Ruiz, H. & Lira Olivares, J., Thick aluminsilicate coatings on carbon steel via sol-gel, *J. Non-Cryst. Solids*, **147 & 148**, (1992), 467.
8. Izumi, K., Murakami, M., Deguchi, T., Morita, A., Tohge, N. & Minami, T., Zirconia coatings on stainless steel sheets from organizirconium compounds, *J. Am. Ceram. Soc.*, **72**, [8], (1989), 1465.
9. Di Maggio, R., Scardi, P. & Tomasi, A., Characterization of Ceria stabilized zirconia coatings on metal substrates, *Mat. Res. Symp. Proc.*, **180**, (1990), 481.
10. Shane, M. & Mecarteney, M. L., Sol-gel synthesis of zirconia barrier coatings, *J. Mater. Science*, **25**, 1537, (1990).
11. Izumi, K., Tanaka, H., Murakami, M., Deguchi, T., Morita, A., Tohge, N. & Minami, T., Coating of florine doped-doped ZrO_2 films on steel sheets by sol-gel method, *J. Non-Cryst. Solids*, **121**, (1990), 344.
12. Guglielmi, M., Fest, D., Innocenzi, P., Mancinelli Degli Esposti, L., Maliavski, N. & Tchekounova, E., Protective ceramic coatings on metals by wet chemistry synthesis, *Proc. of VII Simcer*, Rimini, Italy, (1992), in press.
13. Maliavski, N., Tchekounova, E. & Proshchin, A., *Proc. VII Nat. Congr. Colloid Chemistry & Physics-Chemical Mechanics*, Vol. VI, Tashkent, (1983), 125.
14. Guglielmi, M., Scarinci, G. & Maliavski, N., Preparation and Properties of Silica and Silicate Gels by the Alkoxide, Colloidal and Amine-silicate Methods, *Ceramics Int.*, **14**, (1988), 153.
15. Khripunkov, A., Maliavski, N. & Sidorov, V., *Sov. J. Appl. Chem.*, **62**, (1989), 656.
16. Weldes, H. H., U.S. Patent 3326910 (Philadelphia Quartz Co.) 1967.
17. Enzo, S., Polizzi, S. & Benedetti, A., *Z. Kryst.*, **170** (1985), 275.
18. Prassas, M. & Hench, L. L., Physical chemical Factors in sol-gel processing. In *Ultrastructure Processing of Ceramics Glasses & Composites*, ed. by L. L. Hench & D. R. Ulrich, Wiley, New York, 1984, p. 100.
19. Villegas, M. A., Navarro, J. M. F., *J. Mater. Sci.*, **13** (1988), 2464.
20. Landau, L. D. & Levich, B. G., *Acta Physiochim.* URSS **17**, (1942), 42.
21. Guglielmi, M. & Zenezini, S., The thickness of sol-gel silica coatings obtained by dipping, *J. Non-Cryst. Solids*, **121**, (1990), 303.
22. Brinker, C. J., Hurd, A. J., Shunz, P. R., Frye, G. C. & Ashley, C. S., *J. Non-Cryst. Solids*, Review of sol-gel thin film formation, **147 & 148**, (1992), 424.
23. Innocenzi, P., Thesis of Laurea, Department of Physics 'Galileo Galilei', University of Padova, (1990).

Journal of the European Ceramic Society **15** (1995) 343–348
1995 Elsevier Science Limited
Printed in Great Britain
0955-2219/95/$9.50

Effects of Composition Changes on the Crystallization Behaviour and Properties of SiO_2–Al_2O_3–CaO–MgO (Fe_2O_3–Na_2O–K_2O) Glass-Ceramics

V. K. Marghussian & M. H. Dayi Niaki

Ceramics Division, Department of Materials Science, Iran University of Science & Technology, Narmak, Tehran, Iran

(Received 4 December 1993; revised manuscript received 10 June 1994; accepted 28 July 1994)

Abstract

Several glass-ceramic materials located in the SiO_2–Al_2O_3–CaO–MgO(Fe_2O_3–Na_2O–K_2O) system were formulated by using naturally occurring materials and 1 wt% chromite ore as a nucleant. The crystallization behaviour of specimens was investigated by using dilatometric, DTA and XRD techniques. It was found that the replacement of CaO by MgO has a profound effect on the crystallization behaviour of specimens and some of them show almost complete crystallization. After a two stage heat treatment, an aluminium dioxide phase was identified as the sole crystallization product in all specimens. The microstructures were investigated by SEM.

It was found that phase separation occurs prior to nucleation of dioxide and the latter phase grows into a fibrous shape. The bending strength of crystallized specimens which range from 31 to 76 MPa depends on the degree of crystallinity and on the porosity of specimens. The hardness and chemical durability values depend only on the amount of crystalline phase.

1 Introduction

Glass-ceramic materials which are produced by controlled nucleation and crystallization of glass have received considerable attention in recent years. Among various glass-ceramic materials those of the SiO_2–Al_2O_3–MgO–CaO (Na_2O,K_2O,Fe_2O_3) system are mainly produced from inexpensive natural or synthetic materials such as blast furnace slags,[1–4] basalts,[5–7] oil shales,[8] granite and tuff.[9]

In the present work, an Iranian andesite rock was used as the main constituent to produce a glass-ceramic material and the effect of compositional changes was investigated. All the chosen compositions were part of the system mentioned above.

2 Experimental Procedure

2.1 Starting materials

Local materials, namely andesite rock from the Goorid mine, Birjand (North East Iran), quartz sand from Ghezel-Ghiyeh, magnesite from Birjand, limestone from Boroojerd and chromite from Faryab were used for glass batch preparation. Six batch compositions were selected for study. The chemical compositions of the raw materials and their resultant glasses are given in Tables 1 and 2 respectively.

2.2 Melting and forming

The batch materials were ground into a fine powder, (-60 mesh for all batches, except chromite which was -200 mesh) and after mixing thoroughly were put into preheated fire clay crucibles and melted in an electric furnace at 1300°C for 3–4 h. The melts, which were homogeneous and bubble free, were then cast into stainless steel moulds. The moulds were previously preheated at 440°C which was calculated according to the Coenen procedure.[10]

The glassy specimens (14 × 2 × 1·5 cm) were then properly annealed at the 'annealing temperature' (T_g+5) for 30 min.

2.3 Heat treatment procedure

Differential thermal analysis (DTA) and dilatometric techniques were used in order to follow the changes occurring during the heating of the specimens and thus to determine the suitable nucleation and crystallization temperatures. Differential

Table 1. Chemical compositions of raw materials wt%

Oxide	*Andesite rock*	*Quartz*	*Limestone*	*Magnesite (calcined)*	*Chromite*
SiO_2	63·28	96·62	1·95	0·85	3·52
Al_2O_3	16·15	1·99	—	0·43	9·39
TiO_2	0·76	—	—	—	—
Fe_2O_3	4·12	0·092	0·26	0·07	14·78
CaO	4·38	0·58	54·33	7·79	—
MgO	1·47	0·14	—	90·21	16·97
Na_2O	3·78	0·14	—	—	—
K_2O	3·34	0·21	—	—	—
Cr_2O_3	—	—	—	—	51·13
L.O.I.	2·68	0·25	43·45	0·65	4·21

Table 2. Chemical compositions of prepared glasses[a] wt%

Oxide	*Glass A*	*Glass B*	*Glass C*	*Glass D*	*Glass E*	*Glass F*[b]
SiO_2	50·05	50·05	50·05	50·05	50·05	50·05
Al_2O_3	12·38	12·38	12·38	12·38	12·38	12·38
TiO_2	0·58	0·58	0·58	0·58	0·58	0·58
Fe_2O_3	3·18	3·18	3·18	3·18	3·18	3·18
CaO	27·21	24·71	22·21	19·71	17·21	14·71
MgO	1·29	3·79	6·29	8·79	11·29	13·79
Na_2O	2·75	2·75	2·75	2·75	2·75	2·75
K_2O	2·56	2·56	2·56	2·56	2·56	2·56

[a] 1 wt% Chromite was added to all batches.
[b] Later omitted due to its incomplete melting.

thermal analysis was made in the range 20 – 1100° using powdered samples together with powdered alumina as an inert reference material. The rate of heating in DTA and dilatometer was 10°C/min and 5°C/min, respectively.

Each glassy sample was held at its appropriate nucleation and crystallization temperatures (as determined by DTA and dilatometric techniques) for 3 h.

The heating rate was 10°C/min up to the nucleation temperature and 1°C/min between nucleation and crystallization temperatures.

2.4 X-Ray Diffraction (XRD) and microscopic examinations

The crystallized samples resulting from any of the above mentioned heat treatment schedules were then subjected to XRD and microscopic studies, using a scanning electron microscope (SEM).

2.5 Determination of the physical and chemical properties

The bending strength, micro hardness, density, porosity and chemical durability of the crystallized samples were determined.

3 Results and Discussion

3.1 The crystallization behaviour of glasses

Table 3 shows the glass transition temperatures

Table 3. T_g and T_d values

Specimen	T_g°C	T_d°C
A	663	720
B	660	720
C	657	715
D	655	700
E	653	700

(T_g) and dilatometric softening points (T_d) for glasses A – E. A typical dilatometric curve, represented in Fig. 1 shows the exact locations of T_g and T_d. It can be concluded from Table 3 that by increasing the content of MgO at the expense of CaO, a gradual decrease in both temperatures has occurred. This can be attributed to the gradual decrease of viscosity due to the replacement of CaO by MgO.

Figure 2 gives a typical DTA curve. An endothermic peak is observed beginning at 657°C (T_g) and reaching a maximum at 715°C (T_d), which can be attributed to the glass transition.

The exothermic dip centred at about 915°C is associated with the crystallization of glass. The suitable nucleation temperature (T_n) is usually taken in the 'nucleation range', between T_g and T_d.

The T_n values were determined using 'trial and error', which consisted of holding the specimens at various temperatures within the nucleation range in a gradient furnace, followed by a second hold at 'crystallization temperature' and observing the appearance of specimens. Afterwards, it was found that T_n values determined in this way can also be located approximately at the point where a distinct slope change appeared in the endothermic 'hill' in the DTA curve (Fig. 2). This was later proved to be associated with glass in glass separation.

It is interesting to note the T_n values determined from DTA traces may be fitted into an approxi-

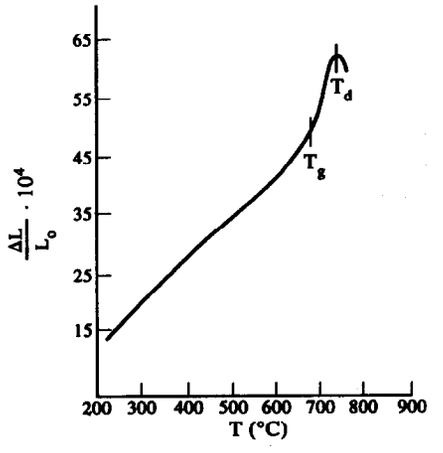


Fig. 1. Dilametric expansion curve of specimen C showing T_g and T_d values.

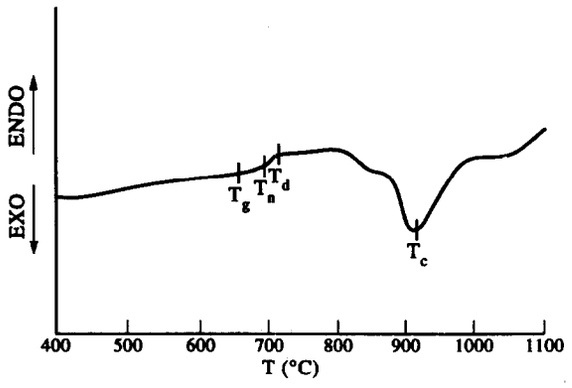


Fig. 2. DTA trace of specimen C showing, T_g, T_d, T_n and T_c values.

mate formula which relates the T_n values to the values to the glass transition and dilatometric softening points:

$$T_n = T_g + \frac{2}{3}(T_d - T_g). \quad (1)$$

Table 4 shows the nucleation and crystallization temperatures for glass samples. The gradual decrease of crystallization temperatures can also be related to the drop in viscosity caused by compositional changes.

3.2 XRD analysis

X-ray diffractometry performed on various heat treated specimens showed that an aluminium dioxide with a pattern very similar to 'Fassaite', Ca $(Mg_{0\cdot8}Al_{0\cdot2})$ $(Si_{1\cdot8}Al_{0\cdot2})O_6$ is the sole crystalline phase observed in all specimens. Regarding the compositions of glass samples, it is likely that some Fe, Na and K have also been substituted in the crystal structure (mainly for Ca). Figure 3 gives the XRD patterns for all specimens. Sample A obviously shows no sign of crystallization and exhibited only slight surface crystallization.

A quantitative X-ray analysis was performed according to the Ohlberg and Stickler method,[11] later revised by Kim *et al.*[12] Figure 4 presents the crystallization results. The amount of crystalline phase rises (Sample B to C), then drops (Sample C to D), finally rising to a very high value (95%). This behaviour can be attributed to competing

Table 4. The nucleation and crystallization temperatures

Specimen	*Nucleation temp from DTA* (T_n)°C	*Nucleation temp Calculated from Eqn. (1)* °C	*Crystallization temp.* °C
A	700	701	920
B	700	700	918
C	693	696	917
D	690	685	910
E	685	684	906

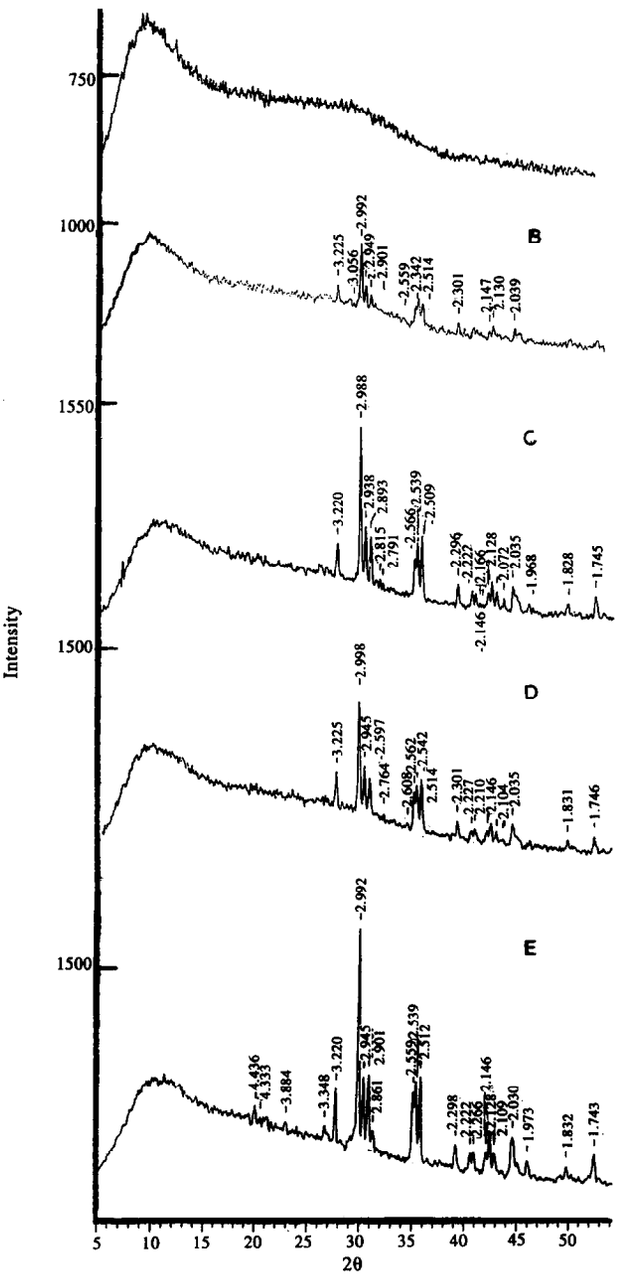


Fig. 3. XRD traces of specimens A to E.

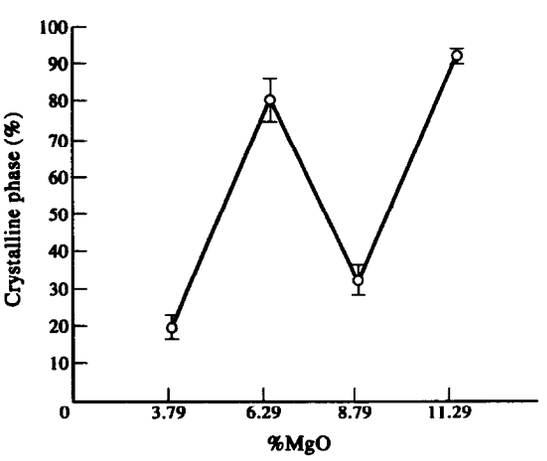


Fig. 4. Percent crystallinity versus composition (wt%).

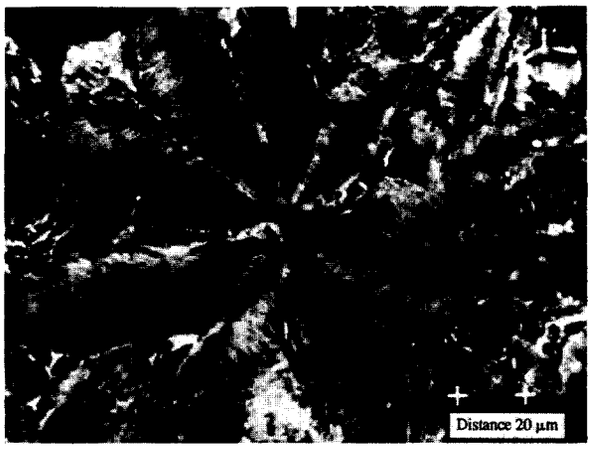


Fig. 5. SEM micrograph of specimen C showing flower-like crystalline aggregates (polished and etched in 2% HF for 5 min.)

thermodynamic and kinetic factors. As was stated previously, the viscosity decreases as a result of replacing CaO by MgO. This increases the crystallization rate. The liquidus temperature is another factor which can affect the crystallization behaviour. The rise of liquidus temperature enhances the crystallization and its drop favours the glass stability. It can be concluded therefore, that the liquidus temperature has probably increased from Specimen B to C and D to E (or if it has decreased the effect of viscosity has predominated), whereas from Specimen C to D the liquidus temperature has dropped. In addition to these factors which affect the growth process, other factors relating to nucleation, such as the effect of composition on surface tension or phase separation, may also be involved.

3.3 Microscopic examinations

Figure 5 shows the micrographs taken by SEM from polished and etched crystallized specimens. The specimens exhibit a special type of dendritic growth giving rise to flower-like crystalline collections. The microstructures of various specimens



Fig. 6. SEM micrograph of glass C after a 3 h hold at nucleation temperature showing extensive phase separation.

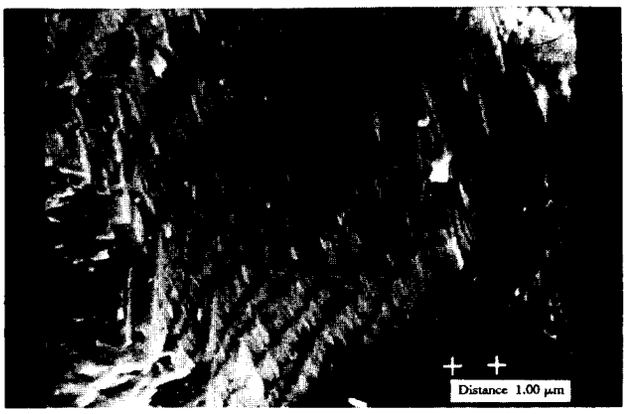


Fig. 7. SEM micrograph of glass C after crystallization showing fibrous morphology of dioxide crystals.

were also studied by SEM using fractured surfaces. Glassy samples which immediately after forming were annealed, did not show any sign of phase separation and inhomogenity up to a magnification of 300 000.

Figure 6 shows that after 3 h hold at the nucleation temperature the glassy sample has became highly phase separated. This observation is in agreement to findings of other investigators.[8,13]

According to McMillan,[13] "chromium in the Cr^{6+} state, being an ion of high field strength is likely to occupy an interstitial position and exert a marked 'ordering' effect upon its surrounding oxygen ions. Under these circumstances a chromium rich phase would separate out from the glass". A mixed spinel of formula $(Mg,Fe)(Al,Fe,Cr)_2O_4$ is then crystallized within the chromium rich phase and acts as a nucleant inducing the crystallization of dioxide.[8] It is likely that the above mentioned nucleation mechanism is also operative in the present investigation, although it was not possible to observe and identify the actual nucleating agents. Figure 7 shows the SEM micrograph of crystallized C glass.

It can be seen that the 'flower like' crystalline collections are themselves composed of 'thread like' fibrous aggregates which have grown in parallel orientation.

The fibrous aggregates consist of tiny, elongated crystals of dioxide, having about 1 μm average length and 0·1 μm average width. These crystals have grown parallel to each other in a direction which makes an angle of about 55–60° with the major axis of 'threads'.

3.4 Mechanical properties

Figure 8 gives the results of three point bending test which was carried out according to ASTM procedure C 158-84 over a span of 10 cm in bars (12 × 2 × 2 cm) cut roughly from original specimens and then ground to size. Each point represents

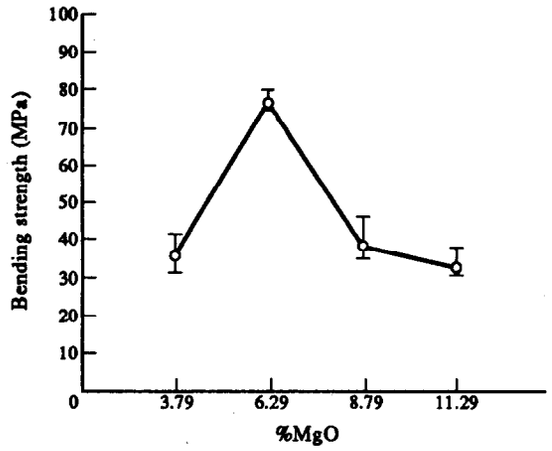


Fig. 8. Bending strength values as a function of composition (wt%). (Each point represents the average value for 10 specimens).

the average value for ten specimens.

It can be concluded that the main factor contributing to the bending strength is the amount of crystalline phase. The relatively low value for Specimen E, in spite of its very high crystallinity, can be attributed to it relatively high value of porosity (see Table 5). It seems that the porosity is mainly formed at the final stage of crystallization. At this stage, the lack of sufficient glassy phase to fill the gaps resulting from crystallization (due to a difference between densities of glassy and crystalline phases) leads to formation of some porosity. The viscous flow of glassy phase at the earlier stage of crystallization, results in pore filling and overall shrinkage of specimens without any considerable pore formation. Our calculations showed that the density of glassy specimens were in the range 2·67–2·69 Mgm^{-3} whereas the mean density of crystalline phase was 3·15 Mgm^{-3}.

From Fig. 9 which shows the knoop hardness values of various specimens, it can be concluded that with increase of crystallinity, the hardness values were also increased. (The hardness tests

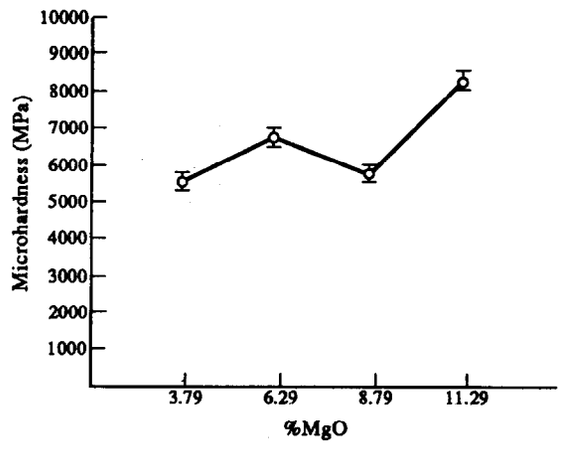


Fig. 9. Knoop hardness values versus composition (wt%). (Each point represents the average value for 3 specimens).

Table 5. Densities and porosities of crystallized specimens

	Specimen			
	B	*C*	*D*	*E*
Bulk density (Mgm^{-3})	2·73	2·97	2·81	2·85
Powder density (Mgm^{-3})	2·77	3·04	2·85	3·12
Total porosity (%) (Calculated)	1·44	2·63	1·40	8·65

Table 6. Chemical durabilities of glass-ceramics

Specimen	*Weight loss in NaOH* $Mgm^{-2} \times 10^{-5}$	*Weight loss*[a] *in HCL* $Mgm^{-2} \times 10^{-5}$
B	Negligible	125·97
C	Negligible	43·61
D	Negligible	85·11
E	Negligible	25·03

[a] Average values for 3 specimens.

were performed at pore-free regions of specimens under a weight of 500 g.) Each point represents the average value for three specimens.

3.5 Chemical durability

Table 6 shows the results of chemical durability of specimens after crystallization. Chemical durabilities were determined by weight loss of polished samples after immersion in 5% NaOH and 5% HCl solutions at 95°C for 24 h.

It is apparent that the resistance to acids is also a function of the crystallinity of material. Specimen E which has the highest amount of crystalline phase shows the highest resistance to acids.

4 Conclusions

Useful glass-ceramic materials can be made by using andesite rock as the primary raw material together with some lime, silica and MgO additions. Chromite ore 1 wt% is sufficient to induce glass in glass phase separation which is a precursor to nucleation in these glasses. A mixed spinel phase precipitating from a chromium rich phase after phase separation, probably acts as a nucleation agent. The replacement of CaO by MgO has a marked effect on the crystallization behaviour of glass compositions studied. There exists an optimum amount of MgO which gives rise to the highest amount of crystalline phase in a standard two stage heat treatment schedule. Although the physical and chemical properties of these glass-ceramic materials generally improve with their degree of crystallinity, the specimen with the highest amount of crystalline phase is not necessarily the strongest one. Specimen C which is almost 80%

crystalline exhibits the highest bending strength. It also possesses acceptable values for hardness and chemical durability and can be used as a suitable, inexpensive construction material.

References

1. Davies, M. W., Kerrison, B., Gross, W. E., Robson, M. J. & Wichall, D. F., Slag ceramics: a glass ceramic from blast-furnace slag. *J. Iron steel Inst.*, **208** (1970) 348–70.
2. Pincus, A. G., Soviet building with slag sitall. *Glass. Ind.*, **53** (1972) 6–9.
3. Hazeldean, G. S. F. & Wichall, D. F., Effect of chemical composition on nucleation and crystallization of slag-based glass-ceramics. *J. Iron steel Inst.*, **211** (1973) 574–80.
4. Topping, J. A., The fabrication of glass-ceramic materials based on blast furnace slag–A review. *J. Can. Ceram. Soc.*, **45** (1976) 63–7.
5. Beall, G. H. & Rittler, H. L., Basalt glass ceramics. *Am. Ceram. Soc. Bull.*, **55** (1976) 579–82.
6. Bahl, D., Roberts, J. A. & Weymouth, J. H., Basalt glass ceramics. *J. Aust. Ceram. Soc.*, **74** (1974) 25–7.
7. Hidalgo, M., Callejas, P. & Rincon, J. M., Microstructure characterization of basalt glass-ceramics. *Mater. Sci. Res.*, **21** (1987) 117–126.
8. Shelestak, L. J., Chavez R. A. & Mackenzie, J. D., Glass & glass ceramics from naturally occuring CaO–MgO–Al_2O_3–SiO_2 Materials. (I) Glass formation & properties. *J. Non-cryst. sol.*, **27** (1978) 75–81; 83–97.
9. Strnad, Z., Glass-ceramic Materials, Elsevier, New York, 1986, p. 112.
10. Coenen, M., Proceedings of the UCDV Conf., Scheweningen, 1965, p. 413.
11. Ohlberg, S. M. & Strickler, D. W., Determination of percent crystallinity of partly devitrified glass by X-ray diffraction. *J. Am. Ceram. Soc.* **45** (1962), 170–2.
12. Kim, H. S., Rawlings, R. D. & Rogers, P. S., Quantitative determination of crystalline and amorphous phases in glass–ceramics by X-ray diffraction analysis. *Br. Ceram. Trans. J.*, **88** (1989) 21–5.
13. McMillan, P. W., Glass-ceramics, 2nd edn., Academic Press, London, 1979, p. 81.

Journal of the European Ceramic Society **15** (1995) 349–355
© 1995 Elsevier Science Limited
Printed in Great Britain. All rights reserved
0955-2219/95/$9.50

Subsolidus Phase Relationships in the Systems Ln_2O_3–Si_3N_4–AlN–Al_2O_3 (Ln = Nd, Sm)

W. Y. Sun, D. S. Yan, L. Gao,

The State Key Lab on High Performance Ceramics and Superfine Microstructure, Shanghai Institute of Ceramics, Academia Sinica, Shanghai, People's Republic of China

H. Mandal, K. Liddell & D. P. Thompson

Wolfson Laboratory, Materials Division, Department of Mechanical, Materials & Manufacturing Engineering, University of Newcastle upon Tyne, UK

(Received 14 April 1994; revised version received 14 July 1994; accepted 1 August 1994)

Abstract

Subsolidus phase relationships in the systems Ln–Si–Al–O–N where Ln = Nd and Sm have been determined. Forty-four compatibility tetrahedra were established in the region Ln_2O_3–Si_3N_4–AlN–Al_2O_3. Within this region, $LnAlO_3$ and M'-phase ($Ln_2Si_{3-x}Al_xO_{3+x}N_{4-x}$) are the only two important compounds which have tie lines joined to β-sialon and AlN polytypoid phases. α-Sialon coexists with the M' phase.

1 Introduction

It is well known that metal oxides are necessary for the densification of silicon nitride ceramics. During sintering, the metal oxide additives and silicon nitride (which unavoidably contains a small amount of silica as an impurity), form an eutectic melt which aids densification. The liquid composition affects the resulting microstructure and hence the properties of the final ceramics; it also determines the nature of grain-boundary crystalline phases after heat-treatment.

The importance of using rare earth oxides for the densification of silicon nitride ceramics has been recognized during recent years. Not only are they very effective for densification, either singly, or in combination with yttria, but also they can be accommodated in the α-sialon lattice, thus providing an opportunity for decreasing the transient liquid phase content after sintering, and hence reducing the amount of residual grain boundary glass. Therefore, phase relationships in Ln–Si–Al–O–N systems are of particular interest. The determination of a whole system, represents a very large amount of work and most previous studies have been restricted to the sub-systems Ln–Si–O–N,[1] Ln–Al–O–N (Ln = Ce, Pr, Nd and Sm)[2] and some planes involving α- and β-sialon.[3,4] In oxygen-rich compositions, there exist two five-component phases,[5–7] U-phase ($Ln_3Si_{3-x}Al_{3+x}O_{12+x}N_{2-x}$) and W-phase ($Ln_4Si_9Al_5O_{30}N$), which have no corresponding counterparts in the Y–Si–Al–O–N system. In the Ln_2O_3–Si_3N_4–AlN–Al_2O_3 sub-system where Ln = Sm, Nd, four compounds: Ln–melilite, $LnAlO_3$, Ln_2AlO_3N and MP ($LnAl_{12}O_{18}N$) have been identified (Fig. 1). The Ln–melilite phase extends into a five-component system, with Si and N being substituted by Al and O to form a solid solution, M', with a range of homogeneity from $x = 0$ to 1 in the formula $Ln_2Si_{3-x}Al_xO_{3+x}N_{4-x}$.[8,9] Work at Shanghai[2] on Ln–Al–O–N systems has shown that the nitrogen-containing magnetoplumbite phase of formula $LnAl_{12}O_{18}N$ is unstable in the pure oxide system.

The purpose of the present work is to complete the study of phase relationships in the region of the Ln–Si–Al–O–N systems defined by the four end-members Si_3N_4, AlN, Al_2O_3 and Ln_2O_3 (Ln = Nd,Sm). This region includes the phases α-sialon, β-sialon and AlN polytypoids, and covers the range of compositions used for the design and processing of commercial multi-phase sialon ceramics.

2 Experimental Procedure

The present paper is the result of two work programmes carried out separately at Shanghai Institute of Ceramics and the University of

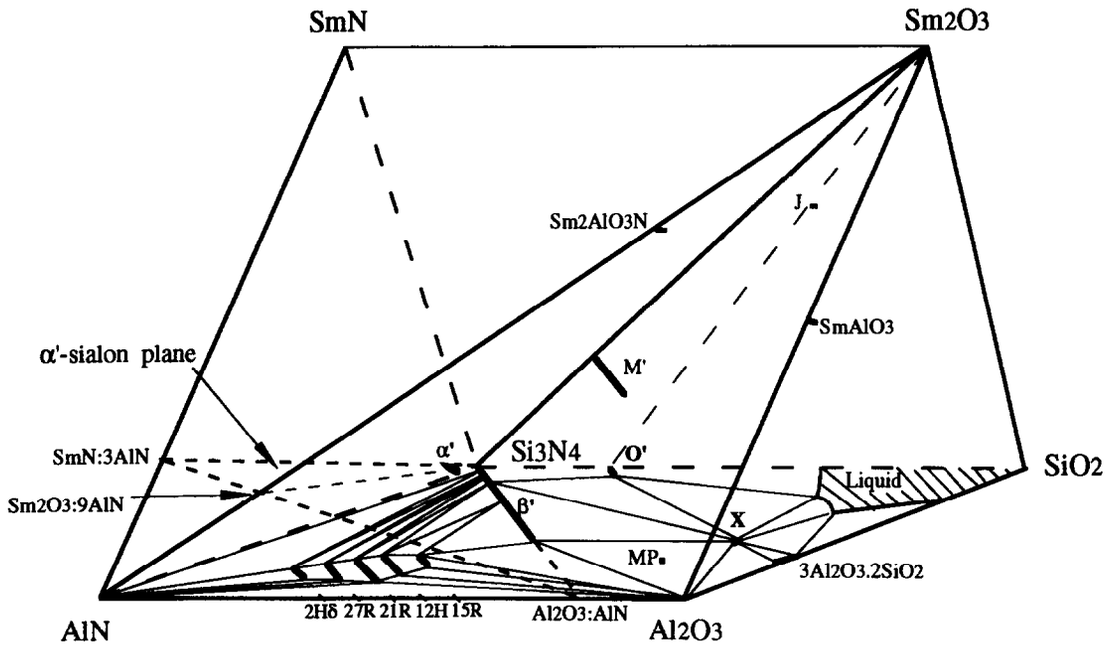


Fig. 1. Representation of Sm(Nd)–SiAlON system showing phases occurring in the region bounded by Si_3N_4, $Sm(Nd)_2O_3$, Al_2O_3 and AlN, and Si–Al–O–N behaviour diagram at 1700°C.

Newcastle. The symbols '#' and '*' are used to represent the experiments carried out at Shanghai and Newcastle, respectively. The starting powders used were α-Si_3N_4 (Starck H1# and Starck LC10*), AlN (supplied by Zhuzhou Institute of Hard Metal Alloys#, containing 1·2% oxygen and Starck Grade B*), Al_2O_3 (99·99%, produced by decomposing ammonium alum# and Alcoa A17*), Nd_2O_3 (99·9%, Yaolung Chemical Works, China# and 99·9%, Aldrick Chemical Co. Ltd*) and Sm_2O_3

Table 1. Compositions studied in the system Si_3N_4–AlN–Al_2O_3–Nd_2O_3

No.	*Compositions (wt%)*				*Firing*	*Phases present*	*Heat*	*Phases present*
	Si_3N_4	*AlN*	*Al_2O_3*	*Nd_2O_3*	*(°C-h)*		*treat.*	
1#	70·75	7·08	8·00	14·17	HP1750-1	β_6s; M'm		
2#	57·19	10·58	18·08	14·16	HP1750-1	β_{15}s; 12Hw	1350-24^	β_{15}s; As; 12Hvw
							1550–5	β_{15}s; 12Hw
3#	55·22	17·25	0·84	26·69	HP1750-1	M'vs; α's; 21Rvw		
4#	53·26	17·99	2·08	26·67	HP1750-1	M'vs; α's; 21Rw; β'vw		
5#	25·95	3·79	23·58	46·68	1500–2	Avs; β'w		
6#	19·75	16·90	27·55	35·65	1550–2	As; 15Rm		
7#	19·61	3·64	6·19	70·56	1700–2	M'vs; Jvw		
8#	14·45	35·30	14·05	35·12	1750–2	M'vs; 21Rm; α'w		
9#	11·77	6·52	—	81·71	1600–2	Jvs; M's		
10#	11·77	—	13·95	74·28	1550–2	As; M's; Hw		
11#	11·77	33·26	—	54·97	1700–2	M'vs; AlNw		
12#	10·57	37·51	43·09	8·74	1750–2	15Rs; MPm; Al_2O_3 vw		
13#	9·77	5·71	14·20	70·31	1550–2	Avs; M's; Hvw		
14#	9·17	41·07	40·95	8·74	1700–2	MPs; 21Rs		
15#	6·10	50·00	—	43·90	1650–2	M's; AlNs; Jm		
16#	4·88	—	13·95	81·17	1600–2	Avs; M's; Jw; Hw		
17#	4·88	6·52	—	88·60	1600–2	Ns; Js; Nd_2O_3s		
18#	80·00	—	4·65	15·35	1700–1	βvs; aw; M'vw	1350–24	βs; Hm; αvw
							1550–5^	βvs; M's; αvw
19*	75·91	1·09	1·85	21·15	1800–1	βvs; M'w	1550·5	M'vs; βs
20*	59·73	16·78	1·52	21·97	1750–1	M's; α'm; 12Hvw	1550–5	M'vs; α'm; 21Rw; βvw
21*	43·75	29·73	6·53	19·99	1750–1	M's; α'm; 21Rw	1550–5	M'vs; α'm
22*	36·96	9·60	23·88	29·56	1600–1	β_{20}s; 15Rm	1350–24	Avs; β_{20}m; 15Rvvw
23*	28·04	17·81	42·61	11·54	1600–1	β_{50}vs; 15Rm; 12Hvw	1150–24	β_{50}vs; Us; 15Rm
							1350–24^	β_{50}s~; As; 15Rm; MPm
24*	26·55	4·91	22·39	46·15	1550–1	M'w 12Hvw	1350–24	Avs; β_{35}W~
25*	14·06	38·89	11·91	35·14	1750–1	M'vs; Am; AlNw; Uvw		

^Used for establishing phase relationships; ~ containing some β' with smaller unit cell dimensions; α = α–Si_3N_4; α'=α-sialon; β = β–Si_3N_4; β', β_6,β_{15}...=β-sialon; A = $LnAlO_3$; N = Ln_2AlO_3N; MP = $LnAl_{12}O_{18}N$; M' = $Ln_2Si_{3-x}Al_xO_{3+x}N_{4-x}$; J = $Ln_4Si_2O_7N_2$; H = $Ln_{10}(SiO_4)_6N_2$; U = $Ln_3Si_3Al_3O_{12}N_2$ (all Ln here represents Nd).

Table 2. Compositions studied in the system Si_3N_4–AlN–Al_2O_3–Sm_2O_3

No.	*Compositions (wt%)*				*Firing*	*Phases present*	*Heat*	*Phases present*
	Si_3N_4	*AlN*	Al_2O_3	Sm_2O_3	*(°C-h)*		*treat.*	
1*	80·00	—	4·52	15·48	1700–1	βvs; M'vw	1350–24	βs; Hm
							1550–5^	βvs; M'w
2*	75·77	1·06	1·81	21·36	1700–1	M'vs; βs; αvw	1550–5	M'vs; βs
3*	70·64	7·07	7·97	14·32	1700–1	β_6s; α'm; M'w	1350–24	β_6s; As; α'w; M'w
							1550–5^	$\beta_6$vs; M's; α'vvw
4*	59·38	16·69	1·49	22·44	1750–1	M's; α'm; β'vw	1550–5	M's; α'm; 21Rvw
5*	57·08	10·56	18·05	14·31	1700–1	β_{13}s; α'w; 12Hvw	1350–24^	β_{13}s; As
							1550–5	β_{13}vs; 12Hw
6*	43·46	29·66	6·49	20·39	1750–1	M's; α'm; 21Rw	1550–5	M's; α'm; 21Rw
7*	36·57	9·50	23·63	30·30	1550–3	β_{20}s; 15Rm	1150–24	Uvs; β_{20}m; 15Rm; $SmSiO_3$?
							1350–24^	Avs; β_{20}m
8*	28·05	17·81	42·51	11·63	1600–1	β_{50}vs; 15Rm	1150–24	β_{50}vs; Us; 15Rm
							1350–24^	Avs; β_{50}S~; MPm; 15Rw
9*	26·56	4·91	22·01	46·53	1600–1	β_{20}s; 15Rm	1150–24	Uvs; β_{20}m; 15Rm; $SmSiO_3$?
							1350–24^	Avs; β_{20}m; Uvw
10*	13·91	38·89	11·91	35·29	1750–1	M'vs; As; AlNw; 27Rvw		
11*	11·82	—	—	88·18	1650–1	Jvs		
12*	9·46	–	2·55	87·99	1650–1	Jvs		
13*	4·73	6·31	—	88·96	1550–1	Avs; Js; Sm_2O_3w		
14*	4·73	—	13·57	81·70	1550–1	Avs; Js; Sm_2O_3w		
15#	10·58	37·44	42·98	9·00	HP1750–1	15Rvs; MPw		
16#	9·17	41·00	40·84	8·99	HP1750–1	12Hvs; MPw; Aw		
17#	3·55	4·21	6·79	85·45	1600–2	Ns; Jm		

All the symbols have the same meaning as in Table 1 except Ln (here Ln represents Sm).

(99·9%, Yaolung Chemical Works, China# and 99·9%, Aldrick Chemical Co. Ltd*). The oxygen contents of the nitride powders were taken into account in calculating the compositions. The starting powders were weighed out and ground in absolute alcohol# or isopropanol* using an agate pestle and mortar. The mixed powders were dried and pressed into pellets 10 mm in diameter and were then isostatically pressed under a pressure of 200 MPa. The specimens prepared at Shanghai were fired in a graphite-resistant furnace with a rather slow cooling rate (~50°C/min) whilst those at Newcastle were fired in graphite-resistant or tungsten element furnaces both of which could be cooled down to room temperature very quickly (~100°C/min). A nitrogen atmosphere was used in all cases. The specimens with the compositions near liquid phase region were prepared in Shanghai and then heat-treated in Newcastle. The heat-treatment was carried out either in a tungsten element furnace (at 1150–1450°C) or in a molybdenum element furnace (at 1550°C). All specimens were examined by X-ray diffractometry# or using a Hägg–Guinier focusing camera*. Only specimens showing less than 3% weight loss after firing were used for data analysis.

3 Results

Twenty five Nd-containing compositions and 17 Sm-containing compositions in the region bounded by Si_3N_4, AlN, Al_2O_3 and Ln_2O_3 were studied to establish compatibility relationships. The binary tie lines established were based on the results listed in Tables 1 and 2. In the region explored, the same phases were observed in both systems, but it was noted that melting temperatures were lower in the samarium system and consequently, at a given temperature, the size of the

Table 3. Subsolidus compatibility tetrahedra in the systems Si_3N_4–AlN–Al_2O_3–Ln_2O_3 (R = Nd and Sm)

Al_2O_3–β_{60}–15R–MP	Al_2O_3–15R–15R'–MP
Al_2O_3–15R'–12H'–MP	Al_2O_3–12H'–21R'–MP
Al_2O_3–21R'–AlN–MP	15R–15R'–12H–12H'–MP
12H–12H'–21R–21R'–MP	21R–21R'–27R–27R'–MP
27R–27R'–$2H^{\delta}$–$2H^{\delta'}$–MP	$2H^{\delta}$–$2H^{\delta'}$–AlN–MP
21R'–27R'–AlN–MP	27R'–$2H^{\delta'}$–AlN–MP
AlN–$2H^{\delta}$–MP–$LnAlO_3$	$2H^{\delta}$–27R–MP–$LnAlO_3$
27R–21R–MP–$LnAlO_3$	21R–12H–MP–$LnAlO_3$
12H–15R–MP–$LnAlO_3$	β_{60}–15R–MP–$LnAlO_3$
β_{60}–Al_2O_3–MP–$LnAlO_3$	β_{60}–β_{25}–15R–$LnAlO_3$
β_{25}–15R–12H–$LnAlO_3$	β_{25}–β_{10}–12H–$LnAlO_3$
β_{10}–12H–$LnAlO_3$–M'	β_{10}–12H–21R–M'
α'–β_0–β_{10}–M'	α'–β_{10}–21R–M'
α'–β_{10}–β_8–21R	α'–β_8–21R–27R
α'–β_8–β_5–27R	α'–β_5–27R–$2H^{\delta}$
α'–β_5–β_2–$2H^{\delta}$	α'–β_2–$2H^{\delta}$–AlN
α'–β_2–β_0–AlN	α'–AlN–$2H^{\delta}$–M'
α'–$2H^{\delta}$–27R–M'	α'–27R–21R–M'
M'–12H–21R–$LnAlO_3$	M'–21R–27R–$LnAlO_3$
M'–27R–$2H^{\delta}$–$LnAlO_3$	M'–$2H^{\delta}$–AlN–$LnAlO_3$
M'–AlN–$LnAlO_3$–J	M'–AlN–J–M
AlN–$LnAlO_3$–J–Ln_2AlO_3N	$LnAlO_3$–J–Ln_2AlO_3N–Ln_2O_3

MP = $LnAl_{12}O_{18}N$; M' = $Ln_2Si_{3-x}Al_xO_{3+x}N_{4-x}$; J = $Ln_4Si_2O_7N_2$; 15R, 12H, 21R, 27R, $2H^{\delta}$ are those on the Si-rich end of AlN polytypoids; 15R', 12H', 21R', 27R', $2H^{\delta'}$ are AlN polytypoids on the Al-rich end.

liquid-forming region is larger. Based on the much more extensive knowledge of phase relationships in the Y–Si–Al–O–N system[10–13] and other information in the literature listed above, 44 compatibility tetrahedra were established in this region for both Nd and Sm (Table 3).

As indicated in this table, tie lines exist between the compound $LnAl_{12}O_{18}N$ and all the AlN polytypoid phases as well as β_{60} (the maximum limit of the β-sialon solid solution). The compound $LnAlO_3$ was found to be compatible with β-sialon in the range $\beta_{10}(z = 0{\cdot}8)$–$\beta_{60}$, and also with the Si-rich terminal compositions of the AlN polytypoid phases. Compatibility tetrahedra are also formed between α-sialon, the Si-rich ends of the AlN polytypoid ranges (from AlN to 21R) and M'-phase. M' was also found to have tie lines with β-sialon from $\beta_0(\beta\text{-}Si_3N_4)$ to β_{10}, forming two $\alpha' + \beta'$ containing compatibility tetrahedra α'–β_0–β_{10}–M' and α'–β_{10}–21R–M'. $LnAlO_3$–AlN polytypoid and α'–β' two-phase regions are represented graphically in Figs 2–4. In the present work, α-sialon is considered as a point composition and its detailed solid solution range has not been determined.

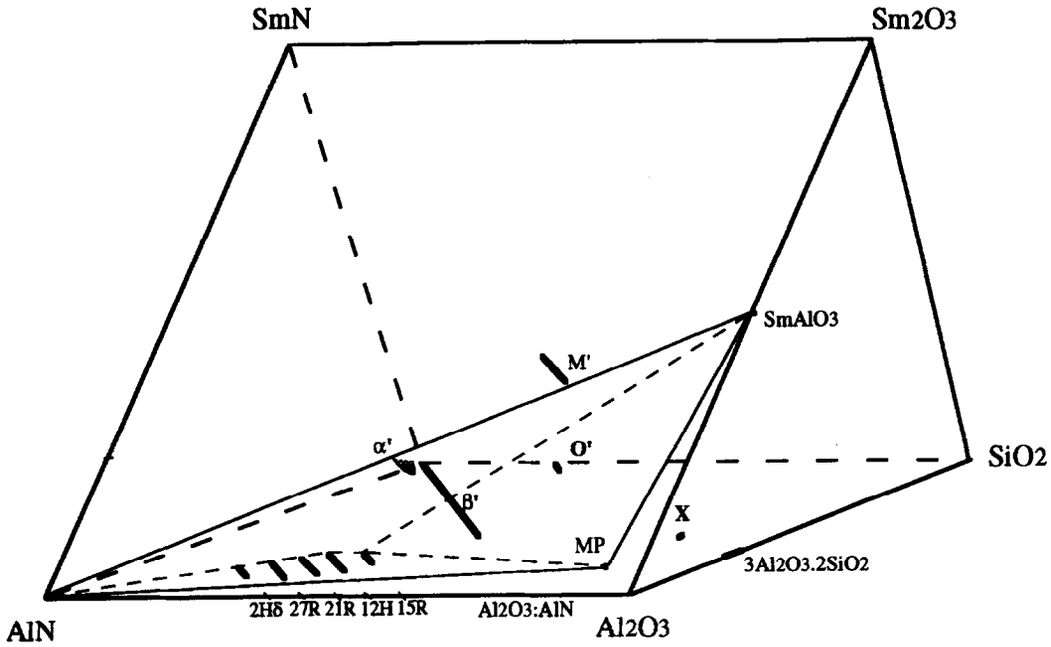


Fig. 2. Sm(Nd)AlO_3 is compatible with all polytypoid phases (Si-rich terminal), AlN and Sm(Nd)$Al_{12}O_{18}N$ (MP-compounds) forming five compatibility tetrahedra: Sm(Nd) AlO_3–15R–MP–12H; Sm(Nd)AlO_3–12H–MP–21R; Sm(Nd)AlO_3–21R–MP–27R; Sm(Nd) AlO_3–27R–MP–2Hδ and Sm(Nd)AlO_3–2Hδ–MP–AlN.

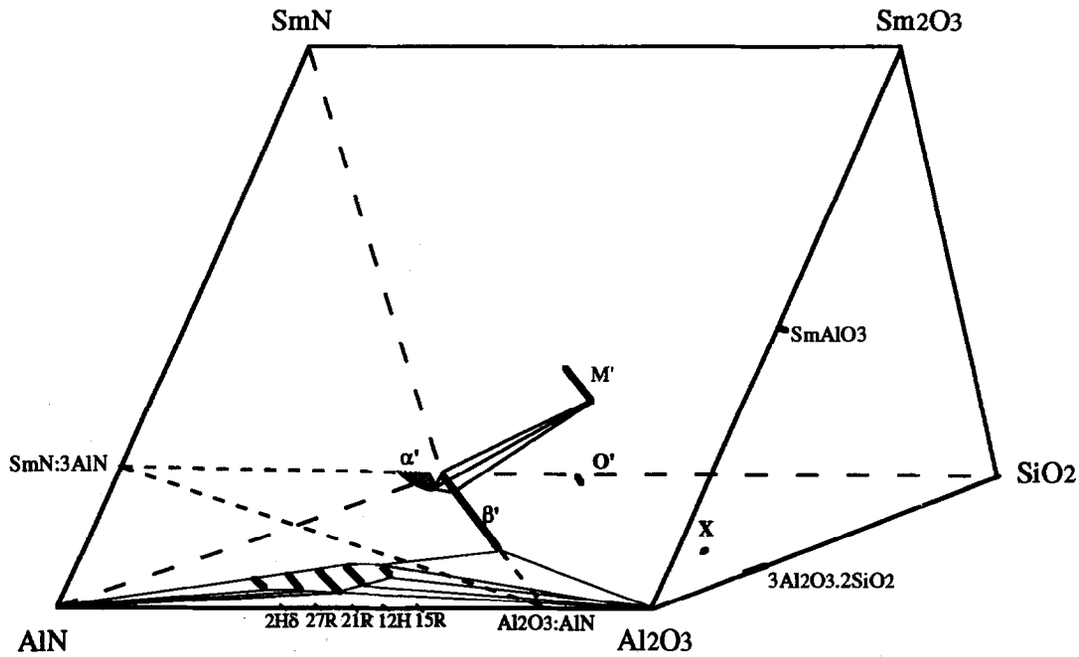


Fig. 3. M'(melilite solid solution) is compatible with β-sialon (β_0–β_{10}) and α-sialon forming α'–β'–M' compatibility tetrahedron.

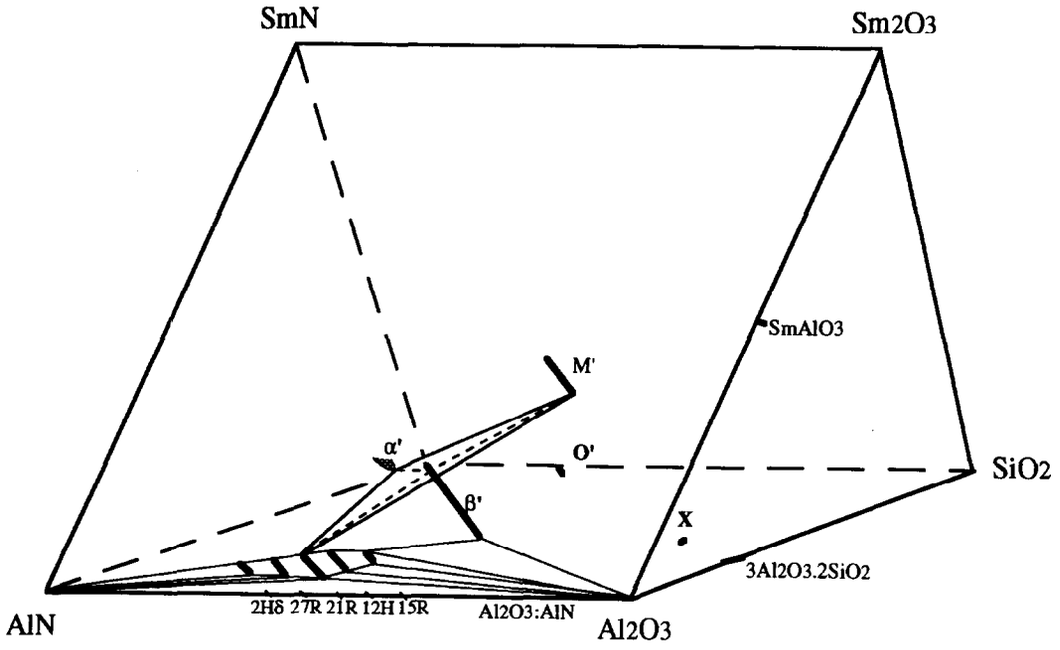


Fig. 4. Compatibility tetrahedron α'–β–21R–M'.

4 Discussion

Previous work in the Nd-system[4] showed that at 1700°C, the liquid phase region in this system intersects the β-sialon–$NdAlO_3$ plane (Fig. 5). Moreover, $NdAlO_3$ does not appear in nitrogen-rich compositions on this plane. These observations are in contrast to the behaviour of YAG ($Y_3Al_5O_{12}$) in the β-sialon–YAG system. The appearance of 12H polytypoid phase on the β-sialon–$NdAlO_3$ plane implies that it must be in equilibrium with a liquid phase of more silica-rich composition than those on the plane. Recently, heat-treatment studies of Ln–Si–Al–O–N (Ln = La–Yb) glasses,[14] have indicated that the resulting crystalline phases vary with the composition of the glass, the atomic number (i.e. ionic radius) of the rare earth element and with the heat-treatment temperature. In the Nd- and Sm-systems, at lower temperatures (1000–1200°C), wollastonite ($LnSiO_2N$) and U-phase are the main crystalline phases formed from glasses in equilibrium with mixed α + β sialons, and with increasing temperature, $LnAlO_3$ appears. U-phase, of composition

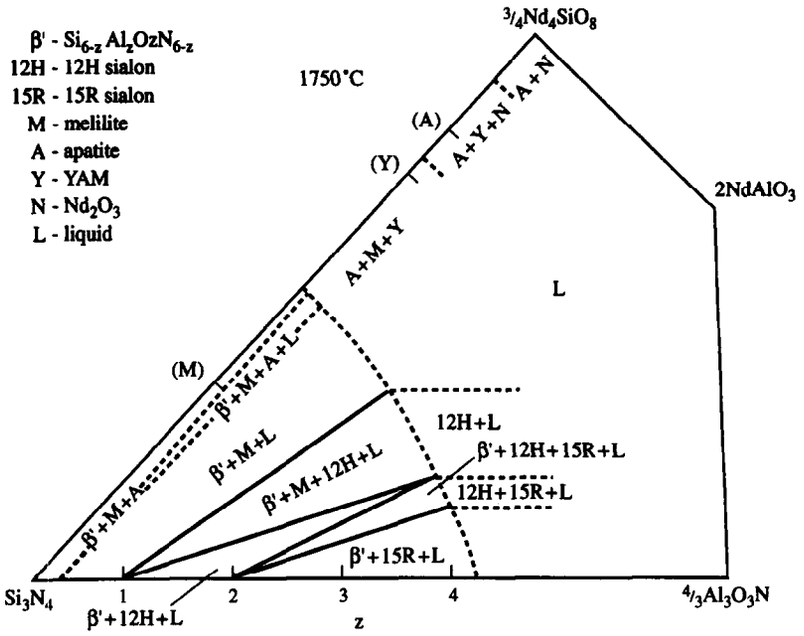


Fig. 5. Phase relationships of β'–$NdAlO_3$ plane at 1750°C.

$Ln_3Si_{3-x}Al_{3+x}O_{12+x}N_{2-x}$, where $O < x < 1$, is a crystallization product of Ln–Si–Al–O–N glasses in equilibrium with β-sialon, heated in the range 950–1400°C. The stability of this phase increases with cation size, and the melting point is around 1390°C.[6]

In the region studied, $LnAlO_3$, M'-phase and U-phase were the main phases observed after heat-treatment in the temperature range 1150–1550°C. Suitable devitrification temperatures for the formation of $LnAlO_3$ are in the range 1250–1450°C. At lower temperatures (1150–1250°C), U-phase occurred instead. In the oxygen-rich compositions explored in the present work, U-phase always occurred after heat-treatment (or even after firing in the Shanghai furnace, which has a slower cooling rate). The occurrence of U-phase in the region studied can not be considered as an equilibrium phase under subsolidus temperature conditions and is only an incompletely recrystallized form of the liquid phase. In Si_3N_4-rich compositions, M'-phase often occurs after sintering, increasing in amount after further heat-treatment at $\approx$1550°C. This is because the composition of M' is nearer to the liquid phase region and therefore M' phase dissolves into the melt during firing. The crystallization temperature for M' is about 1550°C. In establishing subsolidus phase relationships, the judgement on the correct equilibrium phases under subsolidus temperature conditions can sometimes be a difficult problem. Using phase assemblages observed at the same temperature for all conditions studied might lead to mistaken results, since different compositions may need different temperatures to fully crystallize the liquid phase.

In the present work, all starting compositions were designed to fall on supposed tie lines or into supposed compatibility triangles. For examples, in the Sm system, compositions Nos 2, 3 and 5 were on the lines between M' ($Ln_2Si_2AlO_4N_3$) and β-Si_3N_4, β-sialon ($z = 1$) and β-sialon ($z = 2$) respectively; Nos 1, 8 and 9 were on composition lines between $SmAlO_3$ and Si_3N_4, β-sialon ($z = 4$) and β-sialon ($z = 2$), respectively. If the expected phases were obtained after heat-treatment under a particular set of conditions, then equilibrium was believed to have been achieved. Based on this philosophy, compositions marked with the symbol '^' in Tables 1 and 2 were believed to have achieved equilibrium and were used to establish the subsolidus phase relationships. Composition No. 1 (Table 2) only gave M' and apatite ($Sm_{10}(SiO_4)_6N_2$) after heat treatment at 1350 and 1550°C, which indicated that the supposed tie line β-Si_3N_4–$SmAlO_3$ does not exist. In composition No.5(Table 2), the absence of M' phase implies that M' is not compatible with β_{13}. The coexistence of β-sialon with M' was found to be restricted to the range β_0–β_{10}. From the X-ray diffraction data of M' and β-sialon, it seems that Nd- and Sm-melilite ($Ln_2O_3.Si_3N_4$) has priority over β-Si_3N_4 in accommodating Al and O (thereby forming M' phase) and therefore the tie lines between melilite and β-sialon do not run parallel. The oxygen-containing α-sialon phase occurring in the present samples is believed to have a composition close to the oxygen-rich limit of the α-sialon homogeneity range in these systems; this phase is also compatible with M'.

α-sialon, 12H and 15R sometimes occurred in compositions located on the β-sialon–$LnAlO_3$ and β-sialon–M' planes, and decreased in amount or even disappeared after heat-treatment. This is partly because the liquid phase in these compositions shifts in composition with temperature, and also because some $\alpha \rightarrow \beta$ sialon transformation occurs in these samples.[15] J-phase ($Ln_4Si_2O_7N_2$) should occur in compositions along the line joining Ln_2O_3 to Si_2N_2O, but it always appears at the composition $3Ln_2O_3$:Si_3N_4, just as in the Y–Si–Al–O–N system. This could be attributed to the unavoidable existence of a silica layer on the surface of silicon nitride. In the Y–Si–Al–O–N system, J-phase forms a continuous solid solution with YAM ($Y_4Al_2O_9$). In the present work J-phase solid solution (J') was never observed. Composition Nos 11 and 12 (Table 2) were designed to produce J- and J'-phase and the X-ray data did not show visible differences in d-values between these two J-phases.

Of the 44 compatibility tetrahedra established in the present work, the following six which involve α-, β-sialon and AlN-polytypoids (which could be used as reinforcement phase for α', β' or α'-β' because of its fibre-like morphology) and the promising grain boundary phases M' and $LnAlO_3$, are the most useful for the design of multi-phase sialon ceramics. They are: α-sialon–β_0–β_{10}–M'; α-sialon–β_{10}–21R–M'; β_{25}–15R–12H–$LnAlO_3$; β_{25}–β_{10}–12H–$LnAlO_3$; β_{10}–12H–$LnAlO_3$–M' and β_{10}–12H–21R–M'.

5 Conclusions

Subsolidus phase relationships in the systems Ln_2O_3–Si_3N_4–AlN–Al_2O_3 (Ln = Nd, Sm) have been determined. Forty-four compatibility tetrahedra have been established in this region. $LnAlO_3$ coexists with β-sialon, approximately from β_{10} ($z = 0{\cdot}8$) to β_{60}($z = 4$). The liquid phase crosses the tie line between $LnAlO_3$ and β-sialon at firing temperatures (1600–1700°C) and therefore β-sialon–$LnAlO_3$ two-phase materials can only be

obtained after heat-treatment in the range 1250–1450°C. The coexistence of M' with β-sialon is restricted to the range β_0–β_{10}. α-Sialon is also compatible with M'. The compatibility tetrahedra α-sialon–β_0–β_{10}–M'; α-sialon–β_{10}–21R–M'; β_{25}–15R–12H–$LNAlO_3$; β_{25}–β_{10}–12H–$LnAlO_3$; β_{10}–12H–$LnAlO_3$–M' and β_{10}–12H–21R–M' are the most useful for the design and processing of multi-phase sialon ceramic materials.

Acknowledgement

This work was supported by NNSF (National Natural Science Foundation, China) and the ALCS (Academic Link with China Scheme) programme of the British Council, UK.

References

1. Mitomo, M., Izumi, F., Horiuchi, S. & Matsui, Y., Phase relationships in the system Si_3N_4–SiO_2–La_2O_3. *J. Mater. Sci.*, **17** 1982 2359–66.
2. Sun, W. Y., Yen, T. S. & Tien, T. Y., Subsolidus phase relationships in the system Re-Al-O-N (where R = rare earth elements). *J. Solid State Chem.*, **95** 1991 424–9.
3. Huang, Z. K., Tien, T. Y. & Yan, D. S., Subsolidus phase relationships in Si_3N_4–AlN–rare earth oxide systems. *J. Amer. Ceram. Soc.*, **69** 1986 C241–2.
4. Slasor, S., Liddell, K. & Thompson, D. P., The role of Nd_2O_3 as an additive in the formation of α' and β-sialon. In *Proc. Special Ceramics* 8, ed. S. P. Howlett and D. Taylor, British Ceramics Society, UK, 1986, pp. 35–50.
5. Thompson, D. P., New grain boundary phases for Si_3N_4 and sialon ceramics. In *Proc. C-MRS Int. Symp. ('90, Peking)* Vol 2., ed. Y. Ham, Elsevier Science BV, Amsterdam, 1991, pp. 335–42.
6. Mandal, H., Thompson, D. P. & Ekström, T., Heat-treatment of Ln–Si–Al–O–N glasses. In *Proc. 7th Irish Mater. Forum Conf. IMF7*, ed. M. Buggy and S. Hampshire. Trans. Tech. Publications, Switzerland, 1992, pp. 187–203.
7. Thompson, D. P., New grain-boundary phases for nitrogen ceramics. In *Mat. Res. Soc. Symp. Proc. Symposium K* Vol. 287, ed. I.-W. Chen *et al.*, MRS, 1993, pp. 79–92.
8. Cheng, Y.-B. & Thompson, D. P., Aluminium-containing nitrogen melilite phases. *J. Amer. Ceram. Soc.*, **77** (1994) 143–8.
9. Cheng, Y.-B. & Thompson, D. P., Preparation and grain-boundary devitrification of samarium α-sialon ceramics. *J. Eur. Ceram. Soc.*, **14** (1994) 13–21.
10. Thompson, D. P., Phase relationships in Y–Si–Al–O–N ceramics. In *Proc. Int. Symp. Tailoring Multiphase and Composite Ceramics*, ed. R. E. Tressler *et al.* MRS Vol. 20, 1986, pp. 93–102.
11. Sun, W. Y., Tien, T. Y. & Yen, T. S. (Yan, D. S.), Solubility limits of α'-SiAlON solid solutions in the system Si, Al, Y/N, O. *J. Amer. Ceram. Soc.*, **74** (1991) 2547–50.
12. Sun, W. Y., Tien, T. Y. & Yen, T. S. (Yan, D. S.), Subsolidus phase relationships in part of the system Si, Al, Y/N, O: the system Si_3N_4–AlN–YN–Al_2O_3–Y_2O_3. *J. Amer. Ceram. Soc.*, **74** (1991) 2753–8.
13. Sun, W. Y., Yen, T. S. & Tien, T. Y., Graphical representation of the sub-solidus phase relationships in the reciprocal salt system Si, Al, Y/N, O. *Sci. in China(Series A)*, **35** (1991) 877–89.
14. Mandal, H. & Thompson, D. P., Heat-treatment of sialon ceramics densified with higher atomic number rare earth and mixed yttrium/rare earth oxides. In *Proc. Special Ceramics 9*, ed. R. Stevens. The Institute of Ceramics, Stroke-on-Trent, UK, 1992, pp. 97–104.
15. Mandal, H., Thompson, D. P. and Ekström, T., Reversible $\alpha \rightleftharpoons \beta$ sialon transformation in heat-treated sialon ceramics. *J. Eur. Ceram. Soc.*, **12** (1993) 421–9.

Journal of the European Ceramic Society **15** (1995) 357–362
© 1995 Elsevier Science Limited
Printed in Great Britain. All rights reserved
0955-2219/95/$9.50

Tape-casting: Relationship Between Organic Constituents and the Physical and Mechanical Properties of Tapes

M. Descamps,[a] G. Ringuet,[a] D. Leger[b] & B. Thierry[a]

[a]CRITT Céramiques Fines, Laboratoire des Matériaux Avancés Céramiques, Université de Valenciennes et du Hainaut-Cambrésis, France
[b]Laboratoire des Matériaux Minéraux, Conservatoire National des Arts et Métiers Paris, France

(Received 14 March 1994; revised version received 26 June 1994; accepted 1 August 1994)

Abstract

Alumina tapes, obtained by tape-casting, were produced from different slurry compositions. The effects of organic phase concentration on the mechanical and physical properties of green and fired tapes was measured.

The amount of organic phase used did not influence the apparent density of green tapes as long as the volume of organics introduced in the slurry was lower than the pore volume of the tape. Beyond this limit, grain separation occurred, which induced a decrease in material density.

Mechanical properties of tapes, in particular the maximum strength and the rupture elongation, were strongly influenced by the organic phase concentration. Variations in these properties were dependent on the level of filling of the tape porosity by the organic phase.

1 Introduction

Tape-casting is becoming a routine process for the formation of thin ceramic sheets.[1,2] The production of ceramic tapes by this process requires the use of significant amounts of organic compounds (solvents, binders, plasticizers, and dispersing agents).

Studies carried out on tape-casting show that a large diversity of slurry compositions are used.[3] For this process of shaping ceramics, the mechanical and physical characteristics of the green tapes are very important for further processing and the final properties of the material. Indeed, after the drying stage, the tape can be either stored (roller) or made in to the desired shape and dimension (cutting, punching, etc). The ceramic tape must then have the flexibility and strength required for tape handling. On the other hand, the powder compactness inside the green tape will have an effect upon the physical properties of the fired material and in particular upon the tape density. The physical and mechanical properties for a given powder will depend upon the type and quantity of the organic phase introduced inside the suspension.

Generally, work carried out on this theme showed an increase in the mechanical strength of tapes with the rise of the binder content[4] and a tape elongation which increased with the increase of the plasticizer content to the detriment of the mechanical resistance of the material.[5,6]

However, little of the work showed the evolution of mechanical and physical properties as a function of filling level of the porous volume of tape by the organic phase. The purpose of this study was to determine the significant relationship between the physical and mechanical properties of green and sintered tapes, the concentration of organic phases used and the porous volume of tapes.

2 Experimental Study

2.1 Starting material

The raw material used for tape production was an alumina powder (Al_2O_3, CT530SG, Alcoa, USA). Its physical characteristics are shown in Table 1. This powder was a low soda grade (Na_2O = 0·08 wt%) with a nominal purity higher than 99·7% in weight of alumina.

2.2 Slurry composition

Al_2O_3 slurry dispersion was carried out in an azeotropic solvent mixture of trichloroethylene–ethanol (72/28 wt%) using a phosphate ester type (Beycostat C213 CECA, France) dispersing

Table 1. Physical characteristics of Al_2O_3 powders

Specific surface area (m^2/g)	*Mean particle diameter* (μm)	*Density* (g/cm^3)
4·2	1·3	3·98

agent.[7–9] Cohesion between powder grains was ensured with a polyvinylbutyral resin (PVB, Butvar B98 Monsanto) which was plasticized by dibutylphthalate (DBP, Aldrich Chemical). So, the production of a tape-casting suspension requires the use of numerous organic compounds. Competition can occur between the adsorption of the different compounds onto the particle surface to reduce the effectiveness of these products.[10–12] For this reason, the introduction sequence of different organic compounds inside the slurry was important. Thus, the dispersing agent was introduced in order to optimize the slurry defloculation. A first milling, within 4 h, was carried out with the powder, the solvent and the dispersing agent.

The binder and the plasticizer were then added and the suspension was mixed again after 20 h in order to obtain a good homogenization between mineral and organic compounds. These milling operations were carried out with a planetary grinding. Alumina containers and balls were used in order to minimize the pollution.

Slurries were produced with a binder content varying between 2 and 7 wt% (of Al_2O_3 concentration) and a plasticizer content varying between 0 and 300 wt% (of binder concentration). Dry matter content was fixed at 68 wt% and dispersing agent content was equal to 0·8 wt% (of Al_2O_3 concentration) for all experiments. The slurry viscosities were maintained at 1500 ± 100 mPa s using suitable solvent content.

2.3 Casting

Al_2O_3 slurries were cast on a bench by means of the doctor–blade method. The mobile carrier consisted of a polyester film, with the blade height adjusted in order to obtain tapes with a thickness of about 300 μm. Tape drying was carried out at room temperature and in the open air.

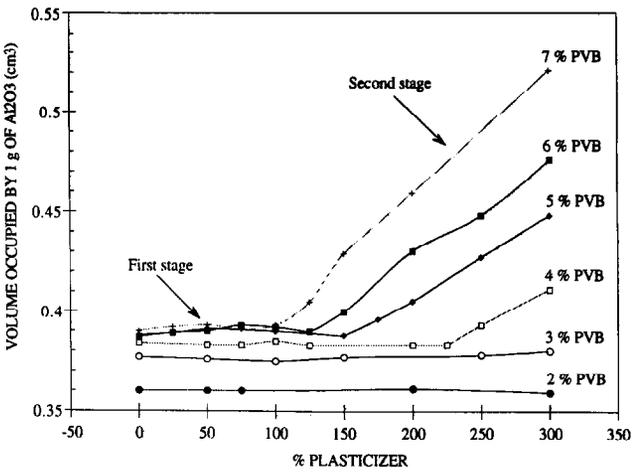


Fig. 1. Evolution of tape volume apparent as a function of plasticizer content at different binder (PVB) concentrations.

Table 2. Volume of the tape containing 1 g of Al_2O_3 and organic limit volume of the tapes (cm^3)

	Tape composition (% binder)					
	2%	*3%*	*4%*	*5%*	*6%*	*7%*
V_{mea} Volume of tape occupied by 1 g of Al_2O_3	0·360	0·376	0·384	0·389	0·391	0·392
V_{lim} Maximum volume to be filled	0·109	0·125	0·133	0·138	0·140	0·141

2.4 Tape characterization

The influence of organic composition on the density of the material was studied by mercury porosimetry (Poresizer 9310 Coultronics). This instrument determines the apparent volume of 1 g of sample (powder + organic). Therefore, the powder weight inside 1 g of tape varies with the amount of organic phase used. For this reason, the accurate volume occupied by 1 g of Al_2O_3 was calculated using the porosimetry results and tape formulations.

Mechanical properties, in particular the maximum strength and the rupture elongation were

Table 3. Organic volume contained in tapes of different formulations (cm^3)

	% Plasticizer						
% Binder	*0*	*100*	*125*	*150*	*200*	*250*	*300*
2	0·0257	0·0449	—	—	0·0641	—	0·0832
3	0·0348	0·0636	—	—	0·0923	—	0·1211
4	0·0439	0·0822	0·0918	0·1014	0·1206	0·1398	0·1589
5	0·0530	0·1009	—	0·1249	0·1488	0·1728	0·1968
6	0·0621	0·1196	0·134	0·1483	0·1771	0·2059	0·2346
7	0·0712	0·1383	0·1550	0·1718	0·2054	—	0·2725

measured for different tape formulations. Measurements, performed 1 week after the slurry casting, were carried out on tapes of 300 μm thickness and dimensions corresponding with NFT51034 standard. Stress and elongation values obtained on the tape, were dependent on the loading rate.[13] For studied compositions, preliminary trials showed a stabilization of these characteristics from rates equal to or higher than 20 mm/min. Thus, the loading rate of the testing machine (Adamel Lhomargy DY30) was then fixed at 20 mm/min, for all experiments.

The rupture elongation of the tapes was measured by the cross-slide movement. Force cells used for these trials were of 10 and 100 N. Twenty specimens of each formulation were tested.

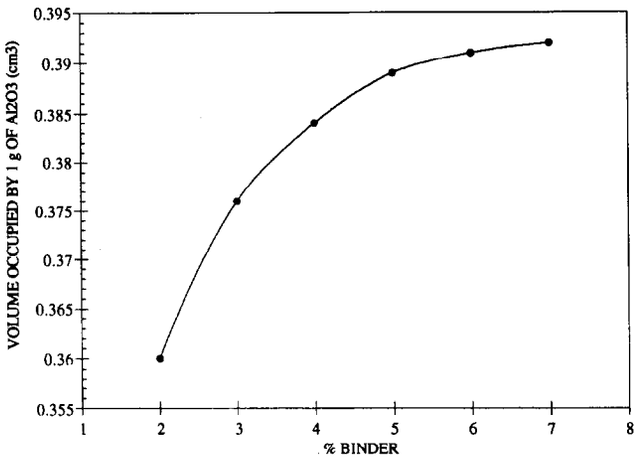


Fig. 2. Evolution of tape volume apparent for different binder contents and plasticizer contents giving an organic volume lower than porous volume of the tape (first stage).

3 Results and Discussion

3.1 Physical properties

The effect on the apparent volume of the tape (volume occupied by 1 g of Al_2O_3) as a function of increasing plasticizer content was studied on tapes fabricated with different binder contents (Fig. 1). When the binder content was equal to or higher than 4 wt% of powder content, two regions were observed as the plasticizer content was increased:

In the first stage, the volume occupied by 1 g of alumina remained constant. Organic compounds (binder, plasticizer, dispersing agent) filled the porous structure of the material without changing the distance between powder grains. In the second stage, a rearrangement of the structure occurred. The distance between the grains increased and there was a significant increase in tape volume. In this stage, the organic volume was higher than the porous volume of the tape.

For binder contents equal to 2 and 3 wt%, only the first stage is observed. The difference between the experimental volume occupied by 1 g of powder inside the tape (volume measured in the first stage, which remained constant up to a certain plasticizer concentration for the different binder contents, V_{mea}) and the theoretical volume of 1 g of Al_2O_3 (V_{th} = 0·251 cm^3) gave the limit value of organic volume (V_{lim}) beyond which structural modification of the tape occurred (Table 2)

$$V_{lim} = V_{mea} - V_{th} \quad (1)$$

Comparison between V_{lim} and V_{org} values for the different compositions (Table 3) shows that total filling of the porous structure of the tape by the organic phase would not be reached for tapes with 2 and 3 wt% of binder content, whatever plasticizer content used. However, for tapes containing 4, 5, 6 and 7 wt% of binder content, V_{org} would exceed V_{lim} for plasticizer amounts of about 250, 200, 150 and 125% respectively. These calculated values, are in agreement with the observed increases of tape volume (Fig. 1).

Whereas increasing plasticizer content did not change the volume filled by 1 g of Al_2O_3 for a given binder amount (when $V_{org} < V_{lim}$), increasing binder content induced an increase in this volume, measured in the first stage. However, for binder concentrations greater than 5% a structure stabilization occurred (Fig. 2). Two hypotheses are proposed in order to explain this behaviour:

(1) Low amounts of binder did not allow a total coating of the Al_2O_3 grain surface. Thus, powder specific surface area had a strong influence.
(2) The binder film adsorbed to the grain surfaces tended to a thickness limit.

Study of the fracture surface of green tapes, with different plasticizer concentrations corroborated the proposed model. For organic compositions lower than the filling volume limit (V_{lim}), the grain surface was 'clean'. When this limit was exceeded, a coating of the powder grain could be observed as well as the formation of granules induced by the organic phase. Micrographs shown in Fig. 3 correspond to a binder concentration of 5 wt%.

Measurements carried out on debinded tapes (1 h at 600°C) and fired tapes (1 h at 1650°C) also showed significant decrease of the tape density when the organic volume was higher than the pore volume of the tape (Fig. 4).

3.2 Mechanical properties of tapes

The maximum strength and the rupture elongation of green tapes were measured on materials introduced from different formulations (Figs 5 and 6).

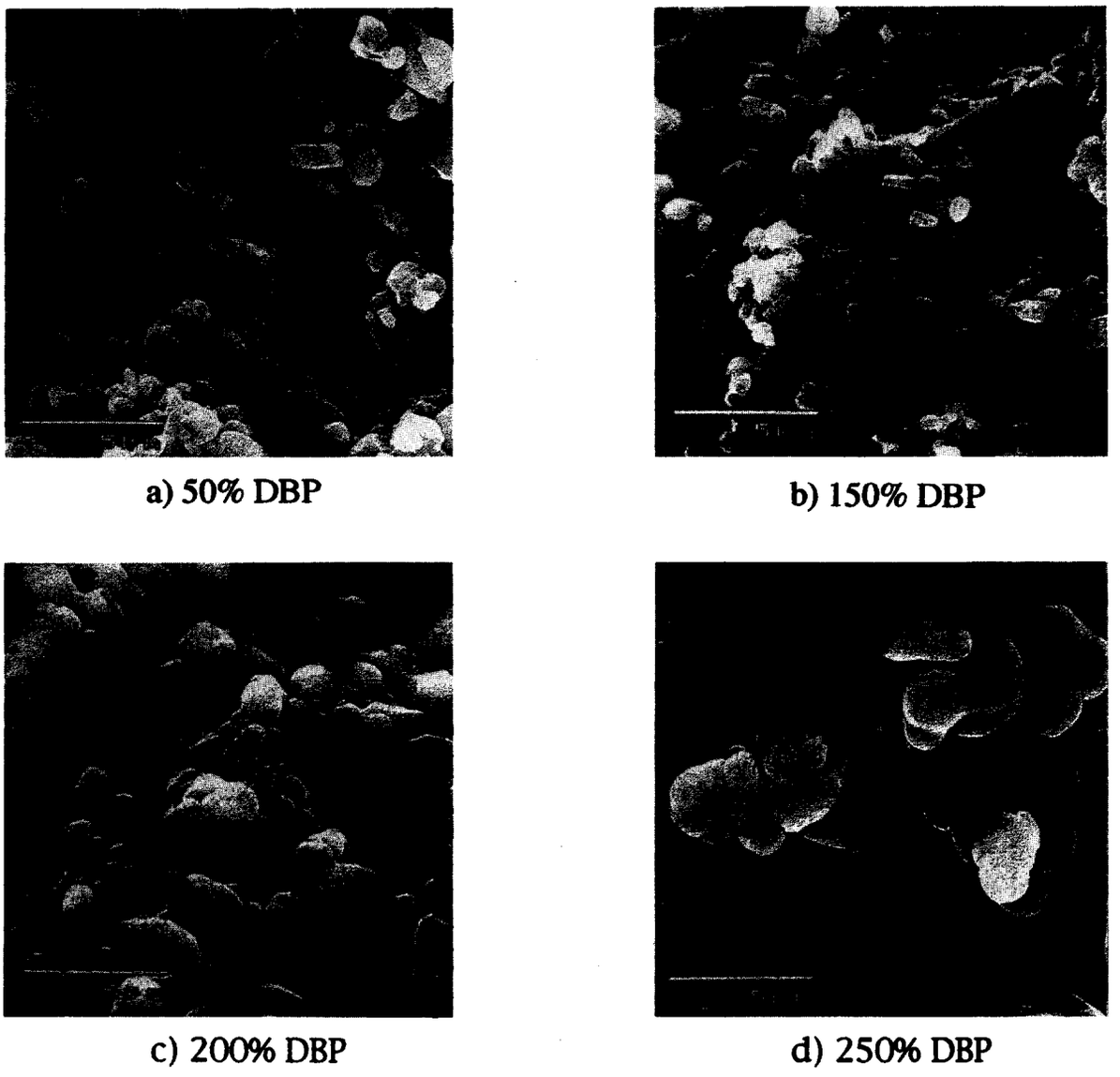


Fig. 3. Fracture surfaces of green tapes produced with 5% of binder and different plasticizer concentrations.

The effect on these properties of the plasticizer amount can be divided into several stages:

(1) In the first stage, results showed a strong decrease of the mechanical strength and a limited increase of tape elongation values. Plasticizer molecules inserted themselves inside the macromolecular network formed by the binder. This insertion destroyed locally intermolecular strength responsible for the mechanical cohesion of the compound. Chain movement is thus facilitated to the detriment of the material resistance.

(2) In the second stage, strength increased (the amplitude of which increased with binder amount). The development of this characteristic is induced by the action of two antagonistic phenomena: On the one hand, the strength decrease of the binder phase was induced by the increasing amount of plasticizer and on the other hand, the reinforcement of the mechanical strength was caused by the filling of the pores in the tape by organic compounds. This reduction in the defect number (pores) increased the mechanical strength of the tape, which occurred all the more for higher binder contents. In this stage, an increase of tape elongation values occurred.

(3) When the organic volume in the slurry was higher than the pore volume of the tape, a third stage was observed. In this stage, the mechanical strength of the tape depended only on the mechanical properties of the binding phase. The characteristics of this phase, saturated by the plasticizer agent, explained the significant decrease in the rupture strength. However, as the plasticizer content was increased, lubrication was improved and this promoted sliding between powder grains, which was manifested by a large increase of tape elongation.

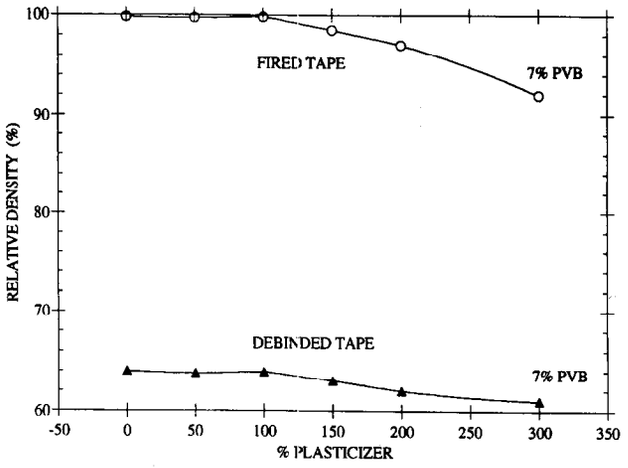


Fig. 4. Evolution of debinded and sintered tape density as a function of plasticizer content for a binder (PVB) concentration equal to 7 wt%.

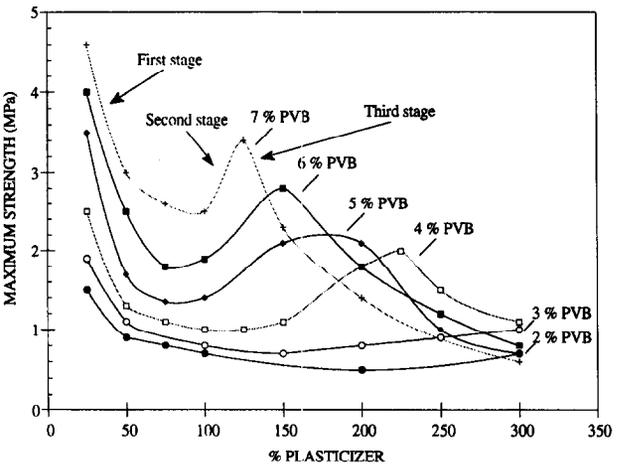


Fig. 5. Evolution of maximum strength as a function of plasticizer content at different binder (PVB) concentrations.

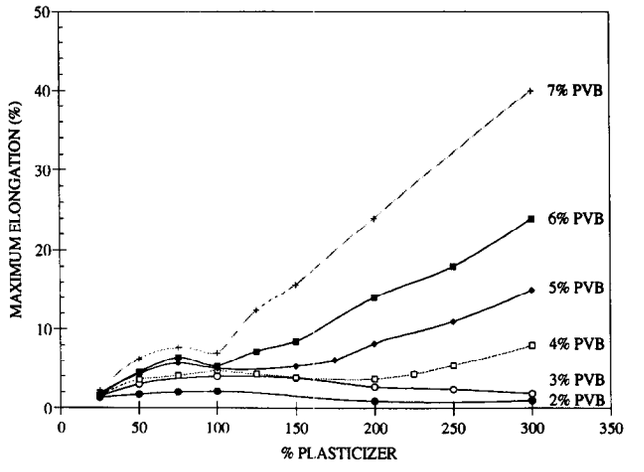


Fig. 6. Evolution of maximum elongation as a function of plasticizer content at different binder (PVB) concentrations.

The variations in rupture strength as a function of percentage binder present showed the importance of the powder particle size on the choice of slurry composition. Figure 7 shows the variation

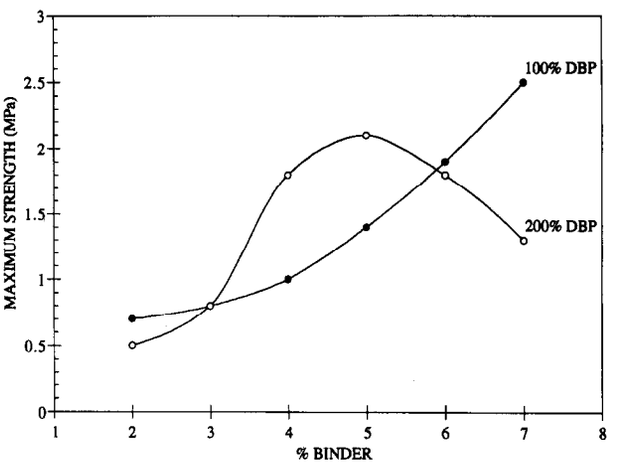


Fig. 7. Evolution of maximum strength as a function of binder content at two different plasticizer (DBP) percentages.

in this property for two DBP concentrations (100%, 200%).

Indeed, for slurry compositions in which the organic volume was lower than the pore volume of the tape, i.e. for the formulation at 100% of plasticizer whatever the content binder and the composition at 200 wt% of plasticizer up to 5% of binder (Tables 2 and 3), increasing the binder content resulted in an increase in the tape mechanical strength. However, when the organic volume was higher than the pore volume (from 5% PVB and 200% DBP) a large decrease of strength was observed, in spite of the increase in binder content.

4 Conclusions

The results of this study showed the important effect of the porous structure of the tapes on their mechanical and physical properties.

When the volume of organics used was lower than the porous volume of the tape, the material volume remained constant whatever the amount of plasticizer used (binder content fixed). On the other hand the volume increased slowly (volume measured in the first stage) when the binder concentration was increased and then tended to stabilise when a critical amount was reached. During this stage, the organic phase filled the tape porosity. When the organic volume was higher than the tape porous volume, powder grains were forced apart which induced an increase of apparent tape volume and a large decrease of fired tape density.

The tape mechanical characteristics were affected by the action of two antagonistic phenomena.

(1) The plasticization and lubrication effects caused by the plasticizer agent produced

an increase in material elongation and a decrease in network resistance.

(2) The reduction in the number of defects caused by the filling of the tape porosity by the organic phases led to an increase of the maximum strength.

The predominance of either effect determines the mechanical behaviour as a function of the amount of organic phases used.

So, for a fixed binder content, increasing of the plasticizer amount induced an increase in the mechanical resistance of the tape. However, from a certain filling level of the tape porosity by the organic phase, this behaviour was inversed and the mechanical resistance reached a maximum corresponding at an organic volume which allowed the complete filling of tape porosity. In this stage, the tape elongation increased appreciably. Beyond this maximum point a drastic reduction of the mechanical resistance appeared, induced by the weak strength of the binder phase (satured in plasticizer agent). These results showed that a judicious choice of the plasticizer concentration allow us to obtain green tapes with optimized mechanical properties, according to the desired application. Plasticizer contents corresponding to an organic volume near to the maximum filling of the tape porosity seems to give a correct compromise between mechanical strength and elongation of the tape. For applications where elongation and flexibility will predominate, significant contents of binder and plasticizer will be required. However these properties will be obtained to the detriment of mechanical resistance of the green tape and the density of sintered material.

On the other hand, increase in binder content for a fixed plasticizer amount, induced the increase of the rupture strength of the tape up to a certain amount of binder. Indeed, for binder concentrations corresponding to organic volumes higher than the porous volume, an important diminution of this characteristic appeared. When particle size distribution of the powder was optimized, the compactness of the powder can be very significant and can produce a very weak, porous volume of tape.[14–15] Thus, low binder content will be sufficient to obtain organic volumes higher than the porous volume of the tape and to induce an important decrease of the network mechanical resistance: behaviour opposed to the desired effect.

This study, carried out on interactions between porous volume and organic content for the production of ceramic tape by tape-casting must allow a better understanding of the evolution of tape properties and an optimization of slurry formulation for a given application.

References

1. Fiori, G. & De Portu. G., Tape-casting: a technique for preparing and studying new materials. *Br. Ceram. Proc.*, **38** (1986) 213–25.
2. Mistler, R. E., Tape-casting: the basic process for meeting the needs of electronics industry. *Am. Ceram. Soc. Bull.*, **69** (1990) 1022–6.
3. Moreno, R., The role of slip additives in tape-casting technology. *Am. Ceram. Soc. Bull.*, **71** (1992) 1647–57.
4. Gardner, R. A. & Nufer. R. W., Properties of multilayer ceramic green sheets. *Solid. State. Technology.*, **17** (1974) 38–43.
5. Roosen, A., Basic requirements for tape-casting of ceramic powders. *Ceramic Transactions, Vol. 1, Ceramic Powder Science II.* Ed. G. L. Messing, E. R. Fullers & H. Hausner. American Ceramic Society, Westerville, OH, 1988, 675–92.
6. Morris, J. R. & Cannon. W. R., Rheology and component interactions in tape-casting slurries. In *Mater. Res. Soc. Symp. Proc., Vol. 60, Defect Properties and Processing of High Technology Nonmetallic Materials.* Ed. Y. Chen, W. D. Kingery & R. J. Stokes, Pennsylvania, 1986, 135–42.
7. Cannon, W. R., Morris, J. R. & Mikeska, K. R., Dispersants for nonaqueous tape-casting. In *Advances in Ceramics, Vol. 19, Multilayer ceramic devices.* Ed. J. B. Blum & W. R. Cannon, American Ceramic Society, Westerville, OH, 1986, pp. 161–74.
8. Chartier, T., Streicher, E. & Boche, P., Phosphate esters as dispersants for the tape-casting of alumina. *American Ceramic Society Bulletin*, **66** (11) (1987) 1653–5.
9. Mikeska, K. & Cannon. W. R., Dispersants for tape-casting pure barium titanate. In *Advances in Ceramics, Vol. 9, Forming of Ceramics.* Ed. J. A. Mangels & G. L. Messing. American Ceramic Society, Colombus. OH, 1983, pp. 164–83.
10. Braun, L., Morris, J. R. & Cannon, W. R., Viscosity of tape-casting slips. *Am. Ceram. Soc. Bull.*, **64**(5) 1985 727–9.
11. Shanefield, D. J., Competing adsorption in tape-casting. In *Advances in Ceramics, Vol. 19, Multilayer ceramic devices.* Ed. J. B. Blum & W. R. Cannon. American Ceramic Society, Westerville, OH, 1986 pp. 155–60.
12. Morris, J. R., Jr., *Organic component interactions in tape-casting slips of barium titanate* Ph.D. Thesis, Rutgers University, New Jersey, 1986.
13. Forte, S., Morris. J. R., Jr. & Cannon, W. R., Strength of tape-casting tapes. *Am. Ceram. Soc. Bull.*, **64**(5) (1985) 724–5.
14. Dinger, D. R. & Funk. J. E., Particle Packing II. Review of packing of polydisperse particle systems. Interceram, **41**(3) (1992) 176–9.
15. Diner, D. R. & Funk. J. E., Particle Packing III. Discrete versus continuous particle sizes. *Interceram*, **41**(5) (1992) 332–4.

Journal of the European Ceramic Society **15** (1995) 363–369
© 1995 Elsevier Science Limited
Printed in Great Britain. All rights reserved
0955-2219/95/$9.50

Densification and Microstructure Development of Alumina/Y-TZP Composite Powder (Y-TZP-rich) Compacts

J. L. Shi & T. S. Yen

State Key Laboratory of High Performance Ceramics and Superfine Microstructure, Shanghai Institute of Ceramics, 1295 Ding-Xi Road, Shanghai 200050, People's Republic of China

(Received 25 November 1993; revised version received 1 June 1994; accepted 11 August 1994)

Abstract

Al_2O_3/Y-TZP composite powders (Y-TZP-rich) were prepared by ball milling submicron-sized alumina and coprecipitated nano-sized Y-TZP powders. The densification behavior of the composite powder compacts is studied and it is shown that the shrinkage rate is reduced at lower temperatures and the composites continue to shrink at elevated temperatures compared to single phase tetragonal Y-TZP. Compacts of the composite powders isostatically pressed at 250MPa at room temperature show duplex pore size distributions due to the presence of alumina, and it is these unusual pore size distributions, rather than the stresses arising from the differential sintering of the secondary particles that are believed to be the source of the retarded densification during constant rate heating. In spite of the retarded densification behavior, the composite powder compacts containing not higher than 30 vol.% alumina, can be sintered in 2 h to above 98% of the theoretical density at 1550°C.

1 Introduction

Alumina/Y-TZP particulate composites are of great interest because of their improved mechanical properties, such as strength, toughness and hardness.[1–5] In particular, alumina-doped Y-TZP materials show unusually high fracture strength.[5] These composites, however, show limited densification when pressureless sintered[4–6] and require hot-pressing or post-hipping to achieve density levels suitable for practical application.

Conventionally, the phase of higher content and smaller particle size is termed the matrix phase and the one of lower content and larger particle size is the secondary phase. The sintering behavior of particulate composites has been studied extensively, and it is well known that the densification of matrices (or composites) is retarded by secondary large particles (inclusions).[6–13] Numerous models have been proposed to account for this retarded densification of the matrix by the secondary phase.[14–21] The early models[14–17] proposed a hydrostatic tensile stress (back stress), believed to counter the normal sintering stress, as the main factor affecting densification. It was later proposed[18,19] that the tensile stress was too small to be the source of retarded densification; instead, the enlargement of pre-existing cracks in the compacts as a result of the tensile stress during sintering was considered to retard densification. Recently a numerical model[20,21] stated that the dense non-deformable region around high-aspect ratio reinforcements and between closely spaced reinforcements constrained the shrinkage of the adjacent, porous matrix, and thus led to the formation of large voids and cracks. These models, in spite of differences in the densification retardation mechanisms, all rely on the effect of stresses due to the presence of the secondary particles.

The retarded densification of particulate composites has also been attributed to the suppressed grain growth of the matrix grains during sintering,[22,23] because it was believed that grain growth enhanced densification.[24]

The proposed stress models are based mostly on the experimental results for composites with very large inclusions as secondary phases, i.e. with size ratios of the inclusions to matrix larger than 100.[10,11,13,21] However, many practical particulate composite systems do not use large size secondary phase particles, so as to avoid large defects in microstructure. For example, in the Al_2O_3/Y-TZP system the size ratio of the second phase to matrix is generally less than 10. For systems of inclusion size to matrix size ratios of around 10, the retarded densification may not be caused by stress alone, as the stresses brought about by the

secondary phase are somewhat limited for small secondary particle size and size ratio.

Recent reports[25,26] have shown that the back stress model[17] does not work in the ZrO_2 inclusions/ZnO matrix system. In their system, the size ratios of ZrO_2 to ZnO matrix varied from about 3 to 30. They proposed that in addition to the interaction between secondary particles and the matrix, the packing properties near the secondary particles may contribute to the retarded densification in the matrix.

In the present study on Al_2O_3/Y-TZP composites, a possible alternative factor affecting densification of composites is identified and a microstructural model based on this finding is introduced.



Fig. 1. TEM micrograph of mixed Al_2O_3/Y-TZP composite powder.

2 Experimental

Alumina powder (Sumitomo Co., AKP-50) with an average particle size of about 0·23 μm as measured by gravity sedimentation by the supplier was used. Y-TZP (3 mol% yttria stabilized tetragonal zirconia polycrystals) powder was obtained by a coprecipitation method using zirconium oxychloride and yttrium chloride as starting materials and ammonia as the precipitation medium. The copreciptation process is described briefly as follows:[27] (1) a mixed solution of zirconium oxychloride and yttria chloride with proper Y^{3+}/Zr^{4+} was prepared; (2) the mixed solution was added to an ammonia solution which resulted in coprecipitation: the pH value was kept above 9·5; (3) the coprecipitates were repeatedly washed to remove Cl^- until the Cl^- content in the filtrate became less than 10 ppm; (4) the coprecipitated cake was dispersed and dried in an oven at 110°C; (5) the powder was calcined at 750°C for 120 min. To avoid the formation of hard agglomerates, the coprecipitates of mixed hydroxide were thoroughly dispersed with a 30 min ultrasonic treatment before drying and calcination. The average primary particle size (equivalent to the crystallite size) of the 3Y-TZP powder is about 22 nm as measured by the X-ray diffraction line broadening method and/or by measuring the specific surface area by BET method (assuming a spherical shape for the particles).[28] Alumina-Y-TZP composite powders were prepared via ball milling for 4 h in a plastic jar using alumina balls as milling media. Five batches of the composite powders were prepared, containing 0, 10, 20, 30, and 40 vol.% alumina, and labelled accordingly as ZA0, ZA10, ZA20, ZA30, and ZA40 respectively. Figure 1 is a typical TEM photomicrograph of ZA30 powder after ball milling, showing a mixture of submicro-sized Al_2O_3 and nano-sized Y-TZP crystallites.

The composite powders were uniaxially dry pressed at 50 MPa, followed by cold isostatic pressing at 250 MPa, and the binder (1·5% polyvinyl alcohol) in the green compacts was burnt out by heating up to 700°C for 2 h. The pore size distributions of the pressed compacts were measured by mercury porosimetry (Model 9200, Micromeritics, USA) which detects pores in the size range 300 μm—3 nm.

The shrinkage behavior of the samples was measured with a dilatometer at a constant heating rate of 10°C/min up to 1550°C, followed by holding at this temperature for 2h. Densities of the sintered samples were measured by the Archimedes method in distilled water. The microstructure of the sintered bodies was observed with scanning electron microscopy (SEM, EPMA-8705, Shimadzu) on the ground and polished surfaces after thermal etching at 1300°C for 150 min.

3 Results

3.1 Duplex pore size distributions in the compacts

Figure 2 shows the pore size distributions of the composite powder compacts after isostatic pressing at 250 MPa. The pure Y-TZP compact exhibits pore size distribution with only one peak illustrating an agglomerate-free state in the compact.[27] Addition of alumina to the Y-TZP powders results in two peaks in the pore size distribution (a duplex distribution). The peaks at smaller pore sizes (Pore I $\leq$ 0·03 μm) are the inter-primary particle pores of the zirconia particles as the zirconia powders are much finer than the alumina powder. Those at larger size (Pore II > 0·03 μm) are the result of the presence of the alumina particles. There are two possibilities for the larger pores. They may be formed between alumina particles

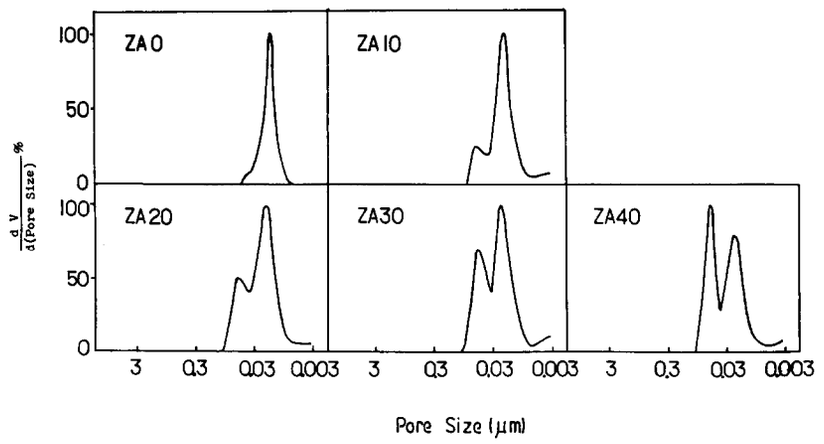


Fig. 2. Pore size distributions of the composite powder compacts at 250 MPa.

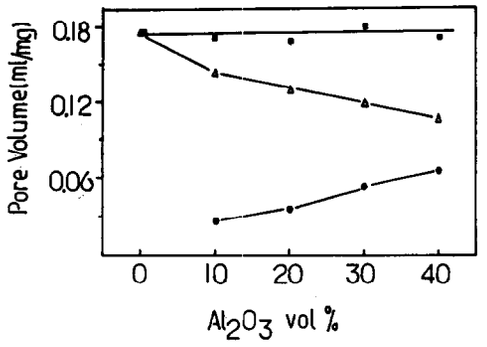


Fig. 3. Volume contents of (■) total pores, (Δ) Pore I and (●) Pore II in the composite powder compacts.

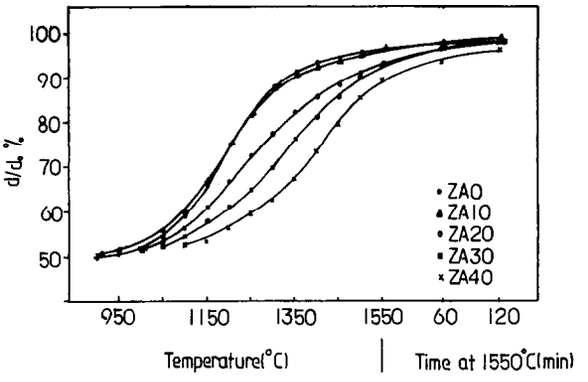


Fig. 5. Densification curves of the composites during constant rate heating of 10°C/min up to 1550°C and holding at 1550°C for 2 h.

(inter-alumina particle pores) and/or formed between alumina particles and Y-TZP matrix (inter-alumina-zirconia particle pores). The former are predicted to be present since agglomerates may also develop from the submicron-sized Al_2O_3 particles if the agglomerates are not fully dispersed especially when the alumina content is high, the latter are sure to exist because the Al_2O_3, particles or agglomerates are surrounded by nano-sized Y-TZP particles at relatively low contents.

Increasing alumina content in the composite powders leads to a volume increase of porosity (Pore II) and a decrease of porosity (Pore 1), while the total pore volume remains essentially unaffected, as shown in Fig. 3. In addition to the pore volume, the average pore sizes (Pores I and II) also increase slightly along with increasing alumina content, as shown in Fig. 4.

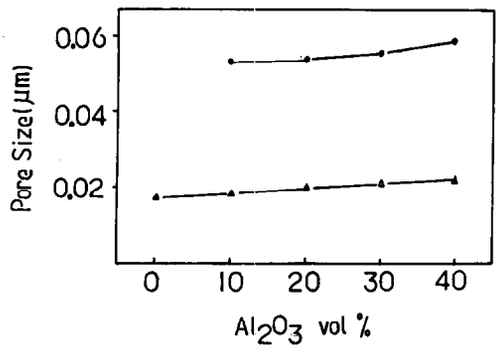


Fig. 4. Effect of alumina content on the size of (Δ) Pore I and (●) Pore II in the compacts.

3.2 Retarded densification of the composite

The densification curves in Fig. 5 show the retarded densification behavior due to the presence of alumina, especially at and beyond 20 vol.%. At the lower temperatures, the shrinkage rates decrease with the increase of alumina content. At higher temperatures and during the high temperature hold, the shrinkage rates increase with the increase of alumina content, as shown in Fig. 6 and, more clearly, in Fig. 7. Although similar final densities can be obtained for composite compacts containing not more than 30 vol.% of alumina (see Fig. 5) when sintered at 1550°C for 2h, the shrinkage rates during constant rate heating and holding depend on the alumina content in the composites.

3.3 Pore structure change during densification

During sintering, the pore volume and size change as densification proceeds. At relatively low tem-

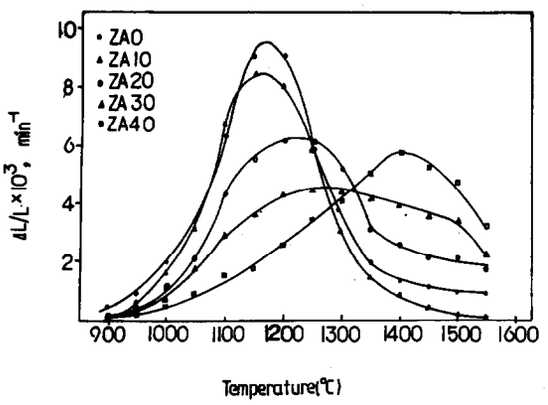


Fig. 6. Shrinkage rate versus temperature during constant rate heating for the composites.

peratures, the change is due mainly to the volume decrease and slight size increase of Pore I. This corresponds to the shrinkage of the green compacts in the early stages of sintering, especially for those with low content of alumina. Beyond 1150°C, there is only one peak (Pore II and size increased Pore I) left as shown in Fig. 8, and the volume diminution (Fig. 9) and size increase (Fig. 10) of the pores continue to relatively high temperatures, which is more evident for the materials with a higher alumina content.

3.4 Microstructure development of the composites

Figure 11 shows the photomicrographs of Al_2O_3/Y-TZP composite bodies sintered at 1550°C for 2 h. For single phase Y-TZP the microstructure is uniform and the grains are submicron-sized (0·3–0·5 μm). Addition of Al_2O_3 particles to the composites leads to a less uniform microstructure: the black particles of relatively large size are Al_2O_3 and the matrix is Y-TZP, as verified by energy dispersive spectroscopy. Both Al_2O_3 and Y-TZP matrix grains in the sintered bodies have grown compared to the powder forms: Y-TZP grains have grown as in the single phase materials by a factor of greater than 10 and the grain sizes are almost independent of the alumina content. The Al_2O_3 grain sizes became larger as the Al_2O_3 content increased, and the rate of increase depended on Al_2O_3 content. So the size ratio of alumina to Y-TZP particles becomes larger for higher Al_2O_3, content in the final sintered bodies. Even for ZA40, however, the size ratios in the final sintered bodies were less than 10, that is to say that Al_2O_3 grains grew at a slower rate than Y-TZP.

In spite of the grain size differences for different Al_2O_3 contents, the sintered bodies were dense and no pores were formed in the vicinity of the larger Al_2O_3, particles, in contrast to results of Tuan[10] and Sudre[13,21] in their particular systems.

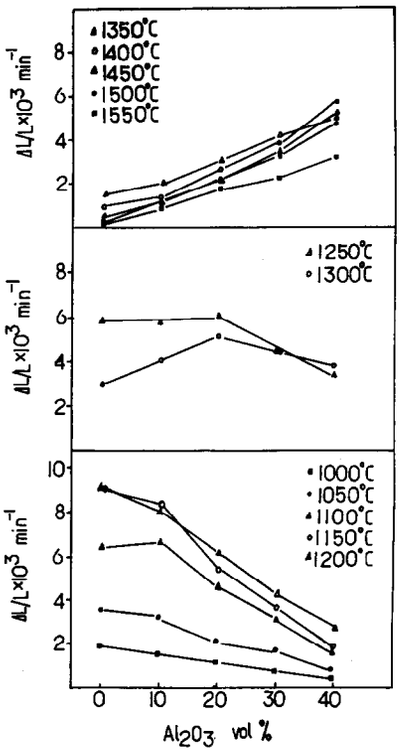


Fig. 7. Shrinkage rate versus alumina content during constant rate heating at various temperatures.

4 Discussion

4.1 Densification retardation by duplex pore size distribution

The effect of bimodal pore size distributions on the viscous sintering of single phase uniform gel compacts has been discussed by Scherer.[14] Altered sintering stress in this system results from the interaction between large and small pores. However, a gel compact with uniform composition is different from a particulate system of multiphase form

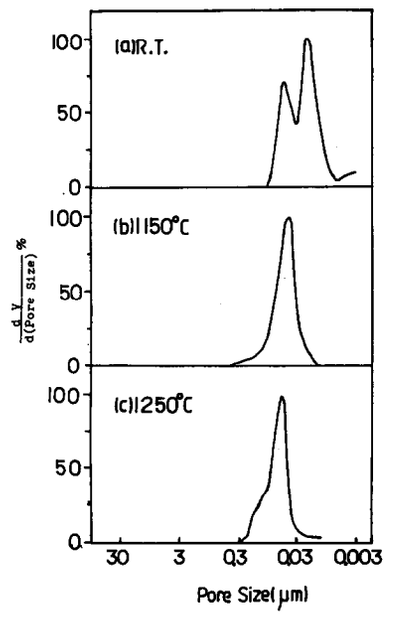


Fig. 8. Pore size distributions of 30 vol.% Al_2O_3/Y-TZP composites during constant rate heating at (a) room temperature, (b) 1150°C, (c) 1250°C.

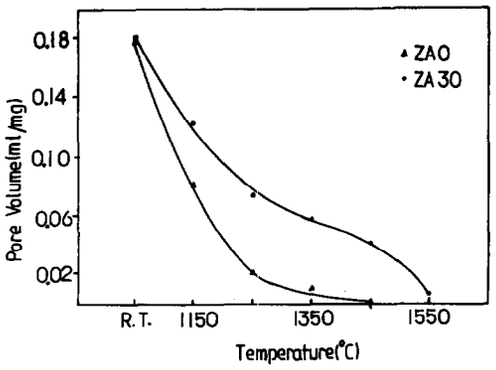


Fig. 9. Pore volume versus temperature during constant rate heating.

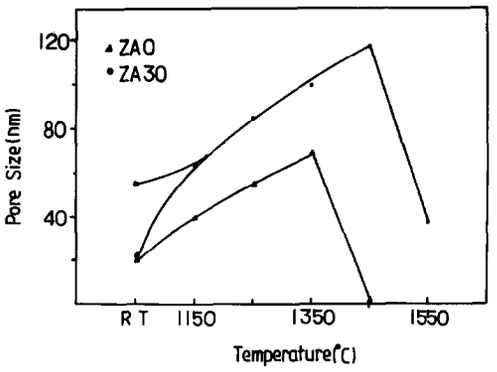


Fig. 10. Pore size versus temperature during constant rate heating.

such as has been studied in this paper. The viscous sintering mechanism of a single phased gel without phase and/or grain boundaries cannot be used to explain the solid state sintering behavior of the present multiphased particulate system.

The presence of large pores in the compacts implies that the particle packing conditions in the multiphase system have been changed. The pores of large sizes (Pore II) may be formed among large alumina particles (inter-alumina particle pores,

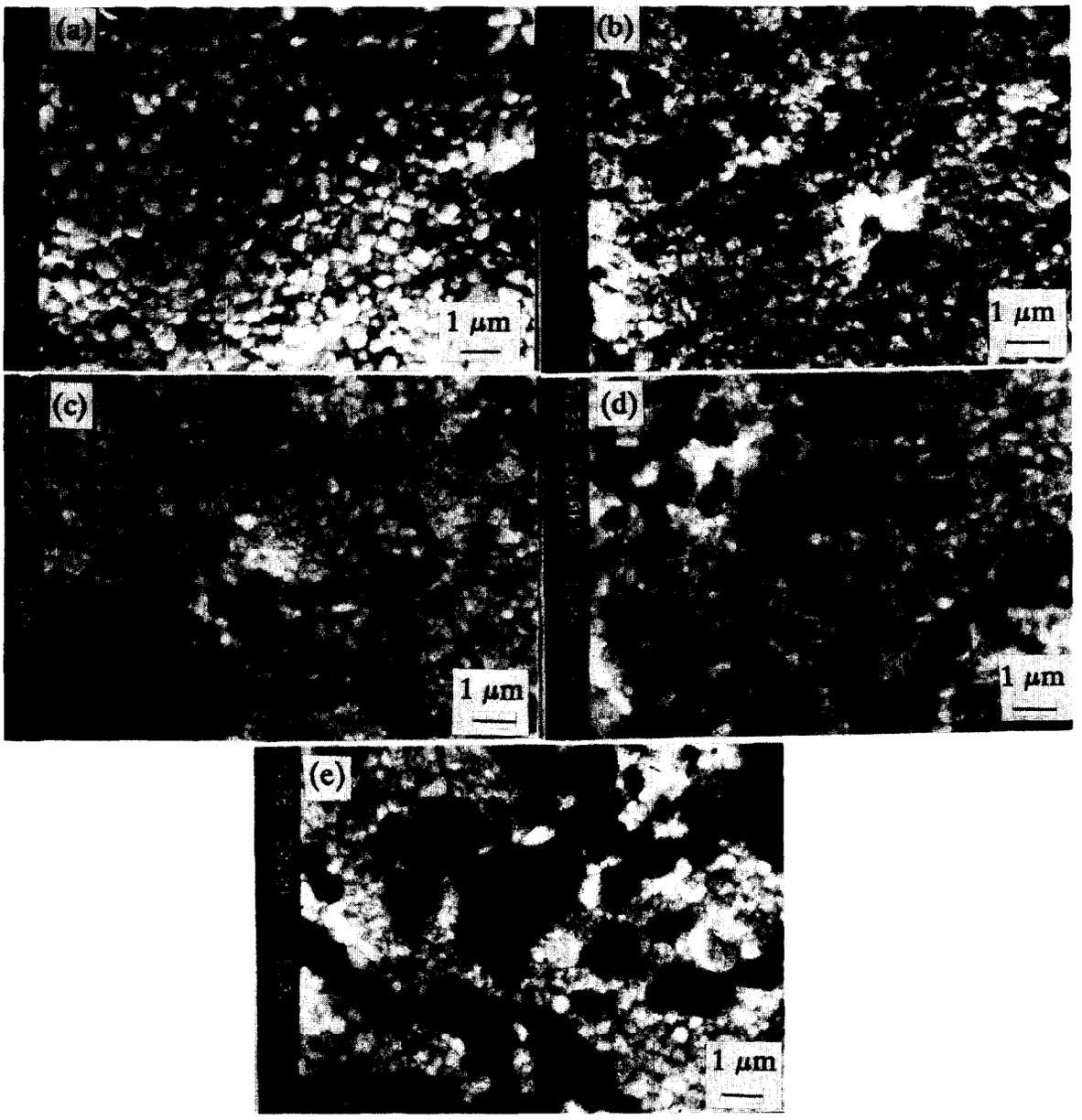


Fig. 11. SEM micrographs on polished and thermally etched surfaces of sintered composite bodies at 1550°C for 120 min, containing (a) 0, (b) 10, (c) 20, (d) 30 and (e) 40 vol.% Al_2O_3.

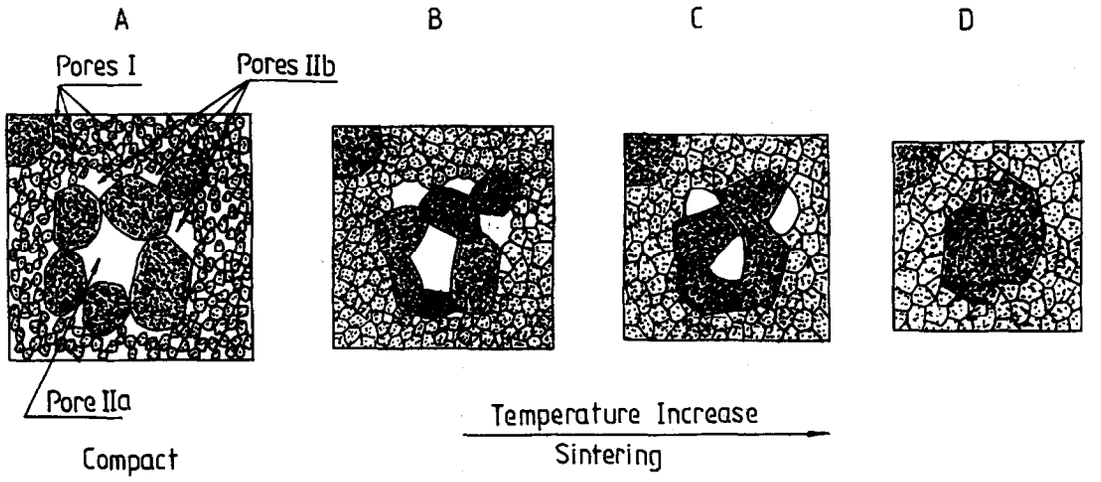


Fig. 12. Microstructure model for the removal of different kinds of pores; (A) pores in compacts; (B) removal of Pore I at relatively low temperature; (C) Pore IIa begin to shrink and Pore IIb become unstable due to the grain growth of Y-TZP as temperature increases, and (D) Pores II were eliminated at a high temperature, e.g. 1550°C.

named as Pore IIa), or between alumina particle(s) and numerous small zirconia particles (inter-alumina-zirconia particle pores, named as Pore IIb), as can be seen in Fig. 1 and shown schematically in Fig. 12(A). Pores I can be removed during sintering at relatively low temperatures, while Pores IIa will not shrink appreciably due to unfavourable kinetic conditions at low temperatures with large alumina particles surrounding the pores. Thermodynamically, Pores IIb may be stable at low sintering temperatures as such pores are coordinated by many very small zirconia particles relative to the alumina particle (Fig. 12(B)), and such pores, as analyzed by Lange,[29] will not shrink at relatively low temperatures before the zirconia particles begin to grow substantially. With the increase of temperature, when the densification process of pure Y-TZP has been completed, Pores IIa will begin to shrink and with the growth of the zirconia particles the coordination number of Pores IIb will decrease and such pores will also become unstable and start to shrink (Fig. 12(C)). So the retarded (and enhanced) densification of the composite powder compacts at relatively low (and high) temperatures, compared to single phase Y-TZP, can be understood. As temperature increases to a certain threshold, e.g. 1550°C, both Pore IIa and Pore IIb in the compacts are removed (Fig. 11, as modelled in Fig. 12(D)) and the sintered densities were rather high when the Al_2O_3 content was not higher than 30 vol.%.

However, the composite powder compact of ZA10 shows a very similar densification behavior with single phase Y-TZP. This is believed to be due to its relatively low amount of alumina. At this low content, Pores II are relatively few, and Pores IIb prevail in the compact as compared to Pores IIa. However, nano-sized zirconia grains grow readily[28] when heated above the calcination temperature of 750°C. Hence the thermodynamic requirements for the shrinkage of pores IIb can be easily satisfied at a relatively low temperature of about 1050°C (Fig. 6). As a result the densification rate of ZA10 was not affected significantly.

4.2 Effect of tensile back stress

The retarded densification of ceramic powder compacts with heterogeneities (inclusions), as a special example of composite powder compacts, has been modelled by calculating the hydrostatic tensile stress in the powder matrix.[15–17] The tensile stress is expected to oppose the sintering stress and therefore impede densification. The concept of back stress has been used[10,11] to explain the limited achievable final density of a composite compact of Al_2O_3, or Y-TZP with very large Al_2O_3 particles of 200 μm by local difference in density, grain size or chemical composition. The back stress concept was developed[20,21] for the system of large ZrO_2 particles in an Al_2O_3 matrix. The size ratio of secondary particles to matrix grains was higher than 100 and the large particles were irregularly shaped or even elongated. The stress caused by the inclusions in matrix may either be compressive or tensile. Densification and grain growth in the compressive region were promoted and formed a so-called non-deformable network. This non-deformable network constrained the shrinkage of the adjacent porous region by exerting tensile stress opposing densification. However, there are three ways where the effect of compressive and/or tensile back stress on densification may be limited in our system. First, the alumina particle size and the size ratio of alumina particles to Y-TZP matrix in the present system are much smaller as compared to those used by Tuan[10,11] and Lange;[20,21] although the stress arising from the secondary particles (or inclusions) is independent of their size,[30] nonetheless as analysed[30] and experimentally

observed by others, the defects (or cracks) are much easier to form around larger inclusions than around smaller. Secondly, the matrix of Y-TZP in this study is very porous and nano-sized, so the tensile stress that resulted from the Al_2O_3, during densification could be effectively absorbed and relaxed by microstructural modification (particle rearrangement, and plastic flow), especially at the initial and intermediate stage of sintering. Thirdly, the secondary Al_2O_3 particles are basically equiaxed and well dispersed in matrix (Fig. 11), so the so-called non-deformable network[20,21] would not form in microstructure and the densification rate in the matrix is expected to be basically the same throughout the specimen.

5 Summary

This study shows that the densification of the Y-TZP powder compacts with the addition of alumina particles (size ratio of Al_2O_3 to Y-TZP is about 10) is retarded by the presence of larger alumina particles. The alumina particles impede the shrinkage of the composites at relatively low temperature $\leq$ 1300°C) at which the single phase Y-TZP undergoes the major shrinkage, and lead to enhanced densification rate at and above 1300°C. Almost full densification is achieved at 1550°C. The retarded densification behavior of the composites are related to the duplex pore size distributions in the green compacts because of the presence of relatively large alumina particles. The presence of inhomogeneities, i.e. larger pores in the compacts for the composite powders, in addition to the smaller pores which the single phase Y-TZP contains, appears to be the main reason for the retarded densification of the composites from both the thermodynamic and kinetic point of view. Back stress effects resulting from secondary Al_2O_3 are argued to be less significant.

References

1. Claussen, N., Fracture toughness of Al_2O_3 with unstabilized ZrO_2 dispersed phase. *J. Am. Ceram. Soc.*, **59** (1976) 49.
2. Lange, F. F., Transformation toughening Part 4: Fabrication, fracture toughness and strength of Al_2O_3–ZrO_2 composites. *J. Mater. Sci.*, **17** (1982) 247.
3. Ruhle, M., Claussen, N. & Heuer, A. H., Transformation and microcrack toughening as complementary process in ZrO_2-toughened Al_2O_3. *J. Am. Ceram. So.*, **69** (1986) 195.
4. Hori, S., Yoshimura, M. & Somiya, S., Strength-toughness relations in sintered and isostatically hot pressed ZrO_2-toughened Al_2O_3. *J. Am. Ceram. Soc.*, **69** (1986) 169.
5. Tsukuma, K., Ueda, K. & Shimada, M., Strength and fracture toughness of HIPed composites of Al_2O_3 and Y_2O_3-partial-stabilized ZrO_2. *J. Am. Ceram. Soc.*, **68** (1985) C–4.
6. Messing, G. L. & Onada, G. Y., Sintering of inhomogeneous binary powder mixtures. *J. Am. Ceram. Soc.*, **64** (1981) 468.
7. De Jonghe, L. C., Rahaman, M. N. & Hsueh, C. H., Transient stresses in bimodal compacts during sintering. *Acta Metall.*, **34** (1986) 1467.
8. Weiser, M. W. & De Jonghe, L. C., Inclusion size and sintering of composite powders. *J. Am. Ceram. Soc.*, **71** (1988) C–125.
9. Rahaman, M. N. & De Jonghe, L. C., Sintering of particulate composites under a uniaxial stress. *J. Am. Ceram. Soc.*, **73** (1990) 602.
10. Tuan, W. H., Gilbert, E. & Brook, R. J., Sintering of heterogeneous ceramic composites, Part I, Al_2O_3–Al_2O_3. *J. Mater. Sci.*, **24** (1989) 1062.
11. Tuan, W. H. & Brook, R. J., Sintering of heterogeneous composites, Part II, ZrO_2–Al_2O_3. *J. Mater. Sci.*, **24** (1989) 1953.
12. Bordia, R. K. & Raj, R., Sintering of Tio_2–Al_2O_3 compsites: a model experimental investigation. *J. Am. Ceram. Soc.*, **71** (1988) 302.
13. Sudre, O. & Lange, F. F., Effect of inclusions on densification: I, Microstructural development in an Al_2O_3 matrix containing a high volume fraction of ZrO_2 inclusions. *J. Am. Ceram. Soc.*, **75** (1992) 519.
14. Scherer, G. W., Viscous sintering of a bimodal pore size distributions. *J. Am. Ceram. Soc.*, **67** (1984) 709.
15. Hsueh, C. H., Sintering behaviour of powder compacts with multi-heterogeneities. *J. Mater. Sci.*, **21** (1986) 2067.
16. Hsueh C. H., Influence of multiple heterogeneities on sintering rates. *J. Am. Ceram. Soc.*, **69** (1986) C–64.
17. Scherer, G. W., Sintering with rigid inclusions. *J. Am. Ceram. Soc.*, **70** (1987) 719.
18. Bordia, R. K. & Scherer, G. W., On constrained sintering. I, II, III, Overview No. 70, *Acta Met.*, **36** (1988), 2392, 2399, 2411.
19. Lange, F. F., Densification of powder rings constrained by dense cylindrical cores. *Acta Metall.*, **37** (1989) 697.
20. Lange, F. F., Constrained network model for predicting densification behavior of composite powders. *J. Mater. Res.*, **2** (1987) 59.
21. Sudre, O., Bao, G., Fan, B., Lange, F. F. & Evans,. A. G., Effect of inclusions on densification: II, Numerical model. *J. Am. Ceram. Soc.*, **75** (1992) 525.
22. Lange, F. F. & Hirlinger, M. M., Grain growth in two phase ceramics, alumina inclusions in Zirconia. *J. Am. Ceram. Soc.*, **70** (1987) 827.
23. Lange, F. F., Yamaguchi, T., Davis, B. I. & Morgan, P. E. D., Effect of ZrO_2 inclusions on the sinterability of Al_2O_3. *J. Am. Ceram. Soc.*, **71** (1988) 446.
24. Lange, F. F. & Kellett, B. J., Thermodynamics of densification: II, Grain growth in porous compacts and relation to densification. *J. Am. Ceram. Soc.*, **72** (1989) 735.
25. Chen-Lung Fan & Rahaman, M. N., Factors controlling the sintering of ceramic particulate composites I, Conventional processing. *J. Am. Ceram. Soc.*, **95** (1992) 2056.
26. Ching-Li Hu & Rahaman, M. N., Factors controlling the sintering of ceramic particulate composites II, coated inclusion particles. *J. Am. Ceram. Soc.*, **75** (1992) 2066.
27. Shi, J. L., Characteristics of the pore structures in the compacts of ultrafine zirconia powders. *J. Solid State Chem.*, **95** (1992) 412.
28. Shi, J. L., Lin, Z. X. & Yen, T. S., Determination of crystallite size of superfine zirconia powders as a function of calcination temperature. *Ceram. Int.*, **18** (1992) 155.
29. Lange, F. F., Sinterability of agglomerated powder. *J. Am. Ceram. Soc.*, **65** (1982) 83.
30. Lange, F. F., Criteria for crack extension and arrest in residual, localised stress fields associated with second phase particles. In *Fracture Mechanics Vol. 2, Microstructures, Materials and Applications*, ed. R. C. Bradt & D. P. H. Hasselman. Plenum, New York, 1974, p. 599.

Journal of the European Ceramic Society **15** (1995) 371–375
1995 Elsevier Science Limited
Printed in Great Britain
0955-2219/95/$9.50

Fabrication of Low-Voltage ZnO Varistors by a Two-Step Process

Joo-Hwan Han, Dong-Heon Lee & Doh-Yeon Kim

Department of Inorganic Materials Engineering, College of Engineering (400), Seoul National University, Seoul 151–742, South Korea

(Received 7 June 1994; accepted 7 July 1994)

Abstract

In order to make a low-voltage ZnO varistor of uniformly large-grained microstructure, a pure ZnO powder compact was first sintered at 1500°C. The abnormal grain growth that occurred during the sintering of the ZnO resulted in a relatively uniform matrix of very large grains. Subsequent heat-treatment in contact with a Bi_2O_3 powder mixture resulted in the formation of a low-voltage ZnO varistor.

1 Introduction

Low-voltage ZnO varistors are now widely used for surge protection in integrated circuits and in automobiles.[1,2] Since the breakdown voltage (V_b) of the varistor is proportional to the number of ZnO grains in series between the electrodes,[3,4] low voltage varistors can be obtained either by decreasing the thickness of the specimen or by increasing the size of ZnO grains. The thin ZnO varistors are, however, difficult to prepare and apt to break. Note also that the energy absorption capability of the thin ZnO varistor is very poor due to its small volume.[5–8] On the other hand, low voltage ZnO varistors with grains of large size have been fabricated by using grain growth-enhancing additives,[6,9] or exceptionally large seed ZnO grains.[7,8] Consequently, its microstructure exhibits a nonuniform distribution of grain size, which causes an irregular current distribution and makes the varistor susceptible to hot spots.[10–12]

In this paper, a new processing technique for the production of a low-voltage ZnO varistor of uniformly large-grained microstructure will be described. Instead of conventional fabrication by sintering of ZnO powder which has been previously mixed with Bi_2O_3 and other oxides, the two-step process consisting of the sintering of pure ZnO alone and subsequent heat-treatment has been adopted for fabrication of the low-voltage ZnO varistor. The uniformity in grain size and low porosity of ZnO varistors obtained by this process are expected to enhance its reliability and lifetime.

2 Experimental Procedures

Commercial grade ZnO powder of 99·9% purity (Aldrich Chem. Co. Inc., Milwakee, Wis., USA) was used. Its average particle size determined by sedimentation technique was 0·5 μm. The powder was pressed to a cylindrical compact (10 mm in diameter) with a hole (3 mm in diameter) in the center, and then pressed hydrostatically at 100 MPa. The obtained compacts were sintered at 1500°C for 1 h in air to induce an extensive grain growth. In order to minimize the ZnO vaporization and consequent pore formation during sintering at such a high temperature, the specimens were put together with the same ZnO powders in a closed alumina crucible. Platinum foil was used to isolate the specimen from the surrounding powders. The sintered specimens were then ground and its thickness was controlled to be 4 mm. On the other hand, high purity Bi_2O_3 and MnO_2 powders were mixed with ZnO to give $1Bi_2O_3$–$1MnO_2$–98ZnO (in mol%). This powder mixture was then manually rubbed into the central hole of the sintered ZnO specimen. The specimen was then heat-treated at 1200°C for 1 h with Bi_2O_3 powders in a closed alumina crucible, as illustrated in Fig. 1. Preliminary experiments showed that this heat-treatment condition is most appropriate for making a varistor of the desirable I–V characteristic.

The photomicrographs of the polished section for pure ZnO, i.e. before the Bi_2O_3 atmosphere treatment were obtained after the thermal etching for 30 min at 1200°C. After the atmosphere treatment, however, etching was not needed for microstructural observation. The presence of the

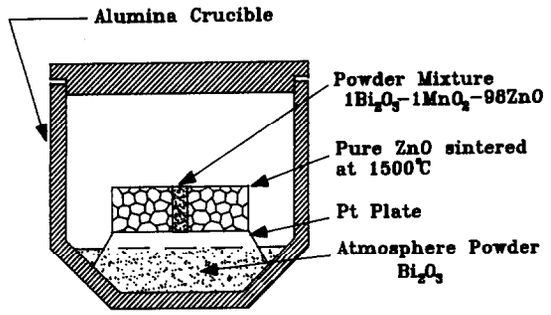


Fig. 1. Schematic illustration for heat-treatment of large-grained pure ZnO specimen in Bi_2O_3 atmosphere.

Bi-rich liquid phase at the grain boundary was observed by transmission electron microscopy. Disks of 3 mm in diameter were cut from the specimen and reduced to a thickness of ≈ 5–10 μm in the center by mechanical grinding and dimpling. A further thinning was carried out by using an ion-miller. The I–V characteristic of the specimen prepared was measured with a picoammeter (Model: 4140B pA Meter/DC voltage source, Yokogawa Hewlett Packard Co., Yokogawa, Japan). The individual specimen was ground on silicon carbide paper (No. 1200) and the electrode was made by sputtering Au on each surface of the cylindrical specimen. The voltage per unit thickness (1 mm) at a current of 1 mA/cm^2 was regarded as the breakdown voltage of the varistor specimen.[10,13,14]

3 Results and Discussion

Previous studies[15–17] on sintering of pure ZnO have shown that its densification begins at a rather low temperature such as 700°C and the full densification is achieved in a few minutes of sintering at 1200°C. On the other hand, a decrease in bulk density, which can be referred to as over-firing has been reported to occur during sintering of ZnO if the sintering temperature is too high.[18] From these works, the optimum temperature for the densification of ZnO powder compact is expected to be around 1100°C. In this investigation, however, the ZnO powder compacts were sintered at 1500°C to induce a rapid grain growth and Fig. 2 (a) and (b) show the microstructure of the specimen sintered for 0·5 and 1 h, respectively. In spite of an excessively high sintering temperature, a notable increase of porosity was not observed in this experiment. It appears likely that the atmosphere powders have minimized the ZnO evaporation from the specimen and consequent pore formation. For the specimen shown in Fig. 2 (a) and (b), most of the pores were trapped inside the grain as a result of extensive grain growth. The

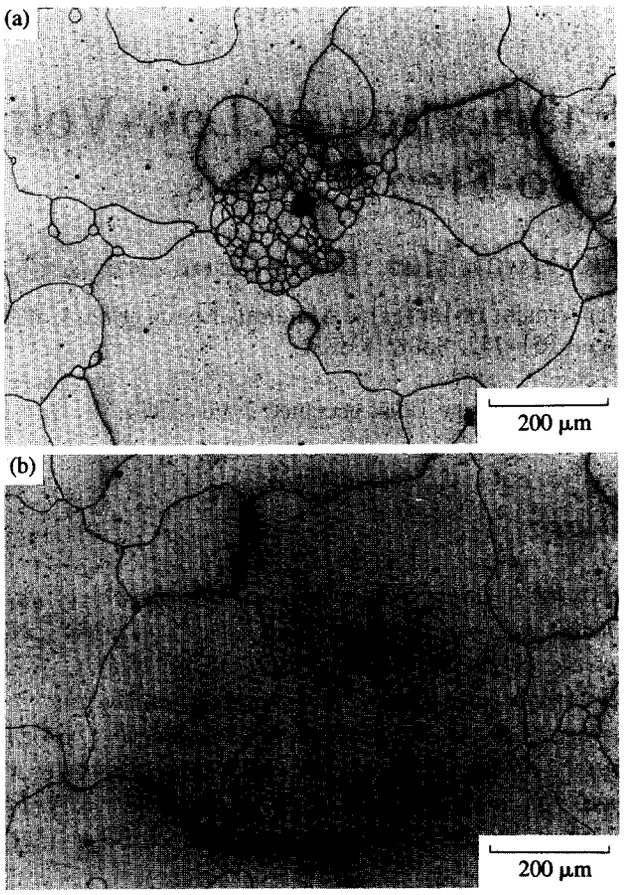


Fig. 2. Microstructures of the pure ZnO specimen sintered at 1500°C for (a) 0·5 and (b) 1 h.

porosities determined by the point counting method were 0·2 and 0·5%, respectively.

In comparison with the initial ZnO particle size (≈ 0·5 μm), the grains observed in the specimen shown in Fig. 2 are exceptionally large. Note that the specimens were made from fine powder and therefore a few particles of a size substantially larger than the average may be present, which acted as embryos for abnormal grain growth.[19,20] It has been suggested that the grains two times larger than the average may be able to start the abnormal grain growth. The assembly of small grains observed in the specimen sintered for 0·5 h (Fig. 2 (a)) may show the initial fine grained structure. Once those few abnormally growing grains reach a size where they impinge each other, the grain boundaries tend to be flat so that the driving force for migration is practically eliminated. Fig. 2 (b) is expected to exhibit such a new set of exceptionally large grains which replace completely the initial fine grained structure. For this specimen, the average grain size was determined to be ≈ 500 μm through the linear intercept method.

Inside those abnormally grown grains, the entrapped small grains were frequently observed as indicated by the arrow in Fig. 2 (b). Such grain entrapment during abnormal grain growth has

also been reported in other ceramic materials and attributed to the very rapid boundary migration.[21] It is expected, however, that the grain entrapment is related to the size and orientation of shrinking grains adjacent to the rapidly growing grains. As the shrinking grains vary in size and have random orientation, the growth rate along the advancing boundary will be uneven from point to point. The slowly shrinking grains and/or the relatively large size grains will become entrapped and be left behind to remain in an apparent metastable state. It is further expected that the grains once trapped shrink rapidly, which may explain their rare experimental observation.

The breakdown voltage of a varistor, V_b, is given by[3]

$$V_b = \nu_{gb} \frac{D}{r} \quad (1)$$

where ν_{gb} is the threshold voltage per grain boundary, which has been estimated to be around 3·6 V,[10,12,13] and D and r are the varistor thickness and average ZnO grain size, respectively. For the low-voltage ZnO varistor, such as V_b = 7 V, it has been consequently reported[22] that the thickness should be less than 100 μm, because the average grain size of ZnO grains in conventionally sintered ZnO–Bi_2O_3 is always below 50 μm. Note also that such coarse-grained ZnO–Bi_2O_3 specimens can be obtained by sintering at 1400°C for several hours during which the vaporization of Bi_2O_3 occurs.[23] The vaporization of Bi_2O_3 and concurrent increase of porosity are known[23] to be significant from 1200°C and to deteriorate the varistor characteristic.

As a consequence, the coarse-grained ZnO varistors ensuring the low V_b have been prepared either by using the grain growth enhancing additives[9,22] such as TiO_2 or by adding large ZnO seed grains.[7,8] The varistors thus prepared, however, showed a large spread of grain size and a very high porosity. The presence of a few large grains may result in the high local currents which give rise to a rapid degradation of the varistor.[10–12] In addition, the harmful effects of pores with respect to the mechanical strength are evident.

Assuming that the microstructure of the ZnO varistor is identical to that of Fig. 2 (b), several advantages may appear. First of all, the thickness of a low-voltage varistor (V_b = 7 V) becomes around 2 mm which can be manufactured and handled without great difficulty. The rather uniform distribution of grain size may provide a uniform current flow, and its low porosity enhances the strength and thermal conductivity of the varistor. The high thermal conductivity and fairly large volume may also increase the energy handling capability of the varistor.[10] However, the addition of Bi_2O_3 is known to be essential for ZnO varistors. The Bi ions segregated in the region of the grain boundary have been attributed for the nonlinear characteristics.[24] In order to make a varistor, it is therefore necessary to form a depletion layer by changing the chemistry of the grain boundaries.

Using the specimen shown in Fig. 2(b), the formation of depletion layer was carried out by the heat-treatment with Bi_2O_3 containing powder mixture. The powder mixture of $1Bi_2O_3$–$1MnO_2$–98ZnO was rubbed into the central hole of the sintered ZnO, and then it was heat-treated at 1200°C for 1 h in Bi_2O_3 atmosphere (Fig. 1). During the treatment, the Bi-rich liquid formed in the powder mixture was expected to penetrate into the grain boundaries of ZnO specimens. Note also that the Bi_2O_3 atmosphere powder in the alumina crucible may provide a high vapor pressure of Bi_2O_3.[10,14,23] In fact, Bi_2O_3 was observed to diffuse into almost all of the grain boundaries of pure ZnO specimen when it was treated at 1200°C for 1 h with a small amount of Bi_2O_3 on its surface.[25]

Figure 3 is the microstructure of the specimen obtained. The region of $1Bi_2O_3$–$1MnO_2$–98ZnO (upper part of Fig. 3) showed a typical liquid-phase sintered structure with the solid grains (white) and pores (dark) dispersed in a Bi-rich liquid matrix. Note that the powder mixture was packed by hand into the hole, which is the cause of the rather large fraction of pores. The originally pure ZnO region can be observed in the lower part of Fig. 3. Although a notable microstructural change compared to Fig. 2 (b) was not observed in this microscopic scale, the liquid was observed to present almost all the triple grain boundary junctions.

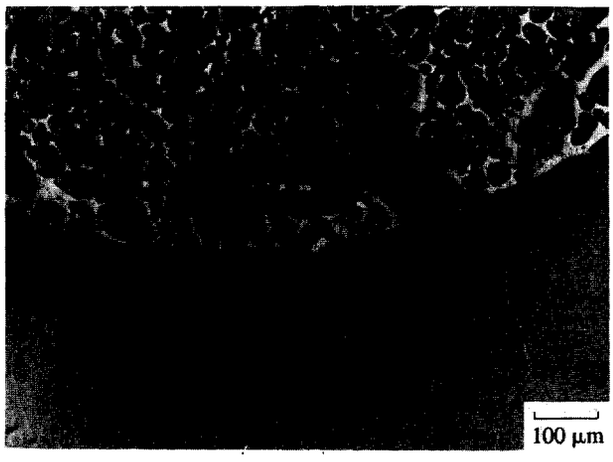


Fig. 3. Microstructure of the ZnO varistor prepared; the pure ZnO was heat-treated at 1200°C for 1 h with the powder mixture ($1Bi_2O_3$–$1MnO_2$–98ZnO in mol%).

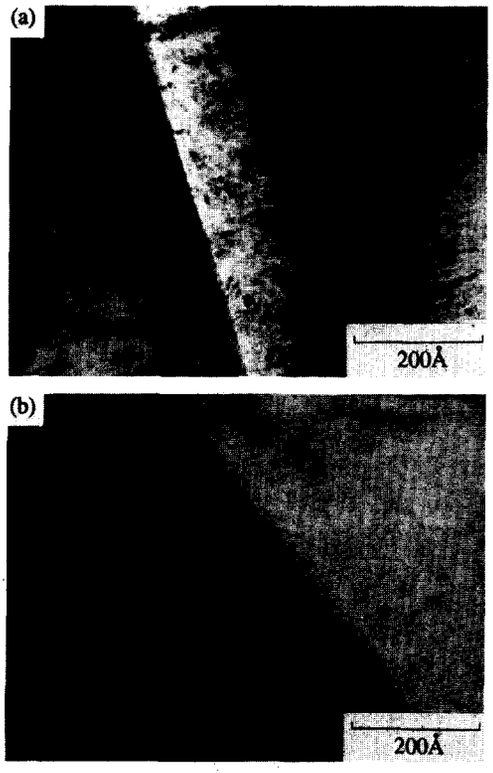


Fig. 4. TEM micrographs of the varistor prepared; (a) some boundaries show the presence of Bi-rich liquid phase and (b) the others show a typical grain boundary.

The grain boundaries and their triple junctions were examined with transmission microscopy. As shown in Fig. 4, some of the grain boundaries showed the presence of a Bi-rich liquid phase (bright region in Fig. 4 (a)), but other boundaries (Fig. 4 (b)) did not show the presence of any Bi-rich liquid phase. Approximately, 80% of the boundaries were observed to be wetted with the Bi-rich liquid and its maximum thickness was around 1 μm. The results may indicate that the grain boundary structure and its energy, which determine the liquid penetration, vary from one grain boundary to another. For ZnO varistors, in fact, three different types of boundary structure were reported,[24] a thick intergranular liquid layer (0·1 ~ 1 μm), a thin intergranular liquid layer (10 ~ 1000 Å), and the grain boundary without any liquid phase.

Figure 5 shows the I–V characteristic of the specimen obtained. The breakdown voltage at a current density of 1 mA/cm^2 is determined to be 3·6 V/mm which is much lower than that of the conventionally fabricated low-voltage varistors. Using ZnO seed grains, for instance, V_b = 6 V/mm has been reported.[7] If the threshold voltage per grain boundary is about 3·6 V, the grain size of the specimen prepared is predicted to be 1000 μm by eqn (1). Note that the current always flows through the easiest path, i.e. the path with the fewest number of grains between the electrodes.

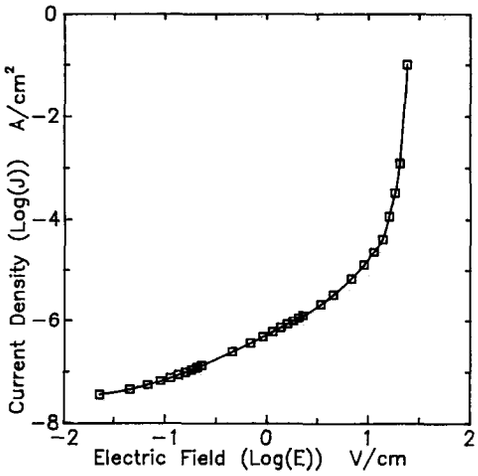


Fig. 5. I–V characteristic of the ZnO varistor prepared.

Therefore, the predicted grain size from the breakdown voltage is always larger than the microstructural average grain size. The nonlinearity coefficient of α for this specimen in the range of 10^{-3} to 10^{-1} A/cm^2 is 20. This value of α is expected to be further increased if other oxides such as CoO, Cr_2O_3, and Sb_2O_3 are incorporated in the Bi_2O_3 containing powder mixture. On the other hand, the amount of leakage current in the pre-breakdown region is acceptable. When the strength of electric field was 10 V/cm, the magnitude of leakage current was 10^{-5} A/cm^2.

4 Conclusions

Low-voltage ZnO varistors have been fabricated by a two-step process consisting of the sintering of pure ZnO and subsequent heat-treatment. The abnormal grain growth that occurred during sintering of ZnO resulted in a relatively uniform matrix of very large grains. After the subsequent treatment with Bi_2O_3 the specimens showed a typical microstructure for a ZnO varistor with a Bi-rich liquid at the triple grain boundary junctions. The breakdown voltage of the specimen obtained was 3·6 V/mm and its nonlinear coefficient α was 20.

Acknowledgement

This work was supported by the Korea Ministry of Education (Research Fund for Advanced Materials in 1992).

References

1. Matsuoka, M., Progress in Research and Development of Zinc Oxide Varistor. In *Grain Boundary Phenomena in Electronic Ceramics, Advances in Ceramics, Vol 1.* ed. L.

M. Levinson. Am. Ceram. Soc., Columbus, OH, 1981, pp. 290–308.
2. Eda, K., Inada, M., Iga, A., Makino, O., Matsuoka, M., Oda, H., Yoshida, N. & Hosokawa, T., High Energy 'ZNR' Surge Absorber for Automotive Use. *Nat. Tech. Rep.* (Matsushita Electr. Ind. Co., Osaka, Japan) **25**(5) (1979) 1024–32.
3. Wong, J., Barrier Voltage Measurement in Metal Oxide Varistors. *J. Appl. Phys.*, **47**(11) (1976) 4071–4.
4. Brückner, W., Bäther, K. H., Moldenhauer, W., Wolf, M. & Lange, F., Inhomogeneities and Single Barriers in ZnO-Varistor Ceramics. *Phys. Stat. Sol. (A)*, **59** (1980) K1–K4.
5. Selim, F. A., Gupta, T. K., Hower, P. L. & Calson, W. G., Low Voltage ZnO Varistor: Device Process and Defect Model. *J. Appl. Phys.*, **51**(1) (1980) 765–8.
6. Bowen, L. J. & Avella, F. J., Microstructure, Electrical Properties, and Failure Prediction in Low Clamping Voltage Zinc Oxide Varistors. *J. Appl. Phys.*, **54**(5) (1983) 2764–72.
7. Eda, K., Inada, M. & Matsuoka, M., Grain Growth Control in ZnO Varistors Using Seed Grains. *J. Appl. Phys.*, **54**(2) (1983) 1095–9.
8. Hennings, D. F. K., Hartung, R. & Reijnen, P. J. L., Grain Size Control in Low-Voltage Varistors. *J. Am. Ceram Soc.*, **73**(3) (1990) 645–8.
9. Trontelj, M., Kolar, D. & Krasevec, Influence of Additives on Varistor Microstructure. In *Additives and Interfaces in Electronic Ceramics (Advances in Ceramics, Vol. 7)*, eds. M. F. Yan & A. H. Heuer. Am. Ceram. Soc., Columbus, OH, 1983, pp. 107–16.
10. Gupta, T. K., Application of Zinc Oxide Varistors. *J. Am. Ceram. Soc.*, **73**(7) (1990) 1817–48.
11. Einzinger, R., Metal Oxide Varistors. *Annu. Rev. Mater. Sci.*, **17** (1987) 299–321.
12. Eda, K., Destruction Mechanism of ZnO Varistors due to High Currents. *J. Appl. Phys.*, **56**(10) (1984) 2948–55.
13. Levinson, Lionel M. & Philipp, Herbert R., Zinc Oxide Varistors — A Review. *Am. Ceram. Soc. Bull.*, **65**(4) (1986) 639–46.
14. Eda, K., Zinc Oxide Varistors. *IEEE Electrical Ins. Mag.*, **5**(6) (1989) 28–41.
15. Gupta, T. K. & Coble, R. L., Sintering of ZnO: I. Densification and Grain Growth. *J. Am. Ceram. Soc.*, **51**(9) (1968) 521–5.
16. Dollimoore, D. & Spooner, P., Sintering Studies on Zinc Oxide. *Trans. Faraday Soc.*, **67**(9) (1971) 2750–9.
17. Whittemore, O. J. & Varela, J. A., Initial Sintering of ZnO. *J. Am. Ceram. Soc.*, **64** (1981) C154–5.
18. Gupta, T. K. & Coble, R. L., Sintering of ZnO: II. Density Decrease and Pore Growth During the Final Stage of the Process. *J. Am. Ceram. Soc.*, **51**(9) (1968) 525–8.
19. Hillert, M., On The Theory of Normal and Abnormal Grain Growth. *Acta Metall.*, **13** (1965) 227–38.
20. Chol, G. R., Influence of Milled Powder Particle Size Distribution on the Microstructure and Electrical Properties of Sintered Mn–Zn Ferrites. *J. Am. Ceram. Soc.*, **54**(1) (1971) 34–39.
21. See, for example: (a) Jeong, In-Kwon, Kim, Doh-Yeon, Khim, Z. G. & Kwon, S. J., Exaggerated Grain Growth During the Sintering of Y–Ba–Cu–O Superconducting Ceramics. *Mat. Lett.*, **8**(3/4) (1989) 91–94. (b) Prochazka, S., Dole, S. L. & Hejna, C. I., Abnormal Grain Growth and Microcracking in Boron Carbide. *J. Am. Ceram. Soc.*, **68**(9) (1985) C235–6.
22. Shohata, N.. Matsumura, T., Utsumi, K. & Ohno, T., Properties of Multilayer ZnO Ceramic Varistors. In *Grain Boundary Phenomena in Electronic Ceramics Advances in Ceramics, Vol. 1*, ed. L. M. Levinson, Am. Ceram. Soc., Columbus, OH, 1981, pp. 349–58.
23. Wong, J., Sintering and Varistor Characteristics of ZnO–Bi_2O_3 Ceramics. *J. Appl. Phys.*, **51**(8) (1980) 4453–9.
24. Clarke, D. R., Grain-boundary Segregation in a Commercial ZnO-based Varistor. *J. Appl. Phys.*, **50**(1) (1979) 6829–32.
25. Morris, W. G., and Cahn, J. W., Adsorption and Microphases at Grain Boundaries in Non-Ohmic Zinc Oxide Ceramics Containing Bismuth Oxide. In *Grain Boundaries in Engineering Materials*, ed. J. Walters *et al.*, 1975, pp. 223–33.

Journal of the European Ceramic Society **15** (1995) 377–383
© 1995 Elsevier Science Limited
Printed in Great Britain. All rights reserved
0955-2219/95/$9.50

Bridging Stress Relations for Ceramic Materials

T. Fett,[a] and D. Munz[b]

[a] Forschungszentrum Karlsruhe, Postfach 3640, Institut für Materialforschung II, D-76021, Karlsruhe, Germany
[b] Universität Karlsruhe, Institut für Zuverlässigkeit und Schadenskunde im Maschinenbau, Karlsruhe, Germany

(Received 2 June 1994; revised version received 12 August 1994; accepted 22 August 1994)

Abstract

In ceramic materials, bridging stresses are generated in the wake of propagating cracks due to crack interactions. Such stresses can be caused by friction of sliding grains or by elastic interactions where the crack surface contact behaves like a spring. Both types of interactions are described and a model is proposed which allows us to combine the two effects.

1 Introduction

Coarse-grained Al_2O_3 shows an R–curve behaviour which is characterised by an increase in crack growth resistance with increasing crack extension. In the past it has been shown by experimental[1] and theoretical investigations[2] that the R–curve is not a unique material property. The shape of the curve depends on the geometry of the test specimens, the initial crack depth, the type of loading (tension, bending) and on the special type of crack extension (stable and subcritical crack propagation).

It was demonstrated experimentally[3–6] that this effect is caused by crack border interactions in the wake of the advancing crack. The bridging interactions were observed mainly in materials with large grains. The crack face interactions localised at single grains can transfer loads which can be modelled in a more homogeneous way by so-called bridging stresses σ_{br} which depend only on the crack opening displacement δ. The bridging stresses shield the crack tip from the external loads.

In the special case of R–curves caused by bridging effects, the relation between bridging stresses and crack opening displacement is a material property which is expected to be much less influenced by special test conditions. In the literature the bridging stresses are mostly considered to be caused by frictional effects.[7] This description is well established for coarse-grained Al_2O_3. In hot-pressed silicon nitride, bridging zones act more like elastic springs of limited extension.[8]

Recently, Dauskardt[9] found experimental evidence for a combination of frictional and elastic behaviour of bridging interactions in alumina.

It is the intention of this investigation to

- present a bridging relation for elastic bridging interactions taking into consideration a distribution for the maximum displacements at which the bridge fails and to
- describe a bridging model that exhibits the main features of load versus displacement curves as measured by Dauskardt.[9]

Therefore, in the first part of this investigation, bridging relations are described which are based on bridging interactions caused by friction and spring effects. In the second part a model is discussed which describes elastic and friction-induced response of crack surface interactions on crack opening displacements.

2 Bridging Relations

2.1 Relation for friction induced bridging stresses

For bridging stresses σ_{br} which are caused by friction effects, Mai and Lawn[7] proposed a relation

$$\sigma_{br,grain} = \begin{Bmatrix} \sigma_0(1-\delta/\delta_c)^m & \text{for } \delta/\delta_c<1 \\ 0 & \text{for } \delta/\delta_c>1 \end{Bmatrix} m = 0,1,2,... \quad (1)$$

as shown in Fig. 1(a) for $m = 1$. If we assume that the characteristic displacement for which the bridging stresses vanish is distributed like a Γ-distribution of first order[2] with a density $f(\delta_c)$

$$f(\delta_c) = \frac{1}{\delta_0}\,\frac{\delta_c}{\delta_0}\exp(-\delta_c/\delta_0) \quad (2)$$

then the macroscopically averaged bridging stresses result from

$$\sigma_{br,aver} = \int_0^\infty \sigma_{br,grain} f(\delta_c)\,d\delta_c \quad (3)$$

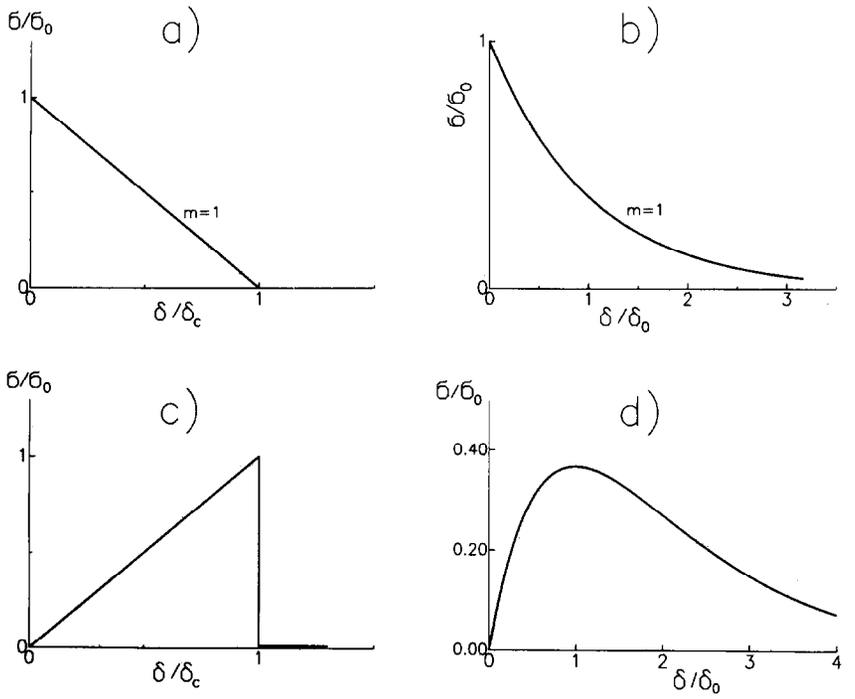


Fig. 1. Bridging stresses. (a) Local stress-displacement relation for frictional crack-surface interactions; (b) global stress-displacement relation for frictional crack-surface interactions; (c) local stress-displacement relation for a single spring; (d) global stress-displacement relation for spring-like crack-surface interactions.

For the mostly used case $m = 1$ the averaged bridging stress relation results

$$\sigma_{br,aver} = \sigma_0 \exp(-\delta/\delta_0) \tag{4}$$

as plotted in Fig. 1(b).

2.2 Bridging relations for springs with limited extensions

In case of spring-like stresses the bridging stresses in a single bridge may be expressed by

$$\sigma_{br,spring} = \left\{ \begin{array}{ll} \sigma_0 \delta/\delta_c & \text{for } \delta/\delta_c<1 \\ 0 & \text{for } \delta/\delta_c>1 \end{array} \right\} \tag{5}$$

with maximum extension δ_c and maximum stress σ_o, shown in Fig. 1(c).

Similar to the bridging effect it is assumed that the characteristic displacement δ_c for which the bridging stresses vanish is also Γ-distributed with a characteristical displacement value δ_0 characterising the 'width' of the distribution. The macroscopically averaged bridging stresses result from

$$\sigma_{br} = \int_0^\infty \sigma_{br,spring} f(\delta_c)\, d\delta_c \tag{6}$$

and one obtains by integration

$$\sigma_{br} = \sigma_0 \frac{\delta}{\delta_0} \exp(-\delta/\delta_0) \tag{7}$$

as given by Fig. 1(d). If we now assume a more narrow distribution of the values of δ_c's we can use the next higher order Γ-distribution, namely

$$f(\delta_c) = \frac{1}{\delta_0} \left(\frac{\delta_c}{\delta_0}\right)^2 \exp(-\delta_c/\delta_0) \tag{8}$$

and we obtain for the bridging-relation

$$\sigma_{br} = \sigma_0 \frac{\delta}{\delta_0} \left(1+\frac{\delta}{\delta_0}\right) \exp(-\delta/\delta_0) \tag{9}$$

For a comparison of eqns (7) and (9) see Fig. 11.

3 A Model for Frictional Bridging Stresses

In the following considerations a model is discussed that allows us to derive a relation for friction-induced bridging effects containing elastic components. As a first step the bridging effect is modelled as a two-dimensional problem for an internal crack in an infinite body, which is bridged by one single grain. In the second step a distribution of bridging grains is considered. In Fig. 2 a section

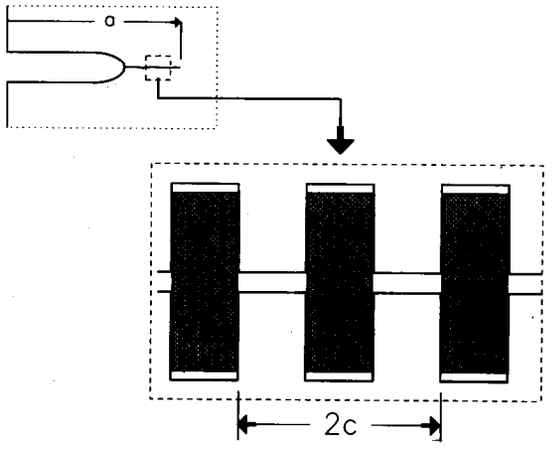


Fig. 2. Bridging model. A crack zone bridged by large grains.

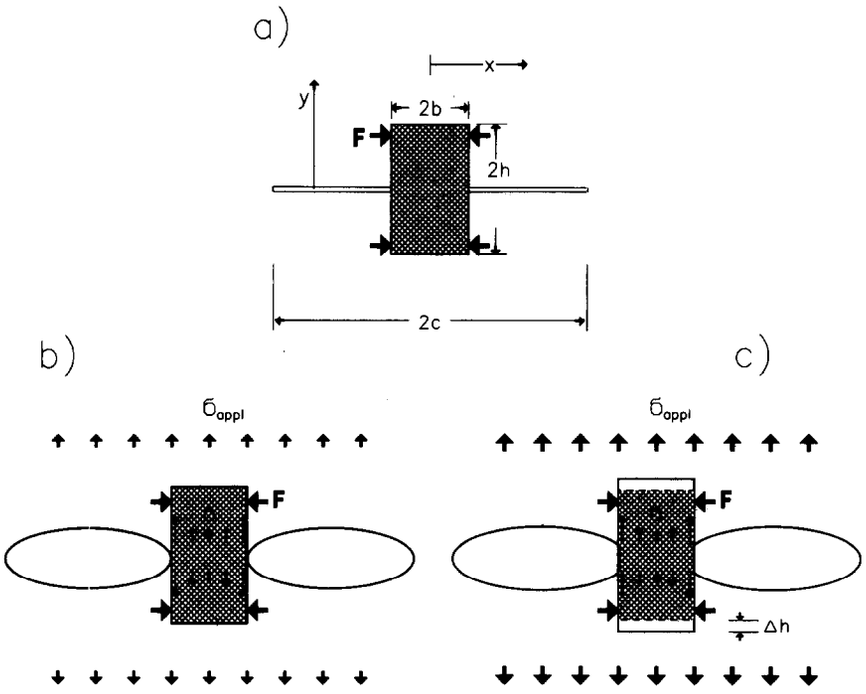


Fig. 3. Bridged crack. (a) Model of a bridged crack (unloaded). (b) Stresses and displacements for low remote loadings (schematic). (c) Stresses and displacements for high remote loadings (schematic).

of the bridged crack is shown. For the model the effect of one grain is considered and the problem can be treated as a crack of length $2c$ (twice the distance between two bridged grains). An elementary cell is shown in Fig. 3(a). Between the bridging grain and the surrounding material a residual stress acts due to mismatch of thermal expansion which creates the force F. This configuration is loaded by a remote stress $\sigma_{\text{appl.}}$ It is the aim of the following considerations to calculate the displacements at a remote location $y = y_0$ as a function of the applied stress. Figure 3(a) illustrates the geometry in the absence of externally applied stresses. For small, externally applied remote stresses σ_{appl} (Fig. 3(b)) the stresses and displacements are governed by the mixed boundary problem

$$\begin{aligned} &\delta = 0 \text{ for } |x| \le b \\ &\sigma = 0 \text{ for } |b| < |x| < |c| \end{aligned} \tag{10}$$

These conditions are valid until the load carried by the grain reaches the maximum friction force μF_0 between the bridging grain and its surroundings, i.e. for

$$2\int_0^b \sigma(x)\,\mathrm{d}x \le \mu F_0 \tag{11}$$

If the load carried by the grain exceeds μF_0, sliding between the bridging grain and the surroundings, with an amount Δh, occurs (Fig. 3(c)), the interaction force reduces to

$$F = F_0\,\frac{h - \Delta h}{h} \tag{12}$$

and the equilibrium condition of forces reads

$$2\int_0^b \sigma(x)\,\mathrm{d}x = \mu F_0 \frac{h - \Delta h}{h} \tag{13}$$

In this case, the boundary problem can be expressed by

$$\begin{aligned} &\delta = \Delta h \text{ for } |x| \le b \\ &\sigma = 0 \text{ for } |b| < |x| < |c| \end{aligned} \tag{14}$$

3.1 Calculation of displacements

Due to the symmetry of the problem with respect to $x = 0$, the computations can be restricted to positive values of x. Using the relation between stresses and displacements,[10] the mixed boundary problem can be written

$$\frac{1}{E'}\int_0^c \int_{\max(x,x')}^c h(c',x)h(c',x')\sigma(x')\mathrm{d}c'\mathrm{d}x' = \Delta h \tag{15}$$
$$\text{for } x \le b \quad \sigma = 0 \quad \text{for } b < x < c$$

The weight function for an internal crack in an infinite body under symmetrical load is[11]

$$h(x,c) = \frac{1}{\sqrt{\pi c}}\left[\left(\frac{c+x}{c-x}\right)^{1/2} + \left(\frac{c-x}{c+x}\right)^{1/2}\right] = \frac{2}{\sqrt{\pi c}}\,\frac{c}{\sqrt{c^2 - x^2}} \tag{16}$$

In the absence of a bridging interaction the crack opening displacement field is given by

$$\delta_0(x) = \frac{2\sigma_{\text{appl}}}{E'}\sqrt{c^2 - x^2} \tag{17}$$

The crack opening displacements caused by the stresses in the grain have to nullify these crack

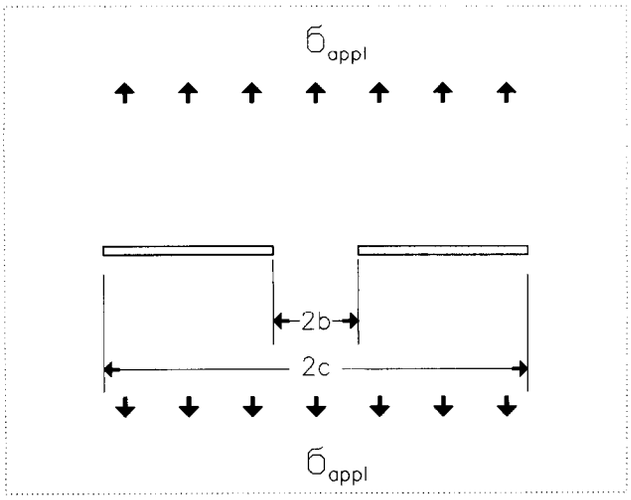


Fig. 4. Partial crack problem. Case 1: pair of collinear cracks.

opening displacements in the range $|x| \le b$. So we have to solve

$$\frac{4}{E'\pi}\int_x^c \frac{t}{\sqrt{t^2-x^2}}\left(\int_0^t \frac{\sigma(x)\,dx}{\sqrt{t^2-x^2}}\right)dt = -\frac{2}{E'}\sigma_{appl}\sqrt{c^2-x^2} + \Delta h \tag{18}$$

There are different possibilities of proceeding: (i) eqn (18) can be solved numerically; (ii) The displacement field can be superimposed by solutions existing for partial problems.

We will choose the second way here. As a first partial problem we compute the crack opening displacements for two neighbouring single cracks, Fig. 4, ensuring zero displacements within $|x| \le b$. The crack opening displacements are (see for example[11])

$$\delta_1(x) = \frac{2\,c\,\sigma_{appl}}{E'\boldsymbol{K}(k)}\,[\boldsymbol{K}(k)\,E(\varphi,k) - \boldsymbol{E}(k)\,F(\varphi,k)] \tag{19}$$

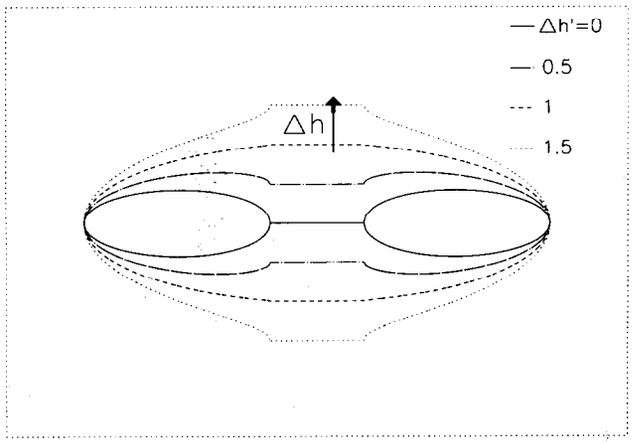


Fig. 5. Bridged crack. Displacements calculated with eqn (22), $b/c = 0{\cdot}2$ and σ_{appl} = constant, $\Delta h' = E'\Delta h/(2\sigma_{appl}c)$.

where $F(\varphi, k)$ and $E(\varphi, k)$ are the first and second elliptical integrals to the modulus k with

$$k = \sqrt{1-(b/c)^2}\quad,\ \varphi = \arcsin\sqrt{\frac{c^2-x^2}{c^2-b^2}} \tag{20}$$

and $\mathbf{K}(k)$, $\mathbf{E}(k)$ are the complete elliptical integrals. In this context, it should be mentioned that in Ref. 11 the elliptical integral $\mathbf{K}$ is missing in the denominator of eqn (19). Equation (19) represents the displacement field for $\Delta h = 0$. In order to satisfy the constant displacements $\Delta h > 0$ in $-b < x < b$, we have to add the displacement field for a parallel rigid wedge of thickness $2\Delta h$ within $-b < x < b$. In order to avoid a separation of the contact surfaces we assume the wedge to be welded with the surrounding material along the interfaces. The displacements are also given in handbooks (e.g. Ref. 11). It holds

$$\delta_2(x) = \frac{F(\varphi,k)}{\boldsymbol{K}(k)}\,\Delta h \tag{21}$$

and, finally, the total solution for the displacements is given by

$$\delta(x) = \frac{2c\,\sigma_{appl}}{E'\boldsymbol{K}(k)}\,[\boldsymbol{K}(k)\,E(\varphi,k) - \boldsymbol{E}(k)\,F(\varphi,k)] + \frac{F(\varphi,k)}{\boldsymbol{K}(k)}\,\Delta h \tag{22}$$

The crack opening displacement field resulting from eqn (22) is shown in Fig. 5.

3.2 Calculation of stresses in the bridging element

The corresponding stresses $\sigma(x)$ in the grain can be calculated numerically with eqn (18). In order to solve eqn (18), we will first calculate as a partial problem the stress distribution for a crack of length $2c$ which is opened by a parallel wedge of length $2b$ and thickness Δh (see Fig. 6). The Westergaard stress function for this problem is given in Ref. 11 as

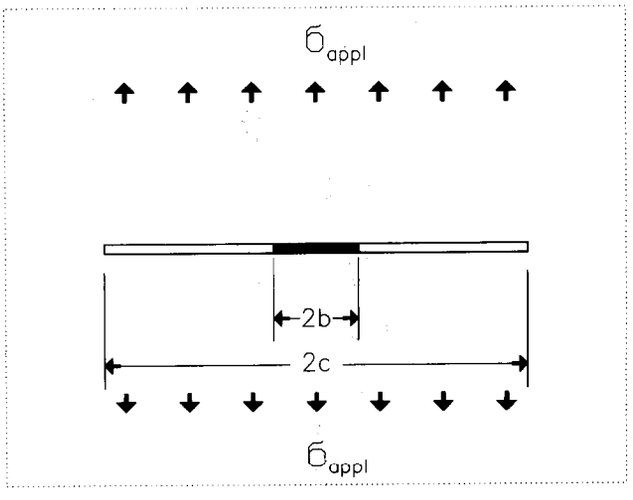


Fig. 6. Partial crack problem. Case 2: single crack opened by a wedge of constant thickness.

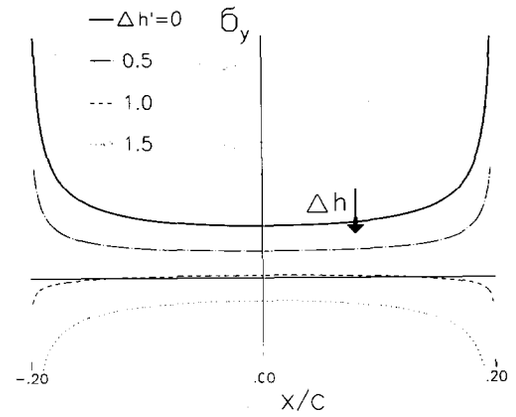


Fig. 7. Stresses in the bridging grain. Stresses calculated with eqn (18), $b/c = 0{\cdot}2$, σ_{appl} = const., $\Delta h' = E'\Delta h/(2\sigma_{appl}c)$.

$$Z(z) = \frac{E'h\,c}{2\boldsymbol{K}(k)} \frac{1}{\sqrt{z^2-c^2}\,\sqrt{z^2-b^2}}, \qquad k = \sqrt{1-(b/c)^2} \tag{23}$$

from which the normal stress σ_y results by

$$\sigma_y = \mathrm{Re}\{Z(z)\} - y\,Im\{Z'(z)\} \tag{24}$$

For $y = 0$ one obtains

$$\sigma_y = \mathrm{Re}\{Z(z)\} \rightarrow \qquad \sigma_y = \frac{E'\Delta h\,c}{2\boldsymbol{K}(k)} \frac{1}{\sqrt{c^2-x^2}\,\sqrt{b^2-x^2}} \tag{25}$$

For the pair of collinear cracks — which result for $\Delta h = 0$ — the stresses in the range $-b \le x \le b$ caused by the remote applied stress σ_{app} are (*see* Ref. 12)

$$\sigma_y = \frac{\sigma_{appl}}{\boldsymbol{K}(k)} \frac{c^2\boldsymbol{E}(k) - x^2\boldsymbol{K}(k)}{\sqrt{(c^2-x^2)(b^2-x^2)}} \tag{26}$$

Superposition of the two partial crack problems yields

$$\sigma_y = \frac{1}{\boldsymbol{K}(k)} \frac{\sigma_{appl}[c^2\boldsymbol{E}(k) - x^2\boldsymbol{K}(k)] - c\Delta hE'/2}{\sqrt{(c^2-x^2)(b^2-x^2)}} \tag{27}$$

The total force P carried by the bridging element is then

$$P = 2\int_0^b \sigma_y\,dx = 2\sigma_{appl}c[2\boldsymbol{E}(k') - \boldsymbol{K}(k')] - E'\Delta h \tag{28}$$

$$k' = \sqrt{1-k^2} = b/c \tag{29}$$

3.3 Load–displacement curve

The total volume resulting from the displacements

$$V = 4b\Delta h = 4\int_{x=b}^{x=c} \delta(x)\,dx \tag{30}$$

is a measure of the externally recorded loading-point displacements. From eqns (11) and (28) we find the applied stress at which the maximum friction force F_0 is reached

$$\sigma_{appl,0} = \frac{\mu F_0}{2c[2\boldsymbol{E}(k') - \boldsymbol{K}(k')]} \tag{31}$$

The volume at $\sigma_{appl} = \sigma_{appl,0}$ is

$$V_0 = \frac{8c\sigma_{appl,0}}{E'\boldsymbol{K}(k)} \left[\boldsymbol{K}(k)\int_b^c E(\varphi,\mathrm{k})\,dx - \boldsymbol{E}(k)\int_b^c F(\varphi,\mathrm{k})\,dx\right] \tag{32}$$

For stresses below this limit the volume is

$$V = V_0 \frac{\sigma_{appl}}{\sigma_{appl,0}} \tag{33}$$

and for higher stresses applied one obtains

$$V = V_0 \frac{\sigma_{appl}}{\sigma_{appl,0}} + 4b\Delta h + \frac{4\Delta h}{\boldsymbol{K}(k)}\int_b^c F(\varphi, k)\,dx \tag{34}$$

with Δh given as

$$\Delta h = h\,\frac{2\boldsymbol{E}(k') - \boldsymbol{K}(k')}{h' - [2\boldsymbol{E}(k') - \boldsymbol{K}(k')]}\left(\frac{\sigma_{appl}}{\sigma_{appl,0}} - 1\right) \tag{35}$$

$$h' = \frac{hE'}{2c\sigma_{appl,0}} \tag{36}$$

The volume — standing for the remote displacement at a given point — as a function of the applied remote stress is shown in Fig. 8. We can identify three regions:

1. For $\sigma_{appl} \le \sigma_{appl,0}$ the displacements are proportional to the applied load, as expressed by eqn (33).
2. At $\sigma_{appl,0}$ the applied stress overcomes the friction forces μF_0. For $\sigma_{appl,0} < \sigma_{appl} \le \sigma_{appl,max}$ the increase in displacements is steeper than in the range $\sigma_{appl} < \sigma_{appl,0}$.

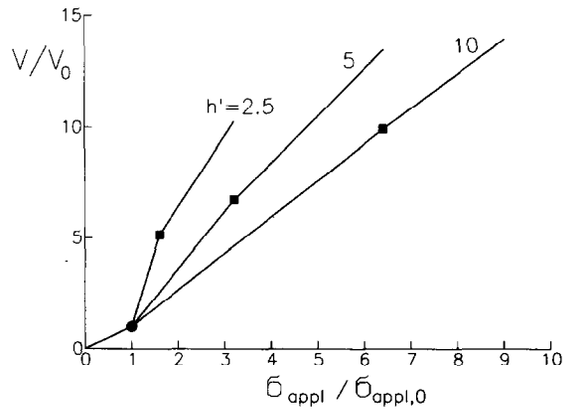


Fig. 8. Volume of the opened crack. Volume of the opened crack as a measure for the loading-point displacements, geometrical data: specimens thickness = 1 (i.e. crack opening area = crack opening volume), $b/c = 0{\cdot}2$, different values of h' as defined by eqn (36).

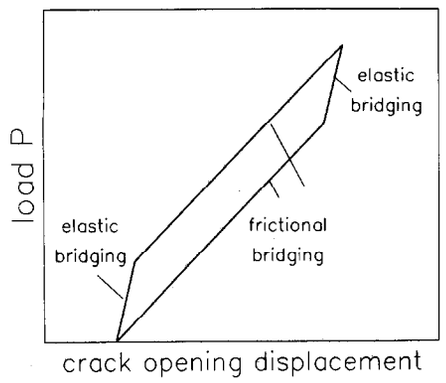


Fig. 9. COD-behaviour. Applied load, P, versus crack opening displacement curves for Al_2O_3 obtained by Dauskardt[9] (schematic).

3. At $\sigma_{appl,max}$ the bridging element is completely pulled out, equivalent to $\Delta h = h$,

$$\frac{\sigma_{appl,max}}{\sigma_{appl,0}} = \frac{h'}{2E(k') - K(k')} \tag{37}$$

and the subsequent curve follows according to

$$V = \frac{\sigma_{appl}}{\sigma_{appl,max}} = V_{appl,max} \tag{38}$$

Dauskardt[9] reports load–COD-curves which are very similar to those represented in Fig. 8. A typical P–COD-curve is schematically shown in Fig. 9 for one cycle of a cyclic test. Dauskardt calls the first steep part (corresponding to the initial flat parts of Fig. 8) 'elastic bridging' and the following phase 'frictional bridging'. Having in mind the COD-calculations made in this section, we can interpret the displacements during *elastic bridging* as the displacements occurring in the crack regions outside the actual bridging element (no elastic strain of the bridging element itself). Obviously, the displacements in Ref. 9 were not large enough ($K_I = K_{Ic}$ may be reached before) to exhibit the third part of the curve, i.e. the unbridged state.

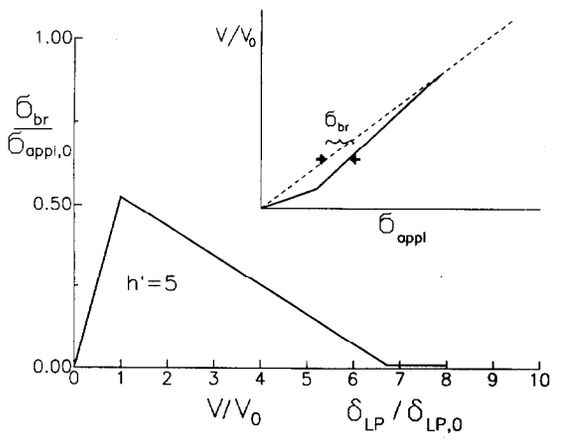


Fig. 10. Bridging stress relation. Bridging stress resulting from Fig. 8.

The bridging stresses result from the difference between the curve plotted in Fig. 8 and that curve which is obtained by prolongation of the line for $\sigma_{appl} \geq \sigma_{appl,max}$ to the origin (representing the completely unbridged state) as symbolised by the insert in Fig. 10. Considering the statistical distribution of the bridging-element lengths h, one obtains a smoother curve. If δ_{c1} is the displacement corresponding to $\sigma_{appl,0}$ and δ_c is the displacement at $\sigma_{appl,max}$, we can write the local bridging stresses as

$$\frac{\sigma}{\sigma_0} \begin{cases} \delta/\delta_{c1} & \text{for } \delta < \delta_{c1} \\ \dfrac{\delta_c - \delta}{\delta_c - \delta_{c1}} & \text{for } \delta_{c1} < \delta < \delta_c \\ 0 & \text{for } \delta < \delta_c \end{cases} \tag{39}$$

In the most general case one may consider the two typical displacements to be distributed independent of each other. But since the maximum friction force F_o characterising the onset of sliding, $\delta = \delta_{c1}$, is proportional to the length h of the bridging element and also the characteristic displacement of complete pull-out is identical to h, it is sufficient to consider the distribution of δ_c by introducing the ratio

$$\lambda = \delta_c/\delta_{c1} = \text{constant} \tag{40}$$

Replacing δ_{c1} in eqn (39) by δ_c λ and introducing this local bridging relation into eqn (3) yields for a Γ-distributed δ_c according to eqn (2) the averaged bridging relation

$$\sigma_{br} = \sigma_0 \frac{\lambda}{\lambda - 1} [\exp(-\delta/\delta_0) - \exp(-\lambda\, \delta/\delta_0)] \tag{41}$$

In Ref. 13 the authors used a Morse-like bridging relation

$$\sigma_{br} = \sigma_0 [\exp(-\delta/\delta_0) - \exp(-2\, \delta/\delta_0)] \tag{42}$$

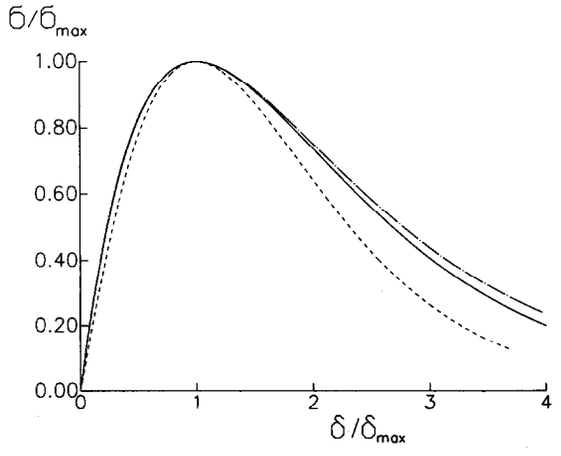


Fig. 11. Comparison of bridging stress relations. Solid curve: eqr (7), dashed curve: eqn (9), dash-dotted curve: eqn (42); δ_{max} is that displacement at which the stress reaches its maximum value.

which is a special case of eqn (41) with $\lambda = 2$. A comparison between the bridging relations described by eqns (7), (9), and (42) is given in Fig. 11.

4 Summary

Bridging stresses in ceramic materials are responsible for the R–curve behaviour. They are generated by crack surface interactions in the wake of a propagating crack and can be caused by friction of sliding grains or by elastic interactions where the crack surface contact behaves like a spring. In this paper, relations for the average bridging stresses as a function of the actual crack opening displacement are proposed and a model is discussed which allows to combine the two effects leading to 'elastic bridging' and 'frictional bridging' as observed by Dauskardt.[9]

The model yields a relation between the bridging stresses and the crack opening displacements. The three free parameters σ_0, λ and δ_0 may be determined

- by direct measurements of the bridging stresses in tensile tests,[14]
- from load–displacement curves as given by Dauskardt,[9]
- by fitting the bridging relation to measured R–curves.

References

1. Steinbrech, R. & Schmenkel, O., Crack-resistance curves for surface cracks in alumina, Comm., *J. Amer. Ceram. Soc.*, **71** 1988 C271.
2. Fett, T. & Munz, D., Evaluation of R–curve effects in ceramics, *J. Mater. Sci.*, **28** 1993 742–52.
3. Knehans, R. & Steinbrech, R. W., Memory effect of crack resistance during slow crack growth in notched Al_2O_3 bend specimens. *J. Mater. Sci. Letters*, **1** (1982) 327–9.
4. Steinbrech, R. W., Knehans, R. & Schaarwächter, W., Increase of crack resistance during slow crack growth in Al_2O_3 bend specimens. *J. Mater. Sci.*, **18** (1983) 265–70.
5. Frei, H. & Grathwohl, G., New test methods for engineering ceramics — in situ microscopy investigation, *Ceramic Forum International, cfi*, **67** 1991 27–35.
6. Rödel, J., Kelly, J. F. & Lawn, B. R., In situ measurements of bridged crack interfaces in the scanning electron microscope. *J. Amer. Ceram. Soc.*, **73** (1990) 3313–8.
7. Mai, Y. & Lawn, B. R., Crack–interface grain bridging as a fracture resistance mechanism in ceramics: II. Theoretical fracture mechanics mode, *J. Amer. Ceram. Soc.*, **70** (1987) 298.
8. Rombach, M., Rißachstum in Si_3N_4, Diplomarbeit, Universität Freiburg, 1992.
9. Dauskardt, R. H., Cyclic fatigue-crack growth in grain bridging ceramics, *J. of Engng. Mater. and Techn.*, **115** (1993) 244–51.
10. Fett, T., Mattheck, C. & Munz, D., On the calculation of crack opening displacement from the stress intensity factor, *Engng. Fract. Mech.*, **27** (1987) 697–715.
11. Tada, H., Paris, P. C. & Irwin, G. R., *The stress analysis of cracks handbook*, Del Research Corporation (1986).
12. Hahn, H. G., Bruchmechanik, B. G. Teubner, Stuttgart 1976.
13. Fett, T. & Munz, D., Influence of crack-surface interactions on stress intensity factor in ceramics, *J. Mater. Sci. Letters*, **9** (1990) 1403–6.
14. Hay, J. C. & White, K. W., Crack face bridging tractions in monolitic spinel. In *Fracture Mechanics of Ceramics* Vol. 9 (1992) 265–76.

Journal of the European Ceramic Society 15 (1995) 385–394
© 1995 Elsevier Science Limited
Printed in Great Britain. All rights reserved
0955-2219/95/$9.50

0955-2219(95)00005-4

Statistical Determination of Surface Flaw Distributions in Brittle Materials

P. D. Warren

Department of Materials, Oxford University, Oxford OX1 3PH, UK

(Received 19 May 1994; revised version received 24 August 1994; accepted 12 December 1994)

Abstract

A computational method is presented for determining the distribution of surface flaws in brittle materials from a series of fracture tests. The number of cracks per unit area with sizes within a range c *to* c + Δc *can be determined by the solution of a system of simultaneous linear equations. As long as the stress intensity factor for the cracks causing fracture can be calculated then results can be obtained from any loading method; the method therefore assumes that the shape of the cracks causing fracture is known. The only data inputs are the fracture loads themselves. Accurate estimates of the flaw density can only be obtained if proper consideration is given to the variation of the stress intensity factor with the angle between the crack-face normal and the tensile stress. Results are shown for computer simulations of 3-point bend testing.*

1 Introduction

The strength of ceramic materials is, unlike that of most metals, inherently variable; fracture occurs over a range of stresses as a result of a distribution of flaw sizes and positions. The most common way of describing the distribution of flaws is that due to Weibull.[1] The Weibull failure probability is defined in its simplest form as:[2]

$$F = 1 - \exp\left[-(\sigma_I/\sigma_o)^m\right] \qquad (1a)$$

where σ_I is the inert strength of the material, m is the Weibull modulus and σ_o a normalizing parameter. In the case where the stress varies with position in the surface of the body, as for instance in a three-point bend test, then the Weibull failure probability becomes:

$$F = 1 - \exp\left[-\int\left(\frac{\sigma_I}{\sigma_o}\right)^m \frac{dA}{A_o}\right] \qquad (1b)$$

σ_o and A_o are normalizing parameters. For equation (1(a)), by forming the cumulative probability of failure, a plot of $\ell n\{\ell n[1/(1-F)]\}$ against $\ell n(\sigma_I)$ should give a straight line of slope m and intercept $-m\ell n(\sigma_o)$. However, it is well known that simple Weibull statistics are not a good description of failure probabilities, particularly if multiple flaw populations are present.[3] Furthermore, this approach gives no direct information about the distribution of the flaws themselves, in terms of the number of flaws in a given size range per unit area, $n(c)\Delta c$.

Argon[4,5] proposed using the Hertzian indentation test as a way of determining surface flaw densities in glass. In this test a hard sphere is pressed against the surface of a solid until fracture occurs (the formation of a ring-crack or ring-cone crack). Argon measured *just* the fracture loads and determined $n(c)\Delta c$ by numerical inversion of Laplace transforms. Wilshaw[6] and Poloniecki and Wilshaw[7], again using Hertzian indentation, presented a different method of analysis. They were motivated by the fact that Argon, 'by analysing only the fracture forces, made the problem unnecessarily complicated'. By measuring the fracture loads *and* the radii of ring-cracks seen on the glass surface *after* fracture, the sizes of the small precursor surface flaws could be determined. For a given test and crack size, the 'searched area' could be defined: 'that area of surface within which, had there been a crack of size c, it would have caused fracture during loading up to a load P'. Thus the searched area, $A(P,c)$, is that area of surface within which $K_I > K_{IC}$ for a crack of size c during loading up to P. The flaw density is simply that number of cracks found within a given size range (c to $c+\Delta c$) divided by the total area searched for flaws of that size (c) in all the tests. This method is not restricted to Hertzian indentation, and is in principle applicable to any test method. It is thus an extremely powerful method of determining flaw densities although it suffers from the disadvantage that it is necessary to find the position from which failure started.

Matthews, McLintock and Shack[8] derived a different method for determining n(c)Δc from *just* the fracture loads measured in 3-point bend tests or Hertzian indentation tests; this method relied on the analytical inversion of an integral equation, which is possible only in limited cases. Evans and Jones[9] extended the work of Matthews *et al.* to include straight-forward tension, the expanding-ring tensile test and biaxial flexure, but again analytical inversion of the fundamental integral equation was crucial to the success of the method.

Alternatively, various analytical forms for the flaw distribution have been proposed. That due to Jayatilaka and Trustrum[10] is:

$$f(a) = \frac{c^{n-1}}{(n-2)!} a^{-n} e^{-c/a} \qquad (2a)$$

where $f(a)$ is the probability density of cracks of semi-length a; c is a scaling parameter (*not* the crack size in this case) and n is a measure of the rate at which the flaw density approaches zero. In fact, $2n\text{-}2=m$, where m is the Weibull modulus. That due to Batdorf and Crose[11] and Batdorf and Heinisch[12] is:

$$N_s(\sigma) = k\sigma^m \qquad (2b)$$

where $N_s(\sigma)$ is the surface crack density function, k is the crack density coefficient and m is the Weibull modulus. Recently, Santhanam and Shaw[13] determined flaw density distributions in ceramic tubes fractured by the crack-off process: by using a weakest-link approach (see below) combined with a flaw distribution function of the form of eqn (2a) (replacing the factorial function with the Γ function to allow for non-integral n) a best-fit of the function $f(a)$ to the fracture data was performed, leading to values for c and n.

In summary, there are three distinct approaches for determining $n(c)\Delta c$, the number of flaws per unit area in a size range Δc centred on c

(1) One can measure a fracture load *and* a fracture position (in which case the size of the crack that caused fracture can be determined); one then uses Wilshaw's[6,7] concept of 'searched area' to determine the flaw density.
(2) Alternatively, one can follow the approach of Matthews *et al.*[8] (or Evans and Jones)[9] where one measures *just* the fracture loads, and then use analytical inversion of an integral equation to determine $n(c)\Delta c$.
(3) Finally, one can follow Santhanam and Shaw's[13] approach, by assuming a functional form for n(c)Δc and obtaining the best values of the adjustable parameters in the expression for $f(a)$.

There are problems with all three approaches. For method (1), in the case of Hertzian indentation it can be extremely difficult to find the ring-cracks formed after fracture, especially on surfaces that are not highly polished. One usually has to resort to the use of chemical etches to bring out the cracks, which in the case of ceramic materials such as alumina means using molten KOH at 360°C. This is not convenient. The second problem with method (1) is that it is not possible to automate it. In principle this means that method (2) is preferable. Unfortunately, the calculations necessary to obtain $n(c)\Delta c$ require (for the analytical inversion of the integral equation) that the form of the stress-field experienced by the cracks is simple, so that the method is not of general application. For Hertzian indentation Argon,[4,5] Wilshaw[6,7] and Matthews *et al.*[8] all assumed that the only stress acting on the crack was the surface radial stress; the steep stress gradients that exist in the Hertzian field were ignored. As pointed out by Lawn,[2] the issue of stress gradients has been largely overlooked by flaw statistics analysts. Finally, in method (3) the problem lies in *assuming* a probability distribution of a particular form. While the form given above, eqn (2) is analytically straightforward, it forces the density of small cracks to be small. For many purposes, (e.g. strength of ceramics), knowledge of the density of small cracks may be irrelevant, but if one is investigating, for example, polishing processes then information about these cracks may be important. Secondly, by forcing the small-crack density to be small, one runs the risk of skewing the distribution at the large crack end.

In the method described below, these problems are overcome. The determination of $n(c)\Delta c$ is accomplished by knowledge of just the fracture loads in a series of tests; no prior assumptions are made about the form of $n(c)\Delta c$, and any loading system can be catered for, as long as K_I can be calculated. Thus the only assumption made here is one about the *shape* of the cracks causing fracture. Finally, most previous methods (with the exception of Santhanam and Shaw)[13] of estimating $n(c)\Delta c$ have ignored the effect of the variation in K_I with the angle between the crack-face normal and the tensile stress axis. It will be shown that this has a pronounced effect on the values of n(c)Δc determined.

2 Weakest-link Statistics

Following Sigl[14] and Danzer[15] we can write the cumulative probability of failure of a body during loading to a load P, $F(P)$, in terms of the *cumulative number of critical flaws* in the surface of the body, N(P):

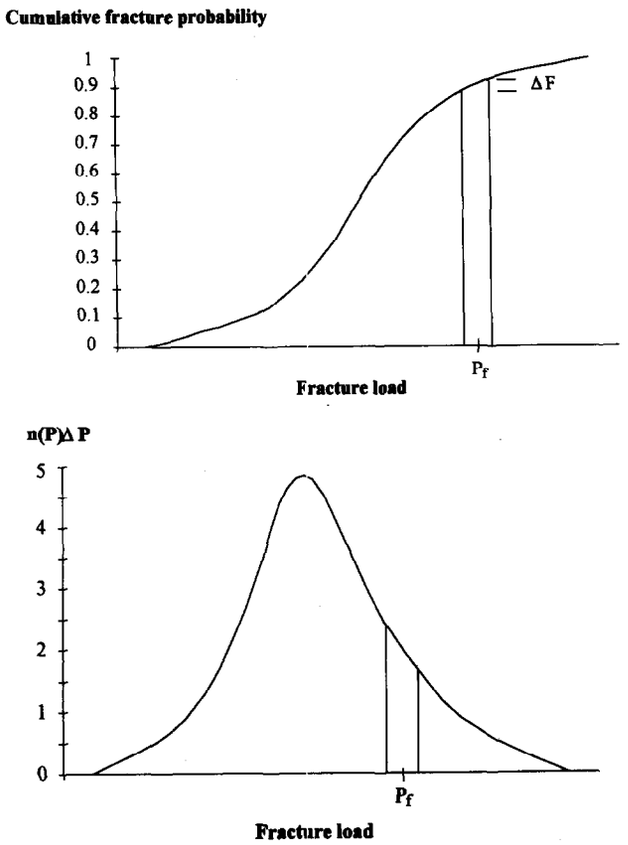


Fig. 1. Generic plots of: (a) cumulative probability of fracture $F(P)$, (b) number of fractures within a given load range $n(P)\Delta P$, both as a function of P.

$$F(P) = 1 - \exp(-N(P)) \tag{3}$$

Figure 1(a) shows a generic plot of $F(P)$, the cumulative probability of failure versus fracture load; Fig. 1(b) is the differential of this, $n(P)\Delta P$, the number of fracture loads in the range P to $P+\Delta P$. We define the number of flaws in a given size range per unit area, $n(c)\Delta c$: it is this quantity that is to be determined. Then, the number of flaws in the size range c to $c+\Delta c$ which are critical when the body is subjected to a load P is:

$$N'(c)\Delta c = A(P, c)\mathrm{n}(c)\Delta c \tag{4}$$

where, following Wilshaw,[6] $A(P, c)$ is the *area searched* for flaws of size c during loading to P i.e. that area of material within which $K_I > K_{IC}$ for flaws of size c during loading to P. It is this quantity $A(P, c)$ that can be calculated for any loading system, assuming that the crack shape is known. For a distribution of crack sizes, we finally obtain:

$$F(P) = 1 - \exp\left[-\sum_j A(P, c_j)\mathrm{n}(c_j)\Delta c\right] \tag{5}$$

A similar equation can obviously be derived for the three-dimensional case by replacing $A(P, c)$ by $V(P, c)$, the *volume* searched for flaws of size c during loading to P and by re-defining $n(c)\Delta c$ as the number of flaws in a given size range per unit volume.

Equation (5) can be re-cast in the form of a matrix equation:

$$\mathbf{b} = \mathbf{A}\mathbf{x} \tag{6}$$

$\mathbf{b}$ is a column vector with, say, m known components $b_i = -\ell\mathrm{n}[1-F(P_i)]$, $\mathbf{A}$ is an mxn matrix, whose known components are the searched areas, $A_{ij} = A(P_i, c_j)$ and $\mathbf{x}$ is a column vector with the n *unknown* components, $x_j = n(c_j)\Delta c$. $\mathbf{A}$ has $i = 1, m$ rows, corresponding to m points on the cumulative probability curve, $F(P_i)$, and $j = 1, n$ columns corresponding to those n crack sizes whose areal densities are to be determined. Strictly, m and n can be chosen arbitrarily, although as will be shown there are certain restrictions on the values that should be used in practice. We give below some examples of the utility of eqn (6).

3 Calculation of Searched Areas

In what follows we assume that the flaws controlling fracture are semi-circular surface-breaking cracks oriented normal to the tensile stress, σ. The stress intensity factor experienced by such a crack, depth c, is:

$$K_I = Y\sigma\sqrt{\pi c} \tag{7}$$

where Y is a shape factor, ~0·713.

3.1 Uniform tension

Figure 2 shows a rectangular parallelepiped pulled with a load P so that the tensile stress $\sigma = P/w^2$ where w^2 is the cross-sectional area of the block. Defining α_1 as:

$$\alpha_1 = \frac{w^2 K_{IC}}{Y\sigma\sqrt{\pi}} \tag{8a}$$

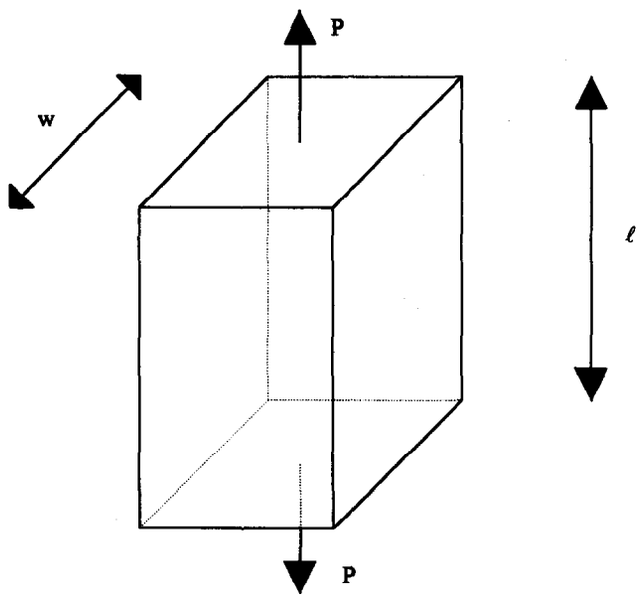


Fig. 2. Parallelepiped pulled by a uniform tension.

then, as long as $P_i \geq \alpha_1/\sqrt{c_j}$, the searched area is:

$$A(P_i, c_j) = 4w\ell \tag{8b}$$

Note that the area searched *during* loading up to P is the same as the area searched *at* a load P. It is perfectly possible to choose $m = n = 3$ (say), and also possible to choose the values of P_i and c_j such that eqn (6) takes the form:

$$\begin{pmatrix} 0 & 0 & A \\ 0 & A & A \\ A & A & A \end{pmatrix} \begin{pmatrix} x_1 \\ x_2 \\ x_3 \end{pmatrix} = \begin{pmatrix} b_1 \\ b_2 \\ b_3 \end{pmatrix} \tag{9a}$$

where the components of **b** are ranked in order of increasing load, and the components of **x** are ranked in order of increasing crack size. The solution is given by:

$$\begin{pmatrix} x_1 \\ x_2 \\ x_3 \end{pmatrix} = \begin{pmatrix} (b_3 - b_2)/A \\ (b_2 - b_1)/A \\ b_1/A \end{pmatrix} \tag{9b}$$

and it is clear that the density of the *largest* cracks, x_3, is controlled by the probability of fracture at the *lowest* load, b_1 as would be expected. Similarly, it is perfectly possible to set $m = n = 4$ and choose the values of P_4 and c_4 such that the matrix **A** has the form:

$$\begin{pmatrix} 0 & 0 & A & A \\ 0 & A & A & A \\ A & A & A & A \\ A & A & A & A \end{pmatrix} \tag{9c}$$

(This could be accomplished by choosing P_4 to be much bigger than P_3 but choosing c_4 to be only slightly larger than c_3). It is immediately clear that **A** is rank-deficient and that no unique solution for **x** exists. Surprisingly, it turns out that if $m = n$ then this is the normal situation; obviously if $m > n$, (i.e. one has more equations than unknowns) then there is never any unique solution for **x**. The method of solution of eqn (6) will be discussed in Section (5).

We now show that the matrix method of solution gives the same answers as those obtained by more conventional methods, at least in the simple case of uniform tension applied to a block. Suppose that a total of N_T fracture tests are performed and N_T fracture loads measured. From eqn (7) one can therefore derive N_T crack sizes. Let $n(P_f)\Delta P$ be the number of fracture loads in a load range ΔP, centred on P_f, this corresponds to the same number of cracks in a size range Δc, centred on c. The area searched for cracks in this size range is the product of the number of tests where the fracture load was greater than or equal to P_f (N_{crit}) with the area searched in each test (A), i.e. $N_{crit}A$. From Figs 1(a) and 1(b) we see that the fraction of tests with $P \geq P_f$ is $1\text{-}F(P_f)$. So, the total searched area is $N_{crit}A = N_T[1\text{-}F(P_f)]A$. But, also from Figs 1(a) and 1(b) the number of fracture loads that found cracks in this range is $N_T[\Delta F(P_f)]$, so that the crack density is:

$$n(c)\Delta c = \frac{\Delta F(P_f)}{[1 - F(P_f)]A} \tag{10}$$

By the matrix method, we can let $m = n$, and we can also choose the values of P and c such that A is triangular, i.e. all the upper-left components of A are 0. In this case, by analogy with eqn (9b) we see that the solution for the jth crack density is:

$$An(c_j)\Delta c = (b_{n-j+1} - b_{n-j}) = -\ell n\left[\frac{1 - F(P_{n-j+1})}{1 - F(P_{n-j})}\right] \tag{11a}$$

where P_{n-j} is the fracture load corresponding to a crack of size c_j. Letting n become large:

$$An(c)\Delta c = -\ell n\left[\frac{1 - F(P+\Delta P)}{1 - F(P)}\right] \tag{11b}$$

or, if $F(P + \Delta P) = F(P) + \Delta F(P)$, then:

$$n(c)\Delta c \approx \frac{\Delta F(P)}{[1 - F(P)]A} \tag{11c}$$

as before, eqn (10).

3.2 3-point bending

Referring to Fig. 3, we see that the tensile stress in the lower surface of the bar is given by:

$$\sigma(x) = \frac{3P(L - x)}{bh^2} \tag{12a}$$

Again, assuming that the only flaws present are semi-circular flaws oriented perpendicular to the tensile stress then the stress intensity factor for a flaw of depth c is as in eqn (7). For a load P_i and a flaw depth c_j the maximum distance that a flaw can be found from the centre of the tensile face is x_m:

$$x_m = L - \alpha_2 / (P_i\sqrt{c_j}) \quad \alpha_2 = \frac{K_{IC}bh^2}{3Y\sqrt{\pi}} \tag{12b}$$

For $P_i \geq \alpha_2/(L\sqrt{c_j})$ the area searched $A(P_i, c_j)$ is:

$$A(P_1, c_j) = \int_0^{x_m} 2b\,dx = 2b\left[L - \frac{\alpha_2}{P_i\sqrt{c_j}}\right] \tag{12c}$$

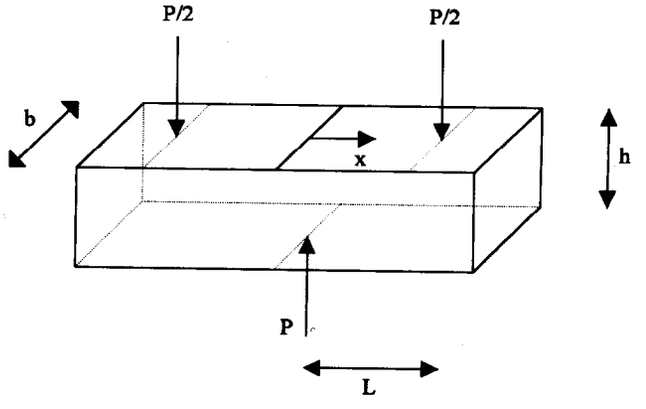


Fig. 3. Three-point bend test.

Note again that the area searched *during* loading up to P is the same as the area searched *at* a load P. In Appendix 1 we show that if eqn (6) is converted to its integral form and then combined with the expression for $A(P_i, c_j)$ from eqn (12c) one obtains the same expression for the flaw density as that originally derived by Matthews *et al.*[8]

3.3 Hertzian indentation

Finally, we consider an example where the area searched during loading to P is not the same as the area searched at a load P, the example of Hertzian indentation. If a sphere, radius R, elastic constants ν_s, E_s, is pressed with a load P into the flat surface of a substrate, elastic constants ν, E, then the two solids touch over a circular contact patch, radius a where:

$$a = \left(\frac{3RP}{4E^*}\right)^{1/3} \qquad \frac{1}{E^*} = \frac{1-\nu^2}{E} + \frac{1-\nu_s^2}{E_s} \quad (13a)$$

The stress state set up outside the contact patch *in the surface of the substrate* is one of radial tension, σ_{rr}, and hoop compression, $\sigma_{\theta\theta}$:

$$\sigma_{rr} = -\sigma_{\theta\theta} = \frac{(1-2\nu)}{2\pi}\frac{P}{r^2} \qquad r \geq a \quad (13b)$$

With K_I given by eqn (7) then for a load P_i and a flaw depth c_j the maximum distance that a flaw can be found from the centre of the indentation is r_m:

$$r_m = \left(\frac{P\sqrt{c}}{\alpha_3}\right)^{1/2} \qquad \alpha_3 = \frac{2\sqrt{\pi}K_{IC}}{Y(1-2\nu)} \quad (13c)$$

For $P_i \geq a^2\alpha_3/\sqrt{c_j}$ then the searched area *at* a load P_i is:

$$A(P_1, c_j) = \int_a^{r_m} 2\pi r dr = \pi(r_m^2 - a^2) \quad (13d)$$

However, as originally shown by Wilshaw[6] $K_I > K_{IC}$ for loads lower than P_i. The minimum load at which $K_I = K_{IC}$, for a crack size c, is P_{min}. The crack must be situated at the position of maximum tensile stress, i.e. at the corresponding contact radius, a_{min}:

$$P_{min} = \left(\frac{3R\alpha_3}{4E^*}\right)^2 \frac{\alpha_3}{c^{3/2}} \qquad a_{min} = \frac{3R\alpha_3}{4E^*c^{3/2}} \quad (13e)$$

The total area searched in loading up to P_i is therefore:

$$A(P_i, c_j) = \pi(r_m^2 - a_{min}^2) \quad (13f)$$

The variation of the maximum value of K_I with distance from the centre of the contact during loading is of importance for Section (4). At a maximum load P (and a corresponding contact radius a), for a given position $r(r \geq a)$ then the maximum K_I at that position is given by:

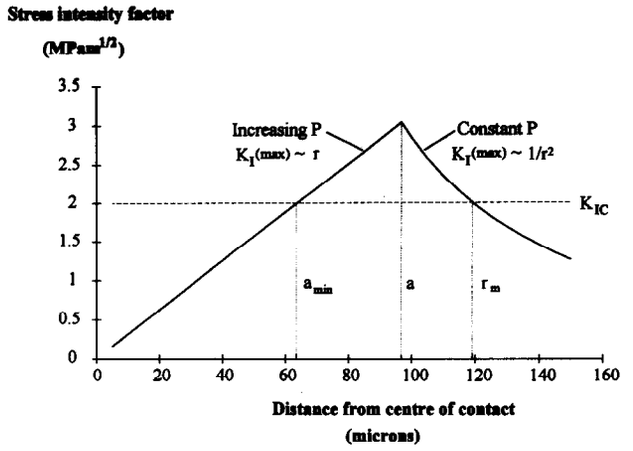


Fig. 4. Hertzian indentation: plot of maximum value of K_I as a function of distance from the centre of the contact using eqns (13g) and (13h), for the particular case $Y = 1{\cdot}12$, $\nu = 0{\cdot}24$, $E = 390$ GPa, $R = 2{\cdot}5$ mm, $K_{IC} = 2$ MPam$^{1/2}$, $P = 100$ N and $c = 3\mu$m.

$$K_I(\max) = \frac{Y(1-2\nu)}{2\pi}\frac{P}{r^2}\sqrt{\pi c} \qquad r \geq a \quad (13g)$$

However, for loads lower than P (but greater than P_{min}), the maximum K_I occurs at $r = a$. Therefore, replacing P by $4E^*r^3/3R$ in eqn (13g) we obtain:

$$K_I(\max) = \frac{Y(1-2\nu)}{2\pi}\frac{4E^*}{3R}r\sqrt{\pi c} \qquad a_{min} \leq r \leq a \quad (13h)$$

Figure 4 shows a plot of $K_I(\max)$ as a function of distance from the centre of the contact for the particular case $Y = 1{\cdot}12$, $\nu = 0{\cdot}24$, $E = 390$ GPa, $R = 2{\cdot}5$ mm, $K_{IC} = 2$ MPam$^{1/2}$, $P = 100$ N and $c = 3$ μm.

4 Angular Variation

We now consider how the expressions for $A(P_i, c_j)$ are modified if the cracks are no longer oriented perpendicular to the tensile stress, but are skewed round at an angle θ. (The cracks are still assumed to be perpendicular to the specimen surface). We now replace the elemental searched area ΔA by the *angularly-weighted* elemental searched area: $\Delta A' = \phi(\Delta A)$ where ϕ is defined as the ratio of the angular range within which $K_I = K_{IC}$ (for a given P and c), $2\phi_c$, to the angular range within which cracks can possibly be found, ϕ_0. Assuming that the angular distribution of the cracks is uniform then $\phi_0 = \pi$; this assumption will be acceptable for normal polishing and lapping procedures but may not be true if the ceramic surface has been machined in one direction only.

For Sections (4.1) and (4.2) below, eqn (7) is replaced by:

$$K_I = Y\sigma\sqrt{\pi c}\cos^2(\theta) \quad (14)$$

We make the assumption that mode I fracture still predominates, i.e. that the skewing of the

crack does not give rise to significant mode II or mode III stress intensity factors.

4.1 Uniform tension

With α_1 as in eqn (8a) we have:

$$\phi_c = \cos^{-1}\left[\left(\frac{\alpha_1}{P\sqrt{c}}\right)^{1/2}\right] \quad (15a)$$

With $P_i \geq \alpha_1/\sqrt{c_j}$ the searched area becomes:

$$A'(P_i, c_j) = \frac{8w\ell}{\pi}\cos^{-1}\left[\left(\frac{\alpha_1}{P_i\sqrt{c_j}}\right)^{1/2}\right] \quad (15b)$$

As P_i or c_j become large then $A'(P_i, c_j)$ tends to $A(P_i, c_j)$, from eqn (8b).

4.2 3-point bending

With K_I given by eqn (14), $\sigma(x)$ by eqn (12a) and x_m as in eqn (12b), we have:

$$\phi_c = \cos^{-1}\left[\left(\frac{L - x_m}{L - x}\right)^{1/2}\right] \quad (16a)$$

For $P_i \geq \alpha_2/(L\sqrt{c_j})$, the searched area $A'(P_i, c_j)$ is:

$$A'(P_1,c_j) = \int_0^{x_m}\left(\frac{2\phi_c}{\pi}\right)(2b\mathrm{d}x) = \frac{4b}{\pi}\left[L\cos^{-1}\left(\sqrt{\frac{L-x_m}{L}}\right) - \sqrt{(L-x_m)x_m}\right] \quad (16b)$$

We note that both $A'(P_i, c_j)$ and $A(P_i, c_j)$, eqn (12c), tend to $2bL$ as either P_i or c_j become large.

4.3 Hertzian indentation

If the flaws are not oriented perpendicular to the radial direction, then the compressive hoop stress must also be taken into account.

The total tensile stress acting across the crack face, oriented at θ to the radial direction is now:

$$\sigma = \sigma_{rr}\cos^2(\theta) + \sigma_{\theta\theta}\sin^2(\theta) = \frac{(1-2\nu)}{2\pi}\frac{P}{r^2}\cos(2\theta) \quad (17a)$$

With a_{min} as in eqn (13e) and r_m as in eqn (13c) we have:

$$\phi_{c1} = \frac{1}{2}\cos^{-1}\left(\frac{a_{min}}{a}\right) \qquad a_{min} \leq r \leq a \quad (17b)$$

$$\phi_{c2} = \frac{1}{2}\cos^{-1}\left(\frac{r^2}{r_m^2}\right) \qquad a \leq r \leq r_m \quad (17c)$$

The searched area up to a load P_i, $A'(P_i, c_j)$, must be calculated in two parts:

$$A'(P_1,c_j) = \int_{a_{min}}^{a}\left(\frac{2\phi_{c1}}{\pi}\right)(2\pi r\mathrm{d}r) + \int_a^{r_m}\left(\frac{2\phi_{c2}}{\pi}\right)(2\pi r\mathrm{d}r) \quad (17d)$$

$$A'(P_1,c_j) = (r_m^4 - a^4)^{1/2} - a_{min}\,a^2 - a^2_{min} \quad (17e)$$

As P_i or c_j become large, the expression for $A'(P_i, c_j)$ does *not* reduce to that for $A(P, c)$ eqn (13f), because the stress state is now different.

If the angular modifications to the searched area, eqns (15b), (16b) and (17e), are not taken into account the searched areas are over-estimated; thus the crack density required to produce a given probability of fracture, $F(P)$, is under-estimated. The calculations below show that this under-estimate can be a large factor, up to $\times 10$.

5 Method of Solution of Eqn (6)

As mentioned above, the solution of eqn (6) is apparently straightforward if one forces $m = n$ so that **A** is a square matrix. Unfortunately, standard routines for inverting matrices show that **A** is rank-deficient unless n is very small, say 3 or 4. A small value for n corresponds to representing $F(P)$ by a few points, which is obviously unsatisfactory. Therefore one chooses m to be large (say 25) and n to be smaller (say 10), in which case the system is over-determined and there is no unique solution; **A** may still be rank-deficient. Singular-value decomposition[16] of **A** may be employed to find a minimal least-squares solution for **x**. Unfortunately, in a number of cases it has been found some of the components of **x**, (i.e. the required flaw densities) are less than zero, which is physically unrealistic. The most satisfactory method has been to use a computer library 'black box' routine, Numerical Algorithms Group E02GBF, which solves over-determined linear equations subject to linear constraints on the unknowns; the routine finds **x** so as to minimise the sum of the absolute values of the residuals **Ax-b**.

6 Computer simulated 3-point bend tests

As a demonstration of the method, we describe the results from a series of computer simulations of three-point bend tests. Semi-circular cracks with randomly chosen depths, positions and orientations were generated. The stress intensity factor for each crack is given by eqn (14). When, under an increasing load, K_I at one crack reached K_{IC}, the load, crack size, position and angle were noted. The whole process was repeated a number of times (typically 100) to give average values. The average flaw spacings for flaws of size c to $c+\Delta c$, $\lambda(c)$, were inputs to the program.

$N(c)$ flaws were distributed in each size range $(c - \Delta c/2) < c < (c + \Delta c/2)$ where Δc was usually 1 μm. The minimum crack size was 1 μm, the maximum 20 μm. The flaws were positioned within a

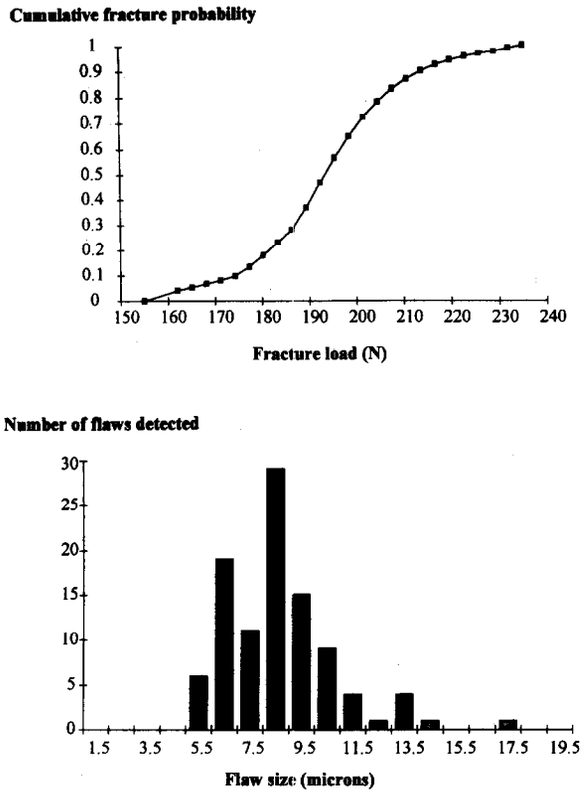


Fig. 5. Results from 100 simulated three-point bend tests: (a) cumulative fracture probability, (b) frequency plot of crack sizes found.

rectangular area, size $2bL$ (Fig. 3), with x-coordinate $-L < x < +L$. Therefore, $N(c) = 2bl/[\lambda(c)]^2$. For $\lambda(c)$ so large that $N(c) < 10$, $N(c)$ was set equal to 10, and cracks generated with x positions $-L' < x < +L'$, where $L' = 10[\lambda(c)]^2/b$.

From the results of 100 tests a cumulative probability of failure curve was constructed, usually at a probability interval of 0·04, i.e. 25 points were chosen. The vector **b** has only 24 components, $-\ln[1-F(P_i)]$; obviously the value $F(P) = 1$ is excluded. The maximum fracture load, P_{max}, sets the lower limit to the crack size, c_{min}, for which it is meaningful to calculate a density: $c_{min} = (\alpha_2/P_{max}L)^2$. The remainder of the cracks, c_j, were spaced 1 μm apart, up to $c_n = 20$ μm. With $m = 24$ values of P_i, and $n = 15$–20 values of c_j **A** and **b** were calculated and NAG E02GBF used to solve for **x**.

Figs 5(a) and 5(b) show the results from 100 simulations; the specimen dimensions were $b = 4$ mm, $h = 1{\cdot}5$ mm and $L = 10$ mm; $Y = 0{\cdot}713$, appropriate to semi-circular surface breaking flaws, and $K_{IC} = 2$ MPam$^{1/2}$. Figure 5(a) shows the cumulative probability distribution, and Fig. 5(b) shows the actual values of the crack sizes detected. (Calculating these crack sizes required knowledge of the crack position.) Figure 6 shows the areas searched for cracks of all sizes during all 100 tests; the upper curve is the searched areas calculated using eqn (12c), the lower curve those areas calculated

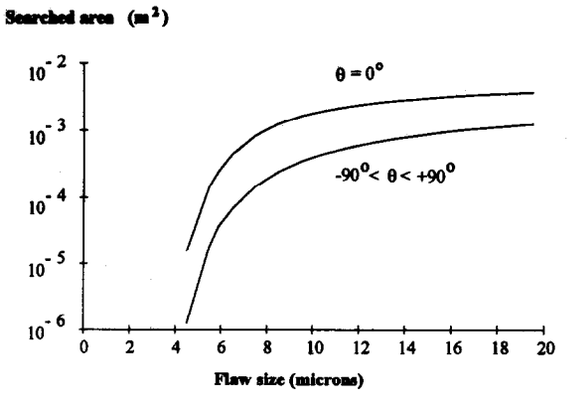


Fig. 6. Areas searched for cracks in 100 tests: upper curve assuming that all cracks are oriented normal to the applied stress; lower curve assuming cracks are randomly oriented with respect to applied stress.

from eqn (16b). The total searched area calculated ignoring the angular variation of K_I with θ is considerably larger than that calculated from eqn (16b), particularly for small crack sizes.

Figures 7(a) and 7(b) show the results of the determination of $n(c)\Delta c$, or equally $\lambda(c)$; clearly $\lambda(c) = 1/\sqrt{n(c)dc}$. Each graph shows three sets of values of $\lambda(c)$: the values input to the computer program, those calculated by Wilshaw's method,[6] and the values returned from the matrix method of calculation. Figure 7(a) shows the results with

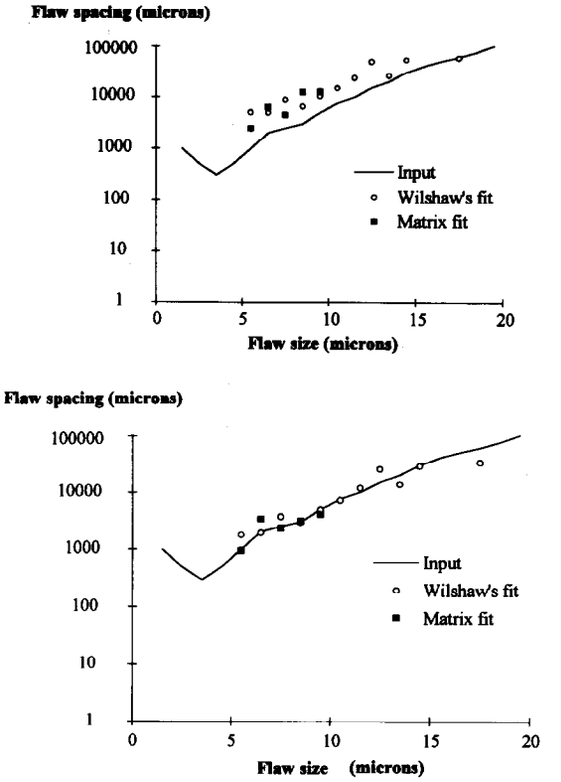


Fig. 7. Reconstruction of the input flaw distribution comparing the known input flaw density with values determined using both Wilshaw's method and the matrix method: (a) Searched areas calculated assuming that cracks are oriented normal to the applied stress. (b) Searched areas calculated assuming cracks are randomly oriented with respect to the applied stress.

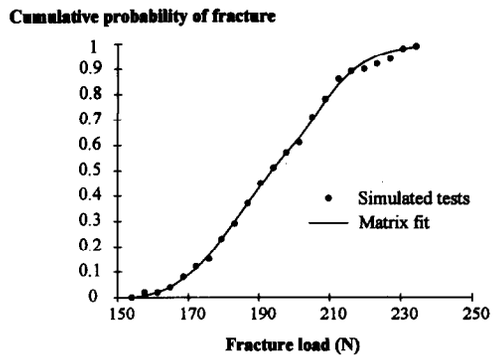


Fig. 8. Reconstruction of cumulative probability of fracture versus fracture load (Fig. 5(a)) using the flaw density distribution calculated by the matrix method.

the searched areas calculated from equation (12c), (ie. all cracks were assumed to lie normal to the tensile stress): the flaw spacings are all too high, i.e. the calculated crack densities are all too small, the discrepancy getting worse as the crack size decreases. Figure 7(b) shows the results with the searched areas calculated from equation (16b). It can be seen that both Wilshaw's method and the matrix method now give accurate estimates of the flaw spacings. Wilshaw's method gives an accurate estimate of the flaw density over almost the entire flaw size range. However, this accuracy is gained at the expense of speed; the position of the flaw actually causing fracture had to be found — to enable the flaw's size to be calculated. In the case of three-pointed bending this may not be a problem, but as mentioned above, this can be difficult in the case of Hertzian indentation. The matrix method of solution gives a reasonably accurate estimate of the flaw density, but only over a limited range of crack sizes. It appears that the best fit for the required components of **b** can be obtained by slightly over-estimating the density of small flaws (around 6–7 microns) and reducing the density of large flaws. This means that this method may not be appropriate for determining flaw densities for 'strength of ceramics' purposes where the large flaws are the ones of interest. The reason for this slight inaccuracy in the estimation of $n(c)\Delta c$ is related to the fact that the searched-area matrix **A** is frequently singular, as mentioned in Section (3(a)). The problem arises for the larger cracks. Figure 6 shows that the searched area no longer varies greatly with the size of the crack for sizes above ~12 μm. This implies that the rows of the matrix **A** may appear to be dependent and the computer routine for inverting the matrix ignores this 'unreliable' data. To compensate, the density of small flaws must be increased somewhat.

Figure 8 shows the results from taking the flaw distribution given by the matrix method, (i.e. the vector **x**) and reconstructing the cumulative probability of fracture curve: $F(P_i) = 1 - \exp(-b_i)$ with $b_i = A_{ij}x_j$. The agreement is quite remarkable.

Conclusions

Using Wilshaw's concept of 'searched area' has enabled a general method for determining the density of surface flaws in brittle materials to be derived, via the solution of a set of over-determined simultaneous equations. Weakest-link statistics are assumed, and it is also assumed that the shape of the cracks causing fracture is known, so that the stress-intensity factor for this crack under any loading situation can be evaluated. The only further inputs necessary are the fracture loads determined from a series of tests. For the three examples presented here (uniform tension, three-point bending and Hertzian indentation, ignoring the stress gradients) analytical expressions for the searched areas can be obtained, including the case where the flaws are assumed to be skewed at an angle with respect to the tensile stress. In general, this will not be possible, and numerical calculations of the searched area will be necessary. The procedure is as follows. First, for a given crack size and a given load it is necessary to calculate the minimum (r_{min}) and maximum (r_{max}) positions within which $K_I > K_{IC}$ at any stage during loading to P, bearing in mind that K_I may be greater than K_{IC} at loads less than P. Secondly, at each of a sufficiently large number of positions within this region, one must calculate the maximum value of K_I for the given crack at any load up to P, and hence determine the maximum angle, ϕ_c, through which the crack can be skewed and still maintain $K_I = K_{IC}$. Then, with the elemental area ΔA:

$$A(P_1, c_j) = \sum_{k=1}^{n} (\Delta A) \left(\frac{2\phi_c (r_k)}{\pi} \right) \qquad (18a)$$

$$r_k = \left(r_{min} + \frac{\Delta r}{2} \right) + (k-1)\Delta r \quad \Delta r = \frac{r_{max} - r_{min}}{n} \qquad (18b)$$

Work is in progress (Warren, Hills and Roberts)[17] applying this method to the determination of the surface flaw densities by Hertzian indentation taking the stress gradients of the Hertzian field into account.

We have deliberately restricted the analysis to consider only surface flaws, because our main interest is in the use of Hertzian indentation for evaluating surface damage following polishing/grinding; in Hertzian indentation the stress field is so strong at the surface that *only* surface flaws are detected. As pointed out by a referee, we recognise

that in three-point bend testing, fracture may initiate from volume flaws. In principle, it is a simple matter to repeat the analysis presented here to deal with the case where only volume flaws are present. However, further work is necessary to determine whether meaningful results can be obtained by this matrix method when *both* surface and volume flaws are present.

Acknowledgements

The author thanks Dr S. G. Roberts and Dr D. A. Hills for very helpful discussions. The work was supported under the SERC/LINK Nanotechnology Project 'Characterisation of surface roughness and sub-surface damage'.

References

1. Weibull, W., A statistical distribution function of wide application. *J. Appl. Mech.*, **18** (1951) 293–7.
2. Lawn, B. R., *Fracture of Brittle Solids* — Second Edition, Chapter 10. Cambridge University Press, 1993.
3. Phani, K. K., A new modified Weibull distribution function for the evaluation of the strength of silicon carbide and alumina fibres. *J. Mater. Sci.*, **23** (1988) 2424–8.
4. Argon, A. S., Distribution of cracks on glass surfaces. *Proc. Roy. Soc.*, **A250** (1959) 422–81.
5. Argon, A. S., Surface cracks on glass. *Proc. Roy. Soc.*, (1959) 482–92.
6. Wilshaw, T. R., The Hertzian fracture test. *J. Phys, D: Appl. Phys.*, **4** (1971) 1567–81.
7. Poloniecki, J. D. & Wilshaw, T. R., Determination of surface crack size densities in glass. *Nature, Lond.*, **229** (1971) 226–7.
8. Matthews, J. R., McLintock, F. A. & Shack, W. J., Statistical determination of surface flaw density in brittle materials. *J. Am. Ceram. Soc.*, **59** (1976) 304–8.
9. Evans, A. G. & Jones, R. I., Evaluation of a fundamental approach for the statistical analysis of fracture. *J. Am. Ceram. Soc.*, **61** (1978) 156–60.
10. Jayatilaka, A. De. S. & Trustrum, K., Statistical approach to brittle fracture. *J. Mater. Sci.*, **12** (1977) 1426–30.
11. Batdorf, S. B. & Crose, J. G., A statistical theory for the fracture of brittle structures subjected to non-uniform polyaxial stresses. *J. Appl. Mech.*, **41** (1974) 459–64.
12. Batdorf, S. B. & Heinisch, H. L. Jr., Weakest link theory reformulation for arbitrary fracture criterion. *J. Am. Ceram. Soc.*, **61** (1978) 355–8.
13. Santhanam, S. & Shaw, M. C., Determination of flaw-size distribution by the crack-off process. *J. Am. Ceram. Soc.*, **73** (1990) 2922–5.
14. Sigl, L. S., Effects of the flaw distribution function on the failure probability of brittle materials. *Z. Metallkd.* **83** (1992) 518–23.
15. Danzer, R., A general strength distribution function for brittle materials. *J. Eur. Ceram. Soc.*, **10** (1992) 461–72.
16. Press, W. H., Teukolsky, S. A., Vetterling, W. T. & Flannery, B. P., *Numerical Recipes (The Art of Scientific Computing)*, Chapter 2. Cambridge University Press, 1992.
17. Warren, P. D., Hills, D. A. & Roberts, S. G., Surface damage in ceramics and Hertzian indentation. *J. Hard. Mater.*, **5** (1994) 213–227.

Appendix 1

Here we demonstrate that in the case of three-point bending, *not* taking the angular variation into account, the concept of searched areas gives the same results for the flaw density as that originally derived by Matthews *et al.*[8] The integral form of eqn (6) is:

$$\int_{c1}^{c2} A(P,c)n(c)\mathrm{d}c = -\ell\mathrm{n}[1 - F(P)] \qquad \text{(A1)}$$

$A(P,c)$ is as given in eqn (12c). The lower limit of the integral, c_1, is the smallest crack that can be detected by a load P: $c_1 = (\alpha_2/PL)^2$. The upper limit of the integral, c_2, is the largest crack that can be detected by a load P, so that by assuming K_I as given in eqn (9) there *is* no upper limit. By differentiating eqn (A1) once with respect to P we obtain:

$$\frac{2b\alpha_2}{P^2}\int_{c1}^{c2}\frac{n(c)}{\sqrt{c}}\mathrm{d}c = \frac{F'(P)}{1 - F(P)} \qquad \text{(A2)}$$

where ' denotes differentiation with respect to P. By differentiating again we obtain:

$$\frac{4b\alpha_2^2\mathrm{n}(c_1)}{P^4L} - \frac{4b\alpha_2}{P^3}\int_{c1}^{c2}\frac{n(c)}{\sqrt{c}}\mathrm{d}c = \left[\frac{F'(P)}{1-F(P)}\right]^2 + \frac{F''(P)}{1-F(P)} \qquad \text{(A3)}$$

By eliminating the integral term between eqn (A2) and (A3) we obtain:

$$n(c_1)\mathrm{d}c_1 = \frac{P^4L}{4b\alpha_2^2}\left\{\frac{2F'(P)}{P[1-F(P)]} + \left[\frac{F'(P)}{1-F(P)}\right]^2 + \frac{F''(P)}{1-F(P)}\right\}\mathrm{d}c_1 \qquad \text{(A4)}$$

where $n(c_1)$ is the number of cracks of size c_1 per unit area per unit size range. If we use the notation of Matthews *et al.*, then S_m is defined as the maximum stress corresponding to a load P and $\Phi(S_m)$ is the cumulative probability of failure. By noting that

$$P = \frac{S_m}{\beta}, \qquad \beta = \frac{3L}{bh^2} \qquad \text{(A5)}$$

$$F(P) = \Phi(S_m), \frac{\mathrm{d}F(P)}{\mathrm{d}P} = \frac{\mathrm{d}\Phi(S_m)}{\mathrm{d}(S_m/\beta)} = \beta\,\frac{\mathrm{d}\Phi(S_m)}{\mathrm{d}S_m} \qquad \text{(A6)}$$

$$\frac{\mathrm{d}^2F(P)}{\mathrm{d}P^2} = \beta^2\,\frac{\mathrm{d}^2\Phi(S_m)}{\mathrm{d}S_m^2} \qquad \text{(A7)}$$

$$c_1 = \left(\frac{\alpha_2 L}{\beta S_m}\right)^2, \qquad \mathrm{d}c_1 = \frac{-2}{S_m^3}\left(\frac{\alpha_2 L}{\beta}\right)^2\mathrm{d}S_m \qquad \text{(A8)}$$

eqn (A4) can be converted to the original result of Matthews *et al.* (their eqn 10), which is written in terms of $g(S_m)$, the number of cracks which give a strength S_m per unit area per unit strength range:

$$g(S_m)dS_m = \frac{S_m}{bL}\left\{\frac{2\Phi'(S_m)}{S_m[1-\Phi(S_m)]} + \left[\frac{\Phi'(S_m)}{1-\Phi(S_m)}\right]^2 + \frac{\Phi''(S_m)}{1-\Phi(S_m)}\right\}dS_m \quad \text{(A9)}$$

ELSEVIER

0955-2219(95)0006-2

Journal of the European Ceramic Society **15** (1995) 395–404
© 1995 Elsevier Science Limited
Printed in Great Britain. All rights reserved
0955-2219/95/$9.50

Reliability of Alumina Ceramics: Effect of Grain Size

Jürgen Seidel, Nils Claussen & Jürgen Rödel[a]

Advanced Ceramics Group, Technische Universität Hamburg-Harburg, Germany

(Received 16 February 1994; revised version received 20 September 1994; accepted 12 December 1994)

Abstract

The grain size dependence of fracture strength and Weibull modulus of alumina using a high purity, commercial starting powder was investigated. In the regime of an average grain size between 1·7 and 11 μm, fracture strength increases with decreasing grain size. This behaviour could be explained quantitatively by modelling the failure-causing defect as either a spherical pore or a hemispherical surface pit with a circumferential crack proportional to the average grain size. No dependence of Weibull modulus on average grain size and hence on R–*curve behaviour could be observed. Theoretical considerations show that the closure stresses in alumina responsible for the* R–*curve behaviour are too low to affect the Weibull modulus.*

1 Introduction

The reliability of ceramics is governed by two factors; the strength and the variability of strength. In developing a material for structural applications, for example a turbo charger for heat engines, a low probability of failure can be realized either by a high Weibull modulus and a moderate characteristic strength or by a high characteristic strength and a lower Weibull modulus.[1]

An approach to increase the strength of polycrystalline ceramics is afforded by the reduction of the average grain size.[2–7] The relationship between strength and grain size has generally been described using a σ versus $G^{-1/2}$ (strength versus inverse square root of the average grain size) diagram. With large grain sizes, an increase in strength with decreasing grain size is observed. In this regime (Orowan-branch) the average grain size is larger than the flaw size due to processing defects (pores, inclusions etc), so the strength determining defect scales with the average grain radius. In the fine grain size regime (Petch-branch) the size of the processing defects is larger than the grain size. In this region only a slight increase of strength[2–6] or even a constant strength level[7] have been observed with decreasing grain size. Due to the relevance of high strength for reliability, (sufficient strength levels could only be achieved in the fine grain size regime), it is of fundamental importance to understand the grain size dependence of flexure strength. Various interpretations of the transition between the two regimes and the failure mechanism at finer grain sizes have been proposed: crack initiation through microplasticity,[2,5] the dominance of processing flaws with a microstructural dependence attributable to a monocrystal to polycrystal increase in crack resistance[3] and the variation of fracture energy with grain size.[3,4] While the early debate was based on a single value toughness for a given grain size; (the influence of a rising *R*–curve on the strength), grain size behaviour has now also been considered.[6] Then the focus remained on the low strength Orowan-branch.[6]

The second feature concerning reliability is the variability of the strength values, generally expressed by the two parameter Weibull statistics.[8] Simple theoretical models lead to the postulate of an increased Weibull modulus if *R*–curve behaviour exists.[9–12] Steinbrech *et al.*[13] demonstrated that the toughness of a coarse grained, 16 μm alumina increases from about 3 MPa $m^{1/2}$ to 6 MPa $m^{1/2}$ over a crack extension of several mm. For alumina it is well appreciated that the plateau value of the *R*–curve increases with the average grain size, due to bridging interaction.[6,13,14]

Possible complications due to residual stresses related to machining damage are considered in a second paper.[15]

In the present study we focus on the grain size dependence of flexure strength in the fine grain

[a]Now at TH Darmstadt, Ceramics Group, FB Materialwissenschaft, GDP, Gebäude D, Hilperstraße 31, Darmstadt, Germany.
This work was supported by the Deutsche Forschungsgemeinschaft under contract number C1 53/13-2.

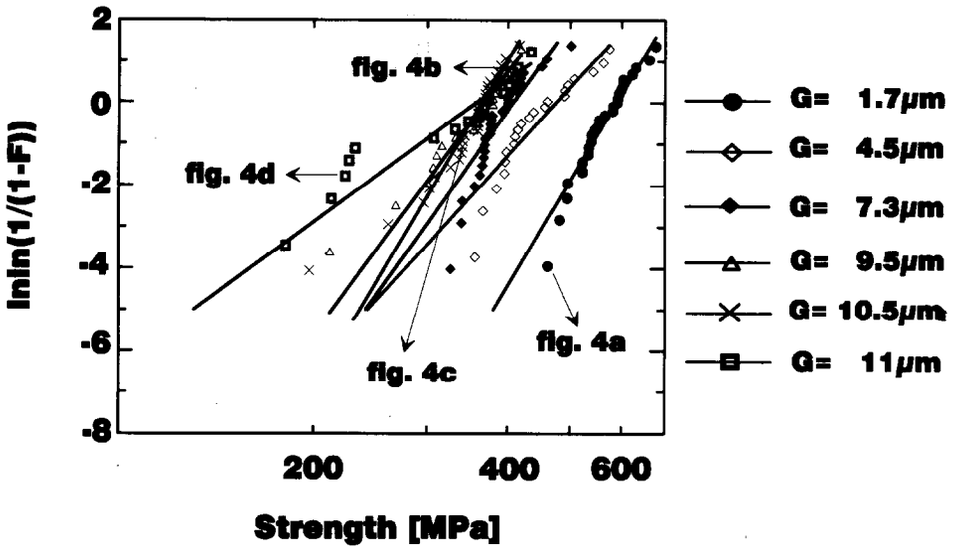


Fig. 1. Strength distributions (Weibull plot) of alumina materials with different grain size.

size regime and present new data, as well as a simple fracture mechanical model which allows rationalization of the observed experimental findings. The general knowledge of grain size dependent R–curve behaviour in alumina is further applied to discuss the influence of the R–curve behaviour on Weibull modulus m, again under application of a simple model to account for the experimental values. Specifically, the key question may be posed as: can the decreasing strength with increasing average grain size be compensated by an enhanced Weibull modulus due to an increasing crack resistance?

2 Experimental Procedure

A commercial, ultrafine Al_2O_3 powder (Taimei Chemical Co., Ltd, TM-DAR) was used to fabricate bars (4 × 5 × 40 mm) by uniaxial pressing the as received powder at 50 MPa in a steel die followed by cold isostatical pressing at 800 MPa. Green densities of 55% of the theoretical density were attained by this procedure. The green bars were sintered at temperatures of either 1350 or 1600°C in air. The lower sintering temperature was used to produce a fine grained material and the coarse grained materials were sintered at 1600°C at different dwell times (10 min to 96 h) to alter the average grain size. The sintered densities measured by the Archimedes method using water as immersion liquid were greater than 99% TD. After preparing the surfaces by grinding and polishing the microstructure was revealed by thermal etching for 30 min at temperatures 20°C below sintering temperature for the fine grained material and 50°C for the coarse grained materials. The average grain diameter were measured using the linear intercept technique. The average grain sizes could thus be adjusted in a regime between 1·7 and 11 μm. Prior to strength testing each bar was ground to 3 × 4 mm by a rotating diamond disk.

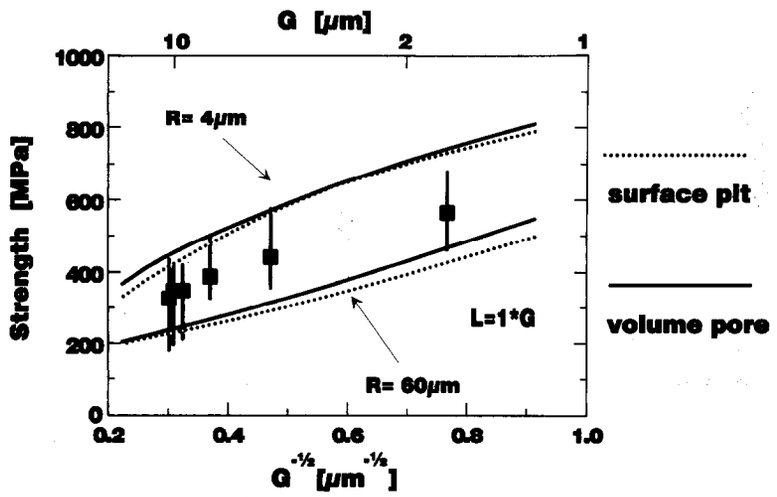


Fig. 2. Strength as function of the average grain size; solid lines represent the computed grain size dependence of strength assuming a spherical pore with an annular crack as fracture origin, dashed lines use the assumption of a hemispherical surface pit with a peripheral crack as a fracture origin.

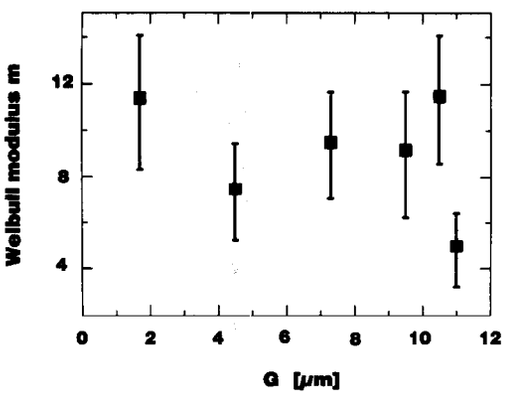


Fig. 3. Weibull modulus and 90%-confidence intervals as function of the average grain size.

The prospective tensile surfaces were finally ground with a 15 μm disk and polished by hand to a 3 μm finish. Uniaxial strength testing was carried out with a four-point bending test device, span lengths 10 and 20 mm with 20–30 bars for each batch in laboratory atmosphere of about 50% relative humidity. The loading rate was 1 mm/min.

The variability of the strength values was analysed corresponding to the 2 parameter Weibull approach, expressed by eqn 1 (with σ the fracture strength and σ_0 the Weibull scale parameter):

$$F = 1 - \exp(-(\frac{\sigma}{\sigma_0})m) \quad (1)$$

The strength values were ranked in ascending order and each strength value was associated with a fracture probability F evaluated by (with n the total number of specimens and i the i'th specimen):

$$F = \frac{i - 0{\cdot}5}{n} \quad (2)$$

The Weibull modulus, m and the 90% confidence intervals were evaluated using the maximum likelihood method.

Scanning electron microscopy was used to examine the fracture surfaces and to identify the strength determining defects.

3 Results

Figure 1 shows the strength distributions of the alumina batches with different grain size. The solid lines through the strength data are the curves representing the fit on the basis of the 2 parameter Weibull approach with the parameters m and σ_0.

Replotting the data as mean strength versus inverse square root of grain size shows the clear trend of an increasing strength with decreasing average grain size G (Fig. 2) with a rise of σ from 325 MPa at an average grain size of 11 μm to 564 MPa at G = 1·7 μm. Evaluation of the Weibull parameter m using the maximum likelihood method yields, with one exception, Weibull moduli ranging from 8 to 11 (Fig. 3). If the confidence intervals are included (Fig. 3) no dependence of m on G in the grain size region up to 11 μm could be observed. Not all the strength data correlate well with the corresponding Weibull parameter fit (Fig. 1). The small grain size materials exhibit a tendency to a low strength cut-off which may be better described by a three parameter Weibull approach, while the material with G = 11 μm might be better fitted by a bimodal strength distribution.

Most of the fracture surfaces investigated reveal volume defects in the form of large voids near the tensile surface as failure source (Fig. 4(a)–(c) see also Fig. 1). In a few cases surface flaws could be identified (Fig. 4(d) see also Fig. 1). There is no indication of a change of the defect character with grain size. Fig. 4(a)–(c) shows the fracture origins from specimens with three different grain sizes. The diameter of the defects (2R) in a batch with identical average grain size ranges from 20 to 80 μm. There is no indication for increasing defect sizes with increasing grain size.

4 Discussion

4.1 Strength as a function of grain size

Our experimental data confirm earlier experimental observations[2–6] of an increasing strength (as in our case by about 240 MPa) with decreasing grain size (in going from 11 to 1·7 μm). In the last decade this increase has been attributed to the increase of fracture toughness (or fracture energy) with grain size.[3,4] Fracture toughness, however, ought to be described by means of toughness as a function of crack length (R–curve), with the toughness at instability, as determined in a fracture test, being of particular interest. Steinbrech stated, that for strength considerations in alumina, the starting value of the R–curve — certainly more than the plateau value — is of special interest.[13,16] Therefore, most of the techniques to measure fracture toughness data are of little significance for strength issues. The starting value of the R–curve could be defined as the crack initiation toughness[13,16–18] as intrinsic,[19] or as crack tip toughness.[20] The term initiation toughness can be misleading, since it can be taken as a measure for a stress magnification before a notch or pore to initiate a crack rather than the stress intensity at the tip of an already existing crack required to define crack equilibrium. Experimental determination of the crack tip toughness is

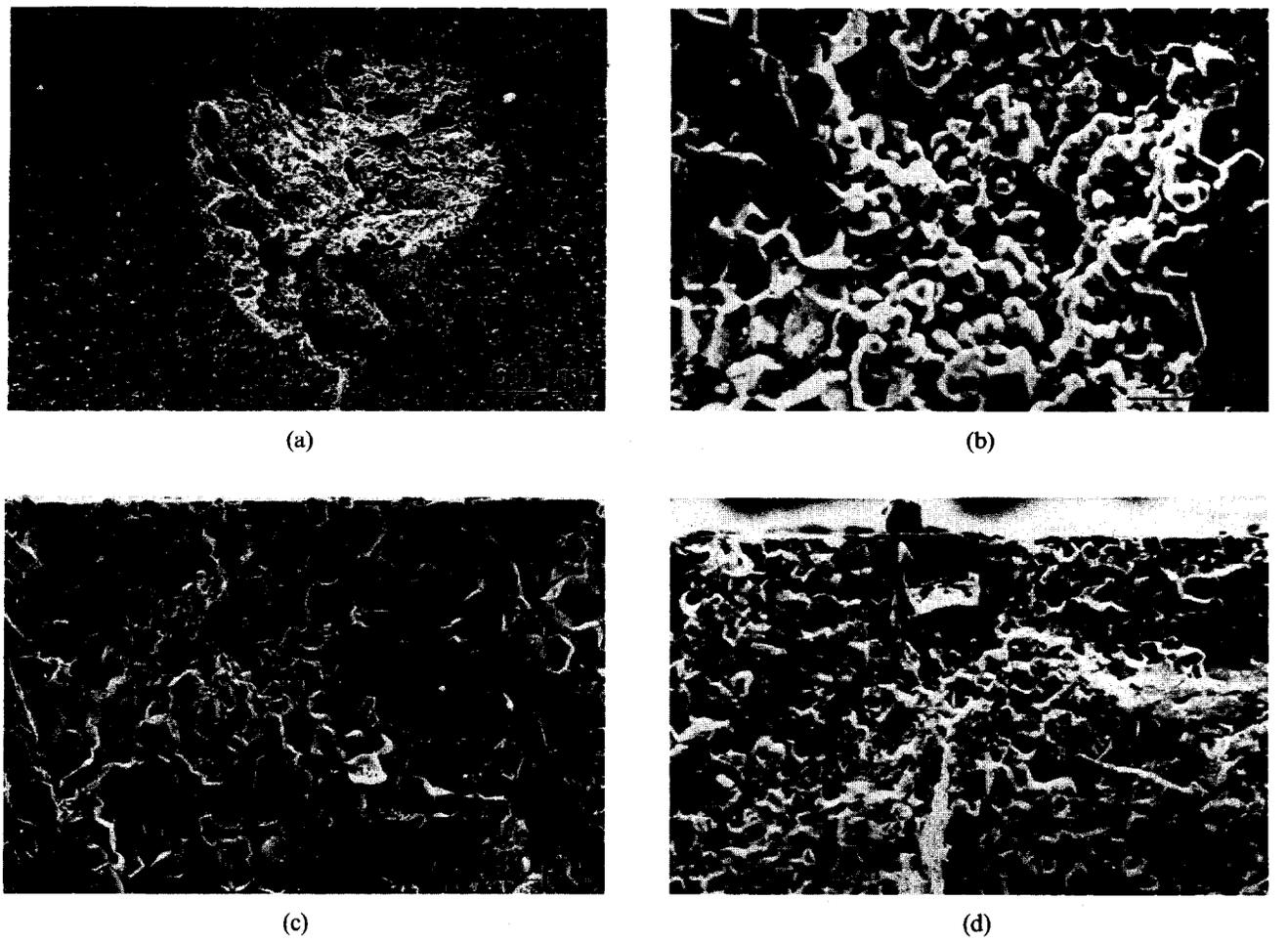


Fig. 4. Fracture surfaces of samples with different grain sizes; (a) G = 1·7 μm, σ = 461 MPa; (b) G = 11 μm, σ = 414 MPa; (c) G = 10·5 μm, σ = 340 MPa; (d) G = 11 μm, σ = 224 MPa; (a)–(c) Volume defects; (d) surface defects.

afforded by measuring the crack opening displacement (COD) near the crack tip.[20–22] This method has been applied to a hot pressed alumina of grain size 11 μm,[21] and a whisker — reinforced alumina.[22] Recently, the dependence of crack tip toughness on grain size in alumina has been investigated[20] and yielded no functional dependence, but an average crack tip toughness, K_0 = 2·3 MPa m$^{1/2}$ for all grain sizes investigated. The concept of a single valued toughness alone is therefore not sufficient to explain the observed dependence of strength on grain size.

Our alumina fractography points to pores (large voids) in the volume as major failure origin, with some occurrence of surface flaws also. Fractography also reveals that the pore size is independent of the grain size. This result can be predicted in applying the knowledge of the current sintering literature,[23] as long as no external pressure is applied and the sintering pressure is thereby only related to grain and pore curvature. In polycrystalline bodies pores should not cause fracture directly, because the stress concentration due to a pore is usually not sufficient to cause specimen fracture from the void surface. Evans and Davidge[24] as well as other authors[25,26] suggested that the pore of radius R is accompanied by a circumferential crack of length L (Fig. 5). The distance $R + L$ is taken as the initial crack length c_0, the crack length after a certain degree of stable crack growth is taken as c. Baratta,[27,28] Green[29]

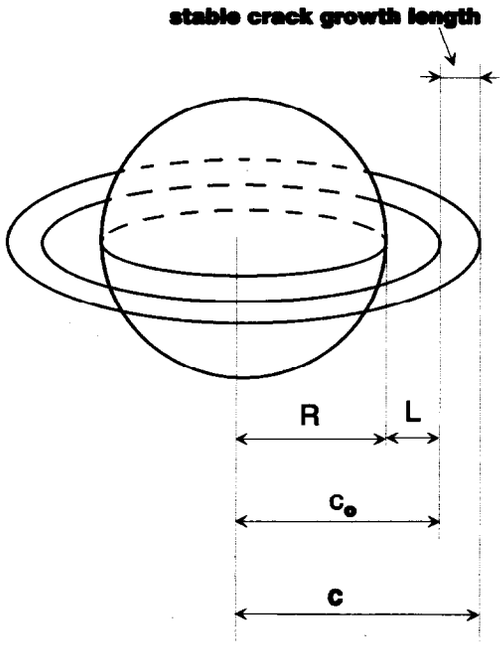


Fig. 5. Pore (void) with a circumferential crack (geometrical parameters).

and Fett[30] modelled this crack configuration and presented solutions for the normalized stress intensity factor in dependence of the ratio of L/R. On this basis it is possible to explain the grain size dependence of fracture strength assuming a pore with a circumferential crack as failure origin. For an evaluation it is assumed that the circumferential crack is proportional to the average grain size, whereas the pore sizes are constant. Equation 3 can then be used to calculate the grain size dependence of strength:

$$K_0 = \sigma \cdot \sqrt{\pi L} f(\frac{L}{R}) \quad (3)$$

The circumferential crack length is discussed in the literature to be a few grains in extent (one to three times the grain size) and perhaps vary with pore size.[3,10] In order to describe the grain size dependence of strength the exact length of the circumferential crack is of secondary nature. The basic assumptions are only that the circumferential crack length is proportional to the average grain size. Further to that, the toughness at instability is equal to the crack tip toughness, K_0. Since the stress in eqn 3 is the stress around the pore or surface pit, which in the first case is not exactly equal to the nominal flexure stress, a further small inaccuracy comes in. This is expected to be irrelevant since the volume flaws were close to the surface and thus differences in stress levels between pore location and surface were minute. To compute the grain size dependent strength for a defect modelled as a spherical pore/circumferential crack pair, we applied eqn 3 in the form given by Baratta[28] with the pore radii, R, then lying between 4 and 60 μm and the circumferential crack length $L = 1{\cdot}G$. To compare our results with possible surface defects as fracture origins, we also performed the equivalent calculation for the peripherally cracked hemispherical surface pit. For both computations, the tabulated values for $f(L/R)$ were utilized and an interpolation function used for the computations.

The solid lines in Fig. 2 show the result of the calculations for these two different pore sizes with the defect modelled as a volume flaw, while the dashed lines give the results for the hemispherical surface pit. The theoretical fits are very similar for both types of defects and in good agreement with the experimentally observed strength values, especially reflecting the decreasing strength with increasing grain size. Discrepancy between this model and the observed strength values can arise from the irregular shape of the pores in the alumina bodies. Uematsu *et al.*[26] measured the size and the size distribution of such irregularly shaped voids in hot isostatically pressed, translucent alumina. They found pore sizes up to 70–80 μm in radius, which is consistent with our calculations.

Although the assumption of a spherical pore or a hemispherical surface pit with a circumferential crack proportional to the average grain size is only an auxilliary means, it provides a plausible model to fit our experimental data. This simple model describes the grain size dependence of strength in both limiting cases, where the grain size is either larger or smaller than the initial flaw size, as well as the transition between the two.

Recently the model of a pore accompanied by a circumferential crack received further credibility by an acoustic emission investigation in alumina of various grain sizes.[31] It was found, that at a critical stress, which decreases with increasing grain size, acoustic events increased rapidly before failure. These events were located in the area where final failure occurred. One may therefore tentatively conclude, that an instability causing pore provides a stress magnification in the surrounding matrix sufficient to cause microcracking which occurs at a stress before final failure results. Physical reality may therefore be a pore with distributed microcracking at its perimeter, which is here modelled with a continuous circumferential crack. However, the actual existence of circumferential cracks around pores, be they complete or incomplete, still needs to be verified.

4.2 Weibull modulus as a function of grain size

The second feature concerning reliability is the variability of strength, normally expressed by the Weibull modulus m. The present study has shown that the Weibull modulus does not change in the grain size regime from 1·7 to 10·5 μm. The alumina of the largest grain size G = 11 μm) exhibited the smallest Weibull modulus with m = 5·8. Here the possibility of localized abnormal grain growth, which introduces a second flaw population, might already come into play. In the literature, systematic studies in the same material on the grain size dependence of the Weibull modulus are rare. Scholten *et al.*[32] for example investigated two different aluminas, a commercially available powder with an average grain size (after sintering) of 50 μm and a laboratory scale alumina with 10 μm. For the uniaxial, four-point bend test, the Weibull modulus for these two different materials was 21·6 and 6·7, respectively. In this context Scholten *et al.* denied the influence of the R–curve to explain the great difference in strength variability. For alumina, a Weibull modulus $m > 20$ has also been reported by Miyashita *et al.*[33] who demonstrated the influence of the compaction pressure on the Weibull modulus. They reported an increasing Weibull modulus with decreasing compaction

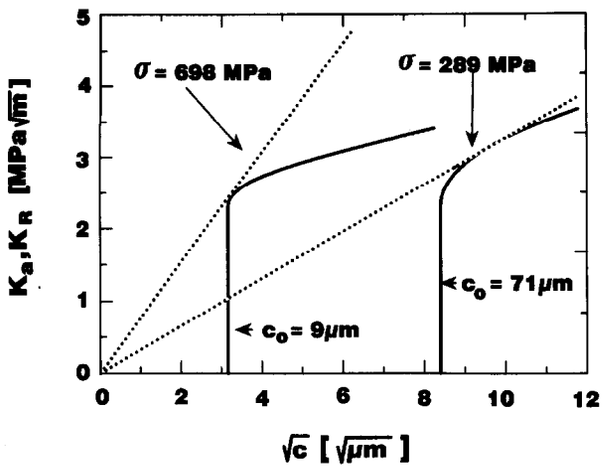


Fig. 6. *R*–curves and instability criterion for different initial flaw sizes (crack is modelled as a penny crack).

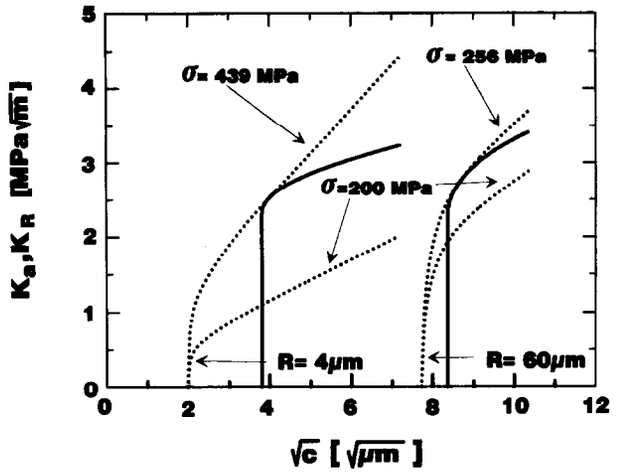


Fig. 7. *R*–curves and instability criterion for different pore sizes for the low strength material (crack configuration: pore + annular crack).

pressure, with a concurrent decrease in strength. Again, it should be emphasized that for reliability both a high strength as well as a high Weibull modulus is aspired. The Weibull moduli reported from other authors[34–36] range between 8 and 13. The important result of this study is that the disadvantage of decreasing strength with increasing grain size could not be compensated by the advantage of an increasing Weibull modulus. The higher plateau toughness of coarse grained, as compared to fine grained alumina, has no influence on the Weibull modulus. In the following section we discuss this result in greater detail.

Long crack *R*–curves of alumina ceramics have been determined by various groups.[13,16,37] In the last few years, efforts were made to measure the *R*–curves from either natural short cracks or radial indentation cracks.[14,38,39] Due to the difficulty of measuring *R*–curves of cracks originating from pores (with the notable exception of Ce–TZP composites)[40] we tried to model the *R*–curve based on the fundamental description of closure stresses. These closure stresses arise from bridging interactions and result in a bridging term R_μ which has to be added to the starting value R_0 of the *R*–curve. For our considerations we resorted to a continuum concept with smoothly varying, delocalized closure stresses (an assumption, which needs to be qualified at a later time). The total crack resistance[19] can then be expressed by eqn 4 (with $p(u)$ the crack closure stress, p as a function of half of the crack opening, u):

$$R(c) = R_0 + R_\mu = R_0 + 2\int_0^{u_b} p(u)\mathrm{d}u \qquad (4)$$

If the COD ($2u$) reaches the value $2u_b$, the closure stresses have diminished to zero and hence the *R*–curve has reached the plateau toughness.

In order to express this relationship in terms of stress intensity factors, R_0 and R_μ[19] can be transformed into K_0 and K_μ by eqns 5 and 6 (E is Young's modulus):

$$K_0 = \sqrt{R_0 \cdot E} \qquad (5)$$

$$K_\mu = \sqrt{K_0^2 + E \cdot R_\mu} - K_0 \qquad (5)$$

In the following calculation we considered the influence of closure stress on the Weibull modulus and on characteristic strength. We used two complementary approaches: Firstly, we modelled the crack as a penny-shaped crack of initial length c_0 (Fig. 6). Secondly, we applied the pore/annular crack configuration as introduced before (Fig. 7).

For mathematical simplicity we started to model the crack configuration pore with an annular crack as a penny crack. When the crack extended stably the closure stresses were only effective between c_0 and c (Fig. 5). Using the weight function of the penny crack geometry the *R*–curve ($K_R(c)$) is described by eqn 7 (where the closure stresses are taken as a function of r only):

$$K_R(c) = K_0 + \int_{c_0}^{c} p(r)\,\frac{r}{\sqrt{c^2 - r^2}}\,\mathrm{d}r \qquad (4)$$

In the very small regime of possible stable crack growth the closure stresses were taken as constant (Dugdale zone), and assumed to be equal to the peak closure stress, p_m (which occurs near the crack tip in alumina).[21]

In order to examine whether the closure stresses cause a deviation from linear behaviour in the Weibull plot we do not resort to the measured strength distributions, since some distributions deviate from exact linear behaviour due to different failure origins. For further calculations we assumed a strength distribution with the Weibull parameter m = 10 and σ_0 = 589 and 365 MPa, similar to the measured distributions with an average grain size of 1·7 and 10·5 μm, respectively,

but without any *R*–curve. Equation 8 was used to transform the strength distribution into a flaw size distribution, providing the initial crack length c_0, whereby a single valued crack tip toughness K_0 = 2·3 MPa $m^{-1/2}$ (independent of grain size) was assumed:[20]

$$K_0 = \frac{2}{\sqrt{\pi}} \cdot \sigma \cdot \sqrt{c_0} \tag{8}$$

The next step is to attach the *R*–curves to the initial crack length c_0. This is demonstrated in Fig. 6. The instability criterion, eqns 9 and 10,

$$K_a = K_R(c) \tag{9}$$

$$\frac{dK_a}{d_c} = \frac{dK_R(c)}{d_c} \tag{10}$$

was taken to calculate the crack length at instability as well as the corresponding strength. This is also shown schematically in Fig. 6.

The calculation was carried out for two peak closure stresses of p_m equal to either 40 or 120 MPa, the upper and lower bounds reported in the literature.[21,41,42] The degree of stable crack growth is found to increase with decreasing strength and increasing closure stress. The stable crack growth length and accordingly the toughness at instability increases with c_0 (Fig. 6). The computation yields a stable crack growth length of 0.5 μm for an initial crack length of 9 μm with a strength increase from 678 to 698 MPa at a K_{Ic} of 2·44 MPa $m^{1/2}$. For a specimen with a large initial flaw size, e.g. c_0 = 71 μm, σ = 243 MPa (without *R*–curve) the stable crack growth length is predicted to be 22·6 μm with instability occurring at 289 MPa at 3·15 MPa $m^{1/2}$. Therefore strength increase due to *R*–curve behaviour is more pronounced for a lower initial strength and hence an increasing

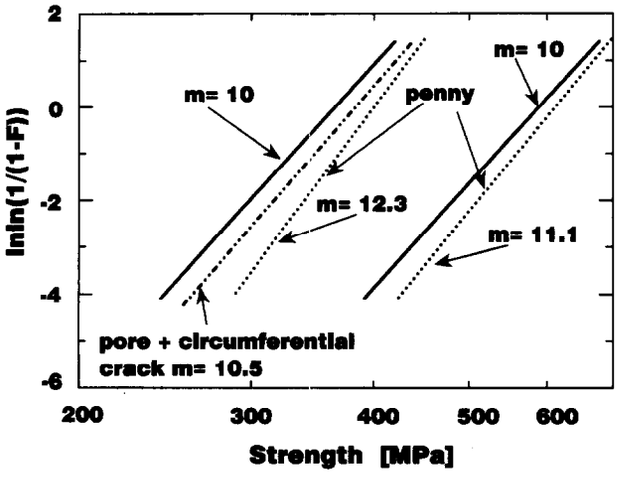


Fig. 8. Influence of constant closure stress of 120 MPa on the strength distributions of material characterized by m = 10 and σ_0 = 365 MPa and 589 MPa, respectively, assuming a penny crack geometry or a pore with an annular crack.

Weibull modulus should be the result. In Fig. 8 the influence of the closure stress of 120 MPa on Weibull modulus and characteristic strength is described. The two initial distributions are shifted to higher strength and the Weibull modulus increases from m = 10 to m = 12·3 for the low strength material and to m = 11·1 for the high strength material. Again, the effect of the closure stress is more evident at lower strength. Still, the increase of the Weibull modulus due to the closure stress of 120 MPa is relatively small. If we carry out the same calculation for a closure stress of 40 MPa the increase in σ_0 and m is negligible. For the high and the low strength material the increase of the characteristic strength is lower than 5 MPa and the Weibull modulus increases from 10 to 10·5. This calculated change would be statistically insignificant in practice for typically 20–30 test pieces. For all computations with the parameter sets used here, the closure stresses do not cause a deviation from linear behaviour in the Weibull plot.

In the calculation presented above the crack configuration was modelled as a penny crack with no bridging interactions at the initially existing crack faces. Different strength values had to be obtained by using different lengths of starting cracks, c_0. In the following section we compute the variation of strength and Weibull modulus for the crack configuration of a pore with a circumferential crack and thereby relate back to the model which could account for grain size dependent strength introduced in the earlier chapter. Again we assume strength distributions with the Weibull parameter m = 10 and σ_0 = 365 MPa (G = 10·5 μm) and σ_0 = 589 MPa (G = 1·7 μm), respectively. For the described crack configuration Barattas solution[28] (eqn (3)) for the stress intensity factor was used to evaluate the pore sizes assuming $L = G$ for the initial circumferential crack length using K_0 = 2·3 MPa $m^{1/2}$. The *R*–curves (eqn (11)) were calculated using a weight function proposed by Fett.[30] It is assumed that the *R*–curves start at $R + 1{\cdot}G$:

$$T(c) = K_0 + p_m \beta \sqrt{\frac{2}{\pi L}} \int_G^L \left(\frac{1}{\sqrt{1-\frac{r}{L}}} + 0{\cdot}6147\sqrt{1-\frac{r}{L}} + 0{\cdot}2502\sqrt{\left(1-\frac{r}{L}\right)^3} \right) dr + \frac{2p_m(1-\beta)}{\sqrt{\pi(L+R)}} \int_G^L \frac{r+R}{(L+R)^2-(r+R)^2}\, dr \tag{11}$$

with β defined by

$$\beta = \frac{1}{(1+2\cdot\frac{L}{R})^2} \tag{12}$$

The instability criterion (eqns 9 and 10) was used to calculate the degree of stable crack growth prior to failure and the corresponding strength. In Fig. 7 the R–curve and the tangency points are sketched for the low strength material for two different pore sizes. The circumferential crack length increases from $L = G = 10{\cdot}5$ μm (starting point of the R–curve) to $L = 15{\cdot}4$ μm at instability ($p_m = 120$ MPa, $R = 60$ μm) with $K_{Ic} = 2{\cdot}73$ MPa $m^{1/2}$ and an increase in strength due to crack bridging from 243 to 256 MPa. The computation for a specimen with small initial pore size ($R = 4$ μm) yields a stable crack growth regime of $1{\cdot}4$ μm and a strength increase from 420 to 439 MPa with instability occurring at 2·52 MPa $m^{1/2}$.

The influence of closure stresses of 120 MPa on the characteristic strength and the Weibull modulus of the low strength material is shown in Fig. 8. σ_0 increases from 365 to 383 MPa and the Weibull modulus from 10 to 10·5. As mentioned above the strength distribution of the high strength material remains unaffected. At a closure stress of 40 MPa the strength distributions of both materials were essentially not influenced.

In summary, the calculation for the crack configuration pore with circumferential crack yields a smaller influence of the closure stresses on the mechanical properties compared to the case when the pore is modelled as a penny crack. This trend may be appreciated if the greater stress concentration at larger pore sizes — in the pore/annular crack model — is taken into account. This results in a stronger increase of K_a with the applied stress σ at larger pore sizes. For the same externally applied stress σ (for example in Fig. 7, $\sigma = 200$ MPa) and the same annular crack length L, K_a is larger at larger pore sizes. Therefore the higher degree of stable crack growth at larger pore sizes associated with a higher crack resistance and with a stronger increase of the initial strength is compensated by a stronger increase of K_a with σ at larger pore sizes. All subleties aside, however, both models are able to reproduce the experimental findings very well and only predict small differences in the increase in Weibull modulus with incorporated R–curve.

The calculations have shown that even at relatively high closure stresses (120 MPa), only a small increase of the Weibull modulus could be achieved, which is consistent with our experimental data. Three qualifications in using our modelling approach should be considered at this point.

Firstly, in assuming a Dugdale zone, we did not specify u_b in eqn 4. Since the instability criteria was met in all computations at very low toughness values ($K_{Ic} < 3{\cdot}2$ MPa $m^{1/2}$), well below commonly reported toughness values for alumina, the plateau value of the R–curve as well as the exact position of the last active bridge are irrelevant in strength considerations of alumina ceramics. Specifically, it is evident, that the long crack toughness values measured in crack bridging materials are not pertinent for strength issues (except for very short, steep R–curves).

Secondly, the computations are strictly relevant only for a continuum with delocalized closure stresses. This condition is not met for grain bridging materials with grain sizes at the order or even larger than our calculated stable crack growth lengths. Since the distribution of bridges in the matrix is unknown, an inclusion of grain-localized stresses in the model, however, would be rather arbitrary. The current model, therefore, serves as the best possible indication for the actual occurring stable crack growth as well as the K_{Ic} values applicable for fracture testing.

Thirdly, the second model of a pore with a circumferential crack hinges critically on the very existence of microcracking around a pore. Indications for the physical reality of this model, however, have been provided recently.[31] This concept can also be understood as a strategy to design high strength materials. These may be manufactured, if microcracking around failure causing pores can be suppressed.

Our results point to the relevance of the ratio of closure stress to failure stress. In material development efforts, both material characteristics need to be appreciated. If microstructural design initially focuses on preparing a relatively weak, but flaw tolerant material, then an increase of strength will not necessarily yield a strong, flaw tolerant material, since the ratio of closure stress to fracture strength decreases. On the other hand, if the effect of closure stress on strength and strength variability is to be considered and even utilized as a measurement tool to compute the closure stresses, a low strength material ought to be employed. This approach was indeed taken by Fett and Munz,[42] who demonstrated a deviation from linear behaviour in the Weibull plot for a low strength, coarse grained alumina. This deviation is only relevant at low strength (about 200 MPa) and is attributed to the R–curve behaviour. This observation supports the result of the present investigation that the closure stresses in alumina do only affect the variability of strength at a very low strength level.

The question posed in the introduction can now be answered: for alumina ceramics a small grain size and therefore high average strength has to be favoured compared to a large grain sized alumina with low average strength, albeit long crack R–curve behaviour. This result is independent of the specific flaw type and specifically holds both

for penny shaped cracks as well as for pores with circumferential cracks. Only in applications where excessive damage may occur[6] and low strengths are tolerable, a large grain sized alumina ought to be chosen as a load bearing material.

Conclusions

(1) The strength in alumina increases with decreasing average grain size from 564 MPa at 1·7 μm to 320 MPa at 11 μm.
(2) This grain size dependence of strength can quantitatively be described by models based on either a spherical pore/circumferential crack combination or a hemispherical surface pit/peripheral crack combination.
(3) Weibull modulus m showed no dependence on grain size.
(4) A simple Dugdale zone model attached to a distribution of flaw sizes can explain the invariability of the Weibull modulus on grain size and R–curve behaviour and points to the importance of the peak closure stress, which, according to literature values appears too low to affect the Weibull modulus of alumina significantly.

Acknowledgements

The authors wish to thank Dr T. Fett for supplying his results concerning the weight function of a void with an annular crack prior to publication, Prof. R. Bordia is thanked for helpful discussions. The reviewers comments are also appreciated for being very helpful.

References

1. Musicant, S., *What every engineer should know about ceramics*. Marcel Dekker, Inc. 1991.
2. Rice, R. W., Strength grain size effects in ceramics. *Proc. Brit. Ceram. Soc.*, **20** (1972) 205–7.
3. Rice, R. W., Microstructure dependence of mechanical behaviour. In *Treatise on materials science and technology.*, Vol. 11, ed. R. K. MacCrone. 1977, pp. 199–381.
4. Dörre, E. & Hübner, H., *Alumina Processing, Properties and applications*. Springer Verlag, New York, 1993.
5. Carniglia, S. C., Reexamination of experimental strength-vs-grain-size data for ceramics. *J. Am. Ceram. Soc.*, **55** (1972) 243–9.
6. Chantikul, P., Bennison, S. J. & Lawn, B. R., Role of grain size in the strength and R–curve properties of alumina. *J. Am. Ceram. Soc.*, **73** (1990) 2419–27.
7. Alford, N. M., Kendall, K., Clegg, W. J. & Birchall, J. D., Strength/microstructure relation in Al_2O_3 and TiO_2. *Advanced Ceramic Materials*, **3**, (1988) 113–7.
8. Weibull, W., A statistical distribution function of wide applicability. *J. Appl. Mech.*, **18** (1951) 293–7.
9. Cook, R. F. & Clarke, D. R., Fracture stability, R–curves and strength variability. *Acta Metall.*, **36** (1988) 555–62.
10. Shetty, D. K. & Wang, Jr, S., Crack stability and strength distribution of ceramics that exhibit rising crack-growth-resistance (R–curve) behavior. *J. Am. Ceram. Soc.*, **72** (1989) 1158–62.
11. Bennison, S. J. & Lawn, B. R., Flaw tolerance in ceramics with rising crack resistance characteristics. *J. Mat. Sci.*, **24** (1989) 3169–75.
12. Tandon, R., Green, D. J. & Cook, R. F., Strength variability in brittle materials with stabilizing and destabilizing resistance fields. *Acta Metall. Mater.*, **41** (1993) 399–408.
13. Steinbrech, R. W., Reichl, A. & Schaarwächter, W., R–curve behavior of long cracks in alumina. *J. Am. Ceram. Soc.*, **73** (1990) 2009–15.
14. Braun, L. M., Bennison, S. J. & Lawn B. R., Objective evaluation of short-crack toughness curves using indentation flaws: case study on alumina-based ceramics. *J. Am. Ceram. Soc.*, **75** (1992) 3049–57.
15. Seidel, J., Claussen, N. & Rödel, J., Reliability of alumina: II. Effect of processing technique and testing procedure. To be submitted to *J. Eur. Ceram. Soc.*
16. Steinbrech, R., Knehans, R. & Schaarwächter, W., Increase of crack resistance during slow crack growth in Al_2O_3 bend specimens. *J. Mat. Sci.*, **18** (1983) 265–70.
17. Mussler, B., Swain, M. V. & Claussen, N., Dependence of fracture toughness of alumina on grain size and test technique. *J. Am. Ceram. Soc.*, **65** (1982) 566–72.
18. Claussen, N., Mussler, B. & Swain, M. V., Grain-size dependence of fracture energy in ceramics. *J. Am. Ceram. Soc.*, **65** (1982) C14–6.
19. Lawn, B., *Fracture of brittle solids*. Cambridge University Press, 1993.
20. Seidel, J. & Rödel, J., Measurement of crack tip toughness in alumina as a function of grain size. To be published in *J. Am. Ceram. Soc.*
21. Rödel, J., Kelly, J. F. & Lawn, B. R., In-situ measurements of bridged crack interfaces in the scanning electron microscope. *J. Am. Ceram. Soc.*, **73** (1990) 3313–8.
22. Rödel, J., Fuller, Jr, E. & Lawn, B. R. In-situ observations of toughening processes in alumina reinforced with silicon carbide whiskers. *J. Am. Ceram. Soc.*, **74** (1991) 3154–7.
23. Slamovich, E. B. & Lange, F. F., Densification of large pores: II. Driving potentials and kinetics. *J. Am. Ceram. Soc.*, **76** (1993) 1584–90.
24. Evans, A. G. & Davidge, R. W., The strength and fracture of stochiometric polycristalline UO_2. *J. Nucl. Mater.*, **5** (1970) 314–25.
25. Rice, R. W., Pores as fracture origins in ceramics. *J. Mat. Sci.*, **19** (1984) 895–914.
26. Uematsu, K., Sekiguchi, M., Kim, J-Y., Saito, K., Mutoh, Y. Inoue, M., Fugino, Y., & Miyamoto, A., Effect of processing conditions on the characteristics of pores in hot isostatically pressed alumina, *J. Mat. Sci.*, **28** (1993) 1788–1992.
27. Baratta, F. I., Stress intensity factor estimates for a peripherally cracked spherical void and a hemispherical surface pit., *J. Am. Ceram. Soc.*, **61** (1978) 490–3.
28. Baratta, F. I., Refinement of stress intensity factor estimates for a peripherally cracked spherical void and a hemispherical surface pit., *J. Am. Ceram. Soc.*, **64** (1981) C3–4.
29. Green, D. J., Stress intensity factor estimates for annular cracks at spherical voids. *J. Am. Ceram. Soc.*, **63**, (1980) 342–4.
30. Fett, T., Stress intensity factors and weight function for a void with an annular crack. To be submitted to *Int. J. of Fract.*
31. Wakayama, S. & Kawahara, M., Evaluation of critical stress of microcracking in alumina. In *Austceram, Proc. of the Int. Conf. on Ceramics*, ed. M. J. Bannister, 1992, pp. 938–43.
32. Miyashita, M., Kim, J.-Y., Kata, Z., Uchida, N. & Uematsu, K., Effect of compaction pressure on the internal structure of sintered alumina. *J. Ceram. Soc. Jap. Int. Ed.*, **100** (1992) 1337–40.

33. Scholten, H., Dortmans, L., De With, G., Weakest-link failure prediction for ceramics: design and analysis of uniaxial and biaxial bend tests II. *J. Eur. Ceram. Soc.*, **10** (1992) 33–40.
34. Quinn, G., Flexure strength of advanced structural ceramics: A Round Robin, *J. Am. Ceram. Soc.*, **73** (1990) 2374–84.
35. Steen, M., Sinnema, S. & Bressers, J., Statistical analysis of bend strength data according to different evaluation methods. *J. Eur. Ceram, Soc.*, **9** (1992) 437–45.
36. Mosser, B. D., Reed, J. S. & Varner, J. R., Strength and Weibull modulus of sintered compacts of spray dried granules. *Am. Ceram. Soc. Bul.*, **71** (1992) 105–9.
37. Fett, T. & Munz, D., Evaluation of *R*-curve effects in ceramics. *J. Mat. Sci.*, **28** (1993) 742–52.
38. Steinbrech, R. W. & Schmenkel, O., Crack-Resistance Curves of Surface Cracks in Alumina. *J. Am. Ceram. Soc.*, **71** (1988) C271–3.
39. Krause, Jr, R. F., Rising fracture toughness from the bending strength of indented alumina beams. *J. Am. Ceram. Soc.*, **71** (1988) 383–43.
40. Ramachandran, N., Chao, L.-Y. & Shetty, D. K., *R*-curve behavior and flaw insensitivity of Ce–TZP/Al_2O_3 composite. *J. Am. Ceram. Soc.* **76** (1993) 961–8.
41. Fett, T. & Munz, D., Influence of bridging interactions on the lifetime behaviour of coarse-grained Al_2O_3. *J. Eur. Ceram. Soc.*, **12** (1993) 131–8.
42. Fett, T. & Munz, D., Estimation of bridging interactions for natural cracks from bending strength of coarse-grained Al_2O_3. Submitted to *J. Am. Ceram. Soc.*

Journal of the European Ceramic Society **15** (1995) 405–413
Elsevier Science Limited
Printed in Great Britain.
0955-2219/95/$9.50

Vickers and Knoop Indentation Behaviour of Cubic and Partially Stabilized Zirconia Crystals

G. A. Gogotsi, S. N. Dub, E. E. Lomonova & B. I. Ozersky

Institute for Problems of Strength of the Academy of Sciences of Ukraine, Timiryazevskaya str. 2, Kiev 252014, Ukraine

(Received 30 December 1993; revised version received 27 June 1994; accepted 22 September 1994)

Abstract

Hardness and fracture toughness of cubic zirconia crystals (CZC) doped with yttria and partially stabilized zirconia crystals (PSZC) doped with yttria, terbia and ceria were studied at indentation loads of 0·1–300 N. MOR and K_{Ic} *of these materials were measured under bending conditions. A maximum hardness value of* H_K *= 21·2 GPa was obtained for CZC at a 0·1 N indentation load when a longer diagonal of the Knoop indenter being directed along <110>. Starting from a 2 N load, PSZC exhibited lateral cracks and phase transition zones. Radial cracks in Vickers indentation tests of Y–Tb–PSZC and Y–Ce–PSZC appeared above 40 N and 50 N respectively. Such cracks in Knoop indentation tests were observed above 300 N. Orientation anisotropy of lateral cracks was noticed in all crystals, radial ones were revealed only in CZC. After grinding off the specimen surfaces, lateral cracks were found to be present under the impressions. The calculations of fracture toughness* K_{Ic}^{v} *using the equation proposed by the authors gave a value corresponding to those materials determined on bending.*

1 Introduction

The fact that zirconia single crystals can be used for medical[1,2] and other cutting instruments stimulates studies on their surface fracture toughness (Fig. 1). The results obtained also appear useful[3] for understanding mechanical behaviour of the materials of such a group. In investigations, both Vickers[4,7] and Knoop indenters[5,8,9] were used. Cubic (CZC), i.e. completely stabilized[5,6,10,11] and partially stabilized crystals (PSZC)[4,9,14] doped with yttria (Y–PSZC) attracted specific interest. The crystals doped with calcia,[4] magnesia,[1,4,8] terbia[9,12] and ytterbia,[2,14] i.e. containing additives with an ionic radius smaller or larger than that of zirconia were also studied. PSZC of lower fracture toughness were tested at indentation loads which did not usually exceed 10 N[3,15] and crystals of higher fracture toughness were investigated at the same loads[1,4,11,16] that are usually for advanced ceramics. The indentation was performed on the (001),[3,5,11] (011)[3,8] or on arbitrarily oriented planes.[2,9,14,17] The comparison of data[2,11] shows no essential differences in K_{Ic} values for Y–PSZC obtained on different indentation planes. The equations used[11,18] give critical stress intensity factors K_{Ic}^{v} obtained in indentation tests which agree with K_{Ic} values determined in SENB bending. Such coincidences were not usually observed in the rest of the cases.

The Vickers indentation caused considerable anisotropy of hardness and fracture toughness for CZC[11] and certain anisotropy of fracture toughness for PSZC.[3] At room temperature, Y–PSZC exhibited[16] considerable influence of the Vickers indenter orientation on phase transition processes on the (001) plane. Similar crystals[15] also revealed phase transition zones around such impression above 200°C. It was found that at room temperature it occured only within the plastic zone of impression. The Knoop indenter caused considerable anisotropy both of hardness and of fracture processes for Y–CZC[5] and Y–PSZC.[2,8]

Y–CZC are the most extensively studied materials. The indentation behaviour of Y–PSZ (though being more interesting for structural applications) is not clear enough and there is no information available which is necessary for their positive practical application. It should be noted that all the data published on PSZC can be divided into two groups: those which was mainly obtained for stronger crystals of Ceros Corp.[3,6,15] and those obtained for tougher crystals produced in the former USSR.[1,2,9,14] The investigations of the first group pursued physical goals, the studies on the latter were aimed at the elucidation of possible practical fields of application of such crystals. In the present work we used a wider range of loads and focused our major attention on PSZC.

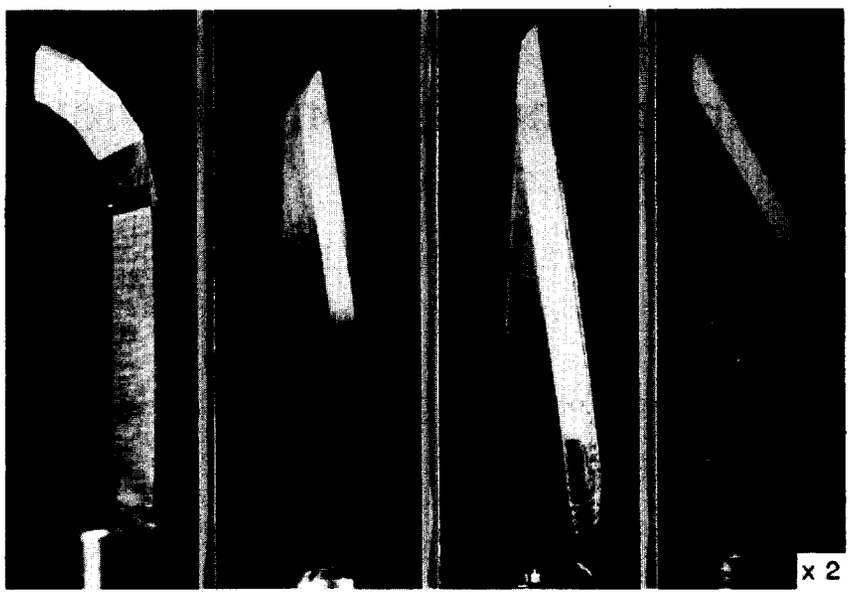


Fig. 1. Experimental samples of surgical knives with blade sharpening radii equal to 0·2–0·5 μm, made of the zirconia crystals studied. They were tested in clinics of Kiev, Moscow and Sydney (×2).

2 Materials and Methods

The crystals under study were grown by a skull melting technique[19] from zirconia powders of a purity over 99·9% (the purity of other components was higher than 99·99%). A K-1 material (Y–CZC) (Table 1) contained 10 mol% Y_2O_3,[20] a K-2 material[12] contained 3·3 mol% Y_2O_3 and less than 0·3 mol% terbia and in a K-3 material[21] ceria was added instead of terbia. After pounding the pieces of specimens in a corundum mortar, they were investigated by X-ray phase analysis. It was established that the K-1 powder consisted of a 100% zirconia cubic phase, the K-2 powder contained 30% monoclinic and 70% tetragonal phases, the K-3 material was 50% monoclinic and 50% tetragonal and cubic.

Test specimens (3·5 × 5 × 45 mm^3 bars) were cut, ground and polished with a diamond instrument. The orientation of specimens was determined by Laue back-reflection which revealed that all their surfaces coincided with the (001) planes. Thus, on mechanical tests, a fracture crack propagated in the (001) plane and tensile stresses and impression also appeared in the same plane.

MOR on four-point bending, static moduli of elasticity and critical stress intensity factors K_{1c} were determined by procedures[22] evaluated earlier in numerous tests of different advanced ceramics and single crystals. For K_{1c} measurements, the specimens were notched for a half-thickness depth and placed with their 3 mm wide surface on supports with a 20 mm span between loading rollers (for MOR measurements the loading surface was 5 mm wide).

The Knoop indentation tests at 0·1–10 N loads were performed in an MXT-70 microhardness meter (Matsuzawa, Japan). For 50–300 N loads a Ceramtest device of our production was used. The hardness was calculated by $H_k = 14{\cdot}23\ P/o^2$, where P is the load on the indenter and d is the length of a larger diagonal of the Knoop impression.

The H/E relationship determined according to the concepts of Ref. 23 was calculated by the equation:

$$H/E = \frac{0{\cdot}14 - b/d}{0{\cdot}45}$$

where b is the length of a shorter diagonal of the Knoop indenter.

The Vickers indentation at 0·1–10 N loads was tested in the same microhardness meter. For high loads, (50–300 N), a TP-2 Vickers hardness meter and Ceramtest device were used.

The values of H_V were calculated by

$$H_v = 0{\cdot}4636\ P/a^2$$

where a is the Vickers impression diagonal half-length.

To calculate critical stress intensity factors K_{1c}^V the following equations were used

$$K_{1c} = 0{\cdot}016\ (E/H)^{0{\cdot}5} P/C^{1{\cdot}5} \quad (1)^{24}$$

$$K_{1c} = 0{\cdot}018\ H\ a^{0{\cdot}5}\ (E/H)^{0{\cdot}4}/C/a - 1)^{0{\cdot}5} \quad (2)^{11}$$

Table 1. Average mechanical characteristics of crystals on fracture in the <001> direction

Material	*Static modulus of elasticity*	*MOR, MPa*	*K_{1c}, Pa $m^{1/2}$ (on bending)*
K-1	327	224	2·01 (1·41)[a]
K-2	350	—	9·96
K-3	369	1250	11·43

[a]Obtained on the specimen with a sharp crack.

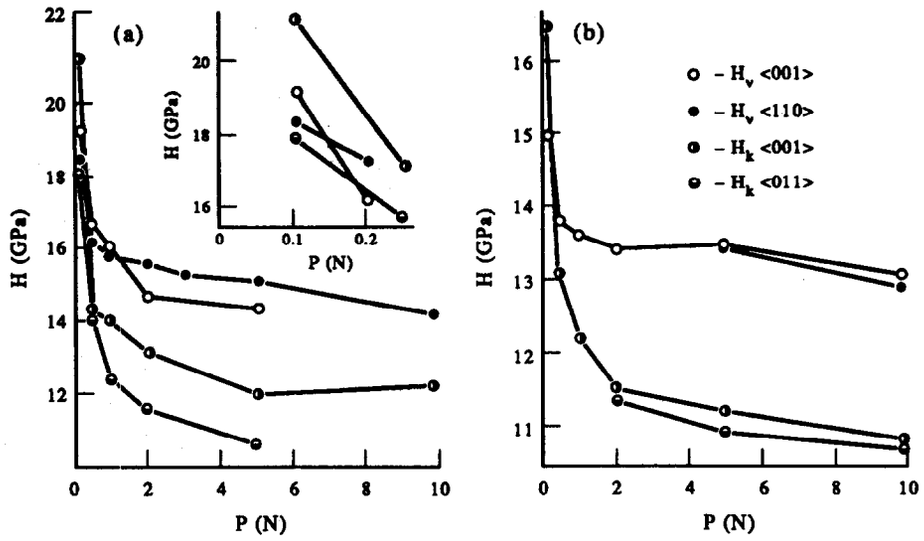


Fig. 2. Microhardness H of K-1 crystals (a) and K-3 crystals (b) as a function of indentation load and indenter orientation (crystallographic directions of the Vickers indenter diagonal (index V) and larger diagonal of the Knoop indenter (index K).

Table 2. Hardness (GPa) at a 4·9 N load

Material	*Interdenter diagonal direction*	
	<001>	*<011>*
K-1	14·4 / 12·0	15·1 / 10·7
K-2	13·6 / 11·4	13·6 / 11·1
K-3	13·6 / 11·2	13·6 / 10·9

The left hand value is the Vickers hardness, the right hand value is the Knoop hardness.

$$K_c^v = 0{\cdot}0424\ (PE/a)^{0{\cdot}5}/(C/a)^{1{\cdot}57} \qquad (3)^{25}$$

Indented specimen surfaces were studied using an NU-2E optical microscope (Carl Zeiss Jena, Germany).

3 Results

Microhardness values for K-1 cubic and K-3 partially stabilized crystals, as a function of applied loads at the orientation of indenter diagonals in the <001> and <110> directions, on the (001) plane for the loads up to 10 N, are shown in Fig. 2. (For K-2 crystals the picture was about the same.) It should be noted that partially stabilized crystals (as opposed to cubic ones) do not practically exhibit any anisotropy of microhardness on the (001) plane for both indenters (Table 2). Vickers impressions on K-1 crystals in the <001> direction of indenter diagonals were almost completely fractured at loads above 5 N; in the <001> direction this fracture occurred at loads above 10 N. (For the Knoop indenter the picture was quite the opposite.)

In Vickers indentation tests, lateral cracks appeared with the indenter diagonals in the <001> direction (Fig. 3(a)) and zones (probably pressure-induced phase transformation[16] of tetragonal phase to monoclinic symmetry) arose if they were in the <110> direction (Fig. 3(b)). In Knoop indentation tests, similar phase transition zones were revealed microscopically in phase contrast with

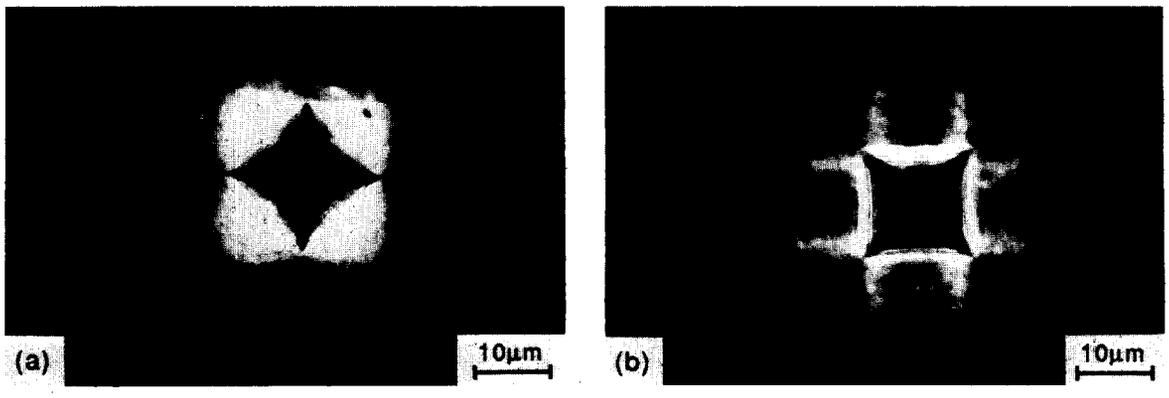


Fig. 3. Vickers impressions on the (001) plane of a K-3 crystal at a 10 N load: the diagonal coincides with the <100> direction (a) and with the <110> direction (b). Illumination: phase contrast.

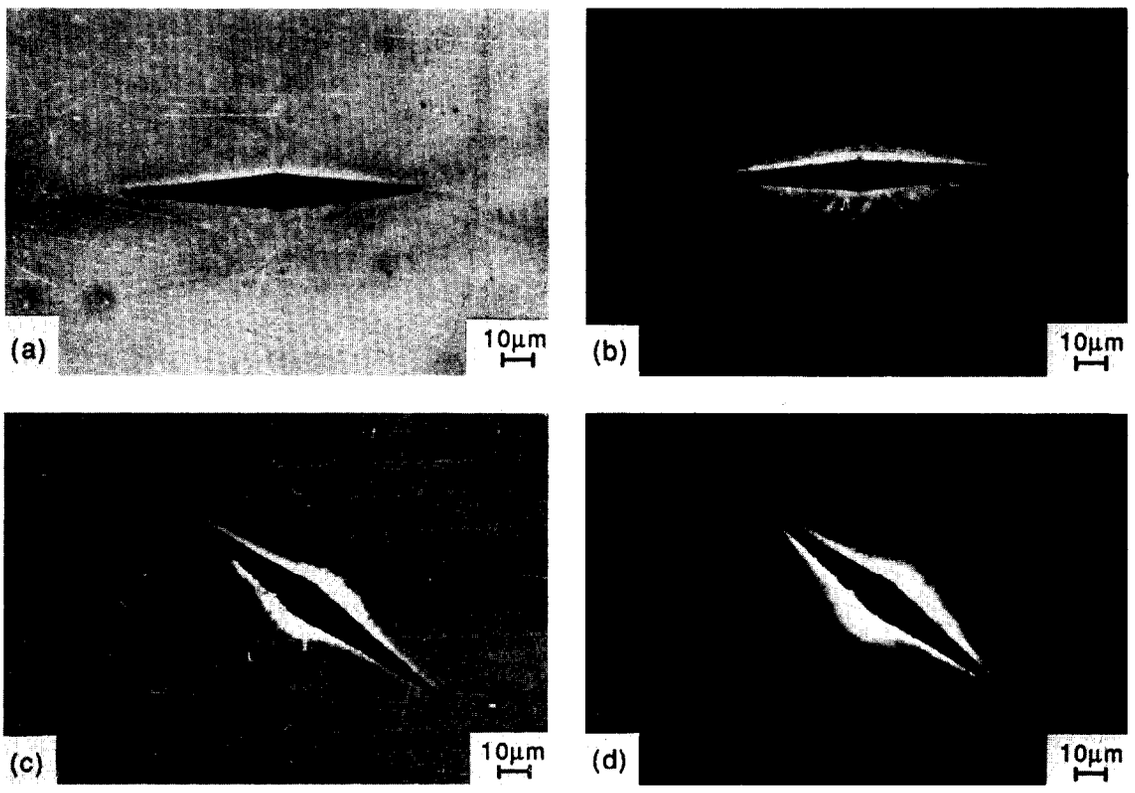


Fig. 4. Knoop impressions on the (001) plane at a 10 N load with a larger diagonal coincides with <001> (a,b) and with <110> (c,d). Illumination: reflected light (a,c), phase contrast (b,c).

the <001> direction of a larger diagonal (Fig. 4(a,b)). When this diagonal was in the <110> direction (Fig. 4(c)), lateral cracks appeared around the impression (more details in Ref. 26).

The results of studying the effect of elastic recovery of Knoop impressions are summarized in Table 3. They demonstrate that the influence of crystal anisotropy on H/E values appeared to be quite noticeable for all the cases.

For the crystals under study, the relationship (up to 10 N loads) between the Vickers impression diagonal half-length and indentation loads is described by the equations:

$$a = 5{\cdot}4\ P^{0{\cdot}52} \quad \text{for K-1}$$
$$a = 5{\cdot}83\ P^{0{\cdot}51} \quad \text{for K-2}$$
$$f = 5{\cdot}81\ P^{0{\cdot}51} \quad \text{for K-3}$$

The Knoop indenter diagonal lengths are described by the equations:

$$d = 31{\cdot}12\ P^{0{\cdot}56} \quad \text{for K-1}$$
$$d = 33{\cdot}22\ P^{0{\cdot}54} \quad \text{for K-2}$$
$$d = 33{\cdot}46\ P^{0{\cdot}55} \quad \text{for K-3}$$

Only PSZC were investigated at higher indentation loads. The results of diagonal and crack measurements and H_V and K_{1c} calculations on the (001) plane, with the <001> direction of indenter

Table 3. Results of investigation of the relation H/E

Material	*Load, N*	*Direction of the larger diagonal of the Knoop indenter*									
		<001>					*<011>*				
		d	*b*	*d/b*	H_K	*H/E*	*d*	*b*	*d/b*	H_K	*H/E*
K-1	1	31·6	3·5	9·03	14·0	14·1	33·6	3·7	9·08	12·4	14·6
	2	46·0	5·0	9·20	13·2	14·0	49·0	5·7	8·97	11·6	18·2
	5	76·2	8·3	9·18	12·0	14·0	80·9	9·4	8·61	10·7	18·1
	10	108·6	12·1	8·96	11·8	15·2	—	—	—	—	—
K-2	1	33·8	3·1	10·90	12·2	9·1	—	—	—	—	—
	2	49·0	5·0	9·80	11·6	11·6	49·5	5·9	8·39	11·4	20·6
	5	78·1	8·2	9·53	11·4	12·5	79·2	9·6	8·25	11·1	22·7
	10	111·7	11·8	9·47	11·2	12·7	113·6	13·9	8·17	10·8	24·2
K-3	1	33·8	3·5	9·66	12·2	12·0	—	—	—	—	—
	2	49·2	5·0	9·84	11·5	11·5	49·4	6·0	8·23	11·4	23·3
	5	79·0	8·6	9·19	11·2	14·0	80·0	10·0	8·00	10·9	28·3
	10	113·9	13·0	8·76	10·8	16·8	114·3	14·4	7·93	10·7	30·0

Table 4. Results of hardness and fracture toughness tests on the (001) plane

Material	*Load, N*	*Half-diagonal length a, μm*	*Crack length c, μm*	*Vickers hardness, GPa*	*Critical stress intensity factor K^v_{Ic}, MPa m calculated by*		
					1	*2*	*3*
	49·1	43·1	77·5	12·2	6·3	6·3	10·9
	98·1	61·1	126·4	12·2	6·0	6·5	10·4
	147·2	76·1	170·8	11·8	5·9	6·6	10·0
K-2	196·2	86·6	202·8	12·1	6·0	6·8	10·1
	245·3	97·0	232·0	12·1	6·1	7·1	10·4
	294·3	107·4	265·9	11·8	6·0	7·2	10·2
	49·1	43·3	67·1	12·1	7·8	7·6	13·7
	98·1	61·5	112·6	12·0	7·2	7·3	12·5
	147·2	75·7	124·2	11·9	9·4	9·2	16·4
K-3	196·2	86·3	180·6	12·2	7·1	7·6	12·1
	245·3	96·4	209·1	12·2	7·1	7·8	12·1
	294·3	106·6	249·9	12·0	6·6	7·5	11·2

diagonals are summarized in Table 4. These data complement our information published earlier (Table 5). The discrepancy between our data and those of other authors observed in this Table may be connected with some distinctions between the technologies of the growth of crystals and raw materials for them.

The radial cracks around Vickers impressions usually aligned with their diagonals, however, in several cases the picture was similar to that shown in Fig. 5.

The cracks around the Knoop impression were mainly lateral up to 300 N loads (Fig. 6). Only single radial cracks were noticed around some of them. The same picture existed in the tests of



Fig. 5. Vickers impression on the (001) plane of a K-3 crystal at a 200 N load (diagonals coincide with the <110> direction). Illumination: phase contrast.

Table 5. Hardness data reported in the literature

Hardness, GPa		*Load, N*	*Indentor orientation*		Y_2O_3 *contains mol.%*	*Authors*
Vickers	*Knoop*		*Plain*	*Direction*		
Y-CZC						
16·1	—	5	—	—	20·0	Ingel *et al.*[4]
—	14·4	5	(100)	<100>		Hannink & Swain[8]
—	12·1	5	(100)	<110>	14,3	
15·2	—		(100)	<100>		
15·2	—			<110>		Pajares *et al.*[5]
—	14·0	2	(100)	<100>	9·4	
—	12·4	2		<110>		
15·6	—		(100)	—		
15·0	—	2-3	(111)	—	9·5	Morscher *et al.*[6]
14·5	—		(110)	—		
15·6	—	2	(100)	<110>	10·0	Dub & Gogotsi[11]
Y-PSZC						
13·6	—	5	—	—	5	Ingel *et al.*[4]
15·0	—	1	(100)	<100>	3·5	Martinez-Fernandez *et al.*[3]
15·0	—	5	(100)	<110>	3·4	Martinez-Fernandez *et al.*[15]
12·0	—	50			2·3	Saiki *et al.*[16]
13·9	—	100	—	—	3+0·3%T_2O_3	
13·4	—	100	—	—	1·5+1·5% Yb_2O_3	Gogotsi *et al.*[9]
13·1	—	100	—	—	3·0	
12·8-13·8	—	10	—	—	—	Gogotsi *et al.*[12]
12·2-13·0	—	100	—	—	3+0·3% Tb_2O_3	
13·2	—	100	—	—	3	Gogotsi & Swain[17]
13·5	—	2	(100)	<110>	3	
12·1	—	49·1	(100)	<110>	3	Dub & Gogotsi[11]

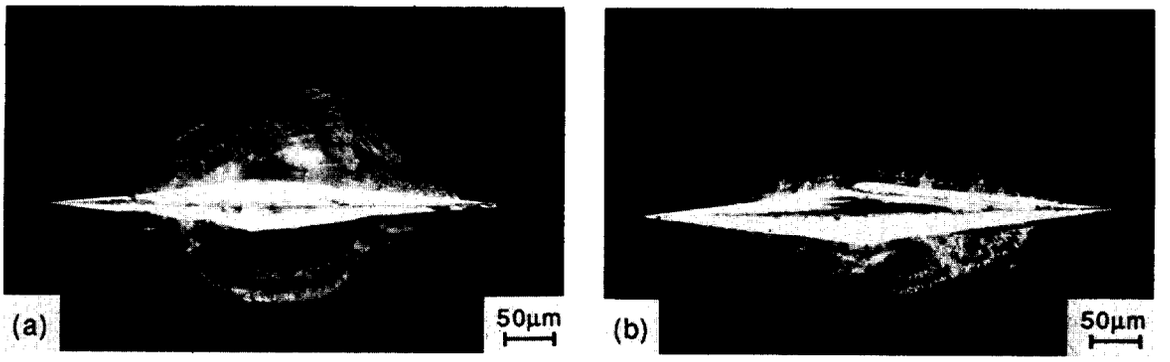


Fig. 6. Knoop impression on the (001) plane of a K-3 crystal at a 200 N load with a larger diagonal coincides with <001> (a) and with <110> (b). Illumination: polarized light.

crystals in Refs 2 and 9, when only at 400 N were pairs of radial cracks observed.

4 Discussion

4.1 Microhardness and hardness

From the analysis of data in Fig. 2, one can see that the maximum values of H_V and H_K we presented for K-1 cubic crystals are higher than those published[16] for the material of the same composition, but it is associated with the fact that in the present work, lower loads were used for indentation. At the same time in Ref. 5, for the <001> direction on (001), the authors obtained H_V = 17·6 GPa and H_K = 19 GPa at 0·5 N, while we obtained 16·5 GPa and 14·3 GPa, respectively. It should be noted that with higher loads this difference becomes less noticable (see Table 5). A descending curve of microhardness versus load is also characteristic of partially stabilized crystals, especially up to 10 N loads. At high loads, as follows from Table 4, it is practically a straight line. The values of H_V for other yttria-stabilized crystals also appear to be quite close.[9] It is interesting that for K-2 crystals the dependence is also about the same, with H_V measurements without strict crystallographic orientation of indentation planes (Table 5). These data point to the fact that H_V values without indication of the load at which they were obtained, should be taken into account with great care.

If the above information on the values of H_V and H_K does not contradict the data published earlier, the relationships for $(E/H)^{1/2}$ given in Table 3 are somewhat different from the results of earlier investigations of cubic crystals, e.g. Ref. 5, where the relationship between these values and the Knoop indenter orientation were not elucidated. As it should be expected, the hardness of crystals is dependent on the orientation of the Knoop indenter (Figs 2 and 6) and they are also characterized by the anisotropy of elastic moduli.[27] Thus the value of H/E determined from the Knoop impression is also orientationally dependent. It should be noted that, e.g. for K-1 crystals, d/D = 8·61 and H/E = 18·1 were obtained in the <001> indentation direction at 5 N loads and in Ref. 5 these values for the same load were 8·3 and 22·0 N respectively. Such differences can be connected with certain differences in the production technology of the crystals under study.

However we could not succeed in getting values of elastic moduli in Knoop indentation tests comparable with those presented in Table 1. There is an impression that the approach[21] to the determination of elasticity (or H/E) of crystals requires a better understanding.

4.2 Fracture

Since the present fracture studies of cubic crystals did not reveal any new results compared to those found earlier[11] and published by other authors, we considered it expedient to discuss and revise only the results for partially stabilized crystals. Single radial cracks in these crystals started appearing around the corners of the Vickers impression at the following loads:

When the Vickers indenter diagonal was parallel to <110>, single radial cracks were observed at 40 N in a K-2 material and at 50 N in a K-3 material.

Table 6

Material	*Indenter diagonal parallel to*	
	<100>	*<110>*
K-2	50	70
K-3	40	50

(Lateral cracks in the <100> direction were discussed earlier.) The difference in sizes on the turn of indenter on the (001) plane at a 100 N indentation load, can be seen in Fig. 7 (the picture was more

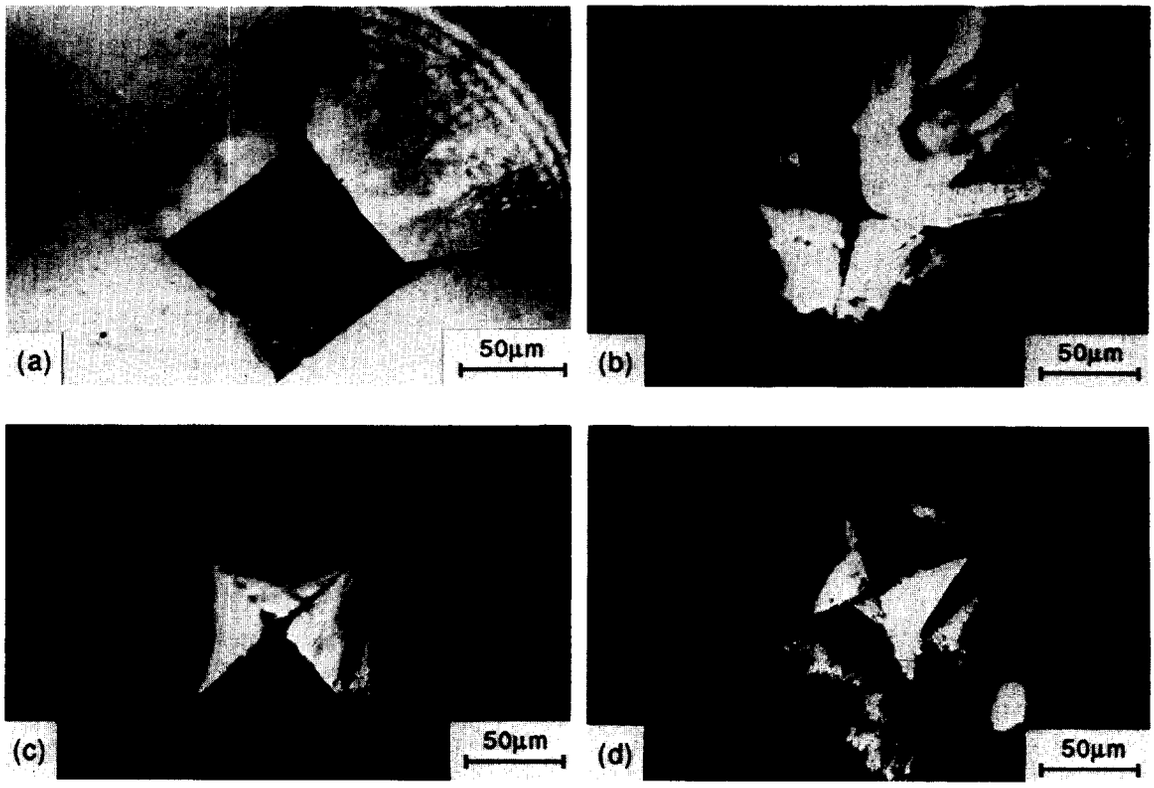


Fig. 7. Vickers impression on the (001) plane of a K-3 crystal at a 100 N load. Diagonals of the indenter correspond to the <100> direction (a,b), to the <110> direction (c) and are deflected through 30° from the <100> direction (d). Illumination: reflected light (a) and polarized light (c,d,e).

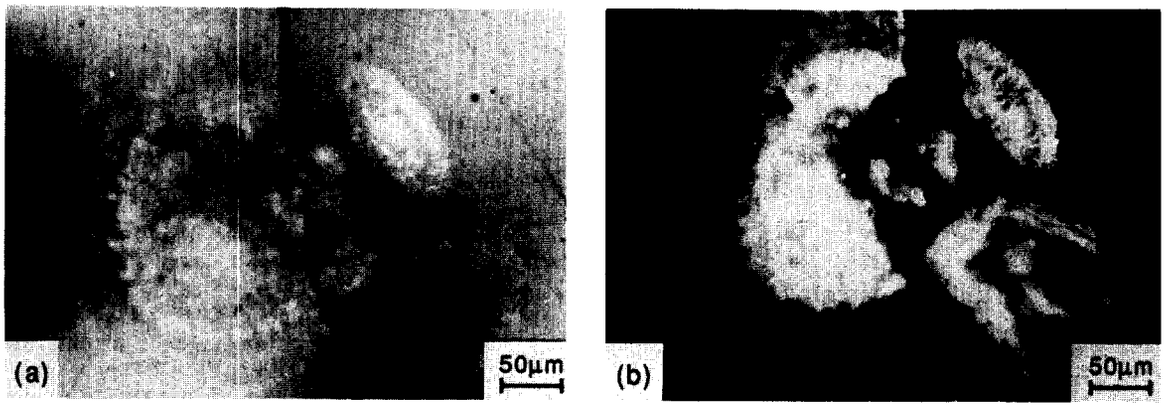


Fig. 8. Vickers impression on the (001) plane of a K-2 crystal after grinding off of its surface at a 100 N load. Illumination: reflected light (a) and polarized light (b).

or less identical for both materials). When the specimen surface is ground off in the indentation zone, lateral cracks can not only reach the surface, but also appear below the indenter impression, as is seen in Fig. 8. It should be noted that in Ref. 2 only lateral cracks reaching the surface are shown in Fig. 10. The lateral cracks in those crystals similar to those shown in Fig. 8 were not analyzed. Radial cracks usually propagating as Palmqvist cracks within the range of loads under study seemed to be branched in the subsurface layer (Fig. 9). Thus, their extent (fractured area) appeared larger than that which could be measured by optical microscope, since only one crack was revealed on the specimen surfaces under study.

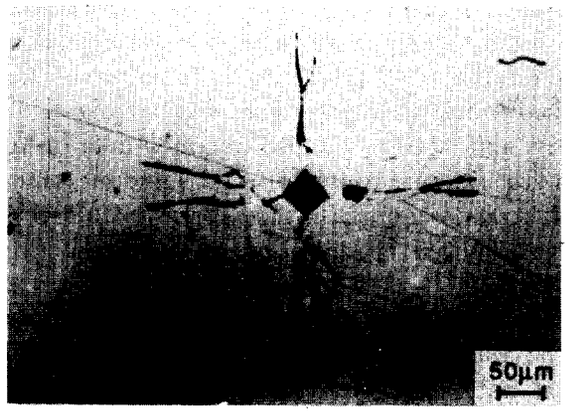


Fig. 9. Vickers impression on the (001) plane at a 200 N load with the diagonal coincides with <001> after partial grinding off of the surface. Illumination: reflected light.

This examination demonstrates that for a well-grounded judgment of the crystal capacity to resist local damages, one should take into account all the real features of their fracture on indentation.[2]

The estimates of their fracture toughness was based only on the measurement of the extent of radial cracks on the surface visible in reflected light in an optical microscope, which is usually done by investigators, (Table 4) and can probably be considered only as a first approach. However, if we take into account that any publications devoted to detailed investigations of PSZC fracture are practically non-existent, the data of the present work can be compared with the known ones only within the framework of this first approach. From Table 4 we can see that the values of K_{1c}^{v} calculated by the equation[11] are quite close to the values of K_{1c} measured on bar bending, (Table 1). If we compare the calculation results for K_{1c}^{v}[25] obtained in the case of arbitrary orientation of the indenter[2] on SC=3b surfaces with the results for Y–PSZC[11] obtained on the (100) plane with the <110> diagonal direction, (Table 4), one can see that they are very close. So we can assume that if elastic moduli of crystals are similar, the anisotropy of local fracture toughness is probably insignificant for practical purposes. The above crystals as well as the crystals in Ref. 11 exhibit higher fracture toughness than those presented, e.g. in Ref. 3 and investigated in an unannealed state. At the same time they display longer (by 20–40%) radial cracks originating on Vickers indentation than those revealed, e.g. in Ref. 9 during the studies on partially stabilised and tetragonal polycrystalline zirconia ceramics[17] doped with 3 mol.% yttria.

5 Conclusion

The investigations of cubic and partially stabilized zirconia crystals resulted in data on their hardness and fracture toughness variations during indentation on the (001) plane as a function of loads applied to the indenters, their diagonal aligned with <001> and <110>. We also obtained data on their strength, fracture toughness and static modulus of elasticity on bending (in this work we studied partially stabilized crystals doped with terbia, ceria and yttria).

It is shown that the equation proposed earlier by the authors for estimating K_{1c}^{v} from the indentation data can give values very close to those determined for K_{1c} in bending tests which cannot be achieved using other similar equations. For example it was noticed that at a 2 N load the Vickers indenter diagonals aligned with <001> lateral crack are formed and when the diagonals are aligned with <110>, phase transition zones appear. When a larger diagonal of the Knoop indenter is aligned with <001>, phase transition zones are also formed. At comparatively high (over 50 N) loads, partially stabilized crystals do not display any noticeable anisotropy of hardness or fracture toughness.

A lower fracture toughness of crystals doped with terbia as compared to those doped with ceria reveals not only lower values of K_{1c}^{v} of the former, but also as lower loads giving rise to lateral cracks in the latter. In both crystals, lateral cracks appeared under the Vickers impression. We consider that the evaluation of fracture toughness on indentation of crystals should account for all their fracture features but not only for the length of radial cracks as it is usually done.

Acknowledgements

This study was supported by the State Committee for Science and Technology of Ukraine. The authors are also grateful to the International Science Foundation of Soros for financial support of this work.

References

1. Gogotsi, G. A., Mechanical behaviour of a new structural material: partially-stabilized ZrO_2 crystals. Informal seminar strength, reliability and quality assurance of components of engineering ceramics, Freiburg. 2–9 July 1992, IPP, Kiev, P. 24.
2. Gogotsi, G. A., Lomonova, E. E. & Pejchev V. G., Strength and fracture toughness of zirconia crystals. *J. Eur. Ceram. Soc.*, **11** (1993) 123–32.
3. Martinez-Fernandez, J., Jimenez-Melendo, M., Dominguez-Rodriguez, A., & Heuer, A., Elevated temperature studies of microindentation of Y–PSZ. In *Structural Ceramics–Processing Microstructural and Properties*, ed, J. J. Bentzen *et al.* Riso National Laboratory, Roskline, Denmarc, (1990) 413–8.
4. Ingel, R., Lewis, R. P. D., Bender, B. A. & Rice, R. W., Physical, microstructural, and thermomechanical properties of ZrO_2 single crystals. In *Science and Technology of Zirconia II. Advanced in ceramics*, **12** (1984) 408–13.
5. Pajares, A., Guiberteau, F., Dominguez-Rodriguez, A. & Heuer, A. H., Microhardness and fracture toughness anisotropy in cubic zirconium oxide crystals. *J. Amer. Ceram. Soc.*, **7** (1988) 332–3.
6. Morscher, G., Pirouz, P. & Heuer, A. H., Temperature dependence of hardness in yttria-stabilized zirconia single crystals. *J. Amer. Ceram. Soc.*, **3** (1991) 491–500.
7. Pajares, A., Guiberteau, F., Dominguez-Rodriguez, A., & Heuer, A. H., Indentation-induced cracks and the toughness anisotropy of 9·4-mol.% yttria-stabilized cubic zirconia single crystals. *J. Amer. Ceram. Soc.*, **4** (1991) 859–62.
8. Hannink, R. H. J. & Swain, M. V., Induced Plastic Deformation of Zirconia. In *Deformation of ceramic materials II*, ed, R. F. Tressler & R. C. Bradt. Plenum Press, N. Y. (1984) 695–708.

9. Gogotsi, G. A., Ozersky, B. A. & Oksametnaya, O. B., Behaviour of poly-and monocrystalline zirconia on indentation. *Refractory*, **33** (1992) 453–461.
10. Cook, R. F. & Pharr, G. M., Direct observation and analysis of indentation cracking in glasses and ceramics. *J. Amer. Ceram. Soc.*, **4** (1990) 787–817.
11. Dub., S. N. & Gogotsi, G. A., Indentation fracture toughness of zirconia crystals. *Materials Forum* (in press).
12. Gogotsi, G. A., Galenko, V. I., Ozersky, B. A., Lomonova, E. E., Myzina, V. A. & Kalabukchova, V. E., Strength and fracture toughness of yttria and terbia-doped zirconia crystals. *Refractory*, **34** (1993) 303–12.
13. Michel, D., Mazerolles, L., Perez, Y & Jorba, M., Fracture of metastable tetragonal zirconia crystals. *J. Mat. Sci.*, **18** (1983) 2618–28.
14. Gogotsi, G. A., Drosdov, A. V. & Pejchev, V. G., Mechanical behaviour of zirconia crystals partially stabilized with yttria. *Strength of Materials*, **23** (1991) 86–91.
15. Martinez-Fernandez, J., Jimenez-Melendo, M., Dominquez-Rodriguez, A. & Heuer, A. J., Microindentation-induced transformation in 3·5 mol.% yttria–partially–stabilized zirconia single crystals. *J. Amer. Ceram. Soc.*, **5** (1991) 1071–81.
16. Saiki, A., Ishizawa, N., Misutani, N. & Kato, M., SEM observation of the stress-induced transformation by Vickers indentation in Y–PSZ crystals. *J. Ceram. Soc. Jpn. Inter. Ed.*, **97** (1989) 41–6.
17. Gogotsi, G. A. & M. Swain, M. V., Comparison of strength and fracture toughness of single and polycrystalline zirconia. In *Science and Technology of Zirconia, V*, ed S. P. S. Badeval, M. J. Bannister & R. H. J. Hannink. Technomic Pub. Co, Lancaster-Basel (1993) 347–59.
18. Liang, K. M., Orange, G. & Fantozzi, G., Evaluation by indentation of fracture toughness of ceramic materials. *J. Mat. Sci.*, **25** (1990) 202–14.
19. Gogotsi, G. A., Lomonova, E. E. & Osiko, V. V., Studies mechanical characteristics of zirconia single crystals for structural application. *Refractory*, **32** (1991).
20. Gogotsi, G. A., Lomonova, E. E. & Ostrovoy, D. Yu., Deformation of ZrO_2 single crystals. *Refractory*, **33** (1992) 152–8.
21. Gogotsi, G. A. & Lomonova, E. E. (in preparation for publication).
22. Gogotsi, G. A., Test method of advanced ceramics: reasonable approaches for standardisation ceramics. *Key Engineering Materials*, **56–7** (1991) 419–34.
23. Marshall, D. B., Noma, T. & Evans, A. G., A simple method for determining elastic modulus to hardness ratios using Knoop indentation measurements. *J. Amer. Ceram. Soc.*, **65** (1992) 175–6.
24. Antis, G. R., Chanticul, B. R., Lawn, B. R. & Marshall, D. B., A critical evaluation of indentation techniques for measuring fracture toughness. *J. Amer. Ceram. Soc.*, **69** (1981) 533–8.
25. Niihara, K., A fracture mechanics analysis of indentation-induced Palmquist crack in ceramics. *J. Mat. Sci. Let.*, **2** (1983) 221–3.
26. Dub, S. N., Gogotsi, G. A. & Lomonova, E. E., Hardness and fracture toughness of ZrO_2 crystals with yttria and terbia (in preparation for publication in *J. Mat. Sci. Let.*).
27. Ingel, R. & Lewis, R. P. D., Elastic anizotropy in zirconia single crystals. *J. Am. Cer. Soc.*, **71** (1988) 265–71.

Journal of the European Ceramic Society **15** (1995) 415–424
© 1995 Elsevier Science Limited
Printed in Great Britain. All rights reserved
0955-2219/95/$9.50

0955-2219(95)00008-9

The Development of Microstructure in Silicon Nitride-Bonded Silicon Carbide

D. P. Edwards,[a,c] B. C. Muddle,[a] Y.-B. Cheng[a] & R. H. J. Hannink[b]

[a]Department of Materials Engineering, Monash University, Clayton, Victoria, 3168, Australia
[b]C.S.I.R.O. Division of Material Science and Technology, Private Bag 33, Rosebank MDC, Clayton, Victoria, 3169, Australia

(Received 6 May 1994; revised version received 14 October 1994; accepted 12 December 1994)

Abstract

The microstructure of a commercial silicon nitride-bonded silicon carbide ceramic composite, formed via the nitridation of silicon powder–SiC preforms, has been characterised using analytical transmission electron microscopy. It comprised coarse particles of SiC dispersed in a matrix which was a mixture of crystalline phases based on Si_2N_2O and β-Si_3N_4, and an amorphous phase. Qualitative microanalysis of amorphous matrix regions revealed the presence of significant concentrations of aluminium, silicon, calcium and oxygen, while aluminium and oxygen were also readily detectable in both of the surrounding crystalline phases. It is thus suggested that the crystalline phases in the matrix are in fact O- and β-sialons respectively. A mechanism, combining reaction bonding and solution-precipitation in a (Ca,K)–aluminosilicate liquid phase at the reaction temperature, is proposed to describe the development of the matrix microstructure.

1 Introduction

The potential for near net shape forming of Si_3N_4 ceramics via the direct nitridation of silicon compacts, together with the economic advantage inherent in the use of silicon powder compared with currently available Si_3N_4 powders, have been major factors in sustaining continued interest in the application of the reaction bonding process to these ceramics in recent years. However, the consolidated densities achieved using this approach are typically only 80% of those obtainable by hot pressing techniques and the lower density, combined with the continuous nature of the porosity typical of reaction-bonded compacts, continue to limit the applications of such materials.

One approach to overcoming these difficulties has involved the development of the nitrided pressureless sintering (NPS) technique,[1–4] which combines the nitridation process with a liquid phase sintering stage, promoted through the addition of oxide sintering aids to silicon/Si_3N_4 compacts. This technique has been shown to be capable of producing Si_3N_4-based materials with near to theoretical densities and, with improved composition control and tailoring of the final microstructure, has the potential to allow more economical production of materials exhibiting reduced shrinkage during sintering and minimal porosity.

The Si_3N_4-based materials developed in this way have potential for application as the bonding constituents in low cost composite refractory materials, typically containing a major fraction of silicon carbide aggregate.[5] Such binders offer potentially superior oxidation and alkali resistance in molten metal environments compared with alumino–silicate matrices in current usage.[6,7] There is thus ongoing interest in the characterisation of the microstructure of such materials and in elucidating the stages of microstructural evolution during the sintering cycle.

The purpose of the present paper is to report on the microstructural characterisation of a commercially produced, reaction-bonded Si_3N_4–SiC composite, containing significant oxide additions, predominantly in the form of a clay binder. This work forms part of a larger project currently being undertaken to examine, using analytical transmission electron microscopy, the microstructural development of Si_3N_4-based ceramics produced by the NPS technique.

2 Experimental Procedures

Fabrication of the composite involved the wet blending of the major components, Si powder (particle size <44 μm) and crushed SiC (70–650

[c]Present address: Defence Science and Technology Organisation, Aeronautical and Maritime Research Laboratories, P.O. Box 4331, Melbourne, Victoria, 3001, Australia.

μm, in the approximate weight ratio of 1:3, with minor additions of organic plasticising agent (Ca–lignosulphonate) and clay (≤5 wt%) to aid plasticity of the slurry prior to moulding of the composite preforms. The cast preforms were allowed upwards of 8 h for material sedimentation and water extraction before mould removal. Sintering of the preforms was carried out in an N_2 atmosphere using a slow heating cycle, with a binder–burnout stage at 400–600°C, a final sintering temperature of 1450°C and a sintering time in excess of 20 h.

Initial phase analysis of the composite was performed in a Siemens D500 powder X-ray diffractometer using Ni-filtered Cu K_α radiation. Lattice parameters of the phases were determined from the measured X-ray diffraction peaks using a least squares fitting routine within the Celsiz program,[8] with calibration performed using silicon as an internal standard.

Composite surfaces for optical and scanning electron microscopy (SEM) were prepared by initial polishing of bulk specimens on a tin lap, followed by final 1 μm diamond polishing. Polished samples were examined in a JEOL 840A scanning electron microscope operating at 20 kV. Specimens for transmission electron microscopy (TEM) were prepared by diamond cutting thin composite slices, grinding and polishing to form 120 μm thick discs, and finally ion milling these discs to electron transparency using 5 kV argon ion beams at an incident angle of 15°. The specimens were coated with a thin carbon film and examined in a Philips CM20 analytical electron microscope operated at 200 kV and equipped with an ultra-thin window Link energy dispersive X-ray spectrometer (EDXS). For comparative X-ray microanalysis, an electron probe of nominally 10 nm diameter was used routinely in the scanning transmission electron microscope (STEM) mode.

3 Experimental Results

3.1 X-ray diffraction

The X-ray diffractometer trace from the reaction-bonded composite, Fig. 1, indicates that, in addition to SiC, the major crystalline phases in the composite are silicon oxynitride (Si_2N_2O) and β-Si_3N_4, with minor fractions of α-Si_3N_4 and unreacted silicon also present. The relative fractions of Si_2N_2O and β-Si_3N_4 in the binder phase were calculated as approximately 0·6 and 0·4 respectively, employing a technique making use of the (002) Si_2N_2O and (210) β-Si_3N_4 peak intensities[9] and ignoring minor phases. Efforts to determine more accurately the phase content of the matrix and the polytypes of SiC present, using available crystallographic data and a Rietveld analysis,[10] proved difficult due to the presence of multiple phases and significant overlap of diffraction peaks. However, analysis of the SiC peaks from both the composite and the starting SiC powder indicated that the 6H structure was the dominant polymorph, with the presence of the cubic (3C) and other α-polytypes as minor constituents suggested by the asymmetry of several major peaks.

A systematic shift in the peak positions for the Si_2N_2O and β-Si_3N_4 phases to lower diffraction

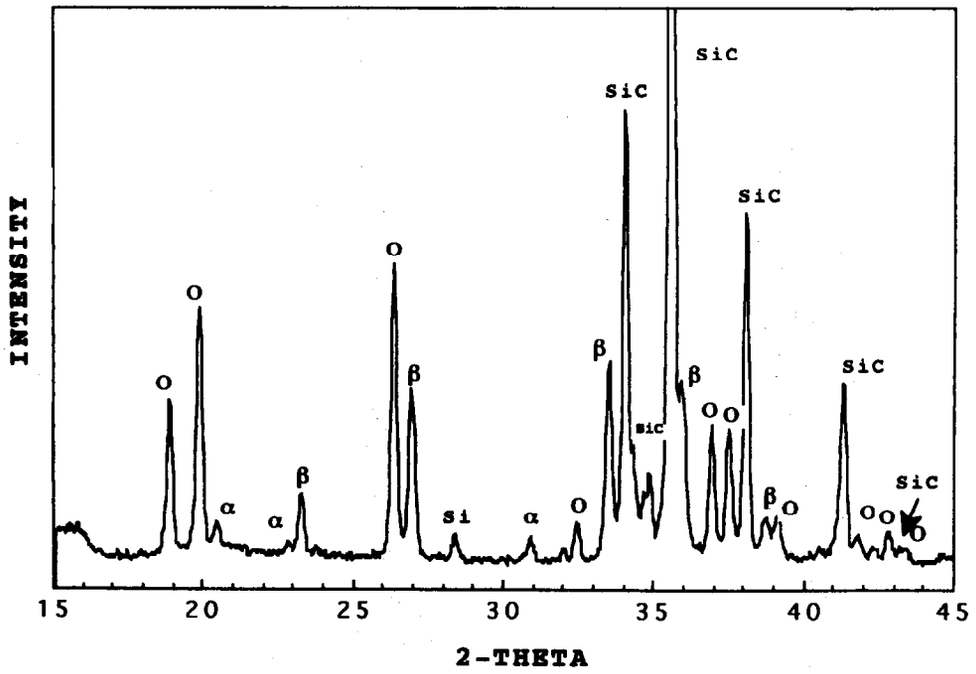


Fig. 1. X-ray diffractometer trace from as-fired material indicating the presence of SiC in a matrix that is predominantly a mixture of crystalline phases based on β-Si_3N_4 and Si_2N_2O (O).

angles (2θ) was noted, when compared with expected positions for the pure compounds. The lattice parameters of the hexagonal β-Si_3N_4 were determined to be a = 0·7617 ± 0·0004 nm and c = 0·2923 ± 0·0003 nm, while those of the orthorhombic oxynitride were measured to be a = 0·8909 ± 0·0003 nm, b = 0·5505 ± 0·0001 nm and c = 0·4861 ± 0·0001 nm. These values are systematically larger than those normally quoted for the pure compounds,[11] and are consistent with an expansion in the unit cell that might arise through Al–O bond substitution for Si–N bonds during sintering.

It is unlikely that the Si_2N_2O within the matrix can be attributed solely to the SiO_2 that is expected to be introduced as a surface layer on both the silicon and SiC powders. The high content of crystalline Si_2N_2O observed, and the almost exclusive appearance of β-Si_3N_4 in preference to α-Si_3N_4, suggest the presence of a liquid phase during the 1450°C reaction bonding process if proposed solution–reprecipitation mechanisms for Si_2N_2O formation are correct.[12–14] This is consistent with the presence in the original powder mixture of additional glass-forming oxides, which will promote the formation of a low melting point liquid and provide a source of oxygen for the formation of Si_2N_2O. However, the lack of a broad low-angle diffraction peak characteristic of an amorphous phase in the X-ray diffractometer trace of Fig. 1 implies that there is a low level of residual glass remaining within the composite after firing.

A few minor peaks remain unidentified in the X-ray diffractometer trace and are suspected to arise from metallic impurities introduced into the raw materials during powder processing.

3.2 Optical and scanning electron microscopy

Figure 2 is an optical micrograph typical of an unetched, polished surface of the as-fired composite, where the large silicon carbide grains in light grey contrast range in size from 20 to 450 μm and constitute approximately 75 vol.% of the composite microstructure. The microstructure of the Si_2N_2O–Si_3N_4 binder is unresolved at this scale, but it appears that it forms a near continuous, cohesive bond around the entire perimeter of the silicon carbide particles. The local dark areas within the binder represent a combination of intrinsic pores and defects introduced during polishing.

Examination in the scanning electron microscope, using backscattered electron contrast, revealed the presence of an impurity phase in light contrast at the SiC boundaries, Fig. 3, while the larger SiC grains often contained a core of slightly darker contrast. Energy dispersive X-ray spectroscopy of the two phases in light contrast (arrowed A and B respectively) indicated significant concentrations of Si, Fe and other metallic impurities, Fig. 3(b), in regions A, while in regions B, unreacted Si alone was detected. Optical and scanning electron microscopy of the raw SiC powder established the presence of the same phases intimately associated with the original SiC particles and it is thus inferred that these phases arise during the processing of the SiC. The use in the composite system of SiC produced by the reaction sintering method is the most likely source of additional metallic impurities in the microstructure, as

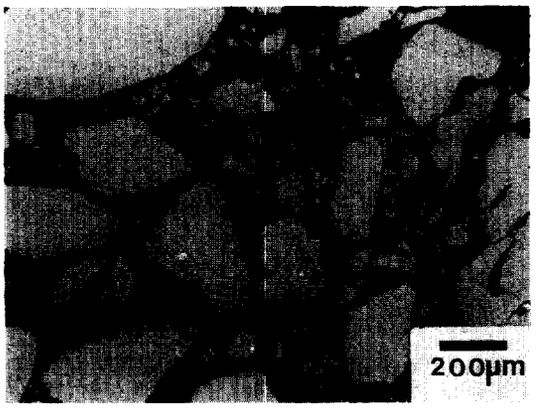
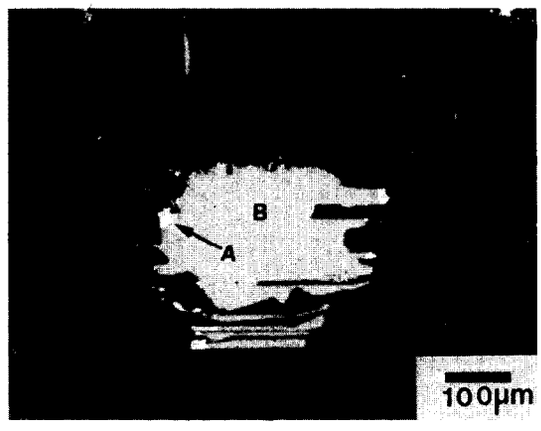


Fig. 2. Reflected light micrograph of unetched, polished surface of as-fired composite.



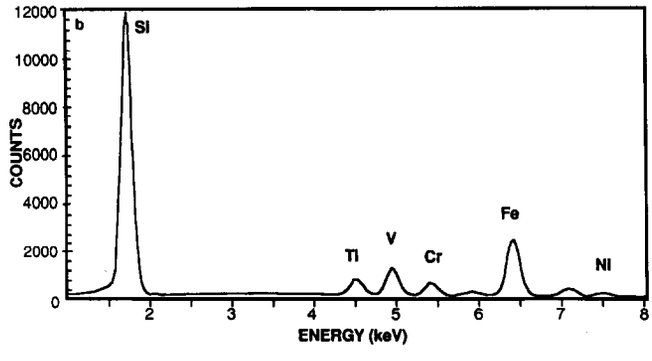


Fig. 3. (a) Backscattered electron image of as-fired composite showing impurity phase (regions A) and unreacted silicon (region B) within SiC grain, and (b) energy dispersive X-ray spectrum typical of impurity phase A.

reaction-sintered SiC is known to contain up to 10% unreacted silicon and other silicide impurities in the final product.[15]

3.3 Transmission electron microscopy

The microstructure of the binder in the composite was complex and varied significantly in grain size and morphology between thin foil specimens and even between adjacent areas within the same sample. Such variability is perhaps related to the relatively large scale of the initial SiC particles, resulting in poor mixing of the raw materials and/or segregation of components during green fabrication, which prevent the formation of a homogeneous structure. Figure 4(a) is a bright field TEM image showing a representative area of the binder microstructure, in which each of the grains in this field has been identified by electron microdiffraction to be either crystalline β-Si_3N_4 (β) or Si_2N_2O (O), while the central region is residual amorphous phase (G). Figures 4(b) and (c) show representative electron microdiffraction patterns used to identify the silicon nitride grains, indexed as (b) [0001] and (c) [$10\bar{1}0$] zone axis patterns from the hexagonal β-Si_3N_4 structure. The Si_3N_4 formed in a variety of morphologies, ranging from approximately equiaxed grains with smoothly curved surfaces and an average diameter of 350 nm, Fig. 4(a), to grains with a faceted, rod-like form. Those elongated grains, which were relatively rare, had a morphology commonly considered typical of the product of the α–β phase transformation in systems containing a liquid phase.[16–18]

In contrast to the Si_3N_4, the Si_2N_2O grains (50–500 nm) were readily distinguished by their elongated, faceted morphology[19,20] and a substructure of stacking faults parallel to the long axis, Fig. 5(a). The Si_2N_2O was also noted to have a tendency to form grains with faceted ends, with the angle of contact between grains apparently being determined by such facet angles. The form of the relationship between such contiguous crystals is at present the subject of further study. Figures 5(b) and (c) show representative electron microdiffraction patterns recorded from the Si_2N_2O grains, which may be indexed as (b) [$1\bar{1}0$] and (c) [$\bar{1}01$] zone axis patterns from the orthorhombic oxynitride structure.[21]

Non-crystalline regions observed within the binder microstructure were also identified by diffraction and diffraction contrast techniques.[22] As shown in Fig. 6, the glass had formed as discrete pockets at three and four grain junctions involving both oxynitride and β-Si_3N_4 grains, and was not readily detectable in the form of continuous intergranular films. The incidence of amorphous

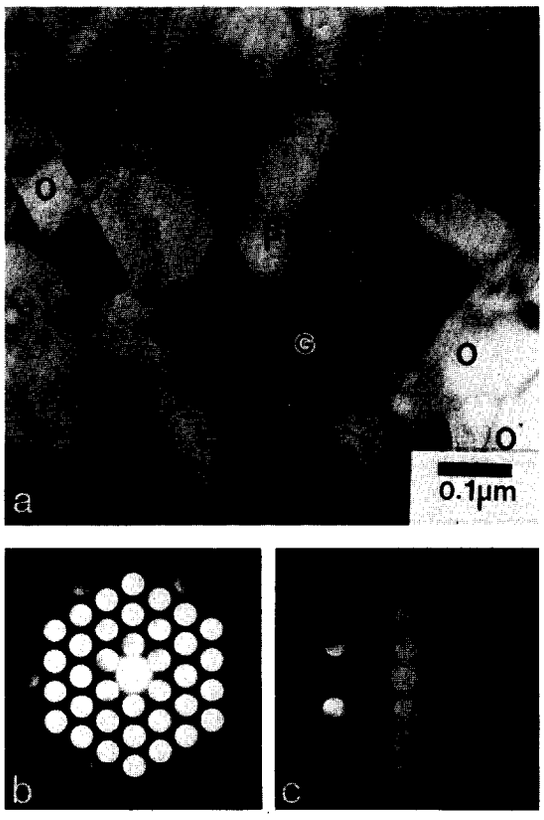


Fig. 4. (a) Transmission electron micrograph showing region of amorphous phase (G) surrounded by a mixture of crystalline phases based on β-Si_3N_4 and Si_2N_2O (O), and electron microdiffraction patterns which can be indexed unambiguously as (b) [0001], and (c) [$10\bar{1}0$] zone axis patterns from the hexagonal β-Si_3N_4 structure.

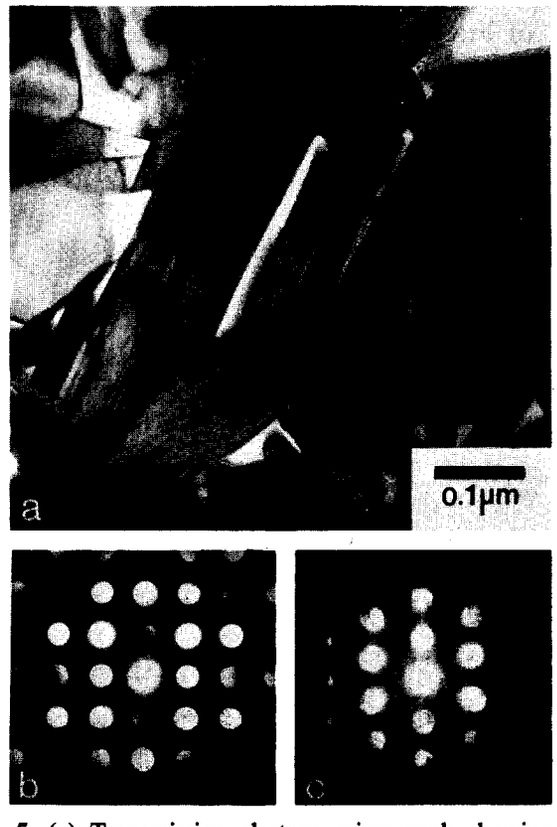


Fig. 5. (a) Transmission electron micrograph showing the morphology typical of elongated grains of the oxynitride-based phase (O), and electron microdiffraction patterns which can be indexed unambiguously as (b) [$1\bar{1}0$], and (c) [$\bar{1}01$] zone axis patterns from the orthorhombic oxynitride structure.

pockets was, however, rare, suggesting that the quantity of such phase within the microstructure was relatively small. Energy dispersive X-ray spectra, Fig. 7(a), recorded from the amorphous regions revealed significant concentrations of Si, Al, O, Ca and K; the C peak is a consequence of specimen coating and contamination. There was some evidence of the presence of nitrogen within the residual glass, but it proved difficult to detect because of the overlap of the adjacent oxygen and carbon peaks.

Microanalysis of the Si_2N_2O grains throughout the binder, Fig. 7(b), indicated the presence of significant concentrations of Al, along with Si, N, and O. It is thus suggested that the phase described thus far as an oxynitride is in fact an O-sialon ($Si_{2-x}Al_xO_{1+x}N_{2-x}$ with $x \leq 0{\cdot}2$). Similarly, significant concentrations of Al were also detected in the nitride grains in the binder, Fig. 7(c), suggesting that this phase is β-sialon ($Si_{6-z}Al_zO_zN_{8-z}$, $z < 4{\cdot}2$), formed by the limited substitution of Al^{3+} for Si^{4+}, with accompanying oxygen–nitrogen substitution for charge compensation.[23,24] The Si : Al ratio was observed to be constant, to within the limits of experimental error, in each of the two crystalline phases throughout the binder microstructure. This uniformity of composition would suggest that the liquid phase, which is the likely primary source of the Al and O, possesses a low viscosity, as would be expected for oxide liquid phases containing significant alkali-metal and alkaline earth concentrations,[25] and is uniformly distributed throughout the microstructure at the final reaction temperature of 1450°C.

Metallic inclusions were also observed occasionally at multiple grain junctions, and Fig. 8(a) shows an area containing a number of inclusions in dark contrast bounded by oxynitride grains. X-ray microanalysis, Fig. 8(b), indicated that the



Fig. 6. Representative transmission electron micrograph of microstructure of the composite matrix, showing discrete pockets of glassy phase (G) at three and four grain junctions.

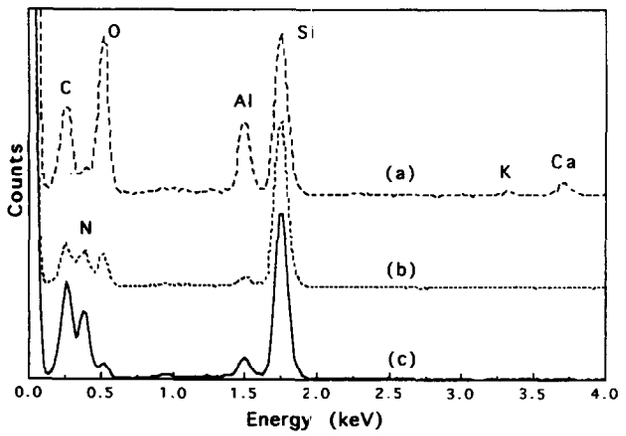


Fig. 7. Energy dispersive X-ray spectra typical of (a) amorphous phase, (b) O-sialon grains, and (c) β-sialon grains within the matrix of as-fired composite.



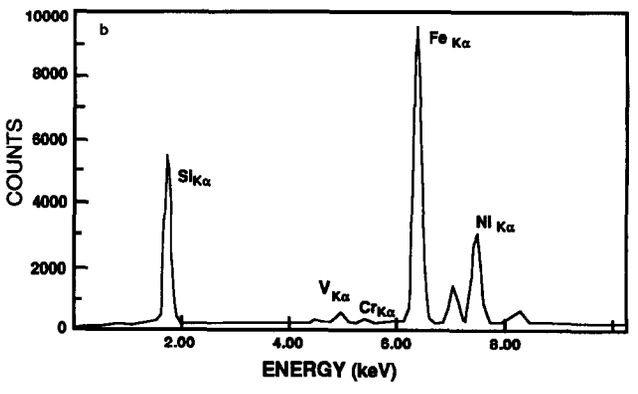


Fig. 8. (a) Transmission electron micrograph showing grains of metallic impurity phase within composite matrix, and (b) energy dispersive X-ray spectrum typical of the impurity phase.

particles contained significant concentrations of Fe, Si, Cr, Ni and V, and it seems likely that such inclusions are introduced during the attrition process, perhaps as a result of the use of stainless steel milling media.

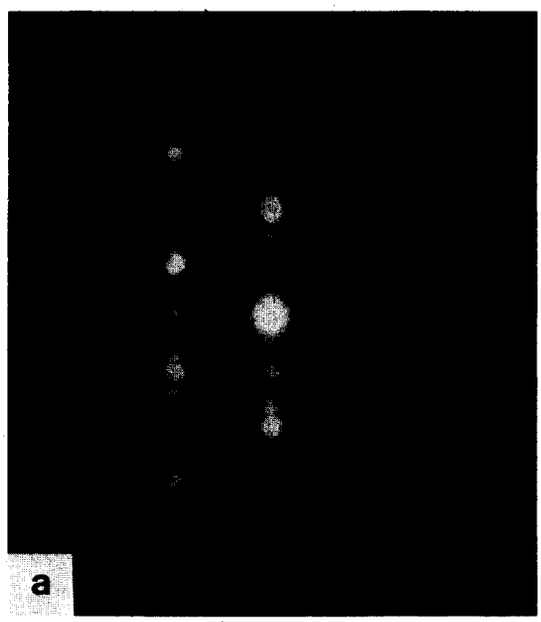
Careful examination of a number of segments of the matrix/SiC interface typically indicated that the interface was cohesively bonded along the entire boundary length. No evidence of crack formation at the interface was observed and it also proved difficult to detect any amorphous thin films between the SiC and the binder phases. More detailed investigations of the interfacial region are in progress to elucidate the interface structure and to check for the presence of the amorphous intergranular films that are often reported in silicon nitride-based ceramics.[26–30]

An interesting feature of the microstructure was the common observation of the preferred nucleation of fine, rod-like O-sialon (O') grains along the boundaries of the coarse SiC particles. Figures 9(a) and (b) show a number of O' crystals extending outwards from their preferred nucleation sites on the SiC surface, with the preferred direction of elongation corresponding to the *c*-axis of the orthorhombic O' phase. Figure 10(a) is a composite electron microdiffraction pattern containing super-





Fig. 9. Transmission electron micrographs showing the preferred nucleation and growth of elongated O-sialon crystals from the surfaces of SiC grains.



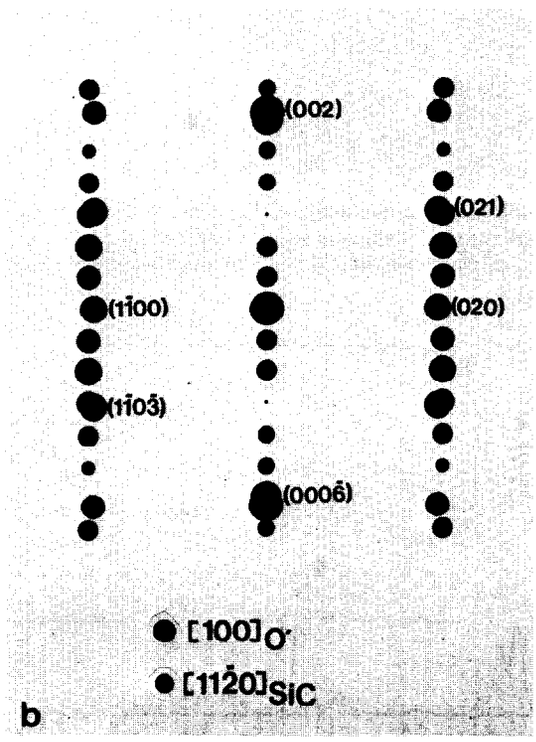


Fig. 10. (a) Composite electron microdiffraction pattern containing superimposed $[100]_{O'}$ and $[11\bar{2}0]_{SiC(6H)}$ zone axis patterns from adjoining regions of O-sialon and SiC, such as shown in Fig. 10, and (b) schematic solution to these patterns.

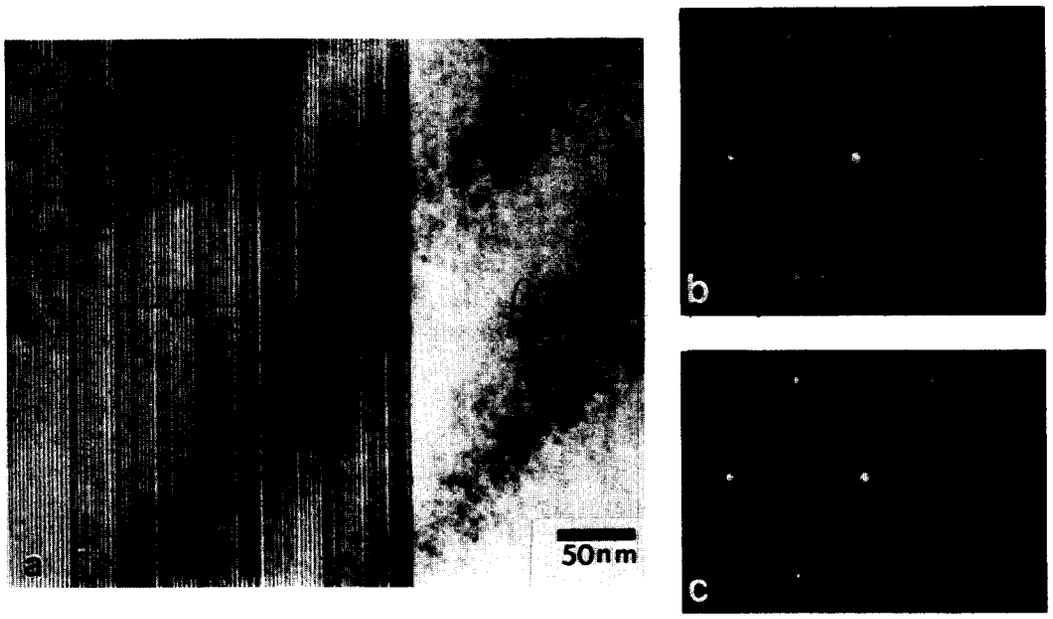


Fig. 11. (a) Transmission electron micrograph showing section of SiC grain containing regions of both the α- and β-SiC polymorphs, and corresponding (b) $[11\bar{2}0]_{SiC(6H)}$ and (c) $[110]_{SiC(\beta)}$ zone axis SAED patterns from the α and β structures respectively.

imposed zone axis patterns from adjoining regions of SiC and the O-sialon. As indicated by the schematic solution to the pattern in Fig. 10(b), the patterns imply an orientation relationship between the O' and the SiC in which:

$$(001)_{O'}// (0001)_{SiC}, \text{ and}$$

$$[100]_{O'}//[11\bar{2}0]_{SiC(6H)}.$$

Several regions in which β-sialon (β') grains were in direct contact with the SiC grains were also examined, but attempts to identify an orientation relationship[31] between the β' and the SiC have thus far been unsuccessful.

Examination of the large SiC particles using electron diffraction and lattice fringe imaging techniques[32] confirmed the existence of a variety of SiC polytypes, as suggested by the X-ray diffraction data from the composite (Fig. 1). The majority of areas examined with the electron beam parallel to a $<11\bar{2}0>$ direction exhibited lattice fringe spacings of 1·52 nm consistent with the 6H polymorph of α-SiC,[33] Fig. 11(a). However, a number of particles were observed to contain alternative α-SiC polytypes and, as illustrated in Fig. 11(a), local regions of β-SiC. The selected area electron diffraction pattern recorded from the α-SiC area in Fig. 11(a) and shown in Fig. 11(b) may be indexed for the hexagonal structure of the α-polytype. The streaking and additional low intensity reflections observed along the $\{10\bar{1}l\}$ diffraction row are characteristic of the faulted substructure of this polymorph.[33,34] In contrast, the SAED pattern in Fig. 11(c) may be indexed as the [110] zone axis pattern from β-SiC.

4 Discussion

Characterisation by analytical electron microscopy, in conjunction with X-ray diffraction, has established that the microstructure of the binder, in what is described as a Si_3N_4-bonded SiC composite, in fact comprises a mixture of crystalline phases based on Si_2N_2O and β-Si_3N_4, with a small volume fraction of residual amorphous phase rich in Si, Al, Ca, K and O. The high content of crystalline oxynitride and the almost exclusive appearance of β-Si_3N_4 (or β-sialon), both suggest the presence of a significant volume fraction of liquid phase during the 1450°C reaction bonding process, as those mechanisms proposed[12,14] for formation of Si_2N_2O invariably involve precipitation from a liquid phase, while the formation of β-sialon also commonly occurs from or in association with a liquid.[16] The residual glassy phase observed within the binder is consistent with the presence of a (Ca,K)–aluminosilicate derived liquid phase at the reaction temperature, although it is noted that the volume fraction of residual glassy phase is small in the as-fired product. These observations lead to a description of the consolidation of the composite in which the microstructure of the composite binder evolves via a modified solution–reprecipitation mechanism, such as that initially proposed for the reactive liquid–phase sintering of hot-pressed silicon nitride.[35,36]

In the case of the present Si/SiC powder composite preform, initial nitridation of the fine silicon powder during heating might be expected to lead to the formation of predominantly α-Si_3N_4 by

the vapour phase reaction of $Si_{(g)}$ or $SiO_{(g)}$ with nitrogen.[37] In the presence of Fe as a significant impurity, formation of the α phase might also arise[38] through Si vaporisation from any $FeSi_x$ liquid phase that may form. However, in studies of the reaction bonding of Si_3N_4 there are numerous reports of the formation of a product containing a significant volume fraction of β-Si_3N_4 at temperatures as low as 1330°C,[38] and it has been suggested[38] that the development of the two modifications may be determined by particular growth mechanisms. The choice of growth mechanism may be strongly influenced by the presence or otherwise of significant fractions of low melting point liquid phase generated from the natural oxide film on the original powder(s) and/or other impurity ingredients.

It is also well established that α-Si_3N_4 transforms to β-Si_3N_4 during heat treatment at temperatures in the vicinity of 1500°C,[17] and that this transformation may be facilitated by the presence of impurity elements and/or a liquid phase of appropriate composition.[16] There are thus at least two mechanisms by which the β-Si_3N_4 observed in the as-fired product may form and increase in volume fraction during the reaction cycle. It is noteworthy that two distinguishable morphologies of the β-nitride were observed within the binder; the major fraction contained rounded, equiaxed grain shapes, but there was a small fraction of grains possessing a faceted and elongated form more typical of a product forming as a precipitate from a liquid phase. These different grain shapes may constitute evidence of two different growth mechanisms contributing to the total fraction of β-Si_3N_4 in the binder.

The EDXS analyses of residual amorphous regions in the composite imply the existence at the reaction temperature of a (Ca,K)–aluminosilicate based liquid phase with a composition derived principally from the clay addition. The timing of the formation of this liquid phase in the reaction sequence may have a strong influence on phase formation within the microstructure. The formation of an extensive liquid phase early in the reaction sequence may, for example, inhibit the formation of Si_3N_4[3] by the premature closure of the pore network necessary for the access of nitrogen to the silicon, if indeed direct access of nitrogen to solid silicon is essential to continuing nitridation. This might be expected to lead to a large residual silicon content in the sintered product. However, both X-ray diffraction and direct microscopic observation indicate that only a small fraction of silicon remains within the present composite. Given that the melting point of the liquid phase is likely to be low (<1450°C) and the liquid phase is thus likely to be present from the earliest stages of the reaction bonding sequence, this suggests that the volume fraction and viscosity of the liquid phase, combined with the low green density of the compact, are such that they do not adversely affect the access of the nitrogen to the silicon.

In the initial stages of nitridation it seems likely that the product is a mix of α-Si_3N_4 formed via a gas phase reaction and β-Si_3N_4 formed perhaps by a combination of mechanisms involving the presence of the (Ca,K)–aluminosilicate liquid phase. Exposed to an increasing fraction of oxygen-rich liquid phase at the reaction temperature, the less stable α-Si_3N_4 present will dissolve to form essentially calcium sialon liquid, and be replaced by the precipitation of the Si_2N_2O-based phase. The large volume fraction of O' compared with β' in the binder is consistent with a substantial proportion of the (α-)Si_3N_4 formed by nitridation being consumed by the liquid phase, while the elongated, faceted morphology and faulted substructure of grains of this phase are characteristic of the oxynitride forming from a liquid phase.[20] It is to be expected that the relatively low solubility of nitrogen combined with a high oxygen activity in the liquid phase will favour formation of O-sialon.

The direct observation of aluminium within the Si_2N_2O-based phase, together with the measurement of lattice parameters systematically larger than the range of lattice constants reported for pure Si_2N_2O, confirm the identity of the phase as O'. The lattice parameter a of O' experiences the most significant expansion as the result of the replacement of Si^{4+} ions with Al^{3+} ions, and comparison of the present measured values with published results[39,40] suggests that the aluminium content of the O-sialon ($Si_{2-x}Al_xO_{x+1}N_{2-x}$) is such that $x \geq 0{\cdot}14$ and, according to some observations,[40] approaching the limit of aluminium solubility in the O' structure. This is consistent with the precipitation of the O' from a liquid phase in which the activity of aluminium is high, i.e. a liquid phase forming in the presence of a high Al_2O_3 concentration.

A unique feature of the present study was the common observation of elongated grains of the oxynitride-based phase extending from the surface of coarse SiC particles and sustaining a well-defined orientation relationship with the SiC. This orientation relationship is such that the long axis of the O', $[001]_{O'}$, is parallel to the c axis of the 6H SiC, and the misfit between $(002)_{O'}$ and $(0006)_{SiC(6H)}$ planes normal to the preferred growth axis is approximately 3·3%, based on lattice parameters determined at room temperature. Normal to the interface between the O' and the SiC, Fig. 10(a),

the planes $(020)_{O'}$ and $(1\bar{1}00)_{SiC}$ are approximately parallel and contain the growth axis, and differ in spacing by only approximately 2·9%. Similarly, the planes $(100)_{O'}$ and $(11\bar{2}0)_{SiC}$ are parallel across the interface and the misfit between them is approximately 3·3%. The form of these O' grains, and the relatively low lattice misfit between the O' and the SiC phases in the observed orientation relationship, imply the preferred heterogeneous nucleation of the Si_2N_2O-based grains on the SiC and their subsequent growth outward into surrounding liquid phase. That they grow into liquid phase is supported by the common observation of small glass pockets surrounding these grains in the as-fired product.

Regardless of the mechanism of formation of the β' phase, the direct observation of aluminium (and oxygen) within the various grain morphologies, together with the magnitudes of the measured lattice parameters, confirm the identification of this phase as β-sialon rather than β-Si_3N_4. There were no significant variations detectable in the aluminium concentration within the different β-sialon morphologies and across many grains of each analysed using EDXS. This suggests that the extended hold time at the final sintering temperature of 1450°C may be sufficient to allow the aluminium and oxygen concentrations within both the β' and O' to approach saturation in the solid state at this temperature. In the case of any β' formed as a solid state reaction product this would seem to imply the diffusion of aluminium and oxygen from the aluminium-rich liquid phase during or immediately following initial nitridation.

If measured values of the lattice parameters for the crystalline binder phases are compared with existing data[41,42] to determine the values of z and x for the β' ($Si_{6-z}Al_zO_zN_{8-z}$) and O' phases respectively, the results support the notion that the aluminium concentration approaches saturation within both phases during the firing treatment. The calculated values of $z = 0{\cdot}45$ and $x = 0{\cdot}14$ are equivalent to aluminium concentrations of 5·72 and 5·34 eq% respectively, indicating that, to within reasonable error limits, the aluminium content of the two phases is essentially identical.

The presence of residual glass pockets in the final microstructure results from a failure to completely exhaust the supply of liquid phase at the reaction temperature. It is noteworthy that the pockets of glass, such as shown in Fig. 4, were relatively rare and that the volume fraction of residual glass was relatively small. There would thus seem to exist, potential for largely eliminating residual glassy phase from the final microstructure through improved design of the composition of the composite and, in particular, improved control of the additions of those minor constituents which generate and stabilise the liquid phase during processing.

5 Summary

(1) The microstructure of the commercial silicon nitride-bonded silicon carbide ceramic composite, formed via the nitridation of silicon powder–SiC preforms, comprises coarse particles of SiC dispersed in a matrix or binder which is a mixture of crystalline phases based on Si_2N_2O and β-Si_3N_4 in the volume ratio of approximately 2:1, together with a small volume fraction of residual amorphous phase.

(2) The direct observation of significant concentrations of aluminium (and oxygen) within both of the crystalline phases, together with measured lattice parameters which are systematically larger than those of the pure compounds, imply that the crystalline phases within the binder are in fact O- and β-sialons respectively.

(3) The O-sialon is observed to nucleate preferentially, but not exclusively, on the 6H SiC particles with an orientation relationship with the SiC of the form:

$$(001)_{O'}// (0001)_{SiC}, \text{ and}$$
$$[100]_{O'}//[11\bar{2}0]_{SiC(6H)}.$$

(4) Direct qualitative microanalysis of amorphous matrix regions indicates the presence of significant concentrations of aluminium, silicon, calcium and oxygen. The regions are interpreted to represent the residue of a reactive, low melting point (Ca,K)–aluminosilicate liquid phase, deriving predominantly from clay binder additions to the original powder mix and present throughout the reaction sequence.

(5) It is proposed that the β-sialon within the binder is predominantly the product of a reaction-bonding sequence, perhaps facilitated by the presence of the liquid phase. The O' is suggested to arise as a result of the dissolution of α-Si_3N_4 in the oxygen-rich liquid phase, followed by precipitation of the O-sialon.

Acknowledgement

One of the authors (D.P.E.) gratefully acknowledges the award of a Postgraduate Research Fellowship under the auspices of the Australian Government Cadet Research Scientist Scheme.

References

1. Falk, L. K. L., Pompe, R. & Dunlop, G. L., Development of microstructure during nitridation and sintering of Si:Si_3N_4 Powder Compacts. In *Science of Ceramics 12*, ed. P. Vincenzini, Ceramurgica S. R. L., Faenza, Italy, 1984, p. 293.
2. Pompe, R., Hermansson, L. & Carlsson, R., Fabrication of low-shrinkage silicon nitride material by pressureless sintering, In *Engineering with Ceramics*, British Ceramics Society, Stoke-on-Trent, ed. R. W. Davidge, 1982, p. 65.
3. Brown, I. W. M., Pompe, R. & Carlsson, R., Preparation of sialons by the nitrided pressureless sintering (NPS) technique. *J. Eur. Ceram. Soc.*, **6** (1990) 191.
4. Falk, L. K. L., Dunlop, G. L. & Pompe, R., The microstructure of Si_3N_4 formed by nitridation and pressureless sintering of Si–Si_3N_4 compacts. *Mater. Sci. Eng.*, **71** (1985) 123.
5. Morrison, F. C. R., Maher, P. P. & Hendry, A., In-situ formation of sialons in refractories containing silicon carbide. *Brit. Ceram. Trans. J.*, **88**(5) (1989) 157.
6. Arrol, A. J., Ceramics for high performance applications. *Proc. 2nd Army Materials Technology Conference*, Hyannis, Massachusetts 1973, p. 729.
7. Zhiping, Z., Hui-Hang, H. & Zhao Hui, H., Sialon-bonded SiC refractories for blast furnace. *Interceram*, **42**(5) (1993) 292.
8. Scott, H., Celsiz program, C.S.I.R.O. Division of Materials Science and Technology, Victoria, Australia.
9. Liddell, K., X-ray analysis of nitrogen ceramic phases, M.Sc. Thesis, University of Newcastle upon Tyne, UK, (1979).
10. Schneider, M., Edv-Vetrieb, WYRIET, Version 3, Starnbergerweg 18, D-8134 Pöcking, Germany.
11. Powder Diffraction File, JCPDS-ICDD, 1990.
12. Trigg, M. B. & Jack, K. H., Silicon oxynitride and O'SiAlON ceramics. *Proc. of International Symposium on Ceramics Components for Engines*, ed. S. Somiya, E. Kanai & K. Ando, Tokyo, Japan, 1983, p. 199.
13. Bergman, B. & Heping, H., The influence of different oxides on the formation of Si_2N_2O from SiO_2 and Si_3N_4. *J. Eur. Ceram. Soc.*, **6** (1990) 3.
14. Huang, Z. K., Greil, P. & Petzow, G., Formation of silicon oxynitride from Si_3N_4 and SiO_2 in the Presence of Al_2O_3. *Ceram. Int.*, **10**(1) (1984) 14.
15. Ness, J. N. & Page, T. F., The structure and properties of interfaces in reaction-bonded silicon carbides. In *Tailoring Multiphase and Composite Ceramics*, Materials Science Research, Vol. 20, ed. R. E. Tressler, G. L. Messing, C. G. Pantano & R. E. Newnham, Penn., USA, 1985, p. 347.
16. Braue, W., Wotting, G. & Ziegler, G., The impact of compositional variations and processing conditions on secondary phase characteristics in sintered silicon nitride materials. In *Ceramic Microstructures '86, Role of Interfaces*, eds J. A. Pask & A. G. Evans. *Mater. Sci. Res.*, **21** 1987, p. 883.
17. Messier, D. R., Riley, F. L. & Brook, R. J., The α/β silicon nitride phase transformation. *J. Mater. Sci.*, **13** (1978), 1199.
18. Ziegler, G., Heinrich, J. & Wotting, G., Review: relationships between processing, microstructure and properties of dense reaction-bonded Silicon Nitride. *J. Mater. Sci.*, **22** (1987) 3041.
19. Siddiqi, S. A. & Hendry, A., The microstructure of dense, low cost silicon oxynitride. *Special Ceramics 8*, (1985) 1.
20. Lewis, M. H., Reed, C. J. & Butler, N. D., Pressureless-sintered ceramics based on the compound Si_2N_2O. *Mater. Sci. Eng.*, **71** (1985) 87.
21. Sjoberg, J., Helgesson, G. & Idrestedt, I., Refinement of the structure of Si_2N_2O. *Acta Cryst*, **C47** (1991) 2438–41.
22. Clarke, D. R., Application of electron microscopy to the processing of ceramic materials. *Ultramicroscopy*, **8** (1982) 95.
23. Jack, K. H., Review: sialons and related nitrogen ceramics. *J. Mater. Sci.*, **11** (1976), 1135.
24. Trigg, M. B. & Jack, K. H., The fabrication of O'-sialon ceramics by pressureless sintering. *J. Mater. Sci.*, **23** (1988) 481.
25. Jastrzebski, Z. D., *The Nature and Properties of Engineering Materials, 2nd Edition*, J. Wiley & Sons Inc., 1977.
26. Das Chowdhury, K., Carpenter, R. W. & Braue, W., A comparative high-resolution study of interface chemistry in silicon-nitride-based ceramic matrix composites reinforced with silicon carbide whiskers. *Ultramicroscopy*, **40** (1992) 229.
27. More, K. L, Koester, D. A. & Davis R. F., Microstructural characterization of a creep-deformed SiC whisker-reinforced Si_3N_4. *Ultramicroscopy*, **37** (1991) 263.
28. Clarke, D. R., Zaluzec, N. J. & Carpenter, R. W., The intergranular phase in hot-pressed silicon nitride: 1. Elemental Composition. *J. Am. Ceram. Soc.*, **64**(10) (1981) 601.
29. Lou, L. K. V., Mitchell, T. E. & Heuer, A. H., Discussion of grain boundary phases in a hot-pressed MgO fluxed silicon nitride. *J. Am. Ceram. Soc.*, **61**(9–10) (1978) 462.
30. Kleebe, H. J., Cinibulk, M. K., Cannon, R. M. & Ruhle, M., Statistical analysis of the intergranular film thickness in silicon nitride ceramics. *J. Am. Ceram. Soc.*, **76**(8) (1993) 1969.
31. Unal, O., Petrovic, J. J. & Mitchell, T. E., CVD Si_3N_4 on Single Crystal SiC: Part 1. Characterization and orientation relationship at the interface. *J. Mater. Res.*, **7**(1) (1992) 136.
32. Clarke, D. R., High-resolution techniques and applications to non-oxide ceramics. *J. Am. Ceram. Soc.*, **5–6** (1979) 236.
33. Dubey, M., Singh, G. & Van Tendeloo, G., X-ray and transmission electron microscopy study of extremely large-period polytypes in SiC. *Acta. Cryst.*, **A33** (1977) 276.
34. Ogbuji, L. U., Mitchell, T. E. & Heuer, A. H., The β–α transformation in polycrystalline SiC: III. The thickening of α plates. *J. Am. Ceram. Soc.*, **64**(2) (1981) 91.
35. Lewis, M. H., Powell, B. D., Drew P., Lumby, R. J., North, B. & Taylor, A. J., The formation of single-phase Si–Al–O–N ceramics. *J. Mater. Sci.*, **12** (1977), 61.
36. Hampshire, S. & Jack, K. H., The kinetics of densification and phase transformation of nitrogen ceramics. *Proc. Brit. Ceram. Soc.*, **31** (1981) 37.
37. Blegen, K., Equilibria and kinetics in the systems Si–N and Si–N–O. *Special Ceramics 6*, Proc. 6th Symp. on Special Ceramics, B.C.R.A., 1974, p. 223.
38. Moulson, A. J., Review: Reaction-bonded silicon nitride: its formation and properties. *J. Mater. Sci.*, **14** (1979) 1017.
39. Trigg, M. B. & Jack, K. H., Solubility of aluminium in silicon oxynitride. *J. Mater. Sci. Let.*, **6** (1987) 407.
40. Lindqvist, O., Sjoberg, J., Hull, S. & Pompe, R., Structural changes in O'-sialons, $Si_{2-x}Al_xO_{1+x}N_{2-x}$, $0{\cdot}04<x<0{\cdot}4$, *Acta Cryst.*, **B47** (1991) 672.
41. Haviar, M. & Johannesen, F., Unit-cell dimensions of β'-sialons, *Adv. Ceram. Mater.*, **4** (1988) 405.
42. Ohashi, M., Hirao, K., Brito, M. E., Takaaki, N., Yasuoka, M. & Kanzaki, S., Solid solubility of aluminium in O'-SiAlON. *J. Am. Ceram. Soc.*, **76**(8) (1993) 2112.

Journal of the European Ceramic Society **15** (1995) 425–434
© 1995 Elsevier Science Limited
Printed in Great Britain. All rights reserved
0955-2219/95/$9.50

0955-2219(95)00013-5

Room Temperature Tensile and Flexural Strength of Ceramics in AlN–SiC System

Houssam A. Toutanji,[a] David Friel, Tahar El-Korchi,[b] R. Nathan Katz, Gary Wechsler[c] & William Rafaniello[d]

[a]University of Puerto Rico, Mayaguez, PR 00681, Puerto Rico
[b]Worcester Polytechnic Institute, Worcester, MA 01609, USA
[c]Army Materials Laboratory, Watertown, MA 02172, USA
[d]Dow Chemical Co., Midland, MI 48674, USA

(Received 12 September 1994; revised version received 12 December 1994; accepted 10 January 1995)

Abstract

Tensile and bend strength were obtained for four compositions in the aluminum nitride–silicon carbide system: AlN, 75%AlN–25%SiC particulate, 50%AlN–50%SiC solid solution and SiC. Room temperature tensile strength, four-point bend strength, and the Weibull parameters for each of the tested materials are presented. Optical and SEM fractography were employed to identify failure initiating flaws for the fractured tensile specimens. The four-point bend strength is predicted using the Weibull tensile parameters and compared to measured values. Accuracy of the predicted results are rationalized based on observed microstructures and failure initiating flaws.

Introduction

Advanced ceramics are being increasingly utilized in a wide variety of demanding structural and electronic applications.[1] The high elastic modulus, excellent wear behavior, low density, high thermal conductivity, and outstanding high temperature strength and oxidation resistance of SiC have led to its use in wear parts, heat exchangers, fixturing for semiconductor manufacturing processes, and armor. AlN has outstanding thermal conductivity and a thermal expansion coefficient near that of silicon. These properties have made AlN the material of choice in electronic packages where heat management is a dominant design issue. However, because of its relatively modest strength and poor oxidation characteristics, except for use in armor systems, AlN receives little consideration in structural applications.

The AlN–SiC binary is somewhat unique among covalent systems in as much as a range of composites and solid solutions are possible depending on the raw materials and the processing conditions employed. If fine powders are processed significantly above 2100°C, a nearly complete range of solid solutions are possible.[2] Alternatively, if coarser materials are processed below 2000°C, where diffusion is slow, a family of two-phase particulate composites are formed.[3] While the mechanical properties of the end members, SiC[4–6] and AlN,[7–10] have been well documented, there have been only limited results reported for AlN–SiC composites and solid solution. Flexural strength data for AlN–SiC solid solutions were first reported by Ruh and Zangvil.[11] The low reported values were attributed to poor mixing. Landon and Thevenot using improved slurry preparation routes formed largely AlN–SiC solid solutions.[12] In general, the strength was higher for the SiC rich compositions. The maximum RT 3-point bend strength was reported as 1000 MPa for a hot pressed AlN–SiC material containing 25 wt% AlN. More recently, researchers at Nagoya University studied the effect of different microstructures on the mechanical properties of a single 30/70 AlN–SiC composition.[13] RT 4-point bend tests of this material demonstrated strengths and Weibull moduli increasing from 589 to 674 MPa and from 7·6 to 10·5 MPa, for the as processed solid solution and a phase separated modulated structure, respectively.[14] Mariano, *et al.*[15] have recently reported limited data on the RT 4-point bend strength of 15 and 45% SiC particulate reinforced AlN composites. They reported strengths of 477 and 347 MPa, respectively.

This work presents a detailed examination of the room temperature tensile and flexural strengths, failure statistics, and strength limiting flaws for four representative materials in the AlN–SiC system. The two end members, one solid solution alloy (50/50), and one particulate strengthened

composite (75/25) were studied. The solid solution and composite were selected based on their performance as ceramic armor materials[16] and potential for other structural applications.

Experimental Procedure

Materials

All of the specimens used in this study were machined from large billets. AlN, the AlN–SiC composite, and the AlN–SiC solid solution were prepared by hot-pressing blocks which were 38 × 104 × 20–40 mm thick in graphite dies. The three hot-pressed materials were pressed at 34·5 MPa and no sintering aids were employed. The exact processing conditions and physical characteristics of these compositions and the pressureless sintered SiC are provided in Table 1. The SiC parts were prepared using the traditional sintering aids of boron and carbon. The sintered dimensions for the SiC tiles were 112 × 112 × 16 mm. Both flexure and tensile specimens were machined out of each billet. The tensile test specimens were cylindrical rods measuring between 103 and 112 mm in length and 9–9·2 mm in diameter. B type bend bars, 3 × 4 × 40 mm, were prepared according to MIL-STD-1942A.[17]

Typical microstructures of the four ceramics studied are shown in Fig. 1. AlN and the 50/50 AlN–SiC solid solutions have uniform, fine-grained microstructures. Despite a processing temperature nearly 500°C higher than AlN, the average grain size was almost a factor of 4 smaller for the solid solution (see Table 1). The TEM micrograph, Fig. 2, of the 50/50 alloy vividly shows this fine grain size. The SiC microstructure is characteristic of other beta SiC materials having transformation induced large (50 × 2 mm) needle-like grains interspersed in a relatively fine microstructure (2 mm). From the optical micrographs, the 75/25 AlN–SiC composite appears to have fine SiC particles uniformly dispersed in an AlN matrix. However, TEM examination revealed that some dissolution of SiC into the AlN matrix grains had occurred. From EDS analysis of individual matrix grains, as much as 8% SiC was present in the AlN.[18]

Mechanical testing

Tensile tests were performed at room temperature utilizing a self-aligning hydraulic technique developed by Baratta and Driscoll[19,20] with a simplified specimen described by Hermansson, *et al.*[21] The tensile test specimens are cylindrical bars measuring between 103 and 112 mm in length and 9·0–9·2 mm in diameter. Forty mm on each end of the ceramic rod is inserted into a steel piston and adhesively bonded in place with a high strength epoxy.[22,23] The specimen–piston assembly is inserted into the pressure chamber of the hydraulic tester.* The pressure is applied and increased until the specimen is broken apart by the hydraulic pressure acting against the pistons. The pressure chamber, with specimen inserted, is shown schematically in Fig. 3. The internal pressurization of the specimen suspended between the O-ring seals minimizes bending stresses. The nominal tensile fracture stress (uncorrected for eccentricity) may be calculated by using the hydraulic pressure at failure and geometric parameters of the specimen–piston assembly.[20] A small degree of triaxiality in the hydrostatic loading of the specimen exists causing a small deviation from the uniaxial stress state, calculated to be less than 5%.[23,24] In addition, to eliminate the effects of stress intensification at the rod to piston bond transition, data from specimens that fractured within one half the radius of the specimen from the piston glue line are not used. Fractures occurring in these locations are considered invalid tests.[21]

Although this tensile method is inherently self-aligning, a small degree of eccentricity or misalignment of the tensile specimens can still occur from two sources. The specimen can be slightly curved or can be glued off-center in the pistons.

*ASCERA Hydraulic Tensile Tester, Robertsfors, Sweden.

Table 1. Processing conditions and physical characteristics

	AlN Hot pressed	*75AlN–25SiC Hot pressed (particulate reinforced)*	*50AlN–50SiC Hot pressed (solid solution)*	*SiC Sintered*
Hot pressing/ sintering temp.°C	1750	2000	2300	2120
Atmosphere	N_2	N_2	N_2	Ar
Density g/cm^3 (%TD)	3·26 (99·9)	3·24 (99·7)	3·22 (99·6)	3·17 (98·8)
Grain size (μm)	1·9 ± 0·6	AlN ≈ 2 μm SiC ≈ 5 μm	0·5 ± 0·2	Bimodal, 2·0 ± 0·6 and 50 × 2 plates
Phases (XRD)	2H AlN very slight AlON	2H AlN (solid sol'n) 3C-SiC	2H (solid sol'n)	3C, 6H minor-other polytypes

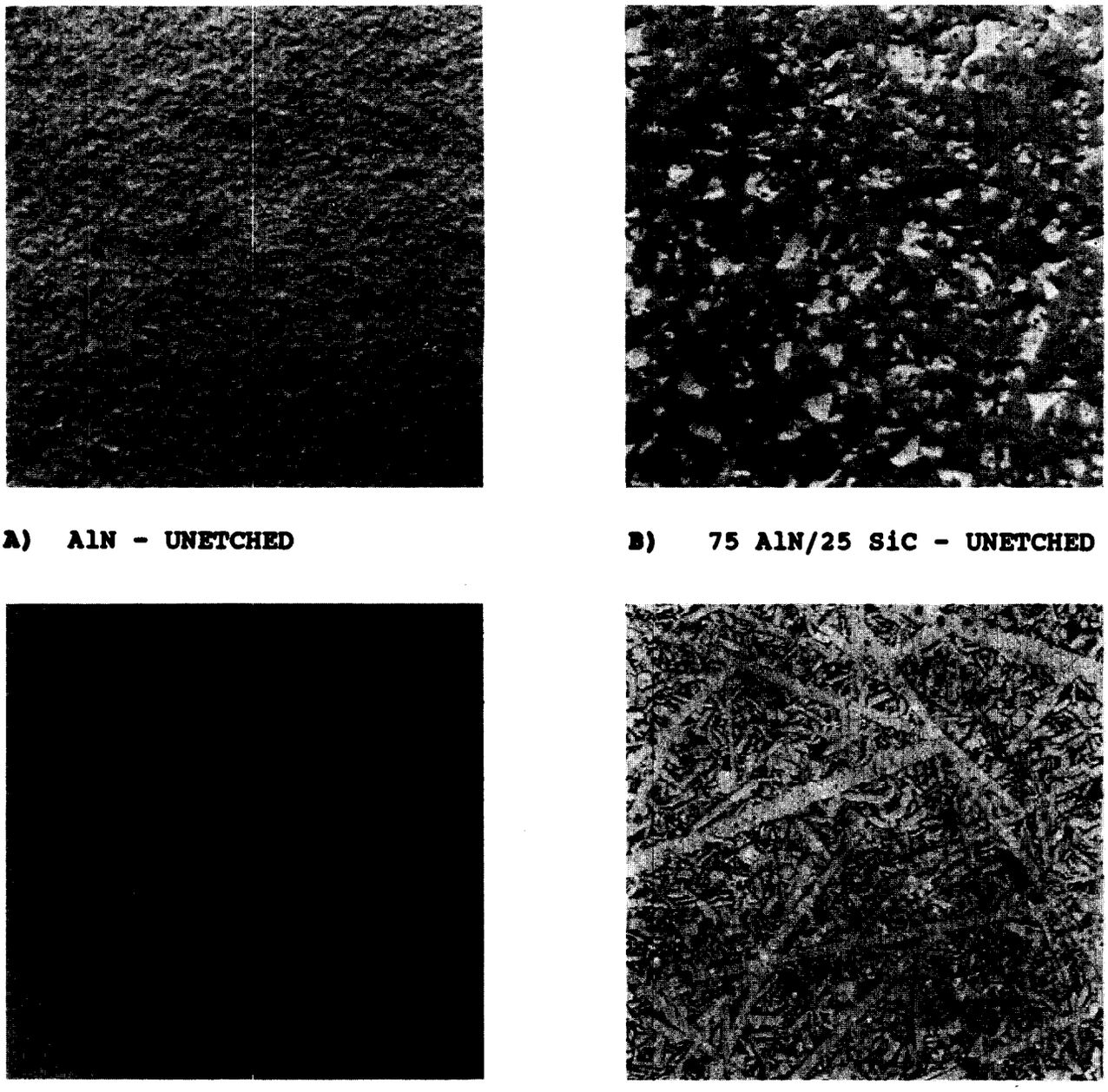


Fig. 1. Optical micrographs AlN–SiC system (original magnification 1000×).

As a result, small bending moments may develop along the gage length. The procedures to correct for this error have been described,[22–25] and were applied to the data reported in this paper.

The stress is related to the hydraulic pressure and test geometry by the following expression:

$$\sigma = \sigma_{nom} + \Delta\sigma = \left(\frac{A - A_s}{A_s}\right) \times P + \Delta\sigma$$

Where: σ_{nom} is the nominal (uncorrected) fracture stress, A is the cross-sectional area of the piston, A_s is the cross sectional area of the specimen, P is the pressure at failure, and $\Delta\sigma$ is the correction for eccentricity which is equal to $\sigma_{nom} \times f$(fracture origin location, specimen eccentricity and diameter).[22–25] The maximum correction for eccentricity in this study was equal to 8·40% with an average correction being approximately 4%.

Four-point bend tests were carried out in accordance with the MIL-STD-1942A standard test.[17] B type bend bars were used, having a size of 3 × 4 × 40 mm with 40 mm outer and 20 mm inner spans as shown in Fig. 4. Tests were carried out on an Instron 4201 universal tensile testing machine.

The fracture surfaces of the tensile specimens were examined by both low magnification optical and high magnification scanning electron microscopy (SEM). SEM fractography and elemental analysis were carried out on a JEOL 840A instrument equipped with an energy dispersive analyzer. The tensile fracture surfaces were ultrasonically cleaned and coated with thin layer of Au–Pd alloy



Fig. 2. TEM of 50/50 solid solution alloy of SiC/AlN showing the sub-micron grain size, ≈ 1/2 μm.

to prevent charging in the SEM. The bend bars shattered into many fragments upon fracture. This made it difficult to do unambiguous fractographic analysis and determine the location of fracture initiation of the bend bars. Consequently, such data will not be reported.

Results and Discussion

Tensile tests

Weibull distributions for the tensile strength of all

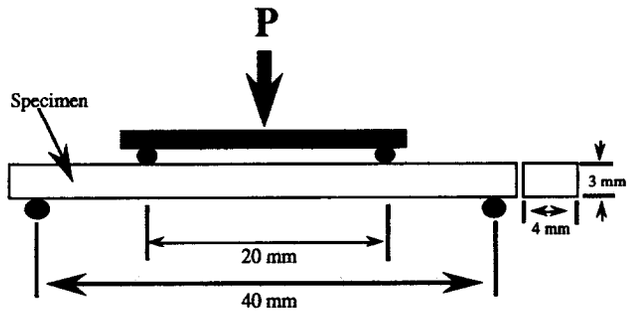


Fig. 4. Four-point bend test.

materials were plotted using the maximum likelihood estimate and are shown in Fig. 5. The characteristic tensile strength of 75%AlN–25%SiC and 50%AlN–50%SiC materials were higher than either of the base materials with values of 371 and 361 MPa, respectively. The AlN material was the weakest among the four materials with a characteristic strength of 234 MPa. The 50%AlN–50%SiC solid solution had the lowest scatter in strength with a Weibull modulus of 26·4. This may be attributed to the uniform nature of this material's microstructure. The other three materials (AlN, SiC, and 75%AlN–25%SiC) all had comparable scatter with Weibull moduli ranging between 9·1 and 12·7, as shown in Fig. 5. The summation of the effective volumes under stress for each set of materials tested is also reported in Fig. 5. 80% of the tested specimens produced valid breaks, 43 out of 53. Details on the tested specimens and the location of the fracture initiating flaws for each material are presented in Table 2.

Fractography of the tensile bars

Low magnification optical fractographs of a typical tensile specimen failure of each of the four materials are presented in Fig. 6, and higher magnification SEM's are presented in Figs 7–11. The AlN samples typically exhibit a well defined

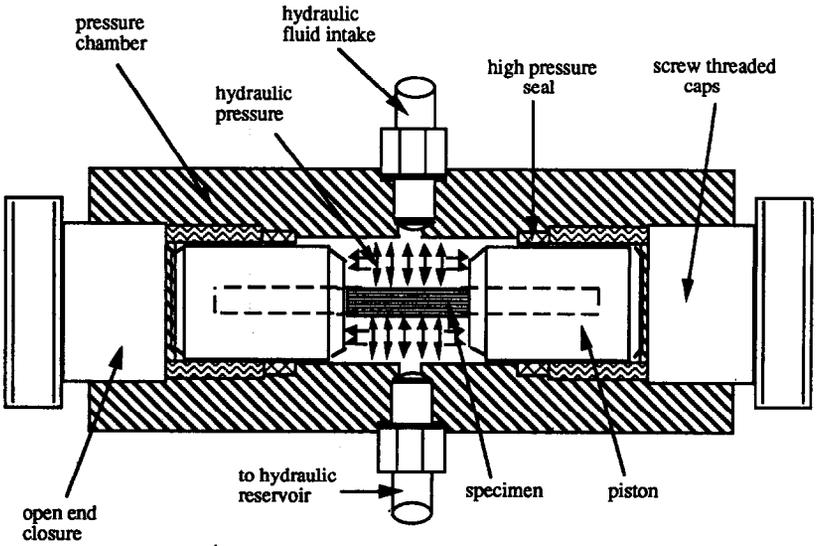


Fig. 3. Hydraulic pressure chamber with specimen–piston assembly.

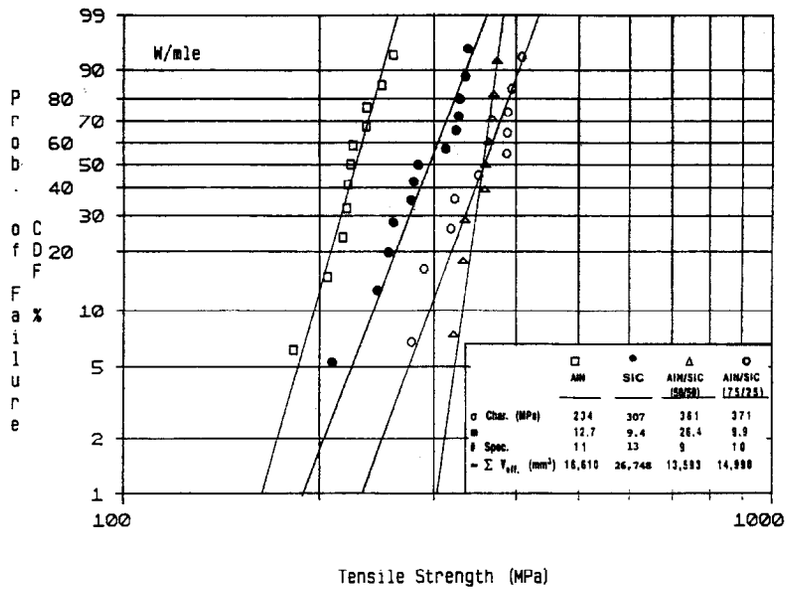


Fig. 5. Weibull strength analysis for ceramics in the AlN–SiC system (tensile tests).

origin, mirror, mist, and hackle as may be seen in Fig. 7(a). The fracture origins in AlN are typically large agglomerates surrounded by high porosity regions (Fig. 7(b)). Figure 8 presents a typical tensile fracture origin in 75%AlN–25%SiC specimens. The initiating flaw agglomerate appears to be highly porous with large grains of irregular morphology which are poorly bonded to the matrix (Fig. 8(b)). EDS results presented in Fig. 9 show a predominance of SiC in the porous region at the origin and an AlN rich region (the 'white area' in Fig. 9(a)) next to the flaw as compared to other regions of the surface. The Fe which is present at the failure origin, may play a role in this apparent segregation of SiC and AlN at the flaw. The fracture mirror in a typical 50%AlN–50%SiC failure origin appears to be smaller than in the case of AlN and 75%AlN–25%SiC (Fig. 6). The usual failure initiating flaw in the 50/50 solid solution alloy was an agglomerate composed of a mass of clustered grains with irregular morphology as shown in Fig. 10. Thus, it was sometimes difficult to locate the initiation of fracture. EDS indicated a lack of SiC at the agglomerate and the presence of pure AlN. The initiating flaw in a typical SiC specimen is also very difficult to locate. The failure initiating flaw appears to be a series of large interconnected pores adjacent to one or more large grains as may be seen in Fig. 11. A summary of the fractography of the four materials is presented in Table 3.

Table 2. Number of tested specimens, valid breaks and their locations

	AlN	*AlN–SiC (75%–25%)*	*AlN–SiC (50%–50%)*	*SiC*
No. specimens tested	15	14	9	15
No. valid breaks	11	10	9	13
Failure origin				
internal	5	6	7	8
near surface	3	2	2	5
indeterminate	1	2	0	0

Prediction of bend strength from tensile data

The four-point bend strength can be predicted from the tensile Weibull parameters by applying the standard Weibull scaling factor.[26]

$$\sigma_b = \sigma_t \left(\frac{\nu_t}{\nu_b}\right)^{\frac{1}{m}} \tag{1}$$

where

σ_t = the strength of the tensile specimens
ν_t = the effective volume of the tensile specimens
ν_b = the effective volume of the flexure specimens
m = Weibull modulus of the tensile specimens

The effective volume in the tensile specimen is the product of the cross-sectional area and the length of the gage section. For four-point bend specimen, the effective volume can be calculated using the following equation:[26]

$$\nu_{\text{eff.}} = \frac{bh}{2}\left(\frac{mL_2 + L_1}{(m+1)^2}\right) \tag{2}$$

where m is the tensile Weibull modulus, and the other parameters are defined in Fig. 4.

The characteristic flexural strength of the four materials were predicted from the tensile strength data. In addition, four-point bend tests of bend bars from the same batches of the four materials used to make the tensile rods were carried out and the Weibull distribution plotted as shown in Fig. 12. The characteristic strength, Weibull modulus,

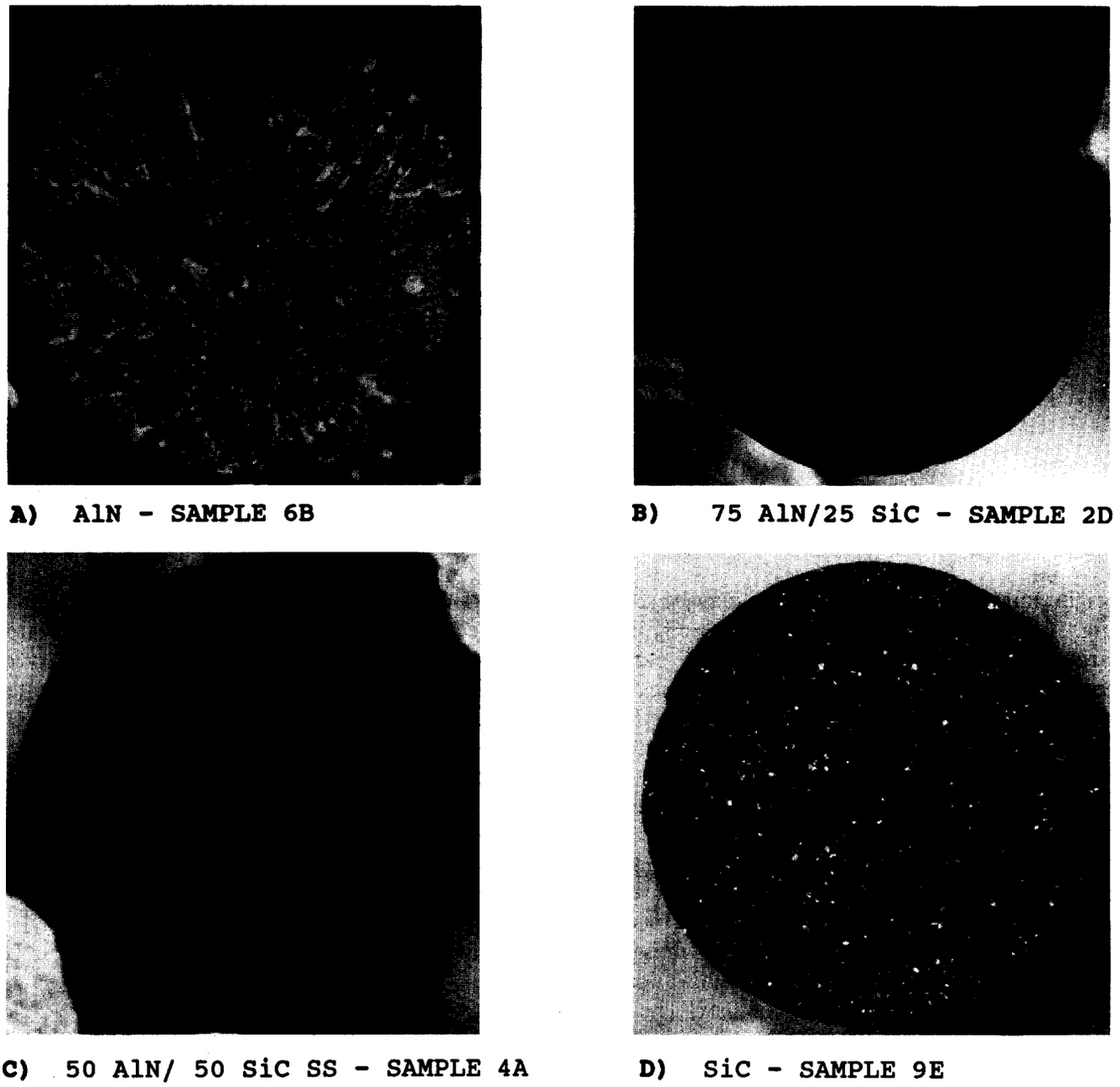
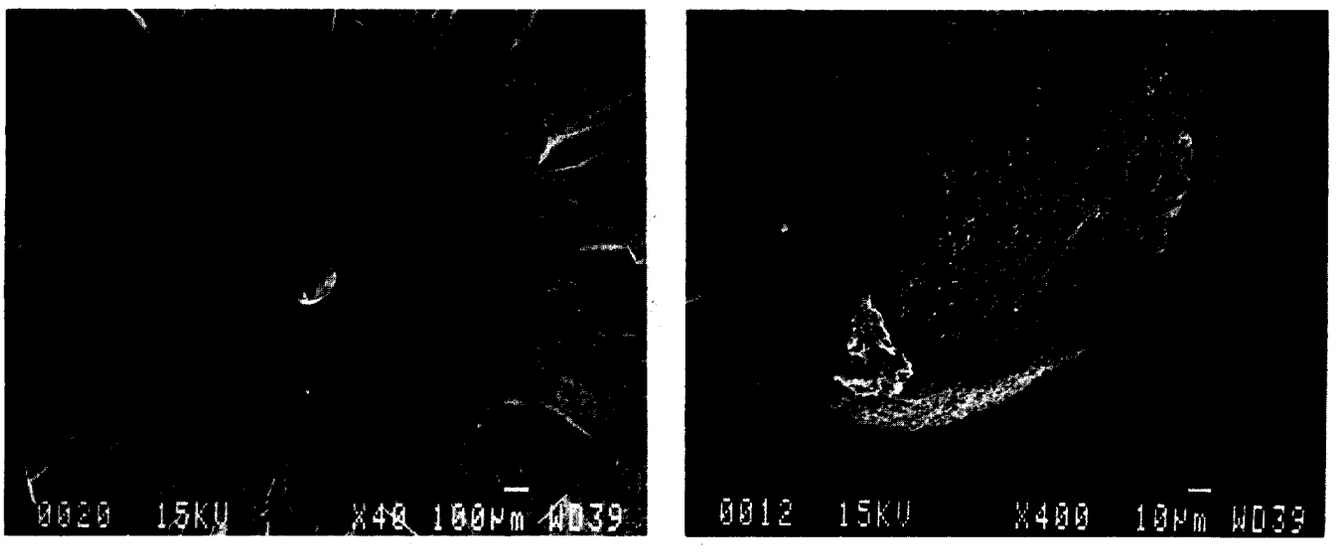
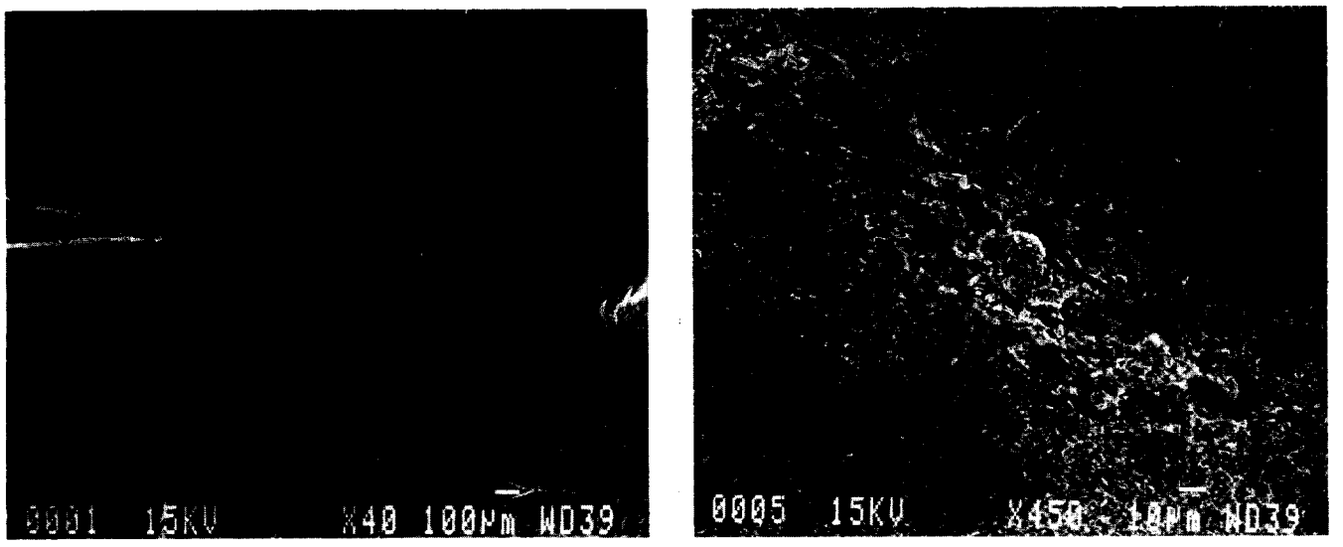


Fig. 6. Optical macro-fractography AlN–SiC system (sample diameter approximately 9 mm).



(A) (B)

Fig. 7. Typical tensile fracture origin in hot pressed AlN: (A) fracture mirror, (B) initiating flaw.



(a) (b)

Fig. 8. Typical tensile fracture origin in 75%AlN–25%SiC: (a) fracture mirror; (b) initiating flaw.

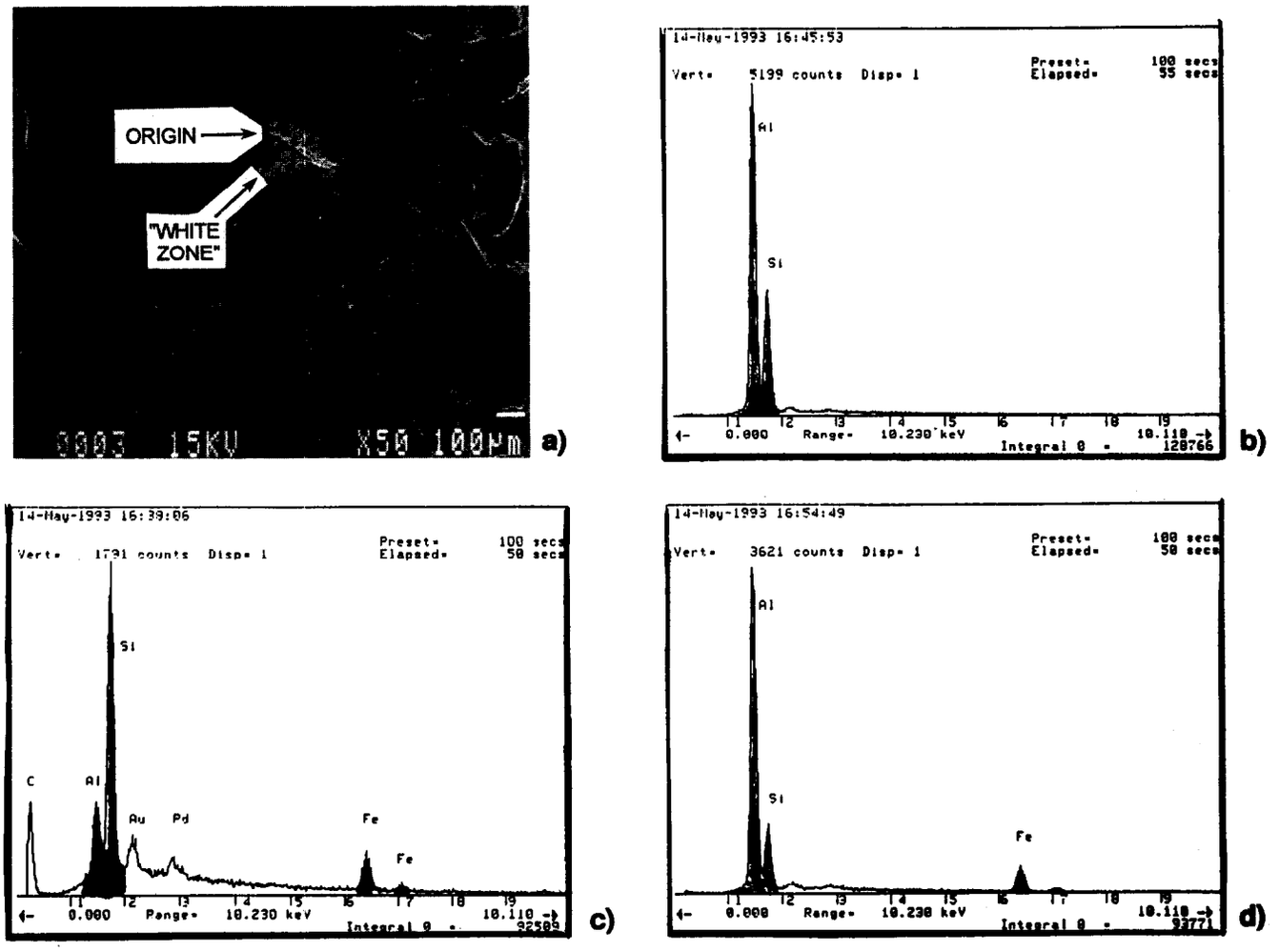


Fig. 9. EDS of failure including flaw in a 75%AlN–25%SiC composite: (a) SEM of initiating flaw and surrounding 'white zone', (b) Normal Si/Al peak height ratio far from origin of failure; (c) Si/Al peak height change indicating Al depletion in failure initiating flaw; (d) Si/Al peak height shift indicates Si depletion in the 'white zone'.

number of specimens, and the sum of the effective stressed volumes for each material are shown on the plot. The predicted and measured four-point bend strengths are compared in Table 4.

As can be seen from Table 4, the predicted flexural strength for the 75%AlN–25%SiC is in close agreement with the measured flexural strength. This is due to the fact that this material has a

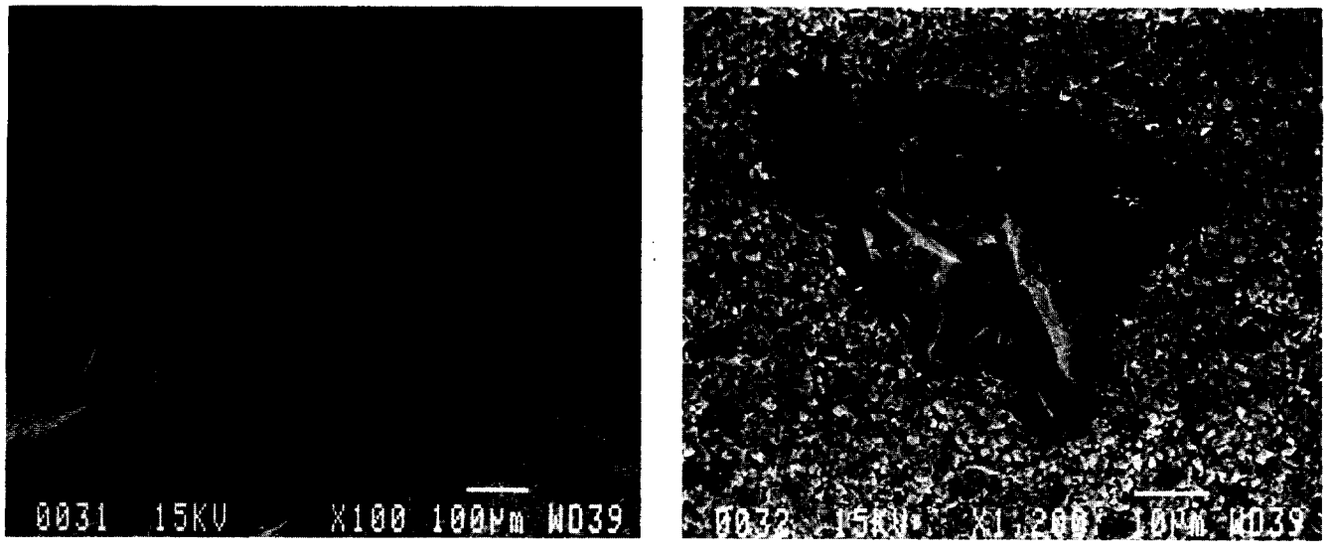


Fig. 10. Typical tensile fracture origin in 50%AlN–50%SiC.

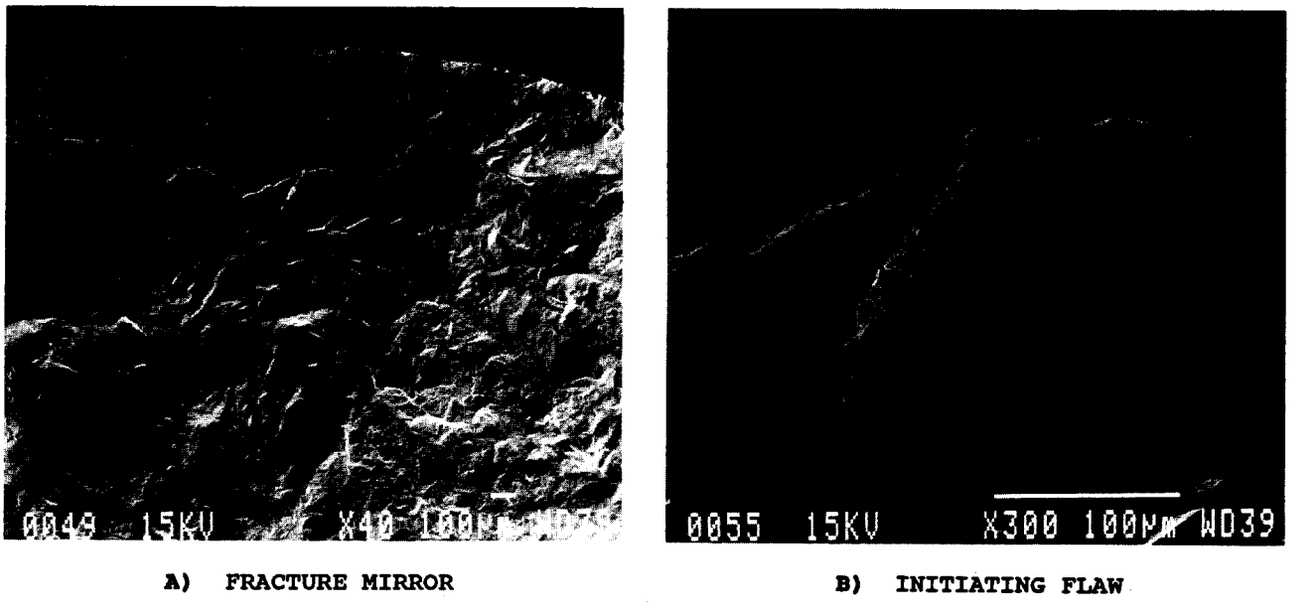


Fig. 11. Typical tensile fracture origin sintered SiC.

Table 3. Fractographical analysis of the ceramic specimens

Material	*Flaw*	*Flaw to matrix bonding characteristics*
AlN	AlN agglomerate circular morphology containing 'large grains' fully dense	Poorly bonded to matrix
75AlN–25SiC (particulate reinforced)	AlN deficient agglomerate irregular morphology 'large grains' highly porous AlN enriched 'white' area surrounding porous agglomerate	Poorly bonded to matrix
50AlN–50SiC (solid Solution)	AlN agglomerate irregular morphology 'large grains' fully dense	Well bonded to matrix
SiC	Large interconnected pores adjacent to large grain	N/A

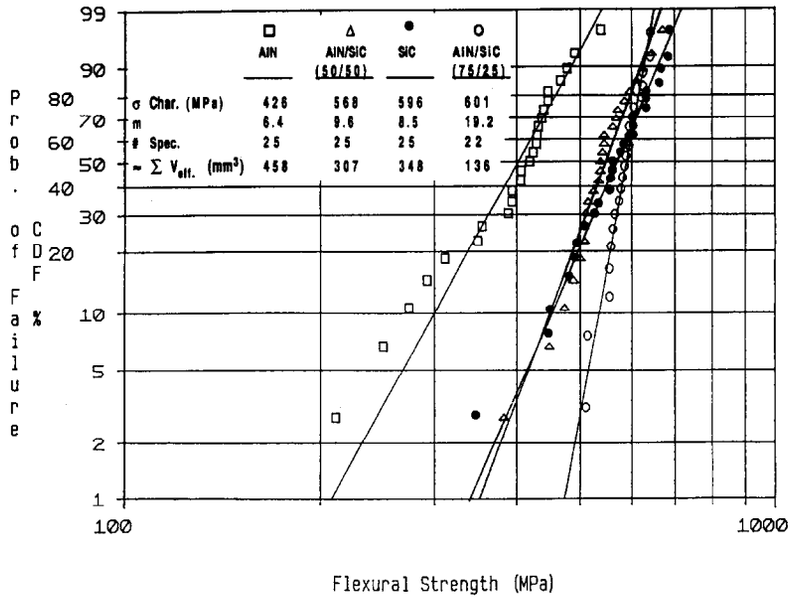


Fig. 12. Weibull strength analysis for ceramics in the AlN–SiC system (4-point bend tests).

Table 4. Predicted and measured flexural strength

Material	*Predicted* $\sigma_{char.}$ *(MPa)*	*Measured* $\sigma_{char.}$*(MPa)*	*Difference (%)*
75AlN/25SiC	605	601	–0·7
SiC	528	596	+11·4
50AlN/50SiC	450	568	+20·8
AlN	349	426	+18

Predictions based on $\sigma_{char.}$, $V_{eff.}$ and m obtained in tensile tests.

bimodal grain/phase structure and this bimodal structure gives rise to flaws that are uniformly dispersed throughout the matrix. The predicted bend strength values for the 50%AlN–50%SiC, AlN, and SiC vary by approximately 21, 18, and 11% of the measured values, respectively. This difference may be attributed to the difference in flaw populations initiating failure as compared to the 75%AlN–25%SiC material. In particular, the large AlN agglomerate which is encountered routinely in the tensile test with its large effective test volume, is likely to be only rarely encountered in bend bars. Identification of the AlN agglomerate as a common failure initiating fracture was obvious in studies of the tensile failures of AlN and 50%AlN–50%SiC, whereas, such a flaw was seen in only one of 25 bend bars. Similarly, the large grains with associated pores which are the failure origins in SiC, may be less frequently encountered in the small stressed volumes of the bend bars whereas, they are commonly encountered in the large tensile specimens. This graphically indicates the importance of obtaining fractographic analysis on tensile specimens as well as bend specimens, in order to be sure to identify all flaw populations.

Conclusions

This study has illustrated the following:

(1) Both the 75%AlN–25%SiC particulate reinforced and 50%AlN–50%SiC solid solution materials showed significantly increased strength as compared to pure AlN and SiC materials.

(2) While the nature of the failure initiating flaws varied for each of the four materials, agglomerates of AlN were common strength determining flaws in the pure AlN and 50%AlN–50%SiC solid solution. The prevalence of this flaw population was clearly evident in the tensile tests but not in the bend tests.

(3) The difference between predicted and measured flexural strength for the AlN, SiC, and 50%AlN–50%SiC materials may indicate that the flaw populations initiating failure differ. Because the tensile test interrogates a significantly larger stressed volume than does the bend test, the tensile test may well include flaw populations that are missed in conventional (10–30 specimens) bend testing. In such cases use of Weibull parameters obtained from tensile testing will tend to underpredict the fracture strength of the smaller component. Thus, the use of tensile data will yield a conservative design.

(4) Finally, the benefit of tensile tests in identifying failure initiating flaw populations was clearly demonstrated. Such information can provide useful feedback to materials' developers.

References

1. Katz, R. N., Opportunity and prospects for the application of structural ceramics. In *Treatise on Materials Science and Technology, 29: Structural Ceramics*. ed. J. B. Wachtman, Jr. Academic Press, Boston, MA, 1989, pp. 1–26.
2. Rafaniello, W., Plichta, M. R. & Virkar, A. V., Investigations of phase stability in the system SiC–AlN. *J. Am. Cer. Soc.*, **66**[6] (1983) 272–6.
3. Ruh, R., Zangvil, A. & Barlowe, J., Elastic properties of SiC, AlN and their solid solutions and particulate composites. *Bull Am. Soc.*, **64**[10] (1985) 1368–74.
4. Dutta, S., Strength distribution in commercial silicon carbide materials. *J. Am. Cer. Soc.*, **71**[11] (1988) C474–9.
5. Srinivasan, M., The Silicon Carbide family of structural ceramics. In *Treatise on Materials Science and Technology, 29: Structural Ceramics*, ed. J. B. Wachtman, Jr. Academic Press, Boston, MA, 1989, pp. 99–159.
6. Woodilla, D., Buonomo, M., Bar-On, I., Katz, R. N. & Whalen, T., Elevated-temperature behavior of high-strength Silicon Carbide. *J. Am. Cer. Soc.*, **76**[1] (1993) 249–52.
7. Boch, P., Glandus, J. C., Jarrige, J., Lecompte, J. P. & Mexmain, J., Sintering, oxidation, and mechanical properties of hot pressed Aluminum Nitride. *Ceramics International*, **8**[1] (1982) 34–40.
8. De With, G. & Hattu. N., Mechanical behavior of hot-pressed Aluminum Nitride ceramics. *Science of Ceramics*, **11** (1981) 489–94.
9. Skeele, F. P., Slavin, M. J. & Katz, R. N., Time–temperature dependence of strength in Aluminum Nitride. In *3rd International Symposium, Ceramic Materials & Components for Engines*, ed. V. J. Tenney, American Ceramic Society, 1989, pp. 710–8.
10. Katz, R. N., Wechsler, G., Toutanji, H., Friel, D., Leatherman, G. L., El-Korchi, T. & Rafaniello, W., Room temperature tensile strength of AlN. *Ceram. Eng. Sci. Proc.*, **14**(7–8). (1993) 282–91.
11. Ruh, R., & Zangvil, A., Composition and properties of hot-pressed SiC–AlN solid solutions. *J. Am. Cer. Soc.*, **65**[5] (1982) 260–5.
12. Landon, M. & Thevenot, F., The SiC–AlN system: Influence of elaboration routes on the solid solution formation and its mechanical properties. *Ceramics International*, **17**[1] (1991) 97–100.
13. Miura, M., Yogo, T. & Hirano, S., Microstructure and mechanical properties of SiC–AlN ceramics after phase separation treatment. *J. Cer. Soc. Jpn.*, **101**[7] (1993) 793–99.
14. Miura, M., Yogo, T. & Hirano, S., Mechanical and thermal properties of SiC–AlN ceramics with modulated texture. *J. Cer. Soc. Jpn.*, **101**[11] (1993) 1281–6.
15. Mariano, S. A., Friel, D. & Bar-On, I., Evaluated temperature mechanical properties of SiC–AlN particulate composites, *Ceram. Eng. Proc.*, **14**[9–10] (1993) 1077–88.
16. Rafaniello, W., Development of Aluminum Nitride: a new low-cost armor, Final Report U.S. Army Research Office, Contract Number DAAL03-88-C-001 2 Dec. 1992.
17. Flexural strength of high performance ceramics at ambient temperature, MIL-STD-1942 (MR), Army Materials Technology Laboratory, Watertown, MA, Nov. 1983.
18. Rafaniello, W., unpublished research, Dow Chemical Co.
19. Baratta, F. I. & Driscoll, G. W., A new axial tension tester for brittle materials, Army Materials and Mechanics Research Center, AMMRC TR 69-02, Watertown, MA, 1968.
20. Driscoll, G. W. & Baratta, F. I., Modifications to an axial tension tester for brittle materials, Army Materials and Mechanics Research Center, AMMRC PTR 71-3, Watertown, MA, 1971.
21. Hermansson, L., Adlerborn, J. & Burstrom, M., Tensile testing of ceramic materials—A new approach. In *High Tech Ceramics*, ed. P. Vincenzini, Elsevier Science Publishers B. V., Amsterdam, 1987, pp. 1161–8.
22. ASEA CERAMA AB, Introduction and Operation Manual for ASCERA Hydraulic Tensile Testing, Robertsfors, Sweden, 1988.
23. Lucas, H. P., Direct tensile testing of brittle materials, Master Thesis, (1991), Worcester Polytechnic Institute, Worcester, MA.
24. Toutanji, H. A., El-Korchi, T., Leatherman, G. L. & Katz, R. N., Tensile strength of Carbon fiber reinforced cement composites. In *Fiber Reinforced Cementitious Composites*, Mat. Res. Soc. Symp. Proc., **245**, 1992, pp. 359–64.
25. Toutanji, H. A., The development of a cementitious composites axial tensile technique and its application to Carbon fiber reinforced cementitious composites, Ph.D. Thesis, Worcester Polytechnic Institute, Worcester, MA, 1992.
26. McLean, A. F. & Hartsock, D. L., Design with structural ceramics. In *Treatise on Materials Science and Technology, 29: Structural Ceramics*, ed. J. B. Wachtman, Academic Press, Inc., 1989 pp. 27–95.

Journal of the European Ceramic Society **15** (1995) 435–443
© 1995 Elsevier Science Limited
Printed in Great Britain. All rights reserved
0955-2219/95/$9.50

Thermal Conductivity Improvement of YAG Added AlN Ceramics in the Grain Boundary Elimination Process

Mitsuo Kasori & Fumio Ueno

Materials & Devices Research Laboratory, Research & Development Center, Toshiba Corporation, Kawasaki, Kanagawa 210, Japan

(Received 26 August 1993; revised version received 14 July 1994; accepted 10 August 1994)

Abstract

The primary cause of the thermal conductivity improvement in Y_2O_3-containing AlN ceramics caused by elimination of the grain boundary phase was investigated. $Y_3Al_5O_{12}$ (YAG)-containing AlN powder compacts were sufficiently densified by firing at 1800°C for 30 min, but had low thermal conductivity (90–110 Wm^{-1} K^{-1}). Improvement to 245 Wm^{-1} K^{-1} and elimination of the grain boundary phases was brought about by annealing in a carbo-reductive atmosphere at 1850°C for up to 100 h. During annealing, $YAlO_3$, $Y_4Al_2O_9$ and Y_2O_3 appeared as a result of the reduction–nitridation of the Al_2O_3 constituent in the YAG. Subsequently, these yttrium rich phases acted as oxygen getters for the dissolved Al_2O_3 which was originally included in the AlN grains. The Al_2O_3 continuously changed into AlN by reduction–nitridation. The cyclic oxygen removal from the AlN through the grain boundary phase composition change is seen as the primary cause for the thermal conductivity improvement.

1 Introduction

AlN ceramic is an insulator having a high thermal conductivity. Applications of AlN ceramics for high power devices and micro electronics packaging materials as heat dissipation substrates are spreading.[1] The heat carrier in AlN is the phonon. Phonon scattering may occur from impurities or lattice imperfections and decrease thermal conductivity. The most harmful impurity has been found to be oxygen. Dissolved oxygen ions in AlN occupy the nitrogen sites, and they generate Al vacancies to compensate the electric charge balance.[2] Commercially available AlN powders have around 1 wt% of oxygen as a surface layer of oxide or oxy-nitride of aluminum.[3,4] Without any oxygen getter, the oxygen in the surface layer dissolves into AlN during sintering. A full densification of AlN by pressureless sintering has been achieved by rare earth or alkaline earth additions.[5] Y_2O_3 and CaO are popular sintering aids. These sintering aids react with the aluminum oxide surface layer at a sintering temperature of around 1800°C. These reactions generate yttrium aluminate or calcium aluminate liquid phases during sintering. These liquid phases are supposed to promote liquid phase sintering of AlN. The aluminates remain in the ceramics as grain boundary phases after sintering. In this way, these sintering aids act as oxygen getters by fixing aluminum oxide as a grain boundary phase. In the case of Y_2O_3 additions, $Y_3Al_5O_{12}$ (YAG), $YAlO_3$(YAL), $Y_4Al_2O_9$ (YAM), and Y_2O_3 were found as grain boundary phases. The kinds of phases remaining depend on the ratio of the amount of oxygen in the starting AlN powder and the amount of Y_2O_3 addition.

Prolonged firing of up to 96 h in a carbo-reductive atmosphere is known to improve thermal conductivity up to around 260 Wm^{-1} K^{-1}.[6] With this kind of firing, the yttrium aluminate grain boundary phases are eliminated from the AlN ceramic. The rate of grain boundary phase elimination from the ceramic is higher when it is fired in a graphite setter than when fired in an AlN setter. A trace amount of carbon gas from the setter or from a graphite heater promotes the reduction–nitridation of the oxides in the yttrium aluminate phases at the ceramic surface. An oxide concentration gradient between the surface and the interior of the ceramics develops during firing; it relaxes by grain boundary diffusion of the oxide.[6] This kind of thermal conductivity improvement and grain boundary elimination has also been observed in other lanthanoide additions but not in alkaline earth additions.[7,8]

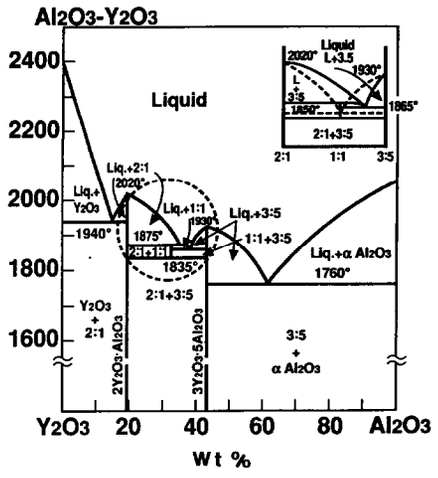


Fig. 1. Phase diagram of Al_2O_3–Y_2O_3 system.

The influence of the grain boundary phase on thermal conductivity has been considered to be slight.[9,10] This is because the grain boundary phases are located at three grain points, thus maintaining sufficient AlN–AlN contacts. AlN grain growth in the ceramics has also been observed in prolonged firing. However, the mean free path of phonons in AlN at room temperature has been estimated to be around 10–30 nm,[11] and the average grain size of AlN in the ceramics is at least around 3 μm even before the prolonged firing. Namely, the mean free path is sufficiently small for the AlN grain size and phonon scattering at the AlN–AlN grain boundaries to have a negligible influence on thermal conductivity.

The aim of this work was to clarify the primary cause of the thermal conductivity improvement in the grain boundary elimination process. The authors have considered that a further oxygen removal from the AlN grains by yttrium aluminates or yttrium oxide grain boundary phases during the grain boundary elimination process might be the primary cause. YAG was used as a sintering aid to test this hypothesis. It was considered from the Y_2O_3–Al_2O_3 phase diagram shown in Fig. 1[12] that YAG should act as a sintering aid if a YAG-containing AlN powder compact is fired at a higher temperature than the liquidus temperature of the YAG. It was also considered that the AlN ceramics densified by YAG addition should have a higher concentration of dissolved oxygen than AlN ceramics densified with Y_2O_3 addition. We can obtain AlN ceramics having a certain amount of dissolved oxygen and having YAG grain boundary phase by this method. Firings of the YAG-containing AlN ceramics in a carbo-reductive atmosphere can be expected to reveal the primary cause of the thermal conductivity improvement in the grain boundary elimination process.

2 Experimental Procedure

2.1 Ceramic preparation

Fine powders of Y_2O_3 (Shinestu Chemical, 4N) an α-Al_2O_3 (Baikowski, 4N) were mixed at a ratio of $3Y_2O_3:5Al_2O_3$. After 0·5 wt% AlF_3 fine powder (Morita Kagaku Kogyo, 3N) was added as a catalyst, the mixed powder was heated at 1500°C for 5 h in an alumina crucible in air. It was then pulverized using an Al_2O_3 mortar. The composition was identified as YAG by XRD. AlN mixed powders, (Tokuyama Soda, F-type, oxygen 0·71 wt%), containing 1, 2, 5, 10, and 20 wt% YAG were prepared. AlN mixed powders containing 1 and 3 wt% Y_2O_3 were also prepared. The mixing was carried out by a wet ball mill using butyl alcohol. After adding a 5 wt% acrylic binder (Tyukyo Oil, SERUNA-SE3000), the mixed powders were fabricated into 30 × 30 × 8 mm compacts by pressing under 50 MPa. Then, they were de-waxed by heating at up to 700°C in N_2 gas.

The mixed powder compacts were sintered at 1800°C for 30 min, in a h-BN setter under an atmospheric pressure of nitrogen using a graphite heater furnace. These ceramics were then annealed at 1850°C for 1, 3, 10, 30, and 100 h respectively, in a graphite setter under an atmospheric pressure of nitrogen in the same graphite heater furnace.

2.2 Characterization

The thermal diffusivity at 23 ± 2°C was measured by the laser-flash method (Shinku Riko, TC-3000). A ruby laser was used for the flash and InSb was used for the infrared detector. Disk samples having 10 mm diameter and around 3·5 mm thickness were coated with a thin gold layer on the surface to prevent the flash penetrating into the ceramics. A carbon black layer was applied over the gold layer to enhance the absorption of the flash energy. Corrections on thermal diffusivity regarding the flash duration time and flash inhomogeneity were carried out according to the Japanese Industrial Standard (JIS-R1611). The thermal conductivity was calculated from the thermal diffusivity, the specific heat measured by differential scanning calorimetry, and the density.

The constituents of the ceramics were identified by powder XRD after being pulverized. The *c*-axis lengths of AlN at room temperature were measured using the internal standard for Si (NIST, 640b). The yttrium contents in the ceramics were measured by the inductively coupled plasma (ICP) method.

Table 1. Comparisons of yttrium concentrations between starting powder compositions and ceramics by ICP.

		Yttrium concentration/wt%	
Additives	*(wt%)*	*Starting composition*	*Analytical result*
YAG	20	8·99	9·03
	10	4·49	3·73
	5	2·25	2·11
	1	0·45	0·44
Y_2O_3	3	2·36	2·26

3 Results

3.1 Sintering by YAG additions

The AlN mixed powder compacts fired at 1800°C–30 min were sufficiently densified without any pores. Table 1 shows the yttrium concentrations in the ceramics measured by ICP and those calculated from the starting compositions. The constituents of the ceramics besides AlN were YAG for YAG added, YAG for 1 wt% Y_2O_3 added, and YAL and YAM for 3 wt% Y_2O_3 added. Figure 2 shows the relationships between the density, the thermal conductivity and the amount of YAG or Y_2O_3 additions. The density increased linearly with the amount of additions in both cases. The thermal conductivity decreased as the amount of YAG addition increased. On the other hand, the thermal conductivity improved as the amount of Y_2O_3 addition increased.

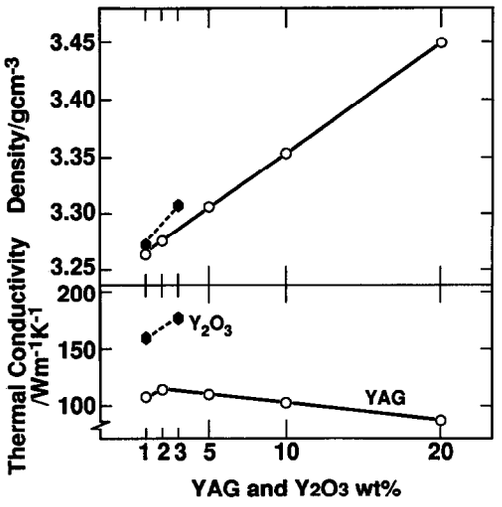


Fig. 2. Relationship between thermal conductivity and density of ceramics and amount of YAG or Y_2O_3 additions.

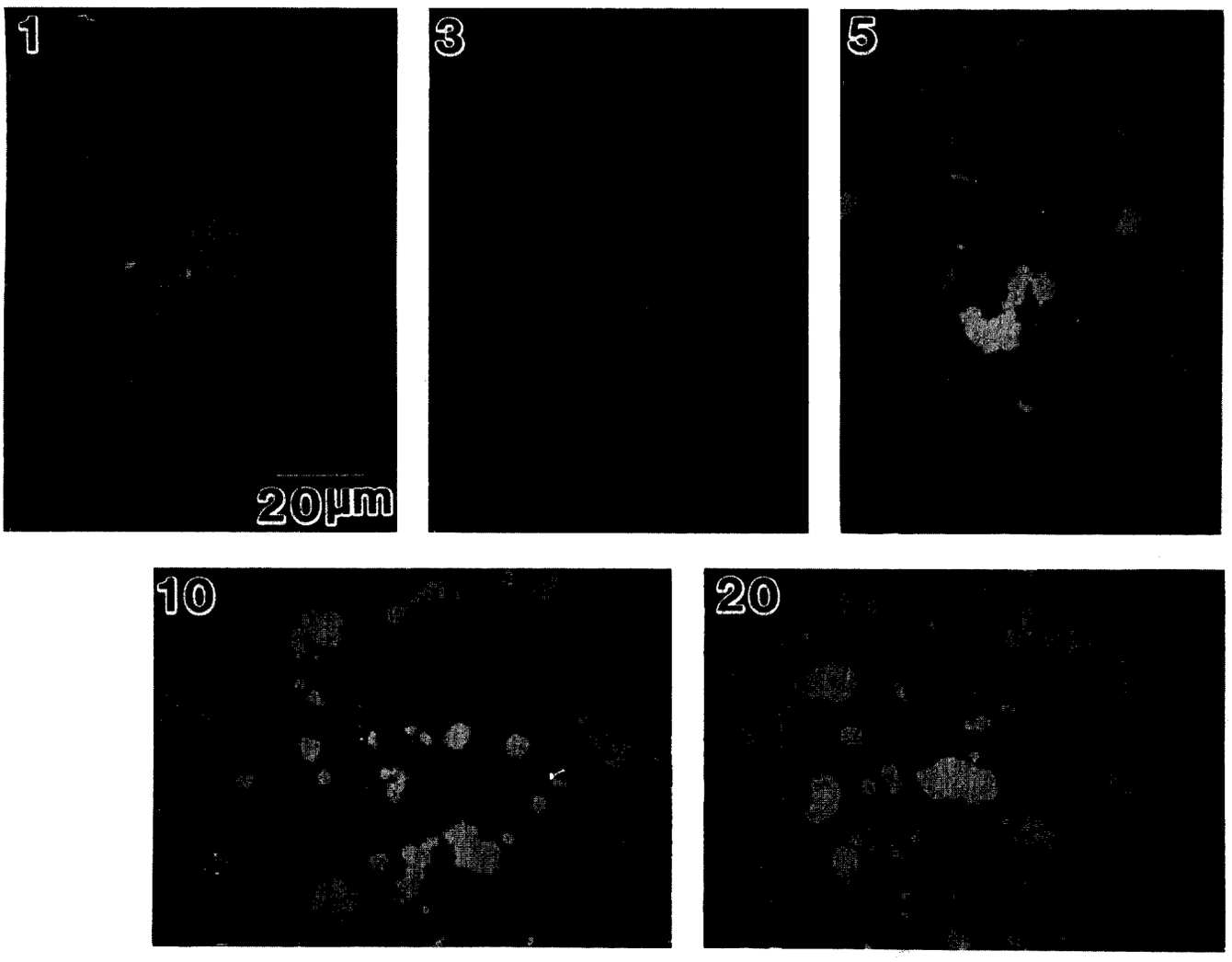


Fig. 3. SEM photographs of polished surfaces of YAG added ceramics.

Considering that the thermal conductivity of the AlN ceramics using Tokuyama Soda F-Type powder which has no additives and have at least 98% theoretical density ranged from 90 to 120 Wm^{-1} K^{-1},[6,13,14] it was considered that the YAG additions contributed to densification but not to thermal conductivity improvement. The thermal conductivity of YAG is around 13 Wm^{-1} K^{-1}.[15] Therefore, the decrease in thermal conductivity by YAG addition is considered to be the result of increase in the amount of poorly conducting phase (YAG) for a given oxygen content in the AlN.[16]

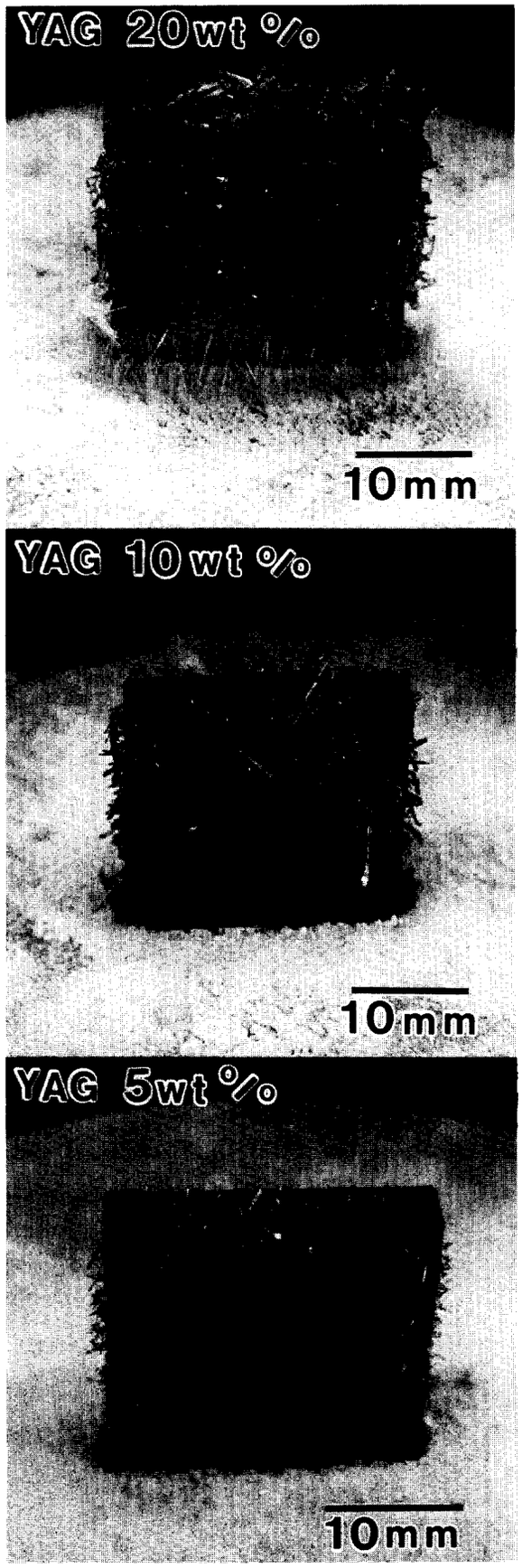


Fig. 4. Annealed appearances of ceramics after 10 h annealings.

The YAG distributions in individual ceramics are shown in Fig. 3. The photographs are SEM images of polished surfaces, and the individual numbers in the photographs represent the amount of YAG addition. The white parts can be attributed to the YAG regions. YAG was distributed as islands ranging from 1 to 20 μm in diameter in the AlN matrix except for the 3 wt% YAG added case. The ratio of $Al_2O_3/(Al_2O_3 + Y_2O_3)$ in the YAG 3 wt% addition case was 0·63, a value very close to the eutectic point composition of Y_2O_3–Al_2O_3. The amount of Al_2O_3 was calculated from YAG and the oxygen content of AlN starting powder.

3.2 Thermal conductivity improvement by annealing in the carbo-reductive atmosphere

The appearances of the as-annealed ceramics are shown in Fig. 4. The photographs show the samples of 5, 10, and 20 wt% YAG, respectively, after 10 h annealing. Needle-like AlN crystals and a black layer on the ceramic surfaces were observed in all cases. The black layer consisted of YN and AlN as determined by XRD. The needle-like AlN crystals grew larger as the YAG content became higher.

Figure 5 shows the relationship between the weight changes of the ceramic constituents besides AlN and the annealing time. The weights were calculated based on the weights of the pre-annealed ceramics, i.e. weight change (%) = (weight before annealed–weight after annealed)/(weight

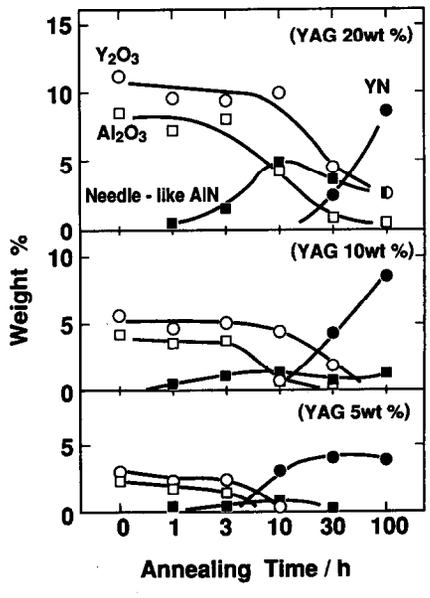


Fig. 5. Weight changes of secondary ceramic constituents during annealings.

before annealed) × 100. The weight changes of the Y_2O_3 and the Al_2O_3 constituents are commensurate with the composition changes of the yttrium aluminate grain boundary phases. The amount of the yttrium aluminate phases were measured from XRD peaks using calibration curves made in advance. Figure 6 shows the yttrium concentrations in the ceramics measured from the ICP and XRD peaks. There was little difference between them. As shown in Fig. 5, the amount of the needle-like AlN crystals increased as the Al_2O_3 constituent in the yttrium aluminate grain boundary phase decreased. The amount of YN also increased as Y_2O_3 constituent in the yttrium aluminate grain boundary phase decreased. From these results, it is considered that the Al_2O_3 constituent in the YAG changed into the needle-like AlN and the Y_2O_3 constituent changed into YN. The amount of the needle-like

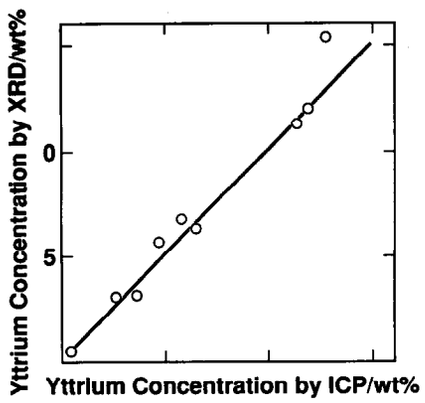


Fig. 6. Comparison of yttrium concentrations in AlN ceramics measured by ICP and XRD.

AlN crystal was maximized at 10 h and decreased over 30 h. It was considered that the enlargement of the surface area by the needle-like AlN crystal generation brought about a substantial sublima-

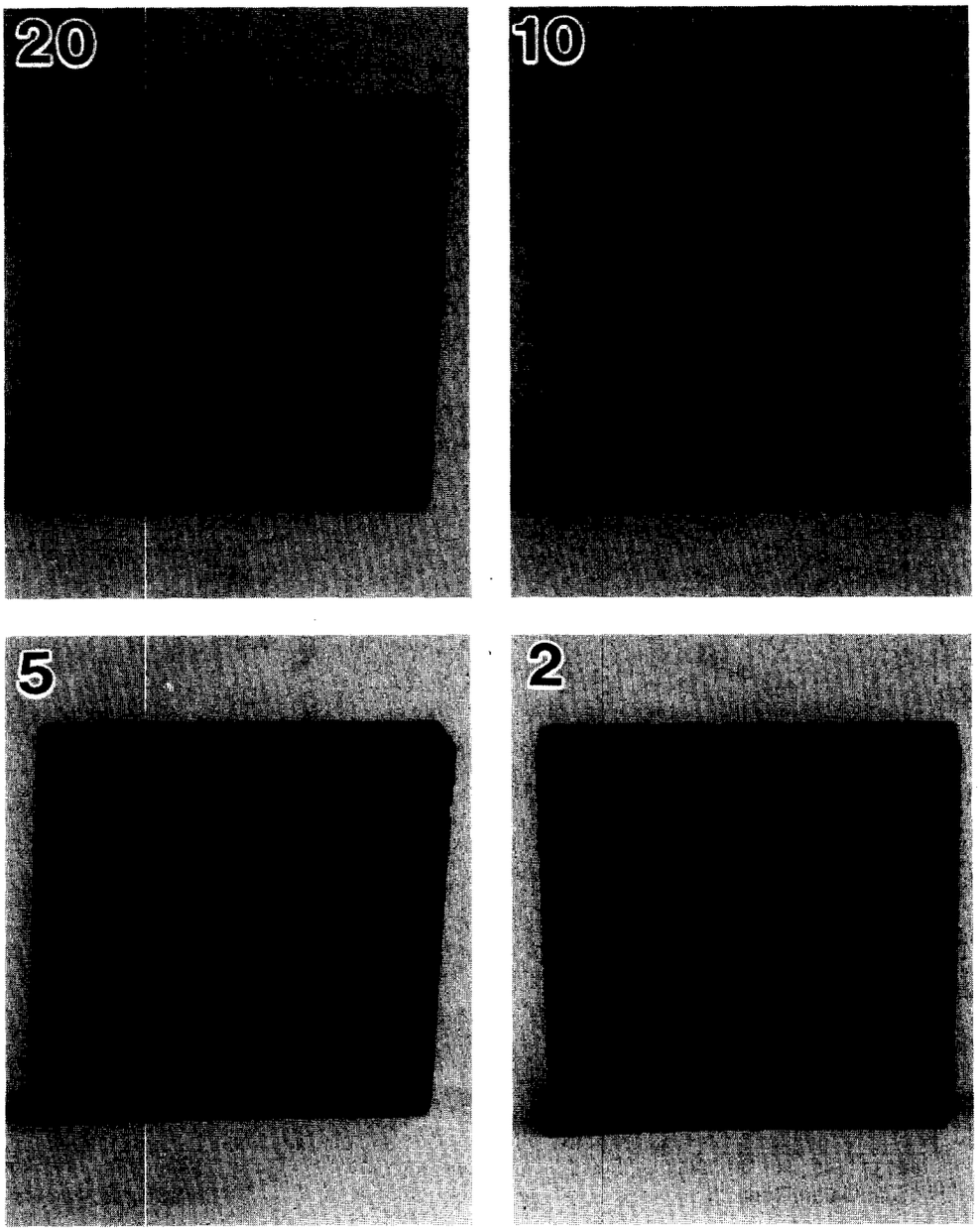


Fig. 7. AlN ceramics surfaces after 3 h annealings. Needle-like AlN crystals were eliminated.

		Firing Time/h					
		0	1	3	10	30	100
YAG	20 wt%	YAG19.7	YAG16.8	YAG15.5 YAP4.5	YAP 9.5 YAM 7.2	YAM 4.5 Y_2O_3 3.1	YAM 1.3 Y_2O_3 2.1
	10	YAG9.9	YAG8.5	YAG6.0 YAP4.1	YAM 4.5 Y_2O_3 0.8	YAM 1.3 Y_2O_3 0.8	
	5	YAG5.3	YAG4.1	YAG1.4 YAP2.4	YAM 0.3 $Y_2O_3$0.02		
	2	YAG1.6	YAG1.6	YAG0.7			
	1	YAG0.8	YAG0.7				
Y_2O_3	3	YAP2.7 YAM2.6					
	1	YAG2.7					

Fig. 8. Interior grain boundary phases changes of AlN ceramics during annealings. Blanks present grain boundary free.

tion of AlN. The YN generation on the ceramic surfaces was striking for the ceramics having lesser YAG contents. The appearances of the ceramics after 3 h annealings are shown in Fig.7. The needle-like AlN crystals were taken off beforehand in these cases. The YN layer covered the whole ceramic surfaces in the case of 1 and 2 wt% YAG additions. Only the upper side of the ceramics was covered with the YN layer, in the case of 5 wt% YAG addition. There was no YN layer on the ceramic surfaces in the case of 10 and 20 wt% YAG additions. It was observed that parts near to the graphite setter tended to form YN quickly.

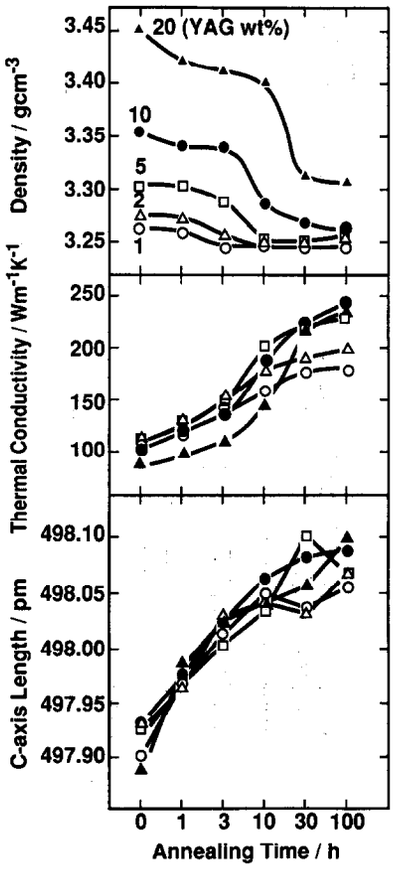


Fig. 9. Relationship between density, thermal conductivity, *c*-axis length and annealing time in different YAG additions.

It was not only the surface layer, but also the interior compositions of the ceramics that were changed during the annealing. It was expected that the grain boundary phase compositions in the vicinity of the ceramic surface were different from the interior.[17] A layer at least 0·5 mm thick was cut from the surface before pulverizing for the XRD measurements. The grain boundary compositions changed during the annealing, as shown in Fig. 8. Blanks indicate the absence of grain boundary phase examined by XRD. YAG turned into phases richer in yttrium as the annealing time was prolonged. Namely, the grain boundary phases changed in the direction of YAG→YAP→YAM→Y_2O_3. Ceramics having a lower YAG content reached the grain boundary phase free state quicker. The grain boundary phases were eliminated completely after 100 h annealing except for YAG 20 wt% addition.

The relationship of the density, the thermal conductivity and the *c*-axis length of AlN to the annealing time is shown in Fig. 9. The numbers in the figure represent the YAG content. The density converged to the theoretical density of AlN (3·26 gcm^{-3}) as the annealing time increased because of the elimination of grain boundary phases with higher densities than AlN. The smaller amount of YAG content made the density decrease earlier. The density decreased in a different manner to the YAG contents. The density decreased noticeably during 10–30 h for 20 wt%, 3–10 h for 10 and 5 wt% and 1–3 h for 2 and 1 wt% YAG. The thermal conductivity improved almost linearly in YAG 1 and 2 wt%. Thermal conductivity improvement

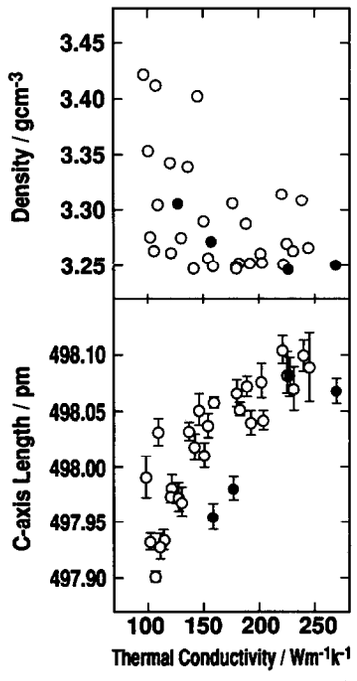


Fig. 10. Relationship between density, *c*-axis length of AlN and thermal conductivity.

occurred during 10–30 h for YAG 20 wt% and 3–10 h for YAG 10 and 5 wt%. These periods coincided with the period of decreasing density. On the other hand the *c*–axis length lengthened gradually during the annealing. Standard deviation of each of the *c*–axis lengths was within 0·10 pm. The *c*–axis lengths ranged from 497·89 to 497·93 pm before annealing and then ranged from 498·07 to 498·10 pm. The *c*–axis length of starting AlN powder was 498·05. The *c*–axis length became shorter at sintering and was then restored by annealing.

In Fig. 10 the relationship between thermal conductivity, density and the *c*–axis length for all samples in this study are shown. The open and the solid circles indicate YAG and Y_2O_3 added, respectively. Even though the density is almost the theoretical of AlN, the thermal conductivity ranged from 90 to 260 $Wm^{-1}\ K^{-1}$. The wide extent of the density range was diminished as the thermal conductivity increased. The *c*–axis length increased as thermal conductivity rose. However, it was found that, a coefficient of correlation to the thermal conductivity was different around the upper and the lower sides of 150 $Wm^{-1}\ K^{-1}$.

Thermal conductivity increased from around 100 to around 250 $Wm^{-1}\ K^{-1}$ by annealing. The *c*–axis length also increased from around 497·3 to 498·8 pm. The highest thermal conductivity within the scale of experiment was 265 $Wm^{-1}\ K^{-1}$. This was obtained by 3 wt% Y_2O_3 addition and 30 h annealing. In the case of YAG additions, the highest was 245 $Wm^{-1}\ K^{-1}$ for 10 wt% YAG after 100 h firing.

4 Discussion

Oxygen occupies nitrogen sites when it dissolves into AlN. The dissolution generates Al vacancies to preserve the electric charge balance. An increase in Al vacancy concentration decreases the *c*–axis.[18] The *c*-axis length of the starting AlN powder was 498·05 ± 0·015 pm. From the results of the *c*–axis length and the thermal conductivity changes, it was considered that the oxygen first dissolved into AlN at 1800°C–30 min sintering and was then gradually removed from the AlN grains by the annealings. Trace amounts of carbon gases are expected in the firing atmosphere. The carbon gas should stimulate the reduction–nitridation of oxides at a high temperature in a nitrogen atmosphere. Therefore, Al_2O_3 and Y_2O_3 in the yttrium aluminate were changed into AlN and YN, respectively, as in the following equations.

$$Al_2O_3 + N_2 + 3C \rightarrow 2AlN + 3CO\uparrow (-40\text{k mol}^{-1}) \quad (1)$$

$$Y_2O_3 + N_2 + 3C \rightarrow 2YN + 3CO\uparrow (80\text{k mol}^{-1}) \quad (2)$$

The YAG located at the ceramic surface reacted with the carbo-reductive atmosphere directly. Subsequently, the Al_2O_3 in the YAG located at the surface changed into AlN according to reaction (1) as a first stage. An oxide concentration gradient between the surface and the interior of the ceramics developed, and was then relaxed by the grain boundary diffusion of the oxide.[6]

The consumption of the Al_2O_3 constituent in the YAG and other yttrium aluminates formed yttrium richer phases, as in the following equations.

$$Y_3Al_5O_{12} + N_2 + 3C \rightarrow 3YAlO_3 + 2AlN + 3CO\uparrow \quad (3)$$

$$4YAlO_3 + N_2 + 3C \rightarrow Y_4Al_2O_9 + 2AlN + 3CO\uparrow \quad (4)$$

$$Y_4Al_2O_9 + N_2 + 3C \rightarrow 2Y_2O_3 + 2AlN + 3CO\uparrow \quad (5)$$

These yttrium rich phases should react with dissolved oxygen in the AlN grain as follows.

$$2Y_2O_3 + Al_2O_3 \rightarrow Y_4Al_2O_9 \quad (6)$$

$$Y_4Al_2O_9 + Al_2O_3 \rightarrow 4YAlO_3 \quad (7)$$

$$3YAlO_3 + Al_2O_3 \rightarrow Y_3Al_5O_{12} \quad (8)$$

The dissolved oxygen in the AlN grains was removed gradually and the thermal conductivity was improved by annealing. The relationship between thermal conductivity and the *c*–axis in Figs 9 and 10 is in agreement with this interpretation, as is the remarkable thermal conductivity improvement at the period of the notable density drop. The reduction–nitridation of the Al_2O_3 at the notable density drop period must be vigorous. The thermal conductivity increase after the grain boundary phase free was believed to be attributed by further oxygen removal with a small amount of yttrium compound less than several hundred ppm.

It is considered that the changes in the yttrium aluminate phase compositions during the annealings were caused by the difference between the reduction–nitridation rate of Al_2O_3 and Y_2O_3 in the YAG. In the case of eqn (2), an excess amount of carbon was in the firing atmosphere, and because the CO gas is exhausted outside the furnace, the reaction should proceed toward the right side. The reactions presented in eqns (3)–(8) should occur simultaneously. It is expected that the migration of Al_2O_3 in the yttrium aluminate should be fast, because the yttrium aluminate was expected to be a liquid at the annealing temperature.[19]

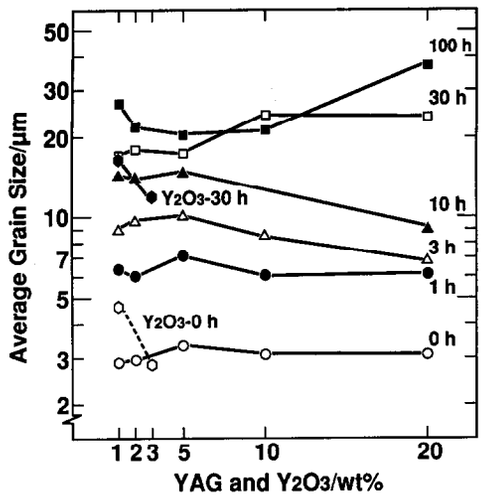


Fig. 11. Relationship between average grain size of AlN and amount of YAG or Y_2O_3 additions during annealings.

Equation (1) describes the AlN powder manufacturing method involving carbo–thermal reaction of Al_2O_3. It is interesting to ask whether oxygen removal without yttrium is possible or not. However, no thermal conductivity improvement was observed even though samples were annealed in the same way.[6,20] Figure 11 shows the grain growth of AlN during the annealings. The grains grew from around 3 μm to a range from 20 to 40 μm after 100 h annealing. One might expect the Al vacancies migrate to the grain boundaries during the grain growth. From the consideration of the mean free path of phonons in AlN, as mentioned earlier, the grain size itself is not directly related to thermal conductivity. Goto *et al.*[20] discussed that thermal conductivity has no relation to grain size ranging from 9 to 21 μm in phase free grain boundary AlN ceramics containing 500 ± 100 ppm oxygen. Watari *et al.*[21] also reported that no relationship was found between thermal conductivity and grain size from characterization of AlN ceramics that has an average grain size of between 4 and 40 μm and has 1·04–0·91 oxygen content.

It should be noted that before annealing, the thermal conductivity of 1 wt% YAG-containing ceramics was slightly lower than that of 3 wt% YAG-containing ceramic. A trace amount of oxygen removal might have occurred even for the 1800°C–30 min firing.

5 Conclusions

The thermal conductivity improvement of 260 Wm^{-1} K^{-1} grade-containing AlN ceramics can be divided into two processes. The first is fixing the original Al_2O_3 impurity in the AlN powder as a grain boundary phase. The second is the grain boundary elimination process by annealing in a carbo-reductive atmosphere. From evaluations on YAG-containing ceramics, we can obtain the conclusions listed below.

(1) The primary cause of thermal conductivity improvement in the grain boundary phase elimination process is considered to originate from a cyclic oxygen removal from the AlN grains by oxygen getters.

(2) The difference in the reduction–nitridation velocity between the Al_2O_3 and the Y_2O_3 constituents in the yttrium aluminate phases generates yttrium rich phase formation during annealing. The Al_2O_3 in the YAG changes into AlN at first. Consequently, yttrium rich phases are formed in the grain boundary phases and then they act as oxygen getters.

(3) Y_2O_3 is better for thermal conductivity than YAG. YAG has been found to be a sintering aid of AlN without any thermal conductivity improvement. The doping should be to form YAP and YAM for thermal conductivity.

References

1. Werdecker, W. & Aldinger, F., Aluminum Nitride—An alternative ceramic substrate for high power applications in micro circuits. *IEEE Trans. Compon., Hybrids. Manuf. Technol.*, 7(4) (1984) 399–404.
2. Slack, G. A., Nonmetallic crystals with high thermal conductivity. *J. Pys. Chem. Solids*, **34** (1973) 321–35.
3. Ponthieu, E., Grange, P., Delmon, B., Lonnoy, L., Leclercq, L., Bechara, R. & Grimblot, J., Proposal of a composition model for commercial AlN powders. *J. Europ. Ceram. Soc.*, **8** (1991) 233–41.
4. Dutta, I., Mira, S. & Rabenberg, L., Oxidation of sintered aluminum nitride at near-ambient temperature. *J. Am. Ceram. Soc.*, **75**(11) (1992) 3149–53.
5. Komeya, K., Inoue, H. & Tsuge, A., Effect of various additives on sintering of aluminum nitride. *Yogyo-Kyokai-shi*, **89**(6) (1981) 330–6, in Japanese.
6. Ueno, F. & Horiguchi, A., Grain boundary phase elimination and microstructure of aluminum nitride. *Proc. Ist. Europ. Soc. Conf. (ECerS'89)*, 1.383, 18–23 June 1989 Maastricht, The Netherlands.
7. Jackson, T. B., Virkar, A. V., More, K. L. & Cutler, R. A., The microstructure of aluminum nitride sintered with yttria. In presentation (11-E-90) of Am. Ceram. Soc. 92nd Annual Meet., 22–26 April, (1990) Dallas, Texas.
8. Horiguchi, A., Kasori, M., Ueno, F. & Tsuge, A., High thermal conductive AlN ceramics by pressureless sintering in reducing atmosphere — investigation of additives. *Proc. Annual Meeting Ceram. Soc. Japan*, 3HO3, 12–14 May 1987, Nagoya, Japan, in Japanese.
9. Lee, R. R., Development of high thermal conductivity aluminum nitride ceramics. *J. Am. Ceram. Soc.*, **74**(9) (1991) 2242–9.
10. Virkar, A. V., Jackson, T. B. & Cutler, R. A., Thermodynamics and kinetic effects of oxygen removal on the thermal conductivity of aluminum nitride. *J. Am. Ceram. Soc.*, **72**(11) (1989) 2031–42.

11. Slack, G. A., Tanzilli, R. A., Pohl, R. O. & Vandeersande, J. W., The intrinsic thermal conductivity of AlN. *J. Phys. Chem. Solids*, **4**(7) (1987) 641–7.
12. Toropov, N. A., Bonder, I. A., Galakhov, F. Ya., Nikogosyan, X. S. & Vinogradova, N. V., *Izu. Akad. Nauk SSSR, Ser. Khim., No. 7*, (1964) 1162. Printed in *Phase diagrams for Ceramists 1969 Supplement* Fig. 2344, Am. Ceram. Soc., (1969).
13. Kuramoto, N. & Taniguchi, T., Transparent AlN Ceramics. *J. Mater. Sci. Lett.*, **3** (1983) 471–4.
14. Kuramoto, N., Taniguchi, H. & Aso, I., Development of translucent aluminum nitride ceramics. *Ceram. Bull.*, **68**(4) (1989) 883–7.
15. Touloukian, Y. S., Powell, R. W., Ho, C. Y. & Klemens, P. G., *Thermophysical Properties of Matter*, Vol. 2 IFI/Plenum, New York-Washington, 1970.
16. Kingery, W. D., Thermal Conductivity: XIV, Conductivity of multicomponent systems. *J. Am. Ceram. Soc.*, **42**(12) (1959) 617–27.
17. Yagi, T., Shinozaki, K., Kato, M., Sawada, Y. & Mizutani, N., Migration of grain boundary phases of AlN ceramics in joined sample of sintered and hot-pressed body. *J. Ceram. Soc. Japan*, **98**(2) (1990) 198–203, in Japanese.
18. Adams, I., AuCoin, T. R. & Wolff, G. A., Luminescence in the system Al_2O_3–AlN. *J. Electrochemical Soc.*, **109**[11] (1962) 1050–4.
19. Yamashita, Y., Shinozaki, K. & Mizutani, N., The temperature measurement of the liquid phase formation in AlN–Y_2O_3 (CaO)–Al_2O_3 system using a self-made high temperature DTA. *Proc. Annual Meeting, Ceram. Soc. Japan.*, 3C05, 5–7 April, 1993, Tokyo, Japan, in Japanese.
20. Goto, Y., Ueno, F., Kasori, H. & Horiguchi, A., The relation between oxygen content of aluminum nitride and its thermal conductivity. *Proc. Annual Meeting, Ceram. Soc. Japan.*, 1A10, 23–25 May 1990, Kobe, Japan, in Japanese.
21. Watari, K., Ishizaki, K. & Fujikawa, T., Thermal conduction Mechanism of Aluminum nitride ceramics. *J. Mater. Sci.*, **27** (1992) 2627–30.

Journal of the European Ceramic Society **15** (1995) 445–453
© 1995 Elsevier Science Limited
Printed in Great Britain. All rights reserved
0955-2219/95/$9.50

0955-2219(95)00004-6

On the Thermal Degradation of Lox-M Tyranno® Fibres

Constantin Vahlas[a] & Marc Monthioux

Laboratoire Marcel Mathieu, CNRS-UPPA, Centre Hélioparc, 2, avenue Angot, F-64000 Pau, France

(Received 21 April 1994; revised version received 30 September 1994; accepted 12 December 1994)

Abstract

A calculational thermodynamic investigation of the thermal degradation of the Lox-M Tyranno® fibre in inert gas flow at atmospheric pressure has been performed, based on the minimization of the Gibbs energy of the Si–C–O–Ti chemical system. The results are compared to a recent characterization of the material by Transmission Electron Microscopy (TEM) which illustrates its sequential structures and nanotextures as a function of treatment temperature. The degradation mechanisms and the corresponding temperature ranges of this and of the NL-202 Nicalon® fibre in the same conditions are compared and the observed differences are attributed to diffusion-based phenomena.

Introduction

The introduction of small amounts of titanium (less than 10 wt%) in silicon oxycarbide ceramic fibres, was first proposed in the early eighties.[1] The aim was to retard crystallization and grain growth at elevated temperatures and hence improve strength retention,[2] and also to improve compatibility for aluminum matrix composites on account of less reactivity but better wettability against molten aluminum.[3] These fibres are produced from organometallic precursors containing Si–O–Ti bonds (polytitanocarbosilane) which are typically obtained using polycarbosilane (PCS) and titanium compounds like tetra-alkoxide,[1,4] tetra-butoxide,[2] or tetra-isopropoxide.[5]

Tyranno® is the family name of a series of non-crystalline Si–Ti–C–O–H fibres fabricated by UBE Industries (Ube, Japan). Since the first publication on this material in 1984,[6] different grades have been presented. Their chemical composition varies between the following values (Ref. 7 and UBE Industries data from Tyranno® fibre, 1986 commercial brochure): Si 45–57, C 25–32, Ti 1·5–4·0, O 12–18, B ≤ 0·15, and N ≤ 0·2 wt%, together with a small amount of hydrogen as a residue of the precursor material. Low oxygen grades of this fibre have recently been commercialized. As for other similar ceramic materials, Tyranno® fibres have valuable mechanical properties up to temperature limits dependent on the operating conditions.

This paper presents a thermodynamic simulation of the behavior of the Lox-M grade of the Tyranno® fibre, under high temperature treatment at atmospheric pressure and inert gas environment. The principle and the different types of calculations as a function of the experimental situation to be simulated are discussed, together with the critical selection of the thermodynamic data for the species considered. The results of calculations are presented by means of yield diagrams, indicating the number of moles obtained at equilibrium for the condensed and the gaseous species as a function of temperature. The theoretical work is associated to a Transmission Electron Microscopy (TEM) investigation which has been presented in part in,[8] with the aim to determine the crystalline structure and nanotexture of the material in the as-received state as well as after thermogravimetric heat treatments at different temperatures, in non-oxidizing environments. This combined approach is expected to allow the stability limit of the fibre, in the investigated conditions, to be determined and to be attributed to corresponding nanotextural changes and chemical reaction mechanisms. The results are compared to the thermal behavior of the NL-202 Nicalon® fibre (Nippon Carbon), which is aimed at similar applications but contains no titanium.

Thermodynamics

The calculations are based on the minimization of the total Gibbs energy (G) of the chemical system generated from combinations of the elements

[a]Permanent address: Laboratoire de Matériaux, URA 445, ENS Chimie, 118 route de Narbonne, F-31077 Toulouse, France.

Si–C–O–Ti–Ar and they were performed by using the GEMINI2 software.[b] Twenty four condensed stoichiometric compounds and three solution phases (liquid and bcc Ti–Si and fcc Ti–C) were involved in the calculations together with twenty gaseous species.

The gas phase was assumed to be ideal. The equation adopted for the free energy of formation, as a function of temperature, T, for each stoichiometric species is:

$$\Delta G^{\circ}(T) = a_1 + a_2T + a_3T\ln T + a_4T^2 + a_5T^3 + a_6T^{-1} + a_7T^4 + a_8T^5 + a_9T^7 + a_{10}T^{-9} + a_{11}\ln T + a_{12}T^{-2} + a_{13}T^{-3} \quad (1)$$

Data were mainly drawn from the Scientific Group Thermodata Europe (SGTE) data bank[9] and from Barin's compilation.[10] Data on Si_xC_y species were drawn from Gurvich *et al.*[11]

The excess free energy of the solid solutions, G^{ex}, was described by a generalized multi-sublattice model as developed by Sundman and Agren,[12] including in particular the classical substitution and the two-sublattice models, applied to the two Ti–Si phases and to the Ti–C phase respectively. For the one sublattice (substitution) model, G^{ex} is written:

$$G^{ex} = x_{Ti}x_{Si}L_{Ti,Si}(x,T) \quad (2)$$

where x_i is the atomic fraction of the component i and $L_{Ti,Si}(x,T)$ is the binary interaction term:

$$L_{Ti,Si}(x,T) = \sum_{\nu}(x_{Ti} - x_{Si})^{\nu}L^{(\nu)}_{Ti,Si}(T) \quad (3)$$

$L^{(\nu)}_{Ti,Si}(T)$ being a binary interaction parameter of order v between Ti and Si, depending on temperature according to the relation (1). Data for these solution phases comes from Vahlas *et al.*[13] In the two sublattice model, applied to the Ti–C phase, the first and the second sublattices are considered to be filled by the carbon atoms or vacancies and by the titanium atoms respectively. In that case, G^{ex} is written:

$$G^{ex} = y_Cy_{vac}L_{C,vac:Ti}(y,T) \quad (4)$$

where y_c, y_{vac} are the atomic fractions of C and of vacancies on their sublattice ($y_c + y_{vac} = 1$) and $L_{C,vac:Ti}$ is the binary interaction parameter between carbon and vacancies within the corresponding sublattice:

$$L_{C,vac:Ti}(y,T) = \sum_{\nu=0}^{\nu}(y_C - y_{vac})^{\nu}L^{(\nu)}_{C,vac:Ti}(T) \quad (5)$$

Although Vincent *et al.*,[14] propose an eight term function for $L_{C,vac:Ti}$, (with $\nu = 4$ and $L^{(\nu)}_{C,vac:Ti} = a +$

[b]Gibbs Energy MINIminimizer (GEMINI2), available from THERMODATA, BP66, F-38402 Saint Martin d'Hères, France.

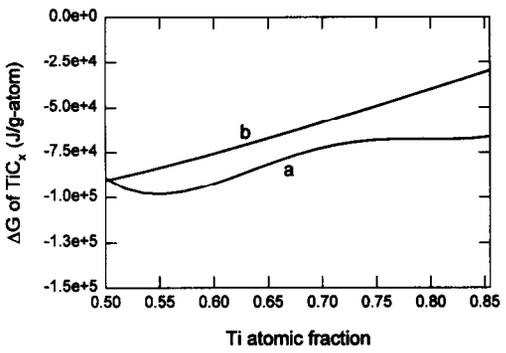


Fig. 1. Free energy of the Ti–C solid solution as a function of Ti atomic fraction for T = 800 K (527°C). (a) Vincent *et al.*[14] model; (b) present model.

bT), in these calculations we used a simpler and more realistic description where $L_{C,vac:\ Ti} = -6000$ J/g-atom. This eliminates demixing artifacts as shown for example in Fig. 1, where the free energy of TiC_x is drawn at 800 K (527°C) as a function of the Ti atomic fraction, using the models adopted in[14] (a), and in this work (b). However, a complete re-calculation of the Ti–C system with regard to available metallurgical and thermodynamic experimental data, as attempted in,[14] remains to be done.

There is no thermodynamic data available for the amorphous SiC_xO_y solid solution although there is strong evidence in the literature for the existence of this phase.[15–20] Consequently, although this phase is possibly present in the as-received material, by analogy with the NL-202 Nicalon® fibre as was shown among others in Ref. 20 it was replaced in calculations by an equivalent mixture of SiC+SiO_2+C. This assumption, the validity of which we have discussed in recent work,[21] does not allow the specific evolution of the fibre during the transition period of degradation to be simulated. However, it is expected to have little influence on the calculated degradation temperature and on the fibre and gas phase composition above it. Indeed, as is evidenced by the elemental analysis and the TEM investigation, there is no SiC_xO_y solid solution left at the end of the degradation process of the NL-202 Nicalon® fibre. By analogy with the above, no $SiTi_xC_yO_z$ solid solution was considered in the calculations.

The models for the ternary Ti_3SiC_2 and $Ti_5Si_3C_x$ compounds come from Racault *et al.*[22] Because of lack of data on the $Ti_5Si_3C_x$ solution phase, the authors considered it as a $Ti_{0.6}Si_{0.34}C_{0.05}$ stoichiometric compound.

Each phase of each chemical element considered (Si, C, O, Ti) was incorporated in the calculations as a G–H_{ser} function of temperature, equivalent to the expression (2). G–H_{ser} is the Gibbs energy relative to the enthalpy of the 'Standard Element Reference', i.e. the reference phase of the element at

Table 1. Species considered in the thermodynamic calculations and the origin of their thermodynamic description.

No.	*Species*	*Ref.*	*No.*	*Species*	*Ref.*	*No.*	*Species*	*Ref.*	*No.*	*Species*	*Ref.*
1	C-diamond	23	14	TiO_2-(S)A	9	26	Ti–Si-bcc	13	38	CO-gas	10
2	C-graphite	23	15	Ti_2O_3-solid	9	27	Ti–Si-liquid	13	39	CO_2-gas	10
3	Si-diamond	23	16	Ti_3O_5-solid	9				40	SiC-gas	11
4	Ti-hcp	11	17	Ti_4O_7-solid	9	28	C-gas	10	41	SiC_2-gas	11
5	SiC-hex., liquid	11	18	TiSi-solid	13	29	C_2-gas	10	42	Si_2C-gas	11
6	SiC-cubic	11	19	$TiSi_2$-solid	13	30	C_3-gas	10	43	SiO-gas	10
7	SiO_2-Lquartz	9	20	Ti_3Si-solid	13	31	O-gas	10	44	SiO_2-gas	11
8	SiO_2-Hquartz	9	21	Ti_5Si_3-solid	13	32	O_2-gas	23	45	TiO-gas	9
9	SiO_2-tridymite	9	22	Ti_5Si_4-solid	13	33	O_3-gas	10	46	TiO_2-gas	9
10	SiO_2-cristobalite	9	23	Ti_3SiC_2-solid	22	34	Si-gas	10	47	Ar-gas	23
11	SiO_2-liquid	9	24	$Ti_5Si_3C_x$-solid	22	35	Si_2-gas	10			
12	TiO-solid	9				36	Si_3-gas	10			
13	TiO_2-(C)R	9	25	Ti-C_x-fcc	14	37	Ti-gas	9			

298 K (20°C). The data adopted for this function come from Dinsdale's compilation.[23]

By analogy with the behavior, in the same conditions, of the NL-202 Nicalon® fibre (as experimentally illustrated in Ref. 20 and simulated in Ref. 21), the de-hydrogenation process is expected to occur in relatively early stages of the thermal treatment yielding molecular hydrogen as the main gaseous by-product. Hence, and since titanium hydrides are not very stable compared to other compounds involved in the calculations, hydrogen and hydrogen-containing species were not considered in this study. The species involved in the calculations and the source of the thermodynamic description adopted are listed in Table 1.

Various quantities of inert gas in contact with the fibre were considered in order to differentiate the chemical environments at the skin and in the core of it. This approach helps to illustrate, in the calculations, the available volume around the fibre and within the pores which may exist within the fibre as was indicated in Ref. 21. Hence, calculations were made with 1 g-atom (skin) and 10^{-4} g-atom of Ar (core) in contact with 1 g-atom of the fibre the initial elemental composition of which was experimentally determined as: Si 52·85 (33·23), C 31·64 (46·42), O 13·07 (14·37), Ti 1·85 (0·68) and H <0·30 (<5·28) wt (at)%.

In Fig. 2 the calculated results are presented for the skin environment (1 g-atom Ar/g atom) as a function of treatment temperature. The evolution of the condensed products is illustrated in Fig. 2(a). In these calculations the fibre is represented by a mixture of SiC, C and SiO_2 which remains stable up to 1500 K (1227°C). Above this temperature there is a slight decrease of the oxygen and of the free carbon content of the material. At 1600 K (1327°C) the free carbon vanishes while SiC increases significantly. At this temperature, the oxygen content reaches a plateau an order of magnitude below its initial concentration and at 1750 K (1477°C) it also vanishes. The above behavior is related to the evolution in the same operating conditions of the gaseous by-products of the heat treatment, presented in Fig. 2(b). From this figure it appears that silicon and especially carbon monoxides, SiO and CO, are the main gaseous species. Their quantities continuously increase with temperature before reaching a plateau at 1600 K (1327°C) for CO and at 1750 K (1477°C) for SiO, corresponding to the exhaustion of the free carbon and of the oxygen reserves of the fibre respectively. At and beyond 1750 K (1477°C) the quantity of CO is ten times higher than that of SiO. Other species, especially CO_2 and Si are present at high temperatures but in very low quantities. They also qualitatively follow the evolution of the free carbon and of the oxygen within the fibre. Beyond 1800 K (1527°C) their increase is delayed or stopped due to the appearance of small quantities of gaseous Si_xC_y species.

From Fig. 2(a) it appears that titanium is found in the fibre exclusively in its carbide form. An expansion on the y axis of the above diagram is presented in Fig. 3, aiming to evidence any minor evolution of TiC_x with temperature. The composition of the TiC_x phase in terms of carbon content for one g-atom of titanium is also presented in this figure. The quantity of TiC_x remains unchanged up to 1650 K (1377°C). Beyond this temperature TiC_x definitively decreases, but not in significant amounts: At 2000 K the number of moles of TiC_x, is $7{\cdot}1997 \times 10^{-3}$ to be compared to $7{\cdot}2 \times 10^{-3}$ in the as-received material. The carbon content of the TiC_x phase follows an equivalent evolution: while up to approximately 1600 K (1327°C) titanium carbide remains stoichiometric, beyond this temperature it continuously loses carbon but again in very small amounts: At 2000 K (1727°C) TiC_x is 10^{-4} g-atom understoichiometric in carbon. No gaseous Ti-containing compounds are shown in Fig. 2(b). As a matter of fact TiO and Ti

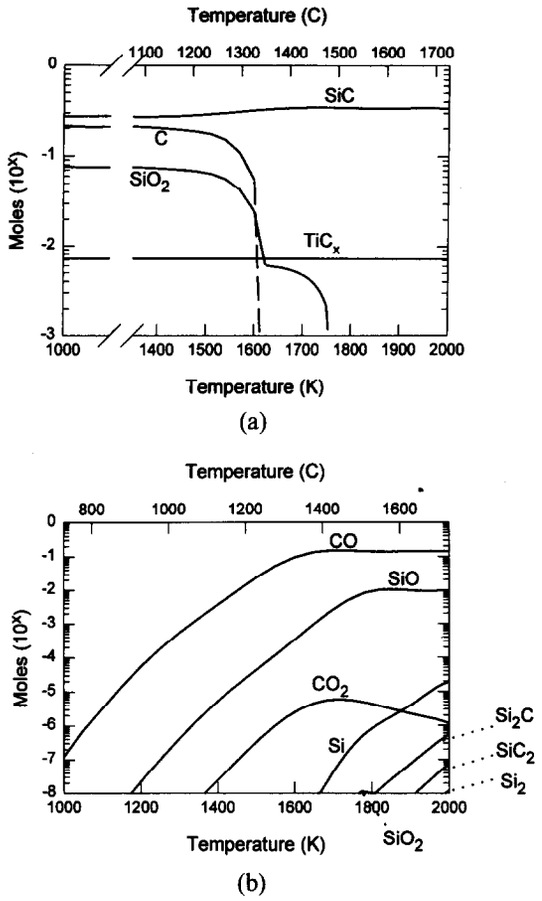


Fig. 2. Thermal evolution of one g-atom of Lox-M. Condensed (a) and gaseous (b) species in contact with one g-atom Ar as a function of treatment temperature.

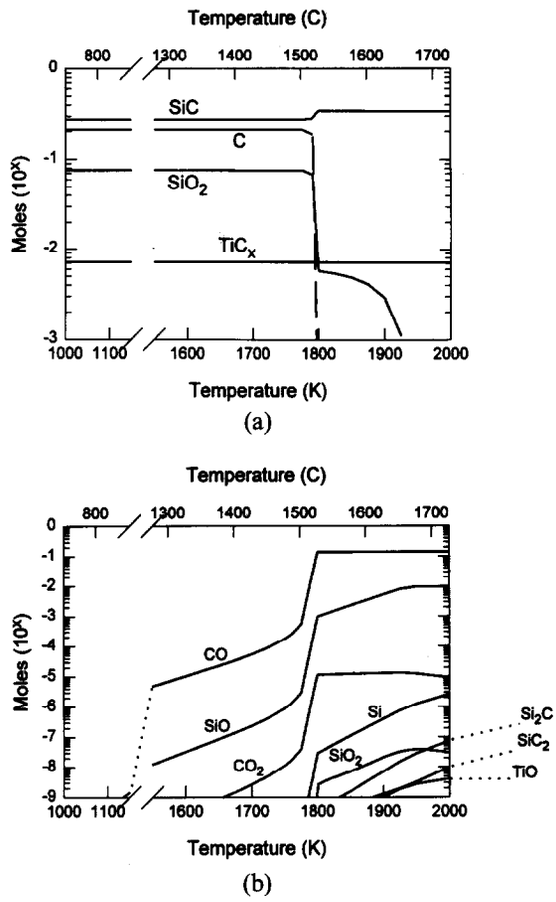


Fig. 4. Thermal evolution of one g-atom of Lox-M. Condensed (a) and gaseous (b) species in contact with 10^{-4} g-atom Ar as a function of treatment temperature.

appear above 1900 K (1627°C) in extremely low quantities ($<2 \times 10^{-9}$ g-atom) illustrating the stability of carbon and silicon oxides towards titanium compounds.

Figure 4 presents the evolution with temperature of the fibre in contact with 10^{-4} g-atom Ar (core), for the condensed species (Fig. 4(a)), and for the gaseous (Fig. 4(b)) species. The general shape of the two figures is equivalent to Figs 2(a) and 2(b) respectively with two main differences: The curves are now flatter with more sharp changes, and the degradation temperature is shifted 200 degrees higher, i.e. 1800 K (1527°C). This is also illustrated in Fig. 4(b) where the rapid increase of CO, SiO, CO_2 and Si also occurs to a higher temperature, i.e. 1800 K (1527°C).

Once again it appears that titanium is entirely linked in its carbide form (Fig 4(a)) and that it has a negligible reactivity in the gas phase (Fig. 4(b)). The quantity of TiC_x remains unchanged up to 1750 K (1477°C) and decreases above it as shown in Fig. 5. The same differences hold for the carbon content where now TiC_x becomes understoichiometric at 1650 K (1377°C). However it has to be pointed out that, as in the conditions of Fig. 3, these variations are extremely weak and, even if they show evidence of the upper stability limit of the material in the corresponding conditions, they are not representative of a significant change in the composition and, consequently in the physical properties of the fibre.

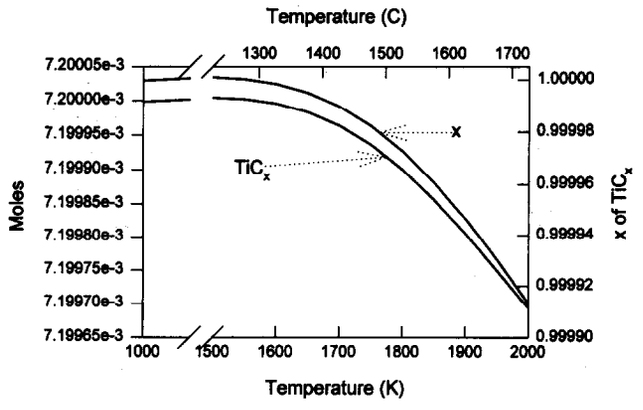


Fig. 3. Thermal evolution of one g-atom of Lox-M. Number of moles of TiC_x (left) and carbon content of TiC_x (right) in contact with one g-atom Ar as a function of treatment temperature.

Experimental

The operating procedure and the main results of the thermogravimetric analysis (TGA) and of the SEM and the TEM characterization are reported

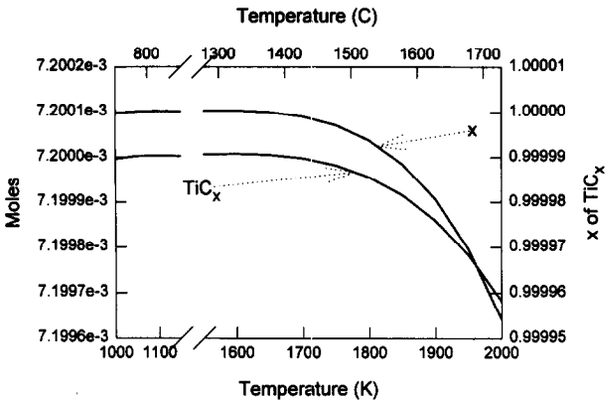


Fig. 5. Thermal evolution of one g-atom of Lox-M. Number of moles of TiC_x (left) and carbon content of TiC_x (right) in contact with 10^{-4} g-atom Ar as a function of treatment temperature.

in.[8] The operating conditions were chosen to be identical to the heat treatment conditions of the Nicalon® fibre, reported in Ref. 20.

In Fig. 6 the TG recordings for treatments at 1623, 1673 and 1773 K (1350, 1400 and 1500°C) are presented. In contrast to the 1573 K (1300°C) sample where the weight loss of the fibre had not reached a plateau at the end of the heat treatment, it appears that the duration of the treatment at each of the above temperatures was long enough to allow the material to reach a stable composition. This stabilization was produced after an almost equal weight loss for the three temperatures: 20·3, 18·3, and 21·8% respectively, to be compared to the reported weight loss of 25·6% for the NL-202 Nicalon® fibre at 2000 K (1727°C).[20]

The SEM characterization indicated that the shape and the dimensions of the 10 μm diameter fibres remain stable after the 1773 K (1500°C) treatment except for a slight increase of the surface roughness compared to the as-received material. However, TEM characterization revealed marked changes between these temperatures regarding the structure and the nanotexture of the fibre, as has been pointed out in Ref. 8 and will be next discussed.

The TEM investigation, showed that the as-received fibre has a nanometric porosity, and that it contains β-SiC nanocrystals and small free carbon units, both having a diameter less than 2 nm. Small stacks of 2–3 fringes of free carbon are shown in the C_{002} Lattice Fringe (LF) image of Fig. 7 (arrows). They are made of basic structural units, (BSUs), i.e. the elemental entities common to many other carbonaceous materials, the diameter of which was determined to be less than 1 nm.[24] Silica was not detected at the extreme surface or within the fibre.

It was not possible to characterize the inner part of samples treated at 1623 K (1350°C) since, because of the high brittleness, ultramicrotomy did not yield any entire section. The 'in-place' particles, i.e. attached to the embedding resin, correspond to the external part of the filament. However, the

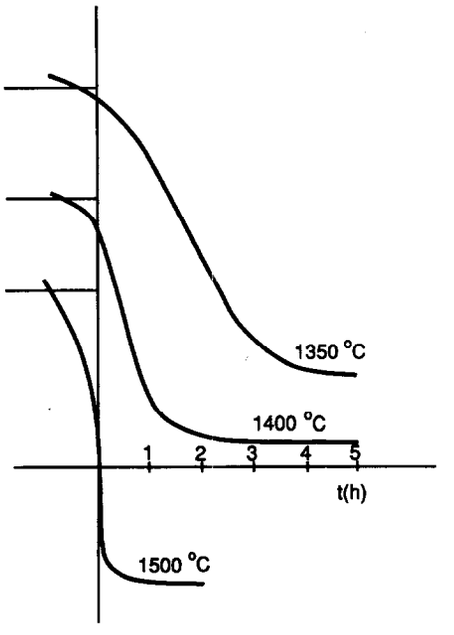


Fig. 6. TG analysis recordings for treatments of Lox-M at 1623, 1673, and 1773 K. From Ref. 8.

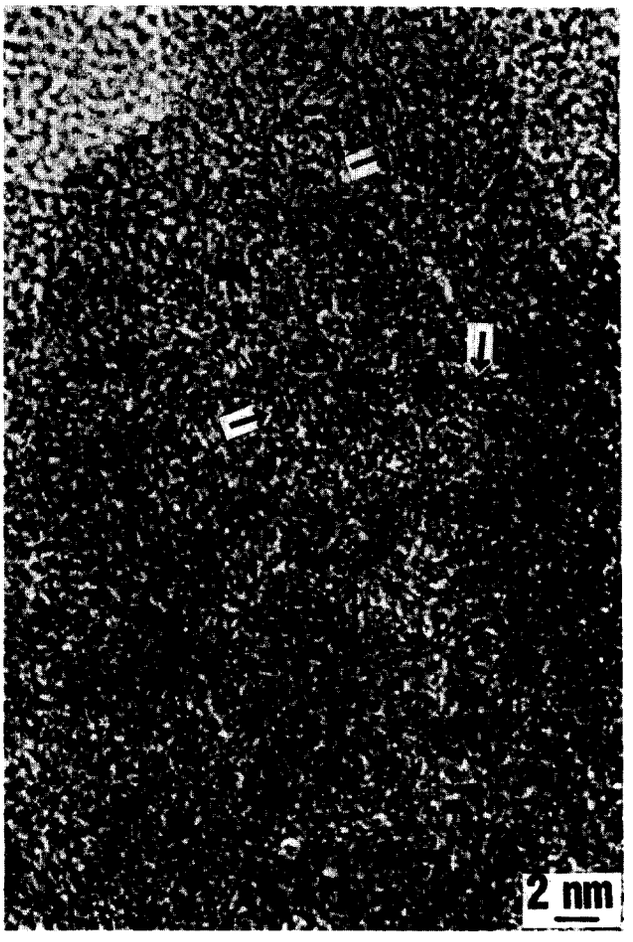


Fig. 7. C_{002} LF image of as-received Lox-M. Arrows indicate BSU's. Similar to Fig. 3 in Ref. 8.

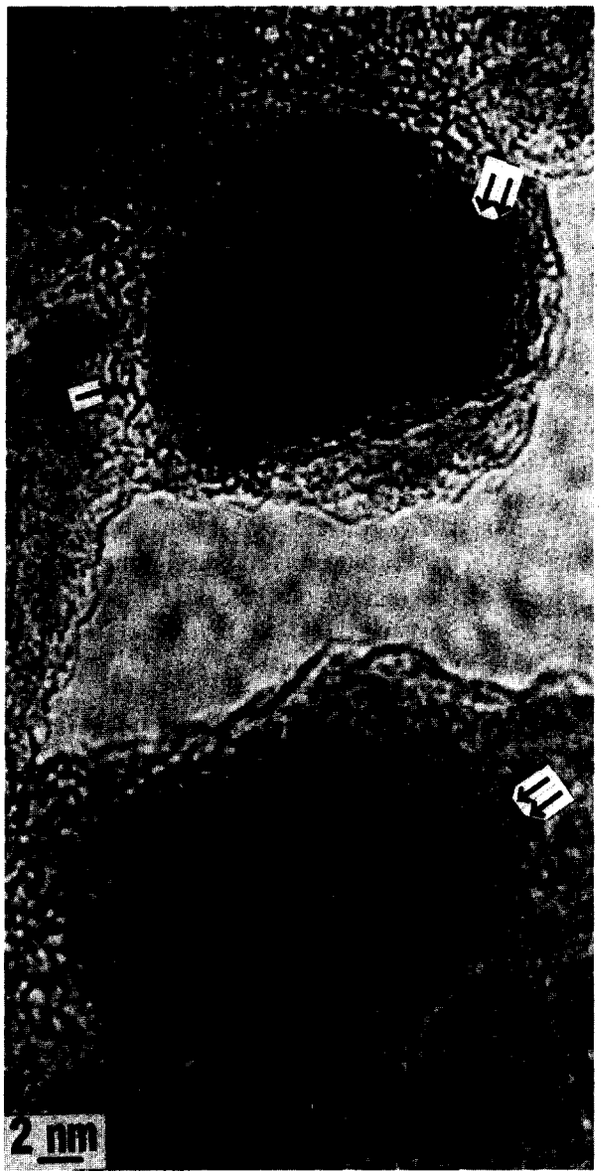


Fig. 8. C_{002} and SiC_{111} LF image of 1673 K heat treated Lox-M. Single arrow point a stack of degraded free carbon, one layer of which was partially consumed. This is a characteristic texture of activated polyaromatic carbon. Double arrows point SiC_{111} lattice fringes. Similar to Fig. 5 in Ref. 8.

investigation of the 'out-of-place' particles provides a statistical idea of the features of the whole fibre. No significant differences were found between random particles and 'in-place' particles from the outer part of the fibre suggesting that the fibre is homogeneous. The major evolution between this and the as-received samples is that carbon is now better organized since BSUs have been associated both face-to-face and edge-to-edge forming stacks of 3–6 distorted layers. This association yields distorted fringes having an average length of ~3 nm. As was shown from 1673 K (1400°C) and 1773 K (1500°C) heat treated fibres, this organization takes place around each SiC crystal, in agreement with other SiC-based material.[20,25]

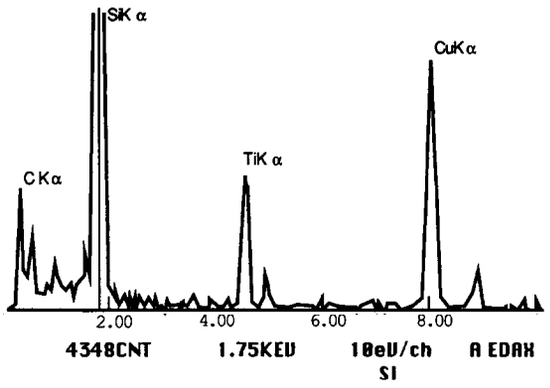


Fig. 9. EDS elemental analysis pattern for 1773 K treated Lox-M.

A C_{002} and SiC_{111} LF image of a 1673 K (1400°C) treated fibre is presented in Fig. 8.[8] At this temperature, SiC crystals have grown markedly up to 60 nm (to be compared to a maximum of 8 nm for the NL-202 fibre in identical conditions),[20] suggesting that the major degradation step has already occurred. Crystal growth is very fast as corresponding SAD patterns show polytypism marks, and free carbon seems degraded, although its aromatic layers remain oriented parallel to the crystalline faces. At 1773 K (1500°C) there is no marked evolution of the fibre except that SiC crystals become larger; their thickness is as high as 90 nm, again with a wide distribution in size.

It was not possible to evidence the titanium carbide either in Electron Diffraction pattern reflections, or in Dark Field (DF) TEM mode. While in the first case TiC reflections are too close to SiC for an unambiguous observation, in the second case TiC grains are not evidenced possibly because of their very small size or because titanium participates (at least in the original fibre) in the intergranular solid solution. The EDS elemental analysis, whose typical pattern is shown in Fig. 9 for a 1773 K (1500°C) treated fibre, did not reveal any significant difference in composition between the skin and the core of the fibre either at 1673 K (1400°C) or at 1773 K (1500°C).

Discussion

The evolution in composition of the condensed species as a function of temperature, which is evidenced in Figs 2(a) and 4(a) illustrates the capacity of the fibre to support, without major alteration, the heat treatments in the selected experimental conditions. This is valid up to a temperature which is a function of the argon dilution and which is detected in the above diagrams by an abrupt change in composition, especially by the

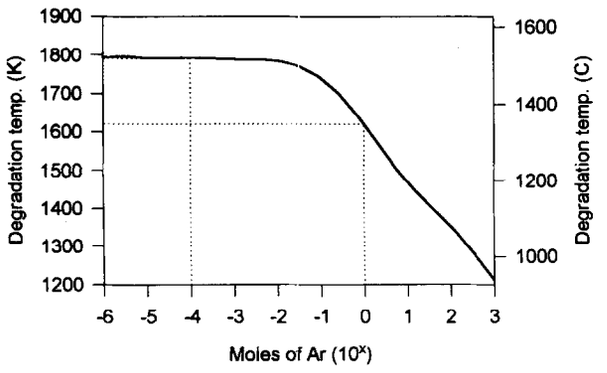


Fig. 10. Thermal evolution of Lox-M. Degradation temperature as a function of the number of moles of Ar available. Dotted lines correspond to the investigated conditions.

elimination of the free carbon, due to an endogenous oxidation mechanism leading to formation of SiC and CO. Following the results of the thermodynamic investigation, the Lox-M Tyranno® fibre is expected to change drastically in composition, morphology and hence physical properties in the range between 1600 and 1800 K (1327 and 1527°C).

The validity of these transition temperatures is studied in Fig. 10, where the degradation temperature is drawn as a function of the number of moles of Ar available in the calculations. As for the NL-202 Nicalon® fibre,[21] the degradation temperature does not depend on the dilution of the reactants up to approximately 10^{-2} g-atom Ar/g-atom. For higher dilution it decreases linearly with the logarithm of Ar quantity. From this figure it appears that, for a material containing no pores or cracks, only calculations made with 10^{-4} g-atom Ar/g-atom have a more general value and can represent the situation in the core, while calculations made with 1 g-atom Ar/g-atom qualitatively indicate that operating conditions are more severe at the external part, leading to lower values of the degradation temperature. It is worth noting that a similar behavior was evidenced by Luthra and Hee Dong[26] in carbon-fibre/oxide-matrix composites: The authors evaluated the chemical compatibility of different oxides with carbon at $T \approx 1873$ K (1600°C) and concluded that these materials are stable if they contain neither cracks nor pores allowing CO to escape.

The fact that the nanotextures of the as-received and of the 1623 K (1350°C) treated fibre are similar while at 1673 K (1400°C) degradation has already occurred, reveals the temperature interval within which degradation is initiated. In the same operating conditions NL-202 was found to be similar to the as-received material at 1523 K (1250°C), to present a skin-and-core effect at 1673 K (1400°C) and to be degraded at 1773 K (1500C).[20] No skin-and-core effect was observed during the degradation of the Lox-M. However, in view of the similarity between the two fibres concerning their precursors, their morphology and their properties, it is presumed that both present a diffusion-limited degradation mechanism. Additionally in the various ceramic materials such as Nicalon® 200 and other experimental Si–C–O and Si–C–N–O fibres investigated in the laboratory, brittleness during ultramicrotomy preparation is systematically important in the as received state and also remains elevated after low temperature treatments. This behaviour yields operating difficulties and often fragmentation. However, as soon as high temperature treatments have degraded the continuum, i.e. the cement between the SiC crystals, the diamond edge progresses among the nanometric crystals and fibres are cut considerably easier. For the investigated family of ceramic materials, this behaviour during ultramicrotomy may thus be considered as an indication of the existence of the interganular solid solution and also of the temperature domain where this solution is degraded. Lox-M behaves in a similar way: it is very brittle below 1623 K (1350°C) and much less above 1673 K (1400°C). Consequently, the degradation of the continuum and the corresponding skin-and-core effect in this fibre must occur between these two temperatures.

The thermodynamic simulation evidenced no difference between the chemical systems corresponding to Tyranno® and Nicalon® fibres. Indeed, Figs 2, 4 and 10 are identical to the corresponding figures for NL-202.[21] It can thus be deduced that degradation of the two fibres is initiated in the same temperature range. In that case, the relatively narrow temperature gap where the presumed skin-and-core effect takes place for Lox-M, compared with NL-202 (degradation of the Nicalon is initiated below 1673 K and is accomplished at 1773 K approximately), indicates that the progression of the skin-reactions to the core is faster in Tyranno®. A more rapid diffusion of the gaseous by-products may be responsible for this behavior due to a higher or more open porosity as is suggested by the lower density of Lox-M relative to NL-202: The two densities are 2·37 and 2·55 g cm^{-3} respectively and only 6% of this difference is due to the difference in composition of the fibres.

Titanium does not seem to modify the chemical behavior of Lox-M relatively to NL-202 except that it combines with an equivalent quantity of carbon. The possible existence of stoichiometric titanium carbide in the original fibre or its formation during the heat treatment is in agreement with the Si–Ti–C phase diagram, whose 1473 K

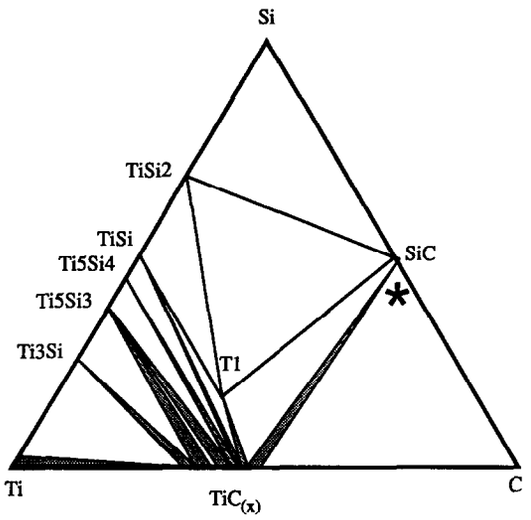


Fig. 11. Si–Ti–C phase diagram. Isothermal section at 1473 K, as calculated in Ref. 22. The initial composition of Lox-M is shown (★).

(1200°C) isothermal section is presented in Fig. 11.[22] As illustrated in this figure, the global composition point of the fibre is located at the interior of the SiC–TiC–C part of this diagram. Since this part of the isothermal section remains stable within a large temperature domain, it can be reasonably assumed that if titanium is not in solution in the original fibre, it will remain present in the form of stoichiometric TiC. The calculations showed that moderate quantities of oxygen are more likely to react with carbon and silicon rather than with titanium or titanium carbide. It is thus possible that in the investigated conditions, only a small shift of the location of the total composition of the fibre within the corresponding quaternary phase diagram takes place, relative to the Si–C–Ti ternary section. However, because of the departure of carbon from the fibre in the form of carbon monoxide but also because of the poor description of the TiC_x phase leading to uncertainties concerning the shape of the phase diagram, a shift of the global composition above the degradation temperature at the exterior of the SiC–TiC–C triangle towards silicon carbide, i.e. a very low other-than-SiC compounds' composition, cannot be excluded.

The difference between the experimentally determined upper limit of 1673 K (1400°C), and the calculated value of 1800 K (1527°C) for the degradation of the fibre, can be attributed to the fact that the concept of a material composed of silicon carbide, carbon and silica, where the core is dissociated from the skin, is not enough powerful to describe and predict more precisely its thermal behavior. However, as was discussed in Ref. 21, the comparison between the thermochemical properties of silicon carbide fibers and of silicon oxycarbide black glass with $SiC+SiO_2+C$ mixed powder, as was investigated by multiple Knudsen cell mass spectrometry in Refs 27 and 28 respectively, showed that the measured pressures of SiO and CO gaseous species above the three materials were comparable. Therefore, the SiC_xO_y solid solution can be replaced as a mixture of $SiC+SiO_2+C$ in the simulation, if the obtained results are considered exclusively in terms of the degradation temperature and of the gas phase composition above the fibre. The thermodynamic simulation is in this case helpful in order to illustrate, understand and predict the major reaction mechanisms responsible for the observed degradation. However, it has to be mentioned that other parameters may also be responsible for the observed difference between experimental results and thermodynamic predictions in similar operating conditions. One is related to the quality of the thermodynamic data adopted to describe the compounds participating in the chemical process. Although important research has already been performed on the chemical behavior of the Si–C–O[28] and of the Si–Ti–C[29] systems, more is needed to be done to improve their thermodynamic description. Other phenomena which have not been taken into account in the present work and which may also participate in the way the material is transformed during heat treatments are solid state diffusion and surface/interface kinetics. The quantification and modelization of their influence is a complex task, especially in the presence of poorly organized constituents.

Conclusions

The evolution of the Lox-M Tyranno® fibre as a function of treatment temperature in inert gas atmosphere and atmospheric pressure was thermodynamically simulated by performing thermochemical calculations in the Si–C–O–Ti chemical system, and was compared to recently performed structural and nanotextural TEM investigations.

The environments in the core and at the skin of the fibre were differentiated in the calculations by considering different inert gas dilution of the reactants. The stability limit of the material was thus calculated to be at 1800 K (1527°C) or lower. At this temperature the available carbon is exhausted and the oxygen content is highly reduced. The main reaction products are silicon carbide and carbon and silicon monoxides. The stable configuration for titanium is expected to be stoichiometric titanium carbide which exhibits a pronounced stability in terms of quantity and stoichiometry

within a large temperature domain, in agreement with the Si–Ti–C phase diagram.

From the comparison of the results of the thermodynamic study and the TEM characterization of the Lox-M Tyranno® and of the NL-202 Nicalon® fibres it appears that the chemical behavior of the Si–C–O–Ti and of the Si–C–O systems is identical in the investigated conditions and that similar mechanisms govern the thermal degradation of the materials. However, the degradation process is completed faster in the case of Lox-M, possibly because of a more rapid diffusion of the gaseous reaction by-products through the core of the fibre.

Acknowledgements

Thanks are due to Evelyne Fischer (THERMODATA) for help with the GEMINI2 software, to Pierre-Yves Chevalier (THERMODATA) for help with the thermodynamic data, to Jean-Paul Tricard (Elf-Aquitaine) for SEM facilities and to Takemi Yamamura (UBE Industries) for supplying the Tyranno® fibres.

References

1. Yajima, S., Iwai, T., Yamamura, T., Okamura, K. & Hasegawa, Y., Synthesis of a polutitanocarbosilane and its conversion into inorganic compounds. *J. Mater. Sci.*, **16** (1981) 1349–55.
2. Murthy, V. S. R., Lewis, M. H., Smith, M. E. & Dupree, R., Structure and degradation of Tyranno fibers. *Materials Letters*, **8** (1989) 263–8.
3. Yamamura, T., Waku, Y., Ishikawa, T., Yamamoto, T., Shibuya, M., Suzuki, M., Nishi, T. & Nagasawa, T., In *Looking Ahead for Materials and Processes*, 8th SAMPE European Chapter, La Baule, France, 1987 pp. 19–28.
4. Hasegawa, Y., Fen C. X., Song, Y. C. & Tan, Z. L., Ceramic fibre from polymer precursor containing Si–O–Ti bonds. *J. Mater. Sci.*, **26** (1991) 3657–64.
5. Yamamura, T., Ishikawa, T., Shibuya, M., Hisayuki, T. & Okamura, K., Development of a new continuous Si–C–Ti–O fibre using an organometallic polymer precursor. *J. Mater. Sci.*, **23** (1988) 2589–94.
6. Yamamura, T., Development of high tensile strength Si–Ti–C fiber as an organometallic polymer precursor. *Am. Chem. Soc. Polymer. Preprints*, **25** (1984) 8–9.
7. Yamamura T. Shibuya, M., Ishikawa, T., Sato, M. & Hisayuki, T., Properties of a continuous Si–Ti–C–O fibers synthesized from an organometallic polymer. In *Japan–US Joint Seminar on Inorganic and Organometallic Polymers,* Nagoya, Japan, 1991.
8. Bourgerette, C., LeCoustumer, P., Monthioux, M. & Vahlas, C., TEM characterization of heat treated Tyranno fibers. In *Proceedings of the International Conference ECCM 6th High Temperature — Ceramic Matrix Composites*, eds R. Naslain, J Lamon & D. Doumeingts, 1993, pp. 67–74.
9. Scientific Group Thermodata Europe, available on line from THERMODATA, BP 66 F-38402 Saint Martin d'Hères, France and Royal Institute of Technology, S-10044, Stockholm, Sweden.
10. Barin, I., *Thermochemical Data of Pure Substances*. VCH, Weinheim, GER, 1989.
11. Gurvich, L. V., Veyts, I. V. & Alcock, C. B., *Thermodynamic Properties of Individual Substances*, 4th edition Vol 1 and 2. Hemisphere Publishing Corp., New York, 1990.
12. Sundman B. & Agren, J., A regular solution model for phases with several components and sublattices, suitable for computer applications. *J. Phys. Chem. Solids*, **42** (1981) 297–301.
13. Vahlas, C. Chevalier, P. Y. & Blanquet, E., Thermodynamic approach to the selective deposition of refractory metal silicides. *Calphad*, **13** (1989) 275–94.
14. Vincent, C., Dazord, J., Bouix, J. & Bernard, C., Calcul de l'energie libre de formation de Gibbs du carbure de titane TiC_y par la methode des sous reseaux. Application a la determination de diagrammes de depot chimique en phase vapeur. *Thermochimica Acta*, **147** (1989) 1–15.
15. Pampouch, R., Ptak, W. S., Jonas, S. & Stoch, J., The nature of ternary Si–O–C phase(s) formed during oxidation of SiC. In *Proceedings of the 9th International Symposium on Reactivity of Solids*, eds. K. Direk, J. Habber & J. Novotny, 1980, pp. 674–84.
16. Yavouz, B. O. & Hench, L. L. Low temperature oxidation of SiC. *Ceram. Eng. Sci. Proc.*, **3** (1982) 596–600.
17. Lipowitz, J., Freeman, H. A., Chen, R. T. & Prack, E. R., Composition and structure of ceramic fibers prepared from polymer precursors. *Adv. Ceram. Mater.*, **2** (1987) 121–8.
18. Porte, L. & Sartre, A., Evidence for a silicon oxycarbide phase in the Nicalon silicon carbide fibre. *J. Mater. Sci.*, **24** (1989) 271–86.
19. Laffon, C., Flank, A. M., Lagarde, P., Laridgani, M., Hagege, R., Olry, P., Cotteret, J., Dixmier, J., Miquel, J. L., Hommel H. & Legrand, A. P., Study of Nicalon-based ceramic fibres and powders by EXAFS spectrometry, X-ray diffractometry and some additional methods. *J. Mater. Sci.*, **24** (1989) 1503–12.
20. LeCoustumer, P., Monthioux, M. & Oberlin, A., Understanding Nicalon® fiber. *J. Europ. Ceramic Soc.*, **11** (1993) 95–103.
21. Vahlas, C., Rocabois, P. & Bernard, C., Thermal degradation mechanisms of the Nicalon® fibre: A Thermodynamic Simulation. *J. Mater. Sci.*, in press.
22. Racault, C., Langlais, F. & Bernard, C., On the CVD of Ti_3SiC_2 from $TiCl_4$–$SiCl_4$–CH_4–H_2 gas mixtures. 1 — A thermodynamic approach. *J. Chemical Vapor Deposition* submitted for publication.
23. Dinsdale, A. T., SGTE Data for Pure Elements, NPL report DMA(A) 195, Sept. 1989.
24. Oberlin, A., High resolution TEM studies of carbonization and graphitization. In *Chemistry and Physics of Carbon*, Vol. 22, ed. P. A. Thrower, Marcel Dekker, NY and Bassel, 1989, pp. 1–143.
25. Monthioux, M., Oberlin, A. & Bouillon, E., Relationship between microstructure and electrical properties during heat treatment of SiC fibre precursor. *Comp. Sci. and Technol.*, **37** (1990) 21–37.
26. Luthra, K. L. & Hee Dong P., Chemical considerations in carbon-fiber/oxide-matrix composites. *J. Am. Ceram. Soc.*, **75**(7) (1992) 1889–98.
27. Rocabois, P., Chatillon, C. & Bernard, C., Mass spectrometry experimental investigation and thermodynamic calculation of the Si–C–O–(N) system and Si_x–C_y–O_z fibre stability. In *Proceedings of the International Conference ECCM 6th. High Temperature — Ceramic Matrix Composites*, eds R. Naslain, J. Lamon & D. Doumeingts, 1993, pp. 93–100.
28. Rocabois, P., Chatillon, C. & Bernard, C., Multiple Knudsen cell mass spectrometric investigation of the evaporation of silicon oxicarbide glass. *Surface and Coatings Technology*, **61** (1993) 86–92.
29. Racault, C, Elaboration par voie solide et gazeuse et caractérisation physico-chimique de céramiques à base de Ti_3SiC_2, Thesis, Université de Bordeaux 1, France, 1993.

Journal of the European Ceramic Society 15 (1995) 455–461
© 1995 Elsevier Science Limited
Printed in Great Britain. All rights reserved
0955-2219/95/$9.50

0955-2219(95)00003-8

Thermal Shock Resistance of Nextel/Silica–Zirconia Ceramic-Matrix Composites Manufactured by Freeze-Gelation

A. Twitty,[b] R. S Russell-Floyd,[c] R. G. Cooke & B. Harris[a]

School of Materials Science, University of Bath, Bath BA2 7AY, UK

(Received 18 October 1993; received in revised form 24 November 1994; accepted 12 December 1994)

Abstract

Ceramic-matrix composites consisting of a silica–zirconia matrix reinforced by 25% by volume continuous Nextel alumino–silicate fibres have been manufactured by a sol–gel route incorporating freeze-gelation and subjected to thermal shock by water quenching from temperatures up to 800°C. Although it was demonstrated that the Nextel fibres exhibited significant degradation of properties during composite processing, they still had a significant reinforcing effect. The material showed a critical temperature of approximately 550°C, below which it was unaffected by water quenching. Above this level there was a 40 and 50% step reduction in modulus and strength respectively. Acoustic emission monitoring showed a significant difference in materials subject to quenching from beyond the critical temperature. There was a lower initial yet higher final AE event rate for a monotonically increasing flexural load, and a bimodal amplitude distribution. This indicated that the material responds in general terms in the manner corresponding to the well-known Hasselmann model of thermal shock of monolithic ceramics, but the presence of fibres appears to improve the thermal shock resistance by raising the predicted critical temperature somewhat.

1 Introduction

The sol–gel process offers the possibility of manufacturing a wide range of ceramic-matrix composites (CMCs) in near-net shape and size by the use of techniques familiar in the processing of polymer-based composites and without the need for such costly manufacturing procedures as are commonly required to process conventional ceramics or CMCs.[1,2] The properties of such composites are more modest than those normally required for aerospace and other high-performance applications, but there are many uses for ceramics in general engineering for which the properties available in sol–gel CMCs are adequate, provided some measure of toughness and resistance to thermal shock can be incorporated. One of the difficulties with any CMC system is that, during either manufacture or subsequent service at elevated temperature, interfacial interactions can lead to deterioration of the fibres so that the full potential strength of the system cannot be realised in practice. An advantage of the sol–gel route in this respect is that it permits lower final firing temperatures and, therefore, the possibility of restraining such adverse reactions during processing. One of the systems that we have been studying as part of a wider program on CMCs manufactured by the sol–gel route is a composite consisting of a silica-based matrix reinforced with Nextel mullite fibres. In this paper we describe a series of experiments to investigate the resistance of this material to water quenching from temperatures up to 800°C.

2 Material

The reinforcing fibre was Nextel 440, manufactured by the 3M Company, a mullite material consisting of 70 wt% alumina, 28 wt% silica and 2 wt% B_2O_3. The manufacturer gives values of 186 GPa for Young's modulus and 2·1 GPa for the tensile strength of this fibre. The matrix ceramic is a silica–zirconia compound prepared from a mixture of Syton HT50, an aqueous sol containing 50 wt% of colloidal SiO_2 and 50 wt% of water, manu-

[a]To whom correspondence should be addressed.
[b]Present address: Johnson Matthey Technology Centre, Sonning Common, Reading, Berks, UK.
[c]Deceased.

factured by Monsanto, and Zircosil, consisting of 61 wt% of ZrO_2, 36 wt% of SiO_2, and small quantities of Al_2O_3, HfO_2, TiO_2, and Fe_2O_3, manufactured by Cookson Minerals.

The matrix components were mixed with a high-shear disperser and the resulting sol was used in a filament-winding process to produce flat plates of unidirectional impregnated sheet. These sheets were then wet-pressed between stainless steel platens to consolidate the windings and to produce plates approximately 100 × 100 mm × 5 mm. The pressed plates were then freeze-gelled by cooling rapidly in liquid nitrogen, following which they were warmed slowly to ambient temperature to produce a porous solid that could be handled. After drying to remove the excess residual water from the sol, the plates were infiltrated three times with Syton D30 silica sol, drying between infiltrations, and then sintered at 950°C for one hour. The sintered plates were then twice re-infiltrated, following which they were cut into 10 mm wide test pieces with a water-cooled diamond saw to provide unidirectionally reinforced composite samples. The cut samples were then re-infiltrated a further three times and finally sintered again at 500°C for 90 min. Three separate batches of the composite were prepared by this procedure with identical processing conditions. Image analysis of composite cross-sections gave average values of the fibre volume fraction, V_f, of 0·26, 0·23 and 0·28, respectively for the batches identified as A, B and C. The fibre distribution was reasonably uniform the final level of matrix porosity was about 30 vol%.

3 Testing Procedures

Mechanical strength and stiffness were determined by flexural testing in three-point bending with a span-to-depth ratio of 16:1 at an Instron crosshead displacement speed of 1 mm.min^{-1}. An indication of the relative toughnesses of the samples was also obtained from the area under the flexural load–deflexion curve. And in order to establish the inherent (undamaged) stiffness of the material, dynamic stiffness values were obtained by time-of-flight and density measurements. All test results reported in this paper are the averages of at least five individual tests.

Thermal shock experiments were carried out by heating samples to different temperatures in the range 200 to 800°C, soaking for 20 min to establish thermal equilibrium, and then quenching into water at 20°C. After the samples were completely cooled, they were furnace dried at 60°C for 24 h. Five samples quenched from each temperature were then used for the determination of the mechanical properties in the quenched condition, as described above. The samples used for these experiments were all from batches A and B. For comparison purposes, a group of samples from batch C were subjected to the same thermal cycle but were slow-cooled from the upper temperature rather than quenched, and samples from batches B and C were heated rapidly from room temperature to the same maximum temperatures as used for the quenching experiments. These samples were also mechanically tested as described above.

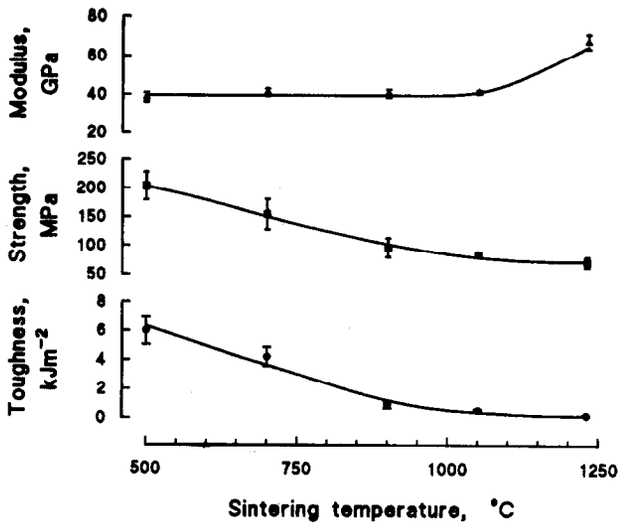


Fig. 1. The effect of raising the sintering temperature on the mechanical properties of freeze-gelled Nextel/silica–zirconia ceramic-matrix composites.

Many of the mechanical tests carried out in this work were accompanied by the monitoring of acoustic emissions. A Marandy MR1004 25-channel amplitude distribution system was used to record emissions received through a PAC U30D-174 PZT transducer and an AECL 2100/pa 60dB preamplifier. The AE data were processed by custom-written software and analysed by means of a conventional spread-sheet program.

The thermal expansion characteristics of the composite over the range 20°C to 650°C were determined in a silica tube dilatometer.

4 Experimental Results

The mechanical properties of the three batches of unidirectional composite after manufacture are given in Table 1.

It can be seen that the strengths and stiffnesses of the three batches of material (which were made by identical procedures, as described earlier) are to all intents and purposes identical, as would be expected. The dynamic stiffness is significantly higher than the flexural modulus measured from

Table 1. Mechanical properties of as-manufactured Nextel/silica–zirconia composite*

Batch	*Fiber volume fraction* V_f	*Dynamic modulus, GPa*	*Flexural modulus, GPa*	*Flexural strength, MPa*	*Work of fracture,* Jm^{-2}
A	0·26 ± 0·01	40 ± 2	31 ± 6	79 ± 18	477 ± 155
B	0·23 ± 0·01	40 ± 1	36 ± 2	84 ± 14	502 ± 111
C	0·28 ± 0·01	44 ± 1	41 ± 4	83 ± 13	871 ± 256

*Errors cited are standard deviations: five test results for each value cited.

the slope of the load–deflexion curve because it effectively assesses the response of an undamaged structure, whereas the mechanical modulus is not a simple elastic property in CMCs, since it inevitably includes some effect of the loss of stiffness due to cracking during loading. It is curious to note, however, that the nominal work of fracture of batch C is almost 50% greater than that of batches A and B. There is little evidence of any kind to explain this difference, the fibre content being only marginally higher, and there being no observable difference in microstructure. The higher fracture work was clearly seen to be the result of a different fracture mode in material of batch C which exhibited a considerable amount of delamination during fracture, whereas the failures of the other two batches were by completely transverse fracture. This difference is also reflected in the higher value of the mechanical flexural modulus. The only possible difference in the processing conditions between batches might be the level of pressure applied during the wet-pressing operation to consolidate the filament-wound material prior to freeze-gelation. This pressure was not controlled, since we had not expected that it would have a significant effect on the properties of the finished composite: this could prove to have been an important processing parameter, however.

On the basis of the manufacturer's value for the fibre stiffness, 186 GPa, the measured composite (dynamic) modulus appears to reflect, almost exactly, a fibre-only contribution (i.e. ¼ of 186 ≈ 46 GPa). In a CMC, this is unlikely, even when the matrix is porous, as in the present case. Earlier work on similar systems[2] suggests that the intrinsic stiffness, E_0, of a dense sol–gel silica matrix may be of the order of 70 GPa, and for a sample with a volume fractional porosity, p, of 0·3 a reasonable value, given by the relationship:

$$E = E_0 \exp(-4p)$$

would be 21 GPa, making an expected composite stiffness of about 65 GPa, some 60% greater than the measured dynamic value. Similarly, a crude estimate of the expected composite strength, based on the manufacturer's figure for the fibre strength (in excess of 2 GPa) and ignoring any matrix contribution, gives a value of the order of 570 MPa, yet the measured strengths in Table 1 imply a fibre strength of the order of only 320 MPa. This enormous loss of strength appears to be a consequence of damage which occurs during processing. Experiments in which tows of the Nextel fibre were passed through the desizing process and then through the guide system through an empty sol bath, for example were found to have lost some 40% of their original bundle strength.[3] Tows of T300 carbon fibre similarly lost about 35% of their original strength during this part of the process. The measured bundle strength of a tow of about 2000 filaments of 11 μm diameter was 198 MPa. Assuming a Weibull modulus of the order of 10, and therefore a bundle strength of the order of 60% of the individual filament strength, a bundle strength of 198 MPa translates to a filament strength of about 330 MPa. Without any more detailed scientific basis for accounting for the difference in gauge lengths in the bundle tests (90 mm) and effective 'gauge length' *in situ* in the composite, this agreement with the measured strength in Table 1 is more than adequate.

As the sintering temperature is raised from 500°C to 950°C the strength declines by about 60%, as shown in Fig. 1, while the modulus (and also the density) increase as consolidation is enhanced. The 950°C sintering temperature was chosen for these experiments to permit the thermal shock experiments to be carried out to a maximum quenching temperature of 800°C. Microstructural evidence, such as that shown in Fig. 2, clearly indicates that significant fibre/matrix interaction does indeed occur during the sintering stage, but it appears that this is not the only



Fig. 2. Electron micrograph showing fibre/matrix interaction in a freeze-gelled Nextel/silica–zirconia ceramic-matrix composite during sintering at 500°C following infiltration.

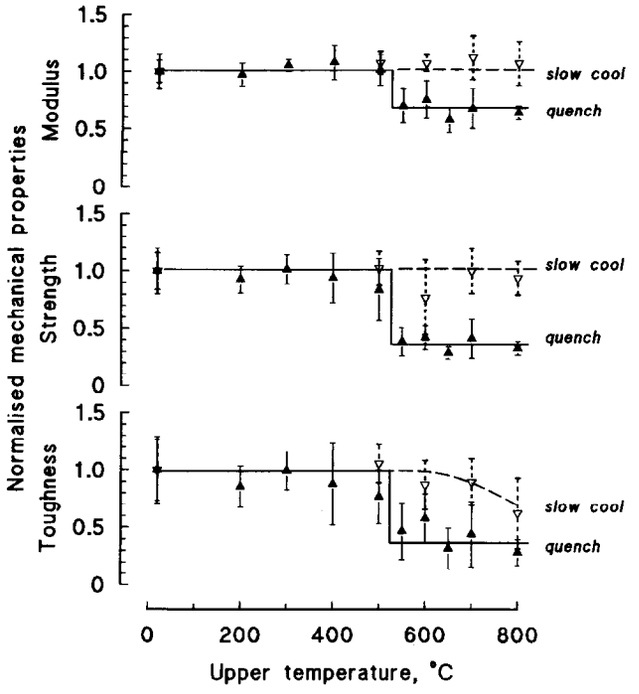


Fig. 3. The effect of slow and rapid cooling on the mechanical properties of freeze-gelled Nextel/silica–zirconia ceramic-matrix composites. The open symbols represent samples of batches A and B (pooled data) water-quenched from the stated soak temperature, while the solid symbols represent samples from batch C slow cooled from the stated temperature. Each point for batches A/B is the mean of ten individual tests, and each point for batch C is the mean of five tests: the error bars are standard deviations.

source of damage. A important secondary advantage of the freeze-gelation process is that the dried but unsintered product has considerable strength as a result of the molecular forces involved in the sol-gel transformation, a situation paralleled to some extent in the 'setting' of the tobermorite gel in cement, and this has important implications for the handling and shaping of pre-sintered products. Thus, we have found that the freeze-gelled material can be tensile tested in the unsintered state after vacuum-drying at a temperature slightly above ambient, followed by further infiltration (but no sintering) to yield a strength of only 155 ± 5 MPa, and this strength falls to 127 ± 7 MPa after sintering at only 500°C. Clearly, then, the Nextel fibre loses most of its reinforcing potential as a result of either corrosion in the sol bath, or abrasion at some stage during the consolidation process. It appears, therefore, that this fibre cannot be considered as a serious contender for use in CMCs manufactured by this process.

The axial coefficient of thermal expansion (CTE) varies strongly with temperature over the range studied, rising from about $2{\cdot}8 \times 10^{-6}(°C)^{-1}$ at ambient temperature to about $6 \times 10^{-6}(°C)^{-1}$ at about 500°C. The variation is approximately linear in temperature, being given by the relationship:

$$\alpha = 2{\cdot}69 \times 10^{-6} + 6{\cdot}44 \times 10^{-9}\, T \qquad (1)$$

The room-temperature CTE of the Nextel fibre is quoted by the manufacturer as $5 \times 10^{-6}(°C)^{-1}$. We have no measured value for the unreinforced matrix material appropriate to its condition in the sol-gel composite, but a value of about $2 \times 10^{-6}(°C)^{-1}$ would, on a crude rule-of-mixtures basis, give the observed CTE of about $2{\cdot}8 \times 10^{-6}(°C)^{-1}$ for the unidirectional composite.

4.1 Thermal shock results

The effects of water quenching on the properties of the composites of batches A and B (filled triangles) are shown in Fig 3. In view of the similarity of properties of batches A and B shown in Table 1, the data for these two batches have been pooled. The A/B data points in Fig. 3 are therefore means of ten individual tests and the error bars represent the standard deviations. Each set of results is normalised with respect to the appropriate property of the as-manufactured composite (i.e. the values given in Table 1) for ease of comparison. It can be seen that the stiffness, strength and mechanical modulus all remain unaffected by quenching until the soaking temperature exceeds 500°C. Above this all three properties fall drastically in step functions to levels that are about 50% of the original values in the case of the strength and toughness, and 60–70% of the initial values for the stiffness. In order to show that it is the thermal shock that is responsible for this sudden loss in properties, samples of batch C were subjected to the same heating and soaking procedure, but were then slow cooled in the furnace from the soak temperature. It can be seen that the strength and stiffness are unaltered by this treatment, but the toughness does change, falling more gradually beyond about 500°C to some 60 or 70% of the initial value. Table 1 shows that the original toughness of batch C was much higher than that of batches A and B, and the corresponding decline in toughness of the material of batches A and B as a result of slow cooling may well be more severe than that shown for batch C in Fig. 3.

As a further check on the role of the downquench, as opposed to other heating effects, in degrading the properties of the composite, a small group of samples was also subjected to the same temperature change by rapid heating up to the soaking temperature. These results are shown in Fig. 4, from which it is clear that the values of all three mechanical properties are substantially unchanged by either slow cooling or rapid heating from 800°C.

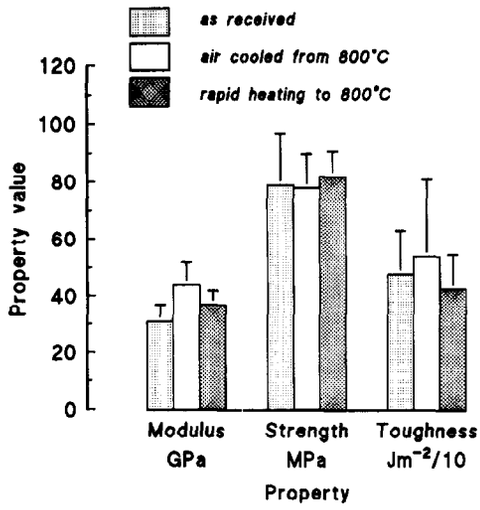


Fig. 4. Effects of slow cooling from 800°C and rapid heating to 800°C on the properties of the Nextel/silica–zirconia CMCs.

The changes in acoustic emission response from quenched and unquenched samples give some insight into the effect of the thermal shock on the damaged state of the material. Figure 5 shows the cumulative total number of AE events emitted by samples during flexural testing as a function of the soak temperature prior to quenching. The data points are the averages of five separate tests and the error bars are the standard deviations. It can be seen that in the as-manufactured state the total AE count is about 800 events, a low output for a unidirectional fibre composite material. There is little change in the total AE count for samples quenched from temperatures up to about 500°C (the slight depression between the as-manufactured level and the level at 500°C is probably not significant, given the variable character of these materials and the general nature of AE phenomena) but beyond 500°C the acoustic response increases markedly, reflecting the sudden deterioration in mechanical properties of samples quenched from above 500°C. Analysis of the amplitudes of the AE events which constitute the general pattern shown in this figure provides further information on the effects of the quench. Figure 6 shows the amplitude distribution histograms for samples loaded to fracture in bending in the as-manufactured state and after quenching from 800°C. These distributions are for the final stages of the two tests, with the samples nearing fracture, a method of AE analysis which emphasises changes in mechanisms by reducing the masking effect of the large numbers of events recorded in the early stages. The bars in the histogram therefore represent the numbers of events emitted during the last few seconds of a test which fall in the amplitude band defined by the amplitude channel number on the abscissa. The width of each amplitude bin is 2·4dB. A voltage of 10 mV at the amplitude sorter for channel 0 represents 10 μV at the transducer. The threshold in these tests was set at channel three to exclude extraneous signals, and hence the actual test threshold was 20·9 mV. In the un-quenched condition, the form of the distribution is roughly exponential, with no significant numbers of events having amplitudes above 832mV (channel 15), the normal kind of distribution found in many types of composite, including CMCs. By contrast, the distribution for the quenched sample shows three distinct features. Apart from the increase in the total event count already referred to, it is clear that there are also many events of much higher amplitude than those in the un-quenched sample, and the distribution has become bi-modal, with a peak at an amplitude of about 363mV (channel 13). This is indicative of the late onset of a different mode of damage, or the operation of an existing damage mode at much higher energy levels.

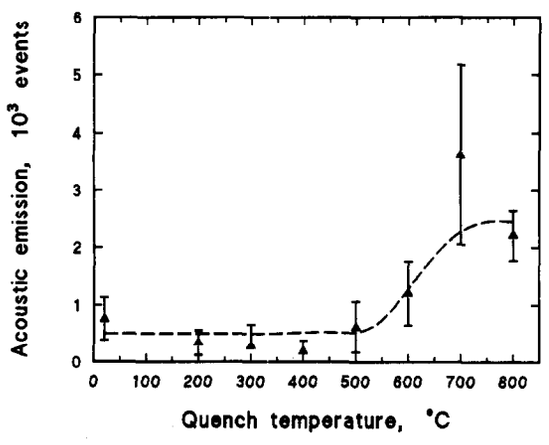


Fig. 5. Cumulative acoustic emission event count during flexural fracture tests on quenched samples of the Nextel/silica–zirconia CMCs.

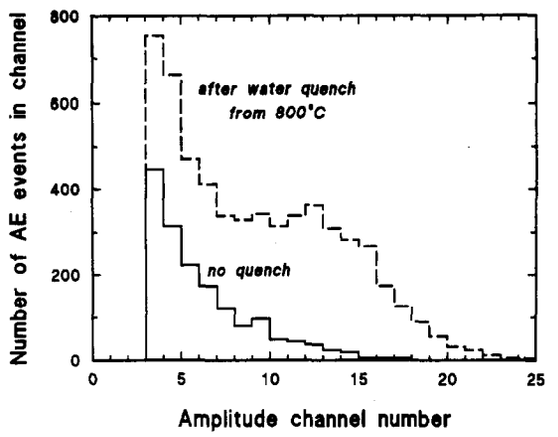


Fig. 6. Acoustic emission amplitude distributions for Nextel/silica–zirconia CMC samples tested to failure in flexure in the as-received condition and after quenching from 800°C.

5 Discussion

It is apparent from Fig. 3 that although, in the quench temperature range below 500°C, the mean strength and toughness values both begin to decline, somewhat more gently than the stiffness values, all of these reductions are still within the overall spread of experimental results and the real effect of thermal shock is more obviously manifested as a step reduction in all three properties at some quenching temperature between 500 and 550°C. Beyond this temperature all three properties remain constant, again within the scatter of the results.

The basic Kingery model[4] for an infinitely rapid quench of a ceramic body gives the maximum temperature difference, ΔT_c, which a material can withstand before the fracture stress, σ_f, is reached as

$$\Delta T_c = (R^I) = \frac{\sigma_f (1 - \nu)}{E\alpha} \quad (2)$$

Since we have no experimental results for the thermal conductivity of our composites, it is not possible to refine the model to account for finite quenching rates and finite sample geometry, but eqn 1 may be used to evaluate the results in Fig. 3, at least to a first approximation. The theoretical value of ΔT_c for a composite exhibiting the properties that would have been predicted from the basic characteristics of the matrix and fibres would have been of the order of 1200°C, assuming a mean value of α of $5{\cdot}5 \times 10^{-6}(°C)^{-1}$. As we have seen, however, the real strength of the composite is a fraction of the predicted value, and if we insert the actual experimental values from Table 1, together with a mean value of α of $4 \times 10^{-6}(°C)^{-1}$, we find that the predicted ΔT_c is about 375°C. The problem is, of course, recursive since, as we showed earlier, the actual value of α, and also its mean value over the predicted quenching range, are themselves functions of that temperature range, and these approximate values of α and ΔT_c must be obtained by successive approximations. The observation that slower cooling does not produce a change in strength implies that the second thermal shock parameter

$$R^{II} = \frac{k\sigma_f (1 - \nu)}{E\alpha} \quad (3)$$

is not significant, i.e. the conductivity, k, is not a contributor to the grading of the materials — they are susceptible only to large, rapid quenches.

It is interesting to note that a very limited number of flexural tests carried out on samples cut transverse to the fibre axis gave values of 6 GPa and 13 MPa, respectively, for the modulus and strength, and these values generate a slightly higher calculated value of ΔT_c, about 406°C, but both predicted values are 150°C or more below the clearly defined experimental value which is between 500 and 550°C.

It appears, therefore, that despite the apparently large loss in strength of the reinforcing fibres during the fabrication process, their presence remains beneficial in increasing the resistance of the material to thermal shock. We note that unreinforced freeze-gelled material has a failure strength of about 20–30 MPa and a work of fracture of 0·05–0·1 kJm^{-2}. Thus, although our experimental material is relatively weak by comparison with high-performance CMCs, it was significantly better than the unreinforced material.

The more complete Hasselmann model[5] predicts that for thermal shocks of severity less than ΔT_c the strength remains unaffected because insufficient strain energy is available to cause propagation of a number of existing flaws (which are assumed to be of a uniform size). The fibres are likely to contribute to the increase of energy required to propagate all of these flaws. When the temperature difference exceeds the critical value, the strength (and, as shown by Fig. 1, any other mechanical property associated with strength as normally defined) falls because a significant proportion of the family of pre-existing cracks has grown as a result of the thermal shock. The process of propagation of these larger cracks is stable, however, and no further drop in strength is expected with further increase in the quenching temperature interval until a second critical temperature difference, $\Delta T_c'$, is reached when the cracks present in the quenched body have become large enough to propagate in quasi-static fashion, with corresponding further decrease in strength as ΔT increases further. It can be seen from Fig. 3, however, that this higher critical temperature interval has not been reached by the time the thermal shock experiments were discontinued at 800°C, above which structural changes in the material would be expected.

The acoustic emission response of the materials in the as-manufactured and quenched states appears to be quite different. During the early stages of loading, samples quenched from above 500°C emit fewer acoustic emissions than un-quenched samples, but as failure approaches the event emission rate increases more rapidly so that, overall, quenched samples produce more events to failure. It has also been shown that a mid-range amplitude peak develops as failure approaches, indicating the possibility of the onset of a micro-failure process that is different from that which occurs normally in un-quenched material. The likelihood

is that this mechanism is the propagation of pre-existing cracks formed or extended by the thermal shock treatment. It appears, then, that cracks are propagating subcritically during thermal shock, presumably from existing defects (pores, perhaps, or reaction damage sites on fibres). During loading of quenched samples, a higher level of strain is then required to cause further propagation and stimulate AE. As failure approaches, however, the number of enlarged cracks results in more AE. The marked decline in composite strength caused by quenching suggests that the thermal shock process must also be causing further damage to the fibres, presumably as a result of the matrix cracks propagating through the fibres as a consequence of the strong interfacial bond.

6 Conclusions

(1) Ceramic-matrix composites consisting of a silica–zirconia matrix reinforced by continuous Nextel mullite fibres have been manufactured by a sol–gel route incorporating freeze-gelation and subjected to thermal shock by water quenching from temperatures up to 800°C.

(2) Nextel alumino-silicate fibres are unsuited to direct inclusion in freeze-gelled ceramic matrix composites, probably because of degradation of the fibres during the desizing and filament winding processes. The lack of appropriate low-cost ceramic reinforcing fibres and the requirement for interface control through the application of interfacial layers is nothing new in the field of CMCs.

(3) Despite 2 above, comparison of reinforced and unreinforced freeze-gelled material shows that the Nextel fibres provide significant reinforcement of the matrix and improvements in the thermal shock resistance. Nextel-fibre-reinforced silica/zirconia CMCs are essentially unaffected by water quenching from temperatures up to 550°C. Beyond this critical value there is a step reduction of strength and modulus to between 50 and 60% of virgin properties.

(4) The changes in mechanical behaviour are accompanied by significant modifications of the acoustic emission response of the materials during post-quench three-point flexural testing. A lower initial event rate during load application gives way to a much higher event rate (and more events in total) at failure. A change to a bi-modal amplitude distribution near failure gives further credence to the hypothesis that thermal shock (beyond a critical value) causes the propagation of probably pre-existing flaws to a longer but stable value. A further, and significantly higher second critical level of thermal shock is then required to cause additional propagation of the flaws and a further reduction in properties. In other words, we believe that our continuous fibre reinforced materials behave in the manner proposed by Hasselmann. We note that earlier work of a similar nature on a freeze-cast short-fibre-reinforced CMC showed that this material also obeyed the Hasselmann model.[6]

(5) Quenching from above the critical temperature results in a significant (but not catastrophic) decline in strength which is not altered by further increasing the quenching temperature. The Hasselmann quenching cracks clearly do not therefore propagate from one side of the sample to the other.

Acknowledgement

This work was carried out as part of a wider program of research on the sol–gel processing of CMC shapes with the financial support of the ACME Directorate of SERC. The authors are grateful for this support and for the encouragement of the Directorate. Sadly, Dr Richard Russell-Floyd, who was a major source of inspiration in this work, died shortly after this paper was submitted for publication.

References

1. Russell-Floyd, R., Harris, B., Jones, R. W., Cooke, R. G., Wang, T. H., Laurie, J. & Hammett, F. W., *Br. Ceram Trans*, **92** (1993) 8–12.
2. Russell-Floyd, R. S., Harris, B., Cooke, R. G., Wang, T. H., Laurie, J., Hammett, F. W. & Jones, R. W., *Journal of the American Ceramic Society*, **76**(10) (1993) 2635–43.
3. Chant, J. M. (1994). University of Bath, private communication of unpublished results.
4. Kingery, W. D., *J. Am. Ceram. Soc.*, **1** (1955) 3–15.
5. Hasselmann, D. P. H., *J. Am. Ceram. Soc.*, **52** (1969) 600–4.
6. Russell-Floyd, R. S., Johnson, R., Cooke, R. G. & Harris, B., *Advanced Composites Letters*, **2** (1993) 57–60.

Journal of the European Ceramic Society **15** (1995) 463–468
© 1995 Elsevier Science Limited
Printed in Great Britain. All rights reserved
0955-2219/95/$9.50

0955-2219(95)00007-0

The Preparation, Characterization and Electrical Properties of Electroceramics made of Copper–Cobalt Manganite Spinel: $Mn_{2\cdot6-x}Co_{0\cdot4}Cu_xO_4$, $0 \leq x \leq 1$

R. Legros, R. Metz[a] & A. Rousset

Laboratoire de Chimie des Matériaux Inorganiques, U.R.A. - C.N.R.S. 1311, 118, route de Narbonne, 31062 Toulouse Cedex, France

(Received 30 November 1993; revised version received 19 July 1994; accepted 12 December 1994)

Abstract

In this paper we report our results on the preparation and characterization of copper–cobalt manganites, $Mn_{2\cdot6-x}Co_{0\cdot4}Cu_xO_4$ ($0 \leq x \leq 1$), obtained from coprecipitated oxalate precursors. Powder and single phase ceramics have been characterized by means of X-ray diffraction (XRD) and electrical conductivity measurements. The results of both characterization techniques are indicative of the ionic distribution for the copper–cobalt manganites solid solution studied: $Mn^{2+}_{0.6-x}Co^{2+}_{0.4}Cu^{+}_{x}\,[Mn^{3+}_{2-x}\,Mn^{4+}_{x}]\,O^{2-}_{4}$; with $0 \leq x \leq 0{\cdot}6$, $Co^{2+}_{0.4}\,Cu^{+}_{0.6}\,[Cu^{2+}_{y}Mn^{3+}_{1.4-2y}\,Mn^{4+}_{0.6+y}]\,O^{2-}_{4}$; with $0{\cdot}6 < x \leq 1$ and $y = x - 0{\cdot}6$.

1 Introduction

Thermistors with Negative Temperature Coefficient of Resistance (NTC) are semiconducting thermally sensitive resistors whose primary function is to exhibit a wide change in electrical resistance with a change in body temperature. These electroceramics are often constituted of spinel structure transition metal manganites with formula: $Mn_{3-x'-x}\,Ni_{x'}\,M_x\,O_4$ ($0 \leq x+x' \leq 1{\cdot}5$; M = Ni, Co, Cu...).

The purpose of this paper is to present the study of manganites without nickel which is often present in industrial NTC thermistors.

The transition metal oxides have aroused considerable interest regarding the valency and the cationic distribution among tetrahedral and octahedral sites in the spinel structure. Many workers using different experimental techniques have sought to resolve this problem. However, the cationic distribution of manganites depends on the preparation conditions. For instance, Kulkarni *et al.*[1] have established from X-ray absorption spectroscopy that the defined compound $CoCuMnO_4$ presents a tetragonal structure with the cationic distribution: $Co^{2+}[Mn^{4+}Cu^{2+}]\,O^{2-}_4$. (the square brackets indicate octahedral sites). However, using a different route Brabers *et al.*[2] prepared a single-phase cubic spinel with the following distribution: $Cu^{+}_{0.65}Mn^{3+}_{0.35}[Cu^{2+}_{0.35}Co^{3+}_{1}Mn^{4+}_{0.65}]O^{2-}_4$. They called into question Kulkarni's preparation.

Hence, to avoid any substantial deviation from an intended composition, it seems necessary to study solid solution rather than defined compounds since one may reasonably assume that the oxidation states and the distribution of cations vary continually with the composition.

Kshirsagar *et al.*[3] studied the solid solution, $Co_xCu_{1-x}[Mn_2]O_4$, and showed that for $x < 0{\cdot}5$ the structure becomes cubic. In this solid solution the manganese is fixed which differs from the present paper in which we have studied the substitution of copper for manganese in the cobalt manganite with formula: $Mn_{2\cdot6}Co_{0\cdot4}O_4$.

Cobalt manganites $Mn_{3-x}Co_xO_4$ for $0 \leq x \leq 1$ have been previously studied.[4–7] These components have tetragonal structure and their cation distribution can be deduced from that of hausmannite as given by $Mn^{2+}\,[Mn^{3+}_2]\,O^{2-}_4$ by substituting essentially Mn with Co on tetrahedral sites implying a structural formula of type $Mn^{2+}_{1-x}Co^{2+}_x\,[Mn^{3+}_2]\,O^{2-}_4$. This structural description accounts for their tetragonal structure characterized by their stability up to very high temperatures and their practical insulating properties.

By analogy with copper manganites, we have tried to create Mn^{3+}–Mn^{4+} couples in octahedral sites which resulted in a dramatic decrease in the electrical resistivity.[8–9]

[a] Present address: Pharmacie Centrale de France, Quai Jean Jaurès - BP 57, 07800 La Voulte-Sur-Rhône, France.

Table 1. Quenched temperatures and lattice parameters of single-phase oxide powders: $Mn_{2\cdot6-x}Co_{0\cdot40}Cu_xO_4$

x	*Quenched*	*Lattice parameters (nm)*			
	temperature °C	*a*	*c*	$a' = 3\sqrt{a^2c}$	*c/a*
·00	1100	·812	·944	·854	1·16
·05	1000	·813	·930	·850	1·14
·10	1050	·813	·932	·851	1·15
·20	1050	·813	·924	·849	1·14
·30	900	·814	·911	·845	1·12
·39	900	·816	·902	·844	1·10
·50	900	·817	·891	·841	1·09
·59	900	·820	·882	·840	1·08
·66	900	·821	·873	·838	1·06
·69	900	·821	·871	·837	1·06
·79	900	·835	·835	·835	1
·90	900	·835	·835	·835	1
1·0	900	·834	·834	·834	1

2 Experimental Procedure

2.1 Sample preparation of powders

The powders were obtained from the decomposition of oxalic precursors prepared by coprecipitation in aqueous solution from $MnCl_2$, $6H_2O$, $CoCl_2$, $6H_20$ and $CuCl_2$, $6H_2O$ and ammonium oxalate $(NH_4)_2C_2O_4$, H_2O at 25°C.

Simple thermal decompositions in air of the precipitated oxalic precursors leads to a mixture of oxides. Therefore, by analogy with the preparation of copper manganite spinels,[9] a long stage at high temperature (to increase the diffusion of the oxides), followed by a quench treatment in water (to stabilize the high temperature structure at room temperature) has been used. These heat treatments in air, with different profiles depending upon the compositions of powders prepared yield metastable single-phase oxides and are depicted in Table 1.

2.2 Sample preparation of ceramics

The earlier preparation of powder with a single-phased spinel structure was of great use in preparing ceramics with a single-phased spinel structure. To obtain well densified ceramics, the previous oxide powders were first pressed into disc form (6 mm diameter and 2 mm thickness) under 7 kbar. Then, the green discs were fired for 4 h at a temperature depending upon the amount of copper. After the sintering the samples were cooled at a rate of 120°C per hour, to the temperature used to obtain single-phased powders and were kept at this temperature for 24 h. The final cooling was a quench in water to stabilize the high temperature structure at room temperature.

It is worth noticing that the single-phased powders were difficult to sinter. Table 2 shows the evolution of densification depending on various sintering temperatures for the given composition: $Mn_{2\cdot20}Co_{0\cdot4}Cu_{0\cdot39}O_4$. It appears that for each composition, there is an optimal sintering temperature (Table 3). Moreover, for certain compositions ($x > 0\cdot5$), we report the phenomenon of exaggerated growth of manganite grains which led to grain sizes up to 500 μm. Eventually, the ceramics cracked or became extremely brittle.

Table 2. Sintering temperatures and densification for the given single-phase ceramic: $Mn_{2\cdot20}Co_{0\cdot41}Cu_{0\cdot39}O_4$

Sintering temperature (°C)	*Densification (%)*
1100	94·5
1130	98
1150	95
1170	94
1200	93

2.3 X-ray diffraction

XRD powder patterns were recorded at room temperature using an automatic diffractometer (Siemens D 501, CoKα radiation). The standard error on parameters was less than ± 0·0005 nm.

2.4 Measurement of electrical properties of ceramics

Samples for electrical measurements were prepared by depositing silver electrodes on the opposite faces of the discs formed and were subjected to thermal treatment at 850°C, so as to make good ohmic contact with the ceramics.

The d.c. resistivity was deduced by classical resistance measurements made at 25 ± 0·05°C and using the relationship $\rho = RS/l$, with R, the electrical resistance in Ohms (Ω); S the area of the specimen in cm^2 and l the thickness of the specimen in cm. Another d.c. resistance measurement was carried out at 85 ± 0·05°C so as to deduce the band gap-related constant B from the classical law of semiconductors $\rho = \rho_0\exp(B/T)$ with $B = \Delta E/2k$.

Table 3. Sintering temperatures used to obtain well densified single-phase ceramics: $Mn_{2\cdot6-x}Co_{0\cdot4}Cu_xO_4$

x	*Theoretical density*	*Densification* (%)	*Sintering temperature* (°C)
·00	4·92	93	1130
·05	4·95	93	1130
·20	5·05	95	1130
·30	5·13	95·5	1130
·39	5·20	98	1130
·50	5·25	95	1130
·59	5·36	97·5	1110
·66	5·40	94·5	1080
·79	5·42	97	1050
·90	5·42	94	1030
1·00	5·44	95·5	1020

3 Results and Discussion

3.1 XRD analyses

3.1.1 Cation distribution of manganite powders

The variation of the lattice parameters of single-phased powders as a function of the copper content is reported in Table 1. Most of the solid solutions $Mn_{2\cdot6-x}Co_{0\cdot4}Cu_xO_4$ were found to be tetragonally distorted from cubic symmetry. The tetragonal distortion $c/a > 1$ decreased with copper content and disappeared for $x \geq 0\cdot79$.

The substitution of copper in the matrix $Mn^{2+}_{0.6}Co^{2+}_{0\cdot4}[Mn^{3+}_2]\ O^{2-}_4$ could be interpreted by one of the four theoretical limiting ionic configurations as follows:

(a) $Mn^{2+}_{0.6-x}Co^{2+}_{0\cdot4}\ Cu^{+}_x\ [Mn^{3+}_{2-x}\ Mn^{4+}_x]\ O^{2-}_4$;
with $0 \leq x \leq 0\cdot6$;

(b) $Mn^{2+}_{0.6-x}Co^{2+}_{0\cdot4}\ Cu^{2+}_x\ [Mn^{3+}_2]\ O^{2-}_4$;
with $0 \leq x \leq 0\cdot6$;

(c) $Mn^{2+}_{0.6}Co^{2+}_{0\cdot4}\ [Cu^{+}_xMn^{3+}_{2-3x}Mn^{4+}_{2x}]\ O^{2-}_4$;
with $0 \leq x \leq 0\cdot66$;

(d) $Mn^{2+}_{0.6}Co^{2+}_{0\cdot4}\ [Cu^{2+}_x\ Mn^{3+}_{2\ 2x}Mn^{4+}_x]\ O^{2-}_4$;
with $0 \leq x \leq 1$.

However, according to the work of Baffier and Huber,[10] the tetragonal distortion in the ferromanganite spinel structure is created by the presence of cations Mn^{3+} on the octahedral sites. Moreover, they have shown that a minimum concentration of Mn^{3+} cations in octahedral sites is necessary to raise a cooperative Jahn–Teller effect. This minimum concentration is about 50%. Thus there is a correlation between the concentration of cations Mn^{3+} in octahedral sites and the macroscopic distortion observed by X-ray diffraction.

The formulae (a), (c) and (d) might explain the decrease of tetragonal distortion as a function of copper content by diminishing the Mn^{3+} ion content in B sites, e.g. by decreasing the Jahn–Teller effect of the cations Mn^{3+} ($t^3_{2g}\ e^1_g$) localized in octahedral sites. However the components (c) and (d) cannot fit with the experimental tetragonal distortion observed for $0 \leq x < 0\cdot79$, because for $x \geq 0\cdot33$ and $x \geq 0\cdot5$ respectively, the distortion of the spinel structure should disappear while the concentration of Mn^{3+} in octahedral sites drops below the 50% critical value necessary to raise a cooperative Jahn–Teller effect. In the case of formula (b), the increased amount of copper (II) in tetrahedral sites must be responsible for a Jahn–Teller effect $c/a < 1$ and thus for the overall decrease of the distortion.

The cubic spinel structure is preserved when different kinds of cation occupy a spinel site. From this Poix[11] defined two parameters: $dCA = \Sigma i\ xi\ (CA_i - 0)$ and $dCB = \Sigma i\ xi/(CBi - 0)/2$ where dCA and dCB are the mean values of the 'oxygen–cation' distance in tetrahedral and octahedral sites respectly. The lattice parameter a of the cubic structure spinel is related to the dCA and dCB according to

$$a = 2\cdot0995\ dCA + (5\cdot8182\ dCB^2 - 1\cdot4107\ dCA^2)^{1/2}$$

Table 4. Anion–cation distance in tetrahedral and octahedral sites of cubic spinel structure[11]

Cations	*Cation–oxygen (nm)*	
	A sites	*B sites*
Mn^{2+}	·2041	·2220
Mn^{3+}	—	·2045
Mn^{4+}	—	·1843
Co^{2+}	·1967	—
Cu^{+}	·2070	·2281
Cu^{2+}	·1940	·2150

It may be seen that the theoretical lattice parameters could be calculated for various cation distributions among the two sublattices. When the phases crystallise in a tetragonally deformed spinel structure it is possible to replace a (cubic parameter) by $a' = \sqrt[3]{a^2c}$ (cubic/root of volume cell). Thus, it is possible, knowing the characteristic bond distances manganese–oxygen, cobalt–oxygen and copper–oxygen (Table 4) to calculate from the cation distributions (a), (b), (c) and (d), the theoretical decrease of the cubic parameter a (or a') as a function of the amount of copper substituted in the manganite: $Mn_{2\cdot6-x}Co_{0\cdot4}Cu_xO_4$.

The variation of the lattice parameter, a', of $Mn_{2\cdot6-x}Co_{0\cdot4}Cu_xO_4$ powders as a function of the copper content, x, calculated for the cation distributions (a), (b), (c) and (d), is compared with the experimental data (Fig. 1). It appears very clear that the hypothetical distributions (b) and (d) cannot fit with the experimental results. It is difficult to choose between the formulae (a) and (c); however the previous discussion about the cooperative Jahn–Teller effect shows that the distribution (c) involves a tetragonal–cubic transition for $x > 0\cdot33$ instead of an experimental transition observed for $x > 0\cdot66$. Thus, the most probable distribution among the four extreme hypothetical substitution processes is:

(a) $Mn^{2+}_{0.6-x}Co^{2+}_{0\cdot4}Cu^{+}_x\ [Mn^{3+}_{2-x}\ Mn^{4+}_x]\ O^{2-}_4$;
with $0 \leq x \leq 0\cdot6$.

According to this last cation distribution with $0 \leq x \leq 0\cdot6$, for $x > 0\cdot6$, the copper should substitute the manganese located in octahedral sites. Two different theoretical substitutions could appear;

(e) $Co^{2+}_{0\cdot4}Cu^{+}_{0\cdot6}\ [Cu^{+}_yMn^{3+}_{1.4-3y}Mn^{4+}_{0\cdot6+2y}]\ O^{2-}_4$;

(f) $Co^{2+}_{0\cdot4}Cu^{+}_{0\cdot6}\ [Cu^{2+}_yMn^{3+}_{1.4-2y}Mn^{4+}_{0\cdot6+y}]\ O^{2-}_4$;
with $y = x\text{-}0\cdot6$ and $0 < y < 0\cdot4$

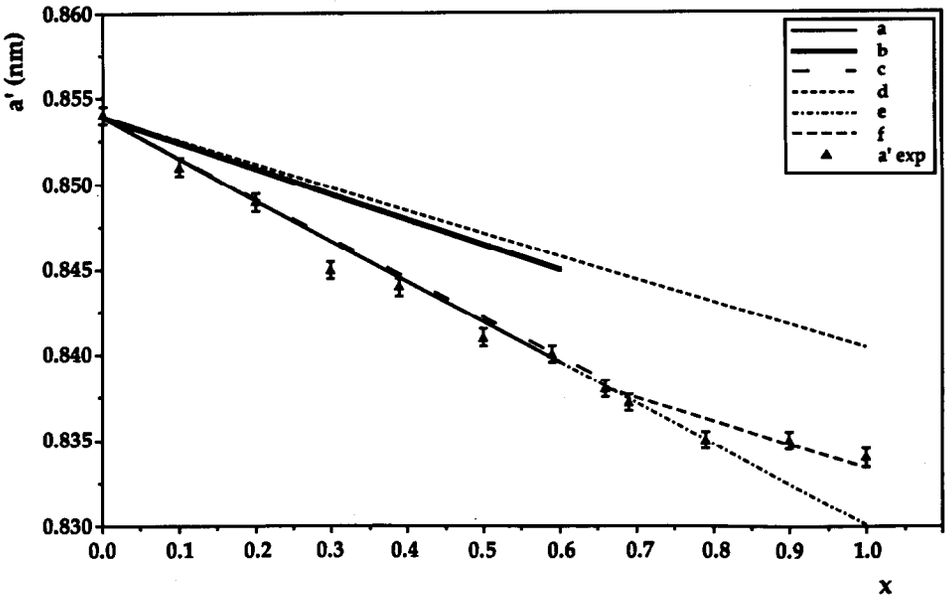


Fig. 1. Theoretical changes of the lattice parameter a' and equations to straight lines calculated for the following cationic distributions:

(a) $Mn^{2+}_{0.6-x}Co^{2+}_{0.4}Cu^{+}_{x}\,[Mn^{3+}_{2-x}Mn^{4+}_{x}]\,O^{2-}_{4}$ → a' = –0·239x + 8·539;

(b) $Mn^{2+}_{0.6-x}Co^{2+}_{0.4}Cu^{2+}_{x}\,[Mn^{3+}_{2}]\,O^{2-}_{4}$ → a' = –0·147x + 8·539;

(c) $Mn^{2+}_{0.6}Co^{2+}_{0.4}[Cu^{+}_{x}Mn^{3+}_{2-2x}Mn^{4+}_{x}]\,O^{2-}_{4}$ → a' = –0·233x + 8·539;

(d) $Mn^{2+}_{0.6-x}Co^{2+}_{0.4}[Cu^{2+}_{x}Mn^{3+}_{2-x}Mn^{4+}_{x}]\,O^{2-}_{4}$ → a' = –0·134x + 8·539;

(e) $Co^{2+}_{0.4}Cu^{+}_{04}[Cu^{+}_{y}Mn^{3+}_{1.4-3y}Mn^{4+}_{0.6+2y}]\,O^{2-}_{4}$ → a' = –0·235y + 8·536;

(f) $Co^{2+}_{0.4}Cu^{+}_{06}[Cu^{2+}_{y}Mn^{3+}_{1.4-2y}Mn^{4+}_{0.6+y}]\,O^{2-}_{4}$ → a' = –0·135y + 8·476.

– Experimental lattice parameters ī as a function of copper content x and equations to straight lines calculated for: $0 < x < 0{\cdot}6$ a' = – 0·238x + 8·534 close to equations (a) and (c); $0 < y < 0{\cdot}4$ a' = – 0·086 + 8·476 close to equation (f).

In contradiction to the formula (e) the experimental data fits well to the (f) line corresponding to the substitution of copper II to manganese in octahedral sites (Fig. 1). Thus, for $x > 0{\cdot}6$ the closer hypothetical cation distribution in these spinels is:

(f) $Co^{2+}_{0.4}Cu^{+}_{0.6}\,[Cu^{2+}_{y}Mn^{3+}_{1.4-2y}Mn^{4+}_{0.6+y}]\,O^{2-}_{4}$

3.1.2 Cation distribution of manganite ceramics

The diffraction analysis revealed the presence of pure spinel structure. The results concerning the lattice parameter values (Table 5), are very close to those observed with spinel powders (Table 1). Hence, we assume that the ionic distribution of the powder samples doesn't differ from the ceramics.

Table 5. Structure and lattice parameters of single-phase ceramics: $Mn_{2.6-x}Co_{0.4}Cu_xO_4$ (to be compared with Table 1)

x	*Spinel structure*	*Lattice parameter (nm)*		
		a	c	a'
·00	tetragonal	·812	·944	·854
·05	tetragonal	·812	·932	·850
·20	tetragonal	·815	·917	·848
·30	tetragonal	·814	·916	·847
·39	tetragonal	·816	·904	·844
·50	tetragonal	·817	·895	·842
·59	tetragonal	·819	·882	·839
·66	tetragonal	·820	·880	·840
·79	cubic	·835	—	—
·90	cubic	·834	—	—
1·00	cubic	·834	—	—

3.2 Electrical properties of ceramics

The experimental data are reported in Table 6. The electrical resistivity of copper–cobalt manganite ceramics decreases with copper ion content until a minimum of resistivity for $x = 0{\cdot}79$ (Fig. 2).

The substitution of copper ions for manganese ions in insulating spinel material, $Mn_{2.6}Co_{0.4}O_4$, gives rise to a semiconductor. The resistivity of the thermistors can reach several Ω cm. The con-

Table 6. Electrical data of monophased ceramics: $Mn_{2.6-x}Co_{0.4}Cu_xO_4$

x	*Spinel structure*	*Densification (%)*	*ρ (Ω·cm)*	*B (K)*
·00	tetragonal	93	$> 2{\cdot}10^6$	—
·05	tetragonal	93	880 000	5360
·20	tetragonal	95	1000	3100
·30	tetragonal	95·5	570	3080
·39	tetragonal	98	310	2970
·50	tetragonal	95	170	2900
·59	tetragonal	97·5	70	2850
·66	tetragonal	94·5	27	2750
·79	cubic	97	7	2490
·90	cubic	94	14	2600
1·00	cubic	95·5	40	2590

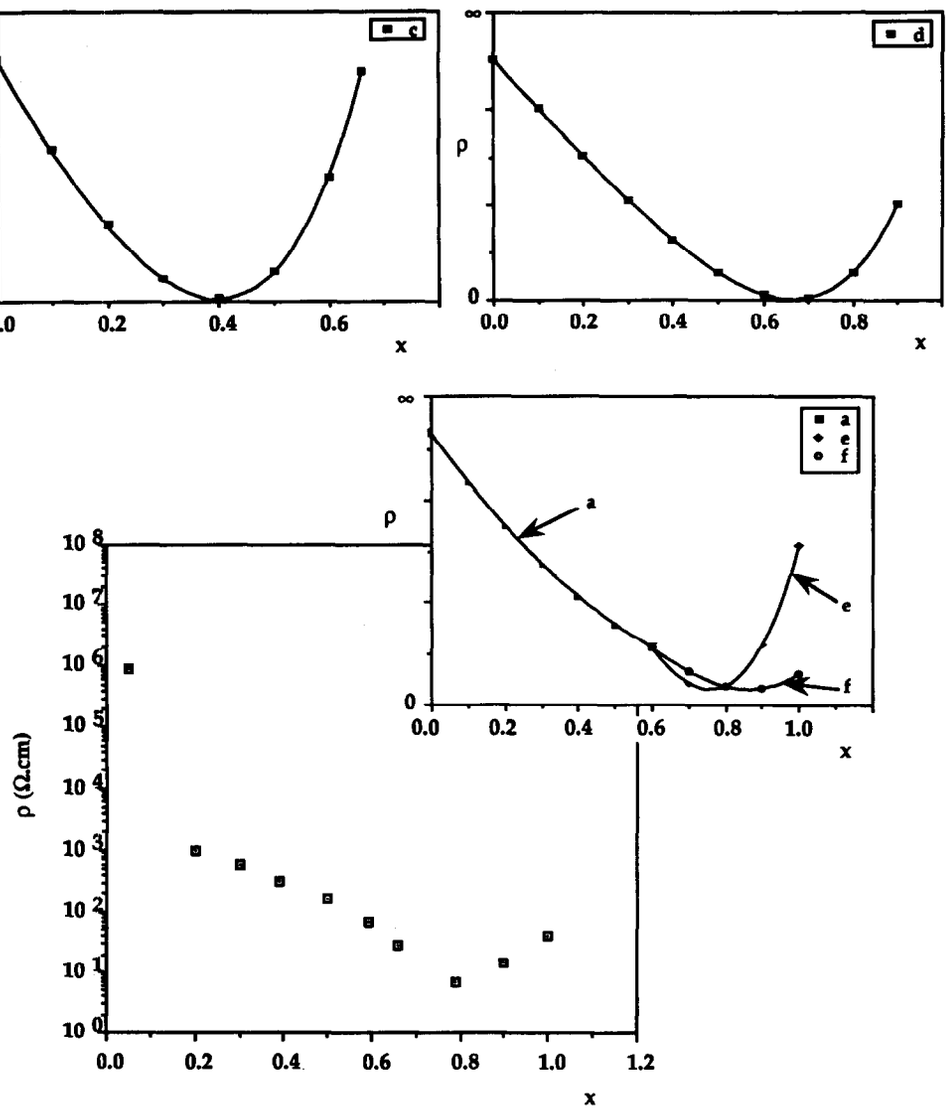


Fig. 2. ⊡ Experimental change of resistivity as a function of the copper content x. Theoretical variation of the resistivity according to the cationic distributions: (a) with $0 < x < 0{\cdot}6$ plus (e) and (f) with $0 < y < 0{\cdot}4$; distributions (c) and (d) with Cu II in octahedral sites.

ductivity of these components is dependent on the presence in the octahedral sites of Mn^{3+} and Mn^{4+}.

The electrical conductivity of a small polaron conductor can be written as[12]

$$\sigma = \frac{\sigma'_o}{T} NC(1-C) \exp\left(\frac{-E_H}{KT}\right) \text{with } \sigma'_o = \frac{N_{oct} e^2 d^2 \nu_o}{K}$$

where N_{oct} is a concentration per cm^3 of octahedral sites, d is a jump distance for the charge carrier, ν_o is the lattice vibrational frequency associated with conduction, K is Boltzmann's constant, e the electronic charge, N is a concentration per formule unit of sites which are available to the charge carriers, C is a fraction of available sites which are occupied by the charge carriers and E_H is a hopping energy.

The term NC (1-C) can be rewritten as

$$NC(1-C) = \frac{(Mn^{3+}_{oct})\,(Mn^{4+}_{oct})}{(Mn^{3+}_{oct}) + (Mn^{4+}_{oct})}$$

which represent the probability of finding Mn^{3+} - Mn^{4+} pairs in octahedral sites.

At first approximation, we take into account only the variation of the last ratio. Thus, the theoretical variation of resistivity can be plotted against copper content and compared to the experimental curve: $\rho = f(x)$. An inspection of the theoretical variations of resistivity with x calculated for the four hypothetical configurations shows an insulating character for formulae (b) (only Mn^{3+} in octahedral site) and a minimum of resistivity ($\partial(C(1-C)/\partial x=0$) with formulae (c) x = 0·4 (Fig. 2 curve *c*) and formulae (d) for x = 0·66 (Fig. 2 curve *d*). The experimental shape of the variation of resistivity (Fig. 2) with copper content does not present a minimum for x = 0·4 or x = 0·66. However, for $0{\cdot}2 \leq x \leq 0{\cdot}4$ the curve presents a slope change and hence, it should be possible that a small amount of copper be present in octahedral sites.

However, the theoretical variation of the resistivity, shown in curve *a* and *f* of Fig. 2, calculated from hypothetical configurations (a) and (f) selected from the earlier XRD study, fits the best

with the experimental data. For $0 \leq x \leq 0{\cdot}6$, the theoretical resistivity is proportional to $(2\text{-}x)x/4$ and the resistivity is expected to decrease continuously for $0 \leq x \leq 0{\cdot}6$. The minimum of resistivity should be for 0·87 ($\partial(C(1\text{-}C)/\partial y=0$) and not for 0·8 (experimental data). This slight misfit could be due to the fact that we have only taken into account the variation of density of charge carriers to calculate the theoretical variation of the resistivity; for instance the variation of the lattice volume (and hence, the hopping distance) which decreases for $0 \leq x \leq 1$ was not considered.

4 Conclusion

Precipitated oxalic have been employed to prepare oxides and ceramics with single-phased spinel structure: $Mn_{2\cdot6-x}Co_{0\cdot4}Cu_xO_4$, $0 \leq x \leq 1$. Powder XRD analysis both from powder and ceramic single-phase sample revealed the presence of a single phase having a tetragonally distorted spinel structure; the tetragonal distortion, $c/a > 1$, decreased with copper content and disappeared for $x \geq 0{\cdot}79$. The XRD powder study and the comparison of experimental curves with the calculated ones for electric resistivity measurements implemented on ceramics indicated that the cation distribution in these spinels is close, both at the powder and ceramic states, to:

$$Mn^{2+}_{0.6-x}Co^{2+}_{0\cdot4}\ Cu^{+}_{x}\ [Mn^{3+}_{2-x}\ Mn^{4+}_{x}]\ O^{2-}_{4};$$
with $0 \leq x \leq 0{\cdot}6$,

$$Co^{2+}_{0\cdot4}Cu^{+}_{0\cdot6}\ [Cu^{2+}_{y}Mn^{3+}_{1.4-2y}Mn^{4+}_{0\cdot6+y}]\ O^{2-}_{4};$$
with $0{\cdot}6 < x \leq 1$ and $y = x - 0{\cdot}6$.

This first structural approach of the solid solution gives a good base for the next step that will be the fine characterization of these components by neutron diffraction and magnetic measurements. With only one solid solution, the electrical resistivities of these thermistors cover a wide range: $>2\ 10^6\ \Omega$ cm – 10 Ω cm and might be interesting for industrial applications.

Acknowledgements

The authors would like to thank H. Minchin for the preparation of several samples and the French scholarship program, 'Lavoisier', without which this paper would not have been written.

References

1. Kulkarni, D. K. & Mande, C., X-ray spectroscopic study of some copper manganites. *Indian Journal of Pure and Applied Physics*, **12** (1974) 60–3.
2. Brabers, V. A. M. & Setten, F., X-ray photoelectron spectroscopy study of ionic configuration of the spinel $CuMnCoO_4$. *J. Phys. D: Appl. Phys.*, **16** (1983) 160–71
3. Kshirsagar, S. T. & Biswas, A. R., Crystallographic studies of some mixed manganite spinels. *J. Phys. Chem. Solids*, **28** (1967) 1493–9.
4. Jabry, E., Elaboration et caractérisation de céramiques semi-conductrices destinées aux thermistances C.T.N., PhD, Toulouse, France (1987).
5. Irani, K., Sinha, A. & Biswas, A., Effect of temperature on the structure of manganites., *J. Phys. Chem. Solids*, **23** (1962) 711–27.
6. Driessens, F. C. M., Place and valence of the cations in Mn_3O_4 and some related manganates. *Inorg. Chemica. Acta*, **I**:1 (1967) 193–201.
7. Wickam, D. G. & Croft, W. J., Crystallographic and magnetic properties of several spinels containing trivalent manganese. *J. Phys. Chem. Solids*, **7** (1958) 351–60.
8. Metz, R., Elaboration et caractérisation de céramiques semi-conductrices à base de manganites de nickel, cobalt et cuivre. Etude des phénomènes de vieillissement des thermistances à coefficient de température négatif. (C.T.N.), PhD, Toulouse University, France, (1991).
9. Metz, R., Caffin, J. P., Legros, R. & Rousset, A., The preparation, characterization and electrical properties of copper manganite spinels $Cu_xMn_{3-x}O_4$, $0 \leq x \leq 1$. *J. Mater. Sci.*, **24** (1989) 83–7.
10. Baffier, N. & Huber, M., Etude par diffraction des rayons X et des neutrons des relations entre distribution cationique et distorsion cristalline dans les ferro–manganites spinelles $x Mn_3O_4$ + (1-x) $Cu(Fe,Cr)O_4$, *Ibid.* **33** (1972) 737–47.
11. Poix, P., Sur une méthode de détermination des distances cation-oxygène dans les oxydes mixtes à structure spinelle, application des valeurs à quelques cas particuliers. *Bull Soc. Chim., France*, **5** (1965) 1085–7.
12. Dorris, S. E. & Masson, T. O., Electrical properties and cation valencies in Mn_3O_4. *J. Ann. Ceram. Soc.*, **71** (1988) 379–85.

Journal of the European Ceramic Society 15 (1995) 469–477
Elsevier Science Limited
Printed in Great Britain.
0955-2219/95/$9.50

0955-2219(95)00009-7

Compaction and Sintering Behaviour of Sol–Gel Powders

Y. Jorand,[a] M. Taha,[a] J. M. Missiaen,[b,d] & L. Montanaro[c]

[a]G.E.M.P.P.M., U.R.A. C.N.R.S. 341, I.N.S.A. Lyon, Bat. 502, 69621 Villeurbanne Cedex, France
[b]C.P.P.I., E.N.S. des Mines de Saint-Etienne, 158 cours Fauriel, 42100 Saint-Etienne, France
[c]Department Materials Science & Chemical Engineering, Politecnico, Corso Duca degli Abruzzi 24, 10129 Torino, Italy.
(Received 4 December 1992; revised version received 11 September 1994; accepted 12 December 1994)

Abstract

Dry pressing is the most common industrial shaping process for ceramic pieces. Sol–gel powders are of high reactivity, but very often agglomeration–aggregation phenomena limit this advantage by inducing poor compaction behaviour. Consequently the goal of sol–gel powder research — to obtain full densification at very low sintering temperature, is not achieved. With the intention of showing the influence of sol–gel powders, specific characteristics on pressing, compaction diagrams and green body characteristics of two experimental zirconia sol–gel powders have been determined. For comparison a well-known commercial product was used as a control. These observations were correlated as densification tests and initial powder characteristics. The sol–gel powder parameters that must be adapted to dry pressing forming and the incidence of the synthesis conditions, have emerged.

1 Introduction

Dry pressing is a method extensively used for the industrial production of ceramics. It is well known that the quality of ceramic bodies is strongly influenced by the characteristics of the starting powder. A powder having good compaction behaviour gives a high-density green compact and, more importantly, a fine and homogenous porosity. This results in a high-density sintered body as already shown in many studies.[1]

The major source of the defects observed in a green body originates in the characteristics of the different constituents of the powder. The different constituents of a powder can be defined in different ways, so we will explain the definitions used in this text. The smallest unit of a powder which can be considered is the crystallite. It can be defined as a coherently diffracting region, and measured by X-ray diffraction line broadening. In a first approximation, the potential reactivity of a powder can be linked to the crystallite size (in fact a crystal can be constituted of several crystallites): this is not far away from the minimal particle size that can be individualised. In classical powder processing these particles do not appear alone, but clustered into either the aggregates or the agglomerates, depending upon the nature of the binding forces. An aggregate is an arrangement of crystallites held together by strong binding forces, e.g. chemical bands in solid bridges. A typical example is the aggregates formed during calcination of Bayer aluminas. Consequently, aggregates retain their identity under a wide variety of severe conditions, and especially under high compaction pressure.[2] The agglomerates are constituted of crystallites and/or aggregates held by weak binding forces, such as Van der Walls or electrostatic forces. Agglomerates, in contrast to aggregates, are much more easily disrupted by external forces.

All fine particle size ceramic powders contain agglomerates, because Van der Walls forces exceed gravitational ones, and very often, depending on the synthesis process, aggregates. When the powder is poured into a compaction die, one can distinguish three porosity types: interagglomerate, interaggregate and intraaggregate porosities. Irregularly shaped particles (agglomerates and/or aggregates) affect the flowability of the powder, and lead to the creation of gross interagglomerates/interaggregate porosities by promotion of arch formations. If agglomerates, or more frequently aggregates, are resistant to compaction forces, this induces packing inhomogeneities in the green

[d]Now at: Laboratoire de Thermodynamique et Physico-Chimie Métallurgiques, E.N.S.E.E.G., B.P. 75, 38402 St Martin D'Hêre Cedex, France.

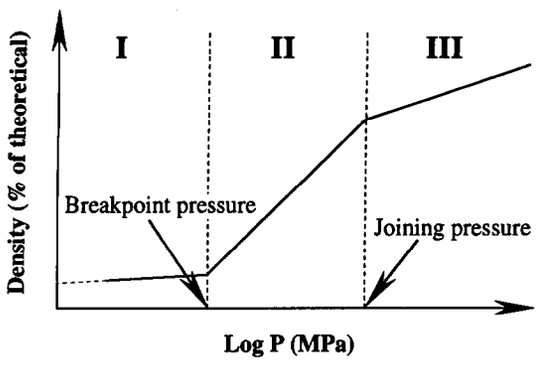


Fig. 1. Typical compaction response diagram for granulated or agglomerated powders.

body associated to important interagglomerates/ interaggregate porosities. During sintering, the denser regions formed by remaining agglomerates/ aggregates will first densify at low temperatures, then the interagglomerates/interaggregate porosities will grow, or more detrimentally, transform into cracklike defects: these porosities will require for their elimination, if it ever happens high temperatures and long sintering times.[3-4]

In classical powder metallurgy processes, the powders are granulated after deagglomeration/ aggregation treatments in order to avoid the problems mentioned earlier. An ideal granulate should be: spherical with the smallest diameter possible while enough to allow good flowability, dense and resistant to industrial manipulations, but plastically deformed under low compaction pressures to fill the intergranulate voids.

Compaction tests are useful tools for characterising the powder pressing operation. Various testing methods have been developed:[5] the most extensively reported is the compaction response diagram that relates the relative density of the compact to the logarithm of the compaction pressure. These tests are quite sensitive to the strength variations of the different particles contained in a powder, and gives good information on the compaction behaviour.[6] The typical compaction response diagram of granulated (or agglomerated) powder is given in Fig. 1. This compaction behaviour has been explained by many authors,[5,7,8] and is summarised below. The curve can be divided into three linear portions. At low pressure the density remains relatively constant which corresponds to granulate rearrangement. The limit between the two first parts defines the breakpoint pressure which is a measurement of granulate (or agglomerate) strength. The second linear portion corresponds to the rearrangements provoked during and after the crushing or deformation of the granulates. The slope remains constant up to a joining pressure where the granules (or the agglomerates) lose their separate identity. Then in the third linear part, the compact behaviour is similar to the same nongranulated (agglomerated) powder. This corresponds to the rearrangement of the crystallites (or aggregates if any). Aggregates, in the sense of the definition given here, cannot be broken under the pressure usually used for compaction tests. Indeed, for example, aggregates formed by calcination in Bayer aluminas require pressures up to 700 MPa to be broken.[8] It can be assumed that the same sequence as for agglomerates is repeated since the aggregates are fractured.

The quality of sintered bodies is also dependent on the physico-chemical characteristics of the powder: the sol–gel methods allow the synthesis of powders having high homogeneity, purity, and reactivity.[9] Sol–gel powders can exhibit crystallite clusters that can be related to granulates in the sense that their morphology and diameters are well controlled. But very often the crystallites contained in these clusters are strongly bonded.[10] This limits their compaction behaviour and does not permit them to benefit from their high reactivity. These pseudo-granules are defined as granules in this paper.

This work compares the compaction and sintering of two sol–gel powders to that of a commercial powder. It is expected that this kind of measurement will give feed-back on how to improve the synthesis process of these powders.

2 Experimental Procedure

Three powders have been studied. The control, labelled P1, is a commercial well-known powder of ZrO_2 + 3 mol% Y_2O_3 (5·8 mol% Y in ZrO_2), TOSOH TZ-3YB. P2 and P3 are ZrO_2 experimental powders. P2 contains 3·6 mol% Y_2O_3 (6·9 mol% Y in ZrO_2). This powder was prepared by a sol–gel technique using monomeric solutions of mixed inorganic salts modified by the addition of high viscosity organic polymers. The resulting viscous solution was sprayed in ammonium hydroxide to form gel particles of mixed hydroxides that were dehydrated by azeotropic distillation. After that the powder was heat-treated at 700°C for 4 h. P3 composition was synthesised with 2 mol% Y_2O_3 (3·9 mol% Y in ZrO_2) by gel coprecipitation starting from inorganic salt solutions[11] $ZrCl_4$ and YCl_3–7 H_2O. The gel obtained was first washed in water, then in ethyl alcohol. The alcohol washing was performed to avoid hard agglomeration occurrence, which derived from the hydroxy-bridges produced by the presence of water on the micelles surface. The alcoholic colloidal suspension obtained was oven-dried at 80°C. Then the resulting agglomerated powder was passed through a 40

μm sieve. This powder was heat-treated at 600°C for 30 min. This calcination temperature was chosen to ensure a development of crystalline phase without a strong decrease of specific surface area.

The powders have been characterised by means of scanning electron microscope (SEM), laser granulometry, BET adsorption method and X-ray diffraction analysis in order to determine the nature and amount of different phases and the crystallite size. The phase (monoclinic and tetragonal ZrO_2) percent composition was evaluated using the relationship presented in Ref. 12 The crystallite size was calculated with the Scherrer formula, after correcting the experimental effect by a parabolic law.[13]

The compaction tests were performed on an INSTRON mechanical testing machine, in the range 0–200 MPa with a crosshead rate of 0·5 mm/min. 2 g powder samples were poured into a cylindrical die of a 10 mm diameter, then the tap density was achieved[14] before conducting the compaction test. The density variation during pressing was deduced from the crosshead continuous displacement. Deviation due to the elastic compliance of the load cell was nullified carrying out a blank test, using the same units of measurement without powder in the die and recording its response in the same pressure range. These compaction tests allowed us to draw the relationship between density and compaction rate versus applied pressure. The tap density is approximated by measuring the density at the early stage of pressing, i.e. at sufficiently low pressure.

Hg porosimetric measurements were carried out on 0·5 g powder samples, uniaxially pressed at 100, 200, and 400 MPa, in order to follow the evolution of pore size distribution during compaction. The data were used to draw the variation of relative and cumulative pore volume as a function of pore radius.

Sintering was studied by dilatometric measurements performed on 2 g pellets obtained by 50 MPa uniaxial pressing, followed by 400 MPa isostatic pressing. Heating rate of 1°C/min and a final temperature of 1500°C were chosen. In addition, pellets were sintered, with the same pressing conditions and heating rate, up to 1350°C and 1500°C respectively, and maintained at these temperatures for 2 h. These samples were characterised by SEM observations and X-ray diffraction analysis, in order to define the nature and amount of phases, using the same protocol as for the starting powders. Hg porosimetry and He pycnometry were also conducted, in order to quantify the open and close porosity respectively, and therefore the apparent density.

Table 1. Powder characteristics

Powder	*Granulate size distribution (μm)*			*Phase composition (%)*	*Mean crystallite size (nm)*	*Specific surface area BET (m^2/g)*
	D_{50}	D_{10}	D_{90}			
P1	53·5	18	84	100% tetra	93	17
P2	34	10	52	100% tetra	9	100
P3	12·5	2·8	37·5	100% tetra	9	80

D_{50}: 50% of the distribution with equivalent diameter below D_{50}.
D_{10}: 10% of the distribution with equivalent diameter below D_{10}.
D_{90}: 90% of the distribution with equivalent diameter below D_{90}.

3 Results and Discussion

The physico-chemical characteristics of the powders are summarised in Table 1. All the powders contained spheroidal granules. But SEM observations show that the P1 powder is constituted of hollow granules characteristic of a spray-drying process. When compared to P1, the P2 and especially P3 granules are finer. It can be seen from Table 1 that the granule size distribution of P3 powder is broader than P1 and P2: the D_{50}/D_{10} and the D_{90}/D_{50} ratios are respectively 3 and 4·5 for P3 and about 1·5 and 3–3·4 for P1 and P2.

The main differences between the three powders are the crystallite size and the specific surface area: both sol–gel powders (P2 and P3) exhibit a smaller crystallite size and a higher specific surface area than the P1 powder. The values obtained are usual for sol–gel powders heat-treated at low temperature (600 and 700°C), because, under these conditions, grain coarsening is negligible.

A relative tap density of 20% is obtained for the P1 powder, while lower values, between 10 and 15%, are obtained with the sol–gel powders. It is well known that tap density is strongly dependent on particle size: with fine powders, the Van der Waals forces between particles are much higher than gravitational forces and this affects the flowability[15] (this is why granulation is required with fine powders). For zirconia it has been calculated that the particulate size limit required for these two forces to be equal is about 20 μm diameter.[16] This means that granulation is efficient for the P1 powder, because it contains a low amount of fine granules with diameter less than this limit (D_{10} value is 18 μm). But in the case of the P2 and P3 powders, the granules are too small, D_{10} values are of 10 and 2·8 μm respectively. A bad filling of the compaction dies is therefore obtained, resulting in low tap densities. These observations were made while P1 contained hollow granules which can reasonably be supposed to be the less dense. Consequently it can be assumed that low flowability due to the P2 and P3 granule sizes when compared to P1 as a predominant effect than granule densities.

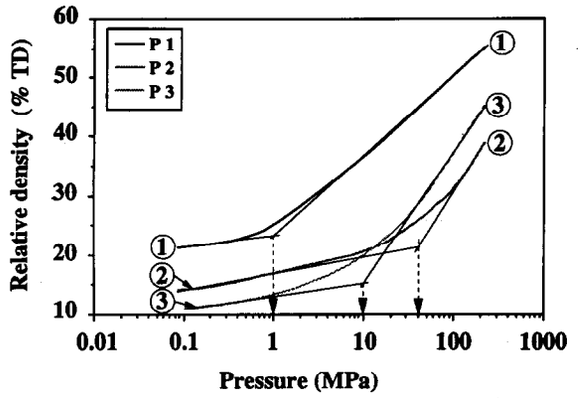


Fig. 2. Compaction response diagram of P1, P2 and P3 powders.

The relative green density (% TD) versus the applied pressure (P) curves (Fig. 2) demonstrate the better compaction behaviour of powder P1: its green density reaches about 50% TD for a pressure of 100 MPa, while 31% TD and 38% TD are reached for P2 and P3 powders. The breakpoint pressure is about 1 MPa, 40 MPa and 10 MPa for P1, P2 and P3 respectively. The compaction rate diagrams (Fig. 3) show that the compaction rate for P1 increases rapidly until 1·5 MPa, and then become stable. This plateau was also observed for the P3 powder, but only starting from 50 MPa. It was not observed for the P2 powder in the range of investigated pressures. It can be assumed that when the maximum compaction rate is obtained, the crushing or deforming of all the granulates is achieved, because they all have successively been submitted to their maximum strength by the net forces developed in the powder arrangement. So the constant compaction rate observed must correspond to reorganisation of the particles provided by the crushed or deformed granulates.

Figure 4 gives the pore size distributions of powders uniaxially pressed at 100, 200, and 400 MPa. A pressure of 100 MPa induces in the P1 sample a monomodal pore distribution of mean radius equal to 16–20 nm. This can be attributed

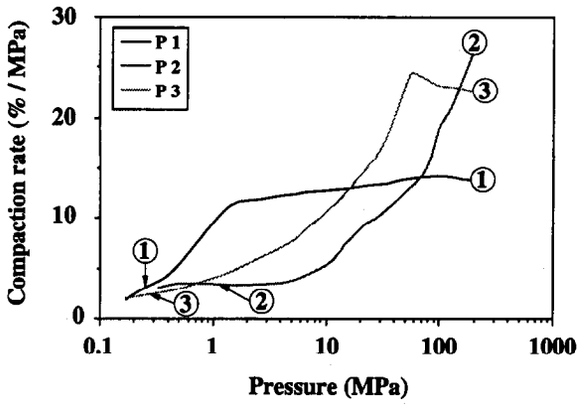


Fig. 3. Compaction rate diagram of P1, P2 and P3 powders.

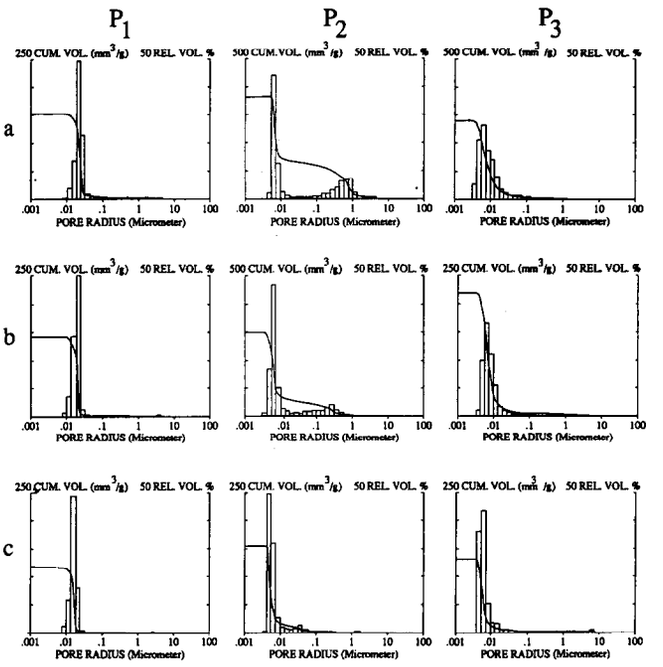


Fig. 4. Pore size distribution for P1, P2 and P3 powders pressed at: (a) 100 MPa, (b) 200 MPa and (c) 400 MPa.

to the fact that only intercrystallite pores (crystallite mean diameter of 93 nm) subsist, since reorganisation of particles due to compaction is still well progressed at this pressure. The pore distribution of the P3 sample pressed at 100 MPa is also monomodal but broader, ranging between 4 and 100 nm. This corresponds to intercrystallite pores that have still not been reduced by particle reorganisation. An increase of the pressure leads to a narrower distribution by reducing the larger intercrystallite pores that are less stable. Consequently higher pressure is required to reach the same green state as the P1 compacts. The porosity evolution of the P2 sample is more complex. At 100 MPa, it shows a bimodal distribution with the maxima at 7 and 800 nm, which correspond respectively to

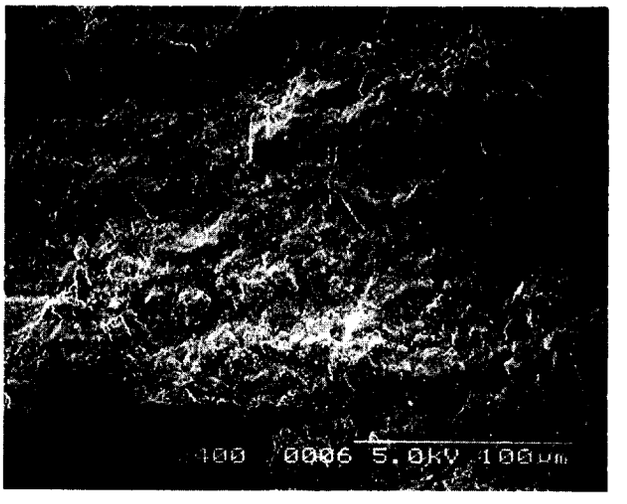


Fig. 5. Green microstructure of P1 powder pressed at 200 MPa, observed by SEM on fracture surface.



Fig. 6. Green microstructure of P3 powder pressed at 200 MPa, observed by SEM on fracture surface.

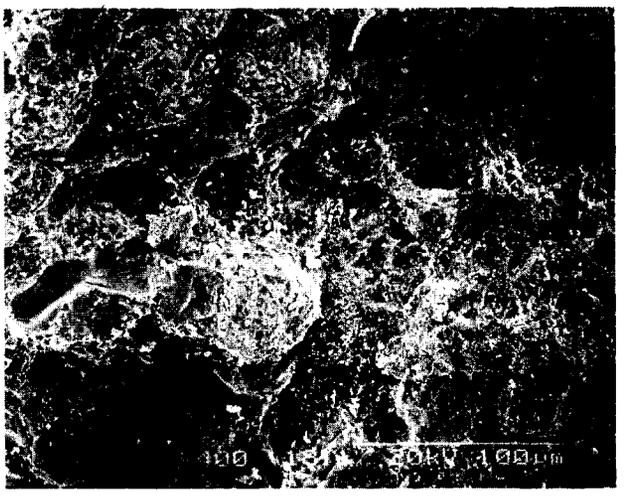


Fig. 8. Green microstructure of P2 powder pressed at 400 MPa, observed by SEM on fracture surface.

intercrystallite pores and intergranulate pores (these granulates are the starting powder granulates weakly deformed by the applied pressure). As pressure is increased, the later pore family is progressively diminished, but at 400 MPa the distribution still presents two maxima, corresponding to intercrystallite pores and intergranulate pores between the widely deformed granulates.

SEM observations substantiate the porosimetric results: at 200 MPa, in both P1 (Fig. 5) and P3 (Fig. 6) samples, the starting granulates lose their identity, although the presence of theses granulates is still well evident in the P2 sample (Fig. 7). At 400 MPa the initial granulates of the P2 powder are sufficiently deformed and the size of the largest intergranulate pores have been reduced but are still visible (Fig. 8).

Numerous relationships have been proposed to predict the tensile strength of monosized spherical particle packing.[17–21] On the basis of these relationships, it can be retained in a first approximation,

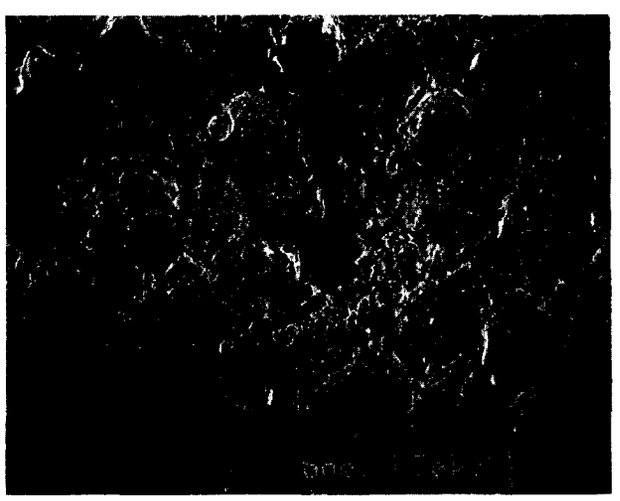


Fig. 7. Green microstructure of P2 powder pressed at 200 MPa, observed by SEM on fracture surface.

that the strength of a green body is related to the packing density, the particle diameter and the interparticle forces. It can be noticed that the JKR model,[20] elaborated on a brittle fracture base, takes also in account the defect size. Nevertheless the notion of defect in a granular material is difficult to define, especially in a granule, so this will not be taken into consideration here. Thus tensile strength is defined as the stress required to fracture a powder compact in simple tension, however these relationships remain useful to evaluate the resistance of a spherical granule under uniaxial compression.

In the case of the P1 powder, the intercrystalline binding generated during the synthesis is fully replaced by 'viscous' binding which depends on the nature of the polymer added. This permits a low breakpoint pressure and a visco-plastic behaviour, but requires some treatment of powder after synthesis.

The strength of P2 and P3 granules is only concerned with powder synthesis since no further treatment was conducted. As the crystallite sizes are the same, the two parameters that have to be considered to explain the difference in granule strength are the packing density and the nature of the intercrystallite forces. The packing density of the granules can be evaluated with consideration of the apparent density of the granules in the compacts. Galakchov[22] has proposed for slip cast green compacts, a method to obtain the apparent density of each powder unit, (aggregate, agglomerate,...), using the pore volume distribution. Indeed each peak of the pore volume distribution can be attributed to a powder unit, thus the apparent density of each unit can be calculated using the following expression:

$$\rho_{i+1} = \rho_i / 1 + \rho_i V_{i+1} \quad (1)$$

where ρ_i is the apparent density of the i^{th} order

unit, V_i is the specific volume of the pores contained in i^{th} unit in cm^3/g.

To obtain the granule density in compacted green samples, the applied pressure must be lower than the breakpoint pressure. This is, of course, to avoid any modification of intragranule porosity. With consideration of the compaction curves, compacts of P2 and P3 powders were obtained with pressures of 20 and 4 MPa respectively. Then Hg porosimetric measurements were conducted on these samples, but the intrusion pressure was limited to 280 MPa because of the fragmentation of the compacts with higher pressures. The pore volume distributions obtained at very low pressures (P < Py) shown a first peak located at large porosities. The pore volume of this peak can be connected with the intergranulate porosity. The pore channel sizes of this peak range from 0·04 to 4 μm for the P2 powder, and from 0·04 to 30 μm for the P3 powder. The first fraction of a second peak is observed, corresponding to intragranule porosities; the location of this peak is coherent with the pore distributions obtained with a compaction pressure of 100 MPa.

Two units in the powders are considered, the crystallites and the granules. Then from the previous expression, the two following expressions are used:

$$\text{apparent density of compacts: } d_o = \rho_g/1 + \rho_g V_{inter} \quad (2)$$

$$\text{first order units (granules) } \rho_g = \rho_o/1 + \rho_o V_{intra} \quad (3)$$

with V_{inter} and V_{intra} respectively the inter and intra-granules porosity. The tetragonal zirconia density (6·10 g/cm^3) was considered for the density of the crystallites ρ_0. The evaluation of the specific porosities (V_{inter} and V_{intra}) and the apparent densities of the granules and the compacts at the different compaction pressures are summarised in Table 2. In the case of low compaction pressures (P < Py), granule densities were obtained using expression (2) since V_{intra} was not measurable. From these calculations it appeared that the granule densities of the P2 and P3 powders were very close (2·168 and 2·095 g/cm^3 respectively). The granule densities are also given for high compaction pressures. Although the use of the term granule is arguable as P > Py, it can be seen from Table 2 that the reduction of intra-granule porosity with compaction pressure is more efficient in P3 granules. At P < Py, the more important inter-granule porosity of P3 compacts compares to P2, confirms that the lower tap density of P3 is due to inadequate granule sizes.

Consequently the granule strength appears to be essentially dependent on the intercrystallite forces induced during powder synthesis. Three kinds of bonds can be considered here: (i) Van der Waals, which concern all fine powders, (ii) solid bridge chemical bonds which may appear during a high temperature calcination step, because of initial sintering, and (iii) Zr–O–Zr chemicals bonds induced on drying after aqueous washing.[23] The Van der Waals bonds are weak and will lead to the formation of soft granules. On the other hand, the two others are strong. It has been extensively reported that hard granules are produced because of these bonds with direct sol–gel process. It can be assumed that solid bridge formation is avoided because of the low calcination temperatures used for powder synthesis. As a consequence of the difference in synthesis processes, we can suppose that Zr–O–Zr chemical bonds are more common in the P2 powder, and Van der Waals forces in the P3 powder.

Figure 9 displays the dilatometric results obtained from P1, P2 and P3 samples showing green densities of 55%, 47% and 49% TD, respectively. P2 and P3 samples exhibited lower starting sintering temperatures than that of sample P1 (1025°C for P1, 875°C for P2 and 950°C for P3): this is due to their smaller crystallite size and related higher reactivity. It can also be observed that the lower the green density, the higher the total shrinkage at 1500°C (18% for P1 <20% for P3 and <22·5% for P2). The high shrinkage may play a negative role in the industrial application of these powders, especially in the case of their utilisation in large and complex die designs.

A complete densification was achieved for the P1 sample at 1500°C and its microstructure was

Table 2. Specific pore volumes and apparent densities in P1 and P2 compacts obtained with different pressures

Compaction pressure (MPa)	*Intra-granules pore volume (cm^3/g)*		*Inter-granules pore volume (cm^3/g)*		*Granule apparent density (g/cm^3)*		*Compact apparent density (g/cm^3)*	
	P2	*P3*	*P2*	*P3*	*P2*	*P3*	*P2*	*P3*
$P < P_y$	—	—	0·181	0·575	2·168	2·095	1·557	0·951
100	0·230	0·257	0·135	0·020	2·540	2·377	1·891	2·267
200	0·243	0·209	0·061	0·010	2·456	2·678	1·137	2·607
400	0·142	0·123	0·014	0·008	3·270	3·481	1·131	3·381

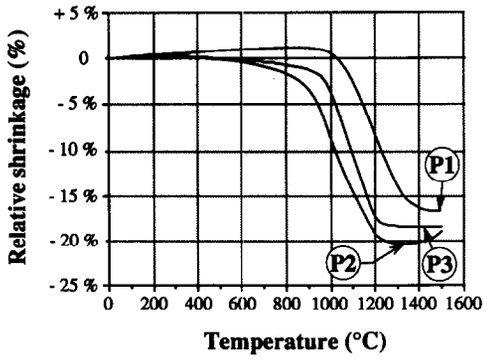


Fig. 9. Dilatometric curves of P1, P2 and P3 samples.

characterised by a uniform submicronic grain size (Fig. 10).

Above 1350°C a 'de-densification' step was observed on the dilatometric curve of the P2 sample. The same, but to a lesser extent, was also noticed on the P3 sample. This phenomenon, characterised by a more or less evident rise on the curves, may be ascribed to a secondary recrystallization, which leads to an abnormal grain growth[24-25] (Fig. 11). In addition, differential sintering phenomena are observed in the P2 sample, leading to circumferential cracks around residual granulates (Fig. 12). Then full densification is impeded by these large pore-like cracks.

So the dilatometric results can be well correlated to the green state: particle arrangements of poor quality in the green parts conducted to a shrinkage curve with a very low slope. In such a case, although the starting sintering temperature is low, the ending sintering temperature is very high because extensive grain growth must arise to allow further shrinkage, as soon as pores larger than the grains are present in the arrangement. At the extreme a total densification will not be possible since abnormal grain growth occurs before which residual porosities disappear by normal grain coarsening. Indeed during abnormal grain growth some pores will be trapped within grains before they have the opportunity to disappear and in noncubic crystalline structures a new class of pores can appear due to the fact that some grains can grow to sizes very much larger than the average particle size.

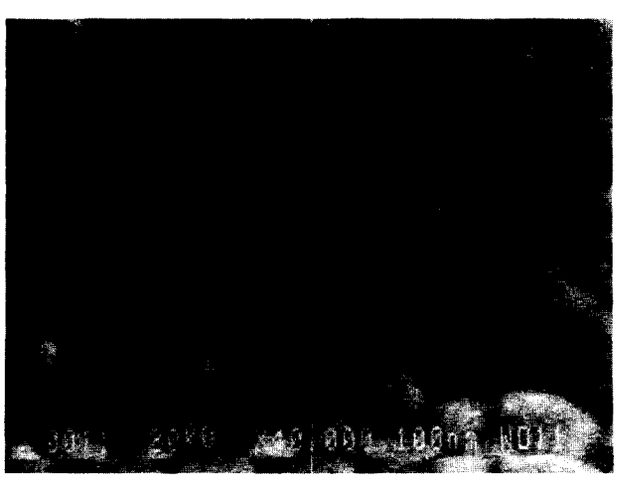


Fig. 10. Microstructure of P1 sample densified 2 h at 1500°C.

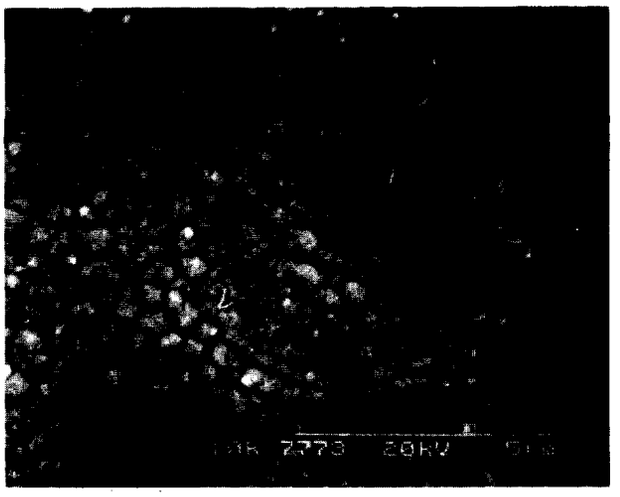


Fig. 11. Abnormal grain growth observed on P2 and P3 samples densified for 2 h at 1500°C.

To determine appropriate sintering conditions, powder pellets were heat treated at 1350°C and 1500°C. The final densities were evaluated and for each sample the relative density was determined on the ground of phase, (monoclinic and tetragonal) composition measured by X-ray diffraction analysis: Table 3 lists the results of XRD and density determinations.

Table 3. Dense material characteristics

Powder	*Sintering temperature (°C)*	*Monoclinic phase (%)*	*Apparent density (g/cm^3)*	*Density in % of theoretical*
P1	1350	0	6·05	99·1
	1500	0	6·05	99·1
P2	1350	0	5·92	97·1
	1500	0	5·35	97·7
P3	1350	42	5·85	99·8
	1500	74	5·62	98·8



Fig. 12. Circonferential cracks due to differential sintering of residual agglomerates observed on P2 densified sample.

For the P2 sample, the density values of the sintered bodies are in agreement with dilatometric curves, and confirm the 'de-densification' phenomenon observed at the higher temperatures. Up to a sintering temperature of 1350°C, no abnormal grain growth is observed in this material, and the grain size stays below 0·1 μm.

In the P3 sample, a density near the theoretical value is reached after sintering to 1350°C, although a high monoclinic zirconia content is present. At 1500°C, the monoclinic zirconia content is largely due to grain growth. This is ascribed to the low yttria content of the P3 powder (2 mol %). However, this is not the case for the P2 powder which contains 3·6 mol % of yttria. As a consequence the Y_2O_3 amount of the P3 powder is too low with respect to the microstructure to avoid the tetragonal–monoclinic transformation during cooling.

4 Conclusions

Each different synthesis process provides specific characteristics to the zirconia powder. The influence of these characteristics on application properties was studied. This allows us to evaluate the potential of sol–gel processes developed here. The significant parameters can be classified as:

— the fineness and reactivity of crystallites

— crystallite arrangement characteristics

— chemical composition

Concerning the first point, sol–gel processes usually allow a great improvement in reactivity. Consequently the starting sintering temperature is lowered.

Nevertheless crystallite size reduction is not a sufficient condition to achieve complete densification. To obtain an end sintering temperature very close to the starting sintering temperature, i.e. full densification at a low temperature, it is necessary to consider the second point and to realise parts with a green state of high quality. For fine powders it is well known that granulation is imperative. Sol–gel process offer many ways to obtain granulates. Two different methods have been tested here and can be summarised as follows:

Granulate sizes

The best results are obtained with large granules, typically 50–100 μm diameter. With minor changes to the process it will be possible to increase the granule diameters of the two sol–gel powders. Tap densities of the same order as the control powder P1 are expected.

Granulate morphology

To ensure good flowability of the powder and an easy reorganisation of the granules during compaction, a spherical geometry is needed. This condition is easily obtained with sol–gel processes. This is the case in the two methods studied here.

Granulate density

Sol–gel processes are able to produce better granules than the classic powders which are frequently spray dried: spray drying has the disadvantage of producing granulates with cavities, so that the tap density and the quality of the reorganisation during compaction are affected.

Granulate strength

The control of the granulate strength is the critical part of sol–gel processes, since industrial processes usually require compaction pressure under 100 MPa. The process used for P3 powder production allows us to produce low strength granules, by suppression of the detrimental chemical bonds Zr–O–Zr between crystallites. This results in compaction curves close to the control. But as it is not possible to use organic additives (a high temperature calcination is necessary after the granulation step), the production of sol–gel granules still encounter two major problems. Firstly, it is difficult to control the strength of the green parts, which is a major problem for industrial products. Secondly, the granule destruction arises by fragmentation instead of plastic deformation, and this is expected to be less efficient for porosity reduction. A process which solves these two problems, without any further treatment after granulation, have to be found, since this constitutes the major interest of sol–gel processes.

Chemical composition

The final point concerns the chemical composition of the powders. This point is of major importance since it has a great influence on the microstructure and phase composition of zirconia products. Sol–gel processes present the advantage of offering a better control of the chemical purity and homogeneity. For example, the stabilising agent distribution can be expected to be more homogeneous. But, as it can be seen with the P3 powder, the stabiliser amount must be optimised with respect to the final grain size.

Acknowledgement

The authors are grateful to CO.TR.A.O. (COmmunauté de TRavail des Alpes Occidentales) for their financial support of this research.

References

1. Zheng, J. & Reed, J. S., Effect of particle packing characteristics on solid state sintering. *J. Am. Ceram. Soc.*, **72**(5) (1989) 810–7.
2. Dynys, F. W. & Halloran J. W., Compaction of an aggregated powder. *J. Am. Ceram. Soc.*, **66**(9) (1983) 655–60.
3. Lange F. F., Sinterability of agglomerated powders. *J. Am. Ceram. Soc.*, **67**(2) (1984) 83–9.
4. Dynys, F. W. & Halloran, J. W., Influence of aggregates on sintering. *J. Am. Ceram. Soc.*, **67** (9) (1984) 596–601.
5. Matsumoto, R. L. K., Generation of powder compaction response diagrams. *J. Am. Ceram. Soc.*, **69**(10) (1986) C246–7.
6. Frey, R. G. & Halloran, J. W., Compaction behavior of spray-dried alumina. *J. Am. Ceram. Soc.*, **67**(3) (1984) 199–203.
7. Matsumoto, R. L. K., Analysis of powder compaction using a compaction rate diagram. *J. Am. Ceram. Soc.*, **73**(2) (1990) 465–8.
8. Niesz, D. E. & Bennett, R. B., Structure and properties of agglomerates. In *Ceramic processing before firing*, ed. G. Y. Onoda & L. L. Hench, Wiley Interscience Publication, 1978, pp. 61–73.
9. Hench, L. L. & Ulrich, D. R., Ultrastructure processing of ceramics, glasses and composites, J. Wiley, New York, 1984.
10. Readey, M. J., Lee, R. R., Halloran, J. W. & Heuer, A. H., Processing and sintering of ultrafine MgO–ZrO_2 and (MgO,Y_2O_3)–ZrO_2 powders, *J. Am. Ceram. Soc.*, **73** (6) (1990) 1499–503.
11. Montanaro, L., Elaboration des poudres ceramiques par voie sol–gel: application au dispersoïde alumine–zircone et à la zircone yttriée. PhD thesis, I.N.P.G. — ENS des Mines de St. Etienne, 1990.
12. Garvie, R. C. & Nicholson, P. S., Phase analysis in zirconia systems. *J. Am. Ceram. Soc.*, **55**(6) (1972) 303–5.
13. Alexander, L. E. & Klugt, H. P., *X-ray diffraction procedures for polycrystalline and amorphous materials*. John Wiley & Sons Ed., New York, 1974.
14. AFNOR French normalization, *Powder metallurgy — determination of tap density*. NF A 95-112 (equivalent to ISO 3953-1977).
15. Vergnon, P., Sur la compressibilité des poudres. *Rev. Int. Hautes Températures et Réfract*, **3** (1966) 399–408.
16. Bortzmeyer, D., Compaction des poudres céramiques. PhD Thesis, E. N. S. des Mines de Paris, 1990.
17. Rumpf, H., *Chem. Intgr. Tech.*, **42** (1970), 538–40.
18. Schubert, H, Tensile strength of agglomerates. *Powder Technol.*, **11** (1975) 107–19.
19. Cheng, D. C. H., *Chem. Eng. Sci.*, **23** (1968) 1405.
20. Johnson, K. L., Kendall, K. & Roberts, A. D., *Proc. Royal Soc. London*, (1961), A324, 301.
21. Thompson, R. A., *Ceram. Bull.*, **60**(2) (1981) 248–51.
22. Galakchov, A. V. & Shevchenko, V. J., Influence of pore structure inhomogeneities in green compacts on strength and reliability of Y-TZP, *J. Europ. Ceram. Soc.*, **6** (1990) 317–22.
23. Kaliszewski, M. S. & Hever, A. H., Alcohol interaction with zirconia powders. *J. Am. Ceram. Soc.*, **73** (1990) 1504–9.
24. Kingery, W. D., *Ceramic fabrication processes*, John Wiley & Sons Ed., New York, 1958.
25. Coble, R. L., *Sintering and related phenomena*. Gordon & Breach Ed., New York, 1967.

Journal of the European Ceramic Society **15** (1995) 479–483
© 1995 Elsevier Science Limited
Printed in Great Britain. All rights reserved
0955-2219/95/$9.50

0955-2219(95)00001-1

The Packing Density of Binary Powder Mixtures

Jingmin Zheng,[a] William B. Carlson & James S. Reed

New York State College of Ceramics, Alfred University, Alfred, New York, USA

(Received 13 July 1993; received in revised form 10 June 1994; accepted 15 July 1994)

Abstract

The maximum particle packing density in a binary powder system can be predicted by the Furnas model. The packing density is lower when the size ratio of coarse particles to fine particles decreases, and is also governed by the volume fraction of coarse or fine particles. Here an empirical equation is derived which describes the packing density as a function of the initial packing efficiencies of particles, the particle size ratio, and the volume fraction variations of the system.

Introduction

The importance of particle packing in ceramic processing is generally appreciated because of its influence on the unfired mechanical properties, the shrinkage and density on sintering, and the microstructure and properties of the final ceramic product. A high maximum packing density* is directly dependent upon the particle size distribution. Many studies have demonstrated the importance of the particle size distribution to obtain dense packing.[1–14] For a two component mixture of coarse and fine particles, the ideal packing density is predicted by the Furnas model[1,3,4] (and sometimes, the Westman and Hugill model[2]), (Fig. 1). The specific packing volume is defined as the reciprocal of the packing efficiency. According to the Furnas model, the theoretical maximum packing efficiency, PE_{max}, of a mixture of coarse and fine particles is:[14]

$$PE_{max} = PE_c + (1 - PE_c)PE_f \quad (1)$$

or

$$PE_{max} = 1 - \phi_c\phi_f \quad (2)$$

where PE_c and PE_f are the packing efficiency of the coarse and fine particle fractions, respectively, and $\phi = 1 - PE$, is the interstitial pore fraction of packed particles of a single size (fine or coarse particles only). Notice that the ratio of two terms of the right side of Eqn (1) is the volume ratio of the coarse to the fine particles to achieve the maximum packing efficiency.

The packing mechanism of the Furnas model is such that smaller particles are introduced and distributed to the interstices of larger packed particles so that the porosity is reduced. The calculation of the ideal packing density is based on the assumption that the size ratio of coarse particles to fine particles is infinitely large. It has been observed in practice by many researchers that when this particle size ratio decreases, the packing efficiency of mixed powders is lower than that predicted by the Furnas model (the Westman–Hugill diagram, Fig. 1). In order to understand the reason for those packing density deviations, Messing and Onoda[15,16] developed a packing model on the notion that the Furnas model may apply locally, but the different volume fractions of coarse and fine particles through the mixture lead to reductions in the overall packing density. Zok and Lange[17] recently studied the effects of the surface of inclusions (the coarse particles) and the contacts of inclusions on the overall packing density. This theoretical analysis was on the scale of the dimension of the fine particles. However, the results from that study are not convenient for the calculation of packing density of a binary particle system with a variable volume fracion, particle size ratio, and different initial packing efficiencies.

Various empirical equations have been developed to predict the particle packing density of a binary system,[18–21] Some equations are either too complicated to apply,[18] or only consider the initial packing efficiency as a constant.[19] Most work in this research field has been reviewed recently.[22]

In this paper, an empirical equation is developed, which takes into account the particle size ratio, the volume fraction of powders, and their initial packing efficiencies. Constants in the proposed equation are adjusted to fit experimental data, which makes predicting the packing density of the mixture more accurate.

[a]To whom correspondence should be addressed at Thermo-Disc, 1981 Port City Boulevard, Muskegon, MI 49443, USA.
*Maximum packing density is used in a macroscopic sense; particles are assumed to be randomly arranged. The term packing density and packing efficiency are used interchangeably.

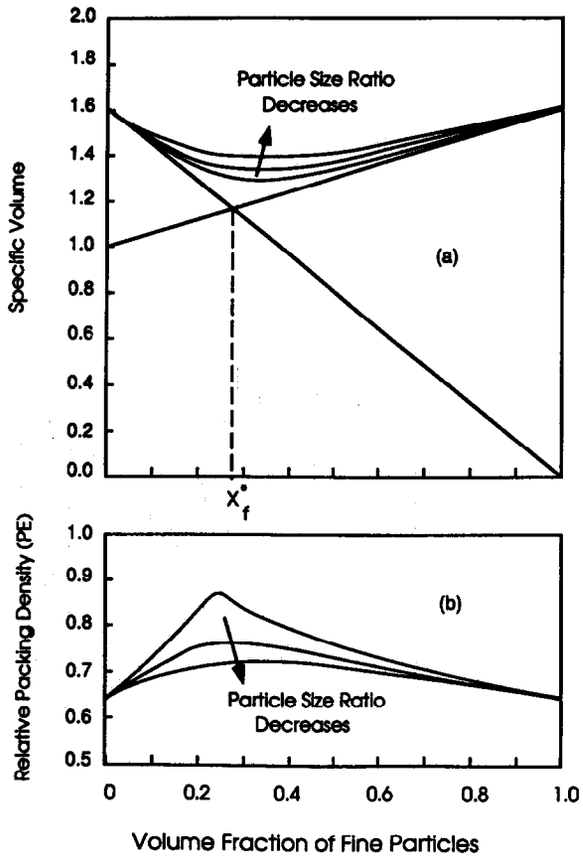


Fig. 1. The Furnas model. Theoretical variation of packing volume for the packing of smaller particles among coarser particles. (a) The Westman–Hugill plot of the Furnas model; straight lines correspond to ideal packing when the size ratio is infinite, and curved lines indicate typical behavior. (b) The Furnas model plotted as the packing density versus particle volume fraction. Figure 1(a) is preferred because the straight lines are easy to draw and their physical meaning is apparent.[15] X_f^* is the volume fraction of fine particles to achieve the maximum packing density.

Derivation of the Equation

For a coarse–fine binary particle size composite, the maximum packing density is predicted by the Furnas model (eqn (1)). The terms on the right side of eqn (1) are the volume fractions of coarse and fine particles, respectively. Starting with coarse powders and adding fine powders, the initial packing density is equal to the first term: the second term indicates the maximum possible density increase when the fine powder is added. For a real binary mixture, the maximum packing density increase should also be a function of the volume fraction and the size ratio of coarse to fine particles. Hence, we propose the following equation to calculate the packing density of a binary mixture (PE_{mix}):

$$PE_{mix} = PE_c + (1 - PE_c)PE_f F_1(X_f) F_2(R) \quad (3)$$

where F_1 is a function of the volume fraction of fine particles, X_f; F_2 is a function of the size ratio of coarse particles to fine particles, R (average particle size ratio if the pure coarse or fine particles are not exactly monosize particles). It is seen, from Fig. 1, that F_1 must be zero when $X_f = 0$ or 1, and F_1 would reach its maximum when $X_f = X_f^*$. (X_f^* is the volume fraction of the fine particles at which maximum packing density is achieved). Figure 1 also indicates that F_2 must be 0 when the size ratio is 1, and F_2 is 1 when the size ratio is infinite.

For solutions to eqn 3 the functions F_1 and F_2 must be assumed or determined.

Table 1. Volume fractions of coarse and fine particles calculated from the theoretical Furnas model

Packing efficiency	*Volume fraction*	
$PE_c = PE_f$	X_c	X_f^*
0·6	0·714	0·286
0·5	0·667	0·333
0·4	0·625	0·375

Selection of F_1

To select F_1, a realistic X_f^* value must first be determined. Table 1 lists the theoretical value of X_f^* calculated from the Furnas model with the assumption that $PE_c = PE_f$. For spherical-like monosize particles, the packing efficiency for random packing is around 0·6; and hence, from Table 1, $X_f^* \approx 0{\cdot}3$. Table 1 shows that X_f^* increases slightly with a decrease of the packing efficiency value for monosize particles. We have also observed that measured data from previous research[1,2] show that as the particle size ratio decreases, the X_f^* value tends to increase slightly. In most cases, the X_f^* is between 0·3 to 0·4.

Bearing this value in mind, F_1 is arbitrarily chosen as:

$$F_1(X_f) = |e\ X_f \ln X_f|^{C_1} \quad (4)$$

where e is the base of a natural logarithm and C_1 is a constant. F_1 versus X_f with different C_1 values are plotted in Fig. 2. It is seen from Fig. 2, that the curve of this equation meets the required criteria, i.e. it is zero when X_f equals 0 or 1, and reaches the maximum when X_f is between 0·3 to 0·4.

It is also seen from Fig. 2, that the constant C_1 affects the shapes and the curvature of the curves. The procedure to determine C_1 is to assign different C_1 values into function F_1; then substitute F_1 and F_2 into eqn (3) and use the data from eqn (3) to plot the Westman–Hugill diagram. The C_1 giving the best match to the experimental data is then selected.

After comparing C_1 values for different binary systems, it was found that by taking C_1 as a function

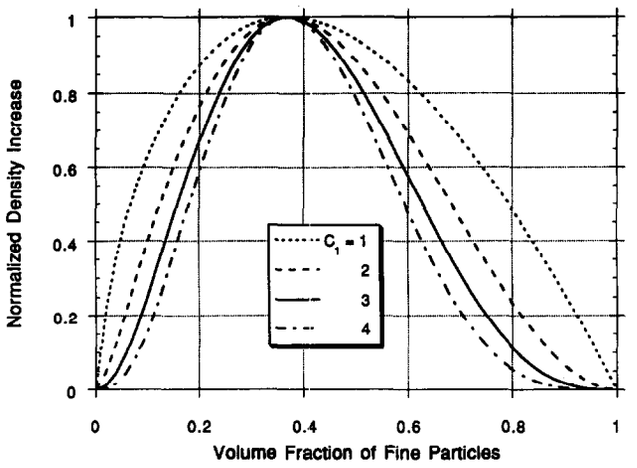


Fig. 2. Normalized packing density variation F_1 as a function of volume fraction of fine particles, X_f. F_1 is zero when X_f equals 0 or 1; F_1 is maximum when X_f is between 0·3 to 0·4. Value of the constant, C_1, alters the shape of the curves.

of PE_c, instead of a constant, a better fit was obtained. The function is:

$$C_1 = \frac{5}{4PE_c} \tag{5}$$

The fact that C_1 is a function of PE_c is actually expected because the curves in the Westman–Hugill diagram are slightly different for binary systems with different PE_c and PE_f values. The Westman–Hugill data approaches the theoretical maximum packing density, the straight lines in Fig. 1(a), when the particle size ratio is infinitely large. When the particle size ratio is small, the data is continuous. In Fig. 2, smooth curves for F_1 show that the empirical equation derived in this paper is only suitable for systems with small particle size ratios. A particle size ratio of 10 or lower is considered small. If the particle size ratio is larger than 10, the packing density of the system is more closely predicted by the theoretical model.

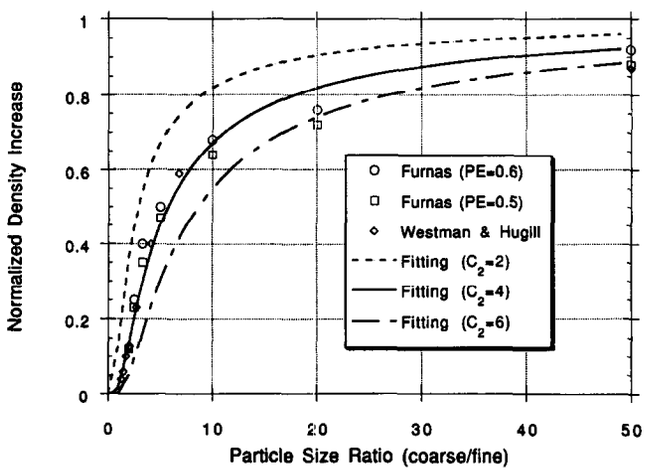


Fig. 3. Normalized packing density variation as a function of the articles size ratio for experimentally measured data and model. $C_2 = 4$ for best fit to measured data.

Selection of F_2

Function F_2 governs the increase of packing density as a function of the particle size ratio. It is seen that the maximum increase in packing density by adding fine particles to coarse, $PE_f(1 - PE_c)$, is a function of the initial packing efficiencies of coarse and fine particles. In order to compare the effects of particle size ratio on the increase in packing density, F_2 is normalized by $PE_f(1 - PE_c)$. Hence, F_2 is usually less than 1 for a real binary powder system. Figure 3 shows the normalized maximum packing density increase versus the particle size ratio of previous researchers.[1,2] According to the distribution of these data, the fitting function F_2 is proposed as:

$$F_2 = \exp\left(\frac{-C_2}{R}\right) \tag{6}$$

where C_2 is a constant. It is seen, from Fig. 3, that a smaller C_2 leads to a more rapid increase of the F_2 value when the particle size ratio increases. It is also seen that when C_2 equals 4, the curve most closely fits the measured data.

After empirically obtaining the functions of F_1 and F_2, eqn (3) is combined with eqns (4), (5) and (6), to get the full descriptive equation for calculating the packing density of a binary mixture:

$$PE_{mix} = PE_c + (1 - PE_c)PE_f[e \cdot X_f \cdot \ln X_f]^{\frac{5}{4PE_c}} \exp\left(-\frac{4}{R}\right) \tag{7}$$

The specific volume of binary mixtures calculated from eqn (7) is plotted in Figs 4 and 5. The calculations are based on the assumption that in the binary mixtures $PE_c = PE_f$, and PE_f equals 0·6 and 0·5, respectively for Figs 4 and 5. It is observed from Figs 4 and 5, that the curves

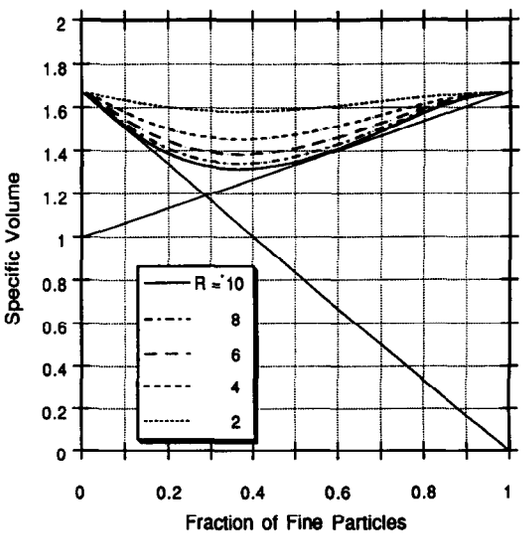


Fig. 4. Calculated specific volume versus particle size ratio using eqn (7). Initial packing efficiency $PE_c = PE_f = 0{\cdot}6$.

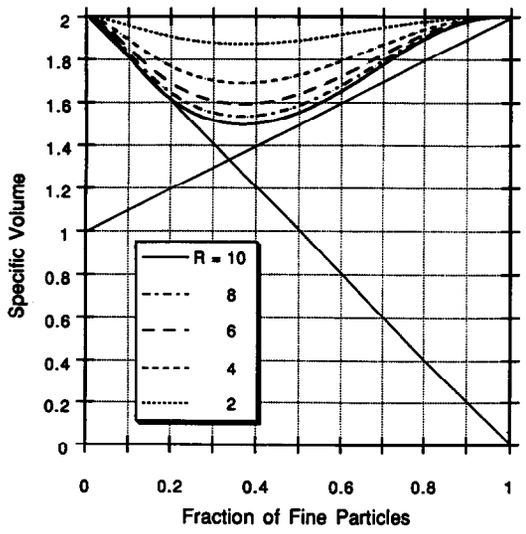


Fig. 5. Calculated specific volume versus particle size ratio using eqn (7). Initial packing efficiency $PE_c = PE_f = 0{\cdot}5$.

calculated by this empirical equation are generally similar to what is observed in practice, except that at a high volume fraction of fine particles, the calculated specific volume is slightly higher than that seen in practice. For example, if the volume fraction of fine particles is 0·8–0·9, in Fig. 5, the calculated packing density by eqn (7) could be about 2% lower than the measured one.

For a binary powder mixture $PE_c \neq PE_f$

For a binary powder system having $PE_c \neq PE_f$, eqn (7) can still be used when the volume of the coarse powders is dominant in the mixture. For a system in which the volume of fine particles is dominant, PE_f may be used as the first term in eqn (7), instead of PE_c. Figure 6 shows the experimentally measured specific volume, as well as the values calculated by eqn (7), using both PE_c or PE_f as the first term. This shows that when the volume fraction of fine particles is less than 0·3, the calculated data using PE_c fits the experimental data. When the volume fraction of fine particles is larger than 0·5, the calculated data using PE_f fits the experimental data. If the volume of fine particles is between 0·3 to 0·5, the experimental data is between the two calculated values.

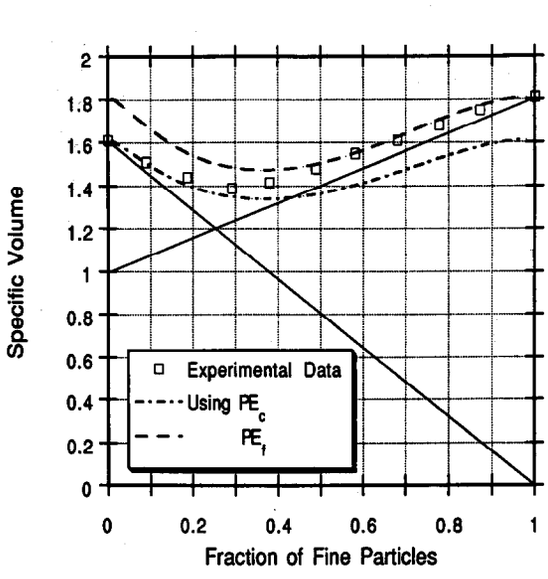


Fig. 6. Calculated specific volume versus particle size ratio using both PE_c or PE_f in the first term of eqn (7) when PE_c is not equal to PE_f.

Summary and Conclusion

The Furnas model describes the ideal particle packing behavior of a binary powder system. The packing density, however, is lower when the size ratio of coarse particles to fine particles decreases. Packing density also depends on the volume fraction of coarse or fine particles. An empirical equation (eqn (7)) was derived to estimate the packing density of a real binary system. This equation, which takes into account the particle size ratio, the compositional variations of the system, and the initial packing efficiencies of particles as variables, enables one to easily predict the packing density of a binary particle system from its particle size ratio and volume fractions of coarse and fine particles.

References

1. Furnas, C. C., *The relations between specific volume voids, and size composition in system of broken solids of mixed size.* In Report of Investigations, Department of Commerce-Bureau of Mines, No. 2894, Oct., 1928.
2. Westman, A. E. R. & Hugill, H. R., The packing of particles, *J. Am. Ceram. Soc.*, **13**[10] (1930) 767–9.
3. Furnas, C. C., Grading aggregates, I—mathematical relations for beds of broken solids of maximum density, *Industrial and Engr. Chem.*, **23**[9] (1931) 1052–8.
4. Anderegg, F. O. Grading Aggregates, II—The application of mathematical formulas to mortars, *Industrial and Engr. Chem.*, **23**[9] (1931) 1058–64.
5. Andreasen, A. H. M. & Andersen, J., Relation between grain size and interstitial space in products of unconsolidated granules, *Kolloid-Z.*, **50** (1930) 271.
6. Schuhmann Jr., R., Principles of comminution: I, size distribution and surface calculation, *Mining Tech.*, **4**[4] (1940) 1–11.
7. McGeary, R. K., Mechanical Packing of Spherical Particles, *J. Am. Ceram. Soc.*, **44**[10] (1961) 513–22.
8. Sohn, H. Y. & Moreland, C., The effect of particle size distribution on packing density, *Can. J. Chem. Eng.*, **44**, (1968) 162–67.
9. Bierwagen, G. P. & Saunders, T. E., Studies of the effects of particle size distribution of the packing efficiency of particles, *Powder Tech.*, **10** (1974) 111–19.
10. Fedors, R. F. & Landel, R. F., An empirical method of estimating the void fraction in mixtures of uniform particles of different size, *Powder Technology*, **23** (1979) 225–31.
11. Patankar, A. N. & Mandel, G., The packing of solid particles, *Trans. Indian Ceram. Soc.*, **39**[4] (1980) 109–117.

12. Lee, D. I., Packing of spheres and its effect on the viscosity of suspensions, *J. Paint Tech.*, **42**[11] (1970) 579–87.
13. Funk, J. E., Dinger, D. R. & Funk, Sr., J. E., Control parameters for a 75 wt% coal-water slurry: Co–Al. In Proceedings of the 4th International Symposium on Coal-Slurry Combustion, Pittsburgh Energy Technology Center/DOE, Pittsburgh, PA, 1982.
14. Zheng, J., Johnson, P. F. & Reed, J. S., Improved equation of the continuous particle size distribution for dense packing, *J. Am. Ceram. Soc.*, **73**[5] (1990) 1392–8.
15. Messing, G. L. & Onoda, Jr, G. Y., Inhomogeneity-packing density relations in binary powders, *J. Am. Ceram. Soc.*, **61**[1–2] (1978) 1–5.
16. Messing, G. L. & Onoda, Jr, G. Y., Inhomogeneity-packing density relations in binary powders — Experimental Studies, *J. Am. Ceram. Soc.*, **61**[7–8] (1978). 363–6.
17. Zok, F., Lange, F. F. & Porter, J. R., Packing density of composite powder mixtures, *J. Am. Ceram. Soc.*, **74**[8] (1991) 1880–5.
18. Westman, A. E. R., The packing of particles: empirical equations for intermediate diameter ratios, *J. Am. Ceram. Soc.*, **19** (1936) 127–9.
19. Yerazunis, S., Cornell, S. W. & Winter, B., Dense random packing of binary mixtures of spheres, *Nature*, **207**[8] (1965) 835–7.
20. Fedors, R. F. & Landel, R. F., An empirical method of estimating the void fraction in mixtures of uniform particles of different size, *Powder Tech.*, **23** (1979) 225–31.
21. Yu, A. B. & Standish, N., Porosity calculation of multi-component mixtures of spherical particles, *Powder Tech.*, **52** (1987) 233–41.
22. German, R. M., *Particle Packing Characteristics*, Metal Powder Industries Federation, Princeton, New Jersey, 1989.

Journal of the European Ceramic Society **15** (1995) 485–502
© 1995 Elsevier Science Limited
Printed in Great Britain. All rights reserved
0955-2219/95/$9.50

0955-2219(95)00035-6

Review

Environmental Degradation of Zirconia Ceramics.

Simon Lawson

School of Engineering & Advanced Technology, University of Sunderland, Sunderland SR1 3SD UK

(Received 5 August 1994; revised version received 2 February 1995; accepted 7 February 1995)

Abstract

This paper critically reviews the existing published experimental evidence for ageing mechanisms in zirconia ceramics. The first part of the paper is concerned with the material and environmental variables affecting the kinetics of the transformation. The current ageing mechanisms are presented and discussed and attention is drawn to the contradictions between the theories. Finally, techniques to retard or prevent the tetragonal–monoclinic phase transformation are presented.

1 Introduction

Partially stabilized zirconia (PSZ), and in particular tetragonal zirconia polycrystalline (TZP) ceramics have excellent mechanical properties such as bending strength and fracture toughness, which are associated with the tetragonal–monoclinic phase transformation around propagating crack fronts. However, a serious limitation to their use, e.g. as cutting tools for microsurgery,[1] is the phenomenon of poor, relatively low-temperature ageing resistance first observed by Kobayashi *et al.*,[2] where surface phase transformations occur and mechanical properties rapidly deteriorate. This phenomenon is widely documented in the literature although there are conflicting views as to the likely ageing mechanism.

Zirconia ceramics stabilized with yttria, ceria, calcia or magnesia are susceptible to various environments such as humid air, water vapour and other aqueous fluids over a temperature range of 65–500°C, but in aqueous solutions the effect is more catastrophic at lower temperatures and in shorter times. It should be noted that hydrothermal corrosion over the same temperature range has been observed in silicon nitride ceramics.[3]

During ageing the degradation of properties is associated with the transformation of metastable tetragonal crystals to the stable monoclinic structure.[4] It has been shown under certain circumstances that almost total strength recovery can occur when aged specimens are annealed, thus re-transforming the monoclinic grains back to the tetragonal phase.[5] It is therefore feasible to use Y–TZPs at higher temperatures or under thermal cycling conditions above the critical ageing temperature regime.

The tetragonal–monoclinic transformation during ageing can benefit certain types of Y–TZP due to the creation of a compressive surface layer of monoclinic phase on the ceramic.[6,7] This layer can, therefore, actually improve mechanical properties, although there is a narrow range between improvement and destruction of mechanical properties, as further ageing results in property deterioration.

The experimental observations on ageing have been summarised by Yoshimura[8] as follows:

1. The degradation proceeds most rapidly at temperatures of 200–300°C and is time dependent.
2. The degradation is caused by the tetragonal–monoclinic transformation accompanied by micro- and macro-cracking.
3. The transformation progresses from the surface to the interior of the specimen.
4. Water or water vapour enhances the transformation.
5. A decrease in grain size and an increase in stabilizer content retards the transformation.

The main variables influencing the stability of the tetragonal zirconia grains are dealt with in the following section.

2 Experimental Observations

The experimental observations of hydrothermal degradation are divided into two main sections, the material variables, and the test conditions under which the zirconia ceramics are examined.

2.1 Material variables

2.1.1 Grain size

One of the principal factors in anti-degradation behaviour is the critical tetragonal grain size which is Y_2O_3 dependent. When the grain size exceeds a critical value for tetragonal phase retention, the monoclinic phase content increases with ageing, as shown in Fig. 1.[9] Tsukuma *et al.*[9] reported that grains larger than 1 μm exhibited a large amount of tetragonal–monoclinic transformation, together with a remarkable decrease in strength. On the other hand, grains of $< 0{\cdot}4$ μm showed no significant change of phase content and strength.

Below a critical tetragonal grain size, it is reported that no tetragonal–monoclinic transformation can occur. Watanabe *et al.*[4] estimated the critical grain size for tetragonal phase retention as a function of Y_2O_3 content as shown in Fig. 2. The critical grain size, D_c, increases from 0·2 to 0·6 μm as the Y_2O_3 content increases from 2 to 5 mol%. Tsubakino *et al.* however, found tetragonal grains with sizes lower than the critical grain size were also subject to ageing induced transformation.[10]

Winnubst and Burggraaf[11] found that a 3·5 mol% Y–TZP with a grain size of 0·1 μm was resistant to the ageing-induced phase transformation, although a 2 mol% Y–TZP with identical grain size was susceptible to the phase transformation. They also found yttrium enrichment at the surface which, therefore, resulted in depletion of the grain interior of yttrium. To compensate for the yttrium loss the critical grain size must be smaller than reported elsewhere for a uniform yttrium distribution. This could perhaps account for Tsubakino's results. Watanabe also found the presence of c-ZrO_2, and that the grain size and c-ZrO_2 content increases with increasing Y_2O_3 content, but the mean t-ZrO_2 grain size remained almost independent of Y_2O_3 content for a given sintering temperature.

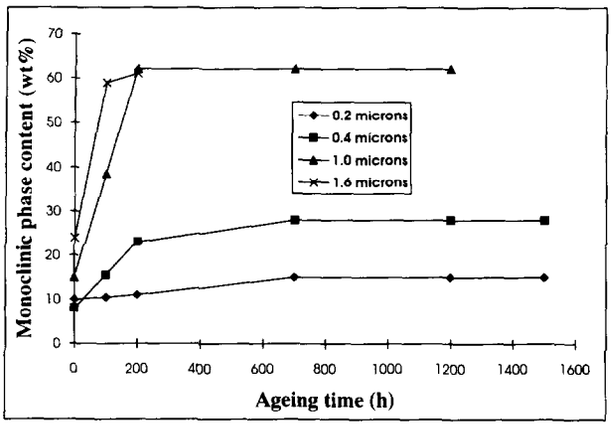


Fig. 1. Grain-size dependence of surface phase transformation on a 3Y–TZP aged at 230°C in air. (After Tsukuma *et al.*[9]).

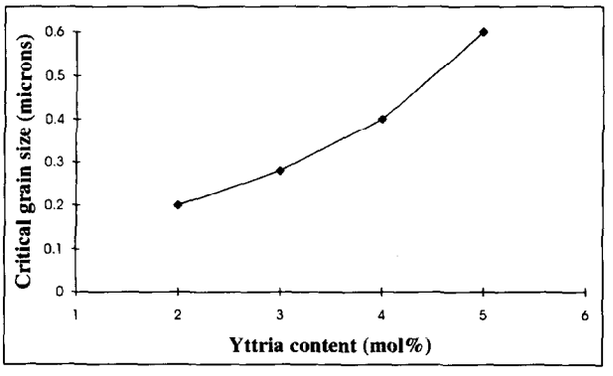


Fig. 2. Critical grain size as a function of yttria content when aged in air at 300°C for 1000 h. (After Watanabe *et al.*[4]).

There have been numerous reports on the stress-states of the tetragonal grains and grain-boundaries, and the effects of grain size and intergranular glassy phases on the residual stresses.[12–15] Schmauder and Schubert[12] used finite element analysis to determine the stress distribution in grains of different sizes. They found that for smaller grains the stresses created by thermal expansion anisotropy decrease more rapidly into the grain than for larger grains. Therefore at a fixed depth into a grain the average stress is higher for larger grains which are, therefore, less stable. Grain-shape also affects the stress levels. Spherical grains exhibit a homogeneous stress level, whereas faceted grains show singularities at the edges. Grains with rounded edges (i.e. when a glassy phase is present) have lower stresses than in perfectly sharp-edged grains. Mecartney[16] investigated the effects of glass content on the ageing resistance and found that materials with the greater glass content degraded the least. This infers that either the glassy phase reduces the residual stresses surrounding the grains, or the glassy phase protects the grain-boundaries from water attack by coating the grains.

Grain size control is normally exercised through the use of ultra fine powders and lowering the sintering temperature. The effect of calcination temperature on the powder crystallite size, the sintered grain size, and hence ageing properties has been investigated by Arai *et al.*[17] They found that of the combinations of calcination and sintering temperatures investigated, only compositions that had been calcined at the lowest temperature (800°C) survived ageing in air and water (200°C in an autoclave).

2.1.2 Stabilizer content

The level of stabilizing oxide also has a profound effect on ageing resistance. The higher the Y_2O_3 level, the more resistant to the ageing-induced tetragonal–monoclinic phase transformation are the Y–TZP ceramics,[9] and this is clearly demonstrated in Fig. 3 (the tetragonal grain sizes of all

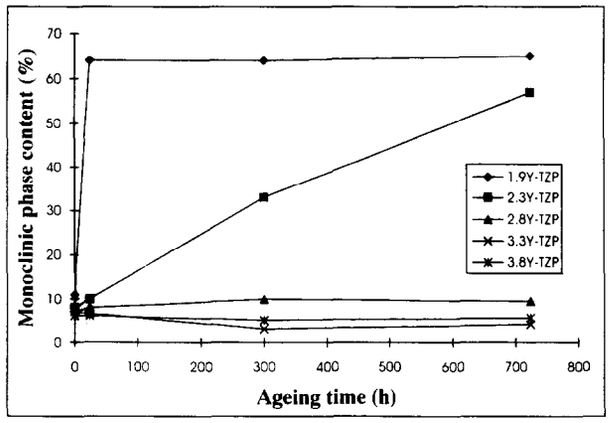


Fig. 3. Phase transformation dependence on yttria content for TZPs (grain size of ~0·4 μm) aged in air at 300°C. (After Tsukuma *et al.*[9]).

the specimens were almost the same ≈0·4 μm). The higher the Y_2O_3 content, then the larger the critical particle size for tetragonal phase retention. Watanabe *et al.*[4] found that as the Y_2O_3 content was raised from 2 to 5 mol%, then the critical particle size for tetragonal phase retention increased from 0·2 to 0·6 μm.

Sato *et al.*[18,19] showed that with increasing levels of Y_2O_3, increasing levels of *c*-ZrO_2 were formed, at the expense of the tetragonal phase. Upon ageing, the level of transformed *m*-ZrO_2 decreased with decreasing initial tetragonal content and in purely *c*-ZrO_2 (6 mol%) no monoclinic phase was detected after ageing. Therefore, they concluded that the monoclinic layer is formed from transformation of the metastable tetragonal phase and not the more stable cubic phase. Yoshimura *et al.*[20] confirmed that the monoclinic phase was a result of the tetragonal–monoclinic phase transformation, and in addition these monoclinic grains had an expanded lattice when compared to the initial lattice, whereas the cubic phase changed neither in content nor lattice parameter, therefore the transformation rate was proportional to the concentration of *t*-ZrO_2 on the surface. They also showed that the final amount of *m*-ZrO_2 decreased with increasing concentration of yttria, but the normalised transformation rate (normalised to the original tetragonal phase content) was almost constant, i.e. increasing the yttria content results in more cubic phase. Nakajima *et al.*[21] assumes that the saturated monoclinic fraction of each specimen is the transformed fraction of the metastable tetragonal phase under the test conditions. It should be borne in mind that the 'nontransformable' fraction of the tetragonal phase is actually *c*-ZrO_2 or *t'*-ZrO_2. Lawson[22,23] has shown that an increase in Y_2O_3 content (2–4 mol %) does not necessarily result in an increase in phase stability and can be detrimental to the ageing resistance of the zirconia.

It is usually thought that only Y–TZP ceramics exhibit the ageing phenomenon. However, Garvie *et al.*,[24] Swain,[25] Sato *et al.*,[26] Hecht *et al.*[27] and Drennan *et al.*[28] have shown that Mg–PSZs are also susceptible to hydrothermal degradation and exhibit the characteristic tetragonal–monoclinic phase transformation accompanied by a reduction in MOR, and Sato *et al.* observed the dissolution of Mg^{2+} ion in water above 200°C. Furthermore, Sato *et al.*[29] aged Ce–TZP in air and water vapour and found an increase in surface monoclinic content with <10 mol% CeO_2. They showed that the rate of transformation decreased with increasing CeO_2 content and smaller grain sizes, and that water vapour accelerated the transformation. The rate of change was slower than for Y–TZP, but the activation energies for transformation were almost identical. Leach and Khan[30] confirmed that <10 mol% CeO_2 exhibited the ageing-induced transformation. Tsukuma's[31] and Matsumoto's[32] results show that 12 mol% Ce–TZPs are highly resistant to the ageing-induced phase transformation. Pampuch *et al.*[33] fabricated Ca–TZP ceramics with sintered densities > 97% theoretical which were aged in air, water vapour (various temperatures) and in an autoclave (230°C). They found that samples of 4·3 mol% CaO sintered at 1300°C (grain size of 0·11 μm) were susceptible to the ageing-induced phase transformation. Samples sintered at lower temperatures were however resistant to degradation. This resistance is attributed to the smaller grain size, 0·09 μm.

Schmauder and Schubert *et al.*[12] showed that stresses caused by anisotropy of thermal expansion are Y_2O_3 dependent. By finite element analysis they showed that the higher anisotropy of the 2 mol% material resulted in higher shear stresses than 3 mol% materials. These stresses are shown schematically in Fig. 4. This figure shows that the stresses in a protruding gram decrease very rapidly

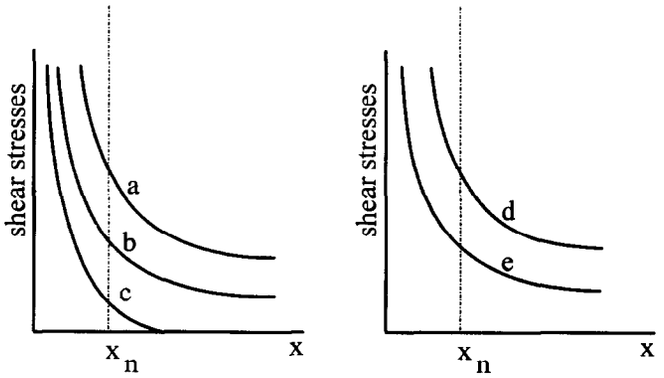


Fig. 4. Maximum shear stresses in the vicinity, *X*, of a grain corner for Y–TZPs. Curve (a) an included grain, 2 mol% Y_2O_3 (position 1 in Fig. 13); (b) an included grain, 3 mol% Y_2O_3 (position 1 in Fig. 13); (c) a protruding grain (position 4 in Fig. 13); (d) a large included grain; (e) a small included grain. (After Schmauder & Schubert[12]).

to zero, that is, these grains relax simply by changing their shape. Also, the stresses in large grains were found to be higher than those in smaller ones. The authors correlate the difference in free energy with various stresses (such as undercooling, residual and transformation stresses) and any increase in internal stresses will decrease the difference in free energy and hence reduce the activation barrier for transformation.

The Y_2O_3 content influences the free energy change of the t-ZrO_2 in two ways:

1. Undercooling is smaller for higher yttria contents,
2. Stresses due to thermal expansion anisotropy increase strongly with reduced yttria content.

Schmauder and Schubert also attach great importance to yttria distribution, and argue that inhomogeneous distribution is detrimental to the ageing resistance. They suggest the existence of a critical composition X_{cr}. For grains with a lower yttria content than X_{cr}, the stresses in the surrounding matrix will be so high as to cause micro cracking. Schubert's results suggest the critical composition X_{cr} for a 0·3 μm average grain size is between 2·2 and 2·8 mol% (4 and 5 wt%) Y_2O_3. It is obvious that the critical composition, X_{cr} will also be controlled by the average grain size of the zirconia ceramics.

The importance of the yttria distribution on stability is shown in Fig 5. The narrow grain size distribution can be achieved by low-temperature sintering. However, a narrow yttria distribution can only be reached with a homogeneous powder. Wang and Stevens[6] also state that a chemically homogeneous TZP will lead to few nucleation events and therefore less opportunity for transformation initiation. Ruhle *et al.* examined and compared commercial Y–TZP ceramics in the TEM[34] and suspected that a higher Y_2O_3 content and thinner grain-boundary layer may retard transformation. They suggest that either a stress corrosion mechanism is in operation at the specimen surface, or a surface-nucleated isothermal martensitic transformation. It is noticeable from their results that the powder which has the greatest inhomogeneous yttria distribution, is readily transformable, and is more resistant to the ageing-induced phase transformation than the other powders evaluated, and has recently been demonstrated by Lawson *et al.*[22,35] and Burger *et al.*[36]

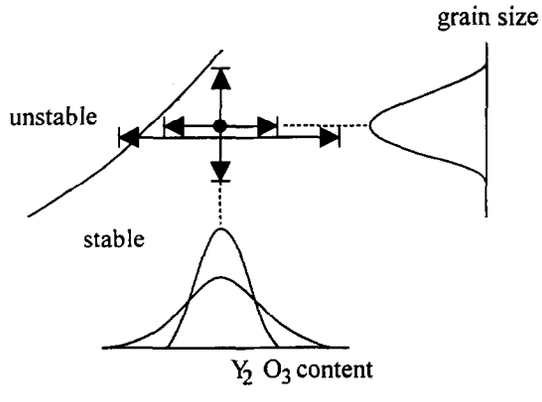


Fig. 5. Schematic of the relationships between grain size and yttria distribution, showing a stable and an unstable region. (After Schubert & Petzow[15]).

Cubic stabilized zirconia (8 mol% Y_2O_3) has been widely accepted as ageing resistant, however recent results obtained by Gibson *et al.*[37] show that such a fully cubic stabilized zirconia ceramic aged in boiling water for 24 h exhibited degradation and a phase change from the stable cubic phase to the monoclinic phase. This could possibly create problems on the use of fully stabilized zirconia in fuel cell applications.

2.1.3 Composition

The composition of the base powders is also of importance to the ageing behaviour of Y–TZP ceramics. Comparisons of commercial powders[34–36,38–41] have been made and the results show that test pieces of equivalent stabilizing oxide, behave differently under hydrothermal conditions. It is an accepted view that a homogeneous yttria distribution and small grain size distribution lead to TZPs with superior anti-degradation performance[12,42] but recent results challenge this view[35,36]

Differences in anti-degradation behaviour occur due to the technique used for incorporating yttria, i.e. co-precipitation, co-coating or milling. The purity of base materials can be of importance and Lange *et al.*[43] investigated the effects of SiO_2 impurities. They found that the intergranular glassy phase does not play a major role in the ageing process, so disproving their initial hypothesis that ageing behaviour is a result of a stress-corrosion type reaction (water vapour reacting with a glassy silicate grain-boundary phase).

Mecartney[16] investigated the effects of intergranular glassy phases on the sintering and mechanical properties of 2·5Y–TZP. She states that the 'omnipresent' glassy phase is due to contamination from two sources: SiO_2 from the powder precursor ($ZrSiO_4$) and SiO_2 and Al_2O_3 from milling media. Mecartney found that an increase in glassy phase content improved the ageing resistance. This behaviour was accounted for by a reduction in the thermal expansion mismatch stresses, and the rounding of grains, thus eliminating the stress concentrations associated with the corners of sharply faceted grains.[12]

Masaki *et al.*[44] state that high purity powders are effective transformation inhibitors. They also conclude that impurities which do not form solid solutions with ZrO_2 or additives such as TiO_2,

Fe_2O_3 and Al_2O_3 can cause strain and thermal stresses which act as transformation nucleation points along grain-boundaries. Masaki goes on to say:

> *"On the other hand these oxides [TiO_2, Fe_2O_3 and Al_2O_3] act as sintering aids, and hence different results will occur depending on their amount. This problem is important subject to be studied in the future."*

2.2 Test conditions

2.2.1 Ageing temperature

It has been found by many researchers that low temperature ageing occurs within the temperature range 65–500°C,[19] with the maximum rate at ≈250°C, and typical results are shown in Figs 6 and 7. The figures show that mechanical properties decrease[45] over the critical temperature range and are accompanied by an increase in the surface monoclinic content.[46]

The temperature limits of the ageing phenomenon are described by Sato *et al.*[47] The upper limit is due to thermodynamic constraints (stabilizer levels, grain size and thermal anisotropy), and the lower limit is due to the kinetics of the transformation. Kim and Jung[13] attribute the lower temperature limit to the onset of thermally activated dipole reorientation.

Sato *et al.*[46] found that the critical temperature below which *m*-ZrO_2 was formed decreased with decreasing sintering temperature. This may be due to the effect of the surface energy of the smaller grains; the resistance to the phase transformation increases with decreasing grain size. Kim and Jung[13] deliberately added destabilizing oxides (Ta_2O_5 and Nb_2O_5 which have little effect on the grain size) to 3Y–TZP in order to study the kinetics of ageing-induced phase transformations. They found that increasing destabilizer levels from 0 to 1·5 mol% increased the monoclinic content and raised the upper temperature limit for no transformation to occur from 250 to 500°C, the lower temperature limit being 80°C regardless of composition.

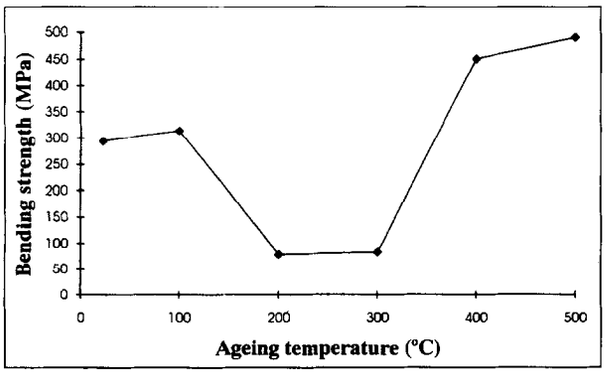


Fig. 6. Relationship between the ageing temperature and bending strength of PSZ ceramics aged in air. (After Miyazawa *et al.*[45]).

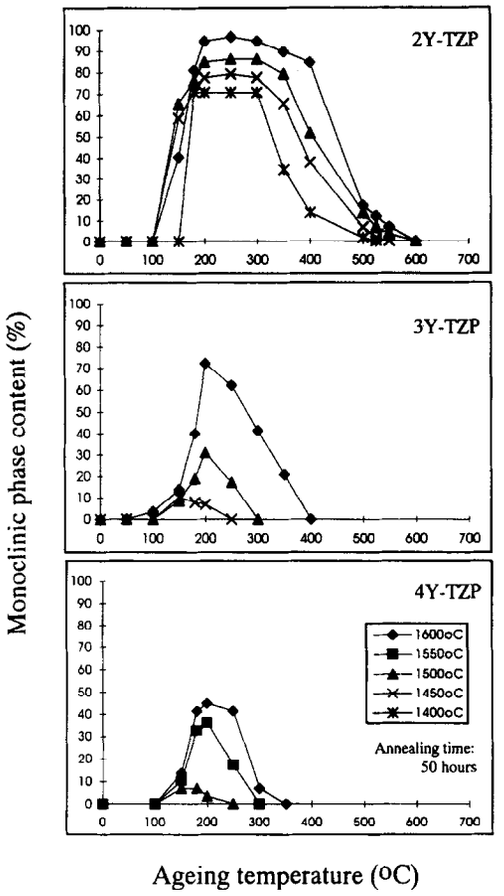


Fig. 7. Relationship between the amount of surface monoclinic phase and the ageing temperature, for a range of Y–TZPs sintered from 1400 to 1600°C and aged for 50 h in air. (After Sato & Shimada[46]).

2.2.2 Test environment

Ageing environments used to study the effects of low-temperature degradation in zirconia ceramics vary from the relatively mild, ageing in humid air (for periods in excess of 3 years[48]), to the much more aggressive autoclave conditions.[34] Generally the autoclave contains water, is heated to temperature (and corresponding pressure) and the test undertaken. The first reported autoclave results were obtained by Nakajima *et al.*[21] who aged a range of Y–PSZs in water from 100 to 180°C. At 180°C the saturation phenomenon was observed in < 5 h. They also dipped the Y–PSZ specimens into sulphuric acid, nitric acid, and caustic soda and found that the phase transformation increased with dipping time.

Sato *et al.*[47] aged specimens in air and in water vapour, and concluded that the water vapour accelerated the rate of reaction, but did not change the reaction equilibrium. The water vapour pressure was also altered and it was found that the monoclinic content increased with increasing vapour pressure. They also aged specimens under

a vacuum and they found that only a trace of monoclinic phase was formed. Sato *et al.*[19] also examined the effect of ageing in various solvents. It was concluded that aqueous solutions and non-aqueous solvents with a molecular structure containing a lone-pair electron orbital opposite a proton donor site also accelerates the tetragonal–monoclinic phase transformation.

The effect of water vapour pressure was investigated by Sato and Shimada[49,50] who found that as the vapour pressure was increased, then the rate of transformation also increased, but the saturation level remained constant. Also, ageing only occurred in water vapour and ammonia gas and not at all in vacuum or carbon dioxide atmospheres. Yoshimura *et al.*[51] investigated the effects of high pressure water (5 to 100 MPa) on the ageing behaviour, and found that transformation proceeds quicker under increasing pressure and over a greater temperature range than for lower pressures.

Perhaps the most interesting observation on the effects of ageing atmosphere was seen by Kuroda *et al.*[52] and is shown in Fig. 8. A sample was aged at 300°C in dry air for 24 h, then subsequently aged at 300°C for 72 h in a dynamic vacuum. The resultant profile (profile 4) was very similar to the one obtained for 96 h at 300°C in dry air (profile 2). Yet when they aged samples in a dynamic vacuum at 300°C they effectively saw no transformation. Therefore, once the transformation had been initiated by the water vapour, autocatalytic propagation then occurs without further chemical attack required.

There have been numerous studies on the effect of *in vitro* and *in vivo* environments on the ageing resistance of Y–TZP. Garvie *et al.*[24] aged Mg–PSZ in Ringer's solution and found that there was a slight decrease in strength and MOR. Their *in vivo* experiments showed that there had been no degradation after 6 months. Drummond found that YSZ ceramics aged in water, saline, and Ringer's solution at 37°C gave a reduction in strength with ageing time,[53] and that autoclaving in water slightly reduced the strength of Mg–PSZ.[54] Thompson and Rawlings found that ageing in Ringer's solution promoted phase transformation and MOR decrease with TZP and ZTA materials.[55]

Surprisingly, there is little data available on the effect of ageing on the wear behaviour of zirconia which is clearly of commercial significance. Preliminary results obtained at the University of Sunderland[56,57] clearly show that wear tests undertaken on aged material exhibit enhanced wear rates.

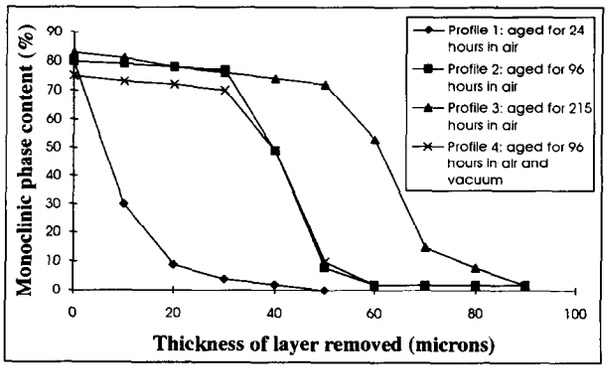


Fig. 8. Relationship between the amount of monoclinic phase and thickness of transformed layer removed for a 2Y–TZP aged in air or vacuum at 300°C. (After Kuroda *et al.*[52]).

3 Ageing mechanisms

There are many conflicting and confusing mechanisms for modelling the ageing behaviour of Y–TZP. Ageing observations have been explained using various mechanical and chemical degradation mechanisms. In the former, stress corrosion cracking of the amorphous intergranular glassy phase or of the t-ZrO_2 grains has been considered, whilst in the latter, the role of water has been suggested to form OH^- by the chemisorption at the surface of Y–TZP grains,[19] or to form $Y(OH)_3$[14,43] perhaps leading to the depletion of yttrium.[43] Part 2 of this paper will present a new ageing mechanism that accommodates all of the experimental observations.[58] The most significant ageing mechanisms are described in the following sections.

It is important, however, to firstly discuss the nature of the monoclinic layer and its kinetics. Tsukuma *et al.*[9] found that the transformation proceeds from the grain boundaries to the grain centres with time. He also suggests that the surface tetragonal grains are more unstable than those in the bulk. Therefore, thermal stability is dependent upon the surrounding grains. However, Schmauder and Schubert[12] observed that unconstrained surface grains were resistant to the ageing-induced phase transformation.

Miyazawa *et al.*[59] polished away the transformed surface layer and measured the monoclinic content with penetration depth for various samples. They found that the monoclinic content decreases with depth from the surface and that penetration depth increases with ageing time as shown in Fig. 9.

These results suggest that there is a gradual decrease in the monoclinic content with depth into the sample. However this is not the case, as the transformed layer has a fixed saturation level[21] dependent on the initial tetragonal and cubic contents of Y–TZPs. Optical microscopy clearly shows that there is a distinct transformed layer boundary with the tetragonal bulk material as shown in Fig. 10[60].

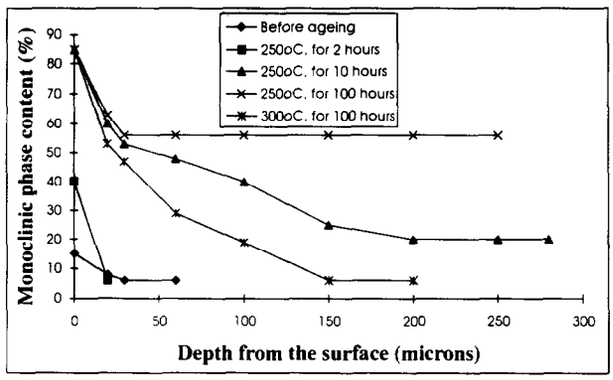


Fig. 9. Relationships between the amount of transformed monoclinic phase as a function of distance from the sample surface for a 5Y–PSZ aged in air. (After Miyazawa *et al.*[59]).

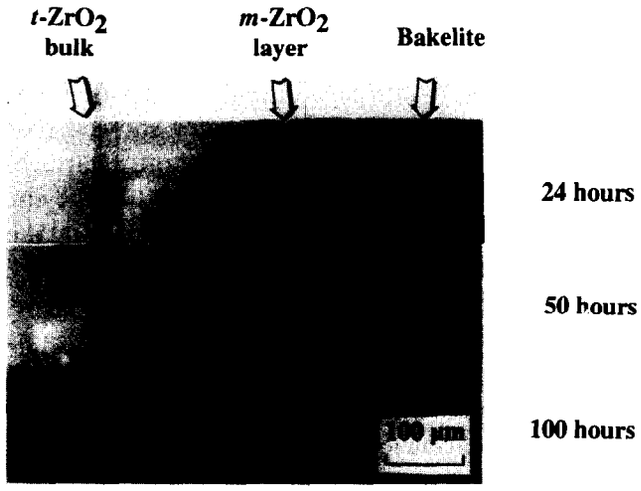


Fig. 10. Optical micrograph showing the growth of the surface monoclinic layer with ageing time for 2·5Y–TZP aged at 180°C in an autoclave containing superheated water (1MPa pressure). (After Lawson *et al.*[22]).

Tsubakino *et al.*,[10,61] Lawson[22] and Zhu *et al.*[62,63] showed that the relationship between the amount of transformation and the ageing time can be expressed by the Johnson–Mehl–Avrami equation:

$$f = 1 - e^{-bt^n} \quad (1)$$

where f is the transformation fraction, t is the time, and b and n are constants.

The value of n obtained was 0·7–1·0 irrespective of grain size or ageing environment. They also show that cracks accompanying the transformation propagate along grain-boundaries. Therefore, an increase in the cohesion of grain boundaries will probably be the most important factor in preventing the propagation of the tetragonal–monoclinic transformation from the surface to the interior.

Sintering aids that promote liquid phase formation do not enhance cohesion, but they help to prevent crack initiation. Kimura *et al.*[64] suggests the

> *"...presence of dopant in grain boundaries [acts] as a protective coating of [the] ZrO_2 grains against water (moisture) attack."*

which will therefore prevent OH^- attack on the grain surfaces.

Chen and co-workers[65–68] identified an incubation region on the kinetic plots of monoclinic content versus ageing time. The first derivative of these kinetic curves shows that generally the rate of transformation gradually increases to a maximum and then decreases. Lu and Chen extrapolated the plot of maximum rate of transformation versus grain size and deduced a critical grain size of 0·37 μm, below which degradation does not occur. Mäntylä *et al.*,[69–71] Lilley[42] and Lawson *et al.*[22,60,72] have shown that there is no incubation time and that the rate of transformation is constant, i.e. the phase transformation reaches saturation immediately and grows inwards linearly with time. Lawson *et al.* found that for 2·5Y–TZP the monoclinic transformation rate was 2–3 μm/h (0·2–0·4 μm grain size respectively) in superheated water in an autoclave at 180°C.

3.1 Corrosion mechanisms

Sato and Shimada[19] based their ageing model on the mechanism of stress corrosion in vitreous silica exposed to water.[73] The authors dismissed the dissolution of yttria or zirconia into the solutions by analysing the solvents used, and also no weight change of the aged specimen was observed. The reaction between water and Zr–O–Zr bonds at the crack tip is shown in Fig. 11. The strain which acts to stabilize the tetragonal phase[74,75] may be released on the surface (due to the reaction in Fig. 11), along with the growth of pre-existing flaws, so inducing the phase transformation.

Sato *et al.*[29] explained the reaction between water and zirconia on the basis of activation energies for transformation in Y– and Ce–ZrO_2. These studies gave similar values for both stabilizers (72·8–93·8 kJ/mol), therefore indicating that the water reacted primarily with Zr–O–Zr bonds on

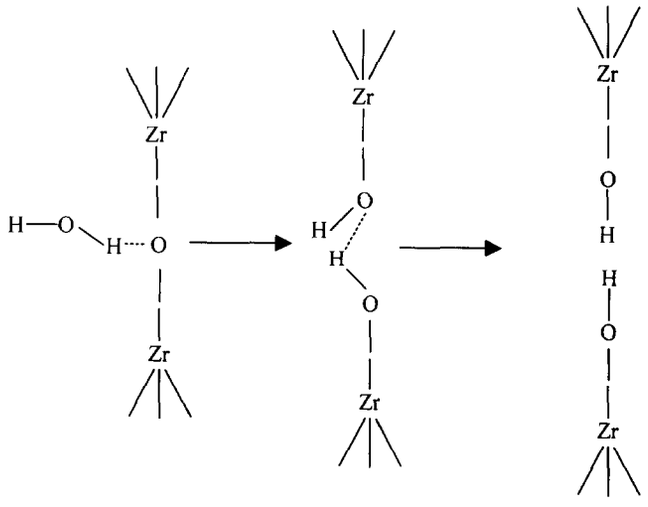


Fig. 11. Reaction scheme expected for the reaction between water and Zr–O–Zr bonds at the crack tip. (After Sato & Shimada[19]).

the surface and not the stabilizing oxide. They also expect solvent environments with a molecular structure containing a lone-pair electron orbital opposite a proton donor site to strongly affect crack growth. Investigation of various solutions[19] lead the authors to conclude that solutions which accelerate crack growth have the greatest effect on the tetragonal–monoclinic transformation.

The role of the water molecule on degradation in Y–TZPs has been investigated by Yoshimura *et al.*[20,51,76] The ageing-induced phase transformation was accompanied by an increase in the crystal lattice. The initial lattice parameters could be restored and a weight loss detected if the aged sample was annealed (400°C for 6 h in vacuum or 1300°C for 1 h in air). This reversible expansion and contraction of the monoclinic lattice seems to be caused by the inclusion and exclusion of OH^- in the lattice. The authors feel that if yttrium depletion by $Y(OH)_3$ formation or by Y^{3+} dissolution had occurred, such a reversible lattice recovery would not be observed at low temperatures and/or in a short period of time. Infrared spectroscopy clearly showed the introduction of OH^- on ageing (also confirmed by Raman spectroscopy) and its subsequent exclusion on annealing.

Yoshimura *et al.* calculate that approximately 60% of oxygen vacancies were occupied by OH^- ions, and that these OH^- ions would migrate faster than O^{2-} because of less charge and similar size. The slow diffusion of Y^{3+} to form $Y(OH)_3$ is thought unlikely by Yoshimura *et al.* and dissolution of Y^{3+} during the hydrothermal dissolution of yttria-stabilized zirconia, YSZ[76] does not occur. Based upon the arguments for anion diffusion, the OH^- ion trigger mechanism was proposed by Yoshimura *et al.*[20,51,76] is described below and shown schematically in Fig. 12.

Step 1 Chemical adsorption of H_2O at the surface.

Step 2 The formation of Zr–OH and/or Y–OH bonds at the surface, at which points stressed sites are created.

Step 3 The accumulation of strain by the migration of OH^- ions at the surface and in the lattice, to prepare nucleating defects.

Step 4 The nucleaton of monoclinic phase in the tetragonal grains: then the tetragonal–monoclinic transformation yields micro- and macro-cracking.

Further investigations[51] into the effect of high-temperature and high pressure-water showed that the activation energy remained constant regardless of temperature or pressure and seemed to be the activation energy for the diffusion of OH^- in the Y–TZP lattice, which further suggests that the degradation is controlled by OH^- diffusion. This model is based upon the accumulation of strains to exceed a critical value, i.e. the energy barrier from tetragonal–monoclinic formation. Therefore the transformation becomes barrierless, and spontaneous nucleation of monoclinic domains occurs.

The mechanism proposed by Sato *et al.*[19] also suggests the formation of Zr–OH at the surface. Sato however, assumes the formation of OH^- causes the release of strain which act to stabilize the t-ZrO_2 whereas Yoshimura *et al.* think that

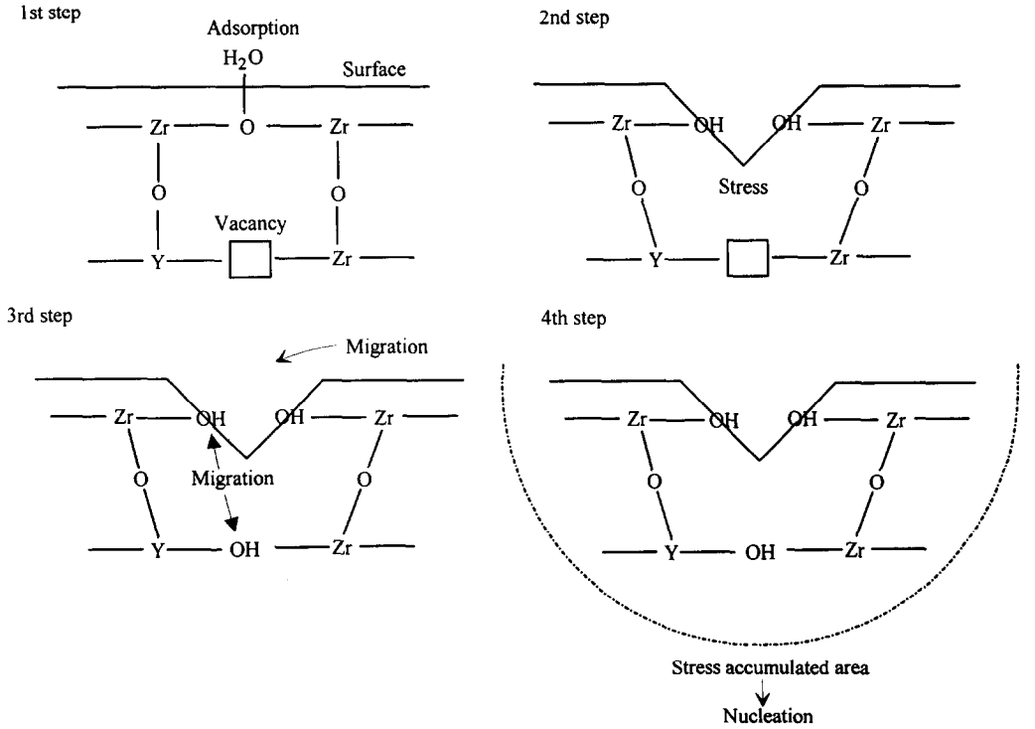


Fig. 12. Proposed degradation process of Y–TZP by the OH^- trigger mechanism. (After Yoshimura *et al.*[20]).

Zr–OH (Y–OH) creates a stressed site. Yoshimura also suggests that the mechanical stresses caused by thermal expansion mismatch as proposed by Schubert *et al.*[12,14,15] also play a role in triggering the tetragonal–monoclinic phase transformation. This mechanism is also supported by Masaki[44] who then proposes that the transformation develops along grain-boundaries causing zirconia particles to lose coherency with the matrix, therefore resulting in great loss in MOR. Masaki attributes inhibition behaviour to higher densities, therefore decreasing the number of cracks and defects for water attack.

Lepisto and Mäntylä have shown by the use of IRS and XPS,[69] that OH^- ions exist on the surface of Y–TZP, but they have also found that the OH^- ions do not extend throughout the transformed layer.[70] It is therefore considered that hydroxide formation throughout the transformed layer is not possible. However it would appear that Zr–OH formation at the specimen surface nucleates the phase transformation which then proceeds autocatalytically, without the requirement of continued hydroxyl ion involvement. Evidence for this mechanism is shown in Fig. 8[52] which shows that the transformation is nucleated in the presence of water vapour and then proceeds at the same rate under a dynamic vacuum.

3.2 Destabilization mechanism

Lange *et al.*[43] initially hypothesized that the ageing phenomenon was a result of a stress–corrosion type reaction, water vapour reacting with a glassy silicate grain-boundary phase. Using specimens with and without silica additions/impurities they found that the presence of a glassy phase at the grain-boundaries had no effect on the ageing behaviour of Y–TZP, which is also supported by Mecartney.[16] Nakajima[21] examined a range of Y–TZP ceramics in the TEM and found no evidence of an intergranular glassy phase. Aged specimens exhibited twinning within grains, and cracks along the grain-boundaries. These cracks seemed to initiate from the triple points and grow along the grain-boundaries. Nakajima attributed these cracks not only to the transformation, but also to corrosion.

TEM studies by Lange *et al.* on a 6·6 mol% specimen (consisting primarily of large cubic grains) before and after ageing revealed an additional microstructural feature that was not present before ageing. Clusters of small yttrium-rich crystallites (20–50 nm) bridged gaps in the TEM foils and were frequently adjacent to the transformed m-ZrO_2 grains as well as the cubic grains. Lange *et al.* found that the crystallites were α-$Y(OH)_3$. In addition, the glassy intergranular phase remained intact and so disproved their initial hypothesis. These crystallites have not been observed by any of the other TEM studies of aged Y–TZP.

Lange *et al.* propose that the tetragonal–monoclinic phase transformation will occur when water vapour draws out an amount of yttrium from a small volume element on the surface of the grain, thus destabilizing this small volume element. As this monoclinic nucleus grows by further yttrium depletion, it will achieve a critical size whereby spontaneous growth can occur without the need for further yttrium diffusion to completely transform the tetragonal grain in which it was growing.

The volume expansion and shear strain associated with the transformation will produce a microcrack if the grain size is greater than a critical value. If the transformed grain is less than the critical size required for microcracking, then nucleation, growth, and thus transformation of subsurface grains will be limited by long-range diffusion of yttrium to the surface. If the transformed grain is larger than the critical size, then microcracks will form and open up subsurface grains to further water vapour attack. Lange comments that only short-range diffusion of the yttrium is required and that this mechanism also explains why transformation only occurs above a critical particle size. However, Tsubakino *et al.*[10] showed that grains smaller than the critical size which should be 'stable' tetragonal grains, do transform when aged under hydrothermal conditions. Yoshimura *et al.*[20] have criticized $Y(OH)_3$ crystallite formation on account of the slow diffusion of yttrium in zirconia.

Winnubst and Burggraaf[11] also favour the formation of α-$Y(OH)_3$. Water reacts with yttrium from the Y–TZP surface grains to form yttrium hydroxide. This results in an yttrium-rich surface layer (observed by AES) and an yttrium depleted region close to the enriched surface. When a critical composition and grain size are reached then the tetragonal–monoclinic transformation will be initiated. Recent work by Azzoni *et al.*[77] who have studied the degradation mechanism using electron paramagnetic resonance (EPR) clearly supports the formation of α-$Y(OH)_3$. Additionally, Kruse *et al.*[78] studied the role of water on the ageing mechanism of Y–TZP using elastic recoil detection analyser (ERDA) and found that hydrogen penetrates deep into 3Y–TZP during ageing, while no penetration was observed for an ageing resistant Y–TZP. This experimental evidence has been used by Boutz[79] as clear confirmation that Y–OH bond formation and diffusion of OH^- into the degrading material occurs. However, Hughes *et al.*[80] who also studied the role of water on the ageing of Y–TZP, concluded that hydroxides of yttrium are only observed after severe treatment and are

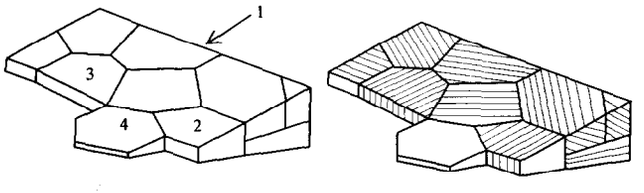
therefore symptomatic of the ageing process rather than initiators of the transformation.

Hernandez *et al.*[81] investigated the surfaces of aged Y–TZP using XPS and deduced that water molecules dissociate and are adsorbed at the surface. Reaction of OH^- ions with Y_2O_3 leads to formation of an oxyhydroxide, YO(OH), species. Simultaneously, tetragonal zirconia embryos form, grow and then transform when their size exceeds a critical value. Microcracking and spalling can then occur opening up new Y–TZP surfaces for continued attack.

3.3 Stress-induced transformation

The effects of internal stresses on the ageing behaviour of Y–TZP ceramics has been extensively investigated by Schubert *et al.*[12,14,15] and also more recently by Kim and Jung.[13] Schmauder and Schubert's[12] experiments were conducted on a 2 mol% Y–TZP, sintered at 1500°C for 2 h and prepared for TEM analysis. The sample was photographed in the TEM, then removed and annealed in air at 250°C for 0·5–168 h, and then remounted in the TEM with the same orientation as before.

The result was that only unconstrained, faceted grains in a protruding position (position 4), Fig. 13, were stable against environmental attack. Grains in positions 2 and 4 have the same surface area in contact with the water and should have the same surface energy. However, if the surface energy determined the stability, these grains would behave in the same way. The observation that the constrained grains behave differently than protruding ones indicates that the stress situation of the grains is the dominant factor governing grain stability. It is known that shear and tensile stresses are destabilizing, whereas compressive stresses stabilize the grains. The shear component is normally the largest and therefore nucleates, or controls, the transformation. They attribute these stresses to the anisotropy of the thermal expansion; the stresses increase with cooling.



as sintered

168 h, 250 °C, humid air

TEM experiment: unconstrained grains did not transform during degradation test.

Fig. 13. Schematic showing the effect of ageing for 168 h, at 250°C in humid air, on constrained and unconstrained grains in 2Y–TZP. (After Schmauder & Schubert[12]).

Schmauder and Schubert propose that the instability of the constrained surface grains is due to stress corrosion attack of these grains by water vapour. They favour the formation of yttrium hydroxide, not however, by diffusion of Y^{3+}, but by the self diffusion of water. The argument is based on the anion vacancies of the distorted fluorite structure coupled with the high anion mobility as a possible path for an uncharged species to diffuse into the lattice. The water molecule is smaller than the O^{2-} ion and could fit therefore into the vacancies. Migration into the lattice is dependent on substitution with an oxygen ion or a vacancy. Schubert calculated that the self diffusion coefficients for the motion of vacancies and for oxygen ions are similar to the linear diffusion coefficient of the transport mechanism for hydroxide formation. Therefore stress–corrosion attack of surface grains by water vapour results in $Y(OH)_3$ formation. The depleted area acts as a monoclinic nucleus which then grows under the influence of thermal expansion anisotropy stresses and propagates autocatalytically and is further aided by water attack via microcracks caused by the volume expansion of transforming grains.

These tensile stresses obviously increase with increasing grain size, and therefore a small grain size is required to prevent microcracking and hence transformation propagation. Schubert also attaches great importance on yttria distribution and attributes an inhomogeneous yttria distribution with reduced ageing performance. An interesting observation by Matsui *et al.*[82] on a 3Y–TZP aged sample with one face in tension and the other in compression, showed that the face in tension had nearly 100% transformation, whereas the rate of change on the other face was lower. Similar studies by Drennan *et al.*[28] on Mg–PSZ also show this behaviour.

The work of Kim and Jung[13] also mentions internal stresses caused by thermal expansion anisotropy, but in this case evidence from the literature points towards relaxation of these internal stresses by dipole rearrangement, which then create localised strains initiating the transformation. Dipole reorientation is a thermally activated process and so according to Kim's mechanism ageing-induced phase transformations would occur in dry air or vacuum. This is not experimentally observed and so this mechanism is not complete without the effect of water vapour taken into account. However, internal friction through dipole rearrangement is a plausible mechanism for aiding ageing-induced transformation initiation and propagation.

Lu *et al.*[65,67] studied the kinetics of the ageing behaviour of Y–TZP and showed that in air the

kinetic curves were sigmoidal, whereas in water they exhibited a linear logarithmic relationship. The sigmoidal kinetic relationship in air was split into three segments; an incubation time, an increase in the rate of transformation, and a reduction in transformation rate with the reaction levelling off. This premise is flawed however, as the sigmoidal shape is simply due to the monoclinic surface layer increasing in thickness until it exceeds the X-ray penetration depth.[22]

They consider that water catalyses the tetragonal–monoclinic transformation by reducing the incubation time. As the more the transformation is induced by the transformation strain, the easier it could be for water to catalyse the phase transformation when it diffuses through microcracks to the interior. Consequently the acceleration of the phase transformation is enhanced by a combination of water-vapour catalysis and subsequent autocatalytic reaction.

3.3.1 Internal friction

An initial reference to the ageing temperature regime and a similar temperature dependence of internal friction was made by Matsui *et al.*[83] Matsui referred to the work of Larsen and Adams[84] who plotted internal friction versus temperature and obtained similar results to Shimada *et al.*[85] and Weller and Schubert.[86] Matsui's results suggest that the tetragonal–monoclinic phase transformation proceeds most rapidly at ≈200°C, which coincides with the optimum internal friction temperature in Larsen's work and is suggested to be due to twin motion in *m*-ZrO_2.[85]

The temperature dependence of Young's modulus and internal friction for various engineering ceramics was studied by Shimada *et al.*[85] They found that for Y-PSZ the internal friction increased rapidly with temperature to a maximum at 200°C then decreased rapidly with temperature up to 400°C where it was a similar value to the room temperature figure. The Young's modulus decreased with decreasing temperature, but an anomolous sudden change was observed accompanied by the internal friction peak. Above 400°C the Young's modulus decreased linearly with increasing temperature up to 650°C and is shown in Fig. 14.

The internal friction, dielectric loss, and ionic conductivity of 3Y–TZP has been studied by Weller and Schuber.[86] Their results were similar to the ones shown in Fig. 14. Mechanical or dielectric loss resulting from reorientation of atomic defects by application of mechanical stress or an electric field, is proportional to the concentration of defects. The experimental results show that the activation enthalpy for mechanical and dielectric

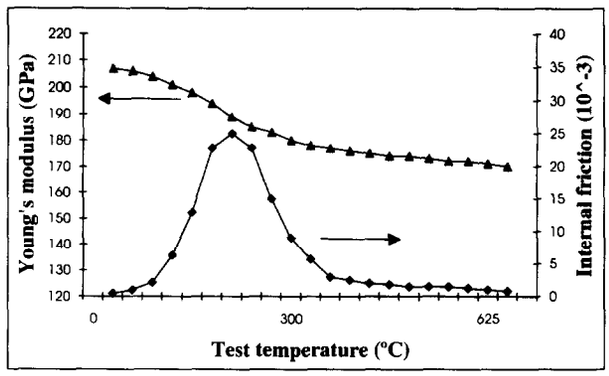


Fig. 14. Temperature dependence of Young's modulus and internal friction in 3Y–TZP. (After Shimada *et al.*[83]).

relaxation is the same (87 kJ/mol), which is similar to the activation energies calculated for ageing-induced phase transformation by Sato *et al.*[29] and Lawson.[22] They conclude that the mechanical and dielectric relaxation is caused by thermally activated reorientation of the same anisotropic defects.

Weller and Schubert propose the following atomistic model for mechanical and dielectric loss in TZP ceramics. During the formation of *c*- and *t*-ZrO_2 solid solutions, substitution of Y^{3+} for Zr^{4+} is accompanied by the introduction of oxygen-ion vacancies (for charge neutrality) in fluorite and distorted fluorite respectively. The coulomb interaction between substituted Y'_{Zr} and oxygen-ion vacancy, V''_o, produces $(Y'_{Zr}V''_o)$ complexes. This complex behaves as an anisotropic electric and elastic dipole, which reorients upon application of an electric or elastic field. It is assumed that dipoles are oriented parallel to [111] lattice direction as in *c*-ZrO_2. The reorientation is caused by oxygen vacancies jumping around the Y'_{Zr} ions for electrical and mechanical fields.

Kim and Jung[13] argue that these dipoles may reorient when residual stresses are relieved due to annealing above the lower temperature limit for ageing. This reorientation produces small localised strains along the [111] direction. When a critical value of strain is reached, the locally strained lattice becomes mechanically unstable, causing nucleation of *m*-ZrO_2. This relaxation temperature is not necessarily sensitive to additive levels or grain size.

The effect of Al_2O_3 additions to 3Y–TZP on the temperature dependence of internal friction were investigated by Ono *et al.*[87] Their results are comparable with those of Weller and Schubert for low Al_2O_3 additions. As the dopant content increased then the internal friction peak became lower and occurred at higher temperatures. They also found that the internal friction peak was accompanied by an inflection point in the Young's modulus.

They conclude that the relaxation phenomenon was concerned with the Y_2O_3 and not ZrO_2.

Nishiyama *et al.*[88] measured internal friction and modulus changes with temperature, and found similar results to those reported above. They attribute the internal friction peak to dipole relaxation (according to Weller and Schubert), to a stress-induced phase transformation, and to water initiated phase transformation (hydrothermal ageing).

3.4 Alternative mechanisms

Lepisto and Mäntylä[69] suggest that zirconia reduction and oxygen vacancy annealing was responsible for the degradation. Zirconia dissolution is initiated at grain-boundaries where the reaction proceeds deeper into the material.

$$Zr_s^{4+} + 2O_s^{2-} + 2V''_o + 4H^+ + 4e^- + 2O^{2-} \rightarrow Zr + 2H_2O$$

The dissolution at grain-boundaries relieves the internal stresses stabilizing the tetragonal structure and thus triggers the phase transformation to monoclinic symmetry.

Kuroda *et al.* suggest that the oxygen anions are responsible for the chemical attack.[52] It is proposed that thermally activated oxygen exchanges take place between the environment and the surface. Oxygen anions occupy monoclinic sites rather than the tetragonal ones, since monoclinic zirconia is thermodynamically more stable at low temperatures. As a result cations shift and therefore cause the tetragonal–monoclinic phase transformation.

Further investigations by this group on the application of an electric potential to induce the tetragonal–monoclinic phase transformation,[89] showed that the surface monoclinic content of the anode and cathode had increased. The reactions at the cathode are as follows:

$$O_2 + 4e^- \rightarrow 2O^{2-} \text{ (in the presence of oxygen)}$$
$$H_2O + 2e^- \rightarrow H_2\uparrow + O^{2-} \text{ (in the presence of water)}$$

Once the above reaction occurs only the oxygen ions can diffuse into the bulk. Oxygen ions then trigger the transformation as explained in the opening paragraph. As the tetragonal grains in the bulk are constrained by the matrix then transformation does not occur despite oxygen ion motion. They conclude that the gas–solid reaction at the surface rather than the anion diffusion through the bulk is essential for the transformation to nucleate.

4 Transformation Inhibition

The free energy change (ΔG_{t-m}) of the tetragonal–monoclinic phase transformation on cooling through the transformation temperature in absence of an applied stress field is given by:[90]

$$\Delta G_{t-m} = (G_c^m - G_c^t) + (G_{se}^m - G_{se}^t) + (G_s^m - G_s^t) \quad (2)$$

where G_c is the chemical free energy, G_{se} the (dilational) strain free energy, and G_s the surface free energy. Superscripts t and m denote tetragonal and monoclinic phases respectively.

Heuer and Lenz, and Heuer *et al.* have modified eqn (2) by taking into account bulk residual shear strains from twinning, interfacial contributions from twin boundaries and particle-matrix microcracking,[91] and an extra nucleation term[92] respectively. The influence of important parameters, however can still be assessed using eqn 2.

The metastable tetragonal phase can only exist when $\Delta G_{t-m} > 0$. The chemical free energy term is always negative, but the addition of stabilizing oxides will make this term less so. The strain free energy term is also negative, and is influenced by the matrix stress according to.[93]

$$G_{se} = 1/2\ \sigma_{ij}\epsilon_{ij}V_{mol} \quad (3)$$

where σ_{ij} is the stress tensor, ϵ_{ij} the strain tensor and V_{mol} the molar volume.

Therefore in the presence of a tensile stress the strain free energy term is negative, making the tetragonal phase less stable. When compressive stresses are present, the tetragonal phase is more stable. Without the presence of compressive stresses, or in general strain contributions, stabilization will only occur when the surface free energy term in eqn 2 is positive and larger than the sum of the first two terms.

Generally speaking, and with reference to eqn 2, the control of the tetragonal–monoclinic phase transformation can be achieved by:

1. An increase in the chemical free energy change by alloying with another stabilizing oxide, e.g. CeO_2.
2. An increase in the strain free energy change by dispersion of a second phase, e.g. Al_2O_3.
3. By increasing the surface free energy change, e.g. reduction in grain size.
4. Coating.
5. Surface microstructural engineering.

It should be noted though that an increased thermal stability by methods 1 and 2 above generally results in a decrease in mechanical properties through over-stabilization of the t-ZrO_2 phase.

4.1 Chemical free energy increase

An increase in the chemical free energy can be achieved quite simply by increasing the yttria content. However this over-stabilization of the t-ZrO_2 phase (and probable c-ZrO_2 phase formation)

leads to a sharp reduction in the mechanical properties of Y–TZP.

An alternative method of increasing the thermal stability of Y–TZP is to alloy with another stabilizing oxide. Sato and Shimada[29,49,94–96] examined the effects of various oxide additions to Y–PSZ. They found that CeO_2 was an effective additive for eliminating degradation, without any reduction in mechanical properties and actually increased the elastic modulus. The authors feel that the effect of CeO_2 may be to increase the size of the transformation zone in the vicinity of a crack front. TiO_2 did reduce the phase transformation but at a cost of increased grain size and reductions in relative density, hardness and fracture toughness. The other oxides evaluated (CaO and MgO) did decrease the surface monoclinic content, but only because of increased cubic formation, which obviously lowered the fracture toughness.

Duh and Wu[97] alloyed 1, 3 and 4 mol% Y–TZPs with 10 mol% CeO_2 and showed that the tetragonal phase could be retained in water at 300°C for up to 1 month. A similar result was obtained by Hirano and Inada[98] but they only alloyed with up to 5·5 mol% CeO_2. Further work by Duh and Wan[99] showed that 9·5 mol% CeO_2 alloyed with 1·5 mol% Y–TZP is required to inhibit ageing.

Hirano and Inada[100] found that hydrothermal stability could only be achieved by (4Y,4Ce)–TZP–25 wt% Al_2O_3 composites, although (4Y,4Ce)–TZP was resistant to ageing in air. Theunissen *et al.*[101] and Boutz *et al.*[79,102] showed improved ageing resistance with CeO_2 additions under autoclave conditions. Theunissen[103] also examined the effects of TiO_2 additions. They found that some samples aged very quickly and others showed good resistance. This variability was attributed to surface enrichment in TiO_2, for the good ageing resistant samples, that may form a TiO_2 overlayer.

4.2 Strain free energy increase

Sato *et al.*[18] added Al_2O_3 (5–10 wt%) to 3 mol% Y–TZP and found that the surface monoclinic content decreased with increasing concentration of dispersed Al_2O_3. They postulated that the Al_2O_3 grains play a major role in resisting the volume expansion of the zirconia grains accompanying the tetragonal–monoclinic phase transformation. Further investigations by Sato and Shimada[29,49,94–96] showed that Al_2O_3 additions reduced the rate of transformation but did not prevent it totally, and increased the elastic modulus. Schmauder and Schubert[12] however, argue that additions of Al_2O_3 create stresses with the bulk ceramic which are detrimental to the ageing behaviour of TZP. Masaki[44] supports this argument and includes TiO_2 and Fe_2O_3 into this category of stress raisers. However neither Schmauder nor Masaki have presented results to support their argument.

Tsukuma and Shimada[104] also found a reduction in monoclinic content with Al_2O_3 additions, and that 40 wt% Al_2O_3 almost perfectly restrained the transformation. They attributed this improvement in thermal stability of the tetragonal phase to an increase in Young's modulus of the matrix due to the Al_2O_3 additions.[105,106] Additions of Al_2O_3 or TiN to 2–6 mol% Y_2O_3–ZrO_2 have been shown to control the phase transformation and so prevent deterioration in modulus of rupture.[107]

Kim and Jung[13] show that composites of transformable and nontransformable TZPs formed in the ZrO_2–Y_2O_3–$Nb(Ta)_2O_5$ systems can act as lattice relaxation inhibitors (increase the lattice stiffness). This composite basically consists of a metastable tetragonal bulk interspersed with large stable grains. Recent research on the role of second phase additions to zirconia ceramics leading to enhanced ageing resistance has been reported for mullite, spinel and Al_2O_3,[108] MgO and Al_2O_3[109] and tungsten carbide.[48]

4.3 Surface free energy increase

The grain size of Y–TZP can be controlled by reducing the sintering (or calcination) temperature. However, unless the powders are ultra fine and highly reactive, the sintered density will not be very high. Hot-pressed or hot-isostatically pressed powders enable a small grain sized, fully dense Y–TZP to be manufactured.

A much cheaper technique is to use sintering additives to ensure a small grain size through lowering the sintering temperature. The effect of additives on the anti-degradation behaviour of Y–TZP has been investigated by Kimura *et al.*[64] and Lawson *et al.*[22,23,110] Transition metal oxide additives were used as sintering aids and resulted in densification occurring at about 1200°C. The doped 2·5 mol% Y–TZPs had a small grain size, were fully dense and were resistant to degradation in air and boiling water.[64] Similar results were also obtained by Lawson *et al.* who showed that strengths in excess of 1000 MPa could be retained after 1000 h in superheated water in an autoclave at 180°C.

Sato and Shimada[49,95] showed that reducing the grain size of the CeO_2-alloyed Y–TZP reduced the surface monoclinic content and lowered the concentration of CeO_2 required for total inhibition.

4.4 Coating

Iio *et al.*[111] coated Al_2O_3 onto the surface of Y–TZP using CVD. When this sample was aged in air at 300°C they found that the tetragonal–monoclinic phase transformation had been restrained. Any coatings however, must be fully

dense and stable against the atmosphere. Such coatings can be produced by CVD but processing is complicated and expensive. If the coating degrades or is fractured in any way, then the susceptible tetragonal grains will be open to water vapour attack.

4.5 Surface engineering

Whalen *et al.* formed a surface layer of very fine-grained tetragonal phase on Y–TZP by surface recrystallization.[112] This had the effect of resisting ageing at 200°C in air for 1000 h. Therefore large grain sized Y–TZP for maximum toughness can be protected from the ageing-induced transformation by simple postsintering treatments.

4.6 Non-transformable tetragonal zirconia (t'-ZrO_2)

The effect of t'-ZrO_2 on ageing of TZPs has been investigated by Noma *et al.*[76] and by Jue *et al.*[113] Noma found that the t'-phase was more resistant to nucleation of the ageing-induced transformation by OH^- trigger mechanism, than a more conventional t-ZrO_2. However, once the transformation had begun it proceeded at the same rate as for the t-ZrO_2 sample. Jue *et al.* showed that t'-ZrO_2 was essentially ageing resistant when it had polished surfaces. However, when surface ground, t'-ZrO_2 exhibited very slight transformation (up to 7% monoclinic content) after ageing at 275°C in air.

4.7 Density

Evidence for a density threshold for ageing was reported by Masaki[44] and is shown in Fig. 15. The solid circles and triangles show the sintered materials, the strength of which decreased greatly after ageing (the extent of the black area in each circle corresponds to the degree of strength reduction). The figure also shows lines of critical densities (thresholds) and grain sizes for the Y–TZP compositions after ageing.

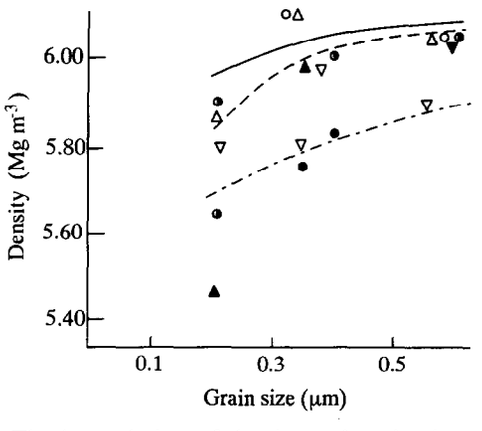


Fig. 15. The interrelation of density and grain size with the degradation of Y–TZPs aged at 200–250°C in air for 2000 h, (O, ——, 2·5 Y_2O_3; Δ, – – –, 3 Y_2O_3; ∇, –·–·–, 4 Y_2O_3. (After Masaki[44]).

According to these results if the density is greater than a critical value (Y_2O_3 dependent) then ageing will not occur. The critical density determined by Masaki will however, be an over-estimate, as his specimens were aged and then cut to the required size before the density and MOR were assessed.

4.8 Lattice spacing

An interesting aspect of Kim and Jung's work[13] is the possible existence of a critical value of d_{111}. Figure 16 shows the tetragonal zirconia (111) lattice spacing, d_{111}, and the amount of monoclinic ZrO_2 resulting from various ageing times (at 250°C). These results show that as a critical value of d_{111} is reached, then localised lattice instability occurs and transformation is initiated. Therefore, t-ZrO_2 grains whose d_{111} is larger than the critical value, transform.

Yoshimura *et al.*[20] observed a reversible expansion and contraction of the zirconia lattice with ageing and subsequent annealing, and concluded that it was caused by the inclusion and exclusion of OH^- in the lattice. Recent results obtained by Lee and Kim[114] have shown that the transformation is reversible upon annealing above 1200°C. The phase recovery was accompanied by healing of micro-cracks, but the macro-cracks remained to a large extent. Therefore the benefit of annealing severely aged zirconia in order to re-establish the tetragonal phase must be questioned.

5 Summary

The experimental evidence of hydrothermal degradation is well documented and there are compositions and conditions under which ageing will not occur. Much more work in developing ageing resistant zirconia ceramics with good mechanical properties has still to be undertaken. The current ageing models do not accommodate all of the

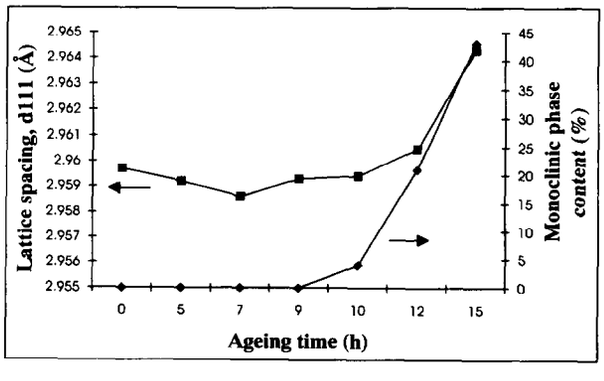


Fig. 16. Monoclinic content and lattice distance vs ageing time for a 3Y–TZP sintered at 1500°C for 5 h and aged in air at 250°C. (After Kim & Jung[13]).

experimental evidence, and there is conflict as to the nature of the attack, and whether there is accumulation or release of strain. The second paper presents a new ageing mechanism which covers all of the published experimental evidence.

Acknowledgements

The author would like to thank the following people who have all helped one way or another in my work and the preparation of this paper: Collin Gill, Malcolm Smith, Graham Dransfield, Tony Jones, Paul McColgan, Neil Mc.N. Alford, Paul Smith, Richard Brook, Ian Birkby, and Mark Rainforth.

References

1. Krajewski, A., Ravaglioli, A., Meschke, F., Azzoni, C. B., Crosignani, E., Scardina, F. & Paleari, A., Transformations on the surface of steam treated TSZ-ceramics. In *Third Euro-Ceramics, Vol. 3: Engineering Ceramics*, eds P. Duran & J. F. Fernandez, Faenza Editrice Iberica S. L., 1993, pp. 518–8.
2. Kobayashi, K., Kuwajima, H. & Masaki, T., Phase change and mechanical properties of ZrO_2–Y_2O_3 solid electrolyte after ageing. *Solid State Ionics*, **3/4** (1981) 489–93.
3. Sato, T., Murakami, T., Endo, T., Shimada, M., Komeya, K., Kameda, T. & Komatsu, M., Corrosion of silicon nitride ceramics under hydrothermal conditions. *J. Mat.Sci.*, **26**[7] (1990) 1749–54.
4. Watanabe, M., Iio, S. & Fukuura, I., Ageing behaviour of Y–TZP. In *Advances in Ceramics, Vol. 12, Science and Technology of Zirconia II*, ed. N. Claussen, M. Ruhle & A. H. Heuer, The American Ceramic Society, Inc., Columbus, Ohio, 1984, pp. 391–8.
5. Matsumoto, R. L. K., Strength recovery in degraded yttria-doped tetragonal zirconia polycrystals. *J. Am. Ceram. Soc.*, **68**[8] (1985) c-213.
6. Wang, J. & Stevens, R., Surface toughening of TZP ceramics by low temperature ageing. *Cer. Int.*, **15** (1989) 15–21.
7. Wang, J. & Stevens, R., Surface transformation and toughening of TZP ceramics by low temperature ageing. In *British Ceramic Proceedings, Vol. 42: Complex Microstructures*. eds R. Stevens & D. Taylor, Institute of Ceramics, 1989, pp. 167–77.
8. Yoshimura, M., Phase stability of zirconia. *Am. Ceram. Soc. Bull.*, **67**[12] (1988) 1950–5.
9. Tsukuma, K., Kubota, Y. & Tsukidate, T., Thermal and mechanical properties of Y_2O_3-stabilized tetragonal zirconia polycrystals. In *Advances in Ceramics Vol. 12, Science and Technology of Zirconia II*, eds N. Claussen, M. Ruhle & A. H. Heuer, The American Ceramic Society, Inc., Columbus, Ohio, 1984, pp. 382–90.
10. Tsubakino, H., Hamamoto, M. & Nozato, R., Tetragonal to monoclinic phase transformation during thermal cycling and isothermal ageing in yttria-partially stabilized zirconia. *J. Mat. Sci.*, **26**[20] (1991) 5521–6.
11. Winnubst, A. J. A. & Burggraaf, A. J., The ageing behaviour of ultrafine-grained Y–TZP in hot water. In *Advances in Ceramics, Vol 24, Science and Technology of Zirconia III.*, eds S. Somiya, N. Yamamoto & H. Yanagida, The American Ceramic Society, Inc., Columbus, Ohio, 1988, pp. 39–48.
12. Schmauder, S. & Schubert, H., Significance of internal stresses for the martensitic transformation in yttria-stabilized tetragonal zirconia polycrystals during degradation. *J. Am. Ceram. Soc.*, **69**[7] (1986) 534–40.
13. Kim, D. -J. & Jung, H.-J., Low temperature degradation of tetragonal zirconia: mechanism and prevention. Presented at Zirconia V, Australia. 1992.
14. Schubert, H., Investigations on the stability of yttria stabilized tetragonal zirconia (Y-TZP). In *Zirconia Ceramics 7*, Uchida Rokokuho, Tokyo, Japan, 1986, pp. 65–81.
15. Schubert, H. & Petzo, G., Microstructural investigations on the stability of yttria-stabilized tetragonal zirconia. In *Advances in Ceramics, Vol 24, Science and Technology of Zirconia III.*, eds S. Somiya, N. Yamamoto & H. Yanagida, The American Ceramic Society, Inc., Columbus, Ohio, 1988, pp. 21–8.
16. Mecartney, M. L., Influence of an amorphous second phase on the properties of yttria-stabilized tetragonal zirconia polycrystals (Y–TZP). *J. Am. Ceram. Soc.*, **70**[1] (1987) 54–8.
17. Arai, T., Yamamoto, T. & Tsuji, K., Transition-free zirconia ceramics. In *Advances in Ceramics, Vol 24, Science and Technology of Zirconia III.*, eds S. Somiya, N. Yamamoto & H. Yanagida. The American Ceramic Society, Inc., Columbus, Ohio, 1988, pp. 517–22.
18. Sato, T. & Shimada, M., Crystalline phase change in yttria-partially-stabilized zirconia by low-temperature annealing. *J. Am. Ceram. Soc.*, **67**[10] (1984) c-212.
19. Sato, T. & Shimada, M., Transformation of yttria-doped tetragonal ZrO_2 polycrystals by annealing in water. *J. Am. Ceram. Soc.*, **68**[6] (1985) 356–9.
20. Yoshimura, M., Noma, T., Kawabata, K. & Somiya, S., Role of H_2O on the degradation process of Y–TZP. *J. Mat. Sci. Lett.*, **6**[4] (1987) 465–7.
21. Nakajima, K., Kobayashi, K. & Murata, Y., Phase stability of Y–PSZ in aqueous solutions. In *Advances in Ceramics Vol 12, Science and Technoloy of Zirconia II*, eds N. Claussen, M. Ruhle & A. H. Heuer, The American Ceramic Society, Inc., Columbus, Ohio, 1984, pp. 399–407.
22. Lawson, S., The sintering, mechanical and ageing properties of transition metal oxide-doped yttria-tetragonal zirconia polycrystals (Y–TZP). Ph.D. thesis, University of Sunderland, UK, 1993.
23. Lawson, S., Gill, C., Smith, J. M., Dransfield, G. P., Egerton, T. A. & McColgan, P., Ageing studies of novel Y–TZPs. In *Third Euro-Ceramics. Vol. 3: Engineering Ceramics*, eds P. Duran & J. F. Fernandez, Faenza Editrice Iberica S. L., 1993, pp. 507–12.
24. Garvie, R. C., Urbani, C., Kennedy, D. R. & McNeuer, J. C., Biocompatability of magnesia–partially stabilized zirconia (Mg–PSZ) ceramics. *J. Mat. Sci.*, **19**[10] (1984) 3224–8.
25. Swain, M. V., Stability of Mg–PSZ in high temperature steam environment. *J. Mat. Sci. Lett.*, **4**[7] (1985) 848–50.
26. Sato, T., Endo, T., Shimada, M., Mitsudome, T. & Otabe, N., Hydrothermal corrosion of magnesia–partially-stabilized zirconia. *J. Mat. Sci.*, **26**[5] (1991) 1346–50.
27. Hecht, N. L., Jang, S. D. & McCullum, D. E., Environmental effects on toughened zirconia ceramics. In *Advances in Ceramics Vol 24, Science and Technology of Zirconia III.*, eds S. Somiya, N. Yamamoto & H. Yanagida, The American Ceramic Society, Inc., Columbus, Ohio, 1988, pp. 133–44.
28. Drennan, J., Hartshorn, A. J. & Thompson, S. W., The effect of low temperature aqueous environments on magnesia–partially-stabilized zirconia (Mg–PSZ). In *Zirconia V*, eds S. P. S. Badwal, M. J. Bannister & R. H. J. Hannink, Technomic Publishing Co. Ltd. 1993, pp. 144–51.
29. Sato, T. & Shimada, M., Transformation of Ceria–doped tetragonal zirconia polycrystals by annealing in water. *Am. Ceram. Soc. Bull.*, **64**[10] (1985) 1382–4.
30. Leach, C. & Khan, N., Stability of zirconia–ceria–yttria

ceramics in hostile environments. *J. Mat. Sci.*, **26**[8] (1991) 2026–30.
31. Tsukuma, K., Mechanical properties and thermal stability of CeO_2 containing tetragonal zirconia polycrystals. *Am. Ceram. Soc. Bull.*, **65**[10] (1986) 1386–9.
32. Matsumoto, R. L. K., Ageing behaviour of ceria–stabilized tetragonal zirconia polycrystals *J. Am. Ceram. Soc.*, **71**[3] (1988) c128–9.
33. Pampuch, R., Pyda, W. & Haberko, K., The obtainment and properties of calcia–TZP. *Cer. Int.*, **14** (1988) 245–9.
34. Ruhle, M., Claussen, N. & Heuer, A. H., Microstructural studies of Y_2O_3-containing tetragonal ZrO_2 polycrystals (Y–TZP). In *Advances in Ceramics Vol. 12, Science and Technology of Zirconia II*, eds N. Claussen, M. Ruhle & A. H. Heuer, The American Ceramic Society, Inc., Columbus, Ohio, 1984, pp. 352–70.
35. Lawson, S., Dransfield, G. P., Jones, A. G., McColgan, P. & Rainforth, W. M. Enhanced performance of Y–TZP materials through compositional zonng on a nano-scale. Presented at the 8th CIMTEC-World Ceramic Congress, Florence, Italy, 1994.
36. Burger, W., Piconi, C., Cittadini, A. & Boccalari, M., Kinetic and thermodynamical investigations on ready to press Y–TZP powders for biomedical applications. Presented at the 8th CIMTEC-World Ceramic Congress, Florence, Italy, 1994.
37. Gibson, I. R., Lachowski, E. E. & Irvine, J. T. S., Hydrothermal degradation of cubic yttria zirconia ceramics., submitted to *Nature*, 1993.
38. Dransfield, G. P., Fothergill, K. A. & Egerton, T. A., The superior ageing properties of a plasma synthesized yttria coated zirconia. 7th CIMTEC-World Ceramic Congress, Montecatini, Italy, 1990.
39. Swabb, J. J., Evaluation of Japanese yttria tetragonal zirconia polycrystal (Y–TZP) materials. *Ceram. Eng. Sci. Proc.*, **8**[7–8] (1987) 886–91.
40. Swab, J. J., Low temperature degradation of Y–TZP materials. *J. Mat. Sci.*, **26** (1991) 6706–14.
41. Hecht, N. L., Goodrich, S. M., McCullum, D. E., Yaney, P. P., Jang, S. D. & Tennery, V. J., Characterization studies of transformation-toughened ceramics. *Am. Ceram. Soc. Bull.*, **71**[6] (1992) 955–9.
42. Lilley, E., Review of low temperature degradation in Y–TZPs. In Ceramic Transactions, Vol. 10: *Corrosion and corrosive degradation of ceramics*, eds R. E. Tressler & McNallan, The American Ceramic Society, 1989, pp. 387–407.
43. Lange, F. F., Dunlop, G. L. & Davis, B. L., Degradation during ageing of transformation-toughened ZrO_2–Y_2O_3 materials at 250°C. *J. Am. Ceram. Soc.*, **69**[3] (1986) 237–40.
44. Masaki, T., Mechanical properties of Y–PSZ after ageing at low temperature. *Int. J. High Tech. Ceram.*, **2** (1986) 85–98.
45. Miyazawa *et al.* Failure of fracture toughness of partially.... *Annual meeting of Jap. Soc. of Powder and Powder Metallurgy*, Tokyo, Japan, **58**[51] (1983) 104–5.
46. Sato, T., Ohtaki, S. & Shimada, M., Transformation of yttria partially stabilized zirconia by low temperature annealing in air. *J. Mat. Sci.*, **20**[4] (1985) 1466–70.
47. Sato, T., Ohtaki, S., Endo, T. & Shimada, M., Transformation of yttria-doped tetragonal ZrO_2 polycrystals by annealing under controlled humidity conditions. *J. Am. Ceram. Soc.*, **68**[12] (1985) c-320–22.
48. Kitano, Y., Iwanaga, H., Oishi, M., Mutsuda, Y. & Masaki, T., Structural and mechanical changes of zirconia and zirconia composites after aging. In *Third Euro-Ceramics, Vol. 3: Engineering Ceramics*, eds P. Duran & J. F. Fernandez, Faenza Editrice Iberica S. L., 1993, pp. 647–52.
49. Sato, T. & Shimada, M., Control of the tetragonal–monoclinic phase transformation of yttria-doped zirconia containing CeO_2, CaO and Al_2O_3 in air and water. In *Ceramic Materials & Components for Engine*, 2nd Int. Symp. eds W. Bunk & H. Hausner, 1986.
50. Sato, T., Ohtaki, S., Endo, T. & Shimada, M., Humidity dependence of phase transformation from tetragonal–monoclinic structure in yttria-doped tetragonal zirconia. In *High Tech Ceramics*, ed. P. Vincenzini. 1987, pp. 281–8.
51. Yoshimura, M., Noma, T., Kawabata, K. & Somiya, S., The effects of high-temperature-and high-pressure-water on the low temperature degradation behaviour of Y–TZP. *J. Ceram. Soc. Jpn. Int. Ed.*, **96**[3] (1989) 263–8.
52. Kuroda, K., Saka, H., Iio, S., Watanabe, M. & Imura, T., Tetragonal to monoclinic transformation in ZrO_2–Y_2O_3 ceramics. In *Proc. of the Int. Confer. on Martensitic Transformations*, The Japan Institute of Metals, 1986, pp. 1161–6.
53. Drummond, J. L., *In vitro* ageing of yttria-stabilized zirconia. *J. Am. Ceram. Soc.*, **72**[4] (1989) 675–6.
54. Drummond, J. L., Effects of *in vitro* ageing of magnesia-stabilized zirconia. *J. Am. Ceram. Soc.*, **75**[5] (1992) 1278-80 .
55. Thompson, I. & Rawlings, R. D., Mechanical behaviour of zirconia and zirconia-toughened alumina in a simulated body environment. *Biomaterials*, **11**[9] (1990) 505–8.
56. Tse, A. W. C., Lawson, S. & Gill, H. C., Low amplitude oscillatory wear of Y–TZP in various environments. Presented at 8th CIMTEC-World Ceramic Congress, Florence, Italy, 1994.
57. Ratnarajan, R., Lawson, S. & Gill, C., Low amplitude oscillatory wear in yttria-stabilized zirconia. Presented at IMF10, Northern Ireland, Sept. 1994.
58. Lawson, S., Environmental degradation of zirconia ceramics, Part II: Ageing mechanism. Submitted to *J. Eur. Ceram. Soc.*, 1995.
59. Miyazawa, T., Mitsuda, H., Toni, H. & Okinaka, H., Deterioration of partially stabilized zirconia (II). *Funtai Oyobi Funmatsu-Yakin*, **32**[4] (1985) 141–4.
60. Lawson, S., Gill, H. C., Dransfield, G. P., Smith, P. A., Button, T. & Alford, N. McN., The monitoring and prediction of the ageing-induced phase transformations occurring in zirconia ceramics using a microwave dielectric loss tangent technique. Presented at the 8th CIMTEC-World Ceramic Congress, Florence, Italy, 1994.
61. Tsubakino, H., Sonoda, K. & Nozata, R., Martensite transformation behaviour during isothermal ageing in partially stabilized zirconia with and without alumina addition. *J. Mat. Sci. Lett.*, **12**[3] (1993) 196–8.
62. Zhu, W. Z., Lei, T. C. & Zhou, Y., Time-dependent tetragonal to monoclinic transition in hot-pressed zirconia stabilized with 2 mol% yttria. *J. Mat. Sci.*, **28**[23] (1993) 6479–83.
63. Lei, T. C., Zhu, W. Z. & Zhou, Y., Behaviour of the tetragonal to monoclinic transition in hot pressed zirconia doped with 2 mol% yttria. *Mat. Chem. & Phys.*, **34** 3/4 (1993) 317–20.
64. Kimura, N., Abe S., Hayashi, Y., Morishita, J. & Okamura, H., Sintering behaviour and anti-degradation property of MO_x-doped Y–TZP (M:Cu, Mn, Co, Ni, Zn). *Sprechsaal.*, **122**[4] (1989) 341–3.
65. Lu, H. -Y. & Chan, S. -Y., Low-temperature ageing of *t*-ZrO_2 polycrystals with 3mol% Y_2O_3. *J. Am. Ceram. Soc.*, **70**[8] (1987) 537–41.
66. Chen, S.-Y. & Lu, H.-Y., Sintering of 3mol% Y_2O_3–TZP and its fracture after ageing treatment. *J. Mat. Sci.*, **23**[4] (1988) 1195–200.
67. Lu, H.-Y., Lin, H.-Y. & Chen, S.-Y., Autocatalytic effect and microstructural development during ageing of 3mol% Y_2O_3–TZP. *Cer. Int.*, **13** (1987) 207–14.
68. Chen, S.-Y., Low-temperature ageing map for 3mol% Y_2O_3–ZrO_2. *J. Mat. Sci.*, **24**[2] (1989) 453–6.
69. Lepisto, T. T. & Mäntylä, T. A., A model for the structural degradation of Y–TZP ceramics in humid atmosphere. *Ceram Eng. Sci. Proc.*, **10**[7–8] (1989) 658–67.
70. Lintula, P., Lepisto, T. T., Reuhkala, P. & Mäntylä, T., Phase transformations in Y–TZP-ceramics in boiling water. In *Euro-Ceramics Vol 1. Processing of Ceramics*,

eds G. de With, R. A. Terpstra & R. Metselaar., Elsevier Applied Science, UK, 1989, pp. 542–6.
71. Lepisto, T. T., Lintula, P. V. & Mäntylä, T. A., TZP-ceramics in humid conditions at 150°C. *Ceram. Eng. Sci. Proc.*, **9**[9-10] (1988) 1517–24.
72. Lawson, S. & Smith, P. A., A new technique for monitoring aging in yttria–tetragonal zirconia polycrystals. *J. Am. Ceram. Soc.*, **76**[12] (1993) 3170–2.
73. Micalske, T. A. & Freiman, S. W., A molecular mechanism for stress corrosion in vitreous silica. *J. Am. Ceram. Soc.*, **66**[4] (1983) 284–8.
74. Mitsuhashi, T., Ichihara, M. & Tatsuke, U., Characterization and stabilization of metastable tetragonal ZrO_2. *J. Am. Ceram. Soc.*, **57**[2] (1974). 97–101.
75. Garvie, R. C., Stabilization of the tetragonal phase in zirconia polycrystals. *J. Phys. Chem.*, **82**[2] (1978) 218–24.
76. Noma, T., Yoshimura, M. & Somiya, S., *Effect of cooling rate on the properties and the nanostructures of Y-TZP.* Report of the Research Lab. of Eng. Mats., Tokyo Inst. of Tech. Number 13, 1988.
77. Azzoni, C. B., Paleari, A., Scadina, F., Krejewski, A., Ravaglioli, A. & Meschke, F., EPR structural study on hydrothermally aged yttria-doped tetragonal zirconia polycrystals. *J. Mat. Sci.*, **28**[14] (1993) 3951–6.
78. Kruse, O., Carstanjen, H. D., Kountouros, P. W., Schubert, H. & Petzow, G., Characterization of H_2O-aged TZP by elastic recoil detection analysis (ERDA). In *Zirconia V*, eds S. P. S. Badwal, M. J. Bannister & R. H. J. Hannink, Technomic Publishing Co. Ltd., 1993, pp. 163–70.
79. Boutz, M. M. R., Nanostructured, tetragonal zirconia ceramics: microstructure, sinter forging and superplasticity. Ph.D. Thesis, University of Twente, Enschede, The Netherlands, 1993.
80. Hughes, A. E., Ciacchi, F. T. & Badwal, S. P. S., Degradation of Y-TZP in moist environments. In *Zirconia V*, eda S. P. S. Badwal, M. J. Bannister & R. H. J. Hannink, Technomic Publishing Co. Ltd., 1993, pp. 152–62.
81. Hernandez, M. T., Jurado, J. R., Duran, P. & Fierro, J. L. G., Subeutectoid degradation of yttria stabilized tetragonal zirconia polycrystal and ceria-doped yttria-stabilized tetragonal zirconia polycrystal ceramics. *J. Am. Ceram. Soc.*, **74**[6] (1991) 1254–8.
82. Matsui, M., Soma, T. & Oda, I., Stress-induced transformation and plastic deformation for Y_2O_3-containing tetragonal zirconia polycrystals. *J. Am. Ceram. Soc.*, **69**[3] (1986) 198–202.
83. Matsui, M., Masuda, M., Soma, T. & Oda, I., Thermal stability and microstructure of Y-TZP. In *Advances in Ceramics, Vol 24, Science and Technology of Zirconia III.*, eds S. Somiya, N. Yamamoto & H. Yanagida, The American Ceramic Society, Inc., Columbus, Ohio, 1988, pp. 607–14.
84. Larsen, D. C. & Adams, J. W., Long-term stability and properties of zirconia ceramics for heavy duty diesel engine components. DOE/NASA/0305-1, NASA, CR-174943.
85. Shimada, M., Matsushita, K, Kuratani, S., Okamoto, T., Tsukuma, K. & Tsukidate, T., Temperature dependence of Young's modulus and internal friction in alumina, silicon nitride, and partially stabilized zirconia ceramics. *J. Am. Ceram. Soc.*, **67**[2] (1984) c-23–4.
86. Weller, M. & Schubert, H., Internal friction, dielectric loss, and ionic conductivity of tetragonal ZrO_2–3%Y_2O_3 (Y-TZP). *J. Am. Ceram. Soc.*, **69**[7] (1986) 573–7.
87. Ono, T., Nurishi, Y., Hashiba, M. & Tanahashi, K., Temperature dependence of internal friction in Al_2O_3–3Y–ZrO_2 composites. *J. Mat. Sci. Lett.*, **8**[5] (1989) 569–70.
88. Nishiyama, K., Yamanaka, M., Omori, M. & Umekawa, S. High-temperature dependence of the internal friction and modulus change of tetragonal ZrO_2, Si_3N_4 and SiC. *J. Mat. Sci. Lett.*, **9**[5] (1990) 526–8.
89. Watanabe, M. & Iio, S., Effect of environmental gas on tetragonal-to-monoclinic transformations in Y-TZP. In *Sintering '87*, Vol. 2, eds S. Somiya, M. Shimada, M. Yoshimura & R. Watanabe, Elsevier Applied Science, UK, 1987, pp. 1162–6.
90. Claussen, N., Microstructural design of zirconia-toughened ceramics (ZTA). In *Advances in Ceramics Vol. 12, Science and Technology of Zirconia II*, eds N. Claussen, M. Ruhle & A. H. Heuer, The American Ceramic Society, Inc., Columbus, Ohio, 1984, pp. 325.
91. Lenz, L. K. & Heuer, A. H., Stress-induced transformation during subcritical crack growth in partially stabilized zirconia. *J. Am. Ceram. Soc.*, **65**[11] (1982) c-192–4.
92. Heuer, A. H., Claussen, N., Kriven, W. M. & Ruhle, M., Stability of tetragonal ZrO_2 particles in ceramic matrices. *J. Am. Ceram. Soc.*, **65**[12] (1982) 642–50.
93. Lange, F. F., Transformation toughening, Part 1, Size effects associated with the thermodynamics of constrained transformation. *J. Mat. Sci.*, **17**[1] (1982) 225–34.
94. Sato, T. & Shimada, M., Control of the tetragonal-to-monoclinic phase transformation of yttria partially stabilized zirconia in hot water. *J. Mat. Sci.*, **20**[11] (1985) 3988–92.
95. Sato, T., Ohtaki, S., Endo, T. & Shimada, S. Improvement of thermal stability of yttria-doped tetragonal zirconia polycrystals by alloying with various oxides. *Int. J. High Tech. Ceram.*, **2** (1986) 167–77.
96. Sato, T., Ohtaki, S., Endo, T. & Shimada, M., Improvement to the thermal stability of yttria-doped tetragonal zirconia polycrystals by alloying with various oxides. In *Advances in Ceramics, Vol 24, Science and Technology of Zirconia III.*, eds S. Somiya, N. Yamamoto & H. Yanagida, The American Ceramic Society, Inc., Columbus, Ohio, 1988, pp. 29–38.
97. Duh, J. G. & Wu, Y. S., Ageing behaviour in Y_2O_3–CeO_2–ZrO_2 ceramics. *J. Mat. Sci. Lett.*, **10**[17] (1991) 1003–6.
98. Hirano, M. & Inada, H., Preparation, sintering, microstructure, and thermal stability of Y_2O_3- and CeO_2-doped tetragonal zirconia ceramics. *Cer. Int.*, **17** (1991) 359–65.
99. Duh, J. G. & Wan, J. U., Developments in highly toughened CeO_2–Y_2O_3–ZrO_2 ceramic system. *J. Mat. Sci.*, **27**[22] (1992) 6197–203.
100. Hirano, M. & Inada, H., Hydrothermal stability of yttria- and ceria-doped tetragonal zirconia-alumina composites. *J. Mat. Sci.*, **26**[18] (1991) 5074–52.
101. Theunissen, G. S. A. M., Winnubst, A. J. A. & Burggraaf, A. J., Effect of dopants on the sintering behaviour and stability of tetragonal zirconia ceramics. *J. Eur. Ceram. Soc.*, **9** (1992) 251–63.
102. Boutz, M. M. R., Olde Scholtenhuis, R. J. M., Winnubst, A. J. A. & Burggraaf, A. J., Preparation, microstructural control and superplasticity of nanostructured yttria/ceria stabilized tetragonal zirconia ceramics. In *British Ceramic Proceedings. Vol. 51: Nanoceramics*, ed. R. Freer, Institute of Materials, 1993, pp. 75–86.
103. Theunissen, G. S. A. M., Microstructure, fracture toughness and strength of (ultra)fine-grained tetragonal zirconia ceramics. Ph.D. thesis, University of Twente, Enschede, The Netherlands. 1991.
104. Tsukuma, K. & Shimada, M., Thermal stability of Y_2O_3-partially stabilized zirconia (Y-PSZ) and Y-PSZ/Al_2O_3 composites. *J. Mat. Sci. Lett.*, **4**[7] (1985) 857–61.
105. Claussen, N. & Ruhle, M., Design of transformation-toughened ceramics. In *Advances in Ceramics, Vol. 3 Science and Technology of Zirconia*, eds A. H. Heuer & L. W. Hobbs, The American Ceramic Society, Inc., Columbus, Ohio, 1981, pp. 137–63.
106. Lange, F. F., Transformation toughening. Part 1: Size effects associated with the thermodynamics of constrained transformations. *J. Mat. Sci.*, **17**[1] (1983) 225–34.
107. Japanese Patent. NGK Spark Plug KK. *Zirconia implant*

material. JP 1040058 (WPI Acc. No. 89-089727/12). JP 87195349. 1987.
108. Hirano, M. & Inada, H., Stability under hydrothermal conditions and fracture strength of Y–TZP/spinel–alumina and Y–TZP/mullite-alumina composites. *Br. Ceram. Trans. J.*, **89**[6] (1990) 214–7.
109. Meschke, F., De Portu, G. & Claussen, N., Microstructure and thermal stability of fine-grained (Y.Mg)–PSZ ceramics with alumina additions. *J. Eur. Ceram. Soc.*, **11**[5] (1993) 481–6.
110. Lawson, S., Gill, H. C. & Dransfield, G. P., The effects of copper and iron oxide additions on the sintering and properties of Y–TZP, accepted for *J. Mat. Sci.*, 1995.
111. Iio, S., Watanabe, M., Kuroda, K., Saka, H. & Imura, T., Tetragonal-to-monoclinic transformation in Y–TZP during low-temperature ageing, and its restraint by coating. In *Advances in Ceramics, Vol 24, Science and Technology of Zirconia III.*, eds S. Somiya, N. Yamamoto & H. Yanagida, The American Ceramic Society, Inc., Columbus, Ohio, 1988, pp. 49–54.
112. Whalen, P. J., Reidinger, F. & Antrim, R. F., Prevention of low-temperature surface transformation by surface recrystallization in yttria-doped tetragonal zirconia. *J. Am. Ceram. Soc.*, **72**[2] (1989) 319–21.
113. Jue, J. F., Chen, J. & Virkar, A. V., Low-temperature ageing of *t'*-zirconia: the role of microstructure on phase stability. *J. Am. Ceram. Soc.*, **74**[8] (1991) 1811–20.
114. Lee, J. K. & Kim, H., Monoclinic-to-tetragonal transformation and crack healing by annealing in aged 2Y–TZP ceramics. *J. Mat. Sci. Lett.*, **12**[22] (1993) 1765–7.

Journal of the European Ceramic Society **15** (1995) 503–511
© 1995 Elsevier Science Limited
Printed in Great Britain. All rights reserved
0955-2219(95)00040-2
0955-2219/95/$9.50

Thermodynamic Assessment of the ZrO_2–$LaO_{1.5}$ System

Yong Du,* Masatomo Yashima, Toshiaki Koura, Masato Kakihana & Masahiro Yoshimura

Research Laboratory of Engineering Materials, Tokyo Institute of Technology, 4259 Nagatsuta, Midori-ku, Yokohama 226, Japan

(Received 2 June 1994; revised version received 7 February 1995; accepted 14 February 1995)

Abstract

Two optimal sets of thermodynamic functions for the ZrO_2–$LaO_{1.5}$ system are obtained by coupling the CALPHAD (CALculation of PHAse Diagrams) technique, the regularity between thermodynamic properties and crystal structure parameters within the family of rare earth oxides, and the Van't Hoff equation. The phases are modelled with the substitutional solution model (liquid, cubic, tetragonal, monoclinic, and hexagonal solid solutions), as the stoichiometric compounds ($Zr_{19}La_{42}O_{101}$, $Zr_2La_2O_7$), and with the sublattice model ($Zr_2La_2O_7$). Two optimizations are performed. In the first optimization, the $Zr_2La_2O_7$ phase is treated as a stoichiometric compound, while in the second one it is described by the Wagner–Schottky model. The eutectoid reaction, high-temperature hexagonal $LaO_{1.5}$ solid solution $\rightleftharpoons$ low-temperature hexagonal $LaO_{1.5}$ solid solution + $Zr_2La_2O_7$, is predicted from the calculation. The calculated phase diagrams and thermodynamic quantities agree well with the experimental data.

1 Introduction

It is well known that accurate thermodynamic information forms the basis of the CALPHAD method.[1–4] The current use of this method consists of evaluating a small number of thermodynamic parameters required to describe binary systems and synthesizing the description of a ternary system from the properties of its corresponding binary ones. The synthetic description for the ternary system can be used to evaluate existing experimental data and design experiments most efficiently. The same is true of going from ternary systems to a quaternary one and so on.

Recently the thermodynamic modelling of zirconia-bearing systems has received considerable attention[5–10] because of the difficulties[11,12] in constructing zirconia-based phase diagrams and thermodynamic properties by means of experimental methods, and the modelling has been justified by its ability to reproduce experimental data in binary systems and to predict experimental results in ternary systems with high certainty. It is interesting to notice that the calculated ZrO_2–$YO_{1.5}$–MgO phase diagrams[9] agree reasonably with most of the experimental data later published,[13,14] and the predicted ZrO_2–CaO–MgO and ZrO_2–$YO_{1.5}$–CaO phase diagrams[15,16] are in good agreement with the experimental data available. This means that the experimental work to measure zirconia ternary phase diagrams can be reduced significantly by using the CALPHAD method. In the case of experimentally well established zirconia binary systems, such as the ZrO_2–$YO_{1.5}$ and ZrO_2–CaO systems, consistent sets of thermodynamic parameters[17,18] can be obtained by only using the CALPHAD method. For most of the technologically important zirconia binary systems, however, experimental information is uncertain, scarce or lacking. Therefore, it is of great interest to optimize and/or estimate phase diagrams and thermodynamic properties in the less well established zirconia binary systems by the combined use of the CALPHAD technique and semiempirical estimation techniques. Similar work can be found for alloy systems, such as the work due to Guillermet and Frisk[19] and Klingbeil and Schmid-Fetzer.[20]

The present work is devoted to providing an optimal set of thermodynamic functions for the ZrO_2–$LaO_{1.5}$ system by coupling the CALPHAD method and semiempirical estimation techniques. This work is part of a research project aimed at developing a thermodynamic database for the ZrO_2–$REO_{1.5}$ (RE = Rare Earth)–CeO_2 systems, which is currently being carried out in our laboratory. The database is of great importance in the production and application of zirconia-based ceramic materials.

*Permanent address: Department of Materials Science and Engineering, Central South University of Technology, Changsha, Hunan, 410083, People's Republic of China.

2 Evaluation of Experimental Data

To conserve space, the cubic, tetragonal, and monoclinic structures of ZrO_2 and the low-temperature hexagonal, high-temperature hexagonal and cubic forms[21] of $LaO_{1.5}$ are denoted c-ZrO_2, t-ZrO_2, m-ZrO_2, A-$LaO_{1.5}$, H-$LaO_{1.5}$ and X-$LaO_{1.5}$, respectively. The solid solution phases based on c-ZrO_2, t-ZrO_2, m-ZrO_2, A-$LaO_{1.5}$, H-$LaO_{1.5}$ and X-$LaO_{1.5}$ are designated as C_{SS}, T_{SS}, M_{SS}, A_{SS}, H_{SS} and X_{SS}, respectively. All temperatures quoted in the present work have been converted into the international temperature scale of 1990.[22]

The liquidus for the ZrO_2–$LaO_{1.5}$ system has been measured by three groups of researchers.[23–25] The most detailed and accurate one is by Rouanet.[25] Except for one liquidus temperature at 38 mol% $LaO_{1.5}$ reported by Wartenberg and Eckhardt,[23] all of the liquidus data points published by them and Rouanet[25] are incorporated in the optimization. The qualitative liquidus data points given by Lin and Yu[24] cannot be used in the optimization.

Since Lefevre *et al.*[26] observed that the pyrochlore-type compound P ($Zr_2La_2O_7$) shows a homogeneity range, a few authors[27–30] have measured its range in a wide temperature range. However, the reported data show large scatter. All of the experimental values[26–30] were nevertheless retained in the optimization, since none of them alone can describe the homogeneity range satisfactorily. In addition to P, Rouanet[25,31] introduced another compound, C_2 (cubic-type Tl_2O_3). Qualitatively narrow range for C_2 has been reported, but definitive ranges are not given. Consequently, this compound is treated as a stoichiometric one, and its stoichiometric composition is palced at 68·8 mol % $LaO_{1.5}$, the average value of the two data points reported by Rouanet.[25,31]

Six groups of authors[24,25,30–33] contributed to the measurement of the solid state phase equilibria. Using X-ray diffraction (XRD) techniques, Brown and Duwez[32] determined the phase relations at 1623 and 2023 K, and Zheng and West[30] reported the phase relation at 1773 K. Based on XRD results, Lin and Yu[24] constructed the equilibrium diagram in the wide range of temperature and composition. All of the experimental values published by the above authors[24,30,32] are qualitative and cannot be utilized in the optimization. However, these data have been used as the checkpoints in the present assessment. By means of thermal analysis and XRD methods, Rouanet[25,31] measured the solidus curve, phase transition temperatures, and invariant equilibria. In the present optimization, all of the solid state phase equilibrium data reported by Rouanet[31] are used. Since the solidus curve is an estimated one and the reducing condition might affect temperature measurements associated with phase transitions, as pointed out by Wilder,[34] these data are attached a low weight in the optimization. Recently, Bastide *et al.*[33] measured the phase relation in the ZrO_2-rich part below about 1623 K in detail. The invariant data[33] for the reaction $T_{SS} \rightleftharpoons C_{SS} + P$ are employed in the optimization.

Using a bomb calorimeter, Korneev *et al.*[35] determined the enthalpy of formation of P at 298 K relative to the elements. This datum is included in the optimization.

3 Thermodynamic Models

3.1 Pure oxides ZrO_2 and $LaO_{1.5}$

The Gibbs free energy function ${}^0G(T) = G(T) - H^{SER}$ (lattice stability) of a pure oxide is expressed by the following equation:

$$ {}^0G(T) = A + BT + CT\ln T + DT^2 + ET^{-1} + FT^7 + GT^{-9} \quad (1) $$

in which H^{SER} is the weighted molar enthalpy of the stable element reference (SER), the pure element in its stable state at 298 K, and T the absolute temperature. For ZrO_2 and $LaO_{1.5}$, H^{SER} are $H^{SER}_{Zr} + 2H^{SER}_{O}$ and $H^{SER}_{La} + 1{\cdot}5H^{SER}_{O}$, respectively. The last two terms in Eqn (1) are used only outside the range of stability,[36] the term FT^7 for a liquid below melting point and GT^{-9} for solid phases above melting point.

As mentioned in the preceding section, $LaO_{1.5}$ has three modifications, A-$LaO_{1.5}$, H-$LaO_{1.5}$, and X-$LaO_{1.5}$. Experimental thermodynamic data are available only for A-$LaO_{1.5}$. In the present work, the lattice stability of A-$LaO_{1.5}$ is evaluated by the weighted least squares method[37] applied to the heat capacity[38–40] and enthalpy increment data.[41–43] The entropy and enthalpy of formation of $LaO_{1.5}$ at 298 K are taken from the recent compilation.[44] Based on the experimental results reported in Refs 21 and 45, the transition temperatures of A-$LaO_{1.5}$ $\rightleftharpoons$ H-$LaO_{1.5}$ and H-$LaO_{1.5}$ $\rightleftharpoons$ X-$LaO_{1.5}$ transitions and the melting temperature are placed at 2314 K, 2384 K, and 2584 K, respectively. The heat capacities of H-$LaO_{1.5}$ and liquid $LaO_{1.5}$ evaluated by Dinsdale[46] are adopted in the present work, and that of X-$LaO_{1.5}$ is assumed to be the average value of them. The H-$LaO_{1.5}$ $\rightleftharpoons$ X-$LaO_{1.5}$ transition enthalpy is estimated to be 29992 J/(mol of cation) by applying the Van't Hoff equation to the annotated ZrO_2–$LaO_{1.5}$ phase diagram.[31] Lacking further information, the A-$LaO_{1.5}$ $\rightleftharpoons$ H-$LaO_{1.5}$ transition enthalpy is assumed to be the same as that of the H-$YO_{1.5}$ $\rightleftharpoons$ C-$YO_{1.5}$ transition.[16,47] Ferro *et al.*[48] have demonstrated that within the family of the rare earth elements plus Y and Sc

constitutional properties (phase diagrams, thermodynamic properties and crystal structures) change according to a simple and systematic pattern. Regular trends of properties of trivalent rare earth oxides, such as transition temperatures[31] and enthalpy of formation of rare earth zirconates,[35] have been reported. In the present work, the enthalpy of melting of $LaO_{1.5}$ is extrapolated by plotting the experimental enthalpies of melting for $YO_{1.5}$[16,47] and $PrO_{1.5}$[44] vs the cation radii.[49] Table 1 lists the lattice stabilities employed in the present assessment.

3.2 Solution phases

Yin and Argent[8] have mentioned that the defect structures in zirconia-based systems are complicated, and for some systems, such as the ZrO_2–CaO system, the defect structure changes from anion vacancies to cation interstitials as temperature increases. Several groups of authors[6,8–10] have shown that the simple substitutional solution model used for metal systems can describe the ZrO_2-based systems satisfactorily. When this model is used to describe solution phases in ZrO_2-bearing systems, it means that clusters, such as associates and neutral species, are not introduced in thermodynamic modelling, and cations and anions were in their simplest forms, such as Zr^{+4}, La^{+3}, O^{-2}. In accordance with the substitutional solution model, the Gibbs free energy of the liquid is expressed by an equation of the form:

$$G^{L}_{m}-H^{SER} = x^{0}G^{L}_{LaO_{1.5}} + (1-x)^{0}G^{L}_{ZrO_2} + RT [x \ln x + (1-x) \ln (1-x)] + x(1-x)[a_0 + b_0T + (a_1 + b_1T)(1-2x) + \ldots] \quad (2)$$

where x is the mole fraction of $LaO_{1.5}$, and R the gas constant. The remaining solution phases are defined in a fashion similar to Eqn (2).

In view of the narrow homogeneity range for C_2, this compound is treated as a stoichiometric one, and its Gibbs free energy is expressed relative to the constituent oxides by the following equation:

$$G^{C_2}_{0.312(ZrO_2)\,0.688(LaO_{1.5})} - H^{SER} = 0.688\,{}^{0}G^{C_2}_{LaO_{1.5}} + 0.312\,{}^{0}G^{C_2}_{ZrO_2} + A + BT \quad (3)$$

In the first optimization, P is also modelled as a stoichiometric compound. For P, the enthalpy of formation at 298 K has been measured.[35] This quantity is directly expressed by A of Eqn (3), if the reference states of ZrO_2 and $LaO_{1.5}$ correspond to the states to which the measured enthalpy of formation is referred. Therefore, it is preferable to choose m-ZrO_2 and A-$LaO_{1.5}$ as the reference states in the Gibbs free energy expression of P.

In the second optimization, the homogeneity range for P is considered. If it is assumed that the cations and anions were in their simplest forms, the two sublattices $(ZO,LO)_1(LO,ZO)_1$ described by the Wagner–Schottky formalism[50] could be used to model this compound. ZO and LO are the abbreviations of ZrO_2 and $LaO_{1.5}$, respectively. According to the Wagner–Schottky formalism, the Gibbs free energy of P is given by the following expression:

$$G - H^{SER} = 0.5\,{}^{0}G^{pyro}_{ZrO_2} + 0.5\,{}^{0}G^{pyro}_{LaO_{1.5}} + RT[0.5\{Y'_{Lo} \ln Y'_{Lo} + (1-Y'_{Lo}) \ln (1-Y'_{Lo})\} + 0.5\{Y''_{Lo} \ln Y''_{Lo} + (1-Y''_{Lo}) \ln (1-Y''_{Lo})\}] + G^{*} + G_{12}n_{12} + G_{21}n_{21} \quad (4)$$

Table 1. Summary of lattice stability parameters[a]

$G^{L\text{-}LaO_{1.5}} - H^{SER}_{La} - 1.5H^{SER}_{O}$
$298 < T < 2584 = -822856.8 + 304.7303T - 59.8354T \ln T - 0.0036025T^2 + 342279.5T^{-1} - 1.7315 \times 10^{-21}T^7$
$2584 < T < 6000 = -894331.4 + 638.1947T - 100T \ln T$

$G^{X\text{-}LaO_{1.5}} - H^{SER}_{La} - 1.5H^{SER}_{O}$
$298 < T < 2584 = -915282 + 567.7316T - 90T \ln T$
$2584 < T < 6000 = -943993.1 + 657.3025T - 100T \ln T + 1.474628 \times 10^{33}T^{-9}$

$G^{H\text{-}LaO_{1.5}} - H^{SER}_{La} - 1.5H^{SER}_{O}$
$298 < T < 2584 = -921434 + 492.5469T - 80T \ln T$
$2584 < T < 6000 = -978856.5 + 671.6888T - 100\,T \ln T + 2.949257 \times 10^{33}T^{-9}$

$G^{A\text{-}LaO_{1.5}} - H^{SER}_{La} - 1.5H^{SER}_{O}$
$298 < T < 2584 = -917924.2 + 343.0925T - 59.8354T \ln T - 0.0036025T^2 + 342279.5T^{-1}$
$2584 < T < 6000 = -1003606 + 682.3301T - 100T \ln T + 3.192479 \times 10^{33}T^{-9}$

$G^{t\text{-}LaO_{1.5}} - H^{SER}_{La} - 1.5H^{SER}_{O}$
$298 < T < 6000 = G^{l\text{-}LaO_{1.5}} - H^{SER}_{La} - 1.5H^{SER}_{O} - 35617.5 + 26.4625T$

$G^{m\text{-}LaO_{1.5}} - H^{SER}_{La} - 1.5H^{SER}_{O}$
$298 < T < 6000 = G^{l\text{-}LaO_{1.5}} - H^{SER}_{La} - 1.5H^{SER}_{O} - 14697.5 + 29.915T$

$G^{H\text{-}ZrO_2} - H^{SER}_{Zr} - 2H^{SER}_{O}$
$298 < T < 6000 = G^{L\text{-}ZrO_2} - H^{SER}_{Zr} - 2H^{SER}_{O} - 71547 + 28.188T$

[a]In J/(mol of cation); temperature (T) in kelvin. L is liquid, X is cubic $LaO_{1.5}$, H is high-temperature hexagonal $LaO_{1.5}$, A is low-temperature hexagonal $LaO_{1.5}$, t is tetragonal ZrO_2 and m is monoclinic ZrO_2. The stable lattice stabilities of ZrO_2 are taken from the recent evaluation by Du *et al.*[18] Lacking further information, it is assumed that the Gibbs free energy difference between L–ZrO_2 and H (A)-ZrO_2 is the same as that[6] of HfO_2.

in which ${}^0G^{pyro}_{ZrO_2}$ and ${}^0G^{pyro}_{LaO_{1.5}}$ are the Gibbs energies of ZrO_2 and $LaO_{1.5}$ in the pyrochlore structure, respectively. Y'_{LO} and Y''_{LO} are the site fractions of the species LO on the first and second sublattices, respectively. G^* is the Gibbs energy of formation of the ideal compound ($Zr_2La_2O_7$), and G_{21} and G_{12} are the Gibbs energies of formation of the fictitious compounds, ZO_1:ZO_1 and LO_1:LO_1, respectively. The colon indicates the end of first sublattice and the start of the second one. n_{ij} is the number of moles of species j on sublattice i.

4 Parameter Evaluation

For convenience, the first and second optimizations in which P is treated as a stoichiometric compound and modelled with the Wagner–Schottky formalism, are referred to as optimizations A and B, respectively. For both optimizations, the other experimental values input are the same.

The evaluation of the parameters is conducted by the program developed by Lukas *et al.*[2] For the liquid it is possible to adjust independently the coefficients a_0 and b_0 of Eqn (2), because the liquidus line has been measured accurately over the whole composition range. In the present work, it was found that the calculated liquidus lines introducing and without introducing b_0 nearly coincide. So in the final optimization, only a_0 was used. The terminal solid solutions C_{SS} and X_{SS} both are cubic[21] and are treated as the same phase in the thermodynamic modelling. The coefficients a and b of Eqn (2) for C_{SS}(X_{SS}) cannot be adjusted independently due to the less well established temperature dependence. To make the excess enthalpy of $LaO_{1.5}$-rich solid solution (X_{SS}) independent from that of ZrO_2-rich solid solution (C_{SS}), a_0 and a_1 need to be introduced. Since the experimental data associated with T_{SS}, H_{SS} and X_{SS} are limited and scatter, each of them is described by one regular parameter. In view of the low solubility of $LaO_{1.5}$ in m-ZrO_2 (0·9 mol % $LaO_{1.5}$ at 1373 K), M_{SS} was approximated as m-ZrO_2. For C_2, it is impossible to adjust A and B of Eqn (3) independently because its Gibbs energies are known only in a narrow temperature range. Since only one coefficient can be adjusted, the value of B was fixed to be 2·75 J/(mol of cation·K). When this value is converted into that corresponding to one mole atom, it is about 1 J/(mol of atom K), which is usually adopted in the assessment of metal systems.[51] In the case of P, the coefficients A and B can be adjusted in optimization A, since the enthalpy of formation and phase diagram data are available. For optimization B, the introduction of two coefficients for G^* and one coefficient for each of G_{12} and G_{21} gives a good compromise to the scatter homogeneity range. The thermodynamic parameters obtained in the present work are shown in Table 2 (optimization A) and Table 3 (optimization B).

5 Results and Discussion

In Fig. 1, the calculated heat capacity of A-$LaO_{1.5}$ is compared with the experimental values.[38–40] Except for the two data points[40] at 800 and 850 K, all of the other experimental values can be reproduced by the calculation within the estimated experimental errors. Basili *et al.*[40] gave a large uncertainty (5%) for their heat capacity data. The large uncertainty corresponds to a low weight in the weighted least squares method.[37] The comparison of the calculated enthalpy increment and the experimental points[41–43] for A-$LaO_{1.5}$ is presented in Fig. 2, which shows a very good agreement.

The estimated enthalpy of melting of $LaO_{1.5}$ is shown in Fig. 3 along with the experimental ones for $YO_{1.5}$[16,47] and $PrO_{1.5}$.[44] In Fig. 3(a), the crystal radius[49] is used, while in Fig. 3(b) the effective ionic radius[49] is utilized. As can be seen from the figures, the estimated enthalpies of melting of $LaO_{1.5}$ are nearly the same in spite of the use of a

Table 2. Optimized thermodynamic parameters for the ZrO_2–$LaO_{1.5}$ system from optimization A (P is modelled as a stoichiometric compound)[a]

Substitutional solution model (Eqn (2))

Phase	i	a_i	b_i	Phase	i	a_i	b_i
Liquid	0	−108326·1	0	C_{SS}(X_{SS})	0	−64239·9	0
T_{SS}	0	−97316·9	0		1	−4658·5	0
A_{SS}	0	−17923·1	0	H_{SS}	0	−52500·6	0

Stoichiometric model (Eqn (3))

Phase	A	B	Phase	A	B
[b]C_2	−83478·8	2·75	P	−54173·8	6·26749

[a] In J/(mol of cation). C_{SS} and T_{SS} are cubic and tetragonal ZrO_2 solid solutions, respectively. X_{SS}, H_{SS} and A_{SS} are the solid solutions based on cubic, high- and low-temperature hexagonal $LaO_{1.5}$, respectively. C_2 and P are $Zr_{19}La_{42}O_{101}$ and $Zr_2La_2O_7$, respectively.
[b] Lacking further information, the Gibbs energy differences for both ZrO_2 and $LaO_{1.5}$ in the cubic-type Tl_2O_3 are simply given a fixed large value (50000 J/(mol of cation)) compared to c-ZrO_2 and X-$LaO_{1.5}$.

Table 3. Optimized thermodynamic parameters for the ZrO_2–$LaO_{1.5}$ system from optimization B (P is modelled with the sublattice model)[a]

Substitutional solution model (Eqn (2))

Phase	i	a_i	b_i	Phase	i	a_i	b_i
Liquid	0	-92098·4	0	$C_{SS}(X_{SS})$	0	-46929·2	0
T_{SS}	0	-77847·9	0		1	-3387·7	0
H_{SS}	0	-34929·3	0				

Stoichiometric model (Eqn (3))

Phase	A	B
C_2	-80286	2·75

Sublattice model (Eqn (4))

Phase	G^*	G_{12}	G_{21}
[b]P	-35126·9 + 1·34452T	-102327	-101998

[a] In J/(mol of cation); Temperature (T) in kelvin. For abbreviations of the phases, see Table 2.
[b] Due to the lack of experimental information, the Gibbs energy differences for both ZrO_2 and $LaO_{1.5}$ in the pyrochlore structure are simply given a fixed large value (100000 J/(mol of cation)) compared to m-ZrO_2 and A-$LaO_{1.5}$.

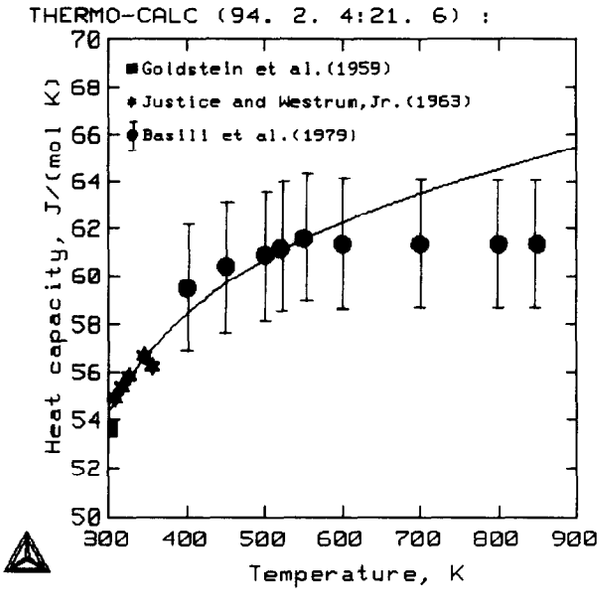


Fig. 1. Comparison of the calculated and measured[38-40] heat capacities of $LaO_{1.5}$.

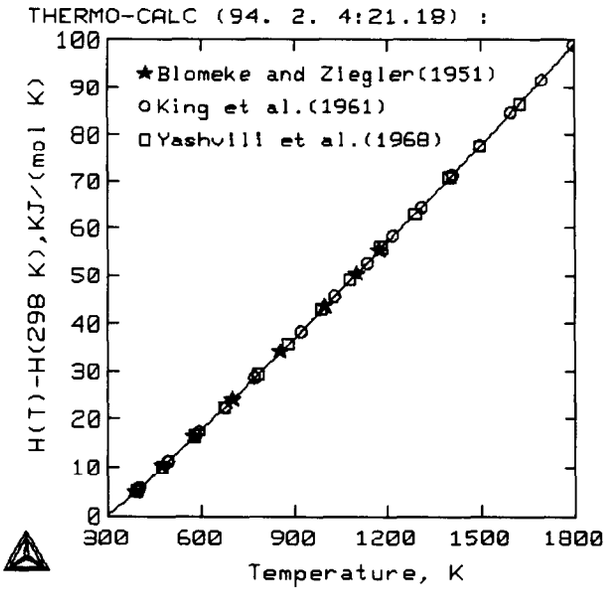
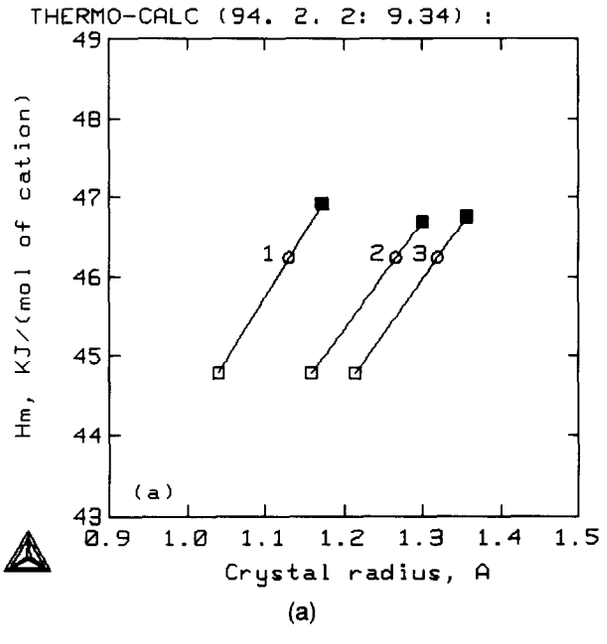


Fig. 2. Calculated enthalpy increment of $LaO_{1.5}$ with the experimental values.[41-43]



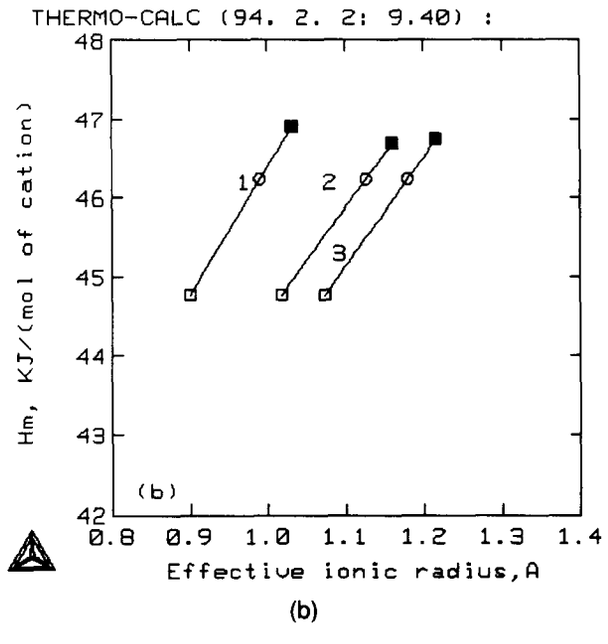


Fig. 3. Estimated enthalpy of melting of $LaO_{1.5}$ (■) along with the experimental enthalpies for $YO_{1.5}$ (□)[16,47] and $PrO_{1.5}$ (○).[44] Curves 1, 2, and 3 correspond to the coordination numbers 6, 8 and 11, respectively. (a) Enthalpy of melting is plotted vs crystal radius, and (b) enthalpy of melting is plotted vs effective ionic radius.

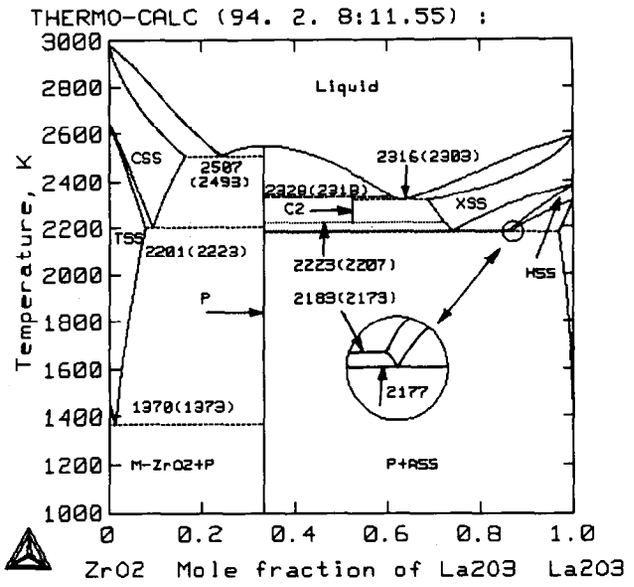


Fig. 4. Calculated ZrO_2–La_2O_3 phase diagram according to optimization A. The temperatures inside the parentheses are the experimental invariant temperatures,[31] and those outside the parentheses are the calculated ones.

different cation radius and a different coordination number. The average value (46790·7 J/(mol of cation)) of the six data points is taken to be the enthalpy of melting. The enthalpy of melting of $LaO_{1.5}$ calculated statistically from related phase diagrams, using the Van't Hoff equation, gives rise to the value of about 35000 J/(mol of cation), which is comparative with that assessed in the present work. Considering the large uncertainty (about 30%) associated with the Van't Hoff equation, the presently estimated value is preferable.

The presently calculated enthalpies of formation of P at 298 K from the elements are -1053187 J/(mol of cation) (optimization A) and -1036303 J/(mol of cation) (optimization B), which agree reasonably with the experimental one (-1020478 J/(mol of cation).[35]

The complete ZrO_2–La_2O_3 phase diagram based on optimization A is shown in Fig. 4. The eutectoid reaction, $H_{SS} \rightleftharpoons P + A_{SS}$, is a result of the calculation. No experimental information is available about this reaction. For the other invariant equilibria, the fit to the experimental data[31] is very good within the estimated errors.

In Fig. 5, the calculated ZrO_2–La_2O_3 phase diagram resulting from optimization A is compared with all of the experimental data available. Except for the homogeneity data for P, most of the other experimental data can be described by the calculation. In particular, the quantitative experimental values[23,25,31,33] are well reproduced. The calculated solidus line in ZrO_2-rich part is a little lower than the estimated one.[31] The present calculation demonstrated that the qualitative liquidus and solidus curves given by Lin and Yu[24] are probably low. Lin and Yu reported the melting temperature of $LaO_{1.5}$ to be 2533 K, which is lower by 51 K than the generally accepted one (2584 K).

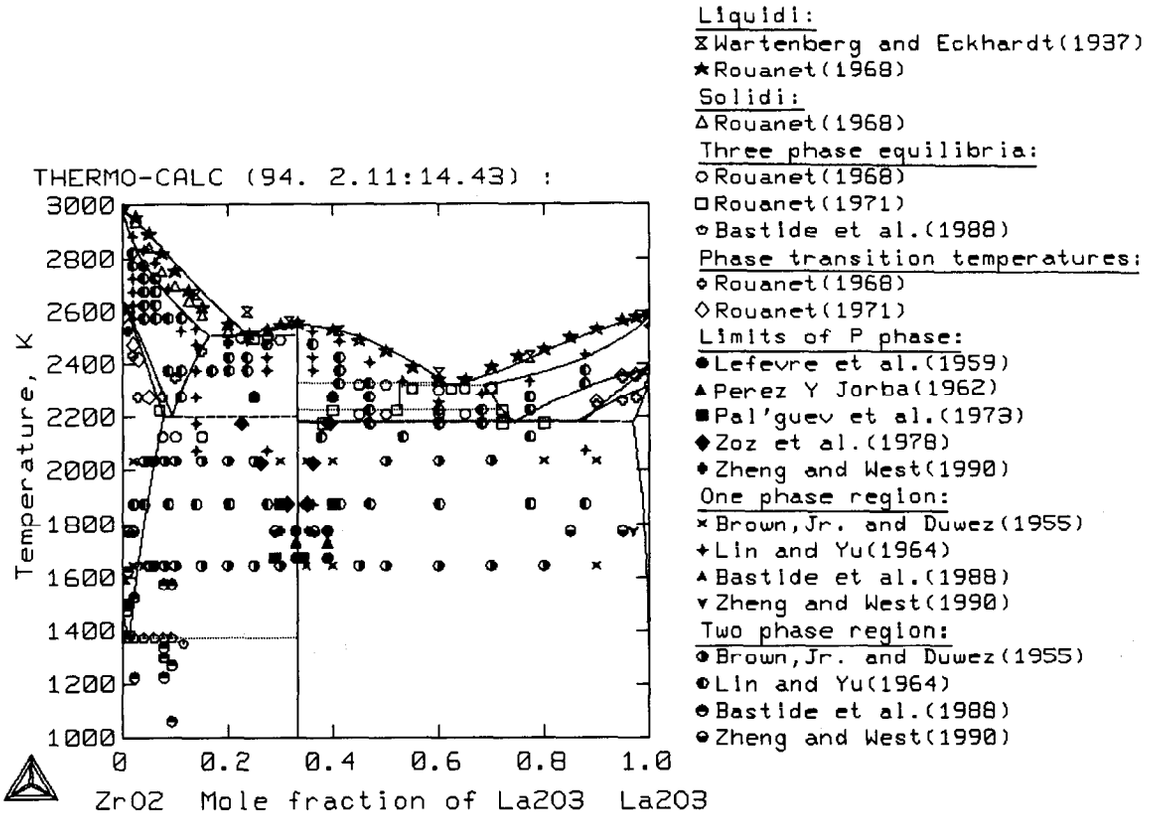


Fig. 5. Calculated ZrO_2–La_2O_3 phase diagram with the experimental phase diagram data. $Zr_2La_2O_7$ is treated as a stoichiometric compound (optimization A).

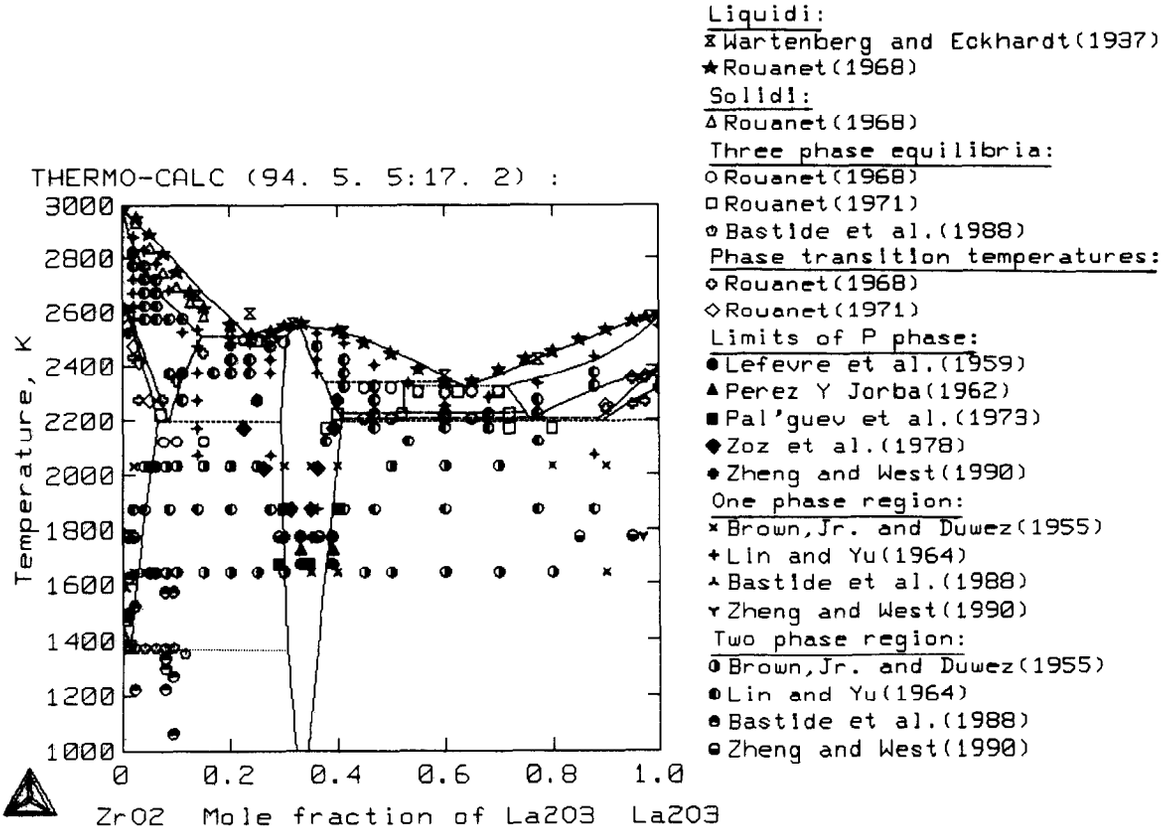


Fig. 6. Calculated ZrO_2–La_2O_3 phase diagram with the experimental phase diagram data. $Zr_2La_2O_7$ is modelled with the sublattice model (optimization B).

The computed ZrO_2–La_2O_3 phase diagram according to optimization B is presented in Fig. 6, which demonstrates an excellent fit to the quantitative experimental data[21,25,31,33] The calculated homogeneity range for P is a good compromise to the available data.[26–30] As mentioned in Section 2, the experimental data for the range of P show large scatter. The calculated limit toward La_2O_3 is located approximately at a curve between the curve reported by Lefevre *et al.*,[26] Perez Y Jorba[27] and Pal'guev *et al.*[28] and the one determined by Zoz *et al.*[29] and Zheng and West.[30] In the case of the limit toward ZrO_2, the computed limit agrees reasonably with the results from Pal'guev *et al.*,[28] Zheng and West,[30] and the datum at 1873 K published by Zoz *et al.*[29] The experimental result given by Lefevre *et al.*[26] and Perez Y Jorba[27] is higher by about 3 mol% La_2O_3 than the calculated one. In contrast, the experimental data at 2023 K and 2173 K given by Zoz *et al.*[29] are lower by about 5 mol% La_2O_3 than the computed one. Better knowledge on the homogeneity range of P is useful for further refinement of the ZrO_2–$LaO_{1.5}$ system. In the case of optimization B, it is found that the calculated solubility of ZrO_2 in $LaO_{1.5}$ is significantly lower than one quantitative datum published by Zheng and West.[30] An attempt to improve the agreement with this datum results in worse agreement with the phase transition temperatures and homogeneity range of P. In consequence, A_{SS} is approximated as A-$LaO_{1.5}$ in the final optimization. In the present work, an attempt to model P with the substitutional solution model was not successful: the calculated homogeneity range deviates significantly from the experimental data.[26–30] This implies the inapplicability of the substitutional solution model to describe P. The substitutional solution model corresponds to the random mixing of two species (ZrO_2, $LaO_{1.5}$) in one sublattice. This is not the case for $Zr_2La_2O_7$. The present work demonstrates that two sublattice model can be used to describe this compound.

The thermodynamic description of the ZrO_2–$LaO_{1.5}$ system obtained in the present work has been combined with the thermodynamic parameters for the ZrO_2–CeO_2[52] and CeO_2–$LaO_{1.5}$ systems to predict the ZrO_2–CeO_2–$LaO_{1.5}$ ternary phase diagrams, which are in reasonable agreement with the experimental data available.

6 Summary

All the phase diagram and thermodynamic data available for the ZrO_2–$LaO_{1.5}$ system have been considered in the present assessment. An attempt has been made to provide the consistent set of thermodynamic parameters describing the system

by coupling CALPHAD method and semiempirical estimation techniques. Two sets of thermodynamic functions have been obtained in the present work. The first one is for a simplified version of the ZrO_2–$LaO_{1.5}$ phase diagram in which $Zr_2La_2O_7$ is treated as a stoichiometric compound. The second one corresponds to the treatment in which $Zr_2La_2O_7$ is modelled with the sublattice model. Comprehensive comparisons with the experimental data available are made, and it is shown that the first parameter set can satisfactorily account for most of the experimental data except for the homogeneity data of $Zr_2La_2O_7$, and the second parameter set gives a good fit to all types of data for the ZrO_2–$LaO_{1.5}$ system except for one solubility datum of ZrO_2 in $LaO_{1.5}$.

Acknowledgements

The use of the program from Dr H. L. Lukas is gratefully acknowledged. One of the authors (Yong Du) is grateful to Professor M. Yoshimura for his nomination to the 29th International Course in Chemistry and Chemical Engineering and to Professors P. Y. Huang, Z. P. Jin and B. Y. Huang for their recommendations to the Course. Partial support from Iketani Science and Technology Foundation are also acknowledged.

References

1. Kaufman, L. & Bernstein, H., *Computer Calculation of Phase Diagrams.*, Academic Press, New York, 1970.
2. Lukas, H. L., Henig, E. -Th. & Zimmermann, B., Optimization of phase diagrams by a least squares method using simultaneously different types of data. *CALPHAD: Comput. Coupling Phase Diagrams Thermochem.*, **1** (1977) 225–36.
3. Pelton, A. D., Computer coupling of phase diagrams and thermodynamics. *Ber. Bunsenges. Phys. Chem.*, **87** (1983) 183–8.
4. Sundman, B., Jansson, B. & Andersson, J. -O., The Thermo Calc databank system. *CALPHAD: Comput. Coupling Phase Diagrams Thermochem.*, **9** (1985) 153–90.
5. Yoshimura, M., Tani, E. & Somiya, S., The confirmation of phase equilibria in the system ZrO_2–CeO_2 below 1400°C. *Solid State Ionics*, **3/4** (1981) 477–81.
6. Kaufman, L., Calculation of multicomponent ceramic phase diagrams. *Physica B+C: (Amsterdam)*, **150** (1988) 99–114.
7. Wu, P., Eriksson, G. & Pelton, A. D., Optimization of the thermodynamic properties and phase diagrams of the Na_2O–SiO_2 and K_2O-SiO_2 systems. *J. Am. Ceram. Soc.*, **76** (1993) 2059–64.
8. Yin, Y. & Argent, B. B., Phase diagrams and thermodynamics of the systems ZrO_2–CaO and ZrO_2–MgO. *J. Phase Equilibria*, **14** (1993) 439–50.
9. Du, Y., Jin, Z. P. & Huang, P. Y., Thermodynamic calculation of the ZrO_2–$YO_{1.5}$–MgO system. *J. Am. Ceram. Soc.*, **74** (1991) 2107–12.
10. Yokokawa, H., Sakai, N., Kawada, T. & Dokiya, M., Phase diagram calculations for ZrO_2 based ceramics: thermodynamic regularities in zirconate formation and solubilities of transition metal oxides. In *Science and Technology of Zirconia V*, ed. S. P. S. Badwal, M. J. Bannister & R. H. J. Hannink. Technomic Publishing Company, Inc., Lancaster, PA 17604, USA, 1993, pp. 59–68.
11. Stubican, V. S. & Hellmann, J. R., Phase equilibria in some zirconia systems. In *Science and Technology of Zirconia*, ed. A. H. Heuer & L. W. Hobbs. American Ceramic Society, Columbus, OH, USA, 1981, pp. 25–37.
12. Yoshimura, M., Phase stability of zirconia. *Am. Ceram. Soc. Bull.*, **67** (1988) 1950–5.
13. Lopato, L. M., Gerasimyuk, G. I., Shevchenko, A. V. & Karpenko, Yu. M., Interaction in the zirconia–yttria–magnesia system. *Izv. Akad. Nauk SSSR, Neorg. Mater.*, **27** (1991) 992–5.
14. Shevchenko, A. V., Lopato, L. M., Karpenko, Yu. M., Gerasimyuk, G. I. & Ruban, A. K., Liquidus surface and polythermal crossections of the zirconia–yttria–magnesia system. *Izv. Akad. Nauk SSSR, Neorg. Mater.*, **27** (1991) 996–1000.
15. Du, Y., Jin, Z. P. & Huang, P. Y., Calculation of the ZrO_2–CaO–MgO phase diagram. *CALPHAD: Comput. Coupling Phase Diagrams Thermochem.*, **16** (1992) 221–30.
16. Jin, Z. P. & Du, Y., Thermodynamic calculation of the ZrO_2–$YO_{1.5}$–CaO phase diagram. *CALPHAD: Comput. Coupling Phase Diagrams Thermochem.*, **16** (1992) 355–62.
17. Du, Y., Jin, Z. P. & Huang, P. Y., Thermodynamic assessment of the ZrO_2–$YO_{1.5}$ system. *J Am. Ceram. Soc.*, **74** (1991) 1569–77.
18. Du, Y., Jin, Z. P. & Huang, P. Y., Thermodynamic calculation of the zirconia–calcia system. *J. Am. Ceram. Soc.*, **75** (1992) 3040–8.
19. Guillermet, A. F. & Frisk, K., Thermodynamic properties of Ni nitrides and phase stability in the Ni–N system. *Int. J. Thermophys.*, **12** (1991) 417–31.
20. Klingbeil, J. & Schmid-Fetzer, R., Terquat: approximate prediction of ternary and quaternary phase diagrams comprising stoichiometric phases. *J. Phase Equilibria*, **13** (1992) 522–31.
21. Foex, M. & Traverse, J. P., Remarques sur les transformations cristallines présentées a haute température par les sesquioxydes de terres rares. *Rev. Int. Hautes Temp. Refract.*, **3** (1966) 429–53.
22. Thomas, H. P., The international temperature scale of 1990 (ITS-90). *Metrologia*, **27** (1990) 3–10.
23. Wartenberg, H. V. & Eckhardt, K., Schmelzdiagramme hochstfeuerfester oxyde. VIII. Systeme mit CeO_2. *Z. Anorg. Allgem. Chem.*, **232** (1937) 179–87.
24. Lin, T. H. & Yu, H. C., Phase equilibria of systems Ln_2O_3 (Rare Earth Oxides) –ZrO_2. I. phase equilibria of the binary system La_2O_3–ZrO_2. *J. Chin. Ceram. Soc.*, **3** (1964) 159–66 (in Chinese).
25. Rouanet, A., Étude de la refractairité et de la structure des phases de haute température présentées par le système zircone–oxyde de lanthane. *C. R. Acad. Sci., Paris, Ser. C*, **267** (1968) 395–7.
26. Lefevre, J., Perez Y Jorba, M. & Collongues, R., Sur les diagrammes d'équilibre zircone–oxydes de terres rares. *Bull. Soc. Chim. France*, **5** (1959) 1969–71.
27. Perez Y Jorba, M., Contribution a l'étude des systèmes zircone–oxydes de terres rares. *Ann. Chim.*, **7** (1962) 479–51.
28. Pal'guev, S. F., Fomina, L. N. & Strekalovskii, V. N., Thermal X-ray diffraction study of the reaction of zirconium dioxide and lanthanum oxide in the region of ccurrence of $La_2Zr_2O_7$. *Tr. Inst. Elektrokhim., Ural. Nauchn. Tsentr. Akad. Nauk SSSR*, **19** (1973) 120–7.
29. Zoz, E. I., Gavrish, A. M. & Gul'ko, N. V., Phase formation in the zirconium oxide (hafnium oxide)–lanthanum oxide systems. *Izv. Akad. Nauk SSSR, Neorg. Mater.*, **14** (1978) 109–11.
30. Zheng, C. & West, A. R., Phase equilibria and electrical properties in the system ZrO_2–La_2O_3–Nd_2O_5. *Br. Ceram. Trans. J.*, **89** (1990) 138–41.

31. Rouanet, A., Contribution a l'étude des systèmes zircone–oxydes des lanthanides au voisinage de la fusion. *Rev. Int. Hautes Temp. Réfract.*, **8** (1971) 161–80.
32. Brown, F. H. Jr. & Duwez, P., The systems zirconia–lanthana and zirconia–neodymia. *J. Am. Ceram. Soc.*, **38** (1955) 95–101.
33. Bastide, B., Odier, P. & Coutures, J. P., Phase equilibrium and martensitic transformation in lanthana-doped zirconia. *J. Am. Ceram. Soc.*, **71** (1988) 449–53.
34. Wilder, D. R., The La_2O_3–ZrO_2 system. In *Phase Diagrams for Ceramists*, Vol. IV, ed. R. S. Roth, T. Negas & L. P. Cook. American Ceramic Society, Columbus, OH, USA, 1981, pp. 133.
35. Korneev, V. R., Glushkova, V. B. & Keler, E. K., Heats of formation of rare earth zirconates. *Izv. Akad. Nauk SSSR, Neorg. Mater.*, **7** (1971) 886–7.
36. Andersson, J. -O., Guillermet, A. F., Gustafson, P., Hillert, M., Jansson, B., Jonsson, B., Sundman, B. & Ågren, J., A new method of describing lattice stabilities. *CALPHAD: Comput. Coupling Phase Diagrams Thermochem.*, **11** (1987) 93–8.
37. Du, Y., Investigation of the ZrO_2–$YO_{1.5}$–CaO–MgO and Co–Ni–Ti phase diagrams. PhD thesis, Central South University of Technology, China, 1992.
38. Gldstein, H. W., Nellson, E. F., Walsh, P. N. & White, D., The heat capacities of yttrium oxide (Y_2O_3), lanthanum oxide (La_2O_3) and neodymium oxide (Nd_2O_3) from 16 to 300 K. *J. Phys. Chem.*, **63** (1959) 1445–9.
39. Justice, B. H. & Westrum, E. F. Jr, Thermophysical properties of the lanthanide oxides. I. Heat capacities, thermodynamic properties, and some energy levels of lanthanum (III) and neodymium (III) oxides from 50 to 350 K. *J. Phys. Chem.*, **67** (1963) 339–45.
40. Basili, R., Sharkawy, A. E. & Atalla, S., Experimental determination of the thermal properties of Nb_2O_5, La_2O_3 and Ce_2O_3 in the temperature range 400–1000 K. *Rev. Int. Hautes Temp. Refract.*, **16** (1979) 331–8.
41. Blomeke, J. O. & Ziegler, W. T., The heat content, specific heat and entropy of La_2O_3, Pr_6O_{11} and Nd_2O_3 between 30 and 900°C. *J. Am. Chem. Soc.*, **73** (1951) 5099–102.
42. King, E. G., Weller, W. W. & Pankratz, L. B., Thermodynamic data for lanthanum sesquioxide. U. S. Bur. Mines, Rept. Invest. No. 5857, 1961, 6. pp.
43. Yashvili, T. S., Tsagareishvili, D. Sh. & Gvelesiani, G. G., Enthalpy and specific heat of the sesquioxides of lanthanum and lutecium at high temperatures. *Teplofiz. Vys. Temp.*, **6** (1968) 817–20.
44. Knacke, O., Kubaschewski, O. & Hesselmarm, K., *Thermochemical Properties of Inorganic Substances*. Springer-Verlag, Berlin, 1991.
45. Shevchenko, A. V. & Lopato, L. M., TA method application to the highest refractory oxide systems investigation. *Thermochimica Acta*, **93** (1985) 537–40.
46. Dinsdale, A., OXUNARY databank, National Physical Laboratory, Teddington, U. K., 1993.
47. Shpil'rain, E. E., Kagan, D. N., Barkhatov, L. S. & Koroleva, V. V., Measurement of the enthalpy of solid and liquid phases of yttria. *High Temp.–High Pressures*, **8** (1976) 183–6.
48. Ferro, R., Delfino, S., Borzone, G., Saccone, A. & Cacciamani, G., Contribution to the evaluation of rare earth alloy systems. *J. Phase Equilibria*, **14** (1993) 273–9.
49. Shannon, R. D., Revised effective ionic radii and systematic studies of interatomic distances in halides and chalcogenides. *Acta Crystallogr., Sect. A*, **32** (1976) 751–67.
50. Wagner, C., *Thermodynamics of Alloys.*, Addison-Wesley Press, Inc., Cambridge, Mass., USA, 1952.
51. Agarwal, R., Fries, S. G., Lukas, H. L., Petzow, G., Sommer, F., Chart, T. G. & Effenberg, G., Assessment of the Mg–Zn system. *Z. Metallkde.*, **83** (1992) 216–23.
52. Du, Y., Yashima, M., Koura, T., Kakihana, M. & Yoshimura, M., Thermodynamic evaluation of the ZrO_2–CeO_2 system. *Scripta Metall. Mater.*, **31** (1994) 327–32.

Journal of the European Ceramic Society **15** (1995) 513–520
© 1995 Elsevier Science Limited
Printed in Great Britain. All rights reserved
0955-2219/95/$9.50

0955-2219(95)00017-8

Creep Properties of Single Crystal Oxides Evaluated by a Larson–Miller Procedure

Shiqiang Deng* & Richard Warren

Department of Materials Science and Production Technology, Luleå University, S-971 87 Luleå, Sweden

(Received 1 June 1994; revised version received 22 September 1994; accepted 26 January 1995)

Abstract

A collation of published results of compressive and tensile creep studies of single and binary oxide single crystals is presented. For the purposes of comparison the results were normalised by means of a Larson–Miller procedure. This method proved to be effective in providing a ranking of the oxides in terms of their creep resistance. Binary oxides with complex crystal structures exhibited the highest creep strengths; no direct correlation with the melting point could be found.

1 Introduction

Composites consisting of an oxide matrix reinforced with continuous oxide fibres are beginning to attract attention in the search for materials capable of withstanding higher temperatures than currently available materials. Thus, many oxides can provide the oxidation-resistance, high melting point and low density that are essential for high temperature aerospace applications. On the other hand, polycrystalline ceramic oxides do not exhibit adequate creep-resistance and high temperature strength. However, several studies have shown that certain single crystal oxides may be capable of providing good creep-resistance and strength; presumably because they lack grain boundaries which are a source of weakness at high temperatures.

Many isolated studies have been made of the creep behaviour of various single crystal oxides, but as far as the present authors are aware, no attempt has been made to carry out an exhaustive, systematic compilation of these. The purpose of the present work was to gather creep data from the many sources for both single and binary oxides in order to assess their relative creep resistance. A direct comparison of creep results from different sources is usually not straightforward since they have usually been obtained under different test conditions, for example, with different combinations of temperature and stress. Moreover, for oxides exhibiting large differences in creep resistance, the position of the stress–temperature regimes employed can vary significantly. To make a meaningful comparison of creep resistance in these cases, the creep data was evaluated here on the basis of a Larson–Miller normalisation procedure[1] as will be outlined in the next section.

Studies of the creep of single crystal oxides have been reported for both compressive and tensile loading and these are treated separately in this paper.

2 Larson–Miller Procedure for Creep Data Evaluation

The basis of the Larson–Miller treatment is that the creep process can be considered to be thermally activated and consequently for a given applied stress the creep rate is described by an Arrhenius-type expression of the form:

$$\dot{\epsilon}_s = A\exp(-Q/RT) \tag{1}$$

where $\dot{\epsilon}_s$ is the steady state creep rate, Q is the activation energy for the creep process, T is the absolute temperature in Kelvin, R is the gas constant and A is a constant. Equation (1) can also be written as

$$Q/R = T(\ln A - \ln \dot{\epsilon}_s) \tag{2}$$

Introducing the concept of a creep life, t_S, defined as the time taken for the steady state creep rate to yield a given arbitrary strain, ϵ_x:

$$t_s = \epsilon_x/\dot{\epsilon}_s \tag{3}$$

Equation (2) can then be written:

$$L = Q/R = T(C + \log t_s) \tag{4}$$

*Permanent address: Third Department, Central Iron and Steel Research Institute, 100081 Beijing, China.

where L is the so-called Larson–Miller parameter and C is a constant. Assuming Q to be independent of temperature, the value of L at a given stress for a given material is considered to be constant, which implies that there is a fixed relationship between T and t_S. Moreover it is generally found that L is inversely proportional to log σ, the applied stress. Thus, L values derived from creep experiments carried out at different combinations of stress and temperature can be plotted against log σ to yield a single straight line. Creep data appropriate to other combinations of stress–temperature–lifetime can then be predicted from the Larson–Miller plot by interpolation or extrapolation. For example, in the present work, the Larson–Miller plots were used to derive a 'creep strength' defined as the stress required at 1600°C to produce a strain, ϵ_x, of 10^{-5} in a time, t_S, of 10^4 s, (i.e. $\dot{\epsilon}_s = 10^{-9}$).

The derived relationship between σ, t_S and T is relatively insensitive to the value of the constant C and it is often set at a fixed value when considering a group of related materials. However, in this work, whenever sufficient experimental data was available, an individual value of C was determined for each oxide, being extracted from a plot of log t_S versus $1/T$ on the basis of a rearrangement of eqn (4):

$$\log t_s = -C + \text{constant}/T \qquad (5)$$

In the present Larson–Miller treatment of published data, values of strain rate corresponding to a steady state were sought, care being taken to avoid values corresponding to primary stages of creep. The values were taken either as reported explicitly or estimated from the published creep curves.

3 Results

Representative plots of log t_S versus $1/T$ used to derive C values are shown in Figs 1 and 2 for ThO_2 and Al_2O_3 single crystals. Several Larson–Miller plots for different oxides are presented in Figs 3–7. Derived C values and values of creep strength together with test details and source references are collected in Tables 1 and 2 for compressive and tensile loading respectively.

It was found that the log t_S versus $1/T$ plots for a given oxide and crystal orientation at different stresses yielded C values with relatively small variations as can be seen from Figs 1 and 2; in these cases average values were used. In some instances small differences in slope were observed (Fig. 2) indicating a variation in the activation energy, Q. This effect was neglected and again an average value of C was used.

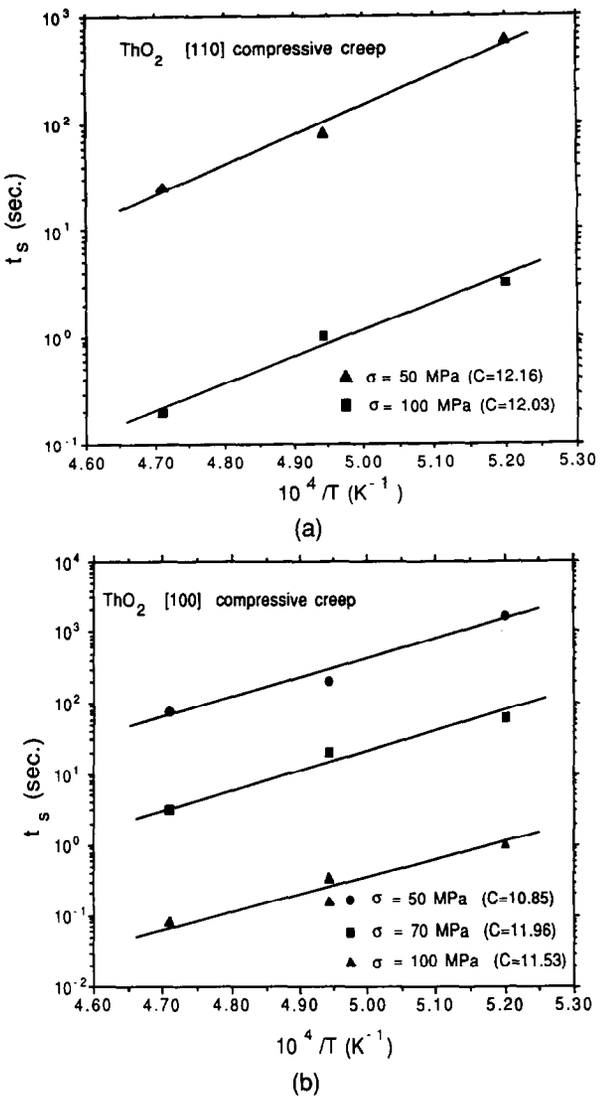


Fig. 1. Plot of log(t_s) versus ($1/T$) of ThO_2 single crystal: (a) [110]; (b) [100].

Figures 3–7 show L values derived from the stated C values using eqn (4) plotted versus the corresponding values of logarithm of applied stress. Linear regression was used to construct the

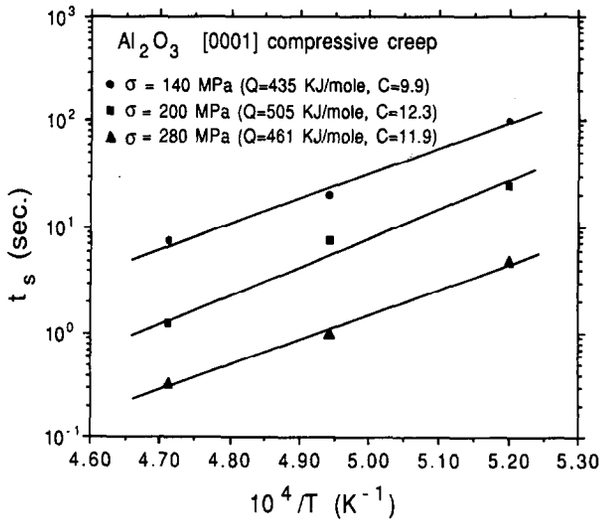


Fig. 2. Log(t_s) versus ($1/T$) of sapphire single crystal for compressive creep.

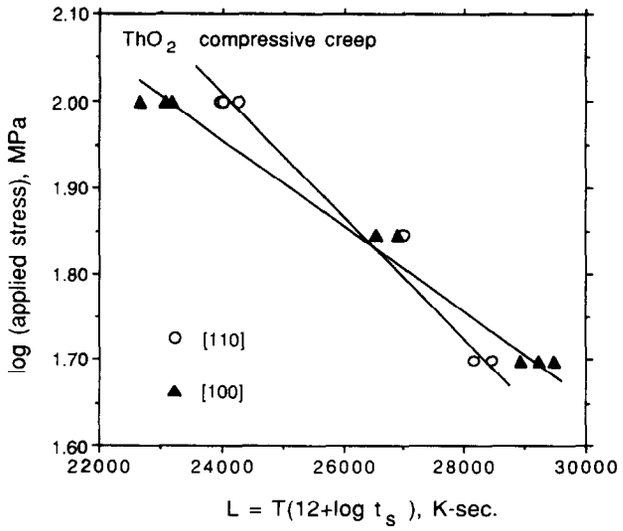


Fig. 3. Larson–Miller plot of ThO_2 single crystal (compressive creep).

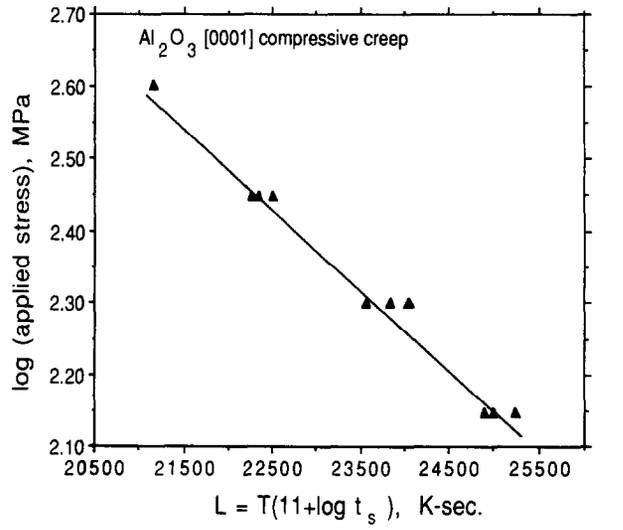


Fig. 4. Larson–Miller plot of single crystal sapphire (compressive creep).

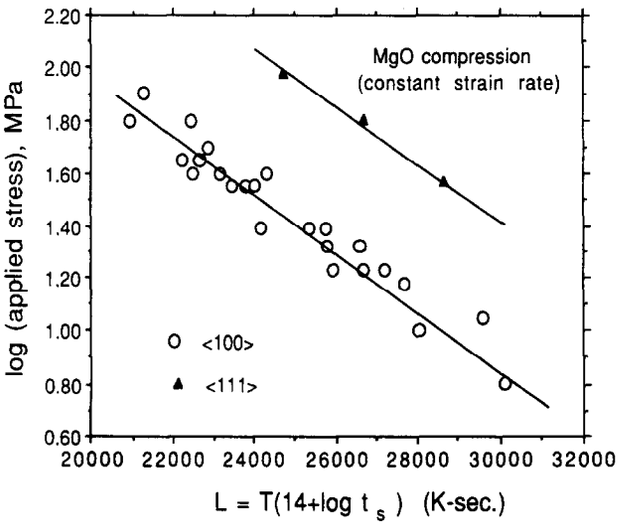


Fig. 5. Larson–Miller plot of MgO single crystal by constant strain rate compression.

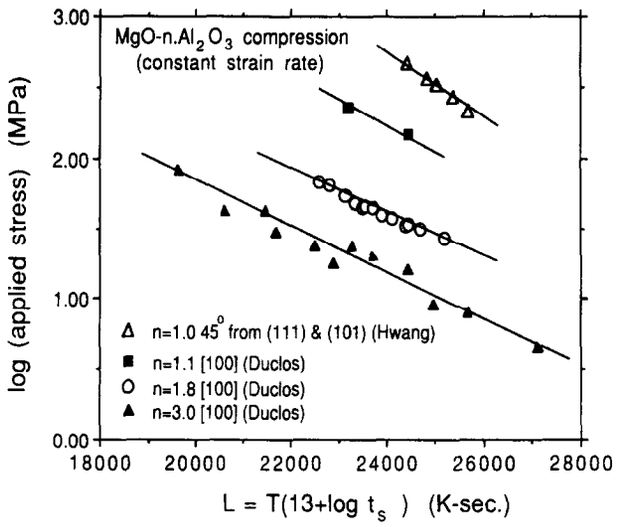


Fig. 6. Larson–Miller plot of spinel with different compositions.

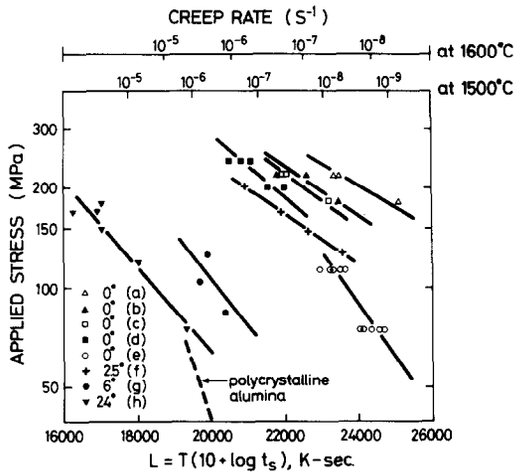


Fig. 7. Larson–Miller plot of sapphire fibres with different deviations from the c-axis. Upper scales indicate equivalent creep rates. Source references as follows: (a),(b),(c)[20], (d)[21], (e)[22], (f)[23] and (g)[24].

straight lines through the data. Where sufficient data is available, good correlation with the assumed linearity is observed. The constructed lines were then used to obtain the creep strength, i.e. the stress corresponding to $t_S = 10^4$s at a temperature of 1600°C. These conditions were based on a criterion for reinforcements in oxide–oxide composites proposed by Courtright.[2] As an example, for ThO_2 crystals (Fig. 3), the values of t_S and T give a Larson–Miller parameter of $L = 29968$ which gives by extrapolation creep strengths of 47 and 41 MPa for the [100] and [110] orientations respectively.

Creep data for crystals exhibiting the same C value can be displayed on plots with identical scales which permits direct comparison of the creep resistance of different crystals over the complete stress–temperature–life regime. This can be seen in Fig. 5 which demonstrates the sensitivity

Table 1. Creep strengths of some single crystal oxides (compression)

(a) Simple oxides

Oxides	*Direction of stress axis*	*Test temp. (°C)*	*Applied stress (MPa)*	*Test method*	*Test atmosp.*	C	*Creep strength (MPa)*	*Ref.*
BeO	$[1\bar{1}00]$	1650–1850	50–140	CLC	He	13	4	(3,4)
	$[11\bar{2}1]$	650–900	12–70	CLC	He	18	<1	(3,4)
MgO (Fe = 70 ppm)	<100>	1300–1500	20–70	CSC	Ar, CO/CO_2	14	2	(5)
MgO (Fe = 4300 ppm)	<100>	1300–1500	20–70	CSC	Ar, CO/CO_2	14	1	(5)
MgO (Fe = 11 900 ppm)	<100>	1300–1500	20–70	CSC	Ar, CO/CO_2	14	1	(5)
MgO	<100>	1665–1735	1·5–6	CSC	—	14	0·3	(6)
MgO	<100>	1300–1800	5–80	CSRC	He	14	3	(7)
	<111>	1700	37–96	CSRC	He	14	11	(7)
Al_2O_3	[0001]	1650–1850	140–400	CLC	He	11	64	(3)
	42° to [0001]	1200–1700	25–100	CLC	He	22	4	(3)
CaO	<111>	1200	5–50	CLC	—	10	1·2	(8)
	<100>	1200	8–40	CLC	—	10	0·6	(8)
CaO	<100>	1350–1450	5–15	CSC	Air	10	1·1	(9)
Y_2O_3	<110>	1550–1800	20–140	CLC	Air	10	36	(10)
YSZ*	[100]	1650–1850	12–100	CLC	Ar-2%H_2	14	16	(3)
	[110]	1650–1850	12–100	CLC	Ar-2%H_2	12	15	(3)
	$[1\bar{1}1]$	1650–1850	12–100	CLC	Ar-2%H_2	10	9	(3)
YSZ*	$[11\bar{2}]$	1300–1550	50–160	CLC	Air	21	13	(11)
YSZ*	<112>	1450–1750	59–300	CSRC	Air	21	44	(12)
					Ar	21	43	
ThO_2	[100]	1650–1850	50–100	CLC	Ar-2%H_2	12	47	(3)
	[110]	1650–1850	50–100	CLC	Ar-2%H_2	12	41	(3)
UO_2 (O/U=2·00	<100>	1100–1300	50–130	CSC	H_2	16	10	(13)
UO_2 (O/U=2·0001)	<100>	1100	80–130	CSC	H_2	16	24	(13)
UO_2 (O/U=2·001)	<100>	1100–1400	60–110	CSC	H_2	16	32	(13)
UO_2 (O/U=2·01)	<100>	1100–1300	50–90	CSC	H_2	16	22	(13)
UO_2 (O/U=2·121)	<100>	1100	30–70	CSC	H_2	16	12	13

(b) Complex oxides

Oxides	*Direction of stress axis*	*Test temp. (°C)*	*Applied stress (MPa)*	*Test method*	*Test atmosp.*	C	*Creep strength (MPa)*	*Ref.*
$BeAl_2O_4$	45° to [100]	1520–1620	25–100	CLC	Ar	18	2	(14)
	[100]	1520–1820	100–280	CLC	Ar	—	>280**	(14)
$MgO–0·9Al_2O_3$	[111]	1650–1850	50–200	CLC	He	11	33	(15)
	[100]	1650–1850	50–200	CLC	He	13	25	(15)
$MgO–Al_2O_3$	45° from (111) & (101)	1790–1850	200–480	CSRC	Ar	13	5	(16)
$MgO–1·1Al_2O_3$	[100]	1530–1630	150–230	CSRC	Ar	13	2·5	(17)
$MgO–1·8Al_2O_3$	[100]	1350–1650	20–70	CSRC	Ar	13	2·5	(17)
$MgO–3·0Al_2O_3$	[100]	1550–1850	5–90	CSRC	Ar	13	1	(17)
Mullite ($3Al_2O_3.2SiO_2$)	3° off c-axis	1400	480	CSC	Air	—	***	(18)
$Y_3Al_5O_{12}$ (YAG)	[110]	1650–1850	100–280	CLC	He	20	128	(3)
	[111]	1650–1850	100–280	CLC	He	20	135	(3)
	[100]	1650–1850	100–280	CLC	He	20	82	(3)

* Yttria stabilised zirconia.
** No detectable creep after 10 h at 1820°C and 280 MPa.
*** No detectable plastic strain at 1400° and 480 MPa for 200 h.
CLC = constant load compression; CSC = constant stress compression;
CSRC = constant strain rate compression (flow stresses were used in Larson–Miller plot for this test method).

of the creep of MgO to crystal orientation. Similarly, Fig. 6 reveals the sensitivity of the creep resistance of spinel to composition.

Figure 7 summarises tensile creep results for sapphire fibres; these have attracted considerable interest as potential reinforcement fibres. The figure illustrates the observed sharp decrease in creep resistance with angular deviation from *c*–axis loading but also a variation in the results from different sources. Such variation could in part be due to small variations in the axial orientation of fibres having a nominal *c*-axis orientation, reflecting the difficulty of growing the fibres with a precise orientation.

The effects revealed by the figures are also reflected in the creep strength values in Tables 1 and 2. Here it can also be seen that certain oxides such as Al_2O_3 and the binary oxides, $BeAl_2O_4$, yttrium aluminium garnet (YAG), mullite and spinel have very high creep resistance in certain crystal directions but exhibit extreme anisotropy. Others such as thoria and stabilised zirconia exhibit moderate strength with less anisotropy. Although there is small scope for direct comparison, the tensile creep results are fairly consistent with the compressive creep results, the former showing a tendency towards somewhat higher strengths. In general the results indicate that certain oxides show promise as high temperature reinforcements.

The creep mechanisms of the oxides are far from well understood and it is not the intention of this work to discuss possible explanations of the observed creep behaviour. Nevertheless, it is of interest to view the results in the light of the methodology proposed by Hillig[29] for predicting the mechanical properties of oxides at high temperature on the basis of such factors as the field strength of the cationic species, the apparent atomic volume of oxygen (V_O), the melting temperature and the crystal structure. Oxides having low values of V_O, high melting point and the most irregular and complicated crystal structure are predicted to offer the greatest strength, stiffness, creep resistance, and high temperature stability. On this basis certain oxides with complex structure, large shear moduli and large Burger's vector such as sapphire, YAG, spinel, mullite, chrysoberyl and BeO were considered to be the most promising candidates. In Table 3, several oxides are listed in the order of their melting points together with the upper and lower bound compressive creep strengths and details of their crystal structure. This confirms that the oxides with complicated structures, such as hexagonal, complex

Table 2. Creep strengths of single crystal oxides (tension)

Oxides	*Direction of stress axis*	*Test temp. (°C)*	*Applied stress (MPa)*	*Test method*	*Test atmosp.*	C	*Creep strength (MPa)*	*Ref.*
MgO	<011>	1200–1500	29–86·2	CLT	Air	10	5	(19)
Al_2O_3 (*c*–axis)	0°–[0001]	1700–1900	182–219	CST	Air	10	161	(20)
	0°–[0001]	1700–1900	182–219	CST	Air	10	138	(20)
Saphikon*	0°–[0001]	1700–1900	182–219	CST	Air	10	114	(20)
Mg–Ti doped	0°–[0001]	1700–1900	182–219	CST	Air	10	77	(20)
Cr–Ti doped	0°–[0001]	1700–1900	182–219	CST	Air	10	81	(20)
Al_2O_3 (*c*-axis)	0°–[0001]	1650–1800	200–240	CST	Air	10	120	(21)
	0°–[0001]	1600–1800	75–114	CST	Air	10	45	(22)
	2·5°–[0001]	1600–1800	132–204	CST	Air	10	89	(23)
	6°–[0001]	1600–1800	85–128	CST	Air	10	10	(23)
Saphikon*	24°–[0001]	1500	120–180	CST	Air	10	11	(24)
Al_2O_3 (*c*–axis)	<2°–[0001]	1760–1875	280–380	CSRT	Air	10	156	(25)
Ti^{4+} doped	<2°–[0001]	1800–1850	190–310	CSRT	Air	10	81	(26)
Sapphire (*a*–axis)	$<11\bar{2}0>$	1550–1850	90–245	CSRT	Vacuum	10	45	(27)
$MgAl_2O_4$ (spinel)	[110]	1871–1927	182–218	CLT	Air	10	70	(28)
YAG	[111]	1500–1850	200	CLT	Air	10	141**	(21)
	[100]	1500–1850	200	CLT	Air	10	~82**	(21)

* Saphikon is the trade name of a commercially-available sapphire fibre.
** Only one stress level. The Larson–Miller plot was drawn parallel to that of the YAG compression plot for the purpose of extrapolation.
CLT = constant load tension; CST = constant stress tension;
CSRT = constant strain rate tension (flow stresses were used in Larson–Miller plot for this test method).

Table 3. Relationship of creep strength with crystal structure and melting point

Oxides	*Crystal system & structure*	*Melting point (°C)*	*Highest creep strength (MPa)*	*Lowest creep strength (MPa)*
Mullite	Orthorhombic	1850	480 (1400°C, 200 h, no plastic deformation)	
$BeAl_2O_4$	Orthorhombic (Olivine)	1870	>280	2
YAG	Cubic (Complex bcc)	1950	135	94
Sapphire (Al_2O_3)	Hexagonal (hcp)	2001–2050	63	4
Spinel $MgO–0·9Al_2O_3$)	Cubic (Complex cubic)	2135	33	25
Y_2O_3	Cubic (Fluorite)	2401–2450 (Fluorite)	36	
BeO	Hexagonal (hcp)	2551–2600	41	<1
CaO	Cubic (NaCl)	2601–2650	1·2	0·6
YSZ	Cubic (α)	2715	14	9
MgO	Cubic (NaCl)	2751–2800	11	0·2
UO_2	Cubic (Fluorite)	2801–2850	32	10
ThO_2	Cubic (Fluorite)	3050	46	39

cubic and orthorhombic, exhibit superior creep resistance but as already noted are often very anisotropic. However, there is no obvious relationship between creep resistance and melting point. Thus, it seems that the effect of crystal structure overrides any correlation with melting point.

The extreme anisotropy of certain oxides presumably originates in an anisotropy of crystal and atomic bond structure. In this respect, a parallel can be drawn with carbon fibres in which the strong graphite basal atomic planes are oriented parallel to the fibre axis, leading to an extreme anisotropy of strength and stiffness in the fibres. In spite of their anisotropy, carbon fibres provide very successful reinforcement in composites, including carbon–carbon composites for high temperature applications.

4 Reliability of the Larson–Miller Procedure

The Larson–Miller method is a procedure that normalises creep data with respect to stress, temperature and strain rate. Its advantage over other normalisation approaches is that it permits convenient comparisons on the basis of relatively little data, only requiring the determination of two constants (the constant C and the slope of the log σ versus L plot). It may be suspected that this convenience is achieved at the expense of precision since the many variables involved in the creep processes are not accounted for individually. A more detailed description of the creep process used by Corman[3] is given by the semi-empirical power law equation:

$$\dot{\epsilon}_s = \frac{A_o D G b}{kT} (\sigma/G)^n \tag{6}$$

where A_o and n are constants, D is the appropriate diffusion coefficient, G the shear modulus, b the Burger's vector, k Boltzmann's constant, and σ is the applied stress. Putting

$$D = D_o \exp(-Q_D/RT) \tag{7}$$

where D_o is the frequency factor and Q_D the activation energy for the diffusion process, and:

$$G = G_o - (\Delta G)T \tag{8}$$

where G_o is the value of the shear modulus obtained by linear extrapolation to absolute zero, eqn (6) becomes after some rearrangement:

$$\dot{\epsilon}_s = A' \frac{G_o - (\Delta G)T}{kT} \left[\frac{\sigma}{G_o - (\Delta G)T}\right]^n \exp(-Q/RT) \tag{9}$$

where A' is a constant. For some of the oxides in Table 1, sufficient data was available for Corman to determine the values of A', Q_D and n by a regression analysis.[3] These values are listed in Table

Table 4. Comparison of the calculated results from semi-empirical equation with the results from Larson–Miller procedure

Oxides	*Direction*	A' *(K/MPa.S)*	n	Q_D *(J/mol)* $\times 10^3$	G_o *(MPa)* $\times 10^5$	ΔG *(MPa/K)*	*Stress (calculated with eqn 9) (MPa)*	*Stress (Larson–Miller method) (MPa)*
Sapphire	[0001]	$1{\cdot}9 \times 10^{7}$	4·54	470	1·70	24·3	63	64
Sapphire	42° to [000$\bar{1}$]	$1{\cdot}14 \times 10^{31}$	4·73	736	1·70	24·3	4	4
BeO	[1$\bar{1}$00]	$1{\cdot}33 \times 10^{15}$	3·38	496	1·654	18·5	39	41
BeO	[11$\bar{2}$1]	$2{\cdot}11 \times 10^{28}$	4·66	376	1·654	18·5	< 1	< 1
ThO_2	[100]	$5{\cdot}21 \times 10^{35}$	10·25	473	1·047	13·9	46	47
ThO_2	[110]	$3{\cdot}04 \times 10^{27}$	6·55	591	1·047	13·9	39	41
YSZ	[100]	$1{\cdot}25 \times 10^{17}$	3·86	519	0·645	18·6	14	16
YSZ	[110]	$3{\cdot}88 \times 10^{17}$	4·40	468	0·645	18·6	13	15
YSZ	[111]	$5{\cdot}56 \times 10^{14}$	3·85	406	0·645	18·6	9	9
YAG	[111]	$5{\cdot}94 \times 10^{25}$	5·64	710	1·195	7·2	115	135

*Values of A', n, Q_D, G_o and ΔG are from Corman.[3]

4 together with the associated values of creep strength calculated from eqn 9 with $\dot{\epsilon}_s = 10^{-9}$ s^{-1} and $T = 1873$ K, the latter being compared with the corresponding values derived using the Larson–Miller treatment. The agreement is sufficient to demonstrate that the Larson–Miller method offers a similar level of reliability.

5 Conclusions

The Larson–Miller method provides a convenient and effective means of comparing and ranking the creep resistance of oxides on the basis of results obtained under different stress and temperature conditions.

The creep of single crystals of several single and binary oxides was compared and it was found that binary oxides with complex crystal structures exhibited the highest creep strengths. However, these oxides were very anisotropic and the high strengths were found only for specific crystal orientations.

No clear correlation between the creep resistance of the oxides and their melting point could be seen.

References

1. Larson, F. R. & Miller, J., A time–temperature relationship for rupture and creep stresses. *Trans. ASME*, **74** (1952) 765–71.
2. Courtright, E. I., Engineering property limitations of structural ceramics and ceramic composites above 1600°C. *Ceram. Eng. Sci. Proc.*, **12**[9–10] (1991) 1725–44.
3. Corman, G. S., High-temperature creep of some single crystal oxides. *Ceram. Eng. Sci. Proc.*, **12**[9–10] (1991) 1745–66.
4. Corman, G. S., Creep of beryllia single crystals. *J. Am. Ceram. Soc.*, **75** (1992) 71–6.
5. Wolfenstine, J. & Kohlstedt, D. L., Creep of (Mg, Fe)O single crystals. *J. Mater. Sci.*, **23** (1988) 3550–7.
6. Ramesh, K. S., Yasuda, E. & Kimura, S., Negative creep and recovery during high-temperature creep of MgO single crystals at low stresses. *J. Mater. Sci.*, **21** (1986) 3147–52.
7. Routbort, J. L., Work hardening and creep of MgO. *Acta Metall.*, **27** (1979) 649–61.
8. Dixon-Stubbs, P. J. & Wilshire, B., Deformation processes during creep of single and polycrystalline CaO. *Phil. Mag. A*, **45** (1982) 519–29.
9. Duong, H. & Wolfenstine, J., Low-stress creep of single-crystalline calcium oxide. *J. Am. Ceram. Soc.*, **74** (1991) 2697–9.
10. Gaboriaud, P. R. J., High-temperature creep of yttrium sesquioxide: Y_2O_3. *Phil. Mag. A*, **44** (1981) 561–87.
11. Martinez-Fernandez, J., Jimenez-Melendo, M., Dominguez-Rodriguez, A. & Heuer, A. H., High-temperature creep of yttria-stabilised zirconia single crystals. *J. Am. Ceram. Soc.*, **73** (1990) 2452–6.
12. Jimenez-Melendo, M., Martinez-Fernandez, J., Dominguez-Rodriguez, A. & Castaing, J., Dislocation climb controlled deformation of Y_2O_3-doped cubic ZrO_2 single crystals. *J. Europ. Ceram. Soc.*, **12** (1993) 97–101.
13. Selterzer, M. S., Clauer, A. H. & Wilcox, B. A., The influence of stoichiometry on compression creep of uranium dioxide single crystals. *J. Nucl. Mater.*, **44** (1972) 43–56.
14. Whalen, P. J., Narasimhan, D., Gasdaska, C. G., O'Dell, E. W. & Morris, R. C., New high-temperature oxide composite reinforcement materials: chrysoberyl. *Ceram. Eng. Sci. Proc.*, **12**[9–10] (1991) 1774–84.
15. Corman, G. S., Creep of MgO-rich spinel single crystals. *J. Mater. Sci. Letters*, **11** (1992) 1657–60.
16. Hwang, L., Heuer, A. H. & Mitchell, T. E., Slip systems in stoichiometric $MgAl_2O_4$ spinel. In *Deformation of Ceramic Materials*, ed. R. C. Bradt & R. E. Tressler. Plenum, New York, 1975, pp. 257–70.
17. Duclos, R., Doukhan, N. & Escaig, B., Study of the origin of the composition influence on the mechanical properties of MgO Al_2O_3 spinels. *Acta Metall.*, **30** (1982) 1381–8.
18. Dokko, P. C., Pask, J. A. & Mazdiyasni, K. S., High-temperature mechanical properties of mullite under compression. *J. Am. Ceram. Soc.*, **60** (1977)150–5.
19. Clauer, A. H. & Wilcox, B. A., High temperature tensile creep of magnesium oxide single crystals. *J. Am. Ceram. Soc.*, **59** (1976) 89–96.
20. Haggerty, J. S., Wills, K. C. & Sheehan, J. E., Growth and poperties of single crystal oxide fibres. *Ceram. Eng. Sci. Proc.*, **12**[9–10] (1991) 1785–801.
21. Corman, G. S., Strength and creep of single crystal YAG fibres, Internal test report, General Electric Corporate Research and Development, Schenectady, NY, 1992.

22. Firestone, R. F., & Heuer, A. H., Creep deformation of 0° sapphire. *J. Am. Ceram. Soc.*, **59** (1976) 24–9.
23. Gooch, D. J., & Groves, G. W., The creep of sapphire filament with orientations close to the c–axis. *J. Mater. Sci.*, **8** (1973) 1238–46.
24. Porter, J. R., Reinforcements for ceramic–matrix composites for elevated temperatures. *Mater. Sci. Eng.*, **A166** (1993) 179–84.
25. Tressler, R. E. & Barber, D. J., Yielding and flow of c–axis sapphire filaments. *J. Am. Ceram. Soc.*, **57** (1974) 13–19.
26. Michael, D. J. & Tressler, R. E., Deformation dynamics of pore-free Ti^{4+}-doped and pure c–axis sapphire crystals. *J. Mater. Sci.*, **9** (1974) 1781–8.
27. Kotchick, D. M. & Tressler, R. E., Deformation behaviour of sapphire via the prismatic slip system. *J. Am. Ceram. Soc.*, **63** (1980) 429–34.
28. Sigalovsky, J., Wills, K. C., Haggerty, J. S. & Sheehan, J. E., Growth characteristics and properties of spinel single crystal fibres. *Ceram. Eng. Sci. Proc.*, **13**[7–8] (1992) 183–9.
29. Hillig, W. B., A methodology for estimating the mechanical properties of oxides at high temperatures. *J. Am. Ceram. Soc.*, **76** (1993) 129–38.

Journal of the European Ceramic Society **15** (1995) 521–526
© 1995 Elsevier Science Limited
Printed in Great Britain. All rights reserved
0955-2219/95/$9.50

0955-2219(95)00016-X

Effect of Vapor Atmosphere on the Formation Reaction of $MSiO_3$ (M = Mg, Ca, Sr and Ba)

Shigeo Hayashi,[a] Ken-ichi Ishizu,[a] Shinya Kikuchi,[a]* Kiyoshi Okada[a]† & Nozomu Otsuka[b]

[a]Department of Inorganic Materials, Faculty of Engineering, Tokyo Institute of Technology, O-okayama, Meguro-ku, Tokyo 152, Japan
[b]Department of Material Engineering, Faculty of Science and Technology, The Nishi Tokyo University, Uenohara, Kitatsuru, Yamanashi 409-01, Japan

(Received 21 July 1994; revised version received 3 September 1994; accepted 10 January 1995)

Abstract

Effect of vapor atmosphere on the formation reaction of $MSiO_3$ (M = Mg, Ca, Sr and Ba) from various precursor powders was investigated by powder X-ray diffraction. Precursors of $MgSiO_3$ and $CaSiO_3$ were prepared by the coprecipitation method by adding NH_4OH to ethanol solution dissolving a respective nitrate and tetraethyl orthosilicate (TEOS). Those of $SrSiO_3$ and $BaSiO_3$ were prepared from respective hydroxide powder and TEOS. Vapor atmosphere showed the most effective influence in the formation of $CaSiO_3$, whereas it showed the least influence in that of $MgSiO_3$ among the four kinds of $MSiO_3$ formation. The difference in effect was mainly attributed to the degree of chemical homogeneity of the precursor powder, the effect being smaller the higher the chemical homogeneity. The samples fired under a vapor atmosphere showed larger specific surface area than those under a dry atmosphere.

1 Introduction

$CaSiO_3$ (wollastonite) has been used and/or studied as a raw material of tile and pottery,[1] a filler to resin,[2] etc. Since sinterability of $CaSiO_3$, is generally not so high, fine and homogeneous powders are necessary as the raw material to prepare dense $CaSiO_3$ ceramics. A conventional synthetic method to mix and calcine raw material powders of $CaCO_3$ and SiO_2 is not appropriate to prepare fine $CaSiO_3$ powders because relatively high temperature is necessary for the formation of $CaSiO_3$ phase due to the sluggish reactivity of SiO_2 component. Several preparation methods from solution have been examined in order to prepare fine and homogeneous $CaSiO_3$ powder. We (Ref 3) reported that good $CaSiO_3$ powder could be prepared by the coprecipitation method from ethanol solution dissolving Ca nitrate and TEOS. No by-product phases were detected during the formation of $CaSiO_3$. We also clarified that fine and homogeneous $MgSiO_3$ powder could be synthesized by the same method as that of $CaSiO_3$, whereas good $SrSiO_3$[4] and $BaSiO_3$ powders could be prepared from a combination of respective hydroxide powder and TEOS.

It is well known that a vapor atmosphere has a certain effect to lower the crystallization temperature of some silicate glasses.[5,6]. Vapor is considered to react to break down Si–O–Si bonds and forms Si–OH groups, thus, weakens the glass structure. It, therefore, lowers the kinetic barrier to nucleation, and increases the mobility of atoms in the glasses.[6] Vapor atmosphere was also reported to be effective for accelerating solid state $CaSiO_3$ formation reaction.[7]

Considering these facts, formation reaction of $CaSiO_3$ and also $MSiO_3$ (M = Mg, Sr and Ba ions) were expected to be lowered by firing under a vapor atmosphere compared with firing in a normal atmosphere. In this paper, formation of $MSiO_3$ from respective precursors under a vapor and a dry air atmosphere was examined to elucidate the effect of the atmosphere on the formation of the various $MSiO_3$ phases.

2 Experimental procedures

2.1 Preparation of the starting powders

Precursor powders of $MgSiO_3$ and $CaSiO_3$ were

†To whom correspondence should be addressed.
*Nihon Cement Co., Ltd., 1-2-23, Kiyosumi, Koutou-ku, Tokyo 135, Japan

prepared using the coprecipitation method.[3] In the $MgSiO_3$ precursor powder, a starting solution was prepared by dissolving $Mg(NO_3)_2 \cdot 6H_2O$ and TEOS in ethanol. The ratio of Mg/Si in the solution was 1 and their respective concentrations were 0·2 mol/l. The same amount of 25% NH_4OH as the starting solution was added to the starting solution by stirring vigorously. The precursor powder was obtained by drying the precipitate and by calcining at 500°C for 2 h.

The precursor powder of $CaSiO_3$ was synthesized using the same method as $MgSiO_3$, using $Ca(NO_3)_2 \cdot 4H_2O$ and TEOS as the starting materials.

$SrSiO_3$ and $BaSiO_3$ precursor powders were prepared using the following method:[4] hydrate powder of $Sr(OH)_2 \cdot 8H_2O$ or $Ba(OH)_2 \cdot 8H_2O$ respectively was dispersed in ethanol, and TEOS was added to this solution. They were mixed and dried on a water bath. The hydrate powder dissolved during this process and was precipitated again by condensation of the solution. The other processes were the same as in the synthesis of the $MgSiO_3$ precursor powder.

Precursor powders of $CaSiO_3$ were also prepared using the three other methods to investigate the influence of the precursors on the formation of $CaSiO_3$ in the vapor atmosphere. They were the alkoxide coprecipitation method, the two-step precipitation method and the solid mixing method. In the first method, Ca ethoxide, $Ca(OC_2H_5)_2$ was used instead of Ca nitrate in the preparation. Ca ethoxide was synthesized by reacting Ca metal powder and ethanol by refluxing in an Ar atmosphere. Then tetramethyl orthosilicate (TMOS) was added to the solution and mixed. The following processes were the same as in the coprecipitation method. The precursor powder prepared by this method was more homogeneous than the powder prepared by the coprecipitation method. In the second method, oxalic acid was added to the starting solution proceeding to the NH_4OH addition. Oxalic acid yielded precipitation of Ca oxalate and NH_4OH yielded precipitation of amorphous silica by the hydrolysis of TEOS. Formation of α-$CaSiO_3$ instead of β-$CaSiO_3$ was the characteristic result in this precursor powder. In the third method, $CaCO_3$ powder and SiO_2 aerogel powder were mixed in ethanol by ball mill for 24 h. The mixture was then dried and calcined at 500°C for 2 h. The powder prepared by this method is less homogeneous than the other ones, i.e. β-Ca_2SiO_4 was formed as the main by-product phase by firing.

2.2 Firing experiments

The precursor powders were fired at various temperatures in a vapor and a dry air atmosphere by an electric furnace. Firing experiments in the vapor atmosphere was performed by flowing a carrier gas (air), which was bubbled in a water bath. Vapor pressure of the carrier gas was controlled at 0·47 atm by adjusting the temperature of the water bath at 80°C. Firing experiments in the dry atmosphere were performed by flowing a carrier gas excluding moisture by a $CaCl_2$ drying agent.

The samples were fired at a set temperature between 400 and 1000°C for a duration of 2 h. All the experiments were performed at the flow rate of 180 ml/min.

2.3 Characterization

After the firing experiments, crystalline phases in the samples were identified by the X-ray powder diffraction method (Rigaku, Geigerflex) using monochromated CuKα radiation. The amount of crystalline phases was estimated semi-quantitatively by comparing the X-ray diffraction intensities. The reflections used were as follows; 310 in $MgSiO_3$ (clinoenstatite), 320 in β-$CaSiO_3$, 112 in α-$CaSiO_3$, 002 in β-Ca_2SiO_4, the reflection at d = 3·08 Å in $SrSiO_3$ (metastable phase), 022 in $SrSiO_3$ (stable phase) and 111 in β-$BaSiO_3$.

Specific surface area was measured by the multipoint B.E.T. method (Carlo Elba Strumentazione, Soaptomatic Series 1800) using nitrogen gas.

3 Results and Discussion

The $MgSiO_3$ precursor powder was amorphous in the as-calcined state and crystallized at around 770°C in both atmospheres. Formation curves of $MgSiO_3$ phase under both firing atmospheres are shown in Fig. 1. The amount of $MgSiO_3$ in the two curves increased very rapidly between 770 and 800°C, and saturated above this temperature. Since the two curves almost coincided with each other, it is concluded that the vapor has no effect on the $MgSiO_3$ formation reaction.

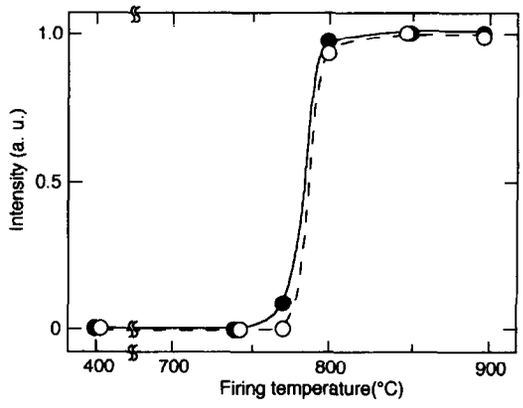


Fig. 1. Formation curves of $MgSiO_3$ by firing the precursor powder under the dry (○) and the vapor (●) atmospheres.

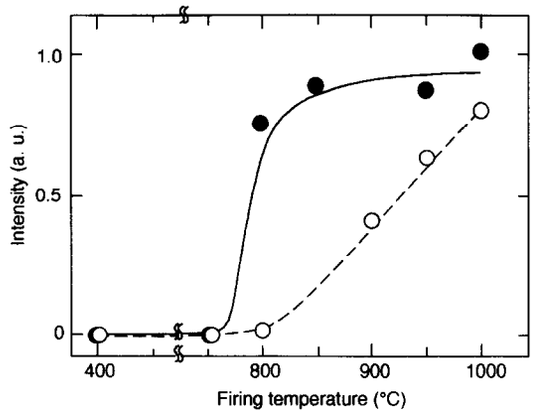


Fig. 2. Formation curves of β-$CaSiO_3$ by firing the precursor powder under the dry (○) and the vapor (●) atmospheres.

The $CaSiO_3$ precursor powder was amorphous in the as-calcined state. Fig. 2 shows the formation curves of β-$CaSiO_3$ phase after firing in the dry and the vapor atmospheres. In the dry atmosphere, crystallization occurred at 800°C and the formation amount increased gradually and linearly between 800 and 1000°C. On the other hand, β-$CaSiO_3$ started to crystallize at 750°C in the vapor atmosphere, the formation amount increased steeply up to 800°C and almost saturated over this temperature. This shows that there is a large difference in the formation of $CaSiO_3$ in the dry and the vapor atmospheres. Vapor is found to accelerate the crystallization of $CaSiO_3$ in this case.

The $SrSiO_3$ precursor powder was amorphous in the as calcined state. Crystalline $3SrO{\cdot}2SiO_2{\cdot}3H_2O$ was detected in the as-precipitated state, but it yielded an amorphous product during the calcination. Figure 3 shows the formation curves of $SrSiO_3$ phases in the two atmospheres. In these samples, the first crystalline phase appeared by firing was a metastable $SrSiO_3$ phase and it transformed to a stable $SrSiO_3$ phase by firing at higher temperature.[4] The sequence of phase changes was the same in the dry and in the vapor atmospheres but reaction temperatures were different in the two atmospheres. The reaction temperatures in the vapor atmosphere were always around 50°C lower than those in the dry atmosphere. Vapor is, therefore, fairly effective in this system.

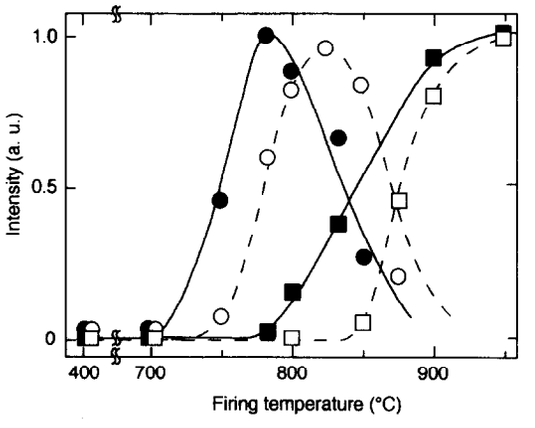


Fig. 3. Formation curves of metastable (○, ●) and stable (□, ■) $SrSiO_3$ by firing the precursor powder under the dry and the vapor atmospheres. Open and solid symbols correspond to the dry and vapor atmospheres, respectively.

In the $BaSiO_3$ samples, crystalline $BaSiO_3{\cdot}H_2O$ was formed in the as calcined state and was converted to crystalline $BaSiO_3$ during the calcination. This was the characteristic point of this sample because all the other samples were amorphous in the as calcined state. A considerable amount of $BaSiO_3$ was already formed in the samples fired at 400°C. However, crystallization to $BaSiO_3$ was not accomplished around that temperature. It means that the as-precipitated sample contains amorphous as well as $BaSiO_3{\cdot}H_2O$. Figure 4 shows the formation curves of $BaSiO_3$. The amount of $BaSiO_3$ started to increase from around 600°C and almost saturated at 800°C. Since the formation curve in the dry atmosphere differed only a little from that in the vapor atmosphere, the effect of vapor is very small in the $BaSiO_3$ samples.

In this way, the effect of vapor on the formation of crystalline $MSiO_3$ phases differed considerably largely among the samples. No significant effect was detected in the $MgSiO_3$ and $BaSiO_3$ samples whereas $MSiO_3$ crystallization was apparently accelerated in the $CaSiO_3$ and $SrSiO_3$ samples. Two different reasons were considered to yield these results. One reason can be attributed to the difference of the character of the M–O bond in the $MSiO_3$ samples. The second reason considered was the influence of the structural state of the precursor powders, i.e. the degree of homogeneity in the mixing state of the two components, and the degree of polymerization state of the silica component. Since the effect of vapor for the respective $MSiO_3$ formation showed no correlation with the order of periodic table of the alkaline earth metal ions, the second reason was considered to be

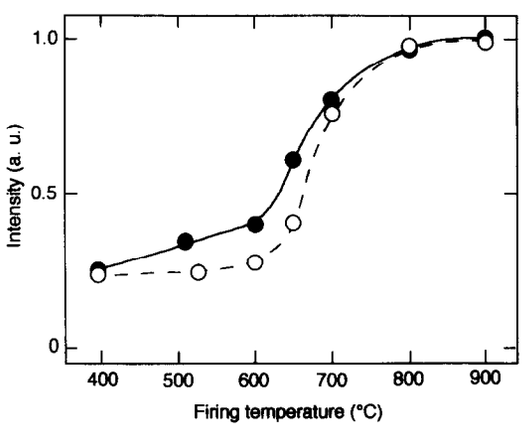


Fig. 4. Formation curves of $BaSiO_3$ by firing the precursor powder under the dry (○) and the vapor (●) atmospheres.

important. Although the precursors of $MgSiO_3$ and $CaSiO_3$ were prepared by the same method, we[8] found by an analytical transmission electron microscopy that the $MgSiO_3$ precursor powder was more homogeneous than the $CaSiO_3$ precursor powder. On the other hand, the precursors of $SrSiO_3$ and $BaSiO_3$ were prepared by the same method and crystalline phase was formed in the as-precipitated state. They were $3SrO{\cdot}2SiO_2{\cdot}3H_2O$ and $BaSiO_3{\cdot}H_2O$, respectively. Since the M/Si ratio of crystalline phase formed in the as-precipitated state was same with that of the objective crystalline phase $MSiO_3$ in the $BaSiO_3$ sample but was different in the $SrSiO_3$ sample, the $BaSiO_3$ sample was more homogeneous than the $SrSiO_3$ sample. In this way, the effect of vapor atmosphere for the crystallization was considered to change by the structural state of the as-precipitated precursor powders. Four kinds of $CaSiO_3$ precursor powders with different structural state were, therefore, prepared to examine the relationship between the effect of vapor and their degree of homogeneity. The $CaSiO_3$ formation curves in the solid mixing method, the two-step precipitation method, the coprecipitation method, and the alkoxide precipitation method are shown in Figs 5, 6, 2 and 7, respectively.

In the solid mixing method, β-Ca_2SiO_4 crystallized preceding to β-$CaSiO_3$. Such a phenomenon to form an alkaline earth metal rich phase is generally known when the formation reaction proceeds mainly by the diffusion of ions and the diffusion paths are long, because the diffusion coefficient of alkaline earth metal is larger than that of silicon. Vapor atmosphere was effective in accelerating the formation of β-$CaSiO_3$ from β-Ca_2SiO_4 and amorphous silica. Vapor is considered to attack surface Si–O–Si bonds in the amorphous silica and yields Si–OH bonds. It is very effective to cause the powder active state.

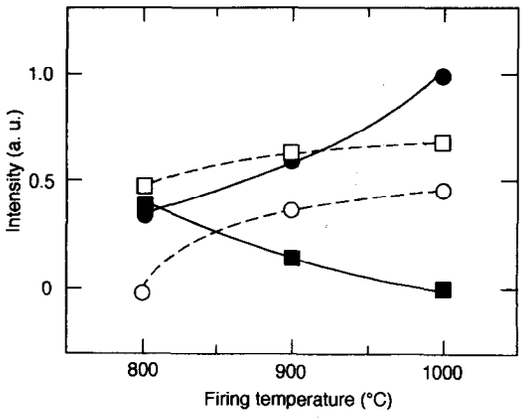


Fig. 5. Formation curves of crystalline phases by firing the solid-mixing $CaSiO_3$ precursor powder under the dry and the vapor atmospheres. Circles and squares correspond to β-$CaSiO_3$ and β-Ca_2SiO_4, and open and solid symbols correspond to the dry and the vapor atmospheres, respectively.

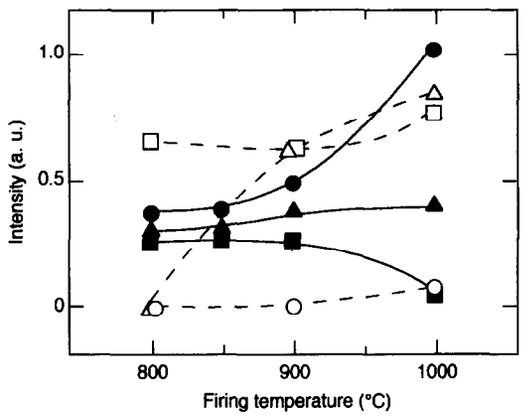


Fig. 6. Formation curves of crystalline phases by firing the two-step precipitated $CaSiO_3$ precursor powder under the dry and the vapor atmospheres. Circles, triangles and squares correspond to β-$CaSiO_3$, α-$CaSiO_3$ and β-Ca_2SiO_4, respectively. Open and solid symbols correspond to the dry and the vapor atmospheres, respectively.

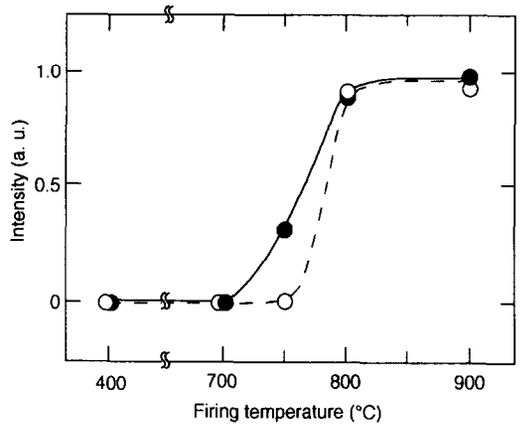


Fig. 7. Formation curves of β-$CaSiO_3$ by firing the alkoxide coprecipitated $CaSiO_3$ precursor powder under the dry (○) and the vapor (●) atmospheres.

Therefore, formation of β-$CaSiO_3$ largely accelerated under the vapor atmosphere.

Crystallization reaction in the two-step precipitation method was much more complicated and not only β-$CaSiO_3$ and β-Ca_2SiO_4 but also α-$CaSiO_3$ (pseudowollastonite) were formed simultaneously. Formation of α-$CaSiO_3$ was the characteristic point of this preparation method. It is the high-temperature phase of $CaSiO_3$ and is stable at the temperature range between 1125 and 1544°C.[9] The actual reason for the formation of this phase was not certain. Since β-Ca_2SiO_4 remained even after firing at 1000°C in the dry atmosphere, vapor was found to be very effective to accelerate the decomposition of β-Ca_2SiO_4 and formation of $CaSiO_3$ in this sample.

The results of the coprecipitation method have already been discussed. In method, only the objective crystalline phase β-$CaSiO_3$ was formed and no by-productive crystalline phase was detected. Therefore, homogeneity of the precursor powder in this method was considered to be better than

those in the solid mixing and the two-step precipitation methods. The formation reaction of β-$CaSiO_3$ was apparently accelerated under the vapor atmosphere as shown in Fig. 2. It may mean that the precursor is not homogeneous in the molecular level and is examined by the ^{29}Si NMR spectra.[10]

In the alkoxide precipitation method, β-$CaSiO_3$ crystallized at the lowest temperature among the four synthetic methods. It may mean that the precursor of this method was in the most homogeneous state. The formation curve showed only a little difference in the vapor and the dry atmospheres and the effect of vapor was the smallest among the various $CaSiO_3$ samples.

Summarizing the results of the four kinds of $CaSiO_3$ precursors, we can conclude as follows:

(1) When the mixing of CaO and SiO_2 components was particle size order, i.e. submicron to micron meter, Ca-rich by-product phase crystallized preceding to the $CaSiO_3$ phase. In this case, vapor played an important role in accelerating the formation reaction of $CaSiO_3$ by attacking Si–O–Si bonds in amorphous SiO_2. The solid mixing and two-step precipitation methods belong to this category.

(2) When the mixing of two components was partly molecular level but remained partly inhomogeneous, vapor was effective in activating the reactivity of the inhomogeneous region. The coprecipitation method may belong to this category.

(3) When the mixing was more homogeneous than the other methods and was molecular level, vapor showed little influence to $CaSiO_3$ formation because no silica-like polymerized structure remained in the precursor.

Figure 8 shows the specific surface area of $CaSiO_3$ samples prepared by the coprecipitation method and fired at various temperatures under the dry and the vapor atmospheres. The surface area fired under the vapor atmosphere was always larger than that under the dry atmosphere irrespective of the firing temperature. Ito[7] reported that the $CaSiO_3$ powder synthesized by the conventional solid reaction method was very easy to grind into fine powder when it was fired under a vapor atmosphere. This is compatible with the present results. Although the formation amount of β-$CaSiO_3$ in the sample fired at 800°C under the vapor atmosphere was almost same with that in the sample fired at 1000°C under the dry atmosphere, the surface area of the former was 5 times as large as that of the latter one. This result shows that the heat treatment under a vapor atmosphere is effective to prepare fine crystalline silicate powder at lower temperatures than that in a dry atmosphere or in a normal atmosphere.

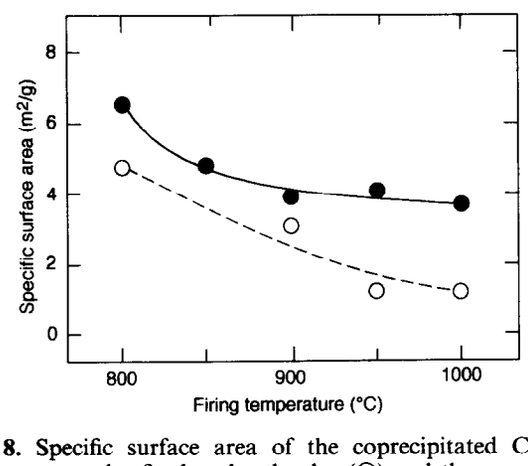


Fig. 8. Specific surface area of the coprecipitated $CaSiO_3$ precursor powder fired under the dry (○) and the vapor (●) atmospheres.

4 Summary

The effect of a vapor atmosphere on the formation of $MSiO_3$ (M = Mg, Ca, Sr and Ba) was examined using the precursor mainly prepared by the coprecipitation method. Among the four kinds of $MSiO_3$, vapor showed most effective influence in the $CaSiO_3$ sample and the least effective influence in the $MgSiO_3$ sample. The reason for these differences was mainly attributed to the chemical homogeneity of the precursor powder. It was further confirmed using the several kinds of $CaSiO_3$ precursor powders prepared by the different methods. The heat treatment of the precursor under the vapor atmosphere was effective to prepare fine crystalline powder compared with that under the dry atmosphere.

References

1. Kurczyk, H. G. & Wuhrer, J., Synthetic wollastonite and its use in ceramic bodies. *Interceram*, **2** (1971) 119–25.
2. Jian, S., Gending, J. & Yuanfu, H., A new method for surface modification of wollastonite. *J. Mater. Sci. Lett.*, **11**, (1992) 409–10.
3. Hayashi, S., Okada, K. & Otsuka, N., Preparation of $CaSiO_3$ powders by coprecipitation method and their sinterability. *J. Ceram. Soc. Jpn.*, **99** (1991) 1224–7.
4. Ueno, A., Hayashi, S., Okada, K. & Otsuka, N., Preparation of $SrSiO_3$ powders from various strontium salts. *J. Mater. Sci. Lett.*, **10** (1991) 9–12.
5. Wagstaff, F. E., Brown, S. D., & Culter, I. B., The influence of H_2O and O_2 atmospheres on the crystallization of vitreous silica. *Phys. Chem. Glass.*, **5** (1964) 76–81.
6. Gonzalez-Oliver, C. J. R., Johnson, P. S. & James, P. F., Influence of water content on the rates of crystal nucleation and growth in lithia–silica and soda–lime–silica glasses. *J. Mater. Sci.*, **14** (1979) 1159–69.
7. Ito, K., Keikaiseki no gousei to mizu no yakuwari. In *Kobutsu Kogaku*, ed. H., Imai, S. Takeuchi, & Y. Fujiki, Asakura shoten, Tokyo, 1976, pp. 111–9.

8. Hayashi, S., Homogeneity of alkaline earth silicate ceramic raw materials prepared by the solution method. Doctoral thesis, Tokyo Institute of Technology, Tokyo, Japan, 1994.
9. Deer, W. A., Howie, R. A. & Zussman, Z., Wollastonite. In *Rock-Forming Minerals Vol. 2A Single-Chain Silicates*. Longman, London, 1978, pp. 547–63.
10. Hayashi, S., Okada, K. & Otsuka, N., Characterization of $MgSiO_3$, $CaMgSi_2O_6$ and $CaSiO_3$ precursor powders by ^{29}Si MAS NMR. *J. Eur. Ceram. Soc.*, in press (1994).

Journal of the European Ceramic Society **15** (1995) 527–535
© 1995 Elsevier Science Limited
Printed in Great Britain. All rights reserved
0955-2219/95/$9.50

0955-2219(95)00014-3

Reactive Formation of Coatings at Boron Carbide Interface with Ti and Cr Powders

P. Mogilevsky,[a] E.Y. Gutmanas,[a]* I. Gotman[b] & R. Telle[c]

[a]Department of Materials Engineering, Technion, Haifa 32000, Israel
[b]Department of Materials Engineering, Drexel University, Philadelphia, PA 19104, USA
[c]Institut für Gesteinshüttenkunde, RWTH, 5-5100 Aachen, Germany

(Received 7 November 1994; revised version received 9 January 1995; accepted 10 January 1995)

Abstract

Boron carbide, B_4C, is an attractive candidate material for reinforcement in metal matrix composites, whose application is severely hampered by its reactions with most engineering alloys at the high processing or service temperatures. The reactivity of B_4C with some of the metals, however, may be made use of to create protective coatings on its surface. In the present research, the microstructure of coatings obtained by the interaction of B_4C with Ti and Cr powders at 1000–1200°C was investigated employing X-ray diffraction, scanning electron microscopy and Auger electron spectroscopy. Coatings obtained by treating B_4C in Ti powder were found to contain Ti carbide, TiC_{1-X}, and Ti borides (TiB_2 and TiB). A relatively thin inner layer of the coating was carbide-free and contained only borides, while the major part of the coating was a mixture of TiC_{1-X} and TiB. In contrast to this, coatings formed by reaction of B_4C with Cr powder contained no carbides, and were shown to consist of Cr borides (CrB_2, CrB, Cr_5B_3 and Cr_2B) and amorphous carbon. A thick outer layer of the coating was carbon-free and consisted almost entirely of CrB. In both cases, the growth of the coatings was controlled by diffusion, the activation energy for the growth of B_4C/Ti coating being approximately 175 KJ/mol. The phase composition, layer sequence and morphology of the coatings obtained were interpreted on the basis of kinetic and thermodynamic data of the ternary systems involved. A good agreement between the experimental results and theoretical predictions was obtained.

1 Introduction

Non-oxide ceramics are important materials having a high potential for advanced structural and electronic applications, as well as reinforcements for metal matrix composites (MMCs). Boron carbide, B_4C, is especially attractive due to its very low density, high hardness and relatively low cost, at least in the particulate form. However, the use of B_4C (as well as other non-oxide ceramics) as a reinforcement for Fe-, Ni- and Co-base alloys is severely hampered by reactions that occur at the ceramic/metal matrix interface at the high processing and/or service temperatures. Although large bulk of evidence exists for the reactivity of non-oxide ceramics with metals,[1–3] the interaction between B_4C and structural Fe-, Ni- and Co-base alloys has practically not been investigated. The solid state reaction between B_4C and nickel at 880°C was reported to yield a complex product at the interface, Ni being a dominant diffusing species.[4] The formation of undesirable reaction products, as well as the dissolution of the ceramic in a metal, result in the degradation of the reinforcement and in the deterioration of the mechanical properties of the matrix and of the MMC as a whole. Since the performance of MMCs is, to a large extent, controlled by the structure and properties of ceramic/metal interfaces, it is important to prevent or, at least, to minimize the reactions at these interfaces. This may be achieved by creating diffusion barriers. The necessity of a diffusion barrier for application of B_4C as a reinforcement for MMCs was emphasized in Ref. 4. One of the possible ways of creating a diffusion barrier is by coating the ceramic prior to inserting it into a metal matrix.

It has been recently shown that non-oxide ceramics such as SiC, Si_3N_4 and B_4C, can be coated employing their interaction with powders of metals having high affinity for carbon, silicon and boron, and a new powder immersion reaction assisted coating method (PIRAC) has been proposed.[5–8] The objective of the present research is to study the microstructure of PIRAC coatings obtained by treating B_4C in Ti and Cr powders.

* To whom correspondence should be addressed.

2 Experimental

In the present research, Cr metal powder (< 150 μm) from Merck, Ti metal powder (~ 100 μm) from Alfa Products and hot pressed boron carbide, B_4C, were used. Plates of B_4C were immersed into the metal powders and heat treated at 1273–1473 K. Heat treatments were conducted in evacuated quartz tubes (10^{-6} Torr at room temperature). After heat treatment, the reacted layers were investigated employing X-ray diffraction, XRD (Philips 1730/10), scanning electron microscopy, SEM, with energy dispersive analysis, EDS (JEOL 840), and Auger electron spectroscopy, AES (Perkin-Elmer PHI 590A).

3 Results and Discussion

3.1 Microstructure of B_4C/Ti powder interface

A representative micrograph of the coating obtained by treating B_4C in Ti powder is shown in Fig. 1. According to the XRD pattern, Fig. 2, the coating consists of a Ti boride, TiB, and the Ti carbide, TiC_{1-X}. The intensities of the TiB peaks do not match the standard intensities, indicating a pronounced (020)-preferred orientation. It should be mentioned that preferred orientation in the direction of the shortest lattice parameter (and [020]/[010] is such a direction for TiB) is often observed during the diffusion growth of compounds with orthorhombic structure.[9] The peaks of TiC_{1-X} are slightly shifted from the standard positions of the stoichiometric TiC, yielding the lattice parameter a ≈ 0·431 nm. This value corresponds to a hypostoichiometric $TiC_{0.6}$ carbide.[10]

Thin coatings obtained after short PIRAC treatments were found to be tightly bonded to the B_4C surface. On the other hand, thicker coatings (> 2–3 μm) tended to spall off the ceramic substrate and stick to the Ti powder, thus revealing the inner surface (coating/B_4C interface) of the reaction layer. A similar behavior was previously observed for PIRAC coatings obtained by treating SiC[7] and Si_3N_4[8] in Ti powder. This allowed to obtain separate AES depth profiles for both the inner, Fig. 3(a), and the outer, Fig. 3(b), layers of the B_4C/Ti coating with good depth resolution. The depth profile in Fig. 3(a) clearly shows that the inner part of the coating is carbon-free and is assumed to be TiB, since this is the only boride detected by XRD. Towards the B_4C surface, however, an increase in the boron content and a corresponding decrease in the Ti content is observed,

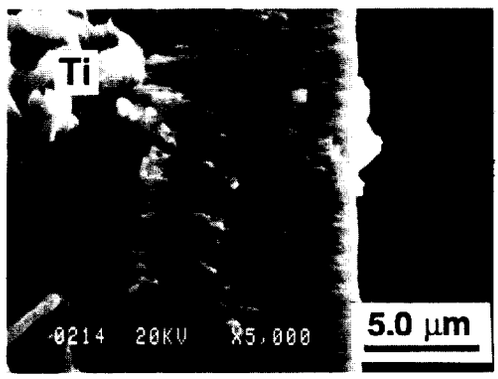


Fig. 1. A representative micrograph of the reaction layer obtained by treating B_4C in Ti powder (1100°C, 6 h), cross section.

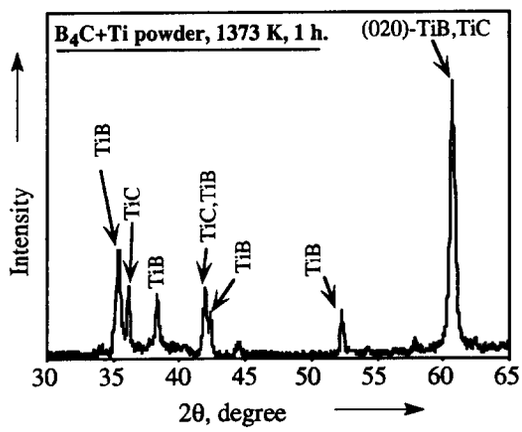


Fig. 2. A typical XRD pattern of the coating obtained by treating B_4C in Ti powder (1100°C, 1 h).

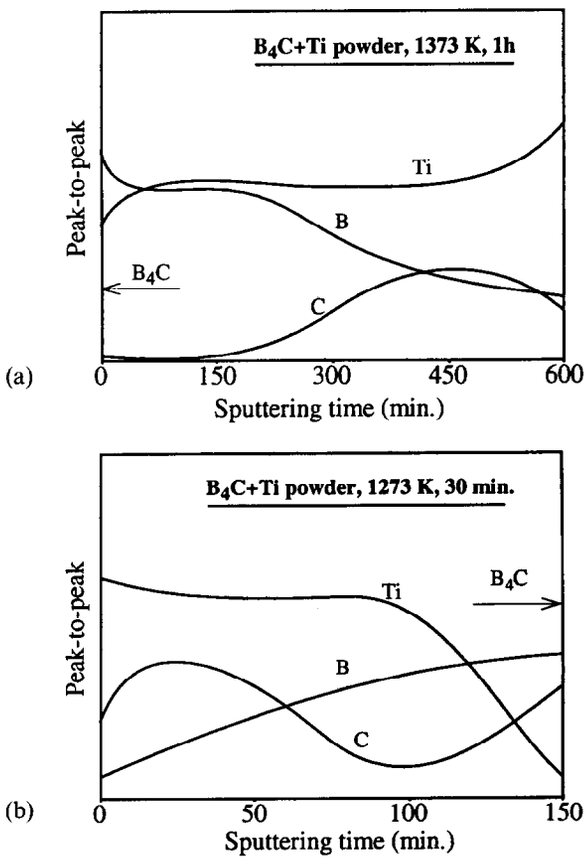


Fig. 3. AES depth profiles of the coatings obtained by treating B_4C in Ti powder: (a) 1100°C, 1 h, sputtering starting from the B_4C/coating interface; (b) 1000°C, 0·5 h, sputtering starting from the coating surface.

Fig. 3(a), suggesting the presence of a thin layer of TiB_2 (or another B-rich boride). Apparently, this layer is too thin to be detected by XRD.

Unlike the inner part of the coating, the outer part contains all the three components — Ti, boron and carbon, Fig. 3(b). It is believed that this part of the coating is a mixture of TiB and TiC_{1-X}, with the amount of TiB gradually decreasing towards the surface. The drop of carbon concentration at the surface of the coating indicates the presence of a layer of TiC_{1-X} with the composition approaching the lower homogeneity limit, i.e. $TiC_{0.5}$. The described sequence of layers in the coating obtained by treating B_4C in Ti powder is schematically shown in Fig. 4.

The results of the kinetic studies, Fig. 5, reveal that the coatings obtained by treating B_4C in Ti powder grow according to the parabolic law, suggesting the diffusion controlled process. The activation energy of growth as calculated from the slope of the Arrhenius plot, Fig. 5(b), is approximately 175 KJ/mol.

In Fig. 6, the diffusion path corresponding to the layer sequence in Fig. 4 is shown superimposed upon the isothermal section of the B–C–Ti system. This diagram has been slightly modified from the one given in[11,12] to reflect the presence of the Ti_3B_4 phase that has been discovered more recently.[13] However, since there is no experimental or theoretical evidence for the stability of this phase at temperatures as low as 1473 K, the Ti_3B_4–TiC_{1-X} tie-line is shown as a dotted line. It can be seen that the experimental results are in a good agreement with the ternary isotherm. The consideration of the diagram shows that TiB_2 is the only phase that forms a stable interface with the stoichiometric B_4C, hence the formation of a thin TiB_2 layer (or TiB_2 and Ti_3B_4 layers) on the B_4C surface. Sections of the diffusion path running along the tie lines from B_4C to TiB_2 and from TiB_2 to TiB are dashed, indicating that B_4C, TiB_2 and TiB single-phase layers are separated by flat interfaces. Similarly, sections of the diffusion path running across a three-phase field to connect a two-phase region to another single-phase region, e.g. (TiB+TiC_{1-X}) to Ti, are drawn with dashed lines, too. This is to indicate that, since no three-phase regions can be formed in course of three component diffusion,[14] the two-phase layer is directly followed (or preceded) by the single-phase layer. (The above comments on the use of dashed lines apply also to the following discussion on the B–C–Cr ternary system). The formation of the

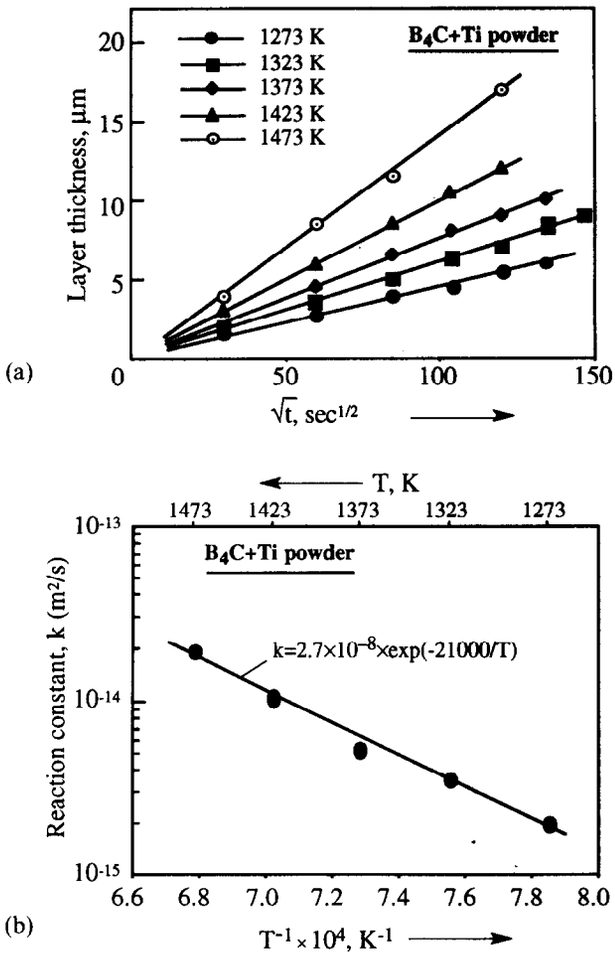


Fig. 5. Kinetics of the coating growth during B_4C/Ti powder interaction: (a) reaction zone thickness versus square root of time at different temperatures; (b) rate of the reaction layer growth versus reciprocal absolute temperature.

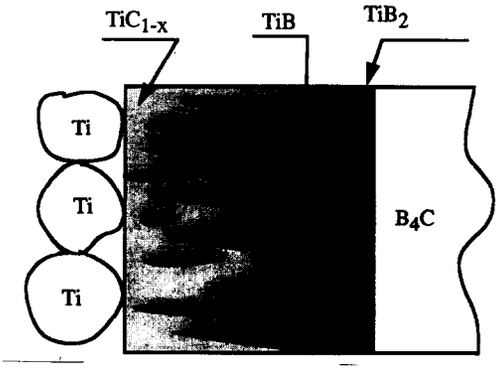


Fig. 4. Schematic of the layer sequence in the B_4C/Ti powder reaction layer obtained at 1000–1200°C.

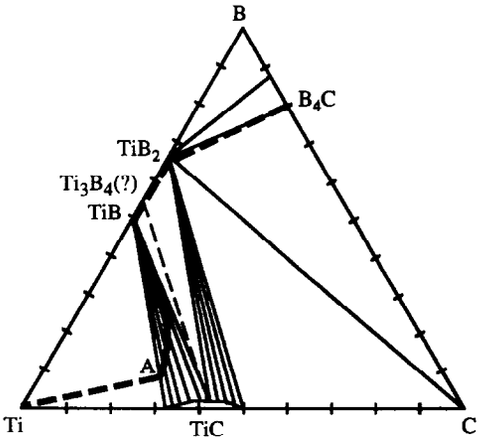


Fig. 6. Isothermal section of the B–C–Ti system at 1500°C.

hypostoichiometric $TiC_{0.6}$ is also in agreement with the diagram, since only a carbon-deficient TiC_{1-x} is in equilibrium with TiB. The same value of (1-x) = 0·6 was obtained by Barsoum *et al.*[15] as the lower limit of (1-x) for TiC_{1-x} in equilibrium with TiB_2 at 1600°C, or, conversely, as the upper limit for TiC_{1-x}in equilibrium with TiB.

In Fig. 6, the major (TiB + TiC_{1-x}) layer of the coating is represented by a section of the diffusion path that passes into a two-phase region (TiB + TiC_{1-x}) from a single phase one (TiB) at an angle to the tie lines and exits into another region. According to Kirkaldy *et al.*,[14] such a diffusion path represents a columnar or a columnar-plus-isolated-precipitate two-phase zone. This suggests that the mixed zone in the B_4C–Ti powder couple contains columnar (and, possibly, some isolated) TiB precipitates in a TiC_{1-x} matrix, the former being rooted in the parent TiB phase, as shown schematically in Fig. 4. Such a microstructure would be consistent both with the observed preferred orientation of TiB, and the columnar-like morphology of the coating cross section, Fig. 1.

The formation of the two-phase (TiB + TiC_{1-x}) layer may be explained by referring to the kinetic model for the formation of an aggregate versus layered morphology in diffusion couples, suggested by Rapp *et al.*[16] Although developed for less complicated diffusion layer sequences, the model seems to be well applicable to our B_4C/Ti powder system. If an initially planar interface between the TiB and TiC_{1-x} layers is assumed, the model predicts[16,17] that it will remain flat provided the growth of the TiB layer is limited by B diffusion through TiB. Alternatively, if the diffusion of Ti through TiC_{1-x} is the rate-limiting step, the two-phase aggregate morphology will result. In our case, the growth of TiB is, most probably, limited by Ti diffusion (the mobile B atoms usually diffuse much faster than the Ti atoms), hence the formation of the two-phase (TiB + TiC_{1-x}) layer in the coating, Fig. 4. Another comment that can be made regarding the relative diffusion rates in the B_4C/Ti couple is that, since the TiC_{1-x} carbide constitutes the major part of the foremost layer of the coating leaving behind the TiB boride, the diffusion of carbon in TiB must be more rapid than that of boron.

3.2 Microstructure of B_4C/Cr powder interface

A representative microstructure of the coating obtained by treating B_4C in Cr powder is shown in Fig. 7. In the micrograph, two morphologically different layers can be distinguished, the outer one having a pronounced 'columnar' structure. Coatings obtained after 1 – 4 h exposures at 1200°C were approximately 14 – 18 μm thick, and they

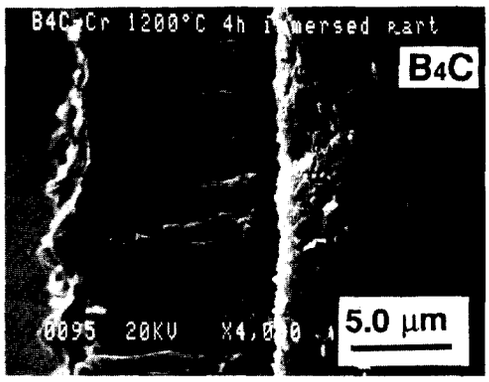


Fig. 7. A representative micrograph of the reaction layer obtained by treating B_4C in Cr powder (1200°C, 4 h), cross section.

easily split (e.g. during polishing) along the sublayer interface. A layer of carbon black was detected on both fracture surfaces. On the other hand, no splitting was observed in the thinner coatings (~7 μm) formed during 0·5 h exposure at 1100°C.

In Fig. 8(a), a typical XRD pattern of the coatings obtained at 1100–1200°C is presented. It can be seen that the coatings consist of different Cr borides: CrB as a major phase, Cr_5B_3 and Cr_2B. The pronounced (002) orientation of CrB suggests that this boride constitutes the outer layer of the

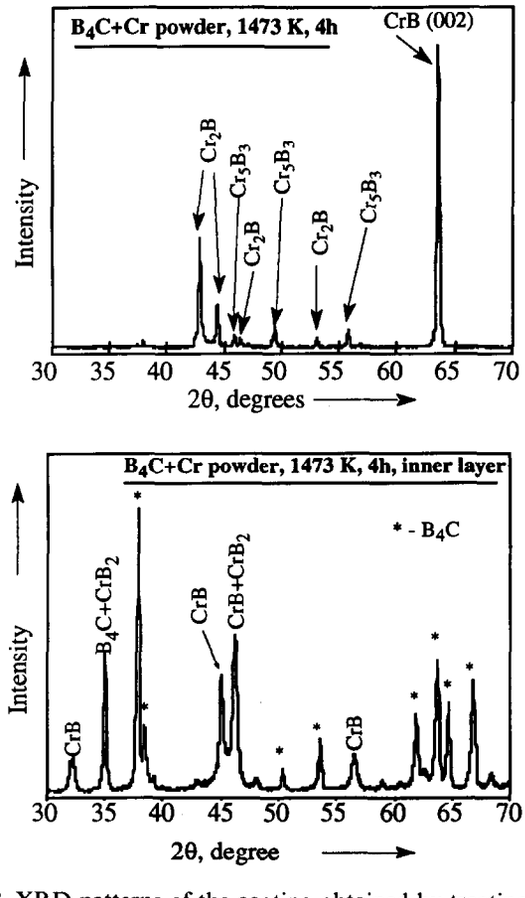


Fig. 8. XRD patterns of the coating obtained by treating B_4C in Cr powder (1200°C, 4 h): (a) the entire coating; (b) the inner layer.

coating having the 'columnar' morphology, Fig. 7. Similarly to the case of TiB, the preferred orientation is in the direction of the orthorhombic unit cell shortest parameter—[002]/[001] for the CrB lattice. The splitting of the coatings obtained at 1200°C made it possible to remove the outer layer and identify the phase composition of the inner layer more accurately. According to the XRD pattern in Fig. 8(b), the inner layer of the coatings obtained at 1200°C consists of CrB (with no preferred orientation) and CrB_2 (It should be mentioned that the XRD detection of CrB_2 is not unequivocal due to the superposition of the lines of CrB_2 and CrB or B_4C. However, the anomalously high intensity of the CrB peak at around $2\theta = 46°$ gives ground to the suggestion that the peak is, in fact, a superposition of the CrB (I/I_{max} = 80%) and CrB_2 (I/I_{max} = 100%) peaks. An alternative assumption that the high intensity of the peak is a result of a certain preferred orientation of CrB is not corroborated by other CrB peak intensities.) Since the coating obtained at 1100°C did not split, no separate XRD analysis of the inner layer phase composition was made. The XRD pattern of the coating as a whole does not indicate the presence of CrB_2 observed in the inner layer of the coating obtained at 1200°C.

The striking feature of the XRD results is the absence of Cr carbides or any other carbon-containing phases including graphite. It is clear, however, that since carbon is one of the products of B_4C decomposition, it should be present in the coating in some form. Indeed, a typical AES depth profile in Fig. 9(a) (1200°C, 4 h) shows that the inner layer of the coating contains, in addition to B and Cr, a large and constant amount of carbon. This mixed C–B–Cr layer is followed by a thin sublayer of pure carbon apparently corresponding to the 'split plane' of the coating. (It should be mentioned, that AES profiling to such a depth (~14 μm) was only made possible due to the splitting of the coating. In fact, three separate depth profiles were obtained: one from the surface of the coating, and two from each 'split surface'. The profile in Fig. 9(a) is a reconstruction based on the three above profiles.) The shape of the carbon KVV-peak in the AES spectrum, Fig. 9(b), was found to match that of the free rather than bound (carbide) carbon.[18] Since no graphite peaks were observed in the XRD pattern, the carbon in the coating is assumed to be amorphous. The profile in Fig. 9(a) clearly shows that the outer layer of the coating is carbon-free thus confirming our early assumption that this is a pure CrB layer. The increase of Cr concentration towards the surface of the coating, coupled with the XRD results, Fig. 8(a) suggests the presence of thin Cr_5B_3 and Cr_2B surface sublayers.

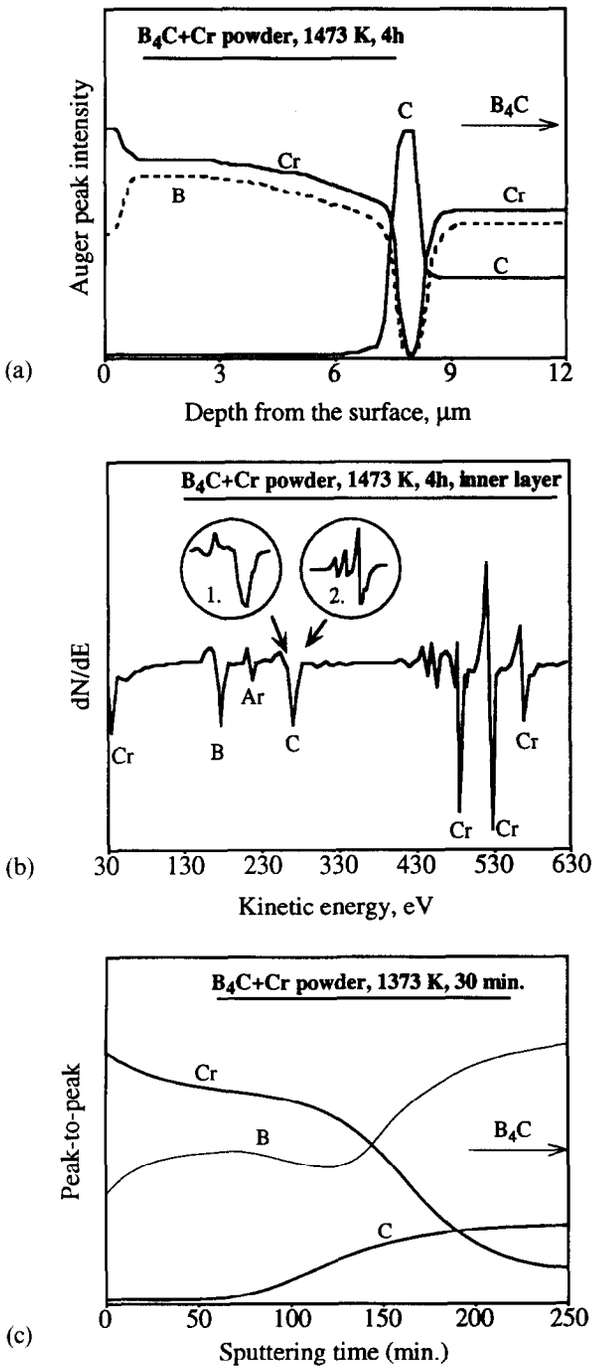


Fig. 9. AES results for the coatings obtained by treating B_4C in Cr powder: (a) 1200°C, 4 h, reconstructed depth profile, depth scale given according to SEM thickness; (b) 1200°C, 4 h, spectrum from the inner layer: 1 — KVV peak of free (unbound) carbon, 2 — KVV peak of bound (carbide) carbon; (c) 1100°C, 0·5 h, depth profile.

AES depth profile of the coating obtained at 1373 K, Fig. 9(c), being in all other respects similar to that in Fig. 9(a), does not reveal the presence of the pure carbon sublayer. This is consistent with the observation that these coatings do not split along the sublayer interface. It should be mentioned, however, that the inability to detect a thin carbon layer may also be the result of an insufficient depth resolution.

Based on the above observations, the sequences of layers in the coatings obtained by treating B_4C in Cr powder at 1100 and 1200°C were suggested

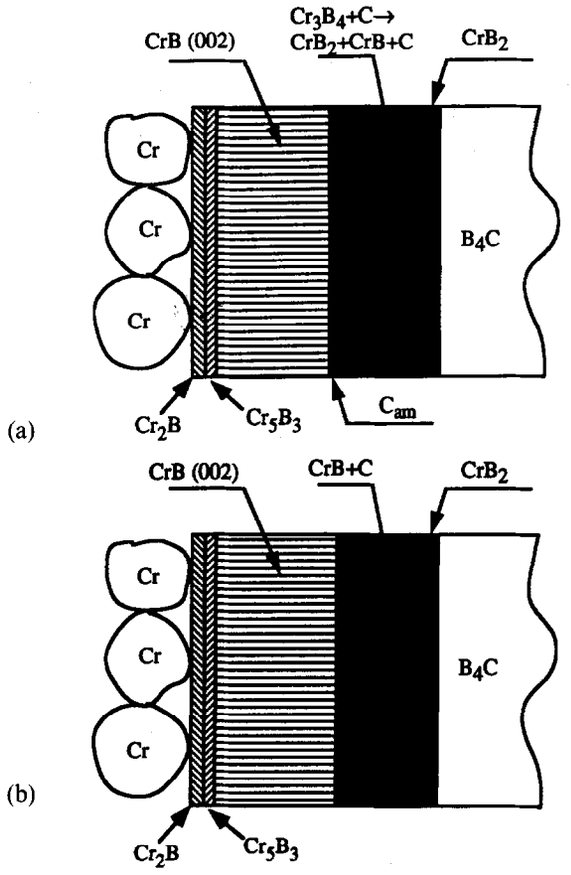


Fig. 10. Schematics of the layer sequences in the coatings obtained by treating B_4C in Cr powder at: (a) 1200°C; (b) 1100°C.

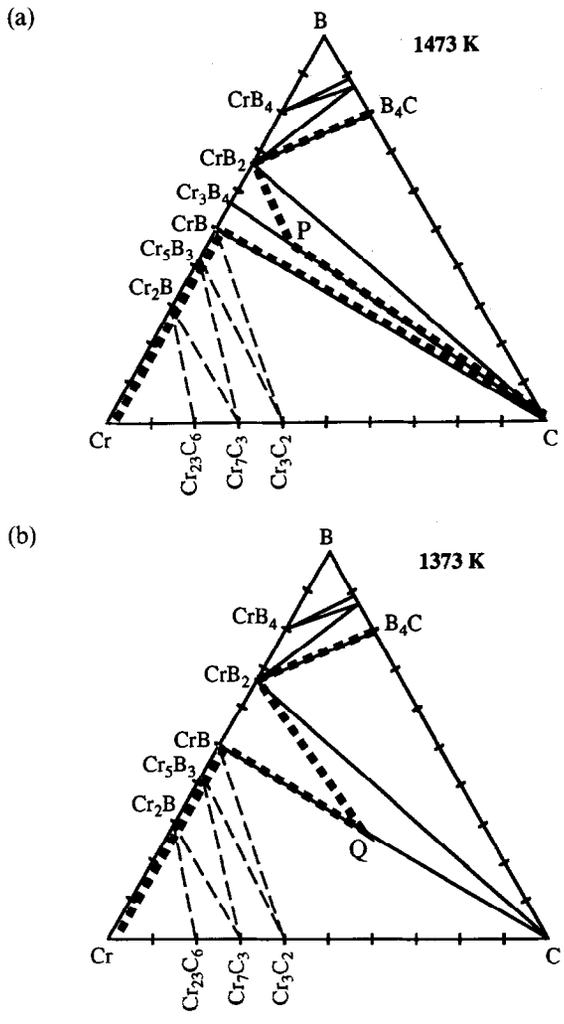


Fig. 11. Tentative isothermal sections of the B–C–Cr system at: (a) 1200°C; (b) 1100°C.

and are shown schematically in Figs. 10(a) and (b), respectively. It can be seen that for the coating obtained at 1200°C, Fig. 10(a), the inner layer containing amorphous carbon, CrB and a small amount of CrB_2, is followed by a thin sublayer of pure carbon black which is, in turn, followed by a layer of columnar (002) oriented CrB grains. Towards the surface of the coating, CrB gives way to the thin sublayers of Cr-rich borides Cr_5B_3 and Cr_2B. For the coating obtained at 1100°C, Fig. 10(b), we assume the inner layer to be a mixture of amorphous carbon and CrB only (since no indication as to the presence of CrB_2 was obtained). The outer carbon-free layer of the coating obtained at 1100°C is similar to that of the 1200°C coating; however, no intermediate sublayer of carbon black is observed in the former.

As seen from Fig. 10, the coatings obtained have rather complex microstructures. Thus, it would be very interesting to try and superimpose the diffusion paths corresponding to the observed phase sequences onto the B–C–Cr ternary diagram. (The 'diffusion path' approach is justified, since the coatings growth in the B_4C–Cr powder system was earlier reported[6] to be controlled by diffusion.) Unfortunately, no isothermal sections of either complete B–C–Cr ternary diagram, or of its B- and C-rich corners are available in the literature. In order to make the discussion of our results possible, an attempt was made to construct tentative isothermal 1100 and 1200°C sections of the B–C–Cr diagram, based on the available literature data as well as on our own experimental results. The tentative isothermal sections are shown in Fig. 11, and they are based on the following assumptions:

- B–C–Cr ternary diagram is, in general, similar to the B–C–Mo[12] and B–C–W[11,12] ternaries, since Cr, Mo and W are transition metals belonging to the same group of the periodic table;
- CrB and CrB_2 are at equilibrium with carbon at temperatures above 1350°C.[19,20] If we assume that the equilibrium pertains to the lower temperatures (down to 1100°C), there are CrB–C and CrB_2–C tie lines on the B–C–Cr ternary isotherms at both 1100 and 1200°C;
- CrB_2 is at equilibrium with B_4C up to 2100°C,[19] i.e. there is a B_4C–CrB_2 tie line on the B–C–Cr ternary isotherms at both 1100 and 1200°C;

- Cr_3B_4 is unstable at temperatures below ~1200°C, and it decomposes at 1100°C < T < 1200°C according to $Cr_3B_4 \rightarrow 2CrB + CrB_2$, similarly to the decomposition of MoB_2 into MoB and Mo_2B_5 at ~1480°C.[21] To establish this, and elemental Cr/B powder blend with the composition corresponding to Cr_3B_4 was compacted, heat treated and analyzed by XRD. The only phase found in the compact annealed at 1200°C for 4 h and rapidly cooled to the room temperature was Cr_3B_4. On the other hand, only traces of Cr_3B_4 were found in the sample slowly cooled from the same temperature, the main peaks being those of CrB and CrB_2. Similarly, the compacts annealed at 1100°C, both rapidly and slowly cooled, consisted of CrB and CrB_2 phases, only. These results suggest that Cr_3B_4 is thermodynamically stable at 1200°C, but is not stable at 1100°C. Therefore, the Cr_3B_4 boride is present in the B–C–Cr ternary isotherm at 1200°C, but it is absent at 1100°C.

Since the Cr-rich corner of the B–C–Cr ternary is very complicated and as it is not this part of the diagram that we're concerned about, its presentation in Fig. 11 is rather simplified (hence the use of dashed lines). An accurate representation of the Cr-rich corner may be found in Ref. 22.

The diffusion paths mapped onto the ternary isotherms in Fig. 11 correspond to the layer sequences shown in Fig. 10. The existence of the CrB_2 – C tie line makes the equilibrium between B_4C and CrB impossible and thus requires the presence of CrB_2 at the B_4C/coating interface. We assume, therefore, that there is a thin interfacial CrB_2 sublayer in the coatings obtained at both 1100 and 1200°C. The layer must be so thin that it could not be detected by XRD, at least for the 1100°C coating. AES depth profiling also proved ineffective in revealing this thin CrB_2 sublayer, apparently as a result of the poor depth resolution in the vicinity of the deeply buried (~7 μm for the 1100°C coating) B_4C/coating interface. (It is worth mentioning, that the detection by AES of the similar TiB_2 sublayer at the B_4C/Ti-base coating, Fig. 3(a), was only made possible due to the spalling of the coating off the ceramic substrate along the B_4C/TiB_2 interface.)

With the above considerations in mind, one can see that the diffusion path in Fig. 11(b) closely follows the layer sequence observed in the coating formed at 1100°C, Fig. 10(b). This is also the case for the coating obtained at 1200°C, with one exception, however. Namely, the diffusion path depicted in Fig. 11(a) requires the presence of a (Cr_3B_4 + carbon) two-phase layer preceding the pure carbon layer, whereas, in the real coating, the (CrB + CrB_2 + carbon) layer is observed, Fig. 10(a). It is apparent that such a three-phase layer could not be formed in our three component system during the process of diffusion growth. This discrepancy can easily be explained by the already mentioned decomposition of Cr_3B_4 at temperatures below 1200°C. We believe that a (Cr_3B_4 + carbon) layer is actually formed at the processing temperature of 1200°C, and is subsequently transformed into the experimentally observed (CrB + CrB_2 + carbon) layer on cooling to the room temperature. Since the exact compositions of the (CrB + CrB_2 + carbon) layer in the 1200°C coating and of the (CrB + carbon) layer in the 1100°C coating have not been measured, the points P and Q representing these layers on the ternary isotherms, Figs. 11(a) and (b), respectively, are given just as a reference.

The formation of the two-phase (Cr_3B_4 + carbon) layer versus the flat carbon/CrB interface in the 1200°C coating is in an agreement with the kinetic model[16] referred to in the previous section. The model predicts that, assuming initially planar interfaces and Cr diffusion as the rate-determining step (that is justified considering the much higher mobility of carbon and boron atoms), the aggregate morphology should develop at the Cr_3B_4/carbon interface yielding the two-phase (Cr_3B_4 + carbon) region, whereas the layered morphology should be preserved at the carbon/CrB interface. These are the morphologies experimentally observed in our diffusion couple, Fig. 10. On the other hand, the attempt to apply the model to the 1100°C coating morphology proved unsuccessful. A more thorough investigation of the microstructure of the coatings obtained by treating B_4C in Cr powder at 1100°C is now in progress. An interesting observation regarding the coatings in the B_4C/Cr powder system is that thick carbon-free pure boride (CrB) surface layers are formed. This suggests that, in contrast to the B_4C/Ti coatings, the diffusion of boron through the reaction products is faster than that of carbon.

4 Summary and Conclusions

It was shown that the interaction of B_4C with Ti and Cr powders at 1000–1200°C yielded complex multi-layer coatings on the ceramic substrate. Coatings obtained by treating B_4C in Ti powder were found to contain the Ti carbide, TiC_{1-X}, and Ti borides (TiB_2, TiB). A relatively thin inner layer of the coating was carbide-free and contained only borides, while the major part of the

coating was a mixture of TiC_{1-X} and TiB. In contrast to this, coatings formed by reaction of B_4C with Cr powder contained no carbides, and were shown to consist of Cr borides (CrB_2, CrB, Cr_5B_3 and Cr_2B) and amorphous carbon. A thick outer layer of the coating was carbon-free and consisted almost entirely of CrB. In both cases, the growth of the PIRAC coatings was controlled by diffusion. The activation energy for the growth of B_4C/Ti coating was found to be approximately 175 Kj/mol. The phase composition and the layer sequences in the coatings obtained were analyzed by mapping the diffusion paths onto the corresponding ternary isotherms. Since no B–C–Cr phase diagram was available in literature, tentative B–C–Cr ternary isotherms were proposed for the temperatures of 1100 and 1200°C. The layer sequence and morphology of the PIRAC coatings were interpreted also on a kinetic basis. The experimental results were found to be in a fair agreement with the kinetic and thermodynamic predictions for the ternary systems involved.

Once PIRAC has been proved useful for coating B_4C ceramic, the next question to be answered is whether the coatings obtained are feasible as protective layers at various B_4C/metal interfaces. To be effective, these coatings should act as diffusion barriers as well as be sufficiently inert with respect to the metal. In addition, thermal expansion coefficients (CTE) of B_4C, the metal and the coating should be considered. Due to the complex structure of the coatings obtained, as well as to the lack of essential data on the diffusion of metals, carbon and boron in borides and carbides and their CTE's, theoretical predictions of the coatings integrity as protective layers are hard to make. Preliminary results have shown that both the Ti- and Cr-based PIRAC coating effectively suppress the interaction of B_4C with iron at 1000–1100°C.[6] Clearly, only relatively thin reaction layers that do not spall off the B_4C surface can be considered as candidates for protective coatings. It would be especially interesting to study the effect of the pure carbon and the mixed carbon/CrB layers on the protective behavior of Cr-based PIRAC coatings on B_4C surface. Carbon coatings are now routinely used as protective layers on SiC fibers (e.g. SCS-6 Textron-AVCO SiC fibers). It should be mentioned, however, that if B_4C-particulate reinforced MMCs (e.g. for wear applications) are considered, the low strength of a pure carbon layer may have an adverse effect on the bonding integrity of B_4C particles in a metal matrix. Further investigation of the coatings' behavior in different metal matrices is required to find out whether they can act as adequate protective layers at B_4C/metal interfaces.

Acknowledgements

The authors would like to thank Dr R. Brener for performing the Auger analysis. This research was supported by G.I.F. Research Grant No. 10069-326.10.87.

References

1. Brito, M. E., Matsumoto, J. M., Hirótusu, Y., Fukuzawa, Y. & Tanaka, K., Solid state reaction of nickel on silicon carbide. In *Joining Ceramics, Glass and Metal*, ed. W. Kraft. DGM Informationgesellshaft, 1984, pp. 305–12.
2. Klomp, J. T., Thermodynamics of ceramic–metal interfaces. In *Designing Interfaces for Technological Applications: Ceramic–Ceramic, Ceramic–Metal Joining*, ed. S. D. Peteves. Elsevier, London, 1989, pp. 127–44.
3. Backhaus-Ricoult, M., Physicochemical processes at metal–ceramic interfaces. In *Designing Interfaces for Technological Applications: Ceramic–Ceramic, Ceramic–Metal Joining*, ed. S. D. Peteves. Elsevier, London, 1989, pp. 79–92.
4. Yang, J. -M., Kao, W. H., & Liu, C. T., Interface characterization of fiber-reinforced Ni_3Al matrix composites, *Metall. Trans.*, **A20** (1989) 2459–69.
5. Gutmanas, E. Y, Gotman, I. & Kaysser, W., Coating of non-oxide ceramics by interaction with metal powders. *Mater. Sci. Eng.*, **A157** (1992) 233–41.
6. Mogilevsky, P., Gotman, I., Gutmanas, E. Y. & Kaysser, W., Microstructure and thermal stability of coatings obtained by interaction of SiC and B_4C with Cr and Ti powders. *Mater. Sci. Eng.*, **A170** (1993) 271–9.
7. Gotman, I., Gutmanas, E. Y. & Mogilevsky, P., Interaction between SiC and Ti powder. *Mater. Res.*, **8** (1993) 2725–33.
8. Gotman, I., Interaction of SiC and Si_3N_4 with metal powders. PhD Thesis, Technion — Israel Institute of Technology, Haifa, Israel, 1991.
9. Van Loo, F. J. J., Multiphase diffusion in binary and ternary solid-state systems. *Prog. Solid St. Chem.*, **20** (1990) 47–99.
10. Kosolapova, T. Ya., *Carbides*. Plenum Press, New York, 1971, p. 98.
11. Rudy, E., *Ternary Phase Equilibria in Transition Metal Boron–Carbon–Silicon Systems*, Part V, Report No. AFML-TR-65-2. Air Force Materials Laboratory, Ohio, 1969, p. 606.
12. Schouler, M., Ducarroir, M. & Bernard, C., Review on constitution and properties of the metal–carbon–nitrogen and metal–carbon–boron systems. *Rev. Int. Hautes Temp. Réfract.*, **20** (1983) 261–311.
13. Spear, K. E., McDowell, P. & MeMahon, F., Experimental evidence for the existence of the Ti_3B_4 phase. *J. Am. Ceram. Soc.*, **69** (1986) C-4 – 5.
14. Kirkaldy, J. S. & Young, D. J., *Diffusion in the Condensed State*. The Institute of Metals, London, England, 1987, pp. 361–99.
15. Barsoum, M. & Houng, B., Transient plastic phase processing of titanium–boron–carbon composites. *J. Am. Ceram. Soc.*, **76** (1993) 1445–51.
16. Rapp, R. A., Ezis, A. & Yurek, G., Displacement reactions in the solid state. *Metall. Trans.*, **4** (1973) 1283–92.
17. Van Loo, F. J. J., van Beek, J. A., Bastin, G. F. & Metselaar, R., The role of thermodynamics and kinetics in multiphase ternary diffusion. In *Diffusion in Solids*, eds. M. A. Dayananda & G. E. Murch. TMS, Warrendale, 1985, pp. 231-59.

18. H. E. Bishop, Auger electron spectroscopy. In *Methods of Surface Analysis*, ed. J. M. Walls. Cambridge University Press, Cambridge, England, 1989, pp. 87–126.
19. Glaser, F. W., Contribution to the metal–carbon–boron systems. Trans. AIME, **194** (1952) 391–6.
20. Markovskii, L. Ya., Vekshina, N. V. & Bezruk, E. T., Interaction of borides with carbon and carbides. In *Chemical Properties and Analysis of Refractory Compounds*, ed. G. V. Samsonov. Consultants Bureau, New York – London, 1972, pp. 114–17.
21. Portnoi, K. I. & Romashov, V. M., Binary constitution diagrams of systems composed of various elements and boron — A review. *Sov. Powder Met. Ceram.*, **11** (1972) 378–84.
22. Pradelli, G., Research on chromium borocarbides. *Met Ital.*, **66** (1974) 551–6.

Journal of the European Ceramic Society **15** (1995) 537–549
© 1995 Elsevier Science Limited
Printed in Great Britain. All rights reserved
0955-2219/95/$9.50

0955-2219(95)00010-0

Experimental Study of the Ti–B–C System Using LPCVD

M. A. Guiban* & G. Malé†

Laboratoire de Science et de Génie des Matériaux et des Procédés du C.N.R.S., BP 5, Odeillo, 66125 Font-Romeu Cedex, France

(Received 29 September 1994; revised manuscript received 6 December 1994; accepted 12 December 1994)

Abstract

The chemical system Ti–B–C–Cl–H was explored experimentally under reduced pressure (10 mbar) starting from a mixture of $TiCl_4$, BCl_3, CH_4 and H_2. The rate of growth, the composition, and the microstructure of the deposited solids were examined. The formation of titanium diboride, present in the entire explored domain, directs the chemical system. Carbon is present only in a small domain and when the concentration of $TiCl_4$ in the gas mixture is very low. Only rhombohedral boron carbide $B_{13}C_2$ and a tetragonal phase noted 'Q' with the general formula $B_{48}Ti_{2-x}C_{2-y}$ were identified, and always in the presence of TiB_2. These solids are distinguished by their very unique and varied microstructures and with the notable existence of nanometric three phase composites.

1 Introduction

The results presented, can be added to other research trying to improve certain properties of boron carbides by adding a third element to the basic boron–carbon system. A small improvement in its reactivity at a high temperature was made using silicon.[1] In this study, titanium was added to the system to evaluate its action on the mechanical properties.

In the domain of high performance ceramic materials, the Ti–B–C system is important because one can hope to obtain *a priori* the main compounds: $B_{13}C_2$, TiC and TiB_2 and their associated characteristics. The system was studied using chemical deposition starting from the gas phase under reduced pressure (LPCVD), which follows the study of the deposition, at thermodynamic equilibrium, of the solid phases starting with mixtures $TiCl_4$, BCL_3, CH_4 and H_2.[2]

It appears that the system is mainly controlled by the strong affinity between titanium and boron. The diagram in Fig. 1 shows that the concentration of $TiCl_4$ strongly influences the nature of the condensed phases and extends their domain boundaries. By contrast, the effect of the CH_4 concentration is minimal and it acts principally on the size deposition domain of the free carbon.

From these results and those of the other authors also cited in Ref. 2, it was determined that the prevailing compound in the system is TiB_2 and that combinations between the carbides of titanium and of boron, although *a priori* interesting, are not thermodynamically possible. Nevertheless, the possibility of codepositing titanium diboride and boron carbide in a narrow region exists.

2 Experimental Methods

The experiments were carried out in a CVD cold wall reactor. The substrates, heated by high frequency induction, are graphite cylinders 16 mm in diameter, and 5 mm high.

$TiCl_4$ titanium precursor, is mixed with the typical reactants used for studying the boron–carbon system (BCl_3, CH_4, and H_2). Being a liquid at ambient temperatures, its vapor is entrained by bubbling hydrogen. The considered parameters are the total pressure in the reactor (P), the temperature of the substrate (T) and the flow rate of the reactants (DX).

For practical reasons, the amount of boron trichloride (D BCl_3) was fixed. This allows one to consider the parameter $R = 100D\ CH_4/(D\ CH_4 + D\ BCl_3)$, representing the variation in the methane flow. Additionally the quantity of $TiCl_4$ participating in the reaction is controlled by the fraction of the flow rate of hydrogen carrying $TiCl_4$.

The characterization of the deposited solids depends on the following:

*New address: Sollac, rue du Compte Jean, Grande-Synthe, BP 2508, 59381 Dunkerque Cedex 1, France
†To whom correspondence should be addressed.

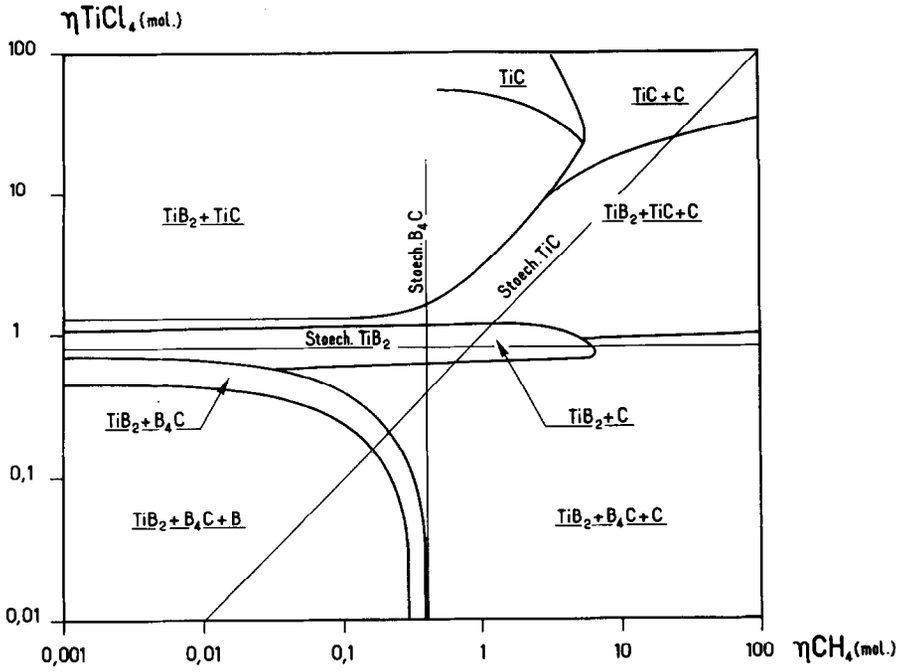


Fig. 1. Theoretical deposition diagram as a function of the gas phase composition.[2] T = 1300 K, P = 10 mbar, n BCl_3 = 1·6 mol, n H_2 = 15 mol.

The determination of the rate of deposit (gain of mass of the substrate per unit time).
The identification of the species by X-ray Difraction (XRD).
The elemental analysis by Electron Microprobe (EM).
The observation of morphology of the surface by Scanning Electron Microscopy (SEM).

3 Influence of the Composition of the Gas Mixture

The initial experiments principally involved control of the concentration of the reactants in the gas phase by varying the flows of $TiCl_4$ and CH_4.

The experimental parameters were the following:

T = 1300 K, P = 10 mbar, D H_2 = 15 lh^{-1}, D BCl_3 = 1·6 lh^{-1}
0·177 < D CH_4 < 9 lh^{-1} is $10^{-2} < D\ CH_4/D_T < 0{\cdot}35$
0·01 < D $TiCl_4$ < 0·4 lh^{-1} is $4 \times 10^{-4} < D\ TiCl_4/D_T < 2{\cdot}4 \times 10^{-2}$
D_T = Total flow

3.1 Identification of the phases

An XRD analysis of the solid deposits obtained from the experiments indicated three phases: titanium diboride (TiB_2), a rhombohedral $B_{13}C_2$ solid solution and a tetragonal phase that we labeled Q, which is of the same type as the phase $B_{50}C_2$ obtained in the B–C system.[3]

The distribution of these phases and their domains are shown in the deposition diagram of Fig. 2,

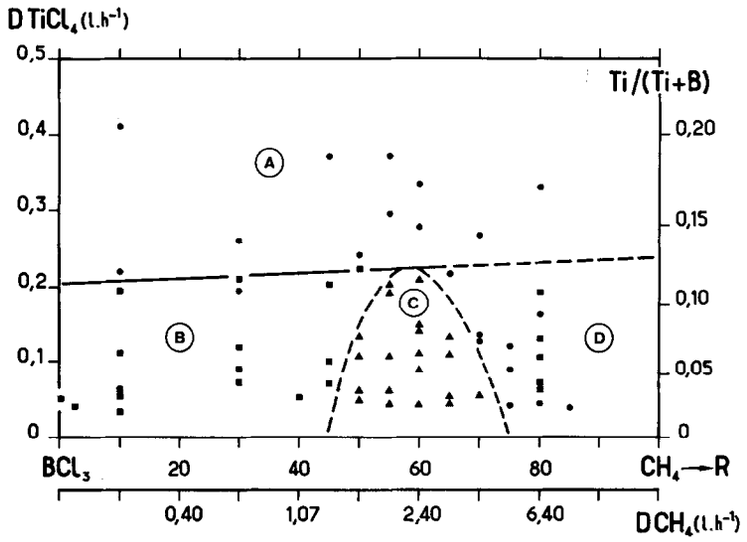


Fig. 2. Experimental deposition diagram as a function of the gas phase composition (XRD). T = 1300 K, P = 10 mbar, D BCl_3 = 1·6 lh^{-1}, D H_2 = 15 lh^{-1}. (A) TiB_2; (B) TiB_2 + Q; (C) $B_{13}C_2$ + TiB_2 + Q; (D) TiB_2 + Q.

which delineates four distinct zones: Zone A: Only TiB_2 is detected for flows of $TiCl_4$ greater than 0·2 lh^{-1} regardless of the value of *R*. For flows below 0·2 lh^{-1}, the phases $B_{13}C_2$ and Q appear. Zone B: The co-deposition of TiB_2 + phase Q is obtained for a ratio *R* less than 45. The proportion of the tetragonal phase in the mixture is more important since the two variables are lower. Zone C: The two compounds $B_{13}C_2$ and TiB_2 and the tetragonal phase Q are deposited simultaneously for values of *R* between 45 and 75. This domain becomes narrower when the flow of $TiCl_4$ is augmented. Zone D: As in Zone B, the TiB_2 and tetragonal phase coexist. Phase Q is present in a very small quantity, and is not always detected by XRD.

In agreement with the thermodynamic predictions,[2] the compound TiB_2 was synthesized in all the explored parametric domain. However, its crystallization in the depositions considered to be monophased is much better, as the gaseous mixture has a low concentration of methane and is rich in $TiCl_4$ (Fig. 3). Indeed an evolution towards the conventional conditions for the production of TiB_2, in which the ratio Ti/B in the gaseous phase is close to that in the condensed phase.

The carbonaceous phases appear jointly with TiB_2 but only for low concentrations of $TiCl_4$ in the gaseous phase. The most frequently encountered phase is the tetragonal (Q) one, probably not containing much carbon.

In fact, this phase clearly has phases very rich in boron such as $B_{50}C_2$, $Ti_{1\cdot87}B_{50}$ or $Ti_{1\cdot3\text{-}2}B_{48}C_2$ as described by Amberger and Ploog.[5–8] Figure 4 compares the RX spectra of the experimental phase Q to those of $B_{50}C_2$, $Ti_{1\cdot87}B_{50}$ or $Ti_{1\cdot86}B_{48}C_2$.

The configuration of the spectrum of the Q phase is identified with that proposed by Amberger, as much by the sequence of the peaks as by their position. The relative intensities of the peaks, by contrast, are not as reported, but the variation can be attributed to the textural effects of our material. In addition, some peaks were found which are not listed in the JCPDS data (no. 29-1356). However, a theoretical calculation of their position based on the lattice parameters determined (Table 1), allowed us to attribute these additional peaks to the tetragonal phase.

During prolonged reheating at 1670 K, this phase dissociated completely, forming $B_{13}C_2$ (the only additional phase detected), but probably also TiB_2 (already present), and boron (not detected because the amounts present are too small).

the spectra of the deposited two and three phases (Fig. 5) show that the proportion of the tetragonal phase decreases rapidly when the flow of $TiCl_4$ increases. Additionally, they show that the XRD peaks relative to the most carbonaceous phase of the system, rhombohedral boron carbide ($B_{13}C_2$), are less numerous, less intense and poorly defined.

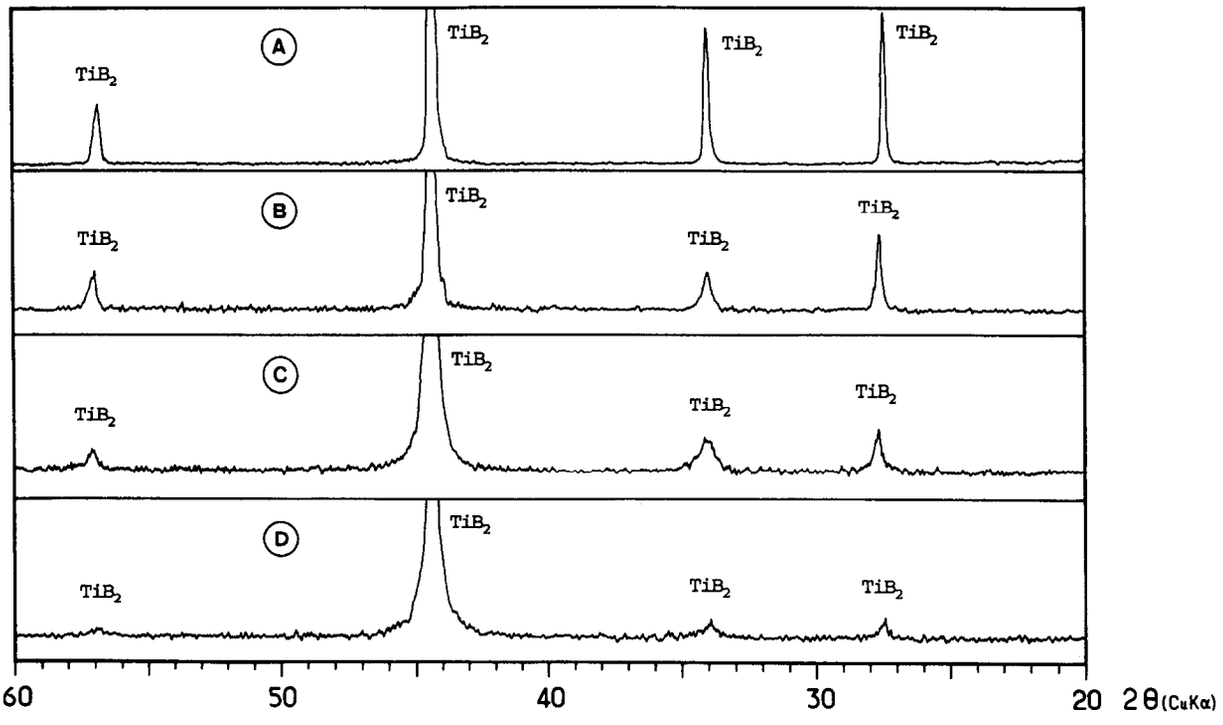


Fig. 3. States of titanium diboride crystallisation. T = 1300 K, P = 10 mbar, D BCl_3 = 1·6 lh^{-1}, D H_2 = 15 lh^{-1}

	A	B	C	D
R	10	55	70	80
D $TiCl_4$ (lh^{-1})	0·40	0·29	0·27	0·16

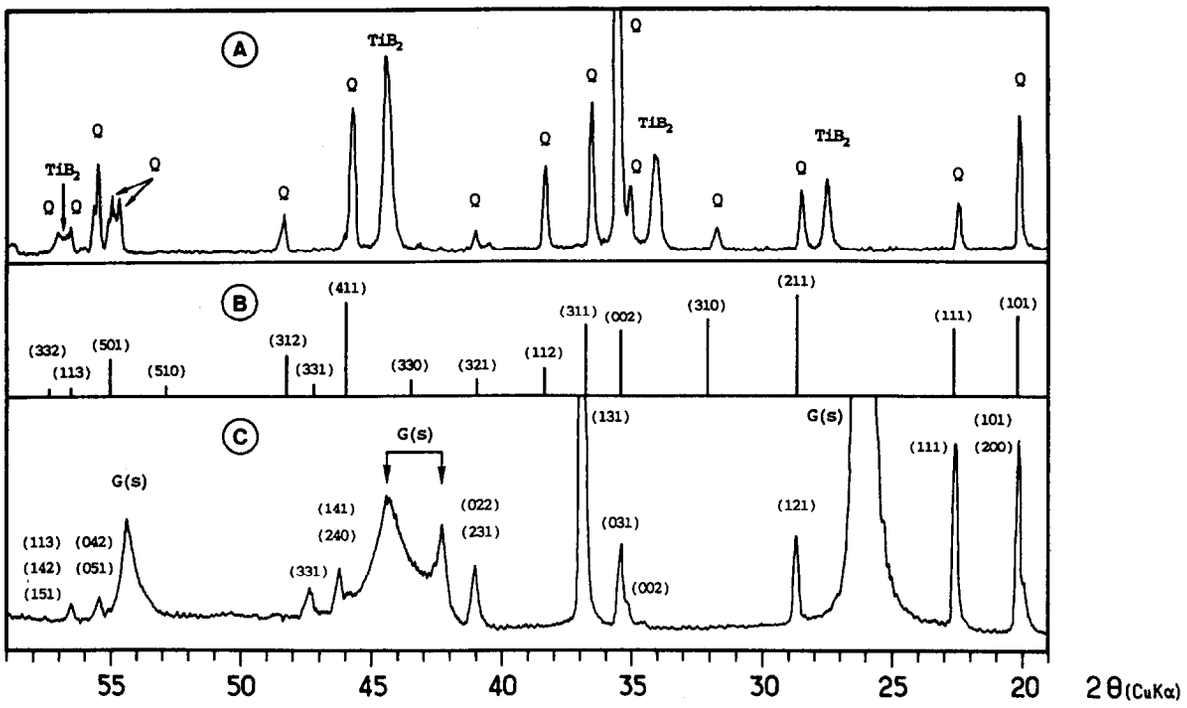


Fig. 4. Identification of the tetragonal phase (Q). (A) RX Spectrum of the B deposition domain (TiB_2 + Q); (B) Theoretical RX Spectrum of $B_{50}Ti_{1\cdot87}$;[6] (C) RX Spectrum of the $B_{50}C_2$ phase (G(s): graphite substrate).

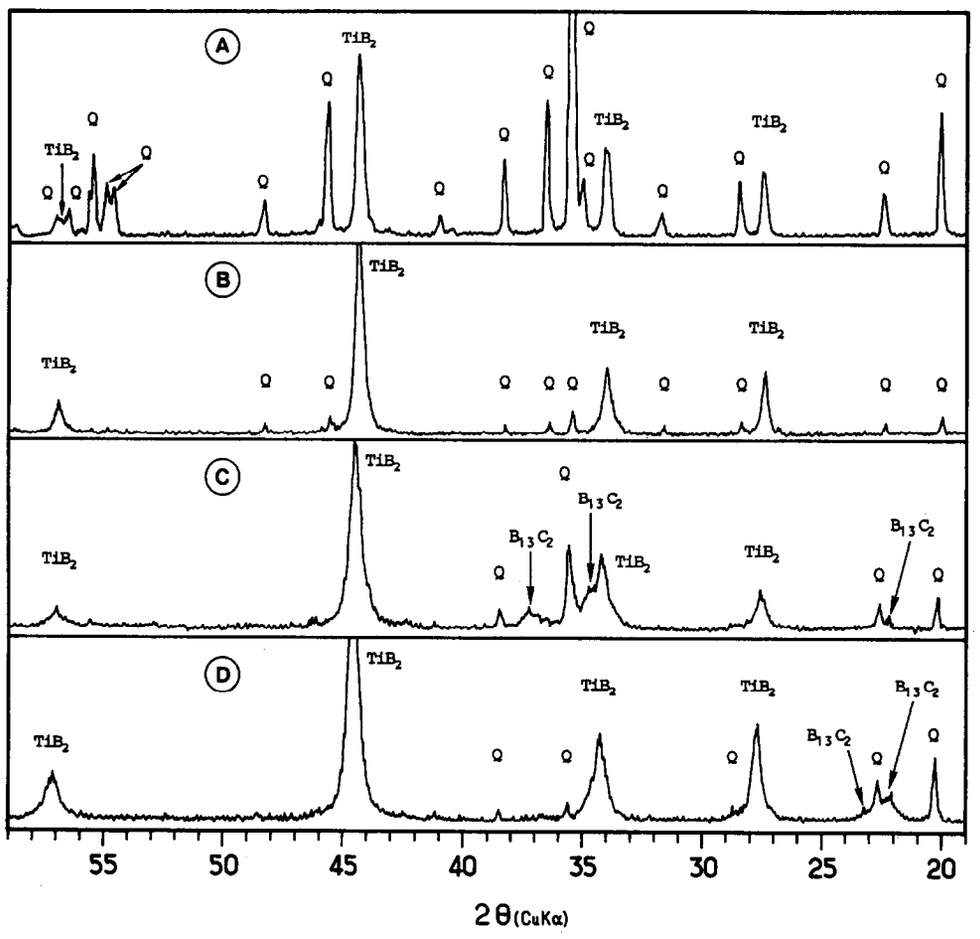


Fig. 5. Evolution of the RX spectra of the two or three phase depositions as a function of the composition in the gas phase:

	A	B	C	D
R	10	10	50	70
D $TiCl_4$ (lh^{-1})	0·014	0·10	0·06	0·054

Table 1. Lattice parameters of the main tetragonal phases

Phase	*a(A)*	*c(A)*	*Reference*
$B_{50}C_2$	8·77	5·07	[5]
$Ti_{1·87}B_{50}$	8·830	5·072	[6]
$Ti_{1·86}B_{48}C_2$	8·870	5·062	[7,8]
Q	8·84 ± 0·01	5·05 ± 0·01	

3.2 Elemental Analysis

Sixteen of the deposited phases distributed throughout the domains of the phase diagram (Fig. 6) were analysed using an electronic microprobe on polished sections. The results of the elementary bulk (defocalization of the electronic beam on a 20 μm diameter) and local analyses on the different visualized phases are averaged from 5 to 10 measurements. The results are grouped in Table 2 and show that the deposits are of a heterogeneous composition at the level of the analysis.

The global compositions are very rich in boron and are found in only a small part of the ternary Ti–B–C diagram. Three types of composition are observed among the local analyses:

(1) The first type corresponds to TiB_2; several percent of carbon are always associated with it.

(2) The second type (92–95 atomic percent boron, 4·5 to 5·5 atomic percent titanium, and 0·5–3 atomic percent carbon) is identified with the tetragonal structure $Ti_{1·3-2}B_{48}C_2$ such that the titanium content is slightly higher and the carbon content is slightly lower as compared to the domain of the solution proposed by Amberger.[8]

(3) The third type of compound which logically corresponds to the $B_{13}C_2$ phase observed by XRD, introduces some important quantities of titanium (from 7–26 atomic percent).

This third composition could be considered as a mixture of the three phases, TiB_2, Q, and $B_{13}C_2$ identified by XRD and forming a dispersed type of material (hereafter designated 'M') for which the size of the crystals would be inferior to the resolution for the spot of analysis.

A deposition diagram was outlined from these analyses (Fig. 7). In this diagram, at the most only two of the three types of the previously defined compositions coexist. The boundary of the monophased zone of the deposition TiB_2 is shifted toward higher flows of the $TiCl_4$ (around 0·3 lh^{-1} as compared with 0·2 lh^{-1} previously). Below this value, the dispersed phase 'M' is always present, either alone or associated with the phases TiB_2 or Q.

3.3 Rate of growth of the coatings

The deposition rates are expressed in units of mass per unit time and area, where the changes in mass were determined by weighing the samples before and after applying the coating.

3.3.1 Effects of varying methane concentration of the deposition rate

Figure 8 shows that for a constant flow of $TiCl_4$, the deposition rate varies little with the methane flow for values of R between 45 and 60, following the flow of $TiCl_4$. For higher values, the deposition rate decreases. This evolution could correspond to the progressive disappearance in the deposited solids of the large crystals of TiB_2 or the Q phase for which the kinetics of growth are elevated. The rate decreases in the zones of the phase diagram where only the dispersed phase 'M' is found.

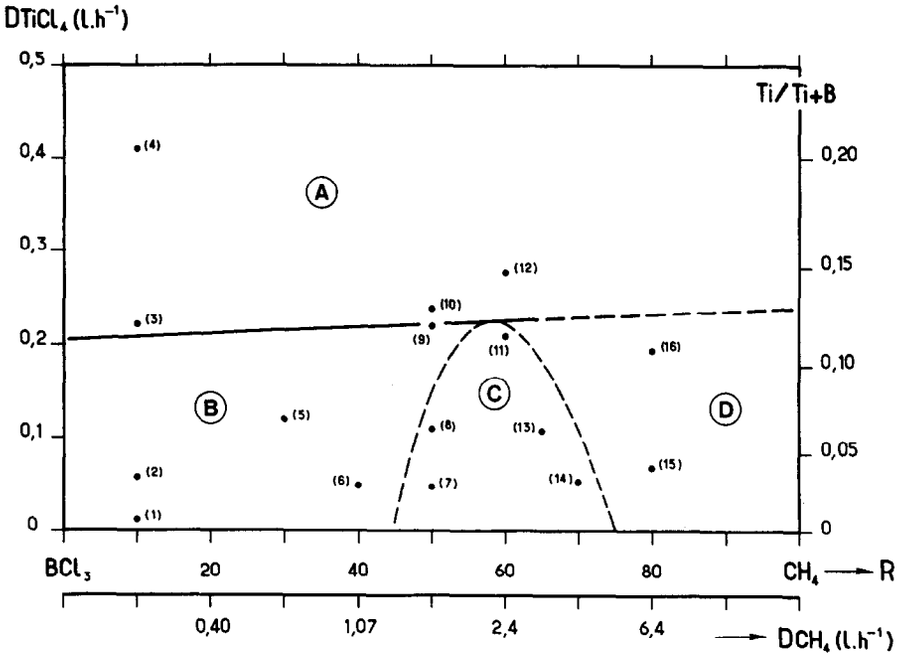


Fig. 6. Position of the analysed samples (electronic microprobe).

Table 2. Elemental analysis of layers

Sample	Bulk analyses (at.%)			Local analyses (at.%)								
				TiB_2			Q			'M'		
	B	Ti	C	B	Ti	C	B	Ti	C	B	Ti	C
1	90·0 ± 2	5·8 ± 1	4·2 ± 1				94·0 ± 2	4·5 ± 0·5	1·5 ± 4	80·0 ± 4	12·0 ± 1	7·0 ± 0·5
2	87·2 ± 3	11·2 ± 1·5	1·6 ± 0·5				95·0 ± 1	4·5 ± 1	0·5 ± 0·5	74·0 ± 3	23·0 ± 1	3·0 ± 0·5
3	78·8 ± 3	18·9 ± 1	2·3 ± 0·5				92·6 ± 3	5·4 ± 1	2·0 ± 0·5	74·0 ± 1	24·0 ± 1	2·0 ± 0·5
4	71·0 ± 3	26·8 ± 2	2·2 ± 0·5	66·0 ± 1	33·0 ± 0·5	1·0 ± 0·5						
5	85·7 ± 4	12·3 ± 0·5	2·0 ± 0·5				93·3 ± 2	4·9 ± 0·5	1·8 ± 0·5	78·6 ± 4	19·4 ± 0·5	2·0 ± 0·5
6	85·3 ± 4	10·3 ± 1·5	4·3 ± 0·5				93·0 ± 1	4·0 ± 0·5	3·0 ± 0·5	80·0 ± 2	17·0 ± 1	3·0 ± 0·5
7	84·3 ± 2	7·0 ± 2	8·7 ± 1							84·3 ± 1	7·0 ± 1	8·7 ± 0·5
8	81·2 ± 4	14·0 ± 2·5	4·8 ± 1							81·5 ± 4	13·5 ± 2·5	5·0 ± 1
9	71·2 ± 5	26·5 ± 1·5	2·3 ± 0·5							71·2 ± 5	26·5 ± 1·5	2·3 ± 0·5
10	75·2 ± 5	17·8 ± 2	7·1 ± 0·5	67·0 ± 1	30·0 ± 0·5	3·0 ± 0·5				72·0 ± 2	21·0 ± 0·5	6·0 ± 0·5
11	72·2 ± 5	21·2 ± 5	6·6 ± 1	64·5 ± 2	34·0 ± 0·5	1·5 ± 0·5				73·0 ± 2	23·0 ± 1	4·0 ± 0·5
12	69·0 ± 2	29·3 ± 1	1·7 ± 0·5	67·6 ± 2	29·4 ± 1	2·2 ± 0·5						
13	78·5 ± 7	16·0 ± 5	5·5 ± 1							76·5 ± 7	19·0 ± 0·5	4·5 ± 1
14	81·2 ± 2	10·9 ± 1	7·9 ± 0·5							81·2 ± 2	10·9 ± 1	7·9 ± 0·5
15	78·9 ± 2	11·3 ± 2	9·8 ± 1							78·9 ± 2	11·3 ± 2	9·8 ± 1
16	69·1 ± 8	25·5 ± 3	5·4 ± 1·5	66·0 ± 2	32·0 ± 1	2·0 ± 0·5				72·0 ± 2	21·0 ± 1	7·0 ± 0·5

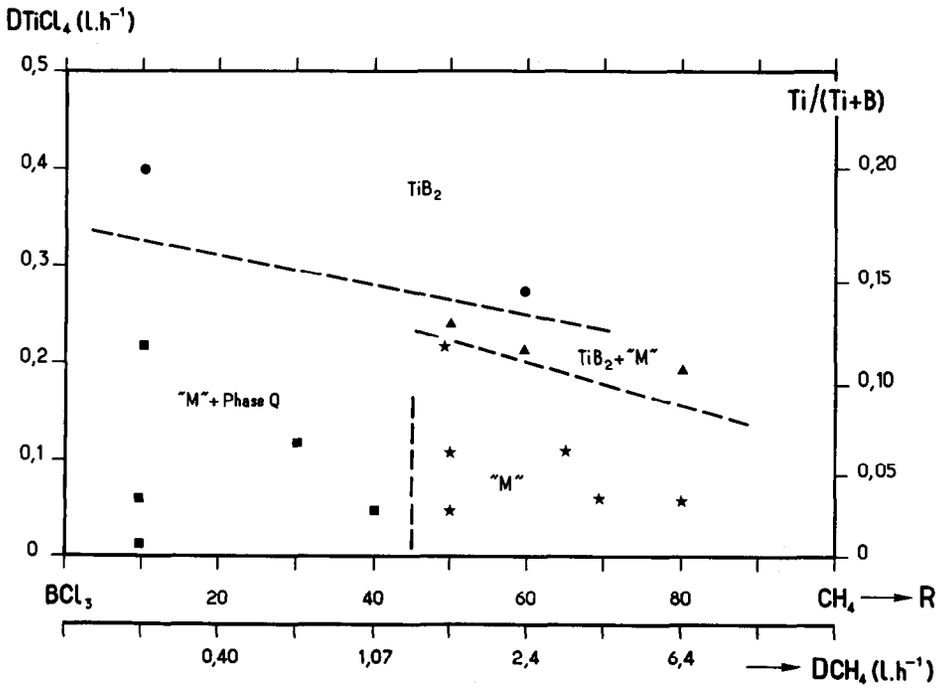


Fig. 7. Diagram of the deposition based an elemental analysis 'M': TiB_2 + $B_{13}C_2$ + Q.

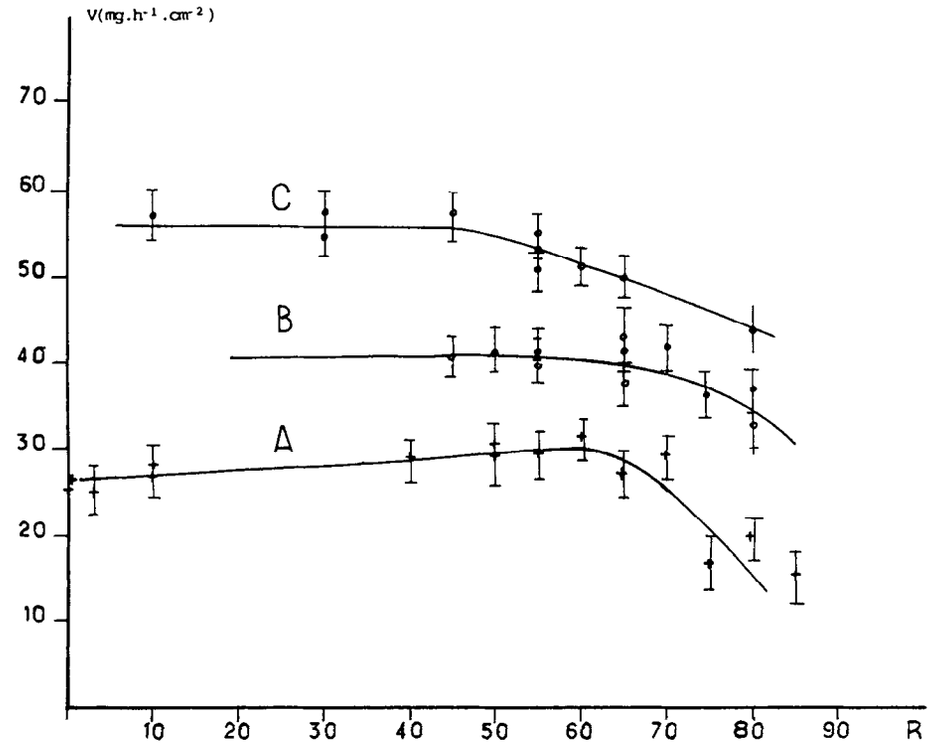


Fig. 8. Evolution of the deposition rate as a function of the methane concentration (R). T = 1300 K, P = 10 mbar, D BCl_3 = 1·6 lh^{-1}, D H_2 = 15 lh^{-1}. (A) D $TiCl_4$ = 0·05 lh^{-1}; (B) D $TiCl_4$ = 0·12 lh^{-1}; (C) D $TiCl_4$ = 0·21 lh^{-1}.

3.3.2 Effects of varying $TiCl_4$ concentration on the deposition rate

The influence of the $TiCl_4$ flow is clearly stronger. The rate of deposition increases rapidly with the flow of titanium tetrachloride. For example, the rate doubles when the flow increases from 0·05 to 0·2 lh^{-1}. The curve in Fig. 9(a) gathers the values obtained for values of R less than 60, which is in the domain where the concentration of CH_4 doesn't have any influence. A maximum rate is obtained for flows of $TiCl_4$ on the order of 0·2–0·25 lh^{-1}.

An analog result was established by Takahashi *et al.*[9] for the system $TiCl_4$–BCl_3–H_2 (Fig. 9(b)), giving evidence of the importance of the formation of diboride in the kinetics of the deposition.

3.4 Microstructure of the deposited layers

The crystallization of the solid phase varies strongly as a function of the composition of the gaseous mixture provoking in particular some unique surface morphologies.

3.4.1 Morphology of the surface

(a) Low flows of $TiCl_4$

If the concentration of the CH_4 is also low, the coatings are rich in the tetragonal phase. The phase $B_{50}C_2$ in the B–C system[4] is present as angular crystals of a large size (up to about 30 μm), but for which the geometry is seldom perfect (Fig. 10(a)). When the flow of methane increases, the crystallization becomes finer, and the growth becomes dendritic. Meanwhile, the concentration of angular crystals in the tetragonal phase decreases sharply and their size is clearly smaller (a few μm).

Near R = 50 (Fig. 9(b)), the surface shows some growth of the order of 10 μm and of a rounded form, characteristic of a mixture with a boron carbide base ('M') when this is the main phase present.

For greater methane flows, the growth increases (~100 μm) (Fig. 9(c), R = 65). Beyond the three phases domain (XRD), the small sub-micronic crystals are very well defined geometrically and are already formed (Fig 9(d), R = 80).

(b) Influence of the $TiCl_4$ flow

When the flow of $TiCl_4$ increases, the titanium diboride has the general tendency to form in large quantities and to become the basic material in the deposition.

In this matrix, with a low flow of methane, the crystals in the tetragonal phase are small in size (a few microns) and become more scattered as the $TiCl_4$ concentration in the gaseous mixture increases. Near R = 60 (Fig. 10(e)) the growths visible at the surface become less and less numerous, and consist of the 'M' mixture.

At high methane concentrations (R > 65) and for a $TiCl_4$ flow on the order of 0·25 lh^{-1}, the surface shows, under small magnification, aspects of an amorphous material. It is in fact comprised of the small crystals remarkably uniform and of a few μm in size (Fig. 10(f)).

3.4.2 Examination of transversal cuts

On the plates shown in Fig. 11, obtained from

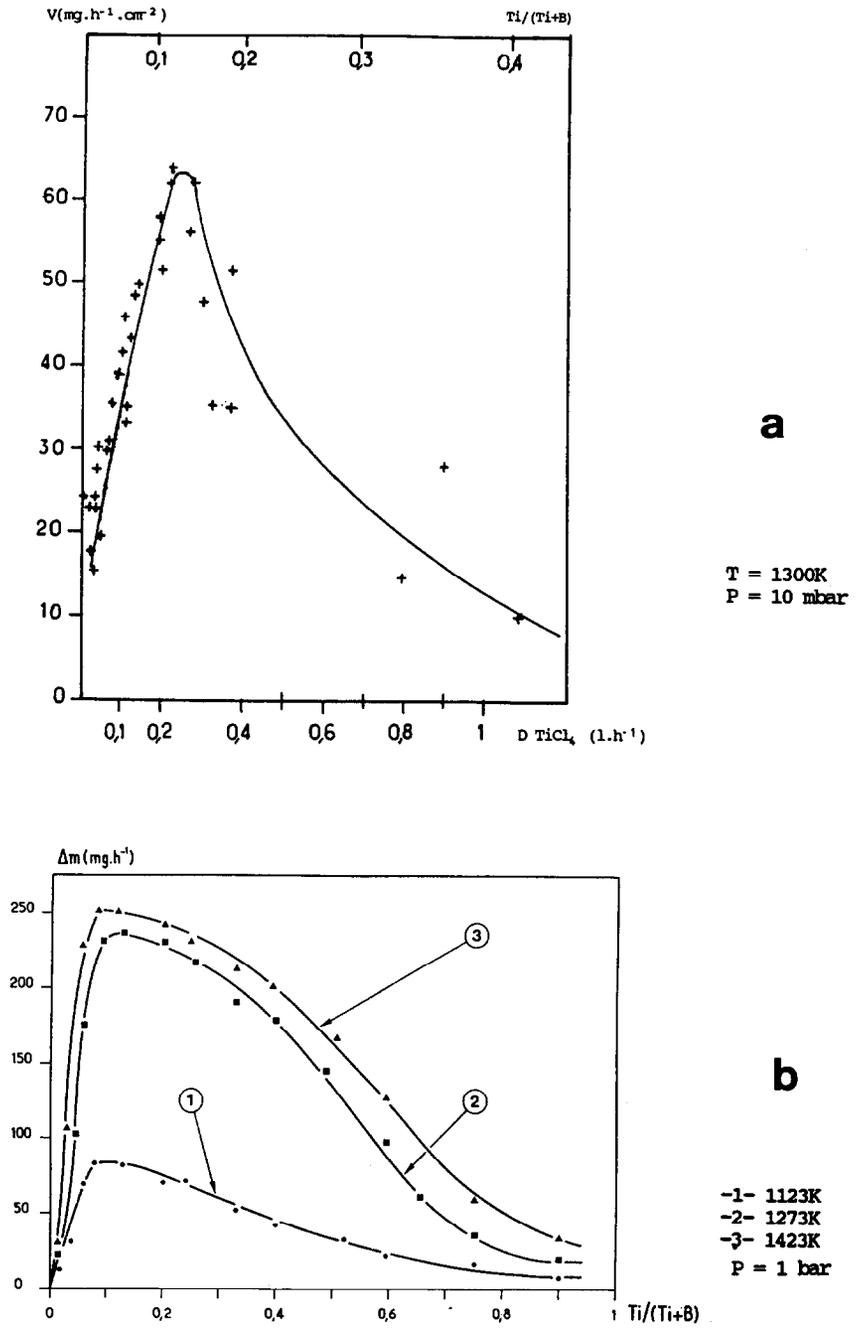


Fig. 9. Influence of the $TiCl_4$ concentration on the deposition rate $R<60$. (a) T = 1300 K, P = 10 mbar, D BCl_3 = 1·6 lh^{-1}, D H_2 = 15 lh^{-1}; (b) Influence according to Takahashi[9] (Ti–B system).

backscattering electrons, the microstructure can be seen clearly: the rich titanium (TiB_2) zones appear clearly and contrast strongly with the shadowed low titanium regions (Q and $B_{13}C_2$). The materials in the 'M' + Q domain are very dense. When the tetragonal phase is preponderant (Fig. 11(a)), the crystals grow perpendicularly to the surface. When it becomes less abundant, the orientation is uncertain (Fig. 11(b)). In the domain 'M', the crystallization is particular. The tetragonal phase is always present in a matrix formed from a mixture of boron carbide and titanium diboride (B_4C + TiB_2), either in the form of filaments without defined geometry (Fig. 11(c)) or under the form of the axis of the grain (Fig 11(d)).

The composition of the matrix is not constant. Near the interface of the substrate and deposition as well as at the center of the nucleation site, the titanium content is higher. When the size of the particles is large, this type of growth leads to the formation of large pores.

The matrix appears homogeneous with the electronic microprobe analysis. The resolution was obtained by field effect microscopy (Fig. 12(a) and 12(b)). It shows that the matrix is constituted of a dispersed mixture of nanometric crystals (about 50 nm) of a boron carbide and titanium diboride ($B_{13}C_2$ + TiB_2). The grains formed here are often found following an axis parallel to the surface with whiskers of phase Q and a cross section of about

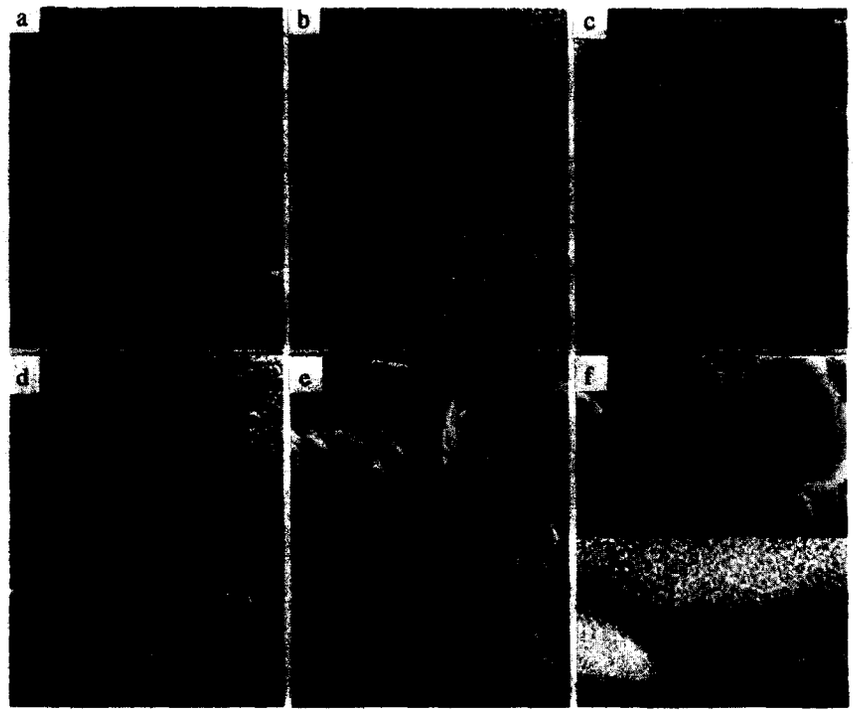


Fig. 10. Morphology of typical deposition surfaces. T = 1300 K, P = 10 mbar, D BCl_3 = 1·6 lh^{-1}, D H_2 = 15 lh^{-1}. (a) Q + 'M' (R = 10); (b) 'M' (R = 50); (c) 'M' (R = 65); (d) 'M' (R = 80); (e) TiB_2 + 'M' (R = 60); (f) TiB_2 + 'M' (R > 65).

0·5 × 0·5 μm. In the domain TiB_2 + 'M', the depositions form over a wide area and have very fine microstructure (Fig. 11(e)). The compounds evolve from 'M' to TiB_2 in forming some zones parallel to the surface. The concentration of TiB_2 is always higher near the interface. The deposits of pure TiB_2 (Fig. 11(f)) equally present a layered structure with very porous periodic layers and are characteristic of those described by Takahashi.[9] These TiB_2 coatings were obtained with weak ratios of Ti/Ti+B.

4 Influence of the Temperature

4.1 Kinetics and the nature of the phases

The results of the experiments with R = 60 and the $TiCl_4$ flow equal to 0·015 lh^{-1}, are shown in Fig. 13(a). At temperatures above 1530 K, the tetragonal phase, which is unstable at high temperatures no longer forms and a codeposit of titanium diboride and boron carbide is found. In contrast, at temperatures below 1280 K, titanium boride is the only phase identified.

The corresponding rate of deposition increases with temperature until 1500 K and then falls quickly at temperatures greater than about 1600 K. This rapid rate decrease can be attributed to the appearance of reactions in the homogenous phase. This tendency was established for the B–C system at the same ratio R.[10,11]. By contrast, the work of Besmann[12] indicates that the TiB_2 deposition rate continues to increase until 2173 K but this increase is lowered as soon as the temperature reaches 1473 K. Thus, the addition of methane essentially limits the deposition rates at high temperatures.

This effect was confirmed when the methane flow was decreased (R = 10, D $TiCl_4$ = 0·05 lh^{-1}). The deposition rate, which was higher than earlier, increased linearly with temperature (Fig. 13(b)). The tetragonal phase was observed up to our highest experimental temperature of 1580 K.

Figure 14(a) shows the deposition rate as a function of temperature for two $TiCl_4$ flow rates. In this case, the flow of BCl_3 was reduced to 0·4 lh^{-1} in order to decrease the kinetics, and R was fixed at 60. The evolution is the same as was described previously (Fig. 13(a)), but an increase in the $TiCl_4$ gas phase concentration displaces the maximum value towards lower temperatures and since the concentration of CH_4 is less, it has a smaller influence on the rate decrease. Figure 14(b) outlines the corresponding deposition diagram. The existence of the two phase region (TiB_2 + Q and TiB_2 + $B_{13}C_2$) and the three phase region (TiB_2 + B_{13} C_2 + Q) appears to be strongly dependent on temperature.

Furthermore, as was mentioned earlier, the carbon phase exist only when $TiCl_4$ concentrations are small. In this case, for flows of $TiCl_4$ > 0·1 lh^{-1}, only TiB_2, is found.

4.2 Surface morphology

The surface morphology, like the composition of the deposits, varies greatly with temperature. For

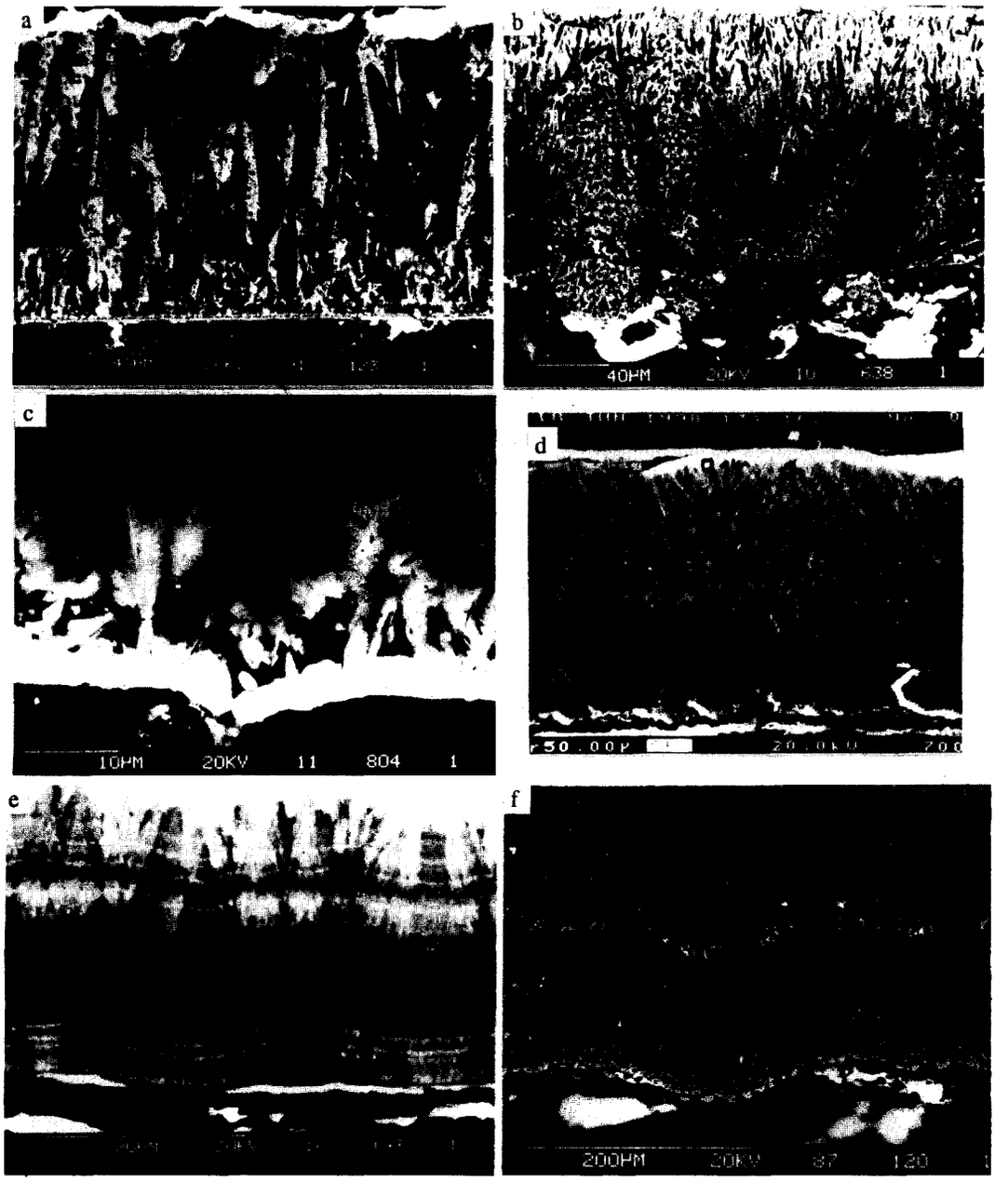


Fig. 11. Metallographic sections of typical deposits (secondary electrons). (a) and (b) 'M' + Q; (c) and (d) 'M'; (e) TiB_2 + 'M', (f) TiB_2.

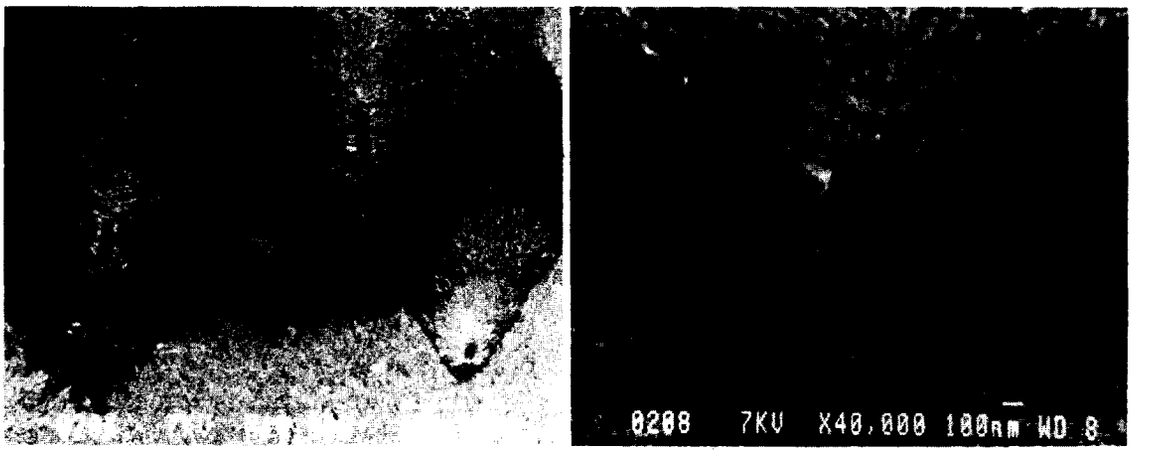


Fig. 12. Microstructural details of a type 'M' deposition (field effect microscopy). R = 65, D $TiCl_4$ = 0·108 lh^{-1}.

R = 60 and D $TiCl_4$ = 0·06 lh^{-1} and at low temperatures (only TiB_2 deposition), the surface has the characteristic partial crystallization (Fig. 15(a)). When the temperature is elevated, the tetragonal phase, which has a tendency to grow in a columnar manner, greatly influences the microstructure

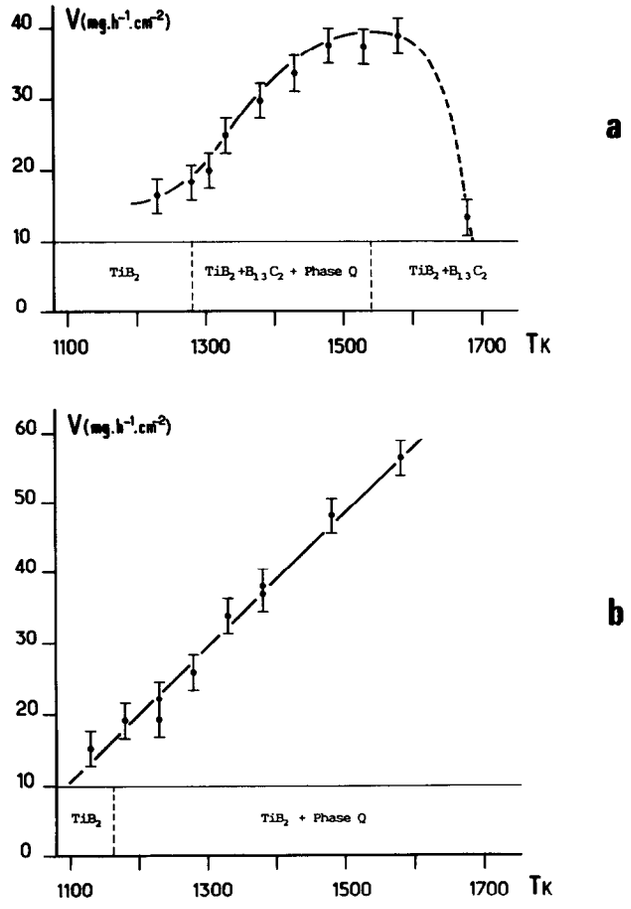


Fig. 13. Influence of the temperature on the deposited phases and on the deposition rate. P = 10 mbar, D BCl_3 = 1·6 lh^{-1}, D H_2 = 15 lh^{-1}. (a) R = 60; D $TiCl_4$ = 0·015 lh^{-1}; (b) R = 10, D $TiCl_4$ = 0·05 lh^{-1}.

of the layers. In particular, a reduction of its content is accompanied by progressive disorientation of the emerging crystals. At 1380 K for example, the surface is typical of a singular crystallization in the previously described 'M' phase (Fig. 15(b)).

Beyond 1580 K, only TiB_2 is identified. This time its crystallization is clearly evident with XRD, but it can be present under a wide variety of morphologies: fine lamellar structure at 1580 K and parallelepipedal crystals at 1685 K (Figs 15(c) and (d)).

5 Conclusions and Comments

The results of this experimental study have little in common with the thermodynamic predictions previously published.[2] The only principal in agreement is the importance of the affinity of the boron and titanium to the behavior of the chemical system. This is evident in all the cases by the omnipresence of titanium diboride in the explored regions. By contrast, the carbon vector has a weak influence experimentally, and it is only for cases with low $TiCl_4$ concentrations in the initial gas mixture that the weakly carbonated phases (Q and $B_{13}C_2$) are deposited.

According to the theoretical results, methane should be almost completely dissociated and accordingly, carbon should be the major element in coatings prepared from a gaseous starting mixture rich in methane. But, neither titanium carbide nor free carbon were ever detected.

If we compare the theoretical deposition diagrams with the experimental ones (Figs. 1 and 2), the experimental region of the $B_{13}C_2$ phase is found largely displaced towards higher values of CH_4 concentrations than in the theoretical diagram (region TiB_2 + B_4C + C) which indicates that an excess of methane (about ten times greater than the amount predicted by thermodynamics) is necessary to form $B_{13}C_2$. Similarly, the limits of the boron carbide domain are found at values less than those predicted by thermodynamics for specific amounts of $TiCl_4$ in the gas phase (Ti/Ti+B < 0·35).

Concerning yields: if one considers that titanium boride is essentially the compound formed when the maximum deposition rate is attained (Figs. 2 and 8), the ratio Ti/B is then about 1 : 6 or a third of the diboride stoichiometry. In this case, 50–60% of the $TiCl_4$ in the gas mixture reacted to form TiB_2. Thus the maximum theoretical yield of 95% as indicated by thermodynamics is not obtained. The discrepancies between the thermodynamic and experimental results can mainly predict the existence of the tetragonal phase Q which could not have been taken into account in the calculations and which also influences the microstructure of the deposited solids. This phase is a new example of the metastable phase which can be obtained far from equilibrium by CVD. It can be identified with the phases described by Amberger and Ploog[7–8] $Ti_{1\cdot87}B_{50}$ and $Ti_{2-x}B_{48}C_2$.

Nevertheless, the huge influence of titanium chloride in comparison to methane on the composition of the solid as well as the results of the local analysis (weak carbon content in the region of the 'Q' phase (Table 2)) leads one to think that, especially in the cases low in methane, the Q phase is more saturated in titanium than in carbon and could be written as $B_{48}Ti_2C_{2-y}$. The more general formulation would be $B_{48}Ti_{2-x}C_{2-y}$.

In other respects, the existence of the carbonaceous phase is also strongly influenced by the synthesis temperature. Their domain of thermal existence is in fact relatively limited (from 1150 to around 1700 K under our experimental conditions). The boundaries evolve however with different parameters. When the tetragonal phase can no longer form (at temperatures less than 1600 K in our work), a codeposit of titanium diboride and boron carbide occurs, which is an interesting *a priori* mixture from the mechanical properties

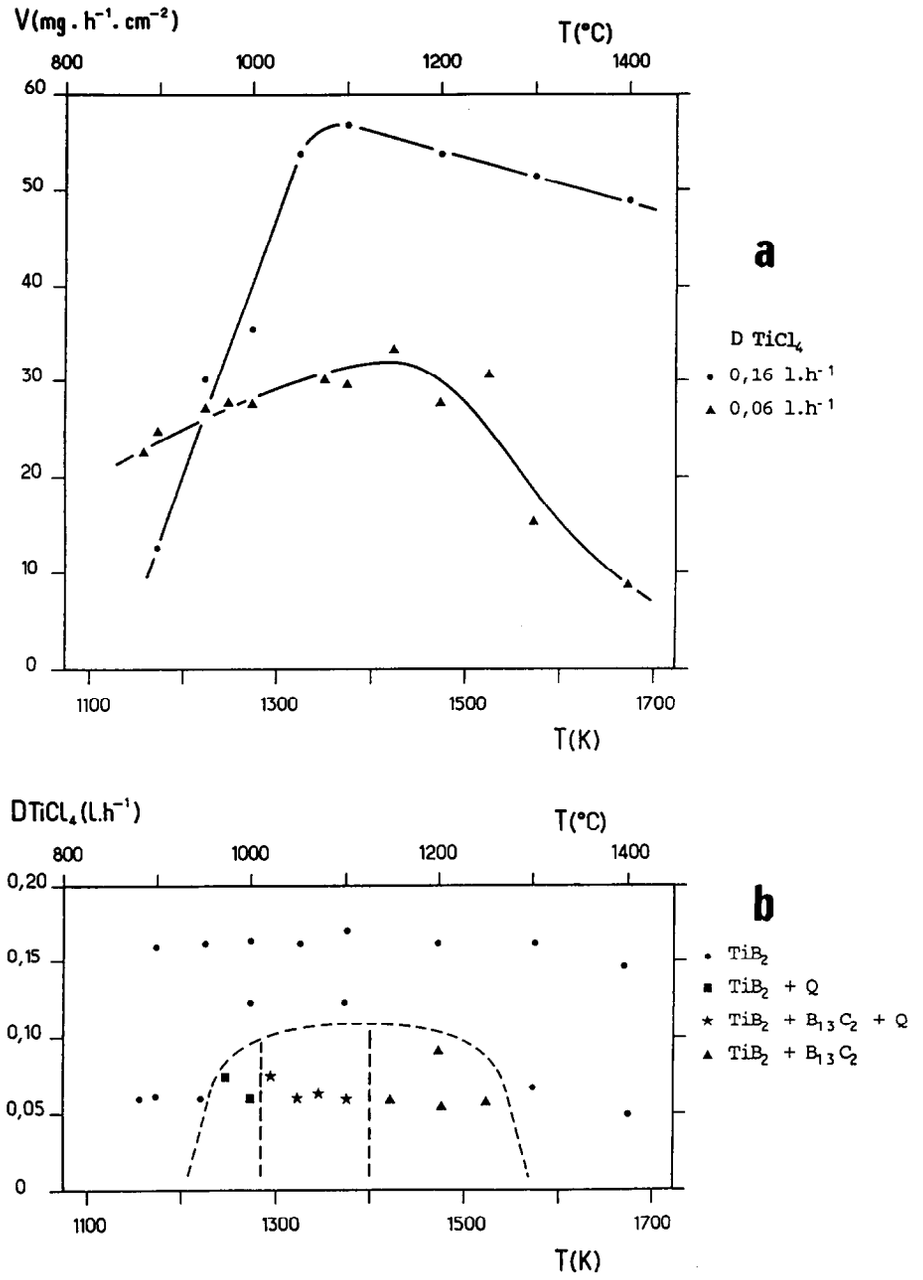


Fig. 14. Influence of temperature and of $TiCl_4$ concentration on the deposition rate (a) and on the nature of the deposited phases (b). P = 10 mbar, R = 60, D BCl_3 = 0·41 lh^{-1}.

stand-point. Since it makes $B_{50}C_2$ in the B–C–H–Cl system,[10,11] this tetragonal phase, very rich in boron, can strongly limit the deposition of non-combined boron at low temperatures. However, the phase obtained in this case differs from $B_{50}C_2$ by its large domain of existence (up to R = 80). Thus, it covers the entire deposition region of boron carbide, and the two phases TiB_2+$B_{13}C_2$ can only be isolated at higher temperatures. By contrast, the deposition domain of the rhombohedral phase is only slightly displaced or not displaced at all on the methane concentration axis as compared to the B–C–Cl–H system.

In conclusion, it can be observed that these carbonaceous phases, using a tridimensional representation of D CH_4 (R), D $TiCl_4$ and temperature, will only be present in a small zone within the large domain of TiB_2 deposition. In contrast, these phases are very interesting because of their very special and unique microstructure. The common basis of these materials is a mixture of nanometric crystals of titanium diboride and rhombohedral boron carbide which wrap the whiskers of phase Q and which also have different configurations. This composite, called 'M', can be mixed with diboride and the Q phase, which are present simultaneously in the same solid under two different crystallizations.

Acknowledgements

This research was supported by the Association Nationale de la Recherche Technique (A.N.R.T.)

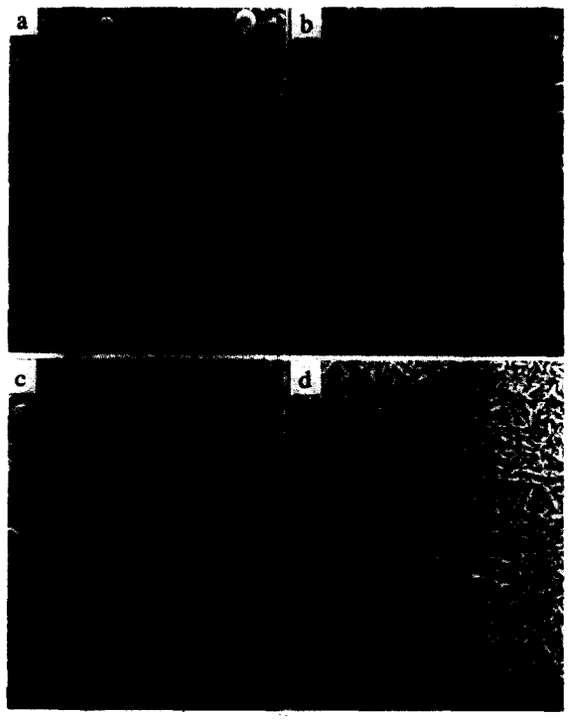


Fig. 15. Surface morphology as a function of temperature. P = 10 mbar, R = 60, D $TiCl_4$ = 0·06 lh^{-1}. (a) 1180 K; (b) 1380 K; (c) 1580 K; (d) 1685 K.

and by Coating Development S.A. (Ciffre convention no 86307).

References

1. Guiban, M. A., Berjoan, R. & Male G., *Ann. Chim. Fr.*, **18** (1993) 159–74.
2. Guiban, M. A. & Male, G., *Calphad*, **17**, 2 (1993) 207–16.
3. Guiban, M. A., Etude par CVD des systèmes Si–B–C–Cl–H et Ti–B–C–Cl–H. *Caractérisation des dépôts*, Thèse de Doctorat, Université de Limoges, 1991.
4. Lartigue, S. & Male G., *J. Mater. Science Letters*, **7** (1988) 153–6.
5. Ploog, K. & Amberger, J., *Less Common Met.*, **23** (1971) 33–42.
6. Amberger, E. & Polborn, K., *Acta Cryst.*, **B31** (1975) 949–53.
7. Ploog K., *Acta Cryst.*, **B32** (1976) 981–2.
8. Amberger, E. & Gerster, *Acta Cryst.*, **B36** (1980) 672–5.
9. Takahashi, T. & Kamia, H., *J. Cryst. Growth*, **26** (1974) 203–9.
10. Lartigue, S., *Elaboration par CVD et caractérisation de dépôts de carbure de bore. Application au revêtement de l'acier*, Thèse de Doctorat, Institut National Polytechnique de Grenoble, 1986.
11. Lartigue, S., Cazajous, D., Nadal, M. & Male, G., *Proc. Euro CVD 5*, Uppsala Sweden, June 17–20 1987 pp. 483–519.
12. Besman, M. & Spear, K. E., *J. Electrochem. Soc., Solid State Science and Technology*, **124**, 5 (1977) 790–7.

Journal of the European Ceramic Society **15** (1995) 551–561
© 1995 Elsevier Science Limited
Printed in Great Britain. All rights reserved
0955-2219/95/$9.50

0955-2219(95)00020-8

On the Chemical Vapor Deposition of Si/B/C-Based Coatings in Various Conditions of Supersaturation

S. Goujard,[a]* L. Vandenbulcke[a] & C. Bernard[b]

[a]Laboratoire de Combustion et Systèmes Réactifs — CNRS, F-45071 Orléans Cedex 2, France
[b]LTPCM, ENSEEG, BP 75, F-38402 Saint Martin d'Hères, France

(Received 22 July 1994; revised version received 21 December 1994; accepted 26 January 1995)

Abstract

The results of a thermodynamic and experimental study concerning the codeposition of three elements — silicon, boron and carbon — by a classical C.V.D. technique in a hot-wall reactor are reported. The thermodynamic approach has been described in a previous study and a first comparison was made with experiments carried out under conditions which favor the control by mass transport, at a relatively high temperature (T = 1400 K) and low mass flow rate. Experimental conditions further from equilibrium have been searched for here for depositing coatings with both good thickness and chemical composition uniformity when the process is more kinetically-controlled. The codeposits were obtained on graphite from various initial gaseous mixtures which were composed of methyltrichlorosilane (MTS), boron trichloride and hydrogen, at a total pressure of 0·395 atm, a total flow rate between 0·1 and 1·0 g/min and a temperature varying in the range 1200–1400 K. Low temperatures and high mass flow rates are shown to favour the deposition of uniform coatings but different results can be obtained as a function of the inlet gaseous composition since different kinetic limitations can arise which favor a boron or a silicon excess in the coating.

1 Introduction

In a new C.V.D. system, generally a thermodynamic study is first undertaken to predict the final composition of the system at equilibrium and to understand the influence of many parameters such as temperature, pressure and inlet gas composition. However, in a C.V.D. reactor, the thermodynamic equilibrium between the gas phase and the solid is always localized at the gas–solid interface, whereas the classic thermodynamic approach assumes that a global equilibrium is reached in a closed isothermal system between the gas phase and deposit. Near equilibrium conditions are actually reached when the chemical kinetics are intrinsically faster than the mass transfer step; generally at high temperature and low flow rate. Local equilibrium is therefore influenced by mass transport, because the material balance is changed by the element segregation transport phenomena and the well-known reactant's consumption and product's formation in downstream positions inside the reactor, especially hot-wall. Not only the influence of fluid mechanical effects has been previously shown, but also the limitations of using global equilibrium calculations to guide C.V.D. experiments. The drawbacks of chemical vapor deposition under near equilibrium conditions in a hot-wall reactor where the gas flows parallel to the surface have also been discussed.[1] As the thickness and chemical composition of the deposit were obviously not uniform, this work has now been extended to conditions which lead to a greater departure from equilibrium or supersaturation at the gas–solid interface, when the process is more kinetically-controlled.

The departure from equilibrium obtained under chemical kinetic limitations is often revealed by the deposition of certain structures differing from stable ones, for either elemental or binary deposits.[2–3] This is also manifested by the deposition of solids whose composition differs significantly from those predicted by thermodynamic calculations.[4–5] Moreover, if the departure from equilibrium or supersaturation were great, it would be easier to obtain coatings exhibiting uniformity in thickness and composition.[5–7]

As already mentioned above, the significance of the amount of supersaturation has been indicated throughout the study of elemental or binary deposits. In this work, the influence of the amount

*Present address: Société Européenne de Propulsion, Les Cinq Chemins — Le Haillan BP 37, F-33165 Saint-Médard-en-Jalles Cedex, France

of departure from equilibrium will be studied for a ternary (Si–B–C) system of deposition as follows:

— a classical comparison between the global thermodynamic predictions and the experimental compositions obtained at different temperatures or mass flow rates, keeping in mind that the material balance was changed as discussed above;

— a study of the influence of the supersaturation on thickness and composition uniformity of the deposits at either variable temperatures and constant mass flow rate, or variable mass flow rates and constant temperature.

2 Theoretical and Experimental Tools of Investigation

2.1 Thermodynamic calculations

The method used for thermodynamic calculations has been explained in another article[8] in which the choice of the solid phases, thermodynamic data and hypothesis for calculations were described in detail. To take into consideration the 'boron carbide' solid solution, the sublattice model developed by Hillert and Staffanson[9] and generalized by Sundmann and Agren[10] was used.[8]

The equilibrium yields, η, of the different gaseous and solid species were calculated. They are defined with respect to n°_{MTS} for silicon-containing species and for carbon-containing species and to $n^{\circ}_{BCl_3}$ for boron-containing species.

$$\eta = n_i\,(Si_yX_z)/n^{\circ}_{MTS},\ \eta = n_i\,(C_yX_z)/n^{\circ}_{MTS} \text{ and } \eta = n_i\,(B_yX_z)/n^{\circ}_{BCl_3}$$

where n_i represents the number of Si, C or B atoms in species i at equilibrium and n°_{MTS} and $n^{\circ}_{BCl_3}$ the initial number of CH_3SiCl_3 (MTS) and BCl_3 moles, ($\Sigma n^{\circ}_i = 1$ mole was chosen for simplicity). The equilibrium yields of the solid or gaseous species will not be represented if they remain smaller than 10^{-6} and it must be overlooked that the concentrations of H_2 and HCl are always high. One element can be incorporated in different solid phases, for example carbon in pure graphite, silicon carbide and boron carbide. From the equilibrium amount of the condensed species, the thermodynamically expected composition of the whole deposit was calculated. It will be presented by the atomic percent of each element.

2.2 Experimental techniques

2.2.1 C.V.D. device

The experimental setup was classic and has been previously described.[1] The desired flow rates of H_2, CH_3SiCl_3 (MTS) or BCl_3 were adjusted by mass flowmeters. The substrates were hung in a graphite susceptor (Fig. 1) which was heated by a high frequency generator regulated by a thermocouple fitted at the top of the susceptor. The maximum temperature fluctuations were ±3 K, but there was a constant difference of +75 K within the [1200–1400 K] range between the temperature of the substrate and that measured by the thermocouple. The gas mixture was introduced by a nozzle from the bottom to associate the natural and forced convections. The mass flow rate (F) varied in the range 0·1–1·0 g/min. Hydrogen used was of 99·995% purity by volume and boron trichloride and MTS of 99·9% purity. The substrates were fine textured polished graphite of 1·75 average density, cleaned in alcohol in an ultrasonic device and dried before weighing. Sample size was (18 × 10 × 2mm).

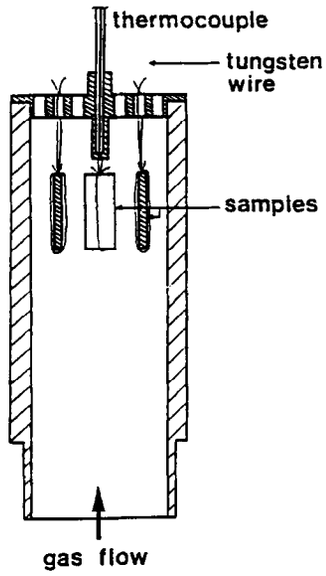


Fig. 1. Graphite susceptor and position of the samples.

2.2.2 Characterization of the deposits

The mass increase of each sample after deposition was measured with a precision balance. The thickness measurements were obtained on polished cross-sections with the help of an optical microscope. The chemical composition of the deposits was determined by the γ prompt photon spectrometry method developed at the C.E.R.I. (CNRS) laboratory in Orléans. The following nuclear reactions were used to measure the concentration of boron and silicon: $^{10}B\ (p, p', \gamma)\ ^{10}B$ and $^{28}Si\ (p, p', \gamma)\ ^{28}Si$ where γ-ray was induced by proton bombardment of ^{10}B and ^{28}Si, with a decrease of proton energy. The atomic percentage of carbon was determined by the difference. This type of measurement is valid because the carbon concentration has been verified on various samples by an independent determination by an activation technique, and because the concentration of impurities was low. The measurement did not depend on the coating density. This method is neither a function

of the crystalline state nor the type of phase, because it concerns only the atomic nuclei. The chemical compositions are given in atomic percentages and their precision, which depended on counting time, was equal to ±5% relative for the present analysis. The details of the method are given elsewhere.[11] X-ray diffraction was also used to attempt to determine the crystalline phases of the coatings.

3 Comparison Between the Thermodynamic and Experimental Studies

The experimental chemical composition was measured at the bottom of the samples, for a h = 3 mm distance from the lower end of the substrate. This position was chosen to try to minimize reactant depletion and maintain an overall material balance as close to the inlet ones as possible. Then a comparison was made between the theoretical and experimental compositions in atomic percent of each element in the coating for various deposition conditions (the coatings were generally badly crystallized and a comparison with the predicted phases cannot be done from X-ray diffraction).

First the influence of the temperature was studied at a constant mass flow rate and pressure for:

$$\alpha = \frac{[H_2]_o}{[MTS]_o} = 20 \text{ and } \beta = \frac{[MTS]_o}{[BCl_3]_o} \text{ varying from } 0{\cdot}6 \text{ to } 8.$$

where $[X]_o$ represents the initial number of X moles.

Thereafter, the same type of study was carried out with a variable mass flow rate, constant temperature and constant pressure for $\alpha = 20$ and $\beta = 1$

3.1 Influence of temperature and inlet gas composition

Figures 2–4 present, for three different temperatures, the relationship between the chemical composition of the coatings and the variation of the β value (0·6 to 8), for a fixed $\alpha = 20$; the pressure was set at 0·395 atm and the mass flow rate was equal to 0·320 g/min. The values of α and the mass flow rate were chosen following the study at $T = 1400$ K because no free carbon was obtained under these conditions.[1]

For three temperatures (T = 1400, 1300 and 1200 K), the chemical compositions predicted by thermodynamic calculations varied in the same way. When β increased, the incorporation of boron decreased, while that of carbon and silicon increased to stoichiometric SiC. For a fixed β value higher than 1, the theoretical incorporation of boron was lower when the temperature decreased, whereas that of carbon became greater when the temperature decreased.

The theoretical equilibrium yields of the solid species showed that, at 1400 K for β varying from 0·4 to 8, no free carbon was formed, whereas at 1300 K, some free carbon was expected from $\beta = 0{\cdot}4$ to $\beta = 0{\cdot}6$ and at 1200 K, free carbon was expected from $\beta = 0{\cdot}4$ to 2 (Figs 5–7).

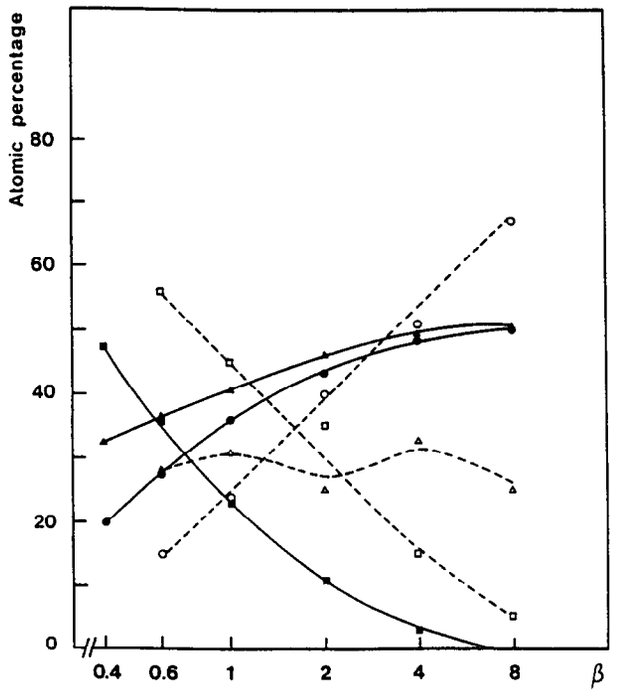


Fig. 2. Comparison between the thermodynamical calculations and the experiments at T = 1400 K, P = 0·395 atm, $\alpha = 20$, β variable. —— thermodynamic, — — — experiment. ■ □ Boron, ● ○ Silicon, ▲ Δ Carbon.

The experimental results (Figs 2-4) were totally the reverse of the thermodynamic estimates because a decrease in the deposition temperature led to a lower incorporation of carbon and to less silicon for all the β values (except for β near 8).

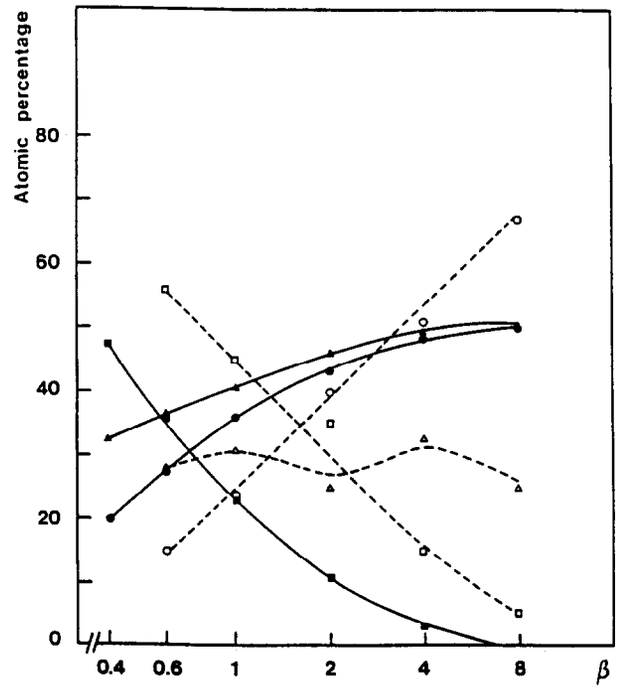


Fig. 3. Comparison between the thermodynamical calculations and the experiments at T = 1300 K, P = 0·395 atm, $\alpha = 20$, β variable. —— thermodynamic, — — — experiment. ■ □ Boron, ● ○ Silicon, ▲ Δ Carbon.

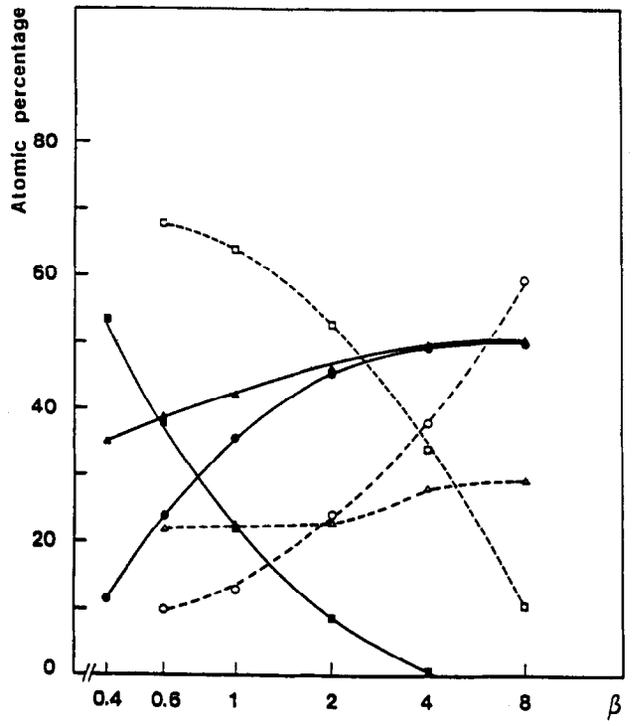


Fig. 4. Comparison between the thermodynamical calculations and the experiments at T = 1200 K, P = 0·395 atm, α = 20, β variable. —— thermodynamic, — — — experiment. ■ □ Boron, ● ○ Silicon, ▲ Δ Carbon.

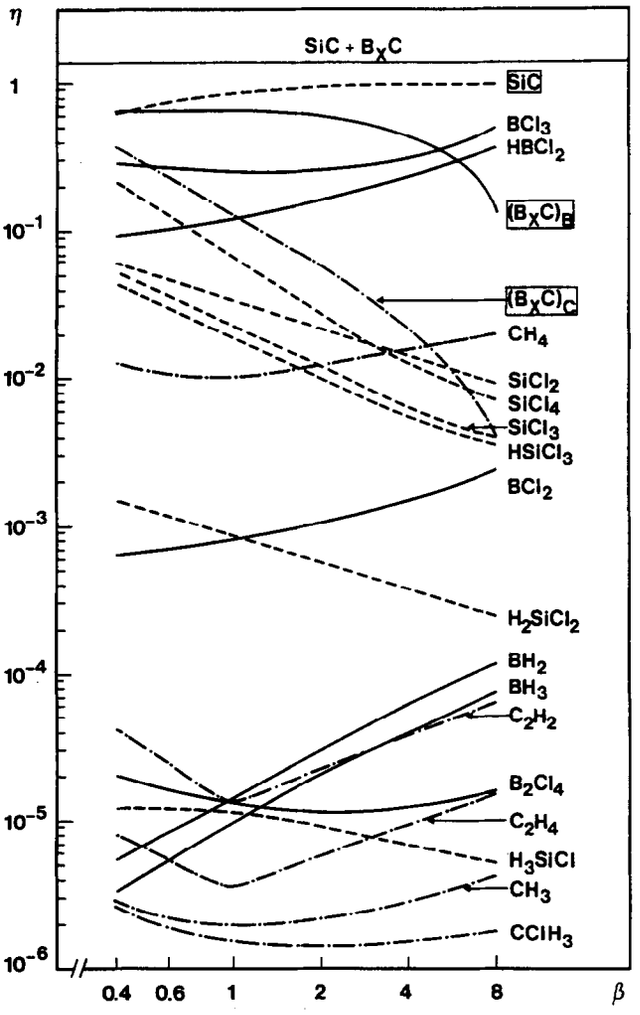


Fig. 5. Equilibrium yields η of the different gaseous and solid species at T = 1400 K, P = 0·395 atm. α = 20, β variable. —— Boron, — — — Silicon, —·— Carbon (containing species). $(B_xC)_B$ and $(B_xC)_C$ are the yields relative to the inlet boron and carbon respectively.

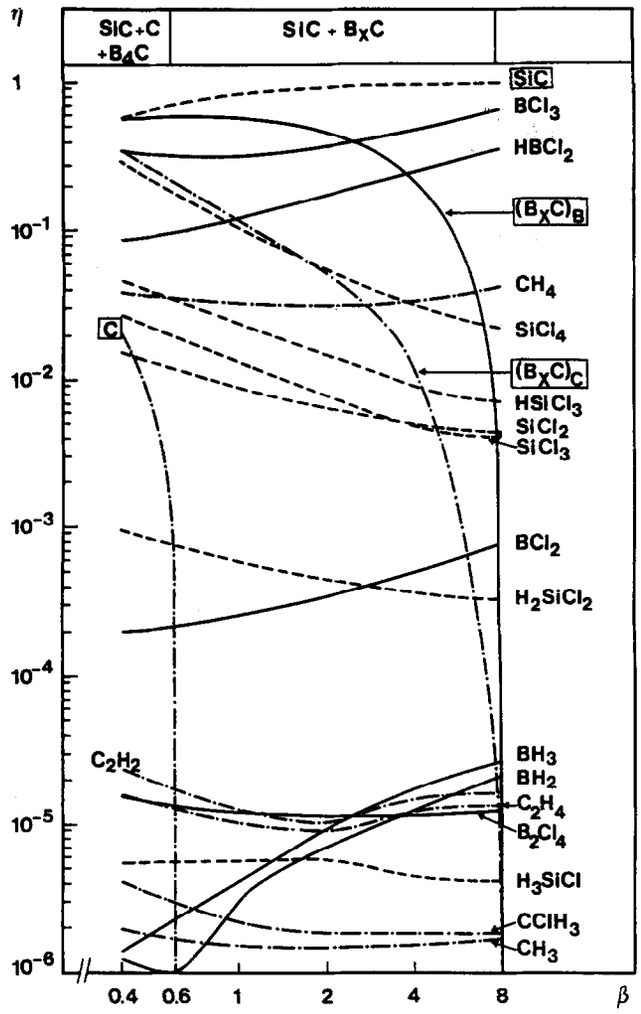


Fig. 6. Equilibrium yields η of the different gaseous and solid species at T = 1300 K, P = 0·395 atm, α = 20, β variable. —— Boron, — — — Silicon, —·— Carbon (containing species).

Simultaneously, the proportion of boron increased when the temperature decreased.

A great departure from the equilibrium predictions was brought to light when the temperature decreased, showing especially a lack of carbon deposition. This phenomenon was already reported for the deposition of boron carbide and titanium carbide where the carbon deposition kinetics from hydrocarbons often limits the process.[12–15]

This departure from equilibrium seems to increase with the deposition of the free elements as boron when $\beta \leq 2$ and silicon when $\beta > 4$.

3.2 Influence of the mass flow rate

Figures 8–10 show, for three different temperatures, the relationship between the chemical composition of the coatings and the mass flow rate when α = 20, β = 1 and P = 0·395 atm.

The compositions predicted by the global thermodynamic calculations do not depend on the mass flow rate and are shown by three straight lines in each figure. For each of the three temperatures, a departure from equilibrium was noticed. The proportion of the incorporated boron was

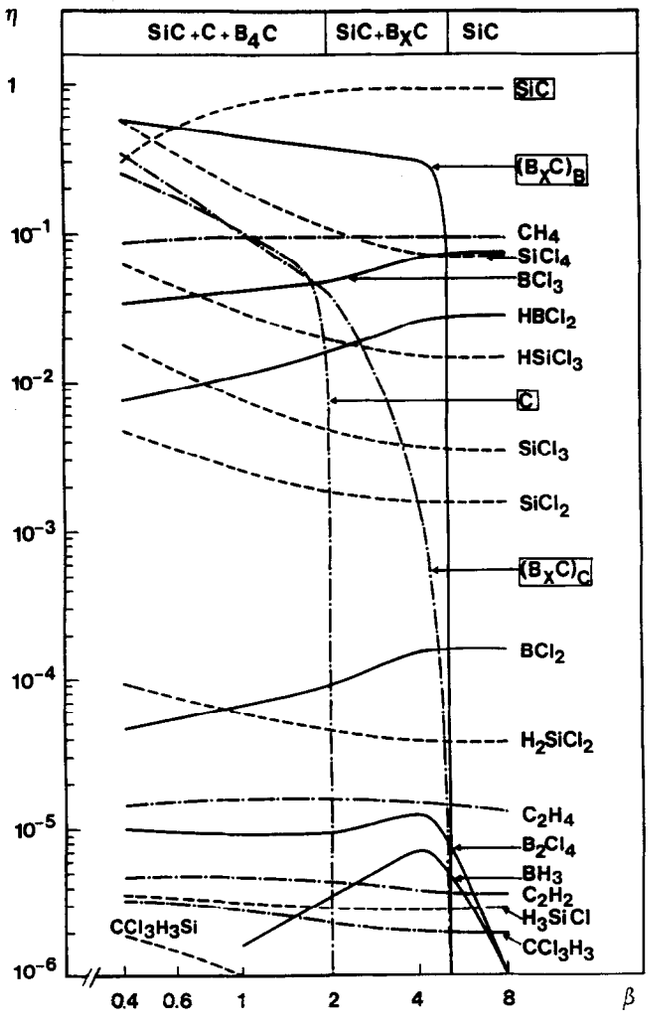


Fig. 7. Equilibrium yields η of the different gaseous and solid species at T = 1200 K, P = 0·395 atm, α = 20, β variable. —— Boron, — — — Silicon, —·— Carbon (containing species).

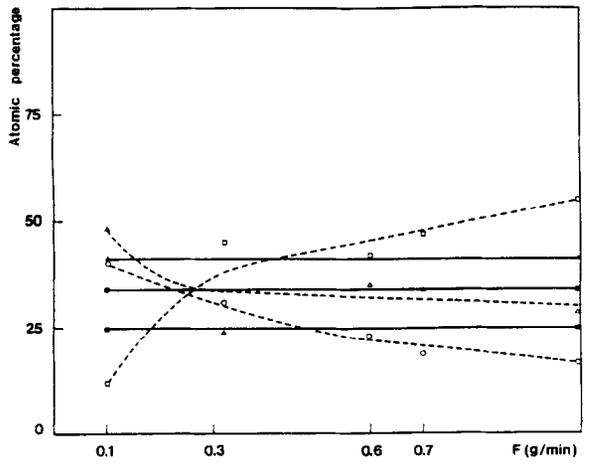


Fig. 8. Influence of the mass flow rate on the chemical composition at α = 20, β = 1, T = 1400 K, P = 0·395 atm. —— thermodynamic, — — — Experiment. ■ □ Boron, ● ○ Silicon, ▲ Δ Carbon.

especially higher than expected (except at a low mass flow rate and T = 1400 K), whereas that of carbon and silicon was lower. In general, it is possible to confirm that the departure from equilibrium increases when the mass flow rate increases.

From these figures, it can be noticed, once again, that the lower the temperature was, the higher the departure from equilibrium for the specific value of β = 1. Obviously, the highest departure from equilibrium was obtained by a low temperature and high mass flow rate, as expected.

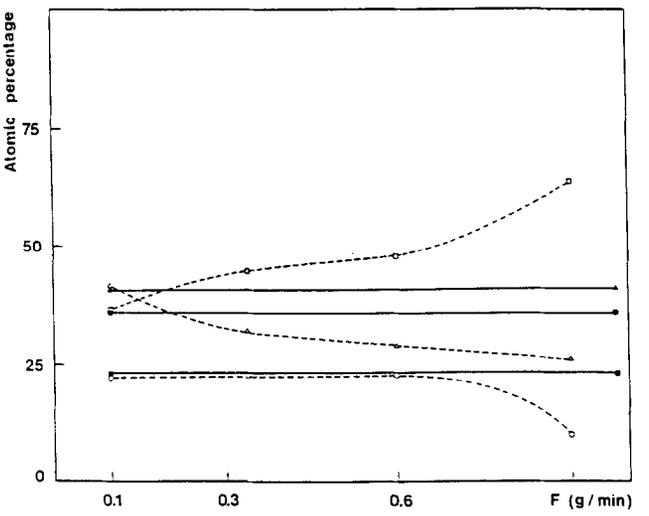


Fig. 9. Influence of the mass flow rate on the chemical composition at α = 20, β = 1, T = 1300 K, P = 0·395 atm. —— thermodynamic, — — — experiment. ■ □ Boron, ● ○ Silicon, ▲ Δ Carbon.

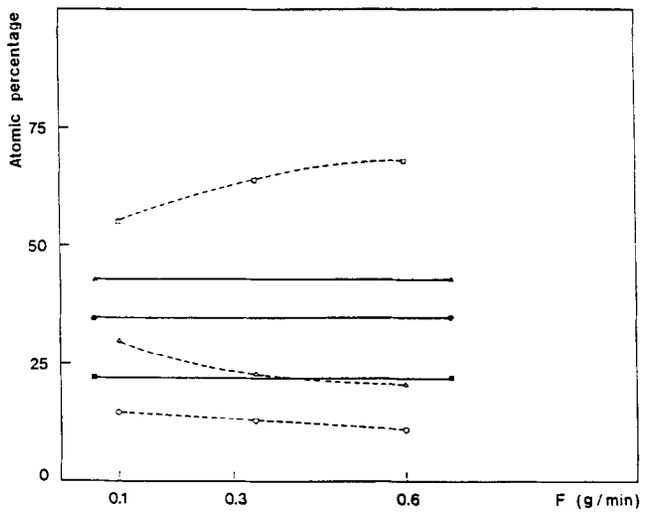


Fig. 10. Influence of the mass flow rate on the chemical composition at α = 20, β = 1, T = 1200 K, P = 0·395 atm. —— thermodynamic, — — — experiment. ■ □ Boron, ● ○ Silicon, ▲ Δ Carbon.

4 Thickness and Composition Uniformity as a Function of the Departure from Equilibrium

4.1 Influence of the inlet gas composition at different temperatures

The experimental conditions that were chosen for this study are the following:

P = 0·395 atm, F = 0·320 g/min, α = 20, β = 0·6-8 and T = 1200, 1300 and 1400 K.

The results are reported in Figs 11–13. The value of T = 1400 K (Fig. 11) corresponds to the

temperature at which the departure from equilibrium was lowest. The deposition rate was relatively high and increased when β increased. At the bottom of the sample (h = 3 mm), it varied from 28 μm/h when β = 0·6 to 59 μm/h for β = 8. At 1400 K, Table 1, which reports the longitudinal uniformity U_L as a function of β ($U_L = t_{15\,mm}/t_{3\,mm}$), indicates that the control of thickness was poor (t_{hmm} = thickness at the position hmm from the lower end of the sample). For a fixed α ratio value and an increase of β, the experimental conditions correspond to both a decrease of the BCl_3 proportion and an increase of the H_2 proportion in the gas phase. Then the U_L ratio decreased when β increased following an increase in the α' ratio:

$$\alpha' = \frac{[H_2]_o}{[MTS]_o + [BCl_3]_o}$$

α' expresses the relationship between the proportion of hydrogen and the chlorinated species which were to be reduced in the initial gas mixtures; the variations of α' are reported in Table 2. This inadequate control of thickness was therefore raised by the dilution, and also by a higher depletion in the reactant concentration as the deposition rate increases at the bottom of the substrates when β increases. It can be associated to a poor control of the chemical composition along each sample. Generally a decrease in the boron content along each sample, with a correspondingly smaller

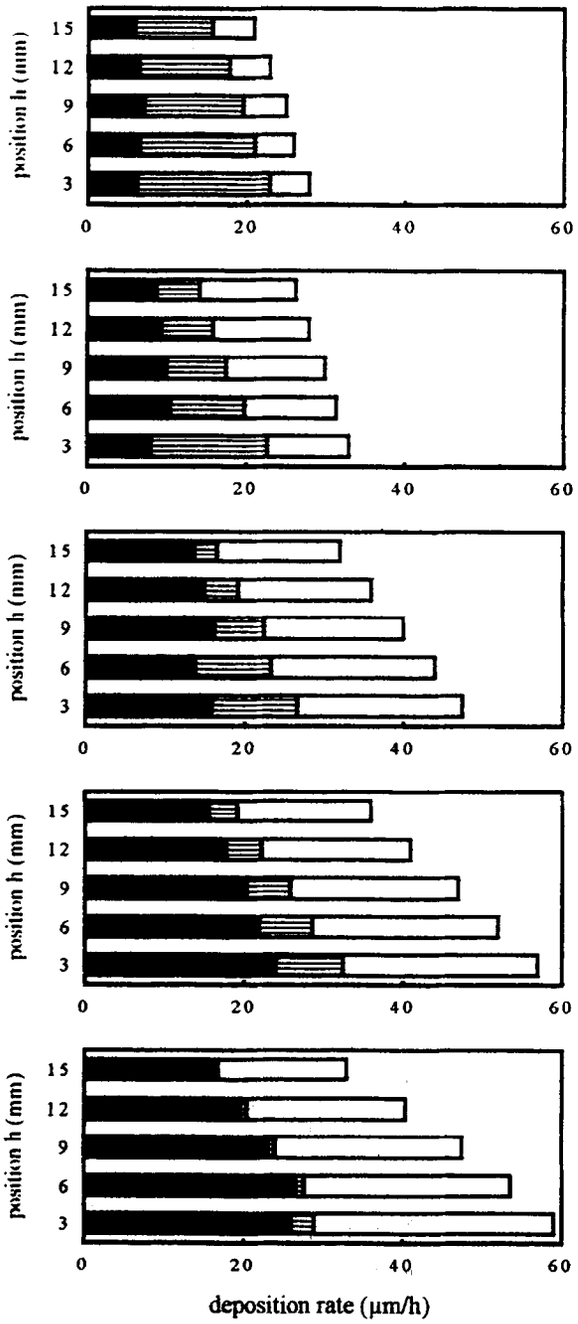


Fig. 11. Thickness and chemical composition (in at %) uniformity at T = 1400 K, P = 0·395 atm, α = 20 and F = 0·32 g/min. From top to bottom, β is equal respectively to: 0·6, 1, 2, 4 and 8. Carbon ■, Boron ▤, Silicon □.

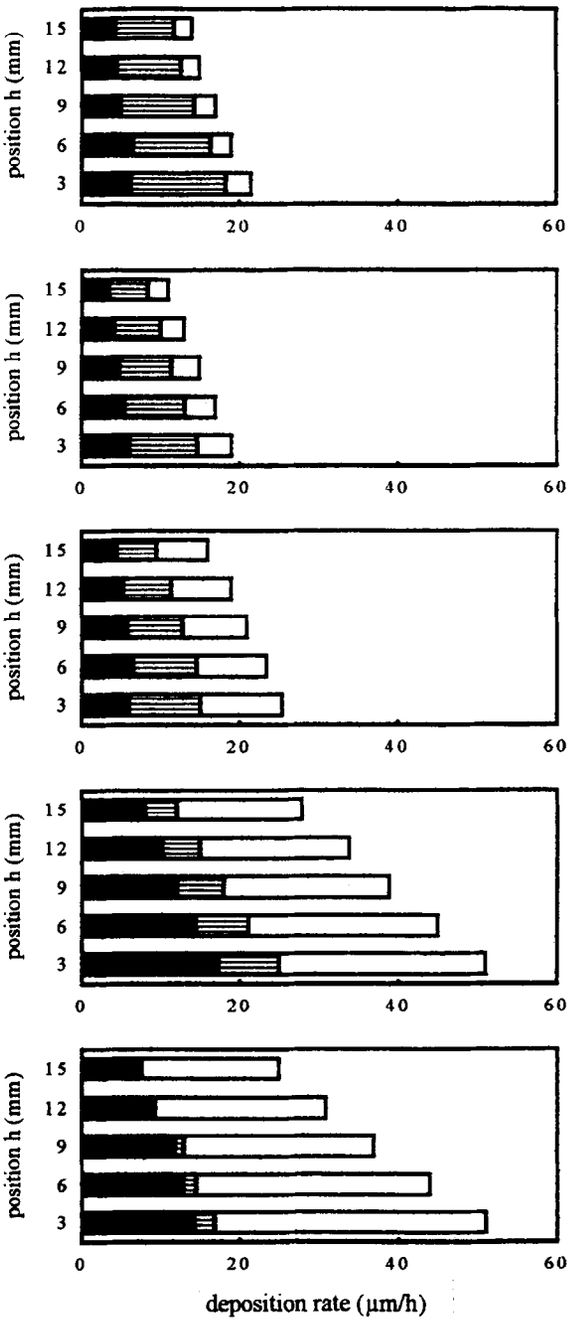


Fig. 12. Thickness and chemical composition (in at%) uniformity at T = 1300 K, P = 0·395 atm, α = 20 and F = 0·32 g/min. From top to bottom, β is equal respectively to 0·6, 1, 2, 4 and 8. Carbon ■, Boron ▤, Silicon □.

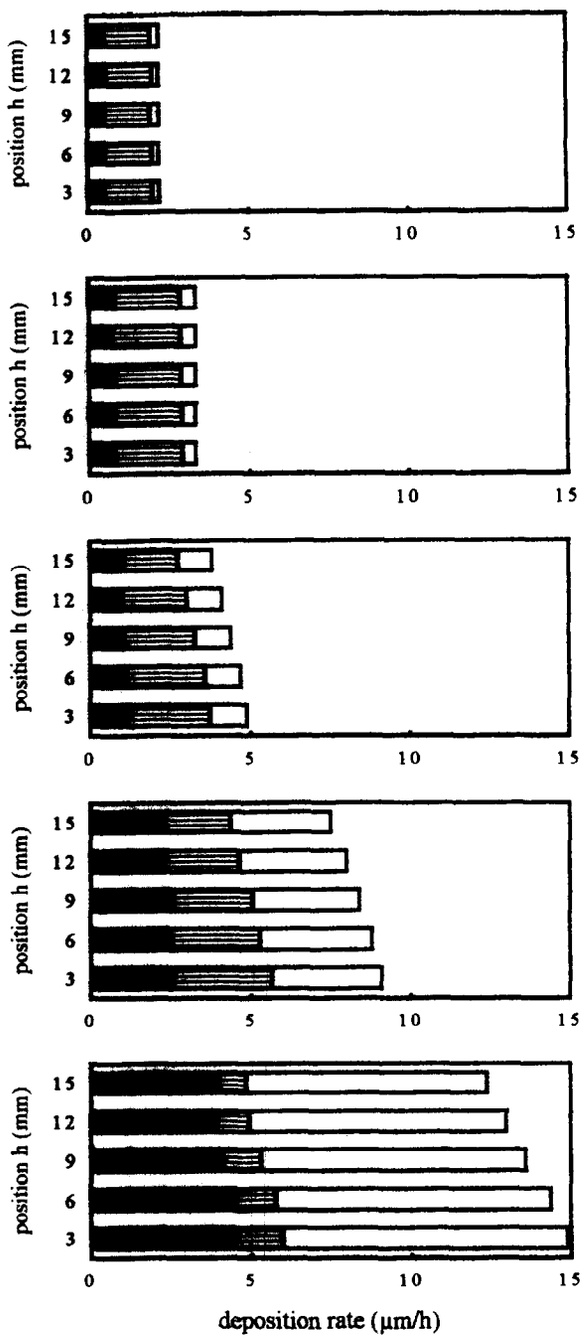


Fig. 13. Thickness and chemical composition (in at %) uniformity at T = 1200 K, P = 0·395 atm, α = 20 and F = 0·32 g/min. From top to bottom, β is equal respectively to: 0·6, 1, 2, 4 and 8. Carbon ■, Boron ▤, Silicon □.

increase in the silicon content, were observed.

At T = 1300 K (Fig. 12), the same comments can be made concerning the uniformity in thickness. The control of thickness is even poorer than at T = 1400 K (Table 1). The U_L ratio decreased, as was the case for T = 1400 K, when β increased. It corresponds to both an increase in the MTS content in the inlet gas composition and in α' (Tables 1 and 2). On the other hand, for T = 1300 K, a better control of the chemical composition was noticed especially for the lowest values of β. The deposition rate was lower than for T = 1400 K but still remained high. The values are 21·5 μm/h

Table 1. Longitudinal thickness uniformity $U_L = t_{15mm}/t_{3mm}$ as a function of ß (where t_{hmm} is the thickness at the h (mm) position from the lower end of the substrate)

	ß = 0·6	1	2	4	8
T = 1400K	U_L = 0·75	0·79	0·67	0·63	0·55
T = 1300K	U_L = 0·65	0·61	0·61	0·55	0·49
T = 1200K	U_L = 1	1	0·78	0·82	0·82

P = 0·395 atm, F = 0·320 g/min, α = 20, ß variable.

Table 2. $\alpha' = [H_2]_o/[MTS]_o + [BCl_3]_o$ values as a function of $\beta = [MTS]_o/[BCl_3]_o$; $\alpha = [H_2]_o/[MTS]_o = 20$

ß	0·6	1	2	4	8
α'	7·5	10	13·3	16	17·8

for β = 0·6, and 51 μm/h for β = 8 at the bottom of the sample, when h = 3 mm.

At T = 1200 K (Fig. 13), for β = 0·6 and 1, a good control of thickness and chemical composition was obtained (U_L = 1), the boron content was high (≈ 65%) and the carbon content remained stable (≈ 23%). Note that this good control was obtained when the deposition rate was low (≈ 2–3 μm/h). When the content of both MTS and H_2 were higher, over β = 2 in the initial gas mixture, thickness and chemical composition uniformity could not be controlled as well. Under these conditions, the deposition rate increased to 15 μm/h and the well-known influence of mass transfer and depletion of reactants arose for such a relatively high rate, when they were not compensated for by using specific reactor geometry.

4.2 Influence of the mass flow rate at different temperatures

The experimental conditions chosen for this study are the following:

$$P = 0{\cdot}395 \text{ atm}; \alpha = 20; \beta = 1; F \text{ variable};$$
$$T = 1200, 1300, 1400 \text{ K}.$$

The results have been reported in Figs 14–16. In section 3.2, it has been verified that the departure from equilibrium increased when the mass flow rate increased.

At T = 1400 K (Fig. 14), the increase in the mass flow rate from 0·1 to 1·0 g/min induced an increase in the deposition rate of the coatings from 15 to more than 70 μm/h. This mass flow rate increase induced a better control of the longitudinal uniformity in thickness U_L (Table 3), but also of the chemical composition of the coatings. This improvement in control goes along with an

Table 3. Longitudinal thickness uniformity $U_L = t_{15mm}/t_{3mm}$ as a function of F (where t_{hmm} is the thickness at the position h_{mm} from the lower end of the substrate)

	F = 0·100	0·320	0·600	0·700	0·900	1·000
T = 1400K	U_L = 0·75	0·79		1		1
T = 1300K	U_L = 0·40	0·61	0·61		0·92	
T = 1200K	U_L = 0·80	1	1			

P = 0·395 atm, α = 20 , ß = 1, F variable.

increase in the boron content for when the mass flow rate increases, as well as with a decrease in the carbon and silicon content. As a result, the final composition obtained was very different from the composition at equilibrium. It is worth noting that a better control in thickness and chemical composition was obtained with a high deposition rate, which could not be reached in an industrial reactor without encountering problems of uniformity.

At T = 1300 K (Fig. 15), the increase in the mass flow rate (0·1 to 0·9 g/min) induced an improvement of the control of the thickness longitudinal uniformity U_L (Table 3) and the chemical composition of the coatings. This better control was obtained when the boron content was highest and the silicon and carbon contents lowest, in other words when the departure from equilibrium of the chemical composition was the highest. Note that an increase in the mass flow rate led, at the end, to a small decrease in the deposition rate for F = 0·9 g/min.

At T = 1200 K (Fig. 16), the increase in the mass flow rate (0·1 to 0·6 g/min) made it possible to obtain a very satisfying control of the thickness longitudinal uniformity U_L (Table 3) as well as the chemical composition of the deposits. Under these conditions, the deposition rates were much lower (2–3·3 μm/h). A good control was obtained when the composition of the coatings was very different from the expected composition at equilibrium. It can be noted that the increase in the mass flow rate led, at the end, to a small decrease in the deposition rate of the coatings as was observed at 1300 K.

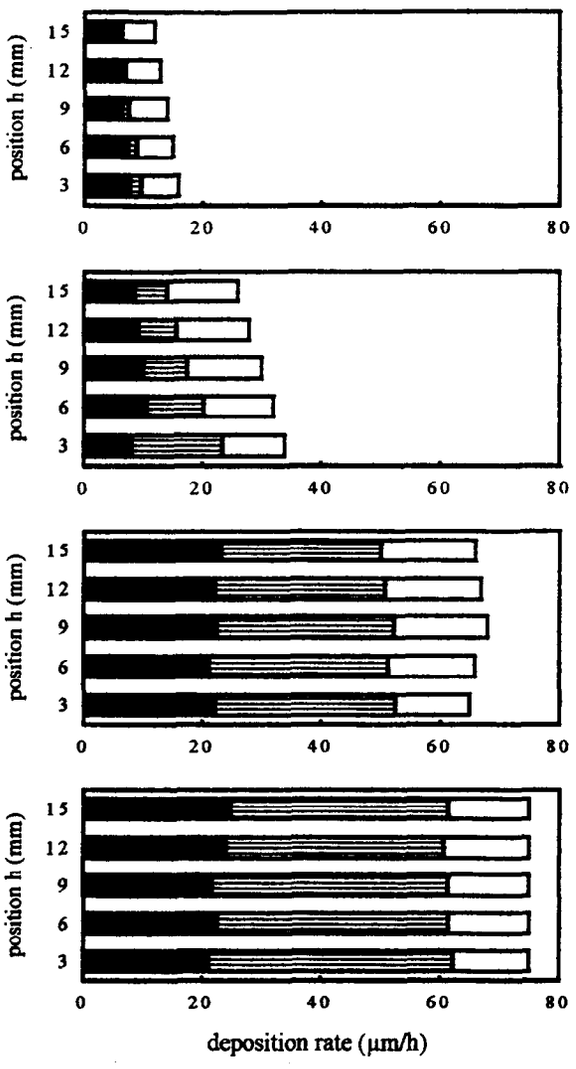


Fig. 14. Thickness and chemical composition (in at %) uniformity at T = 1400 K, P = 0·395 atm, α = 20, β = 1. From top to bottom, F is equal respectively to: 0·1, 0·32, 0·7 and 1·0 g/min Carbon ■, Boron ▤, Silicon □.

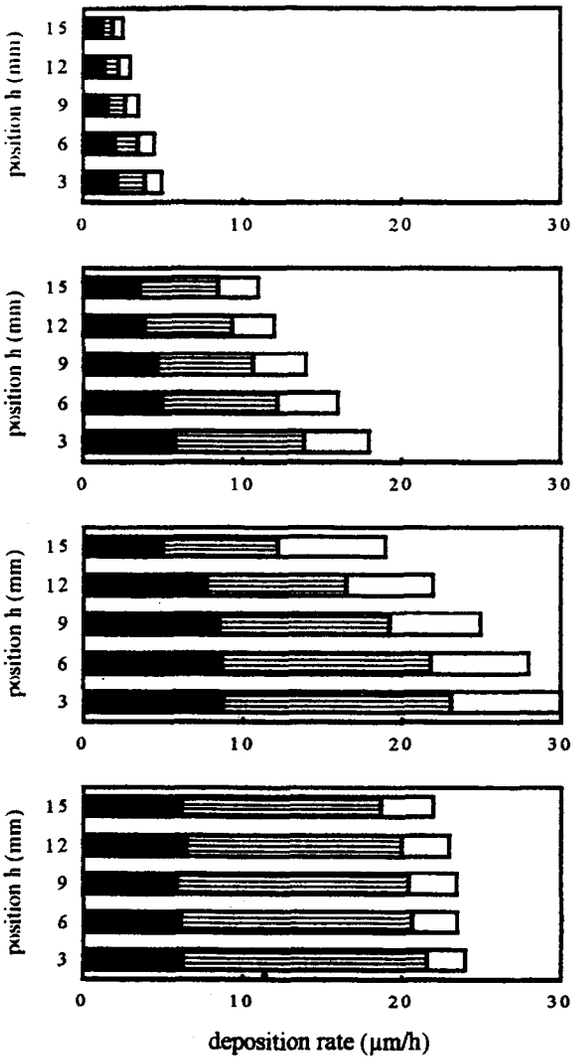


Fig. 15 Thickness and chemical composition (in at %) uniformity at T = 1300 K, P = 0·395 atm, α = 20, β = 1. From top to bottom, F is equal respectively to: 0·1, 0·32, 0·6 and 0·9 g/min. Carbon ■, Boron ▤, Silicon □.

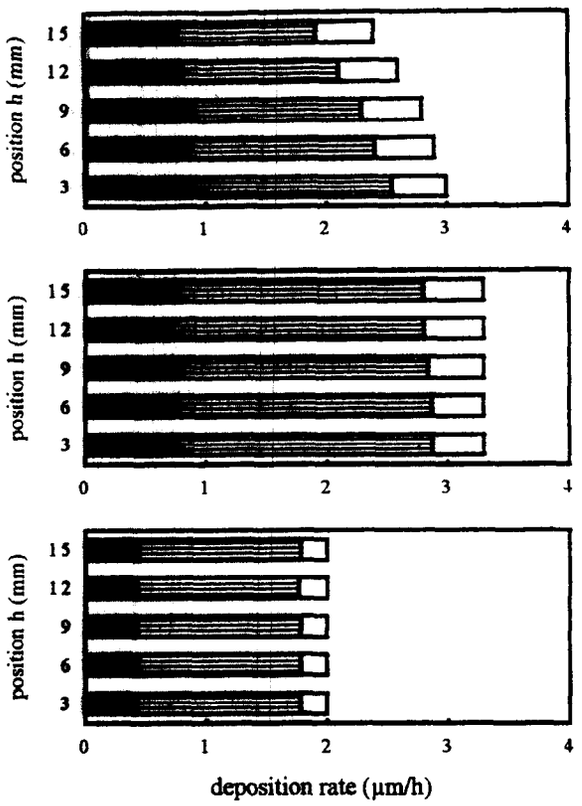


Fig. 16. Thickness and chemical composition (in at %) uniformity at T = 1200 K, P = 0·395 atm, α = 20, β = 1. From top to bottom, F is equal respectively to: 0·1, 0·32, and 0·6 g/min. Carbon ■ Boron ▤ Silicon □.

4.3 Influence of the temperature when β was fixed

When the temperature was lower, whatever the value of the mass flow rate or inlet gas composition was, the deposition rate of the coatings was lower. Moreover, the difference in the chemical composition compared with that of the equilibrium was greater because the content in the free elements (boron and/or silicon) increased.

When the temperature changed from 1400 to 1200 K, the longitudinal uniformity in thickness U_L was worse at 1300 K than at 1400 K. The best uniformity U_L was obtained for T = 1200 K (Figs 14–16).

5 Discussion

It is well-known that the departure from equilibrium at the gas–solid interface of a C.V.D. system increases when the temperature decreases and the mass flow rate increases, as a result of a deposition process which is first controlled by the mass transfer, then by a combination of mass transfer and chemical (reaction) kinetics and finally which is almost only controlled by chemical kinetics alone. When the supersaturation varies, it influences both the thickness and composition in a multicomponent system, hence their uniformity along the surface. This evolution was observed here for the codeposition of three elements (Si–B–C). It can be useful, for this particular system, to specify the relationships between this departure from equilibrium and the final results in terms of chemical composition, thickness and uniformity.

5.1 Influence of the temperature

For a given deposition mechanism, the kinetics of the surface reactions is much more influenced than mass transfer in the gas phase by a change in the deposition temperature. At lower temperatures the deposition is more controlled by the surface kinetics which is the slowest step and a uniform composition at each position on the samples is favored.

But as a function of temperature the deposition mechanism may change because some chemical reactions are favored over others, which was the case described elsewhere for the system (Si–C).[16] At a temperature higher than 1323 K, pure SiC was obtained whereas at 1273 K the coating contained a great amount of free silicon which was deposited at a higher deposition rate than the silicon carbide. A similar phenomenon seemed to occur in the case of the codeposition of the ternary (Si–B–C). When the temperature decreased from 1400 to 1200 K, the atomic percentage of boron and/or silicon increased while the atomic percentage of carbon decreased. This change in the composition may correspond to the deposition of free boron and/or free silicon at T = 1300 or 1200 K. At T = 1400 K, the deposition of a ternary Si–B–C coating with a relatively high carbon content was favored under lower supersaturation conditions.

On the other hand, the chemical kinetics control, which increases at a lower temperature with a high boron or silicon content, leads to greater uniformity of composition under this higher departure from equilibrium. This control was particularly good when T = 1200 K and β was low (0·6–1) (Fig 13). Under these conditions, the departure from equilibrium was high and the depletion in the gas phase and increase concentration of the gas products were reduced along the samples, in accordance with a lower deposition rate obtained for low β values (even at 1300 and 1400 K the results were better for low β values). This kinetic limitation at low temperature and low β values led, accordingly, to the best results for thickness uniformity as the deposition rate was reduced from about 30 μm/h at 1400 K to 3 μm/h at 1200 K when α = 20 and β = 1.

It can be therefore concluded that under a low supersaturation in CH_x species produced by a rel-

atively high α value of 20, which leads to a low carbon content in the solid, the kinetics limitation which is encountered at the lowest temperature of 1200 K depends on the β value. The process is more controlled, with the best uniformity for composition and thickness, when the β value is low. When the β value increases (for inlet concentration of MTS higher than BCl_3), the process is less kinetically controlled by the silicon incorporation in accordance with a higher silicon deposition rate (for example at 1200 K the global deposition rate varied from 2·2 μm/h for boron-rich coatings deposited at β = 0·6 to about 15 μm/h for silicon-rich coatings deposited at β = 8). However the variations of α' with β (Table 2) should not be overlooked in interpreting these chemical kinetics and final uniformity differences. These results were confirmed by the influence of the mass flow rate.

5.2 Influence of the mass flow rate.

It is clear that higher mass flow rates led to a process more controlled by the heterogeneous chemical kinetics and then to a better uniformity in thickness and chemical composition.

Even at 1400 K, a good result was obtained at the highest mass flow rate, but as pointed out previously, it can only be obtained on a small surface inside a small reactor, as the deposition rate was very high (> 70 μm/h) (Fig. 14). The results were surprisingly not improved at T = 1300 K (Fig. 15), in accordance with Fig. 9 where the coating composition does not tend to a limit with the mass flow rate. Also in Fig. 3, the variations of the carbon content appear imprecise. All these results seem to indicate a great sensitivity of the process to the experimental parameters, especially the β value, which could not have been very well controlled at the highest mass flow rates of Fig. 9. A very good control of the final composition and thickness uniformity of the coatings was obtained at T = 1200 K for a mass flow rate equal to or higher than 0·320 g/min (Fig. 16).

In general, an increase in the mass flow rate obviously leads to an increase in the deposition rate to a limit where the deposition is almost only controlled by the surface kinetic step. However for temperatures of 1300 and 1200 K, a small decrease was observed in the deposition rate for mass flow rates of 0·9 and 0·6 g/min, respectively. This phenomenon may be explained by too great a decrease in residence time of the different gaseous species inside the reactor. It can also be attributed to a possible cooling of the substrate due to an increase in the mass flow rate which would decrease the surface kinetics and thus the global deposition rate.

5.3 Influence of the total pressure

The influence of the total pressure was not studied in this work, but it is well-known that lower pressures allow the surface kinetic control of the deposition process to increase. This point is especially interesting for depositing coatings in large scale reactors. It is also important to extend the process to chemical vapor infiltration.[17] One part or the whole matrix of a composite could be composed of such material as Si–B–C which would lead to a great improvement of the oxidation resistance, especially under thermomechanical stresses.[18]

6 Conclusion

It has been shown that a high supersaturation at the gas–solid interface leads to a good uniformity of the thickness and the composition of (Si–B–C) coatings. A higher supersaturation is obviously obtained at lower temperatures and higher mass flow rates, but its amount is also a function of the α and β values, since different kinetic limitations can arise as a function of the inlet gas composition. A decrease in temperature from 1400 to 1200 K produces a change in the deposition mechanism, from near equilibrium conditions at 1400 K where the composition is a function of the element segregation transport phenomena and the reactant consumption, to conditions which deviate from equilibrium at 1200 K where the deposition of excess B or Si is favored under more kinetically controlled conditions. This change is also observed at each temperature when the mass flow rate increases. The best control of both thickness and composition is clearly obtained at the lowest deposition rate (2–3 μm/h), when boron-rich coatings are deposited at 1200 K and $\beta \leq 1$.

The ways of depositing coatings in the whole composition range can be deduced from this study and the desired deposition rate adjusted for a large-scale reactor, however very different coupled combinations of all parameters should be employed. For example, a (Si–B–near stoichiometric C content) solid would be deposited under very different conditions than for a (Si–B–low C content) coating, also as a function of the B/Si ratio in both cases.

This C.V.D. study made it possible to choose experimental conditions with high deposition rates on small substrates, even when the process control was not fully optimized, and to test the oxidation resistance of these coatings as either a (Si–B–C) monolayer or when associated with other compounds in multilayer coatings. These results are published elsewhere.[19]

Acknowledgements

The authors from LCSR gratefully acknowledge the financial support of the Société Européenne de Propulsion (SEP) under contract No. 430 190. This work was part of the thesis of S. Goujard (Orléans, 1990) granted by the SEP and CNRS. We express our thanks to G. Ducouret, G. Blondiaux and J. L. Debrun from C.E.R.I. - CNRS. who carried out the nuclear analysis.

References

1. Goujard, S., Vandenbulcke, L., Bernard, C., Blondiaux, G. & Debrun, J. L., *J. Electrochem. Soc.*, **141** (1994), 452.
2. Blocher, Jr., J. M., *J. Vac. Sci. Technol.*, **11** (1974) 680.
3. Vandenbulcke, L., Vuillard, G., *J. Electrochem. Soc.*, **124**(12). (1977) 1937.
4. Vandenbulcke, L., *I.E.C. Product Research and Development*, **24**, (1985) 568.
5. Arora, R., Rebenne, H., Tirtowidjojo, M. & Pollard, R. In *Proceedings of the 10th Int. Conf. on C.V.D.*, ed. G. W. Cullen & J. M. Blocher, Jr. The Electrochem. Soc. Pennington, NJ, 1987, p. 145.
6. Vandenbulcke, L., Thin Solid Films, **102** (1983) 149–160.
7. Vandenbulcke, L., In *Proceedings of the 4th Euro C.V.D.*, ed. J. Bloem, G. Verspui, L. R. Wolff. Eindhoven, 1983, 44.
8. Goujard, S., Vandenbulcke, L. & Bernard, C., *Calphad*, **18** (1994) 369.
9. Hillert, M. & Staffanson, L. I., *Acta Chem. Scand.*, **24** (1970) 3618.
10. Sundmann, B. & Agren, J., *J. Phys. Chem. Solids*, **42** (1981) 297.
11. Blondiaux, G., Ducouret, G., Debrun, J. L., Goujard, S. & Vandenbulcke, L., *NIM-B*, **B79** (1993) 521.
12. Vandenbulcke, L. & Vuillard, G. E., In *Proceedings of 8th Int. Conf. on C.V.D.*, ed. J. M. Blocher, Jr., G. E. Vuillard & G. Wahl. The Electrochem. Soc., Pennington, NJ, (1981), p. 32.
13. Vandenbulcke, L., Herbin, R., Basutcu, M. & Barrandon, J. N., *J. Less Common Metals*, (1981) 7–22.
14. Vandenbulcke, L., In *Proceedings of 8th Int. Conf. on C.V.D.*, ed. J. M. Blocher, Jr., G. E. Vuillard & G. Wahl. The Electrochem. Soc., Pennington, NJ, (1981) p. 32.
15. Stjernberg, K. G., Gass, H. & Hintermann, H. E., *Thin Solid Films*, **40** (1977) 81–88.
16. Goujard, S., Thesis, Orléans, France, 1990.
17. Naslain, R. In *Introduction aux Matériaux Composites II — Matrices Métalliques et Céramiques*, ed. R. Naslain, Ed. du CRNS/IMC, Bordeaux, (1985).
18. Goujard, S., Vandenbulcke, L., Rey, J., Charvet, J. L. & Tawil, H., Fr patent No. 9013323.
19. Goujard, S., Vandenbulcke, L. & Tawil, H., *Thin Solid Films*, **245** (1994) 86.

Journal of the European Ceramic Society **15** (1995) 563–572
© 1995 Elsevier Science Limited
Printed in Great Britain. All rights reserved
0955-2219/95/$9.50

0955-2219(95)00015-1

The Brazing of Si_3N_4 with Ni–Cr–Si Alloys

G. Ceccone,[a] M. G. Nicholas,[a] S. D. Peteves,[a] A. A. Kodentsov,[b] J. K. Kivilahti[b] & F. J. J. van Loo[b]

[a]Institute for Advanced Materials, CEC, Petten, The Netherlands
[b]Solid State Chemistry and Materials Science, Eindhoven University of Technology, Eindhoven, The Netherlands

(Received 29 July 1994; revised version received 30 October 1994; accepted 10 January 1995)

Abstract

The use of commercially available and laboratory made Ni–Si–Cr brazes for wetting and bonding Si_3N_4 has been explored. The microstructure and chemistry of brazed joints has been characterized by techniques such as optical microscopy, scanning electron microscopy, electron probe micro-analysis and X-ray diffraction. Si_3N_4 was wetted well by all the braze alloys at 1150–1200°C, but the joint quality obtained was poor because of the formation of brittle phases and solid solutions.

1 Introduction

The increasing interest in the application of structural ceramics such as Si_3N_4 and SiC is due to their high-temperature strength and creep resistance, excellent wear, corrosion and thermal shock resistance. However, reliable joining technologies are needed if ceramic inserts are to be used to exploit these properties or complex components are to be made from simple ceramic bodies.

Brazing is an attractive technique for joining ceramic–ceramic and, particularly, ceramic–metal systems. However to profit from the high temperature mechanical properties of ceramics, high temperature brazes have to be employed and several studies[1–3] have suggested Ni-based alloys as suitable brazes for joining Si_3N_4 and SiC.

This paper describes an evaluation of the potential usefulness of some Ni–Cr–Si brazes for joining Si_3N_4, employing a material science approach based where possible on phase stability and thermodynamic factors.

2 Background

Brazing is a versatile and cost-effective technique for joining both similar and dissimilar material systems. However, many of the brazes used for joining metal workpieces do not wet technologically important ceramics and hence a sub-class of brazes, active metal brazes, have been developed for the joining of ceramics. The distinctive feature of these active metal brazes is that they react to change the surface chemistry and wettability of the ceramics.

Commercially available active metal brazes are generally based on the Ag–Cu–(In, Pd)–Ti and Cu–Al–Si–Ti systems and can be used for applications that do not require service temperatures higher than 400°C.[4–7] Si_3N_4 can be joined with these brazes and important applications have been found in the automobile industries. However, many of the proposed future uses of Si_3N_4 involve service temperatures in excess of 700°C. The selection of a high temperature active metal braze involves two tasks: (a) choice of a solvent and, (b), identification of a reactive component. The first task requires consideration of metallurgical and technological factors; the solvent must be sufficiently refractory and chemically inert with respect to the workpieces and the environment so that the joined structures can withstand service conditions such as high temperature oxidizing atmospheres. The development of brazes for high temperature metals such as super alloys can provide some guidance for solvent selection but the second task is often more difficult to accomplish. Identifying a suitable reactive component requires information about what type of products will be formed by the specific workpiece/braze combinations during the joining process. Equilibrium thermodynamics can provide insight about the chemistry of the products, but not about their formation kinetics or properties such as wettability or strength. Thus experimentation is almost always necessary to identify the optimum brazing materials and process conditions.

Several studies of the active metal brazing of engineering ceramics aimed to increase the service temperatures have been reported. In particular, Au–Ni–Ti and Pd–Ni–Ti alloys have been used to

join Si_3N_4 and SiC ceramics.[8] The results obtained indicate that a major problem is the enhanced chemical reaction between the ceramic and the braze.

The present work focused on the utility of Ni–Cr–Si brazes. These are based on the Ni–21%Si eutectic* which melts at 1143°C and were chosen for several reasons: their commercial availability, the expectation that the presence of Si will reduce the dissolution of the Si_3N_4,[9] the successful use of Ni–Cr alloys to diffusion bond Si_3N_4,[10,11] their potentially good high temperature mechanical properties, the ability of Cr to form bonding layers of CrN by reacting with Si_3N_4,[10] and the good oxidation resistance of Ni-Cr alloys. However, a problem to be faced when using Si as a temperature depressant for Ni brazes is the brittleness of the joints caused by the formation of silicides if the Si content exceeds about 10%.

Thermodynamic modelling can be a useful design tool in predicting the behaviour of the ceramic-braze systems and predictions for the SiC/Ni–Cr–Si braze systems are in good agreement with the experimental results.[1,2] Unfortunately Si_3N_4/Ni–Cr–Si systems are more complicated because the reaction processes are strongly influenced by the N_2 local partial pressure.[3,10,11] Furthermore, to understand the behaviour of Si_3N_4/Ni–Cr–Si systems requires a thorough knowledge of the Ni–Cr–Si–N phase diagram. This is lacking but some data, cited below, are available for the Ni–Cr–Si and Ni–Cr–N systems. Furthermore, a few (Ni–Cr–Si)/N_2 nitridation experiments were conducted as a precursor to this brazing study, as discussed later.

Some experimental data for Ni and Cr rich Ni–Cr–Si alloys have been published[12–14] and Ansara *et al.*[13] have assessed the data for Si lean alloys. The Ansara isotherms at 1027 and 1127°C are reproduced in Fig. 1. An obvious deficiency of this evaluation is that even the isotherm for 1127°C does not contain a liquid field, yet the commercial BNi-5, Ni–19Cr–18Si braze has a solidus of 1078°C. Hence, it became clear early on during this study that a more sound knowledge of this system was necessary if braze microstructures were to be interpreted, so a parallel programme[15,16] was initiated to derive a full Ni–Cr–Si diagram and reference to its results will be made in the Discussion.

The stability diagram of nitride phases in various Ni–Cr alloys at 950, 1000 and 1125°C as a function of N_2 fugacity (partial pressure) is given in Fig. 2. More details concerning the thermodynamic calculations and experimental verification of this diagram can be found elsewhere.[17] With

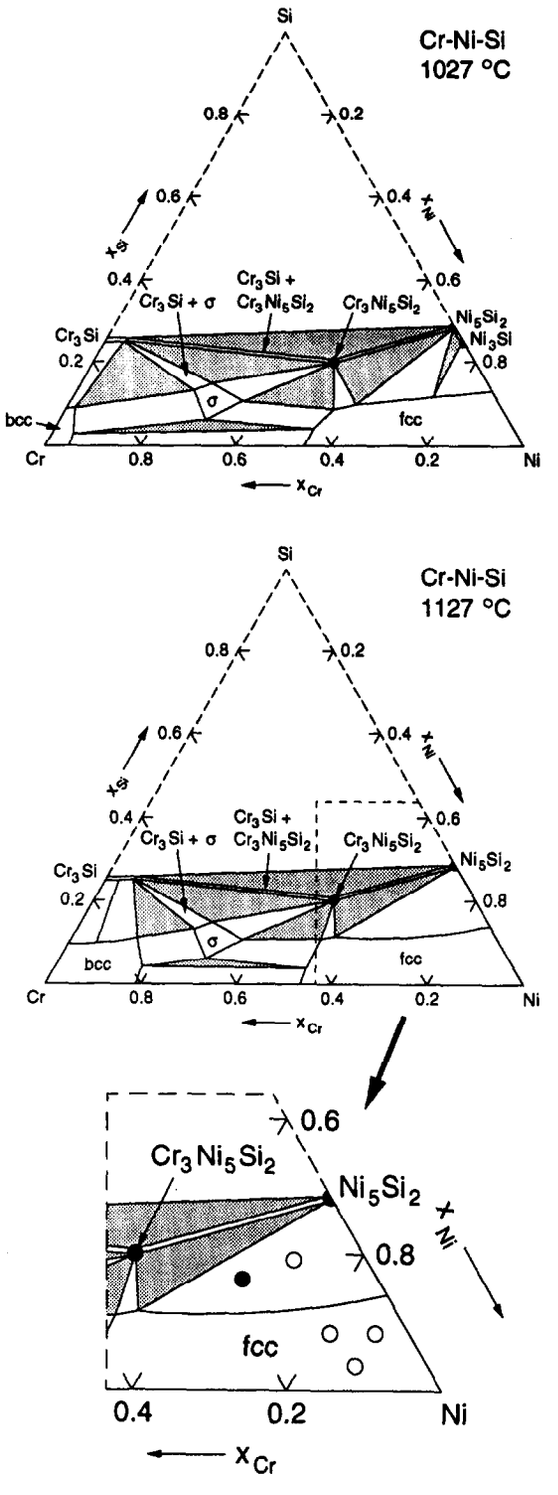


Fig. 1. Calculated partial isothermal section for the Ni–Cr–Si system at 1127°C and 1027°C (after Ref. 13). The insert displays the compositions of the braze alloys used in this study: BNi-5 is shown as a solid circle and the laboratory made alloys as hollow circles.

decreasing temperature down to 1000°C a ternary phase, π, is stable in the Ni–Cr–N system. Nitridation of Ni alloyed with at least 28%Cr produced a π phase, $Cr_{10}Ni_7N_3$[17] or $Cr_{13}Ni_7N_4$,[18] at 1000–1125°C which thermodynamic analyses demonstrated to be in equilibrium with the FCC Ni solid solution and Cr_2N at modest nitrogen activities.[19]

*Unless otherwise specified, composition at% are given.

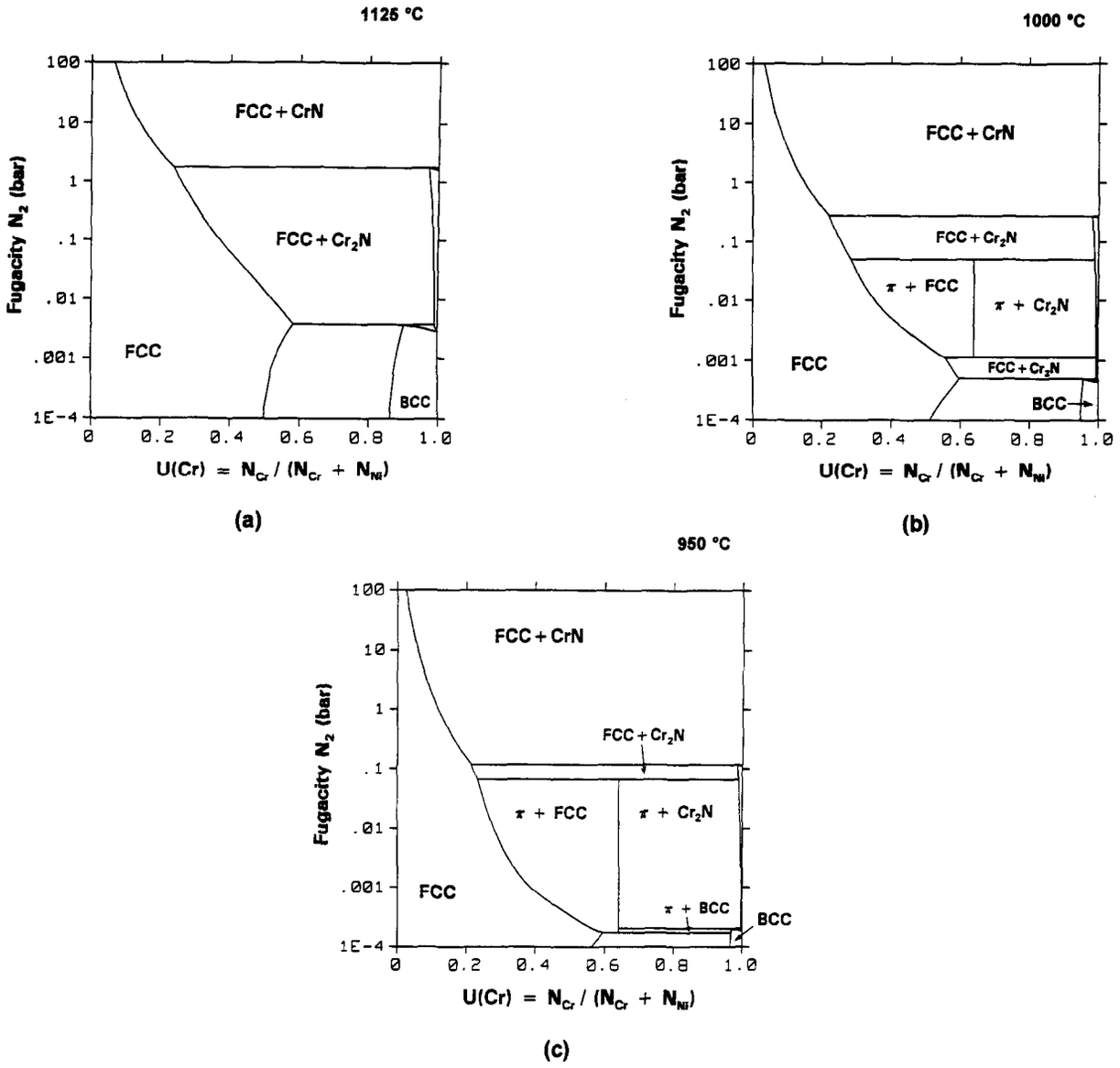


Fig. 2. Calculated stability diagrams of nitride phases in various Ni–Cr alloys as a function of nitrogen fugacity: (a) at 1125°C, (b) at 1000°C, and (c) at 950°C.

3 Experimental

The ceramic used in this work was a commercial hot-pressed Si_3N_4 containing 1·8% Al_2O_3 and 5·1% Y_2O_3 as sintering aids. It was obtained from Ceradyne Inc., Costa Mesa, CA, USA, as a plate from which were cut samples measuring 7 × 15 × 3 mm. The faces to be bonded were polished, using a 1 μm diamond paste, to a final average roughness (R_a) of about 0·3 μm. The braze alloys used were 90 μm thick foils of a commercial BNi-5, obtained from Wesgo Inc., Belmont, CA, USA, and 500 μm thick foils of laboratory produced alloys. Their compositions are indicated in Fig. 1 and summarised in Table 1. Table 1 also includes their liquidus temperatures, which were determined by differential thermal analysis and ranged from 1135°C for BNi-5 to 1400°C for one of the laboratory alloys.

The ceramic pieces and the braze alloy foils were ultrasonically cleaned in methanol, rinsed in water and dried using an air blast immediately before being assembled as a sandwich and placed in the brazing furnace. The brazing experiments were performed under vacuum of 6 × 10^{-4} Pa (1 Pa = 1

Table 1. Composition of the alloys used for wetting and brazing experiments

Alloy Designation	*Liquidus (°C)*	*Composition (at%)*		
		Ni	*Cr*	*Si*
BNi-5 Wesgo	1135	Bal.	18·9	18·4
N-21 Lab. Made	1150	Bal.	6	22
N-4 Lab. Made	1350	Bal.	5	10
N-5 Lab. Made	1345	Bal.	10	10
N-35 Lab. Made	1400	Bal.	10	5

$\times 10^{-5}$ bar) using temperatures of 1150 or 1200°C, times of 0·08–1 h and heating and cooling rates of 10°C/min. In accord with recommended practice for the BNi-5 alloy[20], each brazing cycle included a 1 h sub-solidus dwell at 1050°C during the cooling stage in an attempt to homogenize the seam microstructure. A slight uniaxial force of about 0·5 MPa was applied during brazing to maintain alignment of the workpieces.

Before commencing the main series of brazing experiments, the wetting behaviour of the brazes in vacuum at 1200°C was assessed. The alloy foils were placed on polished and cleaned Si_3N_4 substrates and heated at 10°C/min to 1200°C in a vacuum chamber evacuated to a pressure of less than 5×10^{-4} Pa. The samples were kept for 30 min at temperature and then cooled to room temperature at 10°C/min.

After being used in the wetting or brazing experiments, the samples were cross-sectioned, polished with diamond paste and finished with a 0·3 μm alumina slurry. The contact angles of wetting samples and the interfacial microstructures of brazed samples was characterized by optical microscopy and scanning electron microscopy. Electron probe microanalysis, (EPMA), and X-ray diffraction, (XRD), techniques were used to characterise the micro-chemistry of braze seams. The Vickers hardness of phases within the seams were derived using a 50 g load applied by Zeiss MHT-4 equipment.

Nitridation of the Ni–Cr–Si alloys under total gas pressures up to 100 bars, took place in a sintering furnace (KCE, Germany). Temperature control was carried out with an optical pyrometer within ±5°C accuracy. All experiments were carried out in pure nitrogen ($O_2 \leq 10$ ppm; $H_2O \leq 10$ ppm). After nitridation under these conditions, formation of oxides was not detected at the surface of the samples. The surface of the alloys were examined after nitriding by XRD analysis with a cylindrical texture camera using nickel-filtered Cu–Kα radiation.

4 Results and Interpretation

4.1 Wetting

The contact angles derived from the 1200°C wetting studies are presented in Fig. 3. The commercial BNi-5 braze wetted well with an angle of 10°, while the laboratory produced braze alloys wetted even better with contact angles of virtually zero.

Also included in the figure are some contact angles reported for other Ni braze alloys.[9,21,22] It can be seen that not all Ni brazes wet, the contact angle for BNi-2 (Ni–13B–8Si–7Cr–3Fe) being

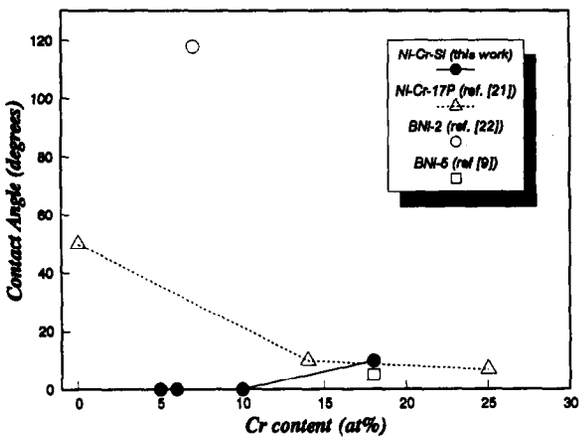


Fig. 3. Wetting behaviour of Ni–Cr–Si brazing alloys on Si_3N_4 substrates at 1200°C (filled circles). The composition of the alloys is given in Table 1. Also included are literature data for BNi-5 (open squares) Ref. 9, for Ni–17P–Cr brazes (open triangles) Ref. 21 and for BNi-2, a Ni–13B–8Si–7Cr–3Fe braze at 1150°C (open circles) Ref. 22.

120°,[22] but our observation of excellent wetting by BNi-5 confirms a literature report.[9] Using the criterion of a maximum contact angle of 30° for effective wetting of a ceramic suggested by Moorhead and Keating,[23] it can be seen that all the Ni–Cr–Si brazes used in this study are adequate but some of the other compositions are unsuitable.

4.2 BNi-5 microstructure

Comparison of the quoted Ni–19Cr–18Si composition of BNi-5 with the phase stability diagrams for both 1027 and 1127°C, Fig. 1, reveals that it lies within the solid–solid Ni_5Si_2–FCC Ni two phase field, yet very close to the boundary of the solid–solid–solid Ni_5Si_2–FCC Ni–$Cr_3Ni_5Si_2$ three phase field. It was surprising, therefore, that the microstructure of the as received BNi-5 braze, shown in Fig. 4, contained three phases. These were: (1) a matrix labelled **M** with a hardness of HV463, (2) a substantial amount of a hard irregular phase labelled **A**, and (3) a small amount of a hard angular phase labelled **B**.

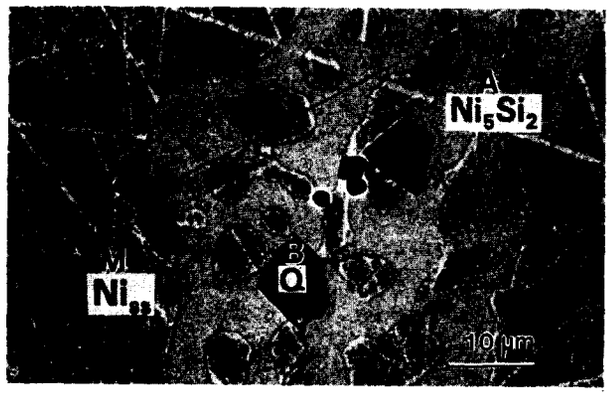


Fig. 4. Scanning electron micrographs of as-received BNi-5 microstructures.

Table 2. Phases identified in BNi-5 foils and braze seams. (Compositions are given in at%). The stoichiometry of the Q-phase was found to be $Ni_{15}Cr_{21}Si_8N_6$

Condition	*Phase M*	*Phase A*	*Phase B*
As -received foil	Ni s.s. Ni–24Cr–15Si	Ni_5Si_2 Ni–26Si–10Cr	Q-phase Ni–45Cr–15Si–3·5N
Melted foil, 1150°C, 15 min	Ni s.s. Ni–24Cr–12Si	Ni_5Si_2 Ni–27Si–7Cr	Q-phase Ni–51Cr–15Si–3·5N
Braze seam, 1150°C, 15 min	Ni s.s. Ni–24Cr–12Si	Ni_5Si_2 Ni–28Si–2·8Cr	Q-phase Cr–29·6Ni– 14·9Si–7·3N
Braze seam, 1200°C, 15 min	Ni_5Si_2 Ni–27Si–8·4Cr	Ni_2Si Ni–32Si–3·5Cr	Q-phase Cr–29Ni– 14·2Si12·2N
Braze seam, 1200°C, 30 min	Ni_5Si_2 Ni–27Si–8·2Cr	Ni_2Si Ni–32Si–4·3Cr	Q-phase Cr–28·2Ni–13·5Si–13·9N

The compositions of the phases in this and other cross-sections are summarised in Table 2. Comparison of these compositions with the Ansara diagrams shown in Fig. 1 identifies the Ni–24Cr–15Si Matrix, **M** as a Cr and Si saturated FCC Ni and the hard irregular Ni–26Si–10Cr phase **A** as a Cr enriched Ni_5Si_2. However, assigning an identity to the Ni–51Cr–15Si–3·5N composition of the angular phase **B** is difficult. The angular phase contains nitrogen and hence cannot be identified validly as any of the ternary compounds shown in the Ansara diagrams. Even if the N content is ignored, the normalised composition is not in accord with any of the phases shown in Fig. 1 but lies within the two phase field between $Cr_3Ni_5Si_2$ and the Cr_3Ni_2Si, or σ, phase. Therefore, it was decided somewhat arbitrarily for the moment, (it will be justified later on), to regard the angular phase (**B**) as a quaternary compound, Q.

The microstructure of the BNi-5 foil was little changed by subjecting it to a simulated brazing cycle by melting in an Al_2O_3 crucible and holding at 1150°C for 15 min, Table 2. The microstructure contained three phases; 53% of the Ni-based solid solution matrix phase, 40% of Ni_5Si_2 and 7% of the quaternary Q-phase. However, major changes occurred when the alloy was subjected to braze cycles in contact with Si_3N_4.

4.3 Si_3N_4/BNi-5 interactions

The good wetting behaviour of BNi-5 ensured that brazed sandwiches were formed successfully at both 1150 and 1200°C. The wetting was so good that the braze also spread over the sides of the ceramic pieces, but the structures of the joints were poor. Optical microscopy revealed that there were voids within the brazed seam and that both the seam and the ceramic–metal interfaces were cracked, presumably due to stresses caused by the mismatch between the $9·5 \times 10^{-6}$ °C^{-1} thermal expansion coefficient of the braze,[9] and the $3·3 \times 10^{-6}$ °C^{-1} of Si_3N_4.

After brazing at 1200°C (Fig. 5) it was found that the Vickers hardness of the braze matrix phase had been increased to about HV 1100 (Table 3), and that the composition of the braze seam had been changed (Table 2).

The matrix became depleted in Cr but Fig. 6 shows that extending the brazing cycle caused the



(a)



(b)

Fig. 5. Microstructure of BNi-5 joints (a) brazed at 1200°C for 15 min, (b) brazed 1200°C for 30 min.

Table 3. Hardness of the matrix phase in Ni–Cr–Si alloys before and after use in various experiments

Alloy or System	*Experiment*	*Hardness (Hv 50gr)*
BNi-5	None	463·5 ± 17·4
Si_3N_4/BNi-5	Brazing at 1200°C	1090·3 ± 40·7
Si_3N_4/N-21	Brazing at 1200°C	1109·0 ± 34·0
Si_3N_4/N-35	Wetting at 1200°C	1061·5 ± 67·8
Si_3N_4/N-4	Wetting at 1200°C	1102·3 ± 31·6

Si content of the braze seam to increase progressively as more Si rich silicides were formed. With increasing the brazing time, the Ni_5Si_2 phase identified in Fig. 4 as A was converted to Ni_2Si, Fig. 7, and became very abundant. Finally, the EPMA studies showed that quite large amounts of a complex Ni–Cr–Si–N phase was formed, the N content of which increased with the brazing temperature and time. By comparison with the microstructure of the as received filler metal this phase was identified as the quaternary Q-phase.

The large amount of Si found in the braze seam clearly demonstrates that Si_3N_4 reacts with the liquid filler metal during the brazing process. The conclusion is reinforced by the fact that decreasing the brazing time to 5 min, still caused the conversion of the matrix to a brittle silicide. Rapid reaction of the ceramic with the molten braze is reported also by Hadian and his co-workers,[9] who used the BNi-5 alloy for brazing Si_3N_4 to Mo at 1200°C. They measured a smaller increase in the Si content of the braze than it was observed in our study, but this difference may be explained by the higher partial pressure of nitrogen in their experiments (~8 Pa) compared to ours (~8 × 10^{-6} Pa), which leads to a lower chemical potential of silicon in Si_3N_4 and, therefore, to lower driving force for diffusion of silicon.

In some final experiments, the configuration of the joints was changed by the introduction of a

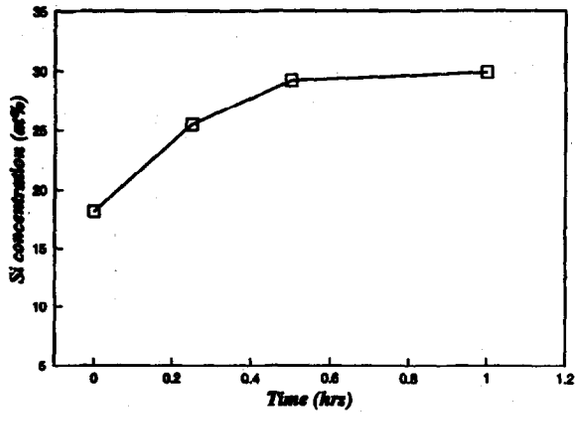


Fig. 6. Concentration of Si in the braze seam of Si_3N_4/BNi-5 joints plotted as a function of the brazing time at 1200°C. Each point is the average of 5 measurements at different 5 × 5 μm^2 locations.

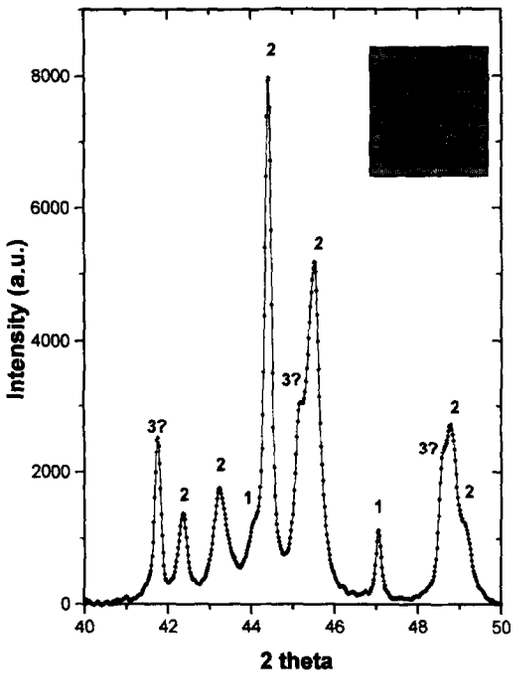


Fig. 7. X-ray diffraction spectrum of a fracture surface of a Si_3N_4/BNi-5 joint brazed at 1200°C for 30 min.

500 μm thick foil of Ni–22Cr, Fig. 8. In this case, δ-Ni_2Si was not found within the braze seam after bonding at 1200°C for 30 min. However, there was an extensive formation of the Q-phase within a matrix of Ni-based solid solution and Ni_5Si_3. In places, the Q-phase was formed as spherical particles, that suggested it had grown in the molten matrix. Another reaction product worth noting was a layer of 'CrN' at the braze–ceramic interface that was observed exclusively in the central region of the joint.

Although the brazing temperature suggested for the commercial BNi-5 alloy ranges between 1150 and 1216°C,[24] the present results demonstrate that a temperature of 1200°C is too high if it is to be used to join Si_3N_4. Hence, further brazing experiments at lower temperatures were performed. The

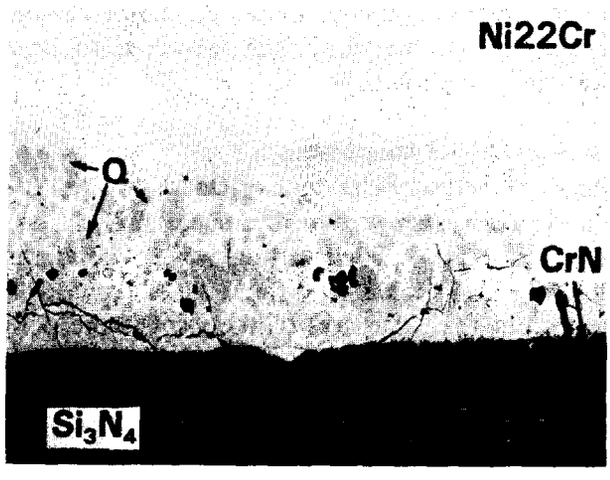


Fig. 8. Microstructure of the Si_3N_4/BNi-5/Ni–22Cr interface (1200°C, 15 min).

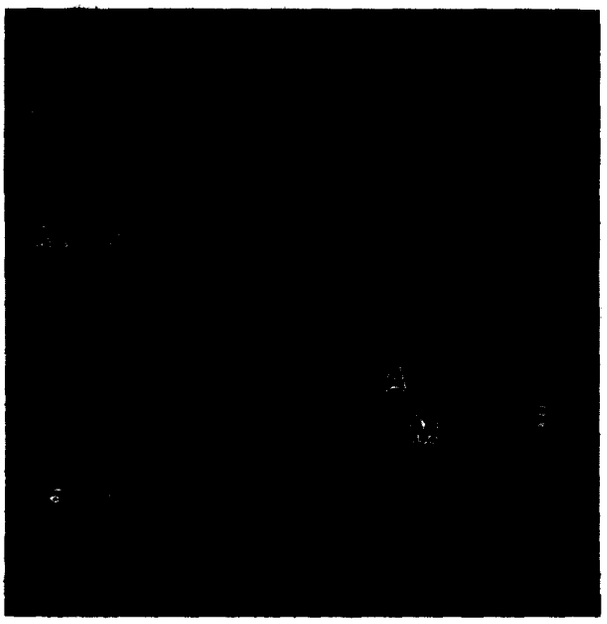


Fig. 9. Scanning electron micrographs of a Si_3N_4/BNi-5 joint brazed at 1150°C for 15 min.

microstructure of a cross-section of a Si_3N_4/BNi-5 joint brazed at 1150°C for 15 min, shown in Fig. 9, is not significantly different to that produced at 1200°C, Fig. 5. Once more, three phases are present in the brazing seam. Quantitative electron probe micro-analysis of the braze seam, summarised in Table 2, showed that the Ni solid solution matrix was still present in the seam even though large amounts of Ni_5Si_2 had been formed; the amount of Cr dissolved in the Ni_5Si_2 was decreased from 8 to about 3%, and the angular Q-phase was even more deficient in nitrogen.

4.4 Interactions of Si_3N_4 with other Ni–Cr–Si brazes

The cross-section of a Si_3N_4/N-21 alloy (Ni–6Cr–22Si) joint bonded at 1200°C for 15 min, shown in Fig. 10(a), has features similar to those observed in Si_3N_4/BNi-5 joints. Once again, the results indicate a brazing temperature of 1200°C is too high because of excessive ingress of Si. This conclusion is supported by results obtained using the other Ni–Cr–Si laboratory alloys, N-4 (Ni–5Cr–10Si), N-5 (Ni–10Cr–10Si) and N-35 (Ni–10Cr–5Si). Melting occurred even though the liquidus temperatures of the alloys are 1350–1400°C, Table 1. The melting was associated with a matrix hardness increase, as shown in Table 3, and the formation of the brittle quaternary, Q-phase.

A significantly different microstructure was produced when the laboratory alloy N-21 (Ni–6Cr–22Si) was used to braze at 1150°C for 15 min, as illustrated in Figure 10(b). In this case a reaction layer with an average thickness 2·4 ± 0·5 μm was formed at the ceramic/braze interface. A quantitative composition cannot be quoted for

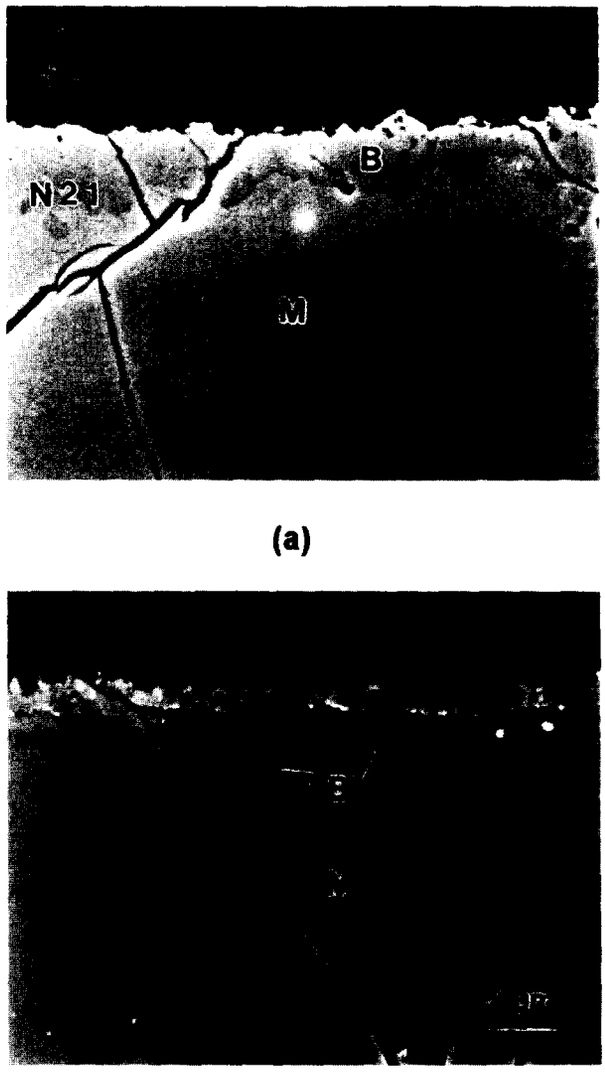


Fig. 10. Cross-sections of Si_3N_4/N-21 joints brazed at, (a) 1200°C for 15 min, (b) 1150°C for 15 min.

this reaction layer because of spatial resolution limitation of the electron probe micro-analysis technique, but from the optical appearance and morphology as well as from qualitative EDX elemental maps we may conclude that this layer is the quaternary Q-phase.

EPMA analysis of the braze seam revealed that the matrix was Ni_5Si_2 and that the angular inclusions shown in Fig. 10 had similar composition with the phases identified as Q in the other joint microstructures. Finally, cracks and voids were present in the seam, so the microstructure was unacceptable as in the case of the Si_3N_4/BNi-5 joints.

4.5 Nitridation of Ni–Cr–Si alloys

In general, as in the case of the Ni–Cr–N system, see Fig. 2, the activity of N_2 largely determines the stability of various phases in the Ni–Cr–Si–N system. Nitridation of Ni–15Cr–10Si alloy at 1125°C under 1 bar N_2 pressure or higher, produced a surface layer and internal precipitates of the

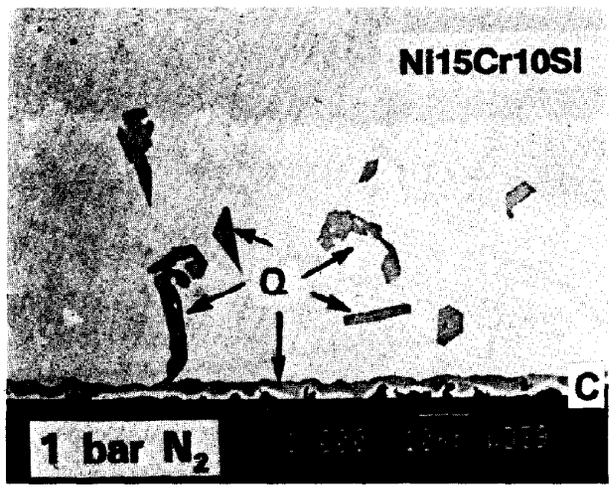


Fig. 11. The formation of the quaternary phase, Q, ($Ni_{15}Cr_{21}Si_8N_6$) after nitriding Ni–15Cr–10Si alloy at 1125°C under 1 bar of N_2 (C = Metal–gas interface).

quaternary phase Q, Fig. 11. Careful EPMA analysis of equilibrated samples pointed out to a $Ni_{15}Cr_{21}Si_8N_6$ stoichiometry for the Q-phase. Additional nitriding experiments of different Ni–Cr–Si alloys (Ni–(20–35%Cr)–(2–5% Si)) have shown that the Q-phase exists as an equilibrium phase in the quaternary Ni–Cr–Si–N system over the temperature range of 1000–1250°C.

5 Discussion

It is clear that Si_3N_4 interacts strongly with Ni–Cr–Si brazes. Thus all the brazes wetted well at 1200°C, and the behaviour of the laboratory-made brazes (N-4, N-5 and N-35) is evidence of a melting temperature depression caused by the ingress of Si from the ceramic. Vigorous workpiece/braze interactions are often associated with good wetting, and all the brazes used in this study wetted very well. The least wetting braze was the commercial BNi-5 alloy which also has the highest Cr content. However, the correlation between Cr content and wetting behaviour is unclear because, for instance, the Ni–Cr–P brazes with the highest Cr contents also formed the lowest contact angles with Si_3N_4.[21]

While braze/ceramic interactions promote wetting, the resultant microstructures are excessively brittle and none of the Ni–Cr–Si brazes used in this study can be considered satisfactory joining materials for Si_3N_4, not even the commercially developed BNi-5.

Upon brazing at 1200°C the liquid filler metal reacts with the ceramic leading to an ingress of Si and nitrogen into the braze. Since the melting point of the Q-phase is higher than 1250°C, as determined by the nitridation experiments, the interaction of the nitrogen with the liquid Ni–Cr–Si filler metal is as follows:

$$Si_3N_4 + L \rightleftarrows Q + L'$$

where L' is the remnant Cr-depleted liquid filler metal. The second eutectic isotherm in the binary Ni–Si system ($L' \rightleftarrows Ni_5Si_2 + \delta\text{-}Ni_2Si$) lies at 1215°C.[25] Chromium that is still present in the liquid may depress the temperature of this eutectic. However, the significant ingress of silicon from Si_3N_4 into the molten braze leads to the formation, inside of liquid, of precipitates of δ-Ni_2Si (or its high temperature modification θ-Ni_2Si) having a higher liquidus temperature.[26] Then, these precipitates grow through the liquid. Such a mechanism seems to be confirmed by the resultant morphology of the reaction zone after brazing at 1200°C for 15–30 minutes (Fig. 5(a), (b)).

At 1150°C the interactions between the ceramic and the braze are less severe. Still the liquid filler metal is enriched with Si and depleted from Cr. Besides the formation of the quaternary Q-phase, excess of Si within the molten filler metal result in the precipitation of Ni_5Si_2 at the brazing temperature rather than upon cooling.

In order to decide whether any other Ni–Cr–Si braze might be suitable, it is necessary to understand the reaction paths followed by the ceramic/braze systems, especially the formation of the nitride phases inside the braze seam. For instance the formation of a continuous layer of CrN at the interface is desirable[11,15] because this could impede the ingress of Si, whereas the formation of the brittle Q-phase in the seam deteriorates the joint quality. Quantitative understanding of the reaction paths cannot be achieved because of the lack of phase equilibrium data for the Cr–Ni–Si–N system but some qualitative guidance can be obtained from considering the recent Ni–Cr–Si phase diagram study in parallel with this brazing work.[15,16]

The ineffectiveness of the Si contents of the brazes in inhibiting further detrimental ingress of Si from the ceramic is further illuminated by these studies. Figure 12 displays two experimentally determined isothermal sections for 1050 and 1125°C that should be relevant to phase structures of molten and solidified brazes. Comparison of this new information with the assessments for Si lean alloys shown in Fig. 1 reveals both similarities and differences which impinge on our observations. There is agreement about the phase structure of the laboratory made alloys: N-4, (Ni–5Cr-10Si), N-5, (Ni–10Cr–10Si) and N-35, (Ni–10Cr–5Si), lie within the Ni solid solution and N-21, (Ni–6Cr–22Si), lies within the two phase field between Ni_5Si_2 and the FCC or γ-Ni solid solution.

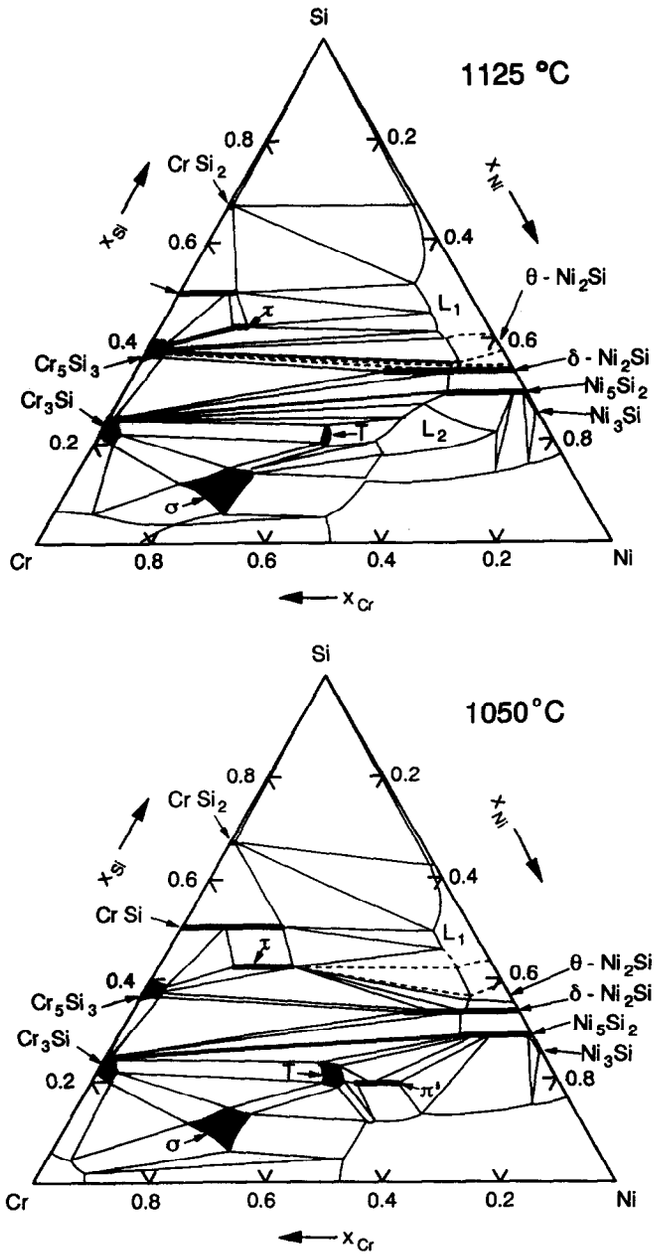


Fig. 12. Experimentally determined isothermal sections for the Ni–Cr–Si system at 1125°C and 1050°C, after Ref. 16.

Similarly, there is agreement that any σ-phase present in the as-received BNi-5 will have been a non-equilibrium or a quaternary phase.

In contrast, the isothermal sections due to Ansara *et al.*,[13] shown in Fig. 1 predict that the commercial BNi-5, Ni–18Cr–19Si, lies on the edge of a solid–solid two phase field between FCC Ni and Ni_5Si_2. This is not confirmed by the new isotherms shown in Fig. 12. In these, the BNi-5 composition lies close to the edge of the L_2 liquid field at 1125°C and presumably will lie on the actual edge of an expanded L_2 liquid field at the braze liquidus of 1135°C. Even more informatively, the new diagram for 1050°C casts light on the microstructure of the solidified braze seams produced by the equilibrium of the brazes and the dissociating ceramic. Ingress of Si will cause the Ni solid solution braze matrix to be replaced progressively by silicides and we have observed the formation of Ni_5Si_2 and Ni_2Si.

The same considerations apply to the interaction of solid Ni–Cr alloys during the diffusion bonding of Si_3N_4, but the approach to equilibrium will be much slower. The diffusion coefficient of Si in Ni–22Cr at 1200°C is $4{\cdot}9 \times 10^{-14}$ m^2s^{-1}, probably 10 000 times slower than in the molten braze because the self diffusion coefficient for molten Ni lies in the range 10^{-8}–$10^{-9}m^2s^{-1}$.[27]

A substantial displacement Cr is caused by the conversion of the Ni–24Cr–12Si matrix of the braze to Ni_5Si_2 and Ni_2Si containing only 8% of Cr. The ingress of Si from the ceramic that causes this displacement of Cr is accompanied also by a release of nitrogen and our experimental results show the displacement to result in a formation of a Cr rich nitride, $Ni_{15}Cr_{21}Si_8N_6$, which can be in equilibrium with the Ni-solid solution and Ni_5Si_2 or Ni_2Si. The presence of $Ni_{15}Cr_{21}Si_8N_6$, therefore provides proof of one logical step in the progress of a reaction path in the uncharted Ni–Cr–Si–N system created when a Ni–Cr–Si alloy is used to braze Si_3N_4.

The 1050°C isotherm in Fig. 12 shows that one or more of the Cr–35Ni–25Si (T), Cr–30Ni–10Si (σ) or Ni–30Cr–20Si (π') phases will be in equilibrium with γNi braze matrices and that the T and π' phases will be in equilibrium with Ni_5Si_2 matrices. Experimental measurements of the Cr enriched angular Q-phase in solidified BNi-5 seams with both γNi and silicide matrices yielded compositions of approximately Ni–42Cr–16Si–12N, intermediate in metal stoichiometry between that of the T and σ phases The σ-phase is not in equilibrium with the Ni_5Si_2 present in all the solidified braze seams, but there are tie lines between the T-phase and both γNi and Ni_5Si_2. Thus the designation of the angular Q-phase in BNi-5 braze seams, and possibly the reaction product layer formed by N-21, as a N modified T phase is a logical, albeit tentative, outcome of the Ni–Cr–Si phase diagram studies.

It is clear that the prospects of improving the joint characteristics by varying fabrication conditions such as time and temperature are bleak. Diffusion barriers will need to be applied to the ceramic surfaces to prevent Si and nitrogen ingress when using Ni–Cr–Si braze alloys.

6 Conclusions

Ni–Cr–Si braze alloys wet and adhere to Si_3N_4 and in some cases spreading is observed. Despite

the large range of brazing conditions explored, the joint quality obtained was very poor. Unbonded areas, cracks and voids were observed in almost all the samples.

Contact between the molten Ni–Cr–Si brazes and Si_3N_4 caused ingress of Si and nitrogen from the ceramic. In the case of the commercial BNi-5 alloy, the relatively ductile γNi matrix of the braze was converted to brittle Ni_5Si_2 or Ni_2Si. Other changes caused by the ingress of Si were the formation of a Ni–Cr–Si–N compound as inclusions or a reaction product layer.

The difficulties encountered when using the Ni–Cr–Si alloys are related to fundamental materials science effects rather than inappropriate choice of brazing conditions. None of the Ni–Cr–Si brazes can offer direct resistance to the embrittling ingress of Si and nitrogen from the ceramic.

Acknowledgements

Part of this work was carried out within the Commission Research and Development Programme. It was also partially supported by the Innovative Programme for Technical Ceramics from the Dutch Finance Ministry (Grant # 91.B230).

References

1. McDermid, J. R. & Drew, R. A. L. *J. Am. Cer. Soc*, **74**(8) (1991) 1855–60.
2. McDermid, J. R., Pugh, M. D. & Drew, R. A. L. Metall. Trans., **20A** (1989) 1803–10.
3. Mehan, R. L., Jackson, M. R., McConnell, M. D. & Lewis, N., *J. Mat. Sci.*, **18**(2) (1983) 508–14.
4. Foley, A. G. & Andrews, D. J., In *Proc. 2nd European Colloquium on Design Ceramic Interfaces*, Petten (NL), 1992, ed. S. D. Peteves, Commission of the European Communities, Luxembourg, EUR 15306 EN, 1993, p. 411–27.
5. Iwamoto, N., Kamay, M., Fujii, K. & Sato, N., *ibid*, p.441–51.
6. Mizuhara, H., *Brazing alloy of copper, silver, titanium, aluminium*, US Patent 5,087,416, February 1992.
7. Santella, M. L., *Advan. Ceram. Mat.*, **3**(5) (1988) 457–62.
8. Lugsheider, E., Boretius, M. & Tillmann, W., DKG **68** No1/2 (1991) 14–22.
9. Hadian, A. M., McDermid, J. R. & Drew, A. L., Ceram. Trans., **19** (1991) 221–7.
10. Peteves, S. D., Moulaert, M. & Nicholas, M. G., *Metall. Trans. A*, **23A** (1992) 1773–81.
11. Moretto, P., Moulaert, M., Glaude, P., Frampton, P., Ceccone, G. & Peteves, S. D. In *Proc. 2nd European Colloquium on Design Ceramic Interfaces*, Petten (NL), (1992), ed. S. D. Peteves, Commission of the European Communities, Luxembourg, EUR 15306 EN, 1993 p. 519–538.
12. Lugscheider, E., Knotek, O. & Klöhn, K., *Thermochim. Acta*, **29**(2) (1979) 323.
13. Ansara, I., Chart, T. G., Chevalier, P. Y., Hack, K., McHugh, G., Rand, M. H. & Spencer, P. J., Report No EUR 9657/1/EN, (1985), Commission of the European Communities, Luxembourg, and references therein.
14. Gupta, K. P., Rajan, N. S. & Beck, P. A., *Trans. TMS-AIME*, **218** (1969) 617.
15. Kodentsov, A. A., Kivilahti, J. K., van Loo, F. J. J. & Peteves, S. D., *Ceram. Trans.*, **35** (1993) 13 516.
16. Kodentsov, A., Kivilahti, J. K., van Loo, F. J. J. & Peteves, S. D., to be published.
17. Kodentsov, A. A., Gulpen, J. M., Kivilahti, J. V. & van Loo, J. F., to be published.
18. Ono, N., Kajihara, M. & Kikuchi, M., *Metall. Trans.* **23A** (1992) 1389.
19. Frisk, K., Ph. D. Thesis, Royal Institute of Technology, Stockholm, Sweden, (1990).
20. Lugscheider, E., Knotek, O & Klöhn, K., *Weld. J., Weld. Res. Suppl.*, **57** (1978) 319s.
21. Nicholas, M. G. & Peteves, S. D., In *Proc. of 4th International Symposium on Ceramic Materials and Components for Engines*, eds. R. Carlsson, T. Johansson & L. Kahlman, Elsevier Applied Science, London, 1992, p. 332.
22. Holmström, M., Ljungberg, L., Warren, A. & Warren, R., In *Proc. of 4th International Symposium on Ceramic Materials and Components for Engines*, eds R. Carlsson, T. Johansson & L. Kahlman, Elsevier Applied Science, London, 1992, p. 364–71.
23. Moorhead, A. J. & Keating, H., Report No ORNL-6262, Oak Ridge National Laboratory, Oak Ridge, TN, March 1986.
24. Metal Handbook, 9th ed, (ASM), Ohio, 6 1983, 1014–21.
25. Massalski, T. B., *Binary Alloy Phase Diagrams*, (ASM), Ohio, 1986 p. 842 & 1756.
26. Nash, P. & Nash, A., *Bull. All. Ph. Diagr.*, **8**(1) 1987 6–13.
27. Iida, T. & Guthrie, R. I. L., *The Physical Properties of Liquid Metals*, Clarendon Press, Oxford, 1988, p. 217.

Journal of the European Ceramic Society **15** (1995) 573–579
© 1995 Elsevier Science Limited
Printed in Great Britain. All rights reserved
0955-2219/95/$9.50

0955-2219(95)00018-6

Transmission Electron Microscopy of Intergranular Regions of Corroded Silicon Nitride

A. D. Stalios,[a] J. Luyten,[a] F. L. Riley[b]* & R. J. Fordham[c]

[a]Materials Department, SCK/VITO, B-2400 Mol, Belgium
[b]School of Materials, The University of Leeds, Leeds LS2 9JT, UK
[c]Materials Centre, JRC Petten, 1755 ZG Petten, The Netherlands

(Received 17 March 1994; revised version received 18 January 1995; accepted 26 January 1995)

Abstract

Two hot-pressed, dense, silicon nitride materials have been exposed to the flue gases of an aluminium smelting furnace heavily contaminated with Al, Ca and K-containing dust and vapours. Transmission electron microscopy (TEM) has been used to examine microstructural changes occurring in the silicon nitride at the interface between corroded and uncorroded material. Extensive diffusion of contaminant metal into the intergranular glass of the silicon nitride occurs, associated with physical and chemical changes in the intergranular regions, and a marked loss of mechanical strength.

1 Introduction

Silicon nitride ceramics are being considered for use as structural components in heat-exchangers in a range of industrial processes. One example is the aluminium remelting furnace where waste heat recovery would be expected to lead to significant energy savings. During the refining operation considerable amounts of a fluoride and chloride flux are added to the metal to form slags. The flue gases can thus contain high concentrations of salts, and silicate byproducts, and they are highly corrosive towards the non-oxide ceramics such as silicon carbide and silicon nitride. Most reported high temperature corrosion studies on silicon nitride have been carried out under closely defined and simplified laboratory conditions. A small number of studies have also been made involving the exposure of silicon carbide and silicon nitride materials to high temperature working industrial environments.[1–3] The work reported here was part of a study carried out to identify the major consequences of corrosive degradation of dense multiphase silicon nitride materials under severe industrial conditions.

Previous detailed studies on silicon nitride[4–8] have concentrated attention on the mechanism of surface oxidative corrosion with relatively thin (~20 μm) layers of corrodent oxide, or with continuous supplies of volatile corrodent at low vapour pressure. It has been shown that surface reactions, and phase equilibrium relationships, involving silicon dioxide and the oxide components of the corrosion film of the type:

$$M_aO_{b(s)} + SiO_{s(s)} = M_aSiO_{(2+b)(l)}$$

are of importance in controlling the rate of corrosion. Surface equilibria can also determine the extent of corrosion caused by a specific amount of corrodent oxide. Liquid silicates of composition not in thermodynamic equilibrium with silicon dioxide (SiO_2) are effectively solvents for SiO_2 and thus prevent the formation of potentially protective films on the silicon nitride surface. These laboratory studies have shown the importance of actual or incipient SiO_2 films at the silicon nitride–silicate film interface as oxygen transport barriers,[9] and therefore able to provide resistance against corrosion. The oxygen conductivity of pure SiO_2 in amorphous and crystalline form is low: silicate glasses and liquids are markedly more permeable towards oxygen.[10]

Detailed attention has not been paid to processes occurring in the silicon nitride beneath the surface oxide film during high temperature corrosion, and under conditions where the formation of a protective SiO_2 layer may be difficult. The microstructure of the silicon nitride is an important factor, and in particular the presence of the interconnecting siliceous intergranular glass. Intergranular cations are particularly important during oxidation in that they are able to diffuse from the intergranular phase to the surface oxide film to react to form silicates. The outwards diffusion of metal cation then becomes an important component of the rate controlling process.[11] However,

*To whom all correspondence should be addressed.

during high temperature oxidative corrosion under conditions where high concentrations of metal cations are deposited on the outer surface of the nitride, inwards diffusion of these cations into the intergranular glass will also occur. One consequence will be a change in composition of the glass, to one richer in contaminant metal oxide and of lower viscosity,[12] and resulting in the silicon nitride having lower high temperature strength and creep resistance. There exists also the possibility of internal oxidation through the rapid transport of oxygen to the silicon nitride grains through the more conductive intergranular glass or liquid. The implications for the long term structural stability and load-bearing capability of the component are thus considerable.

The object of the study reported here was to detect the existence of such inwards diffusion processes by examination of the intergranular regions of the silicon nitrides close to the surface corrosion product film, using transmission electron microscopy (TEM) on thinned foils. Two dense commercial grades of hot-pressed silicon nitrides were used for this study: one (designated SN1) had been densified using yttrium oxide (Y_2O_3); the other (SN2) had been formed using magnesium oxide (MgO). Both contained iron (the SN1 less than the SN2) which had been used possibly either as a silicon nitridation catalyst in the production of the silicon nitride powder, or as a densification aid.[13] The microstructure of the MgO-densified SN2 has already been discussed with regard to the function of iron during the hot-pressing densification stage.[14]

These materials were mounted in refractory concrete holders in an industrial continuous operation aluminium scrap remelting furnace, and exposed for extended times to the flue waste gases at temperatures in the region of 1050°C.

2 Experimental

The chemical compositions of the two commercial hot-pressed silicon nitrides (Feldmühle, Plochingen, Germany), expressed in terms of weight % of oxide constituent (or the equivalent), are given in Table 1.

Small test bars of material, of dimension 14 × 7 × 7 mm^3, were partly embedded in a block of refractory concrete and mounted in the wall of the flue gas duct of a standard large aluminium remelting furnace (Aluminium Foundries, R. Claeys, Lichtervelde, Belgium) fired by three natural gas burners. Two thermocouples were fixed to the concrete blocks with their tips close to the silicon nitride bars. The furnace was operated normally for times up to 1000 h during which time

Table 1. Silicon nitride composition/wt%

	SN1	SN2
Y_2O_3	9·0	0·005
MgO	0·005	1·2
Al_2O_3	0·12	0·20
Fe_2O_3	1·7	2·7
CaO	0·05	0·25
ZrO_2	0·01	0·01
[Si_3N_4	balance	balance]

the temperature fluctuated between 1000 and 1100°C with a mean of 1050°C. Flue gases were contaminated with chlorides and fluorides used as slag-forming fluxes in earlier furnace operating cycles. Exposed bars were removed, and sectioned for examination across the regions which had been fully in the flue gas flow. Scrapings of deposit from corroded surfaces were milled and analyzed by X-ray diffraction (XRD).

TEM examinations (JEOL 200CX equipped with a LaB_6 filament operating at 200 kV) were made of ion-beam thinned discs cut from as-received, and exposed, plates of material 7 × 14 × 0·5 mm^3. The more loosely adhering surface scale was carefully brushed away from each oxidised plate, and the silicon nitride mechanically ground from the unreacted side of the plate to give a maximum thickness of 150 μm. Discs 3 mm in diameter were drilled from the thinned plate and dimpled from both sides until the corrosion layer–bulk material interface was barely visible. Uncorroded materials were prepared in the standard way. Discs were then further ion-milled to perforation in a Gatan 600 dual ion mill using argon ions at 6 kV with a 15° incidence angle, and were finally coated with a 20 nm carbon film to prevent charging in the electron beam. The samples of corroded silicon nitride used for TEM examination were therefore planar sections approximately parallel to the corroded surface (rather than sections normal to the external surface) in the vicinity of the interface between uncorroded, and corroded, material.

The mechanical strengths in four-point bend (Instron Universal test equipment) of as-received and corroded materials were measured before and after exposure to flue gas, using a self-aligning fixture (span 40/20 mm) and a crosshead speed of 6 μm s^{-1}.

3 Results

3.1 The corrosion environment

Two typical random analysis of the flue gases during the course of normal corrosion tests are given in Table 2. These showed that while the tempera-

Table 2. Two examples of typical flue gas exposure conditions

Mean temperature/°C	1020	1090
Gas velocity/m s^{-1}	2·8	3·0
O_2/%	0·1–0·8	1·3–14·2
H_2O/%	19·7	5·4
CO_2/%	9·9–11·5	3·2–12·0
CO/ppm*	19 800–21 900	0–10·5
Cl^-/ppm	1·5	3·5–4·6
F^-/ppm	13	0·5–1·4
SO_2/ppm	0·4–2·0	0·9–1·0
SO_3/ppm	1·2–1·4	0·7–1·6

[*ppm by weight]

ture and gas flow rates remained constant, changes in the combustion air/gas ratio could lead to swings in condition from a high excess oxygen level to marginally oxidising. However, the residual oxygen, together with the oxygen partial pressure arising from the CO_2 and H_2O levels, would have been adequate to ensure stability of the SiO_2 in the oxide film and suppress loss as silicon monoxide (SiO) vapour.

SEM X-ray microspectroscopy (XMS) analyses of flue dust particles showed them to contain predominantly K, Cl, Si, Al and Ca, with lesser amounts of Na, Zn, S, Mn, Ti, Cr, and Fe. Between 70 and 95% of the particles were water soluble, and were mainly the fluorides and chlorides of K, Na, Al, and Ca; there were insoluble silicates of Al and Fe.

The surfaces of the corroded silicon nitride bars were covered with thick deposits of severely blistered material, most probably the result of nitrogen evolution from the underlying silicon nitride. The blisters appeared to consist of a glassy material, which had been liquid at the corrosion temperature, and one or more crystalline phases. XMS elemental analysis of material obtained from the blisters showed that they contained K, Si, Ca, Al, and Cl, and lesser amounts of Zn, S, and either Y, or Fe and Mg, depending on the base silicon nitride composition (Y for SN1, Fe and Mg for SN2). It appeared that the glasses were predominantly a potassium aluminosilicate, and that the crystals, on the bases of XMS analyses, were either a calcium yttrium silicate (SN1), or calcium magnesium silicate (SN2), together with the potassium aluminosilicate, $KAlSiO_4$: strong peaks for sodium potassium sulphate were identified by XRD.

3.2 Corroded SN1

XRD examination showed that the SN1, yttrium oxide-densified, silicon nitride contained β-silicon nitride as the major crystalline phase together with the intergranular yttrium-containing phases, SiY, $Y_2Si_3O_3N_4$ and $YNSiO_2$. A general microstructural

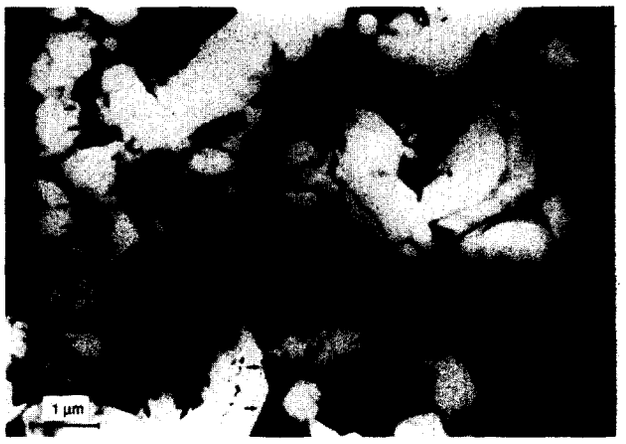


Fig. 1. A general planar view of corroded SN1 silicon nitride at the corrosion layer interface: light regions β-Si_3N_4 grains; the arrowed dark regions Y-rich phases which also contain Fe.

overview of uncorroded SN1 silicon nitride at the corrosion layer interface with unattacked material, and in a plane parallel to the external exposed surface, is provided by the TEM micrograph in Fig. 1. The light regions are β-silicon nitride grains; pockets of a yttrium-rich intergranular phase, which also contained Fe, are shown clearly as the dark regions (arrowed) at higher magnification coupled with XMS analysis (Fig. 2). Many of the yttrium-rich regions appeared to be interconnected. These micrographs are not distinguishable form those of uncorroded material. Figs 3 and 4 show planar sections, but now just within the corroded zone. Figure 3 illustrates the changes taking place in the intergranular region, with the appearance of 100–200 nm dimension regions of foamed glass (liquid at high temperature) at points where the (lighter) silicon nitride grains come into contact with wetting liquids. Because this figure shows a planar section at the corrosion front there is the likelihood that some of the grain boundaries seen are those of uncorroded material. There is here, however, an indication of penetration of a liquid-forming phase at the silicon nitride grain



Fig. 2. Corroded SN1 at high magnification: XMS analysis of dark regions showing the presence of Y and Fe.



Fig. 3. Corroded SN1: 100 to 200 nm regions of foamed intergranular glass at a Si_3N_4 grain, and (smaller arrows) indications of general intergranular attack.

boundary (both features arrowed). At higher magnification (Fig. 4(a)) ~10 nm dimension microvoid formation at a silicon nitride–silicon nitride grain boundary can be seen, leading in extreme cases to the complete grain face separation in Fig. 4(b). On the basis of the lighter colour of the void regions of Fig. 4(b) it is believed that they do not contain glass: whether the nm dimension, more spherical, regions of Fig. 4(a) are voids or glass microspheres is not so certain, but it is assumed that they are again gas-filled bubbles. The very fine scale of all these regions made reliable XMS analyses impossible.

3.3 Corroded SN2

The more heavily iron-contaminated and glassy SN2 silicon nitride also contained predominantly β-Si_3N_4, together with intergranular FeSi, $FeSi_2$, Si_2N_2O, and the Olivine $(Mg,Fe)SiO_4$ forsterite structure solid solution; glass was present at many three grain junctions, and identification of the Mg-containing secondary phase was assisted by XMS analysis. Figs 5(a) and (b) show typical regions of material at the corrosion zone interface after corrosion for 800 h. The MgO-containing silicon nitride was more severely degraded during corrosion than the SN1, Y_2O_3-densified silicon nitride. A marked feature of the microstructure of this material (arrowed) is the regions which appear to be completely depleted of glass, bounded by silicon nitride grains. These are not seen in uncorroded material and suggest the large-scale loss of a liquid (of lowered viscosity) from these regions. Figure 6 shows (arrowed) a crystalline

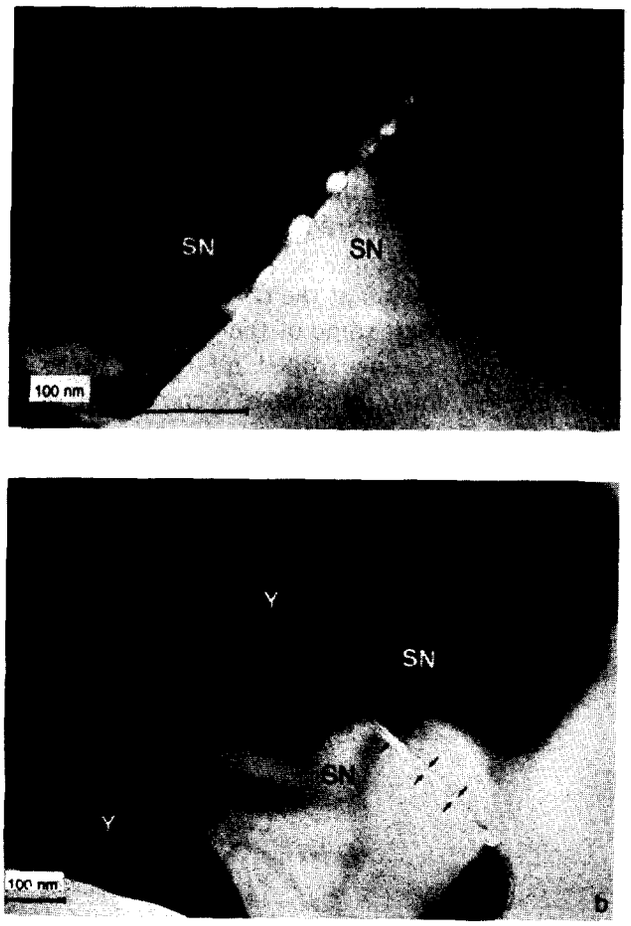


Fig. 4. (a) Nano-void formation at a silicon nitride-silicon nitride grain boundary; (b) complete grain face separation.



Fig. 5. Corroded SN2: typical planar view regions at the corrosion zone interface after corrosion for 800 h; arrows indicate intergranular voids foreign to the uncorroded microstructure.

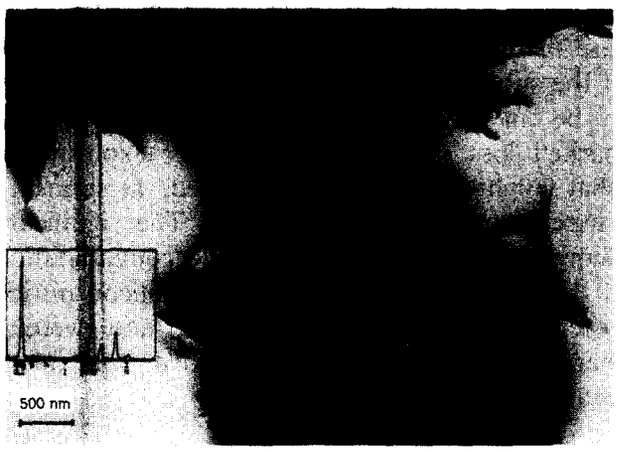


Fig. 6. Corroded SN2 at higher magnification: Fe-rich inclusions and evidence of extensive Zn contamination.

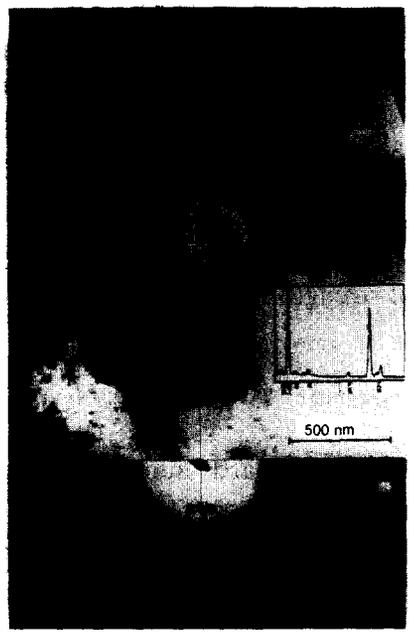


Fig. 7. Corroded SN2: proximity to the corroded external surface; arrowed phase identified by selected area diffraction as β-cristobalite.

Fe-rich intergranular phase, together with the corresponding XMS spectrum, suggesting that it is an iron silicide inclusion, which from the contacting angle with the bounding silicon nitride grains appears to be non-wetting. There is evidence from the XMS spectrum of significant penetration of flue gas Zn into this region of the material. This photograph also shows small neighbouring regions which appear to be devoid of glass.

Figure 7 shows a section of material nearer still to the surface. The arrowed phase was identified by SAD as predominantly β-cristobalite although some reflections could not be indexed. What may be relics of hexagonal symmetry silicon nitride grains are visible in the vicinity, and the appreciable amounts of S present in this film, in association with K and Zn, suggest the presence of sulphates.

Table 3. Strength and residual strength, after exposure at ~1050°C for 100 h

	4-point bend strength/MPa		
Material	*Uncorroded*	*Corroded*	*% loss*
SN1	610 ± 39 [20]	437 ± 62 [8]	28
SN2	610 ± 54 [10]	282 ± 38 [8]	54

3.4 Strength measurements

Bars of both materials, uncorroded and after corrosion for 100 h, were cut from the plates and broken in 4-point bend. The mean strengths and standard deviations, and the numbers of bars used for each series, are shown in Table 3. While both materials lost strength, the more glassy, magnesium oxide densified SN2 material was the most strongly affected by corrosion.

4 Discussion

These examinations using TEM showing details of the silicon nitride oxidative corrosion process under real industrial conditions, and the nature of some of the sub-surface events, indicate the usefulness of this technique for analysis of aspects of the high temperature corrosion of multiphase silicon nitride ceramics. A number of features of interest are revealed, the interpretation of which requires at this stage some speculation. The views put forward in this report are therefore regarded as tentative, but it is hoped that they will stimulate continued and more detailed examination of this type of reaction interface, and lead to a more complete identification of the complex processes occurring.

Analyses of the outer corrosion layer show that the surface at temperatures in the region of 1050°C was predominantly a low viscosity liquid potassium aluminosilicate. The susceptibility of the intergranular glass to reaction with corrodent metal oxide such as Al_2O_3 and K_2O is marked. This effect is seen most strongly with the glassy, MgO-densified, silicon nitride, although there is also very clear evidence for sub-surface attack in the more crystalline material hot-pressed with Y_2O_3 addition. Of significance is the evidence for the inwards diffusion of impurity cations into the intergranular phase of the silicon nitride, where they alter markedly the chemical and physical characteristics of the glass, and in particular its permeability towards oxygen.

The localised, uniform 10–15 nm dimension intergranular spherical features shown in Fig. 4(a) seem most probably to be nitrogen-filled bubbles generated by oxidation of the silicon nitride by

oxygen diffusing through an intergranular film. At this bubble dimension, and assuming a liquid–gas interfacial energy of ~300 mJ m^{-2}, the equilibrium internal gas pressure would be of the order of 600 bar. This is high, but is still insignificant by comparison with the theoretical nitrogen pressure in equilibrium with silicon dioxide and oxygen at 0·2 bar pressure at this temperature, which, on the basis of a standard Gibbs function of reaction at 1400 K of ~–1703 kJ mol^{-1}, would theoretically be of the order of 10^{30} bar. This pressure is clearly an unrealistic one from any practical point of view; the value is of interest in that it serves to indicate the marked tendency for nitrogen to be generated in these regions, and for it to be able to build up a considerable pressures. The internal gas pressure might then be able, in effect, to prise grains apart. This interpretation is, however, clouded by the possibility that internal stresses will be generated also by the considerable volume expansion (~86%) caused by oxidation of silicon nitride to SiO_2, and these stresses will add to those caused by nitrogen generation. The larger voids seen in Fig. 4(b) suggest that with time individual bubbles have indeed linked to form continuous cavities, from which liquid silicate has been expelled by the continuing generation of nitrogen. In the case of the more glassy SN2 material, giving on corrosion much larger liquid-free regions, the process appears to have occurred more extensively. That liquid mobility on this scale should occur at the relatively low temperature of 1100°C would require a very low viscosity, but this would be readily attained by the incorporation of K_2O into the intergranular phase.

Thus, the overall action of the liquid phase assisted corrosion process in generating the intergrain cavities is postulated to be a combination of enhanced oxygen permeation and therefore internal oxidation, and a lowered silicate liquid viscosity associated with K_2O enrichment. That the effect seems to be more marked in the case of the MgO-containing silicon nitride would be explicable partly in terms of a stronger effect of the Mg^{2+} ions on the liquid viscosity, by comparison with the trivalent Y^{3+}, but also because (on the basis of the XRD data) only part of the Y is incorporated into the intergranular glass. Evidence for the greater susceptibility of the MgO-densified silicon nitride to corrosion is provided also by the greater loss of strength of this material after exposure to the flue gas.

It may be speculated therefore that one of the important consequences of the intergranular oxidation of silicon nitride, as shown by this series of TEM photographs, is the loss of bonding of individual silicon nitride grains in the sub-scale region, and thus their incipient detachment. In the case of fully densified materials this deterioration of the sub-surface microstructural quality is likely to be an important factor responsible for the marked loss of strength seen after exposure to what might otherwise be regarded, in terms of temperature, as mild conditions. The significant changes during exposure to oxide contamination of the intergranular liquid in these silicon nitride systems, in composition, fluidity, and wetting characteristics, thus merit extended, and more detailed investigation.

5 Conclusions

Penetration of the intergranular phase of silicon nitride materials by the more mobile cations of a corrodent surface film leads to significant compositional changes in the subsurface intergranular liquid phase, to the development of nm dimension voids within the intergranular phase, and ultimately to local complete loss of contact between adjacent silicon nitride grains. This is postulated to be an important factor leading to the loss of mechanical strength in corroded materials.

Acknowledgement

This work has been partly supported by the Commission of the European Communities through Stimulation Action Contract ST2J-0146-UK(CD).

References

1. Luyten, J. & Stalios, A., In situ corrosion of SiC and Si_3N_4 in the flue gases of an Al-remelting furnace. *Werkstoffe und Korrosion*, **41** (1990) 734–5.
2. Luyten, J., Lemaitre, P. & Stalios, A., High temperature corrosion of silicon nitride and silicon carbide exposed to the flue gases of an aluminium remelting furnace. In *Proc. Eur. Colloquium, High Temperature Corrosion of Technical Ceramics*, ed. R. J. Fordham, Elsevier Applied Science, London 1990, pp. 161–5.
3. Stalios, A., Neyens, L. & Luten, J., In situ corrosion of silicon nitride and silicon carbide ceramics. In *Deutsche Keramische Ges. Symp. Proc. Verschliess und Korrosion–Keramic in der Anwendung*, 22–23 May 1990, pp. 244–50.
4. Mayer, M. I., & Riley, F. L., Sodium assisted oxidation of reaction bonded silicon nitride. *J. Mat. Sci.*, **13** (1978) 1319–28.
5. Mayer, M. I. & Riley, F. L., Sodium ion assisted oxidation of reaction bonded silicon nitride. In *Proc. Brit. Ceram. Soc.*, No. 26, July 1978, pp. 251–64.
6. Fox, D. S. & Jacobson, N. S., Molten salt corrosion of silicon nitride: I. sodium carbonate. *J. Amer. Ceram. Soc.*, **72**(2), (1988) 128–38.
7. Gauthier, G., Lamkin, M. A., Riley, F. L. & Fordham, R. J., High temperature liquid corrosion of silicon nitride based materials. In *Ceramics in Energy Applications*, Pro-

ceedings of the Institute of Energy Conference, Sheffield 9–11 April 1990, Adam Hilger, Bristol 1990, pp. 49–58.
8. Lamkin, M. A., Riley, F. L. & Fordham, R. J., Hot corrosion of silicon nitride in the presence of sodium and vanadium compounds. In *Proc. Eur. Colloquium, High Temperature Corrosion of Technical Ceramics*, ed. R. J. Fordham, Elsevier Applied Science, London 1990, pp. 53–68.
9. Riley, F. L., Phase equilibrium relationships and the liquid phase assisted oxidative corrosion of silicon nitride. In *Corrosion of Advanced Ceramics; Measurement and Modelling*. NATO ASI Series E: Applied Sciences — Vol. 267. ed. K. G. Nickel, Kluwer Academic Publishers. Dordrecht, 1994 pp. 85–96.
10. Lamkin, M. A., Riley, F. L. & Fordham, R. J., Oxygen mobility in silicon dioxide and silicate glasses: a review. *J. European Cer. Soc.*, **10**(5) (1992) 347–67.
11. Andrews, P. & Riley, F. L., The microstructure and composition of oxide films formed during high temperature oxidation of sintered silicon nitride. *J. European Cer. Soc.*, **5**(4) (1990) 245–56.
12. Urbain, F., Cambier, F., Deletter & Anseau, M., Viscosity of silicate melts. *T. & J. Brit. Ceram. Soc.*, **80**(4) (1981) 139–41.
13. Popper, P., Sintering of silicon nitride: a review. In *Progress in Nitrogen Ceramics*, ed. F. L. Riley, Martinus Nijhoff, The Hague, 1983 pp. 187–210.
14. Stalios, A. D., Luyten, J., Hemsley, C. D., Riley, F. L. & Fordham, R. J., The interaction of iron during the hot-pressing of silicon nitride. *J. European Ceram. Soc.*, **7** (1991) 75–81.
15. Kleebe, H. -J., High-resolution electron microscopy studies on Si_3N_4 ceramics. In *Silicon Nitride 93*, Key Engineering Materials Vol. 89–91, Trans Tech Publications, Switzerland 1994 pp. 339–44.

Journal of the European Ceramic Society **15** (1995) 581–590
© 1995 Elsevier Science Limited
Printed in Great Britain. All rights reserved
0955-2219/95/$9.50

0955-2219(95)00011-9

Synthesis of α-Silicon Nitride Powder from a Polymeric Precursor

Ga-er Yu,[a,b] Mohan J. Edirisinghe,[a]* Dudley S. Finch,[a] Brian Ralph[a] & John Parrick[b]

[a]Department of Materials Technology and [b]Department of Chemistry, Brunel University, Uxbridge, Middlesex, UB8 3PH, UK

(Received 20 June 1994; revised manuscript received 15 December 1994; accepted 10 January 1995)

Abstract

Methylcyclosiloxanes and methylcyclosilazanes prepared using dichloromethylsilane have been reacted together to prepare a copolymer which was pyrolysed to give a ceramic powder. The copolymer was characterized using proton nuclear magnetic resonance spectroscopy (^1H NMR) and Fourier transform infra-red spectroscopy (FT-IR). Thermogravimetric analysis of the pyrolysis process and reactions which could occur during conversion of the copolymer to the ceramic are discussed. The product, which was found to be amorphous, was also studied using FT-IR, crystallized by re-heating and characterized using FT-IR, X-ray techniques and scanning electron microscopy. It was identified as α-silicon nitride and its characteristics are compared with a conventionally prepared, widely used, commercially available grade of silicon nitride. The α-silicon nitride synthesised in the present work contains a wide range of particle morphologies, varying from needles (500 nm in length and 100 nm in width) to equiaxed agglomerates (200–500 nm in size with a substructure in the size range 50–120 nm).

1 Introduction

Strength retention at high temperature, high thermal shock, corrosion and wear resistance makes silicon nitride (Si_3N_4) a rapidly emerging engineering material, especially useful for structural applications such as components in advanced engines.[1,2] However, there are several difficulties that must be overcome before the full market potential of Si_3N_4 is realized. A major issue is the lack of suitable Si_3N_4 powder from which ceramic components can be fabricated. Currently, Si_3N_4 powders are manufactured by three main methods:[3]

(1) Nitridation of silicon: $3Si + 2N_2 \rightarrow Si_3N_4$.

(2) Ammonolysis (in the gas phase) of silicon tetrachloride: $3SiCl_4 + 4NH_3 \rightarrow Si_3N_4 + 12HCl$.

(3) Carbothermic reduction of silicon dioxide $3SiO_2 + 6C + 2N_2 \rightarrow Si_3N_4 + 6CO$.

These conventional routes produce powders with the following drawbacks:[4]

(1) Lack of control over crystal structure, phase chemistry and impurity levels, resulting in glass formation at grain boundaries which drastically lower the strength of the materials, especially at high temperatures.

(2) A large average particle size, >1–10 μm, with some powder particles in the 20–100 μm range, thereby giving rise to poor sintering and large grains in the final microstructure.

(3) Irregular morphologies which reduce the packing efficiency during fabrication of components.

(4) A high degree of agglomeration which result in micro-defects in the final microstructure.

Some of the above-mentioned difficulties have been overcome by process modifications, e.g. the use of laser-driven, gas phase reactions which produces finer powders,[4] but it is increasingly acknowledged that chemical processing of ceramic materials could provide the stoichiometry, purity and microstructural control required.[5,6] One such processing method is the pyrolytic conversion of organometallic molecules and polymers to ceramics to produce powders, fibres, coatings and even ceramic artefacts,[7–10] as postulated by Chantrell and Popper[11] in 1964. However, it must be noted that this processing route produces amorphous Si_3N_4 and further heating is necessary to form a crystalline product.

Pioneering work on the synthesis of Si_3N_4 from polymeric precursors was carried out by Seyferth and coworkers[12] who reacted dichlorosilane (H_2SiCl_2), a potentially hazardous material, with NH_3 to produce silazane oil which, when pyrolysed in N_2 at 1150°C, produced α-Si_3N_4 with Si as

*To whom correspondence should be addressed.

an impurity. The yield obtained was approximately 70%wt. Subsequently, Seyferth and Wiseman[13] reported the use of dichloromethylsilane (CH_3SiHCl_2) which was reacted with NH_3 to produce polysilazanes and these were pyrolysed in N_2 at 1420°C to produce ceramics. However, the product was a mixture of Si_3N_4, silicon carbide (SiC) and C (yield of ceramics 80–85%wt.). Further work[14] on mixtures of CH_3SiHCl_2 and $CH_3(CH_2 = CH)SiCl_2$, and CH_3SiHCl_2 and $CH_3(CH_2 = CHCH_2)SiCl_2$, which were ammonolysed to prepare several polysilazanes and pyrolysed in Ar or N_2 at 1000°C, produced a slightly higher yield of ceramics (up to 86%wt.) but still contained a mixture of Si_3N_4 and SiC (about 68%wt. Si_3N_4). In fact, most investigations in this area of research report the preparation of several preceramic polymers which on pyrolysis produce Si_3N_4–SiC mixtures rather than Si_3N_4.[15] Improvement of the Si_3N_4 content was achieved by increasing the N content of the preceramic polymer, e.g. by using mixtures of CH_3SiHCl_2 and H_2SiCl_2 for ammonolysis,[14] and by pyrolysing the precursor in a reactive gas such as NH_3 rather than N_2 or Ar.[14] The first strategy seems to be case-specific as Seyferth and coworkers[14] have also used other types of commercially available $RSiCl_3$ compounds which were mixed with CH_3SiHCl_2, but, overall, there was no appreciable increase in the Si_3N_4 content. Pyrolysis in NH_3 produced Si_3N_4 with 0·29%wt. of C but the phase chemistry of the ceramic obtained is not discussed.

Many other subsequent investigations[16,17] used pyrolysis in NH_3 for the synthesis of nitrogen ceramics, mainly Si_3N_4. In particular, Blum and coworkers[16] give detailed chemical analyses of several ceramic products obtained using different polymers and these clearly indicate that pyrolysis in NH_3, compared with that in N_2, reduces the molar ratio of C by an order of magnitude. Yu and Mah[18] reported the use of a mixture of poly-siloxanes and polysilazanes to produce a 'living' polymer which can be pyrolysed in NH_3 at 1000°C to produce silicon oxynitride (Si_2ON_2). It is worth noting that if the 'living' polymer was pyrolysed in N_2 or Ar, the product obtained was a mixture of Si_3N_4 and SiC.[14] Laine and coworkers[19] report a dehydrocoupling reaction (with an Ru catalyst) to polymerise a silazane oligomer to give a high molecular weight ($\bar{M}_n > 8000$) precursor which can be pyrolysed in NH_3 to produce approximately 97%wt. pure Si_3N_4 with a > 80%wt. yield.

Only a few investigations indicate the phase chemistry of the Si_3N_4 prepared and the product has been mainly a mixture of α-Si_3N_4 and β-Si_3N_4. Burns and Chandra[20] have reported the pyrolysis of several cross-linked polycarbosilanes, polysilanes and polysilazanes in N_2 or NH_3 at 1200°C to produce amorphous Si_3N_4 with a yield of 81–93%wt. but the crystallized product contained only 56%wt. α-Si_3N_4. Schwab and coworkers[21] have also used polysilazanes to produce Si_3N_4 fibres but the product contained a mixture of α-Si_3N_4 and β-Si_3N_4. Recently, Funayama and coworkers[22] used a polyborosilane but pyrolysis in NH_3 and subsequent crystallization in N_2 produced a mixture of α-Si_3N_4 and β-Si_3N_4. Interrante and coworkers[23] report the preparation of α-Si_3N_4 and free C as the main products of pyrolysis of silicon tetradiethylamide produced by condensation polymerisation but no further details are given.

Reports of investigations on the synthesis of ceramics by the pyrolysis of polymeric precursors suffer from the fact that information on polymer synthesis, pyrolysis reactions and the phase and powder characteristics of the ceramic produced are not presented together. In the present work we pyrolyse a copolymer, prepared from methylcyclosiloxanes and methylcyclosilazanes, which have been produced using dichloromethylsilane (CH_3SiHCl_2), in N_2 to synthesise amorphous Si_3N_4 which is heat treated to form crystalline α-Si_3N_4. The copolymer used is a precursor which is suitable for the synthesis of several nitrogen ceramics, as discussed above. Reactions which can occur during pyrolysis are discussed and the resulting crystalline Si_3N_4 powder synthesised is characterized and compared with a conventionally prepared, commercially available grade of Si_3N_4.

2 Experimental Details

2.1 Starting materials

CH_3SiHCl_2 was obtained from Aldrich Chemical Co. (Poole, UK). The middle cut from the distillation of CH_3SiHCl_2 over Mg metal under dry N_2 was used to prepare methylcyclosiloxanes by hydrolysis and methylcyclosilazanes by ammonolysis. Details of these methods and products have been fully described earlier.[24,25]

2.2 Copolymerization

The reaction conditions and procedure described below have been deduced from a detailed investigation on the copolymerization of methylcyclosiloxanes and methylcyclosilazanes.[26] Methylcyclosiloxanes (0·5 g) were added to a THF solution of the methylcyclosilazanes (90 ml, containing 1 g of the silazanes) in a round bottom flask containing a magnetic stirrer. The catalyst/initiator, KH (0·05 g) was added and the reaction was carried out at

60°C for approximately 30 h. Chloromethylsilane (0·2 ml) was injected into the flask to terminate the reaction and about 3 min later a white precipitate appeared. The system was stirred for 3 h and then left for 5 h. Subsequently, the solution was taken in a dry flask and the solvent was evaporated under high vacuum. A redissolvable white solid (the copolymer) was thus obtained.

2.3 Pyrolysis

The copolymer was placed in an alumina holder and pyrolysed in a tube furnace (Lenton Thermal Designs Ltd., Market Harborough, UK) in the presence of flowing N_2 (flow rate approximately 250 ml min^{-1}). The furnace tube was at 120°C when the copolymer was inserted (to minimize any effects of moisture) and heating to 1000°C was carried out at 100°C h^{-1} followed by soaking at this temperature for 2 h. Subsequently, the furnace was switched off and allowed to cool to room temperature. The copolymer was also pyrolysed in a Perkin-Elmer TG2 thermogravimetric balance under similar conditions but at a faster heating rate (20°C min^{-1}).

2.4 Crystallization

The residue after pyrolysis was ground to a fine powder using a mortar and pestle and pressed into a disc shape, (8 mm diameter and a few mm thick). It was encapsulated in a commercially available sub-micrometer size silicon oxynitride powder (supplied by Mandoval Ltd., Surrey, UK) and further pressed to produce a thicker disc which was heated in the tube furnace used for pyrolysis in the presence of flowing N_2 (flow rate approximately 200 ml min^{-1}) to 1600°C at 60°C h^{-1}, soaked at this temperature for 2 h and subsequently cooled to room temperature at 60°C h^{-1}. This encapsulation was carried out to prevent the pyrolytic residue from reacting with any O_2 present in the N_2 during heat treatment at high temperature. Subsequently, the 8 mm disc was separated carefully from the thicker disc and characterized as described below. Crystallization experiments were also carried out at other temperatures (< 1600°C) using a similar temperature ramp.

2.5 X-ray and microscopical characterization

The crystallized ceramic powder and a commercially available Grade LC12 Si_3N_4 powder (supplied by Hermann C. Starck Berlin, Goslar, Germany) were characterized by X-ray diffraction (XRD), X-ray photoelectron spectroscopy (XPS) and scanning electron microscopy (SEM). For the last technique the samples were sputter coated with gold before examination to avoid charging effects.

2.6 FT-IR spectroscopy

A sample of the solution (mentioned in Section 2.2) was taken before the solvent evaporated and used for FT-IR spectroscopy. It was placed on a KBr disc and the solvent was allowed to evaporate under dry N_2. A Nicolet 710 FT-IR spectrometer was used to obtain a spectrum in the range 4000 cm^{-1} to 400 cm^{-1} with a resolution of 4 cm^{-1}. The pyrolytic residue, the crystallized ceramic powder and LC12 Si_3N_4 powder were also investigated using a Nicplan FT-IR microscope to obtain the FT-IR spectrum in the range 4000 cm^{-1} to 600 cm^{-1} with a resolution of 4 cm^{-1}.

2.7 ^{1}H NMR spectroscopy

A JEOL FX200 spectrometer was used and a 10%wt./vol. solution of the copolymer in $CDCl_3$ was studied at 200 MHz. A delay time of 6–10 s was used to ensure that the proton signals were completely relaxed between pulses. Tetramethylsilane (TMS) was used as the internal reference.

3 Results and Discussion

3.1 Copolymer

The molar ratio of Si–H: N–H: Si–CH_3 of the copolymer (from Fig. 1(a)) is equal to 1 : 1·2 : 7·6. We have shown previously[26] that the reaction between methylcyclosiloxanes and methylcyclosilazanes result in a block copolymer dominated by silazane blocks and therefore it is reasonable to compare the ^{1}H NMR spectrum of the copolymer with that of methylcyclosilazanes used in the copolymerization reaction (Fig. 1(b)). The molar ratio of Si–H: N–H: Si–CH_3 of the methylcyclosilazanes (Fig. 1(b)) is 1 : 1 : 3·2. Therefore, it can be concluded that the copolymer contains a much higher concentration of Si–CH_3 groups. Also, comparison of Figs 1(a) and 1(b) shows that the peaks in the former (copolymer) are broader, indicating the complex nature of its chemical structure.

The FT-IR spectra also show the same trends. The relative intensities of Si–CH_3, Si–H and N–H bands of the copolymer (Fig. 2(a)) are compared with similar bands in the reactant methylcyclosilazanes (Fig. 2(b)). Clearly, the relative intensity of the Si–CH_3 bands in the copolymer have increased in comparison with the Si–H and N–H bands. Fig. 2(a) also indicates the presence of Si–NH_2 groups in the copolymer (3450 cm^{-1} for NH_2 stretching and 1540 cm^{-1} for NH_2 deformation, respectively).

3.2 Pyrolytic residue

The pyrolysis of the copolymer results in approximately 70%wt. of residue (Fig. 3). Pyrolysis of

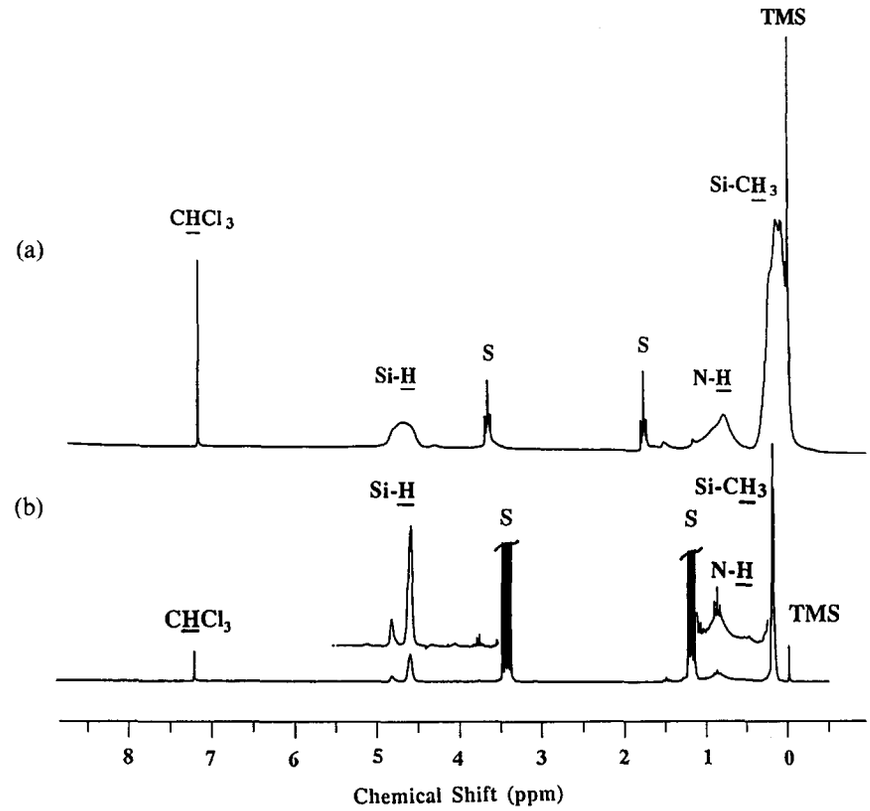
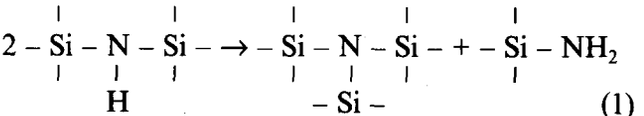


Fig. 1. ^{1}H NMR spectra of (a) the copolymer and (b) the methylcyclosilazanes used to prepare the copolymer (after Refs 25 and 26). TMS and S refer to tetramethylsilane and solvents respectively.

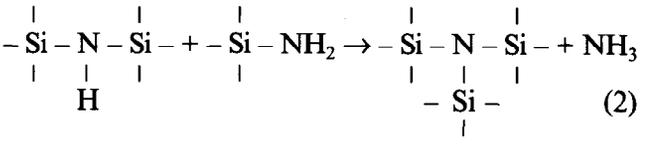
larger quantities in the tube furnace also resulted in the same yield. The residue contained 11·20%wt. C, 21·90%wt. N, and H was not detected (chemical analysis performed using a CHN Elemental Analyser, Carlo Erba, Italy. Chemical analysis to assess Si was not carried out, hence the O content is not reported here). XRD does not show any peaks and therefore the residue is amorphous. The FT-IR spectrum of the residue (Fig. 4(a)) shows the characteristics of Si_3N_4.

The thermogravimetric trace (Fig. 3) indicates that pyrolysis takes place mainly in two stages. The first occurs between approximately 120 and 440°C when about 20%wt. is lost. This is followed by an approximately 10%wt. loss between 440 and 900°C which takes place at a slower rate. The shape of the TGA curve and the %wt. of residue left did not change significantly with variations in the rate of heating, suggesting that cross-linking during pyrolysis is quite fast compared with the thermal degradation of (vinyl SiHNH)$_x$ (MeSiHNH)$_y$ polymers studied by Bahloul *et al.*[27] In a previous paper[28] we used thermogravimetric-Fourier transform infra-red spectroscopy (TG-FTIR) to suggest reactions that take place when a copolymer, very similar to the one used in the work discussed here, is pyrolysed in N_2. However, the resulting ceramic was not identified at that time[28] and we were unable to fully justify the entire scheme of reactions. We can now propose, using the results of the present work, a full scheme of reactions as described below.

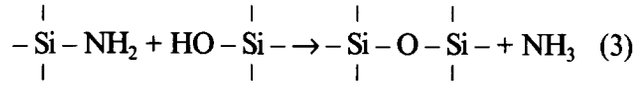
The first stage of weight loss is largely transamination, similar to that occurring during the pyrolysis of polymers of silazanes,[27,29,30] resulting in the formation of the –Si–N–Si– structure according to reaction 1. In addition, –Si–NH_2 and HO–Si– groups are removed according to Reactions 2 and 3, respectively.



(1)

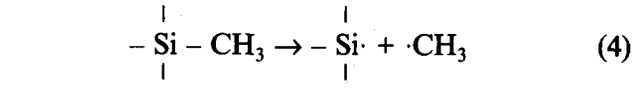


(2)



(3)

These reactions are accompanied by the release of NH_3 as shown by TG-FTIR studies.[28] The second stage of weight loss is accompanied by the evolution of CH_4, as indicated by TG-FTIR studies,[28] and this can occur due to reactions 5 and 6. The $\cdot CH_3$ can be produced initially by Reaction 4.



(4)

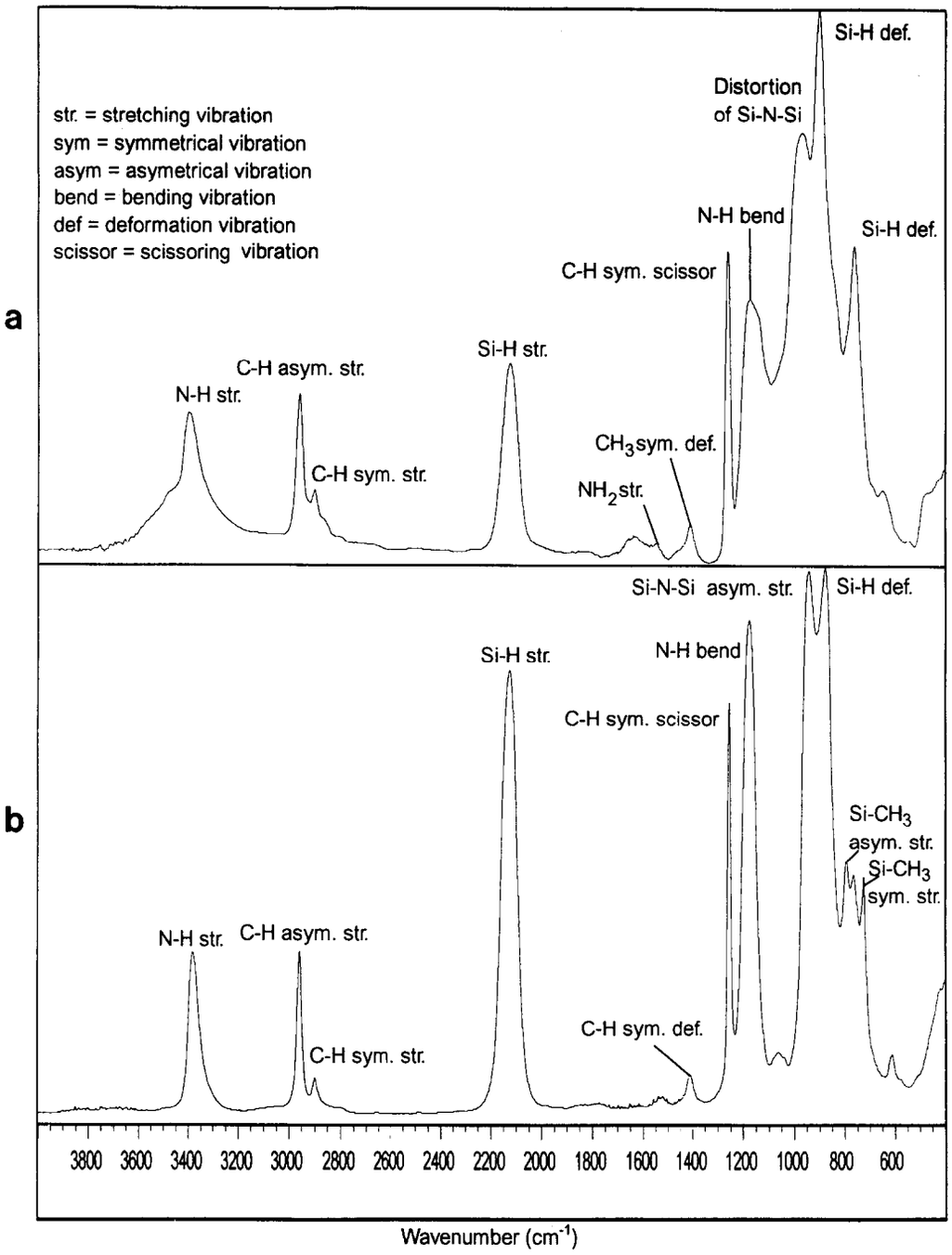


Fig. 2. FT-IR spectra of (a) the copolymer and (b) the methylcyclosilazanes used to prepare the copolymer (after Refs 25 and 26).

$$-\underset{|}{\overset{|}{N}}-\underset{|}{\overset{|}{Si}}-\text{ or }-\underset{|}{\overset{|}{O}}-\underset{|}{\overset{|}{Si}}-+\cdot CH_3 \rightarrow -\underset{|}{\overset{|}{Si}}\cdot + CH_4 \qquad (5)$$

$$-\underset{|}{N}-H + \cdot CH_3 \rightarrow -\underset{|}{N}\cdot + CH_4 \qquad (6)$$

Reaction 7 can also produce CH_4 and –Si–CH_2–Si– groups which have been detected in a recent study where silicon oxynitride was synthesised from a preceramic polymer.[31]

$$2-\underset{|}{\overset{|}{Si}}-CH_3 \rightarrow -\underset{|}{\overset{|}{Si}}-CH_2-\underset{|}{\overset{|}{Si}}- + CH_4 \qquad (7)$$

The products of Reactions 5 and 6 will enable Reaction 8 to take place forming –Si–N–networks.

$$-\underset{|}{N}\cdot + \cdot\underset{|}{\overset{|}{Si}}- \rightarrow -\underset{|}{N}-\underset{|}{\overset{|}{Si}}- \qquad (8)$$

The decomposition of the copolymer can also result in the formation of free C.[32] At higher temperatures (>850°C) C reduces the –Si–O–Si– groups, which are present in the polymer or are formed in reaction 3, eliminating oxygen in the residue and producing both CO and CO_2. In fact in our previous work,[28] TG-FTIR analysis showed that the relative intensities of the CO and CO_2 peaks increased between 850 and 980°C. If the C content available is sufficiently high most of the O should

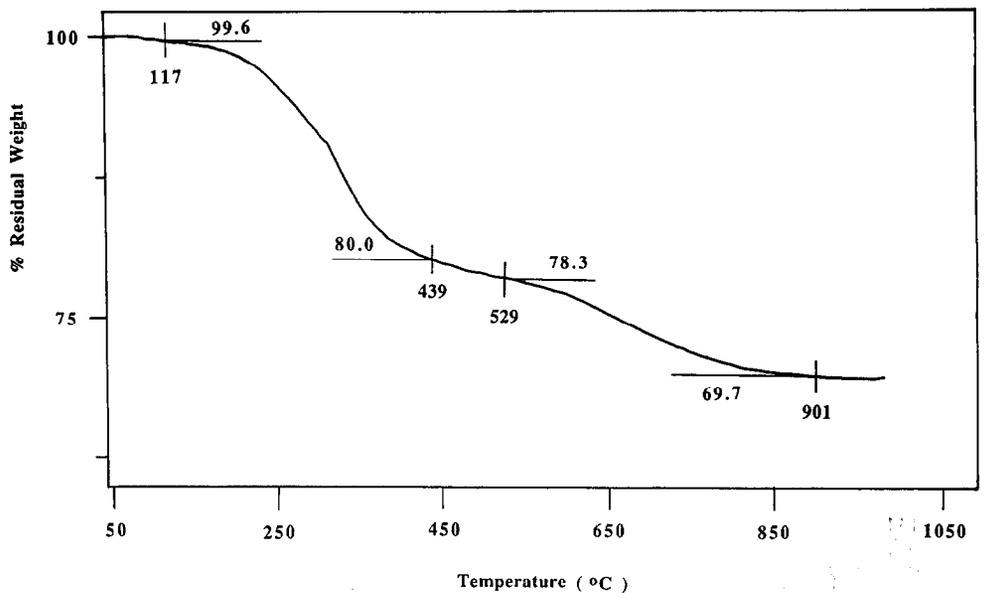


Fig. 3. Thermogram for the degradation of the copolymer in N_2 at a heating rate of 20°C per minute.

be removed and Si_3N_4 with residual O and C is produced as in the present work. The presence of a lower C:O ratio at higher temperatures (>850°C) during pyrolysis will result in a –Si–O–N– ceramic (silicon oxynitride) as observed recently.[31] This confirms the important role C would play during pyrolysis, especially during the final stages of pyrolysis.[33] However, the C content can be controlled by changing the pyrolysis atmosphere.[31]

3.3 Crystalline ceramic

The FT-IR spectra of the crystalline product (Fig. 4(b)) and LC12 Si_3N_4 (Fig. 4(c)) both show the characteristic peak of α-Si_3N_4 at approximately 1100 cm^{-1}. It is well known that Si_3N_4 synthesised from polymeric precursors are amorphous and when heated above 1200°C undergo a diffusion controlled transformation to the crystalline form.[34] In the present work, XRD of the pyrolysis residue heated to various temperatures first showed peaks

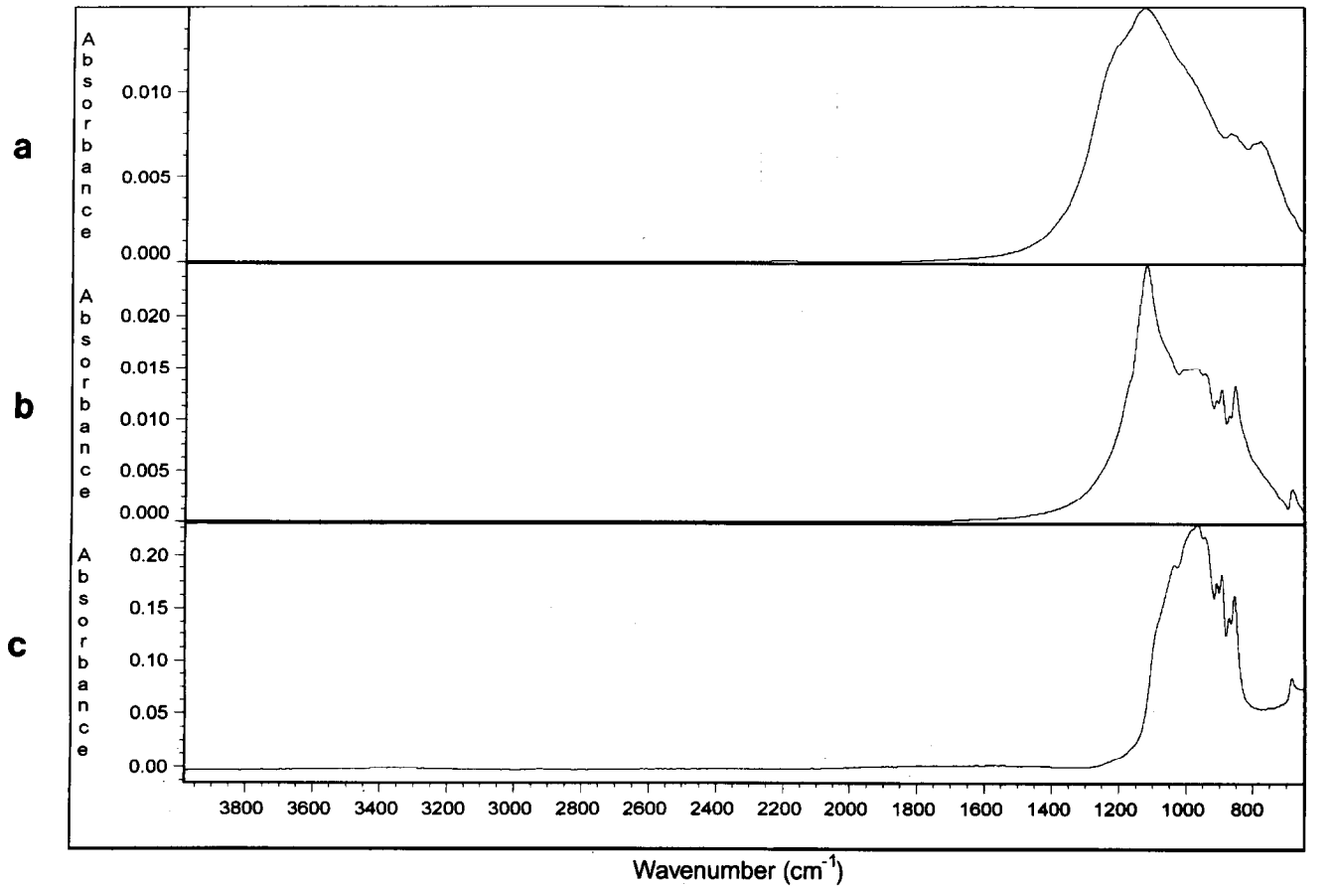


Fig. 4. FT-IR spectrum of (a) the pyrolytic residue, (b) the crystallised Si_3N_4 synthesised in the present work and (c) LC12 Si_3N_4.

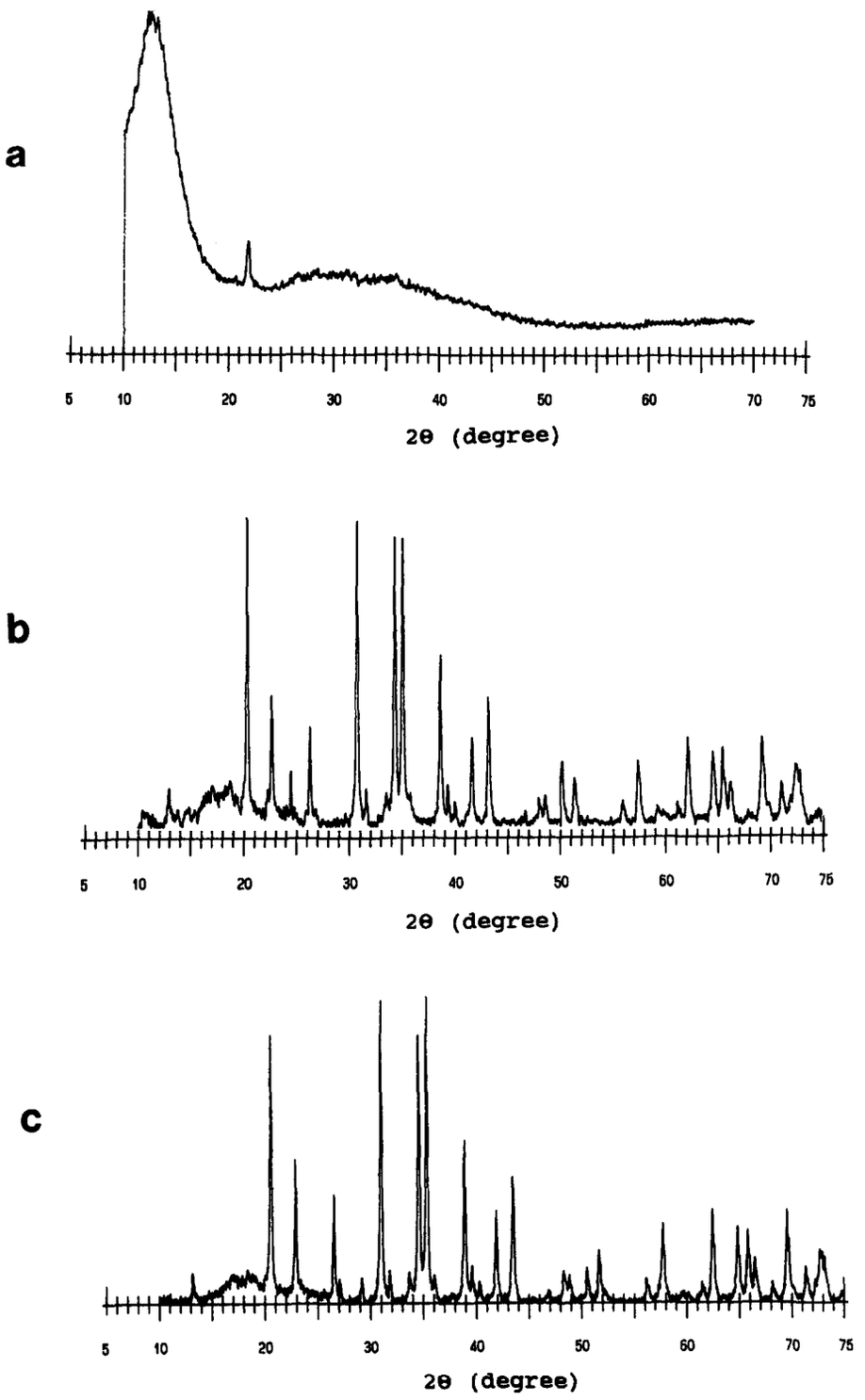
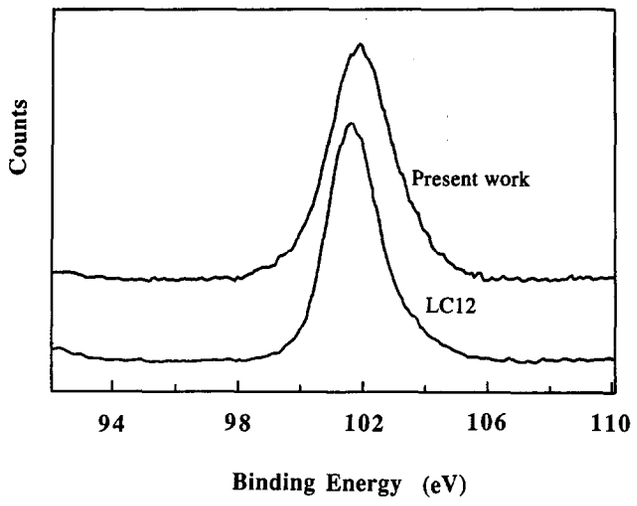


Fig. 5. X-ray diffraction pattern of (a) the pyrolytic residue heated to 1400°C for 5 h, (b) crystallised Si_3N_4 sample synthesised (heated to 1600°C for 2 h) in the present work and (c) LC12 Si_3N_4. A Philips X-ray diffractometer (CuKα radiation of wavelength 0·154 nm and a Ni filter) was used. The step size and scan speed were 0·021° and 0·005° s^{-1} for (a), 0·021° and 0·02° s^{-1} for (b) and 0·01025° and 0·005° s^{-1} for (c).

in the sample heated to 1400°C for 5 h (Fig. 5(a)). Therefore, the crystallization temperature required in the present work was much higher. XRD results of the crystallised product† (after heating to 1600°C for 2 h) are shown in Fig. 5(b). The peaks in Fig. 5(b) correspond to α-Si_3N_4. β-Si_3N_4 and Si were not detected but the diffraction trace shows that some residual C is present. In comparison, LC12 Si_3N_4 was predominantly α-Si_3N_4 containing β-Si_3N_4 and cubic silicon (Fig. 5(c)). The α/β ratio influences sintering behaviour[35] and a high value, as in the powder synthesised in the present work, is a pre-requisite for high technology applications.[36,37]

XPS results of the two samples of Si_3N_4 are shown in Figs 6(a) and (b) where the similarity of

†Recent TEM studies, not reported here, show that complete conversion to the crystalline product was achieved.



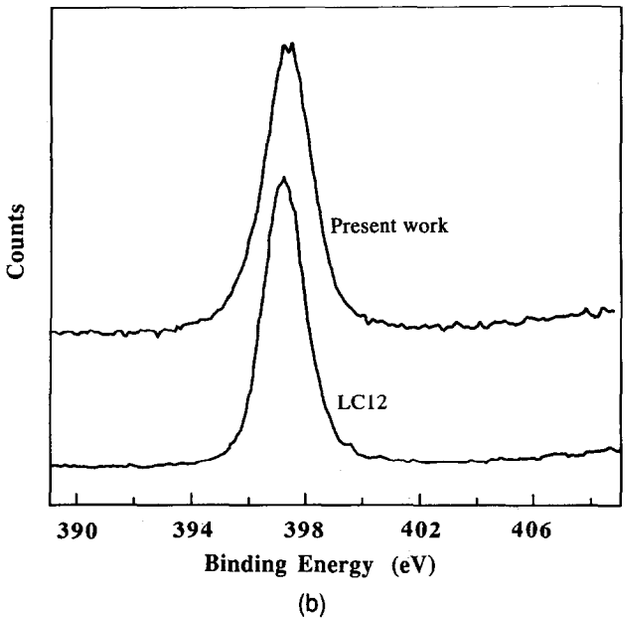


Fig. 6. XPS spectra of the crystallised Si_3N_4 synthesised in the present work and LC12 Si_3N_4 for: (a) Si_{2p} (b) N_{1s}.

Table 1. Summary of XPS results of Si_3N_4 powders. The published binding energy values for Si_{2p} and N_{1s} for Si_3N_4 are 101·9 eV and 397·7 eV, respectively. The area under each curve (given below) is after charge correcting all spectra relative to the C_{1s} peak

	Peak Identity	*Binding Energy (eV)*	*Area*	*Atomic%*
Present work	Si_{2p}	101·9	10·08	32
	N_{1s}	397·5	10·82	34
	O_{1s}	532·4	7·84	25
	C_{1s}	284·6	2·85	9
LC12	Si_{2p}	101·6	15·09	33
	N_{1s}	397·3	18·49	40
	O_{1s}	532·3	8·96	19
	C_{1s}	284·6	3·51	8

the band shape suggest that they exhibit similar chemical binding. Using a full spectrum scan, a summary of all bands present in the two samples are given in Table 1. Both samples contain C and O impurities but the powder prepared in the present work contains a slightly higher level of O. The latter feature is beneficial for sintering[38,39] but the presence of C is not helpful as it can remove O during sintering.[35]

Figure 7 shows that a wide range of particle morphologies, varying from needles to equiaxed lumps, are present in the Si_3N_4 synthesised from the copolymer. The needles are approximately 500 nm in length and 100 nm in width. The lumps are agglomerates, having diameters in the range 200–500 nm. The sub-structure in the agglomerates are in the range 50–120 nm. The particle characteristics of the LC12 Si_3N_4 are well documented.[40] The particles are in the size range 150–1500 nm with a median particle size of 500 nm and these particles are equiaxed in shape and

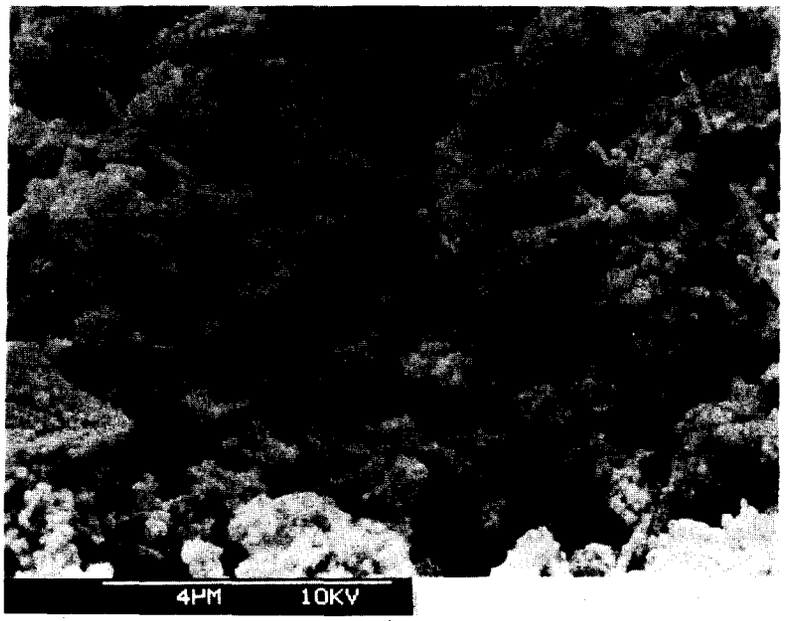


Fig. 7. A scanning electron micrograph of the Si_3N_4 powder in the crystalline form synthesised in the present investigation. A very wide range of particle morphologies is seen. The micrograph was taken using secondary electrons at 10 kV.

appear to be agglomerated to a lesser extent. Clearly, the mixed morphology of the Si_3N_4 prepared using the polymeric precursor indicates that by suitably varying and controlling the pyrolysis and crystallization heat treatments of the amorphous product various particle morphologies can be developed. Strutt *et al.*[41] have synthesised polymerized preceramic nanosized Si_3N_4 by laser irradiation of metalorganic precursors. A near spherical Si_3N_4 powder with a bimodal size distribution corresponding to median diameters of 45 nm and 120 nm was produced and the larger size was thought to be agglomerates. However, the yield of the ceramic powder from the metalorganic powder was about 54%wt. Our yield was approximately 70%wt., typical from the pyrolysis of preceramic polymers in N_2 but higher yields are reported for Si_3N_4 produced by pyrolysis of polymeric precursors in NH_3[14].

4 Conclusions

Crystalline Si_3N_4 powder has been synthesised from a copolymer prepared from methylcylosiloxanes and methylcyclosilazanes.

The complex structure of the copolymer contains a higher concentration of $Si–CH_3$ groups, compared with the reactants. Weight loss in the copolymer occurs mainly in two stages. Between 120 and 440°C the most likely reactions produce –Si–N–Si–, $–Si–NH_2$ and –Si–O–Si– groups and NH_3, which results in about a 20% wt. loss. In the second stage, between 440 and 900°C during which about a 10%wt. loss occurs, release of CH_4 is accompanied by the formation of –Si· and –N· groups. These groups react to produce the –Si–N– structure and hence Si_3N_4. However, the C:O ratio at temperatures > 850°C is a crucial factor in determining the type of ceramic product. A high C:O ratio supports the formation of Si_3N_4.

The product is amorphous and has been crystallised by heat treatment and identified as α-Si_3N_4 containing 9 atomic% of carbon and 25 atomic% of oxygen. The α-Si_3N_4, crystals produced have a wide range of morphologies ranging between 500 nm × 100 nm size needles to 200–500 nm size agglomerates containing 50–120 nm size particles. Comparison of the Si_3N_4 thus produced with conventional, commercially available LC12 Si_3N_4, shows that the former is superior in that it does not contain undesirable β-Si_3N_4 and is free from coarse particles (> 1 μm). Also it has slightly higher oxygen which will aid sintering. However, the LC12 particles are predominantly equiaxed in shape and agglomerated to a lesser extent.

The results of the present investigation show clearly that both the pyrolysis and crystallization process conditions are related closely to the characteristics of the final product. Changes in these process variables seem to determine the type of Si_3N_4 produced. In fact, it should be possible to produce Si_3N_4 with a certain predetermined morphology (needles or equiaxed particles) and this could be of vital importance in the preparation of ceramic composites.

Acknowledgements

The authors are very grateful to S.E.R.C. for financial support of this research (Grant No. GR/H 09904). Dr. S. Woodisse is thanked for help in the X-ray diffraction studies. The staff at the Experimental Techniques Centre at Brunel University are thanked for help with characterization. Mrs Kathy Goddard is thanked for typing the manuscript.

References

1. Riley, F., Silicon Nitride — A review, *Ceramic Technology International*, ed. I. Birkby, 1993, pp. 55–8.
2. Ziegler, G., Heinrich, J. & Wotting, G., Relationship between processing, microstructure and properties of dense and reaction-bonded silicon nitride. *J. Mater. Sci.*, **22** (1987) 3041–86.
3. Rhodes, W. H. & Natansohn, S., Powder for advanced structural ceramics, *Bull. Amer. Ceram. Soc.*, **68** (1989) 1806–12.
4. Danforth, S. C., Symons, W., Nilsen, K. J. & Riman, R. E., Processing of Silicon Nitride powders. In *Advanced Ceramic Processing and Technology*, ed. J. G. P. Binner Vol. 1, 1990, pp. 39–71.
5. Segal, D., *Chemical Synthesis of Advanced Ceramic Materials*, Cambridge Univ. Press, NY, USA, 1989, p. 22.
6. Ulrich, D. R., Chemical Processing of Ceramics, *Chem. and Eng. News*, **68**(1) (1990) 28–40.
7. Mocaer, D., Pailler, R., Naslain, R., Richard, C., Pillot, J. P., Dunogues, J., Gerardin, C. & Taulelle, F., Si–C–N ceramics with a high microstructural stability elaborated from the pyrolysis of new polycarbosilane precursors. Part I: The organic/inorganic transition, *J. Mater. Sci.*, **28** (1993) 2615–31.
8. Fischer, H. E., Larkin, D. J. & Interrante, L. V., Fibre coatings derived from molecular precursors, *MRS Bulletin*, **26** (April 1991) 59–65.
9. Cooke, T. F., Inorganic fibres, *J. Amer. Ceram. Soc.*, **74** (1991) 2959–78.
10. Wright, J. K. & Evans, J. R. G., The manufacture of thin walled ceramic bodies from phenylmethylstyrene dimethylsilylene copolymers (polysilastyrene), *Br. Ceram. Trans. J.*, **89** (1990) 163–7.
11. Chantrell, P. G. & Popper, P., Inorganic polymers and ceramics. In *Special Ceramics*, ed. P. Popper Academic Press, NY, USA, 1965, pp. 87–103.
12. Seyferth, D., Wiseman, G. H. & Prud'homme, C., A liquid silazane precursor to Silicon Nitride, *J. Amer. Ceram. Soc.*, **13** (1983) C13–14.
13. Seyferth, D. & Wiseman, G. H., High-yield synthesis of Si_3N_4/SiC ceramic materials by pyrolysis of a novel polyorganosilazane, *J. Amer. Ceram. Soc.*, **14** (1984) C132–3.

14. Seyferth, D., Wiseman, G. H., Pontasse, C. A., Schwark, J. M. & Yu, Y-F., Organosilicon polymers as precursors for Silicon-containing ceramics: recent developments, *Polym. Prepr. (Div. Polym. Chem., Amer. Chem. Soc.)*, **28** (1987) 389–92.
15. Seyferth, D., Wiseman, G. H., Schwark, J. M., Yu, Y-F. & Pontasse, C. A., Organosilicon polymers as precursors for Silicon-containing ceramics: recent developments. In *Inorganic and Organometallic Polymers*, eds M. Zeldin, K. J. Wynne & H. R. Allcock, Amer. Chem. Soc., Washington DC, USA, 1988, Chapter 11.
16. Blum, Y. D., McDermott, G. A., Wilson, R. B. & Hirschon, A. S., The relationship between the structure of preceramic Polysilazanes, the pyrolysis conditions and their final ceramic products, *Polym. Prepr. (Div. Polym. Chem., Amer. Chem. Soc.)*, **32** (1991) 548–9.
17. Schmidt, W. R., Sukumar, V., Hurley, W. J., Jr., Garcia, R., Doremus, R. H., Interrante, L. V. & Renlund, G. M., Silicon Nitride derived from an organic polymeric precursor: preparation and characterisation, *J. Amer. Ceram. Soc.*, **73** (1993) 2412–8.
18. Yu, Y. & Mah, T. In *Better Ceramics Through Chemistry II*, eds C. J. Brinker, D. E. Clark and D. R. Ulrich, *Proc. Mater. Res. Soc. Symposiums*, PA, USA, 1986, pp. 559–64.
19. Laine, R. M., Blum, Y. D., Chaw, A., Hamlin, R., Schwartz, K. B. & Rowecliffe, D. J., Catalytic synthesis of novel polysilazanes including precursors to Silicon Nitride, *Poly. Prepr. (Div. Polym. Chem., Amer. Chem. Soc.)*, **28** (1987) 393–4.
20. Burns, G. T. & Chandra, G., Pyrolysis of preceramic polymers in Ammonia: preparation of Silicon Nitride powders, *J. Amer. Ceram. Soc.*, **72** (1989) 333–7.
21. Schwab, S. T., Graef, R. C., Davidson, D. L. & Pan, Y., Applications of polysilazanes to precursors to Silicon Nitride, *Polym. Prepr. (Div. Polym. Chem., Amer. Chem. Soc.*, **32** (1991) 556–8.
22. Funayama, O., Kato, T., Tashiro, Y. & Isoda, T., Synthesis of a polyborosilazane and its conversion into organic compounds, *J. Amer. Ceram. Soc.*, **76** (1993) 717–23.
23. Interrante, L. V., Schmidt, W. R., Marchetti, P. S. & Maciel, G. E., Preparation of non-oxide ceramics by pyrolysis of organometallic precursors. In *Better Ceramics through Chemistry V*, eds. M. J. Hampden-Smith, W. G. Klemperer & C. J. Brinker, Vol. 271, 1992, pp. 739–48.
24. Yu, G., Parrick, J., Edirisinghe, M., Finch, D. & Ralph, B, Synthesis of Silicon Oxynitride from a polymeric precursor. Part I: Hydrolysis of dichloromethylsilane, *J. Mater. Sci.*, **28** (1993) 4250–4.
25. *Idem*, Synthesis of Silicon Oxynitride from a polymeric precursor. Part II: The formation of trimethylcyclotrisilazane and tetramethylcyclotetrasilazane from the ammonolysis of dichloromethylsilane in diethyl ether, *ibid*, **29** (1994) 1680–5.
26. *Idem*, Synthesis of Silicon Oxynitride from a polymeric precursor. Part III: Polymerization and copolymerization of methylcyclosiloxanes and methylcyclosilazanes, *ibid*, **29** (1994) 5569–75.
27. Bahloul, D., Pereira, M., Goursat, P., Choong Kwet Yive, N. S. & Corriu, R. J. P., Preparation of Silicon Carbonitrides from an organosilicon polymer. I: thermal decomposition of the cross-linked polysilazanes, *J. Amer. Ceram. Soc.*, **76** (1993) 1156–62.
28. Yu, G., Finch, D. S., Edirisinghe, M. J., Parrick, J. & Ralph, B., Thermal decomposition of a copolymer of methylcyclosiloxanes and methylcyclosilazanes to non-oxide Ceramics. In *Covalent Ceramics II*, eds A. R. Barron, G. S. Fischman, M. A. Fury & A. F. Hepp, Symp. Proc. Mater. Res. Soc., P. A. USA, Vol. 327, 1994, pp. 201–6.
29. Choong Kwet Yive, N. S., Corriu, R. J. P., Leclercq, D., Mutin, P. H. & Vioux, A., Silicon Carbonitride from polymeric precursors: Thermal cross-linking and pyrolysis of oligosilazane model compounds *Chem. Mater.*, **4** (1992) 141–6.
30. *Idem*, Thermogravimetric analysis/mass spectrometry investigation of the thermal conversion of organosilicon precursors into ceramics under argon and ammonia 2. Poly(silazanes) *ibid*, **4** (1992) 1263–71.
31. Yu, G., Edirisinghe, M. J., Finch, D. S., Ralph, B. & Parrick, J., Synthesis of Silicon Oxynitride from a polymeric precursor. Part IV: Pyrolysis of the copolymers, to be submitted to *J. Mater. Sci.*
32. Bahloul, D., Pereira, M. & Goursat, P., Preparation of Silicon Carbonitrides from an organosilicon polymer. II: Thermal behaviour at high temperature under Argon *J. Amer. Ceram. Soc.*, **76** (1993) 1163–8.
33. Burns, G. T., Taylor, R. B., Xu, Y.-R., Zangril, A. & Zank, G. A., High temperature chemistry of the conversion of siloxanes to Silicon Carbide, *Chem. Mater.*, **4** (1992) 1313–23.
34. Riedel, R. & Seher, M., Crystallization behaviour of amorphous Silicon Nitride, *J. Euro. Ceram. Soc.*, **7** (1991) 21–5.
35. Wotting, G. & Hausner, H., Influence of powder properties and processing parameters on the sintering of Silicon Nitride, in progress. In *Nitrogen Ceramics*, ed. F. L. Riley, 1983, Martinus Nijhoff Publishers, Netherlands, pp. 211–8.
36. Mimoto, M., Thermodynamics, phase relations and sintering aids of Silicon Nitride. In *Silicon Nitride I*, eds S. Somiya, M. Mimoto & M. Yoshimu, Elsevier, 1990, pp. 1–11.
37. Tsutsumi, T., Onoda, Si_3N_4 Powders. In *Silicon Nitride I*, eds S. Somiya, M. Mimoto and M. Yoshimu, Elsevier, 1990, pp. 13–23.
38. Ichikawa, K., The influence of Si_3N_4 powder characteristics on sintering behaviour. In *Silicon Nitride I*, eds S. Somiya, M. Mimoto & M. Yoshimu, Elsevier, 1990, pp. 107–16.
39. Kaiser, G. & Schubert, H., The determination of oxygen in Silicon Nitride powder, *J. Euro. Ceram. Soc.*, **11** (1993) 253–62.
40. Powders for high performance ceramics, technical information on Silicon Nitride powders, Private Communication with Hermann C. Stark, Berlin, Goslar, Germany.
41. Strutt, P. R., Gonsalves, K. E. & Xiao, T. D., Synthesis of polymerised preceramic nanoparticle powders by laser irradiation of metalorganic precursors, *Nanostructured Materials*, **1** (1992) 21–5.

Journal of the European Ceramic Society 15 (1995) 591–597
© 1995 Elsevier Science Limited
Printed in Great Britain. All rights reserved
0955-2219/95/$9.50

0955-2219(95)00012-7

Manufacture of Monolithic Ceramic Bodies from Polysilazane Precursor

M. F. Gonon,[a] G. Fantozzi,[b] M. Murat[b] & J. P. Disson[c]

[a]Ceramic Research Unit, University of Limerick, National Technological Park, Limerick, Ireland
[b]Institut National des Sciences Appliquées de Lyon, Groupe d'Etude de Métallurgie Physique et de Physique des Matériaux - URA CNRS 341, 20 avenue Albert Einstein, 69621 Villeurbanne cedex, France
[c]Elf Atochem, Centre de Recherche Rhône-Alpes, rue Henri Moissan, 69310 Pierre-Bénite, France

(Received 16 May 1994; revised version received and accepted 10 November 1994)

Abstract

A low temperature process for the manufacture of non-oxide monolithic ceramic bodies is presented. This process is based on the pyrolysis at temperatures between 1000 and 1400°C of the polysilazane precursor.

The different steps of the process are precisely described. The physical (porosity, density, crystalline phases) and mechanical properties (flexural strength, Young's modulus, toughness and hardness) of the bodies obtained are studied versus the maximum temperature of the pyrolysis. The high temperature oxidation resistance in air is also presented.

1 Introduction

Non-oxide monolithic ceramic bodies, (e.g. SiC, Si_3N_4...) generally result from powders sintering. Materials obtained by this process show interesting mechanical characteristics (e.g. 600–700 MPa for sintered Si_3N_4). However, the very high temperatures (1700°C–2500°C) required to densify ceramic bodies imply expensive energy costs. The homogenisation of the initial slurry (powder + additives) presents difficulties on what effects on the flaw distribution in the final ceramic.

Another way to obtain non-oxide ceramics is the use of organometallic precursors. Indeed, polycarbosilane and polysilazane which lead to SiC or Si_3N_4 derived ceramics, respectively, are frequently used for the manufacture of non-oxide matrix composites. However, only a few experiments have been performed on the elaboration of monolithic bodies from these products.

Such processes may present some interests. The temperatures relative to the precursor's pyrolysis are significantly lower (1000–1400°C) than those required for powder sintering (1700–2500°C). Moreover, powder sintering imposes the use of organic additives which have to be eliminated by heat treatment before sintering. In the present process, no additives are used, therefore very few impurities are present in the final ceramic.

ELF ATOCHEM† has recently developed the synthesis of the polysilazanes PYROFINE PV‡ and PYROFINE PM.[1,2] Research performed on the manufacture of ceramic matrix composites from PYROFINE PV,[3,4] required the optimisation of the ceramic characteristics versus the pyrolysis parameters.[5] The study of mechanical properties needing dense samples, the following process has been developed.

2 The Polysilazane

The following information is more detailed in Refs. 1 and 2.

At room temperature the polysilazane is a highly viscous liquid. Its density is about 1 and its typical elemental composition is given in Table 1 (oxygen originates from the hydrazine used for the synthesis).

Its viscosity decreases with an increase in temperature up to 200°C (Table 2).

The structure of this polymer is cyclic and is shown in Fig. 1.

Upon heating up to 300°C under nitrogen, the opening of the vinyl groups allows the precursor cross-linking. The product obtained is solid, unmeltable and insoluble.

Above 300°C mineralization starts and changes the precursor into an amorphous ceramic. The typical elemental composition of the ceramic obtained after

†ELF ATOCHEM — Centre de Recherche Rhône-Alpes, rue Henri Moissan, 69310 Pierre-Bénite, France
‡PYROFINE PV registered trade mark of ELF ATOCHEM.

Table 1. Elemental composition of polysilazane

	Si	*C*	*N*	*O*	*H*
wt.%	31·5	37·2	20·3	3·2	7·8
at.%	8·2	22·7	10·5	1·4	57·2

Table 2. Variation of the viscosity versus temperature

Temperature	(°C)	50	100	150
Viscosity	(mPa.s)	1000	100	20

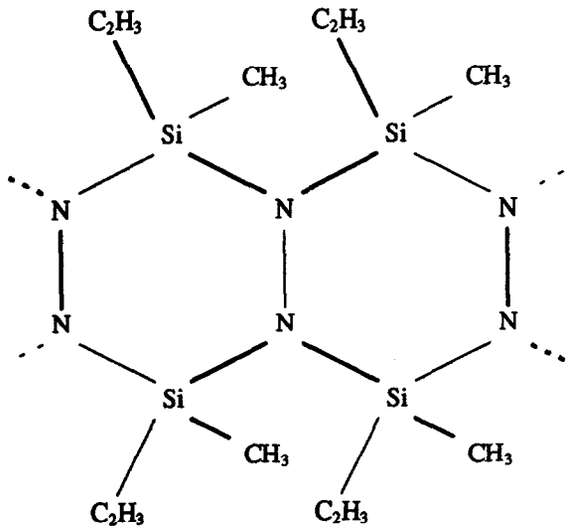


Fig. 1. Structure of the polysilazane.

Table 3. Elemental composition of the ceramic issued from presursor pyrolysis at 1000°C

	Si	*C*	*N*	*O*
at.%	30·0	34·7	27·1	8·2
wt.%	47·5	23·6	21·5	7·4

pyrolysis at 1000°C is given in Table 3. Its absolute density is 2·13 g/cm^3 (measured by He picnometry).

At 1000°C, the ceramic yield is 60–65 wt.%, depending on the heating-up rate used during the cross-linking.[2] The volumetric yield of the transformation is about 30%.

3 Manufacture of Monolithic Ceramic Samples

Due to the foaming of the precursor during pyrolysis,[2] conventional pyrolysis leads in the best case to a ceramic having about 1 g/cm^3 apparent density corresponding to more than 50% porosity.

Such samples cannot be used for the physical and mechanical characterisation of the ceramic, and a specific process has been developed to obtain relatively dense ceramic samples.

3.1 Principle

The basic idea of this process is first to manufacture a mixture of powder and precursor, press it and then pyrolyse it (Fig. 2).

The powder is obtained by heat treatment and milling of the precursor.

To reduce the viscosity of the precursor and to obtain a good homogeneity, toluene is added to the mixture following the ratio a volume toluene per volume precursor. The solvent is then evaporated at 60°C under 500 Pa for 2 h.

Finally the mixture is pressed in a die with a pressure of 150 MPa before proceeding to the pyrolysis.

3.2 Use of ceramic powder

For the first attempts the powder used was obtained by milling the ceramic residue issued from the precursor pyrolysis at 1000°C. The absolute density of this powder is 2·13 g/cm^3 (determined by He picnometry).

The powder alone, pressed under 150 MPa forms a green body having 60% of the absolute density. Therefore the mixture is manufacture in order to obtain a precursor/powder ratio of 40/60 in volume (12/88 wt.%) after toluene evaporation.

The green body obtained after moulding is pyrolysed following the temperature schedule given in Table 4.

The samples obtained have about 30% porosity (apparent density 1·5 g/cm^3) corresponding to the theoretical calculation (28%) based on the volume

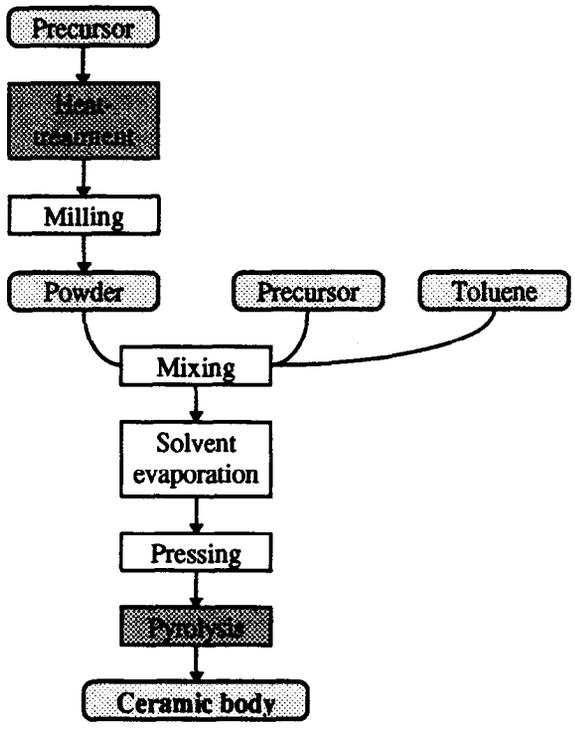


Fig. 2. Elaboration of monolithic ceramic bodies (first process).

Table 4. Pyrolysis temperature schedule

Heating rate	*Temperature*	*Holding time*
(°C/h)	(°C)	(h)
100	20–130	0
5	130–300	0
50	300–1000	4

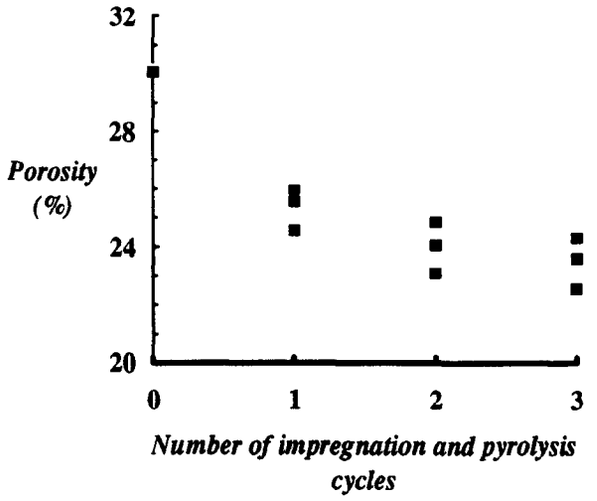


Fig. 3. Variation of porosity of the monoliths versus the number of impregnation and pyrolysis cycles.

ratio of the components, and the volume yield of the precursor to ceramic transformation (about 30 vol.%).

The porosity can be reduced by successive impregnation and pyrolysis cycles with the precursor. However, the larger part of the porosity is closed and a porosity lower than 20–25% cannot be achieved (Fig. 3).

On the other hand numerous cracks are present on the sample surface due to the difference of shrinkage between the precursor (about 70 vol.%) and the ceramic powder (no shrinkage).

To avoid these phenomena and to achieve a lower porosity, new experiments have been completed using a cross-linked precursor powder in place of the ceramic powder.

3.3 Use of cross-linked precursor powder

3.3.1 Theory

A cross-linked precursor powder results from heat treatment under nitrogen at 300°C of the polysilazane. After milling (mortar) the size of the powder grains is about 100–1400 μm in diameter (Fig. 4).

The absolute density of this powder is approx. 1·13 g/cm^3. After pyrolysis at 1000°C its ceramic yield is 72 wt.% corresponding to 38 vol.%.

The powder alone, pressed under 150 MPa,

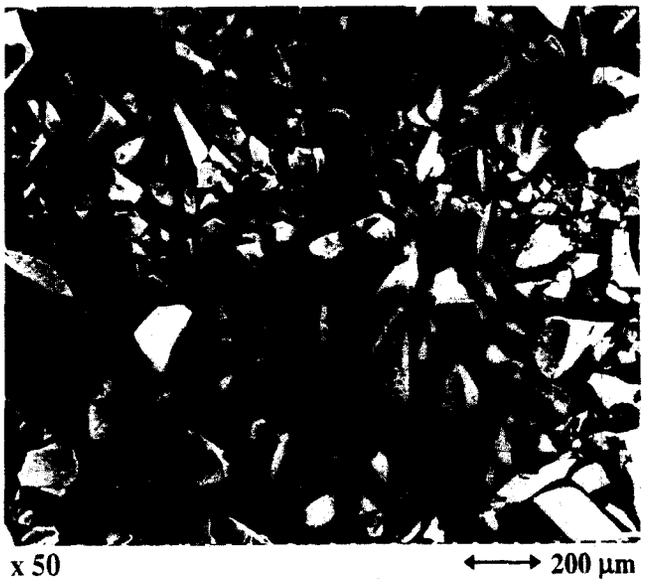


Fig. 4. SEM observation of the cross-linked precursor powder.

forms a green body having 70% of the absolute density. Assuming an apparent sample shrinkage during the pyrolysis equal to that of the precursor powder (about 62 vol.%), the porosity of the ceramic samples would be only 7–8%.

3.3.2 Experiment

(a) Manufacture of the initial mixture

The mixture is obtained following the same process as when using the ceramic powder (see 3.2).

The relative density of the powder in the sample (powder volume/apparent volume of the sample) depends on the precursor amount added (Fig. 5).

As this one remains below 22 wt.%, the relative density of the powder in the sample is equal to the green density of the powder (about 70 vol.%). The precursor fills the spaces separating the powder grains without disturbing their arrangement.

Above 22 wt.% the powder cannot be compacted properly and the relative density of the powder in the sample significantly decreases.

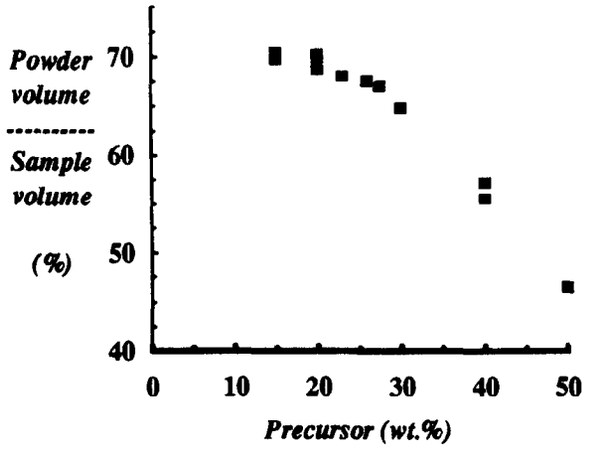


Fig. 5. Variation of the ratio powder volume/sample apparent volume versus the precursor amount added.

Table 5. Cross-linking temperature schedule

Heating rate	*Temperature*	*Holding time*
(°C/h)	(°C)	(h)
100	20–130	0
5	130–300	1

(b) Cross-linking

Using the optimal precursor/powder ratio previously determined, (22/78 wt.%), samples were pressed and cross-linked following the temperature schedule given in Table 5.

After heat treatment, an increase in the apparent volume of the samples is ascertained. This may be due to the precursor 'foaming'.[2] This phenomenon occurs as the precursor amount is higher than 15 wt.%. This value is significantly lower than that corresponding to a complete filling of the intergranular spaces (precursor/powder ratio = 27·5/72·5 wt.%, 30/70 vol.%).

(c) Pyrolysis

Using mixtures having various precursor/powder ratios, samples were pressed, cross-linked and then pyrolysed following the temperature schedule given in Table 4.

The shrinkage of the apparent volume of the sample after cross-linking and after pyrolysis is approximately 60 – 62%, as expected.

The lowest porosity measured is about 24% and corresponds to an initial precursor/powder ratio: 15/85 wt.% (Fig. 6).

This result is not as low as expected due to the apparent volume increase during the cross-linking as the precursor/powder ratio of the initial mixture is high. To avoid this problem and to obtain lower porosity a new step has been added to the process (Fig. 7).

A cross-linked precursor preform is manufactured by moulding and cross-linking the precursor

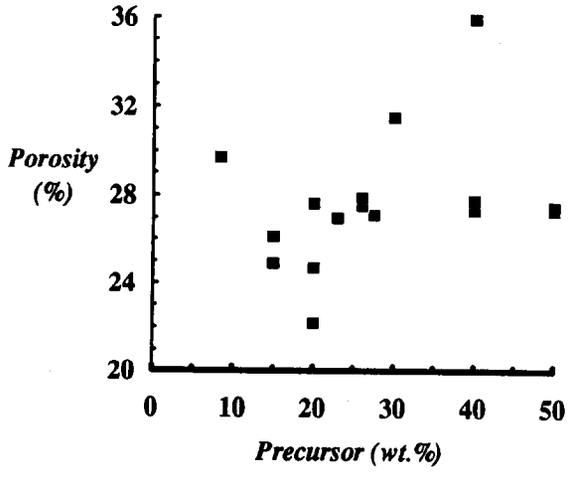


Fig. 6. Porosity of the ceramic monolith versus the initial precursor content.

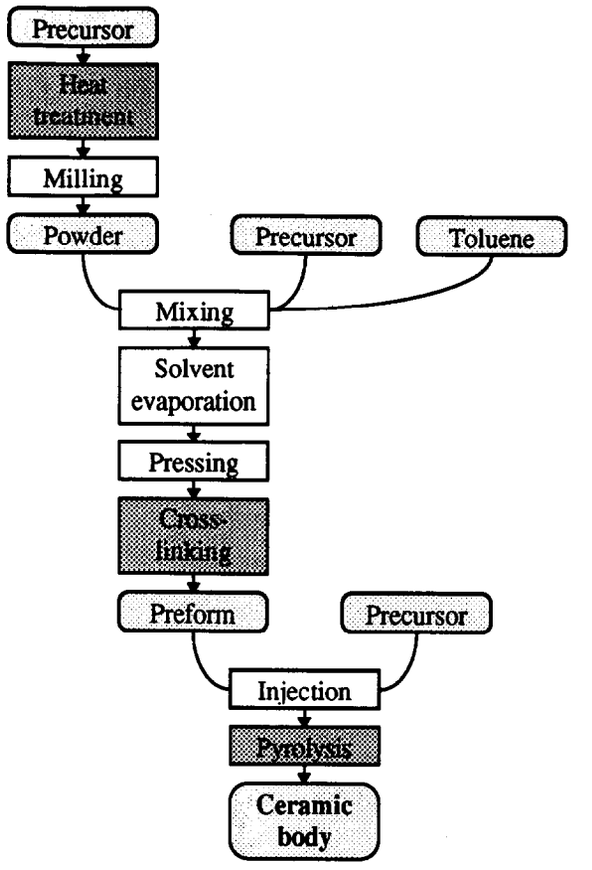


Fig. 7. Elaboration of monolithic ceramic bodies (second process).

+ cross-linked precursor powder mixture. The precursor/powder ratio used is 5/95 wt.% in order to avoid the apparent volume increase of the samples during the cross-linking (see 3.3.2 (b)) and to favour open porosity.

The preform obtained after cross-linking is solid. The high porosity of this preform (about 27%) is filled by precursor impregnation. The preform is charged into a reactor (Fig. 8) and degassed under dynamic vacuum (500 Pa) at 150°C for 2 h.

The precursor, preheated at 150°C to reduce its viscosity, is then injected into the preform by means of the pressure gradient between the outside

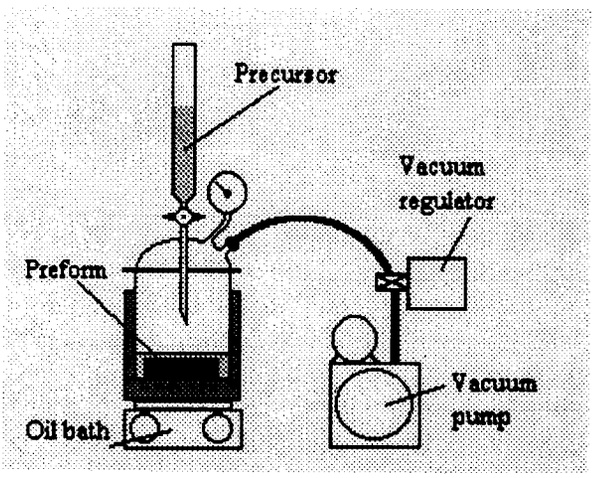


Fig. 8. Diagram of the device used for the precursor injection.

(Nitrogen atmospheric pressure) and the inside of the reactor. After injection the preform is soaked in the precursor for 2 h at 150°C under nitrogen before being removed and placed in the pyrolysis furnace.

The weighing of the performs after the precursor injection and before the pyrolysis indicates that 3–4% of the porosity is not filled. Therefore, the porosity of the monolith obtained after pyrolysis is about 12% instead of 8% as expected from the theoretical calculation.

4 Characterisation of the Monolith Bodies

Seven samples (45 × 40 × 10 mm^3 after pyrolysis) were manufactured using pyrolysis temperatures from 1000°C to 1600°C.

The large size of these samples imposed a very slow heating rate (10°C/h) above 300°C to avoid the crack formation during pyrolysis.

4.1 Porosity

After pyrolysis, the porosity of the monoliths was determined from the ratio between the apparent and absolute density (The absolute density was determined by He picnometry on samples after milling).

A minimum in porosity, about 10–11%, is observed for pyrolysis at 1400°C (Fig. 9).

4.2 Mechanical properties

Ten test bars (40 × 3·5 × 8 mm^3) were cut in each sample. Room temperature flexural strengths were measured in three-point bending on a Schenk RM-T 25 kN using a support span of 50 mm and a crosshead speed of 0·5 mm/min.

Young's modulus was determined from the load/displacement curves. The toughness was determined by the single edge notched beam technique (S.E.N.B.) with $a/w = 0{\cdot}5$ (a = initial crack length; w = thickness of the test bar).

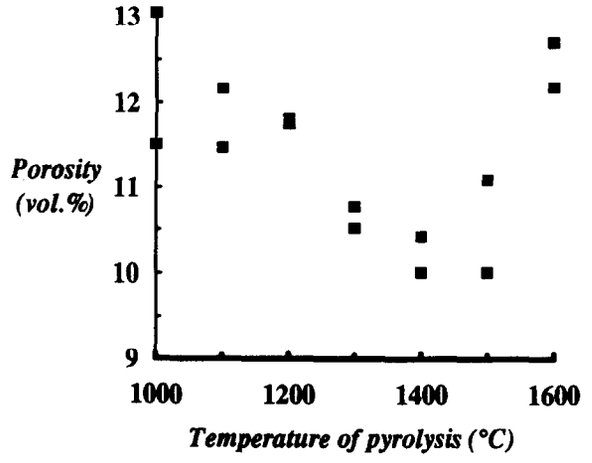


Fig. 9. Porosity of the monoliths versus the highest temperature of the pyrolysis.

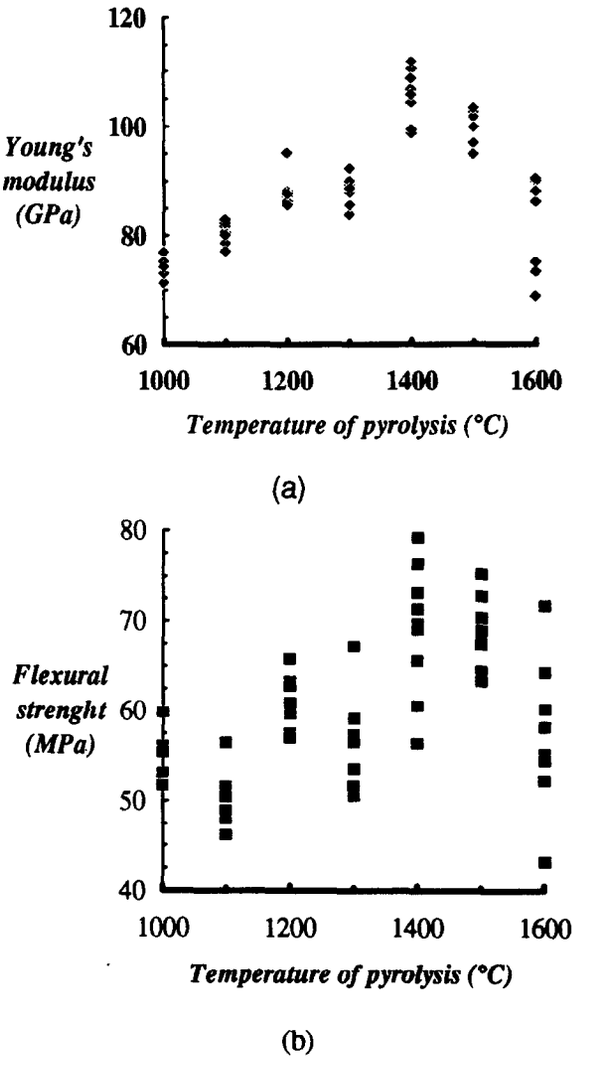


Fig. 10. Evolution of the flexural strength (a) and of the Young's modulus (b) versus the maximum of the pyrolysis.

Highest flexural strength and Young's modulus are observed after pyrolysis at 1400°C corresponding to the minimum in porosity (Figs. 10(a) and (b) and Table 6).

4.3 X-ray diffraction

After milling, the samples were characterised by X-ray diffraction.

Only weak diffractions of SiO_2 are detected on the monoliths pyrolysed at temperatures lower than 1400°C. This SiO_2 is probably polution originating from the milling process and does not belong to the ceramic itself.

On samples pyrolysed at 1500 and 1600°C the X-ray diffraction spectra exhibit signals corresponding to α SiC and α Si_3N_4.

The SEM observation shows the formation of whiskers in the porous volume and of a layer, looking like a skin, on the pore surface (Fig. 11).

This crystallisation may cause the decrease in mechanical properties observed for pyrolysis temperatures higher than 1400°C.

Table 6. Mechanical properties of the composites

Highest temp. (°C)	*Apparent density* (g/cm^3)	*Absolute density* (g/cm^3)	*Porosity* (%)	*Young's modulus* (GPa)	*3-point flexural strength* (MPa)	*Vickers hardness* (MPa)	*Toughness* K_{IC} ($MPa.\sqrt{m}$)
1000	1·87 ± 2	2·13	12	74 ± 3	56 ± 4	888 ± 37	3·33
1100	1·92 ± 3	2·18	12	80 ± 3	51 ± 5	927 ± 31	3·92
1200	2·01 ± 1	2·27	12	90 ± 4	62 ± 4	998 ± 44	4·26
1300	2·05 ± 2	2·31	11	89 ± 4	59 ± 8	955 ± 30	—
1400	2·12 ± 2	2·35	10	106 ± 6	68 ± 11	996 ± 29	—
1500	2·13 ± 2	2·38	11	99 ± 4	69 ± 6	970 ± 28	4·10
1600	2·12 ± 6	2·48	12	69 ± 22	52 ± 20	965 ± 20	—



Fig. 11. SEM observation of the monoliths pyrolysed at 1600°C.

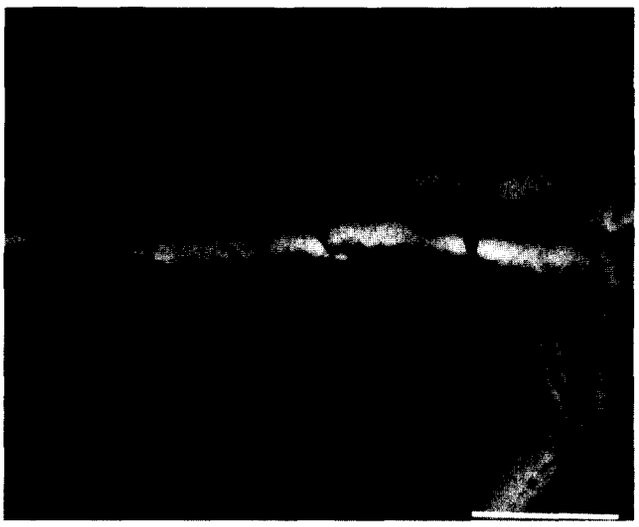


Fig. 13. SEM observation of the surface of the monoliths after 6 h in air at 1400°C.

4.4 Oxidation resistance

The study of the thermal oxidation behaviour by thermogravimetric analysis in air at 1000, 1200 and 1400°C (Fig. 12) shows the high resistance of the ceramic.

After 6 h, no weight deviation is observed at 1000°C and a very low and asymptotic increase is seen at 1200 and 1400°C (respectively + 0·17 wt.% and + 0·28 wt.%).

The SEM observation (Fig. 13) shows that the weight increase observed at 1200 and 1400°C corresponds to the formation of a coating, probably composed of SiO_2, on the sample surface. This coating slows down the oxidation reaction thereby explaining the asymptotic appearance of the TG curves.

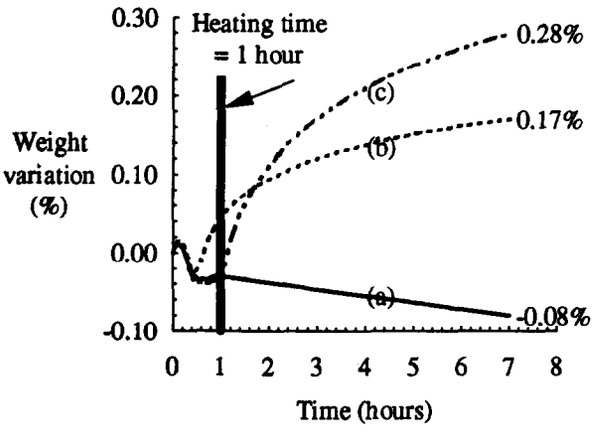


Fig. 12. TGA curves in air at 1000°C (a), 1200°C (b), 1400°C (c) on monoliths pyrolysed at 1000°C (a), 1400°C (b,c).

5 Conclusion

A new process route for ceramic bodies has been developed. Ceramic monoliths with less than 12% porosity can be obtained. As compared to ceramics obtained by sintering of powders, such values are high, but they are relatively good for a liquid precursor processing route. Moreover, the structure of the samples shows no apparent cracks.

The maximal flexural strengths measured in 3 point bending are approximately 70 MPa and Young's modulus 105 GPa. These results are low, but could possibly be improved by a decrease in the pore sizes. Such decrease could be obtained by the use of a cross-linked precursor powder having a lower grain size.

The maximum in mechanical properties is

obtained after pyrolysis at 1400°C, and correspond to the samples having the lowest porosity (about 10%). The decrease observed as the pyrolysis is operated as higher temperatures is probably due to the beginning of the α SiC and α Si_3N_4 crystallisation.

The TGA operated in air at temperatures between 1000–1400°C show the high oxidation resistance of such ceramics due to the formation of a coating (probably SiO_2) on the surface of the samples.

References

1. Colombier, C., *Study of new polysilazane precursors to Si–C–N–O ceramics*, Proceedings of the 1st European Ceramic Society Conference, 18–23 June 1989, Maastricht, The Netherlands. Ed. G. de With, R. Terpstra & R. Metselaar, Elsevier Science Publishers Ltd, Vol. 1, 1989 pp. 143–52.
2. Gonon, M. F., Fantozzi, G, Murat, M. & Disson, J. P., *Pyrofine PV: a polysilazane precursor for Si–C–N–O matrix composites. J. Eur. Ceram. Soc.*, in press.
3. Gonon, M. F., Fantozzi, G., Murat, M. & Disson, J. P., *Association of the C.V.I. process and of the use of polysilazane precursor for the elaboration of ceramic matrix composites reinforced with continuous fibres, J. Eur. Ceram. Soc.*, in press.
4. Gonon, M. F., Fantozzi, G., Murat, M. & Disson, J. P., *Densification of SiC–C–SiC composites preforms by successive impregnation and pyrolysis cycles with a polysilazane*, Proceedings of the 5th HT-CMC Congress, 20–24 September 1993, Bordeaux, France. Woodhead Publishing Ltd, 1993. pp. 450–5.
5. Gonon, M. F., *Elaboration et caractérisation de Composites à fibres longues et à matrice céramique obtenue par pyrolyse d'un précurseur organométallique de type Polysilazane*, Thêse de l'Insitut National des Sciences Appliquées de Lyon, France, 1993, p. 202.

Journal of the European Ceramic Society **15** (1995) 599–604
© 1995 Elsevier Science Limited
Printed in Great Britain. All rights reserved
0955-2219/95/$9.50

0955-2219(95)00012-7

Carbothermal Preparation and Characterisation of Ca-α-sialon

J. W. T. van Rutten, R. A. Terpstra, J. C. T. van der Heijde, H. T. Hintzen & R. Metselaar

Centre for Technical Ceramics, P.O. Box 595, 5600 AN Eindhoven, The Netherlands

(Received 20 September 1994; revised version received 14 December 1994; accepted 10 January 1995)

Abstract

Ca-α-sialon can be synthesised by simultaneous carbothermal reduction–nitridation of a mixture of fine SiO_2, Al_2O_3, $CaSiO_3$ and carbon black powder at 1500°C. For the first time a single phase material is obtained in a one step process. The main intermediate product in these processes is a β-sialon with a low z*-value (z < 1·2). After formation of this β-sialon the calcium is incorporated in the lattice to form the Ca-α-sialon.*

1 Introduction

Si_3N_4 and Si_3N_4 based ceramics like sialon materials are interesting for high temperature engineering applications. These materials have very good thermal shock behaviour, high wear resistance, good corrosion resistivity, oxidation resistance and high strength.[1–4] The preparation of the sialon materials, either α or β, can be performed in several different ways. Reaction sintering is the most widely used method among them. The disadvantages are the relatively expensive starting materials and the limited possibilities to produce complex shapes of fully densified materials. An alternative way of producing sialon starting with relatively inexpensive materials is the route of carbothermal reduction and nitridation of oxide materials. The carbothermal reduction and nitridation of kaolin clay is well known for the synthesis of β-sialon.[5–7] The overall reaction for the production of β-sialon ($Si_{6-z}Al_zO_zN_{8-z}$) when $z = 3$ is:

$$3\,(2\,SiO_2\,Al_2O_3\cdot 2\,H_2O) + 15\,C + 5\,N_2 \rightarrow 2\,Si_3Al_3O_3N_5 + 15\,CO + 6\,H_2O \quad (1)$$

This reaction can be separated into several stages. Some of the intermediate products are mullite and SiC.[5,6]

As mentioned, besides the β-sialon α-sialon also exists. The structure of these latter materials is stabilised by a modifying cation such as Y, Li, Mg and Ca. The general formula for α-sialon is $Me_{m/val}Si_{12-(m+n)}Al_{(m+n)}O_nN_{16-n}$ where m and n indicate the replacement of (Si–N) by (Al–O) and *val* is the valency of the metal ion. The synthesis of α-sialon materials by reaction sintering is widely used, especially for the Y-α-sialon materials which are intensively studied.The carbothermal reduction, however, is hardly ever investigated and reported about. In this paper, the possibility is investigated of preparing Ca-α-sialon by carbothermal reduction in a single step from oxidic starting powders. To determine the most convenient starting materials, it is important to know what kind of intermediate products are formed. This is one of the reasons why the mechanism of the carbothermal reaction has been studied here.

The composition chosen is $Ca_{0.8}Si_{9.2}Al_{2.8}O_{1.2}N_{14.8}$. Starting with $CaSiO_3$ the overall reaction is as follows:

$$0{\cdot}8\,CaSiO_3 + 8{\cdot}4\,SiO_2 + 1{\cdot}4\,Al_2O_3 + 22{\cdot}2\,C + 7{\cdot}4\,N_2 \rightarrow Ca_{0.8}Si_{9.2}Al_{2.8}O_{1.2}N_{14.8} + 22{\cdot}2\,CO \quad (2)$$

This composition has been chosen for practical reasons because it is well within the single phase area of Ca-α-sialon,[8] and single phase material is likely to be obtained.

Some years ago, Mitomo *et al.*[9] prepared α-sialon (Ca and Y) by carbothermal reduction and nitridation. In that study relatively expensive starting materials such as tetraethyl–orthosilicate, aluminium–isopropoxide, calcium–ethoxide and yttrium nitrate were used. These were mixed with carbon black, precipitated and fired at different temperatures. This study showed that α-cristobalite, mullite, Si_2N_2O and β-Si_3N_4 were the main intermediate crystalline products. These were obtained, next to some amount of α-sialon, after firing at temperatures at 1450°C or lower. In a second step the material was transformed to single phase α-sialon by firing it at higher temperatures.

2 Experimental Methods

2.1 Preparation

Pure oxide materials were used to investigate the formation of single phase Ca-α-sialon. The starting materials were SiO_2 (Aerosil OX50, Degussa), C (Elftex 125, Cabot, stoichiometric amount according to reaction eqn (2)), Al_2O_3 (grade 'C', γ + δ Al_2O_3, Degussa) and $CaSiO_3$ (Wollastonite SG, Rheinische Kalksteinwerke). In some experiments $CaCO_3$ (Merck p.a., purity > 99%) or CaO (decomposed $CaCO_3$) were used as a source for calcium. The SiO_2 and Al_2O_3 powders have a high specific surface area (± 50 m^2/g). This means a high reactivity which can cause sintering of particles during the powder preparation.

An important parameter in carbothermal processes is the mixing of the powders to improve the contact between reactants and reduce the diffusion path length. Wet mixing and dry mixing were the two methods that were used. They are described briefly below.

2.2 Wet mixing

The starting powders are dispersed in water or isopropanol in a polyethylene bottle with Si_3N_4 milling balls on a roller bench for ± 48 h. The next stage is evaporating the isopropanol, pressing tablets of the powder, or slip casting the aqueous suspension. For slip casting tablets, the suspension has to meet certain requirements. The powder particle size distribution should be narrow and if possible the particle size should be below 1 μm. It is important that the suspension is stable and not too viscous. To obtain a stable suspension with SiO_2 and Al_2O_3, the pH should be either below pH = 2 (otherwise the SiO_2 and Al_2O_3 will form a gel) or above 9. However in the latter case, a very small amount of the SiO_2 will dissolve and the ionic strength will increase, which will flocculate the suspension. In order to check these properties sedimentation experiments were done in all cases. For dispersing the carbon a surfactant is required. Several surfactants were tried and among these CG-6 (i.e. ammonium salt of poly acrylic acid) supplied by ICI worked best for this system. It also helped to disperse the other powders. The suspensions which were used for slip casting had a pH < 2 because the surfactant worked better at this pH than at higher pH-values. After mixing, the suspension was ultrasonically treated to break the agglomerates and then slip cast in a plastic ring (ϕ 45 mm) placed on a gypsum plate.

2.3 Dry mixing

Pelletising is another way to produce green bodies which can be fired. The starting powders are dry mixed in an Eiger mixer (Labor Mixer R02) until the mixture looked homogeneous. Then water is sprayed on the powder which caused agglomeration of the powder. The size of the pellets obtained is related to the amount of water added and the speed of the mixer (typical values 5–10 mm). These pellets are dried at 100°C and can be used for the synthesis of Ca-α-sialon.

The density of the tablets and pellets are roughly estimated by measuring the weight and volume (pellets = 1·0 g/cm^3, tablets = 0·7 g/cm^3). The slip cast tablets are less dense and more porous than the pellets, so the influence of porosity on the reaction can be observed.

2.4 Synthesis

The different experiments and conditions are summarised in Table 1. For these experiments a constant amount of slip cast tablets were used in a horizontal tube furnace with flowing nitrogen. The exceptions were Experiment A, during which pieces of mixed starting powder bonded with binder were used. (These can be considered as pellets; agglomerates are formed after evaporation of isopropanol) and Experiment E in which pellets were used. The experiments with starting mixtures A–D were carried out in a horizontal tube furnace with a diameter of 25 mm. Experiment E was carried out in a tube furnace with a diameter of 50 mm. The amount of pellets used was 200 g and the bed length was 20 cm. The temperature was in the range 1350 – 1650°C for 3 – 65 h. The progress of the reaction was followed by measuring the CO content in the exhaust gas mixture with a CO-monitor (Defor Gas Analyser, Maihak).

Additionally some of the tablets were refired for 1 or 2 h between 1550 and 1700°C in a graphite resistance furnace in a static nitrogen atmosphere to see if the amount of α-sialon would increase. The tablets were embedded in a mixture of BN, Si_3N_4 and AlN powder to prevent dissociation at these relatively high temperatures. The influence of a milling step between the first and second firing was investigated as well. The milling could be performed in a mortar, because the material was not very hard. This powder was pressed uniaxially followed by isostatic pressing.

To get some insight into the mechanism of the carbothermal reduction, several experiments were carried out at 1500°C as a function of the firing time. In these experiments pellets were used and all the reaction parameters were kept constant, except for the time, which varied from 20 to 1000 min. The volume of the reaction bed in the horizontal tube furnace (ϕ 25 mm) was 10 ml and the N_2 flow was 12·5 l/h.

Table 1. Approximate phase composition after the first firing of a mixture of SiO_2, Al_2O_3, $CaSiO_3$ and C in N_2 at different temperatures

Starting materials	*Temperature [°C]*	*Time [h]*	*N_2-flow [l/h]*	*α/β ratio*	*Composition**
A	1450	14	12	0·27	α-sialon, β-sialon
B	1450	14	12	0·39	α-sialon, β-sialon
B	1450	6	12	0·79	α-sialon, β-sialon
B	1450	6	12	0·25	α-sialon, β-sialon
C	1450	6	12	—	β-sialon
B	1450	5·5	12	—	β-sialon
B	1450	7·5	12	0·49	α-sialon, β-sialon
B	1450	7·5	6	0·67	α-sialon, β-sialon
B	1450	3	12	—	β-sialon
B	1350	6	12	0·33	α-sialon, β-sialon
D	1350	6	12	0·45	α-sialon, β-sialon
D	1450	6	12	—	β-sialon
D	1350	12	12	—	SiO_2
D	1450	6	5	—	Si_2ON_2
E	1500	65	30	>20	α-sialon
E	1500/1650	15/2[+]	30	—	SiC

(A) SiO_2, Al_2O_3, CaO + C in isopropanol with binder.
(B) SiO_2, Al_2O_3, $CaSiO_3$ + C in water.
(C) SiO_2, Al_2O_3, $CaSiO_3$ + C in water, lower mass content.
(D) Same as B but excess of $CaSiO_3$ (2×).
(E) SiO_2, Al_2O_3, $CaSiO_3$ + C, pelletised.
(*) Amorphous and secondary phases neglected.
(+) No cooling inbetween.

3 Characterisation

To investigate the phase compositions in the product material, X-ray diffraction was applied (Rigaku Geigerflex diffractometer) using Cu–Kα radiation. To determine the ratio of α-sialon to β-sialon the following equation was used:[10]

$$\alpha/\beta = [I_{\alpha(102)} + I_{\alpha(210)}] / [I_{\beta(101)} + I_{\beta(210)}] \quad (3)$$

This equation is applicable in the case of pure α and β Si_3N_4 and is assumed to be valid for sialon materials too, because the structures are very similar. To estimate the α-sialon content only α and β sialon phases were taken into account. Amorphous phases and (traces of) secondary phases were neglected. Therefore in Table 1 only an indication is given of the compounds present in the sample; the concentration for each component is not calculated. The lattice parameters of the materials were determined from slow scans (0·0125°/s). The ten strongest reflections observed were applied to calculate the lattice parameters using a computer program based on the SIMPLEX method.[11]

To determine the relation between the nitrogen content and the content of α-sialon the nitrogen content was determined by a reverse Kjelldall titration.[12] The sample is destructed with molten lithium hydroxide, the formed NH_3 is dissolved in boric acid which was titrated with hydrochloric acid to determine the nitrogen-content. Particle size was determined by sedigraph measurements (Micromeritics Sedigraph 5100). The powder was suspended in water and ultrasonically treated to break agglomerates before the measurements.

4 Results and Discussion

4.1 Synthesis of Ca-α-sialon

The conditions of the experiments and the results are displayed in Table 1. As can be seen, the applied conditions at 1450°C or lower temperatures are not appropriate for preparing single phase α-sialon from the starting SiO_2, Al_2O_3 and $CaSiO_3$ powders. The main products in this range of temperatures are α-sialon and a β-sialon when these starting powders are used. Even after a very long time the composition of the samples does not differ significantly. In all samples an amorphous phase is present. This phase cannot be characterised by X-ray diffraction; the phase is assumed to consist of aluminates and silicates. Evaporation of SiO influences the yield of the sialon material. When the reaction time is longer the silicon loss increases. This explains the higher ratio after 6 h compared to the ratio after 14 h (Experiments 2 and 3). Although the circumstances were the same in Experiments 3 and 4, the results were quite different. This is probably due to the fact that two different batches of tablets were used. Apparently one batch was not as homogeneously mixed as it should have been. This could explain the large difference in the α/β ratio. According to the results

of Experiments 13 and 14 (main products SiO_2 and Si_2ON_2) the temperature of 1350°C is not sufficient for the reaction to have proceeded far enough for the sialon materials to be detected. SiO_2 and Si_2ON_2 are well known intermediates in the formation of β-sialon too.[6] In Experiment 14 the N_2-flow is too low to supply a sufficient amount of nitrogen in 6 h to form sialon material. In the samples reacted for a short time there were remains of starting materials present. The z-values of the formed β-sialon material in the samples fired below 1500°C vary between approximately 0·4 and 1·2. A value of 1·4 at the most can be expected from the starting composition. At a temperature below 1500°C the highest content of α-sialon is about 40%, both for the slip cast tablets and pelletised starting material. Increasing the temperature to 1500°C resulted in an almost single phase Ca-α-sialon (> 95 wt%). The rest (5 wt%) is uncertain because of the detection limit of the X-ray diffraction analysis. However, when the holding time at 1500°C is not long enough, a significant amount of residual carbon is left in the mixture. The mixture contains hardly any sialon material (at least not above the detection limit). When the temperature is raised to 1650°C the main product is SiC instead of α-sialon. Refiring the tablets, which were fired at temperatures below 1500°C, at elevated temperatures (1550–1700°C) resulted in a decrease of the α-sialon content. On the contrary, milling and pressing tablets and refiring these tablets in the same temperature range results in products with high α-sialon content. α-sialon contents of up to 95 wt% are achieved (see Table 2).

This means that on the one hand it has been confirmed that Ca-α-sialon can be obtained in a two step process,[9] but on the other hand it has been shown in this paper that it is possible to use a single step process.

Table 2 shows the influence of porosity on the conversion to α-sialon. From this it can be seen that porosity has little or no effect on the reaction (at least in this range of porosity).

Figure 1 shows the transformation percentage to α-sialon after milling and a second firing at higher temperatures. The highest amount of Ca-α-sialon was obtained at 1700°C. No SiC could be detected, indicating a complete consumption of carbon in the first step.

Table 2. Comparison of α-sialon content between first and second firing of tablets and pellets with intermediate grinding. (The numbers are averages)

	First firing (1450°C)	*Second firing (1700°C)*
Tablets	30% α-sialon, 70% β-sialon	> 95% α-sialon
Pellets	35% α-sialon, 65% β-sialon	> 95% α-sialon

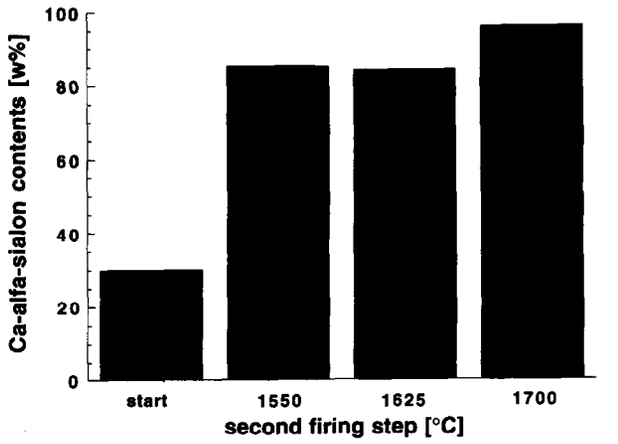


Fig. 1. Transformation to α-sialon after the second firing. (Start = initial amount of Ca-α-sialon before the second firing).

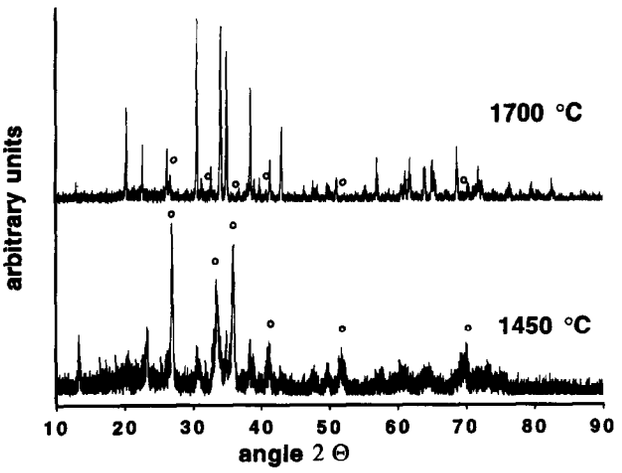


Fig. 2. X-ray diffraction patterns of material after first firing at 1450°C (bottom) and firing at 1700°C (top).The circles indicate peaks of β-sialon.

The phase change during the refiring process is shown in Fig. 2. The lower part presents a diffractogram of a sample fired at 1450°C. According to the baseline (which is not straight) a significant amount of amorphous phase is still present after firing at 1450°C. The diffractogram in Fig. 2 after refiring at 1700°C shows narrow and sharp peaks and a straight baseline. The unit cell dimensions of α-sialon calculated from this diffractogram are a = 0·784 and c = 0·571 nm. From these lattice parameters an m-value in the general formula for α-sialon of ± 1·4 can be estimated. This means that most of CaO is incorporated in the crystalline material and the rest is present in the amorphous or unidentified phase. The powder which is obtained after firing twice is more difficult to mill than powder which is synthesised at 1500°C. The particle size (agglomerate size) of this powder as synthesised is approximately 5–8 μm while the agglomerate size of the refired powder is about 10–20 μm.

4.2 Reaction mechanism

The results from the experiments concerning the investigation of the mechanism of the reaction are presented in Fig. 3 and discussed in the next paragraph. In a relatively short time the sialon products are formed. From X-ray diffraction patterns it follows that in the beginning of the reaction a significant amount of amorphous phase is present. This complicates the identification and quantitative determination of several components during this initial period. The main intermediate product is β-sialon material with low z-values ($z < 1{\cdot}2$). In shortly reacted samples some SiC seems to be present. Sometimes the samples contain O'-sialon. Calcium aluminates or silicates were hardly found except the starting $CaSiO_3$. The intermediate products are consumed very fast otherwise there should have been a plateau at a certain level in the curves.

To monitor the progress of the reaction the cell parameters of Ca-α-sialon are calculated. The values are shown in Table 3. These show that the further the reaction proceeds the smaller the cell parameters become. The cell parameters of the α-sialon converge to the values of the desired product. As expected, if the amount of nitrogen increases the cell parameters will decrease.[13]

In Fig. 4, the data from the nitrogen determination are plotted, showing that even at a low (40 wt%) Ca-α-sialon concentration the nitrogen content is high. This means that nitridation has proceeded so far that most of the nitrogen required for the formation of the Ca-α-sialon is available in the sample. Approaching 100 wt% of Ca-α-sialon the nitrogen content rises up to almost the theoretical value (35·0 wt%)

On the basis of the results mentioned previously the following mechanism of the formation of Ca-α-sialon is proposed. The first step is the formation of a β-sialon with a z-value of 1·2 (Theoretically $z = 1{\cdot}4$, because it was aimed at

Table 3. Cell parameters of Ca-α-sialon calculated during progress of the reaction.

Time [min]	a *[nm]*	c *[nm]*
100	0·787	0·572
125	0·785	0·568
250	0·784	0·569
500	0·785	0·569
750	0·784	0·569
1000	0·784	0·568

$Si_{9.2}/\ Al_{2.8}$). The theoretical value of the nitrogen content of a β-sialon is 33·8 wt% if the z-value is 1·2. In Fig. 4 it is shown that with a low (40 wt%) Ca-α-sialon concentration combined with a high content of β-sialon (60 wt%) the nitrogen content nearly reaches the theoretical value for a β-sialon material with a z-value of 1·2. The end of the curve shows that the nitrogen content rises to the theoretical value of Ca-α-sialon which is 35·0 wt%. The molar concentration of nitrogen is increased from 13·2 to 14·8 (see eqns 4 and 5). In summary, the first step is:

$$4{\cdot}6\ SiO_2 + 0{\cdot}7\ Al_2O_3 + 9{\cdot}9\ C + 3{\cdot}3\ N_2 \rightarrow \underset{(\beta\text{-sialon})}{Si_{4.6}Al_{1.4}O_{1.4}N_{6.6}} + 9{\cdot}9\ CO \quad (4)$$

In the second step calcium and the extra nitrogen are being incorporated:

$$0{\cdot}8\ CaO + 2\ Si_{4.6}Al_{1.4}O_{1.4}N_{6.6} + 2{\cdot}4\ C + 0{\cdot}8\ N_2 \rightarrow \underset{(\alpha\text{-sialon})}{Ca_{0.8}Si_{9.2}Al_{2.8}O_{1.2}N_{14.8}} + 2{\cdot}4\ CO \quad (5)$$

It is assumed that an eutectic liquid of $CaSiO_3$ (providing CaO) and β-sialon promotes the formation of Ca-α-sialon. During this formation it is expected that Si–N as well as Al–O bonds have to be broken but how exactly the formation takes place is not in the scope of this work and is

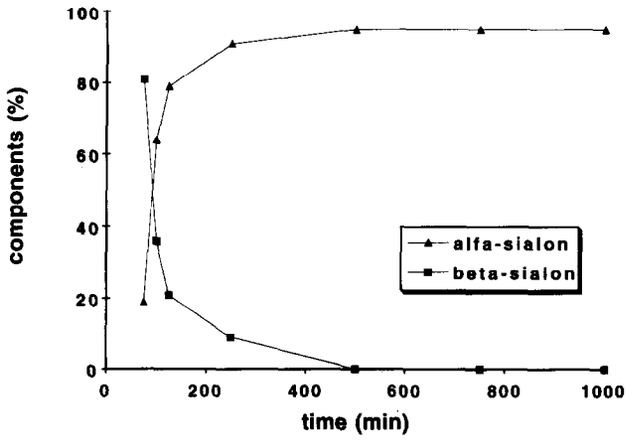


Fig. 3. The α and β sialon content of the mixture after firing at 1500°C for different times.

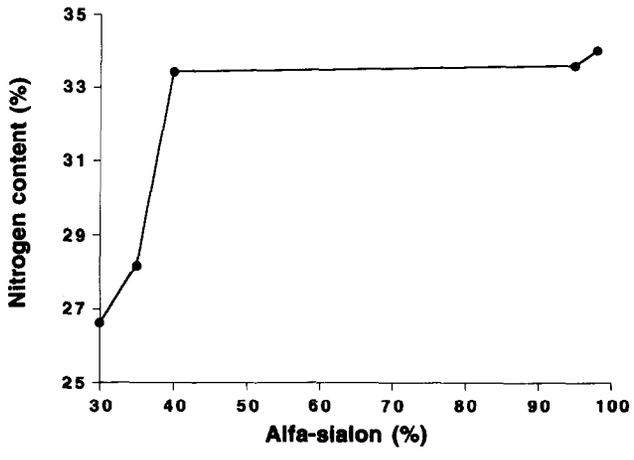


Fig. 4. Relation between nitrogen content and Ca-α-sialon content in the mixture. Experiments were carried out in a large horizontal tube furnace (ϕ 50 mm, 200 g pellets, 30 l/hr N_2-flow, 1500°C).

not investigated. The conversion of the mixed α/β-sialon which was obtained after firing at a temperature lower than 1500°C to a single phase α-sialon by firing it at a higher temperature can be compared to reaction sintering.[13] The carbon was fully consumed in the first step due to complete nitridation. Ca is then incorporated into the material in the second step at a higher temperature without further nitridation, different from the second step of the carbothermal reaction given by eqn (5).

5 Conclusions

The carbothermal reduction and nitridation of oxidic powder precursors is a possible route to prepare single phase Ca-α-sialon in a relatively inexpensive way. There are two methods to obtain single phase material. The first way is firing first at 1450°C, milling the obtained α/β mixture and refiring it at 1550–1700°C. Results from this route are comparable with the results found in Ref.[9] The second way is firing at 1500°C where the reaction can be completed in *one* step to form single phase materials. The main intermediate product in the carbothermal reduction of the oxides is β-sialon with a low z-value ($< 1{\cdot}2$). A proposal for the formation mechanism of single phase Ca-α-sialon has been made. Firstly, a β-sialon with low z-value is formed, followed by the incorporation of the Ca-ions. Nitrogen content determination and calculation of the cell parameters support this proposed mechanism. In contrast with the formation of β-sialon, SiC is not a major intermediate product.

Acknowledgements

The authors want to thank D. Sutanto and J. Klok for performing part of the practical work which resulted in this paper.

References

1. Cao, G. Z. & Metselaar, R., *Chem. Mat.*, **3** (1991) 242–52.
2. Krämer, M., Hoffmann, M. J. & Petzow, G., *Act. Met. Mat.*, **41** (1993) 2939–47.
3. Gogotsi, Y. G. & Grathwohl, G., *J. Am. Ceram. Soc.*, **76** (1993) 3093–104.
4. Cao, G. Z., Preparation and characterization of α'-sialon ceramics. PhD Thesis, Eindhoven University of Technology, Eindhoven, 1991.
5. Higgens, I. & Hendry, A., *Brit. Ceram. Tans. J.*, **85** (1986) 161–6.
6. Kokmeijer, E., Scholten, C., Blömer, F. & Metselaar, R., *J. Mat. Sci.*, **25** (1990) 1261–7.
7. Dijen, F. K. van, Metselaar, R. & Siskens C. A. M., *Sprechsaal*, **117** (1984) 627.
8. JCPDS-card 33-261.
9. Mitomo, M., Takeuchi, M. & Ohmasa, M., *Cer. Int.*, **14** (1988) 43–8.
10. Grand, G., Demit, J., Ruste, J. & Torre, J. P., *J. Mat. Sci. Lett.*, **14** (1979) 1749.
11. Borgwardt, K. H., *The simplex method, a probabilistic analysis*, Springer Verlag, Berlin, 1987.
12. Vogel, A. I., *A Text-book of Quantitative Inorganic Analysis including Elementary Instrumental Analysis*. Longmans, Green and Co, Ltd, London, 1961, p. 257.
13. Hampshire, S., Park, H. K., Thompson, D. P. & Jack, K. H., *Nature*, **274** (1978) 880.

Journal of the European Ceramic Society **15** (1995) 605–615
© 1995 Elsevier Science Limited
Printed in Great Britain. All rights reserved
0955-2219/95/$9.50
0955-2219(95)00025-9

The Barrier Height Formation in ZnO Varistors

P. Q. Mantas & J. L. Baptista

Dep^{to} Eng.^{a} Cerâmica e do Vidro (INESC), Universidade de Aveiro, 3800 Aveiro, Portugal

(Received 2 June 1994; revised version received 27 January 1995; accepted 31 January 1995)

Abstract

The electrical characteristics of ZnO ceramic varistors are interpreted as being due to the existence of potential barriers at the grain boundaries. The two main models describing the origin of these barriers, surface states at the interface, and surface oxidation, are discussed in this work, where the microstructure and the electrical properties at various temperatures (up to 160°C) of a standard varistor composition, are used in an attempt to separate both contributions. The temperature dependence of both the distribution of surface states and the Fermi level, when extrapolated to high temperatures, indicates that the surface states control mainly the shape of the I–V curves, and that the surface oxidation contribution to the barrier, although as high as 0·25 eV, is not sufficient to account for the total energy of the barrier. Values for the density of carriers calculated using the dependence of the Fermi level on temperature, were in good agreement with reported values determined by other techniques.

1 Introduction

The electrical characteristics of ZnO varistors are interpreted as due to potential barriers formed at the grain boundaries of the ceramic material. There are two main models describing the origin of these barriers: (i) surface states at the interface, and (ii) surface oxidation. In the first model, it is considered that the junction between two semiconducting ZnO grains (n-type semiconductor at room temperature) behaves as a p-type semiconductor, and, for the thermodynamic equilibrium, i.e. the equalisation of the Fermi level throughout the junction, a process of charge transfer between the grains and the interface is necessary.[1,2] As a consequence of this process, donors in the grains nearby the interface are ionized, giving electrons to the interface states, which also become ionized. The region near the junction is depleted of charges, and therefore, a potential barrier appears. In equilibrium, there is a simple relation between these three entities, the barrier height, Φ_{Bo}, the ionized donors, N_D, and the ionized charge at the interface, Q_{io}: $\Phi_{Bo} \propto Q_{io}^2/N_D$. Since two opposite Schottky type barriers are formed, this model is also called the Double Schottky Barrier (DSB) model.

In the second model, it is considered that the regions of the ZnO grains near the grain boundaries are much more resistive than the bulk of the grains. The difference in resistivities is due to a non-equilibrium defect chemistry process, arising during the cooling down period. At the sintering temperature (>1200°C), all the material can be considered in thermodynamic equilibrium, and so there is a great concentration of defects, namely those of the Schottky type. When the sample is cooled, these defects must diffuse from the bulk of the grains to the surface where they will be annihilated. Because both the defect formation and the defect diffusion are thermally activated, only the defects near the grains surface are able to reach the interface to be annihilated, the others being frozen in the bulk. The bulk of the grains remains with a high concentration of defects (giving the n-type semiconductor nature), while the interface becomes stoichiometric, i.e. highly resistive (the forbidden band in ZnO at room temperature is about 3·2 eV). For the electron flow across such a junction, a potential barrier is therefore present.[3,4]

Both models, n–p–n and n–i–n, reasonably describe the I–V curves of these materials, if the varistor quality factor α is less than ~25.[5] For higher α values, they need to incorporate other mechanisms of electron flow, based on impact ionization[6–9] or electron tunneling from one grain to the other.[10,11]

In this work we used ZnO varistor samples to measure their electrical characteristics at several temperatures, up to 160°C, and used these experimental results to theoretically derive the distribution of surface states above the equilibrium Fermi level, in an attempt to differentiate the contributions from the two mechanisms for the formation of the varistor potential barriers.

2 Experimental

Varistor samples prepared via a normal ceramic processing route, and sintered at 1300°C, 1 h, in air, were used. The chemical composition of these samples was: 97·0 mol% ZnO and 3·0 mol% of Bi_2O_3, Sb_2O_3, Co_2O_3, MnO_2 and Cr_2O_3, with the molar proportion of 1:2:1:1:1. Samples were used for SEM observation, after polishing and chemically etching the surfaces. Mean grain size was determined by the interseption method, using a computer aided system. Samples used for electrical measurements were sputtered on opposite faces with gold electrodes, after lapping. Electrical measurements were preformed in an oven, heated via an electrically heated wire double wound around a supporting tube. A wire net was used to shield the sample from the tube. Temperatures were controlled with the aid of a programable controller, using cromel–alumel thermocouples. Before electrical measurements, the temperature in the oven was stabilized for 30 min.

I–V measurements were made with a current source (Keithly 225 Current Source), and an electrometer (Keithly 616 Digital Electrometer), up to 100 V. At room temperature, for higher voltages, a pulsed source (AMBO, with 60 μs pulse duration, 13 Hz, up to 1 kV) was used. C–V measurements were done with an ac bridge (Hewlett-Packard 4280A 1MHz C Meter/C-V Plotter), at a fixed frequency of 1 MHz, up to 40 V dc applied voltage.

3 Results and Discussion

3.1 Microstructure

Figures 1 and 2 show the microstructure of the varistor; it can be seen that three phases are present: large ZnO grains, inter/intragranular spinel particles, and a third minor phase, brighter than the other two, that is possibly the reported pyrochlore type phase.[12–18] By EDS, we could hardly detect the presence of Co as the only dopant inside the ZnO grains (Fig. 3(a)). The spinel phase is doped with Co, Mn, and Cr (Fig. 3(b)). The third phase is composed by Zn, Sb, and Bi (Figs 3(c) and 2). This type of microstructure is the one that could be expected from the chemical composition of the sample and the sintering schedule used, as reported by Inada.[13–15] However, it must be

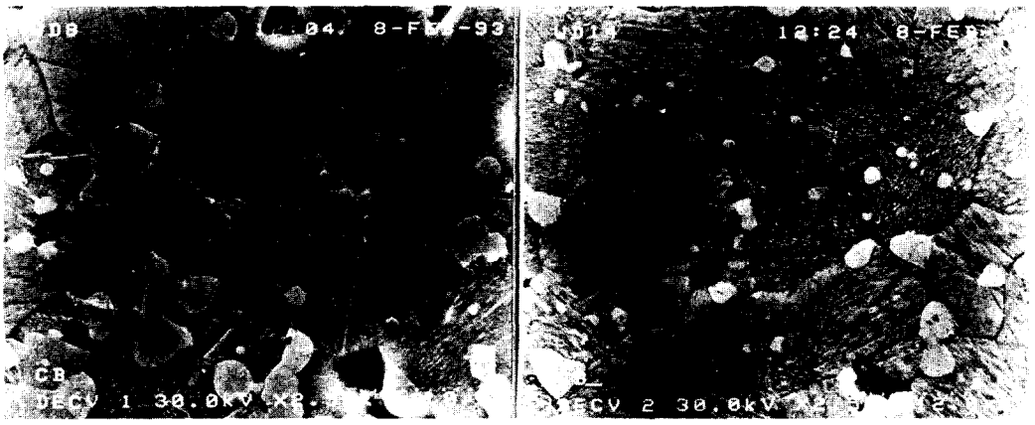


Fig. 1. SEM micrograph of polished and chemically etched sample. The spinel like phase (A) is normally located at the grain boundaries of the ZnO grains with some finer particles inside the grains. A brighter phase (B) can be found near the spinel like phase, and is probably the reported pyrochlore type phase.

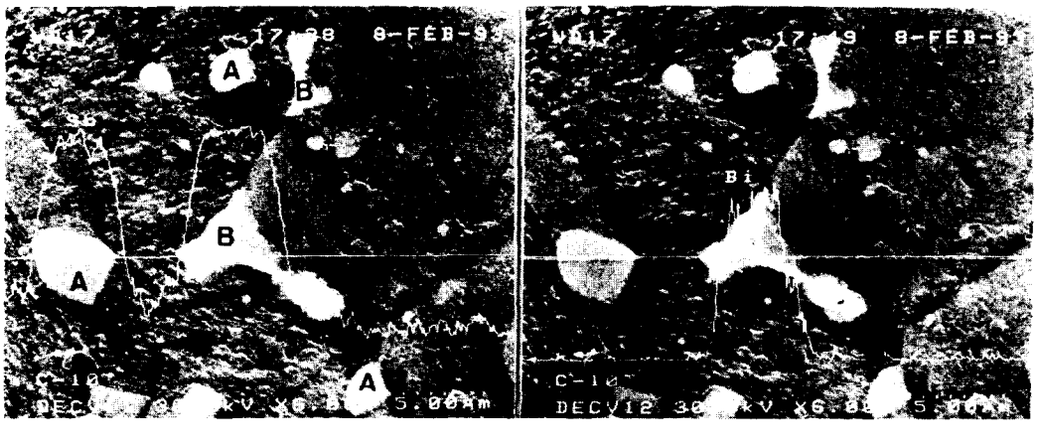


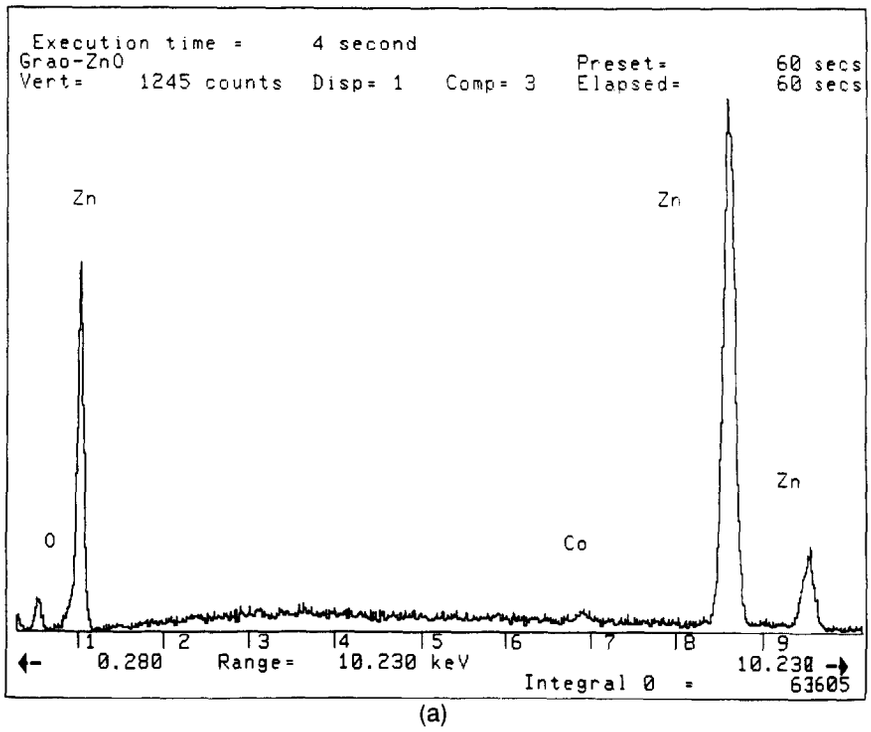
Fig. 2. Antimony and bismuth profiles (by EDS attached to the SEM) of the three phases present in the sample microstructure. Both the spinel like phase (A) and the brighter phase (B) contain Sb, while Bi is only present in the brighter phase.

emphasized that Co, Mn or Cr, were not detected in the third phase. If this phase is the pyrochlore type phase, then it comes with ZnO from the reaction between the spinel like and the Bi-rich liquid phases, during the cooling down of the sample[13–15]

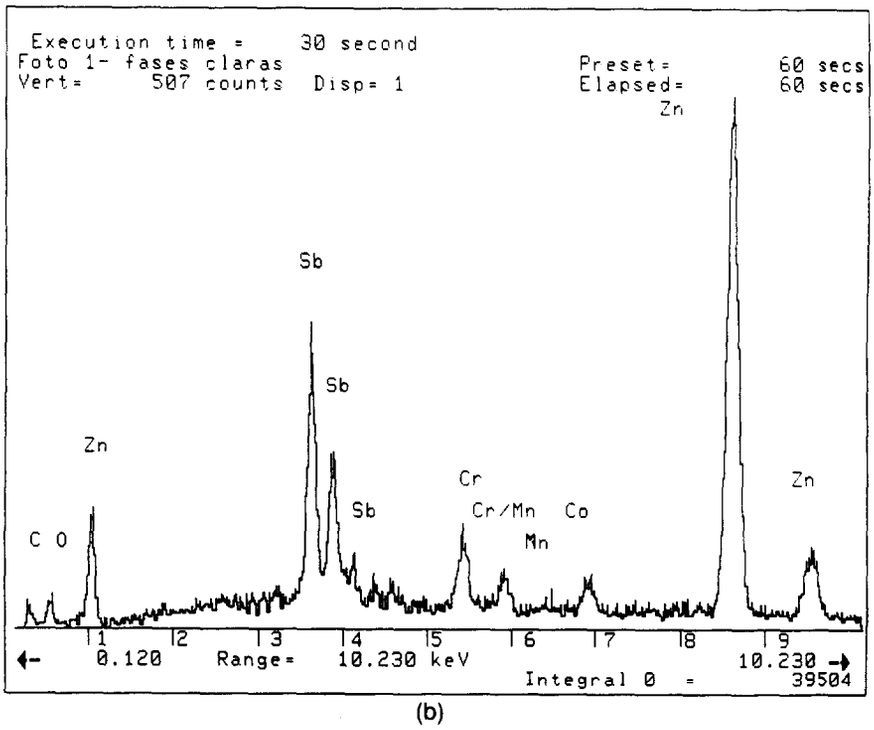
$$3Zn_7Sb_2O_{12}(SP) + 3Bi_2O_3(Liq.) \xrightarrow{950°C} 4Bi_{3/2}ZnSb_{3/2}O_7(PY) + 17ZnO \quad (1)$$

where SP is spinel and PY pyrochlore.

Since the third phase does not contain Co, Mn or Cr, it is possible that these dopants were incorporated in the newly precipitated ZnO. Einzinger[3,4] and Schwing and Hoffmann,[10,11] proposed the build up of the potential barrier in the ZnO grain boundaries as being due to the presence of Co in the grain boundary. For these authors, this mechanism is important for the build up of the potential barrier in the grain boundaries, since foreign atoms segregated near the interface will shift the relative concentrations of zinc and oxygen vacancies. Donor cations (Co, Mn or Cr) will decrease the oxygen vacancy concentration relative to that of zinc vacancy and, consequently, the Fermi level at the interface will be lower in energy, relative to the conduction band edge, than in the bulk of the material; this means that a potential barrier is formed at the interface. The above results could support this mechanism, since a high concentration of these dopants would be in the



(a)



(b)

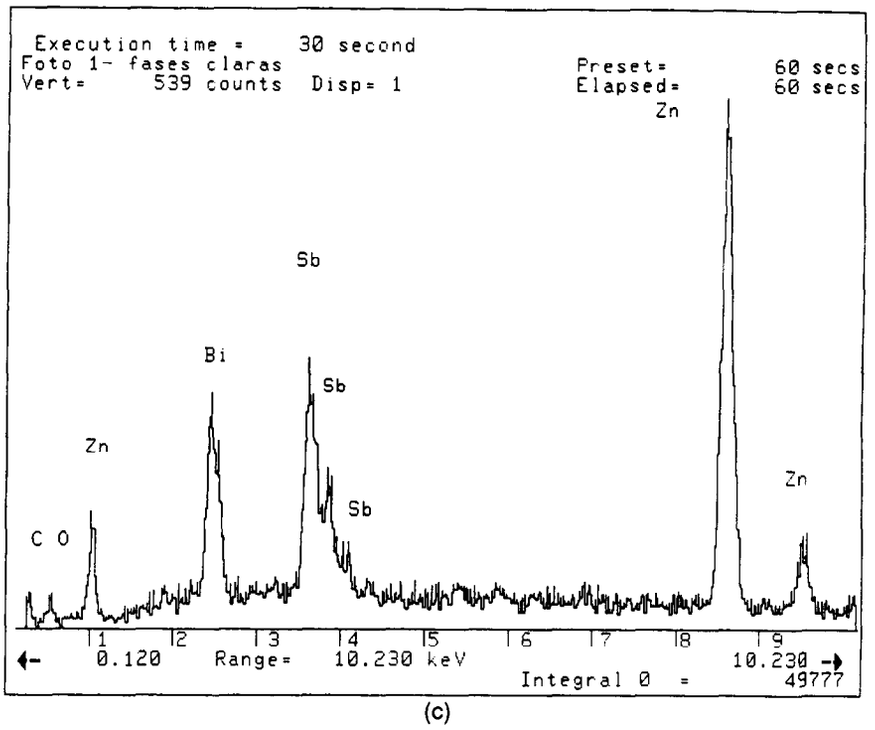


Fig. 3. EDS spectra of the three phases present in the sample microstructure: (A) ZnO phase, showing faintly the presence of Co; (B) spinel like phase, doped with Cr, Co, and Mn; and (C) the brighter phase, composed by Zn, Sb, and Bi, without clear evidence of the dopants.

freshly precipitated ZnO layer. However, in this temperature range (~950°C), most of the ZnO–ZnO grain boundaries are already formed and the material already presents varistor characteristics,[19] and so some doubts can be put on accepting this mechanism as the main contribution to the formation of the potential barriers. It was decided, therefore, to pursue this matter in some detail, and see if there was consistency between the DSB model and the formation mechanism of the potential barriers.

3.2 Varistor parameters

3.2.1 The method used to determine the density of surface states (DOS)

In this work, we firstly determined the equilibrium Fermi level at the interface, E_{Fo}, and thereafter the density of surface states (DOS), at various temperatures, ranging from room temperature up to 160°C. Both parameters, E_{Fo} and DOS, were calculated from each experimentally determined I–V curve, using the double Schottky barrier model (DSB). The procedure was made by successive fittings of the theoretically calculated I–V curves to the experimental ones, until a good fitting between both curves was found. In the following, we describe this procedure step by step.

Using the DSB model, there are two main steps to obtain the electrical parameters that allow the derivation of the I–V curves: in the first step, the relation between the barrier height, Φ_B, and the applied voltage across one junction, V, is found; in the second one, these two parameters are related with the electron flux, J_{DC}. Once the I–V curve is obtained for one junction, it is necessary to relate it to the polyjunction system describing the polycrystalline material. We shall return to this last relation later in this section.

To accomplish the first step, it is necessary to know the density of charge in the junction, $\rho(x)$, and solve the Poisson equation for that case. This has been done by Blatter and Greuter[20,21] who have found a relatively simple relation between the barrier height and the applied voltage

$$\Phi_B = \frac{V_C}{4}\left(1 - \frac{V}{V_C}\right)^2 + \sum_{\nu=1}^{n} N_\nu(\epsilon_\nu - \epsilon_\xi)\left(e\sum_{\nu=0}^{n} N_\nu\right)^{-1} \quad (2)$$

In this equation, the critical voltage, V_C, is related to the accumulated charge at the interface, Q_i, and to the concentration of donors in the grains, N_ν, by the equation

$$V_C = Q_i^2\,(2\epsilon\epsilon_o e\sum_{\nu=0}^{n} N_\nu)^{-1} \quad (3)$$

where ϵ is the relative permitivity of the material, ϵ_o the vacuum permitivity, and e the electron charge. Each donor species, ν, with density N_ν, is in the energy level $E_g - \epsilon_\nu$, where E_g is the forbidden band of the semiconductor; $E_g - \epsilon_\xi$ is the Fermi level in the bulk of the material. The second term of the right hand side in eqn (2), is the contribution of deep donor levels to the barrier height. These

deep levels tend to decrease the barrier height, and have some effect in the I–V curves for high voltages (normally in the breakdown region). As has been pointed out,[20,21] for normal densities of deep levels in ZnO varistors (ca. 10% of the density of shallow donors), the barrier height is reduced by ~0·10 eV, which only represents 10%–20% of the total barrier height; moreover, experimentally it is difficult to observe any smooth change of the I–V curve at high voltages, especially in the breakdown region. Because of that, we have neglected this type of contribution, and so eqn (2) reduces to quite a simple one

$$\Phi_B = \frac{V_C}{4}\left(1 - \frac{V}{V_C}\right)^2 \tag{4}$$

The accumulated charge at the interface, Q_i, represents the total amount of trapped charge,

$$Q_i = e\int_{\xi_i^n}^{n} N_i(E) f_i(E)\,dE \tag{5}$$

where ξ_i^n is a fictitious Fermi level describing the neutral interface, $N_i(E)$ the density of surface states, and $f_i(E)$ their probability of being occupied. Upon the application of the voltage, some of the surface states are ionized, and so the Fermi level at the interface shifts upwards in energy. The voltage dependent barrier height is defined by eqn (2) (or (4)) and by $e\Phi_B(V) = E_g - \epsilon_\xi - E_F(V)$; so any pair of ($\Phi_B$, V) values must be found in a self-consistent way.[20,21]

In the second step for the determination of the I–V curve, it was assumed that the electron flux over the barrier corresponds to the thermionic emission mechanism.[1,2,20,21] It has been shown by Pike[22] that a diffusion mechanism will give similar results, so both mechanisms can be applied to describe the system. Other mechanisms, like the field emission, used by other authors,[23] were not considered here. According to the thermionic emission mechanism, the electrical density across a junction has the form

$$J_{DC} = A^*T^2\exp(-(e\Phi_B(V)+\epsilon_\xi)/kT)(1-\exp(-eV/kT)) \tag{6}$$

where A* is the Richardson constant, T the absolute temperature, e the electron charge, and k the Boltzmann constant; [1– exp(–eV/kT)] corresponds to the net electron flux crossing the junction.[1,2,20,21] In a more accurate description, the electron capture probability must also be taken into consideration in this equation, but since this is a rather minor correction, we have neglected it.[20,21]

Having defined the relation between applied voltage and current density for one junction, i.e. the I–V curve, it is important to relate this to the material characteristics. It is normally accepted that the I–V properties of the material can be described by an equivalent electrical circuit composed of a network or resistors. It is also known that some of the grain boundaries in the material are not electrically active, i.e. they don't have varistor properties. It has been proposed[24] that in such equivalent circuits, it is only necessary to have ~30% of good electrical junctions for the material to behave as a varistor. In view of this result, one can consider that the material is composed of a series of resistors between the electrodes, whose number, m, can be readily calculated by $m \approx d/G$ (d being the sample thickness, and G the mean grain size of the material). This type of approximation can give values of 2–3 volts per grain boundary (V/GB) for the breakdown voltage. If, experimentally, a varistor has α values greater than 25, it is necessary to incorporate a mechanism of impact ionization, or a tunneling mechanism, as already pointed above. For these mechanisms to operate, the breakdown voltage must be ≥3·2 V/GB. This value has been found experimentally for one junction, using microcontacts over a polished surface;[25–28] besides, it is the threshold voltage for the mechanism of impact ionization, also found experimentally.[7] This means that the approximation used for the determination of m, where every grain boundary was counted, can give unrealistic results. However, in these situations where $\alpha \geq 25$, the number of electrically active grain boundaries, m', can be easily found by assuming that the 3·2 V/GB have been reached for these samples, which allows the use of the relation $V_{breakdown}/m' \approx 3{\cdot}2$ V/GB. Once this value has been found, it is thus possible to compare the theoretically calculated (J_{DC}, V) curve with the experimental (J_{DC}, V_{exp}/m') one.

Knowing the relevant electrical parameters for each case, it is then possible to fit a theoretically calculated I–V curve to the experimental one, by manipulating only the distribution of the surface states. In this work, we made this approach with the aid of a computer program, in which the density of surface states (DOS) was introduced as a set of Gaussian distributions. In practice, the type of distribution used is not important, since we could input any number of Gaussians and integrate them to fit the curves.

Since we neglected the contribution of deep donors to the barrier height, N_ν reduces to N_0 (ν = 0). For the density of ionized donors. N_0, we used the values determined by the known relation:[29]

$$\left(\frac{1}{C} - \frac{1}{2C_0}\right)^2 = \frac{2(\Phi_B + V)}{e^2\epsilon\epsilon_0 N_D} \tag{7}$$

where C and C_0 are the capacitance at V and $V = 0$

applied voltage, respectively, and N_D the total density of ionized donors. We assumed that $N_0 \equiv N_D$, since this relation was used with results obtained at a fixed frequency of 1 MHz.[1,3,20,21]

3.2.2 Electrical characteristics

To plot the I–V curves, V/GB was determined by $V_{applied}/m$, where $V_{applied}$ is the voltage applied to the sample, and m is the total number of grain boundaries between the electrodes, m = 189 (with G = 9·8 μm). For this value of m, at a current density of 0·5 mA/mm^2, which is the current density normally accepted for the onset of the breakdown regime,[30] V/GB $\approx$ 2·6 V, and the α value is greater than 25, $\alpha \approx 35$. As already said, for such a high value of α, the voltage applied to each grain boundary exceeds 3·2 V. The calculated value, 2·6 V, is lower than this one, and we can presume that not all the grain boundaries are electrically active. Assuming that this value must be at least 3·2 V, then the number of electrically active grain boundaries is m' = 152. Figure 4 shows the I–V curves, plotted as ln(J) versus ln($V_{applied}/m'$), where J is the current density, for the various temperatures. In this figure m' = 152, which corresponds to ~80% of good junctions in the material and is far above the minimum required for the varistor action. This fraction of good junctions in the material seems to be too high to correspond to the mechanism of segregation of dopants in the ZnO–ZnO boundaries via the formation of the pyrochlore phase by eqn (1), since this phase is a rather minor one, and most of the ZnO grain boundaries must be already formed at ~950°C.[19]

The next step is the determination of the energy of the equilibrium Fermi level at the interface, E_{Fo}, at each temperature. At zero bias, i.e. for lim J_{DC} (V→0) in eqn (6)

$$\sigma = ek^{-1}A^*T\exp[-(e\Phi_{Bo} + \epsilon_\xi)/kT] \qquad (8)$$

and the conductivity, σ, of the material depends essentially on the exponential part of eqn (8). Since $E_{Fo} = E_g - (e\Phi_{Bo} + \epsilon_\xi)$, then E_{Fo} determines the conductivity of the material at each temperature. Assuming a reasonable value for the bulk Fermi energy, ϵ_ξ, E_{Fo} can be calculated for each temperature by simply fitting the ohmic highly resistive part of the I–V curve to the theoretically calculated one. We assumed that ϵ_ξ = 0·05 eV for all the tested temperatures; it is a reasonable energy for the semiconductor, although not necessarily constant for all temperatures. The choice of this energy is to be checked in the following.

Figure 5 represents the variation of E_{Fo} with temperature. It is an almost straight line, with slop $dE_{Fo}/dT = -2{\cdot}3 \times 10^{-3}$ eV K^{-1}. Rossinelli *et al.*[31] have found a similar value for the $SrTiO_3$ based varistors ($-2{\cdot}0 \times 10^{-3}$ eV K^{-1}), and in view of the two quite different chemical systems, it is expected that they have the same physical origin. During heating, the width of the ZnO forbidden band is also decreasing, $E_g = E_{go} - \beta T$, with β = 9·5 × 10^{-4} eV K^{-1}.[32] Instead of calculating the absolute change of E_{Fo} with temperature, we have calculated the relative change of E_{Fo} to E_g with temperature. For each temperature we plotted E_{Fo}/E_g–vs–T, and have then calculated the slope of the obtained curve. We found $d(E_{Fo}/E_g)/dT = -5{\cdot}2 \times 10^{-4}$ K^{-1}. Such temperature dependence can be

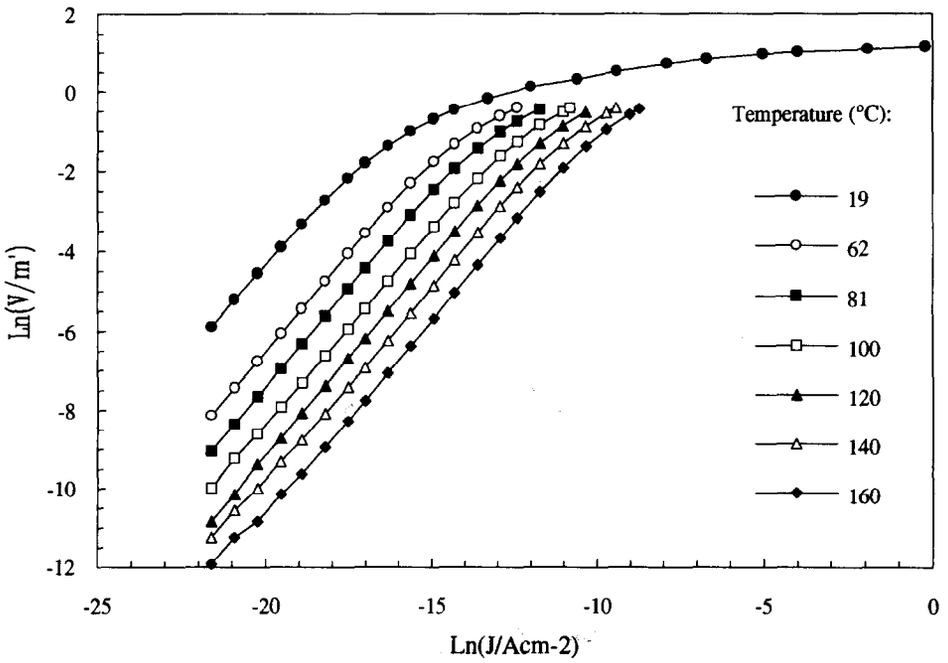


Fig. 4. I–V curves of the samples at the studied temperatures (legend inside the figure). In this Figure, V/GB was determined by $V_{applied}/m'$, where m' = 152 is the number of good junctions (see text).

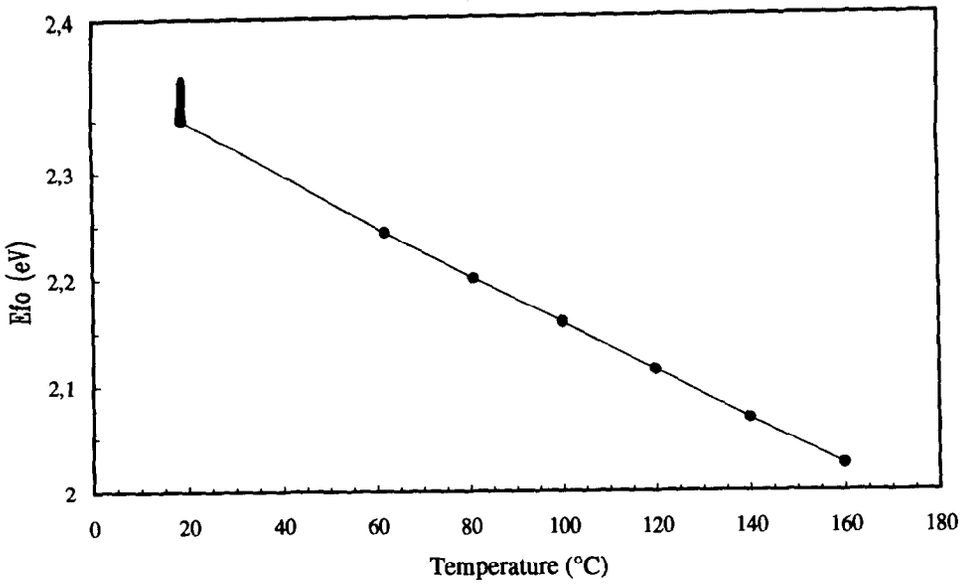


Fig. 5. Variation of the equilibrium Fermi level at the interface, E_{Fo}, with temperature.

assigned to the variation of the bulk Fermi level, assuming that the density of carriers in the ZnO conduction band, in this temperature range, is controlled by donor defects (either intrinsic, like the zinc interstitial, Zn_i, or the oxygen vacancy, V_O, or extrinsic, e.g. due to the presence of Co). As a first approximation, the density of carriers, n, can be considered constant,[33] and ϵ_ξ can be determined by adjusting the n value in the following eqn (9), until it has the same temperature dependence as E_{Fo}/E_g

$$\epsilon_\xi = kT\ln\left(\frac{N_C}{n}\right) \tag{9}$$

where $N_C = 2(2\pi m_e^* kT/h^2)^{3/2}.m_e^*$ is the electron effective mass in ZnO, taken as $m_e^* = 0{\cdot}25m_o$, and h is Planck's constant. Equation (9) is, of course, not entirely correct, since the exact structure of the system is not known (type of donor species, its energy and concentration). However, it gives quite reasonable values for n and for ϵ_ξ: (i) the adjusted n value, $n = 4{\cdot}5 \times 10^{16}$ cm^{-3}, is in close agreement with values determined by other techniques (infrared spectroscopy,[34] high current and high frequency measurements[35]) on commercial varistor samples, $n \sim 1 \times 10^{17}$ cm^{-3}, and (ii) the value of the bulk Fermi level, ϵ_ξ, ranges from 0·10 eV, at room temperature, up to 0·18 eV, at 160°C, values which fall in the range of 0·066 eV[20,21] to 0·32 eV.[36] Knowing the values of E_{Fo} and ϵ_ξ for each temperature, we are now able to calculate the density of states (DOS).

To calculate the DOS we used the parameters listed in Table 1. Figure 6 shows the DOS as a function of the energy at the interface, for all the tested temperatures. For these calculations we introduced four Gaussian curves for each temperature. One of these curves, E_1 in Table 2, corresponds mostly to the ionized surface states in equilibrium, i.e. to Q_{io}. Although the density and distribution of the DOS below the equilibrium Fermi level cannot be known be this method, it is however necessary to use Gaussian curves that extend below the equilibrium Fermi level in order that the DOS very close to it (above and below) can be computed to correctly calculate the DOS for higher energies. This is the reason why this Gaussian curve is shown in Table 2. The Table also shows the parameters of the Gaussian curves, E_i, σ_i, and N_i, representing the energy level, the standard deviation, and the total surface states, respectively, for each tested temperature. It must

Table 1. Used and calculated electrical parameters for the determination of the DOS: the energy of the band gap, E_g, bulk Fermi level, ϵ_ξ, and the concentration of donor species, N_D, were used to calculate the equilibrium values for the interface Fermi level, E_{Fo}, barrier height, Φ_{Bo}, and trapped charge at the interface, Q_{io}. Other important parameters are: electrical permitivity, 8·5, effective mass, $0{\cdot}25m_o$, grain size, 9·8 μm, grain resistivity, 1 Ω cm, and Richardson constant, 30 A cm^{-2}K^{-2}

Temperature (°C)	$E_g(eV)$	$\epsilon_\xi(eV)$	$N_D(m^{-3})$	$E_{Fo}(eV)$	$\Phi_{Bo}(eV)$	$Q_{io}(m^{-2})$
19	3·206	0·103	$1{\cdot}432 \times 10^{24}$	2·349	0·754	$3{\cdot}176 \times 10^{16}$
62	3·165	0·124	$1{\cdot}441 \times 10^{24}$	2·243	0·798	$3{\cdot}278 \times 10^{16}$
81	3·147	0·134	$1{\cdot}542 \times 10^{24}$	2·199	0·814	$3{\cdot}426 \times 10^{16}$
100	3·129	0·144	$1{\cdot}804 \times 10^{24}$	2·158	0·827	$3{\cdot}736 \times 10^{16}$
120	3·110	0·154	$2{\cdot}223 \times 10^{24}$	2·114	0·842	$4{\cdot}184 \times 10^{16}$
140	3·091	0·165	$2{\cdot}084 \times 10^{24}$	2·068	0·859	$4{\cdot}090 \times 10^{16}$
160	3·072	0·175	$2{\cdot}395 \times 10^{24}$	2·025	0·872	$4{\cdot}419 \times 10^{16}$

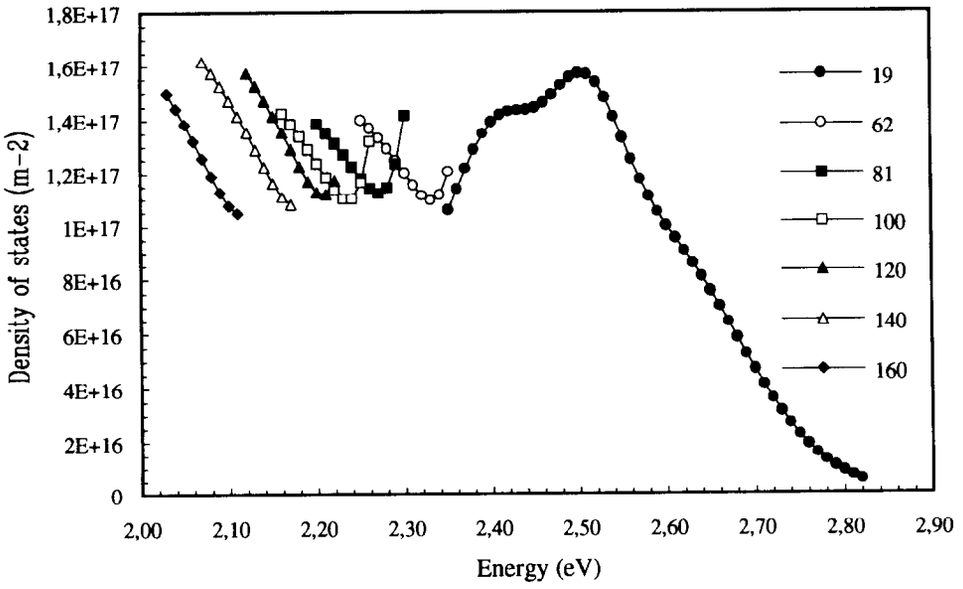


Fig. 6. Energy distribution of surface states (DOS) at various temperatures.

be emphasized that these are guideline parameters and not absolute ones, as pointed out above. The DOS curves in Fig. 6 start at the interface equilibrium energy, E_{Fo}, and end at the energies corresponding to the last experimental point of the I–V curves. Because of this, the room temperature DOS curve is the one with more complete information about the energy distribution. This curve is composed of three main relative peaks, E_2, E_3 and E_4, in Table 2. Their origin is not discussed here, and will be the subject of a forthcoming paper. Although not evident in Fig. 6, with rising temperature, the peaks shift their energy position to lower energies at different rates, and tend to merge together (see Table 2). However, their magnitudes remain unchanged. This observation, together with the linear decrease of E_{Fo}, explains why the values of N_D (Table 1) increase slightly with temperature: as the temperature is rising, some more surface states are being ionized, since they are now below the equilibrium Fermi level, and, to maintain the electrical neutrality condition, eqn (2), N_D must increase. If this behaviour can be extrapolated for higher and lower temperatures, one would expect the following situations:

(i) for higher temperatures, one should see the decrease of the non-ohmic behaviour, since the unionized surface states tend to decrease, and, for some very high temperatures, the system should be ohmic. This behaviour has been experimentally described in the literature;[30,37]

(ii) for lower temperatures, more surface states will be above the equilibrium Fermi level, that is, the sample will show more pronounced varistor characteristics. Concomitantly, there is a higher probability of minor carrier generation by the impact ionization mechanism (or tunneling of electrons from one grain to the other, at the junction). This corresponds to a 'cut-off' of the higher energy surface states, giving the origin of a 'knee' in the I–V curve, or a sharp transition to the breakdown regime. This, in fact, corresponds to much higher α values, that is, the varistor will show α values higher than one could predict *a priori*.[38]

Table 2. Parameters used for the Gaussian curves that describe the DOS for each temperature: E_i, σ_i, and N_i, are the energy level, the standard deviation, and the total surface states, respectively. E_i shift their energy and tend to merge together, while σ_i and N_i remain constant throughout the temperature range. The E_i energies are related to the top of the valence band edge ($E_{VB} = 0$)

Temperature (°C)	*E_1(eV)*	*E_2(eV)*	*E_3(eV)*	*E_4(eV)*
19	2·12	2·41	2·51	2·58
62	2·07	2·28	2·40	2·46
81	2·05	2·21	2·34	2·40
100	2·01	2·14	2·25	2·34
120	1·97	2·05	2·17	2·25
140	1·94	2·00	2·13	2·20
160	1·89	1·92	2·08	2·15
σ_i(eV)	0·15	0·07	0·03	0·10
N_i(m^{-2})	$2{\cdot}9 \times 10^{16}$	$1{\cdot}9 \times 10^{16}$	$4{\cdot}0 \times 10^{15}$	$2{\cdot}3 \times 10^{16}$

It is important to have these observations in mind when attempting to characterize the DOS. In one hand, it is necessary to go to lower temperatures to split the relative peaks of the DOS; on the other hand, at low temperatures some of the DOS will not be 'detected' by the method, namely those at the highest energies. So, the characterization of the DOS is not a straightforward task.

Another important result is the observation that the concentration of donor species in the bulk of

the ZnO grains, is controlling the equilibrium Fermi level at the interface, at least in the temperature range of this work. It is expected that the higher the bulk donor concentration, the lower the temperature coefficient of E_{Fo}, and, since dE_g/dT is constant, this situation leads to a decrease of $E_A = \epsilon_\xi + \Phi_{Bo}$ (E_A is normally determined by the variation of the low voltage ohmic resistivity with temperature, i.e. $\rho = \rho_0 \exp(E_A/kT)$). This means that, unless two different systems are equivalent in their bulk donor concentration, there is no reason to compare the experimentally determined E_A energies in different varistor systems. This is the reason why there is a large range of the determined values for E_A in the literature, $0{\cdot}35 \leq E_A \leq 0{\cdot}94$ eV,[30,39] all of them corresponding to acceptable varistor characteristics.

If the change of E_{Fo} with temperature is only due to the simultaneous variation of E_g and ϵ_ξ, one can extrapolate this result to higher temperatures, and predict what would happen after E_{Fo} reaches the middle of the energy gap, $E_g/2$. For our sample, this situation would happen at ~450°C. Two hypotheses can be considered, either the energy of E_{Fo} continues to decrease after this temperature has been reached, and will be now under the $E_g/2$ value, or E_{Fo} stays at the energy of $E_g/2$.

The first hypothesis would then correspond to a situation where the interface is best described as a p-type semiconductor, while the bulk of the material is still a n-type semiconductor. The junction would then be of the n–p–n type, and, consequently, it would show varistor properties, even at very high temperatures. This is contrary to what has been experimentally observed and reported in the literature.[30,37] The prevision was, of course, a forced one, because even in a p-type semiconductor, at very high temperatures, the Fermi level will tend towards the middle of the band gap, especially if the acceptor concentration is low. However, it must be pointed out that to achieve a p-type conductivity in ZnO, it is necessary to sinter the material at very high oxygen partial pressures,[40,41] or to dope the material with acceptor species. The first condition is not observed in practice, even if one assumes that the Bi-rich liquid phases are good oxygen carriers,[42] since the maximum attainable oxygen partial pressure is *a priori* established by the ambient atmosphere. The second condition can only be observed if the acceptor species are intrinsic in origin, since all the normally used dopants are of the donor type (three- or four-valent cations). The possible intrinsic acceptor species are the interstitial oxygen or the zinc vacancy, the later being invoked, since at the sintering temperatures the Schottky pairs are the predominant defects.[43,44] A surplus of zinc vacancies, or, equivalently, a depression of oxygen vacancies, can arise by the doping process via

$$M_2O_3 \xrightarrow{ZnO} 2M^{\bullet}_{Zn} + 3O_O + V''_{Zn} \qquad (10(a))$$

or

$$M_2O_3 + V_O^{\bullet\bullet} \xrightarrow{ZnO} 2M^{\bullet}_{Zn} + 3O_O \qquad (10(b))$$

(where V_{Zn}'' and $V_O^{\bullet\bullet}$ are the zinc and oxygen vacancy, respectively, both completely ionized, $M_{Zn}^{\bullet}$ is the substitution of a zinc site by the dopant cation, and O_O is an oxygen in its normal site in the ZnO matrix) that is, if the dopants are segregated to the grain boundaries (e.g. M = Bi), it is possible that the interface acts like a p-type semiconductor.

A second hypothesis to consider after E_{Fo} has reached the middle of the band gap, is that it stays at this position when the temperature increases. The interface would then be best described as a n–i–n type junction, where i denotes intrinsic electrical behaviour, or, since the density of majority carriers (electrons) is lower at the interface, it could also be described as a n–insulator–n junction. This model predicts that, at sufficiently high temperatures, the energy difference between the Fermi level and the bottom of the conduction band in both the interface and the bulk of the material, i.e. the barrier height, tends to disappear, and the material will show ohmic behaviour. This is what has been experimentally observed.[30,37] To have intrinsic behaviour at the interface, it is necessary that the material has neither donor nor acceptor levels, or that the net balance of them is null. It is quite unreasonable that there are no defect levels at the interface, since dopants are segregated there from the very beginning of the cooling of the samples.[19] At the sintering temperatures, the Schottky pairs dominate the defect chemistry of the system,[43,44] and, if eqns (10(a, b)) is valid for the formation of associated defects, $(M^{\bullet}_{Zn} - V''_{Zn} - M^{\bullet}_{Zn})^x$, rather than for unassociated species, the condition of net null charge at the interface only requires the annihilation of both oxygen and zinc vacancies following their chemical reaction (Schottky pair equation), during cooling. The elimination of both defects at the interface during cooling, has been the basis for the surface oxidation process.[3,4] Although the formation of the above mentioned associated defects is speculative, it must be emphasized that they could limit the density of unpaired species to a certain extent, which would explain the discrepancy between the density of charged interface defects (10^{12}–10^{13} cm^{-2}) and the concentration of foreign atoms at the interface (~10^{15} cm^{-2}, for Bi atoms), as pointed out by Greuter and Blatter.[20,21]

The second hypothesis discussed above, would

mean that there could be a significant contribution of the surface oxidation process for the barrier height formation. Mahan[42] concluded that the contribution of this process is negligible, ~0·10 eV, which is 10–20% of the total barrier height. Taking his own results (pure ZnO), we have calculated the temperature in which the bulk defects should be frozen, to give $n = 4{\cdot}5 \times 10^{16}$ cm^{-3} at room temperature, and found $T \approx 1050$°C. This seems to be a rather low temperature, since samples quenched from higher temperatures already show varistor characteristics.[19] Taking into consideration that these calculations are reported for pure ZnO, we also calculated the concentration of carriers, n, at the interface, for a frozen temperature of 450°C (temperature at which E_{Fo} in cooling separates from the middle of the band gap), and found $\Delta E_F = kT\ln(n(450°C)/n(1050°C)) \approx 0{\cdot}25$ eV. This contribution can no longer be neglected. Although the contribution of the surface oxidation process, the n–i–n model, to the barrier height formation could then have a significant value, it must be considered that the same type of defect equations (eqns 10 (a, b)) can also be used to explain the contribution to the barrier height formation from a n–p–n model. Subtle differences will be hard to clarify experimentally.

4 Conclusions

Varistor samples sintered at 1300°C in air, developed a microstructure in which the distribution of dopants seemed to indicate that their chemical segregation at the ZnO grain interfaces could be the origin of the electrical potential barrier present in these devices. This type of barrier height formation mechanism should be operative at temperatures below ~950°C, the temperature at which the remaining Bi-rich liquid phase reacts with the spinel phase to give the pyrochlore and ZnO. However, before this temperature most of the ZnO–ZnO grain boundaries are already formed, and the material shows varistor characteristics. Consequently, the contribution of the surface oxidation mechanism to the barrier height formation should only be important at high temperatures, where the diffusion coefficients still allow the migration of the species to the surface of the grains. For temperatures below 950°C, another type of barrier height formation mechanism should then be present.

Taking the double Schottky barrier (DSB) model, we have calculated the distribution of surface states (DOS) above the equilibrium Fermi level for various temperatures, ranging from room temperature up to 160°C. In this temperature range, the equilibrium Fermi level at the interface, E_{Fo}, linearly decreases with temperature, independent of the DOS changes. This variation in relation to the band gap of the semiconductor was assigned to the change of the bulk Fermi level, and so it was possible to derive the density of carriers in the semiconductor conduction band, n. The calculated value, $n \sim 4{\cdot}5 \times 10^{16}$ cm^{-3}, is in good agreement with values, $\sim 1 \times 10^{17}$ cm^{-3}, experimentally determined using other techniques. This procedure can thus be used in any other system, and it also permits the determination of the bulk Fermi level at any temperature. Since the bulk Fermi energy depends on the defect concentration inside the ZnO grains, it is related to the processing of the ceramic, namely to the type and concentration of additives and to the sintering schedule. Consequently, it is expected that each varistor system and processing procedure will give different energy values determined by electrical measurements, which explains the large range of the barrier energy values reported in the literature.

It was also shown that during heating of the samples, the DOS peaks tend to lower energy values, at different rates. This behaviour explains why the interface defect energies also have a large range of reported values. An extrapolation of this behaviour at low temperatures, lead us to the conclusion that the material should show non-linear exponent α at these temperatures, higher than one could predict *a priori*; and also, extrapolating to high temperatures, that the material should show ohmic behaviour.

The temperature dependence of both the band gap of the semiconductor and the energy of the Fermi level, was used to predict the electrical behaviour of the material at high temperatures. The contribution of the surface oxidation mechanism to the formation of the potential barriers, was estimated from the above considerations, and it can be as high as 0·25 eV. According to the results obtained up to now, it seems that the surface states control mainly the shape of the I–V curves. Other contributions to the energy barriers can probably be elucidated by expanding the experimental range of temperatures used to determine the varistor parameters. This is going to be addressed in further publications.

References

1. Pike, G. E. & Seager, C. H., Electronic properties of silicon grain boundaries. In *Grain Boundary Phenomena in Electronic Ceramics*, Advanced Ceramics, Vol. 1, ed. L. M. Levinson. American Ceramics Society, Columbus, Ohio, 1981, pp. 53–66.

2. Pike, G. E. & Seager, C. H., The dc voltage dependence of semiconductor grain boundary resistance. *J. Appl. Phys.*, **50**(5) (1979) 3414–22.
3. Einzinger, R., Grain boundary properties in ZnO varistors. In *Grain Boundary Phenomena in Electronic Ceramics*, Advanced Ceramics, Vol. 1, ed. L. M. Levinson. American Ceramics Society, Columbus, Ohio, 1981, pp. 359–74.
4. Einzinger, R., Grain boundary phenomena in ZnO varistors. In *Grain Boundaries in Semiconductors, Mat. Res. Soc. Symp. Proc.*, Vol. 5, ed. H. J. Leamy, G. E. Pike & C. H. Seager. Elsevier Science Publishers, New York, 1982, pp. 343–55.
5. Bernasconi, J., Klein, H. P., Knecht, B. & Strassler, S., Investigation of various models for metal oxide varistors. *J. Elect. Mater.*, **5**(5) (1976) 473–95.
6. Pike, G. E., Electronic properties of ZnO varistors: A new model. In *Grain Boundaries in Semiconductors, Mat. Res. Soc. Symp. Proc.*, Vol. 5, ed. H. J. Leamy, G. E. Pike & C. H. Seager. Elsevier Science Publishers, New York, 1982, pp. 369–79.
7. Pike, G. E., Kurtz, S. R., Gourley, P. L., Philipp, H. R. & Levinson, L. M., Electroluminescence in ZnO varistors: Evidence for hole contribution to the breakdown mechanism. *J. Appl. Phys.*, **57**(12) (1985) 5512–8.
8. Blatter, G. & Greuter, F., Electrical breakdown at semiconductor grain boundaries. *Phys. Rev. B*, **34**(12) (1986) 8555–72.
9. Blatter, G. & Baeriswyl, D., High-field transport phenomenology: Hot-electron generation at semiconductor interfaces. *Phys. Rev. B*, **36**(12) (1987) 6446–64.
10. Bernasconi, J., Strassler, S., Knecht, B., Klein, H. P. & Menth, A., Zinc oxide based varistors: a possible mechanism. *Solid State Commun.*, **21** (1977) 867–70.
11. Schwing, U. & Hoffman, B., Model experiments describing the microcontact of ZnO varistors. *J. Appl. Phys.*, **57**(12) (1985) 5372–9.
12. Wong, J., Microstructure and phase transformation in a highly non-ohmic metal oxide varistor ceramic. *J. Appl. Phys.*, **46**(4) (1975) 1653–9.
13. Inada, M., Crystal phases of nonohmic zinc oxide ceramics. *Jpn. J. Appl. Phys.*, **17**(1) (1978) 1–10.
14. Inada, M., Microstructure of nonohmic zinc oxide ceramics, *Jpn. J. Appl. Phys.*, **17**(4) (1978) 673–7.
15. Inada, M., Formation mechanism of nonohmic zinc oxide ceramics. *Jpn. J. Appl. Phys.*, **19**(3) (1980) 409–19.
16. Kim, J., Kimura, T. & Yamaguchi, T., Sintering of zinc oxide doped with antimony oxide and bismuth oxide. *J. Am. Ceram. Soc.*, **72**(8) (1989) 1390–5.
17. Olsson, E., Falk, L. K. L., Dunlop, G. L. & Osterlund, R., The microstructure of a ZnO varistor material. *J. Mater. Sci.*, **20** (1985) 4091–8.
18. Kim, J. C. & Goo, E., Morphology and formation mechanism of the pyrochlore phase in ZnO varistor materials. *J. Mater. Sci.*, **24** (1989) 76–82.
19. Mantas, P. Q., Senos, A. M. R. & Bapista, J. L., Varistor–capacitor characteristics of ZnO ceramics. *J. Mater. Sci.*, **21** (1986) 679–86.
20. Blatter, G. & Greuter, F., Carrier transport through grain boundaries in semiconductors. *Phys. Rev. B*, **33**(6) (1986) 3952–66.
21. Greuter, F. & Blatter, G., Electrical properties of grain boundaries in polycrystalline compound semiconductors. *Semicond. Sci. Technol.*, **5** (1990) 111–37.
22. Pike, G. E., Diffusion-limited quasi Fermi level near a semiconductor grain boundary. *Phys. Rev. B*, **30**(6) (1984) 3274–6.
23. Eda, K., Conduction mechanism of non-Ohmic zinc oxide ceramics. *J. Appl. Phys.*, **49**(5) (1978) 2964–72.
24. Tao, M., Ai, B., Dorlanne, O. & Loubiere, A., Different 'single grain junctions' within a ZnO varistor. *J. Appl. Phys.*, **61**(4) (1987) 1562–7.
25. van Kemenade, J. T. C. & Eijnthoven, R. K., Direct determination of barrier voltage in ZnO varistors. *J. Appl. Phys.*, **50**(2) (1979) 938–41.
26. Einzinger, R., Metal oxide varistor action — a homojunction breakdown mechanism. *Appl. Surf. Sci.*, **1** (1978) 329–40.
27. Einzinger, R., Grain junction properties of ZnO varistors. *Appl. Surf. Sci.*, **3** (1979) 390–408.
28. Olsson, E. & Dunlop, G. L., Characterization of individual interfacial barriers in a ZnO varistor material. *J. Appl. Phys.*, **66**(8) (1989) 3666–75.
29. Mukae, K., Tsuda, K. & Nagasawa, I., Capacitance-vs-voltage characteristics of ZnO varistors. *J. Appl. Phys.*, **50**(6) (1979) 4475–6.
30. Matsuoka, M., Nonohmic properties of zinc oxide ceramics. *Jpn. J. Appl. Phys.*, **10**(6) (1971) 736–946.
31. Rossinelli, M., Greuter, F. & Schmückle, F., Electrically active grain boundaries in ceramics: varistors and capacitors. In *Electroceramics, British Ceram. Proc.*, Vol. 41, ed. A. J. Moulson, J. Binner, R. Morell. The Institute of Ceramics, Stoke-on-Trent, U. K., 1989, pp. 177–88.
32. Heilland, G., Mollwo, E. & Stöckmann, F., Electronic processes in zinc oxide. *Solid State Phys.*, **8** (1959) 191–323.
33. Blakemore, J. S., Semiconductor statistics. In *International Series of Monographs on Semiconductors*, Vol. 3, ed. H. K. Henisch. Pergamon Press, Oxford, 1962.
34. Philipp, H. R. & Levinson, L. M., Optical method for determining the grain resistivity in ZnO-based ceramic varistors. *J. Appl. Phys.*, **47**(3) (1976) 1112–26.
35. Levinson, L. M. & Philipp, H. R., High-frequency and high-current studies of metal oxide varistors. *J. Appl. Phys.*, **47**(7) (1976) 3116–21.
36. Hayashi, M., Haba, M., Hirano, S., Okamoto, M. & Watanabe, M., Degradation mechanism of zinc oxide varistors under dc bias. *J. Appl. Phys.*, **53**(8) (1982) 5754–62.
37. Philipp, H. R. & Levinson, L. M., High-temperature behavior of ZnO-based ceramic varistors. *J. Appl. Phys.*, **50**(1) (1979) 383–9.
38. Philipp, H. R. & Levinson, L. M., Low-temperature electrical studies on metal-oxide varistors — A clue to conduction mechanisms. *J. Appl. Phys.*, **48**(4) (1977) 1621–7.
39. Eda, K., Electrical properties of ZnO–Bi_2O_3 metal oxide heterojunction — a clue of a role of intergranular layers in ZnO varistors. In *Grain Boundaries in Semiconductors, Mat. Res. Soc. Symp. Proc.*, Vol 5, ed. H. J. Leamy, G. E. Pike, C. H. Seager. Elsevier Science Publishers, New York, 1982, pp. 381–92.
40. Hagemark, K. I. & Toren, P. E., Determination of excess Zn in ZnO. The phase boundary Zn–$Zn_{1+x}O$. *J. Electrochem. Soc.*, **122** (1975) 992–4.
41. Ziegler, E., Heinrich, A., Oppermann, H. & Stöver, G., Electrical properties and non-stoichiometry in ZnO single crystals. *Phys. Stat. Sol. (a)*, **66** (1981) 635–48.
42. Mahan, G. D., Intrinsic defects in ZnO varistors. *J. Appl. Phys.*, **54**(7) (1983) 3825–32.
43. Göpel, W. & Lampe, U., Influence of defects on the electronic structure of zinc oxide surfaces. *Phys. Rev. B*, **22**(12) (1980) 6447–62.
44. Kröger, F. A., *The Chemistry of Imperfect Crystals*, Vol. 2, 2nd Edn. North-Holland, New York, 1974, p. 743.

Journal of the European Ceramic Society 15 (1995) 617–622
© 1995 Elsevier Science Limited
Printed in Great Britain. All rights reserved
0955-2219(95)00023-2
0955-2219/95/$9.50

Problems Associated with Imaging Resistive Barriers in $BaTiO_3$ PTC Ceramics Using the SEM Conductive Mode

J. D. Russell[a]* & C. Leach[b]

[a]Department of Materials, Imperial College of Science, Technology and Medicine, London, SW7 2BP, UK
[b]Manchester Materials Science Centre, University of Manchester and UMIST, Manchester, M1 7HS, UK

(Received 11 October 1994; revised version received 27 January 1995; accepted 31 January 1995)

Abstract

The micro-electrical properties of $BaTiO_3$ have been studied using the remote electron beam induced current technique. Difficulties associated with applying this technique to low resistance, inhomogeneous ceramics are discussed and illustrated with the example of PTCR materials. At temperatures above the Curie temperature, contrast steps corresponding to resistive interfaces are observed with differing sensitivities according to the imaging conditions used. The image noise decreases and the current sensitivity increases with the sample resistance. Remote electron beam induced current contrast in $BaTiO_3$, showing the high resistivity transition does not occur uniformly as a function of temperature across all grain boundaries.

Introduction

Semiconducting barium titanate and related phases are important electroceramic materials which have been used for their positive temperature coefficient (PTC) of resistance properties in applications such as over-temperature protection and current limiting devices for over thirty years,[1] and are still very important technologically.[2] The most widely accepted model of the PTC effect, due to Heywang,[3] is of back to back Schottky barriers at grain boundaries due to a build up of negative interface charge. This gives rise to a potential barrier whose height depends on the dielectric constant. Since the dielectric constant changes abruptly at the phase transformation, the barrier height and resistivity change accordingly. This model was extended by Jonker who also considered ferroelectric effects below T_c, where spontaneous polarisation reduces the expected potential barrier height.[4]

However, while the gross behaviour is well explained by these models, sensitive structure averaging techniques such as impedance measurements reveal that they do have some shortcomings.[5–7] The introduction of modified models, such as that of Daniels and Wernicke[8] have caused a parallel search for explanations of the PTC effect at the grain level due to the strong effect of heterogeneity on the electrical properties.[9] TEM investigations clearly show the ferroelectric domains below T_c and also that there is no intergranular phase present of width greater than 2–10 nm.[10] Cathodoluminescence microscopy has been used to observe grain boundary potential barriers in PTC material.[11] EBIC has also been used to view the domains and grain boundaries.[12] However, none of these studies offered direct observation of the resistive properties of such materials.

In this paper we discuss the practicalities of the application of a little used variant of the EBIC technique which allows direct observation of the resistivity changes of individual grain boundaries as the resistive transition progresses, allowing detailed determination of device homogeneity.

EBIC Phenomenology in Ceramics

The well-known charge collection imaging mode of the scanning electron microscope (SEM) is often applied to the microcharacterisation of semiconductors. In this mode the impinging electron beam generates a multitude of electron–hole pairs which can then be separated by built-in fields such as those at pn-junctions. By using a suitable contact geometry, charge collection currents several orders of magnitude larger than the beam current

*Now at Manchester Materials Science Centre, University of Manchester and UMIST, Manchester, M1 7HS, UK

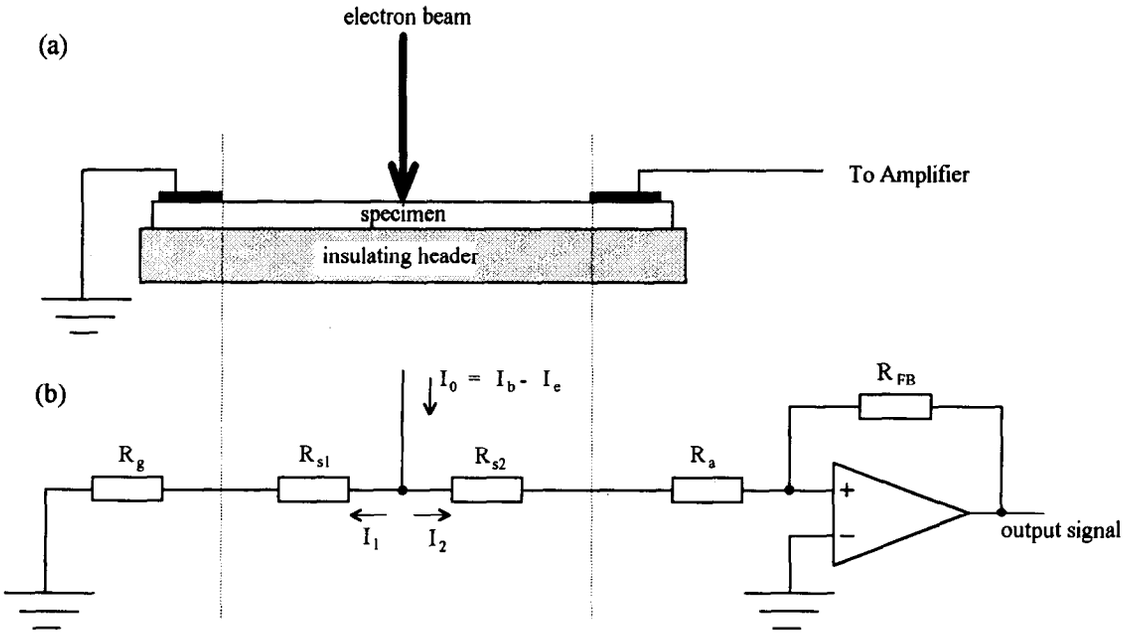


Fig. 1. (a) Specimen configuration and (b) equivalent circuit for REBIC mode imaging. R_g is the resistance from the left of the sample to earth, R_a is from the right of the sample to the amplifier input, I_b is the beam current, I_e the total emitted current, R_{s1} and R_{s2} are the specimen resistances to the left and right contacts from the beam impact point, and $R_{s1} + R_{s2} = R_s$, the specimen resistance. The amplifier is shown schematically, with feedback resistance RFB.

can be obtained in a technique called electron beam induced current (EBIC).[13] In the case of less-well characterised materials such as electroceramics, the absence of suitable built-in fields, and much larger recombination centre densities mean that the usual charge collection mode geometries do not always work as effectively, or at all. However, a technique first used by Matare and Laakso[14] and subsequently termed remote electron beam induced current (REBIC) by Bubulac and Tennant[15] can be employed.

If the specimen has two closely separated contacts as shown in Fig. 1(a), it will have an equivalent circuit as shown in (b), where R_g represents all resistances between the scanned region of the inter-electrode observation area and earth via the earth electrode, and R_a all resistances between the scanned area and earth via the amplifier. R_{s1} and R_{s2} are the components of the scanned area resistance (total R_s) immediately to the left and to the right of the impinging beam. The specimen acts as a current divider with the net current injected by the electron beam flowing either directly to earth through the left contact or to the right through the low input impedance current amplifier. The proportion of I_b reaching the amplifier is used to modulate the signal on the viewing screen and results in a contrast gradient. In some ceramics, electrically active regions cause charge collection contrast due to separated electron–hole pairs. Such contrast would be superimposed on the resistive baseline,[16] and has been observed in ZnO varistor material, for example,[17] where the presence of grain boundary barriers can be satisfactorily explained by grain boundary EBIC models.[18] However, frequently such contrast is not seen and only effects due to the passive resistance component of the interfaces are observed. In this case the imaging method can be referred to as resistive contrast imaging (RCI).[19]

The RCI quality is affected by four factors, as described below.

Current sensitivity

If we consider the case when the scanned area is the total width of sample between the contacts, it can simply be shown, using the terminology of Fig. 1 that the currents which flow through the amplifier when the beam impinges on the sample adjacent first to the left and then the right contact are given by

$$I_{left} = I_o \frac{R_g}{R_g + R_s + R_a} \quad (1)$$

$$I_{right} = I_o \frac{R_g + R_s}{R_g + R_s + R_a} \quad (2)$$

In the case of $BaTiO_3$ the sample resistance, R_s varies widely with temperature, which causes the imaging characteristics to vary. We can define a quantity called the current sensitivity, S,

$$S = \frac{I_{right} + I_{left}}{I_b} \quad (3)$$

where I_b is the beam current. The current sensitivity describes the possible current variation, and hence

contrast, across the sample as a fraction of the beam current, and must be larger than the noise floor for meaningful images to be observed. Although the noise generated by a typical amplifier may only be of the order of picoamperes, as will be seen later, the observed noise can be affected greatly by the sample resistance. It is thus often necessary to work with beam currents of several nA and larger which in turn limits the spatial resolution. The effect of noise is much more important than in charge collection imaging of semiconductors, in which charge multiplication causes a gain of about 1000 over the beam current level. In contrast, RCI of electrical ceramics leads to signals of the order of the beam current. In the case of $BaTiO_3$ PTCR material, a typical sample mounted in the SEM may vary in resistance from 30Ω below the Curie temperature to 30 kΩ above it. From eqns (1–3), using $R_g \approx 10\Omega$, $R_a = 40\Omega$ and $I_o/I_b \approx 0{\cdot}8$ this gives S values of 0·3 and 0·8. Thus the current sensitivity is changed by a factor of 2·7, as is the image contrast, on crossing the phase transition.

Geometrical effects

For a given specimen the largest current sensitivity, and hence the largest current contrast, will be seen if the electrodes are at the image edges. If the field of view spans only part of the electrode separation, the current resolution will be reduced proportionately, i.e. neglecting contact resistances

$$S' = S\frac{w}{D} \tag{4}$$

where w is the image field-width and D the inter-electrode spacing. Thus it is important in detailed work to locate the electrodes as close together as possible. Unfortunately this configuration limits flexibility in aereal imaging and reduces the overall resistance of the sample which gives rise to further difficulties as described in the next section.

Amplifier limitations

For specimen resistances which are small compared with the input impedance of the detecting amplifier, both amplifier noise and the input offset voltage which appear at the inputs of the operational amplifier are magnified in effect. The equation describing the noise amplification is of the form

$$V_{\text{output noise}} = V_{\text{input noise}}\left(1 + \frac{R_{FB}}{R_g + R_s + R_a}\right) \tag{5}$$

where R_s is the sample resistance and R_{FB} is the amplifier feedback resistance (Fig. 1(b)). The value of R_{FB} fixes the amplifier gain, and a typical value for R_{FB} under our experimental conditions would be 100 MΩ. Thus, for the case of the PTCR described previously, the output noise increases by a factor of 1000 in the low temperature, low resistance state compared with its high temperature variant. A similar relationship exists for the amplifier input offset voltage which changes as the sample resistance changes. Although the latter can, in principle, be corrected by applying an appropriate back-off current, in practice for PTCR materials undergoing the phase transformation, the steepness of the change of resistance with temperature means that the signal drifts over a large range with small variations in the sample temperature leading to excessive signal instability.

One way to circumvent this is to add a resistor in series with the sample which will reduce the noise and signal instability. Additionally, this will decrease the total current sensitivity by making the specimen a smaller part of the overall current divider circuit. For example, whilst reducing the noise substantially, adding a 1 kΩ resistor would change the current sensitivity values from 0·3 and 0·8 to 0·022 and 0·77 using the sample resistance values previously cited. It is thus possible to extend downwards the range of sample resistances for which useful images can be obtained. However, because of the close interdependence of the noise and sensitivity, the optimal resistance value required is usually a compromise.

Backscattering contrast effects

On average, around 20% of the beam current is lost from the sample by re-emission as backscattered or secondary electrons. The RCI current will be reduced in regions where a large proportion of the incident beam current is lost. Grains with different backscattering coefficients will, as a consequence, show different contrast in the RCI image for which a correction must be made. This can in principle be achieved by taking a specimen current image (by removing the earth contact so that all the absorbed current must flow to earth through the amplifier) and using it to adjust the measured RCI signal intensity at each point according to

$$I_R = \frac{I'_R}{I_s} \tag{6}$$

where I_R and I_R' are the true and measured RCI currents respectively, and I_s is the local specimen current. Such corrections are small for materials which are predominantly single phase.

Experimental

Polished samples with a 3 mm electrode spacing were prepared from a commercial PTC thermistor device with a Curie temperature of 80°C. These

specimens were mounted on an Oxford Instruments H1001 heating stage, and electrical connections were made using a micromanipulator with fine tungsten probes. A Matelect ISM5 EBIC amplifier was used to amplify the input signal for the SEM.

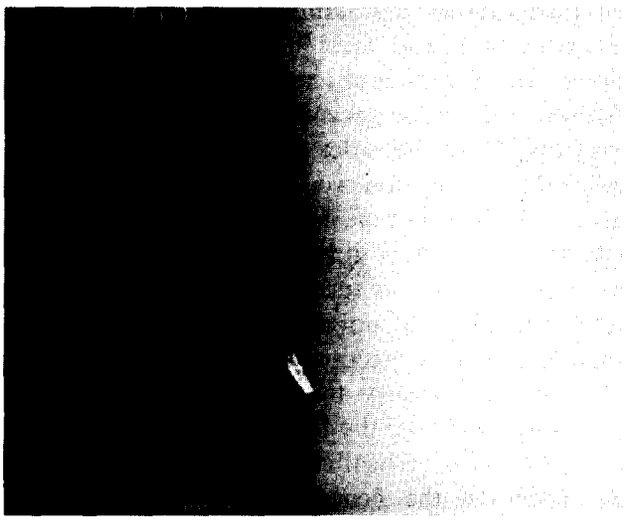
Subsequently the current sensitivity was increased for higher magnification imaging by reducing the contact separation. This was achieved by producing an array of closely spaced ohmic contacts on the sample surface by careful cleaning and evaporation of aluminium onto a polished sample using a fine TEM grid as a mask.

Results and Discussion

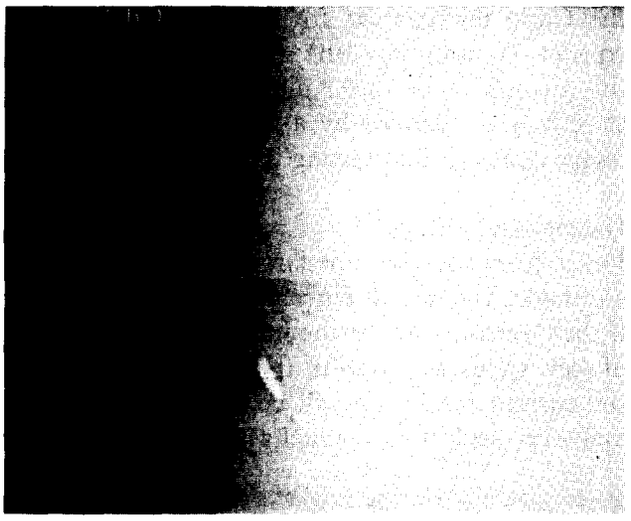
Fig. 2(a) is an RCI image of a region of the polished sample taken with the sample heated to well above the Curie temperature. The inter-electrode spacing is approximately 3 mm left–right in the image. The contrast gradient from left to right is clearly visible, as are the resistive interfaces where abrupt steps in the signal occur. The width of the steps is much larger than the grain size and so at this sensitivity we see clusters of grains of similar grey-level bounded by interfaces with intensity steps. This effect is sometimes referred to as terrace contrast.

As the imaging temperature is decreased, the substantial decrease in sample resistance results in the image becoming more noisy as predicted, along with a parallel decrease in the current sensitivity. However, once this decrease in current sensitivity (Fig. 2(b)), is corrected for, the terraced microstructure can be seen to persist to quite low temperatures until it is lost ultimately in the noise floor. It is thus not clear whether the terraced structure disappears altogether at lower temperatures, or it is simply beyond the capabilities of the imaging technique to observe it. Thus the terrace structure imaged in this way is not necessarily related to the PTCR effect, but may be linked to some intrinsic microstructural feature, such as relics of powder agglomeration prior to sintering.[20] It can be seen from Fig. 2(c) that on increasing the magnification, using this specimen configuration little extra information is seen; contrast is poor with effects only visible at some interfaces. This is due to the lack of current sensitivity when observing a small region between widely spaced contacts (see eqn (4)).

Figure 3 shows the results of a further examination of the same material at higher magnification and higher current sensitivity. This was achieved by using more closely spaced contacts as previously described. A sequence of reproducible



(a)



(b)



(c)

Fig. 2. (a) RCI image between widely separated contacts on $BaTiO_3$ at 140°C showing terrace contrast. (b) is the same area at 110°C where the contrast of the lower half of the image has been scaled to allow for the decreased current sensitivity. The image also shows the increased noise associated with the lower sample resistance. (c) is a higher magnification image of a region from (a). Scale bar (a) and (b) = 100 μm, (c) = 10 μm.

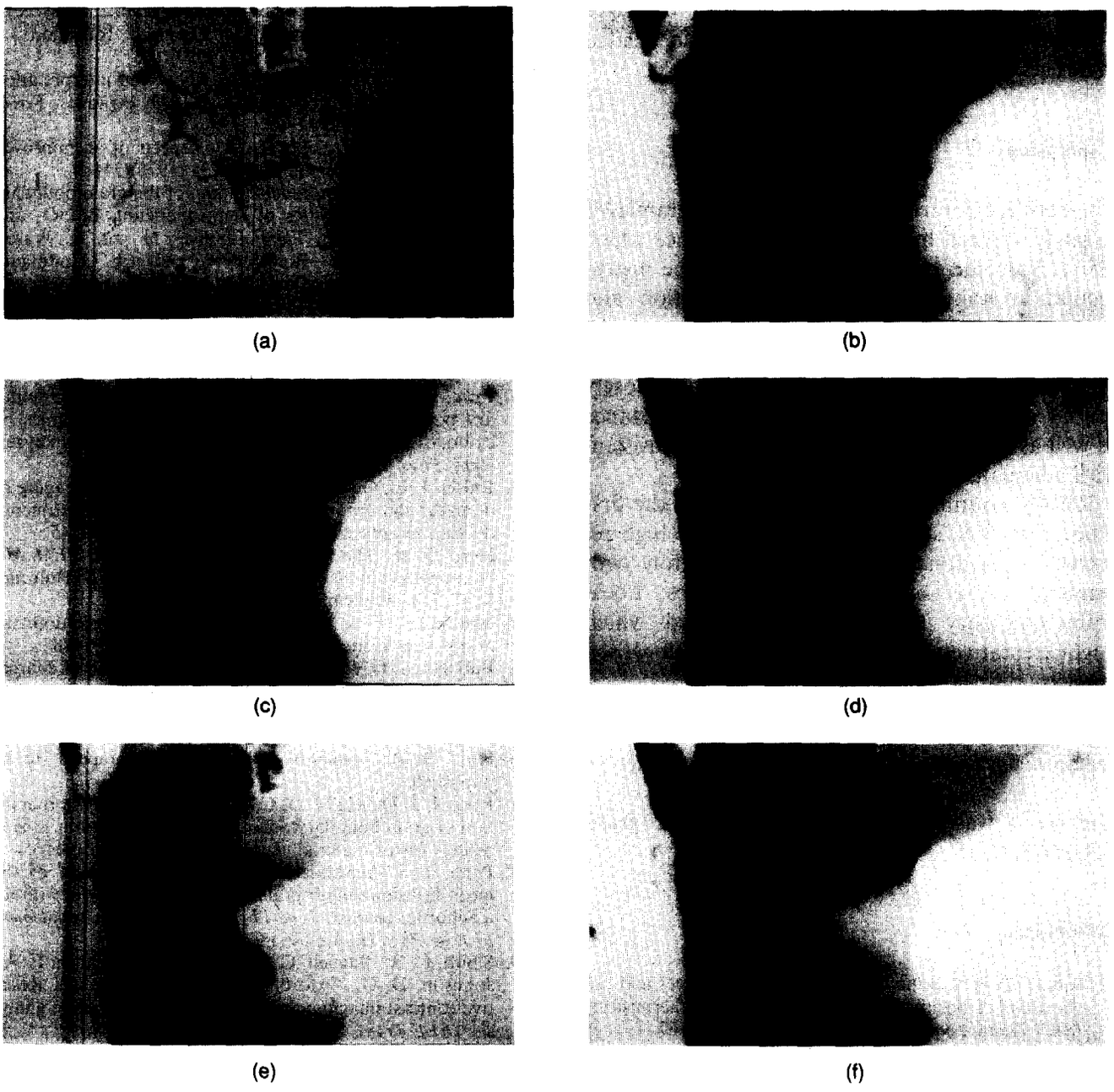


Fig. 3. (a) Secondary electron image showing the grain structure, with the contacts labelled 'L' and 'R'. The left contact is partially covered by a probe. (b–f) are a series of resistive contrast images at 110, 120, 130 and 140°C respectively. In (f) 'A' is an example of a resistive barrier, while 'B' denotes extended regions surrounding grain boundaries also visible in the other images. Scale bar = 10 μm.

images taken in the temperature range 110°C–140°C, where the PTCR effect is active is shown. Figure 3(a) is the corresponding secondary electron image, showing the grain structure and the positions of the two contacts 'L' and 'R', of which the former is covered by one of the micromanipulator probes. Several features are evident.

The REBIC images in Fig. 3(b–f) show that as the temperature increases the image becomes less noisy, and the contrast gets stronger, in accordance with the earlier discussion. This is most clearly evident by comparing (b) and (f).

Each grain boundary that increases its resistance leads to a new contrast step (such as that labelled 'A' Fig. 3(f)) between the contact pads and a slight readjustment of the overall intensity gradient, which is always from approximately left to right. In the later images of the Fig. 3(b–f), more high resistance grain boundaries are introduced compared with the earlier micrographs. It is clearly seen that different barriers become highly resistive at different temperatures, as evidenced by the change in the steps of the contrast profile across the centre of the images with increasing temperature.

Extended regions bounded by resistive barriers spanning grain boundaries occur on the two vertical grain boundaries at the bottom of each image (labelled 'B' in Fig. 3(f)). Backscattered channelling pattern analysis showed that these regions are not crystallographically distinct. Their origin is

unclear, but they might be related to broad impurity diffusion zones as observed in related materials.[21,22]

Conclusions

The resistive contrast shown by electroceramics is strongly affected by the specimen resistance which affects both the current sensitivity and the instrumentation noise. The electrode separation and backscattered electron current loss also need to be taken into consideration. Imaging conditions can be optimised by using specially fabricated, closely spaced electrodes and additional series resistance as well as using the largest beam current consistent with adequate spatial resolution.

REBIC contrast has been observed for the first time in $BaTiO_3$, showing directly that the high resistivity transition does not occur uniformly with temperature across all grain boundaries. Local grain boundary features were observed which might (tentatively) be attributable to a delocalised impurity diffusion phenomenon.

Acknowledgements

This work was carried out under EPSRC grant GR/946783.

References

1. Saburi, O. & Wakino, K., Processing techniques and applications of positive temperature coefficient thermistors. *IEEE Trans. Compon. Parts*, **CP-10** (1963) 53–67.
2. Kulwicki, B. M., Trends in PTC resistor technology. *SAMPE Journal*, **23**(6) (1987) 34–8.
3. Heywang, W., Resistivity anomaly in doped barium titanate. *J. Am. Ceram. Soc.*, **47** (1964) 484–90.
4. Jonker, G. H., Some aspects of semiconducting barium titanate. *Sol. State Electron.*, **7** (1964) 895–903.
5. Sinclair, D. C. & West, A. R., Bulk PTC effect on doped $BaTiO_3$. *J. Mater. Lett.*, **7** (1988) 823–4.
6. Sundaram, S. K., Complex-plane impedance analysis of PTC thermistor–intergranular capacitor transition. *J. Appl. Phys. D: Appl. Phys.*, **23** (1990) 103–7.
7. Michenaud, J.-P. & Gillot, C., About the interpretation of the PTC effect in Nb-doped $BaTiO_3$ ceramics. *Ferroelectrics*, **127** (1992) 41–6.
8. Daniels, J. & Wernicke, R. New aspects of an improved PTC model. *Philips Res. Repts.*, **31** (1976) 544–9.
9. Abelard, P., Present understanding of the grain boundary electrical characteristics of semiconducting $BaTiO_3$ and $SrTiO_3$ ceramics, in *Electroceramics IV*. ed. R. Waser, S. Hoffmann, D. Bonnenberg and Ch. Hoffmann. Augustinus Buchhandlung, Aachen, Germany, 1994, pp. 541–8.
10. Haanstra, H. B. & Ihrig, H., Transmission electron microscopy at grain boundaries of PTC-type $BaTiO_3$ ceramics. *J. Am. Ceram. Soc.*, **63** (1980) 288–91.
11. Ihrig, H. & Klerk, M., Visualization of the grain boundary potential barriers of PTC-type $BaTiO_3$ ceramics by cathodoluminescence in an electron-probe microanalyzer. *Appl. Phys. Lett.*, **35** (1979) 307–9.
12. Ralph, J. E., Gowers, J. P. & Burgess, M. R., Imaging of domains and grain boundaries in a ferroelectric semiconducting ceramic. *Appl. Phys. Lett.*, **41** (1982) 343–5.
13. Holt, D. B., The Conductive Mode. Ch 6 in *SEM Microcharacterisation of Semiconductors*. ed. D. B. Holt and D. C. Joy. Academic Press, London, 1989.
14. Matare, H. F. & Laakso, C. W., Space-charge domains at dislocation sites. *J. Appl. Phys.*, **40** (1969) 476–82.
15. Bubulac, L. O. & Tennant, W. E., Observation of charge-separating defects in HgCdTe using remote contact electron-beam induced current. *Appl. Phys. Lett.*, **52** (1988) 1255–7.
16. Holt, D. B., Insulator EBIC: Basic Phenomena, to be published.
17. Russell, J. D., Halls, D. C. & Leach, C., Direct observation of grain boundary Schottky barrier behaviour in zinc oxide varistor material. *J. Mater Sci. Lett.*, (in press).
18. Palm, J. & Alexander, H., Direct measurement of the local diffusion length grain boundaries by EBIC without a Schottky contact. *J. de Phys IV, Colloq. C6, supplement to J. de Phys III*, **1** (1991) C6-101–6:
19. Smith, C. A., Bagnell, C. R., Cole, E. I., Dibianca, F. A., Johnson, D. G., Oxford, W. V. & Propst, R. H., Resistive contrast imaging: a new SEM mode for failure analysis. *IEEE Trans. El. Dev.*, **ED-33** (1986) 282–4.
20. Halls, D. C. & Leach, C., Processing induced resistive barriers in ZnO material. Submitted to *J. Mater. Sci.*,
21. Hennings, D. & Rosenstein, G., Temperature-stable dielectrics based on chemically inhomogeneous $BaTiO_3$. *J. Am. Ceram. Soc.*, **67** (1984) 249–54.
22. Al-Saffer, R., Azough, F. & Freer, R., A STEM study of core-shell structures in an x7r-type ceramic. *IOP Conf. Ser.* No. 130 (1993) pp. 379–82.

Journal of the European Ceramic Society 15 (1995) 623–629
© 1995 Elsevier Science Limited
Printed in Great Britain. All rights reserved
0955-2219(95)00036-4
0955-2219/95/$9.50

Forming Pressure Dependence of the Ferroelectric Domain Structure in Green Barium Titanate Pellets

P. Sarrazin,[a] B. Thierry[a] & J. C. Niepce[b]

[a]Laboratoire Matériaux Industriels, CRITT Céramiques Fines Techniques, Université de Valenciennes, 59600 Maubeuge, France
[b]Laboratoire Réactivité des Solides, URA CNRS no 23, Université de Bourgogne, BP 138, 21004 Dijon Cedex, France

(Received 7 April 1994; revised version received 31 January 1995; accepted 7 February 1995)

Abstract

Modifications of the X-ray diffraction line profiles by die pressing of fine grained powders of barium titanate have been studied. Two main parameters have been considered: the forming pressure and the mechanical characteristics of the binder. The higher the forming pressure, the greater the modifications of the line profiles. Furthermore, the phenomena seems to be related to pressing only; no significant effect related to the nature of the binder has been shown.

The modifications of the diffraction line profiles are interpreted by considering a reduction of the size of the ferroelectric domains during pressing. In order to confirm this interpretation, the behaviour of the domain structure of a $BaTiO_3$ single crystal under local compression has been studied. The average size of the domain is dramatically reduced by applying local pressure. Moreover, the domain structure modifications produced by the high stress state are largely preserved under a rather low residual pressure. There is a kind of hysteresis as a function of the pressure. This observation may explain the remanent modifications of the line profiles recorded after pressure relaxation.

Introduction

The X-ray diffraction line profiles of fine grained barium titanate powders are modified after the formation of green parts.[1] The effects of the different steps of the green part preparation on the line profile modifications have been determined within an experimental design approach.[2] The forming step is by far the parameter which has the largest influence. Indeed, the line profiles are closely dependent on the forming step and none of the other studied parameters seems to have any direct influence on the profile modifications. Forming was performed by slip casting or die pressing. Thus, the mechanical stress applied during the forming step is responsible for the studied phenomenon.

It is well-known that the line profiles of $BaTiO_3$ powders are quite dependent on the granulometric characteristics.[3–7] It has recently been shown that the diffraction diagram of a fine grained barium titanate is also dependent on the ferroelectric domain structure.[8,9] Thus, a full interpretation of the diffraction line profiles requires consideration of the ferroelectric domain structure with respect to the diffracted intensity.[1,10,11]

The influence of the die pressing pressure on the diffraction line profiles of a micronic barium titanate powder is studied in this paper. In order to fully evaluate the effect of residual stress, the mechanical characteristics of the binder are also considered.

Experimental

1 Sample preparation

A pure $BaTiO_3$ powder, with a narrow grain size distribution ($\varnothing_{10}$ = 1·0 μm, $\varnothing_{50}$ = 2·4 μm, $\varnothing_{90}$ = 4·9 μm), has been used in order to get well separated 002 and 200 diffraction lines (Fig. 1).

Two slips were prepared in organic media with two binders presenting quite different mechanical characteristics (Poly Vinyl Butyral PVB and paraffin 46–48°C). After slip drying and preparation of granules, two sets of discs were formed by die pressing. In both cases, the forming pressure range was 100–1000 MPa.

2 X-ray diffraction characterization

The samples were characterized after die forming by X-ray diffraction using a diffractometer fitted out with an INEL Curved Position Sensitive Detector (CPS120). Cu $K\alpha_1$ radiation has been selected with a focusing quartz monochromator. For each diagram, a 120° 2θ zone was recorded over 8196

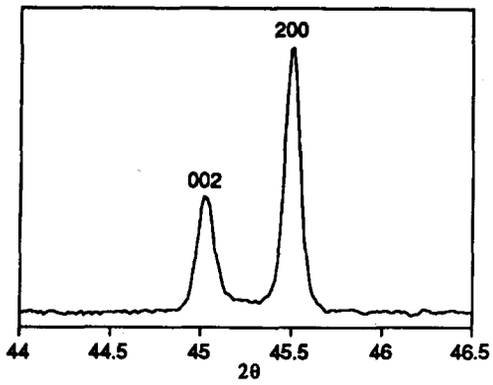


Fig. 1. 002 and 200 X-ray diffraction lines of the $BaTiO_3$ powder used for the sample preparation.

channels during one hour. All the lines of the diagram were fitted.

- The cell parameters' refinement has been carried out with the CELREF Software.
- The mean apparent crystallite size and the mean apparent amount of crystalline lattice distortion have been performed according to the Williamson and Hall[12] method. For this, the half widths (F.W.H.M.) of the 111 and 222 diffraction lines have been determined. They were corrected from the instrumental broadening by considering a Lorentzian approximation of the line profiles. The instrumental broadening approximation for the 111 and 222 lines were the half widths of the two corresponding lines of a well crystallized $BaTiO_3$ previously used as a broadening reference.[1]
- The diffracted intensity profile around the 002 and 200 lines was previously considered for the determination of both the distribution of the cell parameters[5] and the size of the 90° ferroelectric domains.[1,10,11] In the present study, only the two intensity maxima and the minimum of the diffracted intensity between the peaks have been carefully measured.

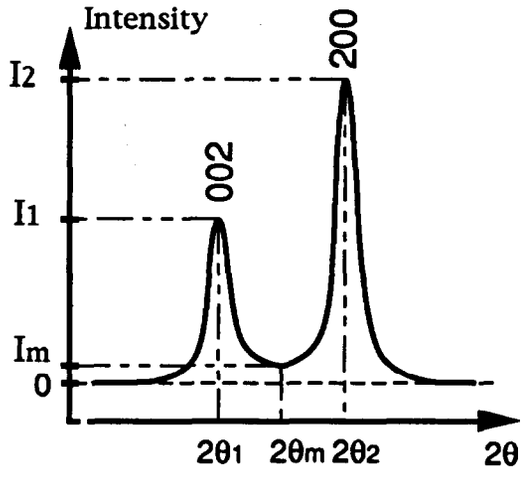


Fig. 2. Characterization by a relative number R of the diffracted intensity between the 002-200 lines.

From these intensities, the R ratios have been calculated in order to characterize the relative intensity between the two lines by a number.

$$R = \frac{(I_m)}{1/2(I_1 + I_2)_{sample}} \Big/ \left(\frac{(I_m)}{1/2(I_1 + I_2)}\right)_{powder}$$

These numbers were normalized by using the corresponding intensities of the initial powder diagram as a reference (Fig. 2).

Results

1 Evolution of the diffracted intensity profile around the 002-200 lines

The 002-200 line profiles obtained with the samples of each of the two sets display the same evolution. Some profiles of various samples prepared with PVB binder are presented in Fig. 3: the diffracted intensity between the two peaks increases with increasing forming pressure.

This first observation of the profiles evolution is numerically shown with the evolution of the R ratio. Figure 4 illustrates the evolution of R as a function of the forming pressure for the two sets of samples. The evolution of R is almost linear with the pressure and on the same straight line whatever the nature of the binder. The binder has no significant influence on the modifications of the line profiles.

Moreover, intensity appears on the two external sides of the line profiles. The two observed modifications are evident in Fig. 5 which presents the superposition of two 002-200 line profiles corresponding to the initial powder and a sample after pressing at 1000 MPa, respectively.

2 Evolution of the cell parameters

The results are presented in Fig. 6. The a parameter does not seem to present any variation whereas the c parameter is slightly decreasing with the forming pressure. The resulting c/a ratio shows a diminution of the cell tetragonality. This is the typical behaviour of a $BaTiO_3$ single crystal under hydrostatic pressure.[13] That means, from a macroscopic point of view, that the uniaxial pressing induces on the powder the same structural modifications as does hydrostatic pressing. This is due to the reaction forces of the die during the pressing and to the fact that the zones of contact between grains are not necessarily oriented perpendicularly to the pressing direction.

3 Evolution of the broadening of the 111 and 222 lines

The 111 line of $BaTiO_3$ and its harmonics are not affected by the tetragonal deformation of the

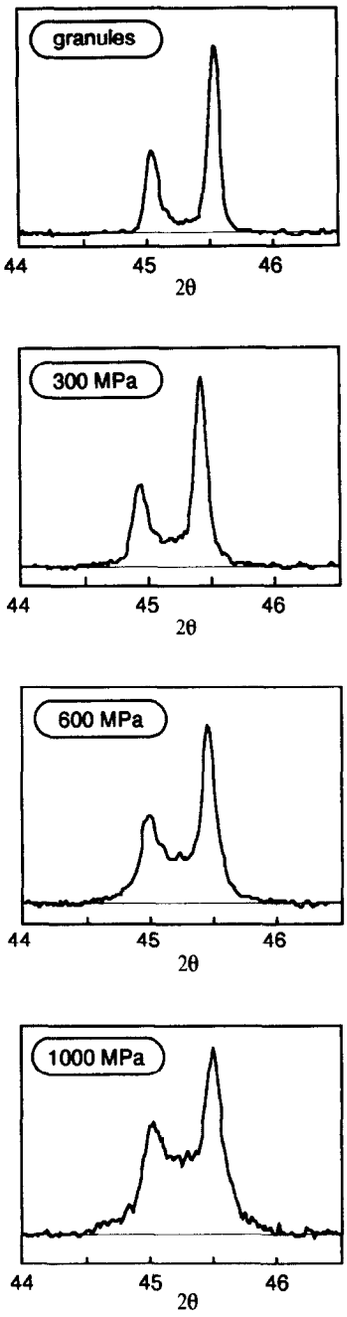


Fig. 3. 002-200 line profiles recorded on granules and discs formed at different pressures (samples prepared with PVB binder).

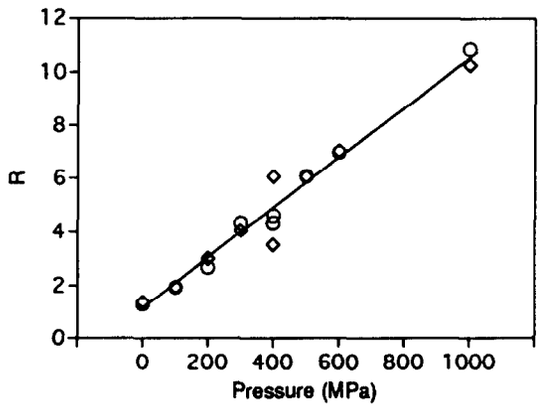


Fig. 4. Evolution of the R ratio with the forming pressure for the two sets of samples. ◇ samples prepared with PVB binder, ○ samples prepared with paraffin binder.

perovskite structure. Thus, 111 and 222 are the only true single lines of the $BaTiO_3$ diagram at room temperature. These lines were used to study the broadening involved by the pressing.

In Fig. 7, the widths of the 111 and 222 lines — corrected from the instrumental broadening — are reported as a function of the forming pressure. The higher the forming pressure, the broader the lines. Moreover, the broadening of the 222 line increases more rapidly than that of the 111 line. This is thought to be attributed to the formation of a kind of lattice distortions in the material.

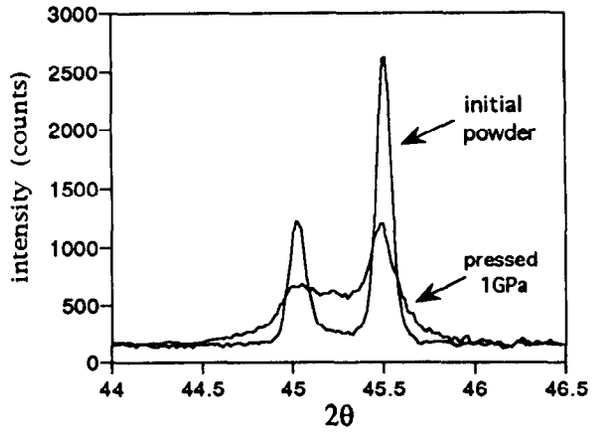
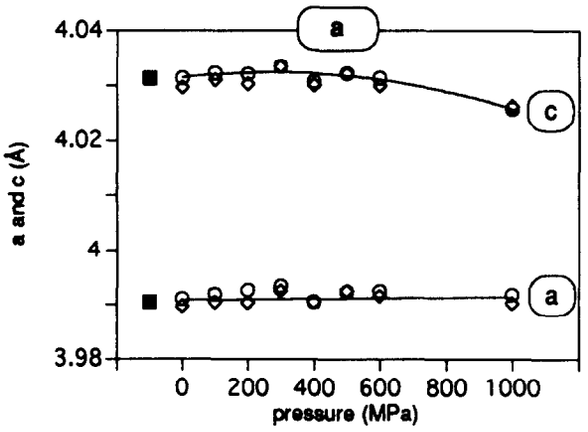


Fig. 5. 002-200 line profiles of the initial powder and of a sample pressed under 1 GPa.



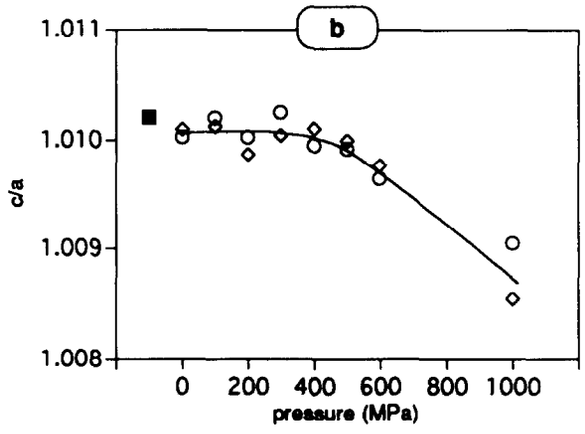


Fig. 6. Evolution of the cell parameters (a) and the c/a ratio (b) with the forming pressure: ■ initial powder; ◇ samples prepared with PVB binder; ○ samples prepared with paraffin binder.

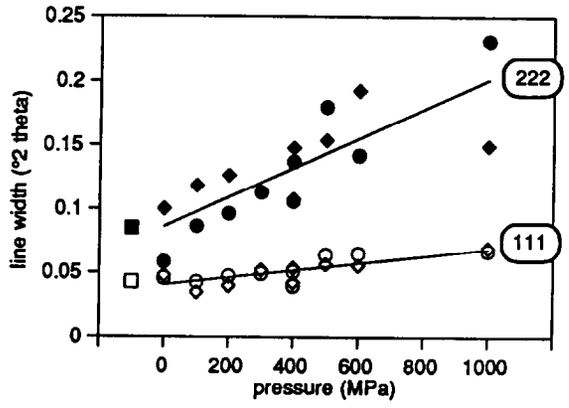


Fig. 7. Evolution of the 111 and 222 line widths with the forming pressure: □■ initial powder; ◇ ◆ samples prepared with PVB binder; ○● samples prepared with paraffin binder.

The Williamson and Hall method has been used to go further with this observation. In this representation, the harmonic lines describe a straight line which the origin ordinate corresponds to the size effect broadening and which the slope is due to the lattice distortion effect broadening. The origin ordinate and slope of each Williamson and Hall straight line are presented in Figs 8 (a) and (b) respectively. The origin ordinate does not exhibit any significant variation, whereas the slope increases with the forming pressure. Therefore, the modifications of the structure involved by the forming are seen as an increase in the lattice defects along the [111] axis without any variation of the size of the coherence domains.

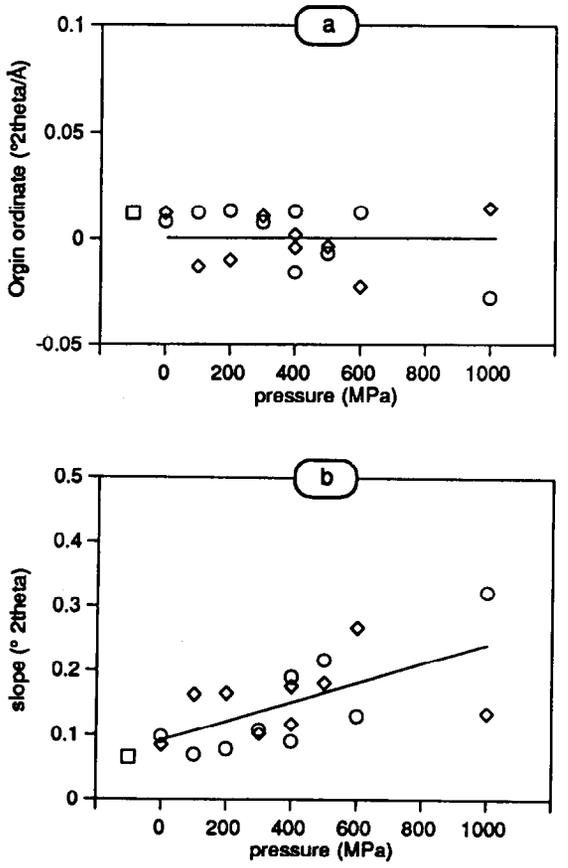


Fig. 8. Origin ordinates (a) and slopes (b) of the Williamson and Hall straight lines: □ initial powder; ◇ samples prepared with PVB binder; ○ samples prepared with paraffin binder.

Discussion and Further Results

1 Diffraction line profiles and organization of the material into ferroelectric domains

At room temperature, the $BaTiO_3$ grains are usually divided into ferroelectric domains which size is commonly correlated to the grain size.[14] This division allows a minimization of the overall deformation and polarisation induced during the paraelectric to ferroelectric transition.

The division into ferroelectric domains has an influence on the X-ray diffraction diagram of $BaTiO_3$ powders.[8,9] In particular, it has been shown that the size of the ferroelectric domains is partly responsible for the broadening of the line profiles:

— The subdivision of the $BaTiO_3$ crystallites into domains at 90° induces a broadening of the 002-200 lines related to the ferroelectric domain size. Moreover, decreasing the domain size increases a particular contribution to the diffracted intensity between these two lines. A model of the 002-200 line profile in relation to the ferroelectric domain size has been proposed.[1,10,11] Figure 9 shows the line profiles obtained with a rough model of a single crystalline grain containing two 90° domains for two different domain sizes.[11] From this figure, the reduction of the domain

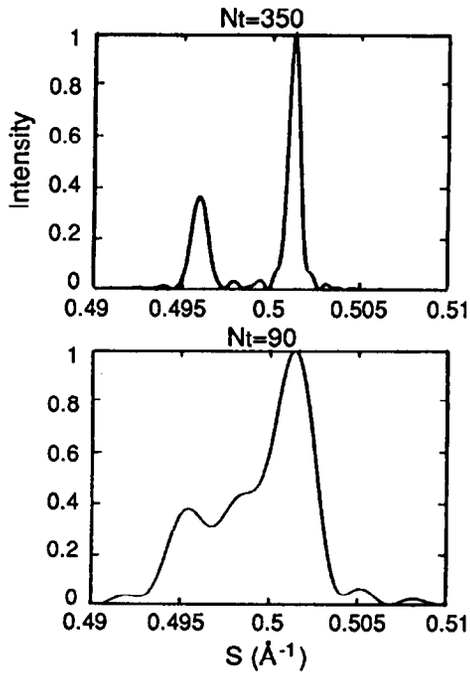


Fig. 9. 002-200 line profile performed with a two 90° domains model for the ferroelectric grain: Nt is the number of 002 and 200 planes in the considered direction.[11]

size involves an increase in the intensity of the middle zone and of the external sides of the line profiles.

— On the contrary, the subdivision of the crystallites into ferroelectric domains does not involve any size effect broadening for lines such as 111 and 222. The division into domains also involves a broadening of these lines but now due to a lattice distortion effect. In fact, along the [111] axes, the lattice periodicity is almost completely preserved from one domain to another. Thus, the diminution of the domain size without any evolution of the grain size involves an increase in the lattice defects content along the [111] axis. Such a modification of the structure should induce a very particular evolution of the Williamson and Hall straight lines built with the 111 and 222 lines: the origin ordinate would be constant while the slope would increase.

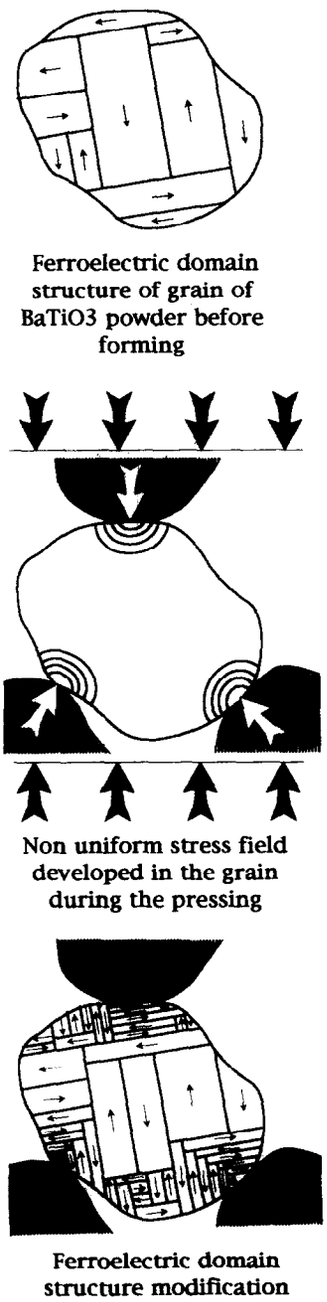


Fig. 10. Proposition for a mechanism of ferroelectric domains fragmentation during the pressing.

2 Influence of the forming pressure on the ferroelectric domains organization of the grains of powder

The Williamson and Hall analysis of the present study has shown that the increase in the forming pressure involves an increase in the apparent lattice defects content while the apparent size of the coherence domains does not vary. This is the expected evolution of the 111 and 222 line profiles in the case of a reduction of ferroelectric domain size. Furthermore, the evolution of the 002-200 line profiles, as a function of the forming pressure, is very similar to that observed with the model of a two domains grain. This is evident by the comparison of Figs 5 and 9.

These observations allow us to interpret the line profile modifications as a reduction of the domain size induced by the pressing of the grains. Figure 10 proposes a diagrammatic mechanism of domain fragmentation. During forming, the grains of the powder develop small zones of contact through which the stress is transmitted. Therefore, the non-uniform stress field developed inside each grain involves local deformations. Since the material plasticity is low, the domain reorganization favours the deformation. These rearrangements are more efficient when increasing the number of domains, thus when the domain size is reduced. The fragmentation into ferroelectric domains allows the minimization of the mechanical energy of the material during forming. A similar mechanism has been proposed by Hennings[15] to explain the grain size dependency on the domain size in fine grained $BaTiO_3$ ceramics.

Nevertheless, this proposition of interpretation is not sufficient to account for the fact that the structural modifications are observed after the forming of the samples. Thus, this mechanism is only valid if the modifications of the domain structure involved during pressing are totally or partially kept after the pressure relaxation.

3 Macroscopic evidence of the pressing influence on the ferroelectric domains

In order to confirm this domain fragmentation, the behaviour of the domain structure of a $BaTiO_3$ single crystal under local compression has been studied. The domain walls of a polished crystal were observed with an optical microscope. Figure 11 shows the special device achieved for studying the local compression of the crystal. A metallic awl is kept in contact with the crystal and applies a compressing force adjusted with a

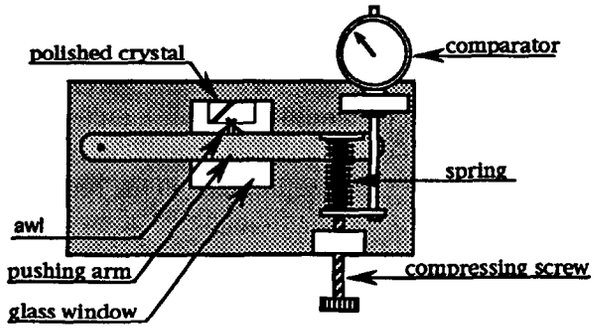


Fig. 11. Diagram of the special device realized for studying the influence of the local compression on the ferroelectric domains of $BaTiO_3$ single crystals.

spring. The compression of the spring is realized with a screw and controlled with a comparator. The calibration of the spring allows the calculation of the force applied on the crystal. This device was placed under an optical microscope to follow the evolution of the domain structure under local pressing.

Figure 12 displays the photographs taken with the microscope during a cycle of increase and decrease in the compressive force. It shows that the pressing of the crystal involves an increase in the density of domain walls around the awl; the higher the force, the broader the zone of high wall density.

Furthermore, the comparison of the pictures relative to the same stress states shows that the domain wall density is not identical depending on whether the pressure is increasing of decreasing. The structure involved under a 12 N force is almost entirely kept right down to a 4 N force. Thus, there is an hysteresis relation between the local pressure and the ferroelectric domain structure. This is in all likelihood due to the ferroelastic properties of $BaTiO_3$. This hysteresis is shown with the curve of Fig. 12 which presents a visual estimation of quantity of domain walls as a function of the force applied on the crystal.

So, a structure generated at high pressure is largely preserved with a rather low residual stress. This might explain the fact that the modifications appearing during the pressing of the $BaTiO_3$ powders are observed after the forming. These last experiments tend to confirm the hypothesis of a fragmentation of the ferroelectric domains during the pressing of the powder.

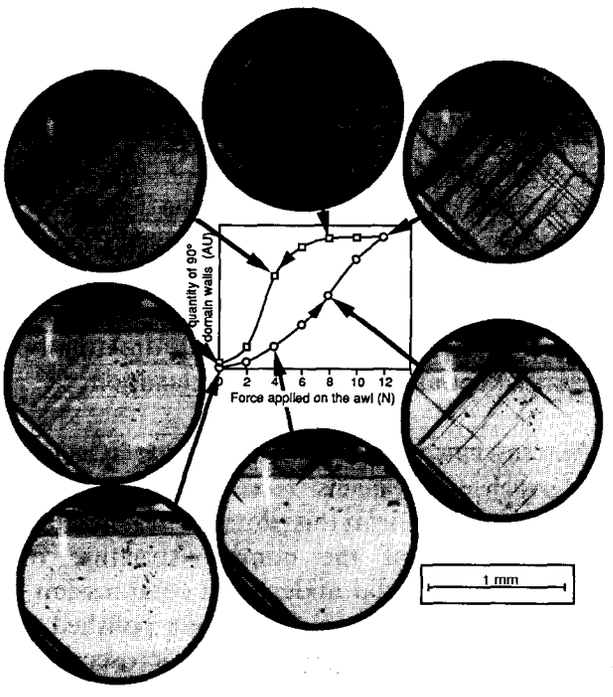


Fig. 12. Optical microscopy photographs of a $BaTiO_3$ single crystal during increase and decrease in the local applied pressure; visual estimation of the quantity of new domain walls as a function of the pressure.

Conclusion

This study has shown that the modifications of the line profiles of barium titanate powders involved during the forming of pellets are essentially due to the pressure applied for the die forming. The nature of the binder, which was suspected to have some influence on this phenomenon, seems to have no noticeable effect. The different results obtained with the X-ray diffraction analysis let us think that a reduction of the ferroelectric domain size inside the material is responsible for these line profile modifications. The mechanism of domain fragmentation proposed is supported by the observation of the domain structure of a $BaTiO_3$ single crystal under local compression. Moreover, this last experiment shows that the modifications involved during the forming may be preserved after the pressure relaxation.

The present results are a new illustration of the influence of the domain structure of barium titanate powders on the X-ray diffraction line profiles. Moreover, this study points out the fact that the granulometric characteristics of the powder are not sufficient to define the domain structure of the grains, the mechanical history of the material has also to be considered.

Acknowledgements

The authors wish to express their thanks to: Region Nord-Pas de Calais and G.I.P. Ceramiques Fines Maubeuge, France, for the financial support of this work, Dr P. Julien and Mr J. P. Troalen, Team Matériaux Ferroélectriques pour l'Optique, URA CNRS 1796, Université de Bourgogne, for providing the barium titanate single crystals. Prof. J. P. Loreau, Centre des Sciences de la Terre,

URA CNRS 157, Université de Bourgogne, for the microscopic observations and Mrs N. Floquet, M. T. Mesnier and C. Valot, Laboratoire Réactivité des Solides, URA CNRS 23, Université de Bourgogne and S. Butow, University of San José, CA, USA, for helpful discussions.

References

1. Caboche, G., Relation structure-dimension des grains monocristallins: cas d'un matériau polaire $BaTiO_3$, thesis, Université de Bourgogne, France, (1991).
2. Sarrazin, P., Lemaitre, J. & Niepce, J. C., Influence des différentes étapes de la préparation des pièces crues de titanate de baryum sur les profils de raies de diffraction. Sil. Indus., (Submitted for publication).
3. Kanzig, W., Space charge layer near the surface of a ferroelectric. *Phys. Rev.*, **98** (1955) 549–50.
4. Uchino, K., Sadanaga, E. & Hirose, T., Dependence of the crystal structure on particle size in barium titanate. *J. Am. Ceram. Soc.*, **72**(8) (1989) 1555–8.
5. Malbe, S., Mutin, J. C. & Niepce, J. C., Distribution des paramètres de maille cristalline dans des échantillons pulvérulents de $BaTiO_3$. *J Chim Phys*, **89** (1992) 825–43.
6. Caboche, G., Boilot, J. P., Chaput, F. & Niepce, J. C., Titanate de baryum à grains fins pour application dielectrique. *Sil. Indus.*, **58** 5–6(1993) 103–7.
7. Caboche, G., Boilot, J. P., Chaput, F. & Niepce, J. C., Crystalline characterization of fine grain sol gel $BaTiO_3$ powders. *J. Europ. Ceram. Soc.*, (to be submitted for publication).
8. Berar, J. F., Caboche, G., Courtois, C., Maglione, M., Mesnier, M. T., Niepce, J. C., Sarrazin, P. & Valot, C. M., Evidence de la contribution de la structure en domaines ferroélectriques dans le diagramme de diffraction d'un matériau ferroélectrique. *Journées d'Etudes Matériaux Piezo-Pyro-Ferroelectriques et leurs applications*. Limoges, France, (1993).
9. Valot, C. M., Berar, J. F., Courtois, C., Maglione, M., Mesnier, M. T. & Niepce, J. C., X-ray diffraction diagram evolution of $BaTiO_3$ ceramic under an electrical field. *Ferroelectric Letters*, **17** (1994) (1–2) 5–12.
10. Caboche, G., Berar, J. F., Pannetier, J., Mesnier, M. T., Niepce, J. C. & Ravet, M. F., Investigation indirecte des domaines ferroelectriques dans $BaTiO_3$ à grains fins. *Sil. Indus.*, **58**(11–12) (1993) 239–243.
11. Caboche, G., Floquet, N., Mesnier, M. T., Niepce, J. C. & Valot, C. M., Fine grain $BaTiO_3$ powders for dielectric applications: ferroelectric domains and diffraction line profiles. *J. Europ. Ceram. Soc.*, (to be submitted for publication).
12. Williamson, G. K. & Hall, W. H., *Acta. Metall.*, **1** 22 (1953).
13. Waesche, R., Denner, W. & Schulz, H., Influence of high hydrostatic pressure on the crystal structure of barium titanate ($BaTiO_3$). *Mat. Res. Bull.*, **16** (1981) 497–500.
14. Arlt, G., Hennings, D. & With, G., Dielectric properties of fine-grained barium titanate. *J. App. Phys.*, **58** (1985) 1619–25.
15. Hennings, D., Barium titanate based ceramic materials for dielectric use. *In. J. High Tech. Ceram.*, **3** (1987) 91–111.

Journal of the European Ceramic Society 15 (1995) 631–635
© 1995 Elsevier Science Limited
Printed in Great Britain. All rights reserved
0955-2219(95)00021-6
0955-2219/95/$9.50

Characterization of $BaTiO_3$ Powder Obtained by a Chemical Route

C. Proust, C. Miot & E. Husson

Laboratoire de Physique et Mécanique des Matériaux, ESEM, Université d'Orléans et CRPHT-CNRS, 45071 Orléans cedex 2, France

(Received 1 December 1994; revised version received 27 January 1995; accepted 31 January 1995)

Abstract

The citric resin method is used to prepare stoichiometric, homogeneous and fine barium titanate powders. The elaboration process is described in detail. Powders are characterized by several methods such as R-ray diffraction, scanning and transmission electron microscopy, thermogravimetric measurements and infra-red absorption and X-photoelectron spectroscopies. Residual carbon content is quantified by nuclear technics and Rosemount method, Raw powders contain small quantities of barium carbonate and residual carbon.

1 Introduction

Today's leading trend in the electronic ceramic industry is to develop component miniaturization. The application of multilayer capacitors implies an increase of the volume efficiency C_v which may be obtained by:

(i) an increase of the relative permittivity ϵ': it may be obtained by grain size control: the dielectric properties are greatly influenced by the grain size; Caboche *et al.*[1] showed that a maximum of ϵ' is observed at room temperature for ceramics having a grain size of about 0·8 μm. The manufacture of such ceramics needs the use of fine powders.
(ii) a decrease of the thickness of the dielectric layers; the production of thin layers again needs fine barium titanate powders.

A wet chemical route to prepare fine and homogeneous powders is interesting compared to conventional solid state reaction processing. In this work, $BaTiO_3$ powders were elaborated by the thermal decomposition of an organic resin produced from a mixed citrate obtained by a method previously described.[2,3] This chemical route allows one to control the Ba/Ti = 1 ratio and the powder morphology and to fix the aggregate size. The Ba/Ti ratio is an important parameter which may dramatically influence microstructural development in high-purity $BaTiO_3$. An excess of BaO involves the formation of Ba_2TiO_4 which inhibits grain growth during sintering and an excess of TiO_2 leads to the formation of an eutectic melt which affects the sintering behaviour because of liquid phase formation at grain boundaries.[4–7]

Different characteristics such as structure, microstructure and residual carbon content must be precise and have been investigated by several methods: transmission electron microscopy (TEM), scanning electron microscopy (SEM), X-ray diffraction (XRD), thermogravimetric analysis (TGA), infra-red (IR) and X-ray photoelectron (XPS) spectroscopies, nuclear analyses, etc.

2 Experimental Procedure

$BaTiO_3$ powders were obtained from a citric resin method, described in previous papers.[2,3] The mixed citrate $BaTi(C_6H_6O_7)_3,6H_2O$ was first prepared, then dissolved in a citric acid, ethylene glycol and water mixture so that the R = $BaTiO_3$ mass/solution mass ratio was 1%. This solution was calcined at 700°C in static air and $BaTiO_3$ powders were produced after 2 h.

The deagglomeration step was performed in two steps:

(i) first the powder was roughly deagglomerated by attrition: the powder was mixed with ZrO_2 balls in isopropanol in the 1/3 balls, 1/3 isopropanol and 1/3 solid phase ratio and shaken for 12 h.
(ii) the powder was then deagglomerated by ultrasonic dispersion. This step was especially studied. Several factors were investigated, for example sonication time (15–30 min), volume of the suspension (20–50 ml) for a solid weight fraction of 1 g. Optimal condi-

tions were found to be 30 min ultrasonication (100 W power) with 30 ml isopropanol per gram of solid phase. After sedimentation, the suspension was dried in a rotovapor and calcined at 700°C for 4 h before yielding raw $BaTiO_3$ powders.

X-Ray diffraction experiments were performed on a Philips PW 1729 diffractometer with the CuK_α wavelength, at room temperature.

Thermogravimetric measurements were made with a Setaram thermobalance, under a flowing oxygen atmosphere. Approximately 100 mg of powder were accurately weighed in a platinum crucible. The temperature was raised from room temperature up to 1000°C at 10°C min^{-1} and then from 1000 to 1400°C at 5°C min^{-1}.

FT-IR absorption spectra were recorded with a Brucker IFS 113+88 interferometer between 4000 and 400 cm^{-1} at room temperature on a sample containing 2 mg of $BaTiO_3$ dispersed in 200 mg of KBr and pressed into pellets.

Carbon analysis: the carbon concentration was determined by two methods:

(i) the Rosemount carbon analysis consisted of heating a weighted sample by flowing O_2 up to 1800°C and analysing the CO_2 evolved with an infra-red detector. This technique gives the volumic carbon content but is not precise enough at ppm levels.

(ii) the $^{12}C(d,p)^{13}C$ nuclear technique using deuterons from the C.E.R.I.'s[1] van de Graaff accelerator. The method has been described in different articles.[8–11] The measurements were performed at 950 keV deuteron energy in a UHV chamber under a vacuum of about 10^{-9} mbar obtained with a cryogenic pumping system on pellet-shaped samples of 4 mm thickness and 13 mm diameter, isostatically pressed at 250 MPa. The detector was a PIPS silicon diode with 100 mm^2 active surface protected by an aluminium foil of 10 μm thickness, situated 64 mm from the sample position with a $\theta = 150°$ detection angle. The beam current was about 10 nA and the counting time was about 2000 s. A theoretical proton spectrum of a material containing C in the bulk with a C-rich surface layer is given in Fig. 1. It can be seen that the shape of the peak gives information about the C content in the surface layer and in the bulk. In the experimental conditions used, taking account of the differential cross-section[12] and the density of the compacted material (50% of the theoretical density of $BaTiO_3$), the surface layer may be estimated about 0·7 μm and the maximal penetration depth about 1·7 μm. This technique is sensitive down to ppm levels.

[1]C.E.R.I. Centre d'Etude sur les Radiations Ionisantes, CNRS Orléans.

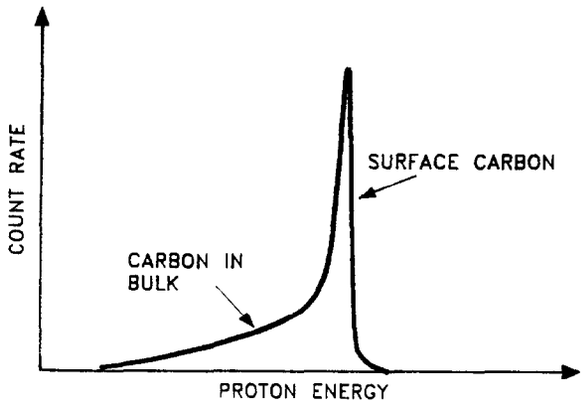


Fig. 1. A theoretical proton spectrum of material containing C with a C-rich surface layer.

X-Ray photoelectron spectroscopy (XPS) analyses were made with an Escalab MK2 of Vacuum Generator system spectrometer using Mg K_α line. The measurements were performed under a vacuum of about 10^{-9} mbar. Samples were obtained by spraying citric precursor on a silica substrate and firing at 700°C. The signal curves were fitted using Gaussian peaks summation and baseline subtraction. Charge compensation was performed using the C_{1s} peak at 284·6 eV.

The SEM images were obtained with a Cambridge stereoscan 100 microscope on samples previously metallized with platinum.

The TEM images were obtained with a JEOL 100 CX microscope on microtomic sections.

3 Results and Discussion

The microstructure is a very important factor which must be controlled during the elaboration of the powder. Figure 2 shows the different agglomeration states of the powder using TEM and SEM techniques. The sample microstructure can be described by (i) microcrystallites of 25–30 nm size (Fig. 2(a)), (ii) crystallites associated into 150 nm spheroid aggregates (Fig. 2(b)) and (iii) aggregates linked in larger agglomerates (platelets about 60 μm in size) (Fig. 2(c)).

Several characterisation methods were used such as XRD, IR absorption and TGA to detect the presence of impurities such as $BaCO_3$. By XRD only one crystalline phase was observed at room temperature, cubic $BaTiO_3$ with cell parameter $a = 4·007$ Å instead of a tetragonal phase as predicted from the phase diagram.[13] This phe-

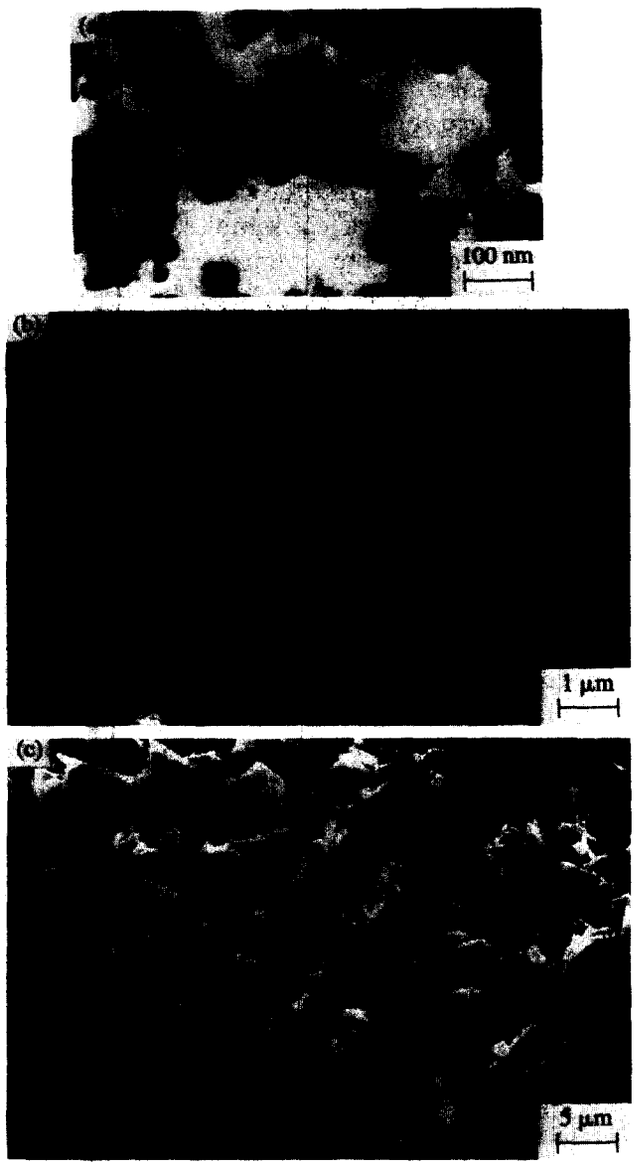


Fig. 2. Microstructure of $BaTiO_3$ powders (a) TEM of ultra-thin sections, (b) SEM of deagglomerated powders, (c) SEM of non deagglomerated powders.

nomenon was already described by Caboche *et al.*[1] They have shown that barium titanate crystallizes at room temperature either in a cubic or a tetragonal phase depending, as well as on cell parameter(s),

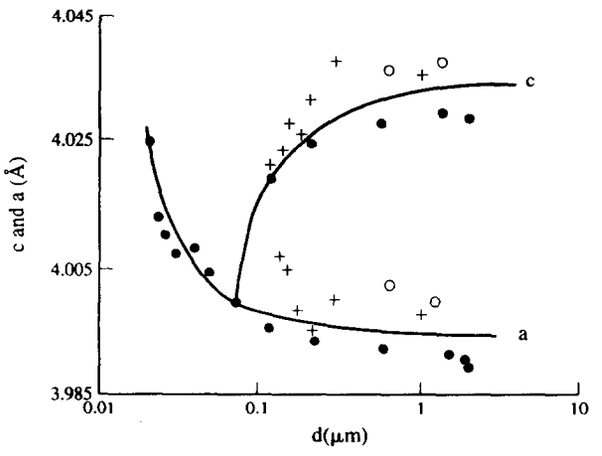


Fig. 3. Variation of cell parameters of fine $BaTiO_3$ powders given by Caboche *et al.*.[7]

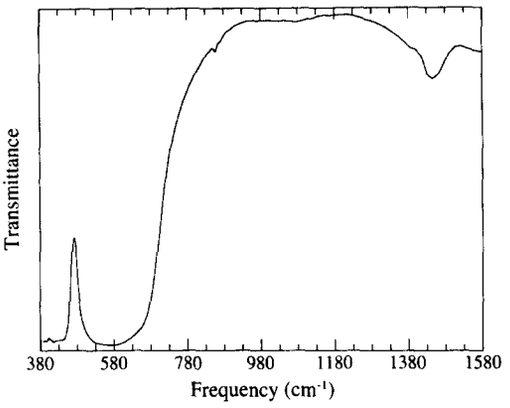


Fig. 4. IR absorption spectra of raw $BaTiO_3$ powders.

on the elementary single crystalline grain size. The cubic cell parameter decreases with this grain size up to a limit of 0·07 μm. Above this limit the crystal cell becomes tetragonal as represented in Fig. 3. Microscopic studies (Fig. 2(a)) have shown that the single crystalline grain size was about 30 nm. According to Caboche *et al.*[1] (see Fig. 3), for such a grain size the powder crystallises in a cubic phase with a cell parameter of about 4·008 Å. Thus, our results are in good agreement with those of Caboche.

The IR absorption spectra recorded at room temperature are presented in Fig. 4 in the 2200–400 cm^{-1} range. The two main absorption bands are characteristic of the vibration frequencies of the TiO_6 octahedra. Two other weak absorption bands, at 1430 and 875 cm^{-1}, reveal $BaCO_3$ traces.

These results are in good agreement with those obtained by XPS. The photoelectron peaks of Ba, Ti and O elements were carefully investigated:

(i) the Ti_{2p} line consists of a single narrow Gaussian peak, meaning that titanium was only present in a single chemical state, $BaTiO_3$.

(ii) the study of the 770–800 eV range shows the presence of two barium types (Fig. 5(a)). The two main peaks at 779·5 and 795 eV after calibration of the charge-shifted energy scale can be associated with barium environment in $BaTiO_3$. The third peak at about 785·5 eV can be assigned to barium environment in $BaCO_3$.[14]

(iii) on the oxygen range (Fig. 5(b)) the first peak at 526·5 eV corresponds to the titanate environment and the second one at 527·5 eV may be due to the carbonate.[14] The XPS results confirm the existence of $BaCO_3$ traces.

More quantitative methods were thus necessary to give the residual carbon content in the form of barium carbonate or other carbonaceous species

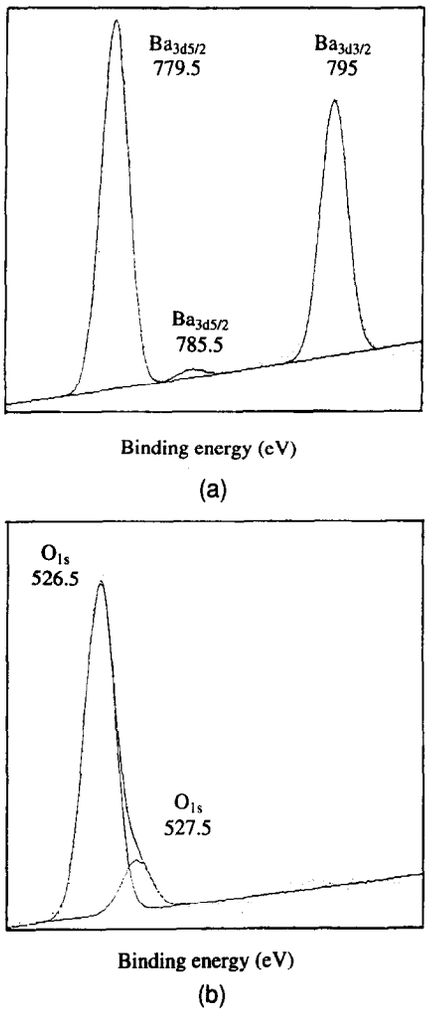


Fig. 5. XPS spectra from raw $BaTiO_3$ powders (a) $Ba_{3d5/2}$ and $Ba_{3d3/2}$, (b) O_{1s}.

more precisely. TGA measurements carried out under flowing oxygen atmosphere gave a curve (Fig. 6) with two weight losses, the first one near 80°C resulting from adsorbed water removal and the second one between 400 and 1100°C which can be due to the CO_2 released during $BaCO_3$ decomposition. Demartin *et al.*[15] and Fang *et al.*[16] have shown that the CO_2 comes mostly from the $BaCO_3$ calcination and that its evolution is observed between 600 and 1300°C on the TGA

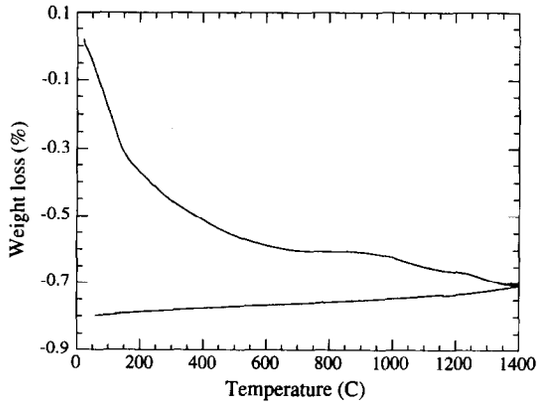


Fig. 6. ATG curve of raw $BaTiO_3$ powders.

curves. In our case the corresponding weight loss was estimated about 0·12%.

The amount of residual carbon in the raw powder determined by the Rosemount method was about 0·25% of the volume.

By nuclear techniques, the carbon content was determined in compacted samples. The surface layer (0·7 μm) of the compacted raw powder exhibits a carbon content of 1·4%. In the volume the C content was estimated at roughly 0·3%.

The results obtained of the volume C content by the two techniques are in very good agreement. The high value of the surface C concentration may be due to the contamination.

If the amount of released CO_2 detected by TGA only originates from the $BaCO_3$ decomposition, we can estimate the $BaCO_3$ concentration at 0·5%. This result is coherent with the XRD results which did not reveal the presence of $BaCO_3$ and the infra-red spectra which displayed two bands of weak intensity assigned to carbonate ions. The carbonate concentration found is low in comparison with those given by different authors for $BaTiO_3$ powders prepared by wet chemical route or hydrothermal synthesis.[14,15,17]

Comparing the results obtained by TGA and carbon content determinations, it can be concluded that the raw powder contains a noticeable residual carbon content in other chemical states than the carbonate one. They could not be found on IR spectra and studies of the XPS C_{1s} peak are now in progress in order to characterize these chemical states.

4 Conclusions

The citric resin method is an interesting way to prepare stoichiometric, homogeneous and fine barium titanate powders. Cubic powders with microcrystallites of 30 nm size were obtained: they contain small quantities of $BaCO_3$ (about 0·5%) which is thermally decomposed between 600 and 1300°C to release CO_2. The total C residual content has been estimated at 00·25–0·30%. Thus a part of the C is in another chemical form than carbonate. Further studies are now in progress to elucidate this point. This synthesis optimization should allow one to obtain dense ceramics with satisfactory bulk capacity.

References

1. Caboche, G., Chaput, F., Boilot, J. P. & Niepce, J. C., Titanate de baryum à grains fins pour application diélectrique. *Silicates Industriels*, **5–6** (1993) 103–7.
2. Coutures, J. P., Odier, P. & Proust, C., Barium titanate

formation by organic resins formed with mixed citrate. *J. Mater. Sci.*, **27** (1992) 1849–56.
3. Le Calvé-Proust, C., Husson, E., Odier, P. & Coutures, J. P., Sintering ability of $BaTiO_3$ powders elaborated by citric process. *J. European Ceram. Soc.*, **12** (1993) 153–57.
4. Kulscar, F., A microstructure study of barium titanate ceramics. *J. Am. Ceram. Soc.*, **39** (1956) 13–17.
5. Sharma, R. K., Chan, N. H. & Smyth, D. M., Solubility of TiO_2 in $BaTiO_3$. *J. Am. Ceram. Soc.*, **64** (1981) 448–51.
6. Choi, J. S. & Kim, H. G., Influence of stoichiometry and impurity on the sintering behaviour of barium titanate ceramics. *J. Mater. Sci.*, **27** (1992) 1285–90.
7. Hutchins, G. A., Galeb, H. M. & Ross, S. D., Control of the Ba : Ti ratio of $BaTiO_3$ at a value of exactly 1 via conversion to $BaO{\cdot}TiO_2{\cdot}3C_6H_8O_7{\cdot}3H_2O$. *Am. Ceram. Soc. Bull.*, **66** (1987) 681–84.
8. Wengeler, H., Knobel, R., Kathrein, H., Freund, F., Demortier, G. & Wolff, G., Atomic carbon in magnesium oxide single crystals. Depth profiling, temperature- and time-dependent behavior. *J. Phys. Chem. Solids*, **43** (1982) 59–71.
9. Oberheuser, G., Kathrein, H., Demortier, G., Gouska, H. & Freund, F., Carbon in olivine single crystals analyzed by the $^{12}C(d,p)^{13}C$ method and by photoelectron spectroscopy. *Geochimica Cosmochimica Acta*, **47** (1983) 1117–29.
10. Mathez, E. A., Carbon abundances in mantle minerals determined by nuclear reaction analysis. *Geophys. Res. Lett.*, **11** (1984) 947–50.
11. Proust, C., Husson, E., Blondiaux, G. & Coutures, J. P., Residual carbon detection in barium titanate ceramics by nuclear reaction technique. *J. European Ceram. Soc.*, **14** (1994), in press.
12. Huez, M., Quaglia, L. & Weber, G., Fonction d'excitation de la réaction $^{12}C(d,p)^{13}C$ entre 400 et 1350 keV. Distributions angulaires. *Nuclear Instruments and Methods*, **105** (1972) 197–203.
13. Rase, D. E. & Roy, R., Phase equilibria in the system $BaO–TiO_2$. *J. Am. Ceram. Soc.*, **38** (1955) 102–113.
14. Hung, C. C., Riman, R. E. & Caracciolo, R., An XPS investigation of hydrothermal and commercial barium titanate powders. *Ceramic Powder Science III*, **12**, (1990) 17–25.
15. Demartin, M., Herard, C., Lemaitre, J. & Carry, C., Grain growth and swelling of hot pressed $BaTiO_3$ during annealing treatments. *Third Euro-Ceramics* **1** (1993) 775–80.
16. Fang, T. T., Lin, H. B. & Hwang, J. B., Thermal analysis of precursor of barium titanate prepared by coprecipitation. *J. Am. Ceram. Soc.*, **73** (1990) 3363–67.
17. Mulder, B., Preparation of $BaTiO_3$ and other ceramic powders by coprecipitation of citrate in alcohol. *Ceram. Bull.*, **49** (1970) 990–993.

Journal of the European Ceramic Society 15 (1995) 637–642
Elsevier Science Limited
Printed in Great Britain.
0955-2219/95/$9.50

0955-2219(95)00024-0

Thermal Spray Spinel Coatings on Steel Substrates: Influence of the Substrate Composition and Temperature

C. Petot,[a] M. Ducos[b] & G. Petot-Ervas[c]

[a]CNRS-LPCM, UPR 211, Université Paris XIII, 93430 Villetaneuse, France
[b]Consultant, Route d'Uchaux, 84550 Mornas, France
[c]CNRS, URA 445, Lab. Physical Metallurgy, ENSCT, 31077 Toulouse, Cedex, France

(Received 24 August 1994; revised version received 24 January 1995; accepted 31 January 1995)

Abstract

Spinel coatings on steel substrates have been obtained by a thermal spraying process. The projection has been done on cold or hot substrates. A further thermal treatment has been performed on some coatings formed on cold substrates. A good adhesion has been observed only on steels rich in oxidizable elements (Z38 CDV5). These coatings have been characterized and tested in a foundry. Adhesion tests have been done by the pulling method and by indentation. The concentration profiles of the most important elements from the metal/oxide interface to the bulk have been determined by EPMA analysis. This set of results has allowed us to show the importance of the coating microstructure and of the diffusion processes on the metal/ceramic bond strength and of the coating stability in contact to Al/Si melted alloys. Such coatings are then good candidates to be used in a foundry to protect the casting tools, mainly when they are performed on heated surfaces.

1 Introduction

Due to the high chemical inertness of ceramics and to the possibility of connecting them to metals, they are increasingly being used as coatings to protect metals in corrosive environments. Some ceramic coatings can also act as thermal barrier. They can both insulate and protect the metal which can then endure extreme thermal cycling under hostile environments. The requirement that the coating must fulfil is dictated by the functions of the device. Nevertheless, its limitations are not due generally to the coating itself but rather by the adhesion quality which is reflected by the fracture resistance of the metal/ceramic interface. Of course, the strength of the metal–ceramic bond is directly linked to the way of formation of the metal/ceramic bonding and to the nature of the material couples but it is also linked to the presence of active species which influence the thermodynamic properties of the interfacial region. Calculating bond strengths is theoretically possible, but at present, results are not available for complex metal/ceramic interfaces. To optimize the metal/ceramic bonding it is then important to have a complete characterization of the interfacial region and to understand as much as possible the correlations between the atomistic configurations and the macroscopic properties.

In the present work, a melted ceramic oxide (Al_2O_3, MgO 70/30 in wt) has been projected in air, using an oxyacetylene flame wire gun fed by a flexible cord, onto previously sanded chromium/molybdenum steels. The spraying has been done on a cold substrate, or on a cold substrate followed by a thermal treatment, or on a hot substrate. Different tests have been performed to characterize these coatings. The adhesion has been controlled by adherence and indentation tests. The metal/ceramic interface has been characterized by EPMA analysis. Furthermore, the coating behavior in contact with Al/Si melted alloys has been studied because such coatings could be used in foundry to protect the casting tools. The set of data obtained has allowed us to identify the main parameters that govern the adhesion and the properties of the coatings.

2 Materials and Coating Procedures

The substrates considered are chromium and molybdenum steels containing different amounts of oxidizible elements (Table 1). They have been coated by the spinel $MgAl_2O_4$ (Al_2O_3/MgO ≈70/30 in wt). The samples for the adhesion tests

Table 1. Composition of the XC38 and Z38 CDV5 steels

Steel XC38									
Al	C	Cr	Cu	Mn	Mo	Ni	P	S	Si
0·06	0·38	0·21	0·22	0·66	0·02	0·02	0·02	0·016	0·27

Steel Z38 CDV5					
C	Cr	Mn	Mo	Si	V
0·34–0·42	4·5–5·5	0·2–0·5	1·2–1·5	0·8–1·2	0·4–0·6

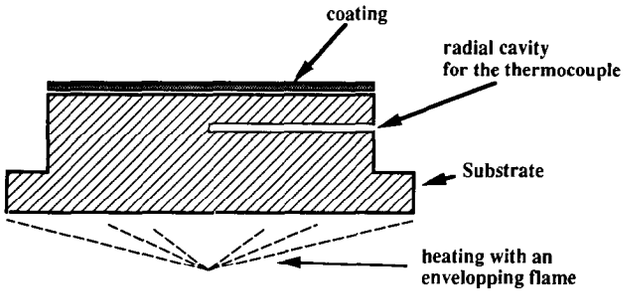


Fig. 1. Sample for the foundry tests.

and EPMA analysis were disks of 50 mm diameter and 3 mm thickness. Those for the foundry tests were cylinders of approximately 50 mm thickness and 50 mm diameter, in order to be able to insert them at the bottom of a casting mould (Fig. 1). All the samples were sandblasted immediately before coating. This allows both cleaning of the substrate surface and creation of surface irregularities giving better adhesion of the coating during the projection (mechanical adhesion).

The projections were performed in air with an oxyacetylene thermal spray flame gun (CYBER-JET model) on which was fitted a ceramic supple string 'SFECORD'. The coating material is melted in the flame and then thrown with a high velocity onto the previously cleaned surface of the substrate. During spraying, the samples were maintained by a steel support. The thickness of the coatings was between 0·1 and 0·2 mm, according to the spraying conditions.

The spinel coatings have been performed on XC 38 and Z38 CDV5 steels, which contain different amounts of oxidizible elements. Three types of coatings have been performed:

- — coatings on cold substrates — samples called IS
- — coatings on cold substrates followed by a thermal treatment under a vacuum of $0{\cdot}5 \times 10^{-2}$ Torr at 800°C, for 100 h — samples called IIS.
- — coatings on a substrate heated at a controlled temperature close to 650–700°C — samples called IIIS

For the coatings IIIS, the temperature of the substrate was controlled with a chromel/alumel thermocouple placed in a radial cavity, as shown in Fig. 1. The heating was performed with an enveloping flame and was maintained during the projection. For the smaller samples an assisted cooling was performed up to 300°C, i.e. for 8 min, in order to prevent thermal shocks. The samples for the foundry (Fig. 1) have a higher calorific capacity. Their temperature decreases naturally from 700 to 300°C, in approximately 17 min.

3 Results

Whatever the type of projection, the coatings on the XC 38 steels crumbled after the projection, during the cooling of the sample. The concentration of oxidizible elements is one of the main differences between the XC38 and the Z38 CDV5 steels. These elements seem to be active species during the projection, performed in air. They can lead to the formation of oxides on the metal surface, in an oxidising atmosphere. These oxides can then react with the coating and create chemical bridges between the metal and the ceramic. The beneficial effect caused by such reactions, due both to the dissolution and to the diffusion of the active species near the metal/ceramic interface, are known in the literature.[1,2] McDonald and Eberhart[1] have found that impurities that are highly oxygen-active can make a major contribution to the adhesion at the interface. Characterizations of the coatings performed on the Z38 CDV5 steel have then been done, in order to establish the main parameters responsible of the adhesion and to check the influence of the oxidizible elements.

3.1 Adhesion tests

The coating adherence is often taken as a criterion which allows definition of the best coating conditions.[3] In the following, two adherence testing methods have been used, in order to compare the adhesion resistance of the spinel coatings on the Z38 CDV5 steels.

3.1.1 Pulling out tests

The adhesion resistance is measured with a traction machine, INSTRON model 1185. The pull

Table 2. Pulling out tests

Sample	Pull out strength (N)	Pull out surface (mm^2)	Adherence (MPa)	Observations
IS	2050	41	50·0	Detachment between the coating and the substrate, in the middle of the sample
	2150	138	15·6	Detachment between the coating and the substrate, from a corner
	2250	103	21·8	Detachment between the coating and the substrate, from an edge
IIS	2550	166	15·4	Coating pulling out
	2750	10	275	The pulling out occurs in the coating thickness
	2850	120	23·8	Coating pulling out
IIIS	3400	130	26·2	The pulling out occurs in the coating thickness
	3950	25	158	Detachment between the coating and the substrate from a corner and partial pulling out of the coating
	4750	20	238	Detachment between the coating and the substrate from a corner and partial pulling out of the coating

rate is equal to 0·5 mm/min. The strength leading to the break at the metal/oxide interface allows the adhesion quality to be known. It is a critical value generally called 'adherence' of the ceramic coating. The results reported in Table 2 show that the adherence is higher for the coatings thermally treated and the best results are obtained for the coatings performed on heated metal substrate (coatings IIIS). Nevertheless, a break sometimes occurs in the thickness of the coatings IIIS. This may be due to changes in temperature during the projection, leading to thermal stresses in the ceramic.[4] Indeed, it is difficult to keep exactly the same experimental conditions from one experiment to the other, with our experimental arrangement. An improvement of the thermal treatment conditions with a better control of the temperature of both the substrate and the coating during the projection can then give promising results. Nevertheless, it may be pointed out that the main use of these coating is to protect steel against corrosion. Therefore, the break inside some coatings observed during the tests does not change the corrosion-preventing performances of the ceramic in service conditions.

3.1.2 Vickers indentation tests

Vickers indentation tests have been performed with a micro-durometer Leitz (HPO-250) at the interface zone of the coatings IS and IIIS. Different loads have been applied on the indenter and the results are in agreement with the pulling out tests. Indeed, we have observed that cracks start to appear for an indenter load of 2 kg for the coatings IS and of 10 kg for the coatings IIIS. Figure 2 shows micrographs of indented samples under a load of 5 kg, applied for 15 s. It illustrates clearly the strong dependence of the coating processing conditions on the mechanical properties of the samples. Indeed, the indentation zone is smaller when the coating is performed on a heated surface (coatings IIIS) and a crack, propagating along the metal/oxide interface, is observed only for the coating IS.

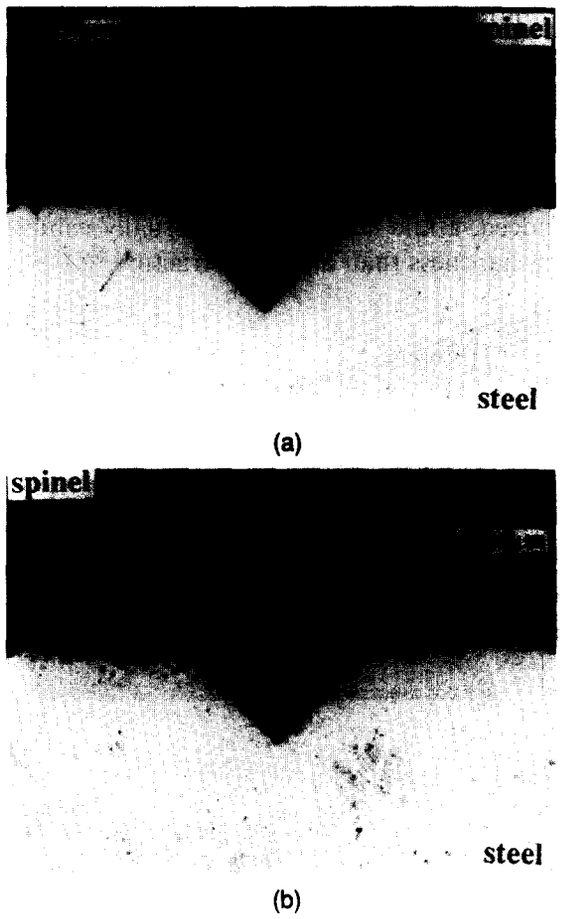


Fig. 2. Spinel coated steel (Z38 CDV5) indented in the interface region (indenter load 5 kg during t = 15 s). (a) Spinel sprayed on an unheated substrate. Note that cracks propagate along the metal/ceramic interface. (b) Spinel sprayed on a heated substrate. Note that the indentation zone is smaller.

3.2 Optical microscopy

Typical cross sections of coatings IS and IIIS on Z38 CDV5 steel are reported in Fig. 3. These micrographs show that the coatings IIIS have a fine microstructure while those performed on an unheated surface (coatings IS) are less dense and microcracks are observed between the particles. Similar observations have been done by Claes and Helgesson[4] who have studied the appearance of alumina droplets sprayed onto cold (20°C) or preheated (600°C) metal substrates. When a droplet hits a cold substrate, it scatters leading to the formation of irregular shape droplets.[4] Indeed, the temperature being too low, the surface tension does not allow them to coalesce and to have a spherical shape. Consequently, they are less mobile and cannot flow into the irregularities of the substrate or of the previous layers. This leads to a porous coating with many interfaces and therefore to a coarse microstructure (Fig. 3(a)). On the contrary, when the droplets hit a preheated substrate they can come together and have time to flow into the irregularities. A more dense coating is then obtained, as shown in Fig. 3(b). It may be pointed out that these microstructural observations are consistent with the indentation tests (Fig. 2). Indeed, a fine microstructure usually exhibits a higher hardness than a coarse structure.[5]

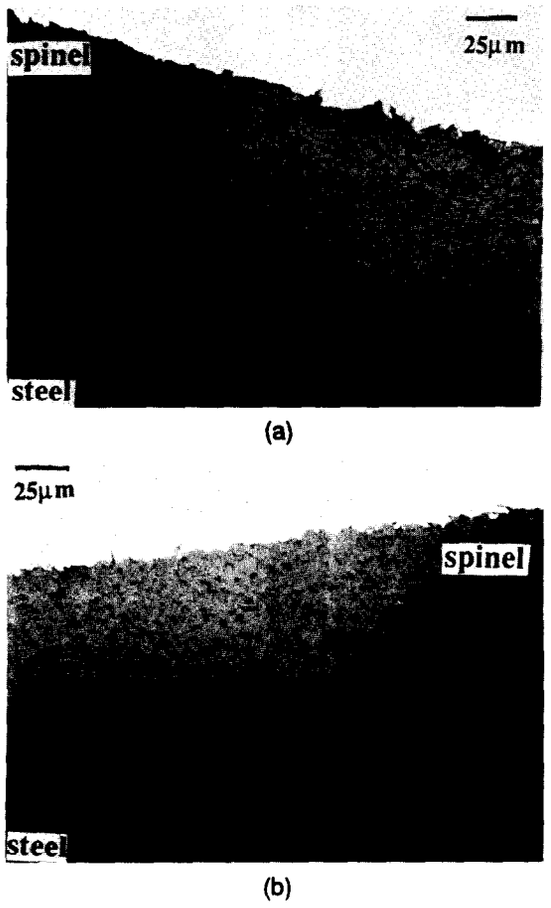


Fig. 3. Cross section micrographs: (a) spinel sprayed on an unheated substrate, (b) spinel sprayed on a heated substrate. Note the perturbation of the metal/oxide interface and the fine microstructure of the coating performed on a heated substrate.

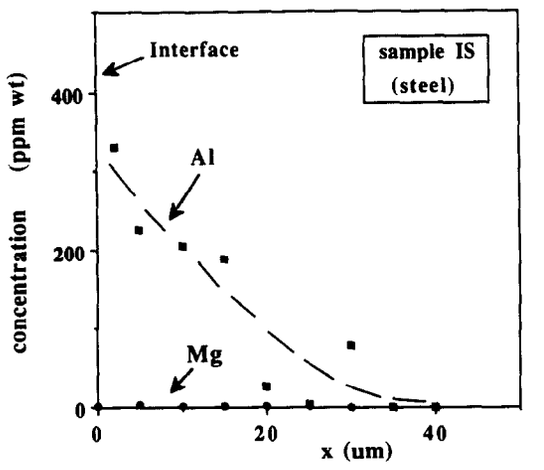
Furthermore, we have observed that the coating IS interface stays planar, whereas at the coating IIIS interface (Fig. 3) perturbations occur in places. Of course, such instabilities have a beneficial effect on the coating adhesion. The initial surface perturbations increase in amplitude when a diffusion process takes place.[6] Consequently, such interface morphologies are consistent with the formation of a 'diffusive coating' when the ceramic is sprayed on heated surfaces.

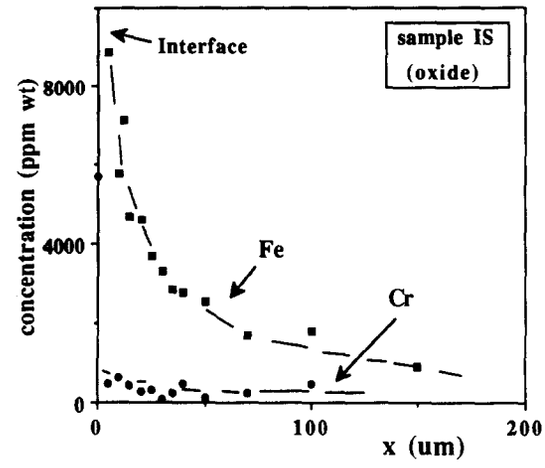
3.3 Electron probe microanalysis

The concentration profiles of the most important elements from the metal/oxide interface to the bulk have been determined by EPMA analysis, in samples IS and IIIS. Typical concentration profiles of Fe, Cr and Si in the oxide and of Al and Mg in the substrate, are reported in Fig. 4. They show clearly the increase of the diffusion zones in the heated coatings. The amount of Fe and Cr close to the interface are nearly the same in samples IS and IIIS. These values seem to be controlled by the solubility limit of these elements in the oxide. The Fe and Cr profiles are very steep in samples IS, whereas they are more extended when the coating is performed on a heated surface (samples IIIS). For silicon, the concentration in the metal seems not to be affected near the interface when the coating is deposited on an unheated substrate and the amount in the oxide is close to the limit of detectability (Fig. 4(a)). In the heated substrate, the silicon concentration increases near the interface both in the metal and in the oxide, due probably to an interfacial reaction between Si and $MgAl_2O_4$ (Fig. 4(b)). For V, Mn and Mo, their amount in the oxide is generally below the limit of detectability.

3.4 Behaviour of the coatings in foundry in contact with an Al/Si melted alloy

The three types of coatings have been studied. The samples (Fig. 1) have been inserted at the bottom of the mould which receives the Al/Si melted alloy, at 700°C. The coating is then subjected to different simultaneous degradations: liquid alloy impact, erosion by the liquid current, thermal shock, thermal stresses and liquid alloy corrosion. The behaviour of the coatings after several casting cycles are described in Table 3. Only the 'diffusive coatings', performed on heated substrate, are very stable. After several casting cycles we have not observed a surface degradation of the ceramic while a scaling is detected, from the first casting cycles, for the coatings performed on unheated substrates. These results are consistent with both the fine microstructure of the coatings IIIS and the strong adherence. Nevertheless, an increase of the quality of the coatings IS is observed after a thermal treat-





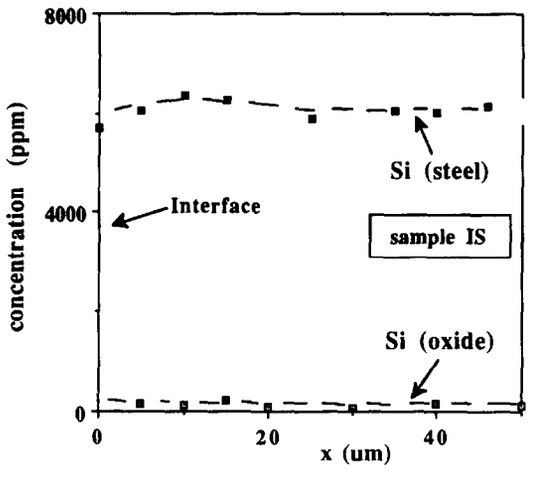
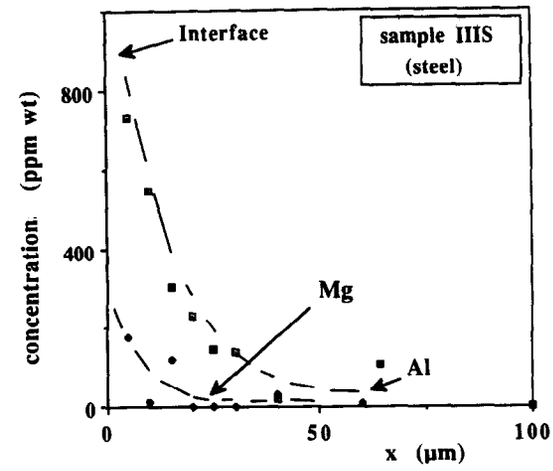
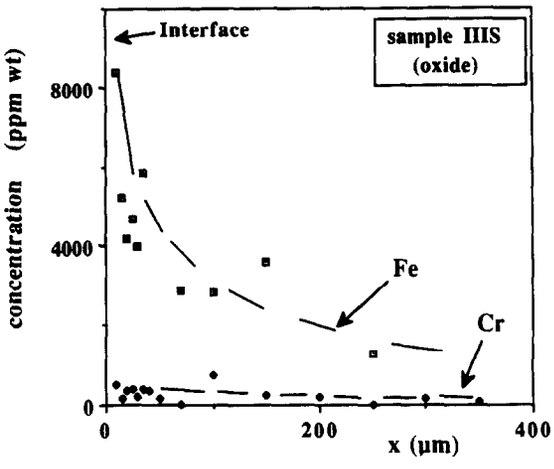


Fig. 4(a). Concentration profiles from the steel/spinel interface of Fe, Cr and Si in the oxide and Al, Mg and Si in the unheated steel.





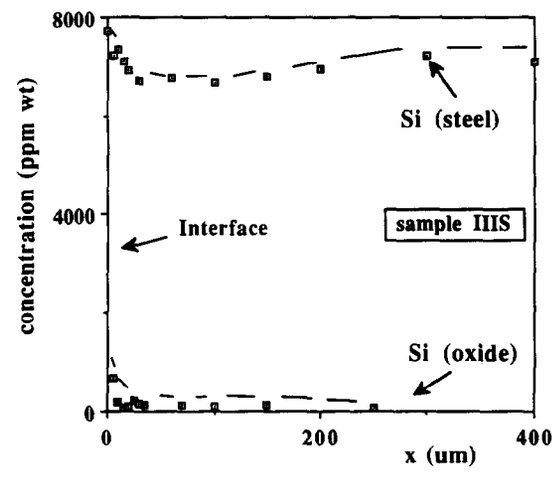


Fig. 4(b). Concentration profiles from the steel/spinel interface of Fe, Cr and Si in the oxide and of Al, Mg and Si in the heated steel.

ment at 700°C (samples IIS). These results show that the degradation of the coating IIS, while continuous, is low (Table 3). An improvement of the coating IS can then be expected by changing the thermal treatment conditions (Section 2).

4 Conclusion

In this work we have first shown the importance of the steel composition on the metal/ceramic bond strength of thermal sprayed coatings. Spinel coatings deposited on XC38 steels crumbled after the projection while spinel coatings on Z38 CDV5 steels are stable. This behaviour has been attributed to the higher amount of oxidizible elements in the Z38 CDV5 steels. Optimization of the properties of the spinel coatings deposited on Z38 CDV5 steel substrates, for use in foundry to protect casting tools against the severe erosion–corrosion conditions encountered when the mould receives the melted alloy, have been performed. The lifetime of the coating deposited on cold substrates increases

Table 3. Coating behaviour in contact with Al/Si melted alloys, after several casting cycles

Spinel coating type	IS	IIS	IIIS
Casting cycles	50	50	730
Observations	Coating scaling from the beginning of the test The interfacial adhesion seems correct	Low and continuous degradation of the coating The interfacial adhesion seems correct	The coating quality widely satisfied the purpose of the test
Coating quality conclusions	Medium	Medium	Satisfactory

when it has been thermally treated at 700°C after deposition, while more promising results have been obtained with coating deposited on heated substrates. Adherence tests, EPMA analysis and microscopical observations have identified the main parameters responsible of the protective properties of the coatings. The fine microstructure, which increases the toughness against the erosion by the melted alloy impact, and the strong metal/ceramic bond contribute to the protective performances of the coatings performed on heated substrates. These properties are in part due to the diffusion processes at the metal/oxide interface as well as the surface instabilities which have a beneficial effect on coating adherence.

Acknowledgements

The authors thank C. Richard (UTC Compiègne) and F. Miard (Université Paris XIII) who have performed the indentation tests and the foundry experiments, respectively.

References

1. McDonald, J. E. & Eberhart, J. G., Adhesion in aluminium oxide–metal systems. *Trans. Metall. Soc. A.I.M.E.*, **233** (1965) 512–7.
2. Loehman, R. E., Interfacial reactions in ceramic-metal systems. *Ceram. Bull.*, **68**(4) (1989) 891–6.
3. Mizuhara, H., Huebel, E. & Oyama, T., High-reliability joining of ceramic to metal. **68**(9) (1989) 1591–9.
4. Claes, I. & Helgesson, I., Influence of coating variables on the properties of flame and plasma sprayed ceramic coatings. *Proc. Xth Int. Ceram. Congress*, Stockholm, Sweden, June 12–18, 1966, pp. 393–412.
5. Tiziani, A., Giordano, L., Matteazi, P. & Badan, B., Laser stellite coatings on austenite stainless steels. *Mater. Sci. Engng.*, **88** (1987) 171–5.
6. Rühle, M. & Evans, A. G., Structure and chemistry of metal/ceramic interfaces. *Mater. Sci. Engng*, **88** (1987) 187–97.

Journal of the European Ceramic Society **15** (1995) 643–650
© 1995 Elsevier Science Limited
Printed in Great Britain. All rights reserved
0955-2219(95)00030-5
0955-2219/95/$9.50

Creep Crack Growth in Alumina with a Glassy Phase

G. Martin, T. Fett & D. Munz

Forschungszentrum Karlsruhe, Institut für Materialforschung II and Universität Karlsruhe, Institut für Zuverlässigkeit und Schadenskunde im Maschinenbau, Karlsruhe, Germany

(Received 22 September 1994; revised version received 19 January 1995; accepted 31 January 1995)

Abstract

Creep-induced crack growth can be described with the C-integral as the relevant load parameter. Several possibilities of evaluating the C*-integral in single specimen tests are discussed, and the constant load and the constant loading-rate are applied to an alumina ceramic containing a glassy phase. The crack-growth rate as a function of the C*-integral is described by a power-law relation with an exponent which agrees very well with the theoretical value.*

1 Introduction

Fracture at elevated temperatures may be caused by subcritical crack propagation, which starts from existing flaws or from creep-induced damage caused by the formation and coalescence of pores. Whereas in the range of subcritical crack growth, which can be described by linear–elastic fracture mechanics, the stress intensity factor is the stress variable at the crack, this is the C^*-integral in the range of noticeable creep.[1] Creep-induced crack growth has very often been studied for metals, but investigations into ceramic materials are sparse.[2–4] It is the aim of this investigation to determine the crack-growth rates as a function of the C^*-integral for macroscopic cracks.

The C^*-integral — proposed by Landes and Begley[1] — is a path-independent energy-rate line integral. In the two-dimensional case (see Fig. 1) it is defined as

$$C^* = \int_\Gamma W^* \mathrm{d}y - T_i \frac{\partial v_i}{\partial x} ds \tag{1}$$

$$W^* = \int_0^{\epsilon_{ij}} \sigma_{ij} \mathrm{d}\epsilon_{ij} \tag{2}$$

where W^* is the strain-energy density rate, T_i is the traction vector, v_i is the displacement vector, and ds is a line length increment along the contour Γ.

The C^*-integral governs the stresses and strains in front of a crack tip. A premise for the applicability of the C^*-integral as a loading parameter is the occurrence of secondary creep, which may be described by a Norton power law

$$\dot{\epsilon}_s = D\,\sigma^n \tag{3}$$

Under this condition, an HRR-stress field occurs ahead of the crack tip.[5,6] The stresses and strain rates are given by

$$\sigma_{ij} = \left(\frac{C^*}{I_n D r}\right)^{\frac{1}{n+1}} \tilde{\sigma}_{ij}(\theta) \tag{4}$$

$$\dot{\epsilon}_{ij} = \left(\frac{C^*}{I_n D r}\right)^{\frac{n}{n+1}} \tilde{\sigma}_{ij}(\theta) \tag{5}$$

where $\dot{\epsilon}$ is the strain rate and $I_n(n)$ and $\tilde{\sigma}_{ij}(\theta)$ are the dimensionless functions, which can be taken from Ref. 6.

Under creep conditions, the application of a load instantly yields an elastic strain reaction. This elastic strain is superposed by creep strains. In the vicinity of the crack tip eqn (5) is immediately valid, but under non-steady-state creep conditions the parameter C^* has to be replaced by the time-dependent parameter $C(t)$.[7]

For very short times after load application, the stress intensity factor K is the relevant loading parameter, which describes the stresses at the crack tip

$$\sigma_{ij} = \left[\frac{\alpha K_I^2}{I_n D r (n+1)\, tE'}\right]^{\frac{1}{n+1}} \tilde{\sigma}_{ij}(\theta) \tag{6}$$

where $E' = E/(1-\nu^2)$ (E = Young's modulus, ν = Poisson's ratio). The numerical factor α is given in Ref. 7 as $\alpha \simeq 1$. With increasing size of the creep zone, the stress field is firstly governed by $C(t)$ and tends asymptotically to the C^*-controlled state. Since

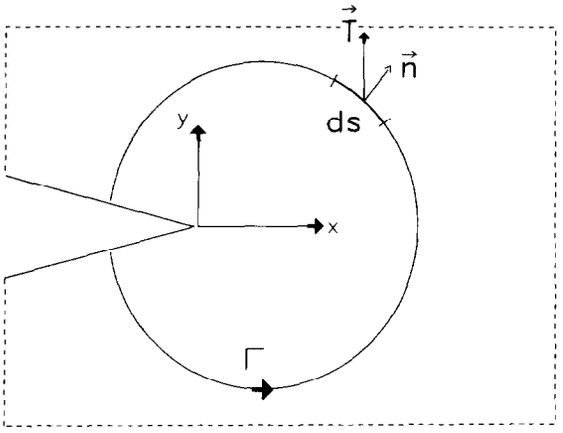


Fig. 1. Definition of the C^*-integral.

$$C(t) \to \frac{\alpha K_1^2}{(n+1)\, t\, E'} \text{ for } t \to 0 \tag{7}$$

and

$$C(t) \to C^* \text{ for } t \to \infty \tag{8}$$

Riedel[7] proposed the interpolation formula:

$$C(t) = \left(1 + \frac{t_1}{t}\right) C^* \tag{9}$$

for the region $t \simeq t_1$ with the characteristic time

$$t_1 = \frac{K_1^2}{(n+1)\, E' C^*} \tag{10}$$

In cases where primary creep dominates an additional integral quantity denoted C_h^* has to be applied. In this investigation we restrict our considerations to C^*.

2 The Experimental Determination of C^*

C^* can be expressed by the power difference of two identically loaded structures containing cracks of depths a and $a + da$, respectively, i.e.

$$C^* = -\frac{1}{B}\frac{dU^*}{da}, \quad U^* = \int_0^{\dot\delta} F\, d\dot\delta \tag{11}$$

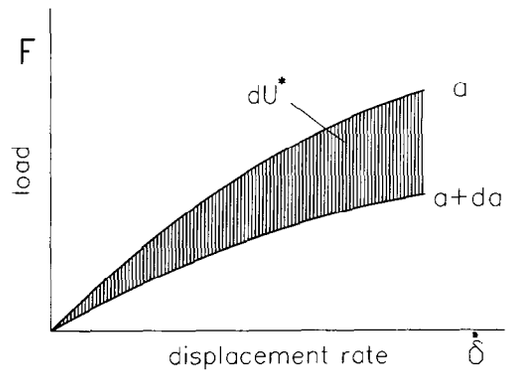


Fig. 2. Increment of energy rate dU^* for two cracks with crack lengths a and $a + da$.

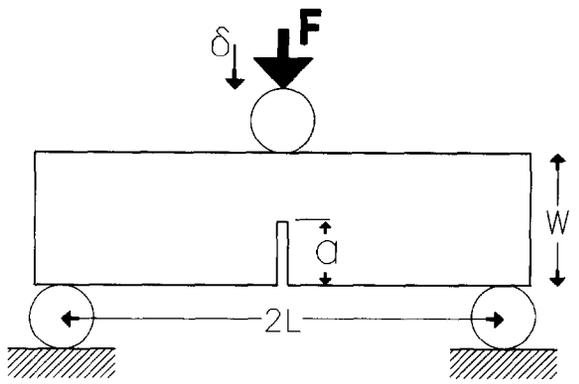


Fig. 3. Geometrical and loading quantities.

(B = specimen thickness). This relationship offers the possibility to determine C^* experimentally. The quantities entering eqn (11) are explained by Fig. 2. Equation (11) is the basis for a number of procedures for determination of C^*. The experimental data necessary for the evaluation of eqn (11) are the force F, the displacement rates $\dot\delta$ of the load application points, and the crack length a.

2.1 Single-specimen evaluation

The application of C^* as the crack-tip parameter was proposed by Landes and Begley[1] in analogy to the J-integral, the loading parameter in case of plastic material behaviour. J-integral solutions are available for numerous types of specimen and loading. In the EPRI-handbook[8] a number of FE-solutions are reported. Due to the analogy between Norton-like creep and strain-hardening plasticity,[9] the data of the EPRI-handbook can be used also for the computation of C^*. By introducing the net stress

$$\sigma_{\text{net}} = \frac{F}{B(W-a)} \tag{12}$$

Riedel[7] proposed the simple relation

$$C^* = aD\sigma_{\text{net}}^{n+1}\, g_1 \tag{13}$$

It should be noted that eqn (13) is only valid if the creep behaviour is correctly described by a Norton-relation. The geometric function $g_1(a/W,n)$ depends on the stress state and differs for plane-stress and plane-strain conditions. A second possibility to determine C^* — also proposed by Riedel[7] — is based on the measurement of the displacement rate at the load-application points

$$C^* = \sigma_{\text{net}}\, \dot\delta\, g_2 \tag{14}$$

with g_2 dependent on a/W and n. Based on the formulation eqn (11), Webster[10] derived

$$C^* = \frac{F^{n+1}}{B(n+1)}\frac{dC_n}{da} \tag{15}$$

with the creep-compliance

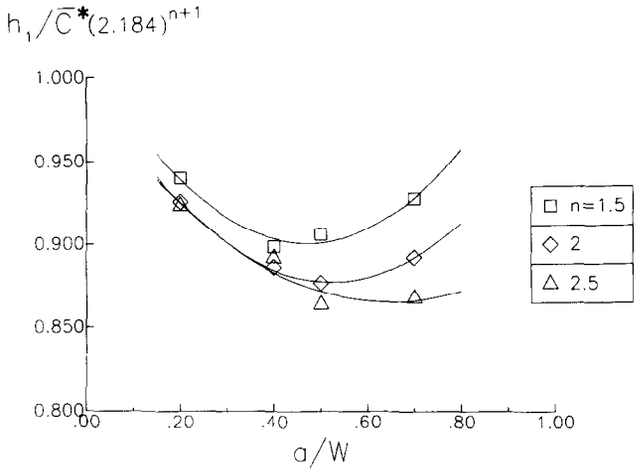


Fig. 4. Ratio of geometric functions from Walz[13] and the EPRI-handbook.[8]

$$C_n = \frac{\dot{\delta}}{F^n} \tag{16}$$

For a static test it results

$$C^* = \frac{F\dot{\delta}}{BW}\left[\frac{W}{n+1}\,\frac{1}{\dot{\delta}}\,\frac{d\dot{\delta}}{da}\right] \tag{17}$$

and in the dynamic loading case with constant displacement rates at the load application points

$$C^* = \frac{F\dot{\delta}}{BW}\left[-\frac{n}{n+1}\,\frac{W}{F}\,\frac{dF}{da}\right] \tag{18}$$

Based on the integral formulation of C^*, Harper and Ellison[11] derived for the static test (F = constant)

$$U^* = \frac{1}{n+1} DL \left(\frac{F}{m_{pl}BW}\right)^n F \tag{19}$$

and in case of constant displacement rates

$$U^* = \frac{n}{n+1} DL \left(\frac{F}{m_{pl}BW}\right)^n F \tag{20}$$

where L is the specimen length, for example the supported length of a bending bar and F is the applied load. m_{pl} is the ratio of the loads necessary to plastify the specimen with and without crack for ideal plastic material behaviour. Consequently, C^* results

$$C^* = -\frac{n}{n+1} DL \left(\frac{F}{m_{pl}BW}\right)^{n+1} \frac{dm_{pl}}{d(a/W)} \tag{21}$$

2.2 Multiple-specimen evaluation

The procedure of Landes and Begley comprises several steps. The detailed description is given in the original paper.[1]

(1) In the first step the load F is plotted as a function of the crack length a and the displacement rate $\dot{\delta}$. The area below the resulting curves gives the energy rate $U^*(a,\dot{\delta})$.

(2) The representation $U^* = f(\dot{\delta}, a)$ provides the derivative $\partial U^*/\partial a$ as a function of $\dot{\delta}$.

(3) From eqn (9) C^* is calculated and plotted versus $\dot{\delta}$.

(4) The basic data directly give $da/dt = f(a, \dot{\delta})$ and, finally, the combination of steps 3 and 4 results in the da/dt versus C^* curve.

This procedure has been applied successfully to Al_2O_3 which contains a glassy phase.[2,4] A further possibility to determine C^* has been proposed by Kanninen and Popelar.[12] Their procedure is based on tests with constant load where the crack length is determined as a function of time. The further procedure is identical with the evaluation according to the procedure proposed by Landes and Begley.[1]

In the present investigation the evaluation of single tests will be applied.

3 Determination of C^* in 3-point bending tests

The procedure of Landes and Begley, Kanninen and Popelar, Harper and Ellison and Webster are directly applicable in 3-point bending. With the relationships proposed in Ref. 7 also the J-integral solutions for bending tests can be used for the determination of C^*. The geometric functions g_1 and g_2 can be written in terms of the h-parameters h_1 h_2 tabulated in:[8]

$$g_{1b} = \left(\frac{W}{a} - 1\right) h_1 \left(\frac{L}{0{\cdot}728\,(W-a)}\right)^{n+1} \tag{22}$$

$$g_{2b} = \frac{h_1}{h_3}\,\frac{L}{0{\cdot}728a} \tag{23}$$

where the subscript b stands for bending. The geometric quantities L, a and W can be seen from Fig. 3. The C^*-integral can also be computed from

$$C^* = D(W-a)\, h_1 \left(\frac{FL}{0{\cdot}728B(W-a)^2}\right)^{n+1} \tag{24}$$

The h-parameters of the EPRI-handbook may be expressed by the following approximations for the range $2 \le n \le 7$

$$h_1 \simeq \alpha \left[1{\cdot}26 + \sum_{\nu=1}^{4}\sum_{\mu=1}^{3} A_{\nu\mu}\,(1-\alpha)^\nu n^{\mu/5}\right]^2 \tag{25}$$

$$h_3 \simeq \frac{1}{\alpha}\left[\sum_{\nu=0}^{3}\sum_{\mu=0}^{2} A_{\nu\mu}\,(1-\alpha)^\nu n^\mu\right]^2 \tag{26}$$

with $\alpha = a/W$ and the coefficients $A_{\nu\mu}$ listed in Table 1 for h_1 and in Table 2 for h_3

It is a well-known fact that ceramics containing a glassy phase exhibit non-symmetry in their creep behaviour. The creep rates under tensile stresses may be substantially higher than under compressive

Table 1. h-parameters. Coefficients for eqn (25)[4]

	$\mu = 1$	2	3
$\nu = 1$	4·4451	−4·552	0·1232
2	8·9083	−9·312	3·9838
3	−23·27	20·225	−3·790
4	13·543	−6·597	−1·333

Table 2. h-parameters. Coefficients for eqn (26)

	$\mu = 0$	1	2
$\nu = 0$	2·1204	−0·196	0·0153
1	−0·809	−0·287	−0·025
2	0·2307	0·7110	0·0519
3	0·4596	−0·326	−0·046

stresses. This behaviour affects heavily the bending creep test in which tension and compression occur. Very often, the non-symmetry is related only to the state of secondary creep. This seems to be the case e.g. for MgO-doped hot-pressed silicon nitride (HPSN).[14] If we take into consideration this non-symmetry, the Norton power law may be modified as

$$\dot{\epsilon}_s = \lambda\, D|\sigma|^n \tag{27}$$

with

$$\lambda = \left\{ \begin{array}{l} 1 \text{ for } \sigma > 0 \\ \dfrac{-1}{\gamma^n} \text{ for } \sigma < 0 \end{array} \right\} \tag{28}$$

and $\gamma > 0$.

In a Finite-Element study Walz[13] determined the C^*-integral in 3 point bending for a number of n-values and γ = 1, 5 and 10. The results are expressed by a geometric function C^* defined as

$$C^* = DW(1 - a/W)^{-(2n+1)}\bar{C}^*\,\sigma^{n+1} \tag{29}$$

where σ is the elastically calculated outer fibre bending stress. In case of symmetric creep behaviour (γ = 1), the geometric functions obtained by Walz[13] can be compared with the C^*-values according to eqn (24). From eqn (24) and eqn (29) one obtains

$$\bar{C}^* = \frac{h_1}{2{\cdot}184^{n+1}} \tag{30}$$

Figure 4 illustrates the quantity $h_1/\bar{C}^*2{\cdot}184^{n+1}$ as a function of α for several n-values. The deviations from the expected value 1 are caused by different values chosen for L/W. Whilst in the EPRI-handbook[8] L/W = 2 is used, the calculations of Walz[13] were performed with L/W = 4·4, as usual for ceramic bending bars. From the computations of Walz the geometric functions C^* were obtained, as listed in Tables 3 and 4.

4 Experiments

4.1 Material and measurements

The tested material was an Al_2O_3 containing a glassy phase. Short characterisation of the material used: density 3·75 g/cm^3, mean grain size 5 μm, composition 96% Al_2O_3 (2·7% SiO_2, 1·3% MgO, 0·02% CaO, 0·02% Fe_2O_3), fracture toughness 20°C: 3·4 MPa $\sqrt{m}$, 1100°C: 4·1–5·2 MPa $\sqrt{m}$, 1200°C: 3·1–5·0 MPa $\sqrt{m}$, elasticity data at 20°C E = 325 GPa, ν = 0·24. In 4-point bending creep tests the parameters of secondary creep were determined as:[4] n = 2·25, $D = 1{\cdot}4 \times 10^{-8}$ (in MPa, h), γ = 5·1. Bending specimens, 3·5 × 4·5 × 45 mm in size, were diamond machined and then annealed in the vacuum for 5 h at 900°C. Then the specimens were damaged by introducing narrow saw cuts of 50 μm width. A second series of bending bars was precracked using the bridge indentation method. The static and dynamic tests were performed in a testing device as used in creep tests.[14] With this device the displacements can be measured within the inner roller span where the bending moment is constant. The 3-point bending tests were carried out with a modified device where the outer displacement pick-ups were applied directly under the outer rollers. All bending tests were performed with $2L$ = 40 mm. The experimental input for the determination of C^*

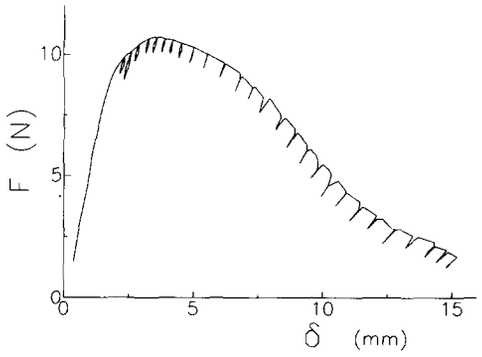


Fig. 5. Partial unloadings in a dynamic bending test.

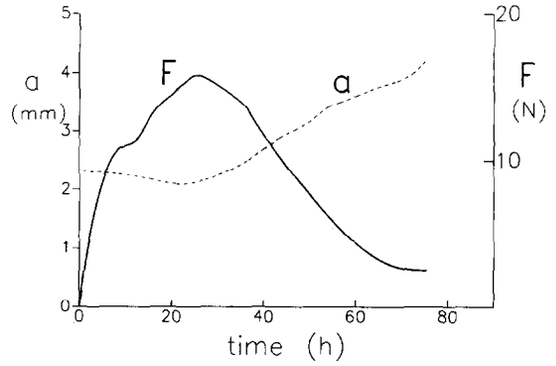


Fig. 6. Dynamic bending test (displacement rate: 2 μm/h).

Table 3. Geometric function $\overline{C}^*$ according to eqn (29) for $\gamma = 5$

a/W	$n = 1{\cdot}5$	2	2·5
0·1	0·0470	0·0242	0·0127
0·2	0·0644	0·0335	0·0163
0·3	0·0664	0·0344	0·0144
0·4	0·0621	0·0314	0·0107
0·5	0·0577	0·0275	0·0077
0·6	0·0553	0·0241	0·0068
0·7	0·0541	0·0215	0·0084
0·8	0·0495	0·0183	0·0120

Table 4. Geometric function $\overline{C}^*$ according to eqn (29) for $\gamma = 10$.

a/W	$n = 1{\cdot}5$	2	2·5
0·1	0·0393	0·0163	0·0065
0·2	0·0577	0·0153	0·0061
0·3	0·0586	0·0109	0·0045
0·4	0·0503	0·0091	0·0030
0·5	0·0403	0·0104	0·0026
0·6	0·0356	0·0126	0·0032
0·7	0·0424	0·0151	0·0043
0·8	0·0662	0·0215	0·0044

are the load–displacement curves and the crack-length data which are determined from partial unloadings. During the periodical partial unloadings the displacements are recorded. An example is shown in Fig. 5. The slopes of the partial unloadings decrease with increasing crack length. During partial unloading and reloading hysteresis effects were observed. Therefore, the usually applied linear–elastic compliance relationship could not be applied. Dynamic bending tests were interrupted in different states and the specimens were broken at room temperature. Then it was possible to measure the crack size on the fracture surface, and one point of the relationship slope of the hysteresis = $f(a)$ has been determined. A series of such tests then yielded the complete calibration curve. The result of a single cynamic bending test performed with a bar containing a saw-cut of 50 μm width and $a/W \simeq 0{\cdot}5$, with a displacement rate $\dot{\delta} = 2$ μm/h, is shown in Fig. 6. The crack starts propagating approximately when the maximum load is reached, and the following crack growth is nearly proportional to the time.

4.2 Evaluation of constant load tests

The loading-point displacements occurring in a creep-crack-growth test consist of three contributions:

- the creep deformations δ_c caused by the singular stress field close to the crack tip;
- the share of global creep deformation occurring in the remote parts of the specimen, δ_{nc}, and
- the contribution caused by an increase in compliance due to crack extension δ_{el}.

The measurable total displacements are

$$\delta_{meas} = \delta_c + \delta_{nc} + \delta_{el} \tag{31}$$

Due to the change of crack length during creep crack growth, an elastical displacement rate $\dot{\delta}_{el}$ occurs. In order to consider only creep effects, the elastic part has to be eliminated, i.e.

$$\dot{\delta} = \dot{\delta}_{meas} - \dot{\delta}_{el}, \quad \dot{\delta}_{el} = F \frac{\partial C}{\partial a} \dot{a} + C\dot{F} \tag{32}$$

or it has to be ensured that the elastic part can be neglected. Displacement rates obtained in a constant load test are plotted in Fig. 7. Whereas the total displacement rate $\dot{\delta}_{meas}$ was experimentally determined, the quantity $\dot{\delta}_{nc}$ was measured in a separate test with an unnotched specimen and $\dot{\delta}_{el}$ was computed from the time-dependent increase in crack length.

As a premise for the correct determination of dU^*/da it has to be ensured that crack propagation had taken place and that the minimum displacement rate in a test has been reached. In Fig. 8 the crack-growth initiation times — the time span between the moment of load application and

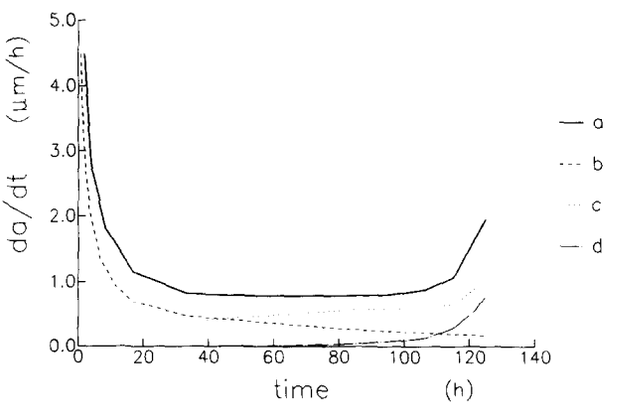


Fig. 7. Displacement rates in a constant load test.; (a) $\dot{\delta}_{meas}$; (b) $\dot{\delta}_{nc}$; (c) $\dot{\delta}_c$; (d) $\dot{\delta}_{el}$.

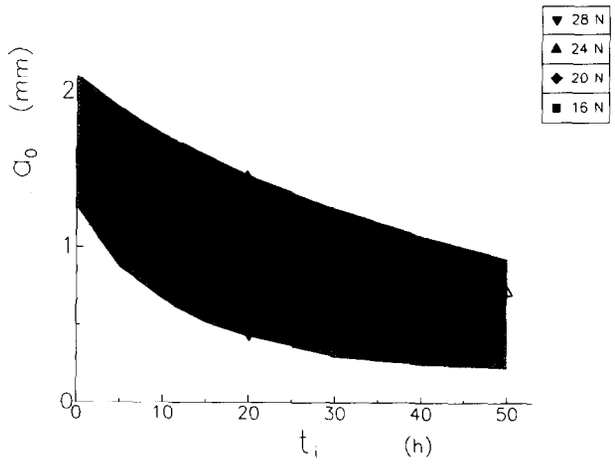


Fig. 8. Initiation times for creep crack growth tests under static load as a function of the initial crack length a_o; solid symbols: cracks introduced by a saw-cut of 50 μm width, open symbols: pre-cracked by the bridging method.

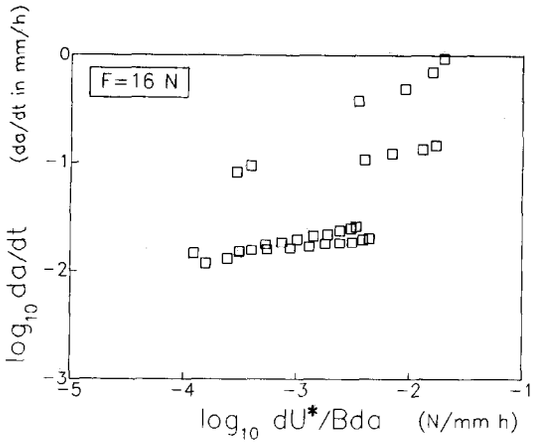


Fig. 9. Crack-growth rate as a function of dU^*/da.

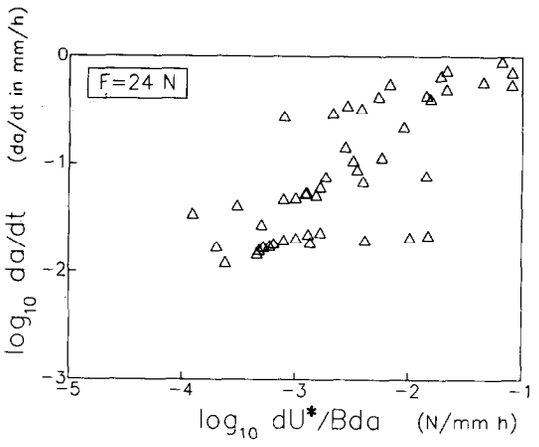


Fig. 11. Crack growth rate as a function of dU^*/da.

the first detectable crack extension — are plotted as a function of the initial crack length a_0.

It can be seen that no significant difference exists between specimens with saw-cut and with precrack. The tendency of decreasing crack-growth initiation time with increasing initial crack size is perceptable and has been expected.

Several series of static bending tests were evaluated with the method proposed by Webster,[10] eqn (17). The change of creep power with crack length was determined for test times $t > 20$ h at 8 h intervals and for times $t < 20$ h in time steps of 1–2 h until the specimens failed or the tests were suspended. All test durations were within 5 h and 340 h. The results are plotted in Figs 9–12.

4.3 Determination of C^*

The values dU^*/da determined in the experiments have to be examined out whether or not they represent valid C^*-values. In order to decide this, we have to compute the characteristic times t_1, using eqn (10). For times $t > 10\ t_1$ we expect the results to be valid C^*-values. Figure 13 shows the results of the constant load tests. The data undergo much scatter. There is some evidence that the very low crack-growth rates may be caused by R-curve effects. The R-curve behaviour shields the crack-tip region from the externally applied loads which results in lower crack-tip loading and, consequently, lower crack-growth rates. A clear indication is the reduction of the scatter band if only the first C^*-data of each test is considered. These data are introduced in Fig. 13 as solid symbols. For these tests the R-curve, for instance caused by crack-bridging effects, does not influence the result since $\Delta a = a - a_0 \to 0$. Fitting the solid symbols we find the power-law relation of creep-crack growth

$$\frac{da}{dt} = 6{\cdot}9\ \frac{\text{mm}}{\text{h}}\ C^{*0{\cdot}77} \tag{33}$$

(C^* in N/mm h). The corresponding straight line is entered in Fig. 13. Figure 14 shows the data resulting from times $t_1/10 \le t \le 10\ t_1$ evaluated according to eqn (9). These data can be expressed by

$$\frac{da}{dt} = 4{\cdot}4\ \frac{\text{mm}}{\text{h}}\ C(t)^{0{\cdot}71} \tag{34}$$

($C(t)$ in N/mm h). For identical crack-growth rates $C(t)$ is slightly lower than C^*. Riedel[7] has shown that the exponent of the creep-crack growth relation should be a simple function of the Norton creep exponent, namely

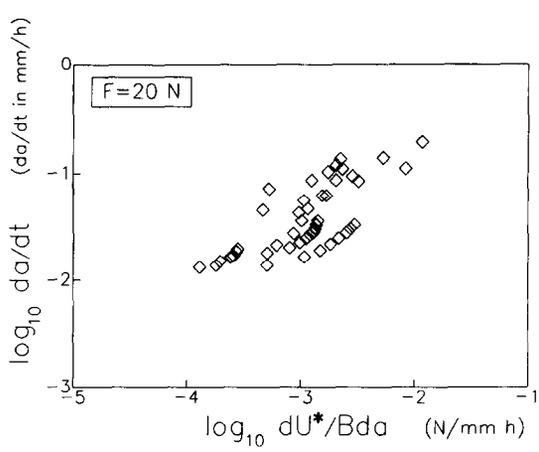


Fig. 10. Crack-growth rate as a function of dU^*/da.

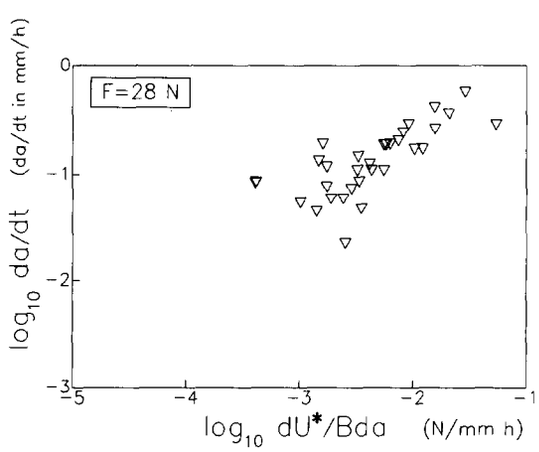


Fig. 12. Crack-growth rate as a function of dU^*/da.

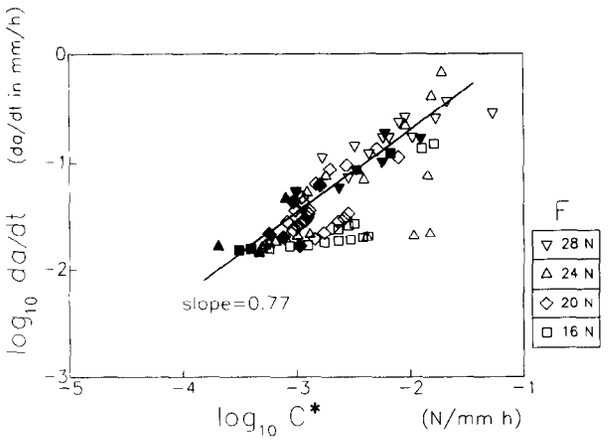


Fig. 13. Crack-growth rate as a function of C^* from static tests. Solid symbols: first values at the beginning of crack extension.

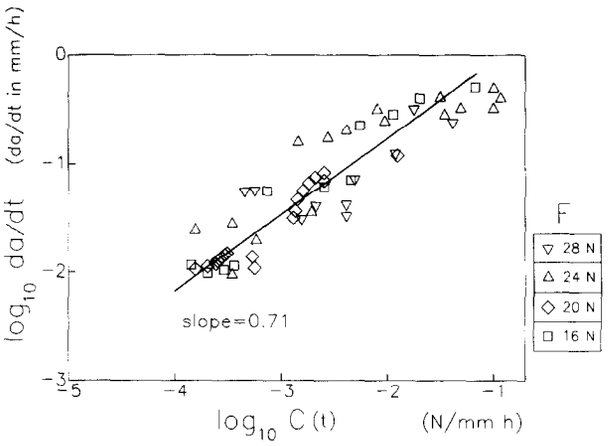


Fig. 14. Crack-growth rate as a function of $C(t)$ from static tests.

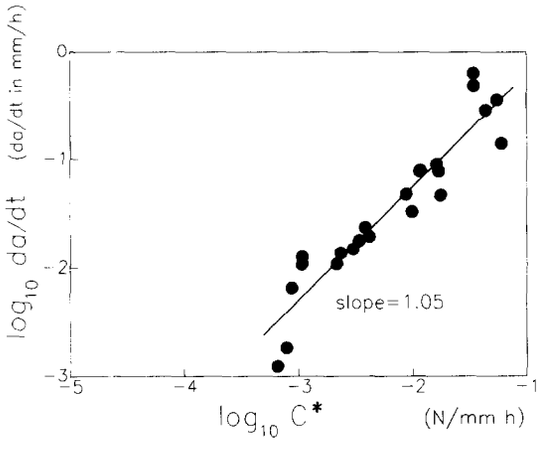


Fig. 15. Crack-growth rate as a function of C^* from dynamic tests.

$$\frac{da}{dt} \propto C^{*n/(n+1)} \tag{35}$$

leading for the investigated material ($n = 2{\cdot}25$) to an exponent of 0·69. This expected value is in very good agreement with the experimental result.

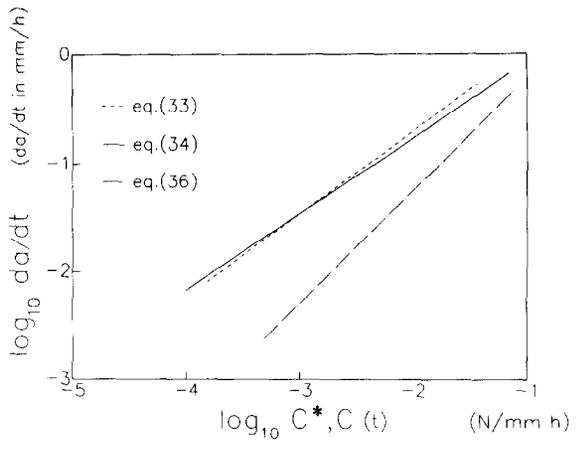


Fig. 16. Intercomparison of the crack-growth relations.

4.4 Evaluation of dynamic bending tests

The single-specimen evaluation from the dynamic tests (tests with constant displacement rates) was performed with eqn (18). It was assumed that in the range of decreasing load steady-state creep conditions are sufficiently fulfilled. The tests were performed with displacement rates in the range from 0·2 μm/h to 10 μm/h. The initial crack sizes were in the range 1 mm $\leq a_0 \leq$ 2·3 mm. In the region where the tests were evaluated the corresponding loads were between 8 and 22 N. Since, unfortunately, the crack-growth rates in the range of decreasing load were found to be highly constant in each test, it was only possible to determine one single C^*-value for one da/dt-value. Figure 15 shows the data obtained. Also in these tests a power law was found

$$\frac{da}{dt} = 6{\cdot}9 \ \frac{\text{mm}}{\text{h}} \ C^{*1{\cdot}05} \tag{36}$$

(C^* in N/mm h). The slightly increased exponent of 1·05 may be caused by R–curve influences. In case of the dynamic tests, the cracks had strongly grown by about 1·4 mm to attain the range of decreasing load. In the static tests the mean crack extension was only $\simeq$ 0·3 mm. Consequently, R–curve effects are stronger in the dynamic tests since $\Delta a \not\to 0$.

A comparison of the crack-growth relations, eqns (33), (34) and (36), is given in Fig. 16.

5 Summary

The paper deals with the determination of the loading quantities C^* and $C(t)$ for creep-crack growth. Different possibilities of evaluating the C^*-integral in single-specimen tests were listed, and the constant load test and the constant loading-rate test were applied to an alumina ceramic

containing a glassy phase. It was found that:

- the crack-growth rate as a function of the loading quantities C^* and $C(t)$ can be described by a power-law relationship;
- the exponents in static tests are about 0·75 and agree very well with the theoretical value (here: 0·69) proposed by Riedel;[7]
- the exponent resulting in tests with constant displacement rate is slightly higher, possibly influenced by R–curve effects.

References

1. Landes, J. D. & Begley, J. A., *ASTM STP 590*, 1976, pp. 128–48.
2. Kromp, K., Haug, T., Pabst, R. F. & Gerold, V., *C* for ceramic materials?, 3. Conf. on Creep and Fracture of Engineering Materials and Structures*, London, 1989, pp. 1021–32.
3. Martin, G., Fett, T. & Munz, D., *Determination of creep crack growth in ceramics*, Proc. 2nd ECRS-Conference, Augsburg, 1991.
4. Fett, T., Mißbach, M. & Munz, D., Failure behaviour of Al_2O_3 with glassy phase at high temperatures. *J. Europ. Ceram. Soc.*, **13** (1994) 197–209.
5. Hutchinson, J. W., Plastic stress and strain fields at crack tip. *J. of Mech. and Phys. of Solids*, **16** (1968) 13–31.
6. Rice, J. R. & Rosengren, G. F., Plane strain deformation near crack tip in power law hardening material, *J. of Mech. and Phys. of Solids*, **16** (1968) 1–12.
7. Riedel, H., *Fracture at high temperatures*, Springer-Verlag, Berlin, 1987.
8. Kumar, V., German, M. D. & Shih, C. F., An engineering approach for elastic–plastic failure analysis. *EPRI-Report NP-1931*, Palo Alto, 1981.
9. Hoff, N. J., Approximate analysis of structures in the presence of moderately large creep deformations *Quarterly of Applied Mathematics*, **12** (1954) 49–55.
10. Webster, G. A., *Crack growth at high temperatures*, Conference on Mechanics and Physics of Fracture, Paper 18. Cambridge, 1975.
11. Harper, M. P. & Ellison E. G., The use of the C^* parameter in predicting creep crack propagation rates. *J. of Strain Analysis*, **12** (1977).
12. Kanninen, M. F., Popelar, C. H., *Advanced Fracture Mechanics*, Oxford Engineering Science Series 15, Clarendon Press, Oxford, 1985 p. 437.
13. Walz, G., unpublished results.
14. Fett, T., Keller, K. & Munz, D., An analysis of the creep of hot-pressed silicon nitride in bending. *J. Mater. Sci.*, **23** (1988) 467–74.

Journal of the European Ceramic Society 15 (1995) 651–653
© 1995 Elsevier Science Limited
Printed in Great Britain. All rights reserved
0955-2219(95)00032-1
0955-2219/95/$9.50

Acoustic Emission Monitoring of Damage Evaluation in Ceramics Submitted to Thermal Shock

F. Mignard, C. Olagnon & G. Fantozzi

Laboratoire GEMPPM, URA CNRS 341, bât. 502, INSA de Lyon, 20 bd. A. Einstein, 69621 Villeurbanne Cedex, France

(Received 27 September 1994; revised version received 3 February 1995; accepted 7 February 1995)

Abstract

In studies conducted on two ceramic materials, namely a porous alumina and a dense zirconia, it is shown that a simple acoustic emission experiment can provide valuable information on the processes of thermal shock degradation in the materials.

Acoustic emission technique for thermal shock damage evaluation of ceramics is particularly attractive because it is non-destructive and it gives *in-situ* information. However, the complexity of the acoustic emission (AE) response of a material makes the quantitative analysis difficult to achieve.[1] Konsztowicz[2,3] used AE for detecting the damaging of refractory or high thermal shock resistance ceramics quenched in silicon oil, but he has not made any direct correlation between the acoustic emission activity and the number of cracks formed. He has also pointed out that not all the signals recorded could be directly related to strength degradation. AE was also used in rising thermal shock by laser irradiation in order to monitor the degradation of thermal barrier coating.[4]

The goal of this work is to show direct relations between AE and thermal shock degradation on relatively dense material, in order to use this technique for monitoring a thermal shock apparatus.

For this purpose thermal shock tests were conducted on two commercial ceramic materials, a coarse grain porous alumina (grade AL24, Degussa, Germany) and a magnesia partially stabilised zirconia (grade Z500, Morgan Matroc, UK). Thermal shock tests consisted of heating the specimens to various high temperatures and to cool them by jet air as described elsewhere.[5] Acoustic emission response of the specimen was recorded with piezoelectric sensor (Bruel & Kjaer sensor, model 8313, resonance frequencies: 250 kHz) connected to a pre-amplifier (Bruel & Kjaer sensor, model 2637, fixed gain: 40 dB) and a main amplifier (Bruel & Kjaer sensor, model 2638, variable gain: 20 dB chosen) leading to a total gain of 60 dB, as described by Peigné.[6] The AE transducer is clamped at the end of a wave guide which plays also the role of a specimen holder (Fig. 1). The envelope of the AE signals delivered by the amplifier is sampled at a frequency of 10 kHz by means of digital/analogical converter driven by a micro-computer. Rectangular flexure specimens of dimensions $4 \times 6 \times 40$ mm^3 were used. The specimens were cooled during 6 s at room temperature by 2 jet air nozzles. This cooling time was shown to be longer than the degradation duration. During the cooling, the acoustic emission was recorded. Alumina specimens were tested as ground and zirconia specimen were polished at 3 μm. Special care regarding subeutectoid ageing treatment was accorded to enhance mechanical properties of Mg—PSZ and to remove residual stresses. The resistance to thermal shock was evaluated in terms of elastic modulus variations and retained strength as shown in Fig. 2. At a critical thermal shock temperature ΔTc, both elastic modulus and retained strength decrease. The number of acoustic emission events is also reported in Fig. 2. Note that the apparition of the first acoustic emission event takes place for the critical thermal shock temperature. This suggests that the degradation is effectively correctly recorded and that it occurs by unstable crack propagation. The number of acoustic peaks increases linearly when increasing the severity of the thermal shock. The critical thermal shock temperature difference is found to be $\Delta Tc = 670$°C for Mg–PSZ and $\Delta Tc = 700$°C for alumina. Thermal, elastic and mechanical properties of these two materials are quite different but their combination leads to similar ΔTc values. It is worth noting that the thermal shock behaviour of the alumina is quite different from that of the Mg–PSZ. After ΔTc, the retained strength of the alumina material is about 0·5 σ_R which is higher than the 0·15 σ_R retained strength measured in Mg–PSZ. The elastic modulus

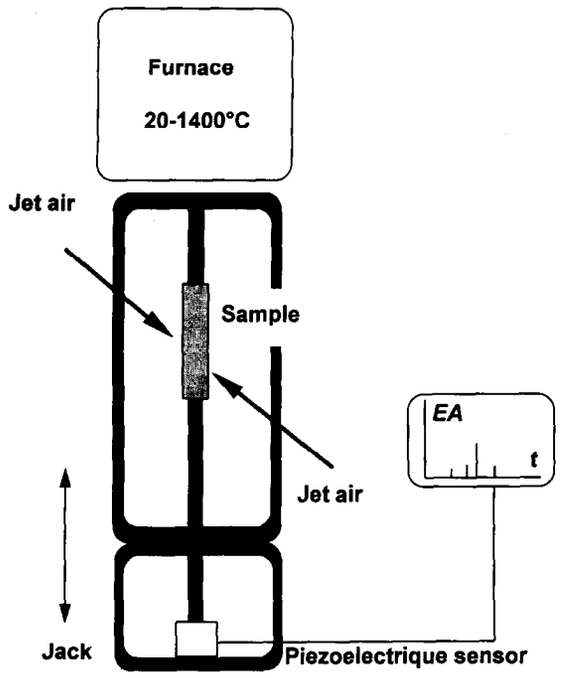


Fig. 1. Thermal shock device.

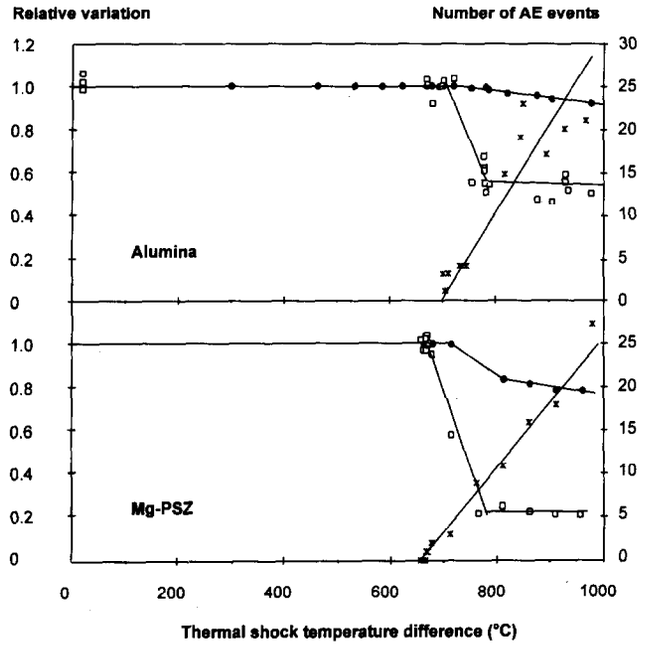


Fig. 2. Relative variation of retained strength (□), modulus of elasticity (●) and number of AE events (×) as a function of thermal shock temperature difference for alumina and Mg–PSZ materials.

exhibits the same phenomena and its decrease with temperature is lower for the alumina than for the zirconia material. This means that the studied alumina behaves like a refractory material.

It is to be recalled that the thermal stress field is such that tensile stresses arise parallel to the surface, which leads to crack initiations from the surface. They could be easily observed by dye penetrant on the nearly dense zirconia material but the high amount of porosity in alumina material did not allow direct crack observation. In the case of zirconia specimen the number of acoustic emission events could be correlated with the number of cracks at the surface of the body. The number of cracks induced by a thermal shock temperature near the critical temperature is low and easy to count. For higher thermal shock temperature differences the number of cracks strongly increases and the counting is difficult to achieve. Pictures were therefore taken from each side of the specimen and assembled together in order to represent a projection of the whole surface and to make the counting easier (see Figs 3(a) and (b)). The number of events in an acoustic emission response was counted with a computer treatment. The surface projection of a Mg–PSZ sample subjected to a thermal shock temperature of 714°C is represented in Fig. 3(a), and its associated acoustic emission response is represented in Fig. 4(a). Note that each crack corresponds to an AE peak. Figures 3(b) and 4(b) show the same phenomena but for a thermal shock temperature of 961°C leading to a higher crack density. Figure 5 shows the correlation between the number of cracks and the number of AE events for all the tested thermal shock temperatures. It appears clear that each crack propagation is associated to an AE peak; the error for the highest thermal shock temperature resulting from the way to count the cracks. This result suggests that the simple AE treatment conducted here can precisely enable us to record the degradation occurring during thermal shock. It might be especially useful for porous material

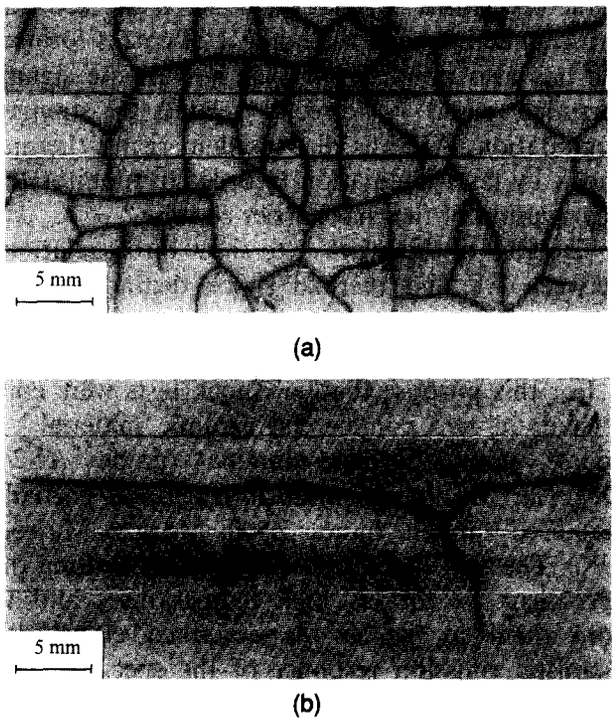


Fig. 3. (a) Damaged surface projection of a Mg–PSZ specimen for a thermal shock temperature difference of 714°C; (b) Damaged surface projection of a Mg–PSZ specimen for a thermal shock temperature difference of 961°C.

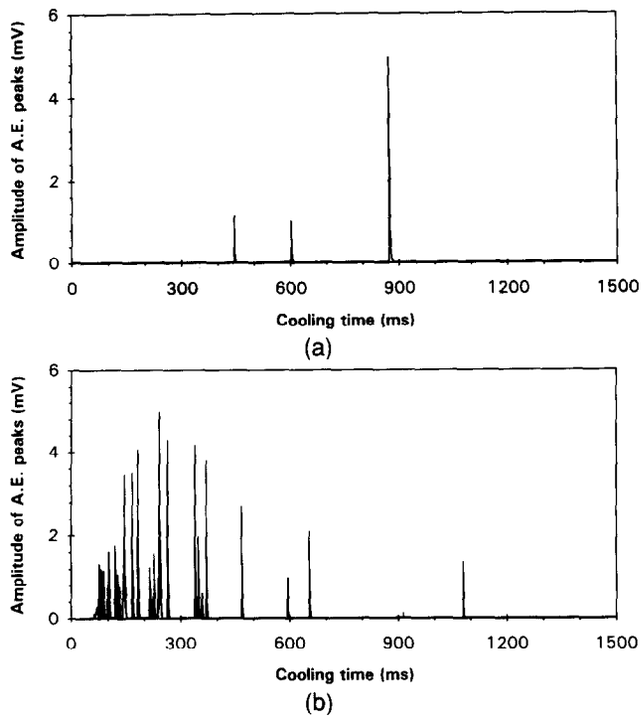


Fig. 4. (a) AE response of a Mg–PSZ specimen subjected to a thermal shock temperature difference of 714°C corresponding to the damaged surface shown in Fig. 3(a) (The amplitude is given in mV at the output of the sensor before the amplification of 60 dB); (b) AE response of a Mg–PSZ specimen subjected to a thermal shock temperature difference of 961°C corresponding to the damaged surface shown in Fig. 3(b) (The amplitude is given in mV the output of the sensor before the amplification of 60dB).

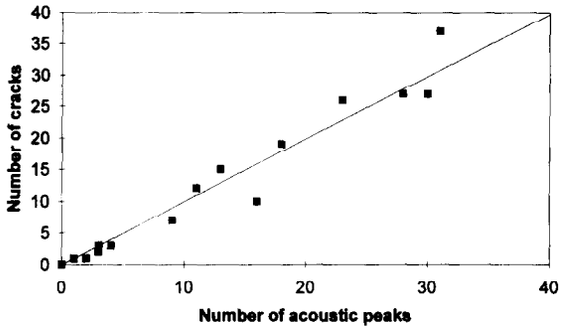


Fig. 5. Correlation between the number of AE peaks and the number of counted cracks in various Mg–PSZ specimens.

such as the alumina studied here and could also be extended to refractory materials.

It is also important to note that AE reflects particular cooling instants that can be associated to damage events. This is of major interest for such a transient problem where only final degradation is otherwise observed.

AE method which gives *in situ* information can be advantageously used for thermal fatigue where the cycling device can be automatically stopped from the apparition of an AE event.

Acknowledgement

The authors wish to acknowledge Dr R. Rezakhanlou and the 'Material Research Division' from Electricité de France (EDF) for their financial support and their interest in this work.

References

1. Ouanezard, N., Etude par émission acoustique de la résistance aux chocs et à la fatigue thermiques des matériaux céramiques, PhD thesis, Institut National des Sciences Appliquées de Lyon, Villeurbanne, France, 1983.
2. Konsztowicz, K. J., Crack growth and acoustic emission in ceramic during thermal shock, *J. Am. Ceram. Soc.*, **73**(3) 1990 502–8.
3. Konsztowicz, K. J., Acoustic emission amplitude analysis in crack growth studies during thermal shock of ceramics. In *Thermal shock and thermal fatigue behaviour of advanced ceramics*, ed. G. A. Schneider & G. Petzow, Kluwer Academic Publishers, The Netherlands, 1993 pp. 429–41.
4. Takahashi, H., Ishikawa, T., Okugawa, D. & Hashida, T., Laser and plasma-arc thermal shock/fatigue fracture evaluation procedure for functionally gradient materials, *ibid*, pp. 543–54.
5. Mignard, F., Olagnon, C., Fantozzi, Chantrenne, P., & Raynaud, M., *Thermal shock behaviour of a coarse grain alumina. Part I: Temperature field determination*, to be published.
6. Peigné, P., Résistance au chocs thermiques des céramiques thermomécaniques, PhD thesis, Institut National des Sciences Appliquées de Lyon, Villeurbanne, France, 1991.

Journal of the European Ceramic Society **15** (1995) 655–660
© 1995 Elsevier Science Limited
Printed in Great Britain. All rights reserved
0955-2219(95)00022-4
0955-2219/95/$9.50

Mechanical Behavior of Porous Glasses Produced by Sintering of Spherical Particles

Savitha C. Nanjangud & David J. Green

Department of Materials Science and Engineering, The Pennsylvania State University, University Park, Pennsylvania 16802, USA

(Received 10 September 1994; revised version received 27 January 1995; accepted 31 January 1995)

Abstract

Young's modulus and biaxial flexure strength were measured for compacts of spherical glass particles sintered to various densities. The aim of the work was to relate the mechanical properties to the sintering process. In particular, changes in the interparticle neck sizes during the sintering process were measured from fracture surfaces. It had been postulated previously that the elastic moduli directly depend on the neck radius to particle radius ratio and such measurements allow the elastic behavior to be directly related to the sintering kinetics. The experimental results were consistent with both the mechanical and sintering models. There was also found to be a strong correlation between Young's modulus and strength of the porous glass bodies.

1 Introduction

One of the aims of the study of sintering science is the development of techniques that allow the experimentalist to characterize the geometric changes that occur in the powder compact as it undergoes sintering. A variety of characterization techniques, such as mercury porosimetry, surface area measurements, small angle neutron scattering etc., have been utilized. In other studies,[1,2] however, it was suggested that the elastic behavior of a porous body could be used to characterize the sintering process. For the case of partially sintered alumina, elastic moduli were measured for specimens that had been subjected to the initial stage of sintering. In this material, there was a rapid increase in the elastic moduli with minimal densification and it was suggested[1,2] that this behavior could be understood by the interparticle neck growth process, and particularly by surface diffusion. An attractive feature of utilizing the elastic behavior of a material to characterize the sintering process, is that the elastic constants can be measured to a high accuracy using nondestructive techniques, such as dynamic resonance or sound velocity measurements.

The aim of the current study was to determine the changes that occur in the mechanical properties of partially sintered glass and to relate these to the changes in the microstructure that occur during the sintering process. In order to simplify the compact geometry, a model system of spherical glass particles was utilized.

2 Background

There has been considerable scientific effort in predicting the elastic behavior of porous materials. In such analyses, the theoretical relationships for the elastic moduli are often expressed solely as functions of the fraction of porosity. In other cases, it has been suggested that pore geometry may play an important role and factors, such as pore shape, have been incorporated into some of the analyses. For materials with moderate or high fractions of porosity, it can be quite difficult to describe the complex nature of the pore structure, especially for materials produced by the sintering of powder compacts. As an alternative approach, Green *et al.*[1,2] have suggested it may be useful to consider the elastic behavior in terms of the interparticle neck growth process and the coordination of the particles. For example, for spherical particles subjected to the initial stage of sintering, it was suggested that[1]

$$\frac{B}{B_o} = \frac{3Nr(1-2\nu_o)}{8kR(1-\nu_o^2)} \tag{1}$$

where B is the bulk modulus of the porous compact, B_o and ν_o are the bulk modulus and Poisson's ratio of the particle, r is the neck radius, N the particle coordination number, R is the radius of the particle and k is an empirical geometric constant. For a given material, eqn (1) can be simplified to obtain

$$\frac{B}{B_0} = CN\left(\frac{r}{R}\right) \quad (2)$$

where C is an empirical constant that can be obtained by comparison with experimental data for a given material. Although the theoretical approach to obtain eqn (2) was considered to be only approximate, the dependence of the elastic constants on the particle coordination number and the ratio of the neck and particle radii is intuitively appealing. The idea of relating the interparticle neck size to the mechanical behavior of porous materials has also been put forward by other researchers[3,4] and in a related idea, Cytermann[5] has postulated that the Young's modulus is directly dependent on the contiguity of the porous solid.

As eqn (2) predicts a dependence of the bulk modulus on (r/R), this allows the sintering theories concerning neck growth in powder compacts to be directly related to the elastic behavior. For example, Frenkel[6] proposed that the sintering mechanism in glass is by viscous flow and derived an expression for the rate of neck growth for glass spheres, i.e.,

$$\left(\frac{r}{R}\right)^2 = \frac{3\gamma t}{R\eta} \quad (3)$$

where γ is the surface energy, η is the viscosity, r is the radius of the neck, R is the radius of the particle and t is the sintering time. Experimental studies by Kuczynski[7] and Kingery and Berg[8] on the sintering of glass beads were in agreement with Frenkel's analysis.

3 Experimental Procedure

Soda–lime–silica glass beads were obtained from a commercial source (Potters Industries Inc., Parsippany, NJ). The average particle size was determined to be 58·6 μm from microscopic observation (750–1000 particles).

3.1 Sample preparation

Twenty grams of the glass powder were mixed with 4 wt% polyethylene glycol (organic binder) which had been dissolved in 20 ml of ethanol at 50°C. The mixture was stirred and the ethanol was removed, by drying at the same temperature for about 6–8 h. The dried powder was crushed to obtain a free flowing glass powder, which was subsequently uniaxially pressed into pellets of 25·4 mm diameter, at a pressure of ~90 MPa. The theoretical density of the glass powder was determined with a helium pycnometer (Multivolume Pycnometer 1305, Micromeritics, Norcross, GA) and found to be 2420 kg m^{-3}.

The glass samples were sintered in two steps. The first step involved binder burnout at 300°C. In the second step, the samples were sintered at various temperatures, ranging, from 620 to 655°C for 2 h and at 625 and 645°C for various times, between 0·5 and 10 h. The density of the samples was calculated from their measured dimensions and weights.

3.2 Mechanical properties

The strength of the glass samples was measured by the biaxial flexure method[9] using a mechanical testing machine (Instron Corporation, Canton, MA). The strength was calculated assuming a constant value of 0·2 for the Poisson's ratio. A 10% error in the Poisson's ratio value gives rise to an error of 4% in the flexural strength value, and this was considered acceptable for the current study.

The Young's modulus of the samples was measured by determining the longitudinal sound velocity.[10] Ultrasonic transducers (2 MHz, Ultran Laboratories, Boalsburg, PA) were used to transmit and receive the signals and no liquid couplant was used between the transducers and the samples. The sound velocity was measured through the thickness of the glass samples and Young's modulus was calculated using[10]

$$E = \frac{V^2\rho(1-2\nu)(1+\nu)}{(1-\nu)} \quad (4)$$

where V is the longitudinal sound velocity, ρ is the density and ν is the Poisson's ratio. As mentioned earlier, a constant value of 0·2 was used for the Poisson's ratio. For typical values of ν, a 10% error will give a ~4% error in the Young's modulus value.

3.3 Microstructural analysis

Neck radius measurements were made on samples sintered in the range 625–645°C and at 625°C for 4, 6, 8 and 10 h. These measurements were accomplished by obtaining a series of micrographs (scanning electron microscope) of the fracture surfaces of four different samples for each of the chosen conditions. For these conditions, the materials fail primarily by the crack passing through the necks. The neck sizes were measured from the micrographs using an image analyzer (ZIDAS, Carl Zeiss, Inc., Thornwood, NY). About 100 necks were measured for each experimental condition and the values were arithmetically averaged to obtain the mean contact radii.

4 Results and Discussion

The average green density of the compacts was determined to be ~64% of the theoretical density.

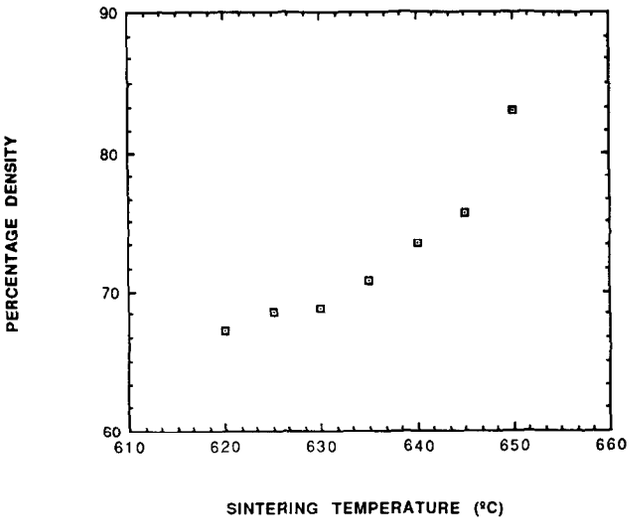


Fig. 1. Density of glass specimens after sintering at various temperatures for 2 h.

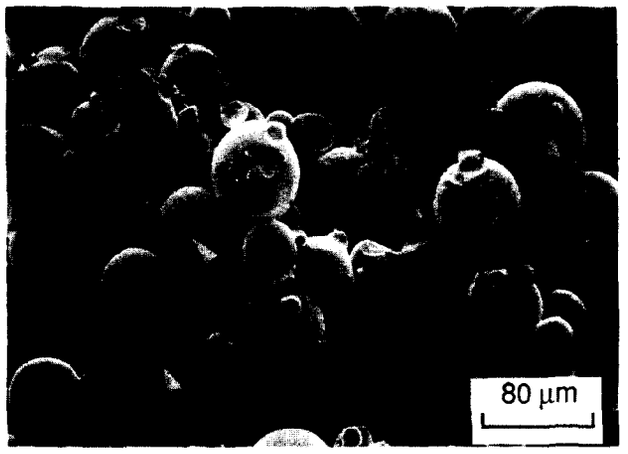


Fig. 3. Fracture surface for a specimen sintered at 620°C (4 h), showing the failed interparticle necks. Some of these necks are indicated by arrows.

The sample densities are shown in Fig. 1 as a function of the sintering temperature. The room temperature Young's modulus values obtained for these specimens are shown in Fig. 2 as a function of the % theoretical density. The Young's modulus values increase continuously with relative density, as expected. This behavior does, however, contrast strongly with the rapid increase in Young's modulus observed in partially sintered alumina.[1,2] For glasses, neck growth is expected to occur by viscous flow with densification, whereas for alumina, in which surface diffusion is prevalent at the lower sintering temperatures, the changes in the elastic moduli should occur without densification. If one considers the Young's modulus of dense soda lime silica glass is ~70 GPa, the data in Fig. 2 is also consistent with the recent analysis of Lam *et al.*,[11] in which the Young's modulus is predicted to be directly dependent on the degree of densification.

The fracture surfaces of the glass samples showed fractured necks which could be seen as small, almost perfect circles on the particles. Figure 3 shows the fracture surface for a glass sintered at 620°C for 4 h and the fractured necks, some of which are arrowed, are small but clearly visible. Transparticle fracture becomes more prevalent in samples sintered at higher temperatures or for longer times, making the neck size measurements more difficult. For example, Fig. 4 shows the fracture surface for a sample sintered at 620°C for 10 h. The ratio of the neck radius to the particle radius was calculated using the average particle size of the glass spheres. The presence of the transparticle failure complicated the current study, in that it may lead to a bias in the measured r/R values. For example, particles with the larger neck sizes may be obscured if the particles fail rather than the necks.

The model by Green *et al.*[1] predicts that the bulk modulus of a partially sintered sample is directly proportional to the product of the coordination of the compact and the radius ratio.

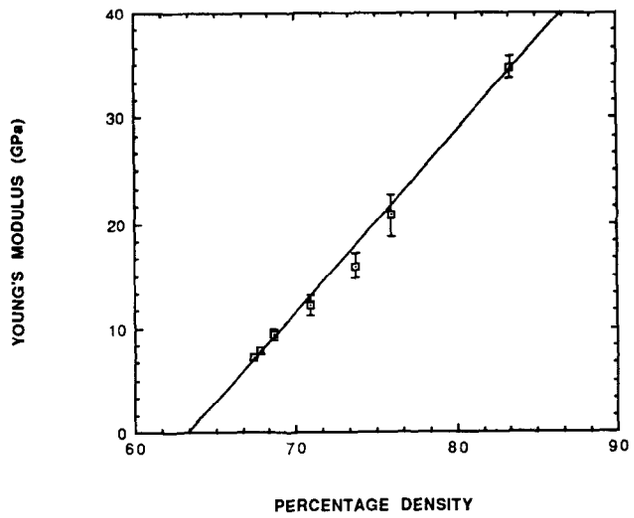


Fig. 2. Room temperature Young's modulus values for porous glass specimens after sintering to various temperatures. The error bars indicate the standard deviation in the data.

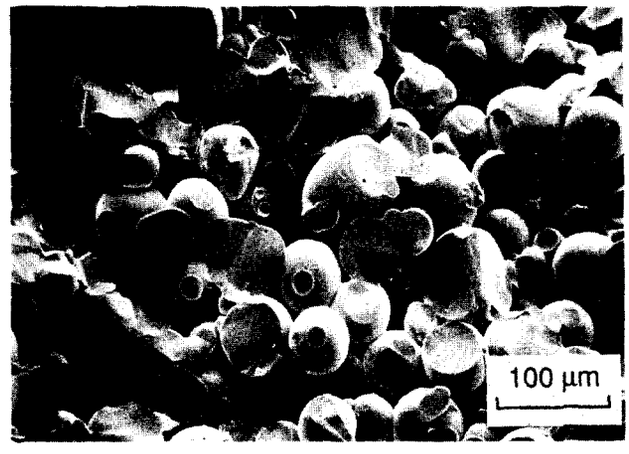


Fig. 4. Fracture surface for a specimen sintered at 620°C (10 h), showing the increase in transparticle failure for the longer sintering times.

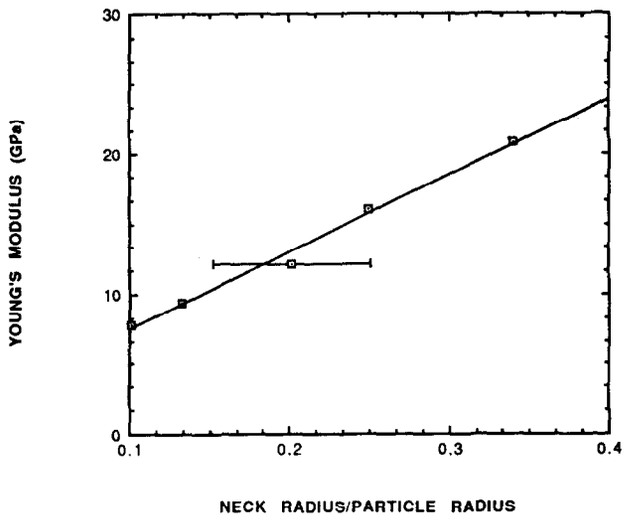


Fig. 5. Young's modulus values for porous glass specimens as a function of the neck to particle radius ratio. The error bar is a typical value of the standard deviation seen in the contact radius measurement.

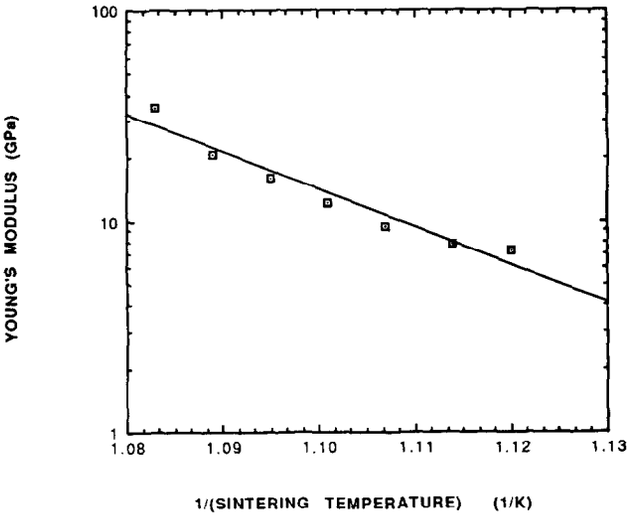


Fig. 6. Arrhenius plot for the (log) Young's modulus values for porous glass specimens as a function of the inverse sintering temperature.

In particular, eqn (2) predicts a linear relationship between the bulk modulus and r/R, assuming there is no change in particle coordination number. If one assumes that the value of Poisson's ratio for the porous glasses does not change significantly with densification, the same linear relationship will be obtained for the relative Young's modulus. To verify this prediction, the Young's modulus values of the porous glasses were plotted as a function of the radius ratio (r/R), as given in Fig. 5. Although the model was derived only for very small contact areas, a linear dependence on r/R is seen to not be unreasonable. From the data in Fig. 5 and eqn (2), if one assumes $(B/B_0) \approx (E/E_0)$ and $E_0 = 70$ GPa, one finds $CN \approx 1$.

In order to relate the elastic behavior to the sintering kinetics, one can combine eqns (2) and (3) to obtain,

$$\frac{E}{E_o} = CN\left(\frac{3\gamma t}{R\eta}\right)^{1/2} \tag{5}$$

where E and E_0 are the Young's moduli of the porous body and the spheres and η is the viscosity of glass at the sintering conditions. In addition, the viscosity is temperature dependent and can be written in the form of an Arrhenius equation near the glass transition temperature, i.e.

$$\frac{\eta}{\eta_o} = \exp\left(\frac{Q}{\mathrm{R}'T}\right) \tag{6}$$

where η_0 is a constant that depends on the glass composition, Q is the activation energy for viscous flow, R' is the universal gas constant and T is the absolute temperature. Substituting for η in Eqn (5), one obtains the following relationship between the Young's modulus and the sintering temperature

$$\frac{E}{E_o} = D\exp\left(-\frac{Q}{2\mathrm{R}'T}\right) \tag{7}$$

where $D = CN(3\gamma t/R\eta_0)^{1/2}$ The results of the analysis are shown in Fig. 6 and the activation energy for viscous flow was calculated from the slope and found to be 690 kJ mol^{-1}. This value is very close to 703 kJ mol^{-1}, which is the activation energy reported in literature[12] for soda lime silica glass in the temperature range 492–541°C.

The biaxial flexure strengths of the porous glasses are given in Fig. 7. The trend in the flexural strength data is very similar to that in the Young's modulus data, suggesting a similar dependence on the compact structure.

The densities of samples sintered at 625 and 645°C for various times are shown in Fig. 8. The density of samples sintered at 645°C increases more rapidly, reflecting the lower viscosity of the glass at this temperature. The Young's modulus and

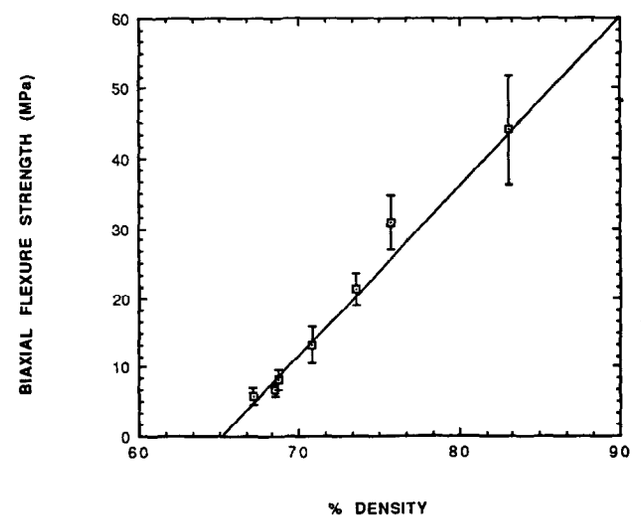


Fig. 7. Room temperature biaxial flexure strength values for porous glass specimens after sintering to various temperatures. The error bars indicate the standard deviation in the data.

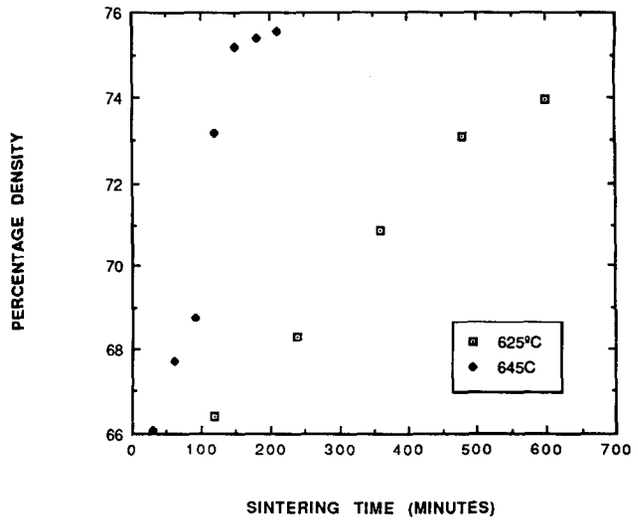


Fig. 8. Density of glass specimens after sintering at 625 and 645°C for various times.

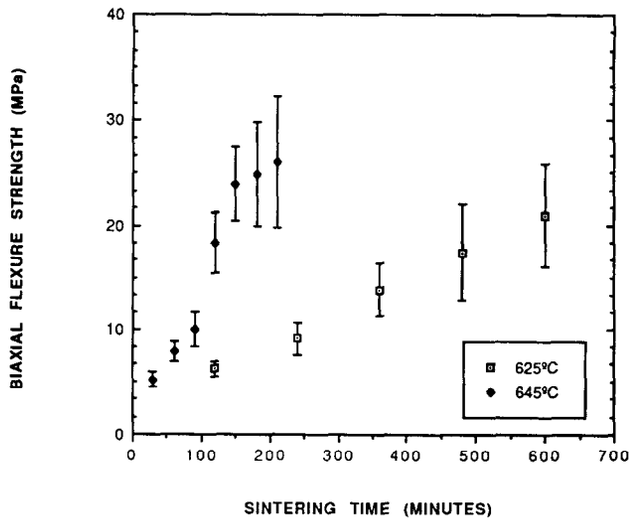


Fig. 10. Biaxial flexure strengths values for porous glass specimens after sintering at 625 and 645°C for various times.

flexure strength of these samples are presented in Figs 9 and 10, and in a similar fashion to the earlier data, show a strong correlation with each other.

From eqn (3), the neck/particle radius ratio is predicted to increase with sintering time with a time exponent of 0.5 and this can be tested using the measured r/R values. Figure 11 shows the data for the samples sintered at 625°C and although the data is rather scattered, a time exponent of 0·51 was obtained, in excellent agreement with the theory and with previous studies.[6,13,14] The data in Fig. 11 can also be used to estimate the glass viscosity at 625°C. From eqn (3), the square of the radius ratio can be plotted as a function of time and the viscosity can be obtained from a linear regression analysis. Using a value of 0·3 J m^{-2}, as suggested by Scherer,[15] the viscosity was calculated to be 10 GPa s. This value is in fair agreement with the value of 1·52 GPa s, reported by Hagy.[16]

The Young's modulus data on samples obtained from the isochronal and isothermal experiments have been combined in Fig. 12 to show the dependence on r/R. One would expect the two data sets to fit a single linear function, assuming there is no change in particle coordination. It appears, however, there is a significant difference between the two data sets. The reason for this difference could be that the particles undergo rearrangements during sintering, thus altering the coordination number and structure of the compact. The extent of these rearrangements may be different at the various sintering temperatures due to the differences in glass viscosity. Alternatively, it should be remembered that the model was only derived for small r/R values; therefore one would expect the agreement to be poor at large r/R values. Thus, although the model tested in this work seems be a reasonable first approximation, it is suspected that further refinements in the model are needed.

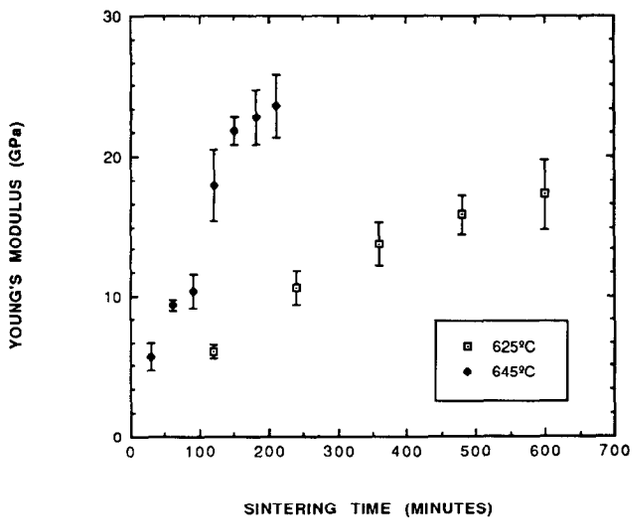


Fig. 9. Room temperature Young's modulus values for porous glass specimens after sintering at 625 and 645°C for various times.

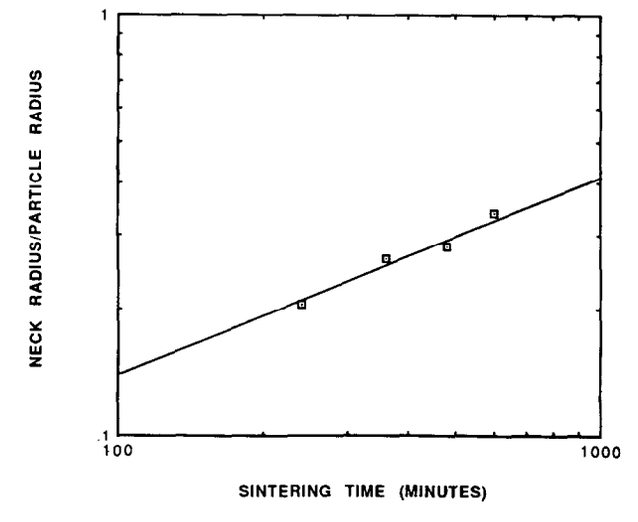


Fig. 11. The ratio of the neck to particle sizes as a function of the sintering time at 625°C. The log–log plot gives a time exponent of 0·51.

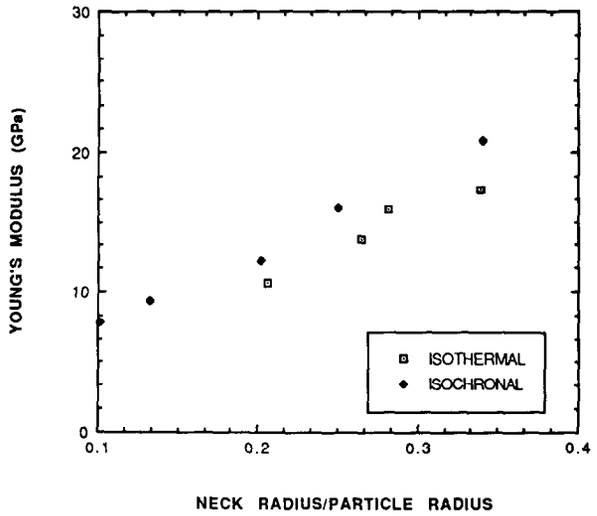


Fig. 12. Young's modulus values for porous glass specimens as a function of the neck to particle radius ratio for the isothermal and isochronal sintering experiments.

5 Conclusions

The Young's modulus and strength were determined for spherical glass particle compacts sintered under various conditions. These properties both increased with increasing density and the changes in the two properties were strongly correlated. The Young's modulus data were also analyzed in terms of the changes in the neck radius/particle radius ratio and an approximate linear relationship was confirmed, in agreement with earlier theoretical predictions. It was also possible to link the sintering kinetics to the elastic behavior and good agreement with the theory was found. Overall, it was found that elastic constant measurements are a very useful approach for characterizing porous ceramic bodies produced from powder compacts and gives insight into the sintering process.

Acknowledgement

The authors would like to acknowledge the Cooperative Program in the Center for Advanced Materials, Penn State, for the financial support of this project.

References

1. Green, D. J., Brezny, R. & Nader, C., The elastic behavior of partially-sintered ceramics. In *Adhesion in Solids*, MRS Symposium Proceedings, Vol 119, ed. by D. M. Mattox, J. E. E. Baglin, R. J. Gotschall and C. D. Batich. Materials Research Society, Pittsburgh, PA, 1988, pp. 43–48.
2. Green, D. J., Nader, C. & Brezny, R., The elastic behavior of partially-sintered alumina. In *Sintering of Advanced Ceramics*, ed. by C. A. Handwerker, J. E. Blendell and W. Kaysser. American Ceramic Society, Westerville, OH, 1990, pp. 347–56.
3. Woignier, T. & Philippou, J. Mechanical strength of silica aerogels. *J. Non-Cryst. Solids.*, **100** (1988) 404–8.
4. Kendall, K., Alford, N. McN. & Birchall, J. D., Elasticity of particle assemblies as a measure of the surface energy of solids. *Proc. R. Soc., Lond.*, **A412** (1987) 269–83.
5. Cytermann, R., A new way of investigating the dependence of elastic moduli on the microstructure of porous materials. *Powder Metall. Int.*, **19** (1989) 27–30.
6. Frenkel, J., Viscous flow of crystalline bodies under the action of surface tension. *J. Phys.*, **9** (1945) 385–91.
7. Kuczynski, G. C., Study of the sintering of glass. *J. Appl. Phys.*, **20** (1949) 1160–3.
8. Kingery, W. D. & Berg, M., Study of the initial stages of sintering by viscous flow, evaporation-condensation, and self-diffusion. *J. Appl. Phys.*, **26** (1955) 1205–12.
9. Wachtman, Jr., J. B., Capps, W. & Mandd, J., Biaxial flexure tests of ceramic substrates. *J. Materials*, **7** (1972) 188–94.
10. Schreiber, E., Anderson, O. L. & Soga, N., *Elastic Constants and their Measurements*. McGraw Hill, New York, 1973.
11. Lam, D. C. C., Lange, F. F. & Evans, A. G., Mechanical Properties of Partially Dense Alumina Produced from Powder Compacts. *J. Am. Ceram. Soc.*, **77** (1994) 2113–17.
12. Scherer, G. W., *Relaxation in Glass and Composites*. John Wiley and Sons, New York, 1986.
13. German, R. M., Simulation of diffusion controlled sphere–sphere sintering. In *Sintering-New Developments*, ed. M. M. Ristic. Elsevier Scientific Publishing Company, Amsterdam, 1979.
14. Scherer, G. W., Sintering of low-density glasses: I Theory. *J. Am Ceram. Soc.*, **60** (1977) 236–9.
15. Scherer, G. W., Viscous sintering of inorganic gels. *Surf. Colloid Sci.*, **14** (1987) 265–300.
16. Hagy, H. E., Experimental evaluation of beam-bending method of determining glass viscosities in the range of 10^8–10^{15} poises. *J. Am. Ceram. Soc.*, **46** (1963) 93–97.

Journal of the European Ceramic Society **15** (1995) 661–666
© 1995 Elsevier Science Limited
Printed in Great Britain. All rights reserved
0955-2219(95)00039-2
0955-2219/95/$9.50

Some Properties of Aluminium-Nitride Powder Prepared by Metal–Organic Chemical Vapour Deposition

Kazuro Kubo, Kiyoshi Itatani,* F. Scott Howell, Akira Kishioka & Makio Kinoshita

Department of Chemistry, Faculty of Science and Engineering, Sophia University, 7–1 Kioi-cho, Chiyoda-ku, Tokyo 102, Japan

(Received 29 September 1994; revised version received 2 February 1995; accepted 7 February 1995)

Abstract

Ultrafine aluminium-nitride (AlN) powders with primary particle sizes of 10–20 nm were prepared by a metal–organic chemical vapour deposition (MOCVD): trimethylaluminium ($Al(CH_3)_3$), triethylaluminium ($Al(C_2H_5)_3$) and triisobutylaluminium ($Al(i\text{-}C_4H_9)_3$)-vapours were reacted with ammonia (NH_3) at 1050°C. The sintered compacts with relative densities of ~95% could be fabricated by firing these compressed powders at temperatures as low as 1600°C. The relative densities of the $Al(CH_3)_3$-derived and $Al(C_2H_5)_3$-derived compacts fired at 1800°C for 10 h attained ~98%. The oxygen contents of these compacts were 1·8 and 4·7%, respectively.

1 Introduction

Aluminium-nitride (AlN) ceramics have high thermal conductivities (theoretical value; 320 $Wm^{-1} \times K^{-1}$)[1] and low thermal expansion coefficients (4·4 $\times 10^{-6}°C^{-1}$; 25–400°C) close to that of silicon.[2] By making use of these properties, AlN ceramics have started to be used as a high-performance ceramic substrate and packaging material. To date, (i) the preparation of high-purity AlN powder and (ii) the fabrication of high-density AlN ceramics with and without a sintering aid have been examined by many researchers.

The high-purity AlN powder may be prepared either by a direct nitridation of metallic aluminium (Al) or by a carbothermal reduction of Al_2O_3.[2,3] Recently, much attention is being devoted to the preparation of high-purity and ultrafine AlN powder by a chemical vapour deposition (CVD), because this AlN powder has a potential application in the fabrication of high-density AlN ceramics without a sintering aid. Various vapourization sources have been proposed by many researchers: metallic Al,[4–8] aluminium chloride ($AlCl_3$)[9–13] and alkylaluminium.[14–16] Among these sources, the vapourization rate of alkylaluminium may be controlled more strictly than those of solid sources, because the commercially available alkylaluminiums: trimethylaluminium ($Al(CH_3)_3$: TMAL), triethylaluminium ($Al(C_2H_5)_3$): TEAL) and triisobutylaluminium ($Al(i\text{-}C_4H_9)_3$: TIBAL) are not solid but liquid at room temperature. The properties of TEAL-derived AlN powder have been reported by Wakimura and Hiai,[15] and Adjaottor and Griffin;[16] those of TIBAL-derived AlN powder by Tsuchida *et al.*[14] But the properties, especially sinterabilities, of AlN powders prepared by the vapour-phase reactions of alkylaluminiums with ammonia (NH_3) have never been examined systematically.

The present authors[8] have examined the properties of AlN powder prepared by a low-pressure CVD (LP-CVD), using metallic Al and NH_3–nitrogen (N_2) gas. This paper deals with: (i) the preparation of AlN powder by a metal organic CVD (MOCVD); (ii) the evaluation of the powder properties and (iii) the comparison of the present data with those of our previous LP-CVD.

2 Experimental Procedure

2.1 Starting materials and reaction apparatus

Three kinds of alkylaluminiums available from Aldrich Chemical Company (Milwaukee, WI, USA) were used as starting materials: (i) TMAL; (ii) TEAL and (iii) TIBAL.

The schematic diagram of the reaction apparatus assembled by ourselves is shown in Fig. 1. The apparatus consisted of: (i) a reacting zone ((a)–(e)); (ii) a collecting zone ((f)–(h)), and (iii) an evacuating

*To whom correspondence should be addressed.

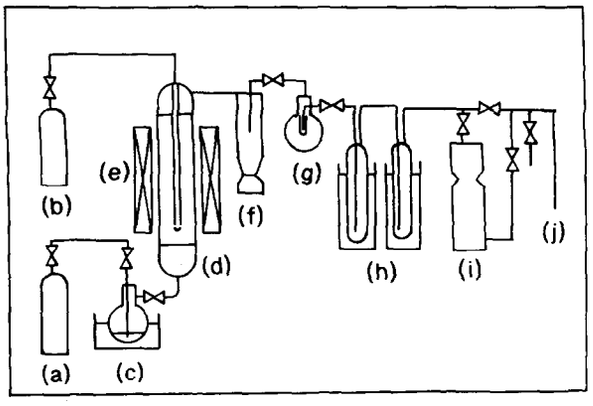


Fig. 1. Schematic diagram of the reaction apparatus: (a) N_2 cylinder (purity: 99·9995%); (b) NH_3 cylinder (purity: 99·99%); (c) Evaporation flask; (d) Mullite tube (diameter: 3 cm, height: 60 cm); (e) Electric furnace (heating zone: 30 cm); (f) Cyclone; (g) Test-tube type filter; (h) Trap; (i) Oil-diffusion pump and (j) Rotary pump.

Table 1. Preparation conditions of AlN powders

(Evaporation)		*(Flow rate)*	
Alkylaluminium	*Temperature (°C)*	*NH_3 gas (dm^3 min^{-1})*	*Carrier gas (N_2) (dm^3 min^{-1})*
$Al(CH_3)_3$	30	50–100	50
$Al(C_2H_5)_3$	110	50	50–100
$Al(i\text{-}C_4H_9)_3$	100	50	100–200

zone ((i)–(j)). The reaction apparatus was first evacuated using the rotary and oil-diffusion pumps. Then alkylaluminium vapour with the partial pressure of 15 mmHg, which was formed by controlling the heating temperature of the liquid alkylaluminium, was introduced into the reaction tube heated at 1050°C, using a carrier gas of nitrogen (N_2) with purity of over 99·9995%; NH_3 gas with purity of 99·99% was simultaneously introduced into the reaction tube. The evaporation conditions of alkylaluminium and the flow rates of NH_3 and N_2 are listed in Table 1. The resulting powder was collected by a cyclone filter and a test-tube type filter. The yield of the powder was ~80% of the theoretical yield.

2.2 Phase identification and quantitative analysis

The crystalline phase of the resulting powder was examined using an X-ray diffractometer with $CuK\alpha_1$ radiation operated at 40 kV and 25 mA (Model Rad IIA, Rigaku, Tokyo). The aluminium content of the resulting powder was determined using an X-ray fluorescence apparatus (Model SXF-1200, Shimadzu, Kyoto); the nitrogen and oxygen contents were determined using a simultaneous nitrogen/oxygen analyser (Model EMGA-550, Horiba, Kyoto).

2.3 Evaluation of powder properties

The specific surface area of the resulting powder was measured by BET technique, using nitrogen (N_2) as an adsorption gas. The particle shape was observed using a transmission electron microscope (TEM; Model H-800; accelerating voltage 200 kV, Hitachi, Tokyo). The particle-size distribution was measured by a laser scattering/diffraction apparatus (Model LA-700, Horiba, Kyoto).

2.4 Evaluation of sinterability

Two kinds of the compacts were fabricated to evaluate the sinterability of the resulting powder; each compact with a diameter of 10 mm and thickness of 10 mm for the dilatometric evaluation was fabricated by pressing ~1·3 g of the powder uniaxially at 50 MPa; each compact with a diameter of 10 mm and thickness of ~3 mm for the measurement of density and microstructural observation was fabricated by pressing ~0·3 g of the powder uniaxially at 50 MPa.

The densification behaviour of the compact was evaluated using a dilatometer from room temperature up to ~1600°C at the heating rate of 5°C min^{-1}. The relative density (bulk density/true density) of the compact fired at a temperature between 1400 and 1800°C for 3 or 10 h, in N_2 flowing at the rate of 2 dm^3 min^{-1}, was calculated using the data on dimensions and weight of the compact; the heating rate from room temperature up to the desired temperatures was 10°C min^{-1}. The fractured surfaces of the sintered compact were observed using a scanning electron microscope (SEM; Model S-430, Hitachi, Tokyo).

3 Results and Discussion

3.1 Crystalline phase of the resulting powder

The powders were deposited not only on the walls (upper parts) of the reaction tube but also on the cyclone and test-tube type filter. The resulting powders were white.

Typical XRD patterns of the powders collected from the cyclone and filter are shown in Fig. 2. Only AlN[17] was detected from the powders, irrespective of the difference in the kind of alkylaluminium. The crystallinities of these powders were almost the same as those collected from the cyclone and filter.

The analytical results of the present powders are listed in Table 2. The molar ratios of Al to N were in the range of 1·00–1·08. The oxygen content varied from 4·6 to 9·9%, according to the kind of alkylaluminium.

The reaction routes of TMAL, TEAL and TIBAL with NH_3 have been examined by several researchers.[14,15,18] Details will be described below:

(i) Reaction route of TMAL with NH_3[18]

$$Al(CH_3)_3 + NH_3 \rightarrow Al(CH_3)_3{\cdot}NH_3 \quad (1)$$

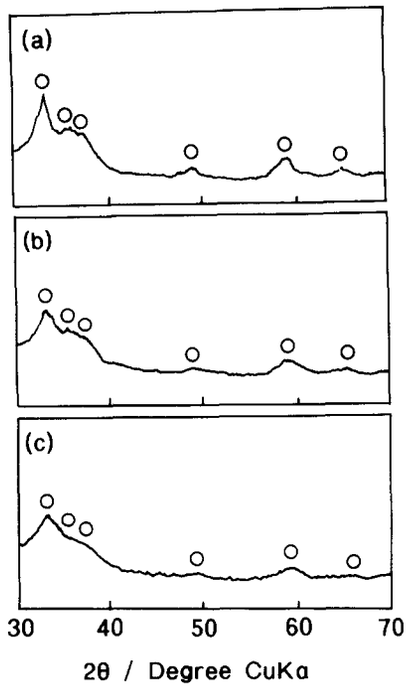


Fig. 2. X-ray diffraction patterns of (a) TMAL-derived powder; (b) TEAL-derived powder and (c) TIBAL-derived powder. ○ AlN — Reaction temperature: 1050°C.

Table 2. Analytical results of the powders and molar ratios of Al to N. Reaction temperature: 1050°C

Alkylaluminium	*Al (wt%)*	*N (wt%)*	*O (wt%)*	$\frac{Al}{N}$
$Al(CH_3)_3$	63·5	31·9	4·6	1·03
$Al(C_2H_5)_3$	61·1	31·7	7·2	1·00
$Al(i\text{-}C_4H_9)_3$	61·0	29·1	9·9	1·08

$$Al(CH_3)_3{\cdot}NH_3 \rightarrow Al(CH_3)_2NH_2 + CH_4 \quad (2)$$
$$Al(CH_3)_2NH_2 \rightarrow AlCH_3NH + CH_4 \quad (3)$$
$$AlCH_3NH \rightarrow AlN + CH_4 \quad (4)$$

(ii) Reaction route of TEAL with NH_3[15]

$$Al(C_2H_5)_3 + NH_3 \rightarrow Al(C_2H_5)_2{\cdot}NH_2 + C_2H_6 \quad (5)$$
$$Al(C_2H_5)_2{\cdot}NH_2 \rightarrow (1/n)\,(AlC_2H_5NH)_n + C_2H_6 \quad (6)$$
$$(AlC_2H_5NH)_n \rightarrow nAlN + C_2H_6 \quad (7)$$

(iii) Reaction route of TIBAL with NH_3[14]

$$Al(i\text{-}C_4H_9)_3 + NH_3 \rightarrow Al(i\text{-}C_4H_9)_3{\cdot}NH_3 \quad (8)$$
$$Al(i\text{-}C_4H_9)_3{\cdot}NH_3 \rightarrow AlN + 3(i\text{-}C_4H_{10}) \quad (9)$$

The upsurges of the X-ray baseline spectra in the range of 30–40° suggest the presence of some amorphous material. The composition of such amorphous material appears to be Al–O–N system, partly because 4·6–9·9% of oxygen are included in the powder, and partly because Al/N ratios above unity indicate somewhat lower nitrogen contents than stoichiometry.

The oxygen may come to be included in the powder during the handling in air.[19] The present oxygen contents (4·6–9·9%) are, however, much smaller than those reported previously; the previous data showed that TEAL-derived and TIBAL-derived powders contain 15–20% of oxygen.[14–16]

3.2 Powder properties

The properties of the resulting powders were examined from the viewpoints of specific surface area, particle shape and particle size.

The specific surface areas of the resulting powders were arranged in the following order: TIBAL-derived powder (175 m^2g^{-1}) > TEAL-derived powder (145 m^2g^{-1}) > TMAL-derived powder (95 m^2g^{-1}). The primary particle sizes calculated on the basis of the surface areas were arranged as follows: TMAL-derived powder (19 nm) > TEAL-derived powder (13 nm) > TIBAL-derived powder (11 nm).

The TEM micrographs and histograms for particle-size distributions of the resulting powders are shown in Fig. 3. The TEM micrographs of TMAL-derived and TEAL-derived powders (Fig. 3(a) and (b)) showed that the polyhedral particles with sizes of < 0·05 μm (50 nm) were adhered to form agglomerates; the histograms for the particle-size distribution indicated that the particles with sizes of < 0·5 μm and with sizes of 1 to 30 μm were present in the powder. The TEM micrograph of TIBAL-derived powder (Fig. 3(c)) showed that the polyhedral particles with sizes of < 0·05 μm (50 nm) were linked to form agglomerates; the histogram for the particle-size distribution revealed that the particle sizes were distributed in the ranges of 0·1–0·2 μm and of 2–30 μm.

The individual particles observed by TEM correspond to primary particles, because the particle

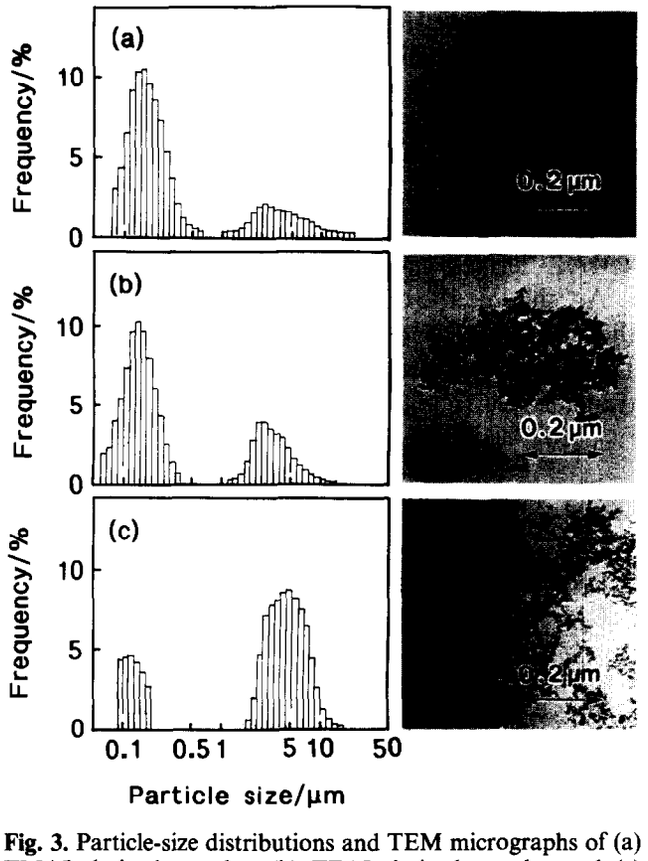


Fig. 3. Particle-size distributions and TEM micrographs of (a) TMAL-derived powder; (b) TEAL-derived powder and (c) TIBAL-derived powder.

sizes (< 50 nm) observed by TEM are in accord with the primary particle sizes of 10–20 nm. These primary particle sizes are smaller than those (30–50 nm) prepared by LP-CVD[8] and those (20–80 nm) by rf plasma.[6]

The particles with sizes of < 0·5 μm correspond to secondary particles where the primary particles are adhered to one another; the particles with sizes of 1–30 μm correspond to ternary particles which are formed by the agglomeration of the secondary particles. The secondary and ternary particles may form spontaneously to lower the excess surface energy which the ultrafine primary particles possess.

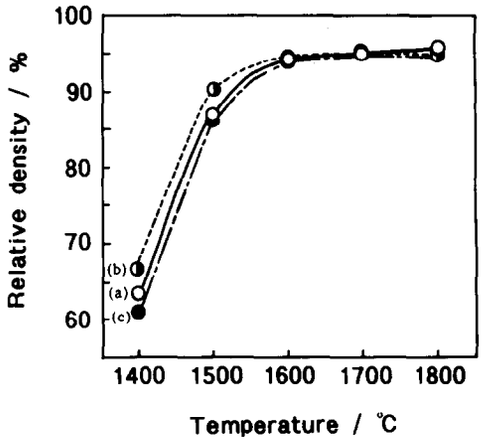


Fig. 5. Effect of firing temperature on the relative density of the compact. (a) TMAL-derived compact; (b) TEAL-derived compact and (c) TIBAL-derived compact. Heating rate: 5°C min^{-1}.

3.3 Sinterability

Before we fabricated the high-density AlN ceramics, we examined the linear shrinkages of these compacts during heating. Results are shown in Fig. 4. The shrinkage of TMAL-derived compact proceeded with temperature and was promoted at temperature exceeding 1200°C. The shrinkage of TEAL-derived compact was similar to that of TMAL-derived compact but was slightly shifted toward the higher temperature side. The shrinkage of TIBAL-derived compact started to occur at ~200°C and was promoted above 1400°C.

The shrinkages during the heating of TMAL-derived and TEAL-derived compacts below ~1200°C and during the heating of TIBAL-derived compact below ~1400°C may be attributed to (i) the elimination of residual carbon formed by the decomposition of alkyl groups and (ii) the elimination of oxygen and H_2O adsorped on the AlN particles. The weight loss (~10%) of TIBAL-derived compact before and after the dilatometric measurement is more appreciable than the weight losses (~5%) of TMAL-derived and TEAL-derived compacts.

As shown above, the rapid shrinkages during the heating of these three compacts above 1200–1400°C indicate the initiation of the mass transfer due to the sintering of AlN particles. On

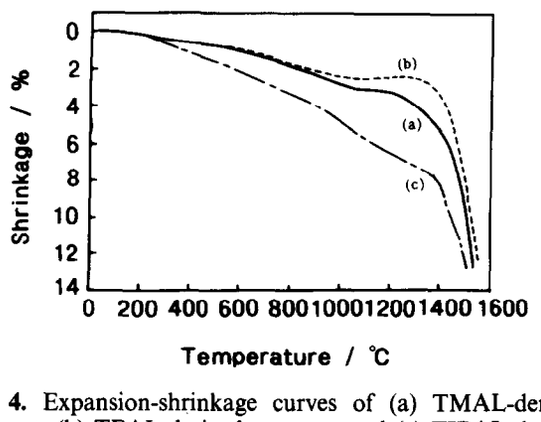


Fig. 4. Expansion-shrinkage curves of (a) TMAL-derived compact; (b) TEAL-derived compact and (c) TIBAL-derived compact. Heating rate: 5°C min^{-1}.

the basis of this information, we decided to fire the compacts at 1400°C or at a higher temperature. The relationship between firing temperature and relative density is shown in Fig. 5. The relative densities for these compacts varied from 60 to 67% at the firing temperature of 1400°C; however, they increased with increasing temperature and attained 95–96% at and above 1600°C.

Although the sintering temperatures of the conventional pure AlN powders with the surface areas of 1–5·3 m^2g^{-1} usually need to be 1850°C or higher,[2,20] those of the present AlN powders with the surface areas of 95–175 m^2g^{-1} are as low as 1600°C. This sintering temperature is in accord with that of AlN powder with the surface area of 92 m^2g^{-1} prepared by rf plasma.[6] Thus, the difference in sintering temperature between conventional pure and present ultrafine AlN powders can be attributed to the surface area or the primary particle size. Moreover, the oxygen in AlN powder may create the cation vacancies to promote the mass transfer during sintering;[19] however, Kuramoto and his coworkers[2,20] state that the particle-size effect, i.e. small particle size and narrow particle-size distribution, contributes much more to the densification of the AlN compact than the oxygen effect does. In actual fact, the relative densities of these sintered compacts are all in the range of 95–96% at and above 1600°C, regardless of the differences in oxygen contents among the starting powders.

The crystalline phases of the compacts fired at 1800°C for 3 h were examined by XRD. Although the data were omitted in this paper, the XRD patterns of these sintered compacts showed that the crystalline phases were not only AlN but also $Al_{(8/3+x/3)}O_{4-x}N_x$[21] (trace).

The oxynitride or $Al_{(8/3+x/3)}O_{4-x}N_x$ results from the reaction of AlN with H_2O and/or O_2 during firing. Although the sintering of AlN powder is promoted by the presence of oxygen,[2] the thermal

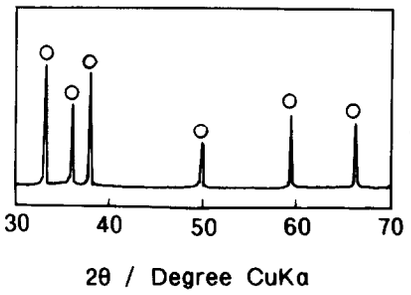


Fig. 6. Typical X-ray diffraction pattern of TMAL-derived compact. ○ AlN — Firing conditions: 1800°C for 10 h.

Table 3. Some properties of the compact fired at 1800°C for 10 h.

Alkylaluminium	*Relative density (%)*	*Phase*[a]	*Oxygen (%)*
$Al(CH_3)_3$	97·9	AlN	1·8
$Al(C_2H_5)_3$	98·2	AlN	4·7
$Al(i\text{-}C_4H_9)_3$	95·1	AlN	5·2

[a] Identified by X-ray diffractometry.

conductivity lowers with increasing oxygen content.[2,22] The oxygen content may be reduced by firing the compact in nitrogen atmosphere.[23] In order to: (i) reduce $Al_{(8/3+x/3)}O_{4-x}N_x$ content and (ii) increase the relative density over ~95%, the firing time was prolonged from 3 to 10 h at the fixed temperature of 1800°C. We examined the crystalline phases of the compacts by XRD. As a typical case, the XRD pattern of TMAL-derived compact is shown in Fig. 6. Only AlN was detected from the sintered compact.

The relative density, crystalline phase and oxygen content are listed in Table 3. The relative density of TIBAL-derived compact was limited to be 95·1%; however, the relative densities of TMAL-derived and TEAL-derived compacts attained ~98%. The crystalline phase was only AlN. The oxygen contents were in the range of 1·8–5·2%.

The SEM micrographs of these sintered compacts are shown in Fig. 7. The SEM micrographs of TMAL-derived and TEAL-derived compacts (Fig. 7(a) and (b)) showed that the grains with sizes of 1–4 μm were closely arrayed. The SEM micrograph of TIBAL-derived compact (Fig. 7(c)) showed that the grains with sizes of < 1 μm were present among the grains with sizes of 2–4 μm.

The fabrication of high-density AlN ceramics without a sintering aid has been examined chiefly by Kuramoto and his coworkers: the relative density of AlN compact fired at 2000°C for 3 h is 93%;[2] the firing of doctor-bladed powder compact at 1850°C for 7 h raises the relative density to 98·7%.[20] Since the relative densities of TMAL-derived and TEAL-derived compacts achieve ~95% at 1600°C for 3 h and ~98% at 1800°C for 10 h, these AlN powders prove to have excellent sinterabilities.

The SEM micrographs (Fig. 7) shows that the uniform-sized grains are closely arrayed, reflecting the high densities (95–98%) of the sintered compacts. Such microstructures demonstrate that the homogenous sintering may proceed among the ultrafine, uniform-sized and weakly-agglomerated AlN particles.[20]

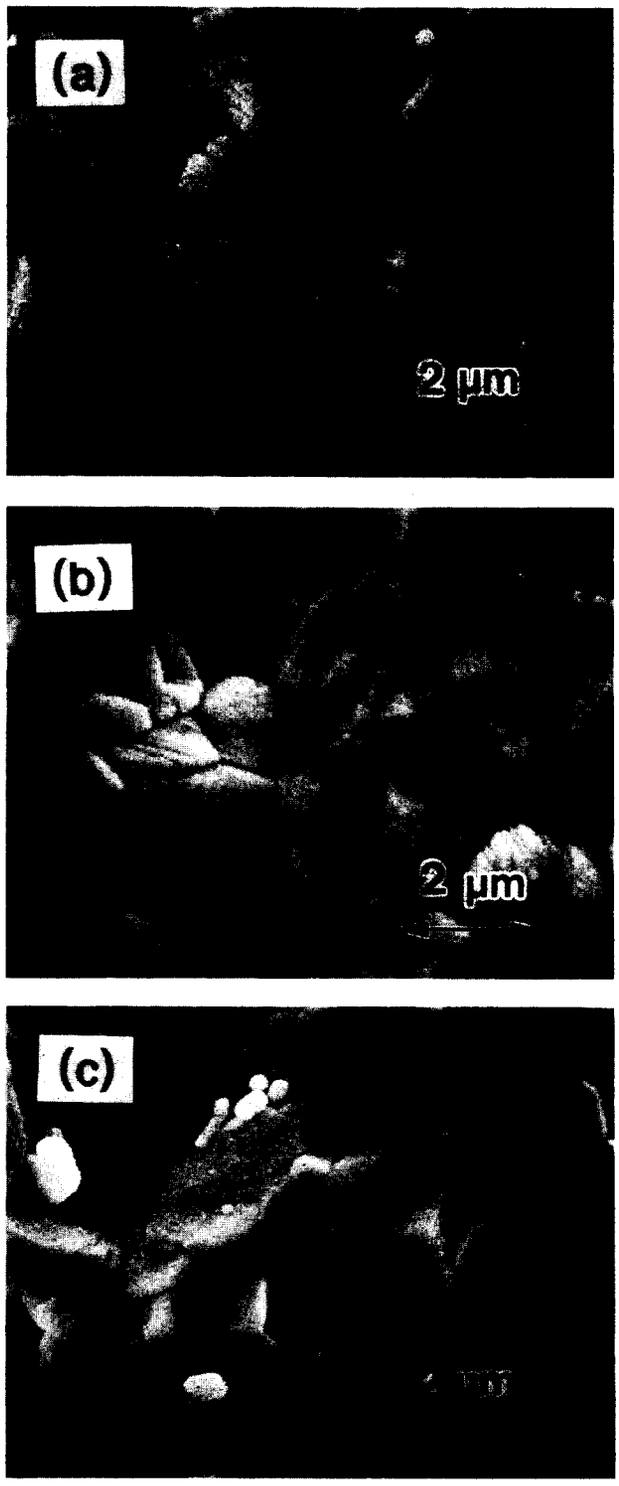


Fig. 7. SEM micrographs of (a) TMAL-derived compact; (b) TEAL-derived compact and (c) TIBAL-derived compact. Firing conditions: 1800°C, 10 h.

4 Conclusion

The aluminium-nitride (AlN) powders were prepared by the metal–organic chemical vapour deposition (MOCVD), i.e. the vapour-phase reactions of trimethylaluminium ($Al(CH_3)_3$: TMAL), triethylaluminium ($Al(C_2H_5)_3$: TEAL) and triisobutylaluminium ($Al(i\text{-}C_4H_9)_3$: TIBAL) with ammonia (NH_3). The properties of the resulting powders are summarized as follows:

(1) The specific surface areas of the resulting powders were 95–175 m^2g^{-1}; the primary particle sizes were in the range of 10–20 nm.

(2) The sintered compacts with the relative densities of ~95% could be fabricated by firing these powders at temperatures as low as 1600°C. When these compacts were fired at 1800°C for 10 h, the relative densities were 98·2% (TEAL-derived compact) > 97·9% (TMAL- derived compact) > 95·1% (TIBAL-derived compact).

(3) After the firing of the compacts at 1800°C for 10 h, only AlN was detected from the sintered compacts; the oxygen contents were 1·8% (TMAL-derived compact) < 4·7% (TEAL-derived compact) < 5·2% (TIBAL-derived compact).

Acknowledgements

The authors wish to express their thanks to Mr K. Nishinaka of Mitsubishi Materials Co. Ltd. for taking the TEM micrographs and to Dr T. Rouxel of Laboratoire de Matériaux Céramiques et Traitements de Surface of U.R.A.—CNRS 320 (France) for dilatometric measurements.

References

1. Borom, M. P., Slack, G. A. & Szymaszek, J. W., Thermal conductivity of commercial aluminum nitride. *Bull. Am. Ceram. Soc.*, **51** (1972) 852–6.
2. Kuramoto, N., Taniguchi, H. & Aso, I., Development of translucent aluminum nitride ceramics. *Am. Ceram. Soc. Bull.*, **68** (1989) 883–7.
3. Mroz, T. J., Aluminum nitride. *Am. Ceram. Soc. Bull.*, **71** (1992) 782, 84.
4. Matsumoto, O., Formation of aluminum nitride by use of a transferred plasma torch. *J. Electrochem. Soc. Jpn.*, **36** (1968) 207–12.
5. Uda, M., Ohno, S. & Okuyama, H., Preparation of ultrafine powders of AlN and (AlN + Al) by nitrogen plasma–Al reaction. *Yogyo-Kyokai-Shi*, **95** (1987) 86–90.
6. Baba, K., Shohata, N. & Yonezawa, M., Synthesis and properties of ultrafine AlN powder by rf plasma. *Appl. Phys. Letters*, **54** (1989) 2309–11.
7. Yokota, M., Yagyu, S., Majima, K. & Nagai, H., Preparation of ultra-fine aluminum nitride by gas phase reaction. *J. Powder and Powder Metall.*, **38** (1991) 382–5.
8. Itatani, K., Sano, K., Howell, F. S., Kishioka, A. & Kinoshita, M., Some properties of aluminium nitride powder synthesized by low-pressure chemical vapour deposition. *J. Mater. Sci.*, **28** (1993) 1631–8.
9. Kimura, I., Hotta, N., Nukui, H., Saito, N. & Yasukawa, S., Synthesis of fine AlN powder by vapour phase reaction of $AlCl_3$ and NH_3, *J. Ceram. Soc. Jpn.*, **96** (1988) 206–10.
10. Nickel, K. G., Riedel, R. & Petzow, G., Thermodynamic and experimental study of high-purity aluminum nitride formation from aluminum chloride by chemical vapor deposition. *J. Am. Ceram. Soc.*, **72** (1989) 1804–10.
11. Riedel, R. & Gaudl, K. -U., Formation and characterization of amorphous aluminum nitride powder and transparent aluminum nitride film by chemical vapor deposition. *J. Am. Ceram. Soc.*, **74** (1991) 1331–4.
12. Park, J. -R., Rhee, S. -W. & Lee, K. -H., Gas-phase synthesis of AlN powders from $AlCl_3$–NH_3–N_2. *J. Mater. Sci.*, **28** (1993) 57–64.
13. Greil, P., Kulig, M., Hotza, D., Lange, H. & Tischtau, R., Aluminium nitride ceramics with high thermal conductivity from gas-phase synthesized powders. *J. Eur. Ceram. Soc.*, **13** (1994) 229–37.
14. Tsuchida, K., Takeshita, Y., Yamane, A. & Kato, A., Preparation of AlN powders by vapor phase reaction of $Al(i\text{-}Bu)_3$–NH_3 system. *Yogyo-Kyokai-Shi*, **95** (1987) 1198–1201.
15. Wakimura, K. & Hiai, A., AlN powders produced by vapour phase reaction from aluminum alkyl. *Function and Materials*, **11**(2) (1991) 13–9.
16. Adjaottor, A. A. & Griffin, G. L., Aerosol synthesis of aluminum nitride powder using metalorganic reactants. *J. Am. Ceram. Soc.*, **75** (1992) 3209–14.
17. Powder Diffraction File Card No. 25-1133, JCPDS International Center for Diffraction Data, Swarthmore, PA, USA, 1975.
18. Interrante, L. V., Carpenter II, L. E., Whitmarsh, C., Lee, W., Garbauskas, M. & Slack, G. A., Studies of organometallic precursors to aluminum nitride. *Mat. Res. Soc. Symp. Proc.*, **73** (1986) 359–66.
19. Sakai, T. & Iwata, M., Effect of oxygen on sintering of AlN. *J. Mater. Sci.*, **12** (1977) 1659–65.
20. Kuramoto, N., Aluminum nitride powder and its situation. *Bull. Ceram. Soc. Jpn.*, **22** (1987) 29–34.
21. Powder Diffraction File Card No. 18–52. JCPDS International Center for Diffraction Data, Swarthmore, PA, USA, 1968.
22. Slack, G. A., Nonmetallic crystals with high thermal conductivity. *J. Phys. Chem. Solids*, **34** (1973) 321–35.
23. Sato, T. & Iwata, M., Preparation of aluminum nitride by electric arc method. *Nippon Kagaku Kaishi*, **1973** (1973) 1869–73.

Journal of the European Ceramic Society 15 (1995) 667–674
© 1995 Elsevier Science Limited
Printed in Great Britain. All rights reserved
0955-2219(95)00034-8
0955-2219/95/$9.50

Characterization and Surface Chemistry of Uncoated and Coated Silicon Nitride Powders

H. Schmidt,[a] G. Nabert,[a] G. Ziegler[a] & H. Goretzki[b]

[a]Institut für Materialforschung (IMA), Universität Bayreuth, D-95440 Bayreuth, Germany
[b]SPECS GmbH, Voltastraße 5, D-13355 Berlin, Germany

(Received 24 June 1994; revised version received 18 January 1995; accepted 7 February 1995)

Abstract

Various Si_3N_4 powders, produced by different procedures, were characterized by imaging (TEM) and analytical methods (EDS, FT-IR, XPS) in the as-received state as well as after doping with a metal oxide (MgO). For the doping, an alternative procedure to the usual methods, was applied, which is based on soluble organometallic compounds. Analytical transmission electron microscopy combined with lateral resolution element analysis and XPS measurements was used for morphological, structural and analytical characterization. The distribution of the dopant was deduced from measurements of XPS sputter depth profiles. These investigations were supplemented by FT-IR measurements in order to determine qualitatively and semi-quantitatively the reactive groups on the particle surfaces of the as-received powders.

For comparison, measurements were performed with Si_3N_4 powders which were doped by the above chemical procedure and by mechanical mixing. The results of the various characterization methods are interpreted in the form of a model display for surface reactions of organometallic doping reagents on the surfaces of ceramic particles. The results show that Si_3N_4 powders with high concentration of OH groups on their particle surface reveal very good distribution of the fluxing element (layer-like coating).

1 Introduction

It is well known that the improvement of homogeneity, reproducibility and sinter activity is an essential objective in the development of structural ceramics. In that context the surface chemistry and structure of sintering powders, which have been developed with even smaller particle sizes and in higher purity degrees, play an important role. Moreover, the distribution of sintering additives in the matrix material has to be improved, which can make it possible to reduce the additive concentration and to enhance the high-temperature properties. Consequently, investigations are necessary to improve the doping techniques, the characterization of the highly sinter active powders, and the homogeneity of (powder + sintering additive)-mixtures.[1] Up to now several techniques, such as mixing/milling processing, the sol-gel method, the precursor route and doping with inorganic metal compounds, have been used in order to introduce inorganic sintering additives (metal oxides).

In the mixing/milling processing frequently used, the raw materials are ground (homogenized) with the sintering additive (mostly metal oxides) in a milling device. Using this technique, the homogeneity of the additive distribution is limited by the particle size distribution (μm-range) of the starting powder and of the dopant. This method is not suited for the doping of silicon nitride powders with small amounts of sintering additives. Additionally, the mixture may be contaminated by abrasion materials.

The sol-gel method is based on the hydrolysis of multivalent metal alkoxides. The gel is subjected to a drying process in order to obtain the material in the powder state.[2,3] Another technique, which is also based on the use of chemical pre-products, is the liquid precursor route. Non-oxide powders have been produced by reaction pyrolysis of inorganic polymers.[4–6] However, both techniques are very expensive.

The disadvantages of inorganic metal compounds is the possibility of forming crystalline phases[7] and the contamination of the powder particles by additional elements from the counterions (N from nitrates, Cl, Br, I from halogenides, P from phosphates, S from sulfates etc.) which may have a detrimental effect particularly on high-temperature properties.[8] Therefore, these elements have to be removed during heating (formation of nitric oxide, sulfur dioxide, halogenic acids etc.).

In the present investigation another method is

used to dope the mostly commercially available powders through soluble organometallic compounds based on Mg as model substance. This method provides several advantages compared to the procedures mentioned above.[9,10] By using Mg-methoxide as the organometallic compound, for example, which can act as the dopant compound, only those elements (in small amounts) are introduced in the matrix powder, which are anyhow incorporated into the raw material through organic additives (carbon, hydrogen and oxygen). This method allows a homogeneous introduction of doping elements even at low concentrations. The development of a chemical bonding between particle surface and organometallic compound suppresses the formation of a separate phase of the dopant metal.

2 Experimental Procedure

Organometallic chemistry was carried out in non-aqueous and water-free solvents; whereby magnesium methoxide as organometallic compound was used. During the mixing process of this solution with a suspension of the raw material in the same liquid, (alcohol), the surface groups of the Si_3N_4 powders act as polar reagent to which the metal alkoxide can be directly bonded generating an alcohol molecule ($Si–OH + (CH_3O)_2Mg \rightarrow Si–O–Mg–O–CH_3 + CH_3OH$). As a result, an excellent distribution of the sintering aids (in solution) may be assumed, which will subsequently be transferred to the particle surfaces in accordance with the distribution and density of the OH-groups. Thus, these are decisive parameters for the homogeneous distribution of the inorganic additives.

The infrared spectroscopy is an ideal method to achieve information about functional groups of molecules[11] through the vibrational excitation. To detect the functional surface groups, powder analysis was performed in the so called Barnes cell (Spectra Tech. Inc.) of an FT-infrared-spectrometer (Digilab FTS 15/80) in the reflection mode, wave numbers ranging from 4000 to 600 cm^{-1}. In the range of 4000–3000 cm^{-1} the stretching vibrations of the surface-OH-groups, which are important for the chemical dopant used here, can be determined. In the range of about 1000 cm^{-1}, the backbone vibrations of the lattices were observed.[12,13]

The silicon nitride powders investigated — either commercially available or special grades from industry — were produced by different procedures (Table 1). These powders were analyzed in the as-received state and after doping with magnesium methoxide with various concentrations between 0·5 and 2 wt% of Mg related to Si_3N_4. Analysis of the dopant reaction concerning the homogeneity of the element distribution was performed by transmission electron microscopy (Philips EM 430; accelerating voltage 300 kV; lateral resolution about 0·2 nm, equipped with EDS, Tracor) and X-ray-photoelectron-spectroscopy (Perkin Elmer PHI 5600). For comparison purposes, a powder mixture (Si_3N_4 grade UBE SN-E10 + 2 wt% MgO grade p.a. Merck) was produced by mixing the powders in a non-aqueous liquid.

Table 1. Oxygen content and specific surface area of the silicon nitride powders most investigated. Additionally, FT-IR measurements were performed with the following powders: HCST S1, Denka SN-9S, HCST LC10-S, HCST LC10-N, Bayer DF0014, HCST LC12-SX, HCST 3918 LC12 (special grade with 3 wt% oxygen), HCST GP, TOSOH TS10.

Product	*UBE SN-E10*	*Starck M11*	*Denka SN-9FW*
Synthesis method	Diimide precipitation	Nitridation	Nitridation
0 (wt%)	1·32	1·78	0·82
Spec. surface (m^2/g) area	11·9	13·5	11·7

3 Results and Discussion

3.1 FT-infrared spectroscopy

The infrared spectrum analysis of the silicon nitride powders investigated provides information about the surface bonded molecules. The height of

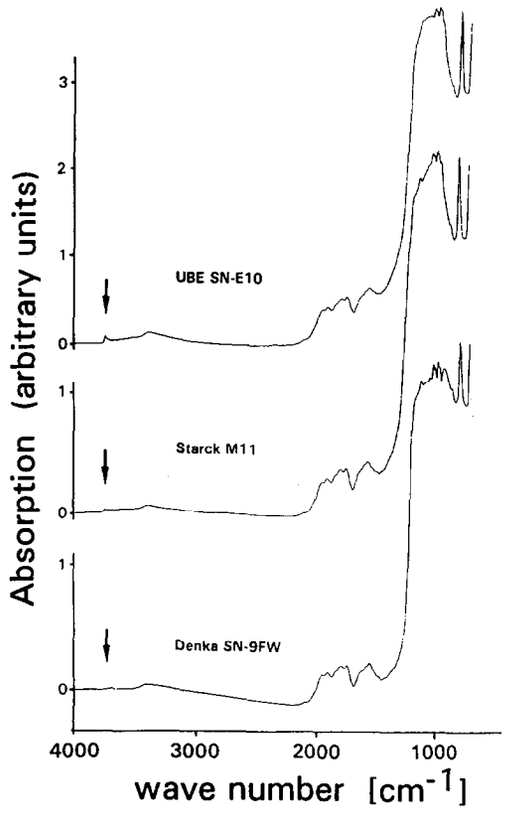


Fig. 1. FT-infrared spectra of various silicon nitride powders investigated (UBE SN-E10, Starck M11, Denka SN-9FW).

the absorption peak of the OH-stretching vibration at 3750 cm^{-1} indicates the amount of the OH-surface groups (Fig. 1). An increasing peak height was found spectroscopically in the sequence of the silicon nitride powders Denka SN-9FW, Starck M11, UBE SN-E10 (see arrows in Fig. 1); in other silicon nitride powders investigated, the intensity of the OH-vibration band increases in the following sequence: HCST Sl (low), Denka SN-9S, HCST LC10-S, HCST LC10-N, Bayer DF0014, HCST LC12-SX, HCST 3918 LC12 (special grade with 3 wt% oxygen), HCST GP, TOSOH TS10 (high). In the range of about 1000 cm^{-1} the backbone vibrations (Si–N–Si, Si–O–Si) of the lattices can be observed (a detailed association of each maximum of the overlapping vibration bands in this so-called 'fingerprint' region is not discussed in connection with the dopant reaction used here).

The silanol groups are used as reactive surface groups for the organometallic compounds. Measuring the extent of the OH-stretching vibrations at 3750 cm^{-1} allows an estimation of the surface occupation of these groups which is not strongly correlated to the total oxygen content of silicon nitride powders (compare Fig. 1 with the total oxygen content in Table 1). Thus, the variation in the intensities of the OH-vibrations gives an indication of suitability and potential for the chemical dopant reaction of each powder.

3.2 Photo-electron spectroscopy

Photo-electron spectroscopy (XPS) is an important analytical technique for surface and thin film characterization of solid materials. It provides qualitative and quantitative information relating to the outermost atom or molecule layers. The depth of information or the thickness of the analyzed surface layer ranges from 1 to 3 nm. This mainly depends on the kinetic energy of the photo-electrons. Sputter depth profiling is applied if concentration variations within a thick surface layer are of interest. The XPS spectra are commonly initiated by Mg K_α or Al K_α radiation. The resulting photo-electron lines can be correlated with the binding energy of the core level states of the atoms. That energy can respond sensitively to a charge transfer between neighbouring atoms. It provides a direct insight into chemical bonding

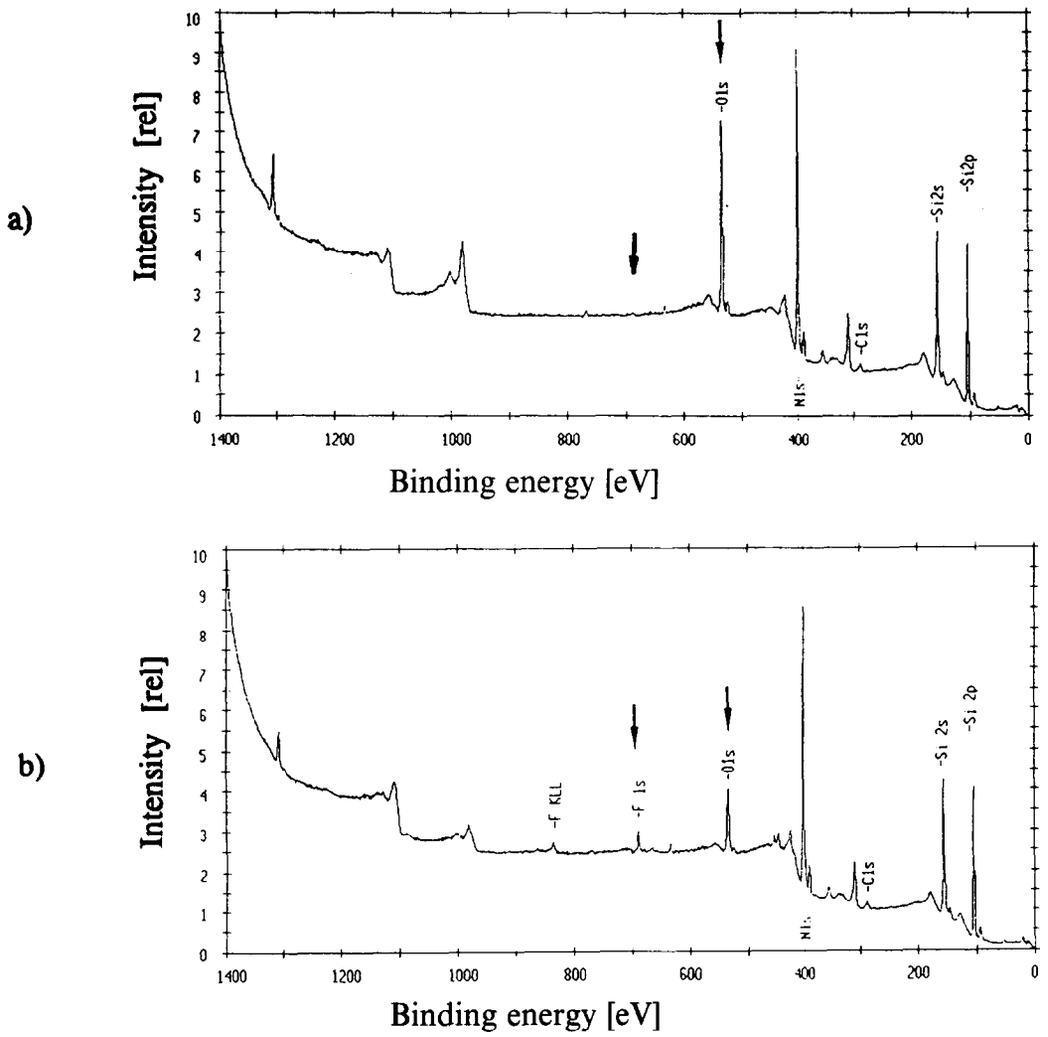


Fig. 2. XPS spectra of two silicon nitride powders with (a) high (UBE SN-E10) and (b) low (Denka SN-9FW) oxygen content.

parameters (chemical shift). XPS is therefore a powerful tool for the identification of chemical compounds and the modification of the electronic structure. A limitation, however, is the overlapping of several bonding states of different compounds.

In the case of the Si_3N_4 powders, a correlation between the XPS data and the TEM studies was found (Figs 2 and 3). The Denka powder SN-9FW reveals a lower oxygen concentration at the surface compared to the powder UBE SN-E10. The low oxygen content connected with the detection of fluorine is obviously caused by HF treatment of the powder. The result coincides with the thickness of the amorphous oxide layer in Fig. 3. The evaluation of the silicon peak in Fig. 4 shows the amount of oxidized Si (SiO_2 at 104·4 eV) in reference to the nitrogen bonded Si (Si_3N_4 at 102·8 eV). This proves that the Si_3N_4 powder synthesized by diimide precipitation has a higher amount of an oxidized phase on the particle surface compared to the Si_3N_4 powder synthesized by direct nitridation (followed by HF treatment). The essential point is that (because of the reaction of HF with the silanol groups) high fluorine contents cause a reduction in the number of OH groups.

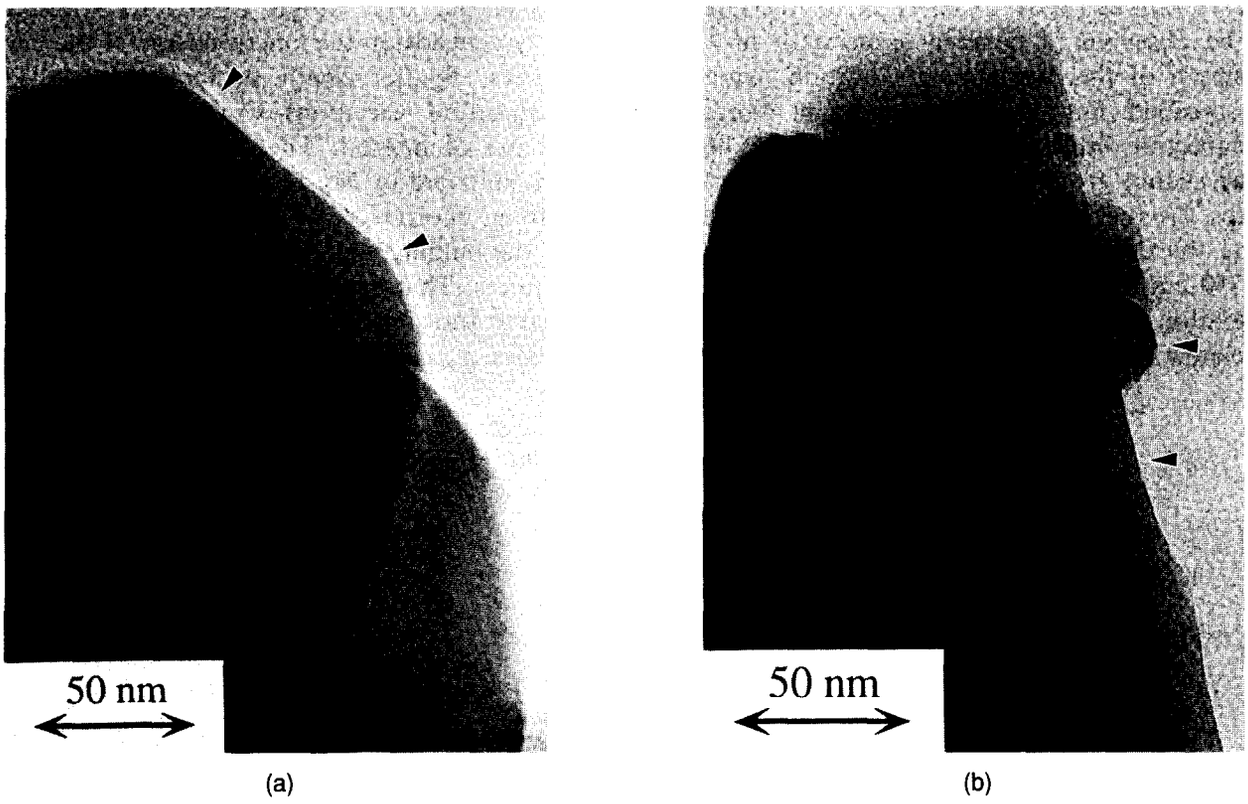


Fig. 3. TEM micrographs of Si_3N_4 particles with (a) a relatively thick and (b) a thin amorphous surface layer. The Si_3N_4 powders are synthesized by (a) diimide precipitation and by (b) direct nitridation.

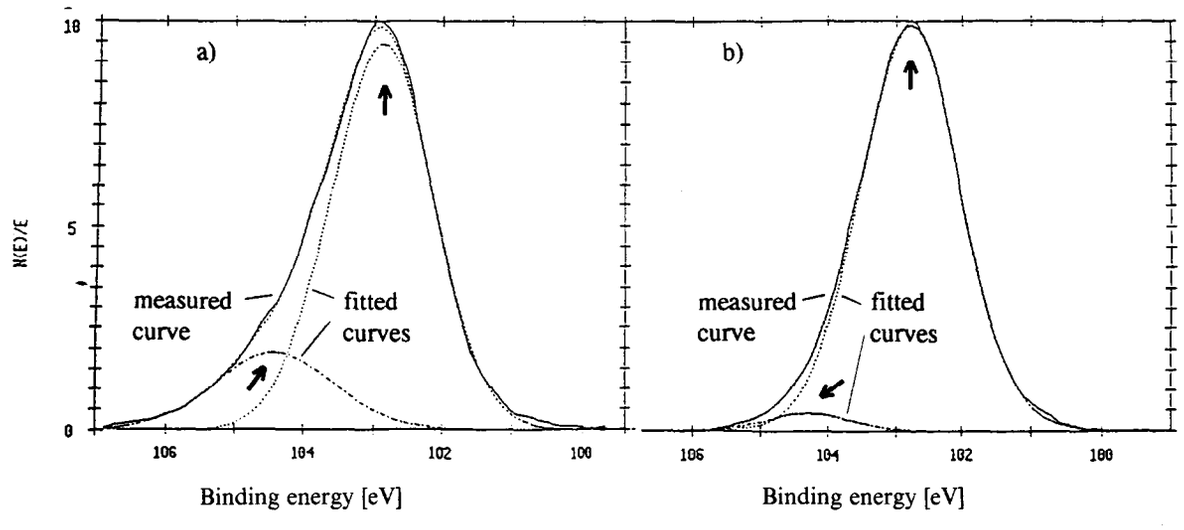


Fig. 4. Deconvolution of the measured peaks and fitted curves of the Si 2p lines (oxidized Si: 104·4 eV; nitrogen bonded Si: 102·8 eV) of XPS spectra of silicon nitride powders with (a) a relatively thick and (b) a thin amorphous surface layer. The Si_3N_4 powders are synthesized by (a) diimide precipitation and by (b) direct nitridation.

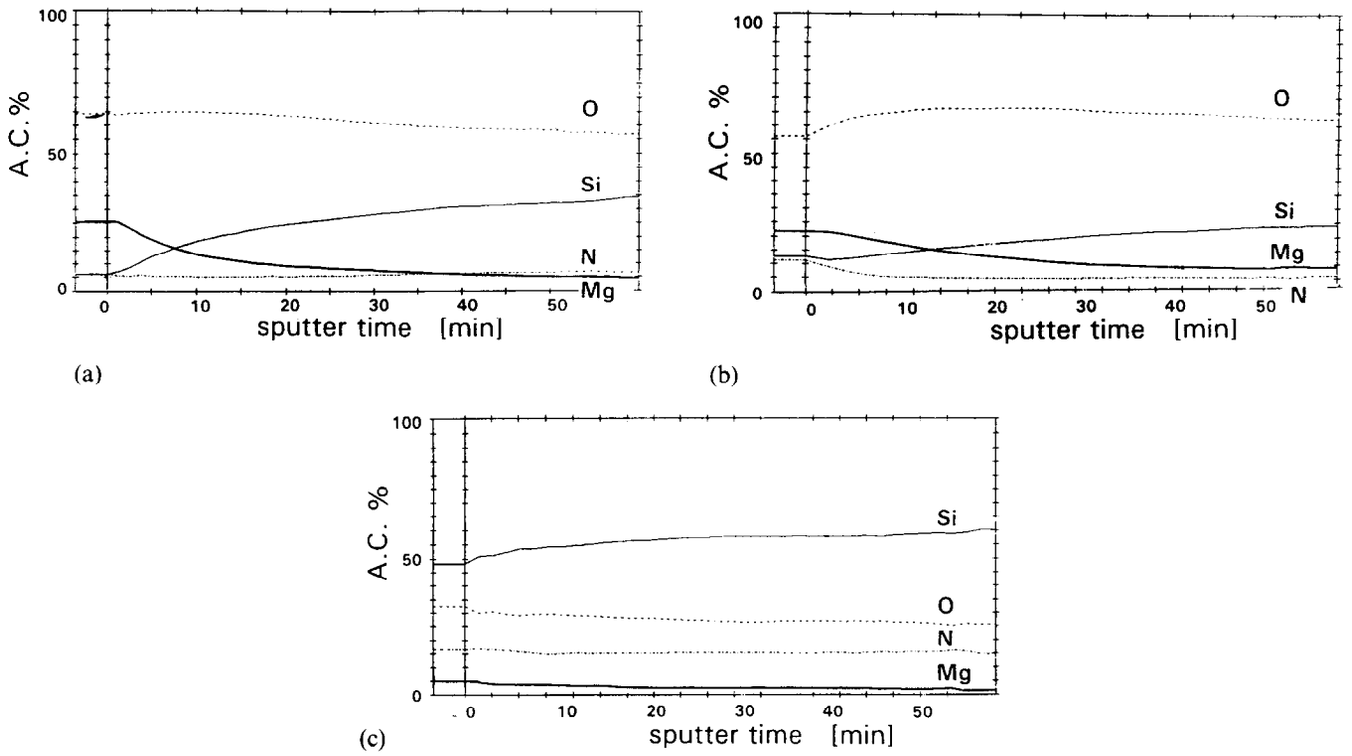


Fig. 5. XPS sputter depth profile measurements (concentration of Si, O, N and Mg as a function of sputter time) of Si_3N_4 powders doped with 2 wt% Mg: (a) chemically doped UBE SN-E10 (high number of OH groups); (b) chemically doped Denka SN-9FW (low number of OH groups); (c) mechanically doped UBE SN-E10.

In Fig. 5, the results of the XPS sputter depth profile measurements of silicon nitride powders, which are chemically and mechanically doped, are presented indicating the Mg-, Si-, O- and N-concentrations. The variation of the element concentration versus sputter time is different for the three

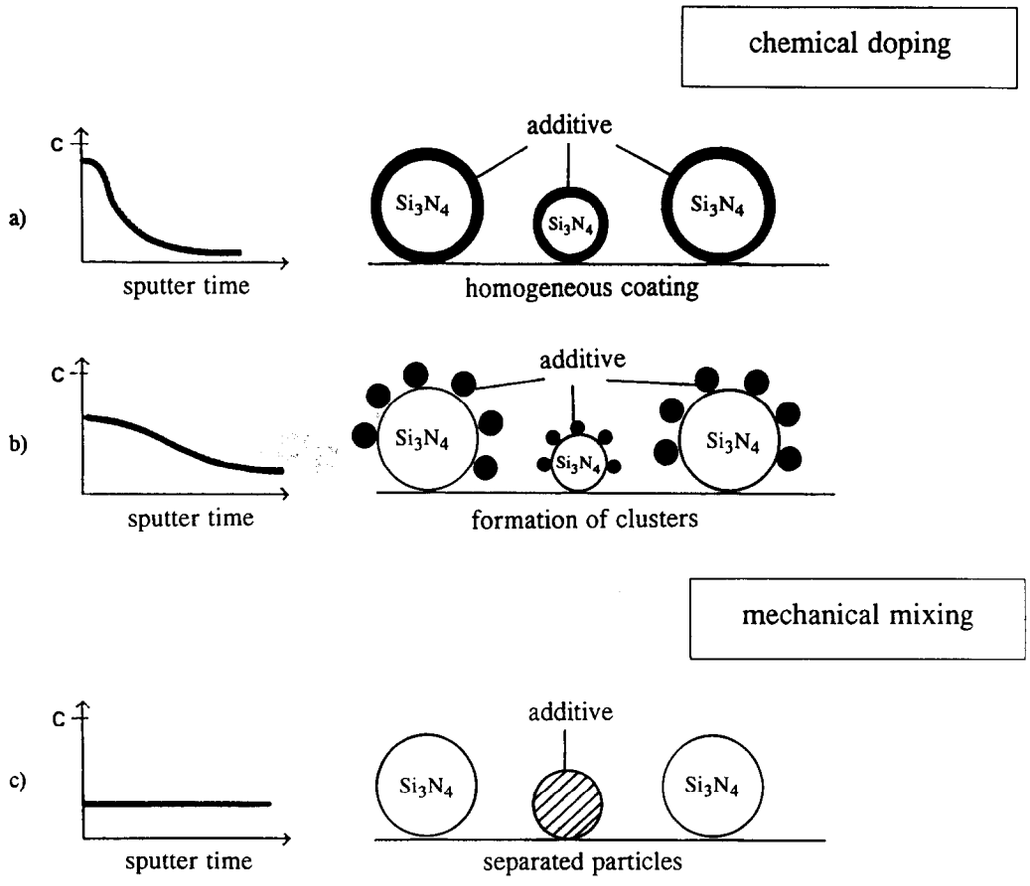


Fig. 6. Model of (a) layer-distribution (additive-coated Si_3N_4 particles), UBE SN-E10; (b) cluster-distribution (additive clusters on Si_3N_4 powder surface), Denka SN-9FW; (c) particle-distribution (additive-particle and Si_3N_4 particles), based on the sputter depth profiles of the dopant element (here schematic; experimental results see Fig. 5).

powder mixtures. From these results, information about the additive distribution in the three systems may be deduced (Fig. 6): a layer distribution (Fig. 6(a)), a particle–particle distribution (Fig. 6(c)) or, as a transition stage between these two, a cluster-like distribution of the dopant element at the powder surfaces (Fig. 6 (b)). For the mechanical doping of raw materials with metal oxide particles, the element concentrations remain mainly unchanged during sputter depth profile measurements because of the simply mixed particles. Powders doped with magnesium methoxide show in the surface-near region a higher magnesium content compared with the added total concentration.

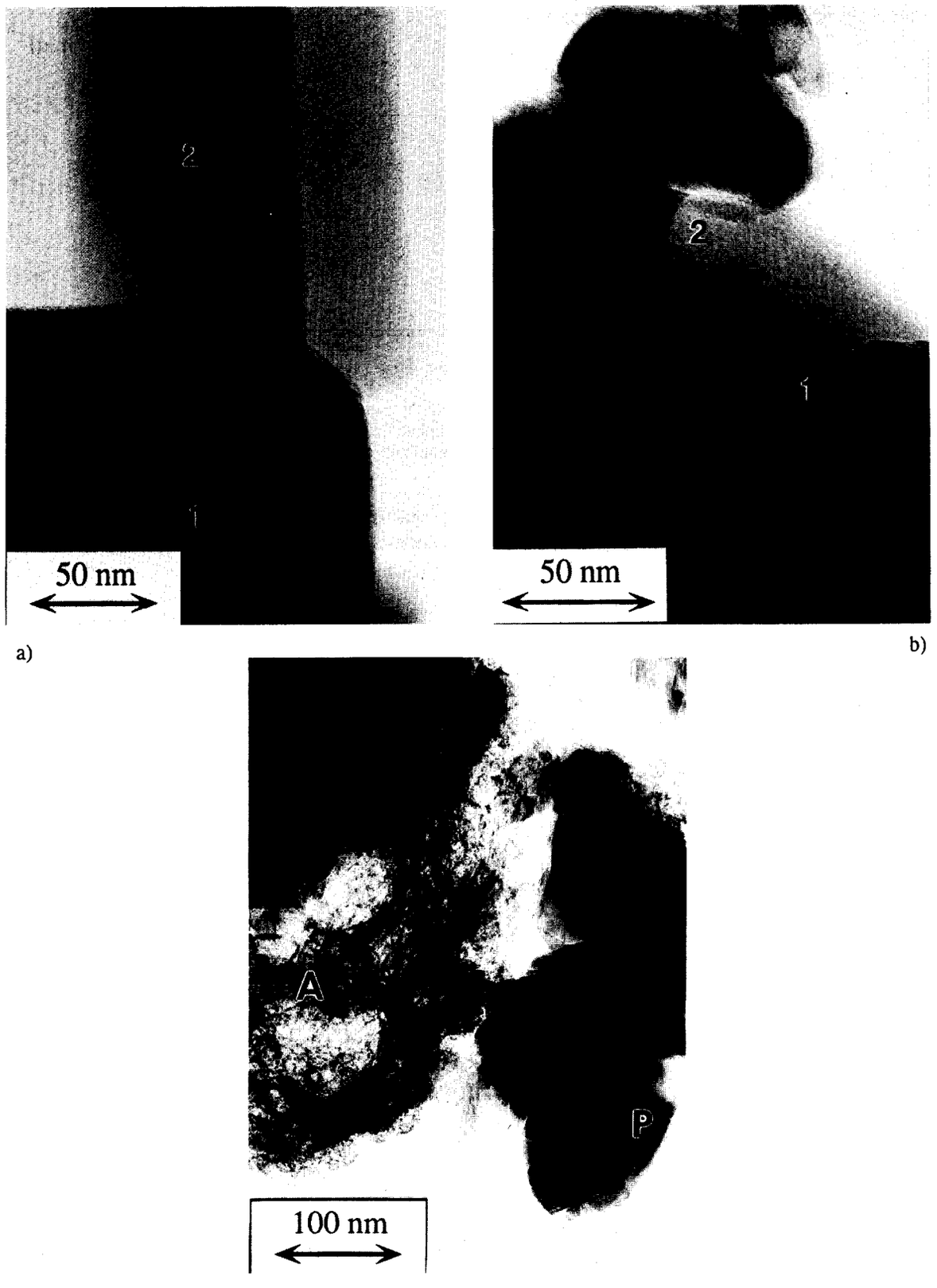


Fig. 7. TEM micrographs of various silicon nitride powders doped with 2 wt% Mg: (a) Si_3N_4 UBE SN-E10, particles 1 and 2; (b) Si_3N_4 HCST M 11, particles 1 and 2; (c) Si_3N_4 Denka SN-9FW, amorphous region A and particle P.

The magnesium concentration decreases with increasing sputtering time. This behaviour may be interpreted in terms of a layered coating or cluster-like doping of the single powder particles with the dopant metal. The higher the slope of the curve Mg = f (sputter time) the more the doping is approaching the layer-like coating.

The results show that the powder UBE SN-E10 with a higher amount of surface-OH-groups reveals a stronger decrease of the magnesium intensity compared to the powder Denka SN-9FW with a lower fraction of surface-OH-groups (see Figs 1 and 5), indicating the desired layer-like doping of each particle.

3.3 Analytical transmission electron microscopy

High resolution and analytical transmission electron microscopy (TEM) offers with extreme lateral resolution the unique possibility for structural, morphological and analytical characterization of powders.[14,15] By using TEM and EDS the local amount of magnesium in the powders was analyzed. Figure 7 shows TEM-micrographs of various silicon nitride powders doped with 2 wt% magnesium; Fig. 8 gives the results of EDS measurements. In the case of the Denka SN-9FW powder doped with 2 wt% Mg, a much higher content of magnesium was found in the amorphous regions (precipitated Mg compound) compared to the Si_3N_4 powder particles (see Figs 7(c) and 8(c)). In contrast to the Denka powder no amorphous region between the particles was observed in the powder mixtures of Si_3N_4-Starck M11 and Si_3N_4-UBE SN-E10 doped with 2 wt% Mg (see Figs 7(a) and 7(b) as well as Figs 8(a) and 8(b)). In these cases, particularly for UBE SN-E10,

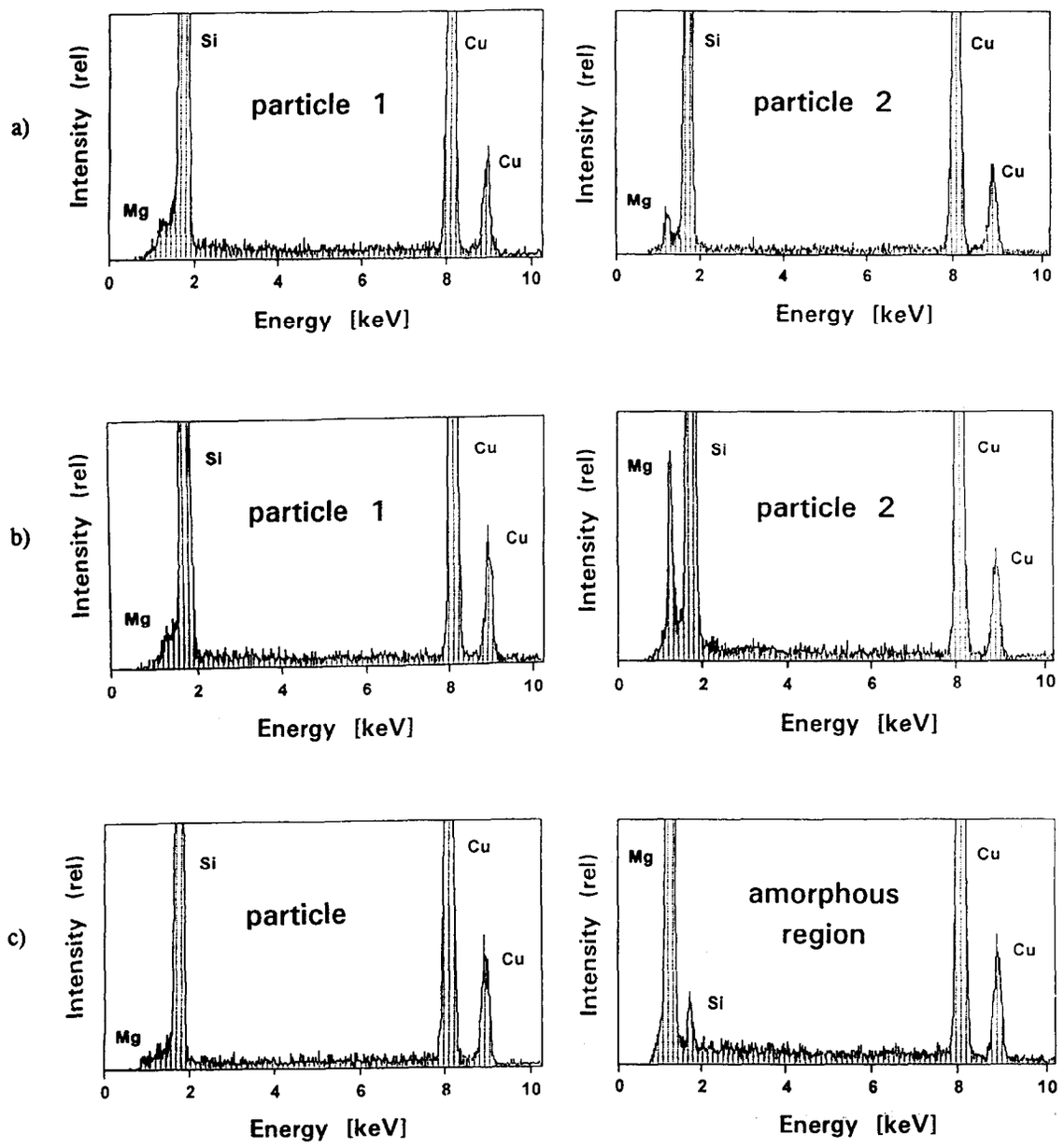


Fig. 8. EDS spectra on local sites of silicon nitride particles doped with 2 wt% Mg (Cu from copper grid): (a) Si_3N_4 UBE SN-E10; (b) Si_3N_4 Starck M 11; (c) Si_3N_4 Denka SN-9FW.

a more homogeneous distribution of the sintering aid was obtained. The reason is the relative high number of silanol groups on the surface as indicated in the FT-infrared spectra (see Fig. 1).

4 Conclusions

The dopant-technique involving organometallic compounds (strong alkaline reagents) provides a more homogeneous distribution of additives like magnesium. The use of analytical transmission electron microscopy, photoelectron spectroscopy and infrared spectroscopy allows an improved characterization of ultra-fine and doped sintering powders. The correlation of the results of the different analytical methods permits an interpretation about the quality of the distribution of sintering aids in ceramic raw materials. From the variation of the element concentration versus sputter time the distribution of the additives in the powder mixtures can be deduced, e.g. layer-like distribution, particle–particle distribution or a transition stage between these two cases, a cluster-like distribution of the additive on the powder surface.

The degree of homogeneity that can be achieved with the aim of eventually producing continuous thin coatings is strongly dependent on the number of OH groups (silanol groups, adsorbed water) on the powder particle surface which are controlled by the type of the Si_3N_4 powder and the pre-treatment as well as the amount of sintering additives. The number of silanol groups cannot be strongly correlated to the total oxygen content in the powders. However, a large specific surface area of the powders and a relatively high amount of oxygen at the particle surface is in general an advantage. In this connection it is important to note that fluorine (because of the reaction of HF with the silanol groups) results in a reduced number of silanol groups.

Based on the character of element distribution as a function of the number of surface groups, the dopant content and the test parameters, three idealized basic models may be deduced:

- a high number of OH-surface groups and low dopant content for dry powders and water-free suspension media result in a layer-like distribution of the sintering additive which is desirable;
- a low number of OH-surface groups and high dopant content for dry powders and water-free suspension media lead to amorphous precipitation of the dopant;
- a number of OH-surface groups nearly equal to the dopant content results in a domain structure of the additives.

In this scope it should be mentioned that in the case of a low number of OH groups relative to the amount of the dopant compound, and small amounts of water in the suspensions (powders with adsorbed water and/or water-containing suspension media) a domain structure of additives is enhanced.

The methodology is not restricted to the described powders, but also appreciable for other oxidic and non-oxidic raw materials. Moreover, it is suited for doping with more than one metal component, especially for low concentrations.

References

1. Ziegler, G., Analytical problems with ceramic materials. *Fresenius Z. Anal. Chem.*, **333** (1989) 360–72.
2. Sanchez, C. & Livage, J., Sol–gel chemistry from metal alkoxide precursors. *New J. Chem.*, **14** (1990) 513–21.
3. Pouskouleli, G., Metalorganic compounds as preceramic materials. II. Oxide Ceramics. *Ceramics International*, **15** (1989) 255–70.
4. Wills, R. R., Markle, R. A. & Mukherjee, S. P., Siloxanes, silanes and silazanes in the preparation of ceramics and glasses. *Ceramic Bulletin*, **62**(8) (1983) 904–15.
5. Schmidt, W. R., Sukumar, V., Hurley, W. J., Garcia, R., Doremus, R. H., Interrante, L. V. & Renlund, G. M., Silicon nitride derived from an organometallic polymeric precursor: preparation and characterization. *J. Am. Ceram. Soc.*, **73**(8) (1990) 2412–8.
6. Mocaer, D., Pailler, R., Naslain, R., Richard, C., Pillot, J. P., Dunogues, J., Gerardin, C. & Taulelle, F., Si–C–N ceramics with a high microstructural stability elaborated from the pyrolysis of new polycarbosilazane precursors. *J. Mater. Sci.*, **28** (1993) 2615–31.
7. Guglielmi, M. M. & Carturan, G., Precursors for sol–gel preparations. *J. Non-Cryst. Solids*, **100** (1988) 16–30.
8. Braue, W., Wötting, G. & Ziegler, G., Influence of impurities in different processed Si_3N_4-powders on high-temperature properties of sintered materials. *Spec. Ceram.*, **8** (1986) 71–80.
9. Bostedt, E., Persson, M. & Carlsson, R., Colloidal processing through surface modification. In *Proceedings of the First European Ceramic Society Conference*, ed. G. de With, R. A. Terpstra & R. Metselaar, Elsevier Applied Science, London, 1989, pp. 1.140–4.
10. Wang, C. M. & Riley, F. L., Alumina-coating of silicon nitride powder. *J. Europ. Ceram. Soc.*, **10** (1992) 83–93.
11. Boehm, H. P., Funktionelle Gruppen an Festkörper-Oberflächen. *Angewandte Chemie*, **12** (1966) 617–52.
12. Socrates, G., *Infrared characteristic group frequencies.* Verlag John Wiley, New York, 1980.
13. Ocana, M., Fornes, V. & Serna, C. J., The variability of the infrared powder spectrum of amorphous SiO_2. *J. Non-Cryst. Solids*, **107** (1989) 187–92.
14. Nabert, G. & Ziegler, G., Characterization of Si_3N_4-powders by transmission electron microscopy. In *Proceedings of the Second European Ceramic Society Conference*, ed. G. Ziegler, H. Hausner, DKG Köln, 1993, pp. 269–75.
15. Kleebe, H. J., Hoffmann, M. J. & Rühle, M., Influence of secondary phase chemistry on grain boundary film thickness in silicon nitride. *Z. Metallkd.*, **83**(8) (1992) 610–7.

Journal of the European Ceramic Society 15 (1995) 675–681
© 1995 Elsevier Science Limited
Printed in Great Britain. All rights reserved
0955-2219/95/$9.50

0955-2219(95)00019-4

Structural Evolution of Non-Crystalline SiC Precursors Prepared from Tetra methoxysilane (TMOS) and Phenol Resin

Hartmut Schneider,[a] Christian Jäger,[b] Alain Mosset,[c] Hidehiko Tanaka[d] & Martin Schmücker[a]

[a]German Aerospace Research Establishment (DLR), Institute for Materials Research, Linder Höhe, D-51140 Köln, Germany
[b]Max-Planck-Institute of Polymer-Research, Ackermannweg 10, D-55128 Mainz, Germany
[c]CEMES-LOE/CNRS, B. P. 4347, F-31055 Toulouse Cedex, France
[d]National Institute for Research in Inorganic Materials (NIRIM), Namiki 1-1, Tsukuba-shi, Japan

(Received 20 June 1994; revised version received 16 August 1994; accepted 26 January 1995)

Abstract

The structural evolution of SiC precursors prepared from tetramethoxysilane (TMOS) and phenol resin by H_2O polymerization and heat-treated between 80 and 1400°C was investigated by X-ray diffractometry (XRD), large-angle X-ray scattering (LAXS), transmission electron microscopy (TEM), and by ^{29}Si and ^{13}C nuclear magnetic resonance spectroscopy (NMR).

After hydrolysis and drying at about 80°C, the samples structurally consist of domains of partially hydrogenated silica and of coexisting phenol resin. Heat-treatments carried out on the predried material yield different stages of structural evolution, though the precursor is non-crystalline throughout the whole temperature field investigated:

— Stage I (≤500°C): gradual temperature-dependent decomposition of phenol resin and simultaneous dehydrolysis of silica.

— Stage II (≥500–≤1400°C): breakdown of the local structural order of phenol resin and formation of C domains with graphite-type short-range-order. C coexists with non-crystalline SiO_2 containing low amounts of OH-groups. The C and SiO_2 domains up to ≈ 1000°C are extremely small (≤1 nm). At higher temperatures, C and SiO_2 domains become larger (≈ 2–3 nm at 1400°C) and develop partial ordering of the short-range structure.

1 Introduction

Different routes have been used to produce SiC, starting with metal organic materials. In an early work Prochazka[1] synthesized β-SiC powders by vapor phase decomposition of halogenated silanes. SiC synthesis by laser or plasma driven CVD methods have also been reported.[2,3] The most widely studied SiC synthesis process using metal organic starting materials is pyrolysis of polysilanes and polycarbosilanes.[4–6] Zhang *et al.*[7] mentioned in a recent paper that the thermal decomposition of polymethylsilane to polycarbosilane takes place at 400°C. Above this temperature a hydrogenated non-crystalline SiC-phase is being formed, transforming to β-SiC at about 1000°C with some small amount of coexisting α-SiC. β-SiC powders can also be processed from tetramethoxysilane and phenol resin by H_2O polymerization.[8] The reaction is believed to take place through an intermediate non-crystalline precursor stage consisting of SiO_2 plus C. Reaction of SiO_2 with C to SiC was observed above about 1200°C. The present study provides additional information on the structural development of the latter precursor prior to SiC crystallization. Nuclear magnetic resonance spectroscopy, X-ray diffraction, transmission electron microscopy, and the large-angle X-ray scattering methods have been used to solve the problem.

2 Processing Conditions

SiC precursors were prepared from tetramethoxysilane ($Si(OCH_3)_4$, TMOS Trichemical Co., Japan), and resol-type phenolic resin (phenol formaldehyde condensate, J-325, Dainippon Ink and Chemicals, Inc., Japan). The molar ratio of water to alkoxide in the starting admixture was 1. The TMOS is 6 N pure and yields SiO_2 after polymerization. The phenolic resin has a molecular weight of 600–650 g/mol. It is thermally set to

Table 1. Description of samples used for the investigations

Sample key	*Heat treatment temperature (°C)*[+]	*Characterization techniques*
ST16 (as-received)	≈80[§]	XRD, LAXS, NMR
ST16-3	300	XRD, NMR
ST16-4	400	XRD, LAXS
ST16-6	600	XRD, NMR
ST16-8	800	XRD, LAXS, NMR
ST16-10	1000	XRD, NMR, TEM
ST16-12	1200	XRD, LAXS, TEM
ST16-13	1300	XRD, TEM
ST16-14	1400	XRD, TEM
ST16-17	1750	XRD

[+]Constant heat-treatment duration: 30 min.
[§]As-received sample, dried in a laboratory furnace.
XRD = Standard X-ray diffraction technique.
LAXS = Large-angle X-ray scattering.
NMR = ^{29}Si and ^{13}C nuclear magnetic resonance.
TEM = Transmission electron microscopy.

polymer resin below 80°C and it transforms to an amorphous carbon at temperatures higher than about 500°C. The carbon yield from the phenolic resin is 35·4 wt% after heat-treatment at 1000°C in N_2 atmosphere. TMOS and phenolic resin were mixed with H_2O and ethyl alcohol, with a weight ratio of TMOS and phenol resin of 1:0·76 to form a gel. After forming a gel by polymerization, the admixture was dried at about 80°C in a laboratory furnace. The resulting product (designated as 'as-received material') appears as a dark brown transparent solid.

The as-received material was heat-treated for 30 min in the temperature range between 300 and 1750°C in flowing N_2 gas. A tabulation of investigations carried out with various samples is given in Table 1.

The plot of weight losses versus heat-treatment temperatures shows that there are 3 distinctive stages leading to SiC formation. During the first stage, from the as-received state to about 500°C,

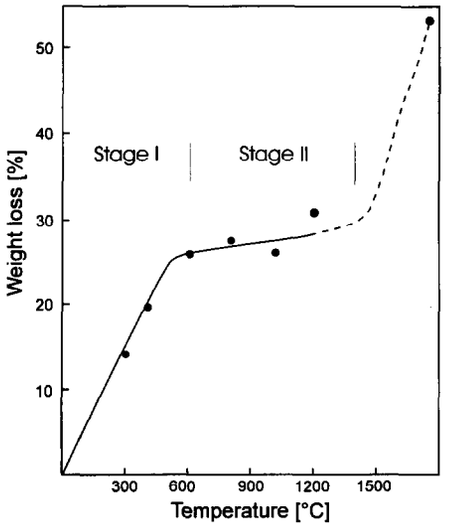


Fig. 1. Weight loss of the as-received SiC precursor material plotted against heat-treatment temperature.

the weight loss increases gradually with temperature. There is no change during the second stage between 500– ≈1400°C. The third stage between 1400 and 1750°C shows again a strong temperature dependency of weight loss (Fig. 1).

3 Experimental Procedure

3.1 X-ray diffractometry (XRD)

Powder XRD studies were carried out at room temperature with a computer–controlled Siemens D5000 powder diffractometer (CuK_α-radiation). The diffractograms were recorded in the 10 to 80° 2θ-range in the step-scan mode (5 s/0·01°, 2θ).

3.2 Large-angle X-ray scattering (LAXS) measurements

The diffuse spectrum scattered by the sample irradiated with graphite-monochromatized molybdenum K_α radiation was obtained by using an automatic diffractometer.[9] 500 intensities corresponding to equidistant s points ($s = 4\pi(\sin\theta/\lambda)$, $\Delta s = 0{\cdot}035363$) were collected in the range $2° < \theta < 65°$ (2θ = diffraction angle). The stability of the X-ray flux and of the sample was checked by frequent repetition of measurements at angles conveniently spread out in the θ range. All measurements were carried out at 22°C.

Scattered intensities were corrected for polarization and absorption effects (namely $I_c(s)$), then normalized by comparison, in the vicinity of high θ angles, with the sum of coherent and incoherent independent intensities. The normalization factor K derived from this data treatment is in good agreement with those determined from Norman's[10] and Krogh-Moe's[11] methods. Atomic scattering factors, $f_i(s)$ for all the atoms, were those proposed by Cromer and Waber.[12] Compton diffusion factors were taken from tables published by Cromer.[13]

Reduced intensities, $I(s)$, were calculated as follows:

$$I(s) = KI_c(s) - \Sigma_i n_i [(f_i(s) + \Delta f'_i)^2 + \Delta f''^2_i + I_{i(inch)}(s)]$$

where K is the normalization constant, $I_c(s)$ is the corrected intensities, n_i is the number of atoms f_i in the chosen unit volume, $f_i(s)$ is the atomic scattering factor, $\Delta f'_i$ and $\Delta f''_i$ are the real and imaginary parts of the anomalous dispersion, and $I_{(inch)}(s)$ is the total incoherent radiation for the atom i.

The radial distribution $D(r)$ is then expressed under the form:

$$D(r) = 4\pi r^2 \rho_o + 2\tau\pi^{-1} \int_i^s si(s)M(s) \sin(rs)\, ds$$

where ρ_o is the average electronic density of the sample and $M(s)$ is a modification function defined by $f^2_{ni}(O)/f^2_{ni}(s)\exp(-s^2/100)$.

All calculations were performed by using our

LASIP program[13] the structure of which is similar to the KURVLR program of Johansson and Sandström.[14]

3.3 Nuclear magnetic resonance (NMR) spectroscopy

MAS NMR measurements were carried out using a Bruker MSL 300 spectrometer operating at 75·4 MHz (^{13}C), and 59·4 MHz (^{29}Si).

^{13}C CP TOSS (CP = Cross polarization, TOSS = Total suppression of spinning sidebands) NMR spectra were acquired with typical cross polarization times of 1 ms and recycle delays of 1 s. About 300 scans were accumulated. The MAS frequency was 3·2 kHz. Additionally, single pulse ^{13}C experiments were carried out for the sample heat treated at 800°C (repetition time: 20 s, number of scans: 1500).

Similar conditions were applied to ^{29}Si measurements. ^{29}Si CP TOSS investigations, and, additionally, a series of single pulse spectra were taken in order to estimate the relative amounts of silica in the different Q^n units. Chemical shifts are referenced to TMS both for ^{13}C and ^{29}Si NMR.

3.4 Transmission electron microscopy (TEM)

TEM was performed with a Philips EM430 analytical microscope (300 kV accelerating voltage, LaB_6 filament). Thin foils were prepared using a tripod polisher and subsequent ion beam milling.

4 Results

4.1 X-ray diffractometry (XRD)

The XRD patterns of the SiC precursors show that up to 1400°C the material is non-crystalline. At 1750°C (ST16-17, Table 1) it consists of β-SiC and a trace of graphite.

Despite being non-crystalline, the XRD diagrams of the SiC precursors below 1400°C exhibit very broad diffraction maxima near 3·95 Å. Another very broad and low intense diffraction maximum appears near 2·08 Å. It gradually becomes more intensive with the increase of the annealing temperature.

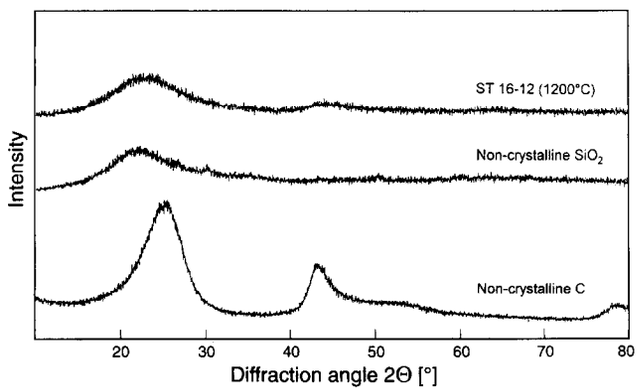


Fig. 2. XRD diagrams of precursor sample ST16-12, heat-treated at 1200°C (Table 1). The XRD patterns of non-crystalline SiO_2 and C are given for comparison.

4.2 Differential radial electron distribution functions (Rdf)

LAXS raw intensity curves of the as-received powder (ST16) and of the sample heat-treated at 1200°C (ST12, Table 1) are drawn in Fig. 3. The LAXS patterns yield strong and broad peaks near 3·95 Å, and weak signals near 2·08 and 1·22 Å. The intensity of the latter peaks increases with temperature. Rdf curves of the as-received and of

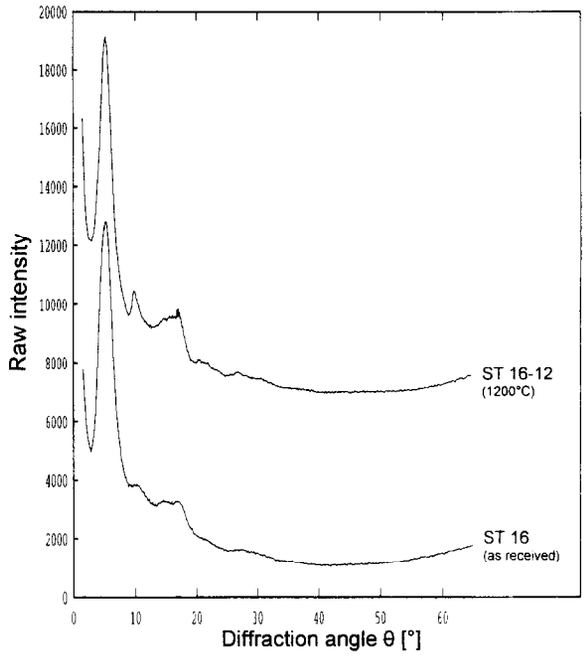


Fig. 3. LAXS raw intensity curves for the as-received sample (ST16) and for the sample heat-treated at 1200°C (ST16-12, Table 1). $Mo_{K\alpha}$ radiation.

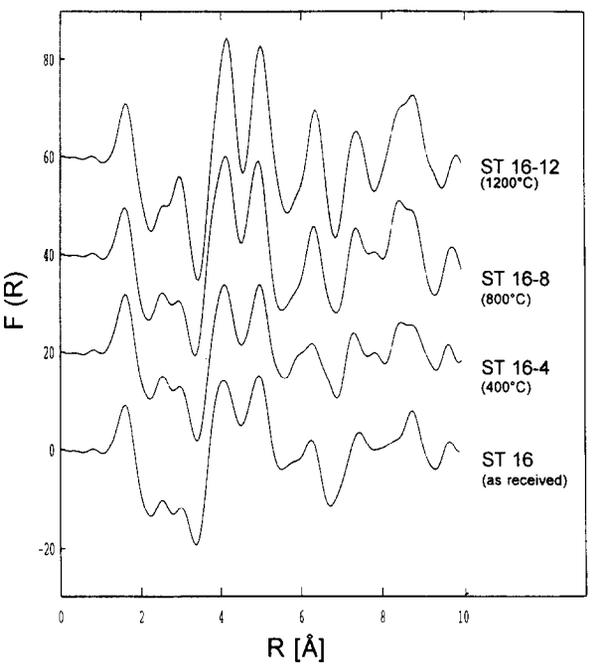


Fig. 4. Differential radial distribution functions (rdf) for the as-received sample (ST16), and for samples heat-treated at 400°C (ST16-4), 800°C (ST16-8), and 1200°C (ST16-12, Table 1).

heat-treated samples show similar features. They can roughly be divided into two domains: below and above R = 5·5 Å (Fig. 4).

- In the first range (R < 5·5 Å), the peaks can readily be assigned to Si–O (1·6 Å), O–O (O_1-Si_1–O_2, 2·6 Å), Si_1–Si_2 (Si_1–O_1–Si_2, 3·3 Å), Si–O_2 (Si_1–O_1–Si_2–O_2, 4·1 Å), and Si_1–Si_3 (Si_1–O_1–Si_2–O_2–Si_3, 5·0 Å). These peak positions lie very close by to those observed for a pure SiO_2 glass.[15-16] The first peak can be taken as internal standard in order to compare the signal intensities, because it always corresponds to the SiO_4 contribution. The peaks at 4·1 Å and 5·0 Å have considerably higher intensities in our samples than in pure SiO_2 glass, except for the samples heat-treated at T ≤ 400°C (samples ST16 and ST16-4, Table 1). This indicates that the short-range-order of the SiO_2 compound is much more regular in our sample as compared to SiO_2. The increase of the intensity of the Si_1–Si_2 peak at 3·3 Å, especially between 800 and 1200°C (samples ST16-8 and ST16-12, Table 1), corresponds to an increase in the size of the partially ordered SiO_2 domains, or to a more narrow distribution of the O–Si–O bonding angles.
- The second range (R > 5·5 Å) in the rdf curves is more difficult to understand, since the peaks cannot be assigned to a specific interaction, but correspond to superpositions of different contributions. However, the main features are also very similar to those observed for pure SiO_2 glass. The samples heat-treated at 800 and 1200°C show an increase of the peak intensities corresponding either to a more regular middle-range-order or to an enlargement of the ordered domains.

4.3 Transmission electron microscopy (TEM)

Bright-field micrographs of samples heat-treated between 1000 and 1400°C appear almost featureless. Dark-field images, however, obtained by a section of the d = 2·08 Å diffraction ring corresponding with non-crystalline carbon (Fig. 5) exhibit remarkable differences between the 1000°C-sample and specimens heat-treated at higher temperature. The latter show domains of few nanometres (Fig. 5), which are assumed to correspond with areas of carbon enrichment. The domain size does not increase significantly from 1200 to 1400°C. No domain-like contrast is detectable in dark field images of samples heat-treated at 1000°C leading to the assumption that carbon clusters, if they exist, are smaller than 1 nm.

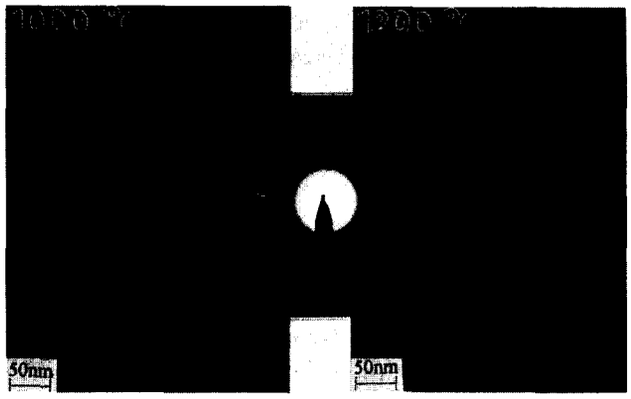


Fig. 5. Dark-field transmission electron micrographs of SiC precursor heat-treated at 1000°C (left) and 1200°C (right) generated by the diffraction ring of d = 2·08 Å (arrow). Bright areas correspond with carbon clusters.

4.4 Nuclear magnetic resonance spectroscopy (NMR)

Figure 6 shows the ^{13}C CP TOSS spectrum. The ^{13}C resonances of the sample ST16 (as-received) and that heat-treated at 300°C (ST16-3, Table 1) can be assigned quite easily using the results of Sojka *et al.*.[17] The signals originate from phenol resin which was used to prepare the samples. Only the low intensity components between 60 and 70 ppm (indicated by stars in Fig. 6) are not yet fully

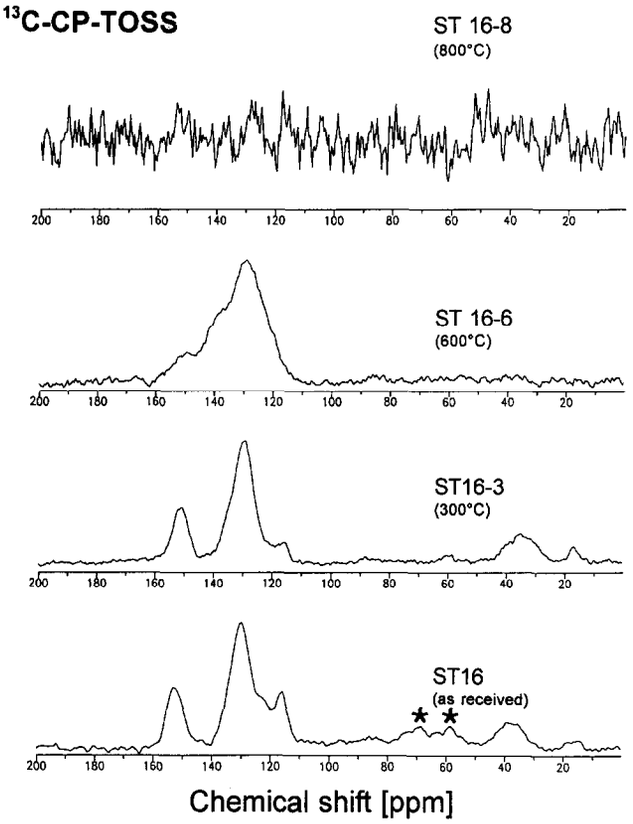


Fig. 6. ^1H–^{13}C CP TOSS NMR spectra (^1H–^{13}C Cross polarization spectra with total suppression of spinning sidebands) of various ST16 samples (Table 1). The spectrum at the bottom corresponds to that of phenol resin (only the two low intensity resonances marked by the stars are not identified as yet, see also text). Phenol resin is decomposed at temperatures above 300°C. At 600°C only sp^2-hybridized C is found. Cross polarization of the sample dried at 800°C gives no signal at all. Hence, there are no CH_x units left.

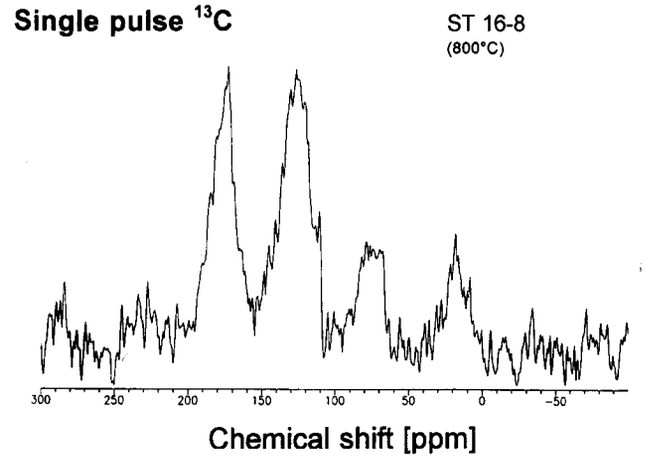


Fig. 7. Single pulse ^{13}C MAS NMR spectrum of sample ST16-8, heat-treated at 800°C (Table 1). The lineshape consists of only one resonance (δ_{iso} = 130 ppm) referring to sp^2-hybridized C with a series of spinning sidebands centered at 180, 75 and 20 ppm.

understood. It is likely that they represent CH_2–O and CH–O units. Heat-treatment of the samples up to 600°C (ST16-6) causes the phenol resin to decompose. A broad resonance at about 130 ppm is found, indicating sp^2-hybridized C. The C is still cross polarized by residual H atoms. However, after heat-treatment of the samples at 800°C (ST16-8) no CP signal is detected, which means that the remaining protons are not associated with C. Single pulse ^{13}C measurements of that sample give only a resonance signal for sp^2-hybridized C with the MAS center band at 120 ppm. The other lines are the spinning side bands equally spaced by the MAS spinning frequency of 4 kHz. They reflect the typical chemical shift anisotropy of about 200 ppm of non-protonated sp^2-hybridized carbon (Fig. 7). There is no hint for sp^3-hybridized carbon.

The situation is different for ^{29}Si NMR. The CP spectra shown in Fig. 8 reveal three different structural units: Q^4 (–112 ppm, SiO_4), Q^3 (–102 ppm, SiO_3OH), and to a minor extent Q^2 groups (–92 ppm, $SiO_2(OH)_2$). In contrast to ^{13}C NMR there is still a CP signal at an annealing temperature of 800°C (ST16-8, Table 1). This indicates that apparently some trace of H atoms is incorporated in the SiO_2 network, forming Q^3 units. The major amount with Q^4 groups, of course, is not cross-polarized. This can clearly be identified by single pulse experiments as shown in Fig. 9 for samples heat-treated at 300 and 800°C. Spectra of single pulse experiments are difficult to deconvolute into three Gaussian lines. But clearly a continuous decrease of the ratios $Q^2:Q^3:Q^4$ is found with increasing temperatures. Estimated ratios are

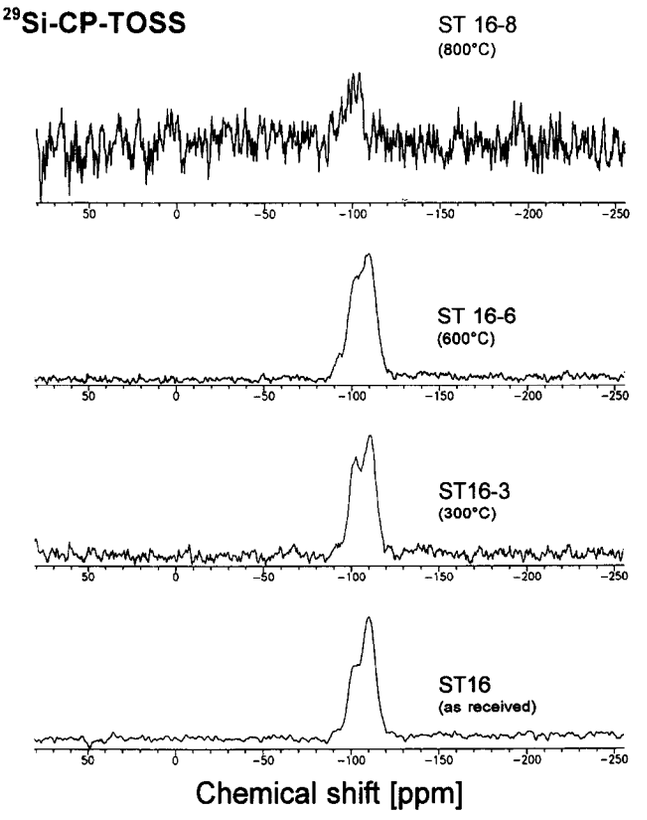


Fig. 8. ^{1}H–^{29}Si CP TOSS NMR spectra (^{1}H–^{29}Si Cross polarization spectra with total suppression of spinning sidebands) of various ST16 samples (Table 1). The spectra for the as-received sample and for the sample heat-treated at 600°C are similar and show Q^4 (SiO_4), Q^3 (SiO_3OH), and a small Q^2 ($SiO_2(OH)_2$) signals (for details see text). At the highest temperature (800°C, ST16-8) only a very weak Q^3 signal is found.

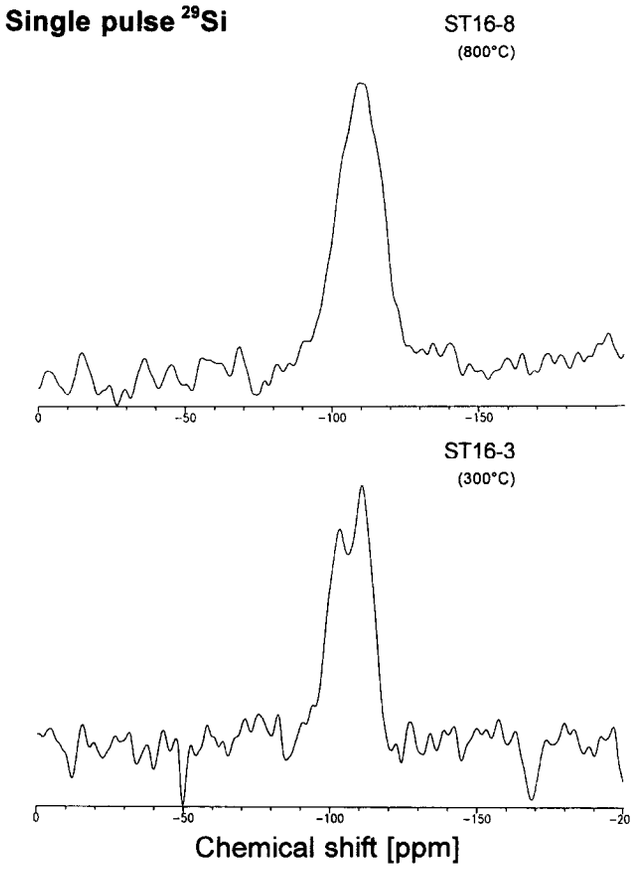


Fig. 9. Single pulse ^{29}Si MAS NMR spectra of the samples ST16-3 and ST16-8 heat-treated at 300 and 800°C, respectively (Table 1). The spectrum at the bottom clearly shows Q^3 (SiO_3OH) and Q^4 (SiO_4) groups in almost equal amounts, whereas only Q^4 units are present after heat-treatment at 800°C.

10:45:45, 5:30:65, and 0:10:90, for the 300, 600, and 800°C samples.

5 Discussion

The Si source material tetramethoxysilane (TMOS) transforms upon hydrolysis and drying at about 80°C to partially hydrogenated SiO_2 (ST16, Table 1). According to the ^{29}Si NMR spectrum, which is very similar to that of dried silica gels,[18] Si occurs as SiO_4 (Q^4), $SiO_3(OH)$ (Q^3) with isolated OH groups, and SiO_2 $(OH)_2$ (Q^2) with two OH groups.[19] There remains the question, whether OH groups are only located in the surface or if they also occur in the bulk of the material. We believe that OH groups are located at the surface and in the volume of the SiO_2 compound.[18] ^{13}C NMR spectra of the sample dried at about 80°C (ST16, Table 1) exhibit peaks which are attributed to phenol resin. Obviously there is no drastic change of the structural short-range-order of the C compound upon hydrolysis and drying the material.

Heat-treatment of hydrolized and dried as-received samples up to 1400°C exhibits 2 different stages in the structural development of the precursors, though all of them are non-crystalline throughout the temperature field investigated (Fig. 2).

Stage I (≤500°C)

Heat-treatment of the as-received material at temperatures to ≤500°C produces strong weight loss (Fig. 1), which is likely due to the gradual decomposition of the phenol resin. This is supported by ^{13}C NMR spectra which gradually and considerably change in this temperature region (Fig. 6). It is especially striking to note that the peaks previously present at about 18 and 35 ppm gradually disappear leaving a rather broad resonance pattern between 120 and 150 ppm in samples heat-treated at 600°C. Rdf curves of the SiC precursor heat-treated at 400°C (ST16-4, Table 1) can also be interpreted in a similar way. Intensities of all rdf peaks, except those at 2·5 and 3·3 Å, become weaker than the peaks of the as-received material (Fig. 4), indicating gradual decomposition of the local structural order in phenol resin.

^{29}Si NMR data (Fig. 8) indicate dehydrolysis of the SiO_x $(OH)_{4-x}$ network to take place. This is evidenced by the deconvolution of the spectra, exhibiting gradual disappearance especially of Q^2 $(SiO_2(OH)_2)$ units.

Stage II (≥500 – ≤1400°C)

Heat-treatment of the SiC precursor in the temperature range of reaction Stage II yields only little weight loss (Fig. 1). ^{29}Si NMR spectra (Figs 8 and 9) and rdf curves (Fig. 4) suggest that non-crystalline SiO_2 is a major compound of the precursors. According to ^{29}Si NMR data (Fig. 8) at 600°C some of the Si bonds are saturated by OH groups distributed throughout the SiO_2 network ('network modifiers'). At 800°C the occurrence of network modifying OH ions becomes less frequent, while at 1200°C the SiO_2 network is OH-ion free. The high intensity of short distance ($R < 5{\cdot}51$ Å) rdf peaks near 4·1 and 5·0 Å suggest that the SiO_2 domains above 400°C have a higher level of structural order than pure fused SiO_2 glasses. The increase of peak intensities in the far distance region ($R > 5{\cdot}5$ Å) of the rdf diagram is interpreted of gradually increasing middle-range-order and of growing sizes of the SiO_2 domains.

^{13}C NMR spectra samples heat-treated at temperatures ≥500°C (Figs 6 and 7) exhibit a complete breakdown of the remaining local structural order of phenol resin and formation of non-crystalline C with sp^2-hybridized graphite-like short-range-order. According to transmission electron microscopic observations the C domains are randomly distributed throughout the SiO_2 matrix (Fig. 5). At 1000°C C domains are below the microscopical resolution (≤1 nm). At 1200°C domain sizes become larger (2–3 nm) though no further increase is observed between 1200 and 1400°C.

Processes taking place at temperatures > 1400°C are beyond the scope of the present study. Referring to weight loss measurements (Fig. 1) and to literature data SiC is formed by reaction of C and SiO_2.[20] The homogeneous mixture of the highly reactive C and SiO_2 compounds yields high SiC formation rates. Ceramics produced from such SiC powders exhibit homogeneous and dense microstructures with favorable fracture toughness, especially in the presence of some finely dispersed graphite particles.[8]

Acknowledgements

H. S. thanks Mr H. Hermanns (Köln) for technical assistance. Dr B. Saruhan (Köln) and S. Schneider (Rheinbach) read the manuscript. This is gratefully acknowledged.

References

1. Prochazka, A., The role of boron and carbon in the sintering of silicon carbide. In *Special Ceramics 6th British Ceramic Research Association*, Stoke on Trent, UK, p. 171, 1975.
2. Kuibira, A., Matsui, A., Hojo, J., & Kato, A., Preparation of SiC and Si_3N_4 powders by RF-plasma. *J. Ceram. Soc. Japan*, **95** (1987) 89.

3. Cannon, W. R., Danforth, S. C., Flint, J. H., Haggerty, J. S. & Mara, R. A., Sinterable ceramic powders from laser driven reactions. I. Process description and modeling. *J. Am. Ceram. Soc.*, (1982) 324–30.
4. West, R., David., L. D., Djurovich, P. I., Yu, H. & Sinclair, R., Polysilastyrene: Phenylmethylsilane – dimethylsilane copolymers as precursors to silicon carbide. *Am. Ceram. Soc. Bull.* **62** (1983) 899–903.
5. Schmidt, W. R., Sukumar, V., Hurley, W. J., Jr. Garcia, R., & Interrante, L. V., Silicon nitride derived from an organometallic polymeric precursor: Preparation and characterization. *J. Am. Ceram. Soc.*, **73** (1990) 2412–8.
6. Wu, H.J. & Interrante, L. V., Preparation of a polymeric precursor to silicon carbide via ring-opening polymerization: synthesis of poly ((methylchlorosilylene)methylene) and poly(silapropylene). *Chem. Mater.*, **1** (1989) 564.
7. Zhang, Z. F., Babonneau, F., Laine, R. M., Mu, Y., Harrod, J. F. & Rahn, J. A., Poly(methylsilane) — A high temperature ceramic yield precursor to silicone carbide. *J. Am. Ceram. Soc.*, **74** (1991) 670–3.
8. Tanaka, H., Kaozhe, J. & Hirota, K., Synthesis and sintering of SiC–C powder mixture from $Si(OCH_3)_4$ and phenol resin. *J. Ceram. Soc. Japan*, **98** (1990) 86–9.
9. Lecante, P., Mosset, A. & Galy, J., LASIP: A liquid and amorphous structure investigation package. *J. Appl. Cryst.*, **18** (1985) 214–8.
10. Norman, N., The fourier transform method for formalizing intensities. *Acta Crystallogr.*, **10** (1957) 370–3.
11. Krogh-Moe, J., A method for converting experimental X-ray intensities to an absolute scale. *Acta Crystallogr.*, **9** (1956) 951–4.
12. Cromer, D. T. & Waber, J. T., Scattering factors computed from relativistic Dirac–Slater wave functions. *Acta Crystallogr.*, **18** (1965) 104–5.
13. Cromer, D. T., Compton scattering factors for aspherical free atoms, *J. Chem. Phys.*, **50** (1969) 4857–60.
14. Johansson, G. & Sandström, M., Computer programs for the analysis of data on X-ray diffraction by liquids. *Chem. Scripta*, **4** (1973) 195–9.
15. Zarzycki, J., *Les Verres et l'Etat Vitreux*, ed. Masson Paris, 1982 p. 83.
16. Himmel, B., Gerber, T. H. & Bürger, H., X-ray-diffraction investigations of silica gel structures. *J. Non-Crystalline Solids*, **91** (1987) 127–36.
17. Sojka, S. A., Wolfe, R. A., Dietz, E. A., Jr. & Dannels, B. F., Carbon-13 nuclear magnetic resonance of phenolic resins. Positional isomers of bis(hydroxybenzyl)phenols and bis-(hydroxyphenyl)methanes. *J. Am. Chem. Soc* **62** (1979) 767–70.
18. Fyfe, C. A., Gobbi, G. C. & Kennedy, G. J. *J. Phys. Chem.*, **89** (1985) 277–81, quoted in: *The physics and chemistry of sol-gel processing*, Sol-Gel Science, Academic Press Inc., San Diego, CA, USA. 1990.
19. Brinker, C. J. & Scherer, G. W., *The physics and chemistry of sol-gel processing*, Sol-Gel Science, Academic Press Inc., San Diego, CA, USA 1990.
20. Tanaka, H. & Kurachi, Y., Synthesis of β-SiC powder from organic precursor and its sinterability. *Ceramics Intern.*, **14**, (1988) 109-15.

Journal of the European Ceramic Society 15 (1995) 683–688
© 1995 Elsevier Science Limited
Printed in Great Britain. All rights reserved
0955-2219(95)00033-X
0955-2219/95/$9.50

A Polysilazane Precursor for Si–C–N–O Matrix Composites

M. F. Gonon,*[a] S. Hampshire,[a] J. P. Disson[b] & G. Fantozzi[c]

[a]Materials Ireland — Ceramic Research Unit, University of Limerick, National Technological Park, Limerick, Ireland
[b]Elf Atochem, Centre de Recherche Rhône-Alps, BP 63, rue Henri Moissan, 69310 Pierre-Bénite, France
[c]Insitut National des Sciences Appliquées de Lyon, Groupe d'Étude de Métallurgie Physique et de Physique des Matériaux, URA CNRS 341, 20 ave Albert Einstein, 69621 Villeurbanne cedex, France

(Received 6 October 1994; revised version received 3 February 1995; accepted 7 February 1995)

Abstract

This paper reports the ability to use a commercial polysilazane† as matrix precursor for the manufacture of ceramic matrix composites.

By pyrolysis under nitrogen in the temperature range 1000–1400°C this polysilazane leads to an amorphous silicon carbonitride with a ceramic yield around 65 wt%.

The rheological behaviour and the thermal decomposition of the polysilazane have been studied. Parameters for the impregnation and pyrolysis cycles required by the manufacture of composites are also proposed.

Introduction

For the last 20 years, the organometallic way for the manufacture of ceramic matrix composites has attracted the attention of many industrial and university laboratories.

Indeed, the low temperatures required by precursor pyrolysis limit the risk of the thermal degradation of the reinforcing materials thereby allowing a large panel of potential materials. Low temperatures also induce low energy costs.

Moreover, times required for composites manufacturing (a few days to few weeks depending on the pyrolysis temperature schedules) are significantly shorter than those needed by the Chemical Vapour Infiltration process (many months).

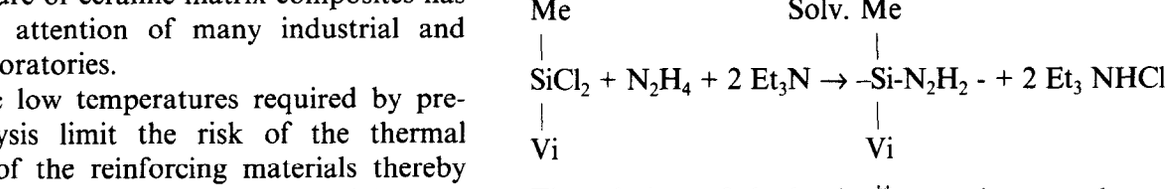
The basic process, using a serial of impregnation and pyrolysis cycles of a fibrous preform by the precursor, appears simple and does not require sophisticated and expensive equipment.[1]

Silicon based ceramics like SiC or Si_3N_4 can be obtained from polycarbonsilanes and polysilazanes.[2] Due to their high mechanical properties and high oxidation resistance, silicon nitride derived materials are interesting as a matrix for thermomechanical composites.[3]

Consequently, research on the synthesis of new polysilazane precursors and the development of a composites manufacturing process using such precursors present a high commercial interest.

1 Synthesis

The synthesis of the polysilazane has already been described in detail by C. Colombier.[4]
PYROFINE PV is a polyvinylsilazane obtained by polymerisation of vinylmethyldichlorosilane with hydrazine in presence of triethylamine.



The choice of hydrazine†† as nitrogen donor instead of ammonia, which is generally used, results in its higher functionality toward vinylmethyldichlorosilane.

For its part, the solvent is chosen among those in which both polysilazane, chlorosilanes and triethylamine are soluble and $(Et)_3NHCl$ is not.

The monomer condenses to form cyclic structures and by further condensation forms high molecular weight cyclic polymers (Fig. 1).

The typical elemental composition of the precursor is given in Table 1, oxygen originating from the hydrazine used for the synthesis:

*To whom correspondence should be addressed.
†PYROFINE PV from Elf Atochem. Centre de Recherche Rhône-Alpes, rue Henri Moissan, 69310 Pierre-Bénite, France.

††Liquide hydrazine, bp: 130°C.

Table 1.

	Si	*C*	*N*	*O*	*H*
wt%	31·5	37·2	20·3	3·2	7·8
at%	8·2	22·7	10·5	1·4	57·2

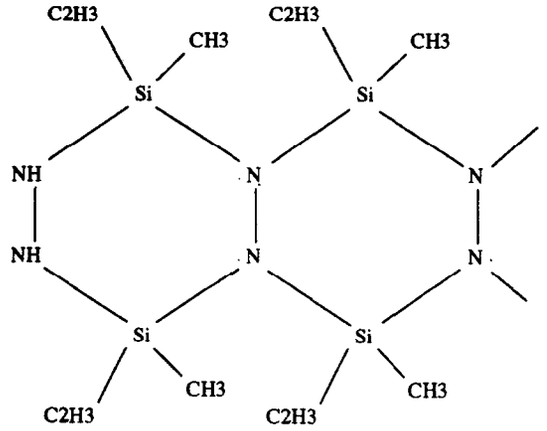


Fig. 1. Structure of the polysilazane.

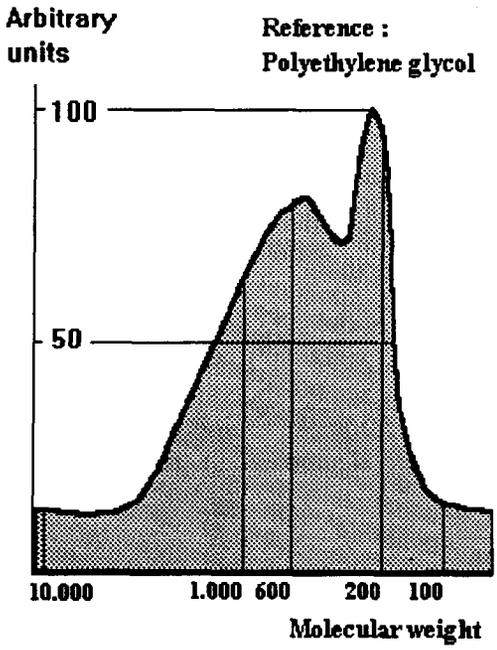


Fig. 2. Molecular weight distribution of the polysilazane.

The gel permeation chromatography shows the large molecular weight distribution of the precursor (Fig. 2). M varies from 0 up to more than 10 000 with a maximum in number between 200 and 1200 corresponding respectively to 1–6 elemental cycles. The average molecular weight in number is 500. A large amount of low molecular weight oligomers ($M < 100$) is also evident.

2 Rheology

At room temperature, the polysilazane is a high viscous liquid with a density close to 1. Upon heating up to 150°C its viscosity decreases with the increase in temperature (Fig. 3) and remains stable during numerous hours (Fig. 4).

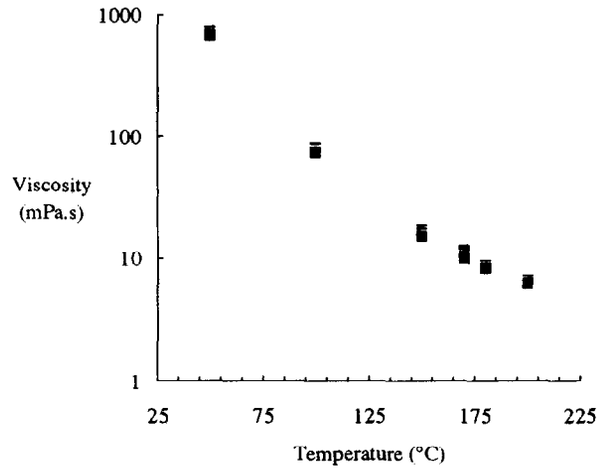


Fig. 3. Variation of the viscosity of the polysilazane versus temperature.

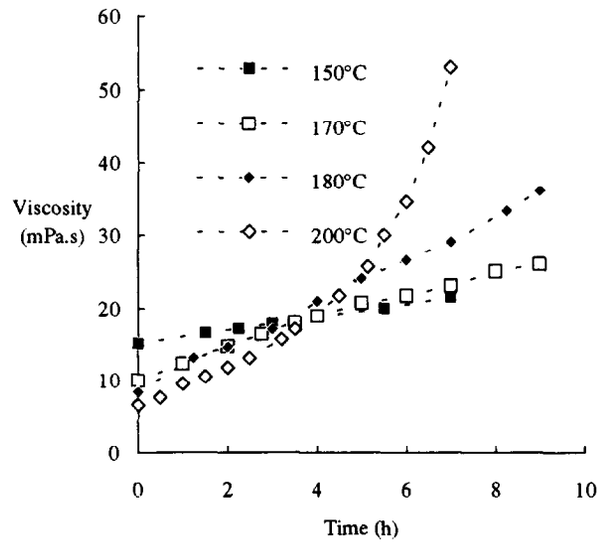


Fig. 4. Variation of the viscosity of the polysilazane versus time at different temperatures.

Above 150°C and up to 220°C, the viscosity still decreases versus temperature but increases quickly versus time. The low molecular weight oligomers may be evaporated or may condense to form longer chains. That increases the average molecular weight of the precursor and consequently, explains the variation of the viscosity versus time.

3 Evolution of the Polysilazane Versus Temperature

3.1 From room temperature up to 300°C

Below 150°C, no weight loss is observed on the TGA curve (Fig. 5, part I). Between 150 and 300°C a 15% weight loss is measured (Fig. 5, part II). The mass spectrometry coupled with the TGA indicates an ammonia release (Fig. 6) which could correspond to the condensation reaction:

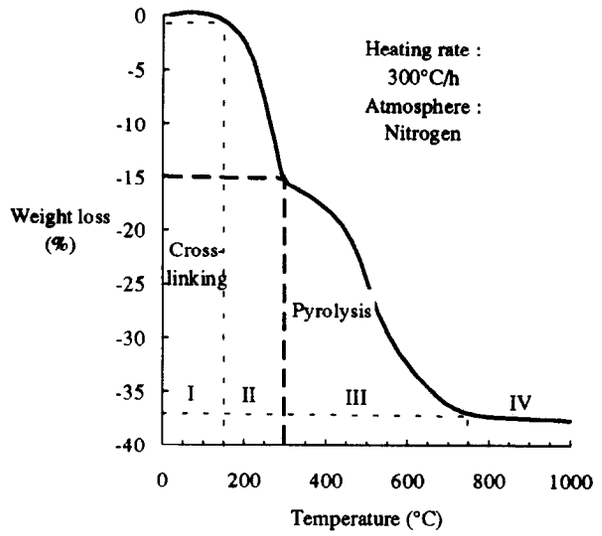


Fig. 5. TGA curve of the polysilazane.

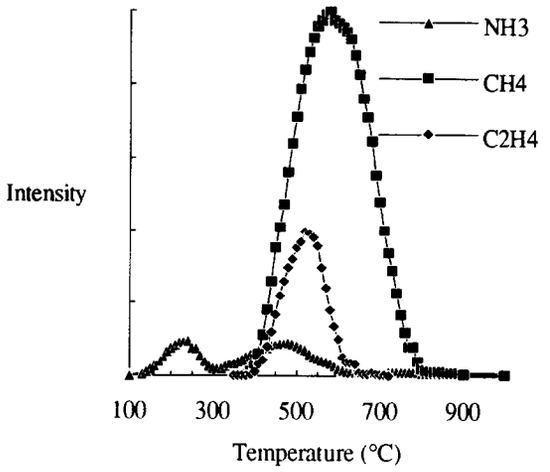


Fig. 6. Mass spectrometry associated to the TGA (Fig. 5).

$$2 \equiv Di\text{–}NH\text{–}NH_2 \rightarrow \equiv Si\text{–}NH\text{–}NH\text{–}Si \equiv + N_2H_4$$

Above 250°C, the hydrazine released may decompose to ammonia and nitrogen with a strong exothermic reaction (–336 kJ/mol):

$$3N_2H_4 \rightarrow N_2 + 4\ NH_3$$

The titrage by reaction in H_2SO_4 of the ammonia generated up to 300°C explains only 1–2% of the 15% weight loss measured by TGA. The evaporation of the light oligomers can explain the bulk of the weight loss. These oligomers are not observed by the mass spectrometry because they condense in the apparatus before the detection.

Between 220 and 300°C the precursor is progressively transformed from a soluble (in toluene) liquid into an unmeltable and insoluble solid.

Table 2.

Heating rate (°C/h)	*Temperatures (°C)*	*Holding time (h)*
100	20–130	0
5	130–*T*°C	1

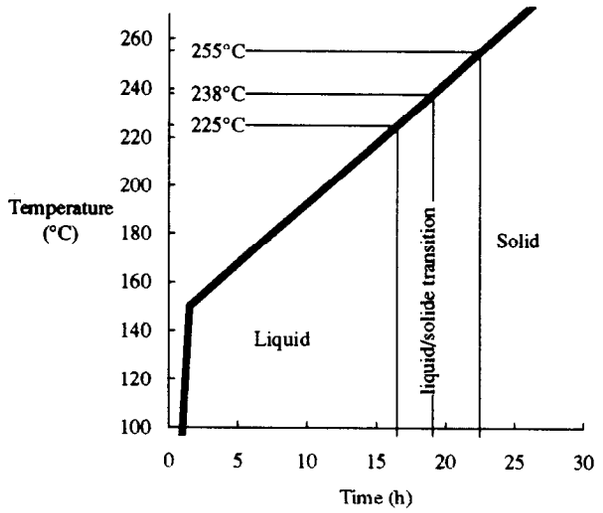


Fig. 7. Temperature range of the precursor cross-linking.

That is evidenced by successive heat treatments on the precursor using the following temperature schedule (Fig. 7 and Table 2):

T = 225°C; the product obtained is a high viscous liquid soluble in toluene.

T = 238°C; the product is solid, soluble in toluene, its melting point is about 100°C. Bubbles are observed on the surface of the sample.

T = 255°C; the product is solid, unmeltable and insoluble. Numerous bubbles are observed in the cross-section of the sample.

The ^{29}Si solid NMR confirms that the cross-linking is due to the opening of the vinyl groups.[5]

$\equiv Si\text{–}CH{=}CH_2$ transforms to $\equiv Si\text{–}CH\text{–}CH_2$

The liquid to solid conversion corresponding to the vinylic cross-linking combined with the generation of gases due to the condensation reaction and the oligomers evaporation, which leads to the

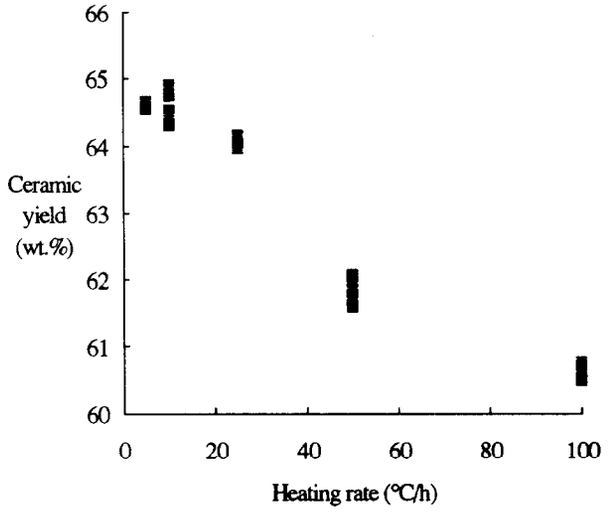


Fig. 8. Variation of ceramic yield at 1000°C versus the heating rate used during the cross-linking (temperature range 130–300°C) the heating rate used from 300–1000°C being 1000°C/h.

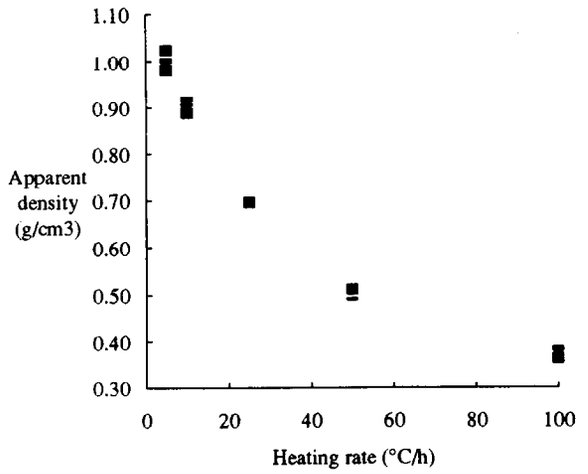


Fig. 9. Apparent density of the ceramic obtained after pyrolysis at 1000°C versus the heating rate used during the cross-linking (temperature range 130–300°C) the heating rate used from 300–1000°C being 100°C/h.

formation of foam, and after pyrolysis to high porous volume ceramics.

As it has previously been shown, the major part of the gas generated arises from the evaporation of the low molecular weight oligomers. This evaporation can be controlled by the heating rate used before and total solidification of the precursor. Indeed, using various heating rates between 130 and 300°C and then achieving the pyrolysis at 100°C/h between 300 and 1000°C we noted that the ceramic yield is higher, when the heating rate used is low.[6] (Fig. 8).

The decrease of the gas released during the solid liquid transition also reduces the foaming and then increases the apparent density of the ceramic residue (Fig. 9).

3.2 Above 300°C

Above 300°C the mineralisation starts. The weight loss between 300 and 800°C is 20–25% (Fig. 5, part III) and the gas release is maximum around 500°C. In the early stage of this step, the ammonia release remains high (Fig. 6) and could be explained by transamination reactions.[5,6]

$$\equiv Si\text{–}NH\text{–}NH\text{–}Si\equiv + \equiv Si\text{–}H \rightarrow \equiv Si\text{–}\underset{\displaystyle Si\equiv}{\overset{|}{N}}\text{–}Si\equiv + NH_3$$

Up to 600°C mainly methane but also methylene, propene and other unsaturated hydrocarbons are generated (Fig. 6).

Methane may originate from the decomposition of the methyl groups.[6]

$$\equiv Si\text{–}CH_3 \rightarrow \equiv Si^* + {}^*CH_3$$

$${}^*CH_3 \xrightarrow{\text{H abstraction}} CH_4$$

The unsaturated hydrocarbon released could arise from the decomposition of isolated vinyl groups which are not in a position to react with another vinyl group.

$$\equiv Si\text{–}CH{=}CH_2 \rightarrow \equiv Si^* + {}^*CH{=}CH_2$$

The $^*CH{=}CH_2$ groups may react with *H, $^*CH_3$ or with another $^*CH{=}CH_2$:

$$^*CH{=}CH_2 + {}^*H \rightarrow C_2H_4$$

$$^*CH{=}CH_2 + {}^*CH_3 \rightarrow C_3H_6$$

$$^*CH{=}CH_2 + {}^*CH{=}CH_2 \rightarrow C_4H_6$$

Above 600°C and up to 800°C only methane is detected. Hydrogen may also be generated from the cleavage of the Si–H, N–H bonds but not detected by mass spectrometry. At higher temperatures the cleavage of the Si–C bonds leads to the formation of Si–N and graphite which is evidenced by ^{13}C solid state NMR after heat treatment at 1000°C. The typical elemental composition of the ceramic obtained after pyrolysis at 1000°C is given in Table 3:

Table 3.

	Si	*C*	*N*	*O*
at%	30·0	34·7	27·1	8·2
wt%	47·5	23·6	21·5	7·4

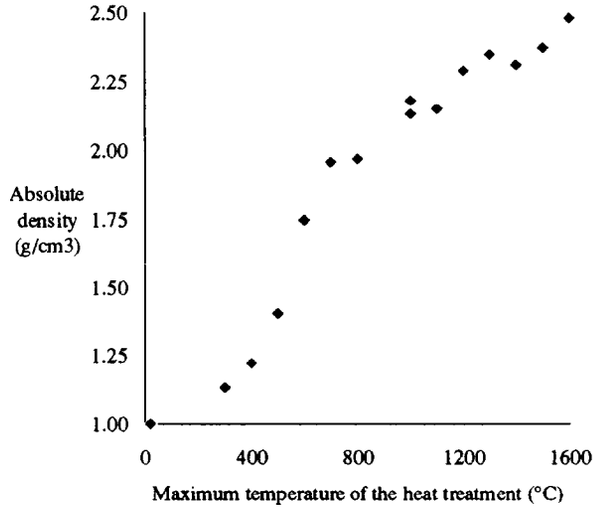


Fig. 10. Absolute density of the residue obtained after heat treatment under nitrogen at various temperatures.

Table 4.

Highest temp. (°C)	*Absolute density (g/cm³)*
1000	2·13
1100	2·18
1200	2·27
1300	2·31
1400	2·35
1500	2·38
1600	2·48

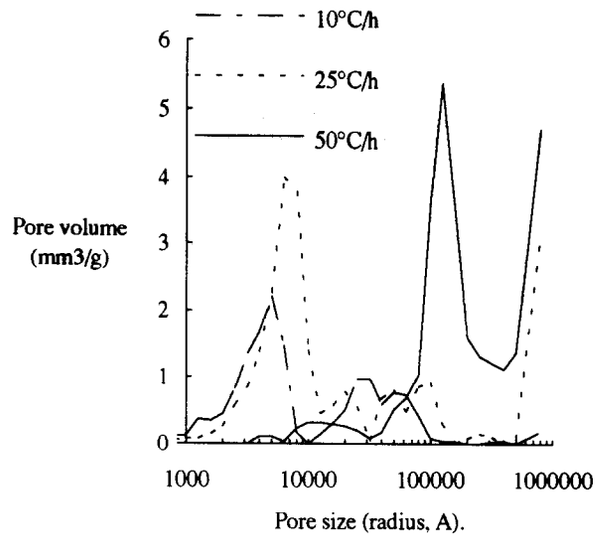


Fig. 11. Pore size distribution in the ceramic samples versus the heating rate between 300 and 1000°C.

The true density of the ceramic has been determined by He picnometry on milled samples. The densities measured depending on the maximum temperature of the pyrolysis as shown (Fig. 10 and Table 4).

3.3 Crystalline structure

Up to 1400°C the ceramic residue remains almost totally amorphous. Only a low signal corresponding to SiO_2 is detected by X-ray diffraction.

Above this temperature, peaks corresponding to α SiC and α Si_3N_4 appear on the graph.[7] It has already been shown that the crystallisation corresponds to the formation of whiskers and of a coating at the pores' surfaces. This leads also to a decrease in the mechanical properties of the ceramic.[8]

3.4 Influence of the heating rate during the mineralisation

Using a specific process for the manufacture of monolithic bodies,[8] ceramic samples were realised using various heating rates (50, 25 and 10°C/h) during the mineralisation step.

After pyrolysis at 1000°C, the true and apparent densities of the samples are similar; 1·91 and 2·15 respectively and correspond to 12–13% porosity. On the other hand, the pore size distribution determined by mercury porosimetry is significantly different versus the heating rate used (Fig. 11). A low heat rate (10°C/h) leads to pores having 2–10 μm radius whereas a faster heating rate (50°C/h) creates pores having more than 20 μm radius.

Moreover, the pores studied by mercury porosimetry correspond to the opened porosity. The porous volume measured on the samples pyrolysed at 10°C/h is significantly lower than that of the samples pyrolysed at 50°C/h. The total porous volume being the same, the ratio open porosity/closed porosity increases as the heating rate is high.

Conclusion

The polysilazane studied appears as an interesting precursor for the manufacture of ceramic matrix composites. Indeed its low viscosity, about 10 mPas at 150°C, and its high stability versus time at this temperature make it particularly suitable for the infiltration of fibrous or particulate preforms.

Moreover, the ceramic yield is high, about 60–65 wt% (About 30 vol%) after pyrolysis at 1000°C, then the number of impregnation and pyrolysis cycles required to obtain low porosity composites would be low. The low true density of the ceramic (2·13 g/cm^3 after pyrolysis at 1000°C) is also interesting.

However, a gas generation, mainly due to the evaporation of low molecular weight oligomers, and taking place simultaneously to the precursor cross-linking leads to the formation of a foam and consequently to a high porous volume in the ceramic after pyrolysis. A low heating rate, 5°C/h, between 130°C–300°C reduces the evaporation of the low molecular weight oligomers and then increases the ceramic yield and the apparent density of the ceramic. Nevertheless in the best case the porosity remains higher than 50%.

Above 300°C the heating rate does not influence the porosity amount in the ceramic but has significant consequences on the pore size distribution. A low heating rate leads to finer pores but creates more closed porosity than a higher one. Therefore, as successive impregnation and pyrolysis cycles will be required, a mean heating rate, about 25°C/h would be used. The ceramic residue remains amorphous up to a pyrolysis temperature of 1400°C. Above this temperature the αSiC and αSi_3N_4 crystallisation leads to a decrease in the mechanical properties of the ceramic.

References

1. Gonon, M. F., Fantozzi, G., Murat, M. & Disson, J. P., Association of the C.V.I. process and of the use of polysilazane precursors for the elaboration of ceramic matrix composites reinforced by continuous fibres. *J. Eur. Ceram. Soc.*, in press.
2. Blum, Y. D., Schwartz, K. B. & Laine, R. M., Preceramic polymer pyrolysis. *J. Mat. Sci.*, **24** (1989) 1707–18.
3. Burns, G. & Chandra, G., Pyrolysis of preceramic polymers in ammonia: preparation of silicon nitride powder. *J. Am. Cer. Soc.*, **72**(2) (1989) 333–7.

4. Colombier, C., Study of new polysilazane precursors to Si–C–N–O ceramics. In *Proceedings of the 1st European Ceramic Society Conference*, Vol. 1. 18–23 June 1989, Maastricht, The Netherlands, Ed. G. de With, R. Terpstra & R. Metselaar, Elsevier Science Publishers Ltd, 1989, pp. 1·43–1·52.
5. Laverdrine, A., Dahloul, D. & Goursat, P., Pyrolysis of polyvinylsilazane precursors to silicon carbonitride. *J. Eur. Ceram. Soc.*, **8** (1991) 221–7.
6. Bahloul, D., Pereira, M. & Goursat, P., Preparation of silicon carbonitride from an organosilicon polymer. I: Thermal decomposition of the cross-linked polysilazane. *J. Amer. Ceram, Soc.*, **76**(5) (1993) 1156–62.
7. Schmidt, W. R., Sukumar, V., Hurley, W. J., Garcia, R., Doremus, R. H. & Interrante, L. V., Silicon derived from an organometallic polymeric precursor: preparation and characterisation. *J. Amer. Ceram. Soc.*, **73**(8) (1990) 2412–8.
8. Gonon, M. F., Fantozzi, G., Murat, M. & Disson, J. P., Manufacture of monolithic ceramic bodies from the commercial polysilazane PYROFINE PV. *J. Eur. Cer. Soc.*, in press.

Journal of the European Ceramic Society 15 (1995) 689–695
© 1995 Elsevier Science Limited
Printed in Great Britain. All rights reserved
0955-2219(95)00026-7
0955-2219/95/$9.50

Study on the Solid Solubility of Al in the Melilite Systems $R_2Si_{3-x}Al_xO_{3+x}N_{4-x}$ with R = Nd, Sm, Gd, Dy and Y

P. L. Wang,[a] H. Y. Tu,[a] W. Y. Sun,[a] D. S. Yan,[a] M. Nygren[b] & T. Ekström[b]

[a]The State Key Lab. on High Performance Ceramics and Superfine Microstructure, Shanghai Institute of Ceramics, Chinese Academy of Sciences, Shanghai 200050, P. R. China
[b]Dept. of Inorg. Chemistry, University of Stockholm, S-106 91 Stockholm, Sweden

(Received 28 September 1994; revised version received 12 January 1995; accepted 31 January 1995)

Abstract

The solubility of aluminium in the nitrogen-containing melilite structure has been studied by preparation of specimens of the general formula $R_2Si_{3-x}Al_xO_{3+x}N_{4-x}$ with R = Nd, Sm, Gd, Dy and Y by hot pressing and pressureless sintering techniques in the temperature interval 1600–1750°C. For elements with large ionic radii, i.e. R = Nd and Sm, up to one Si can be replaced by Al, but the solubility limits in melilite solid solutions decrease with decreasing the ionic radii. Consequently, yttrium–melilite had the lowest observed aluminium solubility ($x \approx 0{\cdot}6$) in rare earth elements–melilite solid solutions.

1 Introduction

Nitrogen-containing melilite phases comprise compounds based on the general melilite composition $Si_3N_4{\cdot}R_2O_3$ with R = Y, and rare earth elements such as Nd, Sm, Gd and Dy, and these compounds have been shown to be refractory and stable ceramics in non-oxidising environments. Yttria and rare earth oxides are frequently used as a sintering aid in the preparation of Sialon ceramics. Consequently nitrogen-containing melilite phases are frequently occurring as a grain boundary phase in α-Sialon and mixed α–β-Sialon ceramics.[1,2] This is expected from phase relationships of the R–Si–Al–O–N systems[3,4] and, apart from the α-Sialon phase, these phases contain more nitrogen than any other phase in these quinary systems. By the formation of crystalline nitrogen-containing rare earth element–melilite (abbreviated R–M below) and/or aluminium and nitrogen-containing rare earth element–melilite solid solution (abbreviated R–M' below) phases, the amount of glassy phase at the grain boundary is reduced and eventually totally eliminated. The ability of the various R–M' phases to act as 'element sink phases' will be discussed below.

The properties of Sialon ceramics at high temperatures are mainly determined by the deterioration of the grain boundary phase. The presence of Y–M in silicon nitride based ceramics has been avoided. Y–M is known to oxidise rapidly at low temperatures (around 1000°C) whereby cristobalite and yttrium disilicate is formed and this process is accompanied with a drastic increase in the specific volume. The specific volume of the latter phases is thus approximately 30% larger than that of Y–M resulting in cracking of the specimen and spalling of the protective oxide layer formed upon oxidation.[5] Thus, although the melting point of Y–M itself is very high (>1850°C) these materials have failed in high-temperature application due to their poor oxidation resistance.[6] Aluminium melilite solid solutions $R_2Si_{3-x}Al_xO_{3+x}N_{4-x}$(R–M') are expected to have an improved stability against oxidation because when Si–N is replaced by Al–O a much smaller relative increase in specific volume of the formed oxidation products is expected and can be used as the best high temperature grain boundary phases for mixed α–β-Sialon ceramics because of their high melting points. Sialon ceramics containing crystalline R–M' phases at the grain boundaries are thus expected to exhibit better oxidation properties than the corresponding materials containing crystalline R–M phases.

The aluminium solid solution range in the Nd–M' system is reported to extend from $Nd_2Si_3O_3N_4$ to around $Nd_2Si_2AlO_4N_3$.[6,7] This range is very similar to the one reported for the Sm–M' system where, also, up to one Si can be replaced by one Al.[8] In order to understand the characteristics of the oxidation behaviour of various R–M' phases, it is necessary, at the first stage, to study

the extension of solubility range of the R–M' phases and the microstructure of the formed compacts and this is reported below.

2 Experimental

The starting powders used were silicon nitride (LC12, H. C. Starck, Berlin) and aluminium nitride (prepared at Shanghai Institute of Ceramics) while R_2O_3 with R = Nd, Sm, Gd, Dy and Y (99·9% pure) were all the products of Yaolung Chemical Works, China. Powder mixtures with the overall nominal composition $R_2Si_{3-x}Al_xO_{3+x}N_{4-x}$ with R = Nd, Sm, Gd, Dy and Y and $0 \leq x \leq 1{\cdot}5$, taking into account surface oxygen of the particles of both Si_3N_4 (1·8 wt%) and AlN (2·0 wt%), were prepared. The powders were mixed in absolute alcohol and milled in an agate mortar for 1·5 h. The compacted samples were fired at the different temperatures in the interval 1600–1750°C for 1 h or 2 h depending on the nominal composition of R–M' to have the samples synthesized, applying both hot-pressing or pressureless sintering techniques in a graphite-resistance furnace in a flowing nitrogen atmosphere.

The phase analysis of the prepared samples was based on X-ray diffraction data obtained in a Guinier–Hägg camera with use of Cu $K\alpha_1$ radiation and Si as the internal standard. The obtained photographs were evaluated with a computerised scanner system and the cell parameters were refined with use of the program PIRUM.[9] The Al content of the prepared R–M' phases were determined from element analysis using either an SEM (Jeol JSM 820) and a TEM (JEM 200CX), both equipped with energy dispersive spectrometers, or an electron probe instrument (8705 QH2). The Si and Al content given below is an average of several (10 or more) spot analysis determinations. The micrographs were obtained in an SEM (Jeol JSM 820) operating in the back scattering mode. The detailed microstructural studies of Sm–, Gd– and DY–M' samples were made in a TEM (JEM 200CX).

3 Results and Discussion

3.1 Phase analysis

The observed crystalline phases in the prepared samples are given in Table 1. The results are given

Table 1. A summary of the phases present in $R_2Si_{3-x}Al_xO_{3+x}N_{4-x}$ compacts according to the X-ray analysis

Sample	*Nominal x value*	*Firing condition (°C/h)*	*Phases present*						
			M	*M'*	*J*	*K*	*H(S)*	*I(Y)*	*A*
	0	1700/1 HP	vs			vw			
	0·5	1700/2 PLS		vs	tr				
Nd–M'	0·75	1700/2 PLS		vs	tr		tr		
	1·0	1700/1 HP		vs	tr		tr		
	1·25	1675/1 HP		vs	vw			w	
	0	1750/1 HP	vs				(vw)		
	0·3	1750/1 HP		vs	tr				
	0·5	1700/2 PLS		vs	tr				
Sm–M'	0·75	1700/2 PLS		vs	vw				
	1·0	1700/1 HP		vs	vw				
	1·5	1600/1 HP		vs	vw			m	
	0	1700/1 HP	vs		vw				
	0·3	1700/1 HP		vs	vw				
Gd–M'	0·5	1750/2 PLS		vs	vw				
	0·75	1700/1 HP		vs	vw				
	1·0	1700/2 PLS		vs	w				
	1·5	1600/1 PLS		vs	vw			ms	
	0	1700/1 HP	vs		vw				
	0·4	1700/1 HP		vs	w				
Dy–M'	0·6	1750/2 PLS		vs	w				
	0·75	1700/1 HP		vs	w				
	1·0	1700/2 PLS		vs	w				
	1·5	1600/1 PLS		vs	w			(ms)	
	0	1750/1 HP	vs		w				
	0·375	1700/1 HP		vs	w				
Y–M'	0·6	1700/1 HP		vs	w				
	1·0	1700/1 HP		vs	mw				tr
	1·25	1700/1 HP		vs	m				w

HP = hot pressing; PLS = pressureless sintering; J = $R_4Si_2O_7N_2$; K = $R_3Si_3O_6N_3$; H = $R_{10}(SiO_4)_6N_2$; S = $R_2Si_2O_7$; I = $RAlO_3$; Y = $Al_5Dy_3O_{12}$; A = AlN-polytypoid.

as a function of the x value of the overall compositions $R_2Si_{3-x}Al_xO_{3+x}N_{4-x}$ with R = Nd, Sm, Gd, Dy and Y and $x \leq 1{\cdot}5$ and as expected the R–M phase or the R–M' phase was found to be the main phase in all samples, but the formed samples contained other phases as well. Thus minor amounts of $Nd_3Si_3O_6N_3$ (Nd–K phase) and $Sm_2Si_2O_7$ was found for $x = 0$ in these systems and trace amounts of $Nd_{10}(SiO_4)_6N_2$ appeared in the Nd–M' system. The J phase, $R_4Si_2O_7N_2$ (or corresponding J'-phase), was found in most other samples. For a given nominal composition, the amount of J phase increased with decreasing the ionic radii of the rare earth element. Finally, the synthesis of Yb–M with the composition $Yb_2O_3{\cdot}Si_3N_4$ was tried by hot-pressing at 1700°C for 1 h and the sample contained the Yb–J phase, $Yb_4Si_2O_7N_2$, as a major component and only minor amounts of Yb–M, which in turn suggests that the R–M' phase is more easily formed for the high ionic radii (low Z) rare earth elements.

In addition, $RAlO_3$ was observed in samples of Nd–M', Sm–M' and Gd–M' with $x > 1{\cdot}0$ while $Al_5Dy_3O_{12}$ was found in samples of Dy–M'. Small amounts of AlN-polytypoid (27R or 2H[6]) appeared in the Y–M' material for $x \geq 1$, which was also confirmed by the SEM/EDS studies (see below).

The occurrence of small amounts of additional phases in samples with $x = 0$ might be attributed to the presence of surface oxide on the silicon nitride powder, which cannot be compensated for at this specific composition. However, we have not been able to prepare monophasic R-M' phases, although these compositions have been compensated for surface oxides on the nitride particles. This can be understood for two reasons. Firstly, the densification process of melilite phase would be the same as Si_3N_4-based ceramics because its composition consists of Si_3N_4 and R_2O_3, i.e. the formation of an oxynitride liquid due to the reaction of rare earth oxides with the silica present on the starting nitrogen-containing powder is an important feature of the densification process, which results in the occurrence of amorphous or crystalline intergranular phases after sintering in R–M/R–M' samples. Secondly, the overall compositions might still be in an oxygen-rich multiphase region, especially for the compositions with high x values. According to the phases analysis, the nominal R–M' compositions with $x > 1{\cdot}0$ and with R = Nd, Sm and Gd might be located in the phase compatible region R–M' – R–J – $RAlO_3$ and for R = Dy in the region R–M' – R–J – $Al_5Dy_3O_{12}$. It is known that in the pseudo-binary systems R_2O_3 – Al_2O_3 (R = rare earth elements), the aluminate phase $RAlO_3$ is formed for low and middle Z rare earth elements, whereas the phase $Al_5R_3O_{12}$ is formed only for Dy and higher Z rare earth elements.[10,11] This is in analogy to the phases found in the present R–M' samples with $x > 1{\cdot}0$. It can also be noted that in spite of the fact that the ionic radii of Y^{3+} is similar to that of Dy^{3+}, $Al_5Y_3O_{12}$ is not formed but AlN-polytypoids are.

3.2 Solid solubility range of R–M' phases

The variations of the a- and c-axis parameters of the tetragonal unit cell of the formed R–M' phases are given as function of the x values of the $R_2Si_{3-x}Al_xO_{3+x}N_{4-x}$ samples in Table 2. The lattice dimensions increase with increasing x-values up to a certain x-value for respective R–M' phases. However, these x-values do not necessarily represent true solubility limits as all samples contained additional phases some of which are rare earth rich. It can, however, be noted that the c/a ratios are almost constant with increasing x-value for each R–M' phase which indicates that the structural changes introduced when Si–N pairs are replaced by Al–O ones are isotropic in all R–M'-phases studied.

SEM-EDS studies have been used to estimate the solubility limits of Al in the various R–M' phases. The findings are compiled in Table 2 and Fig. 1. The maximum Al-content in the various R–M' phases were x = 0·98, 0·90, 0·78, 0·71 and 0·57 for R = Nd-, Sm-, Gd-, Dy- and Y, respectively. Thus, in Nd–M' and Sm–M' systems we find that one Si–N pair per formula unit can be replaced by one Al–O pair in accordance with previous findings[6–8] while the true solubility limits in the Gd–M' and Dy–M' systems seem to be somewhat less (0·75) and even the smaller in the Y–M' system (0·60). The maximum Al-content in the R–M'-phases clearly decreases with the ionic radii[12] of the R-element (see Fig. 2).

The substitution of Si–N by Al–O in the R–M structure produced a lattice expansion. The maximum value of latice expansion is found in the Nd–M' system (1·66%) and the minimum one in the Y–M' system (0·70%) which in turn is due to the fact that these systems exhibit different solid solubility ranges. The slopes of the curves of cell parameters versus the x-value are slightly different for different dopings as shown for Y– and Sm–M' in Fig. 1.

Although the small number of additional phases occurs in the formed samples as mentioned above, the measurements of cell parameters and SEM-EDS studies can be done without difficulty because R–M/R–M' phases were found to be the main phases in all samples and the additional phases can be easily separated from the melilite phase in the back scattering mode of SEM.

In order to understand why the solid solubility decreases with decreasing ionic radii of the R

Table 2. Unit cell dimensions and EDS results for samples of the composition $R_2Si_{3-x}Al_xO_{3+x}N_{4-x}$

Sample	*Nominal x value*	*Cell dimensions (Å)*			*x-value based on EDS measurements*
		a	*c*	*c/a*	
	0	7·7229	5·0327	0·652	0
	0·5	7·7471	5·0401	0·651	–
Nd–M'	0·75	7·7569	5·0439	0·650	–
	1·0	7·7667	5·0520	0·651	0·98
	1·25	7·7685	5·0558	0·651	0·94
	0	7·6830	4·9888	0·649	0
	0·3	7·7026	4·9942	0·648	0·25
	0·5	7·7104	4·9985	0·648	0·41
Sm–M'	0·75	7·7156	5·0056	0·649	0·63
	1·0	7·7174	5·0090	0·649	0·80
	1·5	7·7234	5·0080	0·648	0·90
	0	7·6512	4·9605	0·648	0
	0·3	7·6770	4·9670	0·648	–
Gd–M'	0·5	7·6779	4·9744	0·648	0·41
	0·75	7·6816	4·9797	0·648	–
	1·0	7·6870	4·9816	0·648	0·78
	1·5	7·6870	4·9780	0·648	–
	0	7·6180	4·9221	0·646	0
	0·4	7·6326	4·9307	0·646	–
Dy–M'	0·6	7·6371	4·9422	0·647	–
	0·75	7·6412	4·9448	0·647	0·71
	1·0	7·6430	4·9450	0·647	0·64
	1·5	7·6470	4·9410	0·646	–
	0	7·6137	4·9147	0·646	0
	0·375	7·6184	4·9218	0·646	0·32
Y–M'	0·6	7·6204	4·9255	0·646	0·38
	1·0	7·6262	4·9327	0·647	0·57
	1·25	7·6261	4·9315	0·646	0·54

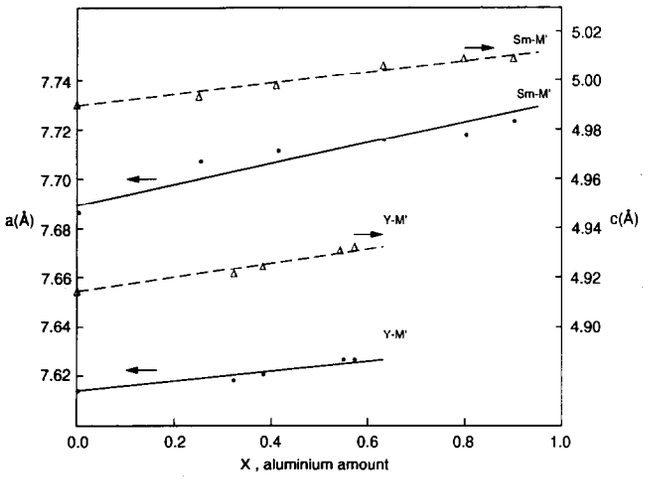


Fig. 1. Variation of the unit cell dimensions plotted vs the actual (SEM-EDS determined) x-values in $R_2Si_{3-x}Al_xO_{3+x}N_{4-x}$ with R = Sm and Y.

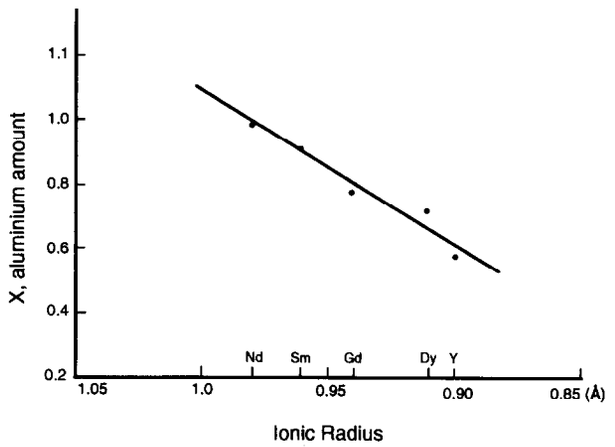


Fig. 2. Maximum solubility of Al in $R_2Si_{3-x}Al_xO_{3+x}N_{4-x}$ plotted vs the ionic radii of the used R element.

element one needs more detailed structural information concerning the metal – non-metal distances of the various R–M' phases. It can, however, be noted that when Si–N is replaced by Al–O the unit cell volume is increased implying that the voids, which accommodate the R element, become larger and eventually they are or will become too large to accommodate the used R element.

3.3 Microstructural studies of compacts containing R–M' phases

The microstructures of R–M' samples containing different amount of Al were studied in an SEM operated in back scattering mode. The micrographs clearly show the multiphase nature of the prepared samples (see in Figs 3 and 4). It is thus clearly seen that large crystals with sharp edges are formed and these crystals are surrounded by a significant

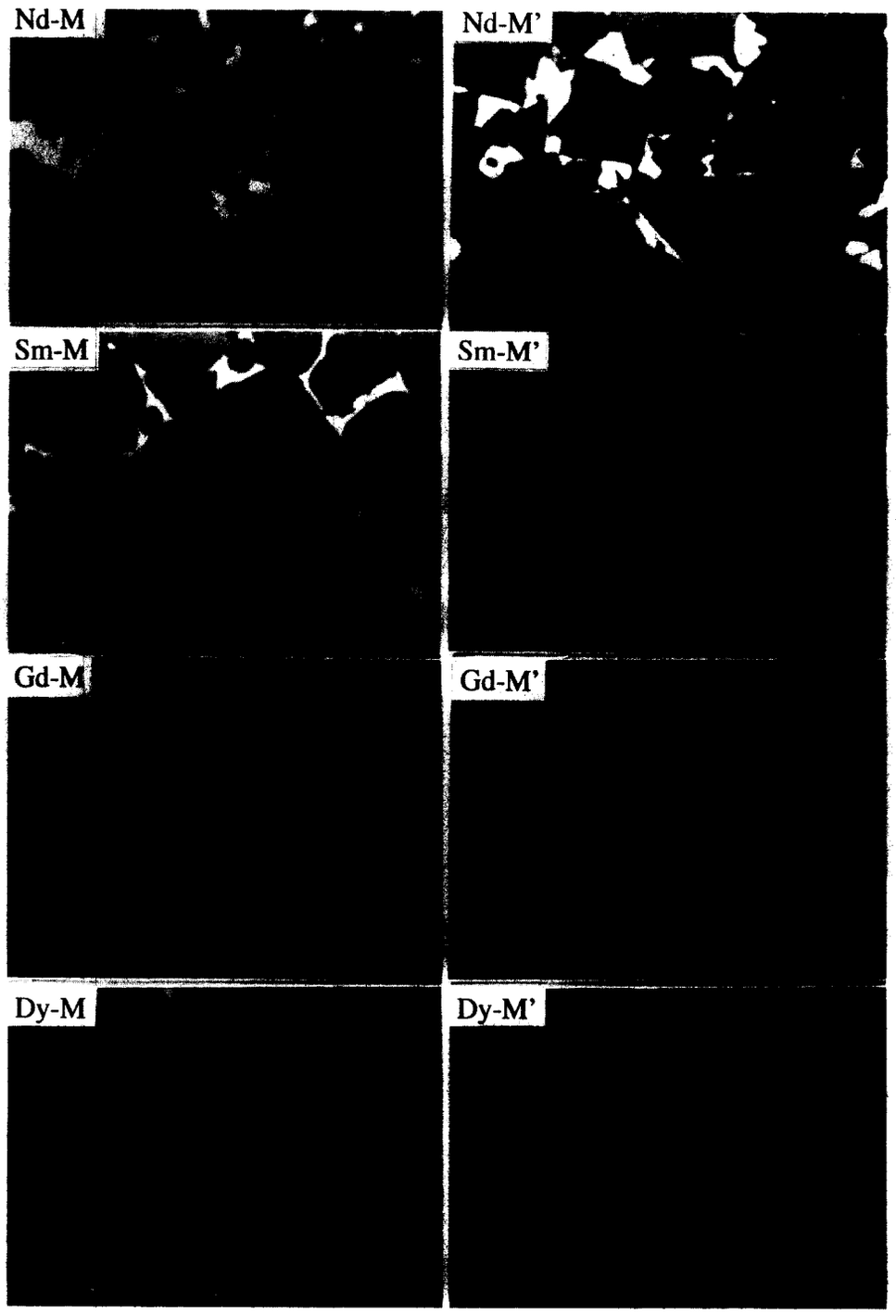


Fig. 3. SEM micrographs of $R_2Si_{3-x}Al_xO_{3+x}N_{4-x}$ with R = Nd, Sm, Gd and Dy and with (a) $x = 0$ and (b) $x = 0{\cdot}5$. The dark grey area represents the R–M' phase and the light grey one the J phase.

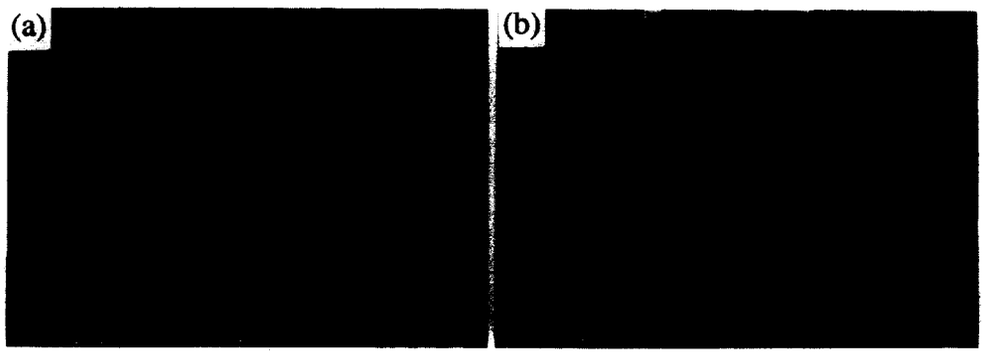


Fig. 4. SEM micrographs of $R_2Si_{3-x}Al_xO_{3+x}N_{4-x}$ with R = Y and with (a) $x = 1{\cdot}0$ and (b) $x = 1{\cdot}25$. The dark grey contrast represents the melilite phase and the light grey one the J phase. The flake and needle-like crystals with black contrast are AlN-polytypoids containing no yttrium.

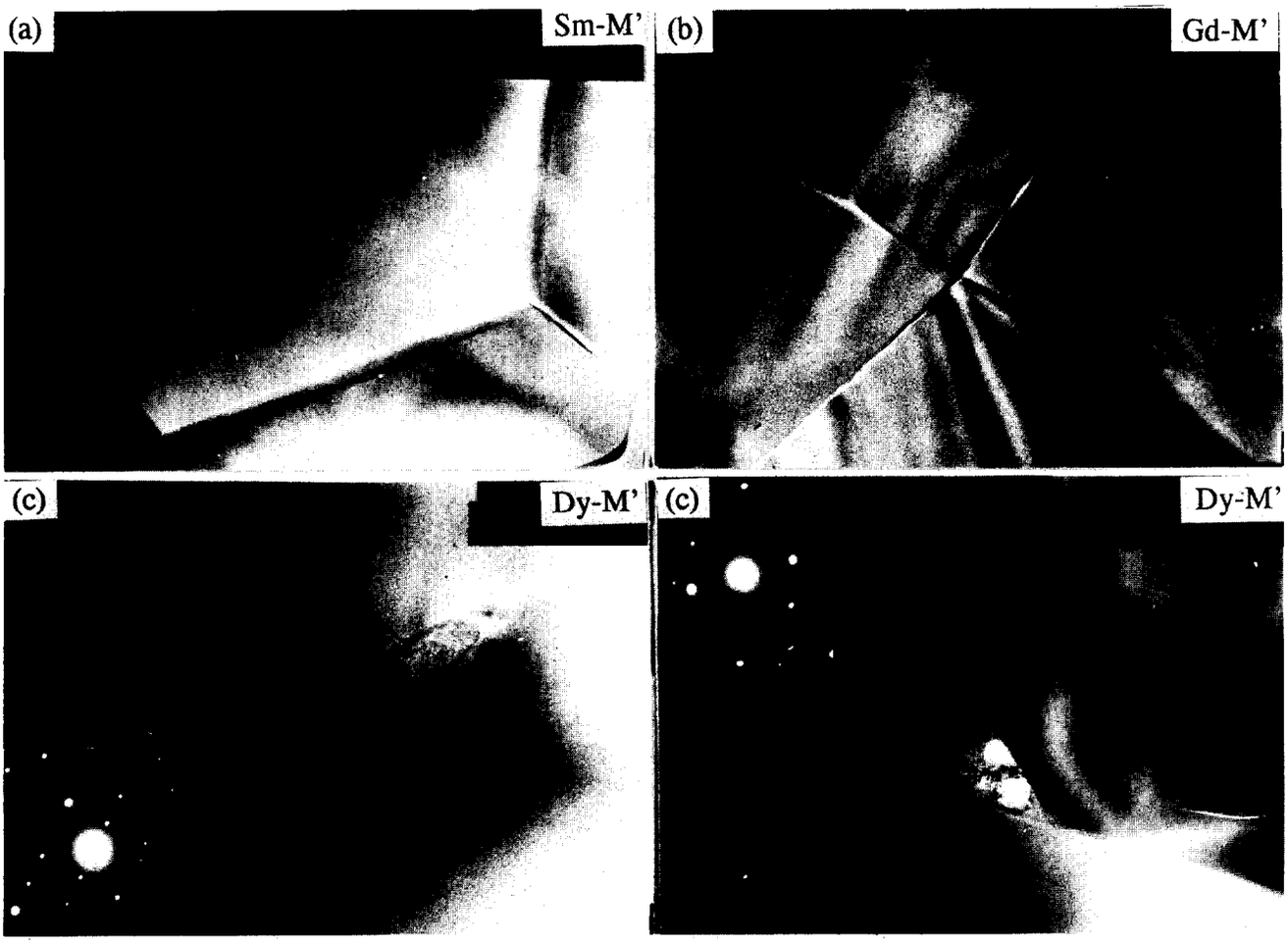


Fig. 5. TEM micrographs of $R_2Si_{3-x}Al_xO_{3+x}N_{4-x}$ samples with (a) R = Sm and x = 0·75, (b) R = Gd and x = 0·5 and (c) R = Dy and x = 0·4.

amount of a rare earth rich grain boundary phase and that the crystallographic morphology of the melilite phase is developed when Si–N are replaced by Al–O in the R–M' samples. This can be understood in terms of the added Al_2O_3 reacting with the silicon oxide on the surface of the nitride particles and with increasing x-value, an increasing amount of liquid phase is formed which in turn promotes the grain growth of the melilite phase.

The SEM micrographs in Fig. 4 show the morphologies of Y–M' phase (dark grey) and J phase (with light grey contrast) in the samples of Y–M' (x = 1·0 and 1·25). The flake and needle-like dark crystals are different AlN-polytypoids containing no yttrium, probably the $2H^{\delta}$ and the 27R modifications respectively. The micrographs also show that the amounts of the J-phase and AlN-polytypoid phases are larger in the sample with x = 1·25 than that of x = 1·0, which agrees with the results of the XRD analysis. The SEM micrographs have revealed that a rare earth element rich grain boundary phase is present in all samples, but more so in the Al containing materials. The XRD analysis has shown that most of it comprises crystalline phases, but the presence of a glassy phase can not be excluded.

TEM studies of triple-grain boundaries in the Sm–M'–(x = 0·75), Gd–M'–(x = 0·5) and Dy–M'–(x = 0·4) samples showed that:

(i) materials prepared with the largest ionic radii element, Sm, exhibited many triple-grain boundaries almost free of any additional phase. Typical triple-grain boundary junctions in this sample are shown in Fig. 5(a);
(ii) in the Gd–M' sample the number of glassy phases in the triple-grain boundaries was increasing but occasionally some multi-grain junctions were observed with no intergranular of glassy phase at all, as shown in Fig. 5(b);
(iii) a mixture of crystalline and glassy phases was always found in the triple-grain boundaries of the Dy–M' material illustrated in the micrographs and electron diffraction patterns given in Fig. 5(c).

These observations are in agreement with the SEM and XRD studies which showed that the homogeneity range of the R–M' phases is largest for the R elements with the largest ionic radii, i.e. these R–M' phases exhibit the best possibility to act as an 'element sink-phase' whereby the amount of glassy phase at the junctions is reduced.

4 Conclusions

The solubility of Al in nitrogen-containing melilite solid solutions according to the formula $R_2Si_{3-x}Al_xO_{3+x}N_{4-x}$ with R = Nd, Sm, Gd, Dy and Y has been studied. The SEM and XRD studies showed that the extension of solid solubility range of the various R–M' phases was largest for the R element with largest ionic radii (Nd and Sm). The TEM studies revealed that the R–M' phase with R = Sm acted as a better 'element sink phase' than R–M' phases containing R elements with smaller ionic radii.

Acknowledgements

The skilful technical assistance of Mrs Y. X. Jia and J. X. Chen is gratefully acknowledged. The State Kay Lab on High Performance Ceramics and Superfine Microstructure, Chinese Academy of Sciences and the Swedish Research Council for Engineering Science are thanked for financial support.

References

1. Wang, P. L., Sun, W. Y. & Yen, T. S., Formation and densification of R-α'-Sialon (R = Nd, Sm, Gd, Dy, Er and Yb). *Mater. Res. Soc. Symp. Proc.*, **287** (1992) 387–92.
2. Persson, J., Ekström, T., Käll, P. O. & Nygren, M., Oxidation behaviour and mechanical properties of β- and mixed α–β Sialons sintered with additions of Y_2O_3 and Nd_2O_3. *J. Eur. Ceram. Soc.*, **11** (1993) 363–73.
3. Huang, Z. K., Tien, T. Y. & Yen, T. S., Subsolidus phase relationships in the Si_3N_4–AlN–rare earth oxide systems. *J. Am. Ceram. Soc.*, **69** (1986) C-241.
4. Sun, W. Y., Tien, T. Y. & Yen, T. S., Subsolidus phase relationships in the part of the system Si, Al, Y/N, O: the system Si_3N_4–AlN–YN–Al_2O_3–Y_2O_3. *J. Am. Ceram. Soc.*, **74** (1991) 2753–8.
5. Patel, J. K. & Thompson, D. P., The low-temperature oxidation problem in yttria-densified silicon nitride ceramics. *Br. Ceram. Trans.*, **87** (1988) 70–3.
6. Slasor, S., Liddel, K. & Thompson, D. P., The role of Nd_2O_3 as an additive in the formation of α' and β' Sialons. *Br. Ceram. Proc.*, **37** (1986) 51–64.
7. Käll, P. -O. & Ekström, T, Sialon ceramics made with mixtures of Y_2O_3–Nd_2O_3 as sintering aids. *J. Eur. Ceram. Soc.*, **6** (1990) 119–27.
8. Cheng, Y. B. & Thompson, D. P., Aluminium-containing nitrogen melilite phases. *J. Am. Ceram. Soc.*, **77** (1994) 143–48.
9. Werner, P. -E., A Fortran program for least-squares refinement of crystal-structure cell dimensions. *Ark. Kemi.*, **31** (1969) 513–6.
10. Sun, W. Y. & Yan, D. S. (ed. Yen, T. S.), Phase relationships in quasi-systems R_2O_3–AlN–Al_2O_3 (R = Ce, Pr, Nd, Sm). *Science in China (Series A)*, **34** (1991) 105–15.
11. Sun, W. Y., Huang, Z. K., Tien, T. Y. & Yen, T. S., Phase relationship in the system Y–Al–O–N. *Mater. Lett.*, **11** (3,4) (1991) 67–69.
12. Vainshtein, B. K., Fridkin, V. M. & Indenbom, V. L., Crystallochemical radii systems, In *Modern Crystallography II, Structure of Crystals*, ed. B. K. Vainshtein, A. A. Chernov, & L. A. Shuvalov, Springer, Berlin, Heidelberg, 1982, pp 78–81.

Journal of the European Ceramic Society 15 (1995) 697–701
© 1995 Elsevier Science Limited
Printed in Great Britain. All rights reserved
0955-2219/95/$9.50
0955-2219(95)00038-0

Mechanical Properties of Hot-Pressed 12H Ceramics

H. X. Li, W. Y. Sun & D. S. Yan

The State Key Lab. on High Performance Ceramics and Superfine Microstructure, Shanghai Institute of Ceramics, Chinese Academy of Sciences, Shanghai 200050, P.R. China

(Received 12 January 1995; revised version received 1 February 1995; accepted 10 February 1995)

Abstract

The mechanical properties of hot-pressed 12H polytypoid phase with YAG as the sintering additive have been studied. The results showed that small amounts of YAG can greatly increase high temperature strength. At room temperature, the 12H with 2·5 wt% YAG possesses a flexural strength of 367 ± 18 MPa, but its high temperature strength can reach above 500 MPa in the temperature range from 1000 to 1300°C. The fracture mechanism has been discussed on the basis of the fracture morphology observed by SEM.

Introduction

It is well known that Sialon ceramics are a family of materials which possess high performance properties at elevated temperatures. In the Si–Al–O–N system, at compositions between β-sialon and AlN, there are six polytypoid phases (8H, 15R, 12H, 21R, 27R and $2H^{\delta}$) with wurtzite-type structures having compositions represented as M_mX_{m+1}.[1-2] These are built up by MX double layers of metal (M) and non-metal (X) atoms stacked with variants of AB and ABC sequences, as in silicon carbide and with MX_2 layers at periodic intervals to account for the different stoichiometries and structures. The crystal structures of AlN-polytypoids have been examined in detail,[3-4] but studies concerning their fabrication and mechanical properties are scarce.[5-6] Komeya[6] studied the formation and mechanical properties for 27R polytypoid and indicated that pure 27R can only be densified by 2000°C presintering and subsequent 2100°C hot-pressing; the ceramics show approximately constant strength values at room temperature to 1700°C(380–470 MPa prepared under the best conditions). This high refractoriness of the 27R polytypoid suggests that other polytypoids such as 21R, 12H and 15R would be also highly refractory. The phase relationships in the Y–Si–Al–O–N system[7] indicate that all AlN–polytypoids are compatible with β-sialon (except 8H), α-sialon (except 8H, 15R) and YAG ($3Y_2O_3{\cdot}5Al_2O_3$). This offers the possibility to incorporate polytypoid phases into α- and/or β-sialons forming composite ceramics simultaneously with YAG as the grain boundary phase. Since AlN-polytypoid phases possess fibre-like or prismatic morphology,[8] it would be interesting to document whether an *in situ* strengthening and toughening effect could be achieved in these composite ceramics. Therefore, the fabrication and mechanical properties of monolithic AlN-polytypoid ceramics prepared under the normal temperatures for nitride ceramics are worth exploration. The sinterability of sialon ceramics strongly depends on the nitrogen content in the starting compositions. In general, the more nitrides in the overall compositions, the more difficult the materials are to be densified. 12H phase contains the lowest nitrogen content among the polytypoids which are compatible with both α-sialon and β-sialon phases and therefore, it poses the greatest attraction among all AlN-polytypoid phases to be studied.

Recently, we studied monolithic 12H ceramics and α'-12H ceramics both with YAG as the sintering additive. A preceding paper[9] has described the effect of YAG on the densification and reaction sequence. The present paper reports the mechanical properties of 12H ceramics. The work on the α'-12H composite ceramics has appeared elsewhere.[10]

Experimental

As indicated in the Si–Al–O–N phase diagram, each AlN-polytypoid phase (M_mX_{m+1}) occurs along a certain line with $M:X$ equal to m:(m + 1). The nominal composition of 12H can be taken as $SiAl_5O_2N_5$. The starting materials used were Si_3N_4(LC12, Stark), AlN(1–2 μm, 1·2 wt% oxygen, (Zhuzhou Institute of Hard-Metals, China), Al_2O_3(99·99%) and Y_2O_3(99·9%). The mixed powder was ball-milled with absolute alcohol for 24 h,

dried and passed through a 120-mesh screen, and then hot-pressed at 1750°C for 1 h in a graphite-resistance furnace under 25 MPa in a flowing N_2 atmosphere. The specimens used for high temperature property determinations were heat treated at 1250°C for 24 h. The phases were identified by X-ray diffraction technique. Hardness and indentation fracture toughness were measured by using a Vickers diamond indenter under a load of 100 N. Flexural strength was tested at room temperature and high temperatures (1000–1400°C) in air by three-point bending with a 30 mm span (20 mm for high temperature test) and a cross-head speed of 0·5 mm/min. A boiling solution of $K_3Fe(CN)_6$ was used for etching the polished specimens. Both polished and fracture surfaces were observed by SEM. TEM study was also performed for revealing the grain boundary structure.

Results and Discussion

1 The effect of YAG on mechanical properties

Table 1 shows the starting compositions and their phase compositions present after hot-pressing and further heat treatment. The room temperature mechanical properties — Vickers hardness, indentation fracture toughness and the flexural strength are shown in Figs 1–3 respectively, and high temperature flexural strength is shown in Fig. 4.

At room temperature, as shown in Figs 1–3, when YAG is below 5 wt%, the flexural strength

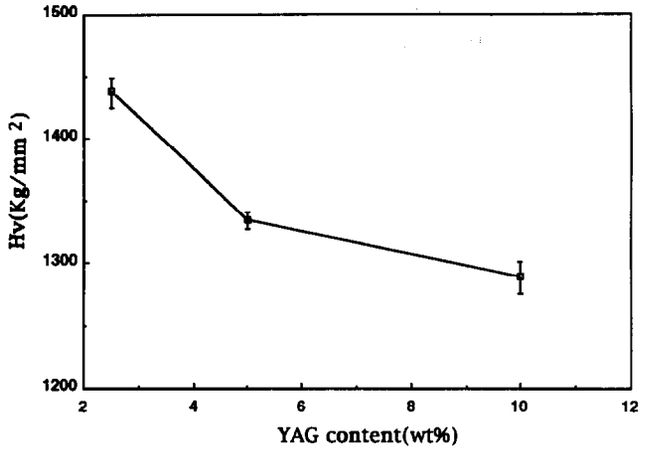


Fig. 1. Hardness of 12H compositions with different contents of YAG addition.

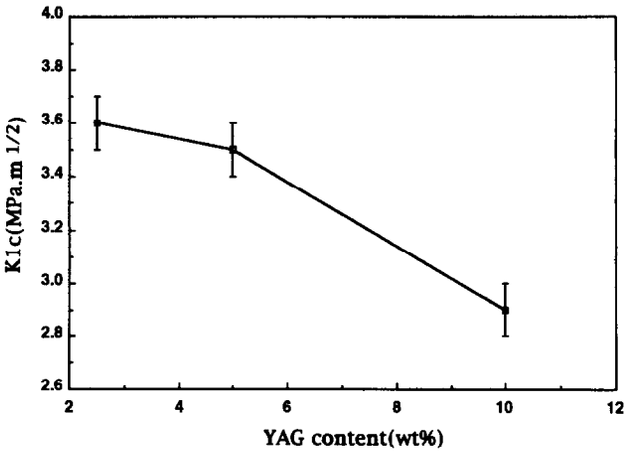


Fig. 2. Indentation fracture toughness of 12H compositions with different contents of YAG addition.

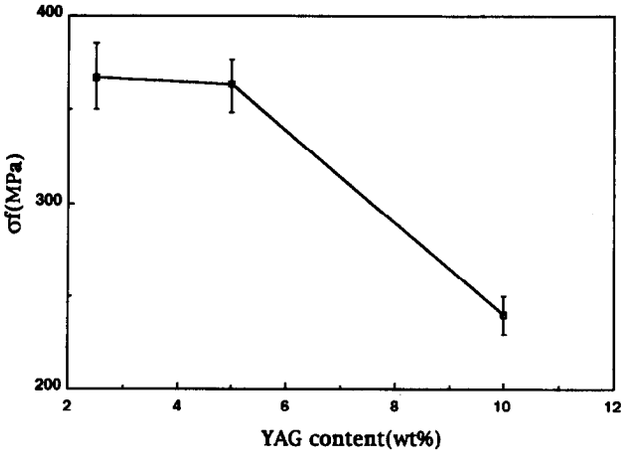


Fig. 3. Flexural strength of 12H compositions with different contents of YAG addition.

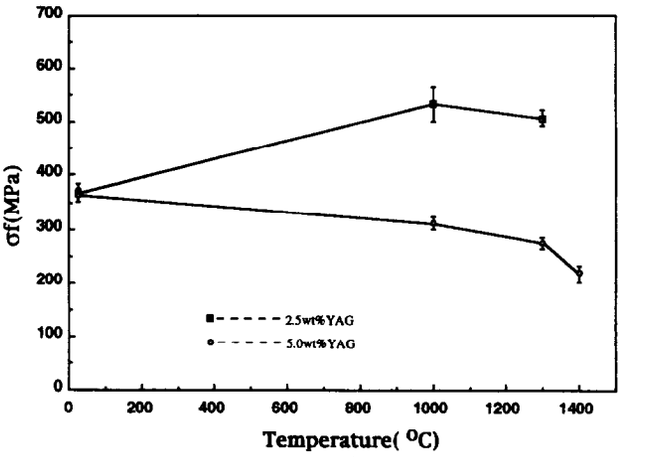


Fig. 4. Flexural strength of 12H with different YAG content versus temperature.

Table 1. The compositions and phases present after hot-pressed at 1750°C for 1 h

Specimens	*Starting compositions*				*Phase compositions*	
	Si_3N_4	*AlN*	Al_2O_3	Y_2O_3	*Before H. T.*	*After H. T.*
12H–2·5 YAG	17·2	57·6	23·8	1·5	12Hvs;YAGvw	12Hvs;YAGw
12H–5 YAG	16·8	56·2	24·2	2·9	12Hvs;YAGw	12Hvs;YAGmw
12H–10 YAG	15·9	53·2	25·2	5·7	12Hvs;YAGm; 15Rw	12Hvs;YAGm; 15Rw

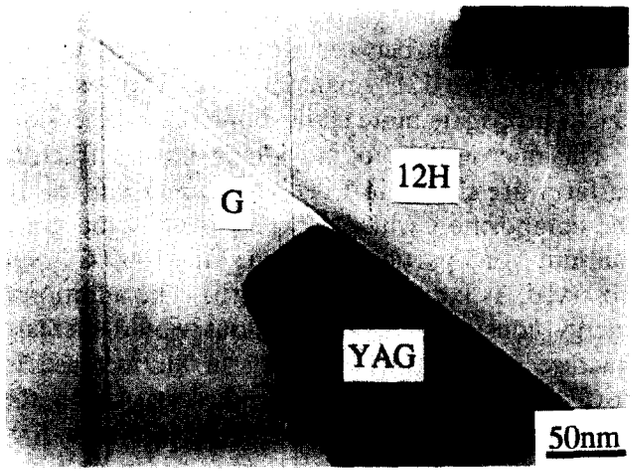


Fig. 5. HREM micrograph of 12H (2·5 wt% YAG) showing YAG and glassy phase at triple grain junction.

and fracture toughness are not sensitive to YAG content and the Vickers hardness decreases with the amount of YAG, but with further increase of YAG, all these mechanical properties become poorer. At high temperatures, as shown in Fig. 4, the effect of YAG on the flexural strength becomes more complex. The flexural strength of 12 H with 2·5 wt% YAG is much higher at high temperatures than at room temperature with an increment of 45 and 37% at 1000 and 1300°C respectively. However, when 5 wt% of YAG is added, the flexural strength decreases gradually with temperature rise.

The grain boundary phases in the 12H materials are YAG and glassy phase as revealed by TEM and X-ray diffraction technique. YAG as a sintering additive in 12H ceramics is more easily crystallized out than in β-sialon where YAG can only be obtained through post heat treatment. Fig. 5 is a TEM grain boundary micrograph of as fired 12H with 2·5 wt% YAG showing YAG with glassy phase existing at the triple grain junction. The microstructures of the compositions with different YAG contents are shown in Fig. 6. With increasing YAG, the content of grain boundary phase composed of both the glassy phase and YAG (white contrast) increases, and the grain size becomes smaller. The grain size change might be the result of having more nucleation sites being developed because of more liquid phase present during hot pressing. Clearly, the variation in the microstructure should be reflected in the mechanical properties. It has been known that the grain size has an obvious effect on the work of fracture in ceramic materials with non-equiaxed grains. The fracture energy can be improved through increasing the grain size.[11,12] Therefore, the higher fracture toughness of 12H materials with smaller amount of YAG addition can be attributed to the smaller quantity of grain boundary phase and to the relatively large grain size. The decreasing hardness in the compositions with higher YAG content can be envisaged by similar reasoning. In the composition with 10 wt% YAG, as indicated in Table 1, there still exists a small amount of 15R(an AlN-polytypoid containing less nitrogen than 12H) which is a transitional phase in the formation of 12H.[9] Whether the small amount of 15R has some effect on the mechanical properties is not clear, but it probably has slightly worse mechanical properties than 12H because of the lower N content in the composition.

The big difference in high temperature flexural strength caused by the amount of YAG must have some indication in their fracture morphology. In general, the glassy phase adversely affects high temperature mechanical properties more severely than at room temperature. But for the composition with 2·5 wt% YAG, the material behaves diff-

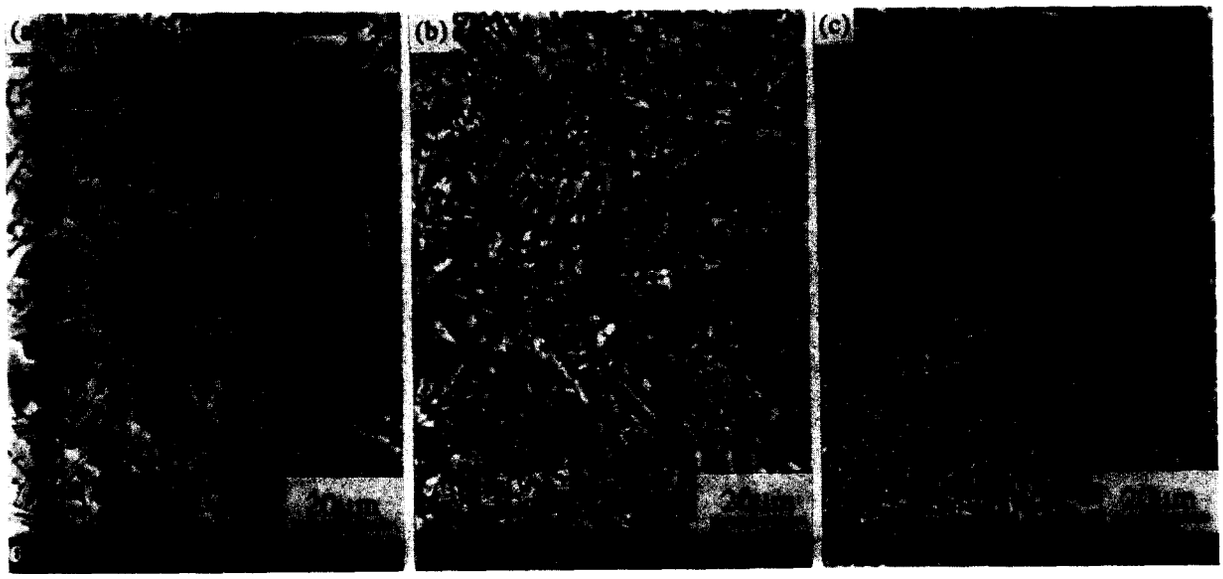


Fig. 6. SEM micrographs of 12H densified with (a) 2·5; (b) 5·0 and (c) 10 wt% YAG.

erently. There must be some strengthening mechanism occurring at high temperatures and this may be found through observing the fracture morphology.

2 The characteristics of fracture morphology

The micrograph of the fracture surface at room temperature for the composition with 2·5 wt% is shown in Fig. 7(a). As observed, 12H materials fractured in a transgranular mode. Some cracks propagated within the 12H grains with a stepwise fracture surface. The transgranular fractural mode is thought to be associated with the interlocking arrangement of 12H grains and their relatively poor strength. The step-like morphology is apparently related to the crystal structure of 12H. The hexagonal AlN-polytypoid phases prefer to grow along the a-dimension, and the width of the grains corresponds to the c-dimension, along which the MX and MX_2 layers stack up. Therefore, the strength of 12H grains varies with their orientation and is weaker along their width due to the poor cleavage strength between structural layers. Consequently, when 12H materials are fractured, the cracks propagate more easily along the c-dimension.

The micrographs of high temperature fracture surfaces are shown in Figs 7 (b–c) and 8 (a–c). In the composition with 2·5 wt% YAG, some grain pull-out or partial pull-out at 1000°C was observed, as indicated in Fig. 7(b). The additional energy consumed by the pull-out would increase fracture energy thus resulting in an increase in flexural strength. At 1300°C, microcracks on the fracture surface were observed, as shown in Fig. 7(c). The formation of microcracks also provides an additional contribution to the energy dissipation, thus improving the strength. Therefore, in the composition with less YAG content, the possible mechanism for the increment of high temperature strength are thought to be grain pull-out and the formation of microcracks. However, when

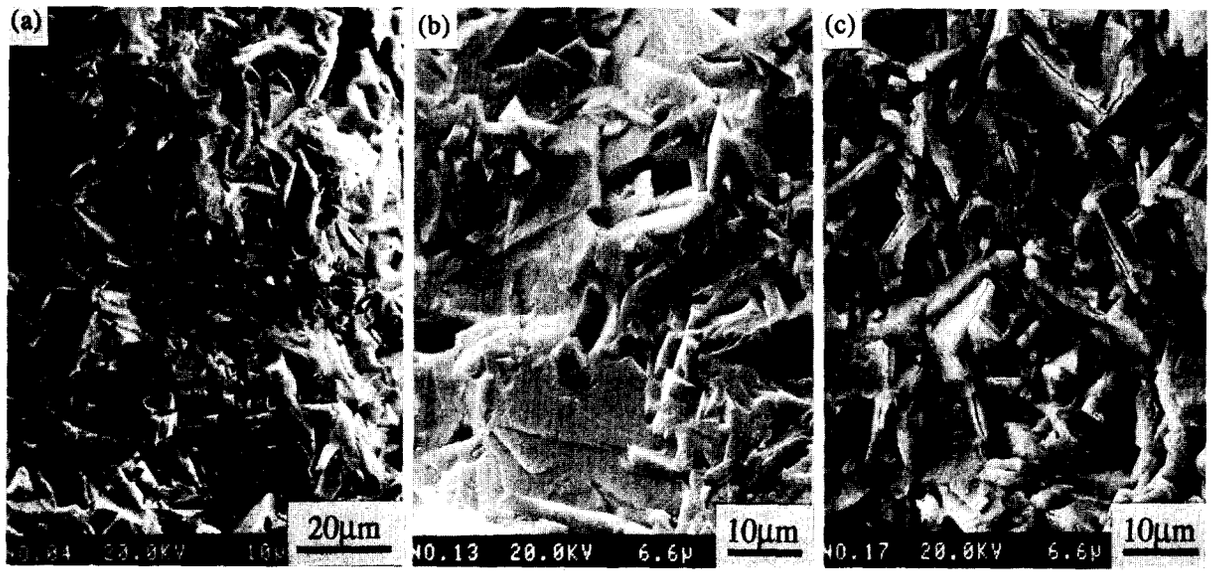


Fig. 7. Micrographs of fracture surface of 12H with 2·5 wt% at (a) room temperature, (b) 1000°C and (c) 1300°C.

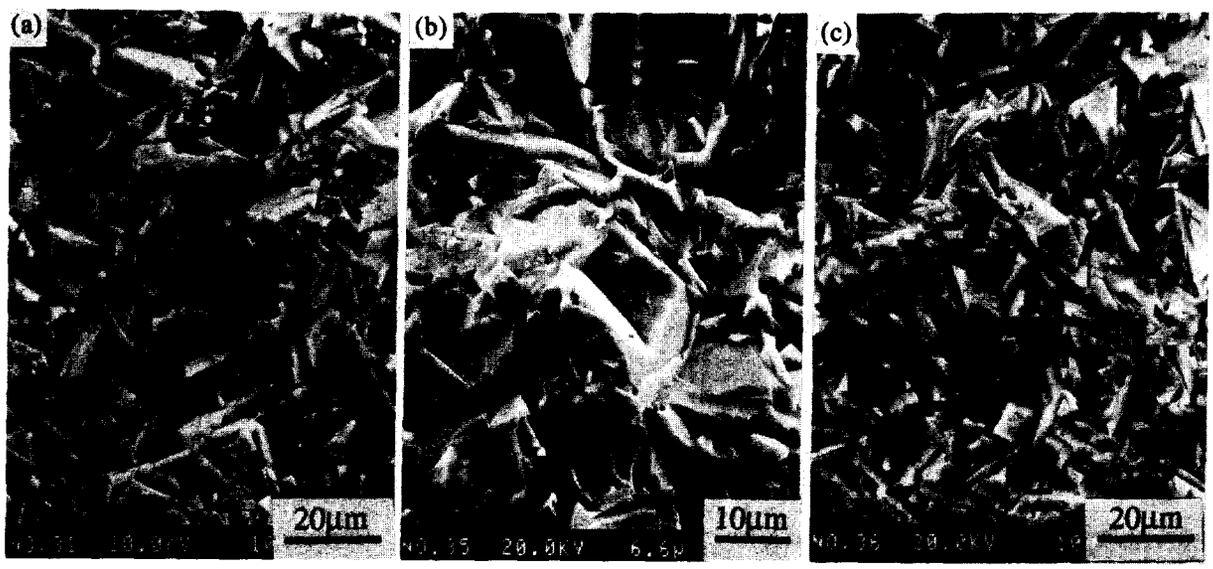


Fig. 8. Micrographs of fracture surface of 12H with 5·0 wt% YAG at (a)1000°C, (b) 1300°C and (c) 1400°C.

more YAG was added, no grain pull-out was observed and the grain boundaries appear to be less sharply defined, as shown in Fig. 8(a–c). The formation of this morphology can be attributed to more glassy phase present at the grain boundaries. Therefore, high temperature mechanical properties are more sensitive to the amount of YAG in the microstructure and better mechanical properties can be obtained through careful control of the grain boundary phases.

Conclusion

YAG as the sintering additive for 12H ceramics plays a decisive role in determining the mechanical properties of the material, especially at high temperatures. The composition with a small amount of YAG (about 2·5 wt%), gives a substantially higher flexural strength at temperatures between 1000 and 1300°C than its room temperature strength. Grain pull-out at 1000°C and microcracks formed in the 12H grains at 1300°C as manifested on the fracture surfaces are supposedly the main mechanisms for the strengthening effect at low additive level of YAG.

Acknowledgements

This work has received financial support from the National Natural Science Foundation of China, Contract No. 59132031. The authors would also like to thank Prof. T. R. Lai for helpful discussions.

References

1. Jack, K. H., Nitrogen ceramics. *J. Brit. Ceram. Soc.*, **72** (1973) 376–86.
2. Gauckler, L. J., Lukas, H. L. & Petzow, G., Contribution to the phase diagram Si_3N_4–SiO_2–AlN–Al_2O_3. *J. Am. Ceram. Soc.*, **58** (1975) 346–7.
3. Thompson, D. P., Korgue, P. & Hendry, A., The structural characterization of sialon polytypoids. In *Progress in Nitrogen Ceramics*, ed. F. L. Riley, Martinus Nijhoff, The Hague, The Netherlands, 1983, pp. 61–74.
4. Bando, Y., Mitomo, M., Kitami, Y. & Izumi, F., Structure and composition analysis of silicon aluminium oxynitride polytypes by combined use of structure imaging and microanalysis. *J. Microscopy*, **142** (1986) 235–46.
5. Cannard, P. J., Ekström, & Tilly, R. J. D., The formation of phases in the AlN-rich corner of the Si–Al–O–N system. *J. Euro. Ceram. Soc.*, **8** (1991) 375–82.
6. Komeya, K. & Tsuse, A., Formation of AlN polytype ceramics and some of their properties. *Yogyo-kyokai-Shi*, **89** (1981) 615–20.
7. Sun, W. Y., Tien, T. Y. & Yan, D. S., Subsolidus phase relationships in part of the system Si,Al,Y/N,O: the system Si_3N_4–AlN–YN–Al_2O_3–Y_2O_3. *J. Am. Ceram. Soc.*, **74** (1991) 2753–8.
8. Tendeloo, G. V., Faber, K. T. & Thomas, G., Characterization of AlN ceramics containing long-period polytypes. *J. Mater. Sci.*, **18** (1983) 525–32.
9. Li, H. X., Sun, W. Y. & Yan, D. S., Fabrication of 12H AlN-polytypoid ceramics. *Eur. J. Solid State Inorg. Chem.*, (in press).
10. Li, H. X., Sun, W. Y., Yan, D. S. & Tien, T. Y., Fabrication and mechanical properties of α'-sialon-12H multiphase ceramics, In *Proc. 5th Int. Sym. on Ceramic Materials & Components for Engines*, 1994, Shanghai, China, (in press).
11. Lange, F. F., Relation between strength, fracture energy and microstructure of hot-pressed Si_3N_4. *J. Am. Ceram. Soc.*, **56** (1973) 518–22.
12. Rice, R. W., Freiman, S. W. & Becher, P. F., Grain-size depend of fracture energy in ceramics: I, experiment. *J. Am. Ceram. Soc.*, **64** (1981) 345–50.

Journal of the European Ceramic Society 15 (1995) 703–715
© 1995 Elsevier Science Limited
Printed in Great Britain. All rights reserved
0955-2219(95)00041-0
0955-2219/95/$9.50

Polymer-Derived Si-Based Bulk Ceramics, Part I: Preparation, Processing and Properties

Ralf Riedel,[a] Martin Seher,[b,c,*] Joachim Mayer[d] & D. Vinga Szabó[d]

[a]Technische Hochschule Darmstadt, Fachbereich Materialwissenschaft, Fachgebiet Disperse Feststoffe, Hilpertstr. 31, D-64295 Darmstadt, Germany
[b]Institut für Anorganische Chemie, Universität Stuttgart, Pfaffenwaldring 55, D-70550 Stuttgart, Germany
[c]Max-Planck-Institut für Metallforschung, Institut für Werkstoffwissenschaft, Pulvermetallurgisches Laboratorium, Heisenbergstr. 5, D-70569 Stuttgart, Germany
[d]Max-Planck-Institut für Metallforschung, Institut für Werkstoffwissenschaft, Seestr. 92, D-70174 Stuttgart, Germany

(Received 2 August 1994; revised version received 7 February 1995; accepted 14 February 1995)

Abstract

The synthesis and processing of dense silicon-based bulk ceramic materials derived from the thermal decomposition of preceramic organosilicon polymers such as polysilazanes and polysilanes was achieved by three different routes A, B, and C. Additive-free silicon carbonitride bodies of the composition $Si_{1.7}C_{1.0}N_{1.6}$ were produced according to route A, with up to 94% relative density by the pressureless pyrolysis of compacted infusible polysilazane powders at low processing temperatures (1000°C). The resulting silicon carbonitride was single-phase and amorphous according to X-ray- and TEM-investigations and exhibited a low solid-phase density of 2·33 g/cm³. The maximum room temperature fracture strength of additive-free silicon carbonitride was 370 MPa. Crystallization of the as-synthesized silicon carbonitride bulk samples occurred at temperatures exceeding 1400°C.

In a second process, route B, densification of polysilazane-derived amorphous silicon carbonitride powder was achieved by liquid phase sintering with alumina and yttria as sintering additives in nitrogen atmospheres and at temperatures up to 1900°C. This process resulted in the formation of dense polycrystalline β-Si_3N_4/β-SiC-composites. The average room temperature fracture strength and fracture toughness of the gas pressure sintered composite were in the range of 650 MPa and 10·2 MPa$\sqrt{m}$, respectively.

Polycrystalline Si_3N_4/SiC-composites were obtained in a third process, route C, by the pyrolysis and subsequent sintering of α-Si_3N_4-powder/polysilane blends. The Si_3N_4-powder serves as an inert filler reducing the volume shrinkage associated with the polymer-to-ceramic transformation. Dense Si_3N_4 and Si_2N_2O bulk ceramics were formed according to route B by the liquid phase sintering of amorphous silicon nitride powder synthesized by the polysilazane pyrolysis under ammonia.

1 Introduction

Advanced non-oxide Si-based materials such as Si_3N_4 or SiC are commonly produced by inorganic solid state reactions at high temperatures. Thus, SiC is synthesized by the reaction of silica with carbon according to the Acheson process at $T \geq 2000$°C. Silicon nitride is fabricated either by the reaction of the elements or by the nitridation of silica in the presence of carbon at $T = 1500$°C. Due to their predominantly covalent nature, high sintering temperatures in the range of 1700–2100°C and the addition of sintering aids have to be used to enhance the densification of compacts prepared from these materials. Since the work of Verbeek *et al.* and of Yajima *et al.* in the mid 1970's, it is known that these ceramics can be produced at unusually low temperatures, i.e. in the temperature regime of 800–1200°C, by the thermal decomposition of organosilicon preceramic polymers.[1,2] This process is known as preceramic polymer pyrolysis and involves the following reaction steps as demonstrated by Seyferth and Wiseman for the formation of Si_3N_4 or Si_3N_4/SiC-composites from polysilazanes.[3,4]

(1) Synthesis of Si-based oligomers or polymers from low molecular weight compounds:

$$RHSiCl_2 \xrightarrow{NH_3} [RHSiNH]_n + 2\ NH_4Cl \quad R = \text{alkyl}$$

(2) Enhanced chemical or thermal cross-linking of the as-synthesized polymers giving high

*Present address: Material-und Energiesysteme, Filderhauptstr. 23, D-70599 Stuttgart, Germany.

molecular weight compounds suitable for polymer-to-ceramic transformation with high yields:

$$[RHSiNH]_n \xrightarrow{\text{strong base}} [RHSiNH]_{n-m}[RSiN]_m + m\ H_2$$

(3) Finally, pyrolysis of the cross-linked polymer providing the desired ceramic material:

$$[RHSiNH]_{n\ m}[RSiN]_m \xrightarrow{1000°C/Ar} Si_xC_yN_z + H_2 + RH$$

$$[RHSiNH]_{n\ m}[RSiN]_m \xrightarrow{1000°C/NH_3} Si_3N_4 + H_2 + RH$$

The preceramic polymer pyrolysis process has been intensively investigated with respect to the production of Si-based non-oxide fibers[2,5] and is already utilized commercially for the fabrication of SiC-, Si_3N_4-, and Si–C–N-fibers. Further potential applications such as infiltration of porous substrates, preparation of ceramic coatings, and joining of ceramics are under research.[6] However, the high potential of molecular preceramic compounds for the production of ceramic powders and bulk materials has been only sporadically demonstrated in the literature. Recently, great interest has been focussed on the *in situ* formation of β-Si_3N_4/β-SiC ceramic micro/nano-composites prepared by the densification of amorphous Si–C–N-powders at $T \gg 1000°C$.[7,8] The amorphous ceramic powders were produced either by the gas-phase decomposition of hexamethyldisilazane $((CH_3)_3Si)_2NH$[8] or by the solid-phase pyrolysis of poly(methyl)silazanes.[3,7,9] Hot-pressing of the Si–C–N-powders can result in β-Si_3N_4/β-SiC-composites which exhibit extraordinary high mechanical strength values ($\geq$1500 MPa)[8] or superplasticity at 1600°C.[10] According to a novel route, Si-containing polymers such as polysilazanes and polycarbosilanes can be processed directly to near dense monolithic ceramic bodies at low temperatures (1000°C) and without using additives by the thermolysis of inorganic polymer powder compacts.[11,12]

Besides the Si-based materials, other non-oxide ceramics such as AlN, BN, B_4C or TiN have also been synthesized by the pyrolysis of appropriate molecular compounds.[13,24] Some representative examples are listed in Table 1. In general, molecular compounds containing more or less direct polar bonds $M^{\delta+} - C^{\delta-}$ between the metal M and carbon are denoted as organometallics. In order to include for consideration the Si-containing polymers, the term organoelement polymer is used for the classification of materials such as polysilanes, polycarbosilanes, polysiloxanes, or polysilazanes.[25]

Generally, preceramic polymer pyrolysis is a process effective at relatively low temperatures and forming in many cases completely amorphous ceramic materials. Polymer-derived multi-component ceramic systems like Si–B–C–N start crystallizing at temperatures exceeding 1600°C, which makes the amorphous ceramics interesting materials for high temperature applications.[26] The controlled crystallization of the amorphous phases can itself be utilized for the synthesis of nano-structured ceramic monoliths or powders. However, the formation of ceramic bulk materials other than fibers starting from preceramic polymers is difficult owing to the fact that the release of the reaction gases formed during the thermolytic conversion of the polymer to the ceramic is associated with a high volume shrinkage, which can lead to crack formation. Furthermore, the use of meltable polymers can result in foaming and bloating of the material during the pyrolysis process. The present work has been undertaken to investigate the processing of organoelement compounds into dense bulk ceramics with the objective of avoiding these problems.

Table 1. A choice of preceramic molecular compounds for the synthesis of non-oxide ceramics

Preceramic molecular compound	*Ceramic product*	*Reference*
$[RAlNH]_n$	AlN	13
$[Cl_2Al\text{-}N(H)Si(CH_3)_3]_2$	AlN	14
$C_5H_5N \times BH_3$	BC_4N	15, 16
$HNC_4H_8NH \times BH_3$	BC_2N	17
$[HNBCl]_3 + ((CH_3)_3Si)_2NH$	BN	18
$H\text{-}[CH_3SiH]_n\text{-}H$	SiC	19
$[CH_3SiH\text{-}CH_2]_n$	SiC/C	2
$[((CH_3)_2Si)_x(CH_3SiC_6H_5)_y]_n$	SiC/C	20
$[CH_3SiHNH]_m\ [CH_3SiN]_n$	$Si_xC_yN_z$	3
$[(CH_3)_2SiO]_m\ [CH_3SiO_{1.5}]_n$	$Si_xC_yO_z$	21
$[B_{10}H_{12}H_2N\text{–}CH_2\text{–}CH_2\text{–}NH_2]_n$	B_4C/BN	22
$[(C_4H_9N)_2Ti]_n$	TiN	23
$Zr[BH_4]_4$	ZrB_2	24

In the present study, dichloro(diorgano)silanes of the general formula $RR'SiCl_2$ with R = H or CH_3 and R' = CH_3 or R = CH_3 and R' = C_6H_5 have been used as the starting materials for the synthesis of the silicon-based polymers and ceramic materials. Dichloro(diorgano)silanes are produced in large quantities by the Rochow synthesis[27] and are commonly used for the preparation of silicones which are produced on the order of 700,000 tons per year.

The organopolysilazanes of the form $[RR'SiNH]_n$ used in this work were synthesized by the reaction of chlorosilanes with ammonia and by subsequent cross-linking of the ammonolysis product with strong bases such as potassium hydride, KH, or with dichloromethylsilane, CH_3SiHCl_2.[3,28] Poly(organo)silanes were obtained by the Wurtz–Fittig analogous reaction of R_2SiCl_2 with Na/K alloys.[20,29] Pyrolysis and subsequent processing of the polysilazanes resulted in the formation of the ceramic materials $Si_xC_yN_z$ (silicon carbonitride),

Si_3N_4 or Si_2N_2O, whereas the thermal decomposition of the polysilanes provided SiC_{1+x}.

In Part I, we report on the synthesis of dense or near dense Si-based bulk ceramics other than fibers from the above organosilicon polymers. Some of the mechanical properties of the materials produced are discussed. In Part II, the polymer-derived bulk ceramic microstructures developed during thermolysis and sintering are investigated by analytical transmission electron microscopy.

2 Experimental

The preparation of various Si-based ceramic bulk materials starting from organoelement polymers was accomplished first by the direct pyrolysis of polymeric shapes (route A) and secondly by the pressureless sintering of polymer-derived amorphous ceramic powders with addition of sintering aids (route B). In a third process, route C, α–Si_3N_4-powder containing Al_2O_3 and Y_2O_3 as sintering additives was mixed with a SiC-forming precursor, pressed and finally sintered. The principal reaction paths used for the synthesis of the organosilicon polymers and the ceramic products derived therefrom are shown in Fig. 1. The different routes applied for the processing of the preceramic polymers to dense bulk ceramics are denoted as A, B, and C as illustrated in Fig. 2. Generally, synthesis and all manipulations of the organoelement polymers were done in glass vessels under Ar. The pyrolysis reactions were conducted in quartz tubes in flowing atmospheres (Ar (99·999% purity) or NH_3 (99·996% purity))[1] with heating rates of 0·5 to 5°C/min.

2.1 Characterization of the polymer-derived ceramics

The chemical analysis of the synthesized ceramic materials was performed by conventional analytical methods.[2]

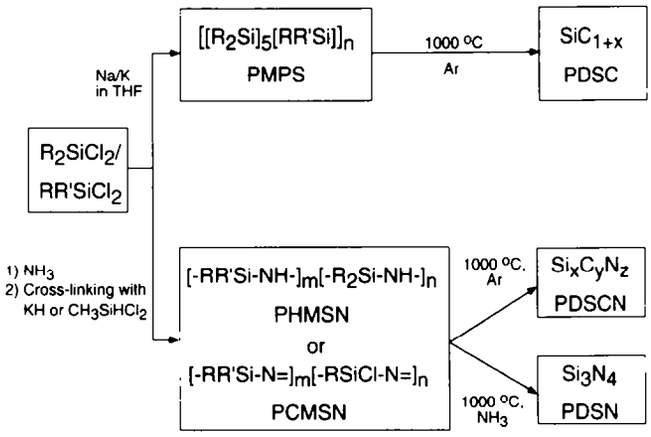


Fig. 1. Synthesis of Si-based polymers and the ceramic products obtained after pyrolysis in different atmospheres. R = CH_3, R' = H (reaction with NH_3) or C_6H_5 (reaction with Na/K); PMPS = poly(methylphenyl)silane; PHMSN = poly(hydridomethyl)-silazane; PCMSN = poly(chlorohydridomethyl)silazane; PDSC = polymer derived SiC; PDSCN = polymer derived silicon carbonitride; PDSN = polymer derived silicon nitride.

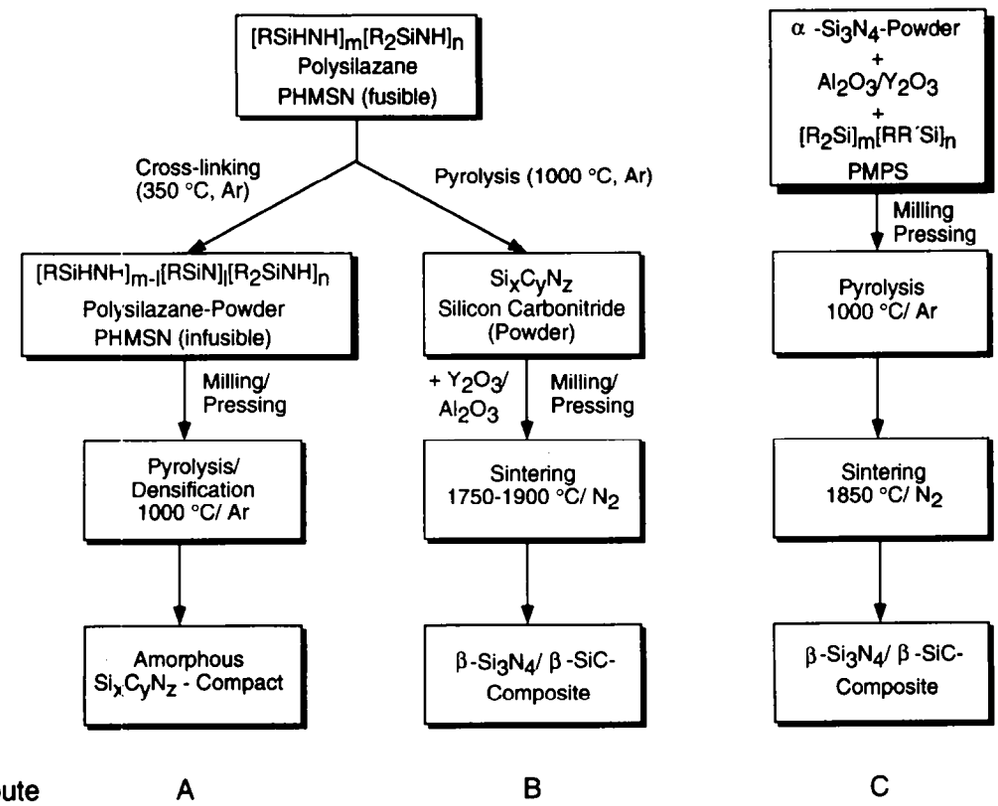


Fig. 2. Flow chart representing the processes A, B and C applied for the preparation of Si-based bulk ceramics derived from organoelement precursors. R = methyl (CH_3); R' = phenyl (C_6H_5H).

Phase compositions were determined by X-ray powder diffraction using monochromated CuK_α radiation (wavelength 154·178 pm).

For the determination of the ceramic solid-phase densities, the densified bulk samples were ball milled to powders. The solid-phase densities of the powders were then measured in a pycnometer using water as the liquid. Silicon carbonitride produced according to route A was analyzed in terms of BET surface area and pore size distribution by the measurement of the adsorption and desorption isotherms using N_2 or Ar as the adsorbing gas to ascertain the influence of possible nanoporosity on the solid-phase density. The solid-phase density of annealed and infusible polysilazane powder (PHMSN) was evaluated by pycnometry with n-hexane as the liquid. The bulk densities were determined by the water displacement method or, in the case of samples with open porosity, by mercury-pressure porosimetry. Relative densities were either based on theoretical densities calculated according to the rule of mixtures or on the ascertained solid-phase densities.

The amorphous silicon carbonitride was analysed by ESCA using Mg-K_α irradiation (1253·6 eV) as the X-ray source.[3] In order to avoid a charge shift due to the low electrical conductivity of the silicon carbonitride, the powder samples were mixed with Cu or Al powder (80 vol%) and uniaxially pressed to tablets.

Flexural strength was determined by the 4-point bend test[4] with an outer and inner span of 40 and 20 mm respectively in the case of room temperature testing and of 20 and 12 mm respectively in the high-temperature case. The flexural strength is given as the mean value calculated from eight specimens. Fracture toughness (K_{IC}) was evaluated by the indentation crack length method (ICL) according to Anstis *et al.*[30] The thermal decomposition of polysilazane-derived silicon oxynitride, Si_2N_2O, was investigated by TGA-MS.[5]

2.2 Synthesis and processing of the materials

2.2.1 Synthesis of additive-free monolithic silicon carbonitride (route A)

The starting material, poly(hydridomethyl)silazane (PHMSN) with the composition $[CH_3SiHNH]_m$ $[(CH_3)_2SiNH]_n$, was commercially available[6] and was used without purification.

In a typical experiment, 50 g of PHMSN were further cross-linked by thermally induced polycondensation for 100 min at 350°C in 0·1 MPa Ar and subsequently for 80 min in vacuum (2×10^{-3} Torr) at the same temperature. During the heat-treatment, a colourless liquid was distilled off and the overall mass loss was determined to be 12 wt%. The annealed PHMSN was infusible and insoluble in organic solvents such as toluene, THF or n-hexane. A solid-phase density of 1·22 g/cm^3 for the infusible polymer was evaluated. The polycondensation was investigated by simultaneous thermo-gravimetric and mass spectrometric (TGA–MS) measurements.[7] The material was then ball milled for 1 h with ZrO_2-balls, sieved through a 32 μm screen and finally compacted by cold isostatic pressing at 640 MPa into cylindrical samples 14 mm in diameter and in height or into rectangular bars having dimensions of 60 × 22 × 14 mm.[3] The relative green densities of the polymer green bodies were in the range of 84–89%. The main part of the pore volume exhibited pore radii of less than 100 nm, as determined by Hg-pressure porosimetry.[8] A minor amount of porosity with radii in the range of 10 μm was also detected. Subsequently, the polymeric green body was heated to 1000°C with a heating rate of 0·5–1°C/min in flowing Ar. Relative linear shrinkages of 25 up to 28% were detected and the overall yield of the black polymer-derived silicon carbonitride was found to be 68% relative to the PHMSN used. According to chemical analysis, the material contained 57·8 wt% Si, 14·3 wt% C, and 26·0 wt% N. From these values, an empirical formula $Si_{1·7}C_{1·0}N_{1·6}$ was derived for the synthesized silicon carbonitride (Table 2). The sample handled in air was contaminated with 0·8 wt% 0. Contamination of the ceramic residues with Zr stemming from the processing of the cross-linked polymer powder with ZrO_2 balls could not be detected. The as-pyrolyzed compacts exhibited relative bulk densities of 90–94% corresponding to a solid-phase density of 2·33 g/cm^3 and to open porosities in the range between 10 and 6% as found by Hg-pressure porosimetry (Table 3). The solid-phase density of PHMSN-derived silicon carbonitride (2·33 g/cm^3) deduced from Hg-pressure porosimetry was in good accordance with that determined by water

[1] Messer Griesheim, Germany.

[2] Optical emission spectrometry with inductively coupled plasma excitation (OES–ICP) was used for the determination of the Si-content; ICP 5500, Perkin Elmer, USA. Carbon and N were detected by carrier gas heat extraction (CGHE); equipment: C, S-analyser 244 and N, O-determinator TC 436, LECO Corp., USA.

[3] Modell ESCA 5300, Perkin Elmer Corp.

[4] Equipment: Zwick, Model 1474, Einsingen, FRG.

[5] Netzsch STA-QMS-system: 409/429-403, Selb, FRG.

[6] $[CH_3SiHNH]_m[(CH_3)SiNH]_n$ was obtained from the Nichimen Corporation, Tokyo, Japan, product name NCP200.

[7] TGA-STA 429, Netzsch Gerätebau, Selb, FRG, coupled with MS QMG 511, Balzers, Balzers, LIE.

[8] Hg-pressure porosimeter model 2000, Carlo Erba Instruments, Milan, Italy.

Table 2. Ceramic yields, elemental composition and solid phase densities of the synthesized organosilicon polymers PHMSN, PCMSN and PMPS (Fig. 1) pyrolysed under Ar and NH_3 without oxide additives

Preceramic organosilicon polymer	*Pyrolysis atmosphere/ temperature (°C)*	*Ceramic yield (wt%)*	*Composition (wt%)* Si	C	N	O	*Empirical Formula*[a]	*Solid phase density*[b] *(g/cm³)*
Cross-linked PHMSN	Ar/1000	68	57·8	14·3	26·0	0·8	$Si_{1.7}C_{1.0}N_{1.6}$	2·33
	NH_3/900	65	60·2	≤0·3	35·5	4·0	$Si_{3.4}N_4$	n.d.
PCMSN	Ar/1000	72	57·4	14·2	25·4	2·4	$Si_{1.7}C_{1.0}N_{1.5}$	2·30
	NH_3/1000	68	n.d.	≤0·5	35·2	3·1	$Si_{3.5}N_4$	n.d.
PMPS	Ar/1000	68	52·4	45·3	—	0·5	$SiC_{2.0}$	2·87[c]

[a]Molar composition neglecting the oxygen content.
[b]Water pycnometry of powdered bulk samples.
[c]Calculated according to the rule of mixtures assuming SiC and C as the phases formed during pyrolysis.

pycnometry of $Si_{1.7}C_{1.0}N_{1.6}$-powder (2·30 g/cm³). In addition, gas adsorption measurements of the as-synthesized silicon carbonitride powder revealed a BET surface area of 5·5 m^2g.Thus, it can be concluded that the pyrolysis of the polysilazane PHMSN gives fully dense amorphous silicon carbonitride powder particles without any detectable nanoporosity.

Pyrolysis of PHMSN-powder in NH_3 up to 900°C provided X-ray amorphous, white silicon nitride in 65% yield. The silicon content was measured to be 60·2 wt% (theoretical value for crystalline Si_3N_4: 60·0 wt%). Due to manipulation of the material in air, an oxygen contamination of 4 wt% was detected. The residual carbon content was below the detection limit of 0·3 wt%.

2.2.2 Synthesis and sintering of polysilazane derived Si-based ceramic powders with additives (route B)

Amorphous polysilazane-derived Si-based ceramic powders were obtained by the pyrolysis of poly(chlorohydridomethyl)silazane PCMSN in flowing Ar or in flowing NH_3. The synthesis of PCMSN is based on the reaction of oligomeric silazanes $[CH_3SiHNH]_n$ with dichlororganosilanes CH_3SiHCl_2[28] and is shown by the following simplified reaction equations:

$$RR'SiCl_2 \xrightarrow{NH_3} [-RR'Si-NH-]_n / R = H;\ R' = CH_3 \quad (1)$$

$$[-CH_3SiH-NH-]_x + yCH_3SiHCl_2 \xrightarrow[H_2/HCl]{30\text{–}300°C} [-CH_3SiH-N=]_m[-CH_3SiCl-N=]_n \quad (2)$$

Pyrolysis of PCMSN in argon at 1000°C gave a black X-ray amorphous silicon carbonitride powder with an empirical composition $Si_{1.7}C_{1.0}N_{1.5}$ and 72 wt% yield (Table 2). Decomposition of PCMSN in ammonia at 1000°C resulted in the formation of X-ray amorphous silicon nitride with 68 % yield. The nitrogen content was measured to be 35·2 wt%. The product was contaminated with 3·1 wt% oxygen and the residual carbon content was less than 0·5 wt%.

Prior to sintering, the different amorphous polymer-derived powders were attrition milled at 1000 rpm either in air or under Ar for 3 h after addition of Al_2O_3 and Y_2O_3 in various amounts. Isopropanol was used as the suspension medium and Si_3N_4-balls as the milling medium. After evaporation of the alcohol, the powder was sieved through a 160 μm-screen and subsequently cold-isostatically pressed at 640 MPa to form green compacts (cylinders 10 mm in length and 15 mm in diameter or rectangular strength-test bars 55 × 25 × 15 mm^3).

A graphite furnace[9] was used for the sintering experiments. Heating rates of 5 and 10°C/min were applied for all samples; the final temperatures were 1750 or 1850°C in 0·1 MPa nitrogen atmosphere.

Besides pressureless sintering of oxide-doped PCMSN-derived silicon carbonitride powder, post-gas-pressure sintering at 1900°C and 10 MPa N_2-pressure[10] was applied to yield polycrystalline Si_3N_4/SiC-composites.

2.2.3 Synthesis and sintering of α-Si_3N_4-powder/ 20 wt% PMPS-blends (route C)

The reaction of a mixture of 5 mol $(CH_3)_2SiCl_2$ and 1 mol $CH_3(C_6H_5)SiCl_2$[11] with Na/K-alloy in THF as the solvent provided poly(methylphenyl)-silane PMPS as shown in eqn 3.

$$5\ R_2SiCl_2 + RR'SiCl_2 \xrightarrow[-NaCl/KCl]{Na/K\text{–}alloy} [[R_2Si]_5[RR'Si]]_n \quad / R = CH_3;\ R' = C_6H_5 \quad (3)$$

Before the preparation of the ceramic-powder/ polymer-blends, as-synthesized PMPS was first heat-treated at 500°C for 5 h under Ar. The resulting product was an amber-coloured polysilane soluble in organic solvents and having a melting range of 100–120°C.

[9]Furnace GERO GmbH, Neuhausen, Germany.
[10]Furnace GERO GmbH, Neuhausen, Germany.
[11]The organochlorosilanes obtained from Merck, Darmstadt, Germany were used without further purification.

Attrition milled α-Si_3N_4-powder[12] containing 2·8 wt% AlN, 7·8 wt% Y_2O_3 and 1·4 wt% Al_2O_3 as sintering additives was mixed with 20 wt% annealed PMPS dissolved in THF. Subsequent evaporation of the solvent THF gave α-Si_3N_4-powder homogeneously coated with the polysilane PMPS. The α-Si_3N_4-powder/PMPS-blend was then cold-isostatically pressed at 640 MPa. Finally, pyrolysis and sintering of the cold-isostatically pressed polymer-powder mixture was conducted under 0·1 MPa Ar at temperatures up to 1000°C in a quartz tube and under 0·1 MPa N_2 up to the final sintering temperature of 1850°C in a graphite furnace.[8]

3 Results and discussion

3.1 Synthesis and processing of the materials

The chlorosilanes were reacted either with Na/K-alloy or with NH_3 providing various types of organoelement ceramic precursors (Fig. 1). Basically, polymers with a high viscosity and a low volatility have to be synthesized to produce dense bulk ceramic materials. Best results, i.e. the highest ceramic yields, are obtained using infusible polymers.[13]

The following different polymer processing routes (A, B, and C) were used to produce dense or near dense bulk ceramics (Fig. 2).

Route A in Figure 2

During the proceeding polycondensation of fusible PHMSN at 350°C, mainly ammonia and hydrogen were evolved as could be determined by simultaneous thermal gravimetric and mass spectrometric (TGA–MS) investigations. The evolution of H_2 indicates that the thermal cross-linking proceeds via the formation of three-dimensional bridging [RSiN]-units:

$$[RSiHNH]_m[R_2SiNH]_n \xrightarrow{350°C/-H_2} \begin{matrix}[RSiHNH]_{m-l}[RSiN]_l \\ [R_2SiNH]_n\end{matrix} \quad (4)$$

Ammonia is formed during the heat-treatment due to condensation of H_2N-polymer end groups. An infusible polysilazane PHMSN was isolated as the reaction product (Fig. 2). The subsequent thermolysis of the compacted infusible polysilazane powder at 1000°C in Ar gave amorphous, additive-free silicon carbonitride compacts with dimensions of 42 × 16 × 10 mm^3. According to our studies, the crack-free polymer to ceramic transformation process succeeds if the following requirements are met:

- The organoelement polymer has to be infusible to enable the compact to shrink while retaining its shape during the heat-treatment.
- After shaping of the polymer-powder, a transient open porosity has to be present to allow the volatile reaction gases to be released without forming cracks and gas bubbles.
- Finally, during ceramisation, the original polymer particles have to form a continuous three-dimensional network by the formation of new covalent bonds between the individual polysilazane powder particles.

Route B in Figure 2

The infusible polysilazane powder was first pyrolyzed in Ar to an amorphous Si–C–N ceramic powder and then processed into dense polycrystalline β-Si_3N_4/β-SiC-composite ceramics by liquid phase sintering at higher temperatures (Fig. 2). Using ammonia instead of Ar during pyrolysis of the polysilazane powders PHMSN and PCMSN results in the formation of X-ray amorphous Si_3N_4-powder (Fig. 1). During attrition milling in wet isopropanol, the reactive amorphous Si_3N_4-powder takes up oxygen by hydrolysis or by alcoholysis in such amounts that pure polycrystalline silicon oxynitride, Si_2N_2O, is formed after densification at 1600°C in 0·1 MPa N_2 when Al_2O_3 and Y_2O_3 were added to this powder. Accordingly, the oxygen content increased from 3·1 wt% in the as-pyrolyzed (NH_3) material to 14·8 wt% in the attrition milled powder. The oxygen content of crystalline Si_2N_2O is calculated to be 14·0 wt%. The oxygen contamination can be reduced to 6·7 wt% by the use of dried isopropanol as the suspension medium and by attrition milling under an Ar atmosphere. In contrast, the oxygen content of the carbon containing silicon carbonitride powder attrition milled in wet isopropanol in air was significantly lower (4 wt%) owing to a strongly decreasing sensitivity of these powders towards moisture.

Route C in Figure 2

Pyrolysis of polysilane PMPS in Ar at 1000°C resulted in the formation of X-ray amorphous SiC_{1+x} with $x = 1$[29] (Fig. 1). In the present investigation, we used PMPS for the *in situ* formation of inter- and intragranular SiC dispersions in a Si_3N_4 matrix.

The ceramic yields, elemental composition and solid-phase densities of the pure organosilicon polymer-derived ceramics are listed in Table 2. Details of the processing of the polymers to dense bulk ceramics and some characteristic data of the densified products such as density, porosity and phase composition are summarized in Table 3.

[12]LC 12 H.C. Starck, Germany.

[13]In contrast, meltable and soluble polymers with lower viscosities are suitable for infiltration processes, for fiber preparation, and for the formation of coatings.

Table 3. Preparation of polymer-derived Si-based bulk ceramics according to the routes A, B, and C in Fig. 2, its final densities and compositions

Processing conditions	*Final ceramic material*			
	$Si_xC_yN_z$	*β-Si_3N_4/β-SiC*	*β-Si_3N_4/β-SiC*	*Si_2N_2O*
Route (see Fig. 2)	A	B	C	B
Starting Materials	PHMSN	PCMSN	α-Si_3N_4-powder +20 wt% PMPS	PCMSN
Additives (wt%) (Al_2O_3/Y_2O_3)	-	15[a]	12[b]	15[a]
Pyrolysis-Temperature (°C)	1000/Ar	1000/Ar	1000/Ar	1000/NH_3
	Sintering conditions and properties			
Temperature (°C)[c]	1000/Ar	1850/N_2	1850/N_2	1600/N_2
Solid phase density (g/cm³)	2·33	3·32	3·33	2·84
Bulk density (g/cm³)	2·15–2·01	3·25	3·22	2·81
Open porosity (%)	6–10	—	—	—
Matrix-composition	$Si_{1.7}C_{1.0}N_{1.6}$[d]	β-Si_3N_4/24 wt% β-SiC	β-Si_3N_4/10 wt% β-SiC	Si_2N_2O

[a] 10 wt% Y_2O_3 and 5 wt% Al_2O_3.
[b] 2·8 wt% AlN, 7·8 wt% Y_2O_3 and 1·4 wt% Al_2O_3.
[c] 1 h isothermal hold at the final temperature. Sintering was conducted at 0·1 MPa gas pressure.
[d] The silicon carbonitride is amorphous according to X-ray and TEM investigations.

3.2 Characterization of the polymer-derived ceramics

3.2.1 PHMSN-derived monolithic silicon carbonitride (route A)

Generally, the volume shrinkage caused by the thermal decomposition of a polymeric compound (*P*) into a ceramic (*C*) with the simultaneous formation of gaseous reaction products (*R*) according to eqn (5)

$$P_{(s,l)} \rightarrow C_{(s)} + R_{(g)} \tag{5}$$

depends on the change in the density of the contributing phases and on the ceramic yield α (≤ 1). The yield α is defined as the ratio of the mass of the polymer-derived ceramic (M_C) to that of the applied polymer (M_P):

$$\alpha = \frac{M_C}{M_P} \tag{6}$$

The overall change in the volume (ΔV) can then be expressed in terms of the mass (M) and solid-phase density (D) of the condensed phases considered in eqn (5):

$$\Delta V = \frac{M_P(D_C - \alpha D_P)}{D_P D_C} \tag{7}$$

or:

$$\Delta V\,[\%] = \frac{D_C - \alpha D_P}{D_C} 100 \tag{8}$$

The polymer to ceramic transformation of shaped PHMSN bodies according to route A in Fig. 2 provided silicon carbonitride compacts with up to 94% rel. density and with the composition $Si_{1.7}C_{1.0}N_{1.6}$. In this case, the densities D_P, D_C, and the ceramic yield α were determined to be 1·22 g/cm³, 2·33 g/cm³, and 77%. From this, the calculated value ΔV of 59·7, however, is about 5% lower than the experimentally determined relative volume shrinkage of 65%. This finding suggests that additional densification processes occur during pyrolysis that enable the porous polymeric body to form dense ceramic materials, even at these low reaction temperatures (800–1200°C).

The SEM micrograph of a polished surface of PHMSN-derived silicon carbonitride bulk sample is shown in Fig. 3. It is evident that pore sizes up to 10–15 μm are present which is in accordance with the pore size distribution measurements from Hg pressure porosimetry.

In order to evaluate the microstructural features of amorphous silicon carbonitride, $Si_{1.7}C_{1.0}N_{1.6}$ obtained after pyrolysis of PHMSN at 1000°C in Ar, ESCA and analytical TEM investigations were performed. The ESCA results support a single phase amorphous material. The ESCA Si(2p)



Fig. 3. SEM micrograph of a polished surface of PHMSN-derived silicon carbonitride bulk material prepared according to route A.

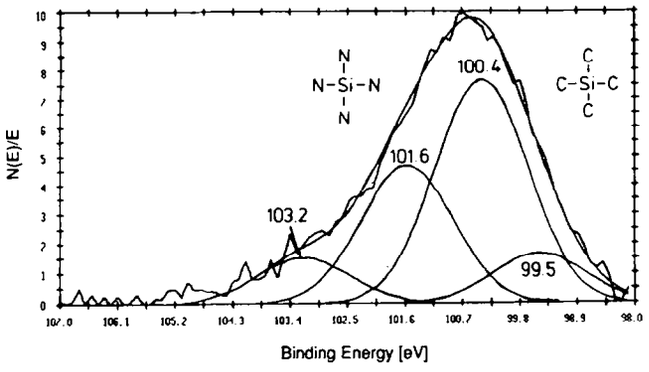


Fig. 4. ESCA Si(2p) spectrum of PHMSN-derived amorphous silicon carbonitride.

spectrum has to be deconvoluted using at least four Gaussian functions as shown in Fig. 4 indicating the presence of Si–N and Si–C bonds in the polysilazane derived material. The bonding energy at 99·5 and at 101·6 eV are associated with SiC_4- and SiN_4-units, respectively, whereas that at 100·4 eV is due to $SiN_{4-x}C_x$-units. The bonding energy located at 103·2 eV is related to the presence of oxygen contamination in the form of silica or silicon oxynitrides. Additionally, no SiC-shoulder can be assigned in the ESCA Si(2p) spectrum in contrast to reports for a mechanical Si_3N_4/SiC mixture.[31] The measured binding energy curve of the N(1s) electron can be deconvoluted into at least two Gaussian peaks with maxima located at 397·4 eV and 398·6 eV corresponding to N–Si and N–C bonds, respectively. The deconvoluted C(1s) peaks clearly indicate the presence of C–C (284·2 eV), C–N (286·4 eV), and Si–C bonds (282·7 eV).

Analytical TEM investigations revealed that the pure silicon carbonitride is completely amorphous and a single phase material. No segregations of C, SiC or Si_3N_4 could be found by the evaluation of the microstructure by means of electron spectroscopic imaging (ESI) in an energy filtering TEM.[32] Even after long annealing times in the order of 50 h under 0·1 MPa N_2 at 1000°C, the material remained amorphous without any phase partitioning. Accordingly, the synthesized silicon carbonitride can be considered as a metastable solid solution. It is worth to mention that such a material cannot be produced by conventional synthesis, i.e. by mixing and heat-treating of SiC and/or C with Si_3N_4.

The determined solid-phase density D_C = 2·33 g/cm^3 of the silicon carbonitride is significantly lower than that of the thermodynamically stable phases of $Si_3N_4$and SiC ($\rho \sim 3{\cdot}2$ g/cm^3). According to the rule of mixtures, solid-phase densities between 2·97 and 3·14 g/cm^3 were expected if the sample is considered to contain amorphous and/or crystalline Si_3N_4, SiC and C (graphite). The low density cannot be explained by nanoporosity since gas adsorption measurements clearly indicated the formation of fully dense silicon carbonitride powder. This phenomenon is associated with a highly disordered solid-phase structure and is in part caused by residual Si–H and C–H bonds which are still present in the material pyrolyzed at 1150°C in Ar as determined by infra-red investigations. In the infra-red spectrum, silicon carbonitride reveals broad vibration bands located at 1250–720 cm^{-1} and 600–415 cm^{-1} indicating the presence of Si–N- and Si–C-bonds. In addition, sharp absorption bands located at 2950–2850 cm^{-1} and at 2164 cm^{-1} are due to aliphatic C–H- and Si–H bonds. The relative openness of amorphous SiC-based ceramics prepared by polymer pyrolysis has also been reported by Soraru *et al.*[33] The solid-phase density of the silicon carbonitride increased from 2·33 g/cm^3 at 1000°C to 2·40 g/cm^3 at 1400°C and is related to the successive loss of residual hydrogen.

The Vickers Hardness, HV, of silicon carbonitride synthesized at 1150°C was determined to be 10 GPa in a sample with 6% open porosity. The median value of the fracture strength σ_B is of the order of 170 MPa with a maximum value of 370 MPa.

Crystallization of $Si_{1{\cdot}7}C_{1{\cdot}0}N_{1{\cdot}6}$ started at temperatures exceeding 1400°C and gave α-Si_3N_4 and α/β-SiC. In contrast, amorphous Si_3N_4 obtained by the mineralization of PHMSN under NH_3 was completely crystallized to α-Si_3N_4 at 1200°C and 30 min soaking time. This behavior reveals a significantly higher thermal stability of the compositionally more complex ternary system Si–C–N. The high thermal stability of precursor-derived Si–C–N ceramics was also observed by D. Mocaer *et al.*[34] The crystallization was accompanied by a weight loss reaching 10·3% after 50 h annealing of the silicon carbonitride bulk material at 1600°C in nitrogen and is associated with the solid state reaction of carbon with silicon nitride partitioned during the course of heat-treatment. Thermodynamically, the excess carbon reacts at temperatures exceeding 1440°C with the Si_3N_4-particles under 0·1 MPa nitrogen pressure according to the following reaction:[35]

$$Si_3N_4 + 3C \rightarrow 3SiC + 2N_2 \qquad (9)$$

3.2.2 PCMSN-derived β-Si_3N_4/24 wt% β-SiC-composites and Si_3N_4-ceramics (route B)

Silicon carbonitride powder with the composition $Si_{1{\cdot}7}C_{1{\cdot}0}N_{1{\cdot}5}$ derived from PCMSN was liquid phase sintered according to route B (Fig. 2, Table 3) with Al_2O_3 and Y_2O_3 (weight ratio = 1 : 2) as sintering aids and at 0·1 MPa N_2-pressure resulting in the in situ formation of β-Si_3N_4 and β-SiC polycrystals as the matrix phase. During the course of densification, β-Si_3N_4- and Si_2N_2O-particles crystallized first as could be determined by

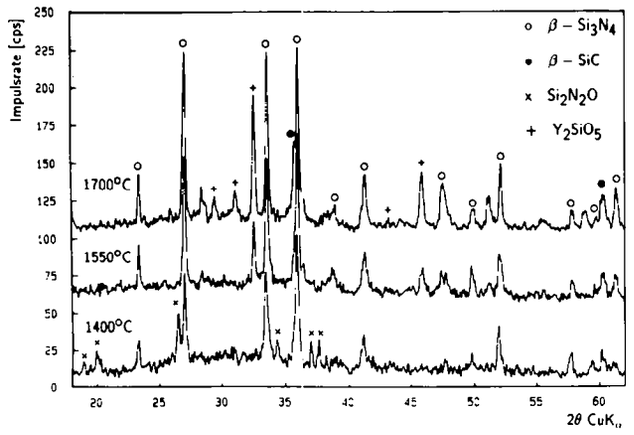


Fig. 5. X-ray diffractograms of cold-isostatically pressed PDSCN powder heat-treated at various temperatures in N_2 without isothermal hold in the presence of 10 wt% Y_2O_3 and 5 wt% Al_2O_3 according to process B.

sintering the cold-isostatically pressed silicon carbonitride powder samples without any holding time at various temperatures. The X-ray diffractograms shown in Fig. 5 clearly show that β-SiC begins to crystallize at temperatures above 1500°C, whereas β-Si_3N_4 is identified at $T \leq 1400$°C. The intermediate generation of silicon oxynitride Si_2N_2O evident at 1400°C cannot be observed at higher temperatures. Crystallization of a part of the amorphous oxide phase in the form of Y_2SiO_5 was also observed in the material annealed at $T \geq 1550$°C. The sintering of the amorphous Si-, C-, and N-containing starting powder has been proposed to proceed via a particle disintegration mechanism.[7] These findings are in accordance with the TEM studies of the microstructure developed at different final temperatures during liquid phase sintering of silicon carbonitride powder.[32]

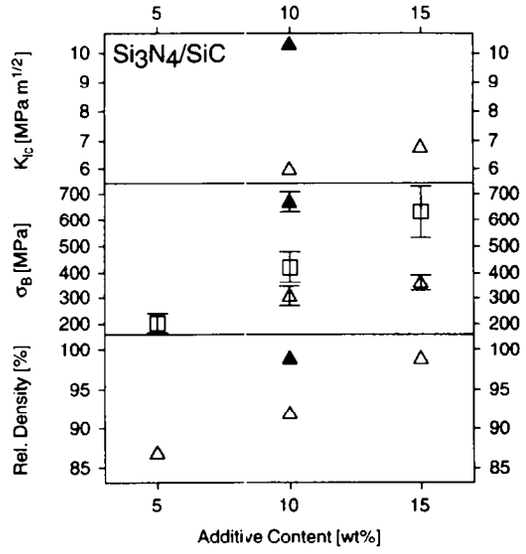


Fig. 6. Sintering densities, fracture strength and toughness (average values) of PCMSN-derived Si_3N_4/SiC-composite versus additive content (Y_2O_3/Al_2O_3 = 2:1). Δ = samples liquid phase sintered at 1850°C and 0·1 MPa N_2-pressure for 1 h according to process B; the filled triangles represent the values of samples which have been subsequently gas-pressure sintered at 1900°C and 10 MPa N_2-pressure for 1 h; □ = fracture strength values measured at 1000°C in air.

In Fig. 6, relative densities and some mechanical properties of the densified samples are shown as a function of additive content. The highest relative density was obtained by the addition of 15 wt% oxides. In the case of 10 wt% sintering aids, similar high densities were measured after gas-pressure sintering of presintered samples. The flexural strength significantly increased from 320 MPa at room temperature to 635 MPa at 1000°C. A maximum value of 700 MPa was attained. This phenomenon may be associated either with the reduction of internal stresses at elevated temperatures or with the reduction of surface defects owing to crack blunting via oxidation during the measurements in air. At temperatures exceeding 1100°C, the strength value strongly decreased due to the beginning of softening of the glassy phase. The room-temperature strength was improved from 280 to 650 MPa for the gas pressure sintered sample. The K_{IC} value was determined to be 10·2 MPa$\sqrt{m}$ which is nearly twice the fracture toughness measured in the presintered material (5·8 MPa$\sqrt{m}$). In Fig. 7, the resulting microstructure and the crack path induced by a Vickers indenter are shown. Due to gas-pressure sintering at a relatively high temperature (1900°C) large rod-like grain sizes up to 40 μm in length were found in

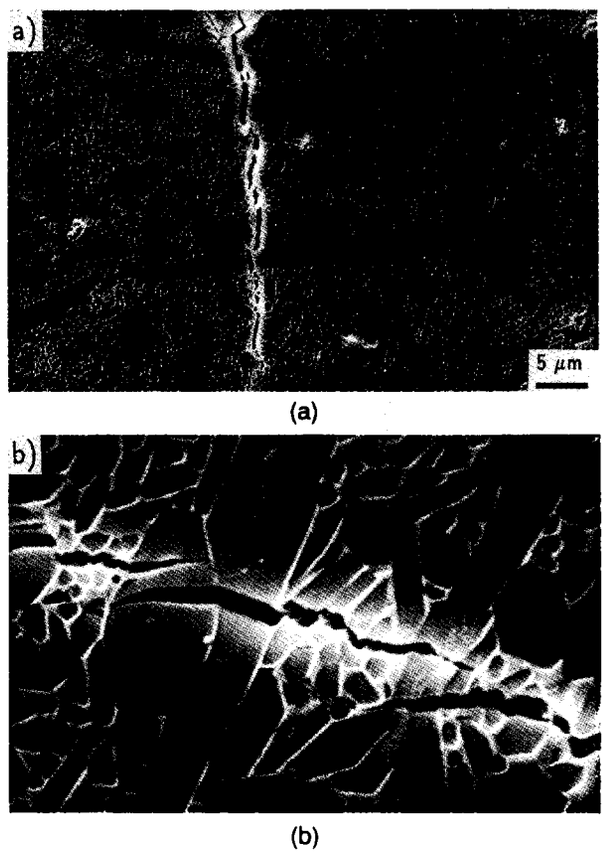


Fig. 7. (a) SEM micrograph of the microstructure of gas pressure and liquid phase sintered β-Si_3N_4/β-SiC composite according to route B (polished and plasma etched surface). The crack has been induced by a Vickers indenter. The micrograph (b) shows a section at higher magnification indicating the occurrence of crack branching. For sintering conditions see Fig. 6.

the β-Si_3N_4/β-SiC microstructure. The rod-like growth is typical for β-Si_3N_4 sintered with 15 wt% additives in the weight ratio Y_2O_3/Al_2O_3 = 2:1.[36] Besides these large, elongated particles, small crystallites in the range of 0·5 μm to several microns were also present.

The crack path induced by a Vickers indenter in the gas pressure sintered sample exhibited both intergranular and transgranular fracture modes as can be seen in Fig. 7. In addition, the crack path reveals the presence of crack branching (Fig. 7(b)) and indicates microcracking causing the relatively high fracture toughness measured. The distance between two crack branches is estimated to be about 5 μm. It is evident that the cracks always stop in a region consisting of small grains as can be also seen in Fig. 7(b). Further investigations on the toughening mechanism operating in the polymer-derived Si_3N_4/SiC-composites are in progress.

The ammonolysis of PCMSN at 1000°C resulted in the formation of amorphous silicon nitride (Fig. 1). Densification of the PCMSN-derived amorphous Si_3N_4-powder (PDSN) containing yttria and alumina as the sintering aids gave dense polycrystalline Si_3N_4-ceramics. X-ray diffraction patterns of the densified samples revealed the presence of the β-modification of Si_3N_4 exclusively. The final densities and mechanical properties vs. the additive content of the sintered PDSN-powder are given in Fig. 8. Figure 9 shows a typical microstructure of the sample densified at 1750°C containing 15 wt% additives. A crack path induced by a Vickers indenter reveals predominant intergranular fracture mode as is represented in Figure 9(b).

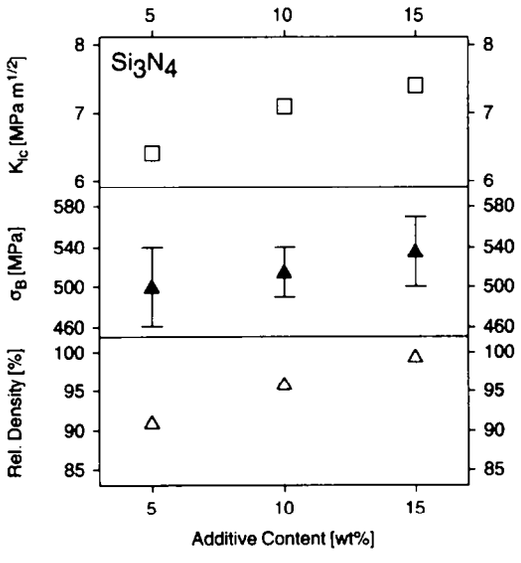


Fig. 8. Mean values of sintering densities, fracture strength and toughness of PCMSN-derived Si_3N_4-ceramic versus additive content (Y_2O_3/Al_2O_3 = 2:1). Sintering was conducted according to process B at 1750°C for 1 h under 0·1 MPa N_2.

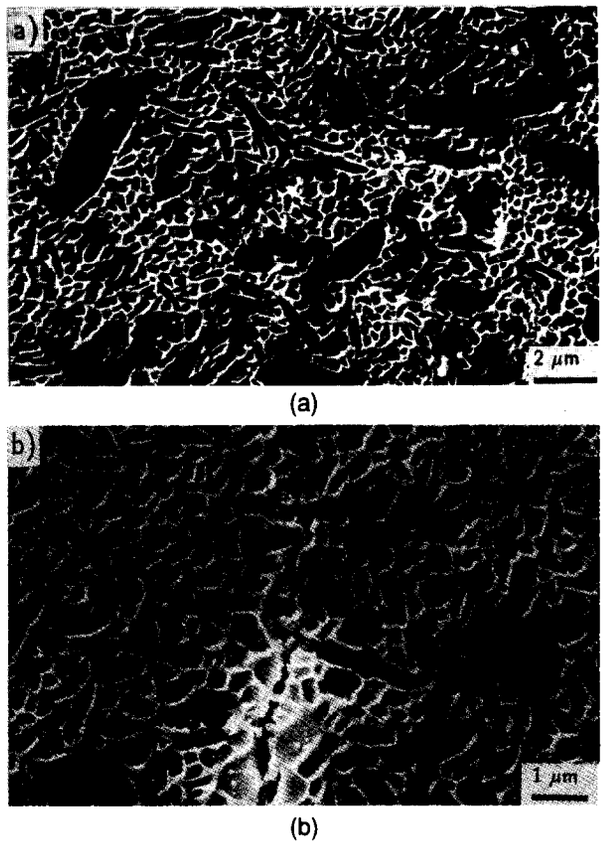


Fig. 9. (a) SEM micrograph of a polished and plasma etched section of the PCMSN derived Si_3N_4 microstructure. The micrograph (b) shows the fracture path induced by a Vickers indenter. The sample was liquid phase sintered after route B at 1750°C for 1 h and 0·1 MPa N_2 pressure with 10 wt% Y_2O_3 and 5 wt% Al_2O_3 as sintering additives.

3.2.3 PCMSN-derived Si_2N_2O (route B)

Besides SiC and Si_3N_4, Si_2N_2O is a potential material appropriate for high-temperature engineering applications. Thermodynamic calculations indicate a superior stability in oxidizing environments,[37,38] compared to Si_3N_4 and SiC. Generally, the pressureless densification of Si_2N_2O-powders is difficult due to its decomposition[39] at temperatures above 1580°C according to eqn (10)

$$3Si_2N_2O \rightarrow 3SiO + Si_3N_4 + N_2 \qquad (10)$$

Therefore, Si_2N_2O-materials with relative densities higher than 95% can only be obtained by hot or hot isostatic pressing of Si_3N_4 and SiO_2 powders at temperatures greater than 1800°C.[38] The use of double oxide sintering aids such as a combination of Al_2O_3 with Y_2O_3 lowers the eutectic temperature and ensures liquid phase sintering yielding final relative densities up to 93%.[39]

We found that PCMSN-derived amorphous silicon oxynitride can be densified at 1600°C in 0·1 MPa nitrogen atmosphere up to 97 and 99% of relative density in the presence of 10 and 15 wt% oxide additives (Figs 10 and 11), respectively. According to X-ray diffraction analysis of the

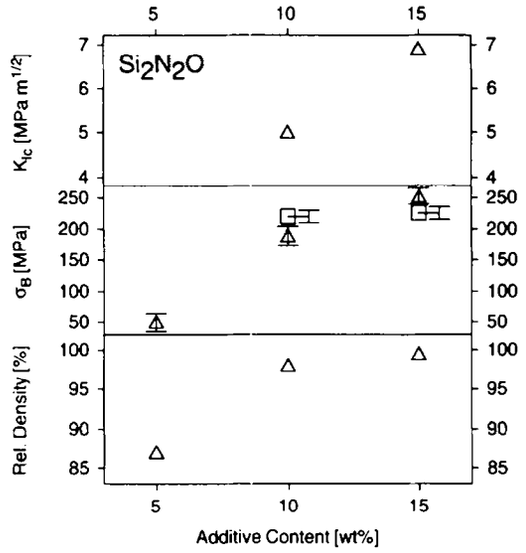


Fig. 10. Average values of sintering densities, fracture strength and toughness of PCMSN-derived Si_2N_2O-ceramic versus additive content (Y_2O_3/Al_2O_3 = 2:1) prepared after process B. Δ = samples sintered at 1600°C for 1 h and 0·1 MPa N_2-pressure; □ = fracture strength values measured at 1000°C in air.

densified sample, the amorphous powder crystallizes to Si_2N_2O, exclusively. No diffraction lines due to silicon nitride polymorphs, indicating the decomposition of the oxynitride phase, could be detected up to 1600°C (Fig. 12). At higher temperatures, β-Si_3N_4 is generated as the crystalline phase. Thermal gravimetric investigations in combination with a mass spectrometer (TGA–MS) of amorphous Si_2N_2O under 0·1 MPa He pressure revealed that the evolution of SiO with m/e = 44 was already detected in small amounts at $T \geq 1400$°C indicating the starting decomposition of the material. Owing to the reduced nitrogen pressure under these conditions, the decomposition of Si_2N_2O occurred at lower temperatures.

The diagrams depicted in Fig. 10 show the relative densities, the mechanical strength, and the K_{IC}

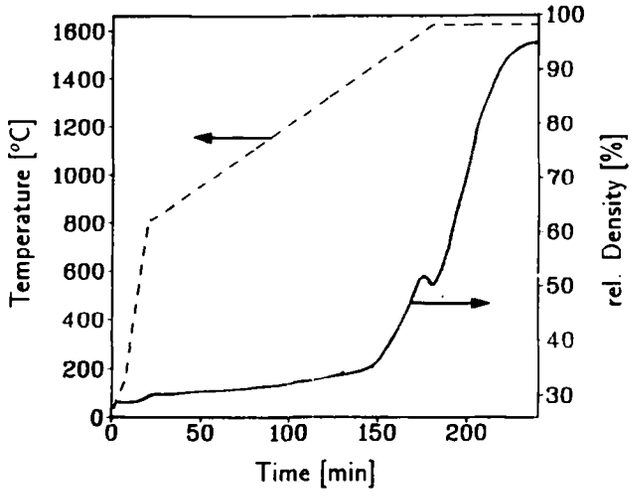


Fig. 11. Density and temperature versus time during sintering according to route B under 0·1 MPa N_2 of PCMSN derived amorphous Si_2N_2O-powder. 10 wt% Y_2O_3 and 5 wt% Al_2O_3 have been used as sintering additives.

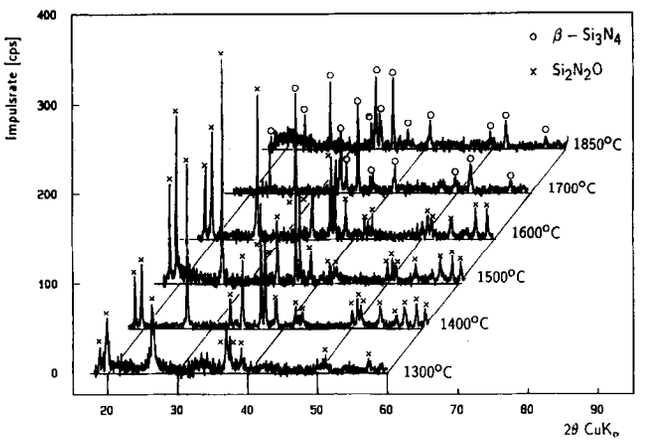


Fig. 12. X-ray diffractogramms of amorphous Si_2N_2O heat-treated for 15 min at various temperatures in the presence of 6·66 wt% Y_2O_3 and 3·33 wt% Al_2O_3 under 0·1 MPa N_2.

values of the sintered Si_2N_2O-material versus the amount of sintering aids. Depending on the final density, the mechanical strength values at room temperature are in the range of 205 (ρ = 97%, 10 wt% additives) and 230 MPa (ρ = 99%, 15 wt% additives) and are retained up to 1000°C. At higher temperatures, the fracture strength rapidly decreases.

3.2.4 α-Si_3N_4-powder/20 wt% PMPS-blend (route C)
The high linear shrinkage of up to 28% found during polymer to ceramic transformation of compacted polysilazane powders (route A in Fig. 2) can be significantly reduced by mixing the polymeric fraction with inreactive powders. Thus a α-Si_3N_4-powder/20 wt% PMPS-mixture prepared according to route C in Fig. 2 and pyrolysed at 1000°C in Ar showed a linear shrinkage of up to 3–4%. The sintered composite sample contained 10 wt% SiC in situ generated from the polysilane PMPS used as determined by chemical analysis (Table 2).

According to TEM studies, the resulting microstructure of the liquid phase sintered samples revealed the presence of SiC crystallites with grain sizes in the range between 20 and 200 nm embedded either intra- or intergranular in the Si_3N_4 matrix; the structure is described in detail in Part II.[32]

Pyrolysis of pure PMPS at 1000°C in Ar without Si_3N_4-powder and without additives gave a ceramic with a molar composition $SiC_{2.0}$. Crystallization started at $T \geq 1200$°C forming nano-sized β-SiC as the crystalline phase.[40] The median crystallite size was derived from the line broadening of the SiC(100)-reflexions in the X-ray powder diffractogram and is plotted versus temperature in Fig. 13. As can be seen in Fig. 13, the grain size of β-SiC heat-treated between 1200 and 2000°C is in the nm-range. Consequently, the β-SiC grain

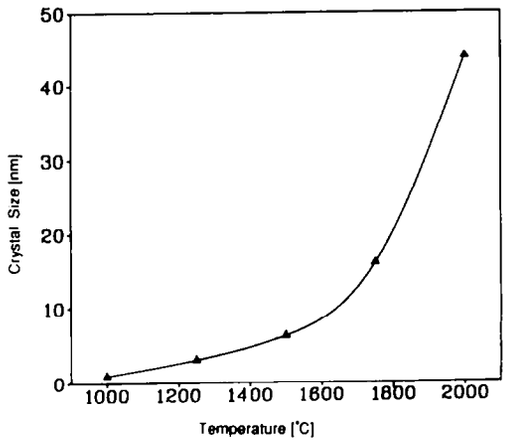


Fig. 13. Temperature dependence of the PMPS-derived β-SiC crystallite size. Isothermal hold at each temperature = 1 h in Ar.

growth is retarded which is related to the excess carbon content present in the polysilane derived SiC (Table 2). In addition, no phase transformation from the β- to the α-modification was observed even by annealing the sample at 2000°C in Ar.

4 Conclusions and outlook

The present studies have shown that dense or near dense silicon-based non-oxide bulk ceramic materials can be synthesized from organosilicon compounds under the following conditions:

(1) The synthesis of crack-free silicon carbonitride ($Si_{1.7}C_{1.0}N_{1.6}$) ceramic parts with 94% rel. density by the direct polymer to ceramic transformation process was demonstrated. An infusible polysilazane prepared by the thermal cross-linking of a commercially available organoelement polymer was used as the starting material. The annealed polymer is ball-milled and sieved, isostatically pressed to polymer green bodies and finally pyrolyzed in Ar. The method is especially suitable for the fabrication of bulk ceramics other than fibers. The main advantages of this novel process compared to the conventional method for the production of Si_3N_4- and SiC-based ceramics are:
- low processing temperature of about 1000°C
- densification without sintering aids,
- low solid-phase density (2·33 g/cm^3) of the resulting ceramic, and
- synthesis of metastable solid solutions in the ternary system Si–C–N.

As-synthesized silicon carbonitride bulk ceramic was amorphous and single phase. The material produced was thermally stable in nitrogen up to 1400°C, had a hardness, HV, of 10 GPa, and a maximum bending strength value of 370 MPa determined in samples with 6% open porosity. Additive-free silicon carbonitride is expected to be a candidate material with high temperature creep resistance.

(2) Bulk ceramics based on crystalline polymorphs comprised of SiC, Si_3N_4, and Si_2N_2O were prepared by the liquid phase sintering of polymer-derived amorphous ceramic powders. Pyrolysis of polysilazanes at 1000°C in Ar gave metastable silicon carbonitride powders with homogeneous distribution of the constituents Si, C and N. During the course of the sintering of these powders attrition milled in isopropanol with Al_2O_3 and Y_2O_3 as oxide additives, the thermodynamically stable phases, β-Si_3N_4 and β-SiC, were formed *in situ* and dense Si_3N_4/SiC-composites were obtained. Similarly, dense Si_3N_4 and Si_2N_2O bodies were produced by the liquid phase sintering of amorphous Si_3N_4 powders obtained by pyrolysis of polysilazane in ammonia.

(3) Polysilane/silicon nitride powder blends have been used to reduce the high shrinkage associated with the density increase from the Si-polymer (ca. 1·1 g/cm^3) to the Si-ceramic (ca. 3·2 g/cm^3) during pyrolysis. The polysilane PMPS used in this work resulted in the *in situ* formation of $SiC_{2.0}$. During liquid phase sintering of the PMPS/Si_3N_4-powder mixture, β-SiC crystals were formed and were embedded inter- and intragranular in the Si_3N_4-matrix.

Due to the fact that Si-based polymers such as polysilanes and polysilazanes are now commercially available, the polymer pyrolysis process can be considered as an alternative method, with respect to the traditional technology, for the production of various Si-based non-oxide ceramics in large quantities. In addition, novel type of non-oxide ceramic materials such as the solid solutions of silicon carbonitrides and *in situ* crystallized Si_3N_4/SiC micro-, nano- and micro/nano-composites can be synthesized.

Acknowledgements

The work has been financially supported by the European Community under the contract No. BREU 0106-C-JR, the Keramikverbund Karlsruhe-Stuttgart, the Deutsche Forschungsgemeinschaft, Bonn, and the Fonds der Chemischen Industrie, Frankfurt, Germany. The authors thank the Hoechst AG, Frankfurt, Germany, for providing the poly(chlorohydridomethyl)silazane (PCMSN) and

Prof. Dr W. F. Maier, Max-Planck-Institut für Kohlenforschung, Mülheim/Ruhr, Germany, for the gas adsorption measurements. The editor, Prof. Dr R. J. Brook, is gratefully acknowledged for his critical revision of the manuscript.

References

1. Winter, G., Verbeek, W. & Mansmann, M., *Shapes of homogenous mixtures of silicon carbide and methods of their production*, Deutsche Offen. 2 243 527 (1974), in German. Verbeek, W. & Winter, G., *Shapes of silicon carbide and methods for their preparation*, Deutsche Offen. 2 236 078 (1974), in German.
2. Yajima, S., Hayashi, J., Omori, M. & Okamura, K., Development of a silicon carbide fiber with high tensile strength. *Nature*, **261** (1976) 683.
3. Seyferth, D. & Wiseman, G., High yield synthesis of Si_3N_4/SiC ceramic material by pyrolysis of a novel polyorganosilazane. *J. Am. Ceram. Soc.*, **67** (1984) C-132.
4. Seyferth, D., Wiseman, G. & Prud Homme, C., A liquid silazane precursor to silicon nitride. *J. Am. Ceram. Soc.*, **66** (1983) C-13.
5. Legrow, G. E., Lim, T. F., Lipowitz, J. & Reaoch, R. S., Ceramics from hydridopolysilazane. *Am. Ceram. Soc. Bull.*, **66** (1987) 363.
6. Wynne, K. J. & Rice, R. W., Ceramics via polymer pyrolysis. *Ann. Rev. Mater. Sci.*, **14** (1984) 297.
7. Riedel, R., Seher, M. & Becker, G., Sintering of amorphous polymer-derived Si. N and C containing composite powders. *J. Europ. Ceram. Soc.*, **5** (1989) 113.
8. Niihara, K., New design concept of structural ceramics — ceramic nanocomposites —. *J. Ceram. Soc. Japan*, **99** (1991) 974.
9. Blum, Y. D., Schwartz, K. B. & Laine, R. M., Preceramic polymer pyrolysis. *J. Mat. Sci.*, **24** (1989) 1707.
10. Wakai, F., Kodoma, Y., Sakaguchi, S., Murayama, N., Izaki, K. & Niihara, K., A superplastic covalent crystal composite. *Nature*, **344** (1990) 421.
11. Riedel, R., Passing, G., Schönfelder, H. & Brook, R. J., Synthesis of dense silicon-based ceramics at low temperatures. *Nature*, **355** (1992) 714.
12. Riedel, R., Alternative routes for the preparation of ceramic materials. *Ingenieur-Werkstoffe*, **3** (1991) 71, in German.
13. Interrante, L. V., Carpenter, L. E., Whitmarsh, C., Lee, W., Garbauskas, M. & Slack, G. A., Studies of organometallic precursors to aluminium nitride. In *Better ceramics through chemistry II, MRS Symposia Proceedings* Vol. 73, eds C. J. Brinker, D. E. Clark & D. R. Ulrich, MRS, Pittsburgh, PA, 1986, p. 359.
14. Riedel, R., Petzow, G. & Klingebiel, U., Characterization of AlN powder produced by the reaction of $AlCl_3$ with hexamethyldisilazane. *J. Mater. Sci. Lett.*, **9** (1990) 222.
15. Riedel, R., Bill, J. & Passing, G., A novel carbon material derived from pyridine–borane. *Adv. Mater.*, **3** (1991) 551.
16. Riedel, R., Passing, G. & Petzow, G., Influence of pyridine borane on the sintering behaviour and properties of α-silicon carbide. *J. Am. Ceram. Soc.*, **74** (1991) C-642.
17. Bill, J., Riedel, R. & Passing, G., Amin-boranes as precursors for boron carbonitride. *Z. Anorg. Allg. Chem.*, **610** (1992) 83, in German.
18. Rye, R. R., Borek, T. T., Lindquist, D. A. & Paine, R. T., Chemical reactions during the thermal processing of borazene polymers. *J. Am. Ceram. Soc.*, **73** (1990) 1409.
19. Zhang, Z.-F., Babonneau, F., Laine, R. M., Mu, Y., Harrod, J. F. & Rahn, J. A., Poly(methylsilane) — A high ceramic yield precursor to silicon carbide. *J. Am. Ceram. Soc.*, **74** (1991) C-670.
20. Mazdiyasni, K. S., West, R. & David, L. D., Characterization of organosilicon-infiltrated porous reaction-sintered Si_3N_4. *J. Am. Ceram. Soc.*, **61**(11–12) (1978) 504.
21. (a) Renlund, G. M., Prochazka, S. & Doremus, R. H., Silicon oxycarbide glasses: Part I. Preparation and chemistry. *J. Mater. Res. Soc.*, **6** 2716 (1991). (b) Renlund, G. M., Prochazka, S. & Doremus, R. H., Silicon oxycarbide glasses: part II. Structure and properties. *J. Mater. Res. Soc.*, **6** (1991) 2723.
22. Rees, W. S. & Seyferth, D., High yield synthesis of B_4C/BN ceramic materials by pyrolysis of polymeric Lewis base adducts of Decaborane (14). *J. Am. Ceram. Soc.*, **88** (1988) C-194.
23. Seyferth, D. & Mignani, G., Preparation of Titanium Nitride and Titanium Carbinitride by the Preceramic Route. *J. Mater. Sci. Let.*, **7** (1988) 487.
24. Rice, G. W. & Woodin, R. L., Zirconium borohydride as a zirconium boride precursor. *J. Am. Ceram. Soc.*, **71** (1988) C-181.
25. Elschenbroich, C. & Salzer, A., In *Organometallics, a concise introduction*, VCH Weinheim, 1992, p. 7.
26. Kienzle, A. & Riedel, R., Synthesis of ceramic materials in the systems SiCB and SiCBN. *Proceedings of the Annual Meeting of the Deutsche Gesellschaft für Materialkunde*, 1–4 June, (1993), Friedrichshafen, Germany, in German.
27. Rochow, E. G., In *Introduction in the chemistry of silicones*, Verlag Chemie, Weinheim, 1952, in German.
28. Gerdau, T., Kleiner, H.-J., Peuckert, M., Brück, M. & Aldinger, F., Polymeric hydridochlorosilazane and methods for their preparation, Deutsche Offen. 37 337 27 (1989), in German. Peuckert, T., Vaahs, T., Brück, M. Ceramics from organometallic polymers. *Adv. Mater*, **2** (1990) 398.
29. Riedel, R., Strecker, K. & Petzow, G., *In situ* polysilane derived SiC particulates dispersed in Si_3N_4 composite. *J. Am. Ceram. Soc.*, **72** (1989) 2071.
30. Anstis, G. R., Chantikul, P., Lawn, B. R. & Marshall, D. B., A critical evaluation of indentation techniques for measuring fracture toughness: I. Direct crack measurements. *J. Am. Ceram. Soc.*, **64** (1981) 533.
31. Suzuki, M., Maniette, Y., Nakata, Y. & Okutani, T., Synthesis of silicon carbide–silicon nitride composite ultrafine particles using a carbon dioxide laser. *J. Am. Ceram. Soc.*, **76** (1993) 1195.
32. Mayer, J., Szabo, D. V., Rühle, M., Seher, M. & Riedel, R., Polymer-derived Si-based bulk ceramics, Part II: Microstructural characterization by electron spectroscopic imaging. *J. Europ. Ceram. Soc.*, **15** (1995) 717.
33. Soraru, G. D., Babonneau, F. & MacKenzie, J. D., Structural evolutions form polycarbosilane to SiC ceramic. *J. Mater. Sci.*, **25** (1990) 3886.
34. Mocaer, D., Pailler, R., Naslain, R., Richard, C., Pillot, J. P., Dunogues, J., Gerardin, C. & Taulelle, F., Si–C–N ceramics with a high microstructural stability elaborated from the pyrolysis of new polycarbosilazane precursor. *J. Mat. Sci.*, **28** (1993) 2615.
35. *JANAF Thermochemical Tables*, 3d ed., p. 14. Eds M. W. Chase, Jr., C. A. Davis, J. R. Downey, Jr., D. J. Fridup, R. A. McDonald & A. N. Syverud, *Journal of Physical Chemistry Reference Data*, 1985.
36. Krämer, M., Investigations of the growth kinetic of β-Si_3N_4 in ceramics and oxynitride glasses, Ph. D. Thesis, University of Stuttgart, Stuttgart, Germany, 1991, in German.
37. Boch, P. & Glandus, J. C., Elastic properties of silicon oxynitride. *J. Mater. Sci.*, **14** (1979) 379.
38. Laker, R., Reaction sintering and properties of silicon oxynitride densified by hot-isostatic pressing. *J. Am. Ceram. Soc.*, **75** (1992) 62.
39. O'Meara, C., Sjöberg, J., Dunlog, G. & Pompe, R., Oxidation of pressureless sintered Si_2N_2O materials. *J. Europ. Ceram. Soc.*, **7** (1991) 369.
40. Strecker, K., Ph.D. Thesis, University of Stuttgart, Stuttgart, Germany.

Journal of the European Ceramic Society **15** (1995) 717–727
© 1995 Elsevier Science Limited
Printed in Great Britain. All rights reserved
0955-2219/95/$9.50

0955-2219(95)00029-1

Polymer-Derived Si-Based Bulk Ceramics, Part II: Microstructural Characterisation by Electron Spectroscopic Imaging

Joachim Mayer,[a] D. Vinga Szabó,[a]* Manfred Rühle,[a] Martin Seher[b,c] & Ralf Riedel[d]

[a]Institut für Werkstoffwissenschaft, Max-Planck-Institut für Metallforschung, Seestr. 92, D-70174 Stuttgart, Germany
[b]Institut für Anorganische Chemie, Universität Stuttgart, Pfaffenwaldring 55, D-70550 Stuttgart, Germany
[c]Pulvermetallurgisches Laboratorium, Institut für Werkstoffwissenschaft, Max-Planck-Institut für Metallforschung, Heisenbergstr. 5, D-70569 Stuttgart, Germany
[d]Fachgebiet Disperse Feststoffe, Fachbereich Materialwissenschaft, Technische Hochschule Darmstadt, Hilpertstr. 31, D-64295 Darmstadt, Germany

(Received 2 August 1994; revised version received 7 February 1995; accepted 14 February 1995)

Abstract

The microstructure of polymer-derived Si-based ceramic materials was characterised with elemental distribution images produced by electron spectroscopic imaging. Depending on the processing conditions, a variety of different microstructures were obtained from the same precursor: without sintering additives, amorphous silicon carbonitride which is stable against crystallisation up to 1400°C is formed. In the presence of Al_2O_3 and Y_2O_3 as sintering additives, Si_3N_4/SiC-composite materials and Si_2N_2O ceramics are produced. Sintering a mixture of Si_3N4 powder with additional polysilane leads to a Si_3N_4/SiC-composite comprising nano-sized SiC inclusions in the Si_3N_4 grains. The development of the microstructure of the Si_3N_4/SiC composite materials was investigated as a function of the sintering temperature and of the concentration of the sintering additives. The observed microstructural changes lead to conclusions on the processes which occur during the sintering of the materials.

1 Introduction

A primary aim in the development of structural ceramics is to obtain control over both the mechanical properties and the macroscopic shape of the ceramic component. The mechanical properties of any material are governed by the microstructure. It is thus desirable to be capable of influencing the microstructure, via the starting material and the processing conditions, and to 'know' the result, via an efficient characterisation technique. In Part I[1] of our studies we have shown that preparing ceramic materials from polymer precursors potentially offers control of both the shape of the final ceramic product and of a variety of microstructural parameters, ranging from the synthesis of monolithic ceramics at low temperatures to the design of composite microstructures with several different phases.

In this paper we report on the results of our microstructural investigations on the polymer derived ceramic materials. In a systematic way we aim to gain insight into the relationships between microstructure and processing parameters. For characterisation, a new technique in transmission electron microscopy was used: electron spectroscopic imaging, (ESI).[2] With ESI, images showing the distribution of various elements in large specimen areas (several μm^2) at high resolution (2–3 nm) can be produced within short times (less than 1 min for one element). ESI is based on the use of an imaging energy filter and makes it possible to image the distribution of a certain element via the characteristic energy losses which an electron beam may suffer in inelastic scattering processes with the atoms in the sample. Hence, Energy Filtering Transmission Electron Microscopy (EFTEM) has become an important tool for the microstructural characterisation of composite microstructures.

In the last ten years considerable research has been devoted to the evaluation of microstructures in Si_3N_4 and SiC ceramics. For the sintering of Si_3N_4 ceramics, Al_2O_3 and Y_2O_3 are used as sintering additives in most cases. Sintering occurs via a liquid phase mechanism in which the solution of α-Si_3N_4 and reprecipitation of β-Si_3N_4 play an important role. Systematic studies with various

*Present address: Kernforschungszentrum Karlsruhe, IMF 3, Postfach 3640, D-76201 Karlsruhe, Germany.

amounts of sintering additive were carried out by Hayashi *et al.*[3] They found that diffusion through the liquid phase is the rate-limiting step in the growth of the Si_3N_4 crystals. Boberski *et al.*[4] investigated the intermediate sintering stages by quenching samples during the sintering process and found that the major densification step is correlated with the melting of the sintering additives at 1389°C and the $\alpha \rightarrow \beta$ transition occurring at 1615°C. Sintering of SiC with Al_2O_3 and Y_2O_3 as sintering additives has first been reported by Omori and Takei.[5] In a systematic TEM study, Kleebe[6] compared SiC and Si_3N_4 ceramics sintered with Al_2O_3 and Y_2O_3 and found that, in contrast to Si_3N_4, the SiC grains are not wetted by the liquid phase formed by the sintering additives. The microstructure of Si_3N_4/SiC-composite materials was investigated by several different groups.[7-11] The densification which can be obtained is significantly influenced by the amount of SiC added.[8] Higher contents of SiC particles inhibit complete densification and a number of pores remain in the final material. Indications for solution and reprecipitation of the SiC particles could only be found at temperatures above 1700°C. Under special conditions, inclusion of the SiC particles in the Si_3N_4 grains could be observed[9-11] which leads to an improvement of the mechanical properties. In the present paper we report on the sintering mechanisms observed in the Si_3N_4/SiC-composite materials prepared from polymer precursors. The temperature dependence of the sintering processes was studied by varying the maximum temperature. The dependence of the microstructure on the concentration of sintering additives was investigated by varying the amount of Al_2O_3 and Y_2O_3 which was added.

2 Experimental

2.1 Energy filtering TEM

In analytical electron microscopy the two methods mainly used, electron energy loss spectroscopy (EELS) and energy dispersive X-ray analysis (EDX), are based on focusing the probe on a small area of interest. The spectroscopic data are then analysed for each probe position. Two-dimensional chemical information can only be obtained by stepping the probe across the sample. For the light elements, EELS analysis is preferable because it offers a much higher detection efficiency. In principle, any EELS spectrometer can be treated as being part of the electron optical system of a TEM with the important property that the information on the image or diffraction pattern of the illuminated sample area is not completely lost but only heavily distorted while the electrons pass through the spectrometer. Within the past ten years, successful attempts have been made to correct these distortions electron-optically. One possibility is to combine four magnetic prisms in an Omega-like geometry where most of the electron optical aberrations are corrected by symmetry.[12] A different approach is to correct the distortions caused by one sector-magnet with an appropriate number of quadrupole and sextupole corrector elements.[13]

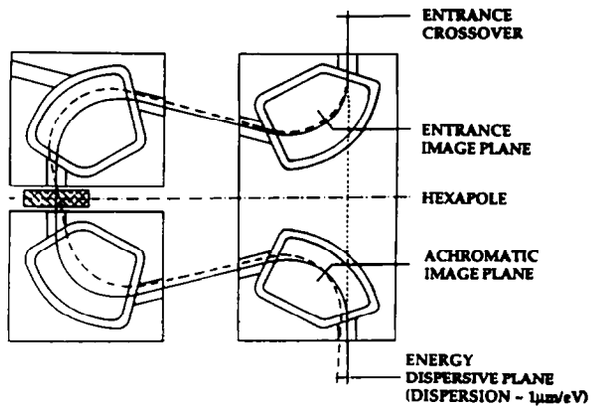


Fig. 1. Schematic drawing of the Omega filter. Through the symmetrical arrangement of magnetic prisms an image is transferred from the entrance image plane to the achromatic image plane. An energy loss spectrum of the illuminated sample area is formed in the energy dispersive plane.

In the present studies we have used a Zeiss EM 912 Omega which is the first commercially available EFTEM with an imaging Omega filter.[14] The design of the Omega filter is schematically shown in Fig. 1. An imaging filter combines two properties: (1) The symmetrical arrangement of prisms transfers an image without distortions to the achromatic image plane. (2) The energy dispersion of the whole arrangement of prisms causes the paths of electrons with different energies to separate and to form an energy loss spectrum at the exit surface of the Omega filter. In this energy dispersive plane, electrons within a defined energy loss interval $\Delta E_1 < \Delta E < \Delta E_2$ can be selected by inserting an energy selecting slit. Only these electrons will contribute to a magnified 'ESI' image which can be produced by focusing the following lenses of the projector system to the achromatic image plane.

2.2 Electron Spectroscopic Imaging (ESI)

Inner-shell excitation of the atoms by the beam electrons leads to characteristic edges in the energy-loss spectrum (Fig. 2). For energy losses above 100 eV the edges are located on top of a nearly exponentially decreasing background and the onset energies of each edge can be used to identify the individual chemical elements. The concentration of an element can be determined from an EELS spectrum if the pre-edge background is extrapolated and subtracted from the signal

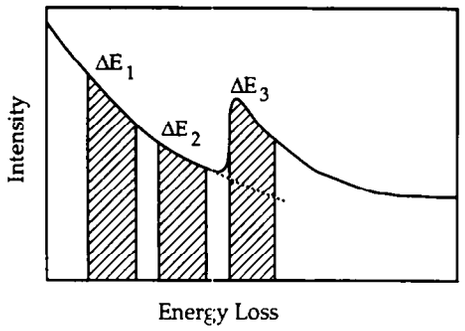


Fig. 2. Illustration of the three-window technique used to produce elemental distribution images. With the two ESI images acquired in front of the edge, an extrapolated background can be calculated and subtracted from the third image containing the element specific signal.

obtained above the edge. In ESI images this has to be done for each individual pixel. The easiest method for background subtraction, the three window technique, is illustrated in Fig. 2. Two ESI images are acquired in the background region before the edge and the extrapolated background is then subtracted from the ESI image containing the signal above the edge. As a result the difference image only contains intensity in the areas where the corresponding element is present in the sample and thus maps the distribution of this element. In the three window technique, however, the intensity in the difference image is not only depending on the concentration of the element but may also vary with thickness or the Bragg orientation of crystalline grains. Owing to the low intensity of the individual ESI images (up to a factor of 100–1000 less than the corresponding bright field image) the difference image will also contain considerable noise which makes it impossible to detect elements in very small concentrations (below 1 at%). The noise in the elemental distribution images can be reduced by special image processing techniques, which may result in a loss of resolution. The detection limits in elemental distribution images are as low as 1–2 monolayers, e.g. for segregants at grain boundaries.[15] The resolution limits are in the order of 2–5 nm, depending on the element and its concentration.

In the three window technique, the optimum position of the energy windows and their width depends on several parameters: (1) the intensity in the energy loss spectrum which decreases strongly with increasing energy loss; (2) the shape of the edge which only shows a sharp onset for the light elements, and (3) the width of the unstructured background region before the edge. The width and positions of the windows which we have used have been determined in an empirical way and are listed in Table 1. In the case of the Si–K edge at 1836 eV the slope of the decreasing background is so small that it can be extrapolated by a horizontal line. In this case, only one background image has to be acquired which is then simply subtracted from the image containing the signal.

Table 1. List of elements investigated by ESI. The energy losses of the edges, ΔE, and the centre of the windows, $\Delta E_1 ... \Delta E_3$, are given in eV.

Element	*Edge*	ΔE	ΔE_1	ΔE_2	ΔE_3	*Window width* ∂E
C	K	284	255	275	295	15
N	K	401	370	390	410	15
O	K	532	500	520	540	15
Si	K	1836	1740	1810	1880	50
Si	K	1836	—	1800	1880	50
Si	L	199	180	194	208	10

In most of the cases, the distribution of several elements will be studied in one sample area. The resulting elemental distribution images can be combined in one image by using different colours for each element and overlaying the individual images. If two or more of the elements under investigation are present in one sample area mixed colours will occur. Mixed colours thus reveal important information on the occurrence of phases which contain more than one of the elements under investigation.

2.3 High-resolution TEM

For some of the materials analysed, high-resolution TEM has been employed in order to distinguish between structurally amorphous and microcrystalline material. These studies were performed on a Jeol 4000 EX operated at 400 kV.

2.4 TEM specimen preparation

The samples sintered at lower temperatures or at a lower concentration of the sintering additives exhibit extremely high brittleness and thus low mechanical stability. Self-supporting TEM specimens could not be made out of these brittle samples and a special technique had to be applied. The method is based on the use of special cylindrical holders which are made out of alumina. The holders contain a slit into which a thin slice of the material (200–300 μm thick) is glued which gives the necessary mechanical support to the brittle material. Subsequently the holders are sectioned into thin discs from which TEM samples are made in the conventional way by polishing, dimpling and ion milling. Details of the technique were published elsewhere.[16]

3 Results and Discussion

As described in Part I of this work,[1] the Si-based materials produced by pyrolysis of Si-containing

Table 2. Empirical formulae of the polymeric precursors used and molar ratio of the final ceramic products (for details see Part I[1])

Empirical formulae†	*Abbreviation*	*Final ceramic material*††
$[-CH_3SiH-NH-]_m[-(CH_3)_2Si-NH-]_n$	PHMSN	$Si_{1.7}C_{1.0}N_{1.6}$
$[-CH_3SiH-N=]_m[-CH_3SiCl-N=]_n$	PCMSN	$Si_{1.7}C_{1.0}N_{1.5}$
$[[(CH_3)_2Si]_5[CH_3Si(C_6H_5]]_n$	PMPS	$SiC_{2.0}$

†Simplified formulae derived from analytical measurements.
††Composition obtained after pyrolysis of the precursor at 1000°C under Ar atmosphere.

polymer precursors can be classified according to the resulting microstructure. Monolithic silicon carbonitrides which consist entirely of an amorphous phase can be produced directly by pyrolysis of the compacted polymer. Dense ceramic composites formed by the crystalline phases Si_3N_4, Si_3N_4 containing SiC, or Si_2N_2O can be produced by adding sintering additives prior to pyrolysis. Both the chemistry of the metal–organic precursors and of the oxidic sintering additives can be varied in wide ranges with resultant changes in the microstructure. For the different precursors the following abbreviations will be used: poly(hydridomethyl)-silazane = PHMSN, poly(chlorhydridomethyl)silazane = PCMSN, poly(methylphenyl)silane = PMPS. The chemical formulae of the polymers have been derived from analytical investigations and are summarised in Table 2. A mixture of Al_2O_3 and Y_2O_3 in various amounts has been used as sintering additives in all cases.

3.1 PHMSN-derived monolithic Silicon Carbonitride

The monolithic silicon carbonitride was prepared by pyrolysis of the shaped infusible polysilazane precursor (PHMSN) at 1000°C under argon. Details of the preparation and characterisation of the material in terms of density and porosity are described in Part I. The TEM investigations showed that the sample material contains pores with diameters between 100 and 1000 nm. By SEM the existence of some larger pores with diameters of up to 10 μm could be seen. By electron diffraction in the TEM it could be verified that the samples are completely amorphous. The analysis of EELS spectra confirmed the presence of Si, N and C in the amorphous ceramic material while oxygen was below the detectivity limit (< 1 at%).

In Fig. 3, a TEM bright field image of the amorphous silicon carbonitride is compared with the ESI images obtained for C and N. The intensity variation in both ESI images is caused by the thickness changes visible in Fig. 3(a). In very thin areas of the specimen, e.g. close to the edge of the sample, the ESI image intensity is low due to the small number of atoms present. For increasing thickness, but below the mean free path for inelastic scattering, the intensity in the ESI images increases. Finally, for thicknesses above 20–30 nm, the intensity decreases again due to the occurrence of multiple inelastic scattering, which increases the background but decreases the intensity gain at the onset energy of an edge in the energy loss spectrum. However, in Figs 3(b) and (c) the same intensity ratio is always obtained for areas of constant thickness. Thus, the distribution of C and N in the amorphous material is homogeneous down to the resolution limit of about 2 nm. No indication for the precipitation or nucleation of Si_3N_4, SiC or pure carbon and elemental silicon was found. According to these electron microscopic findings, the polysilazane-derived silicon carbonitride can be described as a silicon-based amorphous ceramic containing $SiN_{4-x}C_x$ units with $0 < x < 4$.

Finally, quantitative elemental analytical investigations (for experimental details see Part I,[1]) yielded molar ratios which can be represented by the empirical formula $Si_{1.8}N_{1.6}C_{1.0}$ for the PHMSN

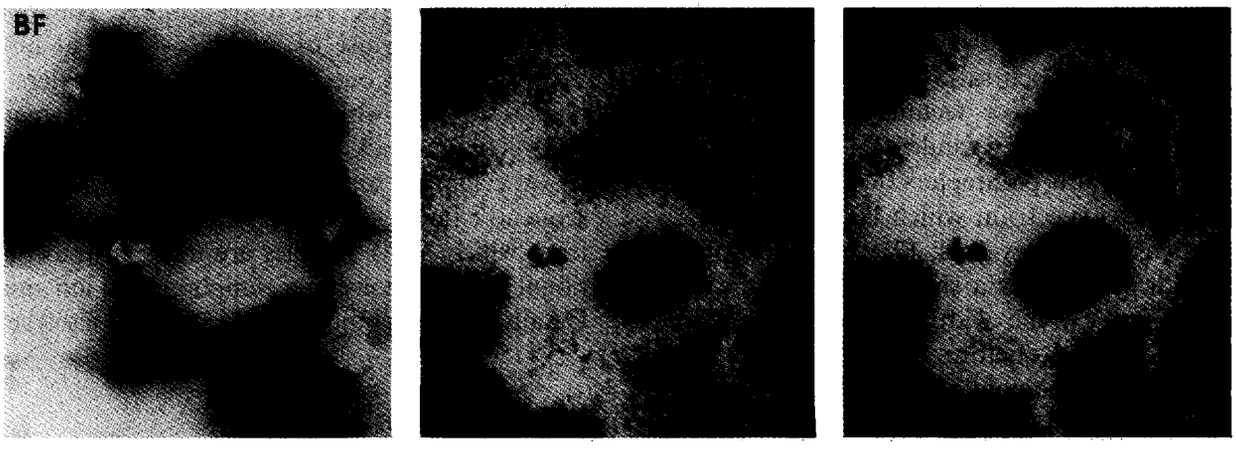


Fig. 3. Monolithic silicon carbonitride after pyrolysis at 1000°C. Comparison between bright field image and the elemental distribution images obtained for carbon and nitrogen. The thickness dependent intensity variation is the same in both distribution images confirming that C and N are distributed homogeneously in the material.

derived silicon carbonitride. Pyrolysis of PCMSN under the same conditions results in a silicon carbonitride with the composition $Si_{1.7}N_{1.5}C_{1.0}$.

3.2 PCMSN-derived Si_3N_4/SiC-composite

Polycrystalline Si_3N_4/SiC composites were produced by sintering of the amorphous PCMSN derived silicon carbonitride at different temperatures under nitrogen atmosphere. Various amounts of Y_2O_3 and Al_2O_3 were added as sintering additives prior to pyrolysis. Details of the processing conditions are described in Part I.[1]

In order to obtain insight into the formation of the microstructure during the sintering process, two series of experiments were carried out. The evolution of the microstructure with increasing sintering temperature and constant additive content was studied at four different temperatures between 1400°C and 1850°C. The dependence of the resulting microstructure on the concentration of the sintering additives at constant sintering temperature was investigated by varying the amount of sintering additives between 5 and 15 wt%. In the following, the microstructure obtained after heat treatment at the highest sintering temperature (1850°C) will be discussed first in order to facilitate comparison with the results obtained in the intermediate stages.

3.2.1 Microstructure after sintering at 1850°C

By sintering the material with 15 wt% sintering additives at 1850°C for 1 h, a ceramic composite with high density and low porosity is obtained. In Fig. 4, a bright field image of a thin area of the TEM specimen is shown. The microstructure consists of crystalline particles with grain sizes ranging from 50 nm to 1 μm and an oxidic glassy phase. The phase composition is revealed by the ESI image in Fig. 4(b). The elemental distribution of C, N and O is imaged in red, green and blue colour, respectively. The corresponding phases are SiC, Si_3N_4 and the amorphous oxide, which can thus clearly be identified. The average size of the SiC grains is generally smaller and less uniform than the size of the Si_3N_4 grains. The ESI images show that there is a tendency of the SiC grains to form clusters. In the material with 15% sintering additives, the Si_3N_4 grains and the individual or clustered SiC grains are separated by extended areas containing the amorphous oxide. X-ray investigations revealed that both crystalline phases are formed in the β-modification, i.e. the materials consist of β-Si_3N_4 and β-SiC.

3.2.2 Evolution of microstructure with temperature

By X-ray diffraction of the heat treated materials (see Part I[1]) it could be shown that, at temperatures below 1400°C, no changes in the phase composition occur and that the amorphous phase produced by the pyrolysis at 1000°C does not start to crystallise nor to react with the sintering additives. At temperatures around 1400°C, however, a rapid onset of crystallisation could be detected. This is presumably caused by the formation of a liquid phase by melting of the sintering additives.

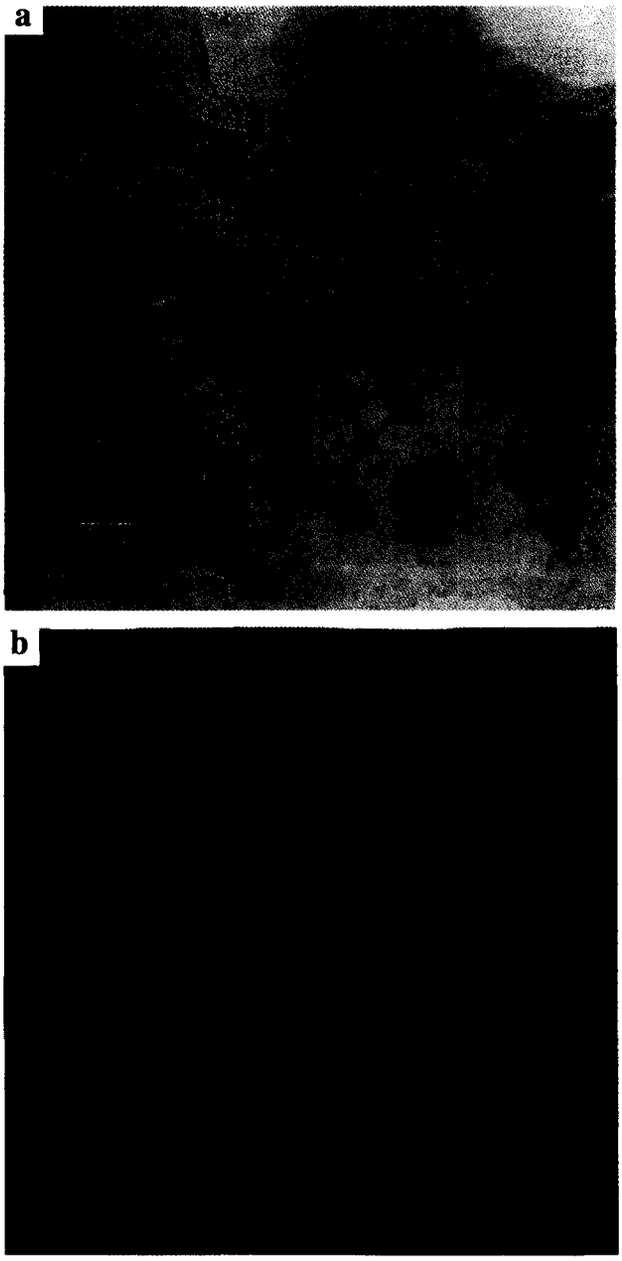


Fig. 4. Si_3N_4/SiC-composite material after sintering for 1 h at 1850°C. (a) Bright field image showing the microstructure; (b) Combined elemental distribution image for carbon (red), nitrogen (green) and oxygen (blue), showing the distribution of the SiC, Si_3N_4 and the amorphous oxide, respectively.

The microstructure which was obtained after a heat treatment of 1 h at 1400°C is shown in Fig. 5 (a). Irregularly shaped grains with dimensions between 50 and 300 nm can be observed. The grains are embedded in a matrix formed by a glassy phase. These areas can clearly be distinguished

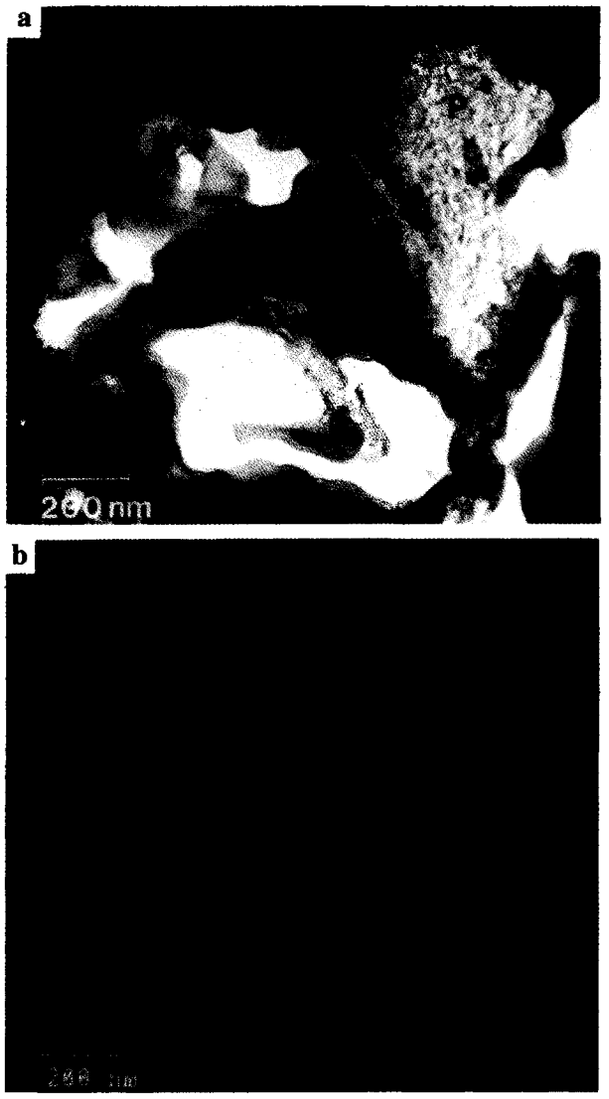


Fig. 5. (a) Microstructure of the material sintered at 1400°C. (b) The elemental distribution image shows that all the carbon (red) remains in pockets (denoted by P), while all the nitrogen (green and light blue) crystallises with an equivalent amount of Si and forms Si_3N_4 grains which are embedded in the glassy phase (dark blue).

from a large number of pockets (denoted by P in Fig. 5(a)) which show fine speckle contrast and have a diameter between 0·5 and 1 μm. Qualitatively, the chemistry of these two morphologically different parts of the microstructure could be clarified by ESI (Fig. 5(b)). The larger irregularly shaped grains all consist of Si_3N_4. The Si_3N_4 grains in the 1400°C material reach about half of the final grain size observed in the 1850°C composite.

Occasionally needle-like grains occur which contain both N and O and presumably consist of Si_2N_2O. They are also embedded within the glassy phase formed by the sintering additives. The pockets (P in Fig. 5(a)) are filled with a material showing speckle contrast and consisting mainly of Si and C. EDX and EELS analysis revealed that small amounts of Al, Y (less than 1 at%) and O

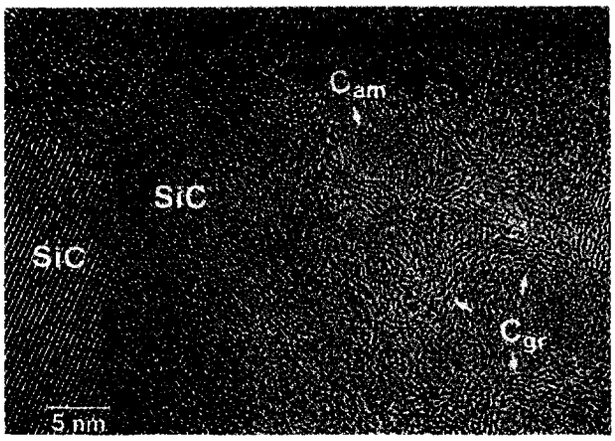


Fig. 6. High resolution image showing the atomic structure of the material contained within the pockets (P in Fig. 5). Nanocrystalline SiC can be identified by the corresponding lattice fringes. The SiC particles are embedded in graphitized and amorphous carbon.

(less than 5 at%) are also present. Electron diffraction patterns from these areas show Debye–Scherrer rings indicating that most of the material is nanocrystalline and that small SiC crystallites exist. In high resolution micrographs (Fig. 6) the SiC grains can be identified by their lattice fringes. Besides these, bent lattice fringes characteristic for graphitized carbon are also present. Both types of precipitate are embedded in amorphous carbon. The observed phase separation in the pockets is in agreement with the phase diagram of the binary Si–C system.[17]

Our microstructural results thus show that during the crystallisation at 1400°C a distinct phase separation takes place which leads to a demixing of the initial silicon-carbonitride into: (1) areas containing crystalline Si_3N_4 and Si_2N_2O grains which are embedded in the glassy phase formed by the sintering additives, and (2) pockets containing all the carbon in the form of nanocrystalline SiC and residual amorphous or graphitized carbon. It is important to note that, in the presence of the sintering additives, the initially amorphous silicon carbonitride has almost completely crystallised at 1400°C (even though the SiC is only nanocrystalline). In contrast to this, the monolithic silicon carbonitride (i.e. without sintering additives) remains amorphous at 1400°C even after 60 h of heat treatment. At 1400°C the sintering additives thus very effectively promote the crystallisation of the amorphous starting material. In the preparation of ceramic composites from polymer precursors the sintering additives are therefore not only required for densification but mainly to promote the crystallisation of the phases forming the composite.

The rapid onset of crystallisation at temperatures between 1300°C and 1400°C can be explained by the melting of the sintering additives.

The microstructure of the material at temperatures below 1300°C presumably consists of large amorphous silicon carbonitride particles which are mixed with crystalline Al_2O_3 and Y_2O_3 particles. In addition the SiNC particles are surrounded by an amorphous SiO_2 layer. In the system SiO_2 + Al_2O_3 + Y_2O_3 a deep eutectic exists at temperatures slightly above 1300°C. Between 1300 and 1400°C the sintering additives thus melt and the SiCN particles are embedded in a liquid phase. The crystallisation of the Si_3N_4 and Si_2N_2O phases is achieved by dissolution of Si and N in the liquid phase and reprecipitation of the crystalline phases. At a temperature of 1400°C only Si and N, but not carbon, diffuse out of the SiCN-particles and dissolve into the liquid phase which explains the observed phase separation into areas containing only Si_3N_4 and Si_2N_2O grains and remaining pockets consisting of nanocrystalline SiC and amorphous C. This result is also in agreement with the observation that sintering of SiC with Al_2O_3 and Y_2O_3 requires much higher temperatures before a solution–reprecipitation mechanism becomes operative.[5,6,8]

At temperatures above 1400°C further reactions are mainly expected in the pockets containing Si and C. At 1550°C grain coarsening occurs in the pockets and clusters of SiC grains form which are surrounded by pure carbon (Fig. 7). The existence of residual carbon can be explained by a surplus of carbon in the initial silicon carbonitride $Si_{3+x}N_4C_{x+y}$ with respect to the formation of stoichiometric Si_3N_4 and SiC. The transformation can be described by the reaction:

$$Si_{3+x}N_4C_{x+y} \xrightarrow{1400°C} Si_3N_4 + (x\ SiC_{nano} + y\ C)_p \xrightarrow{1550°C} Si_3N_4 + x\ SiC + y\ C^{(\uparrow)} \quad (1)$$

The first part of this reaction represents the initial silicon carbonitride, the second part the reaction product at 1400°C, in which the pockets P are filled with a mixture of nanocrystalline SiC and graphitized or amorphous C, and the third part the product at 1550°C, where the pockets are filled with precipitated SiC grains and amorphous carbon. At these temperatures the residual carbon obviously acts as a sintering aid for the SiC grains. At 1550°C the SiC does not seem to be wetted by the liquid phase formed by the sintering additives. Areas containing Si_3N_4 are still well separated from areas containing C and SiC. At 1550°C the residual carbon starts to disappear by forming gases. First indications for the onset of a reaction of the residual carbon with both the oxide phase and the Si_3N_4 grains are given by the gaps between the Si_3N_4 grains and the carbon rich areas. Three chemical reactions can be responsible for this:[18,19]

$$C + SiO_2 \rightarrow SiO\uparrow + CO\uparrow \quad (2)$$

$$3C + SiO_2 \rightarrow SiC + 2\ CO\uparrow \quad (3)$$

$$3C + Si_3N_4 \rightarrow 3SiC + 2\ N_2\uparrow \quad (4)$$

Reactions (2) and (3) lead to a decrease of the oxygen concentration of the material. Thermodynamically, the occurrence of reaction (4) is also expected.[19]

During sintering at 1700°C the amorphous carbon disappears completely. The SiC grains still occur mainly in clusters and the average grain size varies between 10 and 100 nm (Fig. 8). However,

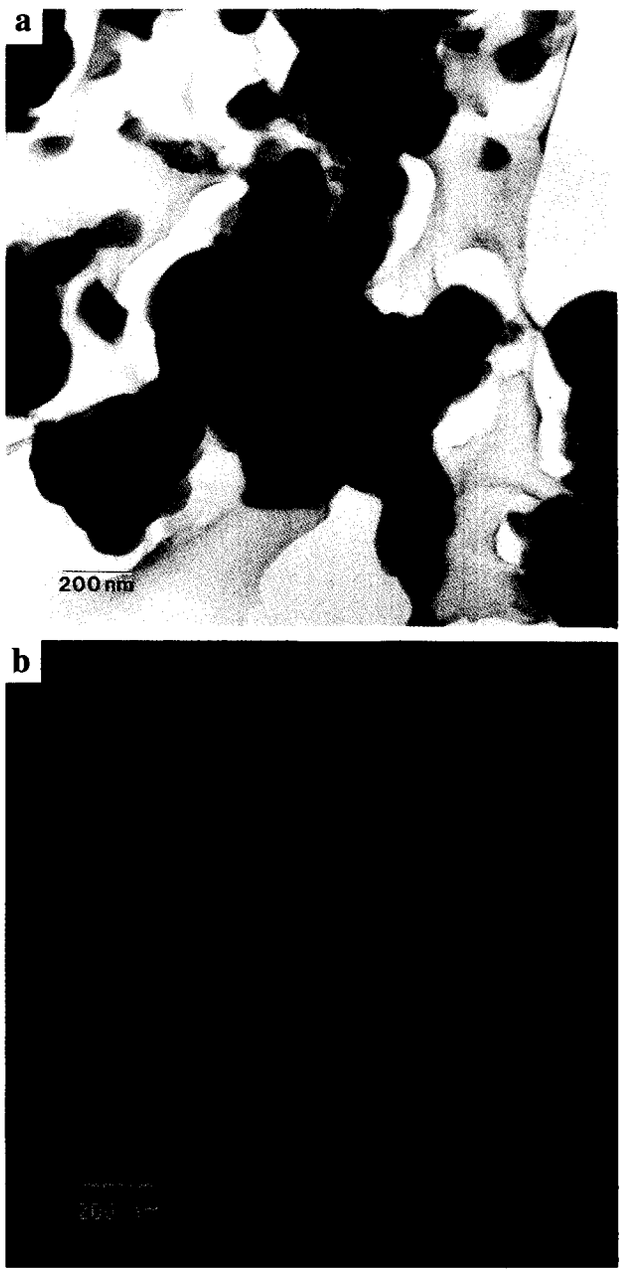


Fig. 7. Bright field (a) and elemental distribution image (b), carbon: red, nitrogen: green, and oxygen: blue) of the material sintered at 1550°C. Grain coarsening of the SiC within the residual C can be observed. At the same time, the residual carbon starts to react with the Si_3N_4 grains and the oxide phase which leaves gaps at the interfaces.

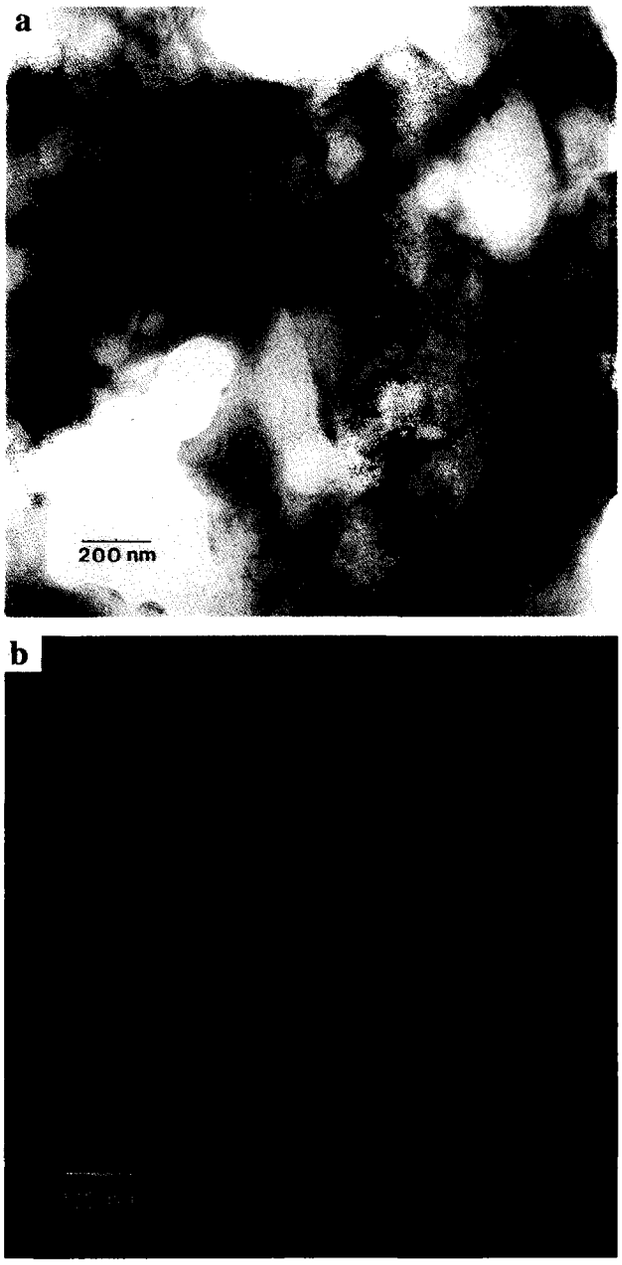


Fig. 8. Bright field (a) and elemental distribution image (b) carbon: red, nitrogen: green, and oxygen: blue) showing the microstructure of the material sintered at 1700°C. Clustering of the SiC particles (red) is still visible and most of the SiC particles have not reached the final grain size observed at 1850°C.

Fig. 8 shows that the SiC grains are now embedded within the glassy phase. From this we conclude that wetting of the SiC grains by the liquid oxides starts between 1550 and 1700°C. At 1700°C no more Si_2N_2O could be observed. This is in accordance with the thermal decomposition of the Si_2N_2O at temperatures above 1600°C:

$$3Si_2N_2O \rightarrow Si_3N_4 + 3SiO\uparrow + N_2\uparrow \qquad (5)$$

Between 1550 and 1700°C the reactions ((2)–(5)) lead to the production of gases which slow down densification.

After the disappearance of the amorphous carbon and the Si_2N_2O at 1700°C only the phases observed in the final product at 1850°C remain, i.e. SiC, Si_3N_4 and the oxidic glassy phase. An increase of the temperature to 1850°C thus only leads to gradual changes in the microstructure. These changes mainly are: a further grain growth of the SiC grains and a further densification. At 1850°C the grain growth of the SiC grains may also involve a solution/reprecipitation mechanism through the liquid phase. This results in an increasing intermixing of the SiC and Si_3N_4 grains leading to the final product described in 3.2.1.

3.2.3 Dependence on concentration of sintering additives

In the preceding section it has been shown that the sintering additives play an important role during the crystallisation of the amorphous silicon carbonitride. Therefore it can be expected that the concentration of the sintering additives also influences the resulting microstructure. In order to investigate this, composites were prepared with 5, 10 and 15% sintering additives under otherwise identical conditions (sintering for 1 h at 1850°C in 0·1 MPa N_2).

In the material with 5 wt% sintering additives, a large amount of open porosity is still present after sintering. This porosity can only be reduced by adding a larger amount of sintering additives, and at 15 wt% an almost completely dense material is obtained. These microstructural observations are in good agreement with the relative densities measured by porosimetry.[1]

In the samples sintered with 5 and 10 wt% sintering additives, a small number of Si_2N_2O grains are still present (Fig. 9). This observation is in contrast with the thermal decomposition of Si_2N_2O above 1600°C (Reaction (5)). However,

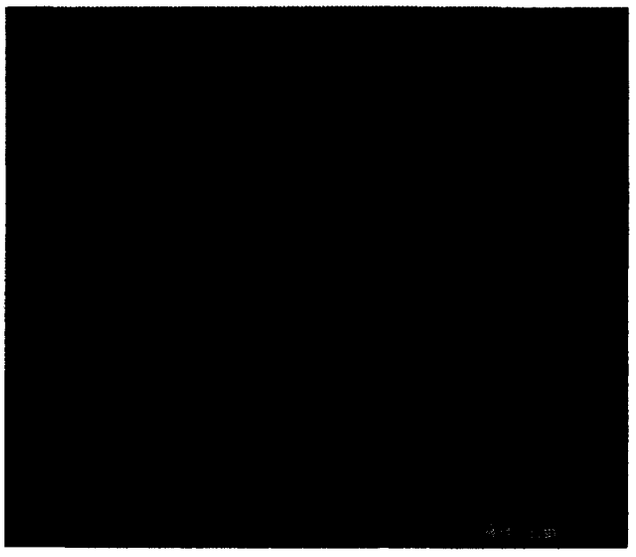


Fig. 9. In the samples sintered with 10 wt% sintering additives at 1850°C the microstructure consists of Si_3N_4 (green), SiC (red) and the amorphous oxide (blue). Occasionally Si_2N_2O grains could be observed, which in the ESI images are characterised by their mixed colour (here: mixed blue and green).

owing to the short annealing time of only 1 h, the Si_2N_2O grains may have survived for kinetic reasons and will disappear after longer heat treatments. The fact that Si_2N_2O is not found in the material sintered with 15% sintering additives indicates that the concentration of sintering additives and thus solution and reprecipitation processes play an important role in the thermal decomposition of Si_2N_2O.

From Fig. 9 it is also evident that the grain sizes of both SiC and Si_3N_4 are smaller in the material sintered with 5 or 10 wt% than in the reference material prepared with 15% additives. Hence, the rate at which the individual grains grow also shows a dependence on the concentration of the sintering additives. This can easily be understood for the Si_3N_4 while the fact that this grain size dependence is also observed for SiC indicates that solution/reprecipitation dominates the grain growth of SiC at 1850°C.

3.3 Sintered PCMSN-derived Si_2N_2O-ceramic

As discussed in Part I,[1] using ammonia during pyrolysis of the PCMSN results in the formation of amorphous silicon nitride powder. By attritor milling in wet isopropanol the reactive amorphous silicon nitride takes up oxygen in such an amount that during the subsequent sintering step polycrystalline Si_2N_2O can be produced. The sintering has to be performed at 1600°C because at higher temperatures Si_2N_2O decomposes according to Reaction (5). A mixture of Al_2O_3 and Y_2O_3 was used as sintering additives in concentrations of 3, 5,10 and 15 wt%.

In the TEM investigations submicron-size pores between the grains could be observed in the samples with 3 and 5% sintering additives. In these materials the low amount of sintering additives is not sufficient to close the pores during pressureless sintering. The individual Si_2N_2O grains are characterised by their elongated shape with an aspect ratio of 3–10 and by the high number of parallel stacking faults. In the materials with 3 and 5 wt% sintering additives only Si_2N_2O grains but no Si_3N_4 grains were found. In the ESI images the Si_2N_2O grains are characterised by their mixed colour (yellow) which is obtained by the superposition of the intensity which is present in both elemental distribution images (nitrogen: red and oxygen: green) (Fig. 10(a)). The oxidic glassy phase between the individual grains is characterised by the green colour.

At a concentration of 10 and 15 wt% of the sintering additives no more pores between the grains could be found. In the 10 wt% material occasionally Si_3N_4 grains could be observed and in the 15 wt% material the Si_3N_4 grains were present more frequently reaching concentrations of up to 10

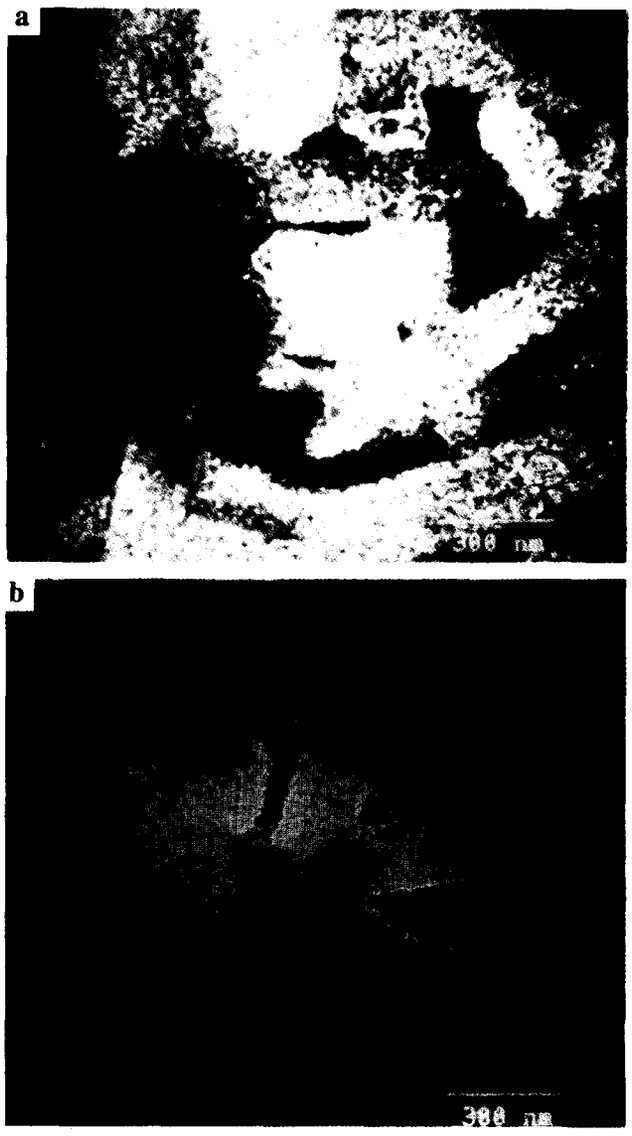


Fig. 10. The microstructure of the Si_2N_2O materials sintered with 3 wt% (a) and 15 wt% (b) sintering additives. In the images the nitrogen distribution is shown in red, the oxygen distribution in green. The Si_2N_2O grains are characterised by their mixed colour (red + green = yellow). At 3 wt% unfilled pores remain. In the 15 wt% samples the microstructure is dense but Si_3N_4 grains were present (red).

vol% (Fig. 10 b). The occurrence of Si_3N_4 grains is thus clearly dependent on the concentration of the sintering additives. This can be understood if it is assumed that during sintering the amorphous silicon nitride at least partly has to be dissolved in the liquid phase formed by the sintering additives. As discussed in the previous section the solution/reprecipitation mechanism may lead to a decomposition of Si_2N_2O into Si_3N_4, therefore increasing the amount of sintering additives increases the probability of Si_3N_4 precipitation.

3.4 Si_3N_4 sintered with 20 wt% Polysilane (PMPS)

According to the results described in Part I[1], an alternative way to produce Si_3N_4/SiC-composites is to mix Si_3N_4 powder with the polysilane PMPS

and an adequate amount of sintering additives. In our studies, 20 wt% of the PMPS and 12 wt% of sintering additives comprising 2·8 wt% AlN, 7·8 wt% Y_2O_3 and 1·4 wt% Al_2O_3 were used.

The resulting microstructure obtained after pyrolysis and sintering of the polymer-powder compact is shown in Fig. 11(a). Large grains with average grain sizes of 0·5–1 μm can be identified. Smaller particles with diameters of 20–200 nm surround these grains (intergranular) but are also embedded within the grains (intragranular). These particles are comprised of SiC as is clearly revealed by the ESI image (Fig. 11(b)). The larger grains consist of β-Si_3N_4. Therefore, besides the intergranular SiC, small intragranular SiC nanoprecipitates in the Si_3N_4 crystals could be detected in our material. A similar composite microstructure belonging to this mixed intra- and inter-type was first reported by Niihara *et al.*.[20] It was found that the fracture strength of these materials is considerably higher than the strength of Si_3N_4/SiC composites without intragranular SiC-precipitates.[9]

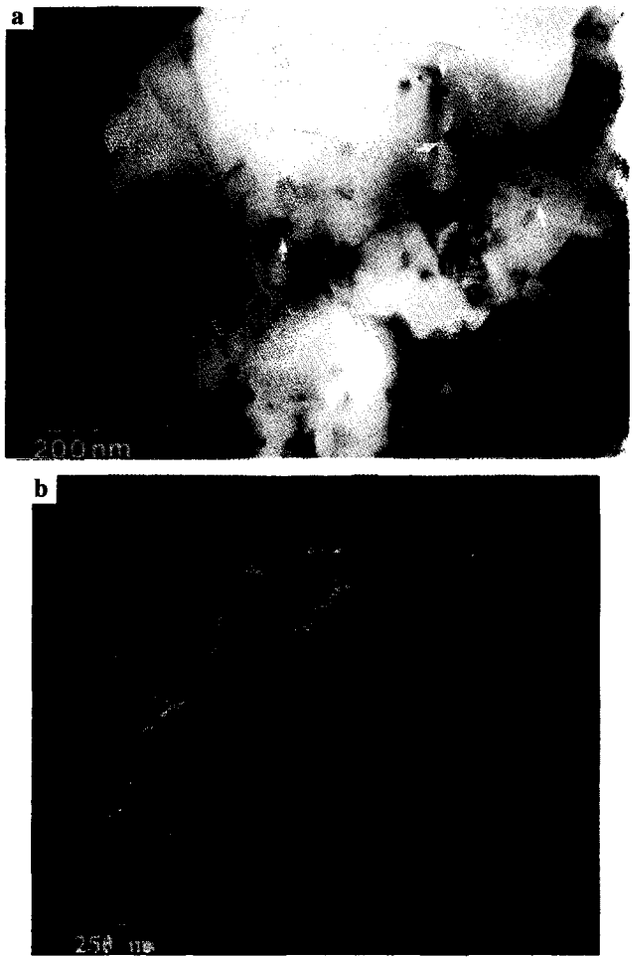


Fig. 11. Si_3N_4/SiC-composite material produced by sintering Si_3N_4 powder with 20 wt% of the PMPS precursor. In the bright field image (left) a number of precipitates can be observed in the large Si_3N_4 grains. The ESI image reveals that these precipitates consist of SiC nanoparticles (red). The Si_3N_4 grains are shown in green, the amorphous oxide in blue.

The results obtained on the Si_3N_4/SiC-composites produced from the polysilazane precursor (see Section 3.2.2) indicate that during sintering considerable amounts of the Si and N present in the starting material are dissolved in the liquid phase. In the material produced from the Si_3N_4-powder/polysilane mixture this solution–reprecipitation process will also take place leading to the growth of larger Si_3N_4 grains. During the reprecipitation of Si_3N_4 from the liquid phase, small polysilane derived SiC particles might become enclosed by the growing Si_3N_4 grains leading to the observed microstructure. The fact that this is not observed in the Si_3N_4/SiC-composites produced from polysilazane as described in Section 3.2.2 could be due to the observed phase separation into regions containing Si_3N_4 grains embedded in the glassy phase and regions containing SiC and residual C. Even though Si_3N_4 might dissolve and reprecipitate at higher temperatures, the SiC is well enough separated from the growing Si_3N_4 crystals and no enclosure is possible.

4 Conclusions

The processing of ceramic composites from polymer precursors involves a complicated sintering mechanism for which we have studied the dependence on the starting material and the processing conditions. The mechanism is based on the formation of a liquid phase from the sintering additives which, by surrounding the amorphous starting material, serves several purposes: (1) the onset of crystallisation occurs much faster and at lower temperatures; (2) the chemical reactions which lead to the formation of the stable, stoichiometric crystalline phases are accelerated by the diffusion through the liquid phase, and (3) complete densification of the material can only be achieved with sintering additives. Based on the results of our microstructural characterisation, a model of the processes occurring during sintering can be proposed (Fig. 12): β-Si_3N_4 grains and Si_2N_2O grains start to form by a solution–reprecipitation mechanism immediately after formation of the liquid phase (1400°C). An increase in temperature leads to grain coarsening by the same mechanism. SiC and C, at least at the lower temperatures, are not dissolved by the liquid phase and are left in pockets which are remnants of the initial SiCN particles. Nucleation and grain coarsening of the SiC grains at the lower temperatures only occurs within the residual carbon matrix. The phases formed are the thermodynamically stable phases β-Si_3N_4 and β-SiC. Chemical reactions at intermediate sintering temperatures result in the disappearance of the

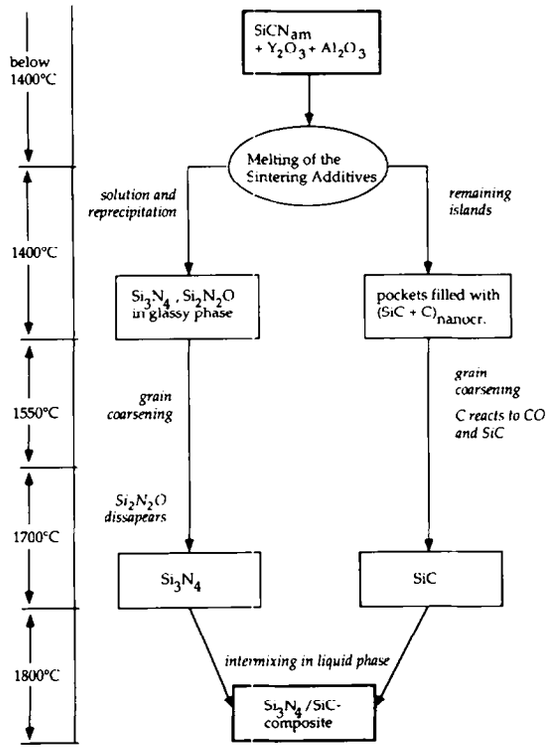


Fig. 12. Schematic diagram showing the processes occurring at increasing sintering temperatures in the Si_3N_4/SiC-composite material.

Si_2N_2O grains and the residual carbon. The gases produced during these reactions slow down densification. Further grain coarsening and rearrangements of the particles at the higher sintering temperatures lead to the final microstructure observed at 1850°C. In the final product the clustering of SiC grains is less pronounced than in the materials obtained at lower temperatures. We attribute this to a solution and reprecipitation reaction which at 1850°C also becomes operative for the SiC and leads to a redistribution of the SiC grains.

In our studies, elemental distribution images obtained with the ESI technique have proven to be a very efficient tool for the analytical characterisation of ceramic microstructures. A comparison with the phases identified by X-ray diffraction (see Part I of our studies[1]) confirms that our TEM results are representative for the overall micro-structure of the materials investigated. However, details of the microstructure, for example the inclusion of SiC precipitates in Si_3N_4 grains which is important for the mechanical behaviour of the resulting composite, could only be identified in the TEM studies.

Acknowledgement

The authors would like to acknowledge helpful discussions with R. Brook. The work was supported by: the Bundesministerium für Forschung und Technologie (NTS 0215/8), the European Community (BREU 0106-C-JR), the Keramikverbund Karlsruhe-Stuttgart, the KSB Foundation, Stuttgart, the Deutsche Forschungsgemeinschaft, and the Fonds der Chemischen Industrie, Frankfurt.

References

1. Riedel, R., Seher, M., Mayer, J. & Szabó, D. V., Polymer derived Si-based bulk ceramics, Part I: preparation, processing and properties. *J. Eur. Ceram. Soc.*, **15** (1995) 703.
2. Reimer, L., Fromm, I. & Rennekamp, R., Operation modes of electron spectroscopic imaging and energy-loss spectroscopy in a transmission electron microscope. *Ultramicroscopy*, **24** (1988) 339–54.
3. Hayashi, T., Munakata, H., Suzuki, H. & Saito, H. Pressureless Sintering of Si_3N_4 with Y_2O_3 and Al_2O_3. *J. Mat. Sci.*, **21** (1986) 3501–8.
4. Boberski, C., Bestgen, H. & Hamminger, R., Microstructural development during liquid-phase sintering of Si_3N_4 ceramics. *J. Eur. Ceram. Soc.*, **9** (1992) 95–9.
5. Omori, M. & Takei, M., Pressureless sintering of SiC. *J. Am. Ceram. Soc.*, **65** (1982) C-92
6. Kleebe, H.-J., SiC and Si_3N_4 materials with improved fracture resistance. *J. Eur. Ceram. Soc.*, **10** (1992) 151–9.
7. Lange, F. F., Effect of microstructure on the strength of the Si_3N_4/SiC composite system. *J. Am. Ceram. Soc.*, **56** (1973) 445.
8. Greil, P., Petzow, G. & Tanaka, H., Sintering and HIPping of silicon Nitride–Silicon carbide composite materials. *Ceramics Intern.*, **13** (1987) 19–25.
9. Sawaguchi, A., Toda, K. & Niihara, K., Mechanical and electrical properties of Silicon Nitride–Silicon Carbide nanocomposite material. *J. Am. Ceram. Soc.*, **74** (1991) 1142–4.
10. Sasaki, G., Nakase, H., Sukanuma, K., Fujita, T. & Niihara, K., Mechanical properties and microstructure of Si_3N_4 matrix composite with nano-meter scale SiC-particles. *J. Ceram. Soc. Japan*, **100** (1992) 536–40.
11. Rouxel, T., Wakai, F. & Izaki, K., Tensile ductility of superplastic Al_2O_3–Y_2O_3–Si_3N_4/SiC composites. *J. Am. Ceram. Soc.*, **75** (1992) 2363–72.
12. Lanio, S., High-resolution imaging magnetic energy filters with simple structure. *Optik*, **73** (1986) 99–107.
13. Krivanek, O. L., Gubbens, A. J., Dellby, N. & Meyer, C. E., Design and first applications of a post-column imaging filter. *Micros. Microanal., Microstruct.*, **3** (1992) 187–99.
14. Bihr, J., Benner, G., Krahl, D., Rilk, A. & Weimer, E., Design of an analytical TEM with integrated imaging Ω-spectrometer. *Proc. 49th Ann. Meeting EMSA*, ed. G. W. Bailey, San Francisco Press Inc., 1991, pp. 354–5.
15. Berger, A., Mayer, J. & Kohl, H., Detection limits in elemental distribution images produced by energy filtering TEM: case study of grain boundaries in Si_3N_4. *Ultramicroscopy*, **55** (1994) 101–12.
16. Salzberger, U., Strecker, A. & Mayer, J., TEM specimen preparation: A universal method for cross sections and brittle materials. *Electron Microscopy 92*, Vol. 2, eds A. Lopez-Galindo & M. J. Rodriguez-Garcia, Granada, Spain, 1992, pp. 743–4.
17. Fitzer, E., Hegen, D., *Angew. Chem.*, **91** (1979) 316.
18. Jong, B. W., Formation of silicon carbide from silica residues and carbon. *Am. Ceram. Soc. Bull.*, **58** (1979) 788.
19. Nickel, K. G., Hoffmann, M. J., Greil, P. & Petzow, G., Thermodynamic calculations for the formation of SiC whisker-reinforced Si_3N_4 ceramics. *Adv. Cer. Mat.*, **3**(6) (1988) 557.
20. Niihara, K., New design concept of structural ceramics — ceramic nanocomposites, *J. Ceram. Soc. Japan*, **99** (1991) 974–82.

Journal of the European Ceramic Society 15 (1995) 729–734
© 1995 Elsevier Science Limited
Printed in Great Britain. All rights reserved
0955-2219/95/$9.50

0955-2219(95)00049-6

Injection Moulding of Silicon Carbide Using an Organic Vehicle Based on a Preceramic Polymer

T. Zhang,[a] J. R. G. Evans[a] & J. Woodthorpe[b]

[a]Department of Materials Technology, Brunel University, West London, Uxbridge, UB8 3PH, UK
[b]T & N Technology, Cawston House, Cawston, Rugby, CV22 7SA, UK

(Received 18 March 1993; revised version received 16 February 1995; accepted 20 February 1995)

Abstract

Large ceramic injection mouldings were prepared using a SiC composition with polycarbosilane and paraffin wax. The material sustained mixing and injection moulding at temperatures up to 230°C. Conventional, modulated pressure and heated sprue techniques were used to produce large sections, some of which were subsequently pyrolysed and sintered. Fired relative densities of 97% were obtained under conditions where the dry compacted powder sintered to 90%.

1 Introduction

Previous work[1] has identified modifications to a ceramic polymer composition suitable for injection moulding in which a transient organic binder is replaced with a polymer which decomposes to silicon carbide. The idea of using polycarbosilane as a binder for silicon carbide was proposed by Yajima[2] and hypostatised by Mutsuddy for extrusion.[3] In the same way Sugawara[4] added polycarbosilane at approximately 40 vol.% to a binder system of ethylene vinyl acetate, wax, dibutyl phthalate and a fatty acid ester for injection-moulding silicon carbide powder. Similarly, Okumara[5] blended polycarbosilane with stearic acid to provide a moulding composition for SiC powder.

By incorporating paraffin wax into the composition, the viscosity is reduced and the danger of temperature-induced crosslinking in the machine is avoided.[1] In the present work, this approach was followed up by using the composition previously developed in an injection-moulding machine to make several components and hence examine the behaviour of the material in the mould-filling and solidification stages.

2 Experimental Stages

The silicon carbide was grade 059S from Superior Graphite Co., Chicago, USA. The powder is shown in Fig. 1 and was equiaxed with irregular shape, with a mean particle size of 0·8 μm. Polycarbosilane (PCS) was supplied by Changsha Institute of Technology, People's Republic of China.

The wax was grade 130/135 from Shell Chemicals UK. The mixture prepared contained 56 vol.% SiC and the composition was 80% SiC, 14% PCS and 6% wax by weight.

Mixing was carried out using a Betol (Luton, Beds, UK) TS40 twin-screw extruder running at 60 rpm with barrel temperatures 190–200–220–210°C feed to exit. When cold, the extrudate was granulated by passing it through the unheated rolls of a twin-roll mill to produce feedstock for the injection-moulding machine.

Viscosity was measured with a Davenport Capillary Rheometer fitted with a 2-mm diameter, 40-mm long die and a 5000 psi pressure transducer. A temperature of 226°C was used and shear rates from 20–150 s^{-1} were studied.

Injection moulding was done on a Negri-Bossi NB90 SM290 machine modified for ceramics use. Three moulds were used producing (i) a centre-gated rectangular bar measuring 15 mm × 10 mm × 113 mm, (ii) an axially gated cylinder measuring 40 mm diameter and 60 mm in length and (iii) a straight-bladed rotor having a diameter of 94 mm with a solid hub. The injection speed was 6·7 × 10^{-5} m^3/s. The injection moulding variables are given in Table 1. Examples of these mouldings made with the SiC–PCS blend are shown in Fig. 2.

The bars were made using conventional static pressure moulding with a sprue bush having a minimum diameter of 10 mm. The cylinders were made using a heated sprue which has been described previously.[6,7] The sprue was heated to 210°C before injection and held at that temperature for 300 s which was calculated[8] to be greater than the time needed for the centre of the cylinder to solidify in a mould at 40°C. The rotors were made using either static pressure or modulated pressure at various pressure amplitudes using the procedure described previously.[9]

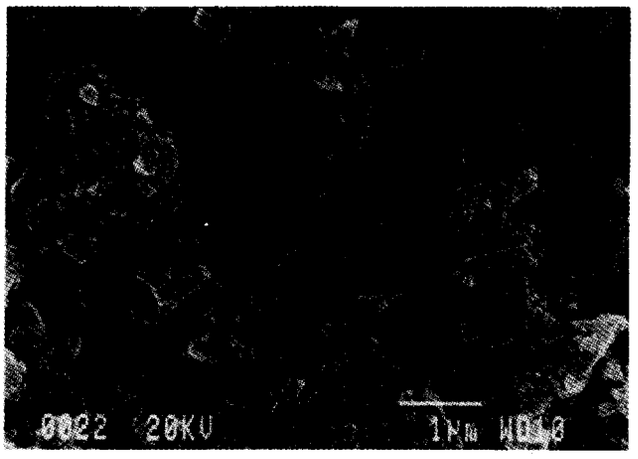


Fig. 1. Scanning electron micrograph of the silicon carbide powder.

The injection-moulding machine was operated with barrel temperatures 210–220–230–230°C feed to nozzle. The mould temperature was varied from 20°C to 50°C and the pressures, which are discussed in Section 3, were varied as shown in Table 1.

Partial pyrolysis of mouldings was carried out in an oxygen-free nitrogen flow of 30 litres/h up to a maximum temperature of 500°C.

Table 1. Injection moulding conditions

Mould temperature (°C)	*Injection pressure (MPa)*	*Hold pressure[a] (MPa)*	*Frequency (Hz)*
Rectangular bars; conventional moulding			
20	108	97	–
20	141	54	–
35	141	54	–
40	141	54	–
50	141	54	–
Rotors; conventional moulding			
38	97	54	–
38	108	54	–
38	141	54	–
38	108	32	–
Rotors; modulated pressure moulding			
38	108	71	1
38	108	71	0·7
38	108	85	0·7
38	108	92	0·7
38	108	99	0·7
38	108	106	0·7
38	108	120	1
40	108	92	0·7
Large cylinders; heated sprue moulding			
30	108	76 (3 s)	–
		then 15 (until end)	
30	108	76 (2 s)	–
		then 15 (200 s)	
		then 10 (100 s)	
		then 5 (200 s)	

[a]For modulated pressure moulding, this column gives the amplitude.

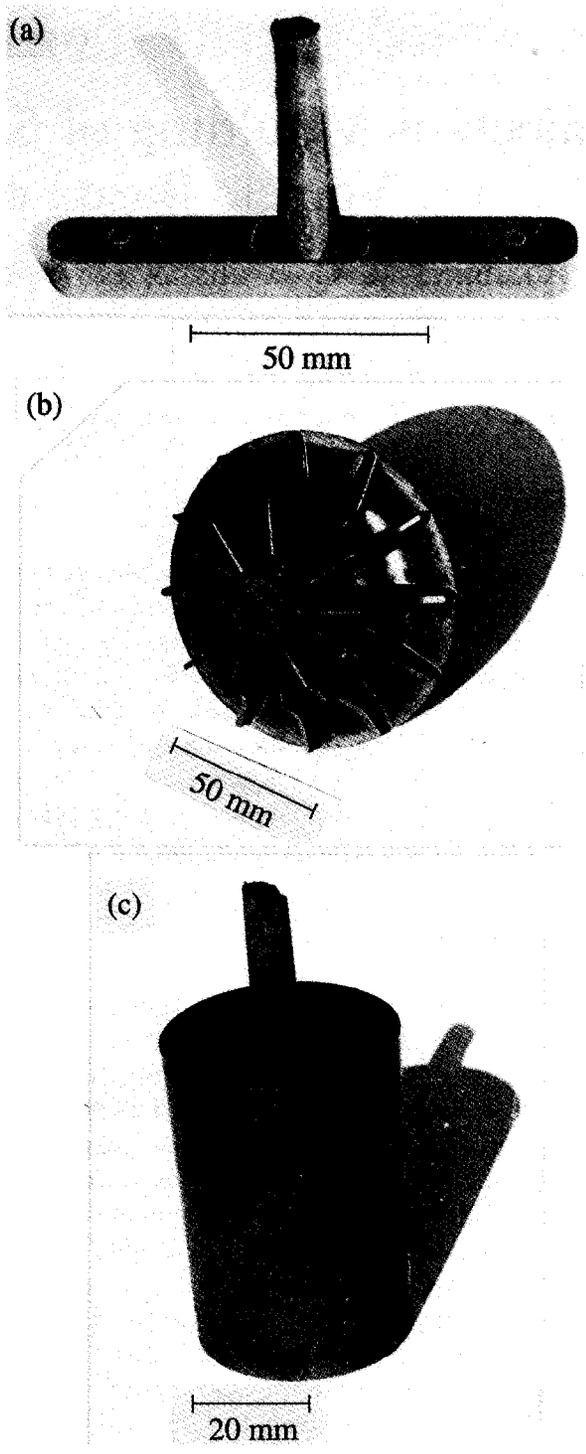


Fig. 2. Injection moulded components: (a) centre-gated rectangular bar, (b) straight-bladed rotor, (c) cylinder.

After initial pyrolysis to 500°C, samples were sintered in a carbon resistance furnace (Jones Vacuum Ltd., Bury, Lancs, UK). The heating rate was 10°C/min to 900°C followed by 5°C/min to 1500°C and a one-hour dwell under vacuum. An argon flow was then established and the temperature was raised to 2050°C at a 5°C/min rate and a 30 min dwell at 2050°C ensued. The density of sintered samples was measured by the Archimedes method in distilled water with a drop of surfactant added.

The sintering behaviour of the pyrolysed bars was compared with that of pressed components of

the SiC powder without organic additives. Rectangular bars (8 × 8 × 51 mm) were made by single-ended die pressing at 70 MPa. Bars of the same size were cut from the pyrolysed injection-moulded material. Pairs of bars were companion-fired in a graphite element vacuum furnace (Lenton, Leics, UK) at 15°C/min to 2000°C and held for 0·5 h and 4 h. An argon flow rate of 0·5 litres/min was maintained. Fracture surfaces were examined in a Cambridge S250 scanning electron microscope.

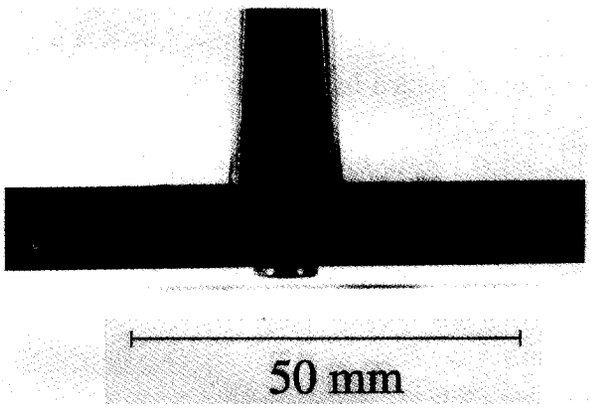


Fig. 3. Polished section of rectangular bar made by the conventional method with a hold pressure of 54 MPa and a mould temperature of 38°C.

3 Results and Discussion

3.1 Injection moulding

When mixed in the proportions tested previously,[1] the suspension had a higher viscosity at the same powder volume loading. This indicates a slightly higher molecular weight for the new sample of PCS, which is made in the laboratory in batches and is not a commercial product.

The composition of the organic vehicle was therefore changed from that used previously so that the ratio of PCS to wax was 7:3 instead of 4:1 and this gave an apparent viscosity at 121 s^{-1} of 800 Pa s and a flow behaviour index of 0·7 at 226°C. Thus the increase in wax fraction had the effect of making the suspension slightly more Newtonian.

In the previous work,[1] mixing was carried out in solvent. The large quantities of material required for injection moulding favoured mixing by twin-screw extrusion at high temperatures. The success of this process shows that the suspension, based on polycarbosilane, can be compounded in plastics processing machinery. This is a necessary but not sufficient condition for admitting a new material to the injection-moulding machine barrel. The other condition is that the apparent viscosity in the region of 100 s^{-1} should be less than about 1000 Pa s.

The mixture had a low softening point of ≈50°C[1] and this meant that shrinkage in the solid state was low. Although this should mean that residual stresses are reduced, it also leads to the tendency to resist ejection. This was a particular problem with the rectangular bars, 50% of which fractured on ejection because of failure to release the sprue when high hold pressures or mould temperatures were used. Rectangular bars made by conventional moulding with a hold pressure of 54 MPa in a mould at 35°C were free from macroscopic defects in the polished section after moulding (Fig. 3). The dimensional reproducibility of the moulded bars is reflected in the coefficient of variation for the length of the bar, which was 0·1%.

Rotors made by conventional moulding were replete with defects over a range of injection and hold pressures as generally observed.[9,10] Figure 4(a) shows the arrangement of defects in a rotor made with a hold pressure of 54 MPa in a mould at 38°C. Variation of the injection pressure did not influence the incidence of defects, which are attributed to the solidification rather than the mould-filling stage. High hold pressures made it very difficult to eject the rotor mouldings without fracture of blades. Modulated pressure rotors with pressure amplitudes in the region 71–92 MPa were free from macroscopic defects in the polished section (Fig. 4(b)) but when the pressure amplitude was increased to 99–120 MPa, large cracks perpendicular to the axis appeared in the hubs of rotors after moulding (Fig. 4(c)). In some cases it was possible to hear and sense the cracking as the rotors were held in the hand after removal from the mould. This phenomenon, attributed to over-packing, has also been reported previously for other systems.[9]

In the frequency region 0·7–1·0 Hz, the frequency had no effect on the appearance of defects. When the frequency was lower than 0·7 Hz, voids appeared even at pressure amplitudes of 120 MPa, an effect that has been attributed to wasted time at the top and bottom of dead centre of piston travel.[11]

Large axially centre-gated cylinders, 40 mm in diameter were made by heated sprue moulding. This method allows large sections to be made without voids at very low pressures. Figure 5 shows the polished section of a cylinder made with a hold pressure of 15 MPa. The sprue was kept molten until the centre of the cylinder was solid. However, the heated sprue process is not yet fully understood and approximately 50% of mouldings showed cracks perpendicular to the axis of the cylinder either on ejection or shortly afterwards. An example is shown in Fig. 6. A similar experience with large heated sprue mouldings with an alumina– polypropylene based system

has been reported.[7] It is suggested that this type of cracking arises from the continuing restraint on shrinkage provided by pressure in the liquid core.

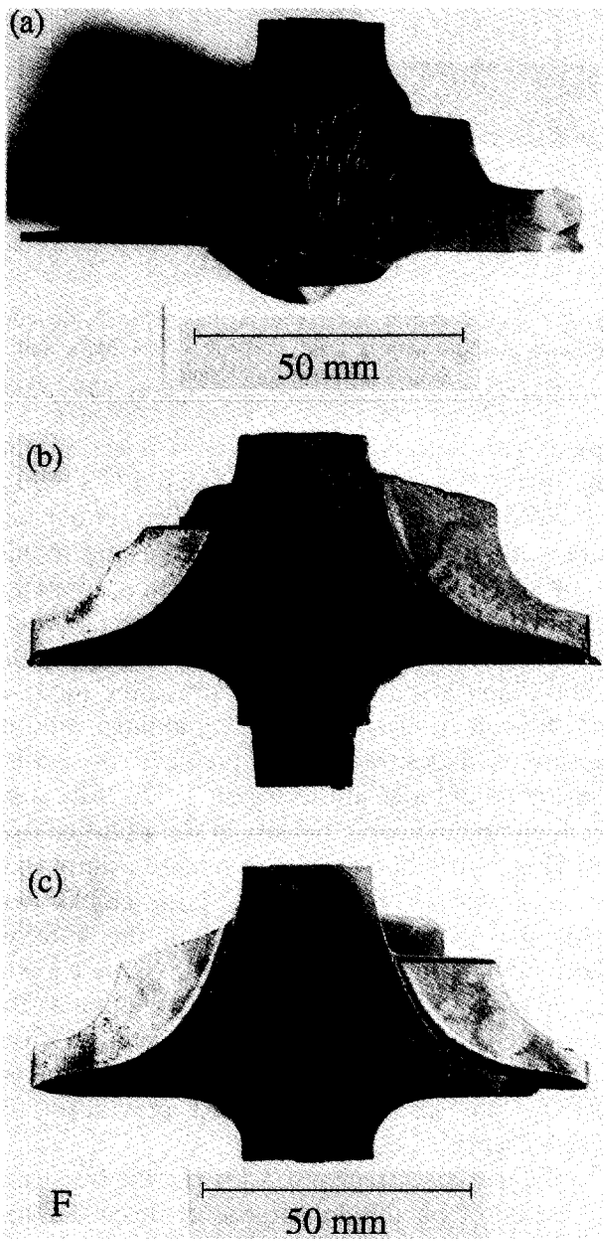


Fig. 4. Polished sections of as-moulded rotors: (a) static pressure 54 MPa, (b) modulated pressure 92 MPa, (c) modulated pressure 120 MPa. The defects are revealed by oblique illumination; no dye was used.

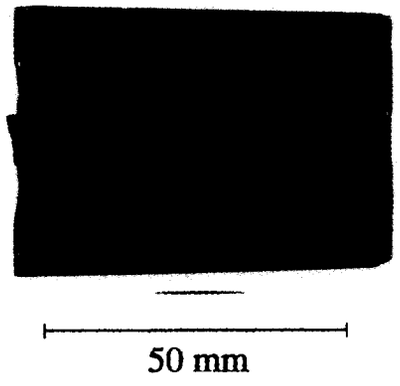


Fig. 5. Section of cylinder made by heated sprue moulding with a 15 MPa hold pressure and mould temperature 30°C.

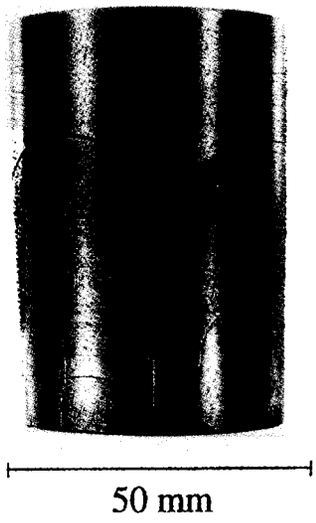


Fig. 6. Cracking in some cylinders made by heated sprue moulding under the same conditions as that in Fig. 5. Flow lines from the axial gating system are also clearly seen in the surface.

3.2 Pyrolysis and sintering of mouldings

Initial pyrolysis was carried out in the temperature range 20–500°C. For the rectangular bar mouldings, the schedule was 60°C/h to 150°C, followed by 2°C/h to 500°C. This produced a weight loss, W_1, of 9·3 ± 0·1 wt%. The bars, which were free from external signs of cracking after moulding, now showed cracks at the junction with the gate. Since the gate had nearly the same diameter as the width of the bar, this region represents the largest overall section. These bars were then broken in half and the sprue was removed before sintering.

Problems were also encountered with the rotor mouldings, which have a much greater section thickness in the hub. These produced a few radial cracks on initial pyrolysis, even at heating rates of 0·5°C/h, which then act as fast transport paths for degradation products. The thinner sections appeared to be sound. A sintered rotor is shown in Fig. 7. There were no external signs of additional defects caused by sintering.

Clearly the overall shrinkage which the component undergoes from the moulded to the sintered state is influenced by the incorporation of a

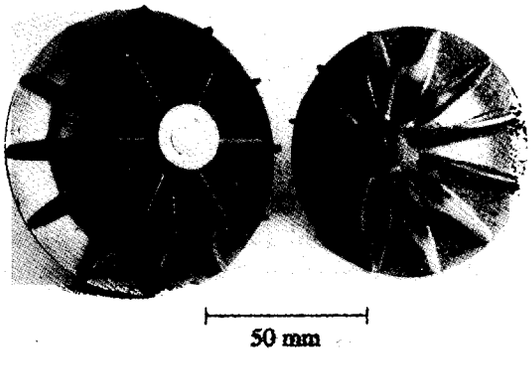


Fig. 7. Rotors, as-moulded (left) and after sintering. Radial cracks appear after pyrolysis of the large section (note the crack at 2 o'clock).

ceramic precursor as binder and by the various weight losses that occur throughout the process. In view of mould tooling costs it is useful to see how well overall shrinkage can be predicted from thermogravimetry.

The average weight loss, W_2, on sintering is made up mainly of the final stage of pyrolysis of the binder, the wax having been expelled earlier. This was 4·1 ± 0·1 wt% measured on 16 samples. The overall weight loss, W_L, is given in terms of the two stages of fractional weight loss by

$$W_L = W_1 + W_2 - W_1 W_2$$

and was 13·0%.

Two stages of shrinkage accompany these processes. The average linear shrinkage after initial pyrolysis was 0·82% measured on the rectangular bar mouldings. The shrinkage attributable to sintering measured on the thickness and width of rectangular bars was 14·0% and 13·8%, respectively. The average overall shrinkage from moulding to sintered body was thus 14·6%.

For samples fired in the Jones furnace, measurement of the sintered density by the Archimedes method in water on 17 bars gave an average of 3122 kg/m^3 with 95% confidence limits based on a 't' distribution of ±10 kg/m^3.

Using the crystallographic density of 3218 kg/m^3 for silicon carbide[12] and assuming the sintered body is free of excess carbon or silica, this corresponds to a relative density of 97%, the same value as that obtained by Mutsuddy.[3]

Since the volume of the moulded material accommodates silicon carbide, wax and PCS exclusively, its specific volume is given by

$$V_0 = \sum_{i=1}^{i=3} W_i/\rho_i$$

where W and ρ are weight fractions and density, respectively, giving $V_0 = 4{\cdot}45 \times 10^{-4}$ m^3/kg.

After sintering, the volume is occupied by silicon carbide and voidage, and

$$V_1 = \frac{(1 - W_L)}{\rho_s}$$

where ρ_s is the apparent density of the sintered body and W_L is the overall fractional weight loss. This gives $V_1 = 2{\cdot}787 \times 10^{-4}$ m^3/kg. The overall volumetric shrinkage is therefore 37·4% and since

$$\frac{\Delta L}{L_0} = 1 - \left(1\frac{\Delta V}{V_0}\right)^{1/3}$$

the linear shrinkage predicted from weight loss and density measurements is 14·5%. This agrees well with the 14·6% measured from the dimensions of bars.

Table 2. Densities and weight losses for companion-fired injection-moulded and pressed SiC (each value is the average for 2 samples)

		Pressed	*Injection-moulded*
Prefired density (%)		54·3	65·7
Sintered 0·5 h	Weight loss	2·2	4·5
	Density	85·9	93·0
Sintered 4 h	Weight loss	1·7	4·0
	Density	90·0	96·8

The overall weight loss is made up of the 6 wt% and the weight loss on pyrolysis of the PCS. Since the overall loss was 13 wt%, the latter represents 50 wt% based on the initial weight of PCS. This is somewhat larger than the 34 wt% loss from PCS noted previously.[1] However, this excludes weight loss of, for example, native silica from the submicron powder on sintering. A weight loss based on the powder of 1·8 wt% would account for this discrepancy and experience shows that losses from this powder are typically 1–2 wt%. Table 2 shows that the weight losses obtained from sintering compacts of this powder without organic additives were 1·7–2·2%.

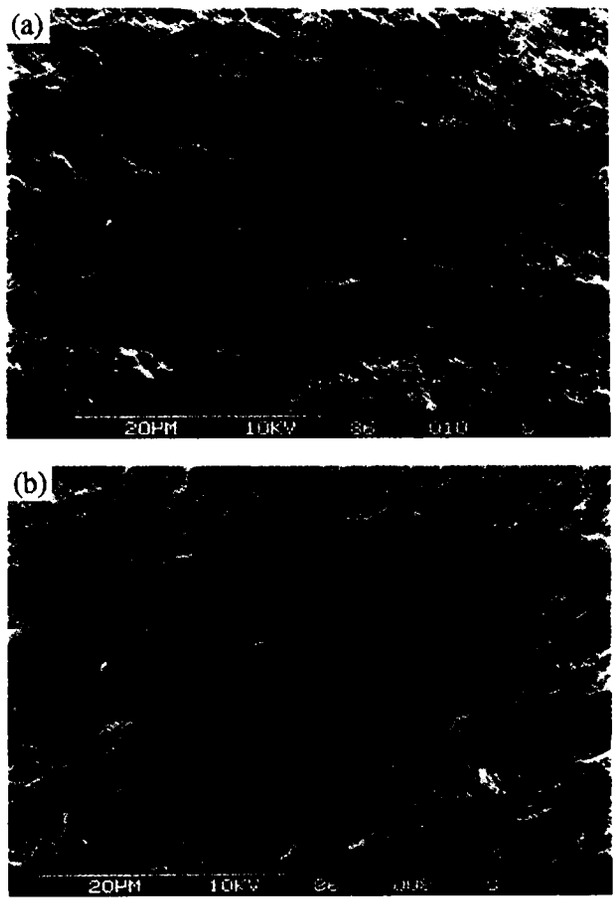


Fig. 8. Scanning electron micrograph of the fracture surfaces of bars companion-fired at 2000°C for 4 h in the Lenton furnace: (a) compacted powder (b) injection-moulded with PCS.

The sintering behaviour of the injection-moulded and pyrolysed bars is compared with that of the die-pressed bars in Table 2. The injection-moulded bars started at a much higher prefired density and reached 97% relative density after 4 h at 2000°C in the Lenton furnace, while pressed bars, fired as companions, reached only 90% relative density. The fracture surfaces of companion-fired bars of both types were examined principally to establish any differences in grain size. Figure 8(a) shows the more extensive porosity in the compacted sample compared with the injection-moulded one (Fig. 8(b)). In both cases, the exaggerated grain growth typical of many silicon carbide artefacts is seen, but there was no evidence of a higher grain size in the sample which had contained PCS.

4 Conclusions

An injection-moulding suspension incorporating a polymeric precursor to silicon carbide diluted with wax can be melt-compounded and injection-moulded at temperatures up to 230°C without premature crosslinking in the machine. Subsequent pyrolysis of large moulded sections produced the same defects that are seen with conventional binder systems, while small sections did not show macroscopic defects. Sintered density was 97% of theoretical and the weight loss and shrinkage were accounted for by the expected SiC residue from the polycarbosilane. Injection-moulded bars, which were companion-fired with compacted bars of the same powder, showed a higher relative density (97%) than the compacted samples (90%). Both samples showed evidence of discontinuous grain growth, but there was no significant difference in grain size.

Acknowledgements

The authors are grateful to the Science and Engineering Research Council for funding this work and to Mrs K. Goddard for typing the manuscript.

References

1. Zhang, T. & Evans, J. R. G., The properties of a ceramic injection moulding suspension based on a preceramic polymer. *J. Eur. Ceram. Soc.*, **7** (1991) 405–12.
2. Yajima, S., Special heat resisting materials from organometallic polymers. *Am. Ceram. Soc. Bull.*, **62** (1983) 893–8.
3. Mutsuddy, B. C., Use of organometallic polymer for making parts by plastic forming techniques. *Ceram. Int.*, **13** (1987) 41–53.
4. Sugawara, J., *Ceramic Compositions for Injection Mouldings*. Jpn. Kokai Tokkyo Koho 61053149 17th Mar. 1986, Assgn. Kurasaki Refractories Co.
5. Okumara, M., Moulded silicon carbide products. German Patent 3 409 385, 20th Sept. 1984. Assign. Shin. Nisso Kako Co.
6. Hunt, K. N. & Evans, J. R. G., A heated sprue bush for ceramic Injection moulding. *J. Mater. Sci. Lett.*, **10** (1991) 730–3.
7. Zhang, T. & Evans, J. R. G., The use of a heated sprue in the injection moulding of large sections. *Br. Ceram. Trans.*, **92** (1993) 146–51.
8. Zhang, T. & Evans, J. R. G., The calculation of temperature distributions during the solidification stage in ceramic injection moulding. *J. Am. Ceram. Soc.*, **75** (1992) 2260–7.
9. Zhang, J. G., Edirisinghe, M. J. & Evans, J. R. G., The use of modulated pressure in ceramic injection moulding. *J. Eur. Ceram. Soc.*, **5** (1989) 63–72.
10. Zhang, J. G., Edirisinghe, M. J. & Evans, J. R. G., The control of sprue solidification time in ceramic injection moulding. *J. Mater Sci.*, **24** (1989) 840–8.
11. Zhang, T. & Evans, J. R. G., The solidification of large sections in ceramic injection moulding: II Modulated pressure moulding. *J. Mater. Res.*, **8** (1993) 345–51.
12. JCPDS Powder Diffraction File, Swarthmore, Penn., USA 1974, file 4-0756.

Journal of the European Ceramic Society **15** (1995) 735–739
© 1995 Elsevier Science Limited
Printed in Great Britain. All rights reserved
0955-2219/95/$9.50

0955-2219(95)00046-1

Synthesis and Densification Behaviour of Bi-Based Superconducting Powder by Organic Precursor

A. Tampieri & G. Celotti

Research Institute for Ceramic Technology (IRTEC-CNR), via Granarolo 64, 48018 Faenza, Italy

(Received 4 July 1994; revised version received 7 February 1995; accepted 14 February 1995)

Abstract

BSCCO (2223) phase superconducting powder was synthesized by pyrolysis of a solution of citrates containing cations in the relative amounts required to prepare compounds with the nominal composition $Bi_{1.84}Pb_{0.35}Sr_{1.9}Ca_{2.1}Cu_3O_x$. *Starting from the pyrolysed precursor, the preparation of (2223) monophasic powder is realized in very short processing time of only 24 h. Reactions among components were investigated by thermogravimetric and differential thermal analysis; the products obtained on treating powders at various temperatures in the range 500–950°C were defined by XRD. The identification of the reaction intermediates that play a crucial role in the synthetic process was systematically performed, and a comparison with the solid-state reaction method was carried out. Hot pressing was performed in order to prepare highly dense superconducting materials. The densification behaviour of the powder obtained by the citrate route was studied in comparison with the solid-state reacted one.*

1 Introduction

Several studies reported the existence of many difficulties in preparing Bi-based superconducting phases, mainly regarding the isolation of the high-T_c phase (2223) as a single phase. Indeed, incomplete reaction, compositional inhomogeneity, very large particle size and long sintering treatment are still typical trademarks of the conventional BSCCO solid-state synthesis. The use of the solution method to prepare organic precursor by pyrolysis overcomes these problems, producing highly homogeneous mixing with good stoichiometric control and constituted by active submicronic particles, characterized by a greater degree of reproducibility.[1,2] It is already known[3] that the pyrolysed precursors and classical mixture of oxides and carbonates, subjected to the same thermal treatments, run along different routes, characterized by different kinetics and generating peculiar reaction intermediates in the two cases.

The present work examines the reactions involved when the pyrolysed precursors are thermally treated and discusses the fundamental role of the Bi–Ca phases as reaction intermediates highly affecting the superconducting phase synthesis rate. Evaluation of the densification behaviour and the sintering efficiency of the citrate powder compared to the solid-state reacted one, during hot pressing, has been performed. Microstructural and electrical characterization of dense materials, produced with the pyrolysed powder, were also carried out.

2 Experimental Procedure

The detailed procedure for powder preparation with a nominal composition $Bi_{1.84}Pb_{0.35}Sr_{1.9}Ca_{2.1}Cu_3O_x$ using a citrate method is reported elsewhere.[1] The obtained powder was calcined at 800°C for 6 h, then fired at 846°C for 5 h and at 858°C for 13 h, with three interposed grindings. The intermediate reaction products obtained after each step were determined by careful interpretation of XRD spectra.

Differential thermal analysis (DTA) and thermogravimetric analysis (TGA) were carried out on the pyrolysed mixture up to 1000°C. To investigate the DTA curve, various thermal treatments up to temperatures in the range 580–930°C were also performed and the products examined by XRD analysis using graphite monochromatized CuK_α radiation.

Morphology of powders and dense samples was investigated by means of Scanning Electron Microscopy (Leica Cambridge Ltd).

The obtained powders were hot-pressed in air using an alumina die with a pressure of 10 MPa; the sintering temperatures were 790 and 800°C and the sintering time under pressure was 2 h. Shrinkage was continuously recorded during sintering and the obtained density reported versus

time. Sample densities were measured by Archimedes' method. The degree of (001) texture orientation (Lotgering factor) in dense samples was also determined by XRD analysis. Electrical resistance of the dense samples was measured by means of the four-probe method with Ag paste contacts which were dried and hardened at 100°C for 10 min.

3 Results and Discussion

Micrograph in Fig. 1 shows spongy agglomerates as the product of the pyrolysis process, consisting of spherical submicronic primary particles (0·2–0·4 μm in diameter) connected to each other by necks partially sintered during the combustion process. Some of these agglomerates are rich in amorphous phases that, hardly detectable even by XRD, are revealed by thermoanalytical investigations.

In Fig. 2 the TG and DTA curves reveal that the precursor powder starts to react at about 500°C and the reaction develops via a complex process. The first step in the TG curve is attributed to the decomposition of $Ca_{0.33}Pb_{0.67}(NO_3)_2$, mainly present in the amorphous state (thus undetectable by XRD), followed by the decomposition of $CaCO_3$, between 580 and 780°C, present with different degree of crystallinity.



Fig 1. SEM micrograph of as-pyrolysed BSCCO powder.

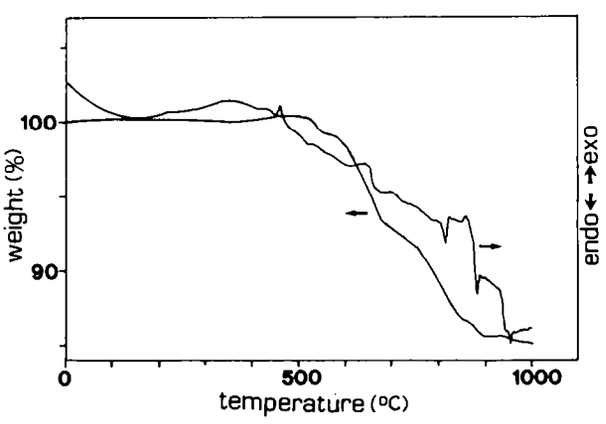


Fig. 2. Thermogravimetric and differential thermal analysis of pyrolysed powder.

The weight loss starting at 780°C is due to the beginning of $SrCO_3$ decomposition that runs out at $T \approx 930$°C. The DTA peaks clearly evident during the thermal analysis of the carbonate and oxide mixing used as a precursor of the solid-state reaction procedure,[4,5] are smoothed and broadened in the thermoanalytical curve of the pyrolysed precursor due to their low crystallinity. The DTA peaks between 630 and 730°C are attributable to various Bi–Ca phase formations and their interconversion from one form to another more stable one.[6] At 730°C, the $Bi_6Ca_4O_{13}$ phase starts to form, in equilibrium with traces of $Bi_6(Ca,Sr)_5O_{14}$; the DTA peak at 815°C is attributed to the transformation of the orthorhombic $Bi_6Ca_4O_{13}$ phase into monoclinic $Bi_6(Ca,Sr)_5O_{14}$. As the decomposition of $SrCO_3$ advances at $T > 820$°C, the CuO species is contemporarily engaged to form $(Ca,Sr)CuO_2$. Taking into account that the methodology used to identify the phases at different temperatures permits only the detection of products of irreversible reactions, it is, however, possible to attribute to the various Ca–Bi phases, and mainly to the 'O_{14}' phase, a dominant role in the superconducting phase formation process.

Table 1 shows the phase evolution, determined by XRD, in the pyrolysed powder, during the various steps of the 24 h processing to obtain 98% pure (2223) phase, as far as the phases belonging to Bi–Sr–Ca–Cu–O system are concerned, the exact amounts of Ca_2PbO_4 and Ca_2CuO_3 cannot be specified, their scattering powders being unknown referred to α-Al_2O_3 standard, but in any case the involved quantities are limited.

The high concentration of 'O_{13}' and especially of 'O_{14}' phases after the calcination treatment is a distinctive factor of the pyrolysed precursor synthetic process with respect to the conventional mixture of oxides and carbonates. The formation and dynamic equilibrium of the $Bi_6Ca_4O_{13}$ and $Bi_6(Ca,Sr)_5O_{14}$ phases cause a retardation in (2212) formation; as a consequence, the phase concentration starts to increase substantially only after the first firing step at 858°C, while the solid-state reacted powder already after calcination exhibits over 80% of (2212) phase. The slackened (2212) formation involves a delay in its grain growth at the considered stage. Taking into account the (2223) formation mechanism proposed by Wang *et al.*,[7] in which after a nucleation on the (2212) particle surface the (2223) growth process is controlled by diffusion, the accelerating effect of the smaller (2212) grain size, typical of calcined pyrolysed powder, becomes clear.

Moreover, the starting submicronic dimension of the pyrolysed precursor grains, promoting the

Table 1. XRD phase analysis of pyrolysed powders after various synthesis steps

		Thermal treatment			
	As pyrolysed	*Calcined*	*5 h/846°C*	*5 h/858°C*	*5+3 h/858°C*
$CaCO_3$	X				
$SrCO_3$	X				
CuO	X	XX			
$Ca_{1-x}CuO_2$	XX				
Bi_2CuO_4	XXX				
Bi_2SrO_4	X				
Bi_2CaO_4	X				
$(Ca,Sr)CuO_2$			X	X	
Ca_2CuO_3			X	X	X
Ca_2PbO_4		XX	XX	XX	XX
Cu_2SrO_3		XX			
$Bi_6(Ca,Sr)_5O_{14}$		XXX			
$Bi_6Ca_4O_{13}$		X			
2201			X	X	tr.
2212		X	XXX	XXX	X
2223			tr.	XX	XXX

Semi-quantitative scale of XRD intensity on a logarithmic base is employed: XXX = 10^3, XX = 10^2, X = 10^1, tr = 10^0.

solid-state diffusion process, stimulates the interfacial reactions responsible for any intermediate and/or final phase growth.[7]

Micrographs in Fig. 3(a,b) show morphology differences between the two completely reacted powders: the one obtained by organic precursor is characterized by reduced average dimension of grains (0·7 μm against 3·5 μm) and definitely less anisotropic shape. These features can explain the differences in green packing of the two powders: the powder by organic precursor shows significantly lower density values of green bodies compared to the solid-state reacted one. This reflects in the different starting points (time = 0) of the densification curves reported in Fig. 4, which shows the densification behaviour of the two powders during hot pressing at different temperatures.

It is evident that the densification rate increases with temperature and at 800°C the density value approach 100% after 2 h. The curves at 790°C were mathematically analysed on the basis of Brook's theory[8] in order to establish the firing behaviour of the two powders in terms of the attainment of high density and the limitation of grain growth. Thus a parameter that relates the

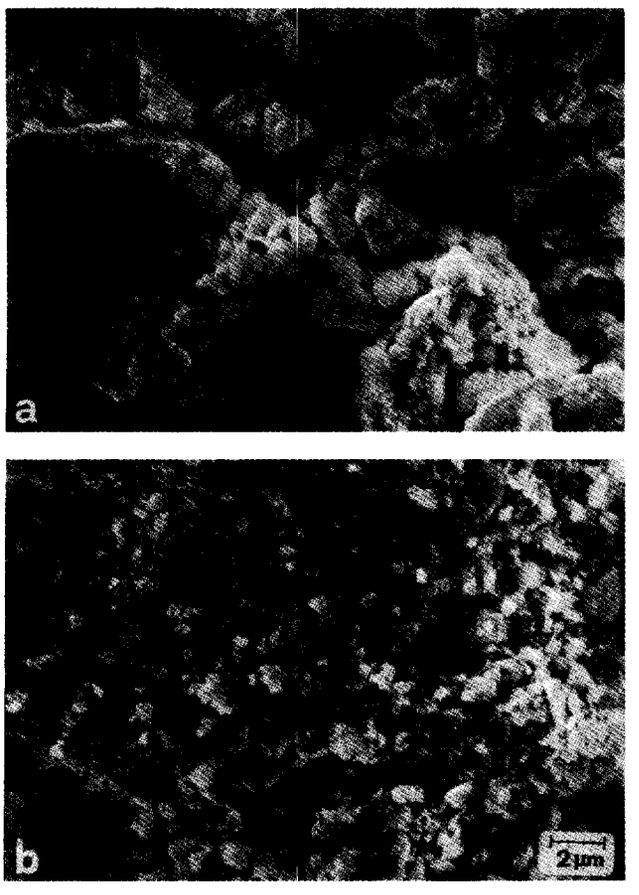


Fig. 3. SEM micrographs of BSCCO completely reacted powders ((2223) phase >95%): (a) solid state (96 h thermal treatment), (b) organic precursor (24 h thermal treatment).

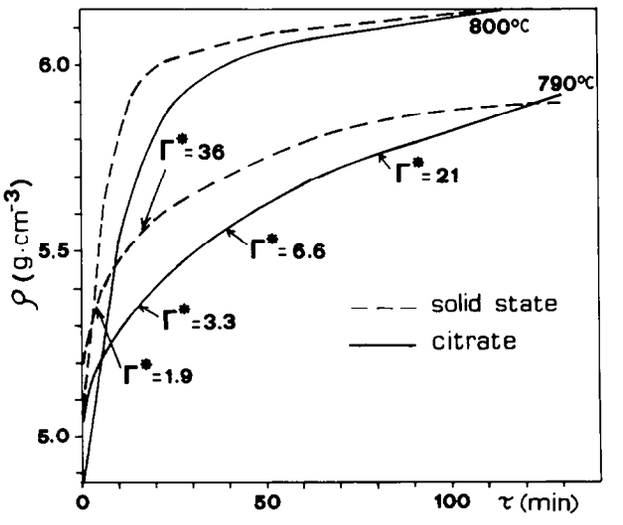


Fig. 4. Densification curves of solid-state reacted and citrate precursor powder; calculated figures of merit Γ^* are reported for some particular density values.

rate of grain growth and the densification rate is a figure of merit defined as:

$$\Gamma^* = -(1/3)\,\dot{\rho}^{\bullet}\,\rho/\dot{\rho}^2$$

where $\dot{\rho}$ is the densification rate and $\dot{\rho}^{\bullet}$ is the densification acceleration. The Γ^* values calculated at different densities along the densification curve (Fig. 4) evidence the behaviour of the two powders: the solid-state reacted powder, which starts the isothermal stage with better particles packing, densifies very rapidly up to 15 min and Γ^* is characterized by a low value, as expected for powders with high densification tendency (and low grain growth rate). At higher densities, Γ^* is lower for organic precursor powder, with respect to solid-state reacted one; in fact, the densification rate of the former increases, leading to the attainment of higher-density values over 120 min of hot-pressing treatment. Γ^* values also show that grain growth in the solid-state reacted powder (highly anisotropic in this case) is markedly enhanced (for densities higher than 80%), causing a reduction in the densification rate. Contemporarily, however, the more anisotropic grain growth allows the attainment of a higher degree of texture orientation (the orientation factor F in this case is $\approx$ 48%, to be compared with 35% for dense sample obtained by organic precursor powder). The citrate powder, characterized by a lower green packing, but able to achieve a higher density in long hot-pressing treatments, produces dense material with a low Lotgering factor, owing to the larger randomness in orientation of less anisotropically grown grains.

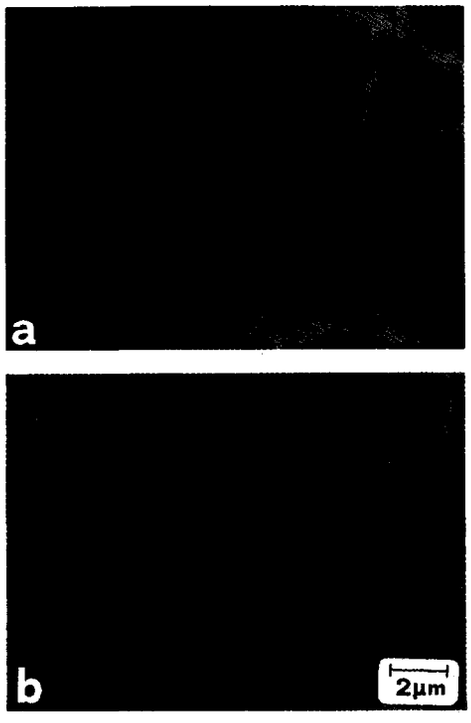


Fig. 5. SEM micrographs of fracture surfaces showing the morphology of hot-pressed dense samples obtained by (a) solid-state reacted powder, (b) citrate precursor powder.

Table 2. Properties of dense samples obtained by pyrolysed powder

Sample	*Sintering temperature (°C)*	*RD (%)*	*F (%)*	$T_{c\ onset}$ *(K)*	$T_{c\ offset}$ *(K)*
1	790	94	35	110	92
2	800	98	38	115	106

In Fig. 5(a,b) the morphology of hot-pressed samples is reported, showing the reduced average dimension of grains (about 2/5) of the sample prepared by organic precursors with respect to that obtained by solid-state reacted powder.

The properties of the hot-pressed samples are reported in Table 2. Critical temperature evaluated on dense samples showed Tc_{onset} values $\approx$ 110 K, proving the substantial (2223) phase purity of the bulk.

The presence of a tailing phenomenon on Sample 1,[9,10] lowering the Tc_{offset} (Table 2), is attributed to the still incomplete densification in comparison with Sample 2 and to the low oxygen income during densification itself. Indeed, it is well known[11] that a scarce diffusion of oxygen into the inner part of the sample causes a lowering of T_{c0} in the (2223) phase: actually the critical temperature of Sample 2 (as densified) was for this second reason very low ($T_{c0} \approx$ 80 K).

Since an oxygen decrease in formula stoichiometry, typical of highly dense materials, could be supposed on the basis of cell parameters evaluated by XRD analysis, Sample 2 was annealed at 820°C for 40 h in flowing air in order to restore the cell parameters themselves, and T_{c0} increased up to 106 K.

4 Conclusions

The citrate solution pyrolysis as an alternative method of preparing precursors for synthesis of BSCCO (2223) superconducting phase was performed and analysed, and inherent differences in comparison with traditional solid-state mixtures of oxides and carbonates were found: intermediate Bi–Ca phases play a determinant role in the organic precursor transformation, retarding the (2212) appearance and allowing the formation of (2223) phase in a total heat-treatment time at least four times shorter.

As expected, grain development is smaller for citrate precursor powder, and their shape is clearly more isotropic; densification exhibits a rather slow rate at the beginning, but within two hours powders by citrates reach and even exceed density values typical of solid-state reacted powders.

Critical temperatures result not too far from

those obtained with solid-state reacted powders, though lesser orientation factors attained by citrate precursor powders point to presumably lower transport current values; anyway, the probable compensating effects of different pinning centre concentrations deserve further investigation.

References

1. Tampieri, A., Celotti, G., Ricciardiello, F. & Russo, G., *Physica C*, **227** (1994) 300–8.
2. Sun, Y. K. & Lee, W. Y., *Physica C*, **212** (1993) 37–42.
3. Shimono, I., Nagata, S., Konishi, H. & Hamaguchi, Y., *Jpn. J. Ceram. Soc.*, **101** (1993) 1018–24.
4. Tampieri, A., Landi, E. & Bellosi, A., *Mater. Chem. and Phys.*, **34** (1993) 157–61.
5. Lo, W., Chen, Y. L., Tang, T. B. & Stevens, R., *Br. Ceram. Trans. J.*, **89** (1990) 218–22.
6. Boehnke, U. C., Heitman, P., Krötzsch, M., Lippold, B. & Zahn, G., *J. Mater. Sci.*, **28** (1993) 111–6.
7. Wang, M., Xiong, G., Tang, X. & Hong, Z., *Physica C*, **210** (1993) 413–6.
8. Pickup, H., Gilbart, E., Brook, R. J., Leriche, A. & Cambier, F., *Proc. 2nd Int. Symp. on Ceramic Materials and Components for Engines*, Lübeck, 14–17 April, 1986, pp. 63–70.
9. Murayama, N., Kodama, Y., Sakaguchi, S. & Wakai, F., *Jpn. J. Ceram. Soc.*, **100** (1992) 236–9.
10. Celotti, G., Tampieri, A., Masini, R. & Malpezzi, M. C., *Physica C*, **225** (1994) 346–52.
11. Nomura, S., Yoshino, H. & Ando, K., *J. Am. Ceram. Soc.*, **76** (1993) 2687–90.

Journal of the European Ceramic Society **15** (1995) 741–758
© 1995 Elsevier Science Limited
Printed in Great Britain. All rights reserved
0955-2219/95/$9.50

0955-2219(95)00047-X

Binder Distribution in Green Ceramic Foils

G. P. van der Beek, U. Gontermann-Gehl & E. Krafczyk

Philips GmbH Forschungslaboratorien, Weisshaustrasse 2, D-52066 Aachen, Germany

(Received 7 November 1994; revised version received 10 February 1995; accepted 14 February 1995)

Abstract

Green ceramic foils with a thickness of 20 μm were tape cast on a doctor-blade machine from an aqueous dispersion of barium titanate powder, containing poly vinyl alcohol, PVA as a binder and triethylene glycol, TEG as a plasticizer. After casting, the wet foils were dried in an oven. The specific aim of this study was to characterize the binder distribution in green foils and to find parameters that affect this distribution. Mercury Intrusion Porosimetry and Nitrogen Adsorption (B.E.T.) were used as techniques to analyse the binder distribution. Experiments were carried out with foils containing either a coarse (d_{50} = 0·75 μm) or a fine barium titanate powder (d_{50} = 0·2 μm). The moment in the drying process of foils, that the binder gets fixed in the ceramic structure determines the binder distribution in green foils. The earlier the PVA fixation process takes place, the more homogeneous is the binder distribution. The plasticizer triethylene glycol (TEG) promotes fixation of PVA by a gelation process. More TEG in the slip leads to a more homogeneous binder distribution in foils. In the case of a low TEG amount, small pores are preferentially filled with binder over large ones and the lower side of foils is enriched with binder. Less hydrolysed PVA types are less susceptible to gelation with TEG, resulting in a more heterogeneous binder distribution.

1 Introduction

Thin green ceramic foils are used for the preparation of several laminated components, e.g. ceramic multilayer capacitors (CMCs)[1–3] and multilayer actuators (CMAs),[4] solid oxide fuel cells (SOFC),[5] heat exchangers,[6] ceramic superconducting elements[7] and laminated composites.[8]

Green ceramic foils consist of inorganic particles, organic substances (binder, plasticizer, dispersants, etc.), air (porosity) and moisture or organic solvent rests. The binder, which is a polymeric substance, has an adhesive function for the ceramic particles within green tapes. The binder is present during a large part of the whole processing route for ceramic components. In most cases, ceramic components are built and shaped in the green state. After that, the binder is burnt out and finally the components are sintered. The constitution and distribution of the binder within green foils influence or determine foil properties that are important for the processing of laminated ceramic components: mechanical characteristics,[9] stress sensitivity, lamination behaviour, porosity and pore sizes. The binder distribution may have a large effect on the mass and heat transfer resistance during thermolysis of green components.[10] These parameters are of crucial importance to prevent crack and defect formation. The amount of binder and the binder distribution in green foils may also affect the porosity in sintered products. Porosity in green bodies can be reduced by pressing; porosity after binder burn-out can only disappear by the sintering procedure. A high local binder content in the pressed green state leaves such a high porosity after binder removal that it cannot be sintered any more to a dense ceramic. Considering all the effects described above, the binder distribution in green foils may have a significant impact on the structural integrity of laminated green components and, eventually, on that of sintered ones as well.[11,12]

The specific aim of this study is to characterize the binder distribution in foils and to determine parameters that affect this distribution. The techniques used for this purpose are Nitrogen Adsorption (B.E.T.) and Mercury Intrusion Porosimetry.

To investigate the binder distribution, as a function of particle size (or pore size), we have analysed foils made from both coarse and fine powders. As a powder system we have taken barium titanate, which is an important material for dielectric layers.[13,14] The influences of the binder concentration, the binder type and the plasticizer content in the slip, on the binder distribution in foils have also been studied. Apart from the materials, the processing conditions (i.e. drying procedure) affect the binder distribution as well.

We will start this paper with a brief description of the drying mechanism of ceramic foils and discern the important parameters for drying. This description appears to be helpful for the interpretation of the results obtained in this study.

2 Theory of Drying

A number of studies on drying of ceramic bodies have been issued over the last few years.[15-21] An excellent paper on this issue has been written by Scherer.[17]

Several stages can be distinguished during drying of ceramic bodies. The drying mechanism, the rate-controlling factors, the stresses that may develop and the dimension changes may all be different in these stages of drying.[17-19] Each stage depends, in a particular way, upon external factors (temperature, air flow and ambient vapour pressure) and on internal factors (such as body geometry, particle packing, pore sizes). For a good controlled drying procedure, the drying conditions have to be set separately for each stage.

The first drying stage is called the *constant rate period* (CRP). Under constant external conditions, the rate of evaporation per unit surface area is independent of time and moisture content in the drying body. During the CRP, the shrinkage of the drying body is equal to the volume of liquid evaporated. The meniscus remains at the exterior surface.

The drying rate during this stage depends upon the external conditions such as ambient vapour pressure, temperature, draught and geometry of the system. In the constant rate period, the evaporation process is by definition the rate-limiting step and not the liquid transport in the green body. Evaporation is an endothermal process and has, therefore, a cooling effect. A reduced temperature upon evaporation leads to a lowering of the drying rate. This feedback process equilibrates when the drying surfaces reach the so-called *wet bulb* temperature. Hence, the drying temperature of water-based ceramic foils is determined by the humidity, the ambient temperature and the air flow.

Liquid from the interior of the green body is transferred to the evaporation surface by flow due to pressure gradients (capillary pressure) as well as by diffusion due to concentration gradients. The flow flux is the most important one in this stage.

The constant rate period ends at the so-called *critical point* where shrinkage virtually stops. At this point, the ceramic structure has been built and further drying occurs by replacing liquid in the ceramic network by air.

A phenomenon often observed during drying of ceramic tapes is the so-called *skin effect*. In such a case, the evaporation process is so fast that the concentration of binder at the surface becomes very high because the diffusion rate is too small. The binder may then precipitate or gelate to an impermeable layer which hinders the transport of the underlying liquid to the evaporation surface. The drying rate may then reduce drastically and the constant rate period is ended by definition. Skin-forming can be prevented by lowering the evaporation rate and/or increasing the diffusion flux. A reduction of the ambient temperature decreases the evaporation rate but also decreases the diffusion flux and is therefore not very effective to counteract binder segregation. Increasing the humidity and/or reducing the air flow lowers the evaporation rate. The diffusion rate may eventually be enlarged because the wet bulb temperature increases due to a lowered evaporation rate. Hence, to overcome the skin effect it is much more effective to reduce the difference between the ambient and equilibrium vapour pressures than to lower the ambient temperature. The skin-forming effect becomes less important for thinner foils because the diffusion distances are smaller.[20]

After the critical point the second drying stage sets in. This stage is called the *first falling rate period* (FRP1). The vapour/liquid interface recedes into the green body and the drying surface may begin to lose its translucency. The drying rate decreases and the temperature of the surface rises above the wet bulb temperature during this stage. Although the meniscus retreats into the green body, most of the evaporation still occurs at the exterior surface due to the fact that the liquid in the pores near the surface is in a funicular condition (i.e. continuous thin liquid pathways along the flow is still possible). Therefore, the temperature of the surface remains under the ambient temperature and the drying rate is still sensitive to external factors as temperature and vapour pressure. The liquid flux from the interior to the surface becomes, however, more and more rate-controlling. At the same time, some liquid evaporates in the unsaturated pores and the vapour is transported by diffusion.

The drying front becomes irregular in instances where different pore sizes are present. At the critical point, the radii of the menisci in different pores are equal and therefore the capillary pressures are equal. Upon further drying, the meniscus radii of the small pores get smaller than those of the large pores. This leads to different capillary pressures in large and small pores. As a consequence, liquid flows from large pores to smaller ones. Hence, large pores are emptied before the small ones.

In the last drying stage, the *second falling rate period* (FRP2), the flux of the liquid is very slow.

Eventually, the flow to the surface stops, the liquid is isolated in pockets (mainly the small pores) and can only be removed from the green body by vapour diffusion. This diffusion process controls the drying rate, which is therefore less dependent upon external factors, and the evaporation process takes place completely inside the body. The temperature of the surface approaches the ambient temperature.

3 Preparation of Foils

Both ceramic foils containing coarse barium titanate powder and foils containing fine barium titanate powder were made and analysed in this study. These foils were prepared by tape casting on a doctor-blade machine.[22-24] The conducted procedure was as follows. Dielectric powder was dispersed into water with the help of a dispersant. The amount of dispersant added was equal to that needed for a minimum value of the yield value and of the viscosity. Of course, more dispersant per weight unit of solid material had to be added to the fine barium titanate powder because of the larger specific surface area (due to smaller particles). The obtained dispersion, which is called a slurry, is then de-agglomerated by ultrasonification (15 min in a US bath of 200/400W) and milling (Attritor-mill filled with 2 mm ZrO_2 balls at 500 rpm; 20 min milling for the fine powder and 40 min for the coarse powder sample). The average diameter of the coarse barium titanate particles in the slurry was about 0·75 μm (= d_{50} as measured by X-ray absorption in a sedimentation experiment using the Micromerites Sedigraph 5000D). This value was equal to 0·2 μm for the fine barium titanate sample. After sieving the slurry, the constituents listed below are added and the suspension is then called a *slip*.

- The binder poly vinyl alcohol, PVA. The rheological behaviour of the slip, which is important for the casting process, may be adjusted by the amount and/or type of binder. When the solvent evaporates after tape casting, the ceramic particles within the foil are held together by the binder. In our study, we used different PVA samples, which are given in Table 1.
- The plasticizer triethylene glycol, TEG. In general, the plasticizer structurally expands the binder and improves the distribution of the binder in the slip. The flexibility of green foils may be increased by the addition of a plasticizer, which lowers the glass transition point, T_g of the binder.

Table 1. Poly vinyl alcohol samples used in this study

PVA sample	$\overline{M_w}$ *(g mol^{-1})*	*hydrolysis ratio*[a] *(mol%)*
PVA 31-88	31 000	87·7 ± 1·0
PVA 27-98	27 000	98·4 ± 0·4
PVA 125-98	125 000	98·4 ± 0·4
PVA 205-88	205 000	87·7 ± 1·0

[a]Poly vinyl alcohol is made from poly vinyl acetate. The hydrolysis ratio is the percentage of acetate groups hydrolysed to alcohol groups.

- Small amounts of an anti-foam agent (to counteract foam formation during mixing), a wetting agent (to have a good wetting behaviour of the slip on the tape casting carrier) and a release agent (to release the green foil from the carrier).

Concentrations of PVA and TEG are always expressed in wt% relative to the solid material throughout this study. After all these additions, the resulting slip was finally degassed before tape casting took place to prevent holes in the foil caused by enclosed air bubbles. Care was taken to prepare the slurry and slip always in the same way in order to be able to compare the foil properties properly.

In this study, 20 μm green foils (unless otherwise stated) were cast from a slip with the help of a doctor-blade machine and subsequently dried in an oven (without air circulation). Because the drying procedure may affect the foil properties, results presented in this study are all based on foils which were dried in the same way, i.e., at 60°C for 30 min. After drying, the foils were carefully released from the substrate.

The binder content and plasticizer concentration in slips are varied in this study. Changes in these concentrations were always compensated for by the amount of water added. In this way, the solid content of all slips could be kept the same (i.e. 45·6 wt%). Variation in the solid content leads to a different drying procedure, which may influence the foil characteristics.

4 Measuring Methods

Both Nitrogen Adsorption (B.E.T.) and Mercury Intrusion Porosimetry may yield information about the binder distribution within a green ceramic foil. Neither of these methods gives, however, a real binder concentration profile over the thickness of the foil.

4.1 B.E.T. nitrogen adsorption

Gas adsorption onto solid phases was first

described by Brunauer, Emmet and Teller (B.E.T.). They derived the following adsorption isotherm:

$$\frac{V}{V_m} = \frac{C(P/P_0)}{[1-(P/P_0)]\,[1 + (C-1)\,(P/P_0)]}$$

where V_m is the volume of one adsorbed monolayer, P is the vapour pressure of the adsorbate and P_0 is the saturated vapour pressure at the temperature of adsorption. The constant C is a measure for the affinity of the adsorbate molecules for the surface. A large C value indicates a strong interaction of the adsorbing molecules to the substrate (so-called 'high energy' surface). Hence, the form of the isotherm depends upon the substrate material. Isotherms with C-values between 1 and 100 are quite usual. Inorganic oxide surfaces have a high C-value most of the time.

The specific surface area (S) can be calculated from the V_m value using the molecular dimension of the adsorbate molecules. Because V_m stays explicitly in the equation of the adsorption isotherm, S can be determined from the experimental adsorption data.

Adsorption hysteresis is frequently found for gas adsorption onto porous media. This hysteresis effect can be explained by capillary condensation. Small pores will be filled with adsorbate at a high vapour pressure, forming a concave adsorbate meniscus. According to Kelvin's law, the evaporation from a flat liquid surface and a concave liquid surface as a function of the vapour pressure is different. Hence, the desorption isotherm will be influenced by capillary condensation. This hysteresis effect is, of course, dependent upon the size of pores. A pore size distribution can, in principle, be determined from the hysteresis effect. Obviously, only small pores (2 nm $\leq d_{pore} \leq$ 50 nm) can be detected in this way.

4.1.1 Analyses

Ceramic foils, with and without binder (after binder burn-out), as well as the ceramic powders were analysed using the ASAP 2000 B.E.T. apparatus from Micromeritics. Nitrogen gas was used as an adsorbate. Before each measurement, the sample was degassed under vacuum at 50°C for about 15 h. The surface affinity to nitrogen adsorption was determined by calculating the C-value from the adsorption isotherm. Changes in the chemical nature of the surfaces inside pores may be detected with the help of this parameter.

As already described in the previous section, small pores can be determined by the B.E.T. adsorption technique. However, we did not pay very much attention to this feature of the B.E.T technique for the following two reasons:

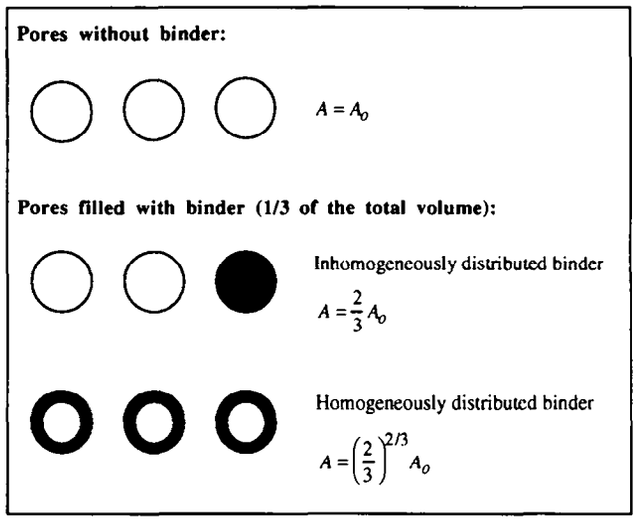


Fig. 1. Surface areas of spherical pores differently filled with binder.

(1) the pore size distribution of most of the foils goes beyond the detection limit of this technique,
(2) the pore size distribution can be measured more accurately by Mercury Intrusion Porosimetry (see next section).

The specific surface area of a green foil depends upon (i) the primary particle size, (ii) the ceramic structure, (iii) the total amount of binder and (iv) the binder distribution. An example of the correlation between the specific surface area of foils and the binder distribution is given in Fig. 1. A foil with an inhomogeneous binder distribution always has a lower surface area than a foil containing a homogeneously distributed binder.

4.1.2 Relationships between the surface area and the binder distribution in foils

Theoretical dependencies of the surface area on the total amount of binder in foils are derived in the Appendix for four special cases. These instances differ in pore geometry and/or binder distribution. The formulas belonging to these different cases are given below. The parameters used in these formulas are:

A_0 The specific surface area of a foil without binder
A The specific surface area of foils containing a certain amount of binder
P_0 The total porosity of foils without binder (not to confuse with the saturated vapour pressure in the B.E.T. adsorption isotherm)
V_i The amount of organic substances (binder, dispersant, etc.), expressed in vol.% with respect to the ceramic material.

4.1.2.1 Spherical pores filled homogeneously with binder. In this case, the added amount of binder with respect to the ceramic is assumed to affect only the radius of the pores (see Fig. 1).

$$A = A_0\left[1-\frac{1-P_0/100}{P_0}V_i\right]^{2/3} \quad (1)$$

4.1.2.2 Pores filled inhomogeneously with binder. In this instance, the amount of added binder with respect to the ceramic is assumed to affect only the number of filled and unfilled pores. This dependency is invariant of the pore geometry. The same relationship holds also for cylindrical pores that are filled from the bottom to the top (the filling height of the cylinders changes with the amount of binder).

$$A = A_0\left[1-\frac{1-P_0/100}{P_0}V_i\right] \quad (2)$$

4.1.2.3 Cylindrical pores filled homogeneously with binder. In this case, the amount of added binder with respect to the ceramic is assumed to affect only the diameter of the cylinder.

$$A = A_0\left[1-\frac{1-P_0/100}{P_0}V_i\right]^{1/2} \quad (3)$$

4.1.2.4 Small spherical pores preferentially filled with binder over large ones. The previous relationships were all based on the assumption that pores are filled equally over the size distribution. Suppose that three different pore sizes (spheres with radii of $0{\cdot}5R$, R, and $2R$) exist in a ceramic foil without binder. The number of pores, for each type, is chosen such that the volume of each class of pores is equal to one third of the total porosity. An inhomogeneous binder distribution is assumed, i.e. pores are filled one by one by the binder. Suppose that first the small pores are filled with binder, then the medium sized ones, and finally the big ones. The total surface area as a function of the amount of binder is then described by the following set of relations:

$$A = A_0\left[1-\frac{12}{7}\left(\frac{1-P_0/100}{P_0}\right)V_i\right] \quad (4a)$$

$$\text{for } 0 \le V_i \le \frac{1}{3}\frac{100P_0}{(100-P_0)}$$

$$A = A_0\left[\frac{5}{7}-\frac{6}{7}\left(\frac{1-P_0/100}{P_0}\right)V_i\right] \quad (4b)$$

$$\text{for } \frac{1}{3}\frac{100P_0}{(100-P_0)} \le V_i \le \frac{2}{3}\frac{100P_0}{(100-P_0)}$$

$$A = A_0\left[\frac{3}{7}-\frac{3}{7}\left(\frac{1-P_0/100}{P_0}\right)V_i\right] \quad (4c)$$

$$\text{for } \frac{2}{3}\frac{100P_0}{(100-P_0)} \le V_i \le \frac{100P_0}{(100-P_0)}$$

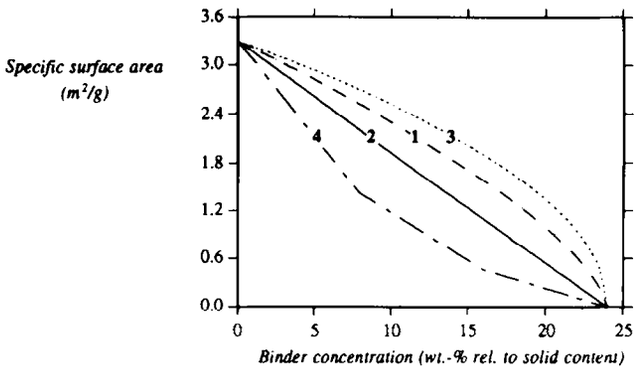


Fig. 2. Theoretical relations between the specific surface area and the amount of added binder relative to the ceramic for foils containing the coarse barium titanate. The numbers correspond to the different cases described above. The following parameters were used for the calculations: P_0 = 55%, A_0 = 3·3 $m^2.g^{-1}$, ρ_{binder} = 1·2 $g.cm^{-3}$, $\rho_{ceramics}$ = 5·9 $g.cm^{-3}$.

All the dependencies given above are visualised by the curves given in Fig. 2. As can be seen in this figure, a high surface area corresponds to a homogeneous binder distribution (cases 1 and 3). Surface area values lower than those given by case 2 can, in principle, only occur if small pores are filled preferentially over large ones.

In order to be able to compare binder distributions of different systems by measuring the specific surface area, we have defined a so-called *binder distribution index*, X:

$$X = \frac{A - A_0\left[1-\frac{1-P_0/100}{P_0}V_i\right]}{A_0\left[1-\frac{1-P_0/100}{P_0}V_i\right]^{1/2} - A_0\left[1-\frac{1-P_0/100}{P_0}V_i\right]} \quad (5)$$

This index is 0 for specific surface areas corresponding to line 2 in Fig. 2, and 1 for values corresponding to curve 3. Hence, the larger the index X, the more homogeneously is the binder distributed. We have to note, however, that high X-values can, in principle, also be due to the fact that large pores are preferentially filled with binder over small ones. In practice, this will rarely occur because large pores are emptied first during drying (by capillary action). On the other hand, negative X values are more probable because of the tendency that small pores are preferentially filled with binder.

4.2 Mercury intrusion porosimetry

The principle of Mercury Intrusion Porosimetry is based on the fact that mercury behaves as a non-wetting liquid towards most substances. Consequently, it does not intrude into the pores of these substances without applying pressure. Mercury porosimetry measurements are conducted by measuring a series of pressures with corresponding

volumes of mercury intruded into the porous body. The pore radius (r) can be calculated from the applied pressure (ΔP), the surface tension of mercury (γ_{LV}) and an assumed wetting angle (θ), using the Washburn equation:

$$\Delta P = \frac{2\gamma_{LV}\cos\theta}{r} \quad (6)$$

The total amount of pores with a certain radius is simply calculated from the volume of intruded mercury at the pressure corresponding to that pore size.[25–28] The total pore volume can be determined if all pores have been filled at the maximum pressure of the equipment. The porosity can then be calculated if the total volume of the sample is known.

A few things should be taken care of using Mercury Intrusion Porosimetry. These items can be summarized as follows:

1. Mercury Intrusion Porosimetry often displays hysteresis phenomena. The pressure-volume relationship is different for penetration and retraction of the mercury. A certain amount of mercury may remain in the porous medium after complete reduction in the pressure. Two causes are mainly responsible for this phenomenon:
   - — The advancing contact angle is often different from the receding one. Different penetration and retraction curves will then be obtained.
   - — Structural hysteresis refers to the presence of the so-called *ink-bottle* pores (i.e. pores with a small opening). During penetration, one big ink-bottle pore is measured as a number of small ones with radii equal to that of the opening of the big pore. In general, the effect of structural hysteresis will be less if the porosity is higher. However, the details of this phenomenon will depend upon the particular geometry of the pore space.
2. If a number of hysteresis loops are recorded, the first penetration curve is different from subsequent ones. A difference in contact angle for a fresh surface and a surface that has already been in contact with mercury may be the reason for this phenomenon.
3. For easily deformable samples, geometrical and pore size changes may occur by the applied pressure (compression).

Assuming that the pores are series of cylinders of different diameters, the surface area can be calculated by integrating the volume–diameter curve. Specific surface areas determined in this way are, in most cases, higher than those obtained from sorption isotherms (B.E.T.) due to the presence of *ink-bottle* pores. We do not use this feature of Mercury Intrusion Porosimetry because the determination of the specific surface area by this technique is less reliable than that of B.E.T. measurements.[25, 28]

4.2.1 Measurements

The measurements were conducted with a Porosimeter 2000 from Fa. Carlo Erba Instruments. Samples that were both analysed by nitrogen sorption and porosimetry were first used for the specific surface area measurement and afterwards put into the porosimeter vessel. Samples of about 15 cm^3 were evacuated for about 1 h before immersing in mercury at a low pressure (0·1 MPa). The Hg-pressure was increased step-wise. The pressure was enlarged only if the volume of intruded mercury had become constant. After a complete reduction in the pressure, a second run was started. All measurements were carried out at room temperature.

We used the following values for the parameters needed to calculate the pore sizes: γ_{LV} = 0·485 N m^{-1} and θ = 140°. For comparison of the porosity and pore sizes between samples of the same nature, it is not really necessary to know the exact values of these parameters. The pore size distribution is indicative of binder distribution in a foil, as can be seen in Fig. 1. Only the number of large pores is diminished for a very inhomogeneous binder distribution. The pore sizes remain unchanged in such a situation. In the case of a homogeneously distributed binder, the pore sizes get smaller with respect to pores in foils without binder.

5 Results

Results from measurements, as mentioned above, are described in this section. Firstly, analyses of the ceramic powders used to process the foils in this study are given. Then the results of foils released from binder are reported, and lastly the characterization of green foils is described. The interpretation and discussion of the results is partly done in a separate paragraph (Section 6).

5.1 Powders

For a correct analysis of green ceramic tapes, characterization of the powders, from which these foils were made, is needed. Porosity measurements were only possible when powders were pressed (or centrifuged) to a coherent pill. The results of the powder analyses are summarized in Table 2.

Table 2. Powder analyses

System	*C*	*B.E.T. surface* ($m^2 g^{-1}$)	*Porosity* (%)	d_{50} *pore size (nm)*
Coarse barium titanate #1:				
Without pre-treatment	103·3	2·91		
Isostatically pressed at 320 MPa	97·7	3·24		
Slurry, 40 min milled, dried	78·5	3·32		
Slurry, 40 min milled, centrifuged	62·3	3·20	37·6	181
Slurry, 40 min milled, dried, pressed at 320 MPa	64·0	3·40	36·1	152
Coarse barium titanate #2:				
Without pre-treatment	108·6	2·87		
Powder-PVA granules	40·4	1·19		
50 wt% powder-PVA granules + 50 wt% powder	76·7	2·14		
Fine barium titanate:				
Without pre-treatment	106·1	9·09		
Isostatically pressed at 3·2 kbar	113·3	9·83	37·9	61
Slurry, 20 min milled, dried	78·7	9·34		
Slurry, 20 min milled, centrifuged	78·6	9·36	38·9	56
Slurry, 20 min milled, dried, pressed at 320 MPa	75·4	9·27	37·6	50
PVA 125-98:				
Crushed granules, dried at 50°C	20·1	–	–	–

5.1.1 B.E.T. analyses

The specific surface areas of the fine and coarse powders without any special treatment are equal to 9·1 $m^2 g^{-1}$ and 2·9 $m^2 g^{-1}$, respectively. No significant difference was found between two different batches of the coarse sample (batch #1 and #2 in Table 2). As expected, the specific surface area of the fine powder sample is much higher than that of the coarse powder due to the smaller particles.

As can be seen in Table 2, the *C*-values of the powders without any pre-treatment are equal to about 105, indicating 'high energy' surfaces. Just isostatically pressing the powders does not change the B.E.T. values very much. The specific surface area seems to increase a little upon this treatment.

We also analysed the powders from the slurries made as described in Section 3. The powders were separated from the slurries either by simply drying or by centrifugation and subsequently drying the centrifuged cake. The specific surface areas of the powders from the slurries are slightly higher than those of the ones without any pre-treatment because of the milling procedure used for the preparation of slurries. This effect is not very large because the surface area of particle aggregates is not very different from that of separated particles. The *C*-values of the slurry powders are all about 75, which is significantly lower than those found for untreated powders. This effect is caused by the adsorption of the dispersant onto the particle surfaces. The chemical nature of the surface, and hence the affinity to nitrogen adsorption, have been changed by this adsorption process.

In order to investigate the influence of the poly vinyl alcohol on the *C*-parameter, we dispersed coarse powder (batch #2) into a PVA solution. The binder concentration with respect to the ceramic material was of the same order as that used in slips (i.e. 8 wt%). Thin films of this dispersion were dried in a oven at 60°C. The product obtained in this way was analysed by the B.E.T. technique. The *C*-value of these powder-PVA granules was equal to 40·4. A mixture of 50 wt% of this product and 50 wt% of untreated powder gave a *C*-value of 76·7 (mixing was done in the dry state). Hence, the B.E.T. technique is sensitive to the degree of powder particle coating with PVA. This effect is graphically shown in Fig. 3.

Finally, we have measured the *C*-value of pure PVA 125-98. This turned out to be about 20, i.e.

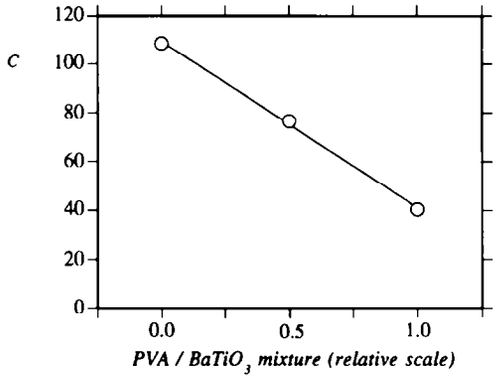


Fig. 3. Surface affinity to nitrogen adsorption (*C*-value) of coarse $BaTiO_3$/PVA mixtures as a function of the PVA concentration: 0.0, pure $BaTiO_3$ powder; 1.0, PVA/$BaTiO_3$ granules (8·0 wt.% PVA with respect to barium titanate); 0·5, pure $BaTiO_3$ powder mixed with the same PVA/$BaTiO_3$ granules as in 1·0 in a weight ratio of 1:1.

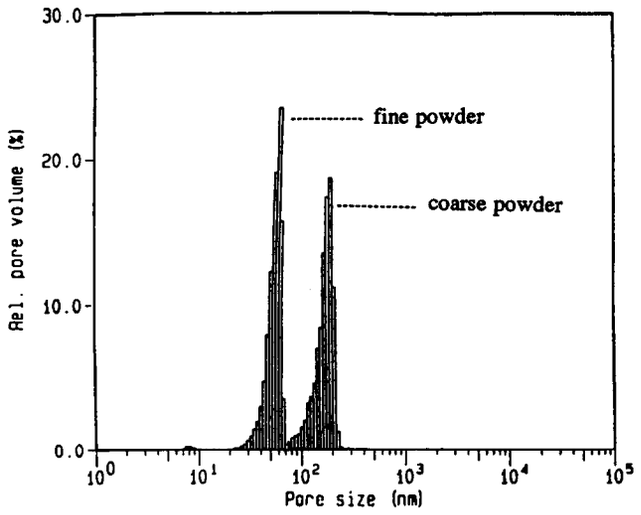


Fig. 4. Pore size diagrams of pills centrifuged from slurries containing the two grades of powder.

the lowest value found so far. Apparently, the nature of the ceramic powder in the dried PVA/$BaTiO_3$ mixture (C = 40) was not fully masked by PVA. The powder particles were, probably, not completely or sufficiently wetted (coated) by the PVA in the dispersion.

5.1.2 Porosimetry

The pore size distributions of powders centrifuged from slurries to a coherent tablet are given in Fig. 4. As can be seen in this figure, the pore sizes for the finer powder batch (d_{50} pore size ≈ 60 nm) are much smaller than for the coarser sample (d_{50} pore size ≈ 190 nm).* A measure of the particle packing is the d_{50} pore size divided by the d_{50} particle size. These numbers lay between 0·20 and 0·30 for both powders. Values of about 0·14 (= 1/7) are found for an ideally closed packed system of monodisperse particles. Hence, both powder pills have the same fairly close particle packing. This is supported by the total porosity measurements. The total porosity for the coarse powder system and the fine powder system are the same, i.e about 37%. For comparison, the porosity of a closed packed system of monodisperse particles is equal to 26%. Apparently, the slurries did not contain large aggregates.

5.2 Foils

A green foil can be conceptualized as a ceramic structure containing organic material. First, the ceramic structure of foils will be discussed. Paragraph 5.2.2. deals with the distribution of organic material within the ceramic structure.

5.2.1 Foils released from organic material

Green foils were released from the organic substances by heating in air at 550°C for 1 h. Both foils consisting of coarse and fine powder were analysed. The influences on the ceramic structure of the binder type, binder concentration and the amount of plasticizer added to the slip have been studied. All results of these measurements are summarized in Table 3.

The C-values and the specific surface areas measured for these burned foils come close to those found for the untreated powders in Table 2.

*The d_{50} value is the pore size at which half of the total porosity is filled with mercury.

Table 3. Analyses of foils released from organic material

PVA type and concentration present in the foils before binder removal	*TEG conc. in the slip (wt%)*	*B.E.T. results*		*Porosity (%)*	*d_{50} pore size (nm)*
		C	*S ($m^2 g^{-1}$)*		
Coarse barium titanate:					
6·5 wt% PVA 205-88	0	83	3·46	55·9	380
6·5 wt% PVA 125-98	0	109	3·63	53·1	364
6·5 wt% PVA 205-88	2·6	96	3·34	55·7	372
6·5 wt% PVA 125-98	2·6	108	3·40	56·5	390
8 wt% PVA 205-88	0	140	3·30	53·6	457
8 wt% PVA 125-98	0	86	3·25	56·9	466
6·5 wt% PVA 205-88 + 1·5 wt% PVA 27-98	0	88	3·38	–	...
6·5 wt% PVA 125-98 + 1·5 wt% PVA 31-88	0	138	3·35	55·7	417
6·5 wt% PVA 125-98 + 1·5 wt% PVA 27-98	0	119	3·33	54·0	463
8 wt% PVA 205-88	3·2	107	2·99	55·0	383
8 wt% PVA 125-98	3·2	118	3·32	52·0	390
6·5 wt% PVA 205-88 + 1·5 wt% PVA 27-98	3·2	108	2·92	55·1	393
6·5 wt% PVA 125-98 + 1·5 wt% PVA 27-98	3·2	117	3·27	56·1	439
12 wt% PVA 125-98	1·6	87	3·13	52·2	408
Fine barium titanate:					
6·5 wt% PVA 20/98	3·2	107	9·27	55·1	136
8 wt% PVA 20/98	1·6	113	8·97	54·0	132
8 wt% PVA 20/98	3·2	109	8·48	55·3	147

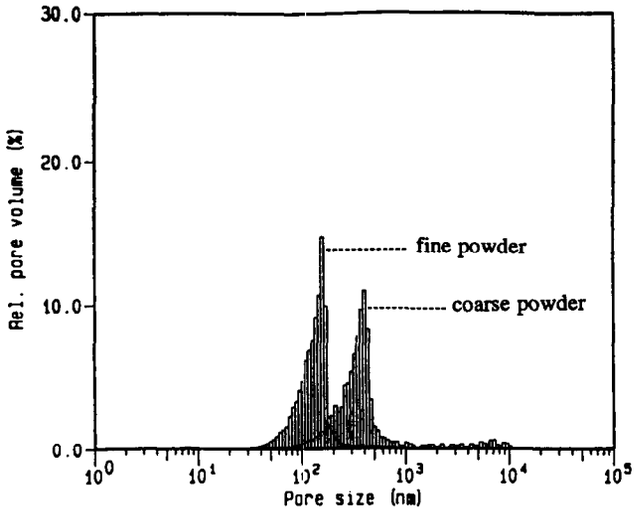


Fig. 5. Pore size diagrams of foils without binder. One foil consists of the fine powder, the other one of the coarse powder.

However, the spread in the *C*-values is quite large. Apparently, the powder surface is not left in a completely reproducible condition after the removal of the organic species. This can possibly be caused by the presence of carbonaceous residues.

As can be seen in Table 3, there is no significant change in either the total porosity or the pore sizes as a function of the slip parameters mentioned above. Hence, the ceramic structure is independent of the PVA type, the PVA concentration, and the TEG concentration within the ranges used in this study. The pore size distributions of a coarse powder and a fine powder foil without organic material are given in Fig. 5. The d_{50} pore sizes in burned foils containing either coarse or fine ceramic powder are 410 nm and 140 nm, respectively.

Both foil types without binder exhibit the same porosity (i.e. about 55%). The average values of the ratio of the d_{50} pore size over the d_{50} particle diameter are equal to 0·54 and 0·69 for the coarse and fine powder foils, respectively. Although this ratio is somewhat larger for fine powder foils than for coarse powder foils, it is questionable whether or not this difference is significant.

Both the porosity and the ratio of pore size to particle size show, however, that the powder particles are less well packed in the foils than in the centrifuged pills. This indicates that the colloidal system in the slip, during the settlement of the powder particles, was most probably not stable. This may be caused by depletion flocculation of particles in the slip due to the presence of the relatively high amount of polymer.

5.2.2 Binder distribution in green foils

The porosimetry and B.E.T. results for green foils, as a function of the binder system, are directly indicative of the distribution of the organic matter in the foils because the ceramic structure is not significantly affected by the constitution of the binder system (see previous section). The influences of the TEG content in the slip, and the PVA type and concentration, on the binder distribution in both coarse powder and fine powder foils are described in the following sections.

5.2.2.1 TEG concentration. Triethylene glycol is a relatively small molecular weight plasticizer which is not very compatible with PVA.[29] As a consequence, TEG can be removed quite easily from thin green foils. Foils may even lose TEG during storage. For instance, most of the TEG can be removed by putting thin green foils between sheets of paper for about 10 days (no plasticizing effect could be observed any more after such storage). The TEG diffuses out of the foils into the paper. All foils used for the experiments described in this section were stored between paper for at least 10 days. Moreover, the foils were evacuating at 50°C or 150°C in the B.E.T. apparatus before a measurement was carried out. So, we can assume that almost no TEG was present any more in the foils during the measurements. This is supported by Fig. 6, which shows porosities of foils prepared with different amounts of TEG. The lines given in

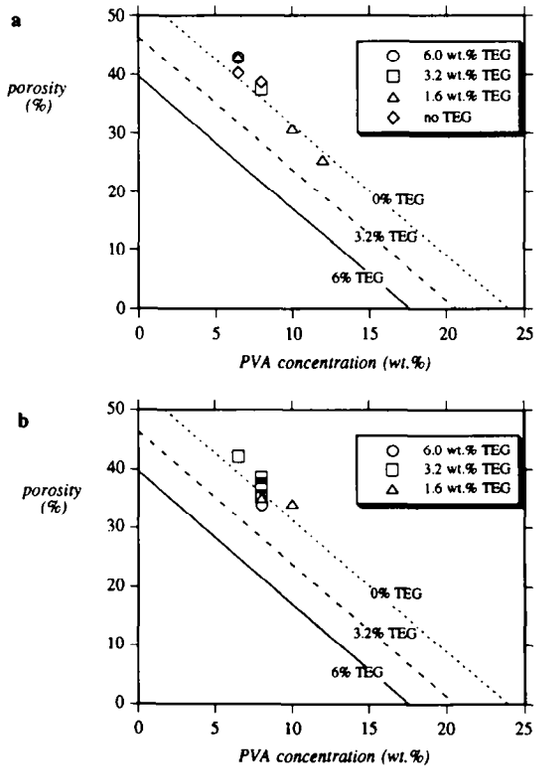


Fig. 6. The porosity of coarse particle green foils (a) and fine particle green foils (b) as a function of the PVA concentration (in wt.-% relative to the ceramic content). The given lines were calculated from the porosity of foils without binder and the densities of the organic substances, the symbols are measured values. Parameters used for the porosity calculation: P_0 = 55%, ρ_{BaTiO_3} = 5·9 g.cm^{-3}, ρ_{TEG} = 1·1 g.cm^{-3}, ρ_{PVA} = 1·2 g.cm^{-3} and 0·4 wt.% other organic substances.

this figure show porosities calculated as a function of the PVA concentration, based on a porosity of the ceramic structure of 55%. These calculations were done for different amounts of TEG present in the foils. The TEG concentrations chosen are equal to those used in several slips. A constant amount of dispersant and other substances is also taken into account (i.e. 0·4 wt% with respect to the ceramics). The measured porosities of foils are compared to calculated values. All the measured porosities (both for the fine and the coarse foils) fall around the line calculated for the case where no TEG is present in the foils. This means that TEG has indeed left the foils and that a direct influence of TEG on the pore size distribution and the specific surface area of foils can be neglected.

Pore size distributions of foils made from slips containing different amounts of TEG are given in Fig. 7. The same trend can be observed for both coarse and fine particle foils. The pore size distribution changes as a function of TEG concentration in the slip. Hence, TEG influences indirectly the binder distribution in foils. In the case where no TEG was used, a fairly thin peak could be found at the same position as the one observed for foils released from binder (see Fig. 5). In the presence of TEG, a second peak at a smaller pore size appears. Sometimes a third very small peak can be observed, especially for coarse foils (position around 1 μm). This peak is, however, independent of the TEG concentration. Whether this peak corresponds to pore sizes with these dimensions or not is doubtful.

We have to note that all pore size diagrams presented in this paper are volume distributions. Hence, one big pore has a much larger contribution to the peak area than one small pore. For a number distribution, the amount of large pores would be much smaller and that of the small pores much larger.

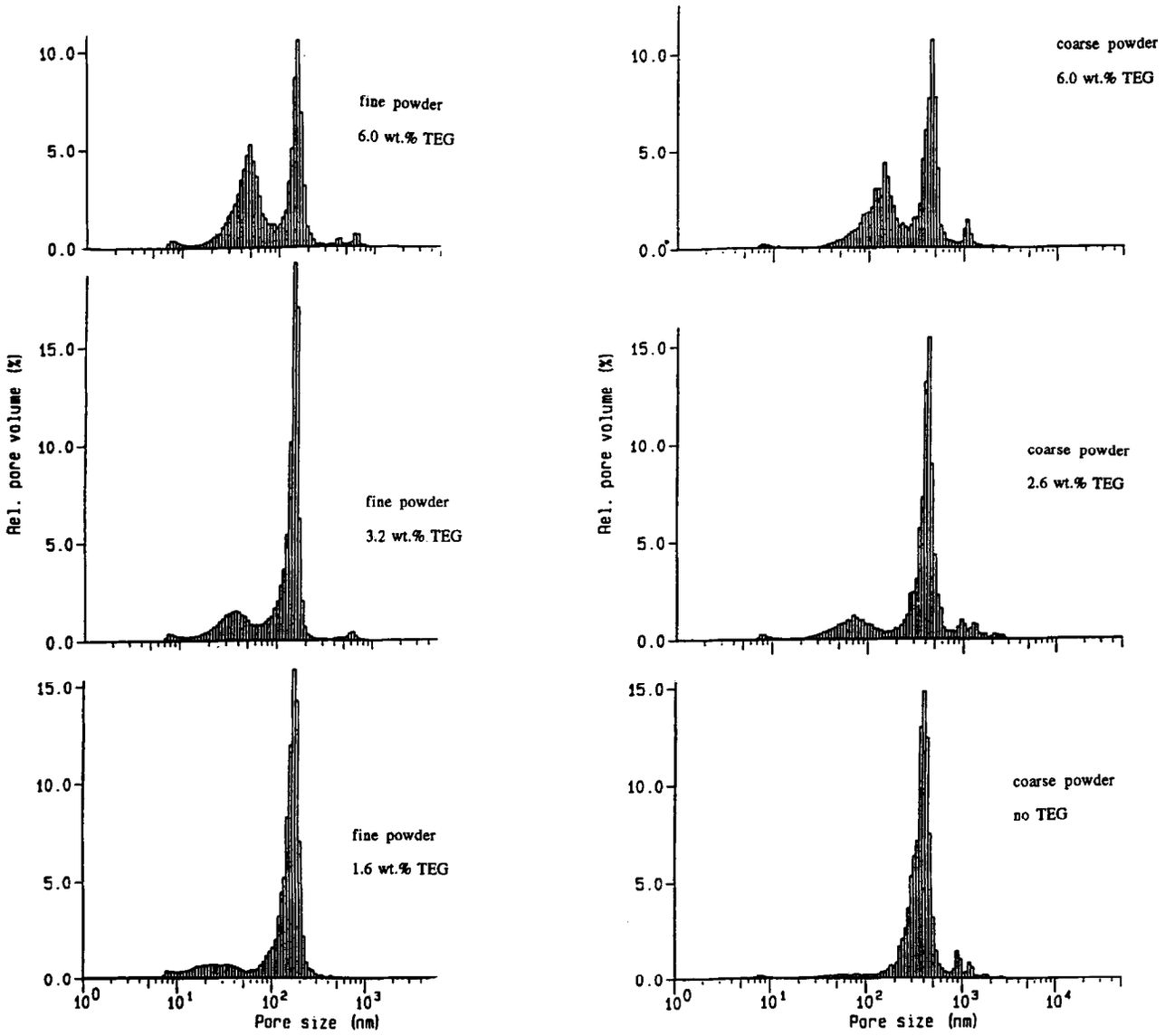


Fig. 7. Pore size distributions of coarse and fine particle green foils as a function of the amount of TEG used in the slip. The TEG concentrations are indicated in the figure (expressed in weight ratio). The PVA 125-98 concentrations were 6·5 wt.-% and 8·0 wt.-% with respect to the solid content for the coarse and fine particle foils, respectively.

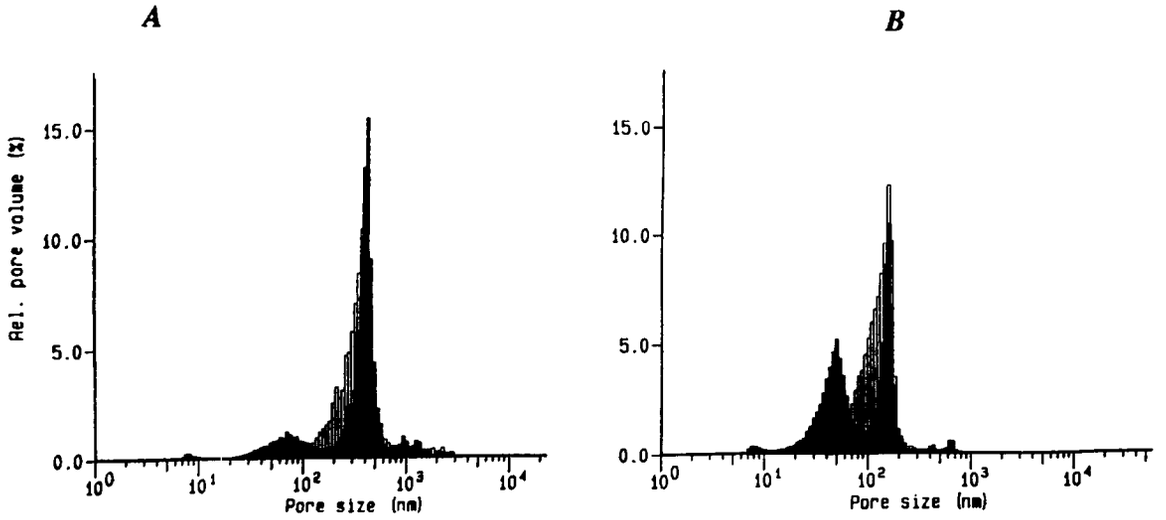


Fig. 8. Pore size distributions of foils with and without binder. A, coarse particle foil made with 6.5 wt.-% PVA 125-98 and 2.6 wt.-% TEG with respect to the ceramic powder (black) and a coarse particle foil released from organic material (white); B, fine particle foil made with 8.0 wt.-% PVA 125-98 and 6.0 wt.-% TEG with respect to the ceramic powder (black) and a fine particle foil released from organic material (white).

Figure 1 is quite helpful for the interpretation of the results of Fig. 7. The large pores (large peak) found in green foils are more or less empty ones and the peak for smaller dimensions are pores partly filled with binder. In the case of no TEG, only large pores exist. This means that some pores are filled completely with binder and others are not filled at all, i.e. there is an inhomogeneous binder distribution. Foils made in the presence of TEG show a more homogeneously distributed binder.

Remarkable is that the peaks of the large pores in the green foils are fairly thin, whereas those found in foils without binder are much broader. Figure 8 compares these two peaks with each other. The peaks of the green foils are drawn in black. It can be seen very clearly that smaller pores are preferentially filled with binder over the larger ones.

In this study, we have used the ratio of the intruded mercury into small pores over that into large pores as a measure of the binder distribution. A larger peak ratio means a more homogeneous binder distribution by this definition. Peak ratios, as a function of TEG concentration in the slip, are given in Fig. 9 for three different types of foil. As can be seen in this figure, the peak ratio increases strongly for larger TEG contents, which indicates a better-distributed binder. The data of the foils presented in Fig. 9 can be more or less described by one single exponential curve.

As already stated in Section 4.2., differences may be found when the same sample is measured for the second time (second run). Figure 10 shows the differences between a first and a second run for both a coarse powder and a fine powder foil. The peak of the small pores is hardly influenced, while the peak of the large ones is quite suppressed in the second run. As a consequence, the peak ratios of the second run are always somewhat larger than those of the first one. This can also be clearly seen in Fig. 9. Both peak ratios determined from the first run and those from the second run are plotted in this figure. The positions of the peaks, however, do not change whether the measurement is carried out the first time or the second time. Not only the height of the peak at small pore dimensions is influenced by the TEG content in the slip but also the position is affected. Figure 11 shows the relative position of the maximum of the peak as a function of the TEG content for different types of foil. The relative position is defined as the pore size at the maximum of the peak divided by the d_{50} pore size of the same foil without binder. The peak maximum of the small pores shifts to larger sizes as the TEG content in the slip becomes higher. Remarkably,

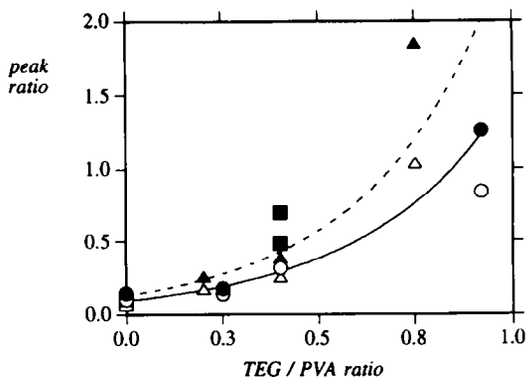


Fig. 9. Peak ratios as a function of the TEG/PVA weight ratio in the slip: circles, coarse particles foils with 6.5 wt.-% PVA 125-98; squares, coarse particle foils with 8.0 wt.-% PVA 125-98; triangles, fine particle foils with 8.0 wt.-% PVA 125-98; open symbols (solid line), data from a first run; filled symbols (dotted line), data from a second run.

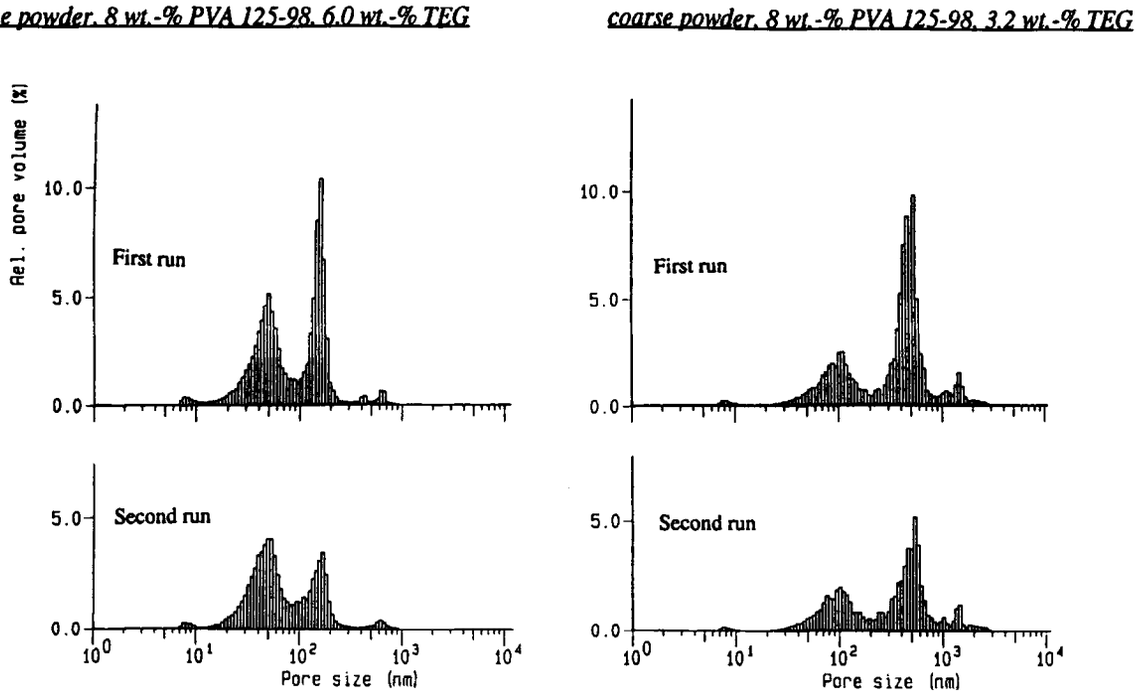


Fig. 10. Pore size distribution differences between a first measuring run and a second one.

the relative positions of these peaks fall on the same curve for both coarse and fine particle foils. Hence, the influence of TEG on the pore sizes in green foils seems to be the same for foils consisting of these two particle sizes.

The B.E.T. results of foils made with different amounts of TEG are given in Fig. 12. The binder distribution index X (see Section 4.1.1) increases with TEG concentration, indicating a more homogeneous binder distribution with increasing TEG content. The X index is negative for low TEG contents, which suggests that small pores are preferentially filled with binder over large ones. The X index reaches a value of unity at a TEG/PVA ratio of about 0·8. Based on the model described in Section 4.1.1, this means a fairly homogeneously distributed binder. The same effect could be seen for the porosity measurement results shown in Fig. 9. The peak ratio increases sharply at TEG/PVA ratios of about 0·8, also indicating a homogeneous binder distribution. Remarkable in Fig. 12 is that the binder distribution index is somewhat lower for the fine particle foils than for coarse particle foils.

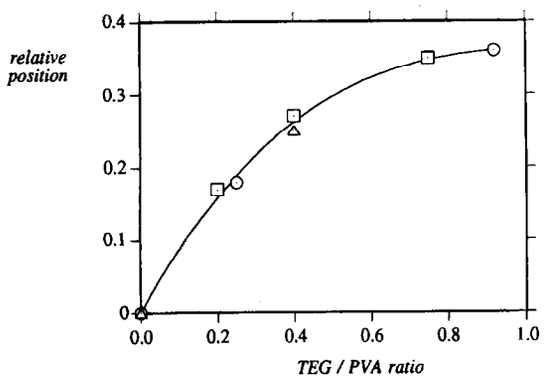


Fig. 11. The relative position of the peak of small pores (i.e. pore size at the maximum of the peak divided by the d_{50} pore size of the same foil without binder) as a function of the TEG/PVA weight ratio: ○, coarse particle foil, 6.5 wt.-% PVA 125-98; Δ, coarse particle foil, 8.0 wt.-% PVA 125-98; □, fine particle foil, 8.0 wt.-% PVA 125-98.

5.2.2.2 PVA type. All the results given above are based on foils made with PVA type 125-98. Do these results also hold for other types of binder? Tables 4 and 5 compare the binder distribution in foils containing either PVA 125-98 or PVA 205-88. Just as in the case of PVA 125-98, foils with PVA 205-88 get a more homogeneous binder distribution when more TEG is used in the slip. The peak ratios from the porosity measurements, as well as the binder distribution indices determined by B.E.T. measurements show,

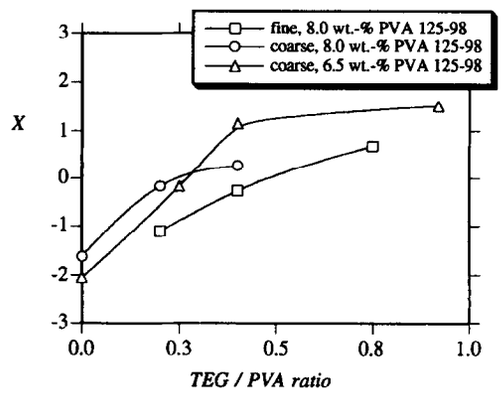


Fig. 12. The binder distribution index as a function of the TEG/PVA weight ratio in the slip.

Table 4. Peak ratios from porosity measurements as a function of the binder type in coarse particle foils

PVA conc. (wt%)	*TEG conc. in the slip (wt%)*	*Peak ratio[a] for PVA 205-88*	*Peak ratio[a] for PVA 125-98*
6·5	0	0·00/0·03	0·10/0·14
6·5	2·6	0·14/0·14	0·31/0·47
8	0	0·06/0·05	0·08/0·10
8	3·2	0·28	0·48/0·70
8 (6·5 + 1·5 PVA 27-98)	3·2	0·25/0·16	0·52

[a]The first number is from a first run, the second is from a second run.

Table 5. The binder distribution index (X) as a function of the binder type in coarse particle foils

PVA con. (wt%)	*TEG conc. in the slip (wt%)*	*X for PVA 205-88*	*X for PVA 125-98*
6·5	0	−2·27	−2·05
6·5	2·6	−1·17	1·15
8	0	−2·16	−1·62
8	3·2	−1·40	0·27
8 (6·5 + 1·5 PVA 27-98)	3·2	−1·42	0·86

however, that at a given TEG concentration in the slip, PVA 205-88 is less homogeneously distributed in foils than PVA 125-98. Even for foils made without TEG, PVA 205-88 is less well distributed. PVA 205-88 differs from PVA 125-98 in two ways, i.e. the molecular weight of PVA 205-88 is higher and the hydrolysis ratio is lower. Which of these properties is responsible for the differences observed? We have plotted the binder distribution index as a function of the relative amount of less-hydrolysed binder in a two-component binder mixture in Fig. 13. As can be seen, the binder distribution index becomes consistently lower for a higher amount of less-hydrolysed PVA types. Hence, most probably, the hydrolysis degree is responsible for the differences found for PVA 125-98 and for PVA 205-88. It is known that some physical properties of PVA (for instance, dissolution behaviour, viscosity, melting point, glass transition temperature) change (drastically) if the hydrolysis ratio reaches 100%.[29]

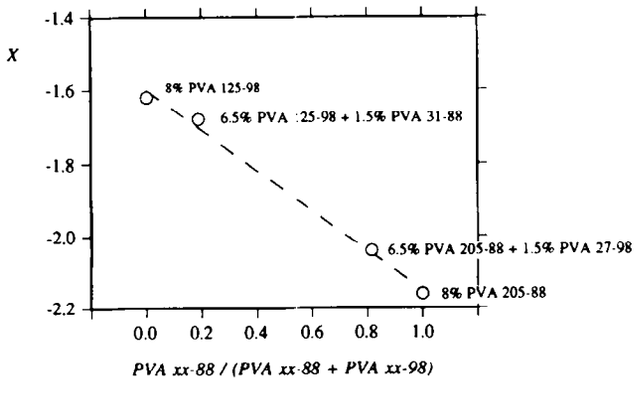


Fig. 13. The binder distribution index as a function of the relative amount of 88% hydrolysed PVA (see Table 1). Foil system: coarse $BaTiO_3$ with 8·0 wt.-% PVA, and no TEG.

5.2.2.3 PVA concentration. The binder distribution index X calculated from the specific surface area of foils is defined in such a way that a comparison between foils containing different amounts of PVA is possible. Table 6 gives X-values for coarse particle foils containing either 6·5, 8·0, 10 or 12 wt% PVA 125-98 with respect to the ceramic material.

The TEG content in the slip is kept constant with respect to the ceramic powder (i.e. 1·6 wt%). This means, however, that the TEG/PVA ratio decreases with increasing amounts of PVA. Hence, a decreasing effect on the binder distribution index may be expected because of a decreasing TEG content with respect to the binder concentration. As can be seen in Table 6, the X-value is negative for the relatively low PVA concentrations and positive for the higher ones. A relatively large difference in binder distribution is found for foils with 8·0 and 10 wt% PVA. To be conclusive, a higher PVA concentration with respect to the ceramic content also leads to a better-distributed binder in the foil.

Table 6. Binder distribution index as a function of binder content in green coarse particle foils; in all cases, the TEG concentration was equal to 1·6 wt% with respect to the ceramics

PVA 125-98 conc. (wt%)	*TEG/PVA (wt/wt)*	*X*
6·5	0·25	−0·17
8·0	0·20	−0·17
10	0·16	0·84
12	0·13	0·57

6 Interpretation/Discussion

In this section, we will try to elucidate the mechanism of how binder is distributed over the foil during drying. Especially, the results obtained for green foils in the previous sections and the drying model as described in Section 2 will be the keys for understanding this mechanism.

Important for the distribution of binder over green foils is the moment in the drying process (i.e. at which part of which drying stage) that the binder gets fixed in the ceramic structure by precipitation, gelation or whatever. Factors that influence this fixation process affect also the binder distribution in foils. Other kinds of factors, such as parameters that influence the accumulation of binder molecules onto ceramic particles due to physical (chemical) interactions, may have also an effect on the binder distribution.

As shown in the previous chapter, several parameters affect the PVA distribution in foils. All of these parameters, however, do not alter the ceramic structure of foils. The porosity of the ceramic structure is even independent of the particle size. The ceramic structure of foils has been built at the end of the constant rate period, i.e. the critical point. This suggests that the binder is not precipitated, gelated or whatever during the constant rate period for the systems analysed in this study. Otherwise, an effect on the ceramic structure of the parameters that influence the fixation process of the binder would have been observed. The supposition that the binder is not yet fixed at the end of the constant rate period is supported by the fact that after complete drying, smaller pores appears to be preferentially filled with binder over the larger ones. This can be explained by the difference in capillary pressures of large and small pores during the first falling rate period. Solution with binder is transferred from large pores to small ones due to this pressure difference. If the totality of the binder had already been fixed in this stage, the binder could not have been transferred in this way. The fact that in some cases binder is observed at the lower side of the foil (the side that has made contact with the carrier) also suggests that the binder is still in solution as the drying process enters the first falling rate period (FRP1). In the FRP1 stage, pores at the upper side of the foil are emptied first and pores that are still filled with solution are enriched with binder by diffusion. This diffusion process is only possible if an amount of the binder is still solved. Hence, for the systems described in this report, the fixation of binder does not notably take place before the critical point is reached.

A very homogeneous binder distribution in green foils will probably be established if the fixation of the binder occurs just at the critical point. In this situation, all pores are still filled with solution with the same binder concentration. The later the point of fixation in the drying process, the less homogeneous is the binder distribution. Binder will then be found more and more in the smaller pores and at the bottom of the foil. This corresponds with very low (negative) X-values.

As shown in the previous section, the binder distribution in foils is influenced by the concentration of TEG and the amount of PVA in the slip. Obviously, the more organic material in the system, the sooner this material is fixed after the critical point in the drying process. However, this certainly does not explain all the results reported in this paper. The binder type also has an influence on the binder distribution. Although not shown in this paper, the drying conditions (external factors) appear to affect the binder distribution in foils as well. Triethylene glycol is known to gelate PVA (one piece of gel may be formed after mixing of PVA and TEG in the appropriate concentrations and waiting for a certain time). With more TEG in the slip, the gelation process will set in earlier, resulting in a more homogeneous binder distribution. PVA types with lower degrees of hydrolysis are somewhat less susceptible to gelation by TEG. These polymers are also better solvable in water than fully hydrolysed ones.[29] Hence, the fixation point is postponed for less-hydrolysed PVA types and, as a consequence, the binder is more heterogeneously distributed.

The external factors for the drying process (air flow, ambient temperature and vapour pressure) can also be expected to have an influence on the fixation process of the binder by TEG. The wet bulb temperature and the speed of drying, which are controlled by these factors, influence the gelation process. Gelation will be set in later when the wet bulb temperature is higher (i.e. a higher ambient temperature and a higher degree of humidity). Most gelation processes are kinetically not very fast. That means that if the drying speed is lowered, the gelation has more time to proceed. Effectively, the gelation point will then be found earlier in the drying process.

The concentration of the binder and that of the plasticizer (provided no plasticizer has been evaporated during drying) at the critical point can be simply calculated using the porosity of foils released from binder, the solid content of the slip and the PVA and TEG concentrations in the slip. The solid content of the system at the critical point can be calculated from the porosity of foils released from binder. The difference in solid content of the slip and that of the system at the critical

point yields the factor with which the concentrations of the organic species have been concentrated at the critical point. In our case, this turns out to be about 5·5. So, the concentrations for gelation at the drying conditions used are probably higher. In principle, an estimate of the gelation concentrations can be made from the peak positions in the pore size distribution diagrams. The volumetric filling percentage of pores with binder can be calculated from the dimensions of an empty pore and those of a filled one. This percentage is then easily transformed into the PVA and TEG concentration at binder fixation, knowing the relative PVA and TEG concentration in the slip. The following uncertainties make this estimate, however, too unreliable:

1. the pore geometry,
2. the way a pore is filled with binder,
3. whether or not TEG has been evaporated before the fixation point is reached during the drying process,
4. the filling degree of pores filled with binder solution when fixation starts,
5. the size of the empty pore (this is not well defined because large pores are emptied firstly during drying).

The peak in the pore size diagram at the small pore size shifts to a larger size when more TEG is used in the slip (see Fig. 11). Two causes may be responsible for this effect:

1. The fixation of the binder starts at a lower PVA concentration in the pores when more TEG is used. After complete drying, less PVA has been left in the individual pores and therefore the open space in pores is larger.
2. When more TEG is used, more TEG will be present in the pores at the fixation point. After removal of TEG from the foil by evaporation or diffusion, more open space will be left.

Another point to remark on is that although a binder distribution may be very inhomogeneous, the *C*-values found were still very close to that of pure PVA. This means that all particles are at least coated with a very thin layer of PVA, even the particles forming empty pores. This may be caused by adsorption of PVA onto the particles. However, the particles are already coated with an adsorption layer of dispersant. Hence, that would mean that PVA adsorbs onto this dispersant layer (displacement is not probable[30]). The effect of a low *C*-value may also be related to the fact that in the first falling rate period, most of the evaporation still occurs at the exterior surface due to continuous thin liquid pathways in pores, along flow is still possible (funicular condition).

We have noticed, that in many cases, the *X*-values for fine particle foils are somewhat smaller than for coarse particle foils, using the same recipe and processing conditions. This may be explained by the differences in capillary pressure that occur within the foil during drying. Pore sizes and the width of the pore distribution are, of course, important in this respect.

7 Conclusions

Both B.E.T. and Mercury Intrusion Porosimetry measurements are useful to characterize the binder distribution in green foils. The results obtained using both techniques are fully in agreement with each other.

Ceramic foils consisting of either a coarse $BaTiO_3$ powder (d_{50} = 0·75 μm) or a fine $BaTiO_3$ powder (d_{50} = 0·20 μm) could be made with the same porosity. The pore sizes in the foils scaled with the particle sizes of the respective powders.

The binder and plasticizer concentrations in the slip used in this study do not change the ceramic structure of foils. Only the binder distribution is influenced by these parameters.

The moment in the drying process of foils that the binder gets fixed in the ceramic structure determines the binder distribution in foils. Factors influencing this fixation process affect the binder distribution. The plasticizer triethylene glycol (TEG) promotes fixation of PVA by a gelation process. More TEG in the slip leads to a more homogeneous binder distribution in foils. In the case of little TEG in the slip, small pores are preferentially filled with binder over large ones and the lower side of foils is enriched with binder. Less-hydrolysed PVA types are less susceptible to gelation with TEG, resulting in a more heterogeneous binder distribution.

All powder particles are covered with PVA molecules, both in foils with a homogeneous binder distribution and in ones with a very heterogeneous binder distribution.

References

1. Ward, P., MLCs — present practices and future trends. In *Ceramic Technology International* 1994, ed. I. Birkby. Sterling Publications Limited, 1994, p. 78.
2. Mistler, R. E., Tape casting: the basic process for meeting the needs of the electronic industry. *Ceram. Bull.*, **69** (1990) 1022–6.
3. Cronin, D. J. & McMarlin, K. A., Tape casting of dielectric substrates. In *Ceramics Today — Tomorrows's Ceramics*, ed. P. Vincenzini. Elsevier Science Publishers B.V., 1991, pp 1963–72.
4. Fransen, B. C. H., Janssen, G. J., Oostra, S. J. J. & de Vries J. W. C., Integration of mechanics and electronics:

low voltage ceramic multilayer actuators. In *6th Capacitor and Resistor Technology Symposium CARTS, '92*, Brugge, 1992, pp. 128–33.
5. Phillips, S. V. & Datta, A. K., Ceramic tape casting for Oxide Fuel Cell (SOFC) electrolyte production. In *Proc. Ceramics in Energy Applications*, Sheffield, 1990, p. 183.
6. Heinrich, J., Huber, J., Förster, S. & Quell, P., Advanced ceramics as heat exchangers in domestic and industrial appliances. *Industrial Ceram.*, **7** (1987) 34.
7. Phillips, S. V., Howard, P. J., Partridge, G. & Datta, A. K., Fabrication routes for superconducting ceramics. *British Ceramic Proceedings No. 40, Superconducting Ceramics*, 1988, p. 31–6.
8. Boch, P., Chartier, T. & Huttepain, M., Tape casting of Al_2O_3/ZrO_2 laminated composites. *J. Am. Ceram. Soc.*, **69** (1986) C-191-2.
9. van der Sanden, M. C. M., Ultimate toughness of amorphous polymers. Thesis, University of Technology Eindhoven, 1993.
10. Cima, M. J., Lewis, J. A. & Devos, A. D., Binder distribution in ceramic greenware during thermolysis. *J. Am. Ceram. Soc.*, **72** (1989) 1192–9.
11. de With, G., Structural integrity of ceramic multilayer capacitor materials and ceramic multilayer capacitors. *J. Eur. Ceram. Soc.*, **12** (1993) 323–36.
12. Bortzmeyer, D., Langguth, G. & Orange, G., Fracture mechanics of green products. *J. Eur. Ceram. Soc.*, **11** (1993) 9–16.
13. Hennings, D. F. K., Schreinemacher, B. & Schreinemacher, H., High-permittivity ceramics with high endurance. *J. Eur. Ceram. Soc.*, **13** (1994) 81–8.
14. Hennings, D., Barium titanate based ceramic materials for dielectric use. *Int. J. High Tech. Ceram.*, **3** (1987) 91–111.
15. Bergholz, A. & Ferber, C., Bedeutung der Strömungstechnik für die Trocknung keramischer Produkte. *Keram. Z.*, **44** (1992) 88–92.
16. Streicher, E. & Chartier, T., Study of cracking and microstructural evolution during drying of tape-cast aluminium nitride sheet. *J. Mater. Sci.*, **26** (1991) 1659–65.
17. Scherer, G. W., Theory of drying. *J. Am. Ceram. Soc.*, **73** (1990) 3–14.
18. Chen, Z.-C., Powder processing of barium titanate ceramics with polyacrylic acid. Thesis, University of Lausanne, 1992.
19. Simpkins, P. G., Johnson, D. W. & Fleming, D. A. Jr., Drying behaviour of colloidal silica gels. *J. Am. Ceram. Soc.*, **72** (1989) 1816–21.
20. Zhang, Y., Tang, X. & Uchida, N., Mathematical simulation for segregation of PVA during drying. *J. Ceram. Soc. Jpn, Int. Edn*, **101** (1993) 177–80.
21. Chiu, R. C. & Cima, M. J., Drying behaviour of granular ceramic films. *Ceram. Trans. (Ceramic Powder Science IV)*, **22** (1991) 347–56.
22. Chartier, T., Tape casting. In *Encyclopedia of Advanced Materials*, ed. D. Bloor, R. J. Brook, M. C. Flemings & S. Mahajan. Pergamon Press, 1994, pp. 2763–7.
23. Spauszus, S. & Rauscher, H.-U., Formgebungs Prinzipien und Arbeitsgrenzen bei der Herstellung dünner Keramikfolien. *Keram. Z.*, **44** (1992) 23–7.
24. Chartier, T. & Bruneau, A., Aqueous tape casting of alumina substrates. *J. Eur. Ceram. Soc.*, **12** (1993) 243–7.
25. van Brakel, J., Modry, S. & Svatá, M., Mercury porosimetry: state of the art. *Powder Technol.*, **29** (1981) 1–12.
26. Whittemore, O. J., Mercury porosimetry of ceramics. *Powder Technol.*, **29** (1981) 167–75.
27. Moscou, L. & Lub, S., Practical use of mercury porosimetry in the study of porous solids. *Powder Technol.*, **29** (1981) 45–52.
28. Opitz, J. & Gontermann-Gehl, U., Porenstruktur dünner keramischer Folien. *Sprechsaal*, **125** (1992) 682–7.
29. Finch, C. A. (ed.), *Polyvinyl Alcohol Developments*. John Wiley & Sons, New York, 1992.
30. van der Beek, G. P., Displacement of adsorbed polymers. A systematic study of segment-surface interactions. Thesis, Agricultural University of Wageningen, 1991.

Appendix: Relationships between the surface area and the binder distribution in foils (eqns (1)–(4))

A1 Spherical pores filled homogeneously with binder

Suppose a porous system has N equal spherical pores of radius R. The empty porous system has a surface area A_0 and a volume V_0 which are given by

$$A_0 = 4\pi R^2 N \tag{A1}$$

$$V_0 = \frac{4}{3}\pi R^3 N \tag{A2}$$

Filling the porous system proceeds in such a way that the radii of all pores decrease equally. The surface area of a system filled with a certain amount of binder is then equal to

$$A = 4\pi r^2 N \quad \text{with } 0 \le r \le R \tag{A3}$$

The volume of added material, V_a, can be expressed in the following way

$$V_a = \frac{4}{3}\pi(R^3 - r^3)N \quad \text{with } 0 \le r \le R \tag{A4}$$

Combining relations (A1)–(A4) yields eqn (A5)

$$A = A_0 \left[1 - \frac{V_a}{V_0}\right]^{2/3} \tag{A5}$$

The volume of the empty porous system, V_0, can also be expressed in terms of the porosity P_0 and the total volume V_{tot} of the system without additions

$$V_0 = \frac{P_0}{100} V_{tot} \tag{A6}$$

In the same way, the volume of the ceramic material is given by

$$V_{cer} = \frac{(100 - P_0)}{100} V_{tot} \tag{A7}$$

A definition of the amount of added organic substances (V_i), expressed in vol.% with respect to the ceramic material, is given in eqn (A8)

$$V_i = \frac{V_a}{V_{cer}} 100 \tag{A8}$$

The factor V_a/V_0 in eqn (A5) can be expressed in the following way, using eqns (A6)–(A8)

$$\frac{V_a}{V_0} = \frac{(1 - P_0/100)}{P_0} V_i \tag{A9}$$

Because the maximum value for the ratio V_a/V_0 is 1, V_i can by definition not be larger than $P_0/(1 - P_0/100)$.

Substitution of the last equation into (A5) yields the following formula, which is identical to eqn (1):

$$A = A_0 \left[1 - \frac{1-P_0/100}{P_0} V_i\right]^{2/3} \quad \text{(A10)}$$

Usually, the concentrations of organic substances in slips and foils are given in wt% with respect to the solid content. The parameter V_i can easily be calculated from the concentrations defined in this way using eqn (A11)

$$V_i = C_i \frac{\rho_{cer}}{\rho_i} \quad \text{(A11)}$$

with ρ_i the specific density of substance i, C_i the concentration of substance i in wt% with respect to the ceramics and ρ_{cer} the density of the ceramic material.

A2 Pores filled inhomogeneously with binder

In this case, filling of the porous system proceeds by lowering the number of empty pores. Pores are completely filled one by one. The number of filled pores is equal to n. The surface area and the volume of one pore are a_0 and v_0, respectively. Relations (A12)–(A15) are of the same kind as eqns (A1)–(A4).

$$A_0 = a_0 N \quad \text{(A12)}$$

$$V_0 = v_0 N \quad \text{(A13)}$$

$$A = a_0(N-n) \quad \text{with } 0 \le n \le N \quad \text{(A14)}$$

$$V_a = v_0 n \quad \text{with } 0 \le n \le N \quad \text{(A15)}$$

Combining the last four equations gives

$$A = A_0 \left[1 - \frac{V_a}{V_0}\right] \quad \text{(A16)}$$

The link between eqns (A16) and (A17) is the same as in the previous case, and

$$A = A_0 \left[1 - \frac{1-P_0/100}{P_0} V_i\right] \quad \text{(A17)}$$

Because we did not assume any pore geometry for the derivation of eqn (A17), this dependency is invariant for the pore geometry!

A3 Cylindrical pores filled homogeneously with binder

In this case, the porous system is modelled as a body containing N cylindrical pores of length z. Addition of organic material reduces the diameter of all cylinders, i.e. this is a homogeneous filling. The same kind of formulas are derived as in the previous cases

$$A_0 = 2\pi R z N \quad \text{(A18)}$$

$$V_0 = \pi R^2 z N \quad \text{(A19)}$$

$$A = 2\pi r z N \quad \text{with } 0 \le r \le R \quad \text{(A20)}$$

$$V_a = \pi(R^2 - r^2) z N \quad \text{with } 0 \le r \le R \quad \text{(A21)}$$

These equations lead to

$$A = A_0 \left[1 - \frac{V_a}{V_0}\right]^{1/2} \quad \text{(A22)}$$

and

$$A = A_0 \left[1 - \frac{1-P_0/100}{P_0} V_i\right]^{1/2} \quad \text{(A23)}$$

A4 Small spherical pores are preferentially filled with binder over large ones

In the previous cases, we have modelled the porous structure as a body containing a number of equally sized pores. Equations (A10), (A17) and (A23) also hold for ceramic structures containing different pore sizes, but the added organic material must then be distributed equally over the size distribution. In this instance, the added organic material is not distributed equally over the size distribution. We assume three different spherical pores with radii $0{\cdot}5R$, R and $2R$. These pore types are denoted in the following relations with one prime, two primes and three primes, respectively. The number of each type of pore is chosen such that the volume of each class of pores is equal to 1/3 of the total volume of pores. Hence,

$$V'_0 = \frac{1}{3} V_0 = \frac{4}{3}\pi (0{\cdot}5R)^3 \frac{64N}{73} \quad \text{(A24)}$$

$$V''_0 = \frac{1}{3} V_0 = \frac{4}{3}\pi R^3 \frac{8N}{73} \quad \text{(A25)}$$

$$V'''_0 = \frac{1}{3} V_0 = \frac{4}{3}\pi (2R)^3 \frac{N}{73} \quad \text{(A26)}$$

The surface area of each class of pore without organic material is given by the following three formulas

$$A'_0 = a'_0 \frac{64N}{73} = \frac{4}{7} A_0 \quad \text{(A27)}$$

$$A''_0 = a''_0 \frac{8N}{73} = \frac{2}{7} A_0 \quad \text{(A28)}$$

$$A'''_0 = a'''_0 \frac{N}{73} = \frac{1}{7} A_0 \quad \text{(A29)}$$

Now added material is not the distributed equally over pores of different sizes. Firstly the small pores are filled, then the medium sized ones and finally the pores with the largest radii. Filling of the porous system proceeds in such a way that the number of pores decreases with the added amount (i.e. inhomogeneous distribution). The surface area A and the added amount of material V_a as a function of the number of occupied pores n are given by the follows equations:

$$\begin{cases} A = A_0 - a'_0 n \\ V_a = v'_0 n \end{cases} \quad \text{for } 0 \le n \le \frac{64N}{73} \tag{A30}$$

$$\begin{cases} A = \frac{3}{7} A_0 - a''_0 (n - \frac{64N}{73}) \\ V_a = \frac{1}{3} V_0 + v''_0 (n - \frac{64N}{73}) \end{cases} \quad \text{for } \frac{64N}{73} \le n \le \frac{72N}{73} \tag{A31}$$

$$\begin{cases} A = \frac{1}{7} A_0 - a'''_0 (n - \frac{72N}{73}) \\ V_a = \frac{2}{3} V_0 + v'''_0 (n - \frac{72N}{73}) \end{cases} \quad \text{for } \frac{72N}{73} \le n \le N \tag{A32}$$

In the same way as in the previous cases, these equations lead to

$$A = A_0 \left[1 - \frac{12}{7} \left(\frac{1-P_0/100}{P_0}\right) V_i\right] \quad \text{for } 0 \le V_i \le \frac{1}{3} \frac{100P_0}{(100-P_0)} \tag{A33}$$

$$A = A_0 \left[\frac{5}{7} - \frac{6}{7} \left(\frac{1-P_0/100}{P_0}\right) V_i\right] \quad \text{for } \frac{1}{3} \frac{100P_0}{(100-P_0)} \le V_i \le \frac{2}{3} \frac{100P_0}{(100-P_0)} \tag{A34}$$

$$A = A_0 \left[\frac{3}{7} - \frac{3}{7} \left(\frac{1-P_0/100}{P_0}\right) V_i\right] \quad \text{for } \frac{2}{3} \frac{100P_0}{(100-P_0)} \le V_i \le \frac{100P_0}{(100-P_0)} \tag{A35}$$

ELSEVIER

0955-2219(95)00002-X

Journal of the European Ceramic Society 15 (1995) 759–768
© 1995 Elsevier Science Limited
Printed in Great Britain. All rights reserved
0955-2219/95/$9.50

Compaction and Sintering Behaviour of Zirconia Powders

M. Taha,[a] J. Paletto,[a] Y. Jorand,[a] G. Fantozzi,[a]
A. Samdi,[b]* M. Jebrouni[b]** & B. Durand[c]

[a]G.E.M.P.P.M., CNRS URA 341, I.N.S.A. de Lyon, F 69621 Villeurbanne, France
[b]Laboratoire de Chimie Minérale III, URA CNRS 116, I.S.I.D.T. Université Claude Bernaud, Lyon I, 69622 Villeurbanne Cedex, France
[c]Laboratoire des Matériaux Minéraux, URA 428, ENSCMu, 68093 Mulhouse Cedex, France

(Received 23 May 1994; revised version received 22 October 1994; accepted 12 December 1994)

Abstract

Four kinds of zirconia powders are prepared in different ways. Their compaction and sintering behaviour are studied extensively. During compaction, the agglomerates or granules present in the powder are broken and/or undergo plastic deformation. The behaviour depends essentially on the strength of links between the particles.

The sol-gel powders are more sensitive to the formation of hard inter-particle links during the synthesis process. So careful control is needed in order to avoid the formation of aggregates, because they favour the presence of large pores which lead to differential sintering and grain coarsening.

In other cases the sintering can also be inhibited by the presence of residual impurities. A powder which has rod-like shaped agglomerates is sintered to regular microstructure.

Introduction

Uniaxial dry pressing is the most common forming process used to obtain green ceramic bodies in technology today. This process is of great interest technologically because it conditions the quality of fired ceramic bodies, which are influenced by the characteristics of the starting powders.

The presence of hard agglomerates in the powders was reported to be the main source of microstructural inhomogeneities in green ceramic bodies.[1–3] They are formed during the synthesis of the powder.

The purpose of this work was to compare the compaction and sintering behaviours of zirconia powder prepared by several laboratories with a commercial zirconia powder P1.† The following synthesis methods were used:

- Sol–gel process[4] was used for the first batches of powder, (P2, P3).
- Drying of amorphous gelatinous precipitates obtained by hydrolysis of solutions containing both zirconium and yttrium acetates[5] for the second batch, (P4).
- Reaction of both zirconyl and yttrium chlorides in molten salt[6] for the final batch, (P5).

The comparison was likely to give some information about the respective processes involved and could help to optimize the physico-chemical parameters in order to produce high quality zirconia powders.

Experimental procedure

The synthesis processes used to prepare the five batches of zirconia are summarized in Fig. 1.

The powder, P1, was prepared by hydrolysis of a solution containing zirconia and yttria chlorides. It was obtained from calcinated gel. It was then milled and atomized.

The powder, P2, was prepared from a solution containing both zirconia and yttria salts. Ammonia was used as the neutralising agent. The gel was first washed using water, then dried using hexanol. The obtained spheroidal xerogel particles were finally calcinated at 700°C.

The powder, P3, was obtained by coprecipitation of gel. This was later prepared from zirconia and yttria chlorides. The gel was washed three times using water, then three times using pure ethanol. It was then, dried at 110°C and calcinated at 600°C.

*Present address: Département de Chimie Université Hassan II, Faculté des Sciences Aïn Chock, B.P. 5366 Maârif, Casablanca, Morocco.
**Present address: Département de Chimie Université Chouaîb Doukkali, Faculté des Sciences, Eljadida, Morocco.
†TZ3YB — Tosoh Corporation Japan.

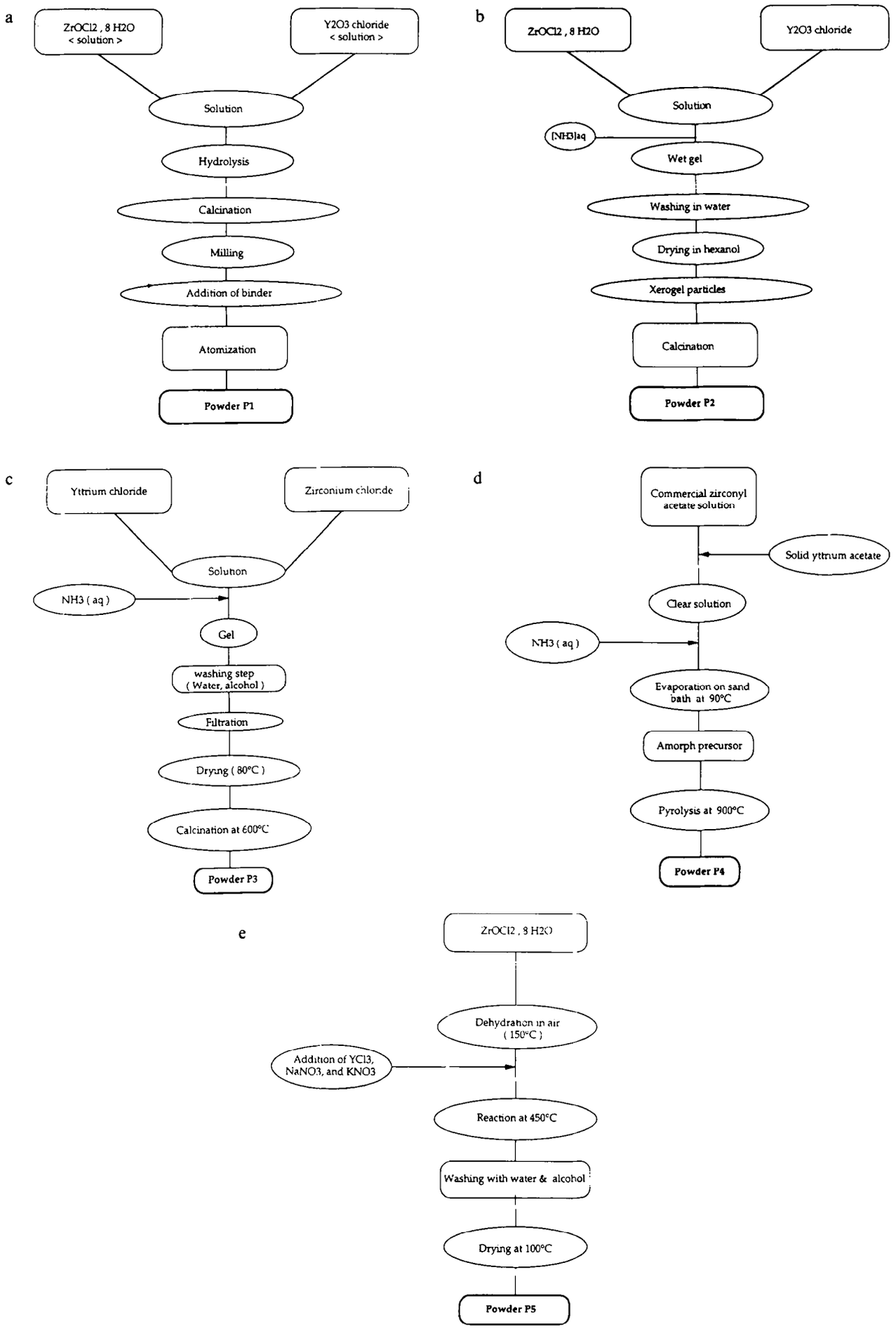


Fig. 1. Flowcharts of synthesis processes involved to prepare the five zirconia powders. (a) Synthesis process of the powder P1; (b) synthesis process of the powder P2; (c) synthesis process of the powder P3; (d) synthesis process of the powder P4; (e) synthesis process of the powder P5.

Table 1. Sample characteristics

Sample	*Synthesis route*	*Y_2O_3 (mol%)*	*Specific surface area (m^2/g)*	*Agglomerates mean size (μm)*	*Crystallite mean diameter (nm)*
P1	—	3	17	53·3	93
P2	Sol–Gel	3·6	100	34	9
P3	Sol–Gel	2	80	12·5	9
P4	Hydroxyacetate	3	6	100	25
P5	Molten salts	3	120	1·7	10

The powder, P4, was prepared from acetates. Solid yttrium acetate was dissolved in commercial zirconyl acetate solution. Then, the clear solution was neutralized by adding ammonia. The wet gel obtained was dried on a sand bath at 90°C and finally calcinated at 900°C in order to obtain white zirconia.

The powder, P5, was prepared by reacting both zirconia and yttria chlorides in molten salts at 450°C.

All the powders are yttrium stabilized zirconia, the amount of Y_2O_3 varying from 2·0 to 3·6 mol% (see Table 1).

The granulometric distribution of the different batches was obtained using a laser particle size analyser† and their morphology was investigated by scanning electron microscopy (SEM). The mean diameter of crystallites was determined from X-ray diffraction line broadening (XRD-LB) using the Scherrer formula for the calculation:

$$D = 0{\cdot}89\ \lambda/(\beta\ \mathrm{Cos}\theta)$$

where D is mean diameter of crystallites, λ the wave length of the X-ray (Cu–Kα), θ is the Bragg angle and β is the calibrated width of the diffraction peak at half maximum at selected 2θ. The proportion between the phases (monoclinic and tetragonal zirconia) was estimated using the empirical equation given by Toraya *et al.*[7] The specific surface area was evaluated by Brunauer–Emett–Teller (BET) nitrogen adsorption method.

Compaction tests were carried out on a mechanical testing machine‡ from 0 to 200 MPa with a crosshead rate of 0·5 mm/min so as to avoid the influence of loading rate.[8] In order to minimize the influence of moisture,[9,10] samples were oven dried at 110°C before compaction. Density variation during pressing was deduced from the crosshead continuous displacement. Deviation due to the elastic deformation of the die and the loading cell was taken into account with a blank test.

Porosity of the green samples was characterized by mercury penetration inside cold isostatic pressed pellets (400 MPa). The open porosity distribution could thus be quantified. Microstructure was also investigated by SEM.

The sintering schedule was optimized by performing dilatometric tests on samples isostatically pressed at 400 MPa; the temperature was raised up to 1500°C, at a rate of 1°C/min and samples were held at this temperature for 2 or 3 h. The porosity and microstructure of sintered samples were also examined.

Results and discussion

The sample characteristics are shown in Table 1. From these results it is shown that:

- Powders P2 and P3, (sol-gel) and P5, (molten salt) exhibit much higher surface areas than powders P1, (commercial) and P4, (hydroxyacetate).
- The crystallite mean diameter of the commercial powder, P1 is consequently larger than that of the other powders.

The X-ray patterns of these powders (Fig. 2) indicates that powders P2, P3, P4 and P5 are fully

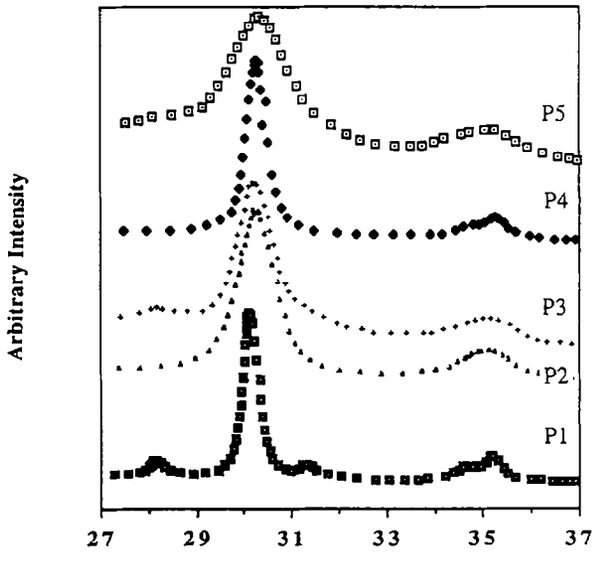


Fig. 2. X-ray patterns of the powders.

†Malvern particle size analyser 2000/3000.
‡Instron Ltd 1195.

stabilized into the tetragonal phase whereas the commercial powder, P1, contains a very low amount of monoclinic zirconia, about 3 vol%.

The SEM micrographs (Fig. 3) can divide the samples into three groups according to the shapes of the agglomerates: spheroidal (P1, P2 and P3), rod-like (P5) and irregular (P4).

The compaction plots (Fig. 4) of all the powders, density versus applied pressure, shows two linear regions separated by a transition zone. The first linear region, localized at low pressures and characterized by a low slope, is consistent with a rearrangement of the agglomerates in the die. This stage is controlled by particle–particle friction,

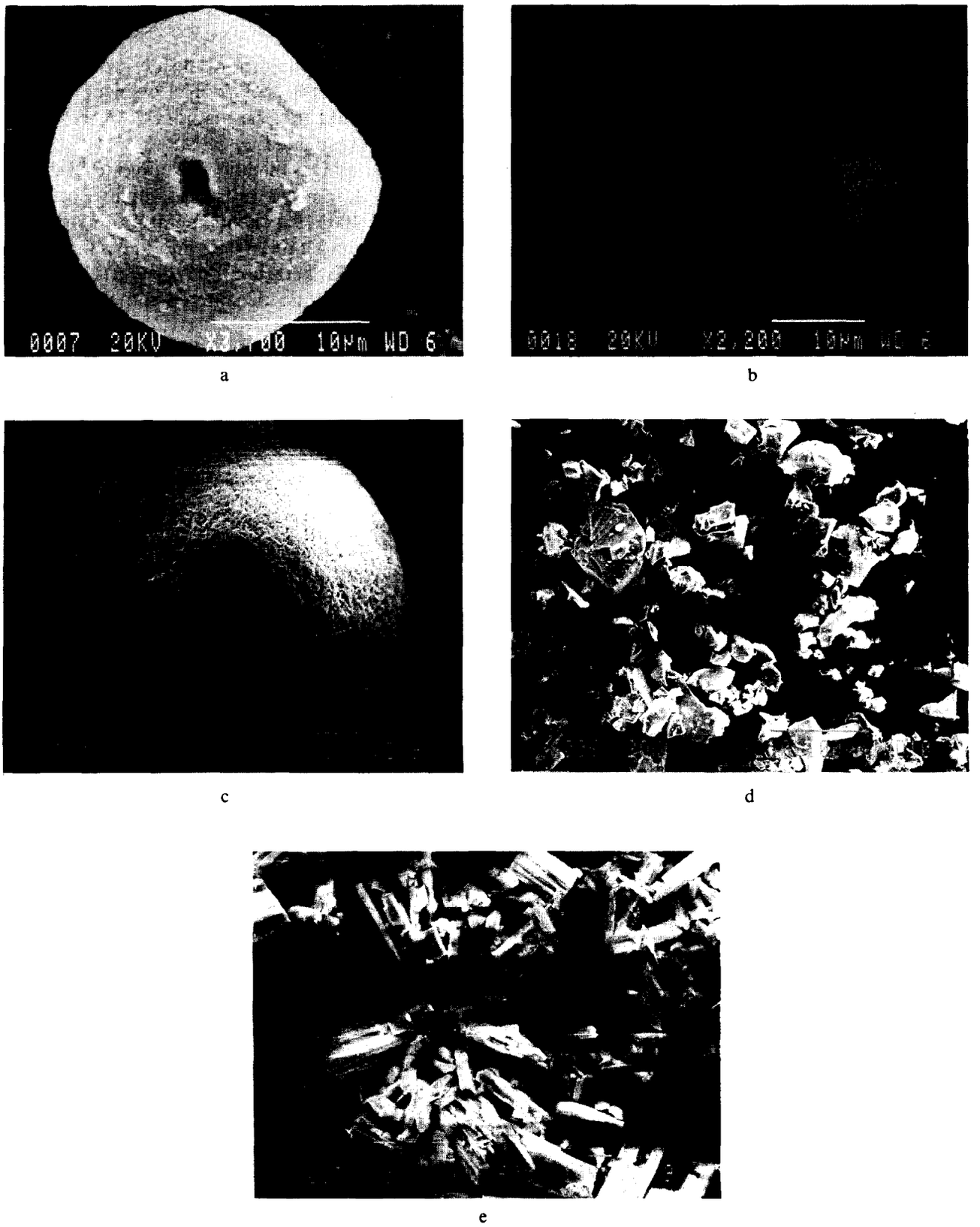


Fig. 3. Scanning electron micrographs of loose powders. (a) powder P1; (b) powder P2; (c) powder P3; (d) powder P4; (e) powder P5.

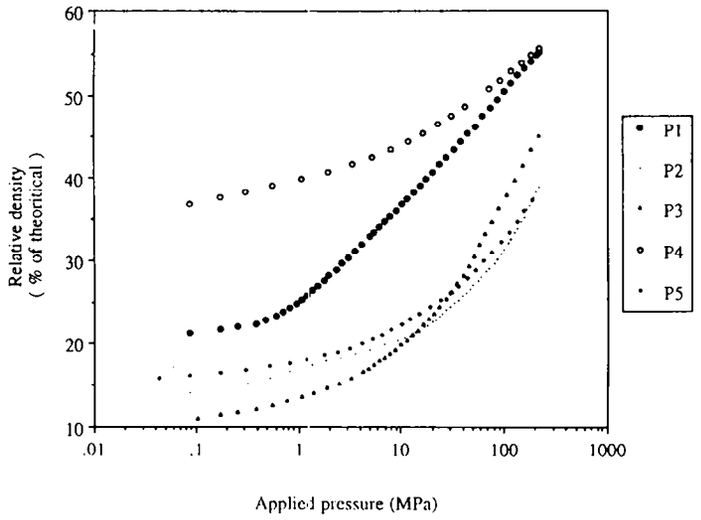


Fig. 4. Compaction behaviour of the five zirconia batches.

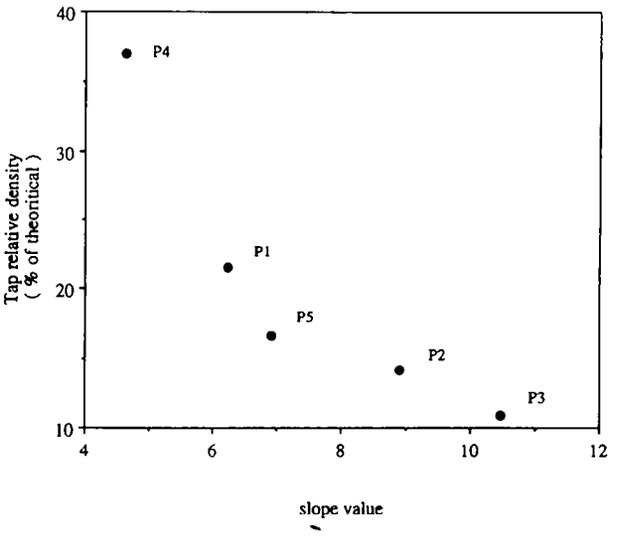


Fig. 5. Plot showing the compaction slope versus tap density. The slope was calculated for each powder in high pressure linear region according to Zheng.

Table 2. Compaction characteristics of the samples

Sample	*P1*	*P2*	*P3*	*P4*	*P5*
Tap density	21·45	14·16	10·83	37·08	16·66
Slope value	6·23	8·90	10·46	4·62	6·90
Pj (MPa)	1	30	11	11	15

until they are on fixed positions to each other.[7,11] The second linear region occurs at higher pressure having a more significant slope, corresponds to the elimination of the interagglomerate porosity.[7,11] The transition zone exhibits a particular pressure value *Pj* for each powder, known as the 'yield point.'[7,11,12] This threshold pressure corresponds to the beginning of the agglomerate deformation and/or crushing. It indicates a transition from discrete agglomerate structure to a coherent compact structure. Compared to the commercial powder, P1, the tap density of powder P4 is about 50% higher whereas for powders P2, P3 and P5 it is lower. For powder P4, even if the shape of agglomerates is irregular, their high density and large size (100 μm) allows this high tap density. For P1 powder, exhibiting the same shape of agglomerates as for the powders P2 and P3, the high tap density is favoured by the large size (53·3 μm) and density of agglomerates. This later allows easy rearrangement in the die. On the contrary, the small size of P2 and P3 agglomerates (mean size 34 and 12·5 μm respectively) and also their porous morphology in the case of the powder P3 favours low tap density. For the powder P5, the rod-like shape of agglomerates involves a bad flowability and consequently a weak green density.

The slopes of the curves in the high pressure linear region have been calculated (Table 2), and plotted versus taped densities (Fig. 5) in the same

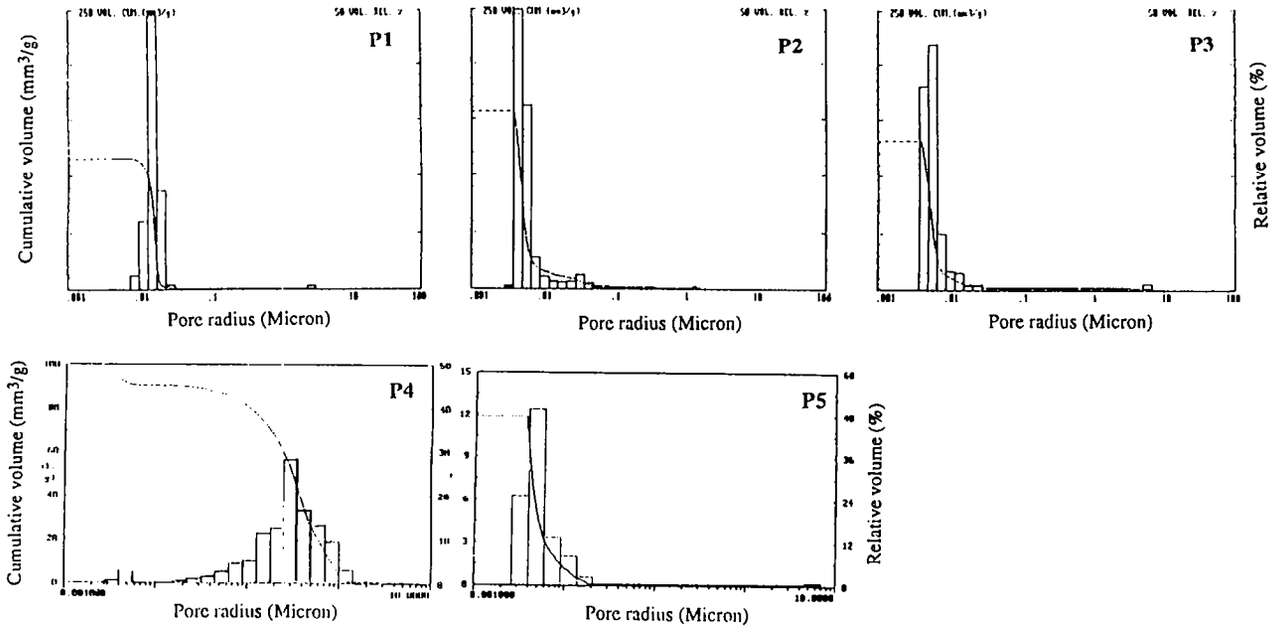


Fig. 6. Pore size frequency distribution in dry isostatically pressed compacts (400 MPa).

way as Zheng and Reed.[13] The compaction rate varies inversely to the powder tap density. The more the powder is constituted of large and dense agglomerates, the more the agglomerates are difficult to deform and/or to crush.

For the powder P1, the yield pressure is about 1 MPa, whereas for the laboratory prepared powders, P2, P3, P4 and P5 it is close to 10 MPa. The difference could be explained by the presence of a binder/plasticizer system in powder P1, allowing

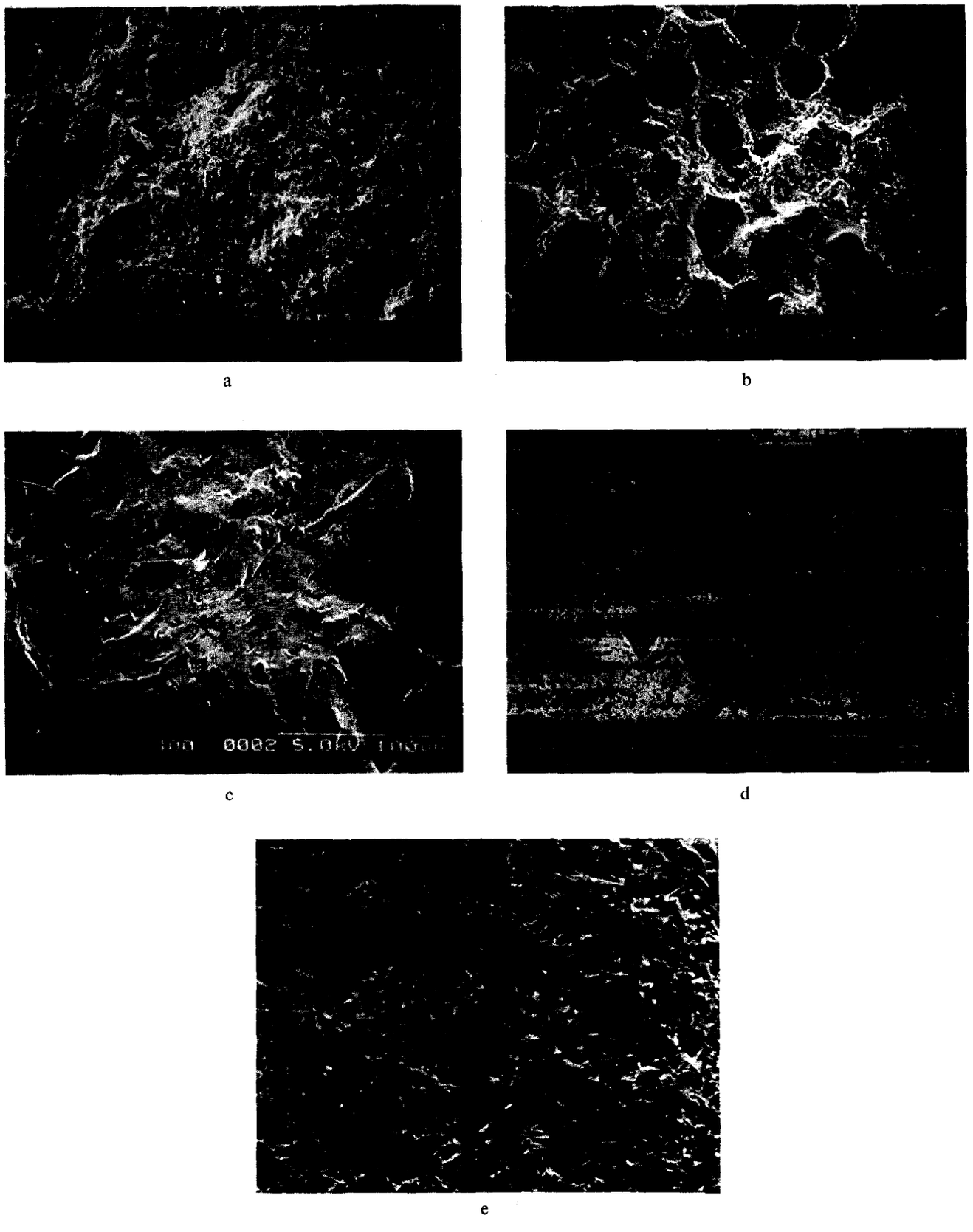


Fig. 7. Series of scanning electron micrographs showing fractured surfaces of green bodies isostatically compacted up to 400 MPa. (a) Fractured surface of green compacted P1; (b) fractured surface of green compacted P2; (c) fractured surface of green compacted P3; (d) fractured surface of green compacted P4; (e) fractured surface of green compacted P5..

easy plastic deformation of agglomerates at low applied pressure. Then, they crush easily and the particles slide onto each other, favouring inter and intra-agglomerate porosity elimination and thus better compaction.

Mercury porosimetry data (Fig. 6) shows a pore distribution radii in the range 0·01–10 μm for all samples isostatically compacted at 400 MPa. The maximum porous volume is localised in the low value side for P1, P2, P3 and P5 (near 0·01 μm) and at the larger side value for P4 (near 0·7 μm). If the pore mean diameter of each powder is compared to crystallite mean diameter obtained from X-ray patterns, we can easily notice that the samples P1, P2, P3 and P5 exhibit mainly intercrystallite porosity. In addition, a very small interaggregate porosity is noticed for samples P2 and P3 with pore radii more than 0·01 μm. On the contrary, the sample P4 exhibits essentially large interaggregate pores. Very weak intercrystallite porosity is also seen at about 5 nm. So, this powder is essentially formed of dense aggregates.

The SEM characterization of green bodies (Fig. 7) shows that:

- The compaction process of powders P1, P3 and P4, at pressures higher than *Pj*, is controlled by a crushing phenomenon of their agglomerates.
- For powder P5, it is also controlled by the crushing of agglomerates but some rod-like shaped agglomerates remain after pressing.
- For powder P2, the integrity of agglomerates is conserved even after pressing up to 400 MPa. Consequently large pores are still present in the green bodies.

The shrinkage of P2, P3 and P5, characterized by a high specific surface area (close to 100 m^2/g),

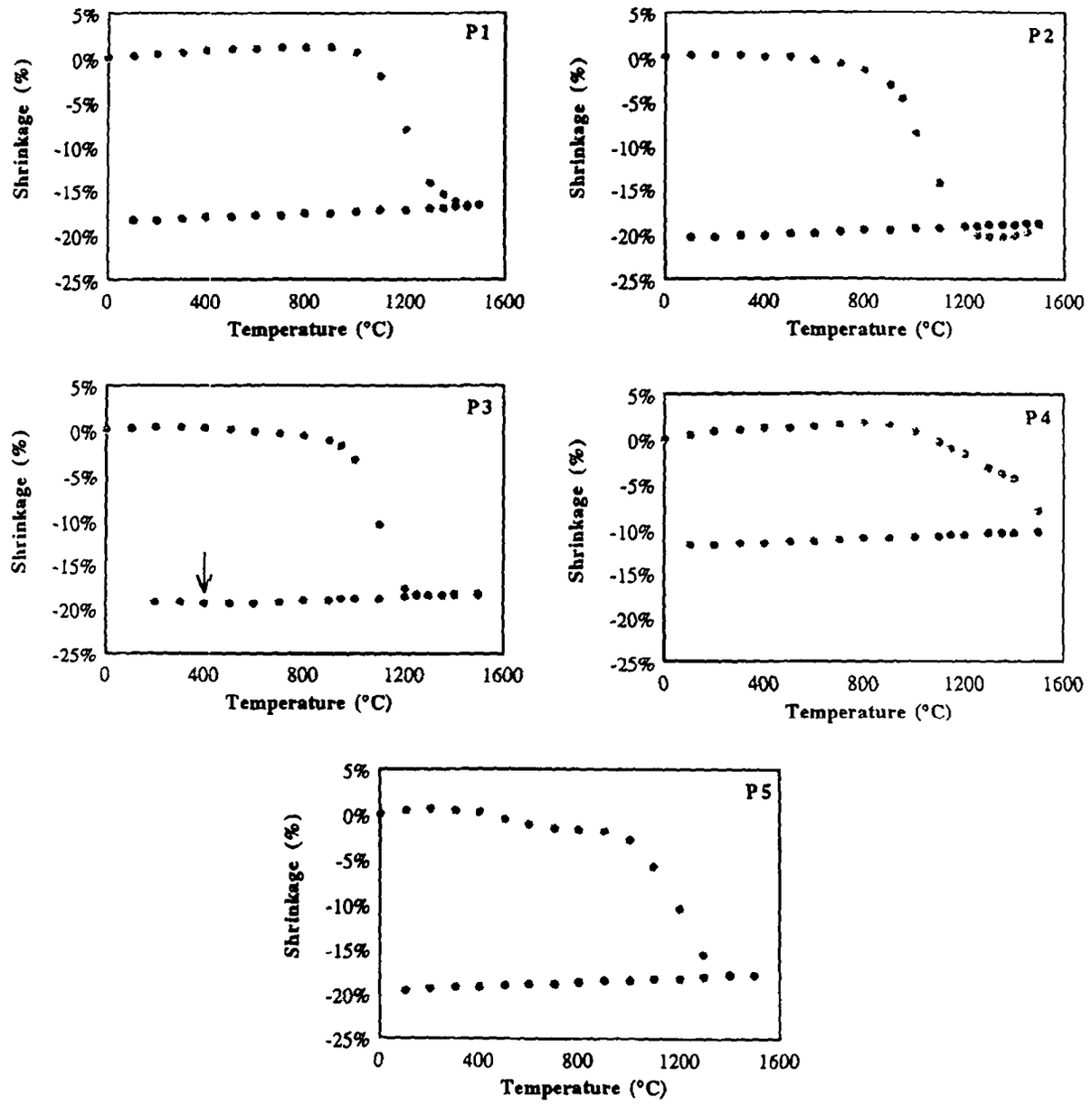


Fig. 8. Dilatometric curves of samples isostatically packed up to 400 MPa and sintered up to 1500°C with a heating rate of 1°C/min.

starts at 400°C and reaches about 20%. Shrinkage is also significant for the powder P1 but begins only at 850°C. Powder P4 has the lowest surface area and shrinkage starts at 850°C and does not exceed 12%, (Fig. 8). Thus, the reactivity of the powders P2, P3 and P5 allows a good densification during the sintering stage, though they have a low green density. The sintering stage of powder P4 is largely delayed by the presence of a large porosity, which is difficult to eliminate at 1500°C

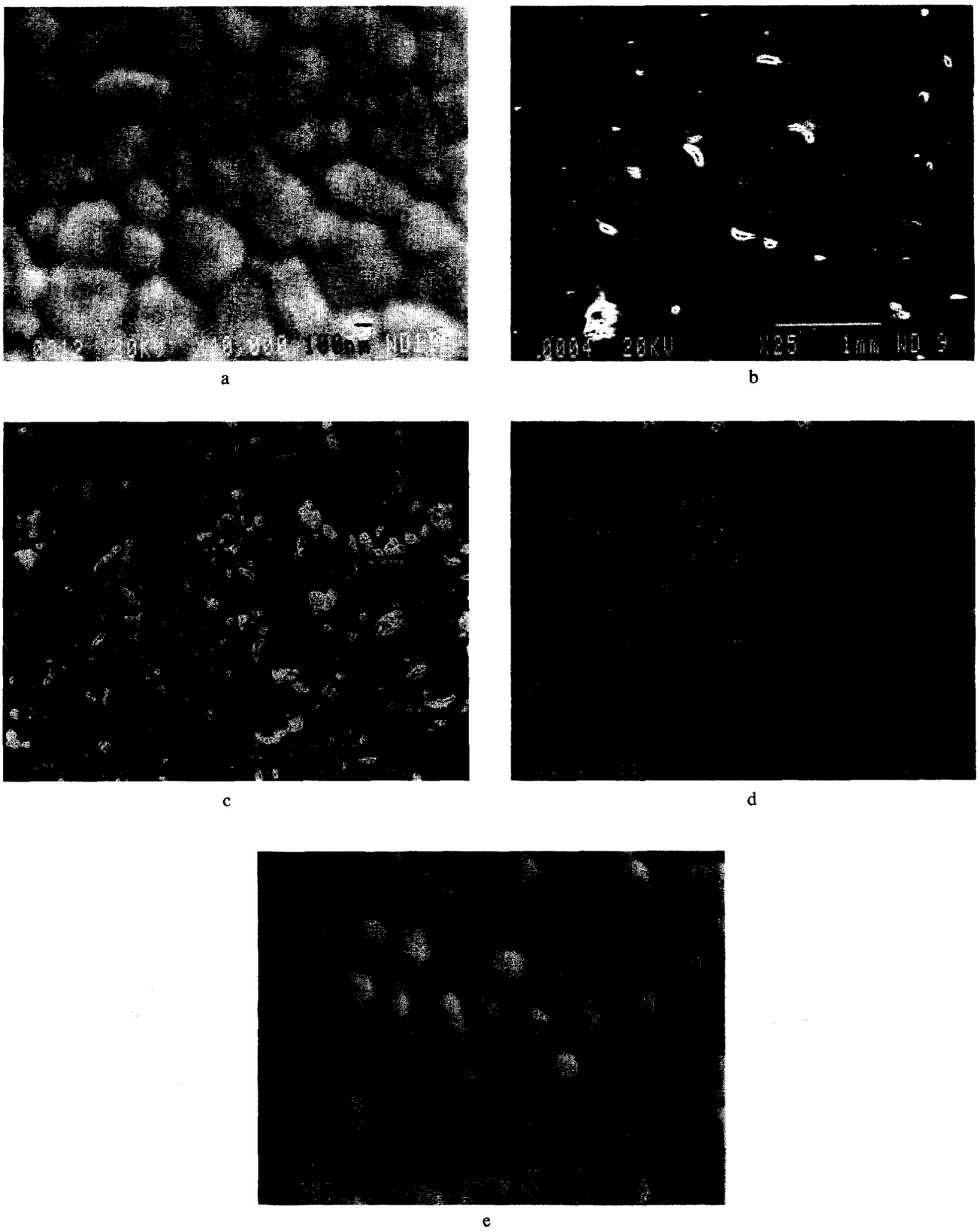


Fig. 9. Series of scanning electron micrographs of sintered (1500°C) pellets made from the powders compacted up to 400 MPa. (a) Micrograph of sintered P1 sample; (b) micrograph of sintered P2 sample; (c) micrograph of sintered P3 sample; (d) micrograph of sintered P4 sample; (e) micrograph of sintered P5 sample.

Table 3. Density of green and sintered samples, % of theoretical

Sample		*P1*	*P2*	*P3*	*P4*	*P5*
Green		54·67	46·78	49·09	58·52	52·17
Sintered	1350°C	—	96·16	94·09	—	—
	1500°C	99·83	88·44	91·99	79·01	98·7

probably owing to the hardness of agglomerates which have not been crushed during pressing. Dilatometric curves of sol–gel powders P3 and principally P2 show a dedensification above 1350°C as previously observed in earlier work.[14,15]

Dilatometric data are confirmed by the measurement of the density of sintered pellets using Arthur's method[16] (Table 3). A density close to 95% of theoretical is reached for samples P2 and P3 sintered at 1350°C. The marked density decrease for the pellets sintered at 1500°C can be explained both by the opening of large pores and the presence of microcracks as shown in SEM micrographs (Fig. 9). Microcracks seen on the micrograph of sample P3, are induced by an increase in monoclinic zirconia content due to grain growth which causes lower density. The tetragonal to monoclinic transformation occurs during the cooling stage as is evident from a dedensification mentioned by the arrow on the dilatometric curve, (Fig. 8) and the presence of monoclinic zirconia on XRD patterns, (Figs 10 and 11).

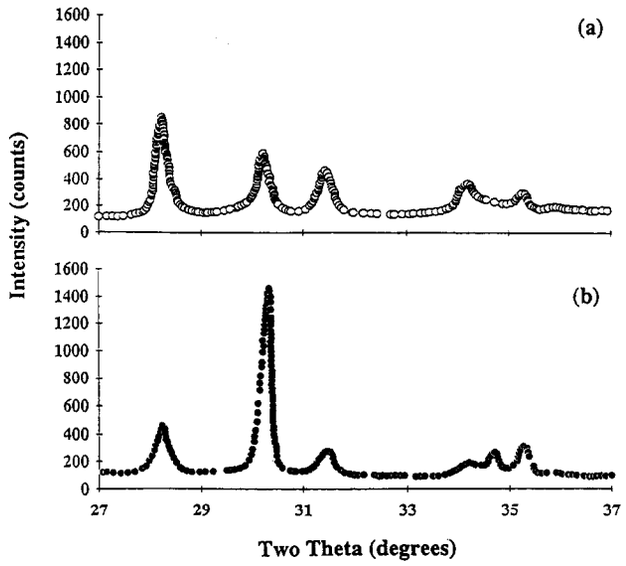


Fig. 11. XRD patterns of P3 sintered (a) at 1500°C, (b) at 1350°C pellets.

The pattern of the other sintered samples indicates only the presence of tetragonal zirconia (Fig. 10). This difference of behaviour is interpreted as a consequence of a lower amount of Y_2O_3 in sample P3. The dedensification phenomenon of sample P2 is a consequence of differential sintering leading to circumferential cracks around hard granules.[17]

A density close to 99 and 98% of theoretical is reached respectively for samples P1 and P5 exhibiting a regular microstructure. The SEM micrograph of sample P4 shows a large porosity which can not be eliminated below 1500°C. TGA experiments (Fig. 12) coupled with gas release

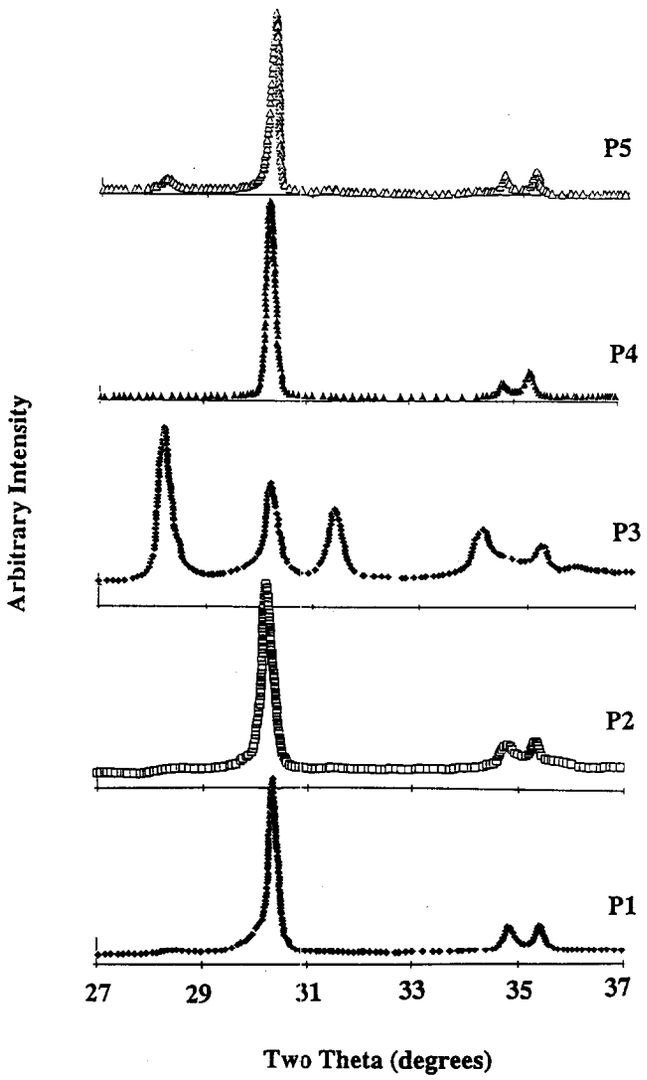


Fig. 10. XRD patterns of compacts sintered at 1500°C.

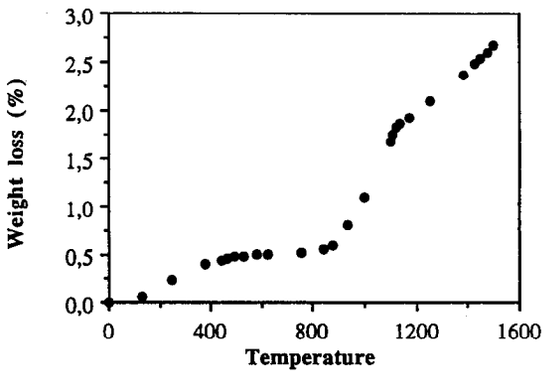


Fig. 12. Thermogravimetric data (TGA) of the sample P4 isostatically packed (400 MPa).

analysis show that the decomposition of residual carbon may be in the form of carbonate or oxycarbonate groups beginning beyond 900°C and not finished at 1500°C. So, a density of 78% of theoretical isn't exceeded.

Conclusions

The commercial powder has a higher mean crystallite size, it sinters quite well and a regular microstructure is obtained. This is due to plastic behaviour of the granules during the compaction stage. The binder favours compaction and allows an earlier crushing of the agglomerates at very low applied pressures. Then, narrower porosity distribution in the green samples leads to good densification.

The reactivity and the fine grain size of sol–gel powders allows a very low sintering temperature. The granulation process involves very good flowability, but it must be controlled carefully to avoid the formation of hard agglomerates. This could be achieved by lowering the calcination temperature down to 400–500 as proposed by Van de Graaf *et al.*[15]

The presence of residual carbon in the form of carbonate or oxycarbonate groups in the sample P4 inhibits the sintering of this powder. Their decomposition begins beyond 900°C and is not finished at 1500°C. Also the presence of aggregates is the second major inconvenience which inhibits the sintering stage.

The molten salt route is interesting because sintered bodies reach the theoretical density. The morphology of this powder must be optimized by changing synthesis parameters so as to enhance flowability.

Acknowledgements

The authors wish to thank Prof. A. Negro, Dr B. Guilhot, Dr J. Dubois, Dr L. Montanaro and Dr J. M. Missiaen for their collaboration and fruitful discussions.

References

1. Dynys, F. W. & Halloran, J. W., Influence of aggregates on sintering. *J. Am. Ceram. Soc.*, **67**(9) (1984) 596–601.
2. Pampuch, R. & Haberko, K., Agglomerates in ceramic micropowders and their behaviour on cold pressing and sintering. In *Ceramic Powders*, Ed by P. Vincenzini. Elsevier Science Ltd, Amsterdam, 1983, pp. 623–34.
3. Ciftcioglu, M., Akinc, M. & Burkhart, L., Effect of agglomerate strength on sintered density for yttria powders containing agglomerates of monosize spheres. *J. Am. Ceram. Soc.*, **70**(11) (1987) C329–34.
4. Montanaro, L., Elaboration des poudres céramiques par voie sol-gel: application aux dispersoïdes alumine-zircone et à la zircone yttriée, PhD thesis, I.N.P.G.-E.N.S.M. de St Etienne, (1990).
5. Samdi, A., Grollier-Baron, T., Durand, B. & Roubin, M., Préparation par hydrolyse de solutions aqueuses, d'acétates de zirconium et d'yttrium précurceurs de zircones dopées à l'yttrium finement divisées, *Ann. Chim., Fr.*, **13** (1988), 517–26.
6. Jebrouni, M., Durand, B. & Roubin, M., Elaboration de zircone pure par réaction en milieu nitrate fondu et caractérisation, *Ann. Chim., Fr.*, **16** (1990) 569–79.
7. Toraya, H., Yoshimura, M. & Somiya, S., Calibration curve for quantitative analysis of the monoclinic–tetragonal ZrO2 system by X-ray diffraction. *J. Am. Ceram. Soc.*, **75**(4) (1984) C119–21.
8. Matsomoto, R. L. K., Analysis of powder compaction using compaction rate diagram. *J. Am. Ceram. Soc.*, **73**(2) (1990) 465–8.
9. Dimilia, R. A. & Reed, J. S., Dependence of compaction on glass transition temperature of the binder phase. *Ceram. Bull.*, **62**(4) (1983) 484–8.
10. Frey, R. G. & Halloran, J. W., Compaction behavior of spray-dried Alumina. *J. Am. Ceram. Soc.*, **67**(3) (1984) 199–203.
11. Holman, L. E., The compaction behaviour of particulate materials. An elucidation based on percolation theory. *Powder Technol.*, **66** (1991) 265–80.
12. Messing, G. L., Markhoff, C. J. & McCoy, L. G., Characterization of ceramic powder compaction. *Ceram. Bull.*, **61**(8) (1982) 857–60.
13. Zheng, J. & Reed, J. S., Particle and granule parameters affecting compaction efficiency in dry pressing. *J. Am. Ceram. Soc.*, **71**(11) (1988) C456–8.
14. Smith, A., Baumard, J. F., Sinterability of tetragonal ZrO2 powders. *Am. Ceram. Soc. Bull.*, **66**(7) (1987) 1114–8.
15. Van de Graaf, M. A. C. G., Ter Maat, J. H. H. & Burggraaf, A. J., Microstructural development during pressing and sintering of ultra fine zirconia powders. In *Ceramic Powders*, ed P. Vincenzini. Elsevier Science Ltd, Amsterdam, 1983 783–94.
16. Arthur, G., Porosity and permeability change during the sintering of copper powder. *J. Inst. Met.*, no. **83**, 1954–5, pp. 329–36.
17. Jorand, Y., Taha, M., Missiaen, J. M. & Montanaro, L., Compaction and sintering behaviour of sol-gel powders. submitted to *J. Euro. Ceram. Soc.*

Journal of the European Ceramic Society **15** (1995) 769–775
© 1995 Elsevier Science Limited
Printed in Great Britain. All rights reserved
0955-2219/95/$9.50

0955-2219(95)00045-3

Mechanical Properties of a Partially Sintered Alumina

Dale Hardy & David J. Green

Department of Materials Science and Engineering, The Pennsylvania State University, University Park, PA 16802, USA

(Received 8 June 1994; revised version received 10 February 1995; accepted 14 February 1995)

Abstract

An experimental investigation was performed to understand the mechanical properties of alumina with moderate amounts of porosity (~20–40%). Young's modulus, strength and fracture toughness showed similar behavior as a function of the degree of sintering. For low sintering temperatures (<1050°C), the mechanical properties were found to change significantly with only minimal densification, and this was considered to be due to neck growth by surface diffusion. At these temperatures, increases in sintering time resulted in further increases in Young's modulus. The Young's modulus and fracture toughness data agreed well with modifications to a recent theory. The critical crack size in these porous materials calculated from the strength and fracture toughness data was found to increase slightly as the sintering temperature was increased. It was concluded that significant improvements in the mechanical properties of porous ceramics can be obtained by control of the sintering process, and in some cases these improvements can be made with minimal densification.

1 Introduction

There are many technological applications in which porous ceramic materials are utilized. For example, high-porosity cellular ceramics can be used for molten-metal filters, radiant burners, lightweight cores for sandwich panels, etc. In other cases, ceramics with moderate amounts of porosity are needed, e.g. as particle filters, catalyst supports and sensors. For structural components, the presence of porosity may be useful in reducing the weight of the component, whereas for non-structural components, porosity may be essential for other functions, such as permeability or a high-surface-area substrate. For both structural and non-structural applications, however, improvements in the mechanical properties and control of strength variability are expected to increase the overall reliability of the material. In order to accomplish this goal, the interrelationship between processing, structure and mechanical properties of porous materials must be understood. The most common way of processing moderately porous ceramic materials is by sintering powder compacts to a fixed degree of densification. During this process, the particles coalesce by the formation of necks, and the particles usually undergo grain coarsening and other geometric changes. The aim of the current study was to measure the room-temperature mechanical properties of a partially sintered alumina, i.e. Young's modulus, fracture toughness and strength, and relate these properties to the sintering process.

2 Background

In order to understand the effect of porosity on mechanical properties, researchers have usually emphasized the volume fraction and geometry of the porosity. In some recent studies,[1–7] however, there has been an attempt to relate the mechanical properties to the microstructure of the *solid* phase, linking the properties to neck growth, particle coordination, solid phase contiguity, etc. Green and coworkers[2,6] have demonstrated a dramatic increase in the strength and elastic moduli of alumina with no change in pore volume. This sharp increase in stiffness with minimal increase in density was attributed to neck growth by surface diffusion, the dominant mechanism in the sintering of alumina at temperatures below ~1000°C. Using a simple model for the initial stages of neck growth that emphasizes the solid microstructure, Green *et al.* suggested[1,2]

$$(B/B_0) = [3Nr(1-2\nu_0)]/[8kR(1-\nu_0^2)] \quad (1)$$

where B is the bulk modulus of the porous compact, B_0 and ν_0 are the bulk modulus and Poisson's ratio of the particle, r is the neck radius, N is the particle coordination number, R is the radius of the particle and k is a geometric constant. According to this model, for a given material the

relative bulk modulus is proportional to the coordination number and the neck-to-particle radius ratio (r/R). By combining eqn (1) with the established relationships for neck growth, it is then possible to relate the elastic moduli of a porous material to the sintering mechanism.[2,7] For the case of alumina, the elastic constants were found to be consistent with the sintering mechanism of surface diffusion at the lower sintering temperatures and volume diffusion at the higher.[2] The increase in strength for alumina without any densification[6] is particularly intriguing, as it implies that one can control the strength of a porous material through manipulation of the sintering process.

In order to obtain further support for eqn (1), Nanjangud and Green[7] measured r/R for partially sintered glass spheres from observations of the fracture surface. The study demonstrated that a linear relationship between Young's modulus and the radii ratio was not unreasonable. Moreover, the study again showed that the elastic properties could be related to the sintering mechanism (viscous flow) and good agreement was obtained between the viscosity data obtained in this manner and previous literature data.[7] In order to understand the strength behavior of a porous material, information is needed on the fracture toughness behavior, and obtaining such data was the primary focus of the current study.

Mechanical property data on porous alumina has recently been gathered by Lam *et al.*[8] and they suggested the elastic constants and fracture toughness should be directly proportional to the degree of densification, i.e.

$$\frac{E}{E_0} = \frac{K_{IC}}{K_{IC}^0} = \left(1 - \frac{P}{P_I}\right) \tag{2}$$

where E and E_0 are the Young's modulus values of the porous and theoretically dense materials, respectively, K_{IC} and K_{IC}^0 are the fracture toughnesses of the porous and dense materials, respectively, P is the fractional porosity and P_I is the fractional porosity in the green state. By postulating an equation for the change in the crack size that initiates failure in these materials, Lam *et al.*[8] also put forward a theoretical relationship for the strength behavior of porous materials. Equation (2) clearly runs into difficulties for materials that undergo sintering without densification, and thus it was suggested recently[7] that the theory for the Young's modulus can be modified to

$$\left(\frac{E - E'}{E_0 - E'}\right) = \left(1 - \frac{P}{P_I}\right) \tag{3}$$

where E' is the Young's modulus at the onset of densification.

3 Experimental Procedure

Porous samples were processed by the partial sintering of powder compacts to various temperatures using a commercially available alumina (Malakoff Industries, TX., >99·99% purity, median particle size = 0·38 μm).

3.1 Sample processing

Bar specimens were used for the Young's modulus and fracture toughness determinations and ~10 individual bars were uniaxially dry-pressed at a pressure of 17 MPa for each batch. The specimens were also isostatically pressed to a pressure of 172 MPa. The specimen dimensions were typically 7 mm × 4 mm × 45 mm. The various batches of material were sintered to different temperatures ranging from 800 to 1600°C. The sintering was conducted in air with a heating rate of 10°C/min and a dwell time of 2 h at the maximum temperature. At the end of the isothermal hold, the samples were allowed to cool at a rate of about 5°C/min. Some isothermal sintering experiments were also conducted at temperatures of 900, 1050, and 1200°C for times up to 78 h.

Specimens for Young's modulus and strength testing were in the form of discs. Powder was introduced into a steel die with a diameter of 25·4 mm and uniaxially pressed to a stress of 45 MPa, but these samples were not isostatically pressed. The sintering procedure was identical to that for the bars. The densities of the bars and discs were both calculated from simple volume and mass measurements and the densities within the batches varied by less than 1%.

3.2 Young's modulus measurements

The Young's modulus of the bars was determined using a dynamic resonance technique from[9,10]

$$E = 0{\cdot}94642C\rho\left(\frac{L^2 f}{h}\right)^2 \tag{4}$$

where E is Young's modulus, L is the sample length, f is the fundamental flexural resonance frequency, h is the beam height, ρ is the density and C is a shape factor. The parameter C is dependent upon Poisson's ratio and values for a porous alumina were taken from a previous study.[2] This approach was considered to be acceptable as Poisson's ratio has only a small effect on the magnitude of C.

The Young's moduli of the discs were determined by an ultrasonic sound velocity technique. Longitudinal sound waves were transmitted through the thickness of the discs by means of a wave pulser and a 12·7-mm diameter, dry contact, 10 MHz transducer (Ultran Laboratories, Boals-

burg, PA). The transit-time measurement was made in the pulse-echo mode and E was calculated using

$$E = \frac{v^2[\rho(1 + \nu)(1 - 2\nu)]}{(1 - \nu)} \quad (5)$$

where v is the longitudinal sound velocity, ρ is density and ν is Poisson's ratio. The Poisson's ratio values for porous alumina were obtained from the literature.[2] Ten samples for each sintering temperature were measured, and the average Young's modulus values were calculated.

3.3 Strength testing

The strengths of the discs were measured using a 'piston on three ball' biaxial flexure test.[11] The load was applied using a commercial mechanical testing machine (Instron Corporation, Model 4200, Canton, MA.). The equation for calculating strength depends on Poisson's ratio, and again values were obtained from literature.[2] The fracture strength for each batch was taken as the average of the strengths of the individual samples. The discs broke into three or four pieces with the cracks originating from the center of the tensile side of the specimens.

3.4 Fracture toughness measurements

Fracture toughness values (K_{IC}) were measured using a four-point bend chevron-notch test.[12,22] This method was chosen to ensure the introduction of sharp cracks in these fragile porous materials. The details of the notching procedure are given elsewhere.[23] Fracture toughness values were determined using the analysis of Munz *et al.*[12] The major and minor spans of the bend fixture were 38·1 and 12·7 mm, respectively, and the crosshead speed was 0·05 mm/min. In the chevron-notch test, crack growth must proceed stably through the maximum load and the presence of stable crack growth was confirmed by the shape of the load–displacement curve obtained for each specimen. If stable growth occurred, the top of the curve would be rounded, whereas a catastrophic failure would give an instantaneous drop in load.

3.5 Microstructural characterization

Scanning electron microscope observations were made on planar sections of the samples to study the microstructural changes as a function of the degree of sintering. It is difficult to polish porous samples without damage, so vacuum impregnation with a cold-mounting epoxy (Epofix HQ, Struers, Westlake, OH) was used to fill the pores and strengthen the samples for polishing. The epoxy was heated to 50°C to reduce the viscosity, and then pieces of the broken discs were dropped into the epoxy in a vacuum chamber. The vacuum was released after 15–30 s to prevent the epoxy from vaporizing. The samples were then mounted for polishing in a different epoxy (M135 Fast Cure Epoxy, Metlab, Niagara Falls, NY). The infiltrated samples were polished to a 0·2-μm diamond paste finish. After polishing, the samples were heated on a hot plate and removed from the softened epoxy. The samples were then heated to 500°C to remove the infiltrated epoxy and, as a final step, were cleaned in acetone prior to microscopic observation.

4 Results and Discussion

Figure 1 shows the changes in the relative density of the alumina bars with sintering temperature. The densities of samples sintered to < 1100°C are relatively unchanged and densification occurs at the higher temperatures. The Young's modulus

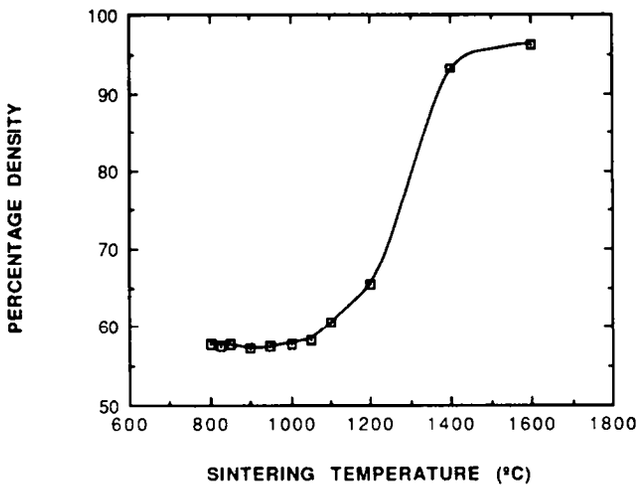


Fig. 1. Density of glass specimens after sintering at various temperatures, showing the onset of densification at ~1050°C.

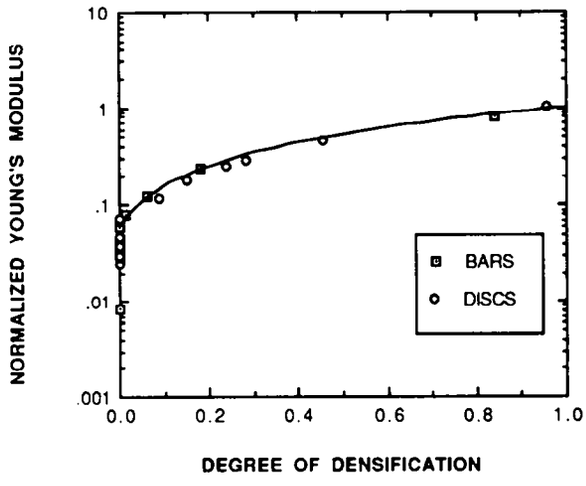


Fig. 2. Comparison of the room temperature Young's modulus values for porous alumina specimens after sintering to various temperatures as a function of the degree of densification with eqn (3).

data for the bars and discs are given as a function of the degree of densification in Fig. 2, i.e. $D = 1 - (P/P_I)$. As with the earlier studies,[2,6] there is a dramatic increase in the Young's modulus for specimens subjected to the initial stages of sintering with very little increase in density, reflecting neck growth by surface diffusion. It is also important to note the E data for both bars and discs fit a single function, even though there was a difference in their respective green densities, i.e. 58% and 54% theoretical density. In terms of eqn (3), the data show an excellent fit, using $E'/E_0 = 0{\cdot}06$. It would appear that the modification to eqn (2) is very useful, but it is still incapable of describing the changes in modulus that occurs for $D = 0$. For these cases, in which non-densifying sintering mechanisms are active, approaches such as that outlined in eqn (1) show more promise, but information on the changes in the r/R ratio and coordination number is difficult to obtain, especially when using sub-micrometer powder as a starting material.

Isothermal sintering was conducted at 900, 1050 and 1200°C and the Young's modulus data are shown in Fig. 3 as a function of the sintering time. For the 900°C and 1050°C sintering schedules, the modulus was substantially increased with no significant change in density (< 1%). This effect could be of technological interest in that Young's modulus can be doubled for this range of sintering times. For the 1200°C specimens, the modulus increased more dramatically, but the density was found to increase at a similar rate. As with the earlier study,[2] the variation in the elastic constants observed in the current study is consistent with a change in the dominant sintering mechanism, i.e. from surface diffusion to volume diffusion at ~1050°C.

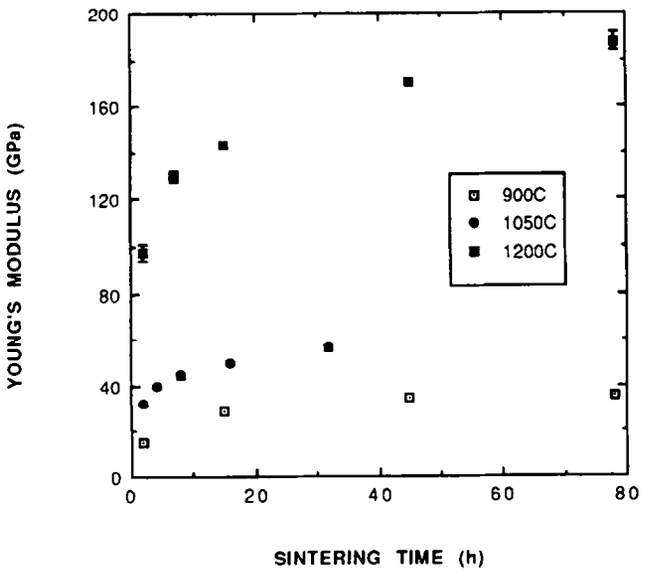


Fig. 3. Room-temperature Young's modulus values for porous alumina specimens after sintering at 900, 1050 and 1200°C for various times. These changes occur without significant densification at the two lower temperatures.

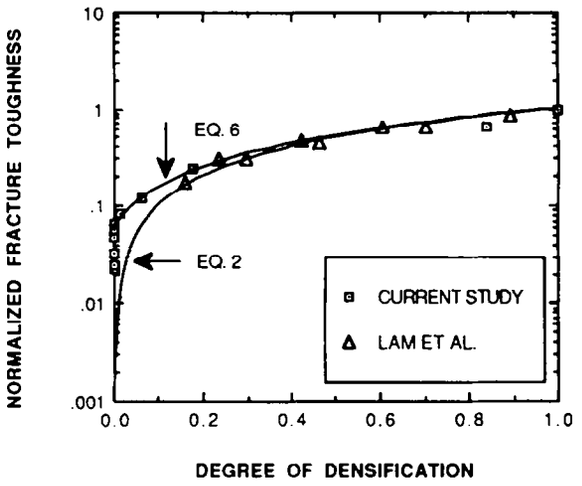


Fig. 4. Room-temperature fracture toughness values for porous alumina specimens after sintering to various temperatures as a function of the degree of densification. For small D, there is significant deviation from the theory of Lam *et al.*[8] Improved agreement is obtained using the proposed modification of eqn (6).

Mode I fracture toughness values (K_{IC}) are given as a function of D in Fig. 4 and are compared with eqn (2). The experimental data of Lam *et al.*[8] is also included in Fig. 4 and comparison with the theory for both data sets shows good agreement for $D \geq 0{\cdot}1$. The growth of the necks for $D = 0$ leads to a significant increase in fracture toughness and shows a strong similarity to the elastic constant data. For a density of 65·4% theoretical, the fracture toughness has increased to 1·06 MPa $\sqrt{m}$, which is a relatively significant value. To place this value in perspective, one should note that the value exceeds that of dense soda-lime-silica glass (~0·7 MPa $\sqrt{m}$). The discrepancy with eqn (2) for small D suggests that eqn (2) for fracture toughness could be modified in the same fashion as the equation for Young's modulus (eqn (3)), i.e.

$$\left(\frac{K_{IC} - K'_{IC}}{K^0_{IC} - K'_{IC}}\right) = \left(1 - \frac{P}{P_I}\right) \qquad (6)$$

where K'_{IC} is the fracture toughness at the onset of densification. The modification to the theory is shown in Fig. 4 using $K'_{IC}/K_{IC}{}^0 = 0{\cdot}06$, and the fit is excellent. A model has been developed that considers the fracture toughness of a partially sintered body in terms of particle neck failure.[23] Such a model would be supported by the increase in fracture toughness seen in Fig. 4 for $D = 0$, similar to the way in which the elastic data in Fig. 2 supports eqn (2). An important difference with the elastic problem is that failure may not necessarily pass through the interparticle necks.[7] For the current work, there was not enough direct evidence to test and support the model.

The biaxial flexural strengths of discs are plotted against relative density in Fig. 5. As with

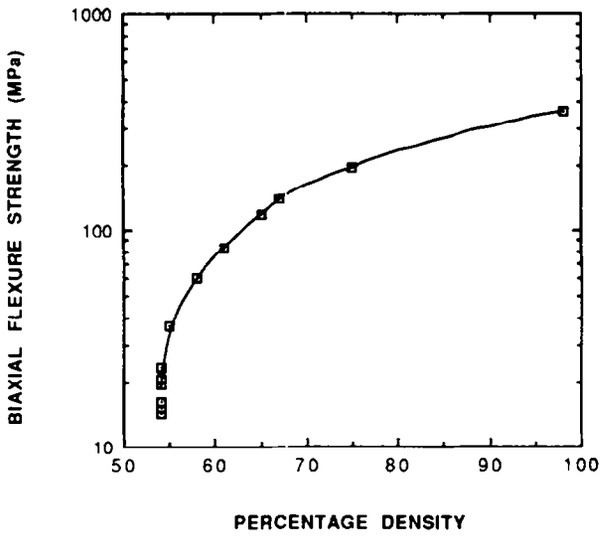


Fig. 5. Room-temperature biaxial flexure strength for porous alumina specimens after sintering to various temperatures as a function of the percentage theoretical density.

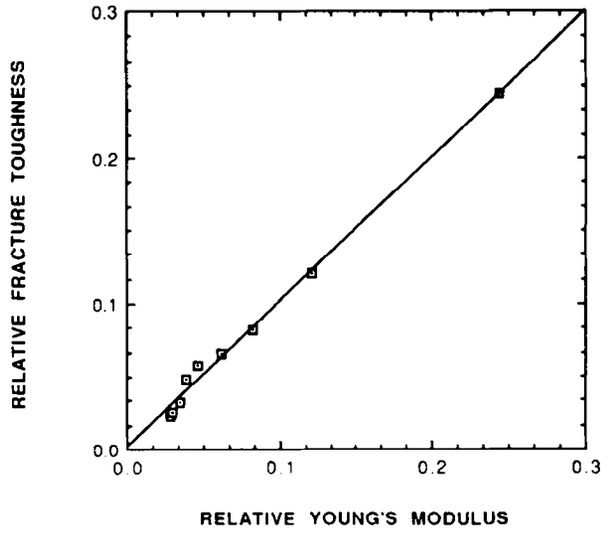


Fig. 6. Correlation between the relative Young's modulus and the relative fracture toughness for bar specimens.

Young's modulus and fracture toughness, there is a relatively large increase in strength for specimens sintered at temperatures below 1100°C. These data show that significant gains in strength of porous ceramics can be obtained with minimal densification. This flexural strength data, along with the Young's modulus and fracture toughness data, is very encouraging in that it demonstrates that the mechanical properties of a porous material can be enhanced at a particular density by control of the sintering mechanism.

The relationship between the strength of a brittle ceramic and its mode I fracture toughness is given as

$$\sigma_f = \frac{K_{IC}}{Y\sqrt{c}} \tag{7}$$

where σ_f is fracture strength, Y is a geometric constant and c is the critical crack length. Thus, the critical crack size can be calculated if σ_f and K_{IC} are known for a given material, and this gives insight into the failure process. In the present study, both σ_f and K_{IC} were measured, but not for the same sample geometry. The fracture toughness tests were conducted on bars, whereas discs were used for the biaxial flexure strength measurements. The difficulty in performing the crack size calculation was that the difference in specimen geometry for the toughness and strength tests gave rise to slight differences in green density. As Young's modulus was measured for both specimen types, it was postulated that K_{IC} could be empirically determined for the strength specimens from the correlation between K_{IC} and E. Equation (2) suggests that $(E/E_0) = (K_{IC}/K_{IC}^0)$ and as shown on Fig. 6, this approach gives a strong correlation even when $D = 0$. Higher-degree polynomials could be used in this fitting procedure, but this was found not to have a strong influence on the crack size calculation. Thus, the fracture toughness of the specimens used in the strength testing was estimated from the E values. The critical crack size, as calculated from eqn (5), is shown in Fig. 7 as a function of the sintering temperature. The value of $Y = 2/\sqrt{\pi}$ was used in the calculation, i.e. the value established for circular cracks of radius c. The critical crack size increased from about 45 to 70 μm as the degree of sintering progressed. At these high porosity levels, it is assumed that the major flaws are interconnected pores and it has been shown previously that pore sizes are expected to increase in alumina during the initial stages of sintering.[24] The data in Fig. 7 contrast strongly with the idea that the critical crack size decreases with increasing D, as suggested by Lam *et al.*[8] One suspects that the critical flaw evolution process may be rather complex and it may be

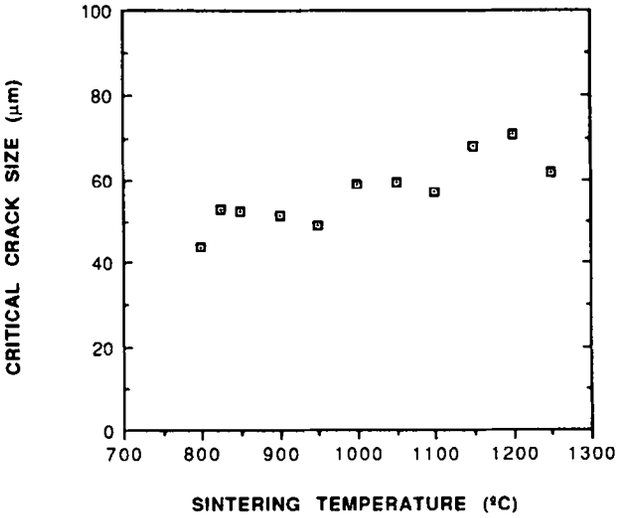


Fig. 7. Critical crack sizes calculated from the biaxial flexure strength and estimated fracture toughness data, assuming a circular flaw geometry, as a function of the sintering temperature.

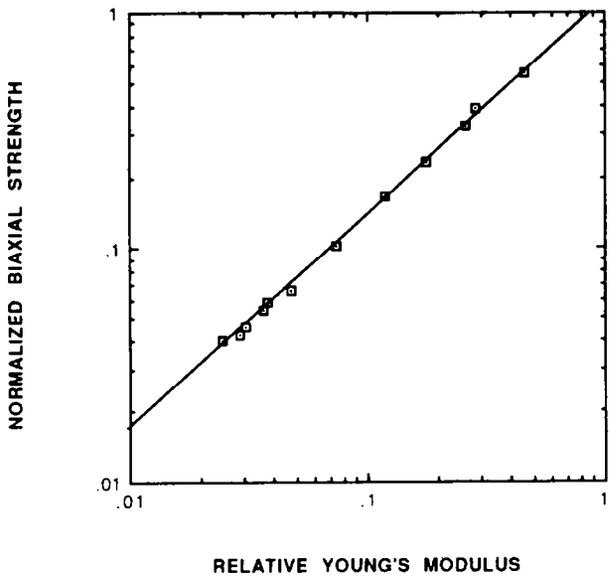


Fig. 8. Empirical correlation between biaxial flexure strength and relative Young's modulus. The strengths were normalized by the strength at the highest density, 357 MPa.

preferable to measure both strength and fracture toughness and obtain empirical information on the changes in critical crack size. For the current work, the critical crack sizes show a fairly smooth variation with increased sintering and as there is a strong correlation between fracture toughness and Young's modulus, one also finds a strong correlation between strength and Young's modulus, as shown in Fig. 8.

Figure 9 shows micrographs for samples sintered at 800, 1000, 1100 and 1200°C. Up to 1050°C, there is no obvious change in particle size or coordination, but some neck growth can be discerned. Above 1050°C, the increased density of the structure becomes apparent as clusters of particles coalesce into a chain-like morphology.

5 Summary and Conclusions

The Young's modulus, strength and fracture toughness of alumina with moderate amounts of porosity (~20–40%) showed similar behavior as a function of the degree of sintering. For low sintering temperatures (< 1050°C), these mechanical properties change with only minimal densification and this was considered to be due to neck growth by surface diffusion. At these temperatures, increases in sintering time can also be used to increase Young's modulus. Modifications to a recent theory that considers the relative Young's modulus and relative fracture toughness to be dependent upon the degree of densification showed very good agreement with the experimental data after densification had initiated. For the present

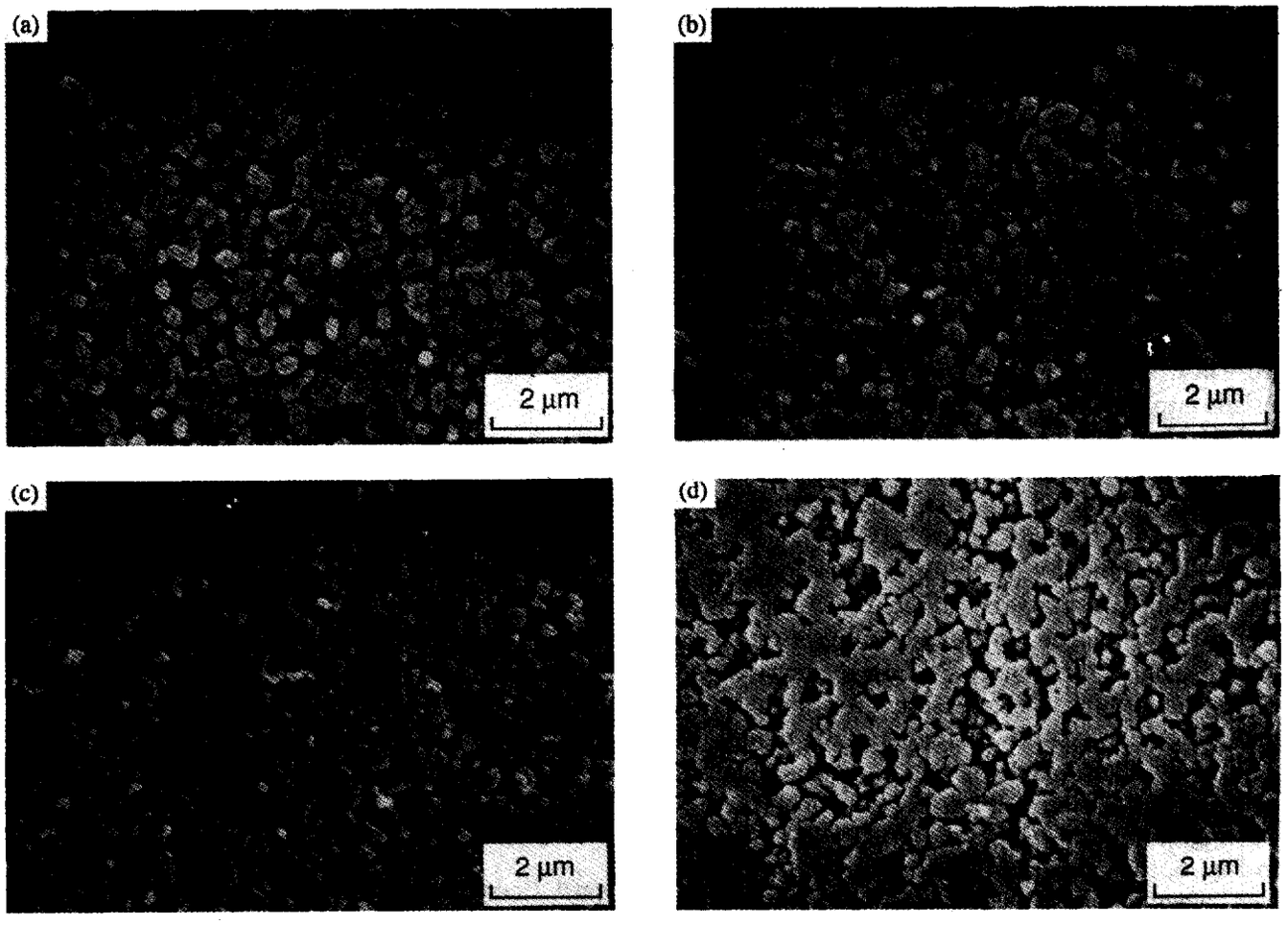


Fig. 9. Scanning electron micrographs showing specimens sintered at (a) 800°C, (b) 1000°C (c) 1100°C and (d) 1200°C.

study, the critical crack size in these porous materials was found to increase slightly as the sintering temperature was increased. Overall, this work shows that significant improvements in the mechanical properties of porous ceramics can be obtained by control of the sintering process and in some cases, with minimal densification.

Acknowledgement

The authors would like to acknowledge the National Science Foundation for financial support under Grant No. DMR. 8818908.

References

1. Green, D. J., Brezny, R. & Nader, C., The elastic behavior of partially-sintered ceramics. In *Adhesion In Solids*, MRS Symposium Proceedings, Vol. 119, eds. D. M. Mattox, J. E. E. Baglin, R. J. Gotschall & C. D. Batich. Materials Research Society, Pittsburgh, PA, 1988, pp. 43–8.
2. Green, D. J., Nader, C. & Brezny, R., The elastic behavior of partially-sintered alumina. In *Sintering of Advanced Ceramics*, eds. C. A. Handwerker, J. E. Blendell & W. Kaysser. American Ceramic Society, Westerville, OH, 1990, pp. 347–56.
3. Woignier, T. & Philippou, J., Mechanical strength of silica aerogels. *J. Non-Cryst. Solids*, **100** (1988) 404–8.
4. Kendall, K., Alford, N. McN. & Birchall, J. D., Elasticity of particle assemblies as a measure of the surface energy of solids. *Proc. R. Soc., Lond., A*, **412** (1987) 269–83.
5. Cytermann, R., A new way of investigating the dependence of elastic moduli on the microstructure of porous materials. *Powder Metall Int.*, **19** (1989) 27–30.
6. Nanjangud, S. C., Brezny, R. & Green, D. J., Strength behavior of a partially-sintered alumina. *J. Am. Ceram. Soc.*, **78** (1995) 266–8.
7. Nanjangud, S. C. & Green, D. J., Mechanical behavior of porous glasses produced by sintering of spherical particles. *J. Eur. Ceram. Soc.*, in press.
8. Lam, D. C. C., Lange, F. F. & Evans, A. G., Mechanical properties of partially dense alumina produced from powder compacts. *J. Am. Ceram. Soc.*, **77** (1994) 2113–17.
9. Davis, W. R., Measurement of the elastic constants of ceramics by resonant frequency methods. *Trans. Br. Ceram. Soc.*, **67** (1968) 515–41.
10. Spinner, S. & Tefft, W. E., A method for determining mechanical resonance frequencies and for calculating elastic moduli from these frequencies. *Proc. ASTM*, **61** (1961) 1221–38.
11. Standard test method for biaxial flexure strength (modulus of rupture) of ceramic substrates. *ASTM F*, **394–78** (1978) 313–17.
12. Munz, D. G., Shannon, J. L. & Bubsey, R. R., Fracture toughness calculation from maximum load in four point bend tests of chevron notch specimens. *Int. J. Fracture*, **16** (1980) R137–41.
13. Bluhm, J. I., Slice synthesis of a three dimensional 'work of fracture' specimen. *Engng. Fract. Mech.*, **7** (1975) 593–604.
14. Munz, D., Bubsey, R. T. & Shannon, J. L. Jr., Fracture toughness of Al_2O_3 using four-point-bend specimens with straight-through and chevron notches. *J. Am. Ceram. Soc.*, **63** (1980) 300–5.
15. Brown, K. R., The chevron notched fracture toughness test, a convenient and inexpensive test at long last. *ASTM Standardization News*, **Nov.** (1988) 66–9.
16. Reddy, K. P. R., Fontana, E. H. & Helfinstine, J. D., Fracture toughness measurement of glass and ceramic materials using chevron-notched specimens. *J. Am. Ceram. Soc.*, **71** (1988) C310–13.
17. Munz, D., Effect of specimen type on the measured values of fracture toughness of brittle ceramics. In *Fracture Mechanics of Ceramics*, Vol. 6, eds. R. C. Bradt, A. G. Evans, D. P. H. Hasselman & F. F. Lange. Plenum Press, New York, 1983, pp. 1–25.
18. Shannon, J. L. Jr. & Munz, D. G., Specimen size and geometry effects on fracture toughness of aluminum oxide measured with short-rod and short-bar chevron-notched specimens. In *Chevron-Notched Specimens: Testing and Stress Analysis*, ASTM STP 855, eds. J. H. Underwood, S. W. Freiman & F. I. Baratta. ASTM, Philadelphia, 1984, pp. 270–80.
19. Bluhm, J. I., Stability considerations in the generalized three dimensional 'work of fracture' specimen. In *Fracture*, Vol. 3. ICF4, Waterloo, Canada, 1977, pp. 409–17.
20. Chuck, L., Fuller, E. R. Jr. & Freiman, S. W., Chevron-notch bend testing in glass: some experimental problems. In *Chevron-Notched Specimens: Testing and Stress Analysis*, ASTM STP 855, eds. J. H. Underwood, S. W. Freiman & F. I. Baratta. ASTM, Philadelphia, 1984, pp. 167–75.
21. Shang-Xian, W., Compliance and stress-intensity factor of chevron-notched three-point bend specimen, *ibid.*, pp. 176–92.
22. Munz, D., Bubsey, R. T. & Shannon, J. L. Jr., Performance of chevron-notch short bar specimen in determining the fracture toughness of silicon nitride and aluminum oxide. *J. Test. Eval.*, **8** (1980) 103–7.
23. Hardy, D., Mechanical properties of partially sintered alumina. MS Thesis, The Pennsylvania State University, 1992.
24. Whittemore, O. J. & Sipe, J. J., Pore growth during the initial stages of sintering ceramics. *Powder Technol.*, **9** (1974) 159–64.

Journal of the European Ceramic Society **15** (1995) 777–785
© 1995 Elsevier Science Limited
Printed in Great Britain. All rights reserved
0955-2219/95/$9.50

0955-2219(95)00048-0

The Interrupted Static Fatigue Test for Evaluating Threshold Stress Intensity Factor in Ceramic Materials: A Numerical Analysis

Vincenzo M. Sglavo & David J. Green

Department of Materials Science and Engineering, The Pennsylvania State University, University Park, PA 16802, USA

(Received 1 August 1994; revised version received 7 February 1995; accepted 14 February 1995)

Abstract

The interrupted static fatigue (ISF) test can be used to evaluate the threshold for sub-critical crack growth, K_{th}. A critical theoretical analysis of this technique is presented in order to elucidate its advantages and limitations and to furnish some suggestions for a more definitive procedure for evaluating K_{th}. It was concluded that a critical parameter in the ISF procedure is the duration of the static hold time. In particular, one should demonstrate that the calculated value of K_{th} does not change when this holding time is increased. Moreover, the applied stress must be chosen such that a significant fraction of samples fail in the hold period. Two different approaches are suggested for calculating the value of K_{th} from experimental data. The first approach is considered preferable for materials with larger Weibull moduli and the threshold is determined from the applied stress intensity factor at which 50% of samples fails during the stress hold. In the second approach, the stress intensity factor applied to the weakest specimen during the stress hold is calculated for various hold times. Once this value becomes independent of hold time, it is equivalent to the threshold.

1 Introduction

The use of glasses and ceramic materials in structural applications can be limited by the phenomenon known as sub-critical crack growth. For ceramics that exhibit this fatigue behaviour, strength becomes dependent upon time and environmental conditions. The design of structural components consisting of materials that exhibit fatigue behaviour must proceed by the estimation of a design stress, which corresponds to a required minimum failure time.

Some studies on sub-critical crack growth in glasses and ceramics have shown that this phenomenon seems to have a lower limit in the sense that crack propagation velocities tend to zero for some particular value of the applied stress intensity factor, K_{th}. This is termed the fatigue limit or the threshold stress intensity factor.[1–15] From an engineering design point of view, the existence of a fatigue limit turns out to be extremely desirable, as it allows an applied stress to be defined, below which delayed failure does not occur.

In spite of the importance of the fatigue threshold, no comprehensive test methodology has been presented for its determination. In early works on sub-critical crack growth in glasses and ceramics, specimens, usually pre-cracked, were loaded at different stress levels and the lifetime was determined.[1–7,9] The 'endurance limit' was defined as the stress at which the fatigue curve shows an asymptotic limit. For glass in a moist environment, values ranging from 0·2 to 0·4 times the strength measured in liquid nitrogen were obtained.[5] The same approach has also been used in more recent works.[16–18]

Studies devoted to sub-critical crack velocity determination as a function of the applied stress intensity factor showed, in some cases, the existence of a threshold below which crack motion did not occur. In these cases, fracture mechanics specimens such as the double cantilever beam (DCB) and double torsion geometries were used and crack advancement was measured as a function of time.[8,10,13,14,19–21]

The difficulty with the methodologies described above is that extremely long experimental times are necessary to evaluate the crack growth at these low stress levels. In fact, the fatigue limit is usually extrapolated from stress or stress intensity factor data to obtain information at long times.

The difficulties, outlined above, can be by-passed by using some indirect methods. For example, in the work of Michalske, DCB glass specimens were loaded in water at a stress intensity factor value of

0·225 MPa √m and aged in this state for fixed periods.[22] The stress intensity factor was then raised and crack motion as a function of time was recorded. The existence of a stress corrosion limit in glass, postulated to be the result of crack tip blunting, was exhibited by observing a delay in the crack growth upon reloading. A fatigue limit $<0{\cdot}25$ MPa √m in soda lime silicate glass was proposed.[22]

An approach that is experimentally easier was presented by Dutton and Rogowski[23] and Wilkins and Dutton.[24] In their studies, alumina and glass samples were loaded in a 'corrosive' environment and the load was maintained for times of the order of a few hours. The strength was then measured and compared to the initial strength. This has been termed the interrupted static fatigue (ISF) test. The same technique has been used by Hayashi *et al.* to measure the fatigue limit of borosilicate glass rods in water.[25]

Tressler and coworkers[26–29] have further developed the approach proposed by Dutton and Rogowski.[23] In studies on silicon carbide and silicon nitride ceramics at high temperatures, they measured the average strength of samples aged under different loads. The threshold stress intensity factor was calculated from the stress level above which samples failed during the static hold part of the test. Nevertheless, the lack of a solid theoretical background sometimes made the interpretation of the data difficult.[26–29] Tanaka and Pezzotti pointed out that some of the data proposed by Tressler and coworkers do not represent the real fatigue limit but are the result of a typical time-to-failure test.[30]

In the following study, a theoretical analysis on the interrupted static fatigue test is presented. The behaviour of silicon carbide at high temperatures and of glass in water is simulated using fracture mechanics so that the conditions for the correct evaluation of the fatigue limit can be highlighted. The results of the theoretical analysis allow some suggestions regarding the methodology for threshold stress intensity factor determination to be proposed.

2 Theoretical Approach

In order to describe the strength degradation that occurs in the interrupted static fatigue test, a function describing the sub-critical crack propagation velocity is required. The crack growth behaviour is usually expressed as a power function of the stress intensity factor K and can be written as follows:

$$v = \frac{dc}{dt} = v_0 \left(\frac{K}{K_c}\right)^n \quad \text{if } K > K_{th} \tag{1a}$$

$$v = 0 \quad \text{if } K < K_{th} \tag{1b}$$

where K_c corresponds to the fracture toughness, v_0 and n are constants which depend upon the material and the environment, K_{th} is the threshold for sub-critical crack growth and c is the crack length.

The stress intensity factor K, associated with a 'crack-like' flaw subjected to an applied stress σ, is given by

$$K = \sigma \Psi \sqrt{c} \tag{2}$$

where Ψ is the geometric factor that includes the effect of flaw shape, boundary interactions and loading geometry. In the absence of residual stress fields, the strength S, associated with a crack of length c, can be written as

$$S = \frac{K_c}{\Psi \sqrt{c}} \tag{3}$$

According to eqn (1a), when a constant stress, σ_h, is applied for a time t and $K > K_{th}$, the flaw size increases from the initial value c_0 to a final value c_1. Correspondingly, strength decreases from S_0 to S_1. Substitution of eqn (2), with $\sigma = \sigma_h$, into eqn (1) and subsequent integration allows one to evaluate S_1 as a function of hold time t as

$$S_1 = \left(S_0^{n-2} - \frac{\sigma_h^n t}{B}\right)^{1/(n-2)} \quad \text{if } K > K_{th} \tag{4a}$$

$$S_1 = S_0 \quad \text{if } K < K_{th} \tag{4b}$$

where

$$B = \frac{2K_c^2}{(n-2)\Psi^2 v_0} \tag{5}$$

When n is a real number, eqn (4a) is not defined for $\sigma > \sigma^* = (B\, S_0^{n-2}/t)^{1/n}$, the condition for which $S_1 = 0$.

Equation (4) can also be expressed in terms of the stress intensity factor K_h, applied at the start of the static hold. From eqns (2) and (3),

$$\sigma_h = S_0 \frac{K_h}{K_c} \tag{6}$$

and thus, for $K_h > K_{th}$, eqn (4a) becomes

$$S_1 = S_0 \left(1 - \frac{S_0^2 K_h^n t}{K_c^n B}\right)^{1/(n-2)} \tag{7}$$

In this case, S_1 is not defined for $K_h > K^* = K_c\,[B/(S_0^2 t)]^{1/n}$. The importance of this condition resides in the fact that, when a stress intensity factor larger than K^* is applied for a time t, the final strength S_1 is zero. This condition can also be defined in terms of the ratio $\kappa = K_h/K_c$, as

$$\kappa^* \left(\frac{2c_0}{(n-2)tv_0}\right)^{1/n} \tag{8}$$

3 Simulation Results

On the basis of the theoretical background developed in the previous section, the behaviour of silicon carbide at 1400°C and soda-lime silicate glass in water at room temperature was simulated. The properties used in the calculations are given in Table 1.[31,32] In these initial calculations, average strength values were used. The effect of strength variability will be explored later.

Figure 1 shows the strength of SiC after the ISF test as a function of the applied stress for three different holding times, as calculated from eqn (4), in the absence of a threshold. Sub-critical crack growth is responsible for the strength decrease that occurs over a small range of applied stress values. This behaviour demonstrates that, even in absence of a threshold for fatigue, strength remains practically constant for most of the lifetime of the sample. It can also be observed that the stress value (σ^*) at which strength 'drop-off' occurs, decreases for increasing hold time.

Diagrams such as Fig. 1 can also be given in terms of the stress intensity factor (eqn (7)), as shown in Fig. 2. In this case, the threshold for sub-critical crack growth was assumed to be 1 MPa $\sqrt{m}$.[31] A distinct strength drop-off is still evident and K^* decreases for increasing hold times until the threshold is reached. At this point, further increases in hold time do not have any influence on the stress intensity factor corresponding to the strength drop-off.

Figures 1 and 2 illustrate some important features regarding threshold measurement by the ISF test. When S_1 is measured to be equal to the initial strength S_0, it is not possible to definitely conclude that this is the effect of K being lower than the threshold. In addition, as shown in Fig. 2 for SiC at 1400°C, hold times during the ISF test must be longer than 44·2 h in order to guarantee that the strength degradation is only a result of the stress intensity factor being above the threshold.

Table 1. Properties of SiC and soda-lime glass considered in this study[31,32]

S_0 (MPa)	K_c (MPa $\sqrt{m}$)	n	B (MPa^{2}s)
470	2·7	21	14·23
130	0·75	19·3	0·19

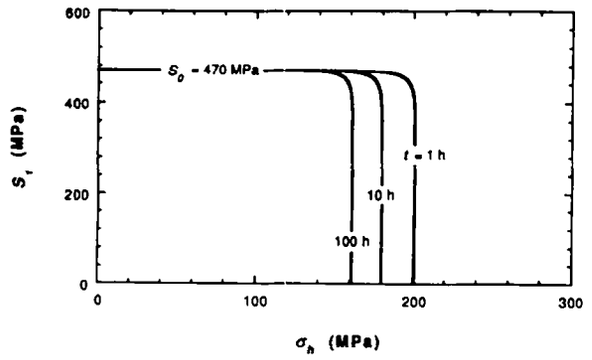


Fig. 1. Strength S_1 of SiC after the ISF test as a function of the applied stress σ_h for three different holding times.

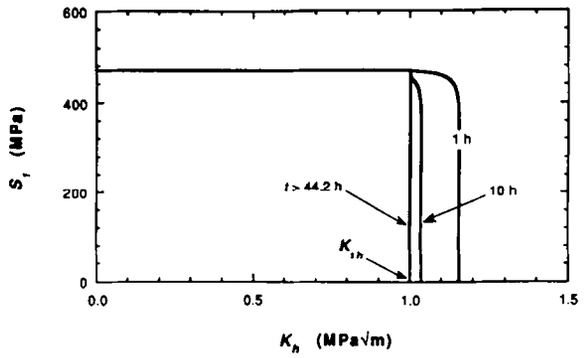


Fig. 2. Strength S_1 of SiC after the ISF test as a function of the applied stress intensity factor K_h for increasing holding times. A fatigue threshold equal to 1 MPa $\sqrt{m}$ was assumed.

The importance of the hold time on the performance of the ISF test can be highlighted further by Fig. 3, in which the stress intensity factor at which strength drop-off occurs (K^*) is plotted as a function of t. It is clear that if the material possesses a threshold, it is critical to ensure the strength loss due to sub-critical crack growth is occurring at the threshold conditions. Diagrams in Fig. 3 were calculated starting from initial strength values of 470, 149 and 47 MPa. The first of these values was that used in Table 1 while the other two were calculated by assuming that the initial crack size was 10 and 100 times larger. Such behaviour would be obtained if cracks were purposely introduced into the test specimens. The behaviour in Fig. 3 indicates that the presence of larger flaws leads to an increase in the time necessary for defining the threshold behaviour in the ISF test. Indeed, the introduction of artificial larger cracks, in order, for instance, to reduce the strength scatter, has a negative impact on the efficiency of the test methodology in terms of time management.

Calculations similar to those presented for SiC at 1400°C were also performed for soda-lime silicate glass in water at room temperature. The most

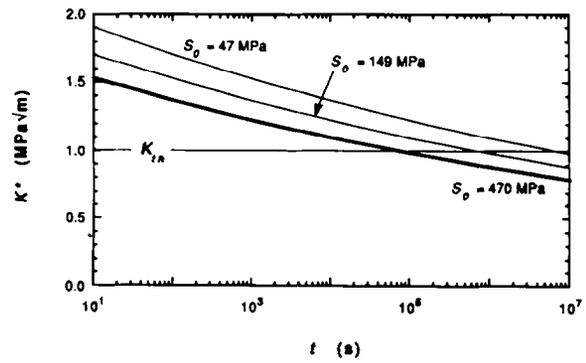


Fig. 3. 'Drop off' point K^* for SiC as a function of the holding times for different initial strengths S_0.

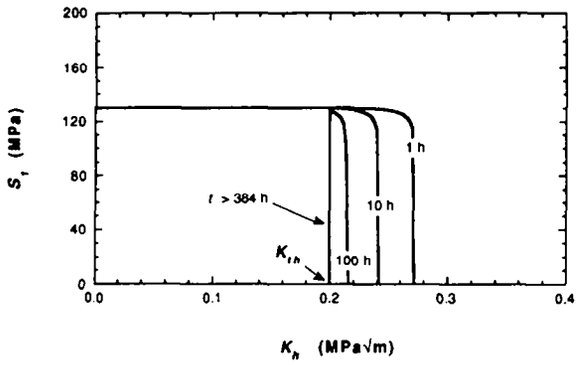


Fig. 4. Strength S_1 of soda-lime silicate glass after the ISF test as a function of the applied stress intensity factor K_h for increasing holding times. A fatigue threshold equal to 0·2 MPa √m was assumed.

significant result is shown in Fig. 4, where the strength after holding under constant stress is plotted as a function of K, for different dwell times. In this case a threshold for sub-critical crack growth was assumed to be 0·2 MPa √m.[11] For this case, hold times in excess of 384 h were found to be necessary to ensure the threshold is being measured properly for soda-lime silicate glass. Clearly, lower values of the ratio K_{th}/K_c would further increase the necessary hold times for threshold detection.

Simulation of the strength degradation behaviour of soda-lime glass was analysed further in order to point out the influence of an interrupted static fatigue test on the strength distribution. Thus far, calculations were developed by considering only the average strength (Table 1). Due to the typical large scatter shown by the strength of ceramic materials, a complete analysis should not leave out of consideration the variation in the initial crack sizes. This is an important feature as it implies a variability in K_h.

Glass strength was assumed to follow a Weibull distribution, as defined by the relationship[33]

$$F = 1 - \exp\left[-A\left(\frac{S}{\sigma_0}\right)^m\right] \tag{9}$$

where F is the failure probability, A is a constant depending on the geometry of the specimen and of the test, while σ_0 and m represent the scale parameter and the shape factor, or Weibull modulus, respectively. The constant A was assumed to be equal to 1 for easier calculation, but this does not compromise the generality of the analysis. The strength distribution was generated by assuming a mean strength S_m and a Weibull modulus equal to 130 MPa (Table 1) and 5, respectively.[33] The scale parameter σ_0 was determined by the relation[33]

$$\sigma_0 = \frac{S_m}{\Gamma(1 + 1/m)} \tag{10}$$

where Γ is the gamma function. Two situations, corresponding to a number of test specimens (N) equal to 10 and 100, respectively, were considered. Failure probability was calculated as $F = j/(N + 1)$, j being the rank in the ascending strength distribution.[33] Discrete values of the strength were obtained from eqn (9). The simulation of strength distribution variations after ISF testing was performed by considering holding times (t) ranging from 1 to 1000 h and applied stresses (σ) of 15, 30, 45 and 60 MPa. As earlier, a threshold stress intensity value of 0·2 MPa √m was assumed. Each element of the initial strength distribution S_{0j} (j = 1,N) was associated with a particular initial flaw size c_{0j}. This value was used to evaluate the stress intensity factor K_j applied to each specimen by eqn (2), once the hold stress was defined. Depending on the K_j value, the strength S_{1j} was calculated by eqn (4) as a function of hold time and applied stress.

Figure 5(a) shows the Weibull plot of the strength distributions after the holding at different stress levels for 1 h, for N = 100. The failure probability of specimens surviving the static hold were calculated as a censored distribution. The initial distribution, corresponding to an applied stress equal to 0, is obviously represented by a straight line.[33] Increased values of σ lead to significant changes in the strength distribution. This appears

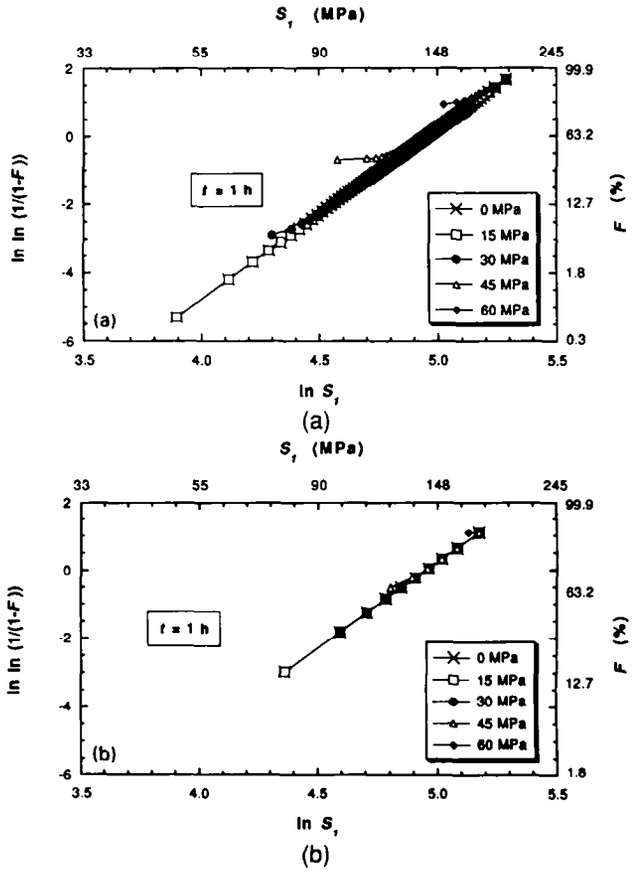


Fig. 5. Weibull plot of the strength distribution of soda-lime silicate glass after the holding at different stress levels for 1 h. The initial strength distribution corresponds to the applied stress of 0 MPa. (a) Number of specimens, N = 100, (b) N = 10.

as a 'twist' in the distribution, which is truncated for specimens that fail during the static hold. Sub-critical growth accounts for these effects. The larger the defect, the higher the stress intensity factor applied during the hold and this increases the amount of sub-critical crack growth. Thus, larger flaws can grow significantly or even fail during the constant stress period. Similar trends were also observed when $N = 10$, although the 'twisting' becomes more difficult to distinguish, as shown in Fig. 5(b). Clearly, the behaviour in a real experimental test would be further complicated by the actual scatter in the c_0 values and statistical sampling effects.

The effect of increasing hold time is shown in Fig. 6, for $N = 100$ and, as expected, a larger number of specimens fail during the stress hold for a given applied stress (all specimens fail when $\sigma = 60$ MPa and $t \geq 100$ h). A limit is reached when an increased hold time does not affect the distributions further, i.e. the twist in the distribution disappears, as shown in Fig. 6(c) and (d). This implies that all the specimens that fail in the hold had K values above the threshold, while those that survived were below the threshold. The same behaviour was also observed for $N = 10$.

Changes in strength distribution after specimens have been held at particular stress levels have been used in some previous studies as a means to identify the threshold for sub-critical growth in glass.[24,25] For example, Wilkins and Dutton[24] and Hayashi *et al.*[25] determined K_{th} for soda-lime glass at 400°C and for borosilicate glass in water at room temperature, respectively. In these studies the threshold was defined as the point in the strength distribution at which the 'twisting' starts. This approach is based on the assumption that the element of the distribution from which 'twisting' starts corresponds to the specimen subjected to a stress intensity factor equal to or lower than the threshold. If the data output used to draw Figs 5 and 6 are considered, the elements subjected to $K = K_{th}$ can easily be identified. The points corresponding to these specimens are marked with the letter X in Fig. 7, which shows three of the distributions presented in Fig. 5(a). It is evident that the points denoted as X_1 and X_2 are not the same as the points at which the twisting becomes significant. As already pointed out in the earlier analysis, specimens that do not show any strength degradation may not have been subjected to a stress intensity factor value lower than K_{th} (Fig. 1). When experimental data are considered, detection of the points denoted as 'X' in Fig. 7 is an even more formidable task as the current analysis did not include the type of scatter seen experimentally. If points like those marked with 'Y' in Fig. 7, are considered in place of 'X', this leads to an overestimation of the fatigue limit. For example, the use of points Y_1 and Y_2 leads to threshold estimates of

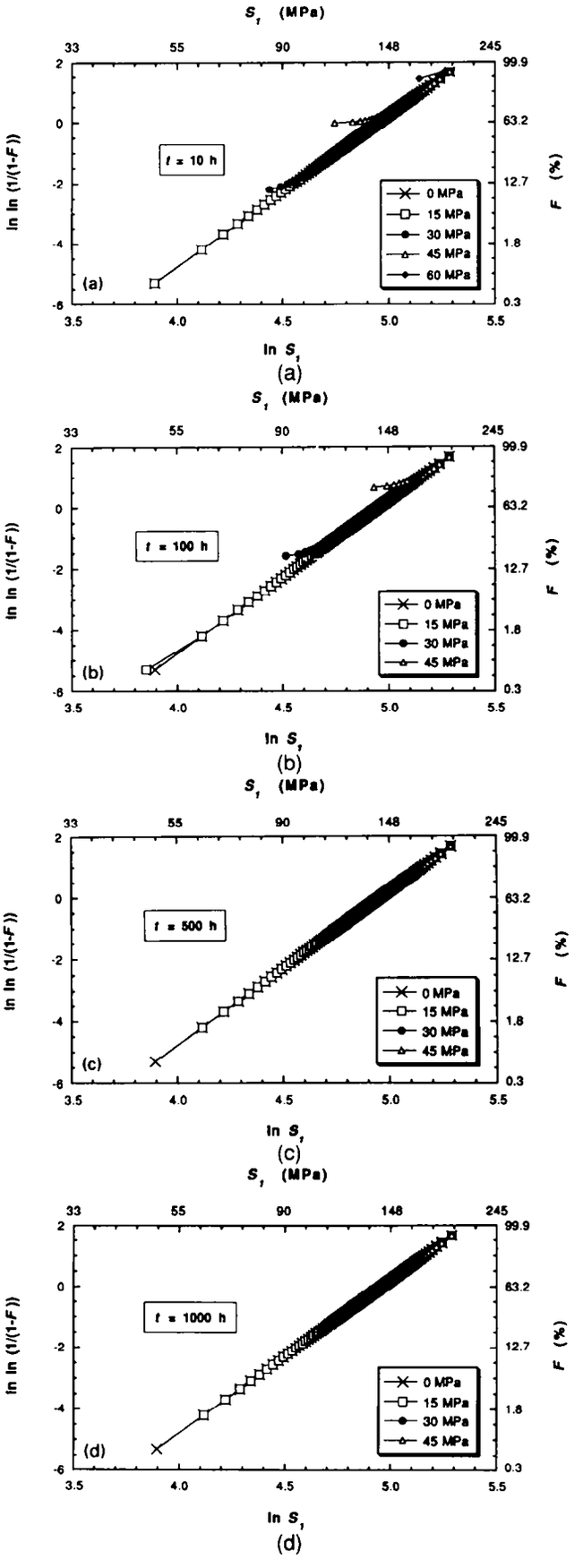


Fig. 6. Weibull plot of the strength distribution of soda-lime silicate glass after the holding at different stress levels for (a) 10 h, (b) 100 h, (c) 500 h and (d) 1000 h. The initial strength distribution corresponds to an applied stress of 0 MPa.

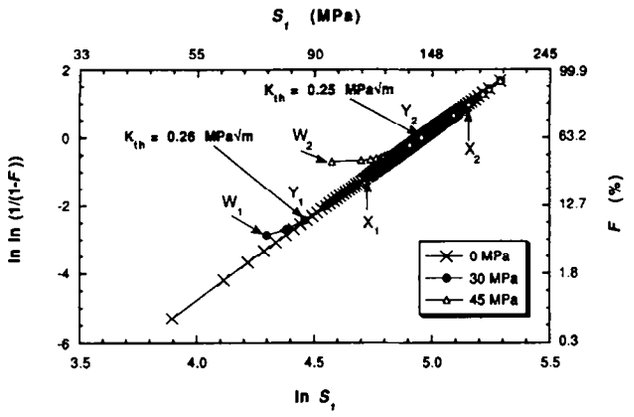


Fig. 7. Weibull plot of the strength distribution after the holding at two different stress levels for 1 h (Fig. 5(a)). The initial strength distribution corresponds to the applied stress of 0 MPa. Some elements of the distributions were removed around points marked with 'X' and 'Y' for better clarity. Explanation of points 'X', 'Y' and 'W' is given in the text.

0·26 and 0·25 MPa √m, respectively, instead of the value assumed in the analysis (0·2 MPa √m).

On the basis of the presented simulation (Figs 5 and 6), a different approach to threshold estimation is proposed. If the weakest specimen of the distribution (marked as 'W' in Fig. 7) is considered, the corresponding stress intensity factor K_W tends to, and then equals, the threshold, as the holding time is increased, as shown in Fig. 8. This shows that calculated K_W values correspond to the previously assumed fatigue limit (0·2 MPa √m) for $t \geq 500$ h, when $N = 100$. One would expect that the number of specimens used for each test condition would be important, as this increases the range of K_h values (Fig. 5); that is, one is more likely to obtain $K_h < K_{th}$ and more specimens would break during the constant stress phase. Clearly, using a larger number of specimens influences both economics and duration of the experimental work.

A final step in the simulation was performed by using data shown in Fig. 6 in order to plot the strength as a function of the applied stress intensity factor. Average values (K_{av}) of the stress intensity factor applied during the hold were calculated from the initial average strength from eqn (6). The average strength after holding, and

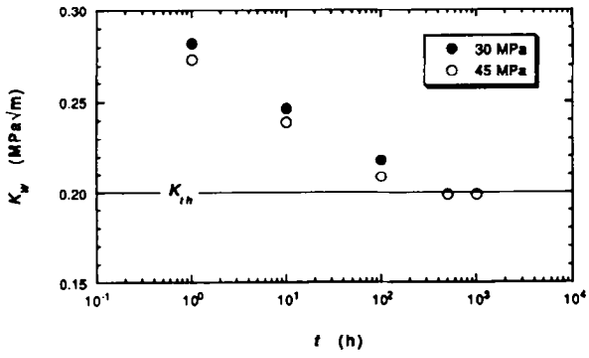


Fig. 8. Stress intensity factor K_w corresponding to the weakest sample of the strength distributions after the ISF test at stress levels of 30 and 45 MPa (Figs. 5(a) and (6)) as a function of the holding time t. Symbols at t equal to 500 and 1000 h are overlapped.

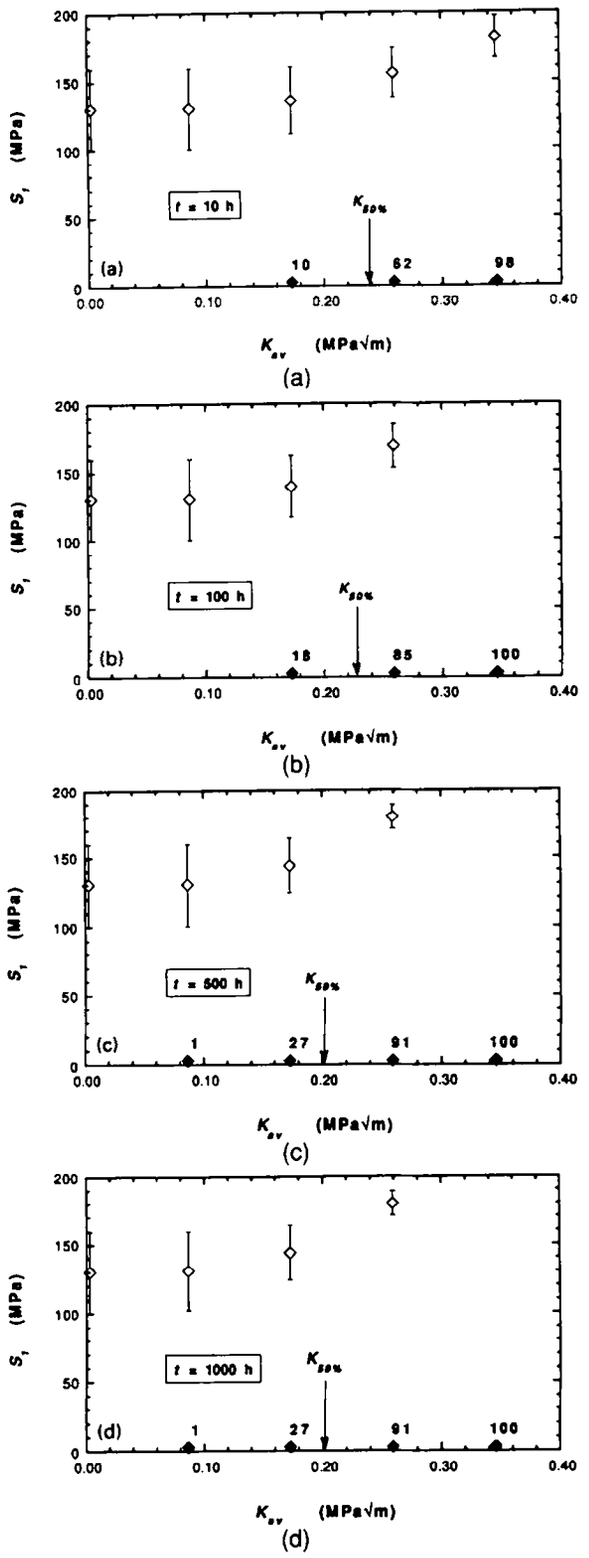


Fig. 9. Average strength S_f after the holding at different stress levels as a function of the applied stress intensity factor K_{av} for holding times of (a) 10 h, (b) 100 h, (c) 500 h and (d) 1000 h. The initial strength is shown at $K_{av} \approx 0$ MPa √m. Both S_f and K_{av} were calculated on the basis of results shown in Fig. 6. The numbers close to the solid symbols represent the number of specimens failing during the hold. The stress intensity factor $K_{50\%}$ corresponding to failure of 50% of the specimens during the hold, was calculated by linear interpolation.

corresponding standard deviation, were determined from data in Figs 5 and 6. Figure 9 shows the results for $N = 100$. The number of samples failing during the stress hold is also shown and the stress intensity factor ($K_{50\%}$) corresponding to the failure of 50% of the specimens during the hold is shown. $K_{50\%}$ is meant to represent the value of the stress intensity factor at which the average of the strength S_1 tends to zero in eqn 4(a). In Fig. 9, $K_{50\%}$ was calculated, by linear interpolation, as the stress intensity factor at which 50 specimens failed. As was previously pointed out, it is evident that $K_{50\%}$ tends to, and then equals, the fatigue limit as t increases. These calculations suggest a second approach to threshold determination, i.e. design the ISF test such that specimens break during the hold time and then increase the hold time.

4 Suggestions for a Correct Procedure for the ISF Test

The results presented in the last section suggest appropriate procedures for the measurement of the fatigue limit for sub-critical crack growth.

Two different approaches have been suggested. The first one is related to the determination of the strength distribution changes for specimens that survive the hold period, while the second one considers the changes in the average strength values. Suggested procedures for these two approaches are given below.

4.1 Strength of weakest specimen approach

The initial strength distribution (S_{0j}) must be determined in an inert environment. Samples are then subjected to the ISF test using constant stress σ for a time t. Knowledge of the fatigue parameters n and B from dynamic fatigue experiments is very useful as it allows one to estimate σ^* and K^* values from eqns (4) and (7). If an estimated value of the threshold is available, σ and t can be decided on the basis of σ and K^*, such that some failures will occur during the static hold. Strengths are also measured in the inert environment after the ISF test to obtain the distribution S_{1j}. A strength of zero is assigned to samples that fail during the stress hold and this allows one to obtain the censored distributions such as those illustrated in Figs 5 and 6. The weakest sample is identified and its rank in the strength distribution allows its strength (S_{0w}) to be defined from the previously determined initial strength distribution. The stress intensity factor K_w applied to this weakest sample can then be calculated as:

$$K_w = K_c \left(\frac{\sigma}{S_{ow}} \right) \tag{11}$$

Knowledge of the toughness K_c is essential for a precise definition of K_w. The value of K_w is then determined at the same hold stress but with increasing hold times. When K_w becomes invariant with hold time, $K_w = K_{th}$.

This first approach is considered to be preferable for materials with lower Weibull moduli. In fact, due to the large strength scatter when m is low, only a few trials are necessary to identify the stress and times required for the hold periods. Conversely, for very narrow strength distributions, several trials could be necessary before the optimal applied stress value can be identified.

It has been outlined that the strength measurement should be performed in an inert environment. Determination of K_w from eqn (11) requires the inert strength to be known. Unfortunately, inert conditions are sometimes difficult to obtain, especially when the behaviour of materials at high temperatures is considered. When the strength is measured in an active environment, it is usually lower than the inert value and this results in an overestimation of the threshold.

4.2 Hold period failure approach

In this alternative approach, the average initial strength S_{0av} is measured. Then samples are subjected to some ISF tests in which different stress levels are used for a certain time t. In this case, values of σ and t can be a decided on the basis of the assumption of a particular value for the threshold and from a knowledge of n and B. The number of samples failing during the hold at each stress level is recorded and the applied stress corresponding to 50% of samples failing during the hold ($\sigma_{50\%}$) can be calculated by easy linear interpolation. The corresponding stress intensity factor is given by

$$K_{50\%} = K_c \left(\frac{\sigma_{50\%}}{S_{0av}} \right) \tag{12}$$

As in the previous case, the hold time is increased and, once $K_{50\%}$ becomes invariant with hold time, $K_{50\%} = K_{th}$.

This second approach is considered to be appropriate for materials with large Weibull moduli. First of all, the precision of the average strength and of the number of samples failing during the hold is higher for larger values of m. In addition, several trials could be necessary to determine $\sigma_{50\%}$ precisely for wider strength distributions. Interestingly, in this approach, determination of the strength after the holding is not even necessary unless the purpose of the study is also to detect some strengthening effect taking place during the hold, for instance a strength increase could be correlated to crack tip blunting.[34–37]

5 Conclusions

A theoretical simulation of the interrupted static fatigue (ISF) tests, used for the evaluation of the fatigue threshold K_{th}, was presented. The behaviour of SiC at 1400°C and soda-lime glass in water at room temperature was analysed using fracture mechanics principles. The analysis considered changes in both the average strength values and strength distribution as a result of a period of constant stress. The duration of the ISF test and the applied stress turned out to be extremely important for a correct evaluation of the threshold. Optimal values for these two parameters can be calculated *a priori* from the fatigue parameters n and B, and from the assumption of a particular value of K_{th}. Two different approaches were proposed for fatigue limit determination. In the first case, a stress level is applied in order to obtain some failures during the hold, which then allow the 'interrupted' strength distribution to be determined. The stress intensity factor corresponding to the weakest sample that survives the hold is calculated as the estimate for K_{th}, and this value is then determined as a function of increased hold time. In the second approach, sample sets are subjected to various stress levels. The stress intensity factor corresponding to 50% of failures occurring during the stress hold is assumed as the estimate K_{th}. The value of K_{th} is than re-determined as a function of hold time until it becomes invariant. The two approaches outlined above were considered to be preferable for materials with lower and higher Weibull moduli, respectively.

References

1. Stuart, D. A. & Anderson, O. L., Dependence of ultimate strength of glass under constant load on temperature, ambient atmosphere and time. *J. Am. Ceram. Soc.*, **36**(12) (1953) 416–24.
2. Shand, E. B., Experimental study of fracture of glass: I, The fracture process. *J. Am. Ceram. Soc.*, **37**(2) (1954) 52–60.
3. Mould, R. E. & Southwick, R. D., Strength and static fatigue of abraded glass under controlled ambient conditions: II, Effect of various abrasions and the universal fatigue curve. *J. Am. Ceram. Soc.*, **42**(12) (1959) 582–92.
4. Watanabe, M., Caporali, R. V. & Mould, R. E., The effect of chemical composition on the strength and static fatigue of soda-lime glass. *Phys. Chem. Glasses*, **2**(1) (1961) 12–23.
5. Mould, R. E., Strength and static fatigue of abraded glass under controlled ambient conditions: IV, Effect of surrounding medium. *J. Am. Ceram. Soc.*, **44**(10) (1961) 481–91.
6. Shand, E. B., Strength of glass — the Griffith method revised. *J. Am. Ceram. Soc.*, **48**(1) (1965) 43–9.
7. Hillig, W. B. & Charles, R. J., Surfaces, stresses-dependent surface reactions and strength. In *High Strength Materials*, ed. V. F. Zakay. John Wiley and Sons, New York, 1965, pp. 683–705.
8. Wiederhorn, S. M. & Bolz, L. H., Stress corrosion and static fatigue of glass. *J. Am. Ceram. Soc.*, **53**(10) (1970) 543–8.
9. Ritter, J. E. & Sherburne, C. L., Dynamic and static fatigue of silicate glasses. *J. Am. Ceram. Soc.*, **54**(12) (1971) 601–5.
10. Evans, A. G., A method for evaluating the time-dependent failure characteristics of brittle materials — and its application to polycrystalline alumina. *J. Mater. Sci.*, **7** (1972) 1137–46.
11. Evans, A. G., A simple method for evaluating slow crack growth in brittle materials. *Int. J. Fract.*, **9**(3) (1973) 267–75.
12. Wiederhorn, S. M. & Johnson, H., Effect of electrolyte pH on crack propagation in glass. *J. Am. Ceram. Soc.*, **56**(4) (1973) 192–7.
13. Wiederhorn, S. M., Subcritical crack growth in ceramics. In *Fracture Mechanics of Ceramics*, Vol. 2, eds. R. C. Bradt, D. P. H. Hasselman & F. F. Lange. Plenum Press, New York, 1974, pp. 613–46.
14. Wan, K., Lathabai, S. & Lawn, B. R., Crack velocity functions and threshold in brittle solids. *J. Eur. Ceram. Soc.*, **6** (1990) 259–68.
15. Chan, K. S. & Page, R. A., Origin of the creep-crack growth threshold in a glass-ceramic. *J. Am. Ceram. Soc.*, **75**(3) (1992) 603–12.
16. Pavelchek, E. K. & Doremus, R. H., Static fatigue in glass — a reappraisal. *J. Non-Cryst. Solids*, **20** (1976) 305–21.
17. Gehrke, E., Ullner, C. & Hähnert, M., Correlation between multistage crack growth and time-dependent strength in commercial silicate glasses. Part 1. Influence of ambient media and types of initial cracks. *Glastech. Ber.*, **60**(8) (1987) 268–78.
18. Gehrke, E., Ullner, C. & Hähnert, M., Correlation between multistage crack growth and time-dependent strength in commercial silicate glasses. Part 2. Influence of surface treatment. *Glastech. Ber.*, **60**(10) (1987) 340–5.
19. Gehrke, E., Ullner, C. & Hähnert, M., Effect of corrosive media on crack growth of model glasses and commercial silicate glasses. *Glastech. Ber.*, **63**(9) (1990) 255–65.
20. Fett, T., Germerdonk, K., Grossmüller, A., Keller, K. & Munz, D., Subcritical crack growth and threshold in borosilicate glass. *J. Mater. Sci.*, **26** (1991) 253–7.
21. Gehrke, E., Ullner, C. & Hähnert, M., Fatigue limit and crack arrest in alkali-containing silicate glasses. *J. Mater. Sci.*, **26** (1991) 5445–55.
22. Michalske, T. A., The stress corrosion limit: its measurement and implications. In *Fracture Mechanics of Ceramics*, Vol. 5, eds R. C. Bradt, D. P. H. Hasselman & F. F. Lange. Plenum Press, New York, 1983, pp. 277–89.
23. Dutton, R. & Rogowski, A. J., A theoretical study of crack propagation during high temperature static fatigue. *J. Can. Ceram. Soc.*, **41** (1972) 53–61.
24. Wilkins, B. J. S. & Dutton, R., Static fatigue limit with particular reference to glass. *J. Am. Ceram. Soc.*, **59**(3–4) (1975) 108–12.
25. Hayashi, K., Easler, T. E. & Bradt, R. C., A fracture statistics estimate of the fatigue limit of a borosilicate glass. *J. Eur. Ceram. Soc.*, **12** (1993) 487–91.
26. Minford, E. J. & Tressler, R. E., Determination of threshold stress intensity for crack growth at high temperature in silicon carbide ceramics. *J. Am. Ceram. Soc.*, **66**(5) (1983) 338–40.
27. Minford, E. J., Kupp, D. M. & Tressler, R. E., Static fatigue limit for sintered silicon carbide at elevated temperatures. *J. Am. Ceram. Soc.*, **66**(11) (1983) 769–73.
28. Foley, M. R. & Tressler, R. E., Threshold stress intensity for crack growth at elevated temperatures in a silicon nitride ceramic. *Adv. Ceram. Mater.*, **34** (1988) 383–6.
29. Yavuz, B. O. & Tressler, R. E., Threshold stress intensity for crack growth in silicon carbide ceramics. *J. Am. Ceram. Soc.*, **76**(4) (1993) 1017–24.
30. Tanaka, I. & Pezzotti, G., Evaluation of slow crack growth resistance in ceramics for high-temperature applications. *J. Am. Ceram. Soc.*, **75**(4) (1993) 772–7.

31. Evans, A. G. & Lange, F. F., Crack propagation and fracture in silicon carbide. *J. Mater. Sci.*, **10** (1975) 1659–64.
32. Jakus, K., Coyne, D. C. & Ritter, J. E., Analysis of fatigue data for lifetime predictions for ceramics materials. *J. Mater. Sci.*, **13** (1978) 2071–80.
33. DeSalvo, G. J., Theory and structural design application of Weibull statistics, Westinghouse Electric Corporation, Astronuclear Laboratory, Technical Report WANL-TME-2688, May 1970.
34. Ito, S. & Tomozawa, M., Crack blunting of high-silica glass. *J. Am. Ceram. Soc.*, **65**(8) (1982) 368–71.
35. Hirao, K. & Tomozawa, M., Dynamic fatigue of treated high-silica glass: explanation by crack tip blunting. *J. Am. Ceram. Soc.*, **70**(6) (1987) 377–82.
36. Hirao, K. & Tomozawa, M., Kinetics of crack tip blunting of glasses. *J. Am. Ceram. Soc.*, **71**(1) (1987) 43–8.
37. Han, W.-T. & Tomozawa, M., Mechanism of mechanical strength increase of soda-lime glass by aging. *J. Am. Ceram. Soc.*, **72**(10) (1989) 1837–43.

Journal of the European Ceramic Society 15 (1995) 787 794
© 1995 Elsevier Science Limited
Printed in Great Britain. All rights reserved
0955-2219(95)00042-9
0955-2219/95/$9.50

Preparation of Dispersed Zirconia Barium Aluminosilicate Composites

A. Nordmann, Y.-B. Cheng* & B. C. Muddle

Department of Materials Engineering, Monash University, Clayton, Victoria, 3168, Australia

(Received 18 May 1994; revised version received 7 February 1995; accepted 14 February 1995)

Abstract

The potential for preparing a ZrO_2-containing ceramic composite based on barium feldspar ($BaAl_2Si_2O_8$) using the reaction sintering of zircon has been investigated. It is demonstrated that, through the reaction of $ZrSiO_4$, Al_2O_3 and $BaCO_3$ above 1400°C, a distribution of ZrO_2 particles in a $BaO{\cdot}Al_2O_3{\cdot}2SiO_2$ matrix can be achieved. A glassy phase rich in Si and Ba surrounds the zirconia particles and infiltrates the grain boundaries of the polycrystalline feldspar matrix. The tendency of the ZrO_2 particles to agglomerate within the matrix can be reduced by incorporating additional silica into the reaction, while limited stabilisation of tetragonal ZrO_2 can be achieved by additions of Y_2O_3 which partition between the ZrO_2 and the glassy boundary phase.

Introduction

Zircon ($ZrSiO_4$) is a natural mineral resource known to react with certain oxides to produce a dispersion of zirconia particles within ceramic or glass–ceramic matrices. The reaction of zircon with alumina results, for example, in a ZrO_2–mullite composite material, while the reaction of zircon with alumina and magnesia or alumina and calcia produces ZrO_2-containing cordierite and anorthite, respectively.[2–5] These composite materials, obtained by the reaction sintering method in which consolidation of individual particles is accompanied by a chemical reaction, have often been shown to possess high thermal stability and improved fracture toughness, the latter being a direct consequence of the transformation toughening effect associated with the included ZrO_2 particles.[7]

Barium aluminosilicates, particularly the celsian polymorphs of $BaO{\cdot}Al_2O_3{\cdot}2SiO_2$, display oxidation resistance and refractory characteristics commensurate with the properties required of high temperature materials.[8–10] The orthorhombic (α) and hexagonal (β) phases of hexacelsian ($BaAl_2Si_2O_8$) possess thermal expansion coefficients of $7{\cdot}1 \times 10^{-6}$/°C and $8{\cdot}0 \times 10^{-6}$/°C, respectively,[11] while the monoclinic phase, simply termed celsian, has a melting point of 1760°C and a thermal expansion coefficient as low as $2{\cdot}29 \times 10^{-6}$/°C.[11] Zirconia has a thermal expansion coefficient of $6–10 \times 10^{-6}$/°C[12] which is comparable to that of the hexacelsian polymorphs and is therefore expected to minimise the thermal expansion mismatch within a composite material comprised of hexacelsian and zirconia. Such thermal properties, coupled with the high melting point of ZrO_2 (2680°C) suggest that barium aluminosilicates and zirconia are an ideal combination from which to fabricate high temperature materials. A recent study has indicated that a barium aluminosilicate containing up to 40 mol% ZrO_2 can be prepared via a sol–gel process.[13] However, the desire to utilise a natural resource in the form of zircon in the present work has led to the choice of reaction sintering as an alternative processing route. Reaction sintering is becoming increasingly attractive as a ceramic processing technique because of its simplicity and cost efficiency, and reaction sintering of zircon is a particularly effective means of dispersing zirconia grains into ceramic matrices. The current work was undertaken to investigate the possibility of forming a zirconia-containing barium feldspar composite material using the reaction sintering of zircon and assuming the following stoichiometric reaction:

$$2ZrSiO_4 + BaCO_3 + Al_2O_3 \rightarrow 2ZrO_2 + BaO{\cdot}Al_2O_3{\cdot}2SiO_2 + CO_2 \uparrow \quad (1)$$

Experimental Procedures

The starting powders used were $ZrSiO_4$ (Cerac 99% pure, average particle size approximately 3·5 μm), $BaCO_3$ (AJAX Chemicals, 99% pure), SiO_2

* To whom correspondence should be addressed.

(AJAX Chemicals, precipitated) and Al_2O_3 (AJAX Chemicals). Stabilisation of ZrO_2 was achieved through the addition of Y_2O_3 (Cerac 99·9% pure). The powders were hand-mixed for 20 min in an alumina mortar and pestle with a small amount of isopropanol added for lubrication. Batches of about 2·5 g were compressed uniaxially in a compaction die to produce pellets approximately 14 mm in diameter. The pellets were placed in a high purity alumina crucible and fired in a rapid heating furnace in which temperatures of up to 1600°C could be achieved in 80 min, and a cooling rate of 20°C/min was employed. The mercury displacement method was used to determine the bulk density of sintered samples.

Phase identification for the sintered samples was carried out using X-ray diffraction (XRD) on a Rigaku Geigerflex diffractometer with Cu K_α radiation and a Ni filter. Samples for scanning electron microscopy (SEM) were mounted, ground on SiC paper and polished prior to being carbon coated and examined in a JEOL JSM840A scanning electron microscope operating at 20 kV. Samples for transmission electron microscopy (TEM) were cut, polished, ion-beam milled to perforation, carbon coated and then examined in a Philips EM420 TEM operating at 120 kV and equipped with an EDAX PV9900 energy dispersive X-ray spectrometer.

Results and Discussion

Sample preparation

Initial nominal compositions of the samples prepared are shown in Table 1. The progress of reaction sintering, the densification behaviour of the samples and the microstructures produced were studied in detail using a variety of techniques.

Crystalline phases

The reaction sequence of the system was studied by obtaining XRD spectra from samples sintered for 2 h at temperatures of 1000–1600°C at 100°C intervals. The positions of characteristic peaks at each of the given temperatures allowed for the identification of phases as the reaction progressed. With changes in the sintering temperature the starting powders reacted to form intermediate phases as well as the final products. By comparing the intensities of peaks corresponding to the reactants it was possible to obtain an indication of when these phases disappeared. Similarly, the emergence of new phases could also be monitored as the reaction progressed, and the relative intensities of corresponding characteristic peaks were used to define approximately the proportions of the phases as a function of sintering temperature. Representative XRD spectra of samples sintered for 2 h at 1300 and 1600°C are shown in Fig. 1(a) and (b), respectively, while the results in Fig. 2 illustrate the relative proportions of phases detected at different sintering temperatures.

The onset of zircon dissociation is evident at approximately 1100°C. This compares favourably

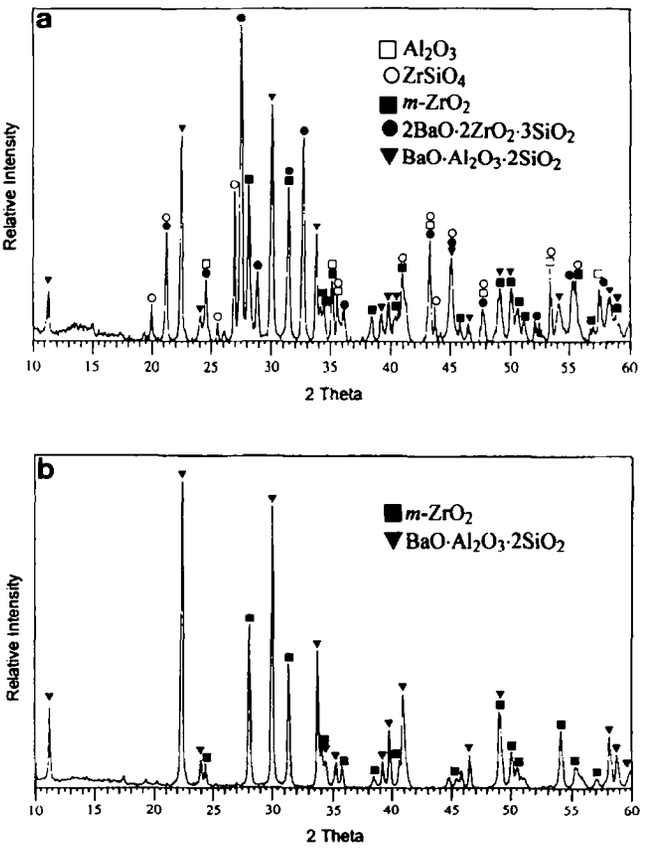


Fig. 1. XRD traces of samples sintered for 2 h at (a) 1300°C and (b) 1600°C.

Table 1. Nominal compositions of samples prepared (wt%)

Sample	*$ZrSiO_4$*	*Al_2O_3*	*$BaCO_3$*	*SiO_2*	*Y_2O_3*
1—Reaction 1	55·1	15·3	29·6	—	—
2—Reaction 2	33·8	18·9	36·4	11·1	—
3—Yttria stabilised (4%)	54·2	15·0	29·2	—	1·5
4—Yttria stabilised (8%)	53·3	14·8	28·7	—	3·1
5—Yttria stabilised (12%)	52·4	14·6	28·2	—	4·8

Reaction (1) is defined by the stoichiometric equation while reaction (2) incorporates additional silica into the reaction. Compositions 1 and 2 correspond to reactions (1) and (2), respectively, while compositions 3, 4 and 5 are free of additional silica and lead to sintered products in which the Y_2O_3 concentration corresponds to 4, 8 and 12 wt% of the anticipated ZrO_2 content.

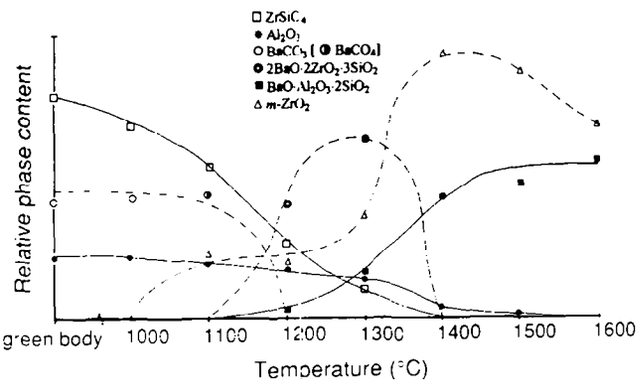


Fig. 2. Reaction sequence showing approximately the relative proportion of major phases present as a function of sintering temperature.

with the dissociation temperature of pure zircon of 1670°C, indicating that the presence of the other components significantly lowers the temperature at which the constituents, ZrO_2 and SiO_2, are obtained. The dissociation of zircon at 1100°C is accompanied by the appearance of monoclinic zirconia, m-ZrO_2. The SiO_2 obtained from the dissociation is not detected as a crystalline phase and is thus assumed to exist in an amorphous state. At this temperature, barium carbonate has undergone a structural change from $BaCO_3$ to a phase identified as $BaCO_4$,[14] but no evidence of decomposition of this phase was observed.

At 1200°C, the zircon content has further diminished and the barium carbonate has completely decomposed. The ZrO_2 and BaO thereby attained manifest themselves in the formation of an intermediate phase, $2BaO{\cdot}2ZrO_2{\cdot}3SiO_2$,[15] which also utilises the SiO_2 formed at lower temperatures. Furthermore, a slight reduction in Al_2O_3 is observed at this temperature, a barium aluminosilicate phase (hexacelsian) starts to emerge and a barium silicate phase, $2BaO{\cdot}3SiO_2$,[16] is also detected. However, since the latter phase was only observed at 1200°C it is not represented by a separate curve in Fig. 2.

At 1300°C, the Al_2O_3 and $ZrSiO_4$ contents continue to decrease, the transitory barium silicate phase has disappeared and the proportions of m-ZrO_2, hexacelsian and $2BaO{\cdot}2ZrO_2{\cdot}3SiO_2$ have increased. On heating to 1400°C, the decomposition of $ZrSiO_4$ is essentially complete and the Al_2O_3 content shows a marked reduction. This coincides with a maximum in the ZrO_2 content and increasing formation of hexacelsian. These observations may be explained by the complete dissociation of the barium zirconium silicate ($2BaO{\cdot}2ZrO_2{\cdot}3SiO_2$), which reacts with Al_2O_3 and thereby allows for the formation of hexacelsian.

At 1500°C only a trace of Al_2O_3 is detected, with the dominant phases being the reaction products, hexacelsian and ZrO_2. Zirconia is present only as the monoclinic phase since no stabilising oxide has been added at this stage to allow for the stabilisation of tetragonal zirconia. It is noted that a reduction in the ZrO_2 content occurs and this may be explained by the dissolution of ZrO_2 in the residual liquid. The solubility of ZrO_2 increases with increasing temperature and hence a further reduction in ZrO_2 is observed at 1600°C. By 1600°C, the initial powders have completely reacted to form hexacelsian and m-ZrO_2.

The detection of hexacelsian in these samples is interesting and perhaps raises questions concerning the existing understanding of this material. It is commonly reported that the barium aluminosilicate of composition $BaAl_2Si_2O_8$ may exist as one of three crystallographic phases: α-hexacelsian (orthorhombic), β-hexacelsian (hexagonal) and celsian (monoclinic).[8–11] Monoclinic celsian is stable thermodynamically below 1590°C, whereas β-hexacelsian is stable above 1590°C. However, the transformation between β-hexacelsian and celsian occurs sluggishly, so that β-hexacelsian may persist as a metastable phase below 1590°C.[8] Furthermore, it has been reported that at approximately 300°C, β-hexacelsian undergoes a rapid, reversible displacive transformation to metastable orthorhombic α-hexacelsian and that this transformation is accompanied by a 3–4% volume expansion, which is large enough to potentially cause deterioration of the material during cooling.[17] The α and β forms of hexacelsian are based on similar lattices and, given the similarity in interplanar spacings for the two phases, it proved impossible to distinguish between them in the current samples using X-ray diffraction.[18] However, there was little metallographic evidence of significant cracking in the matrix of the sintered samples suggesting that the β-hexacelsian may have been retained as a metastable phase, and that the transformation to orthorhombic α-hexacelsian may have been suppressed on cooling to room temperature.

The preferential formation of metastable hexacelsian rather than monoclinic celsian has previously been ascribed to structural differences.[8] The high symmetry hexagonal and orthorhombic forms may be described in terms of infinite two-dimensional hexagonal sheets consisting of two layers of $(Si,Al)O_4$ tetrahedra, whereas the low symmetry celsian consists of a three-dimensional structure in which the four vertices of the tetrahedra are shared. In both structures, some substitution of Al for Si occurs in the tetrahedra and charge compensation by Ba is provided through its location either between the sheets, in the case of hexacelsian, or in the larger interstices of the celsian structure. The

two-dimensional high symmetry forms therefore have lower kinetic barriers for nucleation and are consequently formed first. Nevertheless, with a suitable additive it may be possible to stabilise monoclinic celsian in these materials.[19]

Densification

The sintering behaviour was further monitored by measuring the density of the sintered samples as a function of temperature and the results are presented in Fig. 3. The initial reduction in the density up to 1200°C may be the result of the decomposition of $BaCO_3$. The CO_2 gas evolved during this decomposition will, if trapped in the sample, expand with further heating, and thereby cause an expansion of the specimen. With continued heating, chemical reaction begins accompanied by particle coalescence and sample shrinkage occurs. A significant increase in the rate of densification is observed above 1300°C and a maximum density of 3·52 g/cm^3 is obtained at 1500°C. It is thought that the melting of the intermediate phase ($2BaO{\cdot}2ZrO_2{\cdot}3SiO_2$) above 1300°C provides a low temperature eutectic liquid which facilitates the rapid densification. The relatively lower density measured at 1600°C is attributed to the bloating effect prevalent in these samples, a phenomenon which may be a result of the instability of the low temperature eutectic liquid phase. In addition, the transformation of zirconia from tetragonal to monoclinic symmetry on cooling produced cracks in samples sintered above 1200°C and this may also have contributed to a reduction in the measured density. The trends observed in the densification process were substantiated by dilatometry measurements, although the results obtained are not presented here.

Scanning electron micrographs were obtained at various stages of the reaction sequence to illustrate particle arrangement and distributions at each temperature. Since little microstructural change occurred on sintering below 1300°C, only those samples prepared at the higher sintering temperatures ($T \geq 1300$°C) where the most significant changes occurred, are represented in Fig. 4.

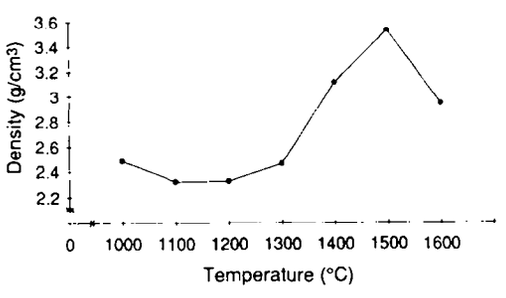


Fig. 3. Density as a function of temperature for samples prepared according to reaction 1. Rapid densification is seen to take place at temperatures immediately above 1300°C.

The emergence of a liquid phase occurs at 1300°C (arrowed, Fig. 4(a)); however, since only a small amount of this phase is formed, no significant densification is achieved at this temperature. At 1400°C, Fig. 4(b), there are significant pores present but individual grains of starting powder are no longer distinguished. The lighter contrast regions in Fig. 4(b) are ZrO_2-rich and comprise clusters of small spheroidal grains with a morphology typical of a product forming in the presence of a liquid phase. The microstructural observations are consistent with both density and X-ray results which suggest that chemical reaction and densification are significantly accelerated between 1300 and 1400°C. At 1500°C, Fig. 4(c), the dispersion of ZrO_2 particles is clearly evident, although the tendency to form agglomerates is common. At 1600°C, Fig. 4(d), the reaction is essentially complete and spherical ZrO_2 particles, between 1 and 3 μm in diameter, remain as agglomerates within the feldspar matrix.

The results to this stage support the feasibility of using a reaction sintering approach to fabricate a ZrO_2/hexacelsian composite material. A significant porosity is observed in all samples and the ZrO_2 particles remain in localised clusters, often in association with pores. In addition, as a result of the tetragonal (*t*) to monoclinic (*m*) transformation within the ZrO_2 grains on cooling, these particles are of monoclinic symmetry with the ensuing cracks in the samples being a direct consequence of the volume expansion associated with this transformation.

Stabilisation of ZrO_2

In order to prevent cracking of the samples, it was necessary to suppress the spontaneous *t* to *m* transformation in the ZrO_2 particles on cooling through the addition of a suitable stabilising oxide. As shown in Table 1, the compositions were adjusted to incorporate additions of Y_2O_3 corresponding to 4, 8 and 12 wt% of the expected ZrO_2 content, and subsequent sintering was performed at 1500°C for 2 h. According to the ZrO_2–Y_2O_3 phase diagram,[20] at 1500°C the 4 wt% composition is located in the tetragonal phase field; the 8 and 12 wt% compositions lie in the tetragonal/cubic phase field. Provided that the Y_2O_3 partitions to the ZrO_2 during reaction sintering, the precipitation of transformable metastable *t*-ZrO_2 might therefore be expected on cooling and hence phase transformation toughening may become possible at room temperature.

In contrast to the yttria-free samples, all the samples with additional yttria displayed negligible cracking after sintering. As shown in Table 2, X-ray diffraction suggested that increasing fractions

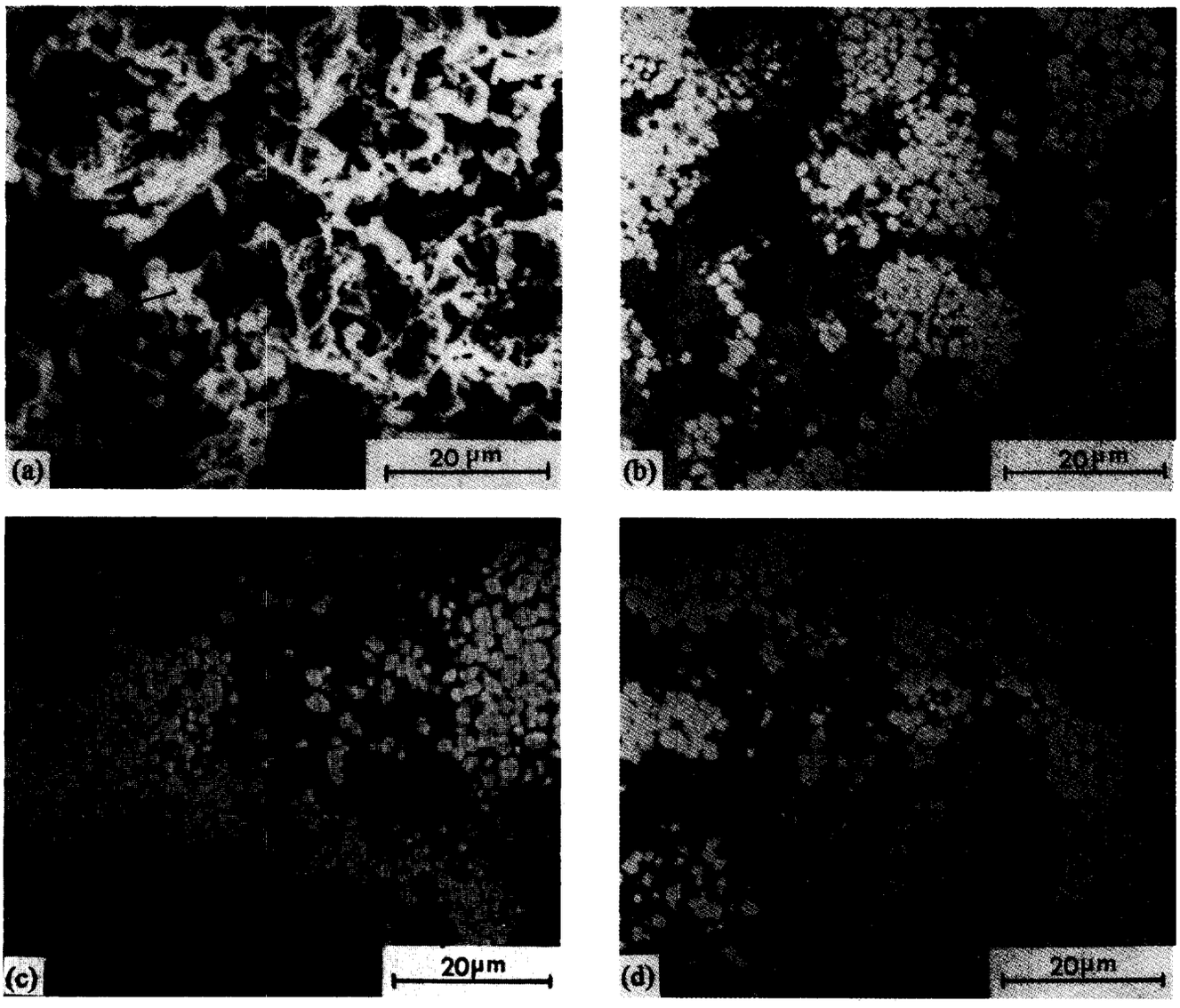


Fig. 4. SEM images depicting the microstructures obtained when sintering for 2 h at (a) 1300°C (b) 1400°C (c) 1500°C and (d) 1600°C.

of zirconia were stabilised as tetragonal phase with increasing yttria content. Moreover, in samples containing 4 and 8 wt% Y_2O_3, the ratio of monoclinic to tetragonal zirconia was found to be increased after grinding the samples to a fine powder using a mortar and pestle, see Table 2. Since the mechanical stresses associated with this grinding are comparable to the stresses located around a crack tip, these results are indicative of the potential for a toughening increment to be achieved through the stress-induced transformation of zirconia dispersed within the composite. It is noted that analysis of the XRD data was complicated by overlap between the (111) t-ZrO_2 peak and what is either the (112) peak of α-hexacelsian or the (102) peak of β-hexacelsian. However, a comparison of peak intensities corresponding to m- and t-ZrO_2 is still useful, since the intensity of the feldspar peaks should be unaffected by grinding and any changes in the peak intensity at this location can be attributed entirely to changes in the fraction of t-ZrO_2.

Table 2. Ratio of monoclinic to tetragonal zirconia in the yttria-modified samples before and after grinding. Samples were sintered for 2 h at 1500°C

Y_2O_3 content	$I_m(11\bar{1})/I_t(111)$ before grinding	$I_m(11\bar{1})/I_t(111)$ after grinding
4%	29/100	41/100
8%	0/100	9/100
12%	0/100	0/100

Microstructural observation

A sample containing 4 wt% Y_2O_3 and sintered at 1500°C for 2 h was further characterised using transmission electron microscopy and energy dispersive X-ray spectroscopy (EDXS). As shown in Fig. 5(a), the microstructure contained local clusters of spheroidal ZrO_2 particles dispersed in an amorphous matrix. The domain substructure of the particles and the corresponding selected area diffraction pattern, Fig. 5(b), confirm that they are m-ZrO_2. The substructure of approximately twin-related domains arises during the displacive t to m transformation, in order to accommodate the shear

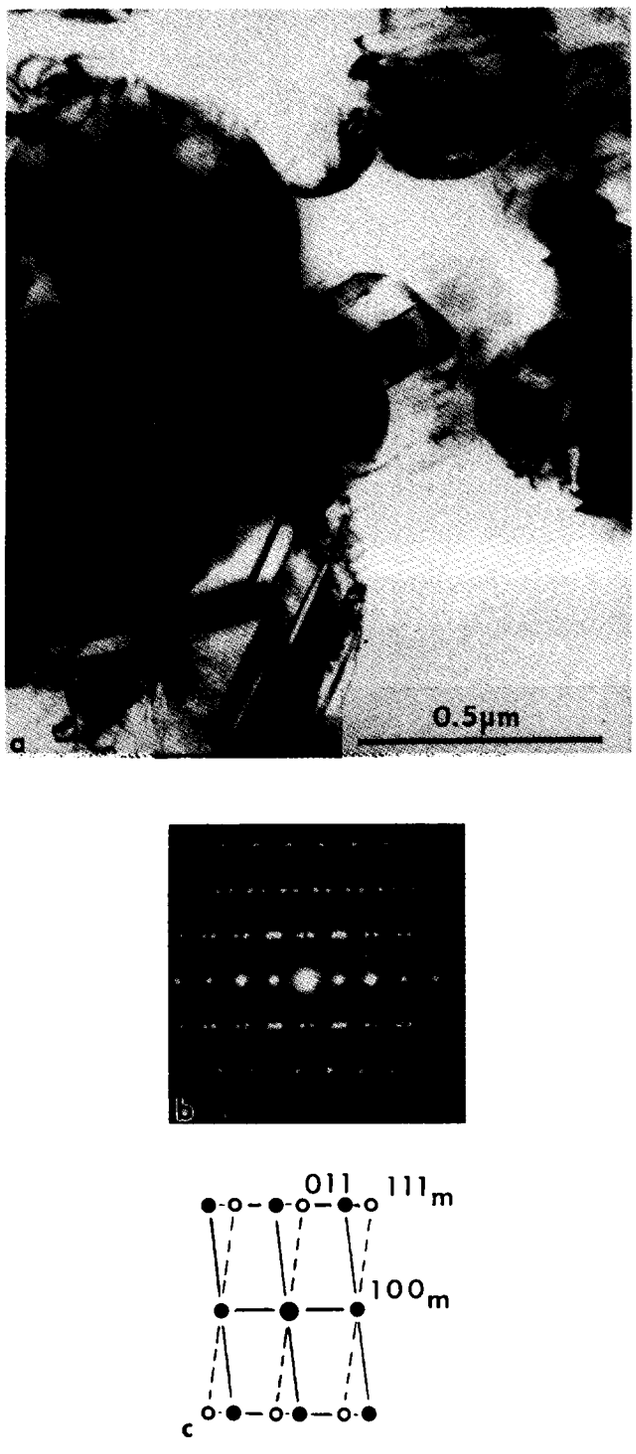


Fig. 5. (a) Bright field TEM micrograph of a sample containing 4 wt% Y_2O_3 and sintered for 2 h at 1500°C; (b) corresponding SAED pattern from single ZrO_2 particle, and (c) schematic solution to pattern containing two variants of the monoclinic phase twin-related about $(100)_m$. The zone axis is $[0\bar{1}1]_m$.

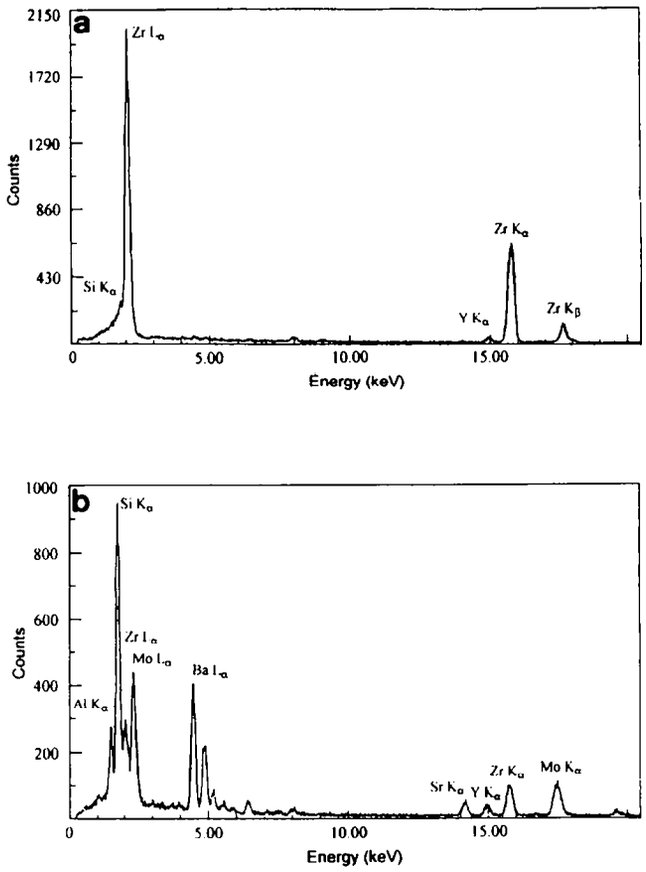


Fig. 6. EDX spectra from a sample containing 4 wt% Y_2O_3, sintered for 2 h at 1500°C. Spectra were recorded from (a) a zirconia grain shown in Fig. 5(a) and; (b) the glassy region seen in Fig. 5(a). The molybdenum recorded in Figure 5(b) is a contaminant resulting from ion-beam milling.

component of transformation. The absence of extensive microcracking around the particles indicates that the residual misfit strains around the particles may be accommodated by the glassy matrix.

X-ray microanalysis, Fig. 6(a), indicated that detectable concentrations of Y_2O_3 were present within the ZrO_2 grains. However, there was also a significant concentration of Y_2O_3 in the surrounding amorphous phase, indicating that an excess of Y_2O_3 may be necessary to stabilise the ZrO_2 as tetragonal phase. The detection of a significant fraction of tetragonal phase in X-ray diffraction patterns from this sample, and the failure to observe tetragonal phase in thin foil specimens, can probably be attributed to the tetragonal to monoclinic transformation occurring during preparation of the thin foil specimens upon relaxation of matrix constraint.

Figure 7 includes bright field images recorded from matrix regions of the same sample. In this case the structure is polycrystalline and the mixture of elongated and equiaxed grains were identified as metastable hexacelsian using electron microdiffraction. However, the diffraction patterns recorded from such grains, Fig. 8, could commonly be interpreted as being from either the high temperature hexagonal β form or the low temperature orthorhombic α phase. The pattern in Fig. 8(a) may, for example, be indexed as representing either a hexagonal $[2\bar{1}\bar{1}0]$ zone axis pattern or a [100] orthorhombic zone, while that in Fig. 8(b) is either a $[\bar{2}4\bar{2}3]$ zone axis pattern from the hexagonal phase or a $[\bar{2}01]$ pattern from the orthorhombic α. In the absence of detailed information on the crystal structures for the two phases it proved

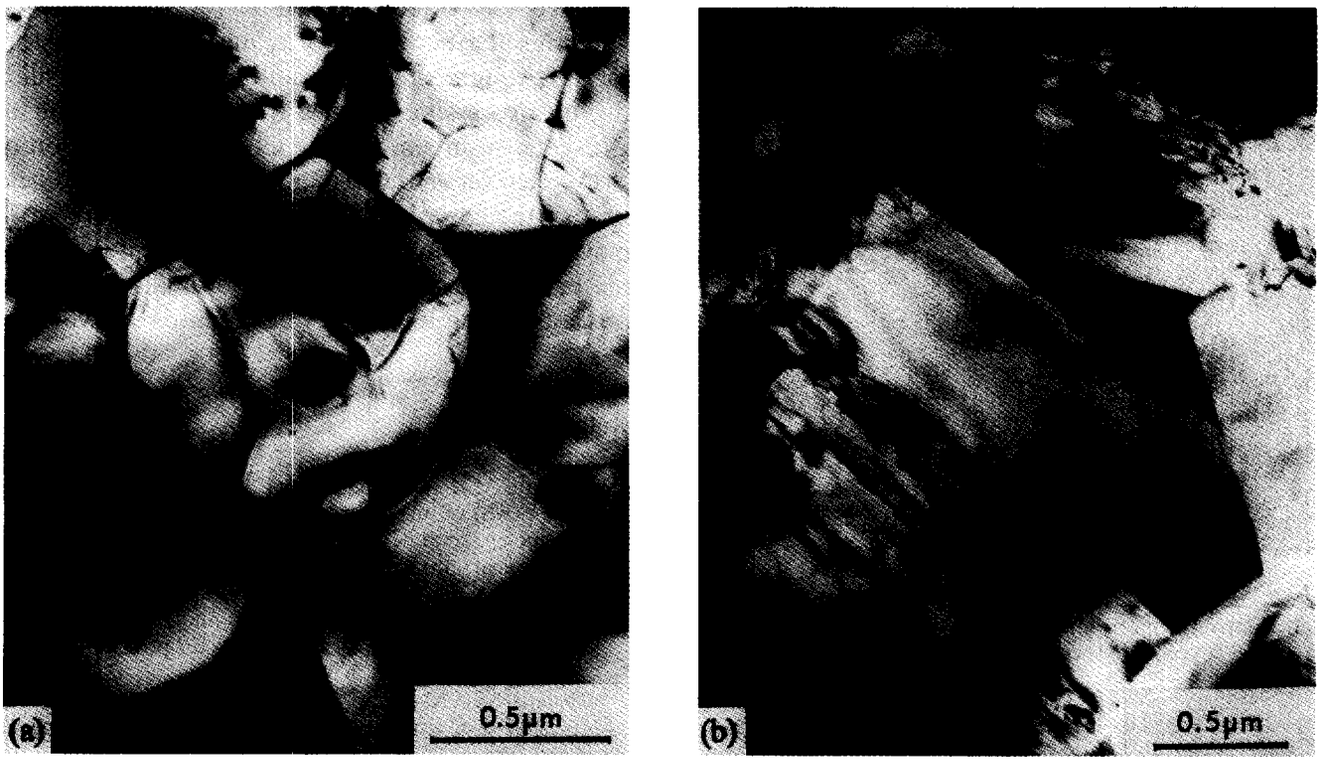


Fig. 7. Bright field TEM images showing (a) equiaxed and (b) elongated grains of hexacelsian.

impossible to identify zone axes for which patterns might be distinguishable for the two structures and thus impossible, in this preliminary study, to distinguish between the phases using electron diffraction. However, there was little or no evidence in the microstructure of the matrix of a solid state displacive transformation to the orthorhombic α-hexacelsian, or of the cracking or microcracking that might be expected to accompany such a transformation involving a 3–4% volume change. It is thus suggested that the hexagonal β-hexacelsian may have been retained as the dominant metastable phase at ambient temperature.

The micrographs of Fig. 7 indicate that the grains of hexacelsian were separated by a thin film of the same glassy phase as that surrounding the zirconia particles, and that there were pockets of glassy phase at grain triple junctions. Diffraction patterns recorded from such triple junctions contained diffuse rings consistent with an amorphous structure, and EDX spectra from such pockets, Fig. 6(b), indicated that the phase was Si-rich, with a high content of Ba. The composition is consistent with a glassy phase that is liquid during sintering to facilitate consolidation and the spheroidal form of the ZrO_2 grains is characteristic of the morphology that would be expected to develop during liquid phase sintering.

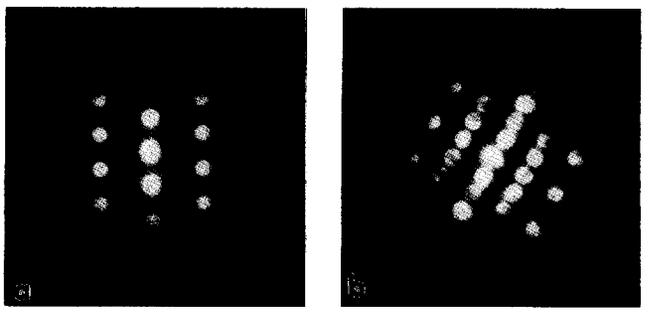


Fig. 8. Electron microdiffraction patterns recorded from hexacelsian grains which may be indexed as representing (a) a hexagonal $[2\bar{1}\bar{1}0]$ zone axis pattern or a [100] orthorhombic zone; and (b) a $[\bar{2}4\bar{2}3]$ zone axis pattern from the hexagonal β phase or a $[\bar{2}01]$ pattern from the orthorhombic α hexacelsian.

Effect of additional SiO_2

The stoichiometric reaction (1) yields a product with a molar ratio of zirconia to feldspar of 2:1. On the basis that the excess zirconia concentration may contribute to the inhomogeneous dispersion of zirconia agglomerates, additional SiO_2 was added in an attempt to improve the sinterability and homogeneity of the composites, assuming a reaction of the form:

$$ZrSiO_4 + BaCO_3 + Al_2O_3 + SiO_2 \rightarrow ZrO_2 + BaO{\cdot}Al_2O_3{\cdot}2SiO_2 + CO_2 \uparrow \quad (2)$$

It was anticipated that addition of SiO_2 would serve to form extra low temperature eutectic liquid phase and a comparatively lower zirconia concentration. A further series of samples was thus prepared under similar processing conditions, but with the composition of Sample 2 given in Table 1.

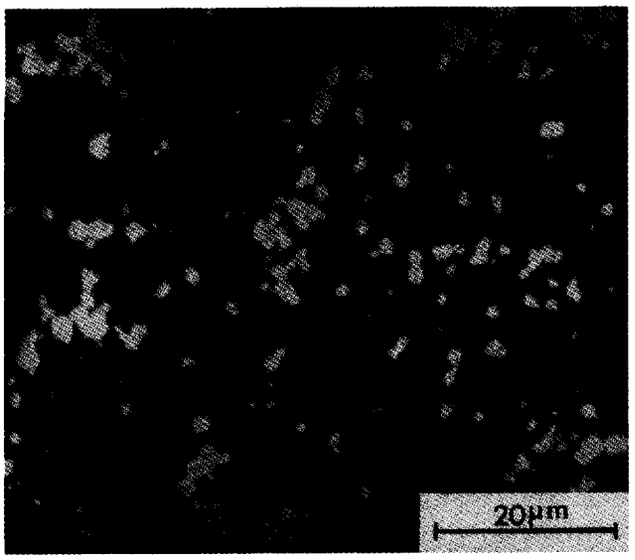


Fig. 9. SEM micrograph of Sample 2 sintered at 1500°C for 2 h, showing a more uniform distribution of ZrO_2 particles compared with that shown in Fig. 4.

The scanning electron micrograph recorded from the resulting sample is shown in Fig. 9 and indicates that the effective reduction in zircon content has resulted in a lower volume fraction and more uniform distribution of zirconia particles within the matrix. However, the improved distribution of the ZrO_2 particles seems to occur at the expense of the densification achieved. In fact, the highest density attained for the silica modified reaction was 2·87 g/cm^3 when sintering was carried out at 1500°C for 2 h. A possible explanation of this effect may lie in the origin of the silica. A finer, more uniform dispersion of amorphous SiO_2 produced from the dissociation of zircon may permit a more uniform formation of liquid phase that in turn facilitates densification more readily.

Conclusions

Reaction sintering of zircon with alumina and barium carbonate produces a composite material comprising distributed ZrO_2 in a continuous barium feldspar matrix. The spheroidal particles of ZrO_2 are in clusters surrounded by an amorphous phase rich in Si and Ba, and there is evidence that this glassy phase also infiltrates the grain boundaries of the polycrystalline feldspar matrix. Electron and X-ray diffraction results suggest that the matrix consists of either hexagonal (β) or orthorhombic (α) forms of hexacelsian ($BaO{\cdot}Al_2O_3{\cdot}2SiO_2$), or a combination of these two phases. Yttria added during processing partitions in part to the ZrO_2 allowing a significant fraction of the ZrO_2 to be retained as tetragonal phase at room temperature and thus the potential for a measure of transformation toughening. The addition of extra silica during processing reduces the volume fraction of ZrO_2 and results in a more uniform distribution of ZrO_2 particles. However, in this case the densification of the composite is less effective. Future work may focus on improving the dispersion of the zirconia particles by the use of attrition milling or other mixing–milling techniques of the initial powders.

References

1. Anseau, M. R., Leblud, C. & Cambier, F., Reaction sintering (RS) of mixed zircon-based powders as a route for producing ceramics containing zirconia with enhanced mechanical properties. *J. Mater. Sci. Lett.*, **2** (1983) 366–70.
2. Pilate, P. & Cambier, F., Synthesis and reaction sintering with alumina of plasma sprayed zircon powder. *Silicates Industriels*, **7–8** (1986) 95–8.
3. Holmström, M., Chartier, T. & Boch, P., Reaction-sintered ZrO_2-mullite composites. *Mater. Sci. Engng.*, **A109** (1989) 105–9.
4. Boch, P. & Giry, J. P., Preparation of zirconia-mullite ceramics by reaction sintering. *Science of Sintering*, **20**(2/3) (1988) 141–8.
5. Descamps, P., Sakaguchi, S., Poorteman, M. & Cambier, F., High-temperature characterisation of reaction-sintered mullite-zirconia composites. *J. Am. Ceram. Soc.*, **74**(10) (1991) 2476–81.
6. Cheng, Y. -B. & Thompson, D. P., Zirconia toughening of cordierite and anorthite glass ceramics. *British Ceramic Proceedings — Complex Microstructures*, ed. R. Stevens & D. Taylor, **42** (1989) 149–58.
7. Garvie, R. C., Hannink, R. H. J. & Pascoe, R. T., Ceramic steel? *Nature*, **258** (1975) 703–4.
8. Drummond, C. H., Lee, W. E., Bansal, N. P. & Hyatt, M. J., Crystallization of a barium aluminosilicate glass. *Ceram. Engng. Sci. Proc.*, **10**(9–10) (1989) 1485–502.
9. Drummond, C. H., Crystallization behaviour and properties of $BaO{\cdot}Al_2O_3{\cdot}2SiO_2$ glass matrices. *Ceram. Engng. Sci. Proc.*, **11**(7–8) (1990) 1072–86.
10. Bansal, N. P. & Hyatt, M. J., Crystallization kinetics of $BaO{\cdot}Al_2O_3{\cdot}SiO_2$ glasses. *J. Mater. Res.*, **4**(5) (1989) 1257–65.
11. Moya Corral, J. S. & Garcia Verduch, A., The solid solution of silica in celsian. *Trans. J. Br. Ceram. Soc.*, **77** (1978) 40–4.
12. Green, D. J., Hannink, R. H. J. & Swain, M. V., *Transformation Toughening of Ceramics*. CRC Press Inc., Boca Raton, Florida, 1989, pp. 222–3.
13. Debsikdar, J. C., Effect of zirconia addition on crystallinity, hardness and microstructure of gel-derived barium aluminosilicate, $BaAl_2Si_2O_8$. *J. Mater. Sci.*, **27** (1992) 5320–4.
14. JCPDF card no. 3–659.
15. JCPDF card no. 25–1466.
16. JCPDF card no. 27–1035.
17. Yoshiki, B. & Matsumoto, K., High-temperature modification of barium feldspar. *J. Am. Cer. Soc.*, **34**(9) (1951) 283–6.
18. JCPDF card nos. 12–725, 12–726.
19. Chen, M., Lee, W. E. & James, P. F., Synthesis of monoclinic celsian glass-ceramics from alkoxides. *J. Non-Cryst. Solids.*, 147–148 (1992) 532–6.
20. Scott, H. G., Phase relationships in the zirconia-yttria system. *J. Mater. Sci.*, **10** (1975) 1527.

Journal of the European Ceramic Society 15 (1995) 795–800
© 1995 Elsevier Science Limited
Printed in Great Britain. All rights reserved
0955-2219(95)00043-7
0955-2219/95/$9.50

Ca-acceptors in Dielectric Ceramics Sintered in Reducive Atmospheres

D. F. K. Hennings & H. Schreinemacher

Philips GmbH, Research Laboratories Aachen, P. O. B. 1980, 52021 Aachen, Germany

(Received 15 November 1994; revised version received 7 February 1995; accepted 14 February 1995)

Abstract

Dielectric ceramics of the system (Ba,Ca)(Ti,Zr)O_3 (BCTZ) have been fired with BaO-excess in reducive atmosphere. By the influence of BaO-excess the Ca^{2+}-ions are shifted from the Ba- to the Ti-sites of the perovskite lattice. The solubility of Ca^{2+} on Ti-sites is largely independent of the firing atmosphere, but shows a pronounced temperature dependence. At 1400°C ≅ 2 at.% Ca can be dissolved on the Ti-sites. Ca-ions on Ti-sites are strong electron acceptors. Highly insulating materials can be thus prepared in reducive atmospheres. The Ca-acceptors are electrically compensated by large numbers of ionized oxygen vacancies. Electromigration of the oxygen vacancies gives rise to ionic conductivity, resulting in low life stability of multilayer capacitors, sintered in reducive atmosphere.

1 Introduction

Up to now most of the dielectric materials used in ceramic multilayer capacitors (MLCs) are based on barium titanate. For a long time the dielectric ceramics have been cofired with inner electrodes of expensive palladium or palladium silver alloys. After decades of research and development[1,2] the manufacturers of MLCs are now capable of replacing the expensive noble metals by cheaper base metals, e.g. Fe, Co, Ni. Base metal electrodes (BME), however, have to be fired in a protective atmosphere of N_2/H_2 or CO/CO_2. In reducing atmosphere the $BaTiO_3$ forms large numbers of ionized oxygen vacancies,[2] $V(o)^{\bullet\bullet}$. Large numbers of conduction electrons then give rise to high electronic conductivity of the dielectric material, according to the reaction

$$V(o)^{x} \rightarrow V(o)^{\bullet\bullet} + 2e.$$

The semiconductance of reducive sintered $BaTiO_3$ ceramics can be, however, very effectively suppressed by addition of acceptor dopes. Classical acceptor dopes[1] for $BaTiO_3$ are the ions of Al, Cr, Mn, and Fe. These ions enter the B-sites (Ti-sites) of the perovskite lattice, forming there acceptor-type point defects, like $[Mn^{2+}{}_{(Ti)}]''$, $[Fe^{3+}(Ti)]'$ which strongly trap the conduction electrons.[3] Highly insulating dielectric materials can be thus prepared in reducing atmosphere. BME capacitors, made from acceptor doped $BaTiO_3$ dielectrics exhibit very high insulation resistances (IR) of $\geq 10^{12}\Omega$.[4]

One of the principal problems of transition metal acceptors is the valence instability of transition metal ions, e.g. Cr^{3+}, Mn^{2+}, Fe^{3+}, at a change of the oxygen partial pressure during heat treatment of the MLCs. For this reason manufacturers of BME–MLCs make use of calcium ions on Ti-sites, $[Ca^{2+}{}_{(Ti)}]''$, which have been reported as being very strong acceptors.[5,6] Chan *et al.*[7] found that Ca^{2+}-ions which are well known as A-site substituents may also enter the B-sites of $BaTiO_3$. In the case of BaO-excess a certain number of the Ca^{2+}-ions is shifted from the Ba- to the Ti-sites. Zhuang *et al.*[8] studied the effect of Ca-acceptors on the conductivity and dielectric properties of $BaTiO_3$. They observed a decrease of the tetragonal distortion (c/a) of the perovskite unit cell and a lowering of the Curie point, T_C, at the incorporation of $[Ca^{2+}{}_{(Ti)}]''$ in $BaTiO_3$. Zhang *et al.*[9] reported a maximum solubility of ≅ 5% $[Ca^{2+}{}_{(Ti)}]''$ in $BaTiO_3$.

High-permittivity dielectrics of the temperature specification Y5V are usually prepared from ceramic mixed crystals of the system $(Ba_{1-x}Ca_x)[Ti_{1-y}Zr_y]O_3$ (BCTZ). In BCTZ the Ca^{2+}-ions strongly prefer the Ba-sites of the perovskite lattice,[10] too. At 1300°C a maximum solubility of ≅ 20% $[Ca^{2+}{}_{(A)}]$ was found in $BaTiO_3$.[11] Incorporation of Ca^{2+} on the A-sites yields only slight changes of the lattice parameters and Curie point of $BaTiO_3$.

1.1 Aim of the investigation

The solubility of Ca on the Ti-sites of BCTZ is not yet known. Changes of the Curie point and

the unit cell volume will be therefore studied as function of the concentration of $[Ca_{(Ti)}]''$ in BCTZ. Subject of investigation are further the temperature dependence of the solubility of $[Ca_{(Ti)}]''$ and a possible change of the Ca^{2+}-ions from the B-sites back to the A-sites, $Ca_{(Ti)} \rightarrow Ca_{(Ba)}$, in CO_2 or oxidizing atmosphere. The insulation resistance and life stability of reducively sintered BCTZ is studied, using accelerated life tests (ALT).

2 Experimental

2.1 Preparation of BCTZ

The standard experimental material was BCTZ of the composition $(Ba_{0.95}Ca_{0.05})[Ti_{0.88}Zr_{0.12}]O_3$. The atomic ratio of A-site (Ba, Ca) and B-site ions (Ti, Zr) was carefully fixed by analytical means (XFA) at $A/B = 1 \pm 0.0015$. For this the raw materials TiO_2 ('TM1', Fuji Titanium Industries, Ltd, Osaka, Japan) and ZrO_2 ('EF-ULTRA', Z-Tech, Bad Homburg, Germany) had to be analysed for impurities, using ICP analyses and heated for 1 h at 1000°C in O_2 to remove slight oxygen deficits and traces of water. $BaCO_3$ and $CaCO_3$ (both analytical grade, Merck Darmstadt, Germany) were heated for 1 h in a CO_2 stream at 500°C. The small Sr-content of $\cong$ 0·2 wt% of the $BaCO_3$ was also considered at weighing in. The raw materials were mixed in isopropanole, using an agate ball mill and then calcined to perovskite at 1200°C (6 h) in air.

2.2 Sintering of ceramics

The atomic ratio A/B of the BCTZ was systematically varied by addition of appropriate amounts of TiO_2 or $BaCO_3$ in the range 0·005 mol TiO_2 to 0·15 mol $BaCO_3$. TiO_2 and $BaCO_3$ additives were finely distributed over prereacted BCTZ by wet milling in isopropanole, using 2 mm∅ ZrO_2 balls. Because of the poor sintering behaviour at $A/B > 1$ the powders must be intensively milled to $d_{50} \cong 0.4$ μm. The powders were uniaxially pressed at 3 kbar to discs of 6 mm diameter and 600 μm thickness. The predensified samples were fired for 2 h at 1400°C in a reducing atmosphere of moist (H_2O-20°C) N_2H_2-95/5. Theoretical densities were determined, using the lattice constants of sintered ceramics. Relative densities of 96–99% of the theoretical value were observed. The highest densities (≥99%) were found at the atomic ratio $A/B \cong 1$. With increasing $BaCO_3$ additions the densities decreased. After sintering the diameter of the discs was $\cong$ 5 mm and the thickness $\cong$ 500 μm.

2.3 XRD experiments

The lattice parameters of BCTZ ceramics were determined by means of X-ray diffraction (XRD), using Cu–K_α radiation. Due to the large size difference between Ca^{2+}- and Ti^{4+}-ions, strong changes of the lattice parameters are expected to occur at the incorporation of Ca^{2+} on the B-sites. The solubility of Ca on the B-sites was thus determined from the change of the unit cell volume in dependence of the molar amount of added $BaCO_3$.

2.4 Electrical measurements

For electrical measurements 500 μm thick ceramic discs were evaporated with CrNi–Au electrodes. The temperature dependence of the relative dielectric constant K was studied in the range -50°C to +150°C, using an automatic capacitance bridge (HP 4278 A). Similar to the lattice parameters also the Curie point T_C of BCTZ is assumed to change with the number of Ca-ions on B-sites. Hence, the solubility of $[Ca^{2+}{}_{(Ti)}]''$ was also determined from T_C changes as function of the BaO-excess in BCTZ.

The life stability of dielectric materials is commonly evaluated from long time measurements of the insulation resistance (IR) under electric field and temperature stress. The long time measurements were abbreviated by employing so-called accelerated life tests (ALT) under specially high temperature stress. The IR of such tested ceramics then breaks down after rather a short time. ALT experiments on BCTZ discs were performed at 250 V and 200°C.

2.5 Thermogravimetric (TGA) experiments

The incorporation of Ca on the B-sites of BCTZ was thermogravimetrically studied on powders, containing various additions of $BaCO_3$. $BaCO_3$-excess pushes the Ca^{2+}-ions from the A- to the B-sites, according to the reaction:

$$(Ba_{1-x}Ca_x)[Ti_{1-y}Zr_y]O_3 + z\ BaCO_3 \quad (1)$$

$$\rightleftharpoons$$

$$(Ba_{(1+z-x)}Ca_{(x-\frac{z}{2})})\ [Ti_{(1-y)}Zr_yCa_{\frac{z}{2}}]O_{3+z} + z\ CO_2$$

From eqn (1) it can be derived that for each Ca on B-sites two extra Ba-ions have to be incorporated on the A-sites. Thus, formation of $z/2$ $[Ca_{(Ti)}]$ corresponds to the addition of z $BaCO_3$. The weight loss due to evaporation of z CO_2 at the incorporation of z $BaCO_3$ was determined by means of TGA. One of the important questions to be answered by TGA were the extent and the reversibility of reaction (1) in different atmospheres.

According to reaction (1) the total number of perovskite unit cells increases by $z/2$ new units at the addition of z BaO to BCTZ. For $z/2$ new perovskite units a corresponding number of $3/2z$ oxygen ions would be necessary to fill up the oxygen sublattice. However, only a number of z O^{2-} is

available at the incorporation of z BaO. Hence, at the incorporation of z BaO a corresponding number of $z/2$ oxygen vacancies (V(o)) is generated. For each Ca^{2+} on B-sites therefore one oxygen vacancy is formed. In $BaTiO_3$ the Ca-acceptors are compensated by doubly ionized[3] oxygen vacancies.

$$[Ca^{2+}{}_{(B)}]'' \cong [V_{(o)}]^{\bullet\bullet} = z/2$$

The actual composition of BCTZ, containing Ca on A- and B-sites and oxygen vacancies is:

$$(Ba_{(A)1-x}Ca_{(A)x})[Ti_{(B)1-y-z}Zr_{(B)y}Ca_{(B)}{}''_z]O_{3-z}V_{(o)}{}^{\bullet\bullet}{}_z \quad (2)$$

After saturation of the B-sublattice with $[Ca^{2+}(B)]''$ an orthotitanate 2nd phase, similar to Ba_2TiO_4, is most probably formed on further addition of δ $BaCO_3$. The formation of orthotitanate is assumed to be analogous to the known reaction in $BaTiO_3$:

$$BaTiO_3 + \delta\ BaCO_3 \Leftrightarrow \delta\ Ba_2TiO_4 + (1-\delta)\ BaTiO_3 - \delta\ CO_2 \quad (3)$$

In BCTZ most probably a mixed crystal of $(Ba,Ca)_2TiO_4$ is formed.

For TGA experiments mixtures of BCTZ and z mol $BaCO_3$ in the range $z = 0{\cdot}01$ to $z = 0{\cdot}15$ were prepared. The powder mixtures were prereacted for 2 h at 1400°C in moist (H_2O-20°C) N_2/H_2-95/5. In the thermobalance the crushed powders were several times heated to 1250°C and cooled down to room temperature in streaming CO_2 ($\cong$ 1 bar). The weight changes due to uptake or loss of CO_2 were thus repeatedly measured.

3 Results

3.1 Unit cell volume

Corresponding to the expected shift of Ca^{2+} from A- to B-sites the unit cell volume strongly increased at the incorporation of BaO in BCTZ, see Fig. 1. Up to $BaCO_3$ additions of $z = 0{\cdot}05$ the volume of the perovskite unit cell almost linearly increased (Végards law). The volume increase did not directly start at $z = 0$, but at $z \cong 0{\cdot}005$, indicating a small impurity excess of $\cong$ 0·5% on the B-sites of BCTZ which had to be balanced by the corresponding amount of $\cong$ 0·5% $BaCO_3$. The slight B-excess most probably results from the wear of ZrO_2 milling balls. By interpolation of the Végard lines a maximum solubility of $z = 0{\cdot}045$ BaO in BCTZ was derived.

The XRD diagram of BCTZ fired with $z = 0{\cdot}06$ mol $BaCO_3$ exhibited weak reflexions of a 2nd phase which were almost identical to those of $BaCaTiO_4$.[12] Thus, at $z = 0{\cdot}06$ orthotitanate is formed, analogous to reaction (3). The BCTZ is most probably saturated with BaO already at $z < 0{\cdot}06$. From the value of $z = 0{\cdot}045$ the slight B-excess due to $\cong$ 0·005 mol ZrO_2 wear has to be subtracted. Thus, a maximum solubility of $z \cong 0{\cdot}040$ mol BaO in BCTZ results at 1400°C.

According to eqn (1), the maximum solubility of Ca^{2+} on the B-sites of BCTZ is $z/2 \cong 2$ at.% at 1400°C. This value is considerably lower than the $\cong$ 5 at.% $[Ca^{2+}{}_{(B)}]''$ reported for pure $BaTiO_3$ by Zhang *et al.*[9] In samples containing 0·5% TiO_2-excess, the maximum solubility of Ca^{2+} on the A-sites of BCTZ was found to lie at $[Ca^{2+}{}_{(A)}] \cong$ 16% at 1400°C, see Fig. 2.

3.2 Curie point changes

Similar to the observed changes of the unit cell volume the Curie point T_C is also strongly shifted towards lower temperatures by the incorporation of BaO, see Fig. 3. Due to the slight ZrO_2 wear, the T_C shift starts at $z \cong 0{\cdot}005$ again. The T_C of BCTZ is almost linearly decreasing from +75°C at $z = 0$ to −35°C at $z = 0{\cdot}045$. From this a maximum

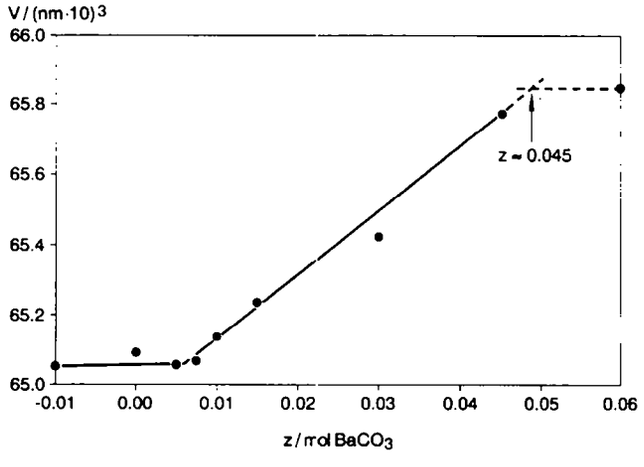


Fig. 1. Change of the unit cell volume of $Ba_{0.95}Ca_{0.05}(Ca_{0.88}Ti_{0.12})O_3$ (BCTZ) at the addition of z mol $BaCO_3$ to 1 mol BCTZ; 1400°C, moist (H_2O-20°C) N_2/H_2-95/5.

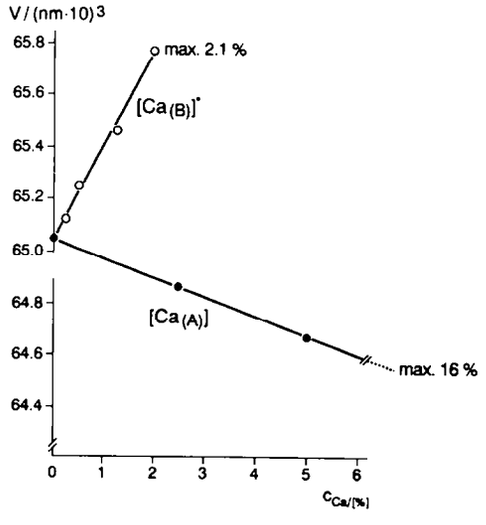


Fig. 2. Change of the unit cell volume of $Ba_{0.95}Ca_{0.05}(Ca_{0.88}Ti_{0.12})O_3$ as function of the Ca concentration on A- and B-sites of the perovskite lattice (1400°C).

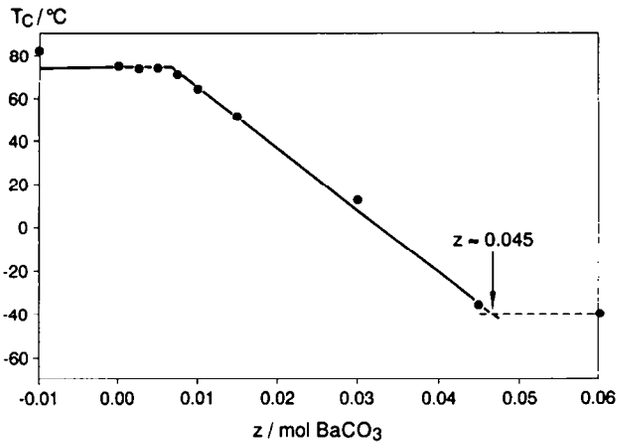


Fig. 3. Curie point shift of $Ba_{0.95}Ca_{0.05}(Ca_{0.88}Ti_{0.12})O_3$ at the addition of z mol $BaCO_3$ to 1 mol BCTZ; 1400°C, moist (H_2O-20°C) N_2/H_2-95/5.

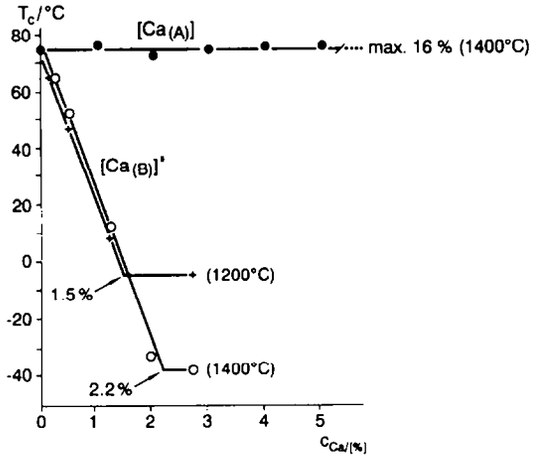


Fig. 4. Curie point shift of $Ba_{0.95}Ca_{0.05}(Ca_{0.88}Ti_{0.12})O_3$ as function of the Ca concentration on A- and B-sites of the perovskite lattice; 1200°C and 1400°C.

solubility of $\cong$ 2% [Ca^{2+}(B)]" at 1400°C was again evaluated, see Fig. 4. The maximum solubility of [Ca^{2+}(B)]" decreased to $\cong$ 1·5% after annealing the samples for 2 h at 1200°C. Firing of the samples at various partial pressures of oxygen, (N_2/H_2-95/5 to ~99·9/0·1, air and pure O_2) had no measurable influence on T_C. Incorporation of Ca^{2+} on the A-sites of BCTZ had in accordance to the known phase diagrams[10] negligible influence on T_C, see Fig. 4.

3.3 TGA results

The TGA experiments were carried out with pre-reacted mixtures of BCTZ and $BaCO_3$ in pure CO_2 at 1250°C. At a partial pressure of 1 bar CO_2 the orthotitanate phase Ba_2TiO_4 begins to decompose into $BaCO_3$ and $BaTiO_3$ at temperatures of $T \leq 1135$°C.[13] The decomposition of $(Ba,Ca)_2TiO_4$ into $BaCO_3$, $CaCO_3$ and $(Ba,Ca)TiO_3$ is expected to occur at comparable temperatures.

The TGA experiments revealed negligible weight changes for a BaO excess of $z \leq 0{\cdot}03$, see Fig. 5. At

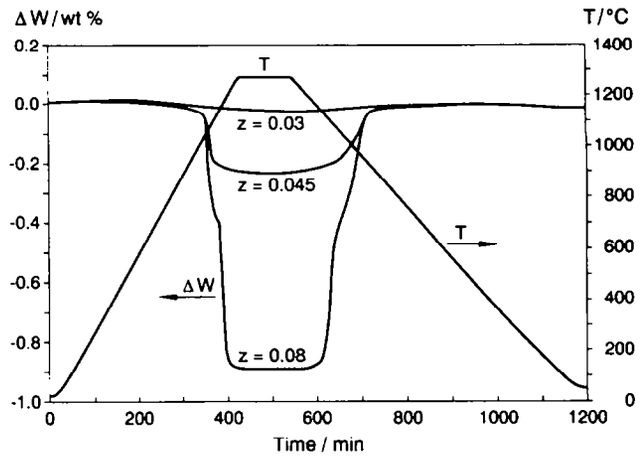


Fig. 5. TGA of $Ba_{0.95}Ca_{0.05}(Ca_{0.88}Ti_{0.12})O_3$ at the addition of z = 0·03, z = 0·045, and z = 0·08 mol $BaCO_3$; 20–1250°C, CO_2 atmosphere.

larger BaO-excess ($z > 0{\cdot}03$) a reversible uptake and loss of CO_2 was observed at *ca* 1050°C due to formation of orthotitanate. The lower equilibrium temperature of 1050°C, compared to 1135°C of pure Ba_2TiO_4, suggests a modification of Ba-orthotitanate by dissolved Ca and Zr. With increasing BaO-excess in BCTZ, the weight changes due to uptake and loss of CO_2 also become larger and larger, see Fig. 5. The TGA experiments revealed an irreversible incorporation of Ca^{2+}-ions on the B-sites of BCTZ for $z \leq 0{\cdot}03$, even in CO_2 at $T \leq$ 1250°C. The (Ba,Ca)-orthotitanate phase formed at larger $BaCO_3$ additives, $z > 0{\cdot}03$, is obviously in equilibrium with $(Ba,Ca)CO_3$ and BCTZ at $T \cong$ 1050°C and $p(CO_2) \cong 1$ bar.

The reversible weight change Δw, due to the uptake or loss of CO_2 in BCTZ + z $BaCO_3$ at 1250°C was plotted as function of z, see Fig. 6. Most of the measured values of Δw lie on a straight line which becomes $\Delta w = 0$ at z = 0·035. Considering a ZrO_2 wear of $\cong$ 0·5%, a maximum solubility of z = 0·03 mol BaO of $\cong$ 1·5% Ca^{2+} on the B-sites of BCTZ was derived for 1250°C. The

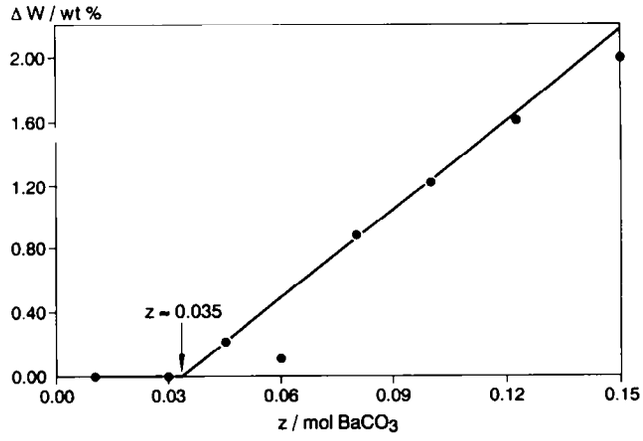


Fig. 6. Reversible weight change of $Ba_{0.95}Ca_{0.05}(Ca_{0.88}Ti_{0.12})O_3$ at the addition of z mol $BaCO_3$ in CO_2 atmosphere; 20–1250°C.

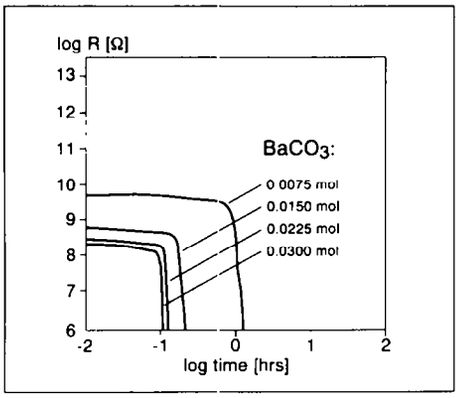


Fig. 7. Life stability at 200°C, 0·5V/μm of $Ba_{0.95}Ca_{0.05}(Ca_{0.88}Ti_{0.12})O_3$ containing various $BaCO_3$ additives, fired at 1400°C in moist (H_2O-20°C) N_2H_2-95/5.

lower solubility of [Ca(B)]" determined at 1250°C confirms the temperature dependence of the solubility of $[Ca^{2+}{}_{(B)}]$, already detected by means of T_C measurements.

3.4 Insulation resistance (IR) and life stability

Accelerated life tests (ALT) have been performed on ceramic discs at 200°C and 0·5V/μm, see Fig. 7. The discs have been sintered at 1400°C with various $BaCO_3$ additives of $z = 0{\cdot}0075$ to $z = 0{\cdot}03$ in moist (H_2O-20°C) N_2/H_2-95/5 atmosphere. The insulation resistance of such treated samples show rather high values of IR = 10^8 Ω to 10^{10} Ω at 200°C. The pale yellow colour as well as the high IR indicate the strong electron trapping effect of the Ca-acceptors. Increase of the BaO-excess from $z = 0{\cdot}0075$ to $z = 0{\cdot}03$, however, lowers the IR by more than one decade. This effect can be ascribed to the ionic conductivity, caused by electromigration of charged oxygen vacancies,[14] $[V(o)]^{\bullet\bullet}$.

Electromigration of ionized oxygen vacancies in dc fields was found to be the major reason for the electrical degradation of $BaTiO_3$-based perovskite dielectrics.[15,16] Charged oxygen vacancies, formed for compensation of the Ca-acceptors are thus assumed to be responsible for the rather poor life stability of BCTZ, fired with BaO-excess. As can be seen in Fig. 7, the life time of BCTZ strongly decreases with increasing amount of BaO-excess, z.

4 Summary and Discussion

The investigation of $(Ba_{0.95}Ca_{0.05})(Ti_{0.88}Zr_{0.12})O_3$ (BCTZ) confirmed earlier results obtained on pure $BaTiO_3$, that Ca^{2+}-ions are shifted from the A- to the B-sites by the influence of BaO-excess. Even at 1400°C the maximum solubility of $\cong$ 2% $[Ca^{2+}{}_{(B)}]$ in BCTZ is below that reported for pure $BaTiO_3$[9] (5%). The solubility of Ca^{2+}-acceptors on the B-sites of BCTZ shows a distinct temperature dependence, but was found to be independent of the oxygen partial pressure of the firing atmosphere. It has been also confirmed that $[Ca^{2+}{}_{(B)}]$" is a strong electron-acceptor in BCTZ. Ba-excess (A/B > 1) can be thus successfully employed for suppressing the electronic conduction in BCTZ-based dielectric materials cofired with Ni electrodes in reducive atmosphere. While the electronic conductivity of Ca-acceptor doped BCTZ is very low, a large number of charged oxygen vacancies, $[V(o)]^{\bullet\bullet}$ gives rise to a considerably high ionic conductivity. The mobility of the ionized oxygen vacancies $[V(o)]^{\bullet\bullet}$ in the electrical field is considered as responsible for the rapid degradation of Ca-acceptor doped BCTZ under dc field and temperature stress. Hence, additional dopes are needed to suppress the ionic conduction in BME multilayer capacitors prepared from BCTZ dielectric materials with BaO-excess.

References

1. Burn, I. & Maher, G., High resistivity $BaTiO_3$ ceramics sintered in CO–CO_2 atmospheres. *J. Mater. Sci.*, **10**(4) (1975) 633–40.
2. Daniels, J., Härdtl, K. -H., Hennings, D. & Wernicke, R., Defect chemistry and electrical conductivity of doped barium titanate ceramics. *Philips Research Reports*, **31** (1976) 487–559.
3. Hagemann, H. -J. & Hennings, D., Reversible weight change of acceptor-doped $BaTiO_3$. *J. Am. Ceram. Soc.*, **64** (1981) 590–594.
4. Hagemann, H. -J., Hennings, D. & Wernicke, R., Ceramic Multilayer Capacitors. *Philips Techn. Rev.*, **41** (1983) 89–98.
5. Wakino, K., Minai, K. & Sakabe, Y., High-dielectric constant ceramics for base metal monolithic capacitor. *Proc. Japan U.S. Study Seminar on Dielectric Piezoelectric Ceramics*, Roppongi, Tokyo 1982, p. W-1.
6. Sakabe, Y., Dielectric materials for base-metal multilayer ceramic capacitors. *Ceram. Bull.*, **66**(9) (1987) 1338–41.
7. Chan, H. M., Harmer, M. P., Lal, M. & Smyth, D. M., Calcium site occupancy in $BaTiO_3$. *Mater. Res. Soc. Symp. Proc.*, Vol 31. Elsevier Science Publ. Co. Inc., 1984, pp. 345–50.
8. Zhuang, Z. Q., Harmer, M. P., Smyth, D. M. & Newnham, R. E., The effect of octahedrally-coordinated calcium on the ferroelectric transition of $BaTiO_3$. *Mater. Res. Bull.*, **22** (1987) 1329–35.
9. Zhang, X. W., Han, Y. H., Lal, M. & Smyth, D. M., Defect Chemistry of $BaTiO_3$ with Additions of $CaTiO_3$. *J. Am. Ceram. Soc.*, **70** (1987) 100–3.
10. Jaffe, B., Cook, W. R. & Jaffe, H., Piezoelectric ceramics. In *Non-Metallic Solids*, ed. J. P. Roberts & P. Popper. Academic Press, London, 1971, p. 91.
11. Hennings, D. & Schreinemacher, H., Temperature dependence of the segregation of calcium titanate from solid solutions of $(Ba,Ca)(Ti,Zr)O_3$ and its effect on the dielectric Properties. *Mater. Res. Bull.*, **12** (1977) 1221–6.
12. Kwestroo, W. & Paping, H. A. M., The systems BaO–SrO–TiO_2, BaO–CaO–TiO_2, and SrO–CaO–TiO_2. *J. Am. Ceram. Soc.*, **42** (1959) 292–9.

13. Heit, W., Phase relations and thermodynamics of solid state reactions in barium oxide containing systems. Doctoral Thesis, University Saarbrücken, Germany, 1972.
14. Waser, R., Bulk conductivity and defect chemistry of acceptor-doped strontium titanate in the quenched state, *J. Am. Ceram. Soc.*, **74**(8) (1991) 1934–40.
15. Waser, R., Baiatu, T. & Härdtl, K. -H., Dc electrical degradation of perovskite type titanate ceramics: I. *J. Am. Ceram. Soc.*, **73**(6) (1990) 1645–53.
16. Hennings, D., Klee, M. & Waser, R., Review advanced dielectrics: bulk ceramics and thin films. *Adv. Mater.*, **3** (1991) 334–40.

Journal of the European Ceramic Society **15** (1995) 801–809
© 1995 Elsevier Science Limited
Printed in Great Britain. All rights reserved
0955-2219/95/$9.50

0955-2219(95)00044-5

Interfacial Reaction in Carbon Fibre–Sialon Ceramic Composites

P. Dupel & A. Hendry

Department of Metallurgy & Engineering Materials, University of Strathclyde, Glasgow, UK

(Received 7 June 1994; revised version received 10 February 1995; accepted 14 February 1995)

Abstract

Sintering and interfacial reaction have been studied in a composite of sialon matrix with chopped carbon fibre reinforcement. It has been shown that at relatively low temperature (1500°C) there is a little α *to* β *transformation in the reaction sintered matrix, no interfacial reaction (the carbon fibre is unaltered by the firing cycle) and 20% apparent porosity. As the temperature is increased to 1550°C and 1600°C, a corresponding increase in both transformation and density occur but accompanied by significant interfacial reaction. The nature of these changes is quantified and the microstructures determined by electron microscopy. The observations are interpreted in terms of interface chemistry, and transport mechanisms in both the gas and liquid phases are explained. Optimised procedures for fabrication are suggested.*

1 Introduction

The development of silicon nitride engineering ceramics over the last two decades has been devoted to the pursuit of maximum sintered density and therefore to the highest levels of mechanical strength. However, of equal importance is the need for reliability and reproducibility in the fabricated component, and for a means of crack inhibition to improve the relative toughness. Both of these aspects can be addressed through the use of composite action in the ceramic matrix, although this will necessarily lead to some decrease in fracture strength. A number of papers devoted to these aspects of the mechanical behaviour of ceramic matrix composites have been published in recent years and these are best summarised in the proceedings of the conferences at Riso[1] and that specifically devoted to silicon nitride in Stuttgart in 1993.[2]

Before detailed modelling of fracture behaviour can be attempted, however, it is necessary to address the problems of composite fabrication. This is necessary because, in general, the systems of interest are chemically incompatible, i.e. a reaction occurs between the matrix and the reinforcement during high-temperature fabrication or high-temperature use. The specific problem of carbon-fibre-reinforced silicon nitride materials was first discussed by Kyotoku *et al.*[3] where the nature of the interfacial reaction was identified and methods of inhibition or prevention devised. The critical factors are the interaction of the sintering gas atmosphere with the composite in the early stages of sintering when open porosity is present, and the rate of pore closure. However, in that work[3] and in subsequent investigations at Strathclyde, the detailed nature of the carbon–sialon interaction was not elucidated and therefore the micromechanisms at the interface are not known. There are specific requirements for knowledge of (i) the influence of temperature on the interfacial reaction, (ii) the interaction between sintering mechanisms and interfacial reaction, and therefore (iii) the role of the sintering liquid phase on material transport at the interface.

In order to have a simple, rapid densification, it was decided to use hot pressing as the fabrication method and to use a limited range of temperatures, 1500–1600°C, in which it was evident that both sintering and interfacial reaction were relatively rapid. The hot-press environment of a graphite die initially heated in air gives rise to a gas atmosphere with total pressure slightly in excess of one atmosphere with a chemical composition of 35 vol.% CO and 65 vol.% N_2 from the conversion of air to nitrogen and carbon monoxide. An investigation was therefore carried out to determine the answers to the three headings above and to provide guidance on the optimum fabrication routes for strong, reliable composites.

2 Experimental Procedure

The composites were prepared from β'-sialon 201 supplied by Cookson Group and containing un-reacted α-Si_3N_4, 6 wt% Al_2O_3, 8 wt% Y_2O_3 (as a densifying aid) and 10 wt% AlN polytypes. During sintering, this material forms a β'-sialon

of composition $Si_{5.25}Al_{0.75}O_{0.75}N_{7.25}$ (β'; $z = 0.75$). Reinforcing material used was chopped carbon fibre supplied by Osaka Gas Co. and two different proportions of carbon fibre have been added to the matrix : 10 vol.% and 20 vol.% The appropriate quantities of matrix and reinforcement material were wet-mixed for 2 h in propan-2-ol using alumina balls. After evaporating the alcohol, the powder was remixed dry for 1 h. Samples were uniaxially cold-compacted in a steel die to approximately 60% of the theoretical density to produce cylindrical pellets (15 mm diameter × 5 mm; 1·5 g). The pellets were embedded in boron nitride powder and hot-pressed in a graphite die under a stress of 30 MPa at different temperatures (1500, 1550 and 1600°C). Temperature was monitored by a two-colour optical pyrometer. The sintering time used was generally 1 h but lower times have also been used to determine the sequence of the reaction. Samples were subsequently sectioned and polished for micro-examination. Densities were measured by Archemedes' method using distilled water. Crystalline phases present were identified by X-ray powder diffraction using a Hägg–Guinier focusing camera (CuK_α, 50 KV, 20 mA). The microstructure of the samples has been studied by scanning electron microscopy (SEM, Jeol 840) and by transmission electron microscopy (TEM, Philips 400T) equipped with a windowless energy-dispersive X-ray analysis system (EDX).

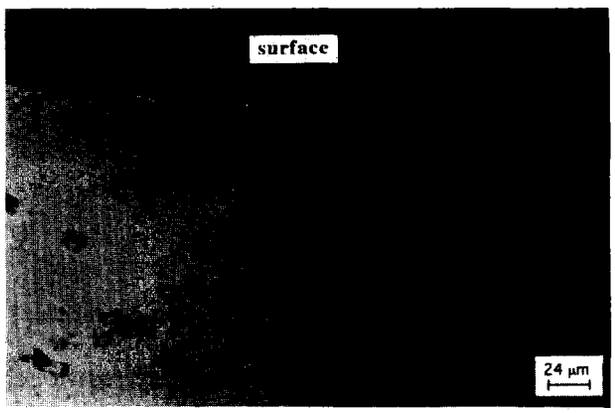


Fig. 1a. Optical micrograph of a 10 vol.% fibre composite sintered at 1550°C for 1 h, showing the external surface of the compact.



Fig. 1b. Optical micrograph of a 10 vol.% fibre composite sintered at 1600°C for 1 h.

3 Results

3.1 Density, weight losses and optical observations of the samples

Table 1 gives the densities and weight losses of samples sintered for 1 h at various temperatures and containing 10 or 20 vol.% carbon fibres.

The weight loss and density increase slightly for a given temperature with the amount of fibre in the sample. At 1500°C, the weight loss is negligible and density is very low, while the maximum density is obtained from 1550°C and the weight loss increases slightly with temperature. It should be noted that the percentage of theoretical density is sensitive to the value assumed for theoretical density. The value for density of carbon fibre given by the manufacturer is an overestimate of the true value, and samples fired at 1600°C are effectively fully dense. All weight losses are very small.

Table 1. Sample density and weight loss for various sintering temperatures and carbon fibre loadings

	Vol.% fibre		*Vol.% fibre*	
	10	*20*	*10*	*20*
Temperature (°C)	*Density (% theoretical)*		*Weight loss (%)*	
1500	81	83	0·2	0·4
1550	92	94	1·3	1·7
1600	94	95	2·0	2·5

Accuracy of density ±1%, weight loss ±0·2%.

Samples sintered at 1600°C exhibit a grey colour in contrast to the black colour at lower temperatures. Optical micro-observations show that at 1600°C and 1550°C a reaction has taken place between the matrix and the carbon fibre and at 1600°C an external surface layer is formed as shown in Figs 1a and 1b, respectively.

3.2 SEM observations

Electron microscopy observations of samples sintered for 1 h at 1500°C confirm a weak reaction between fibres and matrix. Cross-sectional and surface appearance of fibres do not reveal any attack, and the matrix appears to be adherent to the fibres as shown in Figs 2a and 2b. At 1550°C with 10 vol.% fibre, two kinds of fibre are observed. First, fibres with a reaction layer between the carbon core and the matrix, as shown in Fig 3. Usually small pores are also present between the matrix and the reaction layer. Second, some fibres do not seem to have reacted with the matrix and

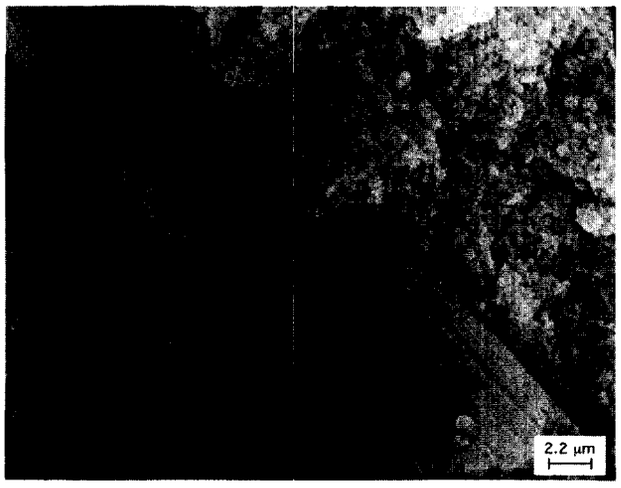


Fig. 2a. SEM micrograph of the external surface of a fibre in a 10 vol.% fibre composite sintered at 1500°C for 1 h.

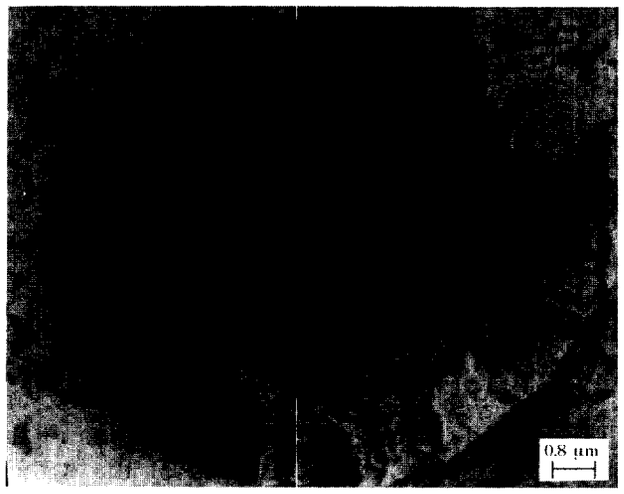


Fig. 2b. SEM micrograph of a cross-section of a fibre in a 10 vol.% fibre composite sintered at 1500°C for 1 h.

show the same appearance as in Figs 2a and 2b. Samples with 20 vol.% fibres and fired at the same temperature exhibit a similar comportment but the reaction between the matrix and the fibre is less extensive. It should also be noted that independent from the fibre loading, fibres near the



Fig. 3. As in Fig. 2 sintered at 1550°C for 1 h.



Fig. 4. As in Fig. 2 and 3 sintered at 1600°C for 1 h.

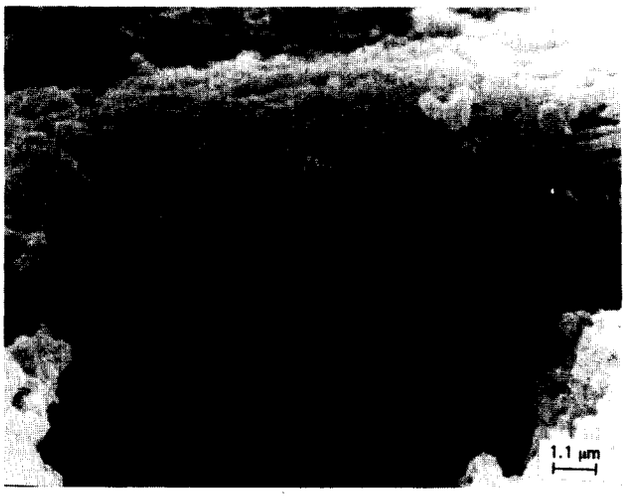


Fig. 5. SEM micrograph of the external surface of a reacted fibre in a 10 vol.% fibre composite sintered at 1600°C for 1 h.

surface of the pellet appear to be more heavily attacked than at the centre (see also Fig. 1b).

At 1600°C for 1 h with 10 vol.% of fibres, the reaction is more extended and complete for most of the fibres, i.e. the initial structure of the carbon fibre is no longer apparent, as shown in Fig 4. In this case, there is extensive porosity around the fibre and the surface of the fibres exhibit holes due to gas emission, as shown in Fig. 5. There is no difference between the surface and the centre of the pellet after 1 h, but a sample fired at 1600°C for only 5 min reveals a less extensive reaction and a clear difference between the surface and the centre of the pellet. As at 1550°C, samples with 20 vol.% fibres sintered at 1600°C create a less-extended reaction than the 10 vol.% fibres.

3.3 T.E.M. and X-ray analysis

3.3.1 Matrix

Figure 6 shows the X-ray diffraction patterns obtained from samples containing 10 vol.% fibres

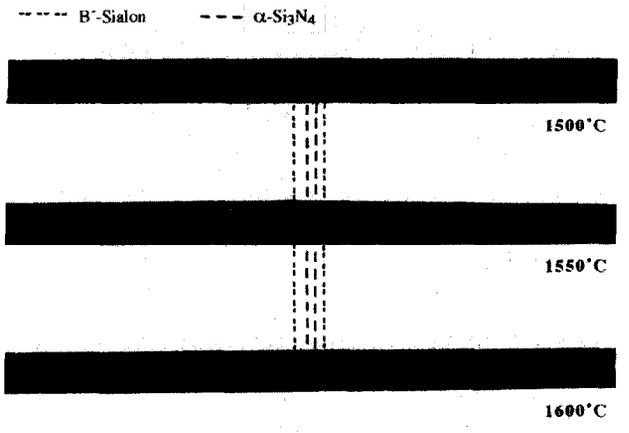


Fig. 6. X-ray Guinier camera photographs of 10 vol.% fibre composites fired at three different temperatures for 1 h.

and sintered at various temperatures for 1 h. As expected, there is a large variation in the sample composition with temperature since at 1500°C α-Si_3N_4 is the main phase, whereas at 1600°C β'-sialon is in the majority. The z-value of the β' phase calculated from the β' lines of the diffraction patterns presented in Fig. 6 follows the variation with temperature as shown in Table 2. The lower the temperature, the higher the z-value. A variation is also observed with the amount of carbon fibres.

TEM observations of the matrix corroborate the X-ray analysis. At 1500°C, large α-Si_3N_4 grains are surrounded by smaller grains and the

Table 2. β'-sialon z-value and main phases versus sintering temperature and fibre content

Temperature (°C)	*v/o fibre*		*Main phases*
	10	*20*	
	z-Value		
1500	0·92	1·33	α-Si_3N_4 (tr. β'-sialon)
1550	0·77	1·06	α-Si_3N_4 + β'-sialon
1600	0·46	0·72	β'-sialon

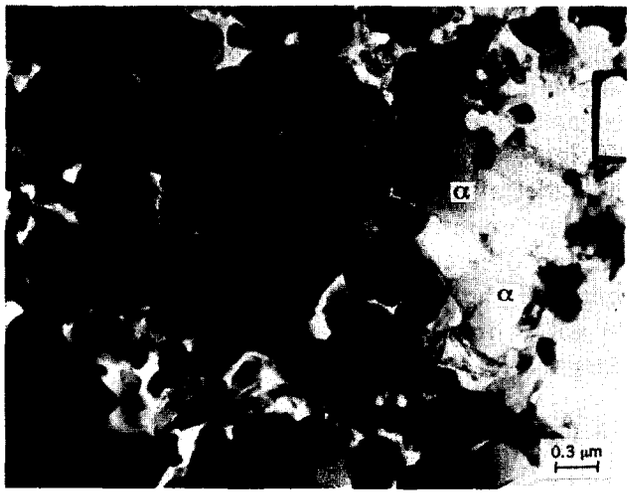


Fig. 7. TEM bright field micrograph of the matrix of a 10 vol.% fibre composite sintered at 1500°C for 1 h, showing residual α-$Si_3x/4$ grains.



Fig. 8. TEM bright field micrograph of the matrix of a 20 vol.% fibre composite sintered at 1600°C for 1 h.

sample exhibits a low density as shown in Fig. 7. Some elongated β'-sialon crystals are also present. At higher temperature, the matrix is more dense and no large α-Si_3N_4 grains are observed, as shown in Fig. 8.

3.3.2 Carbon fibre–matrix interface

At 1500°C, whatever the content of fibre, most of the carbon fibres have not reacted with the matrix. A typical interface between the two components is shown in Fig. 9. The fibre and the matrix are clearly unreacted and the low densification of the matrix is obvious. EDX analysis of the carbon fibre gives only a carbon peak and a small silicon peak (see Fig. 10). However, in some places in the sample, two other features of the fibres can be observed. First, the carbon fibre reveals a weak reaction with the components of the matrix, particularly the liquid phase, giving rise to very tiny grains at the interface or within the fibre, as shown in Fig. 11a. EDX analysis shows that these



Fig. 9. TEM bright field micrograph of a fibre–matrix interface in a 10 vol.% composite sintered at 1500°C for 1 h.

small grains and the fibre itself contain a larger amount of silicon than the unreacted fibre, as shown in Fig. 11b. In rare places, some large pieces of silicon carbide with intergrowths are observed, as shown in Fig. 12.

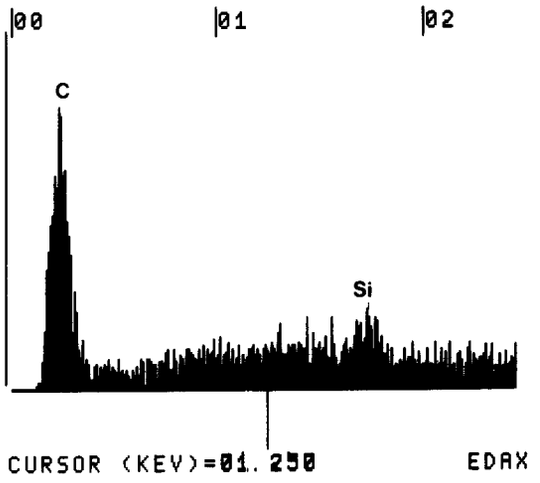


Fig. 10. Energy-dispersive analysis trace of the carbon fibre shown in Fig. 9.

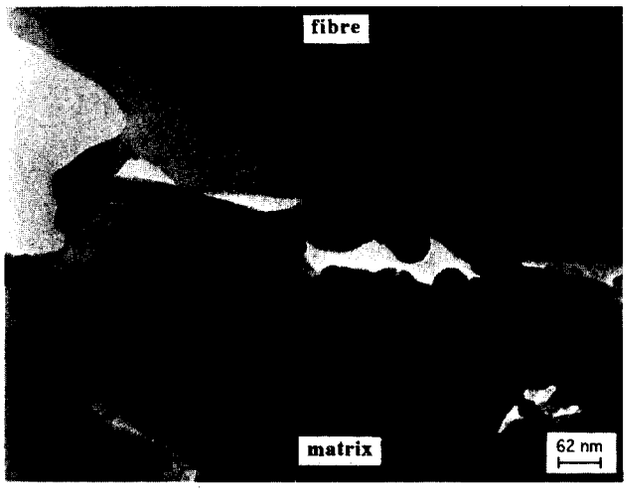


Fig. 11a. TEM bright field micrograph of the fibre–matrix interface in a 10 vol.% fibre composite fired at 1550°C for 1 h.

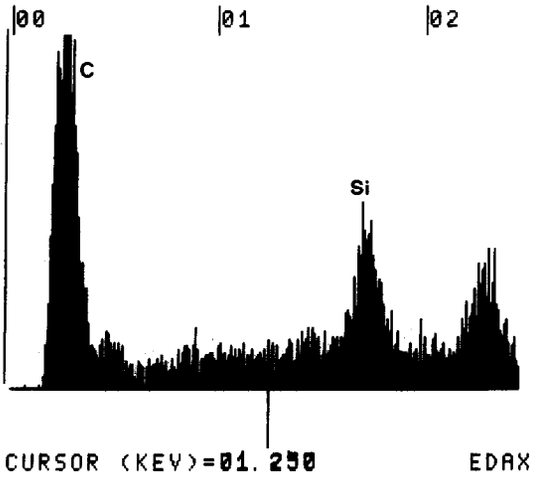
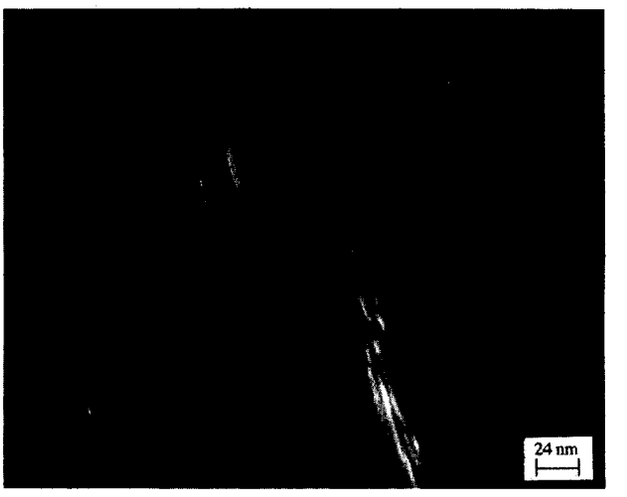
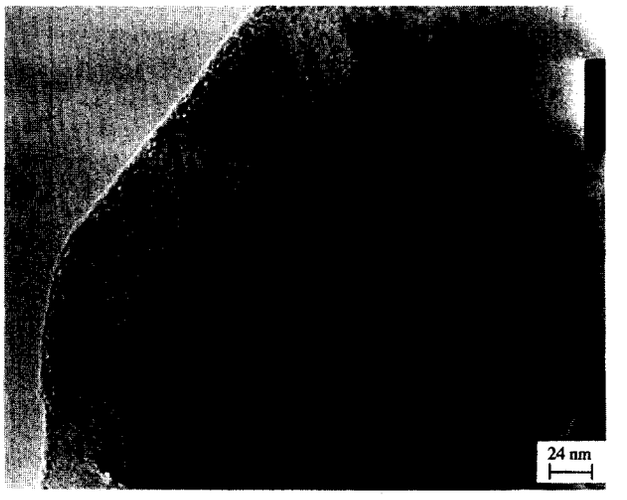


Fig. 11b. Energy-dispersive analysis trace of the carbon fibre shown in Fig. 11a.

A higher temperature, 1600°C, yielded a noticeably different microstructure in that extensive reaction had taken place between matrix and fibre. Two main structures are observed in the samples. First, some net interfaces between the fibre and



(a)



(b)

Fig. 12. Bright field (a) and dark field (b) TEM micrographs of fibre containing faulted silicon carbide.



Fig. 13. TEM bright field micrograph of the fibre–matrix interface in a 20 vol.% fibre composite sintered at 1600°C for 1 h.

the matrix are seen, as shown in Fig 13. As at lower temperatures, the carbon fibre contains silicon. The matrix contains a large amount of liquid phase containing Y, Si, Al and O (see Fig. 14) and small grains are embedded in this solidified liquid as shown in Fig 15a. Generally, few silicon carbide grains are observed in the samples fired at 1600°C for 1 h, and in this case they are located in the matrix or surrounded by the solidified liquid phase (see arrow in Fig. 15a). However, when the sintering time is shorter, 5 min, some large areas containing a lot of SiC grains are found as shown in Fig. 15b (silicon carbide grains are clearly evident from the high incidence of faulting). The second main structure observed is presented in Fig. 16a. This reacted carbon fibre shows a peculiar appearance with very small grains within the structure. The EDX analysis of the carbon fibre shows the presence of silicon and more surprisingly of molybdenum. These products are found again in some other places in the matrix, as shown in Fig. 16b (see arrow). The diffraction patterns of both such areas show that the small grains are SiC. These types of reacted carbon fibre are often observed as a thin film in the matrix, as shown in Fig 17. Whatever the temperature and the carbon content in the sample, some bubbles in the liquid phase are often observed near the fibre–matrix interfaces as, shown in Fig. 18.

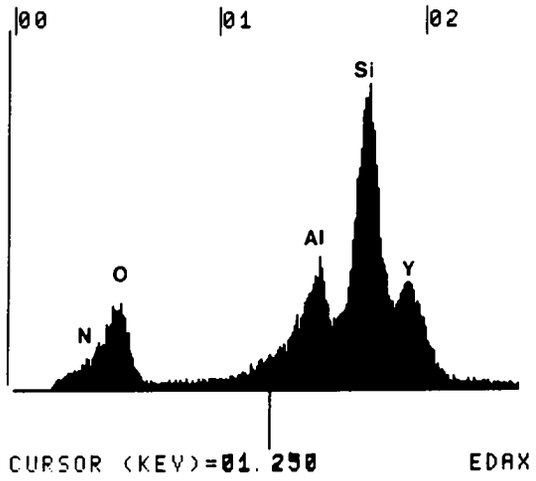


Fig. 14. Energy-dispersive analysis of a glassy phase area in Fig. 13.



Fig. 15a. Bright field TEM micrograph of precipitation of SiC (arrow) from the liquid phase in a 20 vol.% fibre composite sintered at 1600°C for 1 h.



Fig. 15b. TEM bright field micrograph of silicon carbide grains in a 10 vol.% fibre composite sintered at 1600°C for 5 min.

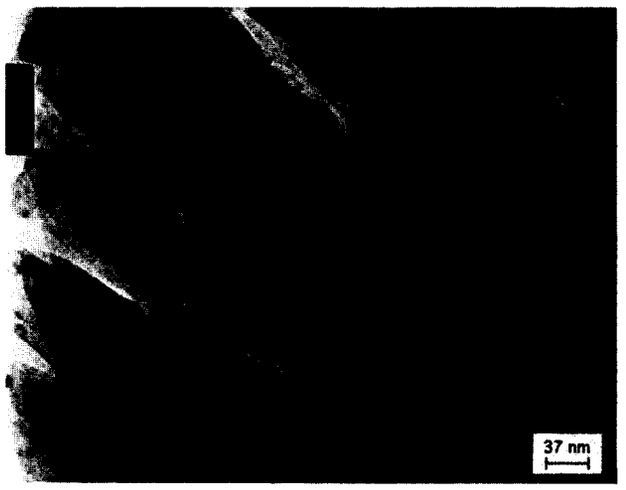


Fig. 16a. TEM bright field micrograph c/a reacted fibre in a 10 vol.% fibre composite sintered at 1600°C for 1 h.

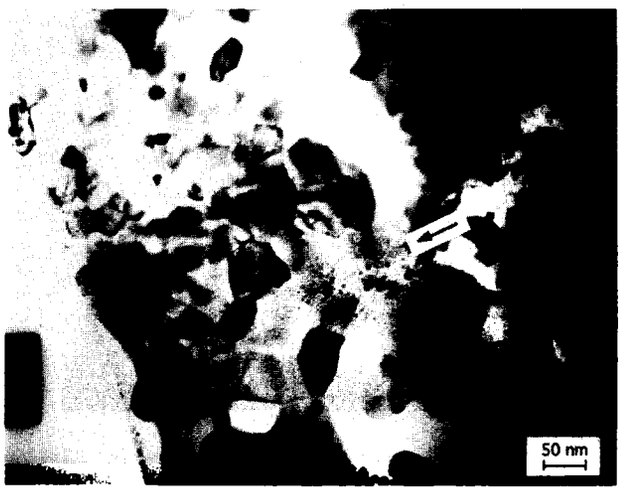


Fig. 16b. TEM bright field micrograph of a 20 vol.% fibre composite sintered at 1600°C for 1 h.

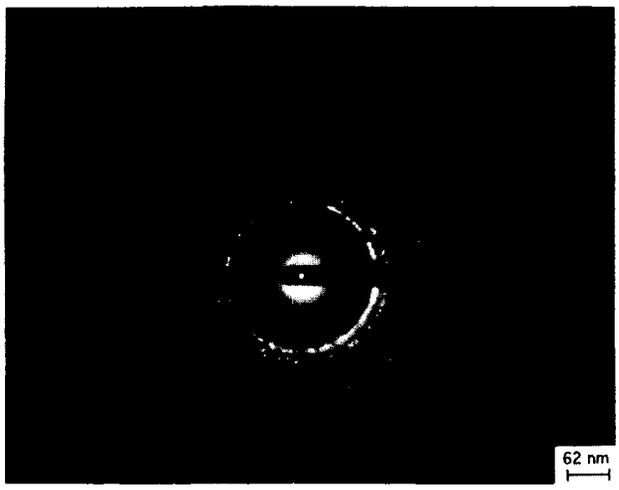


Fig. 16c. Electron diffraction pattern of silicon carbide grains in a fibre from a composite sintered at 1600°C for 1 h.

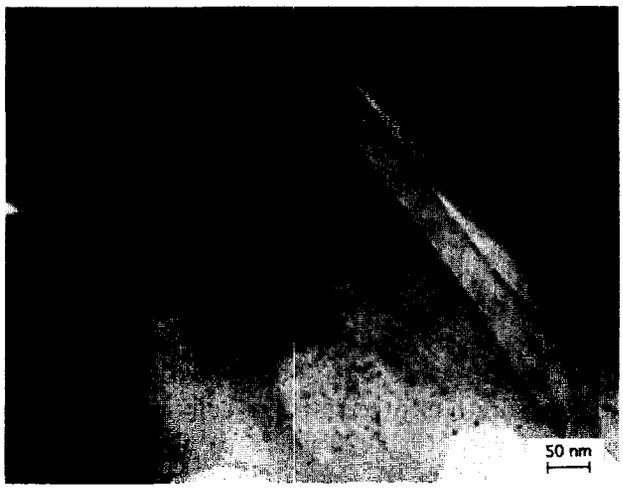


Fig. 17. TEM bright field micrograph of a 10 vol.% fibre composite sintered at 1600°C for 5 min.

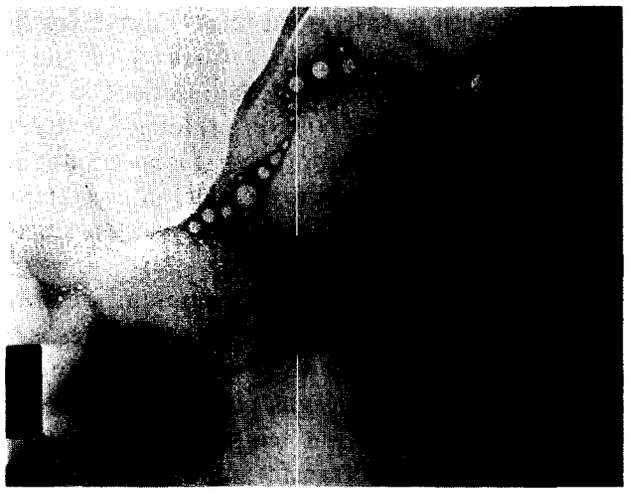


Fig. 18. TEM bright field micrograph of gas pores in the liquid phase of a 20 vol.% fibre composite sintered at 1600°C.

4 Discussion

It is clear that temperature affects both sintering of the matrix and reaction between the components of the composite, and that sintering only occurs if the temperature is equal to or higher than 1550°C. The interesting result regarding sintering is the variation of the β'-sialon z-value with temperature and with the fibre content. When temperature increases, z decreases. According to Kim and coworkers,[4] this is due to the transformation of α to β' in the matrix. At the beginning of sintering, the liquid phase and the precipitated β'-sialon grains are very Al rich. Because the aluminium in the liquid phase is consumed with the formation of β'-sialon by reaction of α-Si_3N_4 grains, the liquid contains less and less aluminium as the transformation progresses and the Al content in the β'-sialon grains decrease with time. Moreover, the Al-rich β'-sialon grains precipitated at the beginning of sintering redissolve as the Al concentration in the liquid phase decreases. In short, as α dissolves the z-value decreases, and therefore the average z-value of the β'-sialon in the composites decreases with time and temperature. However, some silicon is also consumed by formation of SiC within the fibres during sintering and there the z-value of the matrix β' is expected to decrease with increasing fibre content. That is, the dependence of z with the amount of carbon fibre in the sample is related to the reaction between the matrix and the fibres. Two factors have to be considered. First, the more carbon fibre in the composite, the less liquid phase is present. Second, silicon is incorporated in the attacked fibres (see Fig. 11). So, at a given temperature, the 20 vol.% composite contains more fibres, less liquid phase and Si reacts partly with the fibres. As a consequence, the ratio Si/Al in the liquid phase is lower, the transformation α to β' slower and the z-value is higher for a given sintering time.

From the results, it is clear that the extent of reaction increases with temperature of sintering and is related to the sintering behaviour in that it is promoted by the presence of liquid phase. At low temperature, the extent of sintering is limited and little α to β' transformation occurs, but the β' which is formed is of higher z-value than expected, as discussed above. There is no reaction at 1500°C and the fibre is unaffected by the sintering process. As the temperature and extent of densification increase, so the z-value of β' decreases and the attack on the carbon fibre becomes more pronounced. Two effects on the fibre are clear from the results. First, there is surface degradation due to the attack at the liquid/fibre interface which results in increased porosity in the fibre (compare Figs 5 and 2a). The second effect is reaction within the fibre, which converts the carbon from an amorphous phase to a micropolycrystalline state and includes formation of silicon carbide (Figs 12a and 16a). At the same temperature, as

shown in Fig. 15, there is reaction within the ceramic phase to form grains of silicon carbide as discreet crystals close to the interface. In the relatively short time duration of the present experiments (1 h) it is unlikely that such effects can be explained by liquid-phase diffusion and therefore gaseous transport must be involved both within the ceramic matrix pore network and in the increasingly porous fibres. The gases involved in the sintering environment are N_2 and CO and these must be involved in the process at the earliest stages when open porosity is present. This behaviour has been discussed by Kyotoku *et al.*[3] and it has been shown that in the presence of a significant CO pressure, the interfacial reaction is inhibited and weight losses are therefore expected to be small, as is found in the gas atmosphere of the hot press used in the present experiments. Similarly, open porosity is necessary for a gas evolution reaction (see weight losses in Table 1) at the fibre surface. In addition, however, the strongly reducing environment at the fibre/matrix interface (solid carbon, gaseous CO and N_2) will lead to carbothermal reduction of the predominantly oxide sintering liquid with formation of silicon monoxide (SiO) and carbon monoxide (CO)

$$SiO_2 + C_{(s)} \Leftrightarrow SiO_{(g)} + CO_{(g)} \quad (1)$$

where SiO_2 represents silica at reduced activity in the liquid phase. By this means carbon is consumed at the fibre surface and silicon is transported into the fibres by gaseous diffusion of SiO within the fibre pore network. This reacts with the fibres producing SiC in the fibre structure:

$$SiO_{(g)} + 2C_{(s)} \Leftrightarrow SiC_{(s)} + 2CO_{(g)} \quad (2)$$

while silicon carbide may be formed in the liquid phase either by direct reduction:

$$SiO_2 + 3C_{(s)} \Leftrightarrow SiC_{(s)} + 2CO_{(g)} \quad (3)$$

or by gaseous reaction with the carbon monoxide

$$SiO_2 + 4CO_{(s)} \Leftrightarrow SiC_{(s)} + 3CO_{2(g)} \quad (4)$$

The latter reaction is unlikely, however, both on thermochemical grounds (at 1600°C) and from electron microscopy, which shows that SiC crystals in the ceramic matrix are only found in the immediate vicinity of the interface, indicating reaction with solid carbon. As sintering proceeds and closed porosity develops, all of the above gas-generating reactions will be inhibited as the internal pore pressures increase and further reaction will not occur. Indeed, it should be noted that weight losses are small (Table 1) and that the above reactions are limited in extent even at the highest temperature studied; this is reflected in the high density achieved at 1550 and 1600°C even when reaction occurs.

In a second, later stage of the sintering process, silicon carbide crystals in the matrix redissolve as the system tends toward chemical equilibrium. At 1600°C and below, silicon carbide is thermodynamically unstable with respect to carbon, β'-sialon and the liquid phase.[5–7] The latter is assumed to be in equilibrium with the crystalline solid β' precipitated from it as part of the reaction sintering process.

The optimum manufacturing conditions for such composites require a rapid sintering process and sufficient time at a temperature high enough to equilibrate β'-sialon/liquid. Therefore, to produce a composite with minimum interfacial reaction, the sintering conditions should be arranged so as to provide rapid pore closure, i.e. a fast heating rate and adequate liquid phase. Prolonged sintering should not affect the reaction but is necessary for maximum density and phase transformation. The results also suggest that the fibre composites can be sintered to maximum density at 1600°C, which is 50–100°C less than that recommended for the monolithic ceramic.

5 Conclusion

The present work has shown that good-quality carbon-fibre-reinforced sialon composites can be prepared with 10 or 20 vol.% of fibre. Interfacial reaction between the constituents only takes place above 1500°C, in the temperature range required for liquid-phase sintering of the sialon matrix. The interfacial reaction therefore accompanies the α to β' transformation. Interfacial reaction involves the liquid phase and results in formation of silicon carbide in the matrix side of the interface at short times, but these redistribute on prolonged sintering times. Gas phase transport by silicon monoxide from the matrix to the fibres results in conversion of part of the amorphous fibre to crystalline silicon carbide.

The data suggests that the optimum sintering procedure for these chopped fibre composites is to use a rapid heating rate to provide fast pore closure, thereby preventing gas phase transport, and a maximum densification temperature of 1600°C for 1 h to give α to β' transformation and complete sintering of the matrix.

Acknowledgement

The authors are grateful for the provision of support by the University of Strathclyde Research Fund.

References

1. Bentzen, J. J., Bilde-Sovensen, J. B., Christiansen, N., Horsewell, A. & Ralph, B. (eds), *Structural Ceramics: Processing, Microstructure and Properties*. Riso National Laboratory, Roskilde, 1990.
2. Hoffman, M. J., Becker, P. F. & Petzow, G. (eds), *Silicon Nitride 93*. Trans Tech Publications, Aedesmannsdorf, 1993.
3. Kyotoku, H., Morrison, F. C. R. & Hendry, A., Prediction and control of interface reaction. In *Ceramic–Ceramic Composites*. Silicate Industriel, 53, 1988, p. 143.
4. Kim, N. K., Kim, D. Y., Kranzmann, A., Bischoff, E. & Kang, S. J., Variation of aluminium concentration in β'-sialon grains formed during liquid-phase sintering of Si_3N_4–Al_2O_3–Nd_2O_3. *J. Mater. Sci.*, **28** (1993) 4355–8.
5. Hendry, A., Thermodynamics of silicon nitride and oxynitride. *Proc. NATO-ASI Nitrogen Ceramics*, ed. F. L. Riley. Noordhot, Leyden, 1976, p. 183.
6. Hillert, M. & Jonsson, S., Thermodynamic calculation of the Si–N–O system. *Z. Metallk.*, **83** (1992) 648.
7. Hillert,M. & Jonsson, S., Thermodynamic calculation of the Si–N–O system. *Z. Metallk.*, **83** (1992) 720.

Journal of the European Ceramic Society 15 (1995) 811–821
© 1995 Elsevier Science Limited
Printed in Great Britain. All rights reserved
0955-2219(95)00053-4
0955-2219/95/$9.50

Alumina of High Reliability by Centrifugal Casting

W. Huisman, T. Graule & L. J. Gauckler

Nichtmetallische Werkstoffe, ETH Zürich, Sonneggstr. 5, 8092 Zürich, Switzerland

(Received 8 September 1994; revised version received 14 February 1995; accepted 20 February 1995)

Abstract

Centrifugal casting is a powerful colloidal processing route for massive ceramic parts of high strength and high reliability. Aqueous α-alumina slurries with up to 56·8 vol.% solids content with a mean particle size of 0·46 μm were deagglomerated by ultrasonic treatment and subsequent filtration. Consolidation was performed at various centrifugal accelerations. Differential sedimentation during centrifugal casting was studied and found to be negligible for slurries with high solids loadings exceeding 50 vol.%. Green bodies with very good particle packing, showing high green densities of 68%TD (theoretical density), as well as narrow pore size distributions were obtained. High sintered densities (≥99·4%TD) with homogeneous and fine microstructures were achieved at sintering temperatures as low as 1400°C. Four-point-bending tests showed an average strength of 540 MPa with a Weibull modulus m *of 24.*

1 Introduction

Despite the outstanding properties of advanced ceramic materials, their lack of reliability still remains the highest barrier to a wider range of engineering applications.

The lack of plastic deformation in combination with flaws often up to 100 times larger than the average grain size, makes ceramic parts very susceptible to stress peaks. Thus, surface and volume flaws can lead to catastrophic failure of an entire component.[1–3] Critical flaws can be introduced via the starting powder, (e.g. impurities and hard agglomerates), during the formation of the green body (organic or inorganic inclusions, drying-induced cracks)[3,4] or during service of the component via surface damage, as well as slow crack growth.

The homogeneity of the particle packing in the green compact has a great influence on the microstructural evolution during sintering, rather than actual sintering mechanisms.[5–10] For in the case of solid state sintering, inhomogeneous (unreliable) green bodies lead to unreliable fired products. The amount and distribution of large flaws present in the green body are retained throughout the sintering process unless further flaws are introduced, e.g. due to differential shrinkage or due to exaggerated grain growth.[11] In the worst case, this can lead to an undesirably wide strength distribution in a set of ceramic components. The spread of strength values of a batch of samples is expressed by means of the Weibull Modulus m, which, for ceramic compounds (alumina, zirconia (Y-TZP), ZTA) has a value around 10, whereas metallic components show values around 100. Design engineers require values between 20 and 30.[1,2]

Hence the formation of a homogeneous, densely packed green body is one of the most important steps in the manufacturing of engineering ceramics. Average strength and reliability, especially of the low-toughness-type advanced ceramics, which obey the Griffith fracture criterion, will then be strongly increased.[12–14]

In recent years it has become evident that wet processing of powders has many advantages over dry processing in respect of reliability.

The wet processing route provides the possibility of breaking up agglomerates by milling or ultrasonic treatment or by removing them and other flaw sources from the slurry by filtration, decantation or sedimentation.

This route also allows optimal particle packing and thus a minimum in flaw size and number of flaws.[4,6,15,16] Well-known examples are slip casting, pressure filtration and electrophoretic deposition of ceramic slurries. Centrifugal casting, compared with other colloidal-forming methods, has the advantage of producing massive ceramic objects combined with a reduced risk of stress gradients in the formed part.

Stresses during the centrifugal forming process act on every volume element.[13,15,17] During sedimentation the particles move in the direction of gravity, whereas the liquid flows in the opposite

direction. This means that the total volume of liquid in the dispersion does not have to be transported through the sedimented body leaving defects such as filtration channels as in the case of slip casting and pressure filtration.

The drawback of this technology, however, is that particle size separation might occur due to differential settling during the consolidation stage.[16,18,19] There are three approaches to overcome this problem: consolidation of the system (1) in the flocculated state[18] or (2) in the coagulated state,[19] or (3) the use of highly concentrated dispersed slurries.[20] The first two approaches have been successfully used in various single-phase[18,19] and binary powder systems[19] but lead to an open structure showing bimodal porosity (intra-agglomerate: small, inter-agglomerate: large) which is undesirable for subsequent densification[5–10,21,22] because higher temperatures are needed to approach the theoretical density. It is well known that higher sintering temperatures can lead to exaggerated grain growth in the well packed regions which is equivalent to the introduction of new flaws. Several investigations severely questioned the flocculated approach by theoretically and experimentally proving an inhomogeneous density profile in centrifuged sediments from as-prepared slurries.[23–27] The third approach produced very good results for one component system with high solids loadings (≥50 vol.%).[20,28–31] Mass segregation could be avoided by hindered sedimentation in these high-solids-content slurries. Such suspensions with repulsive, nontouching particles led to green bodies with high densities and narrow pore size distributions. They show good sintering behaviour and reach high final densities at much lower sintering temperatures.[6,28–31]

The aim of the present study was to improve the mechanical properties of alumina via centrifugal casting. Of special interest for the production of such high-quality ceramic objects were the processing parameters such as solids loading, suspension conditions, sedimentation velocity and centrifugal acceleration. Green and sintered densities, sintering behaviour and microstructures were studied as well. All these results were compared to those obtained from isostatically pressed α-alumina.

2 Experimental Procedure

A commercial α-alumina powder (Ceralox HPA-0·5 with MgO, Condea, Tucson, USA) was used with a surface area of 9·4 m^2/g (BET method) and an average particle size d_{50} of 0·46 μm (d_{90} = 0·2 μm, d_{10} = 1·3 μm, Malvern Mastersizer). Chemical analysis revealed a purity of >99·97%, with the following major impurities (in ppm): Mg 293, Na 20, Si 17, Fe 13 and Ca 7, according to the supplier.

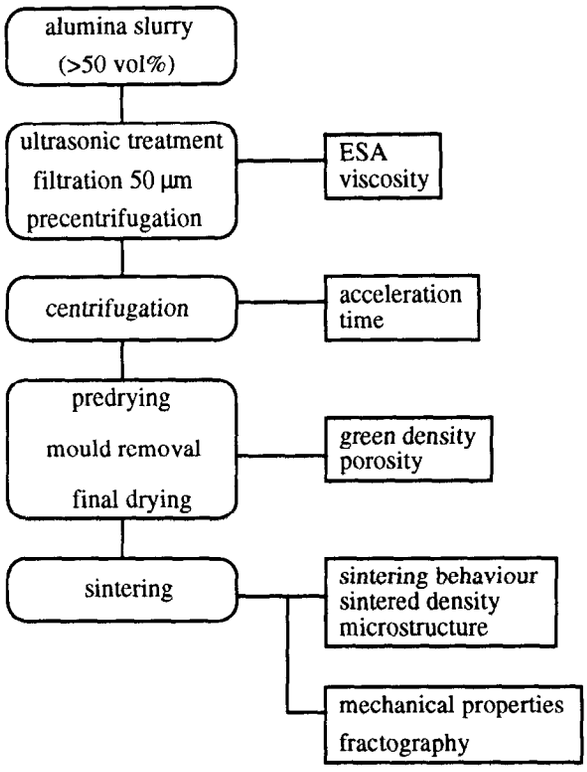


Fig. 1. Flow chart of centrifugal casting process.

Surface charge measurements were performed with 2 vol.% suspensions using an Electrokinetic Sonic Analysis System (ESA) (Matec ESA 8000, Matec Applied Science, USA). The ESA system was calibrated with Ludox TM (DuPont) 33 vol.% solids in water at a value of –3·67 mPa m/V. Viscosities of highly loaded suspensions were studied using a rotational viscosimeter (Rheomat 115A, Contraves AG, Zürich) equipped with a DIN125 testing device which varied the shear rate from 0 to 700 s^{-1} under isothermal conditions at 25°C.

The centrifugal casting process flow chart is shown in Fig. 1. Electrostatically stabilized aqueous suspensions of up to 56·8 vol.% Al_2O_3 were prepared at a pH between 4 and 4·2 using HNO_3, and subsequently dispersed by 50% pulsed ultrasonic cavitation for 8 min at 20 kHz and a power input of 420 W (Vibra Cell VC600, Sonics & Materials Inc., Danbury, USA). As the alumina used in this study is not derived by the Bayer process and therefore it is very low in Na-content, the pH did not change in between the limits given above during the subsequent preparation time. Large agglomerates, which could not be destroyed during ultrasonication, were removed by filtration (50 μm sieve) which led to slurries free of large agglomerates. These slurries were consolidated by cen-

trifugal casting (ZK 510, Berthold Hermle GmbH & Co., D-7209 Gosheim) in aluminum tubes with a diameter of 38·4 mm and a height of 110 mm. Objects with different geometries were cast in anodized aluminium moulds of which the ball-shaped one (d = 45 mm) could be disassembled into two halves along the acceleration axis. Centrifugal acceleration was varied from 150 to 4000 g to give compacts of up to 8 cm height. Centrifugation time to compact a given slurry volume of 90 cm^3 was dependent upon acceleration and ranged from 75 min to 64 h. Standard conditions were chosen, if not otherwise mentioned, with 53·4 vol.% solids content, densified at 4000 g for 90 min. Cast specimens were dried under controlled temperature and humidity conditions and then sintered in air at 1400°C with 6 h holding time. The heating and cooling rate was 1°C/min. Green and sintered densities were measured by the Archimedes principle in both mercury and water. Pore size distributions in green compacts were determined by mercury porosimetry with pressures up to 2000 bar (Hg-Porosimeter 2000, Carlo Erba Strumentazione, I-Milano). For analysis the cylindrical model was used,

Other samples using the same alumina powder were prepared by isostatic pressing at 350 MPa for 3 min. The sintering temperature for those samples was 1500°C with a 2 h holding time. The sintering behaviour in air was monitored with a differential dilatometer (Type 802, Bähr Gerätebau GmBH, D-4971, Hüllhorst), using a sapphire reference.

Bending test specimens of 4 × 3 × 45 mm (width, height, length) were cut out of a sintered cylinder in the direction of the acceleration axis. Strength measurements were performed according to the four-point-bending test method DIN 51 110 (Instron 8652, Instron Ltd., HP12 3SY, England) with 20/40 mm spans and a crosshead speed of 2 mm/min. Microstructures were observed by LM and SEM on polished and thermally etched surfaces. Mean grain sizes were obtained by measuring the intercepts of about 200 grains per sample and multiplying the average value by 1·5.[32] K_{Ic} measurements were performed in air by the Vickers indentation method (Zwick, D-7900, Ulm) using the Evans and Charles approach to evaluate fracture toughness.[33]

3 Results and Discussion

3.1 Suspension stability and viscosity

To avoid preferential segregation during centrifugal casting, highly stabilized dispersed systems with high solids content are required.[19,28–30] It is well known that the stability of suspensions increases with increasing electrokinetic sonic amplitude signal (ESA) which is directly proportional to the Zeta potential. Figure 2 shows the change in ESA signal in the pH range from 3 to 11 for an Al_2O_3 suspension containing 2 vol.% solids. The region of highest ESA signal lies around pH 4 and the isoelectric point at pH 9. Below pH 4 the solubility of Al_2O_3 increases drastically. Since the formation of dissolved Al^{3+} ions has a deteriorating effect on the sintering behaviour of alumina,[31] the plateau region around pH 4 was chosen to stabilize the suspensions.[19,28,29]

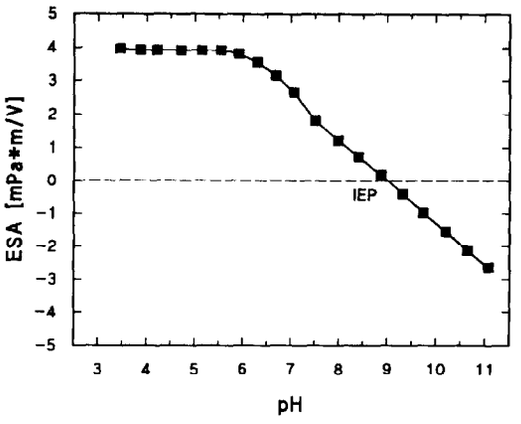


Fig. 2. ESA signal versus pH for a 2 vol.% alumina suspension.

The highest possible powder content is desirable for centrifugal casting in order to prevent separated sedimentation, but also to save space (for supernatant water) and weight (of the moulds) during the centrifugation step. On the other hand, high solids loadings are limited by the increase in viscosity (Fig. 3), and by rising pseudoplasticity. In addition, higher powder contents in the slurry result in increased losses of material during filtration and increased difficulties during mould filling.

In order to explore an optimum solids content of the suspension, slurries with 50·1, 53·4 and 56·8

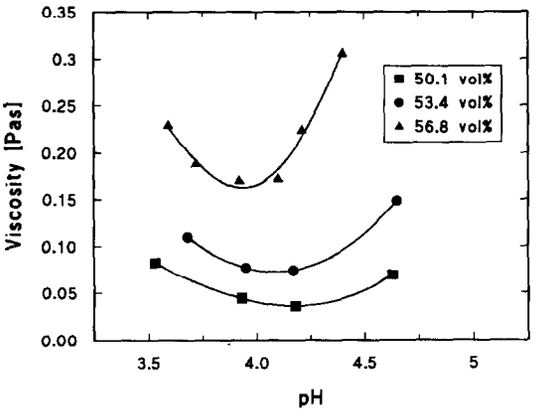


Fig. 3. Viscosity (at shear rate 100 s^{-1}) versus pH for alumina suspensions with different solids loadings.

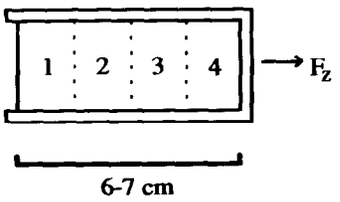


Fig. 4. Segmentation and numbering of cylindrical green compact.

vol.% solids were made at various pH values around pH 4. Figure 3 shows the viscosities at a shear rate of 100 s^{-1} (η_{100}) for slurries with different solids loadings around the optimal pH (≈ 4) found in ESA measurements. With rising powder content, the minimum of lowest viscosity will increase from 3 mPa s (50·1 vol.%, at pH 4·2) to 160 mPa s (56·8 vol.%, at pH 3·95). In addition, the viscosity/pH curve's minima shift slightly to lower pH values while narrowing considerably with augmenting powder content.

3.2 Solids content, green density and porosity

To define the limits of hindered sedimentation, slurries of different powder contents from 36·9 to 56·8 vol.% were cast in aluminum tubes at 4000 *g* for 90 min. All suspensions were stabilized at a pH between 4 and 4·2. The dried compacts were cut into segments of about 1·5 cm height to determine their green density and porosity. The numbering of the segments is shown in Fig. 4. Green densities and average pore radii (r_{50}) are summarized in Table 1.

All top segments show a green density that is lower than that of segments closer to the bottom of the cylinder. This difference is negligible for all parts that were cast from slurries with a powder content higher than 51·7 vol.%. If the solids loading was chosen below this value, a much larger deviation in green density could be measured. Obviously, differential sedimentation occurred in those slurries and finer particles were packed at the top corresponding to smaller pores found as well. Porosimetry measurements revealed a different mean pore size (Table 1), a different cumulative volume and a different surface area for top and bottom parts of compacts made from those low-

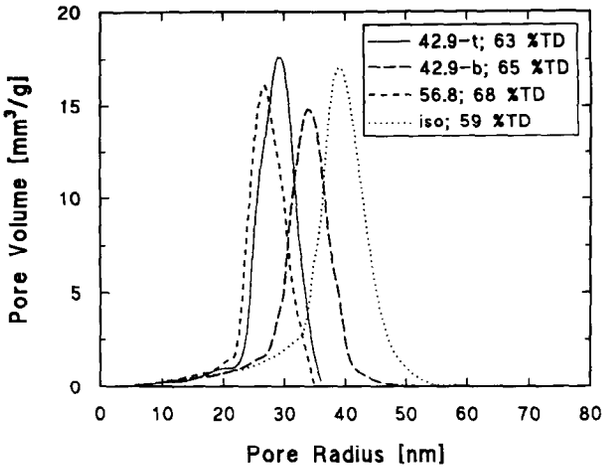


Fig. 5. Porosimetry data of 42·9 vol.%-slurry compact, 56·8 vol.% compact and isopressed compact (segments).

loaded slurries (<50 vol.% powder). It is well known, that monosized particles do pack more homogeneously but lead to lower densities (63 versus 68 %TD) than multisized powders. The change in surface area is due to the fact that larger particles pack at the bottom (smaller BET) and finer ones pack at the top (larger BET) in the case of particle size separation. As can be seen from Fig. 5, the average pore radius decreases from the bottom to the top segment of a 42·9 vol.% slurry-cylinder from 35 to 29 nm. In contrast to these findings, a 56·8 vol.% slurry-compact shows an average pore radius of 28 nm over the entire length of the cylinder, as well as a homogeneous and high green density of 68%TD. This indicates that no separation occurred during the centrifugation process. For comparison reasons, the pore size distribution of an isostatically pressed sample is also displayed. This dry processed sample (59%TD) has a broader pore size distribution than all wet processed samples and the highest average pore radius of 41 nm. Thus, the particle packing of colloidally processed samples is much better (63–68%TD) than that of an isostatically pressed sample (59%TD).

Shih *et al.*[25,27] have elaborated a theoretical approach to predict the density profiles of centrifuged cakes from flocculated suspensions by

Table 1. Green density (GD, in %TD) and average pore size (r_{50}, in nm) of segmented cylinders

Slurry (Vol.%)	*Segment 1*		*Segment 2*		*Segment 3*		*Segment 4*	
	GD	r_{50}	*GD*	r_{50}	*GD*	r_{50}	*GD*	r_{50}
36·9	62·8	27·0	64·2	30·0	66·2	33·5	66·5	39·3
42·9	63·0	27·1	63·7	33·1	64·0	36·0	66·0	34·6
50·1	64·2	27·0	65·0	28·7	66·5	28·9	66·5	29·9
51·7	65·0	27·5	65·2	29·8	68·5	28·7	67·7	28·8
53·4	65·0	29·3	65·7	30·6	66·7	30·0	66·5	30·0
56·8	67·6	27·5	68·1	28·3	68·3	28·2	68·1	27·5

implementing their experimentally obtained power-law pressure–density relationship[23] into the general differential equations for centrifugation[17] with appropriate boundary conditions. Their calculations were formulated in the equation

$$\frac{\Phi(z)}{\Phi_{max}} = \left[1 - \left(\frac{z}{z_m}\right)\right]^{\frac{1}{(n-1)}} \quad (1)$$

where $\Phi(z)$ is the volume fraction of solids at elevation z (measured from the bottom of the tube), Φ_{max} is the maximum solids volume fraction (measured at $z = 0$) and z_m is the elevation at equilibrium state. The exponent n indicates the flocculation state of a system during compaction. Generally, n decreases as the degree of flocculation increases. Their predictions agreed very well with the pronounced density profiles they measured in cakes that were centrifuged from flocculated alumina and boehmite suspensions. The uniform density profiles found in this investigation can be described by their equation as well. Green densities GD(z) instead of volume fractions $\Phi(z)$ were used for the calculations made in this study. This is, especially for the high loaded suspensions, a tolerable approximation. A linear drying shrinkage of 0·5–1·0% equals a volume reduction of 1·5–3·0%, indicating that the actual volume fraction for a green density of 0·68 would then be 0·67 or 0·66. Due to the high green densities obtained in this investigation, Φ_{max} was set to 0·685 (instead of 0·64 for random packed spheres[25,27]). Green densities of cylinders compacted from a 36·9 vol.% and a 56·8 vol.% slurry are displayed in Fig. 6. Three curves calculated according to Ref. 27 are shown as well. The n values chosen are $n = 9$ for a flocculated suspension[25,27] and $n = 100$ to fit the dispersed suspension with low (36·9 vol%) solids content. Hereby it has to be emphasized that for dilute alumina suspensions, a density gradient is

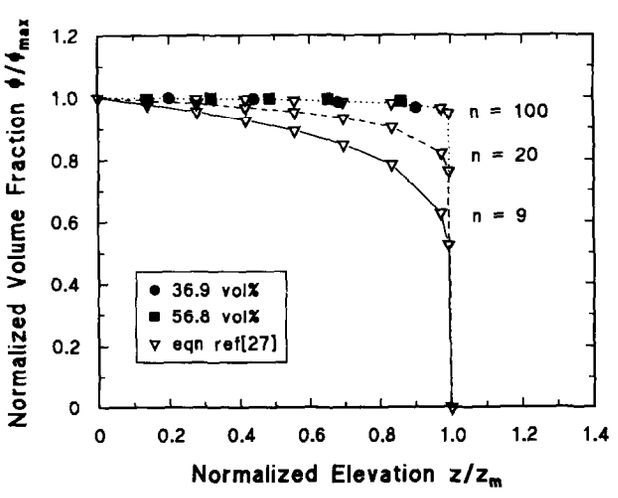


Fig. 6. $\Phi(z)\Phi_{max}$ versus z/z_{max} for green densities of compacts made from 36·9 and 56·8 vol.% slurries. Triangles are calculated values according to Ref. 27.

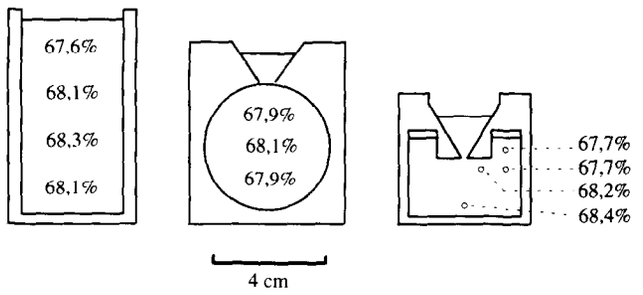


Fig. 7. Green density distribution of compacts shaped in different moulds: (a) cylinder; (b) ball; (c) with extreme constriction (53·4 vol.% slurry).

found due to particle size separation and not due to a pressure gradient in the centrifuged cylinder. For dispersed suspensions containing high volume fractions, the density–elevation relationship can be described if $n = 150$ is applied, which expresses virtually a step function and therefore a negligible density gradient.

Based on the results obtained so far, a solids loading of 53·4 vol.% was chosen for further experiments to be the best compromise between good handling of the suspensions and highest possible powder content.

During centrifugation the centrifugal force on the particles acts radially to the centre of the centrifuge. The question arises as to how a mould with undercuts can be filled properly with solids. Beylier *et al.*[20] have shown that the casting process can properly fill past constrictions in their spool and screw moulds. In order to elucidate the limits of mould filling, a mould containing an extreme undercut (Fig. 7c) was constructed. Centrifugal casting was performed with a 53·4 vol.% slurry. After centrifugation, the undercut was filled up to 65% of its height (10 mm) with alumina, leaving the upper part filled with clear water. The cast undercut was of stable shape and did not flow away after immediate removal of the top part of the mould. There was no evident difference in green density in this highest annular-shaped segment compared to the rest of the compact (Fig. 7(c)). Sintering led to a compact that showed no cracks and a homogeneous density. As can be seen from Fig. 7, high and homogeneous green densities of about 68%TD could be achieved in all moulds used throughout this investigation.

3.3 Mould-filling factor

To study dependence of the velocity of sedimentation upon the maximum applied acceleration, a slurry with 53·4 vol.% solids content was centrifuged at different accelerations for various times. The time t_{eq} to reach the equilibrium-state height z_m of a suspension by centrifugation is proportional to the initial slurry column height H_0

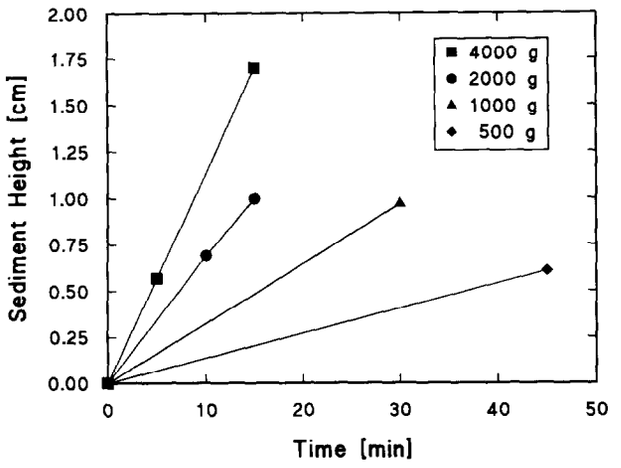


Fig. 8. Sediment height versus centrifugation time of a 53·4 vol.% slurry at various centrifugal accelerations.

and inversely proportional to the centrifugal acceleration $\omega^2 R$ where R is the radius of the centrifuge ($z = 0$).[24]

$$t_{eq} \approx H_0/\omega^2 R \quad (2)$$

At 4000 g the settling rate of the suspension in a cylindrical mould with a diameter of 38·4 mm is 0·12 cm/min, as shown in Fig. 8. To settle down the same amount of slurry and reach the same green density at 500 g, the centrifugation time is 6·6 times longer, and at 150 g, 26 times longer. No evident difference in homogeneity of the compact density was detected. After 15 min centrifugation at 4000 g the body does not show any plastic deformation under its own weight anymore. With lower solids contents, the settling rate will increase but differential sedimentation will occur due to increased inter-particle distances.

3.4 Drying and drying shrinkage

After centrifugation, the supernatant water is removed. Then the centrifuged green bodies still contain between 9 and 11 wt% water, which will evaporate during drying. It is well known that fast evaporation of the liquid during and especially at the end of the constant rate period (CRP) can lead to the formation of cracks in the green body, resulting in a low yield after sintering.[34] To detect the limits of successful, (i.e. crack-free) drying of centrifuged compacts, drying was performed while varying the parameters of temperature and relative humidity (RH). Cast compacts were dried under the following conditions: (1) in an oven at 50°C, (2) at ambient, (3) in a temperature-controlled humidity chamber at 25°C and 97%RH and (4) totally protected from direct convection at 25°C/97%RH. After casting, one-half of the ball-shaped mould was removed immediately after casting and the compacts were dried under the aforementioned conditions. The weight loss of the drying compacts was monitored over time and is displayed in Fig. 9. The final weight (dry body) was subtracted from that of the starting weight (wet body without supernatant) to give the value for the total water content in the cast compact (≡100%, Fig. 9). The fastest drying rates were achieved under oven and ambient conditions, followed by the nonconvection-protected compact under climatized conditions (25°C/97%RH) and with the slowest rate for the full convection-protected ball. As soon as drying rates are faster than 1·5% of the total water content of the green body per hour, the possibility of crack formation in the sintering body will be strongly increased. Compacts dried in the oven or under ambient conditions could not be sintered without cracking. In addition to that, it is important to protect the drying green bodies from direct convection as the CRP drying rate will be decreased with increasing layer of standing air over the compact. Normally, after a drying period of 4–5 days under climatized conditions, compacts could be sintered without cracking.

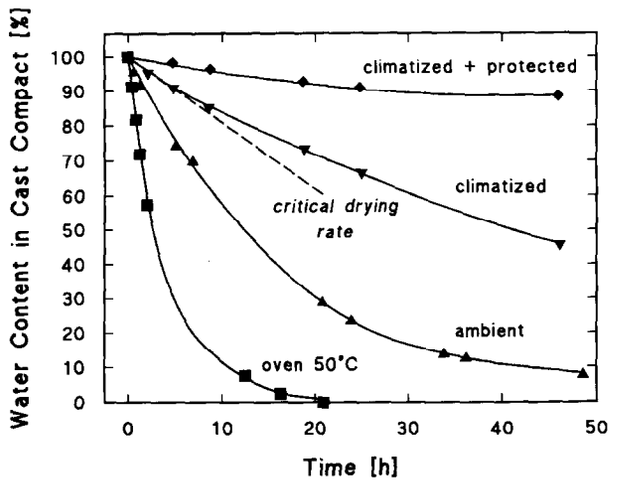


Fig. 9. Drying behaviour of ball-shaped cast compacts under various conditions.

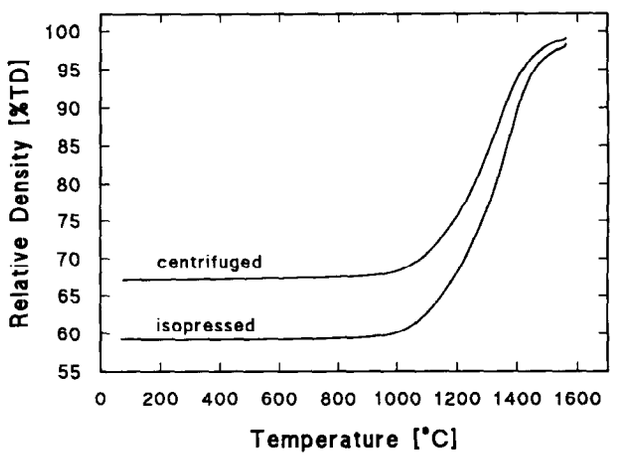


Fig. 10. Sintering curve of isopressed and cast alumina (53·4 vol.% slurry, 4000 g/90 min) at a constant heating rate of 5°C/min.

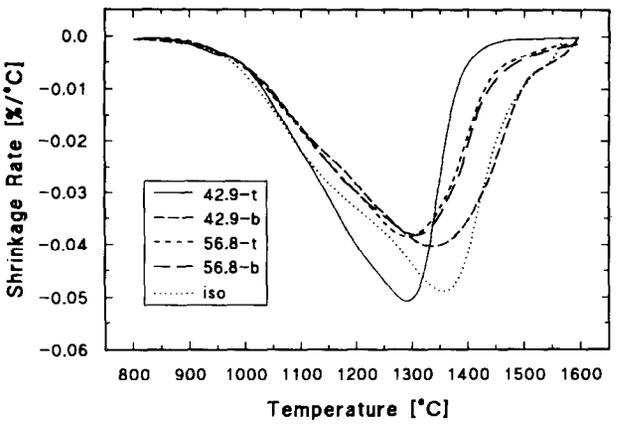


Fig. 11. Shrinkage rates of segments of cast alumina parts produced from 42·9 and 56·8 vol% slurries and of isopressed alumina.

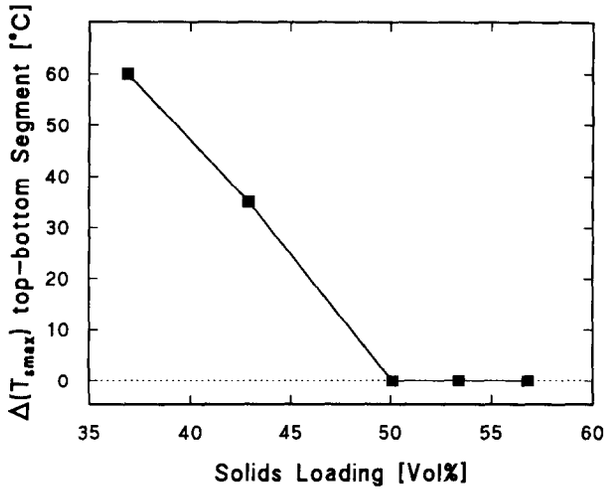


Fig. 12. Influence of solids loading on the difference of temperature of the maximum shrinkage rate $\Delta(T_{smax})$ between top and bottom segments of the centrifuged cylinders.

Linear shrinkage during drying was in the range 0·5–1·0% for compacts produced from high-solids-content slurries. This is equal to a volume reduction of 1·5–3·0% for compacts produced from high-solids-content slurries. Assuming a straight line of average-sized particles, this corresponds to an inter-particle distance of 5 nm in the sedimented wet state which is, according to the DLVO theory, just of the order of the distance of the primary minimum barrier. This calculation model, however, is very simplified and does not take into account the three-dimensional rearrangement behaviour of a drying particle system.

3.5 Sintering behaviour

The change in relative density during constant-heating-rate sintering (5°C/min) is shown in Fig. 10. The wet processed sample, which was produced from a 53·4 vol.% slurry, starts from a higher green density (68%TD) and reaches a higher final density at lower temperature than the dry processed sample (59%TD). This is due to the fact that larger pores disappear or get smaller, reaching an equilibrium size at higher temperatures and at a lower rate than small pores.[22,23] The isopressed part shows a wide pore size distribution from 0 to 60 nm around an average pore radius of 41 nm, whereas the centrifuged part has a smaller r_{50} of 29 nm and a narrow pore size distribution (Fig. 5). This proves that the finer the pores and the narrower the pore size distribution, the faster and earlier ceramic parts will sinter to maximum density.[6] Hence, centrifugal casting leads to a good sintering behaviour due to homogeneous particle packing in the case of high-solids-content slurries.

For a further illustration of the sintering kinetics, the shrinkage rates of three green compacts are compared in Fig. 11. A compact made from a relatively low solids loading slurry (42·9 vol.% Al_2O_3) showed different shrinkage rates at the top (t) and the bottom (b) of the compact. Due to differential sedimentation in this compact, the top consists of finer particles and finer pores (as illustrated in Fig. 5) than the bottom and therefore shows sintering at lower temperatures than the bottom part. This difference becomes negligible in the case of compacts made from high-solids-loading (56·8 vol.%) slurries. Both parts, top and bottom, show identical shrinkage rates over the whole sintering regime (Fig. 11). For comparison reasons, the shrinkage rate of an isostatically pressed sample is shown too. In the beginning (up to 1100°C) well-densified intra-agglomerate regions are responsible for the shrinkage, and the shrinkage rate is very similar to that of the 42·9 vol.% top segment. However, due to the larger inter-agglomerate pores, the temperature for the maximum shrinkage rate is not reached until 1375°C and the final density even at 1600°C is not as high as that of the cast compact (Fig. 10).

The findings from Fig. 11 can be illustrated in a different manner. Fig. 12 shows the influence of solids loading on the difference in temperature of the maximum shrinkage rate for the top and bottom segments of the cylindrical compacts. With rising solids loading, this temperature difference decreases from 60°C in the case of a 36·9 vol.% slurry over 35°C at 42·9 vol.% and becomes negligible for green bodies made from suspensions with solids loadings higher than 50 vol.%. This means that for a solids content above 50 vol.% no differential shrinkage over the length (8 cm) of a compact occurs. These findings agree with the results of the porosity measurements (Table 1), crack formation (Table 2) and the gradient degree in light scattering of polished cross sections (lengthways

Table 2. Density and appearance of sintered cylinders (1400°C/6 h)

Slurry (vol.%)	*Sintered density (%TD)*	*Sintered compact*
36·9	99·72	Cracks, gradient
42·9	99·50	Cracks, gradient
50·1	99·44	OK
51·7	99·47	OK
53·4	99·40	OK
56·8	99·35	OK

of centrifugation axis) of sintered cylinders produced from slurries containing less than 50 vol.% solids.

3.6 Sintered density

Table 2 shows the differences in sintered density after 6 h at 1400°C for the entire cylinders. Centrifugal casting leads to sintered densities of more than 99·3%TD which are significantly higher than those of isostatically pressed material (98·6 %TD). Highest densities were reached with cylinders made from slurries with low solids contents (36·9 and 42·9 vol.%), but, however, the particle separation led to the formation of cracks during the firing process, as well as to a gradient degree of

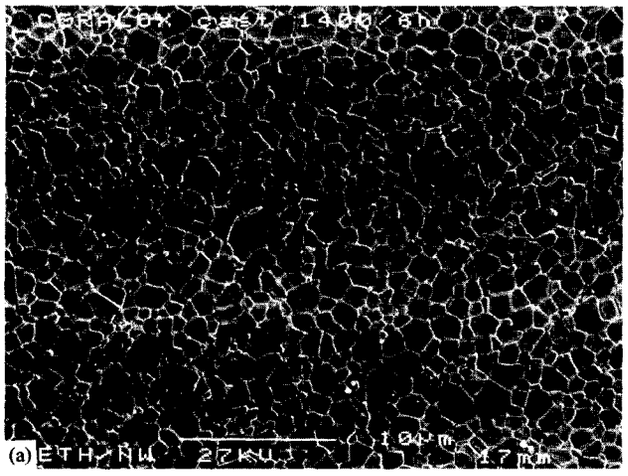


Fig. 13. Microstructures of sintered compacts: (a) centrifugally cast (53·4 vol.% slurry, 4000 *g*/90 min); (b) isostatically pressed.

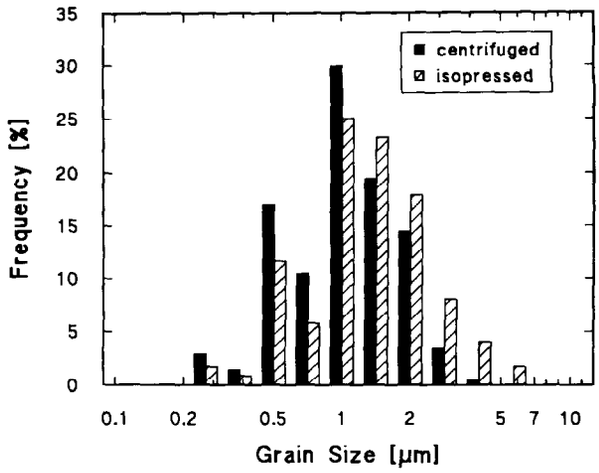


Fig. 14. Statistical evaluation of microstructures of sintered compacts.

light scattering over the length of the cylinder. This is due to the different sintering kinetics of larger and smaller particles (and larger and smaller pores) at the top and bottom part of the cylinder, respectively. Slurries containing more than 50 vol.% solids gave crack-free sintered parts that showed densities of about 99·4%TD and homogeneous light scattering throughout the entire length of a cylinder.

3.7 Microstructure

At the same final density (99·4%TD) a finer and more homogeneous microstructure is achieved by centrifugal casting compared to isopressed samples, as can be seen from Fig. 13. A statistical evaluation of the micrographs is shown in Fig. 14. The average grain size measured was 1·1 μm for the centrifuged samples and 1·6 μm for the isopressed alumina. The most important difference lies in the homogeneity of the microstructure. Isostatically pressed alumina shows grains of up to 10 μm in size, whereas the maximum grain size in cast alumina does not exceed 6 μm. Grain growth can occur in densified regions and its speed is strongly dependent upon the temperature. The lower the sintering temperature to reach a high final density, the better for the microstructural evolution which will be finer and more homogeneous.

3.8 Flaw size distribution

Figure 15 shows polished surfaces of cast and isostatically pressed alumina of comparable density (99·4%TD). By colloidal processing the number and size of larger pores could be drastically reduced. This can be more clearly seen from Fig. 16 which shows a statistical evaluation of the flaw distribution of centrifugally cast and isopressed samples. The largest pores in sintered compacts from cast alumina reach a size of 20–30 μm, which is about 4–5 times smaller than the largest

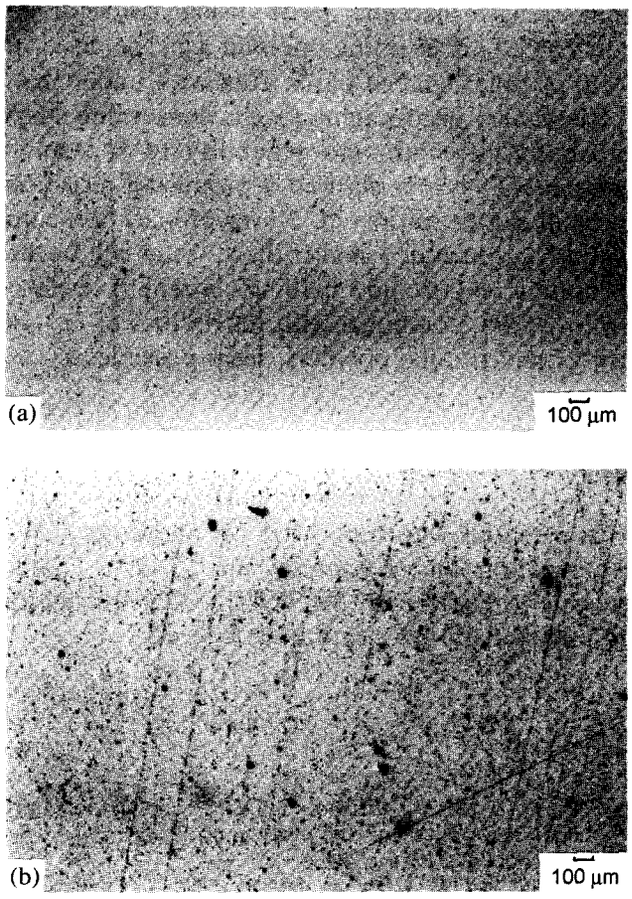


Fig. 15. Polished surfaces of sintered compacts: (a) centrifugally cast (53·4 vol.% slurry, 4000 *g*/90 min); (b) isostatically pressed.

pores found in isopressed material (90–120 μm). The area investigated on both samples was 5·6 mm^2. The total pore volume equals 5 ppm of the total volume.

Fracture surfaces of centrifuged bending test specimens were examined with SEM (Fig. 17) and the fracture origins were recognized to be agglomerates having a size of 20–30 μm. This is typical for the maximum flaw size of the centrifuged compacts of this study and is in accordance with the Griffith relationship for the case of a fracture

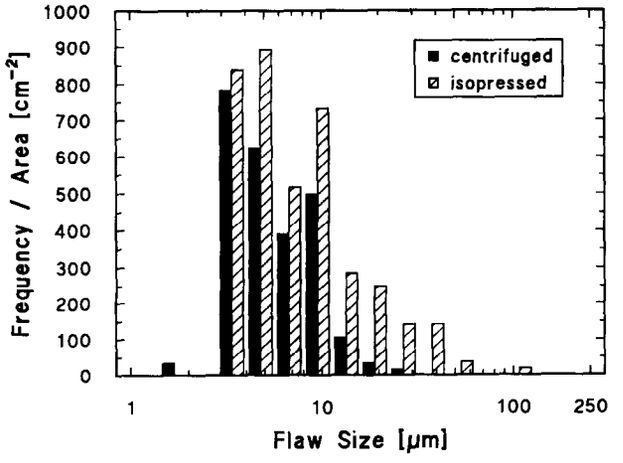


Fig. 16. Statistics of flaw distribution in sintered compacts.



Fig. 17. Typical fracture surface of centrifuged bending test specimen showing the fracture origin.

toughness of 3·8 MPa $\sqrt{m}$ and an average bend strength of 540 MPa, (geometry factor Y-1168).

3.9 Mechanical properties and reliability

The advantages of centrifugal casting are obvious when comparing the mechanical properties, as shown in Fig. 18. These data were acquired from four-point-bending tests of batches of at least 21 specimens. The number of specimens is large enough to give good Weibull statistics.[35] The average strength of cast alumina was 540 MPa; an increase of 60% compared to isostatically pressed material (340 MPa). The Weibull modulus m of the centrifuged material was more than tripled, reaching 23·9. For the statistical calculation, the fracture probability estimator with the largest bias (mean rank value: $P_{if} = i/(n + 1)$) was chosen, leading to the lowest m-values of all known estimators.[36,37] These results prove that centrifugal casting provides the possibility of increasing the reliability of α-alumina ceramics up to the level requested by design engineers.

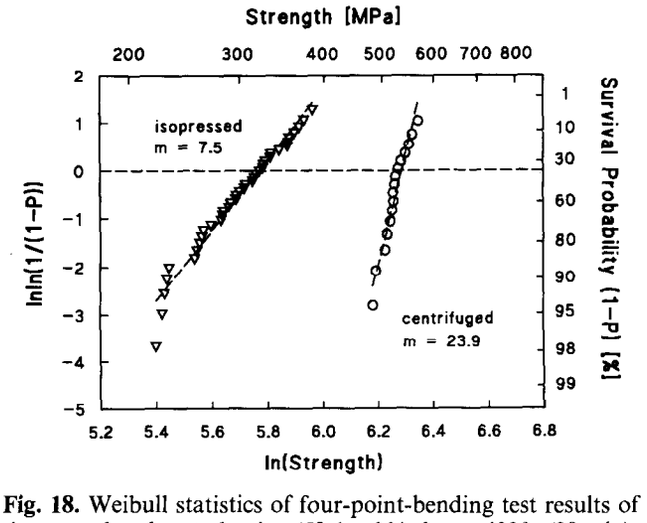


Fig. 18. Weibull statistics of four-point-bending test results of isopressed and cast alumina (53·4 vol.% slurry, 4000 *g*/90 min).

Table 3. Comparison of typical properties for cast and isostatic-pressed compacts

Property	*Centrifugal casting*	*Isostatic pressing*
Green density (%TD)	68	59
Sintered density (%TD)		
1400°C/6 h	99·4	98·6
1500°C/2 h	99·7	99·5
Linear shrinkage (%)	12	17
Average grain size (μm)	1·1	1·6
Maximum grain size (μm)	6	10
Maximum flaw size (μm)	20–30	90–120
Average strength (MPa)	540	340
Weibull modulus m	23·9	7·5

3.10 Comparison of centrifugal casting and isostatic pressing

In Table 3 some properties of compacts made via centrifugal casting and isostatic pressing are shown. The cast sample sinters to ≥99·4%TD at 1400°C with 6 h holding time, whereas the pressed sample requires a sintering temperature of 1500°C and 2 h to reach the same density. Centrifugal casting of high-solids-content slurries provides ceramic parts which have high green densities (15% higher than isopressed) and narrow pore size distributions and therefore closing of the structure is completed at lower temperatures and shrinkage is smaller. Higher green densities in combination with narrow pore size distributions leads to smaller grain sizes due to lower sintering temperatures. The largest flaws in the centrifuged parts are due to agglomerates not eliminated in the slurry preparation sequence. It can be expected that even better slurry preparation combined with smaller sieve size (from 1 to 5 μm) will reduce the maximum flaw size even more, leading to even higher strength values at higher reliabilities.

4 Summary and Outlook

α-Alumina ceramic components showing high reliability at high bend strength levels can be obtained from commercially available powders via centrifugal casting. Wet processing of ceramic powders and subsequent centrifugal casting of high-solids-content suspensions provides a route to producing parts that show better particle packing and a smaller number and size of flaws than dry processed components. High green and sintered densities as well as homogeneous microstructures were achieved by centrifugal casting α-alumina with a four-point-bend strength of 540 MPA and a reliability characterized by a Weibull modulus of m = 23·9 could be obtained. Centrifugal casting of high-solids-loading slurries is a very promising way to form highly reliable, high-strength ceramic parts using conventional powders. This forming method can be used to form complex shaped parts, even with undercuts.

These very encouraging results concerning shape capability, strength and reliability of α-alumina components clearly showed a promising direction, but still can be improved. Slurry preparation eliminating agglomerates smaller than 30 μm will further increase strength and reliability. Strength levels of up to 1 GPa, combined with reliabilities of m = 40 using conventional powders, seem possible.

Acknowledgements

This research was supported by the Swiss KWF organization under contract no. 2243.1. Thanks are due to Dr Rieger, METOXIT AG, for helpful discussions and his continuous interest.

References

1. Alford, N. McN., Birchall, J. D. & Kendall, K., Engineering ceramics — the process problem. *Mater. Sci. Technol.*, **2**(4) (1986) 329–36.
2. Birchall, J. D., High strength ceramics: problems and possiblities. *J. Phys. Chem. Solids*, **49**(8) (1988) 859–62.
3. Gauckler, L. J., Processing and properties of advanced ceramics. In *High-Tech Ceramics: Viewpoints and Perspectives*, ed. G. Kostorz. Academic Press, 1989, pp. 59–105.
4. Lange, F. F., Fabrication reliability of ceramics: controlling of flaw populations. *Mater. Res. Soc. Symp.*, **60** (1986) 143–52.
5. Ross, J. W., Miller, W. A. & Weatherly, G. C., Computer simulation of sintering in powder compacts. *Acta Metall.*, **30** (1982) 203–12.
6. Rhodes, W. H., Agglomerate and particle size effects on sintering yttria-stabilized zirconia. *J. Am. Ceram. Soc.*, **64**(1) (1981) 19–22.
7. Petzow, G. & Exner, H. E., Particle rearrangement in solid state sintering. *Z. Metall. K.*, **67** (1976) 611–17.
8. Exner, H. E. & Bross, P., Material transport, rate and stress distribution during grain boundary diffusion driven by surface tension. *Acta Metall.*, **27** (1978) 1007–12.
9. Barringer, E. A. & Bowen, H. K., Formation, packing, and sintering of monodispersed TiO_2 powders. *J. Am. Cer. Soc.*, **65**(12) (1982) C-199.
10. Occhionero, M. A., Influence of particle packing on microstructural development during sintering. Case Western Reserve University, PhD 8611452, 1986.
11. Kendall, K., Alford, N. McN. & Birchall, J. D., The strength of green bodies. *British Ceramic Proceedings, Special Ceram.*, **8**(37) (1986) 255–65.
12. Alford, N. McN., Birchall, J. D. & Kendall, K., High-strength ceramics through colloidal control to remove defects. *Nature*, **330**(5) (1987) 51–3.
13. Persson, M., In *Surfactant and Colloid Chemistry in Ceramic Processing*, eds R. J. Pugh & L. Bergström. Marcel Dekker Inc., New York, 1994, pp. 292–4.
14. Kendall, K., Alford, N. McN., Tan, S. R. & Birchall, J. D., Influence of toughness on Weibull modulus of ceramic bending strength. *J. Mater. Res.*, **1**(1) (1986) 120–3.
15. Pober, R. L., Product and process integration: the need for a ceramics manufacturing science. In *High-Tech Ceramics: Viewpoints and Perspectives*, ed. G. Kostorz. Academic Press, 1989, pp. 17–28.

16. Lange, F. F., Powder processing science and technology for increased reliability. *J. Am. Ceram. Soc.*, **72**(1) (1989) 3–15.
17. Buscall, R., The sedimentation of concentrated colloidal suspensions. *Colloids and Surfaces*, **43** (1990) 33–53.
18. Lange, F. F., Forming a ceramic by flocculation and centrifugal casting. US Patent 4 624 808, 25.11.1986.
19. Chang, J. C., Velamakanni, B. V., Chang, J. C., Lange, F. F. & Pearson, D. S., Centrifugal consolidation of Al_2O_3 and Al_2O_3/ZrO_2 composite slurries versus interparticle potentials: particle packing and mass segregation. *J. Am. Ceram. Soc.*, **74**(9) (1991) 2201–4.
20. Beylier, E., Pober, R. L. & Cima, M. J., Centrifugal casting of ceramic components. In *Ceramic Powder Science III, Ceramic Transactions*, **12**, eds G. L. Lessing, S. Hirano & H. Hausner. American Ceramic Society Inc., Westerville, Ohio, 1990, pp. 529–36.
21. Lange, F. F., Sinterability of agglomerated powders. *J. Am. Ceram. Soc.*, **67**(2) (1984) 83–9.
22. Salmovich, E. B. & Lange, F. F., Densification of large pores: I. Experiments. *J. Am. Ceram. Soc.*, **75**(9) (1992) 2498–508.
23. Shih, W. H., Kim, S. I., Shih, W. Y. & Aksay, I. A., Consolidation of colloidal suspensions. *Mater. Res. Soc. Symp.*, **180** (1980) 167–72.
24. Bergström, L., Schilling, C. H. & Aksay, I. A., Consolidation behavior of flocculated alumina suspensions. *J. Am. Ceram. Soc.*, **75**(12) (1992) 3305–14.
25. Shih, W. H., Shih, W. Y., Kim, S. I. & Aksay, I. A., Equilibrium-state density profiles of centrifuged cakes of flocculated suspensions. *Mater. Res. Soc. Symp.*, **289** (1993) 251–8.
26. Abel, J. S., Stangle, G. C., Schilling, C. H. & Aksay, I. A., Sedimentation in flocculating colloidal suspensions. *J. Mater. Res.*, **9**(2) (1994) 451–61.
27. Shih, W. H., Shih, W. Y., Kim, S. I. & Aksay, I. A., Equilibrium-state density profiles of centrifuged cakes. *J. Am. Ceram. Soc.*, **77**(2) (1994) 540–6.
28. Nagae, H., Ito, A. & Toriyama, M., Forming of ceramics by centrifugal casting. *Kinki Chem. Soc. Jpn Chem. Express*, **5**(3) (1990) 173–6.
29. Huisman, W., Graule, T. & Gauckler, L. J., High quality ceramics by centrifugal slip casting. *Third Euro-Ceramics*, **1** (1993) 537–42.
30. Huisman, W., Graule, T. & Gauckler, L. J., Centrifugal casting of zirconia (TZP). *J. Eur. Ceram. Soc.*, **13**(1) (1994) 33–9.
31. Hidber, P., Baader, F., Graule, T. & Gauckler, L. J., Sintering of wet milled centrifugal slip casting. *J. Eur. Ceram. Soc.*, **13**(4) (1994) 211–19.
32. Underwood, E. E., *Quantitative Stereology*. Addison-Wesley Publ. Co., Reading, Mass., 1970, pp. 24, 140.
33. Evans, A. G. & Charles, E. A., Fracture toughness determination by indentation. *J. Am. Ceram. Soc.*, **59**(7–8) (1976) 371–2.
34. Scherer, G. W., Theory of drying. *J. Am. Ceram. Soc.*, **73**(1) (1990) 3–14.
35. Balaba, W. M., Stevenson, L. T. & Wefers, K., Probability estimators for Weibull statistics of the failure strengths of brittle powder compacts. *J. Mater. Sci. Lett.*, **9** (1990) 648–9.
36. Bergmann, B., On the estimation of the Weibull modulus. *J. Mater. Sci. Lett.*, **3** (1984) 689–92.
37. Bergmann, B., On the variability of the fracture stress of brittle materials. *J. Mater. Sci. Lett.*, **4** (1985) 1143–6.

Journal of the European Ceramic Society 15 (1995) 823–831
© 1995 Elsevier Science Limited
Printed in Great Britain. All rights reserved
0955-2219(95)00054-2
0955-2219/95/$9.50

The Production of Reinforced Aluminium/Alumina Bodies by Directed Metal Oxidation

X. Gu & R. J. Hand

Department of Engineering Materials, University of Sheffield, Sir Robert Hadfield Building, PO Box 600, Mappin Street, Sheffield, S1 4DU, UK

(Received 19 August 1994; revised version received 21 February 1995; accepted 10 March 1995)

Abstract

Both unreinforced and model filler reinforced aluminium/alumina bodies have been produced by directed metal oxidation from pure aluminium parent metal blocks externally doped with magnesium. It is shown that there are some differences between the growth processes in the two cases and that in particular the presence of the filler in the production of reinforced bodies restricts the supply of oxygen to the reaction front and that an oxygen-depleted atmosphere may arise locally, leading to areas where aluminium nitride is produced rather than alumina.

1 Introduction

The production of ceramic materials by the directed metal oxidation process developed by the Lanxide Corporation, Delaware, USA, has received increasing attention recently. The process involves the oxidation of a bulk molten metal by a gas through a directed growth process to produce an interconnected ceramic reaction product, that may contain several percent of residual metal. Reinforcements may be readily incorporated in the ceramic/metal body by allowing the oxidation reaction product to grow through, and thereby incorporate, a filler material such as ceramic particles, platelets or fibres. Dopants are required to initiate and maintain the growth process and it is this feature that distinguishes it from other reaction bonding processes. Growth is limited by the presence of inert (barrier) powders which may used to define the shape of the desired product.

Much of the published work[1–3] in this area has concentrated on the production of unreinforced Al_2O_3/Al bodies grown from specially prepared aluminium alloys containing both Mg and Si as dopant elements. Nagelberg[4] has studied directed growth from an Al–Mg alloy, but in this case initiation required scratching the initial oxide scale to expose the molten Al alloy directly to the air atmosphere. Xiao and Derby[5,6] have shown that MgO may be used as an external dopant to initiate growth with pure Al.

In this paper, we concentrate on the effects of reinforcement on the production of Al_2O_3/Al bodies from pure Al with Mg as an external dopant element. To this end both unreinforced and model reinforced bodies have been produced. The model reinforced bodies were produced by growth into coarse alumina fillers (this filler could be readily distinguished from the alumina reaction product generated by the oxidation process). The microstructural development and the relationships between the growth mechanisms for both unreinforced and reinforced directed metal oxidation bodies have been investigated and are discussed below in some detail.

2 Experimental Procedure

99·8% pure Al (Alcan) blocks were placed on a bed of fine alumina powder (A17, Alcoa) contained within a mullite crucible. A mullite tube was placed on top of the Al block and further fine alumina was packed round the outside of this tube. Powdered reagent-grade Mg (5 wt%, Fisons) was either placed inside the tube directly on the surface of the Al block as a dopant (in the production of unreinforced bodies) or mixed with coarse tabular alumina (8–14 mesh, Alcoa) and the mixture placed in the tube above the Al block (to produce model reinforced bodies). In either case the tube was then withdrawn leaving the arrangements are shown in Fig. 1.

The prepared systems were heated in air at 200°C per hour in a muffle furnace to a soak temperature of 1180°C. This temperature was maintained for 15 or 24 h, after which the samples were cooled to room temperature inside the furnace.

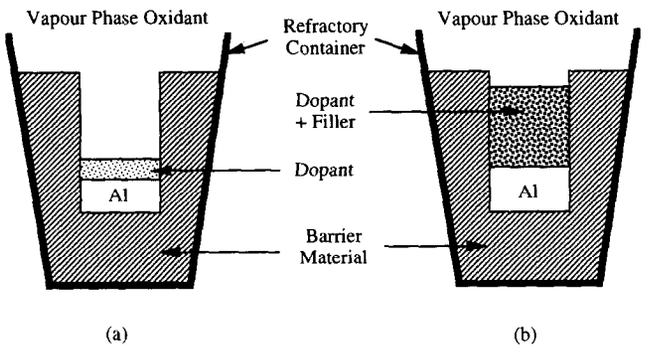


Fig. 1. Experimental arrangements used; (a) unreinforced body system: dopant directly placed on Al block, (b) reinforced body system: dopant mixed with filler and mixture placed above Al block.

Qualitative phase analysis of both the starting materials and fired specimens was undertaken by X-ray diffraction (XRD). Fired samples were sectioned parallel or perpendicular to the growth direction and the different regions analysed by XRD. These samples were subsequently mounted in epoxy resin, ground and diamond-polished to 1 μm, before carbon coating for examination with both scanning electron microscopy (SEM) (Jeol JSM 6400) and energy dispersive spectroscopy (EDS) (Link Analytical 6276).

3 Results

3.1 Unreinforced Al_2O_3/Al composites

After 24 h oxidation at 1180°C, the Al-block was partially consumed; the reaction product had an irregular shape with a smooth surface. Cross sections of this reaction product showed that it contained substantial amounts of aluminium in wide channels 3–5 μm in diameter, it is clear that the oxidation process was not completed. XRD showed that the product was predominantly Al and $MgAl_2O_4$, (magnesium aluminium spinel) with some Al_2O_3 present (Fig. 2).

SEM and EDS indicated the presence of several regions within the sample. The bulk of the sample consisted of unoxidised aluminium interspersed with a ceramic phase that contained both Al and Mg and which was presumed to be spinel (Fig. 3) as XRD failed to detect either Mg or MgO. On the outer surface of the product, there was a denser Mg-containing layer, which was about 10 μm thick; the lack of Mg or MgO detected by XRD indicated that this was also spinel (Fig 4).

3.2 Reinforced Al_2O_3/Al bodies

On heating the system with filler to 1180°C for 15 h, a small amount of growth product was obtained. Macroscopic inspection of a cross-section of the growth product showed that although infiltration of the filler/dopant mixture by the molten metal occurred during the initial stages of the oxidation reaction, it was limited in extent and most of the mixture (filler and dopant) remained unimpregnated by either metal or ceramic. XRD (Fig. 5) showed that the unimpregnated mixture contained Al_2O_3, $MgAl_2O_4$ and MgO but no free Mg. In the growth product, although both α-Al_2O_3 and Al were present, the filler was the main source of α-Al_2O_3; Mg and $MgAl_2O_4$ were also present; again no MgO was detected.

Microanalysis of the oxidised sample provided further confirmation that Al infiltrated into the base of the filler mass close to the metal reservoir (Fig. 6). Within the metallic phase, inclusions containing Al, Mg and O were observed by EDS, which again suggested that they consisted of $MgAl_2O_4$. In the upper region of the growth product, ceramic

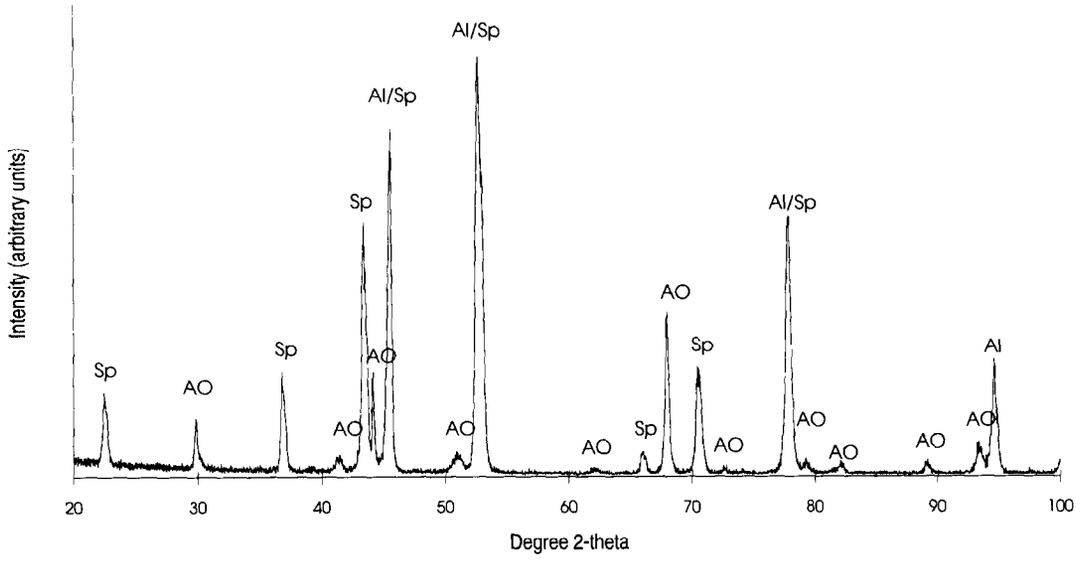


Fig. 2. XRD pattern from unreinforced body produced by firing for 24 h at 1180°C AO: Al_2O_3; Sp: $MgAl_2O_4$.

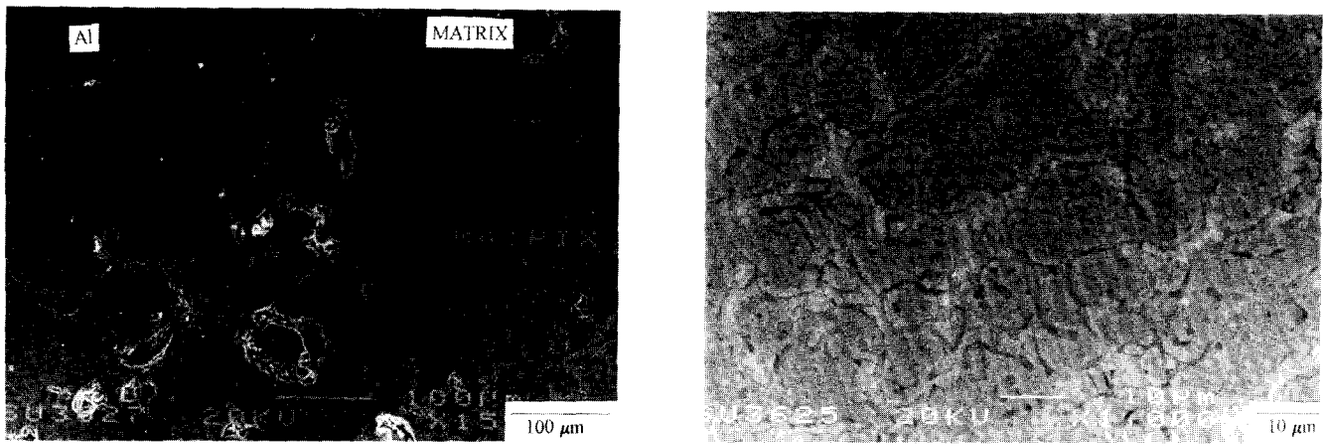


Fig. 3. SEM image from unreinforced growth body fired for 24 h at 1180°C. (a) Secondary electron image of product which consists of both unoxidised Al closest to metal reservoir and ceramic matrix growth; (b) back-scattered image of matrix region which contains connected ceramic (dark) inter-spersed with metal (light) channels.

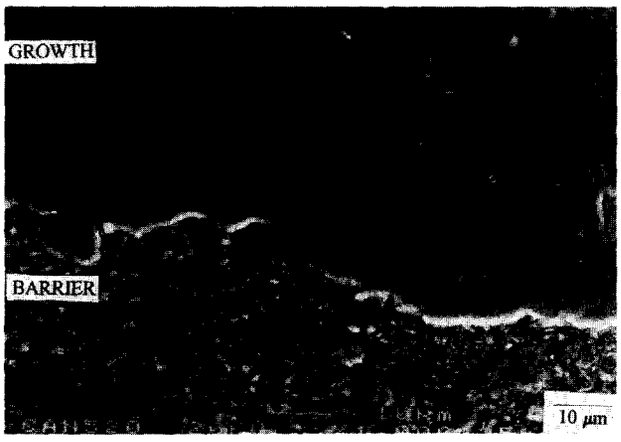


Fig. 4. SEM image of top region of unreinforced growth body fired for 24 h at 1180°C; the outermost layer in the product is spinel.

particles were developing within the metallic phase. The oxidation front was rather porous and extended over a scale of several particle diameters, with the extent of the reaction product increasing towards the central axis of the sample. It appears that layers of matrix grew outwards from the surface of the filler particles (Fig. 7a). The growth matrix contained unoxidised aluminium channels and was covered by a Mg-containing layer thought to be $MgAl_2O_4$ (Fig. 7b).

By comparison, after 24 h at 1180°C the Al-block was totally consumed, and the resultant reaction product encapsulated the filler particles. It was also observed that, in the completely oxidised sample, the distribution of Al_2O_3 filler particles was quite uniform, although some large holes

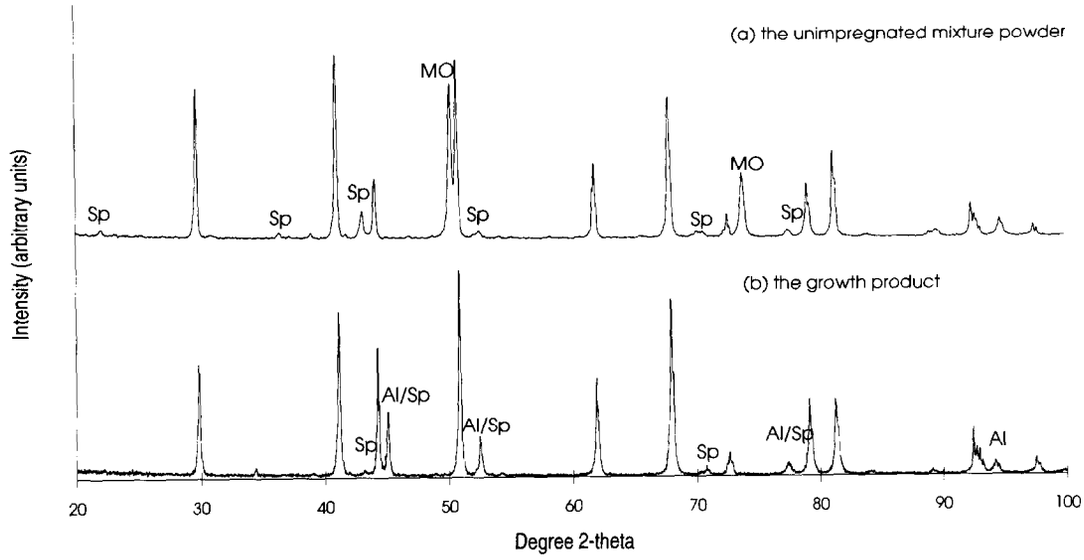


Fig. 5. XRD pattern from reinforced body system fired for 15 h at 1180°C. (a) Unimpregnated mixture powder, (b) growth product. Al: aluminium, Sp: $MgAl_2O_4$, spinel; MO: MgO; unlabelled peaks are Al_2O_3.

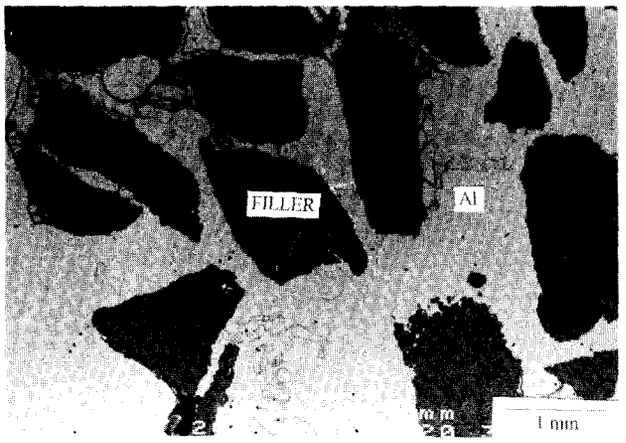
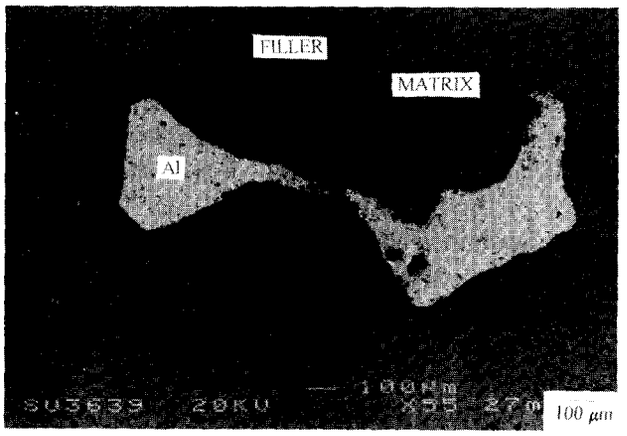


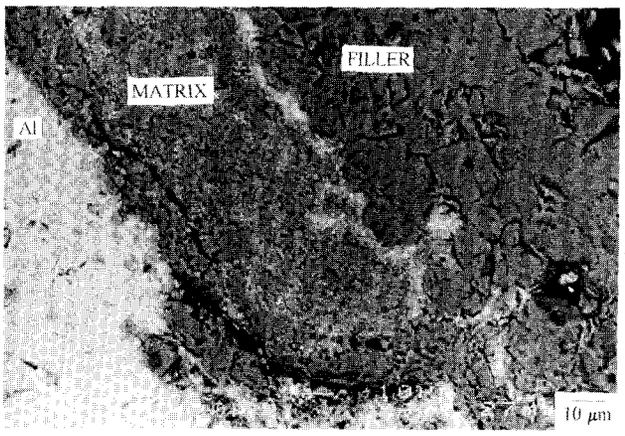
Fig. 6. SEM image from bottom region of reinforced growth body fired for 15 h at 1180°C showing aluminium (white) infiltrated into filler mass (dark) and some ceramic traces (grey) formed within metallic phase.

were present, especially towards its base. In this case XRD (Fig. 8) showed that Al, α-Al_2O_3 and $MgAl_2O_4$ were all present but there was still no MgO and there was also no longer any free Mg. Significantly, aluminium nitride, AlN, was also detected by XRD in this sample.

Microanalysis of the sample fired for 24 h at 1180°C showed that it consisted of an Al_2O_3/Al matrix with some $MgAl_2O_4$. In the middle of part of the product, AlN instead of Al_2O_3 matrix could be observed (Fig. 9). Three different structures could be clearly distinguished. The first was filler particles; whilst the second, close to the filler, was the matrix growth, which consisted of Al_2O_3 with a surface layer about 5 μm thick, of $MgAl_2O_4$. The third structure which was immediately next to the $MgAl_2O_4$ layer, consists of needles which EDS indicates contain both Al and N and which were



(a)



(b)

Fig. 7. SEM image from upper region of reinforced growth body fired for 15 h at 1180°C showing (a) that matrix grew outwards from individual filler particles and (b) metal channels covered by a $MgAl_2O_4$ layer.

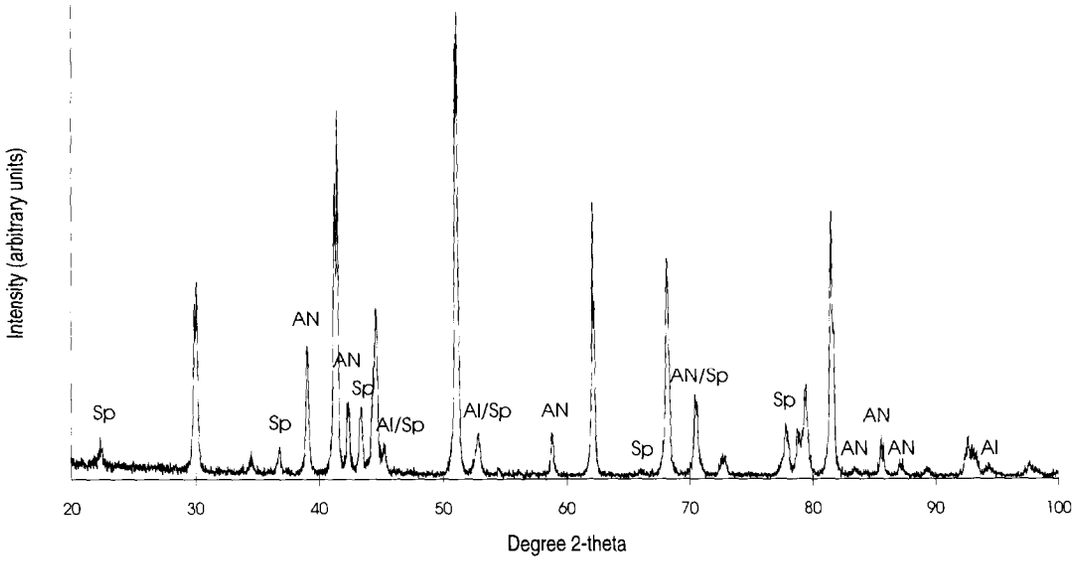
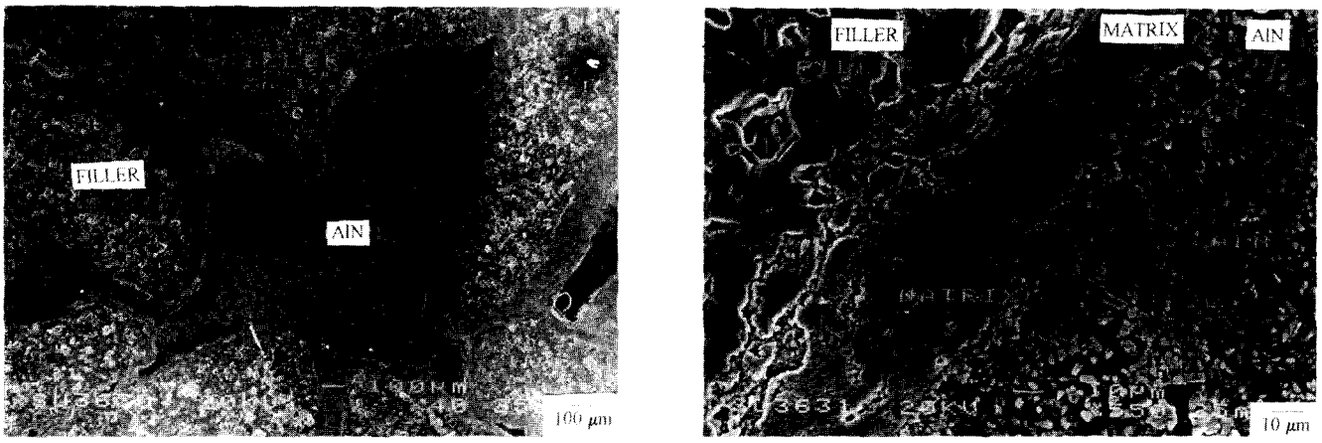


Fig. 8. XRD pattern from reinforced body system fired for 24 h at 1180°C. Al: aluminium; AN: aluminium nitride; Sp: $MgAl_2O_4$ spinel; unlabelled peaks are Al_2O_3.



(a) (b)

Fig. 9. SEM image from middle region of reinforced growth body fired for 24 h at 1180°C showing (a) AlN instead of Al_2O_3 formed amongst filler particles; (b) enlargement of part of (a).

thus identified as the aluminium nitride detected by XRD in this sample.

4 Discussion

In the current work, directed metal oxidation from a pure aluminium block with a surface doping of Mg particles has been studied, rather than growth from an aluminium alloy which has been reported elsewhere. Differences in microstructure between these two types of system have been observed, implying that there are differences in growth mechanism between Al–Mg alloy systems and an externally doped pure Al system.

Some mechanisms have been proposed to explain the directed oxidation of the Al–Mg–Si alloy system.[4,7,11] These are, in general, based on the initiation of the reaction sequence in the aluminium/alumina system by magnesium. For example, Xiao and Derby reported that when pure MgO was placed on the surface of a commercial-purity Al alloy (>99·5%) and oxidised at 1200°C for 7 h, a reaction occurred. Nagelberg[4] pointed out that oxidation product can also be obtained from the Al–Mg alloy; however, the initiation of composite growth required the mechanical disruption of the protective oxide formed during initial heating to the growth temperature.

When aluminium is exposed to oxygen in the atmosphere, a persistent oxide film is soon formed by the following reaction:

$$2Al(s) + \frac{3}{2} O_2(g) \rightarrow Al_2O_3(s). \qquad (1)$$

However, if Mg is present on the surface of the Al-block then, according to the Ellingham diagram,[12] Mg is oxidised first. For example, Bahadur[13] reported that the addition of 0·9 wt% Mg to pure Al at temperatures of more than 500°C caused the formation of MgO at the surface instead of α-Al_2O_3. In addition Al–Mg alloys favour the formation of both MgO and $MgAl_2O_4$ for Mg concentrations above 0·02% and thus Mg is thought to prevent the normal passivation of aluminium by the formation of aluminium oxide film. Haginoya[14] demonstrated by XRD that during the initial oxidation of Al–Mg alloys, the amount of MgO first increased and then decreased with time, while the $MgAl_2O_4$ content increased continuously with time as bulk depletion of Mg in the alloys results in the eventual conversion of nearly all the MgO to $MgAl_2O_4$.

In the present study MgO was not observed, but EDS has shown that most of the Mg was found in regions which also contained Al and these regions are thereby presumed to be the $MgAl_2O_4$ identified by XRD. This is the case even for reaction products formed by heating to 1180°C followed immediately by furnace cooling. Those workers who have observed MgO have air-quenched their samples. This difference in cooling rate implies that $MgAl_2O_4$ is more stable than MgO for alloy compositions containing 5% Mg. This is in agreement with the thermodynamic calculations of Xiao and Derby,[5] which show that spinel ($MgAl_2O_4$) is the most stable oxide in contact with liquid aluminium alloys containing greater than about 0·5 wt% Mg.

Based on these observations the following growth mechanisms for both unreinforced and reinforced bodies are proposed. In the following argument all the thermodynamic data has been calculated using the SGSUB database in the MT-DATA package.

4.1 Unreinforced directed metal oxidation

In this case the system is pure aluminium with a surface layer of 5 wt% of powdered Mg. Initially Mg powder is oxidised by the air to form MgO (this occurs before the aluminium melting temperature is reached):

$$2Mg(s) + O(g) \Leftrightarrow 2MgO(s). \quad (2)$$

An interdiffusion reaction between the MgO so formed and the layer of alumina that will be present on the aluminium surface can then convert the MgO layer to spinel:

$$MgO(s) + Al_2O_3(s) \Leftrightarrow MgAl_2O_4(s) \quad (3)$$

This spinel layer is non-protective and because it is easily wetted by aluminium permits infiltration by aluminium. At the aluminium melt surface, the oxygen partial pressure is determined by the equilibrium between Al and Al_2O_3:

$$Al(l) + \frac{3}{2} O_2(g) \Leftrightarrow \frac{1}{2} Al_2O_3(s)$$

for which $\Delta G = 1{\cdot}21842 \times 10^6$ J mol^{-1} at 1453 K. Thus, assuming that condensed materials have unit activity, the partial pressure of oxygen in this region is fixed and low at about $9{\cdot}064 \times 10^{-30}$ atm. The spinel in this region will be in equilibrium with magnesium and alumina. Considering the following equilibrium:

$$MgAl_2O_4(s) + 2Al(l) + O_2(g) \Leftrightarrow 2Al_2O_3(s) + Mg(g) \quad (4)$$

for which $\Delta G = -7{\cdot}27010 \times 10^5$ J mol^{-1} at 1453 K. Again, taking the condensed materials to be at unit activity, this gives an equilibrium constant of $K = P_{Mg}/P_{O_2} = 1{\cdot}36458 \times 10^{26}$ and thus the partial pressure of magnesium at the aluminium melt interface is $1{\cdot}237 \times 10^{-3}$ atm. This is sufficient to move magnesium away from the melt interface to a region with a higher partial pressure of oxygen, where it will recombine to form magnesia:

$$Mg(g) + \frac{1}{2} O_2(g) \Leftrightarrow MgO(s). \quad (5)$$

At 1453 K $\Delta G = -4{\cdot}33283 \times 10^5$ J mol^{-1} for this reaction, and thus using $\Delta G = -RT\ln K$ the equilibrium constant is:

$$K = \frac{1}{P_{Mg} P_{O_2}^{1/2}} 3{\cdot}76703 \times 10^{15}.$$

Recombination will therefore occur when the magnesium reaches a region where the oxygen partial pressure is greater than $4{\cdot}6068 \times 10^{-26}$ atm. As the partial pressure of magnesium drops, a proportionately higher oxygen partial pressure will be required to cause the formation of magnesia. The magnesia formed by this reaction will subsequently react with the Al that reaches it by penetrating the non-protective spinel layer that lies immediately beneath it.

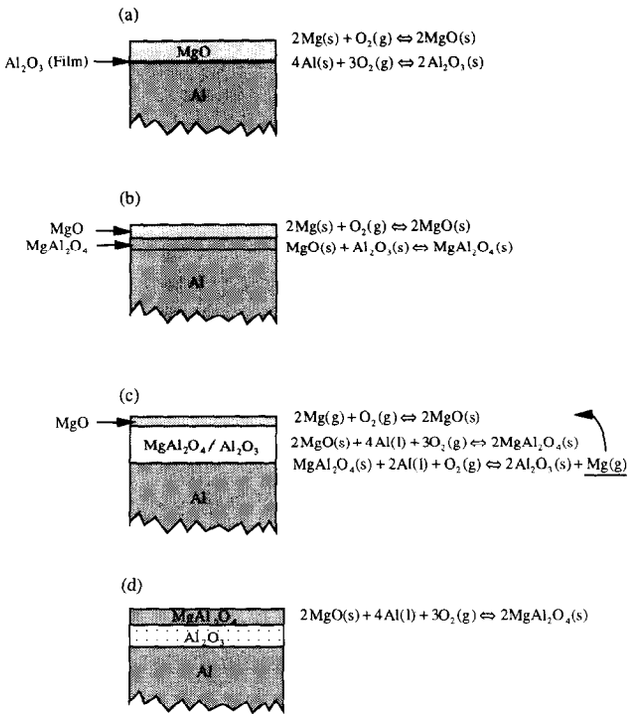


Fig. 10. Schematic diagram of development of cyclic reaction sequence in unreinforced DMOX bodies (time increases from (a)–(d)).

Removal of magnesium from the melt interface will favour the decomposition of the spinel to form alumina and thus a reaction system is set up with a thin magnesia layer overlaying a spinel layer, which in turn overlays an alumina layer. The spinel layer is continually being decomposed at its lower surface to form the next layer of alumina and it is continually being replenished at its upper surface by the reaction of the lower surface of the magnesia layer. The upper surface of the magnesia layer is in turn being replenished. The reaction process, which is shown schematically in Fig. 10, agrees in essence with that given elsewhere.[7,9,10]

Although this reaction sequence implies the existence of a magnesia layer on the growth surface, this was not seen in this work, although it has been reported elsewhere on air-quenched samples. Air-quenching will tend to freeze the sample in the high-temperature state, whereas during furnace cooling there is sufficient time for lower-temperature equilibria, which favour the formation of spinel from magnesia, to develop.

4.2 Reinforced directed metal oxidation Al_2O_3/Al

The introduction of a filler has several effects on both the process reactions and the microstructure of the product. For growth to be possible, the filler must both be wettable by the molten metal

and allow matrix growth through the pores amongst its particles. If there were no wetting of the filler particles by the matrix, the effective reactive surface area of the growing matrix would be reduced in proportion to a volume fraction of the filler. Conversely, if the filler is easily wetted by the growing matrix, the matrix/atmosphere surface area can be increased significantly and this should give enhanced growth rates. The coarse filler used in this work has a very rough surface texture, which according to the Wenzel model implies a high degree of wettability of the filler by molten Al.[15]

In this work, filler particles mixed with magnesium powder are placed on the Al-block. During firing, within the mixture, Mg powder is firstly oxidised to form MgO (reaction (1) above). As well as reacting with the protective alumina layer on the aluminium reservoir surface Mg may also react with the Al_2O_3 filler surface to form $MgAl_2O_4$ by either:

$$MgO(s) + Al_2O_3(s;\ \text{filler}) \Leftrightarrow MgAl_2O_4(s), \quad (6)$$

$$Mg(s) + Al_2O_3(s;\text{filler}) + \frac{1}{2}O_2(g) \rightarrow MgAl_2O_4(s). \quad (7)$$

This is in agreement with the observation of Hitchcock *et al.*[15] who reported that in the wetting of alumina by Al–Mg alloys, the interface was characterised by formation of spinel, which considerably enhanced the wettability of aluminium liquid for alumina.

As described above, the Al-rich melt may also dissolve Mg from spinel to nucleate Al_2O_3 (reaction (4) above), thereby releasing magnesium and thus setting up the same basic reaction sequence that is outlined above. A reaction front will thus gradually propagate through the filler body, leading to the encapsulation of filler in the alumina product.

This time, however, the gas phase reaction between Mg and O_2 can also lead to the deposition of magnesia on the surface of the alumina filler. This magnesia then reacts with the filler to produce spinel. Molten aluminium will react with the spinel layer to produce alumina, thereby freeing magnesium, and the cycle of reactions can proceed locally round each filler particle so that growth proceeds outwards from each filler particle.

This process will, however, deplete oxygen locally; this is especially significant if the filler particles in question are behind the main reaction front. The presence of the filler limits the ingress of oxygen to the growth surface. As a result, when the matrix grows and wetting of the filler proceeds upwards, unreacted regions may remain between filler particles where the oxygen content is very

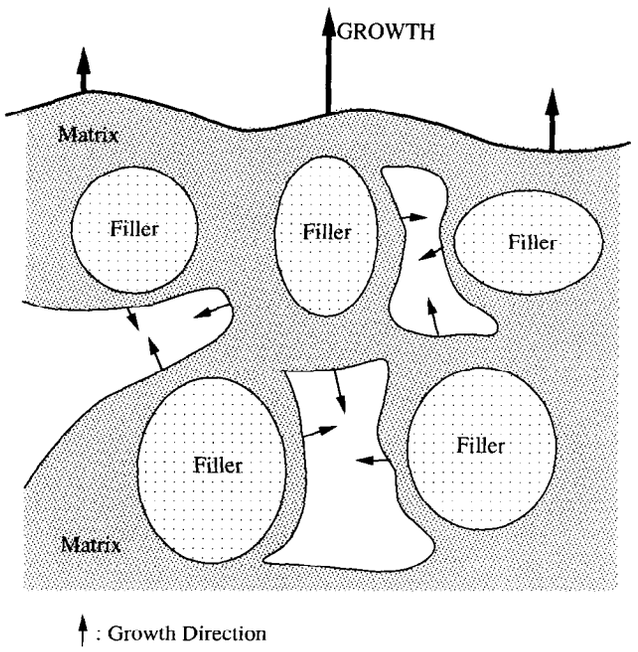


Fig. 11. Schematic diagram of growth mechanism in reinforced DMOX bodies.

low (shown schematically in Fig. 11). If the oxygen content is sufficiently low, with nitrogen (in air) as the diluent, Al liquid reacts with nitrogen to form AlN amongst the filler particles:

$$Al(l) + \frac{1}{2}N_2(g) \Leftrightarrow Aln(s). \quad (8)$$

In fact, high-purity AlN can be prepared by complete nitridation of molten Mg–Al alloys[17] at temperatures above the boiling point of magnesium (1363 K). Scholz and Claussen[17] suggested that magnesium plays a similar role in the nitridation of aluminium as it does in the oxidation, it prevents the formation of a dense nitride layer and thus turns a surface reaction into a volume reaction. For the pure alumina, a threshold oxygen-to-nitrogen ratio exists, above which the oxide and below which the nitride become stable, according to the reaction:

$$2AlN(s) + \frac{3}{2}O_2(g) \Leftrightarrow Al_2O_3(s) + N_2(g). \quad (9)$$

For this reaction at 1453 K $\Delta G = -8{\cdot}94725 \times 10^5$ J mol^{-1} and as long as the $P_{N_2} : P_{O_2}$ ratio is greater than $1 : 3{\cdot}07 \times 10^{-20}$, then the nitride formed by reaction (8) will not be converted to alumina. This condition is achieved because of the tortuous oxygen diffusion path and the removal of oxygen from the local atmosphere within the filler body as either alumina or spinel. Hence both Al_2O_3 and AlN are observed in the central region of the final product. Enough oxygen reaches the top of the reaction product to ensure that only Al_2O_3 or spinel is seen in this region.

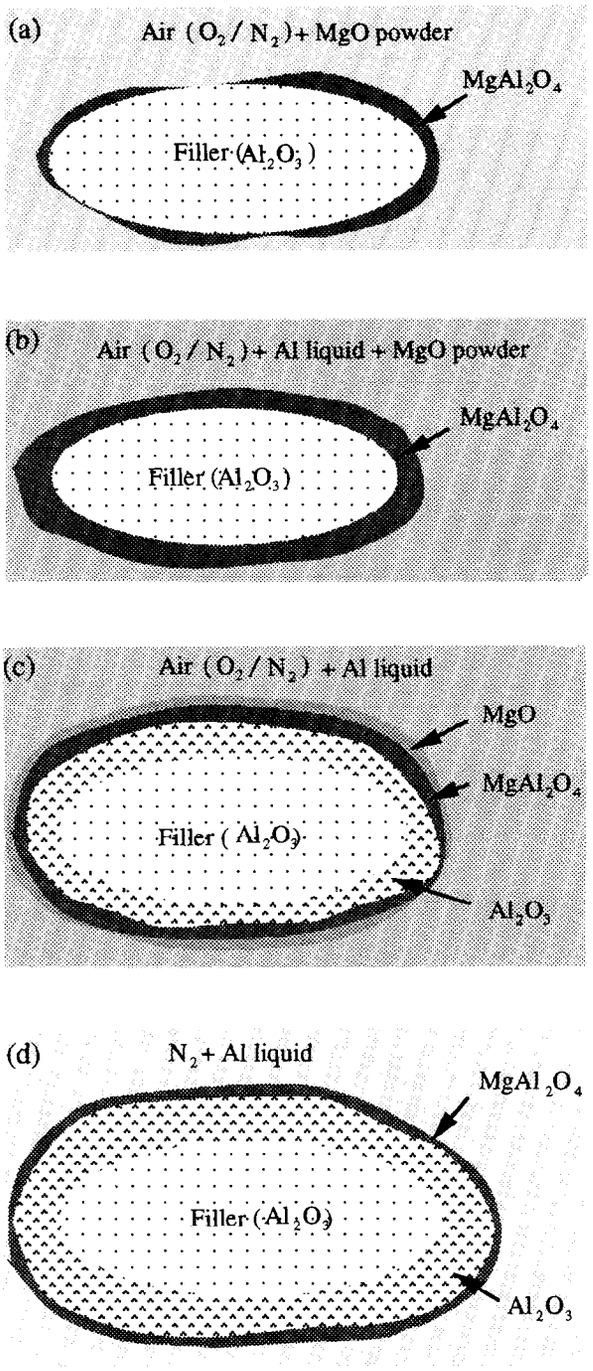


Fig. 12. Schematic diagram of stages of growth with time around filler particles in reinforced DMOX bodies (time increases in going from (a)–(d)).

Thus, although the presence of a filler does not change the overall reaction sequence in the Mg doped Al/Al_2O_3 system, it can give rise to local reaction sequences behind the main reaction front. The local growth mechanism is shown schematically in Fig. 12.

5 Conclusions

The directed metal oxidation growth of both unreinforced and reinforced Al_2O_3/Al bodies from pure Al with an external dopant of Mg has been investigated. The role of the dopant Mg is to promote the formation of a non-protective oxide layer at the surface of the reaction product. This layer is instrumental in developing the subsequent cyclic reaction sequence.

The proposed mechanism is consistent with the experimental results observed, and has the following stages: firstly, $MgAl_2O_4$ is formed via the reaction between MgO which is produced by oxidation of Mg dopant and the passive Al_2O_3 layer which is present on the surface of the Al-block. This ruptures the stable oxide film Al_2O_3; as it thickens, some of the $MgAl_2O_4$ is dissolved by Al melt, and Al_2O_3 is subsequently nucleated. Mg produced via the decomposition of $MgAl_2O_4$ moves to regions of higher oxygen partial pressure, where it forms magnesia and subsequently reacts with Al to reform $MgAl_2O_4$. The cyclic reaction sequence results in the observed product growth.

In the case of reinforced Al_2O_3/Al composite, the filler bed placed on the parent metal affects both reactions and microstructure. With an alumina filler, the magnesia formed during the reaction sequence may react with either aluminium metal or with the filler itself to form spinel. The latter reaction locally consumes oxygen and as the filler limits the ingress of oxygen to oxidation growth reaction fronts that are between the filler particles and behind the main reaction front, oxygen may become locally exhausted, leading to the formation of AlN instead of Al_2O_3. Thus the presence of a filler preform has led to changes in the observed reaction products. The details of such changes obviously depend upon the material used, but they should be considered in the production of ceramic matrix composites by this route.

Acknowledgments

We thank Professor B. B. Argent for his help with calculating the free energy changes in the directed metal oxidation process and for his critical reading of the first draft of this paper. This work was undertaken whilst one of us (X. G.) was in receipt of a scholarship from the University of Sheffield.

References

1. Newkirk, M. S., Urquhart, A. W. & Zwicker, H. R., Formation of Lanxide ceramic composite materials. *J. Mater. Res.*, **1** (1986) 81–9.
2. Urquhart, A. W., Novel reinforced ceramics and metals: a review of Lanxide's composite technologies. *Mater. Sci. & Engng*, **A144** (1991) 75–82.
3. Pickard, S. M., Manor, E., Ni, H., Evans, A. G. & Mehrabian, R., The mechanical properties of ceramic composites produced by melt oxidation. *Acta. Metall. Mater.*, **40** (1992) 177–84.

4. Nagelberg, A. S., Observations on the role of Mg and Si in the directed oxidation of Al–Mg–Si alloys. *J. Mater. Res.*, 7 (1992) 265–8.
5. Xiao, P. & Derby, B., The formation of Al_2O_3/Al composites by controlled oxidation of Al. *Proc. Br. Ceram. Soc.*, **48** (1991) 153–9.
6. Xiao, P. & Derby, B., The formation of Al_2O_3/Al composites by oxidation. *Proc. Br. Ceram. Soc.*, **50** (1993) 191–9.
7. Sindel, M., Travitzky, N. A. & Claussen, N., Influence of magnesium–aluminum spinel on the directed oxidation of molten aluminum alloys. *J. Am. Ceram. Soc.*, **73** (1990) 2615–18.
8. Vlach, K. C., Salas, O., Ni, H., Jagaram, V., Levi, C. G. & Mehrabian, R., Thermogravimetric study of the oxidative growth of Al_2O_3/Al alloy composites. *J. Mater. Res.*, **6** (1991) 1982–95.
9. Salas, O., Ni, H., Jayaram, V., Vlach, K. C., & Levi, C. G., Nucleation and growth of Al_2O_3/metal composites by oxidation of aluminum alloys. *J. Mater. Res.*, **6** (1991) 1964–81.
10. Antolin, S., Nagelberg, A. S. & Creber, D. K., Formation of Al_2O_3/metal composites by the directed oxidation of molten aluminum–magnesium–silicon alloys: Part I. Microstructural development. *J. Am. Ceram Soc.*, **75** (1992) 447–54.
11. Nagelberg, A. S., Antolin, S. & Urquhart, A. W., Formation of Al_2O_3/metal composites by the directed oxidation of molten aluminum–magnesium–silicon alloys: Part II. Growth-kinetics. *J. Am. Ceram. Soc.*, **75** (1992) 455–62.
12. Gaskell, D. R., *Introduction to Metallurgical Thermodynamics*. Scripta Publishing Company, Washington, DC, 1973, pp. 253–68.
13. Bahadur, A., Behaviour of Al–Mg alloys at high temperature. *J. Mater. Sci.*, **22** (1987) 1941–4.
14. Haginoya, I., On oxidation of molten Al–Mg alloys in air. *J. Jpn. Inst. Light Metal.*, **24** (1974) 364–71.
15. Hitchcock, S. J., Carroll, N. T. & Nicholas, M. G., Some effects of substrate roughness on wettability. *J. Mater. Sci.*, **16** (1981) 714–32.
16. McEvoy, A. J., Williams, R. H. & Higginbotham, I. G., Metal/non-metal interfaces. The wetting of magnesium oxide by aluminium and other metals. *J. Mater. Sci.*, **11** (1976) 297–302.
17. Scholz, H. & Claussen, N., Nitridation reactions of molten Al–(Mg, Si) alloys. *J. Mater. Sci.*, **26** (1991) 667–77.

Journal of the European Ceramic Society 15 (1995) 833–839
© 1995 Elsevier Science Limited
Printed in Great Britain. All rights reserved
0955-2219(95)00055-0
0955-2219/95/$9.50

Study of Mechanical and Physicochemical Properties of Polycrystalline Alumina Implanted with Titanium

F. Halitim,[a] S. Paletto,[a] G. Fantozzi[a] & D. Treheux[b]

[a] INSA-GEMPPM, URA 341, 69621 Villeurbanne, France
[b] ECL — Départ Matériaux Mécanique Physique Ecully, France 69631

(Received 10 June 1994; revised version received 21 February 1995; accepted 10 March 1995)

Abstract

A study of ion implantation in polycrystalline alumina has been undertaken aimed at two principal areas. Firstly the measurement of the evolution of mechanical properties in the treated surface, such as hardness and fracture toughness, was undertaken using a Vickers indentation method. These properties are very sensitive to the presence of residual stresses and to the surface microstructure. Secondly a physicochemical study of the treated surface using XRD and SEM techniques in order to identify the parameters that influence the mechanical changes was undertaken.

1 Introduction

The thermomechanical properties of structural ceramics depend strongly on their surface state: e.g. fracture in brittle materials is frequently due to the flaws present on the surface Ion implantation is one of the methods currently used to overcome this difficulty, since the method has the advantage that the net shape and dimensions of the samples are preserved even after the treatment. Most of the studies on ion implantation up to now have been carried out on single crystals.[1–3] We report here on a study of ion implanted polycrystalline alumina. In the case of ion implantation with zirconium, an element which readily oxidises to ZrO_2, which is not miscible in alumina, the formation of a zirconia reinforced alumina composite layer has been observed.[4] It is therefore equally interesting to study the case of titanium implantation in alumina since titanium also oxidises very easily to TiO_2 which has considerable solubility in alumina.[5] Earlier studies on the ion implantation of Ti^+ and Y^+ ions in single crystals has revealed that compressive stresses are created in the implanted zone.[6] These stresses provide a possibility of reducing the spreading of radial cracks on the sample surface, which leads to variations in the surface mechanical properties. It is also possible under certain conditions, to form an amorphous surface layer by this technique. In the case of titanium implantation into sapphire, the amorphous layer is not formed until the fluence is less than 10^{17} ions/cm^2 (at room temperature) or until the temperature is lowered to 77 K with smaller doses.[7] The microstructure of the implanted zone depends generally on the fluence level and the ion energy, as well as on the temperature of implantation, the nature of the ion implanted and the state of the substrate surface.[8] A post-thermal treatment could allow the possibility of other changes in the microstructure and in the phases present in the implanted layer which, in turn, could lead to changes in the mechanical properties. It is therefore necessary to understand the processes that follow the thermal treatment of the ion implanted layers.

2 Experimental

2.1 Sample preparation

Polycrystalline alumina samples (MATROC D995 F) of 99·95% purity and a grain size <3 μm was used in this study. The samples were polished rigorously to the same reference level (fixed roughness).

Polishing grinding

The samples were ground to levels of assured planarity by fixing them on rotating metallic disks and using a diamond paste of 6 μm size for a period of about 20 min under a pressure of 1 bar.

Polishing

Final polishing was done on a felt disc using polycrystalline diamond paste of 3 μm, followed by a diamond paste of 1 μm, the different operations led to a surface roughness < 0·02 μm. To reduce the damages induced by polishing, the samples were post annealed in air for 1 h at 1200°C.

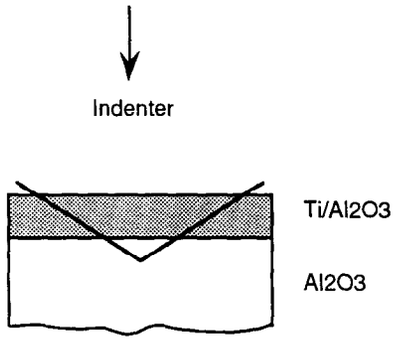


Fig. 1. Indenter into the implanted layer.

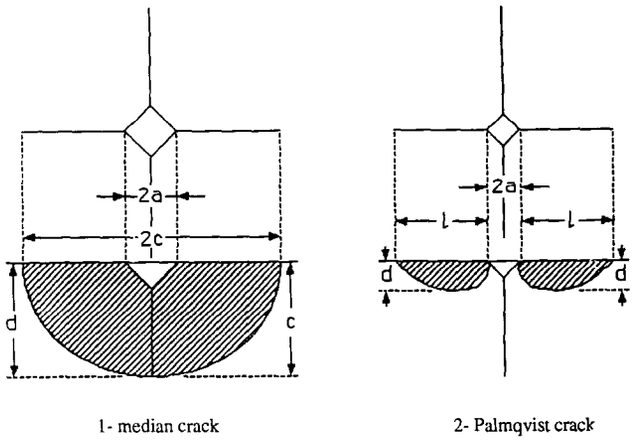


Fig. 2. Crack system.

2.2 Ion implantation

Ion implantation was conducted using monocharged ions produced by an isotopic separator which permits separation of monocharged ions possessing a maximum energy of 110 Kev; doses of 2×10^{16} ions/cm^2 and 10^{17} ions/cm^2 are used in this study. The higher dose is the limit, for this energy, to obtain an implanted layer without amorphisation.[7] During the implantation, the temperature of the target was maintained at the ambient level using a water circulation system for the target holder. After implantation, thermal treatment at three different temperatures 1000, 1200 and 1500°C was conducted for 1 h in air in all cases.

2.3 Vickers hardness

The hardness of the implanted alumina samples was obtained by the ratio of the load to the surface contact area. The Vickers microhardness was measured on a non-instrumented microhardness tester (WOLPERT VTD 11 Type) using loads in the range of 0·1–10 N. The loads were applied to the sample for a period of 30 s in all cases. The unit was fitted with an optical system with two scales of magnification. The samples were subjected to 10 indentations under different loads (0·1, 0·25, 0·5, 1, 2, 3, 5 and 10 N). For the smallest load, the indents were of the order of 3 μm, thus we are unable to observe them accurately. Hence an indirect method has been used, where an optical microscope with its immersion objective attached camera with a high resolution film is used. This permits a magnification of 10000 and increases the possibility of measuring such small indents, without, however, increasing the resolving power of the microscope. The photography enables us to measure the indents with a higher definition (a few %). The implanted layer is about 1000 Å thick and the lowest charge of 0·1 N was used for the indentation, shown schematically in Fig. 1. As stated above, this arrangement indicates the direction of the changes in the hardness value, but not the exact value of the hardness of the implanted layer. If the hardness of the implanted layer increases this increases the measured hardness as well.

2.4 Fracture toughness

The Vickers indentation is particularly suitable to measure the toughness of brittle materials. Recently Liang *et al.*[9] have proposed a unified formula which enables the determination of toughness in both cases of median or Palmqvist's cracks, shown schematically in Figs 2.1 and 2.2.

$$\frac{K_c\Phi}{Ha^{1/2}}\left(\frac{H}{E\Phi}\right)^{0.4}\alpha = \left(\frac{c}{a}\right)^{(c/18\,a)-1.51}$$

$$\alpha = 14\left[1{\cdot}8\left(\frac{4\nu - 0{\cdot}5}{1+\nu}\right)^4\right]$$

where a and c are respectively: the semidiagonal length of indent and the half length of the cracks produced by indentation. Φ is a constant ≈ 3, ν is Poisson's ratio, H the hardness and E the Young's modulus of the material. The load at which the crack is initiated is 2 N. A knowledge of the length of the crack, $2c$, and the hardness of the material, H, would enable the determination of toughness K_{1C}. The polycrystalline material used in this study is an industrial product and possesses a heterogeneous microstructure; this leads to a

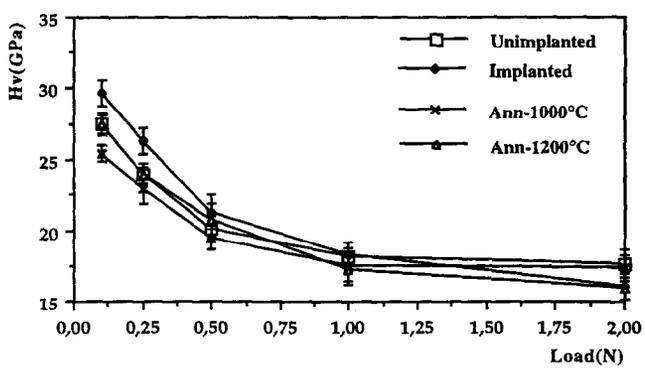


Fig. 3. H_v versus load in Ti^+ implanted Al_2O_3, dose 2×10^{16} ions/cm^2.

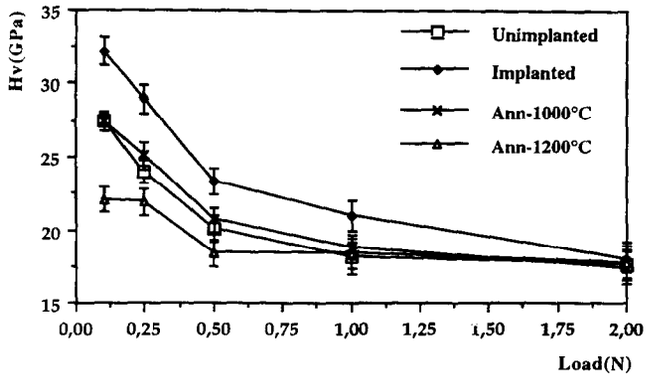


Fig. 4. H_v versus load in Ti^+ implanted Al_2O_3, dose 10^{17} ions/cm^2.

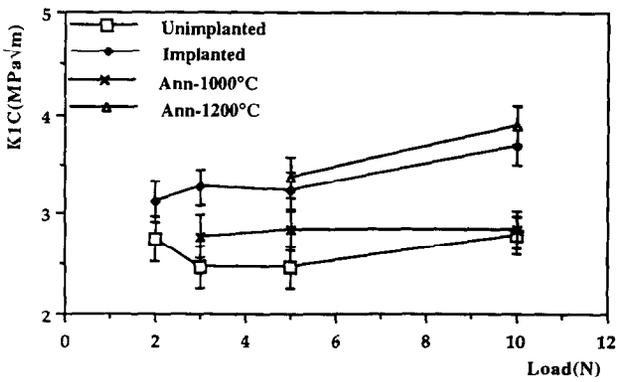


Fig. 6. Variation of K_{1C} as a function of applied load on Ti^+ implanted Al_2O_3, dose 10^{17} ions/cm^2.

dispersion in the measured values of toughness. For this reason, the results showing a large deviation from the mean values are excluded in this study. The mean values derived give an indication of the changes to the material toughness.

3 Experimental Results

3.1 Hardness

The curves of Figs 3 and 4 present the variation of hardness as a function of the load used for different temperatures of annealing and for the two implantation doses mentioned. As stated earlier, the most significant values of hardness are obtained at a load of 0·1 N.

3.2 Toughness

Figures 5 and 6 present the evolution of toughness as a function of load and the temperature of annealing. Cracks occur only after a particular applied load. The K_{1C} values have been calculated for different loads.

3.3 Physicochemical analyses

Figure 7 presents the evolution of the superficial microstructure observed in a scanning microscope at the two implantation dose levels and for different temperatures of annealing. (Fig. 7(a–d)) for the dose 2×10^{16} ions/cm^2 and Fig. 7(e–h) for the dose 10^{17} ions/cm^2 respectively).

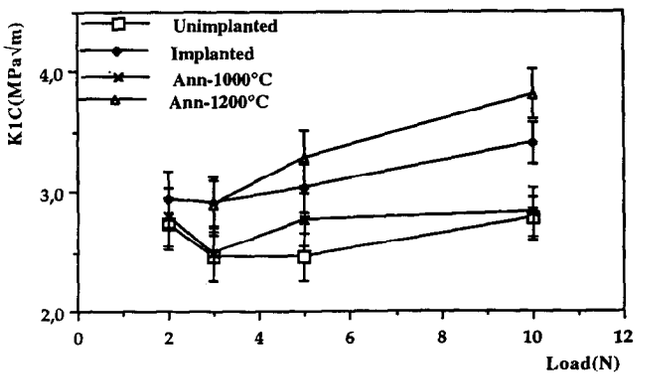


Fig. 5. Variation of K_{1C} as a function of applied load on Ti^+ implanted Al_2O_3, dose 2×10^{16} ions/cm^2.

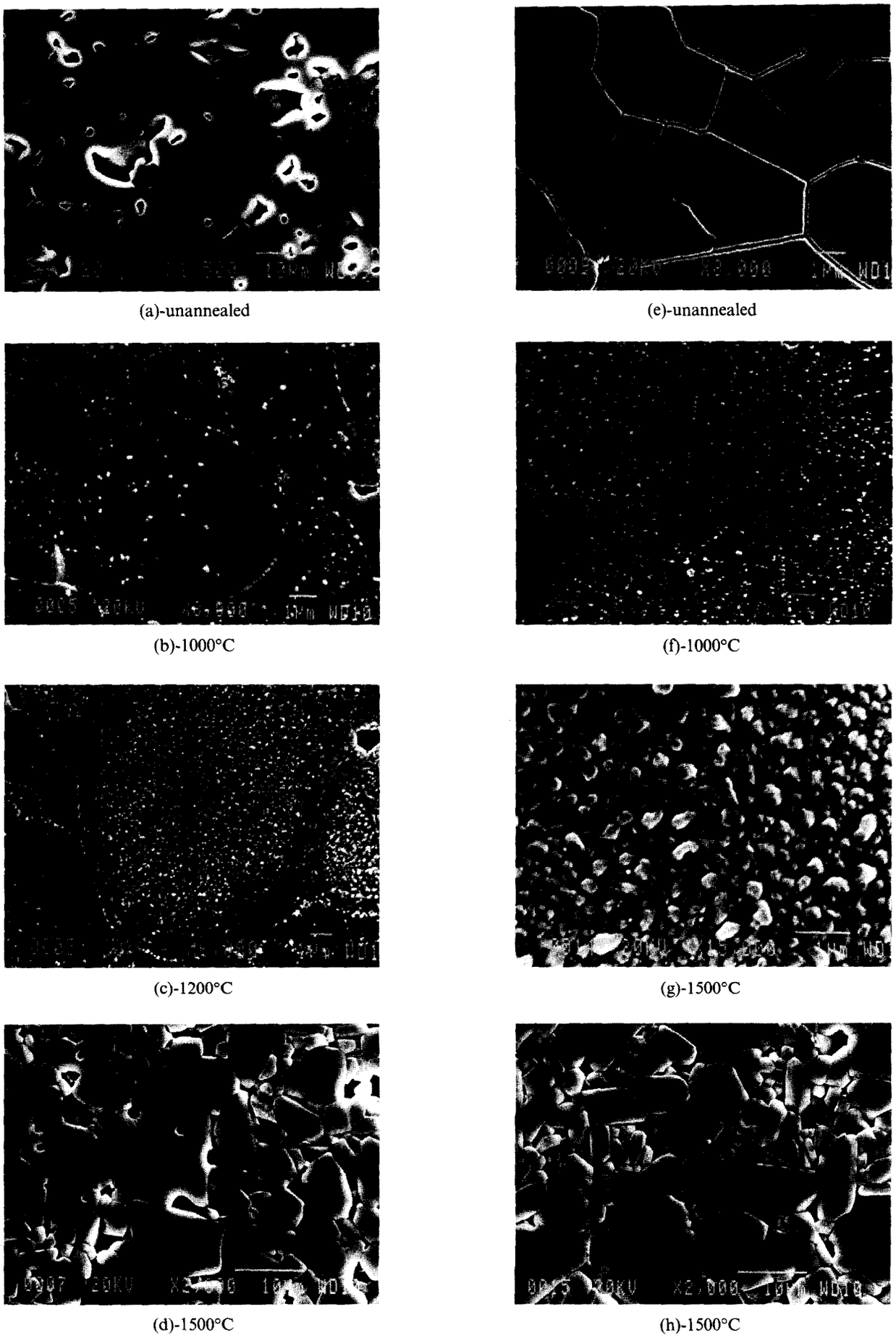
It can be seen that for the unannealed samples the surface is free of precipitates, (Fig. 7(a–e)). These precipitates only appear at 1000°C and grow at 1200°C, (Fig. 7(c–g)). Annealing at 1500°C removes the precipitates so that only the grain boundaries remain, (Fig. 7(d–h)).

Figure 8 presents the X-ray diffraction diagrams at grazing incidence (GXRD) obtained for the implanted sample (Fig. 8(a)) for both doses of 2×10^{16} ions/cm^2 and 10^{17} ions/cm^2 annealed at 1000°C and Fig. 8(b) for both doses of 2×10^{16} ions/cm^2 and 10^{17} ions.cm^2 annealed at 1200°C respectively). The peaks without indices correspond to α-Al_2O_3 and the others indicate the presence of the tetragonal TiO_2 obtained after annealing.

4 Discussion of the Results

The result of titanium implantation into polycrystalline alumina is an enhancement of the hardness of 8 and 18% for dose levels of 2×10^{16} ions/cm^2 and 10^{17} ions/cm^2 respectively. When the implanted samples are thermally annealed at 1000°C, the hardness was found to decrease for both doses. However, while thermal annealing at 1200°C recovers the hardness value to that of the unimplanted alumina in the case of the smaller dose, the hardness value lies much below that of the unimplanted alumina in the case of the higher dose. It should be noted also that changes in the toughness K_{1C} in the case of both doses follow a trend similar to the case of hardness (Fig. 6).

An appreciable increase in the value of K_{1C} could be noticed in the case of both doses (22% for the smaller dose and 32% for the larger dose). Thermal annealing at 1000°C lowers the values of K_{1C} in both cases while thermal annealing at 1200°C finally leads to an increase in the value of toughness (32 and 40% for the small and the high doses respectively).



(a)-unannealed (e)-unannealed

(b)-1000°C (f)-1000°C

(c)-1200°C (g)-1500°C

(d)-1500°C (h)-1500°C

Fig. 7. Microstructure of the implanted alumina before and after annealing at different temperatures: a–d — dose: 2×10^{16} ions/cm^2 and e–h — dose: 10^{17} ions/cm^2.

The scanning electron microscopic (SEM) studies show that the microstructure of all the implanted alumina samples is similar and the porosities present in alumina are visible (Fig. 7(a)–(b)). Thermal annealing at 1000°C creates precipitates in the grain and on the grain boundaries (Fig. 7(b)). Annealing at 1200°C increases the quantity of precipitates which have a size less than 1 μm (Fig 7(c–g)). At 1500°C, the precipitates disappear and only the grains remain visible (Figs 7(d–h)) the surface becomes irregular and measurement of the indent or cracks dimensions is no longer possible. It is also observed that implantation at the larger dose leads to rupture of the grain boundaries (Fig. 7(e)) as an increase in the size and number of precipitates at the lower dose level (Fig. 7(f–h)).[10]

The principle of X-ray diffraction at grazing incidence is the same as for classical X-ray diffraction studies. The X-ray beams of constant intensity fall on the sample under grazing incidence (a few tenths of 1 or 2 degrees). The penetration of X-ray beams is a function of this angle and the depth of analysis is variable. These diagrams reveal the presence of TiO_2 at 1000 and 1200°C (Fig. 8(a–b)) for both doses. At room temperature and at 1500°C the XRD reveals only the presence of α-Al_2O_3. These X-ray diffraction studies show that the oxidation of titanium occurs during the heat treatment and may be due to the oxygen ions displaced from the substrate by the ion implantation, or an external ingress of oxygen.[11]

On the basis of the XRD and SEM studies, these results can be explained in the following manner:

(i) For the two doses used, the increase of hardness observed on the implanted samples which remain crystalline,[12] could be attributed to the compressive stresses induced by implantation.
(ii) When the annealing temperature is increased, two phenomena are induced simultaneously, namely stress relaxation and TiO_2 formation.

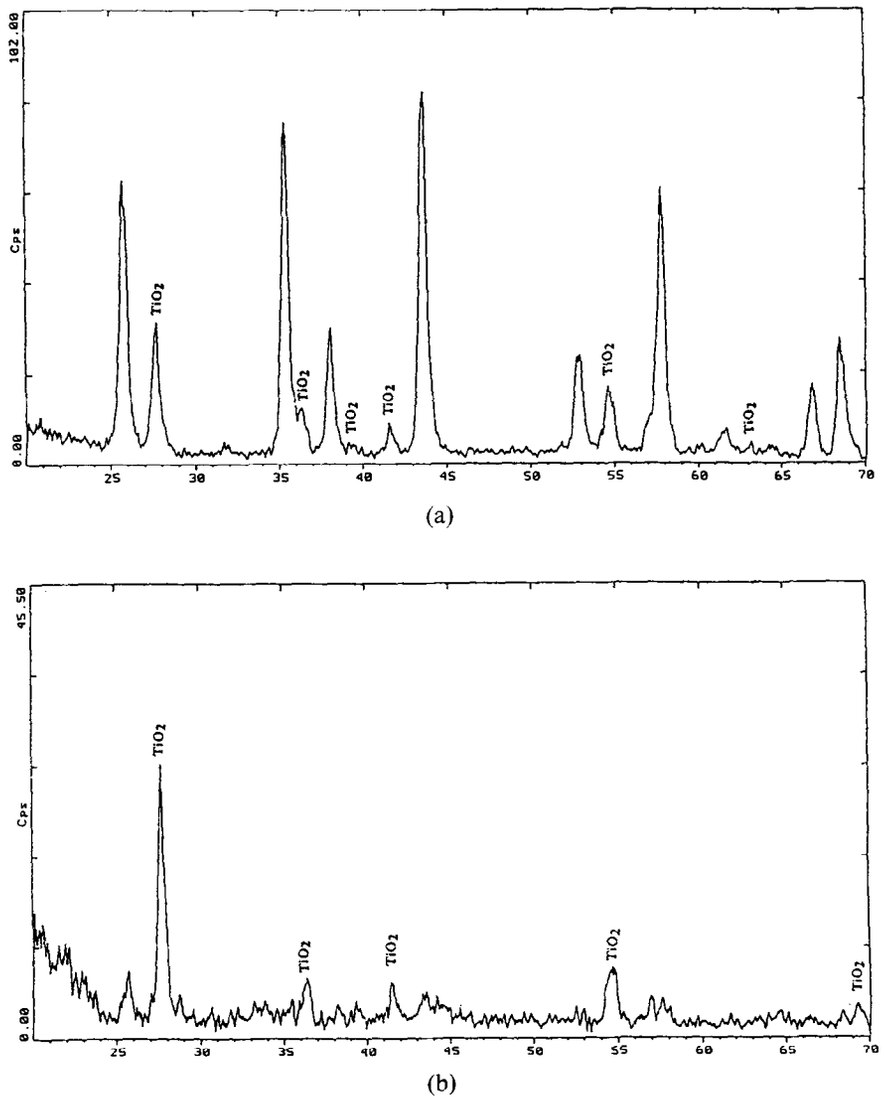


Fig. 8. GXRD patterns showing the effect of annealing for ion implanted alumina. (a) Doses 2×10^{16} ions/cm^2 and 10^{17} ions/cm^2, annealed at 1000°C, (α = 0·3°). (b) Doses 2×10^{16} ions.cm^2 and 10^{17} ions/cm^2, annealed at 1200°C, (α = 0·5°).

One can see that for implantation at the 2×10^{16} ions/cm^2 dose followed by thermal annealing at 1200°C there is very little formation of TiO_2 and the initial hardness of the unimplanted sample is recovered. For the 10^{17} ions/cm^2 dose, the hardness obtained is much less since there is an appreciable formation of TiO_2, whose hardness is less than that of pure alumina. At a temperature which is close to the sintering temperature of alumina (1500°C), the implanted ions are entirely ejected from the implanted surface.

According to Burnett and Page,[6] the residual stresses introduced in the implanted layer are compressive in nature. These stresses were observed by the beam embedding of thin samples method,[13] and also by the measurement of variation of the radial crack length around the Vickers indent. Lawn and Fuller[14] have given a relationship which gives the values of these stresses.

$$1 - \left(\frac{C_0}{C}\right)^{3/2} = \frac{2\Psi\sigma_s\, d^{1/2}}{K_c}$$

where K_c is the substrate toughness, C_0 is the radial crack length at $\sigma_s = 0$, C is the crack length at stress σ_s, and ψ is a constant taken as unity (= 1). In the case where $C < C_0$, σ_s is negative, and the stresses are compressive. The following tables show the values of σ_s (residual stress) obtained for three values of the crack length.

The results obtained with different indentation loads give slightly different values of stress. The method of Lawn and Fuller gives lower values of stress than the method of Krefft and Eernisse.[15]

Generally, implanted samples become amorphous and this leads to the enhancement of the toughness,[10] but the fluences used in this study are not sufficient to amorphise alumina.[6] Hence, we should consider again the idea developed here that the toughness increase for the as-implanted samples is due to the compressive stresses induced by the implantation.

Annealing at 1000°C relaxes these stresses and we obtain a value of toughness close to that of unimplanted alumina. At 1200°C, there is a formation of TiO_2 which gives a toughness value higher than that of alumina. In particular the case where a load of 5 N has been applied, (Figs 5 and 6) an enhancement of 32% for the dose of 2×10^{16} ions/cm^2 and of 36% for the dose of 10^{17} ions/cm^2 is observed. We propose that the residual stresses increase with the implanted dose. This could be attributed to a large concentration of induced defects, point defects and dislocations.[10]

Figure 9 shows a schematic representation of the evolution of the implanted layer composition as a function of annealing temperature and a pictorial representation of the results obtained in the SEM studies.

Table 1. Values of σ_s obtained for the two doses. (a) 2×10^{16} ions/cm^2. (b) 10^{17} ions/cm^2

Load (N)	*10 (N)*	*5 (N)*	*3 (N)*
Co (μm)	84	54	38
C (μm)	72	48	34
σ_s (MPa)	−1040	−800	−770

(a)

Load (N)	*10 (N)*	*5 (N)*	*3 (N)*
Co (μm)	83	54	38
C (μm)	68	43	31
σ_s (MPa)	−1534	−1638	−1422

(b)

5 Conclusion

The surface mechanical properties of ceramics could be modified by ion implantation. Such modifications are a result of the change in material microstructure and in the residual stresses produced in the implanted layer.

The specific case of Ti^+ ions implanted in polycrystalline alumina is studied here at 2×10^{16} and 10^{17} ions/cm^2, an increase in hardness due to the effect of compressive stresses is noted at room temperature. These stresses relax with the formation of a layer of TiO_2 when implanted samples are annealed at 1000°C, leading to a decrease of the sample hardness. However, this relaxation effect is compensated by the formation of a large quantity of titanium oxide, in the case of the higher fluence, followed by annealing at 1200°C. Since the toughness of TiO_2 is higher than that of alumina, it is normal that the toughness increases with annealing temperature. At a certain temperature the oxide layer disappears from the implanted layer, which in the present case takes place at 1500°C. Most previous work has been carried out in single crystal alumina and the present work confirms that previous knowledge is equally applicable to polycrystalline aluminas.

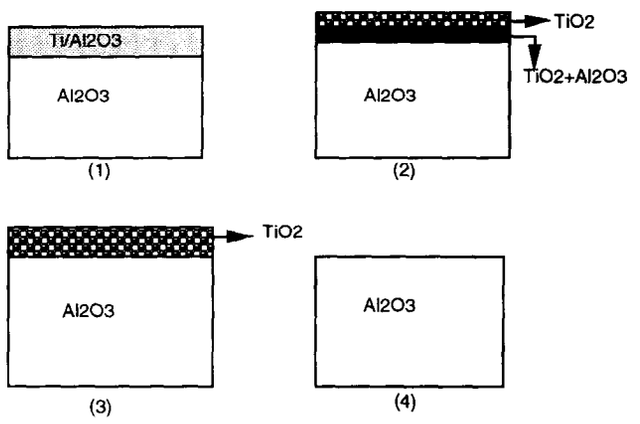


Fig. 9. Schematic representation of the evolution of implanted layer (1) Room-T (2) 1000°C (3) 1200°C (4) 1500°C.

It can therefore, depending on the desired applications, either increase the hardness by implantation, or the toughness by a combination of implantation doses followed by annealing at an optimum temperature. In the last case there is a great possibility of the creation of a third phase. Thus the surface could be suitably treated to obtain surface layers favourable for tribological application.

Acknowledgements

The authors wish to express thanks to the Direction Recherche Etudes et Techniques for their financial help, in the form of a research contract, the Groupe de Traitement de Surface, Institut de Physique Nucléaire de Lyon for ion implantation and to the Laboratoire Métallurgie et Physique des Matériaux de L'Ecole Centrale de Lyon for the X-ray analyses.

References

1. McHargue, C. J., Farlow, G. C., White, C. W., Williams, J. M., Appleton, J. M. & Naramoto, H., The amorphisation of the ceramics by ion beams. *Mater. Sci. Eng.*, **69** (1985) 123–7.
2. Bull, S. J. & Page, T. F., Thermal effects on the microstructure and mechanical properties of ion implanted xceramics. *J. Mater. Sci.*, **26** (1991) 3086–106.
3. Bull, S. J. & Page, T. F., The friction and wear of ion-implanted ceramics: the role of adhesion. *Nucl. Ins. Meth.*, North-Holland, **B32** (1988) 91–5.
4. Paletto, S., Moutel, A. & Fantozzi, G., *Annealing effects on mechanical properties of implanted alumina and zirconia.* SMT 4, Paris (1990).
5. McHargue, C. J., Appleton, B. R. & White, C. W., Structure property relationships in ion implanted ceramics. NATO, Les Arcs France (1983).
6. Burnett, P. J. & Page, T. F., An investigation of ion implantation induced near surface stresses and their effects in sapphire and glass. *J. Mater. Res.*, **20** (1985) 4624–46.
7. McCallum, J. C., White, C. W., Sklad, P. S. & McHargue, C. J., Annealing environment effect in solid-phase epitaxial regrowth of Fe-implanted Al_2O_3. *Nucl. Ins. Meth.*, North-Holland, **B46** (1990) 137–43.
8. Donnet, C., Caractérisation physico-chimique de céramiques thermomécaniques traitées par implantation ionique. PhD thesis, University of Claude Bernard Lyon 1, France, 1990.
9. Liang, K. M., Torecillas, R., Orange, G. & Fantozzi, G., Evaluation by indentation of fracture toughness in ceramics. *J. Mater. Sci.*, **25** (1990) 207–14.
10. McHargue, C. J., The mechanical properties of ion implanted ceramics: a review. *Defect and Diffusion Forum*, **57–58** (1988) 359–80.
11. Bourdillon, A. J., Bull, S. J., Burnett, P. J. & Page, T. F., The charge state of Ti ions implanted into sapphire: an EXAFS study. *J. Mater. Sci.*, **21** (1986) 1547–52.
12. McHargue, C. J., Structure and mechanical properties of ion implanted ceramics, *Nucl. Ins and Meth. in Phys. Res.*, North-Holland, **B19** (1987) 171–5.
13. O'Hern, M. E., McHargue, C. J., White, C. W. & Farlow, G. C., The effect of chromium implantation on the hardness, elastic modulus, and residual stress of Al_2O_3, *Nucl. Ins. Meth.*, North-Holland, **B46** (1990) 171–5.
14. Lawn, B. R. & Fuller, E. R., Measurement of thin-layer surface stresses by indentation fracture. *J. Mater. Sci.*, **19** (1984) 4061–7.
15. Kreft, G. B. & Eernisse, E. P., Volume expansion and annealing compaction of ion bombarded single-crystal and polycrystalline α-Al_2O_3. *J. Appl. Phys.*, **49** (1978) 2725–30.

Journal of the European Ceramic Society 15 (1995) 841–849
© 1995 Elsevier Science Limited
Printed in Great Britain. All rights reserved
0955-2219(95)00056-9
0955-2219/95/$9.50

Effect of Y_2O_3 Addition on Alumina–Hex Boron Nitride Composites

A. Abreal,[a] D. Goeuriot,[a] F. Thevenot,[a] M. Lagace,[b] B. Gueroult[b] & M. Rigaud[b]

[a]Ecole Nationale Supérieure des Mines de St-Etienne, 158 Cours Fauriel, 42023 St-Etienne cedex 02, France
[b]Ecole Polytechnique de Montréal, CIREP CRIQ, 8475 rue Christophe Colomb, Montréal (Québec), H2N 2N9, Canada

(Received 4 July 1994; revised version received 20 February 1995; accepted 10 March 1995)

Abstract

Hot-pressing is the only process to densify alumina–hexagonal boron nitride composites. It must be applied at 1750°C — 40 MPa, under nitrogen, but it does not reduce the porosity lower than 8% for composites with alumina contents lower than 70 vol%, and leads to anisotropic composites due to the orientation of the boron nitride platelets perpendicular to the pressing axis. Furthermore, the composites' behaviour during their use in the continuous steel casting is mainly due to the porosity and anisotropy.

To increase their resistance to oxidation by oxygen and corrosion by molten steel, and to change the effect of their microstructure, some yttrium oxide additions have been used. Yttrium oxide, by helping the alumina sintering, increases the composite's densification and so its mechanical strength, and by increasing the grains cohesion, it allows us to change the hot-pressing programme to obtain a more isotropic composite. Also, by reaction with alumina, it forms yttrogarnet (YAG) which protects the composite from oxidation by forming a protective liquid phase at the surface, following the reaction with boron oxide formed by the boron nitride oxidation. However, this liquid phase is eroded by the molten steel and so, cannot increase the corrosion resistance, but it is possible to stop this corrosion by an addition of neodymium oxide.

1 Introduction

The alumina–hexagonal boron nitride composites have interesting properties used in the continuous casting of low carbon steel, substituting to alumina–graphite. Indeed, boron nitride brings to the composites its good thermal shock resistance and its low wettability by the molten metals.

But it resists poorly to the oxidation and acts as a sintering inhibitor. So, the composite's densification, that needs hot-pressing shaping, does not exceed 92% of the theoretical density for alumina contents lower than 80 wt% (70 vol%). So a considerable porosity is maintained into composites that allows the gas exchanges and so, enhances the oxidation too. For that reason, some yttria additions have been tested to increase the densification of these composites and their oxidation resistance.

This oxide addition was chosen because yttria is a sintering help for alumina by the aluminum vacancies formation, characteristic of an electron donor.[1–5] This effect is attributed to its ionic radius which is larger than the aluminum radius ($r\ Y^{3+}$ = 0·093 nm, $r\ Al^{3+}$ = 0·05 nm) and the phenomenon follows the mechanism:

$$\frac{3}{4}O_2 + 3\,Y_{Al}^{x} \leftrightarrows \frac{3}{2}O_0^{x} + 3\,Y_{Al}^{\circ} + V_{Al}'''$$

Moreover, these vacancies increase the alumina plasticity and so, can help the BN flakes orientation when the pressure is applied during hot-pressing, and limit the vaults formation between these platelets that creates a considerable porosity in the composites.

Also, the Y_2O_3 addition can lead to the appearance of yttrogarnet $Y_3Al_5O_{12}$ (YAG) by *in situ* reaction with Al_2O_3: yttrogarnet whose corrosion resistance in molten steels was shown to be better than BN, W. Sinclair and M B. Trigg.[6–8]

2 Experimental Procedure

Commercial grade powders, 772 SB PECHINEY Alumina and GREPSI Hexagonal Boron Nitride flakes were used to prepare the composites. Starting from a 4 μm homogeneous BN powder after attrition, two slurries were prepared in the 66 vol% methyl ethyl ketone-34 vol% ethanol azeotrope, with specific dispersants, 0·8 wt% phosphate ester for alumina and yttria, and 2 wt% Polyvinyl Pyrrolidone for BN. After 10 min of ultrasonic disintegration, necessary to crumble these powders,

both slurries were mixed together for 42 h by ball-milling and 5 h by a slow attrition before to be dried and sieved.

The powder was hot-pressed at 1750°C and 40 MPa for 30 min in nitrogen atmosphere with a heating rate of 30°C/min.[9-10] All these parameters are controlled by a computer which allows us to obtain the shrinkage rate during sintering.

The properties of Y_2O_3 doped alumina–BN composites were determined: density, flexural strength, SEM observations and XRD analysis. For flexural strength measurements, the crack propagation is parallel to the pressing axis of hot-pressing.

The composites, whose behaviour were studied at high temperatures, were chosen with 60 wt% alumina and 0, 0·5 and 2·5 wt% Y_2O_3 in reference to Al_2O_3 content.

These composites were tested for resistance to thermal shocks. After having been cut into bars of $20 \times 3 \times 4$ mm^3, they were heated in a vertical tube furnace at a chosen temperature and then dropped into agitated oil at room temperature. Then, the samples were broken by the 3 point bending test; the variation of the flexural strength versus the temperature difference ΔT, between the initial hot temperature and the quenching medium, allows to determine the critical value ΔT_c.

The oxidation resistance was studied on cubic samples of $10 \times 10 \times 10$ mm^3 treated in oxygen at 1300°C, by measurements of the oxidized layers depths versus soaking time, for the two main directions, parallel and perpendicular to the pressing axis.

Also, the corrosion resistance was obtained by studying the corroded layers on fingers with dimensions $45 \times 10 \times 10$ mm^3 immersed into liquid steel at 1580°C ± 10°C for 30 min (Fig. 2).[10-11] The steel oxidation is limited by the addition of a slag whose composition is given in Table 1. An erosive condition is maintained by the forced movement of steel due to the furnace induction and the rotation of the samples at the speed of 2 rpm.

The oxidized and corroded samples were studied by SEM observations and XRD analysis.

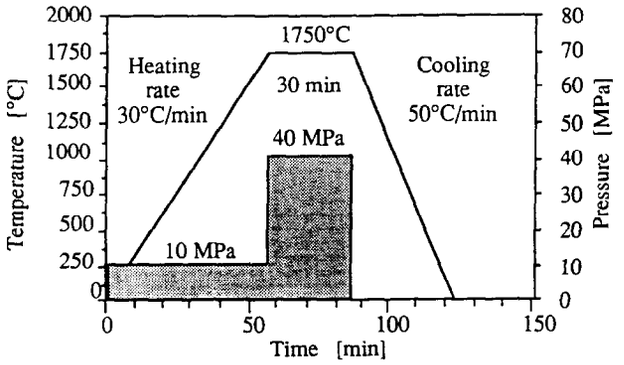


Fig. 1. Hot pressing cycle.

Table 1. Chemical composition of the slag

Components	*Contents*
SiO_2	34·3 ± 2·0
CaO	33·0 ± 2·0
MgO	1·3 ± 0·5
Na_2O	5·8 ± 1·0
F_2	8·6 ± 1·5
Fe_2O_3	0·4 ± 0·5
Al_2O_3	10·0 ± 1·0
MnO	1·3 ± 0·5
C	6·1 ± 1·5

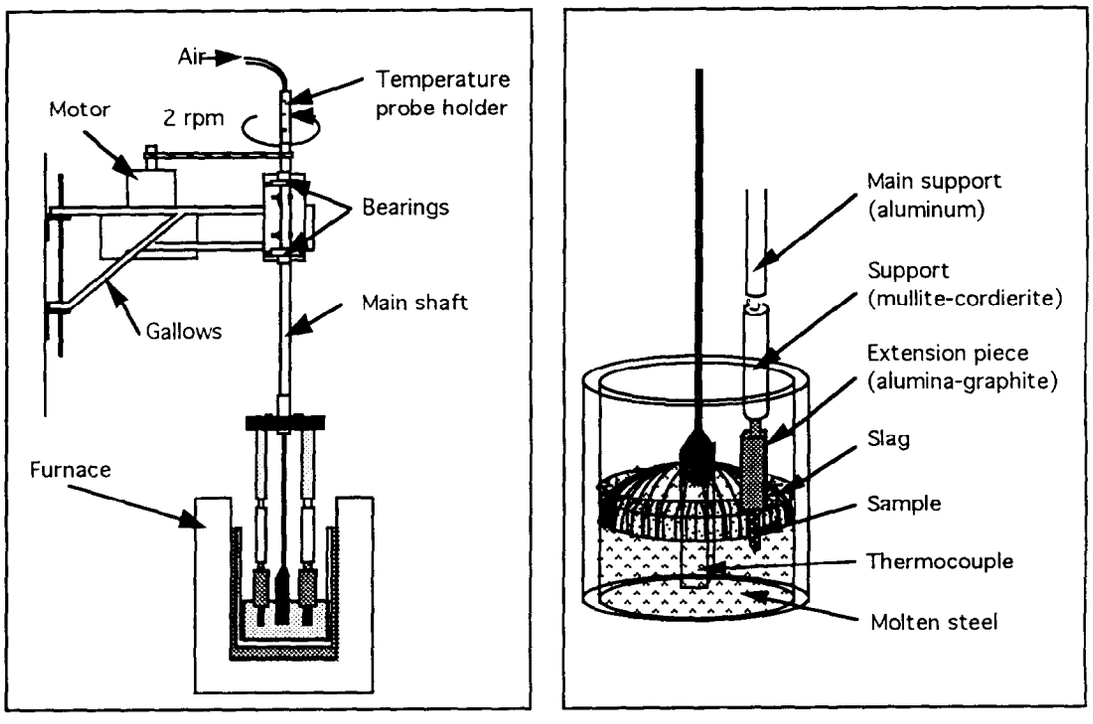


Fig. 2. Corrosion test set-up.

3 Results and Discussion

3.1 Densification and flexural strength

3.1.1 Undoped composites

Without Y_2O_3, the composite densification is limited to 92% of the theoretical density, for alumina contents lower than 70 wt%, due to vault formations between the BN platelets during hot-pressing[5] (Fig. 3). To reduce this drawback and densify composites, a pressure of 40 MPa must be applied at the soaking temperature which must be at least 1750°C, to achieve a sufficient plasticity of the alumina grains and so to allow orientations of the BN flakes. So, the material has an anisotropic microstructure with BN flakes orientated perpendicularly to the pressing axis and separated by strata of alumina grains between these platelets.

The reference hot-pressing cycle, presented in Fig. 1 and optimized by D. Goeuriot,[9] allows us to minimize the unfavourable orientations of BN platelets. It is divided into three successive segments:

— Heating in N_2 atmosphere at 30°C/min rate under a pressure of 10 MPa to limit the chemical reaction between Al_2O_3 and BN to form AlN and B_2O_3.

— Temperature soaking at 1750°C under a pressure of 40 MPa for 30 min, to allow the BN flakes to orient perpendicular to the pressing axis.

— Cooling to room temperature at 50°C/min rate without applied pressure.



Fig. 3. Fracture faces of an undoped composite with an important porosity due to a bad BN platelets orientation.

3.1.2 Yttria doped-composites

3.1.2.1 Sintering shrinkage of doped-composites. The sintering shrinkage curves, presented in Fig. 4, show differences between the composites' behaviour depending on their boron nitride and yttria contents:

— For composites with alumina content lower than 70 wt%, the curves for Y_2O_3 additions indicate that the beginning of densification and the temperature of the maximum of densification rate are shifted back by about 150°C.[12] Furthermore, these composites are particularly sensitive to the alumina plasticity for the BN platelets orientation. So, with yttria, the vacancies formation in alumina grains increases their plasticity and so allows the BN platelets orientation at lower temperatures.

— For composites containing 80 wt% Al_2O_3, the shrinkage beginning temperature is also decreased by the yttria presence, but the maximum shrinkage rate temperature and that of the end of the 'rapid' step of densification at 1400°C are not changed by yttria additions. For these composites which contain only 30 vol% of BN, the BN flakes dispersion is already sufficient to limit the contacts between them, and the vaults formation is so limited. The flakes orientation is so easy under a pressure of 40 MPa at 1750°C, that the yttria effect does not appear.

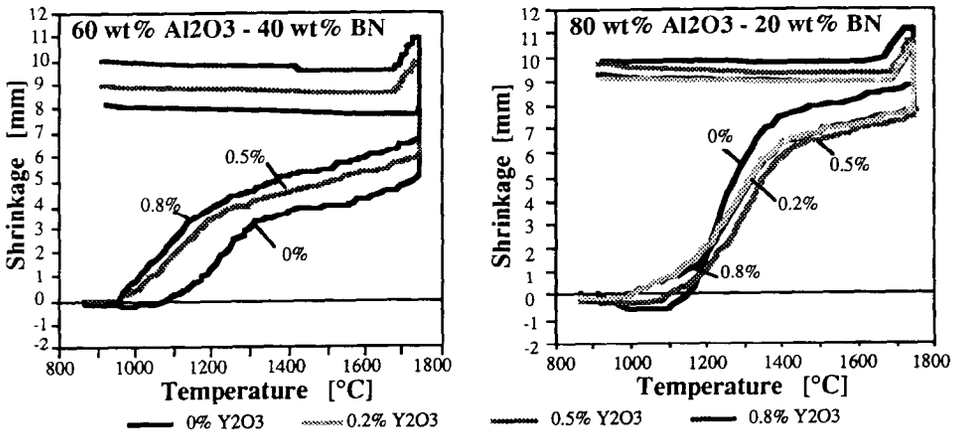


Fig. 4. Shrinkage of the Y_2O_3 doped composites during hot-pressing.



Fig. 5. Fracture faces of 0·5 wt% yttria doped composites (30 wt% BN–70 wt% Al_2O_3). Presence of strata of alumina and BN.

3.1.2.2 Doped composites microstructures. Due to the favourable effect of yttria on alumina sintering, the composites hot-pressed at 1750°C under 40 MPa following the reference cycle of Fig. 1 present a very nice orientation of the BN flakes. The microstructure is so composed by successive strata of BN platelets and alumina grains (Fig. 5).

3.1.2.3 Optimal addition of yttria. Despite the effect of yttria on composite shrinkage (mentioned before), it has a low influence on the final densification at 1750°C. For all alumina contents, the densities of doped composites and hot-pressed composites with the reference cycle, show a maximum increase of their densification of about 1% in comparison with undoped samples (Fig. 6). This increase obtained for additions of 0·5 wt% yttria considering Al_2O_3.

3.2 Hot pressing cycles influence (Fig. 7)

As the shrinkage temperature could be decreased by 150–200°C, different hot-pressing cycles were tested, with soaking temperature reduced to 1550°C and two different moments of pressure rise, at soaking temperature to obtain a favourable orientation of BN platelets, and at 1050°C below the alumina sintering temperature.

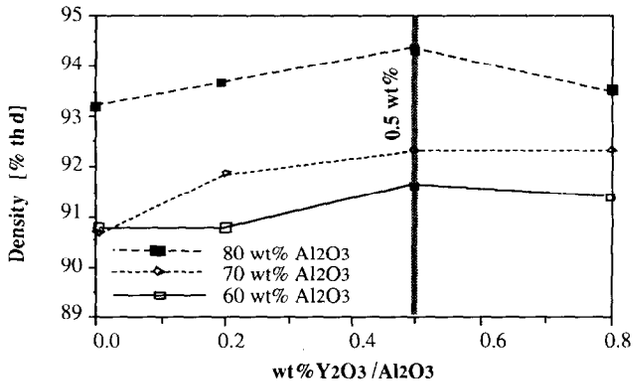


Fig. 6. Y_2O_3 additions effects on the composite densities after hot-pressing at 1750°C–40 MPa for 30 min.

So, four hot-pressing cycles were tested to densify the alumina–BN composites.

- 1750: the reference cycle presented in Fig. 1, with a soaking temperature of 1750°C and a pressure of 40 MPa applied during this temperature soaking.
- 1750–40: 40 MPa pressure is applied at 1050°C, below the soaking temperature at 1750°C.
- 1550: is the same cycle as 1750 with a soaking temperature reduced by 200°C, at 1550°C.
- 1550–40: is the same cycle as 1750–40 with a soaking temperature reduced to 1550°C.

The densification rates and flexural strengths were determined for two Y_2O_3 contents: 0·1 wt% and 0·5 wt% Y_2O_3 in reference to alumina and two alumina contents: 70 wt% and 80 wt%. The results are presented in Fig. 7.

3.2.1 Composites doped with 0·1 wt% Y_2O_3

There is not enough Y_2O_3 to densify the composites with 70 wt% alumina and only the reference cycle, 1750, allows us to obtain the most densified composites with the highest flexural strength.

For this temperature, applying high pressure (40 MPa) before the alumina shrinkage, which happens above 1100°C, leads to a poor orientation of BN flakes. This disorientation remains when the temperature rises and so impedes the densification, so that, the porosity of the sintered composite that follows the 1750–40 cycle is higher and it shows a lower flexural strength.

Samples sintered at 1550°C are less dense and so present lower flexural strengths too.

For the 80 wt% Al_2O_3 composite, there exists no important difference between the cycles in regard to their densification. For this composition, the low content of BN has little effect on the densification, as has been explained in Section 3.1.2.1.

But the flexural strengths are significantly higher if the soaking temperature is 1750°C. This difference is not only due to the porosity, but also certainly to a higher anisotropy of the material at 1750°C owing to a sufficient plasticity of alumina that allows the BN orientation during the pressure application. This plasticity which only occurs above 1100°C, does not allow us to obtain anisotropic composites at 1550°C and corresponding to these composites possess lower strengths.

For this composition also, applying 40 MPa at 1100°C is unfavourable to the BN orientation and so to the flexural strength.

3.2.2 Composites doped with 0·5 wt% Y_2O_3

Hot-pressing with 0·5 wt% Y_2O_3/Al_2O_3, allows us to densify the alumina–boron nitride composites

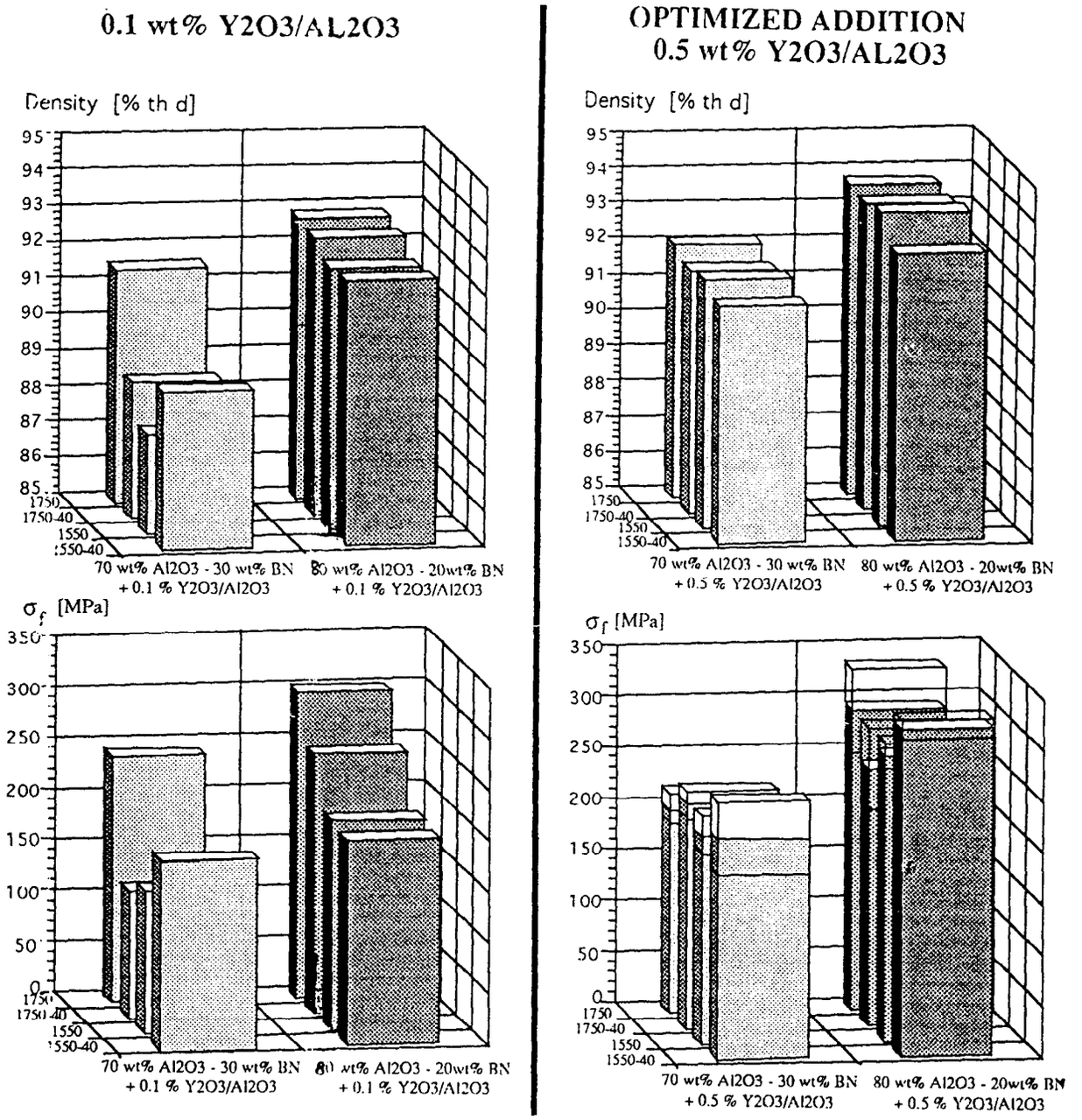


Fig. 7. Densities and flexural strengths of composites with 0·1 and 0·5 wt%/Y_2O_3 considering Al_2O_3.

and even the 70 wt% Al_2O_3 composites. Also, flexural strength is considerably increased by the addition of 0·5 wt% Y_2O_3 for all the applied cycles.

Part of these increments can be due to higher densification. But we can show that the highest strengths are measured for composites for which the pressure was applied at low temperatures, (1750–40 and 1550–40 cycles), even though the densities are a little lower than for the 1750 and 1550 cycles. The yttria addition has a significant favourable effect on the flexural strength of the alumina– boron nitride composites.

3.2.3 Discussion

3.2.3.1 Undoped composites. In the case of a high anisotropic composite formed by strata of alumina between the BN platelets, the fracture is propagating during flexural bending tests perpendicularly to the orientation of the platelets through the alumina boundaries or grains. When the crack meets a BN platelet, it by-passes along the Al_2O_3–BN boundary. This case corresponds to the 'pull-out' phenomenon of reinforcement.

But if the platelets are not perpendicularly orientated to the pressing axis, the fracture can follow it and propagate through this platelet between the 001 crystallographic planes.

So, less energy is spent to limit the fracture propagation, and the flexural strength of the composite is significantly decreased.

So, to reach the highest flexural strengths for undoped composites, BN platelets must be oriented. This needs the reference cycle to be used, with a soak at 1750°C under 40 MPa.

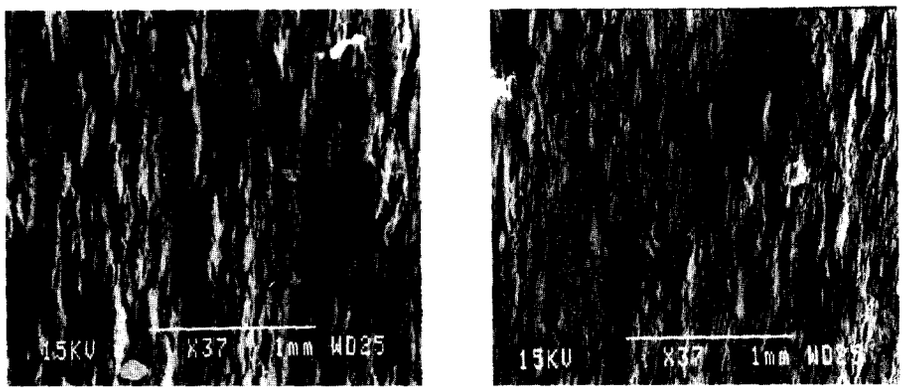


Fig. 8. Fracture faces of hot-pressed (1800°C — 40 MPa) boron nitride: (a) pure boron nitride; (b) BN with 2·3 vol% of Y_2O_3.

3.2.3.2 Doped composites. Samples that have been hot-pressed with a pressure rise at 1050°C (cycles 1750–40 and 1550–40) are considerably more porous due to the formation of vaults between the BN platelets. However, they have higher flexural strength due to the presence of yttrium at the boundaries, increasing the adhesion between alumina grains and BN platelets and cohesion between the BN platelets themselves, as shown on the fracture faces of Fig. 8. The fracture is more transgranular into the doped samples. In fact, the energy, spent to propagate the fracture through the BN flakes is more significant than that of by-passing. A. G. Evans[13] presented his theory (Fig. 9) on the reinforcement of boundaries in composites and the fiber or platelets debonding. There is a critical value of the ratio between the fracture energies of the interface and the platelet, for that, the fracture propagates either along the boundary or through the platelet.

The mechanism of crack deflection also occurs for these high energy boundaries and can thereby increase the flexural strength too (Fig. 10).

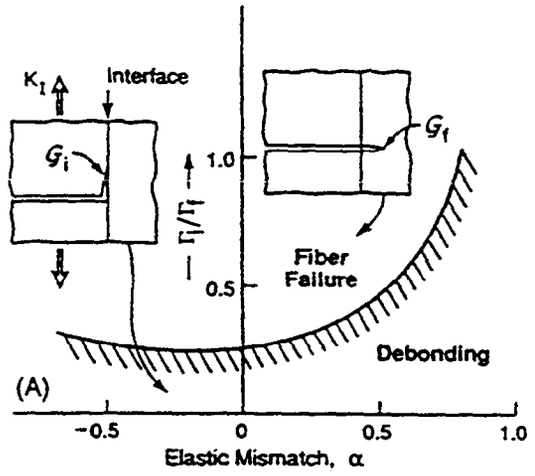


Fig. 9. Conditions of debonding of a fiber, perpendicular to the fracture (Ref. 13).

3.2.4 Conclusions

Without yttria, the alumina–boron nitride composites need to be hot-pressed at least at 1750°C under 40 MPa under nitrogen with a pressure rise during temperature soaking, to reach the highest flexural strengths. So the composites have an anisotropic microstructure constituted by strata of alumina between the BN platelets.

With yttria, composites can also be shaped without orientation of the BN platelets, also having a good flexural strength, and by the reinforcement of boundaries due to the presence of yttrium. So, we can suppose that it is easier to sinter these composites, perhaps by hot isostatic pressing.

3.3 Other properties

With yttria, property studies were performed to find out the composition that seems to be the best compromise on the different properties that composites need for the molten-steel casting, like good resistance to thermal shocks, oxidation and corrosion by the molten metals. This composition is 40 wt% BN and 60 wt% Al_2O_3.

3.3.1 Thermal shock resistance (Fig. 11)

Without yttria, the thermal shock resistance was



Fig. 10. Deflection of cracks into doped composites (30 wt% BN–70 wt% Al_2O_3) hot-pressed following the 1750–40 cycle.

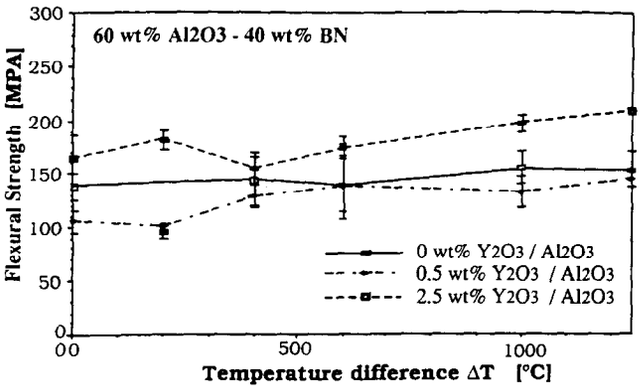


Fig. 11. Thermal shock resistance of yttria doped composites after oil quenching at 25°C.

studied for all the compositions between 50 and 90 wt% alumina contents. No drop of flexural strength in plotting it against temperature difference ΔT was observed, except perhaps for the highest alumina content.

With yttria, in spite of the temperature difference that exceeds 1200°C for some tests, the flexural strength curves of Fig. 11 show no fall, a slight increase can even be noticed for the highest yttria content.

In fact, all these composites have about 8 vol% of porosity, that is favourable to the thermal shock resistance. Moreover, microcracks appear during hot-pressing due to the significant thermal expansion coefficients mismatch between alumina (7–10 × 10^{-6} K) and boron nitride (0·7 × 10^{-6} K in the direction perpendicular to the pressing axis). The initial low flexural strengths prove that the microcrack length and density are high. So, it could be expected that the thermal shocks cause only quasi-static crack propagations. That does not affect the composites' flexural strengths.

So, the alumina–boron nitride composites' properties make them highly resistant to thermal shocks and no deterioration of the mechanical properties could be observed.

3.3.2 Oxidation

3.3.2.1 Undoped composites. Without yttria, composites are readily oxidized above 1100°C, according to the following mechanism, divided into two successive steps:[10,14]

$$2\ BN + 3/2\ O_2\ (g) \rightleftarrows B_2O_3(1) + N_2\ (g)$$

$$9\ Al_2O_3 + 2\ B_2O_3(g)(1) \rightleftarrows 9\ Al_2O_3 \cdot 2\ B_2O_3\ (A9B2)$$

The plotting of the oxidation depth versus time at 1300°C under O_2 (Figs 12 and 13) shows the oxidation kinetics in the two directions, perpendicular and parallel to the pressing axis for anisotropic materials.

3.3.2.2 Perpendicular to the pressing axis. Without yttria, and perpendicular to the pressing axis, the oxygen can migrate between the debonding 001 planes of the hexagonal boron nitride and oxidizes their platelets very quickly and forms significant quantities of B_2O_3. A part of this boron oxide is unable to react with alumina and so migrates to the surface along with the nitrogen formed. There, it forms a protective liquid layer that closes the pores and thereby stops the gas exchange (Fig. 14). So, the oxidation protection is assumed to be that of boron oxide alone and, in this direction, the effect of yttria on the oxidation rate could not be observed.

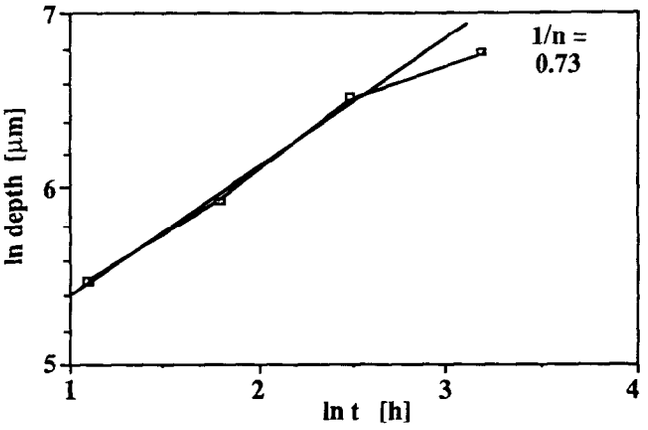


Fig. 13. Evolution of the oxidized layer depth with 0·5 wt% Y_2O_3/Al_2O_3 (parallel to the pressing axis).

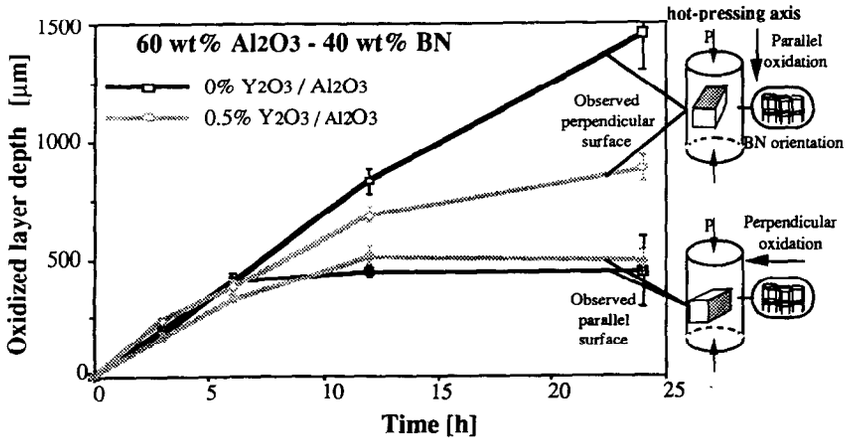


Fig. 12. Evaluation of the oxidized layer depths versus time with and without yttria additions.



Fig. 14. Cross-section of the oxidized scale in the case of oxidation perpendicular to the pressing axis. Presence of a dense liquid layer.

Also, at the surface, above this protective layer, the boron oxide's evaporation leads to enrichment in alumina and A9B2 chimneys can form. This chimney shape is caused by the exhaustion of volatile boron oxides and nitrogen (Fig. 14).

3.3.2.3 Parallel to the pressing axis. Without yttria, the oxidation follows a linear kinetic, that means there is a reaction limiting step:

$$\text{Depth} = kt$$

Following this oxidation direction, oxygen meets the BN flakes oriented perpendicularly and only oxidizes some first 001 planes. So, there is little boron oxide, B_2O_3, formed by oxidation of the boron nitride, that dissolves the alumina grains. Then, there is a crystallization of A9B2 in the form of bars of about $10 \times 0{\cdot}8 \times 0{\cdot}8$ μm^3 in dimension, following the remaining nonoxidized BN planes. So this crystallization occurs perpendicularly to the pressing axis as shown in Fig. 15. Then there is a penetration of the oxygen between these A9B2 bars, and the mechanism happens again.

With Y_2O_3, the mechanism is more complex. The composite is, before oxidation, composed of Al_2O_3, BN and yttrogarnet, $Y_3Al_2(AlO_4)_3$, formed *in situ* by the reaction between Al_2O_3 and Y_2O_3 during hot-pressing. EDS analysis showed the yttrium migration to the surface during oxidation. Then, this material forms at the surface as a protective amorphous layer constituted of Al, B, Y, O, N, present around and under the A9B2 crystals. That allows part of the open pores to close due to the A9B2 crystallization, so limiting the gas exchange and thereby the oxidation rate. But the kinetic law does not follow a parabolic curve as for an O_2 diffusion-controlled mechanism, but this law follows:

$$\text{Depth}^{1{\cdot}4} = k't$$

So the oxidation mechanism with yttria is dual, consists of kinetics of O_2 diffusion mechanism due to the protective layer and of reaction-controlled mechanism.[10,14]



Fig. 15. Oxidized scale for oxidation parallel to the pressing axis: A9B2 crystals and open porosity.

3.4 Corrosion by molten steel

The same samples tested for oxidation were dropped into molten steel covered with a slag containing $34{\cdot}3 \pm 2{\cdot}0$ wt% SiO_2 and $33{\cdot}0 \pm 2{\cdot}0$ wt% CaO, as presented in Table 1. This test combines two corrosive mechanisms.[10–11]

- — oxidation of boron nitride by the dissolved oxygen in iron and by FeO
- — alumina dissolution by the slag which is particularly reactive with Al_2O_3, forming mullite or calcium aluminates with SiO_2 and CaO respectively.

In iron, the yttria-doped composites are oxidized by a mechanism similar to the one in oxygen with the A9B2 crystallization. But there is an erosion of the protective layer observed after the tests of oxidation by the movement of the molten steel. So, although the corroded layer depths with yttria (Table 2) are smaller, the attack is significant as can be observed in Fig. 16, because this liquid layer at the surface is eroded and the alumina grains are carried off along with it.

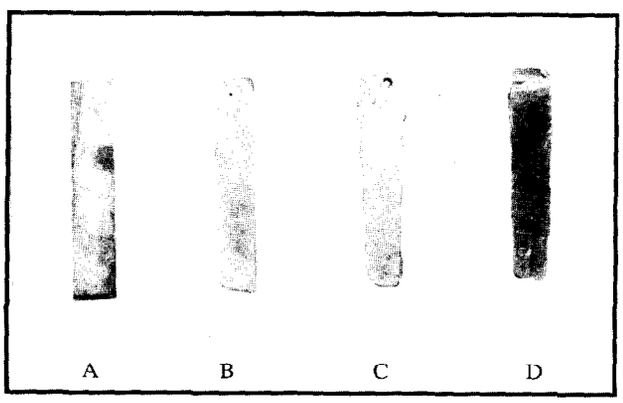


Fig. 16. Corroded samples cross-section: (A) uncorroded sample (reference); (B) 0 wt% Y_2O_3; (C) 0·5 wt% Y_2O_3; (D) 2·5 wt% Y_2O_3.

Table 2. Corroded layer depthes depending on the yttria contents

Sample (60 wt% Al_2O_3–40 wt% BN)	*Corroded layer depth in slag (μm)*	*Corroded layer depth in iron (μm)*
0 wt% Y_2O_3/Al_2O_3	10–20	500–600
0·5 wt% Y_2O_3/Al_2O_3	100	300
2·5 wt% Y_2O_3/Al_2O_3	30	150

In the slag, the corrosive attack is slightly more significant with yttria too. The reaction between yttria and alumina to give YAG, consumes a part of the alumina grains that are smaller and so more reactive to react with the slag.

Moreover, the 2·5 wt% yttria content composite has cracks, mostly longitudinal and 'V' shaped. They indicate that this composite did not withstand the thermal shock induced by immersion in liquid steel. That was not detected in its behaviour during thermal shock at 1250°C. So, either the yttria content must be limited in order to avoid considerable deterioration of the mechanical properties of the composite in contact with iron, or it should be necessary to pre-heat the composite specimen prior to this contact.

Although, yttria addition offers much resistance to oxidation by O_2 resistance, but does not protect the alumina–boron nitride composites from the corrosion by slag and molten steel. But other studies allow us to increase this corrosion resistance by neodymium oxide additions to lead to very inert composites.[10–12]

4 Conclusions

Without Y_2O_3 additions, the improvement of mechanical properties of the Al_2O_3–BN composites is maximum; if the BN platelets are oriented perpendicularly to the pressing axis during hot-pressing. This microstructure is attained by hot-pressing at 1750°C with a pressure rise from 10 to 40 MPa at this soaking temperature.

With 0·5 wt% Y_2O_3/Al_2O_3, it is possible to modify the microstructure by changing the hot-pressing cycle to obtain a more isotropic material by a pressure rise at only 1050°C. This yttria addition allows us to reduce the soaking temperature by 200°C, from 1750 to 1550°C, leading to more densified composites with increased mechanical strengths, due to the more stronger cohesion caused by Y_2O_3.

This 0·5 wt% Y_2O_3 addition increases the oxidation resistance of the composite too, by reaction at the surface between YAG, alumina and B_2O_3, forming a liquid phase that protects the material by closing the pores created by the A9B2 crystallization.

But Y_2O_3 decreases the corrosion resistance to molten steel, because this liquid phase is easily eroded and unable to protect the material. Moreover its concentration should not exceed 0·5 wt%/Al_2O_3, in order to limit the damage caused by the thermal shock during the immersion in liquid steel.

References

1. Saadi, B., Ochin, P., Petot-Ervas, G., Lesage, B. & Huntz, A. M., Propriétés de transport dans l'alumine à dopee à l'yttrium et au titane. *Ann. Chim. Fr.*, **10** (1985) 257–60.
2. Loudjani, M., Lesage, B. & Huntz, A. M., Influence du dopage et du mode d'élaboration sur la microstructure de l'alumine à polycristalline. Relations avec les propriétés de transport. *L'Indusrie Ceramique*, **801** (1986) 53–60.
3. Delaunay, D., Huntz, A. M. & Lacombe, P., The influence of yttrium on the sintering of Al_2O_3. *J. of the Less-Common Metals*, **70** (1980) 115–17.
4. Lagrange, M. H., Huntz, A. M. & Laval, J. Y., Effect of yttrium on the microstructure and diffusion properties of alumina. *Ann. Chim. Fr.*, **12** (1987) 9–21.
5. Gautier, G. & Bernache-Assolant, D., Evolution of the inter- and intra-agglomerate porosity during hot-pressing of aluminium nitride. *Science of Ceramics*, **14** (1988) 249–54.
6. Sinclair, W., McDonald, A. M. & Trigg, M. B., Evaluation of non-oxide ceramics for steel making. *Materials Forum*, **10**(3) (1987) 211–13.
7. Sinclair, W. & Trigg, M. B., Corrosion of non-oxide ceramics in liquid steel. *High Techn. Ceramics*, ed. Vincenzini, Elsevier Science Publishers, BV., Amsterdam, 1987, pp. 2672–82.
8. Trigg, M. B., Ellson, D. B. & Sinclair, W., Corrosion of selected non-oxide ceramics in liquid steel. *Br. Ceram. Trans. J.*, **87** (1988) 153–7.
9. Goeuriot-Launay D., Brayet, G. & Thevenot, F., Boron nitride effect on the thermal shock resistance of an alumina based ceramic composite. *J. Mat. Sciences Letters*, **5** (1986) 940–2.
10. Abreal, A., Propriétés réfractaires des composites céramiques alumine-nitrure de bore. Thesis No 103TD, Ecole Nationale Supérieure des Mines de St-Etienne, France, (1994).
11. Lagace, M., Gueroult, B., Rigaud, M., Abreal, A., Goeuriot, D. & Thevenot, F., Corrosion test on Al_2O_3–BN samples in contact with mold flux and steel. In *Proceedings of the UNITECR'93 Congress*, Sao Paulo, Brazil, 1993, pp. 314–23.
12. Abreal, A., Goeuriot, D., Thevenot, F., Lagace, M., Gueroult, B. & Rigaud, M., Effect of neodymium and yttrium oxides on alumina–BN composites. In *Proceedings of the 11th International symposium on boron, borides, and related compounds*, Tsukuba, Japan, 1993, in press.
13. Evans, A. G., He, M. Y. & Utchinson, J. W., Interface debonding and fiber cracking in brittle matrix composites. *J. of Amer. Ceram. Soc.*, **72**(12) (1989) 2300–3.
14. Abreal, A., Goeuriot, D., Thevenot, F., Lagace, M., Gueroult, B. & Rigaud, D., Additions to improve the oxidation resistance of alumina–boron nitride composites. In *Proceedings of the 3rd Euro-Ceramics*, eds P. Duran & J. F. Fernandez, Faenza Editrice Iberica, Madrid, 1993, Vol. 3, pp. 231–6.

Journal of the European Ceramic Society **15** (1995) 851–858
© 1995 Elsevier Science Limited
Printed in Great Britain. All rights reserved
0955-2219/95/$9.50

0955-2219(95)00050-X

Surface Segregation and Morphology of Mg-Doped α-Alumina Powders

D. Monceau,[a] C. Petot,[a] G. Petot-Ervas,[a] J. W. Fraser,[b] M. J. Graham[b] & G. I. Sproule[b]

[a]CNRS/LPCM-UPR 211, Univ. Paris XIII, 93430 Villetaneuse, France
[b]Inst. for Microstructural Sci., N.R.C., Ottawa, Canada K1A 0R6

(Received 7 November 1994; revised version received 16 February 1995; accepted 20 February 1995)

Abstract

This work considers the effect of a thermal treatment, at a temperature equal to or higher than 1200°C, on the physical and chemical characteristics of submicron α-alumina powders, doped with 550 and 1650 ppm in weight of MgO. The powders have been characterized by TEM, SEM, BET, XPS and chemical analysis. TEM observations show that the grains have elongated and rounded forms and exhibit considerable agglomeration. The BET surface area of the powder decreases with increasing annealing time and temperature and increases with the amount of MgO. XPS analysis shows a strong segregation of Mg and this effect is more pronounced when the size of the grains increase. In some cases XPS also detected the presence of Na, Ca and Si in the surface region of the grains.

1 Introduction

The fabrication of reliable, high-performance ceramics is an important industrial challenge, and it has long been recognized that further progress will be made by an increased understanding of the role played by the microstructure and microchemistry of the starting powders. Indeed, the processing of a ceramic generally involves the manufacture of a powder, with a suitable composition and microstructure, followed by its compaction and sintering. The characteristics of powders, such as size distribution, agglomeration, purity and surface area, are of course crucial in controlling the densification and therefore the microstructure of the finished material, which may give rise to specific properties. Nevertheless, in the different processing steps leading to the sintered ceramic, surfaces and interfaces play a critical role. At the macroscopic level, a requirement for densification is that the interfacial energy of the sintered material is lower than the surface energy of the powder. However, at the microscopic level it is the rapid movement of atoms that leads to the closeness of the center of the particles and to the densification. The influence of curved surfaces on these atom fluxes has long been recognized. Local variations in surface curvature give rise to local gas partial pressure differences and this in turn leads to local chemical potential gradients which drive the atom transport. For an atom to move, however, it is necessary that point defects be in close proximity. The point-defect concentration is of course related to the surface curvature, but also depends strongly upon the surface composition and the thermodynamic equilibrium conditions (T and P_{O_2}). Various papers have been devoted to the effect of dopants on the microstructure and characteristics of powders and sintered materials.[1–9] To our knowledge, however, there is a lack of data concerning the microchemistry of the powder and therefore the effect of variations in composition at or near the powder surfaces on the early stages of sintering, controlled mainly by surface diffusion, and ultimately on the ceramic densification. This is mainly due to experimental difficulties encountered until recently in characterizing insulating materials, particular in the form of powders.

In the case of alumina, an intensification of research was observed after the discovery by Coble in 1957 concerning the beneficial effect of magnesia on the alumina sintering. Small additions of MgO allow the theoretical density to be achieved without both abnormal grain growth and pores entrapped within grains. In subsequent studies,[5–9] authors have tried to understand the role of MgO and also to determine how to extend those results to other systems. It is now unquestioned that the presence of impurities, such as CaO or SiO_2, also play an important role in the alumina sintering.[5–9] Nevertheless, difficulties arise in understanding the influence of these additives on the mobility of grain boundaries and pores. The results are generally controversial[7] and it is now

recognized that an improved characterization of powders and compacts,[10] and a better knowledge of the microstructure evolution during densification, would be beneficial for further progress to be made in predicting the influence of dopants on sintering and grain growth.

This study mainly concerns the influence of the thermal treatment conditions on the nanochemistry and microstructure of α-alumina powders doped with magnesia. In previous papers the authors[11–14] have analysed kinetic demixing effects near surfaces in ceramics under a thermodynamical potential gradient or during cooling. They have also examined the segregation of additives (Y, Zr or Mg) and impurities (Si, Ca,...) to the surface of alumina powders and the effect of dopants on both the microstructure of alumina particles and the sintering kinetics.[15] More recently, XPS analysis of alumina powders doped with magnesium have allowed the determination of the extent of magnesium surface segregation as a function of the thermal treatment conditions and of the amount of dopant.[16] In this paper, we report a systematic study of cation redistributions (dopants and impurities) near the surface of alumina powders, in order to try to understand the parameters that play a critical role in the powder microchemistry.

2 Materials

The alumina powders studied have been prepared from the alum. They are doped with MgO: 550 ppm (0·07 at% Mg with respect to the cationic site number) or 1650 ppm in weight (0·21 at%). In the alum method, the dopants are added before the thermal decomposition of the starting materials (sulfates), close to 400°C. The change by a liquid phase promotes a uniform distribution of the additives in the grains because the nascent crystallites of γ-alumina have a high reactivity due to their high surface area. The next calcination occurs at temperatures higher than 1150°C. This

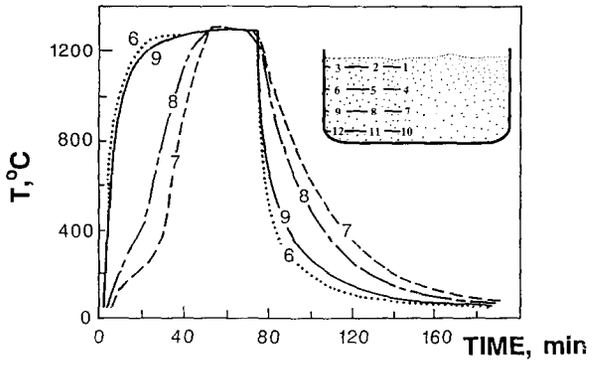


Fig. 1. Position of the thermocouples (1–12) in the silica crucible and thermal history of the powder for positions 6–9.

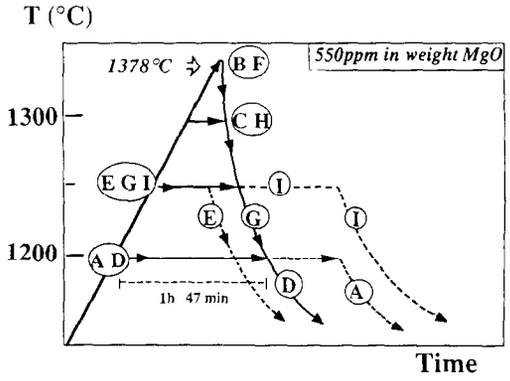


Fig. 2. Thermal history of the powder treated in air in an alumina crucible. Powders B, F, C, D, H, G and D have been maintained for the same time (1 h 47 min) at a temperature equal to or higher than 1200°C and cooled at the furnace cooling rate.

results in the commercial α-alumina. The quality of the powder depends strongly upon this step of the process. Consequently, in the present work we have examined the influence of the conditions of this last thermal treatment on the microchemistry and microstructure of the powder. The calcination was first performed in air at 1300°C, in large silica crucibles which contain approximately 700 g of powder. Pt/Pt–Rh10% thermocouples are placed in the silica crucible, as shown in Fig.1 (positions 1–12), to monitor the thermal history of the powder. As an example, we have reported in Fig. 1 the thermal history of powders from positions 4–9. Chemical analysis, surface area measurements and SEM examinations have been performed on powders taken in the vicinity of the different thermocouples (1–12). Only samples from position 6 and 7, with the largest difference in thermal treatment conditions (Fig. 1), have been analysed by XPS and TEM. Complementary treatments have been carried out between 1200 and 1378°C, in small alumina crucibles containing approximately 7 g of powder, in order to try to separate the role played by different parameters, such as the temperature of calcination, the cooling rate and the size of the grains. Figure 2 shows the thermal history of different samples treated in alumina crucibles and which have been cooled at the furnace cooling rate, i.e. more slowly than the powders treated in the silica crucible.

3 Results and Discussion

3.1 Chemical analysis, surface area measurements (BET), SEM and TEM observations

The main impurities found in the powders by inductive coupled plasma spectrometry (ICPS analysis) are: Si, Na, K, Ca and Fe. Their concentration range is reported in Table 1. Whatever the

Table 1. Concentration range of the main impurities (ppm in weight) found in different α-alumina powders (treated in alumina or silica crucibles) doped with 1650 and 550 ppm (by weight) of MgO (0·21 and 0·07 at% Mg), respectively

Amount of MgO	*Fe*	*Na*	*K*	*Si*	*Ca*
1650	3–12	11–27	8–48	13–120	3–11
550	2–9	12–34	12–33	18–143	3–6

type of treatment (alumina or silica crucible), the repartition of impurities is found to be relatively homogeneous, except for Si and Na. When the powder is treated in a silica crucible, the amount of Si increases in the powder taken near the edges of the crucible (Fig. 3), while the opposite is observed for Na. The amount of Na is generally close to 15 ppm for the powders taken near position 6 and between 22 and 34 ppm for powders near position 7. When the powder is treated in a small alumina crucible, the amount of Si is independent of position, but depends upon MgO content: 27 ppm in weight for powders doped with 550 ppm

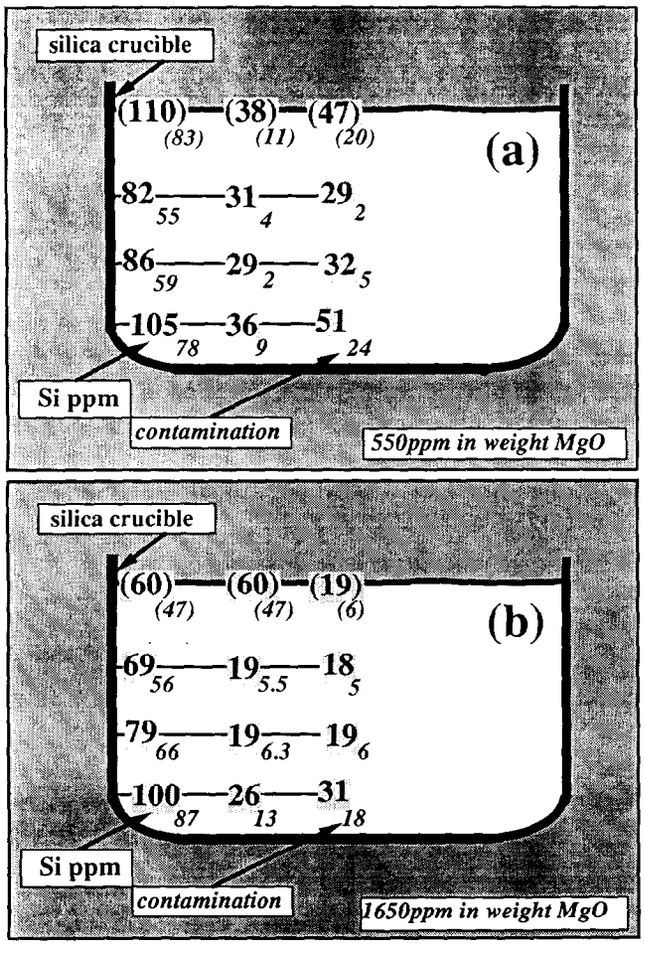


Fig. 3. Amount of silicon in the magnesium-doped alumina powder, as a function of the position in the silica crucible and silicon contamination due to the silica crucible. The surface values are given in parentheses: (a) 550 ppm MgO (average of two experiments); (b) 1650 ppm MgO (average of three experiments).

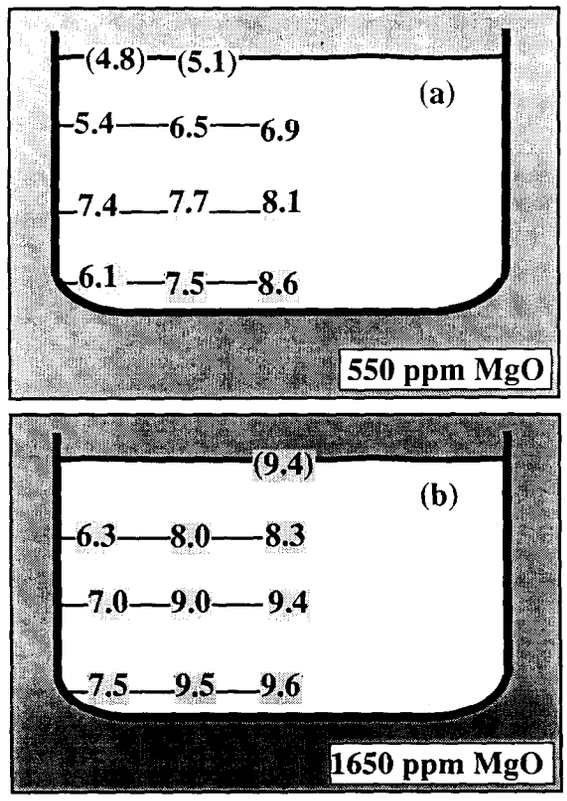


Fig. 4. BET surface area of the alumina powders doped with 550 and 1650 ppm MgO, as a function of the position in the silica crucible. Surface areas of powder near the outer surface are given in parentheses.

MgO and 13 ppm for those doped with 1650 ppm MgO. A comparison of the results of the amount of silicon from samples in the silica crucible (Fig. 1) with those for powders treated in the alumina crucible, allows determination of the amount of additional Si due to the contamination (Fig. 3).

BET analyses have been performed only on powders treated in the silica crucible. The surface area depends upon the position of the powder in the crucible, as shown in Fig. 4. The powders from position 7 have the largest surface area, while those taken near position 6 have the lowest values. One can recall that a decrease in surface area seen by BET corresponds to an increase in the grain size. In agreement with the BET analysis, SEM (JEOL 840 microscope) and TEM (80 kV Zeiss Model 902 electron energy loss (EEL) imaging microscope) observations show that the size of the grains increases with annealing time at 1300°C and when the amount of magnesium decreases (Fig. 5). The TEM observations also show that the grains have elongated and rounded forms and that they are highly agglomerated. Their size is between 50 and 400 nm, depending on the thermal treatment. A texture has been observed at the surface of some grains which may be due to spinel precipitates (cf. XPS analysis) but complementary observations must be performed to better define this texture.

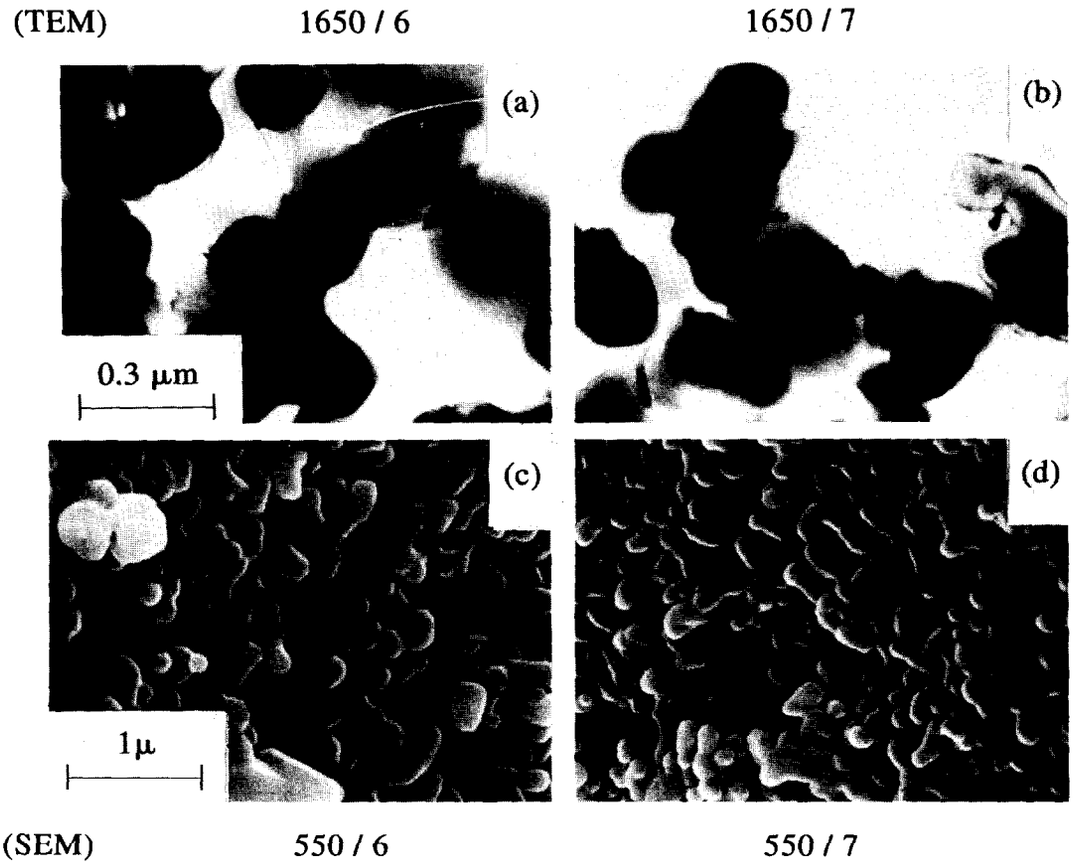


Fig. 5. Influence of the amount of magnesium and thermal treatment conditions on the size and microstructure of the alumina grains. TEM: (a) 1650 ppm MgO/position 6; (b) 1650 ppm MgO/position 7; SEM; (c) 550 ppm MgO/position 6; (d) 550 ppm MgO/position 7.

3.2 Nano-chemical analysis

XPS and EELS analysis has been performed to obtain information concerning the distribution of magnesium near the surface of the grains. Experimental details of these analyses are reported in a previous paper.[16] The trends of the two sets of results are similar. However, the error in quantifying the EELS data is large, and this method allows only an estimate of the magnesium concentration.[16] Consequently, we have concentrated on XPS analysis to examine the surface composition of the powders. Observations have been made on a perfectly flat surface of compacted powder. The results are obtained from a surface area of 0·8 × 0·8 mm. It may be pointed out that it is not possible to distinguish by XPS the Mg segregated in alumina grains from the Mg present in a second phase. Therefore, according to the amount of magnesium we have found, $MgAl_2O_4$ has been used as a standard. By analysing the magnesium lines (Mg_{1s}, Mg_{2s} and Mg_{2p}) it has been possible to obtain information on the total magnesium concentration near the surface of the grains. The escape depth of the Mg_{1s} electrons is about 0·5 nm (kinetic energy = 187 eV), while for the Mg_{2s} and Mg_{2p} electrons (with kinetic energies of 1387 and 1437 eV, respectively) it is about 2·0 nm. The Mg_{1s} signal allows us to determine a mean concentration of magnesium over the first 2 or 3 monolayers at the surface of the grains, while the Mg_{2s} and Mg_{2p} signals give a mean concentration over a depth of about 2·0 nm. The error in quantification is quite large because of the morphology of the samples and can be estimated to be 0·3–0·4 at%. Nevertheless, it should be noted that the reproducibility of the results is generally better than 0·1 at%. Furthermore, the Mg_{2s} peak gives more accurate data than the Mg_{2p} peak, because of peak overlaps.

3.2.1 Powders treated in silica crucibles

The XPS results obtained with the powders treated in the silica crucible (positions 6 and 7) are given in Table 2. They show a high magnesium concentration over the first two or three monolayers (Mg_{1s}) at the surface of the grains and this

Table 2. Amount of magnesium (at%) determined by XPS at the near surface of the alumina powder treated in a silica crucible. These results represent the mean of 6 different experiments. The reproducibility of the data is better than 0·1 at%

Analysis depth / *Sample*	*0·5 nm* (Mg_{1s})	*2 nm* (Mg_{2s})	*2 nm* (Mg_{2p})
Al_2O_3–1650/6	4·7	1·0	0·9
Al_2O_3–1650/7	4·4	1·0	1·0
Al_2O_3–550/6	3·4	1·0	0·7
Al_2O_3–550/7	2·4	0·6	0·5

enrichment is related to both the amount of magnesium in the powder and to its position in the crucible. Less surface segregation is observed in the alumina powder doped with 550 ppm MgO (0·07 at% Mg with respect to the cationic site number), and the powder from position 7 appears to have less segregation than the powder from position 6. The magnesium enrichment factor (atomic surface concentration in Mg divided by the average atomic concentration in Mg) over the first 2 or 3 monolayers calculated from these results is about 30 for the powder doped with 0·21 at% Mg (1650 ppm) and 80 for the powder containing 0·07 at% Mg (550 ppm). It is likely that precipitates of $MgAl_2O_4$ are also present at the surface of the grains, according to the limit of solubility of Mg in alumina.[17]

Figure 6 shows the mean concentration of magnesium in a depth of 2·0 nm (Mg_{2s}) as a function of the mean concentration in the first 2 or 3 monolayers (Mg_{1s}). The data exhibit a straight line whose gradient is 1/4. This value corresponds to the ratio of the analysis depth, and therefore suggests that the magnesium segregated mainly on a depth lower than or equal to 0·5 nm, leading to a Mg-enriched near-surface layer including the precipitation of the spinel phase. Figure 7 shows the different information that can be deduced from Mg_{2s}/Mg_{1s} relationships, according to the position of the experimental results in the graph. When the magnesium segregation increases, a saturation effect occurs near the surface (depth equal to 0·5 nm) and this leads to an increase in the segregation depth. The experimental results deviate then

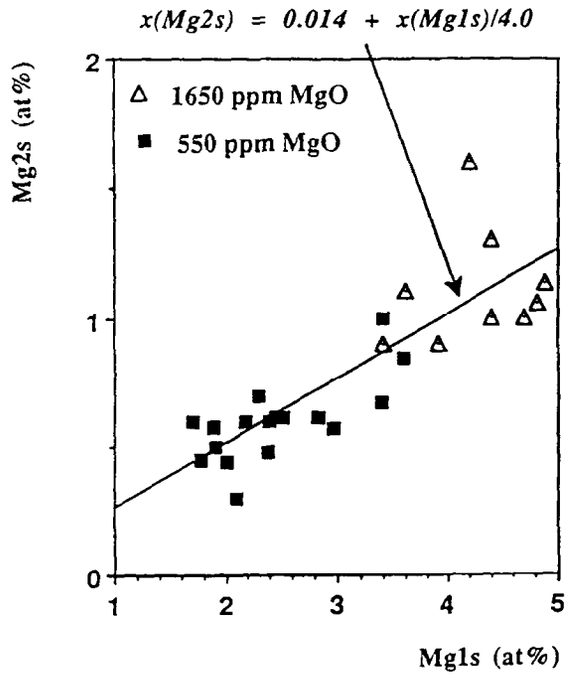


Fig. 6. Concentration of magnesium in a depth of 2·0 nm (Mg_{2s}) as a function of the concentration in a depth of 0·5 nm (Mg_{1s}).

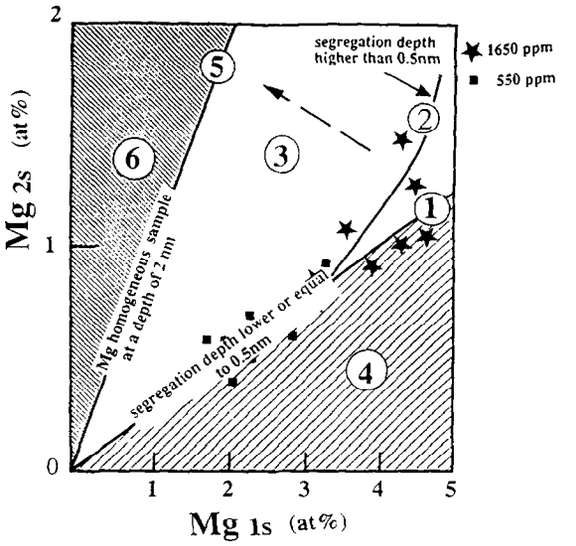


Fig. 7. Information that can be obtained from a representation of the concentration of magnesium in a depth of 2 nm (Mg_{2s}) as a function of the concentration in a depth of 0·5 nm (Mg_{1s}). When the Mg segregation increases, a saturation effect occurs at a depth of 0·5 nm (line 1) and the segregation depth increases (line 2 or in a general way area 3). When the experimental results are in area 6, the concentration of Mg decreases near the surface. The sample is homogeneous on a depth of 2 nm when the experimental results are on line 5.

from the straight line 1, whose gradient is equal to 1/4 (Fig. 7). In agreement with the results reported in Fig. 6 and Table 2, the saturation effect observed at a depth of 0·5 nm is of course more likely when both the magnesium concentration in the powder and the size of the particles increase.

The previous results (Fig. 6) are in agreement with the estimate of the repartition of magnesium in the grains (Fig. 8). Indeed, taking into account the amount of magnesium in the powder and the XPS results, it has been possible to determine the mean concentration of magnesium at a depth of 0·5 and 2 nm, respectively, in the particles assumed to be spherical. Their size has been estimated from

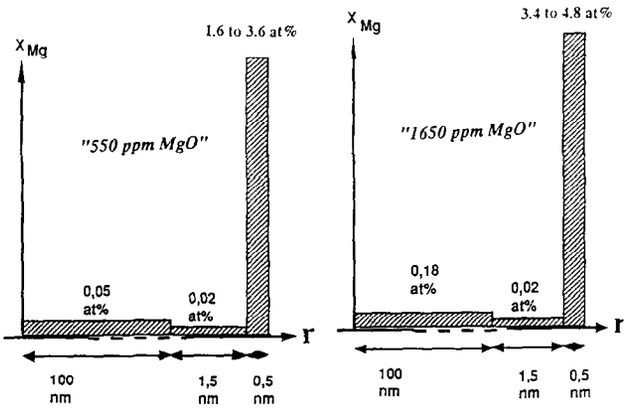


Fig. 8. Distribution profile of magnesium through an alumina grain treated at 1300°C, in a silica crucible for both 550 and 1650 ppm MgO-doped powders. This estimation has been performed assuming the grains to be spherical and taking into account the mean concentration of Mg in the powder (chemical analysis) and the XPS results at 0·5 and 2 nm.

the BET surface-area results. The results reported in Fig. 8 represent schematically the distribution of Mg across the grain. A lowering of the magnesium concentration is observed at a depth higher than 0·5 nm. This observation is consistent with a Mg kinetic demixing during the cooling of the powder. Nevertheless, complementary experiments must be performed to check the influence of this parameter on the Mg redistribution in the alumina grains.

XPS also detected the presence of Na, but the other impurities (Si, Ca, Fe and K) were not found in these powders. It may be noted that the amount of Na in powders from position 6 (0·6 at%) is lower than in powders from position 7 (1·4 at%), in agreement with the chemical analysis reported in the last section.

3.2.2 Powders treated in alumina crucibles

As shown in Fig. 2, samples B, C, D, F, G and H have been maintained for the same time (1 h 47 min) at temperatures equal to or higher than 1200°C, in order that the size of the grains be of the same order of magnitude after the different thermal treatments. They have then been cooled at the furnace cooling rate, i.e. more slowly than the powders treated in the silica crucible. The XPS results reported in Table 3 seem to show a decrease in the magnesium segregation when the maximum temperature of annealing decreases. However, a small increase in the size of the grains seems to occur when the annealing temperature increases (Table 3) and complementary experiments must be performed to substantiate this conclusion, as we shall see in the next section. Concerning the effect of the annealing time, the results at 1250°C are consistent with those obtained in the silica crucible at 1300°C (positions 6 and 7). The segregation of Mg increases when the annealing time increases and the TEM observations show that this effect is accompanied by an increase in the size of the grains.

3.3 Effect of grain size and cooling rate

According to the results reported in Figs 4 and 5 and in Table 3, the size of the grains is strongly related to the thermal history of the powder. Consequently, it was important to check the influence of this parameter on the segregation phenomena. Figure 9 reports the mean concentration of magnesium in the first 2 or 3 monolayers (Mg_{1s}), as a function of the size of the grains, assumed to be spherical. The size has been estimated from the BET surface area measurements. In a few cases this has also been measured on the SEM images. Whatever the amount of magnesium in the powder, the segregation increases with the size of the grains. This effect is so important that it overshadows the influence of the other parameters. It is thus difficult to draw definite conclusions with regard to the influence of annealing temperature and cooling rate on magnesium surface segregation. However, it seems that a decrease in cooling rate favors the segregation of silicon. Indeed, this impurity has been detected by XPS only in powders treated in alumina crucibles, which have a lower amount of silicon (around 13 and 26 ppm in the powders doped with 1650 and 550 ppm of MgO, respectively), than those treated in a silica

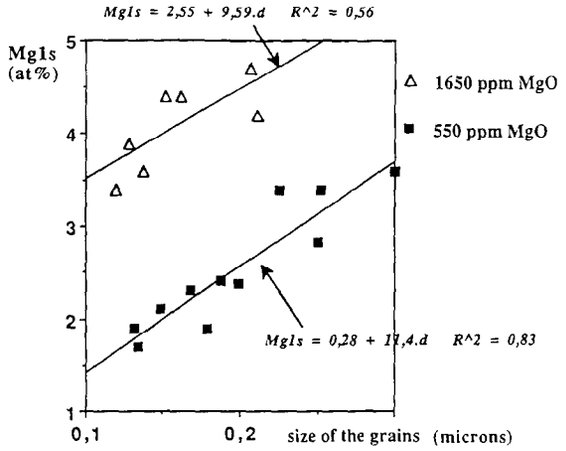


Fig. 9. Influence of the amount of magnesium and of the size of the grains on the magnesium concentration in the first 2 or 3 monolayers (depth 0·5 nm) at the surface of the grains.

Table 3. Amount of magnesium, silicon and sodium (at%) determined by XPS at the near surface of the alumina powder treated in an alumina crucible and cooled at the furnace cooling rate. (Concentration of Si over a depth of 2·4 nm; concentration of Na over a depth of 1·0 nm)

Experiment	*Temperature (°C)*	*Time*	*Grain size (SEM)*	*XPS Mg_{1s} (at%)*	*XPS $Mg_{2s,2p}$ (at%)*	*XPS Na_{1s} (at%)*	*XPS Si_{2s} (at%)*
A1	1200		0·3 μm	3·57	0·85–1·13	2·30	–
A2				3·60	0·82–0·67	2·19	0·56
D	1200	1 h 47 min	0·18 μm	1·89	0·58–0·58	1·06	0·25
E	1250	1 h		2·00	0·44–0·56	0·65	–
G	1250	1 h 22 min		2·18	0·60–0·69		
I	1250	2 h 30 min		3·39	0·67–0·53	1·53	0·20
C	1300	56 min	0·2 μm	2·38	0·48–0·60	0·52	–
H	1300	56 min		2·52	0·61–0·57	1·39	–
B	1378	1 s	0·25 μm	2·83	0·61–0·52	1·01	0·23
F	1378	1 s		2·97	0·57–0·64	0·88	–

crucible (Fig. 1) but which have been cooled more slowly (furnace rate).

It may be pointed out that the results reported in Fig. 9 are consistent with the estimation of the repartition of Mg through the grain, assumed to be spherical (Fig. 8). Indeed, if we take into account that practically all the dopant has segregated at the near surface of the grain, i.e. over a thickness equal to 'e' (0·5 nm, for example), with $e<<R_{grain}$, it is possible to write, for a given amount of dopant: $V_{total}/V_{grain})4\ \pi\ R^2 e\ C_{surf}$ = constant (where V_{total} is the total volume of the powder, C_{surf} the near-surface concentration of the dopant in a thickness 'e' and R is the grain radius). One obtains from this expression:

$$C_{1surf}/R_1 = C_{2surf}/R_2 = \text{constant}$$

Then one can verify that the surface concentration is proportional to the grain radius (R_{grain}).

4 Conclusions

This study has allowed us to illustrate the influence of the thermal treatment conditions on the microchemistry and microstructure of alumina powders doped with 550 and 1650 ppm by weight of MgO. SEM and TEM observations, as well as surface-area measurements, have allowed us to show that the size of the grains is strongly related to the amount of magnesium and to the thermal treatment conditions (temperature and annealing time). Quantitative XPS analysis shows that Mg, Na and Si are segregated at the near surface of the grains. In the case of Mg, this is likely to lead to the formation of $MgAl_2O_4$ precipitates. Furthermore, the results obtained show clearly that the magnesium surface enrichment increases with the size of the grains. However, it is difficult to draw conclusions regarding the influence of the cooling rate, as well as the effect of the temperature and annealing time. These effects are overshadowed by the effect of grain size. Complementary experiments must be performed on powders of the same grain size, in order to eliminate the important influence of this parameter. For Si and Na, their surface concentration seems to increase when the cooling rate decreases.

Finally, this study shows that it is possible to control the concentration of dopants or impurities at the near surface of the grains by changing only the thermal treatment conditions of the powder. Of course, such segregation phenomena, which can lead to the precipitation of a second phase at the near surface of the grains, confer specific properties to the powder. Nevertheless, complementary experiments must be performed in order to obtain a better understanding of the role played by parameters such as the cooling rate and the surrounding atmosphere.

Acknowledgements

This work has been sponsored by the Ministère de la Recherche et de la Technologie-département Matière et Matériaux, contract no. 90 A 0220. The authors are indebted to J. C. Droguet and L. Du Repaire (Baikowski-Chimie-Annecy/France) for their collaboration and fruitful discussions.

References

1. Brook, R. J., The Materials science of ceramic interfaces. In *Surfaces and Interfaces in Ceramic Materials*, eds. L. C. Dufour, C. Monty & G. Petot-Ervas. Kluwer Acad. Press, 1989, E 173, pp. 23–37.
2. Clarke, D., Intergranular phases in polycrystalline ceramics. In *Surfaces and Interfaces in Ceramic Materials*, eds. L. C. Dufour, C. Monty & G. Petot-Ervas. Kluwer Acad. Press, 1989, E 173, pp. 57–79.
3. Carter, C. B., Structure of interfaces in ceramic materials. In *Surfaces and Interfaces in Ceramic Materials*, eds. L. C. Dufour, C. Monty & G. Petot-Ervas. Kluwer Acad. Press, 1989, E 173, pp. 29–53.
4. Kingery, W. D., Segregation phenomena at surfaces and at grain boundaries in oxides and carbides. *Solid State Ionics*, **12** (1984) 299–308.
5. Handwerker, C. A., Cannon, R. M. & French, R. H., A retrospective. *J. Am. Ceram. Soc.*, **77**(2) (1994) 293–7.
6. Badley, R. D. & Johnson, D. L., Effect of magnesia on grain growth in alumina, structure and properties of MgO and Al_2O_3 ceramics. *Adv. in Ceram.*, **10** (1984) 666–78.
7. Bennison, S. J. & Harmer, M. P., A history of the role of MgO in the sintering of α-alumina, sintering of advanced ceramics. *Ceram. Trans.*, **7** (1990) 13–49.
8. Handwerker, C. A., Morris, P. A. & Coble, R. L., Effects of chemical inhomogeneities on grain growth and microstructure in Al_2O_3. *J. Am. Ceram. Soc.*, **72**(1) (1989) 130–6.
9. Bae, S. I. & Baik, S., Critical concentration of MgO for the prevention of abnormal grain growth in alumina. *J. Am. Ceram. Soc.*, **77**(10) (1994) 2499–504.
10. Coble, R. L., Song, H., Brook, R. J., Handwerker, C. A. & Dynys, J. M., Sintering and grain growth in alumina and magnesia, structure and properties of MgO and Al_2O_3 ceramics. In *Advances in Ceramics*, Vol. 10, ed. W. D. Kingery. The American Ceramic Society, 1984, pp. 839–52.
11. Petot-Ervas, G. & Petot, C., Surface segregation in ceramic materials during cooling or under a temperature gradient. *J. Eur. Ceram.*, **6** (1990) 323–30.
12. Monceau, D., Petot, C. & Petot-Ervas, G., Kinetic demixing profile calculations in oxide solid solutions under a chemical potential gradient. *Solid State Ionics*, **45** (1991) 231–7.
13. Monceau, D., Petot, C. & Petot-Ervas, G., Kinetic demixing profile calculation under a temperature gradient in multi-component oxides. *J. Eur. Ceram.*, **9** (1992) 193–204.
14. Monceau, D., Modélisation des phénomènes de 'ségrégation dynamique' dans les céramiques — Conséquences sur l' élaboration des poudres et des monocristaux d'alumine-α dopée. Thesis, University Paris XIII (1992).

15. Petot-Ervas, G., Lartigue, S., Severac, C., Barj, M. & Petot, C., Surface impurity segregation in submicronic alumina. In *Structural Ceramics, Proceeding, Microstructural and Properties*, eds J. J. Bentzen & J. B. Sorensen. Risø National Laboratory, Roskilde, Denmark, 1990, pp. 459–63.
16. Monceau, D., Petot-Ervas, G., Petot, C., Fraser, J. W., Graham, M. J. & Sproule, G. I., Influence of the thermal treatment on the microstructure and microchemistry of α-alumina powders doped with magnesium, *J. Eur. Ceram. Soc.*, **12** (1993) 337–41.
17. Roy, S. K. & Coble, R. L., Solubilities of magnesia, titania and magnesium titanate in aluminum oxide. *J. Am. Ceram. Soc.*, **51** (1968) 1–6.

Journal of the European Ceramic Society **15** (1995) 859–865
Elsevier Science Limited
Printed in Great Britain
0955-2219/95/$9.50

0955-2219(95)00027-5

Quality Assessment of MgO Substrate Materials for High T_c Superconductor Thin Films using Cathodoluminescence Microscopy

P. R. Fletcher[a] & C. Leach[b]

[a]Department of Materials, Imperial College, Prince Consort Road, London, SW7 2BP, UK
[b]Manchester Materials Science Centre, University of Manchester, Grosvenor Street, Manchester, M1 7HS, UK

(Received 10 June 1994; revised version received 10 February 1995; accepted 14 February 1995)

Abstract

Cathodoluminescence (CL) microscopy has been used to investigate the luminescence response of MgO single crystal substrates intended for high T_c *superconductor applications. Wavelength resolved CL spectra have been collected from both the surface and the bulk of the MgO single crystals, under different preparatory treatments. It was found that annealing the MgO resulted in the reduction of luminescent surface defect states present in the as-received and ion milled samples and at sites of surface damage. The surface treatment given to MgO single crystals can significantly affect the electrical properties of high* T_c *superconducting thin films deposited on them.*

Introduction

$YBa_2Cu_3O_{7-\delta}$ high T_c superconducting thin films, produced by laser ablation or sputtering, are frequently grown in an epitaxial relationship on MgO single crystals. The substrate/film lattice mismatch, however, will give rise to coherent or semi-coherent heterophase boundaries that can affect the performance of the thin film. In this respect the surface quality of the substrate is an important parameter in the construction of good epitaxial thin films as any disturbance in the substrate will ultimately be incorporated in the film structure.[1,2] Optimisation of deposition parameters maximises the number of *c*-axis oriented grains.

In a previous study, the observation of CL in the scanning electron microscope (SEM) and the light microscope was applied to the problem of locating and determining the nature of impurity phases within YBCO polycrystalline pellets.[3] Here the technique has been applied to the study of MgO single crystals intended as substrates for the production of superconducting thin films. MgO has a band gap of 7·7 eV[4] which is too big for direct CL emission, but the presence of impurities at parts per million (ppm) levels, local deformation, or defect structures can give rise to extra states in the band gap that allow a number of luminescent emissions to be observed in the visible range via electron beam excitation.

Slip planes in deformed and compressed single crystals display bright contrast in CL emission.[5–8] Datta *et al.*[5] recorded blue emission from the slip planes with a CL band at 466 nm; the undeformed crystal containing two CL bands at 425 nm and 488 nm. Changes in the slip plane luminescence intensity can be brought about by annealing, causing some planes to appear in dark contrast.[8] An excitation peak at 500 nm[7] in compressed crystals is attributed to the generation of F centres.

Vickers indentations in MgO have also been analysed in CL[8–10] and luminescence variations attributed to differences in the density of point defects. Piqueras *et al.*[9] observed CL intensity variation across indentations which appeared dark at the centre and bright at the edge of the deformation band. The dark CL contrast was attributed to a high density of defects at the centre, quenching the CL emission. Annealing caused the centre of the indent to luminesce as a result of the diffusion and annihilation of these point defects.[8] A broad band of emission at 400–420 nm was observed from some of the dislocation etch pits due to the impurities or point defects that surrounded them.[6] Away from the dislocations, two CL peaks were present at 400 and 430 nm. Frictional damage of MgO by 2 mm tungsten carbide balls gave rise to a non-luminescent region within the track with luminescence at the edges due to the highly distorted layer beneath the surface containing defects.[11]

Impurities contained within the MgO, particularly iron, have been shown to play a role in defining both the overall CL intensity and spectral response. Emissions in the red region have been found to increase with higher Fe doping in some cases[5] but not others.[6] Without knowing the precise overall impurity levels within the MgO crystals, correlation between workers'[1] sets of results for the band structure can only be speculative. This occurs because some impurities act to increase luminescence, whilst others can 'quench' or 'kill' emissions. In fact, a non-linear relationship of CL intensity versus concentration can be seen with some impurity atoms where increasing concentrations at first increase CL intensity, but then at some critical defect density, the introduced states interact and CL can be lost.

Other luminescence techniques such as fluorescence, radioluminescence, photoluminescence, thermoluminescence (TL), and gamma irradiation[12–19] have also been used to attempt to correlate the occurrence of certain impurities in MgO with observable peaks in the visible region. Ni^{2+} doping has been related to the emissions at 478, 482, 486, and 491 nm.[12] This idea has been supported by Delgado[14] who proposed the $^1T_{2g}$–$^3A_{2g}$[14,17,19] transition in substitutional Ni^{2+} ions. Chromium ions have been associated with the peaks in the 700 nm region.[15–19] However, there is some controversy about the role of the iron impurities and some suggest[18] that this impurity gives rise to red luminescence as well as chromium. However, Sathyamoarthy *et al.*[19] found in his samples that Fe acts to quench the observed TL intensity. Other impurity elements such as cobalt and copper also reduce the luminescence from MgO, whereas manganese has been seen to increase luminescence with a band at about 600 nm.[19]

For superconducting thin film fabrication, some workers[1,21,22] have considered pre-treatments before deposition. Of these, the most successful has been annealing the MgO at 1273–1473 K either in air or in oxygen. Awaji *et al.*[21] reported the removal of CL spots by annealing suggesting that any contamination layer on the MgO was removed. Moeckly *et al.*[22] concluded that films on annealed MgO substrates produced the higher T_c and J_c response. This finding has also been reproduced in previous work.[23] The reason is connected to improved surface crystallinity in the substrate.

The effect of substrate defects on thin films has been studied by Barkay *et al.*[24] They determined that cleavage slip steps in the substrate, observable by CL, disrupted the thin film. The step defects that they observed were of the order of microns in height and hence should be observable by normal optical microscopy.

This paper describes the CL technique as a method for assessing the surface structure quality of the MgO single crystals prior to superconducting film deposition and addresses the problem of characterising defects too small to be seen by light microscopy, but which are believed to affect the film microstructure.[23]

Experimental Method

MgO single crystals, 99·99% purity, were obtained from PI-KEM. The major impurity was ~5 ppm iron, with all other elements at lower levels than this. A piece of single crystal MgO was cleaved into three strips for each of the following surface treatments:

- annealed at 1273 K for 10 h in O_2 then cooled to RT in oxygen,
- ion milled for 30 h using argon,
- as-received (the control sample).

Using strips from the same MgO sample was necessary to obtain samples with identical impurity contents. This allowed the effect of the treatments on the CL emission to be compared. The samples were cleaned in ethanol using an ultrasonic bath and then rinsed with acetone. A light carbon coat was applied to eliminate charging in the SEM.

Panchromatic CL images of the samples were recorded in colour using a Technosyn Cold Cathode Luminescence stage, model 8200MK11, fitted to a light microscope. This was operated at 15 keV and 200 μA load current, illuminating approximately 1 cm^2 of the sample surface.

Collection of the CL emissions was carried out using an Oxford Instruments CL detector and wavelength resolved by a Bentham monochromator with a slit width of 0·4 mm. The MgO samples were cooled to 77 K which reduced band broadening and increased the overall CL intensity. Higher order diffraction peaks were eliminated by the use of two optical filters at 400 and 700 nm respectively. A linear response GaAs solid state detector with a useful wavelength range of 400–900 nm amplified any emissions. Noise output from the detector was reduced by cooling to 273 K. The secondary electron and CL images were generated in a Jeol JSM 840A scanning electron microscope. For each analysis, the CL collection mirror was optimally focused and accurate beam currents were measured using a Faraday cage. The electron beam conditions ranged from 5 to 20 keV and 3 to 9 nA.

Results

Some variability in CL emission (both chemically and mechanically induced) was noted between as-received MgO crystals from different batches and so obtaining single crystals from the same melt and to a good polished quality is very important in any comparative work.

The colour micrographs in Fig. 1(a) (transmitted light optical) and Fig. 1(b) (CL) demonstrate the benefits of CL microscopy over optical for observing fine surface damage in MgO single crystals. Figure 1(b) clearly shows sharply defined blue lines in CL at the surface of the substrate. No surface damage can be seen in the optical image of Fig. 1(a).

Figure 2(a–c) illustrates the effects on the CL images of ion milling and annealing MgO single crystals. The micrograph in Fig. 2(a) shows dark red lines, possibly at the sites of subgrain boundaries, running throughout the as-received sample. Ion milling the surface (Fig. 2(b)) resulted in a pronounced increase in the light blue excitations generated from the surface layer. Annealing decreased the intensity of these CL excitations which resulted in the sample having strong luminescent emission in the red region. The dark red lines are now unresolved.

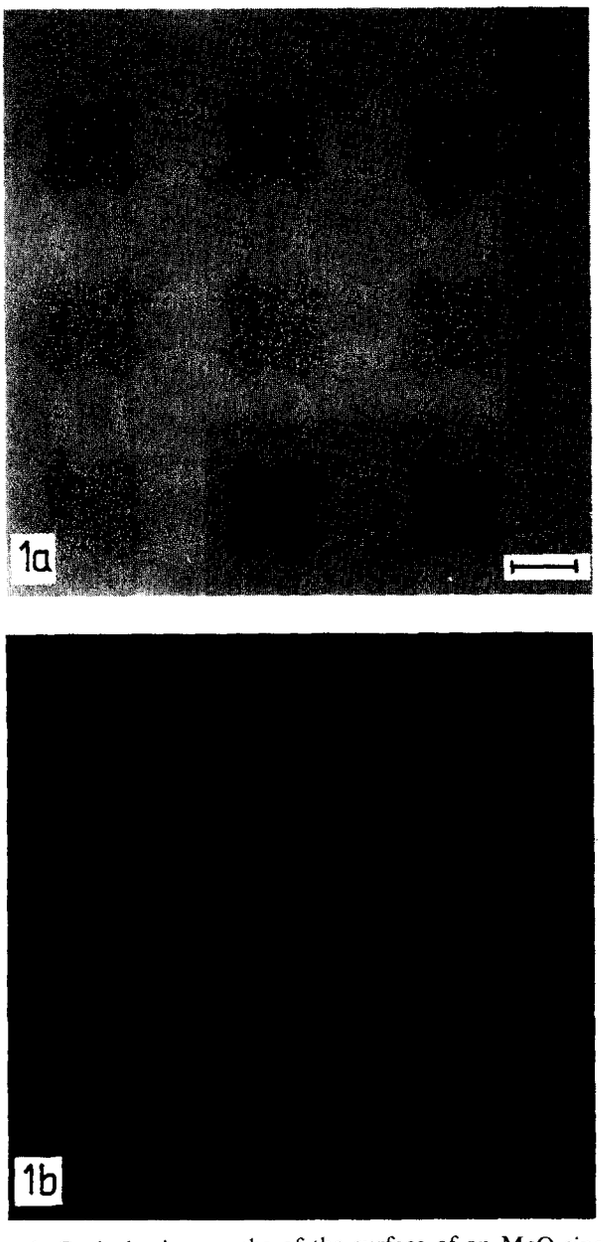


Fig. 1. Optical micrographs of the surface of an MgO single crystal: (a) normal mode and (b) CL mode (scale bar = 200 μm).

Wavelength resolved CL examination of the substrates in the SEM is illustrated in Fig. 3(a–d). The luminescence response generated from the bulk and from the surface were determined by using accelerating voltages of 5 and 20 keV. Using the Kanaya equation[25] 5 keV corresponded to 0·07 μm penetration depth and 20 keV to 0·78 μm depth, for the surface and bulk analysis respectively. On comparing Fig. 3(a) and (c), sharp peaks are observed from the bulk but not the surface around the 480 nm region. The spectra collected at 20 keV in Fig. 3(c) all display sharp peaks at 477, 481, 486 and 490 nm. The low CL emission at 5 keV meant that spectral resolution was poor, and hence no peaks could be resolved in Fig. 3(a).

Comparison of Fig. 3(a) with the colour micrographs (Fig. 2(a–c)), indicate good CL correlation between the systems. Ion milling the surface results in the highest proportion of luminescent defect states at wavelengths above 500 nm, with bands at 540, 560 and 630 nm. The annealed sample had the lowest CL intensity. Consideration of Fig. 3(b) and (d), analysing the surface and bulk luminescence generation respectively, illustrate similar spectra between the ion milled and as-received samples. Several peaks are present in the red region, between 696 and 740 nm. One unusual feature is the presence of a broad excitation band stretching from 750–850 nm. However, the annealed spectrum differs in one major respect from the as-received and ion milled samples, as the peak intensity at 867 nm is greatly reduced.

The wavelength resolved data in Fig. 4(a) and (b) show the effect of surface damage. Using spot mode at 10 keV and 6 nA resulted in the CL signal to noise ratio being sufficient for data collection without appreciable sample damage. In Fig. 4(a), the spectrum collected from the scratch has around 10 times the CL intensity of that from an undamaged area. Numerous luminescent states are generated throughout the visible range demonstrating that the electronic band structure is greatly disrupted. The 540, 560 and 630 nm bands are all clearly visible. However annealing the surface damage (Fig. 4(b)) returns the spectrum close to that of the undamaged surface.

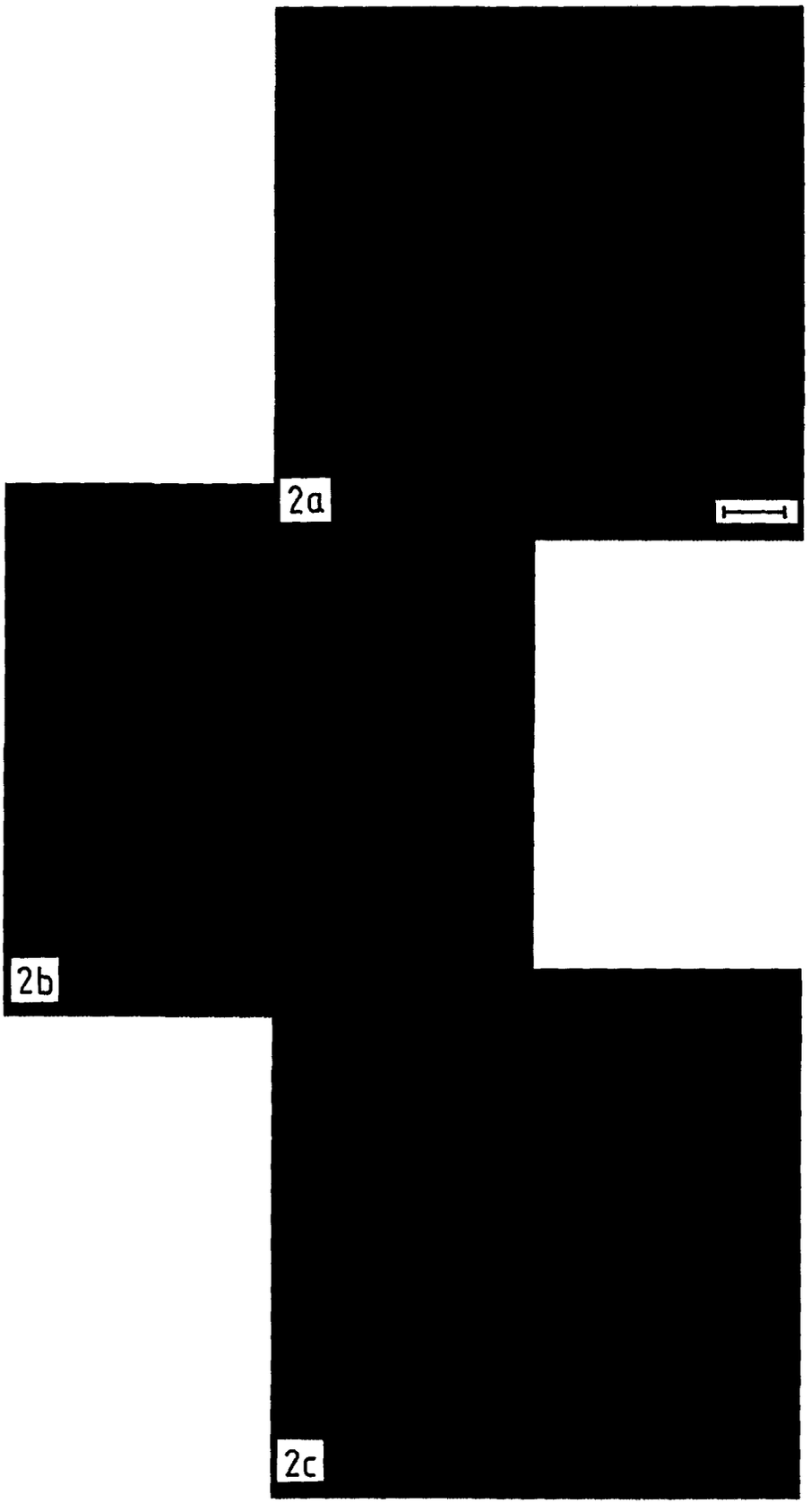


Fig. 2. CL micrographs showing the luminescent emissions of the MgO under the surface treatments of: (a) as-received, (b) ion milled and (c) annealed (scale bar = 200 μm).

Discussion

Assessment of the quality of MgO substrates, suitable for high T_c thin film deposition, can be carried out quickly by optical CL. Surface damage, which greatly affects the quality of epitaxial thin film growth, is easily observed due to local disruption of the electronic band structure at the site of flaws giving rise to bright CL contrast. However, other workers have reported the CL intensity to

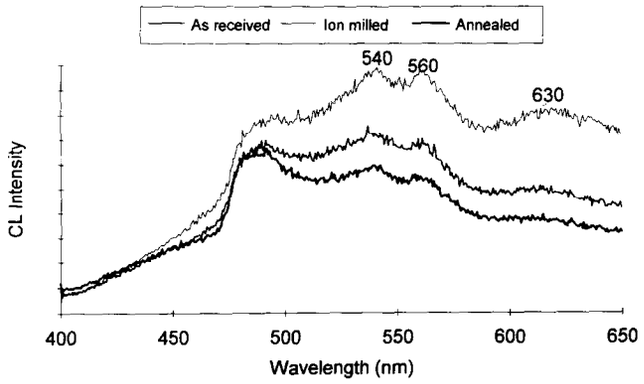


Fig. 3(a). CL intensity versus wavelength for the three surface treatments collected under the conditions of 5 kV, 9 nA in the SEM at 77 K using spot mode.

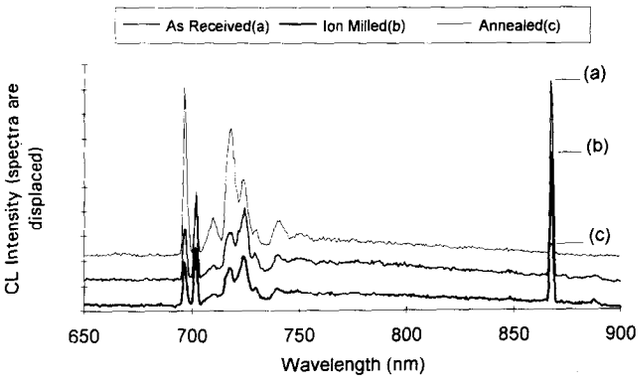


Fig. 3(b). CL intensity versus wavelength for the three surface treatments collected under the conditions of 5 kV, 9 nA in the SEM at 77 K using spot mode.

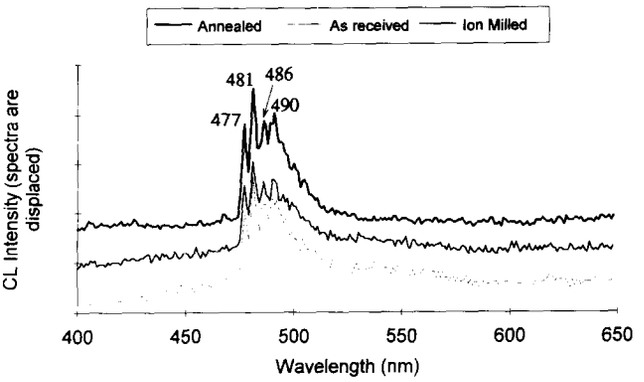


Fig. 3(c). CL intensity versus wavelength for the three surface treatments collected under the conditions of 20 kV, 3 nA in the SEM at 77 K using spot mode.

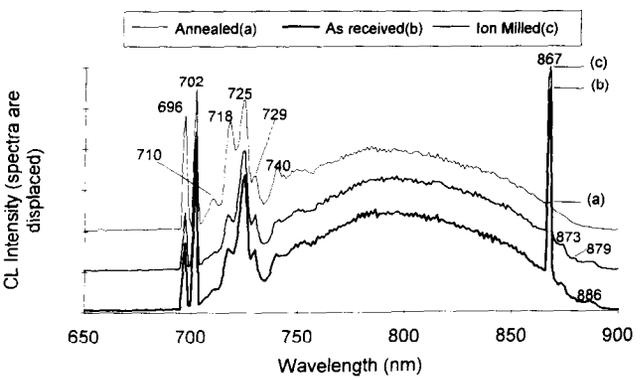


Fig. 3(d). CL intensity versus wavelength for the three surface treatments collected under the conditions of 20 kV, 3 nA in the SEM at 77 K using spot mode.

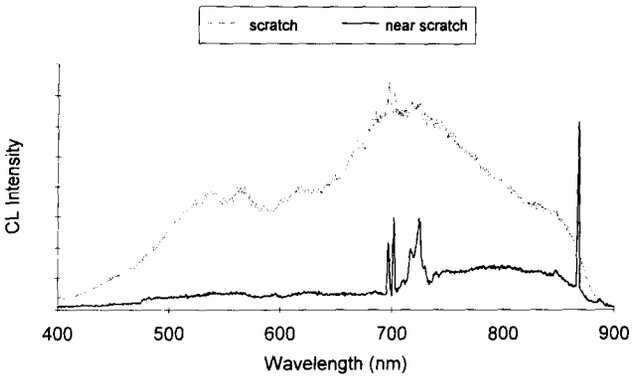


Fig. 4(a). CL wavelength analysis near and at a surface scratch in the as-received MgO. Conditions: 10 kV, 6 nA, spot mode.

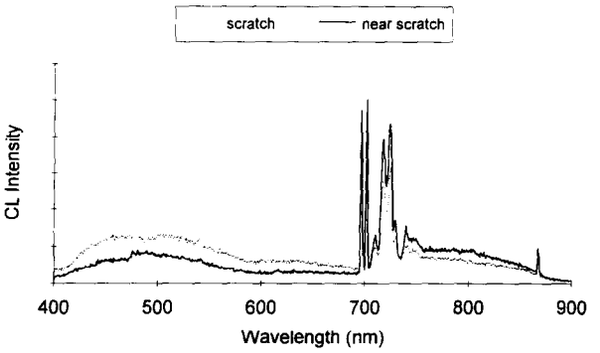


Fig. 4(b). CL wavelength analysis near and at a surface scratch in the annealed MgO. Conditions: 10 kV, 6 nA, spot mode.

be dependent upon the density of defect sites, with a high density giving rise to low CL emission.[8] Analysis of other single crystals, with optically visible surface flaws, confirmed that the surface damage displays a characteristic luminescence emission. Hence, in this study, the sharp blue lines in MgO single crystals are concluded to be due to fine surface flaws, that cannot be resolved using normal light microscopy. The damage observed by CL and described in this paper is much finer than that previously studied[24] and is generally not observable by normal light microscopy. Other researchers have also observed dislocations in CL contrast,[6,24] but were not able to correlate them with red luminescence. It is well documented that substitional Cr^{3+} ions are responsible for the red peaks between 696 and 701 nm. The direct transition is believed to be ^2E–$^4A_2$.[13,18] From the data presented here, it is not easy to judge the true position of the direct electronic transition as no system response correction was made to the data, but it is reported to lie at 698 nm.[13]

The peaks at 710, 718 and 724 nm resemble a direct transition with vibrational side bands. These could be connected to Fe^{3+} ions, but there is no evidence of this in the literature, although it has been suggested that Fe^{3+} gives rise to red luminescence.[18]

The broad blue emissions, in the colour micrographs of the as-received and ion milled samples occur uniformly within the samples. The spectroscopic analysis reveals four distinct excitations (476, 481, 486 and 490 nm), from the bulk (20 kV), which correlate very well with the TL data of Ralph *et al.*[12] for substitutional Ni^{2+} ions undergoing the $^1T_2$–$^3A_2$ transition.[14,17,19] Monochromatic CL imaging in the SEM at 480 and 700 nm was not able to identify the dislocations, because of the detector's small area of focus, hence any differences in the CL excitation spectra at the dark red lines, believed to be sub-grain boundaries, could not be determined.

Spectroscopic analysis of the surface at 5 keV beam energy, however, showed the band attributed to the Ni^{2+} ions together with luminescent transitions giving rise to bands at 540, 560 and 630 nm. The intensity of these emissions was found to be dependent upon the surface treatment suffered by the MgO, with the ion milled surface showing an increased CL intensity compared with the other two. Figure 3(a) shows that the as-received sample also has some defect band transitions. Residual lattice strain in the surface, caused by mechanical polishing prior to their supply, would be expected to alter the electronic band structure. This may be connected to the three luminescent bands. Ion milling appears to have enhanced these defects. The CL spectrum from the annealed specimen shows some recovery of the surface deformation and elimination of defects resulting in the CL intensity of the defect bands being much lower. These bands at 540, 560 and 630 nm are possibly connected to surface defect states associated with atomic scale surface roughness, as the bulk spectra displayed no such bands above noise levels. Annealing would result in the reconfiguration of the surface layers, reducing the density of defect states, thus giving a reduced CL intensity for these bands.

The spectra in Fig. 3(b) and (d) contain two peaks that have not been previously described. The emission at 867 nm is dominant in both, but annealing reduces its intensity considerably. Associated with this are four small peaks at 873, 880 and 886 nm, all of which are removed during annealing. The narrow width of the peak at 867 nm suggests a direct transition, with the small peaks being vibrational side bands. This could possibly be the result of surface contamination, as MgO suffers degradation when exposed to the atmosphere through chemisorption of H_2O and CO_2[20], but for the presence of peaks at 20 keV in the as-received and ion milled samples. Presumably, either the electronic configuration of the MgO is being affected by the anneal, which acts to remove vacancy sites, or an impurity ion is diffusing through the sample.

The presence of surface flaws in the MgO substrate greatly affects the local electronic band structure. Similar defects, albeit larger, from cleavage steps, have been described by Barkay *et al.*[24] However, their use of large excitation volumes (beam energies of 30 keV) meant that CL collection was predominately from the bulk and not from the surface. The spectra in Fig. 4(b) show that the CL intensity is reduced by annealing the substrate. The CL emissions from an annealed flaw are now very similar to that of the undamaged substrate. However, the gross flaws that can be seen optically are not removed by the anneal; only the luminescent defect states associated with the flaw have been removed, whilst the flaw itself remains.

Superconducting thin films of YBCO have been grown onto similarly treated MgO substrates which contain defects, and the film morphologies determined.[23] At the site of a defect, porosity was observed in the film microstructure. For example, the defect width in an YBCO film deposited on an annealed substrate was about 200 nm. Hence it is seen that fine defects in the substrate, not easily observable by optical methods can affect the thin film nucleation and growth processes, resulting in unwanted defects in the final microstructure. This is undesirable for electronic device applications.

Conclusions

The preparation of MgO single crystals has been successfully monitored by the CL technique. The optical and spectroscopic CL systems have enabled the identification of both Ni and Cr impurities, and the assessment of surface quality, with respect to treatment. Annealing has resulted in the removal of surface defect states, which are responsible for the luminescence in both the untreated and ion milled samples. Also luminescent defects states associated with surface scratches are virtually removed on annealing. It is concluded that, with respect to high T_c thin films, the process of annealing results in a marked improvement in the thin film electrical properties.

Acknowledgements

The authors acknowledge the support of a SERC postgraduate studentship with additional CASE support from the National Physical Laboratory, Teddington, UK.

References

1. Norton, M. G. & Carter, C. B., Growth of $YBa_2Cu_3O_{7-\delta}$ thin films — nucleation, heteroepitaxy and interfaces. *Scanning Microscopy*, **6** (1992) 385–98.
2. Zandbergen, H. W., Wen, J. G., Traeholt, C. & Svetchnikov, V., Nanostructural characterisation of interfaces of thin films of $YBa_2Cu_3O_7$ with various kinds of substrates. *J. Alloys Compounds*, **195** (1993) 85–92.
3. Fletcher, P. R. & Leach, C., Impurity phase recognition in YBCO high T_c superconductors by cathodoluminescence spectroscopy. *J. Mater. Sci.*, **28** (1993) 6774–8.
4. Kuusmann, I. L. & Fel'dbakh, E. Kh., Edge cathodoluminescence of MgO crystals in the vacuum ultraviolet. *Sov. Phys. Solid State*, **23** (1981) 259–62.
5. Datta, S., Aeberli, K. E., Boswarva, I. M. & Holt, D. B., SEM analyses of cathodoluminescence in MgO, CdS and $GaAs/Ga_x\ Ak_{1-x}$ As crystals. *J. Microscopy*, **118**(3) (1980) 367–73.
6. Llopis, J., Piqueras, J. & Ballesteros, C., Influence of purity on cathodoluminescence from dislocations in MgO. *Phys. Stat. Sol. A*, **70** (1982) 739–46.
7. Namba, H. & Murata, Y., Surface discloation of MgO(100) studies by secondary electron emission spectroscopy and cathodoluminescence spectroscopy. *J. Physical Soc.*, **53** (1984) 1888–98.
8. Llopis, J., Ballesteros, C., Piqueras, J., Remon, A. & Gonzalez, R., Thermally induced changes in the cathodoluminescence image of deformed MgO. *Phys. Stat. Sol. A*, **78** (1983) 679–84.
9. Piqueras, J., Llopis, J. & Delgado, L., Cathodoluminescence from defects in of indented MgO. *J. Appl. Phys.*, **52** (1981) 4341–4.
10. Nazarova, T. A., Nazarov, M. V., Rau, E. I. & Saparin, G. V., Scanning microscopies of indented MgO crystals. *Scanning*, **14** (1992) 91–9.
11. Enomoto, Y. & Yamanaka, K., Cathodoluminescence at frictional damage in MgO single crystals. *J. Mater. Sci.*, **17** (1982) 3288–92.
12. Ralph, J. E. & Townsend, M. G., Fluorescence and absorption spectra of Ni^{2+} in MgO. *J. Phys. C Solid State Phys.*, **3** (1970) 8–18.
13. Chao, C. C., Charge-transfer luminescence of Cr^{3+} in magnesium oxide. *J. Phys. Chem. Solids*, **32** (1971) 2517–28.
14. Delgado, L., Charge transfer mechanisms in the thermoluminescence of MgO. *Nuclear Instr. Methods Phys. Res.*, **B1** (1984) 219–22.
15. Ziniker, W. M., Merrow, J. K. & Meuller, J. I., Thermally stimulated luminescence in MgO. *J. Phys. Chem. Solids*, **33** (1972) 1619–30.
16. Williams, R. T., Williams, J. W., Turner, T. J. & Lee, K. H., Kinetics of radiative recombination in magnesium oxide. *Phys. Rev. B*, **4** (1979) 1687–99.
17. Duley, W. W., Multiphonen excitation of visible and vuv luminescence in MgO crystals. *Optics Commun.*, **51** (1984) 160–2.
18. Clement, S. & Hodgson, E. R., Correlation between Fe, Cr and the broad red emission band in γ-ray-irradiated MgO. *Phys. Rev. B*, **30** (1984) 4684–8.
19. Sathyamoarthy, A. & Luthra, J. M., Mechanism of thermoluminescence in magnesium oxide. *J. Mater. Sci.*, **13** (1978) 2637–44.
20. Henderson, B. & Wertz, J. E., *Defects in Alkaline Earth Oxides*. Taylor and Francis, 1977, pp. 142–4.
21. Awaji, T., Sakuta, K., Sakaguchi, Y. & Kobayashi, T., Improved surface crystallinity of MgO crystal substrate through annealing in oxygen atmosphere. *Jpn. J. Appl. Phys.*, **31** (1992) 5B L642–L645.
22. Moeckly, B. H., Russek, S. E., Lathrop, D. K., Buhrman, R. A., Li, J. & Mayer, J. W., Growth of $YBa_2Cu_3O_7$ thin films on MgO: the effect of substrate preparation, *Appl. Phys. Lett.*, **57** (1990) 1687–9.
23. Fletcher, P. R., Leach, C., Wellhofer, F. & Woodall, P., Defect analysis in substrate materials for high T_c superconducting thin films. *MRS Symposium Proc., Epitaxial Oxide Thin Films and Heterostructures*, (accepted for publication).
24. Barkay, Z., Racah, D., Grunbaum, E. & Deutscher, G., Effect of substrate defects on the properties of high T_c superconducting thin films. *J. Appl. Phys.*, **73** (1993) 7585–90.
25. Yacobi, B. G. & Holt, D. B., *Cathodoluminescence Microscopy of Inorganic Solids*. Plenum, New York, 1990, pp. 58.

Journal of the European Ceramic Society 15 (1995) 867–874
© 1995 Elsevier Science Limited
Printed in Great Britain. All rights reserved
0955-2219(95)00050-X
0955-2219/95/$9.50

Electrical and Thermal Transport Properties of (La,Ca)(Cr,Co)O_3

Rasit Koc[a] & Harlan U. Anderson[b]

[a]Southern Illinois University, Department of Mechanical Engineering and Energy Processes, Carbondale, IL 62901, USA
[b]University of Missouri-Rolla, Ceramic Engineering Department, Rolla, MO 65401, USA

(Received 19 September 1994; revised version received 14 February 1995; accepted 20 February 1995)

Abstract

DC electrical conductivity and Seebeck data as functions of temperature and oxygen activity were used to explain the electrical and thermal transport properties of (La,Ca)(Cr,Co)O_3. The electrical conductivity data of La(Cr,Co)O_3 suggested that it depends upon Co content. At Co concentrations less than 20 mol%, Co acted as traps for the carriers and decreased the electrical conductivity of the compositions at temperatures less than 900°C. As the Co concentration increased to above 20 mol%, electrical conductivity increased significantly due to a connecting path of available Co sites. Additional Ca substitution for La increased the electrical conductivity in accordance with Verway's principle. Defect models derived from the electrical conductivity data were found to relate the carrier concentrations to the Ca, Co and oxygen vacancy concentrations. The measured Seebeck coefficients were found to be positive even for the most reducing conditions, indicating that (La,Ca)(Cr,Co)O_3 compositions with Co ≤ 0·3 and Ca ≤ 0·3 were as stable as $LaCrO_3$. The Heikes formula was adopted to interpret the Seebeck coefficient results. These results indicated that electrical conduction in La(Cr,Co)O_3 and (La,Ca)(Cr,Co)O_3 occurs via the non-adiabatic and adiabatic small polaron mechanisms, respectively.

1 Introduction

The demand for materials that possess the chemical stability and electrical conductivity required in high-temperature solid oxide fuel cells (SOFC) and oxygen-separation cells has led to the investigation of the substantially mixed perovskite-type (La,Ca)(Cr,Co)O_3 system.[1,2] The basic perovskite crystal structure is given by the formula ABO_3 in which A, the large cation site, may be an alkali, alkaline earth, or rare earth ion and B represents a transition metal cation. The (La,Ca)(Cr,Co)O_3 system has a pseudo-perovskite crystal structure because its crystal structure deviates from the ideal cubic perovskite structure, (i.e. orthorhombic and rhombohedral). This system is composed of both Cr and Co B-site ions in an attempt to retain the desirable properties found in the end members, (e.g. $LaCrO_3$ — chemical stability in both air and in highly reducing atmospheres at 1000°C, $LaCoO_3$ — high electrical conductivity and sinterability). Ca is substituted for a fraction of the La on the A lattice site, in order to increase the small-polaron carrier concentration according to the Verway controlled ionic valency principle.

Both $LaCrO_3$ and $LaCoO_3$ are believed to show a thermally activated electrical conductivity due to p-type small-polaron hopping among B-site cations. $LaCrO_3$ is chemically stable to high temperatures over a wide range of oxygen activity. $LaCoO_3$ has a significantly greater electrical conductivity than $LaCrO_3$. However, $LaCoO_3$ is not chemically stable under reducing conditions at high temperatures.

The present author's recent results on $La_{1-x}Ca_xCr_{1-y}Co_yO_3$ have shown that compositions with $x \geq 0{\cdot}1$ and $y \geq 0{\cdot}1$ can be sintered to densities above 94% of theoretical in air at 1400°C and below.[1] The electrical conductivity as measured in air from room temperature to 1100°C increased with increasing Co and Ca content. At 1000°C, values from 1·5 S/cm (for $LaCr_{0.9}Co_{0.1}O_3$) to 50 S/cm (for $La_{0.7}Ca_{0.3}Cr_{0.9}Co_{0.1}O_3$) were measured.[2] However, the room-temperature electrical conductivity minima occurs at a Co concentration of approximately 20%. The Seebeck coefficients were positive, indicating p-type conductivity. The substitution of Co for Cr significantly decreased the Seebeck coefficients, indicating that Co substitution for Cr increased the carrier concentration. Additional Ca substitution for La resulted in a further decrease in the Seebeck coefficient.

Seebeck coefficients then exhibited a temperature-independent behavior, indicating that the carrier mobility, rather than carrier concentration, was thermally activated.[2] However, published works regarding the electrical behavior with respect to oxygen activity of $(La,Ca)(Cr,Co)O_3$ ceramics are virtually non-existent.

The objectives of the present paper are to explain the electrical and thermal transport properties of $(La,Ca)(Cr,Co)O_3$ ceramics and provide information on electrical conductivity and Seebeck coefficients as a function of oxygen activity for the material system at 1000°C.

2 Experimental Procedure

Specimens in the $(La,Ca)(Cr,Co)O_3$ system were prepared by a polymer precursor method similar to that first described by Pechini.[3] The starting chemicals were reagent-grade materials and were standardized by thermogravimetric methods to determine the actual cation contents. The desired compositions were prepared by dissolving measured amounts of selected carbonates and nitrates in solutions of citric acid, ethylene glycol, and water. The mixtures were heated on a hot plate at about 95°C until polymerization had occurred. Subsequent heating at higher temperatures resulted in the decomposition of the polymer resin and allowed conversion into the desired oxide. Final calcination was done at 850°C for 8 h. The resulting powders were milled and subjected to X-ray diffraction to ensure that they were single-phase. Samples for electrical conductivity and Seebeck measurements were formed by dry pressing at 2500 kg/cm^2 and then sintering the compacts at 1500°C for 10 h in a SiC heated furnace. Bulk densities of about 95% of theoretical were obtained. Rectangular specimens, usually 0·3 × 0·3 × 2 cm, were cut from the sintered bars. To reduce the effects of barrier layers and non-ohmic contacts, Pt paste was applied to the contact faces of the specimens.

Four-wire DC electrical-conductivity and Seebeck measurements were performed simultaneously in an apparatus that could measure three samples at a time. The specimens were mounted between two platinum blocks, which had type-S thermocouples (Pt versus Pt–10% Rh) as electrical contacts; the Pt wire heater was wound on the lower end of the holder to generate a temperature gradient along the vertical direction. Three sets of specimens and holders were contained in Al_2O_3 tubes within a $MoSi_2$ furnace, where the temperature was controlled by a Eurotherm temperature controller. The oxygen activity over the samples was controlled by using flowing gas mixtures composed of either O_2–N_2 or CO_2-forming gas (10% H_2–90% N_2). A Y_2O_3-stabilized ZrO_2 oxygen sensor was used to monitor the oxygen partial pressure of the gas mixture. Electrical conductivity measurements were made using the two-probe, four-wire Kelvin technique in which two leads carry the test signal (1 mA) and the other two measure the voltage drop. The Seebeck coefficients were determined by measuring temperature gradients and thermal emf's through the common leads of the thermocouples. The measurements were made using a data logger (Hewlett Packard 3497A data acquisition/control unit), which employs a HP-85 computer both as a control and readout device.[4]

3 Results and Discussion

3.1 Temperature dependence

DC electrical conductivity of $La(Cr,Co)O_3$ was measured in air as a function of temperature, with results shown in Fig. 1. The electrical conductivity increased with increasing temperature and Co content. The electrical conductivity of the end members of the $La(Cr,Co)O_3$ series exhibits the activated behavior expected from small-polaron transport over a wide temperature range. Previous investigations[5–7] have indicated that $LaCrO_3$ and $LaCoO_3$ perovskites conduct by the diffusion of p-type small polarons among Cr and Co ions. A small polaron is associated with a particular Cr or Co site if the ion is in the +4 valence state, rather than the stoichiometric +3 valence state.

Transport of the carrier to an adjacent unoccupied site requires transport of the lattice distortion as well. The activation energy is associated with small-polaron transport, and charge migration through the crystal occurs by an activated hopping mechanism. Two different types of small

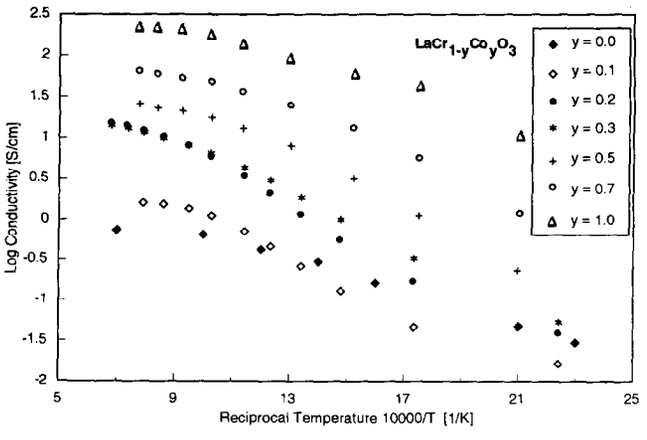


Fig. 1. DC electrical conductivity versus 10 000/T in air for $La(Cr,Co)O_3$.

polaron have been determined. The carrier is always able to jump to an adjacent unoccupied site whenever an atomic displacement favoring the jump occurs, which is called the adiabatic case, while in the non-adiabatic case the carrier can only occasionally take advantage of a favorable atomic configuration and change sites.

The mobility of charge carriers, μ, of adiabatic small polarons is given as[8]

$$\mu = [(1-C)\, e\, a^2 \nu / kT] \exp(-E_A/k/T) \qquad (1)$$

where C is the fraction of available sites occupied by charge carriers, e is the unit charge, a is the lattice spacing, ν is the vibrational frequency, k is the Boltzmann constant, T is absolute temperature, and E_A is the activation energy for hopping. The electrical conductivity, σ, is expressed as

$$\sigma = (NC)\, e\, \mu \qquad (2)$$

where N is the density of available sites. The expression for the temperature-dependent electrical conductivity of an adiabatic small-polaron material becomes

$$\sigma = [NC\,(1-C)\, e^2\, \nu\, a^2/kT] \exp(-E_A/kT) \qquad (3)$$

For materials that obey non-adiabatic small-polaron conduction, the mobility expression is given by

$$\mu = [(1-C)\, e^2\, a^2/kT]\, (4\, \pi^2 j^2/h^2)\, (\pi/4\, kTE_A)^{1/2} \exp(-E_A/kT) \qquad (4)$$

where j is the electron transfer energy and h is Planck's constant. The electrical conductivity of a non-adiabatic small-polaron material becomes

$$\sigma = [NC(1-C)\, e^2\, a^2/kT]\, (4\, \pi^2 j^2/h^2)\, (\pi/4\, kTE_A)^{1/2} \exp(-E_A/kT) \qquad (5)$$

If all of the variables in the pre-exponential term of eqns (3) and (5) are independent of temperature (or slightly temperature-dependent), a plot of log (σT) (for the adiabatic case) or log ($\sigma T^{3/2}$) (for the non-adiabatic case) versus reciprocal temperature should give a straight line, with a gradient proportional to the activation energy associated with small-polaron hops.

Plots of log (σT) versus 10 000/T and log ($\sigma T^{3/2}$) versus 10 000/T for La(Cr,Co)O_3 compositions covering the entire temperature range studied are shown in Figs 2 and 3, respectively. The two plots are very similar, showing substantial linearity for the compositions. Linear regression was applied to calculate the activation energies and evaluate the linearity of plots for the compositions. Calculated values for the activation energies are given for each case in Table 1. The conductivity of the compositions of the La(Cr,Co)O_3 series does exhibit the activated behavior expected from small-polaron transport over a wide temperature range, with $\sigma T^{3/2}$ giving a slightly better fit than σT. Linear regression was used to evaluate the linearity of the plots. The linearity was slightly higher for the non-adiabatic case (Fig. 3) than for the adiabatic case (Fig. 2). R^2 values are included in Table 1 for

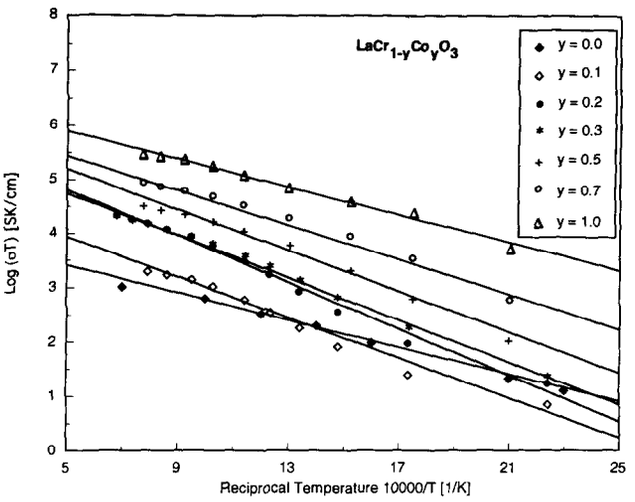


Fig. 2. Log σT versus 10 000/T for La(Cr,Co)O_3.

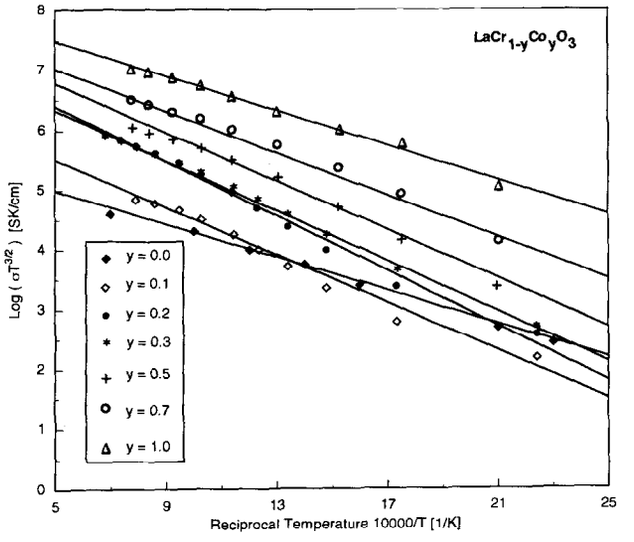


Fig. 3. Log $\sigma T^{3/2}$ versus 10 000/T for La(Cr,Co)O_3.

Table 1. Activation energies for La(Cr,Co)O_3

	Activation energy (eV)			
Composition $LaCr_{1-y}Co_yO_3$	*Adiabatic case*	*Non-adiabatic case*	*Adiabatic case*	*Non-adiabatic case*
$y = 0.0$	0·25	0·28	0·9930	0·9966
$y = 0.1$	0·37	0·40	0·9786	0·9805
$y = 0.2$	0·42	0·46	0·9894	0·9900
$y = 0.3$	0·39	0·42	0·9958	0·9972
$y = 0.5$	0·37	0·41	0·9869	0·9912
$y = 0.7$	0·32	0·35	0·9843	0·9903
$y = 1.0$	0·26	0·29	0·9875	0·9915

both cases. The greater the magnitude of R^2, the better the fit of the data to the linear function. Evaluation of the linearity of plots for compositions in La(Cr,Co)O_3 indicated that the electrical conduction occurs via the non-adiabatic small-polaron mechanism.

Although the activation energies of the end members are similar, $LaCoO_3$ has a high-temperature conductivity value much higher than that of $LaCrO_3$. Despite the larger intrinsic electronic conductivity of $LaCoO_3$, a small substitution of Co for Cr in $LaCrO_3$ resulted in a sharp drop in low-temperature conductivity from that exhibited by either end member (see Fig. 1). This minimum occurs at a Co concentration of 10 mol%. This small substitution of Co also resulted in a strong temperature dependence with increased gradient. The maximum gradient observed occurs in the 20 mol% Co composition and corresponds to an activation energy of 0·46 eV. As can be seen from Table 1, the activation energy increases with Co content to a maximum at 20 mol% and then linearly decreases as Co content increases. The substitution of small amounts of Co for Cr has been found to cause the low-temperature electrical conductivity to drop orders of magnitude below that of either end member and increase in activation energy. This is probably due to the difference in the electronic structure of Co and Cr ions. The Co sites also have lower small-polaron site energies as compared to Cr sites. In the case of a low concentration of Co, the lower-energy Co sites act as traps for carriers diffusing among Cr sites at low temperature. Therefore, the activation energy for conduction is increased from that of $LaCrO_3$. At higher Co concentrations, direct transport among Co sites becomes possible and conductivity increases and activation energy decreases. The electrical conductivity of all compositions increased to an asymptotic value dependent upon the amount of Co present as the temperature was increased. A possible explanation for this involves considering the different spin states of Co. The low spin (s = 0) state is the most stable and predominates at temperatures below 900°C. As the temperature increases, higher spin states of Co^{3+} (s = 1, s = 2) become populated. This transition probably leads to hopping between Co-sites and neighboring Cr-sites. Therefore, the electrical conductivity at higher temperatures increased with Co concentration.

The DC electrical conductivity of $La_{1-x}Ca_xCR_{0.9}Co_{0.1}O_3$ and $La_{1-x}Ca_xCr_{0.8}Co_{0.2}O_3$ (with x = 0·1 and 0·2) was measured in air as a function of temperature, with the results shown in Figs 4 and 5, respectively, as log(σ) as a function of reciprocal temperature. Plots of log (σT) versus 10 000/T and log ($\sigma T^{3/2}$) versus 10 000/T for

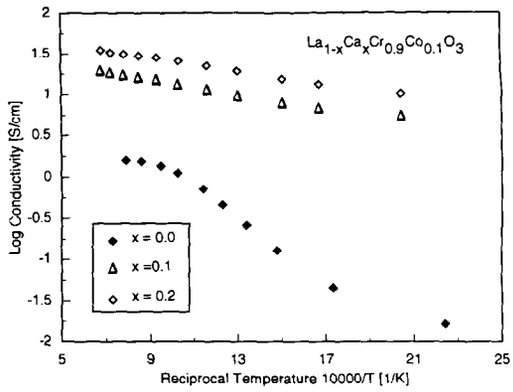


Fig. 4. DC electrical conductivity of $La_{1-x}Ca_xCr_{0.9}Co_{0.1}O_3$ as a function of Ca content and temperature.

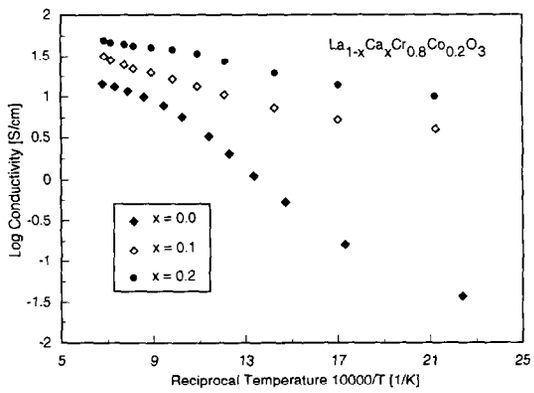


Fig. 5. DC electrical conductivity of $La_{1-x}Ca_xCr_{0.8}Co_{0.2}O_3$ as a function of Ca content and temperature.

$La_{1-x}Ca_xCr_{0.9}Co_{0.1}O_3$ are shown in Figs 6 and 7, respectively. The two plots are very similar, showing slightly higher linearity for the adiabatic case. Thus, for the system $La_{1-x}Ca_xCr_{0.9}Co_{0.1}O_3$, the high linearity of the plots is consistent with the assumption that electrical conduction in these compositions occurs via the adiabatic small-polaron mechanism (see Table 2). Log (σT) versus 10 000/T and log ($\sigma T^{3/2}$) versus 10 000/T for $La_{1-x}Ca_xCr_{0.8}Co_{0.2}O_3$ are also plotted in Figs 8 and 9, respectively. The linearity of the plots are again consistent with the assumption that electrical

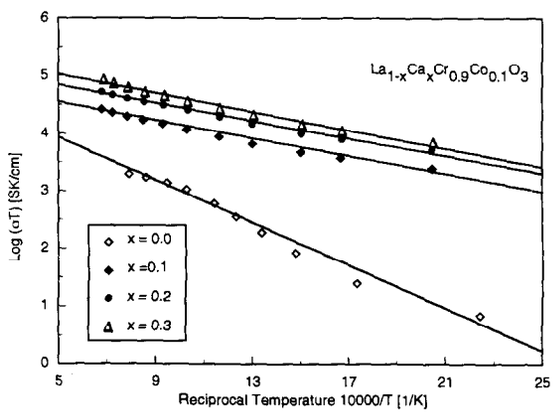


Fig. 6. Log σT versus 10 000/T for $La_{1-x}Ca_xCr_{0.9}Co_{0.1}O_3$.

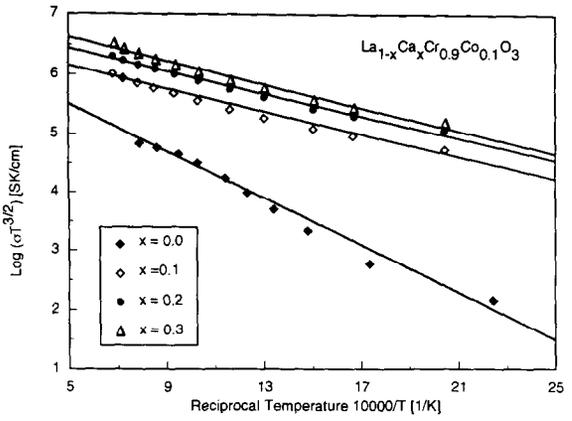


Fig. 7. Log $\sigma T^{3/2}$ versus 10000/T for $La_{1-x}Ca_xCr_{0.9}Co_{0.1}O_3$.

conduction occurs via the adiabatic small-polaron mechanism. There was only one composition (x = 0·1) which had the greater magnitude of R^2 in the non-adiabatic case. This might be due to the experimental error, since the rest of the compositions yielded a better fit of the data to the linear function with the adiabatic small-polaron mechanism.

Activation energies for hopping for adiabatic and non-adiabatic cases were calculated from Figs 6–9 and tabulated in Table 2. The activation energies were slightly higher for the non-adiabatic case than for the adiabatic case. As can be seen, with a

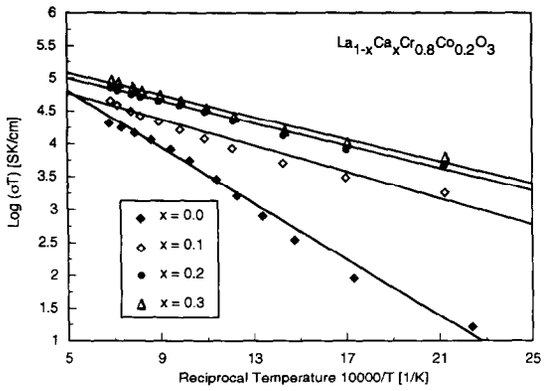


Fig. 8. Log σT versus 10000/T for $La_{1-x}Ca_xCr_{0.8}Co_{0.2}O_3$.

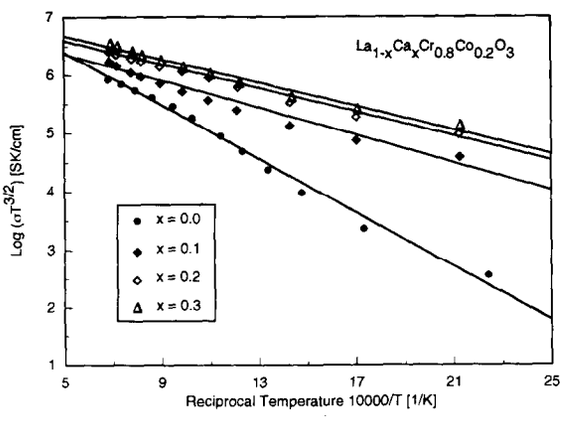


Fig. 9. Log $\sigma T^{3/2}$ versus 10000/T for $La_{1-x}Ca_xCr_{0.8}Co_{0.2}O_3$.

Table 2. Activation energies for (La,Ca)(Cr,Co)O_3

Composition $La_{1-x}Ca_xCr_{1-y}Co_yO_3$	*Activation energy (eV)*			
	Adiabatic case	*Non-adiabatic case*	*Adiabatic case*	*Non-adiabatic case*
x = 0·1; y = 0·1	0·16	0·19	0·9825	0·9818
x = 0·2; y = 0·1	0·15	0·19	0·9912	0·9895
x = 0·3; y = 0·1	0·16	0·19	0·9850	0·9836
x = 0·1; y = 0·2	0·20	0·23	0·9678	0·9688
x = 0·2; y = 0·2	0·17	0·20	0·9915	0·9905
x = 0·3; y = 0·2	0·17	0·20	0·9817	0·9811

Ca content of 10–30 mol%, all Co-content levels have essentially the same activation energy. The additional substitution of Ca for La in the La(Cr,Co)O_3 eliminated the increase in activation energy that was observed with Co substitution for Cr. The substitution of 10 mol% Ca for La in the La(Cr,Co)O_3 series increased the conductivity by approximately 10%, which was anticipated in view of a carrier density increase of 10% in accordance with Verway's principle. As in the case of $La_{1-x}Ca_xCrO_3$ and $La_{1-x}Ca_xCO_3$, the substitution of Ca for La in La(Cr, Co)O_3 should result in the formation of Cr^{4+} and Co^{4+} in order to preserve the electrical neutrality. Formation of both Cr^{4+} and Co^{4+} increases the small-polaron concentration and decreases the activation energy for conduction.

Thermopower measurements were made to determine the type and concentration of charge carriers. Figures 10–12 show the Seebeck coefficient plotted as a function of temperature for La(Cr,Co)O_3, $La_{1-x}Ca_xCr_{0.9}Co_{0.1}O_3$, and $La_{1-x}Ca_xCr_{0.8}Co_{0.2}O_3$, respectively. In La(Cr,Co)O_3, the substitution of Co for Cr significantly decreased the Seebeck coefficient, indicating that Co substitution for Cr increases the carrier concentration. As the Co content increased, the Seebeck

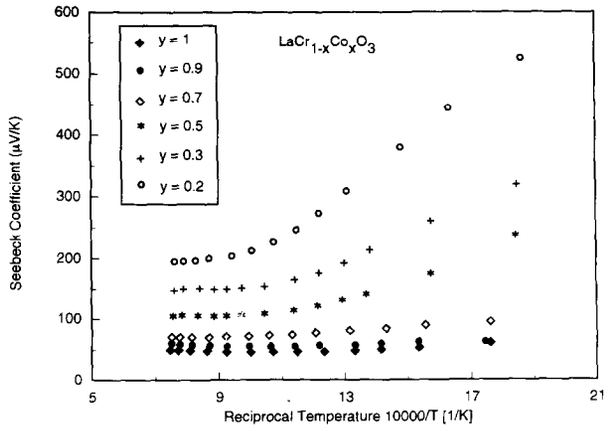


Fig. 10. Seebeck coefficients of La(Cr,Co)O_3 as a function of Co and temperature.

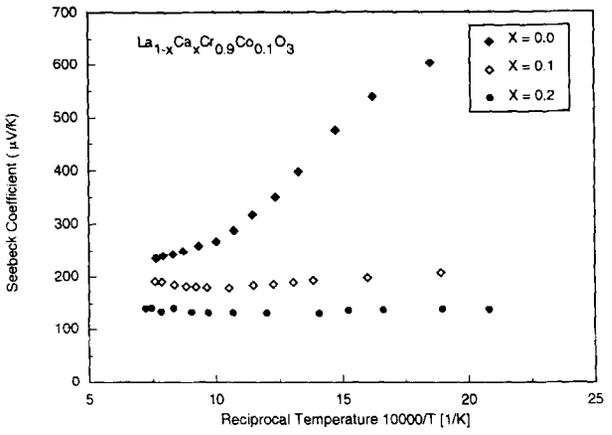


Fig. 11. Seebeck coefficients of $La_{1-x}Ca_xCr_{0.9}Co_{0.1}O_3$ as a function of Ca and temperature.

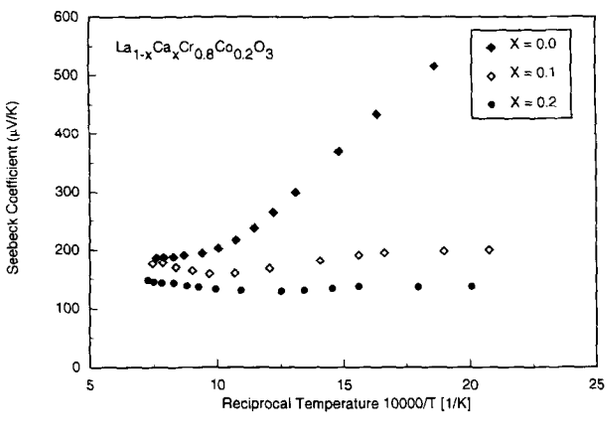


Fig. 12. Seebeck coefficients of $La_{1-x}Ca_xCr_{0.8}Co_{0.2}O_3$ as a function of Ca and temperature.

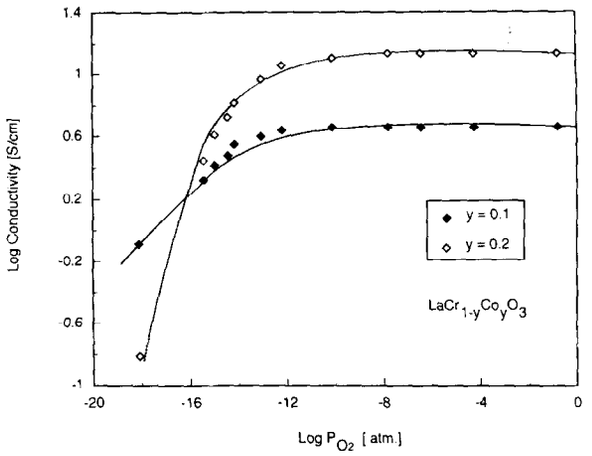


Fig. 13. Log σ versus log oxygen activity for La(Cr,Co)O_3 at 1000°C.

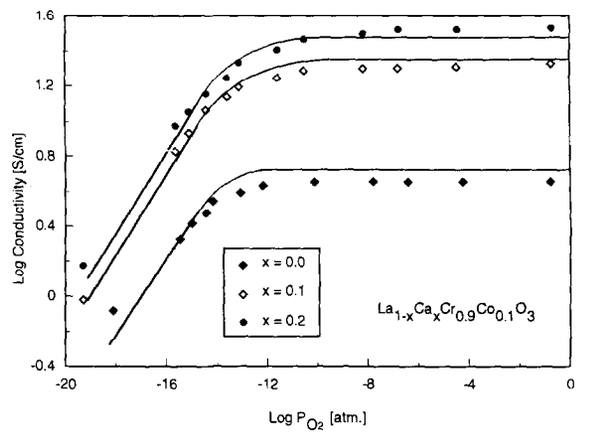


Fig. 14. Log σ versus log oxygen activity for (La,Ca)(Cr,Co)O_3 at 1000°C.

coefficient showed temperature-independent behavior, indicating that the carrier mobility, rather than the carrier concentration, was thermally activated. According to Heikes' formula, this type of behavior indicates a small-polaron conduction mechanism which agrees with electrical conductivity measurements. In the cases of $La_{1-x}Ca_xCr_{0.9}Co_{0.1}O_3$ and $La_{1-x}Ca_xCr_{0.8}Co_{0.2}O_3$, introduction of Ca significantly decreased the Seebeck coefficient, which became temperature-independent.

3.2 Oxygen-activity dependence

DC electrical conductivity measurements for $La_{1-x}Ca_xCr_{1-y}Co_yO_3$ (x = 0·0, 0·1, 0·2, 0·3 and y = 0·1, 0·2) were made as a function of oxygen activity at 1000°C. The results are shown in Figs 13 and 14. The electrical conductivity data showed similar oxidation–reduction behavior. In the high oxygen-activity region, within the experimental error the electrical conductivity was nearly constant. The electrical conductivity decreased as a function of oxygen activity to the one-quarter power as reduction progressed. The constant electrical conductivity that exists in the high oxygen-activity region may be easily understood if it is assumed that the carrier concentration and electronic compensation predominates. In the low oxygen-activity region, oxygen vacancies are formed and the electrical conductivity begins to decrease as a result of ionic compensation.

The defect chemistry of oxides shows how the defect structure and electrical conductivity change as they equilibrate under various oxygen activities at elevated temperatures. The following model is adopted from the model developed for Mg-doped $LaCrO_3$[5] in order to explain the electrical conductivity of $La_{1-x}Ca_xCr_{1-y}Co_yO_3$ (where y is less than 0·3) as a function of oxygen activity. In the $La_{1-x}Ca_xCr_{1-y}Co_yO_3$, the Co^{3+} substitutes for Cr^{3+}, and Ca^{2+} substitutes for La^{3+}. The acceptor Ca^{2+} substitutes for La^{3+}. The acceptor Ca^{2+} possesses one effective negative charge which can be compensated for either by Cr^{3+}–Cr^{4+} or Co^{3+}–Co^{4+} transitions, or by the formation of oxygen vacancies. If such a substitution is compensated for by the formation of oxygen vacancies, no contribution to the electronic conductivity is anticipated.

Since cations and anions are of comparable size, it can be assumed that Schottky is native defect, and the Schottky reaction (using the Kroger–Vink notations[9]) for this composition is expressed by

$$\text{nill} = V'''_{La} + V'''_{Cr,Co} + 3\ V^{\cdot\cdot}_{O} \quad (6)$$

$$K_s = [V'''_{La}][V'''_{Cr,Co}][V^{\cdot\cdot}_{O}]^3 \quad (7)$$

Since this is a closed system, the cation stoichiometry must remain constant, therefore, $[V_{La}] = [V_{Cr,Co}] = [V_M]$ throughout the entire region.

$$K_s = [V'''_M]^2\,[V^{\cdot\cdot}_O]^3 \quad (8)$$

The p-type non-stoichiometric reaction is given by

$$3/2\ O_2 = V'''_{La} + V'''_M + 6\,\dot{h} + 3\ O_o \quad (9)$$

$$K_9 = [V'''_{La}]\,[V'''_M]\,p^6\,P_{O_2}^{-3/2} \quad (10)$$

When Ca^{2+} is substituted for La^{3+}, the Ca^{2+} will possess one effective negative charge which can be compensated for either by a B^{3+}–B^{4+} transition or by the formation of oxygen vacancies. This leads to the following electrical neutrality condition:

$$2\,[V^{\cdot\cdot}_O] + p = 6\,[V'''_M] + [Ca'_M] \quad (11)$$

At high oxygen activity, assuming that both $[V_O]$ and $[V_M]$ are smaller than the acceptor content, the neutrality condition becomes

$$p = [Ca'_M] \quad (12)$$

and from eqns 8, 10 and 12

$$[V'''_M] = K_9^{1/2}\,P_{O_2}^{3/4}/[Ca'_M]^3 \quad (13)$$

$$[V^{\cdot\cdot}_O] = K_S^{1/3}\,[Ca'_M]^2\,P_{O_2}^{-1/2}/K_9^{1/3} \quad (14)$$

respectively.

At low oxygen activities, oxygen may be lost and ionic compensation takes place through the formation of oxygen vacancies. In this case the electrical neutrality condition becomes

$$p = [Ca'_M] - 2[V^{\cdot\cdot}_O] \quad (15)$$

This condition can be expressed by

$$La_{1-y}Ca'_yM^x_{1-y}M^{\cdot}_yO_3 = La_{1-y}Ca'_yM^x_{1-y+2x}M^{\cdot}_{y-2x}V^{\cdot\cdot}_{Ox}O_{3-x} + \tfrac{1}{2}\,xO_2$$

or

$$O_O + 2\ M^{\cdot}_M = 2\ M_M + V^{\cdot\cdot}_O + 1/2\ O_2 \quad (16)$$

where y is the amount of acceptor and x is the concentration of oxygen vacancies. The equilibrium constant for reaction (16) can be expressed as

$$K_{16} = [M_M]^2\,[V^{\cdot\cdot}_O]\,P_{O_2}^{1/2}/[M^{\cdot}_M]^2 \quad (17)$$

which in terms of mole fractions becomes

$$K_{16} = (1-y+2x)^2\,x\,P_{O_2}^{1/2}/(y-2x)^2 \quad (18)$$

Equation (18) can be solved to yield

$$2x = y - \{P_{O_2}^{1/2}\,[(8y\,K_{16}\,P_{O_2}^{-1/2} + 1)^{1/2} - 1]/4\,K_{16}\} \quad (19)$$

The electrical conductivity for p-type materials is given by

$$\sigma = e\,p\,\mu \quad (20)$$

where e is the electron charge, μ is the mobility, and p is the concentration of carriers which, from the model, is equal to $(y–2x)$. Thus eqn (19) can be rearranged to give

$$\sigma = e\mu P_{O_2}^{1/2}\{[(8\,yK_{16}\,P_{O_2}^{-1/2} + 1)^{1/2} - 1]/4\}K_{16} \quad (21)$$

At the high oxygen-activity region, eqn (19) reduces to $x = 0$ and eqn (21) reduces to $\sigma = e\,y\,\mu$, whereas in the low oxygen-activity region the respective equations are reduced to

$$p = (y\text{-}2x)/y = P_{O_2}^{1/4}/(2y\,K_{16})^{1/2} \quad (22)$$

or

$$\sigma = (e\,\mu\,y^{1/2}\,P_{O_2}^{1/4})/2K_{16} \quad (23)$$

and

$$\sigma/\sigma_R = P_{O_2}^{1/4}/(2y\,K_{16})^{1/2} \quad (24)$$

where σ_R is the electrical conductivity at 1 atm oxygen.

The equilibrium constant K_{16} can be found by combining the electrical conductivity experimental data and eqn (24). The theoretical curves can be generated by using eqn (24) and the calculated values of K_{16}. The individual symbols in Figs 13–14 represent the experimental data, while the lines are the calculated curves. The equilibrium constants used to generate these lines are listed in Table 3. It is clear that the electrical conductivity decreases with decreasing oxygen activity as $P_{O_2}^{1/4}$, as the electrical compensation changes from electronic to ionic. All of the compositions showed the same behavior. The oxygen-activity dependence on conductivity was small at high oxygen activities; as oxygen activity decreased, a break in electrical conductivity at 10^{-10} atm and 1000°C was observed, then the electrical conductivity decreased as $P_{O_2}^{1/4}$. Compositions $La_{1-x}Ca_xCr_{1-y}Co_yO_3$ with x = 0·0–0·3 and y = 0·0–0·2 are stable towards dissociation

Table 3. Equilibrium constants calculated from defect model at 1000°C

Composition	*Log equilibrium constant*
$LaCr_{0.9}Co_{0.1}O_3$	–4·8
$La_{0.9}Ca_{0.1}Cr_{0.9}Co_{0.1}O_3$	–5·8
$La_{0.8}Ca_{0.2}Cr_{0.9}Co_{0.1}O_3$	–6·1
$LaCr_{0.8}Co_{0.2}O_3$	–4·1
$La_{0.9}Ca_{0.1}Cr_{0.8}Co_{0.2}O_3$	–4·8
$La_{0.8}Ca_{0.2}Cr_{0.8}Co_{0.2}O_3$	–5·2

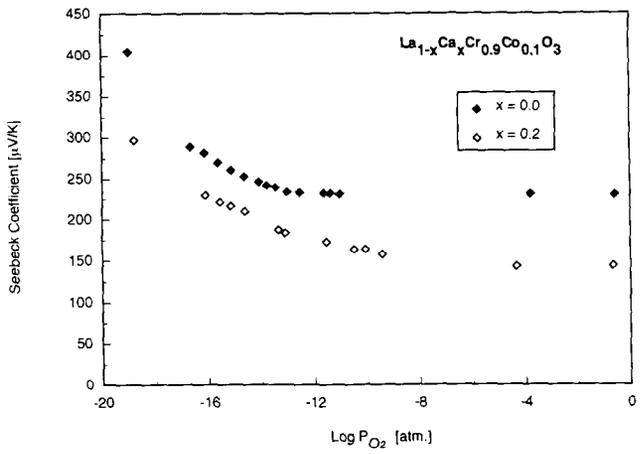


Fig. 15. Seebeck coefficient as a function of oxygen activity for $LaCr_{0.9}Co_{0.1}O_3$ at 1000°C.

in forming gas at 1000°C, even though the electrical conductivity decreases.

Seebeck measurements were also made as a function of oxygen activity at 1000°C. The results for compositions $(La,Ca)(Cr,Co)O_3$ are shown in Fig. 15 . The Seebeck coefficients in all cases were positive, indicating p-type conductivity. Increasing the Co substitution for Cr decreased the Seebeck coefficients. In accordance with the electrical conductivity, the Seebeck coefficient remains constant until the low P_{O_2} region is reached. At this point, the Seebeck coefficient rapidly increases at the transition knee because of its inverse relationship with the carrier concentration. The location of the transition knee shifted to a higher P_{O_2} with increasing Co and Ca concentration in both the Seebeck and electrical conductivity data. For the high P_{O_2} region, the carrier concentration is controlled by the acceptor content p = [Ca'] and electronic compensation predominates. Any temperature dependence of the electrical conductivity is therefore determined by mobility. It should be noted that in eqn (24), the mobility was assumed to be independent of oxygen activity. This is an important feature of the model if the calculated equilibrium constants are to be regarded as correct.

4 Conclusions

The electrical conductivity as measured in air from 100 to 1100°C increased with increasing Co and Ca content. At 1000°C, values from 1·5 S/cm (for $LaCr_{0.9}Co_{0.1}O_3$) to 50 S/cm (for $La_{0.7}Ca_{0.3}Cr_{0.9}Co_{0.1}O_3$) were measured. The Seebeck coefficients were positive, indicating p-type conductivity. The substitution of Co for Cr significantly decreased the Seebeck coefficients, indicating that Co substitution for Cr increased the carrier concentration. Additional Ca substitution for La resulted in a further decrease in the Seebeck coefficient. Seebeck coefficients then exhibited a temperature-independent behavior, indicating that the carrier mobility, rather than carrier concentration, was thermally activated. The results indicated that the electrical conduction in $La(Cr,Co)O_3$ and $(La,Ca)(Cr,Co)O_3$ occurs via the non-adiabatic and adiabatic small-polaron mechanisms, respectively.

At 1000°C the oxygen activity dependence upon conductivity was small at high oxygen activities; as oxygen activity decreased, a break at 10^{-10} atm was observed, at which point the electrical conductivity began decreasing as $P_{O2}^{1/4}$, following the model previously proposed for $LaCrO_3$.

References

1. Koc, R. & Anderson, H. U., Liquid phase sintering of $LaCrO_3$. *J. Eur. Ceram. Soc.*, **9** (1992) 285–92.
2. Koc, R. & Anderson, H. U., Electrical conductivity and Seebeck coefficient of $(La,Ca)(Cr,Co)O_3$. *J. Mater. Sci.*, **27** (1992) 5477–82.
3. Pechini, M., Method of preparing lead and alkaline earth titanates and niobates and coatings using the same to form a capacitor. US Patent 3 330 697, 1967.
4. Carini, G., An apparatus for the measurement of DC electrical and seebeck coefficient of semiconductors as a function of high temperature and oxygen activity. MS Thesis, University of Missouri-Rolla (1988).
5. Flandermeyer, B. K., Thermogravimetric and electrical conductivity studies of Mg-doped $LaCrO_3$ and La-doped $SrTiO_3$. PhD Thesis, University of Missouri-Rolla (1984).
6. Karim, D. P. & Aldred, A. T., Localized level hopping transport in $La(Sr)CrO_3$. *Phys. Rev. B*, **20**(6) (1979) 2255–63.
7. Taguchi, H., Shimada, M. & Koizumi M., Electrical properties in the system $(La_{1-x}Ca_x)CoO_3$ $(0{\cdot}1<x<0{\cdot}5)$. *J. Solid State Chem.*, **44** (1982) 254–6.
8. Stevenson, W. J., Electrical and structural properties of compositions in the systems $Y_{1-x}Ca_xMnO_3$ and $La_{1-x}Ca_xMnO_3$. PhD Thesis, University of Missouri-Rolla (1991).
9. Kroger, F. A. & Vink, H. J., *Solid State Physics*, Vol. 3, eds F. Seitz & D. Turnbull. Academic Press, New York, 1965, p. 307.

Journal of the European Ceramic Society **15** (1995) 875–886
© 1995 Elsevier Science Limited
Printed in Great Britain. All rights reserved
0955-2219/95/$9.50

0955-2219(95)00057-7

Analysis of the Isothermal Forced Flow Chemical Vapour Infiltration Process. Part I: Theoretical Aspects

Y. G. Roman,[a] J. F. A. K. Kotte[a] & M. H. J. M. de Croon[b]

[a]TNO, Centre for Technical Ceramics, PO Box 595, 5600 AN Eindhoven, The Netherlands
[b]Eindhoven University of Technology, Department of Chemical Engineering, PO Box 513, 5600 MB Eindhoven, The Netherlands

(Received 24 June 1994; revised version received 2 March 1995; accepted 10 March 1995)

Abstract

In this paper the densification of a cylindrical pore due to a first order heterogeneous deposition reaction on the wall is described. The basic understanding of these mechanisms can aid in the prediction of the infiltration time and composite porosity after densification. The results of the modelling are compared with experimental results which are reported in an additional paper, i.e. Part 2 of this study. The main characteristic parameter that determines the infiltration behaviour is the gas velocity.

1 Scope

The drive to gain 'tough' ceramic material led to the development of the so-called thermal gradient FCVI (TGFCVI) technique some ten years ago.[1–4] With this method, thick walled ceramic component structures can be made. A drawback however, is that for each different sample geometry, a new fixture needs to be developed through which a thermal gradient can be applied across the fibrous preform.

The isothermal FCVI (IFCVI) method does not have this problem, so the fixture can have a much simpler design. For thin walled structures like hot gas filters, heat shields, burner tubes, seal rings and heat exchanger panels, this isothermal method can thus provide a great improvement towards industrial application of the FCVI technique. Optimisation of IFCVI process conditions however is of great importance to be able to homogeneously fill the porous substrate, especially in the direction parallel to the gas flow.

The modelling of both ICVI and FCVI processes is a topic of much effort and a first attempt to optimise conditions rapidly. However, the experimental validation of these models (especially FCVI) is still very limited and a basic insight into the process mechanisms is often arduous. As far as is known, there are no publications on the effect of the different process variables of the FCVI process on the infiltration efficiency in terms of composite density and infiltration time. This study is an attempt to fill this gap and reach a better understanding in the IFCVI process using on one hand a very simple model (*viz.* in Part 1) and on the other hand, experimental validation (Part 2).[5]

2 Introduction

When reactive precursor gas is forced through a heated porous fibrous preform, a chemical reaction takes place on the fibre surface and a solid matrix material is deposited onto the fibres: the forced flow chemical vapour infiltration (FCVI) process.

In this study, silicon carbide (SiC) is deposited onto the fibres as a result of a heterogeneous decomposition of methyl-trichlorosilane (MTS) in hydrogen:

$$SiCH_3Cl_{3(g)} + H_{2(g)} \rightarrow SiC_{(s)} + 3HCl_{(g)} + H_{2(g)}$$

As the material is growing onto the fibres, the density of the preform increases and the pores get smaller. The preform microstructure is thus changing with time.

In principle, the preform can be visualised simply as a cylindrical plate in which cylinder holes (pores) are present. Through these pores the gas flows, due to the pressure gradient that is present across the plate. The diffusion due to concentration gradients along the pore axis can be neglected, because it is much smaller than the mass transport of the species due to the pressure driven convection.

The FCVI process is dependent on two kinds of parameters, i.e. the process conditions such as:

- Temperature of the preform
- Total pressure
- Gas velocity

- Precursor concentration

and the microstructural properties of the starting preform such as:

- Preform permeability
- Preform porosity
- Average pore size and pore size distribution
- Preform thickness
- Pore tortuosity
- Specific surface area available for deposition.

For a complete understanding of the FCVI process it is necessary to know the effect on the infiltration process when one or more of these parameters are varied.

The purpose of this manuscript is to gain more understanding of the infiltration behaviour and this paper describes the effect of the different process conditions and microstructural properties of the preform under isothermal conditions. Although the model presented is a simplification of reality, it can provide insight into the basic principles of the FCVI process.

3 One-dimensional analysis of the isothermal CVI process

The three dimensional raw fibrous preforms used in Part 2 of this study, contain pores of three size ranges and contain an average total porosity of 50 vol%. The smallest pores are smaller than 0·01 μm, bigger pores between 2–30 μm represent the pores within the bundles and large pores with a diameter between 100–1000 μm are the voids between two crossing tows and the pores between the tows.

When it is assumed that the relative contribution in void space of the two smallest pores is negligible, then the porosity will depend on the large pores only. As such, the infiltration time and densification of the preform is dependent on these large pores, since they determine the preform permeability and pressure drop and thus the moment that the process is terminated, i.e. when the pore entrances of these big pores are (almost) closed due to matrix deposition.

For the description of the CVI process. the preform can then be represented simply as a plate with continuous monosized pores of 500 μm in diameter under isothermal conditions. The pores are straight and open on both sides. Such a model preform is visualised in Fig. 1.

Distinction should be made in the way the gas species are transported into the pore cavity using one of the different CVI methods. During isothermal isobaric CVI (ICVI) processing, the gas flows around the model preform and the gas species are transported into the pores by diffusion.

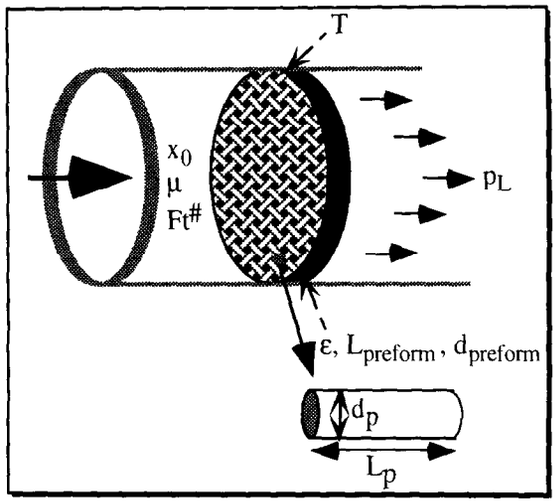


Fig. 1. The cross-section of the reactor tube with a porous model preform consisting of n monosized cylindrical pores. Known initial adjustable process and microstructural parameters are indicated.

On the other hand, in the case of isothermal forced flow CVI (IFCVI), the gas mixture enters the preform from one side and flows in axial direction due to forced convection.

For both ICVI and IFCVI densification, silicon carbide (SiC) is deposited onto the pore wall. The deposition rate of SiC is controlled by either the chemical reaction rate or one of the two mass transport mechanisms.

Two dimensionless numbers, i.e. the mass Peclet number (Pe) and the Damköhler (Da) number[1,2] describe the competition between the chemical reaction rate at the fibre surface and the mass transport rate of the precursor species into the pore.

The Peclet number describes the ratio of mass transport due to convection into the pore relative to diffusive transport. The Damköhler number is the ratio of the chemical deposition rate of the matrix material relative to the rate of mass transport into the pore. For a porous preform consisting of cylinder pores in which deposition takes place, the Pe number for a cylindrical pore is defined as:

$$Pe = \frac{\text{convective mass transport}}{\text{diffusive mass transport}} = \frac{u_p d_p}{D_{eff}} \quad (1)$$

D_{eff} is the effective gas diffusion coefficient ($m^2.s^{-1}$), d_p is the pore diameter (m) at the gas entrance side and u_p is the average superficial gas velocity ($m.s^{-1}$) for laminar flow within a horizontal cylindrical straight pore and will be described later on.

At low Peclet numbers, (i.e. if $u_p d_p << D_{eff}$), diffusion is the mass transport mechanism whereas at large Pe numbers convection is dominant.

The Damköhler number is dependent on the mass transport mechanism and therefore distinction is made between the first and second

Damköhler number Da I and Da II, respectively). For a first order reaction (in MTS) on the pore wall, these are defined as:

$$Da\ \mathrm{I} = \frac{\text{chemical reaction rate}}{\text{convective mass transport rate}} = \frac{4k_s}{u_p} \quad (2)$$

$$Da\ \mathrm{II} = \frac{\text{chemical reaction rate}}{\text{diffusive mass transport rate}} = \frac{4k_s d_p}{D_{eff}} \quad (3)$$

Here, k_s is the first order reaction rate coefficient based on surface area ($m.s^{-1}$).

When the Damköhler numbers are small (i.e. if numerator << denominator), the chemical reaction is rate limiting whereas at large values the rate of mass transport is controlling the SiC growth.

Four idealised, extreme cases can be given:

(1) The growth rate is mass transport limited and mass transport is dominated by:
   (a) gas phase diffusion; Pe small, *Da* II high;
   (b) forced convection; Pe high, *Da* I high.

(2) The chemical reaction rate is limiting the growth and mass transport is due to:
   (a) gas phase diffusion; Pe small, *Da* II small;
   (b) forced convection; Pe high, *Da* I small.

Cases 1(a) and 2(a) are conditions during the ICVI process (isothermal and isobaric CVI, low Pe) and 1(b) and 2(b) (high Pe) are common for FCVI. In the former cases, the gas flows around the substrate and the concentration gradient is the driving force for the diffusion of the precursor gas into the pores. In the latter cases, a pressure gradient across the substrate forces the gas to flow through the pores.

For both situations an equation can be found for the MTS concentration profile (or effectiveness factor ζ) within a cylindrical pore (open on both sides) where gas molecules enter the pore from one side. For ICVI (cases 1(a) and 2(a)), diffusion and reaction the effectiveness factor is given in literature.[3–5]

For FCVI (cases 1(b) and 2(b)), forced convection and chemical reaction in a straight pore, the effectiveness factor is defined as (Appendix A):

$$\frac{C_z}{C_0} = \exp\left(\frac{-4k_s z}{d_p u_p}\right) = \exp\left(\frac{-Da\ \mathrm{I} z}{d_p}\right) \quad (4)$$

The decrease of the layer thickness or precursor conversion (depletion) along the pore axis from opening ($z = 0$) to end ($z = L$) can be represented by Δ, defined as:[4]

$$\Delta = \frac{G_0 - G_L}{G_0} = 1 - \frac{C_L}{C_0} \quad (5)$$

with G being the first order SiC growth rate ($mol.m^{-2}.s^{-1}$) and is:

$$G_{SiC} = k_s\, C_{MTS,z} \quad (6)$$

For FCVI, the deposition layer gradient or depletion can be expressed as:

$$\Delta = 1 - \exp\left(\frac{-4k_s L}{d_p u_p}\right) = 1 - \exp\left(\frac{-Da\ \mathrm{I} L}{d_p}\right) \quad (7)$$

For a uniform deposited layer, Δ equals zero. As the precursor conversion is low, the SiC layer uniformity and composite density will thus be large.

For both ICVI and FCVI this means that respectively *Da* II and *Da* I should be small. Infiltration should therefore be performed in the reaction rate limited growth regime to enhance uniform deposition.

Furthermore, for ICVI a small Δ implies a large diffusion coefficient and pore diameter and small pore length. The modelling of the ICVI process is performed by many[4–8] and is no topic of this study.

4 The Infiltration Behaviour Versus IFCVI Process Conditions. Introduction

In this section, some general relationships are derived that are applicable for the description of the IFCVI process. The FCVI process has been modelled by many, using complex and powerful computer models.[9–12] However, basic insight in the controlling phenomena of the FCVI process is often lost and the model is a black box where a certain input will yield an output that is not well understood. Furthermore, these models are often based upon process variables that are impossible to alter in real experiments. The operator of the IFCVI process is only able to vary four input process conditions, i.e. preform temperature: T, total gas flow rate at STP: $Ft^{\#}$, total pressure at the gas exit side of the preform: p_L and the reactant mole fraction in the gas mixture at the gas inlet side: X_0. Furthermore, the shut off point of the process can be adjusted. The latter is a certain pressure difference between the pressure at the gas inlet side at $t = 0$ and the pressure at the same location after a densification time period.

In the next section, some simple analytical tools are presented[16] that can aid in the prediction of trends in matrix growth rate at the gas inlet and outlet position of the preform. First (Section 4.1–4.3), the effects of the four input process conditions are examined. Subsequently, a correlation of the microstructural parameters of the raw (uninfiltrated) preform on the infiltration behaviour is presented in Section 5.

4.1 General description of the growth rate during FCVI in a cylindrical model pore

The growth rate G_z ($mol.m^{-2}.s^{-1}$) of the solid matrix material SiC in axial direction z in the pore is given by:

$$G_z = C_z k_s = C_0 k_s \exp\left(\frac{-4k_s z}{d_p u_p}\right) \quad (8)$$

As infiltration proceeds, the pore mouth — of diameter d_p (m) (at z = 0) — will become smaller due to deposition, hence:

$$d_{pt} = d_{p0} - \frac{2t_i G_0 m_{SiC}}{\rho_{SiC}} \quad (9)$$

Here, m_{SiC} is the molar mass of SiC = 0·040 kg.mol^{-1} and $\rho_{SiC} = 3{\cdot}2 \times 10^3$ kg.m^{-3}, t_i is the infiltration time (s).

4.2 Kinetically controlled matrix growth

At very large gas velocities (u_p > infinity), eqn 8 reduces to $G_z = C_0 k_s = G_0$, indicative of kinetically controlled growth. Within this growth regime, Δ (eqn 7) equals 0.

$$G_z = k_s C_z = k_0 \frac{X_0 p_0}{Rg\ T} \exp\left(\frac{-Ea}{Rg\ T}\right) \quad (10)$$

with Rg (J.mole^{-1}.K^{-1}) as the gas constant and Ea (J.mole^{-1}) the activation energy of the heterogeneous reaction. Clearly, neither the total gas flow rate does not affect the growth rate within the pore. Increase of total inlet pressure p_0, temperature T or molar fraction of the precursor X_0, will increase the growth of SiC.

Theoretically, compared with kinetically controlled growth during ICVI, FCVI will not allow complete densification of the preform due to the imposed pressure gradient that yields a deposition gradient.

4.3 Forced convection controlled matrix growth

The effect of the process conditions in case of mass transport limited SiC growth, is not as straightforward as for kinetically controlled growth. The gas velocity is the prime parameter that determines the growth rate of SiC along the pore axis.

Gas velocity

Clearly, the gas velocity is of prime importance during convective mass transport. The gas velocity determines the mass transport rate of the MTS and depletion along the pore axis. This pressure driven velocity of the precursor species is represented by the gas velocity u_p of the gas through a pore p of the preform.

As a starting point, the superficial gas velocity u (m.s^{-1}) for a hollow cylinder tube of constant diameter, based on the mass flux of the species is defined as:

$$u = \frac{Ft}{A} = \frac{Ft^{\#}\ T\ p^0}{T^0\ \bar{p}\ A} \quad (11)$$

Here, $Ft^{\#}$ is the total gas flow rate at STP conditions (m^3.s^{-1}), A is the cross flow area of the cylindrical tube and is thus $0{\cdot}25\pi d^2$ (m^2), d is the tube diameter (m), T^0 and p^0 are the standard temperature (273 K) and standard pressure (10^5 Pa) respectively, $\bar{p}$ is the arithmetic mean pressure, averaged across the preform width (Pa). This description of the gas velocity in the reactor tube or pore is linearly dependent on the gas inflow rate Ft.

As a first approximation it is assumed that the pressure within the pore decreases linearly from gas inlet to outlet of the preform and the gas velocity through the pore is the gas velocity based upon the pore mouth diameter. In other words, these assumptions imply that the pore becomes smaller, but remains of uniform diameter.

The average total pressure in the pore $\bar{p}$ is:

$$\bar{p} = \frac{p_0 + p_L}{2} \quad (12)$$

where p_0 is the pressure at the gas inlet side of the preform and p_L the pressure at the gas outlet side (Pa).

The average† gas velocity u_p (m.s^{-1}), according to the Hagen–Poiseuille relationship[1] for a hollow cylindrical straight pore p where laminar flow is present and the gas density is constant (incompressible flow) is given by:

$$u_p = \frac{d_p^2\ \Delta p}{32\ \mu L} \quad (13)$$

Here L (m) is the pore length and equals (in this case, Fig. 1) the preform thickness, μ (Pa.s) is the dynamic viscosity of the gas mixture flowing through the pore, and Δp (Pa) is the pressure drop across the pore or preform:

$$\Delta p = p_0 - p_L \quad (14)$$

The pore gas velocity, (i.e. the average gas velocity through each of the total of n single monosized straight pores) is linked with the superficial gas velocity through a hollow IFCVI reactor tube u, through the preform total porosity ϵ:

$$u_p = \frac{u}{\epsilon} \quad (15)$$

The preform porosity ϵ (volume fraction) is derived from the total pore volume equation. The total pore volume of a preform equals $n \times V_p$ or $\epsilon \times V_{preform}$ and hence the (constant) number of pores n, with constant diameter d_p is:

$$n = \frac{\epsilon d^2_{preform}\ L_{preform}}{d_p^2\ L_p} \quad (16)$$

where $L_{preform}$ can be considered to equal L_p, when the tortuosity of the pore equals one. V_p is the

†The average velocity of the parabolic velocity profile in the hollow tube or pore.

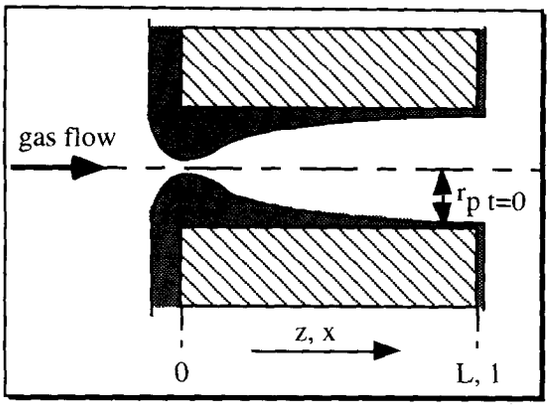


Fig. 2. A cross-section of one cylinder pore.

single raw pore volume (m^3), $V_{preform}$ is the total raw preform volume (m^3) and $d_{preform}$ is the preform disc diameter (m).

The preform diameter remains relatively unchanged whereas the porosity changes during infiltration. Due to deposition on the pore wall and depletion of the precursor from the gas mixture at mass transport limited conditions, the pore diameter gets larger from the gas inlet side ($z = 0$) further down the pore and thus will be dependent on z. This effect is visualised in Fig. 2 (Section 6).

Combination of (11) with (15) gives the velocity through one pore u_p ($m.s^{-1}$):

$$u_p = \frac{Ft}{\epsilon A_{preform}} \tag{17}$$

During the FCVI process, the driving force for the gas flow is dominated mainly by forced convection due to a pressure difference.

The FCVI operator can only adjust the total gas flow rate $Ft^{\#}$ and the outlet pressure p_L to gain a certain u_p setpoint. An expression for the pore gas velocity, similar to the Hagen–Poiseuille relation, in terms of outlet pressure can be derived through combination of eqns 13 and 17:

$$u_p = \frac{d_p^2}{32\mu L} p_L \left\{ \sqrt{1 + \frac{256 Ft^{\#} p^0 T \mu L}{\pi n d_p^4 T^0 p_L^2}} - 1 \right\} \tag{18}$$

Here, the term within brackets times p_L, equals the pressure drop across the pore.

5 Effect of the Preform Microstructure on the Infiltration Behaviour

The effect of the microstructural properties on the infiltration behaviour can be performed through correlation of these properties with the gas velocity. This latter is the prime process parameter for the description of the layer uniformity and thus density during mass transport limited growth.

In the next section, the microstructural properties are presented in detail with their effects on the infiltration behaviour of the preform.

The microstructure of the preform changes with time due to deposition within the pore network. Unless stated otherwise, the initial ($t = 0$) microstructural parameters of the raw preform are meant in all cases.

The total description of the initial preform microstructure is performed through the definition of:

- Preform permeability, indicative of the resistance of the preform for gas flow;
- Preform open porosity, the total open pore volume of the preform that is to be filled with matrix material;
- Diameter of the pores, giving the size of the openings through which the gas flows;
- Deposition area, giving the total surface area available for deposition;
- Preform thickness, the length of the path the gas molecules have to travel;
- Tortuosity, giving the complete path length in case of curved pores.

Preform permeability

The permeability K (m^2) is defined as the fluid conductivity of the porous material.[13,14]

The permeability of a porous system is supposed to be a constant in Darcy's law.

In case the fluid is an incompressible liquid, K is indeed a constant. In the case of gases, the permeability is dependent on pressure at low absolute pressure. (More details about the permeability are given in Part 2 of this study in Section 5). Because of this fact and because the liquid permeability K_l is not a realistic useful FCVI quantity, it is necessary to express the preform microstructure in other more suitable parameters like porosity, pore size, thickness and to be more complete also in terms of tortuosity.

The permeability of the preform is, despite the facts mentioned above, still the sole parameter that gives an impression of the resistance of the structure to the gas flow.

A constraint of infiltration is that the gas permeability of the structure should be sufficiently large to be able to force the gas through it, without having the pressure at the inlet side reaching excessively high values in a short period of time.

Initial preform tortuosity

The tortuosity of a porous material $\tau(-)$, is defined[15] as the square of the ratio of the average distance traversed by a particle of fluid, L_{eff} to the

direct distance through the preform, $L_{preform}$ and hence $(L_{eff}/L_{preform})$.[2] The mean tortuous velocity through the bed u_{bed} (m.s^{-1}) is:

$$u_{bed} = \frac{uo\ \tau}{\epsilon} \tag{19}$$

Where uo is the superficial gas velocity.

It is hard to anticipate what the effect of the tortuosity will be on the density of the composite after infiltration without knowing the exact microstructure. As a first approximation it is anticipated that a preform with $\tau > 1$ can be compared with a thicker preform and that effects are similar. Large tortuosity will yield low density due to larger depletion effects.

As the pores are not straight and uniform in diameter, the section with the largest resistance (small diameter or high angle) can cause early blocking of the pore resulting in early termination of the infiltration process and thus low density.

6 The Relative Composite Density as a Function of Process and Microstructural Parameters

During the densification process, matrix material is deposited onto the pore wall and the layer thickness of the matrix will decrease exponentially with z, see Fig. 2.

Obviously, during the infiltration process, the deposition behaviour changes due to the reduction of the pore size and non-uniform deposition on the pore wall.

Modelling of the infiltration process is therefore more accurate when all conditions and pore dimensions are described both time and position dependent.

The simple equations derived in the previous sections are no longer sufficient. For position dependence, some basic differential equations were derived. This is described in Appendix B.

In summary, for a pore of length L (m) and radius r (m) at temperature T (K) where MTS (denoted with S) reacts at the pore wall, the three principal differential equations are:

$$\frac{\partial p_x}{\partial x} = \frac{-8\ \mu\ L\ K\ Ft^{\#}}{n\ \pi\ p_x\ r_x^4} \tag{20}$$

$$\frac{\partial C_{Sx}}{\partial x} = -2LC_{Sx}\left[\frac{n\ \pi\ k_s\ r_x\ p_x}{Ft^{\#}\ K} + \frac{4\ \mu\ K\ Ft^{\#}}{n\ \pi\ p_x^2\ r_x^4}\right] \tag{21}$$

$$\frac{\partial r_x}{\partial t} = \frac{-m_{SiC}}{\rho_{SiC}} k_s\ C_{Sx} \tag{22}$$

$$\text{with } K = \frac{Tp^0}{T^0}\ (\text{Pa}) \tag{23}$$

and x (–) is the dimensionless axial distance in the pore.

Simultaneous solution of these equations with the variables p_x (Pa), C_{Sx} (mole.m^{-3}) and r_x (m), allows the calculation of the evolution of the pore diameter as a function of time and position in axial direction. After the simulated infiltration process has ended the resulting composite microstructure can be estimated.

The open volume V_0 within the preform after infiltration (m^3) is given by the general expression for a solid of revolution:

$$V_0 = n\pi L \int_0^1 r_x^2\ dx \tag{24}$$

with n the (constant) number of pores in the preform (eqn 16) and r_x represents the pore radius after infiltration.

The mass of the total amount of deposited matrix in the preform M_{in} (kg), is the matrix volume multiplied by the theoretical density of the SiC matrix material ($3{\cdot}2 \times 10^3$ kg.m^{-3}).

$$M_{in} = \rho_{SiC}\ (n\ V_p - V_0) \tag{25}$$

where V_p is the volume of one raw cylindrical pore and equals $\pi r_p^2 L$.

Furthermore, the SiC matrix is not only deposited in the porous preform but moreover, on the front surface of the preform as well. The mass of the deposited SiC on its front side, neglecting the initial surface porosity, can be roughly estimated with:

$$M_{on} = \rho_{SiC}\ \pi r^2_{preform}\ (r_p - r_a) \tag{26}$$

with r_a the radius of the pore mouth after infiltration (m) and r_p the radius of the raw pore (m). The porosity of the preform after infiltration ϵ_c (vol%) is:

$$\epsilon_c = \frac{V_0}{V_{preform}} \tag{27}$$

Here, $V_{preform}$ is the volume (m^3) of the raw preform (without the coating on the front side). The relative bulk composite density is defined here as:

$$\rho_{brel} = 100 - \epsilon_c \tag{28}$$

7 The Model Set-up

General assumptions and model input

In the simulation results described in Section 8, assumptions are made in order to gain a model that can be solved easily and is easy to use and understand. These assumptions are:

(1) Mass transport of the gaseous species takes

place by forced convection in axial direction only. Axial dispersion and radial convection or diffusion (either ordinary or Knudsen) are not taken into account. This model is thus ID.

(2) The forced convection takes place in the viscous laminar flow regime.
(3) The gas behaves ideally.
(4) Stefan flow due to the reaction stoichiometry is neglected since dilution of the precursor compound in the gas mixture is generally large.
(5) The surface kinetics follow a first order relationship with respect to the MTS concentration. The reaction rate coefficient is assumed to be independent of total pressure.
(6) Homogeneous gas phase reactions do not occur.
(7) The initial pores are cylindrical and monosized and the tortuosity equals 1.

The required input parameters for the modelling are:

Initial preform porosity (volume fraction), initial preform thickness (m), diameter of the preform disc (m), activation energy of the first order deposition reaction (J.mole^{-1}), pre-exponential factor (m.s^{-1}), preform temperature (K), outlet pressure (Pa), precursor inlet molar fraction, total gas flow rate at STP (m^3.s^{-1}) and pressure shut off point (Pa). The latter is defined in Part 2 of this study (eqn 10).

The only input microstructural parameter that is required and initially unknown is the pore radius r_p at $t = 0$ (m). Through comparison of experimental infiltration durations and simulation results, this r_p can be fine-tuned to gain a matching between experiments and model.

Calculation algorithm

After input of the process conditions, the constants are calculated: k_s, μ at the selected temperature and the number of pores n (eqn 16). An initial pore diameter is selected and an initial iteration step of 5 s was chosen. At these conditions, the pressure within the pore as a function of position is calculated through numerical integration of eqn 21. Hereto, the total pore is split into 40 equal length segments. Simultaneously, the MTS concentration (eqn 22) within the pore is calculated numerically and allows the estimation of the deposition rate in the pore and the local reduction in pore radius (eqn 23).

With this reduced pore size, a next time step is selected and again the pressure, concentration and growth rate are calculated for each of the 40 segments.

As the inlet pressure starts to increase more rapidly, the time step is reduced to gain higher accuracy. The whole iteration is terminated when the selected shut off pressure drop setpoint is reached. At the final pore dimensions, the relative density or porosity of the preform, the deposited mass of SiC in and on the preform and final pore mouth radius are calculated.

The results of the model calculations as a function of process conditions are presented in Section 8.

8 Modelling Results

Due to the large amount of assumptions and simplifications made, this model can only simulate rough trends in infiltration time and composite density as a function of time and process or microstructural conditions. It is thus not intended to give quantitative information.

Nominal simulation conditions

In the following figures the results are summarised of the simulations performed at nominal process conditions using a standard preform model plate:

Temperature: 1273 K, outlet pressure: 50 torr, total gas flow rate: 1 slm, MTS inlet mole fraction: 0·15, preform porosity: 50%, initial preform thickness: 3 mm, preform diameter 8 cm, initial pore diameter: 500 μm, pressure shut off difference: 100 ± 10 torr, activation energy: 400 kJ.mole^{-1} and pre-exponential factor: $2{\cdot}1 \times 10^{14}$ m.s^{-1} of the first order reaction.[16] The dynamic viscosity of the gas mixture is estimated through: $\mu(T) = 2{\cdot}9 \times 10^{-7} + 4{\cdot}8 \times 10^{-8}T - 1{\cdot}6 \times 10^{-11}T^2 + 3{\cdot}2 \times 10^{-15}T^3$ in Pa·s. Initial iteration step size: 5 s.

IFCVI process as a function of time

As infiltration proceeds and the pores become smaller, the process conditions change.

In Fig. 3, the simulated change in inlet pressure and inlet and outlet MTS concentration are presented.

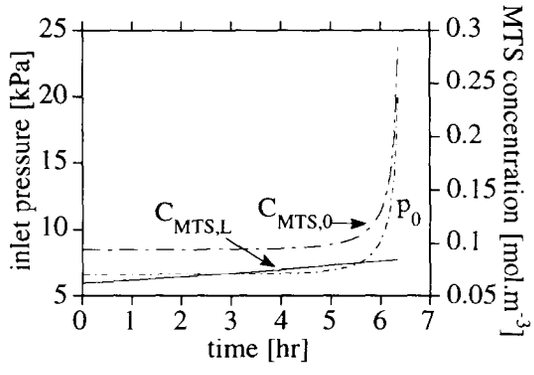


Fig. 3. Simulation result of the inlet pressure, the inlet and outlet MTS concentration (resp. $C_{MTS,0}$ and $C_{MTS,L}$) of a model preform at nominal conditions.

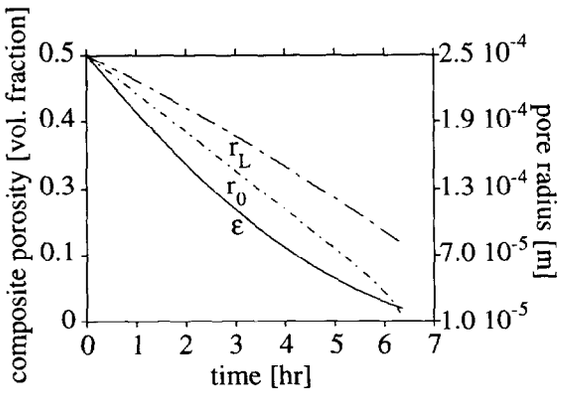


Fig. 4. Simulation result of the inlet and outlet radius (respectively r_0 and r_L and porosity of a model preform at nominal conditions.

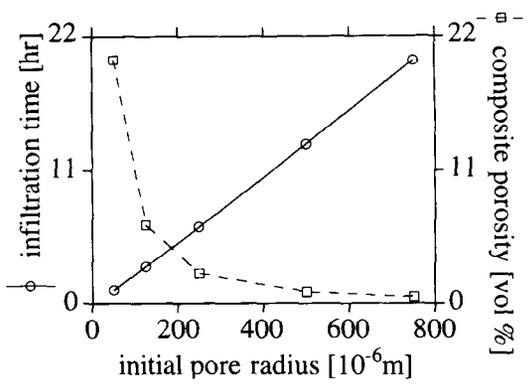


Fig. 6. The simulated infiltration time and composite porosity after infiltration of a model preform at nominal conditions versus initial pore radius.

The outlet pressure remains constant at 6·65 kPa (= 50 torr). Initially the inlet pressure hardly rises, but as soon as a critical pore size is reached, the pressure increases rapidly.

Combined with the increase of the inlet pressure, the inlet concentration and the gas velocity are increasing.

In general, more uniform deposition occurs due to the increase in gas velocity through the pores so that depletion effects are less severe in a later stage of the infiltration process.This effect is demonstrated in Fig. 3 by the increase of $C_{MTS,L}$.

Clearly, as the pore is becoming smaller, the porosity decreases (Fig. 4). At first, decrease is rapid, but due to the reduction of the deposition (pore mantle) area, porosity is only decreasing relatively slowly later on.

Total gas flow rate

Increase in total gas flow rate and thus increase of the mass transport rate, yields a larger matrix growth rate and reduction in infiltration time (Fig. 5). Subsequently, the uniformity of the layer profile is enhanced, since the gas velocity is enlarged.

When the kinetics are becoming rate controlled, further increase of $Ft^{\#}$ no longer has an effect on the layer uniformity, but the increase of the initial pressure drop at large $Ft^{\#}$ will yield a reduction in G_L/G_0 ratio and thus increase the composite porosity. In summary, a minimum will exist in composite porosity.

Initial pore size

When L/d_p is relatively small, matrix growth is limited by the chemical reaction (eqn 8) and thus occurs at large r_p. Increase of r_p as demonstrated in Fig. 6, linearly increases infiltration time, whereas composite porosity decreases through the increase of the gas velocity (eqn 13).

Outlet pressure

Similar to Fig. 5, in Fig. 7 an optimum (at 6·65 kPa outlet pressure) in composite density is found when the outlet pressure is increased from 13·3 to $1{\cdot}0 \times 10^5$ Pa (0·1–760 torr). At high outlet pressure, (i.e. ≥ 20 kPa), the gas velocity is low (eqn 11) so that depletion of the precursor gas is high along the pore length. Non-uniform deposition is the consequence. At low outlet pressure (p_L = 0·133 kPa) and thus at large gas velocity, the pressure drop value across the preform is of similar magnitude as the outlet pressure.

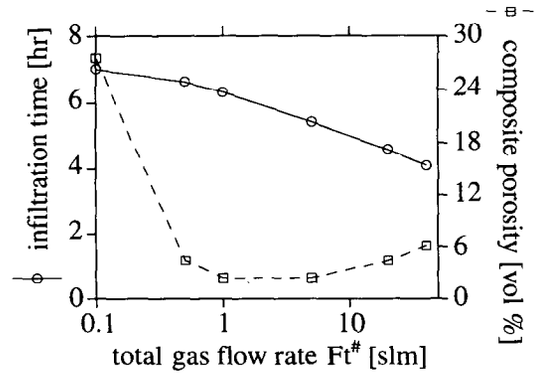


Fig. 5. The simulated infiltration time and composite porosity after infiltration of a model preform at nominal conditions versus total gas flow rate.

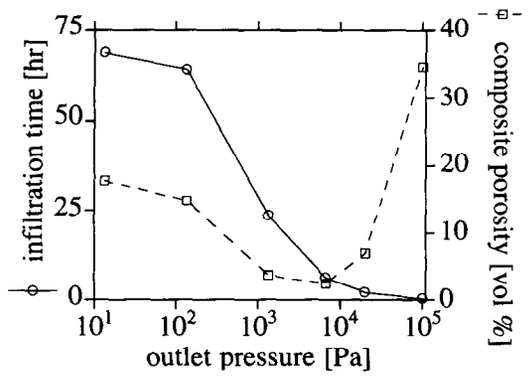


Fig. 7. The simulated infiltration time and composite porosity after infiltration of a model preform at nominal conditions versus total outlet pressure.

The large gas velocity will yield large density, but on the other hand when $p_0 > p_L$ and thus $G_0 > G_L$ uniformity will be poor. It is speculated that growth is limited by the chemical kinetics at these large gas velocities, since mass transport to the surface is very fast. Here, the matrix growth is not dependent on the gas velocity but on the local total pressure only.

Infiltration time is reduced if the total pressure and thus concentration is increased, because matrix growth is enhanced.

Temperature

At low temperature, deposition is kinetically controlled. Increase of temperature decreases infiltration time rapidly, whereas growth becomes mass transport limited infiltration time is less severely reduced (Fig. 8). As stated before, kinetically controlled growth is preferred because depletion (at low T) is low and uniformity is high.

Precursor input mole fraction

Increase of the MTS fraction in the gas mixture has no effect on the relative composite density. In relative terms, the uniformity is not affected by the absolute value of the MTS fraction within the gas mixture, neither in the mass transport limited nor in the kinetically controlled regime, as coincides with theoretical considerations.

However, infiltration time is reduced inversely proportional with the MTS fraction due to the increase of precursor concentration.

Preform porosity

The raw preform porosity is changed by alteration of the amount of pores. The gas stream is split into smaller portions, so that when the porosity is increased it will have to flow through a larger pore area. This reduction in gas velocity (eqn 11) yields a larger composite porosity in an almost linear fashion.

At low mass transport rate (high porosity) infiltration will take more time.

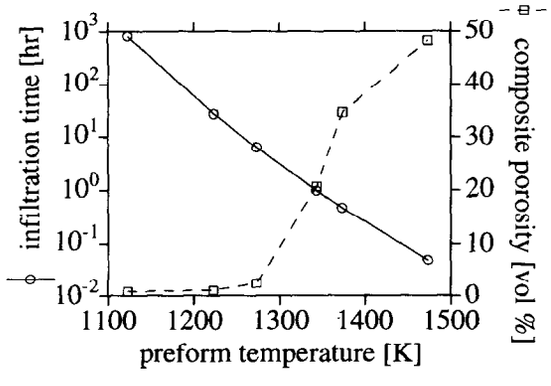


Fig. 8. The simulated infiltration time and composite porosity after infiltration of a model preform at nominal conditions versus preform temperature.

Initial preform thickness

A thicker preform disc will be infiltrated in the same time as a thin disc, as long as the deposition rate in the pore mouth is unaffected, i.e. p_0 remains unchanged.

A thick preform will, however, yield a larger initial pressure drop across the preform as compared to a thin preform at the same flow rate. Depletion of the MTS from the gas mixture is more severely affecting the composite density when the pores are longer.

Preform diameter

As the preform diameter or cross flow area A gets larger, the gas velocity is decreased (eqn 11). Subsequently, composite porosity is increased. As a consequence, the infiltration time will increase since mass transport of the gas species is reduced.

9 Discussion and Conclusions

Despite the better and more comprehensive numerical 2D models used by others, the developed simple ID model gives a good insight in the relative complex FCVI process without using a black box approach. The simulation variables correspond to the process variables that can be adjusted by the operator providing a direct correlation between experiments and model.

The capability of this model is to predict trends in filtration time and composite density that might be expected when process conditions, preform structure or dimensions are varied.

The general model trends are summarised in Table 1.

The simulation results show that uniformity of the matrix deposition can be improved by allowing

Table 1. The infiltration behaviour parameter dependence on initial process conditions and raw preform structure. The matrix growth is either limited by the surface kinetics or the mass transport rate.

		Composite density	
Parameter increase	*Infiltration time*	*Kin. contr.*	*Conv. contr.*
u_p	↓	↓	↑
$Ft^{\#}$	↓	↓	↑
p_L	↓	↑	↓
T	↓	*—	↓
X_{MTS}	↓	—	—
d_p	↑	—	↑
$d_{preform}$	↓	—	↓
ϵ	↑	—	↓
L	↓	—	↓

*Assuming a first order reaction.

a large pore gas velocity in combination with a low inlet to outlet pressure ratio.

The first Damköhler number should be small. This implies operation where the gas velocity is so fast that matrix growth is just within the kinetically controlled growth regime. This generally occurs at: medium total gas flow rate, medium outlet pressure, low temperature and arbitrary precursor content in the gas mixture (with the constraint however that pure SiC will be formed, so the ratio H_2/MTS must not be too low).

The preform microstructure that is best suited for FCVI processing to gain a large composite density has a low open porosity, is thin and contains pores of large diameter. In general the gas permeability of the porous structure should be sufficiently large to enable the gas to flow through the structure easily. The best starting preform microstructure (without considering mechanical aspects) implies: low porosity, thin walled structures, large pore diameter, straight continuous pores and sufficient permeability.

For economical reasons, the infiltration time required to reach a certain homogeneous density should be kept as low as possible. Obviously, a high matrix growth rate across the entire pore length is essential. Increase of the matrix growth rate can be tailored by increase of the precursor molc fraction in the gas mixture without affecting the uniformity of the deposition profile. Increase of the temperature will also enhance densification rates, but will negatively affect the uniformity of the matrix distribution. Rapid infiltration is also enhanced through increase of the gas velocity. Lowering the total pressure will negatively affect the matrix growth rate and thus increase of the total gas flow rate is more suitable for this purpose.

In summary, the global optimum process settings for both rapid and dense composites are thus:

- high total gas flow rate;
- medium outlet pressure;
- medium temperature;
- high precursor molar fraction;

the best starting preform microstructure implies:

- low porosity;
- thin walled structures;
- straight continuous pores;
- medium pore size;
- sufficient permeability.

Unfortunately, it can be concluded that rapid densification does not coincide with high composite homogeneity and density.

For industrial application of the FCVI process, the real processing optimum depends on the specification of the desired composite material, especially its density. A high density can be achieved, but the time consumption will be large. This extra energy and material consumption should thus be compared with the extract value of the material for the specific application.

References

1. Janssen, L. P. B. M. & Warmoeskerken, M. M. C. G., *Transport Phenomena Data Companion*, Delftse Uitgevers Maatschappij, Delft, (1991).
2. Levenspiel, O., *Chemical Reaction Engineering*, Wiley, New York, (1972).
3. v.d. Brekel, C. H. J., Fonville, R. M. M., van der Straten, P. J. M. & Verspui, G., *Proc. 8th Int. Conf. on CVD*, Electrochem Soc., (1981).
4. Rossignol, J. Y., Langlais, F. & Naslain, R., *Proc. 9th Int. Conf. on CVD*, ed. Mc. D. Robinson, The Electrochem. Soc. (1984), p. 596–614.
5. Roman, Y. G., de Croon, M. H. J. K. & Metselaar, R., submitted to the *J. Eur. Ceram. Soc.*
6. Chung, G. Y. & McCoy, B. J., *J. Am. Ceram. Soc.*, **74** (1991) 746–51.
7. Tai, N. & Chou, T., *J. Am. Ceram. Soc.*, **72** (1989) 414–20.
8. Fedou, R., Langlais, F. & Naslain, R., *J. Mat. Synthesis and Processing*, **1** (1993) 43–52. *ibid* Ref. 2. 61–74.
9. Lin, Y. S. & Burggraaf, A. J., *Chem. Eng. Sci.*, **46** (1991) 3067–80.
10. Gupte, S. M. & Tsamopoulous, J. A., *J. Electrochem. Soc.*, **137** (1990) 1626–38.
11. Starr, T., *Ceram. Sic. Eng.*, **9** (1988) 803–12.
12. Starr, T., *Proc. 10th Int. Conf on CVD*, ed. G. W. Collen, The Electrochem. Soc. (1987), p. 1147–55.
13. Bear, J., *Dynamics of fluid in porous media*, Elsevier, New York, (1972).
14. Collins, R. E., *Flow of fluids through porous materials*, Reinhold Publ. Corp., (1961).
15. Carman, P. C., *Trans. Inst. Chem. Eng. London*, **15** (1937) 150.
16. Roman, Y. G., Forced flow chemical vapour Infiltration, PhD thesis Eindhoven University of Technology, Eindhoven, The Netherlands, (1994).

Appendix A. Time Dependent Precursor Concentration in a Cylindrical Model Pore

The cylindrical model pore can be assumed to be a steady state plug flow reactor in which forced convection is present and chemical reaction takes place on the pore wall. Stefan flow is neglected since the dilution of the $SiCH_3Cl_3$ in the carrier gas (hydrogen) is high. If it is assumed that the pore gas velocity is constant throughout the pore and independent of axial position, the following simplified analytical solution of the concentration of MTS within the pore can be derived.

The mass balance for a differential element of the pore with volume dV:

$$F_{Sz} = (F_S + dF_S)_z + (-r_S dV) \qquad \text{(A1)}$$

where 'S' denotes $SiCH_3Cl_3$, F_{Sz} the molar flow rate S (moles.s^{-1}) and equals $C_{Sz}\, u_z\, A_z$ since S is heavily diluted in the carrier gas. C_{Sz}, u_z and A_z are respectively the concentration of S (moles.m^{-3}),

the gas velocity ($m.s^{-1}$) and the cross flow area (m^2) at a location in axial direction z within the pore. Also:

$$C_{Sz} = \frac{F_{S0}(1 - Y_{Sz})}{u_z A_z} \tag{A2}$$

where Y_S is the conversion of S.

The reaction rate ($moles.m^{-3}.s^{-1}$) of S on the pore wall is:

$$-r_S = k_v C_{Sz} = \frac{k_v F_{S0}(1 - Y_{Sz})}{u_z A_z} \tag{A3}$$

where k_v is the volumetric reaction rate coefficient for the first order reaction (s^{-1}).

Rewriting A1 yields:

$$-dF_{Sz} = F_{S0}\, dY_{Sz} = -r_S dV \tag{A4}$$

and combination with A3 gives:

$$dY_{Sz} = \frac{-r_S\, dV}{F_{S0}} = \frac{k_v(1 - Y_{Sz})dV}{u_z A_z} \tag{A5}$$

After grouping of the terms and with $dV = A dz$ for a straight pore:

$$\int_0^{Y_{Sz}} \frac{1}{1 - Y_{Sz}}\, dY_{Sz} = \int_0^z \frac{k_v}{u_z} dz \tag{A6}$$

Here, the reaction rate coefficient k_v is based on the volume of the pore. In terms of surface area of the pore k_s ($m.s^{-1}$) is calculated through: $k_v V = k_s A$ with A representing the deposition or mantle area of the straight pore (m^2). k_v is thus $4k_s/d_p$, where d_p is the pore diameter of the straight pore (m).

Equation A6 can be integrated from pore mouth to length z and combined with (eqn A2):

$$1 - Y_{Sz} = \frac{C_{Sz} u_z A_z}{C_{S0} u_0 A_0} \tag{A7}$$

to yield:

$$\frac{C_{Sz} u_z A_z}{C_{S0} u_0 A_0} = \exp\left(-4k_s \int_0^z \frac{1}{u_z d_{pz}} dz\right) \tag{A8}$$

This equation reduces to a simpler one when the pressure across the pore axis is assumed to be linearly decreasing from p_0 towards p_L and the pore is straight so that u_z and d_{pz} are independent of z. At constant pressure and for an incompressible gas, the continuity equation is $\rho_z u_z A_z = \rho_0 u_0 A_0$. A very rough estimation of the concentration profile is:

$$\frac{C_{Sz}}{C_{S0}} = \exp\left(\frac{-4k_s z}{d_p u_p}\right) \tag{A9}$$

where u_p and d_p are based upon the entrance pore diameter conditions ($z = 0$).

Appendix B. Time and Position Dependent Precursor Concentration in a Cylindrical Model Pore

It may be clear that due to non-uniform deposition on the pore wall (as a consequence of depletion and the pressure gradient), the total gas flow rate, total pressure, MTS concentration and pore radius are all a function of position along the pore axis z.

The next section presents the derivations of three differential equations and are: the total gas flow rate, total pressure within the pore, the MTS concentration and the pore radius as a function of position in axial direction. These equations are solved simultaneously using a Mathematica† numerical routine based upon the Runge Kutta method.

Recall the inflow gas velocity (eqn 11):

$$u_{pz} = \frac{Ft^{\#} T p^0}{n A T^0 p_z} = \frac{Ft^{\#} T p^0}{n \pi r_z^2 T^0 p_z} \tag{B1}$$

and the Poiseuille flow eqn 13 as:

$$u_{pz} = \frac{-r_z^2}{8\mu} \frac{\partial p_z}{\partial z} \tag{B2}$$

Rewriting the equations in terms of dimensionless axial distance x: $x = z/L > dz = L dx$, equation B2 becomes:

$$u_{pz} = \frac{-r_x^2}{8\mu L} \frac{\partial p_x}{\partial x} \tag{B3}$$

A combination of (B1) and (B3) yields the position dependent pressure differential equation:

$$\frac{\partial p_x}{\partial x} = \frac{-8\mu\, LK\, Ft^{\#}}{n\pi p_x r_x^4} \quad \text{with } K = \frac{Tp^0}{T^0} \tag{B4}$$

The mass balance for a differential element of the pore with volume dV:

$$F_{Sz} = (F_S + \partial F_S)_z + (-r_S\, \partial V) \tag{B5}$$

where $SiCH_3Cl_3$ is denoted as 'S' and F_{Sz} is the molar flow rate of S ($moles.s^{-1}$).

The first order reaction rate of disappearance of S, r_S ($moles.m^{-3}.s^{-1}$) on the pore wall is:

$$r_S = -k_v C_{Sz} \tag{B6}$$

Here, the reaction rate coefficient k_v is based on the volume of the pore. In terms of surface area of the pore, k_s ($m.s^{-1}$) is calculated through: $k_v V = k_S A$, where A represents the deposition (or pore mantle) area (m^2) and thus $k_v = \frac{2k_s}{r_z}$. Rewriting B5 yields:

$$\partial F_{Sz} = r_S A_z\, \partial z = r_S \pi r_z^2 \partial z \tag{B7}$$

†Mathematica is software of Wolfram Research Inc.

$$\partial F_{Sz} = -k_S\, C_{Sz}\, 2\pi\, r_z\, \partial z \text{ with } \partial z = L\partial x \quad \text{(B8)}$$

$$\frac{\partial F_{Sx}}{\partial x} = -2\,\pi\, k_s\, L\, C_{Sx}\, r_x \quad \text{(B9)}$$

F_{Sx} equals ($C_{Sx}\ u_x\ A_x$) if the dilution of S in the carrier gas is high. C_{Sx}, u_x and A_x are respectively the concentration of S (moles.m^{-3}), the gas (m.s^{-1}) velocity and the cross flow area (m^2) at a location in axial direction within the pore. It is known that:

$$C_{Sx} = \frac{nF_{Sx}}{Ft_x} = \frac{nF_{Sx}p_x}{Ft^{\#}\,K} \quad \text{(B10)}$$

where F_{Sx} is the molar and Ft_x is the volumetric flow rate and equals (u_xA_x) and p_x is the total pressure in the pore as a function of x. Differentiation on both sides yields:

$$\frac{\partial F_{Sx}}{\partial x} = \frac{Ft^{\#}\,K}{n}\ \frac{\partial \dfrac{C_{Sx}}{p_x}}{\partial x} \quad \text{(B11)}$$

and with the chain rule:

$$\frac{\partial F_{Sx}}{\partial x} = \frac{Ft^{\#}\,K}{n}\left[\frac{1}{p_x}\,\frac{\partial C_{Sx}}{\partial x} - \frac{C_{Sx}}{p_x^2}\,\frac{\partial p_x}{\partial x}\right] \quad \text{(B12)}$$

Combination of equations (B9) and (B12) yields:

$$\frac{Ft^{\#}\,K}{n}\left[\frac{1}{p_x}\,\frac{\partial C_{Sx}}{\partial x} - \frac{C_{Sx}}{p_x^2}\,\frac{\partial p_x}{\partial x}\right] = -2\,\pi\, k_s L r_x C_{Sx} \quad \text{(B13)}$$

hence:

$$\frac{1}{p_x}\,\frac{\partial C_{Sx}}{\partial x} = \frac{-2n\pi\, k_s L r_x C_{Sx}}{Ft^{\#}\,K} + \frac{C_{Sx}}{p_x^2}\,\frac{\partial p_x}{\partial x} \quad \text{(B14)}$$

combination with equation (B4):

$$\frac{\partial C_{Sx}}{\partial x} = -2\,L\,C_{Sx}\left[\frac{\pi\, n\, k_s\, r_x\, p_x}{Ft^{\#}\,K} + \frac{4\,\mu\,K\,Ft^{\#}}{n\,\pi\,p_x^2\,r_x^4}\right] \quad \text{(B15)}$$

with the boundary condition that at $x = 0$:

$$C_{S0} = \frac{p_{S0}}{RgT} = \frac{S_{S0\,p0}}{RgT} \quad \text{(B16)}$$

For the change in pore radius due to deposition on its wall:

$$\frac{\partial r_x}{\partial t} = \frac{-m_{Sic}}{\rho_{Sic}}\, k_s\, C_{Sx} \quad \text{(B17)}$$

(B4), (B15) and (B17) and the three principal equations that depend on the three variables p_x, C_x, r_x and can be solved simultaneously as a function of both position x and time t to yield the development of the matrix deposition within a cylindrical pore.

Journal of the European Ceramic Society **15** (1995) 887–898
© 1995 Elsevier Science Limited
Printed in Great Britain. All rights reserved
0955-2219/95/$9.50
0955-2219(95)00062-3

Analysis of the Isothermal Forced Flow Chemical Vapour Infiltration Process. Part II: Experimental Study

Y. G. Roman,[a] M. H. J. M. de Croon[b] & R. Metselaar[a]

[a]TNO, Centre for Technical Ceramics, PO Box 595, 5600 AN Eindhoven, The Netherlands
[b]Eindhoven University of Technology, Department of Chemical Engineering, PO Box 513, 5600 MB Eindhoven, The Netherlands

(Received 24 June 1994; revised version received 2 March 1995; accepted 10 March 1995)

Abstract

The preparation of homogeneously dense fibre reinforced SiC composites in a rapid way was the main objective of this study. Furthermore, densification should proceed as fast as possible. In Part 1 of this study,[1] some theoretical concepts were proposed of the infiltration mechanisms. The simple model was verified qualitatively using the results of experiments as is reported in this manuscript. Model and experiments do generally coincide. The trends predicted and found experimentally during alteration of the process or microstructural conditions appear to justify the theoretical concepts. Optimum infiltration conditions to gain largest density gain in the shortest time frame are 1320 K, outlet pressure of 6·65 kPa, total gas flow rate of 4 × 10^{-5} m^3 s^{-1}, MTS fraction of 16 vol% and pressure shut off point of 10 kPa.

1 Introduction

This paper is the continuation of the study to find the optimum process and microstructural conditions to gain high density ceramic composites using the Isothermal Forced Flow Chemical Vapour Infiltration (IFCVI) technique. In the previous paper, a simple mechanistic model was presented. In this manuscript the results are presented of an experimental study to verify the derived concept of the first paper.

2 Experimental Details

During the IFCVI of a porous carbon fibre preform, a CVD reaction takes place on the hot fibre surface. In this study, methyl-trichlorosilane (MTS) was used as both the silicon and carbon donor for the silicon carbide matrix. In the presence of a large amount of hydrogen it is known to form stoichiometric SiC.[2] The CVD reaction is:

$$CH_3SiCl_{3(g)} + H_{2(g)} \rightarrow SiC_{(s)} + 3HCl_{(g)} + H_{2(g)} \quad (1)$$

Raw materials

Disc shaped substrates with a diameter of 80 mm and a thickness of approximately 3 mm are used for the infiltration experiments. They were manufactured at DASA Aerospace,[3] Germany. They consist of Torayca T-300 (3K) fibres in plain woven layers that are stacked upon each other in a 0/90° orientation and woven together through a tow in the z direction. This orthogonally woven preform thus contains fibres in a 3D configuration.

Since the preform is very sensitive to handling and has a low stiffness, it is prefixed through impregnation with an alkali free liquid phenolic resin and compressed. After pyrolysis of the resin, the plates are cut into discs of 80 mm diameter using a water cutting machine. The carbon fibre content of the preforms varied from approximately 40–55 vol.% with respective thicknesses of 3·2–2·5 mm.

Infiltration experiments

Before infiltration, the preform plate is washed ultrasonically in acetone for 15 min and then positioned on top of a graphite support ring into a graphite holder. This holder is placed on top of a graphite injector tube through which the gases enter the holder and after flowing through the preform mainly axially, exit via the exhaust tube and pump (see Fig. 1). The graphite injector and holder are situated in a vacuum tight reactor chamber which is kept at a constant pressure and temperature by external resistance heating. This reactor is checked for leaks prior to each run. The preform is heated under a flow of nitrogen to 1200 K overnight at a rate of 120 $K.hr^{-1}$ and thereafter ramped to process temperature. After temperature stabilisation of at least 30 min, the process is started through introduction of the CVI gases at the process pressure.

The preform temperature is monitored by a thermocouple that is located in the bottom of the holder. All process settings (temperatures,

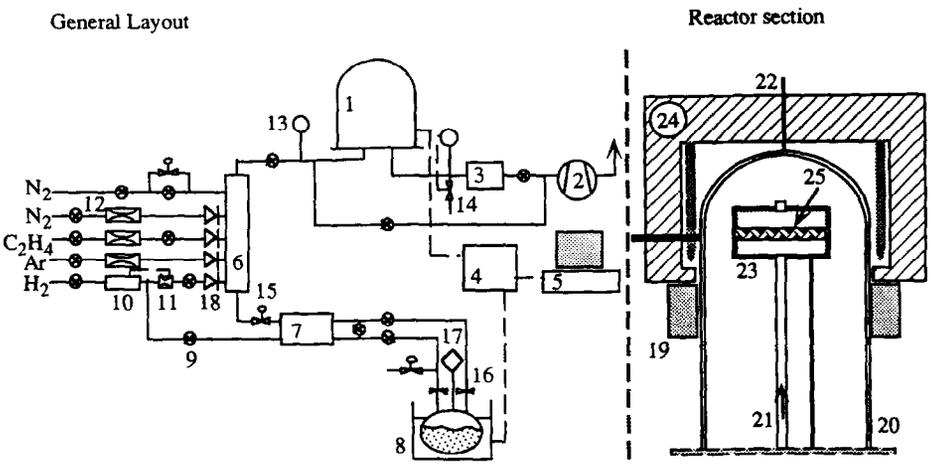


Fig. 1. A schematic layout of the FCVI reactor system; 1. bell jar reactor; 2. pump; 3. particle trap; 4. digital process and temperature controller; 5. P.C. data logger; 6. gas mixing box; 7. vapour source controller; 8. temperature controlled MTS bubbler; 9. pneumatic valve; 10. mass flow meter; 11. controller device of mass flow meter; 12. mass flow controller; 13. pressure gauge; 14. automatic nitrogen injection; 15. manual needle valve; 16. manual valve; 17. vacuum manometer; 18. check valve; 19. alumina wool; 20. alumina bell jar; 21. gas injector pipe; 22. thermocouple; 23. graphite preform holder; 24. furnace, 25. preform.

pressures, gas flows) during the infiltration are monitored by a data logging system attached to the FCVI apparatus which logs at 5 min intervals.

The methyltrichlorosilane (MTS) precursor flow rate is controlled by a vapour source controller. The MTS bubbler is weighed before and after each run to check the MTS flow rate. The 'weighed' MTS flow is used as the actual MTS flow value. The total amount of hydrogen gas, (i.e. the carrier gas for the bubbler and the bypass) is kept constant during the entire infiltration duration and additional argon is added for obtaining both a constant H_2/MTS ratio and total gas flow rate. The pressures at the injector and outlet side are monitored with two baratrons.

The pressure in the outlet is maintained at a constant value during the entire infiltration experiment. When the pressure in the injector at the start and the pressure at the end exceeds a certain shut off value, the infiltration is terminated and the gas flows are shut off. The preform is cooled to room temperature at 120 $K.hr^{-1}$ under a flow of argon.

In Table 1, the standard IFCVI process conditions are summarised.

Table 1. Standard IFCVI process conditions

Preform temperature (K)	1273
Outlet pressure (kPa)	6·65
MTS bubbler temperature (K)	288
Total gas flow rate (slm)	1
H_2 fraction at inlet (vol.%)	54
Ar fraction at inlet (vol.%)	37
MTS fraction at inlet (vol.%)	9
H_2/MTS ratio at inlet	6
Shut off pressure difference (kPa)	9·44 or 26·6

3 Characterization of the Preform

Raw preform

The outer dimensions and the weight of the disc shaped carbon fibre substrates with an initial diameter of 80 mm and a thickness of approximately 3 mm were measured before and after each run respectively with vernier callipers and an analytical balance. For the calculation of the fibre content V_f (volume fraction) of the preform relation[2] was used in which the small amount of pyrolised resin was neglected.

$$V_f = \frac{M_{preform}}{V_{preform}\,\rho_C} \tag{2}$$

Here, $M_{preform}$ (kg) is the mass of the raw preform and $V_{preform}$ is the volume of the raw preform disc in m^3 and ρ_C is the density of the carbon fibre ($1{\cdot}75 \times 10^3$ $kg.m^{-3}$).

Hereafter, the theoretical ideal density ρ_i ($kg.m^{-3}$) of a densified preform where the total pore volume is completely filled with silicon carbide matrix material ($\rho_m = 3{\cdot}2 \times 10^3$ $kg.m^{-3}$) can be calculated according to:

$$\rho_i = V_f\,\rho_c + (1 - V_f)\,\rho_m \tag{3}$$

The initial deposition area A_{dep} (m^2) is the weight $M_{preform}$ (kg) of the raw preform multiplied by the specific surface area S_C ($m^2.kg^{-1}$) of the carbon fibres (550 $m^2.kg^{-1}$). Assuming that there is no trapped porosity:

$$A_{dep} = S_C M_{preform} \tag{4}$$

Permeability

The preform permeability K, is defined as the conductance of the preform for the gas flow. The

initial permeability of the raw preform is dependent on its microstructure only and thus dependent on its fibre content. The gas permeability K_g (m^2) of a porous structure is given by Darcy's law as:[4]

$$K_g = \frac{uo\ \mu\ L}{\Delta p} \tag{5}$$

where L is the preform thickness (m), uo is the average superficial gas velocity ($m.s^{-1}$), μ is the dynamic gas viscosity (Pa.s) and ΔP is the pressure difference across the preform plate (Pa). This form of Darcy's law has, however, a very narrow range of validity.[5]

The permeability of a porous system is supposed to be a constant by definition. In case the fluid is an incompressible liquid and inertial effects can be neglected,[6] K is indeed a constant. In the case of gases, especially at low total pressure, the fluid does not always stick to the wall of the pores as required in Darcy's law (Poiseuille type flow) and a phenomenon termed 'slip' can occur. This slipping of the fluid along the pore walls gives rise to an apparent dependence of permeability on pressure. This dependence is called the Klinkenberg effect and occurs typically at low total pressure and corresponding Knudsen numbers[7] between 0·1 and 1.

Because the gas permeability is thus dependent on the pressure (drop) and not solely a microstructural constant, for the sake of comparison within the range of a process condition, it is necessary to express the evolution of the preform microstructure during CVI in other parameters like porosity, pore size, fibre diameter, fibre arrangement and wall thickness and to be more complete also in terms of tortuosity. Still, the permeability of the raw preforms is measured as a function of fibre content (and preform thickness), outlet pressure and total gas flow rate to obtain an order of magnitude of the conductance to gas flow. Hereto, argon gas flowed through the raw preform in the IFCVI apparatus at a temperature of 1273 K. The argon flow rate was varied stepwise from 0 to 2 slm at 2·66, 6·65 and 9·31 kPa outlet pressure and the pressure drop across the preform plate was measured using two matched pressure gauges.

Dimensionless numbers

The Peclet and the first Damköhler numbers can aid in the description of the IFCVI process conditions that were used for the experiments. These are defined in Part 1 of this study for a hollow cylindrical pore. For a more realistic definition of the preform the following definitions[9] were applied that are indicative for the raw preform and process conditions at $t = 0$.

$$Pe_{bed} = \frac{u d_f\ \tau^2}{\epsilon\ (1 - \epsilon)\ D_{multi}} \tag{6}$$

$$DaI_{bed} = \frac{4\ k_s\ \epsilon}{\tau\ u} \tag{7}$$

with τ (–) is the tortuosity of the preform and assumed to equal 2, k_s ($m.s^{-1}$) is the first order reaction rate coefficient, ϵ (vol. fraction) is the raw preform porosity, d_f (m) is the fiber diameter = 7×10^{-6} m, D_{multi} ($m^2.s^{-1}$) is the multi component diffusion coefficient.

Infiltrated preform

After the infiltration experiments, the composite discs were weighed to calculate the overall MTS conversion or total yield of MTS: η in the preform into solid matrix material. This η (%) is estimated by:

$$\eta = \frac{M_{m,dep}}{M_{m,max}} \times 100 \tag{8}$$

where $M_{m,dep}$ (kg) is the total deposited mass of matrix material and $M_{m,max}$ (kg) is the mass of matrix material that would be deposited at a complete conversion of MTS. Note that (reaction 1) 1 mol of MTS yields 1 mol of SiC.

This definition of η is very similar to Δ (eqn 5 part 1), whereas the first represents the conversion based upon the whole preform volume and the latter one represents the conversion across the length of a cylinder pore. This similarity implies that large η will yield low composite density due to low uniformity of the deposited matrix in axial direction.

After weighing of the composite preforms, they were cut into bars. Out of each disc, four samples from the middle section were cut, with typical dimensions of $60 \times 10 \times 3$ mm^3 using a diamond blade. The bars were ultrasonically cleaned in ethanol for 15 min and dried at 400 K for at least one night. Since the samples absorb moisture from the air, each bar was weighed directly after drying on an analytical balance. The outer dimensions of each bar were measured with callipers and the percentage of the ideal density expressed as the relative bulk composite density $\rho_{b\ rel}$ (vol.%) was estimated through:

$$\rho_{b\ rel} = \frac{M_b}{V_b\ \rho_i} \times 100 \tag{9}$$

with V_b (m^3) being the bulk volume of the bar and M_b (kg) the weight of the infiltrated bar. The arithmetic mean of the relative density of the four bars indicates the $\rho_{b\ rel}$ of each preform disc.

Analysis of the matrix composition

For the determination of the phase structure of the deposited matrix material, XRD analysis was

used with CuKα radiation at 35 kV and a 2θ diffraction angle between 20 and 80°. The SiC matrix was further analysed using a microprobe (EPMA, Jeol type JXA-8600SX). The composition of the matrix as a function of infiltration temperature, i.e. the silicon, carbon and oxygen content were measured quantitatively using an acceleration voltage of 10 kV. Both sides of the composite discs were measured *viz.* the gas inlet side and gas outlet side.

4 Results and Discussion

The effect of the different process variables such as preform temperature, total gas flow rate, MTS fraction in the inlet gas mixture and the outlet pressure on the infiltration time and composite density was studied. Furthermore, the effect of the fibre content and the densification stage (pressure drop) as a function of infiltration time are presented.

First, the reproducibility of the process and of the characterization methods are tested.

Reproducibility

A blank run was performed in which a preform plate was heated up to the typical process temperature of 1273 K and subjected to a mixture of H_2 and Ar, at a rate of respectively 500 and 100 sccm for 5 h. After cooling according to the normal procedure, the preform dimensions and weight were checked. No significant difference in weight or volume was detected.

So, it can be concluded that the changes of the preform, described hereafter, are solely the consequence of the infiltration procedure.

Before the effect of any process variable was tested, the reproducibility of the IFCVI process was estimated by carrying out twice, three repeated runs, (i.e. three runs under the same conditions). The relative bulk density (average of four bars out of one sample, $n = 4$) varied 0·5%, whereas it varied more when measured with a whole composite disc ($n = 1$), i.e. 2·2%. The latter error is larger, because of the error that is made in the measurement of the composite thickness, due to a radial thickness gradient of the deposited coating on the gas inlet side of the sample of approximately 10%.

Process conditions during the run

The data logging system allows continuous monitoring of the process settings. A typical result is given in Fig. 2. The total hydrogen flow rate is the summation of the hydrogen flow rate through the bubbler and the 'back up' hydrogen flow rate that is added additionally. All process conditions

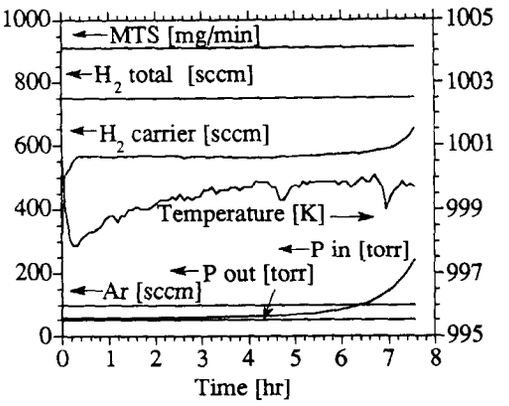


Fig. 2. The process conditions as a function of infiltration time as monitored with the data logging system. 'H_2 carrier' is the H_2 flow through the MTS bubbler. It increases due to increase in injector pressure 'pin'.

remain constant during the run with the exception of the injector pressure. Temperature typically varies ±2 K.

Pressure difference shut off point

During the infiltration process the gas permeability of the preform decreases due to the deposition of the SiC on the pore walls. Consequently, the pressure drop across the preform starts to rise. For comparison of the preforms after the infiltration process and especially of the infiltration time, a shut off point is required.

Therefore, the pressure drop across the preform is used as the shut off quantity and despite changing the process conditions it is kept at a constant shut off value. Its definition is:

$$\Delta p_{\text{shut off}} = (p0_{t=\text{end}} - p0_{t=0}) \qquad (10)$$

For the bulk density estimation, the average of the four bars, cut from the middle section of the composite disc were used, thus $n = 4$. The printed dots in the plots presented hereafter, are the arithmetic means of the relative densities of the four bars from one experiment and the error bars are indicative of the 95% confidence interval, assuming that the data is normally distributed.

Axial uniformity

It is clear that within the goal of achieving homogeneous composite density, the axial gradient of the SiC deposition within the preform plays an important role. The direct quantitative measurement of the uniformity in axial direction with the purpose of comparison of the samples, appeared however to be impossible for these thin samples.

Therefore, the simplest method was used, which is the estimation of the overall bulk density by eqn 9. Due to the fact that the (theoretical) density of the SiC matrix is larger than of the composite

material C/SiC, the relative bulk density of a composite with a thick SiC coating on the gas inlet side will be lower compared to one with a thin layer, assuming that the C/SiC composites without the thin layer have the same density. The relative bulk density is therefore not only a tool for measuring density but in a sense for homogeneity as well.

4.1 Effect of the total gas flow rate

Matrix composition at high flow rate

It was noticed that at high total gas flow rate, (i.e. >1·8 slm) the deposited SiC layer on the gas inlet side had a black appearance. The coatings produced at low gas flow rate had a shiny silvery appearance. The composition of the black deposit was measured using EPMA at an acceleration voltage of 6 kV. Although oxygen free, the Si/C ratio was in the order of 1·5, (i.e. 20 at.% free silicon). It is anticipated that the silicon forms more easily as compared with carbon at this high gas velocity.

Infiltration behaviour

From Fig. 3, it is evident that increase of the total gas flow rate results in a decrease of the infiltration time. As in CVD, it is anticipated that at low total gas flow rates, mass transport limitations— either convective or diffusive — are dominating growth. For clarification, if either convective or diffusive mass transport has been dominating matrix growth, the following concepts were audited.

During FCVI processing, the gas flows through the pores. The transport of the species is driven by convection. A boundary layer develops along the wall of the pores through which diffusive mass transport (low Peclet number) of the gas species occurs.

Consequently,[1] t_i is proportional to the reciprocal of the square root of $Ft^{\#}$. On the other hand, if convection in the remaining pore cavity — surrounded by the boundary layer — is faster than diffusion (large Peclet number), the infiltration time is proportional to exp $(c \times Ft^{\#-1})$.

Unfortunately, on this basis it is not possible to distinguish which of the two transport mechanisms has controlled matrix growth. Therefore, the magnitude of the Peclet number should indicate if either diffusive or convective mass transport has taken place in the regime of low total gas flow rate. Since the calculated Peclet numbers for the packed bed at the process conditions used — indicated in the figure caption of Fig. 3 — are relatively large, i.e. larger than 10^{-3} *viz.* $3{\cdot}8 \times 10^{-3}$, it is assumed that forced convection has been more dominant than diffusion. At large gas flow rates, the growth is limited by the kinetics of the deposition reaction at the fibre surface and becomes independent of flow rate.

The transition between the two growth regimes in Fig. 3, e.g. mass transport (at large Damköhler numbers and low flow rates) towards kinetically controlled growth (at small Damköhler numbers and large flow rates) was estimated by the intersection of the two slopes of the curves of the growth regimes. Surface reaction limitation starts at a rate of approximately 0·8 slm and at a corresponding calculated DaI_{bed} number of approximately 0·06–0·05.

It is anticipated that the infiltration time will decrease until a minimum is reached asymptotically when the growth is totally kinetically controlled, whereas at very low flow rate (close to 0) the infiltration time will reach infinity. Although the error of the measurements presented in Fig. 4 is relatively large, it may be stated that there is an increasing trend in density as a function of total gas flow rate. At zero gas flow rate, beyond the scope of the fire, the bulk density equals the raw relative bulk density of the starting preform (typically 36·5%).

Large total gas flow rates are thus advantageous in achieving large bulk densities. This is not

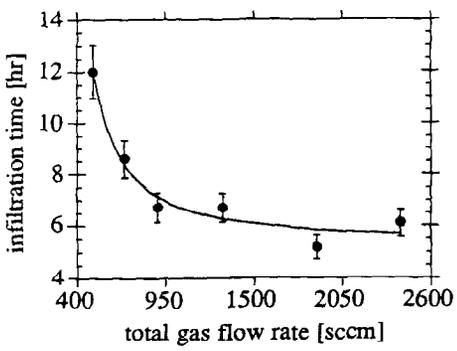


Fig. 3. The infiltration time versus total gas flow rate $Ft^{\#}$. T = 1273 K, H_2/MTS = 6·15, V_f = 51·2 vol%, $L = 2{\cdot}89 \times 10^{-3}$ m, p_L = 6·65 kPa, $\Delta p = 9{\cdot}44 \times 10^3$ Pa $Pe_{bed} = 3{\cdot}88 \times 10^{-3} - 2{\cdot}20 \times 10^{-2}$, $DaI_{bed} = 6{\cdot}81 \times 10^{-2} - 1{\cdot}74 \times 10^{-2}$.

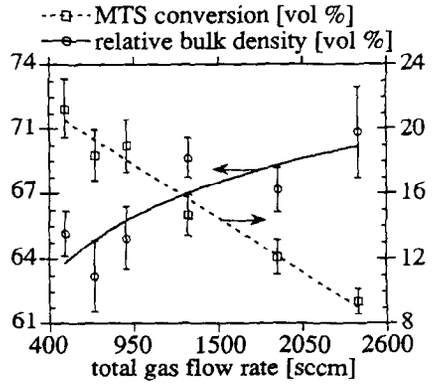


Fig. 4. The relative bulk density and MTS conversion versus total gas flow rate $Ft^{\#}$. T = 1273 K, H_2/MTS = 6·15, V_f = 51·2 vol%, L = 2·89 mm, p_L = 6·65 kPa, $Pe_{bed} = 3{\cdot}88 \times 10^{-3} - 2{\cdot}20 \times 10^{-2}$, $DaI_{bed} = 6{\cdot}81 \times 10^{-2} - 1{\cdot}74 \times 10^{2}$, $\Delta p = 9{\cdot}44 \times 10^3$ Pa.

surprising, considering the fact that through increase of flow rate, the gas velocity within the pores will increase and the uniformity of the matrix distribution will enlarge. At even larger flow rates, i.e. >0·8 slm (Fig. 3), the growth is limited by surface kinetics.

The enhancement of the matrix deposition uniformity is also demonstrated by the MTS conversion that decreases linearly with flow rate. Despite the fact that density is reaching a more or less constant value above 1·5 slm, the MTS conversion is still decreasing. This is explained as follows. During kinetically limited growth only a certain limited amount of molecules can be converted into solid matrix material. The numerator in eqn 8 ($M_{m,dep}$) will remain constant. Larger mass transfer fluxes will, however, increase the denominator $M_{m,max}$. The MTS conversion will decrease until the denominator reaches infinity.

At very large gas velocities, this phenomenon can reach an extreme. When the residence time t_r of the gas in the preform structure gets very short, the critical reaction time t_{cr} can become larger than the residence time of the gas. If so, the MTS has insufficient time to react. This explains the fact that in the centre part of the discs, infiltrated at flow rates exceeding 1·5 slm and/or at outlet pressures ≤1·33 kPa, poor deposition was achieved. The residence time of the gaseous species in the centre of the disc is based upon the Poiseuille gas velocity. On the axis of the preform $u_{bed,ax} = 2u_{bed}$. In general terms as $t_r < t_{cr}$ (s) deposition will be severely hindered and hence in the centre of the preform disc:

$$\frac{\epsilon L_{preform}}{2\,\tau\,uo} < \frac{1}{k_s \times av} \qquad (11)$$

where av is defined[1] as $4 \times d_f^{-1}$. Calculation of t_r and t_{cr} (with assumed tortuosity τ of 2) indicated that at mean gas bed velocities larger than 3 m.s^{-1} this phenomenon can occur.

During kinetically controlled growth, theoretically uniform deposition should occur. However, due to the pressure gradient across the preform, deposition will always be larger at the gas inlet side as compared to the outlet side. Therefore, complete homogeneity can never be reached using the IFCVI technique. Best uniformity can be gained at large flow rates when the process is just kinetically limited. At larger gas flow rates, beyond the scope of the plot, it is anticipated that density can decrease again if the MTS has insufficient time to react at the fibre surface, or due to the following phenomenon.

The pressure drop across the preform is a function of the square root of the total gas flow rate. Experiments performed at high total gas flow rate will consequently start at a high value of the inlet pressure. The corresponding SiC growth rate at the high pressure side will thus be much larger than the growth rate at the opposite side of the preform, i.e. $G_0 >> G_L$ ($t = 0$).

All experiments are finished at the same pressure drop value (eqn 10). Consequently the amount of uniformly deposited matrix will be larger when the flow rate is small ($G_0 \approx G_L$), resulting in a higher density. According to this consideration — that coincides with the model predictions of Part 1 of this study — the relative bulk density presented in Fig. 4 should reach a maximum at the point where growth is kinetically limited and the infiltration process begins at the condition that $p_0 \approx p_L$. These theoretical considerations could not experimentally be verified due to practical limitations. The p_0 over p_L ratio — as measured at the largest experimental flow rate — is 1·6 at the start of the infiltration process and is not sufficient to negatively affect the deposition uniformity.

4.2 Effect of the outlet pressure

In Fig. 5 the results are presented of the study on the effect of outlet pressure on the infiltration time. Increase of the outlet pressure results in decrease of the infiltration time in a non-linear way. It is known that the precursor concentration is a linear function of the total pressure. Increase in (outlet) pressure therefore results in a larger growth rate of the matrix.

The gas velocity is also affected by the total pressure. At low pressure, when the gas velocity is high, it is assumed that chemical kinetics control matrix growth. In the other regime at high total pressure, mass transport governs matrix growth and decrease in infiltration time is less severe.

On the other hand, when diffusive mass transport — across the boundary layer that is present along the pore wall — would control matrix growth, infiltration time would be independent of total pressure.

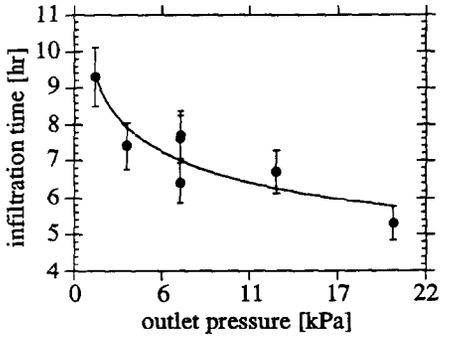


Fig. 5. The infiltration time versus total outlet pressure p_L. T = 1269 K, H_2/MTS = 4·97, V_f = 45·9 vol%, $L = 2{\cdot}96 \times 10^{-3}$ m, $Ft^{\#} = 1{\cdot}67 \times 10^{-5}$ m^3.s^{-1}, $Pe_{bed} = 5{\cdot}03 \times 10^{-3}$, $Dal_{bed} = 1{\cdot}17 \times 10^{-2} - 9{\cdot}50 \times 10^{-2}$, $\Delta p = 2{\cdot}66 \times 10^4$ Pa.

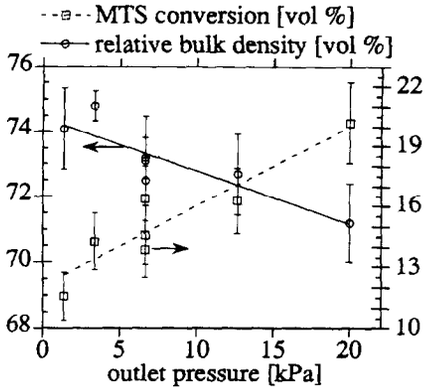


Fig. 6. The relative bulk density and MTS conversion versus total outlet pressure p_L. T = 1269 K, H_2/MTS = 4·97, V_f = 45·9 vol%, L = 2·96 × 10^{-3} m, $Ft^{\#}$ = 1·67 × 10^{-5} $m^3.s^{-1}$, Pe_{bed} = 5·03 × 10^{-3}, DaI_{bed} = 1·17 × 10^2 – 9·50 × 10^{-2}, Δp = 2·66 × 10^4 Pa.

Comparison of these theoretical concepts with the experimental results that are presented in Fig. 5, shows that convection has been the mass transport mechanism at the corresponding Peclet number of 5 × 10^{-3}.

In Fig. 6, the relative bulk density decreases with increasing outlet pressure. When the outlet pressure is increased — during convection controlled growth — the gas velocity through the pores will reduce and the uniformity of the matrix distribution is lowered. This results in a reduction of the relative bulk density and is also demonstrated by the increase in MTS conversion.

One may conclude that the experiments have predominantly been performed within the mass transport limited regime, since density and eventually MTS conversion would remain constant with pressure otherwise. From the effect of the total gas flow rate it is known that transition between the two growth regimes is in between a DaI_{bed} of 0·05 and 0·06. This implies that only the first three data points of the experiments in Fig. 6, have been performed at surface reaction limited conditions where the effect of outlet pressure on relative density is indeed negligible.

4.3 Effect of the preform temperature

Matrix composition

The composition of the SiC matrix of all preform discs on both gas inlet and outlet side were measured using EPMA. The coatings were oxygen and chlorine free, i.e. within the error of the detection limit. The SiC coating on the gas inlet side of all specimens had a shiny silvery appearance. The Si/C ratio varied slightly from 1·0 to 1·1 corresponding to a maximum free silicon content of 5 at.%. No effect of the SiC location (either gas inlet or outlet) was detected.

XRD measurements on both sides of the samples indicated that the coating was crystalline β-SiC and contained mainly cubic crystals. Traces of hexagonal SiC were observed at the gas inlet side of the preform.

Consequently, it is assumed that the density of the matrix material is independent of the deposition temperature and equal to the theoretical density of silicon carbide.

Infiltration behaviour

In Fig. 7 the infiltration time is presented as a function of preform temperature.

At high temperatures, matrix growth is fast. In accordance with theoretical considerations, the infiltration time reduces with increasing temperature due to the Arrhenius behaviour of the deposition reaction. Since the first Damköhler number is smaller than 0·054 within the whole range of experiments, it is anticipated that kinetics have been controlling the formation of SiC.

In Fig. 8 relative composite density is independent of temperature and possibly even positively affected by an increase of temperature. On the other hand, the MTS conversion is a linear increasing function of temperature.

The independence of the relative bulk density on temperature can be explained if chemical kinetics are governing matrix growth. This statement is

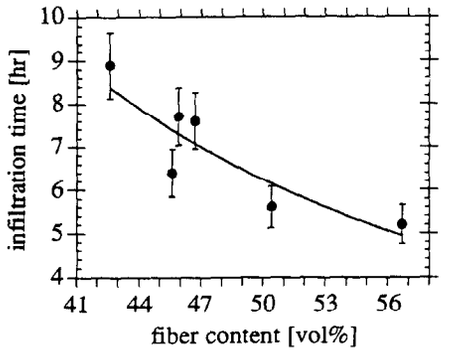


Fig. 7. The infiltration time versus preform temperature T. H_2/MTS = 4·98, V_f = 44·8 vol%, $Ft^{\#}$ = 1·67 × 10^{-5} $m^3.s^{-1}$, L = 3·06 × 10^{-3} m, p_L = 1·33 kPa, Pe_{bed} = 1·32 × 10^{-2}, Δp = 2·65 × 10^4 Pa, DaI_{bed} = 3·49 × 10^{-3} – 5·41 × 10^{-2}.

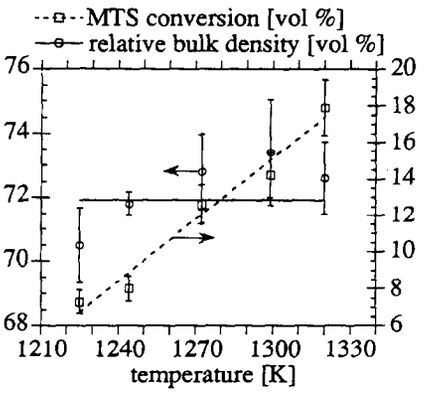


Fig. 8. The relative bulk density and MTS conversion versus preform temperature T. H_2/MTS = 4·98, V_f = 44·8 vol %, $Ft^{\#}$ = 1·67 × 10^{-5} $m^3.s^{-1}$, L = 3·06 × 10^{-3} m, p_L = 1·33 kPa, Pe_{bed} = 1·32 × 10^{-2}, Δp = 2·65 × 10^4 Pa, DaI_{bed} = 3·49 × 10^{-3} – 5·41 × 10^{-2}.

in accordance with the value of $DaI_{bed} < 0{\cdot}05$–$0{\cdot}06$. In general terms, at low temperature, SiC growth is kinetically controlled.

The relative bulk density will remain unaffected as long as the initial pressure gradient ($t = 0$) is not too large, (i.e. $G_0 \approx G_L$).

Depletion effect can be excluded and deposition is uniform. Hereafter, at higher temperatures, density will decrease because mass transport limitations dominate matrix growth and depletion of the MTS — that flows in axial direction through the pores — is rising and the resulting deposition profile is less uniform. At very high temperatures, when the MTS is almost completely depleted from the bulk gas stream, no SiC is deposited deeper into the preform. What remains is an only partially infiltrated preform.

4.4 Effect of the MTS fraction in the gas mixture

Experimental examination of the dependence of the infiltration time as a function of MTS fraction — shown in Fig. 9 — is in accordance with theoretical predictions (see Part 1 of this study). The concentration of the precursor is a linear function of its mole fraction in the gas mixture. The infiltration time is thus proportional with X_{MTS}^{-1}. The input fraction of the MTS has no effect on the resulting relative bulk density.

Theoretical concepts indicate that neither in the mass transport controlled regime nor during kinetically controlled growth is an effect of the MTS fraction on the composite density expected. In Fig. 10 this theory is experimentally verified for the kinetically controlled growth regime since DaI_{bed} is smaller than 0·05 for all experiments. This independence of MTS content in the gas mixture on the composite density is also confirmed by the fact that the first Damköhler number is independent of precursor concentration as long as first order reactions apply.

Depletion of the precursor is independent of absolute concentration and hence the relative density

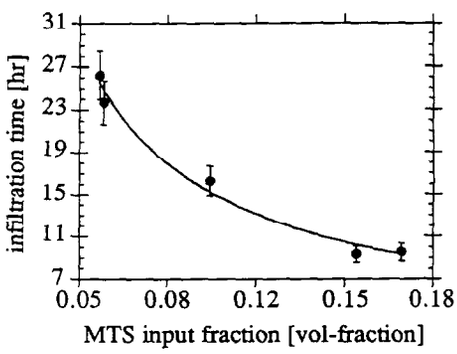


Fig. 9. The infiltration time versus input MTS fraction in the gas mixture x_{MTS}. $T = 1269$ K, $V_f = 44{\cdot}8$ vol%, $L = 3{\cdot}03 \times 10^{-3}$ m, $Ft^{\#} = 1{\cdot}67 \times 10^{-5}$ m^3 s^{-1}, $p_L = 1{\cdot}33$ kPa, $Pe_{bed} = 1{\cdot}33 \times 10^{-2} - 3{\cdot}57 \times 10^{-3}$, $DaI_{bed} = 1{\cdot}22 \times 10^{-2}$, $\Delta p = 2{\cdot}66 \times 10^4$ Pa.

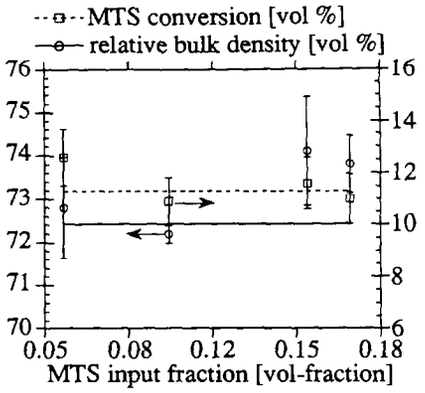


Fig. 10. The relative bulk density and MTS conversion versus input MTS fraction in the gasmixture x_{MTS}. $T = 1269$ K, $V_f = 44{\cdot}8$ vol%, $L = 3{\cdot}03 \times 10^{-3}$ m, $Ft^{\#} = 1{\cdot}67 \times 10^{-5}$ m^3.s^{-1}, $p_L = 1{\cdot}33$ kPa, $Pe_{bed} = 1{\cdot}33 \times 10^{-2} - 3{\cdot}57 \times 10^{-3}$, $DaI_{bed} = 1{\cdot}22 \times 10^{-2}$, $\Delta p = 2{\cdot}66 \times 10^4$ Pa.

is constant. Clearly, the MTS content should be sufficiently high to overcome almost complete conversion of the MTS before the gas has arrived at the other end of the preform.

4.5 Effect of the fibre content and preform thickness

Increase of the fibre content in the preform volume is achieved by exerting higher pressure on the preform during its prefixing stage, resulting in not only larger fibre content per volume (V_f), and tortuosity (τ), but also in lower thickness (L) and smaller average pore size (d_p). These quantities are measured and presented in Table 2 as a function of fibre content. It appears that even the surface area available for deposition (A_{dep}) is increased.

Due to these microstructural changes, the gas permeability of the porous structure K_g will also differ between the samples.

Permeability of the raw preform: experimentally and analytically

The gas permeability K_g (m^2) was measured as a function of raw preform fibre content, outlet pressure and argon flow rate at 1273 K. The details of the raw preforms used for the permeability test are given in Table 2.

The results can be fitted according to Darcy's law (eqn 5) for incompressible fluids, since for a constant outlet pressure, $uo\mu L$ follows a linear relationship with Δp and the slope represents K_g.

However, the data obtained at different outlet

Table 2. Raw preform characteristics for the permeability test at 1273 K under argon flow.

Exp no.	V_f (vol %)	Thickness (m)	A_{dep} (m^2)
52	42·6	$3{\cdot}17 \times 10^{-3}$	6·54
50	45·6	$2{\cdot}95 \times 10^{-3}$	6·66
53	49·4	$2{\cdot}74 \times 10^{-3}$	6·68
51	56·7	$2{\cdot}53 \times 10^{-3}$	6·94

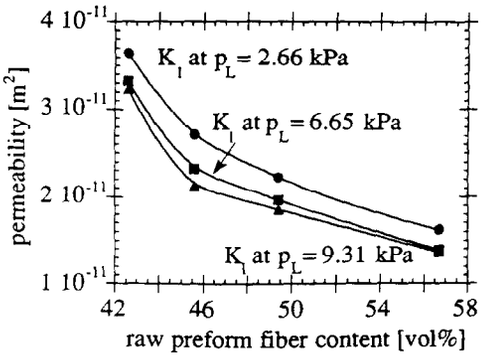


Fig. 11. The permeability K_l versus raw preform fibre content V_f and outlet pressure p_L at 1273 and argon flow.

pressures resulted in different slopes, so that K_g is a function of average pressure. Best fit was achieved with the permeability expression for compressible gas flow with slip.[1] It was found that the experimental data could not be fitted within the whole range of process variables and no complete elucidation of the proper permeability equation was gained. Deviations were noticed at the lowest outlet pressure of 6.65 kPa and are probably due to inertial effects.[7]

From Table 2 and Fig. 11 it can be concluded that permeability decreases with increasing fibre content, due to the less open structure.

Also, it was found that permeability at the low absolute total pressure conditions used, increases linearly with decreasing outlet pressure or increasing pressure drop.

A constraint for proper infiltration is the fact that sufficiently high permeabilities are required to overcome excessive inlet pressures (or Δp) so that infiltration can proceed sufficiently long to be able to grow matrix into the structure. More generally stated, $LA^{-1}K^{-1}$ should be small (eqn 5) with A representing the cross flow area (m^2).

Infiltration behaviour

As illustrated in Fig. 12, when the fibre content of the raw preform is increased, the infiltration time

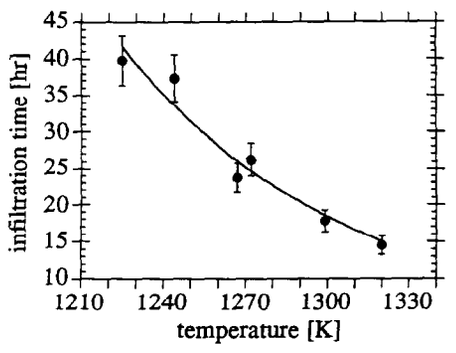


Fig. 12. The infiltration time versus raw preform fibre content. T = 1271 K, H_2/MTS = 5·02, V_f = 42·6–56·7 vol%, $Ft^{\#}$ = 1·67 × 10^{-5} $m^3.s^{-1}$, L = 3·17 × 10^{-3}–2·96 × 10^{-3} m, Pe_{bed} = 5·05 × 10^{-3}, DaI_{bed} = 3·97 × 10^{-2}–3·32 × 10^{-2}, A_{dep} = 6·54–6·94 m^2, Δp = 2·65 × 10^4 Pa.

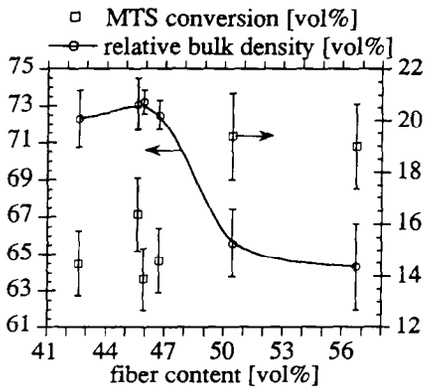


Fig. 13. The relative bulk density and MTS conversion versus raw preform fibre content. T = 1271 K, H_2/MTS = 5·02, V_f = 42·6–56·7 vol%, $Ft^{\#}$ = 1·67 × 10^{-5} $m^3.s^{-1}$, L = 3·17 × 10^{-3}–2·96 × 10^{-3} m, Pe_{bed} = 5·05 × 10^{-3}, DaI_{bed} = 3·97 × 10^{-2}–3·32 × 10^{-2}, A_{dep} = 6·54–6·94 m^2, Δp = 2·65 × 10^4 Pa.

is reduced. Yet, the variation of the raw preform fibre content is a combined effect of more than only one variable. Pore size is reduced, whereas the surface area and tortuosity of the structure is increased (Table 2). So, the filling of the pores is relatively fast at large fibre content. This effect is mainly due to the small pore diameter of the preform of high fibre content.

The relative bulk density of the composite is a decreasing function of the fibre content and is presented in Fig. 13. Apparently, the deposition uniformity is enhanced when V_f is decreased. This effect cannot be explained in terms of decreasing τ or A_{dep} or increasing L, but only in increasing pore diameter d_p.

The pore gas velocity that controls the uniformity of the matrix distribution along the pore axis is a positive function of the pore diameter (eqn 13, Part 1 of this study). And since the mean pore diameter is a decreasing function of the fibre content, the density will thus decrease with increasing V_f.

For achieving the same composite density, a preform with low fibre content and high permeability should be infiltrated up to a lower pressure shut off point as compared with a preform of high fibre content and low permeability. An optimum in density gain, i.e. the largest density in the shortest time is reached at a fibre content of 46 vol.%.

4.6 Apparent reaction rate equation

Introduction

Premature homogeneous decomposition[8] of MTS in the gas phase in front of the preform can rule the kinetic equation. Therefore, the amount of decomposed MTS in the gas phase prior to and in the preform was calculated and appeared to be smaller than 10% for all experiments.[1] It is

therefore assumed that the kinetic equation derived in the following, is caused by the direct reaction of MTS to SiC without prior decomposition.

Experimental results

The overall apparent reaction rate equation within the porous structure that relates the infiltration time with the process conditions within the regime of kinetically controlled growth was quantified. The results of the effect of temperature (Section 4.3) and MTS fraction in the gas mixture (Section 4.4) were used for the estimation of the overall apparent reaction rate equation. First, the activation energy (E_a) of the surface reaction was derived from plotting the logarithm of the matrix growth rate versus the reciprocal temperature in Fig. 14(a).

The matrix growth G_{SiC} (mol.m^{-2} s^{-1}) is calculated according to:

$$G_{SiC} = \frac{M_{m,dep}}{m_{SiC} A_{dep} t_i} \tag{12}$$

where $M_{m,dep}$ (kg) is the weight increase of the preform due to SiC deposition, m_{SiC} is the molar mass of SiC (kg.mole^{-1}), A_{dep} (m^2) is the deposition area (eqn 4) and t_i (s) is the infiltration time. The slope of the plot Fig. 14(a) represents $-E_a/R_g$, from which an apparent activation energy of 135 kJ.mol^{-1} was calculated. The experiments where the MTS input fraction was varied, were used for the estimation of the partial reaction order and pre-exponential factor. In Fig. 14(b) it is demonstrated that the SiC matrix growth follows a first order dependence in MTS.

The slope of the plot equals the partial reaction order, whereas the intercept represents $\ln(k_s)$. From k_s (m.s^{-1}) and the activation energy, k_0 is calculated to equal 16·45 m.s^{-1}.

This results in the overall apparent reaction equation for the silicon carbide growth rate G_{SiC} (mol.m^{-2}.s^{-1}) within a porous structure using MTS in an excess of H_2 and Ar:

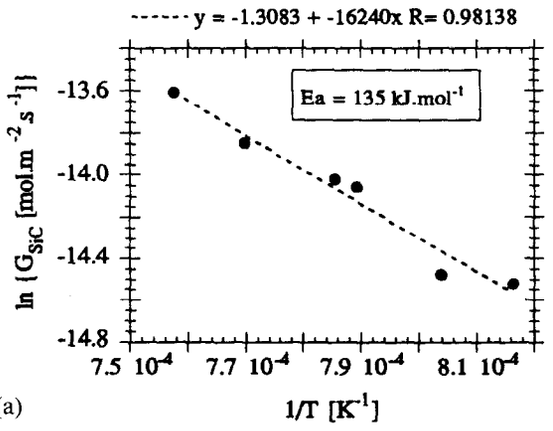


Fig. 14(a). The logarithmic SiC growth rate versus the reciprocal preform temperature; H_2/MTS = 5.

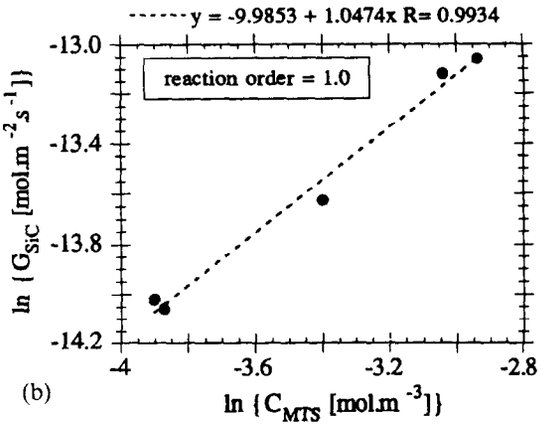


Fig. 14(b). The logarithmic SiC growth rate versus the logarithmic MTS concentration at input.

$$G_{SiC} = 16{\cdot}45 \exp\left(\frac{-135 \times 10^3}{T\ Rg}\right) C_{MTS}^{1{\cdot}0} \tag{13}$$

Because the experiments were performed at $DaI_{bed} < 0{\cdot}054$, it is assumed that surface kinetics have been dominating growth.

4.7 Effect of the shut off pressure drop on the infiltration time and composite density

The effect of the pressure difference across the preform (shut off point) on the infiltration time and the composite density was studied. The results are presented graphically in Figs 15 and 16.

After termination of the experiments, the permeability of the composite at the end of the process was calculated using eqn 5 at the pressure drop shut off point, temperature and gas composition used.

Initially, during the first 4 h of infiltration, the pressure drop across the preform hardly rises *viz.* from 0·13 to 1·2 kPa. After approximately 7 h, the injector pressure (and pressure drop) start rising rapidly, because the pores in the preform reach a critical size. Within approximately an hour the injector pressure rises from 5 to 55 kPa.

In this time lapse hardly any additional matrix is deposited within the small pores (Fig. 16). Here, not

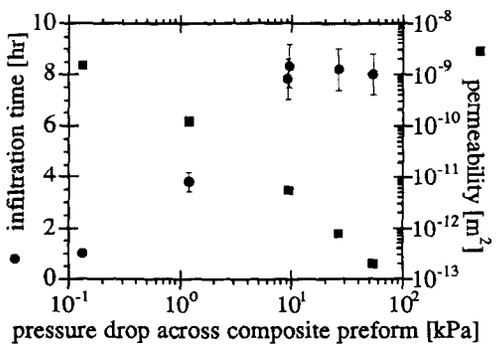


Fig. 15. The infiltration time and composites permeability versus shut off pressure difference. T = 1255 K, H_2/MTS = 6·00, V_f = 47·4 vol%, $Ft^{\#}$ = 2·49 × 10^{-5} m^3.s^{-1}, L = 2·90 × 10^{-3} m, p_L = 1·33 × 10^3 Pa, Pe_{bed} = 5·05 × 10^{-3}, DaI_{bed} = 3·97 × 10^{-2}–3·32 × 10^{-2}, A_{dep} = 6·54 m^2.

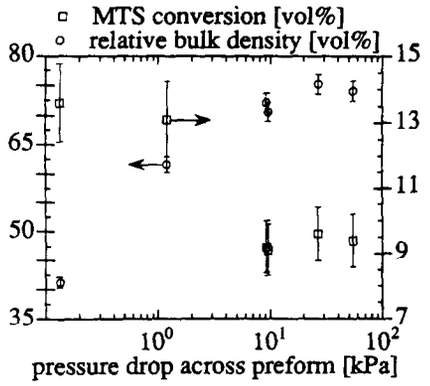


Fig. 16. The relative bulk density and MTS conversion versus pressure difference and infiltration time. T = 1255 K, H_2/MTS = 6·00, V_f = 47·4 vol%, $Ft^{\#}$ = 2·49 × 10^{-5} $m^3.s^{-1}$, L = 2·90 × 10^{-3} m, pL = 1·33 × 10^3 Pa, Pe_{bed} = 5·05 × 10^{-3}, DaI_{bed} = 3·97 × 10^{-2}–3·32 × 10^{-2}, A_{dep} = 6·54 m^2.

only density, but the uniformity expressed in terms of MTS conversion is also constant. It appears that a pressure drop of about 10 kPa is sufficient to reach maximum density at the selected infiltration conditions. Further densification will only yield a thicker coating on the gas inlet side of the sample.

The permeability of the composite is a decreasing function of the pressure drop. Even when composite density is not further enlarged, permeability still decreases. This drop in conductance for the gas flow will, however, be attributed to the deposited coating on the gas inlet side and narrowing of the pore mouth of the sample instead of the whole preform structure. At the point of just reaching maximum density, the permeability of the preform structure is decreased at least two orders of magnitude.

General remarks

The FCVI process can be represented as a two stage process in which both the small pores in a fibre bundle and the bigger pores inbetween the bundles have to be infiltrated. Convection is present in the big pores between the bundles (FCVI), whereas mass transport of the gaseous species into the bundles will be dominated by diffusion since there is no Δp from outer to inner volume of the bundle (this is in fact ICVI).

During the first hours of infiltration, the matrix deposits onto the available surface area and density increases rapidly (Fig. 16). Each filament is coated with a layer of SiC. As soon as a fibre bundle has grown together, the available surface area is greatly reduced and the larger pores between the bundles will become smaller. As a result, density gain is less rapid. During this time lap, a pressure increase is observed. As soon as the resistance for the gas flow is getting too big, the injector pressure increases very rapidly and the experiment is shut off.

5 General Discussion and Conclusions

The results presented above are consistent with the general concepts that are described in Part 1 of this study. For homogeneous densification, matrix growth within the kinetically limited growth regime is preferred. For rapid infiltration, forced convection should control matrix growth.[9]

Comparison with the FCVI model

The infiltration characteristics as a function of process variables were investigated and appear to qualitatively coincide with the FCVI model predictions of Part 1 of this study. Therefore, infiltration trends may be predicted using a 1D cylinder pore approach.

The transition point (x-value) of kinetically controlled towards convective controlled growth conditions of the model and of the experiments coincide (compare Fig. 5 Part 1 with Figs 3 and 4 Part 2, Fig. 7 Part 1 with Figs 5 and 6 Part 2, and Fig. 8 Part 1 with Figs 7 and 8 Part 2).

However, the effect of the preform temperature on the infiltration time as experimentally observed — in the kinetically limited growth conditions — is less pronounced than simulated with the model (Fig. 8 Part 1). The trend that the composite density is unaffected by temperature increase in the kinetically limited growth conditions is in agreement with model predictions. Increase of the total gas flow rate or decrease in outlet pressure — in the mass transport limited growth regime—yields an increase of the gas velocity and hence uniformity of the deposited SiC layer within the pores. The model (Figs 5 and 7 Part 1) and experimental observations are in agreement.

The MTS content in the gas mixture has no effect on the resulting composite density for both model and experiments. The increase of injector pressure with time as experimentally observed and calculated with the model (Fig. 3 Part 1) are in good agreement. Also, when infiltration proceeds densification is rapid initially, but levels off later on.

According to the model, high raw preform porosity yields low composite density. As such, experimental observations indicate the opposite. However, decrease of the raw preform porosity without affecting other microstructural parameters such as tortuosity, pore diameter, preform thickness and deposition area cannot be achieved. In terms of pore diameter, model (Fig. 6 Part 1) and experimental results do coincide.

Experimental observations

It appeared that a Peclet number (for a packed bed) larger than 4 × 10^{-3} corresponds with convective mass transport. $Pe_{bed} < 4 \times 10^{-3}$ and DaI_{bed}

$<5 \times 10^{-2}$ coincide with kinetically limited SiC growth conditions. The apparent overall reaction rate of the heterogeneous controlled conversion of MTS to SiC follows a first order dependence in MTS with an apparent activation energy of 135 kJ.mole^{-1}. The pre-exponential factor equals 16·45 m.s^{-1}.

In principle, for this first order reaction, low first Damköhler numbers and MTS conversion are in agreement with large IFCVI composite density. The highest composite density gained in this study was 75% of the ideal density at a MTS conversion smaller than 15%. Since the determination of the relative bulk density of the composite samples is subjected to many errors and its measurement is even impossible for complete geometries, the simple total MTS conversion appears to be a powerful tool in the estimation of the optimum process conditions.

It should be noted that the transition values of the Peclet and first Damköhler number itself should be treated with care. Their order of magnitude or moreover its transition value is very much dependent on the definition used, especially its characteristic length. The optimum pressure shut off point is dependent on the permeability of the raw preform. A poorly permeable preform structure requires a larger pressure drop to reach the same density as compared to a preform of large permeability. A constraint of the FCVI technique is that only preforms with high permeability without closed porosity are suitable to gain large composite density and strength. More generally stated, $LA^{-1}\ K^{-1}$ should be small.

Optimum infiltration, i.e. the largest density gain for a 80 mm diameter, 3 mm thick preform in the shortest time, occurs with a preform of 46 vol.% fibre, a temperature of 1320 K, outlet pressure of 6·65 kPa, total gas flow rate of 4×10^{-5} m^3.s^{-1}, MTS fraction of 16 vol.% and a pressure drop shut off point of 10 kPa. Clearly, these specific conditions are only applicable for preforms of exactly the same microstructure as the one studied and a first order heterogeneous decomposition reaction at the pore walls.

In general, high composite density is reached at IFCVI conditions of kinetically controlled matrix growth and hence implies: high total gas flow rate, low preform temperature, low outlet pressure, arbitrary precursor fraction in the gas mixture, high pressure shut off difference, low raw preform fibre content and high raw preform gas permeability. A negative effect of the initial pressure drop ($t = 0$) on the composite density was not observed at least as long as $p_0/p_L < 1{\cdot}6$. On the other hand, rapid IFCVI is achieved at mass transport limited matrix growth conditions and generally at: high total gas flow rate, high preform temperature, high outlet pressure, high precursor fraction in the gas mixture, low pressure shut off difference, high raw preform fibre content and low raw preform gas permeability.

Unfortunately, these two criteria — with the exception of the total gas flow rate and MTS fraction in the gas — obviously are contradictory. It should be noted that again a too large gas velocity — typically $u_{bed} > 3$ m.s^{-1} — can lead to poor infiltration, because the residence time of the MTS precursor in the preform is insufficient to cause a deposition reaction at its fibre surface.

References

1. Roman, Y. G., Kotte, J. F. A. K. & de Croon, M. H. J. M., *J. Eur. Ceram. Soc.*, **15** (1995) 875–86.
2. Schlichting, J., *Powder Metallurgy International*, **12** (1980) 141–200.
3. Patent DASA: in preparation.
4. Collins, R. E., *Flow of fluids through porous materials*, Reinhold Publ. Corp. New York, Ed. C. R. Wilke (1961).
5. Scheidegger, A. E., *The physics of flow through porous media*. University of Toronto Press, 1957.
6. Philipse, A. P. & Schram, H. L., *J. Am. Ceram. Soc.*, **74** (1991) 728–32.
7. Kaviany, M., *Principles of heat transfer through porous media*, Springer Verlag, 1991.
8. Burgess, J. N. & Lewis, T. J., *Chem. and Ind.*, **19** (1974) 76–7.
9. Roman, Y. G., Forced flow Chemical Vapour Infiltration, PhD Thesis Eindhoven University of Technology, Eindhoven, The Netherlands (1994).

Journal of the European Ceramic Society 15 (1995) 899–903
© 1995 Elsevier Science Limited
Printed in Great Britain. All rights reserved
0955-2219(95)00059-3
0955-2219/95/$9.50

Influence of the Debinding Method on the Mechanical Properties of Plastic Formed Ceramics

Thierry Chartier, Marc Ferrato & Jean-François Baumard

LMCTS, URA 320, ENSCI, 47 Av. Albert Thomas, 87065 Limoges, France

(Received 7 June 1994; revised version received 23 February 1995; accepted 10 March 1995)

Abstract

A new method of extraction of organic additives, by a supercritical fluid, is presented. Flexural strengths and Weibull moduli of extrusion molded alumina, debinded by classical pyrolysis and by supercritical CO_2 extraction are compared. Better mechanical properties are obtained after a short time (3 h) of supercritical treatment (σ = 277 MPa, m = 13·7) than after 18 h of pyrolysis (σ = 253 MPa, m = 12·4). The binder extraction from green pieces by supercritical fluids is limited by two factors, solubility and diffusivity of organic compounds. The major factors causing defects in the pyrolytic binder removal, such as binder redistribution in the liquid phase and the outward diffusion of degradation products, do not take place in the supercritical debinding method.

1 Introduction

Ceramic components are made by applying ceramic processing techniques to ceramic materials. One of the main difficulties that structural engineering ceramics have to overcome to find industrial applications lies on the fabrication of shapes from powders. The forming of green pieces is critical, because it affects both final properties of materials, for example because it introduces cracks, and the characteristics of components, for example because it alters the size accuracy of the shapes.

Most high technology ceramic processings require the use of transitory, organic compounds, which are eliminated by subsequent treatments before sintering. A compromise must be found between the ease of shape forming and the necessity of removing the binders. Therefore, the optimization of ceramic processing techniques must take not only the forming method, but also the removal of the organic additives into account.

Plastic forming methods as injection and extrusion-molding are attractive for producing complex shapes of high dimensional accuracy and high uniformity at a rather low cost. These techniques require the use of a large amount of organic compounds in order to confer properties as cohesion, flexibility and workability in the green state.[1] Amounts as large as 50 vol.% of organic are sometimes added to the ceramic powder. A major drawback of these processing methods remains the removal of these organics.

Although thermal decomposition is the method currently used, studies of pyrolytic removal of organic additives in a green ceramic body, are very recent.[2–8] In the last few years, an effort was made to understand the many physico-chemical processes that occur during binder removal. Binder removal by thermal treatment involves: (i) chemical mechanisms with the thermal degradation of organic compounds into volatile species and, (ii) physical mechanisms as the diffusion of these species to the surface as well as the changes in the binder distribution within the green body. Changes in the binder distribution, governed by diffusion and capillary migration, and the magnitude of the mass- and heat-transfer limitations are critical parameters for the design of the efficient heating cycle to prevent stresses and the formation of defects in ceramic parts.[6]

Thermal debinding remains one of the most critical steps of ceramic processing, especially in the case of large size parts for three main reasons: (i) defects are generated which affect properties of the sintered pieces, (ii) it is very time-consuming, the binder removal time being directly proportional to square of the section thickness[2] and (iii) residues of pyrolytic degradation can be detrimental during the subsequent sintering stage.

Alternative techniques are needed to produce defect-free green bodies and to reduce debinding time. In this respect, approaches including chemical degradation, evaporation or sublimation, solvent extraction and capillary action can be beneficial. In the present work, we have used an original

method of extraction of organic compounds based on the unique dissolving characteristics and transport properties of fluids at temperatures and pressures beyond the critical point, i.e. supercritical fluids. While the densities of liquids and supercritical fluids are more or less similar, the diffusion coefficients are expected to be much larger in the later media. The binder extraction by the supercritical fluid is controlled by the solubility and the diffusivity of the polymeric compounds. The largest solubility of a binder in the supercritical fluid can be estimated using solubility parameters and the diffusivity of dissolved organic species in green samples has been modelled.[9]

The purpose of this paper is to compare mechanical properties (flexural strength and Weibull modulus) of extrusion-molded ceramics debinded by classic pyrolysis and by supercritical extraction of organics.

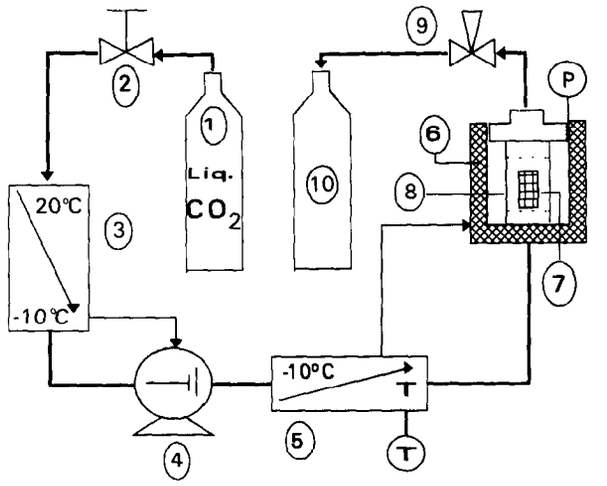


Fig. 1. Schematics of the equipment: (1) CO_2 storage cylinder; (2) shutoff valve; (3) cooling circulator; (4) high pressure pump; (5) thermostated oil bath; (6) extraction vessel; (7) ceramic sample; (8) cylindrical basket; (9) micrometering valve; (10) collector cylinder.

2 Experimental

2.1 Preparation of green samples

Samples with a square section (4 × 4 mm^2) were prepared by extrusion-molding of a mixture containing 86 wt.% alumina, 2 wt.% polystyrene and 12 wt.% paraffin oil (Prolabo, France). The alumina (P172SB, Péchiney, France) was 99·7 wt% purity, 0·6 μm mean particle size and 10 $m^2.g^{-1}$ specific surface area. The molecular weight of the polystyrene (Lacqrene 4801, Elf Atochem, France) was 150000. The green density was 56% of theoretical density.

2.2 Removal of organic compounds

Two routes were used to remove organic compounds: pyrolysis and treatment with a supercritical fluid.

The pyrolysis was carried out with four heating rates up to 550°C; 0·5, 1, 2 and 4·5°C.mn^{-1} without dwell.

Extraction of binders was performed by using carbon dioxide in a supercritical state. Carbon dioxide, which is extensively used in the food or perfume industry, has shown promising possibilities for the extraction of light organic compounds in ceramic forming processes.[10] The main advantages of carbon dioxide lie in a low cost, low critical temperature and pressure (Tc = 31°C, Pc = 7·37 MPa) as well as in absence of toxicity and flammability.

The schematics of the equipment used during the present work are shown in Fig. 1. Green samples to be debinded (7) are introduced in a cylindrical basket (8) fitted with sintered metallic parts at both ends. This basket, located into the extractor (6), acts as a sample holder for the polymer-containing materials, and remains quite permeable to the fluids. Carbon dioxide, taken from a storage tank (1), is cooled down to –10°C by means of a heat exchanger (3). The resultant liquid carbon dioxide is pressurized up to the working pressure, by means of the pump (4). Then, the pressurized liquid is heated up to the working temperature (15–120°C) with a second heat exchanger (5), leading to supercritical carbon dioxide. The carbon dioxide, in the supercritical state, is flowing through the extractor, dissolving binders from the green sample. The dissolved binders are recovered in a collector cylinder (10). The process temperature of the extractor (6) and the temperatures of the two heat exchangers (3 and 5) are regulated by thermostated baths.

2.3 Sintering

The two series of samples, e.g. those submitted to supercritical treatment, thus still containing a low amount of non-soluble binder, and those debinded by pyrolysis, were sintered in an electric furnace with $MoSi_2$ heating elements, with the same heating cycle, i.e. 5°C.mn^{-1} up to 1600°C with a dwell time of 3 h.

2.4 Characterization

The density of sintered samples was measured by the Archimedes method in distilled water.

The room temperature strength was measured by the classical four-point bend test (outer span: 40 mm, inner: 20 mm) at a cross head speed of 0·5 mm.min^{-1}. The tensile face was polished and the edges were bevelled.

The fracture of a homogeneous brittle material depends on the stress necessary to propagate an existing critical flaw or crack present in it. Variable sizes and shapes of flaws in ceramic materials are responsible of the scatter of failure strengths observed when 'identical' specimens are tested under identical loading conditions. The Weibull statistics[11,12] were commonly used in the analysis of strength of brittle materials. This method, based on the 'weakest link of a chain', assumes that the most critical flaw under a given stress distribution leads to failure.

The major defects included in injected molded ceramics, in particular in the case of thick parts with submicrometer particle sizes, can be associated with removal of organic compounds[13,14] The Weibull statistics were used to provide a means of comparison of strength distribution, and then of flaw size distribution, between the two series of samples.

The strength data (N = 20 samples) was analysed using the usual two-parameter empirical formula relating the probability of failure, P_f, to the stress, σ_f:

$$P_f = 1 - \exp\left[-\left(\frac{\sigma_f}{\sigma_0}\right)^m\right] \quad (1)$$

where m is the Weibull modulus and σ_0 a normalizing factor. Flexural strengths were ranked in order and assigned a probability of failure according to the formula:

$$P_f = (i\text{–}0{\cdot}5)/N \quad (2)$$

where i is the i^{th} specimen. The Weibull modulus is the slope of a plot of LnLn $(1/P_f)$ versus Ln σ_f.

3 Results and Discussion

The supercritical treatment of the green pieces was carried out at 88°C under 28 MPa for 3 h. Under these conditions, supercritical CO_2 is a relatively good solvent for paraffin oil, but the high molecular weight polystyrene was not dissolved. The molecular weight distribution of the paraffin used is large, and only 67% of the paraffin introduced, probably corresponding to the lighter backbone, was dissolved. It is noteworthy that a small amount of undissolved polystyrene presents the advantage of maintaining a cohesion of ceramic green bodies, and that it does not seem to affect properties of sintered parts.

Extruded samples pyrolyzed with a heating rate higher than 1°C.mn^{-1} exhibit macro-defects as blistering, bloating and cracking (Fig. 2). Hence, the strength analysis was performed on samples pyrolyzed at rates of 0·5 and 1°C.mn^{-1}.

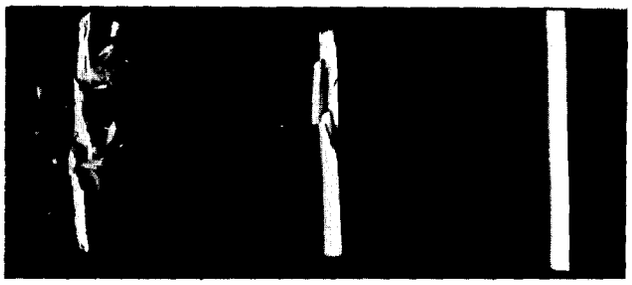


Fig. 2. Samples (4 × 4 mm^2) after removal of the organic compounds by heating at a rate of (a) 4·5°C.min^{-1}, (b) 2°C.min^{-1} and (c) 1°C.min^{-1}.

Weibull diagrams of sintered samples previously debinded by pyrolysis and by supercritical treatment are given in Fig. 3. The relative density of the sintered samples was 97%. Taking into account that testing bars were polished, it can be assumed that critical defects are volumic ones. Samples submitted to thermal and supercritical treatments were prepared using the same forming technique. Hence, differences in strength-controlling defects can be associated with the removal of organic compounds and not with the forming method. The mean failure strengths, in the four-point bend test, were 219, 253 and 277 MPa for samples pyrolysed at rates of 1 and 0·5°C.mn^{-1}, and for samples submitted to supercritical treatment, respectively. The Weibull modulus was low, i.e. 5·4, for samples thermally debinded at a rate of 1°C.mn^{-1}, whereas samples thermally debinded at a rate of 0·5°C.mn^{-1} and those supercritically treated exhibited a larger and similar value of the Weibull modulus, i.e. 12·4 and 13·7, respectively.

A first comment concerns the higher strength of samples debinded by supercritical treatment. This

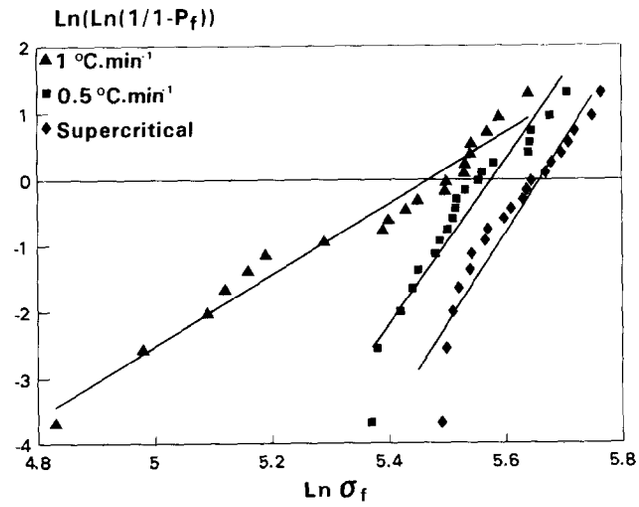


Fig. 3. Weibull diagrams of sintered samples previously debinded by pyrolysis with heating rates of 0·5°C.mn^{-1} (σ = 253 MPa, m = 12·4) and 1°C.mn^{-1} (σ = 219 MPa, m = 5·4), and by supercritical treatment (σ = 277 MPa, m = 13·7).

suggests that this method of binder removal leads to a more homogeneous green state before firing, with smaller critical defects than after classical thermal debinding.

A second comment concerns the higher Weibull modulus of samples debinded with a very slow heating rate and for samples debinded by supercritical treatment. The scatter of failure strengths, hence the scatter of defect sizes and/or shapes, was lower for samples debinded by a supercritical fluid.

As far as the treatment duration is concerned, better mechanical properties were achieved after 3 h of supercritical treatment than after about 18 h of thermal treatment on similar extruded samples. The time parameter then becomes critical for large ceramic parts.

Mutsuddy[15] reported a three-point flexural strength of 260 MPa and Fanelli *et al.*[16] a four-point flexural strength of 309 MPa for injection molded alumina (A16SG, AlCoA, Pittsburgh, PA) after thermal debinding and sintering. This alumina has similar characteristics to the one used in this study. Three-point bend tests generally lead to higher values of flexural strength than four-point bend tests, due to the Weibull effect. Concerning the Weibull modulus, G. D. Quinn[17] reported values ranging between 7 and 13 for nearly fully densified alumina. The values of four-point flexural strength (277 MPa) and of Weibull modulus (13.4), obtained after 3 h of supercritical debinding, are slightly higher than those generally quoted in the literature.

Pyrolytic binder removal is controlled by two main phenomena,[2,18] namely capillary migration in the liquid phase and diffusion in the gas phase. These two mechanisms lead to a redistribution of the binder in the green body, which determines the path length over which molten binder or volatile species must migrate or diffuse.[8,19] Due to capillary forces, molten binder, in the early stage of removal, segregates to the smallest pores of the green body, leading to the apparition of stress gradients. The magnitude of capillary forces depends on the surface tension and of the viscosity of the organic liquid. At higher temperature, cracking occurs if the generation of volatile species produced by thermal decomposition of organics is in excess of the amount removed by outward diffusion and evaporation at the surface.[20] The major factor causing defects was attributed to the diffusion of degradation products in solution in the binder.[3,4] Then, the formation of defects is dependent on balancing the rates of diffusion and degradation/evaporation. The thermogravimetric analysis of extruded samples (Fig. 4) shows that about 10 wt% of organics are removed over a very narrow temperature range during pyrolysis, making kinetics control

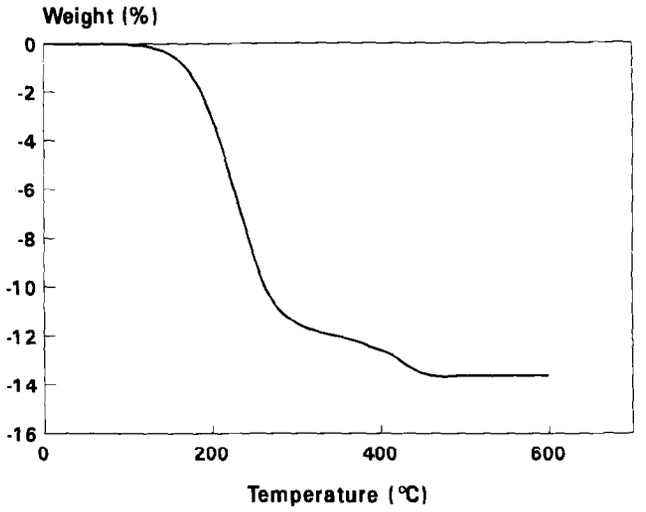


Fig. 4. Thermal gravimetric analysis for alumina–polystyrene–paraffin extruded samples (in air with a heating rate of 5°C.min^{-1}). The total amount of organic compounds is 14 wt%.

difficult. To summarize, chemical kinetics, liquid diffusivity, vapour phase transport and binder redistribution are critical parameters of the pyrolytic binder removal process. These parameters can hardly fulfil requirements together in order to avoid the formation of defects in the green body.

The supercritical debinding method was performed at a rather low temperature, (i.e. lower than 120°C), at which no redistribution of the binder in the green body, due to capillary forces, takes place and at which no degradation of organic compounds occurs. For example, in the case of the polypropylene-based binder system studied by Pinwill,[5] defects occur at temperatures higher than 160°C.

Extraction by the supercritical fluid acts through two steps, namely solubilization of organics without degradation and diffusion of dissolved species through the porous medium. On one hand, the density of the supercritical fluid, which depends on pressure and temperature, leading to the largest solubility of a binder can be estimated using solubility parameters. On the other hand, a model based on diffusion equations was recently developed to estimate diffusivity of dissolved organic species in green samples.[9] Solubility and diffusivity control the binder extraction with opposite pressure and temperature dependencies. The limiting mechanism of supercritical debinding is the diffusion of dissolved species, here soluble paraffin, through the space available between ceramic particles, keeping in mind that a large portion of this space (about 50 vol.%) is still occupied by undissolved binder (non-soluble paraffin and polystyrene). The diffusion coefficient is also reduced by the tortuosity factor.

The small amount of undissolved polystyrene by the supercritical CO_2 maintains the cohesion of the ceramic green body. Organic bridges between ceramic particles are preserved, avoiding the deformation of the green part during and after the extraction of the largest amount of organics. According to calculations based on a diffusion model,[9] the amount of organics which have to be removed, by supercritical treatment, to reach an open and interconnected porosity over the whole sample was evaluated at 42% of the initial organic content. Then volatile species produced during the subsequent pyrolysis can diffuse more freely between ceramic particles and escape to the gas phase without causing large stresses. The supercritical treatment, by itself, allows the extraction of 50 vol.% of binders under the present conditions. Then, it remains possible that the unavoidable pyrolysis of residual organics at a heating rate of 5°C min^{-1} could affect mechanical properties of sintered specimens through the mechanisms involved earlier in this section, and thus a reduced heating rate during the presintering stage could possibly improve the strength to failure and the Weibull modulus to some extent. This is presently under investigation, but nevertheless it is noteworthy that interesting benefits can be expected from a 'soft' technique of binder removal such as supercritical extraction.

4 Conclusions

Organic removal from green ceramic parts is a crucial stage in ceramic processing, especially when large pieces are produced. This work has demonstrated that organic removal by supercritical carbon dioxide leads to plastic formed materials with higher mechanical properties than thermally treated ones. Higher values of strength to failure and Weibull modulus were obtained after 3 h of supercritical treatment (σ = 277 MPa, m = 13·7) than after 18 h of thermal treatment (σ = 253 MPa, m = 12·4).

This original method offers the great advantage of removing binders from ceramic green pieces without melting and without degradation of these organic compounds. Binder redistribution due to capillary forces and outward diffusion of degradation products, which are the major factors causing defects in the pyrolytic binder removal, does not take place during the supercritical extraction. Supercritical debinding involves two mechanisms, namely solubility of organics and diffusion of dissolved species through the porosity created.

The selective solvent properties of supercritical carbon dioxide allow a small amount of high molecular weight binder to be kept in order to maintain the cohesion of the ceramic green bodies after the extraction treatment.

References

1. Boch, P. & Chartier, T. Ceramic processing techniques: the case of tape casting. *Ceramic. Forum Int.*, **4** (1989) 55–67.
2. German, R. M., Theory of thermal debinding. *Int. J. Powder Metall.*, **23**(4) (1987) 237–45.
3. Calvert, P. D. & Cima, M. J., Theoretical models for binder burnout. *J. Am. Ceram. Soc.*, **73**(3) (1990) 575–9.
4. Evans, J. R. G., Edirisinghe, M. J., Wright, J. K. & Crank, J., On the removal of organic vehicle from moulded ceramic bodies. *Proc. Roy. Soc. (London)*, **A432** (1991) 321–40.
5. Pinwill, I. E., Edirisinghe, M. J. & Bevis, M. J., Development of temperature-heating rate diagrams for the pyrolytic removal of binder used for powder injection moulding *J. Mat. Sci.*, **27** (1992) 4381–8.
6. Cima, M. J., Lewis, J. A. & Devoe, A. D., Binder distribution in ceramic greenware during thermolysis. *J. Am. Ceram. Soc.*, **72**(7) (1989) 1192–9.
7. Wright, J. K. & Evans, J. R. G., Removal of organic vehicle from moulded ceramic bodies by capillary action. *Ceram. Int.*, **17** (1991) 79–87.
8. Barone, M. R. & Ulicny, J. C., Liquid-phase transport during removal of organic binders in injection-molded ceramics. *J. Am. Ceram. Soc.*, **73**(11) (1990) 3323–33.
9. Chartier, T., Ferrato, M. & Baumard, J. F., Supercritical debinding of injection molded ceramics, to be published in *J. Am. Ceram. Soc.*
10. Hawthorne, S. B., Analytical-scale supercritical fluid extraction, *Anal. Chem.*, **62** 633–42A (1990).
11. Jayatilaka, A. S. & Trustum, K., Statistical approach to brittle fracture. *J. Mat. Sci.*, **12** (1977) 1426–30.
12. Trustum, K. & Jayatilaka, A. S., Applicability of Weibull analysis for brittle materials. *J. Mat. Sci.*, **18** (1983) 2765–70.
13. Zhang, J. G., Edirisinghe, M. J. & Evans, J. R. G., A catalogue of ceramic injection molding defects and their causes. *Ind. Ceram.*, **9**(2) (1989) 72–82.
14. Dong, C. & Bowden, H. K., Hot Stage bubble formation during binder burnout. *J. Am. Ceram. Soc.*, **72**(6) (1989) 1082–7.
15. Mutsuddy, B. C., Mechanical properties of injection molded ceramics. *Powder Met. Int.*, **19**(2) (1987) 43–5.
16. Fanelli, A. J., Silvers, R. D., Frei, W. S., Burlew, J. V. & Marsh, G. B., New aqueous injection molding process for ceramic powders. *J. Am. Ceram. Soc.*, **72**(10) (1989) 1833–6.
17. Quinn, G. D., Flexural strength of advanced structural ceramics: a round robin. *J. Am. Ceram. Soc.*, **73**(8) (1990) 2373–84.
18. Ferrato, M., Chartier, T., Baumard, J. F. & Coudamy, G., Le déliantage des céramiques. *L'Industrie Céramique*, **864**(10) (1991) 656–61.
19. Stangle, G. C. & Aksay, I. A., Simultaneous momentum, heat and mass transfer with chemical reaction in a disordered porous medium: application to binder removal from a ceramic green body. *Chem. Eng. Sci.*, **45** (1990) 1719–31.
20. Mangin-Fritsch, A., Modélisation et optimisation de la dégradation themique de liants utilisés en injection de céramiques, PhD thesis, Ecole Nationale Supérieure des Mines de Paris, 1992.

Journal of the European Ceramic Society **15** (1995) 905–908
© 1995 Elsevier Science Limited
Printed in Great Britain. All rights reserved
0955-2219/95/$9.50

0955-2219(95)00061-5

The Accuracy of Failure Predictions Based on Weibull Statistics

S. L. Fok* & J. Smart

Department of Engineering, University of Manchester, Manchester, M13 9PL, UK

(Received 3 October 1994; revised 2 March 1995; accepted 10 March 1995)

Abstract

The mechanical failure of ceramic materials is usually characterised by probability equations based on Weibull's weakest link theory. To evaluate these for components in a varying stress field, postprocessors have been developed by us as well as others. The effect of the errors which arises from the postprocessing on the fractional errors in the nominal failure load, the probability of failure or the probability of survival are found and discussed.

Introduction

The mechanical failure of ceramics is usually considered to be governed by failure laws which are based on the original ideas of Weibull[1] in 1939. Since then the theory has been developed to allow for multiaxial stress fields and for different failure criteria. Essentially, the ceramic is considered to have many small flaws (cracks) distributed throughout the body and failure depends upon the first crack to fail: hence the concept of the weakest link. These small cracks will have different sizes and will be randomly orientated. The largest crack may not cause failure as it may occur in an area of low stress or it may be orientated so that, for example, the stress normal to the crack is small and hence is less likely to fail when compared to the crack which is orientated so that the stress normal to the crack is high.

To account for these variations, the mechanical failure of ceramics is normally described by a probability distribution and typically the failure probability will be described by the equation

$$P_f = 1 - e\left\{-\left(\frac{\sigma_{nom}}{\sigma_0}\right)^m \Sigma_v\right\} \quad (1)$$

where Σ_v is a stress volume integral given by

$$\Sigma_v = \int_v \frac{1}{4\pi} \int_0^{2\pi} \int_0^{\pi} \left(\frac{\sigma_e}{\sigma_{nom}}\right)^m \sin\phi \, d\phi \, d\psi \, dv \quad (2)$$

for a body with a random distribution of crack orientations.

The stress volume integral accounts for the variation of stress throughout the body and also, through σ_e, the different failure criteria. In these equations, σ_0 and m are material properties which correspond to the strength of the ceramic and to the spread in the failure loads and σ_{nom} is a nominal stress. As well as stress volume integrals in which the stress is evaluated over the volume, there are also failure laws based on the stress distribution over the surface of the component.

In order to determine the failure probability of a structure in which the stress varies, the normal procedure is to perform a finite element analysis and then using the data from this analysis evaluate the failure probability using a postprocessor based on (1) and (2). How our postprocessor worked is described in Ref. 2.

To compare the performance of various postprocessors a numerical round robin was performed and the results have been published by Dortmans *et al.*[3] To compare the errors a measure called $\bar{S}_{nom}$ was used. This is the predicted mean nominal stress and is directly related to σ_{nom} in eqn (1). This was chosen as it is not too sensitive to errors in the postprocessor.

However, a designer is probably more interested in properties such as probability of failure or nominal failure stress for a given probability of failure (or survival). The purpose of this paper is to discuss the relationships between these values and the relationship with the errors arising from the postprocessor when evaluating the stress volume (or area) integral.

Theory

The probability of failure as given by (1) can be generalised so that Σ represents either a stress volume, Σ_v, or stress area, Σ_A, integral, i.e.

*Now at Nuclear Electric Plc, Berkeley Technology Centre, Gloucs., UK.

$$P_f = 1 - e\left\{-\left(\frac{\sigma_{nom}}{\sigma_0}\right)^m \Sigma\right\} \quad (3)$$

and for the survival probability

$$P_s = e\left\{-\left(\frac{\sigma_{nom}}{\sigma_0}\right)^m \Sigma\right\} \quad (4)$$

Now, for a particular value of survival probability

$$\sigma_{nom} = \sigma_0 \left(\frac{\ln(1/P_s)}{\Sigma}\right)^{1/m}$$

or

$$\sigma_{nom} \propto (1/\Sigma)^{1/m} \quad (5)$$

This gives a relationship between the nominal failure stress, the stress integral and the Weibull parameter. Now, because of errors in the postprocessing

$$\frac{\sigma^*_{nom}}{\sigma_{nom}} = \left(\frac{\Sigma}{\Sigma^*}\right)^{1/m} \quad (6)$$

where the asterix denotes the numerically derived values. This provides a measure of the error in the nominal failure stress which depends on the Weibull modulus and the numerical error from the postprocessing step in calculating the stress integral. Equation (6) also applies to $\bar{S}_{nom}$.

On the other hand, if the survival probability, P_s, is required then from (4)

$$P_s = e\left\{-\left(\frac{\sigma_{nom}}{\sigma_0}\right)^m \Sigma^*\left(\frac{\Sigma}{\Sigma^*}\right)\right\} = P_s^{*(\Sigma/\Sigma^*)}$$

or

$$\frac{P_s^*}{P_s} = P_s\left(\frac{\Sigma^*}{\Sigma} - 1\right) \quad (7)$$

This now provides a measure of the error in the survival probability which depends on the survival probability and the error in the stress integral.

For the failure probability and using (7) gives

$$\frac{P_f^*}{P_f} = \frac{1 - P_s^{\Sigma^*/\Sigma}}{P_f}$$

or

$$\frac{P_f^*}{P_f} = \frac{1 - (1-P_f)^{\Sigma^*/\Sigma}}{P_f} \quad (8)$$

This provides a measure of the error in the failure probability which depends on the failure probability and the error in the stress integral.

Results and Discussion

Equations (6), (7) and (8) have been evaluated to examine the effect of errors in determining the stress integrals and the results are given in Figs 1, 2 and 3.

For the nominal failure stress, Fig. 1 shows the dependency on the Weibull parameter and that the errors in evaluating the stress integral are reduced when calculating the nominal failure stress, particularly for high values of Weibull modulus. However, as has been shown elsewhere,[3] the errors in evaluating Σ are greater for higher values of m.

From Fig. 2 it can be seen that to evaluate the survival probability accurately, it is important for low survival probabilities that the stress volume integral is evaluated accurately. However, for high survival probabilities, which is the realistic region for design, the errors are smaller.

From Fig. 3 it can be seen that a high failure probability reduces the fractional error of failure probability caused by errors in evaluating the stress integral. The error in the failure probability is always lower than that in the stress integral.

The equations given above have been derived using a 2-parameter Weibull model. However, a

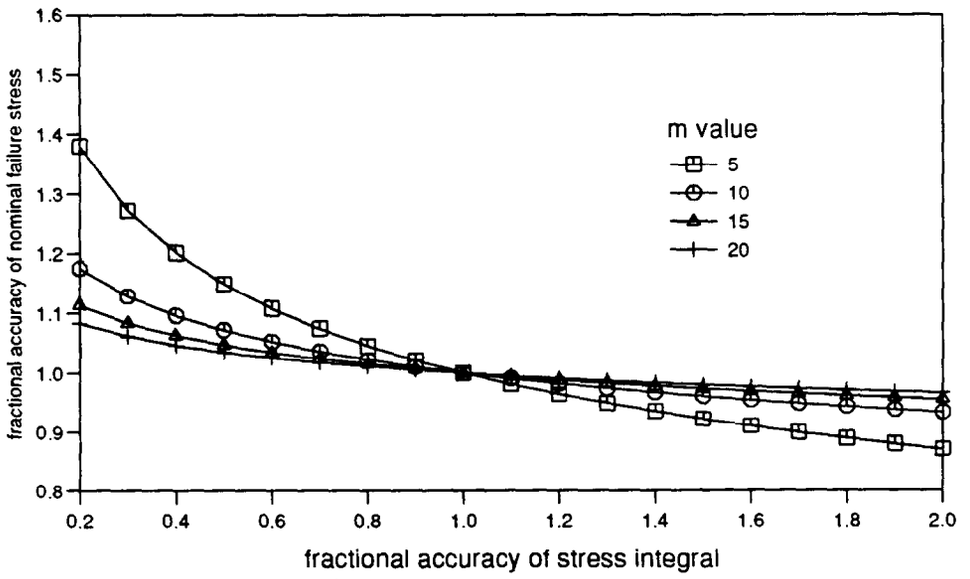


Fig. 1. Accuracy of nominal failure stress.

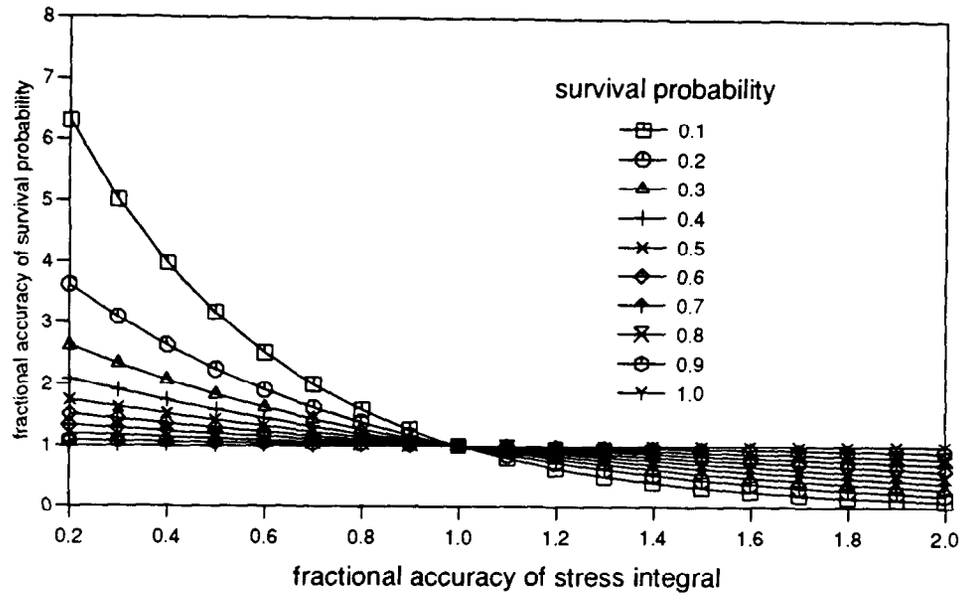


Fig. 2. Accuracy of survival probability.

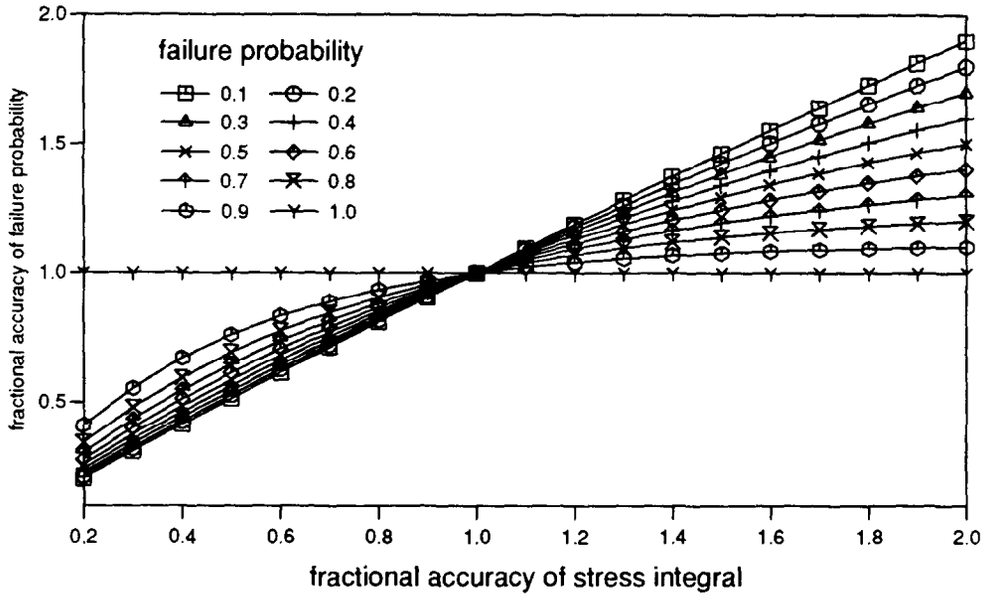


Fig. 3. Accuracy of failure probability.

3-parameter model using a threshold stress is also used in describing the mechanical failure distribution of ceramics. In this case the relationship given by (6) is no longer valid although the relationships (7) and (8) still hold.

A further measure of error is the absolute error, i.e.

$$| P_s^* - P_s | = | P_s^{\Sigma^*/\Sigma} - P_s | \tag{9}$$

Also

$$| P_f^* - P_f | = | (1 - P_s^*) - (1 - P_s) |$$

$$\therefore | P_f^* - P_f | = | P_s^{\Sigma^*/\Sigma} - P_s | \tag{10}$$

It can be seen from (9) and (10) that, not surprisingly, the absolute error in the failure and survival probabilities is the same. This is probably a better indicator of error because, for example, the practical difference between a failure probability of 1×10^{-5} and 2×10^{-5} is negligible even though the fractional error is 50%.

The results of evaluating (9) are shown in Fig. 4 for the region of high survival probability which is the realistic design range.

Equation (10) can be further developed as

$$P_f^* - P_f = (1 - P_f)^{\Sigma^*/\Sigma} - (1 - P_f)$$

For small probabilities of failure and when Σ^*/Σ is approximately 1, then

$$P_f^* - P_f = 1 - \frac{\Sigma^*}{\Sigma} P_f - 1 + P_f$$

$$\therefore P_f^* - P_f = P_f \left(1 - \frac{\Sigma^*}{\Sigma} \right) \tag{11}$$

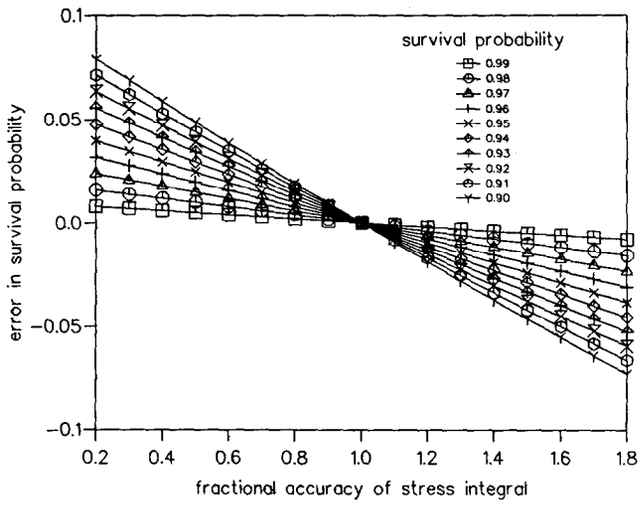


Fig. 4. Error in survival probability.

An examination of Fig 4 shows that this simplified equation is a good representation of the data and will enable the error in the failure probability caused by an error in determining the stress integral to be readily determined.

Conclusions

Relationships have been developed which give the fractional error in the mean nominal failure stress, the survival probability, the failure probability and the error in survival probability caused by errors in evaluating the stress integrals in the Weibull failure laws used for ceramic materials.

These have been evaluated to provide guides for the accuracy required in calculating the stress integrals in postprocessors.

References

1. Weibull W., *A statistical theory for the strength of materials*. Ingeniors Vetenskaps Akademien Handlinger, No 152, 1939.
2. Smart, J. & Fok, S. L., The numerical evaluation of failure theories for brittle materials. In *Life prediction methodologies and data for ceramic materials*, ASTM1201, eds C.R. Brinkman & S. F. Duffy, 1994, pp. 143–60.
3. Dortmans, L., Thiemeier, Th., Brückner-Foit, A. & Smart. J. WELFEP: a round robin for weakest-link finite element postprocessors, *J. Euro Ceram. Soc.*, **9** (1993) 17–22.

Journal of the European Ceramic Society **15** (1995) 909–912
© 1995 Elsevier Science Limited
Printed in Great Britain. All rights reserved
0955-2219/95/$9.50

0955-2219(95)00060-7

The Efficient Integration of the Orientation Integral in Weakest Link Finite Element Postprocessors

S. L. Fok* & J. Smart

Department of Engineering, University of Manchester, Manchester, M13 9PL, UK

(Received 3 October 1994; revised 2 March 1995; accepted 10 March 1995)

Abstract

In evaluating the failure probability of ceramics it is usually necessary to numerically integrate an orientation integral which accounts for the random orientation of cracks with respect to the stress field. The procedure for performing this efficiently is discussed and recommendations are given.

Introduction

To evaluate the failure probability or nominal failure load of a ceramic component in a varying stress field a postprocessor is normally used. This takes the results from a finite element analysis and evaluates the failure laws which are typically written as[1]

$$P_f = 1 - e\left\{-\left(\frac{\sigma_{nom}}{\sigma_0}\right)^m \Sigma_v\right\} \quad (1)$$

where Σ_v is a stress volume integral given as

$$\Sigma_v = \int \frac{1}{4\pi} \int_0^{2\pi} \int_0^{\pi} \left(\frac{\sigma_e}{\sigma_{nom}}\right)^m \sin\phi \, d\phi \, d\psi \, dv \quad (2)$$

In eqn (2), σ_e and σ_{nom} are the equivalent and nominal stress respectively and the angles ϕ and ψ are defined in Fig 1.

In order to provide some benchmarks and to investigate how various postprocessors work, a numerical round-robin was carried out and a questionnaire circulated by WELFEP.[2] One question asked referred to the numerical integration of (2). Essentially, this equation accounts for the stress variation within the component and for the possibility that a crack may be orientated in any direction with respect to the stress field.

If eqn (2) is examined it can be seen to comprise of 2 parts; an integration over a unit sphere within an integration over the volume of the component. Previously,[1] we have investigated the integration rule within the volume of the component but have not discussed the integration over the unit sphere.

The purpose of this paper therefore, is to discuss the problem of how to efficiently and accurately integrate

$$I = \int_0^{2\pi} \int_0^{\pi} \left(\frac{\sigma_e}{\sigma_{nom}}\right)^m \sin\phi \, d\phi \, d\psi \quad (3)$$

As this is over a unit sphere and is to account for the orientation of the cracks with respect to the stress field it is often called the orientation integral. In the questionnaire,[2] it was found that 'generally Gauss–Legendre integration is applied with 10, 15 or 20 Gauss points'.

However, the question arises, is this the best method?

Theory

If the maximum principal stress, σ_1, is taken as the nominal stress then (3) can be rewritten as

$$I = \int_0^{2\pi} \int_0^{\pi} f\left(\frac{\sigma_2}{\sigma_1}, \frac{\sigma_3}{\sigma_1}, m, \phi, \psi\right) d\phi \, d\psi \quad (4)$$

and if the integration is performed numerically then

$$I = \sum_{i=1}^{N} \sum_{j=1}^{N} f_{ij} W_i W_j \quad (5)$$

where N is the number of sampling points and W_i and W_j are the weighting factors associated with the integration scheme.

For the Gauss–Legendre method, a linear transformation has to be performed to make the limits of integration +1 and −1. The sampling points are non-uniformly distributed and the values of the weighting factors vary.[3]

For the rectangular rule, the weighting factors are constant and the sampling points are evenly distributed through the domain. When integrating in 1-D this is equivalent to dividing the area under the curve into equal strips with the weighting

*Now at Nuclear Electric Plc, Berkeley Technology Centre, Gloucs, UK.

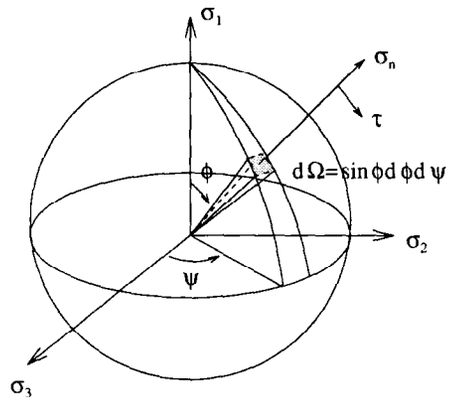


Fig. 1. Unit sphere in principal stress space.

factor the strip width and the sampling point being the centre of each strip. (Often, numerical integration is called quadrature and the Gauss–Legendre method is called Gaussian quadrature).

To investigate the efficiency of the evaluation of the integral both the Gaussian and rectangular rules will be used. Also, as (4) shows that the ratios σ_2/σ_1 and σ_3/σ_1 are important, various cases are considered, i.e.:

(i) uniaxial tension $\sigma_2/\sigma_1 = \sigma_3/\sigma_1 = 0$
(ii) equi-biaxial tension $\sigma_2/\sigma_1 = 1; \sigma_3/\sigma_1 = 0$
(iii) tension-compression $\sigma_2/\sigma_1 = 1; \sigma_3/\sigma_1 = -1$
(iv) equi-triaxial tension $\sigma_2/\sigma_1 = \sigma_3/\sigma_1 = 1$

Results and Discussion

The results are shown in Figs 2–5 for a shear insensitive equivalent stress, i.e. $\sigma_e = \sigma_n$.
In this case

$$\sigma_e = \sigma_1\cos^2\phi + \sigma_2\sin^2\phi\sin^2\psi + \sigma_3\sin^2\phi\cos^2\psi \quad (6)$$

From these figures, it can be seen that the calculated orientation integrals converge with increasing integration order and that, as for the integral over the volume,[1] the higher the Weibull modulus, m, the more sampling points are required for the integral to converge. For both rules, a quadrature order of 10 or less appears to be sufficient for the ranges of m values and stress ratios tested. However, in contrast to the calculation of the stress integrals, the rectangular rule can be seen to give a faster convergence than Gaussian quadrature with the exception being the case of equi-triaxial tension.

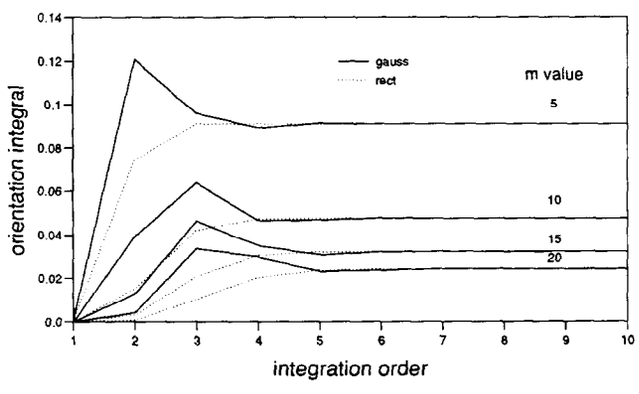


Fig. 2. Convergence of orientation integral for uniaxial tension.

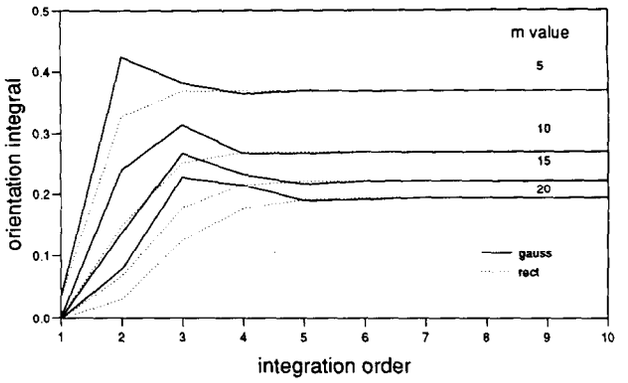


Fig. 3. Convergence of orientation integral for equi-biaxial tension.

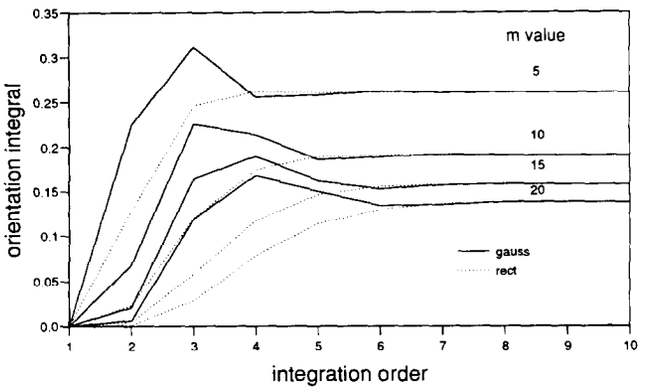


Fig. 4. Convergence of orientation integral for tension–compression.

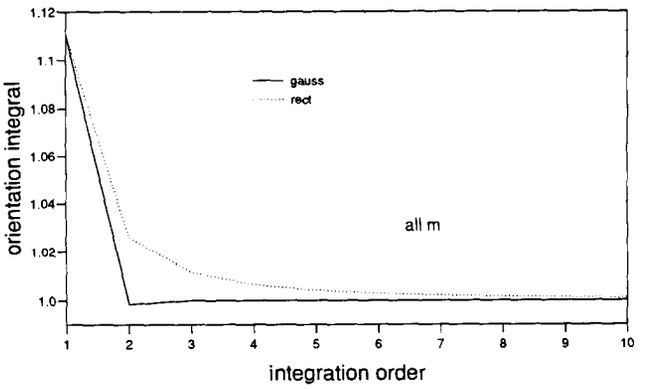


Fig. 5. Convergence of orientation integral for equi-triaxial tension.

At first sight, the results may seem surprising considering the superiority of Gaussian quadrature in evaluating the volume integral.[1] However, if the integral, eqns (3) and (6), is examined it can be found to contain terms such as $\cos^m\phi$ and $\sin^m\phi$ because of the stress transformations. When plotted, these functions have shapes similar to a ramp function as shown in Figs 6 and 7. If the

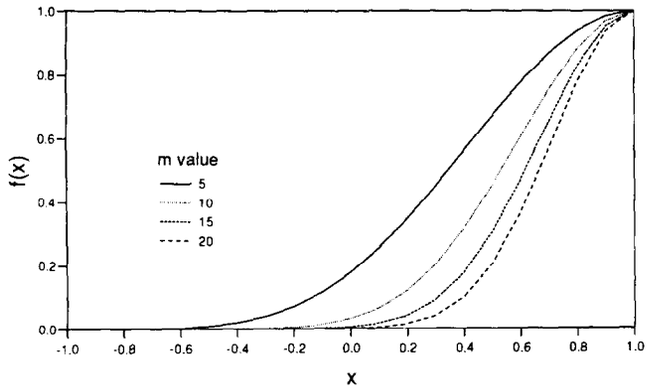


Fig. 6. $f(x) = \sin^m \frac{\pi}{4}(x + 1)$

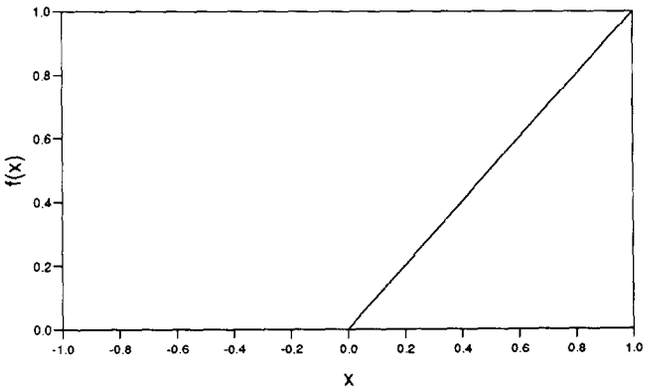


Fig. 7. Ramp function.

rectangular rule is used to integrate the ramp function, the use of 2 or any other even number of sampling points will give the correct answer. On the other hand, when the number of sampling points is odd a higher integration order is required to obtain a converged result. Figs 8 and 9 compare the performance of the rectangular and Gaussian rule in integrating the functions in Figs 6 and 7 and it can be seen that in both cases the rectangular rule is more efficient.

For a shear sensitive criterion, e.g.

$$\sigma_e = (\sigma_n^4 + 6\sigma_n^2 \tau^2 + \tau^4)^{1/4} \qquad (7)$$

similar results are obtained, although the convergence is not so rapid with the value of the orienta-

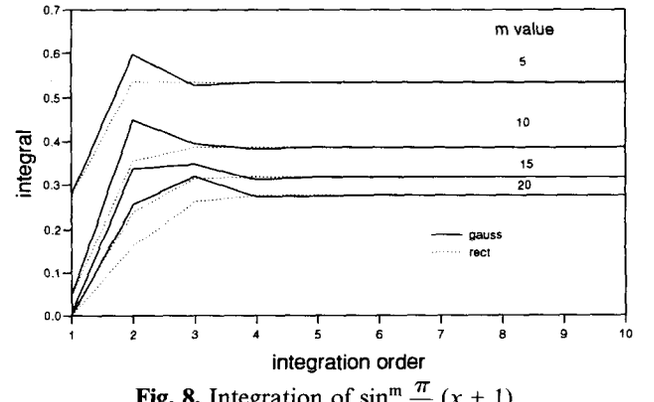


Fig. 8. Integration of $\sin^m \frac{\pi}{4}(x + 1)$

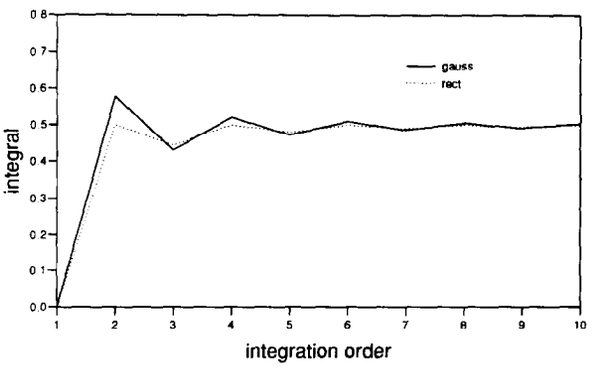


Fig. 9. Integration of ramp function.

tion integral oscillating more before converging. This is particularly so for case (iii), i.e. tension–compression and for $m = 5$. Convergence is also affected by the way in which negative values of stress are treated. If

$$\sigma_e = 0 \text{ for } \sigma_n < 0$$

then convergence is not so good and higher integration orders may be needed.

The effect of any errors in calculating the error in probability of failure, probability of survival or nominal stress has also been examined by the authors.[4] For high survival probabilities, the fractional error in the survival probability is considerably less than the fractional error in the stress integral. It was shown that

$$\frac{P_s^*}{P_s} = P_s\left(\frac{\Sigma^*}{\Sigma} - 1\right)$$

where P_s is the survival probability, Σ is the value of the stress integral and the *superscript denotes the numerically derived values. So, for example, for a fractional error of 10% in Σ, i.e. $\Sigma^*/\Sigma = 1{\cdot}10$, then P_s^*/P_s for a survival probability of 0·99 is 0·999, i.e. a 0·1% error. Alternatively, the absolute error is given as

$$| P_s^* - P_s | = | P_s^{\Sigma^*/\Sigma} - P_s |$$

and the absolute error is 0·000994.

In view of these results, an integration order of 10 is recommended as sufficient for practical applications and there is little difference between Gaussian and rectangular quadrature.

Conclusions

To evaluate the orientation integral in the failure laws for ceramic materials, it is recommended that an integration order of 10 is used. The rectangular rule and Gaussian quadrature give almost identical results.

References

1. Smart, J. & Fok, S. L., The numerical evaluation of failure theories for brittle materials. In *Life prediction methodologies and data for ceramic materials*, ASTM, STP 1201, eds C. R. Brinkman & S. L. Duffy, 1994, pp. 143–60.
2. Dortmans, L., Thiemeier, Th., Brückner-Foit, A. & Smart, J., WELFEP: a round robin for weakest link finite element postprocessors. *J. Eur. Ceram. Soc.*, **9** 1993 17–22.
3. Stroud, A. H. & Secrest, D., Gaussian Quadrature Formulas. Prentice Hall, 1966.
4. Fok, S. L. & Smart, J., The accuracy of failure predictions based on Weibull statistics. *J. Eur. Ceram. Soc.*, **15** 1995 905–8.

Journal of the European Ceramic Society 15 (1995) 913–920
© 1995 Elsevier Science Limited
Printed in Great Britain. All rights reserved
0955-2219(95)00039-9
0955-2219/95/$9.50

Effect of Mullite–Zirconia Additions on the Creep Behaviour of High-Alumina Refractories

C. Wolf,[a] R. Kauermann,[a] H. Hübner,[a] J. A. Rodrigues[b] & V. C. Pandolfelli[b]

[a]Arbeitsbereich Werkstoffphysik, Technische Universität Hamburg-Harburg, D-21071 Hamburg, Germany
[b]Departamento de Materiais, Universidade Federal de São Carlos, 13.565–905 São Carlos — SP, Brazil

(Received 20 December 1994; accepted 10 February 1995)

Abstract

The creep behaviour of high-alumina refractories containing increasing amounts of a fused mullite–zirconia aggregate (MZA) of eutectic composition was studied experimentally. The MZA has been added with the intention of improving the work of fracture and the thermal shock resistance through microcrack toughening. The creep resistance was found to decrease with increasing MZA content. This was attributed to the formation of an increasing fraction of a substructure composed of small grains and an amorphous binder phase situated between the large agglomerate particles. Creep deformation mainly occurred within these fine-grained interagglomerate regions, but rate controlled by mullite formation kinetics as an accommodation process. This interpretation is substantiated by the measured values of the stress exponent (n = 1·2–2·7) and the activation energy for creep ($Q \approx$ 720 kJ/mol) and by the finding that the creep rate was distinctly reduced by a preceding heat treatment.

1 Introduction

During the last decade, modern refractories have been developing into a class of highly sophisticated multiphase composite materials. As pointed out recently by Bradt[1] in a review on present day refractories, the manyfold and complex reactions between the constituents of the microstructure which are dynamic and transient in nature must be understood when a critical assessment of the physical and mechanical properties is to be obtained.

Among the mechanical properties of refractories, the deformation behaviour at high temperature under compressive load is of particular interest. Knowledge of the creep data of refractories is a prerequisite for selecting materials that exhibit a minimum of creep in a given application, as well as for establishing engineering design parameters for the construction of stoves and furnaces, as has been clearly demonstrated by Ainsworth and Kaniuk.[2] Furthermore, it has been pointed out by Evans *et al.*[3] that the availability of creep data is an indispensable basis when stresses and strains in refractory components and structures in service are to be calculated. By using the Θ projection concept developed by Evans and Wilshire[4] they demonstrated that the creep strength of refractories under service conditions can be extrapolated from the creep data determined in the laboratory within a limited range of test conditions.[3] Finally, the investigation of basic creep mechanisms is the key for developing new materials of improved creep resistance for use in refractory settings where creep is to be minimized.

A series of experimental creep studies on a variety of refractories of different compositions have been reported in the literature.[2, 5–13] It is generally recognized that creep of refractories is strongly affected by the microstructure. Fundamentally, there are three microstructural features which influence the creep behaviour, i.e. (1) the mineral content (size and distribution of the crystalline aggregates); (2) the flux content (amount, composition and distribution of the glassy phase), and (3) the apparent porosity.

The aim of the work presented here was to evaluate the creep behaviour of an experimental high-alumina refractory particularly designed for high thermal shock resistance.[14] To achieve this, different amounts of a mullite–zirconia aggregate (MZA) were added with the purpose of taking advantage of the zirconia toughening effect on room temperature mechanical properties. In fact, an increase in both the work of fracture and the retained strength after thermal shock was observed as the MZA content was increased, pointing at an increased microcrack density caused by the presence of zirconia particles.[14] Likewise, a pronounced loss of high-temperature strength was found to occur at 1400°C. This was attributed to increasing fractions of glassy phase

Table 1. Compositions of the refractory materials

Materials	*Grain size range (mm)*	*Composition (wt%)*				
Tabular alumina*	0·044–2	90	80	70	60	50
Calcined alumina†	<0·01	10	10	10	10	10
Mullite–zirconia aggregate	0·21–1	—	10	20	30	40

*T-60, Alcoa (Germany).
†APC-2011 SG, Alcoa (Brazil).

introduced by the MZA additive.[14] It was to be expected that the increase in glass phase content should also degrade the creep resistance of the material which was actually found in this paper.

2 Experimental Details

2.1 Materials and sample preparation

Five different high-alumina refractories were tested. These consisted of a basic mixture of a tabular and a calcined alumina to which varying amounts of a fused mullite–zirconia aggregate (MZA) have been added. The pressed bricks were fired at 1510°C for 12 h as indicated in Ref. 14. Table 1 shows the compositions of the materials tested, as well as their grain-size ranges. In the following, these five materials are identified by the weight fraction of their MZA content. Samples for compressive testing having dimensions of 20 × 20 × 40 mm^3 and 12 × 12 × 20 mm^3 were prepared by cutting blocks from the as-fired bricks and grinding them to the final dimensions. Specimens for microstructural examinations were ground and polished using a diamond paste down to a size of 1 μm. Micrographs were obtained by scanning electron microscopy on as-polished microsections.

2.2 Mechanical testing

Experimental techniques used in the literature for generating creep data are: (1) the refractoriness-under-load test (RUL test) where under a constant load and at a constant heating rate the temperature of the onset of plastic deformation is determined, and (2) compressive creep tests under constant load and temperature. Both techniques were applied in the present study. RUL tests were carried out according to DIN 51053 using a heating rate of 5°C/min and a compressive stress of 0·2 MPa.

Creep tests were performed in a constant-load creep machine in air at 1400°C and 3 MPa until failure occurred. Both as-received materials (all compositions) and samples annealed for 10 days at 1400°C (compositions 0, 10 and 30% MZA content) were tested. Stress change tests at 1400°C from 1 to 10 MPa and temperature change tests at 3 MPa from 1300 to 1450°C were made to obtain the stress exponent, n, and the activation energy for creep, Q, respectively (see eqn 1).

3 Results

3.1 Micrographic examinations

The microstructures of the five refractories studied in this work are shown in Figs 1 and 2. Figs 1(a) and (b) compare the materials without MZA and with 20% of MZA at a low magnification. In both micrographs, the large grains of tabular alumina prevail. These particles are considered to be rigid even under creep conditions and therefore do not contribute to the deformation. Between these large crystalline components, there is a substructure consisting of small grains and an amorphous binder phase. A fine-grained interaggregate substructure of similar appearance was also reported by Wiederhorn and Krause[13] in a magnesium–chromite refractory. The comparison of Figs 1(a) and (b) demonstrates that the volume fraction occupied by the interaggregate substructure is increased and that the grain size of the small grains within this substructure is decreased when MZA is added.

In Figs 2(a), (b) and (c), micrographs of the refractories containing 10, 20, and 40% of MZA

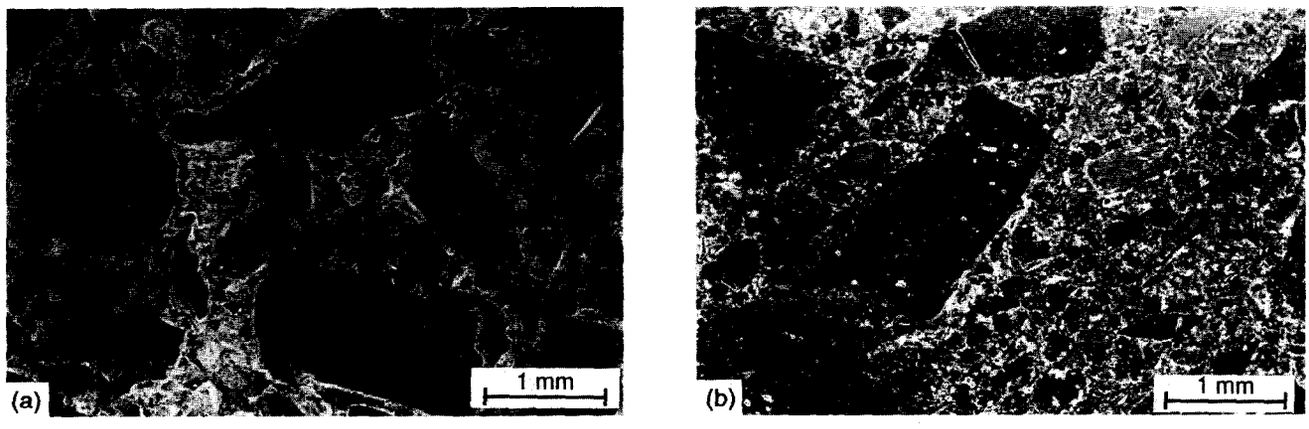


Fig. 1 SEM micrographs of refractories studied: (a) 0% of MZA content; (b) 20% of MZA content.

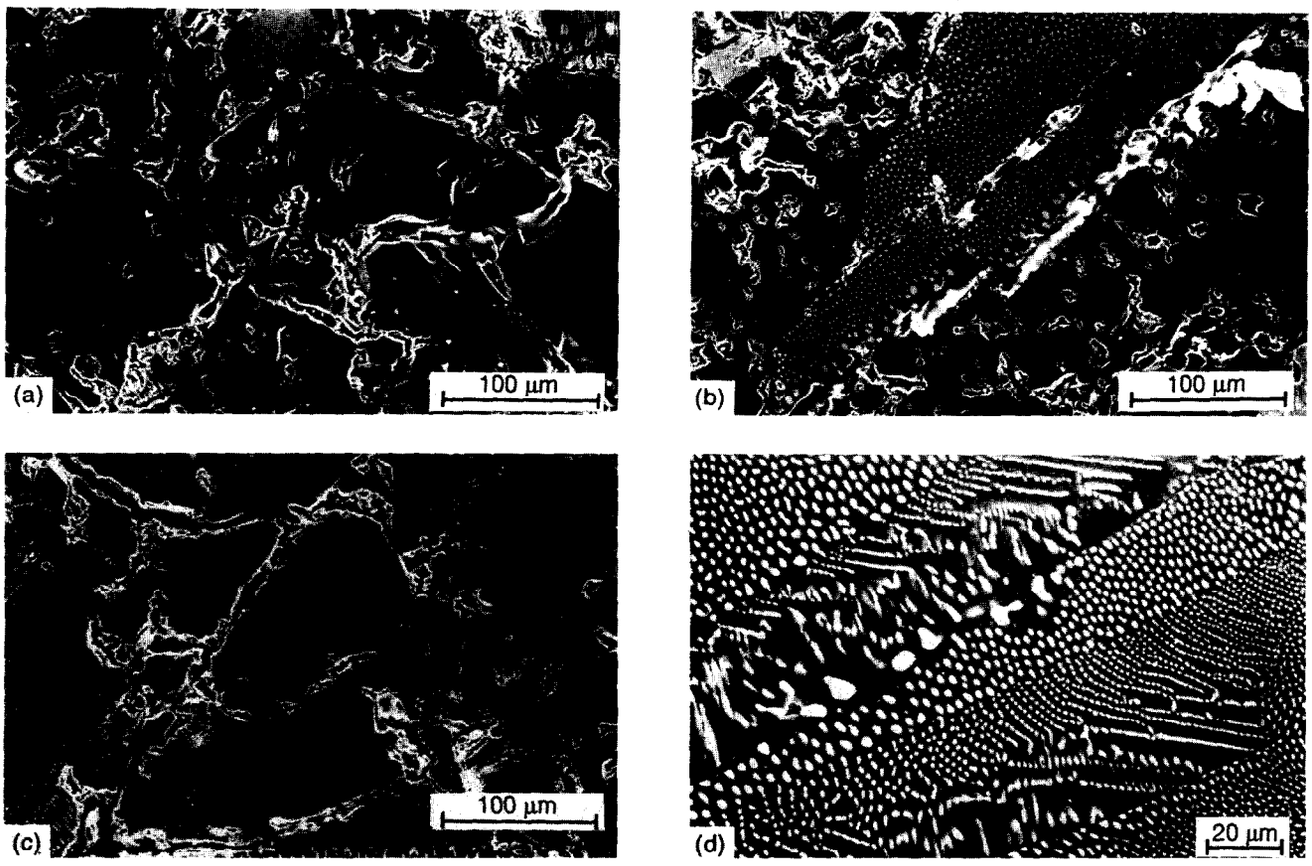


Fig. 2 Microstructure development with an increasing amount of MZA: (a) 10% of MZA content; (b) 20% of MZA content; (c) 40% of MZA content; (d) 20% of MZA content at higher magnification.

are shown at a higher magnification. The microstructure is composed of large particles of tabular alumina and the mullite–zirconia aggregate. These two components represent the major part of the crystalline phase content of the refractories.

The MZA can easily be detected in Fig. 2 by its dotted or striped appearance. The light phase is zirconia and the dark phase is mullite, as was proved by an EDX analysis. It is the mullite–zirconia eutectic which is formed in the Al_2O_3–SiO_2–ZrO_2 phase diagram. It has a eutectic temperature of 1750°C.[15] Within the MZA particles, the zirconia phase has a rod-like shape and forms periodic arrays of parallel orientation which are embedded in the continuous mullite matrix, as is shown in Fig. 2(d). This micrograph also demonstrates that there is a reasonable fit between the two phases of the eutectic since no microcracks can be detected within the MZA particles. However, considering the thermal expansion coefficients of mullite and zirconia, α_M and α_Z, ($\alpha_M = 5{\cdot}3 \times 10^{-6}\ K^{-1}$ and $\alpha_Z = 10{\cdot}0 \times 10^{-6}\ K^{-1}$ [16]), the value for the embedded phase is nearly twice that of the matrix phase. Thus, it may be concluded that thermally induced residual stress is created on cooling. In fact, evidence of microcrack formation at the ZrO_2/mullite interface was obtained on several micrographs.

Beside the rod-like zirconia component, there are also larger zirconia particles present in the micrographs of Figs 2(a), (b) and (c). These particles may be responsible for the toughening effect found in Ref. 14. Figures 2(a), (b), and (c) also show that the aggregate particles are surrounded by small layers of amorphous phase.

3.2 RUL tests

RUL test plots of the compositions 0, 20, and 40% MZA are presented in Fig. 3. The curves show a regime of linear thermal expansion and, at temperatures >1200°C, small deviations caused by the very onset of plastic deformation, the 20 and 40% materials going through a strain maximum at about 1400°C. According to DIN 51053, the upper temperature limit of the test is 1500°C and the softening temperature $T_{0{\cdot}5\%}$ is defined as that temperature where the compressive deformation attains a value of 0·5% with respect to the strain reached at the maximum. As can be seen from Fig. 3, $T_{0{\cdot}5\%} > 1500$°C for all compositions.

Since the sample deformation was very small when the temperature limit of 1500°C was reached the tests were continued at this temperature and stress for an additional 24 h to get a first idea of the creep resistance. By that means, creep curves $\epsilon(t)$ are developed which are also plotted in Fig. 3. From these curves the time $t_{0{\cdot}5\%}$ to reach a deformation $\epsilon = 0{\cdot}5\%$ was taken for each composition

Table 2. Comparison of mechanical properties at high temperatures

Aggregate (wt%)	*MOR* (MPa)*	$t_{0.5\%}$† *(h)*	ϵ_r‡ *(%)*	t_r‡ *(h)*	$\dot{\epsilon}_s$‡ *(s^{-1})*	$\dot{\epsilon}_{ann}$‡ *(s^{-1})*	*n*	*Q (kJ/mol)*
0	11·1	17	>10	>185·4	$1{\cdot}1 \times 10^{-7}$	—	1·3–2·0	692
10	8·5	—	7·63	6·3	$1{\cdot}7 \times 10^{-6}$	$4{\cdot}6 \times 10^{-7}$	1·7–2·7	668
20	6·8	3·9	6·06	2·2	$3{\cdot}9 \times 10^{-6}$	—	1·6–2·4	715
30	5·0	—	8·03	10·2	$1{\cdot}2 \times 10^{-6}$	6×10^{-7}	1·3–2·0	735
40	4·5	4·0	8·54	9·6	$1{\cdot}3 \times 10^{-6}$	—	1·2–2·1	778

* At 1400°C, Ref. 14.
† At 1500°C and 0·2 MPa.
‡ At 1400°C and 3 MPa.

and listed in Table 2. For the material without MZA content, this time is about 4 times that of the two other materials, indicating its superior creep resistance.

3.3 Creep tests

Creep curves plotted as creep rate $\dot{\epsilon}$ versus strain ϵ are shown in Fig. 4 for all materials in the as-received state at 1400°C and 3 MPa. The form of the creep curves is typical of many other ceramics and also refractories, exhibiting a primary, secondary or steady-state and tertiary creep stage. In some cases, no steady-state creep stage was found. The material without MZA had the lowest creep rate and did not exhibit any signs of creep damage up to ϵ = 10% where the test was stopped. The other compositions crept much more readily and exhibited failure by creep rupture at strains between 6 and 9%. Values of rupture strain ϵ_r, rupture time t_r and the steady-state or minimum creep rate $\dot{\epsilon}_s$ are listed in Table 2 for comparison.

The steady-state creep rate of a material is usually described by the equation

$$\dot{\epsilon}_s = A(S) \cdot \sigma^n \cdot \exp\left(-\frac{Q}{RT}\right), \qquad (1)$$

where $A(S)$ is a structure-dependent constant, σ is the stress, n is the stress exponent, Q is the activation energy for creep, and R and T have their usual meaning. To determine n and Q of eqn (1), stress and temperature change tests were performed. Examples of such tests are shown in Fig. 5 (stress changes) and Fig. 6 (temperature changes) for the refractory containing 30% of MZA. The stress exponent is calculated from the height of the $\dot{\epsilon}_s$ steps of Fig. 5 and the activation energy from the step height of Fig. 6. The n and Q values which were thus obtained are listed in Table 2.

The stationary creep rates measured at different stress levels at 1400°C are presented in Fig. 7 in a log–log plot. In this type of presentation, all five materials tested are close together, the difference increasing a little with increasing stress and reaching a factor of 5 at 10 MPa. The stress exponent derived from the slope of the curves has values between 1 and 2 and increases slightly with increasing applied stress level.

Figure 8 is an Arrhenius plot of the creep rates of the five materials at 3 MPa. Straight and nearly parallel lines were obtained which point at an activation energy for creep that is independent of temperature and equal for all compositions.

The effect of the MZA content on the steady-state creep rate at 1400°C and 3 MPa is shown in Fig. 9. It can clearly be recognized that the addition of MZA accelerates the creep deformation process. The maximum increase (by a factor of 25) was observed for the samples containing 20%

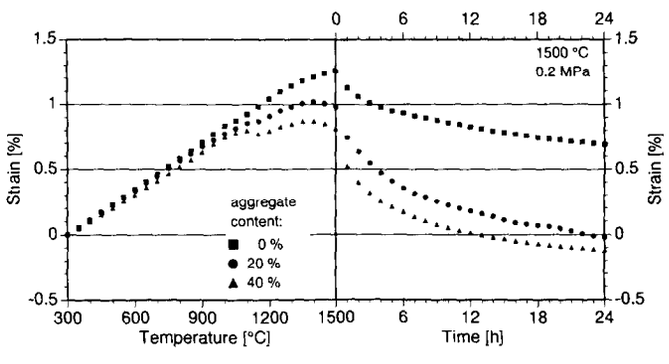


Fig. 3 RUL test plots.

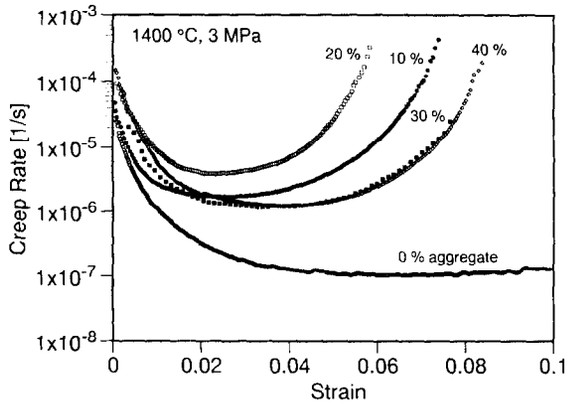


Fig. 4. Creep curves of high-alumina refractories in the as-received state.

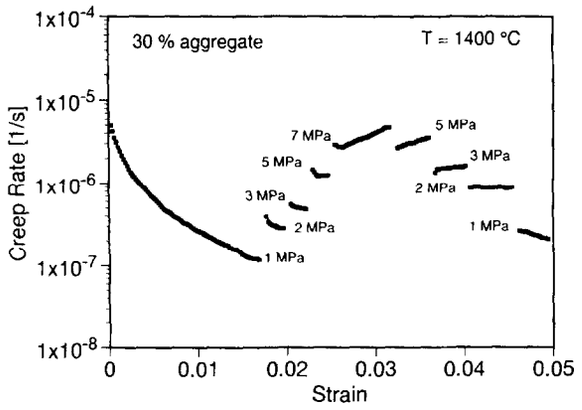


Fig. 5. Stress changes to determine the stress exponents, n.

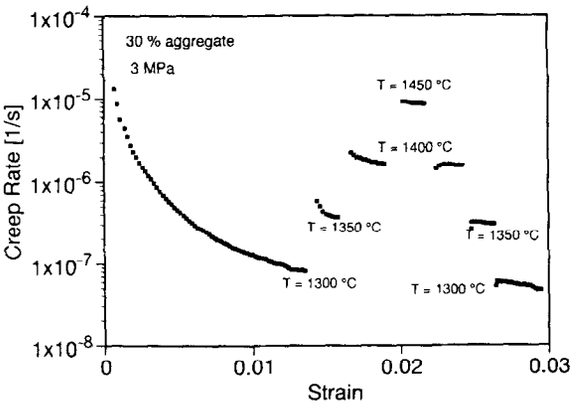


Fig. 6. Temperature changes to determine the activation energy for creep, Q.

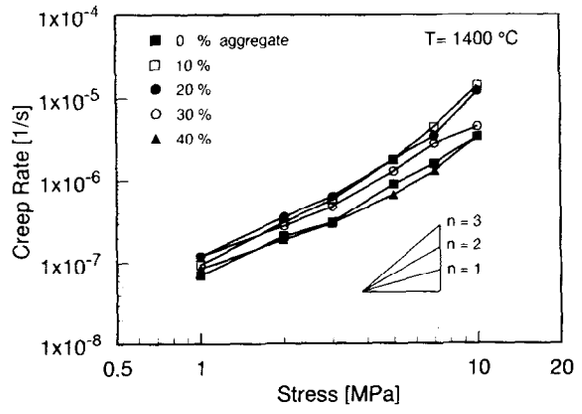


Fig. 7. Stress dependence of the stationary creep rate.

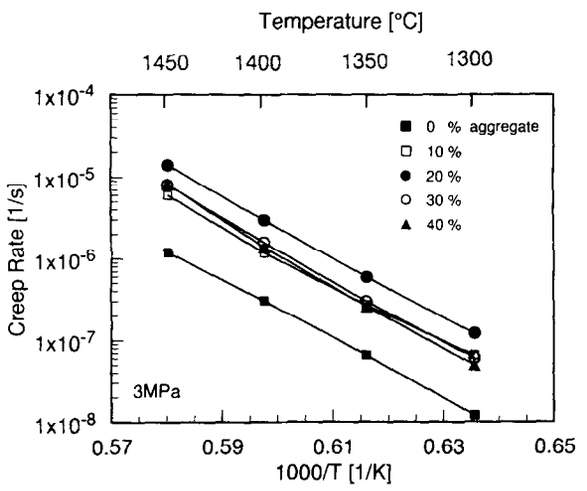


Fig. 8. Arrhenius diagram for the stationary creep rates.

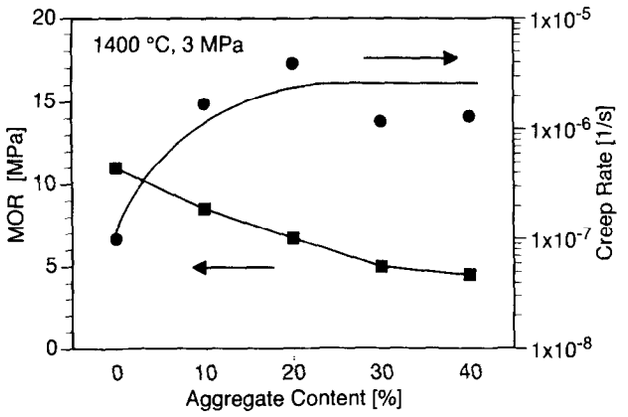


Fig. 9. Effect of MZA content on creep behaviour and high-temperature strength.

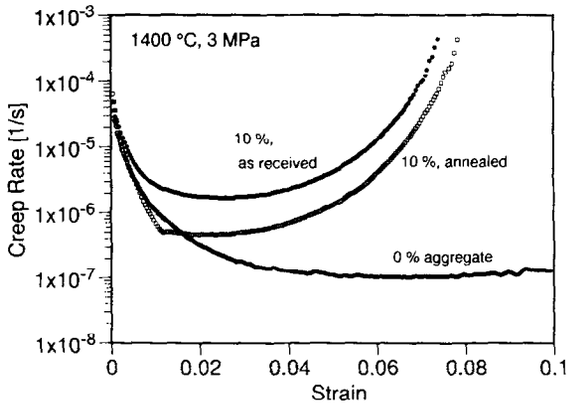


Fig. 10. Effect of heat treatment on the creep behaviour of 10% MZA refractory.

MZA. Figure 9 additionally contains modulus-of-rupture (MOR) data taken from Ref. 14. The MOR data are also listed in Table 2. The comparison of the two curves of Fig. 9 demonstrates that the high-temperature strength is degraded by the MZA addition in the same way that the creep rate is increased. From this finding it may be argued that the two mechanical parameters are controlled by the same microstructural features.

It has been reported by many investigators[5–7,10] that a post-fabrication heat treatment or hard firing condition reduces the creep rates of fired bricks. To examine the validity of this observation for the refractories studied here, compositions of 10 and 30% MZA were annealed at 1400°C for 10 days prior to creep testing. In Fig. 10 the creep curves of 10% MZA materials after the heat treatment and in the as-received state are compared. Minimum creep rate data of the two annealed

refractories are contained in Table 2. It was found that annealing altered the shape of the creep curve considerably, reducing minimum or steady-state creep rate by a factor of 4 in the material containing 10% and by a factor of 2 in the 30% MZA refractory.

4 Discussion

The creep behaviour of fired high-alumina refractories is strongly affected by their microstructure. There exists agreement in the literature that the two most important microstructural parameters are the crystalline phase content and the intergranular glassy phase. The results of the present research will be discussed in terms of these two features.

4.1 Crystalline phase content

According to the silica–alumina phase diagram, the equilibrium phases formed at elevated temperatures are mullite and corundum. Therefore, in high-alumina refractories mullite may be formed from alumina and excess silica by the reaction

$$3Al_3O_3 + 2SiO_2 \rightarrow 3\ Al_2O_3 \cdot 2SiO_2 \qquad (2)$$

The amount and morphology of the mullite phase controls the creep strength of high-alumina refractories since mullite formation increases the fraction of crystalline phases and reduces the amorphous phase content in the microstructure. Clements and Vyse[5] pointed out that best creep resistance is achieved when a three-dimensional network of mullite laths is present. Hulse and Pask[6] arrive at the same conclusion; namely that creep is controlled by the continuous mullite microstructure. Similar observations were made by Burdick and Day[7] and by Matsumara *et al.*[10] who found that all means of accelerating the rate of mullite formation resulted in a decrease of the creep rate. Other crystalline phases, such as large aggregate grains, are thought to be rigid and therefore do not contribute to the deformation. Furthermore, all four of these studies[5–7,10] agree upon the observation that the mullite content and hence the creep resistance of high-alumina refractories is increased through a heat treatment, either during initial firing or afterwards. A further observation concerning the effect of the crystalline phase content on the creep strength of refractories was made by Coath and Wilshire[9] and by Evans *et al.*[11] They reported that the creep rate of CaO/MgO doloma refractories decreased by up to an order of magnitude when the magnesia content was increased by admixing additional MgO powder to the raw material.

There is strong evidence that the creep behaviour of the refractories studied here is controlled by their mullite formation kinetics as well, as may be seen from the following arguments: (1) In metallographic observations a mullite lath network was observed at the interface between large alumina grains and MZA particles[14] where most of the local deformation is likely to occur. (2) The activation energy for creep is nearly the same for all five grades tested (Fig. 6). It has an average value of 720 kJ/mol and is very close to the activation energy for creep of mullite which has been reported to be 740 kJ/mol.[6] On the other hand, creep control by one of the other main constituents of the microstructure, i.e. the glassy phase and the large alumina grains, can be excluded since both of them have activation energies for creep much smaller than the measured figure of 720 kJ/mol. After Hulse and Pask,[6] silica-based glass has an activation energy in the range of 210–340 kJ/mol, whereas that of pure polycrystalline alumina is about 580 kJ/mol.[17] (3) The creep resistance was found to increase after a prolonged heat treatment (Fig. 8). This can be explained by temperature-activated mullite formation and silica consumption according to eqn (2). (4) Creep of the high-alumina refractories studied here is not a merely viscous process that would exhibit a stress exponent of $n = 1$. Instead, n values significantly greater than unity were found (Table 2 and Fig. 5). This finding indicates that the deformation additionally involves an accommodation process which probably actuates at the mullite–mullite and mullite–glass junctions and interfaces and which has a non-linear stress dependence.

4.2 Intergranular glassy phase

Even though the mullite phase is regarded to be rate-controlling in the creep of high-alumina refractories the properties of the glassy phase also affect the deformation behaviour. As pointed out by Hulse and Pask,[6] refractories with a high glass content will have a high deformation rate. Evidence of the effect of glassy phase content on the creep behaviour was also found in this study: (1) The MZA content caused the creep rate to be increased (Figs 2 and 7). This is attributed to an increased fraction of the amorphous phase in the microstructure because it was found in Ref. 14 that the addition of MZA resulted in an increased glass content. (2) In the presence of MZA, tertiary creep was observed to occur (Fig. 2) which is indicative of creep damage formed during deformation. The formation of creep damage generally decreases the rupture time t_r and reduces the ductility ϵ_r as indicated by the respective data in Table 2. It is well known that creep cavitation in

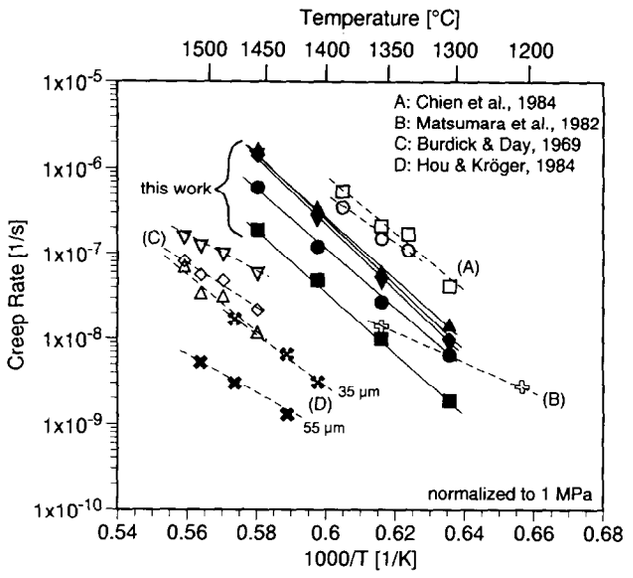


Fig. 11. Comparison of creep data from previous creep studies — data taken from Burdick and Day,[7] Matsumara *et al.*[10] Chien *et al.*,[19] and Hou and Kröger.[20]

structural ceramics is extraordinarily promoted by the presence of an amorphous phase. (3) The increase in creep rate and the decrease of rupture time must have the same origin. This follows from the fact that the $\dot{\epsilon}_s$ and t_r data of the four MZA containing refractories (Table 2) obey the Monkman–Grant relationship:[18]

$$\dot{\epsilon}_s \cdot t_r = \text{const.} \quad (3)$$

The $\dot{\epsilon}_s \cdot t_r$ product of the four data sets of Table 2 is about 0·040. The basic idea of the Monkman–Grant relationship is that, for a given failure mechanism, the strain at rupture is a constant.[18] Thus, if eqn (3) is valid for a given material, both the acceleration of the creep process and the reduction of the failure time are solely two different aspects of the same underlying mechanism. The Monkman–Grant relationship was found to hold for a series of glass-containing structural ceramics.[13]

The role of the intergranular glass phase in the creep of refractories was further elucidated by Wiederhorn and Krause.[13] They recognized that a substructure of small grains plus binder phase is present between the large rigid aggregate particles, and that it is this fine grain-size interaggregate microstructure which represents an easy path for dissolution and mass transport of the rate-controlling crystalline phase. After Ref. 13 the deformation occurs more easily within the fine grain-size bonding structure, leading to an effective interagglomerate viscosity of the bond phase that is smaller than in the absence of the fine interagglomerate grains. In the present investigation, evidence of increasing volume fractions of the fine grain-size interagglomerate microstructure with increasing MZA content were found in metallographic examinations as described in Section 3.1. This observation is taken as a further explanation of the decrease of the creep resistance due to the addition of MZA.

A further experimental result that emphasizes the role of the intergranular amorphous phase in the creep process of refractories is the work of Evans, Wilshire and co-workers.[9,11,12] In both CaO/MgO-based doloma refractories[9,11] and in magnesia refractories[12] it was observed that the creep rate increased drastically (up to a factor of 30) when the impurity level, specifically Fe_2O_3, was increased by intentional doping. It must be supposed that the Fe_2O_3 impurities were dissolved in the silicate-based glass phase. Due to its trivalent state, Fe^{3+} is known to substitute Si–Si bonds, thereby reducing the viscosity of the glass and accelerating the creep process.

4.3 Comparison with previous creep studies

In Fig. 11, the results of the present creep investigation are compared with creep data from previous creep studies. The comparison is limited to materials of similar basic compositions, i.e. other high-alumina refractories. Creep data of such materials were reported by Burdick and Day,[7] Matsumara *et al.*,[10] Chien *et al.*[19] and Hou and Kröger.[20]

To compare the results measured at different applied stresses, the data were normalized to a common stress of 1 MPa before plotting them in Fig. 11. For that, the stress exponent n given in the respective paper was used, or, if no stress exponent was indicated, $n = 1$ was assumed. As can be seen from Fig. 11, the creep data at a given temperature cover a range of about three orders of magnitude.

The spread of the data must be attributed to differences in both the grain size and glassy phase content of the various materials investigated. Unfortunately, the grain size is not reported in most of the papers, with the exception of Ref. 20 where creep rates of three different aluminas having grain sizes of 6, 35 and 55 μm, respectively, were measured. For the comparison of Fig. 11 the data of the 35 and 55 μm grain size material were selected since this figure is close to the lower limit of the grain-size range of the tabular alumina given in Table 1.

The glass-phase content of the high-alumina refractories studied in Refs 19 and 20 was 33–44% and 1%, respectively. For the refractories of the present investigation, a value between 10 and 20% seems to be a reasonable assumption. The creep data of these three studies are ranked in the same sequence in Fig. 11: the data sets of Refs 19 and

20 form the upper and lower boundary of the experimental data whereas the creep data of the present study are intermediate. Thus, it may be concluded that the fundamental microstructural feature that controls the creep rate of these refractories is the volume content of the glassy phase.

5 Conclusions

It was shown previously in Ref. 14 that the addition of a fused mullite–zirconia aggregate results in a considerable improvement of the work of fracture and the thermal shock resistance of high-alumina refractories. Unfortunately, high-temperature mechanical properties such as the strength and creep resistance are deteriorated by increasing amounts of MZA in the microstructure as is demonstrated by Fig. 9. Thus, to take full advantage of zirconia-induced microcrack toughening of the high-alumina refractories studied here, a balance must be achieved between the opposing influences of MZA on the mechanical properties. This may be obtained by optimizing the MZA content for a given application.

Acknowledgement

The authors are grateful to Magnesita, Alcoa, FAPESP, CNPq, and DAAD for providing materials and funds for this work. The authors also thank Professor R. C. Bradt for comments regarding the manuscript.

References

1 Bradt, R. C., Twenty first century refractories. In *Refractory Raw Materials and High Performance Refractory Products*, (Proceedings of the Second International Symposium on Refractories), eds Z. Xiangchong, L. Jiaquan, Y. Xingjian, & L. Maoqian. International Academic Publishers, Beijing, 1992, pp. 15–21; for a Chinese translation see: *J. Chinese Ceram. Soc.*, **21** (1993) 169–75.

2. Ainsworth, J. H. & Kaniuk, J. A., Creep of refractories in high temperature blast furnace stoves. *Am. Ceram. Soc. Bull.*, **57** (1978) 657–9.
3. Evans, R. W., Scharning, P. J. & Wilshire, B., Constitutive equations for creep of a fired doloma refractory. *Br. Ceram. Trans. J.*, **85** (1986) 63–5.
4. Evans, R. W. & Wilshire, B., *Creep of Metals and Alloys*. The Institute of Metals, London, 1984.
5. Clements, J. F. & Vyse, J., Creep measurements on some high-alumina refractories. *Trans. Brit. Ceram. Soc.*, **65** (1966) 59–85.
6. Hulse, C. O. & Pask, J. A., Analysis of deformation of a fireclay refractory. *J. Am. Ceram. Soc.*, **49** (1966) 312–18.
7. Burdick, V. L. & Day, D. E., Creep of high-alumina refractories. *Am. Ceram. Soc. Bull.*, **48** (1969) 1109–13.
8. Trostel, L. J., Deformation of oxide refractories. In *Deformation of Ceramics Materials*, eds R. C. Bradt & R. E. Tressler. Plenum Press, New York & London, 1974, pp. 339–60.
9. Coath, J. A. & Wilshire, B., The influence of variations in composition on the creep behaviour of doloma. *Ceramurgia Int.*, **4**, (1978) 66–70.
10. Matsumura, I., Hayashi, Y., Hiyama, Y. & Ijiri, A., Refractoriness under load and hot creep measurements. *Taikabutsu Overseas*, **2** (1982) 36–42.
11. Evans, R. W., Scharning, P. J. & Wilshire, B., Creep of CaO/MgO refractories. *J. Mater. Sci.*, **20** (1985) 4163–8.
12. Evans, R. W., Scharning, P. J. & Wilshire, B., Factors affecting the creep strength of magnesia refractories. *Br. Ceram. Trans. J.*, **84** (1985) 108–10.
13. Wiederhorn, S. M. & Krause, R. F., Effect of coal slag on the microstructure and creep behavior of a magnesium–chromite refractory. *Am. Ceram. Soc. Bull.*, **67** (1988) 1201–10.
14. Pandolfelli, V. C., Salvini, V. R., Brant, P. O. R. C., Noronha, R. T. T. & Mattos, U., Influence of mullite zirconia aggregate addition on the thermomechanical properties of high-alumina refractories. *Proc. Unified International Technical Conference on Refractories — UNITECR 93*, ed. Alafar, São Paulo, Brazil, 1993, pp. 282–91.
15. *Phase Diagrams for Ceramists*, ed. M. K. Reser. The American Ceramic Society, Columbus, USA, 1980.
16. Kingery, W. D., Bowen, H. K., & Uhlmann, D. R., *Introduction to Ceramics*. 2nd Edition, John Wiley & Sons, New York, 1976, p. 589 f.
17. Dörre, E. & Hübner, H., *Alumina. Processing, Properties and Applications*. Springer-Verlag, Berlin, 1984, pp. 154–73.
18. Monkman, F. C. & Grant, N. J., An empirical relationship between rupture and minimum creep rate in creep-rupture tests. Proc. *ASTM*, **56** (1956) 593–620.
19. Chien, Y. T., Lee, T. F., Pan, H. C. & Ko, Y. C., Effect of Cr_2O_3 on creep resistance of high alumina bauxite refractories. *Am. Ceram. Soc Bull.*, **63** (1984) 915–18.
20. Hou, L. D. & Kröger, F. A., Creep in Polycrystalline Al_2O_3: Si. *Mater. Sci. Lett.*, **3** (1984) 993–6.

Journal of the European Ceramic Society 15 (1995) 921–928
© 1995 Elsevier Science Limited
Printed in Great Britain. All rights reserved
0955-2219(95)00052-6
0955-2219/95/$9.50

Yttria–Alumina–Silica Glasses with Addition of Zirconia

P. Vomacka & O. Babushkin

Department of Engineering Materials, Luleå University of Technology, S-951 87 Luleå, Sweden

(Received 25 May 1994; revised version received 18 February 1995; accepted 29 February 1995)

Abstract

ZrO_2-free glasses and glasses containing ZrO_2 in the system Y_2O_3–Al_2O_3–SiO_2 have been investigated. Properties of compositions fired in nitrogen at 1600, 1650 and 1700°C have been assessed. The solubility limit of ZrO_2 in yttrium aluminosilicate liquids with a high content of Y_2O_3 at 1700°C was determined to be 6 wt%. The hardness and density of the ZrO_2-containing glasses were slightly increased compared to the ZrO_2-free glass; y-$Y_2Si_2O_7$ (at temperatures <1300°C) and β-$Y_2Si_2O_7$ (at temperatures >1300°C) monoclinic phases are the main products formed during the crystallization. An unidentified intermediate phase rich in Y, Al and Si was observed to undergo a transformation at temperatures ≥1200°C resulting in the formation of the β-$Y_2Si_2O_7$ phase.

1 Introduction

Silicon nitride and sialon ceramics are among the most promising materials for use in structural applications at high temperatures due to their outstanding combination of mechanical, chemical and thermal properties. Processing of these materials to near-theoretical density requires the use of sintering aids to provide a medium for liquid-phase sintering since the low self-diffusivity of Si_3N_4 does not allow densification by solid-state sintering.[1] Among the many oxides studied, Y_2O_3 is one of the most useful as a sintering additive, both in terms of the refractory nature of the resulting microstructures and in terms of its oxidation resistance. Alumina is often added to enhance sinterability. On cooling, these two oxides, together with SiO_2, appearing naturally on the surface of all silicon nitride powders, form a glass.[2] The softening of this glassy phase at high temperatures reduces mechanical strength and the upper-use temperature.

Two possible approaches to eliminate the glassy phase from the final microstructure are: (i) heat treatment to promote crystallization of the amorphous phases and (ii) alteration of the glass composition to increase the ease of crystallization.[3] Two-stage heat treatment, using the temperature of maximum nucleation rate for the first stage, followed by a higher annealing temperature to induce growth, has been suggested.[2] Other parameters also affect crystallization in the intergranular regions of Si_3N_4 ceramics such as the thickness of these regions. While crystallization of the secondary-phase pockets is possible in most systems, glassy material always remains at the grain boundaries with only the exception of special boundaries.[4] Clarke[5] proposed that an equilibrium intergranular film thickness exists for each material composition.

The amorphous grain-boundary phase composition in Si_3N_4 containing yttria and alumina as sintering additives can be simulated by glasses in the Y_2O_3–Al_2O_3–SiO_2 system. The first major study of the Y_2O_3–Al_2O_3–SiO_2 system was reported by Bondar and Galakov,[6] who developed a phase diagram in 1964. Recently Arita *et al.*[2] reviewed the crystallization studies in yttria–alumina–silica glasses. Several investigations have been carried out on other properties of yttria–alumina–silica glasses.[7–15] It was found that the density, refractive index, microhardness and thermal expansion of these glasses vary significantly with the Y_2O_3 content. The yttria–alumina–silica glasses have high thermal expansion considering their high T_g. The high microhardness indicates good abrasion resistance. The chemical durability in distilled water is very high.

Typical glass compositions for sialons are in the ternary eutectic 'trough' of the Y_2O_3–Al_2O_3–SiO_2 system with nitrogen solubility and stable glass-forming ability extending to between 20 and 30 eq.%.[16] The amorphous grain-boundary phase composition in Y-sialon materials can be simulated

by oxynitride glasses in which nitrogen is substituted for oxygen in the Y_2O_3–Al_2O_3–SiO_2 system to produce a more tightly linked glass network. It has been shown that the glassy phase in β-sialon material, with additions of yttria, can be crystallized to yttrium aluminum garnet—YAG—by a post-sintering heat treatment. The YAG crystallization requires either simultaneous Si_2N_2O formation or accommodation of excess Si and N within β-sialon.[17] Crystallization behaviour in oxynitride glasses has been investigated by several researchers. Leng-Ward and Lewis[7] studied glasses having compositions with a constant Y:Si:Al ratio of 1·04:1·27:1·27 with nitrogen contents ranging from 0 to 30 eq.% and reported the replacement of the yttrium disilicate ($Y_2Si_2O_7$) by yttrium aluminum garnet with increasing nitrogen content at 1250°C for 40 h when nitrogen was mainly incorporated into Si_2N_2O. Annealing of the nitrogen glasses at 1100°C produced partial crystallization involving an intermediate phase related to nitrogen-wollastonite ($Y_2Si_2O_4N_2$). Loehman[14] investigated glasses lying on the Y_2O_3–SiO_2–AlN plane of the Y–Si–Al–O–N system and found a general trend to formation of $Y_2Si_2O_7$ as the predominant crystalline phase at 1000, 1100 and 1200°C and longer times. Five intermediate phases (yttrium silicates, yttrium aluminum silicates or nitrogen apatite — $Y_4Si_4O_{11}N_2$) were also observed. Dinger *et al.*[18] studied crystallization of a glass having a composition of $Y_{0.26}Si_{0.30}Al_{0.11}ON_{0.11}$ with the crystallization proceeding by a heterogeneous nucleation mechanism, with intermetallic iron silicides acting as nuclei for the columnar dendritic y-$Y_2Si_2O_7$ species. After secondary crystallization of $YSi_2AlO_4N_2$ in interdendritic regions at 1200°C, the high-temperature polymorph of $Y_2Si_2O_7$ (δ_2–$Y_2Si_2O_7$) formed and became the predominant crystalline phase in glass crystallized at 1300°C and 1400°C. Besson *et al.*,[19] investigating a glass with a similar composition to that of Dinger *et al.*[18] containing 17 eq.% of nitrogen, observed $Y_2Si_2O_7$ in the α form below 1200°C and the β form above this temperature. Crystallization of the YAG phase at 1100°C and $AlYO_3$ with Si_2N_2O at 1250°C and 1300°C was also observed. O'Meara and Dunlop[20] studied crystallization of glass with the composition 53 wt% Y_2O_3, 17 wt% Al_2O_3 and 30 wt% SiO_2 with additions of 8–15 wt% Si_3N_4 at 1200°C for 12 h and found $Y_2Si_2O_7$ (α, β) Si_2N_2O and YAG.

Since nucleation and growth of secondary crystalline phases are unlikely processes in grain boundaries or pockets in Si_3N_4-based ceramics, the full crystallization of the glassy phase in these materials may be difficult. Complete elimination of this glassy phase might be achieved by another mechanism, namely the remaining intergranular phase may form a crystalline solid solution phase. Zirconia provides a good example of this behaviour since its structure can accept considerable amounts of oxides in solid solution. The microstructure of sintered Si_3N_4–$ZrO_2(Y_2O_3)$ ceramics contains extremely small amounts of intergranular phase.[21–25]

Zhao *et al.*[26] found that addition of ZrO_2 to yttria–alumina–silica glasses as a nucleating agent could shorten the incubation period of nucleation and increase the rate of nucleation. Crystallization studies reported by Drummond[3] on three different systems showed that the addition of nucleating agents can result in crystallization of the intergranular phases.

The present study attempts to simulate the intergranular phase in silicon nitride-based ceramics by an yttria–alumina–silica glass with an addition of zirconia. First, three ZrO_2-free powder mixtures were fired at different temperatures to assess their glass-forming tendency on furnace cooling and the obtained glasses were characterized. Following this, the solubility limit of ZrO_2 in a chosen composition at 1700°C was determined by producing a series of glasses with between 0 and 11 wt% ZrO_2. These ZrO_2-containing glasses were characterized. The crystallization behaviour at different temperatures of an appropriate glass with the addition of 6 wt% zirconia was studied.

2 Experimental Procedure

2.1 Sample preparation

The experimental conditions and the composition of all the samples are given in Table 1.

Three powder mixtures in the Y_2O_3–Al_2O_3–SiO_2 system located as indicated in Fig. 1 were fired at 1600, 1650 and 1700°C to determine the glass-forming tendency on furnace cooling (compositions 1A–3C). Samples were prepared from high-purity Y_2O_3, Al_2O_3 and SiO_2 powders (Rhone Poulenc, Alcoa Chemicals, and Johnson Matthey Alfa Products, respectively). The powders were weighed in a precision balance, dry-mixed in polyethylene containers on a Siemens roller mill for 10 h and sieved. Batches of approximately 20 g each were then mechanically compacted into molybdenum crucibles and fired in a nitrogen atmosphere (pressure 0·17 MPa) at temperatures of 1600, 1650 and 1700°C for 3 h. The heating rate up to the firing temperatures was 5°C/min, the cooling rate from the firing temperatures to 1400°C was 20°C/min, from 1400–950°C, 15°C/min and from 950 to 500°C, 10°C/min. The

Table 1. Composition and experimental condition of the studied glasses

	Composition (wt%)					*Experimental conditions*		
No.	Y_2O_3	Al_2O_3	SiO_2	Si_3N_4	ZrO_2	*Firing temp. (°C)*	*Fired in*	*Phases after cooling from firing temp.*
1A	55·3	16	28·8			1600	Nitrogen	$Y_{4.67}(SiO_4)_3O$ $Al_5Y_3O_{12}$ AlYO3 amorphous
1B	55·3	16	28·8			1650	Nitrogen	$Y_{4.67}(SiO_4)_3O$ $Y_2Si_2O_7$ amorphous
1C	55·3	16	28·8			1700	Nitrogen	$Y_{4.67}(SiO_4)_3O$ amorphous
2A	51·4	19·9	28·8			1600	Nitrogen	$Al_5Y_3O_{12}$ Y_2SiO_5 $Y_2Si_2O_7$ amorphous
2B	51·4	19·9	28·8			1650	Nitrogen	$Y_{4.67}(SiO_4)_3O$ $Y_2Si_2O_7$ amorphous
2C	51·4	19·9	28·8			1700	Nitrogen	$Y_2Si_2O_7$ amorphous
3A	46·9	24·3	28·8			1600	Nitrogen	$Al_5Y_3O_{12}$ $Y_2Si_2O_7$ amorphous
3B	46·9	24·3	28·8			1650	Nitrogen	Amorphous
3C	46·9	24·3	28·8			1700	Nitrogen	Amorphous
4	43·1	22·4	26·5	8		1650	Nitrogen	Amorphous
5	46·9	24·3	28·8			1600	Air	Amorphous
6	46	23·8	28·2		2	1700	Nitrogen	Amorphous
7	44·6	23·1	27·3		5	1700	Nitrogen	Amorphous
8	44·1	22·8	27·1		6	1700	Nitrogen	Amorphous
9	43·7	22·5	26·8		7	1700	Nitrogen	$Y_{0.15}Zr_{0.85}O_{1.9}$ amorphous
10	43·1	22·4	26·5		8	1700	Nitrogen	$Y_{0.15}Zr_{0.85}O_{1.9}$ amorphous
11	42·7	22·1	26·2		9	1700	Nitrogen	$Y_{0.15}Zr_{0.85}O_{1.9}$ amorphous
12	42·2	21·9	25·9		10	1700	Nitrogen	$Y_{0.15}Zr_{0.85}O_{1.9}$ amorphous
13	41·7	21·6	25·6		11	1700	Nitrogen	$Y_{0.15}Zr_{0.85}O_{1.9}$ amorphous

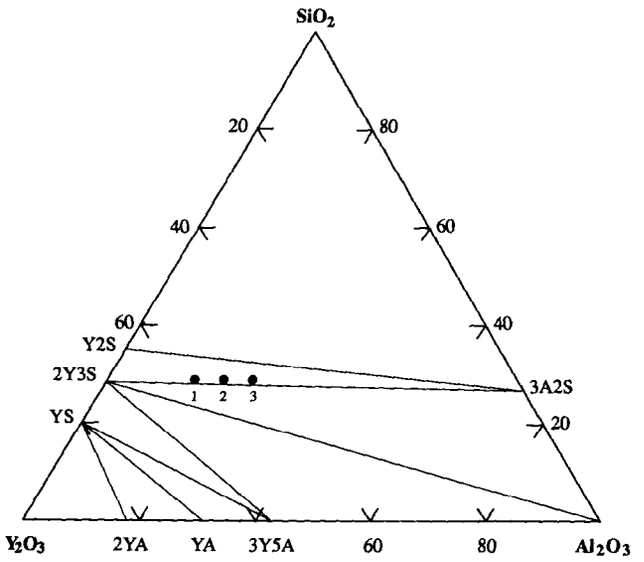


Fig. 1. The Al_2O_3–Y_2O_3–SiO_2 subsolidus phase diagram[6] with the powder mixtures (1, 2, 3) (YS = $Y_2O_3{\cdot}SiO_2$; Y2S = $Y_2O_3{\cdot}2SiO_2$; 2Y3S = $2Y_2O_3{\cdot}3SiO_2$; YA = $Y_2O_3{\cdot}Al_2O_3$; 2YA = $2Y_2O_3{\cdot}Al_2O_3$; 3Y5A = $3Y_2O_3{\cdot}5Al_2O_3$; 3A2S = $3\ Al_2O_3{\cdot}2SiO_2$).

cooling rate was the natural cooling rate of the furnace (cold wall vacuum/pressure furnace with a graphite heater) after it has been switched off. No mass changes were observed.

A glass with composition 4, i.e. with the addition of 8 wt% Si_3N_4 (KemaNord Industrikemi) was prepared at 1650°C using the same procedures as described above; this was used for comparison of the hardnesses of the produced glasses. Glass with composition 5 was prepared in air, also for comparison when subsequently characterizing glasses made in nitrogen. A batch of 20 g was fired in an alumina crucible at 1600°C for 1 h using a rapid high-temperature furnace (maximum temperature of 1600°C).

To evaluate the solubility of zirconia in the yttrium aluminosilicate liquid at 1700°C, increasing amounts of unstabilized zirconia powder (Sigma Chemical) were added to composition 3C to give compositions 6–13 of the type $x ZrO_2$ + (100-x) (46·9 Y_2O_3 · 24·3 Al_2O_3 · 28·8 SiO_2) where x (in

wt%) varied between 0 and 11. The above mixing and firing procedures were used with batches of approximately 10 g each. The firing temperature was 1700°C.

A large 100g batch of composition 8 with 6 wt% of zirconia was also fired applying the same procedures. This glass was used to investigate crystallization of an yttria–alumina–silica glass containing zirconia. To improve the mixing efficiency of such a large batch, propanol was used as the mixing medium.

2.2 Glass characterization

Powder X-ray diffraction (Phillips X-ray diffractometer, CuK_α radiation) was performed on the furnace-cooled specimens to check for crystallization during cooling, to determine the solubility limit of zirconia and to identify crystalline phases in zirconia-containing glass-ceramics after the heat treatment. The lower limit of detectability of the technique lies around 2–5 wt% of a given phase. Differential thermal analysis (DTA) was carried out in a nitrogen atmosphere using an Al_2O_3 powder reference standard and a heating rate 10°C/min. The infrared spectra (IR) were measured using a Perkin-Elmer 1760 X Fourier transform spectrometer equipped with a triglycine sulphate (TGS) detector. The measurements were carried out on discs pressed from powdered samples mixed with KBr. A microhardness tester with a diamond indenter was used to measure Vickers hardness. A load of 200 g was applied for 15 s on the sample whose surface had been polished with a 3-μm spray diamond. At least 10 indentations were made on each sample, the hardness being calculated on the basis of the average length of the indentation diagonals. The density was measured with Archimedes' method, using water as the suspending medium. SEM investigations were carried out using a CamScan S4-80DV electron microscope. The nitrogen contents of the glasses were determined on powdered samples using commercially available equipment, the Leco nitrogen determinator TN-414.

2.3 Crystallization of an Yttria–Alumina–Silica glass containing zirconia

The investigation was carried out on glass composition 8 with 6 wt% of zirconia using an alumina tube furnace with flowing nitrogen. Pieces of approximately 1 g (7 × 7 × 4 mm) were placed in a Si_3N_4 powder bed in alumina–silica boats and heat-treated at 50°C intervals between 950 and 1400°C for 1 h with a heating rate of 250°C/h. After the heat treatment, the samples were removed from the high-temperature zone and cooled rapidly to room temperature in the cold zone, while still in the nitrogen atmosphere.

Table 2. Glass transition temperatures for compositions 3B and 3C from DTA analysis

Composition	*Firing temp. (°C)*	T_g *(°C)*
3B	1650	900
3C	1700	920

3 Results and Discussion

3.1 Yttria–alumina–silica glasses

Table 1 summarizes the results of phase identification of samples furnace-cooled after firing. Only compositions 3B and 3C fired at 1650 and 1700°C gave fully amorphous material (transparent grey-coloured glasses). According to the equilibrium phase diagram,[6] phases expected after cooling from the firing temperatures were yttrium oxide silicates (Y2S = $Y_2O_3.2SiO_2$ and 2Y3S = $2Y_2O_3{\cdot}3SiO_2$) and mullite (3A2S = $3Al_2O_3{\cdot}2SiO_2$). With the exception of Y2S, these phases were not found after the furnace cooling, probably because the cooling conditions were far from equilibrium; it should also be noted that the existence of the 2Y3S phase has not been confirmed and has been questioned.[8,10] In some cases another yttrium oxide silicate phase ($Y_{4.67}[SiO_4]_3O$—JCPDS: 30-1457) was identified instead.

Results from DTA analysis of glasses 3B and 3C are shown in Table 2 and indicate a shift in glass transition temperature. Loehman[13–15] and Ding *et al.*[27] have reported a similar shift of T_g to a higher temperature with increasing nitrogen content.

Hardness of glass can also be an indicator of composition changes. For example, Makishima *et al.*[11] compared the Vickers hardness (200 g, 15 s) of an optical glass containing PbO (4·6 GPa) with an yttria–alumina–silica glass (8·2 GPa). It was found by Hyatt and Day[9] that glasses of high Y_2O_3 content were harder. As shown by Loehman,[13–15] increasing the nitrogen content increases the hardness of the yttria–alumina–silica glasses due to the nitrogen substitution for oxygen in the network to produce a more highly cross-linked structure. Here, the hardnesses of four glasses with the compositions 3B, 3C, 4 and 5 fired under different conditions were examined (Table 3). As expected, the lowest value of Vickers hardness was found for the glass fired in air and the highest for the glass prepared in nitrogen with the addition of Si_3N_4 and containing 1 wt% of nitrogen. Glasses fired in 1650 (≤ 0·1 wt% of

Table 3. Vickers hardness (200 g, 15 s) and density of the selected glasses

Composition	*Firing temp. (°C)*	*VH (GPa)*	*Density (g cm^3)*	*Fired in*
3B	1650	7·69 ± 0·24	3·59	Nitrogen
3C	1700	7·96 ± 0·46	3·63	Nitrogen
5	1600	7·06 ± 0·32	3·54	Air
4	1650	9·22 ± 0·11	3·84	Nitrogen

nitrogen) and 1700°C (≤0·1 wt% of nitrogen) exhibited intermediate values. The results in the present work are therefore comparable to those reported in the above-mentioned studies.[9,11,13–15] Results of the density measurements are also included in Table 3 and are in a good agreement with previously reported data.[27]

The infrared spectra (Fig. 2) of glasses with compositions 3A, 3B, 3C and 5 revealed their structure to be a continuous, closed network. The spectrum of the sample melted at 1600°C (3A) is characterized by the presence of two absorption bands located at 920 and 1100 cm^{-1}. They are associated with the cooperative antisymmetric stretching motion of silica tetrahedra containing bridging Si–O–Si and non-bridging Si–O$^-$ oxygen bonds.[28] The number and sequence of another group of absorption bands (770, 715, 680, 580 and 535 cm^{-1}) can be related to the YAG phase sintered as a standard at 1600°C in air. The spectra of glasses melted at 1650 and 1700°C (3B and 3C, respectively) are characterized by a broad absorption band at 890 cm^{-1}. This broad band is a result of stretching modes of both the Si–O–Si and the Si–O–Al(Y) bonds. These two spectra are very similar to the spectrum of glass melted in air (5). The small shift of this band at 1700°C to 870 cm^{-1} might be related to the contribution of the Si–N bonds,[27,29] but in view of the chemical analysis of the glasses, this contribution to the IR spectrum is

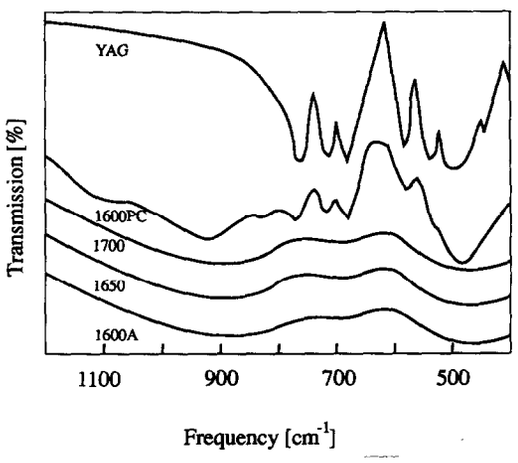


Fig. 2. IR spectra of glasses with compositions 3A, 3B, 3C and 5 prepared at different temperatures and YAG crystalline phases.

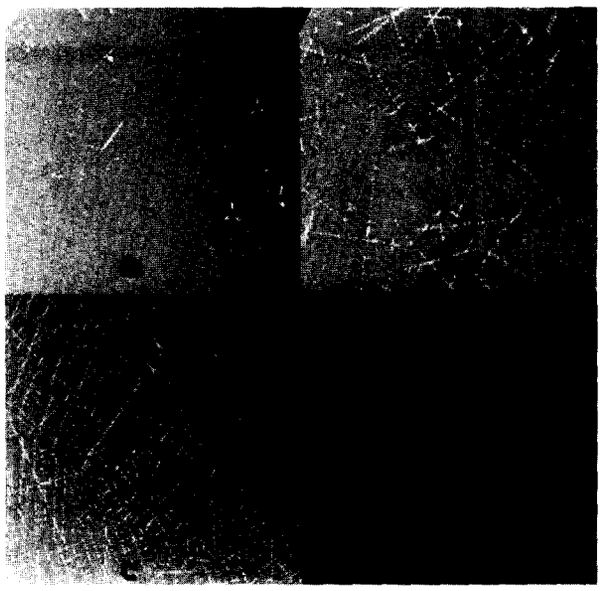


Fig. 3. Microstructures of zirconia-containing yttria–alumina–silica as-quenched glasses (backscatter image — 100×): (a) 7 wt% ZrO_2, (b) 9 wt% ZrO_2, (c) 11 wt% ZrO_2.

probably negligible. However, in general the location of the bond absorption at 870 and 890 cm^{-1} is determined by a strong contribution of Si–O–Al(Y) stretching.

3.2 Addition of zirconia

The X-ray diffraction patterns of compositions 6–8 revealed no crystalline phases to be present. A cubic phase of 'yttria-stabilized zirconia' having a composition of $Y_{0.15}Zr_{0.85}O_{1.93}$ was identified in compositions 9–13 containing more than 6 wt% of zirconia. SEM investigations revealed a dendritic structure of this phase as indicated in Fig. 3.

Results from DTA analysis are shown in Fig. 4. When evaluating the glass transition temperature (T_g) of the ZrO_2-containing glasses, no significant peak above background could be identified on the DTA charts but two endotherms were recorded at 1410 and 1425°C. No mass change occurred in association with the endotherms and therefore they were interpreted as representing melting reactions. The eutectic temperature of the base mixture of oxides without zirconia has been determined as 1430°C (Fig. 4). The lowest endotherm indicates that this eutectic is lowered to 1410°C by the addition of zirconia. The melting process is assumed to proceed as follows:

$$C_1 + C_2 + \ldots \rightarrow L_I + C(\text{compound(s)}) \rightarrow L_{II}$$
$$1410°C \qquad 1425°C$$

This implies that the second melting temperature is due to a monotectic reaction and that consequently liquids L_I and L_{II} are immiscible.[20] Table 4 includes Vickers hardness and density measurements. The densities of samples containing 7 and 8 wt% of zirconia are higher due to the

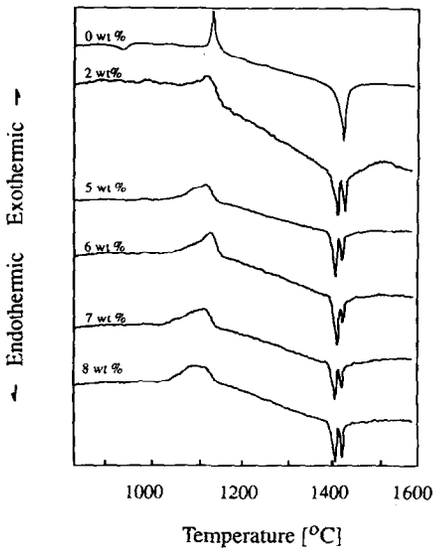


Fig. 4. DTA curves of glasses prepared at 1700°C with different ZrO_2-content.

higher density of the dendritic crystalline phase (5·959 g/cm^3).

3.3 Crystallization of a zirconia-containing glass

Composition 8 with the addition of 6 wt% of zirconia was subjected to heat treatments described in Section 2 in order to investigate the behaviour of ZrO_2 in the glass.

Samples treated at 950 and 1000°C still remained as clear transparent glasses. A sample treated at 1050°C was opaque but no traces of crystalline phases could be detected in its X-ray pattern. Heat treatments at higher temperatures resulted in glass-ceramics with a small amount of glassy phase retained in the structure. Peaks of cubic yttria-stabilized zirconia were found in all of the X-ray diffraction patterns. Other crystalline phases identified by X-ray diffraction analysis are listed in Table 5. They are consistent with those found in previous studies.[2] Yttrium disilicate ($Y_2Si_2O_7$) crystallized from the glass in the form of two polymorphs β (JCPDS-22-1103) and y (JCPDS-32-1448). Small traces of mullite ($Al_6Si_2O_{13}$) were present in all X-ray diffraction patterns.

The Al_2O_3 phase, expected because the existence

Table 4. Vickers hardness and density of zirconia-containing glasses

Composition	*ZrO_2 content (wt%)*	*VH (GPa)*	*Density (g cm^3)*
3C	0	7·96 ± 0·46	3·63
6	2	7·89 ± 0·20	3·69
7	5	8·09 ± 0·18	3·73
8	6	8·65 ± 0·22	3·76
9	7	8·73 ± 0·21	4·43
10	8	8·42 ± 0·53	4·44

Table 5. X-ray powder diffraction analysis for composition 8 with the addition of 6 wt% of zirconia heat treated in nitrogen for 1 h

Crystallization temp. (°C)	*Phase*
950	Clear amorphous glass
1000	Clear amorphous glass
1050	Opaque amorphous glass
1100	y-$Y_2Si_2O_7$, s; β-$Y_2Si_2O_7$, w; $Al_6Si_2O_{13}$, vw;
1150	y-$Y_2Si_2O_7$, s; β-$Y_2Si_2O_7$, w; $Al_6Si_2O_{13}$, vw;
1200	y-$Y_2Si_2O_7$, s; β-$Y_2Si_2O_7$, m $Al_6Si_2O_{13}$, vw;
1250	β-$Y_2Si_2O_7$, s; y-$Y_2Si_2O_7$, w; $Al_6Si_2O_{13}$, vw;
1300	β-$Y_2Si_2O_7$, s; y-$Y_2Si_2O_7$, w; $Y_3Al_5O_{12}$, vw; $Al_6Si_2O_{13}$, vw; $Al_6Si_2O_{13}$, vw
1350	β-$Y_2Si_2O_7$, s; y-$_3Al_5O_{12}$, vw; $Al_6Si_2O_{13}$, vw

s is strong, m is medium, w is weak and vw is very weak.

of the 2 $Y_2O_3{\cdot}3SiO_2$ phase has been questioned, was detected neither by X-ray nor SEM analysis, which confirms results by Hyatt and Day.[9] A very small amount of YAG ($Y_3Al_5O_{12}$) was identified after the 1300 and 1350°C treatments by X-ray analysis. It is important to emphasize that the specimens were heat-treated at the elevated temperatures for only 1 h and then quenched very rapidly. Therefore, equilibrium conditions mean reached and consequently some additional, probably intermediate, phases were observed. Although they could not be identified using JCPDS tables, the existence of such phases has been reported in earlier studies.[2,3] Dinger *et al.*[18] reported the existence of a low-temperature, impurity-stabilized y-polymorph of $Y_2Si_2O_7$, that transforms to α-$Y_2Si_2O_7$ upon heating at 1200°C and to δ_1 and δ_2 upon heating above 1200°C. Drummond[3] observed the formation of the β-$Y_2Si_2O_7$ polymorphs when adding zirconia as a nucleating agent. The crystallographic data for the compounds in the Y_2O_3–$NSiO_2$ system have been summarized recently by several investigators (see, e.g. Refs 30 and 31).

SEM investigations in this study revealed that the crystallization of the glass is probably governed by a number of mechanisms acting at different temperatures. The different types of phase transformation observed in the glass can be summarized as follows:

(i) crystallization of β-$Y_2Si_2O_7$;
(ii) crystallization of y-$Y_2Si_2O_7$;
(iii) crystallization of yttria stabilized ZrO_2 (Y–ZrO_2);
(iv) transformation of y-$Y_2Si_2O_7$, to β-$Y_2Si_2O_7$;
(v) transformation of a Y–Al–Si-rich phase to β-$Y_2Si_2O_7$.

At 1100°C, the sample is almost fully crystallized, with only a small amount of retained glassy

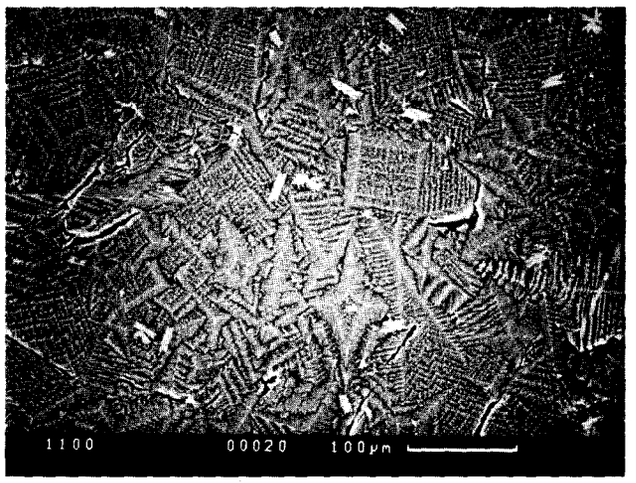


Fig. 5. Crystallization at 1100°C. (backscatter image — 200×).

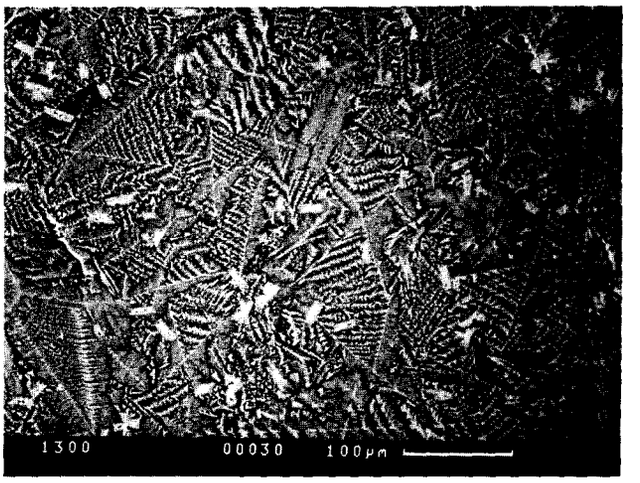


Fig. 7. Crystallization at 1300°C (backscatter image — 200×).

phase (Fig. 5). The y-$Y_2Si_2O_7$ is the dominant phase at this treatment temperature. At 1150 and 1200°C, a Y–Al–Si-rich phase appears in the microstructure and starts to transform to β-$Y_2Si_2O_7$ and probably mullite (Fig. 6). At 1300°C, the β-$Y_2Si_2O_7$ phase begins to dominate the microstructure (Fig. 7) and the y-$Y_2Si_2O_7$ phase also starts to transform to the β-$Y_2Si_2O_7$ phase while the phase transformation of the Y–Al–Si-rich phase continues. At 1350°C, the dominant phase is β-$Y_2Si_2O_7$. The microstructure begins to loose its dendritic appearance and the transformation of the y-$Y_2Si_2O_7$ phase to the β-$Y_2Si_2O_7$ phase continues (Fig. 8).

The transformation of the y- to the α-polymorph was not observed. At higher temperatures the y-$Y_2Si_2O_7$ polymorph starts to transform to the β-$Y_2Si_2O_7$ polymorph (stable at temperatures between 1225 and 1445°C in the binary Y_2O_3–SiO_2 system.[3,10]

4 Conclusions

Properties of yttria–alumina–silica compositions fired in nitrogen at 1600, 1650 and 1700°C have been assessed. The results are consistent with previous studies. ZrO_2 (6 wt%) can be dissolved in the investigated composition of the yttria–alumina–silica liquid at 1700°C. When larger amounts are added, a cubic crystalline phase of 'yttria-stabilized zirconia' with a composition of $Y_{0.15}Zr_{0.85}O_{1.9}$ forms. The hardness and density of the glass increased slightly with addition of ZrO_2·y-$Y_2Si_2O_7$ (at temperatures <1300°C) and β-$Y_2Si_2O_7$ (at temperatures >1300°C) monoclinic phases formed during the crystallization. Very small amounts of mullite in all cases, and yttrium aluminium garnet at 1300 and 1350°C, were also observed. An unidentified intermediate phase rich in Y, Al and Si was observed to undergo a transformation at temperatures ≥ 1200°C, probably resulting in the formation of the β-$Y_2Si_2O_7$ phase.

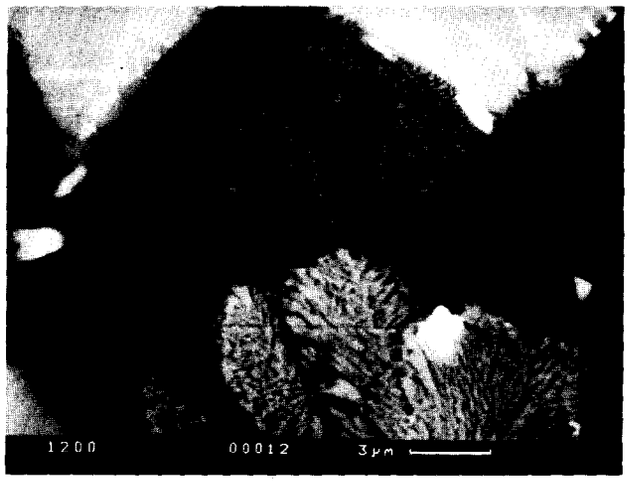


Fig. 6. Y–Al–Si-rich phase at 1200°C with part of a y-$Y_2Si_2O_7$ loose network and Y–ZrO_2 particles (backscatter image — 5000×).

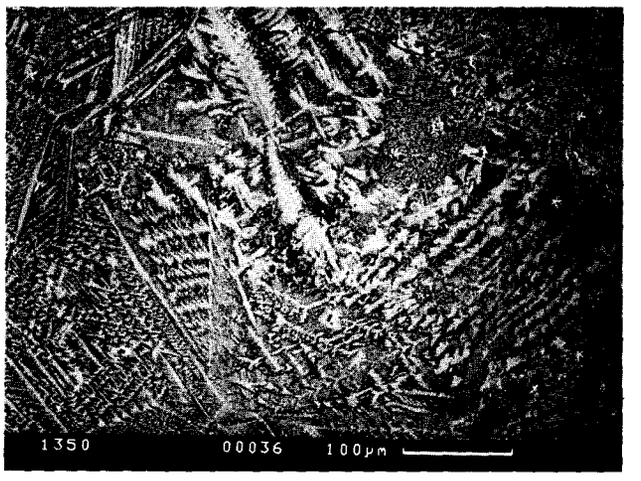


Fig. 8. Crystallization at 1350°C (backscatter image — 200×).

References

1. Cinibulk, M. K. & Thomas, G., Grain-boundary-phase crystallization and strength of silicon nitride sintered with a YSiAlON glass. *J. Am. Ceram. Soc.*, **73**(6) (1990) 1606–12.
2. Arita, I. H., Wilkinson, D. S. & Purdy, G. R., Crystallization of Yttria–alumina–silica glasses. *J. Am. Ceram. Soc.*, **75**(12) (1992) 3315–20.
3. Drummond, C. H., III, Glass-formation and crystallization in high-temperature glass-ceramics and Si_3N_4. *J. Non-Cryst. Solids*, **123** (1990) 114–28.
4. Kleebe, H.-J., Cinibulk, M. K., Cannon, R. M. & Ruhle, M., Statistical analysis of the integranular film thickness in silicon nitride ceramics. *J. Am. Ceram. Soc.*, **76**(8) (1993) 1969–77.
5. Clarke, D. R., On the equilibrium thickness of intergranular glass phases in ceramic materials. *J. Am. Ceram. Soc.*, **70**(1) (1987) 15–22.
6. Bondar, I. A. & Galakov, F. Y., Phase equilibria in the system Y_2O_3–Al_2O_3–SiO_2. *Izv. Akad Nauk. SSSR Ser Khim.*, **7** (1964) 1325–6.
7. Leng-Ward, G. & Lewis, M. H., Crystallization in Y–Si–Al–O–N glasses. *Mater. Sci. Engng.*, **71** (1985) 101–11.
8. Meara, C. O., Dunlop, G. L. & Pompe, R., Phase relationship in the system Y_2O_3–Al_2O_3–SiO_2. In *Proc. World Congress on High Tech Ceramics (6th CIMTEC)*, Milan, Italy, ed. P. Vincenzini. Elsevier Science Publishers, Amsterdam, 1986, pp. 265–70.
9. Hyatt, M. J. & Day, D. E., Glass properties in yttria–alumina–silica system. *J. Am. Ceram. Soc.*, **70**(10) (1987) C-283–7.
10. Drummond, C. H., III & Lee, W. E., Crystallization and characterization of Y_2O_3–SiO_2 glasses. *Ceram. Engng. Sci. Proc.*, **9**(9–10) (1988) 1343–54.
11. Makishima, A., Tamura, Y. & Sakaino, T., Elastic moduli and refractive indices of aluminosilicate glasses containing Y_2O_3, La_2O_3 and TiO_2. *J. Am. Ceram. Soc.*, **61**(5–6) (1978) 247–9.
12. Sedych, T. S., Pustilnik, A. I. & Mikheikin, V. I., Refractive indices in the system Y_2O_3–Al_2O_3–SiO_2 in the vitrification region. *Akad. Nauk SSSR, Neorg. Mater.*, **11**(6) (1975) 1153–4.
13. Loehman, R. E., Preparation and properties of yttrium–silicon–aluminum oxynitride glasses. *J. Am. Ceram. Soc.*, **62**(9–10) (1979) 491–4.
14. Loehman, R. E., Oxynitride glasses. *J. Non-Cryst. Solids*, **42** (1980) 433–46.
15. Loehman, R. E., Preparation and properties of oxynitride glasses. *J. Non-Cryst. Solids*, **56** (1983) 123–34.
16. Lewis, M. H., Crystallisation of grain boundary phases in silicon nitride and sialon ceramics. *Key Engng Mater.*, **89–91** (1994) 333–8. Trans Tech Publications, Switzerland.
17. Lewis, M. H., Bhatti, A. R., Lumby, R. J & North, B., The microstructure of sintered Si–Al–O–N ceramics. *J. Mater. Sci.*, **15** (1980) 103–13.
18. Dinger, T. R., Rai, R. S. & Thomas, G., Crystallization behaviour of a glass in the Y_2O_3–SiO_2–AlN system. *J. Am. Ceram. Soc.*, **71**(4) (1988) 236–44.
19. Besson, J. L., Billieres, D., Rouxel, T., Goursat, P., Flynn, R. & Hampshire, S., Crystallization and properties of a Si–Y–Al–O–N glass-ceramic. *J. Am. Ceram. Soc.*, **76**(8) (1993) 2103–5.
20. O'Meara, C. & Dunlop, G. L., Formation, crystallization and oxidation of selected glasses in the Y–Si–Al–O–N system. *J. Eur. Ceram. Soc.*, **8** (1991) 161–70.
21. Ekström, T., Transient liquid phase sintering of silicon nitride. In *Proc. Int. Ceramic Conference Austceram 90*, Perth, Australia, eds P. J. Darragh and R. J. Stead. Trans. Tech. Publications, 1990, pp. 586–91.
22. Knutson-Wedel, E. M., Falk, L. K. L. & Ekström, T., Si_3N_4 ceramics formed by HIP using additions of ZrO_2. In *Ceramics Today–Tomorrow's Ceramics*. Elsevier Science Publishers B.V., 1991.
23. Knutson-Wedel, E. M., Falk, L. K. L. & Ekström, T., Si_3N_4–ZrO_2 Composites with small Y_2O_3 and Al_2O_3 additions prepared by HIP. *J. Mater. Sci.*, **26** (1991) 4331–40.
24. Knutson-Wedel, E. M.., Falk, L. K. L. & Ekström, T., Microstructures and properties of Si_3N_4 ceramics formed by HIP using different oxide additives. In *Proc. 11th Risø Int. Symp. on Metallurgy and Materials Science*, Denmark, 1990.
25. Knutson-Wedel, E. M., Falk, L. K. L. & Ekström, T., Pressureless-sintered Si_3N_4–ZrO_2 composites with Y_2O_3 and Al_2O_3 additions. *J. Mater. Sci.*, **9** (1990) 823–6.
26. Zhao, J., Wang, L., Peng, G. & Wu, J. G., Effect of zirconia on the crystallization of grain boundary. *Proc. 4th Int. Symp. on Ceramic Materials and Components for Engines*, Gothenburg, Sweden, 1990.
27. Ding Yuquan, Ding Zishang & Jiang Zhonghua, Formation and properties of Y–Al–Si–O–N system in the grain boundaries of Si_3N_4 ceramics. *J. Non-Cryst. Solids*, **112** (1989) 408–12.
28. Lazarev, A. N., *Vibrational Spectra and Structure of Silicates*. Plenum Press, New York, 1972.
29. Sato, R. K., Bolvin, J. & McMillan, P. F., Synthesis and characterization of a SiAlON glass. *J. Am. Ceram. Soc.*, **73**(8) (1990) 2494–7.
30. Lee, W. E., Drummond, C. H. III, Hilmas, G. E. & Kumar, S., Microstructural evolution in near-eutectic yttrium silicate compositions fabricated from a bulk melt and as an intergranular phase in silicon nitride. *J. Am. Ceram. Soc.*, **73**(12) (1990) 3575–9.
31. Kumar, S. & Drummond, C. H. III, Crystallization of various compositions in the Y_2O_3–SiO_2 system. *J. Mater. Res.*, **7**(4) (1992).

Journal of the European Ceramic Society 15 (1995) 929–933
© 1995 Elsevier Science Limited
Printed in Great Britain. All rights reserved
0955-2219(95)00058-5
0955-2219/95/$9.50

Thermal Shock Resistance of $KZr_2P_3O_{12}$–$SrZr_4P_6O_{24}$ Ceramics

Biao Zhang & Jingkun Guo

Shanghai Institute of Ceramics, Chinese Academy of Sciences, Shanghai 200050, People's Republic of China

(Received 29 July 1994; revised 7 March 1995; accepted 10 March 1995)

Abstract

The thermal shock resistance of potassium strontium zirconium phosphate (KSZP) ceramics was investigated by quenching in water. The retained strength of the compositions with very low thermal expansion increased greatly after quenching. These compositions can withstand water quench from 1000°C and still retain their strength before quenching. The relationships between thermal shock resistance and strength, Young's modulus, thermal conductivity, thermal stress, and thermal expansion coefficient was discussed. The thermal shock resistance data measured was compared with that of calculated.

1 Introduction

Materials having high thermal shock resistance are needed for high-temperature applications. Generally, there are two principal ways to design and select materials to achieve high thermal shock resistance.[1] The first way involves the avoidance of fracture initiation, and the second is avoidance of catastrophic crack propagation. A figure of merit for thermal shock resistance is given by

$$R = \sigma/\alpha E \propto \Delta T_c \quad (1)$$

where ΔT_c is the maximum step change in temperature without causing fracture, σ the strength of the material, E Young's modulus and α the thermal expansion coefficient. To avoid fracture initiation by thermal shock, the favorable material characteristics include high strength and thermal conductivity (such as Sialon[2]), and low thermal expansion coefficient (such as LAS glass-ceramic and cordierite ceramic). Most of the structural ceramics have a high Young's modulus and a typical catastrophic decrease in the retained strength. However, to minimize the extent of crack propagation, high Young's modulus and low strength are required. These requirements of Young's modulus and strength are just opposite to those necessary for preventing crack initiation.[3] Hence, the microstructures that exhibit both high thermal shock resistance and high thermal shock damage resistance must be carefully designed. In this respect, ceramics with fine grain size, no defects on grain boundary and small porosity (homogenously distributed) are needed for obtaining high thermal shock resistance. In the case of aluminum titanate,[4] Si_3N_4–BN composite,[5] and Y–TZP,[6] low thermal expansion, microcrack, and large grain size are responsible respectively for their high thermal shock damage resistance. High anisotropic expansion induced microcracks at grain boundaries can restrain crack propagation caused by thermal shock. The increase of the contribution of the transformation toughening of large grain size Y–TZP prevent the thermal stress fracture. The present study was concentrated on the effects of thermal expansion on the thermal shock resistance of two KSZP compositions, $K_{1/2}Sr_{1/4}Zr_2P_3O_{12}$ and $K_{1/4}Sr_{3/8}Zr_2P_3O_{12}$, with magnesia (MgO) additions of 0–8 wt%.

2 Materials and Experimental

Compositions of KSZP with 0–8 wt% MgO are given in Table 1. The KSZP powders were synthesized through coprecipitation and the ceramics were prepared by pressureless sintering. Details of the preparation procedure were described in previous papers.[7,8] Sintering conditions and selected properties are shown in Table 1.

Thermal shock tests were conducted by measuring the retained bending strength after quenching samples from successively increasing temperatures into water at 0°C. The specimens were 2·5 × 5 × 25 mm in dimension. The strength and Young's modulus were measured by three point bending over a 20 mm span at a cross-head speed of 0·5 mm/min (Instron 1195). Each number is the mean

Table 1. Compositions and properties of KSZP ceramics

	Composition	*Sintering condition*		*Density*	*Young's modulus*	*Thermal conductivity at 500°C*	*Phases identified*
		T(°C)	*t(h)*	*(g/cm³)*	*(GPa)*	*(W/mK)*	
K2	$K_{1/2}Sr_{1/4}Zr_2P_3O_{12}$	1300	8	3·01		1·43	Single
K2M2	+2% MgO	1200	1	3·20	109	1·64	Single
K2M2H*	+2%MgO	1200	0·5	3·21	138		Single
K2M5	+5%MgO	1150	1	3·22	108	1·56	+ glass
K2M8	+8%MgO	1110	8	3·25	76	1·62	Two phases
K1	$K_{1/4}Sr_{3/8}Zr_2P_3O_{12}$	1350	2	3·11	—	—	Single
K1M2	+2%MgO	1200	8	3·25	95	—	+ glass
K1M5	+5%MgO	1200	2	3·26	79	—	Two phases
K1M8	+8%MgO	1100	8	3·30	84	1·65	Two phases

*Hot pressed.

result over 5 samples with a maximum dispersion of ±15 MPa.

The measurements for bulk thermal expansion were made on rectangular bars (4 × 4 × 50 mm) using a dilatometer (Model 402-3, Netzsch) from room temperature (RT) to 1000°C at a heating rate of 10°C/min.

The stresses of specimens were determined by using X-ray diffraction method[9] at fixed Ψ (Model D/Max-3A). Strains were determined from 142–143° diffraction angle (2θ) using CrKα radiation at $\Psi = 0°$ and $\Psi = 45°$ on a Φ 40 × 2·5 mm specimen. The total residual stresses (σ_s, includes macrostresses and microstresses) were calculated from the simplified equation:

$$\sigma_s = E \cdot \cot\theta \cdot \Delta 2\theta \cdot \pi/((2(1+\nu) \cdot \Delta \sin\Psi \cdot 180) \quad (2)$$

where Ψ the angle between sample surface and diffraction crystal plane, θ the diffraction angle, $\Delta 2\theta$ the difference of diffraction angle when $\Psi = 0°$ and $\Psi = 45°$, E Young's modulus, and ν Poisson's ratio.

Additionally, thermal conductivities were measured by using a laser heat-conductometer and a differential scanning calorimeter (Model DSC-4, Perkin Elmer).

3 Observations and Discussion

Figure 1 shows the flexural strength of the specimens with various compositions after quenching. The initial strength of K2M5 ceramic is retained up to a critical temperature difference ΔT_c (about 600–800°C) where a sudden decrease in the retained strength occurs. Other ceramics exhibit no instantaneous decline in strength prior to what might be interpreted as a ΔT_c, but do exhibit a more gradual reduction because of microcrack initiation and subcritical crack propagation before ΔT_c is reached. For K2M2 the thermal shock behavior is more complicated.

The retained strength of K2M2 increased markedly after thermal shock. A slight increment of retained strength after thermal shock were observed for K1M2, like that of low thermal expansion aluminium titanate ceramic.[10] It is clear that thermal shock predictions based on so many factors are critically dependent upon the accuracy of that data. The remarkable characteristics of K2M2 ceramic is its low thermal expansion and phase transition. Thermal expansion coefficients of KSZP ceramics are indicated in Table 2. K1 series

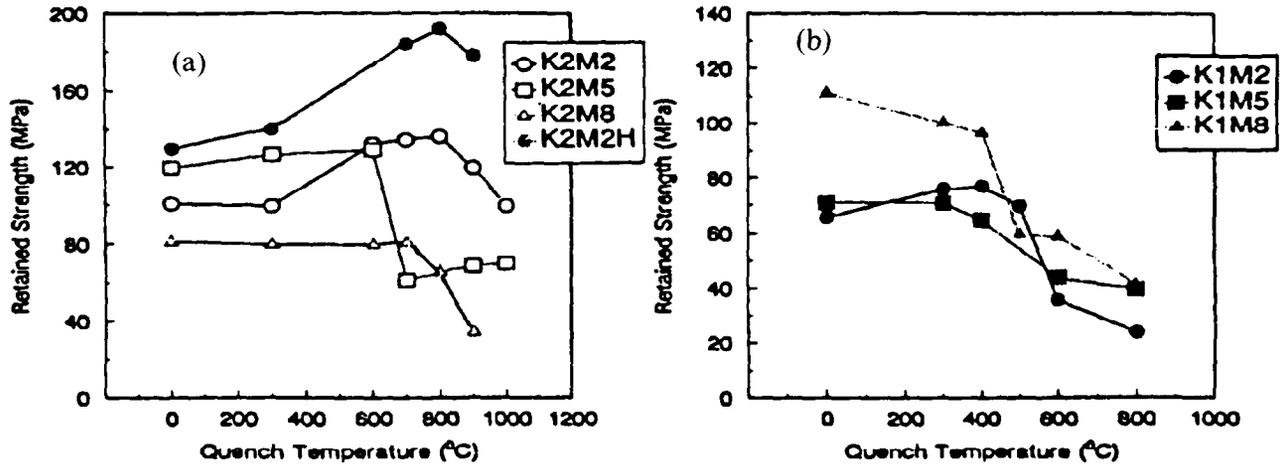


Fig. 1. Thermal shock resistance of (a) K2 series and (b) K1 series of ceramics.

Table 2. Thermal expansion coefficients ($\times 10^{-6}$/°C, RT–T°C) of KSZP ceramics

No.	100 (°C)	200 (°C)	300 (°C)	400 (°C)	500 (°C)	600 (°C)	700 (°C)	800 (°C)	900 (°C)	1000 (°C)
K2	-4·68	-4·16	-3·85	-3·16	-2·23	-1·43	-1·37	-1·44	—	—
K2M2	-1·81	-1·21	-0·55	0·39	1·05	1·19	1·25	1·35	1·46	1·52
K2M2H	-2·38	-1·54	-0·76	-0·25	0·97	1·05	0·75	0·93	1·11	1·72
K2M5	-0·93	-0·35	0·42	0·83	1·08	1·33	1·53	1·79	2·13	2·05
K2M8	-1·41	-1·10	-0·31	0·85	1·24	1·76	2·61	3·53	3·80	3·97
K1	0·21	0·62	0·99	1·30	1·57	1·81	1·92	2·01	—	—
K1M2	1·34	1·65	1·92	2·22	2·43	2·52	2·58	2·68	—	—
K1M5	1·85	2·12	2·44	2·78	2·95	3·03	3·17	3·13	—	—
K1M8	0·77	1·10	2·19	2·39	2·50	2·61	3·05	3·50	4·04	3·24

of ceramics exhibit an overall positive and high thermal expansion, while the thermal expansion coefficients of K2 series of ceramics are low or negative below 300°C. The thermal expansion anisotropy of KSZP is low compared with that of KZP.[8]

To clarify the thermal shock fracture behavior of K2 series ceramics, residual stresses after water quench were measured. The results are shown in Fig. 2. The negative value means compressive stress. The more negative the value, the larger the strength. The stress dependence of quenching temperature stand in direct contrast with each other between K2M2 and K2M5. Compressive stress of K2M2, the lower thermal expansion ceramic, increase with quenching temperature increase and has a sharp change from 300 to 600°C, and is in good agreement with strength variation (Fig. 1(a)). Compressive stress of K2M5, the larger thermal expansion ceramic, decrease with quenching temperature increase, and has a gradual decline. It is also corresponding to its thermal shock result.

Residual stress in single-phase polycrystalline ceramics are of two types: macrostresses and microstresses. Macrostresses generally are near the surface because of differences in processing (such as cutting, grading and quenching) between the surface and the interior. Microstresses arise because grains constrain if the grain is anisotropic. Experimental methods to be used for the determination of residual stress should take into account the two types of residual stress as well as the depth over which the method averages the measurements.[11] A method for separating the macrostresses from the microstresses has been developed by Noyan and Cohen.[12] In this work, the stresses were calculated approximately from eqn (2) as total stresses. Although unable to separate macrostresses from microstresses at these moments, the general trend of stress variation is enough to explain the thermal shock behavior.

As illustrated in Fig. 1(a), the pressureless sintered and hot pressed K2M2 ceramics exhibit similar behavior. Under optical and scanning electron microscope, no obvious cracks were observed. The reason why the significant improvement of residual strength of the K2M2 ceramic after thermal shock is that the ceramic has a very low thermal expansion and phase transition. Below 400°C, the ceramic exhibits negative expansion, whereas above 400°C, it is positive. A phase transformation occurs at 600°C in $K_{1/2}Sr_{1/4}Zr_2P_3O_{12}$ ceramic.[8] The cell volume of the high-temperature phase is larger than that of the low-temperature phase. The phase transition still exists in the K2M2

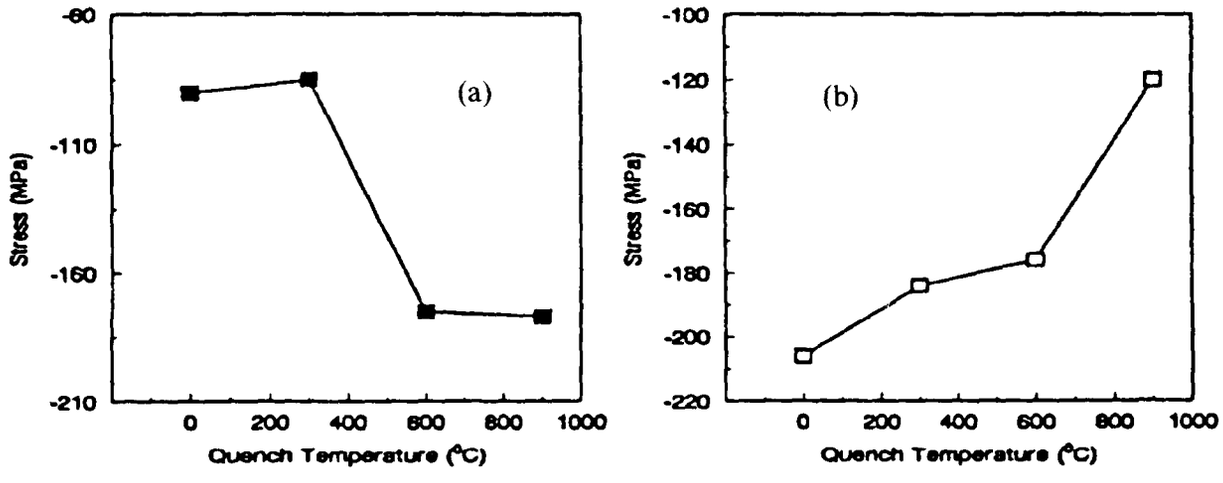


Fig. 2. Total stresses of (a) K2M2 and (b) K2M5 ceramics after water quench from high temperature.

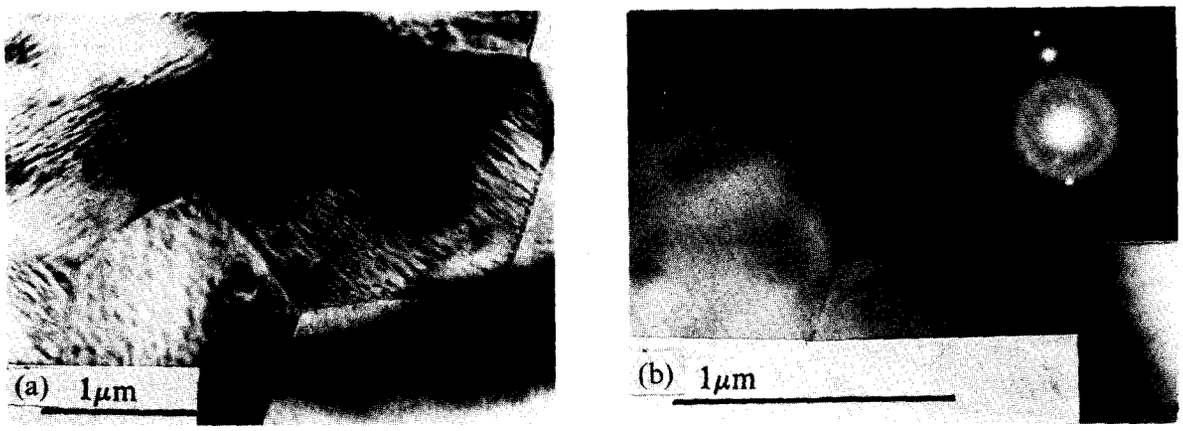


Fig. 3. Microstructure of grain boundaries: (a) bright-field micrograph showing clear boundaries K2M2, and (b) amorphous phase at triple-grain junction and electron diffraction pattern of K2M5 being attached.

ceramic, but it is restrained in K2M5 ceramic. During quenching, the surface region of the specimen cools quickly and shrinks until the temperature reaches 400°C and expands, but the core of the sample cools slowly and still contracts when the surface expands. The surface remains the high-temperature phase and the core transforms to the low-temperature phase. Therefore, the surface is constrained and compressive stresses were formed on the surface. The increment of retained strength occurred just as in strengthened glass. Another reason for high thermal shock resistance of the K2M2 ceramic is no glass phases at the intergranular regions, as suggested by Hoffmann[13] that the ΔT may be connected with the softening of glass phase. TEM micrographs (Fig. 3) show the clear boundaries and junctions of grains for the K2M2 ceramic, but for the K2M5 ceramic, an amorphous phase is observed at triple grain junctions. The residual strength of K2M5 after 1000°C water quenching was a little larger than that of 700°C water quench. This is because that the density of cracks caused by thermal shock increased with increasing ΔT.

For other ceramics, a gradual strength decay is observed. Normally, with most large-grain and large pore ceramics, the retained strength declines slowly when ΔT just exceeds ΔT_c. Relatively, the strength and density of the KSZP ceramics are low and are difficult to sinter, especially for K1 and K2 which have no addition of MgO. For this reason, the thermal shock tests were not conducted on K1 and K2 ceramics.

The application of eqn (1) to KSZP ceramics is shown in Fig. 4(a). The data shows a good fit to eqn (1). Precise theoretical calculations for thermal shock resistance based on material parameters is very difficult. The disagreement between experimental observations and predictions can be attributed to the difference in test methods and inexact property data,[14] especially temperature dependence of mechanical and thermal properties.

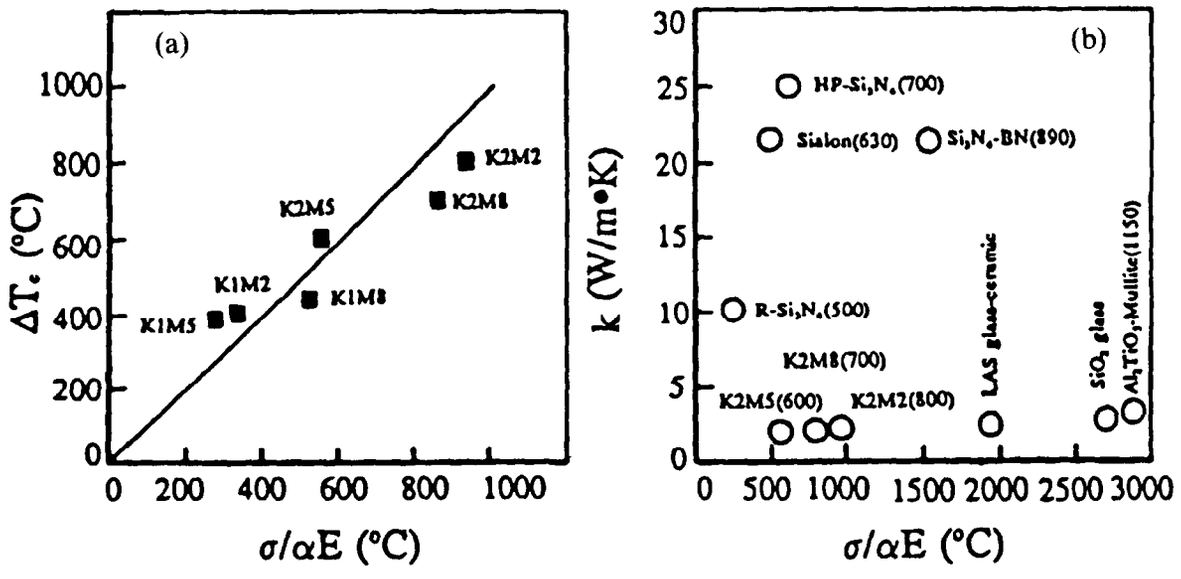


Fig. 4. (a) Thermal shock resistance of KSZP ceramics measured and described in eqn (1), (b) thermal conductivity and thermal shock resistance of SKZP and other ceramics (Refs 2, 5, and 10. The values in parentheses mean ΔT_c).

As is illustrated in Table 2, thermal expansion coefficients, especially low thermal expansion material, are not constant over all the temperature range. They vary significantly in different temperature ranges. It is not clear what an appropriate value for α and σ should be.

Figure 4(b) summarizes the most important properties (k, thermal conductivity, σ, strength, α, the coefficient of thermal expansion, and E Young's modulus) of high thermal shock resistant ceramics. It is indicated that there are two major categories of high ΔT_c ceramics, one with high strength and thermal conductivity, and another with low thermal expansion coefficient. To make an optimum material design and selection of high thermal shock resistant ceramics, guidelines on some factors are needed: high strength, toughness, thermal conductivity, low thermal expansion, less thermal expansion anisotropy resulting in microstructures that can cope with thermal stresses without developing creep cavitation.

4 Conclusions

$KZr_2P_3O_{12}$–$SrZr_4P_6O_{24}$ (0–8 wt% MgO) ceramics possessing low thermal expansion, high thermal shock resistance and high strength have been studied. Thermal expansion coefficients varied in the range of $-4{\cdot}68 \sim 3{\cdot}97 \times 10^{-6}$°C. The thermal shock behavior of low thermal expansion ceramics exhibited some interesting features. The retained strength and compressive stress on the surface of the K2M2 ceramic increased with increasing quench temperature (from 100 MPa at RT to 136 MPa at ΔT = 800°C for pressureless sintered and from 130 MPa at RT to 192 MPa at ΔT = 800°C for hot pressed K2M2 ceramic). The thermal expansion behavior, single phase microstructure, and phase transformation are responsible for its thermal shock behavior. The critical quenching temperature difference varied from 400 to 800°C for KSZP ceramics, which might be used as thermal barrier materials.

References

1. Hasselman, D. P. H., Figures of merit for the thermal stress resistance of high temperature brittle materials: a review. *Ceram. Int.*, **4** (1978) 147–50.
2. Raj, R., Fundamental research in structural ceramics for service near 2000°C. *J. Am. Ceram. Soc.*, **76** (1993) 2147–74.
3. Lutz, E. H., Swain, M. V. & Claussen, N., Thermal shock behavior of duplex ceramics. *J. Am. Ceram. Soc.*, **74** (1991) 19–24.
4. Hamano, K., Ooya, Y. & Kakagawa, Z., Microstructure and mechanical strength of aluminum titanate ceramic prepared from a mixture of aluminum and titania. *Yogyo Kyokaiski*, **91** (1983) 94–101.
5. Sinclair, W. & Simmons, H., Microstructure and thermal shock behavior of BN composites. *J. Mater. Sci. Lett.*, **6** (1987) 627–9.
6. Ishitsuka, M., Sato, T., Endo, T., Shimada, M., Ohno, H., Igawa, N. & Nagasaki, T., Grain-size dependence of thermal shock resistance of yttria-doped tetragonal zirconia polycrystals. *J. Am. Ceram. Soc.*, **73** (1990) 2523–5.
7. Zhang, B., Guo, J. K. & Zhu, P. N., Synthesis of $NaZr_2P_3O_{12}$ powder. *J. Chinese Ceram. Soc.*, **22** (1994) 246–52.
8. Zhang, B., Guo, J. K. & Zhu, P. N., Synthesis and thermal expansion of $M_{1/2}Sr_{1/4}Zr_2P_3O_{12}$ (M = Li, Na, K) compounds. *Ceram. Int.*, **20** (1994) 287–92.
9. Predecki, P., Abuhasan, A. & Barrett, C. S., Residual stress determination in Al_2O_3/SiC whisker composites by X-ray diffraction. *Adv. X-Ray Anal.*, **31** (1988) 231–43.
10. Morishima, H., Kato, Z., Uematsu, K., Saito, K., Yano, T. & Ootsuka, N., Development of aluminum titanate–mullite composite having high thermal shock resistance. *J. Am. Ceram. Soc.*, **69** (1986) C-226–7.
11. Abuhasan, A., Balasingh, C. & Predecki, P., Residual stresses in alumina/silicon carbide whisker composites by X-ray diffraction. *J. Am. Ceram. Soc.*, **73** (1990) 2474–84.
12. Noyan, I. C. & Cohen, J. B., An X-ray diffraction study of the residual stress–strain distribution in shot peened two phase brass. *Mater. Sci. Eng.*, **75** (1985) 179–93.
13. Hoffman, M. Y., Schneider G. A. & Petzow G., The potential of Si_3N_4 for thermal shock applications, in thermal shock and thermal fatigue behavior of advanced ceramics, eds G. A. Schneider & G. Petzow, 1993, Kluwer, Academic Publishers, The Netherlands, pp. 229–44.
14. Becher, P. F., Lewis, III, D., Carman, K R. & Gonzalez, A. C., Thermal shock resistance of ceramics: size and geometry effects in qeunch tests. *Am. Ceram. Soc. Bull.*, **59** (1980) 542–5.

Journal of the European Ceramic Society 15 (1995) 935–938
© 1995 Elsevier Science Limited
Printed in Great Britain. All rights reserved
0955-2219(95)00071-2
0955-2219/95/$9.50

Fast Firing of Alumina

D. E. García, J. Seidel, R. Janssen & N. Claussen

Technische Universität Hamburg-Harburg, Advanced Ceramics Group, D-21071 Hamburg, Germany

(Received 2 August 1994; revised version received 16 March 1995; accepted 31 March 1995)

Abstract

Densification behavior and mechanical performance of alumina fast fired at relatively low temperatures were evaluated and compared to those of conventionally sintered alumina. A density of about 99% of the theoretical value and a grain size of 1·2 μm were achieved by firing pure alumina powder compacts at 1350°C for 20 min. Fast fired alumina exhibits room temperature strengths (520 MPa) and Weibull moduli (10·4) nearly comparable to those of conventionally sintered alumina although very high heating/cooling rates were used. A qualitative densification model is presented based on the beneficial effects of transient mismatch stresses.

1 Introduction

Rapid sintering (fast firing), which is known to provide equivalent densities at smaller grain sizes in a less energy-consuming process, has been reported for a number of materials.[1–8] It generally involves rapid insertion of a specimen into a preheated furnace at high temperatures followed by soaking for shorter times than used in conventional sintering. Although the validity of the fast firing concept has been confirmed for several ceramic materials, the mechanism has not been fully identified. Basically the superior densification is attributed to the rapid passage of a specimen through the low temperature regime where grain coarsening dominates into the region where densification mechanisms prevail, resulting in dense products in very short firing times. Using this concept, Johnson[9] modeled rapid initial stage sintering of Ag and found that the heating rate and particle size parameters have a large effect on the sintering behavior. He concludes that rapid sintering and its beneficial effects are uniquely associated to fine particles sizes.

During fast firing, energy is absorbed in the surface of the material which is then transferred into the bulk of the sample by heat conduction. Because thermal conduction takes a finite amount of time, temperature gradients within the sample exist until the sample achieves thermal equilibrium. The importance of temperature gradients in mass transport was stressed by Braudeau *et al.*,[10] and calculations of Searcy[11] suggest that temperature gradients are essential in driving densification during fast firing. Enhanced diffusion is therefore held to be responsible for accelerated sintering in fast firing.

In contrast to these findings, Morgan and Yust,[12] studying the rapid heating of ThO_2 compacts, observed that the increase in densification rate was much greater than the corresponding increase in the diffusion coefficient of the slower diffusing species. They explain their results in terms of material transport by dislocation movement or 'plastic flow'. Furthermore, it is interesting to point out that fast firing and the well known rate controlled sintering concept[13] are somehow in conflict, although both approaches are aimed at the fabrication of advanced ceramics with high density and small grain size. Whereas the first one requires very fast densification rates, the second one is based on the control of densification rates within certain limits through all stages of densification in order to avoid, e.g. premature pore closure, gas entrapment and rapid grain growth.

In the present paper, we focus on fast firing of Al_2O_3 with respect to the benefits in energy savings and production time. Harmer *et al.*[4] have already shown that pure alumina can be fired in 2 min to 95·5% of the theoretical density (T.D.), however, at 1850°C which is a major disadvantage. Therefore, the feasibility of fast firing pure Al_2O_3 at lower temperatures was studied. The intent of the present paper is to further understand fast firing and to compare the mechanical performance of rapidly and conventionally sintered alumina.

2 Experimental Procedure

Commercial Al_2O_3 powder† of high purity (99·99%) and small grain size (~0·2 μm) was used to fabricate bars (4 × 5 × 40 mm) by uniaxial pressing of

†Taimei Chemical Co. LTD, TM-DAR.

the as-received powder at 50 MPa in a steel die followed by cold isostatic pressing at 800 MPa. Green densities of 57% T.D. were attained. The specimens were heated to 200°C prior to firing in order to remove adsorbed water. The fast firing process was carried out at 1350°C using a standard box furnace. To obtain the highest heating rates possible, the samples were introduced rapidly into the preheated furnace. After sintering for various times, the samples were taken out of the furnace and cooled in air. The free cooling to room temperature took about 15 min. Polished specimens cut from samples sintered for 20 min were thermally etched in air at 1300°C for 30 min in order to examine the microstructure and to identify possible strength-determining defects. The average grain diameter was measured using the linear intercept technique.

Fracture strength was measured in 4-point bending according to German standard DIN 51110 but with rectangular bars of reduced length (25 × 4 × 3 mm) and loading spans of 10 and 20 mm. The tensile side was polished to a 3 μm surface finish and the edges were bevelled. The scatter of strength data and Weibull moduli was analyzed as described elsewhere.[14]

3 Results and Discussion

Fast firing of pure alumina by rapid insertion and removal using a preheated furnace includes extremely high heating and cooling rates, and a certain soaking time at maximum temperature. In Fig. 1, final mean densities are summarized as a function of soaking time at 1350°C. A density of 95·4% T.D. was obtained by conventional firing using a heating rate of 15 K min^{-1} and a soaking time of 20 min. Even without densification during the heating period, fast firing yielded final densities of about 99% T.D just by soaking for 20 min. The average grain size is 1·2 μm about 30% smaller than those reported by Seidel *et al.*[14] after conventional sintering using low heating rate (10 K min^{-1}) and soaking for 120 min at 1350°C. The morphology of the microstructure, however, is very close to conventionally sintered pure alumina as shown in Fig. 2. Therefore, the fast firing approach as outlined by Brook *et al.*[4-7] can be used to fabricate highly dense and fine grained alumina within very short periods of time, e.g. cycle time from room temperature to room temperature of ~30 min.

In a strict discussion, however, the density distribution during the initial stages of fast firing must also be considered. For example, Fig. 3 represents a part of the cross section of fast fired alumina after soaking for 8 min at 1350°C showing a dense

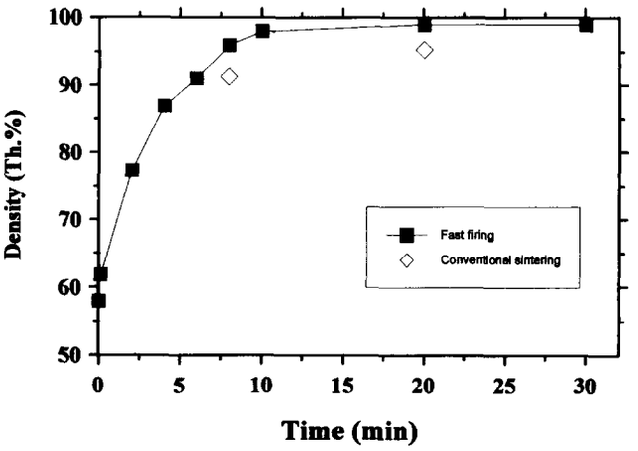


Fig. 1. Average density versus soaking time at 1350°C (note: densities plotted are determined after quenching to room temperature).



Fig. 2. Microstructure of alumina fast fired at 1350°C for 20 min.

outer layer and a porous inner core of the sample as well as a transition from dense to porous within less than 100 μm. Neglecting small gradients within the porous and dense region, the transition can be termed as interface 'porous/dense'. During soaking, this interface migrates from the surface to the center of the sample. Optical microscopy of

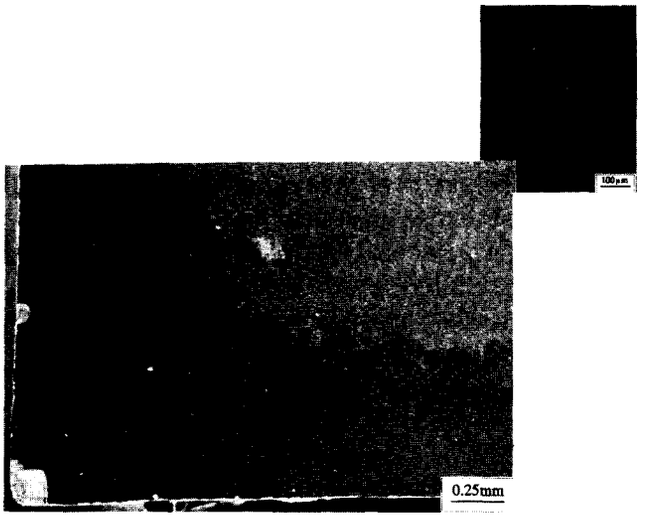


Fig. 3. Cross section of fast fired alumina after 8 min at 1350°C. The interface dense/porous is shown in the upper right at higher magnification.

samples quenched after various soaking times corroborates the evidence for a migrating interface 'porous/dense'. However, micrographic reproduction proved difficult due to low contrast and the small scale of pores and grains. In contrast to fast firing, conventional sintering at 1350°C/8 min using a heating/cooling rate of 15 K min^{-1} results in homogeneous microstructures without density gradient.

It is necessary to point out that the creation of an interface 'porous/dense' in fast fired samples is associated with the formation of transient stresses due to the shrinkage mismatch. Considering these stresses, a schematic of our understanding of the densification progress during fast firing is given in Fig. 4 contrasting the migrating densification front with the transient mismatch stresses during a given fast firing experiment at various times. For simplicity, the interface is considered as infinite. In the following, each situation is discussed in turn.

t_0: The green sample is just inserted into the preheated furnace. The surface of the sample is heated to temperatures close to the temperature of the furnace predominantly by radiation heat transfer, whereas the core remains almost at room temperature (assuming heat conduction as the velocity determining mechanism). However, a notable densification and, therefore, transient stresses caused by shrinkage mismatch are not yet formed. Considering the calculations of Searcy[11] the large

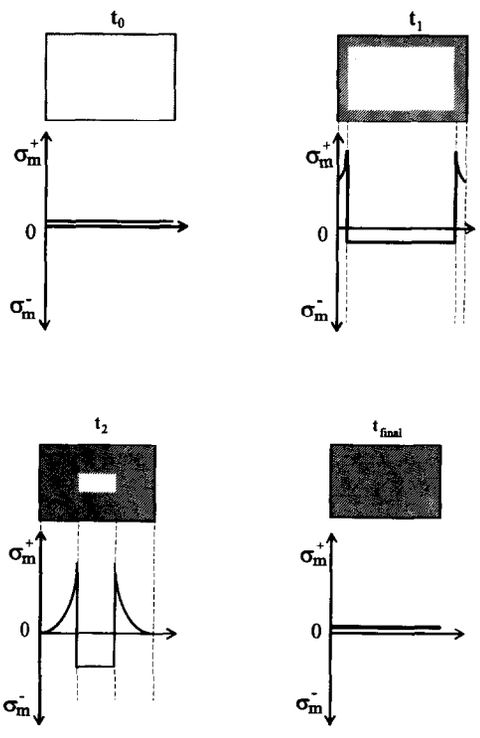


Fig. 4. Schematics contrasting densification progress and transient mismatch stresses during fast firing for the (a) porous compact, (b) initial and (c) medium state during fast firing and (d) final product after prolongated soaking at T_{max}, (note: stress relaxation effects are neglected and the interface is considered as infinitesimal thin).

thermal gradient formed may cause an enhanced mass transport although the following scheme holds also assuming conventional mass transport.

t_1: A small surface layer is densified to a certain extent. Tensile stresses are formed in this layer, however, they are overruled by high sintering potential resulting in a first densification of the outer layer (the rate of densification is neglected for this simplified discussion). The compressive stresses at the interface enhance the densification of the porous region. Due to easy stress relaxation, the stresses are only effective within a small area considering the grain size as characteristic length of microstructure.

t_2: The interface has moved further and, therefore, densification caused by transient stresses proceeds in the interior. The center core, however, is still porous (cf. Fig. 3). The densification already present is associated with volumetric shrinkage of the sample and, therefore, with mass transport from the outer dense to the inner porous part.

t_{final}: The sample is almost fully densified, i.e. after 20 min soaking at 1350°C. Furthermore, transient stresses caused by constrained sintering are diminished due to creep relaxation. The microstructure of the final product (Fig. 2) is similar to conventionally sintered pure alumina.

In summary, besides the densification mechanism mentioned generally for fast firing, transient stresses play an important role improving densification. We should point out that subleties like densification by stress induced diffusion are not included here and may provide an additional effect for the very fast densification observed. Specimen composition and size effects are also not included since these do not effect the basic influence of transient stresses, however, they can be used to improve our understanding of fast firing. For instance, the specimen thickness can be used to calculate the rate of interface movement. Considering the present results (cf. Fig. 1), we can estimate an interface movement of 4 $\times 10^{-6}$ ms^{-1}. For a quantitative analysis, one would have to face for example the rate of heat transfer to the surface, the heat conduction within the sample as well as stress relaxation kinetics. Calculations of heat conductivity, however, are particularly difficult due to non constant parameters during fast firing, i.e. pore size distribution.

Nevertheless, while appreciating that we present a simplified picture of fast firing, the results can be linked to previous work. For instance, Johnson[9] concluded in his review that rapid sintering is a phenomena unique to fine particle sizes. Considering the model presented, it is obvious that reactive fine particles are required in order to overrule the tensile stresses in the dense region by high sintering potential as well as to enhance stress relaxation by creep phenomena.

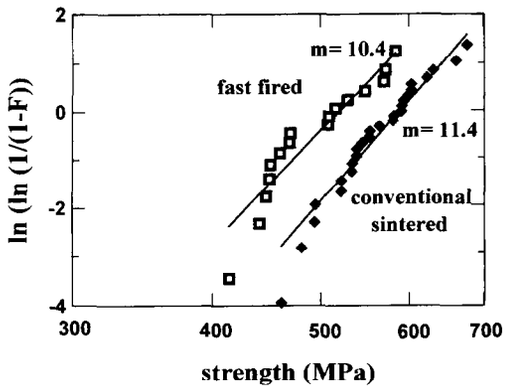


Fig. 5. Bending strength distribution (Weibull plot) of alumina fast fired at 1350°C for 20 min and conventional alumina sintered at 1350°C for 2 h.[14]

The preliminary results of fracture strength of fast fired alumina indicate that there is almost no severe strength degradation when compared to conventionally sintered alumina. Fig. 5 shows the strength distributions of fast fired and conventionally sintered alumina,[14] with an average strength of 520 and 564 MPa and Weibull moduli of 10·4 and 11·4, respectively. The solid lines through the strength data are curves representing the fit on the basis of a two parameter Weibull approach.

Polished surfaces investigated reveal defects of about 10–15 μm in the form of voids, as shown in Fig. 6, probably originating from powder agglomerates in the green compact. However, there is no indication of a change of the defect character when compared to conventional sintering. The small drop in strength and the corresponding increase in flaw size may be attributed to the transient tensile stresses in the surface region during fast firing, resulting in an expansion of flaws already present prior to heat treatment. With this hypothesis, nearly defect-free green bodies as well as further enhanced stress relaxation by creep is required for obtaining high strength alumina by fast firing.

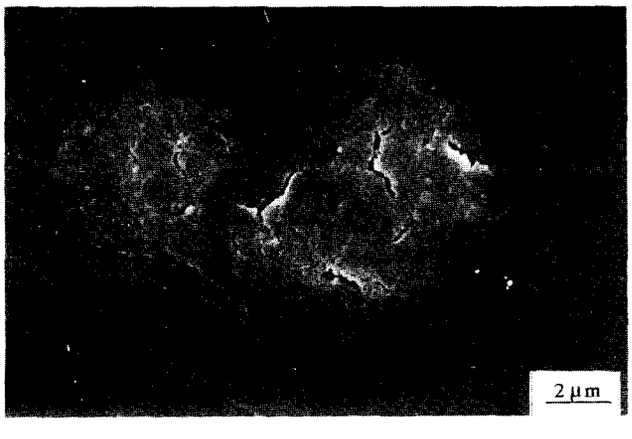


Fig. 6. SEM micrograph of polished surface showing typical defects in fast fired alumina.

4 Conclusions

Using fine reactive powders, the fast firing approach can be used to fabricate alumina within very short production times at low temperature. Transient stresses caused by constrained sintering are formed during fast firing. These stresses accelerate densification and enhance the formation of a dense, fine grained microstructure. The mechanical performance of the final product is, in first approximation, comparable to conventionally sintered alumina.

Acknowledgement

Financial support by German Research Foundation (DFG) under contract Ja 655/4-1 is gratefully acknowledged.

References

1. Vergnon, P., Juillet, F. & Teichner, S. J., Effect of increasing rate of temperature on sintering of pure alumina homodispered particles, *Rev. Int. Hautes Temp. Refract*, (in French), **3** (1966) 409–19.
2. Jones, W. & Miles, L. J., Production of β-Al_2O_3, *Proc. Br. Ceram. Soc.*, **19** (1971) 161–78.
3. Morrel, A. & Hermosin, A., Fast firing of soft Mn–Zn and Ni–Zn ferrite pot cores, *Amer. Ceram. Soc. Bull.*, **59**(6) (1980) 626–9.
4. Harmer, M. P., Roberts, E. W. & Brook, R. J., Rapid sintering of pure and doped α-Al_2O_3, *Trans. Br. Ceram. Soc.*, **78**(1) (1979) 22–5.
5. Mostaghaci, H. & Brook, R. J., Fast firing of non-stoichiometric $BaTiO_3$, *Trans Br,. Ceram. Soc.*, **80** (1981) 148–9.
6. Mostaghaci, H. & Brook, R. J., Production of dense and fine grain size $BaTiO_3$ by fast firing, *Trans. J. Br. Ceram. Soc.*, **82** (1983) 167–70.
7. Brook, R. J., Fabrication principles for the production of ceramics with superior mechanical properties, *Proc. Br. Ceram. Soc.*, **32** (1982) 7–24.
8. Baumgartner, C. E., Fast firing and conventional sintering of lead zirconate titanate ceramic, *J. Am. Ceram. Soc.*, **71**(7) (1988) C-350–3.
9. Johnson, D. L., Ultra rapid sintering. In *Sintering and heterogeneous catalysis*, eds G. C. Kuczynski, A. E. Miller & G. A. Sargent, Plenum Publ. Corp., New York, 1984, pp. 243–52.
10. Braudcau, P., Morell, A. & Monty, C., Effect of temperature gradient on material transport in alumina, *Ann. Chim. Fr.* (in French), **10** (1985) 261–3.
11. Searcy, A. W., Theory for sintering in temperature gradients — role of long-range mass transport, *J. Am. Ceram. Soc.*, **70**(3) (1987) C-61–2.
12. Morgan, C. S. & Yust, C. S., Material transport during sintering of materials with fluorite structure. *J. Nucl. Mater.*, **10**(3) (1963) 182–90.
13. Huckabee, M. L. & Palmour III, H., Rate controlled sintering of fine grained alumina, *Am. Ceram. Soc. Bull.*, **51**(7) (1972) 574–6.
14. Seidel, J., Claussen, N. & Roedel, J., Reliability of Alumina Ceramics. I: Effect of Grain Size, *J. Eur. Ceram. Soc.* (in press).

Journal of the European Ceramic Society **15** (1995) 939–950
© 1995 Elsevier Science Limited
Printed in Great Britain. All rights reserved
0955-2219/95/$9.50

0955-2219(95)00063-1

Effect of Solid Solution Additives on the Sintering of Ultra-fine CeO_2 Powders

M. N. Rahaman[a] & Y. C. Zhou[b]

[a]University of Missouri–Rolla, Department of Ceramic Engineering, Rolla, Missouri 65401, USA
[b]Institute of Metal Research, Academia Sinica, Shenyang 110015, P. R. China

(Received 12 September 1994; revised 6 March 1995; accepted 10 March 1995)

Abstract

Ultra-fine CeO_2 powders (particle size ≈10–15 nm) containing up to 20 at% of various divalent and trivalent cations (Mg^{2+}, Ca^{2+}, Sc^{3+}, Y^{3+} and Nd^{3+}) were prepared by chemical precipitation under hydrothermal conditions. The effects of the cation concentration, size and valency on the densification and grain growth of the compacted powders were examined during sintering at a constant heating rate of 10°C/min. Compared to undoped CeO_2, all of the additive cations caused a shift in the densification curve to higher temperatures. However, the density and grain size achieved after sintering depended significantly on the elemental composition of the additive. When the radii of the additive cations were larger than that of the host Ce^{4+} cation, (i.e. Ca^{2+}, Y^{3+} and Nd^{3}), nearly full density and ultra-fine grain size were achieved. Under identical sintering conditions, lower density (≈93–95% of the theoretical) and larger grain size were achieved when the radii of the additive cations were smaller than that of the host, (i.e. Mg^{2+} and Sc^{3+}). Powders doped simultaneously with two cations, (e.g. Ca^{2+} and Mg^{2+}) showed sintering and grain growth characteristics which were intermediate between those for the powders doped with single cations at the equivalent concentration.

1 Introduction

Materials with ultra-fine grained microstructure (sometimes referred to as nanocrystalline materials) have been the subject of much recent investigation.[1–8] While considerable attention has been devoted towards the preparation of ultra-fine particles and the production of thin films by vapor phase or sol–gel techniques, the production of bulk materials with controlled density and grain size by the sintering of ultra-fine particles has received little attention. Due to their ultra-fine size, typically of the order of 10 nm or so, nanocrystalline powders have a fairly large fraction of molecules residing in the surface of the particles. Nanocrystalline solids also contain a large number of grain boundaries per unit volume. The consequences of these characteristics for sintering and grain growth have not been determined.

An understanding of the sintering behavior of ultra-fine powders is also important for the application of nanocrystalline materials. The driving force for densification increases and the diffusion distance for matter transport decreases with a decrease in the particle size. From the point of view of materials fabrication, a key benefit of ultra-fine powders, therefore, is the reduction in the sintering temperature. Many properties are dependent on the grain size of the fabricated body. Another key benefit is the production of ultra-fine grained microstructures. Such microstructures are of great practical interest for the investigation of structure–property relationships in polycrystalline materials. A problem is that non-densifying processes such as vapor transport and surface diffusion are also enhanced with a decrease in the particle size.[9] These processes lead to coarsening of the microstructure and, consequently, to the reduction in the driving force for densification. The benefits of the ultra-fine particle size for sintering are therefore not clear.

The reduction in the sintering temperature of ultra-fine powders has been observed in a number of studies.[3,7,8] However, the production, by sintering, of materials with high density and ultra-fine microstructure has experienced difficulties. Rapid grain growth in the final stage of sintering has been a common problem so that the achievement of high density has normally been accompanied by relatively large grain size.[3,7]

In an earlier study, the present authors investigated the sintering of ultra-fine CeO_2 powders which were prepared under hydrothermal conditions.[10] Nearly full density and ultra-fine grain size

(less than ≈200 nm) were obtained by careful control of the heating schedule or with the use of powders doped with yttrium. The present paper describes a more detailed study of the preparation and sintering of doped, ultra-fine CeO_2 powders. The effects of substituting cations differing in valency and ionic size were investigated. Of particular interest was the effect of the additive cations on the morphology and chemical homogeneity of the synthesized powders and on the sintering and grain growth of the compacted powders. CeO_2 was considered to be a useful model system for these studies because of its relatively simple cubic fluorite crystal structure[11] and its high solid solubility for many cations.[12] In addition, it does not undergo any known crystallographic transformation during the normal range of heating. The results are expected to be relevant to the general understanding of the sintering behavior of ultra-fine powders and to the elucidation of the role of dopants in sintering. Solid solutions of CeO_2 have also been attracting considerable interest as solid electrolytes with high ionic conductivity for applications in fuel cells.[13,14] The present study may also be useful for the microstructure control of CeO_2 solid electrolytes.

2 Experimental

2.1 Hydrothermal synthesis of CeO_2 powders and doped CeO_2 powders

Powders of undoped CeO_2 and of solid solutions of CeO_2 containing up to 20 at% of Mg, Ca, Sc, Y and Nd were prepared by hydrothermal techniques. The starting materials for the preparation of the powders consisted of Analar Grade nitrate or chloride salts of the appropriate metals with a purity greater than 99.9%: cerium (III) nitrate hexahydrate,* $Ce(NO_3)_3.6H_2O$, magnesium nitrate hexahydrate,† $Mg(NO_3)_2.6H_2O$, calcium nitrate tetrahydrate,† $Ca(NO_3)_2.4H_2O$, scandium nitrate hexahydrate,† $Sc(NO_3)_3.6H_2O$, yttrium chloride hexahydrate,* $YCl_3,6H_2O$, and neodymium nitrate hexahydrate,† $Nd(NO_3)_3.6H_2O$.

In the hydrothermal synthesis of the powders, the appropriate amounts of cerium nitrate (for the undoped CeO_2) or a mixture of cerium nitrate and the desired metal salt, (e.g. yttrium chloride, for the CeO_2 solid solution containing yttrium) were dissolved in distilled water and ammonium hydroxide solution was added, under vigorous stirring, to produce a sol at pH = 10. The gelatinous precipitate was filtered, washed with distilled water and then transferred to a Teflon tube which was sealed with a cap and placed in an autoclave. Hydrothermal synthesis was performed for 4 h at ≈300°C and under a pressure of ≈10 MPa. After rapid cooling, the product was washed with distilled water, dried in air at room temperature and then ground lightly in an agate mortar and pestle. Finally, the powder was calcined at 200°C for 2 h. The preparation conditions were kept almost identical for each powder composition.

2.2 Sintering of the compacted powders

Powder compacts (6 mm diameter by 4 mm) were formed by uniaxial pressing in a die at ≈50 MPa in a tungsten carbide die. The compacts were sintered in air in a dilatometer which allowed continuous monitoring of the shrinkage kinetics. The sample holder and pushrods of the dilatometer were made of high purity alumina. Sintering was performed at a constant heating rate of 10°C/min to 1350–1400°C. The density of the sample at any temperature was determined from the initial density and the measured shrinkage. The final density was checked by Archimedes' method.

2.3 Characterization of the powders and sintered materials

The ultra-fine powders prepared by hydrothermal synthesis were characterized by X-ray diffraction (XRD), thermogravimetric analysis (TGA), differential thermal analysis (DTA) and transmission electron microscopy (TEM). The TGA and DTA analyses were performed at a heating rate of 10°C/min. Analysis of the crystal structure of the powder was performed in a diffractometer (Scintag XDS 2000) using Cu K_α radiation at a scan rate of 2° 2θ min^{-1}. Crystallite size was measured from XRD patterns at a scan rate of 0·5° 2θ min^{-1}. The crystallite size, H, was calculated from the Scherer formula:

$$H = \frac{0{\cdot}9\,\lambda}{\beta \cos\theta} \tag{1}$$

where λ is the wavelength of the X-rays, θ is the diffraction angle, and β is the corrected half width given by:

$$\beta^2 = \beta_m^2 - \beta_s^2 \tag{2}$$

where β_m is the measured half width and β_s is the half width of a standard CeO_2 sample with a crystal size greater than 100 nm. The reflection from the (422) plane, occurring at 88° 2θ, was used for the crystallite size measurement.

Transmission electron microscopy was also used to characterize the powders. Samples were prepared by dispersing the powder in ethanol and then putting a drop of the suspension on a holey

*Aldrich Chemical Co., Milwaukee, WI, USA; †Johnson Matthey, Seabrook, NH, USA.

carbon film and allowing it to dry. The microstructure of the powders was observed in a Philips EM-420 transmission electron microscope. In addition, the microstructure of the CeO_2 powders doped with Y and Ca was observed in a JEOL-2000FXII high resolution electron microscope. The distribution of the dopants in the doped powders were analyzed by energy dispersive X-ray analysis (EDX).

The microstructure of the sintered samples was observed using scanning electron microscopy (SEM) of fracture surfaces. The grain size was measured by the line intercept method. The microstructure of selected samples were also observed in a JEOL-2000FXII high resolution electron microscope. The samples for TEM were prepared by cutting to a thickness of ≈0·5 mm, followed by mechanical polishing to ≈25 μm and finally ion beam milling at 5 kV using an incident angle of 15°. Phase composition of the sintered materials was analyzed by XRD of powder samples at a scan rate of 2° 2θ min^{-1}.

3 Results

The results of the present work allowed an investigation of the effects of solid solution additives on the sintering of compacted CeO_2 powders. Since the characteristics of the synthesized powder can have a significant influence on the sintering behavior, it is important to determine how these characteristics are controlled by the concentration and elemental composition of the additive. Figure 1 shows the effect of dopant concentration on the characteristics of the powder doped with yttrium. The TEM micrographs show powders of undoped CeO_2 (a), and CeO_2 doped with Y^{3+} at concentrations of 6 at% (b), 10 at% (c) and 20 at% (d). The undoped CeO_2 powder consists of polyhedral shaped particles with an average size of ≈12 nm (as measured by X-ray line broadening). The average size measured by TEM was ≈14 nm, which agrees well with the value obtained by X-ray line broadening. The powders doped with 10 and 20 at% yttrium have an average size and shape that are close to that for the undoped powder. However, the powder containing 6 at% Y^{3+} shows a fairly significant difference in size. The average particle size obtained from X-ray line broadening measurements for the powder doped with 6 at% Y^{3+} was 9 nm.

The effect of the elemental composition of the dopant on the characteristics of the synthesized powder is shown in Fig. 2 for undoped CeO_2 powder (a) and for doped CeO_2 powder containing

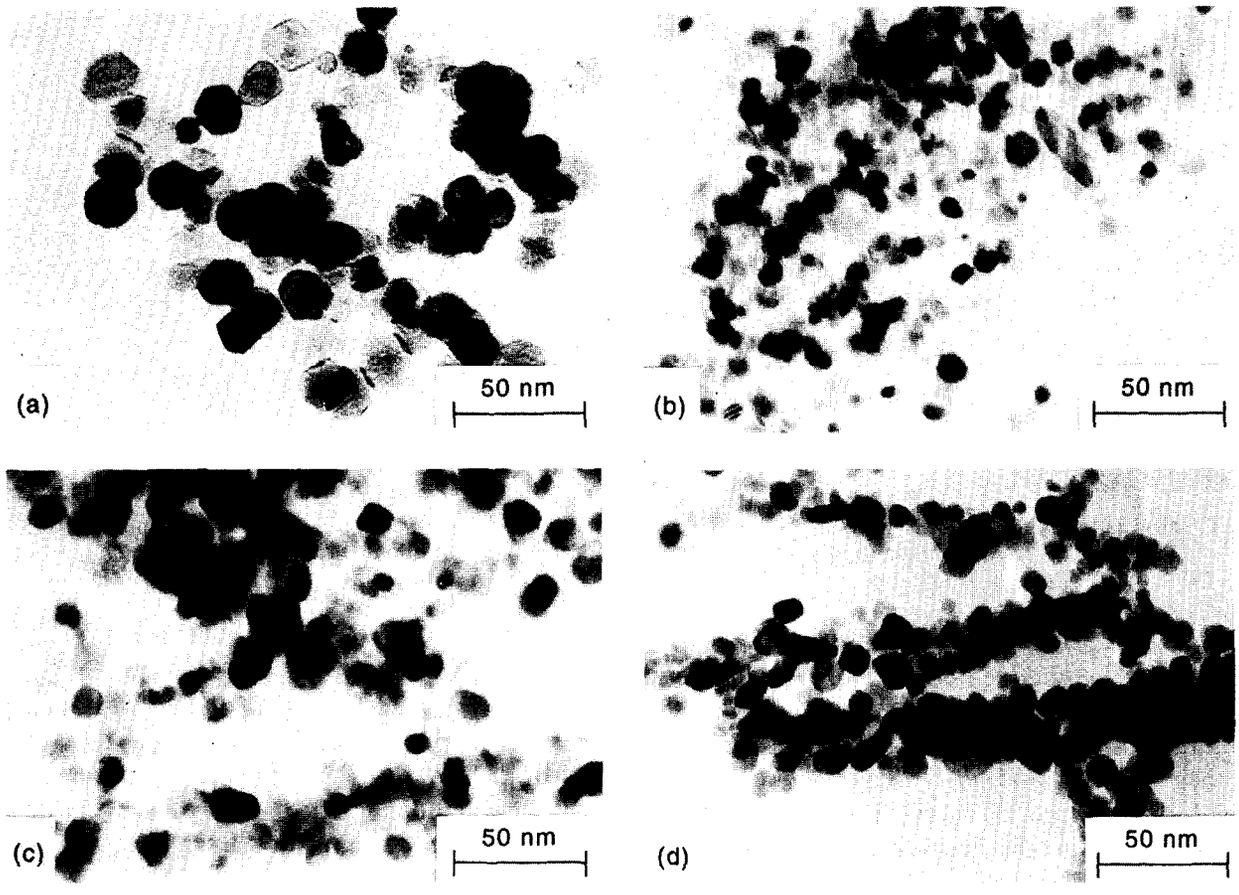


Fig. 1. TEM of the CeO_2 powder doped with Y^{3+} at concentrations of (a) 0; (b) 6; (c) 10 and (d) 20 at% prepared under hydrothermal conditions.

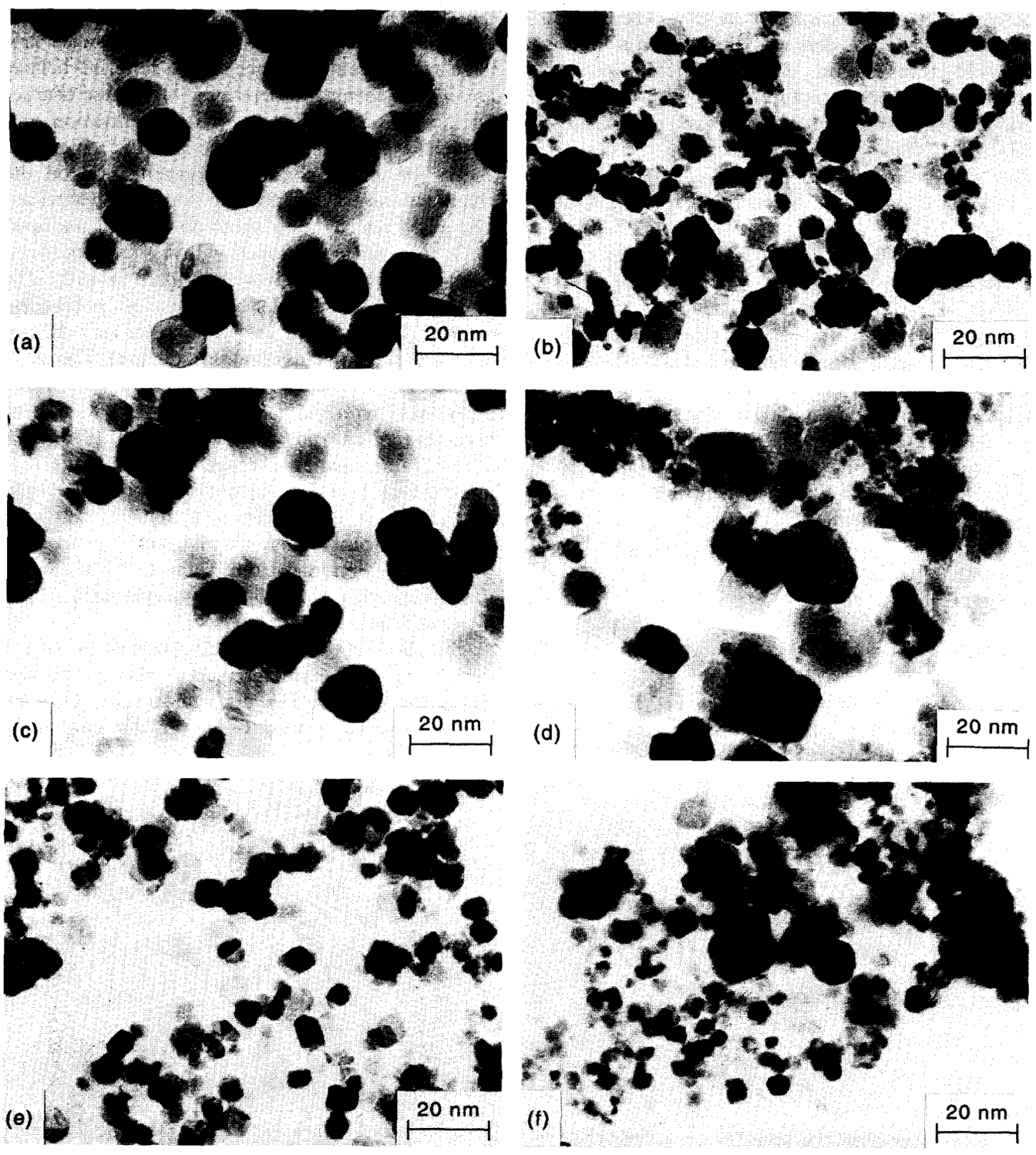


Fig. 2. TEM of the powders prepared under hydrothermal conditions showing (a) the undoped CeO_2 powder and the doped CeO_2 powder containing 6 at% of (b) Mg^{2+}; (c) Ca^{2+}; (d) Sc^{3+}; (e) Nd^{3+} and (f) Y^{3+}.

6 at% of Mg^{2+}, Ca^{2+}, Sc^{3+}, Nd^{3+} and Y^{3+} (b–f) respectively). The undoped powder and the powders doped with Ca^{2+} and Nd^{3+} have a fairly narrow distribution of sizes. However, the powders doped with Mg^{2+}, Sc^{3+} and Y^{3+} have a noticeable bimodal distribution of sizes. The effect of the dopants on the size distribution of the powders is further illustrated in Fig. 3. Particle size distribution histograms determined by measuring maximum diameters of more than 100 particles in TEM micrographs are shown for (a) undoped CeO_2 and CeO_2 doped with (b) 6 at% Ca^{2+} and (c) 6 at% Sc^{3+}. The histogram of the Ca-doped powder is approximately similar to that of the undoped powder. The powder doped with Sc^{3+} has a bimodal distribution of larger particles (average size $\approx$20 nm) and finer particles (average size $\approx$8 nm).

The distribution of the dopant in the particles of the powder may also have important conse-

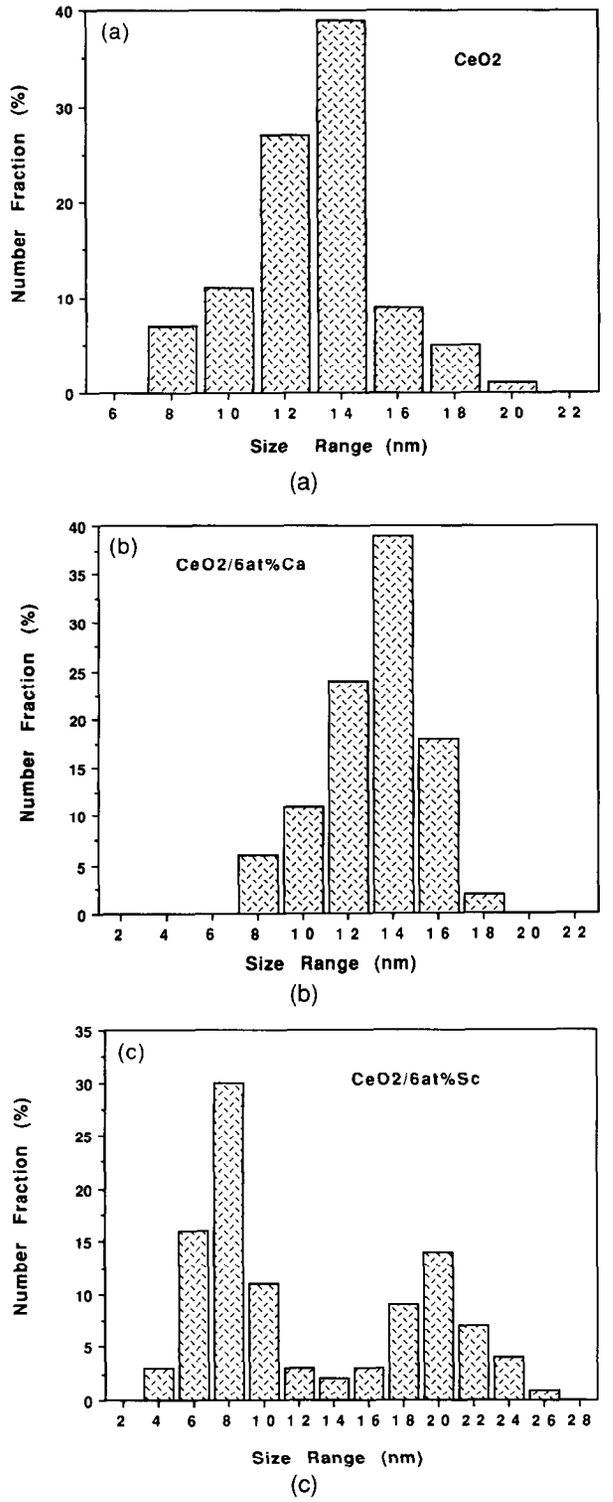


Fig. 3. Histogram showing the particle size distribution of (a) the undoped CeO_2; (b) the CeO_2 powder doped with 6 at% Ca and (c) the CeO_2 powder doped with 6 at% Sc.

quences for sintering. Figure 4 shows high resolution TEM micrographs of the synthesized powder doped with 6 at% Ca^{2+}. The particles are observed to have faceted shapes and, within the limits of resolution, fully crystalline. EDX analysis revealed no difference in the chemical composition of the individual particles. As outlined above, the powders doped with Mg^{2+}, Sc^{3+} and Y^{3+} have a bimodal distribution of sizes. High resolution micrographs

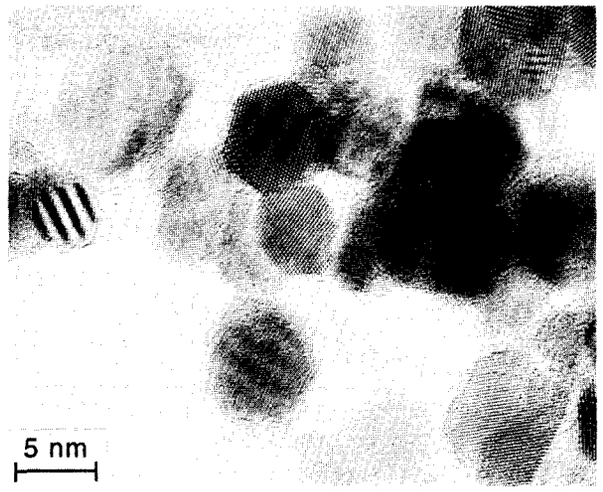


Fig. 4. HREM of the CeO_2 powder doped with 6 at% Ca^{2+}.

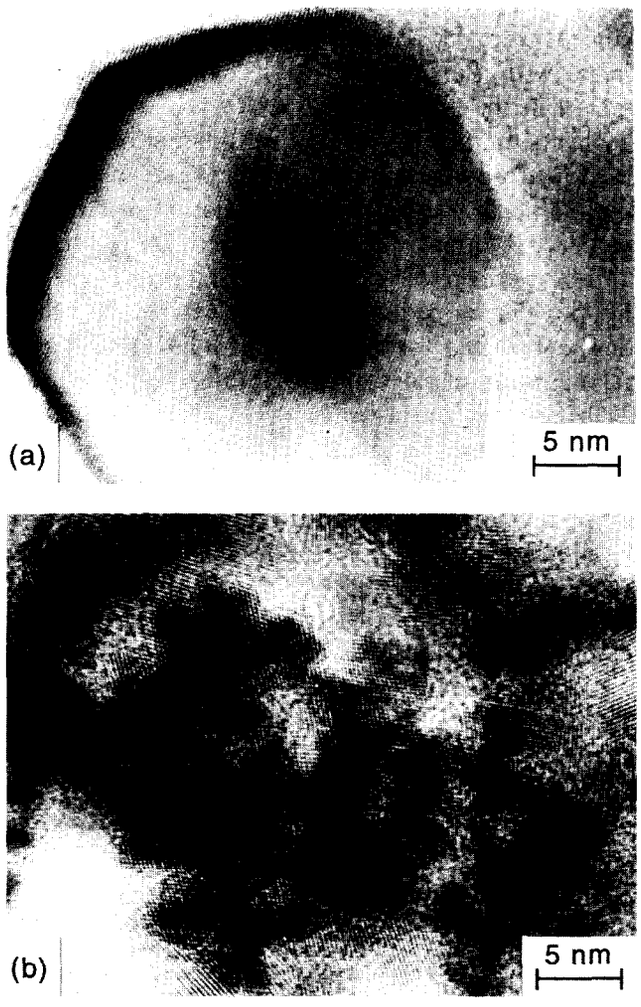


Fig. 5. HREM of the CeO_2 powder doped with 6 at% Y^{3+} showing (a) a larger particle with a lower concentration of Y^{3+} and (b) smaller particles with a higher concentration of Y^{3+}.

of the powder doped with 6 at% Y^{3+} are shown in Fig. 5 for (a) a larger particle and (b) smaller particles in the distribution. The highly crystalline nature of the larger particle is very noticeable. However, for these powders, EDX analysis revealed a significant difference in the dopant

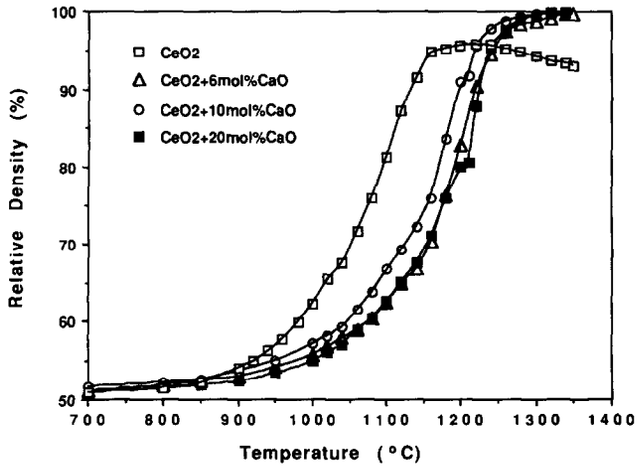


Fig. 6. Relative density versus temperature for the compacted CeO_2 powder doped with 0, 6, 10 and 20 at% Ca^{2+} during sintering at 10°C/min to 1350°C.

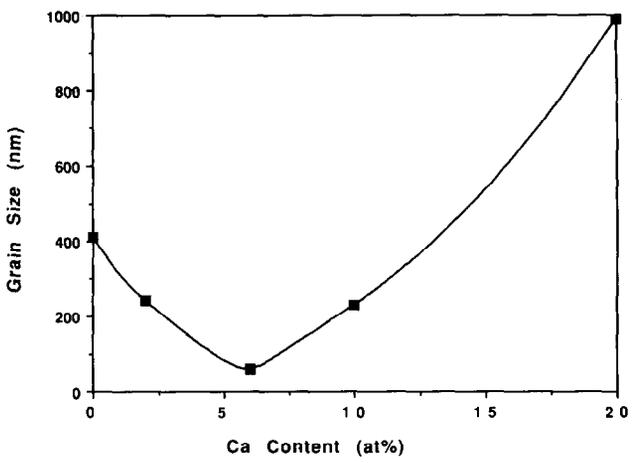


Fig. 7. Grain size versus Ca^{2+} concentration for the powder compacts sintered under identical conditions of 10°C/min to 1350°C.

concentration between the larger and smaller particles, with the concentration being significantly greater in the finer particles.

The sintering curves for the undoped and Ca-doped powders are shown in Fig. 6, where the relative density is plotted as a function of the temperature. Dopant concentrations of 2, 6, 10 and 20 at% were investigated. The sintering curve for the powder doped with 2 at% Ca^{2+} was nearly identical to that for sample doped with 6 at% and, to maintain clarity of the figure, was omitted. Each curve is the average of two runs under the same conditions, and the density at any temperature is reproducible to ±0·01. The sintering behavior of the undoped powder has been described in detail elsewhere.[10] The undoped CeO_2 powder starts to sinter at ≈800–900°C and reaches a density of 0·95 of the theoretical at ≈1200°C, after which the density decreases slightly. It is seen that one effect produced by the dopants is a shift of the sintering curves to higher temperature. Furthermore, the sintering curves for the doped powders lie within a narrow band, which indicates that for the range of values investigated (2–20 at%), the Ca^{2+} concentration has a relatively insignificant effect on the densification. It is also seen that the doped samples reach nearly full density below ≈1300°C.

For the Ca-doped powders, the final grain size of the compacts sintered under identical conditions (10°C/min–1350°C) is shown in Fig. 7 as a function of the dopant concentration. It is seen that the dopant concentration has a significant effect on the final grain size. With increasing Ca^{2+} concentration, the final grain size decreases from ≈400 nm for the undoped sample and reaches a minimum value of ≈30 nm at 6 at%, after which it increases to ≈1 μm for a concentration of 20 at%. SEM of the fracture surfaces of the sintered bodies are shown in Fig. 8. The effect of the Ca concentration on the grain size and microstructure is very striking.

Figure 9 shows the effect of yttrium dopant on the sintering of the compacted powders. Dopant concentrations of 2, 6, 10, 14 and 20 at% were investigated but the data for the powder doped with 14 at% Y^{3+} were omitted to maintain clarity of the figure. As observed above for the powders doped with Ca^{2+}, doping produces a shift in the sintering curves to higher temperature. However, the effect of the Y^{3+} appears to be somewhat more complex than that observed for Ca^{2+}. The shift in the curves increases with increasing Y^{3+} concentration so that higher temperatures are required in order to achieve the same final density. The sintering curve for the sample doped with 20 at% Y^{3+} shows a trend which is different from those of the others. No densification occurs below ≈1300°C, after which the curve increases rapidly. Furthermore, the curve shows a small expansion at ≈1200°C. A small expansion was also observed for the powder doped with 14 at% Y^{3+}. The cause of the expansion is not understood clearly at present. As outlined earlier, X-ray analysis and high resolution electron microscopy show no evidence of free Y_2O_3 in the powders. However, electron microscopy shows that the powder doped with Y^{3+} has a bimodal size distribution and that the smaller particles in the distribution have a higher yttrium concentration (Fig. 5). A possibility is that the expansion is caused by a solid state reaction driven by the yttrium concentration difference between the smaller and larger particles in the powder. After the yttrium concentration has equilibrated, densification occurs rapidly.

The effect of the elemental composition of the dopant on the sinterability of the compacted powders is shown in Figs 10 and 11 for a fixed dopant

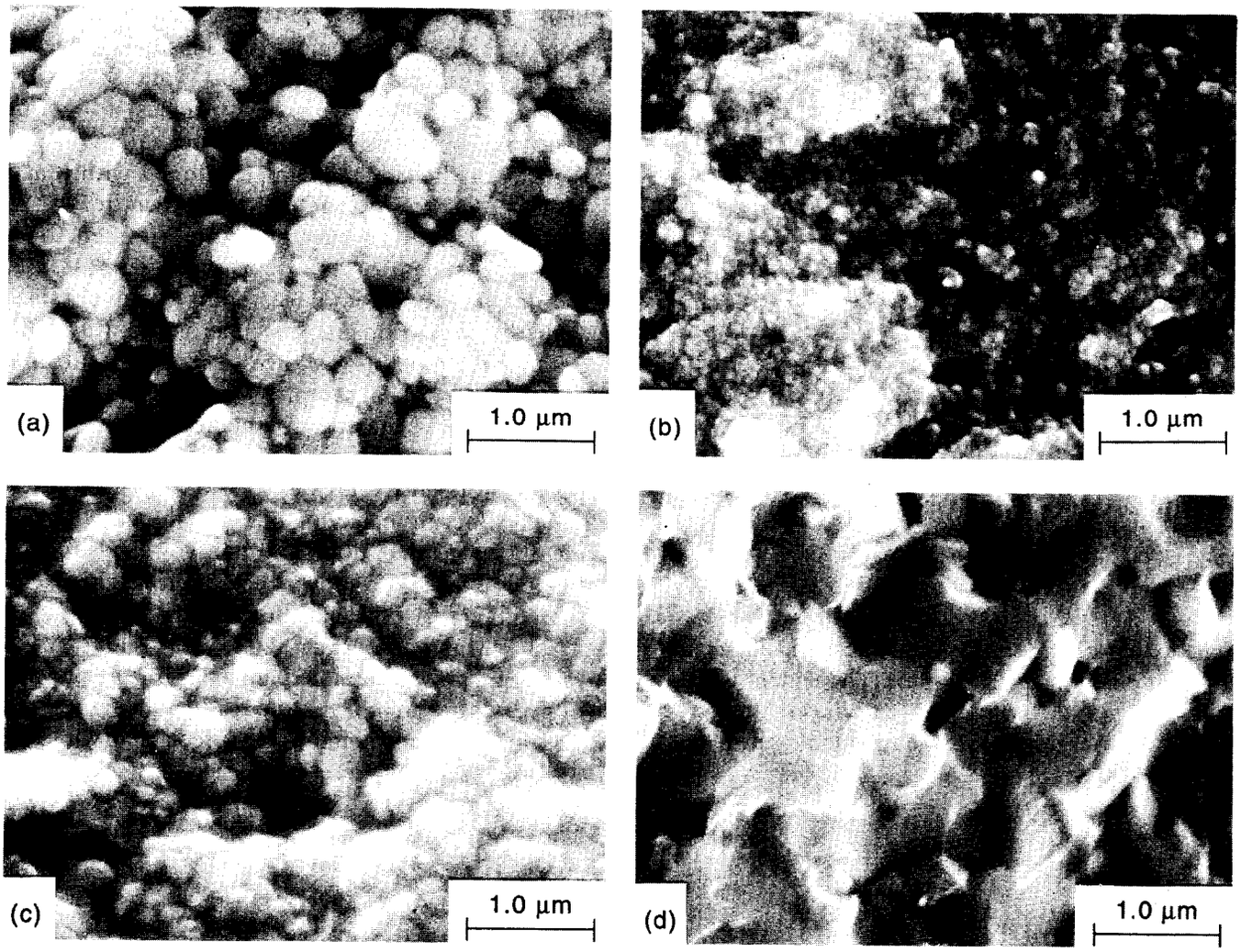


Fig. 8. SEM of the fracture surfaces of the Ca-doped powder compacts after sintering at 10°C/min to 1350°C for Ca^{2+} concentrations of (a) 2; (b) 6; (c) 10 and (d) 20 at%.

concentration of 6 at%. For the divalent cations investigated, i.e. Mg^{2+} and Ca^{2+}, it is seen that both cations lead to a shift of the sintering curve to higher temperature (Fig. 10). However, the final densities obtained under identical sintering conditions are different. The Mg-doped sample reaches a limiting density of ≈95% of the theoretical while the Ca-doped sample reaches almost full density. For the trivalent cations, i.e. Sc^{3+}, Y^{3+} and Nd^{3+}, the shift of the sintering curves to higher temperatures is also observed (Fig. 11).

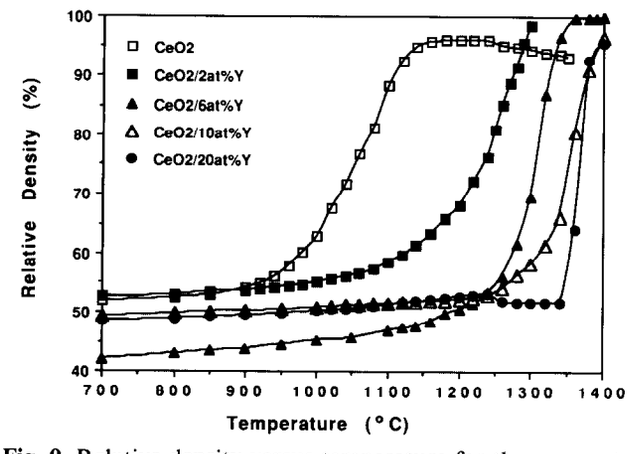


Fig. 9. Relative density versus temperature for the compacted CeO_2 powder doped with 2, 6, 10 and 20 at% Y^{3+} during sintering at 10°C/min.

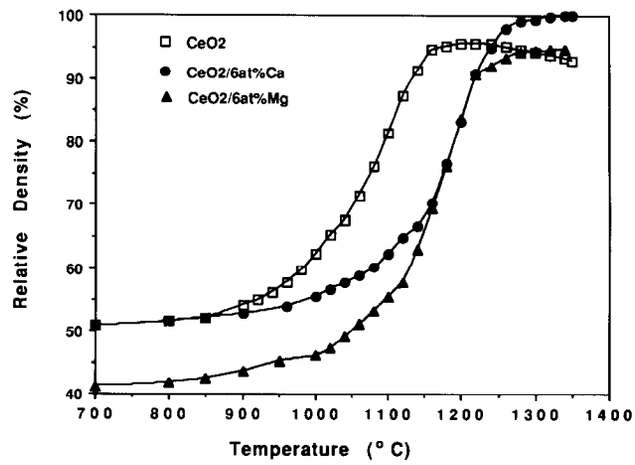


Fig. 10. Relative density versus temperature for the CeO_2 powder compacts doped with 6 at% of the divalent cations, Mg^{2+} and Ca^{2+}, during sintering at 10°C/min to 1350°C. For comparison, the data for the undoped CeO_2 powder compact are also shown.

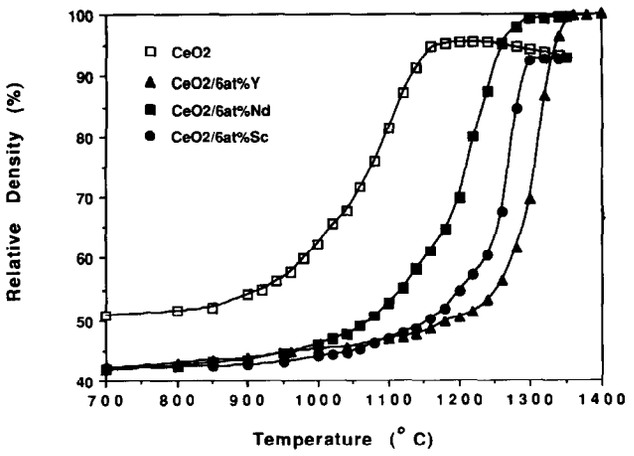


Fig. 11. Relative density versus temperature for the CeO_2 powder compacts doped with 6 at% of the trivalent cations, Sc^{3+}, Y^{3+} and Nd^{3+}, during sintering at 10°C/min. For comparison, the data for the undoped CeO_2 powder compact are also shown.

The extent of the shift is dependent on the elemental composition of the dopant; the smallest shift is caused by Nd^{3+} while Y^{3+} produces the largest shift. As observed for the divalent cations, the final density depends on the elemental composition of the dopant. Almost full density is achieved for the powders doped with Nd^{3+} and Y^{3+} while the powder doped with Sc^{3+} reaches a limiting density of only ≈93% of the theoretical.

SEM of the sintered samples doped with 6 at% of Mg^{2+}, Ca^{2+}, Y^{3+} and Nd^{3+} are shown in Fig. 12. The grain size and microstructure are seen to be highly dependent on the elemental composition of the dopant. Relatively large grain size is obtained with the Mg^{2+} dopant. The microstructure of the Sc-doped sample, not shown here, is close to that for the Mg-doped sample. While Ca^{2+}, Y^{3+} and Nd^{3+} are very effective for achieving small grain sizes, the smallest grain size was obtained for the powders doped with Ca^{2+}.

The sintering behavior of CeO_2 doped with two metal cations, (i.e. double dopants) was also investigated. Figure 13 shows the sintering curves for the compacted powders doped with 3 at% Ca^{2+} + 3 at% Mg^{2+} and 2 at% Ca^{2+} + 4 at% Mg^{2+}. For comparison, the sintering curves for the powders doped with 6 at% Ca^{2+} and with 6 at% Mg^{2+} are also included in the figure. It is seen that while the

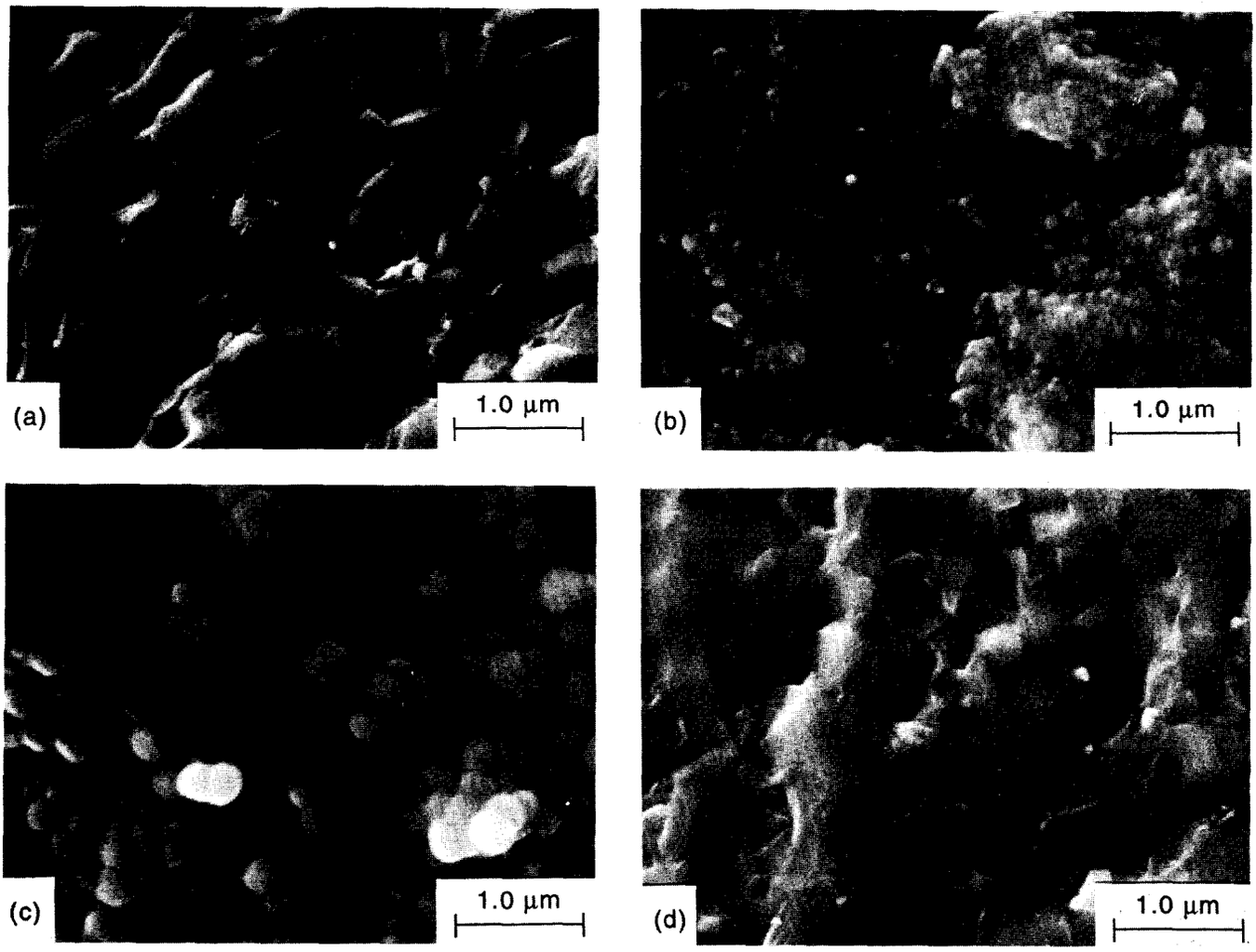


Fig. 12. SEM of the fracture surfaces of the CeO_2 powder compacts doped with 6 at% of (a) Mg^{2+}, (b) Ca^{2+}, (c) Y^{3+} and (d) Nd^{3+} after sintering at 10°C/min to 1350°C.

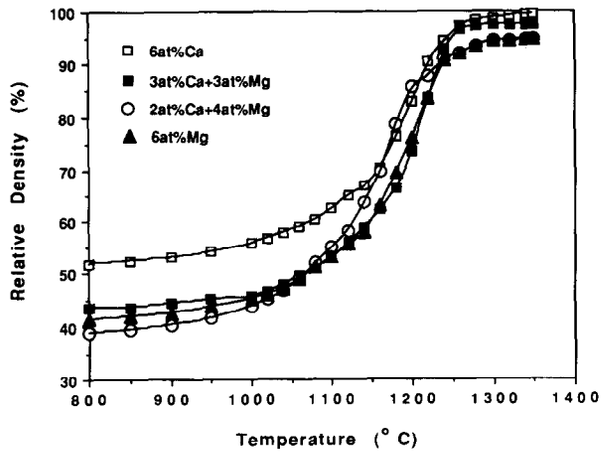


Fig. 13. Relative density versus temperature for the CeO_2 powder compacts doped with double cations, Mg^{2+} + Ca^{2+}, during sintering at 10°C/min to 1350°C. For comparison, the data for CeO_2 powder compacts doped with the single cations at the equivalent concentration are also shown.

green density of the Ca-doped powder compact is somewhat higher than those for the other samples, soon after the onset of densification the data fall within a narrow band. The data therefore indicate that for a fixed concentration of these two dopants, the elemental composition of the dopant does not have a significant effect on the sintering kinetics. The final densities of the doubly-doped samples have values which are intermediate between those for the Mg-doped and Ca-doped samples.

Figure 14 shows scanning electron micrographs of the samples containing double dopants after sintering to 1350°C. The micrograph shown in Fig. 14(a) (for the sample doped with 3 at% Ca^{2+} + 3 at% Mg^{2+}) does not represent the true fracture mode of the dense sample. The powder compact used to produce the microstructure contained a small crack (formed during the powder compaction stage). After sintering, the surface of the crack was observed in the SEM. The micrograph reveals a classical microstructure produced by solid state sintering where the flat grain boundaries have clearly developed. Figure 14(b) shows the true fracture surface of the dense sample (containing 2 at% Ca^{2+} + 4 at% Mg^{2+}). The fracture mode is predominantly transgranular. Generally, for the equivalent dopant concentration, the microstructures for the samples containing double dopants show features which are intermediate between those for the Ca-doped sample (Fig. 12(b)) and the Mg-doped sample (Fig. 12(a)).

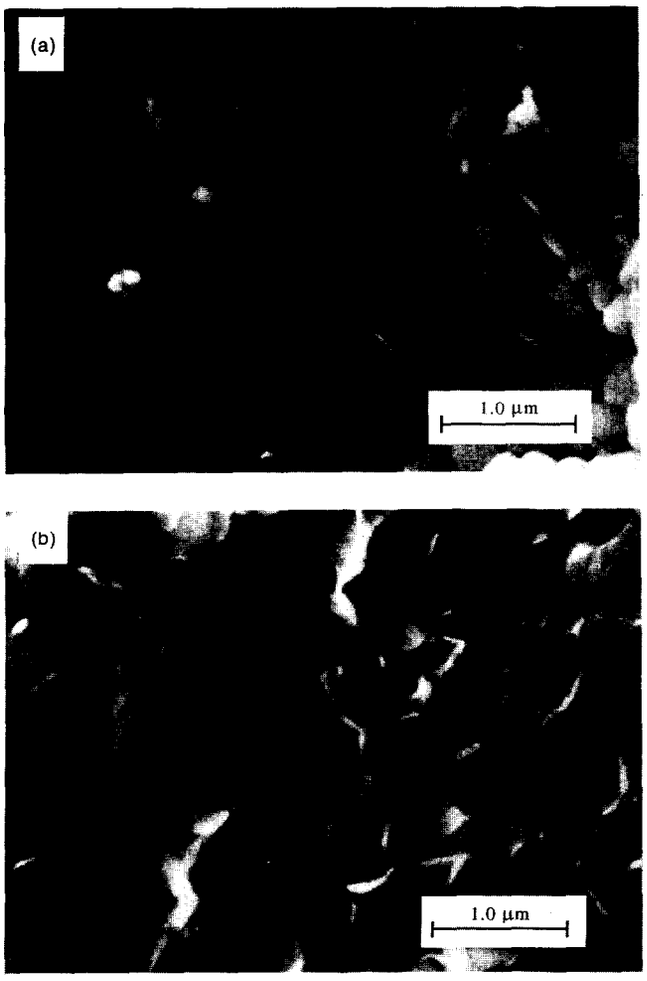


Fig. 14. SEM of the samples described in Fig. 13 containing double dopants of (a) 3at% Ca^{2+} + 3 at% Mg^{2+} and (b) 2 at% Ca^{2+} + 4 at% Mg^{2+}. Part (b) shows the fracture surface of the dense sample but (a) shows the surface of an internal flaw in the dense sample.

4 Discussion

The results indicate that the incorporation of dopants produce subtle microstructural effects in CeO_2 powders prepared by hydrothermal processing. The major processes occurring in the hydrothermal technique employed in the present work are the dissolution of an amorphous, gelatinous product and its precipitation in the form of crystalline particles. X-ray diffraction of the powders after the hydrothermal treatment revealed no evidence of free oxides of any of the dopant elements investigated (Mg, Ca, Sc, Y and Nd). Furthermore, high resolution electron microscopy of the doped powders (Figs 4 and 5) revealed that the powders were crystalline in nature. On the basis of the X-ray and electron microscopy data, the dopants may be assumed to be incorporated into the CeO_2 solid solution during the hydrothermal process.

Electron microscopy also indicates that the incorporation of dopants into the CeO_2 powders during hydrothermal synthesis influences the powder morphology and the distribution of the dopant within the powder. Powders doped with Ca^{2+} or Nd^{3+} have a relatively narrow distribution in sizes. Furthermore, EDX analysis of the Ca-doped powder indicates that the chemical composition of the individual particles is the same.

Dopants such as Mg^{2+}, Sc^{3+} and to a lesser extent Y^{3+}, lead to a bimodal distribution of particle sizes. EDX analysis of the powder doped with Y^{3+} also revealed that the dopant concentration was significantly higher in the particles with the smaller sizes. Further work is necessary in order to understand the effect of the dopants on the microstructure and microchemistry of the powders.

The sintering results indicate that the dopants investigated have a profound effect on the densification and grain growth of the compacted powders. All of the dopants lead to a shift in the sintering curve for CeO_2 to higher temperatures (Figs 10 and 11). While the mechanism of densification of CeO_2 is not clear, predictions based on Herring's scaling laws[9] indicate that grain boundary diffusion is enhanced with decreasing particle size. Compared to diffusion through the lattice, grain boundary diffusion is also expected to be more rapid at lower temperatures. For the ultrafine powders and relatively low sintering temperatures used in the present work, it seems reasonable to assume that grain boundary diffusion is the rate-controlling mechanism for densification. The shift in the sintering curves to higher temperatures indicates that the dopants reduce the rate of grain boundary diffusion. This reduction in the grain boundary diffusion, compared to undoped CeO_2, further indicates that the additive cations modify the structure of the grain boundary region.

The dopants were also found to have a dramatic effect on grain growth phenomena during sintering. Dopants can influence the structure of the grain boundary and, hence, the mobility of the grain boundary by two main processes. First, the additive may form a separate phase at the grain boundary by precipitation or by chemical reaction. The second phase can be solid or liquid at the sintering temperature. In the second process, the concentration of the additive cations may be enhanced or diminished in the grain boundary without the formation of a second phase. The term segregation will be used in a limited sense to describe the second process. For the present work, the first process appears unlikely. Detailed microstructural analysis by conventional and high resolution TEM of the sintered Ca-doped sample showed no evidence of a second phase at the grain boundaries (Fig. 15). It will be recalled (Fig. 7) that the Ca-doped samples show the most dramatic change in grain growth behavior. CeO_2 is also known to have a high solid solubility for many dopants, including those investigated in this work.[12–14] Furthermore, the presence of a liquid phase during sintering appears unlikely because of the low final sintering temperature (1350°C) used for most of the experiments in this work.

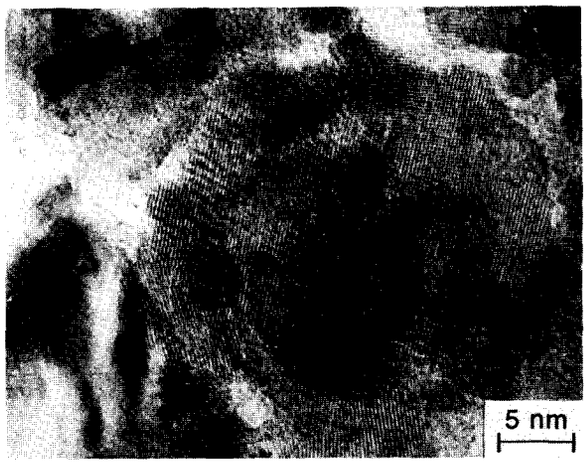


Fig. 15. HREM of a sintered sample of CeO_2 doped with 6 at% Ca^{2+}. The sample was sintered at 10°C/min to 1350°C.

The evidence described above strongly suggests that segregation of the dopants to the grain boundary (referred to as solute segregation) might be an important process by which the dopants influence the sintering and grain growth of CeO_2. The characterization of the microchemistry of the grain boundaries in the sintered samples is currently in progress. However, a number of observations pertinent to the use of solid solution additives in the sintering of ceramics can be made at this stage. One mechanism which is believed to control solute segregation to the grain boundary involves the concept of a space charge.[15–17] It has been shown recently that the effect of dopants on the grain growth of tetragonal zirconia polycrystals (TZP) can be satisfactorily rationalized in terms of the space charge concept.[18] In the space charge theory, surfaces, boundaries and dislocation cores in an ionic crystal may possess a net charge resulting from the presence of excess ions of one type. This charge is compensated by a region of space charge of the opposite sign adjacent to these lattice discontinuities. For ionic crystals doped with aliovalent cations, the magnitude and sign of the space charge are expected to be controlled by the effective charge of the solute. In the present experiments, the dopants present in the bulk of the lattice have a negative effective charge so that, in thermal equilibrium, the boundary will possess a positive charge. The dopants must then segregate to the boundary as a space charge so that the bulk of the crystal remains neutral.

For the aliovalent dopants investigated in this work we may expect, on the basis of the space charge concept, that the divalent cations (Mg^{2+} and Ca^{2+}) are more strongly segregated to the grain boundaries compared to the trivalent cations (Sc^{3+}, Y^{3+} and Nd^{3+}). However, the grain size data show that Ca^{2+}, Y^{3+} and Nd^{3+} are effective for

controlling grain growth, with Ca^{2+} being the most effective, while Mg^{2+} and Sc^{3+} are not effective. The grain size data cannot therefore be rationalized in terms of the space charge concept only.

An interaction between the moving grain boundary and the dopant cations can also originate from the strain energy caused by the mismatch in size between the dopant cations and the host cations.[19] Because of the size mismatch, there will be a difference in strain energy between a dopant cation situated at or near the grain boundary and one in the crystal lattice. For aliovalent dopants, the interaction between the strain field and the boundary must be coupled with the space charge field because of the effective charge of the dopant cations. The distribution of the dopant cations and defects within the space charge cloud can therefore be significantly affected by the strain field due to the size mismatch.

Assuming eight-fold coordination, the ionic radii of Ce^{4+}, Mg^{2+}, Ca^{2+}, Sc^{3+}, Y^{3+} and Nd^{3+} are 0·097, 0·089, 0·112, 0·087, 0·102 and 0·112 nm, respectively.[20] The cations Mg^{2+} and Sc^{3+} which have ionic radii smaller than that of host Ce^{4+} ion, (i.e. the undersize cations) are not effective for grain growth control while Ca^{2+}, Y^{3+} and Nd^{3+} with ionic radii larger than that of the Ce^{4+} ion, (i.e. the oversize cations) are effective for grain growth control. For the oversize cations, Ca^{2+} with the highest effective charge is most effective for grain growth control. It is clear that both the charge and the size mismatch of the dopant cations are important factors for grain growth control by divalent and trivalent cations.

Assuming that the segregated dopants control the grain boundary mobility by the solute drag mechanism proposed by Cahn,[21] the mobility of the grain boundary is given approximately by an equation of the form:

$$M = \frac{D}{\Delta C\, kT} \tag{3}$$

where D is the diffusivity of the dopant cation, ΔC is the excess concentration of the dopant cation in the grain boundary, k is the Boltzmann constant and T is the absolute temperature. Taking the case of the divalent dopants, the effectiveness of Ca^{2+}, compared to Mg^{2+}, for grain growth control may be due to an increased segregation to the grain boundary due to a larger size mismatch or a decrease in the diffusivity of the dopant due to its larger ionic radius or a combination of the two. The concentration of the dopants in the grain boundary is currently being investigated. However, the effectiveness of the Ca^{2+} dopant, compared to Mg^{2+}, can be rationalized in terms of its larger ionic size. For cations of nearly the same size, e.g. Ca^{2+} and Nd^{3+}, the greater effectiveness of Ca^{2+} can be rationalized in terms of its greater effective charge. Thus, based on the space charge concept and the strain mismatch, Ca^{2+} is expected to be most effective for grain size control, as is observed.

For Ca^{2+} which forms the most effective dopant for grain growth control, the data of Fig. 7 for the grain size after identical sintering conditions show that the concentration of the dopant has a significant effect on the grain size. The variation of the grain size with dopant concentration is not uniform. With increasing Ca^{2+} concentration, the grain size decreases monotonically and reaches a minimum at ≈5–6 at%, after which it increases monotonically. There is therefore an optimum Ca^{2+} concentration which is most effective for grain growth control. Grain size data for the CeO_2 doped with Y^{3+} also reveal an optimum dopant concentration for grain growth control at ≈6 at%. As outlined earlier, high resolution TEM of the sintered body doped with 6 at% Ca^{2+} did not reveal the presence of a discrete second phase at the grain boundaries. For samples containing low concentrations of dopants, (e.g. below the optimum concentration of ≈6 at%), the grain growth behavior can be rationalized in terms of the solute drag mechanism. However, the mechanism cannot be used to explain the grain growth behavior at large dopant concentrations where the grain size of the doped samples are greater than that for the undoped CeO_2 (Fig. 7).

For the same concentration of dopants (6 at%), the data indicate that the effect of double dopants (Mg^{2+} + Ca^{2+}) on the sintering and grain growth is intermediate between those of the single dopants. Under identical sintering conditions, the grain size for the sample doped with 3 at% Mg^{2+} + 3 at% Ca^{2+} is ≈0·5 μm which is approximately half-way between those for the samples doped with 6 at% Mg^{2+} and 6 at% Ca^{2+} (≈30 nm) but approximately twice that for the sample doped with 3 at% Ca^{2+} (200 nm). Both Mg^{2+} and Ca^{2+} are expected to substitute at the regular Ce^{4+} lattice sites and the nature of the charged defects produced by Mg^{2+} and Ca^{2+} substitution is therefore expected to be the same. Compensation of one type of defect by another cannot occur for the double dopants used in this study. The data for the double dopants therefore indicate that the dopants act to influence the grain boundary structure.

5 Conclusions

Divalent and trivalent dopants (Mg^{2+}, Ca^{2+}, Sc^{3+}, Y^{3+} and Nd^{3+}) produced subtle changes in the microstructure and microchemistry of ultra-fine

CeO_2 powders prepared under hydrothermal conditions. The powders doped with Mg^{2+}, Sc^{3+} and, to a lesser extent Y^{3+}, had a bimodal size distribution. EDX analysis of the Y-doped powder showed that the dopant concentration was significantly higher in the smaller particles. The undoped powder and the Ca-doped and Nd-doped powders had a fairly narrow size distribution. For the Ca-doped powder, no difference in the chemical composition of the individual particles was detected by EDX analysis.

The dopants had a dramatic effect on the sintering and grain growth behavior of the compacted powders. Compared to the undoped CeO_2, all of the dopants produced a shift in the sintering curve to higher temperature. The effect of the dopants on grain growth was dependent on both the cation charge and the cation radius. The undersize cations, Mg^{2+} and Sc^{3+} were not effective for grain growth control. Grain growth was suppressed in the samples doped with the oversize cations, Ca^{2+}, Nd^{3+} and Y^{3+}, with Ca^{2+} being the most effective for grain growth control.

At low concentrations, the influence of the dopants on the sintering and grain growth behavior can be rationalized in terms of segregation to the grain boundary by a space charge mechanism and solute drag on the grain boundary. However, this mechanism cannot explain the enhanced grain growth at large dopant concentrations where the grain size of the doped sample is significantly greater than that for the undoped CeO_2.

References

1. Gleiter, H., Nanocrystalline materials, *Prog. Mater. Sci.*, **33**(4) (1989) 223–315.
2. Birringer, R., Gleiter, H., Klein, H.-P., & Marquard, P., Nanocrystalline materials: an approach to a novel solid structure with gas-like disorder, *Phys. Lett.*, **102A** (1984) 365–9.
3. Hahn, H., Logas, J. & Averback, R. S., Sintering characteristics of nanocrystalline TiO_2, *J. Mater. Res.*, **5**(3) (1990) 609–14.
4. Mayo, M. J., Siegel, R. W., Narayanasamy, A. & Nix, W. D., Mechanical properties of nanophase TiO_2 as determined by nanoindentation, *J. Mater. Res.*, **5**(5) (1990) 1073–82.
5. Nieman, G. W., Weertman, J. R. & Siegel, R. W., Mechanical behavior of nanocrystalline Cu and Pd, *J. Mater. Res.*, **6**(5) (1991) 1012–27.
6. Komarneni, S., Roy, R., Breval, E., Ollinen, M. & Suwa, Y., Hydrothermal route to ultrafine powders utilizing single and diphasic gels, *Adv. Ceram. Mater.*, **1**(1) (1986) 87–92.
7. Komarneni, S., Fregeau, E., Breval, E. & Roy. R., Hydrothermal preparation of ultrafine ferrites and their sintering, *J. Am. Ceram. Soc.*, **71**(1) (1988) C26–8.
8. Somiya, S., Yoshimura, M., Nakai, Z., Hishinuma, K. & Kumaki, T., Hydrothermal processing of ultra-fine single-crystal zirconia and hafnia powders with homogeneous dopants, *Advances in Ceramics*, **21** (1987) 43–55.
9. Herring, C., Effect of change of scale on sintering phenomena, *J. Appl. Phys.*, **21** (1950) 301–3.
10. Zhou, Y. C. & Rahaman, M. N., Hydrothermal synthesis and sintering of ultrafine CeO_2 powders, *J. Mater. Res.*, **8**(7) (1993) 1680–6.
11. Blumental, R. N., Brugner, F. S. & Garnier, J. E., The electrical conductivity of CaO-doped nonstoichiometric cerium oxide from 700 to 1500°C, *J. Electrochem. Soc.*, **120** (1973) 1230–5.
12. Distine, R. T., Blumenthal, R. N. & Kuech, T. F., Ionic conductivity of calcia, yttria, and rare earth-doped cerium oxide, *J. Electrochem. Soc.*, **126**(2) (1979) 264–9.
13. Yahiro, H., Eguchi, K. & Arai, H., Electrical properties and reducibilities of ceria–rare earth oxide systems and their application to solid oxide fuel cell, *Solid State Ionics*, **36** (1989) 71–5.
14. Yahiro, H., Ohuchi, T., Eguchi, K. & Arai, H., Electrical properties and microstructure in the system ceria–alkaline earth oxide, *J. Mater. Sci.*, **23** (1988) 1036–41.
15. Kingery, W. D., Plausible concepts necessary and sufficient for interpretation of ceramic grain boundary phenomena: I. grain-boundary characteristics, structure, and electrostatic potential, *J. Am. Ceram. Soc.*, **57**(1) (1974) 1–8; II. solute segregation, grain-boundary diffusion, and general discussion, *J. Am. Ceram. Soc.*, **57**(2) (1974) 74–83.
16. Lehovec, K., Space charge layer and distribution of lattice defects at the surface of ionic crystals, *J. Chem. Phys.*, **21** (1953) 1123–8.
17. Frenkel, J., *Kinetic theory of liquids*, Oxford University Press, New York, NY, 1946, p. 36.
18. Hwang, S.-L. & Chen, I-W., Grain size control of tetragonal zirconia polycrystals using the space charge concept, *J. Am. Ceram. Soc.*, **73**(11) (1990) 3269–77.
19. Yan, M. F., Cannon, R. M. & Bowen, H. K., Grain boundary migration in ceramics, Ceramic Microstructures '76. Eds R. M. Fulrath & J. A. Pask. Westview Press, Boulder, CO, 1977, pp. 276–307.
20. Shannon, R. D., Revised effective ionic radii and systematic studies of inteatomic distances, halides and chalcogenides, *Acta Crystallogr.*, **A32** (1976) 756.
21. Cahn, J. W., The impurity drag effect in grain boundary motion, *Acta Metall.*, **10**(9) (1962) 789–98.

Journal of the European Ceramic Society **15** (1995) 951–958
© 1995 Elsevier Science Limited
Printed in Great Britain. All rights reserved
0955-2219(95)00073-9
0955-2219/95/$9.50

Grain Growth of Differently Doped Zirconia

J. A. Allemann,[a] B. Michel,[a] H.-B. Märki[a], L. J. Gauckler[a] * & E. M. Moser[b]

[a]Nonmetallic Materials, Swiss Federal Institute of Technology, CH-8092 Zürich, Switzerland
[b]EMPA, Überlandstr. 129, CH-8600 Dübendorf, Switzerland

(Received 13 September 1994; revised version received 26 March 1995; accepted 31 March 1995)

Abstract

Grain growth has been characterized for various zirconia alloys and cation segregations have been measured with AES and ESCA. The samples were prepared by coprecipitation, followed by compacting and sintering at 1400°C for different times. Grain growth was found to depend strongly on the dopants, e.g. on their radius and valence state. However, segregation factors of these cations did not reveal significant differences. Impurities up to 1 wt% are found to control grain growth via a grain boundary layer. Large amounts of Cr_2O_3 and SnO_2 tend to suppress grain growth effectively by the spherical shaped precipitations. The results are discussed in relation to the existing grain growth models.

Introduction

Polycrystalline tetragonal zirconia is a ceramic that combines both high strength and outstanding toughness, caused by a mechanism known as transformation toughening. One of the most important parameters for this toughening mechanism is the material's grain size. For good mechanical properties it must have a well defined value slightly smaller than a critical grain size being typically in the order of 1 μm for Y–TZP. In order to control grain growth in a ceramic body during processing, a profound knowledge of grain growth parameters is needed.

Grain growth of zirconia alloys depends very strongly on composition and is related to the phase content. The growth of cubic grains in zirconia doped with Y^{3+} is 30–250 times faster than that of tetragonal grains alloyed with the same cation.[1] Grain growth is strongly suppressed if both phases are coexistent. Furthermore it is well known, that Y^{3+} and Gd^{3+} suppress the grain growth very efficiently whereas Ce^{4+} does not. Up to now, the influence of a variety of alloying elements on the grain growth has been investigated, but there is still a strong controversy about the mechanisms involved in this process.

Two models are proposed up to now. **Model 1**: Theunissen *et al.*[2] proposed a solute drag model based on the observed enrichment of Y^{3+} at the surface of both Y–TZP and Y–FSZ. Hwang and Chen[3] confirmed this observation qualitatively and explained the segregation behavior of different dopants using a space charge concept. **Model 2**: Based on the large differences in Y_2O_3 content from grain to grain during sluggish partitioning, Lange *et al.*[4] suggested that coherency strains arise when boundaries between grains with different compositions move, suggesting one possible correlation between sluggish phase partitioning and slow grain growth. Stoto, Nauer and Carry[5] confirmed the sluggish grain growth during phase partitioning and observed an enhanced grain growth after phase segregation had occurred.

There are still some discrepancies in both of these models. **Model 1**: Hwang and Chen[3] found an enrichment factor for Y^{3+} of 1·9 whereas a much stronger enrichment factor of 4·3 has been found by Theunissen. On the other hand, Nauer and Carry found yttria segregation at grain boundaries only in combination with a 2 nm thick amorphous intergranular phase. The influence of such a glasslike layer on the segregation of dopants is said to be negligible by Hwang and Chen and not taken into consideration by Theunissen.[6,7] **Model 2**: The most significant decrease in grain growth occurs generally with concentrations up to the solubility limit. Model 2 cannot explain the strong decrease of grain growth within the homogeneity range, as there is no compositional difference between the grains. In addition, it is difficult to explain with Model 2 the observation that the grain growth of samples within the two phase field is approximately constant. This in spite of the fact, that the compositional inhomogeneities might increase with increasing dopant concentration.

*To whom correspondence should be addressed.

The aim of this study was to investigate the influence of alloying elements on the grain growth of tetragonal zirconia and based on these results to differentiate between the validity of the different models.

Experimental

Sample preparation and characterization

Doped zirconia powders were made by coprecipitating $ZrOCl_2 \cdot H_2O$ (Corustar, Frankfurt, D) and metal chlorides (Fluka AG, grade p.a.) in aqueous solutions with ammonia. The filtered hydroxides were washed chlorine free, spray dried and calcined at 700°C for 1 h. Finally these powders were attrition milled at 1500 rpm for 30 min and again spray dried. The commercial powder 6 Y–ZrO_2 (Alusuisse-Lonza Services AG, P021) has been fabricated with a similar technique, but calcined at 750°C for 8 h. For explanation: an alloy 3 7 AB–ZrO_2 has the composition 3 ct% A^{a+}, 7 ct% B^{b+} and 90 ct% Zr^{4+} (ct% = cation%). Solely the grain growth experiment at 1550°C was carried out with an other 6Y–ZrO_2 powder (Tosho, Tokio, Japan; TZ-3YB/PVA).

All powders were pressed uniaxially to cylinders (Ø15 mm, h ≈ 8 mm) without adding any binder and compressed isostatically at 250 MPa. Subsequently they were heated with 10 K/min to 1400°C and sintered for 5 min or 8, 24 or 72 h, respectively. Afterwards they were quenched in air down to room temperature.

The phases in the sintered samples were analyzed with a X-ray diffractometer (D 5000, Siemens). The diffraction patterns were collected with Cu Kα radiation (γ = 1·5405 Å) over an angular range of 10–80° 2θ. Those samples which disintegrated during cooling were ground and measured in powdered form. Measurements have been carried out on the uncracked samples before and after removing a surface layer by polishing; no change in the m : t : c phase ratio has been found between bulk and layers.

The grain size has been measured on fracture surfaces with a scanning electron microscope (SEM) and evaluated based on the mean intercept method. The results were fitted with the phenomenological equation:

$$D^n - D_o^n = kt \quad (1)$$

In this equation, grain size D depends on the starting grain size D_o, the exponential parameter n, the preexponential factor k and the time t. The exponent n depends on the microstructure.[8] Therefore, the data were evaluated for both n = 2, and n = 3. In addition, the best fitting n was determined for each material using an approximation algorithm. No significant difference could be found between these methods. In order to be able to compare the different grain growth coefficients k to each other and to published data, it has been fixed at n = 3.

Segregation measurements

Scanning electron images (SEI) and depth profiles on inter- and intracrystalline fractures at the selected areas of <0·01 μm^2 have been performed with a Perkin Elmer PHI Model 4300 SAM spectrometer operating with a primary beam energy of 3 kV and an electron beam current of 0·01 μA. Small pieces of the ceramic samples were pressed into a gold foil and heated up to 450°C by resistivity in order to enhance the electrical conductivity of the material while its thermal stability is still maintained.[9] A residual pressure lower than $9–10^{-10}$ mbar has been maintained in the analytical chamber during the measurements. The sensitivity factors of the oxides[6,7] have been used to calculate the cation's concentration with the exception of calcium,[10] where that of the oxide is unknown. The ion gun was operated with an Ar^+ ion energy of 2 keV, corresponding to an etching rate of 0·93 nm/min with an interface resolution of 2·8 nm for a 33 nm SiO_2/Si (111) standard reference which corresponds to a sputtering rate of 0·46 nm/min for a ZrO_2/Si (111) reference.

Photoelectron spectroscopy measurements have been recorded with a Perkin Elmer PHI 5400 small spot ESCA apparatus equipped with a channel plate detector and a Mg X-ray source operated at 400 W (15 kV; 26,7 mA). The pass energy of the analyzer has been set to 35·75 eV, resulting in a full width at half-maximum (FWHM) value of 1·0 eV for the Ag($3d_{5/2}$) line. The Zr($3d$) line at 182·2 eV was used as a reference to correct for sample charging.[11]

Generally, AES and XPS concentration measurements agreed only roughly with chemically determined concentrations. The estimation of errors of the measured concentrations takes only those errors into account which are due to uncertainties of data evaluation. Several factors can cause additional deviations. It was not possible to hold the incidence angle between the electron beam and different grains' surfaces constant. The deviations amount to about ±10°. Therefore, the information depth of the investigated layer varies and so does the measured cation concentration. By changing this angle, the concentration was found to alter in the order of ±3 ct%. The quantitative analysis of Y(MNN) and Ce(MNN) was difficult to perform due to a peak overlapping with Zr(MNN). If only the first half of the Y(MNN) AES-peak was taken

into consideration and this concentration was multiplied with 2, influences of the overlapping Zr(MNN)-lines could be excluded. The XPS signals were merely integrated and no deconvolution has been carried out. For such an evaluation Ce(MNN) concentrations of AES and XPS measurements showed similar results. During the enhanced exposure of the grains to the electron beam, a loss of calcium was observed. In case of Ti, Ce, Y and Zr, the sensitivity factors of the oxides have been used to calculate the cation's concentrations.[6,7] Excluding preferential sputtering,[12] the measured concentrations are compatible to the concentrations determined by chemical analysis. Since the sensitivity factor of CaO was not available, that of the metal has been taken; the absolute concentrations of the titanium is also affected. Thus, these values are not comparable with chemically determined concentrations and can be regarded just relatively to each other.

Results and Discussion

Grain growth of differently doped zirconia

Grain size of differently doped zirconia has been measured as a function of soaking time at 1400°C (Fig. 1). The grain size D increases with the soaking time t according to a law, best described by eqn (1). Undoped tetragonal ZrO_2 at 1400°C has a grain growth coefficient $k = 2{\cdot}4 \times 10^{-22}$ m^3/s. The grain growth is enhanced by doping with smaller cations whereas it becomes sluggish by doping with larger ones (Table 1). In addition, the grain growth is more effectively suppressed by large cations, if they have a lower valence state. That explains why Ce^{4+} suppresses the grain growth only weakly whereas the grain growth slows down significantly by doping with Gd^{3+} and Y^{3+}. The same relationship has been demonstrated by Hwang and Chen[2] for 12 Ce–ZrO_2 doped with ternary cations of different size and valence state. Their grain growth coefficients k are slightly larger than ours due to the smaller concentration of doping cations. However, their data depends on both the size as well as the valence of the doping cation. k factors as small as $0{\cdot}01 \times 10^{-22}$ m^3/s to $0{\cdot}02 \times 10^{-22}$ m^3/s were found for Y–TZP. This extreme grain growth suppression had not been observed in the other alloying systems.

Table 1. Grain growth coefficients k of eqn 1 and $n = 3$ for alloyed tetragonal ZrO_2 at 1400°C in units of 10^{-22} m^3/s

Valence	*Ionic size: smaller than Zr^{4+}*	*Ionic size: larger than Zr^{4+}*
	For pure ZrO_2	2·4
2^+	MgCe: 1†	CaCe: 0·3†
		Y: 0·02
3^+	Cr: 12	(0·12 at 1500°C, 0·49 at 1550°C)
		Y: 0·01...0·02*
		Gd: 0·1 #
		YCe: 1...2†
		RECe: 1...3†
4^+	Ti: 17	Ce: 1·2

†Ref. 3: Grain growth at 1420°C was measured in a ternary systems by adding 1ct% of a dopant to 12 Ce–ZrO_2.
*Ref. 22: 1400°C, Ref. 5: 1450°C.
Ref. 13: 1400°C.

Y–TZP has been annealed at different temperatures. The grain growth coefficients k of Y–TZP were found to be 0·02, 0·12 and $0{\cdot}49 \times 10^{-22}$ m^3/s at 1400, 1500 and 1550°C, respectively. The study was done more carefully at 1550°C up to 300 h (Fig. 2) as the mechanical properties generally are tailored at this temperature. No increased grain growth has been observed at all during and after the partitioning of an oversaturated tetragonal phase to stable (t + c) phases (a phase analysis has not been carried out, but the long annealing times at 1550°C suggest an extensive progress in phase partitioning). This is in clear contradiction to

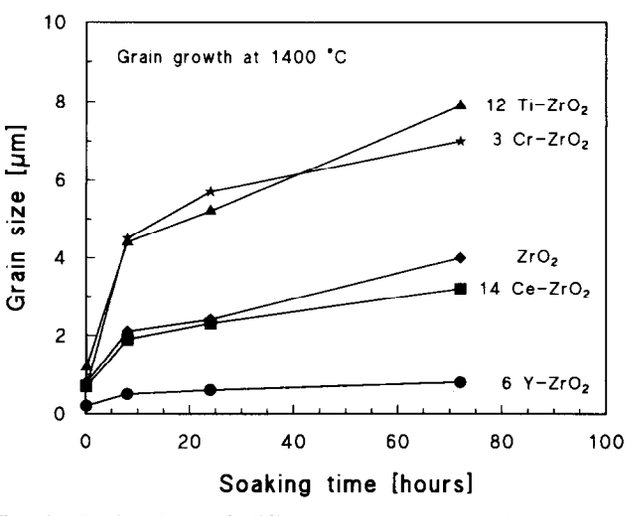


Fig. 1. Grain sizes of differently doped zirconia alloys in function of the annealing time at 1400°C.

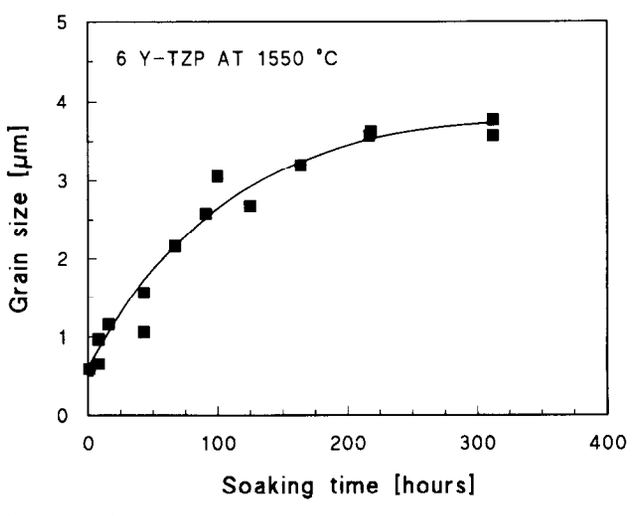


Fig. 2. Grain sizes of 6 Y–TZP as a function of the soaking time at 1550°C.

observations made by Nauer *et al.*[5] at 1400 and 1450°C up to 200 h. It is assumed that their findings are caused by another unknown growth mechanism. Our results suggest that phase partitioning has at least not a strong influence on grain growth.

Solid solutions of zirconia with 6, 10 and 12 ct% Ti^{4+} have been prepared using the described coprecipitation method. The grain growth of the annealed samples resulted in k values of 16·9, 16·7 and 16·2 10^{-22} m^3/s, respectively. This suggests that grain growth does not depend on the concentration within the investigated range. It is therefore assumed that the grain growth of zirconia doped with small cations is concentration independent above a threshold value which up to now is not known. In addition, zirconia doped with 3 ct% Cr^{3+} has a grain growth coefficient k = 12·3 10^{-22} m^3/s, which is not significantly different from that found in the samples Ti–ZrO_2. In contrast, Gd^{3+} inhibits the grain growth effectively up to a concentration of 1·5 ct%[13] (Fig. 3), which is close to the solid solubility limit of 1·1 ct%. The decrease of the grain growth in the homogeneity range is inverse proportional to the concentration as predicted by the solute drag model of Lücke.[14] In the two phase regions, the grain growth is pretty much constant. A similar behavior has been found also in other systems such as in Y–ZrO_2,[15] La–ZrO_2,[16] Ca–ZrO_2[3] and YCe–ZrO_2.[17]

The above results suggest that cations smaller than Zr^{4+} increase the grain growth, independent on both their concentration and valence. In contrast, larger cations suppress it very strongly. Grain growth coefficients decrease mainly within the homogeneity range and do not depend on the concentration in the two phase region. Our results do not give evidence for a enhanced grain growth during or after the phase partitioning process.

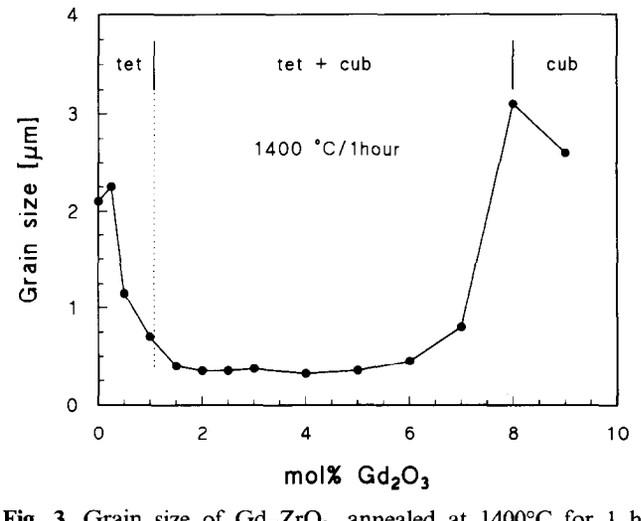


Fig. 3. Grain size of Gd–ZrO_2, annealed at 1400°C for 1 h as a function of the Gd^{3+} concentration (after Leung *et al.*)[13]

Therefore it is proposed that phase partitioning has not an essential influence on grain growth.

Segregation of dopants

Segregations of doping cations within a zirconia grain have been investigated using AES (Auger Electron Spectroscopy) and XPS (X-ray Photoelectron Spectroscopy). Surface concentrations have been ascertained on several intercrystalline broken grain facets. The observed concentrations reveal the same tendencies and are reproducible within some ct%, governed by the resolving limit of the applied method. Concentration profiles have been worked out by sputtering off layer by layer up to the grains' interior. For some samples it was possible to confirm these bulk concentrations by AES measurements on transcrystalline fracture faces. The obtained values agreed well to each other. Concentration measurements of Ca^{2+} are not compatible with values obtained from chemical analysis, as the sensitivity factor of the oxide is unknown and thus that of the metal had to be taken. Therefore, these results can be regarded just relatively to each other.

The surface and bulk concentrations were used to determine the segregation factors of the different dopants (Table 2). They are summarized briefly in the following:

Y^{3+} has a segregation factor of 2·4. The enrichment of Y-ions is observed in the uppermost layers at the surface of the grains. The surface concentration has been confirmed on several grains.

Ti^{4+}: In all binary alloys as well as in the ternary sample 7 8 CeTi–ZrO_2, the Ti^{4+} has a segregation factor of about 5. Furthermore it has been observed, that the segregation generally occurs within a broad layer, extending up to 6 nm into the grain. In a ternary alloy together with Ca^{2+}, segregation of Ti^{4+} clearly is less pronounced.

Ce^{4+} has a segregation factor of 2·2. This factor does not change significantly in ternary alloys with titanium oxide.

Ca^{2+}: The determined surface and bulk concentrations of these alloys are much too high. One explanation is, that this discrepancy is caused because the sensitivity factor of the metal is used rather than that for the oxide. We exclude that our data are collected on possible second phases, because the same values were also gathered on X-ray single phase materials. Whatever originated this error, the segregation factor of Ca^{2+} should not be affected significantly. It has been determined to about 1·5 for both the binary and ternary alloy and has been confirmed on other alloys as well.

Table 2. Concentrations of various cations at the surface (C_s) and in the bulk (C_b) and the resulting segregation factors C_s/C_b for zirconia alloys

Sample	C_s *(cat%)*	C_b *(cat%)*	*Thickness (nm)*$^+$	C_s/C_b	*Method*
6 Y–ZrO_2	19±1	8±1	1	2·4	AES/XPS
6 Ti–ZrO_2	43·1±0·6	8·1±1·8	6	5·3	AES
12 Ti–ZrO_2	47·3±0·6	9·6±1·8	6	4·9	AES
14 Ce–ZrO_2	22±4	10±3*	2	2·2	AES/XPS
7 8 CeTi—ZrO_2	11±3 Ce	4±3 Ce	2	2·8	AES/XPS
	45·2±0·5 Ti	11·2±1·8 Ti	3	4	
17 Ca–ZrO_2 (c)♦	51·3±0·2	34·9±0·4	2	1·5	AES
6 8 CaTi–ZrO_2♦	33·3±0·6 Ca	25·5±1·2 Ca*	1	1·3(Ca)	AES
	28·7±0·6 Ti	20·3±1·8 Ti*	3	1·4(Ti)	

*Confirmed on transcrystalline fracture faces: 26·9 (1·2) ct% Ca, 17·2 (1·7) ct% Ti.
♦Sensitivity factor of Ca-metal was taken rather then that of the oxide. See test for explanation.
$^+$Thickness of the segregation zone.

Segregation factors for all doping cations vary between 1 and 5·3 and seem to be relatively small for those cations which suppress grain growth and large for those which promote it. In addition, the segregation factors may not depend strongly on the dopant's concentration (Ti–ZrO_2). Furthermore, the segregation factor of Ti^{4+} is altered by alloying Ti–ZrO_2 with Ca^{2+} (6 8 CaTi–ZrO_2), but it appears not to be affected by Ce^{4+}, e.g. in the alloy 7 8 CeTi–ZrO_2. This behavior might be explained by the formation of an overcoat as mentioned by Theunissen *et al.*[6] The cations of titanium and cerium do form such an overcoat, i.e. behave in a similar way, but not that of calcium.

The segregation factors of Ce^{4+}, Ti^{4+} and Ca^{2+} in all binary and ternary alloys do not change markedly with increasing cation concentration, but the surface concentration of these cations increase if the bulk concentration is enhanced. This is consistent with the measurements of Hwang and Chen,[3] but not with those of Theunissen,[6,7] who found a constant Y^{3+} enrichment at the surface for all investigated concentrations.

Segregation factors of Ca^{2+} do not change strongly between tetragonal (at the time of soaking) and cubic grains. Similar segregation factors in these two crystal structures have also been found by Theunissen *et al.*[6,7] for yttria doped zirconia. Nevertheless, the grain growth of the tetragonal and cubic single phase microstructures are clearly different. This is surprising because the cation's segregation barrier cannot be responsible for such a large difference. One possible explanation is that lattice misfits between randomly oriented tetragonal grains inhibit grain growth. The lattice parameters of two touching grains are different and must be changed abruptly if one of that grains is growing into the other. Such lattice misfits do not exist in cubic grains and their grain growth is therefore faster.

The above results support therefore the idea that the segregation factors are similar for all cations in binary and ternary zirconia alloys. No evidence has been found for the suggestion of Hwang *et al.*,[3] that cations with a larger effective charge are more strongly attracted to the grain boundary than others. However, it is well known that cations alter diffusion significantly by their size and valence. The segregation of slowly diffusing cations thus is able to pin a grain boundary whereas the equally strong segregation of fast diffusing cations cannot do this.

Grain growth of polyphase zirconia

Second phases alter the grain growth of doped zirconia significantly. Main parameters are their mobilities, concentrations and morphologies. It is demonstrated in the following, that impurities influence the grain growth in a fundamentally different manner than second phases in amounts exceeding few mol%.

Impurities of SiO_2 and Al_2O_3 up to 1 wt% are added in various ratios to Y–TZP (Table 3(a)). The applied processing procedure is described in Ref. 18. Generally, it is found that increasing amounts of impurities lead to increased grain growth coefficients k (Fig. 4(a)). However, in the sample doped with only SiO_2, grain growth was insensitive to the amount of added SiO_2. By mixing SiO_2 and Al_2O_3 in a ratio of 1 : 1, abnormal grain growth was observed, leading to grains 10 times larger than those of the matrix. The resulting k value, evaluated merely based on the small matrix grains, does not reflect a proper grain growth mechanism and thus cannot be compared with the normal grain growth coefficients of the other samples.

Insoluble impurities have an impact on grain growth mainly by forming a grain boundary phase (Fig. 4(b)). The thickness of such grain boundaries has been measured by Impedance Spectroscopy

Table 3 (a) Grain growth coefficients k of Y–TZP with impurities of varying $SiO_2 : Al_2O_3$ ratios. (b) Grain growth coefficients k of zirconia alloys with large amounts of second phases and the characteristics

(a)

$SiO_2 : Al_2O_3$	$SiO_2 + Al_2O_3$ (wt%)	$k/10^{-22}$ (m^3/s)	δ_{GB} (nm)
0:0	<0·03	0·12	0·04
1:0	0·92	0·06	0·33
4:0	0·96	0·36	5·23
1:1	0·48	0·30	2·48
1:4	0·72	0·36	1·88
0:1	0·95	0·18	0·31

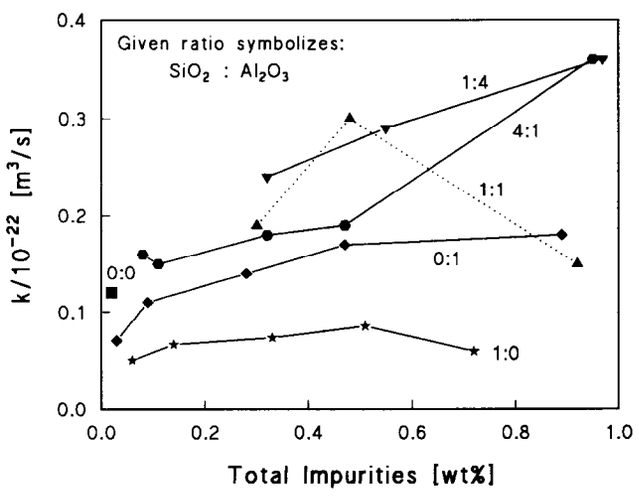
(b)

Sample	$k/10^{-22}$ (m^3/s)	Correlation r	Solubility	Precipitations	Morphology
ZrO_2	2·42	0·990		No	
3 Cr–ZrO_2	12·3	0·97		Nearly none	
10 Cr–ZrO_2	0·42	0·96	Cr: 1·4[23]	Cr_2O_3	*
12 Cr–ZrO_2	0·06	0·65		Cr_2O_3	*
5 In–ZrO_2	0·24	0·97	In: 3·4[24]	In_2O_3	#
6 8 CaTi–ZrO_2	2·25	0·997	Ca: 5[25]	M + c	
9 8 CaTi–ZrO_2	0·63	0·98	Ti: 15[26]	M + c + CZ	
10 15 CaTi–ZrO_2	7·19	0·996		M + c + CZ + ZT	
5 Bi–ZrO_2	34·5	0·95	Bi: 0[21]	Bi_2O_3	*
10 Sn–ZrO_2	1·2	0·98	Sn: ?	SnO_2	*

CZ: $CaZr_4O_9$, ZT: $ZrTiO_4$.
*Spherical, in triple points.
#Enlongated crystals.

and evaluated with a 'brick layer model' described elsewhere.[19] High purity Y–TZP has no grain boundary layer (0·04 nm) and a grain growth coefficient of k = 0·12 10^{-22} m^3/s, both determined on samples annealed at 1500°C. The addition of pure SiO_2 or Al_2O_3 lead in both cases to 0·3 nm thin grain boundary layers. In spite of that similarity, these layers alter the grain growth differently, namely they suppress it by SiO_2 and enhance it by Al_2O_3 additions. This behavior is surprising as SiO_2 is thought to form a viscous layer whereas Al_2O_3 is known as unyielding. However, due to the high annealing temperature of 1500°C, the formation of $ZrSiO_4$ is plausible. Due to the small dimension of its layer, the composition could not be determined. Mixed SiO_2–Al_2O_3 impurities caused much thicker grain boundaries as well as enhanced grain growth. The thickness of the grain boundary layers increased with increasing $SiO_2 : Al_2O_3$ ratio.

The viscosity of the grain boundary layer dominates the influence on grain growth. Due to the lack of viscosity data, the latter can be estimated with the help of melting temperatures T_M. Based



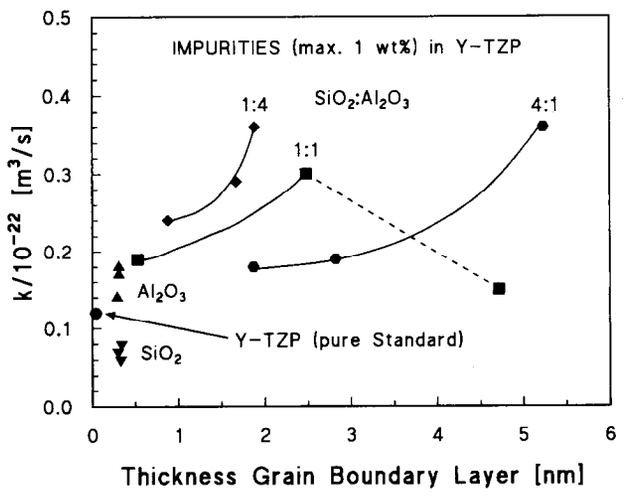


Fig. 4. (a) Grain growth coefficients k of Y–TZP containing up to 1 wt% impurities such as Al_2O_3, SiO_2 or mixtures of both as a function of the total amount of the impurities (Al_2O_3 + SiO_2). (b) Grain growth coefficients k as a function of the grain boundary layers formed.

on the ternary Y_2O_3–SiO_2–Al_2O_3 phase diagram,[18] the following relations are found: $T_{M,1:0}$ (liquidus of $ZrSiO_4$) > $T_{M,0:1}$ > $T_{M,1:4}$ > $T_{M,1:1}$ > $T_{M,4:1}$. The grain growth is enhanced in the same sequence.

If considerable amounts of a second phase are present, precipitations rather than grain boundary phases become crucial for grain growth. The grain growth coefficients k were determined for several systems containing large amounts of second phases (Table 3) and their influence could roughly be estimated. Chromium oxide in solid solution increases the grain growth but its precipitation decreases k by a factor of 200, despite the fact that chromium starts to volatilize around 1400°C. The same holds qualitatively also for tin oxide. 6 8 CaTi–ZrO_2 contained at room temperature substantial portions of monoclinic (at 1400°C tetragonal) and just few % cubic grains. Its grain growth is comparable to that of pure zirconia. The addition of 3 mol% more Ca^{2+} results in the formation of $CaZr_4O_9$. The grain growth is clearly suppressed by this second phase. Increase of the titanium oxide concentration to 7 mol% results in the formation of an additional $ZrTiO_4$ phase, i.e. the sample now contains 4 different phases. The grain growth of this sample is strongly increased, indicating a grain growth accelerating influence of $ZrTiO_4$. Bismuth additions increased the grain growth, too. This behavior must be caused by forming mobile Bi_2O_3 precipitations in triple points (as observed by SEM) and by a volatile phase. The large radius of Bi^{3+}, its valence and its low solubility[21] exclude a grain growth accelerating influence in solid solution of zirconia.

In summary, SiO_2 impurities probably in form of $ZrSiO_4$ decrease the grain growth whereas large amounts of SiO_2 increase it. In contrast, Al_2O_3 impurities enhance grain growth only slightly, whereas large amounts suppress it very efficiently. Cr_2O_3 and SnO_2 inhibit grain growth very efficiently but they evaporate at temperatures around 1400°C. These findings suggest that impurities influence grain growth over a grain boundary layer whereas larger amounts of a second phase control grain growth based on its morphology, mobility and amount.

Conclusions

Grain growth is found to be varied by the doping cations up to a factor of 10.[4] Large, low valence cations are most effective to reduce grain growth in agreement with the solute drag model whereas small ones increase it independent of their valence state and concentration. The cations' segregations are similar for all investigated alloys and do not reveal any correlation with the grain growth coefficients k. It is therefore suggested that segregations generally occur independent of the cations valence state, e.g. not with a space charge mechanism. However, the pinning of the grain boundaries is most effective in alloys doped with large cations of low valence, indicating, that the diffusion of the segregated cations is the controlling mechanism. The grain growth behavior of Y–TZP is not altered during and after phase partitioning, excluding it as a growth controlling mechanism. Impurities were found to govern grain growth by forming grain boundary layers, whereas larger amounts of a second phase controls the grain growth by mobility, morphology and amount of the precipitations. Thus, SiO_2 impurities (probably in form of $ZrSiO_4$) decrease the grain growth whereas large amounts increase it. In contrast, Al_2O_3 impurities increase grain growth, whereas considerable amounts of it suppress it very efficiently. Furthermore, grain growth could be suppressed by spherical Cr_2O_3– and SnO_2-precipitations.

Acknowledgements

We are grateful to Prof. Dr G. Bayer for his suggestions and helpful discussions. This study was partially supported by Alusuisse-Lonza Services Ltd.

References

1. Lee, I., Sintering and grain growth in tetragonal and cubic zirconia, Dissertation, University of Michigan, 1990.
2. Theunissen, G, Winnubst, A. & Burggraaf, A., Segregation aspects in the ZrO_2–Y_2O_3 ceramic system, *J. Mat. Sci. Lett.*, **8** (1989) 55–7.
3. Hwang, S. & Chen, I., Grain size control of tetragonal zirconia polycrystals using the space charge concept, *J. Am. Ceram. Soc.*, **73**(11) (1990) 3269–77.
4. Lange, F., Marshall, D. & Porter, J., Controlling microstructures through phase partitioning from metastable precursors: the ZrO_2–Y_2O_3 System. In *Ultrastructure Processing of Advanced Ceramics*, eds J. Mackenzie & D. Ulrich. Wiley, New York, 1988, pp. 519–32.
5. Stoto, T., Nauer, M. & Carry, C., Influence of residual impurities on phase partitioning and grain growth processes of Y–TZP materials, *J. Am. Ceram. Soc.*, **74**(10) (1991) 2615–21.
6. Theunissen, G., Microstructure, fracture toughness and strength of (ultra)fine-grained tetragonal Zirconia ceramics, Dissertation der Universität Tweente, Niederland, Februar 1991.
7. Theunissen, G., Winnubst, A. & Burggraaf, A., Surface and grain boundary analysis of doped zirconia ceramics studied by AES and XPS, *J. Mat. Sci.*, **27** (1992) 5057–66.
8. Brook, R., Controlled Grain Growth. In *Treatise on Materials Science and Technology*, Vol. 9, Ceramic Fabrication Processe, Academic Press (1976) 331–64.

9. Hamminger, R., SIA, **12** (1988) 519–26.
10. Davis, L., MacDonald, N., Palmberg, P., Riach, G. & Weber, R., *Handbook of Auger Electron Spectroscopy*, Perkin Elmer Corporation, Eden Prairie, (1979).
11. Hughes, A. & Sexton, B., *J. Mater. Sci.*, **24** (1989) 1057.
12. Moser, E. M., Metzger, M. & Gauckler, L. J., SAM/AES Analysis of Grain Boundaries in Zirconia Ceramics, submitted to *Fresenius' J. Anal. Chem.*, **8** Working conference on applied surface analyses, Kaiserslautern (1994).
13. Leung, D., Chan, C., Rühle, M. & Lange, F., Metastable crystallization, phase partitioning, and grain growth of ZrO_2–Gd_2O_3 materials processed from liquid precursors, *J. Am. Ceram. Soc.*, **74**(11) (1991) 2786–92.
14. Lücke, K., Rixen, R. & Rosenbaum, F., The impurity drag theory. In *The nature and behavior of grain boundaries*, ed. H. Hu, Plenum Press, 1972, p. 256–73.
15. Lange, F., Transformation-toughened ZrO_2: correlations between grain size control and composition in the system ZrO_2–Y_2O_3, *J. Am. Ceram. Soc.*, **69**(3) (1986) 240–2.
16. Bastide, B., Odier, P. & Coutures, J., Phase equilibrium and martensitic transformation in lanthana-doped zirconia, *J. Am. Ceram. Soc.*, **71**(6) (1988) 449–53.
17. Duh, J. & Lee, M., Fabrication and sinterability in Y_2O_3–CeO_2–ZrO_2, *J. Mat. Sci.*, **24** (1989) 4467–74.
18. Michel, B., Korngrenzenglasphasen in tetragonalem Zirkonoxid, Diss. ETH Nr. 10247.
19. Gödickemeier, M. *et al.*, Effect of intergranular glass films on the electrical conductivity of 3Y–TZP, *J. Mater. Res.*, **9**(5) (1994) 1228–40.
20. Bondar, I. A. & Galakhov, F. Y., Phase equilibria in the system Y_2O_3–Al_2O_3–SiO_2, *Izv. Akad. Nauk. SSSR, Ser. Khim*, **7** (1964) 1231–2.
21. Tcheichvili, L. & Marques, M., Systeme ZrO_2–Ti_2O_3, ZrO_2–In_2O_3 und ZrO_2–Bi_2O_3, *Keramische Zeitschrift*, **33**(5) (1982) 294.
22. Nieh, T. & Wadsworth, J., Dynamic grain growth during superplastic deformation of yttria-stabilized tetragonal zirconia polycrystals, *J. Am. Ceram. Soc.*, **72**(8) (1989) 1469–72.
23. Jayaratna, M. & Yoshimura, M., Hot pressing of Y_2O_3–stabilized ZrO_2 with Cr_2O_3 additions, *J. Mat. Sci.*, **21** (1986) 591–6.
24. Sasaki, K., Bohac, P. & Gauckler, L., Phase equilibria in the system ZrO_2–$InO_{1.5}$, *J. Am. Ceram. Soc.*, **76**(3) (1993) 689–98.
25. Stubican, V., Phase equilibria and metastabilities in the systems ZrO_2–MgO, ZrO_2–CaO and ZrO_2–Y_2O_3. In *Advances in Ceramics, Vol. 24, Science and Technology of Zirconia III*, eds S. Somiya, N. Yamamoto & H. Yanagida, American Ceramic Society, 1988, pp. 71–82.
26. Noguchi, T. & Mizuno, M., Phase change in the ZrO_2–TiO_2 System, *Bull. Chem. Soc. Jpn.*, **41**(12) (1968) 2895–9.

Journal of the European Ceramic Society **15** (1995) 959–965
© 1995 Elsevier Science Limited
Printed in Great Britain. All rights reserved
0955-2219/95/$9.50

0955-2219(95)00065-8

Processing of Nano-Y–TZP/Al_2O_3 Composites. I: Preparation and Characterization of Nano-Y–TZP/Al_2O_3 Composite Powders

J. L. Shi, B. S. Li, M. L. Ruan & T. S. Yen

Shanghai Institute of Ceramics, Chinese Academy of Sciences, 1295 Ding-Xi Road, Shanghai, 200050, P.R. China

(Received 31 August 1994; revised 9 March 1995; accepted 20 March 1995)

Abstract

Nano-sized and well dispersed Y–TZP/alumina (Y–TZP-rich) composite powders have been prepared via a chemical method. It has been found that alumina exists metastably in the Y–TZP lattice in the composite powders at relatively low temperatures before the crystallization of α-alumina from the composites started at around 1200°C. Alumina in the composite powders impedes the crystallite growth of Y–TZP and increases the specific surface area of the composite powders. This effect is discussed and attributed to the lattice distortion of Y–TZP by alumina.

1 Introduction

Ceramic composites are of great interest to ceramists because they exhibit better performance than their individual component materials, for example, fibre and whisker-reinforced ceramics.[1,2] However, as it is well known, fibers and whiskers are expensive and sometimes toxic, and these composites are technically difficult to densify because of the impedance of the second phase to the densification of the matrix phases. Generally hot-pressing or hot isostatic-pressing techniques are used, and thus the cost of fabricating these composites are relatively high. Another kind of ceramic composite, the particle/particle composites are, however, relatively easy technically to fabricate and are thus cheap.

Zirconia (or Y–TZP, yttria stabilized tetragonal zirconia polycrystals)/alumina composite is one of the most investigated ceramic composites, from their phase stability to mechanical properties.[3–10] Zirconia is usually used as the reinforcement agent in alumina.[6–7] However, for Y–TZP matrix/alumina particles composites, the mechanical properties of the composites were also found to be significantly better than single phase Y–TZP material.[8–10] The sinterability of the composites depends on the particle properties. Defining R as the size ratio of the second phase to the matrix phase, (the matrix Y–TZP phase assumed to be easy to densify), the densification of the matrix is greatly impeded when $R \approx 100$,[11–13] which results from the inner back stress around the second particles opposite to the sintering stress; if $R \approx 10$, the back stress is believed to be smaller, and the composite can be pressurelessly sintered, but higher sintering temperatures are needed because of the bimodal pore size distributions in the composites.[14] Supposing that the R value decreases further to about 1 — the two factors affecting the densification: back stress and the duplex pore size distribution can be minimized or even cleared out, so the sinterability of the composites will not be affected significantly.

Composite powders of $R = 1$ can be prepared by chemical methods. Rejandran *et al.*[15] Exter[16] and others[17] have prepared the composite powders using the coprecipitation method resulting in very large specific areas. However, these composite powders were still difficult to fully densify via pressureless sintering. We believe that the problem is due to the agglomeration effect of the composite powders, and hardly any individual particles in the powder can be identified.

To obtain good powder properties, the composite powders were prepared using the coprecipitation method and care was taken with the coprecipitation and washing processes. In this paper, the preparation and characterization of the Y–TZP/alumina composite powders will be reported; the compaction and sintering behavior will be presented in the next paper.

2 Experimental Procedure

2.1 Powder preparation

The Y–TZP/alumina composite powders were prepared using a common coprecipitation method,

which is described as follows: (1) Preparation of the solutions of Zr^{4+}, Y^{3+} and Al^{3+} from zirconium oxychloride (chemical grade), respectively, with their concentrations determined by chemical methods. (2) Preparation of the mutual solutions with designated ratios of Zr:Y:Al. (3) Putting the solution into a 12 vol% concentrated ammonia solution and yielding the coprecipitates. The pH value of the solutions after coprecipitation was maintained at around 8–9. (4) Washing the coprecipitates with distilled water until the concentration of Cl^- in filtrates were less than 10 ppm. (5) Washing the cake further with ethanol for approximately six times until the water content in the filtrates measures less than 6 vol%. (6) Drying the coprecipitates overnight at 80°C, followed by calcination in air at different temperatures from 420 to 1350°C for 120 min. After the above steps, the composite oxide powders were obtained.

2.2 Powder characterization

The composite powders were characterized as follows:

2.2.1 Specific surface area

The specific surface area of the composite powders was measured with multi-point nitrogen adsorption BET method (Micromeritics, 220/50000/OX). The particle sizes of the composite powders were calculated by assuming the spherical shape of the powder particles.

2.2.2 Crystallite size determination

X-ray diffraction-line broadening (XRD-LB, Rigaku Denki, RAX-10) method was used for the determination of the average crystallite size of the composite powders. As a matter of fact, only the diffraction peaks of Y–TZP crystals could be obtained at less than about 1200°C, so only the crystallite sizes of Y–TZP in the composite powders were determined using its (111) diffraction peak. The half intensity breadth of the diffraction peak was calibrated by subtracting the instrumental broadening.

2.2.3 Micro-morphology observation

The crystallite size and micro-morphology of the composite powders were observed using transmission electron microscopy, (TEM, JEM-200CX, JEOL) and the composite powders were also analyzed of their components in a micro-area with energy dispersive spectroscopy (EDS) which is part of the microscope. The detailed structure of the composite crystallites were observed with a high resolution electron microscope (HREM, JEM-200CX, JEOL).

2.2.4 Phase analysis

X-ray-diffraction (Rigaku Denki, RAX-10) was used for the analysis of the phase structures. To detect the possible phases of very weak diffraction ability, very high X-ray intensity was used when the diffraction peaks of the main phase were largely out of scale.

To investigate the possible effect of alumina on the lattice distortion of Y–TZP, the (200) lattice plane distance of Y–TZP was measured using the XRD method. To prevent an instrument error, pure Y–TZP samples prepared under the same conditions as the composite powders were measured, together with other samples in every batch.

3 Results

3.1 Specific surface area as a function of alumina content

As reported by other researchers,[15,16] the specific surface area of the coprecipitated composite powders was greatly increased by the addition of alumina. This was also true for the composite powders prepared in this study, as shown in Fig. 1. Figure 2 shows the calculated particle size of

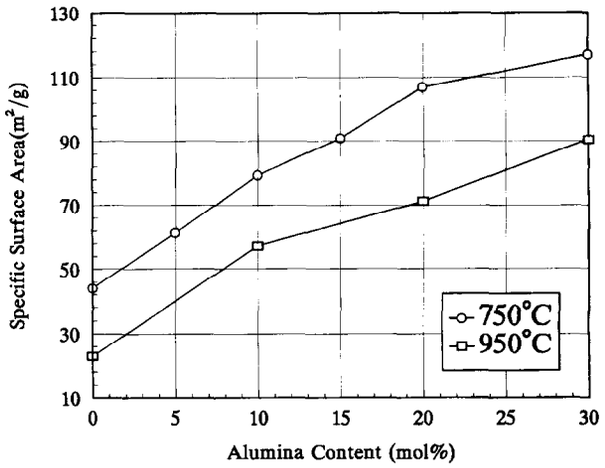


Fig. 1. Specific surface area of the composite powders as a function of alumina content, the powders were calcined at 750 and 950°C for 120 min.

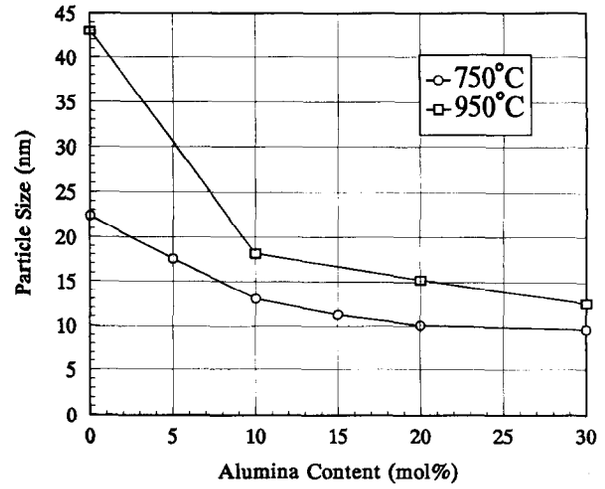


Fig. 2. Particle size calculated from the specific surface area versus alumina content.

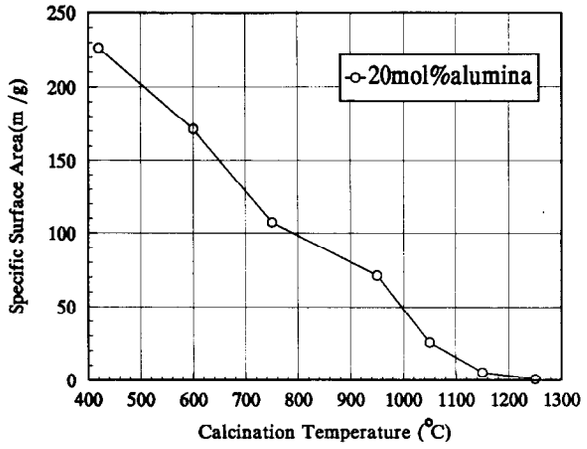


Fig. 3. Temperature dependence of the specific surface area of the Y–TZP/20 mol% alumina composite powders.

the composite powders from the specific surface area. The composite powders were very fine with extraordinarily high surface area when calcined at low temperatures such as 420 and 600°C, and decreased rapidly at elevated temperatures as illustrated in Fig. 3, which was accompanied by crystallite growth, particle coarsening and partial sintering.

3.2 Phase structure and crystallite size

The results of the XRD study for Y–TZP/20 mol% alumina composite powders (Fig. 4) shows that at less than about 1200°C, only the diffraction peaks of Y–TZP were detected but not those of alumina, even at the maximum X-ray power output of 15 kW; although γ-alumina (or other forms except for the α phase) using the same process can be detected easily under ordinary diffraction conditions.

Based on the above reason, only the crystallite sizes of Y–TZP could be determined with the

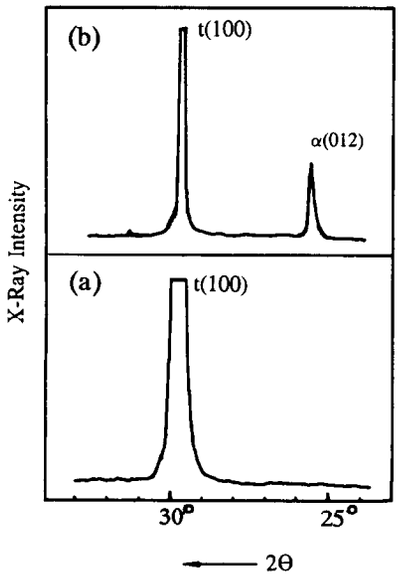


Fig. 4. XRD spectra of the Y–TZP/20 mol% alumina composite powders calcined at (a) 750°C and (b) 1250°C for 120 min.

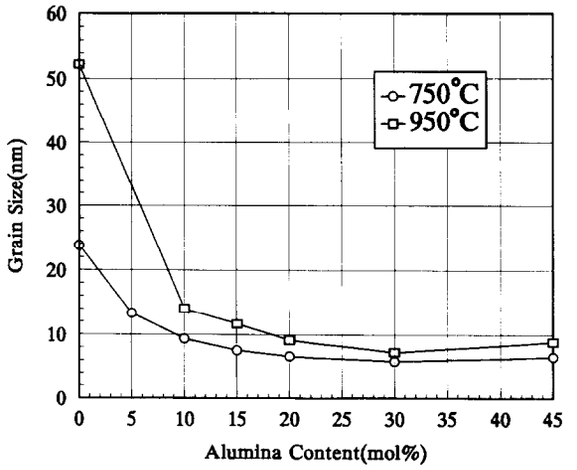


Fig. 5. Crystallite size of Y–TZP as a function of alumina content in the composite powders calcined at 750 and 950°C for 120 min.

method. The results are shown in Fig. 5 illustrating the effect of alumina on the crystallite size of Y–TZP, and such an effect was most important at relatively low alumina contents of 5 and 10 mol%.

3.3 Micromorphology of the composite powders

The effect of the addition of alumina on the crystallite size is shown in Fig. 6. The decrease of the crystallite size with increasing alumina content is apparent. Different from the powder micromorphology reported by Rajendran,[15] the particles were well dispersed and therefore could be identified separately from the micrographs, due to the careful control of the processes of the powder preparation. The temperature dependence of the particle size and morphology of Y–TZP/20 mol% alumina is illustrated in Fig. 7. At temperatures lower than 1250°C, there seems to be only one kind of particle present in the powders, which means no component separation can be observed under the conditions. At elevated temperatures of 1250°C or higher, the component contrasts can be seen in the micrographs, which means the component separation takes place. As shown in Fig. 7(f), the dark grains are Y–TZP and the lighter ones are alumina, as indicated by the EDS results in Fig. 8.

4 Discussion

4.1 Existing form of alumina in the composite powders

According to the phase diagrams, alumina and zirconia are insoluble with each other both at ambient and high temperatures. In the present study, this is true for the composite powders calcined at temperatures of around 1200°C when α-alumina crystallized out, as can be seen in Figs 4 and 7.

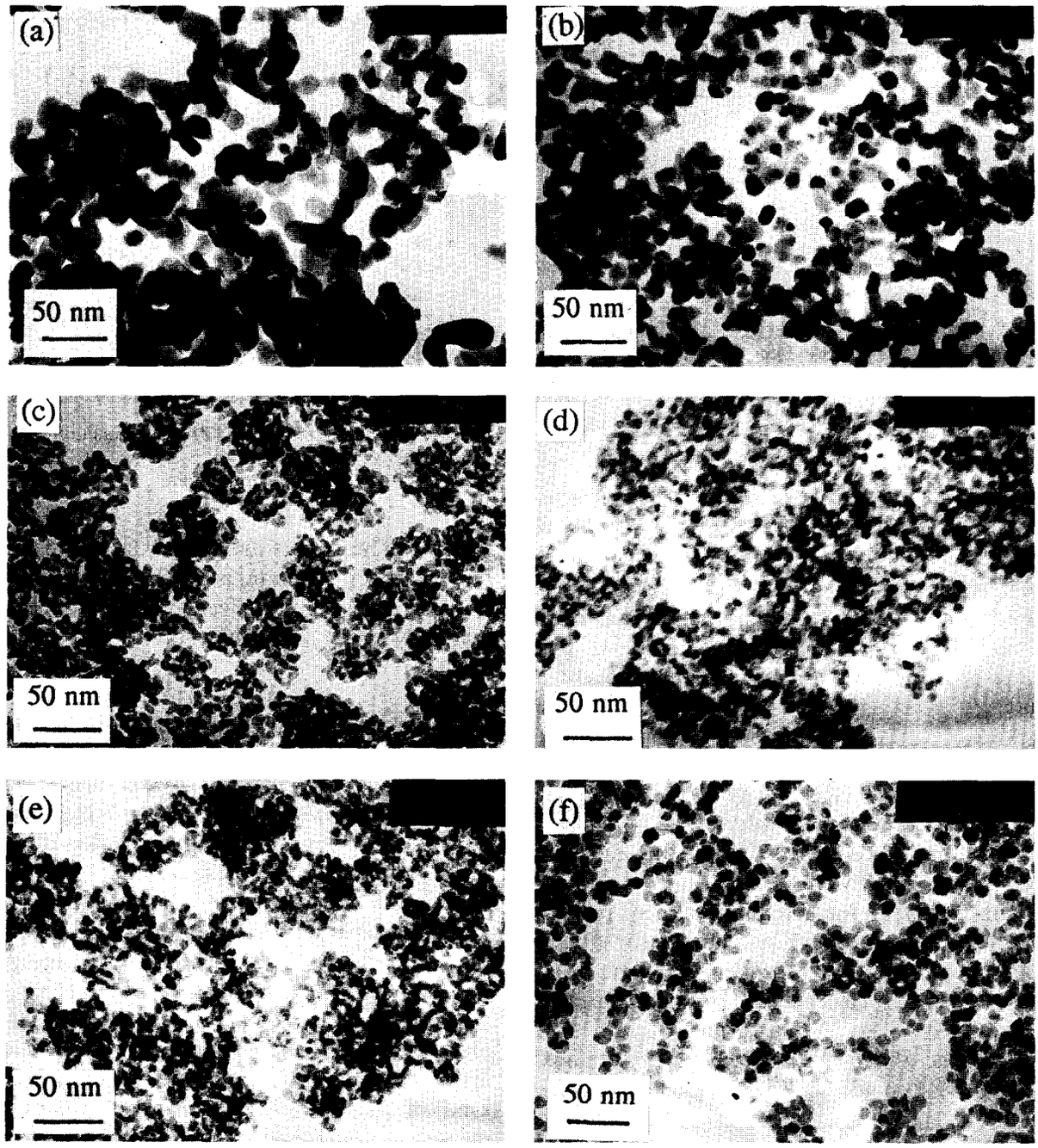


Fig. 6. TEM micrographs of the 750°C calcined composite powders containing (a) 0, (b) 5, (c) 10, (d) 20, (e) 30 and (f) 45 mol% alumina.

However, the two components (supposing yttria always dissolves in the Y–TZP lattice) were not found to exist separately from Y–TZP at lower temperatures than the crystallization point of the α phase. The detailed observation by HREM of the micromorphology of the composite powders containing 20 mol% alumina (Fig. 9) shows no alumina in the Y–TZP grains or around the grains, although alumina may be amorphous-like. However, if it existed separately from Y–TZP, there should have been a contrast between alumina and Y–TZP and between alumina and the background of carbon films which was used to support the particles. So it is believed that alumina existed in the Y–TZP lattice before the crystallization of α-alumina from the composites at around 1200°C. Direct evidence of this conclusion has been found by measuring the lattice parameters of Y–TZP, (as shown in Fig. 10), of the differences of the (200) lattice plane distances between pure Y–TZP and alumina added composite powders. Such a lattice distortion could only be attributed to the alumina existing in the Y–TZP lattice, since the lattice parameters of Y–TZP cannot be affected by alumina particles around them even in the sintered bodies.[14] Such an effect was most significant at a relatively low alumina content, which corresponded to the crystallite size decreasing effect of Y–TZP by the addition of alumina. When α-alumina crystallized out from the

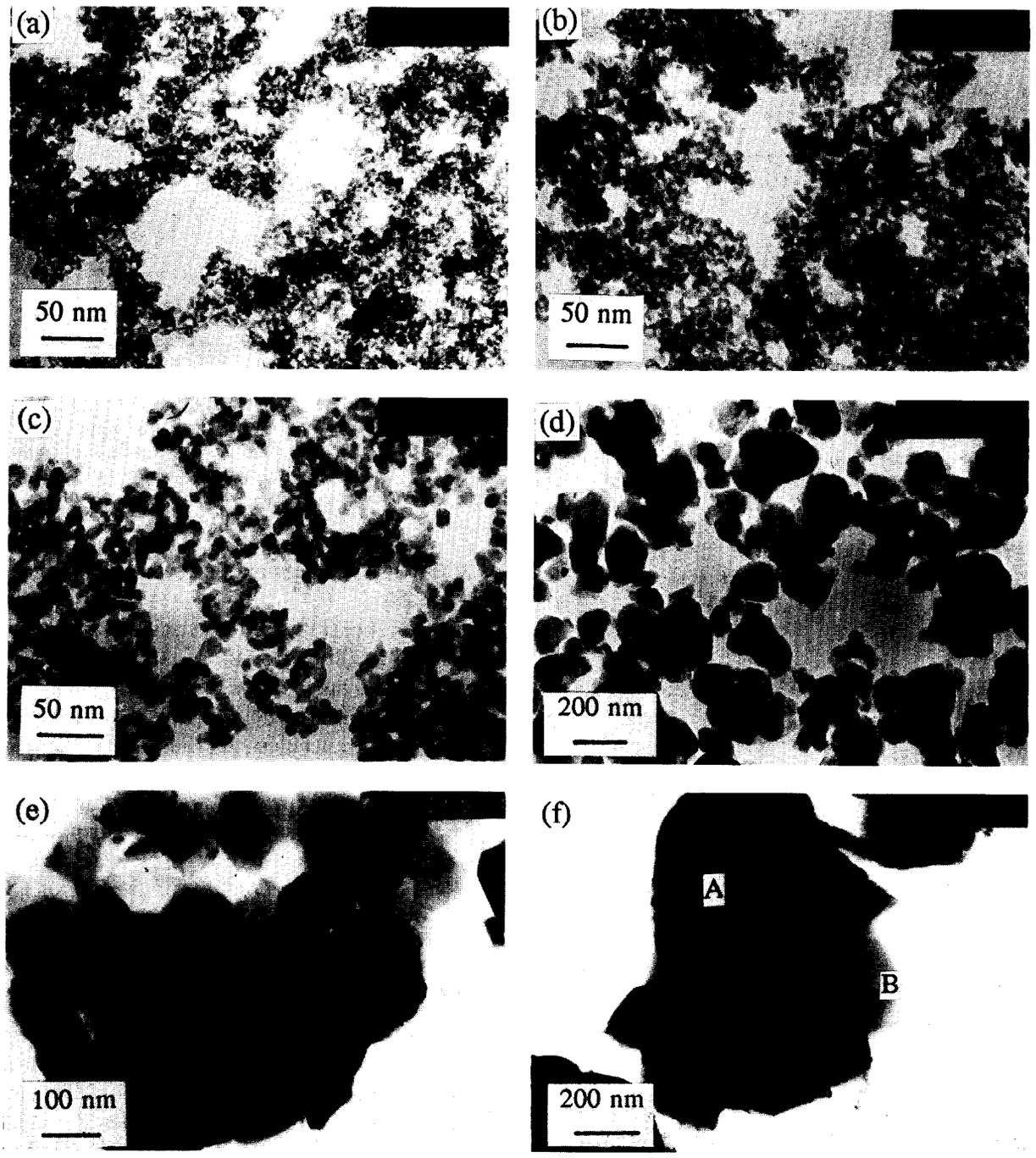


Fig. 7. TEM micrographs of the Y–TZP/20 mol% alumina composite powders calcined at (a) 420, (b) 600, (c) 950, (d) 1050, (e) 1250 and (f) 1350°C for 120 min.

composite, the difference of the lattice plane distances returned to zero, as shown in Fig. 11 for the composite powders containing 20 mol% alumina.

4.2 Crystallization process of alumina in the composite powders

Al_2O_3 presents as the γ phase (or other forms except the α phase) when decomposed from the hydroxides or other salts of aluminum at around 1200°C. These forms are amorphous-like and therefore are metastable themselves. As the phase transformation from these forms to the thermodynamically stable α phase needs a big structure rearrangement, usually a temperature range around 1200°C is required for such a transformation. For the composite powder investigated in this study, the three components were mixed homogeneously on a molecular level in their mutual solutions and such a homogeneity could be maintained in the hydroxide coprecipitates and amorphous oxides at less than about 360–400°C. Y–TZP are very easy to crystallize from its amorphous oxide at only around 400°C.[3] At this low temperature, the diffusion of alumina molecules through Y–TZP to form a separate alumina phase are difficult. This was because, firstly, the thermodynamic driving force for this process was small, as a separate alumina phase at less than 1200°C was metastable

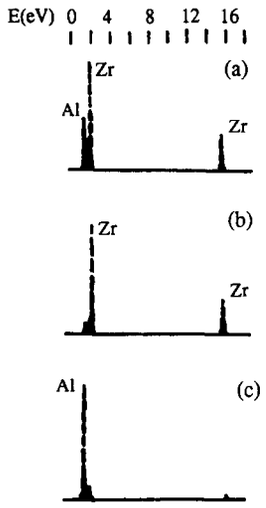


Fig. 8. EDS spectra: (a) for the sample shown in Fig. 7(c); (b) for the sample shown in Fig. 7(f) on dark area 'A' and (c) on the lighter area 'B'.

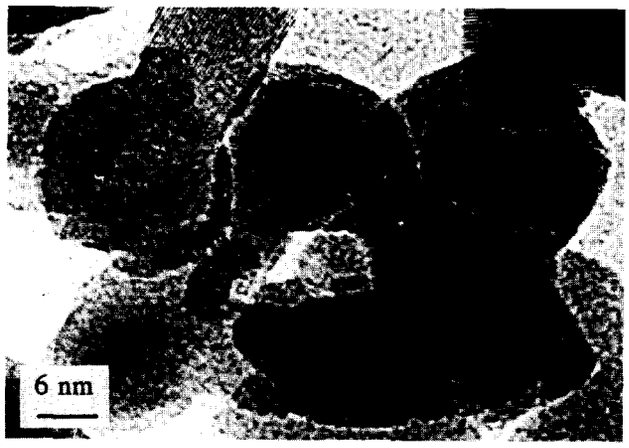


Fig. 9. HREM micrographs of Y–TZP/20 mol% alumina composite powders calcined at 950°C.

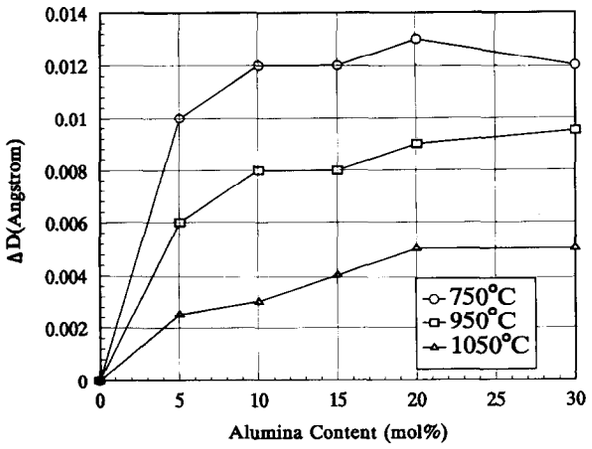


Fig. 10. Differences of the (200) lattice plane distance between pure Y–TZP and composite powders.

itself; secondly, the kinetic resistance was great because of such a low temperature and Y–TZP impedance. As temperature increases, the diffusion resistance became less and the driving force became large. At around 1200°C, thermodynamically stable α phase crystallized out and the two components became separate to one another.

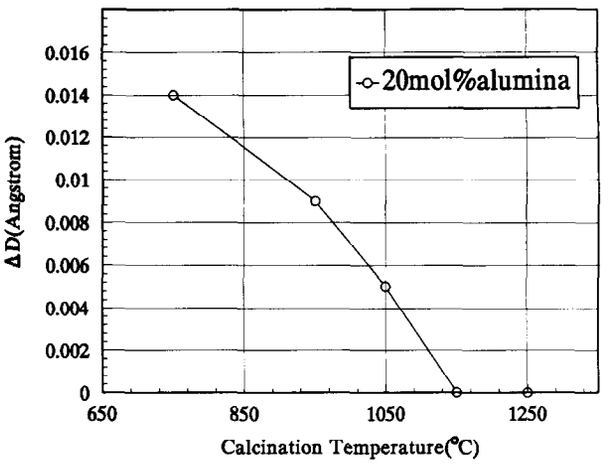


Fig. 11. Difference of the (200) lattice plane distances of Y–TZP/20 mol% alumina composite powders as a function of calcination temperature.

4.3 Influence of alumina on the crystallite growth of Y–TZP

There are possibly two reasons for the hindrance of the crystallite growth of Y–TZP by alumina: lowering the surface tension of the Y–TZP particles, or increasing the resistance for the diffusion of Y–TZP molecules. As has been argued, alumina existed homogeneously in the Y–TZP lattice before the crystallization of α-alumina from the composite powders, and the most strong effect on the crystallite growth of Y–TZP was at the relatively low alumina content of 5–10 mol%. Even so, it was still possible that some alumina components at, or near the particle surface of Y–TZP could affect the surface tension. However, this effect is believed to be limited if the homogeneous distribution of the alumina molecules in the Y–TZP lattice was true, because the amount of alumina species at the particle surface were not concentrated, which could not alter the crystallite growth behavior so much, as shown in Fig. 5. In contrast, the presence of alumina in the Y–TZP lattice caused the lattice distortion of Y–TZP, mostly at the relatively low alumina level of 5 mol%, corresponding to the dependence of crystallite size on the alumina content. The lattice distortion led by the aluminum ions would lead to the considerable additional energy fluctuations in the lattice. Such an energy fluctuation would act as the energy barrier for the diffusion of Y–TZP, so the diffusion resistance of Y–TZP species would be increased, and therefore the crystallite growth which depends on the diffusion would be impeded. So it is believed that the lattice distortion by the presence of alumina in the Y–TZP lattice is the main reason for the impedance of the crystallite growth of Y–TZP in the composite powders.

5 Conclusions

(1) Nano-sized and well dispersed Y–TZP/Al_2O_3 composite powder could be prepared by coprecipitation method with careful control of the processes.

(2) Alumina co-existed in the Y–TZP lattice at relatively low temperatures before the crystallization of the α phase from the composite powders at about 1200°C, leading to the lattice distortions of Y–TZP.

(3) The crystallite growth of Y–TZP was greatly impeded by the addition of alumina in the composite powders. The reason for this phenomenon is believed to be caused mainly by the lattice distortion led by alumina.

References

1. Maschall, D. B. & Evans, A. G., The tensile strength of uniaxially reinforced ceramic fibre composites. In *Fracture Mechanics of Ceramics, Vol. 7*, eds R. C. Bradt, A. G. Evans, D. P. H. Hasselman & F. F. Lange, Plenum, New York–London, 1986, pp. 1–16.
2. Becher, P. F., Tiegs, T. N., Ogle, J. C. & Warwick, W. H., Toughening of ceramics by whisker reinforcement, *ibid.* pp. 61–74.
3. Shi, J. L., Lin, Z. X. & Ten, T. S., Effect of alumina restraining on the stability of tetragonal zirconia composite powders. *J. Europ. Ceram. Soc.*, **9** (1992) 27–33.
4. Murase, Y., Kato, E. & Dlaiman, K., Stability of ZrO_2 phase ultrafine ZrO_2–Al_2O_3 mixtures, *J. Am. Ceram. Soc.*, **69**(2) (1986) 83.
5. Yoshimatsu, H., Kamasaki, H. & Osaka, A., Stability of tetragonal ZrO_2 phase in Al_2O_3 prepared from Zr–Al organometallic compounds, *J. Mater. Sci.*, **23** (1988) 332.
6. Masaki, T. & Shino, K., Mechanical behaviour of ZrO_2–Y_2O_3 ceramics formed by hot-isostatic pressing. In *Advances in ceramics, science and technology of zirconia III*, eds S. Somiya, N. Yamamoto & H. Hanagida, The Am. Ceram. Soc. Inc., Columbus, OH, 1988, p. 709.
7. Lange, F. F., Transformation toughening. Part 4: fabrication, fracture toughness and strength of Al_2O_3–ZrO_2 composites, *J. Mater. Sci.*, **17** (1982) 247.
8. Tsukuma, K., Takahata, T. & Shiomi, M., Strength and fracture toughness of Y–TZP, Ce–TZP, Y–TZP/Al_2O_3 and Ce–TZP/Al_2O_3. In *Advances in ceramics vol. 24, science and technology of zirconia*, eds S. Somiya, N. Yamamoto, H. Hanagida, The Am. Ceram. Soc., Columbus, OH, 1988, p. 721.
9. Shi, J. L., Li, B. S. & Yen, T. S., Mechanical properties of Al_2O_3 particle-Y–TZP matrix composite and its toughening mechanism, *J. Mater. Sci.*, **28** (1993) 4019–22.
10. Rajendran, S., Swain, M. V. & Rossell, H. J., Mechanical properties and microstructures of co-precipitation derived tetragonal Y_2O_3–ZrO_2–Al_2O_3 composites, *J. Mater. Sci.*, **23** (1988) 1805–12.
11. Tuan, W. H. & Brook, R. J., Sintering of heterogeneous composites, Part II: ZrO_2–Al_2O_3, *J. Mater. Sci.*, **24** (1989) 1953.
12. Sudre, O. & Lange, F. F., Effect of inclusions on densifications. I: microstructural development in an Al_2O_3 matrix containing a high volume fracture of ZrO_2 inclusions, *J. Am. Ceram. Soc.*, **75**(3) (1992) 519.
13. Tuan, W. H. & Brook, R. J., Sintering of heterogeneous ceramic composites, Part I: Al_2O_3–Al_2O_3, *J. Mater. Sci.*, **24** (1989) 1062.
14. Shi, J. L. & Yen, T. S., Densification and microstructure development of alumina/Y–TZP composite powder (Y–TZP-rich) compacts, *J. Euro. Ceram. Soc.*, in press.
15. Rejandran, S., Rossell, H. J. & Sanders, J. V., Preparation and characterization of precursors powders for yttria-doped tetragonal zirconia polycrystals (Y–TZP) and Y–TZP–Al_2O_3 composites, *J. Mater. Sci.*, **24** (1989) 1195 202.
16. der Exter, P., Winnubst, A. J. A. & Burggraaf, A. J., The preparation and characterization of Y–TZP/20 vol% Al_2O_3, *J. Euro. Ceram. Soc.*, **11** (1993) 497.
17. Navarro, L .M., Recio, P., Jurado, J. R. & Duran, P., Development of high density Y_2O_3–ZrO_2–Al_2O_3 composites as solid electrolyte for SOFC. In Proceedings of Third Euro-Ceramics Vol. 2, ed. P. Duran & J. F. Fernandez, Faenza Editrice Iberuca S. L., 1993, p. 281–6.

Journal of the European Ceramic Society 15 (1995) 967–973
© 1995 Elsevier Science Limited
Printed in Great Britain. All rights reserved
0955-2219(95)00067-4
0955-2219/95/$9.50

Processing of Nano-Y–TZP/Al_2O_3 Composites. II: Compaction and Sintering Behaviour of Nano-Y–TZP/Al_2O_3 Composite Powders

J. L. Shi, J. H. Gao, B. S. Li & T. S. Yen

Shanghai Institute of Ceramics, Chinese Academy of Sciences, 1295 Ding-Xi Road, Shanghai, 200050, P.R. China

(Received 31 August 1994; revised version received 9 March 1995; accepted 20 March 1995)

Abstract

The compaction and sintering behaviour of nano-sized and well-dispersed Y–TZP/Al_2O_3 composite powders have been investigated. It has been found that the composite powders contained no hard agglomerates, and after compaction, all soft agglomerates are fragmented. The green density of the compact was found to decrease with the increase of alumina content. The composite powder compacts containing less than 20 mol% alumina can be sintered at not higher than 1350°C to 99% of their theoretical densities. The densification behaviour of the composite powders show duplex shrinkage peak characteristics for the composites containing not less than 15 mol% alumina.

1 Introduction

Reports have shown that zirconia (or Y–TZP)/alumina composites exhibit higher performance than single phase alumina or TZP ceramics.[1–7] For the alumina matrix based composite ceramics, the main toughening and strengthening mechanisms are zirconia phase transformation and microcracking.[1–4] Another kind of composite is TZP, (mainly Y–TZP) based composite; this kind of composite also shows higher toughness and strength than single TZP ceramics. The toughening effect of the composite has been found to be increased phase transformation volume of Y–TZP by the addition of alumina particles in the Y–TZP matrix.[9]

As stated in the previous paper, the composites were more difficult to densify than the single matrix phase.[9–11] So depending on the powder properties, hot-pressing or hot-isostatic pressing techniques may be required[5–7] for the full densification. This is because the second phase usually acts as an impedance to the densification if the particles of the second phase were too large compared to the matrix phase, or if the composite powders were possibly strongly agglomerated. Pressureless sintering may also be useful if the particles of the second phase are not much larger than that of the matrix,[12] but the sintering temperature must be higher than the matrix because of the duplex pore size distribution led by the larger second phase.[13] Providing that the hard-agglomerate-free composite powders with roughly the same particle sizes between the second and matrix phases can be prepared, they could have good sinterability comparable to the matrix. In the previous paper, such a composite powder has been successfully prepared[14] and the sintering behaviour will be studied in this paper.

2 Experimental Procedure

The preparation process of the composite powders has been reported in the previous paper.[14] The powders were afterwards compacted first by uniaxial pressing at 50 MPa and followed by cold isostatic pressing at 250 MPa. The green densities of the composite powder compacts were calculated by their weights and the geometric volumes measured, and the theoretical densities were calculated according to the volume percentages of the composites. The compacts were also characterized by their pore size distributions to find if the agglomerates, (i.e. inter-agglomerate pores) were present in the compacts.

The shrinkage behaviour was recorded by a constant heating rate of 5°C/min on a linear dilatometer to 1550°C. Isothermal sintering was also conducted in a molybdenum silicide furnace at various temperatures for 120 min.

The sintered bodies were observed of their microstructure with scanning electron microscope (SEM, JCXA-733, JEOL) and transmission electron microscope (TEM, JEM-200CX, JEOL).

3 Results

3.1 The compaction behaviour

The agglomeration behaviour of the powders can be characterized by the pore size distributions of their compacts.[11-12] For agglomerate-free powder compacts, there are only one kind of pores—inter-primary particle pores could be detected in the compacts. Fig. 1 shows the pore size distribution of the compacts of the composite powders calcined at 750°C. There was only one distribution peak detected in every kind of powder compact and therefore, there was only one kind of pore present in the compacts, which were the interprimary particle pores, meaning that no agglomerates were present in the compacts. Figure 2 gives the mean pore sizes and the size ratios of the pores to the grains as a function of alumina content. The pore size decreased with the increase of alumina content when the alumina content was less than 20 mol%, corresponding to the reducing effect of alumina on the crystallite size of Y-TZP;[14] however it increased slightly when above 20 mol%. The size ratio of the pores to the crystallites increased with the addition of alumina at not higher than 30 mol%, meaning the compaction properties of the primary particles of the composite powders have changed, as proved by the measurement of the green densities of the compacts (Fig. 3).

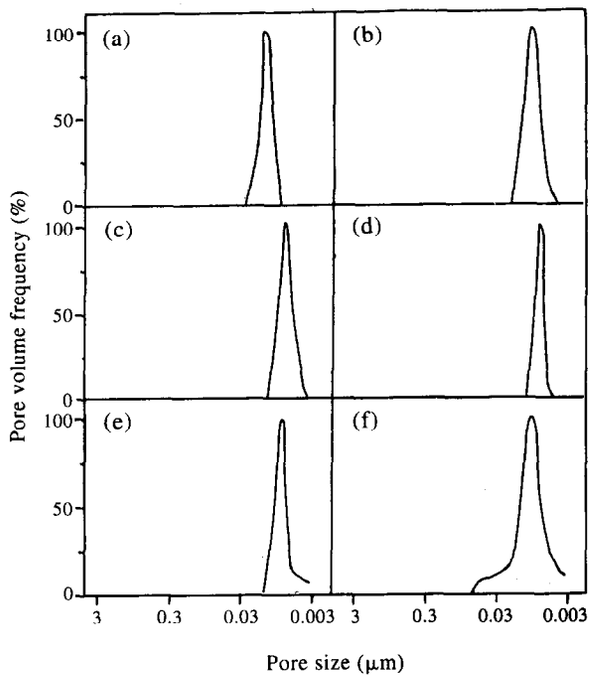


Fig. 1. Pore size distributions of the 750°C calcined composite powder compacts (250 MPa) containing (a) 0, (b) 10, (c) 15, (d) 20, (e) 30, (f) 45 mol% alumina.

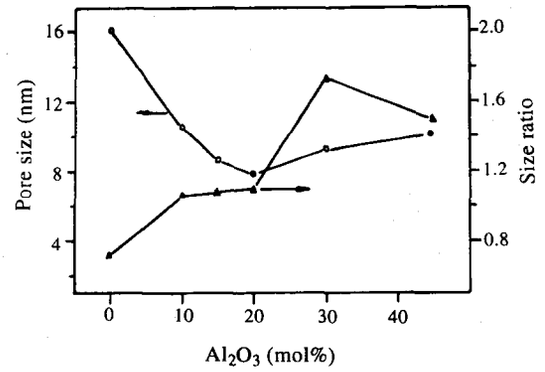


Fig. 2. Dependence of the pore size and the size ratio of pores to particles on the alumina content in the composite powder compacts (750°C calcined, 250 MPa compacted).

3.2 Densification with constant heating rate

The densification behaviour of the composite powder compacts with constant heating rate measured is shown in Fig. 4. The figure shows that the

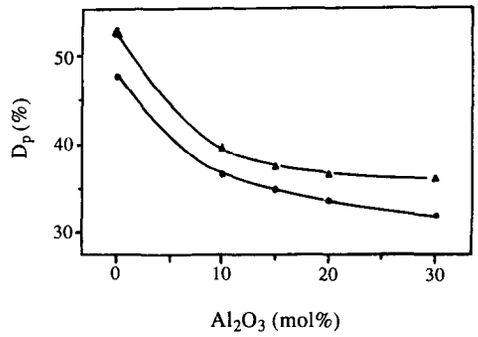
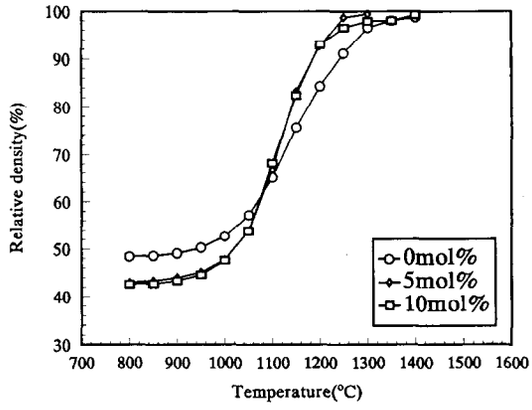


Fig. 3. Green densities of the composite powder compacts as a function of alumina content, (●) 750°C, (▲) 950°C.



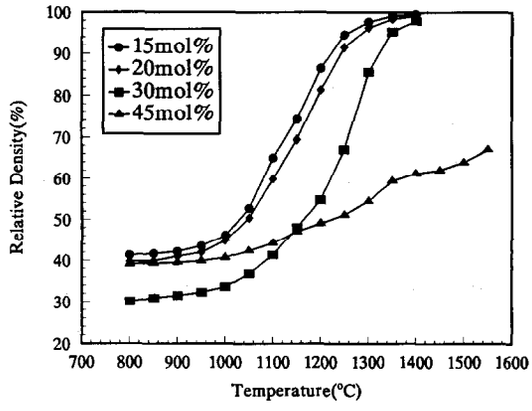


Fig. 4. Relative densities (ρ) versus temperature profile of the composite powder compacts during sintering by a constant heating rate of 5°C/min at different alumina contents.

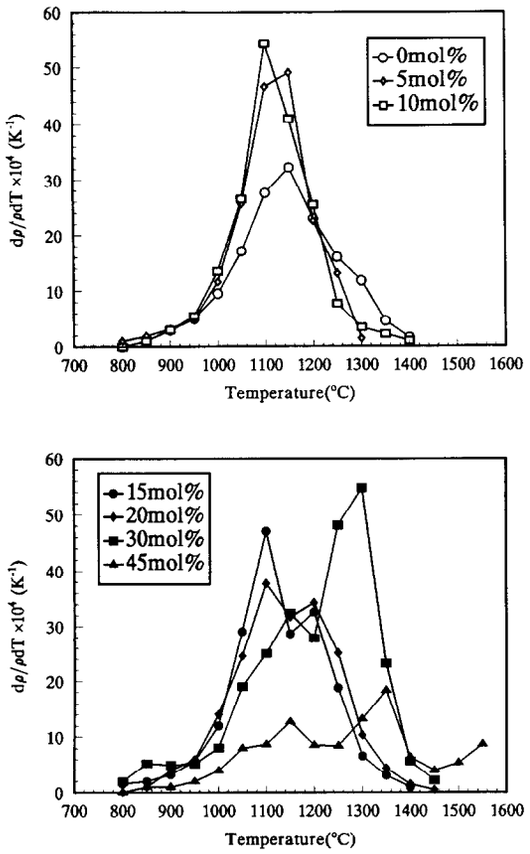


Fig. 5. Densification rate ($d\rho/\rho dT$) versus temperature profile of the composite powder compacts during sintering by a constant heating rate of 5°C/min at different alumina contents.

addition of 5–10 mol% alumina lowered the densification temperature from about 1350°C to about 1250–1300°C, but the densification process finished at higher temperatures when the composite powders contained a higher percentage of alumina. For the composite powders containing 45 mol% alumina, full densification could not be reached.

Figure 5 gives the densification rates of the composite powder compacts. The densification rates were greatly raised by the addition of 5 or 10 mol% alumina in the composites, and temperatures for the end-point of densification were lowered. Much more interestingly, when the composites contained 15 or higher mol% of alumina, there were two maximum points of the densification rates, (duplex shrinkage peaks), during heating: one at about 1050–1100°C and another at around 1200°C or higher. Despite this phenomenon, the composite powders could still be densified at about 1400–1450°C, but if the alumina content was any higher, (45 mol%), there was only a small densification effect.

3.3 Densification with isothermal sintering

Figure 6 shows the sintering densities of the composite powder compacts at different temperatures. The results show again that nearly full densification could be obtained for the composites containing 5–20 mol% alumina at sintering temperatures as low as 1250–1350°C; the sintered densities were roughly the same as or even higher than those of single phase Y-TZP in the temperature range of 1150–1350°C except for the composite containing 30 mol% alumina. At 1450°C, the sintering densities decreased for the composites containing 15 mol% or a high content of alumina.

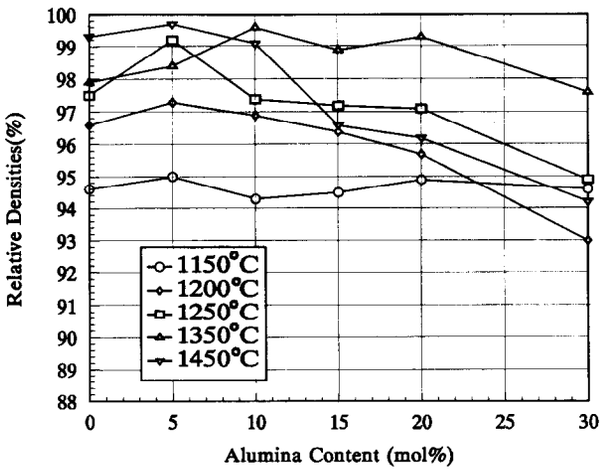


Fig. 6. Sintering densities of the composites at different sintering temperatures by isothermal sintering for 120 min.

3.4 Microstructure development

The presence of alumina does not only decrease the crystallite size in the coprecipetated composite powder, it also inhibits the grain growth in the composites, as shown in Fig. 7 and 8. The micrographs in Fig. 7 were obtained on the polished and thermally etched surface of the sample sintered at lower temperatures and no apparent contrast difference between the components could be distinguished in the micrographs. Those in Fig. 8 were the natural surfaces of the composite sintered at higher temperatures, and the contrasts between the particles can be clearly seen: the dark grains were alumina and others were Y-TZP. It is obvious from the micrographs that the microstructure is fine and homogeneous, and the grain size of the two phases of alumina and Y-TZP are almost the same.

Figure 9 shows the microstructure of a Y-TZP/45 mol% alumina composite sintered at 1350°C. The composite was not densified and the microstructure was highly porous.

Figure 10 shows the TEM microstructure of Y-TZP/20 mol% alumina composite sintered isothermally at different temperatures. In contrast to the micrographs shown in Fig. 8, in TEM micrographs, the dark grains are Y-TZP, the bright ones alumina. The grains of both Y-TZP and alumina grew with increasing sintering temperature.

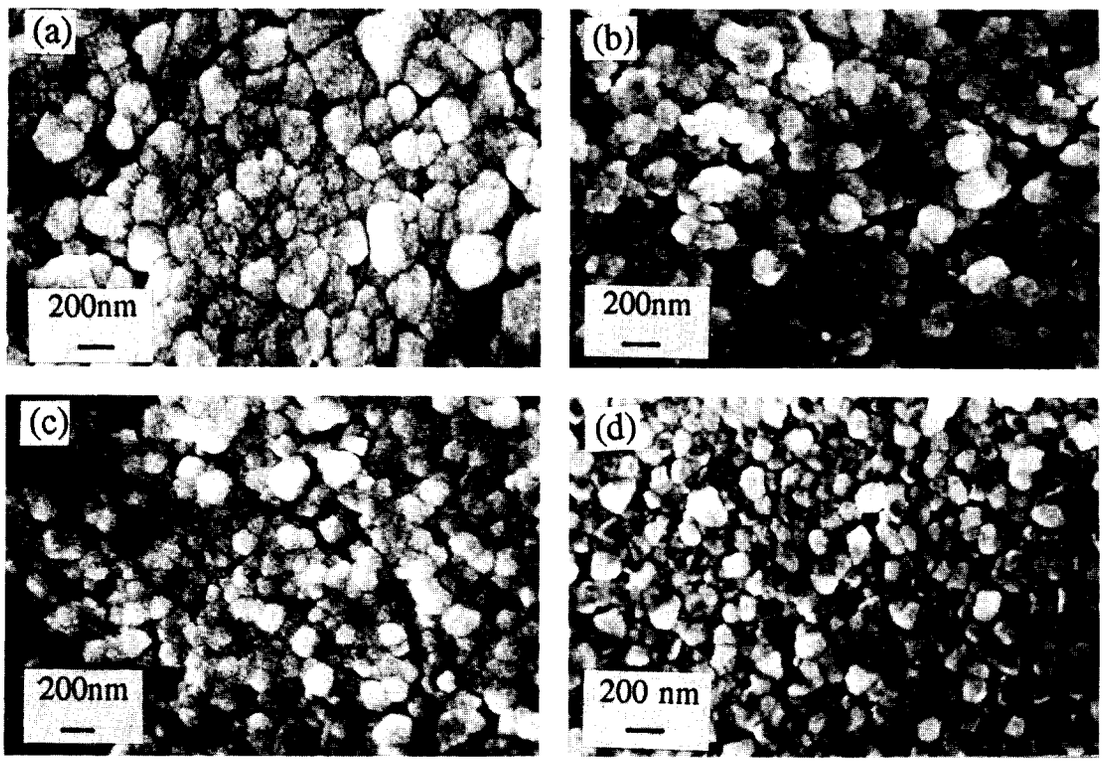


Fig. 7. Microstructure of the composites sintered at 1250°C for 120 min with alumina content of (a) 0, (b) 10, (c) 20 and (d) 30 mol%.

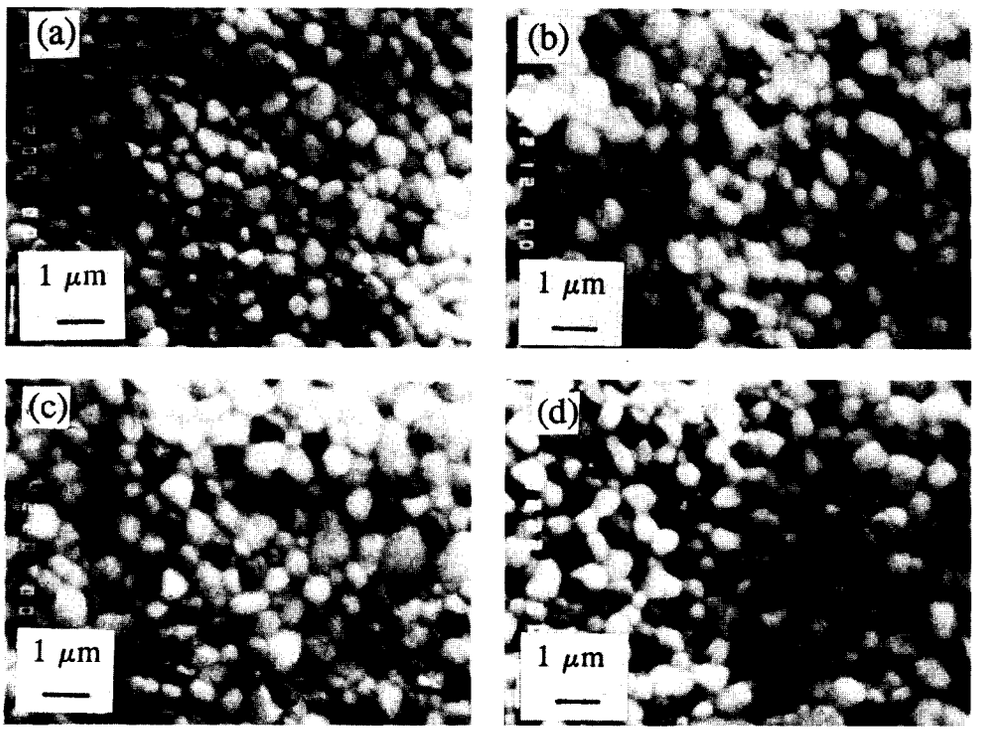


Fig. 8. Microstructure of the composites sintered at 1550°C for 120 min with alumina content of (a) 0, (b) 10, (c) 20 and (d) 30 mol%.

4. Discussion

4.1 Particle arrangement in the compact

Although the composite powders prepared are hard agglomerate-free and could be compacted with only one kind of pores — inter-primary particle pores left in the compacts — the packing properties between the primary particles were dependent on the alumina content. The size ratios of the pores to primary particles increase with the increase of alumina content, corresponding to the decrease of the compaction densities. This phenomenon, if the agglomeration properties were not affected by the alumina addition, could be mainly attributed to the decrease of particle size when alumina was added. The dependence of the packing densities on the particle size is well known to ceramists, the poor flowability of fine powders

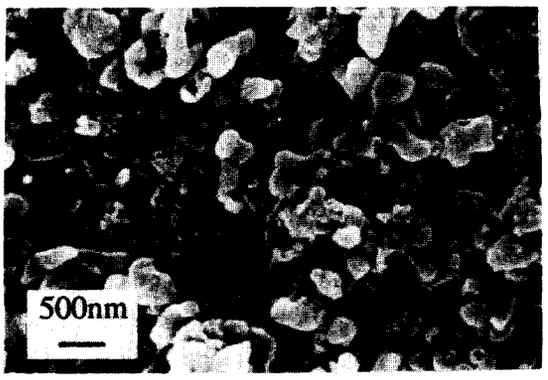


Fig. 9. Microstructure of Y-TZP/45 mol% alumina sintered at 1350°C for 120 min.

is the reason for their low packing densities. The dependence of compaction densities can be explained in a similar way. With the decrease of particle size, the contact between the particles in the unit area increases. Because of the non-deformability of the ceramic particles, the contact area for every contact is independent of particle size, so under a certain external pressure, the more contact between the particles causes lower effective internal pressure, which is the driving force for the rearrangement between particles. Thus, the compaction density would decrease with the decreasing of particle size. Higher applied pressure is needed for powders of finer particle sizes for the same density than that for powders of larger particle sizes.

4.2 Densification characteristics as influenced by alumina

The great increase of the densification rate of the composite powders at 5 and 10 mol% alumina is not fully understood. Probably it is due to the smaller grain size of the composites than the single phase Y-TZP in the compacts during sintering. Generally there is only one maximum value of the densification rate during sintering, with a constant heating rate of homogeneous powder compacts. This is true for the composites with not higher than 10 mol% alumina, the maximum temperature for this is around 1100°C. The occurence of the second maximum value occurs at around 1200°C or higher (in addition to the first maximum value), for the composite powder compacts with higher alumina content can be understood by the phase transformation of alumina in the composite powder during sintering. As this process did not take place at a calcination temperature as low as 750°C but at around 1100–1200°C.[14] When the first maximum value was reached, the crystallization of

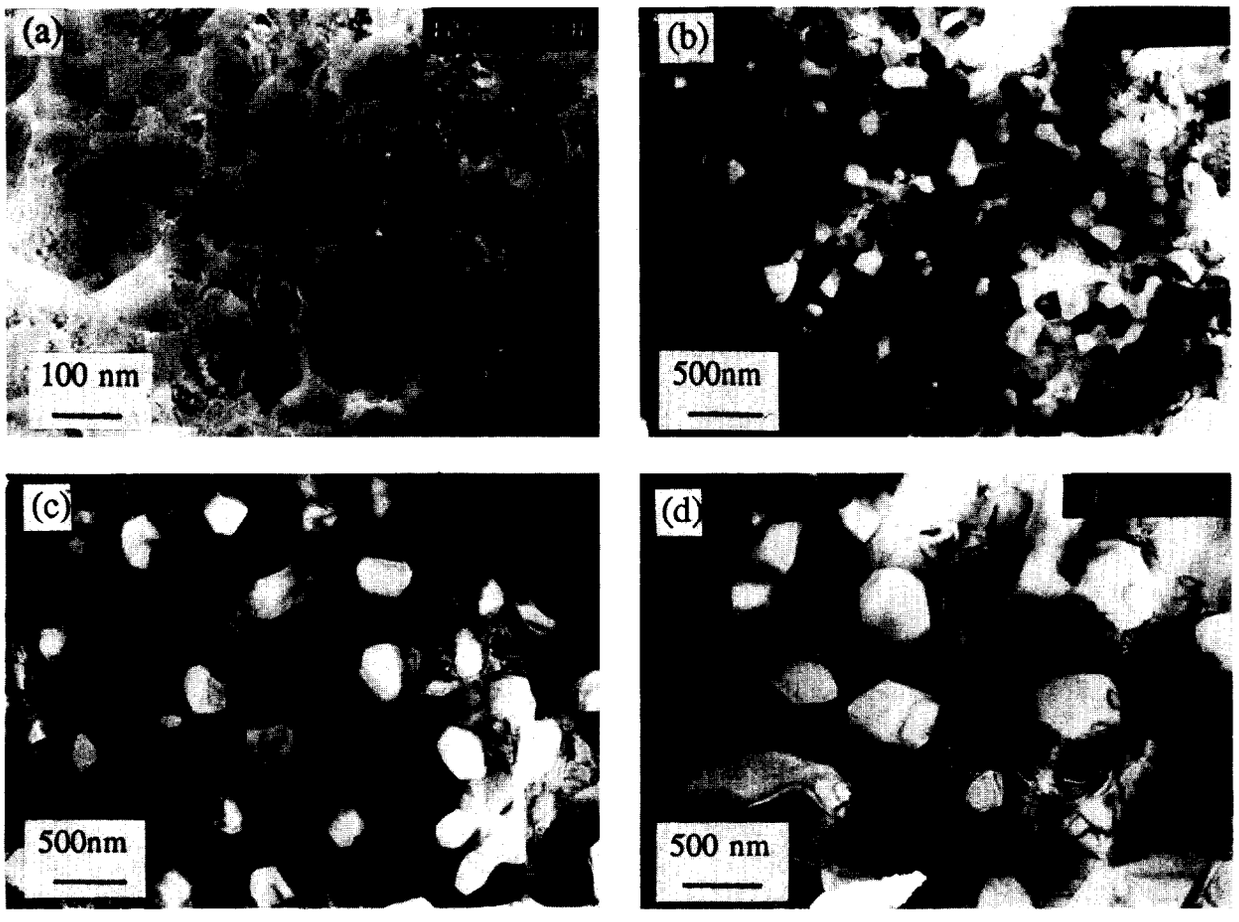


Fig. 10. TEM microstructure of the composites containing 20 mol% alumina sintered at (a) 1250, (b) 1350, (c) 1450 and (d) 1550°C for 120 min.

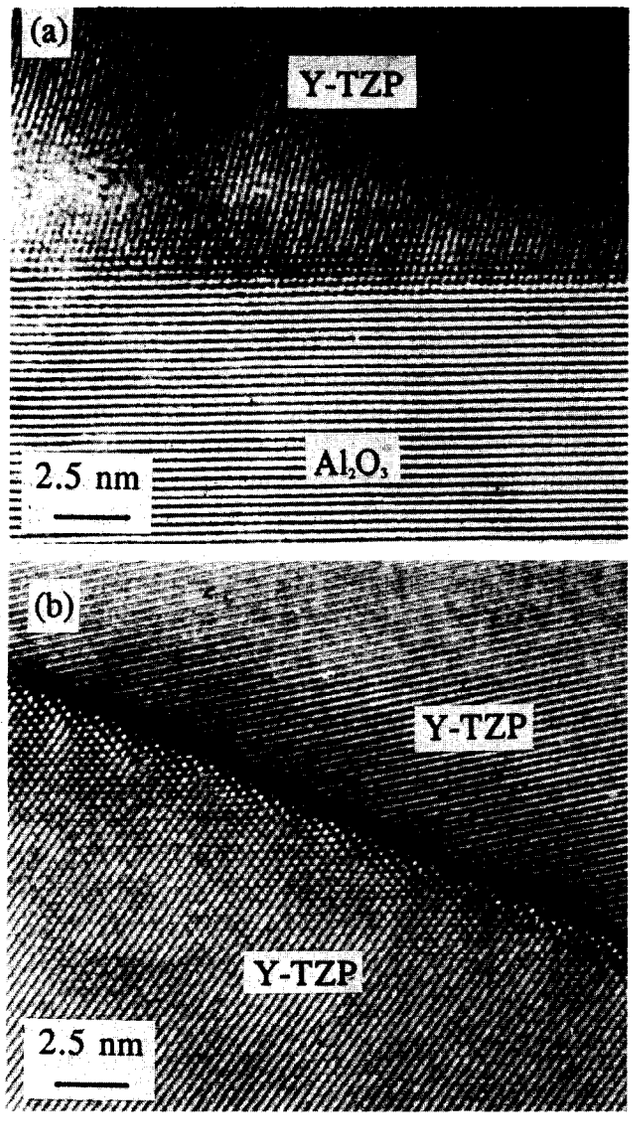


Fig. 11. Lattice images of the Y–TZP/20 mol% alumina composites sintered at 1450°C for 120 min for (a) Al_2O_3/Y–TZP interface, (b) Y–TZP/Y–TZP interface.

α-alumina from the Y–TZP matrix during sintering impeded the densification process of the composite and densification rate was lowered through the formation of the inter alumina Y–TZP pores, and/or the 'vermicular' structure between alumina particles, inhibiting matrix diffusion. As the temperature increased, the densification rate reached another maximum value through the enhancement of the diffusion ability at elevated temperatures. An alternative explanation for the second maximum densification rate may be that as the alumina content reaches 15 mol% or higher, the contacts between alumina particles increase and the alumina clusters may form, and the densification of the alumina cluster, together with the not necessarily retarded densification of Y–TZP, causes the second maximum rate. The temperatures for the second maximum were dependent on alumina content, and more alumina that is added, then the impedance effect by alumina is larger and the second maximum densification rate occurs at higher temperatures.

The composite powder compacts could be densified to near full density when alumina content is not higher than 20 mol%. 30 mol% alumina in the composite has already prevented the composite from reaching full densification; at 45 mol% of alumina, the composite compact showed only very limited densification effect, partially because of the low green density, but mainly because higher alumina content, which forms an extensive 'vermicular' structure or even a network in the body. This vermicular network leads to a large amount of inter-alumina or inter-alumina-Y–TZP pores and densification becomes greatly impeded.

4.3 The role of alumina in the development of the microstructure

The crystallization of alumina from Y–TZP grains during sintering leads to a two phase structure: alumina particles become homogeneously distributed in the Y–TZP matrix. Different from the similar composed but differently processed composites,[9–13] the particle size of the second alumina phase in this study was almost the same for those with the Y–TZP matrix (so no alumina particles could be trapped in a matrix grain or vice-versa), so the microstructure inhomogeneity was greatly suppressed. The particle size of the Y–TZP matrix was considerably affected by the presence of alumina particles at 1250°C: the matrix grain growth was inhibited by alumina. Figure 10 is the lattice image of a composite containing 20 mol% alumina. It can be seen that the interface between the two phases is very clear and no glass phase can be detected, so the inhibiting effect of grain growth by alumina is mainly from the pinning effect of the *in situ* formed second alumina phase. At a higher sintering temperature of 1550°C, the effect of grain growth inhibition of Y–TZP by alumina was not so strong as that at 1250°C.

5 Conclusions

(1) The composite powders prepared are hard, agglomerate-free and can be compacted without agglomerates left in the compacts.
(2) The composites can be densified to full densities at relatively low temperatures of 1250–1350°C for 2 h when alumina content is not higher than 20 mol%.
(3) The densification rate of the composite compacts with alumina content of 5 and 10 mol% is greatly increased because of the inhibited grain growth of the Y–TZP matrix.

Two maximum values of the densification rate (duplex shrinkage peaks) occur when alumina content is equal to or larger than 15 mol%, which is attributed to the phase transformation of alumina and/or the alumina particle clusters formed in the compacts during sintering.

(4) The homogeneous microstructure of the composite was obtained with the same grain size of the matrix Y–TZP and the second phase of alumina. The inhibiting effect of alumina on the grain growth of Y–TZP is probably led by the pinning effect.

References

1. Heuer, A. H., Claussen, N., Krive, W. M. & Ruehle, M., Stability of tetragonal ZrO_2 particles in ceramic matrices, *J. Am. Ceram. Soc.*, **65**(2), (1982) 642.
2. Lange, F. F., Transformation toughening Part 4; fabrication, fracture toughness and strength of Al_2O_3–ZrO_2 composites. *J. Mater. Sci.*, **17** (1982) 247.
3. Green, K. J., Critical microstructure for microcracking in Al_2O_3–ZrO_2 composites. *J. Am. Ceram. Soc.*, **65**(12) (1982) 610.
4. Ruehle, M., Claussen, N. & Heuer, A. H., Transformation and microcracking as complementary process in ZrO_2 toughened Al_2O_3. *ibid.*, **69**(3) (1986) 195.
5. Hori, S., Yoshimura, M. & Somiya, S., Strength-toughness relations in sintered and isostatically hot-pressed ZrO_2-toughened Al_2O_3 composites. *ibid.*, **69**(3) (1986) 169.
6. Masaki, T. & Shino, K., Mechanical behaviour of ZrO_2–Y_2O_3 Ceramics formed by hot-isostatic pressing. In *Advances in ceramics, science and technology of zirconia III*, eds S. Somiya, N. Yamamoto & H. Hanagida, The Am. Ceram. Soc. Inc., Columbus, OH. (1988), p. 709.
7. Tsukuma, K., Takahata, T. & Shiomi, M., Strength and fracture toughness of Y–TZP, Ce–TZP, Y–TZP/Al_2O_3 and Ce–TZP/Al_2O_3. In *Advance in Ceramics Vol 24: science and technology of zirconia*. eds S. Somiya, N. Yamamoto & H. Hanagida, The Am. Ceram. Soc., Columbus, OH, (1988), p. 721.
8. Rajendran, R., Swain, M. V. & Rossell, H. J., Mechanical properties and microstructure of co-precipitation derived tetragonal Y_2O_3–ZrO_2–Al_2O_3 composites. *J. Mater. Sci.*, **23** (1988) 1805–12.
9. Shi, J. L., Li, B. S. & Yen, T. S., Mechanical properties of Al_2O_3 particle-Y–TZP matrix composite and its toughening mechanism. *J. Mater. Sci.*, **28** (1993) 4019–22.
10. Tuan, W. H. & Brook, R. J., Sintering of heterogeneous composites. Part II: ZrO_2–Al_2O_3. *ibid.*, **24** (1989) 1953.
11. Sudre, O. & Lange, F. F., Effect of inclusions on densifications. I: microstructural development in an Al_2O_3 matrix containing a high volume fraction of ZrO_2 inclusions. *J. Am. Ceram. Soc.*, **75**(3) (1992) 519.
12. Tuan, W. H. & Brook, R. J., Sintering of heterogeneous ceramic composites. Part I: Al_2O_3–Al_2O_3. *J. Mater. Sci.*, **24** (1989) 1062.
13. Shi, J. L. & Yen, T. S., Densification and microstructure development of alumina/Y–TZP composite powder (Y–TZP-rich) compacts. *J. Europ. Ceram. Soc.*, **15** (1995) 363.
14. Shi, J. L., Ruan, M. L. & Yen, T. S., Processing of Nano-Y–TZP/Al_2O_3 Composites. I: preparation and characterization of nano-Y–TZP/Al_2O_3 composite powders. *J. Europ. Ceram. Soc.*, **15** (1995).

Journal of the European Ceramic Society 15 (1995) 975–981
© 1995 Elsevier Science Limited
Printed in Great Britain. All rights reserved
0955-2219(95)00069-0
0955-2219/95/$9.50

Alumina/Zirconia Multilayer Composites Obtained by Centrifugal Consolidation

E. Lucchini & O. Sbaizero

Dipartimento di Ingegneria dei Materiali e Chimica Applicata, Università di Trieste, Via Valerio 2, 34127 Trieste, Italy

(Received 4 May 1994; revised version received 21 February 1995; accepted 20 March 1995)

Abstract

An attractive method for the fabrication of Al_2O_3–ZrO_2 laminar composites is described in this paper. The process consists in the centrifugation of colloidal suspensions containing alumina and zirconia particles. With this procedure, it is possible to grow thin layers with different composition and smooth interfaces. The effects of the slurry compositions, as well as aging times and centrifuging conditions on the morphology of the laminae are discussed.

Introduction

Laminar ceramic composites are attractive materials because superior mechanical performances can be achieved by tailoring the properties, geometry and interfaces of the different layers.[1–3]

In particular, brittle ceramics can be toughened by introducing weak interfaces transverse to the growing crack or by developing internal stresses.[4–6] These tensile and compressive stresses are a consequence of the different thermal contractions and determine a deviation of the propagating cracks.

From this point of view the Al_2O_3–ZrO_2 system is interesting because the thermal expansion coefficients of the oxides are quite different, therefore, it is possible, by changing the ratios between alumina and zirconia in the layers, to obtain laminar composites with high internal stresses. Furthermore Al_2O_3–ZrO_2 based ceramics are known to be high toughness materials due to the stress-induced transformation of the metastable tetragonal zirconia inclusions.

So far, ceramic laminates have been prepared through chemical methods, the doctor blade technique and the slip casting route.[6–10] In this paper an alternative methodology is presented. It consists of the centrifugation of a relatively dilute aqueous suspension, in the removal of the supernatant liquid and in the addition, on the consolidated layer, of a new suspension with a different Al_2O_3–ZrO_2 ratio. Further, centrifugation induces the consolidation of a new layer and the process is repeated until the composite has the desired number of laminae.

The advantage of this method consists of obtaining thin layers of powders free of aggregates. In fact, during suspension preparation, repulsive interactions are generated between the particles, consequently the aggregates, which are deleterious for the sinterability of the powders and for the microstructure homogeneity, are broken down. Finally, this procedure results in smooth interfaces between the laminae and therefore a sharp variation of the sign of the internal stresses. This variation causes the deviation of the propagating cracks when they cross the interfaces. Furthermore, if the outer layers are in compression, the materials are damage resistant and therefore both mechanisms give rise to better mechanical properties.

Experimental

The starting materials were commercial submicron powders of Al_2O_3 (Sumitomo AKP-20) with an average particle size of 0·5 μm and t-ZrO_2 with 3 mol.% of Y_2O_3 (ICI Advanced Ceramics) with an average particle size of 0·3 μm.

Mixtures of Al_2O_3 and ZrO_2 powders were dispersed with a blender for 20 min in distilled water (6000 r.p.m). The pH values of the suspensions were adjusted to 4·0 using HNO_3 (1 M). This pH was chosen on the basis of previous work[11] and corresponds to the minimum viscosities for both alumina and zirconia slurries.[6]

Under these conditions, the submicron oxides' particles were positively charged, electrostatic repulsive interactions were generated, the aggregates

broken down and the solid phase sedimentation inhibited.[12]

After different aging times, the solutions were ultrasonically homogenized for 15 min at 300 W in order to break down the hard aggregates.[13] The duration of this treatment was decided on the basis of a previous study.[14]

After ultrasonication the pH of several slurries were changed to 8 using NH_4OH.

Under these conditions the zeta potential of Al_2O_3 and ZrO_2 particles was close to zero and the solid phase flocculates[15,16]. In other slurries, before the ultrasonication, NH_4NO_3 was introduced to induce strong short range repulsive forces between the particles. The reasons, as well as the effects of these additions will be discussed in the next section.

Quantities of slurry sufficient to yield the desired layer thickness were placed in a teflon cylindrical container (diameter = 50 mm). The vessel was put in a centrifuge and spun at various speeds for various periods.

After centrifuging, the supernatant aqueous solution was removed and another volume of suspension, containing a solid phase with different composition, was placed in the container in order to deposit the next layer. This procedure was repeated until multilaminar symmetric composites were obtained. The sequence of the operations is shown in Fig. 1.

After water removal, the samples were kept in the container at room temperature for several hours. During this stage, a certain quantity of water evaporated and the material contracted and consolidated. The laminates were removed from the container, dried at 60°C for 24 h, cold pressed at 1000 MPa and fired at 1580°C for 3 h.

Density was measured by immersion in distilled water and the microstructure was examined on polished samples with a scanning electron microscope.

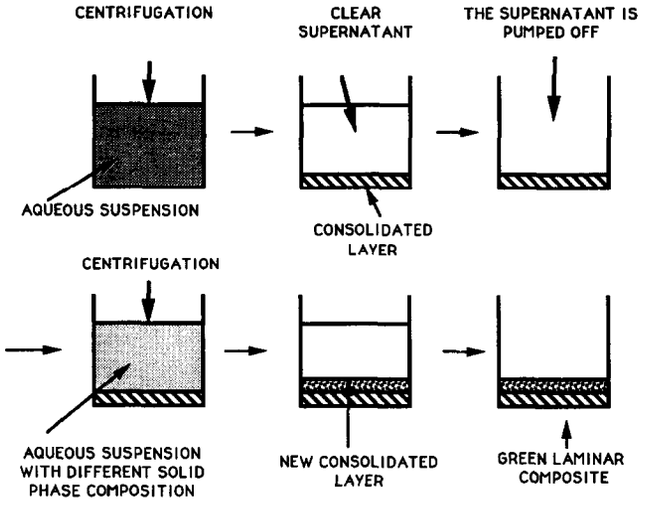


Fig. 1. Flow sheet of the procedure used for the preparation of compacts.

The suspension viscosities were measured at 25°C with a Rotowisko RV 100 viscometer. The zeta potential (ζ) was determined with a Rank Brothers Mark II equipment. For this purpose the slurries were prepared in 10^{-1} M KNO_3 solution in order to maintain a constant electrical double layer thickness.

The sedimentation rate was measured in a 100 ml graduated cylinder by observing the height of the interface between the settling suspension and its supernatant over an 8 h period.

Results and Discussion

For the the preparation of suspensions we used four powder mixtures with the following compositions:

Al_2O_3 85 vol.% – ZrO_2 15 vol%,
ZrO_2 85 vol% – Al_2O_3 15 vol.%,
Al_2O_3 65 vol.% – ZrO_2 35 vol.%,
ZrO_2 65 vol.% – Al_2O_3 35 vol.%.

The above compositions were chosen on the basis of previous experiments which showed that higher composition differences lead to the obtainment of composites containing laminae with very different thermal expansion coefficients. During the cooling, this thermal mismatch causes thermal stresses exceeding the tensile resistance of zirconia reach layers.

The influence of the chemical composition and thickness of the laminae on the composite mechanical properties is discussed elsewhere.[17]

The solid phase content of the suspensions was set to 15 vol%. This value was chosen on the basis of previous experience and on the basis of practical considerations, in fact, slurries with a high solid loading (>20 vol.%) are not able to break down the aggregates[8] and therefore homogeneous microstructures cannot be obtained.

On the other hand, high volumes of dilute suspensions are needed in order to develop layers of sufficient thickness. Therefore the considerable distance between the suspension surface and the container bottom can induce, during spinning, a concentration gradient of the oxides in the lamina.

Centrifugation conditions

The first attempts were made by centrifuging at 3000 r.p.m. for 30 min immediately after dispersion and ultrasonication pH = 4 suspensions. The results were not satisfactory because the supernatant liquid was cloudy. Longer spinning times did not cause the complete sedimentation of the solid phase. The layer thickness varied across the

diameter and reached a maximum near the walls of the container, therefore after drying and sintering the samples warped (Fig. 2) and exhibited delamination phenomena.

Furthermore, the ZrO_2 reach suspensions (85 vol.% of zirconia and 15 vol.% of alumina) exhibited on the surface a high quantity of 'bubbles'. These inhomogeneities remained also on the surfaces of the consolidated layers and were not destroyed by the deposition of other laminas (Fig. 3). Therefore, after sintering the composites exhibited irregular and porous interfaces.

Measures were taken in order to overcome the above mentioned shortcomings. An appropriate sequence in the spinning operations was studied in order to decrease the thickness differences across the samples. The best results were obtained by centrifuging the suspensions at 800 r.p.m. for 2 h and increasing the speed to 3000 r.p.m. during the last 5 min of the operation. With this procedure, the warping phenomenon was avoided.

During the centrifugation, in order to provoke complete separation of the solid phase the suspension pH was adjusted to 8 after ultrasonication. Under these conditions the zeta potential of the particles approaches zero value and the solid phase flocculates.[11]

By adopting this procedure, the supernatant liquid was clear after centrifugation, but the SEM examination of sintered samples showed the presence of large aggregates at the interfaces between the laminas, therefore no smooth interfaces were obtained using flocculated suspensions (Fig. 4). The examination of micrographs also showed a higher concentration of ZrO_2 aggregates in the bottom of layers.

These results are not in agreement with those found in another study.[18] In fact, in the paper mentioned above, homogeneous microstructures were observed in the compacts obtained with flocculated and centrifuged slurries. At present, no explanation can be given for this discrepancy.

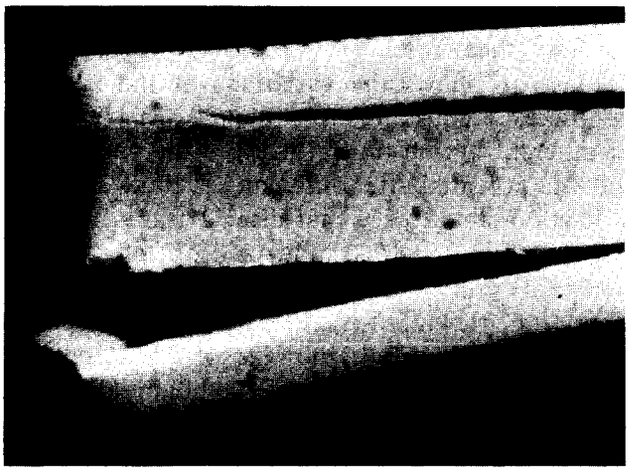


Fig. 2. Warping and delamination at the end of a sintered laminate, ZrO_2 content in the central layer 65 vol.%, in the external layers 35 vol.%. Warping and delamination are due to the different thicknesses throughout the length.

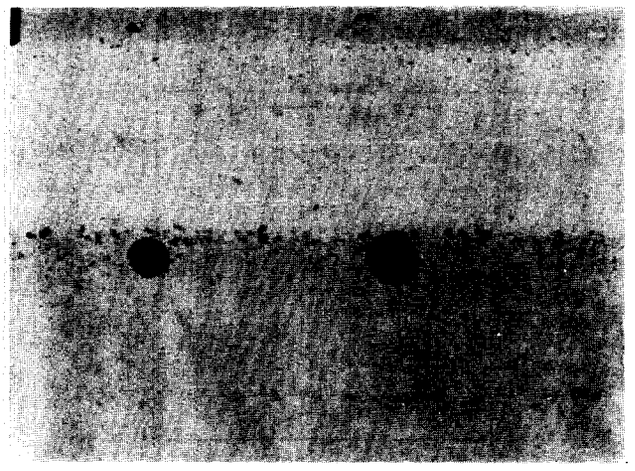


Fig. 3. Optical photomicrograph of the interface between a layer containing 15 vol.% of ZrO_2 (gray stratum) and another one containing 85 vol.% of ZrO_2. The presence of 'bubbles' is evident.

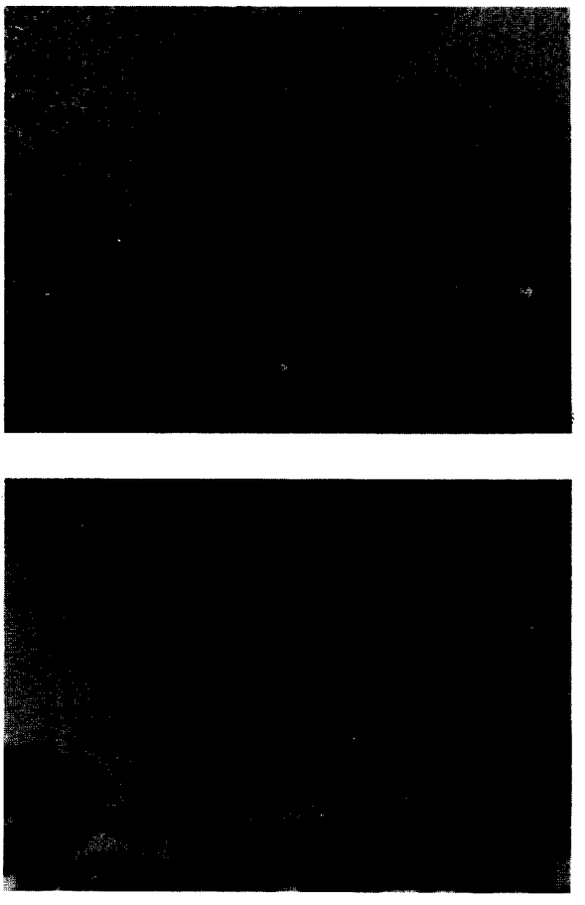


Fig. 4. SEM back-scattered micrograph of the interface between a layer containing 15 vol.% of ZrO_2 (gray stratum) and a layer containing 85 vol.% of ZrO_2 (brighter stratum). The powders were flocculated at pH = 8 before centrifugation. The presence of a large alumina aggregate is evident (darker particle).

Ageing of the suspensions

In order to eliminate the bubbles present on the surface of the zirconia reach suspensions, anti-foaming agents were used, but the best results were obtained by submitting the slurries to gentle mixing with an electric stirrer for 4 h. This treatment enabled the bubbles to deflate. After ultrasonication, the suspensions were centrifuged: smooth surfaces and an almost clear supernatant liquid were obtained. The good separation of the solid phase was surprising; therefore a short investigation was undertaken in order to explain this behavior.

For this purpose we examined the rheological behavior as a function of different ageing times of a zirconia reach suspension (ZrO_2 85 vol.%).

The results are summarized in Fig. 5 where the shear stresses measured after different rest times and at different shear rates are reported. The measurements were taken every 30 min over a period of 4 h, but in the graph, for sake of clarity, only the curves relative to 0, 90, 120, 150, 210 and 240 min of ageing times are reported. The slurry was prepared and aged using the procedures mentioned above and ultrasonicated immediately before the measurements.

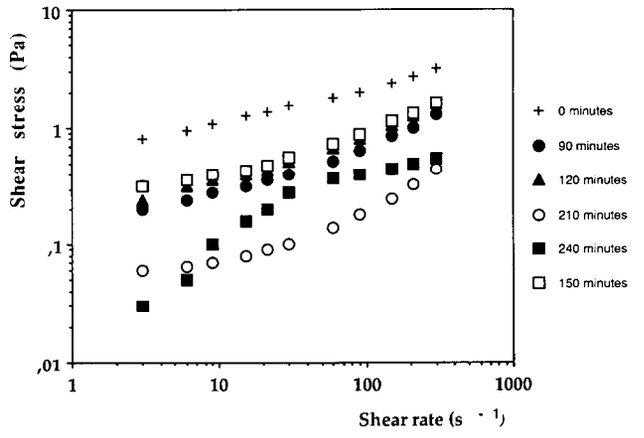


Fig. 5. Rheological behavior of aqueous suspensions aged for different times. Solid phase content = 15 vol.%, solid phase composition: ZrO_2 = 85 vol.%, Al_2O_3 = 15 vol.%, pH = 4).

The hysteresis loop method was used in order to ascertain the presence in the suspensions of a time-dependent behavior, but no thyxotropic phenomena were observed. According to the results reported by other authors for slurries of similar composition, the Herschel–Bulkley model is suitable to describe the rheological behavior of this system.[19]

$$\tau = \tau_0 + K\,\gamma^n \qquad (1)$$

Where τ is the shear stress, τ_0 is the yield value, γ the shear rate and n a constant.

However the Herschel–Bulkley equation cannot describe the behavior of suspensions aged for 4 h (see the curve in Fig. 3 indicated with full squares). Other models were used, (Casson, Bingham), in order to characterize this slurry, but the experimental and calculated data were at variance. In addition, fluctuation of the shear stress values (τ) were observed during the measurements at constant shear rate.

Figure 6 shows the variations of the apparent viscosities at constant shear rate (30 s^{-1}) as function of different ageing times. In Fig 7 the variation of the zeta potential after different rest times is shown.

It is possible to see that after 210 min, the suspensions exhibited a sudden drop of the zeta potential and a consequent viscosity increase. Therefore, the repulsive interactions between the particles are lowered, the size of the aggregates increases and the stability of the colloidal suspensions decreases. This fact can explain the obtainment of clear supernatant liquid when suspensions aged for 4 h are centrifuged. In this manner, it is also possible to explain the difficulties in characterizing the slurries aged for 4 h from the rheological point of view and the fluctuation of the τ values. Both inconveniences can be imputed to the friction of the aggregates on the walls of the measurement device.

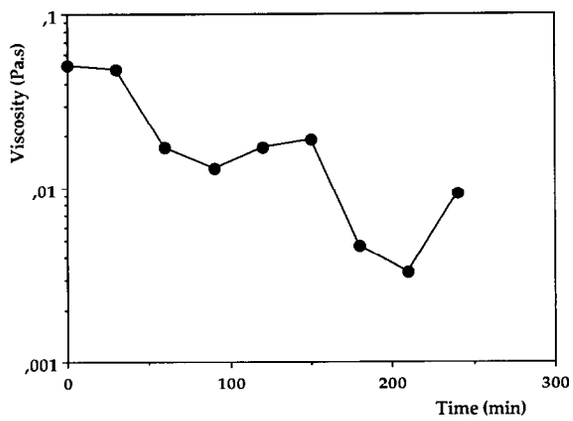


Fig. 6. Influence of the ageing times on the suspension viscosity (constant shear rate = 30 s^{-1}). The slurry composition is the same as that reported in the caption of Fig. 5.

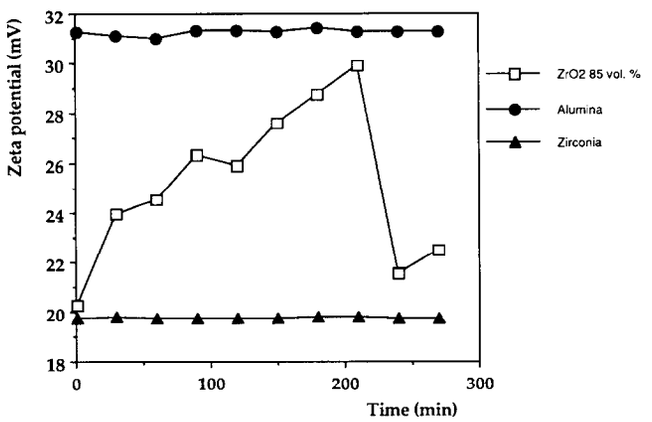


Fig. 7. Variation with the time of the zeta potential of alumina, zirconia and a mixture of 85 vol.% of ZrO_2 and 15 vol.% of Al_2O_3. Solid phase content 15 vol.%, pH = 4.

Figure 7 also shows the variations of the zeta potential of suspensions containing only zirconia and alumina powders. The preparation method and the solid phase content are the same as those used for the Al_2O_3–ZrO_2 systems. Because the zeta potentials of oxide particles remain constant during ageing, one can suppose that the variations of ζ in the suspension containing the Al_2O_3–ZrO_2 mixtures are essentially due to the interactions between the Y^{3+} ions and the surfaces or the double layers of the alumina particles. The yttrium ions in fact are released from the tetragonal stabilized zirconia in acidic conditions[20] and can decrease the stability of the slurries.

The kinetics of the interaction of Y^{3+} with the alumina are probably complicated and the observation of Figs 6 and 7 revealed the presence of several steps.

Improvement of the solid phase separation

The results obtained with flocculated and ultrasonicated suspensions aged for 4 h were encouraging and the laminae appeared homogeneous to SEM observations. These results are not in agreement with the paper of Velamakanni *et al.* [20] which showed that the centrifugation of Al_2O_3–ZrO_2 deflocculated slurries leads to a non-uniform distribution of the components; we would point out however that we did not undertake a systematic study on the distribution of the two oxides across the consolidated layers.

In Fig. 8, the microstructure of a laminar composite prepared using the procedure mentioned above is shown. The compositions of the alternating layers were 15 vol.% of ZrO_2–85 vol.% of Al_2O_3 and 15 vol.% of Al_2O_3–85 vol.% of ZrO_2 respectively.

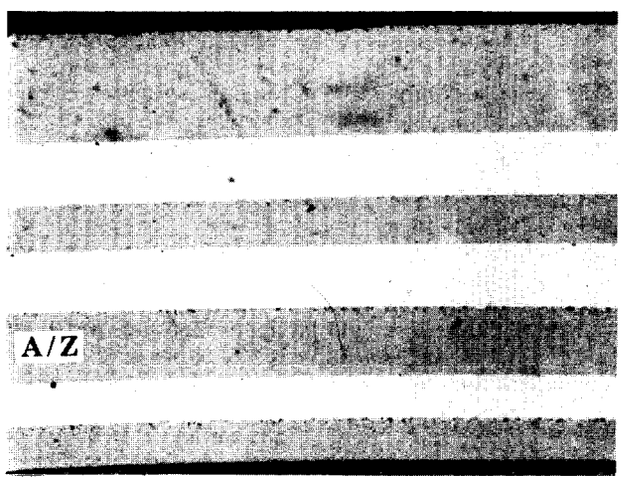


Fig. 8. Optical photomicrograph of a composite obtained by centrifugation of an aqueous suspension at pH = 4 after a gently mixing for 4 h. The slurry was ultrasonicated immediately before centrifugation. For the composition's layers, see the text.

In order to obtain a complete separation of the solid phase we added NH_4NO_3 to the suspensions. In fact the presence in the slurry of a high quantity of electrolite strongly decreases the long range electrostatic repulsive interactions and develops strong short range hydration repulsions.[20]

The salt addition provokes a viscosity increase and a destabilization of the suspension, but the permanence of a repulsive lubricating hydration layer allows the obtainment of high density bodies with well packed particles (coagulated suspensions).

The slurries were prepared using the previously discussed methods and the ammonium nitrate was added, after a certain rest time, immediately before ultrasonication. The salt concentration in the liquid phase was 1 M.

The sedimentation rate of a coagulated suspension was compared to that of a deflocculated one with the same solid phase composition (ZrO_2 85 vol.%), (Fig. 9).

Also in this case, the suspensions were aged in order to eliminate the bubbles, therefore, the evolution of the rheological behavior of the zirconia reach slurries was studied.

In order to avoid the problems related to the solid phase sedimentation, the viscosity measurements were performed immediately after the salt addition.

Again the Herschel–Bulkley model is suitable in order to describe the rheological behavior of the slurries, the only difference being that in the case of the coagulated suspensions the yield value (τ_o) is near to zero.

Good results were obtained by centrifuging the salt added slurries aged for times ranging from 1 to 4 h. Figure 10 shows the microstructures of a multilayer composite with the same composition as that of Fig. 8. Using this procedure laminae with less than 30 μm were easily obtained.

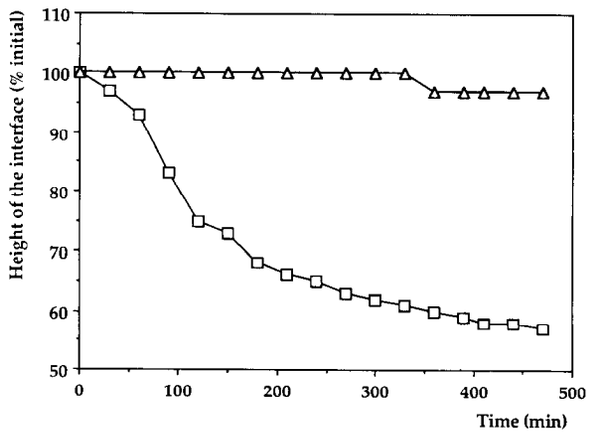


Fig. 9. Sedimentation rate of an aqueous suspension containing NH_4NO_3 1 M (squares) and without salt addition (triangles). For the slurry composition, see the text.

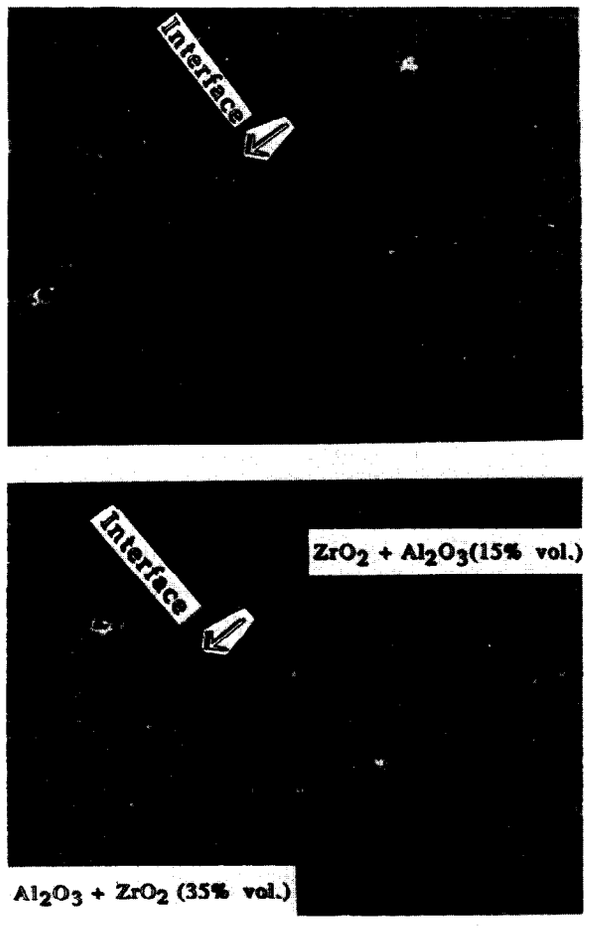


Fig. 10. SEM back-scattered micrograph of a laminar composite obtained by centrifugation of $NHNO_3$ added suspensions. The smoothness of the interface and the homogeneity of the layers are evident.

Sintering of multilayer composites

Densities of about 98–99% were reached by sintering the composites obtained from deflocculated slurries at 1580°C for 3 h (heating rate 5°C/min).

In the case of NH_4NO_3 added materials, a more complicated sintering process was needed in order to gently decompose the salt. The powder compacts were heated at 2°C/min up to 200°C and kept at this temperature for 45 min. Successively, the heating rate was increased by 5°C/min and the composites were fired for 3 h at 1580°C. With this thermal cycle, densities close to the theoretical value were obtained.

Conclusions

Zirconia and alumina based laminar composites can be fabricated by centrifuging aqueous suspensions containing the two oxide powders.

Good results were obtained using relatively dilute slurries (solid phase = 15 vol%). Strong repulsive interactions were generated by adjusting the pH at 4 with HNO_3 additions.

Centrifugation was performed in two different steps. The first one at low g and the other one, shorter, at high g. In this manner, samples with homogeneous thickness were obtained. Before centrifugation, the zirconia reach suspensions required long ageing times in order to eliminate the bubbles present in the suspensions. After 4 h, a decrease of the zeta potential of these suspensions was observed, together with a viscosity increase. The centrifugation of these aged suspensions led to an almost complete solid phase separation. This behavior at present cannot be explained. The best results were obtained with coagulated suspensions (containing NH_4NO_3 1 M) aged for several hours. With these slurries thin laminae with smooth interfaces were obtained.

Acknowledgement

The authors gratefully acknowledge the funding provided by P.N.F.M.T.A.

References

1. Chartier, T., Besson, J. L. & Boch, P., Mechanical properties of ZrO_2–Al_2O_3 laminated composites. In *Advances in Ceramics, Science and Technology of Zirconia III*, Vol. 24, eds S. Somiya N. Yamamoto & H. Yanagida, Amer. Ceram. Soc., Westerville, Ohio, 1988, pp. 1131–8.
2. Chartier, T. & Besson, J. L. , Behaviour of ZrO_2–Al_2O_3 laminated composites loaded by various mechanical arrangements. In *Science of Ceramics*, Vol. 14, ed. D. Taylor, The Institute of Ceramics, UK, 1988, pp. 639–44.
3. Russo, C. J., Harmer, M. P., Chan, H. M. & Miller, G. A., Design of laminated ceramic composite for improved strength and toughness. *J. Amer. Ceram. Soc.*, **75**(12) (1992) 3396–400.
4. Clegg, W. J., The fabrication of failure of laminar ceramic composites. *Acta Metall. Mater.*, **40**(11) (1992) 3085–93.
5. Harmer, M. P., Chen, H. M. & Miller, G. A., Unique opportunities for microstructural engineering with duplex and laminar ceramic composites. *J. Am. Ceram. Soc.*, **75**(7) (1992) 1715–28.
6. Requena, J., Moreno, R. & Moya, J., Alumina and alumina/zirconia multilayer composites obtained by slip casting. *J. Am. Ceram. Soc.*, **72**(8) (1989) 1511–13.
7. Adair, J. H., Touse, S. A. & Melling, P. J., Chemically derived multilayer ceramics. *Am. Ceram. Soc. Bull.*, **52**(11) (1973) 850–4.
8. Misler, R. E., High strength alumina substrates produced by a multi-layer casting technique. *Am. Ceram. Soc. Bull.*, **52**(11) (1973) 850–4.
9. Boch, P., Tape casting of layered composites. In *Processing of Advanced Ceramics.*, eds J. S. Moya & S. De Azza, Soceidad Espanola de Céramica y Vidrio. Madrid, Spain, 1987, pp. 103–12.
10. Fiori, C. & De Portu, G., Tape casting: a technique for preparing and studying new materials. In *Novel Ceramic Fabrication Process*, ed. R. W. Davidge, Institute of Ceramics, Stoke-on-Trent, UK, 1986, pp. 213–25.
11. Lucchini, E. & Maschio, S., Alumina–zirconia ceramics: preparation and properties. In *Zirconia 88*, eds S. Meriani & G. Plamonari, Elsevier Applied Science, London – New York, 1989, pp. 161–70.

12. Verwey, E. J. & Overbeek, J. Th. G., *Theory of Stability of Lyophobic Colloids*, Elsevier Publ., Amsterdam, 1948.
13. Chartier, T., Jorge, E. & Boch, P., Ultrasonic deagglomeration of Al_2O_3 and $BaTiO_3$ for tape casting. *J. Phys.*, **III** (1991) 689.
14. Langlois, R. & Konstowicz, K. J., Effects of soft agglomeration on the mechanical properties of zirconia — toughened alumina ceramics. *Trans.*, **19** (1991) 723–9.
15. Gosky, D., Kwak, J. T. & Konstowicz, K. J., Electrokinetic behaviour of zirconia alumina colloidal suspensions in water and in electrolyte. *Ceram. Eng. Sci. Proc.*, **12** (9–10) (1991) 2075–83.
16. Moreno, R., Requena, J. & Moya, J. S., Slip casting of yttria-stabilized tetragonal zirconia polycristals. *J. Am. Ceram. Soc.*, **71**(12) (1988) 1036–40.
17. Sbaizero, O. & Lucchini, E., Influence of residual stress on the mechanical properties of a layered ceramic composite. To be published.
18. Srinivasa Rao, A., Effect of pH on the suspension stability of alumina, titania and their mixtures. *Ceramic Int.*, **13** (1987) 233–41.
19. Farinas, C., Moreno, R., Requena, J. & Moya, J. S., Acid-basic stability of Y–TZP ceramics. *J. of Mat. Sci. and Eng*, **A109** (1989) 97–9.
20. Velamakanni, B. V., Chang, J. C., Lange, F. F. & Pearson, D., New method for efficient colloidal particle packing via modulation of repulsive lubricating hydration forces. *Langmuir*, **6** (1990) 1323–5.

Journal of the European Ceramic Society 15 (1995) 983–988
© 1995 Elsevier Science Limited
Printed in Great Britain. All rights reserved
0955-2219(95)00070-4
0955-2219/95/$9.50

Microstructure and Creep Properties of Alumina/Zirconia Ceramics

José María Calderón-Moreno,[a] Antonio R. de Arellano-López,[a] Arturo Domínguez-Rodríguez[a] & Jules L. Routbort[b]

[a]Departamento de Física de la Materia Condensada & Instituto de Ciencias de Materiales de Sevilla, Universidad de Sevilla-CSIC, Sevilla, Spain
[b]Materials Science Division, Argonne National Laboratory, Argonne, Illinois 60439, USA

(Received 18 May 1994; revised version received 20 March 1995; accepted 31 March 1995)

Abstract

High temperature creep of two zirconia toughened alumina ceramics, fabricated by powder processing and sol–gel precursors processing, has been studied in order to determine plastic deformation mechanisms. Compressive creep tests were carried out between 1300 and 1450°C, under stresses from 10 to 150 MPa. For the sample fabricated from powders, a stress exponent of 1·4 and an activation energy of 580 kJ/mol were found below a critical stress of 40 MPa. For larger stresses, accelerated creep rates developed. In the specimens processed from precursors, values of 1·8 for the stress exponent and 540 kJ/mol for the activation energy, over the entire range of stresses have been determined. Creep parameters and microstructural evolution of the samples during the experiments have been correlated with models to establish the dominant creep mechanism.

Introduction

ZrO_2 has a very high fracture toughness and its addition to other ceramics, zirconia toughened ceramics (ZTC), has many advantages.[1] In the last eighteen years, a number of investigations of the mechanical and microstructural features of ZTCs, in particular in the system Al_2O_3–ZrO_2, also called zirconia toughened alumina, ZTA, have been performed.[2,3] The major application of ZTAs has been metal cutting tools.[4]

Available results on mechanical properties of ZTA are mainly on fracture, strength, and elasticity. All properties show a strong dependence on the volume fraction of each component, on the ratio of tetragonal and monoclinic zirconia, as well as on zirconia grain size (GS). The review by Green *et al.*,[5] summarizes most of these results.

Fracture studies[3] on ZTA, have shown an increase in K_{Ic} (up to 10 MPa.m$^{1/2}$) with increasing zirconia volume fraction, in particular for small grain sizes (< 1 μm). These authors have claimed that the total increment in fracture toughness is a combination of transformation and microcrack mechanisms of toughening. The first is only possible if t-ZrO_2 particles are present, and the second actuates if zirconia particles at the grain boundaries are transformed to monoclinic by cooling down from the sintering temperature.

In some cases, microcracking resulted in a reduction of strength which is particularly deleterious for large zirconia GS, and volume percentages.[6] To avoid flaws, some researchers have HIP-ed sintered samples,[6] and obtained improved strength, in particular for t-ZrO_2. Some improvement in flexural strength has been also reported for volume percentages of mainly t-ZrO_2 up to 10%.[3] Other authors have studied the retained strength after thermal shock.[7] A sharp decrease in this parameter occurs if samples are heated over the phase transformation temperature and then cooled down. Both room-temperature Vickers hardness, and Young's modulus decrease with increasing zirconia content, in particular, in specimens with high microcracking activity.[8]

In this study our objective is to obtain knowledge on plastic deformation mechanisms in composite systems, as well as on the microstructural effects of creep. Only a few high-temperature mechanical properties data are available. Due to such lack of data, we will compare our results with related materials, like monolithic Al_2O_3 or ZrO_2.

Experimental Techniques

(a) Material

Creep of two polycrystalline ZTA ceramics with 94·5 vol% of Al_2O_3 and 5·5 vol% of ZrO_2 has been

studied. In one case, processing was conducted by wet mixing of powder raw materials and dispersants. The alumina was in the form of α-Al_2O_3 and the zirconia powder was of high purity (99·995%), in the form of monoclinic m-ZrO_2, with a typical particle size of 0·5 μm. Densification took place after drying by uniaxial hot-pressing, at 1600°C, achieving full density. This type of material will be called pd-ZTA.

In the other materials, the processing was carried out by a sol–gel technique using an Al_2O_3 solution and a ZrO_2 precursor, which should result in a better mixing of components. After calcination, screening and drying, uniaxial hot-pressing was performed at 1600°C, obtaining fully dense samples. Throughout this paper, this material will be called pc-ZTA.

(b) Mechanical testing

Mechanical tests have been carried out under compression on 3 × 3 × 5 mm^3 samples, both at constant strain rate (CSR) of 1·7 × 10^{-5} s^{-1}, and or constant load (CL) between 10 and 150 MPa (engineering stress). Temperatures ranged from 1300 to 1450°C. All tests were performed in air.

(c) Microstructural observations

Polished surfaces of as-received and deformed samples were observed by SEM. Some were thermally etched in air at 1450°C to reveal grain morphology. Several microstructural parameters (zirconia distribution, GS, and shape) were studied by means of an image analyzer.

Other microstructural features (dislocations, cracks,...), have been studied by TEM in as-received and deformed specimens. TEM samples were prepared using standard techniques and were carbon coated before observation.

Microstructure of As-Received Samples

(a) ZTA prepared from powders

ZrO_2 grains are homogeneously distributed throughout the Al_2O_3 matrix, with a typical log–normal distribution of GS. 20% of the total volume fraction of zirconia are small particles (<0·5 μm) and are normally embedded in large alumina grains having an average GS of 4·7 ± 0·7 μm, as seen by TEM (Fig. 1). Another 60% of ZrO_2 are grains between 0·5 and 7 μm diameter, located at grain boundaries (GB) and triple point junctions. Finally, the remaining 20% of ZrO_2 are large conglomerates (>7 μm, with a maximum size of 38 μm) located between Al_2O_3 grains. These conglomerates have a lenticular shape oriented perpendicularly to the hot-pressing axis (HPA) (Fig. 2).

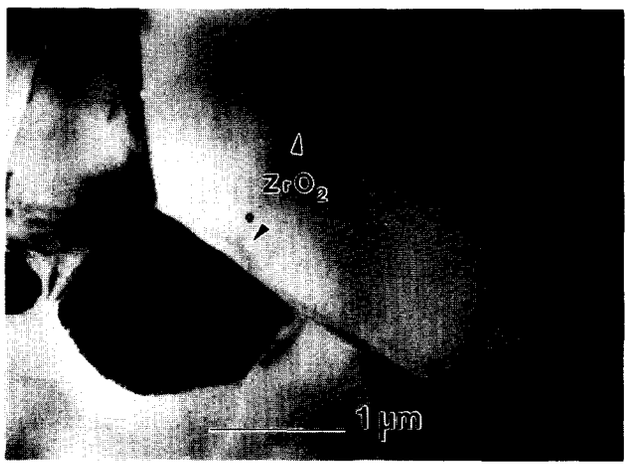


Fig. 1. TEM micrograph of pd-ZTA showing small zirconia particles.

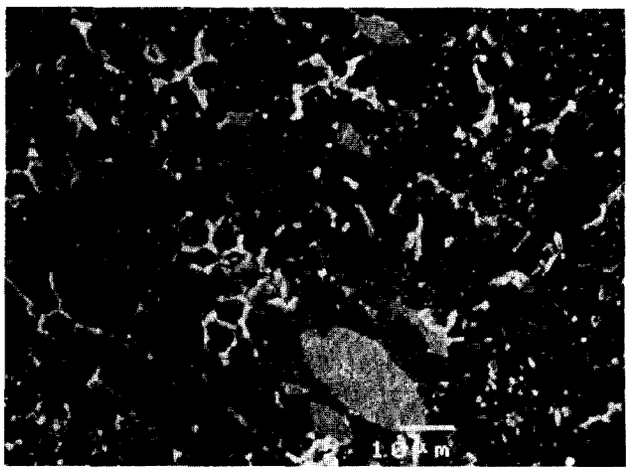


Fig. 2. SEM micrograph of polished pd-ZTA showing alumina GS and one of the lenticular agglomerates of zirconia oriented perpendicularly to the HPA axis.

Several studies have reported similar microstructures. Kibbel and Heuer,[9,10] for instance, indicated that the presence of zirconia, enhances in some cases the growth of alumina usually resulting in small-trapped ZrO_2 particles. Heuer *et al.*[11] showed that trapped grains, with GS smaller than 0·5 μm, are mostly tetragonal, and are very unlikely to transform to monoclinic in a rigid matrix like Al_2O_3,[12] while larger particles, normally placed at grain boundaries, are mainly monoclinic. When the dispersion of zirconia in matrix is not good enough, the monoclinic particles can agglomerate, and form the larger particles reported in this and other studies.[13]

The effect of the m-ZrO_2 along grain boundaries promotes poor thermal shock resistance. When heated up for sintering, etching or creep-testing, m-particles transform to tetragonal (over 1100°C for undoped zirconia). When cooled-down, they become monoclinic again, creating cracks, in particular around the large ZrO_2 particles previously mentioned.[7,8]

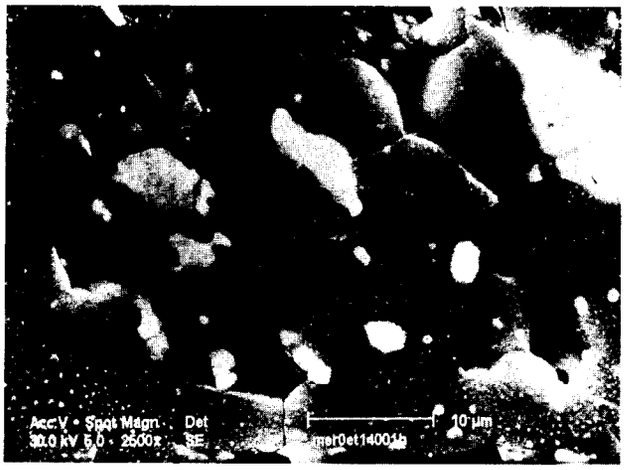


Fig. 3. SEM micrograph of polished and etched pd-ZTA showing a crack inbetween zirconia grains, and significant pull-out, due to microcracking.

In Fig. 3, a SEM micrograph taken on a polished and thermally etched surface, it is easy to observe the formation of extensive cracks between the large ZrO_2 particles. All observations confirm the activity of the martensitic transformation during etching, and, in general, during any thermal cycling over the transformation temperature.

The microstructure of the ZTA prepared by powder techniques is, therefore, 'intragranular–tetragonal/intergranular–monoclinic' as expected from all the above mentioned investigations.[1]

(b) ZTA prepared from precursors

In these samples, ZrO_2 particles are also homogeneously distributed through the matrix (Fig. 4). Nevertheless, an observed major difference compared with pd-ZTA is a much narrower log–normal distribution of zirconia grains, with 95% of the total number of particles smaller than 1 μm, mostly embedded into the Al_2O_3 grains which average a GS of $2{\cdot}6 \pm 0{\cdot}3$ μm.

When the samples were polished and etched for microstructural analysis, the features of grain pull-out, and microcracking due to thermal cycling, were not observed as in pd-samples. The absence of large monoclinic zirconia grains is responsible for this better microstructure. The ZrO_2 grains are small enough, even if they are located at grain boundaries, to keep their tetragonal structure. Therefore, we can characterize this pc-ZTA as 'intra-granular tetragonal'.[1]

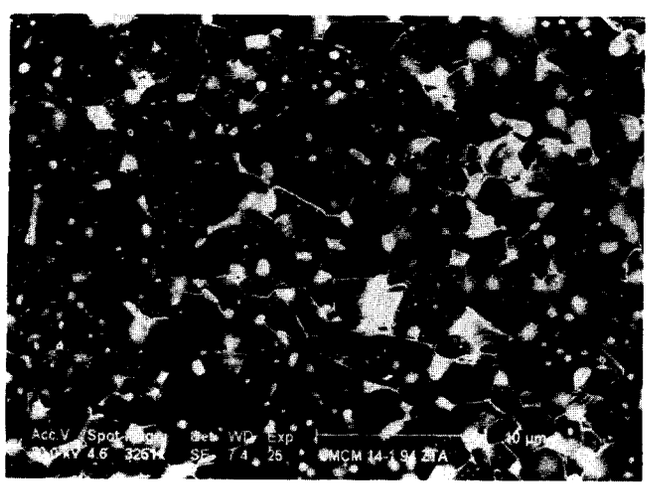


Fig. 4. SEM micrograph of pc-ZTA, showing the homogeneous GS and distribution of zirconia particles, and alumina GS.

Results

Figures 5 and 6 show results of CSR tests on pd-ZTA and pc-ZTA. At 1300 and 1350°C the samples fractured after 6–7% deformation. At the lower temperature strain/stress plots showed brittle fracture for σ = 385 MPa for pd-ZTA, and 434 MPa for pc-ZTA, while at 1350°C the samples fracture for σ = 231 MPa and 296 MPa, respectively, but exhibited plastic behavior. At 1400°C, 95 MPa was reached without fracture after 8% strain for the powder-processed samples. Some softening is detected in the final part of the plot, but without failure. Such behavior was also

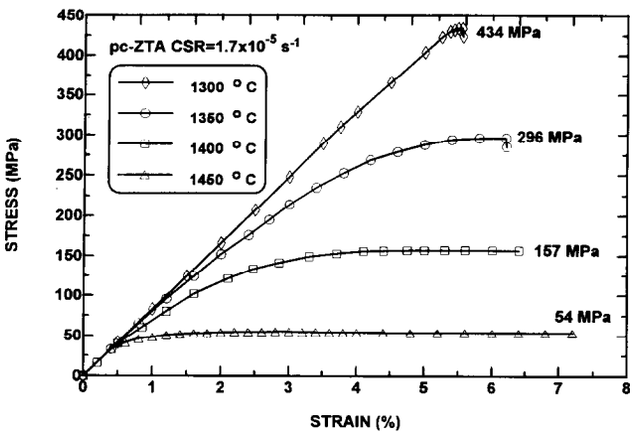


Fig. 5. Results of constant strain rate tests on pc-ZTA at different temperatures as shown.

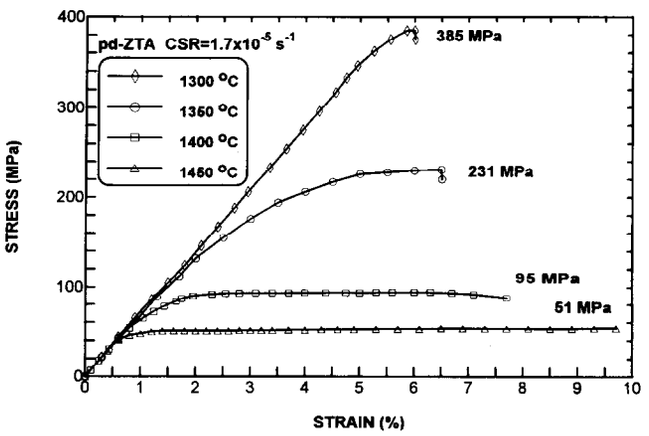


Fig. 6. Results of constant strain rate tests on pd-ZTA at different temperatures as shown.

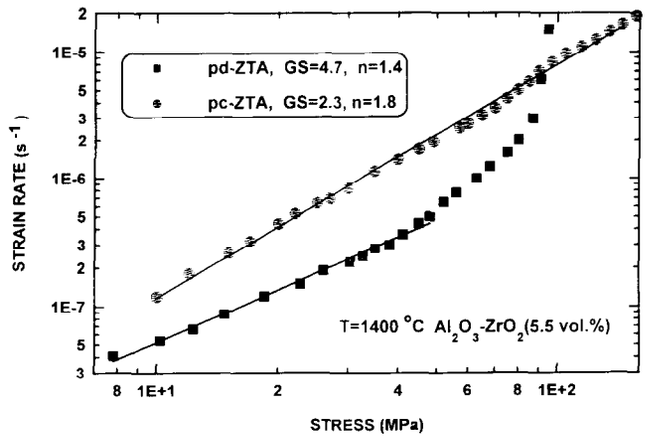


Fig. 7. Steady state strain rates reached on constant load tests versus true stresses.

observed in the tests performed on the precursor-processed samples, with a zero-work hardening stress of 157 MPa, in this case. At this last temperature, several CL tests were performed on different samples. For increasing stresses from 10 to 150 MPa, strain rates ranged between 4×10^{-8} and 2×10^{-5} s^{-1}. Steady-state strain rates are plotted in Fig. 7 versus the applied stress. The effect of temperature on creep rate, at constant load was studied between 1300 and 1450°C. An Arrhenius plot of (ln $\dot{\epsilon}$) versus (1/T) is shown in Fig. 8.

All of these results are analyzed using the phenomenological equation:

$$\dot{\epsilon} = A\sigma^n d^{-p}{}_{\exp}(-Q/RT) \qquad (1)$$

where $\dot{\epsilon}$ is the strain rate, σ is the stress, d is the grain size, A is a constant, and R and T have their usual meaning. The parameters n (stress exponent) and Q (activation energy) and p (grain size exponent) can be determined and correlated with plastic deformation mechanisms.

For the pd-ZTA material, two regimes of deformation were detected, with a change in the stress exponent from 1·4 ± 0·2 at low stresses, to variable values larger than two for higher stresses.

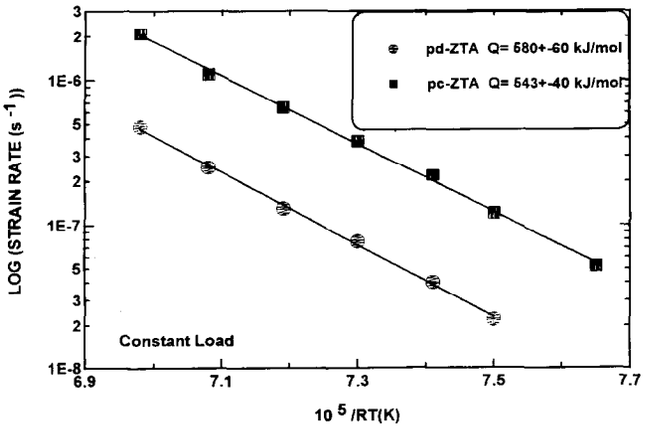


Fig. 8. Steady state strain rates reached on constant load tests versus (1/RT) in an Arrhenius plot.

The critical σ_c is above 40 MPa. On the other hand, in the range of stresses studied, a constant n = 1·8 ± 0·2 is measured for the pc-ZTA material.

We have determined the activation energy, Q, for both materials. 580 ± 60 kJ/mol is obtained for pd-ZTA, under 23 MPa ($< \sigma_c$), and 540 ± 40 kJ/mol for pc-ZTA, under 25 MPa.

However, in a complex material, like the one in this study, the meaning of these parameters in terms of creep mechanisms, is not clear without analyzing the microstructural evolution of the samples during plastic deformation. A complete discussion will follow.

Microstructural analysis was performed on samples deformed at 1400°C, from both CSR and CL tests. After the test, CSR deformed specimens showed extensive intergranular cracking. We can also see large cracks formed by coalescence of pre-existing cavities near ZrO_2 particles at grain boundaries (Fig. 9). After the CL experiments, we only observed samples deformed in the n = 1·4–1·8 regime. Some cavities were observed. However they should not control plastic deformation because it was possible to measure quasi-steady states of creep. A more detailed analysis of the role of cavitation in the creep of composite ceramics is out of the scope of this paper.

Grain size and morphology of deformed samples was studied. Neither alumina, nor zirconia grains appear to suffer major geometric changes. GS remains constant. The grains form factors, defined as

$$FF = 4\pi.(\text{area})/(\text{perimeter})^2,$$

remains around 0·8 up to 20% strain.

Discussion

For the compression rate used, with $T < 1400$°C,



Fig. 9. Cracks formed by coalescence of cavities developed at the surroundings of zirconia particles at grain boundaries during plastic deformation.

the pc-ZTA samples suffer brittle fracture at stresses typically higher than the ones measured for pd-ZTA samples. For temperatures over 1400°C both kinds of samples are plastic.

We have specifically studied plasticity at 1400°C, using a wide range of stresses. pc-ZTA specimens show a single deformation regime characterized by n = 1·8 and Q = 540 kJ/mol, while for pd-ZTA samples two regimes have been detected. In these samples, below $\sigma_c \approx 40$ MPa, approximately, the plastic deformation mechanisms is characterized by a sequence of steady states with calculated n = 1·4 and Q = 560 kJ/mol. For $\sigma > \sigma_c$ values for n and Q have little meaning. This non-steady state regime is a consequence of coalescence of cavities whose origin we have not investigated and will not be considered in the following analysis.

Absolute values of the strain-rate are between 2 and 5 times faster in pc-materials than in pd-samples, but this can be explained, in the light of eqn (1), by the difference in GS (d). If the $\dot{\epsilon}$ values are normalized for grain size differences using p = 2 or 3, the strain rates become, within the experimental scatter, equal. Figure 10 shows such a comparison for p = 2, for illustrational purposes. Also included in Fig. 10 is a comparison with results of a monolithic alumina of 3·3 μm GS, reported in a previous work.[14] Good concordance is found in the stress exponent (1·3 ± 0·1) and in the activation energy (510 ± 20 kJ/mol), and in the normalized strain rates (also included in Fig. 10). The accord might suggest that diffusion in both ZTA and Al_2O_3 is extrinsically controlled. The most important conclusion though is that no significant improvement in creep resistance in the steady-state region for either material is found.

The unchanged form factors indicate that grain boundary sliding (GBS)[15] is the dominant mechanisms of deformation since a pure diffusion mechanism requires a change of grains' shape. Additionally, large cracks can nucleate from

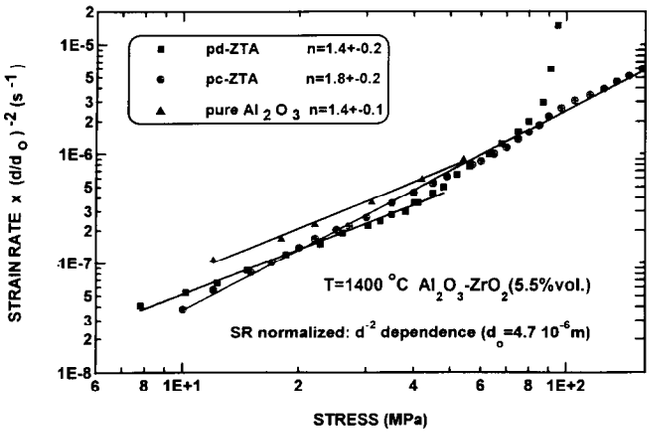


Fig. 10. Steady state strain rates normalized using p = 2, for a common grain size of 4·7 μm, for pd-ZTA, pc-ZTA and monoclinic alumina.[15]

ZrO_2-related microcracks, and will limit the utility of these materials over a certain critical strain (ϵ_c).

There are two mechanisms of diffusion accommodated GBS creep.[16] One is the mechanisms known as interface-reaction controlled (IRC) grain boundary sliding (with n = 2) and the other is transport of matter controlled (TMC) grain boundary sliding (n = 1), the first is more active in polycrystals with small grains. The creep parameter p can be either 2 or 3 in TMC creep, depending on the path of the creep controlling diffusion (p = 2 for lattice diffusion and p = 3 for grain boundary diffusion). In IRC creep the grain size exponent aries from 1 to 3. Both IRC and TMC, have been used to describe GBS in pure alumina[16,17] The parameter p in Al_2O_3 was found to be between both theoretical extremes, 2 and 3.

A range of n's from 1·1 to 2, and Q values from 410 to 568 kJ/mol has been reported in polycrystalline alumina specimens.[18] Although there is a general agreement that GBS is the dominant mechanism in Al_2O_3, there is much controversy on the meaning of the measured activation energies in terms of controlling diffusion species. Most authors claim that the higher values of Q are related to the diffusion of O^{2-} through the lattice, which is in agreement with p = 2, and has been detected in samples with large grain sizes (> 5 μm). On the other hand, the lower values of Q are claimed to result from grain boundary diffusion of Al^{3+}. A value of p = 3 is reported in these cases, usually found in samples with small grain sizes. However, comparisons are difficult because diffusion dynamics can be seriously altered by the presence of impurities,[19] and these are unknown in our samples. Our calculated creep parameters for ZTA, are consistent with the values reported for monolithic alumina. The values of n, and the microstructural observations, agree with the mechanism of unaccommodated GBS, with a mix of IRC and TMC. The largest values of n = 1·8, is found for the samples with the smallest grain size, and the lower n = 1·4 is found for samples with the largest grain size, in good agreement with predictions. The high values of Q found in this study support the control of the creep by O^{2-}, and the lattice is very likely to be the path of this transport of matter.

ZrO_2 agglomerates at grain boundaries are probably the origin of damage, and limit the strain to failure. The samples processed using the precursors technique contain less of these particles, and even though the unaccommodated GBS causes the formation of cavities, the samples remain intact with up to 40% strain. On the other hand, powder processed samples, which contains large zirconia particles, exhibit a critical stress over which the samples fail.

Baddi *et al.*[20] have studied the diffusional creep regime in a material of symmetric composition to the one in our work (zirconia matrix with alumina inclusions) and found that at low stresses IRC–GBS was dominating, while a TMC–GBS was active for the high stress range. Their microstructural analysis showed significant changes in the shape of the grains, without any cavitation. Other authors have proposed the same mechanisms (superplastic) acting in monolithic zirconia. The activation energy determined by Baddi and co-authors, also agreed with the one reported for monolithic zirconia In the material studied by Baddi *et al.*, the dominant component is then ZrO_2.

In our materials, it appears then, that the controlling component which determines the creep response is the harder phase: alumina. The role of the ZrO_2 phase is important in the brittle behavior and probably plays a role in the damage which accumulates in the plastic regime.

The better dispersion of the zirconia into the matrix in pc-TA, avoiding the formation of large intergranular monoclinic particles, results in better high-temperature mechanical response

Conclusions

It has been shown that the addition of 5·5 vol% of zirconia particles to an alumina matrix does not improve its resistance to creep. Creep takes place by grain boundary sliding and is accompanied by the formation of cavities. In the pd-samples, where large m-zirconia grains are present at grain boundaries, the linkage of the cavitation is easier because the inherent microcracking present in the samples, and results in a limited strain to failure and in a critical stress over which the formation of damage is too severe to allow measuring steady states of creep. On the other hand, for pc-samples, where a narrower GS distribution of smaller t-ZrO_2 particles has been measured, a single plastic regime of steady-states was detected. Cavities are also present in these crept samples, but the less microcracking activity promotes a better mechanical response.

We may conclude that the precursors-processed ZTA, with less microcracking, is a better candidate for high temperature applications than powder-processed ZTA, where microcracking is introduced by the presence of monoclinic zirconia grains.

Acknowledgements

The authors thank Lori Leaskey, from MER Corporation, Phoenix, Arizona, for supplying the samples. The work in Spain was supported by CICYT Project MAT91-0978 of the Spanish Ministerio de Educación y Ciencia. JLR was supported by the US Department of Energy, BES, Division of Materials Science under contract W-31-109-ENG.

References

1. Claussen, N., Microstructural design of zirconia-toughened ceramics. In *Science and Technology of Zirconia II, Advances in Ceramics*, vol. 12, eds N. Claussen, M. Rühle & A. H. Heuer. American Ceramic Society, Columbus, Ohio, 1984, pp. 325.
2. Claussen, N., Fracture toughness of Al_2O_3 with an unstabilized ZrO_2 dispersed phase, *J. Am. Ceram. Soc.*, **59** (1976) 49.
3. Claussen, N., Steeb, J. & Pabst, R. F. Effects of induced microcracking on fracture toughness of ceramics. *Am. Ceram. Soc. Bull.*, **56** (1977) 559.
4. Garvie, R. C., Microstructure and performance of an alumina–zirconia tool-kit, *J. Mat. Sci. Lett.*, **3** (1984) 315.
5. Green, D. J., Hannick, R. H. J. & Swain, M. V. In *Transformation toughening of ceramics*, CRC Press, Boca Raton, (1989), pp. 157–92.
6. Hori, S., Yoshimura, M. & Somiya S., Strength-toughness relations in sintered and isostatically hot-pressed ZrO_2 toughened Al_2O_3, *J. Am. Ceram. Soc.*, **69**(3) (1986) 169.
7. Becher, P. F., Transient thermal stress behaviour in ZrO_2–toughened Al_2O_3, *J. Am. Ceram. Soc.*, **64** (1981) 37.
8. Green, D. J., Critical microstructure for microcracking in Al_2O_3–ZrO_2 composites, *J. Am. Ceram. Soc.*, **65** (1982) 610.
9. Kibbel, B., Heuer, A. H., Ripening of inter- and intragranular ZrO_2–Toughened Al_2O_3. In *Science and Technology of Zirconia II, Advances in Ceramics*, vol. 12, eds N. Claussen, M. Rühle & A. H. Heuer, American Ceramic Society, Columbus, Ohio, (1984), pp. 415.
10. Kibbel, B. & Heuer, A. H., Exaggerated grain growth in ZrO_2–Toughened Al_2O_3, *J. Am. Ceram. Soc.*, **69** (1986) 231.
11. Heuer, A. H., Claussen, N., Kriven, W. M. & Rühle, M., Stability of tetragonal ZrO_2 particles in ceramic matrices, *J. Am. Ceram. Soc.*, **65**(12) (1982) 642.
12. Yuan, L. J. & Yen, T. S., Major influences on the particle size–transformation temperature relation in Al_2O_3–ZrO_2 composites, *J. Am. Ceram. Soc.*, **75**(9) (1992) 2576–80.
13. Witek, S. R. & Butler, E. P., Zirconia particle coarsening and the effects of zirconia additions on the mechanical properties of certain commercial aluminas, *J. Am. Ceram. Soc.*, **69**(7) (1986) 523.
14. DeArellano-López, A. R., Cumbrera, F. L., Domínguez-Rodriguez, A., Goretta, K. & Routbort J., Compressive creep of SiC-whisker-reinforced Al_2O_3, *J. Am. Ceram. Soc.*, **73**(5) (1990) 1297.
15. DeArellano-López, A. R., Domínguez-Rodriguez, A., Goretta, K. & Routbort, J., Plastic deformation mechanisms in SiC-whiskers-reinforced alumina, *J. Am. Ceram. Soc.*, **76**(6) (1993) 1425.
16. Ashby, M. F. & Verrall, R. A., Diffusional flow and superplasticity, *Acta Metall.*, **21** (1973) 149.
17. Cannon, R. M., Rhodes, W. H. & Heuer, A. H., Plastic deformation of fine grained Al_2O_3. I: Interface-controlled diffusional creep, *J. Am. Ceram. Soc.*, **63**(1–2) (1980) 46.
18. Heuer, A. H., Tighe, N. J. & Cannon, R. M., Plastic deformation of fine grained Al_2O_3. II: Basal slip and unaccommodated grain boundary sliding, *J. Am. Ceram. Soc.*, **63**(1–2) (1980) 53.
19. Castaing J., Domínguez-Rodríguez, A. & Monty, C., Oxygen diffusion and its relationship to high-temperature deformation of ceramic oxides, *Jpn. J. Appl. Phys., Ser. 2*, **28** (1989) 97–103.
20. Baddi, R., Clarisse, L., Duclos, R. & Crampon, J., Diffusional creep of alumina–zirconia composites: mechanical behavior and microstructure. In *Third Euroceramics*, vol. 3, eds P. Durán & J. F. Fernández, Faenza Editorial, Spain, (1993), pp. 641–6.

Journal of the European Ceramic Society 15 (1995) 989–996
© 1995 Elsevier Science Limited
Printed in Great Britain. All rights reserved
0955-2219(95)00075-5
0955-2219/95/$9.50

Influence of Whisker Reinforcement on the Creep Behaviour of Zirconia Matrices

R. Baddi,* J. Crampon & R. Duclos

Laboratoire de Structure et Propriétés de l'Etat Solide, URA CNRS 234, Université de Lille 1, 59655 Villeneuve d'Ascq Cedex, France

(Received 23 June 1994; revised version received 10 April 1995; accepted 16 May 1995)

Abstract

Zirconia matrices reinforced with 13 vol% SiC whiskers, obtained either by hot-pressing or by extrusion, have been deformed by compressive creep. The composite behaviour is similar to that of the matrix alone and suggests identical deformation mechanisms. The creep rate was not much affected by the whiskers; in particular the creep rate was not dependent on the direction of the compression axis. By contrast, for some directions of the compression axis, a strain anisotropy appeared in the plane perpendicular to the compression axis. The influence of whisker orientation on deformation has been explored by considering the matter flows in the vicinity of whiskers and the whisker distribution.

1 Introduction

This paper deals with the high temperature creep behaviour of zirconia matrices reinforced with SiC whiskers. Its main concern is with the understanding of the interactions occurring between a creeping matrix and a hard, nondeformable phase when large strains are achieved.

In particular, in a recent study concerning the superplastic deformation of an alumina–zirconia matrix reinforced with 25 vol% SiC whiskers,[1] a strong influence of the whisker orientation on the creep rate and on the shape of strained samples was observed. For instance, samples whose compression axis (CA) was perpendicular to the hot-pressing axis (HPA) showed a strain anisotropy in the plane perpendicular to the compression axis, the two transverse strains (the one parallel to the HPA over that in the perpendicular direction) being in the ratio 2.

Such results have been rarely reported in studies concerned with the deformation of ceramic matrices reinforced with SiC whiskers either because deformation was conducted in four-point bending,[2–5] a test whose analysis is complex, or, for the few studies conducted in compression, because the orientation effect was not systematically studied.[6,7] Only Lorenz[8] and Swan *et al.*[9] investigated the influence of whisker orientation on the resultant creep rates. Lorenz studied the effect of whisker orientation for two whisker contents: 20 and 29 vol%. For the first quantity no influence of the compression axis orientation was observed, while for the second, the creep rate of specimens with the CA perpendicular to the HPA was found to be about 4 times faster than the creep rate of samples parallel to the HPA in agreement with our own results.[1] Concerning Swan *et al.*'s work, no effect of sample orientation on the creep rate was observed by these authors. These various results show the complexity of the influence of whisker orientation on the resultant deformation.

From the theoretical point of view, models accounting for enhancement of creep resistance are mainly based on stress transfers across the matrix–whisker interfaces.[10–13] At a high temperature, however, diffusion can be fast enough to partially release shear stresses on the interfaces. Moreover, models predicting an influence of the whisker orientation are seldom in agreement with experimental results.

In point of fact, the above results show that the effect of whiskers on the deformation rate cannot be reduced to a simple stress transfer effect across interfaces but that secondary effects such as whisker interaction, local plasticity or direction of matter flow, must be taken into account. It is partially with this object that this work was undertaken.

In this paper the results of creep tests on a SiC_w-reinforced zirconia composite compacted by various techniques are reported. Mechanical results and microstructure observations are first

*Permanent address: Université Mohamed 1er, Faculté des Sciences, Oujda, Morocco.

presented. Then, the anisotropy effects are discussed, not specially for this material but more generally with reference to literature data.

2 Experimental Procedure

The material studied was a 3 mol% yttria stabilized zirconia matrix (Tosoh, Japan) reinforced with 13 vol% of both α and β SiC whiskers (Tokai Carbon, Japan). Two kinds of dense materials (ρ = 5·72 g/cm^3) were obtained at the Ecole Polytechnique Fédérale de Lausanne (Switzerland): either disks, hot-pressed at 1450 or 1550°C (to obtain various zirconia grain sizes), or cylinders extruded at 1600°C through a conical graphite die.[14] This last method partially explains why a zirconia matrix and a relatively low whisker content were used. These two techniques entail different whisker distributions. In the first case, the whiskers were almost perpendicular to the hot-pressing axis whilst in the second case, they were more or less aligned in the extrusion direction (ED).

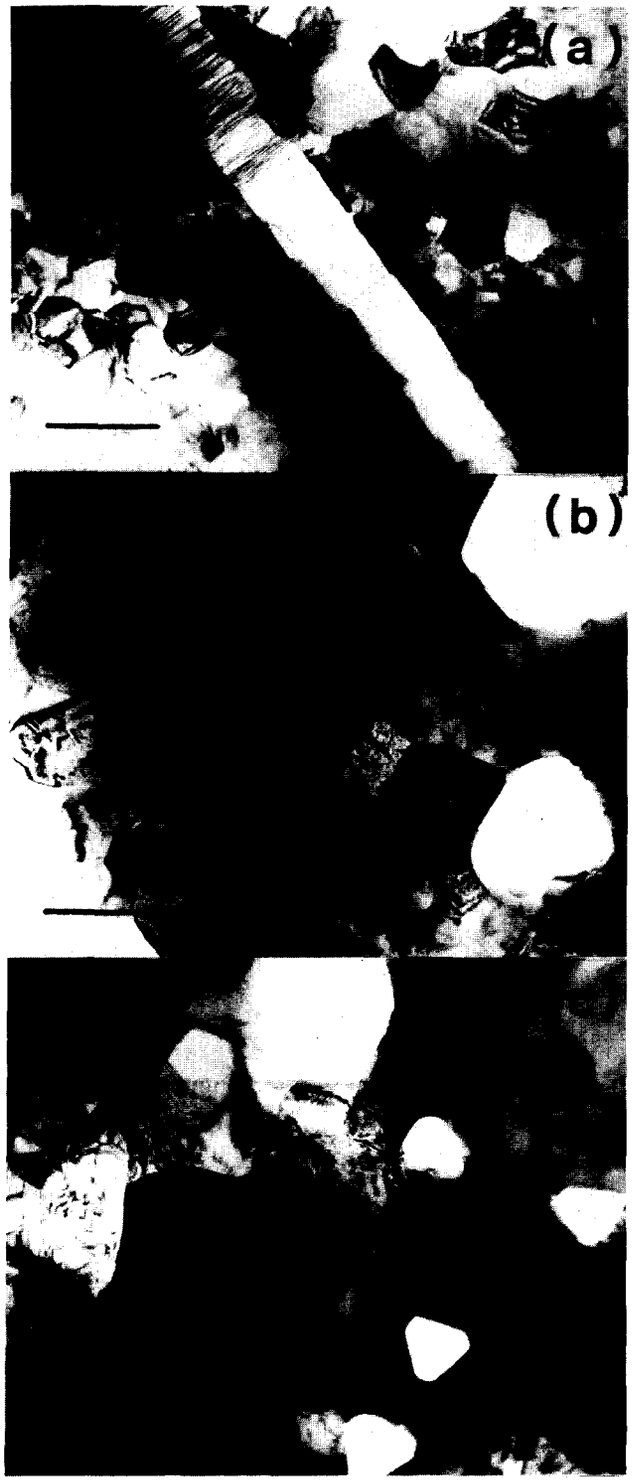


Fig. 1. Typical sample microstructures (scale bar = 0·5 μm): (a) HP at 1450°C; (b) HP at 1550°C; (c) extruded at 1600°C.

Microstructures of the three reinforced materials are shown in Fig. 1. The mean grain sizes of zirconia were respectively 0·33 and 0·54 μm in the disks hot-pressed at 1450 and 1550°C and 0·85 μm in the extruded material. The whisker diameter varied between 0·2 and 1 μm and the maximum length was 10 μm. The average aspect ratio was about 10. No glassy phase was detected by conventional transmission electron microscopy (TEM) at the matrix–whisker interfaces or in the matrix, but the presence of a thin intergranular film (~1 nm) in this kind of material is not to be excluded.

Due to the preferential whisker orientations, specimens with the compression axis either parallel or perpendicular to the hot-pressing axis or to the extrusion direction were cut, resulting in the four sample configurations of Fig. 2, called respectively P//, P⊥, E// and E⊥. These configurations correspond

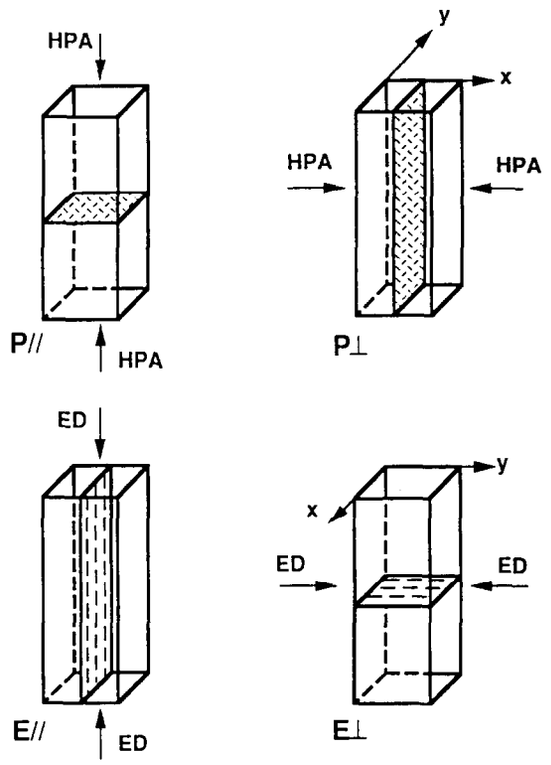


Fig. 2. Configurations of samples used in this study. P stands for hot-pressed specimen (HPA: hot-pressing axis) and E means extruded specimen (ED: extrusion direction). In each instance, the compression axis lies parallel to the long dimension of the sample.

to whiskers lying in planes perpendicular or parallel respectively to the compression axis for P samples, or to whiskers respectively parallel or perpendicular to the compression axis for E specimens. Sample size was typically $3 \times 3 \times 7$ mm^3.

Compressive creep experiments were conducted in an argon atmosphere between 1260 and 1330°C over a stress range of 20–120 MPa. Final strains varied typically between 20 and 40%. Two or even three specimens were tested for each deformation condition.

After creep tests, microstructure observations were made by TEM at 200 kV or SEM (scanning electron microscopy) at 15 kV on polished and thermal etched surfaces.

3 Experimental Results

3.1 Macroscopic behaviour

At first, to test the effect of whisker orientation on the creep rate, experiments were conducted on the two kinds of materials (hot-pressed or extruded) at several temperatures in the same stress conditions. Figure 3(a) is a plot of creep rate versus true strain for two specimens, a P// and a P⊥, deformed at 1300°C and 40 MPa. The two curves are very similar. The same inference can be drawn for E specimens as presented in Fig. 3(b) for two tests conducted at 1330°C and 30 MPa. These results do not show a significant influence of the compression axis orientation relative to the whisker direction on the creep rate. Under these conditions, the different specimen configurations can be neglected and we will assume later on, in particular in the creep rate analysis, that various specimens differed only by their grain sizes.

By contrast, in the case of P⊥ and E⊥ samples, transverse strains were whisker orientation dependent. As previously observed,[1] for these two kinds of specimens the transverse strain in the x direction in Fig. 2, the direction perpendicular to the whiskers, was systematically larger than that in the other transverse direction (y direction). The corresponding strain ratio, ϵ_x/ϵ_y, was approximately 1·5 whatever the deformation conditions. *A priori*, the insensitivity of creep rates to whisker orientation may seem to be inconsistent with the above strain anisotropy. This will be discussed later.

The experimental steady-state creep rates $\dot{\epsilon}$ were analysed according to the phenomenological relationship:

$$\dot{\epsilon} = A\,(\sigma^n/d^p)\exp(-Q/RT) \qquad (1)$$

where σ is the stress, d is the zirconia grain size, n and p are the stress and grain size exponents respectively, Q is the creep activation energy, R and T having their usual meaning. A is a constant depending on the microstructure and on the controlling rate mechanism.

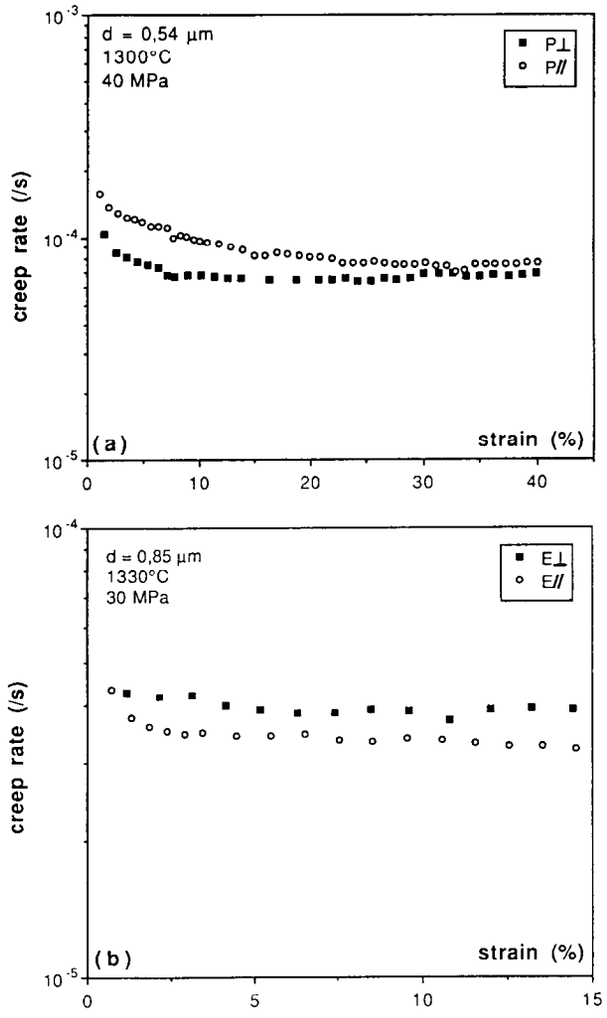


Fig. 3. Influence of whisker orientation on the creep rate: (a) case of two hot-pressed specimens deformed at 1300°C, one parallel and one perpendicular to the hot-pressing direction; (b) case of two extruded specimens deformed at 1330°C, one parallel and one perpendicular to the extrusion direction.

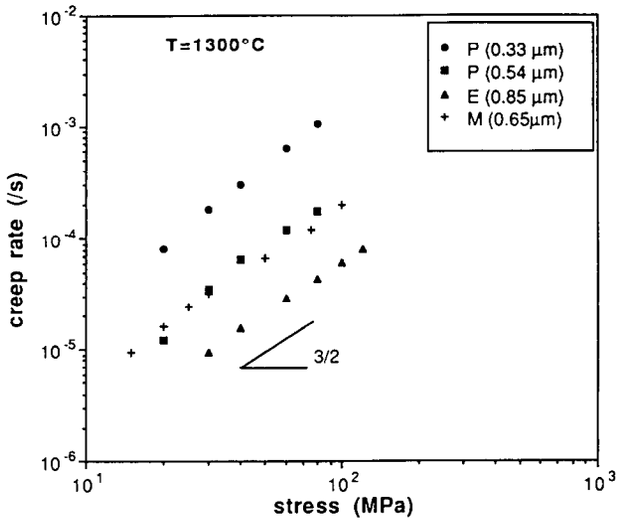


Fig. 4. Influence of stress on the creep rate at 1300°C of the three reinforced materials (P and E specimens). The curve with the open points represents the matrix behaviour (grain size = 0·65 µm).

The effect of the stress on the creep rate is presented in Fig. 4 as a log–log plot of the steady state creep rate versus stress for the three tested grain sizes. On this diagram, the experimental points concerning the zirconia matrix[15] (grain size 0·65 μm) have been added. A great similarity with the present experimental curves is observed. For the high stress range (typically higher than 40 MPa), the stress exponent has a value of 1·6. At the lowest stresses, especially for the two kinds of hot-pressed samples which have finer grain sizes than the extruded material, the stress exponent n slightly increases, as for the matrix.[15] However, the difficulties associated with conducting creep tests at very low stresses (5–10 MPa) do not allow us to investigate this stress range and to study the possibility of an increasing stress exponent in this domain or the occurrence of a threshold stress such as has been observed in creep studies of alumina–zirconia matrices reinforced with 27 vol% of SiC whiskers.[1,16,17]

From Fig. 4, the effect of the grain size on the creep rate was determined over the range 30–80 MPa (Fig. 5). The grain size exponent has a value between 3 and 4, being relatively constant throughout the entire stress range.

The temperature dependence has been analysed from temperature changes performed during tests at a constant stress of 30 MPa. The resultant activation energy does not depend on the specimen kind and ranges between 550 and 600 kJ/mol, the same activation energy as found for the matrix in the high stress regime.

3.2 Structure development

TEM and SEM examinations showed that the microstructure of crept samples was nearly identical to the microstructure of undeformed specimens. No glassy phase related to whisker oxidization

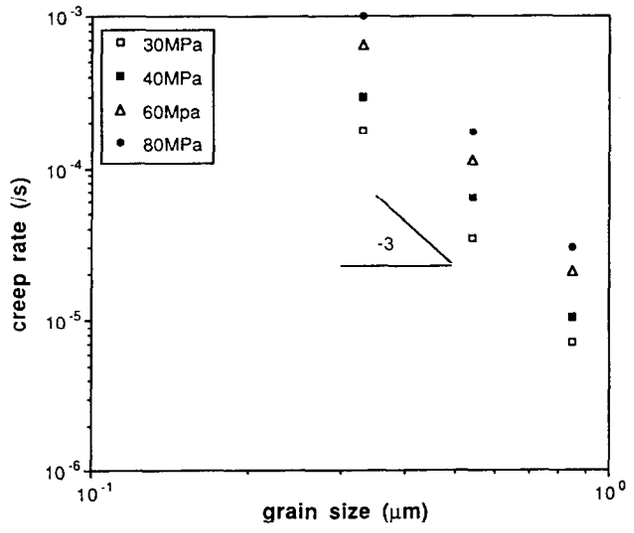


Fig. 5. Influence of grain size on the creep rate at 1300°C of reinforced materials.



Fig. 6. Microstructure inside the zirconia matrix after a strain of 40% at 1300°C for a specimen pressed at 1550°C. Scale bar = 0·5 μm.

during the deformation test, was detected at the whisker–zirconia interfaces or in the matrix by conventional TEM. SiC whiskers presented no evidence of plastic deformation such as shape change or intragranular dislocation activity. Zirconia grains which retained their initial equiaxed shape and size were generally dislocation free (Fig. 6). On the other hand, boundary dislocations were observed, especially in the extruded material. The main structure changes concerned the whisker orientation relative to the compression axis and the cavity nucleation.

During deformation of P⊥ and E// specimens, for which whiskers do not lie in planes perpendicular to the compression axis at the test onset, the angle between compression axis and mean whisker direction increased with strain. Thus, at a strain of 40%, more than 70% of the whiskers were about perpendicular to the compression axis, in good agreement with our previous results.[1] Moreover, in the case of P⊥ specimens, whiskers tended to stay in the planes perpendicular to the initial hot-pressing axis, rotation of whisker occurring more or less isotropically in the E// specimens. This means that during deformation the whisker distribution in P⊥ specimens became identical to that of E⊥ samples while E// specimens tended to be similar to P// samples.

Cavity formation was observed at every stress with an increasing tendency at high stress. The cavitational component of creep strain was determined by density measurements. According to the deformation conditions, the observed decrease in density ranged from 0·9 to 3·6% as shown in Table 1. Cavities were mainly observed at the matrix–whisker interfaces in the matrix phase (Fig. 7) but sometimes also inside the zirconia phase itself. They were generally located at triple points but could also be developed along boundaries. In this

case, porosity was preferentially oriented parallel to the stress direction. When a creep acceleration was observed, it was correlated to pore coalescence and microcrack formation (Fig. 8).

Table 1. Decrease in density $\Delta\rho/\rho o$ at 1300°C as a function of experimental conditions. P* means hot-pressed at 1550°C

Specimen	*Stress (MPa)*	*Creep strain*	$\Delta\rho/\rho o$ (%)
P//	20–30–40	0·41	1·9
P//	30	0·36	2·1
P//	40–60–80	0·36	3·1
P⊥	20–30–40	0·43	1·6
P⊥	40	0·40	2
P⊥	40–60–80	0·36	3
P*//	20–30–40	0·34	1·8
P*//	40–60–80	0·34	3·2
P*⊥	40	0·40	0·9
E//	30	0·33	1·3
E//	30–40–60	0·26	2·4
E⊥	30–40–60	0·19	1·9
E⊥	40–80–120	0·29	3·6



Fig. 7. Crack at a matrix–whisker interface in an extruded sample deformed at 1330°C up to a strain of 34%. The arrow is parallel to the compression axis. Scale bar = 0·5 μm.



Fig. 8. Observation of microcrack coalescence during the tertiary creep of a specimen deformed at 1300°C under a stress of 120 MPa. Scale bar = 1 μm.

4 Discussion

4.1 Creep mechanism

As shown in Fig. 4, the stress influence on the creep rate of the three reinforced materials is nearly identical to that of the zirconia matrix. The creep rate is characterized by a stress exponent whose mean value of $n \sim 1{\cdot}6$ does not reflect a single mechanism, but rather a combination of two or more active mechanisms.

TEM examinations and density measurements showed that the contributions of intragranular dislocations and cavitation to creep strain was likely to be too weak to account for such a stress exponent. In addition, any tendency to an increase in the stress exponent should be observed at high stress and not at low stress, if cavitation and/or dislocation contributions were significant.

The activation energy, 550–600 kJ/mol, is similar to that of the matrix in the high stress range;[15] this suggests:

(1) That whiskers do not have a significant influence on the controlling mechanism of creep, in agreement with the fact that the creep behaviour was only little affected by the whiskers.

(2) That only mechanical interactions between matrix and whiskers and not chemical interactions (with consequent changes in the diffusion mechanisms and activation energy) took place during deformation.

The grain size exponent is also coherent with the value obtained in the high stress range for the matrix.

Finally, except for the A factor in eqn (1), all the thermomechanical parameters of the composites, n, p and Q, are approximately the same as for the matrix. The deformation mechanisms are therefore believed to be identical for the reinforced and unreinforced materials: grain boundary sliding and a grain rearrangement process are responsible for a large amount of deformation. If the specific nature of the accommodation mechanisms cannot be unambiguously established on the basis of the exponents and activation energy observed and owing to the lack of reliable diffusion data, some informations can be obtained from literature:

(i) a comparison of our creep rates with those expected from Nabarro–Herring diffusion creep[18] shows that ours are faster by more than two orders of magnitude suggesting in agreement with Chokshi's conclusion[19] that N–H diffusion creep should not contribute significantly to deformation of our materials;

(ii) in addition, according to several authors[20–22] the grain size of our specimens lies in the range where grain boundary diffusion should be expected.

Nevertheless, the effect of impurities and the possible presence of a thin intergranular film must not be neglected in the deformation accommodation.

With respect to the matrix behaviour,[15] whiskers behaved as an inert and non-plastic phase; their effect appears mainly: (i) in the difference of transverse strains for P⊥ and E⊥ samples and (ii) in the creep damage. For the first point, this means that the whiskers reduce the deformation in the direction parallel to the whisker axis. This point is more specially discussed in the next part. Concerning the second point, this confirms the absence of plasticity of the whiskers at the test temperatures resulting from the low diffusion coefficients and from stress levels insufficient to activate dislocation glide in the SiC phase.[23,24] Under these conditions, stress concentrations in the vicinity of the whiskers can be released only by plastic deformation in the zirconia phase. When zirconia plasticity is not efficient enough, cavity nucleation occurs.

4.2 Effect of whisker orientation on the creep rate

In contrast to our previous results,[1] the creep rates obtained in the present study were not significantly affected by the orientation of the compression axis relative to the whisker direction.

Nevertheless, in these two works, a similarity has been noted that concerns the strain anisotropy in the planes perpendicular to the compression axis in P⊥ and E⊥ specimens. (Recall that in these specimens, the whiskers were, or became during deformation, parallel lying in planes perpendicular to stress). The ratio between the two transverse strains, the strain in a direction perpendicular to the whiskers (ϵ_x in Fig. 2) over the strain in a parallel direction (ϵ_y), is dependent on the whisker content, 1·5 presently versus 2 previously.[1] This anisotropy results from a greater ease of grain rearrangement perpendicular to the whiskers, due to an easier rotation of whiskers around their own axis than around a perpendicular axis.[25] The effect of the whisker content can be understood if we consider that the influence of a given whisker on the matrix deformation decreases with the distance from the whisker. Consequently at a distance r_0 of a few grain sizes, one can assume that the whisker has no more effect on the matrix behaviour and deformation becomes again isotropic in a plane perpendicular to the compression axis. That influence occurs in a cylindrical volume of radius r_0 and length approximately equal to the whisker length, called interaction volume in what follows. In this interaction volume, the rearrangement rate in a direction parallel to the whisker axis slowed down more and more with respect to the perpendicular rate as the distance from the whisker decreases. At a low whisker content, two neighbouring interaction volumes do not overlap; as a result, the composite behaviour is little modified by the presence of the whiskers and the ratio between the two transverse strains, ϵ_x/ϵ_y, is roughly equal to one. But, as the whisker content increases, the overlapping, or interaction, between these volumes increases and the matrix deformation is more and more disturbed in the direction parallel to the whiskers relative to that in a perpendicular direction. Under these conditions, the strain anisotropy of P⊥ and E⊥ specimens must effectively increase with the whisker content.

Concerning the effect of whisker orientation on the sample strain rate, it can be partly understood by some earlier considerations.[1] The achievement of large strains results from matter flows whose direction is controlled by the applied stresses. As previously mentioned, in the vicinity of the whiskers, i.e. in the interaction volumes, the flows can be separated into two elementary flows (Fig. 9), one parallel to the whisker and the other one perpendicular, corresponding respectively to average contributions to the macroscopic strain rate R// and R⊥, with R⊥ > R// and R⊥ / R// increasing with the whisker content. According to the whisker content and distribution, the need to maintain the strain compatibility throughout the specimen imposes that the flows around a whisker are more or less coupled. This results also from the fact that the deformation in a layer perpendicular to the stress direction is dependent on deformation occurring in the layers just above and below due to the rearrangement or intercalation mechanism that increases the grain number in a cross sectional area and requires grain exchanges between neighbouring layers.

When all the whiskers are parallel, the same kinds of flow, those parallel or those perpendicular to the whiskers, occur around each whisker in the whole specimen. Consequently, the two matter flows can be treated independently and the resultant

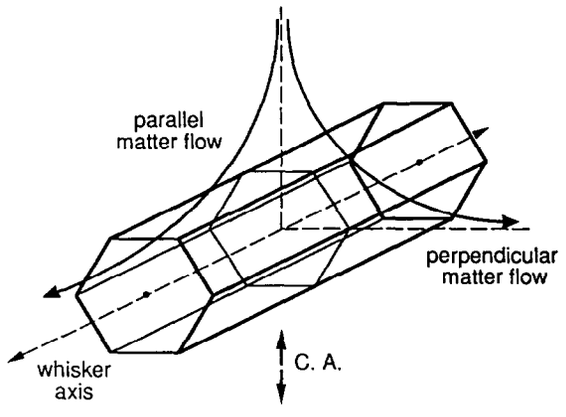


Fig. 9. Definition of parallel and perpendicular matter flows around a whisker.

strain rate should be simply the sum of R// and R⊥.

When the whisker orientations are more or less homogeneously distributed in the planes perpendicular to the compression axis, the two flows can be no more treated separately. The two extreme cases correspond to:

(i) the two flows act in parallel but the fastest one (R⊥) is slowed down by the slowest one (R//) and the resultant creep rate is estimated to twice the slowest rate. This occurs at a whisker content low;

(ii) the two flows act in series and the creep rate in them half the slowest contribution. This must correspond to high whisker contents.

Such assumptions can account, at least qualitatively, for our results at low and high whisker contents. However the above estimations assume that after hot-pressing all the whiskers laid perpendicular to the hot-pressing direction. When it is not the case, for instance when whiskers with a high aspect ratio, for which the interference threshold is reached at a relatively low content,[26] are used, the deformation of specimens with the compression axis perpendicular to the hot-pressing direction is then dependent on the whiskers out of planes perpendicular to the hot-pressing axis. Consequently in such specimens, the behaviour anisotropy related to the compression axis orientation should lessen or even disappear. The influence of whiskers on the creep rate is then strongly dependent on their orientation and morphology and cannot be simply related to their content.

5 Conclusion

The deformation of zirconia matrices reinforced with 13 vol% of SiC whiskers has shown that the creep behaviour was not strongly affected by the presence of the whiskers. The activation energy, the stress exponent and the grain size exponent were found to be similar to those of the matrix, suggesting that the same microscopic mechanisms were rate controlling. Cavity formation made a limited contribution to the deformation (a few percent for strains of 40%).

The influence of whiskers on deformation was particularly observed on the strain anisotropy of samples where the compression axis was perpendicular to the directions of hot-pressing or extrusion. The strain in a direction parallel to the whisker axis was systematically lower than that in a perpendicular direction. This observation was analysed by a greater ease of grain rearrangement when it occurs in a direction perpendicular to the whiskers. By comparison with our previous results,[1] it appeared that an increase in whisker content increased the interaction between the matrix and the whiskers and had a more pronounced effect on deformation in the direction parallel to the whiskers than in the perpendicular direction: the strain anisotropy was then dependent on the whisker content for these kinds of specimens.

The influence of specimen orientation on the creep rate has been explored by estimating the more or less high connection between the two elementary matter flows around the whiskers as a function of the whisker content.

Acknowledgements

The authors are indebted to Claude Carry (ISM, Université de Paris XI, France) for help in material processing.

References

1. Bernard-Granger, G., Baddi, R., Duclos, R. & Crampon, J., Superplastic deformation of an alumina–zirconia matrix reinforced with SiC whiskers. *J. Eur. Ceram. Soc.*, **10** (1992) 13–20.
2. Chokshi, A. H. & Porter, J. R., Creep deformation of an alumina matrix composite reinforced with silicon carbide whiskers. *J. Am. Ceram. Soc.*, **68** (1985) C144–5.
3. Porter, J. R., Lange, F. F. & Chokshi, A. H., Processing and creep performance of SiC–whisker-reinforced Al_2O_3. *Ceram. Bull.*, **66** (1987) 343–7.
4. Liu, D. S. & Majidi, A. P., Creep behaviour of SiC_w/Al_2O_3 composites. In *Ceramic Materials & Components for Engines*, Am. Ceram. Soc., Westerville, OH, 1989, pp. 958–67.
5. Lin, H. T. & Becher, P. F., Creep behavior of a SiC–whisker-reinforced alumina. *J. Am. Ceram. Soc.*, **73** (1990) 1378–81.
6. De Arellano-Lopez, A. R., Cumbrera, F. L., Dominguez-Rodriguez, A., Goretta, K. C. & Routbort, J. L., Compressive creep of SiC–whisker-reinforced Al_2O_3. *J. Am. Ceram. Soc.*, **73** (1990) 1297–300.
7. Lipetzky, P., Nutt, S., Koester, D. A. & Davis, R. F., Atmospheric effects on compressive creep of SiC–whisker-reinforced alumina. *J. Am. Ceram. Soc.*, **74** (1991) 1240–7.
8. Lorenz, O.-K., Creep behaviour of SiC–whisker-reinforced alumina, Ph. D. thesis, Technical University Hamburg-Harburg, Germany, 1991.
9. Swan, A. H., Swain, M. V. & Dunlop, G. L., Compressive creep of SiC–whisker-reinforced alumina. *J. Eur. Ceram. Soc.*, **10** (1992) 317–26.
10. Kelly, A. & Street, K. N., Creep of discontinuous fibre composites II: Theory for the steady state. *Proc. Roy. Soc. London*, **328** (1972) 283–93.
11. Pachalis, J. R., Kim, J. & Chou, T. W., Modelling of creep of aligned short-fiber-reinforced ceramic composites. *Comp. Sci. Technol.*, **37** (1990) 329–46.
12. Pachalis, J. R. & Chou, T. W., Modelling of creep of misaligned short-fiber-reinforced ceramic composites. *J. Appl. Mech.*, **59** (1992) 27–32.
13. Yoon, C. K. & Chen, I. W., Superplastic flow of two-phase ceramics containing rigid inclusions: zirconia/mullite composites. *J. Amer. Ceram. Soc.*, **73** (1990) 1655–65.
14. Nauer, M., Carry, C. & Duclos, R., Processing of SiC whisker-reinforced zirconia by extrusion at elevated temperature. *J. Eur. Ceram. Soc.*, **11** (1993) 205–10.

15. Amana, B., Duclos, R. & Crampon, J., Stress influence on the deformation mechanisms of tetragonal zirconia polycrystals. *Ceramics International*, **18** (1992) 385–90.
16. Duclos, R. & Crampon, J., Diffusional creep of a SiC–whisker-reinforced alumina/zirconia composite. *Scripta Met.*, **23** (1989) 1673–8.
17. Backhaus-Ricoult, M. & Eveno, P., Creep properties of an alumina–zirconia composite reinforced with silicon carbide whiskers. *J. Eur. Ceram. Soc.*, **11** (1993) 51–62.
18. Dimos, D. & Kohlstedt, D. L., Diffusional creep and kinetic demixing in yttria-stabilized zirconia, *J. Amer. Ceram. Soc.*, **70** (1987) 531–6.
19. Chokshi, A. H., Superplasticity in fine grained ceramics and ceramics composites: current understanding and future prospects, *Mat. Sci. Eng.*, **A106** (1993) 119–33.
20. Nauer, M. & Carry, C., Creep parameters of yttria-doped zirconia materials and superplastic deformation mechanisms, *Scripta Met. Mater.*, **24** (1990) 1459–63.
21. Von Minden, C. & Hübner, H., Creep of tetragonal zirconia polycrystals (TZP) reinforced by alumina platelets, In *Euro-Ceramics II*, Vol 2, eds G. Ziegler & H. Hausner, Deutsche Keramische Gesellschaft e. v., Köln, 1991, pp. 1553–7.
22. Boutz, M. M. R., Winnubst, A. J. A., Burggraaf, A. J., Nauer, M. & Carry, C., Low temperature superplastic flow of yttria stabilized tetragonal zirconia polycrystals, *J. Eur. Ceram. Soc.*, **13** (1994) 103–11.
23. Fujita, S., Maeda, K. & Hyodo, S., Dislocation glide motion in 6H SiC single crystals subjected to high temperature deformation. *Phil. Mag. A*, **55** (1987) 203–15.
24. Corman, G. S., Creep of 6H α silicon carbide single crystals. *J. Amer. Ceram. Soc.*, **75** (1992) 3421–4.
25. Beeré, W., Stresses and deformation at grain boundaries. *Phil. Trans. Roy. Soc. London A*, **288** (1978) 177–96.
26. Holm, E. A. & Cima, M. J., Two-dimensional whisker percolation in ceramic matrix–ceramic whisker composites. *J. Amer. Ceram. Soc.*, **72** (1989) 303–5.

Journal of the European Ceramic Society 15 (1995) 997–1006
© 1995 Elsevier Science Limited
Printed in Great Britain. All rights reserved
0955-2219(95)00074-7
0955-2219/95/$9.50

Thermomechanical Stability of Nicalon Fibres in a Carbon Monoxide Environment

R. Bodet,[a]* N. Jia[b] & R. E. Tressler[c]

[a]Laboratoire des Composites Thermostructuraux (UMR 47 CNRS-SEP-UB1), Domaine Universitaire - 3, allée de la Boëtie, 33600 Pessac-France
[b]Analytical Sciences Laboratory, Allied Signal Inc., Morristown, New Jersey 07962-1021, USA
[c]Department of Materials Science and Engineering, The Pennsylvania State University, University Park, Pennyslvania 16802, USA

(Received 25 March 1994; revised version received 26 March 1995; accepted 31 March 1995)

Abstract

Microstructural changes and the related strength degradation were investigated for the Nicalon ceramic fibre heat-treated in argon and in a CO/Ar mixture (with a CO partial pressure of 40 kPa) at 1200–1400°C and for different periods of time (0·5–30 h). Detailed structural and compositional analyses were carried out using X-ray diffraction, TEM, SEM, and Auger electron spectroscopy. Strength degradation of the Nicalon fibre after heat-treatments in argon resulted from the fibre decomposition and CO gas escape which produced surface defects, grain growth and intergranular porosity. On the other hand, the strength degradation was effectively reduced for fibres heat-treated in an appropriate atmosphere of argon and CO, as long as the heat-treatment temperature was kept below 1400°C. Such conditions of heat-treatment in CO/Ar showed little effect on the grain size.

1 Introduction

Commercially available and developmental ceramic fibres are stimulating extensive research on the fabrication of ceramic and metal matrix composites for high temperature applications. To determine whether or not the composites can first be produced and then successfully used in a high temperature environment, the microstructure, microchemistry, mechanical properties, and thermal stability of the fibres are important parameters that need to be characterized. This characterization also provides information which will help to develop appropriate processes to produce fibres for high temperature use. There have been many studies of the effects of thermal exposure on the properties of polymer derived ceramic fibres, especially on Nicalon† Si–C–O fibres. It is now clear from the literature that the major factors which will influence the mechanical properties of these fibres at high temperature are microstructural instability and surface reaction. The thermodynamic calculations performed by Luthra[1] and Greil[2] indicate that the Nicalon fibre is inherently unstable at high temperatures, and other investigators[3] have proposed that the ternary amorphous SiO_xC_y phase in Nicalon would be primarily responsible for this instability. The decomposition of the silicon oxycarbide phase in the Nicalon fibre[4–6] and in other polycarbosilane based ceramics[7] results in weight loss associated with CO(g) and perhaps SiO(g) evolution and β-SiC grain growth. With or without involvement of excess carbon, this decomposition will result in the formation of gas and SiC. This means that one can anticipate the following reactions to take place in fibres at high temperature and, essentially, in any environment:

$$SiO_xC_y(a) \rightarrow n_{SiC}SiC(s) + n_{CO}\,CO(g) + n_{SiO}\,SiO(g) \quad (1)$$

or

$$SiO_xC_y(a) + C(s) \rightarrow n_{SiC}\,SiC(s) + n_{CO}\,CO(g) + n_{SiO}\,SiO(g) \quad (2)$$

and

$$SiO(g) + 2C(s) \rightarrow SiC(s) + CO(g) \quad (3)$$

According to eqns (1)–(3), the decomposition, crystallization, and gas evolution must occur simultaneously. If one of them can be suppressed, it should suppress them all, until all the SiO_xC_y species reach an equilibrium. A strong support for this assumption can be found from fibres heat-treated under various pressures. Jaskowiak *et al.*[8]

*Now with Institute of Advanced Materials, Joint Research Center, Petten, The Netherlands.

†From Nippon Carbon Co., Tokyo, Japan.

noticed that under vacuum or at normal pressure, both rapid weight loss and grain growth of Nicalon fibres start at 1200°C. A strong correlation between the grain growth and weight loss was observed. While oxidizing CVD SiC powder, Pampuch *et al.*[3,9] observed a ternary phase of Si, C, and O which was only stable for oxidation temperatures below 1200°C. It decomposed to SiO_2 and Si with the evolution of CO(g) at higher temperatures. Mah *et al.*[4] studied the decomposition of Nicalon, and the major out-gassing species was CO(g). Johnson *et al.*[5] measured the partial pressure of gases over Nicalon, and the major vaporization species were SiO(g) and CO(g). Previous investigations[10] had shown that grain growth and porosity increased with time of heat-treatment at 1300°C. Recently, the high temperature creep behavior of these fibres in argon has been characterized by a rheological model based on the viscous flow of a concentrated suspension of SiC particles in an unstable viscoelastic matrix. As a result of the decomposition of the SiO_xC_y phase, the viscosity of the fibre increased which caused the continuously decreasing creep rate and the steady-state creep impossible under such conditions.[11]

Considering the instability of Nicalon fibre leads to an important question: could the decomposition of SiO_xC_y be stopped? Two methods have proved to be effective in reducing the decomposition of SiO_xC_y: high total pressures and a carbon monoxide partial pressure. The first method was used by Jaskowiak and DiCarlo,[8] and Jaskowiak[12] with high pressure argon and nitrogen gas. However, the decomposition of the ternary phase occurred again when the high pressure argon heat-treated fibre was subsequently reheated at normal argon pressure. The second method attempted by Bibbo *et al.*[13] involves treatments of Nicalon in argon/CO mixtures with a range of CO partial pressures. A maximum effect on the strength of the fibre was found for pCO = 0·4 atm after a 30 min heat-treatment at 1300°C. However, no microstructural characterization was performed in this study. Bender *et al.*[14] have also mentioned the benefits of CO treatments (P_{CO} = 1 atm). After 3 h at 1600°C, the Nicalon fibre retained an average strength close to 1·4 GPa whereas in nitrogen at the same temperature the fibre retained less than 5% of its original strength. Bender *et al.* showed that the fibre underwent few microstructural changes in CO, i.e. limited grain growth and the beginning of the development of microporosity.

The purpose of the study was to investigate the long-term thermomechanical behavior of Nicalon fibres in a so-called chemically stable environment, i.e. by achievement of the fibre stability via suppressing SiO_xC_y decomposition and grain growth during heat-treatments in flowing CO. The results of these experiments helped to further establish the steady-state creep behavior of those fibres.[15]

2 Experimental Procedure

2.1 Material

The thermomechanical stability of Nicalon was investigated on a ceramic grade type fibre,† obtained from a polycarbosilane precursor. The Nicalon fibre contains Si, C, O as its major elements and some traces of hydrogen in it have been also reported.[16] Nicalon NLP 201 is a nanocrystalline β-SiC based-fibre. It has an average diameter of 15 μm. The fibres were received in spool form and coated with an epoxy sizing. This sizing was removed prior to the mechanical and structural characterization by washing the fibre bundle in ultrasonically agitated baths of acetone, ethyl alcohol and distilled water, successively, except for those exposed to high temperature treatments which were kept for 1 h at 550°C under vacuum prior to the temperature raise. Traces of carbon resulting from the sizing decomposition were detected by Auger analysis on the surface of the thermally desized fibres. It was verified that this method of desizing does not influence the initial strength distribution of the as-received fibres.

2.2 Heat-treatment furnaces and procedures

The custom built furnace used for the argon heat-treatments consisted of a vertical alumina tube heated by six SiC heating elements. Temperature was maintained via a controller and monitored using a Pt/Pt–10% Rh thermocouple located near the outer surface of the alumina tube and in the center of the hot zone. Fibre bundles were suspended by sewing them through a carbon cloth placed inside the cold, top part of the tube. A preliminary step consisting of vacuuming the furnace (down to $\approx 10^{-1}$ Pa) was performed at the beginning of the heat-treatment (up to 550°C). A first dwell time for at least 45 min (sometimes up to 2 h) with flowing UHP argon gas (oxygen $< 10^{-9}$ ppm) at 550°C was programmed prior to the final ramp. This was used to burn off the sizing. An in-line oxygen sensor (zirconia cell) connected to a voltmeter for a better accuracy was used to determine the oxygen level. As the temperature rose, the sensor indicated a decrease in the oxygen content. Different equipment was used for heat-treating

†Ceramic grade NLP 201.

Nicalon fibres at elevated temperatures in a very specific CO/Ar atmosphere (P_{CO} = 40 kPa). The apparatus used to heat up to 1200°C was a thermogravimetric balance consisting of a vertical fused quartz tube over which a furnace could slide. Fibre bundles were bound together by using an extra fibre bundle and were suspended in the tube by a silica hook to a platinum wire. The furnace was then raised and heat-treatment temperatures were reached within 30 min. A high temperature/atmosphere controlled tube furnace was used for heat-treating Nicalon fibres in CO at higher temperatures. Fibres were placed in a SiC boat and heated at 30°C min^{-1} in a horizontal alumina tube using Super Kanthal elements. Both furnace setups utilized mass flow controllers for the exact control of gaseous species entering the furnace tube. While the total pressure of the gases remained at one atmosphere, the partial pressures of individual gases (argon and carbon monoxide) could be adjusted through the flow-rate control of the mass flow controllers. The flow rate was adjusted to 5 standard cm^3 min^{-1}. Oxygen degassing was accomplished prior to each run by flowing argon for 30 min, and pre- and post-furnace oxygen traces were detected with an in-line zirconia cell.

2.3 Materials characterization

X-ray diffraction patterns were generated with a diffractometer* using Cu-Kα radiation. As-received and heat-treated fibres were ground into powder using an alumina mortar and pestle. Grinding was performed in acetone. The peaks in the diffraction patterns were identified using the JCPDS† files.

Auger electron analyses were performed with an AES microanalyser†† using the depth profiling mode on CO-heat-treated fibre samples mounted on indium foil. The spectra were recorded from the filament surfaces (spot size ~ 1 μm). The intensities of selected Auger electron transitions, (i.e. LVV for silicon, KLL for carbon, and KLL for oxygen) were recorded as a function of the thickness of the material which has been sputtered (established for a Ta_2O_5 standard).

Individual filament fracture surfaces after strength tests and surface degradation after heat-treatments were examined in a scanning electron microscope.[a]

TEM analyses were obtained with a 120 kV microscope.[b] The three main techniques of conventional TEM, i.e. bright field imaging (BF), dark field imaging (DF), and selected area diffraction (SAD), were used to characterize the fibre microstructure. TEM specimen preparation used two complementary techniques, i.e. ion milling to obtain longitudinal sections of the fibre core and microtomy to get cross-sections for the information concerning the fibre surface. The ion milling technique was performed using a dual ion mill,[c] whereas thin sections of fibres first embedded in a resin were cut using a diamond knife[d] and mounted on microtome.[e]

2.4 Strength tests

The room temperature strength tests on Nicalon fibres were performed on a table-top tester[f] with a small capacity Type A load cell (10, 20, 50 g full scale). Gripping of the filament was accomplished by mounting the fibre ends to paper tabs with epoxy. High temperature tests were performed in a small, custom-built furnace (Kanthal heating elements) using the same apparatus and the same cold gripping technique. All high temperature tests were begun within about 1 min after temperature stabilization because the furnace slit made the fibre loading easier. To determine fibre diameter, a portion of the test fibre was placed on a microscope slide and examined using an optical microscope.[g] All fibres were tested at the same cross-head speed of 0·5 mm/min, corresponding to a strain rate of 3·28 10^{-4} s^{-1} for the 25·4 mm gauge length for room temperature strength tests, and 5·56 10^{-5} s^{-1} for the 152·4 mm gauge length for the high temperature tests.

3 Results and Discussion

3.1 Microstructural analyses

Microstructural analyses were performed using TEM and XRD. Figure 1 represents the XRD spectra for fibres heat-treated at 1300°C at 0 and 40 kPa of CO, respectively. In the pure argon, SiC crystallization increased with time of heat-treatment, as seen in Fig. 1(a). Although image analysis using TEM dark field is not a reliable technique for ceramics containing very small grain sizes, it was just used here to evidence an increase of the

*Rigaku Denki Co., Japan.
†Joint Committee on Powder Diffraction Standards, Swarthmore, PA, USA.
††Model PHI-590 SAM, Perking-Elmer Corp., Norwalk, CT, USA.

[a]Model SX-40A, International Scientific Instruments, Santa Clara, CA, USA.
[b]Model 420 T, Philips Electronic Instruments Inc., Mahwah, NJ, USA.
[c]Gatan Inc., Warrendales, PA, USA.
[d]E.I. du Pond de Nemours, Wilmington, De, USA.
[e]Microtome, Inc., Sweden.
[f]Model 1102, Instron Corp., Canton, MA, USA.
[g]Bausch and Lomb, Rochester, NY, USA

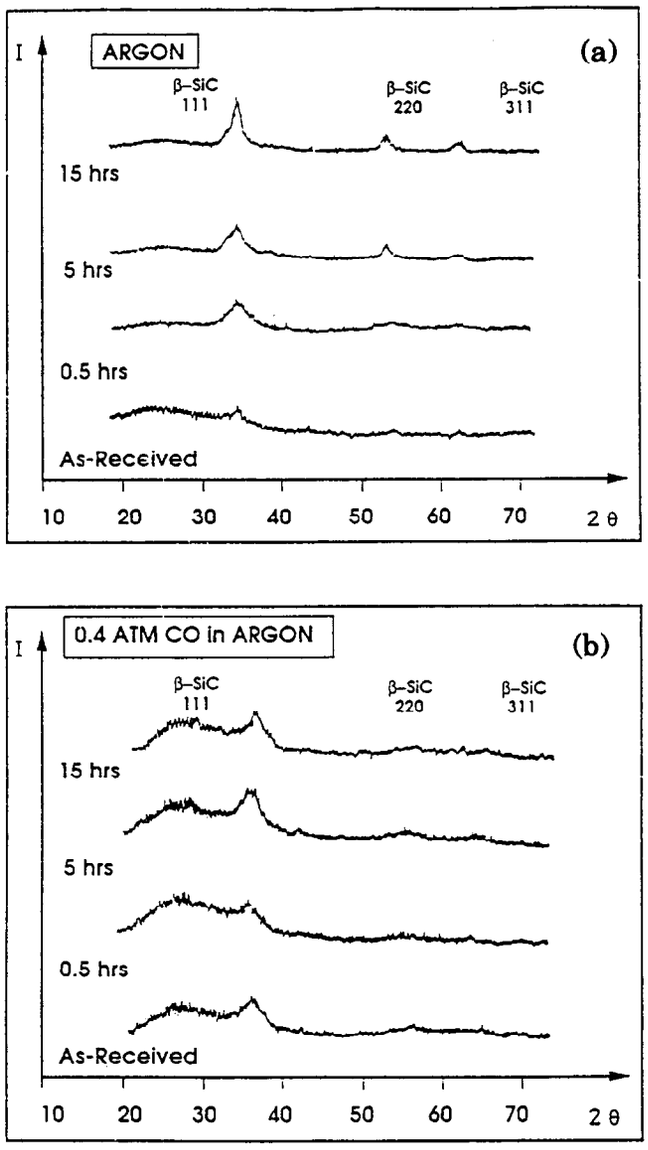


Fig. 1. XRD analysis of argon/CO heat-treated Nicalon fibres as a function of heat treatment time at partial pressures of CO of (a) 0 kPa and (b) 40 kPa.

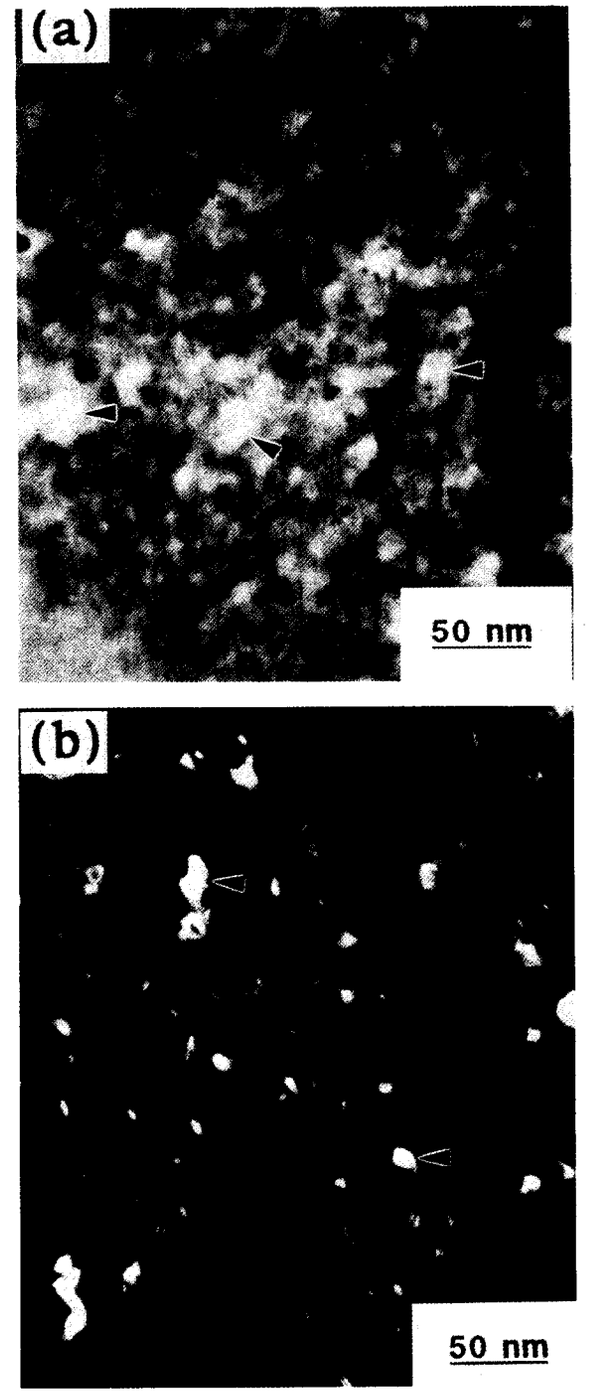


Fig. 2. BF and associated 111-SiC DF image of the cross section of a Nicalon fibre heat-treated in pure argon at 1300°C for 15 h showing (a) evidence of porosity and (b) grain growth, as indicated by arrows.

mean β-SiC grain size in Nicalon as a function of the heat-treatment time in argon. The mean grain size changed from 2·7 nm in the as-received fibre to ~10 nm after 15 h at 1300°C in argon. Figure 2 shows the grain growth and porosity resulting from this heat-treatment. It was previously mentioned that β-SiC grain growth could arise from SiO_xC_y decomposition, according to eqns (1)–(3). If one can assume that the escape of gas species, (i.e. CO or/and SiO) is faster near the fibre surface than near the center, one will assume that the same will be true for the grain growth. Thus decomposition and related grain growth will proceed further in the fibre with time of heat-treatment. On the other hand, the structural stability of Nicalon fibres was greatly enhanced when heat-treated at 1300°C with CO partial pressure of 40 kPa, as evidenced in Fig. 1(b). Figure 3, through a series of TEM micrographs of fibre cross-sections, shows evidence of carbon build-up on the Nicalon fibre. The two micrographs in Figs 3(a) and (b) indicate that carbon actually formed layers stacked parallel to the fibre surface. Figure 3(c) shows the turbostratic structure of this carbon, and the 004 reflection on the SAD pattern (inset of Fig. 3(c)) shows its orientation. The thickness of this carbon layer is about 500 nm. This carbon deposit may arise from the decomposition of CO(g) into C(s) and CO_2(g) during the cooling of the chamber at the end of the heat-treatment.

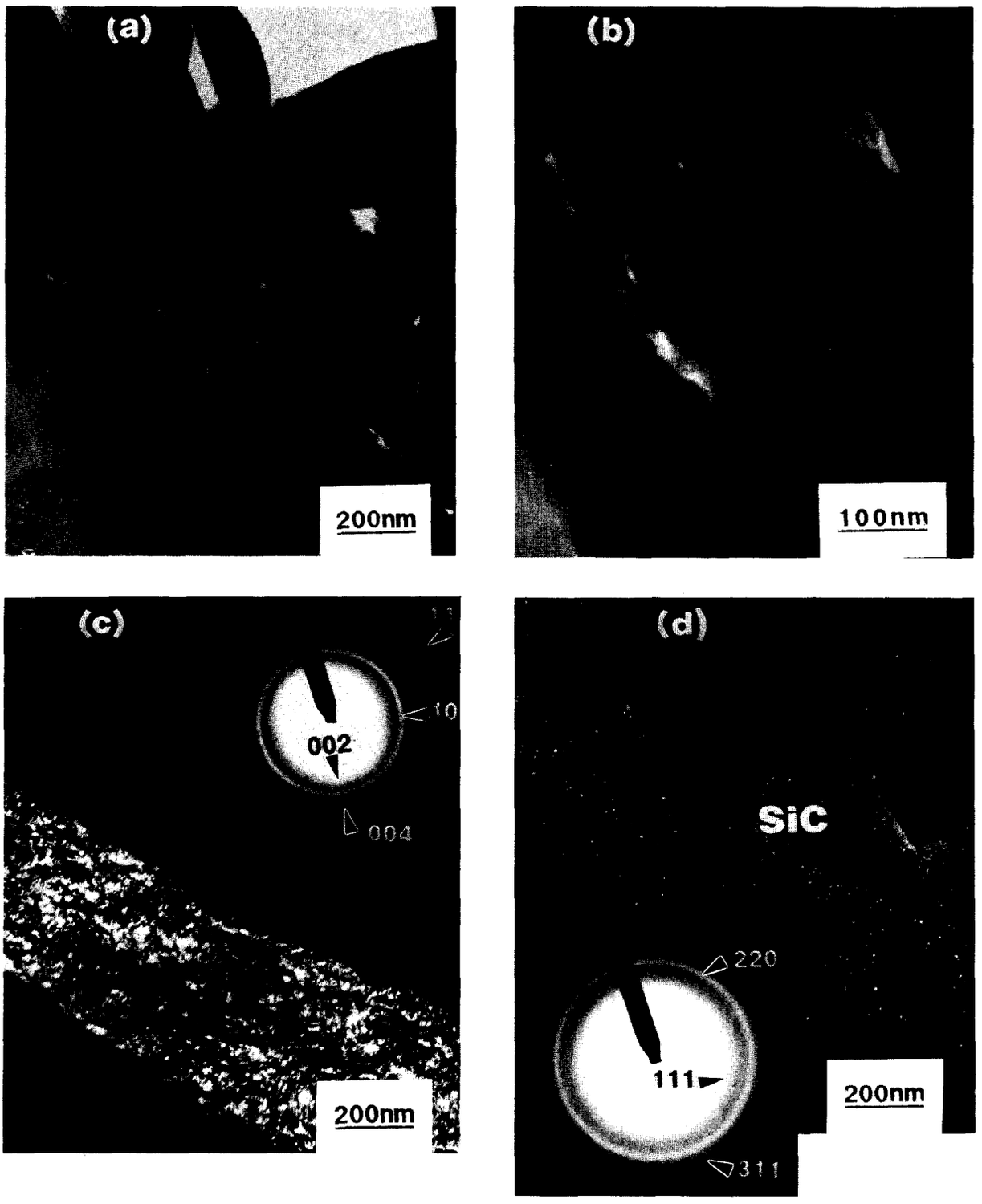


Fig. 3. TEM analysis of a CO heat-treated Nicalon fibre at 1300°C for 15 h. (a) and (b) are BF micrographs of the fibre surface, (c) and (d) are DF and SAD patterns of (c) carbon and (d) SiC.

Bibbo *et al.*[13] also observed a build-up of carbon on the fibre surface in the case of a 1 h heat-treatment at 1300°C. The thickness of this carbon layer was seen to increase with the initial CO partial pressure. The SiC-111 dark field image, in Fig. 3(d), shows that little grain growth occurred after 15 h at 1300°C in 40 kPa of CO, indicating that the thermal decomposition of the fibre could be indeed minimized in 40 kPa CO. Fibres heat-treated at 1200°C behaved similarly. An example of a fibre surface is seen in Fig. 4. The previous figures, for fibres that were heat-treated at 1300°C, can be compared with Fig. 5, for fibres heat-treated at 1400°C at the same partial pressure of CO. Figure 5 indicates that, despite the presence of carbon build-up on the fibre surface (see arrows in Fig. 5(a)), an extensive crystallization of SiC occurred at higher temperatures, which showed no

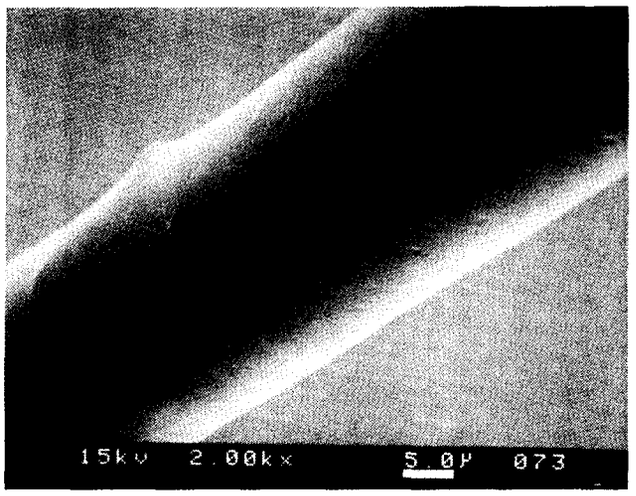
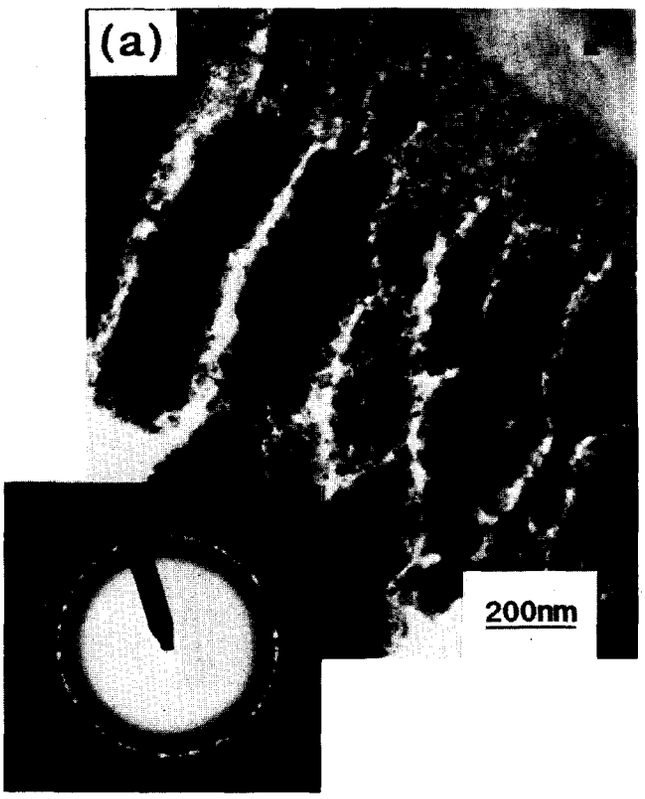


Fig. 4. SEM micrograph of a Nicalon fibre heat-treated in CO (40 kPa) at 1200°C for 0·5 h.

difference with heat-treatments in pure argon.[10] The spotty rings on the SAD pattern correspond to well developed SiC grains beneath the carbon. Some cracks are also apparent on the bright field micrograph in Fig. 5(a). It is unsure whether these cracks preexist or originate from the TEM specimen preparation. Internal pressure in the fibre is likely to build-up until the gas products resulting from fibre decomposition are released, causing a network of cracks beneath the carbon sheath. During the cutting operation by microtomy, the diamond knife can also induce damage in the degraded fibre by relieving these internal stresses. A well-developed crack network has been observed in fully decomposed fibres after prolonged heat-treatments in pure argon.[10] Because of the difference in textures (which behave differently regarding the stresses induced by the diamond knife) the cracks apparently vanish in a $\approx$ 400 nm wide region of different contrast, intermediate between the outer carbon layer and the fibre bulk. Figure 5(b) shows that the SiC grains are smaller in this transition region (indicated by double arrows) than those in the fibre bulk. This could be explained by a carbon penetration, which inhibited grain growth in the fibre surface. The microstructural changes that Nicalon underwent from 1300 to 1400°C while the partial pressure of CO was maintained at 40 kPa can be explained through thermodynamic calculations. Luthra[1] has shown that the equilibrium CO partial pressure above Si–C–O fibres at 1400°C is close to 100 kPa. Thus, it is believed that the exposure of the fibre at 1400°C to an environment containing a lower CO partial pressure than this equilibrium partial pressure will result in a more pronounced degradation of the fibre microstructure, (i.e. grain growth, porosity and gas evolution).



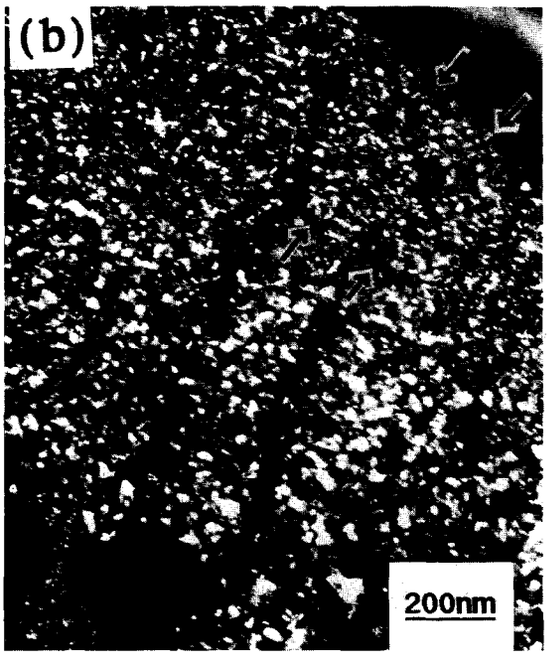


Fig. 5. TEM analysis of a CO heat-treated Nicalon fibre at 1400°C for 5 h. (a) BF micrograph of the fibre surface and SAD pattern. Single arrow shows the carbon layer. (b) DF of SiC. Double arrows show the region of limited grain growth.

3.2 Scanning auger electron analyses

SAM analyses were performed on Nicalon fibres to evaluate more precisely the composition change resulting from surface reactions occurring after heat-treatment in CO/Ar. Results of surface composition for heat-treatments performed at 1300°C for 15 h, and at 1400°C for 5 h, both at the same partial pressure of 40 kPa, are shown in Fig. 6

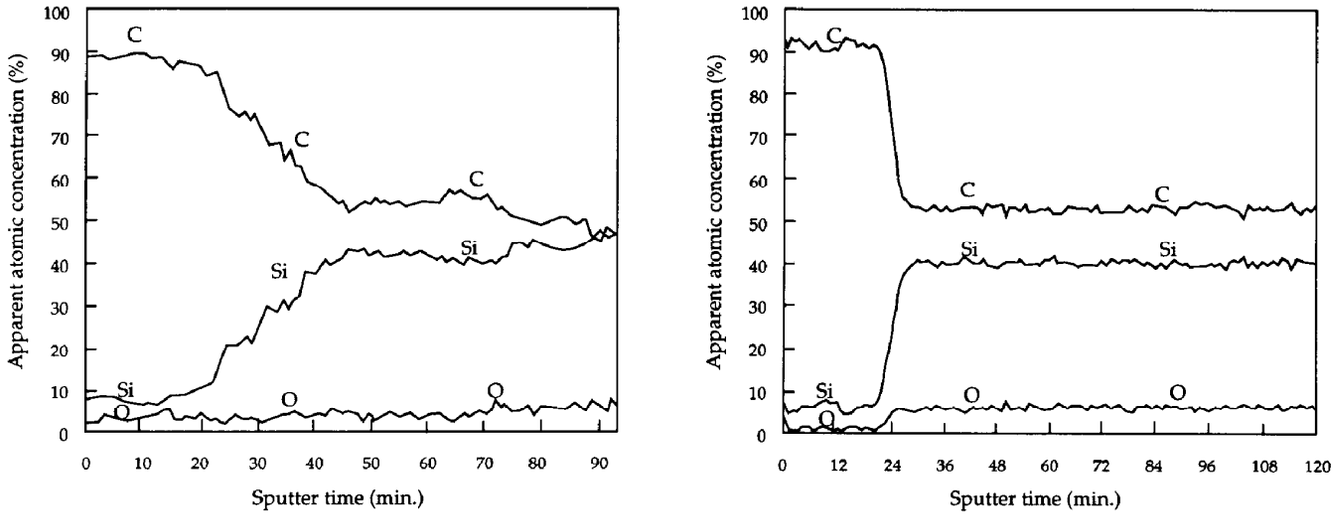


Fig. 6. AES analyses on Nicalon fibres after heat-treatment in CO and argon at CO partial pressure of 40 kPa. Fibres were heat-treated at (a) 1400°C for 5 h and (b) 1300°C for 15 h. Profiles show a carbon build-up on the surface (sputtering rate 25 nm/min; reference Ta_2O_5).

(a),(b). Both fibres developed a carbon rich layer of about 0·45 μm on their surface, according to an estimated sputtering rate of 25 nm/min (notice that this result agrees well with the TEM analysis in Fig. 3(c)). However, the sample heated at 1400°C did not show a sudden change in the composition profile compared to the other specimen. Instead, the carbon was found to decrease progressively with depth while at the same time silicon, probably as SiC, was increasing. On the other hand, the sample heated at 1300°C had a stable composition beneath the build-up of carbon. Moreover, this sub-layer composition was found to match that of the as-received fibre, i.e. 40 at% (Si), 53 at% (C), and 7 at% (O), proof that decomposition had been suppressed. After heat-treatment in the CO atmosphere at 1300°C, there was in fact only a deposition of carbon on the surface of the fibres.

3.3 Effect of heat-treatment on fibre strength

Room temperature strength tests were performed on heat-treated Nicalon fibres in CO/Ar at 0 and 40 kPa of CO. Results are reported in Table 1. In Fig. 7(a), the strength of Nicalon fibres at room temperature is plotted versus time of exposure in various environments, and follows a logarithmic decay for all heat-treatment conditions. The effect of CO partial pressure on the fibre stability is obvious. Fibres heat-treated in the CO/Ar mixture exhibit much less strength reduction compared to those heat-treated in pure argon. After a 30 h heat-treatment at 1200°C in CO, the Nicalon fibre exhibited only a 25% loss in strength, while for the

Table 1. Room temperature tensile strength and modulus of as-received and argon/CO heat treated Nicalon fibres versus heat treatment time

Heat treatment temperature (°C)	*Partial pressure CO (kPa)*	*Heat treatment time (h)*	*Number of fibres tested*	*Tensile strength (MPa)*	*Standard deviation (MPa)*	*Strength retention (%)*	*Young's modulus (GPa)*	*Standard deviation (GPa)*
—	—	—	15	2262	445	—	233	32
1000	0	15	12	1830	465	81	205	34
		30	12	1623	456	72	171	25
1200	0	15	10	1204	187	53	183	17
		30	9	743	652	33	165	46
1300	0	0·5	17	1241	404	55	206	25
		5	14	964	591	43	214	58
		15	12	545	189	24	180	34
		30	11	363	234	16	145	67
1400	0	2	5	818	556	36	186	9
		15	9	211	83	9	85	12
1200	40	0·5	14	1826	521	81	254	57
		5	16	1764	748	78	225	51
		15	17	1633	399	72	207	22
		30	10	1642	341	73	218	32
1300	40	0·5	13	2023	283	89	218	49
		5	17	1762	468	78	193	52
		15	15	1710	516	76	209	48

same temperature and time in argon, the loss was close to 70%. When comparing the data for a 15 h treatment at 1300°C, the losses became 22 and 76%, for CO and pure argon heat-treatments, respectively. The effect of argon and CO annealing treatments on the elastic modulus is shown in Fig. 7(b). Whereas the Young's modulus decreased from 230 to 160 GPa after 30 h at 1200°C in argon (the drop is even more drastic at 1300°C), its value never dropped below 200 GPa in CO. The observed increase after about 15 h at 1200°C and after only a few hours at 1300°C was probably due to the high stiffness of the fibre surface since a thick and oriented carbon layer ((001) carbon planes parallel to the surface) developed on the fibre surface. Figure 8 is an SEM micrograph of the fracture surface of a Nicalon fibre heat-treated at 1200°C for 0·5 h. The fibre had a rupture strength (2010 MPa) slightly above the average (1820 MPa). A notable feature observed on this figure as well as on other fracture surfaces is the evidence of debonding of the carbon layer. In some cases, fracture originated from bubbles beneath the carbon sheath perhaps because gaseous species generated by some late local decomposition

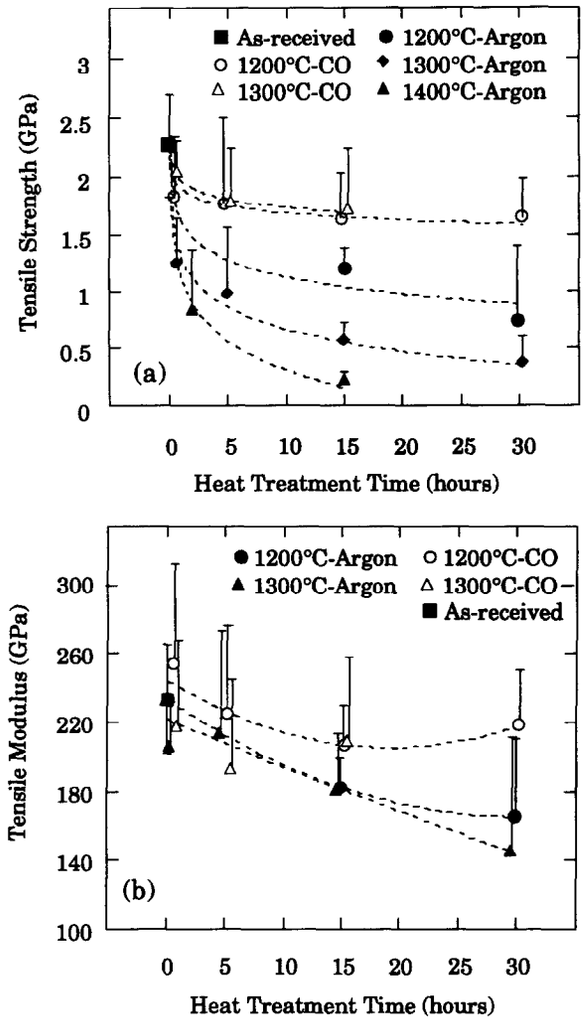


Fig. 7. Effect of CO and argon heat-treatments on (a) the rupture strength and (b) the Young's modulus of Nicalon at room temperature. The single sided bars represent the standard deviations.

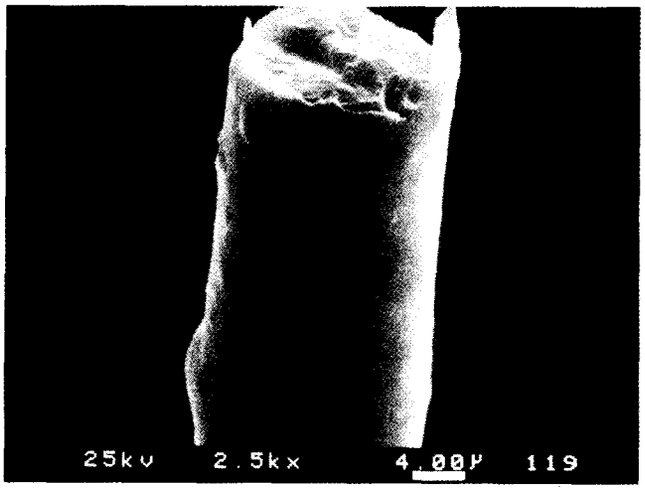


Fig. 8. Fracture surface of a Nicalon filament tested at room temperature after the fibre was heat treated in CO/Ar (P_{CO} = 40 kPa, T = 1200°C, t = 0·5 h). The fibre had a strength of 2010 MPa (standard deviation = 533 MPa, 14 tests, average strength = 1820 MPa).

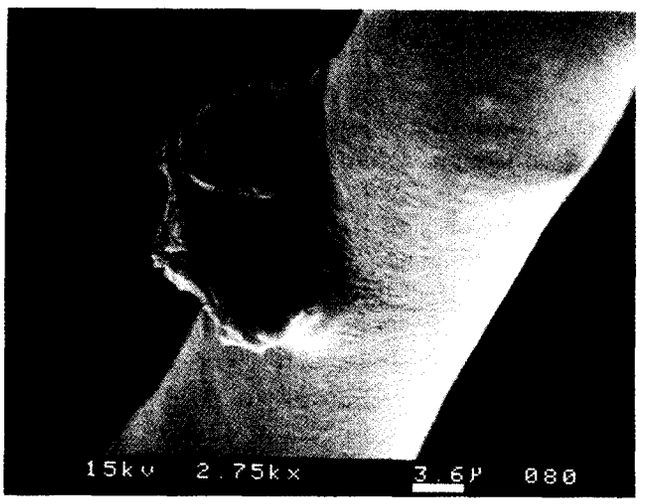


Fig. 9. SEM micrograph of a Nicalon fibre heat-treated in CO (40 kPa) at 1300°C for 5 h showing local surface decomposition.

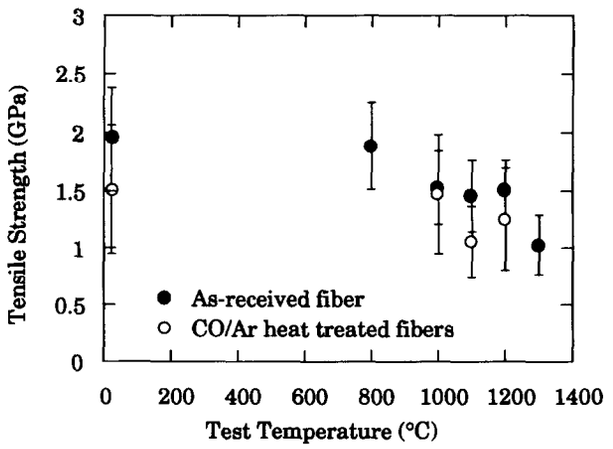


Fig. 10. Effect of CO treatments on the short term strength of Nicalon fibres at high temperatures. The error bars represent the standard deviation.

Table 2. Short term strength tests on as-received and CO/Ar heat-treated Nicalon fibres in air at high temperature[¶]

	As-Received			*CO/Ar Heat Treated*		
T[¶¶] (°C)	$\sigma u^{\dagger}$ (GPa)	$st D\sigma^{\dagger\dagger}$ (GPa)	$n^{\S}$	σ_u (GPa)	$st D\sigma$ (GPa)	*n*
1000	1·53	0·30	10	1·47	0·51	11
1100	1·46	0·30	10	1·06	0·31	4
1200	1·51	0·25	10	1·25	0·44	5

[¶]Condition of heat treatment: pCO +pAr = 1 atm, T = 1200°C, t = 20 h.
[¶¶]Testing temperature.
†Mean strength.
††Standard deviation.
[§]Number of specimens tested.

had been stopped by the carbon build-up (Fig. 9). This rare feature of the heat-treated fibres was never observed on the as-received fibres.

High temperature strength tests were performed in air on as-received Nicalon fibres as well as on those that were annealed in CO/Ar at 1200°C for 30 h. Results shown in Fig. 10 and reported in Table 2 indicate that the two sets of fibres have lost part of their strengths at high temperatures. A slightly greater strength loss is sometimes observed for the fibres previously annealed in CO/Ar, which might be related to the exposure of the defectuous surface of the fibres to oxidation after the carbon sheath was burned off.

4 Conclusions

The goal of CO treatments was to investigate the feasibility of suppressing the Nicalon fibre decomposition and more precisely to evaluate the effects of the long term and temperature variation of such annealing treatments on the thermochemical stability and the strength of the fibre. Heat-treatments at 40 kPa of CO in argon were performed in the range 1200–1400°C at times between 0·5 and 30 h. At the end of the heat-treatment, the reduction of CO from the atmosphere during the cooling of the furnace always formed a carbon-rich layer on the fibre surface. Little effect of the CO heat-treatments on the grain size was found up to 1300°C, but extensive crystallization, with ~60 nm large grains, and pronounced porosity were observed at 1400°C. An intermediate carbon-rich region with limited SiC grain growth was found beneath the carbon layer at the highest temperature. The strength degradation could be effectively reduced for Nicalon fibres heat-treated at 1200 and 1300°C in Ar/CO, with a CO partial pressure of 40 kPa. However, this gas mixture was no longer effective in preserving fibre strength when heat-treated at higher temperatures. Part of this investigation confirm the results of other authors that the presence of oxygen-rich phases inside PCS-derived fibres is responsible for the degradation of their thermo-mechanical properties. The Si–C–O fibre is inherently unstable in air and argon beyond about 1200°C but its decomposition can be delayed at higher temperatures in an atmosphere of carbon monoxide as long as the CO partial pressure is high enough. Additional studies on the fibre behavior in CO are presently being done to characterize their intrinsic creep-rupture properties.

Acknowledgements

The authors acknowledge the financial support of the Gas Research Institute to this project, through the Center for Advanced Materials at Penn State University, and that of Société Européenne de Propulsion, Bordeaux, France.

References

1. Luthra, K. L., Thermomechanical analysis of the stability of continuous 'SiC' fibers. *J. Am. Ceram. Soc.*, **9** (1986) C-231–33.
2. Greil, P., Thermodynamic calculations of Si–C–O fibre stability in ceramic matrix composites. *J. Eur. Ceram. Soc.*, **6** (1990) 53–64.
3. Pampuch, R., Ptak, W., Jonas, S. & Stoch, J., Formation of ternary Si–O–C phase(s) during oxidation of SiC. *Mater. Sci. Monographs*, **6** (1980) 435–48.
4. Mah, T., Hecht, N. C., McCullum, D. E., Hoenigman, J. R., Kim, H. M., Katz, A. P. & Lipsitt, H. A., Thermal stability of SiC fibres (Nicalon). *J. Mater. Sci.*, **19** (1984) 1191–201.
5. Johnson, S. M., Brittain, R. D., Lamoreaux, R. H. & Rowcliffe, D. J., Degradation mechanisms of silicon carbide fibres. *J. Am. Ceram. Soc.*, **71** (1988) C-132–135.
6. Delverdier, O., Monthioux, M. and Oberlin, A., Understanding Nicalon™ fibre. *J. Eur. Ceram Soc.*, **11** (1993) 95–103.
7. Bouillon, E., Mocaer, D., Villeneuve, J. F., Pailler, R., Naslain, R., Monthioux, M., Oberlin, A., Guimon, C. & Pfister, G., Composition-microstructure-property relationships in ceramic monofilaments resulting from the pyrolysis of a polycarbosilane precursor at 800°C to 1400°C. *J. Mater. Sci.*, **26** (1991) 1517–30.
8. Jaskowiak, M. H. & DiCarlo, J. A., Pressure effects on the thermal stability of silicon carbide fibres. *J. Am. Ceram. Soc.*, **72** (1989) 192–7.
9. Pampuch, R., Ptak, W. S., Jonas, S. & Stoch, J., The nature of ternary Si–O–C phase(s) formed during oxidation of SiC. In *Proceedings of the 9th International Symposium on Reactivity of Solids*, Vol. 2, eds K. Direk, J. Habber & J. Novotng, Elsevier, New York, 1980, pp. 674–7.
10. Bodet, R., Jia, N. & Tressler, R. E., Effects of microstructural instability on the rupture strength of Si–C–O (Nicalon) and Si–N–C–O (HPZ) fibres. *J. Eur. Ceram. Soc.* (submitted).
11. Jia, N., Bodet, R. & Tressler, R. E., Effects of microstructural instability on the creep behavior of Si–C–O (Nicalon) fibres in argon. *J. Am. Ceram. Soc.*, **76** (1993) 3051–60.

12. Jaskowiak, M. H., Effects of high pressure nitrogen on the thermal stability of SiC fibres. Technical memorandum no. NASA TM-103245, NASA Lewis Research Center, Cleveland, Ohio 44135-3191 (1991).
13. Bibbo, G. S., Benson, P. M., & Pantano, C. G., The effect of carbon monoxide partial pressure on the high temperature decomposition of Nicalon fibre. *J. Mater. Sci.*, **26** (1991) 5075–80.
14. Bender, B. A., Wallace, J. S. & Schrodt, D. J., Effect of thermochemical treatments on the strength and microstructure of SiC fibres. *J. Mater. Sci. Letters*, **26** (1991) 970–6.
15. Bodet, R., Lamon, J. & Tressler, R. E., Effects of chemical environments on the creep behavior of Si–C–O fibres. In *Proceedings of the 1st International Conference on High Temperature Ceramic Matrix Composites (HT-CMC-1)*, Bordeaux, eds R. Naslain, J. Lamon & D. Doumeingts. Woodhead Publishing Limited, Abington Cambridge, 1993, pp. 75–83.
16. Lipowitz, J., Freeman, H. A., Chen, R. T. & Prack, E. R., Composition and structure of ceramic fibres prepared from polymer precursors, *Adv. Ceram. Mater.*, **2** (1987) 121–8.

Journal of the European Ceramic Society **15** (1995) 1007–1014
© 1995 Elsevier Science Limited
Printed in Great Britain. All rights reserved
0955-2219(95)00077-1
0955-2219/95/$9.50

Effect of Gaseous Environment on the Corrosion of β-Sialon Materials

R. Ramesh,[a] M. J. Pomeroy,[a] H. Chu[b] & P. K. Datta[b]

[a]Department of Materials Science and Technology, University of Limerick, Limerick, Ireland
[b]Department of Mechanical Engineering and Manufacturing Systems, University of Northumbria at Newcastle, Ellison Building, Ellison Place, Newcastle upon Tyne, UK.

(Recieved 28 June 1994; revised version received 26 April 1995; accepted 16 May 1995)

Abstract

This paper reports the effects of different gaseous environments on the corrosion behaviour of β*-sialon materials. Six* β*-sialon materials with* z*-values of 0·2, 0·5, 1·0, 1·5, 2·0 and 3·0 were prepared by pressureless sintering. Corrosion results obtained at 1350°C in environments comprising (i) Laboratory air; (ii) Argon – 20% oxygen – 2% chlorine; (iii) hydrogen – 10% hydrogen sulphide – 2% water vapour and (iv) nitrogen – 15% carbon dioxide – 4% oxygen – 0·2% sulphur dioxide showed that for each of the four environments the* z *= 3·0 material exhibited the best corrosion resistance. The mechanism of corrosion at 1350°C in each of the four environments involves the formation of large volumes of low viscosity liquid phases. These large volumes of liquid enable the solution of* β*-sialon grains to occur and it is this process which is responsible for corrosion.*

1 Introduction

There are a wide range of fossil fuel conversion systems, eg. coal gasifiers, conventional and advanced coal-fired power generation systems and industrial incinerators where silicon nitride components may afford cycle efficiency increases due to either the employment of higher cycle temperatures or the obviation of inefficient component cooling. Whilst the excellent oxidation resistance of silicon nitride materials has been documented[1] and the effects of condensed sodium sulphate deposits assessed[2] no significant body of literature exists relating to the corrosion of such materials in gaseous environments typifying coal gasifiers, conventional/advanced power generation plant and waste incinerators. Oxychlorine and sulphur containing environments, which normally prevail in such industrial processes, can cause accelerated corrosion through the formation of volatile oxychlorides,[3,4] and SiS/SiO compounds,[5] respectively.

The corrosion of silicon based ceramics in corrosive gases at high temperatures has been investigated but it has been mainly confined either to hot pressed or hot isostatically pressed materials. The oxidation of such silicon nitride materials has been shown to be strongly dependent on the level of oxidant in the ambient gases.[6,7] When a high level of oxidant is present, a protective silicate layer is formed which separates the underlying ceramic from the environment. Oliveira *et al.*[5] defined the limits of pO_2 and pS_2 and temperature for the safe usage of hot pressed/HIPped silicon nitride by testing in gas mixtures similar to those that are likely to be encountered in coal gasifiers. An assessment of the effect of similar environments on the mechanical behaviour has also been made for hot pressed silicon nitride materials.[8] In contrast, no significant body of information is available for pressureless sintered materials.

The corrosion of silicon nitrides by gases representative of flue gases emanating from gas-, oil- or coal-fired combustion plant has not been directly studied. However, Demaison, *et al.*[9] have compared the corrosion of two similar β-sialon materials in oxygen and carbon dioxide. The results obtained by Demaison *et al.* indicate that the carbon dioxide environment encourages the development of oxide scales which are considerably more fluid than those which form during corrosion.

In studying the corrosion of materials by aggressive media it is important to understand the process by which simple oxidation takes place. The mechanism by which the oxidation of silicon-nitride based materials occurs is thus important and has been shown to depend upon temperature.[10,11] For temperatures typically in the range 1000–1150°C oxygen diffusion across a protective silica layer is rate controlling. For higher temperatures (up to 1400°C) the diffusion of sintering

additive cations and impurities from the interior of the ceramic into the surface silicon rich oxide scale is considered to be the rate controlling step. The rate controlling step in the mechanism by which silicon nitride oxidises at even higher temperatures has not been fully elucidated. In the intermediate temperature range, oxidation rates as determined from straight line relationships between the square of specific weight gain and time are observed to depend on the type and level of additives employed during sintering.[10–12] This is unfortunate since additive types and levels which facilitate pressureless sintering give rise to accelerated oxidation. One exception to this general rule is the oxidation behaviour of certain sialon materials.[12] In addition, attention has been drawn to the fact that additive rich oxide liquids, possibly containing nitrogen, are formed during the oxidation process.[9,13] Whether or not the formation of such liquids is an effect of the oxidation process or its cause has not been fully rationalised even though it is clear that the formation of such liquids and their volume is dependent on the diffusion of additive and impurity cations into the surface scales.

The research presented in this paper addresses the effect of the z-value of pressureless sintered β-sialons ($Si_{(6-z)}Al_zO_zN_{(8-z)}$) on the corrosion of these ceramics in environments typical of those arising in coal conversion and waste incineration plants.

2 Experimental Detail

The starting compositions of the materials employed in this work are given in Table 1 together with theoretical densities achieved and phase assemblages observed after firing. Weighed amounts of the relevant powders were ball milled for 24 h under isopropanol in a polypropylene container using sialon milling media. The mixtures were then homogenised for 30 min, dried and sieved to <212 μm. They were then cold isostatically pressed at 2000 atm. in a rubber mould. The cold pressed bars, typically 15 × 15 × 50 mm, were then located in a powder bed (50:50 boron nitride:silicon nitride) which was contained in an alumina crucible. The bars were then fired for 2 h at 1700°C in flowing nitrogen. The fired densities were measured by the Archimedes principle using both water and mercury as working fluids. The densities observed were compared with theoretical densities derived from the mass fractions and densities of the relevant sialon and Y–Si–Al–O–N glass phases present in the ceramic. The phase assemblages of the fired materials were determined using X-ray diffraction (XRD) and the z-value of the sialon ceramics determined using correlations and data published by Ekstrom *et al.*[14]

Following fabrication, corrosion experiments were performed in tube furnaces using specimens typically 10 × 10 × 3 mm, polished to a 1 μm finish. A heating and cooling rate of 8°C min^{-1} was employed for each experiment.

Corrosion experiments were conducted in different gaseous environments under the following conditions for all the materials chosen:

(1) Laboratory air at a temperature of 1350°C for 128 h.
(2) A chloridising environment comprising argon – 2% chlorine, 20% oxygen at a temperature of 1350°C for 100 h.
(3) A sulphidising environment comprising hydrogen – 10% hydrogen sulphide – 2% water vapour at a temperature of 1350°C for 100 h.
(4) A simulated flue gas environment comprising nitrogen – 15% carbon dioxide, 4% oxygen, 0·2% sulphur dioxide at a temperature of 1350°C for 96 h.

Corroded coupons were weighed following their removal from the relevant environment and extents of corrosion expressed as weight gain per unit area, i.e. specific weight gain. For materials exposed to the chloridising and sulphidising environments thickness loss measurements were used to assess extents of corrosion because weight losses were observed to occur in certain instances as stated below. The phase assemblage of the surface layers of the corrosion scales was determined using XRD and the surface morphology using scanning electron microscopy (SEM). Large

Table 1. Compositions (wt%), densities and phase assemblage for materials

Nominal z-value	Y_2O_3	Si_3N_4	*AlN*	Al_2O_3	*% theor. density*	*% β-sialon*	*Analysed z-value*	*Other phases*
0·2	7·00	87·98	0·65	4·37	96	100	0·22	none
0·5	7·03	83·33	1·73	7·91	98	100	0·54	none
1·0	7·08	75·59	3·53	13·80	98	100	0·85	none
1·5	7·13	67·50	5·16	20·21	98	100	—	none
2·0	7·18	60·17	7·13	25·52	98	100	2·05	none
3·0	7·28	44·82	10·70	37·20	100	100	2·70	YAG

All compositions are based on 88·9 v/o of relevant sialon–11·1 v/o Y-sialon glass of composition (in equivalent %) 28 Y; 56 Si; 16 Al; 80 O; 20 N.

(1·6 × 1·0 mm) energy dispersive X-ray analyses (EDX) of the surface layers of selected specimens were conducted in order to determine the cation (Y, Al, Si) compositions of these scales.

3 Results

3.1 Fabrication and phase assemblage

From the results presented in Table 1, it is seen that as the nominal z-value of the materials increases, greater densification occurs during firing. The data shown in Table 1 also shows that full conversion of the α-silicon nitride powder to β-sialon occurs during firing. In only one instance (z = 3·0 matrix) was a residual crystalline phase observed. This phase was yttrium aluminium garnet and it is thought that the formation of this phase contributes to the discrepancy between nominal and observed z-value. For other compositions the z-values determined from the lattice parameter shifts agree fairly well with the nominal values.

3.2 Corrosion

3.2.1 Laboratory air

The variation in weight gain as measured after 128 h at 1350°C shows that z-values in the intermediate range ($0{\cdot}5 \geq z \leq 1{\cdot}5$) are the least resistant to oxidation at 1350°C (Fig. 1). The phase assemblages as identified by XRD indicate yttrium disilicate or cristobalite as the major surface phases for the z = 0·2–1·0 materials, while for the higher z-value materials mullite is the predominant phase. Typical surface textures observed for the z = 0·2, 1·0 and 2·0 materials are shown in Fig. 2. As can be seen, both z = 0·2 and 2·0 materials show a marked level of crystallinity in terms of yttrium disilicate and needle like mullite crystals respectively. The z = 1·0 material is typified by the occurrence of needle like mullite crystals and a grey cristobalite phase located in an amorphous phase. Superposition of the large area surface analyses on the Y_2O_3–SiO_2–Al_2O_3 phase diagram[15] showed that for the z = 0·2 and 0·5 materials the compositions lay in the yttrium disilicate–silica–eutectic phase field. For the z = 1·0, 1·5, 2·0 and 3·0 the compositions lay within the mullite–silica–eutectic phase field. Indeed the surface compositions for the latter three materials lay on a line joining the eutectic and mullite.

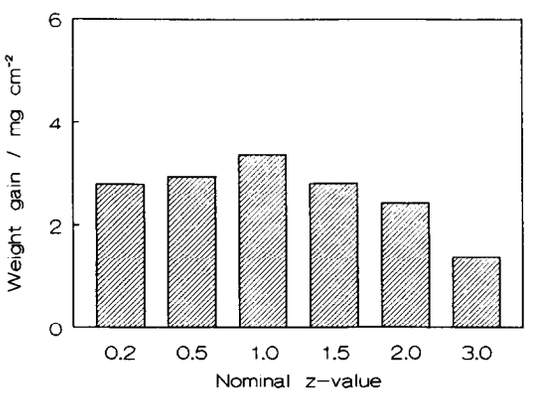


Fig. 1. Weight change data as a function of z-value after 128 h oxidation at 1350°C.

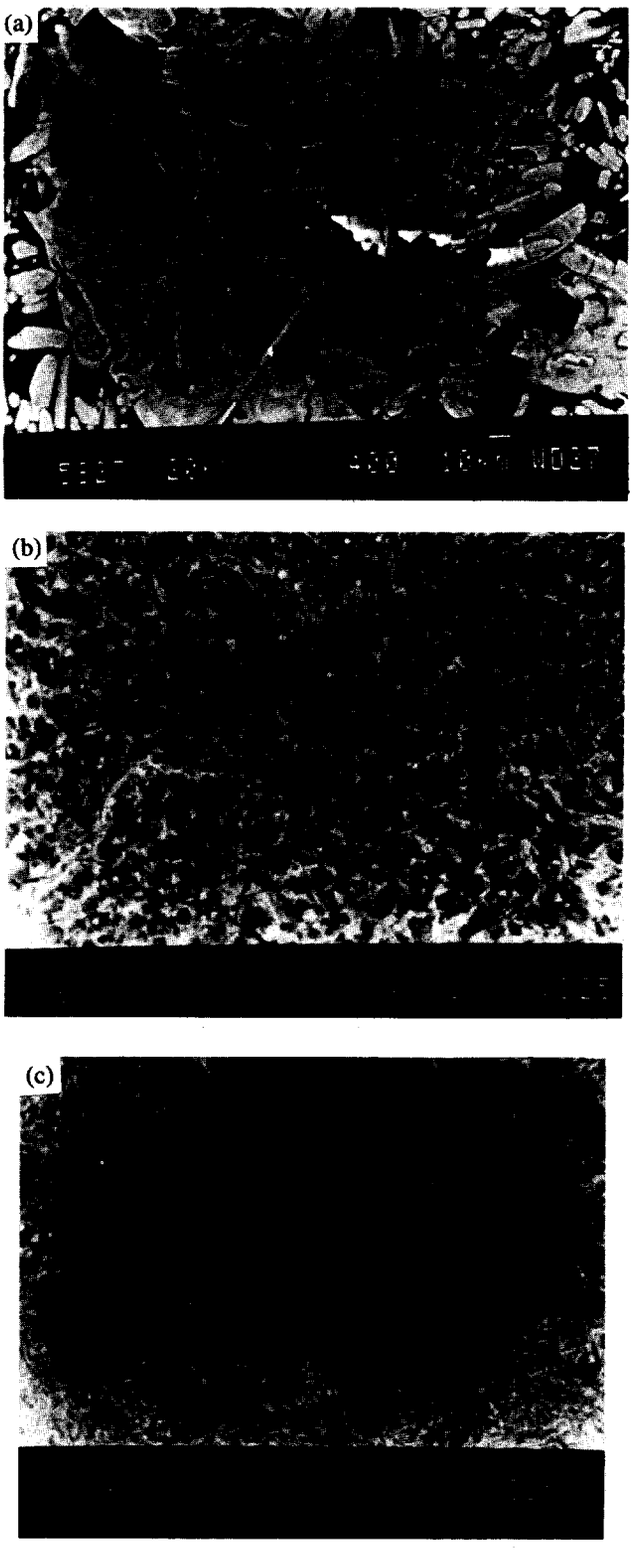


Fig. 2. Surface morphology of oxidation products formed on β-sialon materials after 128 h oxidation at 1350°C (a) z = 0·2, (b) z = 1·0 and (c) z = 2·0.

3.2.2 Chloridation environment

Figure 3 shows the weight change data for $z = 0{\cdot}2$ material following exposure to $2\%Cl_2/20\%O_2/Ar$ gas mixture at 1350°C for time periods up to 100 h. It is seen from this figure that the specific weight gain increases with time up to 50 h duration and then decreases for longer time periods. This decrease in weight gain was considered to be due to the volatilisation of corrosion products as most chloride and oxychloride reaction products are volatile at elevated temperatures.[16] Similar effects were observed in the sulphidising environments. Accordingly, it was decided that the use of specific weight change data as a measure of corrosion could be erroneous and hence thickness loss measurements were subsequently used to establish extents of corrosion after 100 h exposure. Figure 4 shows thickness loss data obtained for the β-sialons of different z values exposed to the argon – 20% oxygen – 2% chlorine environment at 1350°C. It is seen that as z-value increases the extent of corrosion after 100 h initially increases with z-value and then decreases. The most corrosion resistant material is that with a z-value of 3·0.

The morphology of the corrosion scales formed after 100 h corrosion was observed to be dependent on z-value. The scales were amorphous for materials with z-values of 0·2, 0·5, 1·0 and 1·5. For the $z = 2{\cdot}0$ material sillimanite and mullite

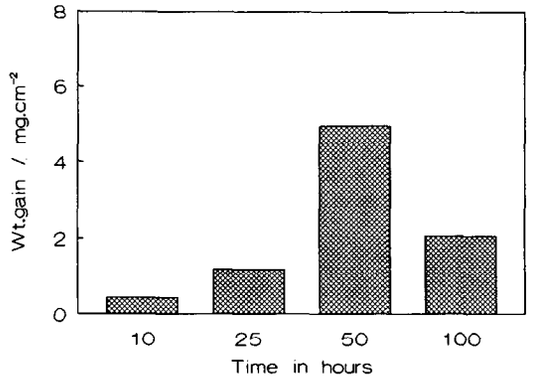


Fig. 3. Weight gain–time relationship for z = 0·2 sialon exposed to $2\%Cl_2/20\%O_2/Ar$ mixture at 1350°C.

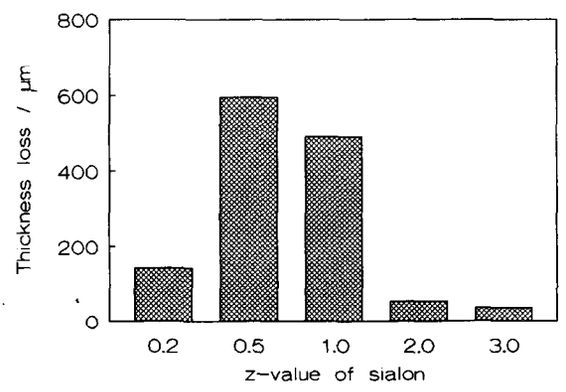


Fig. 4. Thickness loss data obtained for different sialon materials exposed to chloridising environment for 100 h at 1350°C.

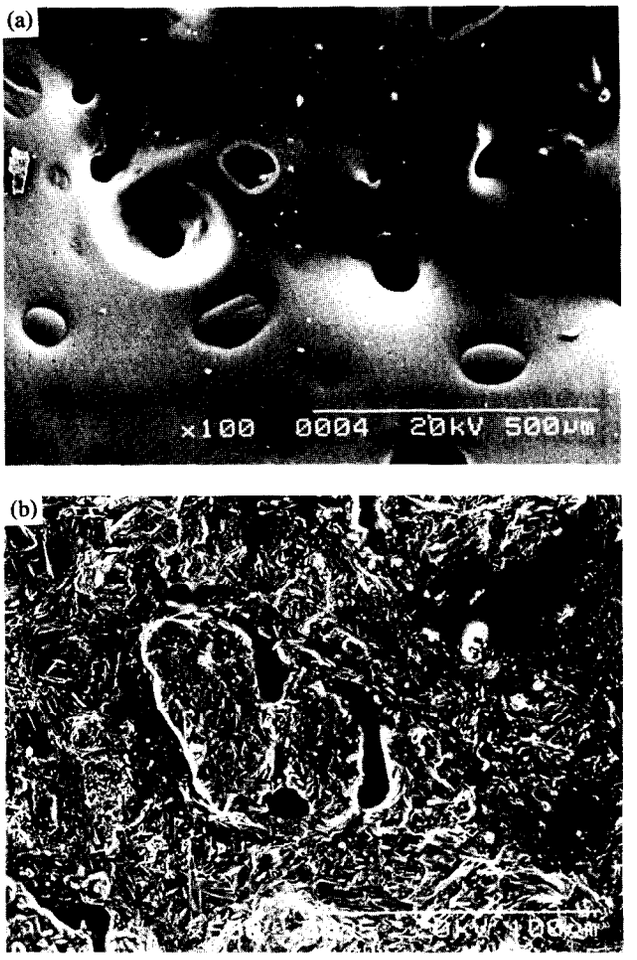


Fig. 5. Surface morphologies of the corrosion products formed following exposure to $2\%Cl_2/20\%O_2/Ar$ gas mixture at 1350°C (a) $z = 1{\cdot}0$ and (b) $z = 3{\cdot}0$.

crystals were observed in an amorphous scale and mullite crystals were observed to be present in an amorphous scale in the case of the $z = 3{\cdot}0$ material. Figure 5 shows representative surface morphologies of the corrosion products formed on the $z = 1{\cdot}0$ and 3·0 materials.

3.2.3 Sulphidising environment

The effect of z-value on corrosion thickness loss in the $H_2 - 10\%\ H_2S - 2\%H_2O$ environment is shown in Fig. 6. This figure shows that the extent of

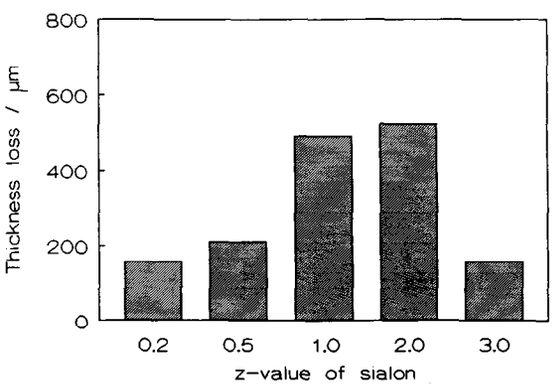


Fig. 6. Thickness loss data obtained for different sialon materials exposed to sulphidising environment for 100 h at 1350°C.

corrosion increases with increasing z-value up to 2·0 and then decreases with z = 0·2 and 3·0 materials undergoing least corrosion. The phase assemblages and surface morphologies observed for the different materials were similar to those observed for the chloridising environment.

3.2.4 Simulated flue gas environment

The form of the specific weight gain–time curve obtained for the z = 0·2 material exposed to the simulated flue gas environment at 1350°C was parabolic with rates of weight gain diminishing with time. Accordingly, it was assumed that no weight losses occurred during 96 h exposure and that weight gain data gave a true reflection of extent of corrosion. Figure 7 shows specific weight gain data as a function of z-value after exposure for 96 h at 1350°C. It is seen from this figure that as z-value increases from 0·2 to 1·0 the extents of corrosion increase. For z-values in excess of 1·0, the extent of corrosion decreases with increasing z-value.

The phase assemblages of the surface layers were observed to dependent on z-value. For the z = 0·2 material the predominant phase formed was β-yttrium disilicate which coexisted with silica and γ-yttrium disilicate. For the z = 0·5 material the predominant phase in the surface layers was silica. For the z = 1·0, 2·0 and 3·0 materials the predominant phase formed was mullite. Silica was also observed for these materials. A comparison of the amounts of liquid formed in the simulated flue gas environment with those formed during oxidation of similar materials for a similar length of time showed that the presence of carbon dioxide and sulphur dioxide in the simulated flue gas encouraged liquid formation (Fig. 8). The surface morphology of the z = 0·5 material exposed to the simulated flue gas environment for 48 h at 1350°C shown in Fig. 8 clearly demonstrates the occurrence of a large volume of liquid on the surface of the corroding sialon. The bright crystals seen in both Fig. 8 (a) and (b) are yttrium disilicate. z = 3·0 materials exhibit little liquid formation (Fig. 9) and this is consistent with the lowest corrosion rates observed (Fig. 7). Furthermore, large scale EDX analyses showed that for the low z-value materials (z = 0·2, 0·5 and 1·0) the surface layers of the corrosion scales formed in the simulated flue gas environment were richer in aluminium than

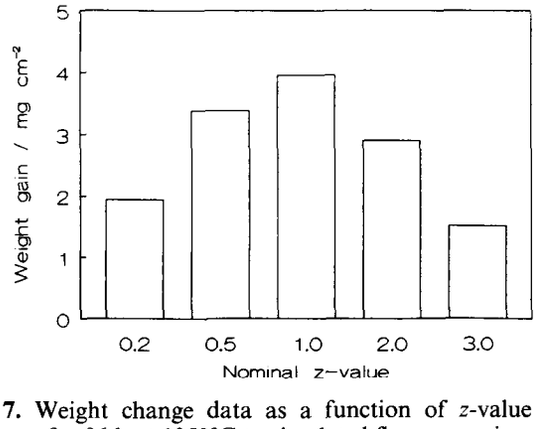


Fig. 7. Weight change data as a function of z-value after exposure for 96 h at 1350°C to simulated flue gas environment.

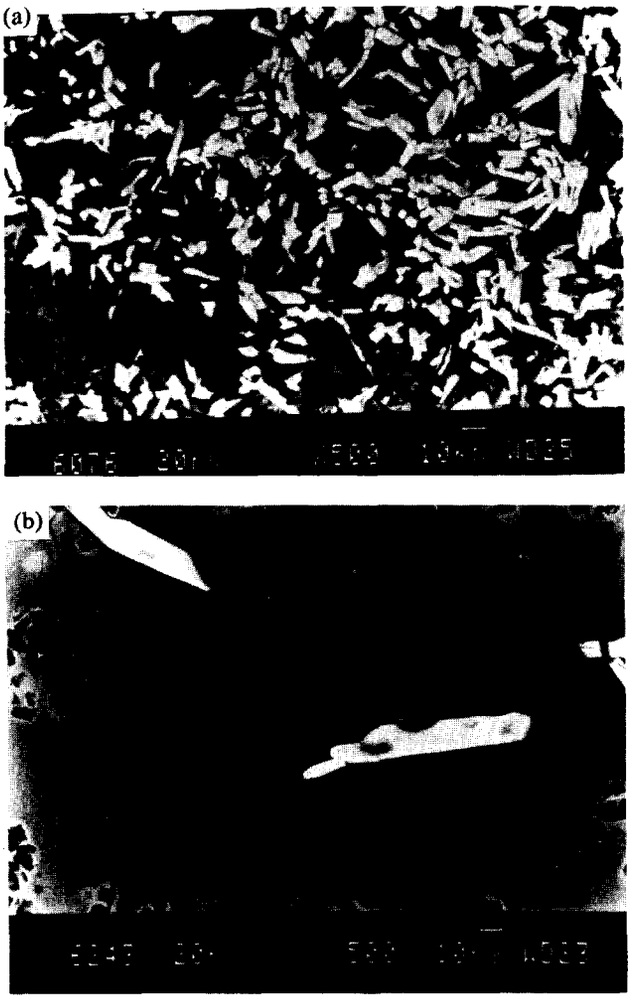


Fig. 8. Surface morphology of 0·5 sialon material after 48 h exposure at 1350°C in (a) laboratory air environment and (b) simulated flue gas environment.

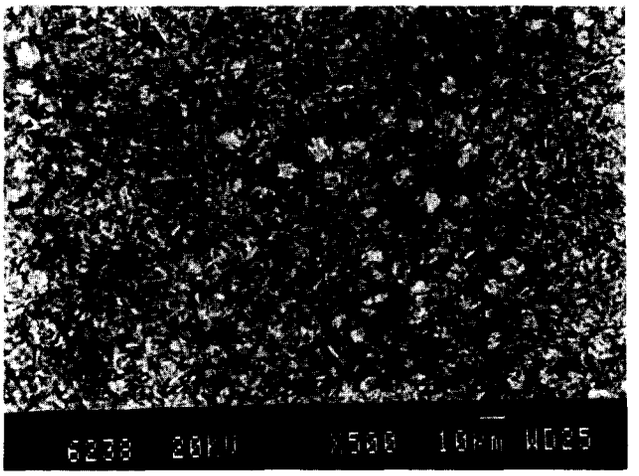


Fig. 9. Surface morphology of 3·0 sialon material after 48 h exposure at 1350°C in simulated flue gas environment.

those formed during oxidation. It is to be noted however that the crystalline phases formed were the same in both environments.

4 Discussion of Results

4.1 Relative corrosion resistance

Of the materials tested the $z = 3{\cdot}0$ material appears to be the most resistant to oxidation/corrosion by laboratory air. This material is also without doubt the most corrosion resistant material in the other three environments used in this work. The fact that the mullite forming $z = 3{\cdot}0$ material exhibits little liquid formation during corrosion in any of the environments investigated is most probably the reason for its excellent corrosion behaviour. In general the $z = 1{\cdot}0$ material undergoes the most extensive corrosion in each of the four environments studied.

4.2 Effect of environment on corrosion scales developed

From the results presented above it is clear that liquid phases are formed on the surfaces of the materials investigated during exposure to laboratory air. In the chloridising environment, chlorine is the only reactive gas addition which can account for the accelerated oxidation and significant extent of corrosion observed. In addition, the extent of liquid phase formation is greater in the chloridising environment than the laboratory air environment; indeed the scales formed on the $z = 0{\cdot}2$, $0{\cdot}5$, $1{\cdot}0$ and $1{\cdot}5$ materials are wholly amorphous. It is to be expected that the corrosion scales formed in the chloridising environment are more fluid than those formed in laboratory air since Hetherington *et al.*[17] noted marked decreases in the viscosity of fused silica contaminated with trace amounts of chlorine. In the case of the sulphidising environment the situation is more complex since both hydrogen and sulphur vapour are present in addition to the oxygen provided as water vapour. In order to ascertain the exact effect of hydrogen sulphide on the corrosion process, additional experiments were conducted at 1350°C in a gaseous environment comprising hydrogen–2% water vapour using the $z = 0{\cdot}2$ material. The results obtained from this work demonstrated that the corrosion rate was less than that observed for the environment containing hydrogen sulphide and that the corrosion products showed some crystallinity. It may therefore be concluded that the large volumes of low viscosity liquid formed in the sulphidising environment, compared to those formed in laboratory air, arise from the synergistic effects of hydrogen and sulphur. Combining the findings of Demaison *et al.*[9] and the results obtained for the simulated flue gas environment strongly suggests that carbon dioxide and sulphur dioxide exert a similar synergistic effect on liquid volume and viscosity. This is clearly demonstrated by comparison of the micrographs shown in Figs. 8(a) and (b). As stated above, the exterior layers of the corrosion scales formed on the $z = 0{\cdot}2$ and $0{\cdot}5$ materials in the simulated flue gas environment were observed to contain more aluminium than those formed in the laboratory air environment. Since the crystalline phases formed ($Y_2Si_2O_7$ and SiO_2) do not contain this element, more liquid is expected to form in the former environment as observed above.

4.3 Corrosion mechanisms

Combining the above rationalisation of the effects of environment on the volume and fluidity of liquid corrosion products with the extents of oxidation and corrosion suffered by the different sialon materials indicates that for large volumes of a fluid corrosion product, (i.e. chloridising and sulphidising environments) extents of corrosion are significantly greater than those observed when lower volumes of liquid are formed, (i.e. simulated flue gas and oxidising environments). This correlation indicates that the role played by liquids in the oxidation and corrosion mechanisms operating at 1350°C is extremely important. Additional experiments with RBSN have shown that the $\beta/(\alpha + \beta)$ silicon nitride ratio observed in the layers beneath the cristobalite corrosion product formed in the simulated flue gas environment is greater than in the starting material. It was also observed that in addition to cristobalite a calcium containing amorphous phase was present in the surface layers of the corrosion product. In order for the α-/β-phase transformation to occur, a liquid phase must be present to facilitate the solution–precipitation reaction.[18] It would therefore appear that α-silicon nitride is dissolved by the calcium containing liquid present at 1350°C and reprecipitated as β-silicon nitride. This finding suggests that silicon nitride can be dissolved by liquid corrosion products. In order to validate the fact that the α/β transformation could occur at such a low temperature a green sample of the $z = 0{\cdot}2$ material was sintered for 96 h in flowing nitrogen at a temperature of 1350°C. The density of the material increased from 62% of theoretical to 90% and the initial β-content of 5% increased to 65% clearly demonstrating that densification and associated solution–precipitation effects could occur over long time periods at 1350°C. If α-silicon nitride can dissolve in a liquid corrosion product it seems plausible to assume that β-silicon nitride and sialons can also. However, dissolved β-silicon

nitride and β-sialons cannot be reprecipitated as α. Accordingly, if the β-silicon nitride dissolves in the corrosion scale it is likely that the resulting nitrogen saturated liquid will decompose into a liquid containing little nitrogen and the relevant crystalline silicates or silica. If this mechanism of oxidation and corrosion is accepted then the rate of corrosion should be dependent on the volume and viscosity of the liquid formed during oxidation. Greater liquid volumes will result in greater extents of silicon nitride/sialon solution and lower viscosities will enable the dissolution products to be transported away from the liquid – nitride interface more rapidly. The extensive corrosion of the various materials in the chloridising and sulphidising environments is thus easy to comprehend.

As stated in the introduction, although rates of oxidation at temperatures of the order of 1350°C are controlled by the diffusion rate of additive and impurity cations from the bulk of the ceramic into the surface scale the exact reasons for this are not fully appreciated. The above arguments relating to corrosion mechanisms enable a fuller appreciation to be put forward if it is realised that the diffusion of additive and cation impurities into the surface scale increases its liquid content and lowers the viscosity of the liquid formed. Such an argument is consistent with observations that the type and level of additive employed during densification control oxidation rate[11,12] since additive types and levels which give rise to large volumes of low viscosity liquids during densification will give rise to large quantities of low viscosity liquids in oxide scales.

In designing silicon nitride ceramics for high temperature corrosion resistant applications the selection of additive and sialon z-value are critical as the results presented show. The optimum ceramic will comprise constituents which will give rise to little liquid formation during corrosion. The observation that the mullite forming $z = 3{\cdot}0$ material exhibits less liquid formation during corrosion in any of the environments investigated and that this is consistent with the lowest corrosion rates endorses such a design criterion.

5 Conclusions

(1) In general, the most corrosion resistant material in oxidising, chloridising, sulphidising and simulated gas environments at 1350°C is a $z = 3{\cdot}0$ sialon material.

(2) The presence of gaseous impurities (sulphur vapour, chlorine, hydrogen, sulphur dioxide, carbon dioxide) in the corrosion environments employed have the effect of increasing the volumes of liquid phase formed in the corrosion scales.

(3) The occurrence of increased volumes of liquid phase results in increased corrosion rates.

(4) The mechanism by which corrosion and indeed oxidation of silicon nitride–based ceramics occurs appears to involve the solution of sialon grains by such liquids, the extent and rates of liquid formation are controlled not only by the gaseous environment but also by cation diffusion effects.

Acknowledgements

The authors thank the commission of the European Communities for the grant given under BRITE-EURAM contract No. BREU/0180-C (EDB). The help rendered by Ms A. Flannery and Mr R. Bartley with regard to specimen fabrication and preparation is acknowledged.

References

1. Ekstrom, T. & Nygren, M., Sialon ceramics. *J. Am. Ceram. Soc.*, **75**(2) (1992) 259–76.
2. Blachere, J. R. & Pettit, F. S., *High Temperature Corrosion of Ceramics*, Noyes Data Corporation, Park Ridge, New Jersey, 1989.
3. Marra, J. E., Kriedler, E. R., Jacobson, N. S. & Fox, D. S., Reactions of silicon-based ceramics in mixed oxidation chlorination environments. *J. Am. Ceram. Soc.*, **71**(12) (1988) 1067–73.
4. Hsu, P., Sikyin, I., Park, C. & McNallan, M. J., Oxidation of silicon, silicon carbide and silicon nitride in gases containing oxygen and chlorine. *J. Am. Ceram. Soc.*, **76**(6) (1993) 1621–3.
5. Costa Oliveira, F. A., Edwards, R. A. H., Fordham, R. J. & De Wit, J. H. W., Factors limiting the application of silicon nitride ceramics in sulphur containing environments of low oxygen potential at high temperatures. In *Corrosion of Advanced Ceramics*, ed. K. G. Nickel, Kluwer Academic Publishers, 1994, pp. 177-88.
6. Sheehan, J. E., Passive and active oxidation of hot pressed silicon nitride materials with two magnesia contents. *J. Am. Ceram. Soc.*, **65** (1982) C111–4.
7. Costa Oliveira, F. A., Fordham, R. J. & De Wit, J. H. W., Degradation mechanisms of a silicon nitride in H_2–H_2O environments. In *Euroceramics II*, eds G. Ziegler & H. Hausner, Deutsche Keramische Gesellschaft e.V., 1991, pp. 1351–6
8. Martins, C. S., Steen, M. Bressers, J. & Rosa, L. G. High temperature flexure strength degradation of HP–Si_3N_4 pre-exposed to sulphidising aggressive environments. In *Euroceramics II*, eds G. Ziegler & H. Hausner, Deutsche Keramische Gesellschaft e.V., 1991, pp. 1357–61.
9. Demaison, J., Brossard, M., Demaison-Brut, M. & Goursat, P., Oxidation behaviour of β'-sialons in oxygen and carbon dioxide. In *Progress in Nitrogen Ceramics* ed. F. L. Riley, Martinus Nijhoff, The Hague, 1983, pp. 439–46.
10. Bouarroudj, A., Goursat, P. & Besson, J. L., Oxidation resistance and creep behaviour of a silicon nitride ceramic densified with Y_2O_3. *J. Mat. Sci*, **20** (1985) 1150–9.

11. Babini, G. N., Bellosi, A. & Vincenzini, P., A diffusion model for the oxidation of hot pressed Si_3N_4–Y_2O_3–SiO_2 materials. *J. Mat. Sci*, **19** (1984) 1029–42.
12. Pomeroy, M. & Hampshire, S., Oxidation processes in silicon-nitride-based ceramics. *Mat. Sci & Eng*, **A109** (1989) 389–94.
13. Pomeroy, M & Ramesh, R., Understanding the morphological development of oxidation products formed on β-sialon materials with different z-values. In *Microscopy of Oxidation-2*, eds S.B. Newcomb, & M. J. Bennett, Cambridge, UK, 1993, pp 566–75.
14. Ekstrom, T. & Olsson, P-O., β-sialon ceramics prepared at 1700°C by hot isostatic pressing. *J. Am. Ceram. Soc.*, **72**(9) (1989) 1722–4.
15. Bondar, A. & Galakov, F. Ya. In *Phase Diagrams for Ceramists*, ed. M. K. Reser, The American Ceramic Society, Columbus, Ohio, 1969, p. 165.
16. Daniel, P. L. & Rapp, R. A., Halogen corrosion of metals. In *Advances in Corrosion Science and Technology*, eds M. G. Fontana & R. W. Staehle, Plenum Press, NY, **6** 1976, pp. 55–72.
17. Hetherington, G., Jack, K. H., & Kennedy, J. C., The viscosity of vitreous silica. *Physics and Chemistry of Glasses*, **5**(5) (1964) 130–6.
18. Hampshire, S. & Jack, K. H., The kinetics of densification and, phase transformations of nitrogen ceramics. In *Special ceramics*, Vol. 7, eds P. Popper & D. E. Taylor, Proc. Brit. Ceram. Soc., **31** 1981, pp. 37.

Journal of the European Ceramic Society **15** (1995) 1015–1024
© 1995 Elsevier Science Limited
Printed in Great Britain. All rights reserved
0955-2219(95)00064-X
0955-2219/95/$9.50

Oxidation Behaviour of Yttrium and Neodymium Oxynitride Glasses

M. Sebai,[a] J. Sjöberg,[a] P. Goursat,[a] E. Nestor,[b] R. Flynn,[b] R. Ramesh[b] & S. Hampshire[b]

[a]Laboratoire de Matériaux Céramiques et Traitements de Surface, URA CNRS 320, 123, Avenue Albert Thomas Université de Limoges 87060, France
[b]Materials Research Centre, University of Limerick, Limerick, Ireland

(Received 7 November 1994; revised 9 March 1995; accepted 20 March 1995)

Abstract

The oxidation behaviour of oxynitride glasses in M–Si–Al–O–N system (M = Nd, Y) has been studied in air and under various oxygen pressures. The influence of glass composition on the oxidation resistance was studied at 1075°C by varying Y/Al or Si/Al ratios and also by substituting Y by Nd and by varying the nitrogen content. The reactivities in air of the YSiAlON system is studied in the temperature range of 1000–1150°C. The oxidation resistance of YSiAlON glasses is better than for glasses containing Nd. A pressure law is determined for the YSiAlON system based upon data from oxidation at 1050 and 1075°C at oxygen pressures in the range of 15–100 kPa. The nature and morphology of oxidised samples were characterised by optical microscopy, XRD and SEM. These investigations reveal that the oxidation of the studied oxynitride glasses is governed by a reaction process where the progress of the internal interface is the limiting step.

1 Introduction

It is well established that oxidation and high temperature mechanical properties of silicon nitride ceramics are strongly dependent on the residual secondary phases. These can be glass or crystalline phases and are formed as a result of sintering additives or impurities in the material powders used in the synthesis of the ceramics. This has aroused a considerable interest in oxynitride glasses both as bulk materials and as grain boundary secondary phases in the nitride ceramics. Jack[1] was the first to report the existence of oxynitride glasses in the YSiAlON system. Additional information on the preparation and characterisation of glasses in this system has been given by Shillito *et al.*[2] and Loehman.[3,4] Subsequently, considerable investigations were carried out to determine the extent of vitreous regions in a wide range of M–Si–O–N and M–Si–Al–O–N systems[5–21] (M = either Ba, Ce, Ca, La, Li, Mg, Mn, Na, Nd or Y) including the effects of increasing nitrogen content on the properties of these glasses. The first systematic investigation of the effects of nitrogen on properties of alumino-silicate glasses was carried out by Drew *et al.*[11–13] who found that glass transition temperature, viscosity, microhardness and refractive index all increased as nitrogen was substituted for oxygen in the glass network. Another interest in oxynitride glasses is their ability to form glass-ceramics for potential thermomechanical applications. However, the mechanisms governing their transformation are still unknown. The products of glass crystallisation are also sensitive to nitrogen content and the results obtained by different authors vary.[22–26] The high temperature use of oxynitride glasses, in air, is limited by their oxidation resistance but relatively little data on their oxidation resistance are available in the literature[26–29] for a limited number of glass systems.

The present work is part of a European collaboration between four partners on the preparation and characterisation of a wide range of compositions of oxynitride glasses in various systems. This study has been undertaken to investigate the oxidation behaviour of some glasses in order to define their use under isothermal conditions and to explain the degradation mechanisms of sintered silicon nitride materials at high temperatures. In this paper some data on the influence of glass composition, heat treatment conditions and

oxygen pressure on the oxidation resistance and the morphology of glasses are reported. In contrast to CaSiAlON and MnSiAlON systems studied[27-28] the exploitation of the results was facilitated by the fact that samples preserve their geometry under oxidation. A second paper is devoted to explaining the mechanisms governing the oxidation of oxynitride glasses in the YSiAlON system.

2 Materials and Procedure

2.1 Glass preparation

The Jänecke triangular prism representation is used to represent glass composition within these M-sialon systems with concentrations of components expressed in equivalents (as shown in Fig. 1). Constant oxygen:nitrogen ratios can be represented by vertical triangular planes within the prism parallel to the oxide and nitride faces. $4N^{3-}$ are replaced by $6O^{2-}$ on moving from left to right and the distance x represents the concentration of nitrogen and the distance y represents the concentration of oxygen, in equivalents, such that $x/(x + y) = (3[N])/(2[O] + 3[N])$ where [O] and [N] are, respectively, the atomic concentration of oxygen and nitrogen within any composition. For any plane, the O : N ratio is fixed and the concentrations of the cations are calculated in equivalents in the normal way for a 3-component system. The compositions used for this study are shown in Table 1.

Glasses were prepared using the melting procedure described by Hampshire *et al.*[16] from mixtures of 99.99% pure silicon nitride powder with high purity oxides (Al_2O_3, Nd_2O_3, SiO_2 and Y_2O_3). They were mixed in isopropanol, dried, and pressed into pellets. Large batches of 40–70 g were melted in a boron nitride lined graphite crucible under 100 kPa nitrogen at 1700°C for 1 h. The glass was poured into a pre-heated graphite mould and annealed at 850–900°C for 1 h and allowed to cool slowly.

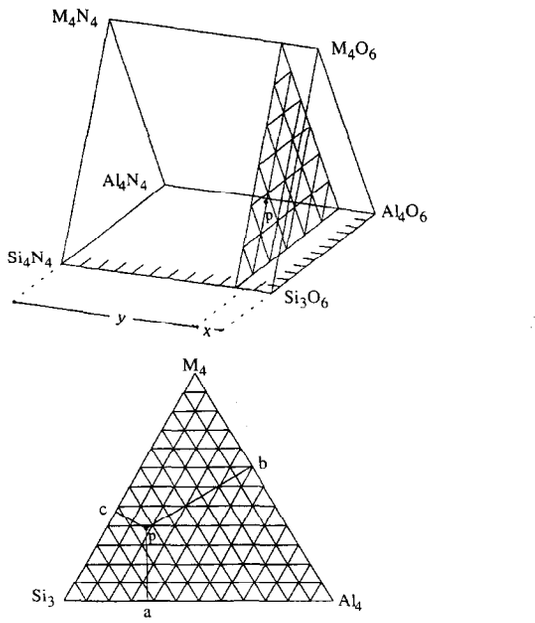


Fig. 1.. Jänecke prism representation of the M–Si–Al–O–N system.

2.2 Glass characterisation

Specimens were examined by optical microscopy (Olympus PMG3) and subjected to X-ray diffraction using a diffractometer (Philips PW1130) and a Guinier camera to confirm their amorphous nature, while chemical analysis of the nitrogen content was performed by a gas chromatographic analyser (Carlo Erba 1106). The oxidised samples were also characterised using X-ray diffraction, optical microscopy, SEM (Philips XL30) with integrated EDAX. Bulk glass densities were measured by an archimedean displacement using water as the immersion liquid, the accuracy of the measurement is ±0·05.

The nominal compositions in equivalent percent (e/o) cations/anions, glass densities and the values of nitrogen content found by analysis of the prepared glasses are detailed in Table 1.

Table 1. Glass compositions

	Composition (e.o)					*N (weight %)*		*Density*
Glasses	*Y*	*Si*	*Al*	*O*	*N*	*Cal.*	*Exp.*	
YSi17G4	40	56	4	83	17	3·377	3·32 ± 0·08	4·13
YSi17G8	36	56	8	83	17	3·502	3·415 ± 0·1	4·03
YSi17G12	32	56	12	83	17	3·638	3·59 ± 0·11	3·87
YSi1G16	28	56	16	83	17	3·775	3·43 ± 0·19	3·75
YSi10G16	28	56	16	90	10	2·22	2·19 ± 0·09	3·69
YY17G12	28	60	12	83	17	3·76	3·53 ± 0·10	3·71
YY17G20	28	52	20	83	17	3·78	3·59 ± 0·1	3·73
YY17G22	28	50	22	83	17	3·78	3·61 ± 0·12	3·74
Glass	*Nd*	*Si*	*Al*	*O*	*N*	*cal*	*exp*	*Density*
NdSi17G16	28	56	16	83	17	3·03	3·08 ± 0·05	4·56

2.3 Oxidation experiments

Cubic samples ($4 \times 4 \times 4$ mm^3) were cut from the pellets using a low-speed diamond saw and then carefully polished with diamond pastes and cleaned in an ultrasonic bath. The oxidation resistance of glasses in air and under controlled atmosphere was carried out using a thermobalance (Ugine Eyraud B60).

While the furnace was heated at a constant rate of 20°C min^{-1} to the oxidation temperature, the sample was kept in a cold zone then lowered quickly into the hot zone where it was kept only during the isothermal oxidation treatment.

3 Results

The oxidation reaction of oxynitride glasses, in the quinary systems, is very complicated due to the formation of a number of crystalline phases in the oxide layer. The nature and morphology of the oxidation products will be explained later. The crystalline phases are formed according to the following general reactions:

$$YSiAlON + aO_2 \rightarrow bY_2Si^2O^7 + cY_2SiO_5 + dAl_2O_3 + eAl_6Si_2O_{13} + \text{amorphous oxide} + N_2\nearrow$$

From weight changes it is possible to determine the fractional weight gain according to the equation:

$$\alpha = {}^{\Delta W_t}/_{\Delta W_\infty}$$

where ΔW_t is the weight gain for a given time t and ΔW_∞ is the weight gain which corresponds to a complete oxidation of the oxynitride glass. In this case ΔW_∞ corresponds to the experimental values of nitrogen content seeing that we obtain a complete oxidation when all nitrogen is substituted by oxygen in the glass network.

3.1 Influence of the glass composition

The behaviour at high temperature of oxynitride glasses is closely linked to the total composition. The nature and the concentration of each element are important parameters which influence the structure of the glass network. Oxidation resistance varies from one system to another[27–29] but the role of the different elements in the oxidation resistance of these glasses remains unknown. Considering that the structure controls the viscosity, the physical properties and the degradation of oxynitride glasses, systematic investigations were carried out to study the influence of glass composition on their oxidation resistance and to explain the contribution of each constituent. The experiments were carried out using the following series of samples:

(a) constant ratio Y/Si/Al and varying O/N ratio in order to evaluate the influence of nitrogen content;

(b) constant ratio M/Si/Al/O/N and varying the type of metallic cation;

(c) constant ratio Y/O/N and varying Si/Al to explain the role of silicon and aluminium in the network;

(d) constant ratio Si/O/N and varying Y/Al to explain the role of yttrium and aluminium as network modifiers.

The oxidised samples at 1075°C preserve their geometry. After oxidation of glasses we have seen no changes in the morphology of samples or the plasticity of the substrates.

The oxidation behaviour of oxynitride glasses is strongly dependent on the glass composition as shown in Fig. 2. The incorporation of nitrogen increases the oxidation resistance (Fig. 2(a)). As it will be shown later the oxidation starts above the glass transition temperature. When oxygen is replaced by nitrogen in silicon co-ordination tetrahedra, the increase of the degree of reticulation and the individual negative charge leads to an increase in the coulombic forces between these tetrahedra and the cations, thus enabling a higher refractoriness and compactness of the network.

The same effect is observed on the substitution of neodymium by yttrium (Fig. 2(b)). This could imply that the size of the cation alone is responsible for the behaviour changes at high temperatures; it can be explained by the fact that the strength of the bond between the metallic ion and the surrounding oxygen ions in the glass structure (M–O) where (M = Nd, Y) increases with increasing field strength of the metallic ion. It is known that the field strength varies with the reciprocal of the ionic radius which means that the Y–O bonds are stronger than Nd–O ones. As the M–O bonds are weaker than the Al–O and Si–O bonds, a more compact glass network is obtained with the stronger M–O bonds. The same results were observed by Shelby *et al.*[31] on the properties of oxide alumino-silicate glasses and by Persson *et al.*[30] while oxidising silicon nitride with Y_2O_3 and Nd_2O_3 additives.

Results for glasses that are oxidised at 1075°C for 20 h are shown in Figs 2(c) and (d). The role played by aluminium in the glass structure depends strongly on its concentration. For the low concentrations, aluminium is expected to exist in fourfold coordination with oxygen where the presence of (AlO_4) tetrahedra confers to aluminium the role of network former. As the aluminium content increases, it seems that the glass structure becomes more disordered[32–34] which could explain the decrease of the oxidation resistance. A negative effect of aluminium on the oxidation resistance of silicon nitride is also revealed by Gogotsi *et al.*[35]

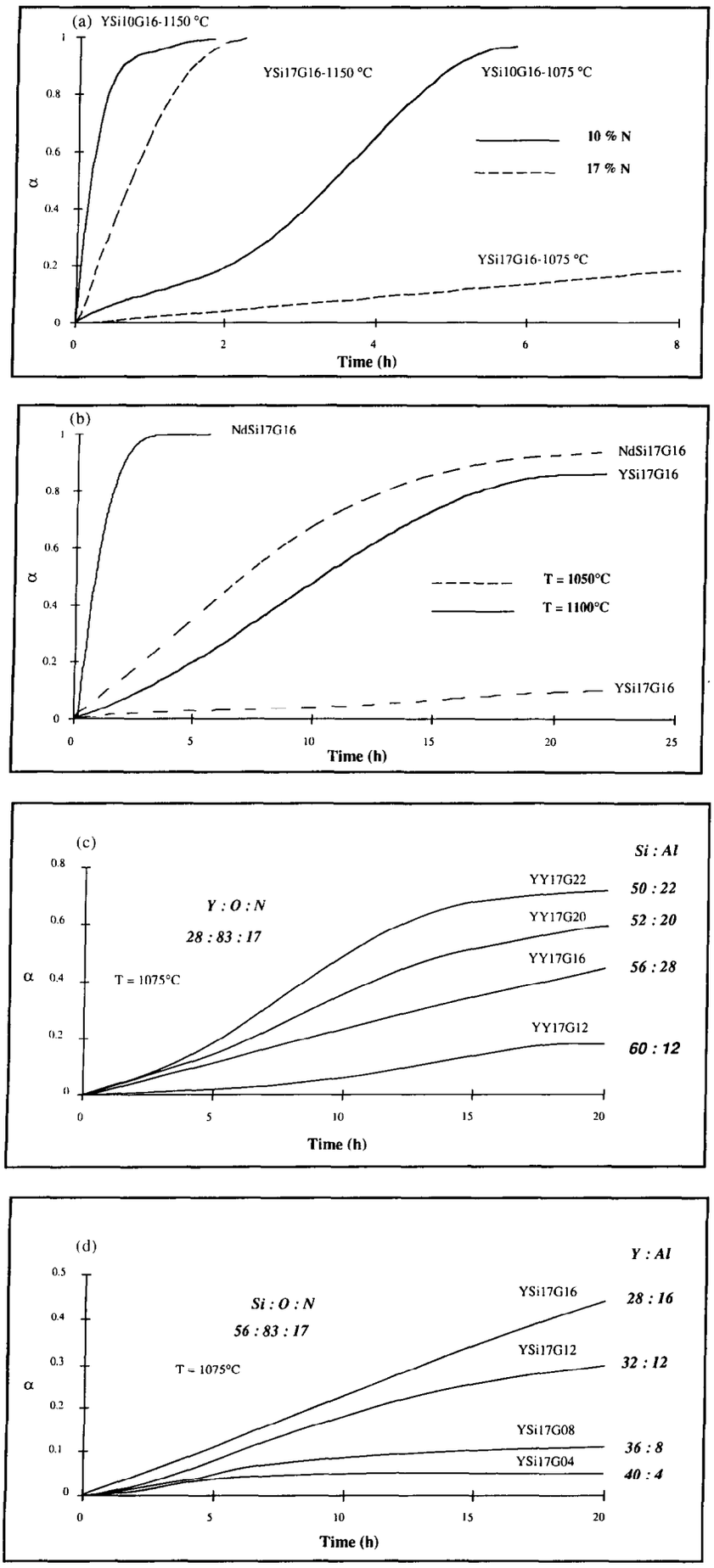


Fig. 2. Oxidation kinetics in air of oxynitride glasses: (a) with a constant ratio Y/Si/Al = 28/56/16 and various nitrogen contents; (b) with a constant ratio Si/Al/O/N=56/16/83/17 and changing rare earth element; (c) with a constant ratio Y/O/N=28/83/17 and varying Si/Al; (d) with a constant ratio Si/O/N=56/83/17 and varying Y/Al.

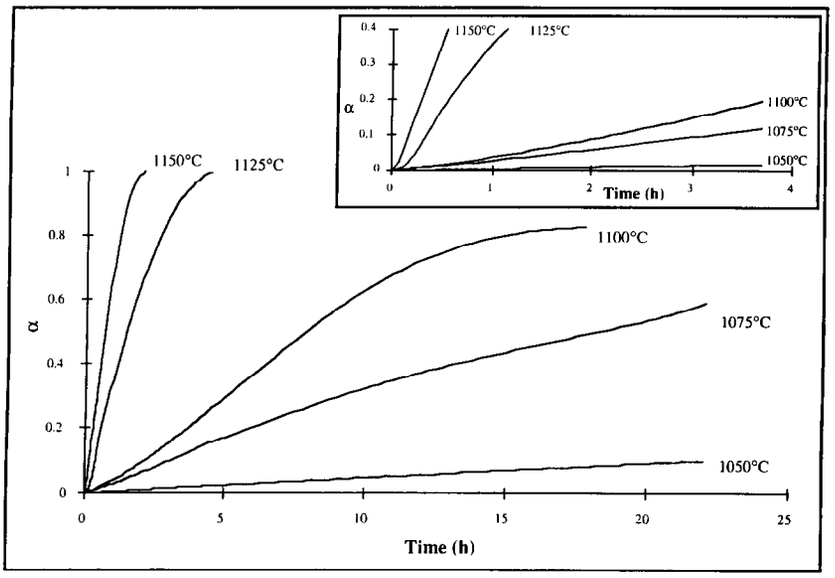


Fig. 3. Oxidation kinetics in air of YSi17G16 oxynitride glasses.

If we compare the oxidation curves of YSi17G12 and YY17G12 specimens which are characterised by a constant ratio Al/O/N and a varying Y/Si ratio, we observe that the oxidation resistance of the glasses decreases when yttrium replaces silicon. This is due to the fact that the substitution of silicon (network forming) by yttrium (network modifying) tends to make the glass structure more random. The other explanation is that, for glasses with a constant ratio Al/O/N, the increase of Y/Si ratio is followed by a slight increase in the concentration of aluminium in five-fold coordination.[33] Thus, oxynitride glasses containing more nitrogen and silicon and less aluminium are characterised by higher oxidation resistance.

3.2 Influence of the oxidation temperature

Oxidation of oxynitride glasses was investigated in air between 1000 and 1150°C for YSi17G16.

(a) Oxidation kinetics

The reactivity of YSiAlON glasses with oxygen starts around 1000°C with a weak weight gain (Fig. 3). For higher temperatures, the oxidation rate increases significantly and the oxidation is almost complete in a few hours at 1150°C. The oxidation curves of the studied glasses exhibit a sigmoïdal shape and the latent period of the reaction decreases with the increase of the oxidation temperature. For each isotherm, the oxidation rate has a maximum and the time of appearance of this maximum changes with the temperature. No initial weight loss was observed in the lower temperature range, which is not in agreement with results reported by Desmaison-Brut *et al.*[27-28] for the CaSiAlON and MnSiAlON systems.

(b) Nature and morphology of the reaction products

In order to explain the mechanisms governing the oxidation of oxynitride glasses, we have studied the nature and the morphology of the reaction products.

The oxide scale changes continuously with oxidation conditions (temperature and time). The reaction of the glasses with oxygen leads to the release of nitrogen and the formation of voids at the internal interface, which is followed by the growth of a white oxide layer.

At low temperatures, samples are covered by a thick oxide layer which increases with the oxidation time and temperature (Figs 4 and 5). The oxide layer thicknesses, measured from the micrographs (Figs 5(a), (b) and (c)) are 15, 360 and 760 μm for samples oxidised for 22 h respectively at 1000, 1050 and 1075°C. The increase of temperature favours the formation of nitrogen bubbles and the creation of porosity in the oxide scale and at the internal interface, as seen in Figs 5 (b) and (c). The presence of the bubbles leads to the formation of an irregular interface and favours the access of oxygen. The continuous changes in the morphology of oxidised samples is accompanied by the formation of a number of crystalline phases in the oxide layer. For the first oxidation temperatures, a crystalline phase transformation is observed as a function of time or temperature (Table 2). This successive change in the nature of the oxidation products indicates the non-recovering character of the formed oxide layer. The difference in mechanical properties between the oxide layer and the substrate favours the relaxation of stresses at the internal interface which leads to cracking at the edges of the samples to induce a maltese cross symmetry (Fig. 4(b)).

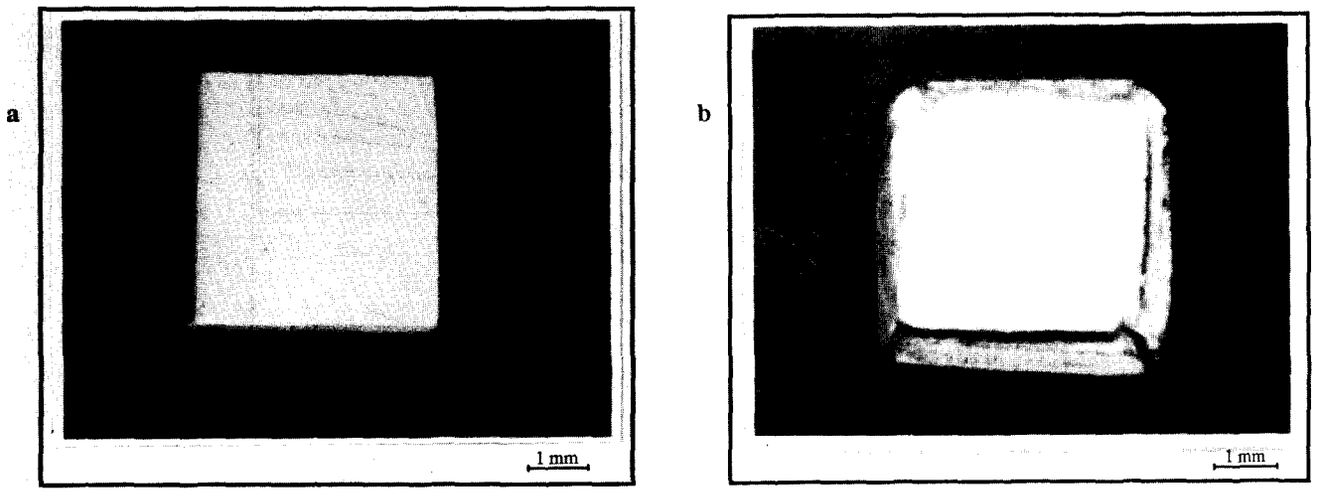


Fig. 4. Optical micrographs of oxidised glasses: (a) YSi17G16 at 1000°C (22 h); (b) YSi17G16 at 1075°C (22 h).

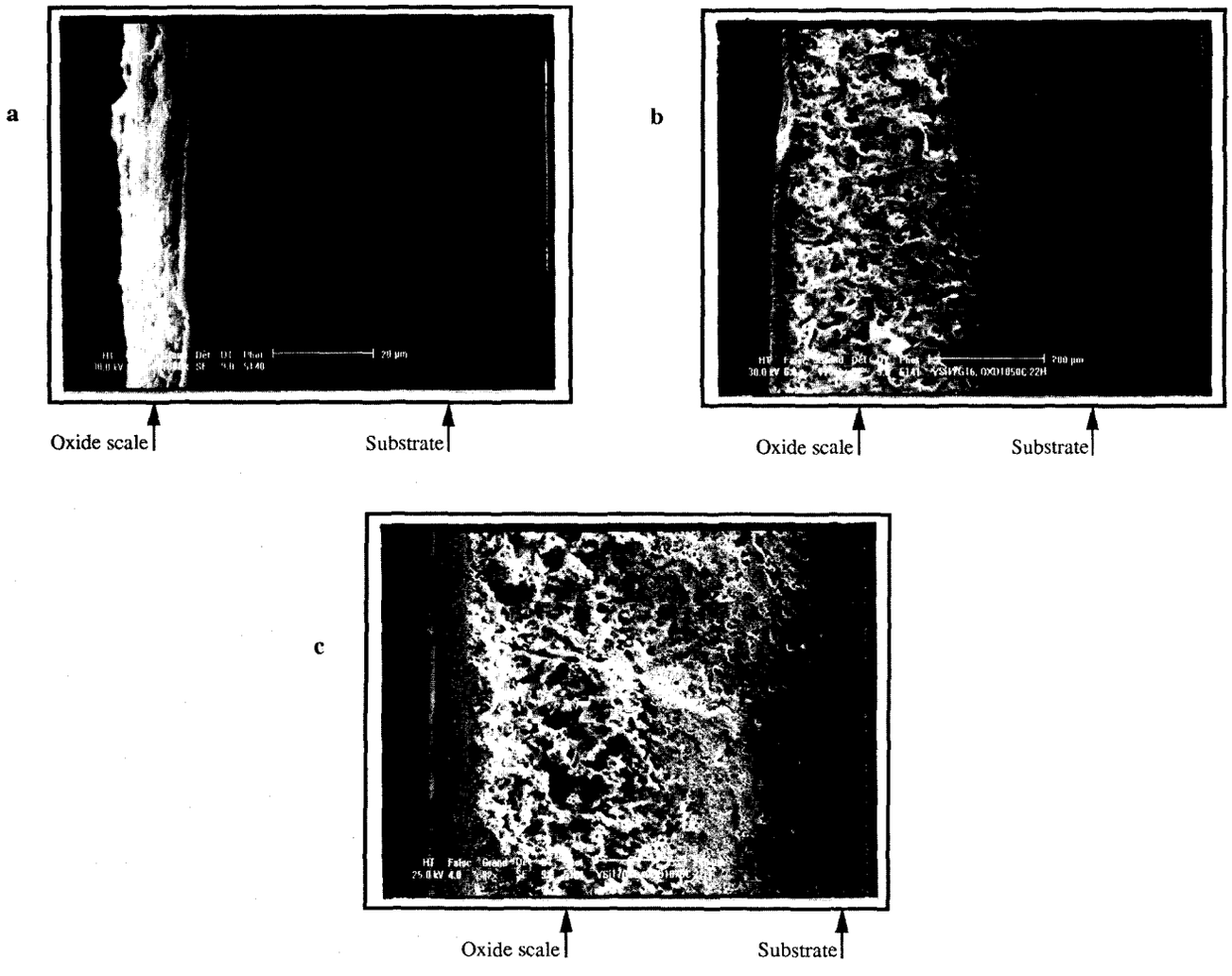


Fig. 5. Cross-section SEM photomicrographs of oxidised glasses: (a) YSi17G16 at 1000°C (22 h); (b) YSi17G16 at 1050°C (22 h); (c) YSi17G16 at 1075°C (22 h).

At high temperatures, oxidation occurs very quickly with the formation of very large bubbles and extensive porosity in the oxide layer and the substrate. The presence of this porosity in the oxide layer increases the volume of oxide scales (Fig. 6) and facilitates the rapid access of oxygen to the centre of samples.

The crystalline phases present in the oxide scales, detected by X-ray diffraction, are given in Table 2.

At 1000°C and for 22 h of heat treatment, the oxide layer contains $\alpha Y_2Si_2O_7$ and a small amount of yttriallite ($yY_2Si_2O_7$) and corundum. With the increase of oxidation time a gradual substitution of $\alpha Y_2Si_2O_7$ by yttriallite occurs. After 100 h of

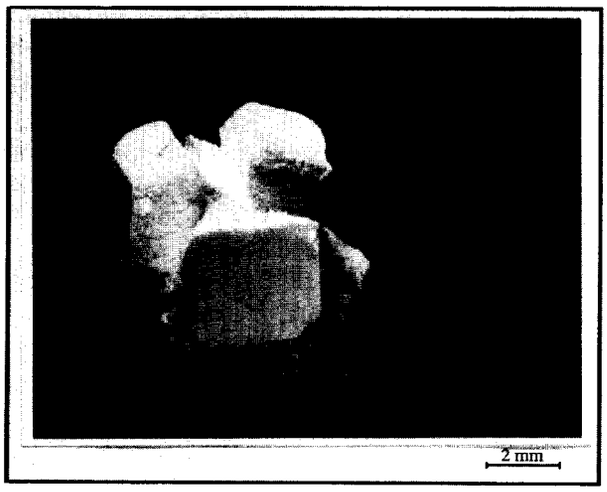


Fig. 6. Optical micrographs of YSi17G16 oxidised at 1150°C (18 h).

heat treatment the oxide layer is formed by yttrialite as the main oxide, with the presence of small quantities of mullite, corundum, cristoballite and $\alpha Y_2Si_2O_7$. The simultaneous presence of α and $yY_2Si_2O_7$ is in agreement with the crystallisation results of Hampshire *et al.*[16] and Dinger *et al.*[25] where they observe the presence of yttrium dissilicates for glasses heat treated with the same conditions. For the higher oxidation temperatures, X-ray diffraction data of oxidised samples, reveal no change in the nature of crystalline phases present in the oxide layer and confirm the absence of any transformation in the oxide layer.

A small amount of crystallisation of the substrates is detected above 1050°C ($yY_2Si_2O_7$).

(c) Kinetics modelling

For cubic samples the oxidation reaction rate is calculated up to the edge a of the cube using the following equations:

$-da/dt = 2k$

where, $a = a_0 - 2kt$

and a_0 is the initial cube edge, k is the rate constant which corresponds to the growth of the oxide layer along the time ($mm.s^{-1}$) and t the time.

α can be expressed by: $\alpha = 1 - a^3/a_0^3$)

$a = a_0 - (1 - \alpha)^{1/3}$

and we obtain the following kinetics equation:

$$F(\alpha) = 1 - (1-\alpha)^{1/3} = 2kt/a_0 \quad (1)$$

The sigmoïdal shape of the oxidation curves, the texture and the morphology of the porous oxide scale which show a direct access of oxygen to the internal interface and the growth of the maltese cross symmetry imply that the oxidation of YSi17G16 is governed by a reaction process where the progress of the internal interface is the limiting step. This assumption is confirmed by the determination of $F(\alpha).a_0/2t$ which increases from the beginning of the reaction to become constant after a few minutes or by the linearity of the transformations as a function of time as shown in Fig. 7. The

Table 2. Crystalline phases in the oxide layer after a heat treatment in air at various temperatures

Temperature	*Time (h)*	*Crystalline phases*
1000°C	22	$\alpha Y_2Si_2O_7$, $yY_2Si_2O_7$, Al_2O_3
1000°C	100	$yY_2Si_2O_7$, $\alpha Y_2Si_2O_7$, $Al_6Si_2O_{13}$, Al_2O_3, SiO_2
1050°C	22	$yY_2Si_2O_7$, $Al_6Si_2O_{13}$, Al_2O_3, SiO_2
1075°C	22	$yY_2Si_2O_7$, $Al_6Si_2O_{13}$, SiO_2
1100°C	22	$yY_2Si_2O_7$, $Al_6Si_2O_{13}$, SiO_2
1125°C	5	$yY_2Si_2O_7$, $Al_6Si_2O_{13}$, SiO_2
1150°C	18	$yY_2Si_2O_7$, $Al_6Si_2O_{13}$, SiO_2

$Al_6Si_2O_{13}$ (mullite); SiO_2 (α-cristoballite); Al_2O_3 (corundum).

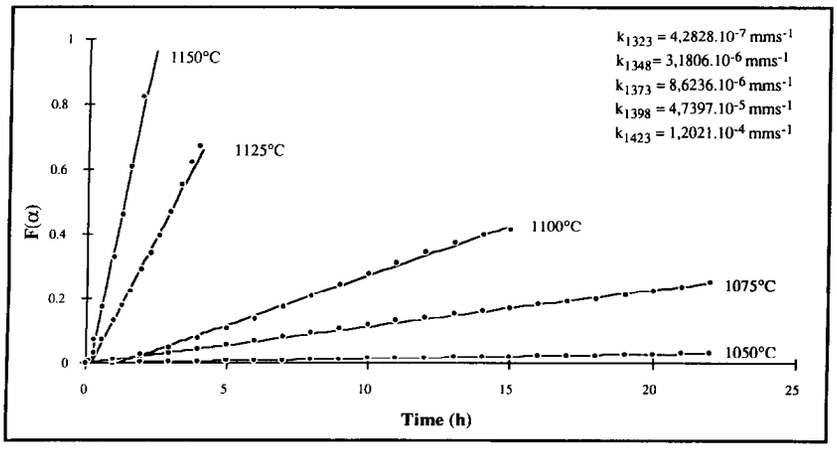


Fig. 7. Transformation as a function of time (YSi17G16).

apparent activation energy calculated from the slope of the transformation curves is $E = 848 \pm 50$ kJ/mol.

3.3 Influence of the oxygen pressure

The influence of oxygen pressure on the oxidation resistance of oxynitride glasses was studied at 1075°C on YSi17G16 at oxygen pressures in the range 15–100 kPa with nitrogen added up to atmospheric pressure. Two experiments were carried out:

(1) Samples were oxidised for 8 h at different oxygen pressures since $\alpha_0 = 0$ (Fig. 8(a)).

(2) Samples were first oxidised in air for 4·5 h corresponding to $\alpha_0 = 0{\cdot}153$, after which they were put in the cold zone while the furnace was evacuated and lowered again into the hot zone when the mixture of oxygen and nitrogen had been introduced (Fig. 8(b)).

The kinetics of oxidation of YSi17G16 are affected by the oxygen pressure. The transformation as a function of time calculated using expression (1) are linear in the studied interval which permits the determination of a pressure law as:

$$k = k_0 P^n$$

where k is the oxidation rate constant ($mm.s^{-1}$), k_0 a constant, P is oxygen pressure and n is a coefficient determined from the slope of the curve $\log_{10}k$ as a function of $\log_{10}P$ (Fig. 9). For the experiments in this study $n = 0{\cdot}5 \pm 0{\cdot}05$ which is in agreement with the presence of a porous oxide layer which facilitates the access of oxygen to the internal interface.

4 Discussion

The influence of the glass composition, oxidation conditions and oxygen pressure on the oxidation resistance of oxynitride glasses have been studied. The wide range of glass compositions investigated permits us to explain the role played by each constituent on the oxidation behaviour of oxynitride glasses. As for the glass transition temperature (T_g) the incorporation of nitrogen increases the oxidation resistance of glasses. The aluminium concentration has a direct influence on the oxidation of these glasses which is due to the influence of aluminium on viscosity which decreases as aluminium content increases[36] and this results in a higher reactivity of the glass network. A high concentration of silicon is necessary to improve the oxidation resistance of oxynitride glasses, as seen

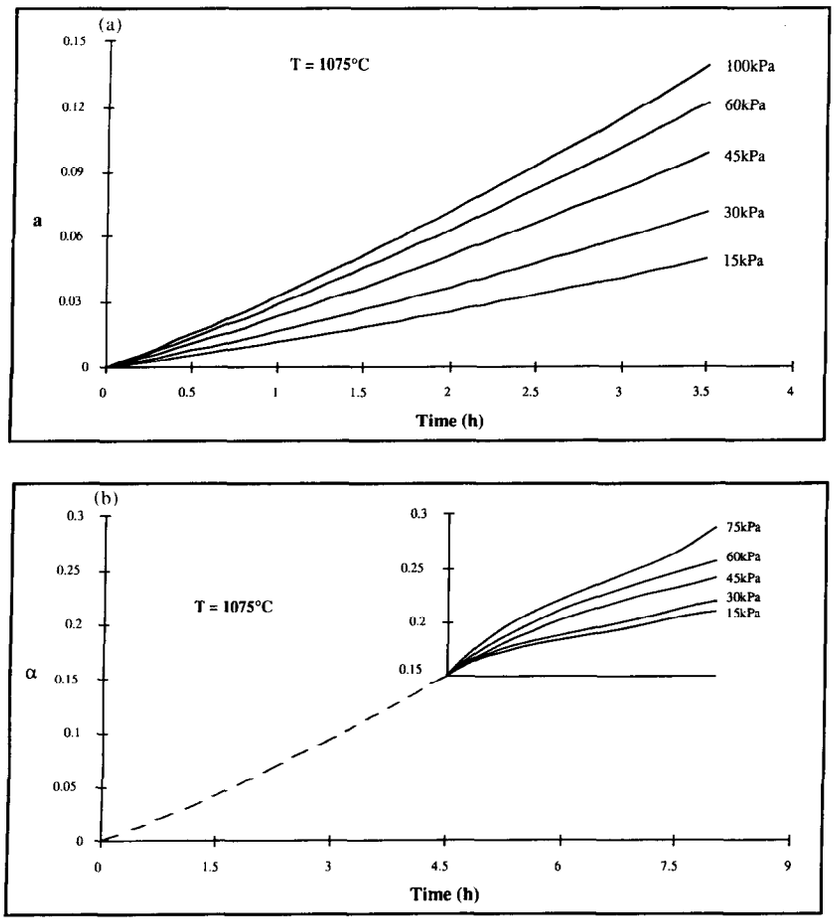


Fig. 8. Oxidation curves of YSi17G16 at different oxygen pressures: (a) $T = 1075°C$ ($\alpha_0 = 0$); (b) $T = 1075°C$ ($\alpha_0 = 0{\cdot}153$)

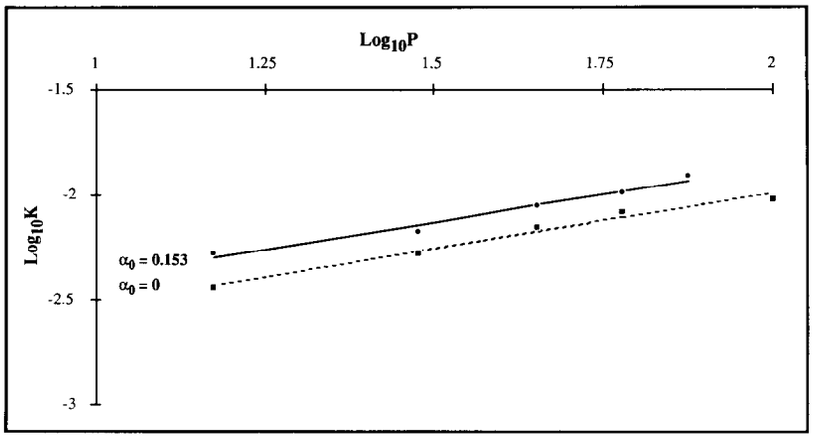


Fig. 9. $Log_{10}k$ as a function of $log_{10}P$.

also for the physical properties of yttrium alumino-silicate glasses.[37]

Temperature has a strong influence on the oxidation behaviour of the studied oxynitride glasses. At low temperatures ($T < 1075°C$), the oxidation is low and the samples preserve their cubic geometry. For higher temperatures, an extensive oxidation is produced, even during the initial stages of heat treatment, which favours the formation of a very porous and expanded product.

Study of the influence of pressure has confirmed the direct access of oxygen to the internal interface of samples.

The sigmoïdal shape of the oxidation curves of the all studied glasses suggests that oxidation is governed by a similar mechanism which is a reaction-controlled process as found for YSi17G16. The increase of temperature or time of oxidation leads to the formation of disorder in the glass structure. This disorder is followed by an increase in the average number of non-bridging oxygens per polyhedron which decreases the glass viscosity. Considering that at a fixed temperature above the glass transition temperature, the glass viscosity decreases with time, a little enhancement of the mobility of the glass constituents can be observed. The mobility of the glass constituents results in glass crystallisation under inert atmospheres and favours oxidation in the presence of oxygen. This hypothesis correlated with the formation of a non-covered oxide layer and the continuous changes in the oxidation products can be used as a basis to explain the presence of a reaction controlled process for global oxidation.

These investigations provide a guide for understanding the effects of the nature and concentrations of sintering additives in silicon nitrides on their oxidation behaviour. Yttria is preferred to neodymia and the Al_2O_3 concentration must be lower than that of Y_2O_3. The sintering of silicon nitride with a low concentration of additives allows an increase in its oxidation resistance.

5 Conclusions

The oxidation behaviour in air of oxynitride glasses is strongly dependent on the composition. The oxidation resistance increases when nitrogen content increases, when aluminium is substituted by yttrium or silicon and when yttrium replaces neodymium.

The oxynitride glasses oxidised rapidly in air at temperatures above the glass transition temperature by forming a porous oxide scale, probably due to the evolution of gaseous nitrogen during the oxidation. X-ray investigations of the oxide scale reveal the presence of different forms of yttrium silicates and mullite.

The sigmoïdal shape of the oxidation curves, the porous oxide scale which grows with the maltese cross symmetry and the linearity of the transformations as a function of time indicate the presence of a reaction process where the progress of the internal interface is the limiting step. The oxidation of oxynitride glasses is very sensitive to the oxygen partial pressure.

Acknowledgements

The authors wish to acknowledge financial support for this work under the EC BRITE-EURAM programme, contract no. BRE2-CT92-0272. We wish to thank our partners Dr D. P. Thompson, University of Newcastle upon Tyne and Prof. J. L. Besson and Dr T. Rouxel, ENSCI, Limoges for valuable discussions.

References

1. Jack, K. H., Review: sialons and related nitrogen ceramics. *J. Mater. Sci.*, **11** (1976) 1134–58.
2. Shilito, K. R., Wills, R. R. and Bennet, R. B., Silicon metal oxynitride glasses. *J. Am. Ceram. Soc.*, **61** (1978) 537.

3. Loehman, R. E., Preparation and properties of yttrium–silicon–aluminium oxynitride glasses. *J. Am. Ceram. Soc.*, **62** (1979) 491–4.
4. Loehman, R. E., Oxynitride glasses. *J. Non-Cryst. Sol.*, **42** (1980) 433–46.
5. Verdier, P., Pastuszak, R. & Laurent, Y., Préparation de verres azotés dans les systèmes M–Si–Al–O–N (M = Nd, Ca, Mn) étude comparative de quelques propriétés. *Verre et Réfract.*, **36**(3) (1982) 547–56.
6. Messier, D. R. & Broz, A., Microhardness and elastic moduli of Y–Si–Al–O–N glasses. *J. Am. Ceram. Soc.*, **65** (1982) C123.
7. Tredway, W. K. & Risbud, S. H., Melt processing and properties of barium–sialon glasses. *J. Am. Ceram. Soc.*, **66** (1983) 324–7.
8. Makhishima, A., Mitomo, M., Ii, N. & Tsutsumi, M., Microhardness and transparency of an La–Si–O–N oxynitride glasses. *Comm. Am. Ceram. Soc.*, **66** (1983) C55–6.
9. Kenmuir, S. V. J., Thorp, J. S. & Kulesza, B. L. J., The dielectric behaviour of Mg–Al–Si, Ca–Al–Si, Y–Al–Si, Nd–Al–Si, oxynitride glasses. *J. Mater. Sci.*, **18** (1983) 1725–30.
10. Loehman, R. E., Preparation and properties of oxynitride glasses. *J. Non-Cryst. Sol.*, **56** (1983) 123–34.
11. Drew, R. A. L., Hampshire, S. & Jack, K. H., The preparation and properties of oxynitride glasses. In *Progress in Nitrogen Ceramics*, ed. F. L. Riley, 1983, pp. 323–30.
12. Hampshire, S., Drew, R. A. L. & Jack, K. H., Viscosities, glass transition temperatures, and microhardness of Y–Si–Al–O–N glasses. *Comm. Am. Ceram. Soc.*, **67** (1984) C46–7.
13. Hampshire, S., Drew, R. A. L. & Jack, K. H., Oxynitride glasses. *Phys. Chem. Glass.*, **26** (1985) 182–6.
14. Rocherulle, J., Guyader, J., Verdier, P. & Laurent, Y., Li–Si–Al–O–N and Li–Si–O–N oxynitride glasses study and characterization. *J. Mater. Sci.*, **24** (1989) 4525–30.
15. Rocherulle J., Verdier P. & Laurent Y., Preparation and properties of gadolinium oxide and oxynitride glasses. *Mater. Sci. and Eng.*, **B2** (1989) 265–8.
16. Hampshire, S. Nestor, E. Flynn, R. Besson, J.-L., Rouxel, T., Lemercier, H., Goursat, P. Sebaï, M., Thompson D. P. & Lidell, K., Yttrium oxynitride glasses: Properties and potential for crystallisation to glass-ceramics. *J. Europ. Ceram. Soc.*, **14** (1994) 261–73.
17. Ohashi, M. & Hampshire, S., Formation of Ce Si O N glasses. *J. Am. Ceram. Soc.*, **74** (1991) 2018–20.
18. Unuma, H., Kawamura, K., Sawaguchi, N., Maekawa H. & Yokokawa, T., Molecular dynamics study of Na–Si–O–N oxynitride glasses. *J. Am. Ceram. Soc.*, **76** (1993) 1308–12.
19. Wusirika, R. R. & Chyung, C. K., Oxynitride glasses and glass-ceramics. *J. Non-Cryst. Sol.*, **38 & 39** (1980) 39–44.
20. Ball, R. K., Lewis, M. H., Szweda, A. & Butler, E., Ceramics and glasses in the Sc–Si–Al–O–N system. *Mater. Sci. and Eng.*, **71** (1985) 137–45.
21. Homeny, J. & McGarry, D., Preparation and mechanical properties of Mg–Al–Si–O–N glasses. *J. Am. Ceram. Soc.*, **67** (1984) C225–7.
22. Rouxel, T., Besson, J.-L., Gault, C., Goursat, P., Leigh, M. & Hampshire, S., Viscosity and Young's modulus of an oxynitride glass. *J. Mater. Sci. Lett.*, **8** (1989) 1158.
23. Thomas, G. & Ahn, C., Characterization and crystallization of Y–Si–Al–O–N glass. *Comm. Am. Ceram. Soc.*, **68** (1982) C294–7.
24. Leng-Ward, G. & Lewis, M. H., Crystallization in glasses. *Mat. Sci. and Eng.*, **71** (1985) 101–11.
25. Dinger, T. R., Rai, R. S. & Thomas, G., Crystallization behaviour of a glass in the Y_2O_3–SiO_2–AlN system. *J. Am. Ceram. Soc.*, **71** (1988) 236–44.
26. O'Mara, C., Dunlop, G. L. & Pompe, R., Formation, crystallisation and oxidation of selected glasses in the Y–Si–Al–O–N system. *J. Euro. Ceram. Soc.*, **8** (1992) 161–70.
27. Desmaison-Brut, M., Desmaison, J. G. & Verdier, P., Oxidation behaviour of an oxynitride glass in the system Ca–Si–Al–O–N. *Sol. Sta. Ionics*, **105** (1988) 323–9.
28. Desmaison-Brut, M., Desmaison, J. G. & Verdier, P., The reactivity in oxygen of two M–Si–Al–O–N oxynitride glasses. *Sol. Sta. Ionics*, **32/33** (1989) 843–51.
29. Wusirika, R. R., Oxidation behavior of oxynitride glasses. *Comm. Amer. Ceram. Soc.*, **68** (1985) C294–7.
30. Persson, J., Ekström, T., Käll, P. O. & Nygren, M., Oxidation behaviour and mechanical properties of β- and mixed α–β sialons sintered with additions of Y_2O_3 and Nd_2O_3. *J. Euro. Ceram. Soc.*, **11** (1993) 363–73.
31. Shelby, J. E. & Kohli, J. T., Rare-earth aluminosilicate glasses. *J. Am. Ceram. Soc.*, **73** (1990) 39–42.
32. Kohli, J. T., Condrate, R. A. & Shelby, J. E., Raman and infrared spectra of rare earth aluminosilicate glasses. *Phys. Chem. Glass*, **34**(3) (1993) 81–7.
33. Kohli, J. T., Shelby, J. E. & Frye, J. S., A structural investigation of yttrium aluminosilicate glasses using ^{29}Si and ^{27}Al magic angle spinning nuclear magnetic resonance. *Phys. Chem. Glass.*, **33** (1992) 73–8.
34. Morikawa, H., Miwa, S., Miyake, M., Marumo, F. & Sata, T., Structural analysis of SiO_2–Al_2O_3 glasses. *J. Am. Ceram. Soc.*, **65** (1982) 79–81.
35. Gogotsi, Yu. G., Grathwohl, G., Thümmler, F., Yaroshenko, V. P., Hermann, M & Taut, C., Oxidation of yttria- and alumina-containing dense silicon nitride ceramics, *J. Am. Ceram. Soc.*, **11** (1993) 375–86.
36. Hamphire, S., Thompson, D. P., Besson, J. L. & Goursat, P., Optimisation of nucleation and crystallisation in oxynitride glasses to develop novel glass-ceramics for advanced thermomechanical and optical applications. 2nd 12-monthly report to European commission, contract No. BRE2-C792-0272, 1994.
37. Shelby, J. E., Minton, S. M., Lord, C. E. & Tuzzolo, M. R., Formation and properties of yttrium aluminosilicate glasses, *Phys. Chem. Glass.* **33** (1992) 93–8.

Journal of the European Ceramic Society 15 (1995) 1025–1029
© 1995 Elsevier Science Limited
Printed in Great Britain. All rights reserved
0955-2219(95)00068-2
0955-2219/95/$9.50

Thermal Properties and Devitrification Behaviour of $(2-x)CaO \cdot x/3Y_2O_3 \cdot 2SiO_2$ Glasses

A. Costantini, F. Branda & A. Buri

Dipartimento di Ingegneria dei Materiali e della Produzione, Università de Napoli 'Federico II', 80125 Napoli, Italy

(Received 23 July 1993; revised version received 7 March 1995; accepted 20 March 1995)

Abstract

The thermal properties (glass transformation, T_g, softening, T_s, and exo-peak, T_p, temperatures), and the devitrification behaviour of glasses in the system $CaO–Y_2O_3–SiO_2$ are reported. The T_g, T_p and E_c results can be explained on the basis of the increased structural rigidity when Ca^{+2} ions are substituted by Y^{+3} ions, with the formation of stronger bonds to the oxygen.

For the molar ratio of Ca/Si = 0·7 or more, wollastonite is no longer formed; at the same time a new and as yet unidentified phase appears. Surface nucleation occurs preferentially, but, in finely powdered samples, which soften and sinter before devitrifying, surface nuclei behave virtually as bulk nuclei.

Introduction

In this paper the thermal properties and the study of the devitrification behaviour of glasses of the system $CaO–Y_2O_3–SiO_2$ are reported. In particular the effect of the substitution of Y_2O_3 to CaO in a glass of composition $CaO–SiO_2$ (wollastonite) has been studied.

The devitrification process has been studied by differential thermal analysis (DTA).

CaO and SiO_2 in a molar ratio $CaO/SiO_2 \simeq 1$ are the basic components of bioactive glasses and glass-ceramics.[1,2] Otherwise it is known that the addition of yttrium oxide to silicates allows us to obtain glasses with high elastic moduli and hardness.[3] The addition of Y_2O_3 has proved to be useful in also obtaining glass-ceramics which have interesting properties. Machinable glass ceramics have been obtained in the system $CaO–Al_2O_3–Y_2O_3–SiO_2$.[4] Refractory glasses have been obtained in the system $Y_2O_3–Al_2O_3–SiO_2$.[5]

The non-isothermal devitrification of glasses in this system is interesting because, in the temperature range of efficient devitrification, powder sintering occurs. As will be shown, this has consequences on the devitrification mechanism.

Experimental

Glasses of composition expressed by the following formula

$$(2-x)CaO.(x/3)Y_2O_3.2SiO_2 \text{ where } 0 \leq x \leq 1{\cdot}0$$

were prepared by melting analytical grade reagents, Y_2O_3, $CaCO_3$ and SiO_2 in a platinum crucible in an electric furnace for 4 h, in the temperature range 1400–1600°C. The melts were quenched by plunging the bottom of the crucible into cold water.

Differential thermal analysis (DTA) was carried out by means of a Netzsch Differential Scanning Calorimeter (DSC) model 404M on about 50 mg powdered samples at various heating rates (2–20°C/min). Fine (63–90 μm) and coarse (500–315 μm) powdered samples were used. Powdered Al_2O_3 was used as reference material.

Devitrified samples were analyzed by computer-interfaced X-ray (CuKα) powder diffractometry (XRD) using a Philips Diffractometer model PW1710, with a scan speed of 1°min^{-1} and a built-in computer search program. The crystalline phases were identified by means of JCPDS cards.

Results

The DTA curves of the studied glasses, together with the derivative curve (DDTA) for one of them, are reported in Figs 1 and 2 as recorded at 10°C/min heating rate; the data are for fine, (63–90 μm), (Fig. 1) and coarse, (315–500 μm), (Fig. 2) powdered samples. When a glass is heated in a DTA apparatus a slope change appears on the recorded curve when passing through the glass transformation temperature range. The glass transformation temperature, T_g, has been taken from the derivative curve as indicated in Fig. 1.

As can be seen in many cases, the first slope change in the glass transformation range is followed by a second one at a temperature lower than the onset of the devitrification exo-peak.

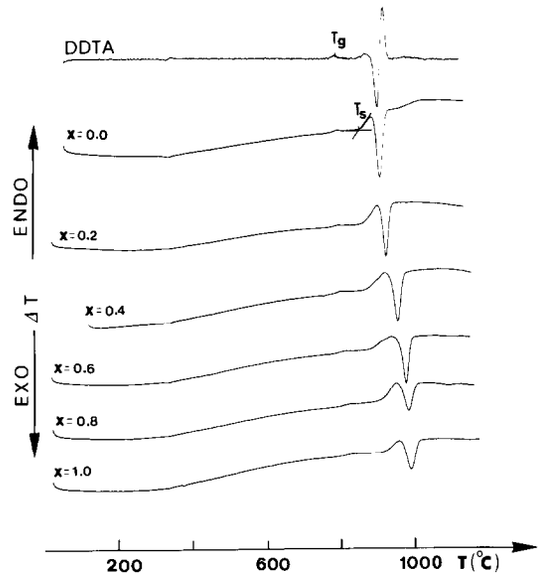


Fig. 1. DTA and DDTA curves recorded at 10°C/min heating rate on fine (63–90 μm) powdered samples.

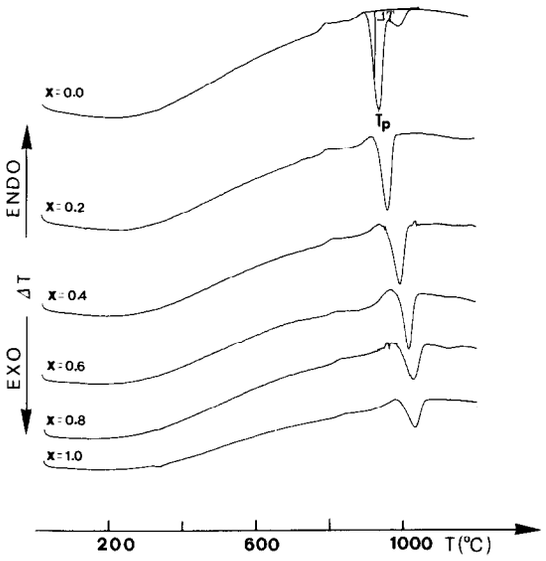


Fig. 2. DTA curves recorded at 10°C/min heating rate on coarse (315–500 μm) powdered samples.

As a matter of fact in these cases the initially powdered samples were recovered from the DTA sample holder as porous bodies. Therefore the second slope change is to be linked to the change in the thermal exchange coefficients when powders soften and sinter. The effect is much more pronounced in the case of the fine powders. The softening temperatures can be taken from the DTA curves as indicated in Fig. 1.

In Figs 3, 4 and 5 the glass transformation, T_g, softening, T_s, and DTA exo-peak, T_p, temperatures are reported as a function of composition. In Table 1 the values of the onset and peak temperatures of the devitrification exo-peaks are reported. As can be seen, all of them increase as the Y_2O_3 content is increased.

In Fig. 6 the X-ray diffraction patterns are

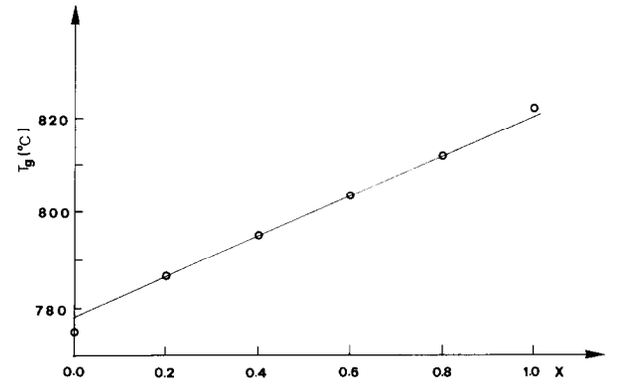


Fig. 3. Plot of the glass transformation temperature T_g versus composition.

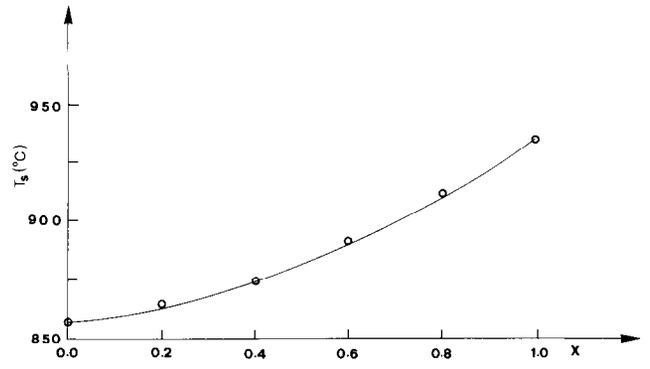


Fig. 4. Plot of the softening temperature T_s versus composition.

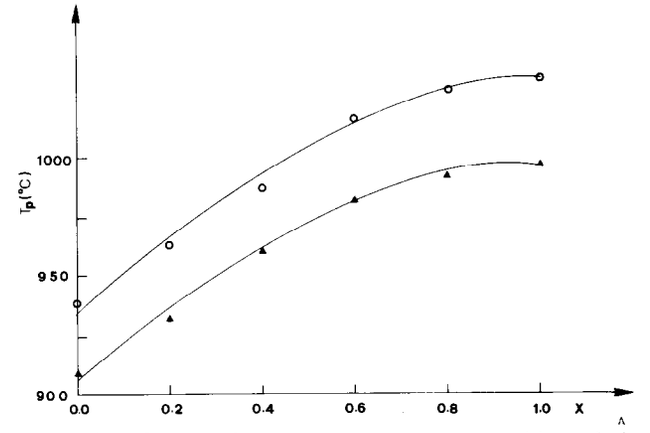


Fig. 5. Plot of exo-peak temperature versus composition relative to fine powdered (▲) and coarse powdered (○) samples.

Table 1. Onset and peak temperature of devitrification exo-peaks relative to fine (T_{of}, T_{pf}) and coarse (T_{oc}, T_{pc}) powders

Composition	T_{of}(°C)	T_{pf}(°C)	T_{oc}(°C)	T_{pc}(°C)
$x = 0$	880	910	895	940
$x = 0{\cdot}2$	903	929	918	962
$x = 0{\cdot}4$	926	962	938	993
$x = 0{\cdot}6$	945	984	970	1018
$x = 0{\cdot}8$	961	991	985	1028
$x = 1{\cdot}0$	970	997	990	1034

reported relative to the pattern of a sample submitted to a DTA run which was stopped just after the exo-peak. As can be seen in the (a)–(d) patterns, the lines of wollastonite (JCPDS card

29/372) appear, but their intensity progressively reduces as the Y_2O_3 is substituted for CaO. In the (b) and (c) patterns the lines of pseudo-wollastonite, CaO.SiO_2, (JCPDS card 19/248) are also present. In the (c) pattern another, unidentified, phase appears, whose lines progressively substitute those of wollastonite phase.

In Table 2 the *d*-spacings' values and relative intensity of the lines of the unknown phase are reported.

The non-isothermal devitrification was also studied. The kinetic parameters were determined by using the following two equations:

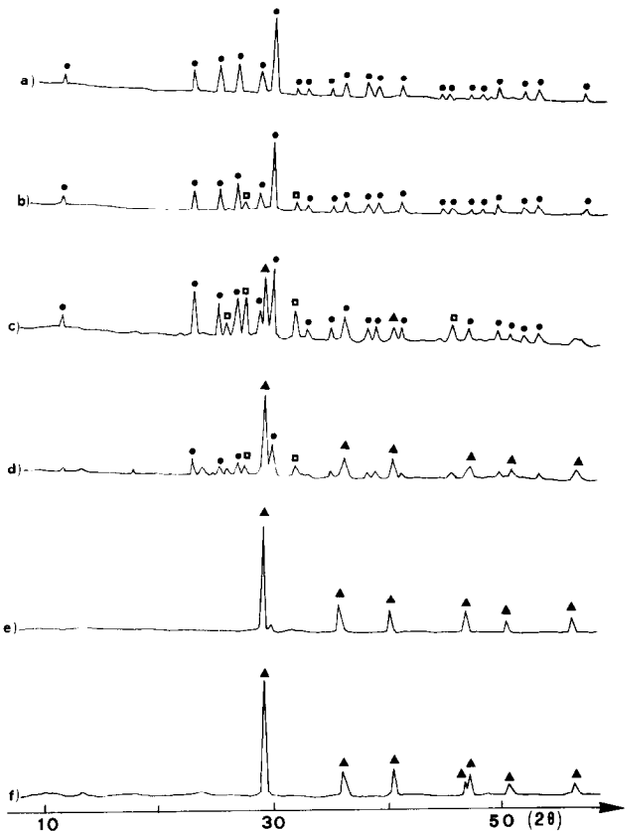


Fig. 6. X-ray diffraction patterns of samples devitrified during a DTA run: (a) $x = 0$; (b) $x = 0{\cdot}2$; (c) $x = 0{\cdot}4$; (d) $x = 0{\cdot}6$; (e) $x = 0{\cdot}8$; (f) $x = 1{\cdot}0$. (●) wollastonite (JCPDS card 29/372); (□) pseudowollastonite (JCPDS card 19/248); (▲) unknown phase.

Table 2. *d*-spacings and relative intensity of the lines of diffraction pattern of Fig. 6(f) that have not been attributed (S = strong; W = weak)

Unknown phase Distance plane (A)	*Relative intensity*
3·045	S
2·494	W
2·487	W
2·222	W
1·931	WW
1·920	W
1·631	WW
1·626	WW

$$\ln\beta = -E_c/RT_p + \text{const} \quad (1)$$

$$\ln \Delta T = -mE_c/RT + \text{const} \quad (2)$$

Eqns 1 and 2 can be derived from the well known following eqn:[6,7]

$$-\ln(1 - \alpha) = (AN/\beta^m)\exp(-mE_c/RT) \quad (3)$$

where α is the crystallization degree, N is the nuclei number and A is a constant, β is the heating rate, ΔT and T_p the deflection from the base line and the peak temperature taken as indicated in Fig. 2 and T is the temperature. As in inorganic glasses, the devitrification exo-peak occurs in a temperature range higher than that of efficient nucleation,[6] E_c is the crystal growth activation energy. The parameter m depends upon the mechanism and morphology of crystal growth; it ranges from $m = 1$ for 1-dimensional growth (or growth from surface nuclei) to $m = 3$ for 3-dimensional growth.[6,7]

Eqns 1 and 2 can be derived from it by supposing: (1) α at peak temperature is not dependent on the heating rate;[8] (2) ΔT is proportional to the instantaneous reaction rate:[9,10] and (3) in the initial part of the DTA crystallization peak, the change in the temperature has a much lower effect than α on the T.[11]

In Fig. 7 the plots of $\ln\beta$ versus $1/T_p$ are reported for the fine powdered samples. In Figs 8 and 9 the plots of $\ln\Delta T$ versus $1/T$ are reported for fine and coarse powdered samples taken from DTA curves recorded at 10°C/min. According to eqns 1 and 2, straight lines were obtained. Their slopes allow, therefore, to evaluate the E_c and mE_c

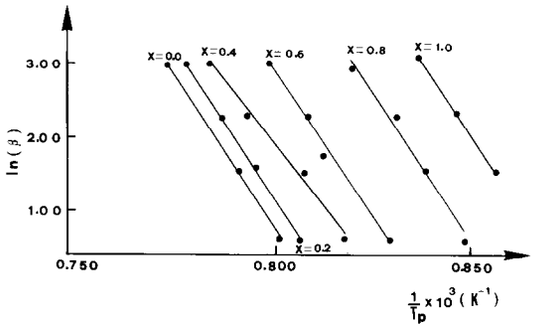


Fig. 7. Plot of $\ln\beta$ versus $1/T_p$.

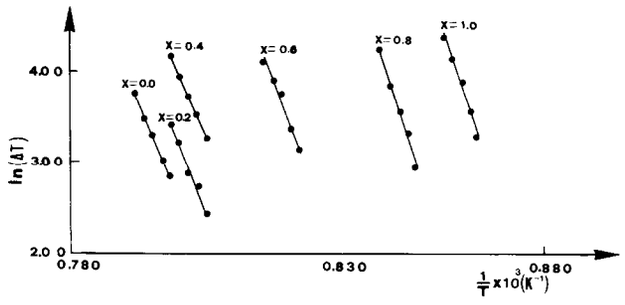


Fig. 8. Plot of $\ln\Delta T$ versus $1/T$ relative to fine powered samples (63–90 μm).

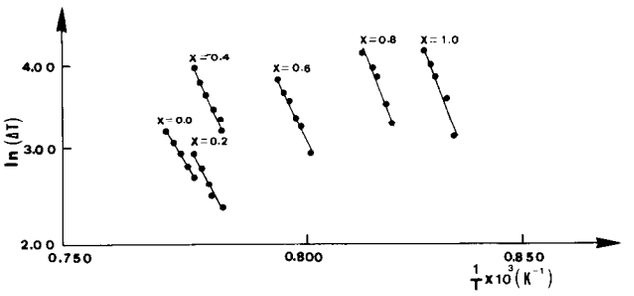


Fig. 9. Plot of ln ΔT versus $1/T$ relative to coarse powdered samples (315–500 μm).

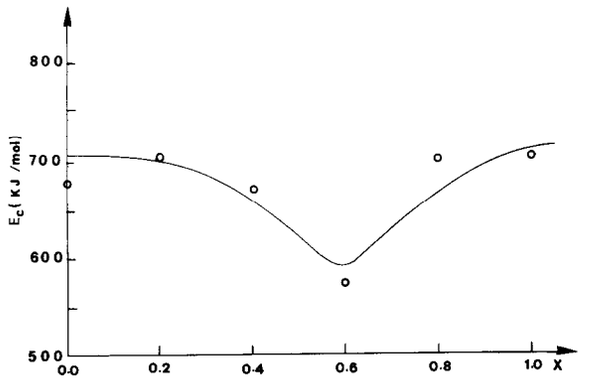


Fig. 10. Plot of the activation energy for crystalline growth E_c versus composition.

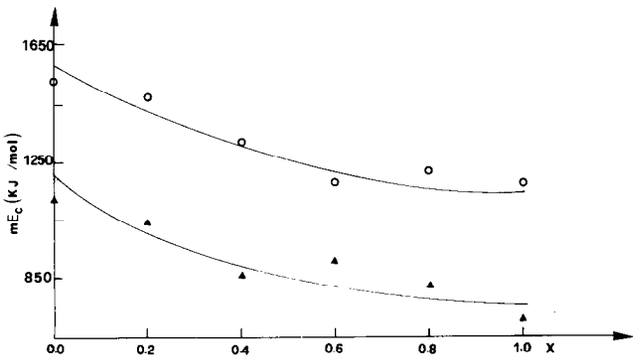


Fig. 11. Plot of the mE_c values versus composition relative to fine powdered samples (63–90 μm). (○) and coarse powdered samples (315–500 μm) (▲).

values reported in Figs 10 and 11. The curve of E_c versus composition shows a minimum. As can be seen in Fig. 11, for each glass, the mE_c values appear to increase as the specific surface of the samples is increased. When comparing the values of E_c with the mE_c relative to fine powdered samples, values of $m \approx 2$ are obtained for all glasses of the studied system. In the case of coarse powdered samples values $1 \leq m \leq 2$ are always obtained.

Discussion

The increase of T_g as the Y_2O_3 is substituted to CaO can be explained by taking into account that, according to Ray,[12] the glass transformation temperature depends on the density of covalent cross-linking and the number and strength of the cross-links between the cation and oxygen atoms. It's worth remembering that CaO and Y_2O_3 are reported to be modifier oxides;[13] therefore, in the studied series, the density of covalent cross-linking doesn't change because the molar ratio O/Si is constant. When this happens, it was found that the changes of T_g when a modifier oxide is substituted for another one can be related to their coordination number and strength of bonds to oxygen atoms, linked to the field strength Z/r^2, where Z is the charge and r the radius of the cation.[13] Ca^{+2} and Y^{+3} have the same coordination number in their pure oxide structures;[13] otherwise Y^{+3} has a greater field strength (3·76 A–2 instead of 2·04 A–2) and a greater single bond strength in the pure oxide structure (210 KJ/mol instead of 130 KJ/mol.[13]) The T_g increase can therefore be ascribed to the greater strength of the cross-links between the Y^{+3} cation and oxygen atoms.

With this in mind we can also find an explanation for the increasing trend of the T_p curve.

In Fig. 10, it must be taken into account that the crystal growth activation energy, E_η, is usually equal to the viscous flow activation energy, E_η,[14] the viscosity depends upon the temperature according to the VFT equation,[15] which implies that E_η continuously decreases as the temperature increases:

$$\log\eta = A + B/(T-To)$$

where η is the viscosity, T is the temperature, A, B and To are constants whose values depend on the glass composition.

Otherwise E_η should increase as Y_2O_3 is substituted to CaO, as long as this involves the structure rigidity being increased, as discussed earlier. The trend in Fig. 10 gives an explanation for these 'temperature' and 'compositional' effects. Therefore, initially the 'temperature' effect could overwhelm the 'compositional' one, which should become dominant starting from x = 0·6. In fact, Table 1 shows that until x = 0·6, a continuous increase of T_p is observed; the maximum difference being as great as 80°C. Figure 5 shows that when x = 0·6 the slope of the T_p/x plot changes and the 'compositional' effect can became dominant.

XRD results (Fig. 6) indicate that, in the presence of Y_2O_3, starting from the molar ratio Ca/Si = 0·7 (x = 0·6), more wollastonite does not form; at the same time a new phase appears that is not reported on the JCPDS cards.

The mE_c values appear to increase as the

specific surface of the samples is increased. Usually the opposite result is obtained owing to the fact that the greater the specific surface, the greater the tendency to devitrify by growth from surface nuclei so that m is progressively reduced to the value $m = 1$. In the case of diopside glass[16] it was found that nucleation preferentially occurs at the surface of the sample, but surface nuclei formed in the glass transformation range behave as bulk nuclei in finely powdered samples that efficiently sinter before devitrifying. This hypothesis appears to be effective in explaining the devitrification behaviour of all the studied glasses. In fact in the case of coarse powdered samples that sinter badly (see Figs 1 and 2), a value $1 \leq m \leq 2$ were obtained. On the contrary, in the case of finely powdered samples that sinter well before devitrifying, higher values of the m parameter have been obtained. The value $m \approx 2$ for wollastonite agrees with the reported result that its crystals are often in the form of tablets.[17]

Conclusions

The following conclusions can be drawn from the experimental results:

(1) T_g, T_p, and E_c results suggest that the substitution of Y_2O_3 for CaO causes the structure rigidity to increase.

(2) Starting from the molar ratio Ca/Si = 0·7, more wollastonite does not form; at the same time a new phase appears that is not reported on the JCPDS cards.

(3) The homogeneous nucleation rates are very low; nevertheless surface nuclei can behave as bulk nuclei in powdered samples that sinter before devitrifying. In this case values $m \approx 2$ were found for all the studied glasses.

References

1. Hench, L. L., Bioceramics: from concept to clinic. *J. Am. Cer. Soc.*, **74**(7) (1991) 1487–510.
2. Kokubo, T., Novel bioactive materials derived from glasses. Proc. XVI International Congress on Glass, Madrid, Vol. 1, *Bol. Soc. Esp. Ceram. Vid.*, **31-C1** (1992) 119–37.
3. Makishima, A., Tamura, Y. & Sakaino, T., Elastic moduli and refractive indices of aluminosilicate glasses containing Y_2O_3, La_2O_3 and TiO_2, *J. Am. Cer. Soc.*, **61**(5–6) (1978) 247.
4. Makishima, A., Asami, M. & Ogura, Y., A machinable calcia–alumina–yttria–silica glass-ceramic, *J. Am. Cer. Soc.*, **72**(6) (1989) 1024.
5. Arita, I., Wilkinson, D. & Purdy, G., Crystallization of yttria-alumina–silica glasses, *J. Am. Cer. Soc.*, **75**(12) (1992) 3315.
6. Matusita, K. & Sakka, S., Kinetic study of non-isothermal crystallization of glass by thermal analysis, *Bull. Inst. Chem. Res. Kyoto Univ.*, **59** (1981) 159–71.
7. MacFarlane, D. R., Matecki, M. & Poulain, M., Crystallization in fluoride glasses devitrification on reheating. *J. Non-Cryst. Solids*, **64** (1984) 351–62.
8. Boswell, P. G., On the calculation of activation energies using a modified Kissinger method. *J. Thermal Anal.*, **18** (1980) 353–8.
9. Borchardt, H. J. & Daniels, F., The application of differential thermal analysis to the study of reaction kinetics. *J. Am. Chem. Soc.*, **79** (1957) 41–6.
10. Akita, K. & Kase, M., Relationship between the DTA peak and the maximum reaction rate. *J. Phys. Chem.*, **72** (1968) 906–13.
11. Piloyan, F. O., Ryabchica, I. V. & Novikova, O. S., Determination of activation energies of chemical reactions by differential thermal analysis. *Nature*, **212** (1966) 1229.
12. Ray, N. H., Composition-property relationships in inorganic oxide glasses. *J. Non-Cryst. Solids*, **15** (1974) 423–34.
13. Rawson, H., Inorganic glass forming systems. Academic Press, London & New York, 1967 pp. 24–5.
14. Matusita, K. & Sakka, S., Kinetic study on crystallization of glass by differential thermal analysis — criterion on application of Kissinger plot. *J. Non-Cryst. Solids*, **38–39** (1980) 741–6.
15. Scholze, H. (ed.). *Le Verre*, Institut du Verre, Paris, 1980, p. 69.
16. Branda, F., Costantini, A. & Buri, A., Non-isothermal devitrification behaviour of diopside glass. *Thermochim. Acta*, **217** (1993) 207–12.
17. Winchell, A. N. & Winchell, H., The microscopical characters of artificial inorganic substances: optical properties of artificial minerals, Academic Press New York and London, 1964, p. 291.

Journal of the European Ceramic Society **15** (1995) 1031–1035
© 1995 Elsevier Science Limited
Printed in Great Britain. All rights reserved
0955-2219(95)00072-0
0955-2219/95/$9.50

Constitution of Porcelain Before and After Heat-Treatment. I: Mineralogical Composition

S. P. Chaudhuri & P. Sarkar

Special Ceramics Section, Central Glass & Ceramic Research Institute, Calcutta — 700 032, India

(Received 2 February 1994; revised version received 8 July 1994; accepted 31 March 1995)

Abstract

Porcelain compositions were prepared with and without the addition of mineralizers/nucleating agents and their phase assemblages were studied before and after subjecting them to heat-treatment. Mullite, quartz and glass were detected in the compositions before heat-treatment, but cristobalite appeared as an additional phase after heat-treatment. Heat-treated compositions were comparatively rich in mullite following crystallization from the glassy phase. Nb_2O_5 was the most efficient nucleating agent among those tried.

1 Introduction

Porcelain is the vitrified product of mixtures of clay, quartz and feldspar, and chemical porcelain[1] is one such product having 60–65 wt% clay. Mullite and glass constitute the major phases[2] of porcelain which also contains some quartz,[3] cristobalite, tridymite and corundum are rarely found in it.

Although mullite is endowed with excellent mechanical, creep, thermal and chemical properties,[4] the electrical properties are not well studied. It has been shown in earlier work[5] that the electrical resistivity of porcelain decreases with increase in mullite content. The electrical resistivity of mullite depends on the $Al_2O_3 : SiO_2$ molar ratio. While mullite of composition $2Al_2O_3.SiO_2$ (2 : 1 mullite) is an electrical insulator[6] comparable to siliceous phases,[7] the $3Al_2O_3.2Sio_2$ composition, i.e. 3 : 2 mullite has poor electrical resistivity especially above 1000°C.[6] The 2 : 1 mullite has a band gap energy 7·7ev,[6] but 3 : 2 mullite has a band gap energy 1·43 ev.[8,9] Mullite crystals in porcelain have $3Al_2O_3.2SiO_2$ composition as these are derived from the solid state decomposition of the clay component and are formed by nucleation and crystallization from the feldspathic glass.

It consequently seems possible to make porcelain more conducting by increasing its mullite content. This can be accomplished by promoting reaction between the residual quartz and glass in the presence of mineralizers, e.g. Fe_2O_3 or TiO_2 by a two step reaction,[10,11] *viz.* replacement of Al^{3+} ion from glass by the cation of the mineralizer and subsequent diffusion of Al^{3+} ion into the residual silica.

The glassy phase in the porcelain body lies mainly in the Al_2O_3–SiO_2 system and is prone to crystallization[12] to mullite. This needs incorporation of suitable oxides, such as Fe_2O_3, TiO_2 or Cr_2O_3 into the glass and subsequent heat-treatment of the nucleated glass.

The glass in porcelain contains alkalis (K_2O + Na_2O) and when it is exposed to elevated temperatures, crystallization of cristobalite and tridymite phases[13] is also possible. These phases have high electrical resistivity and thereby counter balance the effect of mullite.

In the literature concerning semi-conductor and dielectric porcelain,[14] ceramic heating elements,[15,16] and glass-ceramic heating elements,[17] no mention is made of the constitution of these heating elements and its effect on electrical properties. It has, however, been observed[18] that a mullite porcelain body can be employed as a temperature indicator-cum-controller.

In the present work, chemical porcelain samples, with and without the addition of mineralizers/nucleants have been prepared and their constitution has been studied before and after subjecting them to heat-treatment. The mineralogical compositions (phase assemblages) of the porcelain samples are reported in this paper.

2 Experimental

2.1 Raw materials

The chemical analyses of the china clay, glass sand and potash feldspar are shown in Table 1. The porcelain samples were prepared from a mixture of clay (63 wt%), quartz (12 wt%) and feldspar (25 wt%).

Table 1. Chemical analyses of raw materials

Raw Material	Concentration (wt.%) of constituent oxides								
	SiO_2	Al_2O_3	Fe_2O_3	TiO_2	CaO	MgO	K_2O	Na_2O	LOI
Clay	45·2	39·1	0·65	0·22	Trace	Trace	0·38	0·03	14·82
Quartz	99·9	—	—	—	—	—	—	—	—
Feldspar	64·43	18·05	0·30	Trace	0·89	Trace	13·55	2·22	0·30

2.2 Mineralizers/nucleating agents

The transition metal oxides, Fe_2O_3, TiO_2, Cr_2O_3, V_2O_5 and Nb_2O_5 were incorporated into the basic composition individually to the extent of 2–8 wt% and also in combinations of (V_2O_5 + TiO_2) and (V_2O_5 + Fe_2O_3). The concentrations of the oxides are given in Table 2.

2.3 Sample preparation

A good casting slip was obtained by milling a mixture of clay, quartz and feldspar. Discs of 25 mm diameter × 6 mm height were cast, dried and fired in an electric furnace at 1400°C for 1 h followed by overnight cooling.

The mineralised compositions are obtained by incorporating the oxides into the base composition during milling.

2.4 Heat-treatment

The glassy phases in the porcelain samples resembled very closely feldspathic glass and a strong exothermic peak11 characteristic of crystallization of mullite occurred in their DTA traces. This peak temperature (1150°C) was accepted as heat-treatment temperature for the 50 h duration for glass crystallization. This was carried out in an electric furnace with 10°C/min heating rate to 1150°C, held for 50 h and cooled overnight.

2.5 Identification and estimation of phases

The crystalline phases were identified and estimated by X-ray diffractometry. The quantity of glass was calculated by difference.

Table 2. Concentration (wt.%) of mineralizers/nucleating agents

Sample no.	Mineralizers/nucleating agents	Concentration (wt.%) of nucleating agents/ mineralizers
1	—	—
2	TiO_2	8
3	V_2O_5	3
4	Fe_2O_3	2·6
5	TiO_2	2·6
6	(V_2O_5 + Fe_2O_3)	V_2O_5–1·5 + Fe_2O_3–1·3
7	(V_2O_5 + TiO_2)	V_2O_5–1·5 + TiO_2–1·3
8	Cr_2O_3	2·5
9	Nb_2O_5	2

2.5.1 Crystalline phase

The identification was done in the usual manner from the peaks by running the diffractometer from 15–65° (2θ) at 2° (2θ)/min.

The quantitative analysis was done by the internal standard technique, NaF being the internal standard. Three calibration curves were drawn by scanning the zones (2θ): 37–43° for mullite, 48–58° for quartz and 20·5–23·5° and 37·5–40·5° for cristobalite and by plotting the peak-height ratios against phase concentrations. The experimental samples were similarly scanned and concentrations of phases were computed from the calibration curves.

2.5.2 Glassy phase

The SiO_2 and Al_2O_3 in porcelain occur in mullite, quartz, cristobalite and in the glass formed in combination with the other oxides. Knowing the quantities of crystalline phases, the quantity and composition of the glass can be estimated.

The feldspathic matrix glass comprised SiO_2, Al_2O_3 and K_2O to the extent of (90 ± 5) wt% in the samples before heat-treatment and (85 ± 5) wt% in the samples after heat-treatment.

3 Results

The concentrations of the crystalline and glassy phases in the samples before and after heat-treatment are compiled in Tables 3 and 4, respectively. Mullite and quartz were detected in all the samples whether heat-treated or not. Cristobalite was virtually absent in the samples before heat-treatment except the one containing Nb_2O_5. However, cristobalite appeared in all the samples after heat-treatment in sufficient quantity and mullite content also increased significantly.

The calculated chemical compositions of the glassy phases in the samples before and after heat-treatment are tabulated in Tables 5 and 6, respectively. These compositions can be represented in terms of their major constituents on the SiO_2–Al_2O_3–K_2O ternary diagram.

It was observed that the compositions of glasses of almost all the samples before heat-treatment lie

Table 3. Mineralogical compositions of porcelain samples before heat-treatment

Sample no.	*Description*	*Concentration (wt.%) of phases*			
		Crystalline phases			
		Mullite	*Quartz*	*Cristobalite*	*Glassy Phase*
1B	B.C.	32·7	4·5	0·2	62·6
2B	B.C. + 8% TiO_2	28·5	6·5	0	65·0
3B	B.C. + 3% V_2O_5	39·7	7·5	0·3	52·5
4B	B.C. + 2·6% Fe_2O_3	33·5	10·7	0	55·7
5B	B.C. + 2·6% TiO_2	33·5	3·0	0	63·5
6B	B.C. + (1·5% V_2O_5 + 1·3% Fe_2O_3)	36·0	8·3	0·4	55·4
7B	B.C. + (1·5% V_2O_5 + 1·3% TiO_2)	32·7	6·3	0·3	60·7
8B	B.C. + 2·5% Cr_2O_3	29·7	5·5	0·4	64·3
9B	B.C. + 2% Nb_2O_5	43·0	9·7	24·8	22·4

B.C. = Base Composition.

Table 4. Mineralogical compositions of porcelain samples after heat-treatment

Sample no.	*Description*	*Concentration (wt.%) of phases*			
		Crystalline phases			
		Mullite	*Quartz*	*Cristobalite*	*Glassy Phase*
1A	B.C.	41·5	5·4	22·8	30·4
2A	B.C. + 8% TiO_2	35·5	3·7	27·8	33·0
3A	B.C. + 3% V_2O_5	43·0	5·7	28·6	22·6
4A	B.C. + 2·6% Fe_2O_3	41·5	6·2	25·2	27·2
5A	B.C. + 2·6% TiO_2	40·7	5·3	31·0	23·0
6A	B.C. + (1·5% V_2O_5 + 1·3% Fe_2O_3)	43·0	5·6	25·6	25·8
7A	B.C. + (1·5% V_2O_5 + 1·3% TiO_2)	43·0	5·7	27·0	24·3
8A	B.C. + 2·5% Cr_2O_3	43·0	5·0	24·4	27·6
9A	B.C. + 2% Nb_2O_5	42·3	5·0	29·0	23·7

in the ternary system within the mullite phase field but those of almost all the samples after heat-treatment are distributed within the tridymite phase and K–feldspar phase fields only.

4 Discussion

Mullite is the primary crystalline phase in the porcelain samples. The amount of clay that is present in the batch composition can provide 39·9 wt% (maximum) mullite and the maximum concentration of mullite to be available from the entire batch is 46·2 wt%. It is observed from Table 3 that the mullite content of all the samples before heat-treatment with the exception of the one with Nb_2O_5 was less than 39·9 wt%. This suggests that clay had been the only source of mullite in these samples. A small amount of mullite, about 3·1 wt%, in the Nb_2O_5 containing sample in excess of the theoretical clay-derived value originated from the glassy phase. This might be due to the highly charged Nb^{5+} cation of Nb_2O_5 which is also a more efficient nucleating agent than the other oxides used. Nb_2O_5 showed remarkable efficiency by effecting crystallization of mullite in considerable amount from the glassy phase within an hour of initial firing of the sample at 1400°C. The mullite content (43 wt%) of this sample almost reached the theoretical value. The V^{5+} ion of V_2O_5 was almost equally efficient.

The other nucleating agents also enhanced mullite formation. Higher concentration of TiO_2, however, reduced mullite content of the base compositions as also found with Cr_2O_3. TiO_2 being a fluxing agent and growth inhibitor retarded mullite formation at higher concentration but at lower concentration improved mullitization by producing a little amount of liquid phase that assisted decomposition of clay to mullite. Due to its refractory nature Cr_2O_3 failed to provide a liquid phase and thereby the mullite content of the Cr_2O_3-containing sample dropped. Small amounts of Fe_2O_3 and combinations of (Fe_2O_3 + V_2O_5) or (TiO_2 + V_2O_5) also favoured more mullite formation in these samples by generating liquid phase.

Table 5. Compositions of glassy phases in porcelain samples before heat-treatment

Sample no.	*Description*	*Concentrations (wt.%) of constituent oxides*										
		SiO_2	Al_2O_3	Fe_2O_3	TiO_2	CaO	MgO	K_2O	Na_2O	V_2O_5	Cr_2O_3	Nb_2O_5
1B	B.C.	77.28	13.82	0.86	0.25	0.39	Trace	6.36	1.02	—	—	—
2B	B.C. + 8% TiO_2	64.70	15.85	0.72	12.13	0.33	Trace	5.40	0.86	—	—	—
3B	B.C. + 3% V_2O_5	77.60	6.54	0.94	0.28	0.44	Trace	7.13	1.13	5.90	—	—
4B	B.C. + 2·6% Fe_2O_3	71.76	13.84	5.83	0.27	0.41	Trace	6.79	1.08	—	—	—
5B	B.C. + 2·6% TiO_2	75.03	12.23	0.81	4.60	0.37	Trace	6.00	0.95	—	—	—
6B	B.C. + (1·5% V_2O_5 + 1·3% Fe_2O_3)	74.40	10.83	3.35	0.27	0.42	Trace	6.82	1.08	2.82	—	—
7B	B.C. + (1·5% V_2O_5 + 1·3% TiO_2)	72.92	13.56	0.84	2.48	0.38	Trace	6.24	0.99	2.59	—	—
8B	B.C. + 2·5% Cr_2O_3	71.52	16.10	0.80	0.24	0.36	Trace	5.94	0.94	—	4.09	—
9B	B.C. + 2% Nb_2O_5	63.43	5.33	2.15	0.64	0.98	Trace	16.05	2.55	—	—	8.85

Table 6. Compositions of glassy phases in porcelain samples after heat-treatment

Sample no.	*Description*	*Concentrations (wt.%) of constituent oxides*										
		SiO_2	Al_2O_3	Fe_2O_3	TiO_2	CaO	MgO	K_2O	Na_2O	V_2O_5	Cr_2O_3	Nb_2O_5
1A	B.C.	73·91	7·86	1·75	0·52	0·80	Trace	13·07	2·08	—	—	—
2A	B.C. + 8% TiO_2	49·76	15·97	1·28	21·37	0·58	Trace	9·52	1·51	—	—	—
3A	B.C. + 3% V_2O_5	61·05	5·06	2·05	0·61	0·93	Trace	15·25	2·42	12·61	—	—
4A	B.C. + 2·6 Fe_2O_3	64·10	7·94	11·33	0·53	0·81	Trace	13·20	2·10	—	—	—
5A	B.C. + 2·6% TiO_2	56·24	11·28	2·06	11·74	0·94	Trace	15·31	2·43	—	—	—
6A	B.C. + (1·5% V_2O_5 + 1·3% Fe_2O_3)	65·72	4·56	6·74	0·55	0·84	Trace	13·72	2·18	5·69	—	—
7A	B.C. + (1·5% V_2O_5 + 1·3% TiO_2)	63·79	4·81	1·95	5·75	0·89	Trace	14·49	2·30	6·00	—	—
8A	B.C. + 2·5% Cr_2O_3	68·44	4·34	1·75	0·52	0·80	Trace	13·06	2·08	—	9·00	—
9A	B.C. + 2% Nb_2O_5	63·19	7·12	2·05	0·61	0·93	Trace	15·25	2·43	—	—	8·42

The glassy phase of the samples before heat-treatment contained 10–30 wt% Al_2O_3 (Table 5) and aluminosilicate glass of similar Al_2O_3 content could be suitably nucleated and crystallized[12] to mullite by heat-treatment. Moreover, the compositions of glass in the samples before heat-treatment exist within the mullite phase field. These criteria strongly favoured the separation of mullite from the glassy phase in these samples and this fact was supported by the results presented in Table 3 and Table 4. The mullite content of each sample in Table 4 exceeded the amount which was available from its clay component only.

The glass compositions of the samples after heat-treatment became more siliceous (Table 6) and entered the tridymite and K–feldspar zones. Good amount of cristobalite also appeared here. By virtue of their low Al_2O_3 and high K_2O content, these glassy phases almost reached mineralogically stable state but longer heat-treatment might cause microstructural changes in the samples.

5 Conclusions

(1) The glassy phase in porcelain is prone to nucleation and crystallization by incorporation of metal oxides and heat-treatment.

(2) Mullite content of porcelain can be increased by 6–7 wt%: over that is theoretically available from the clay component only.

(3) Cristobalite precipitates out along with mullite by heat-treatment.

Acknowledgements

The authors wish to thank Dr B. K. Sarkar, Director of the Institute, for his permission to publish the paper. One of the authors (P.S.) is grateful to CSIR, India for providing him with a research fellowship to carry out this study.

References

1. Norton, F. H., *Fine Ceramics*, McGraw Hill, New York, 1970, p. 178
2. Singer, F. & Singer, S., *Industrial Ceramics*, Chapman & Hall, London, 1970.
3. Schüller, K. H., Reactions between mullite and glassy phase in porcelains. *Trans. Brit. Ceram. Soc.*, **63** (1964) 103–17.
4. Davis, R. F. & Pask, J. A., Mullite. In *High Temperature Oxides*, Vol. 5, Part IV, ed. A. M. Alper. Academic Press, New York, 1971, pp. 37 76.
5. Chaudhuri, S. P., Sengupta, K. & Mitra Nita, Ceramic properties of hard porcelain in relation to mineralogical

composition and microstructure, V: Electrical resistivity. *J. Can. Ceram. Soc.*, **61** (1992) 243–8.
6. Saalfeld, H. & Guse, W., Mullite single crystal growth and characterization. In *Mullite and Mullite Matrix Composites* (Ceramic Transactions, Vol. 6), eds S. Sómiya, R.F. Davis & J. A, Pask. American Ceramic Society, Ohio, 1990, pp. 73–101.
7. Buchanan, R. C., Properties of ceramic insulators. In *Ceramic Materials for Electronics*, ed. R. C. Buchanan, Marcel Dekker, Inc., New York, 1986, pp. 1–77.
8. Bárta, R. & Bártuska, M., Mullite studies. *Techn. Sil.*, **4** (1957) 146–85.
9. Chaudhuri, S. P., Bandyopadhyay, S. & Mitra Nita, Electrical resistivity of mullite samples prepared by sintering Al_2O_3–SiO_2 mixtures. *Interceram*, in press.
10. Chaudhuri, S. P., Influence of mineralizers on the constitution of hard porcelain. I: Mineralogical Compositions. *Amer. Ceram. Soc. Bull.* **53** (1974) 169–71.
11. Chaudhuri, S. P., Crystallization of glass of the system $K_2O(Na_2O)$–Al_2O_3–SiO_2. *Ceramics Int'l.*, **8** (1982) 27–33.
12. McDowell, J. F. & Beal, G. H., Immiscibility and crystallization in Al_2O_3–SiO_2 glasses. *J. Amer. Ceram. Soc.*, **52** (1969) 17–25.
13. Levin, E. M., Robbins, C. R. & McMurdie, H. F., *Phase Diagrams for Ceramists*. American Ceramic Society, Ohio, 1964, p. 156.
14. Kumagai, M., Kato, K., Takeuti, H., *et al.*, Semi-conductor porcelain substrate, Dielectric porcelain substrate and Capacitor. US 5,006, 959, 9 Apr. 1991, *Ceram. Abst.*, **70** (1991) 10803P.
15. Bard, M. & Cremer, G., Space heating element comprising a ceramic shaped body provided with an electrically resistive coating, in particular in the form of a tile. US 4, 868, 899, 19 Sept. 1989, *Ceram. Abst.*, **69** (1990) 02568P.
16. Wang, T., Ceramic heating element. US D304, 230, 24 Oct. 1989, *Ceram. Abst*, **69** (1990) 06446P.
17. Baudry, H., Moneraye, M & Morhaim, C., US 4, 973, 826, 27 Nov., 1990, *Ceram. Abst.*, **70** (1991), 05595P.
18. Chaudhuri, S. P. & Sengupta, K., An inexpensive temperature indicator-cum-controller with sensor of mullite porcelain. Unpublished work.

Journal of the European Ceramic Society **15** (1995) 1037–1041
© 1995 Elsevier Science Limited
Printed in Great Britain. All rights reserved
0955-2219(95)00076-3
0955-2219/95/$9.50

Characterisation of the Join of Electric Discharge Pulse Welded Ceramics

J. G. P. Binner,[a] P. A. Davis,[a] J. A. Fernie[b] & I. D. Dubovetskü[c]

[a]Department of Materials Engineering and Materials Design, University of Nottingham, University Park, Nottingham, NG7 2RD, UK
[b]TWI, Abington, Cambridge, CB1 6AL, UK
[c]E. O. Paton Electric Welding Institute, Kiev, Ukraine

(Received January 1992; revised version received 13 April 1995; accepted 16 May 1995)

Abstract

A series of sialon, silicon carbide (SiC) and lead zirconium titanate (PZT) ceramics joined by an electric discharge pulse-welding process have been examined to provide information on joint characteristics. Techniques used include X-ray diffraction, scanning electron microscopy and energy dispersive X-ray analysis. Results indicate that joints with variable degrees of interfacial contact, interlayer porosity and thermal stress have been produced, depending on the precise conditions used. Titanium was found to provide better wetting characteristics than aluminium when used as an interlayer material.

Introduction

Advanced ceramics have developed to become major contenders for a number of high temperature, high strength applications.[1] The versatility of these materials is becoming more and more extensive as research programmes reduce the problems of brittleness and insufficient reproducibility of properties. Currently of high interest are the family of ceramic materials based on silicon nitride, including reaction bonded, pressureless sintered and hot pressed silicon nitride with a variety of sintering aids and the sialon group of ceramics based on solid solution between silicon nitride and alumina. Silicon carbide ceramics also possess the required characteristics for many structural engineering applications and are available in the same forms as silicon nitride.[2]

As the demand for larger and more complex shaped components increases, it becomes more difficult to fabricate ceramics using a single step shaping process and economically unfavourable to machine simple blocks to complex shapes. Thus, commercial use becomes dependent upon the availability of reliable techniques for ceramic–ceramic and ceramic–metal joining.[2–3] Various techniques for chemically joining ceramics have been investigated, the most common are active metal brazing and diffusion bonding.[1–3] Both processes can be carried out with or without intermediary layers. The purpose of the intermediary layer is to absorb the effects of the mismatch in thermal expansion between the components to be joined. Other processes which may offer a potential route for ceramic bonding include ceramic adhesives and electric discharge welding.[4] Of these the former offers high temperature stability but little mechanical strength, the latter involves a high energy pulse passing through a conductive interlayer, converting it into a plasma. A ceramic–metal interaction occurs and a bond is formed. The process is exceptional for its speed, bonding typically occurring in < 60 μs, compared to many minutes for conventional brazing and diffusion bonding.

A schematic diagram of the process is shown in Fig. 1(a), and an example of a typical electric discharge pulse welded ceramic piece is shown in Fig. 1(b). A metallic foil approximately 5 μm in thickness is clamped between the ceramic specimens. No special surface condition is necessary in terms of polishing, but the surface must be clean. When the capacitor is discharged, the interlayer is vaporized and bonds to the ceramic. The process is currently under investigation at the E.O Paton Electric Welding Institute (E.O.P.E.W.I) in Kiev, Ukraine.[4]

The technique has been used principally to examine the bonding of silicon nitride based ceramics using various metallic interlayers. The properties of a good interlayer can be listed as:

(a) low electrical resistance;
(b) must wet the ceramic;
(c) must be clean and free from inclusions, porosity and gases.

Within the discharge zone the energy density is

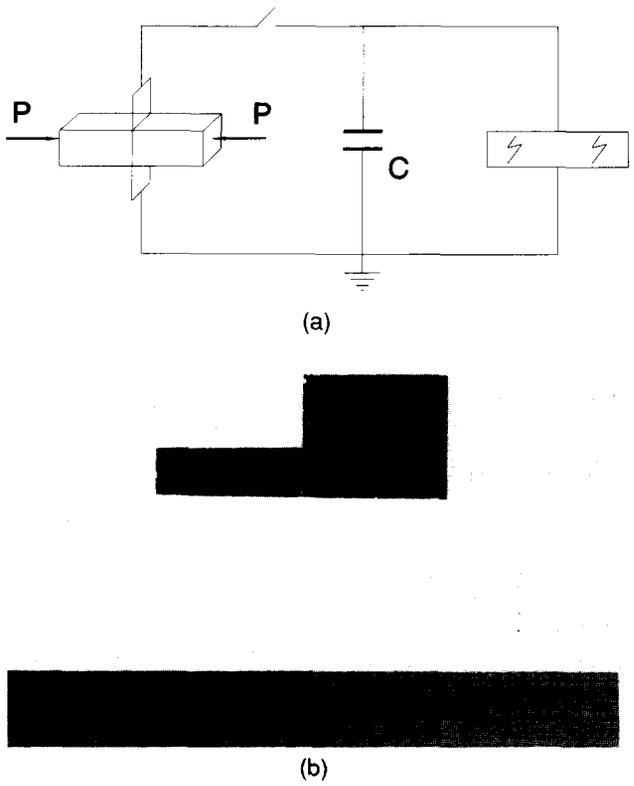


Fig. 1. (a) A schematic diagram of the electric discharge pulse welding process. P = pressure (< 20 MPa), C = capacitance (1–100 μF). Adapted from Ref. 4. (b) An example of a typical electric discharge pulse welded sialon ceramic joined using a 1·5 μm thick sputtered aluminium interlayer. Shown on a scale where each division is equal to 1 mm.

1–100 kJ/m^3, the plasma temperature approaches 10^4–10^5 K and pressures of 10^3–10^5 MPa are induced. All other conditions being equal, experiments have shown that the quality of a joint decreases with a decrease in charge energy below a minimum level. However, excess energy can result in either:

(a) fracture due to the high pressure pulse which accompanies the discharge, especially if the ceramic possesses low strength; or
(b) metallisation of the surfaces of the ceramic.

In the present study, sialon, silicon carbide and lead zirconium titanate ceramics joined by such a process, in which either an aluminium or titanium foil or sputtered interlayer was used, have been investigated.

Experimental

Ten joined ceramic–ceramic specimens were provided by the E.O.P.E.W.I. together with details corresponding to the materials involved and their respective processing parameters. This information is given in Table 1. The cross-sectional areas of all ten bonded ceramics were 5 × 5 mm and the length of each ceramic piece prior to joining was typically 6 mm.

Table 1. Composition and processing characteristics of electric discharge pulse welded specimens.

Specimen	*Material*	*Potential difference applied (V) (capacitance 12 μF, Time 40 μs)*	*Interlayer form*
1	Sialon/Al/Sialon	2100	5 μm foil
2	Sialon/Al/Sialon	2500	5 μm foil
3	Sialon/Ti/Sialon	3100	5 μm foil
4	SiC/Al/SiC	2500	5 μm foil
5	SiC/Ti/SiC	3200	5 μm foil
6	Sialon/Al/Sialon	1100	1·5 μm sputtered
7	Sialon/Al/Sialon	1500	1·5 μm sputtered
8	SiC/Al/Sic	2000	1·5 μm sputtered
9	SiC/Ti/SiC	1100	1·5 μm sputtered
10	PZT/Al/PZT	1100	5 μm foil

The specimens numbered 1–9 were sectioned perpendicular to the join, then one half mounted in a conductive resin and polished. Specimen 10, incorporated into the investigation at a later date, had previously been polished and was ready for use in the scanning electron microscope.

Three characterisation techniques were used to investigate the specimens, namely X-ray diffraction, scanning electron microscopy and energy dispersive X-ray analysis. The former was performed on both the dense, sintered samples provided and also on portions of the same samples ground into fine powder. Samples were carbon coated prior to examination on the SEM and both bulk analysis and spot analysis across the join were carried out using EDX. The latter permitted the degree of interlayer material diffusion into the bulk ceramics to be estimated. No analysis was undertaken to measure the bond strength of the joined ceramics as the number of specimens provided was too small to have any statistical merit.

Results and Discussion

X-ray diffraction analysis on both the monolithic, sintered samples and subsequently powdered material indicated that the sialon samples were composed of the X-phase ($Si_{12}Al_{18}O_{39}N_8$) as the primary phase with small amounts of (Si_3N_4)14H as a secondary phase. The primary phase present in the silicon carbide samples was (SiC)33R, however the secondary phase was too small to identify. Specimen 10 was identified as being the single phase $Pb(Z_{0.52}Ti_{0.48})O_3$. Table 2 indicates the principal impurities found in the samples.

The scanning electron microscope investigations

Table 2. Quantitative analysis of the impurities found in the samples.

Material	*Impurities*	*Relative proportions of impurities*
Sialon	Iron, calcium	Si : Al : Fe : Ca = 1 : 0·6 : 0·08 : 0·06
Silicon carbide	Aluminium	Si : Al = 1 : 0·20
Aluminium	Copper, nickel	Al : Cu : Ni = 1 : 0·2 : 0·05
Titanium	Vanadium	Ti : V = 1 : 0·2
Lead zirconium titanate	—	—

carried out have indicated that all of the specimens display a degree of poor contact at the ceramic–metal interface. This suggests that the optimum conditions for joining have not been met for any of the specimens examined. However, a positive feature of the process is that at distances greater than 20 μm from the join there is no indication in any of the specimens that the process has effected the properties of the bulk ceramic.

The aluminium foil on melting appears to wet the surface of the sialon better than the silicon carbide, resulting in improved adherence. The process has produced a highly porous interlayer material, with the pressure generated at the join pushing the Al into the pores at the interface of the ceramic, hence enlarging the surface area of contact (Fig. 2). Spot analysis* across the join for both the sialon/Al/sialon and SiC/Al/SiC specimens suggests, by the sharp transition of elemental intensities shown in Figs 3 and 4, that diffusion in either direction across the interface has not occurred as would be expected for such a short joining time.

The adherence of the titanium foil interlayer at the silicon carbide interface is far superior to that at the sialon interface and for both ceramics the joint characteristics are a significant improvement on those achieved when an aluminium interlayer is used. For the SiC/Ti/SiC specimens, bonding at the ceramic–metal interface is evident from the presence of cracks running through the titanium perpendicular to the join as in Fig. 5. These cracks are thought to be caused by the differences in coefficients of thermal expansion between the two materials creating stresses at the interface on cooling. Spot analysis across the join indicates a more gradual transition of elemental intensities (Fig. 6), suggesting the existence of reaction products at the interface. For the sialon/Ti/sialon specimen, spot analysis across the join does not distinguish either way whether reaction products exist or not.

In agreement with Ref. 4, at too low a charge energy no join is formed. The limit has not been

*The spot analysis, carried out at 25 keV under a magnification of × 1000 for 100 s, can only be considered as an estimate of the element distribution. The graphs which indicate the composition variation across the join for each specimen possess errors of ±1·0 in terms of intensity. The accuracy in positioning of the spot lies within ±2 μm, which when considering the total width of the interlayer is only 5 μm, then this error is considerable.



Fig. 2. Sialon ceramic joined using a 5 μm thick aluminium foil.

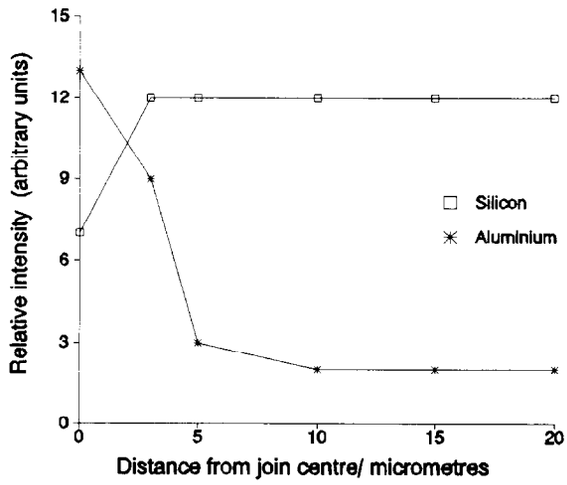


Fig. 3. Composition variation across the join for sialon ceramics joined using an aluminium interlayer.

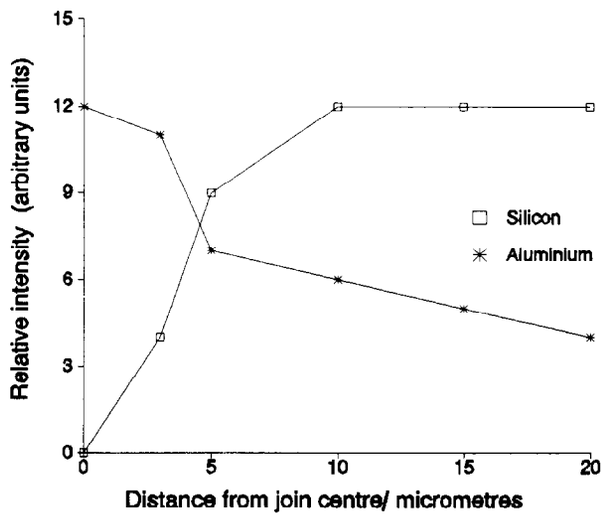


Fig. 4. Composition variation across the join for silicon carbide ceramics joined using an aluminium interlayer.

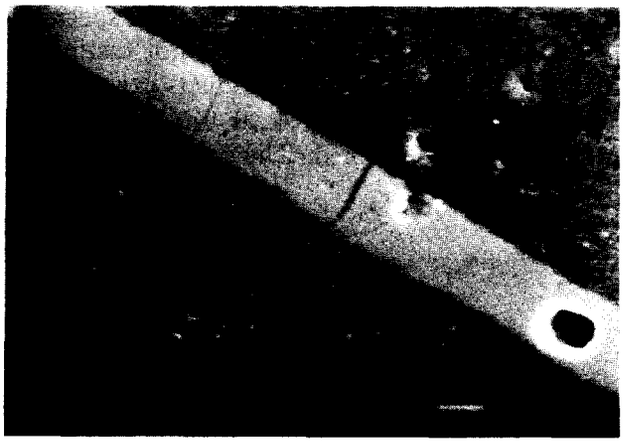


Fig. 5. Silicon carbide ceramic joined using a 5 μm thick titanium foil.

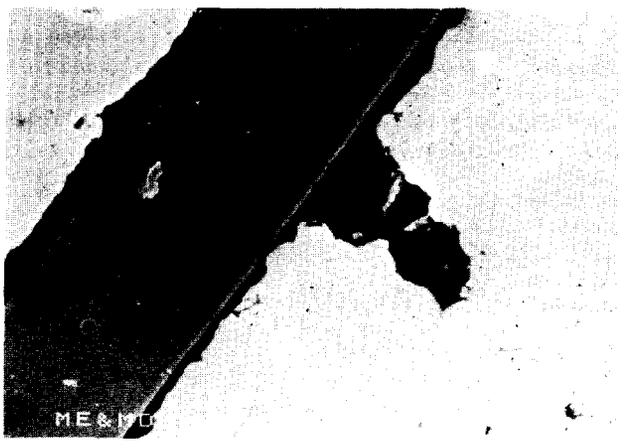


Fig. 7. Lead zirconium titanate ceramic joined using a 5 μm thick aluminium foil.

determined in the current work, however 1100 V appears to be too low for a sputtered interlayer 1·5 μm thick. The interlayer has melted but not bonded with the ceramic. Exceeding an applied voltage of 2500 V to join both sialon–sialon and SiC–SiC ceramics using an aluminium interlayer resulted in the fracture of the ceramic parallel to, and at distances of typically 10 μm from, the join. Using a titanium interlayer meant that the upper limit to the applied voltage was raised; fracture of the ceramic adjacent to the join was not observed until 3100 V was applied. At this voltage the behaviour of the ceramic is similar to that observed for aluminium at 2500 V.

The sialon and SiC ceramics have similar thermal expansion coefficients of approximately 5 MK^{-1}. Typical values for aluminium and titanium are 24 and 9 MK^{-1} respectively.[5] The variation in level of applied voltage required for damage to occur corresponds to the greater thermal expansion mismatch at the aluminium–ceramic interface compared to that at the titanium–ceramic interface. It is this mismatch which in turn results in the fracture of the ceramic. Further work is clearly required using a multilayer system, with the intention of reducing the thermal stresses developed due to the difference in materials used.

No direct comparison can be made between the two interlayer thicknesses used as the charge energy had also been varied in the samples analyzed. However the results suggest that the sputtered interlayer yields improved joins. This could be because the layer is thinner or because the sputtering process will have increased the initial ceramic–metal contact prior to joining.

The lead zirconium titanate specimen displays a similar degree of joining as the engineering ceramics (Fig. 7). The edges of the aluminium interlayer are very uniform and no evidence exists of mechanical keying by the aluminium in the pores at the ceramic interface. The electrical pulse has not weakened the ceramic adjacent to the join and thus no cracking is apparent. Spot analysis across the join (Fig. 8) shows a variation in intensity for

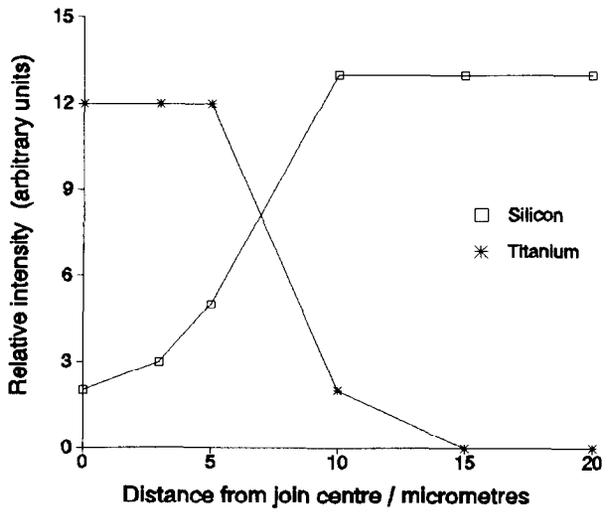


Fig. 6. Composition variation across the join for silicon carbide specimens joined using a titanium interlayer.

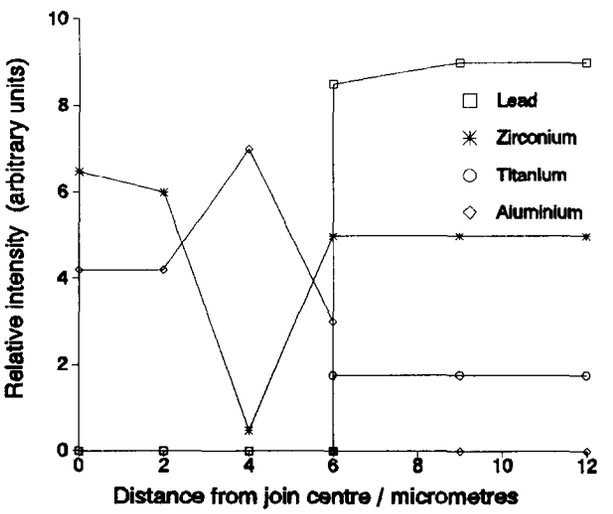


Fig. 8. Composition variation across the join for lead zirconium titanate ceramics joined using an aluminium interlayer.

the Al and Zr across the ceramic–metal interface that suggests some diffusion has occurred across the interface and reaction products exist.

Conclusions

For a ceramic–ceramic join with the aid of an active metal interlayer, then the processing parameters chosen must ensure that the metal melts, wets and chemically bonds to the surface of the ceramic interfaces. Control of the reaction zone variables such as thickness, thermal expansion coefficients and thermal stability, allows optimisation of the bond properties. Although this degree of control has not been achieved in any of the specimens provided, evidence has been found which illustrates the potential for this new processing technique.

The present study has indicated the greater wetting capabilities, and hence superior performance, of Ti-alloys over Al in electric discharge welding of sialon and silicon carbide ceramics. This agrees with the theory given in Ref. 2, in which aluminium and titanium interlayers were used in an attempt to join silicon nitride ceramics.

Limits to the range in charge energy used are: too low and bonding will not occur, too high and the ceramic fractures or metallization of the ceramic surfaces occurs. The optimum for both the foil and sputtered interlayers with the engineering ceramics studied appears to lie within the range 1·1–3·2 kV.

Since charge energy was varied simultaneously with interlayer thickness, no real indication of the effect of the latter was obtained, though the results do indicate a preference towards the use of a sputtered interlayer. A continuation in this investigation would be the introduction of a multilayer system, with the intention of reducing the thermal stresses developed due to the difference in materials used.

References

1. Nicholas, M. G., Joining Structural Ceramics. In *Designing Interfaces For Technological Applications: Ceramic–Ceramic, Ceramic–Metal Joining*, ed. S. D. Peteves, Elsevier Applied Science, 1989, pp. 49–65.
2. Fernie, J. A., Joining Ceramic Materials. In *Welding and Metal Fabrication*, July 1990.
3. Doyama, M., Sōmiya, S. & Chang, P. H., In *Proceedings of the MRS International Meeting on Advanced Materials*, Vol. 8, 1988, p. 35.
4. Yushchenko, K. A., Nesmikh, U. S. & Dubovestskü, I. V., Application Of Conductor Electric Explosion In Joining Ceramics. In *Advances In Joining Newer Structural Materials*, 1990, pp. 109.
5. Ashby, M. F. & Jones, D. R. H., In *Engineering Materials 2, An Introduction To Microstructures, Processing and Design*, pp. 10–11.

Journal of the European Ceramic Society **15** (1995) 1043–1046
© 1995 Elsevier Science Limited
Printed in Great Britain. All rights reserved
0955-2219/95/$9.50

0955-2219(95)00066-6

Joining of $Y_1Ba_2Cu_3O_{7-x}$ and Pb(Zr, Ti)O_3, and their Interfaces

Sunao Sugihara* & Hiroshi Fujitani

Department of Materials Science and Ceramic Technology, Shonan Institute of Technology, 1–1–25, Tsujido Nishikaigan, Fujisawa 251, Japan

(Received 1 February 1994; revised version received 4 October 1994; accepted 20 March 1995)

Abstract

The joining of the superconducting oxide, YBCO, with the piezoelectric ceramic, Pb(Zr,Ti)O_3, was studied using a thick film of YBCO. The electrical resistivity of the composite was evaluated from liquid nitrogen temperature to room temperature; the resistivity was 0·1 Ω cm at 80 K without a clear critical temperature. Furthermore, Pb(Zr, Ti)O_3 was sandwiched by YBCO electrodes to measure the piezoelectricity.

A slurry of YBCO was pasted on a sintered Pb(Zr,Ti)O_3 pellet followed by sintering for 5, 60 and 420 min at 1193 K. The YBCO film thicknesses were 5, 17 and 35 μm as determined by scanning electron microscope (SEM). An electron probe microanalyzer (EPMA) revealed diffusion of Ba into Pb(Zr,Ti)O_3. The hetero-joining was achieved, although the YBCO film was porous as investigated by SEM. A higher density film can be obtained by optimizing the sintering conditions for the composite.

1 Introduction

In considering an electrode for ceramics, the wettability of the metal for the ceramic is of importance. A glass frit is commonly employed for joining a metal to a ceramic. Sugihara *et al.* have widely studied the wettability and bondability of metal/ceramics and ceramics/ceramics for electronic ceramics in particular.[1,2]

The joining of a superconductor to a semiconductor has been theoretically studied in terms of boundary effects by P. G. De Gennes;[3] superconducting electrons migrate towards the semiconductor in the proximity effect. There have been several studies of the proximity effect in superconductors;[4] a Y–Ba–Cu–O based multilayer for optoelectronic devices was investigated on the sapphire and Al_2O_3 as as IR detector.[5] The YBCO films were hundreds of nm thick and employed for the counterelectrode and base.

On a more macroscopical scale, Srivastava *et al.* reported that $Y_1Ba_2Cu_3O_{7-x}$ (hereafter YBCO) adhered to $BaTiO_3$ and to Pb(Zr,Ti)O_3 (hereafter PZT); electrical properties of the devices were characterized.[6] Furthermore, Moya *et al.* formed YBCO composites on Ce–TZP, Y–TZP and spinel substrates.[7] The interfaces between YBCO and other ceramics are very important for devices or composites when one uses YBCO as an electrode.

The first purpose of the present work is to join YBCO thick film to piezoelectric ceramics, then to find the appropriate thickness and the best contact of the film to give satisfaction for both piezoelectricity and superconductivity. The second aim is associated with the use of YBCO electrode for a field effect transistor at the temperature even if the temperature is not below the transition.

2 Experimental

2.1 Fabrication of PZT

The PZT powder with composition of Pb ($Zr_{0.53}$, $Ti_{0.47}$)O_3 (Fuji Titanium Ind. Co. Ltd, Japan) was pressed at 180 MPa followed by sintering for 2 h at 1503 K. The sintering was carried out in an atmosphere of lead or lead oxide in the crucible. The size of the sintered pellets was 15 mm in diameter and 0·8–1·0 mm thickness. The sintered density was 95–96% of the theoretical value.

2.2 Slurry of YBCO

The YBCO powder (Seimi Chemical Co. Ltd, Japan) calcined at 873 K was milled with the solvent and ZrO_2 balls (3 mm in diameter) for 24 h. The slurry was painted on the PZT fabricated above, then sintered at 1193 K in an oxygen atmosphere (0·5 litre/min) for each sintering time; 5, 60, 420 min. The samples were cooled down to

*To whom correspondence should be addressed.

room temperature at the rate of about 1·5 K/min. The surface of the thick films was examined by X-ray diffraction analysis (XRD).

2.3 Interfaces between YBCO and PZT

The morphological analysis of the interfaces was carried out by a scanning electron microscope, and the element distributions through the interfaces were qualitatively investigated by mapping with an electron probe micro analyzer.

2.4 Electrical properties

Electrical resistivity was measured with a four-probe method from the temperature of liquid nitrogen to room temperature. YBCO-sandwiched PZT(SIS) was investigated for the frequency dependence of the composite response by impedance analyzer (YHP 4192A).

3 Results and Discussion

3.1 Interfaces of YBCO/PZT and YBCO surfaces

Figs 1(a–c) show the SEM photographs at the interfaces of the YBCO/PZT system sintered for 420, 60 and 5 min at 1193 K, respectively. The bonding of YBCO grains is seen, although there seems to be porosity in the YBCO thick film sintered for 420 min. The thickness of the film was about 17 μm. The system maintained for 60 min had a very porous structure with a film thickness of about 33 μm; the 5 min sintered system showed a denser morphology. The SEM photographs of the surfaces of the YBCO/PZT system are shown in Fig. 2 (a–c) maintained for 420, 60 and 5 min in sintering, respectively. As shown in Fig. 2(a), well-developed bonding of the YBCO occurred with porous microstructure on the 17 μm film sin-

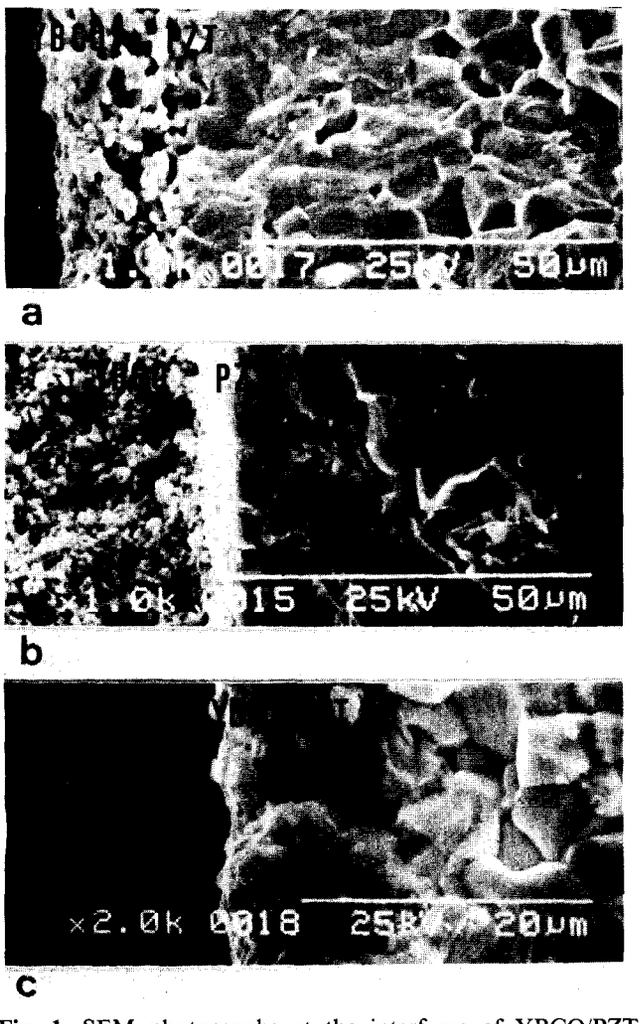


Fig. 1. SEM photographs at the interfaces of YBCO/PZT systems for each sintering time: (a) 420; (b) 60 and (c) 5 min.

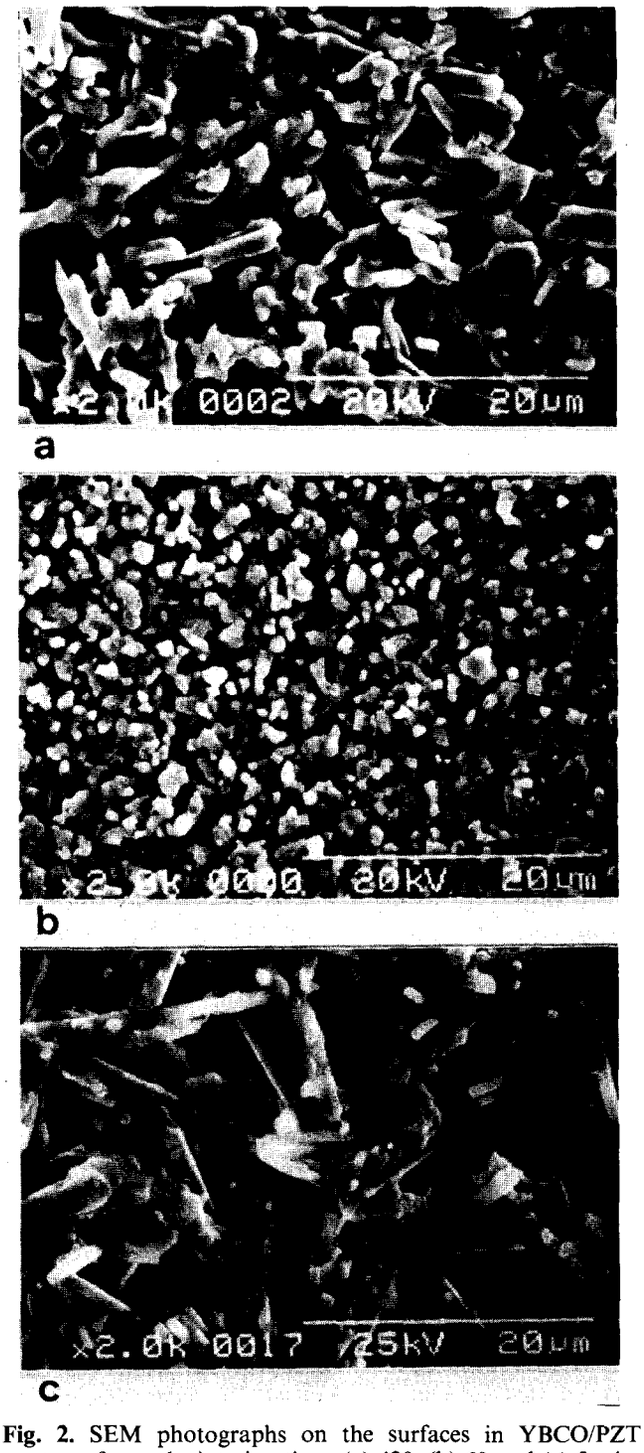


Fig. 2. SEM photographs on the surfaces in YBCO/PZT systems for each sintering time: (a) 420; (b) 60 and (c) 5 min.

tered for 420 min. The inter-particle bonding did not develop in the film which had a thickness of about 33 μm after 60 min sintering (Fig. 2(b)); this seemed to be more porous with a different microstructure from those of the 5 and the 420 min sinterings. It is not clear at this moment why the 60 min sintering shows a pronounced difference in microstructure. In the 5 min sintering, the film was thinner (5 μm) and more dense (Fig. 2(c)); the thinner film seems to be better from the viewpoint of morphology.

3.2 Diffusion of barium from YBCO to PZT

Y_2BaCuO_5 and $BaCuO_2$, as well as YBCO were found by XRD analysis in samples sintered for 420 min at 1193 K, and Y_2BaCuO_5 of green colour and non-superconducting character was detected together with YBCO peaks in the film sintered for 5 min. Figs 3(a and b) show the EPMA line analyses indicating a Ba diffusion distance of 35 and 5 μm into the PZT from the interfaces, respectively. The length of Ba diffusion is illustrated in Fig. 4.

3.3 Electrical resistivity and piezoelectric properties

The resistivities were measured at temperatures from that of liquid N_2 to 296 K. They indicated semiconductive temperature dependences. The

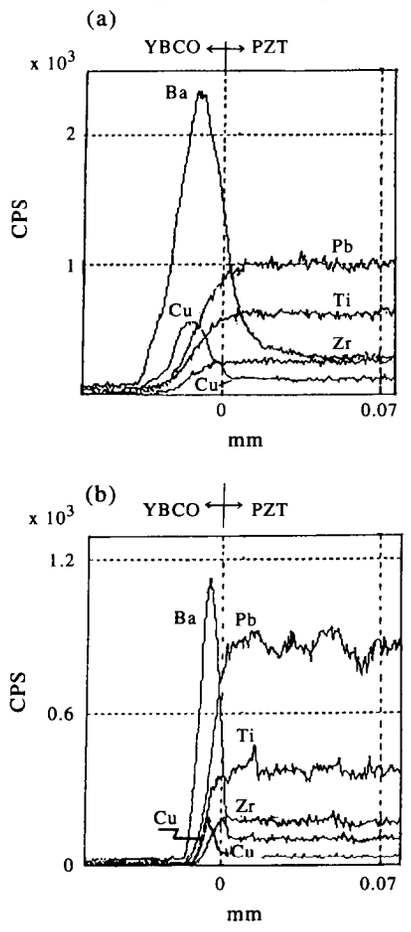


Fig. 3. EPMA line analysis at the interfaces between YBCO and PZT in each sintering time: (a) 420; (b) 60 and (c) 5 min.

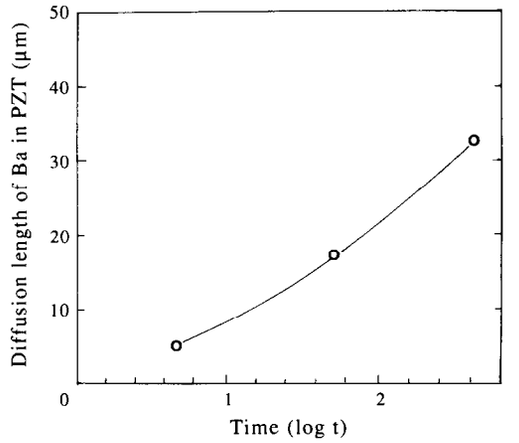


Fig. 4. Change of Ba diffusion length in PZT with sintering time at 1193 K.

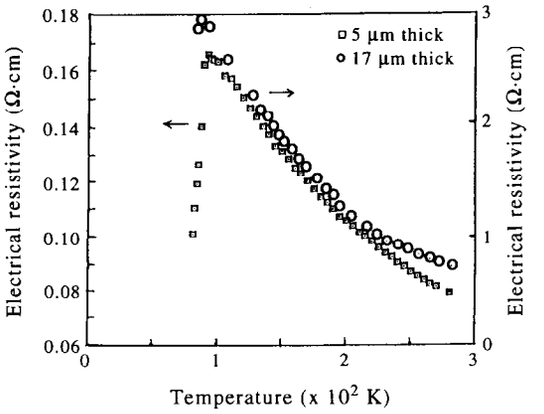


Fig. 5. Electrical resistivity changes with temperature.

critical temperature of the 5 μm YBCO film was not clear although 0·1 Ω cm was shown at a temperature of 80 K, and the resistivity at 296 K was 0·08 Ω cm. The $BaCuO_2$ produced in the 60 min sintering is a non-superconductive material. More Ba and Y were detected on the surface of the YBCO than in the bulk, due to a large amount of CO_3^{2-} ions; these elements and the ions concentrated on the surface are estimated to reduce the superconductivity.[8]

The composite piezoelectricity with electrodes of 5 μm thickness YBCO is shown in Fig. 6.

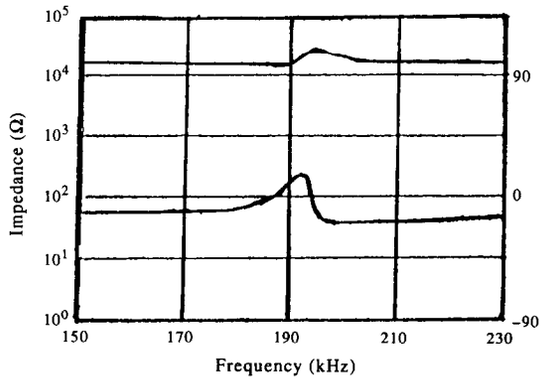


Fig. 6. Impedance analyses with frequency: (a) starting material; (b) Ba-doped PZT (electrodes were Ag).

Absorption of energy by PZT was low at a frequency around 190 kHz as indicated by impedance analysis suggesting poor piezoelectricity. The poor film density and Ba diffusion may cause the poor piezoelectricity in the YBCO/PZT/YBCO system. It is suggested that the density of the YBCO thick film is not high enough for the material to act as electrode for a device.

4 Conclusions

(1) YBCO thick films (5–33 μm) adhered onto PZT. Investigation of the interfaces revealed diffusion of Ba from YBCO to PZT; the length of the diffusion zone depended on the sintering time at 1193 K.
(2) YBCO thick film of 5 μm indicated semiconductive properties rather than superconductivity with no clear indication of a critical temperature.
(3) The thick film should be denser to function as successful electrodes for the composites consisting of superconductor/PZT/superconductor; also a film thickness of 5 μm or less can be suggested as well as a short sintering time.

References

1. Sugihara, S. & Okazaki, K., *Proc. of the 7th International Sym. of Application on Ferroelectrics*, June 6–9, 1993, Urbana Champaign, USA, pp. 429–31.
2. Sugihara, S. & Okazaki, K., *Proc. of the 7th International Sym. of Application on Ferroelectrics*, June 6–9, 1993, Urbana-Champaign, USA, pp. 432–4.
3. DeGenes, P. G., *Rev. Mod. Phys.*, **36** (1965) 225–37.
4. Nishino, T., Yamada, E. & Kawabe, U., *Phy. Rev.*, **B33** (1986) 2042–5.
5. Villegier, J. C., Moriceau, H., Boucher, H., DiCiocio, L., Ghis, A., Jaeger, A., Levis, M., Pourtier, F., Schwerdtfeder, M., Vabre, M. & Villard, C., *Mat. Sci. and Engineering*, **B15** (1992) 92–100.
6. Srivatava, A., Bhalla, A. & Cross, L. E., *Ferroelectrics*, **123** (1991) 243–51.
7. Saiz, E., Osendi, M. I., Miranzo, P., Requena, J. & Moya, J. S., *J. Less-Comm. Metals*, **164** and **165** (1990) 458–63.
8. Shigematsu, J. S., Ishikawa, M. & Nakanishi, N., *Powder and Powder Metall.*, **34** (1987) 647–50.

Journal of the European Ceramic Society **15** (1995) 1047–1059
© 1995 Elsevier Science Limited
Printed in Great Britain. All rights reserved
0955-2219(95)00095-X
0955-2219/95/$9.50

Toughness of Damage Tolerant Continuous Fibre Reinforced Ceramic Matrix Composites

Bent F. Sørensen[a] & Ramesh Talreja[b]

[a]Materials Departrnent, Risø National Laboratory, 4000 Roskilde, Denmark
[b]School of Aerospace Engineering, Georgia Institute of Technology, Atlanta, GA 30332-0150, USA

(Received 30 March 1995; revised version received 24 May 1995; accepted 25 May 1995)

Abstract

A simple shear-lag model is used to estimate the toughness of a unidirectional fibre reinfored ceramic matrix composite. In the model, which includes the residual axial stresses, the stress transfer across the fibre/matrix interface is by a constant shear stress. The estimates from the model are compared to experimental measurements for four composites and good agreement is found. The effects of distributed and localized energy uptake on fracture stability are discussed, and it is concluded that for most applications the toughness, rather than the pull-out energy absorption, should be maximized.

Nomenclature

a	fibre radius
A	cross-section area
B	specimen width
c	crack length
E	Young's modulus
f	fibre volume fraction
G	(critical) energy-release-rate
L	specimen length
l_s	sliding length
l_p	pull-out length
P	applied load
s	spacing of matrix cracks
U	toughness (energy per unit volume) of composite
v	displacement
W_{sl}	energy dissipated (per unit volume) due to frictional sliding
W_p	energy dissipated (per unit area) due to fibre pull out
γ_{WOF}	work of fracture
δ	matrix crack opening
Δ	specimen elongation
ϵ	axial strain
ϵ_u	ultimate tensile strain
Π	potential energy
σ	stress
τ_s	interfacial sliding shear stress
ϕ	strain energy density

Subscript

db	debonding
f	fibre
m	matrix
max	value at specimen separation
mc	matrix cracking
u	value at ultimate stress
FS	full sliding along the interface

Superscript

ACK	fully and multiply cracked matrix
ini	initiation of matrix cracks
res	residual
*	value after specimen separation
0	initial state
I–IV	stages of damage

1 Introduction

Monolithic ceramics are brittle, flaw-sensitive, and of low energy absorption capacity before and during fracture. However, a class of ceramic composites with continuous reinforcement is emerging, which has much more attractive damage and fracture behaviour. Materials in this class are *damage tolerant*, in the sense that the first mode of damage (matrix cracking) does not lead to final fracture. Instead, the strength of the materials is controlled by the strength of the reinforcement. This flaw-insensitive behaviour is a remarkable property of materials that are made of brittle constituents. As a consequence, fracture toughness is not a proper parameter to characterize such materials. Rather, the stress at the onset of multiple matrix cracking, the failure stress, and total energy uptake until failure constitute a set of property parameters.

Most theoretical works on continuous fibre reinforced ceramics focus on two topics: progression of multiple matrix cracking[1–3] and energy dissipation due to fibre pull out.[4–7] Multiple matrix cracking is of importance since it leads to non-linear constitutive behaviour that must be taken into account when these materials are used, see e.g. ref. 8. It is equally important to point out that in general there is no correlation between the 'proportional limit', i.e. the stress level at which multiple matrix cracking causes non-linearity in the stress-strain curve and the fatigue limit.[9] The energy dissipation due to pull out is important for assessment of the final fracture behaviour. A central part of all these models is the role of the interface (see ref. 10 for a recent review).

The energy uptake by distributed mechanisms (i.e. prior to localization) has not been addressed sufficiently in the previous works. Experimentally, a remarkably non-linear stress–strain response has been found for several continuous fibre-reinforced ceramics composites.[9–14] However, the details of the associated evolution of damage have been studied only recently.[15–19] On the basis of these recent findings, this paper develops a model for the energy uptake by distributed mechanisms, defined here as toughness, i.e. the total energy uptake until failure in volume-distributed mechanisms. This energy comprises both the recoverable and non-recoverable parts. It is of major importance, because this is the maximum energy that can be absorbed per unit volume without causing fracture of a component, i.e. (the component will be damaged but will retain its integrity such that it can still continue to carry loads).

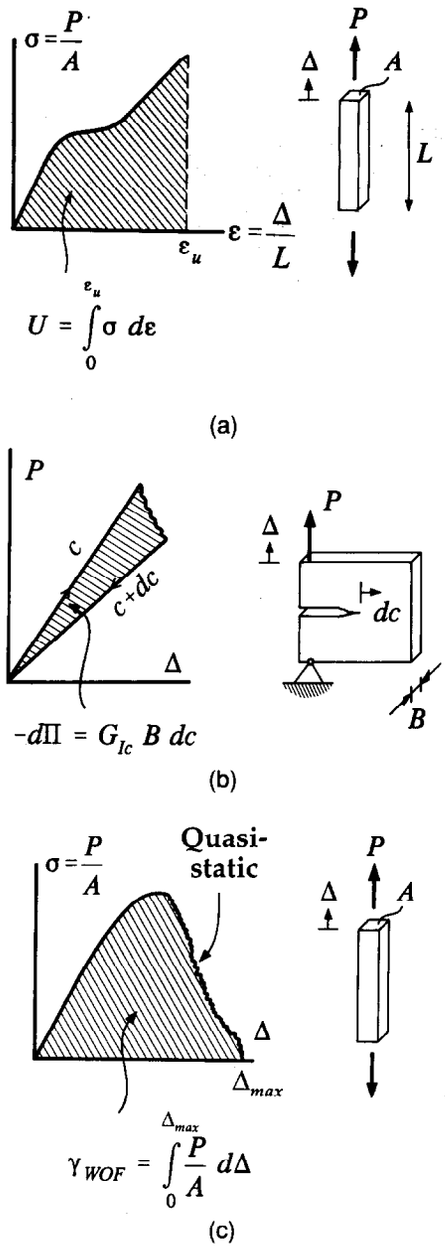


Fig. 1. Energy measures for materials: (A) the toughness, U, (B) the critical energy release rate, G, and (C) the work of fracture, γ_{WOF}.

2 Measurements of energy for material characterization

2.1 Energy quantities

Firstly, for clarity, we start off reviewing some energy concepts and quantities that are often used to characterize the fracture behaviour of materials. For simplicity the considerations are limited to the case where a specimen is loaded by a single tension force. Figure 1 illustrates three commonly used quantities: the toughness, the critical energy release rate (fracture toughness) and the work of fracture.

The toughness[20] is the ability of a material to uptake energy (per unit volume) prior to failure, i.e. the strain energy density to failure[20];

$$U = \int_0^{\epsilon_u} \sigma(\epsilon)\, \mathrm{d}\epsilon, \tag{1}$$

where σ and ϵ are stress and strain, respectively, and ϵ_u is the failure strain (onset of localization). It is the area under the stress–strain curve, and has the SI unit J/m^3.

The *energy release rate* is defined in fracture mechanics by the decrease of the potential energy per new crack area during a quasi-static crack increment[21]

$$G = -\frac{1}{B}\frac{\mathrm{d}\Pi}{\mathrm{d}c}, \tag{2}$$

where Π is the potential energy, and c and B are the length and the width of the crack, respectively. The critical value of G is equivalent to the energy absorbed per unit new crack area, during an incremental (stable) crack growth. The SI unit for G is

J/m^2. Alternatively, the critical value of G is called the fracture toughness. Sometimes in the literature the term toughness is used loosely when fracture toughness is meant. This may cause confusion. In our paper toughness is defined by (1) and fracture toughness by (2).

The *work of fracture* is defined by the total energy absorped (during a quasi-static fracture process) by the specimen per unit fracture area, i.e. the area under the load–displacement curve, per cross-sectional area (see e.g. ref. 22),

$$\gamma_{WOF} = \int_0^{\Delta_{max}} \frac{P(\Delta)}{A} \, d\Delta, \qquad (3)$$

where A is the cross-sectional area of the specimen, P is the load and Δ is the elongation. γ_{WOF} has the SI unit J/m^2.

From the definitions it follows that the quantities mentioned are suited for characterizing different phenomena. U relates the energy uptake (prior to localization) to the volume, and is the proper measure of the *fracture initiation energy*. G is a measure related to characterizing phenomena appearing with *growth of a single crack*. Work of fracture relates the *total energy absorped* (fracture energy) to the full crack area.

2.2 Distributed versus localized energy absorption of uniaxial fibre composites

When unidirectional fibre composites are loaded in the fibre direction a range of *distributed damage* mechanisms occur before final failure. The *fracture* occurs as a *localized* phenomenon, since fibre fracture and pull out only take place at a single matrix crack, namely where the specimen separates into two pieces. Throughout this paper distinction will be made between distributed energy uptake and energy absorped during localization. Distributed energy uptake should be measured by a quantity that reflects that the energy uptake is by distributed phenomena, such as the area under the stress–strain curve, U. The energy dissipation during localization also involves distributed and localized mechanisms. It is of importance to measure and calculate these contributions separately, since they do not scale in the same manner with specimen geometry, as will be elaborated later.

2.3 Choice of test method — bending or pure tension

Having recognised the importance of distinguishing between distributed and localized mechanisms, we now proceed with a discussion of test methods for measurements of the toughness. Materials having distributed damage are characterized by non-linear constitutive laws. Per definition a constitutive law is the relationship between the stress and strain states at any point in the material. For continuum mechanics to be applicable for materials experiencing distributed damage, the test volume (gage length of extensometer or strain gauge) must be much larger than any microstructural dimensions (e.g. matrix crack spacing), such that the measured volume behaviour is scale-independent, and the definitions apply. Moreover, the test *volume* must have *uniform stress and strain fields.*

In bending tests the normal stress distribution is non-uniform (going from tension on one side to compression on the other), and so is the damage evolution, as sketched in Fig. 2. The true stress–strain curve cannot be determined, since the stress and strain distributions across the specimen depth are not known (when damage takes place, the distribution of normal stress is not linear, but depends on the type of damage mechanism and degree of damage). Furthermore, at the peak load, localized fibre failure takes place at the tensile surface, multiple matrix cracking takes place in the central region of the specimen, and the compression side may still be undamaged. From the *bending load–displacement curve it is not possible to distinguish between the effects of distributed mechanisms* (matrix cracking, fibre/matrix debonding and interfacial sliding) and *localized* (fibre breakage and pull out). Furthermore, a shear stress field is present in bending tests. Thus, the damage evolution and failure may be due to shear or compressive stress components, rather than tension.[23]

It is unfortunate that bending tests have been so widely used for characterizing ceramic composites, since this has led to incorrect conclusions concerning the material behaviour. For instance, it has sometimes been suggested that the tail (the downgoing part) of the load–displacement curve (measurable in displacement controlled experiments only) represents the energy dissipation due to fibre

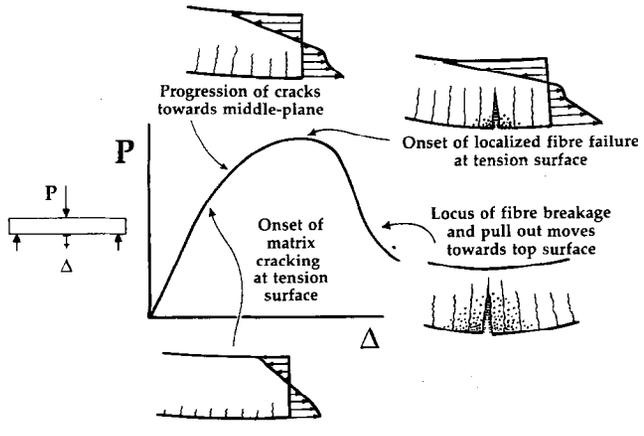


Fig. 2. A schematic illustration of various damage mechanisms operating simultaneously during a bending experiment. The damage evolution is not uniform throughout the depth of the specimen.

pull out. This is incorrect, since matrix cracking, fibre/matrix debonding, fibre sliding and fibre failure continue to take place during this part of the bending response, as the failure locus moves across the depth of the specimen towards the compression side.

Uniaxial tension experiments, on the other hand, allow an unambiguous interpretation, since the damage mechanisms initiate and develop at identifiable stress or strain levels,[15–19] and take place uniformly over the entire volume of the gage section of the specimen.

Unfortunately, tensile tests are difficult to perform, since an accurate alignment is needed to prevent bending effects.[24] Also, although tensile tests are performed with much care, it is not unusual that failure takes place at tabs,[19] so the true strength of the composite cannot always be measured. However, if there is no bending in the test section, then the relationship between stress, strain and damage mechanisms can readily be identified.

2.4 Experimental characterization of damage in uniaxial tension

Figure 3 shows an experimental stress–strain curve of a hot pressed unidirectional SiC-fibre-reinforced calcium alumino silicate (denoted CAS II from Corning Inc., NY, USA) glass–ceramic matrix composite, tested in uniaxial tension along fibres[19] at a strain rate of 4×10^{-4} min^{-1}. Throughout this paper we will refer the evolution of damage to the axial strain of the composite rather than the composite stress, since the axial stress component in the fibres resulting from the external load and the axial stress component in the matrix before matrix cracking are proportional to the axial strain of the composite. This approach also makes it easier to compare behaviour of unidirectional and cross-ply composites. For the SiC/CAS II composite shown in Fig. 3, U was measured to be 3.1 MJ/m^3, which is almost 40 times that of the pure matrix material. However, due to loading rate effects on the monotonic stress–strain behaviour,[25] the value for SiC/CAS II can vary from 1·7 MJ/m^3 (at 0·01 MPa/s) to 5·4 MJ/m^3 (500 MPa/s).

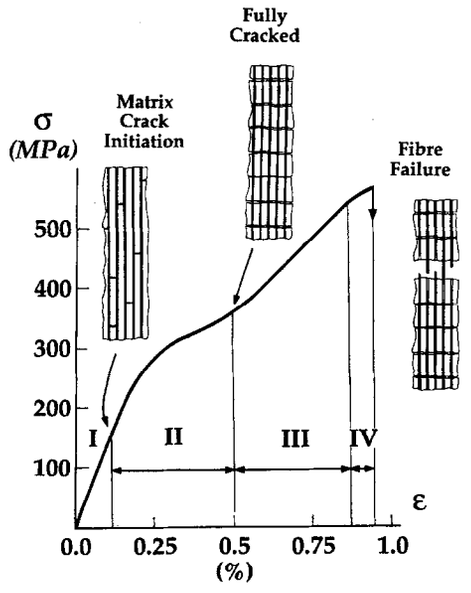


Fig. 3. The non-linear stress–strain curve of SiC/CAS II measured in uniaxial tension along fibres (strain rate of 4×10^{-4}/min). Applied stress as function of strain. The stages of damage evolution are indicated (after ref. 19).

The non-linear stress–strain curve reflects the various stages of damage (see ref. 19 for a detailed discussion). At low strain the material response is linearly elastic and reversible (Stage I). At higher strain matrix cracks initiate and evolve into fairly regularly spaced multiple matrix cracks (Stage II). This takes place over a certain strain range, rather than at a specific strain value. Fibre/matrix debonding also takes place during Stage II, and facilitates frictional sliding along the fibre/matrix interface. These damage processes cause the non-linear part of the stress–strain curve. The corresponding changes in the overall unloading modulus and Poisson's ratio in Stage II can be modelled by a continuum damage model.[8] Increasing the applied stress further leads to a second linear response (Stage III), where the stiffness is mainly due to the fibres. However, significant hysteresis appears during unloading due to effects from interfacial friction. For some specimens a small amount of distributed fibre fracture (Stage IV) may take place just prior to failure. Final failure occurs by localized fibre fracture. Recalling the preceding discussion, the area under the stress–strain curve represents the energy that the material has absorbed per unit volume of the composite up to failure. The energy quantity measured by U is the energy that has been absorbed by *distributed* mechanisms. Mechanisms operating during the *localized* fracture, such as fibre fracture and pull out do *not* contribute to this quantity.

3 Model of Energy Uptake

3.1 Basic considerations

In the following the energy uptake by distributed mechanisms of a unidirectional ceramic fibre reinforced ceramic composite is estimated, based on the damage mechanisms and scenario identified above. The tensile stress–strain curve represents the response of the material to a quasi-static loading in equilibrium with the stresses in the material, and therefore, according to the first law of thermodynamics, the work of the external force must be equal to the change of the energy in the specimen.

In many cases the stress–strain curve does not show non-linearity immediately before failure, indicating that the presence of Stage IV (distributed fibre failure) can be neglected. Thus, our analysis concerns only energy uptake in Stages I, II and III, with Stage III extended until failure. In Stage I the energy uptake per unit volume of the composite, the area under the stress–strain curve up to $\epsilon = \epsilon_{mc}^{ini}$, is denoted U^I. According to the principle of virtual work (or the first law of thermodynamics) the energy uptake U^I is equal to the increase in strain energy density in the matrix and fibres, Φ_m^I and Φ_f^I, respectively, where superscript 0 and I denote the start and end of Stage I, respectively

$$U^I = \int_0^{\epsilon_{mc}^{ini}} \sigma \, d\epsilon = \Phi_m^I + \Phi_f^I - \Phi_m^0 - \Phi_f^0. \quad (4)$$

In Stage II the external work per unit volume is, again, according to the principle of virtual work, equal to the sum of the changes in strain energy density of fibre and matrix, the fracture energy of multiple matrix cracks, fibre/matrix debonding and the energy dissipation due to interfacial frictional sliding in Stage II. Denoting superscript II for the end of Stage II ($\epsilon = \epsilon_{mc}^{ACK}$), the energy uptake in Stage II is

$$U^{II} = \int_{\epsilon_{mc}^{ini}}^{\epsilon_{mc}^{ACK}} \sigma \, d\epsilon = \Phi_m^{II} + \Phi_f^{II} - \Phi_m^I - \Phi_f^I + U_{mc} + U_{db} + W_{sl}^{II}, \quad (5)$$

where W_{sl}^{II} stands for the frictional energy dissipation per unit volume in Stage II, U_{mc} is the energy consumed due to the formation of matrix cracks and U_{db} is the debond energy per unit volume. Assuming that the deformation of fibre and matrix continues in Stage III, the energy uptake in Stage III is

$$U^{III} = \int_{\epsilon_{mc}^{ACK}}^{\epsilon_u} \sigma \, d\epsilon = \Phi_m^{III} + \Phi_f^{III} - \Phi_m^{II} - \Phi_f^{II} + W_{sl}^{III}, \quad (6)$$

where superscript III stands for the end state, when localization sets in ($\epsilon = \epsilon_u$), and W_{sl}^{III} is the frictional energy dissipation in Stage III. This gives the total energy uptake as

$$U = U^I + U^{II} + U^{III} = \Phi_m^{III} + \Phi_f^{III} - \Phi_m^0 - \Phi_f^0 + U_{mc} + U_{db} + W_{sl}, \quad (7)$$

where W_{sl} is the total energy dissipation per unit volume due to frictional sliding in Stages II and III. Note that U can be calculated from the stress and strain states in the *initial and end states*. The frictional energy dissipation can also be calculated from the strain distributions in the end state, assuming the fibre sliding to occur monotonically.

3.2 Basis of unit cell model

In this paper the strain densities and frictional sliding are calculated from a simple shear-lag model, similar to Aveston *et al.*;[1] the effect of residual stresses are added (details are given in the Appendix). The model is a simple one-dimensional analysis, i.e. only the changes in the *axial* stresses and strains are considered, and the interfacial friction shear stress τ_s is assumed to be constant throughout the experiment. This is a good assumption for the accuracy of modelling presented here, since it has been found that the effects of fibre Poisson's contraction and roughness more or less cancel out.[26,27]

Initially, i.e. in the virgin state, the composite is free from external stresses, but has axial residual stresses, σ_f^{res} and σ_m^{res} in the fibre and matrix, due to a thermal expansion mismatch between fibre and matrix. Before fibre/matrix debonding has taken place, there is no slip between fibre and matrix at the interface. During multiple matrix cracking the fibre and matrix debond during the loading, the matrix retracts and, relatively, the fibres slide along the interface monotonically (Fig. 4). It is assumed that the fibres slide symmetrically inside the matrix cylinder from both ends, such that there is sliding along the *entire* interface except at the middle of the matrix cylinder ($0<x<s/2$, Fig. 4), where sticking friction is assumed due to symmetry (the condition for full slip is given in the Appendix).

3.3 Geometrical considerations

A unit cell model is depicted in Fig. 4. The cylindrical volume cell represents a single fibre of radius, a, surrounded by a matrix cylinder. The length of the cell is s, corresponding to the matrix crack spacing, and the outer radius of the matrix cylinder is such that the fibre volume fraction is f. The cross-section area A_f of the fibre is

$$A_f = \pi a^2. \quad (8)$$

The interfacial surface area A_s is

$$A_s = 2\pi a s, \quad (9)$$

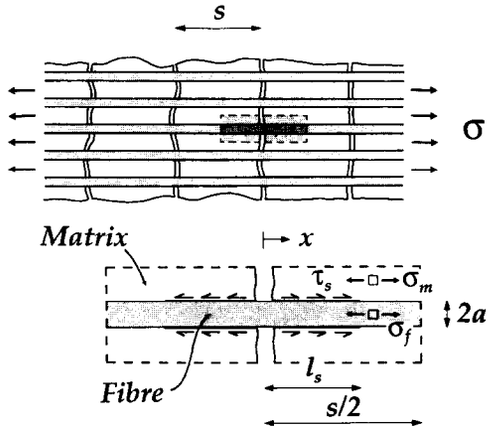


Fig. 4. The axisymmetric unit cell used in the analysis.

the cross-section area of the matrix is

$$A_m = \frac{1-f}{f}\pi a^2 \tag{10}$$

and the total volume of the cell is

$$V = \frac{\pi a^2 s}{f}. \tag{11}$$

3.4 Multiple matrix cracking

During multiple matrix cracking one crack is formed within each volume cell (Fig. 4). Thus the energy absorped per unit volume of the composite is

$$U_{mc} = \frac{G_m A_m}{V} = \frac{G_m}{s}(1-f), \tag{12}$$

where G_m is the critical energy release rate of the matrix, and eqns (10) and (11) have been used.

3.5 Fibre/matrix debonding

For each unit cell there is debonding over the surface A_s, such that the energy absorbed due to fibre/matrix debonding per unit volume of the composite is

$$U_{db} = \frac{G_{db} A_s}{V} = 2f\frac{G_{db}}{a}, \tag{13}$$

where G_{db} is the critical (mode II) energy release rate of the interface, and eqns (9) and (11) have been used. Note that an advantage of this approach is that the estimates of U_{mc} and U_{db} are independent of the load level at which matrix cracking and debonding take place.

3.6 Strain energy in matrix and fibre

The strain energy densities due to residual stresses are

$$\Phi_m^0 = \frac{A_m s}{V}\frac{1}{2}\frac{(\sigma_m^{res})^2}{E_m} = \frac{1-f}{2}\frac{(\sigma_m^{res})^2}{E_m}, \tag{14}$$

and

$$\Phi_f^0 = \frac{A_f s}{V}\frac{1}{2}\frac{(\sigma_f^{res})^2}{E_f} = \frac{(1-f)^2}{2f}\frac{(\sigma_m^{res})^2}{E_f}, \tag{15}$$

where the force balance of the residual stress components in the axial direction,

$$f\sigma_f^{res} + (1-f)\sigma_m^{res} = 0, \tag{16}$$

and eqns 8 and 11 have been used. The strain energy density in the matrix during full sliding along the fibre/matrix interface can be derived from the strain state in the matrix (Appendix), using eqns (10) and (11),

$$\Phi_m^{III} = \frac{A_m}{V/2}\int_0^{s/2}\frac{1}{2}E_m\epsilon_m^2(x)\,dx = \frac{1}{6}\frac{f^2}{1-f}\frac{s^2}{a^2}\frac{\tau_s^2}{E_m}, \tag{17}$$

where the strain is defined to be zero at the stress free state at room temperature. The factor 2 in the denominator before the integral is to account for the integration being only over half the volume of the unit cell shown in Fig. 4 (from the fibre end to the centre of the matrix block).

Likewise, the strain energy density in the fibres during full slip is (by eqns 8 and 11)

$$\Phi_f^{III} = \frac{A_f}{V/2}\int_0^{s/2}\frac{1}{2}E_f\epsilon_f^2(x)\,dx = \frac{1}{2}\frac{\sigma_u^2}{fE_f} + \frac{f}{6}\frac{s^2}{a^2}\frac{\tau_s^2}{E_f} - \frac{1}{2}\frac{\sigma_u}{E_f}\frac{s}{a}\tau_s, \tag{18}$$

where the composite strength is given by the failure strain (Appendix)

$$\sigma_u = f\epsilon_u E_f + \frac{f}{2}\frac{s}{a}\tau_s + f\sigma_f^{res}. \tag{19}$$

3.7 Interfacial frictional sliding

The energy dissipation due to frictional sliding can be assessed by considering the difference in displacement fields between the matrix and fibre at the end state (the maximum applied stress at the point of failure) and the initial state (prestressed with the residual stresses), i.e. from the difference in the displacement fields of fibre and matrix of half the volume cell,

$$W_{sl}(\sigma) = \frac{2}{V}\int_0^{s/2} |\, v_m(\sigma, x) - v_f(\sigma, x)\,|\, 2\pi a\,\tau_s\,dx, \tag{20}$$

where v_m and v_f are the displacement fields of the matrix and fibre at the applied stress σ, defined to be zero before loading (i.e. v_f and v_m are zero when the residual stresses act alone). The factor 2 in front of the integral is to account for the integration being only over the half volume of the unit cell. Using the displacement fields derived in the Appendix, the energy dissipation due to sliding is found by combining eqns (11), (19) and (20),

$$W_{sl} = \frac{f}{2}\frac{s}{a}\left(\epsilon_u + \frac{\sigma_m^{res}}{E_m}\right)\tau_s - \frac{f}{12}\frac{s^2}{a^2}\left(\frac{4f}{1-f}\frac{\tau_s^2}{E_m} + \frac{\tau_s^2}{E_f}\right). \tag{21}$$

Table 1. Properties of fibres, matrices and composites

		SiC/CAS II	*SiC/LAS III*	*SiC/MAS*	SiC/1723
Fibre					
	E_f (GPa)	200	200	200	200
	a (μm)	7·5	7·5	7·5	7·5
Matrix					
	E_m (GPa)	98	85	75[a]	86
	G_m (J/m^2)	25[b]	30[c]	40[a]	40
Composite					
	f	0·35	0·3[d]–0·50	0·45	0·35–0·4
	τ_s (MPa)	5–15[e]	2	1·5[a]	86
	G_{db} (J/m^2)	0·04[f]	0·04[f]	0·04[f]	0·04[f]
	s (μm)	160	400	100	100
	ϵ_u (%)	0·9	0·77[c]	0·36	1·2
	σ_m^{res} (MPa)	70	−50[c]	175	69

The data for SiC/MAS are from ref. 34, [a]supplemented by data for SiC/MAS-L[36].
Data for SiC/CAS II are from ref. 19, except for [b](ref. 17).
The data for SiC/LAS III are from ref. 32; [c]from ref. 33.
[d]Value calculated from the initial composite modulus, E_c.
[e]Lowest value from ref. 31, highest value from ref. 14.
[f]Data from ref. 28.
[g]The data for SiC/1723 are from ref. 12.

4 Results

4.1 Available material data

Table 1 shows the available material data for four continuous fibre-reinforced ceramic composites. The values of G_{db} were taken from Marshall and Oliver,[28] who measured this property on SiC/LAS III with a single fibre push-in method. Since the interphases of most composites consist mainly of carbon,[29,30] an identical value of G_{db} was assigned for all composites. In the literature there is some variation on the values of the interfacial sliding friction for SiC/CAS II, ranging from τ_s = 5 MPa (estimated from the energy dissipation calculated by the fatigue hysteresis loop method[31]) to 15 MPa (found by a single fibre indentation method[14]). For the SiC/LAS III composite[32] Cao *et al.*[33] reported the measured composite modulus E_c to be 120 GPa and a fibre volume fraction of f = 0·5. However, using the rule of mixtures, (eqn 29), f can be calculated from E_c to be f = 0·3. For the SiC/MAS composite[34] a value of $\alpha_m = 5 \times 10^{-6}$ °C^{-1} was used in the calculation of the residual stresses.[35] However, Martin *et al.*[36] reported $\alpha_m = 3 \times 10^{-6}$ °C^{-1} for a MAS-L matrix.

4.2 Comparison of predictions to experiments

Using the material data given in Table 1 and eqns (12)–(15), (17)–(19) and (21), the individual contribution of each mechanism can be calculated, and using eqn (7) the total energy uptake, the value of U can be predicted (Table 2). The experimental results lie close to the theoretical predictions. Some deviations, however, are found, particularly for the SiC/MAS composite. For this material the predicted value is lower than the measured. However, this may be attributed to poor estimates of the residual stresses, since there appears to be some disagreement on the reported values of the thermal expansion mismatch. Neglecting the residual

Table 2. Toughness, predictions and experiments

	SiC/CAS II	*SiC/LAS III*	*SiC/MAS*	*SiC/1723*
U_{mc} (MJ/m^3)	0·10	0·04–0·05	0·22	0·26–0·28
U_{db} (MJ/m^3)	0·004	0·003–0·005	0·005	0·003–0·004
Φ_m^0 (MJ/m^3)	0·016	0·007–0·010	0·11	0·018–0·19
Φ_f^0 (MJ/m^3)	0·015	0·002–0·003	0·05	0·012–0·014
Φ_m^{III} (MJ/m^3)	0·036–0·33	0·003–0·011	0·00–0·007	0·33–0·48
Φ_f^{III} (MJ/m^3)	2·44–2·45	1·90–3·16	0·29	3·95–4·61
W_{sl} (MJ/m^3)	0·17–0·42	0·10–0·16	0·02–0·10	0·84–0·89
U (MJ/m^3)				
Predicted	2·7–3·0	2·0–3·4	0·37–0·46	5·4–6·2
Experiment	3·1	2·7	0·57	5·4

Experimental data for U are from ref. 19 for SiC/CAS II, ref. 33 for SiC/LAS III, ref. 34 for SiC/MAS and from ref. 12 for SiC/1723.

stresses completely gives $U = 0{\cdot}82$ MJ/m^3, which is higher than the experimental value. Thus, it appears that the residual stresses in SiC/MAS, (Table 1), are overestimated. Therefore, it is concluded, that the agreement between prediction and experimental results is satisfactory.

It is interesting that for all the composites the strain energy in the fibres represents more than half of the total energy uptake. Therefore, the most important parameters to raise in order to maximize the toughness are the failure strain and volume fraction of the fibres (see eqns 18 and 19). The contributions from frictional sliding and distributed matrix cracking are significant, whereas the energy absorbed due to debonding is low.

5 Discussion

5.1 Localized energy absorped by fibre pull-out

The energy absorped due to fibre fracture is fG_f per unit cross-section area (assuming, reasonably, that each fibre fails only once during pull-out), where G_f is the critical energy release rate of the fibre. This product is usually very small[6] compared to the energy dissipation due to frictional sliding, and will be neglected in the following. The energy absorption due to fibre pull out can be assessed by the concept of a bridging law (see e.g. ref. 37), where the extra energy absorped due to bridging, ΔG, is given by

$$\Delta G = \int_0^{\delta_{max}} \sigma(\delta)\, d\delta, \tag{22}$$

where δ is the opening of the matrix crack and $\sigma(\delta)$ is the bridging law, i.e. the bridging stress as function of the crack opening. Although eqn 22 was originally derived for bridging in connection with a crack tip,[38] the result is also valid for our problem (in our case the crack can be considered to be infinitely long). For a fibre broken at an average distance l_p away from the matrix crack, the stress in the fibre across the matrix crack (x=0) is (Fig. 5)

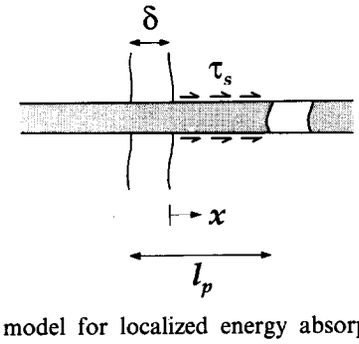


Fig. 5. The model for localized energy absorption by fibre pull-out.

$$\sigma_f(x = 0, \delta) = 2\,\frac{l_p - \delta}{a}\,\tau_s. \tag{23}$$

The bridging stress is $\sigma(\delta) = f\sigma_f(\delta)$, such that the energy absorped due to pull out, W_p, becomes (eqn 22)

$$W_p = \int_0^{l_p} 2_s \frac{l_p - \delta}{a}\,\tau_f\, d\delta = \frac{f l_p^2 \tau_s}{a}, \tag{24}$$

as also obtained elsewhere.[4,7]

Many theoretical efforts have been made to express $\sigma_f(\delta)$ and l_p by the strength variation of the fibres, described by a Weibull distribution, and the interfacial friction.[4–7] This will not be pursued here. Rather, for the purpose of comparing the magnitudes of distributed and localized energies absorped, we simply take the estimates of the mean pull out length by observations from the fracture surfaces. For the SiC/CAS II composite l_p has been reported[17,39] to be in the order of 0·2 mm, giving $W_p = 28$ kJ/m^2.

5.2 Fracture stability and total energy absorption of test specimens

Consider a specimen subjected to uniaxial tension in the fibre direction. Distributed damage (matrix cracking, fibre/matrix debonding and interfacial sliding) operates until the maximum load (the failure load) is reached. From then on the history depends on loading mode. If the test is performed under constant loading rate (load control), the specimen fractures unstably. If the experiment is controlled by the opening of the matrix crack where specimen separation occurs, fracture may take place in a quasi-static manner (solid line, Fig. 6). Although the crack opening, δ, increases monotonically, the overall elongation, Δ, decreases initially, as 'elastic' contraction takes place (due to decreasing load) in the specimen away from the localization. During this unloading the fibres away from the fracture locus contract more in the axial direction than the matrix, leading to energy dissipation by reverse interfacial sliding. In the final stages the overall elongation, Δ, may increase again, if the δ increases with a faster rate than the 'elastic' contraction. In case the experiment is conducted at constant displacement rate, a non-equilibrium load-drop will occur during localization (dashed line, Fig. 6). Depending upon the bridging law and specimen length, L, a tail may occur during separation if the maximum pull out length, $(l_p)_{max}$, is larger than the length change (contraction) due to unloading of the specimen (see Appendix), i.e. if

$$\epsilon_u - \frac{s}{2a}\frac{\tau_s}{E_f} + \frac{\sigma_f^{res}}{E_f} \le \frac{(l_p)_{max}}{L}. \tag{25}$$

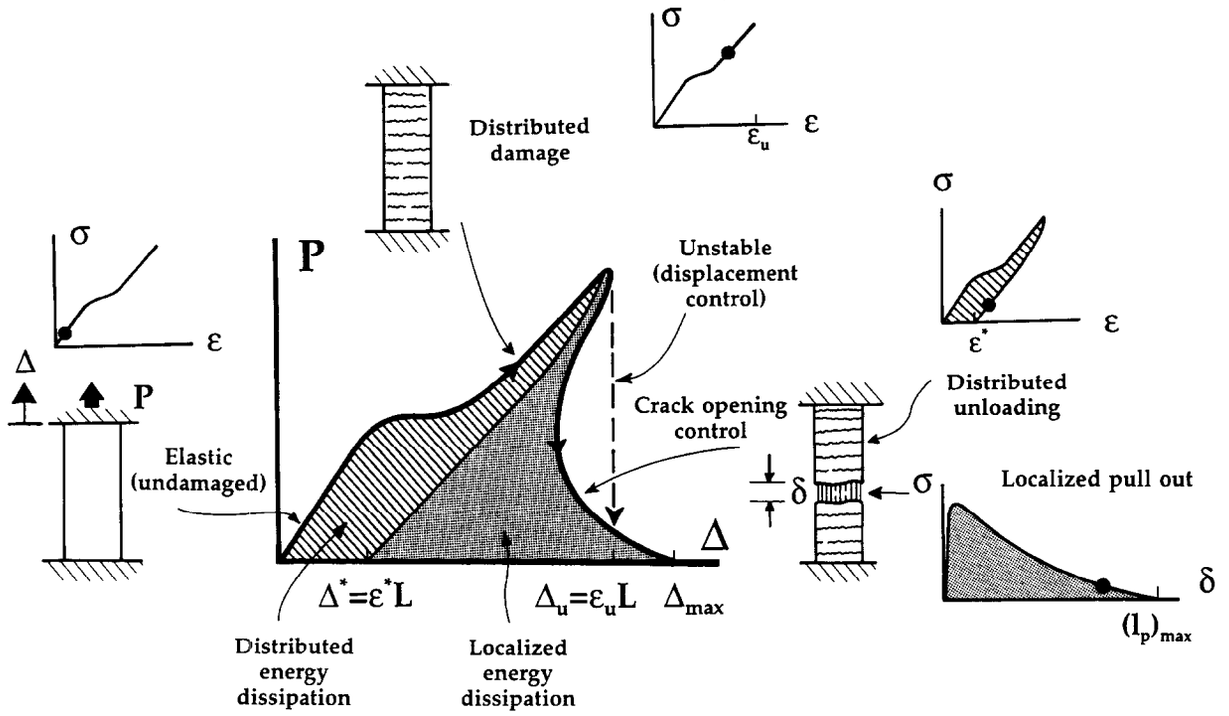


Fig. 6. Schematic illustration of overall load–displacement curve, distributed and localized energy dissipation during loading, fracture and separation of a tensile specimen. The solid line is the load–displacement curve that would occur if the experiment was conducted under crack opening (δ) control, while the dotted line indicates the unstable fracture that takes place under control of the displacement of the specimen. The deformation during loading is due to distributed phenomena, while the down-going part comprises distributed deformation ϵL and localized crack opening δ.

Thus, regarding ϵ_u and $(l_p)_{max}$ as material constants, a tail (stable fracture) will only appear if the specimen length is sufficiently short. Using the material data for SiC/CAS II and SiC/LAS III (Table 1) and $(l_p)_{max}$ = 0·4 mm for the SiC-fibres, the critical length is calculated to be $L \approx 50$ mm. The experimental results of Cao *et al.*[32] were obtained with a gauge length of 15 mm, and a small tail was measured by extensometer. The experiments of Sørensen and Talreja[19] were also conducted in displacement control, but on specimens with longer gage section (80 mm). The fracture occurred unstably (i.e. no tail), although fibre pull out occurred. These results are in agreement with eqn (25). There are examples in the literature where a tail, the down-going part of the load–displacement curve, has been termed as a tough behaviour, contrasting materials that did not show a down-going tail (unstable fracture). Such interpretation is incorrect and should not be accepted. As described above there is no correlation between U and the fracture stability, since *fracture stability is not a material property*, but depends on specimen length and loading condition. Instead, we suggest that attention should be focused on whether amaterial is damage tolerant or flaw sensitive.

As indicated in Fig. 6, the total energy dissipation (the area under the quasi-static load–displacement curve (solid line)) comprises two sources, distributed energy dissipation and localized pull out energy dissipation. During loading the energy dissipation per unit volume by distributed mechanisms is the non-recoverable part of the toughness, i.e. U_{mc}, U_{db}, and W_{sl}. During unloading the reverse sliding that takes place along the fibre/matrix interface dissipates additional energy, W_{sl}^* per unit volume (superscript* indicate unloaded state). When the composite is completely free of external forces, residual stresses exist in fibre and matrix due to interfacial friction, such that strain energy is stored in fibre and matrix. Therefore, the total energy dissipation, from initial undamaged state until the specimen is fully separated, can be calculated as the sum of distributed energy dissipation and localization

$$\int_0^{\Delta_{max}} P(\Delta)\mathrm{d}\Delta = L\,A\,W_D + A\,W_p, \tag{26}$$

where W_D is the energy absorbed per unit volume of the composite by distributed mechanisms,

$$W_D = U_{mc} + U_{db} + W_{sl} + W_{sl}^* + \Phi_m^* + \Phi_f^* - \Phi_m^0 - \Phi_f^0, \tag{27}$$

and W_p is the pull-out energy per unit area. The energy dissipation due to reverse sliding (full slip) per unit volume of the composite is

$$W_{sl}^{*} = \frac{2}{V}\int_{0}^{s/2} | (v_m - v_m^{*}) - (v_f - v_f^{*}) | 2\pi a \tau_s \, dx =$$

$$\frac{s}{2a}\frac{\sigma_u}{E_f}\tau_s - \frac{2}{3}\frac{f}{1-f}\frac{s^2}{a^2}\frac{E_c}{E_m}\frac{\tau_s^2}{E_f}, \quad (28)$$

where E_c is

$$E_c = f E_f + (1-f) E_m. \quad (29)$$

The strain energy of the fibres per unit volume of the composite is (in similar fashion to eqn (18) on noting that the applied stress is zero and the sign in front of τ_s is changed since the slip direction is reversed)

$$\Phi_f^{*} = \frac{f}{6}\frac{s^2}{a^2}\frac{\tau_s^2}{E_f} \quad (30)$$

and that of the matrix is $\Phi_m^{*} = \Phi_m^{III}$. From eqn (26) it follows that the energy dissipation by distributed mechanisms increases with an increasing specimen length, while the pull out energy dissipation does not. An important consequence of this is that the distributed energy dissipation can be raised as much as one desires simply by increasing L. Therefore, the concept of work of fracture, γ_{WOF} (eqn 3), is not applicable for this class of materials.

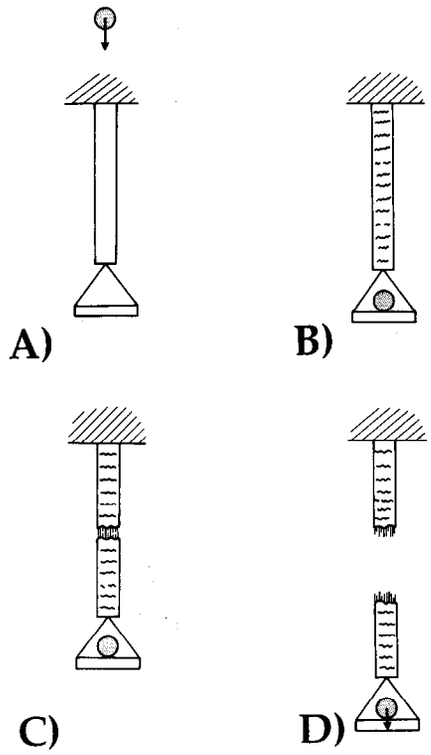


Fig. 7. (A) An impact loading at a component made of a damage tolerant ceramic matrix composite. (B) All the kinetic energy is absorbed by distributed energy uptake. (C) The kinetic energy is absorbed by distributed and localized energy mechanisms. (D) The kinetic energy is higher than what can be absorbed by distributed and localized mechanisms, so the component fractures.

5.3 Energy absorption and fracture stability of components

Now consider an *impact loading of a component* in service (Fig. 7A). This situation is different from a displacement controlled tensile test. In this case it is the actual amount of kinetic energy transferred to the specimen in the form of deformation energy that determines how the fracture behaviour will be. Consider an object hitting the composite component such that the direction of the moving object is in the fibre direction, and that during the impact the object causes uniform tension in the composite. Will the composite break, and in case it does, in which manner?

The first possibility is that the kinetic energy is lower than the total available distributed energy uptake, $U_L A$ (Fig. 7B). Then the composite will absorb the energy without fracture (it will be damaged, but it will not break). Alternatively, when the kinetic energy is higher than $U_L A$, the composite will fracture; the fibres will break, and the composite will lose strength. In this scenario, however, two possibilities exist: (1) If the kinetic energy is higher than the total fracture initiation energy but lower than the total energy dissipation (eqn 26), the component will be damaged and partly fractured (Fig. 7C); with fibres broken and partly pulled out. The composite will lose strength, because the two parts of the composite are only kept together by frictional stresses acting at the broken fibres. (2) If the impact energy is higher than the total fracture initiation energy and higher than the total energy absorped (eqn 26) (Fig. 7D), then the component will fracture unstably, since it cannot absorb the kinetic energy of the object.

Imagine that the component was a turbine blade in a jet-engine (this is a typical considered application for ceramic matrix composites). In such an application it is very important whether or not the component fractures, since a fractured blade may lead to total failure of the engine (this could be fatal for the aircraft). Now, if a turbine blade was hit by a bird or a stone having a specific amount of kinetic energy, what would happen to the component? If $U_L A$ was sufficient to absorb the energy, then the component would be *damaged*, but it would *retain its strength*. Thus, the aircraft would be able to land safely and the damaged component could be replaced. If the impact energy was so high that the component fractured, the pull out energy might stop the object, but now the component strength has decreased. The inertia forces of the rotating component could be sufficiently high that the blade could fracture completely, and the engine would

fail. It follows, that for such applications, the pull-out energy has little importance for the consequences of failure. Therefore, it can be concluded that for such applications it *is not the pull-out energy, W_p, that should be optimized, but the toughness, U.*

6 Conclusions

This paper has analyzed the energy absorption of unidirectional fibre reinforced ceramic composites. A simple model has been used to assess the energy uptake of the individual damage mechanisms. Special attention has been paid to separate energy uptake by distributed and localized mechanisms, since they scale differently with specimen dimensions. The distributed energy uptake, i.e. the toughness, has been found to be mainly due to strain energy in the fibres (this represents more than half of the energy uptake), but contributions from frictional sliding and distributed matrix cracking have also been found to be important, whereas the contribution from fibre/matrix debonding has been found to be very small. The predictions have been compared to experimental values for several composites, and a good agreement between the predictions and the measured values is found. Finally, arguments have been forwarded to conclude that in some applications the energy uptake due to the distributed mechanisms should be maximized rather than the energy for fibre pull-out, giving the most desirable material response.

Acknowledgement

B.F.S. was supported by the Risø Engineering Science Centre for Structural Characterization and Modelling of Materials.

References

1. Aveston, J., Cooper, G. A. & Kelly, A., Single and multiple fracture, *The Properties of Fibre Composites, Conference Proceedings*. IPC Science and Technology Press, Guildford, UK (1971) 15–26.
2. Budiansky, B., Hutchinson, J. W. & Evans, A. G., Matrix fracture in fiber-reinforced ceramics. *J. Mech. Phys. Solids*, **34** (1986) 167–78.
3. McCartney, L. N., New theoretical model of stress transfer between fibre and matrix in a uniaxially fibre-reinforced composite. *Proc. R. Soc. Lond.*, **A425** (1989) 215–44.
4. Sutcu, M., Statistical fibre failure and single crack behaviour in uniaxially reinforced ceramic composites. *J. Mater. Sci.*, **23** (1988) 928–33.
5. Thouless, M. D. & Evans, A. G., Effects of pull-out on the mechanical properties of ceramic-matrix composites. *Acta Metall.*, **36** (1988) 517–22.
6. Curtin, W. A., Theory of mechanical properties of ceramic matrix composites. *J. Am. Ceram. Soc.*, **74** (1991) 2837–45.
7. Cousland, S. McK., The contribution of fibre pull-out to the work of fracture of a metal-matrix composite, for the case of non-interacting fibres. *Materials Forum*, **16** (1993) 327–34.
8. Talreja, R., Continuum modelling of damage in ceramic matrix composites. *Mechanics Materials*, **12** (1991) 165–80.
9. Holmes, J. W. and Sørensen, B. F., Fatigue behavior of continuous fiber reinforced ceramic matrix composites. In *Elevated Temperature Behavior of Ceramic Matrix Composites*, eds S. V. Nair and K. Jakus. Butterworth Heineman, (1995) in press.
10. Evans, A. G., Zok, F. W. & Davis, J., The role of interfaces in fiber-reinforced brittle matrix composites. *Compos. Sci. Technol.*, **42** (1991) 3–24.
11. Prewo, K. M., Fatigue and stress rupture of silicon carbide fiber-reinforced glass-ceramics. *J. Mater. Sci.*, **22** (1987) 2695–701.
12. Mandell, J. F., Grande, D. H. & Dannemann, K. A., High temperature testing of glass/ceramic matrix composites, *Test Methods for Design Allowable for Fibrous Composites*, Vol. 2, ASTM STP 1003, ed. Chamis, C. C. American Society for Testing and Materials (1989) 3–15.
13. Holmes, J. W., Kotil, T. & Foulds, W. T., High temperature fatigue of SiC fibre-reinforced Si_3N_4 ceramic composites. In *Proceedings, Symposium on High Temperature Composites*. Technomic, Basel, (1989) 176–86.
14. Wang, S.-W. & Parvizi-Majidi, A., Mechanical behaviour of Nicalon fiber reinforced calcium aluminosilicate matrix composites. *Ceram. Engng. Sci. Proc.*, **11** (1990) 1607–16.
15. Kim, R. Y. & Pagano, N. J., Crack initiation in unidirection brittle-matrix composites. *J. Am. Ceram. Soc.*, **74** (1991) 1082–90.
16. Barsoum, M. W., Kangutkar, P. & Wang, A. S. D., Matrix crack initiation in ceramic matrix composites, part I. Experiment and test results. *Compos. Sci. Technol.*, **44** (1992) 257–70.
17. Beyerle, D. S., Spearing, S. M., Zok, F. W. & Evans, A. G., Damage and failure in unidirectional ceramic-matrix composites. *J. Am. Ceram. Soc.*, **75** (1992) 2719–25.
18. Karandikar, P. & Chou, T.-W., Characterization and modelling of microcracking and elastic moduli changes in Nicalon/CAS. *Compos. Sci. Technol.*, **46** (1993) 253–63.
19. Sørensen, B. F. & Talreja, R., Analysis of damage in a ceramic matrix composite. *Int. J. Damage Mech.*, **2** (1993) 246–71.
20. Hertzberg, R. W., *Deformation and Fracture of Engineering Materials*, 3rd Edn. John Wiley and Sons, New York, (1989) 26.
21. Kanninen, M. F. & Popelar, C. H., *Advanced Fracture Mechanics*. Oxford University Press, New York, (1985) 159.
22. Sakai, M. & Bradt, R. C., Fracture toughness of brittle materials. *Int. Mater. Rev.*, **38** (1993) 53–78.
23. Marshall, D. B. & Evans, A. G., Failure mechanisms in ceramic-fiber ceramic-matrix composites. *J. Am. Ceram. Soc.*, **68** (1985) 221–31.
24. Holmes, J. W., A technique for tensile fatigue and creep testing of fiber-reinforced ceramics. *J. Compos. Mater.*, **26** (1992) 915–32.
25. Sørensen, B. F. & Holmes, J. W., Effect of loading rate on the monotonic tensile behavior and matrix cracking of a fiber-reinforced ceramic. *J Am. Ceram. Soc.*, (1995) accepted.
26. Marshall, D. B., Shaw, M. C. & Morris, W. L., Measurement of interfacial debonding and sliding resistance in fiber reinforced intermetallics. *Acta Metall. Mater.*, **40** (1992) 443–54.
27. Sørensen, B. F., Effect of fibre roughness on the overall stress–transverse strain response of ceramic composites. *Scrip. Metall. Mater.*, **28** (1993) 435–9.

28. Marshall, D. B. & Oliver, W. C., Measurements of interfacial mechanical properties in fiber-reinforced ceramic composites. *J. Am. Ceram. Soc.*, **70** (1987) 542–8.
29. Bischoff, E., Rühle, M., Sbaizero, O. & Evans A. G., Microstructural studies of the interface zone of a SiC-fiber-reinforced lithium aluminum silicate glass-ceramic. *J. Am. Ceram. Soc.*, **72** (1989) 741–45.
30. Bonney, L. A. & Cooper, R. F., Reaction layer interfaces in SiC-fiber-reinforced glass-ceramics: a high-resolution scanning transmission electron microscopy analysis. *J. Am. Ceram. Soc.*, **73** (1990) 2916–26.
31. Cho, C., Holmes, J. W. & Barber, J. R., Estimation of interfacial shear in ceramic composites from frictional heating measurements. *J. Am. Ceram. Soc.*, **74** (1991) 2808–8.
32. Cao, H. C. & Thouless M. D., Tensile tests of ceramic-matrix composites: Theory and experiments. *J. Am. Ceram. Soc.*, **73** (1990) 2091–4.
33. Cao, H. C., Bischoff, E., Sbaizero, O., Rühle, M., Evans, A. G., Marshall, D. B. & Brennan, J. J., Effect of interfaces on the properties of fiber-reinforced ceramics. *J. Am. Ceram. Soc.*, **73** (1991) 1691–9.
34. Ricca, N., Guette, A., Camus, G. & Jouin, J. M., SiC (ex. PCS)/MAS composite with a BN interphase: microstructure, mechanical properties and oxidation resistance. In *High Temperature Ceramic Matrix Composites, HT-CMC1*, eds R. Naslain, J. Lamon & D. Doumeingts. Woodhead UK (1993) 455–62.
35. Khodakovskaya, R. Y. & Pavlushkin, N. M., Structure and properties of metastable quartzitic phases in sitalls in the SiO_2–Al_2O_3–MgO–TiO_2 system. *Inorg. Mater.*, **3** (1967) 1662–8.
36. Martin, B., Benoit, M. & Rouby, D., Interfacial sliding strength in fibre reinforced ceramic matrix composites mvolving positive radial thermal misfit. *Scripta Metall. Mater.*, **28** (1993) 1429–33.
37. Suo, Z., Bao, G., & Fan, B., Delamination R-curve phenomena due to damage. *J. Mech. Phys. Solids*, **40** (1992) 1–16.
38. Rice, J. R., A path independent integral and the approximate analysis of strain concentrations by notches and cracks. *J. Appl. Mech.*, **35** (1968) 379–86.
39. Rousseau, C. Q., Davidson, D. L. & Campbell, J. B., The micromechanics of ambient temperature cyclic loading fatigue in a composite of CAS glass ceramic reinforced with Nicalon fibers. *J. Comp. Tech. Res.*, **16** (1994) 115–26.
40. Pryce, A. W. & Smith, P. A., Matrix cracking in unidirectional ceramic matrix composites under quasi-static and cyclic loading. *Acta Metall. Mater.*, **41** (1993) 1269–81.

Appendix

A.1 Strain fields

Before matrix cracking and interfacial debonding the composite exhibits residual stresses, e.g. due to thermal expansion mismatch. We define the strains to be zero at stress free state at room temperature. Then the strain fields in matrix and fibres due to the residual stresses are

$$\epsilon_m^{res} = \frac{\sigma_m^{res}}{E_m}, \qquad \text{(A1)}$$

and

$$\epsilon_f^{res} = \frac{\sigma_f^{res}}{E_f}. \qquad \text{(A2)}$$

When matrix cracking and fibre/matrix debonding take place frictional sliding takes place along the interface as the matrix retracts. After application of the external force the strains in the slip region are, with reference to the coordinate system in Fig. 4,

$$\epsilon_m(\sigma, x) = 2\frac{f}{1-f}\frac{x}{a}\frac{\tau_s}{E_m} \quad 0 \le x \le l_s(\sigma) \qquad \text{(A3)}$$

and

$$\epsilon_f(\sigma, x) = \frac{\sigma}{fE_f} - 2\frac{x}{a}\frac{\tau_s}{E_f} \quad 0 \le x \le l_s(\sigma). \qquad \text{(A4)}$$

In these expressions, l_s is the sliding length along the interface, measured from the matrix crack (Fig. 4). The sliding length can be found as the position x along the interface where the fibre and matrix strain changes are identical, $\epsilon_f(l_s) - \epsilon_f^{res} = \epsilon_m(l_s) - \epsilon_m^{res}$, giving

$$\frac{l_s(\sigma)}{a} = \frac{1-f}{2}\left[\frac{\sigma}{f\tau_s}\frac{E_m}{E_c} - \frac{\sigma_f^{res}}{\tau_s}\frac{E_m}{E_c} + \frac{\sigma_m^{res}}{\tau_s}\frac{E_f}{E_c}\right], \qquad \text{(A5)}$$

as also found by Pryce and Smith.[40] From eqns (A5) and (29) it follows that there is sliding along the *entire* interface ($l_s = s/2$), when the applied stress exceeds a characteristic value, σ_{FS} (subscripts indicate Full Slip)

$$\frac{\sigma_{FS}}{fE_f} = \frac{\sigma_f^{res}}{E_f} - \frac{\sigma_m^{res}}{E_m} + \frac{1}{1-f}\frac{s}{a}\frac{\tau_s}{E_f}\frac{E_c}{E_m}. \qquad \text{(A6)}$$

Above this stress level, the stress and strain states in the matrix do not change. This is a consequence of the assumption in the model that τ_s does not change. When the terms of the residual stresses are dropped in eqns (A5) and (A6), they become identical to the results in ref. 31. Inserting the strains gives the strain densities in eqns 17 and 18.

A.2 Displacement fields during loading

The displacement fields at a stress σ (after multiple matrix cracking and debonding) are, for the case of full sliding, then found by integration of the strains,

$$\int_{v_m(x)}^{v_m(x=s/2)} dv_m = \int_x^{s/2}\left[\epsilon_m(\sigma, x) - \frac{\sigma_m^{res}}{E_m}\right]dx \qquad \text{(A7)}$$

and

$$\int_{v_f(\sigma, x)}^{v_f(x=s/2)} dv_f = \int_x^{s/2}\left[\epsilon_f(\sigma, x) - \frac{\sigma_f^{res}}{E_f}\right]dx, \qquad \text{(A8)}$$

where the last terms represent the displacements due to the release of the residual stress during debonding, eqns (A1) and (A2). In eqns (A7) and (A8) $v_m(x=s/2)$ and $v_f(x=s/2)$ are the displacements at the centre of the matrix block. They are identical, since there is no sliding at the centre of the matrix block, and cancel out, when inserting into

eqn (20). Inserting eqns (A3) and (A4) into (A7) and (A8) gives

$$v_m(x) = v_m(x=s/2) - \frac{f}{1-f}\frac{\tau_s}{E_m}\left(\frac{s^2}{4a} - \frac{x^2}{a}\right) + \frac{\sigma_m^{res}}{E_m}\left(\frac{s}{2} - x\right) \quad \text{(A9)}$$

and

$$v_f(\sigma, x) = v_f(x=s/2) + \frac{\tau_s}{E_f}\left(\frac{s^2}{4a} - \frac{x^2}{a}\right) + \left(\frac{\sigma_f^{res}}{E_f} - \frac{\sigma}{fE_f}\right)\left(\frac{s}{2} - x\right). \quad \text{(A10)}$$

Inserting these displacements into eqn 20 gives the frictional energy dissipation (eqn 21).

A.3 Displacement fields during unloading

After fracture, as the specimen unloads the sliding direction changes, as the fibres contract and slide into the matrix. Then, the sign in front of τ_s changes in eqns (A3) and (A4). When the specimen is completely free of external load, the displacement fields are

$$v_m^*(\sigma = 0, x) = v_m^*(x=s/2) + \frac{f}{1-f}\frac{\tau_s}{E_m}\left(\frac{s^2}{4a} - \frac{x^2}{a}\right) + \frac{\sigma_m^{res}}{E_m}\left(\frac{s}{2} - x\right) \quad \text{(A11)}$$

and

$$v_f^*(\sigma = 0, x) = v_f^*(x=s/2) - \frac{\tau_s}{E_f}\left(\frac{s^2}{4a} - \frac{x^2}{a}\right) + \frac{\sigma_f^{res}}{E_f}\left(\frac{s}{2} - x\right). \quad \text{(A12)}$$

Inserting these displacements gives the frictional energy dissipation, W_{sl}^* (eqn 28).

A.4 Overall composite strain

The maximum composite strain during loading can be estimated by the average elongation of the unit cell, using eqn A4 (assuming full sliding),

$$\epsilon_u = \frac{2}{s}\int_0^{s/2} \epsilon_f(\sigma_u, x) - \frac{\sigma_f^{res}}{E_f}\,dx = \frac{\sigma_u}{fE_f} - \frac{s}{2a}\frac{\tau_s}{E_f} - \frac{\sigma_f^{res}}{E_f}. \quad \text{(A13)}$$

The strain offset after unloading is (full sliding)

$$\epsilon^* = \frac{s}{2a}\frac{\tau_s}{E_f} - \frac{\sigma_f^{res}}{E_f}, \quad \text{(A14)}$$

on noting that the sign of in front of τ_s is changed and σ vanishes. Subtracting these two strain values gives the strain change during unloading, i.e. the left hand side of eqn 25.

Journal of the European Ceramic Society **15** (1995) 1061–1064
© 1995 Elsevier Science Limited
Printed in Great Britain. All rights reserved
0955-2219(95)00080-1
0955-2219/95/$9.50

On the Paradox Between Crack Bridging and Crack Interaction In Quasi-Brittle Materials

Kai Duan[a], Yiu-Wing Mai[b] & Brian Cotterell[c]

[a]CSIRO Division of Exploration and Mining, PO Box 883, Kenmore, QLD 4069, Australia
[b]Centre for Advanced Materials Technology, Department of Mechanical and Mechatronic Engineering, University of Sydney, Sydney, NSW 2006, Australia
[c]School of Mechanical and Production Engineering, Nanyang Technological University, Nanyang Avenue, Singapore 2263

(Received 16 January 1995; revised version received 18 May 1995; accepted 19 May 1995)

Abstract

Discontinuous cracks observed in quasi-brittle materials subjected to fracture mechanics testing may be idealised by two mechanical models, i.e. an interaction model between the main crack and collinear small cracks, and a crack-wake bridging model. A study on these two models is presented in this paper and it shows that the instability of the crack system is significantly dependent on the model used. While the interaction model leads to unstable crack propagation, the crack bridging model predicts stable crack growth. It is concluded that the crack bridging model is more consistent with experimental observations on fracture in quasi-brittle materials.

Introduction

Crack-bridging due to ligament and grain pull-out has been recognized as an important toughening mechanism in quasi-brittle materials such as the non-transformable ceramics and cementitious materials, and has been successfully used to explain the non-continuous crack phenomenon observed in fracture mechanics testing of such materials.[1–13] In the idealized form, however, the bridged crack may be seen as a series of collinear cracks lying ahead of the main crack tip. As a result, two ways may be used to model or analyse the stress intensities of the crack system. One considers the interaction of the microcracks with the main crack where the singularities at each crack tip are retained and the other assumes finite stresses acting over the bridges. These are referred to as the interaction model and the bridging model, respectively. As will be shown later two completely different conclusions result from these two models.

Stress Intensity Factor Analyses

Figure 1(a) shows the interaction which consists of a semi-infinite crack along the negative x axis and a finite crack located in $a<x<b$. The stress fields in the vicinity of the main crack tip can be significantly intensified because of the presence of the finite crack. In the bridging model, Fig. 1(b), the ligament between the main crack and the finite crack is considered as a bridge and its effects on crack growth can be modelled by the actual stress distribution $\sigma_b(x)$ on the bridge.

Systematic solutions for the interaction model have been obtained by using the complex potential technique.[14–17] The stress intensity factors K_t^O, K_t^a and K_t^b at the crack tips O, a and b are normalised by the applied stress intensity factor at the main crack tip K_a^O and are given by[14,16]

$$\begin{aligned} K_t^O/K_a^O &= C/k \\ K_t^a/K_a^O &= (C-k^2)/kk' \\ K_t^b/K_a^O &= (1-C)/k' \end{aligned} \tag{1}$$

where

$$\begin{aligned} C &= E(k')/K(k') \\ k^2 &= a/b \\ k' &= (1-k^2)^{1/2} \end{aligned} \tag{2}$$

E and K denote the complete elliptic integrals of the second and first kinds, respectively. The normalised true stress intensity factors are plotted in Fig. 2 where it is found that the true stress intensity factor at the main crack tip K_t^O is always the largest. Therefore, for homogeneous brittle materials, crack growth will always start from the main crack tip, and if K_a^O is constant, the link-up of the main crack with the collinear microcrack will proceed unstably.[16]

Further study by Rubinstein[14] found that the above analysis holds also for collinear multi-

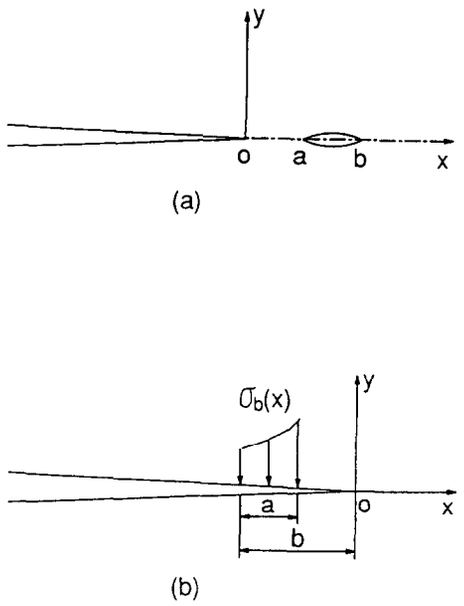


Fig. 1. Two models to study the collinear crack problem: (a) crack interaction model between a semi-infinite crack and a microcrack and (b) crack-wake bridging model.

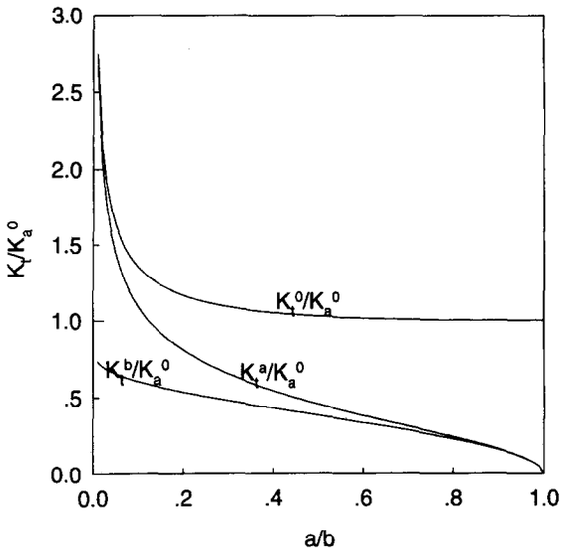


Fig. 2. True stress intensity factors normalized by the applied stress intensity factor.

microcracks. However, the stress intensity factor at the main crack tip is enlarged even further when the number of microcracks increases.

For the bridging model the ligament between the two cracks is considered as a bridge, Fig. 1(b). The true stress intensity factor K_t^O at the crack tip can be expressed as the superposition of the applied stress intensity factor K_a^O and stress intensity factor increment ΔK induced by the bridging stress on the ligament, i.e.

$$K_t^O = K_a^O + \Delta K \tag{3}$$

ΔK is usually negative and is referred to as the fracture resistance increment denoted by ΔK_R. Previous studies showed that ΔK_R due to the bridging stress $\sigma_b(x)$ can be written as[18]

$$\Delta K_R = \sqrt{\frac{2}{\pi}} \int_{b-a}^{b} \frac{\sigma_b(x)}{\sqrt{x}}\, dx \tag{4}$$

For quasi-brittle materials such as non-transformable ceramics and cements, the bridging stress $\sigma_b(x)$ usually decreases with crack face separation $w(x)$, i.e. it obeys a strain-softening law which can be approximated by[2]

$$\sigma_b(x) = \sigma_m [1 - w(x)/w_c]^n \tag{5}$$

where σ_m is the maximum bridging stress, n, softening exponent and w_c is the critical crack face separation corresponding to the saturated bridging zone length X, at which the bridging stress is zero. Further assumption that the crack faces remain straight during crack propagation leads to a simpler relationship between the bridging stress $\sigma_b(x)$ and the distance x to the crack tip, [6]

$$\sigma_b(x) = \sigma_m(1 - x/X)^n \tag{6}$$

The stress intensity factor increment due to the bridging stress can be estimated by substituting eqn (6) into eqn (4) and completing the integration. For the purposes of discussion ΔK_R for two bridging stress distributions: linear strain-softening and constant bridging stress, i.e. n = 1·0 and 0 in eqn (6), respectively are calculated. Substitute eqn (6) with n = 1·0 into eqn (4) and complete the integration, ΔK_R due to the linear strain-softening bridging stress can be obtained as

$$\Delta K_R = \sqrt{\frac{8}{\pi}}\, \sigma_m \sqrt{b}\, \{1 - k' - \frac{b}{3X}[1-(k')^3]\} \tag{7}$$

For the constant bridging stress σ_m, i.e. $n = 0$, we have

$$\Delta K_R = \sqrt{\frac{8}{\pi}}\, \sigma_m \sqrt{b}\, (1 - k') \tag{8}$$

As expected, the bridging stress reduces the stress intensity factor at the crack tip. The amount of crack shielding due to the bridging stress is related to the material parameters n and σ_m. This is different to the interacting collinear microcrack model where the stress intensity factors only depend on the dimensions of the microcracks and their spatial distribution. Corresponding to the multi-microcrack problem, the incremental resistances ΔK_R due to N ligaments with these two bridging stress functions are

$$\Delta K_R = \sqrt{\frac{8}{\pi}}\, \sigma_m \sqrt{b} \sum_{i=1}^{N} \{(\sqrt{i} - \sqrt{i - a/b} - \frac{b}{3X}[i^{3/2} - (i - a/b)^{3/2}]\} \tag{9}$$

for n = 1·0 and

$$\Delta K_R = \sqrt{\frac{8}{\pi}}\, \sigma_m \sqrt{b} \sum_{i=1}^{N} \{(\sqrt{i} - \sqrt{i - a/b})\} \tag{10}$$

for $n = 0$.

Instability of Crack System

The instability of materials containing cracks is dependent on the resistance to crack propagation. For ideally brittle materials, unstable crack propagation would proceed if the net stress intensity factor at a crack tip is equal to or above the critical stress intensity factor K_{Ic}. In the interaction model, the true stress intensity factor K_t^0 at $x = 0$ is always the largest. Therefore, the instability of the system is always preceded by unstable propagation of the main crack. This implies that the interaction situation can not be observed unless there are pre-existing microcracks ahead of the main crack. Based on eqn (1), it is also seen that the fracture resistance reduces because of the presence of the collinear microcrack.

For the bridging model with $n = 1{\cdot}0$, the fracture resistance increment ΔK_R can be expressed as

$$\Delta K_R / \sqrt{\frac{8}{\pi}}\,\sigma_m \sqrt{X} = \sqrt{\frac{b}{X}}\left\{1-k' - \frac{b}{3X}[1-(k')^3]\right\} \tag{11}$$

and for $n = 0$, one has

$$\Delta K_R / \sqrt{\frac{8}{\pi}}\,\sigma_m \sqrt{X} = \sqrt{\frac{b}{X}}(1-k') \tag{12}$$

Shown in Fig. 3 is the change of ΔK_R, due to a bridge of fixed width a with increasing distance from the crack tip. It can be seen that ΔK_R decreases as the crack advances. This indicates that the single bridging ligament can not result in stable crack propagation when subjected to steady-state loading even if it enhances the effective fracture toughness. However, if discrete bridges are developed continuously as the crack advances, an increasing ΔK_R can be obtained because the bridging stress effects from the bridges near the crack tip are much larger than those far away from it. As a result, stable crack growth can be observed when ΔK_R is larger than the crack driving stress intensity factor increment, ΔK_a.

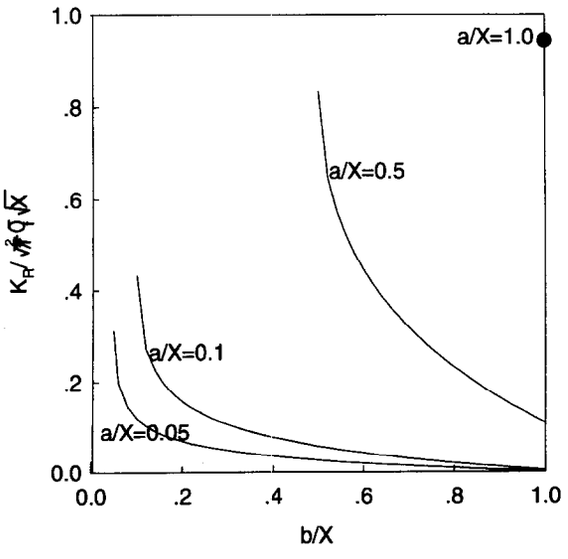


Fig. 3. Fracture resistance curves due to linear strain-softening bridging stress.

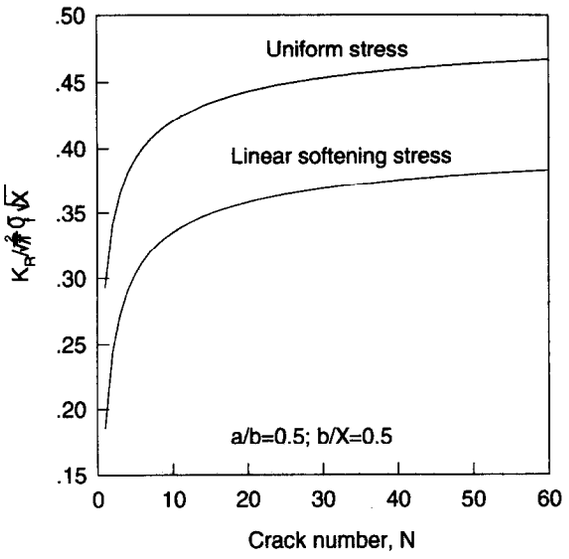


Fig. 4. Change of fracture resistance increment ΔK_R with microcrack number N.

The effect of crack number N on ΔK_R is shown in Fig. 4 where the distance between main crack tip and the most remote microcrack tip is assumed to be a constant b ($b/X = 0{\cdot}5$). For a given a/b ($0{\cdot}5$), the crack shielding effects due to bridging stresses of the ligaments increase with increasing crack number N and tend to a plateau value dependent on a/b.

Conclusions

The collinear crack problem can be simplified as two idealised mechanics models: crack interaction and crack bridging. But the two simplifications lead to two completely different conclusions. Crack propagation based on the interaction model is unstable. However, stable crack propagation can be achieved based on the crack bridging model if discrete bridges are continuously developed with the advancing crack. The increased fracture resistance from the bridging model are dependent on both geometry and material properties. Unless pre-existing microcracks are observed the collinear crack system found in the fracture of quasi-brittle materials is usually caused by crack bridging.

References

1. Krehans, R. & Steinbrech, R. W., Memory effect of crack resistance during slow crack growth in notched Al_2O_3 bend specimens. *J Mater. Sci. Lett.*, **1** (1982) 327–9.

2. Foote, R. M. L., Mai, Y.-W. & Cotterell, B., Crack growth resistance curves in strain-softening materials, *J. Mech. Phys. Solids*, **34** (1986) 593–607.
3. Swanson, P. L., Fairbanks, C. J., Lawn, B. R., Mai, Y.-W. & Hockey, B. J., Crack-interface grain bridging as a fracture resistance mechanism in ceramics: I, experimental study on alumina. *J. Am. Ceram. Soc.*, **70** (1987) 279–89.
4. Mai, Y.-W. & Lawn, B. R., Crack-interface grain bridging as a fracture resistance mechanism in ceramics: II, theoretical fracture mechanics model, *J. Am. Ceram. Soc.*, **70** (1987) 289–94
5. Mai, Y.-W., Fracture resistance and fracture mechanisms of engineering materials, *Mater. Forum*, **11** (1988) 230–67.
6. Cotterell, B. & Mai, Y.-W., Modelling crack growth in fibre-reinforced cementitious materials, *Mater. Forum*, **11** (1988) 341–51.
7. Steinbrech, R. W., Reichl, A. & Schaarwachter, W., *R*-curve behaviour of long cracks in alumina, *J. Am. Ceram. Soc.*, **73** (1990) 2009–15.
8. Hu, X.-Z. & Wittmann, F. H., Experimental method to determine extension of fracture process zone, *J. Mater. Civil Engng., (ASCE)*, **2** (1990) 15–23.
9. Duan, K., Mai, Y.-W., Swain, M. V. & Cotterell, B., Mechanical properties of a sintered Al_2O_3/ZrO_2 composite, *Key Engng. Mater.*, **48–50** (1990) 130–6.
10. Hu, X.-Z. & Wittmann, F. H., An analytical method to determine the bridging stress transferred within the fracture process zone: I, general theory, *Cement and Concrete Research*, **21** (1991) 1118–28.
11. Hu, X.-Z. & Wittmann, F. H., An analytical method to determine the bridging stress transferred within the fracture process zone: II, application to mortar, *Cement and Concrete Research*, **22** (1992) 559–70.
12. Hu, X.-Z. & Mai, Y.-W., General method for determination of crack–interface bridging stresses, *J. Mater. Sci.*, **27** (1992) 3502–10.
13. Mai, Y.-W., Hu, X.-Z., Duan, K. & Cotterell, B., Crack-resistance curve and cyclic fatigue in ceramic materials. In *Fracture Mechanics of Ceramics*, Vol. 9, eds. R. C. Bradt, D. P. H. Hasselman, D. Munz, M. Sakai and V. Ya. Shevchenko, Plenum Press, New York, 1992, pp. 387–422.
14. Rubinstein, A. A., Macrocrack interaction with semi-infinite microcrack array, *Int. J. Fract.*, **27** (1985) 113–19.
15. Rubinstein, A. A., Macrocrack-microdefect interaction, *J. Appl. Mech. (ASME)*, **53** (1986) 505–10.
16. Rose, L. R. F., Effective fracture toughness of microcracked materials, *J. Am. Ceramic Soc.*, **69** (1986) 212–14.
17. Rose, L. R. F., Microcrack interaction with a main crack, *Int. J. Fract.*, **31** (1986) 233–42.
18. Tada, H., Paris, P. C. & Irwin, G. R., *Stress Analysis of Crack Handbook*, 2nd, Paris Production Inc., St. Louis, Missouri, 1985.

Journal of the European Ceramic Society 15 (1995) 1065–1070
© 1995 Elsevier Science Limited
Printed in Great Britain. All rights reserved
0955-2219(95)00094-1
0955-2219/95/$9.50

Influence of 1 vol% Ni_3Al Addition on Sintering and Mechanical Properties of Reaction-Bonded Si_3N_4.

B. R. Zhang[a]* & F. Marino[b]

[a]Department of Inorganic Materials, Shandong Institute of Light Industry, 250100 Jinan, People's Republic of China
[b]Dipartimento di Scienza dei Materiali e Ingegneria Chimica, Politecnico di Torino, 10129 Torino, Italy

(Received 5 December 1994; revised version received 24 May 1995; accepted 25 May 1995)

Abstract

The sintering-aid effect of 1 vol% Ni_3Al powder addition on the nitridation of silicon at 1300–1350°C for 5–20 h and its influence on mechanical properties of the reaction sintered material have been studied. The addition of 1 vol% Ni_3Al accelerates the nitriding rate of silicon and promotes the formation of β-Si_3N_4; no free silicon phase was detected by X-ray diffraction in the 1 vol% Ni_3Al-added sample nitrided at 1350°C for 20 h. The 1 vol% Ni_3Al-added sintered material has higher relative density, higher Vickers hardness and indentation fracture toughness but lower Young's modulus and flexural strength than the contemporaneously processed reaction-bonded silicon nitride.

1 Introduction

Reaction-bonded silicon nitride (RBSN) is formed by reacting a silicon powder preform with either nitrogen or ammonia. Its outstanding characteristic is that net shape components can be prepared because no shrinkage occurs during the process, which leads to the formation of complex shapes without the expensive machining associated with sintering and hot-pressing processes. Another important advantage of reaction bonding is the absence of oxide sintering aids which degrade the high-temperature mechanical properties of sintered and hot-pressed materials.[1] In addition, combination of the advantages of the reaction-bonding process (lower shrinkage rate during sintering and lower raw material costs, compared with Si_3N_4 powder compacts) with those of hot isostatic pressing (HIP) (high density and excellent mechanical properties) has been considered,[2–4] using RBSN as starting material for HIP or sintering. The post-sintering and post-HIP of RBSN have resolved the high porosity (12–30 vol%) problem of RBSN.[5]

RBSN formation from conventional powders typically requires several days at temperature ranging up to 1420°C,[5] resulting in mainly α-Si_3N_4 phase. Our previous studies[6,7] on reaction-bonded sintering of Si_3N_4 intermetallic composite have demonstrated that the addition of Ni_3Al powder accelerates the nitridation of silicon and promotes the formation of β-Si_3N_4 phase at a low temperature such as 1250°C through the presence of some liquid phase resulting from the reaction between Ni_3Al and Si, accompanied by the formation of intermetallic compounds of the type Ni_xSi_y. Accordingly, the anomalous thermal hardening nature of Ni_3Al, i.e. the strength increases with temperature,[8] cannot be utilized. On the other hand, when the amount of Ni_3Al addition was small, e.g. 1 vol%, the nitriding rate of silicon and the resulting relative density of the Si + 1 vol% Ni_3Al sample were higher than that of the contemporaneously processed silicon compact without Ni_3Al;[7] but it was also found that there was still free silicon phase being detected in the Si + 1 vol% Ni_3Al sample nitrided at 1250°C for up to 80 h. Therefore, in this paper, a new nitriding process of the Si + 1 vol% Ni_3Al system is investigated, in which Ni_3Al is used as a sintering aid. The resulting micro-structure as well as the influence of the Ni_3Al addition on mechanical properties are reported.

2 Experimental Procedure

Commercial silicon powders were ball-milled to a particle size of < 1 μm and mixed with 1 vol% of rapidly solidified Ni_3Al particles (about 20 μm) with respect to the final Si_3N_4. These intermetallic powders, produced by vacuum gas atomization and with the composition 73·12 Ni–18·82 Al–8·06 Cr–0·019 Mo–0·10 B at% (kindly supplied by

*Present address: Dipartimento di Scienza dei Materiali e Ingegneria Chimica, Politecnico di Torino, 10129 Torino, Italy.

R. N. Wright and J. R. Knibloe[9]), have a ductile behaviour. The powder mixtures were cold-pressed using a single-action stainless steel die and formation pressure of 250 MPa, producing green compacts with a density of about 62% of the theoretical value. The reaction sintering was carried out at 1300–1350°C for 5–20 h; the nitriding gas was a mixture of purified N_2+5% H_2, at atmospheric pressure. Pure silicon compacts were nitrided under the same conditions as reference material. The samples without Ni_3Al and with 1 vol% Ni_3Al are named SN and SN/NA1, respectively. The extent of nitridation was determined by the ratio between the weight of the nitrided sample (minus the weight of Ni_3Al added) and its theoretical weight assuming that all the silicon is converted into Si_3N_4.

The nitrided phases were identified by X-ray diffraction (XRD), using Cu$K\alpha$ radiation monochromated in the diffracted beam, on the core of samples; the α/β ratio was determined by the quantitative X-ray analysis method outlined by Gazzara and Messier.[10] Microstructure was characterized by scanning electron microscopy (SEM) on polished surfaces and on samples etched using a 10% HF+15% HNO_3 solution for 14 h. Densities of samples were determined before and after nitriding by weight and volume measurements and by Archimedes' principle. Bending strength of rectangular bars (3 mm × 4 mm × 45 mm) was measured at room temperature by four-point bending using spans of 40 and 20 mm at a crosshead speed of 1 mm min^{-1}. The Vickers microhardness was measured using loads from 9·8 to 196 N. The elastic modulus was measured by dynamic mechanical analysis (DMA) at room temperature. Fracture toughness was determined by the indentation crack length technique, calculated using the formula of Anstis *et al;*[11] the induced crack length and its propagation were observed by optical microscopy and SEM. Both the fracture toughness and the hardness were measured using five indentations for each specimen.

3 Results and Discussion

3.1 Effect of Ni_3Al addition on nitridation of Si and resulting microstructure

The reaction-sintering processes applied and the resulting nitrided fraction are shown in Table 1, which indicates that the nitrided fraction of the SN/NA1 sample is much higher than that of SN sintered in the same process. These values are consistent with the results reported in our previous work,[7] which concluded that the acceleration effect of Ni_3Al addition on the nitriding rate of Si was mainly due to the presence of some liquid phase resulting from the reaction between Si and Ni_3Al, leading to the formation of low melting intermetallics of the type Ni_xSi_y. The nitrided fraction of Si in SN/NA1 has been determined by the ratio between the weight of the nitrided sample and its theoretical weight minus the weight of Ni_3Al added (both at numerator and denominator), assuming that all the silicon in the sample is completely nitrided, as listed in Table 1. It is also supposed that the weight of Ni_3Al remains the same before and after sintering.

Higher temperatures and shorter times (1300–1350°C; 5–20 h) are employed in the present study and higher nitriding rates obtained, compared with the processes (1250°C; 5–80 h) and the nitrided fraction reported in our previous work.[7] Typically, no free silicon phase is detected in SN/NA1 nitrided at 1350°C for 20 h; the X-ray diffraction patterns of SN/NA1 and, for comparison, SN nitrided under the same condition are shown in Fig. 1. The α/β ratio in reaction-sintered SN/NA1 is about 6/4. In addition, no Ni_3Al but some nickel silicides have been detected which melt at about 1000°C and are considered to be responsible for the formation of β-modification Si_3N_4. In this work, it was difficult to identify the formulae of the nickel silicides accurately, because their amount is very small. For the SN sample, the nitrided fraction increases with increasing temperature and, as shown in Fig. 1, a small amount of β-Si_3N_4 has been found in SN nitrided at 1350°C for 20 h.

As the reaction between silicon and nitrogen is exothermic, it may result in overheating of the sample and this phenomenon would be more important when the nitriding temperature applied is sufficiently high. On the other hand, the presence of a small amount of metallic impurities can also decrease the melting temperature of silicon and accelerate the formation of β-Si_3N_4.[12,13] However, a large amount of free silicon has been also detected

Table 1. Nitrided fraction of the samples obtained under different sintering processes

Sample	*Nitrided fraction (%) under following processes*			
	1300°C, 5 h	*1300°C, 15 h*	*1300°C, 5 h+ 1350°C, 5 h*	*1350°C, 20 h*
SN	77·2	79·2	82·0	89·1
SN/NA1	85·3	89·2	91·3	95·2

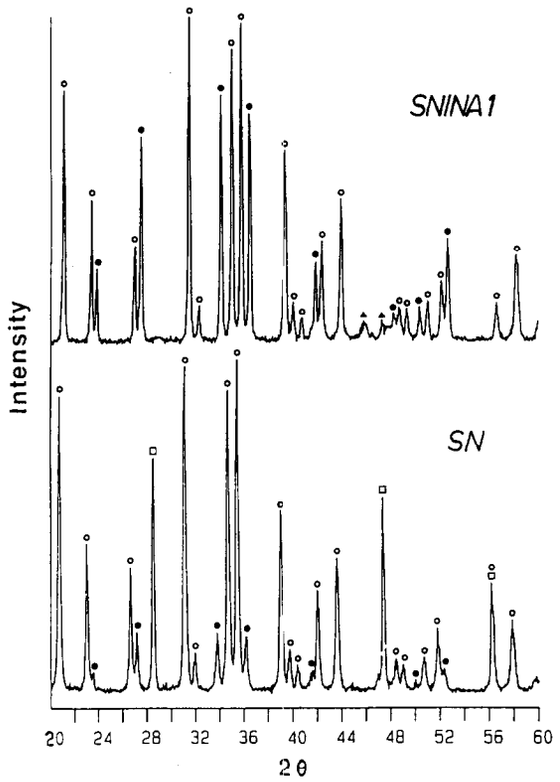


Fig. 1. X-ray diffraction patterns of the samples nitrided at 1350°C for 20 h: (○) α-Si_3N_4, (●) β-Si_3N_4, (□) Si, (▲) Ni_xSi_y.

by X-ray diffraction on the inner region of a cross-sectioned sample. This indicates that the surface is nitrided more rapidly than the bulk region for the pure silicon compact. On the contrary, no difference was found by X-ray diffraction analyses on the surface or the inner part of the SN/NA1 nitrided compact.

Figure 2 shows the morphology of SN/NA1 sintered at 1350°C for 20 h. The light particles are intermetallics, mainly nickel silicides, whose formulae have been determined on the sample containing 10 vol% Ni_3Al[6] and chiefly correspond to NiSi, $Ni_{31}Si_{12}$, Cr_3Si. It must be emphasized

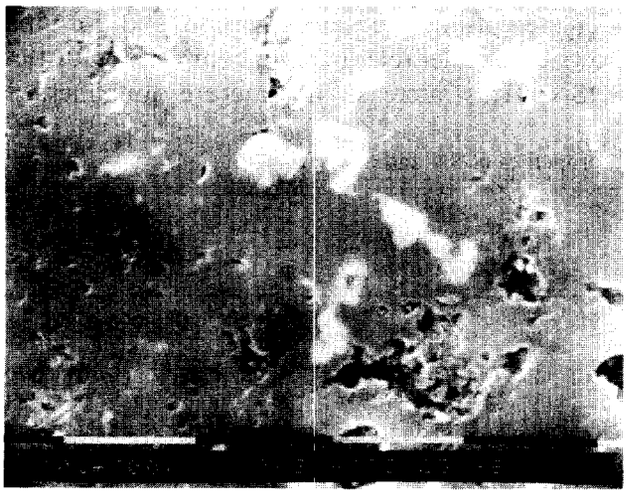


Fig. 2. SEM micrograph showing the morphology of SN/NA1 sample nitrided at 1350°C for 20 h.

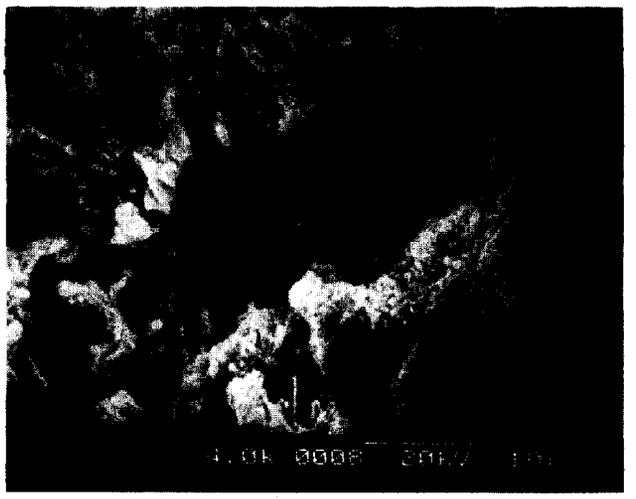


Fig. 3. SEM micrograph of an etched SN/NA1 sample, showing the cavity left by an intermetallic particle.

that more macropores (1–3 μm) were found in SN/NA1, probably owing to the reaction between Si and Ni_3Al, and this results in a less homogeneous microstructure than in SN. As indicated by X-ray diffraction analyses in Fig. 1, the microstructure of SN/NA1 consists of α-Si_3N_4, β-Si_3N_4 and traces of Ni_xSi_y intermetallics. SEM observation reveals that α-phase present in SN/NA1 contains α-grains and α-whiskers; α-grains are generally formed in zones far from intermetallic particles. On the contrary, α-whiskers and β-modification Si_3N_4 are preferably generated close to macropores and intermetallic particles because of the occurrence of some liquid phase. This is consistant with the formation mechanism of α-whisker and β-modification Si_3N_4 indicated in the literature.[5,14] Figure 3 shows a SEM micrograph of an etched SN/NA1 sample; in the cavity left by an intermetallic particle, α-whiskers and the rod-like β-Si_3N_4 are observed, as shown more clearly in Fig. 4 for α-whiskers and Fig. 5 for β-phase.



Fig. 4. SEM micrograph showing α-whiskers formed in macropores.



Fig. 5. SEM micrograph showing β-Si_3N_4 formation in zone close to an intermetallic particle.

3.2 Influence of Ni_3Al addition on densification and mechanical properties of the composite

Table 2 shows the densities and mechanical properties of the SN/NA1 sample compared with two different samples of RBSN: one nitrided under the same conditions (1350°C, 20 h), the other having about the same nitrided fraction.[7]

The relative densities of SN and SN/NA1 nitrided at 1350°C for 20 h are about 80 and 90%, respectively, obtained from the ratio of the measured density and $3{\cdot}16 \times 10^3$ kg m^{-3} for SN and $3{\cdot}20 \times 10^3$ kg m^{-3} (calculated) for SN/NA1. SN/NA1 is denser than SN obtained under the same nitriding process due to the higher conversion rate of the silicon and the $\alpha \rightarrow \beta$ phase transformation of Si_3N_4,[15] although it has a less homogeneous microstructure than SN.

It should be mentioned that the values of flexural strength are not reported in Table 2 because of high scattering of the experimental data, which however show a decreasing trend of the flexural strength from SN to SN/NA1. Thus, for the mechanical properties, it can be said that the addition of 1 vol% Ni_3Al increases the Vickers hardness and the fracture toughness, but decreases the Young's modulus and the flexural strength, compared with both RBSN samples. The hardness of SN/NA1 was expected to decrease because both the Ni_3Al and Ni_xSi_y intermetallic phases are softer than silicon nitride, but the experimental results have shown a little increase, probably owing to the improvement of the relative density. As regards the decrease of the flexural strength of SN/NA1, a very significant influencing factor is the microstructure, especially the pore size. As indicated by Ziegler *et al.*[5] a homogeneous microstructure with a narrow pore-size distribution at moderate densities is better than a high-density material which contains large voids in order to achieve high-strength materials. Furthermore, the decrease in strength caused by large pores, formed during reaction bonding of the coarse-grained silicon powder, was demonstrated in the same paper. Thus, the presence of more macropores in the SN/NA1 sample results in the decrease in strength; on the other hand, it may be also responsible for the decrease of Young's modulus in SN/NA1. Even though a study on hot-pressed Si_3N_4[16] has illustrated an increase of strength with increasing amount of β-fraction and although a large amount of β-grains was found in SN/NA1, no improvement of strength was observed for this sample, perhaps owing to the inhomogeneous distribution of β-phase.

However, in contrast to reduced flexural strength, the indentation fracture toughness of SN/NA1 is higher than that of SN. Although it must be kept in mind that many formulae for the determination of K_{IC} from indentation are proposed in the literature,[17] each of them leading to different indentation toughness values,[18] the indentation crack length technique is still widely applied for toughness measurement of Si_3N_4 ceramics.[18,19] In the present work, the values of indentation fracture toughness for SN, ranging from 1·99 to 2·20 Mpa $m^{1/2}$, fall in the typical range of K_{IC} values, 1·5–2·8 MPa $m^{1/2}$, for RBSN.[5] The K_{IC} value of SN/NA1, calculated using the same method and formula, shows a considerable increase compared with that of SN. This increase in fracture toughness is

Table 2. Relative densities and mechanical properties of SN and SN/NA1

Property	*SN (1350°C, 20 h)*	*SN*[7] *(1250°C, 50 h + 1450°C, 10 h)*	*SN/NA1 (1350°C, 20 h)*
Nitrided fraction (%)	89·1	94·9	95·2
Relative density (%)	79·75	85·44	89·80
Vickers microhardness (GPa)	7·86	8·10	8·35
Young's modulus, E (RT, GPa)	110	120	100
Fracture toughness, K_{IC}(MPa a $m^{1/2}$)	1·99	2·20	2·54

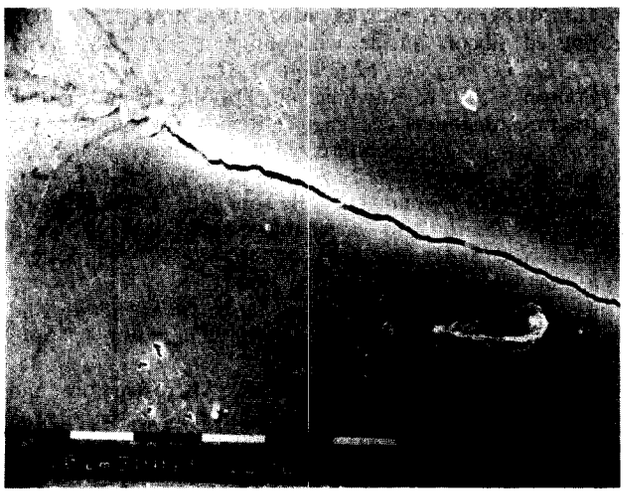


Fig. 6. SEM micrograph showing the crack propagation in SN sample.

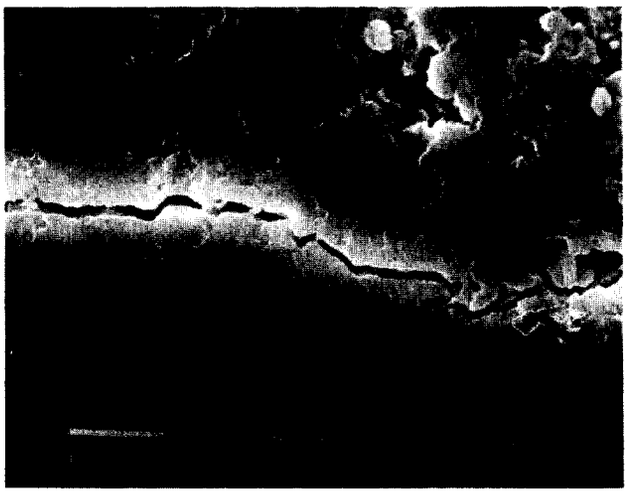


Fig. 7. SEM micrograph showing the crack propagation in SN/NA1 sample.

probably due to the formation of rod-like β-Si_3N_4 phase in SN/NA1 which, as reported in the literature,[19–22] shows the self-reinforcement and crack-bridging effects of the *in situ* formed β-Si_3N_4. Figures 6 and 7 show the propagation of the crack induced by the indentation in SN and SN/NA1, respectively, using a load of 196 N. It can be observed that the crack propagates smoothly in the SN sample and that it has an indented path, which causes energy consumption, around the weak intermetallic/matrix interface in SN/NA1.

4 Conclusions

The reaction-sintering processes of Si+1 vol% Ni_3Al at 1300–1350°C in purified N_2+5% H_2 atmosphere have been investigated. The addition of 1 vol% Ni_3Al accelerates the nitriding rate of silicon and increases the relative density of the resulting nitrided samples. No free silicon phase is detected by XRD in 1 vol% Ni_3Al-added samples nitrided at 1350°C for 20 h. The resulting nitrided fraction and the relative density are 95·2% and 89·80%, respectively, compared with 89·1% and 79·75% for the contemporaneously processed RBSN. The microstructure of SN/NA1 consists of α, β-Si_3N_4 with an α/β ratio of about 6/4, and a small amount of nickel silicide intermetallics; but SN/NA1 has more macropores than SN.

The Vickers hardness and the indentation fracture toughness of SN/NA1 are respectively 8·35 GPa and 2·54 MPa $m^{1/2}$, higher than those of SN owing to the higher relative density and the formation of rod-like β-modification Si_3N_4; but the Young's modulus and the flexural strength are slightly lower than in SN probably due to the presence of more macropores in SN/NA1.

Acknowledgements

This work was partially supported by Alenia Spazio spa Torino (Italy) and the authors gratefully acknowledge the collaboration of Dr B. Fornari, Alenia Spazio spa Torino. We would like also to thank Professor O. Sbaizero, Università di Trieste (Italy) for his help in the four point-bending tests, Dr M. Ferraris and M. Raimondo, Dipartimento di Scienza dei Materiali e Ingegneria Chimica del Politecnico di Torino, for their help with the SEM observations.

References

1. Sheldon, B. W., Szekely, J. & Haggerty, J. S., Formation of reaction-bonded silicon nitride from silane-derived silicon powders: macroscopic kinetics and related transport phenomena. *J. Am. Ceram. Soc.*, **75** (1992) 677–85.
2. Kleebe, H. J. & Ziegler, G., Influence of crystalline secondary phases on the densification behaviour of reaction-bonded silicon nitride during postsintering under increased nitrogen pressure. *J. Am. Ceram. Soc.*, **72** (1989) 2314–17.
3. Heinrich, J., Backer, E. & Bohmer, M., Hot isostatic pressing of Si_3N_4 powder compacts and reaction-bonded Si_3N_4. *J. Am. Ceram. Soc.*, **71** (1988) C28–9.
4. Mangels, J. A. & Tennenhouse, G. J., Densification of reaction-bonded silicon nitride. *Am. Ceram. Soc., Bull.*, **59** (1980) 1216–22.
5. Ziegler, G., Heinrich, J. & Wotting, G., Relationships between processing, microstructure and properties of dense and reaction-bonded silicon nitride. *J. Mater. Sci.*, **22** (1987) 3041–86.
6. Zhang, B. R., Gialanella, S. & Marino, F., Chemical aspects of reaction-bonded sintering of Si_3N_4 intermetallic composite. In *Proc. of the 8th CIMTEC. Int. Conf. on Modern Materials Technologies.* Techna, Faenza, Italy, 1994,
7. Marino, F., Zhang, B. R. & Fornari, B., Processing and microstructural development of reaction-bonded sintering of a Si_3N_4 intermetallic composite. *J. Mater. Sci.*, submitted.

8. Guard, R. W. & Westbrook, J. H., Alloying behaviour of Ni_3Al. *Trans. TMS-AIME*, **215** (1959) 807.
9. Wright, R. N. & Knibloe, J. R., The influence of alloying on the microstructure and mechanical properties of P/M Ni_3Al. *Acta Metall. Mater.*, **38** (1990) 1993–2001.
10. Gazzara, C. P. & Messier, D. R., Determination of phase content of Si_3N_4 by X-ray diffraction analysis. *Am. Ceram. Soc. Bull.*, **56** (1977) 777-80.
11. Anstis, G. R., Chanticul, P., Lawn, B. R. & Marshall, D. B., A critical evaluation of indentation techniques for measuring fracture toughness: I, Direct crack measurements. *J. Am. Ceram. Soc.*, **64** (1981) 533–8.
12. Mitomo, M., Effect of Fe and Al additions on nitridation of silicon. *J. Mater. Sci.*, **12** (1977) 273–276.
13. Messier, D. R., Riley, F. L. & Brook, R. J., The α/β silicon nitride phase transformation. *J. Mater. Sci.*, **13** (1978) 1199–1205.
14. Messier, D. R. & Wong, P., Kinetics of nitridation of Si powder compacts. *J. Am. Cream. Soc.*, **56** (1973) 480–5.
15. Mitomo, M. & Mizuno, K., Sintering behaviour of Si_3N_4 with Y_2O_3 and Al_2O_3 addition. *Yogyo Kyokaishi*, **94** (1986) 106–11.
16. Himsolt, G. & Knoch, H., Mechanical properties of hot-pressed silicon nitride with different grain structures. *J. Am. Ceram. Soc.*, **62** (1979) 29–32.
17. Ponton, C. B. & Rawlings, R. D., Vickers indentation fracture toughness test Part 1: Review of literature and formulation of standardized indentation toughness equations. *Mater. Sci. Technol.*, **5** (1989) 865–72.
18. Rossignol, F., Goursat, P., Besson, J. L. & Lespade, P., Microstructure and mechanical behaviour of self-reinforced Si_3N_4 and Si_3N_4 – SiC whisker composites. *J. Eur. Ceram. Soc.*, **13** (1994) 299–312.
19. Travitzky, N. A. & Claussen, N., Microstructure and properties of metal infiltrated RBSN composites. *J. Eur. Ceram. Soc.*, **9** (1992) 61–5.
20. Pyzik, A. J. & Beaman, D. R., Microstructure and properties of self-reinforced silicon nitride. *J. Am. Ceram. Soc.*, **76** (1993) 2737–44.
21. Becher, P. F., Microstructural design of toughened ceramics. *J. Am. Ceram. Soc.*, **74** (1991) 255–69.
22. Mitomo, M. & Uenosono, S., Microstructural development during gas-pressure sintering of α-silicon nitride. *J. Am. Ceram. Soc.*, **75** (1992) 103–8.

Journal of the European Ceramic Society **15** (1995) 1071–1077
© 1995 Elsevier Science Limited
Printed in Great Britain. All rights reserved
0955-2219(95)00091-7
0955-2219/95/$9.50

Preparation of Fine Amorphous Silicon Nitride Powder in the System SiH_4–Ar–NH_3

Sadananda Sahu,[a] Štefan Kavecký[b] & János Szépvölgyi[c]

[a]Institute of Inorganic Chemistry, Slovak Academy of Sciences, 842 36 Bratislava, Slovakia
[b]Institute of Materials and Mechanics of Machines, Slovak Academy of Sciences, 836 06 Bratislava, Slovakia
[c]Research Laboratory of Inorganic Chemistry, Hungarian Academy of Sciences, H-1112 Budapest, Budaörsi út 45, Hungary

(Received 20 January 1995; revised 19 May 1995; accepted 22 May 1995)

Abstract

Amorphous silicon nitride powders have been prepared in a tube reactor in the system silane–argon–ammonia in the temperature range 500–1100°C. The powders prepared at 500°C show the presence of elementary silicon. The powders prepared above 650°C are near stoichiometric in composition, isometric in morphology and the particle size distribution is in the range of 0·05–0·2 μm. The powders prepared at 1100°C are nearly monodispersive, having the particle size 0·1 μm. The influence of molar ratio of ammonia to silane shows that silicon nitride powder of near stoichiometric composition can be prepared above 11·62 and below this ratio the powders contain elementary silicon. The change in total gas flow rate shows that below 300 cm^3 min^{-1} the powders again contain elementary silicon and with further increase in flow rate the powders are near stoichiometric at 400 cm^3 min^{-1} and little hyperstoichiometric in nitrogen content at and above the flow rate of 500 cm^3 min^{-1}. Surface characterization by X-ray photoelectron spectroscopy indicates that most of the oxygen is confined on the surface and is present in the form of SiO_2.

1 Introduction

Silicon nitride based ceramics are well recognized as the material of the next generation, suitable for high temperature structural applications. Although there is a fast development in achieving superior high temperature mechanical properties, bending strength up to 950 MPa and fracture toughness 7·5 $MPa.m^{1/2}$,[1] however there are still opportunities left to improve these properties. It is commonly accepted that to prepare good quality ceramics the powder should have the following properties: low cationic impurity (< 2 wt%), low oxygen (< 2 wt%), > 95 wt% α phase content and average particle size in the range of 1 μm and close to monodispersive. Generally silicon nitride powders are prepared in four different ways: 1. nitriding of powdered silicon by nitrogen or ammonia; 2. silicon diimide, $Si(NH)_2$ decomposition; 3. carbothermal reduction and nitridation of silica; 4. gas phase reaction of silane or its halogen derivatives with nitrogen or ammonia.[2] Besides the described methods which are used in an industrial scale, there are several other synthesis methods which are under development at present, e.g. plasma synthesis, laser induced reaction etc.. The impurity contents are inherent to the method of preparation. The last mentioned method is usually applied in the deposition of thin coatings by chemical vapor deposition. Nevertheless, recently a lot of attention has been paid to prepare high quality silicon nitride powders from the gas phase reaction route.[3–8] There are three different ways in which the gas phase reactions are carried out: 1. laser induced reaction; 2. R.F. plasma synthesis;[5–8] 3. electrically heated reaction tube.[4] Each system has its own advantages and disadvantages. However, the powders prepared by the last technique are submicron and isometric. Addition of 20 wt% of this amorphous powder to the commercial powder (H. C. Stark, LC12 S) leads to the homogeneous nucleation of β-Si_3N_4, resulting in fine microstructure and improved mechanical property of sintered body.[9,10] The various gas phase systems in the deposition of thin coatings by chemical vapor deposition for application in electronics are: $SiCl_4$–NH_3, SiH_4–NH_3, $SiCl_4$–N_2–H_2, SiF_4–NH_3, SiH_2Cl_2–NH_3, $SiBr_4$–NH_3. But recently some work has been carried out to prepare ultra-fine nitride powders in the system SiH_4–N_2–NH_3[4] and SiH_4–Ar–NH_3.[3]

The main aim of the present work is to study extensively the influence of different parameters

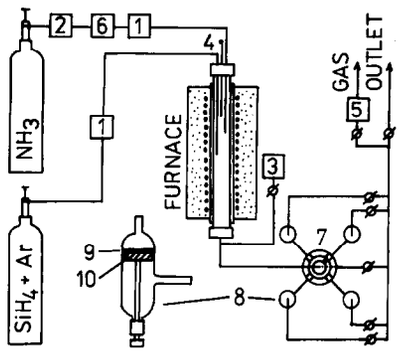


Fig. 1. Experimental set-up for the synthesis of silicon nitride from a silane–argon–ammonia gas mixture: 1. mass flow meter; 2. drying column (KOH); 3. manometer; 4. thermocouple; 5. rotary vacuum pump; 6. drying column (Na); 7. sample collector–distributor; 8. sample collecting chamber; 9. glass frit; 10. powder stripper.

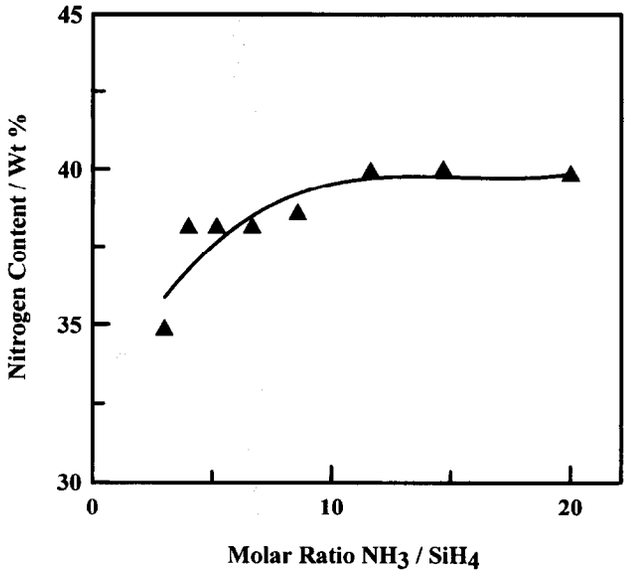


Fig. 2. The change of nitrogen content of powders against ammonia/silane molar ratio prepared at 650°C.

such as temperature, ratio of NH_3 to SiH_4, flow rate of the total gas and influence of the carrier gas Ar with respect to N_2 on the particle size, morphology and the quality of the product in the system SiH_4–Ar–NH_3.

2 Experimental

Ammonia gas of technical purity (99·5%), electronic grade silane (15 wt% in argon) and argon (purity 99·5%) were used for the experiment. The details of the experimental set up of the hot wall reactor is described in an earlier publication.[4] The reactor dimensions are as follows: internal diameter = 46 mm and length = 500 mm. There was a little modification made in the sample collector to improve the collection efficiency and avoid choking of the glass frit. In the present experiments a new multiple sample collector was designed with the mechanical scrubber and rotary valve to get multiple number of samples synthesized in different conditions in one run. The schematic description of the apparatus is given in Fig. 1. The first set of experiments were carried out by varying the mole ratio of NH_3 to SiH_4 (r) in the range of 3–20 keeping the total flow of gas across the reactor at 400 cm^3 min^{-1} and temperature of reaction at 650°C. In the second set of experiments the total gas flow varied in the range of 200–600 cm^3 min^{-1} simultaneously maintaining the ratio of NH_3 to SiH_4 at 11·62 and reaction temperature at 650°C. In the third set of experiments r was constant at 11·62 and the total flow of gas increased from 400–1000 cm^3 min^{-1} by the introduction of argon stepwise and keeping the reaction temperature at 650°C. The last set of experiments were carried out in the temperature range between 500–1100°C at fixed ratio of NH_3 to SiH_4 at 11·62. In all the experiments the pressure of the reactor was kept at 110 kPa.

The properties of the powders were studied by XRD analysis, SEM, FTIR spectroscopy. The elemental analysis of silicon was done by neutron activation analysis, oxygen by LECO TC-136 and nitrogen by titrimetric method (Kjelldahl method). The surface composition of the powders were analyzed by XPS.[11]

3 Results and Discussion

In the earlier study,[4] it was revealed that in the system SiH_4–N_2–NH_3, nitrogen acts merely as a carrier gas, since in the system SiH_4–N_2 on Si_3N_4 formation was observed up to 1400°C. The molar ratio of NH_3 to SiH_4 of about 11, temperature at 650°C and total gas flow rate of 400 cm^3 min^{-1}

Table 1. Chemical composition of the products prepared at various mole ratios NH_3/SiH_4 at a constant temperature of 650°C and a flow rate of 400 cm^3 min^{-1}

r	*3*	*4*	*5·18*	*6·66*	*8·57*	*11·62*	*14·66*	*20*
N (wt%)	34·81	38·09	38·06	38·0	38·53	39·89	39·95	39·88
O (wt%)	1·31	1·51	1·47	2·44	1·19	1·43	2·23	6·91
Si (wt%)	65·13	58·92	59·57	59·53	59·43	59·39	60·13	51·88
Σ	101·1	98·52	99·1	99·97	99·15	100·71	102·3	98·67
Colour	Brown	Light brown	Light brown	White	White	White	White	White

were suggested as the optimum conditions for the production of amorphous silicon nitride powder of near stoichiometric composition in the system SiH_4–N_2–NH_3. On the basis of these results the conditions for the present experiments were chosen.

3.1 Influence of NH_3/SiH_4 ratio, (r)

The effect of the molar ratio of ammonia to silane was studied in the range from 3–20 at a constant temperature of 650°C and total flow rate of gases at 400 cm^3 min^{-1} across the reactor. The characteristics of the products are given in Table 1.

From the nitrogen content analysis it is observed that at lower r value the nitrogen content is below the stoichiometric composition (39·96 wt% of N_2) of silicon nitride. When the r value is 11·62 and above, the products contain the stoichiometric amount of nitrogen. The trend in nitrogen content with the change in molar ratio is plotted in Fig. 2. It can be seen that for the synthesis of nearly stoichiometric silicon nitride powder a relatively excess amount of ammonia is required. Low molar ratio products are brown to light brown in colour indicating the presence of elementary silicon. As the r value is increased to 11·62 and above, the products are white and near stoichiometric in composition. However, when a high excess amount of ammonia is present, the product is a little hyperstoichiometric in nitrogen content. In the present experiments, no decrease in the nitrogen content was observed by increasing the molar ratio (r) above 11, which was distinctly observed in the previous work in the system SiH_4–N_2–NH_3.[4] The present result is in agreement with the earlier results:[3,4] that near stoichiometric silicon nitride can be prepared at a molar ratio of ammonia to silane 11. SEM studies of the powders show that powders prepared at a lower molar ratio (r), i.e. 3 and 4, are agglomerated. The particles have a tendency to agglomerate and form necks and rings.

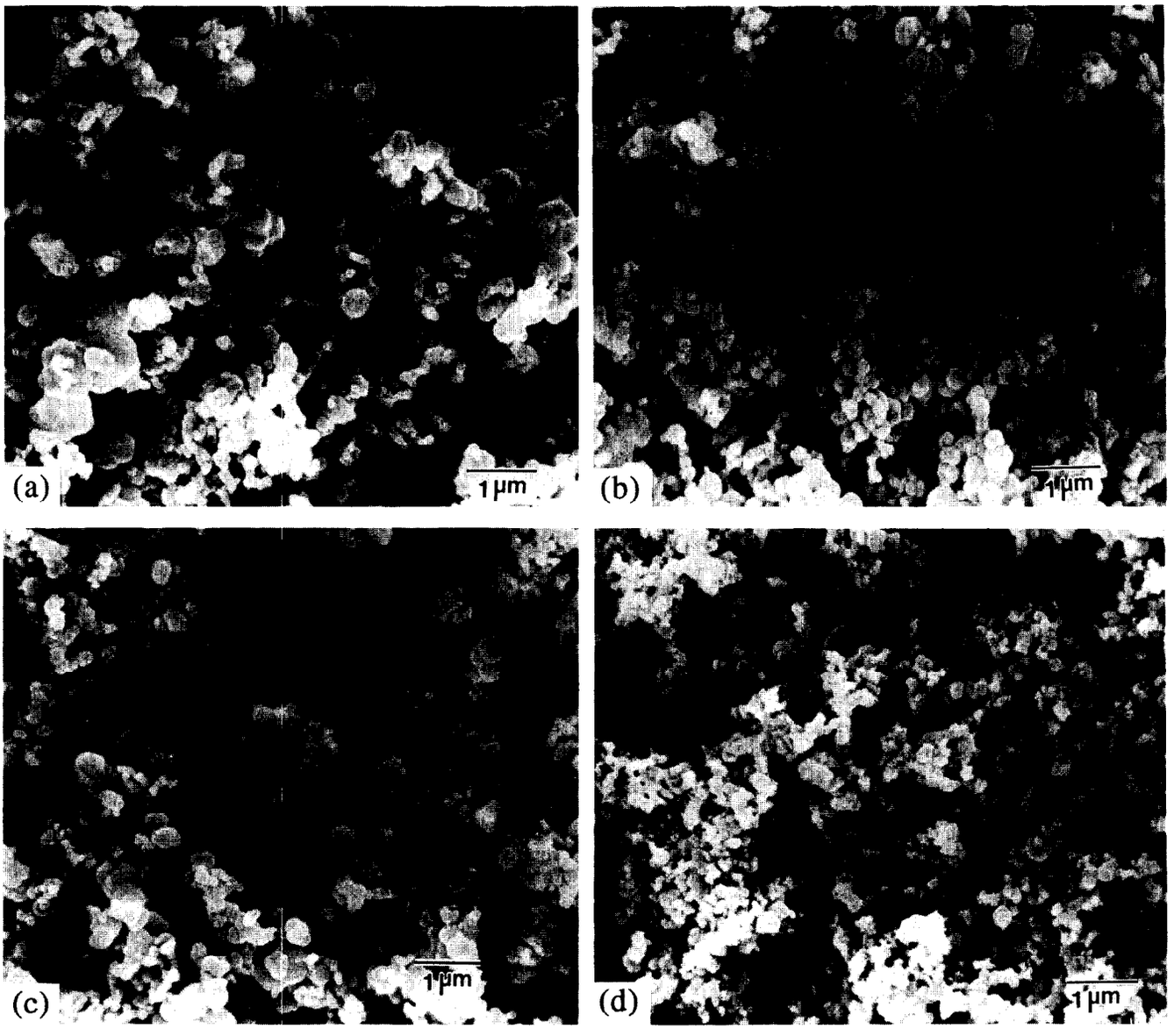


Fig. 3. SEM photographs of powders: (a) prepared at 650°C, total gas flow rate 400 cm^3 min^{-1} and ammonia/silane ratio = 11·62; (b) at 650°C, total gas flow rate 400 cm^3 min^{-1} and ammonia/silane = 20; (c) at 650°C, total gas flow rate 600 cm^3 min^{-1} and ammonia/silane ratio = 11·62; (d) at 1100°C, total gas flow rate 400 cm^3 min^{-1} and ammonia/silane ratio = 11·62.

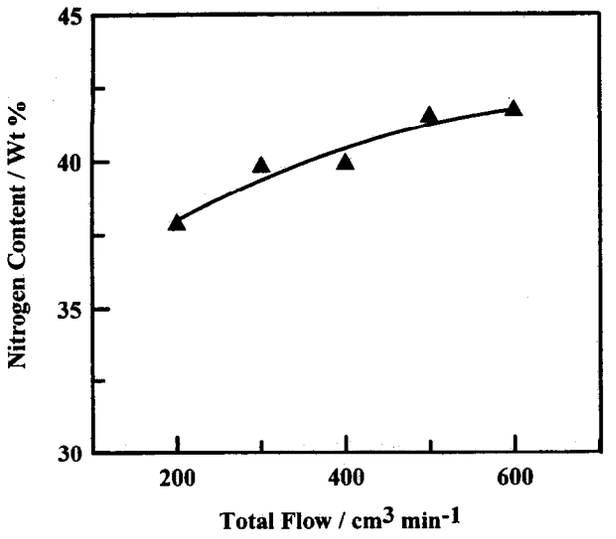


Fig. 4. The change of nitrogen content against total gas flow rate at 650°C and ammonia/silane = 11·62.

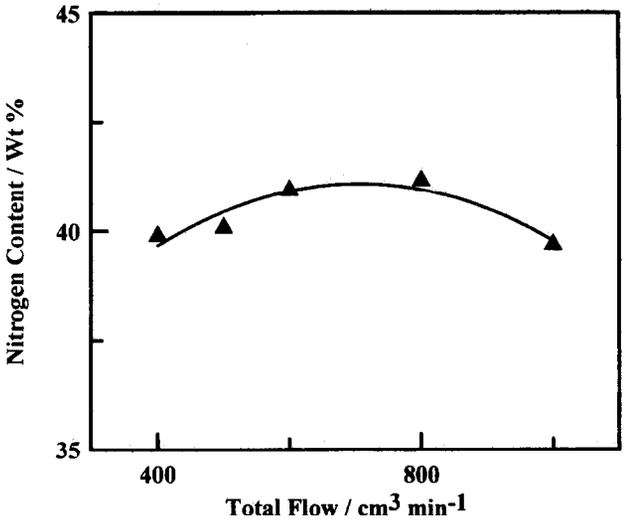


Fig. 5. The change of nitrogen content against total gas flow rate by the addition of argon to 400 cm^3 min^{-1} of the original gas mixture at 650°C and ammonia/silane ratio = 11·62.

At molar ratio of 5·18 and 6·66 the products are less agglomerated. At a further increase of molar ratio, the size of particles are in the range of 0·05–0·2 μm and practically without agglomeration. An SEM photograph of a product at molar ratio 11·62 is shown in Fig. 3(a). There is no large change in the particle size and morphology with further change in the molar ratio up to 20, which can be observed from Fig. 3(b).

Considering the stoichiometry in composition and quality of the product the powder prepared at r = 11·62, seems to be the optimum. So these synthesis conditions have been adopted as the basis for the next experiments.

3.2 Influence of total gas flow rate

In order to investigate the effect of the total flow rate of gases across the reactor, the temperature and molar ratio of ammonia to silane (r) were kept constant at 650°C and 11·62 respectively and the total flow rate, i.e. NH_3 (g) + SiH_4 (g) was varied from 200–600 cm^3 min^{-1}. The characteristics of the powders are presented in Table 2. The nitrogen content is plotted against the flow rate in Fig. 4. Increase of the flow rate above 300 cm^3 min^{-1} increased the nitrogen content gradually above the stoichiometric composition. When the total flow rate is 200 cm^3 min^{-1}, the nitrogen content is well below the stoichiometry. In this case the elementary silicon was increased and the colour of the product was light brown. This indicates that at a lower total gas flow, the rate of formation of elementary silicon is promoted. On the other hand, its recombination with ammonia leading to the formation of silicon nitride is limited at lower temperatures.

SEM observation shows, Fig. 3(c), that a finer product was obtained at a higher flow rate of 600 cm^3 min^{-1} (compare Fig. 3(a) and (c)). This fact is also confirmed by the specific surface area measurement by BET: the product prepared at 400 cm^3 min^{-1}, shown in Fig. 3(a) has a specific surface area of 12 m^2 g^{-1} whilst the product prepared at 600 cm^3 min^{-1}, shown in Fig. 3(c) has a specific area of 14 m^2 g^{-1}. The particle size distribution of this finer product is narrow and varies in the range from 0·05 to 0·2 μm.

In another series of experiments, the total gas flow rate has been increased by the addition of argon stepwise to the original total flow of gas 400 cm^3 min^{-1} of NH_3(g) + SiH_4(g) + Ar(g) to 1000 cm^3 min^{-1} keeping temperature at 650°C and the molar ratio of ammonia to silane at 11·62.

Table 2. Chemical composition of the products at various total gas flow rates and at constant molar ratio of NH_3/SiH_4 = 11.62, T = 650°C

Total gas flow rate (cm^3 min^{-1})	*200*	*300*	*400*	*500*	*600*
N (wt%)	37·85	39·80	39·89	41·49	41·70
O (wt%)	7·57	2·08	1·43	3·03	3·85
Si (wt%)	52·87	56·75	59·39	52·85	51·20
Σ	98·29	98·63	100·71	97·37	96·75
Colour	Light brown	White	White	White	White

Table 3. Chemical composition of products at various total gas flow rate of carrier gas (Ar) and constant molar ratio of NH_3/SiH_4 = 11·62, T = 650°C (The total gas flow rate was changed by the addition of argon to the original total flow of 400 cm^3 min^{-1})

Total gas flow rate (cm^3 min^{-1})	*400*	*500*	*600*	*800*	*1000*
N (wt%)	39·89	40·07	40·93	41·15	39·69
O (wt%)	1·43	2·34	1·98	2·25	1·60
Si (wt%)	59·39	57·31	57·96	56·60	60·39
Σ	100·7	99·72	100·8	100	101·7
Colour	White	White	White	White	White

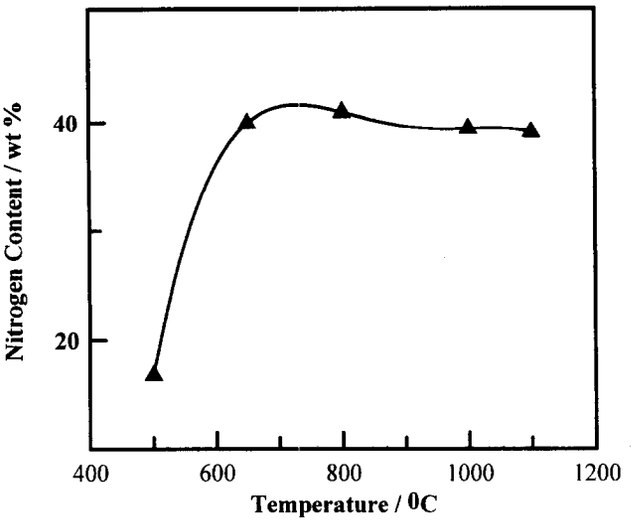


Fig. 6. The change of nitrogen content against temperature of synthesis at total gas flow rate 400 cm^3 min^{-1} and ammonia/silane = 11·62.

The chemical composition of the products are given in the Table 3, and the change of nitrogen content with respect to the total flow rate is shown in Fig. 5. From these results, it is obvious that with an increase in the flow rate there is a slight tendency to increase the nitrogen content up to 800 cm^3 min^{-1}.

3.3 Influence of temperature

For this series of experiments, the total gas flow rate was kept at 400 cm^3 min^{-1} and the mole ratio of ammonia to silane at 11·62. The chemical composition and characteristics of the products prepared in the temperature range between 500 and 1100°C are given in Table 4 and the dependence of nitrogen content on the temperature is shown in Fig. 6. From Table 4 and Fig. 6 it is clear that silicon nitride of near stoichiometric composition can be prepared at and above 650°C. At 500°C the product contains only 16·79 wt% of nitrogen and a proportionately higher amount of silicon. It seems that 650°C is the critical temperature for the formation of silicon nitride in this system. Below this temperature there is a tendency of the formation of elementary silicon. From the thermodynamic analysis (Table 5), it is obvious that the enthalpy of reaction 1 is negative, that means silicon nitride should have formed at this temperature without elementary silicon. The fact that elementary silicon is present in the product at 500°C is due to kinetic reasons. At this temperature, the decomposition rate of silane is higher than the recombination of elementary silicon to silicon nitride.

Table 5. Thermodynamic data of the different reactions

Reactions	ΔG *at 700 K* *kcal/mol*	ΔG *at 900 K* *kcal/mol*
1. 3 SiH_4 + 4 NH_3 → Si_3N_4 + 12 H_2	−212·65	−232·90
2. SiH_4 → Si + 2 H_2	−21·29	−25·97
3. 3 Si + 4 NH_3 → Si_3N_4 + 6 H_2	−148·78	−154·98

Table 6. Surface chemical composition of powders as determined by XPS (in at%)

Total gas flow rate (cm^3 min^{-1})	*Si*	*N*	*O*	*C*	*N/Si*	*O/Si*
200	28·42	24·87	38·47	8·24	0·88	1·40
300	27·44	28·69	33·13	10·74	1·05	1·20
400	28·45	26·21	38·79	6·55	0·92	1·36
500	28·39	26·60	36·48	8·52	0·94	1·28
600	28·09	24·50	39·70	7·71	0·87	1·41

The product prepared at 650°C is not agglomerated and the particles are isometric with the size from 0·05 to 0·2 μm, Fig. 3(a). On the other hand with an increase of the reaction temperature, the refinement of the product was observed. At 1100°C, superfine almost monodispersive isometric powder was prepared with the particle size ranging from 0·05 to 0·1 μm, Fig. 3(d)

The formation of finer powders at higher temperatures is most probably due to the creation of more nucleation centers. The powders are still mainly amorphous at 1100°C with partial crystallization, at about 5–10%.

4 XPS studies

According to the wide scan spectra registered for the samples prepared at 650°C r = 11·62 and with varying total gas flow rates from 200 to 600 cm^3 min^{-1}, Si, N, O and C could be detected on the surface (The characteristics of the powders are presented in Table 2). As an example the wide scan spectra of samples prepared at 400 cm^3 min^{-1} is presented in Fig. 7. The surface chemical composition and the N/Si and O/Si atomic ratios were calculated from the relevant wide scan spectra and

Table 4. Chemical composition of the products prepared at a constant molar ratio NH_3/SiH_4 of 11·62 and total gas flow rate of 400 cm^3 min^{-1} at various reaction temperatures

Temperature (°C)	*500*	*650*	*800*	*1000*	*1100*
N (wt%)	16·79	39·89	40·90	39·36	39·04
O (wt%)	2·13	1·43	1·83	1·41	1·22
Si (wt%)	80·50	59·39	58·58	59·49	59·30
Σ	99·5	100·71	101·31	100·26	99·56
Colour	Brown	White	White	White	Light tan

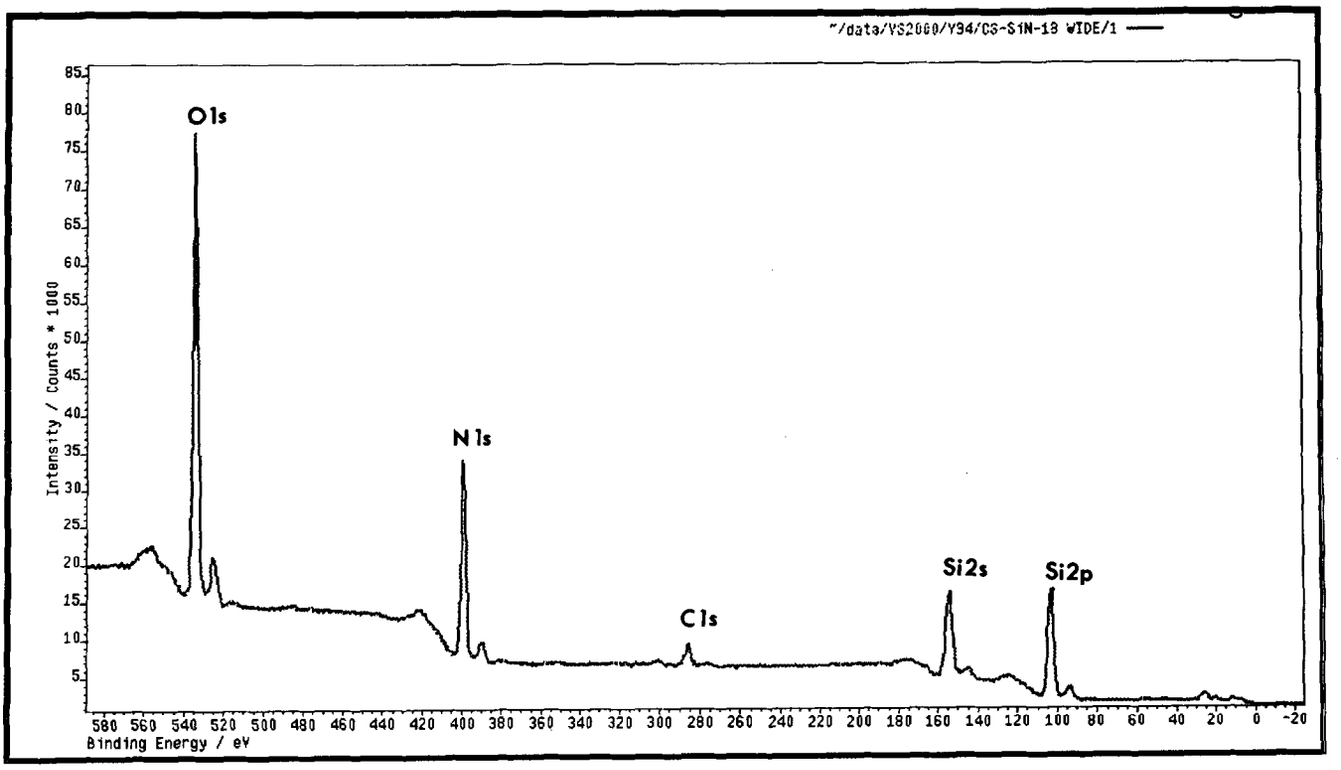


Fig. 7. Wide scan XPS spectrum of the powder prepared at 650°C, total gas flow rate 400 cm^3 min^{-1} and ammonia/silane ratio = 11·62.

summerized in Table 6. It is evident that all samples are characterized by a high surface oxygen content. In addition the tendencies in the changes of the bulk and surface compositions against the total flow rate of gases are similar (see Tables 2 and 6).

Deconvolution of the Si 2*p* peak (Fig. 8) refers to the simultaneous presence of Si–N and Si–O bonds. So most of the oxygen on the surface is present in the form of SiO_2.

5 Conclusions

Effects of the NH_3/SiH_4 molar ratio, total gas flow rate and reaction temperature on the properties of

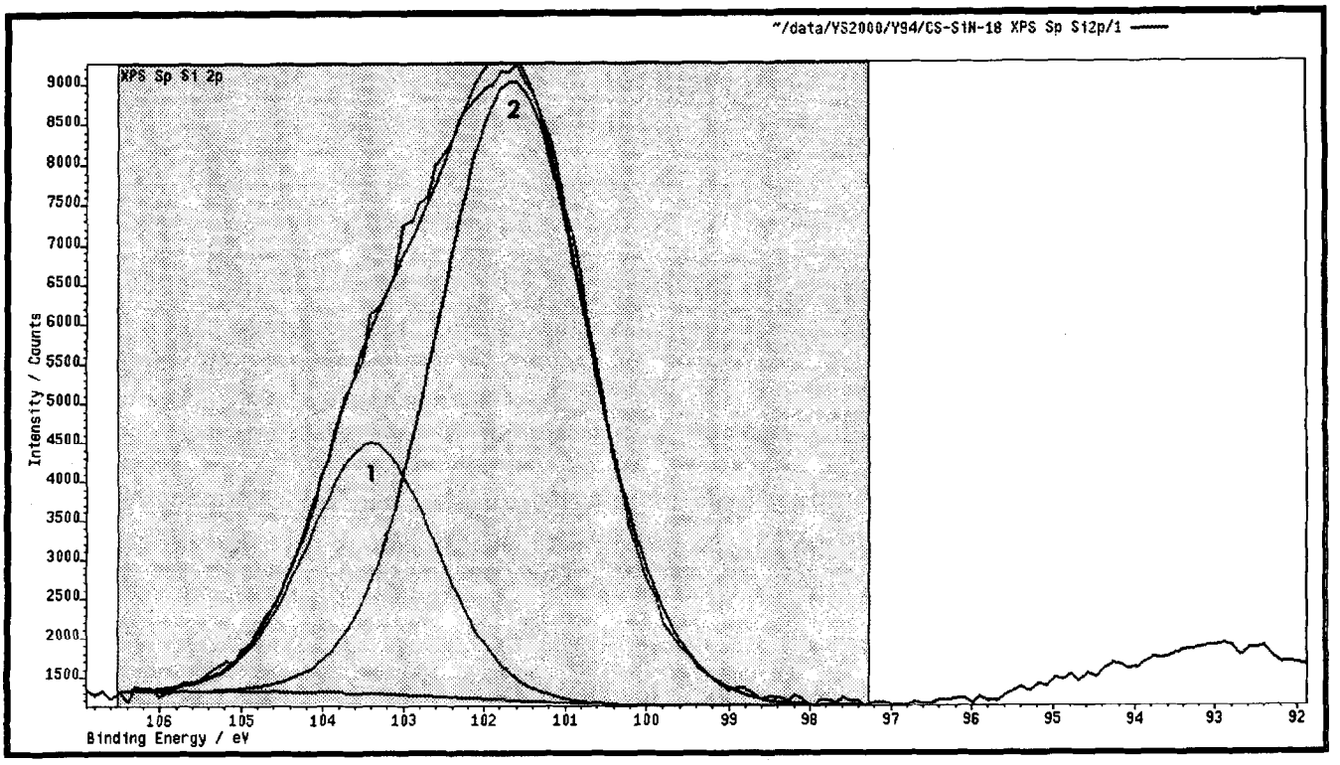


Fig. 8. Deconvolution of Si 2*p* peak; peak 1 corresponds to Si–O; peak 2 to Si–N bonds.

Si_3N_4 powders prepared in the system SiH_4–NH_3–Ar in a tube reactor have been investigated. It was found that for the formation of a stoichiometric silicon nitride powder, the NH_3/SiH_4 molar ratio should be kept at about 11. The total gas flow rate above 400 cm^3 min^{-1} creates more finer fractions of the powder without changing the morphology of the particles. However, powders of hyperstoichiometric in nitrogen content are being formed at higher flow rates. The temperature of synthesis has a substantial influence both on the nitrogen content as well as the mean particle size of the products. The optimum conditions for the preparation of nanosized, isometric, mainly amorphous silicon nitride powders in the given system are: NH_3/SiH_4 molar ratio = 11·62, total flow rate = 400 cm^3 min^{-1}, temperature 650°C.

Acknowledgements

The authors are thankful to Dr P. Šajgalik and Dr M. Haviar for valuable discussions. The work was supported by the Slovak Grant Agency (GAV 2116994).

References

1. Niihra, K. & Nakhira, A., New design concept of structural ceramics, ceramics nanocomposites, *J. Ceram. Soc. Japan*, **99**(10) (1991) 974.
2. Schwier, G., Nietfeld, G. & Franz, G., *Production and characterization of silicon nitride powders*, Materials Science Forum, Trans Tech Publications, Switzerland, 1989, pp. 1–20.
3. Prochazka, S. & Greskovich, C., Synthesis and characterization of pure silicon nitride powder, *Am. Ceram. Soc. Bull*, **57**(6) (1978) 579–81.
4. Janiga, J., Sin, K.-P. & Figush, V., Synthesis of silicon nitride powder by gas phase reaction. *J. Eur. Ceram. Soc.*, **8**(3) (1991) 153–60.
5. Szépvölgyi, J. & Mohai-Tóth, I., *Factorial experimental investigation of the formation of nitride powder in an RF plasma torch*, 11th Int. Symp. on Plasma Chem., Loughborough University, England, Vol. 4 (1993) 1549–54.
6. Szépvölgyi, J., Mohai-Tóth, I., Bertoti, I., Gilbart, E. & Riley, F. L., Synthesis of silicon nitride powder in an RF plasma torch and studies of their sintering behavior, Silicon Nitride 93, In *Key Eng. Materials*, Vol. 89–91, Trans Tech Publication, Switzerland, 1994, pp. 35–40.
7. Tani, T., Yoshida, T. & Akashi, K., The synthesis of ultrafine SiN in a hybrid plasma, *J. Appl. Phys.*, **94**(1) (1986) 7–11.
8. Lee, H. J., Eguchi, K. & Yoshida, T., Preparation of ultra fine silicon nitride and silicon nitride and silicon carbide mixed powders in a hybrid plasma, *J. Am. Ceram. Soc.*, **73**(11) (1990) 3356–62.
9. Šajgalik, P. & Dusza, J., Preparation and properties of fine Si N ceramics, Silicon Nitride 93, In *Key Eng. Materials*, Vol. 89–91, Trans Tech Publication, Switzerland, 1994, pp. 171–74.
10. Šajgalik, P. and Galusek, D., α/β phase transformation of silicon nitride: homogenous heterogenous nucleation, *J. Mat. Sci. Lett.*, **12** (1993) 1937–39.
11. Bertoti, I., Varsanyi, G., Mink, G., Szekely, T., Vaivads, J., Millers, T. & Grabis, J., XPS characterization of ultrafine Si_3N_4 powders, In *Surface and Interface Analysis*, Vol. 12, 1988, pp. 527–30.

Journal of the European Ceramic Society 15 (1995) 1079–1085
© 1995 Elsevier Science Limited
Printed in Great Britain. All rights reserved
0955-2219(95)00089-5
0955-2219/95/$9.50

Surface Characterization of Chemically Treated Aluminium Nitride Powders

R. Metselaar, R. Reenis, M. Chen,* H. Gorter & H. T. Hintzen

Centre for Technical Ceramics, Eindhoven University of Technology, PO Box 513, Eindhoven, The Netherlands

(Received 30 January 1995; revised version received 19 May 1995; accepted 22 May 1995)

Abstract

The surface characteristics of pure AlN powders are compared with those of so-called water stabilized powders. Both commercially available powders and stearic acid coated powders are used. By means of XPS, diffuse reflectance infrared spectroscopy and thermally programmed desorption mass spectrometry, information is obtained about the presence of surface groups. The behaviour of the different powders in aqueous suspension is compared by means of pH measurements and determination of the isoelectric points.

1 Introduction

The behaviour of powder suspensions is largely controlled by the surface chemistry of the solid. Also the sintering behaviour is influenced by the presence of physisorbed and chemisorbed surface groups. In nitride powders the surface oxygen content is also of particular importance for the sinterability. In case of AlN the oxygen content also influences the heat conductivity of the dense material. The chemical stability of AlN powders against oxidation and hydration is low and in water hydrolysis takes place. The reaction with water molecules is so fast that slip casting in aqueous suspensions is in fact not possible. For this reason some manufacturers produce AlN powders which have been treated chemically to increase the water resistance. Little is known about the surface chemistry of such AlN powders. Bowen *et al.*[1] showed the hydrolysis of uncoated AlN using diffuse reflectance infrared spectroscopy (DRIFT). A surface layer of stoichiometry close to AlOOH is formed, which gradually transforms into $Al(OH)_3$ according to the reactions:

$$AlN + 2H_2O \rightarrow AlOOH_{amorph} + NH_3 \quad (1)$$

$$NH_3 + H_2O \rightleftharpoons NH_4^+ + OH^- \quad (2)$$

$$AlOOH_{amorph} + H_2O \rightarrow Al(OH)_3 \quad (3)$$

This reaction is strongly dependent on pH and temperature.[2] Egashira *et al.*[3,4] suppressed the surface reactivity using carboxylic acid adsorption. They assume that surface hydroxyl groups play an important role during the adsorption, according to a reaction

$$\equiv Al\text{–}OH + HOOC\text{–}R \rightarrow \equiv Al\text{–}O\text{–}\underset{\underset{O}{\|}}{C}\text{–}R + H_2O$$

To obtain more insight in the surface chemistry we have used different surface characterization techniques. In this paper we present results of characterization of pure and so-called water-resistant AlN powders.

2 Experimental

Table 1 gives a survey of the specifications of the powders used. Powders C and D (A100 and A200 from Advanced Refractories Technologies, ART, Buffalo, NY, USA) and E (Toyalnite WF from Toyo Aluminium K.K., Osaka, Japan) are commercially available water-resistant powders. AlN powder A (grade C from Starck, Berlin, Germany) was tested as-received and compared with the water resistant powders. Powders B were the Starck C powders coated by us according to the procedure described by Egashira *et al.*[3] Powder B1 was coated with stearic acid by refluxing in benzene, for powder B2 cyclohexane was used as a solvent. Further details are given in Ref. 5.

The reactivity in water was measured by following the change in pH for 0·05 wt% suspensions. To obtain a stable suspension of the powders C and D 1 wt% of the deflocculant Triton X100 (a polyoxyethylene alkylether) was added to these powders.

*On leave of absence from Guanxi University, Nanning, PR China.

Table 1. Specification of AlN powders

Sample No.	*A*	*B1, B2*	*C*	*D*	*E*
Origin	Starck Germany	Powder A coated with stearic acid	ART USA	—	Toyo Aluminium, Japan
	Grade C		A100	A200	Grade WF
FSSS, μm	1·2	as A	3–4	3–4	1·94
BET, m^2/g	3·7	as A	2·5–4	2·5–4	4·30
Al wt%	64·7	as A	66·05	66·0	—
N wt%	33·5	as A	33·0	32·7	32·9
O wt%	1·7	—	1·0	1·1	1·39
Si ppm	—	—	1000–2000	1000–2000	58
Water resistance (h)	—	6–12	2·5–4	—	>72

To measure the pH_{iep} at the isoelectric point the powders were dispersed in water (again with Triton deflocculant in case of the powders C and D), containing 0·01 M KNO_3 electrolyte. The suspensions were stabilized at pH = 2·5 and titrated with 0·1 M KOH under vigourous stirring. The pH_{iep} was found from the zero crossing of the electroacoustic signal, using a Matec ESA analyser. For three powders XPS measurements were performed using a PHI Model 550 system and Al Kα radiation. On four powders diffuse reflectance infrared Fourier transform spectroscopy (DRIFT) was used. The region 4000–800 cm^{-1} was scanned with 4 cm^{-1} resolution, using 500 scans to improve the signal to noise ratio. Powders were diluted in KBr and measured against KBr as reference.

Finally we used thermally stimulated desorption (TPD) to obtain information about adsorbed species and their binding energies to the surface. Similar experiments for the characterization of Si_3N_4 powders have been published earlier.[6,7] In the TPD equipment the sample is heated under high vacuum, while the desorbed gases are monitored by a mass spectrometer. A loosely pressed powder sample of about 20 mg is placed in a sample holder in the first vacuum chamber, which is pumped by a turbomolecular pump to 10^{-7} mbar. After one night, the sample holder is transferred to the main vacuum chamber, which is pumped with an ion getter pump to a vacuum of $<5 \times 10^{-8}$ mbar. In this chamber the sample can be heated by means of an electron gun heater at a rate controlled by a PID controller. Presently the sample is surrounded by stainless steel radiation shields. This limits the maximum sample temperature to about 900°C, due to outgassing of the radiation shields. The desorbed gases are monitored by means of a quadrupole mass spectrometer (Balzers QMG511). Using the relative ionization cross sections for the different molecules, measured curves were corrected. No attempts were made to calculate ion concentrations.

3 Experimental Results

3.1 XPS measurements

Results of the XPS measurements on pure and coated AlN powders are summarized in Table 2. The peaks at 77 and 400 eV are ascribed to Al and N respectively. The energies correspond to Al^{3+} and N^{3-}, and thus these peaks are due to bulk AlN. The carbon peaks at 288 eV are due to contamination; probably the same holds for the oxygen peak at 535 eV. Powder C shows silicon peaks at 105 and 180 eV. According to the supplier 1000–2000 ppm Si is present in these powders. Evidently this silicon is present in the surface coating. The carbon peak in this material is shifted over 0·7 eV; however, it is uncertain if this indicates the presence of organic carbon atoms. The spectra of powder E contain peaks at 199·2 and 149·2 eV

Table 2. XPS peaks for different AlN powders

Sample	*Peak centre (eV)*	*Element*
Starck Grade C (uncoated) powder A	76·7	Al
	400·0	N
	534·7	O
	287·8	C
ART A100 powder C	76·9	Al
	400·0	N
	534·7	O
	287·1	C
	105·0; 180·0	Si
Toyalnite powder E	77·4	Al
	119·02; 149·2	P (from phosphate)
	400·3	N
	535·6	O
	287·8	C

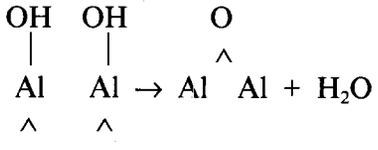
which are assigned to P in phosphate groups. The shift of the oxygen peak with 0·9 eV may also be due to the bonding in the phosphate group. The presence of phosphate is in accordance with a remark in Ref. 8.

3.2 DRIFT spectra

All powders show about 8 strong bands between 600 and 1400 cm^{-1} which can be assigned to lattice phonons of AlN.[9] A weak band at 1973 cm^{-1} in powder E agrees well with the $3TO_1$ mode found in Ref. 9. Broad IR bands at 1600 cm^{-1} and around 3400 cm^{-1} are due to weakly bonded water molecules. Powders B clearly show the CH_2 stretching bands around 2800 cm^{-1}, originating from the stearic acid coating. The spectra of the powders C and D show two extra peaks which could not be assigned unambiguously. For instance a peak at 2160 cm^{-1}, present in both C and D may be assigned to a metal–hydrogen band. Ref. 10 attributes this band on pure AlN to Al–H stretching, although the authors note that the frequency is rather high in comparison with AlH in aluminium hydrides. However, the same frequency is observed for Si–H on Si_3N_4 powders.[11] The band is not present in the uncoated powder, and since XPS shows the presence of Si on the surface of powder C this suggests that it is due to an SiH vibration. However, the absorption is also present in powder E, where no Si was found with XPS. A broad band in both powders at 3200 cm^{-1} may be due to NH,[9] while a sharper peak at 2965 cm^{-1} may indicate the presence of carbon. These assignments remain uncertain, however.

3.3 Temperature programmed desorption

TPD spectra of the different powders are shown in Figs 1–5. All powders show a high desorption peak of water at about 100°C. This is clearly physisorbed water. However, the water desorption continues up to about 600°C. By analogy with the reaction of silanol groups on silicon nitride, this may be due to the surface reaction



After coating with stearic acid (powders B) the physisorbed water peak has a much lower intensity. As could be expected, the stearic acid coated material shows many peaks due to decomposition products of the organic coating, e.g. C_6H_{11}, C_6H_7, C_6H_5, C_4H_9, C_4H_7, C_3H_7, C_3H_5, C_2H_5, and lower masses. Figure 2 shows two of these peaks, at mass 41 and 55 respectively. The hydrocarbons show a desorption maximum at about 400°C,

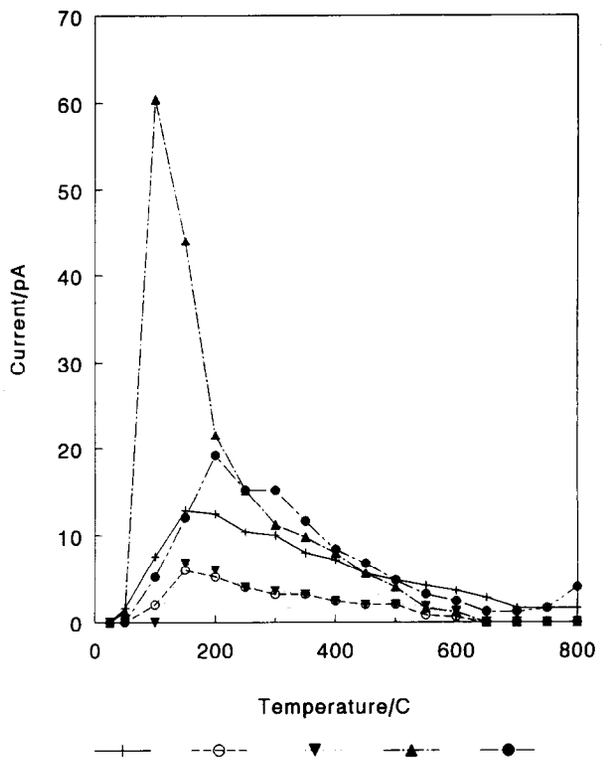


Fig. 1. TPD mass spectrum of uncoated AlN (powder A). Legends from left to right + M = 2, H_2; ○ M = 16 and ▼ M = 17 overlapping peaks NH_2, NH_3; ▲ M = 18, H_2O; ● M = 28, N_2.

indicating that the coating is chemically bonded to the AlN surface. No difference was observed between the powders coated from stearic-acid benzene or stearic-acid cyclohexane solutions.

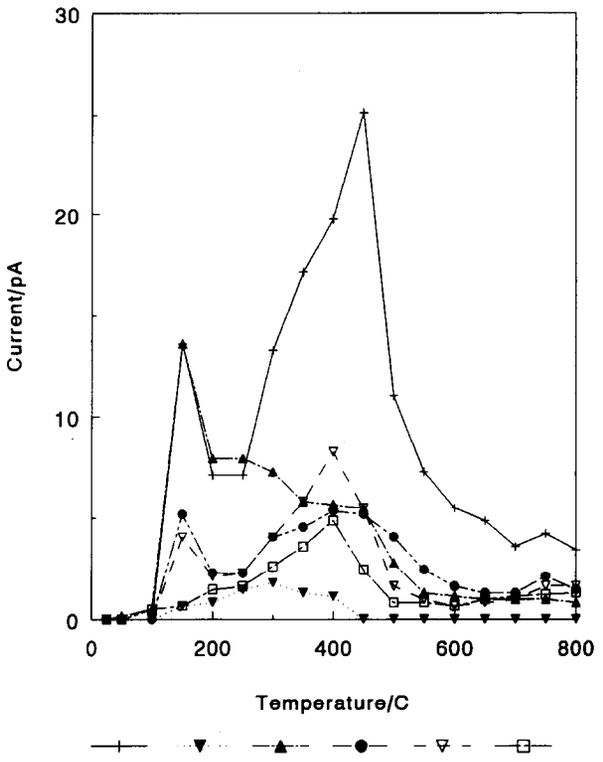


Fig. 2. TPD mass spectrum of stearic acid coated AlN (powder B). Legends from left to right + M = 2, H_2; ▼ M = 17, NH_3; ▲ M = 18, H_2O; ● M = 28, N_2; ∇ M = 41, C_3H_5; □ M = 55, C_4H_7.

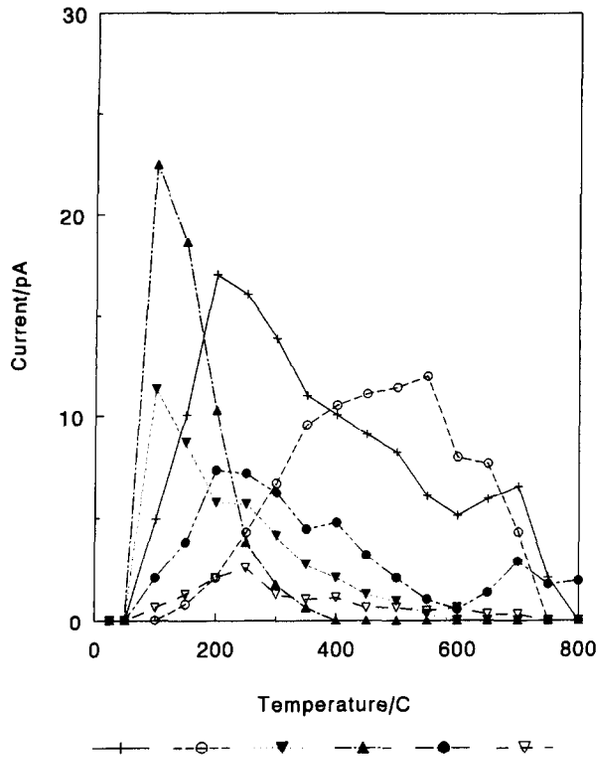


Fig. 3 TPD mass spectrum of water resistant AlN (powder C). Legends from left to right + M = 2, H_2; ○ M = 16, NH_2; ▼ M = 17, OH; ▲ M = 18, H_2O; ● M = 28, N_2; ▽ M = 41, C_3H_5.

Powder C shows a peak at mass 41, which may be due to hydrocarbon (note that in blank runs hydrocarbons have never been found, due to the clean vacuum system). The TPD spectrum of D shows a strong peak at mass 28 above 700°C, which is not observed in the other powders. This may be due to Si instead of N_2, as shown by the XPS and suggested by the DRIFT spectra, however, the fact that it is not observed with powder C contradicts this. Powders A, C, D and E all show desorption of NH_3 at about 150°C, indicating a weak bonding. As mentioned above, AlN reacts with water to form AlOOH and NH_3. Part of the ammonia formed by reaction of AlN with water vapour will remain adsorbed at the surface and may cause the low temperature desorption peak.

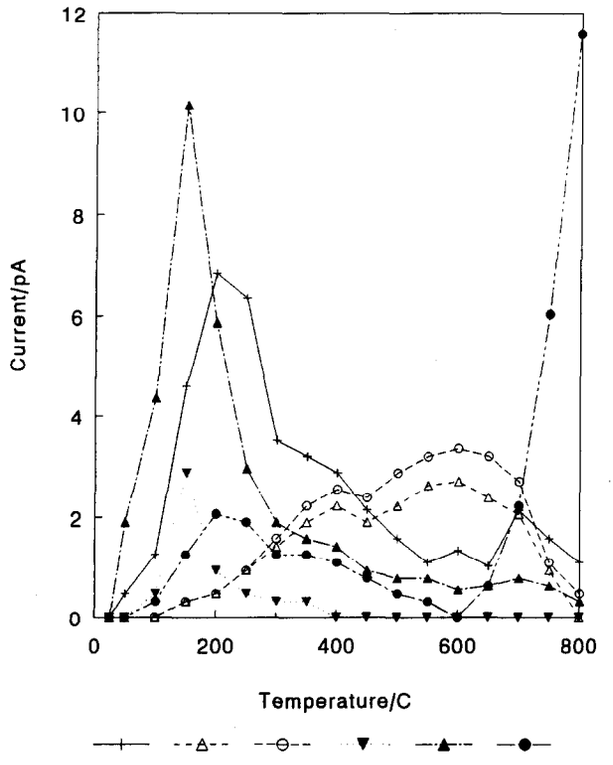


Fig. 4. TPD mass spectrum of water resistant AlN (powder D). Legends from left to right + M = 2, H_2; Δ M = 15, NH; ○ M = 16, NH_2; ▼ M = 17, OH; ▲ M = 18, H_2O; ● M = 28, N_2.

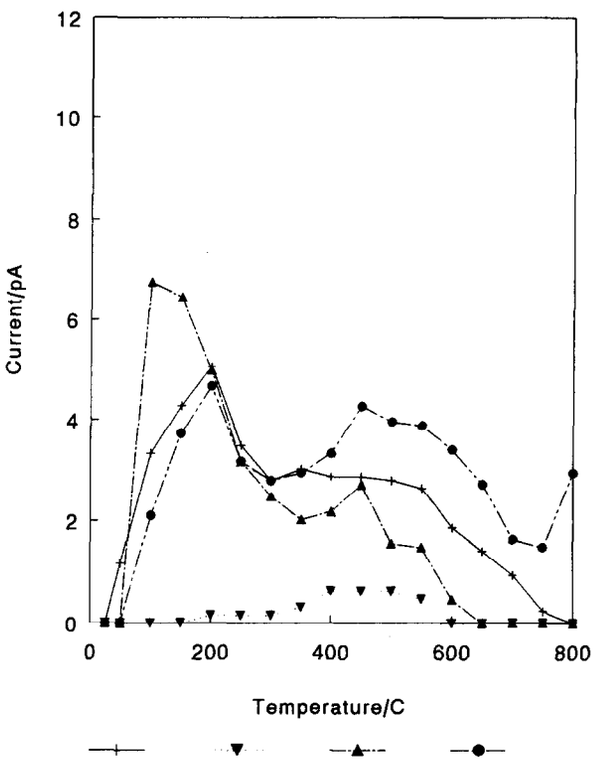


Fig. 5. TPD mass spectrum of water resistant AlN (powder E). Legends from left to right + M = 2, H_2; ▼ M = 16 and 17 overlapping peaks NH_2, NH_3; ▲ M = 18, H_2O; ● M = 28, N_2.

In all powders we find desorption of H_2 and N_2. The peaks are closely correlated and show maxima at 200 and about 400°C. A similar behaviour was found in Si_3N_4 powders.[7] In silicon nitride there is ample evidence for the presence of OH and NH surface groups.[13,14] Therefore we assume that the desorption of hydrogen and nitrogen from the AlN powders is also due to the presence of NH groups at surface sites. Powders C, D and to a lesser extent E all show a peak at about 500–600°C for mass 15 and 16. These peaks are also closely correlated and are therefore attributed to NH and NH_2. Desorption of powder E is low over the whole temperature range. No hydrocarbon peaks were detected for this powder. In view of the XPS results this may indicate a coating with phosphate without organic groups.

Milling of the uncoated AlN powder for 70 h in dry propanol gives a TPD spectrum identical with that of the untreated powder, i.e. the adsorbed species are not removed by this treatment. It also shows that AlN is quite stable in propanol, in agreement with the observation in Ref. 1.

We have also measured the TPD spectrum of uncoated Starck powder after heat treatment at 1000°C in nitrogen. Most of the H_2, N_2, and H_2O are removed, while the NH_3 and NH_2 peaks disappear almost completely.[12] A similar observation was made for silicon nitride powders.[7]

3.4 Electroacoustic measurements

The stability of the powders was measured by following the pH of aqueous suspensions at room temperature. Figure 6 shows the change in pH for 0·5 wt% suspensions of five different powders. The uncoated powder A starts to react from the very beginning. The end value for these dilute suspensions is about pH 11. As shown earlier the addition of Triton surfactant does not influence these results.[5] The figure shows that both the stearic acid coated powder B and powder E are stable for long times at room temperature. This confirms earlier results of Egashira *et al.*[3] No difference was observed between B1 and B2. Powders C and D are stable up to about 30 h, as specified by the supplier. One may suspect that the stability depends on the starting pH of the dispersions. Therefore we repeated the experiment with powder E, the most stable powder, using different initial pH values. Figure 7 shows the results. Suspensions of powder E show a decrease in stability at high pH values. For slip casting one uses much higher solid loadings. Therefore we followed the pH of 30 vol% (58 wt%) suspensions as a function of time (Fig. 8). The decomposition rate is considerably enhanced and hydrolysis of the uncoated

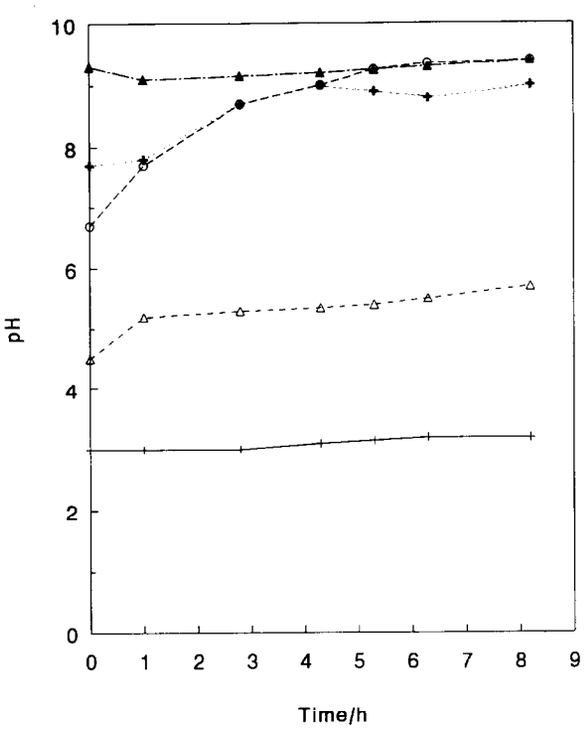


Fig. 7. Stability of powder E in water with different starting pH.

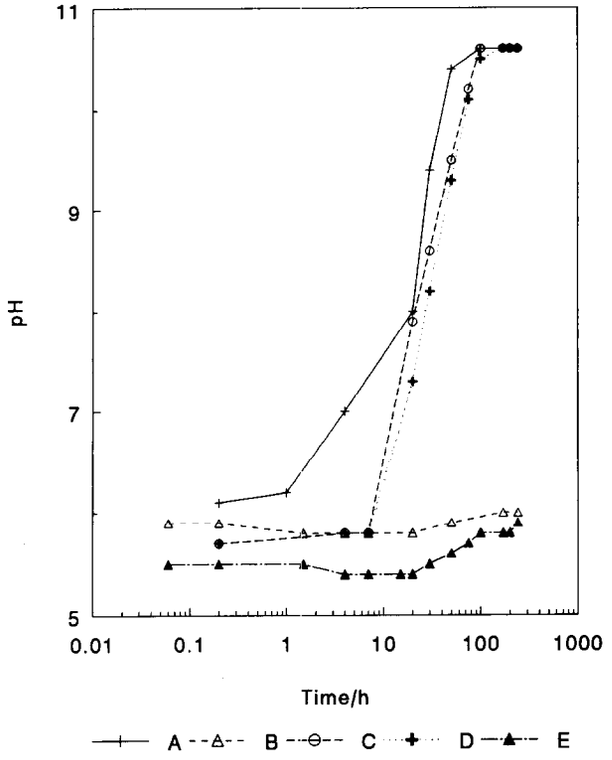


Fig. 6. Time dependence of pH of 0·05 wt% dispersions of AlN (powders A–E) in water.

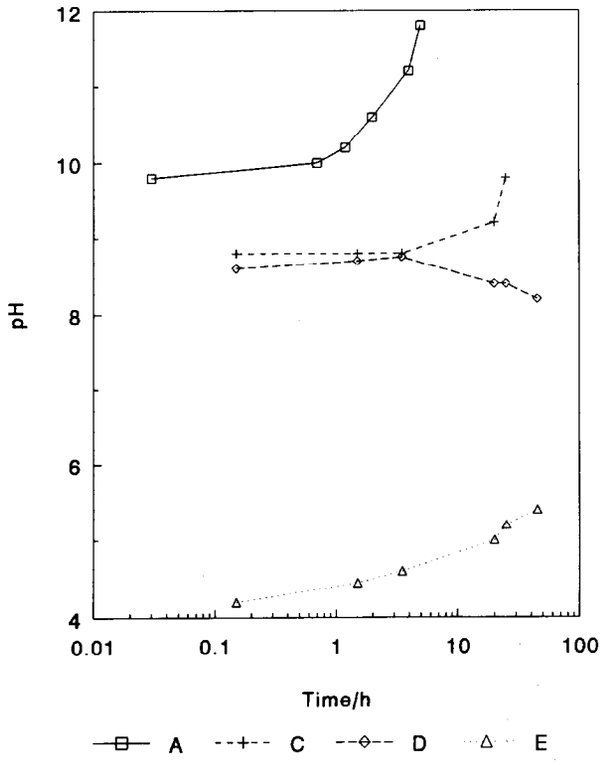


Fig. 8. Time dependence of pH of 30 vol% slips of AlN powders in water.

Table 3. Isoelectric point for suspensions with different solid contents

Sample	*Conc. wt%*	pH_{iep}
Starck Grade C	4	9·7
(powder A)	10	8·9
	25	8·8
	50	8·8
ART A100	4	8·5
(powder C)	10	8·5
	25	8·4
	50	8·1
ART A200	4	7·9
(powder D)	10	7·8
	25	7·7
	50	7·5
Toyalnite	4	6·0
(powder E)	10	6·0
	25	6·0
	50	5·8

powder is visible within 1 h. For powder B the reaction starts between 24 and 48 h. Due to the exothermal nature of the reaction the rate rapidly increases and the slip even became a solid mass. Note that although suspensions are made with water of pH = 7, the pH at the first measuring point after 2 min has changed considerably. Suspensions of powder E become acidic, powders C and D slightly basic. Results of the determination of the isoelectric point by means of ESA measurements are shown in Table 3. Measurements were performed for four different concentrations of the suspensions, *viz.* 4, 10, 25 and 50 wt% AlN in water. There is a slight tendency towards decreasing pH_{iep} values for increasing concentrations. The surface charge is positive below the isoelectric point and negative above. The pH_{iep} value of 8·9 for the uncoated powder is in close agreement with the value of 9·0 found by Seitz *et al.*[15] From a comparison with alumina these authors concluded that Al_2O_3 and AlN exhibit a similar surface. This would mean that the surface contains amphoteric AlOH groups, which may be ionized in solution according to the following reactions:

$$AlOH_2^+ \rightleftharpoons AlOH + H^+ \text{ (aq)}$$
$$K_1 = (H^+)(AlOH)/(AlOH_2^+) \quad (4)$$
$$AlOH \rightleftharpoons AlO^- + H^+ \text{ (aq)}$$
$$K_2 = (H^+)(AlO^-)/(AlOH) \quad (5)$$

The point of zero charge (pzc) is found when $(AlOH_2^+) = (AlO^-)$. From eqns 4 and 5 it follows that this is the case when $pH_{pzc} = (pK_1 + pK_2)/2$. Assuming $pH_{iep} = pH_{pzc}$ we find $pK_1 + pK_2 = 17{\cdot}8$. One also finds the ratio of basic to acid sites as a function of pH:

$$\log(AlOH_2^+)/(AlO^-) = pK_1 + pK_2 - 2pH = 17{\cdot}8 - 2\,pH \quad (6)$$

Powder E has a pH_{iep} of 6·0, which indicates the presence of acidic surface groups. This is in accordance with the observation of phosphate groups in the XPS and IR spectra. The behaviour of powder D indicates that the organosilicon coating results in a pH_{iep} of about 7·5. The pH_{iep} of powder C is in between the value of uncoated powder A and powder D, suggesting that the surface is incompletely covered. The higher water sensitivity of C compared to D points in the same direction. Both powders were poorly dispersable in water which is related to the hydrophobic coating.

4 Summary and Conclusions

The surface of coated and uncoated AlN powder has been investigated by means of XPS, DRIFT spectroscopy, TPD and electrokinetic measurements. Uncoated AlN has a surface similar to alumina with amphoteric AlOH groups. The stability of AlN in water increases in the sequence pure AlN<ART coated<stearic acid coated<Toyalnite coated. The surface of ART powder C seems to be only partially covered by a coating containing both silicon and organic carbon. Stearic acid gives a better protection, but a considerable quantity of this organic compound is present on the surface, which has to be removed before sintering. The Toyalnite powder contains phosphate groups. Due to the coatings the isoelectric point shifts from pH 9 for pure AlN via 7·5 for ART powder to 5·8 for the Toyalnite powder.

Acknowledgements

T. Verhoeven is acknowledged for the XPS measurements and interpretation, J. Vaessen and G. Koekebier for help with ESA measurements and C. Verhagen for advice on the DRIFT spectra.

References

1. Bowen, P., Highfield, J. G., Mocellin, A. & Ring, T. A., Degradation of aluminium nitride powder in aqueous environment. *J. Am. Ceram. Soc.*, **73** (1990) 724–8.
2. Reetz, T., Mönch, B. & Saupe, M., Aluminium hydrolysis. *cfi/Ber. DKG*, **69** (1992) 464–5.
3. Egashira, M., Shimizu, Y. & Takatsuki, S., Chemical surface treatments of aluminium nitride powder suppressing its reactivity with water. *J. Mater. Sci. Letters*, **10** (1991) 994–6.
4. Egashira, M., Shimizu, Y., Takao, Y., Yamaguchi, R. & Ishikawa, Y., Effect of carboxylic acid adsorption on the hydrolysis and sintered properties of aluminium nitride powder. *J. Am. Ceram. Soc.*, **77** (1994) 1793–8.
5. Gorter, H., Gerretsen, J. & Terpstra, R. A., *3rd Euro Ceramics*. Vol. 1, eds P. Duran & J. F. Fernandez. Faenze Editrice Iberica, 1993, pp. 615–20.
6. Kawamoto, M., Ishizaki, K & Ishizaki, C., Characterization

of silicon nitride powders by a temperature programmed desorption study. In *Euro-Ceramics*, Vol. 2, eds G. de With, R. A. Terpstra & R. Metselaar. Elsevier Appl. Sci., London, 1988, p. 2·120.

7. Chen, M., Van Rutten, J. W. T. & Metselaar, R., Study of temperature programmed desorption of silicon nitride and sialon by means of mass spectrometry. In *3rd Euro-Ceramics*, Vol. 1, eds P. Duran & J. F. Fernandez. Faenza Editrice Iberica, 1993, p. 597–602.
8. Sheppard, L. M., *Recent developments and the outlook for electronic ceramics: Surge in electronic materials continues* — Part 1. Silicates Industr., 1993, pp. 83–9.
9. Collins, A. T., Lightowlers, E. C. & Dean, P. J., Lattice vibration spectra of aluminum nitride. *Phys. Rev.*, **158** (1967) 833–8.
10. Merle-Méjean, T., Baraton. M-I., Quintard, P., Laurent, Y. & Lorenzelli, V., Fourier-transform infrared characterization of an aluminium nitride surface. *J. Chem. Soc. Faraday Trans.*, **89** (1993) 3111–5.
11. Busca, G., Lorenzelli, V., Porcile, G., Baraton, M. I., Quintard, P. & Marchand, R., FT-IR study of the surface properties of silicon nitride. *Mater. Chem. Phys.*, **14** (1986) 123–40.
12. Chen, M. & Metselaar, R., Study of temperature programmed desorption of aluminium nitride powders by means of mass spectrometry. In *Charting the Future, Proc. 8th CIMTEC Conference*, ed. P. Vincenzini. Techna, Faenza, 1995, pp. 2125–36.
13. Bergström, L. & Bostedt, E., Surface chemistry of silicon nitride powders: Electrokinetic behaviour and ESCA studies. *Coll. and Surfaces*, **49** (1990) 183–197.
14. Hackley, V. A. & Malghan, S. G., The surface chemistry of silicon nitride powder in the presence of dissolved ions. *J. Mater. Sci.*, **29** (1994) 420–30.
15. Seitz, K., Hessel, F., Güther, H.-M., Roosen, A. & Aldinger, F., Comparison of the surface characteristics of alumina and aluminium nitride. In *Ceramic Trans. 22, Ceramic Powder Sci. IV*, eds S. Hirano, G. L. Messing & H. Hausner. Am. Ceram. Soc., Westerville, 1991, pp. 227–34.

Journal of the European Ceramic Society **15** (1995) 1087–1100
© 1995 Elsevier Science Limited
Printed in Great Britain. All rights reserved
0955-2219(95)00078-X
0955-2219/95/$9.50

Carbothermal Synthesis of Aluminium Oxynitride (ALON) Powder: Influence of Starting Materials and Synthesis Parameters

Jie Zheng & Bertil Forslund

Department of Inorganic Chemistry, Arrhenius Laboratory, University of Stockholm, S-106 91 Stockholm, Sweden

(Received 6 February 1994; revised version received 9 May 1995; accepted 16 May 1995)

Abstract

Carbothermal synthesis of cubic aluminium oxynitride (ALON) have been performed in a graphite furnace at different temperatures (1700–1860°C) and pressures (0.1–10 MPa). The products were characterized by XRD, SEM and elemental analyses, and the overall compositions were determined by reoxidation in air. The control of excess nitridation was a crucial task in the preparation of ALON. A two-step procedure, first annealing at about 1550°C then at about 1800°C, was found to be effective to this end. CO additions to the N_2 gas stimulated ALON formation, but a pressure increase resulted in a lower nitridation rate. The particle size and morphology of ALON depended on raw material type and synthesis parameters such as temperature program, pressure, CO content in the N_2 gas, and sample compartment type. Thermodynamic calculations in the Al–O–C–N system have been performed in order to explain the experimental results.

1 Introduction

The acronym 'ALON' is used for an aluminium oxynitride, of composition $Al_{(64+x)/3}O_{(32-x)}N_x$ ($0 \leq x \leq 8$)[1] — a pseudo-binary solid solution of AlN in Al_2O_3, which may be regarded as a nitrogen-stabilized cubic γ-Al_2O_3 phase (spinel). It has interesting optical, mechanical and chemical properties, making it potentially useful as a high-performance ceramic material.

There is some controversy in the literature as to the extent of solid solubility. McCauley and Corbin[2] found the ALON field to range from about 27 to 40 mol% AlN, with fairly constant limits in the temperature range 1700 – 2000°C. They reported the lattice parameter of the cubic structure, in samples quenched from 1975°C, to vary from 7.938 Å for the most oxygen-rich composition to 7.951 Å at the other extreme. According to Lejus,[3] on the other hand, the ALON solid solution extends from about 16 to 33 mol% AlN at 1700°C, and the cell edge varies between 7.927 and 7.950 Å. In a recent study Willems *et al.*[4] established that the homogeneity range is 19–34 mol% AlN at 1850°C, becoming successively more narrow at lower temperatures, reaching zero at 1640°C.

In a comprehensive article by Corbin,[5] the physical properties of ALON are reviewed, and also various preparation methods employed since the first paper on the compound in 1959.[6] A tentative phase diagram of the AlN–Al_2O_3 system is presented, valid at 1 bar of nitrogen pressure. In total, thirteen different oxynitride phases have been reported to date. ALON is the only stable binary phase below 1900°C although other oxynitride or nitrogen stabilized alumina phases are apt to form also in this regime under specific synthesis conditions.[7,8]

Of the ALON synthesis methods tried so far, those demanding the highest temperatures (> 1500°C) are: direct reaction of an alumina + aluminium nitride powder mixture, and reduction/nitridation of alumina with carbon, aluminium metal or hydrogen in nitrogen or ammonia. Oxidation/nitridation of aluminium in air has been used at ca. 1500°C, and the gas phase reaction between aluminium chloride and ammonia is effective below 1000°C.

Carbothermal nitridation of alumina, according to:

$$\left(\frac{64+x}{3}\right)Al_2O_3 + 3xC + xN_2(g) \rightarrow 2Al_{(64+x)/3}O_{(32-x)}N_x + 3xCO(g) \quad (1)$$

is a well established preparation procedure for ALON. Several patents have been issued, some of

them describing a two-step heat-treatment process in a nitrogen atmosphere; first at 1500–1600°C, then at 1700–1800°C.[9]

The synthesis of ALON powder according to the reaction (1) might seem straightforward but control of the product stoichiometry may be a difficult task. There are several reasons for this. Firstly, at the very high preparation temperatures required, around 1800°C, evaporative losses of aluminium and aluminium suboxides from the charge are likely to be high, particularly in a dynamic atmosphere. Secondly, the reducing conditions prevailing in a graphite furnace, which is a convenient reactor type, may have a large influence on the final O/N ratio in the powder, as was early recognized.[6] Willems *et al.*[10] calculated the composition (oxygen, carbon and nitrogen activities) of the gas phase in stable coexistence with ALON, and concluded that it should be extremely difficult to prepare pure ALON in a flowing N_2 atmosphere without partial reduction or oxidation to AlN or Al_2O_3. A contributing difficulty is that we presently do not know the exact ALON formation mechanism: is it mainly a solid state reaction between aluminium nitride and alumina, or are there important reaction steps occurring *via* the gas? The relatively slow advancement of the ALON formation, even at high temperatures; and observations such as those of Ish–Shalom,[11] that the relative amount of ALON in the product mixture goes through a maximum at a certain annealing time, favour the view that ALON formation is mainly controlled by solid state diffusion. On the other hand, the high activities expected for some aluminium-bearing gas species at the reaction temperatures make it necessary to consider also gas phase reaction steps. Lefort and Billy[12] have suggested that AlN forms on the surface of the Al_2O_3 grains by nitridation of Al vapour, and that ALON subsequently forms at temperatures above ca. 1600°C as a result of solid–solid interactions at the Al_2O_3/AlN interface.

The main purpose of the present investigation of ALON synthesis, by carbothermal nitridation of alumina, was to study the effect of variation of different synthesis parameters on conversion rate, sample stoichiometry and particle morphology, and to elucidate the optimal conditions for synthesis of a monophasic ALON powder in a graphite furnace. To this end, powder mixtures of different alumina and carbon starting materials were heat-treated according to different temperature programs and annealed at 1700–1860°C in flowing nitrogen. Of particular interest was to find out if the nitrogen pressure could be a useful synthesis parameter, as previously found to be the case with Si_3N_4[13] and AlN.[14,15]

2 Experimental

2.1 Sample preparation

Raw materials were alumina and carbon black ('N330', Nordisk Philblack AB, Malmö, Sweden), having a surface area of 82 $m^2\ g^{-1}$ and a mean particle diameter = 30 nm. Alumina materials used were coarse α-Al_2O_3 ('A-591', mean particle diameter 5 μm, Fisher Scientific Co., New Jersey, USA) and fine γ-Al_2O_3 (made in-house), with a surface area of 0.6 and 138 $m^2\ g^{-1}$, respectively. The latter was a poorly crystallized decomposition product of ammonium alum. Aluminium nitride ('Grade A', Hermann C. Starck Berlin Gmbh, Goslar, Germany) was used in some comparison experiments. The nitrogen gas ('Nitrogen Plus', AGA Co., Lidingö, Sweden), specified to contain < 5 ppm O_2 and < 5 ppm H_2O, was used without further purification. An N_2 + 10% CO mixture of the same purity level and Ar ('Argon 4.8', AGA Co., Lidingö, Sweden) were used in some experiments.

Starting materials were seven mixtures of alumina and carbon black powders, denoted 'A' – 'G' (Fig. 1). Besides, 'H' was a mixture of Al_2O_3 and AlN, while 'I' was prepared from $AlCl_3 \cdot 6H_2O$ and starch by a sol–gel procedure. Their compositions, theoretical relative weight changes for full conversion and modes of preparation are given in Table 1. The water contents of the aluminas have been compensated for in these calculations.

Three charge types were used: powders, pellets and granules. Powders were obtained by drying an ethanol slurry, milled in a mortar or in a plastic bottle with SiAlON balls for 4 days. About 0.5 g of the dried, yet plastic powders was pressed into cylindrical pellets of 11 mm diameter and 4–8 mm thick, using a pressure of 840 MPa for 30 s. Granules of diameter 1.5 mm and length 1–6 mm were formed by extrusion. Residual alcohol was subsequently removed by further drying.

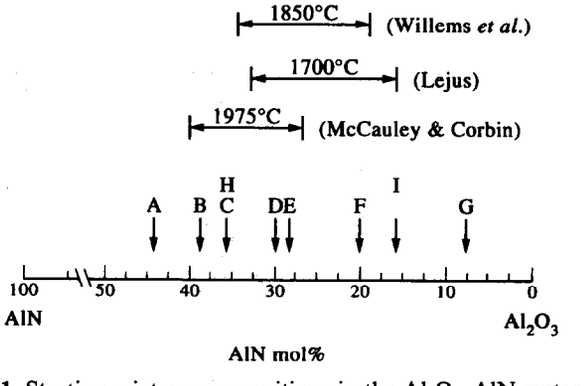


Fig 1. Starting mixture compositions in the Al_2O_3–AlN system. ALON homogeneity ranges suggested by previous authors (Refs 2, 3, and 4) are indicated.

Table 1. Compositions and theoretical relative weight changes of starting mixtures

Symbol	*Wt. ratio*	*Composition (mol% AlN)*	$(-\Delta m/m_0)_{theo.}$ (%)	*Mixing by*
A	α-Al_2O_3/C = 10·0	44·2	14·1	Ball milling
B	γ-Al_2O_3/C = 12·3	38·5	14·1	Milling in mortar
C	α-Al_2O_3/C = 13·0	35·7	11·1	Ball milling
D	γ-Al_2O_3/C = 16·0	29·9	11·3	Ball milling
E	α-Al_2O_3/C = 17·0	28·6	8·6	Ball milling
F	α-Al_2O_3/C = 25·4	20	5·9	Ball milling
G	α-Al_2O_3/C = 70·4	7·7	2·2	Milling in mortar
H	γ-Al_2O_3/AlN = 4·5	35·7	0	Milling in mortar
I	Al_2O_3/C = 33·4	15·7	8·2	Sol–gel procedure

2.2 Synthesis procedure

The carbothermal nitridations of alumina at different nitrogen pressures (0.1–10 MPa) were performed in a gas autoclave with a vertical graphite furnace, described previously.[13,14] The granules or pellets were placed in a graphite sample holder, some of them with a BN (ABB Cerama, Robertsfors, Sweden) liner. Powders were charged in alumina or molybdenum crucibles in the sample holder.

In order to eliminate air from the autoclave before nitridation, the autoclave was flushed several times with nitrogen (1 MPa) at room temperature and on heating up to 600°C. During the whole experiment the nitrogen gas was forced through the sample holder at a controlled flow rate (0–10 $l_{stp.}$ min^{-1}), and then the shortest way out *via* a reducing valve and a flowmeter.

The sample temperature was measured with a W/(W, Re) thermocouple, calibrated against the melting points of Au, Pd and Pt. The plateau temperature could be kept within ± 1 K.

Two kinds of temperature programs, controlled by a PID regulator, were used in our synthesis experiments: a 'one step reaction' with one plateau temperature and a 'two step reaction' with two plateaus. The heating rate was normally 20 K min^{-1}, the cooling rate 30 K min^{-1}. Usually the gas outlet valve was opened at 1400°C on heating and closed at 1450°C on cooling.

2.3 Characterization

The surface area of the materials was measured by an independent laboratory using the BET method. The phase compositions of the reaction products were determined by X-ray powder diffraction (XRD, Guinier-Hägg-type focusing cameras) using Cu $K\alpha_1$ radiation and Si as an internal standard. The cell dimensions of the ALON phase were calculated with the PIRUM program[16] on the basis of, at most, 11 reflexions, representing *d*-values in the range 1.1–4.6 Å. The particle size was estimated by scanning electron microscopy (SEM, JEOL JSM-820, Tokyo, Japan). A few samples were subjected to elemental (N, O, C) analyses by a commercial laboratory using a fusion-gas analysis method.

In order to determine the overall composition of a product, this was ground into powder, charged in a platinum crucible and then heat treated at 1400°C for 2 h in air. Such an oxidation procedure has been reported[7] to completely transform the sample to α-Al_2O_3, expelling all nitrogen, for example according to:

$$4Al_{23}O_{27}N_5(s) + 15O_2(g) \rightarrow 46Al_2O_3(s) + 10N_2(g) \quad (2)$$

Judging from the colour of the oxidized samples, white in all cases, the residual carbon was efficiently removed by this simple procedure. This was also confirmed by chemical analysis of some samples, showing the C content to be less than 0.2 wt%. By accurate weighing of the sample before and after oxidation, the original composition, given as the AlN molar ratio $X_{AlN} = n_{AlN}/(n_{AlN} + n_{Al_2O_3})$, could be determined with an estimated accuracy better than ± 0.01, in most cases.

3 Thermodynamic Calculations

In order to interpret some of our results, we have performed thermodynamic calculations on the system Al–O–C–N by means of the computer program 'SOLGASMIX',[17] based on the principle of free energy minimization. The system was described by 35 different gas species and 8 condensed phases (Al, C, AlN, α-Al_2O_3, γ-Al_2O_3, Al_4C_3, Al_4O_4C and ALON). All $\Delta G°_f$ data were taken from the JANAF Tables[18] except those of Al_4O_4C and ALON which are from Refs 19 and 10, respectively. In all calculations ALON was regarded as a stoichiometric phase with the composition $Al_{23}O_{27}N_5$, due to the absence of data for other compositions.

Figures 2 and 3 give the calculated partial pressures of Al(g) and $Al_2O(g)$ in equilibrium with nitrogen gas and the solid product phases after reaction between Al_2O_3 and AlN, at 2100 K and

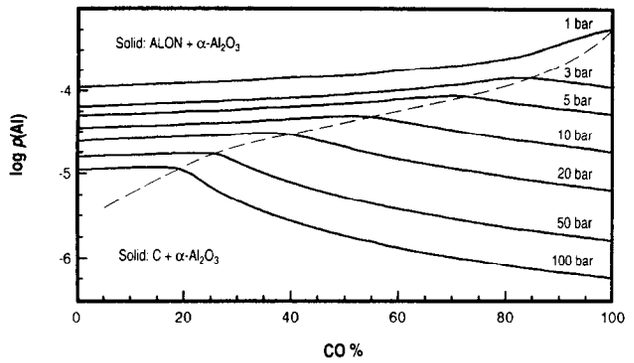


Fig. 2. Calculated equilibrium partial pressures (bar) of Al in a mixture of the products of the reaction between Al_2O_3 and AlN at 2100 K, at different pressures and CO contents in nitrogen (Al_2O_3: 9 mol, AlN: 5 mol, N_2+CO: 100 mol).

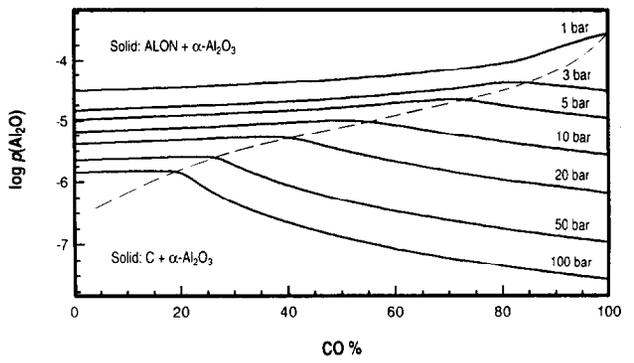


Fig. 3 Calculated equilibrium partial pressures (bar) of Al_2O in a mixture of the products of the reaction between Al_2O_3 and AlN at 2100 K, at different pressures and CO contents in nitrogen (Al_2O_3: 9 mol, AlN: 5 mol, N_2+CO: 100 mol).

different pressures and CO contents (Al_2O_3: 9 mol, AlN: 5 mol, N_2 + CO: 100 mol). The partial pressures p(Al) and $p(Al_2O)$ are not sensitive to the relative amounts of starting materials. ALON ($Al_{23}O_{27}N_5$) and α-Al_2O_3 are stable products in the field above the dashed curve. Below this line, C and α-Al_2O_3 become the product phases. In the ALON formation field, p(Al) and $p(Al_2O)$ increase slightly with CO content but decrease with increasing total pressure.

4 Results

4.1 Single step runs

A large number of synthesis experiments were carried out with the simple temperature program, the 'one step reaction', on the starting mixtures 'A'–'I', with Al_2O_3/C ratios between 10 and 70 (Fig. 1). Plateau temperatures and nitrogen pressures were in the ranges 1600–1860°C and 0.1—10 MPa. The results of only a selected number of runs are shown in Table 2. Also included are some 'two step reactions', as well as runs with recharged samples.

ALON appeared as a reaction product in all experiments at temperatures above 1700°C, although it turned out to be virtually impossible to prepare single phase ALON in a 'one step reaction'. The reason was that further nitridation of alumina easily occurred, yielding aluminium nitride even for a mixture with a high Al_2O_3/C ratio, such as 'G'.

Fine γ-Al_2O_3, for example in mixtures 'B' and 'D', was more reactive than coarse α-Al_2O_3, but also easily underwent substantial excess nitridation. Using the Al_2O_3–C precursor, made by the sol–gel method ('I') and expected to be highly reactive, ALON could actually be prepared at 1700°C in 3 h, but AlN formation occurred in spite of a starting composition at low X_{AlN}.

With coarse α-Al_2O_3 as in 'A', 1 h at 1750°C, 0.5 MPa was not sufficient for ALON formation in granules, which however was accomplished at 0.1 MPa. As is exemplified in Table 2, increasing the pressure hampered ALON formation for all compositions, but the difference in nitridation rate between high- and low-pressure runs was more marked with mixtures of fine-grained γ-Al_2O_3 (*cf.* runs No.5 and 6). Run No.3 with mixture 'B' demonstrates the rapid *onset* of the ALON formation reactions at T > 1800°C.

Heating at a rate of 5°C min^{-1}, instead of the normal 20°C min^{-1}, did not make much difference as to the synthesis result. A run with Ar as the furnace atmosphere during heating, and N_2 for the subsequent 1 h on the 1820°C plateau, yielded the same sample composition as an 'all nitrogen' comparison run. This suggests that the result is not very sensitive to the choice of heating rate (It is noteworthy though, that ALON failed to form in No.7, after very slow heating, 2°C min^{-1}, to 1800°C and then 1 h tempering). Neither did we find 'charge type', i.e. pellet, granule or loose powder, to be very important for the conversion rate with the starting materials used in this study.

The relative weight change (RWC), $-\Delta m/m_O$ (m_O is the charge weight), can be chosen as a general measure of conversion. However, RWC is not exclusively due to losses of CO following eqn (1), but also to extra reduction of the sample by the gas atmosphere and irreversible evaporative losses of Al-containing gas species, (e.g. aluminium or aluminium suboxides). It can be seen from Table 2 that the experimentally obtained RWC-values were always higher than the $(RWC)_{theo.}$, calculated for full conversion according to reaction (1), even for short time runs at low temperatures. The RWC ratio values given in parentheses were calculated from the analyzed AlN contents (X_{AlN}). They should be approximately equal to the experimental RWC ratios, if the weight decrease is exclusively due to reduction/nitridation of Al_2O_3 by the C reactant or the furnace atmosphere.

Table 2. The synthesis parameters and the results of the first series of nitridation runs

Run No.	*Mixture sample*	*T(°C) t (h)*	*p(N_2) (MPa)*	*Φ(N_2) (1 min^{-1})*	*Sample holder*	*Product phases**	*X_{AlN} (%)*	*RWC ratio (%)***	*Comment*
1	Mix. A pellet	1800°C 1 h	5·0	5	BN	N, O	—	104	
2	Mix. B granule	1800°C 1 h	5·0	5	BN	ALON, N, O	46·6	133 (109)	
3	Mix. B pellet	1600 + 1820°C, 2 + 0 h	0·2	0·5	Mo	ALON, O, N	—	118	C granules as support charge
4	Mix. C pellet	1800°C 1 h	5·0	5	BN	N, O	33·8	104 (103)	
5	Mix. D pellet	1820°C 0.83 h	0·1	0·2	BN	ALON, N_w	51·2	152 (127)	Whiskers
6	Mix. D pellet	1820°C 0.83 h	1·0	1	BN	ALON, O_w,N_w	39·9	142 (112)	
7	Mix. E pellet	1800°C 1 h	0·5	1	BN	O, N	32·0	116 (105)	2°C min^{-1} (heating), whiskers
8	Mix. E pellet	1800°C 1 h	5·0	5	BN	O, N, $ALON_w$	—	111	
9	Mix. E pellet	1800°C 1 h	5·0	0	BN	ALON, O, N	30·9	112 (104)	Sample 8 recharged
10	Mix. E pellet	1600°C 1 h	1·0	5	BN	O, N	—	111	Whiskers
11	Mix. E pellet	1820°C 4 h	0·2 (Ar)	0	BN	ALON, N	43·0	134 (123)	Sample 10 recharged, whiskers
12	Mix. E pellet	1600+ 1820°C, 1+ 0.7h	1·0	5 + 0, 1+ 0.7h	BN	ALON, O_w,N_w	38·7	113 (119)	
13	Mix. F granule	1800°C 1 h	5·0	5	C	ALON, O, N	31·5	122 (124)	
14	Mix. F pellet	1800°C 1 h	3·0	5	BN	O, N, ALON	23·6	112 (107)	
15	Mix. F pellet	1800°C 1 h	5·0	5	BN	O, N, ALON	—	100	
16	Mix. F pellet	1800°C 1 h	5·0	0	BN	ALON, O, N	25·7	—	Sample 15 recharged

* O = Al_2O_3, N = AlN, O_w= weak XRD lines of alumina, N_w = weak XRD lines of aluminium nitride.
** RWC ratio = $(RWC)_{exp.}/(RWC)_{theo}$. Figures in parentheses are RWC values based on analyzed X_{AlN}.

When a graphite sample holder was used, this material reduced the sample appreciably, even without direct contact, resulting in an extra high RWC, e.g. in run No.13. In most runs, therefore, the charge was separated from the graphite sample holder by a BN liner.

Figure 4 shows that resulting RWC versus reaction time under different conditions for compositions 'A', 'C', 'E', and 'F'. It is clear that $-\Delta m/m_O$ increases with reaction time, particularly for samples charged in the graphite holder. Increasing CO concentration in the gas to 10% caused an overall decrease of RWC, but not a lower nitridation rate (see 'special tests' below) as in the carbothermal syntheses of AlN and Si_3N_4.[13,14] No obvious dependence of conversion on gas flow rate was found. Neither was this expected, as the major effect of increasing the gas flow should be to diminish the CO concentration in the sample space. The product phase assemblage was generally ALON + AlN. In mixtures 'E' and 'F', run for short times, unreacted Al_2O_3 could also be detected.

No accurate determination of the amounts of different phases in the samples was undertaken in this study. As a rough measure of the relative contents of ALON and AlN, and in order to follow the progress of reaction, the X-ray intensity ratio $I_{ALON(400)}/I_{AlN(100)}$ was used. Figure 5 shows this ratio as a function of reaction time for pelletized starting mixtures 'A' and 'F', run in graphite sample

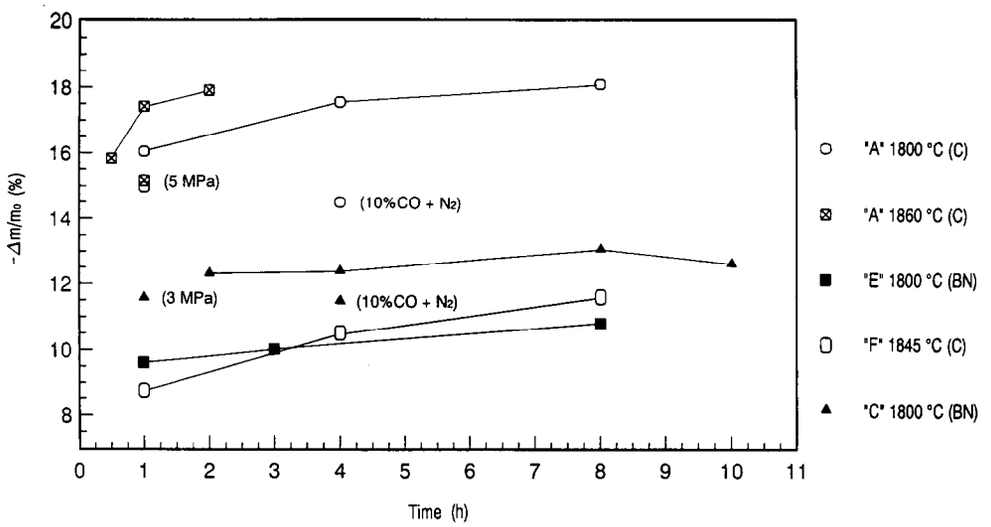


Fig. 4. RWC ($-\Delta m/m_O$) as a function of reaction time for starting mixtures A, C, E and F, run at $p(N_2)$ = 0.5 MPa, $\Phi(N_2)$ = 5 l min^{-1}, with different temperatures and sample holders (graphite or boron nitride). The furnace atmosphere and the pressure for some special runs are indicated in parentheses.

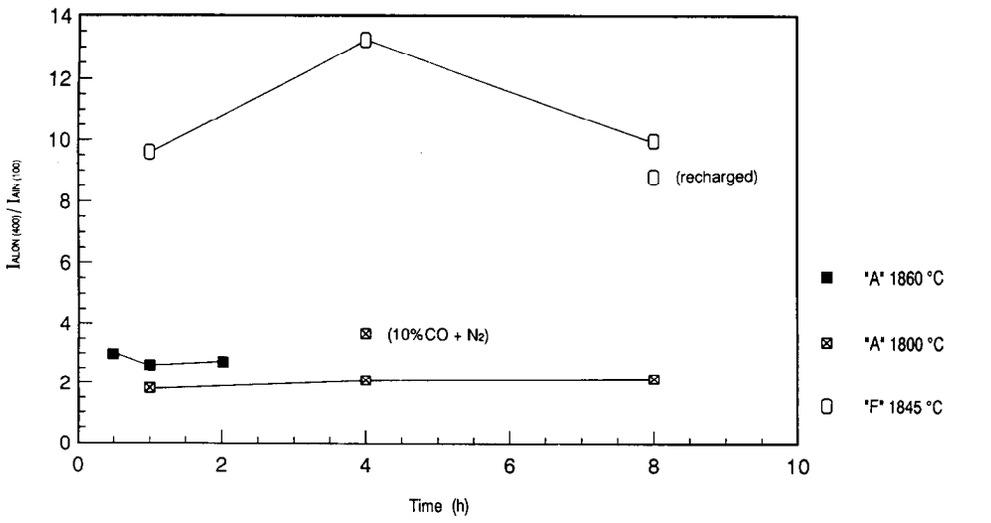


Fig. 5. The measured intensity ratio $I_{ALON(400)}/I_{AlN(100)}$ as a function of reaction time for starting mixtures A and F, run in graphite sample holders at 0.5 MPa, 51 min^{-1} and different temperatures.

holders at 0.5 MPa and different temperatures. The ratio for 'F' samples first increases with time but then decreases. Such a trend was not observed for composition 'A', possibly due to the Al_2O_3/C ratio of 'A' being much lower than that of 'F'. One sample, which had been run for 8 h, was recharged without further homogenization and the heat-treatment repeated for another 8 h, but I_{ALON}/I_{AlN} did not increase. Figure 6 shows the intensity ratio as a function of reaction time for pellets of compositions 'C' and 'E' run at 1800°C, 5 MPa, in sample holders with BN liners. For both compositions the ratio increases with time, but the rate of increase is smaller for 'C', which contains more AlN. The adverse effect on the ALON formation of an increase in pressure is evident. On the other hand, introduction of carbon monoxide into the nitrogen gas seems to slightly favour ALON formation, at the expense of AlN (Figs 5 and 6).

As stated above, none of our runs with a simple temperature programme resulted in a single-phase ALON powder. Homogenization and recharging of incompletely reacted samples and repeated heat-treatment was neither a successful means to reach this goal (compare runs No.15, and No.16 with No.14 in Table 2). Either unreacted Al_2O_3 remained, due to insufficient tempering, or AlN formed due to excessive reduction. The nitridation proceeded too far even when nitrogen was excluded during the second heat-treatment, as in runs No.10 and No.11. Nevertheless, this couple of runs, with the first annealing at only 1600°C, was an improvement upon the double run No.8 and No.9, at 1800°C. Better still was a two-step run, with a first annealing at 1600°C and a second at 1820°C without recharging, e.g. run No.12. In this case both the evaporative losses and the composition shift were smaller than in the corresponding 'single step reaction'.

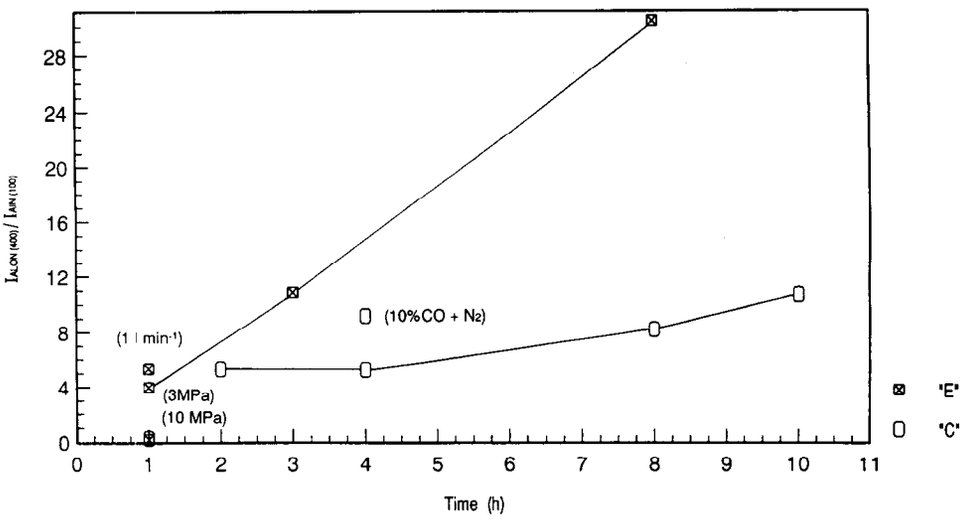


Fig. 6. The measured intensity ratio $I_{ALON(400)}/I_{AlN(100)}$ as a function of reaction time for starting mixtures C and E, run at 1800°C, 5 MPa, 5 l min^{-1} in a sample holder with BN liner. The conditions for some special runs are shown in parentheses.

4.2 Special tests

Careful control of the nitridation of Al_2O_3 thus turned out to be crucial to the carbothermal synthesis of ALON. Mainly in order to clarify the rôle of gas phase reactions in this respect, a series of special tests on pure Al_2O_3 and AlN powders were carried out. Table 3 gives the details of the experimental conditions and the results.

In all runs except No.1 and No.8, the sample was covered to prevent contamination by carbon, occasionally released from the furnace and carried away by the gas flow.

Under the experimental conditions in Nos 1–6, the Al_2O_3 charge was found to react with N_2 in the absence of C, to form substantial amounts of ALON and AlN in 4 h at 1820°C. At least qualitatively, the same results were obtained with alumina and molybdenum crucibles. Elemental analyses gave clear evidence that addition of 10% CO to the N_2 in No.6 stimulated nitridation (*cf.* No.2), while an increase in pressure had an adverse effect (No.3). Fine γ-Al_2O_3 was found to be somewhat more reactive than coarse α-Al_2O_3.

Experiment No.7, with AlN powder in a Mo

Table 3. The synthesis parameters and the results of the special tests

Run No.	*Raw material*	*Container*	*Gas*	*T (°C) t (h)*	*p(N_2) (MPa)*	*Φ(N_2) (1 min^{-1})*	*Product phases**	*ALON a_o(Å)***	*N (wt%)*
1	γ-Al_2O_3	Al_2O_3 crucible without cover	N_2	1820 4	0·2	0·6	s: N, ALON, O i: O, ALON, N	7·951 (1) 7·945(3)	—
2	γ-Al_2O_3	Mo crucible Al_2O_3 cover	N_2	1820 4	0·15	0·6	m: O, N, ALON	7·944 (2)	7.4
3	γ-Al_2O_3	Mo crucible Al_2O_3 cover	N_2	1820 4	5·0	0·6	m: O, ALON	7·948 (2)	0.8
4	γ-Al_2O_3	Mo crucible Al_2O_3 cover	N_2	1820 8	5·0	0·6	m: O, ALON	7·945 (2)	—
5	α-Al_2O_3	Mo crucible Al_2O_3 cover	N_2	1820 4	0·15	0·5	s: O, ALON, N i: O, ALON, N	7·946 (1) 7·945(2)	5.1
6	γ-Al_2O_3	Mo crucible Al_2O_3 cover	N_2+ 10% CO	1820 4	0·15	0·5	m: N, ALON, O	7·948 (2)	14.6
7	AlN		Ar	1820 4	0·15	0			—
	γ-Al_2O_3	Mo crucible and cover					i: N, ALON	7·949 (2)	
8	AlN	Mo crucible without cover	Ar	1820 4	0·15	0	m: N	—	—

* s = surface, i = interior, m= mean, N= AlN, O = Al_2O_3.
** Figures in parentheses are ± 3σ (σ ≡ the standard deviation).

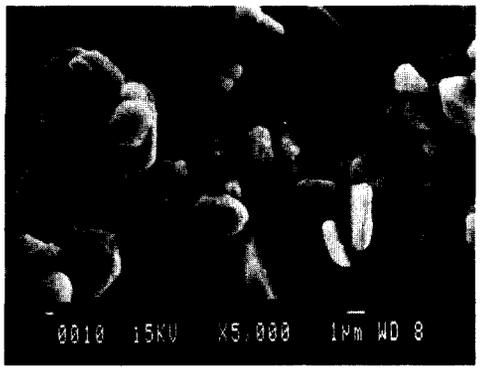


Fig. 7. SEM micrograph of the coarse α-Al_2O_3 raw material.

crucible resting on an Al_2O_3 powder bed, shows that with the reaction times and temperatures used in this series, AlN powder is affected by Al_2O_3, even at a distance of several mm, to form ALON. This reaction was mediated by gas species in the Ar atmosphere, as there was no direct contact between the two solids. Run No.8 is the 'blank' corresponding to No.7, proving that the Ar used was pure enough not to oxidize AlN.

4.3 Optimization of the ALON synthesis procedure

Based on the results of the first series of carbothermal nitridation, experimental attempts were made to optimize the synthesis parameters, aiming at monophasic powders of two different compositions within the ALON field. The 'two-step procedure' was chosen in a series of runs, with the temperature and nitrogen pressure varied, as well as the holding time at each temperature plateau. The mixtures 'B', 'C', 'D' and 'E' were selected as starting materials, either in pellet form or as loosely packed powders. The first two had the compositions X_{AlN} = 0.39 and 0.36; with 'B' made of fine-grained γ-Al_2O_3 and 'C' of coarse α-Al_2O_3. Mixtures 'D' with γ-Al_2O_3 and 'E' with α-Al_2O_3 had X_{AlN} = 0.30 and 0.29 (Fig. 1).

In order to prevent excessive reduction/nitridation, a BN compartment was used for the samples, which in most cases were contained in alumina crucibles. In some experiments the sample was also covered by Al_2O_3 powder or enclosed in an Mo capsule, embedded in a 'support charge' consisting of granules of the Al_2O_3 + C mixture in question. The effects on the synthesis result of changes in gas flow rate, heating rate and CO additions to the nitrogen gas were also studied in a few runs.

Some results of the optimization procedure are shown in Table 4. In many cases, samples for XRD were taken both from the surface and the bulk of the product pellet or powder bed. The overall composition (X_{AlN}) was determined by oxidation in air of the whole sample, as previously described.

Starting at the relatively low X_{AlN} = 0.30, it was possible to produce a single-phase ALON powder, both with mixtures made of fine γ-Al_2O_3 ('D') and coarse α-Al_2O_3 ('E'), and equally well with pellets and powders. Heating a 'D' pellet at 1600°C for 2 h and then at 1820°C for 40 min at atmospheric pressure in a BN environment produced a mixture of ALON + AlN and made the sample composition shift to X_{AlN} = 0.44. Limiting the first plateau holding time to one hour, though, was enough to retain the sample composition within the permissible limits (run No.1 in Table 4), demonstrating once more that the major reduction occurs already below ALON formation temperatures. Yet, this heat treatment was enough to yield pure ALON, although the top surface layer was found to contain small amounts of AlN as well. The large cell edge, 7.948 Å, calculated for this layer compared with the bulk, 7.945 Å, is consistent with the surface being more easily nitridized than the interior part of the pellet under the prevailing synthesis conditions. Monophasic ALON was also obtained (run No.2) using a lower heating rate from the first plateau to the second, but otherwise a temperature programme identical to that of run No.1. The effect of the slower heating was probably just to increase the annealing time. When using a higher pressure, 1.0 MPa (run No.3), a three-phase mixture was left, due to the decreased reactivity.

With the powder charge in run No.4, a longer reaction time was needed than with a pellet (run No.1). The overall composition became X_{AlN} = 0.40, but an excess of AlN formed in the surface parts. With Al_2O_3 powder covering the charge, the reduction/nitridation was hampered; 3.5 h heating resulted in a three-phase mixture (run No.5). In this case, the ALON cell edge was shorter in the surface layer (7.943 Å) than in the interior of the sample (7.945 Å). By the combined use of an elevated pressure (0.5 MPa), expected to reduce the nitridation rate, and a 10% CO addition to the nitrogen, a pure ALON powder was produced in run No.6 with a mean cell edge of 7.946 Å.

Optimization of the ALON synthesis based on mixture 'E' pellets typically started with runs such as No.7 and No.8, which did not yield fully reacted samples in spite of high gas flow rates and ca. 2 h tempering at 1.0 MPa. Lowering the pressure to 0.1 MPa resulted in increased nitridation (X_{AlN} = 0.41), although unreacted Al_2O_3 still remained (run No.9). To obtain pure ALON with a pellet charge slightly more than 2 h heat treatment was required at atmospheric pressure (run No.10).

If instead a powder of mixture 'E' was used, loosely packed in an alumina crucible, the reactivity decreased, as expected. In run No.11, heating

Table 4. The synthesis parameters and the results of runs by the 'two-step procedure'

Run No.	*Mixture sample*	*T (°C) t (h)*	*$p(N_2)$ (MPa)*	*$\Phi(N_2)$ (l min^{-1})*	*Sample holder*	*Product phases**	*X_{AlN} (%)*	*ALON a_o(Å)***	*RWC ratio (%)****	*Comment*
1	Mix. D pellet	1500 + 1820°C, 1 + 0·7 h	0·1	0·2	BN	s: ALON, N_w i: ALON	40·4	7·948 (1) 7·945 (1)	145 (113)	
2	Mix. D pellet	1600 + 1820°C, 1 + 0·7 h	0·1	0·2	BN	s: ALON, N i: ALON	—	7·947 (1) 7·943 (1)	147	Whiskers, 2°C min^{-1} to 1820°C
3	Mix. D pellet	1400 + 1820°C, 2 + 0·7 h	1·0	0·5	BN	i: ALON, N, O	—	7·944 (1)	134	
4	Mix. D powder	1600 + 1820°C, 1 + 1·5 h	0·1	0·2	Al_2O_3	s: ALON, N_w	40·4	7·948 (1)	130 (113)	
5	Mix. D powder	1550 + 1820°C, 2 +1·5 h	0·16	1	Al_2O_3	s:ALON, O_w, N_w i: ALON, O_w, N_w	—	7·943(1) 7·945 (1)	—	Covered by Al_2O_3
6	Mix. D powder	1600 + 1820°C, 1 + 2 h	0·5	0·8 + 0, 0·5 + 2·5 h	Al_2O_3	i:ALON	—	7·946(1)	140	N_2 + 10% CO
7	Mix. E pellet	1600 + 1820°C, 1 + 0·7 h	1·0	5 + 0, 1 + 0·7 h	BN	s: ALON, O_w, N_w i: ALON, O_w, N_w	38·7	7·947 (2) 7·945 (1)	113 (119)	
8	Mix. E pellet	1400 + 1820°C, 2 + 0·7 h	1·0	0·5	BN	i: ALON, O, N_w	39·4	7·944 (1)	123 (118)	
9	Mix.E pellet	1600 + 1820°C, 1 + 0·7 h	0·1	0·2	BN	s: ALON, O_w, N_w i: ALON, O_w, N_w	41·2	7·948 (2) 7·947 (2)	121 (120)	Whiskers, 2°C min^{-1} to 1820°C
10	Mix. E pellet	1600 + 1820°C, 2 + 0·7 h	0·1	0·2	BN	s: ALON, O_w, N_w i: ALON	40·6	7·946 (1) 7·948 (1)	119 (119)	Whiskers
11	Mix. E powder	1600 + 1820°C, 1 + 2 h	0·5	0·8 + 0, 0·5+ 2·5 h	Al_2O_3	i: ALON, O, N	36·5	7·945 (1)	112 (112)	N_2+ 10% CO
12	Mix. E powder	1600 + 1850°C, 2 + 5 h	5·0	1·2	Al_2O_3	s: ALON, N i: ALON, O_w	41·1	7·948 (1) 7·948 (2)	113 (119)	
13	Mix. E powder	1600 + 1850°C, 1 + 1·5 h	0·16	1	Al_2O_3	i: ALON	39·1	7·947 (1)	115 (116)	Whiskers

* s = surface, i = interior, O = Al_2O_3, N = AlN, O_w = weak XRD lines of alumina, N_w = weak XRD lines of aluminium nitride.
** Figures in parentheses are $\pm 3\sigma$.
*** RWC ratio = $(RWC)_{exp.}/(RWC)_{theo.}$. Figures in parentheses are RWC values based on analyzed X_{AlN}.

for 3 h at 0.5 MPa was insufficient to produce a monophasic powder, in spite of CO being added to the nitrogen in order to facilitate ALON formation. At 5.0 MPa, unreacted Al_2O_3 could still be found, even after 5 h heating at 1850°C (run No.12). The overall composition had shifted to $X_{AlN} = 0.41$. In this sample, as in most of the others, the surface layer was more nitridized than the interior. This difference, however, as can be judged from the calculated ALON cell edge, seems to be somewhat less pronounced for mixture 'E' than for 'D'.

At $p(N_2) = 0.16$ MPa, pure ALON powder could be prepared after 1.5 h at 1850°C (run No.13).

All our attempts hitherto to prepare pure ALON powders from the 'B' and 'C' mixtures, with starting compositions up to $X_{AlN} = 0.40$, have been unsuccessful. Excessive reduction/nitridation, leading to ALON + AlN mixtures, could not be avoided when open sample containers were used,

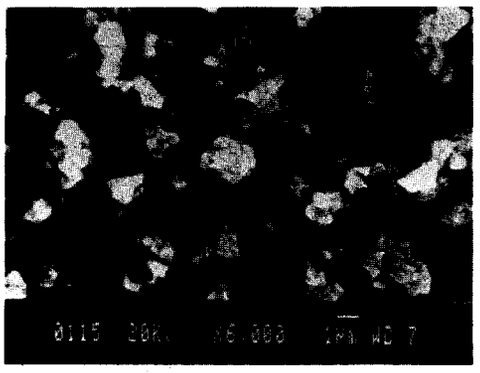


Fig. 8. SEM micrograph of the product of a two-step run with mixture E (powder) at 0.1 MPa, 0.2 l min^{-1}, 1600°C for 2 h and 1820°C for 0.67 h.

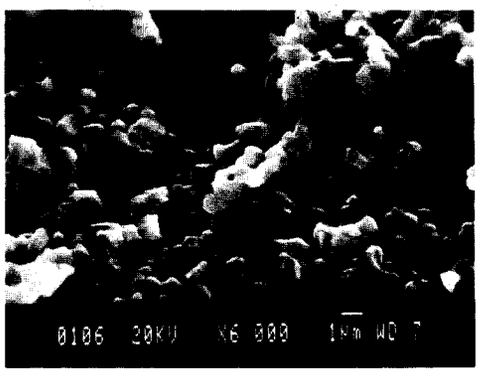


Fig. 9. SEM micrograph of the product of a one-step run with mixture D (pellet) at 1820°C for 0.83 h, 1 MPa, 1 l min^{-1}.

even in an Al_2O_3 and BN environment, and with moderate synthesis temperatures (1820°C)

By use of an elevated pressure (5 MPa), a 'support charge' or an Al_2O_3 cover, it was possible to partly control the compositional shift, also for several hours of heat-treatment at 1850°C, but even so, AlN and residual Al_2O_3 were found in the samples.

For a number of samples at the compositional limits ALON/AlN and ALON/Al_2O_3, the cell edge values of ALON, calculated with the PIRUM program, were found to be 7.938 ± 0.0001 Å (O-rich) and 7.951 ± 0.001 Å (N-rich). These were in fact the minimum and maximum cell parameters observed in the whole series of experiments, at 1750–1860°C and with cooling rates of ca. 30°C min^{-1}. Judging from Table 4 the ALON–AlN phase boundary seems to be close to X_{AlN} = 0.40 at ca. 1800°C, as determined by reoxidation of ALON samples in air.

The ALON diffraction lines on the XRD films always appeared sharp, even on close inspection of the peak profiles, excluding extended compositional variation over the samples. Yet, the cell parameter values presented in Table 4 were not sufficiently representative for the overall composition to allow a precise relationship between X_{AlN} and a_O to be established. A linear relationship between nitrogen content in ALON and cell parameter has previously been determined by Guillo.[20]

4.4 Powder morphology

Typical SEM photos (Figs 8–12) of ALON materials from this study reveal morphological differences

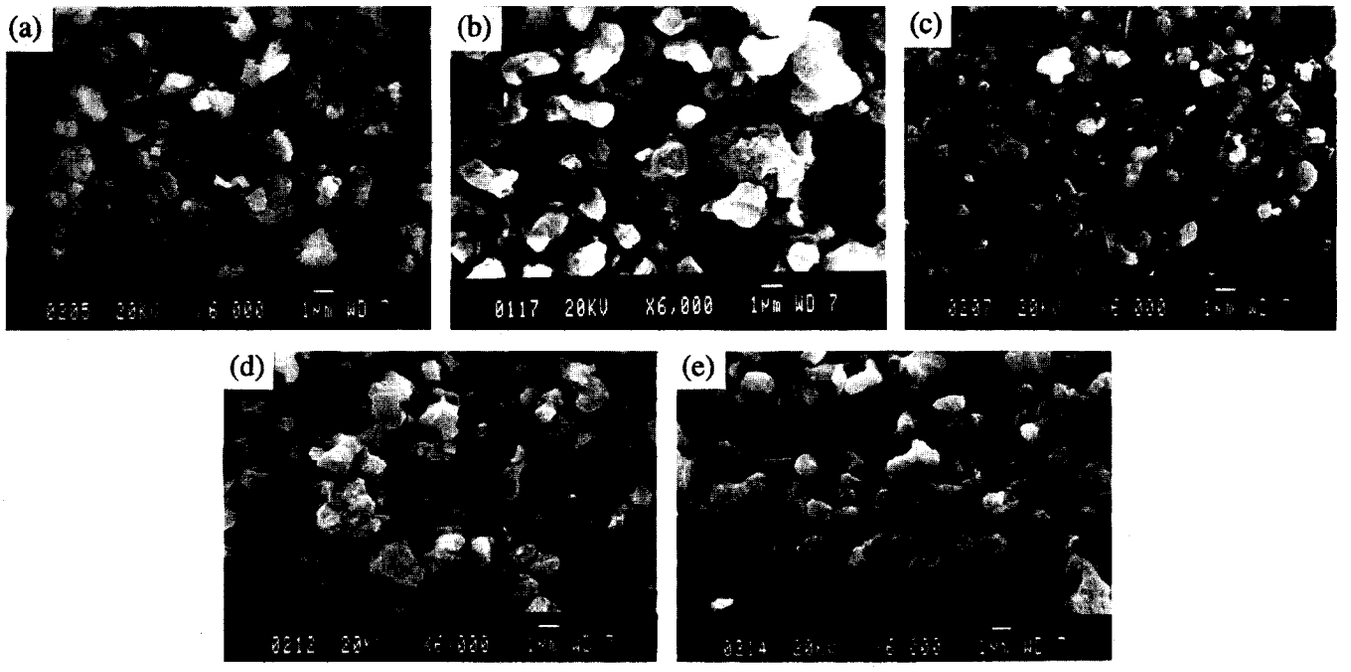


Fig. 10. SEM micrographs of the products of mixture D: (a) pellet run (two-step) at 1600°C for 2 h and 1820°C for 0.67 h, 0.1 MPa, 0.2 l min^{-1}, (b) powder run (two-step) at 1600°C for 1 h and 1820°C for 1.5 h, 0.1 MPa, 0.2 l min^{-1}, (c) powder charge covered by α-Al_2O_3 powder, run (two-step) at 1550°C for 2 h and 1820°C for 1.5 h, 0.16 MPa, 1 l min^{-1}, (d) powder run (two-step) at 1600°C for 1 h and 1830°C for 1.5 h, 5 MPa, 0.7 l min^{-1}, (e) powder run (two-step) at 1600°C for 1 h and 1820°C for 2 h in 10% CO + N_2 gas, 0.5 MPa, 0.8 l min^{-1} for 0.5 h then 0 l min^{-1}.

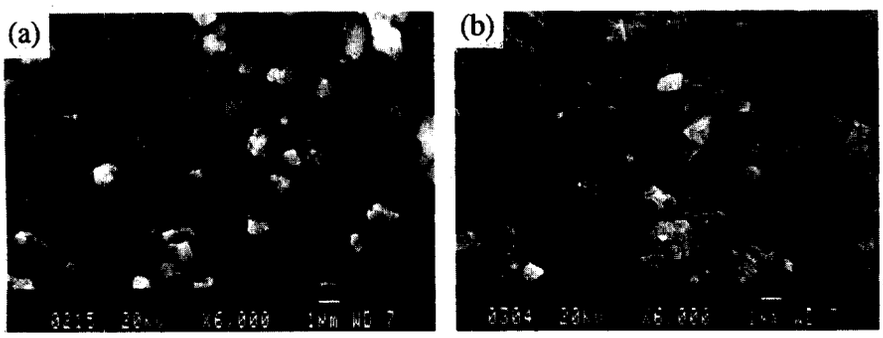


Fig. 11. SEM micrographs of the products of mixture D: (a) pellet run at 1600°C for 1 h, 1 MPa and 5 l min^{-1}, (b) product of (a) recharged and run at 1820°C for 4 h in pure N_2 gas, 0.2 MPa.

between powders prepared under different conditions.

Whether coarse or fine-grained alumina powder was the starting material made a large difference. The first type persistently yielded aggregates of irregularly shaped ALON particles, with a wide size distribution (Fig. 8), irrespective of the choice of process parameters. Yet, they proved to be finer, on an average, than the α-Al_2O_3 particles of the raw material (Fig. 7).

With fine γ-Al_2O_3 in the starting mix, the temperature programme turned out to be decisive for the ALON morphology. A 'single-step' process always resulted in densely sintered particle agglomerates (Fig. 9). On the other hand, use of a 'two-step' programme apparently was a means to reduce agglomeration, and typically to produce relatively fine-grained ALON with a moderately wide size distribution. Within this class of samples some SEM-pictures reveal small morphological differences, though, and these can be related to the different sets of process parameters used.

The slightly different features of the samples seen in Figs 10(a) and (b) suggest that the grain size is somewhat better controlled in a pellet than in a powder, loosely packed in an open crucible. However, as is shown by Fig. 10(c), a fine grain size could be achieved also with a powder bed, provided it is covered by an Al_2O_3 powder layer.

Neither the pressure, between 0.1 and 1 MPa, nor the gas flow rate and heating rate from the first to the second plateau temperature were found to be important parameters for sample morphology. On the other hand, close inspection of SEM pictures such as Figs 10(d) and (e) reveals that both application of a nitrogen pressure in excess of 2 MPa and a 10% CO-addition to the reaction gas have some influence on particle morphology; the resulting ALON particles become medium-sized, possibly with a relatively narrow distribution. Besides, the grains appear more 'crystalline', with sharp edges and corners, than other ALON powders, which are typically devoid of symmetrical features.

Figure 11(a) shows the AlN + Al_2O_3 powder that results on annealing a C + Al_2O_3 mixture at the first plateau, ultimately leading to the ALON powder in Fig. 11(b). A somewhat finer powder, similar to the starting powder in Fig. 11(a), was obtained when Ar replaced N_2 at the second plateau.

It can be seen that the products (Fig. 12(a)) obtained from fine γ-Al_2O_3 and a commercial AlN raw material are non-homogeneous and that the morphology is related to that of the starting AlN powder (Fig. 12(b)).

5 Discussion

Our experimental results exemplify some difficulties, likely to be encountered in the preparation of

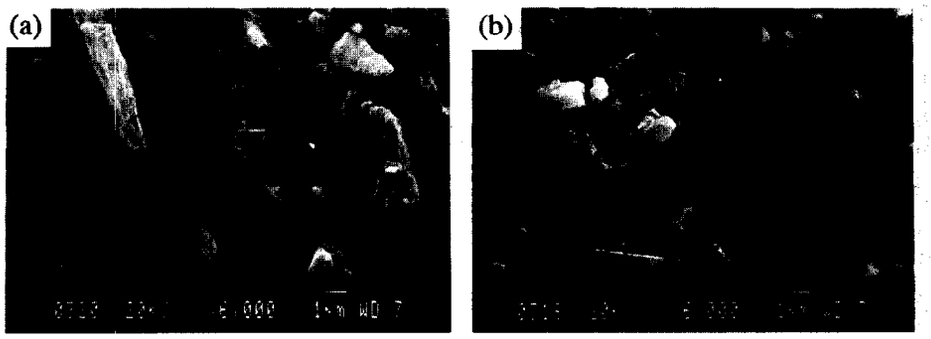


Fig. 12. SEM micrographs of (a) the product of a pellet of mixture H, run (two-step) at 1500°C for 1 h and 1820°C for 0.67 h, 0.1 MPa and 0.2 1 min^{-1}, and (b) the starting AlN material.

monophasic ALON powder by the carbothermal route. However, some possible means are also presented, to circumvent the difficulties and carry out the synthesis from mixtures of carbon and alumina powders, of ordinary grade and homogenized by simple mechanical mixing. Very fine-grained reactants do not seem to be required for a successful synthesis. Use of fine powder mixtures or a sophisticated homogenization procedure, such as sol–gel, improves reactivity but will not eliminate the problem with drifting composition inherent in the high-temperature synthesis of ALON without strictly controlled O, N, C gas phase activities.[4] A common feature of carbothermal runs in a graphite furnace is namely the tendency for continuous reduction and nitridation of the sample, beyond the point determined by the carbon content of the starting mixture. As a consequence, there will also be an extra weight loss above that expected from eqn (1), and excess AlN may form.

This problem is overcome if one starts with C + Al_2O_3 mixtures with compositions corresponding to oxygen-rich ALON, thus having some tolerance for extra reduction. Such an approach was successfully used in this study and has also been the method preferred by previous workers. However, our attempted syntheses of monophasic ALON, starting with compositions near the ALON–AlN phase boundary failed, and this was due to the inability to control the reduction strictly enough. Use of a two-step heating program, an elevated pressure, CO additions to the nitrogen gas and a 'support charge' or a cover of Al_2O_3 were measures taken to achieve compositional control of the charge. All of these were effective to some degree and will be taken advantage of in future preparative work.

From a comparison of ALON cell dimensions in different parts of the samples, we conclude that application of an Al_2O_3 cover has the extra advantage of improving the charge homogeneity. Generally, a better homogeneity was obtained with coarse α-Al_2O_3 starting material than with fine γ-Al_2O_3.

When 10% CO was added to the feed gas we noted a somewhat increased intensity ratio $I_{ALON(400)}/I_{AlN(100)}$ in the products (Figs 5 and 6). This is probably a result of hampered formation of aluminium nitride,[14] as thermodynamic calculations (Figs 2 and 3) show that the formation of AlON should not be hampered by addition of CO to the N_2 gas. The increase in nitridation rate with rising CO content, found for pure Al_2O_3 powders at 1820°C (special run No.6, Table 3), is expected from thermodynamic considerations, provided gas species such as $Al_{(g)}$ and $Al_2O_{(g)}$ are somehow involved in the nitridation process. Thermodynamic calculations show that the partial pressures of these species will increase almost 100-fold when the CO content is increased from 0 to 10% in N_2 over Al_2O_3 at 2100 K.

One reason for the lower ALON formation rate at 5 MPa than at 0.1 MPa (Fig. 6 and special run No.3, Table 3) is a slower mass transport in the gas phase at the higher pressure. Furthermore, the thermodynamic calculations show that p(Al) and $p(Al_2O_3)$ will decrease on raising the total pressure (Figs 2 and 3).

5.1 The two-step procedure

The improvement achieved with the 'two-step procedure', compared with the 'single-step runs', highlights the reaction chemistry below ALON formation temperatures.

From previous studies of carbothermal reduction and nitridation of Al_2O_3 at different temperatures and pressures[14] we know that in the ranges 0·1–5 MPa, 1400–1600°C the only solid compound formed is AlN. Because this phase will inevitably form prior to ALON on heating an Al_2O_3 + C mixture in N_2, ALON formation must somehow be connected with the AlN particles present, as these will remain also at 1800–1900°C. The Al_2O_3 particles in the reacting mixture are relatively stable, although partial pressures of species such as $Al_{(g)}$ and $Al_2O_{(g)}$ can be appreciable. This has been confirmed experimentally, e.g. by Lefort and Billy,[12] who established the presence of Al vapour over alumina at 1550°C in vacuum, by means of an emission spectrograph. They also observed a drastic decrease in p(Al) when nitrogen was introduced in the reactor to form AlN. We therefore anticipate partial dissociation of Al_2O_3 and net losses of oxygen from the sample, particularly under the reducing conditions prevailing in a graphite furnace. These losses are expected to be higher in the surface layer of a pellet, or powder charge, than in the interior.

The gaseous aluminium is probably retained to a high degree by reaction with nitrogen, and this manifested itself in the AlN whiskers, which grew radially outward from the pellets in many of our experiments (Tables 2 and 4). (They did not grow at elevated pressure, > 1 MPa, however, which probably reflects the reduced mobility of $Al_{(g)}$ and $Al_2O_{(g)}$ following an increase in total pressure). Consequently, the surface layer of the charge will be depleted of oxygen, compared with the interior, and the resulting ALON powder will contain excess AlN near the surface. Such a segregation was observed in most of our samples, particularly in runs with high-surface area γ-Al_2O_3 at low (atmospheric) pressure, high temperature, high gas

flow rate, and in a graphite sample holder. By use of a 'support charge' or an Al_2O_3 powder covering the reaction mix, this segregation could be diminished, and in some cases even an oxygen excess was left in the surface layer. Compositional variations over ALON samples, as a consequence of the gaseous environment affecting the surface parts, have been observed previously.[4]

AlN formation by the carbothermal route is not a very rapid process;[14] it is to some extent controlled by p(CO), and would demand more than 1 h for a full conversion in our set-up, even at 1600°C. While the onset of ALON formation seems to be immediate, at least 0.5 h is needed for full conversion. Dissociation of 'extra' Al_2O_3 not converted to AlN by the C reagent, proceeds concurrently and may cause considerable 'over reduction' at T > 1800°C. We therefore conclude that the benefit of a primary annealing at low temperature, ≤ 1600°C in the 'two-step procedure' is that a maximum amount of AlN with respect to the C/Al_2O_3 ratio can form at temperatures low enough to cause minimum evaporative loss of oxygen. This should be a more efficient way to prepare ALON than the 'one-step procedure', implying less excessive nitridation.

The RWC values calculated from the analyzed overall compositions (X_{AlN}) in Tables 2 and 4 are rather close to the experimentally obtained values for mixtures 'F', 'C' and 'E'. Samples of mixtures 'B' and 'D', on the other hand, gave noticeably higher experimental RWCs than expected from mere reduction/nitridation of the Al_2O_3 content. Apparently these mixtures, made up of high surface area γ-Al_2O_3, were subjected to an extra weight decrease, which may be due to an irreversible loss of Al-containing gas species, such as $Al_{(g)}$ and $Al_2O_{(g)}$. If this is the case, the difference in RWC between runs No.1 and No.4 in Table 4 shows that such losses may be minimized if an Al_2O_3 crucible is used as sample container.

Part of the excess nitridation observed in most runs could be a result of a continuous decomposition of ALON with time in the graphite furnace. A dissociation process of ALON into AlN has been suggested by previous workers.[12] As a matter of fact, the compositional variation within the ALON may be described as a substitution of oxygen for nitrogen and vice versa, and hence:[10]

$$\text{ALON} + N_2(g) \rightarrow \text{AlN} + O_2(g) \qquad (3)$$

The results of our special test series (Table 3), suggesting ALON to be the primary product phase with AlN subsequently appearing, seem to show that some decomposition mechanism is operating.

5.2 Particle size and morpholoy

The special tests (Table 3) tell us that in an AlN + Al_2O_3 powder mixture ALON may form, either by oxidation of the former or nitridation of the latter, without direct contact between particles. As the ALON particles bear no resemblance to the original Al_2O_3 particles, it is likely that the main direction of mass transport in the gas at ALON formation temperatures is from Al_2O_3 to AlN. In support of this view is the observation that ALON particles obtained in a two-step process from mixtures of C and fine γ-Al_2O_3 were relatively uniform, compared with powders made from coarse α-Al_2O_3 (Fig. 7). This was actually the size-dependence of process parameters previously found for AlN.[15] Consequently, mixtures of fine-grained γ-Al_2O_3 and a non-uniform, standard grade commercial AlN powder (Fig. 12(b)) produced non-uniform ALON powders (Fig. 12(a)).

The mechanism for the subsequent ALON forming reaction between the AlN matrix and the Al–O species, however, still remains to be elucidated. It should also be stressed that ALON easily forms by nitridation of Al_2O_3, even in the absence of AlN (Table 3). This may occur by the mechanism suggested in Ref. 12, and mentioned in the Introduction.

The small, yet noticeable morphological differences between powders prepared from mixtures with γ-Al_2O_3 (Figs 9–11) suggest that the rate of dissociation of Al_2O_3 is of some importance for the AlN particle size and thus the final ALON morphology. Rapid heating (single-step) led to a highly sintered powder (Fig. 9), while slow heating hampered ALON formation (run No.7 in Table 2). Possibly, the degree of supersaturation of Al or Al–O species in the gas, which is governed by the specific surface area and dissociation rate of Al_2O_3, is the crucial parameter. If so, the general tendency for particles in a pellet charge to be a little smaller than in a loose powder (*cf.* Figs 10(a) and (b)) can be understood, as well as the small grain size obtained, also with a powder charge, when an Al_2O_3 cover was used (Fig. 10(c)). This is supposed to minimize leakage of gas species from the sample, and thus to favour build-up of p(Al) and $p(Al_2O)$.

A relatively large AlN particle size is expected in runs at an increased pressure and a low gas flow rate (1 l min^{-1}),[15] and a similar trend was actually observed for ALON (Fig. 10(d)).

The relatively coarse powder obtained in a two-step run in an N_2 + 10% CO atmosphere (Fig. 10(e)) is probably due to a reduction of the Al_2O_3 surface area during the first annealing at 1600°C. For thermodynamic reasons,[14] the AlN formation rate is very low in 10% CO at this temperature,

but will increase on further heating to the second plateau.

6 Conclusions

- Preparation of monophasic ALON powder by carbothermal nitridation of Al_2O_3 is complicated due to the difficulties of keeping compositional control during the process. In a graphite furnace, excess nitridation is likely to occur, mediated by Al-containing gas species generated at relatively high activities at the high synthesis temperatures required > 1600°C.
- A means to prepare pure ALON powder, without excessive reduction and AlN formation, and also to obtain a reasonably narrow particle size distribution, is to perform the synthesis in two steps; first annealing for 1 or 2 h at 1600°C, and then at 1800–1850°C for another hour. Direct heating to ALON formation temperatures, ≥ 1750°C, did not yield monophasic powders with a reasonably narrow particle size distribution.
- A high pressure in the synthesis generally lowered the nitridation rate, and may therefore be used for control of sample stoichiometry, and also particle size to some degree. To this end an Al_2O_3 sample holder with Al_2O_3 covering the charge may also be used.
- Increasing the CO content in the reaction gas (up to a certain level) has an enhancing effect on ALON formation, at the expense of AlN.
- The ALON particle morphology seems to be related to the AlN (precursor) particle morphology.
- ALON formed slowly at 1850°C in the absence of carbon, by the reaction of N_2 with a pure Al_2O_3 powder. It also formed on AlN, in the presence of Al_2O_3, without direct contact, in an Ar atmosphere.
- The crystallographic unit cell edge of the ALON samples prepared in this study at about 1800°C was found to vary between 7.938 + 0.001 Å (high-O) and 7.951 ± 0.001 Å (high-N).

Acknowledgements

We are grateful to Professor Lars Kihlborg for critical reading of the manuscript and for valuable comments. Dr Sven Westman is thanked for revision of the English text, and Mr Lars Göthe for his kind help with the X-ray diffraction. This work has been sponsored by the Swedish Natural Science Research Council (NFR).

References

1. McCauley, J. W., A simple model for aluminum oxynitride spinels. *J. Am. Ceram. Soc.*, **61** (7–8) (1978) 372.
2. McCauley, J. W. & Corbin, N. D., Phase relations and reaction sintering of transparent cubic aluminum oxynitride spinel (ALON). *J Am. Ceram. Soc.*, **62**(9–10) (1979) 476.
3. Lejus, A.-M., Sur la formation a haute température de spinelles non stoechiométriques et des phases dérivées. *Rev. Hautes Tempér. et Réfract.*, **1** (1964) 53.
4. Willems, H. X., Hendrix, M. M. R. M., de With, G. & Metselaar, R., Thermodynamics of Alon II: Phase relations. *J. Eur. Ceram. Soc.*, **10** (1992) 339.
5. Corbin, N. D., Aluminum oxynitride spinel: a review. *J. Eur. Ceram. Soc.*, **5** (1989) 143.
6. Yamaguchi, G. & Yanagida, H., Study on the reductive spinel—A new spinel formula AlN-Al_2O_3 instead of the previous one Al_3O_4. *Chem. Soc. of Japan Bull.*, **32**(11) (1959) 1264.
7. Goursat, P., Billy, M., Goeuriot, P., Labbe, J. C., Villechenoux, J. M., Roult, G. & Bardolle, J., Contribution a l'etude du systeme Al/O/N. II. Retention d'azote dans les produits d' oxydation de l'oxynitrure d'aluminium γ. *Mater. Chem.*, **6** (1981) 81.
8. Long, G. & Foster, L. M., Crystal phases in the system Al_2O_3–AlN. *J. Am. Ceram. Soc.*, **44**(6) (1961) 255.
9. Hartnett, T. M., Gentilman, R. L. & Maguire, E. A., Aluminum oxynitride having improved optical characteristics and method of manufacture. US Patent No. 4481300, 6 November 1984.
10. Willems, H. X., Hendrix, M. M. R. M., Metselaar, R. & de With, G., Thermodynamics of Alon I: Stability at lower temperatures. *J. Eur. Ceram. Soc.*, **10** (1992) 327.
11. Ish-Shalom, M., Formation of aluminium oxynitride by carbothermal reduction of aluminium oxide in nitrogen. *J. Mater. Sci. Letters*, **1** (1982) 147.
12. Lefort, P. & Billy, M., Mechanism of AlN formation through the carbothermal reduction of Al_2O_3 in a flowing N_2 atmosphere. *J. Am. Ceram. Soc.*, **76**(9) (1993) 2295.
13. Ekelund, M. & Forslund, B., Carbothermal preparation of silicon nitride: Influence of starting material and synthesis parameters. *J. Am. Ceram. Soc.*, **75**(3) (1992) 532.
14. Forslund, B. & Zheng, J. Carbothermal synthesis of aluminium nitride at elevated nitrogen pressures. I—Effect of process parameters on conversion rate. *J. Mater. Sci.*, **28** (1993) 3125.
15. Forslund, B. & Zheng, J., Carbothermal synthesis of aluminium nitride at elevated nitrogen pressures. II—Effect of process parameters on particle size and morphology. *J. Mater. Sci.*, **28** (1993) 3132.
16. Werner, P.-E., A FORTRAN program for least-squares refinement of crystal-structure cell dimensions. *Arkiv Kemi.*, **31**(43) (1969) 513.
17. Eriksson, G., Thermodynamic studies of high temperature equilibria. XII. SOLGASMIX, a computer program for calculation of equilibrium compositions in multiphase systems. *Chemica Scripta*, **8** (1975) 100.
18. Stull, D. R. & Prophet, H. (eds), *JANAF Thermochemical Tables 2nd edn.*, NSRDS-NBS, National Bureau of Standards, Washington D.C., USA, 1971.
19. Frank, R. A., Finn C. W. & Elliott, J. F., Physical chemistry of the carbothermic reduction of alumina in the presence of a metallic solvent: Part II. Measurements of kinetics of reaction. *Metall. Trans.*, **20B** (1989) 161.
20. Guillo, P., Thesis No. 32-85, University of Limoges, France (1985).

Journal of the European Ceramic Society **15** (1995) 1101–1109
Elsevier Science Limited
Printed in Great Britain
0955-2219(95)00084-4
0955-2219/95/$9.50

At-Temperature Observation of Phase Development in Yttrium α-Sialon

A. Ashkin,[a] D. Ashkin,[a] O. Babushkin[a] & T. Ekström[b*]

[a]Department of Engineering Materials, Luleå University of Technology, S-951 87 Luleå, Sweden
[b]Department of Inorganic Chemistry, Arrhenius Laboratory, Stockholm University, Sweden

(Received 14 February 1995; revised version received 19 May 1995; accepted 22 May 1995)

Abstract

A powder mixture of α-Si_3N_4, AlN and Y_2O_3 corresponding to an yttrium α-sialon composition, $Y_{0.4}Si_{10.2}Al_{1.8}O_{0.6}N_{15.4}$, was sintered both in a high temperature X-ray diffraction unit and in a regular sintering furnace. X-ray analysis was performed and it was shown that high temperature X-ray diffraction can be used to monitor the kinetics of the α-sialon phase formation during sintering at temperatures between 1450 and 1580°C as the reactions take place. A variety of yttrium-rich intermediate and secondary phases are formed during sintering; those formed in the HT-XRD unit were not the same as those formed in the regular sintering furnace, but they do not significantly influence the overall reaction sequence or the amount of α-sialon formed. Quantitative analysis of the acquired data was used to evaluate the kinetics of the α-sialon phase formation; the estimated activation energy of the initial stage α-sialon formation was 330 kJ/mol. After this initial stage of relatively rapid α-sialon formation the process became inhibited.

1 Introduction

The sialons are a group of ceramic compounds corresponding to the α and β form of silicon nitride, in which silicon and nitrogen atoms have been substituted in part by aluminium and oxygen.[1] Unlike α silicon nitride which transforms to β silicon nitride at high temperatures, α sialon can be stabilized by metal ions such as yttrium. The α sialons are characterized by good thermal shock resistance and high hardness which is retained to quite high temperatures.[2] They therefore have potential as materials for high temperature applications.

*Present address: Industrial Research Limited, Lower Hutt, New Zealand.

The present work concerns the formation of a yttrium α-sialon with the ideal composition $Y_{0.4}Si_{10.2}Al_{1.8}O_{0.6}N_{15.4}$ by reactive sintering of an appropriate mixture of silicon nitride, aluminium nitride and yttria powders. This composition is predicted to yield pure α sialon with some glassy phase upon completion of the reaction. Reactions of similar compositions have been studied earlier by means of sintering plus quenching experiments and the general sequence of reactions at temperatures between 1000 and 1750°C has been documented.[3–7] It involves the formation of an oxide liquid and then solution of Si_3N_4 and AlN into it, forming an yttrium-containing oxynitride melt from which α-sialon is precipitated. Besides α-sialon, intermediate and secondary phases like YAM ($Y_4Al_5O_9$), J-ss ($Y_4Al_{2-x}Si_xO_{9-x}N_x$), YAG ($Y_3Al_5O_{12}$) and N-melilite ($Y_2Si_3O_3N_4$) are found depending on temperatures and starting compositions. α-sialon forms at as low a temperature as 1400°C when dissolution of the two nitrides, Si_3N_4 and AlN, becomes significant.[4,6] At this temperature the amount of liquid is still low but it increases with temperature as the extent of the liquid phase field increases. However, for a given temperature the amount of available liquid decreases as the reaction to α-sialon proceeds and yttria, oxygen and aluminum are substituted into the structure.

In studies of crystallization of the intergranular glass phase in sialon ceramics it has been noted that the O/N ratio of both the bulk composition and the liquid phase as well as the temperature play a major role in determining which phases crystallize out.[8,9] The composition, quantity, and viscosity of the liquid phase has also been reported to strongly influence densification.[10] These factors might be expected to complicate the kinetics of α-sialon formation. In the present work, the sensitivity of α-sialon formation to intermediate and secondary phases, sintering conditions and controlled changes in compositions was studied.

The study of phase formation in ceramic materials is often impeded by difficulties in following the course of reactions at elevated temperatures. Generally reactions are studied by 'quenching' a series of samples at different stages of the reaction. This approach is adequate for slower reactions such as those controlled solely by solid state diffusion. If fast transformations occur during cooling, it is hard to retain a high-temperature state unless special experimental conditions are used. For example it has recently been shown that the α-sialon phase with large stabilizing ions decomposes unexpectedly rapidly upon cooling when a liquid phase is present.[11] An alternative to the quenching technique is offered by high temperature X-ray diffraction (HT-XRD). This permits study of reactions as they proceed; the uncertainty associated with quenching is avoided and the kinetics of reactions can be determined far less arduously. A potential drawback of the method is that it can only observe a thin zone of material close to the free surface of a sample which may not give a true representation of realistic bulk sintering conditions. One of the purposes of this work was to apply HT-XRD to a study of the reactions during the sintering of the α-sialon and to compare the observations with the results of conventional sintering.

2 Experimental

Powder mixtures were prepared from the starting materials, silicon nitride (H.C. Starck, Berlin, Grade LC1), aluminum nitride (H.C. Starck, Berlin, Grade A) and yttrium oxide (H.C. Starck, Berlin, Grade > 99·8% Y_2O_3) to correspond to x = 0·4 in the formula $Y_x(Si_{12-4.5x},Al_{4.5x})(O_{1.5x},N_{16-1.5x})$ for yttrium α-sialon (corresponding to 78·0 wt% silicon nitride, 14·4 wt% aluminium nitride and 7·6 wt% yttria). The oxide contents of the aluminum nitride and silicon nitride were compensated for to best approximate the above formula as discussed in a previous article by two of the authors.[12] Samples for the HT-XRD were prepared by cutting powder bodies, CIPed at 200 MPa, into thin slices with a razor, presintering them at 1350°C for 1 h in 0·11 MPa nitrogen atmosphere and then dry grinding them to a dimension of 12 × 8 × 1 mm.

HT-XRD measurements were then conducted at temperatures 1450, 1500, 1530 and 1580°C in a static atmosphere of 0·11 MPa N_2 in a specially constructed graphite furnace coated with silicon nitride. This coating was stable to a temperature of 1600°C. Furnace and HT-XRD conditions have been described earlier.[13] During a soaking time at temperature the reactions were followed by repeating a set of two scans . The first scan over a 2θ range of 28–45° at a rate of 0·04°/s was used to follow the sequence of formation of all phases and to calculate the AlN content by integrating intensities of major peaks. The second scan over a 2θ range of 42–44° and a rate of 0·01°/s was used for profile analysis of one α-Si_3N_4 peak (hkl = 301) and the corresponding peak of α-sialon. These peaks were not overlapped by peaks of other phases and could be used for quantitative estimates of the α-silicon nitride to α-sialon conversion. After the HT-XRD runs, selected samples were analysed by room temerature XRD (RT-XRD) at different depths into the sample to assess any differences between top surface and inner reactions.

Quantitative phase analysis was performed through careful calculation of the XRD peak areas. Correction for overlap of the diffraction peaks as well as the integration of the peak areas were performed by fitting of the experimental diffraction profile using a Marguardt non-linear least squares algorithm.[14] The same algorithm was also used to determine the positions of the α and α' (301) peaks and AlN (101) peak. (α and α' denote α-silicon nitride and α-sialon respectively). The highest accuracy of peak areas and positions was achieved at 1580°C, where the peak separation was largest. The amounts of aluminium nitride, silicon nitride and yttria were estimated by reference to the peaks of an unsintered sample.

The amount of α-sialon was measured in terms of the degree of conversion from α-silicon nitride to α sialon:

$$f = S\alpha'/(S\alpha'+S\alpha) \quad (1)$$

where f is the relative mass fraction α-sialon, $S\alpha'$ the area of the α-sialon (301) peak and $S\alpha$ the area of the α-Si_3N_4 (301) peak. Low amounts of α' were indicated only by an asymmetry of the α peak and therefore required careful deconvolution. It should also be noted that this estimate of the degree of conversion implies that it occurs merely as a crystallographic transformation without any change of composition or change of the total quantity of $\alpha+\alpha'$. Thus the increase in the mass of α' by incorporation of AlN and Y_2O_3 is neglected in the definition of f and consequently the fraction of α' is somewhat overestimated. However, the amounts of AlN and Y_2O_3 involved are relatively small and this approximation has relatively little effect on the values of f obtained. The small amount of β silicon nitride ($\approx$5%) in the starting powder is also disregarded in this analysis.

To verify the HT-XRD results, parallel sintering experiments were conducted in a graphite sintering

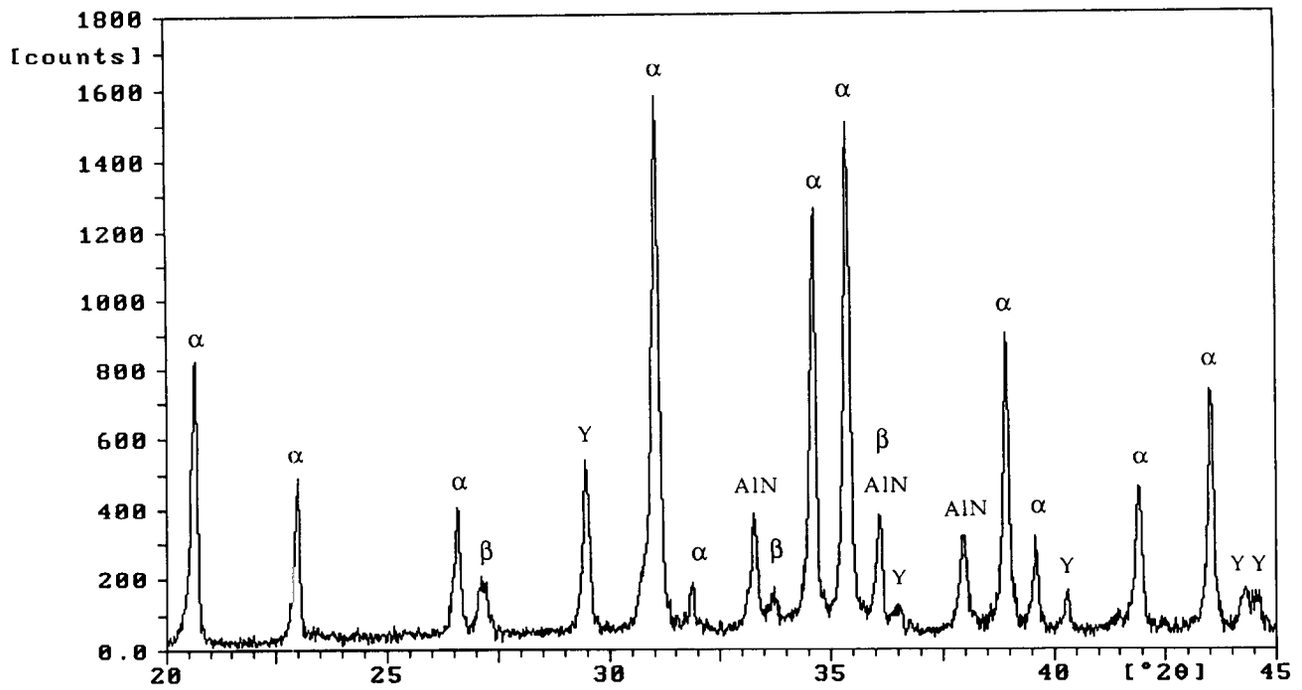


Fig. 1. RT-XRD pattern of sample presintered at 1350°C for 1 h. Where Y = $Y_{10}Al_2Si_3O_{18}N_4$ and/or a J–ss phase ($Y_4Al_{2-x}Si_xO_{9-x}N_x$), and α = α-Si_3N_4 and β = β-Si_3N_4.

furnace with samples of the same composition. Both as-pressed samples and samples presintered as above were sintered at a temperature of 1560°C in 0·15 MPa N_2 for 3 h in a silicon nitride powder bed. All samples were analysed for phase content by XRD at room temperature. The cooling rates between the sintering temperature and 1000°C were approximately 100°C/min in the HT-XRD unit and 20°C/min in the sintering furnace.

In the HT-XRD, the investigated sintering surface is totally open to the furnace atmosphere. To assess the possible effects of this, another two sets of samples were prepared for comparison. In the first set (A) additions of 0·5–3·0 wt% silica were made to the original composition. The second set (B) was given the same nominal composition but with different raw materials. The powders used for the second set of samples had a higher oxide content than those used in the original HT-XRD study and were AlN (H.C. Starck, Berlin Grade B) and Si_3N_4 (Kemanord, Grade P95). The silica used in all the mixtures was derived from an ammonia stabilized colloidal silica, destabilized by propanol. After drying this was easily comminuted to a fine-grained silica by use of an agate spex mill. The atomic composition of the two sets of samples is shown in Table 1. To allow comparison between the two sets, the Al + Si content was adjusted to 12 in the atomic formula. The second set had a higher Si:Al ratio and this was further increased slightly by the addition of silica.

3 Results

3.1 HT-XRD analysis

The XRD diffraction pattern of the original composition presintered for 1 h at 1350°C is shown in Fig. 1. Presintering resulted in formation of yttrium-rich aluminosilicate phase(s) and no detectable α-sialon. The yttrium-rich aluminosilicate phase could be identified as $Y_{10}Al_2Si_3O_{18}N_4$ but

Table 1. Normalized atomic compositions of α-sialon mixtures with different amounts of silica added

	% SiO_2	*Y*	*Al*	*Si*	*O*	*N*
Composition (A)	0	0·400	2·099	9·901	1·099	14·968
	0·5	0·398	2·090	9·910	1·193	14·906
	1	0·397	2·083	9·917	1·287	14·842
	2	0·393	2·064	9·936	1·479	14·721
	3	0·390	2·048	9·952	1·669	14·594
Composition (B)	0	0·404	1·802	10·198	1·286	14·946
	0·5	0·402	1·794	10·206	1·380	14·884
	1	0·400	1·788	10·212	1·475	14·821
	3	0·393	1·754	10·246	1·856	14·572

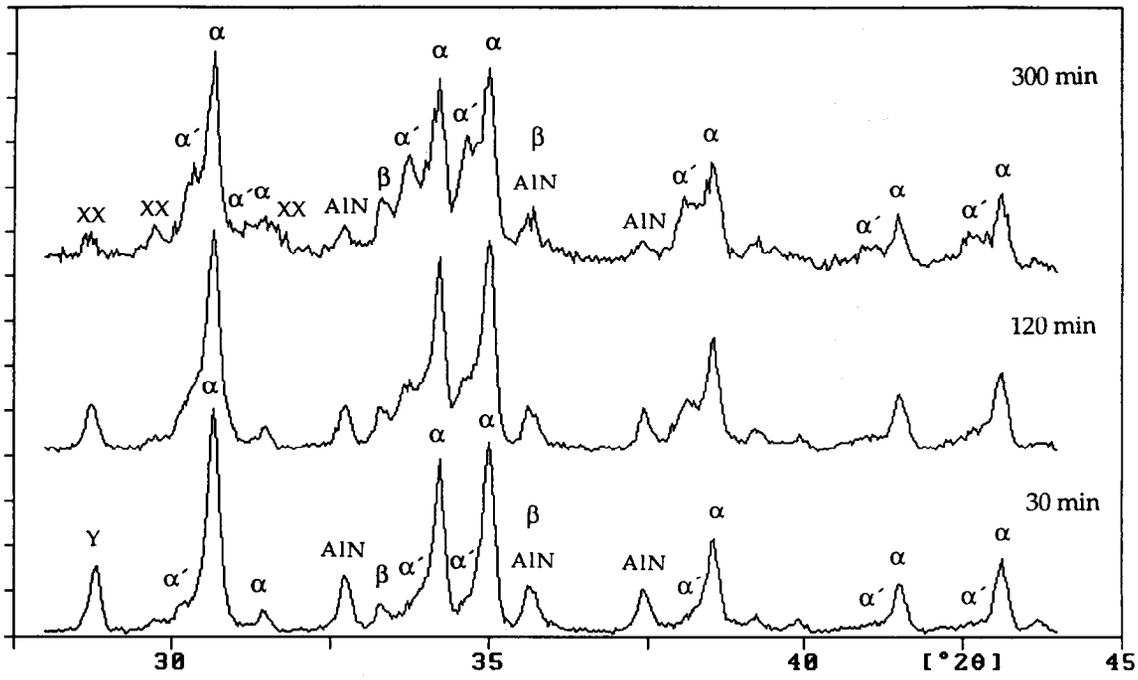


Fig. 2. Phase development with time at 1580°C as-measured at temperature in the HT-XRD, where XX = unidentified secondary phase(s).

with small shifts in the peak positions indicating a shift from stoichiometry or the incorporation of other ions. The major peaks of this phase, however, overlap the peaks of the J–ss phase. Some additional minor diffuse peaks might belong to a J–ss type phase. Their simultaneous presence therefore cannot be excluded. Nevertheless all these phases are characterized by being yttria- and oxygen-rich and will for convenience be denoted $Y_{10}Al_2Si_3O_{18}N_4$ in this paper. The formation of $Y_{10}Al_2Si_3O_{18}N_4$ suggests either the initial formation of an oxynitride melt or a direct reaction between yttria and the oxynitride layers that can be assumed to exist on the surfaces of the Si_3N_4 and AlN powders.

Figure 2 gives an example of how the phase composition develops during sintering in the HT-XRD (at 1580°C in this case). The initial formation of α-sialon was indicated only by an asymmetric broadening of the α-Si_3N_4 peaks. Times up to 5 h were needed for a clear peak shift to occur. Only very small amounts of β-Si_3N_4 could be detected. The evolution of the phase composition with temperature (5 h sintering) as measured at room temperature after sintering in the HT-XRD is summarized in Fig. 3. The results agree well with the HT-XRD measurements as regards the

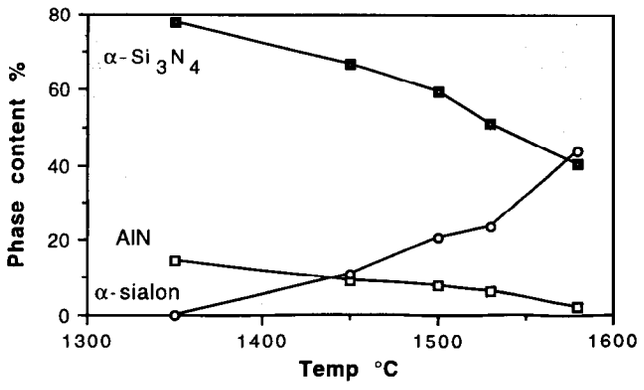


Fig. 3. Amounts of phases measured at room temperature after sintering in the HT-XRD unit for 5 h. The relative amounts of α-sialon and α-Si_3N_4 were calculated from asymmetry of the (301) XRD diffraction peak.

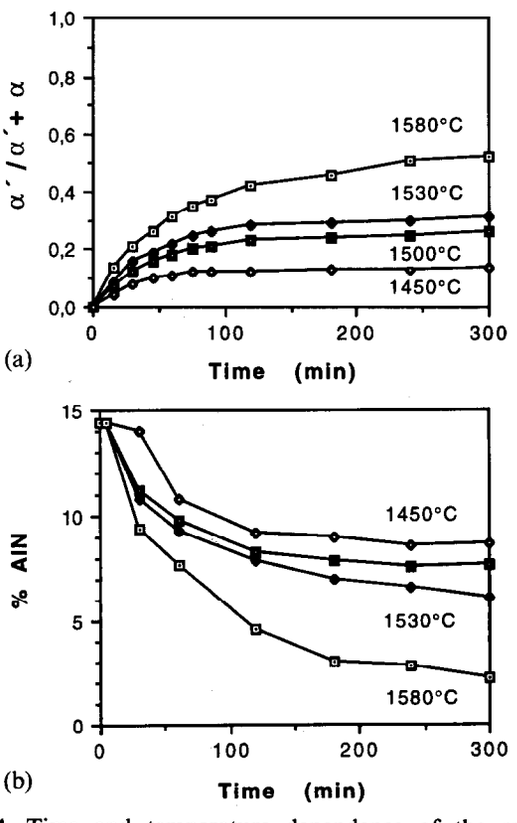


Fig. 4. Time and temperature dependence of the relative amount of (a) α-sialon ($\alpha'/\alpha'+\alpha$) and (b) AlN as-measured at temperature.

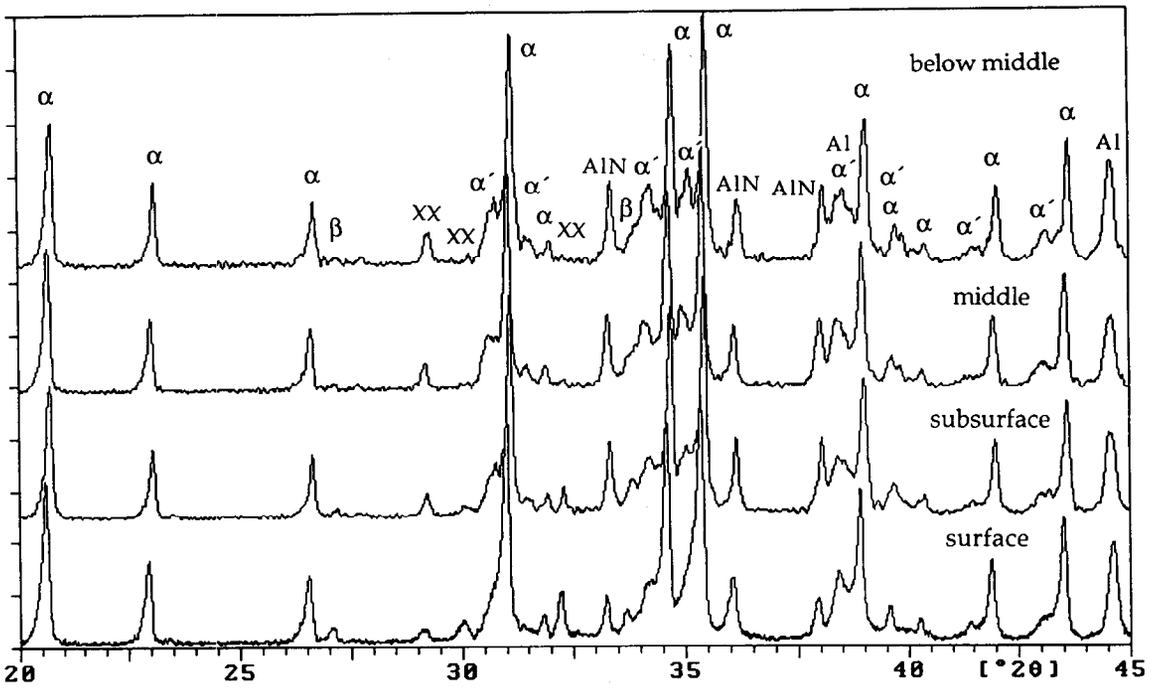


Fig. 5. RT-XRD of sample sintered at 1530°C for 5 h in the HT-XRD at different distances from the surface.

relative amounts of α and α' and with the results of other investigations of α-sialon formation.[5,6] Figures 4(a) and (b) show the increase in α-sialon and decrease of AlN with time at the different sintering temperatures. The trend in rate of formation of α-sialon corresponds well with the trend of the dissolution rate of AlN.

The amount of $Y_{10}Al_2Si_3O_{18}N_4$ was observed to decrease with both time and temperature (*cf.* Fig. 2). Instead, another phase, or possibly two phases, are formed. These are difficult to identify as they do not fit well with any single known pattern. They could however be based on a solid solution of yttrium silicates or yttrium aluminosilicates, similar to the J–ss phase or apatite.

Figure 5 shows RT diffraction patterns taken at different distances from the surface of the sample subjected to HT-XRD investigation for 5 h at 1530°C, while Table 2 shows the phase composition at corresponding distances for samples studied at different temperatures. The amounts of silicon nitride, α-sialon and $Y_{10}Al_2Si_3O_{18}N_4$ did not seem to differ significantly between the surface and the interior, except in the 1450°C sample, where the level of $Y_{10}Al_2Si_3O_{18}N_4$ is lower on the surface of the sample. The aluminum nitride content on the other hand is consistently higher in the interior. The reduced aluminum nitride content on the surface of the sample is probably due to its having a higher susceptibility to oxidation than silicon nitride. The surface of the sample showed some evidence of glassy phase after HT-XRD.

Although the differences in the amounts of α-sialon between the surface and the interior were small the nature of the α-sialon peaks was different. The peaks on the surface were broader and showed smaller separation from the α-Si_3N_4 peak than those in the interior. This was especially true for the 1530°C samples in which the peak separation in the interior was much larger than at any other temperature investigated (Table 2). This result can be compared with results reported by Walls *et al.*,[6] which showed that the cell parameters of the α-sialon are higher at the beginning of α-sialon formation than at equilibrium. They attributed this to a lower dissolution of silicon nitride than aluminum nitride in the liquid at the beginning of α-sialon formation, allowing a more highly substituted sialon to form. In this investigation the higher peak separation in the interior of the samples coincided with higher amounts of unreacted AlN than were observed at the surface. This implies that AlN does oxidize on the surface

Table 2. Relative amounts (wt fractions) of α-sialon and AlN and the α-sialon/α-Si_3N_4 peak separation at the surface and in the interior of samples sintered 5 h at different temperatures in the HT-XRD unit

Temp°C	*Position*	α'/α + α'	α'–α (2Θ) *separation*	AlN
1450	Surface	0·15	—	0·085
1450	Middle	0·14	—	0·124
1500	Surface	0.31	—	0·08
1530	Surface	0·39	0·434	0·06
1530	Subsurface	0·30	0·520	0·09
1530	Middle	0·31	0·537	0·1
1530	Below middle	0·32	0·525	0·095
1580	Surface	0·52	0·414	0·02
1580	Middle	0·47	0·442	0·06

of the sample and that this influences the peak separation, while the amount α-sialon formed does not change significantly.

3.2 Conventionally sintered compositions

As explained above, samples of the same composition as those studied in HT-XRD were sintered in a powder bed in a conventional furnace. First, a comparison was made between samples pressed directly from powders and samples presintered at 1350°C with the HT-XRD samples. There was no detectable difference in the overall phase composition of the two samples.

A difference, however, was found between the surface and interior of the conventionally sintered samples. The surface consisted of α- and β-Si_3N_4 and YAG, while the interior contained α-sialon, N-melilite, unreacted α-Si_3N_4 and AlN. The samples had also gained weight slightly ($\approx$ 1%) during sintering. This implies a mass transfer from the powder bed to the sample probably caused by a higher partial pressure of oxygen or silicon monoxide in the powder bed. The reduced AlN content on the surface of HT-XRD samples suggests that a similar effect occurred in the HT-XRD unit.

Figure 6 compares the room temperature phase composition of the interior of presintered + conventionally sintered sample sintered at 1560°C with the surface compositions of presintered + HT-XRD sintered samples treated at 1530 and 1580°C. It is seen that the α-sialon content of the interior of the sample sintered at 1560°C is similar to that of the surface of the 1580°C HT-XRD sample. The intermediate phases in the HT-XRD sample were however different from those both in the surface and interior of the conventionally-sintered sample. In the 1530°C HT-XRD sample the α-Si_3N_4 to α-sialon conversion had not proceeded as far but the yttrium-rich intermediate phase(s) is the same as in the 1580°C HT-XRD sample. These experiments show that the furnace coating in the HT-XRD unit provides a reasonable atmosphere for the sample but does not interact with the sample in the same way as a powder bed.

3.3 Conventionally sintered compositions with silica additions

Since the observed decrease in AlN content on the surfaces of the HT-XRD and conventionally sintered samples might be attributed to an oxidation, it was of interest to see how an increase in oxide content of the starting compositions would influence the phase formation. The two sets of samples shown in Table 1 were sintered at 1560°C for this purpose.

Table 3 shows the room temperature phase contents of the cross sections of the different sets of samples with 0·5 to 3·0 wt% extra silica. For (A) samples, i.e. those based on the original mixture, the phase composition comprised α-sialon, melilite, β-Si_3N_4 and unreacted Si_3N_4 and AlN; with increasing silica content, the YAG phase began to develop and the fraction of melilite decreased. In the (B) samples, based on the comparison composition, the development was very similar but instead of melilite the $Y_{10}Al_2Si_3O_{18}N_4$ phase formed; moreover it disappeared faster than the melilite in the (A) samples. The amount of α-sialon was not significantly affected, except for the 3% silica addition samples in set (B).

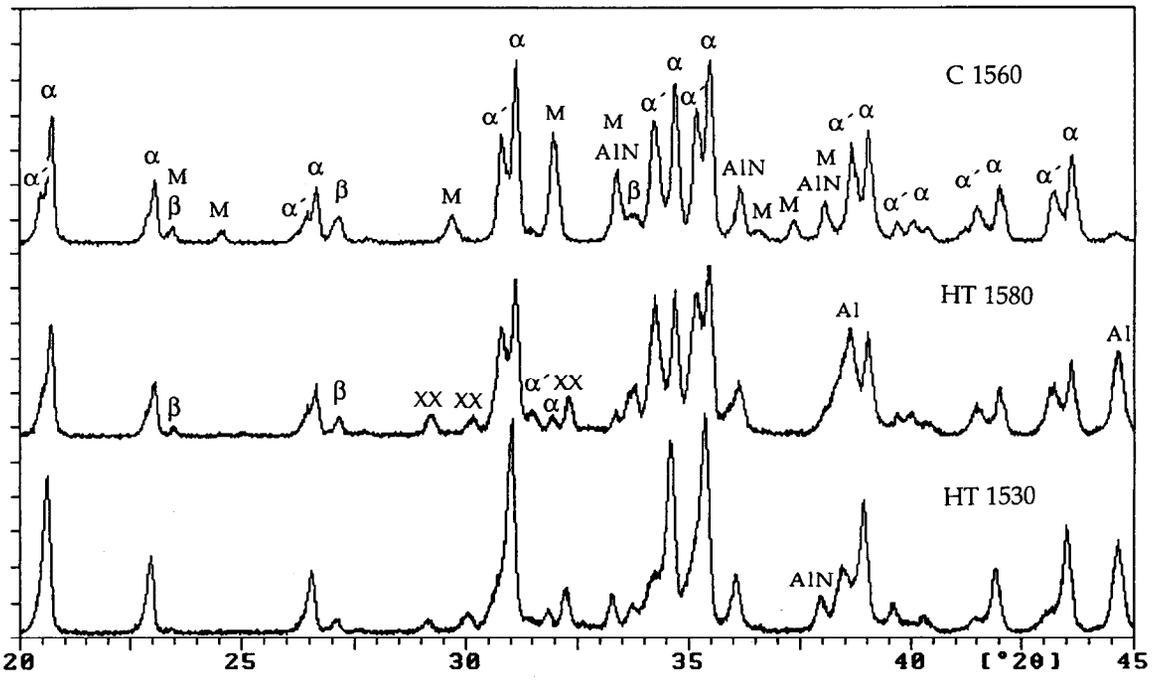


Fig. 6. RT-XRD patterns of samples presintered at 1350°C and then sintered at 1560°C in a conventional furnace (C1560), at 1530°C in the HT-XRD (HT1530) and at 1580°C in the HT-XRD (HT1580). M = $Y_2Si_3N_4O_3$.

Table 3. Phase compositions of conventionally sintered samples as a function of silica additions. Series A is the original HT-XRD composition and series B the comparison composition. α = α-Si_3N_4, α' = α-sialon, β = β-sialon, M = N–melilite, Y = $Y_{10}Al_2Si_3O_{18}N_4$. Brackets indicate very small amounts

Composition	*Phases observed*	*α–α' shift(2θ)*	*α'/α + α'*
A/0%SiO_2	α/α'/β/M/AlN	0·359	0·31
A/0·5%SiO_2	α/α'/β/M/AlN	0·375	0·35
A/1%SiO_2	α/α'/β/M/AlN	0·381	0.38
A/2%SiO_2	α/α'/β/M/YAG/AlN	0·369	0·37
A/3%SiO_2	α/α'/β/(M)/YAG/AlN	0·371	0·39
B/0%SiO_2	α/α'/β/Y/(YAG)/AlN	0·372	0·46
B/0.5%SiO_2	α/α'/β/(Y)/YAG/AlN	0·367	0·44
B/1%SiO_2	α/α'/β/YAG/AlN	0·358	0·42
B/3%SiO_2	α/α'/β/YAG/AlN	0·292	0·30

The most significant effect observed when slightly increasing the O/N-ratio of both series of samples, were the changes in the yttrium-rich intermediate phases that formed. Nitrogen-rich melilite in the A-series samples and $Y_{10}Al_2Si_3O_{18}N_4$ in the B-series gave way to oxygen-rich YAG as the overall oxygen content of the material increased.

3.4 Kinetics of α-sialon formation

The above sintering experiments showed that within the range of sintering conditions used here the degree of conversion to α-sialon is not very sensitive to small changes in oxygen content or to the intermediate phases formed. It is therefore possible to use the HT-XRD data to examine the kinetics of α-sialon formation under these circumstances. The isothermal plots of sialon formation in Fig. 4(a) show that the conversion rate is greatest within the first 90–120 min of the sintering, decreasing markedly at longer times. The reaction is considered to occur by dissolution and transport of the reactants in the liquid oxide phase and the formation of the α-sialon at the surfaces of α-Si_3N_4. The inhibition of the reaction could occur by a decrease in the fraction of the liquid phase, necessitating increased degree of solid state diffusion, or covering of silicon nitride surfaces. To describe the rapid early stage of the process, only the first period of 120 min was used in determining a reaction rate constant. In this stage the transformation was assumed to be described by a simple reaction law:

$$df/dt = k(1 - f)^n \qquad (2)$$

where n is the index of reaction, f the fraction of α sialon formed and k the reaction rate constant. To evaluate the results, a best-fit n-value was determined for the 1580°C data. It was then assumed that the reaction mechanism for all other temperatures was the same and consequently this n-value (3·64) was used to estimate the k values for all temperatures. The k values thus derived are 0·0023 (1450°C), 0·0045 (1500°C), 0·0061 (1530°C) and 0·0102 (1580°C). Reaction curves based on the above assumption are drawn in Fig 7(a) and indicate the extent to which the assumed kinetic description is reasonable. The temperature dependence of the reaction rate is expressed in the form of an Arrhenius diagram in Fig. 7(b) and yields an effective activation constant of 330 kJ mol^{-1} which is consistent with a liquid diffusion process.

An alternative approach to determining the activation energy, requiring no assumptions about the process kinetics, is to construct an Arrhenius plot on the basis of ln $1/t$ versus $1/T$ where t is the time required to give a fixed degree of reaction. Here a satisfactory linear relationship was achieved for t corresponding to a conversion of 10% and this confirmed the activation constant of 330 kJ mol^{-1}. This corresponded to a reaction time

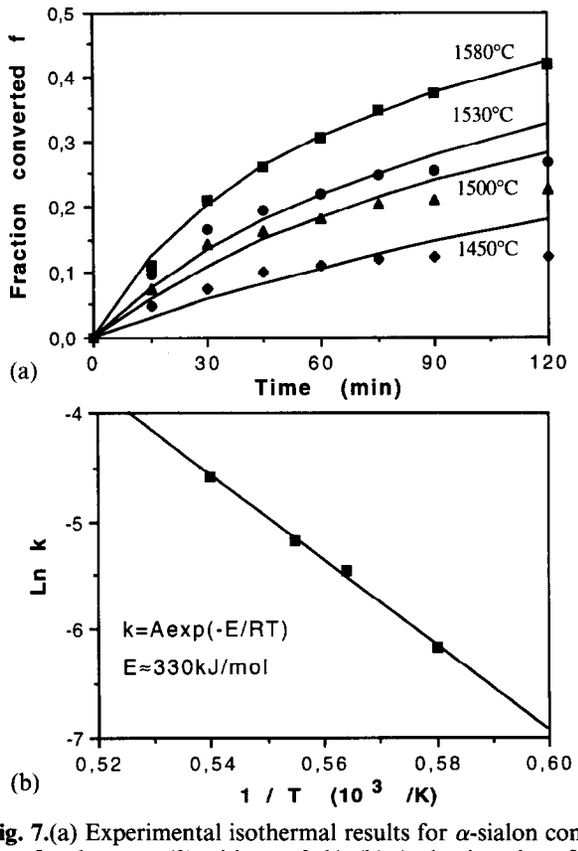


Fig. 7.(a) Experimental isothermal results for α-sialon conversion fitted to eqn (2) with n = 3·64; (b) Arrhenius plot of rate constants derived from 7(a).

of 45 min at 1450°C. Beyond this time, the results for 1450°C were no longer consistent with the linear Arrhenius plot implying an inhibiting change in reaction mechanism.

4 Discussion

As already indicated, the reaction sintering of the material studied here occurs by a complex combination of associated mechanisms occurring both in parallel and in series. After formation of an oxide liquid from surface oxides and yttria these mechanisms will include dissolution of AlN and α-Si_3N_4, transport of reactant atoms through the liquid, formation of sialon on the α-Si_3N_4 and subsequently solid state diffusion of reactants through the sialon. In addition a number of intermediate and secondary phases form depending on sintering conditions and composition. A microstructural study by Hwang *et al.*[15] has indicated that α-sialon formation occurs predominantly by heterogeneous nucleation and preferential growth on undissolved silicon nitride grains.

One of the interesting aspects of this investigation is that in the range of temperatures and conditions studied the rate and extent of α-sialon formation was relatively insensitive to small changes in oxygen content and was not influenced by the intermediate phases formed. Thus the α-sialon formation was determined mainly by the temperature and time. This is in accordance with previous findings. For example, Cao *et al.*[16] in studying the effect of extra alumina additions to an α-sialon composition concluded that, while densification was affected by the liquid phase, the early formation of α-sialon was not significantly influenced by small changes in the composition, amount or the viscosity of the liquid. The intermediate phase that formed changed from melilite to YAG with addition of alumina, but this did not influence the overall reaction sequence.

In the present work, the fact that the amount of α-sialon did not seem to change significantly with small changes in composition, while the peak separation did, suggests that the number of growing α-sialon grains was fairly constant at a given temperature but that its composition could vary. The rate of sialon formation is probably determined by the rate of dissolution and transport of silicon nitride and AlN, and therefore strongly dependent on temperature. The lower availability of AlN on the surface of the HT-XRD samples on the other hand probably only leads to a lower substitution of the α-sialon and does not affect the number and growth of grains.

β-Si_3N_4 only seem to form in very small amounts at the temperatures studied here unless major compositional changes occur, for example through a significant increase in oxygen activity, as on the surface of a sample in contact with a powder bed containing only silicon nitride and silica. It is therefore likely that the α-sialon has the lowest energy of formation at high nitrogen activities and at these relatively high temperatures. It has been suggested in the past that the α-Si_3N_4 structure is a low-temperature modification, but with yttria stabilization it readily forms.

The above observations imply that, although small compositional changes on an open surface are unavoidable, high-temperature X-ray diffraction is still an appropriate method to study the kinetics of α-sialon formation or decomposition. On the other hand, HT-XRD may not always be suitable as a means of monitoring all the products of the reactions since the intermediate and secondary phases are strongly dependent on sintering conditions. Thus, in the present study the $Y_{10}Al_2Si_3O_{18}N_4$ formed during presintering gradually disappeared during treatment in the HT-XRD while other intermediary phases formed. These were different from those formed during sintering in a powder bed in a conventional graphite furnace.

A very characteristic feature of the kinetics of sialon formation was the dramatic inhibition of growth after a certain fraction of transformation. The range of inhibition moved to higher fractions of transformation and longer times with increasing temperature suggesting that the effect may be caused by a decrease in the amount of liquid.

5 Conclusions

The reaction sintering of an yttria α-sialon from a mixture of yttria, AlN and α-Si_3N_4 has been studied at temperatures between 1450 and 1580°C. The rate of α-sialon formation was significant during an initial reaction stage but became inhibited after a limited fraction of conversion had occurred. The rate of reaction as well as the fraction of conversion and time at which inhibition set in all increased with temperature. The activation energy of the initial reaction stage was 330 kJ/mol.

A variety of intermediate and secondary phases were observed to form during sintering depending on variations in the sintering conditions such as the oxygen level of the sintering environment and small variations in the starting composition. The rates of α-sialon formation were however not affected significantly by these variations in conditions or secondary phases.

Since the rate of α-sialon formation is relatively insensitive to other sintering conditions than the

temperature, HT-XRD is considered to be a suitable technique for studying the kinetics of α-sialon formation and was applied for this purpose in this study. The technique is however considered unsuitable for the study of the formation of secondary phases since these are very sensitive to the sintering conditions.

Acknowledgements

The authors extend thanks to Professor Richard Warren for valuable advice. The work was supported financially by The Research Council of Norrbotten. T. Ekström acknowledges the support of the Swedish Research Council for Engineering Sciences.

References

1. Jack, K. H. & Wilson, W. I., Ceramics based on the Si–Al–O–N and related systems. *Nature, Phys. Sci.*, **238** (1972) 28–9.
2. Cao, G. Z. & Metselaar, R., α'-Sialon ceramics: A review. *Chem. Mater.*, **3** (1991) 242–52.
3. Nagel, A., Greil, P. & Petzow, G., Reaction sintering of yttrium containing α-silicon nitride solid solution. *Revue de Chimie Minérale*, **22** (1985) 437–48.
4. Ishizawa, K., Ayuzawa, N., Shiranita, A., Takai, M., Uchida, N. & Mitomo, M., Some properties of α-sialon ceramics. In *Proc. Ceramic Materials and Components for Engines*, eds W. Bunk & H. Hausner. Deutsche Keramische Gesellschaft, 1986, pp. 511–18.
5. Slasor, S. & Thompson, D. P., Preparation and characterisation of yttrium α'-sialons. In *Proc. Non-oxide Technical and Engineering Ceramics*, Limerick, Ireland, 1985, pp. 223.
6. Walls, P. A. & Thompson, D. P., Reaction mechanisms in the formation of calcium and yttria α'-β'sialon composites. In *Br. Ceram. Proc. Special Ceramics.*, **8**, 1986, pp. 35–50.
7. Cao, G. Z., Metselaar, R. & Ziegler, G., Preparation and properties of α' and α' + β'-sialon ceramics. *Mater. Forum*, **16** (1992) 299.
8. Winder, S. M. & Lewis, M. H., Nitrogen content of the intergranular glass phase in syalon ceramics. *J. Mater. Sci. Lett.*, **4** (1985) 241–3.
9. Mandal, H., Thompson, D. P. & Ekström, T., Heat-treatment of Ln–Si–Al–O–N glasses. *Key Engin. Mater.*, **72–74** (1992) 187.
10. Cao, G. Z., Metselaar, R. & Ziegler, G., Formation and densification of α'-sialon ceramics. *Material Science Monographs*, 66B, ed. P. Vincenzini, Amsterdam, 1991, pp. 1285–93.
11. Mandal, H., Thompson, D. P. & Ekström, T., Reversible α↔β sialon transformation in heat-treated sialon ceramics. *J. Eur. Ceram. Soc.*, **12** (1993) 421.
12. Bartek, A., Ekström, T., Herbertsson, H. & Johansson, T., Yttrium α-sialon ceramics by hot isostatic pressing and post-hot isostatic pressing. *J. Am. Ceram. Soc.*, **75** (1992) 432–9.
13. Ashkin, A., Ashkin, D. & Babushkin, O., Investigation of α-sialon formation by high temperature X-ray diffraction. In *Proc. Int. Conf. on Silicon Nitride Based Ceramics*, Trans Tech Publications, Switzerland, eds M. J. Hoffmann, P. F. Becher & G. Petzow, 1993, pp. 373–7.
14. Schreiner, W. N. & Jenkins, R., *Adv. X-ray Anal.*, **26** (1983) 141–8.
15. Hwang, S. L. & Chen, I. W., Nucleation and growth of α'-sialon on α-Si_3N_4. *J. Am. Ceram. Soc.*, **77** (1994) 1711–18.
16. Cao, G. Z., Metselaar, R. & Ziegler, G., Effects of the characteristics of silicon nitride powders on the preparation of α'-sialon ceramics. *J. Mater. Sci. Lett.*, **11** (1992) 1685.

Journal of the European Ceramic Society 15 (1995) 1111–1117
© 1995 Elsevier Science Limited
Printed in Great Britain. All rights reserved
0955-2219(95)00086-0
0955-2219/95/$9.50

Zirconia as a Nucleating Agent in a Yttria–Alumina–Silica Glass

P. Vomacka, O. Babushkin & R. Warren

Department of Engineering Materials, Luleå University of Technology, S-951 87 Luleå, Sweden

(Received 13 February 1995; revised version received 19 May 1995; accepted 22 May 1995)

Abstract

The crystallization behaviour of a ZrO_2-containing glass and a ZrO_2-free glass in the Y_2O_3–Al_2O_3–SiO_2 system prepared at 1700°C were compared in order to study the influence of ZrO_2 on the nucleation and growth processes. Techniques used included SEM, DTA and XRD analysis. The microstructural development of the ZrO_2-containing material during crystallization was more complex than that of the ZrO_2-free material. In the crystallization treatments no phase separation prior to crystallization could be observed and no precursor crystalline phase was observed to form in the ZrO_2-containing glass. Thus the added zirconia could be considered to act as a growth modifier rather than a catalyst nucleating agent.

1 Introduction

During the sintering of Si_3N_4 materials by liquid-phase sintering an oxynitride liquid forms through reaction of oxide sintering aids (such as Y_2O_3 and Al_2O_3) with surface silica on the starting Si_3N_4 powder particles and some of the Si_3N_4. Upon cooling from the sintering temperature an intergranular glassy phase forms from the liquid. The compositions of this phase in, for example, materials with yttria and alumina as sintering aids lie within the Y_2O_3–Al_2O_3–SiO_2 system. In general, the presence of such glassy phases has a deleterious influence on the mechanical properties and oxidation behaviour of Si_3N_4 ceramics.[1–5] One approach to reducing these effects is to induce a crystallization of the amorphous phase by means of a suitable heat treatment. Experimental studies of intergranular phases to better understand their crystallization behaviour and associated property changes are difficult to perform *in situ*; for this reason it is of interest to study bulk glasses with compositions that simulate such phases.[6–10]

Nucleation catalysts are widely used in glass systems to promote crystallization. Thermal treatment at a temperature necessary for precipitation of a crystalline phase, which acts as primary nucleation centers, leads to the devitrification of the glass.[11] Another catalysis mechanism which leads to a subsequent volume crystallization and which is not yet entirely understood is phase separation leading to the formation of a fine dispersion. Phase separation can be induced by a number of oxides (such as, e.g. TiO_2 and ZrO_2).[11] Crystallization studies made by several investigators[2,12,13] have shown that ZrO_2 added to yttria–alumina–silica glasses can catalyse their crystallization.

The aim of the present work was to study the influence of ZrO_2 on crystallization of an yttria–alumina–silica glass prepared at 1700°C. The crystallization behaviour of a high Y_2O_3-content glass with and without the addition of 6 wt% zirconia was studied.

2 Experimental

The solubility limit of ZrO_2 at 1700°C in an yttrium aluminosilicate liquid with the composition of 46·9 wt% Y_2O_3, 24·3 wt% Al_2O_3 and 28·8 wt% SiO_2 was in the previous study determined as 6 wt%.[14] Therefore two glasses (A and B) with compositions x ZrO_2 + (100–x) [46·9 Y_2O_3, 24·3 Al_2O_3, 28·8 SiO_2] (where x in wt% was 0 and 6) were chosen for the present study. Both compositions were subjected to the same heat treatments as described below.

Samples were prepared from high-purity Y_2O_3, Al_2O_3, SiO_2 and unstabilized ZrO_2 powders (Rhone Poulenc, Alcoa Chemicals, Johnson Matthey Alfa Products and Sigma chemical respectively). The powders were weighed in a precision balance, mixed in polyethylene containers on a Siemens roller mill for 10 h using prophanol as mixing medium, dried and sieved. Batches of 100 g each were then mechanically compacted into molybdenum crucibles and fired in a nitrogen

Table 1. Results of heat treatment* in this study and in the previous work[14] (s is strong, m is medium, w is weak and vw is very weak)

Heat treatment		*Phase analysis*	
Time (h)	*Temp. (°C)*	*Sample A*	*Sample B*
1	900	Clear amorphous glass	Clear amorphous glass
	950	Clear amorphous glass	Clear amorphous glass
	980	Clear amorphous glass	Clear amorphous glass
	1010	Clear amorphous glass	Clear amorphous glass
	1040	Opaque amorphous glass	Clear amorphous glass
	1100	y - $Y_2Si_2O_7$, m; β - $Y_2Si_2O_7$, m; amorphous glass, w	y - $Y_2Si_2O_7$, m; amorphous phase, m
	1150[14]		y - $Y_2Si_2O_7$, s; β - $Y_2Si_2O_7$, w; Y–ZrO_2; w; $Al_6Si_2O_{13}$, vw;
	1200[14]		y - $Y_2Si_2O_7$, s; β - $Y_2Si_2O_7$, m; Y–ZrO_2; w; $Al_6Si_2O_{13}$, w
	1250[14]		β - $Y_2Si_2O_7$, s; y - $Y_2Si_2O_7$, m; Y–ZrO_2; w; $Al_6Si_2O_{13}$, w
	1300[14]		β - $Y_2Si_2O_7$, s; y - $Y_2Si_2O_7$, w; Y–ZrO_2; w; $Al_6Si_2O_{13}$, w
	1350[14]		β - $Y_2Si_2O_7$, s; y - $Y_2Si_2O_7$, w; Y–ZrO_2; w; $Al_6Si_2O_{13}$, w
6	900	Clear amorphous glass	Clear amorphous glass
	950	Clear amorphous glass	Clear amorphous glass
	980	Opaque amorphous glass	Clear amorphous glass
	1010	y - $Y_2Si_2O_7$, w; β - $Y_2Si_2O_7$, w; amorphous phase, s	Opaque amorphous glass
	1040	y - $Y_2Si_2O_7$, m; β - $Y_2Si_2O_7$, m; amorphous phase, w	y - $Y_2Si_2O_7$, m; amorphous phase, m;
	1100	y - $Y_2Si_2O_7$, s; β - $Y_2Si_2O_7$, m; amorphous phase, vw $Al_6Si_2O_{13}$, vw	y - $Y_2Si_2O_7$, s; β - $Y_2Si_2O_7$, w; amorphous phase, w; Y–ZrO_2; vw $Al_6Si_2O_{13}$, vw
12	900	Clear amorphous glass	Clear amorphous glass
	950	Clear amorphous glass	Clear amorphous glass
	980	Opaque amorphous glass	Clear amorphous glass
	1010	y - $Y_2Si_2O_7$, w; β - $Y_2Si_2O_7$, w; amorphous phase, s	Opaque amorphous glass
	1040	y - $Y_2Si_2O_7$, m; β - $Y_2Si_2O_7$, m; amorphous phase, w	y - $Y_2Si_2O_7$, m; β - $Y_2Si_2O_7$, m; amorphous phase, m
	1100	y - $Y_2Si_2O_7$, s; β - $Y_2Si_2O_7$, m; $Al_6Si_2O_{13}$, vw	y - $Y_2Si_2O_7$, s; β - $Y_2Si_2O_7$, m; Y–ZrO_2; vw; $Al_6Si_2O_{13}$, vw
	1300	β - $Y_2Si_2O_7$, s; $Al_6Si_2O_{13}$, w	β - $Y_2Si_2O_7$, s; Y–ZrO_2; m; $Al_6Si_2O_{13}$, w

*Starting materials were amorphous glasses, as evidenced by X-ray diffraction.

atmosphere (pressure of 0·17 MPa) at a temperature of 1700°C for 3 h. The heating rate up to the firing temperature was 5°C/min, the cooling rate was that given by the furnace after switching off (firing temperature to 1400°C, 20°C/min; 1400–950°C, 15°C/min and 950–500°C, 10°C/min). The furnace was a cold wall vacuum/pressure furnace with a graphite heater.

Pieces of the as-prepared glass (approximately 7 × 7 × 7 mm) were heat-treated at selected temperatures and times (see Table 1); they were placed in a Si_3N_4 powder bed in Mo crucibles and heated in a 0·17 MPa nitrogen atmosphere in the same furnace as above. The heating rate was 5°C/min and cooling was furnace cooling (see above). As-melted samples and heat-treated samples were examined by X-ray diffraction to check for crystallization and to identify crystalline phases. Powder samples of the as-melted glasses were also subjected to differential thermal analysis (DTA) at a heating rate of 10°C/min in a nitrogen atmosphere using an alumina powder reference standard. Dilatometric measurements were made on selected samples in a Netzch dilatometer 402E at a heating rate of 2°C/min. The microstructure of the samples were examined by scanning electron microscopy (SEM) using a CamScan S4-80DV instrument and attached energy dispersive spectrometer (EDS).

3 Results and Discussion

3.1 Phase identification

Crystalline phases identified by X-ray diffraction of glass cubes devitrified at temperatures between 900 and 1350°C are compiled in Table 1. These temperature limits were dictated by the measured

Table 2. Dilatometric measurements (glass transition temperatures — M_g and dilatometric softening points — M_s) and DTA measurement (the maximum of endothermic peaks indicating melting temperatures — T_L)

Sample	M_g(°C)	M_s(°C)	T_L(°C)
A	867	912	1430
B	842	900	1410, 1425*

*Two melting temperatures because of the immiscibility.[14]

glass transition temperatures and melting temperatures of the glasses (Table 2). For composition A the detected phases are in general agreement with those expected from the equilibrium phase diagram.[2,6,7,15–17] namely $Y_2Si_2O_7$ and $Al_6Si_2O_{13}$, without the appearance of the Al_2O_3 phase reported in previous studies.[6,9,14] In composition B the cubic yttria stabilized ZrO_2 ($Y–ZrO_2$) phase also appeared in all the X-ray diffraction patterns of samples heat treated at temperatures >1100°C (Fig. 1). Some unidentified phases were also detected for some heat treatments. They are probably intermediate phases and are not included in Table 1.

3.2 Microstructural changes

The EDS analysis of as-prepared glasses of both compositions revealed impurities of Fe and Mo in the microstructure probably coordinating from the starting powders and from the Mo crucibles. They appeared as small (<2 μm) particles probably of iron silicides[18] and molybdenum oxides.



Fig. 2 Glass with composition A after heat treatment at 980°C for 6 h (backscatter image—500 ×).

They influenced the crystallization process during the heat treatment to some extent but it is important to emphasize that they appeared in both glass compositions and they were of a very small amount.

At 900–950°C, no observable crystallization of composition A or B occurred. At 980°C, glass A had an opaque appearance when heat-treated for 6 and 12 h; this appeared to be due to the formation of small (1–10 μm) crystals, probably of y-$Y_2Si_2O_7$ and β-$Y_2Si_2O_7$ species (Fig. 2). They occurred to approximately the same extent for both treatment times. Their crystallization appeared to be heterogeneously nucleated by the impurities in the glass.

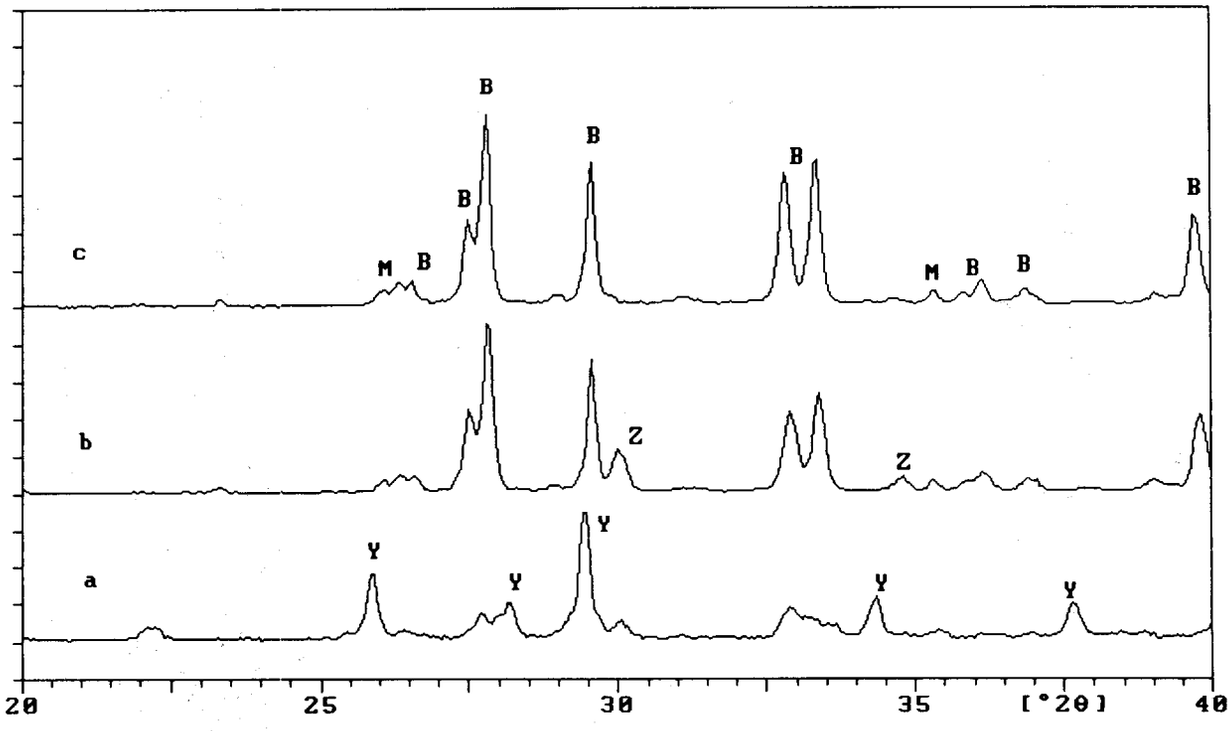


Fig. 1. X-ray diffraction patterns of the investigated glasses: (a) with 6 wt% ZrO_2 (composition B) heat treated at 1100°C for 1 h, (b) with 6 wt% ZrO_2 heat treated at 1300°C for 12 h and (c) without the addition of ZrO_2 (composition A) heat treated at 1300°C for 12 h. The symbols represent identified phases: (Y) y - $Y_2Si_2O_7$, (B) β - $Y_2Si_2O_7$, (M) mullite and (Z) cubic yttria stabilized ZrO_2. At $2\theta = 30°$ the ZrO_2 (111) peak coincides with a y - $Y_2Si_2O_7$ peak.

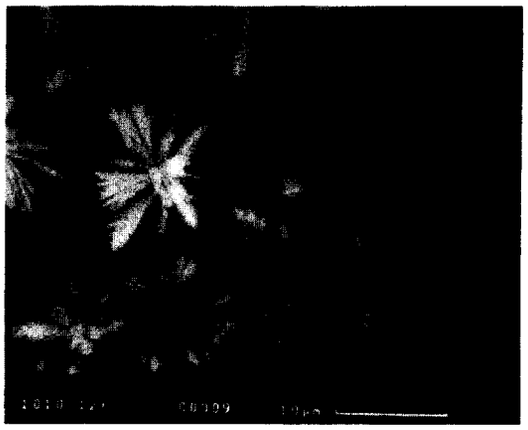


Fig. 3. Micrograph of composition A heat treated at 1010°C for 12 h with spherulitic dendrites of $Y_2Si_2O_7$ (backscatter image—2500 ×).

At 1010°C, composition A treated for 6 and 12 h exhibited an increased rate of crystallization and the occurrence of small spherulites (≈ 10–20 μm in diameter) consisting of radially growing dendrites of $Y_2Si_2O_7$ (Fig. 3). Spherulites are transient morphological forms produced during the rapid growth of crystals when the rate of growth exceeds that of diffusion and are often observed during the crystallization of highly supercooled viscous liquids. Composition B heat-treated at this temperature exhibited a similar degree of crystallization to composition A treated for 6 h at 980°C. However, in this glass the crystals were double platelike precipitates of $Y_2Si_2O_7$ in some cases with Y–ZrO_2 particles in their centers serving as nucleating catalysts (Fig. 4). These Y–ZrO_2 particles might either have been nucleated by the impurities in the glass or originated from the parent glass surviving the melting process.

At 1040°C, the crystallization rate increased for both compositions; in samples treated for 6 and 12 h the spherulites in composition A and plate crystals in composition B extended to larger dimensions (≈ 20–30 μm in diameter for spherulites and



Fig. 4. Glass B after heat treatment at 1010°C for 12 h with Y–ZrO_2 particles in centres of double platelike crystals of $Y_2Si_2O_7$ (backscatter image—2500 ×).

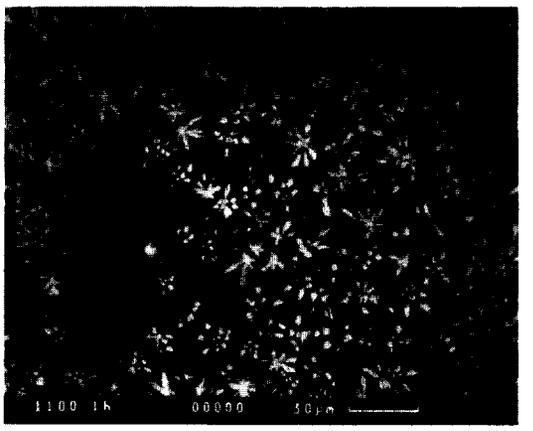


Fig. 5. Spherulites of $Y_2Si_2O_7$ in composition A after 1 h at 1100°C (backscatter image—500 ×).

20–30 μm in length for plates respectively). The microstructure of B began to be characterized by a dendritic morphology of the $Y_2Si_2O_7$. Such a morphology has been observed in the surface oxide layer of hot-pressed Si_3N_4–Y_2O_3–SiO_2 materials by Babini *et al.*[19] These authors attributed the dendrite formation to constitutional supercooling caused by a larger concentration of yttrium in the glass than in stoichiometric $Y_2Si_2O_7$. In the present case, the crystallization of y-$Y_2Si_2O_7$ requires the rejection of Al (solubility of Al in the y-$Y_2Si_2O_7$ phase decreases as a function of increasing crystallization temperature[18]), Si, O and Zr to the glass phase ahead of the glass/crystal interface. This effect would cause the constitutional supercooling resulting in dendrite formation. Glass A treated for 1 h had an opaque appearance due to a microstructure similar to those developed at 980°C after 6 and 12 h.

At 1100°C, the crystallization rate for both compositions increased dramatically with only small amounts of amorphous glassy phase retained in the microstructure (Table 1, Figs 5 and 6). The Y–ZrO_2 phase appears in the micrographs of B samples as small dendrites. In the B-glass the y-$Y_2Si_2O_7$ crystals grew to large dimensions

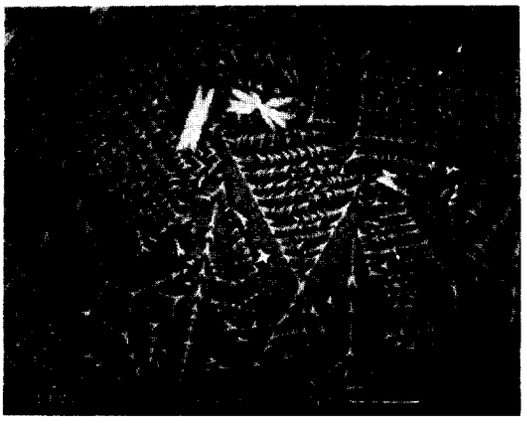


Fig. 6. Glass B after 1 h at 1100°C (backscatter image—500 ×).



Fig. 7. Crystallization of glass B at 1300°C after 12 h (backscatter image—500 ×).

presumably because they nucleated on the relatively few residual, undissolved ZrO_2 and possibly on impurity particles.

In the temperature range, 1150–1350°C (only B compositions were studied),[14] the samples were almost fully crystallized. The observations revealed different phase transformations such as crystallization of y-$Y_2Si_2O_7$, crystallization of β-$Y_2Si_2O_7$, transformation of y-$Y_2Si_2O_7$ to β-$Y_2Si_2O_7$ and crystallization of cubic yttria stabilized ZrO_2(Y–ZrO_2) occurring at different temperatures.

At 1150 and 1200°C, the microstructure of the crystallized samples was very complex with the $Y_2Si_2O_7$ occurring in the form of dendrites and fibrelike branches with an interfibrillar material which is probably amorphous.[6] At 1300°C, the y-$Y_2Si_2O_7$ phase transforms to the β-$Y_2Si_2O_7$ phase which begins to dominate the microstructure. At 1350°C, the transformation of the y-$Y_2Si_2O_7$ phase to the β-$Y_2Si_2O_7$ phase results in a β with blocky morphology to be seen growing from what were originally y-$Y_2Si_2O_7$ dendrite branches (Fig. 7). Aspects of the y $\rightarrow$ β transformation and the role of Y–ZrO_2 and its appearance in the microstructure will be discussed in the following section.

3.3 Influence of ZrO_2 on crystallization behaviour

The solubility of ZrO_2 in the investigated glass prepared at 1700°C is limited to 6 wt%.[14] As shown in Table 2 the addition of ZrO_2 leads to a decrease of the dilatometric glass transition temperature (M_g) and the dilatometric softening point (M_s) of the glass. DTA measurements on glasses with various ZrO_2 contents (0–8 wt%)[14] showed only one exothermic peak. However, this does not mean that only one crystal species is crystallizing. The broadness of the peak in ZrO_2-containing glasses indicates that ZrO_2 and other phases, mainly the $Y_2Si_2O_7$ phase, crystallize within a narrow temperature interval. The shape and lower intensity of the exothermic peak for composition B indicate a lower crystallization rate of this glass.

The crystallization of $Y_2Si_2O_7$ in composition B requires the rejection, not only of Al, Si and O but also Zr at the glass/crystal interface. The enrichment of Zr in the glass ahead of the interface would lead to a higher local viscosity of the glass near the interface than would be the case in glass A, thereby causing inhibition of the crystal growth of the $Y_2Si_2O_7$ phase. Thus, under these conditions ZrO_2 acts as a growth modifier during crystal growth.[20] The local enrichment of Zr at the glass/crystal interface might be expected to lead to the formation of ZrO_2 crystals. However, the growth of the ZrO_2 particles beyond colloidal dimensions is limited by slow diffusion of Zr in the glass at lower temperatures. In this study ZrO_2 particles growth at the glass/crystal interface was observed at higher temperatures (> 1100°C), the particles being detected by XRD and in SEM (Figs 1 and 7 and Table 1). Some of ZrO_2 remains trapped in the $Y_2Si_2O_7$ phase during cooling from the heat treatment temperature and appears as a decoration of the $Y_2Si_2O_7$ crystals in the microstructure (Fig. 8).

It has been suggested that ZrO_2 promotes liquid immiscibility because of its high cationic field strength.[21] In the present case, DTA measurements revealed two endothermic peaks in glass B around 1400°C without any mass changes occurring during the measurement.[14] They were interpreted as representing melting reactions and therefore it was concluded that the addition of ZrO_2 does enhance liquid immiscibility in this system. On the other hand, in the crystallization treatments no phase separation prior to crystallization could be observed possibly because the temperatures lay outside the appropriate range. Nevertheless, at high heat treatment temperatures (1200–1350°C) the Zr entrapped in the interfibrillar glass phase, which is rich in Al, Si and O (due to the phenomenon described above and no

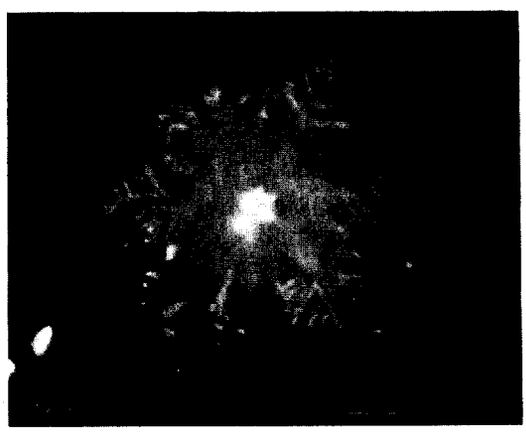


Fig. 8. Decoration of an $Y_2Si_2O_7$ crystal with ZrO_2. Composition B heat treated at 1250°C for 1 h (backscatter image—3500 ×).



Fig. 9. Zr-rich droplets in glass B heat treated at 1300°C for 1 h (backscatter image—2500 ×).

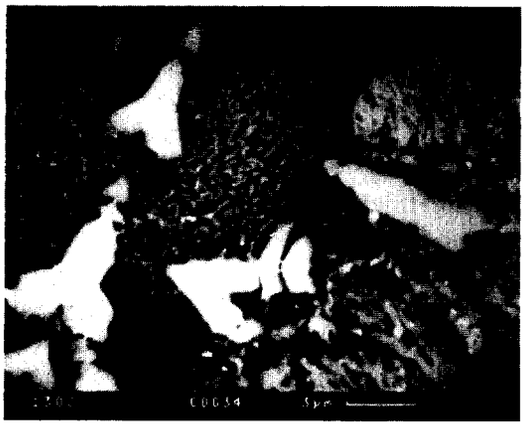


Fig. 10. Crystallization of glass B (1300°C for 1 h). Zr-rich droplets in an area that was originally y-$Y_2Si_2O_7$ fibres with the interfibrillar glass phase (backscatter image—5000 ×).

Al-containing phase having yet crystallized out) precipitated to form small Zr-rich droplets (Fig. 9). These droplets then provided nucleation sites for the β-$Y_2Si_2O_7$ and mullite crystals which then grew from the original y-$Y_2Si_2O_7$ fibres and interfibrillar glass phase (Fig. 10). Whether or not this process was initiated by phase separation[22] of the interfibrillar glass phase could not be ascertained by the available SEM analysis.

4 Conclusions

The crystallization of the ZrO_2-free glass proceeded by the formation of spherical aggregates (spherulites) consisting of radially growing dendrites. In contrast, only a small number of spherulites were observed in the ZrO_2-containing glass, the crystallization proceeding by the formation of extended dendrites rather than spherulites and being accompanied by the formation of double platelike crystals. Therefore it is believed that Zr acts as a growth modifier in this glass. As in studies of the devitrification mechanisms in $Li_2O{\cdot}Al_2O_3{\cdot}6SiO_2$ glasses[23] containing ZrO_2 as a nucleating agent, no precursor crystalline phase was observed to form in the investigated yttria–alumina–silica-glass. ZrO_2 precipitates observed in some cases, probably remaining from the glass melting, served as nucleating centers for the crystallization of the $Y_2Si_2O_7$ phase. Some of the $Y_2Si_2O_7$ crystals were probably also nucleated by impurities in the glass. The low frequency of these impurity particles and of ZrO_2 particles that survived the melting led to the formation of large $Y_2Si_2O_7$ grains. The addition of ZrO_2 might increase the rate of the y $\rightarrow$ β transformation occurring at higher temperatures compared to the ZrO_2-free glass but present results do not confirm this.

References

1. Falk, L. K. L. & Dunlop, G. L., Crystallization of the glassy phase in an Si_3N_4 material by post-sintering heat treatments. *J. Mat. Sci*, **22** (1987) 4369–76.
2. Drummond, III, Ch. H., Glass formation and crystallization in high-temperature glass-ceramics and Si_3N_4. *J. Non-Cryst. Solids.*, **123**, (1990) 114–28.
3. Kleebe, H.-J., Cinibulk, M. K., Cannon, R. M. & Ruhle, M., Statistical analysis of the intergranular film thickness in silicon nitride ceramics. *J. Am. Ceram. Soc.*, **76**(8) (1993) 1969–77.
4. Lewis, M. H., Crystallization of grain boundary phases in silicon nitride and sialon ceramics. In *Key Engineering Materials*, **89–91**, Trans Tech Publications, Switzerland, 1994, pp. 333–8.
5. Lewis, M. H., Bhatti, A. R., Lumby, R. J. & North, B. The microstructure of sintered Si–Al–O–N ceramics. *J. Mat. Sci.*, **15** (1980) 103–13.
6. Arita, I. H., Wilkinson, D. S. & Purdy, G. R., Crystallization of yttria–aluminia–silica glasses. *J. Am. Ceram. Soc.*, **75**(12) (1992) 3315–20.
7. Bondar, I. A. & Galakov, F. Ya., Phase equilibria in the system Y_2O_3–Al_2O_3–SiO_2. *Izv. Akad Nauk. SSSR Ser Khim.*, **7** (1964) 1325–6.
8. Meara, C. O., Dunlop, G. L. & Pompe, R., Phase relationship in the system Y_2O_3–Al_2O_3–SiO_2. In *Proceedings of the World Congress on High Tech Ceramics (6th CIMTEC)*, Milan, Italy, 1986, ed. P. Vincenzini, Elsevier Science Publishers, Amsterdam, pp. 265–70.
9. Hyatt, M. J. & Day, D. E., Glass properties in yttria–alumina–silica system. *J. Am. Ceram. Soc.*, **70**(10) (1987) C-283–7.
10. Loehman, R. E., Preparation and properties of oxynitride glasses. *J. Non-Cryst. Sol.*, **56** (1983) 123–34.
11. Zarzycki, J., *Glasses and the Vitreous State*. Cambridge University Press, Cambridge, 1991, 422–4.
12. Zhao, J., Wang, L., Peng, G. & Wu, J. G., Effect of zirconia on the crystallization of grain boundary. In *Proceedings of the 4th International Symposium on Ceramic Materials and Components for Engines*, Gothenburg, Sweden, 1990.
13. Thomas, G. & Ahn, C., Characterization and crystallization of Y–Si–Al–O–N glass. *Communications of the Am. Cer. Soc.* November 1982, C-185-8.
14. Vomacka, P. & Babushkin, O., Yttria–alumina–silica glasses with addition of zirconia. To be published in *J. Europ. Cer. Soc.*
15. Drummond, III, Ch. H. & Lee, W. E., Crystallization and characterization of Y_2O_3–SiO_2 glasses. *Ceram. Eng. Sci. Proc.*, **9**(9–10), (1988) 1343–54.

16. Lee, W. E., Drummond, III, Ch. H., Hilmas, G. E. & Kumar, S., Microstructural evoluation in near-eutectic yttrium silicate compositions fabricated from a bulk melt and as an intergranular phase in silicon nitride. *J. Am. Ceram. Soc.*, **73**(12) (1990) 3575–9.
17. Kumar, S. & Drummond, III, Ch. H., Crystallization of various compositions in the Y_2O_3–SiO_2 system. *J. Mater. Res.*, **7**(4) (1992).
18. Dinger, T. R., Rai, R. S. & Thomas, G., Crystallization behavior of a glass in the Y_2O_3–SiO_2–AlN system. *J. Am. Ceram. Soc.*, **71**(4) (1988) 236–44.
19. Babini, G. N., Bellosi, A. & Vincenzini, P., Factors influencing structural evolution in the oxide hot-pressed Si_3N_4–Y_2O_3–SiO_2 materials. *J. Mater. Sci*, **19** (1984) 3487–97.
20. Zdanieski, W. A., Microstructure and kinetics of crystallization of MgO–Al_2O_3–SiO_2 ceramics. *J. Am. Ceram. Soc.*, **61**(5-6) (1977) 199–204.
21. Yuan-Jang, S., Pouyan, S., San-Yuan, Ch. & Hong-Yang, L., Spherulitic growth from phase-separated vitreous matrix in a cordierite-Y-stablized zirconia glass-ceramics. *J. Am. Ceram. Soc.*, **74**(1) (1991) 85–91.
22. Aksay, I. A. & Pask, J. A., System Al_2O_3–SiO_2. *J. Am. Ceram. Soc.*, **58**(11–12) (1975) 507–12.
23. Hsu, J. & Speyer, R. F., Influences of zirconia and silicon nucleating agents on the devitrification of $Li_2O{\cdot}Al_2O_3{\cdot}6SiO_2$. *J. Am. Ceram. Soc.*, **73**(12) (1990) 3585–93.

Journal of the European Ceramic Society 15 (1995) 1119–1124
© 1995 Elsevier Science Limited
Printed in Great Britain. All rights reserved
0955-2219(95)00093-3
0955-2219/95/$9.50

Crystallization of Metastable Tetragonal Zirconia from the Decomposition of a Zirconium Alkoxide Derivative

David E. Collins, Kirk A. Rogers & Keith J. Bowman*

School of Materials Engineering, Purdue University, West Lafayette, IN 47907, USA

(Received 24 February 1995; revised version received 19 May 1995; accepted 22 May 1995)

Abstract

A zirconium alkoxide derivative, dibutoxybis(acetylacetonato) zirconium, was polymerized at 120°C and 300 millitorr for 3 h to form oligomers, as characterized by gel permeation chromatography and Fourier transform infra-red spectroscopy. Pyrolysis of the precursor at 675°C in flowing 5% H_2 in N_2 followed by cooling to room temperature, produced nano-scale, tetragonal ZrO_2 considerably below the tetragonal-to-monoclinic transformation temperature (approximately 1200°C). Subsequent heat treatment of the same precursor in flowing air under otherwise identical conditions produced approximately 8 vol% monoclinic ZrO_2. The possible formation of oxygen vacancies from polymer pyrolysis and their role in nucleating the metastable tetragonal phase are discussed.

1 Introduction

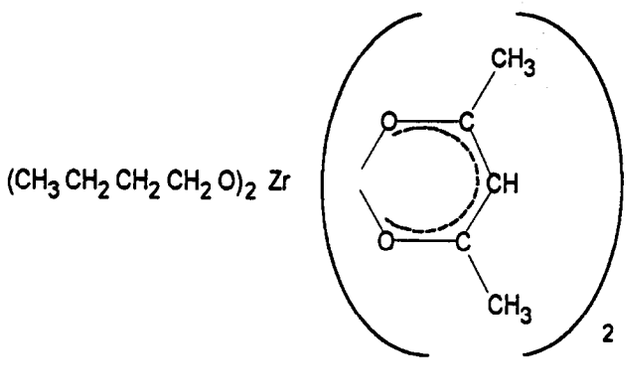
It has been well documented[1–4] that the pyrolysis of zirconium-based precursors produces a metastable tetragonal phase below the monoclinic–tetragonal transition temperature (approximately 1200°C) with crystallite sizes reported in the range of 5 to 460 Å.[2,3] Several investigators,[5–7] including Livage *et al.*[1] and Clearfield,[8] have speculated that the metastability of tetragonal zirconia (t-ZrO_2) is attributed to the structural similarities between the precursor phase and the tetragonal phase. In conjunction with these structural similarities, Livage *et al.*[1] and Osendi *et al.*[3] discussed the nonstoichiometry associated with the metastable tetragonal phase. By crystallizing ZrO_2 from zirconyl chloride *in vacuo*, Livage *et al.*[1] showed that a nonstoichiometric tetragonal phase predominated, whereas crystallization in air produced the monoclinic phase. From electron paramagnetic resonance studies on ZrO_2 crystallized from zirconyl chloride, Osendi *et al.*[3] concluded that tetragonal metastability results from lattice defects, specifically anionic vacancies, created upon crystallization. More recently, Igawa *et al.*[9] refined crystal structure calculations for the metastable tetragonal phase using neutron diffraction and Rietveld analysis on ZrO_2 crystallized from $Zr(O(CH_2)_3CH_3)_4$. They concluded that the crystal lattice coincided with those of doped tetragonal structures rather than pure t-ZrO_2 at 1200°C. However, in all of these cases, the origin of nonstoichiometry is unclear.

In spite of this ambiguity, these conclusions suggest that ZrO_2 crystal structure might be tailored by the choice of precursor and processing. An appealing application would be the formation of t-ZrO_2 with a preferred orientation caused by the processing of oriented, zirconium-based polymers. For such a processing strategy to be successful, the molecular configuration of the polymer must influence the final crystal structure. Establishing the existence of such a relationship relies on a full understanding of the precursor-to-ceramic transition. However, what factors influence structure on the molecular level during pyrolysis remain a critical issue not resolved in the literature. Although our intent is to control zirconia crystallization, the underlying goal is to address metallo-organic decomposition from a molecular standpoint. In this paper, we describe a mechanism by which the molecular configuration of a zirconium-based polymer might influence structural features in the pyrolysis product.

2 Experimental Procedure

Dibutoxybis(acetylacetonato) zirconium (BAZ), represented as:

*To whom correspondence should be addressed.



was obtained in a 60 wt% solution of n-butanol (97% pure 2:1 (alkoxide-to-zirconium); the remaining 3% is 1:1) from Gelest Inc., Tullytown, PA, USA. The excess n-butanol was distilled from the solution *in vacuo*, resulting in a yellow oil. Similar to the method described by Yogo,[10] the remaining BAZ was refluxed for 3 h at 120°C and 300 millitorr such that a reddish-brown gel was formed upon cooling to room temperature. To remove the retained solvent, samples were dried in flowing 5% H_2 in N_2 (300 cm^3 min^{-1}) at 200°C for 12 h, producing a fine orange powder. Samples were then fired at 675°C in a flowing gas, either H_2 in N_2 or air (300 cm^3 min^{-1}), and then allowed to cool to room temperature.

Fourier transform infra-red spectroscopy (FTIR), performed on a Nicolet 550 infra-red spectrometer, was used to identify structural features of the polymerized complex. The analysis was restricted to vibrational energies in the mid-infra-red spectrum, corresponding to a wavenumber range of 4000–400 cm^{-1}. For this study, neat samples were prepared by dispersing ground samples onto NaCl plates. Gel permeation chromatography (GPC), by Lark Enterprises, Webster, MA, USA, was used to determine the relative molecular weight and shape of the polymerized complex in solution as compared with a polystyrene standard. Styragel HR 2, 1, and 0·5 columns, employed for the analysis, were operated at 37°C using tetrahydrofuran as the mobile phase. A low molecular weight oligomer mix of polystyrene was used as a standard for calibration. Transmission electron microscopy (TEM) samples were prepared by grinding the samples with a mortar and pestle into a powder that could be applied to a graphite-coated Cu grid using acetone as the carrying medium. A JEOL 2000 FX operated at 200 kV was used to conduct bright-field imaging and selected-area diffraction (SAD) studies.

X-ray diffraction (XRD) performed on a Siemens D500 diffractometer with CuKα radiation was used to determine the phases present and the crystallite size using the Scherrer equation with respect to the {1 1 1} reflections.[11] The monoclinic volume fraction, v_m, was calculated from the linear intensity relationship

$$v_m = \frac{I_m(\bar{1}\,1\,1) + I_m(1\,1\,1)}{I_m(\bar{1}\,1\,1) + I_m(1\,1\,1) + I_t(1\,1\,1)} \quad (1)$$

where the subscripts m and t represent monoclinic and tetragonal, respectively. Although eqn (1) is consistent with literature on this topic, several investigators[12–14] have demonstrated that v_m calculated from eqn (1) can deviate from the actual v_m as much as 20% at $v_m = 0{\cdot}46$. Modifications based on structure factor calculations have been suggested,[12] unfortunately, an accurate diffraction model for metastable ZrO_2 that addresses stoichiometry and corresponding ionic position remains to be developed.

3 Results and Discussion

3.1 Molecular structure

The FTIR spectra in Fig. 1 impart information regarding the molecular structure and the precursor-to-ceramic transition of this organozirconium complex. The peak assignments were made by comparison to similar metal alkoxides[15,16] and metal bisacetylacetonate complexes.[17–19] Table 1 lists the observed frequencies and band assignments for this zirconium complex.

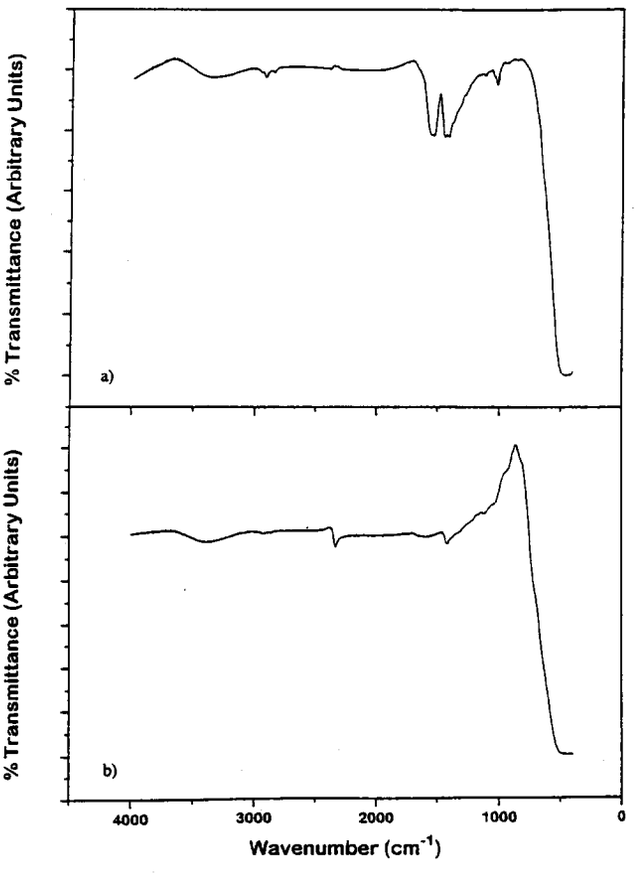
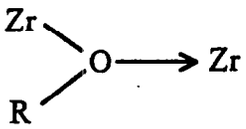


Fig. 1. Fourier transform infra-red (FTIR) spectra of (a) dried sample and (b) sample pyrolysed at 675°C.

Table 1. Observed frequencies and band assignments of *cis*-oligo[dibutoxybis(acetylacetonato) zirconium] (COBAZ) dried at 200°C; ν denotes stretching frequencies, δ denotes deformation frequencies

Observed frequencies (cm^{-1})	*Band Assignments*
3350	ν –OH
2920	ν –CH
2850	ν –CH
1550	ν C = O
1453	δ $-CH_3$
1420	δ –CH
1120	ν C – O
1025	ν Zr = O
452	ν Zr – O – Zr

The residual–OH bands in the spectra of the dried sample (Fig. 1(a)) result from possible hydrolysis of butoxy groups. The absence of bands ascribed to acetylacetonate (acac), such as Zr =O and $-CH_3$, in the spectra taken of the pyrolysed sample at 675°C in air (Fig. 1(b)) signify bidentate ligand decomposition during the pyrolysis process, leaving only the Zr–O–Zr bonds. These oxo bonds are consistent with investigations by Barraclough *et al.*[15] and Bradley *et al.*[20] which have shown that zirconium atoms, similar to other metal atoms, can be electrostatically bonded as follows:



where R represents $CH_3(CH_2)_3$ in this case.

Figure 2 shows the resulting GPC chromatograph of the precursor. The broad peak corresponds to a wide range of molecules having similar molecular weights, whereas the distinct peaks correspond to large concentrations of specific low molecular weight molecules. Preliminary GPC data indicated that the precursor molecular weight was less than the monomer

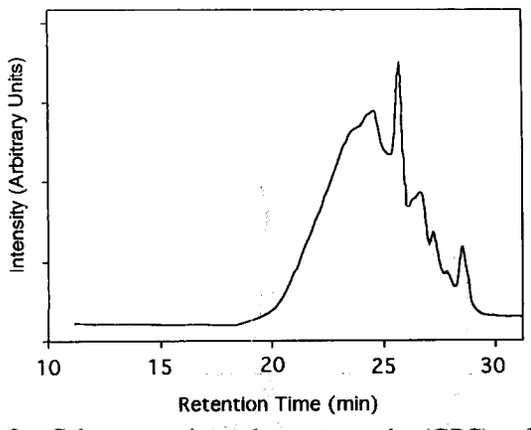


Fig. 2. Gel permeation chromatograph (GPC) of *cis*-oligo[dibutoxybis(acetylacetonato) zirconium] (COBAZ) in tetrahydrofuran.

Table 2. The molecular weight and average degree of polymerization as determined by gel permeation chromatography (GPC)

Retention time (min)	*Molecular weight (g mol^{-1})*	*Degree of polymerization*	*Average degree of polymerization*
29·15	335·99	0·77	
28·65	434·91	1·00	0·98
28·35	507·75	1·17	
27·60	747·76	1·72	
27·50	787·36	1·81	1·91
27·12	957·97	2·20	
27·00	1019·18	2·34	
26·80	1130·00	2·60	2·90
26·08	1638·58	3·77	
26·04	1672·80	3·85	
25·80	1893·35	4·35	4·24
25·72	1973·16	4·54	
25·23	2540·95	5·84	
24·68	3375·03	7·76	19·52
24·38	3940·24	9·06	
24·10	4552·87	10·47	
23·53	6110·13	14·05	
20·42	30419·85	69·93	

molecular weight, suggesting that the precursor was retained in the column more readily than the polystyrene standard; possibly due to apparent molecular size or packing interactions. From this observation, the molecular weight distribution was normalized to the last eluted peak, corresponding to the monomer molecular weight. Table 2 lists the molecular weight ranges assigned to the remaining peaks. Once normalized, the values of the adjacent peaks 2, 3 and 4 correspond to a dimer, trimer and tetramer, respectively.

The molecular architecture of these oligomers depends on the *cis*- or *trans*-configuration of the monomer as shown by Bradley and Holloway in an analogous system.[21,22] In their study, proton nuclear magnetic resonance (H^1 NMR) analysis of titanium bisacetylacetonate derivatives $(Ti(acac)_2(OR)_2$ where R represents Me, Et, Pr^i, Bu^t groups, etc.) demonstrated that the *cis*-isomer is favoured over the *trans*-isomer. Following this premise, the *cis*-monomers combine by alkoxy bridges, as described by Thomas,[23] forming oligomers during polymerization. The resulting oligomers, *cis*-oligo[dibutoxybis(acetylacetonato) zirconium] (COBAZ), have a host of structural isomers dependent on this *cis*-configuration and steric factors associated with the organic ligands. Two possible structures, a 'linear' and a cyclic configuration, of a tetrameric oligomer are depicted schematically in Fig. 3. For clarity, the $CH_3(CH_2)_3$ groups bonded to the oxygens that bridge the zirconiums together have been left off. Within the COBAZ backbone, each zirconium has an eight-fold coordination with oxygen; however, each zirconium in

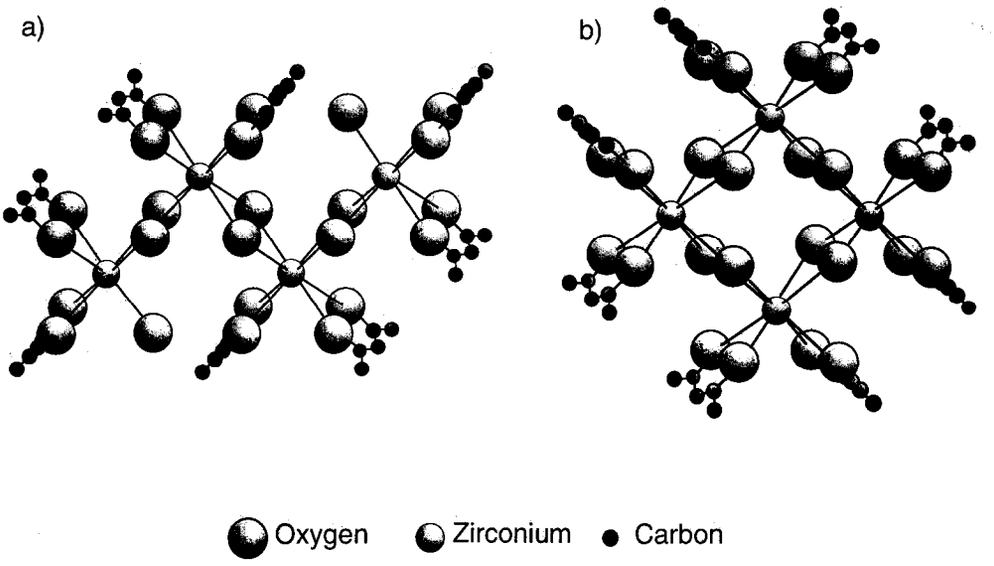


Fig. 3. Molecular structures of (a) 'linear' and (b) cyclic tetrameric *cis*-oligo[dibutoxybis(acetylacetonato) zirconium] (COBAZ). Hydrogen atoms and alkyl groups have been omitted for clarity.

the terminal positions has a seven-fold coordination due to an unshared alkoxy ligand not used in bridging, see Fig. 3(a). The acetylacetonate ligands, which hinder reaction due to steric obstruction during the polymerization process,[24] form the perimeter of the oligomer.

3.2 Pyrolysis

Although the COBAZ XRD data do not demonstrate any long-range order, brightfield imaging and SAD in TEM show (see Fig. 4) COBAZ to comprise nano-scale crystallites. Pyrolysing these COBAZ crystallites under reducing conditions of flowing 5% H_2 in N_2 produces a completely tetragonal oxide (see Fig. 5(a)), black from incomplete combustion of the organic material. The average crystallite size, approximately 110 Å, falls within such a range that line broadening masks resolution of the {200}, {220} and {113} peaks. The same sample annealed in flowing air under otherwise identical conditions shows the emergence of the (1 1 1) and ($\bar{1}$ 1 1) peaks of the monoclinic phase as can be seen in Fig. 5(b). XRD data indicate that



Fig. 4. Transmission electron micrograph (TEM) and selected-area diffraction (SAD) data of the dried precursor.

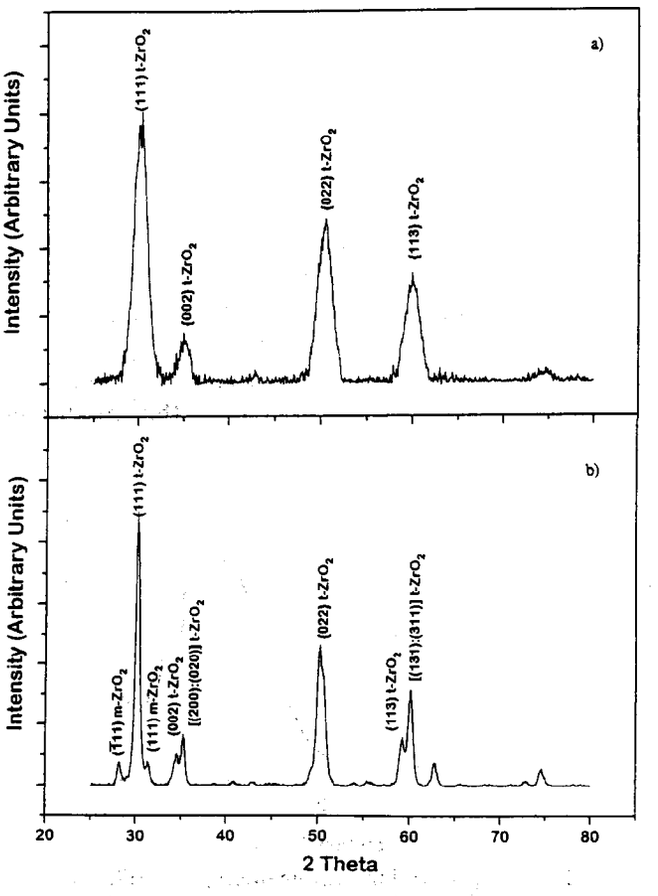


Fig. 5. X-ray diffraction (XRD) data of sample pyrolysed at 675°C in (a) flowing 5% H_2 in N_2 and (b) flowing air.

after 12 h of exposure to oxygen in air, 8 vol% of the tetragonal phase with an average crystallite size of approximately 480 Å underwent a phase transformation to m-ZrO_2 with a crystallite size of 570 Å. Furthermore, the resulting white powder was more friable after exposure to oxygen, indicative that the transformation had occurred.

Interpretation of this outcome can be related to significant structural features on the molecular level. Analogous to zirconyl chloride, COBAZ has a similar molecular structure to the t-ZrO_2 crystal lattice with the exception of the terminal positions. Upon heat treatment, the organic material decomposes, allowing the alkoxy bridges to undergo oxolation, the process by which the alkoxy bridges convert to oxygen bridges. At this point, the eight-fold coordination of zirconium within the oligomeric chain is retained, which is also true of the seven-fold coordination of the terminal zirconium. Upon pyrolysis, the terminal positions become likely sites for lattice defects, more specifically oxygen vacancies. We propose that these defects retained from the COBAZ structure are instrumental in producing the tetragonal phase during nucleation of the ZrO_2 crystallites under oxygen-deficient conditions. A similar phenomenon has been documented for other martensite systems in which point defects sustain tetragonality.[25] This inception of lattice defects based on the initial structure of the precursor may also explain the nonstoichiometry that Livage *et al.*[1] and Osendi *et al.*[3] saw in their investigations.

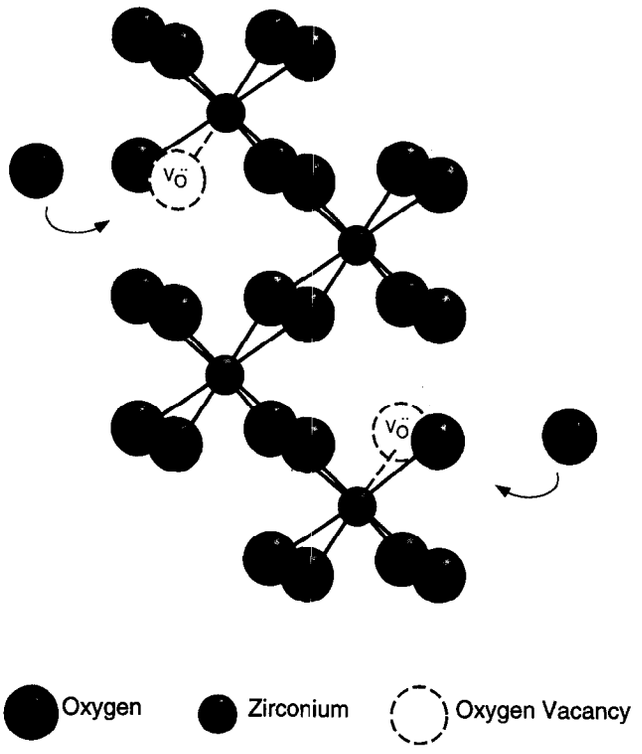


Fig. 6. Schematic of oxygen movement into oxygen vacancies that act as dopants to stabilize the tetragonal phase of zirconia during crystallization of a zirconium-based polymer. The polymer is at a point in pyrolysis in which the organic material has decomposed.

Akin to the work of Igawa *et al.*,[9] the resulting nano-crystallite, metastable t-ZrO_{2-x} should have lattice parameters similar to those of doped zirconias at room temperature. The probability of transformation to the monoclinic phase during this onset of nucleation may be relatively small due to the crystallite size.[26] Upon further heat treatment in the presence of oxygen, the anionic vacancies fill as depicted in Fig. 6. A sufficient decrease in the number of these vacancies should facilitate instability in the metastable tetragonal phase. Our results also show that crystallite coarsening and residual carbon accompany the pyrolysis. Because the metastable phenomenon also occurs in the zirconyl chloride system which is devoid of residual carbon, its actual influence is questionable; however, evidence that carbon may stabilize nonstoichiometry has been found in the literature and cannot be ignored.[27] Unfortunately, assessing the role that these factors play in nucleation, transformation and stability of metastable, tetragonal crystallites is not easily accomplished.

4 Summary

To address metallo-organic decomposition on the molecular level, we have found that the molecular configuration of the precursor, COBAZ, and the resulting oxide after pyrolysis are intimately related. We propose that zirconium, within the COBAZ backbone, has an eight-fold coordination to oxygen, similar to the t-ZrO_2 unit cell; whereas terminal zirconium has a seven-fold coordination. When pyrolysed in the absence of oxygen, COBAZ nucleates a completely t-ZrO_{2-x} bearing oxygen vacancies retained from the COBAZ structure, particularly from the terminal zirconium positions. These vacancies play an integral role in tetragonal nucleation. When t-ZrO_{2-x} is heat treated in the presence of oxygen under otherwise identical conditions, a fractional amount of monoclinic phase develops. This introduction of oxygen diminishes the number of vacancies such that tetragonal instability occurs, facilitating monoclinic growth.

Acknowledgments

We would like to thank H. Lackritz, K. Trumble and E. Slamovich for their insightful contributions to this investigation. This research was supported by The National Science Foundation DMR-91-21948.

References

1. Livage, J., Doi, K. & Mazieres, C., Nature and thermal evolution of amorphous hydrated zirconium oxide. *J. Am. Ceram. Soc.*, **51**(6) (1968) 349–53.
2. Mitsuhashi, T., Ichihara, M. & Tatsuke, U., Characterization and stabilization of metastable tetragonal ZrO_2. *J. Am. Ceram. Soc.*, **57**(2) (1974) 97–101.
3. Osendi, M., Moya, J., Serna, C. & Soria, J., Metastability of tetragonal zirconia powders. *J. Am. Ceram. Soc.*, **68**(3) (1985) 135–9.
4. Tani, E., Yoshimura, M. & Somiya, S., Formation of ultrafine tetragonal ZrO_2 powder under hydrothermal conditions. *J. Am. Ceram. Soc.*, **66** (1983) 11–14.
5. Fryer, J., Hutchison, J. & Paterson, R., An Electron microscopic study of the hydrolysis products of zirconyl chloride. *J. Colloid Interface Sci.*, **34**(2) (1970) 238–48.
6. Mamott, G., Barnes, P., Tarling, S., Jones, S. & Norman, C., Dynamic studies of zirconia crystallization. *J. Mater. Sci.*, **26** (1991) 4054–61.
7. Turrillas, X., Barnes, P., Tarling, S., Jones, S., Norman, C. & Ritter, C., Neutron thermodiffractometry and synchrotron energy-disperive diffraction studies of zirconium hydroxide calcination. *J. Mater. Sci. Let.*, **12** (1993) 223–6.
8. Clearfield, A., Structural aspects of zirconium chemistry. *Rev. Pure Appl. Chem.*, **14** (1964) 91–108.
9. Igawa, N., Ishii, Y., Nagasaki, T., Morii, Y., Funahashi, S. & Ohno, H., Crystal structure of metastable tetragonal zirconia by neutron powder diffraction study. *J. Am. Ceram. Soc.*, **76**(10) (1993) 2673–6.
10. Yogo, T., Synthesis of polycrystalline zirconia fiber with organozirconium precursor. *J. Mater. Sci.*, **25** (1990) 2394–8.
11. Klug, H. & Alexander, L., *X-Ray Diffraction Procedures.* John Wiley & Sons Inc., New York, 1954.
12. Toraya, H., Yoshimura, M. & Somiya, S., Quantitative analysis of monoclinic-stabilized cubic ZrO_2 systems by X-ray diffraction. *J. Am. Ceram. Soc.*, **67**(6) C183–121.
13. Evans, P., Stevens, R. & Binner, J., Quantitative X-ray diffraction anaylsis of polymorphic mixes of pure zirconia. *Br. Ceram. Trans. J.*, **83**(2) (1984) 39–43.
14. Schmid, H., Quantitative analysis of polymorphic mixes of zirconia by X-ray diffraction. *J. Am. Ceram. Soc.*, **70**(5) (1987) 367–76.
15. Barraclough, C., Bradley, D., Lewis, J. & Thomas, I., The infrared spectra of some metal alkoxides, trialkylsilyloxides, and related silanols. *J. Chem. Soc.*, (1961) 2601.
16. Lynch, C., Mazdiyasni, K., Smith, J. & Crawford, W., Infrared spectra of transition metal alkoxides. *Anal. Chem.*, **36** (1964) 2332.
17. Mikami, M., Nakagawa, I. & Shimanouchi, T., Far infra-red spectra and metal–ligand force constants of acetylacetonates of transition metals. *Spectrochim. Acta*, **23A** (1967) 1037.
18. Nakamoto, K., *Infrared Spectra of Inorganic and Coordination Compounds.* John Wiley & Sons, Inc., New York, 1970.
19. Barraclough, C., Lewis, J. & Nyholm, R., The stretching frequencies of metal–oxygen double bonds. *J. Chem. Soc.*, (1959) 3552.
20. Bradley, D., Mehrotra, R., Swanwick, J. & Wardlaw, W., Structural chemistry of the alkoxides. Part IV. Normal alkoxides of silicon, titanium, and zirconium. *J. Chem. Soc.*, (1953) 2025–30.
21. Bradley, D. & Holloway, C., Some Labile cis-dialkoxybis (aceylacetonato) titanium (IV) compounds. *Chem. Commun.*, (1965) 284.
22. Bradley, D. & Holloway, C., Nuclear magnetic resonance and infrared spectral studies on labile cis-dialkoxy-bis (acetylacetonato) titanium (IV) Compounds. *J. Chem. Soc. (A)*, (1969) 282.
23. Thomas, A., *Colloid Chemistry* McGraw-Hill Book Co., Inc., New York, 1934.
24. Papet, P., Le Gars, N., Baumard, J., Lecomte, A. & Dauger, A., Trasparent monolithic zirconia gels: effects of acetylacetone content on gelation. *J. Mater. Sci.*, **24** (1989) 3850–4.
25. Winchell, P. & Speich, G., Point-defect-supported martensite tetragonality. *Acta Met.*, **18** (1970) 53–62.
26. Garvie, R., The occurrence of metastable tetragonal zirconia as a crystallite size effect. *J. Phys. Chem.*, **69**(4) (1965) 1238–43.
27. Ackermann, R., Garg, S. & Rauh, E., High-temperature phase diagram for the system Zr–O. *J. Am. Ceram. Soc.*, **60** (7–8) (1977) 341–5.

Journal of the European Ceramic Society 15 (1995) 1125–1134
© 1995 Elsevier Science Limited
Printed in Great Britain. All rights reserved
0955-2219(95)00083-6
0955-2219/95/$9.50

Moisture Sensitive Degradation in TiO_2–Y_2O_3–ZrO_2

A. E. Hughes,[a]* H. St John,[b] P. Kountouros[c]† & H. Schubert[c]

[a]C.S.I.R.O., Division of Materials Science and Technology, Private Bag 33, Rosebank MDC, Clayton, 3169, Victoria, Australia
[b]C.S.I.R.O., Division of Chemicals and Polymers, Private Bag 33, Rosebank MDC, Clayton, 3169, Victoria, Australia
[c]Max-Plank-Institut für Metallforschung, Institut für Werkstoffwissenschaft, Pulvermetallurgisches Laboratorium, Heisenbergstraße 5, 7000 Stuttgart 80, Germany

(Received 19 January 1995; revised version received 18 May 1995; accepted 19 May 1995)

Abstract

Sintered discs (1450°C) of yttria–stabilised tetragonal zirconia (3 mol% Y_2O_3) with additions of 1, 10 and 20 mol% TiO_2, were treated in distilled water in an autoclave at 170°C for times up to 144 h. X-ray diffraction (XRD) and X-ray photoelectron spectroscopy (XPS) were used to monitor changes which occurred at the surface of the discs during autoclave treatment. The addition of TiO_2 retarded the transformation of the tetragonal (t)-phase to monoclinic (m)-phase as determined by XRD. During autoclave treatment an increase in the Ti/Zr ratio, decrease in the Y/Zr ratio and a peak in the percentage Zr^{3+} were observed using XPS. Furthermore, at long autoclave treatment times there was a surface oxygen enrichment in excess of that expected from the stoichiometry. The data have been interpreted in terms of vacancy annealing and the rate of transformation to m-ZrO_2 appears to be related to the presence of Zr^{3+}, adsorbed water and substitutional cations such as Ti^{4+} in modifying adsorption sites at the surface.

1 Introduction

Sintered and fully dense Y_2O_3–stabilized tetragonal zirconia polycrystal (Y–TZP) undergoes an unusual surface degradation at low temperatures (100–500°C) during exposure to air saturated with water vapour or autoclave treatment. The degradation is most pronounced at ~250°C and is characterized by a loss of mechanical properties[1–4] as a result of microcracking, spalling or even complete collapse of the sintered body.[5–8] The surface degradation has been shown to be due to transformation of the surface tetragonal (t) grains to monoclinic (m) phase and the microcracking results from the volume expansion associated with the transformation to the m-phase. Hence the longer the exposure time to moist environments the deeper the transformation zone and the more dire the consequences for the mechanical properties of the sintered bodies.[2,6–11]

The amount of transformation depends on grain size and yttria content of the Y–TZP.[5,11] For example, Watanabe *et al.*[3] found that the critical grain size below which no transformation occurred, increased from 0·2 to 0·6 μm as the yttria content of the Y–TZP increased from 2 to 5 mol% Y_2O_3. As the yttria content is increased the t-phase becomes more stable on a thermodynamic basis and consequently there is less transformation to the m-phase.[2,5]

Various models have been proposed to explain the low-temperature degradation of Y–TZP. Lange *et al.*[11] suggested that α-$Y(OH)_3$ formation created yttria-poor regions at grain surfaces which act as nucleation sites for the m-phase. Sato and Shimada[12] proposed that water vapour attack at pre-existing flaws resulted in crack propagation by scission of Zr–O–Zr bonds and formation of Zr–OH, releasing the strain which stabilizes the t-phase thus promoting the t→m transformation. Similarly, Yoshimura[13,14] proposed that water attack produces scission of the bridging surface oxygen groups resulting in Zr–OH or Y–OH formation thus opening up the subsurface region to further attack by H_2O and eventual crack propagation. However, in his case it was a stress corrosion cracking mechanism since the stress field at the crack tip induces the t→m transformation.

Another class of models considers the destabilization of the t-phase via annealing of the anion vacancies with a range of species, i.e. occupation

*Author to whom correspondence should be addressed.
†Present Address: Research Centre Jülich, Institute for Materials in Energy Systems, D-52425, Jülich, Germany.

of the anion vacancies with anions. Narita *et al.*[15] suggested that water reacts with anion vacancies to produce interstitial hydrogen ions and oxygen anions which occupy anion vacancies (annealing) leading to the destabilization of the t-phase. Hughes *et al.*[8] also concluded that the moisture sensitivity of Y–TZP was related to annealing of anion vacancies by O^{2-} anions. In their experiments they observed an increase in the oxygen anion/zirconium ratio during exposure to moist air at 200°C using X-ray photoelectron spectroscopy (XPS). Lepitso and Māntylā[10] also concluded that anion vacancy annealing by O^{2-}accompanied by grain boundary attack, promoted the t→m transformation. Kountouros and Petzow[16] have shown that oxygen vacancies play a decisive role in the stability of the t-phase (and c-phase) and argue that vacancy annealing by oxygen anions promotes the t→m transformation. Furthermore elastic recoil detection analysis (ERDA) spectra on TZP-samples degraded in D_2O-rich water have shown that H- and D-atoms penetrate the lattice.[17]

Much effort has been devoted to reducing or even eliminating the low-temperature degradation effect. In a number of studies the effects of different substitutional cations have been examined. For example, Sato and Shimada[18] observed that Al_2O_3 or CeO_2 additions provided some degree of control of the moisture sensitive degradation. Based on free energy considerations they concluded that the t-phase was stabilized, in the case of Al_2O_3 addition, by increasing the strain energy of the constraining matrix and for alloying with CeO_2 by increasing the chemical free energy. XPS studies by Theunissen *et al.*[19] and Duran *et al.*[20] suggested that protection of the t-phase in ternary systems containing CeO_2 and TiO_2 was imparted by surface segregation of Ce^{4+} and Ti^{4+} and formation of protective overlayers on the external surface and possibly in the grain boundary. Kountouros and Petzow[16] have noted that the activation energy for total ionic conductivity increases significantly in the presence of Ti^{4+} hence oxygen anions may become 'locked' in lattice sites due to changed bonding conditions. Under such circumstances, if there is surface enrichment of Ti^{4+} a semi-impenetrable 'vacancy-annealed barrier' may be set up protecting the interior of the grain from further vacancy annealing and consequently retarding the transformation to the m-phase.

The development of such a large variety of models to describe the one phenomenon is a consequence of the limited control over processing variables during sample preparation which significantly alter the microstructure and consequently the extent of transformation. Processing variables such as sintering times, temperatures and atmospheres can significantly alter; grain growth, average grain size, grain size distributions, yttria disproportionation, impurity phase distribution within the grain boundary network and soluble impurity distributions within grains. Furthermore, many spectroscopic studies have examined the surfaces of degraded specimens only after severe treatments rather than during transformation. For example, it is only *after* extensive autoclave or moist air treatment that either hydroxide formation has been observed using XPS[7,10,20] or significant OH^- formation has been observed using Fourier Transform Infrared (FTIR) spectroscopy.[13,15,21]

In this paper the authors have examined the effects of the addition of Ti^{4+} as a substitutional cation for Z^{4+}, on the stability of Y–TZP during autoclave treatment at 170°C. X-ray diffraction (XRD) has been used to monitor the generation of the m-phase, while XPS has been used to study chemical changes at the surface.

2 Experimental

2.1 Sample preparation

The details of preparation of the TiO_2–Y_2O_3–ZrO_2 samples has been given in detail elsewhere.[22] Briefly, powders were prepared by co-precipitation during spraying of chloride solutions of $ZrOCl_2.8H_2O$, $YCl_3.6H_2O$ and $TiCl_3$ mixed in the required stoichiometry into ammonia solution. The precipitate was then washed several times in distilled water to ensure that it was Cl^- free, distilled azeotropically to dehydrate the powder and dried at 70°C. The powder was calcined at 950°C for 3 h, wet milled in ethanol with TZP balls, dried at 70°C and pressed into 1 × 1 cm cylinders at either 200 or 630 MPa. These cylinders were sintered in air by ramping at 100–1450°C, cooled, then cut, lapped and polished to a 1 μm finish. The three compositions of interest here had 3 mol% Y_2O_3 and either 1, 10 or 20 mol% TiO_2 and are designated Z3Y1T, Z3Y10T and Z3Y20T respectively. The samples were prepared in Germany and transported to Australia for analysis.

2.2 Autoclave treatments

The discs were subsequently placed in 40 cc of distilled water in an autoclave for times up to 144 h, which represented surface saturation of m-ZrO_2, at 170°C (0·792 MPa). After each treatment time the specimens were removed, examined by XRD and XPS, then given further autoclave treatment in fresh distilled water.

2.3 X-ray diffraction (XRD)

The m-phase content was determined by XRD using the (111)m, (11$\bar{1}$)m and (111)t reflections (Cu Kα radiation). In a preliminary series of experiments the development of m-ZrO_2 in the polished surface of Z3Y10T was monitored using XRD without any XPS experiments being made on the specimens. In subsequent series of experiments both XRD and XPS measurements were made on specimens of all compositions at each autoclave treatment time. No difference was found in the amount of m-phase generated with either the XRD or the XRD followed by XPS series of experiments, therefore the XPS has no effect on the generation of m-phase.

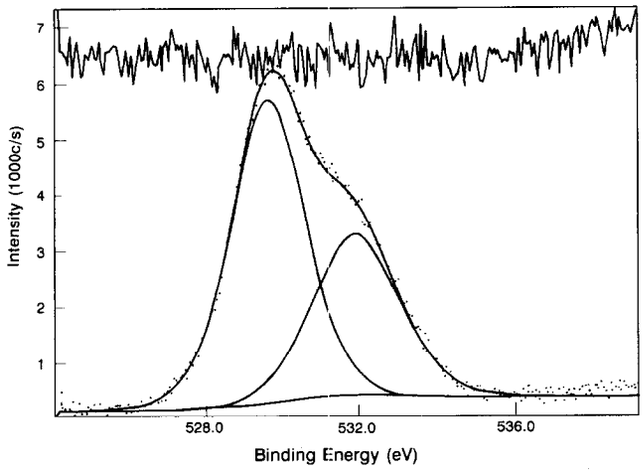


Fig. 1. Typical fit of Gauss/Lorentz product functions to an O 1*s* spectrum. Spectrum of Z3Y10T after 7 h treatment in an autoclave at 170°C. Oxygen anions contribute to the low binding energy component while adsorbed water or O_2^- contribute to the high binding energy component. Reduced χ^2 = 1·012 with 170 degrees of freedom.

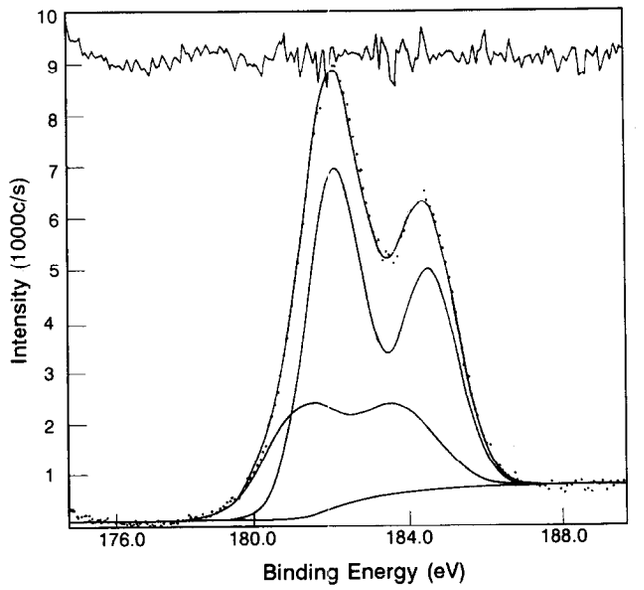


Fig. 2. Typical fit of doublets comprised of two Gauss/Lorentz product functions to a Zr 3*d* spectrum. Spectrum of Z3Y10T after 0·5 h treatment in an autoclave at 170°C. Zr^{3+} moieties contribute to the low binding energy component while Zr^{4+} cations contribute to the high binding energy component. Reduced χ^2 = 1·099 with 140 degrees of freedom.

2.4 X-ray photoelectron spectroscopy (XPS)

The experimental setup and quantification of results for XPS has been described previously.[23] Extensive analysis was made of the O 1*s* and Zr 3*d* spectra by curvefitting Gauss/Lorentz product functions. Two components, without any constraints, were fitted to each O 1*s* spectrum (Fig. 1). Two unconstrained Zr 3*d* doublets were fitted to the Zr 3*d* spectra. The Z_r^{4+} doublet had a fixed separation of 2·42 eV and relative intensity of 0·686, whereas the Zr^{3+} doublet had the same separation but the relative intensity was allowed to float and typically reached values of 0·8. The origin of this small additional intensity is not clear. A typical fit to the Zr 3*d* region is shown in Fig. 2.

3 Results

The %m-ZrO_2 generated in Z3Y1T, Z3Y10T and Z3Y20T as a function of treatment time in the autoclave at 170°C is presented in Fig. 3. It is clear that the development of the m-phase is retarded by increasing the TiO_2 content of the Y_2O_3–ZrO_2. Z3Y1T reached a saturation value of around 78%m-ZrO_2 after only 20 h treatment whereas the times to saturation with m-ZrO_2 for Z3Y10T and Z3Y20T was increased to around 70 and 144 h respectively.

It is important to note that because of the surface sensitivity of XPS, changes in the atomic ratios only reflect changes that occur in the surface grains. Hence it is worth attempting to estimate at what stage all surface grains have transformed to the m-phase. Assuming the analysis depth of XRD is approximately 7 μm[24] and the grain size and saturation value of m-phase are 1·3 μm and 78% respectively then the surface should be fully transformed between 7 and 8% m-ZrO_2, assuming transformation to a depth corresponding to half average grain size. (Recall that the surface is

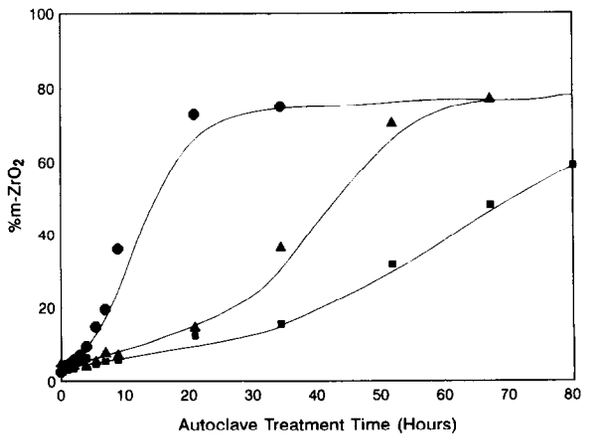


Fig. 3. %m-ZrO_2 phase content of the surface determined by XRD versus the autoclave treatment time at 170°C. (●) Z3Y1T; (▲) Z3Y10T and (■) Z3Y20T.

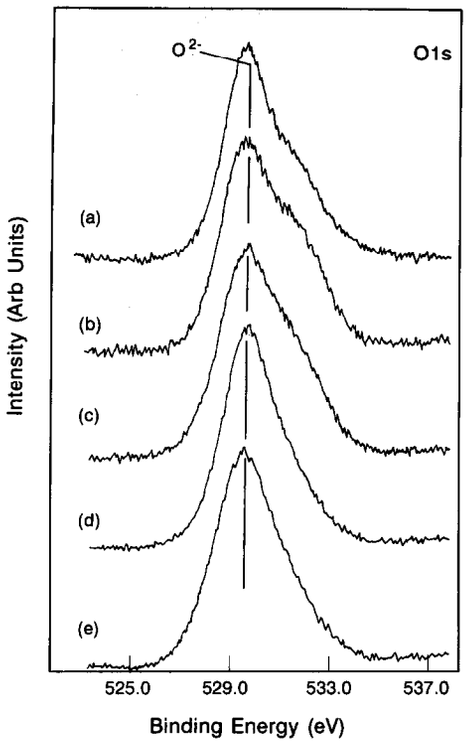


Fig. 4. Series of O 1*s* spectra displaying changes which occur as a result of autoclave treatment. (a) 0; (b) 4; (c) 7; (d) 9 and (e) 34 h.

polished so the surface layer is only half the average grain size in thickness.)

XPS measurements were made on the discs of Z3Y1T, Z3Y10T and Z3Y20T after each treatment time in the autoclave. It can be seen in Fig. 4 that significant changes occurred to the O 1*s* spectra as a function of autoclave treatment time as indicated by a change in the relative intensity from low to high binding energies. Curvefitting of the O 1*s* spectra revealed the presence of two components at 529·8 eV (O_I) and 532·2 eV (O_{II}). Previously four component fits were made to 3 mol%Y_2O_3–ZrO_2 after treatment in moist air at 200°C,[8,24] however, in this case no statistically significant fits could be obtained with either three or four components. The component O_I at 529·8 eV is typical of oxygen anions in lattice sites.[23,25] Adsorbed water[26] or O_2^-[27] are likely candidates for the O_{II} component at 532·2 eV. Hernandez *et al.*[7,20] attributed a high binding energy component at 532·8 eV in autoclave treated CeO_2–Y_2O_3–ZrO_2 to bound hydroxyl groups based on hydroxylation of transition metal compounds. However surface hydroxides on zirconia or yttria occur around 531 eV[28] and are unlikely to contribute to the O_{II} intensity. Likewise O_2^{2-}, which may be present on the surface, occurs at around 531·2 eV and therefore is unlikely to contribute to O_{II}.[28]

The dependence of the total oxygen to zirconium (O_{TOT}/Zr) atomic ratio as well as O_I/Zr and O_{II}/Zr on the autoclave treatment time are plotted

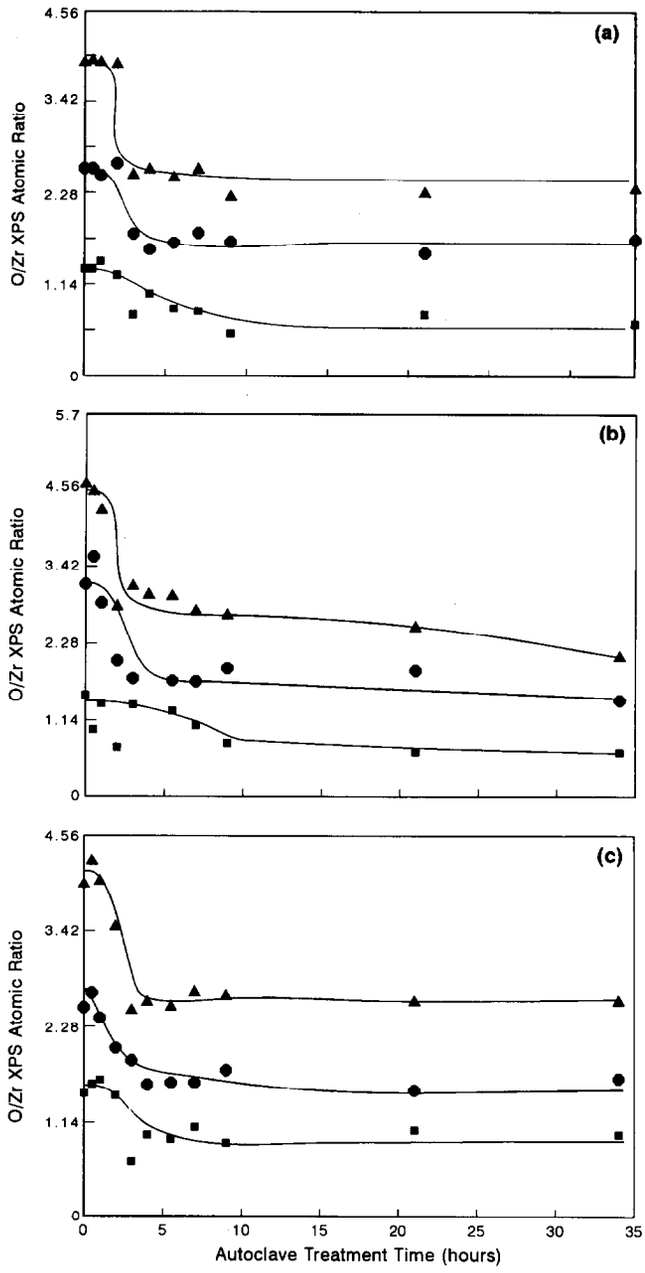


Fig. 5. (▲) O_{TOT}/Zr; (●) O_I/Zr low binding energy component due to oxygen anions and (■) O_{II}/Zr high binding energy component due to adsorbed water as a function of autoclave treatment time. (a) Z3Y1T; (b) Z3Y10T and (c) Z3Y20T.

in Figs 5(a)–(c). The O/Zr ratios displayed stepwise decreases between 1 and 2 h treatment time for Z3Y1T (Fig. 5(a)) and 2 and 3 h for Z3Y10T (Fig. 5(b)) and Z3Y20T (Fig. 5(c)) respectively. The stepwise decrease was partially obscured when the data were plotted as a function of %m-ZrO_2 suggesting that the loss of oxygen is not caused by the development of the m-phase. Indeed, the decreases occurred at much shorter times than those expected for surface saturation of the m-phase and most likely resulted from the removal of some surface carbon contamination of the specimens which may have originated during polishing and/or storage and transport. In the

presence of a carbon overlayer the high O/Zr ratios are most likely explained on the basis that the XPS is sampling a much smaller volume of the actual ceramic surface than for a material without the contaminating layer. (This was confirmed in repeat experiments on freshly polished surfaces where very little carbon was detected on the surface and the O/Zr ratio was around 1·8.) This would enhance the O/Zr signal since the external surface of the ceramic is oxygen rich. The O_{II} component displayed only a gradual decrease with increasing treatment time indicating an apparent reduction in the amount of adsorbed water. However, the $\%O_{II}$ of O_{TOT} goes through a peak as a function of autoclave treatment (Fig. 6).

Increasing autoclave treatment time also resulted in a loss of resolution in the normally well resolved Zr 3*d*5/2–3*d*3/2 spin-orbit doublet of the Zr 3*d* spectra, suggesting the presence of additional components (Fig. 7). These changes can be demonstrated, for example, by comparing the apparent loss of resolution of the Zr 3*d*5/2 and 3/2 doublet in Z3Y10T before autoclave treatment (Fig. 7(a)) with 4 and 7 h autoclave treatment at 170°C (Figs 7(b) and (c) respectively). Curve fitting of the Zr 3*d* spectra revealed two components corresponding to Zr^{4+} (182·2 ± 0·1 eV) and a second component at 181·4 ± 0·2 eV most probably due to the presence of Zr^{3+} (Fig. 2).[29,30]

Hughes *et al.*[24] have previously argued that the origin of the Zr^{3+} signal is most likely related to trapping of electrons at associated cation-vacancy pairs. Electron spin resonance (ESR) measurements indicate that associated vacancy-Zr cation moieties are efficient traps for low energy electrons.[31,32] The electron becomes trapped in the *d*-orbital resulting in a $4d^1$ configuration and Zr^{3+}. One source of low-energy electrons is the XPS experiment itself where photoelectrons undergo inelastic interactions within the solid thereby losing much of their kinetic energy. A second source of low energy electrons may arise with the exchange of O^{2-} with O_2. The broad 1/2 width of the low

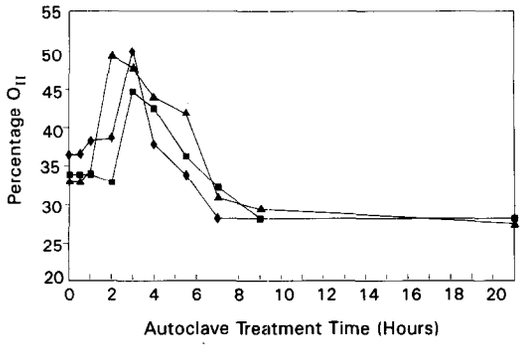


Fig. 6. Variation of $\%O_{II}$ with autoclave treatment time. (■) Z3Y1T, (▲) Z3Y10T and (♦) Z3Y20T.

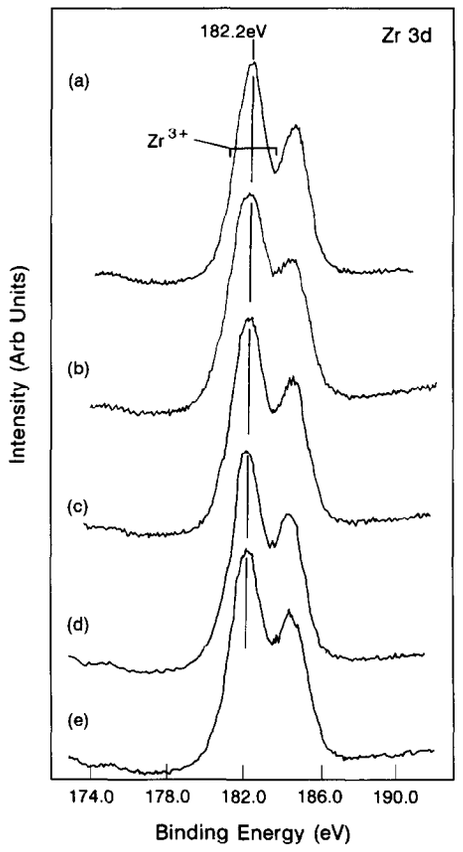


Fig. 7. Series of Zr 3*d* spectra displaying changes which occur as a result of autoclave treatment. (a) 0; (b) 4; (c) 7; (d) 9 and (e) 34 h.

binding energy Zr 3*d* component reflects a variety of Zr^{3+} configurations (Fig. 2). Regardless of their origin, these Zr^{3+} sites are important from the viewpoint of surface chemistry since ESR measurements indicate that they are co-ordinatively unsaturated but can co-ordinatively saturate through adsorption of species such as H_2O.[33,34]

The % Zr^{3+} determined from curvefitting, as a function of treatment time at 170°C is presented in Fig. 8. (As with the O/Zr ratios the $\%Zr^{3+}$ displayed no correlation with $\%m\text{-}ZrO_2$ phase content.) Although there is some scatter in the data it would seem that at short autoclave treatment

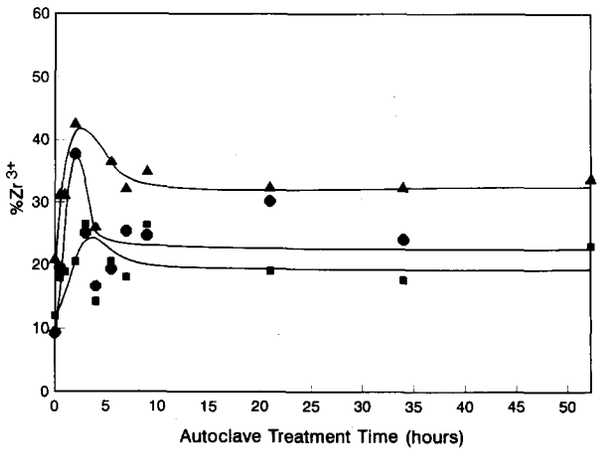


Fig. 8. % Zr^{3+} as a function of the autoclave treatment time at 170°C. (▲) Z3Y1T, (●) Z3Y10T and (■) Z3Y20T.

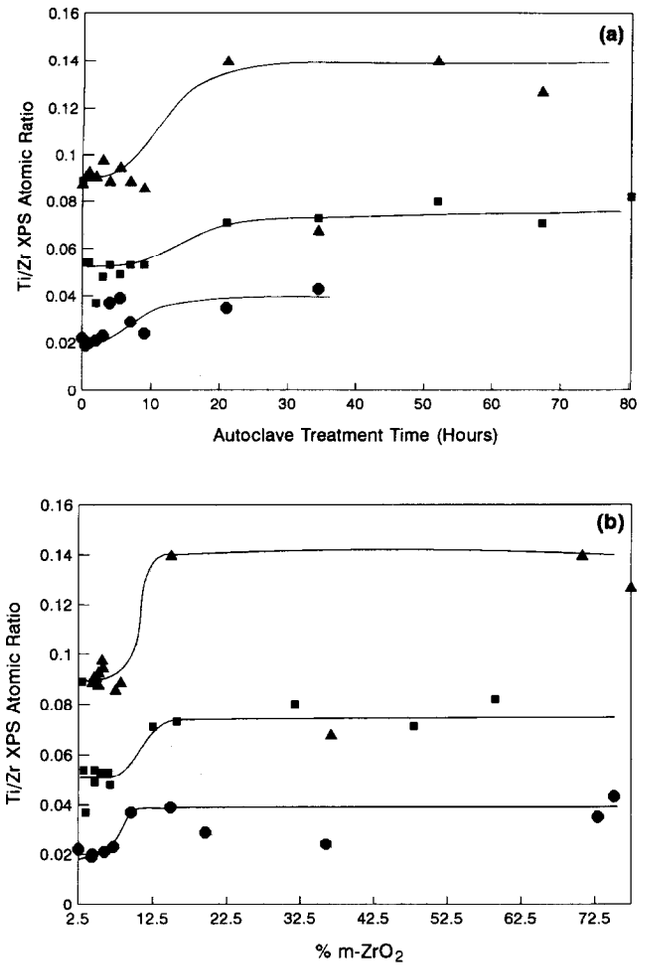


Fig. 9. Ti/Zr ratio versus (a) autoclave treatment time and (b) %m-ZrO_2. (●) Z3Y1T (■) Z3Y10T and (Δ) Z3Y20T.

times (between 2 and 4 h) there is a peak in the $\%Zr^{3+}$ but thereafter it remains constant. The peak maxima appear to be highest for Z3Y1T and Z3Y10T at around 40% Zr^{3+} but considerably less for Z3Y20T at approximately 25% Zr^{3+}.

While the O/Zr ratios and $\%Zr^{3+}$ appeared to depend primarily on the autoclave treatment time, the Ti/Zr ratios were a function of the m-phase content of the surface as clearly demonstrated in Fig. 9. The Ti/Zr ratios remained constant over the first few hours of autoclave treatment then exhibited a stepwise increase to new equilibrium values but this step was staggered in the time domain for the different compositions (Fig. 9(a)), but occurred in the single range 7–13%m-ZrO_2 for all compositions (Fig. 9(b)) which spans the region where there is complete saturation of the surface with m-phase.

The initial and final Ti/Zr atomic ratios are presented in Table 1 and compared to those expected from the stoichiometries of the different ceramics. For Z3Y1T all measured values of the Ti/Zr ratio indicate a surface enrichment of Ti^{4+}. The Ti/Zr ratio for untreated Z3Y10T indicated a small surface depletion of Ti^{4+}, which changed to enrichment after autoclave treatment. Severe surface depletion of Ti^{4+} was observed under all conditions for Z3Y20T. Z3Y10T exhibited nearly twice the level of surface Ti^{4+} compared to Z3Y20T which itself was twice the level of the Z3Y1T specimen, suggesting that there is a TiO_2 content which will give a maximum surface Ti enrichment. This is demonstrated in Fig. 10 where the Ti/Zr ratio displayed a clear maximum at 5 mol% TiO_2 for the as-sintered specimens.

Table 1. XPS and calculated Ti/Zr ratios after various treatments

Sample	*Untreated*[1]	*Treated*[2]	*Expected*[3]
Z3Y1T	0·022	0·038	0·010
Z3Y10T	0·088	0·14	0·115
Z3Y20T	0·055	0·079	0·26

[1]XPS atomic ratio measured on the surface prior to autoclave treatment.
[2]XPS atomic ratio measured after autoclave treatment for longer than 30 h.
[3]Calculated on the basis of bulk stoichiometry.

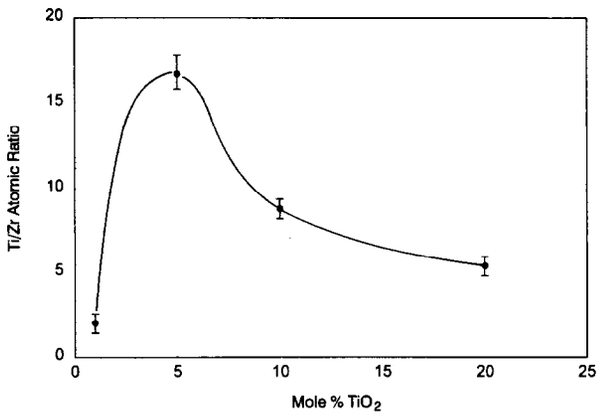


Fig. 10. Surface Ti/Zr ratio (by XPS) versus the bulk mol% TiO_2.

The Y/Zr ratios also displayed significant changes around 7% m-ZrO_2 phase content of the surface (Fig. 11). The initial and final values of the Y/Zr ratios are compared to the expected values in Table 2. The Y/Zr ratios for the untreated samples

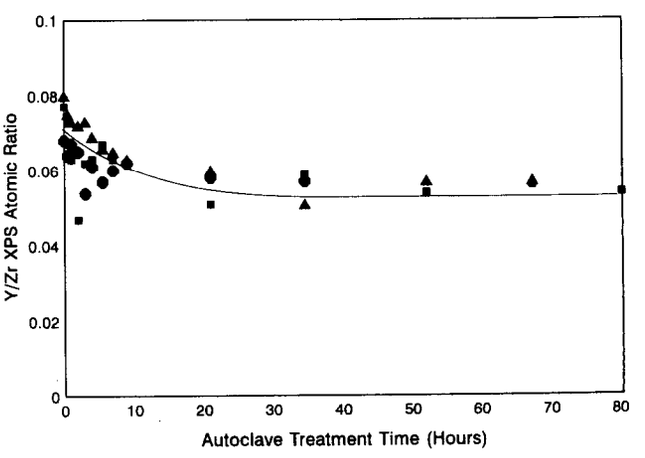


Fig. 11. Y/Zr ratio versus autoclave treatment time. (●) Z3Y1T, (▲) Z3Y10T and (■) Z3Y20T.

Table 2. XPS and calculated Y/Zr ratios after various treatments

Sample	*Untreated*[1]	*Treated*[2]	*Expected*[3]
Z3Y1T	0·068	0·058	0·0625
Z3Y10T	0·080	0·057	0·0690
Z3Y20T	0·077	0·055	0·0780

[1]XPS atomic ratio measured on the surface prior to autoclave treatment.
[2]XPS atomic ratio measured after autoclave treatment for longer than 30 h.
[3]Calculated on the basis of bulk stoichiometry.

all displayed either surface enrichment or ratios similar to the expected bulk values. After autoclave treatment all compositions displayed a depletion to a common value of around 0·057 ± 0·004.

4 Discussion

The most notable features of the XPS data were the decrease in the Y/Zr ratio and peaks in the $\%Zr^{3+}$ during the first 3 h treatment for all samples. Furthermore, there was an increase in the Ti/Zr ratio between 7 and 13%m-ZrO_2, a range which represents the complete transformation of surface grains to m-phase. These changes suggest that some local surface rearrangements must occur with respect to the starting compositions of the material. It would appear that these changes occur during a period where the surface is undergoing transformation to the m-phase but thereafter no further changes are observed.

The XPS data clearly deals with two different phenomena:

(i) Changes in the O/Zr ratios, particularly the $\%O_{II}$, and the % Zr^{3+}, which only depend on the autoclave treatment time and thus may herald changes in the surface chemistry which lead to the t→m phase transformation;
(ii) Changes in the Ti/Zr and possibly the Y/Zr ratios which are associated with cation redistribution as part of the m-phase transformation.

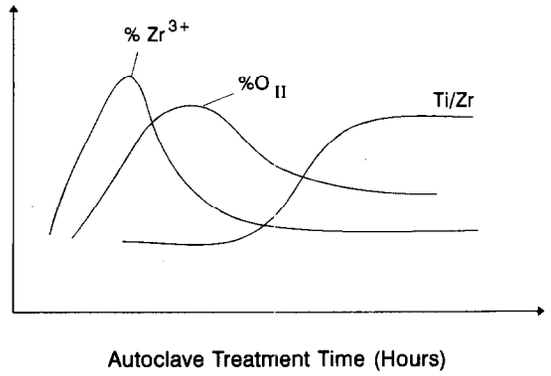


Fig. 12. Schematic representation of the temporal evolution of changes in the surface chemistry.

These changes are summarised schematically in Fig. 12.

4.1 Generation of Zr^{3+} and O_2^-

Changes in the surface chemistry appear to begin with an increase in the level of Zr^{3+} which is followed by an apparent change in the degree of occupation of surface anion sites by the O_{II} species (adsorbed water and probably superoxide). At much longer autoclave treatment times, where the surface is fully saturated with m-ZrO_2, the Ti/Zr ratios increase suggesting cation redistribution as a result of phase transformation.

In order to understand these changes this discussion will begin with the role of the Zr^{3+} sites and their influence on the O_{II} species drawing on the ESR studies of adsorbed H_2O and O_2^- on m-ZrO_2. Morterra *et al.*[33,34] have identified a number of different surface species and adsorption sites on m-ZrO_2. One of the important adsorption sites being the co-ordinatively unsaturated (cus)-Zr^{3+} centres which can co-ordinatively saturate in the presence of water without oxidizing to Zr^{4+}. Furthermore, the Zr^{3+} centres were not quenched by the presence of superoxide from which they concluded that the electron donating centres which gave rise to O_2^- at the surface, must be ESR silent. (They suggested that O_2^- was formed by donation of electrons from the conduction band.) This indicates that the Zr^{3+} centres which co-ordinatively saturate with H_2O and sites where O_2^- occur must coexist. In addition, they found that superoxide (O_2^-) formation on m-ZrO_2 is an activated process which only occurred in appreciable amounts at 150°C. In the presence of water, the activation barrier for superoxide formation was reduced and considerable quantities of superoxide were formed at room temperature.

In the work of Morterra *et al.*[33] the Zr^{3+} centres were generated by annealing in vacuum or O_2 at temperatures between 375 and 825°C. In the autoclave, the Zr^{3+} centres are most likely produced in the normal process of exchange of O^{2-} with atmospheric O_2 except that, in the autoclave environment, water molecules are also present and compete for surface sites. Consequently, it is likely that a considerable proportion of the surface Zr^{3+} sites become coordinatively saturated with water. In the presence of an increased density of adsorbed water on the surface of the ceramic much more O_2^- will be generated. Since the generation of O_2^- is the first step in the reduction of oxygen it is assumed that the presence of superoxide will lead ultimately, to much more O^{2-} than would occur on a surface largely free of adsorbed water. Some indirect evidence for the relationship between adsorbed water and the cus-Zr^{3+} sites is provided

Table 3. O_{TOT}/Zr, $\%O_I/Zr$, $\%O_{II}/Zr$ and $\%Zr^{3+}$ for Z3Y20T after 80 h autoclave treatment at 170°C versus examination time under X-ray source

Time (min)[1]	O_{TOT}/Zr	$\%O_I/Zr$	$\%O_{II}/Zr$	$\%Zr^{3+}$
0–10	2·34	61·5	38·5	26·6
30–40	2·29	65·7	34·3	24·0
60–70	2·29	70·6	29·4	21·8
90–100	2·21	71·5	28·5	19·8

[1]It takes approximately 5 min to measure each of the Zr 3*d* and O 1*s* spectra hence a 10 min window is given for each entry in the table.

by the data in Table 3. During dehydration under the X-ray source, O_{II}/Zr (adsorbed water and superoxide) decreased with a consequent loss of Zr^{3+}. In addition there was evidence to suggest that the O_{II} species may have been converted to O^{2-} since there is a 26% reduction in O_{II} but only a total reduction in O_{TOT} of 5·5%. Furthermore, there is also a 26% reduction in the $\%Zr^{3+}$ indicating that the Zr^{3+} have been oxidized up to Zr^{4+} concurrently with the decomposition of the O_{II} species to oxygen anions. As a result of O^{2-} generation there is rapid annealing of surface vacancies and likely penetration of O^{2-} into the lattice, destabilizing the t-phase and resulting in either transformation to the m-phase or the nucleation of domains of m-phase. The likelihood of m-phase nucleation domains is further improved by surface depletion of Y (Fig. 10).

4.2 Anion annealing

Evidence for anion annealing comes from the data collected at longest autoclave treatment times where all compositions have reached surface saturation with m-phase. The saturation values of O_{TOT}/Zr, O_I/Zr and O_{II}/Zr at these long treatment times are presented in Table 4 along with expected values based on the stoichiometry. Two points need to be made with respect to the table. First, the measured O_{TOT}/Zr ratios are much larger than the ratios calculated on the basis that all the anion vacancies are filled (O/Zr), suggesting the presence of oxygen rich species such as some form of molecular oxygen, perhaps superoxide (O_2^-). Furthermore, O_{TOT}/Zr is higher than the stoichiometries that take into account vacancies due to the presence of either Y^{3+} (O^{Y}_{Vac}/Zr) or Y^{3+} and Zr^{3+} ($O^{Y,Zr3+}_{Vac}/Zr$) suggesting that many of the oxygen vacancies have been filled. Second, O_I/Zr, which only accounts for the oxygen anions in the lattice, falls far short of any of the calculated stoichiometries. It is only with the contribution of O_{II}/Zr that the experimental values approach the values calculated from the stoichiometry suggesting that a significant proportion of the surface oxygen anion sites are occupied by the O_{II} species, i.e. adsorbed H_2O or O_2^-. It is difficult to distinguish adsorbed H_2O from O_2^- using XPS core levels, however, preliminary static secondary ion mass spectrometry (SIMS) spectra confirm the presence of O_2^- after autoclave treatment whereas no O_2^- was evident before treatment on freshly polished surfaces. The SIMS results indicate that superoxide must therefore partially contribute to the O_{II} species observed in XPS.

Table 4. Comparison of XPS O/Zr ratios after long treatment time with the calculated O/Zr ratios

Treatment	*Z3Y1T*	*Z3Y10T*	*Z3Y20T*
O_{TOT}/Zr*	2·36	2·65	2·65
O_I/Zr*	1·66	1·80	1·66
O_{II}/Zr*	0·684	0·857	0·964
O/Zr¶	2·14	2·37	2·68
O^{Y}_{Vac}/Zr§	2·12	2·33	2·63
$O^{Y,Zr3+}_{Vac}/Zr$†	1·82	2·03	2·33

*Average XPS atomic ratio determined after surface saturation with m-phase.

¶Calculated with known molar concentration of oxides assuming that each oxide has its full oxygen stoichiometry, e.g. for Z3Y10T there is 87 mol% ZrO_2, 6 mol% $YO_{1.5}$ and 10 mol% TiO_2 hence the O/Zr ratio is $(2 \times 87 + 2 \times 6 + 2 \times 10)/87 = 2{\cdot}37$.

§Calculated with known molar concentration of oxides assuming that each oxide has its fill oxygen stoichiometry, e.g. for Z3Y10T there is 87 mol% ZrO_2, 6 mol% $YO_{1.5}$ and 10 mol% TiO_2 hence the O/Zr ratio is $(2 \times 87 + 1{\cdot}5 \times 6 + 2 \times 10)/87 = 2.33$.

†Calculated on the basis of bulk stoichiometry but taking into account vacancies created by the presence of Y^{3+} and Zr^{3+}, e.g. for Z3Y10T $(2 \times 87 - 0{\cdot}2 \times 87 + 2 \times 10)/87 = 2{\cdot}03$ where the second term takes account of 20% Zr^{3+} in the Zr 3*d* spectra and assumes that one vacancy is associated with each Zr^{3+}.

4.3 Substitutional cations

The role of substitutional cations emerges; replacement of surface or bulk Zr^{4+} cations by Ti^{4+} or other cations will modify adsorption conditions on the surface. For example, on the rutile form of TiO_2, water adsorption has been reported up to 300°C[35] whereas on anatase water desorbs around 200°C and is dependent on the surface crystallography.[36] On m-ZrO_2 molecular water desorbs from the surface below 200°C.[37] Hence it is possible that stronger binding of chemisorbed water in the presence of Ti^{4+} may suppress the rate of formation of O^{2-}. Furthermore, it has been noted by Kountouros and Petzow[16] that the activation energy for ionic conductivity increases when TiO_2 is used as an alloying component. This suggests that oxygen may be more tightly bound in the modified neighbourhood of Ti^{4+}. Clearly, however, the surface Ti/Zr ratio has little direct bearing on the rate of transformation to the monoclinic phase since Z3Y10T had the highest surface concentration of Ti but transformed at autoclave times intermediate between those of Z3Y1T and Z3Y20T.

It should be noted that while this model is based on the XPS results of the external surface, it is likely that the same species are involved in the grain boundary network, although the mechanisms are likely to be much more complex due to the presence of impurity phases. Further, a different composition of the surface of grains due to cation segregation will lead to a significant modification of the reaction kinetics. The role of impurities is at least twofold; in modifying the defect distribution near the surface and in providing a grain boundary protective coating via the presence of the grain boundary impurity phase. Grain boundary impurity phases and grain surface composition, which vary considerably in different ceramics,[37-40] could therefore be just as critical as grain size or yttria content in determining the stability of sintered Y–TZP.

It is worthwhile considering whether there is any significant difference between moist air and autoclave treatments. It was previously reported by Hughes *et al.*[8,24] that vacancy annealing occurred during moist air treatment of Y–TZP but very little adsorbed water was present during these experiments by contrast to the significant quantities of adsorbed water during the autoclave experiments reported here. During autoclave or moist air treatment both O_2 and water vapour will be present but in different relative ratios. The different relative ratios of the two species in the gas phase as well as the higher pressure in the autoclave environment may well influence the distribution of surface adsorbed species. For example, it would appear that in an autoclave environment significantly more Zr^{3+} is generated suggesting the potential for a much higher density of adsorbed water.[24] If the formation of O_2^-, which is the first step in the reduction of O_2 to O^{2-}, is enhanced in the presence of water on m-ZrO_2[34] then it might be expected that molecular oxygen or superoxide migrates across the surface to a site adjacent to the adsorbed water.[41] Consequently, the rate of reduction of O_2 to O^{2-} will be increased if the density of adsorbed water is higher. On this basis alone, it could be expected that autoclave treatment will result in more rapid transformation to m-phase than moist air treatment.

While the route from O_2 to O^{2-} is conceptually clear, it is unclear what role the decomposition of H_2O has to play. In the case of adsorbed water it might be expected that some surface hydroxyl group are formed, however, surface OH^- was not evident in the XPS suggesting that if OH^- is formed then it must react quickly to give O^{2-} and either H_2 or interstitial H^+. Krouse *et al.*[17] have demonstrated, using ERDA, that hydrogen penetrates the lattice, and given the weight gain and desorption of H_2 from autoclave treated Y–TZP measured by Narita *et al.*[15] it seems likely that interstitial hydrogen is produced. Interstitial hydrogen ions would provide charge balance for the excess O^{2-}.

5 Conclusions

The XRD results indicate that the addition of TiO_2 to Y_2O_3–ZrO_2 as an alloying oxide retards the onset of the t→m transformation during autoclave treatment at 170°C. XPS and SIMS results further indicate that the only oxygen species on the surface of autoclave treated TiO_2–Y_2O_3–ZrO_2 are adsorbed water, superoxide and oxygen anions. XPS results indicate that treatment in an autoclave environment gives rise to the generation of Zr^{3+} sites which co-ordinatively saturate with water. The presence of adsorbed water on the surface increases the rate of formation of O_2^- which, it is assumed, leads to a much larger amount of O^{2-} than would be the case in the absence of the adsorbed water. It is thought that the excess O^{2-} anions anneal anion vacancies thus destabilising the t-phase and promoting the t→m phase transformation. The observed enrichment of Ti^{4+} occurs as a result of the t→m phase transition and does not appear to retard bulk transformation by creating a protective overlayer which retards the t→m phase transformation.

Acknowledgement

The authors would like to thank Dr M. J. Bannister and Prof. G. Petzow for useful discussions, Ms G. Roderick and Mr M. Fergus for assistance with drafting the diagrams and photography. We are also grateful to the University of Queensland for providing time on their surface analysis instrument for SIMS analysis.

References

1. Whalen, P. J., Reidinger, F. & Antrim, R. F., Prevention of low temperature surface transformation by surface recrystallisation in yttria-doped tetragonal zirconia. *J. Am. Ceram. Soc.*, **72** (1989) 319–21.
2. Tsukuma, K., Kubota, Y. & Tsukidate, T., Thermal and mechanical properties of Y_2O_3-stabilised tetragonal zirconia polycrystals. In *Adv. Ceram., Vol. 12. Science and Technology of Zirconia II.* eds N. Claussen, M. Rhule & A. H. Heuer, The American Ceramics Society, Columbus OH., 1984, pp. 382–90.
3. Watanabe, M., Iio, S. & Fukuura, I., Aging behaviour of Y–TZP. *ibid.*, pp. 391–8.
4. Matsui, M., Soma T. & Oda I., Effect of microstructure on the strength of Y–TZP components. *ibid.*, pp. 371–81.
5. Wang, J. & Stevens, R., Surface transformation and

toughening of TZP ceramics by low temperature aging. *Proc. Br. Ceram. Soc.*, **42** (1989) 167–78.
6. Sato T. & Shimada, M., Crystalline phase change in yttria–partially-stabilised zirconia by low temperature annealing. *J. Am. Ceram. Soc.*, **67**(10) (1984) C212–13.
7. Hernandez, M. T., Jurado, J. R., Duran P. & Fierro, J. L. G., Subeutectoid degradation of yttria–stabilised tetragonal zirconia polycrystal and ceria–doped yttria–stabilised tetragonal zirconia polycrystal ceramics. *J. Am. Ceram. Soc.*, **74** (1991) 1254–8.
8. Hughes, A. E., Ciacchi, F. T. & Badwal, S. P. S., Degradation of Y–TZP in moist environments. In *Proceedings of the Fifth International Conference on the Science and Technology of Zirconia*, eds S. P. S. Badwal, M. J. Bannister & R. H. J. Hannink, Technomic Publishing Co., Lancaster, Pennsylvania, 1993, pp. 152–62.
9. Wang J. & Stevens, R., Preferred $ZrO_2(t) \rightarrow ZrO_2(m)$ transformation on the aged surface of TZP ceramics, *J. Mater. Sci. Letts.*, **8** (1989) 1195–8.
10. Lepisto T. T. & Mäntylä, T. A., A model for structural degradation of Y–TZP ceramics in humid atmosphere. *Ceram. Eng. Sci. Proc.*, **10** (1989) 658–67.
11. Lange, F. F., Dunlop G. L. & Davis, B. I., Degradation during aging of transformation-toughened ZrO_2–Y_2O_3 materials at 250°C. *J. Am. Ceram. Soc.*, **69** (1986) 237–40.
12. Sato, T. & Shimada, M., Transformation of yttria-doped tetragonal ZrO_2 polycrystal by annealing in water. *J. Am. Ceram. Soc.*, **68** (1985) 356–9.
13. Yoshimura, M., Noma, T., Kawabata, K. & Sōmiya, S., Role of H_2O on the degradation process of Y–TZP. *J. Mater. Sci.*, **6** (1987) 465–7.
14. Yoshimura, M., Phase stability of zirconia. *Am. Ceram. Soc. Bull.*, **67** (1988) 1950–5.
15. Narita, N., Leng, S. Inada T. & Higashida, K., Environmental effect on phase stability in Y–TZP ceramics. In *Sintering '87*, Proceedings of the 4th International Symposium on Science and Technology of Sintering in Tokyo (1987), eds S. Sōmiya, M. Shimada, M. Yoshimura & R. Watanabe, Elsevier Science Publishers, London, 1988, pp. 1130–5.
16. Kountouros, P. & Petzow, G., Defect chemistry, phase stability and properties of zirconia polycrystals. In *Proceedings of the Fifth International Conference on the Science and Technology of Zirconia*, eds S. P. S. Badwal, M. J. Bannister & R. H. J. Hannink, Technomic Publishing Co., Lancaster, Pennsylvania, 1993, pp. 30–48.
17. Kruse, O., Corstanjen, H. D., Kountouros, P. W., Schubert H. & Petzow, G., Characterization of H_2O–aged TZP by elastic recoil detection analysis (ERDA). In *Proceedings of the Fifth International Conference on the Science and Technology of Zirconia*, eds S. P. S. Badwal, M. J. Bannister & R. H. J. Hannink, Technomic Publishing Co., Lancaster, Pennsylvania, 1993, pp. 163–70.
18. Sato T. & Shimada, M., Control of the tetragonal-to-monoclinic phase transformation of yttria–doped tetragonal ZrO_2 polycrystals (Y–TZP) by annealing in water. *Proc. Br. Ceram. Soc.*, **37** (1986) 151–8.
19. Theunissen, G. S. A. M., Winnubst, A. J. A. & Burggraaf, A. J., Effects of dopants on the sintering behaviour and stability of tetragonal zirconia ceramics. *J. Eur. Ceram. Soc.*, **9** (1992) 251–64.
20. Duran, P., Hernandez, T., Moure, C., Gonzalez, M., Recio, P., Pascual, C. & Jurado, J. R., Aging behaviour properties of SOFC electrolytes. In *Ceramics Today–Tomorrow's Ceramics*, ed. P. Vincenzini, Elsevier Science Publishers, Amsterdam, 1991, pp. 2219–28.
21. Shigematsu, T., Nakao, Y. & Nakanishi, N., Effect of water on the tetragonal to monoclinic phase transition of ZrO_2 with Y_2O_3. In *Shape Memory Materials*, Vol. 9, eds M. Doyama, S. Somiya & R. Chang, Materials Research Society. Pittsburgh, 1989, pp. 549–54.
22. Kountouros, P. & Schubert, H., Bloating Effect During Sintering of TZP. In *Proc. 2nd Europ. Ceram. Soc. Conf.*, Augsburg, 1991.
23. Hughes, A. E. & Badwal, S. P. S., Impurity and yttrium segregation in yttria–tetragonal zirconia. *Solid State Ionics*, **46** (1991) 265–74.
24. Hughes, A. E., Ciacchi, F. B. & Badwal, S. P. S., Role of O^{2-}, OH^- and anion vacancies in the degradation of Y–TZP in moist environments. *J. Mater. Chem.*, **4**(2) (1994) 257–63.
25. Leonov, A. I., Kostikov, Yu. P., Ivanov, I. K., Andreeva, N. S. & Trusova, E. M., The nature of electrical conductivity of solid solutions in the ZrO_2–Y_2O_3 system. *Iz. Akad. Nauk SSSR, Neorg. Mat.*, **16** (1980) 1076–9.
26. Miller, M. L. & Linton, R. W., X-Ray photoelectron spectroscopy of thermally treated SiO_2 surfaces, *Anal. Chem.*, **57** (1985) 2314–19.
27. Dolle, P., Drissi, S., Besançon, M. & Jupille, J., Application of a point-charge model to the O^{2-}, O_2^{2-} and O_2^- ions formed in the presence of Li, K and Cs. *Surf. Sci.*, **269/270** (1992) 687–90.
28. Barr, T. L., An ESCA study of the termination of the passivation of elemental metals. *J. Phys. Chem.*, **82** (1978) 1801–10.
29. De González, C. O. & García, E. A., An X-ray photoelectron spectroscopy study of the surface oxidation of zirconium. *Surf. Sci.*, **193** (1988) 305–20.
30. Morant, C., Sanz, J. M., Galán, L., Soriano, L. & Rueda, F., An XPS study of the interaction of oxygen with zirconium. *Surf. Sci.*, **218** (1989) 331–45.
31. Orera, V. M., Merino, R. I., Chen, Y., Cases, R. & Alonso, P. J., Intrinsic electron and hole defects in stabilized zirconia single crystals. *Phys. Rev. B*, **42** (1990) 9782–9.
32. Azzoni, C. B. & Paleari, A., EPR study of electron traps in X-ray-irradiated yttria–stabilised zirconia, *Phys. Rev. B*, **40** (1989) 6518–22.
33. Morterra, C., Giamello, E., Orio, L. & Volante, M., Formation and reactivity of Z^{3+} centers at the surface of vacuum annealed monoclinic zirconia, *J. Phys. Chem.*, **94** (1990) 3111–16.
34. Giamello, E., Volante, M., Fubini, B., Geobaldo, F. & Morterra, C., *Mater. Chem. Phys.*, **29** (1991) 379.
35. Jackson, P. & Parfitt, G. D., *Trans. Far. Soc.*, **67** (1971) 2469–83.
36. Tanaka, K. & White, J. M., Characterisation of species adsorbed on oxidized and reduced anatase. *J. Phys. Chem.*, **86** (1982) 4708–14.
37. Hughes, A. E. & Badwal, S. P. S., The effects of sintering atmosphere on impurity phase formation and grain boundary resistivity in Y_2O_3–fully stabilized ZrO_2. *J. Eur. Ceram. Soc.*, **10** (1992) 115–22.
38. Hughes, A. E., Segregation in single crystal fully-stabilized yttria–zirconia. *J. Am. Ceram. Soc.*, **78**(2) (1995) 369–78.
39. Ingo, G. M. & Padeletti, G., Segregation aspects at the fracture surfaces of 8 wt% yttria–zirconia thermal barrier coatings, **21** (1994) 450–4.
40. Chaim, R., Brandon, D. G. & Heuer, A. H., A diffusional phase transformation in ZrO_2-4 wt% to Y_2O_3 induced by surface segregation. *Acta Metall.*, **34**(10) (1986) 1933–9.
41. Taylor, R. J. & Humffray, A. A., Electrochemical studies on glassy carbon electrodes: II. oxygen reduction in solutions of high pH (pH > 10). *J. Electroanal. Chem.*, **64** (1975) 63–84.

Journal of the European Ceramic Society 15 (1995) 1135–1140
© 1995 Elsevier Science Limited
Printed in Great Britain. All rights reserved
0955-2219(95)00082-8
0955-2219/95/$9.50

Dielectric Properties of the Mixed Aurivillius Phases $M^{II}Bi_8Ti_7O_{27}$ (M^{II} = Ca, Sr, Ba and Pb)

R. Maalal, M. Manier & J. P. Mercurio*

Laboratoire de Matériaux Céramiques et Traitements de Surface, URA CNRS no. 320, Faculté des Sciences, Université de Limoges, 123, Avenue Albert-Thomas, 87060 Limoges Cedex, France

(Received March 1995; revised version received 18 May 1995; accepted 19 May 1995)

Abstract

Ceramic materials have been prepared by natural sintering and hot-forging $M^{II}Bi_8Ti_7O_{27}$(M^{II} = Ca, Sr, Ba and Pb) powders synthesized using a molten salt technique. The materials are ferroelectric at room temperature and show strong dielectric anisotropy in connection with the crystal structure. In each case, a double anomaly of the dielectric permittivity was found as a function of temperature. The temperatures at which it occurs are dependent on M^{II}. The origin of this phenomenon is assumed to be closely related to a sequence of phase transitions like those already observed in other mixed Aurivillius phases.

1 Introduction

The so-called Aurivillius phases are a family of layer bismuth compounds generally formulated as $Bi_2A_{m-1}B_m O_{3m+3}$. Their crystal structure can be regarded as a regular intergrowth of $(Bi_2O_2)^{2+}$ layers and $(A_{m-1}B_mO_{3m+1})^{2-}$ perovskite-type slabs.[1,2] In these compounds, A is a mono-, di- or trivalent element allowing dodecahedral coordination, B is a transition element suited to octahedral coordination and m an integer ($1 \leq m \leq 8$) which represents the number of perovskite-like slabs intercalated between the $(Bi_2O_2)^{2+}$ layers. As they generally show ferroelectric behaviour, a number of them, e.g. $Bi_2PbNb_2O_9$ (m = 2), $Bi_4Ti_3O_{12}$ (m = 3), $BaBi_4Ti_4O_{15}$ (m = 4), have been thoroughly investigated from the point of view of both structural and electric properties.[3–7] The frequent occurrence of disordered intergrowths — corresponding to different values of m — suggested that ordered intergrowths would be obtained in suitable systems and under appropriate thermal treatment. In fact, various ordered intergrowths have been recently prepared as macroscopic pure phase.[8,9] They always correspond to a regular intergrowth of one half the unit cell of a m member structure and one half the unit cell of a m + 1 member structure, so that they have the general formula $Bi_4A_{2m-1}B_{2m+1}O_{6m+9}$, e.g. $Bi_5TiNbWO_{15}$ (intergrowth 1 + 2), $Bi_7Ti_4NbO_{21}$ (intergrowth 2 + 3) and $M^{II}Bi_8Ti_7O_{27}$ (intergrowth 3 + 4). Several papers have been devoted to the dielectric properties of $Bi_7Ti_4NbO_{21}$: the main characteristic of this ferroelectric phase is the occurrence of a double anomaly of the dielectric permittivity as a function of temperature.[9,10] An interpretation of this phenomenon was recently given from single crystal structure investigations.[11] On the contrary, there is only few literature dealing with dielectric properties of phases with 1 + 2 or 3 + 4 intergrowths.

The aim of this paper is to present the results of the investigation of the dielectric properties of $M^{II}Bi_8Ti_7O_{27}$(M^{II} = Ca, Sr, Ba and Pb) as a function of temperature and frequency and to discuss their evolution within the Aurivillius family.

2 Experimental

Polycrystalline powders were prepared by molten salt synthesis. Stoichiometric mixtures of reagent grade $M^{II}CO_3$, Bi_2O_3 and TiO_2 were thoroughly mixed with excess NaCl–KCl eutectic and ground in agate mill for 2 h. The mixtures, placed in closed platinum crucibles were heated up to 650°C for 1 h to ensure homogeneization and then soaked at 800–900°C (depending on the composition) for 1 h. After cooling, the salt was eliminated by washing with hot water until the last washing water does not react with silver nitrate and the powders finally dried at 100°C.

Ceramic samples were obtained by natural sintering of uniaxially pressed pellets at 1050–1120°C for 1–3 h in air. High oriented materials were elaborated by a hot-forging technique (920–1060°C, 4–12 MPa, 1–3 h) described elsewhere.[10]

*To whom correspondence should be addressed.

The morphology of powders and the microstructure of hot-forged ceramics were observed with a Philips XL30 scanning electron microscope. X-ray diffraction patterns were obtained with a Siemens D5000 powder diffractometer (CuKa) and the cell parameters refined by a least-squares method. Dielectric measurements were made between room temperature and 1000°C by impedance spectrometry using a HP 4194A impedance analyser. Disk-shaped samples (10 mm diameter and 1 mm thick) of naturally sintered ceramics and parallelepipedic bodies of hot-forged materials ($1 \times 1 \times 3$ mm^3) were polished and coated with platinum paste (Cerdec Pt 576402/1, 1000°C, 30 min), aged overnight at 110°C and left for at least 24 h before measurements. For hot-forged ceramics, electrodes were put on faces either parallel or perpendicular to the forging direction. D-E hysteresis loops were obtained at room temperature using a classical Sawyer–Tower device operating at 20 mHz. Piezoelectric coefficients d_{33} were determined with a Berlincourt-meter and the electromechanical coupling factors were derived from resonance–antiresonance measurements.

3 Results and Discussion

3.1 Powders

Strongly anisotropic platelet-like powders were obtained using molten salt synthesis. As shown in Fig. 1 for calcium and lead compounds, they develop large faces with areas in the range 1–10 μm^2 and thickness less than 0·1 μm. As expected, X-ray diffraction patterns confirmed that the direction perpendicular to the main faces correspond to the stacking direction of the Bi_2O_2 sheets. All the compounds are orthorhombic with lattice parameters a and b close to 0·54 nm ($\approx \sqrt{2}\, a_{perovskite}$) and c inherently long ($\approx$ 7·3 nm) due to the number of perovskite and Bi_2O_2 slabs involved in the unit cell. The evolutions of the lattice parameters are

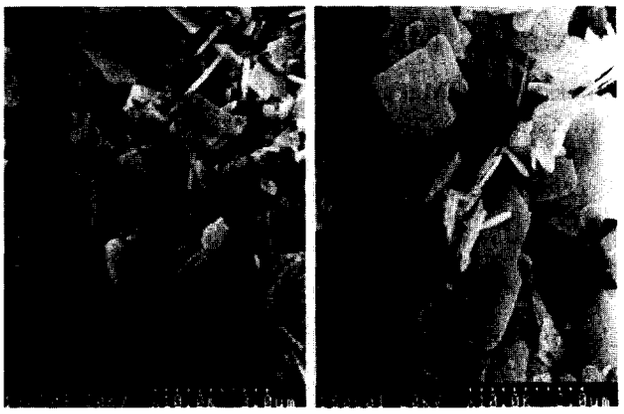


Fig. 1. SEM micrographs of $CaBi_8Ti_7O_{27}$ and $PbBi_8Ti_7O_{27}$ powders prepared by molten salt synthesis.

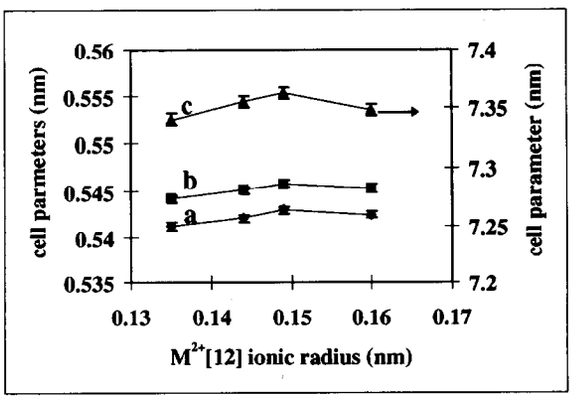
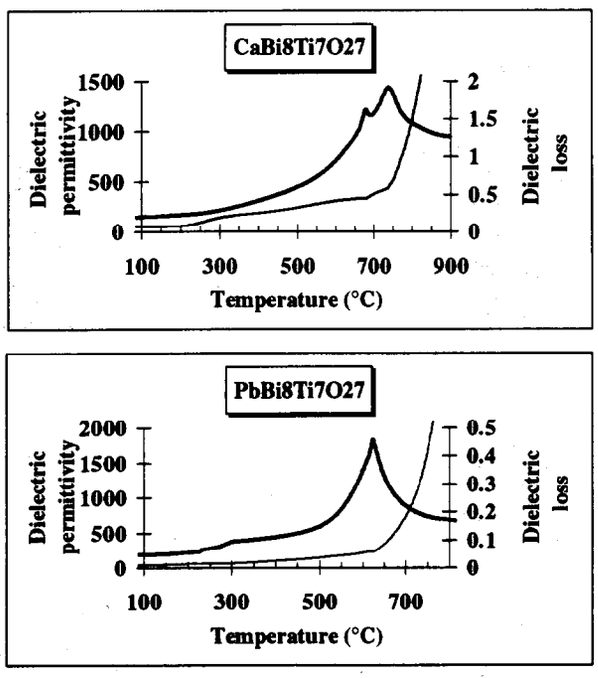


Fig. 2. Lattice parameters of $M^{II}Bi_8Ti_7O_{27}$ as a function of M^{2+} ionic radii in coordinence.[12]



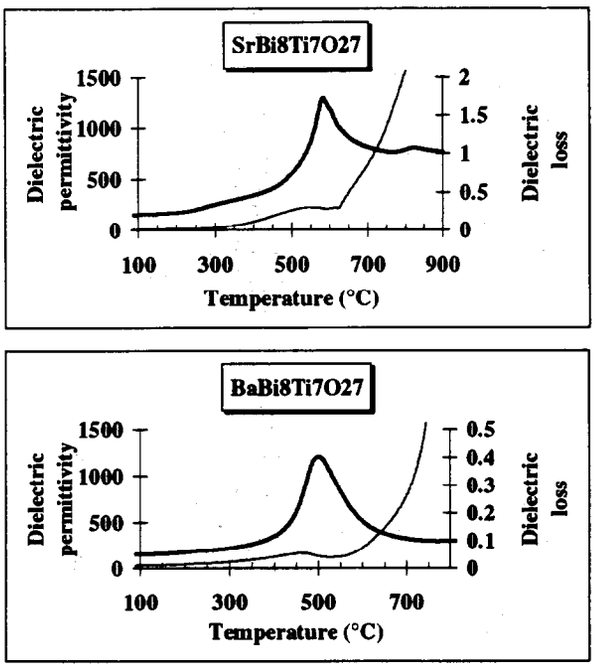


Fig. 3. Thermal variation of dielectric permittivity and loss of naturally sintered $M^{II}Bi_8Ti_7O_{27}$ ceramics at 1 MHz.

given in Fig. 2 as a function of the ionic radii in coordinence [12] of the M^{2+} cations.[12] From calcium to barium, the lattice parameters roughly increase, but the behaviour of the lead compound appears to be out of the general trend. The abnormally high values obtained for this compound would be undoubtly related to the strong polarizability of Pb^{2+} due to the $6s^2$ lone pair which is absent in the alkaline earth compounds. Such a trend was already observed in M^{II}-containing Aurivillius phases, e.g. $M^{II}Bi_2Nb_2O_9$, $M^{II}Bi_4Ti_4O_{15}$ or $(M^{II})_2Bi_4Ti_5O_{18}$.[3,4]

3.2 Naturally sintered ceramics

After natural sintering in air atmosphere, ceramic materials achieved densities lying within 92–96% of theoretical and X-ray patterns did not show any significant preferential orientation.

The thermal variations of the dielectric permittivity and dielectric loss at 1 MHz of $M^{II}Bi_8Ti_7O_{27}$ are given in Fig. 3. For M^{II} = Sr, Ba and Pb, one dielectric anomaly is observed at 580, 480 and 610°C respectively for both ϵ_r and tan δ. This behaviour was already found by Kikuchi *et al.*[9] On the contrary, the calcium compound is characterized by a double anomaly at 660 and 720°C, similar to that observed in the 'mixed phase' $Bi_7Ti_4NbO_{21}$.[9,10] For all compounds, the anomaly temperatures of ϵ_r and tan δ are frequency independent and only a slight decrease of ϵ_r as the frequency increases from 100 kHz to 5MHz is observed as shown in Fig. 4.

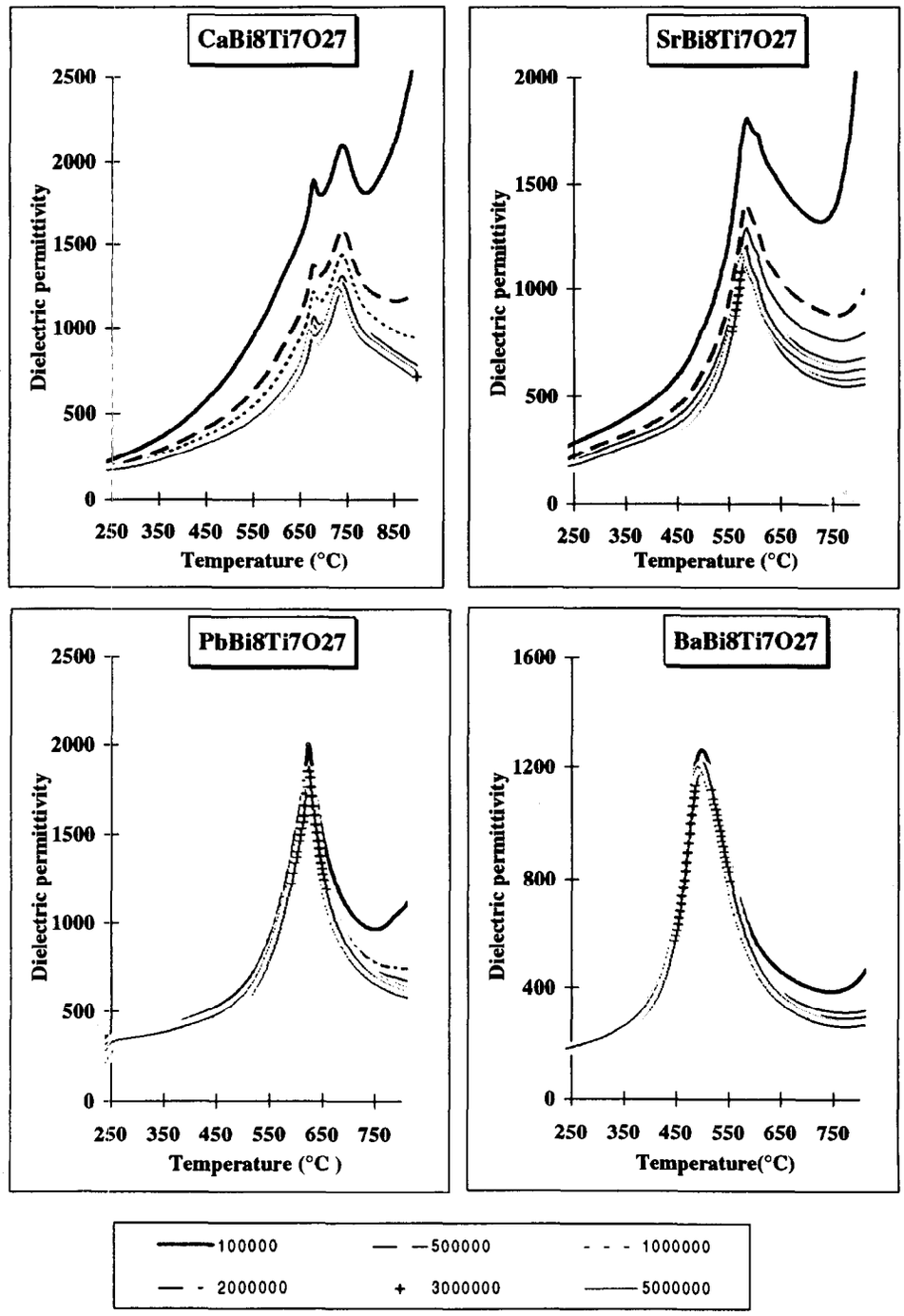


Fig. 4. Thermal variation of dielectric permittivity of naturally sintered $M^{II}Bi_8Ti_7O_{27}$ ceramics as a function of frequency.

Polarization–electric field curves confirm the ferroelectric behaviour of these compounds at room temperature. The observed loops are not fully saturated due to experimental difficulties (Fig. 5). Nevertheless they allow determination of coercive field (42–58 $kVcm^{-1}$) and remnent polarization (2·3–3·9 $\mu C\ cm^{-2}$), (Table 1). These values are slightly lower — but of the same order of magnitude — than those obtained for $Bi_7Ti_4NbO_{21}$.

Table 1 also shows the piezoelectric constants d_{33} and the planar electromechanical coupling coefficients measured on samples poled at 200°C for 10 min in silicone oil under 8 kV mm^{-1}. As for other Aurivillius phases, the obtained values are quite low, but are kept almost the same up to about 450°C.

Table 1. Selected ferroelectric and piezoelectric data of $M^{II}Bi_8Ti_7O_{27}$ naturally sintered ceramics

	Coercive field (kV/mm)	*Remanent polarization ($\mu C/Cm^2$)*	d_{33} *(pC/N)*	k_p *(%)*
$CaBi_8Ti_7O_{27}$	58	3·3	7·4	3·3
$SrBi_8Ti_7O_{27}$	48	3·9	8	3·2
$PbBi_8Ti_7O_{27}$	45	3·35	6·3	2·2
$BaBi_8Ti_7O_{27}$	42	2·3	7·5	2·8

3.3 Hot-forged ceramics

The hot-forging technique gave strongly oriented highly densified ceramics. Orientation factors — calculated using the Lotgering method — higher than 90% were currently obtained at 1050°C under 12 MPa.[13] The corresponding densities were 96–99% of theoretical. Figure 6 shows a SEM micrograph of the lead compound taken in a direction perpendicular to the forging axis. The strong anisotropy was confirmed by X-ray diffraction experiments performed along two perpendicular directions (// and ⊥ to the forging axis) and compared with the powder pattern. As expected, the ⊥ pattern shows only (001) lines which are absent in the // pattern (Fig. 7).

The thermal variations of the dielectric permittivity of hot-forged samples were measured along both // and ⊥ directions. As previously noticed for naturally sintered materials, the temperatures of

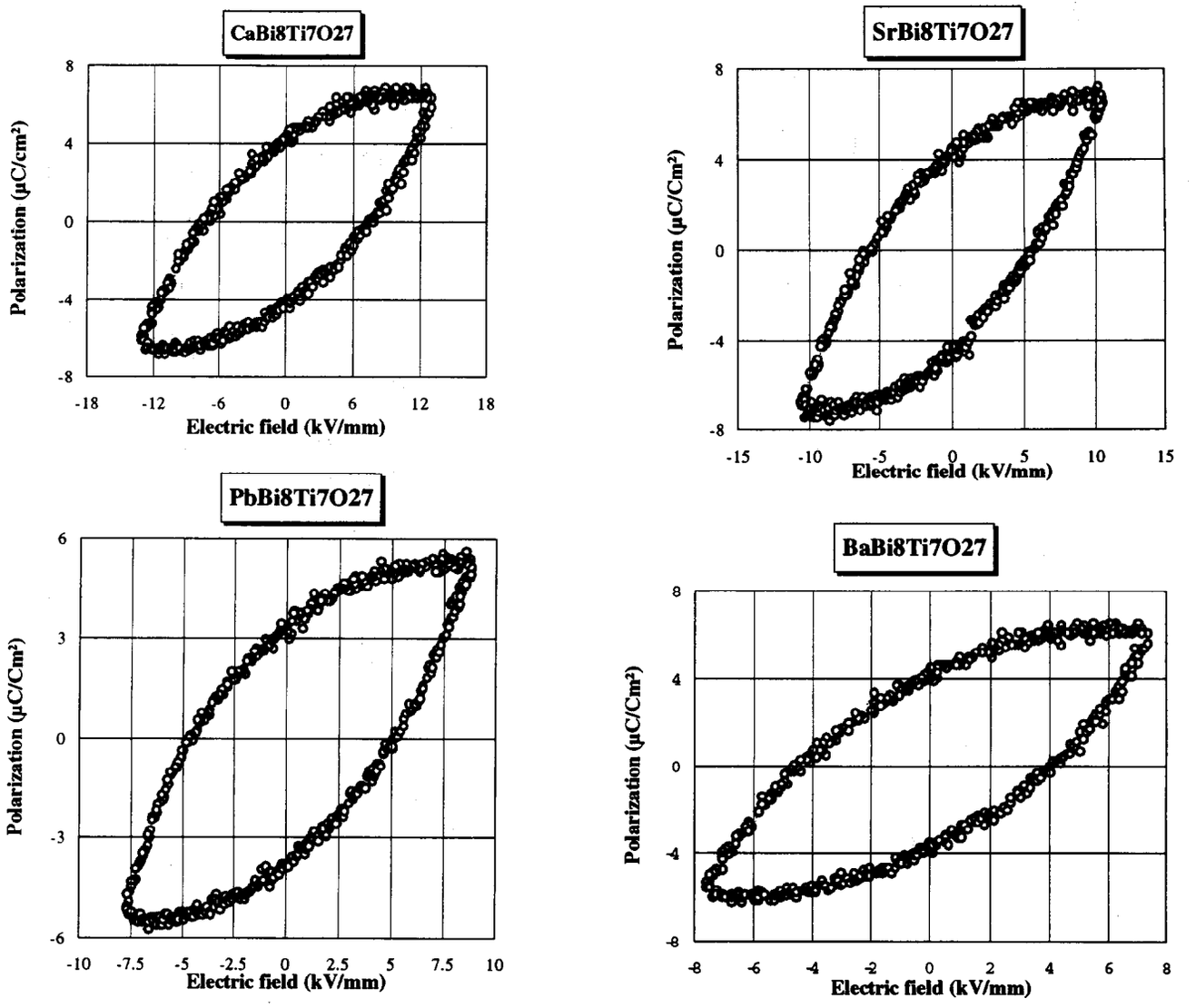


Fig. 5. Polarization-electric field loops of naturally sintered $M^{II}Bi_8Ti_7O_{27}$ ceramics.



Fig. 6. SEM micrograph of hot-forged $PbBi_8Ti_7O_{27}$ ($\perp$ to the forging direction)

the permittivity anomalies are frequency independent. From Fig. 8, which gives the results obtained at 1 MHz, two main features can be emphasized:

(i) in each case, $\epsilon_\perp$ is higher than $\epsilon_{//}$, the ratio being maximum at anomaly temperatures. Such a behaviour was already observed for other hot-forged materials, e.g. $M^{II}Bi_4Ti_4O_{15}$ and $Bi_7Ti_4NbO_{21}$, and was attributed to the strong anisotropic microstructure of the materials.[10,14] As a matter of fact, the high $\epsilon_\perp$ value was correlated to the direction of the polarization which lies, for most Aurivillius phases, in or close to the planes of the Bi_2O_2/perovskite sheets, i.e. perpendicular to the forging direction. In the same way, the slight maxima observed for $\epsilon_{//}$, would indicate the presence of a small component of the polarization along the direction parallel to the forging direction (the *c*-axis of the unit cell).[15]

(ii) in contrast with the results obtained on naturally sintered ceramics, all ϵ(T) curves show a double anomaly more or less defined according to the M^{2+} cation (for M = Pb, there is only a small hump just before the maximum). In any case, when M is an alkaline earth element, the gap between the temperatures of the anomalies decreases when the ionic radii increase.

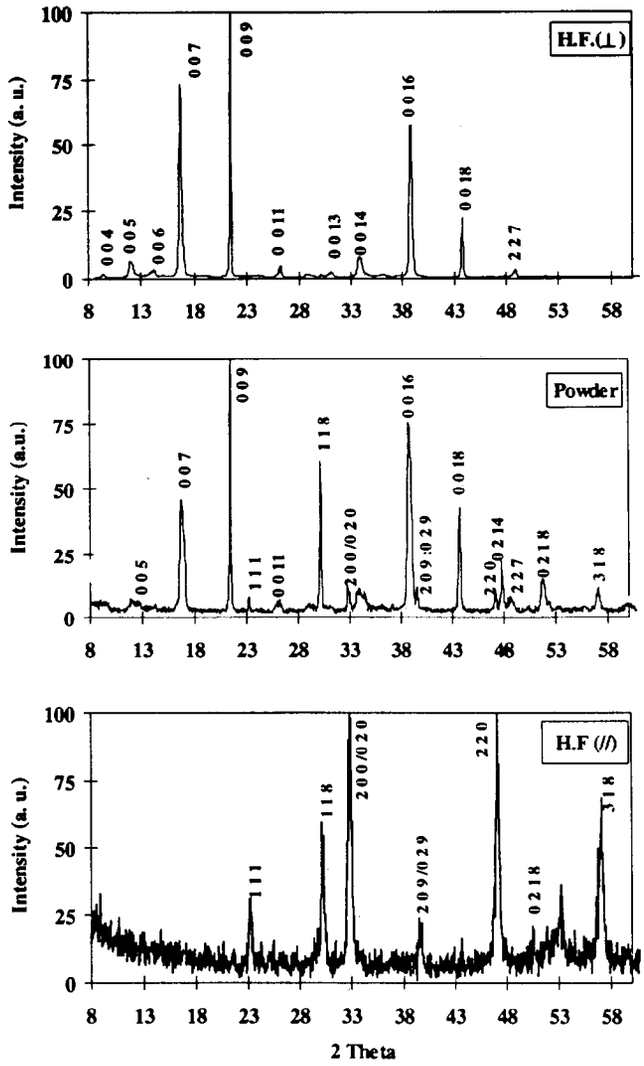


Fig. 7. X-ray diffraction patterns of hot-forged $PbBi_8Ti_7O_{27}$ ceramics.

By reference to $Bi_7Ti_4NbO_{21}$ (mixed 2–3 Aurivillius phase), one may suppose that the double anomaly would originate in a sequence of phase transitions of the following type: orthorhombic ferroelectric-(elastic) state I $\rightarrow$ orthorhombic ferroelectric-(elastic) state II $\rightarrow$ tetragonal paraelectric-(elastic) state.

The first phase transition within the orthorhombic symmetry might not occur for the lead compound because the behaviour of the lone pair Pb^{2+} cannot be strictly likened to the spherical alkaline earth cations.

4 Conclusion

Dielectric experiments on naturally sintered and highly oriented hot-forged ceramics of the so-called mixed Aurivillius family $M^{II}Bi_8Ti_7O_{27}$ have shown that all materials:

— are ferroelectric with Curie temperatures in the range 500–740°C depending on the nature of M^{II};

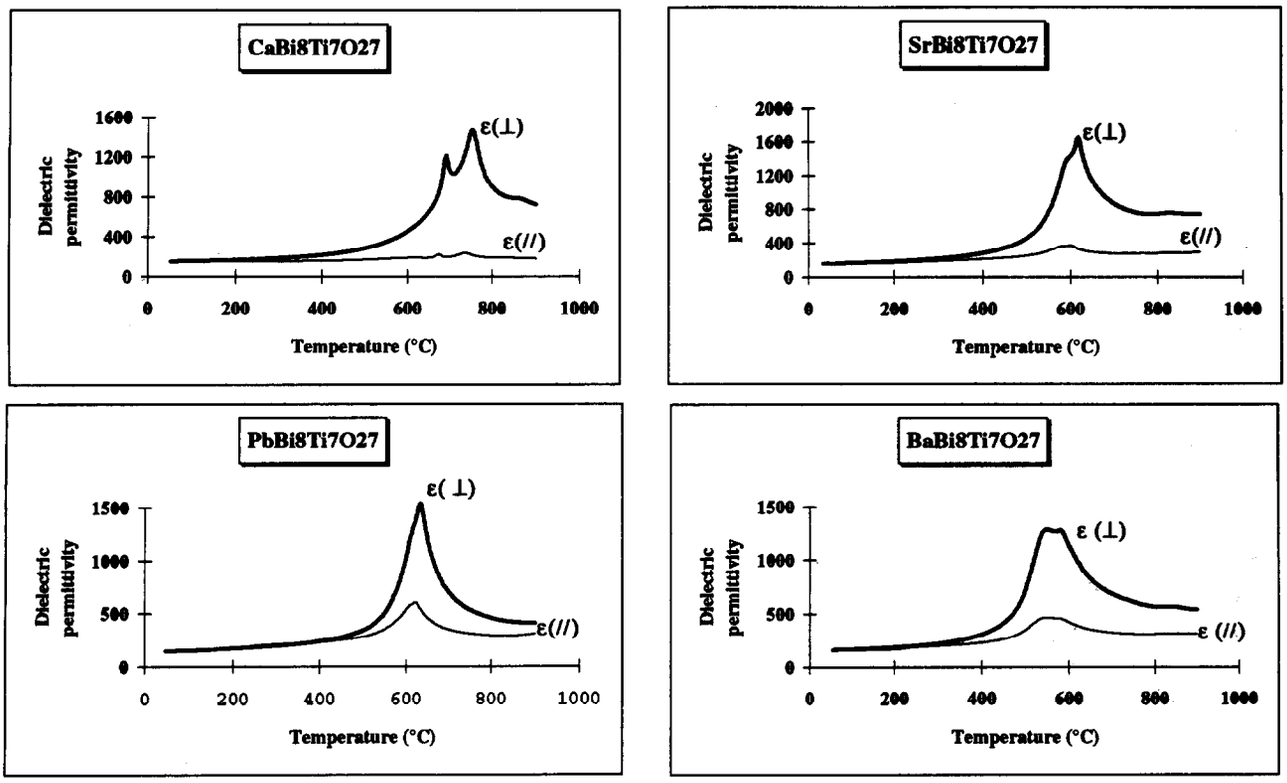


Fig. 8. Thermal variation of the dielectric permittivity of hot-forged $M^{II}Bi_8Ti_7O_{27}$ ceramics at 1 MHz (⊥ and // to the forging direction).

— present a double dielectric anomaly as a function of temperature.

The overall behaviour of the ceramics is likely to that already observed in other mixed Aurivillius phases. To confirm the assumptions about the nature of the phase transitions, further investigations (crystal structure determination, dielectric and optical microscopy measurements as a function of temperature) are now in progress on $CaBi_8Ti_7O_{27}$ single crystal.

Acknowledgement

The authors would like to thank E. Lattard for her help in dielectric hysteresis measurements.

References

1. Aurivillius, B., Mixed bismuth oxides with layer lattices I. The structure type of $CaNBi_2B_2O_9$. *Arkiv Kemi*, **1** (1949) 463–80.
2. Aurivillius, B., Mixed bismuth oxides with layer lattices II. Structure of $Bi_4Ti_3O_{12}$, *Arkiv Kemi*, **1** (1949) 499–512.
3. Smolenskii, G. A., Isupov, V. A. & Agranovskaya, A. I., Seignettoelectrics of the octahedral type with a layer structure, *Fiz. Tverdogo Tela*, **3**, (1961) 895–901.
4. Subbarao, E. C., Crystal chemistry of mixed bismuth oxides with layer-type structure, *J. Amer. Ceram. Soc.*, **45** (1962) 166–9.
5. Newnham, R. E., Wolfe, R. W. & Dorrian, J. F., Structural basis of ferroelectricity in bismuth titanate family, *Mat. Res. Bull.*, **6** (1971) 1029–39.
6. Kubel, F. & Schmid, H., X-ray room temperature structure from single crystal data, powder diffraction measurements and optical studies of the Aurivillius phase $Bi_5(Ti_3Fe)O_{15}$, *Ferroelectrics*, **129** (1992) 101–12.
7. Withers, R. L., Thompson, J. G. & Rae, A. D., The crystal chemistry underlying ferroelectricity in $Bi_4Ti_3O_{12}$, $Bi_3(TiNbO_9$ and Bi_2WO_6, *J. Solid State Chem.*, **94** (1991) 404–17.
8. Horiuchi, S., Kikuchi, T. & Goto, M., Structure determination of a mixed-layer bismuth titanate $Bi_7Ti_4NbO_{21}$ by super-high-resolution electron microscopy, *Acta Crystallogr.*, **A33** (1977) 701–5.
9. Kikuchi, T., Watanabe, A. & Uchida, K., A family of mixed-layer type bismuth compounds, *Mat. Res. Bull.*, **12** (1977) 299–304.
10. Maalal, R., Manier, M., Mercurio, J. P. & Frit, B., Grain-oriented $Bi_7Ti_4NbO_{21}$ ceramics, *Silicates Ind.*, **5-6** (1994) 161–3.
11 Maalal, R., Propriétés diélectriques et structurales de la phase d'Aurivillius mixte $Bi_7Ti_4NbO_{21}$, PhD thesis, University of Limoges, France, 1994.
12. Shannon, R. D. & Prewitt, C. T., Effective ionic radii in oxides and fluorides, *Acta Crystallogr.*, **B25** (1969) 925–46.
13. Lotgering, F. K., Topotactical reactions with ferrimagnetic oxides having hexagonal crystal structures—I, *J. Inorg. Nucl. Chem.*, **9** (1959) 113–23.
14. Takenaka, T. & Sakata, K., Grain orientation and electrical properties of hot-forged bismuth titanium oxide ($Bi_4Ti_3O_{12}$) ceramics, *Jpn. J. Appl. Phys.*, **19(1)** (1980) 31–9.
15. Cummins, S. E. & Cross, L. E., Electrical and optical properties of ferroelectric $Bi_4Ti_3O_{12}$ single crystal, *J. Appl. Phys. Lett.*, **39(5)** (1968) 2268–74.

Journal of the European Ceramic Society **15** (1995) 1141–1147
© 1995 Elsevier Science Limited
Printed in Great Britain. All rights reserved
0955-2219(95)00088-7
0955-2219/95/$9.50

Structural and Electrical Properties of Iron Manganite Spinels in Relation with Cationic Distribution

T. Battault, R. Legros & A. Rousset*

Laboratoire de Chimie des Matériaux Inorganiques, URA CNRS 1311, Université Paul Sabatier, 118 route de Narbonne, 31062 Toulouse Cedex, France

(Received 5 December 1994; revised version received 19 May 1995; accepted 22 May 1995)

Abstract

Single-phase iron manganite spinels, $Mn_{3-x}Fe_xO_4$ with $O \leq x \leq 1{\cdot}05$, were prepared by thermal processing of iron–manganese co-precipitated formate precursors. Powder X-ray diffraction (XRD) analysis shows a cubic–tetragonal transition for x = 1·05. *The Mössbauer spectroscopy indicates the presence of only trivalent iron ions in both sites of the spinel structure. The electrical measurements show that these iron manganites have the characteristics of negative temperature coefficient thermistors. Moreover, in these solid solutions, the resistivity* ρ *decreases with increasing of iron content* x. *Correlation of the results obtained by XRD, Mössbauer spectroscopy and electrical measurements permits one to infer the cationic distribution, given by* $Mn^{2+}_{1-y}\ Fe^{3+}_{y}\ (Fe^{3+}_{z}\ Mn^{3+}_{2-x}\ Mn^{2+}_{y})\ O^{2-}_{4}$ *with* x = y + z.

1 Introduction

Results obtained in recent years have led to much progress in the development of high performance negative temperature coefficient (NTC) thermistors[1–4] and particularly thin layer ceramics.[5] Generally, these NTC ceramics are based on Mn-spinels. Since both manganese and iron assume multiple valences in oxide structure, it is possible to elaborate spinels over a continuous range of composition from Mn_3O_4 to Fe_3O_4.[6] Thus, in determining the phase diagram of the solids present in the system $Fe_2O_3 - Mn_2O_3 - O_2$ at equilibrium in air, Wickham[7] described the chemical composition of the mixed oxides of iron and manganese which have the spinel crystal structure and proposed the formula $Fe_{3-x}Mn_xO_{4+\delta}$. The value of δ for most of the spinel compositions is very close to zero, yet relatively large for x equal to zero. Pelton *et al.*,[8] through analysis of the phase equilibrium diagram of the Fe_3O_4–Mn_3O_4 spinel system, obtained information on the thermodynamic properties and inferred the distribution of divalent and trivalent cations between the octahedral and tetrahedral sites.

Until now, many papers have been devoted to manganese ferrite $Fe_{3-x}Mn_xO_4$ with $0 \leq x \leq 1$.[9–14] But studies are rare for iron manganite (excess of manganese) and only for the defined compound Mn_2FeO_4. Thus, measurements of magnetic-moment data enabled Eschenfelder[6] to propose a cationic distribution for this compound $Mn^{2+}(Fe^{2+}Mn^{4+})O^{2-}_4$. Using the Mössbauer technique, Tanaka *et al.*[15] introduced both Fe^{3+} and Fe^{2+} ions in octahedral sites following the distributions $Fe^{3+}_{0{\cdot}09}\ Mn^{2+}_{0{\cdot}91}(Fe^{2+}_{0{\cdot}09}\ Fe^{3+}_{0{\cdot}82}\ Mn^{3+}_{1{\cdot}09})\ O^{2-}_4$. More recently, Kulkarni and Darshane,[16] by Mössbauer investigation of $FeMn_2O_4$, showed the equal distribution of Fe^{3+} ions between tetrahedral and octahedral sites and the absence of Fe^{2+} ions in the lattice. Their conductivity and thermopower measurements led them to express the cation distribution of this compound by the formula $Fe^{3+}_{0{\cdot}5}\ Mn^{2+}_{0{\cdot}5}\ (Fe^{3+}_{0{\cdot}5}\ Mn^{2+}_{0{\cdot}5}\ Mn^{3+}_{1-y}\ Mn^{2+}_{y/2}\ Mn^{4+}_{y/2})O^{2-}_4$.

The approach of Rousset *et al.*[17] is to optimize all the manufacturing and electrical parameters of NTC thermistors by a chemical process to establish correlations between composition, structure and electrical properties, so as to understand and rationalize the conventional process. In this respect, the present work reports our results on the preparation of single-phase iron manganite $Mn_{3-x}Fe_xO_4$ with $0 \leq x \leq 1{\cdot}05$. A cation distribution in the compound defined is proposed that takes account of the results obtained for the complete range of these solid solutions. This method appears to be more relevant than the one that only considers only the defined compound Mn_2FeO_4.

*To whom correspondence should be addressed.

2 Experimental

2.1 Preparation of iron manganite powders

Co-precipitated formate precursors were obtained by the addition of water–ethanol solutions at 25°C from $MCl_2.4H_2O$ (with M = Mn, Fe) and ammonium formate. After 30 min, the precipitates were filtered and washed with water–ethanol solution. The different compositions of formate solid solutions studied, $Fe_y\ Mn_{1-y}\ (O_2CH)_2.\ 2\ H_2O$, are listed in Table 1.

After several thermal decomposition tests on formate precursors, we succeeded in obtaining the desired spinel structure phase directly: $Fe_xMn_{3-x}O_4$ (with $x = 3y$). The conditions applied were: rate of temperature increase 150°C h^{-1}, ageing for 4 h at 1000°C, and quenching in air from 1000°C to room temperature.

2.2 Preparation of ceramic samples

To prepare the ceramics, the spinel powders were mixed with an organic binder and pressed into discs under 400 MPa pressure. The resulting discs were fired at 1180°C in air, with 4 h sintering time, and then quenched in air.

The densification of the ceramics was improved by optimizing the percentage of binder. The highest densification, about 95%, was obtained for a ratio of 40 wt% of binder.

2.3 Measurements

X-ray powder diffraction (XRD) measurements were performed at room temperature using an automatic diffractometer (Siemens D501).

The ^{57}Fe Mössbauer spectra were recorded at room temperature with a spectrometer using a 25 mCi ^{57}Co source in Rh matrix. Absolute velocity calibration was carried out with an Fe foil (25 μm thick); isomer shifts (IS) are reported with reference to Fe. The spectra were computer-fitted using a general Lorentzian routine, and a nonlinear least-squares curve-fitting procedure was employed to obtain the best fit to the experimental data. We used IS and quadrupole splitting (QS) to characterize the species.

Table 1. Composition of the formate precursors $Fe_yMn_{1-y}(O_2CH)_2.2H_20$ and the corresponding iron manganites $Fe_xMn_{3-x}O_4$

y	0	0·04	0·13	0·19	0·26	0·35
x	0	0·12	0·39	0·58	0·78	1·05

To determine the electrical characteristics, the ceramic samples were electroded with silver paint and fired at 850°C. Resistivity measurements, ρ, were taken at (25 ± 0·05)°C using a Philips PM2525 multimeter. A second measurement at 85°C gave us the thermal sensitivity B.

3 Results

3.1 XRD analysis

All $Mn_{3-x}Fe_xO_4$ ($0 \leq x \leq 1{\cdot}05$) solid solutions crystallize with a spinel structure. Figure 1 and Table 2 give the overall results, the variation in the lattice parameters a and c, and the c/a ratio. For $0 \leq x \leq 0{\cdot}78$, XRD powders revealed a single tetragonally distorted cubic symmetry spinel phase. This tetragonal distortion, characterized by the ratio c/a, decrease as a function of increasing iron, x, and disappears for x equal 1·05. For $x = 1{\cdot}05$, $Mn_{1.95}Fe_{1.05}O_4$ crystallized with a cubic single phase.

The same results were observed for the ceramics, see Table 3.

3.2 Mössbauer spectroscopy

The Mössbauer spectra of all iron manganite powders have the same form; Fig. 2 shows the Mössbauer spectrum of $Mn_{2.42}Fe_{0.58}O_4$. All the

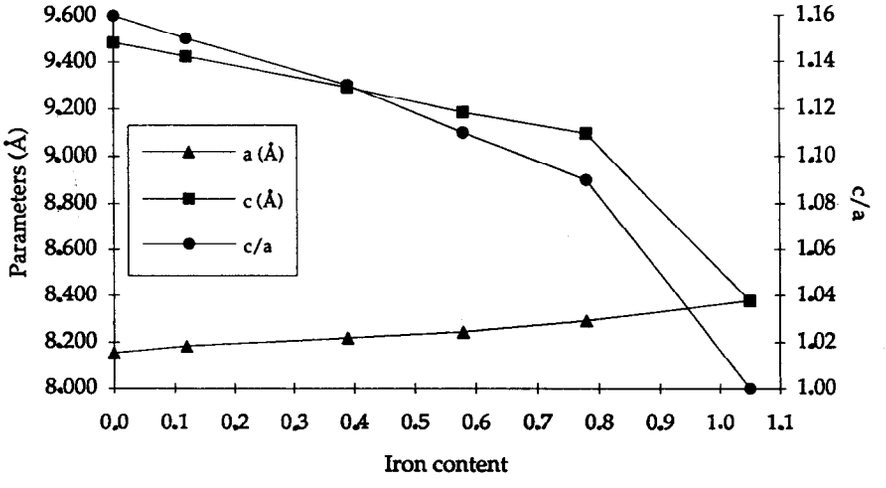


Fig. 1. Variation of the lattice parameters, a and c, and the c/a ratio as a function of iron content.

Table 2. Lattice parameters and *c/a* ratio as a function of iron content, *x*, for the iron manganite powders

x	0	0·12	0·39	0·58	0·78	1·05
a(Å)	8·155	8·183	8·217	8·243	8·291	8·377
c(Å)	9·484	9·423	9·290	9·184	9·096	
c/a	1·16	1·15	1·13	1·11	1·09	1

Table 3. Lattice parameters and *c/a* ratio as a function of iron content, *x*, for the iron manganite ceramics

x	0·12	0·39	0·58	0·78	1·05
a(Å)	8·219	8·215	8·259	8·274	8·341
c(Å)	9·400	9·300	9·181	9·019	
c/a	1·14	1·13	1·11	1·09	1

spectra exhibit two doublets with an isomer shift of between 0·3 and 0·5 mm s^{-1}, indicating the presence of two non-equivalent sites of the Fe^{3+} ion. This could be associated with the presence of Fe^{3+} ions in octahedral and tetrahedral sites. Singh *et al.*[18]

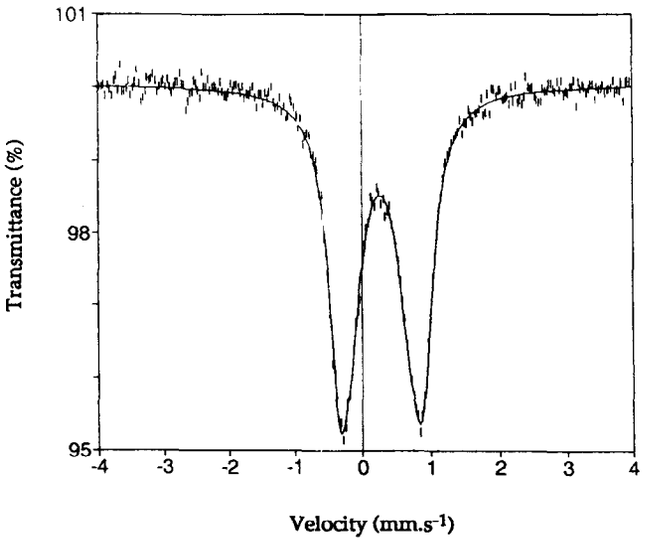


Fig. 2. Mössbauer spectrum of $Mn_{2.42}Fe_{0.58}O_4$.

Table 4. Analysis of the Mössbauer spectra. IS = isomer shift; QS = quadrupole splitting; A = tetrahedral site; B = octahedral site

x	IS_A (mm s^{-1})	IS_B (mm s^{-1})	QS_A (mm s^{-1})	QS_B (mm s^{-1})	% Fe_A^{3+}	% Fe_B^{3+}
0·12	0·369	0·406	1·503	0·978	76·0	24·0
0·39	0·380	0·380	1·336	1·012	57·2	42·8
0·58	0·382	0·372	1·231	0·875	49·9	50·1
0·78	0·383	0·367	1·301	0·891	37·2	62·8
1·05	0.384	0·364	1·297	0·912	21·7	78·3

Table 5. Electrical characteristic data

x	0·39	0·58	0·78	1·05
ρ (Ω cm)	$1{\cdot}431\times10^7$	$0{\cdot}988\times10^7$	$0{\cdot}244\times10^7$	$0{\cdot}202\times10^7$
B (K)	5981	5722	5510	5468

showed that quadrupole splitting is less in octahedral sites than in tetrahedral sites. By quantitative analysis, we can calculate the percentage of Fe^{3+} ions in each site. The percentages are given in Table 4.

3.3 Electrical measurements

Electrical measurements were carried out on the ceramics. Figure 3 shows the variation in dc resistivity, ρ, as a function of iron content, *x*, while Table 5 summarizes the electrical data. The dc resistivity of the composition for $x \leq 0{\cdot}12$ was too high for measurement in our laboratory. For $x > 0{\cdot}12$, resistivity decreased until *x* is equal to 0·78, then remained constant. The substitution of ferric ion in Mn_3O_4, an insulating compound, changed the resistivity from 1 GΩ cm[19] to 2 MΩ cm. The values of thermal sensibility, *B*, also decreased with decreasing resistivity, dropping from 5980 to 5470 K for $0{\cdot}39 \leq x \leq 1{\cdot}05$.

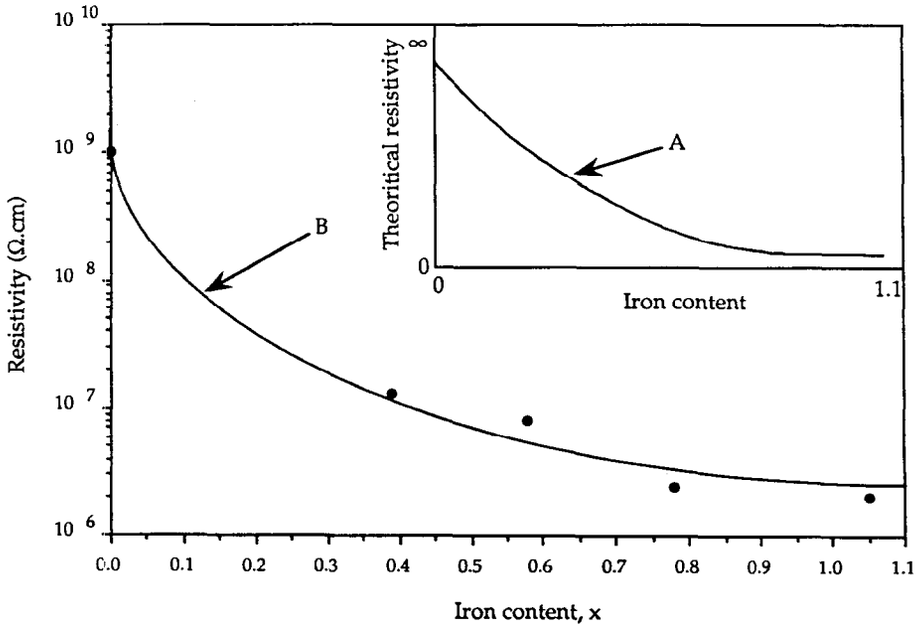


Fig. 3. Variation of resistivity as a function of iron content: (A) theoretical curve and (B) experimental curve.

4 Discussion

4.1 Valency and position of iron cations

Iron manganites were prepared by substituting iron ions for manganese ions in hausmannite Mn_3O_4, the basic crystal structure of manganites. It is now commonly accepted[20,21] that the cation distribution in Mn_3O_4 is Mn^{2+} (Mn_2^{3+}) O_4^{2-}. Thus the iron cation can occupy either the tetrahedral sites (A sites, Mn^{2+} substitution) or octahedral sites (B sites, Mn^{3+} substitution). The Mössbauer results indicate the presence of Fe^{3+} ions only (i.e. no Fe^{2+} ions) located in both octahedral and tetrahedral sites. The introduction of Fe^{3+} ions at octahedral sites does not disturb the overall electrical neutrality of the material, whereas Fe^{3+} in tetrahedral sites does. In the latter case, to preserve electrical neutrality, some Mn^{3+} at B sites change valency to Mn^{2+}. Moreover, the number of Mn^{2+} in octahedral sites is equal to the number of Fe^{3+} in tetrahedral sites. The following ionic configuration can thus be proposed for iron manganites:

$$Mn^{2+}_{1-y}\ Fe^{3+}_{y}\ (Fe^{3+}_{z}\ Mn^{3+}_{2-x}\ Mn^{2+}_{y})\ O^{2-}_{4} \text{ with } x = y + z \quad (I)$$

Using quantitative Mössbauer results, the values of the coefficients x, y and z can be calculated. For example, for $x = 0{\cdot}58$:

$$Mn^{2+}_{0{\cdot}71}Fe^{3+}_{0{\cdot}29}(Fe^{3+}_{0{\cdot}29}\ Mn^{3+}_{1{\cdot}42}\ Mn^{2+}_{0{\cdot}29})\ O^{2-}_{4}$$

The cationic distributions obtained for the other values of x are given in Table 6. Whatever the value of x (total number of iron ions) above 0·12, the number of Fe^{3+} ions in A sites is almost constant, about 0·23 – 0·29, whereas the number of Fe^{3+} ions in B sites increases with the increasing total number of iron ions.

4.2 Cubic–tetragonal transition

Most of the $Mn_{3-x}Fe_xO_4$ solid solutions were found to be tetragonally distorted from cubic symmetry. Hausmannite exhibits a tetragonal distorsion explained by the presence of Mn^{3+} ions in octahedral positions (Jahn–Teller effect). Moreover, Baffier and Huber[22] showed that a minimum concentration of Mn^{3+} ions in octahedral sites is necessary to promote a cooperative Jahn–Taller effect. The minimum is about 50%. Thus a correlation exists between the concentration of Mn^{3+} cations in B sites and the macroscopic distorsion observed by X-ray diffraction. The cationic distribution (I) could explain the decrease in tetragonal distortion as a function of iron content (x) by diminishing the Mn^{3+} ion content in B sites.

Particularly when $x = 1{\cdot}05$, the Mn^{3+} concentration in octahedral sites is below 50% and cubic symmetry appears. These results are in good agreement with the studies of Brabers[23] who pointed out the cubic–tetragonal transition in manganese ferrites $Mn_xFe_{3-x}O_4$ for $x = 1{\cdot}9$, corresponding in this work to iron manganites $Mn_{3-x}Fe_xO_4$ to $x = 1{\cdot}1$.

X-ray diffraction analysis of manganite ceramics revealed the presence of a pure spinel structure. The results concerning the lattice parameters (Table 3) are very close to those observed with spinel powders. Hence we can assume that the ionic distribution of the powder samples does not differ from that of the ceramics.

Table 6. Cationic distributions of the iron manganites $Mn_{3-x}Fe_xO_4$

x	*Cationic distributions*
0	$Mn^{2+}_1(Mn^{3+}_2)O^{2-}_4$
0·12	$Mn^{2+}_{0{\cdot}91}Fe^{3+}_{0{\cdot}09}(Fe^{3+}_{0{\cdot}03}Mn^{3+}_{1{\cdot}88}Mn^{2+}_{0{\cdot}09})O^{2-}_4$
0·39	$Mn^{2+}_{0{\cdot}77}Fe^{3+}_{0{\cdot}23}(Fe^{3+}_{0{\cdot}17}Mn^{3+}_{1{\cdot}60}Mn^{2+}_{0{\cdot}23})O^{2-}_4$
0·58	$Mn^{2+}_{0{\cdot}71}Fe^{3+}_{0{\cdot}29}(Fe^{3+}_{0{\cdot}29}Mn^{3+}_{1{\cdot}42}Mn^{2+}_{0{\cdot}29})O^{2-}_4$
0·78	$Mn^{2+}_{0{\cdot}71}Fe^{3+}_{0{\cdot}29}(Fe^{3+}_{0{\cdot}49}Mn^{3+}_{1{\cdot}22}Mn^{2+}_{0{\cdot}29})O^{2-}_4$
1·05	$Mn^{2+}_{0{\cdot}77}Fe^{3+}_{0{\cdot}23}(Fe^{3+}_{0{\cdot}82}Mn^{3+}_{0{\cdot}95}Mn^{2+}_{0{\cdot}23})O^{2-}_4$

4.3 Electrical properties of ceramics

Electrical conduction in ferrites and manganites is assumed to occur according to the 'hopping' mecanism.[24] It has been determined that hopping will occur if ions of the same element, differing in valency by one unit only, are present in crystallographically equivalent lattice sites.

According to the cationic distribution proposed for iron manganites, formulae I, both Mn^{2+} and Mn^{3+} are present in B sites so that the conditions are correct for electron hopping from Mn^{2+} to Mn^{3+}. The conductivity of the material is determined by the number of ions capable of either donating or accepting electrons in this electron transfer. Thus the electrical conductivity can be written[25]:

$$\sigma = \frac{\sigma_o}{T} NC(1-C) \exp\left(\frac{-E_H}{kT}\right) \text{ with } \sigma'_o = \frac{N_{oct} e^2 d^2 \nu_o}{k}$$

where N_{oct} is a concentration per cm^3 of octahedral sites, d is a jump distance for the charge carrier, ν_o is the lattice vibrational frequency associated with conduction, k is Boltzmann's constant, e the electronic charge, N is a concentration per formulae unit of sites which are available to the charge carriers, C is a fraction of available sites which are occupied by the charge carriers, and E_H is a hopping energy.

The term $NC(1 - C)$ can be rewritten:

$$NC(1-C) = \frac{(Mn^{3+}_{oct})(Mn^{2+}_{oct})}{[(Mn^{3+}_{oct})+(Mn^{2+}_{oct})]^2}$$

Table 7. Comparison between iron manganites and nickel manganites

	Cationic distribution	NC(*1* – C)[a]	d(Å)[b]
$Mn_{2.42}Fe_{0.58}O_4$	$Mn^{2+}_{0.71}Fe^{3+}_{0.29}(Fe^{3+}_{0.29}Mn^{3+}_{1.42}Mn^{2+}_{0.29})O^{2-}_4$	0·141	3·021
$Mn_{2.43}Ni_{0.57}O_4$	$Mn^{2+}_1(Ni^{2+}_{0.57}Mn^{3+}_{0.86}Mn^{4+}_{0.57})O^{2-}_4$	0·240	2·989

$$^{a}NC(1\text{-}C) = \begin{cases} \dfrac{(Mn^{3+}_{oct})\,(Mn^{2+}_{oct})}{[(Mn^{3+}_{oct}) + (Mn^{2+}_{oct})]^2} \\ \text{or} \\ \dfrac{(Mn^{3+}_{oct})\,(Mn^{4+}_{oct})}{[(Mn^{3+}_{oct}) + (Mn^{4+}_{oct})]^2} \end{cases}$$

^{b}d = distance of $\begin{cases} Mn^{2+} - Mn^{3+} \text{ carriers in iron manganites} \\ \text{or} \\ Mn^{3+} - Mn^{4+} \text{ carriers in nickel manganites} \end{cases}$

$$= \begin{cases} \dfrac{a\sqrt{2}}{4} \text{ for cubic phase} \\ \text{or} \\ \dfrac{a'\sqrt{2}}{4} \text{ for tetragonal phase with } a' = \sqrt[3]{a^2c} \text{ (average value)} \end{cases}$$

which represents the probability of finding Mn^{3+} Mn^{2+} pairs in octahedral sites.

As a first approximation, we shall consider only the variation in the last ratio. Thus, the theoretical variation in resistivity can be plotted against iron content and compared with the experimental curve: $\rho = f(x)$. The theoretical variation in resistivity shown in Fig. 3 curve A, calculated for hypothetical configuration I, selected from a previously Mössbauer study, fits well with the experimental data (Fig. 3 curve B). Thus for $0 < x < 0{\cdot}8$, both theoretical and experimental resistivities decrease then remain constant. Table 5 summarizes the electrical data. Note that the substitution of iron ions in hausmannite ($x = 0$) insulating material (resistivity about 10^9 Ω cm) changes the resistivity by only about 10^6 Ω cm. Compared with the substitution of the same number of nickel ions in Mn_3O_4, for example $x = 0{\cdot}57$ nickel ions, the resistivity is about 1650 Ω cm. Two parameters can influence the hopping process: the number and/or the distance of carriers. The higher resistivity in iron manganite can be explained on the one hand by a small number of carriers, 0·141 compared with 0·240 carriers in nickel manganites with approximately the same total number of substituted ions (see Table 7), and, on the other, by the distance of Mn^{2+}–Mn^{3+} carriers in iron manganites (3·021 Å), which is higher than the distance of Mn^{3+}–Mn^{4+} carriers in nickel manganites (2·989 Å).

Figure 4 shows that a plot of log resistivity against the reciprocal of absolute temperature gives a straight-line relationship between these

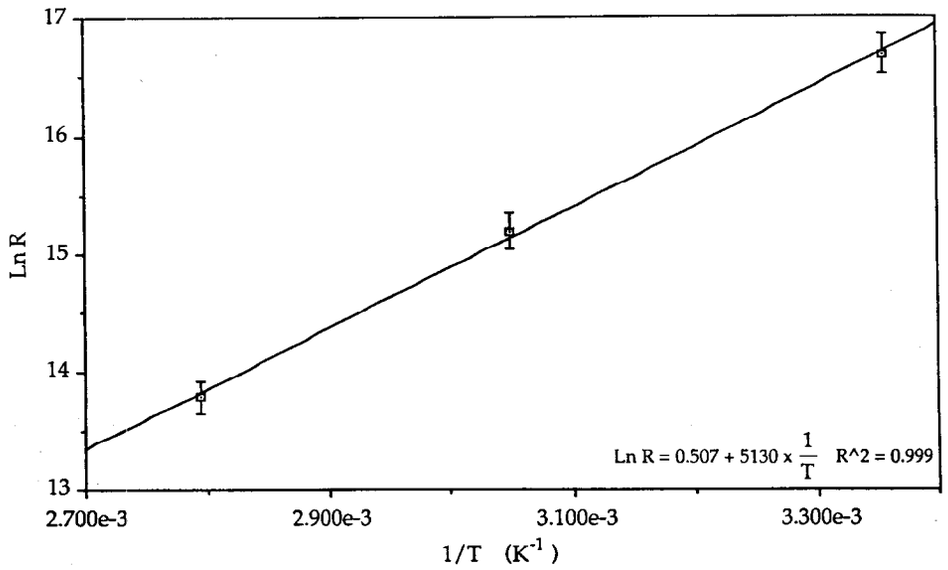


Fig. 4. Variation of ln *R* as a function of inverse of the temperature between 25 and 85°C.

parameters. This result indicates that, in spite of the high resistivity, iron manganites have thermistor characteristics. Moreover, the thermal sensibility is also very high, ranging from 5468 to 5981 K in all solid solutions.

4.4 Cationic distributions

Mössbauer studies indicate that only Fe^{3+} ions are located in both sites of the spinel structure of iron manganites $Mn_{3-x}Fe_xO_4$. Using quantitative results, a cationic distribution is proposed for all solid solutions. In these latter, the number of Mn^{3+} ions in B sites corresponds to the tetragonal distortion, observed by X-ray diffraction, and explains the cubic–tetragonal transition when $x = 1{\cdot}05$.

The electrical resistivity also correlates with the theoretical resistivity calculated by the number of charge carriers from proposed cationic distributions. These results suggest the following ionic distribution model for iron manganite solid solutions:

$$Mn^{2+}_{1-y}\ Fe^{3+}_{y}(Fe^{3+}_{z}\ Mn^{3+}_{2-x}\ Mn^{2+}_{y})\ O^{2-}_{4} \text{ with } x = y + z \quad (1)$$

Differences of opinion exist regarding the distribution and valency states of the cations on the tetrahedral and octahedral sublattices of the spinel structure of iron manganites.[6,15,16] These discrepancies may result from their preparation, since iron manganite are usually prepared by mixtures of oxides. Thus the difficulty of synthesizing single-phase compounds often limits the correlation of structure and properties.

5 Conclusions

Co-precipitated iron–manganese formate was employed to prepare single-phase iron manganite spinels, $Mn_{3-x}Fe_xO_4$ with $0 \leq x \leq 1{\cdot}05$. XRD analysis of these spinels revealed the presence of a single phase having a tetragonally distorted spinel structure for $x < 1{\cdot}05$ and a single cubic spinel phase for $x = 1{\cdot}05$. Mössbauer spectroscopy showed the presence of iron ions in both sites of the spinel structure but only with oxidation degree III. XRD results, combined with Mössbauer spectroscopy, and comparison of experimental and theoretical curves of electrical measurements indicated that the cationic distribution in these spinels approached:

$$Mn^{2+}_{1-y}\ Fe^{3+}_{y}(Fe^{3+}_{z}\ Mn^{3+}_{2-x}\ Mn^{2+}_{y})\ O^{2-}_{4} \text{ with } x = y + z$$

These electro-ceramics display high resistivity and, above all, high thermal sensibility, and should accordingly find interesting industrial applications as NTC thermistors.

References

1. Carnet, R., Etude et développement industriel de céramiques semi-conductrices destinées à la fabrication de thermistances à coefficient de température négatif (CTN) à hautes performances. *Thesis*, University Paul Sabatier, Toulouse, France (1986).
2. Lagrange, A., Caffin, J. P., Fau, P., Legros, R., Metz, R. & Rousset, A., Composition pour thermistances à coefficient de température négatif et de très faible résistivité électrique. *French Patent 8912890* (3 October 1989).
3. Feltz, A., Töpfer, J. & Schirrmeister, F., Conductivity data and preparation route for $NiMn_2O_4$ thermistor ceramics. *J. Eur. Ceram. Soc.*, **9** (1992) 187–91.
4. Martinez Sarrion, M. L. & Morales Sanchez, M., Preparation and characterization of thermistors with negative temperature coefficient, $Ni_xMn_{3-x}O_4$ ($1 \geq x \geq 0{\cdot}56$), from formate precursors. *J. Mater. Chem.*, **3** (1993) 273–7.
5. Lindner, F. & Feltz, A., Thin layer NTC semiconductor ceramics based on $NiMn_2O_4$ and $Zn_zNiMn_{2-z}O_4$ (z = 1/3,2/3). *J. Eur. Ceram. Soc.*, **11** (1993) 269–74.
6. Eschenfelder, A.H., Ionic valences in manganese–iron spinels. *J. Appl. Phys.*, **29** (1958) 378–80.
7. Wickham, D. G., The chemical composition of spinels in the system Fe_3O_4–Mn_3O_4. *J. Inorg. Nucl. Chem.*, **31** (1969) 313–20.
8. Pelton, A. D., Schmalzried, H. & Sticher, J., Thermodynamics of Mn_3O_4–Co_3O_4, Fe_3O_4–Mn_3O_4 and Fe_3O_4–Co_3O_4 spinels by phase diagram analysis. *Ber. Bunsenges. Phys. Chem.*, **83** (1979) 241–52.
9. Tsuji, T., Asakura, Y., Yamashita, T. & Naito, K., Phase equilibria of the Mn–Fe–O system (Fe/Mn = 2). *Solid State Chem.*, **50** (1983) 273–80.
10. Tailhades, Ph., El Guendouzi, M., Rousset, A. & Gillot, B., Sur le comportement des ions du manganèse lors de l'oxydation de magnétites substituées finement divisées., *C. R. Acad. Sci. Paris*, **299** (1986) 13–16.
11. Gillot, B., El Guendouzi, M., Tailhades, Ph. & Rousset, A., Oxidation mechanism of manganese substituted magnetites. *Reactivity of Solids*, **1** (1986) 139–52.
12. Tailhades, Ph., Rousset, A., Bendaoud, R., Fert, A. R. & Gillot, B., Structural study of new defect manganese ferrites. *Mater. Chem. Phys.*, **17** (1987) 521–9.
13. Kolk, B., Albers, A., Hearne, G. R. & Le Roux, H., Evidence of a new structural phase of manganese–iron oxide. *Hyperfine Interactions*, **42** (1988) 1051–4.
14. Jimenez Mateos, J. M., Jones, W., Morales, J. & Tirado, J. L., Composition and cation-valency distribution of cation-deficient Mn/Fe spinel oxides. *J. Solid State Chem.*, **93** (1991) 443–53.
15. Tanaka, M., Mizoguchi, T. & Aiyama, Y., Mössbauer effect in $Mn_xFe_{3-x}O_4$. *J. Phys. Soc. Japan*, **18** (1963) 1091.
16. Kulkarni, J. A. & Darshane, V. S., Effect of high temperature on cation distribution: $NiMn_2O_4$–$FeMn_2O_4$ system. *Thermochim. Acta*, **93** (1985) 473–6.
17. Rousset, A., Legros, R. & Lagrange, A., Recent progress in the fabrication of ceramic negative temperature coefficient thermistors. *J. Eur. Ceram. Soc.*, **3** (1994) 185–95.
18. Singh, V. K., Khatri, N. K. & Lokanathan, S., Mössbauer study of $Co_xMn_{3-x-y}Fe_yO_4$ and $Ni_xMn_{3-x-y}Fe_yO_4$ systems. *Ind. J. Pure & Appl. Phys.*, **20** (1982) 83–9.
19. Castelan, Ph., Contribution à l'étude des propriétés électriques et du phénomène de vieillissement des thermistances C.T.N. à base de manganites à valence mixtes. *Thesis*, University Paul Sabatier, Toulouse, France (1993).
20. Goodenough, J. B. & Loeb, A. L., Theory of ionic ordering crystal distorsion and magnetic exchange due to covalent forces in spinels. *Phys. Rev.*, **98** (1955) 391–408.
21. Driessens, F. C. M., Place and valence of the cations in Mn_3O_4 and some related manganates. *Inorg. Chim. Acta*, **1** (1967) 193–201.
22. Baffier, N. & Huber, M., Etude par diffraction des rayons

X et des neutrons. Des relations entre distribution cationique et distorsion cristalline dans les ferro-manganites spinelles. *J. Phys. Chem. Solids*, **33** (1972) 737–47.
23. Brabers, V. A. M., Infrared spectra of cubic and tetragonal manganese ferrites. *Phys. Stat. Sol.*, **33** (1969) 563–72.
24. Macklen, E. D. *Thermistors.* Electrochemical Publications Limited, Ayr, Scotland, 1979.
25. Dorris, S. E. & Mason, T. O., Electrical properties and cation valencies in Mn_3O_4. *J. Am. Ceram. Soc.*, **71** (1988) 379–85.

Journal of the European Ceramic Society **15** (1995) 1149–1156
© 1995 Elsevier Science Limited
Printed in Great Britain. All rights reserved
0955-2219(95)00079-8
0955-2219/95/$9.50

Study of $Li_{1+x}Al_xTi_{2-x}(PO_4)_3$ for Li^+ Potentiometric Sensors

M. Cretin, P. Fabry & L. Abello

Laboratoire d'Ionique et d'Electrochimie du Solide de Grenoble, CNRS URA D1213, ENSEEG, B.P. 75, 38402 Saint Martin d'Heres, Cedex, France

(Received 21 January 1995; revised version received 18 May 1995; accepted 19 May 1995)

Abstract

Mineral compounds $Li_{1+x}Al_xTi_{2-x}(PO_4)_3$ (x = 0 and x = 0·3) have been made by co-grinding and soil–gel processes. Structural characterizations by X-ray diffraction and Raman spectroscopy indicate that alumina substitution (x = 0·3) does not modify the crystallographic structure, whatever the synthesis process: compounds crystallize in the rhombohedral system with an R-3C space group. The use of the sol–gel route makes low-temperature sintering (950°C) easier and, moreover, leads to ceramics with a high water stability. $Li_{1.3}Al_{0.3}Ti_{1.7}(PO_4)_3$ compounds are fast ionic conductors: $\sigma_{25°C}$ varies from 15^{-5} to 10^{-4} S cm^{-1}, depending on the synthesis process. They have been used as ionic membranes for lithium-selective electrodes. Sensors prepared with sol–gel membranes have the best performance: the detection limit is 1·4 × 10^{-4} mol dm^{-3}. The potassium and the protonic selectivity properties are attractive for such electrodes. For sodium, they need to be improved for biomedical applications.

1 Introduction

During the last few years, numerous studies on lithium ionic conductors of NASICON-type structure have been published. Because of their significant ionic conductivity, the high reduction potential and low atomic mass of lithium, these materials were destined to be used as solid electrolytes for secondary batteries.[1–5] These ionocovalent compounds, of general formula $Li_{1+x}M'x$ (III)$_{2-x}$(IV)$(PO_4)_3$, have a particular crystallographic structure: the NASICON framework consists of a 3D network of PO_4 tetrahedra sharing corners with TiO_6 octahedra and a 3D linked interstitial space occupied by Li^+ ions.[1] These materials may have good selectivity properties as membranes for ion-selective electrodes. The possibility of similar systems has already been shown with the NASICON $Na_{1+x}Zr_2Si_xP_{3-x}O_{12}$, a sodium conductor used in sodium potentiometric sensors.[6,7]

To realize crystallized membranes for lithium electrodes, we have synthesized $Li_{1+x}M'_x$(III)M_{2-x}(IV)$(PO_4)_3$ type compounds, with M' = Al and M = Ti, by different routes. First, we have chosen the most conducting compound of this group: $Li_{1.3}Al_{0.3}Ti_{1.7}(PO_4)_3$. We have also synthesized $LiTi_2(PO_4)_3$ to compare the properties of the doped (x = 0·3) and the undoped (x = 0) ceramics. We have used two processes for their preparation: co-grinding (A) and a sol–gel (B) route. Various physico-chemical characterizations have been carried out on rough and calcined powders, and sintered materials. Afterwards, the samples were used in potentiometric sensors. The results obtained with the different methods are compared.

2 Synthesis and Structural Properties

2.1 Co-grinding synthesis (method A)

Starting materials were Li_2CO_3 (Janssen®, 99% pure), Al_2CO_3 (Baikowski®, 99·99% pure), TiO_2 (Merck®, 99% pure) and $(NH_4)_2HPO_4$ (R.P.®, 99% pure). A stoichiometric mixture was ground for ~100 h with zirconia grinding balls in ethanol. The approximate ratio was 1/3 powder, 1/3 grinding balls and 1/3 ethanol. Then, it was dried and calcined for 2 h at 900°C to decompose the precursors. Afterwards the resulting material was reground.[4] For total decomposition, we had to reheat at 900°C and regrind the product. Specific area of the obtained mixture (measured by the B.E.T. method) is 1·7 m^2 g^{-1} for dried powder. The granulometry is dispersed so that the particle sizes vary from 0·5 to 2 μm (Fig. 1(a)).

The synthesized powder was pressed into pellets at a pressure of 2500 bar (250 MPa) and sintered for 2 h at 1000°C. As seen from a micrograph of a $Li_{1.3}Al_{0.3}Ti_{1.7}(PO_4)_3$ broken pellet obtained by scanning electron microscopy (SEM) (Fig. 1(b)),

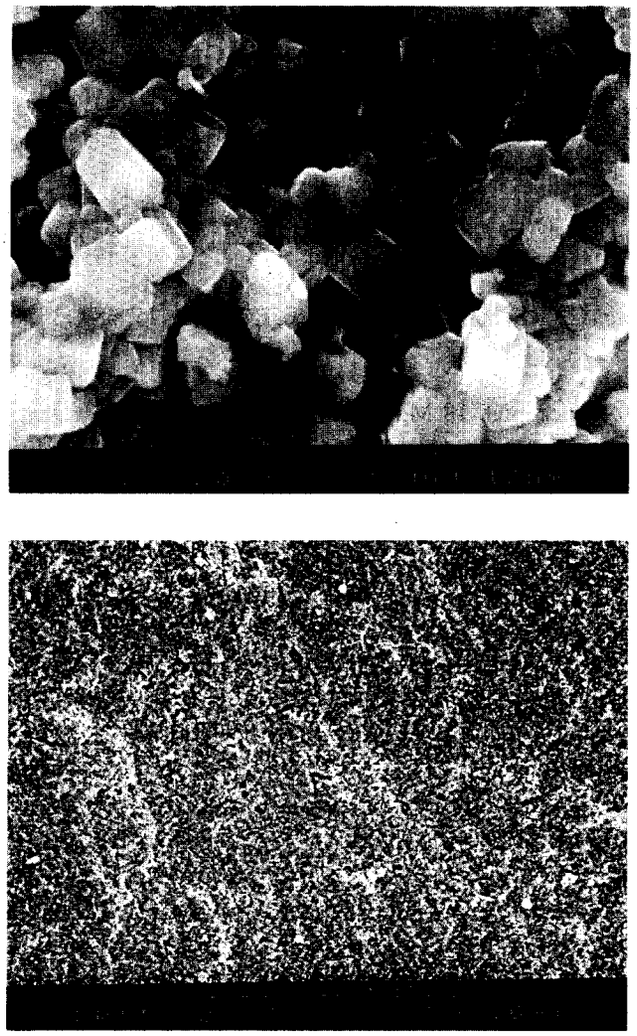


Fig. 1. Scanning electron micrographs of (a) $Li_{1\cdot3}Al_{0\cdot3}Ti_{1\cdot7}(PO_4)_3$ powder synthesized by the co-grinding process and calcined at 900°C and (b) $Li_{1\cdot3}Al_{0\cdot3}Ti_{1\cdot7}(PO_4)_3$ pellet synthesized by theco-grinding process (sintered at 1000°C).

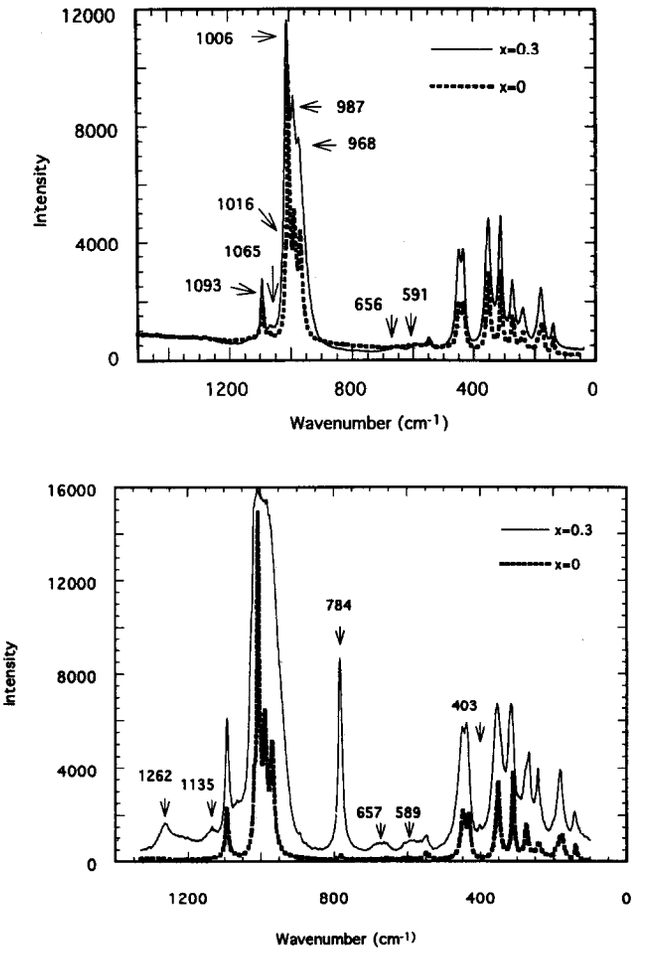


Fig. 2. Raman spectra of (a) co-ground pellet sintered at 1000°C and (b) sol–gel pellet sintered at 950°C.

the ceramic is compact with a packing density of 92%. On the other hand, the $LiTi_2(PO_4)_3$ samples are porous: packing density is about 75%. This result is in agreement with those of Aono *et al.*[4] X-ray diffraction analysis (using $K_{\alpha 1}$ Cu radiation, λ = 0·15406 nm) was conducted with a Siemens D500® $\theta/2\theta$. Doped and undoped ceramics are single-phase materials based on the $LiTi_2(PO_4)_3$ type, with a rhombohedral structure in the R-3C space group. X-ray microanalysis connected with SEM has shown heterogeneity in the composition because of the incomplete decomposition of Li_2CO_3.

To complete the structural analysis, we studied the sintered samples by Raman scattering spectroscopy. Spectra were obtained using a Dilor® *XY* multi-channel spectrometer. The excitation source was an argon-ion laser (excitation wavelength of 514·5 nm and power of 60 mW). Raman spectra of undoped $LiTi_2(PO_4)_3$ (x = 0) and doped $Li_{1\cdot3}Al_{0\cdot3}Ti_{1\cdot7}(PO_4)_3$ (x = 0·3) polycrystalline samples synthesized by co-grinding are shown in Fig. 2(a). Assignment of the different bands of the $LiTi_2(PO_4)_3$ spectra followed the works of Barj.[9,10] Table 1 compares the Raman frequencies of this material and of $NaTi_2(PO_4)_3$.[10] Concerning the co-ground compound, the vibrational frequencies of the internal modes (wavenumber > 400 cm^{-1}) of both compounds are in agreement (Table 1). The intensity inversion between ν_1 and ν_3 has been observed previously and is due to the high electrical charge of PO_4 tetrahedra.[10] For the external modes (< 400 cm^{-1}), the assignment is delicate because of the possibility of frequency coupling between the different ions. Consequently the lithium signature, which should appear at about 300 cm^{-1}, has never been identified. In this range, the correlation with $NaTi_2(PO_4)_3$ is more difficult. For the substituted compound (x = 0·3), the intensities of the unknown bands at 656 and 591 cm^{-1} increase slightly (Fig. 2(a)). This alumina doping also induces a significant modification of the relative intensities of the bands at 1006, 987 and 968 cm^{-1}, and a general enlargement of the spectrum which is due to distortion of the $(Ti/Al)O_6$ octahedra and the PO_4 tetrahedra. Doped and undoped materials are homogeneous: Raman spectra on different areas of the pellets are identical. Li_2CO_3, identified by X-ray microanalysis, did not appear in the spectra.

Table 1. Comparison between the Raman frequencies of the different compounds

$LiTi_2(PO_4)_3$ Raman wavenumber (cm^{-1})		$NaTi_2(PO_4)_3$ Raman wavenumber (cm^{-1}) (Ref. 10)	
Co-ground (Fig. 2(a))	*Sol–gel (Fig. 2(b))*		
1093	1093	1098	$\nu 3$: $A_{1g} + 3E_g$
1065	1065	1070	(antisymmetric
1016	1016	1037	stretching vibration)
1006	1006	1009	
987	987	985	ν_1:$A_{1g}+E_g$
968	968	970	(symmetric stretching vibration)
	784		
656 and 591	657 and 589		
547	548	547	ν_4:$A_{1g} + 3E_g$
		525	(anti symmetric bending vibration)
		455	ν_2:$2A_{1g} + 2E_g$
448	448	440	(symmetric bending vibration)
432	431	432	
		418	
		382	
352	352	350	(Ti–O) vibration mode
		337	
310	310	305	vibration
274	274	273	and
239	240	255	translation
195	195	222	of
177	177	195	phosphorus ions
139	139	155	T^1 and R^1 (PO_4)
		67 and 42	vibration mode of N_a^+

2.2 Sol–gel synthesis (method B)

$LiTi_2(PO_4)_3$ and $Li_{1.3}Al_{0.3}Ti_{1.7}(PO_4)_3$ have already been successfully prepared by this process. Tohge *et al.*[11] used organic precursors for lithium and titanium: $LiOC_2H_5$ and $Ti(OC_4H_9)_4$. They also tested different sources of phosphorus: $PO(OC_2H_5)_3$ and H_3PO_4. It was shown that the use of $PO(OC_2H_5)_3$ leads to a heterogeneous gel and to a material containing TiO_2 after calcination. On the other hand, Ando *et al.*[12] synthesized the above ceramics from CH_3COOLi, $Ti(OC_4H_9)_4$, H_3PO_4, $AlCl_3.6H_2O$ and CH_3COONH_4. The use of CH_3COONH_4 gave a single-phase material without TiO_2 because acetate anions replace the OR groups and form a stable titanium–acetate complex.[13]

The precursors that we chose are $Ti(OC_4H_9)_4$ (Janssen®, 99% pure) and $Al(OC_4H_9)_3$ Janssen®, 97% pure), $NH_4H_2PO_4$ (Fluka®, >99% pure) and CH_3COOLi (Schuchardt®, 98% pure). We avoided the use of chloride precursors, because Cl_2 is generally difficult to eliminate during the sintering. We also tested other starting materials for Li precursors: $LiNO_3$ and LiOH. The pellets obtained were single-phase type $LiTi_2(PO_4)_3$, but the samples had very poor ionic conductivity, almost certainly because of lack of a part of the lithium due to Li_2CO_3, formation[14] and $LiNO_3$ departure during the drying stage. Consequently, we stopped using these type of precursors and chose CH_3COOLi.

The different stages of our sol–gel process are:

- a C_2H_5OH solution of $Ti(OC_4H_9)_4$ and $Al(OC_4H_9)_3$ is heated for 1 h at 70°C;
- an aqueous solution of CH_3COOLi and $NH_4H_2PO_4$ at 70°C is added to the first mixture;
- an excess of H_2O (70°C) (more than the stoichiometric amount required for hydrolysis of the alkoxides) is also used.

As soon as the solutions are mixed, a fine powder forms immediately. Strong stirring is used for 2 h at 70°C.

Then, the drying stage is conducted at low temperature. To facilitate the sublimation process, the product is frozen at –40°C with a Christ Alpha 2-4® freeze dryer. With this technique, the initial morphology of the powder is preserved, contrary to the usual hot or room temperature drying processes such as evaporation, centrifugation with acetone[15] or azeotropic distillation,[16] which can induce powder agglomeration. The specific area of this xerogel powder dried with our process is 52 $m^2\ g^{-1}$ and the particle size is about 0·25 μm diameter.

During a temperature analysis of the sol–gel pellets, very high shrinkage took place between 200 and 450°C (Fig. 3). In this range of temperature, differential scanning calorimetry (DSC) and thermogravimetric analysis (TGA) (Fig. 4) of the sol–gel compounds show exothermic peaks and considerable weight loss. All these phenomena are

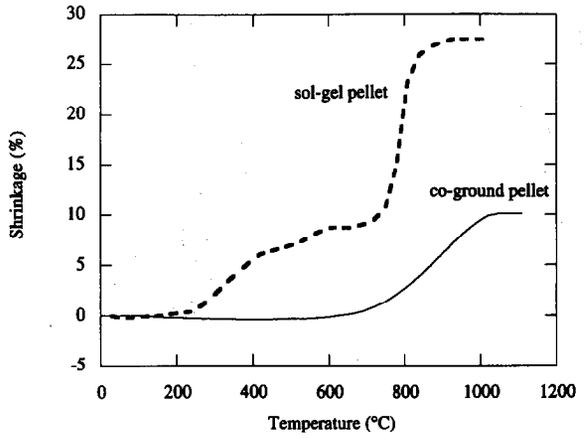


Fig. 3. Shrinkage study during the sintering of $Li_{1.3}Al_{0.3}Ti_{1.7}(PO_4)_3$ synthesized by the co-grinding and sol–gel processes.

due to the combustion of organic groups. As a consequence, to facilitate sintering, it is better to burn off the organic groups. So the powder was calcined at 550°C for 4 h. It remained amorphous according to X-ray diffraction and Raman spectroscopy but the specific area decreased (35 m^2 g^{-1}) due to low temperature sintering of the gel. Nevertheless, the particles are finer than those synthesized by the co-grinding process (Fig. 5).

Sintering is much faster for the sol–gel compounds and moreover takes place at a temperature 100°C lower than that for co-ground compounds (Fig. 3). These properties are required for very high densification. They are due to the very good reactivity of the sol–gel powder, because of its homogeneity and narrow granulometry. Subsequently, doped pellets sintered at 950°C have a packing density of about 93%. At about 640°C, compounds start to crystallize as evidenced by an exothermic peak on the DSC trace (Fig. 4). Pellets sintered at 950°C for about 2 h are mono-phase $LiTi_2(PO_4)_3$.

Raman spectra of $LiTi_2(PO_4)_3$ synthesized by both processes are in agreement (Figs 2(a) and 2(b) and Table 1), except for the presence of a

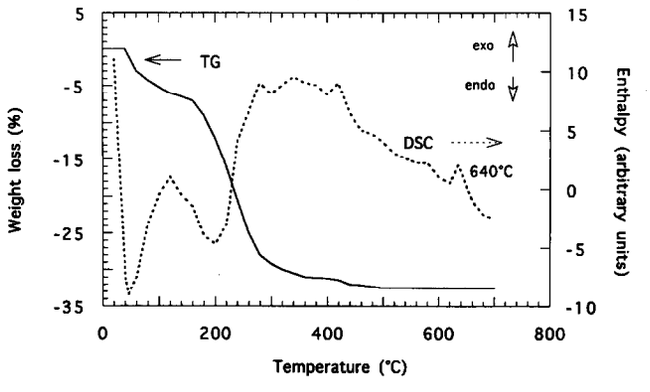


Fig. 4. Thermogravimetric and differential scanning calorimetry analysis of a doped powder synthesized by the sol–gel route.

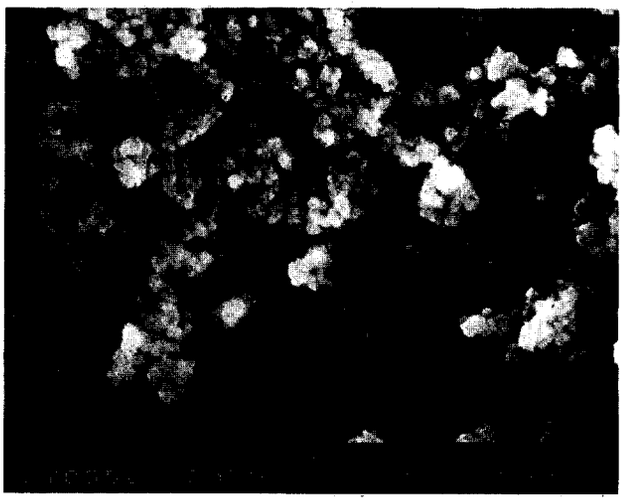


Fig. 5. Scanning electron micrograph of a $Li_{1.3}Al_{0.3}Ti_{1.7}(PO_4)_3$ powder synthesized by the sol–gel process and calcined at 550°C.

very weak band at 784 cm^{-1} on the sol–gel sample spectra. The general spectrum modifications due to the substitution do not depend on the synthesis process: for x = 0·3, we notice for both compounds the relative intensity modifications of the ν_3 and ν_1 bands and a general enlargement of the spectrum. We note the presence of new bands at 1262, 1135 and 403 cm^{-1} on the sol–gel doped material (Fig. 2(b)). Analysis of different samples and powders of $Li_{1.3}Al_{0.3}Ti_{1.7}(PO_4)_3$ have shown that intensity of the bands at 784 and 403 cm^{-1} is a function of the sample and of the analysis area, whereas the relative intensities of the other bands are constant. Consequently, the sol–gel samples contain a small amount of a second phase. This phase seems to be more important for the doped material and it is difficult to know its nature because it is invisible to X-ray diffraction. The complete assignments of the Raman spectra bands for $LiTi_2(PO_4)_3$ and $Li_{1.3}Al_{0.3}Ti_{1.7}(PO_4)_3$ are the subject of current work.

3 Physico-chemical Properties Study

3.1 Ionic conductivity

Ionic conductivity has been measured by the AC impedance method in the range 5 to 13 MHz (impedance analyser HP 4192A®). The measurements were made in a vaccum cell between 25 and 200°C, using gold evaporation electrodes. The utilization of Au blocking electrodes allows a correct separation between the bulk and electrode impedances. An example is given in Fig. 6. The respective contributions of the grains and the grain boundaries have not been separated because their characteristic frequencies are close. As a consequence, Table 2 gives the total conductivity at

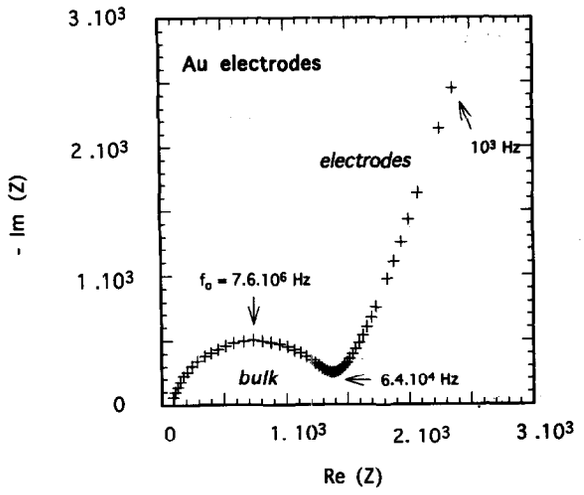


Fig. 6. Example of impedance diagram obtained at 130°C on a $Li_{1.3}Al_{0.3}Ti_{1.7}(PO_4)_3$ pellet synthesized by the sol–gel process using Au electrodes.

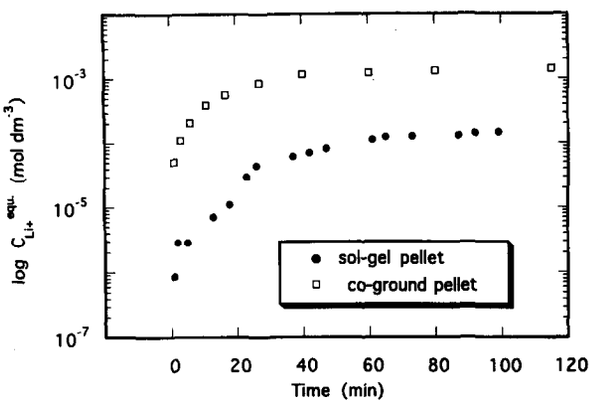


Fig. 7. Evolution of the lithium concentration in solution as a function of time for $Li_{1.3}Al_{0.3}Ti_{1.7}(PO_4)_3$ sintered pellets.

25°C and the activation energy of the different sintered samples, extracted from the Arrhenius plots.

For $x = 0$, the co-ground compound (75% packing density) and the sol–gel compound (82% packing density) are poor ionic conductors. Moreover, the sol–gel material has a high activation energy. On the other hand, $Li_{1.3}Al_{0.3}Ti_{1.7}(PO_4)_3$ ceramics have good electrical properties: very high lithium conductivity and low activation energy. These properties are better for the co-ground samples (95% packing density). The lithium conductivity enhancement for doped materials can be explained by the fact that conductivity depends on different factors:

- the carrier concentration — partial substitution of Ti (IV) by Al (III) has required lithium enhancement to maintain electroneutrality of the compound. This doping has been corroborated by the value of the lithium concentration in the ceramic, which was measured by the analysis laboratory of the CNRS (Vernaison, France);
- the carrier mobility — the octahedral substitution $(Ti/Al)O_6$ has led to a distortion of the structure, confirmed by Raman spectroscopy. Consequently, like in NASICON compounds, carrier diffusion is facilitated by structural transformation,[17] because of the slight decrease of the size of the conduction sites;
- the packing density of the sample — Aono *et al.*[4] have shown that the partial substitution of the Ti^{4+} site with Al^{3+} was very effective for enhancement of the conductivity, mainly because of the densification of the sintered pellets.

3.2 Stability in water

To determine the stability in water of the ceramics, we have recorded the lithium loss from the pellet to the solution. Samples were immersed in distilled water and the lithium concentration was measured every 10 min using a Varian AA1275BD® atomic absorption spectrometer (Fig. 7). Results in function of time are given in Fig. 7.

The values tend to a constant, with stability being achieved after about 40 min for the co-ground pellet and 60 min for the sol–gel pellet. The lithium concentration equilibrum value is $1{\cdot}4\ 10^{-3}$ mol dm^{-3} for the co-ground ceramic. We can think that the lithium concentration corresponds to equilibrum phenomena (solubility, ionic exchange, etc.). After about 100 h of immersion, we recorded 5% weight loss for this pellet. This very poor stability in water is due to the preferential solubility of parasite phases, invisible by X-ray diffraction. Li_2CO_3, identified by X-ray microanalysis, is certainly the origin of this solubility. On the other hand, sol–gel ceramics have a better stability: the equilibrum value is low, $1{\cdot}5 \times 10^{-4}$ mol dm^{-3}. In this case, weight loss is about 0·9%.

Table 2. Conductivity at 25°C and activation energy (E_a) of sintered pellets

	$LiTi_2(PO_4)_3$ ($x = 0$)				*$Li_{1.3}Al_{0.3}Ti_{1.7}(PO_4)_3$ ($x = 0{\cdot}3$)*			
	Co-ground		*Sol–gel*		*Co-ground*		*Sol–gel*	
$\sigma_{25°C}$ ($S\ cm^{-1}$)	2×10^{-6} Ref. 4	7×10^{-7}	$2{\cdot}4 \times 10^{-8}$ Ref. 12	4×10^{-8}	7×10^{-4} Ref. 4	9×10^{-5}	$3{\cdot}2 \times 10^{-4}$ Ref. 12	10^{-5}
E_a(EV)	0·37		0·51		0·37		0·40	

4 Utilization of Ceramics as Ionic Membranes in Potentiometric Sensors

The development of lithium-selective potentiometric electrodes for the determination of Li^+ activity in biological systems has already been realized, especially when using polymeric membranes.[18–23] However, the lifetime of this type of electrode is short; moreover polymers are not suitable for sterilization. Consequently, it is attractive to use ceramic membranes in potentiometric sensors for such applications. Experimentally, the specific electrode is made with the ionic ceramic, stuck at the extremity of the electrode isolant body. Inside, a silver wire covered with a silver chloride layer and immersed in lithium salt solution constitute the internal reference. Tested membranes are $Li_{1\cdot3}Al_{0\cdot3}Ti_{1\cdot7}(PO_4)_3$ synthesized by co-grinding and sol–gel processes, because of their high ionic conductivity.

The electrochemical cell is:

Ag–AgCl/Lithium salt/Ionic conductor/Analyzed solution//Saturated Calomel Electrode (SCE)

When lithium activity in the internal reference is constant, the cell potential obeys the Nernst equation:

$$E=E^0+2\cdot3RT/F \log a_{Li^+}$$

where E^0 is a constant depending on the internal (Ag–AgCl) and external (SCE) references, and consequently on temperature. R and F are the usual constants, T the absolute temperature and a_{Li^+} the lithium activity in the analysed solution. For measurements, we use generally a supported electrolyte and we have made the approximation that the ionic strength is a constant. So, as a first approximation, a_{Li^+} can be substituted for the concentration (activity coefficient is included in E^0).

4.1 Detection limit

Referring to the IUPAC recommendations, the detection limit (DL) is the crossing point of the Nernst asymptote ($2.3RT/F$ slope) and the horizontal line, corresponding to the insensitive range of the sensor. Figure 8 gives an example of a calibration curve. We used a $BaCl_2$ 10^{-1} mol dm^{-3} solution to keep constant ionic strength and also to decrease the analysed solution impedance (Ba^{2+} is not an interfering ion). Consequently, the experimental procedure for this operation is the following: the external reference electrode is equipped with an extension (double junction) containing $BaCl_2$ 10^{-1} mol dm^{-3}. The lithium salt contained in the internal reference is LiCl 10^{-1} mol dm^{-3} + $BaCl_2$ 10^{-1} mol dm^{-3}. Both electrodes are immersed in a $BaCl_2$ 10^{-1} mol dm^{-3} solution. The addition of LiCl solutions (10^{-3} to 1 mol dm^{-3} + $BaCl_2$ 10^{-1} mol dm^{-3}) and recording of the cell potential allow the calibration curve to be plotted (Fig. 8).

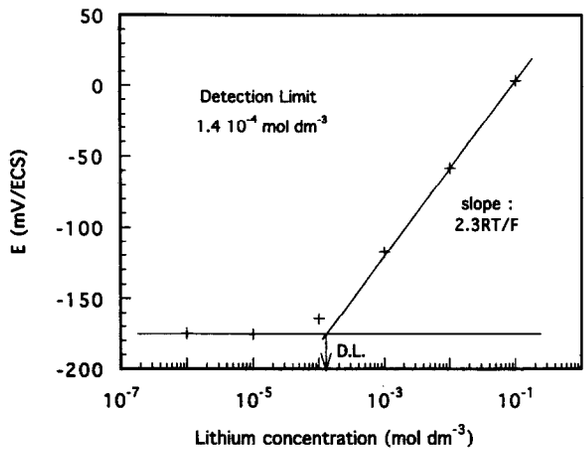


Fig. 8. Example of calibration curve and detection limit (DL) determination obtained on a Li^+ electrode using a $Li_{1\cdot3}Al_{0\cdot3}Ti_{1\cdot7}(PO_4)_3$ sol–gel membrane.

Electrodes using $Li_{1\cdot3}Al_{0\cdot3}Ti_{1\cdot7}(PO_4)_3$ membranes have a Nernst response for high lithium concentration, with a slope of $2\cdot3RT/F$ V per concentration decade. Moreover, the detection limit depends on the membrane synthesis process (Table 3): sensors using sol–gel membranes are more sensitive than those made with co-ground ones. These first type of specific electrodes are based on ionic exchanges at the membrane–solution interface. Consequently, the cell potential is a function of the ionic equilibrum at this interface. As we have seen before (stability in water), part of the lithium contained in the ceramic leaves the membrane for the solution. As a consequence, lithium concentration is more important at the interface than into the analysed solution. The detection limit of both types of sensor and the lithium solubility equilibrium value for each membrane (from Fig. 7) are compared in Table 3. The sensor sensibility is linked to the stability in water of the ceramics. Accordingly, the lithium solubility of the material is the principal limiting factor for lithium analysis with the first kind of electrodes using $Li_{1\cdot3}Al_{0\cdot3}Ti_{1\cdot7}(PO_4)_3$ ceramics. For biological appli-

Table 3. Comparison of the sensor sensibility with the concentration of Li^+ in water after about 1 h of use for co-ground and sol–gel membranes

	Co-ground membrane	*Sol–gel membrane*
Detection limit of sensors (mol dm^{-3})	$1\cdot6 \times 10^{-3}$	$1\cdot4 \times 10^{-4}$
Lithium equilibrium in water (mol dm^{-3})	$1\cdot4 \times 10^{-3}$	$1\cdot5 \times 10^{-4}$

cations, where lithium measurements in the range from 10^{-4} to 5×10^{-3} mol dm^{-3} are required,[24] sensors using co-ground membranes are not sensitive enough (DL = $1{\cdot}6 \times 10^{-3}$ mol dm^{-3}), whereas those made with sol–gel ones are usable because of their higher sensibility (DL = $1{\cdot}4 \times 10^{-4}$ mol dm^{-3}).

4.2 Ionic selectivity

The selectivity for ionic electrodes is the ability to recognize one ion amongst others. It is never perfect, because interfering ions can disturb ionic exchange at the interface. The electrode responds to the empirical Nickolskii relation:

$$E = E^{o} + 2{\cdot}3RT/z_iF \log (a_i + K_{i,j}^{pot} a_j^{zi/zj})$$

where i is the primary ion, j an interfering ion and $K_{i,j}^{pot}$ the potentiometric ion-selectivity coefficient for ion j. An example of the potentiometric ion-selectivity coefficient determination for a_{Li^+} = constant is given in Fig. 9. There are two asymptotes:

(1) $$\text{for } a_j \to 0$$
$$E^* = E^{o} + 2{\cdot}3RT/z_iF \log a_i$$

(2) $$\text{for } K_{i,j}^{pot} a_j^{zi/zj} >> a_i$$
$$E' = E^{o} + 2{\cdot}3RT/z_iF \log K_{i,j}^{pot} a_j^{zi/zj}$$

At the crossing point (Fig. 9) of both asymptotes: $K_{ij}^{pot} = a_i/(a_j^{*zi/zj})$. For the $a_j^{*zi/zj}$ value, the variation between the curve and the intersection point is 18 mV at 25°C. a_j^* is generally determined with this 18 mV variation because of the difficulty in defining the Nernst asymptote (Fig. 9).

To determine the sodium and potassium ion-selectivity coefficients, we made successive additions of a solution containing the interfering ion (LiCl 10^{-2} mol dm^{-3} + $BaCl_2$ 10^{-1} mol dm^{-3} + NaCl or KCl 10^{-1} mol dm^{-3}) in a solution of LiCl 10^{-2} mol dm^{-3} + $BaCl_2$ 10^{-1} mol dm^{-3}. To determine the protonic influence, we changed the pH of the solution by chloride acid addition. Recording and plotting of the cell potential as a function of the interfering ion lead to a_j^* determination and to $K_{i,j}^{pot}$ calculation.

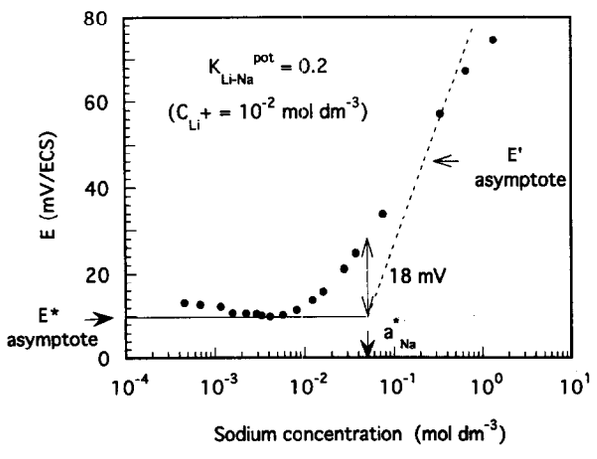


Fig. 9. Example of the determination of K_{Li-Na}^{pot} of a Li^+ electrode using a $Li_{1{\cdot}3}Al_{0{\cdot}3}Ti_{1{\cdot}7}(PO_4)_3$ co-ground membrane.

Table 4. Principal potentiometric ionic-selectivity coefficients

	Co-ground membrane	*Sol–gel membrane*
K_{Li-Na}^{pot}	0·5–1	0·2
$K_{Li\ K}^{pot}$	3×10^{-2}	5×10^{-2}
K_{Li-H}^{pot}	0·2–2	2

The synthesis process does not have a great influence on the principal potentiometric ionic-selectivity coefficients (Table 4). Both types of electrode are more selective to potassium than to sodium. This result is in agreement with Fabry and Siebert's assumption[25] that selectivity depends on the size of the interfering ion (ionic radii of Li^+, Na^+ and K^+ in 6 coordinance are 0·76, 1·02 and 1·38 Å, respectively.[8] We can explain this property by the particular structure of NASICON-type ceramics: there are two types of conduction site in the network. The way between different sites is achieved through bottlenecks, the size of which is adjustable: lattice constants depend on the stoichiometry and the composition of the material.[5] In the composition $Li_{1{\cdot}3}Al_{0{\cdot}3}Ti_{1{\cdot}7}(PO_4)_3$ the sodium mobility in the membrane is high, because the opening of the bottlenecks is sufficiently large [as a comparison, the optimal value for Na^+ diffusion is obtained for $Na_3Zr_2Si_2P_2O_{12}$ for which lattice parameters are approximately a = 9·05 Å, c = 22·9 Å (Refs. 15,16)]. As a consequence, the interface equilibrum is etablished with the contribution of the sodium contained in the analysed solution. On the other hand, the potassium is too large for the bottlenecks and then the K^+ contribution decreases greatly.

Concerning the pH effect on the sensor response, it is not due to a structural ionic exchange but arises from ionic (H^+ or OH^-) adsorption at the surface of the membrane.[26] Then, for very high protonic concentration, the electrode operates like a glass one. We note that the values of the protonic potentiometric coefficient (Table 4) are lower than those obtained with the Na^+ NASICON used in sodium-selective electrodes.[15,16,25]

5 Conclusion

The use of the sol–gel process for the synthesis of $Li_{1+x}Al_xTi_{2-x}(PO_4)_3$ (x = 0·3) is fully justified. The morphology of the sol–gel powders leads to attractive sintering properties, without modification of

the structure of the sintered samples. In spite of a lower ionic conductivity than the co-ground material, the sol–gel ceramic has a better stability in water.

For aqueous analyses, ion-selective electrodes using a doped ceramic synthezised by the sol–gel process is the more attractive: the detection limit is $1{\cdot}4 \times 10^{-4}$ mol dm^{-3}. For biomedical measurements, the ion-selective electrode must be very selective for Na^+ and K^+ (low values of $K_{Li,Na}^{pot}$ and $K_{Li,K}^{pot}$) because of the important concentration of these elements in the body. Consequently, actual values of the potentiometric coefficients, especially for Na^+, are too high for lithium analysis in blood. However, the low protonic interference is very interesting for measurements in systems such as gastric juice.

Acknowledgements

This work was supported by the 'Région Rhône-Alpes' in collaboration with RADIOMETER-ANALYTICAL S.A. The authors thank particularly Mr J. J. Fombon for his assistance in this field. They would like to acknowledge the technical assistance of M. Henault and N. Rosman.

References

1. Subramanian, M.A., Subramanian, R. & Clearfield, A., Lithium ion conductors in the system $AB(IV)_2(PO_4)_3$(B = Ti, Zr and Hf). *Solid State Ionics*, **18 & 19** (1986) 562–9.
2. Lin, Z. X., Yu, H. J., Li, S. C. & Tian, S. B., Lithium ion conductors based on $LiTi_2P_3O_{12}$ compound. *Solid State Ionics*, **31** (1988) 91–4.
3. Aono, H., Sugimoto, E., Sadaoka, Y., Imanaka, N. & Adachi, G. Y., Ionic conductivity of the lithium titanium phosphate ($Li_{1+x}M_xTi_{2-x}(PO_4)_3$, M = Al, Sc, Y and La) systems. *J. Electrochem. Soc.*, **136** (1989) 590–1.
4. Aono, H., Sugimoto, E., Sadaoka, Y., Imanaka, N. & Adachi, G. Y., Ionic conductivity of solid electrolytes based on lithium titanium phosphate. *J. Electrochem. Soc.*, **137** (1990) 1023–7.
5. Aono, H., Sugimoto E., Sadaoka, Y., Imanak, N. & Adachi, G. Y., Ionic conductivity and sinterability of lithium titanium phosphate system. *Solid State Ionics*, **40/41** (1990) 38–42.
6. Engell J. & Mortensen, S., Ion sensitive measuring device. Int. Patent WO 84:01829, Radiometer (1984)
7. Fabry, P., Gros, J. P., Million-Brodaz, J. F. & Kleitz, M., NASICON, an ionic conductor for solid-state Na^+-selective electrode. *Sensors and Actuators*, **15** (1988) 33–49.
8. Shannon, R. D., Revised effective ionic radii and systematic studies of interatomic distances in halides and chalcogenides. *Acta Cryst*, **A32** (1976) 751–67.
9. Barj, M., Perthuis, H. & Colomban, Ph., Domaines d'existence, distorsions structurales et modes de vibration des ions conducteurs dans les réseaux hotes de type NASICON. *Solid State Ionics*, **11** (1983) 157–77.
10. Barj, M., Etude de la structure statique et dynamique de quelques matériaux à mobilité ionique par spectroscopie de vibration et par diffusion de neutrons. *Thesis*, University of Paris-Nord (1987).
11. Tohge, N., Zhu, J. & Minami, T., Low-temperature preparation of $LiTi_2(PO_4)_3$ by the sol–gel process. *Chemistry Express*, **5** (1990) 973–6.
12. Ando, Y., Hirose, N., Kuwano, J., Kato, M. & Otsuka, H., Preparation of lithium ion conducting solid solutions based on $LiTi_2(PO_4)_3$ by sol–gel method. *Ceram. Today — Tomorrow's Ceram.*, (1991) 2242–52.
13. Doeuff, S., Henry, M., Sanchez, C. & Livage J., Hydrolysis of titanium alkoxides:modification of the molecular precursor by acetic acid. *J. Non-Cryst. Solids*, **89** (1987) 206–16.
14. Smaihi, M., Céramiques tritigènes à base d'orthosilicate de lithium: préparation sol–gel, mobilité du lithium et relâchement du tritium. *Thesis*, University of Paris-Sud (1990).
15. Caneiro A., Fabry, P., Khireddine, H. & Siebert, E., Performance characteristics of sodium super ionic conductors prepared by the sol–gel route for sodium ion sensors. *Anal. Chem.*, **63** (1991) 2550–7.
16. Khireddine, H., Etude des performances de capteurs potentiométriques à ions sodium utilisant des membranes de NASICON. *Thesis*, INP Grenoble (1992).
17. Boilot, J. P., Collin, G. & Colomban, Ph., Relation structure–fast ion conduction in the NASICON solid solution. *J. Solid State Chem.*, **73** (1988) 160–71.
18. Kirsch, N. N. L., Funck R. J. J., Pretsch, E. & Simon, W., Ionophore für Li^+: Membranselektivität, Darstellung und Stabilitätskonstanten in Äthanol. *Helv. Chim. Acta.*, **60** (1977) 2326–33.
19. Metzger, E., Ammann, D., Asper, R. & Simon, W., Ion selective liquid membrane electrode for the assay of lithium in blood serum. *Anal Chem.*, **58** (1986) 132–5.
20. Gadzekpo, V. P. Y., Hungerford, J. M., Kadry A. M., Ibrahim, Y. A., Xie, R. Y. & Christian, G. D., Comparative study of neutral carriers in polymeric lithium ion selective electrodes. *Anal. Chem.*, **58** (1986) 1948–53.
21. Kitazawa S., Kimura, K., Yano, H. & Shono, T., Lithium-selective polymeric membrane electrodes based on dodecylmethyl-14-crown-4. *Analyst*, **110** (1985) 295–9.
22. Kimura, K., Sakamoto, H., Kitazawa, S. & Shono, T., Novel lithium-selective ionophores bearing an easily ionizable moiety. *J. Chem. Soc., Chem. Commun.*, (1985) 669–70.
23. Sugihara, H., Okada, T. & Hiratani, K., Lithium ion-selective electrodes based on 1,10-phenanthroline derivatives. *Chem. Lett.*, (1987) 2391–2.
24. Samuel, D. & Gottesfeld, Z., Le lithium, la manie dépressive et la chimie du cerveau. *Endeavour*, **32** (1973) 122–8.
25. Fabry, P. & Siebert, E., NASICON: a sensitive membrane for ion analysis. In *Chemical Sensor Technology*, ed. Yaminhi, Kodansha, Tokyo, 1992, Vol. 4, pp. 111–24.
26. Sandifer, J. R., Theory of interfacial potential differences: effects of adsorption into hydrated (gel) and non hydrated surfaces. *Anal. Chem.*, **60** (1988) 1553–62.

Journal of the European Ceramic Society 15 (1995) 1157–1161
© 1995 Elsevier Science Limited
Printed in Great Britain. All rights reserved
0955-2219(95)00092-5
0955-2219/95/$9.50

AC-Conductivity Measurements on γ-Aluminium Oxynitride

H. X. Willems,* P. F. Van Hal, R. Metselaar & G. de With†

Eindhoven University of Technology, CTK, POB 513, 5600 MB Eindhoven, The Netherlands

(Received 2 February 1995; revised version received 18 May 1995; accepted 22 May 1995)

Abstract

AC-conductivity measurements were performed on aluminium oxynitrides (Alons) because of their interesting defect structure. Although it became apparent that these Alons are not stable in the temperature range used, the electrical properties of the materials could be measured with impedance spectroscopy using a special procedure. The activation energy for charge transport in Alons with 67·5, 73 and 77·5 mol% Al_2O_3 at temperatures between 1173 and 1373 K was 2·78, 2·85 and 2·97 eV, respectively, while the pre-exponential factors increased with increasing number of aluminium vacancies. The conductivity shows a more-than-linear dependency on the amount of aluminium vacancies. Charge is transported via aluminium vacancies but the large amount of vacancies does not result in greatly changed mobilities: the interesting defect structure of Alon does not lead to extraordinary electrical properties.

1 Introduction

γ-Aluminium oxynitride (Alon) is a ceramic material with a spinel-type crystal structure.[1] The ideal composition for this system (Al_3O_3N) is outside the homogeneity region of Alon[2,3] and the actual Alon phase can be described with the constant anion model, in which all anion sites are occupied by oxygen or nitrogen and the cation sites are partly occupied by aluminium.[4] As about one aluminium atom is missing in each unit cell,[5] Alon is a highly defective material. Because it might be possible to have high ion mobilities in such a material and because the electrical properties of Alon were largely unknown, we decided to investigate these properties for three Alons with different compositions. During these investigations it became apparent, however, that Alon has only a limited stability, as is reported in detail elsewhere.[6] However, interesting Alon/Al_2O_3 and Alon/Al_2O_3/SiC composites can be obtained in spite of these restrictions[7,8]

The conductivity for ionic conductors is thermally activated and can be described by $\sigma = \sigma_0/T \times \exp(-\Delta H_m/kT)$, in which σ is the specific conductivity (S m^{-1}), σ_0 is a scaling constant (K S m^{-1}), T is the temperature (K), k is Boltzmann's constant, and ΔH_m is an activation enthalpy (J mol^{-1}). To determine ΔH_m, $\ln(\sigma T)$ is plotted against $1/T$ in an Arrhenius plot; the slope in this plot is equal to $\Delta H/k$, provided that the number of charge carriers is constant over the temperature range considered.[9]

2 Experimental

Details of the preparation of the Alons were reported earlier.[10] The Alons had compositions corresponding to 67·5, 73 and 77·5 mol% Al_2O_3 and will be designated 'L', 'M' and 'R', respectively, in this paper. Mechanical and optical properties of these materials were reported earlier.[11] Samples were flat discs, typically 8 mm in diameter and 0·5 to 1 mm thick. These were polished, cleaned in boiling nitric acid (60%), neutralized with ammonia, rinsed thoroughly with deionized water and dried. Platinum electrodes (diameter 5·5 mm, thickness ~3 μm) were deposited on the samples by sputtering and subsequent painting (Demetron 308 A paste). The electroded samples were annealed at 873 K for 2 h in air.

AC-measurements were performed with a set-up based on a Solartron 1174 Frequency Response Analyzer which was interfaced to a computer. The computer was also used to control a DC-driven tube furnace containing a spring-loaded alumina conductivity cell, comparable to that of Metselaar and Larsen.[12]

*Presently affiliated with Philips Research Laboratories.
†To whom correspondence should be addressed. Also affiliated with Philips Research Laboratories, Prof. Holstlaan 4, 5656 AA, Eindhoven, The Netherlands.

The partial oxygen pressure was kept low because the oxidation of Alon to Al_2O_3 is faster than the decomposition of Alon into Al_2O_3 and AlN. Experiments were done in flowing nitrogen (pressure 10^5 Pa, purity 99·999%) which was led over graphite powder at a temperature of 1273 K before it entered the measurement set-up.

For each temperature a new sample was used which was heated to the desired measuring temperature (heating rate 344 K h^{-1}) and kept there for 20 min to stabilize. For composition M, stabilization times of 6 h were also used for comparison. After this stabilization the frequency response of the material was measured in the frequency range 1 MHz–0·1 Hz, which took about 30 min, the greater part of which was spent in measuring the lower frequencies. This cycle of stabilizing and measuring was repeated two times or more (typically three impedance diagrams were taken) and the resulting impedance diagrams were extrapolated linearly to t=0, which is the time at which the sample reaches the measuring temperature for the first time. The stabilization time was chosen in such a way that the impedance–time plot for any frequency was well approximated by a straight line. Temperatures used ranged from 1123 to 1373 K. Measurements were performed with a measuring voltage of 50 mV (voltages of 100 and 200 mV gave the same results).

No Nernst potential measurements were performed because the material degrades fairly rapidly. In our equipment specimens have to be mounted at high temperature to obtain a gas–tight seal before the measurements can take place. As a result of this, the material would already change considerably before any measurement could be performed.

3 Results

A number of typical complex impedance diagrams of Alon with composition M are stacked together in Figs 1(a) and 1(b). Both diagrams show several measurements on one specimen each and the extrapolation that was made to t=0. Measurements with a stabilization time of 20 min always showed one arc only. Measurements with a stabilization time of 6 h showed results similar to Fig. 1(b) at all temperatures, although the second and third arcs were not always as clearly visible as in this figure. At t=0 the complex impedance diagram consists of one depressed arc only. As the sample is held at the measuring temperature, the intersection of the arc with the real axis shifts to higher values. At still longer holding times, a second and a third arc appear in the diagram. Table 1 lists the

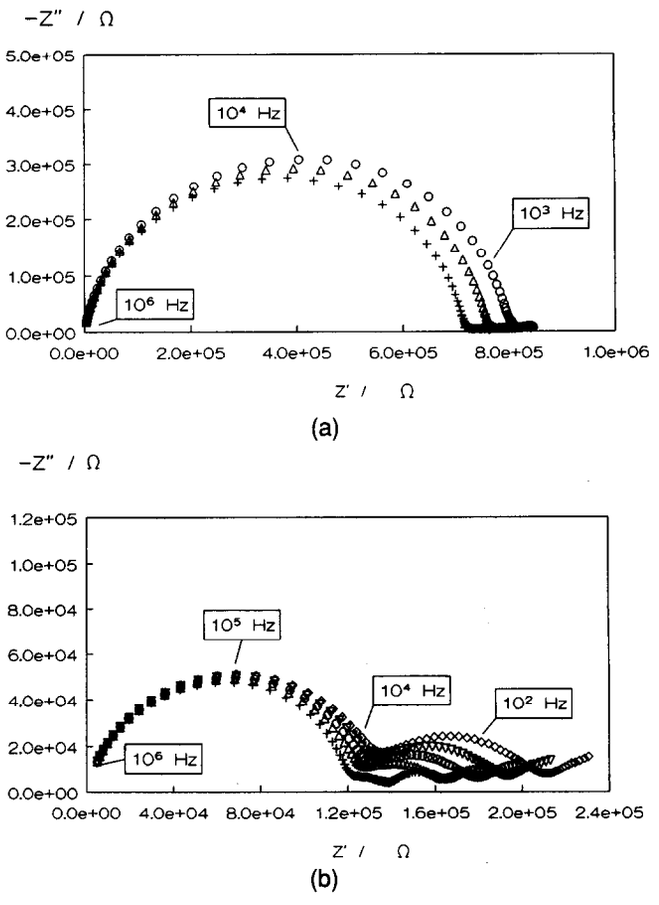


Fig. 1. Two typical sets of measurements on Alon with composition M together with extrapolations to t=0 (inner circle, +): (a) shows measurements at 1248 K with a stabilization time of 20 min); (b) measurements at 1348 K with a stabilization time of 6 h (Δ = first measurement, ○ = second measurement, ∇ = third measurement and ◇ = fourth measurement).

results of the measurements with a stabilization time of 20 min on the three types of Alon. Each entry represents the value of the real part of the complex impedance at t=0.

At temperatures above 1373 K no reliable extrapolation to t=0 could be made (degradation is too fast). Moreover, the characteristic frequency of the first arc was about 1 MHz and as this is the maximum measuring frequency, half of the arc

Table 1. Extrapolated values of the specific resistance at t=0 (the time at which the measuring temperature was reached for the first time) at various temperatures for L, M and R Alons. The stabilization time used for the measurements was 20 min.

Temperature (K)	*Specific resistance (Ω m)*		
	Composition L	*Composition M*	*Composition R*
1173	$2·32 \times 10^5$	$1·86 \times 10^5$	$1·16 \times 10^5$
1198	$1·25 \times 10^5$	$1·00 \times 10^5$	$6·63 \times 10^4$
1223	$8·06 \times 10^4$	$6·79 \times 10^4$	$3·76 \times 10^4$
1248	$4·29 \times 10^4$	$3·58 \times 10^4$	$2·34 \times 10^4$
1273	$2·93 \times 10^4$	$2·11 \times 10^4$	$1·40 \times 10^4$
1298		$1·34 \times 10^4$	$7·65 \times 10^3$
1323		$9·00 \times 10^3$	$4·66 \times 10^3$
1348		$5·74 \times 10^3$	
1373		$3·35 \times 10^3$	

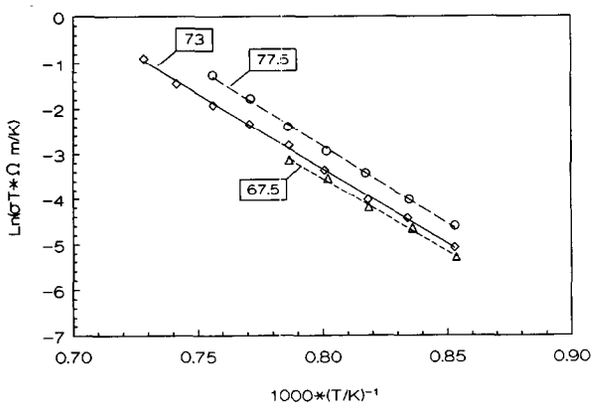


Fig. 2. Arrhenius plot for all measurements with a stabilization time of 20 min (Δ = L, ◇ = M and ○ = R).

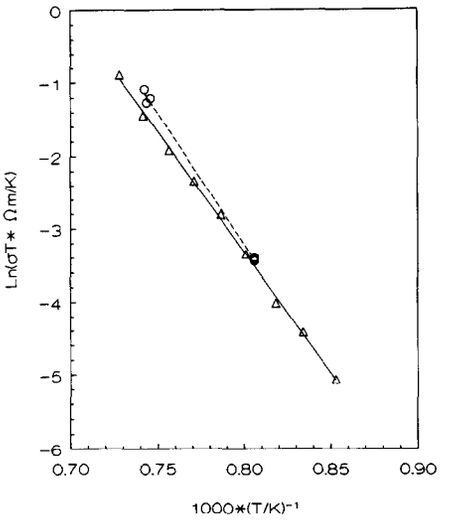


Fig. 3. Comparison between measurements on M Alon with short stabilization times (20 min, Δ) and those with long stabilization times (6 h, ○)

could not be measured. Below 1123 K, the DC-resistance of the samples was > 10 MΩ. As it is not possible to measure these impedances accurately with the set-up used, no measurements were performed in this region. At temperatures below 1173 K equilibration was too slow and reliable extrapolation was not possible.

An Arrhenius plot containing all measurements is given in Fig. 2. Activation energies of 2·78, 2·85 and 2·97 eV were obtained for L, M and R, respectively. These values were determined with a linear least-squares fit of the data. Correlation coefficients were 0·998, 0·999 and 0·999, respectively.

Table 2 lists the results of the measurements on Alon with composition M with a stabilization time of 6 h. As can be seen in Fig. 3, the measurements at 1240 K give almost the same results as the measurements with the short stabilization time and the measurements at 1340–1350 K resulted in slightly higher conductivity values than the measurements with the short stabilization time.

X-ray diffraction (XRD) on specimens before and after testing showed that the lattice parameters had decreased slightly during the experiments. Unfortunately, the uncertainty of the XRD measurement is of the same magnitude. No other phases than Alon were observed with XRD. Alons of composition L and M were still translucent after testing but specimens of composition R were afterwards slightly more opaque than before.

Table 2. Extrapolated values of the specific resistance at t=0 of M Alon at several temperatures with a stabilization time of 6 h

Temperature (K)	*Specific resistance (Ω m)*
1241	$3{\cdot}80 \times 10^4$
1241	$3{\cdot}80 \times 10^4$
1242	$3{\cdot}70 \times 10^4$
1341	$4{\cdot}5 \times 10^3$
1344	$4{\cdot}8 \times 10^3$
1347	$4{\cdot}0 \times 10^3$

If Alon specimens were kept for some days at the measuring temperature, α-Al_2O_3 was found on the outer surface of the specimens.

4 Discussion

At first, there is only one arc in the impedance diagrams, corresponding to the bulk material, while after a certain period of time one or two additional arcs appear. The bulk material decomposes because of the instability of the material at the measuring temperature. The additional arcs can, for instance, be due to accumulation of oxygen on the grain boundaries (probably the first step in the oxidation of the material) or to electrode reactions. The slight decrease of the lattice parameters also indicates an increase in the oxygen content. The opaqueness of the R specimens can be due to the formation of Al_2O_3-rich regions in the material.

The results of the experiments with long stabilization times are only different from those with short stabilization times at high temperature. At high temperature, degradation does not proceed linearly with time when the time between observation is too long and reliable extrapolation is not possible.

If the amount of intrinsic aluminium vacancies is plotted against the specific conductivity for various temperatures, Fig. 4 is obtained. As can be seen, the conductivity is higher when the amount of vacancies increases, which is an indication that the migrating species are the aluminium vacancies.

The literature data on electrical properties of Alon are limited to one publication of Kim and Richards[13] who measured the AC-conductivity of Alon with compositions corresponding to 70 and 76·3 mol% Al_2O_3 at temperatures of 1573, 1673

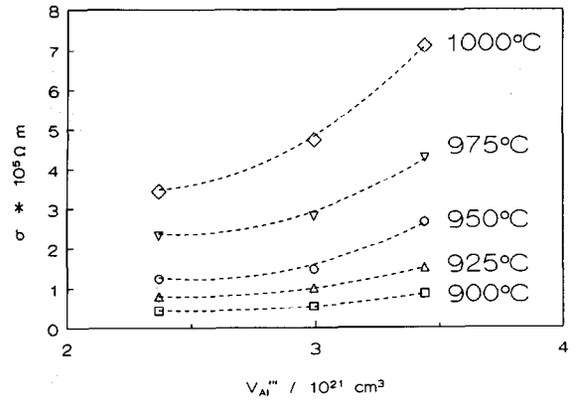


Fig. 4. Electrical conductivity of Alon as a function of concentration of aluminium vacancies at various temperatures.

and 1773 K in flowing nitrogen. They report an activation energy of 116 kJ mol^{-1}, which we were unable to reconstruct from their data. If their data are fitted with the equation for ionic conductors we obtain an activation energy of 329 kJ mol^{-1} (3·41 eV). The differences between their results and this investigation are probably due to faster degradation of the materials at the higher measuring temperatures used by Kim and Richards.

There are some data on the electrical behaviour of $MgAl_2O_4$, which has the same crystal structure as Alon. Sonder[14] showed that conduction in $MgAl_2O_4$ is almost purely ionic in character and argued that the transporting species most probably are cation vacancies. It was also shown that the conductivity between 700 and 2000 K is not greatly influenced by either ambient oxygen pressure (10^5–10^{11} Pa) or iron impurities up to 0·1%.[14,15] The activation energies ranged between 1·50 and 2·74 eV, dependent on the temperature range considered. Bates and Garnier[16] observed nearly the same range of activation energies with measurements on single crystal and polycrystalline $MgAl_2O_4$ at temperatures between 650 and 1260 K. Comparison between diffusion coefficients of magnesium, aluminium and oxygen in MgO, Al_2O_3 and $MgAl_2O_4$ show that the mobility of oxygen is several orders of magnitude lower than that of magnesium and aluminium.[17] From these literature data it can be concluded that the charge transport in $MgAl_2O_4$ takes place via cation vacancies. Because Alon has the same type of crystal structure as $MgAl_2O_4$ and nitrogen ions are even larger than oxygen ions, it seems plausible that the same situation exists in Alon. The influence of impurities on the amount of cation vacancies will also be limited in Alon because the intrinsic defect concentration is already quite high.

If we assume that aluminium vacancies are the transporting species, it is possible to calculate the diffusion coefficient of these vacancies from the Nernst–Einstein relation. If we take for instance the specific resistance of Alon with composition M at 1373 K, a diffusion coefficient of 8×10^{-15} m^2 s^{-1} can be calculated. This diffusion coefficient is of the same order of magnitude as the diffusion coefficient for Mg^{2+} in stoichiometric magnesium aluminate spinel.[17] However, the conductivity shows a more-than-linear dependency on the amount of aluminium vacancies (Fig. 3). A similar phenomenon was observed by Aggarwal and Dieckmann[18] in their investigation of non-stoichiometric cobaltous oxide, in which the mobility of the cationic defects also increased with increasing deviation from stoichiometry. They tentatively attribute this effect to a decrease in the lattice parameter and/or to changes in the type of defects, but at the moment the physics behind this phenomenon are not understood.

Let us assume for a moment that Alon is a semiconductor instead of an ionic conductor. In this case, energies of 2·64, 2·74 and 2·86 eV can be calculated for L, M and R, respectively, using $\sigma = \sigma_s \times \exp(-\Delta H_s/kT)$. The correlation factors remain unchanged. A possible mechanism could be extrinsic electron conduction due to silicon impurities (about 800 ppm) that can act as donors. If we assume complete ionization, the amount of free electrons (n) is equal to the amount of silicon atoms ($n = [Si_{Al}] = 6{\cdot}3 \times 10^{25}$ m^{-3}) which gives a mobility (b) of 3×10^{-11} m^{-2} V^{-1} s^{-1} (from $\sigma = n \times e \times b$). Although low values for the electron mobility are known to exist in small polaron semiconductors, this value is so small that it makes electron conduction improbable. Also, the activation energy of 2·8 eV is high for the activation energy of a donor. In comparison, Lee and Kröger reported a value of about 1·7 eV for the activation energy of silicon donors in Al_2O_3.[19] If we take also Fig. 4 into account we conclude that electronic conductivity can be ruled out.

5 Conclusions

AC-conductivity measurements were performed on Alons because of their interesting defect structure. Although it became apparent that Alons are not stable in the temperature range used, the electrical properties of the materials could be measured with impedance spectroscopy using a special procedure. The activation energy for charge transport at temperatures between 1173 and 1373 K was shown to be 2·78, 2·85 and 2·97 eV for compositions L, M and R respectively, while the pre-exponential factors increased with increasing number of aluminium vacancies. The conductivity shows a more-than-linear dependency on the amount of aluminium vacancies. Charge is trans-

ported via aluminium vacancies but the large amount of vacancies does not result in greatly changed mobilities: the interesting defect structure of Alon does not lead to extraordinary electrical properties.

Acknowledgement

This research has partly been supported by the Commission for the Innovative Research Program Technical Ceramics (IOP-TK) of the Ministry of Economic Affairs in the Netherlands (IOP-TK research grant 88.A022).

References

1. Goursat, P., Billy, M., Goeuriot, P., Labbe, J. C., Villechenoux, J. M., Roult, G. & Bardolle, J., Contribution a l'etude du systeme Al/O/N II: retention d'azote dans les produits d'oxydation de l'oxynitrure d'aluminium γ. *Mater. Chem.*, **6** (1981) 81–94.
2. Lejus, A .M., Sur la formation à haute température de spinelles non stoechiométrique et des phases dérivées. *Rev. Hautes Tempér. et Réfract.*, **1** (1964) 53–95.
3. McCauley, J. W., & Corbin, N. D., Phase relations and reaction sintering of transparent cubic aluminium oxynitride spinel. *J. Am. Ceram. Soc.*, **62** (1979) 467–9.
4. McCauley, J. W., A simple model for aluminium oxynitride spinels. *J. Am. Ceram. Soc.*, **61** (1978) 372–3.
5. Willems, H. X., de With, G., Metselaar, R., Helmholdt, R. B. & Petersen, K. K., Neutron diffraction of γ-aluminium oxide. *J. Mater. Sci. Lett.*, **12** (1993) 1470–2.
6. Willems, H. X., Hendrix, M. M. R. M., de With, G. & Metselaar, R., Thermodynamics of Alon II: Phase relations. *J. Eur. Ceram. Soc.*, **10** (1992) 339–46.
7. Sappei, J., Goeuriot, D., Thevenot, F., Laurent, Y., Guyader, J., & L'Haridon, P., Alumina-γ-aluminium oxynitride composites from alumina nitrided by ammonia. *J. Eur. Ceram. Soc.*, **8** (1991) 257–62.
8. Thevenot, F., Espérance, E., & Goeuriot, D., Three phase ceramics composites: Al_2O_3–Alon–SiC. In *Third Euro-ceramics*, Vol. 3, Eds. P. Durán and J. F. Fernández, Faenza Editrice Ibérica, Castellón, 1993, pp. 577–94.
9. Macdonald, J. R. (Ed.), *Impedance Spectroscopy*. Wiley, New York, 1987.
10. Willems, H. X., Hendrix, M. M. R. M., de With, G. & Metselaar, R., Production of translucent γ-aluminium oxynitride. In *Euro ceramics III*, Eds. G. Ziegler and H. Hausner, Deutsche Keramische Gesellschaft, Köln, 1993, pp. 2443–7.
11. Willems, H. X., van Hal, P. F., de With, G. & Metselaar, R., Mechanical properties of γ-aluminium oxynitride. *J. Mater. Sci.*, **28** (1993) 6185–9.
12. Metselaar, R. & Larsen, P. K., Diffusion of oxygen vacancies in yttrium iron garnet investigated by dynamic conductivity measurements. *J. Phys. Chem. Solids*, **37** (1976) 599–605.
13. Kim, I. U. & Richards, V. L., High temperature conductivity of aluminium oxynitride spinel. *J. Am. Ceram. Soc.*, **68** (1985) C210–2.
14. Sonder, E., Ionic transference numbers and electrical conduction in $MgAl_2O_4$ spinel. *J. Am. Ceram. Soc.*, **66** (1983) 50–3.
15. Weeks, R. A. & Sonder, E., Electrical conductivity of pure and Fe-doped magnesium–aluminium spinel. *J. Am. Ceram. Soc.*, **63** (1980) 92–5.
16. Bates, J. L. & Garnier, J. E., Electrical conductivity of $MgAl_2O_4$ and $Y_3Al_5O_{12}$. *J. Am. Ceram. Soc.*, **64** (1981) C138–41.
17. Bratton, R. J., Initial sintering of $MgAl_2O_4$. *J. Am. Ceram. Soc.*, **52** (1969) 417–9.
18. Aggarwal, S. & Dieckmann, R., Non-stoichiometry and point defect structure of cobaltous oxide. *Ceram. Trans.*, **24** (1991) 23–30.
19. Lee, C.H. & Kröger, F. A., Electrical conductivity of polycrystalline Al_2O_3 doped with silicon. *J. Am. Ceram. Soc.*, **68** (1985) 92–9.

Journal of the European Ceramic Society 15 (1995) 1163–1170
© 1995 Elsevier Science Limited
Printed in Great Britain. All rights reserved
0955-2219(95)00090-9
0955-2219/95/$9.50

Dense Ceramics of $BaTiO_3$ Produced from Powders Prepared by a Chemical Process

C. Miot, C. Proust & E. Husson*

Laboratoire de Physique et Mécanique des Matériaux, ESEM, Université d'Orléans et CRPHT-CNRS, 45071 Orléans Cedex 2, France

(Received 24 January 1995; received in revised form 19 May 1995; accepted 22 May 1995)

Abstract

A sintering optimization of barium titanate ceramics from fine-grained and homogeneous reproducible powders obtained by the citric process is presented. Different sintering parameters are studied: heating rates, final temperature, dwelling times at this final temperature, and influence of the powder deagglomeration step. The sintering is followed by dilatometric measurements. The ceramics obtained by sintering at 1230 or 1300°C are free of barium carbonate, the residual carbon content being estimated at about 400 ppm in the surface layer. They exhibit a grain size close to 1 μm, a structure in which the cubic and tetragonal phases coexist, and a density of about 96% of the theoretical density. Their permittivity and loss factor are respectively about 5000 and 2·5 × 10⁻² at 25°C.

1 Introduction

Barium titanate ceramics are extensively used in the manufacture of ceramic multilayer capacitors. These applications require materials with a good density, a high dielectric constant and a low loss factor. Synthesis of materials with these properties needs fine-grained ceramics, which may be obtained from fine-grained and homogeneous reproducible powders. In a previous paper, we have presented the elaboration of such a powder from a citric resin process.[1] Here is given a sintering optimization study to obtain ceramics with good dielectric properties. The different physical and chemical characteristics of the ceramics obtained were investigated by several methods: dilatometric measurements, X-ray diffraction (XRD), scanning electron microscopy (SEM), thermogravimetric analysis (TGA), infra-red spectroscopy (IR) and nuclear analyses.

2 Experimental Procedure

$BaTiO_3$ powders were obtained from a citric resin method, described in previous papers.[1–3] The mixed citrate $BaTi(C_6H_6O_7)_3.6H_2O$ was first prepared, then dissolved in a citric acid, ethylene glycol and water mixture so that R = ($BaTiO_3$ mass)/(solution mass ratio) was 1%. This solution was calcined at 700°C in static air and $BaTiO_3$ powders were produced after 2 h. Powders elaborated by this method exhibit a Ba/Ti ratio equal to 1. After a careful deagglomeration step,[1] powders were calcined at 700°C for 4 h before being isostatically pressed at 250 MPa in the form of discs and then sintered.

X-ray diffraction patterns of crushed ceramics were obtained using a Siemens D500 diffractometer with the CuK_α wavelength at room temperature. The 400–004 diffraction lines were accurately recorded in the range $98{\cdot}5° < 2\theta < 102{\cdot}5°$ in steps of 0·01° (2θ) with a counting time of 80 s per data point.

Thermogravimetric measurements were made with a Setaram thermobalance under flowing oxygen atmosphere. Approximately 100 mg of ceramic was accurately weighted in a platinum crucible. The temperature was raised from room temperature to 1000°C at 10°C min^{-1} and then from 1000 to 1400°C at 5°C min^{-1}.

FTIR reflection spectra were recorded with a Brucker IFS 113+88 interferometer between 4000 and 400 cm^{-1} at room temperature on a sample containing 2 mg of $BaTiO_3$ dispersed in 200 mg of KBr and pressed into pellets.

The residual carbon concentration was determined by the $^{12}C(d, p)^{13}C$ nuclear technique using deuterons from the CERI's† Van de Graaff generator. The

*To whom correspondence should be addressed.
†CERI. Centre d'Etude sur les Radiations Ionisantes, CNRS Orléans.

method has been described elsewhere.[4–6] The measurements were performed at 950 keV deuteron energy in an ultra-high vacuum chamber under a vacuum of about 10^{-9} mbar obtained with a cryogenic pumping system. The disc samples were sintered ceramics of about 3 mm in thickness and 11 mm in diameter. In the experimental conditions used,[7] taking into account the differential cross-section[8] and the density of the material, the maximal penetration depth is estimated to be about 1 μm and the carbon in the surface layer (about 0·4 μm) may be determined with a precision of 10%.

The SEM images were obtained with a Cambridge stereoscan 100 microscope on the fracture surfaces of samples previously metallized with platinum. The transmission electron microscopy (TEM) images were obtained with a Philips SM20 microscope.

Final densities were evaluated by geometrical measurements and confirmed by: (i) mercury intrusion data (Micrometric 9300 apparatus); (ii) helium pycnometry data (Accupic 1330 apparatus).

Dilatometric measurements were made in a Setaram vertical dilatometer with a constant force load equivalent to 1 g. The derivative curve of shrinkage versus temperature may be calculated electronically. The measurement of the shrinkage, reported for room temperature, allows the estimation of the final density from the green compact one. The value of 6·02 g cm^{-3} was used as the theoretical density, d_{th}.

Dielectric measurements of the ceramics were carried out on an automated Hewlett-Packard impedancemeter HP 4194A. The relative dielectric constant ϵ' and loss factor tg δ were measured between 160 and 120°C at various frequencies (100 Hz, 1 kHz, 10 kHz, 100 kHz and 1 MHz) with a cooling rate of 1°C min^{-1}.

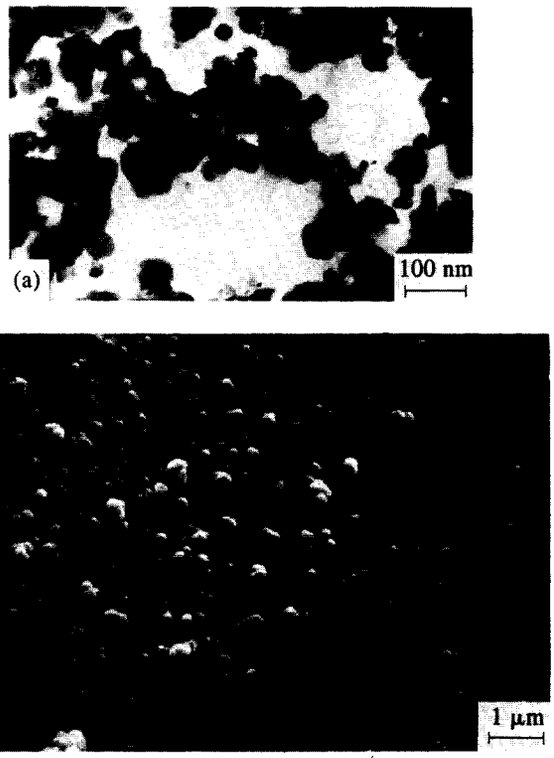


Fig. 1. Microstructure of deagglomerated $BaTiO_3$ powder: (a) 40 nm crystallites observed by TEM; (b) 150 nm spheroide aggregates observed by SEM.

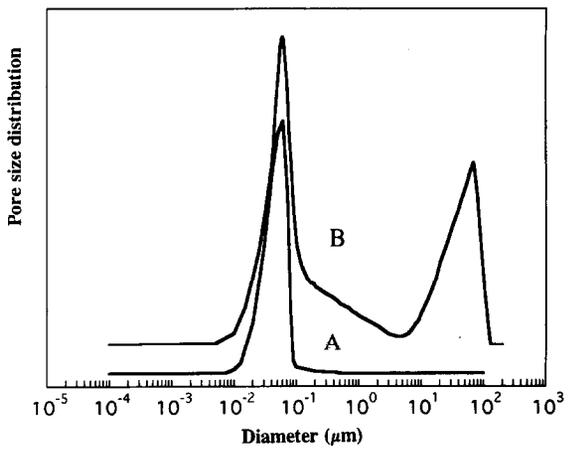


Fig. 2. Pore-size distribution for green compacts of (a) a deagglomerated powder and (b) a raw powder.

3 Results and Discussion

3.1 Raw powders

The sintering behaviour strongly depends on the green states, thus it was very important to know the powder characteristics. The latter were studied and described in detail in a previous paper.[1] Here only the microstructure of the raw deagglomerated powder is given again: it can be described by crystallites associated into 150 nm spheroid aggregates (Fig. 1).

The results obtained by mercury intrusion, for deagglomerated and non-deagglomerated powders are presented in Fig. 2. The curve obtained with a non-deagglomerated powder shows two pore-size distributions centred on 0·05 and 80 μm (Fig. 2(b)) whereas only one peak, centred on 0·05 μm, is observed on the curve obtained with a deagglomerated powder (Fig. 2(a)).

3.2 Sintering optimization

The green compacts were sintered in air at different temperatures up to 1400°C, using various heating rate conditions reported in Table 1. According to our previous studies,[2,3] it appeared that the best sintering temperature to obtain dense ceramics with fine grain size was approximately 1250°C. Thus, for this final temperature of the sintering cycle, different heating rates were

investigated. The sintering conditions, geometrical densities and grain sizes estimated from SEM observations are reported in Table 1. It can be observed that:

(i) a decrease of the heating rate between 1000 and 1250°C induces an increase of the density and grain size;

(ii) for a slow heating rate (4°C h^{-1} between 1000°C and the final temperature), an increase of the final temperature (up to 1300°C) induces an increase of the density and grain size. In this case, the higher the final temperature, the larger the grain size distribution;

(iii) for sintering steps with a final temperature of 1400°C the ceramics showed a classical bimodal grain-size distribution with large grains (100–200 μm) embedded in a fine-grained matrix. This phenomenon was evidenced by several authors[9–12] and the anomalous grain growth occured when samples were heated up to a final temperature greater than 1380°C.

It appeared that to obtain a good density and a small grain size, the final sintering temperature could be reduced to 1230°C with a slow heating rate between 1000 and 1230°C, for example 4°C h^{-1} (Table 1). The best conditions were the following: heating from 20 to 700°C at 350°C h^{-1}, then from 700 to 1000°C at 50°C h^{-1} and finally from 1000 to 1230°C at 4°C h^{-1}. These sintering conditions will be called '1230°C sintering' in the following text. The ceramics had a geometrical density greater than 96% of d_{th}, and an average grain size of 1·6 μm with 80% of the grains between 0·25 and 2·5 μm size (Fig. 3(a)). At this final temperature, the anomalous grain growth was inhibited.

With these optimized sintering conditions, the effect of the deagglomeration step was studied by sintering a green compact made with a non-deagglomerated raw powder. The resulting ceramics were not densified (61·5% of d_{th}) and showed two grain-size distributions, the first one centred on 0·3 μm and the second one on 2 μm (Fig. 3(b)). A high density (99% of d_{th}) might be obtained by sintering for 2 h at 1400°C; then the grain size was homogeneous but with grains of 100–200 μm size.

Table 1. Sintering conditions investigated around the final temperature of 1230°C. Density (in d_{th} %) and average grain size

Final sintering temperature (°C)	*Sintering rates*	*% d_{th}*	*Grain size (μm)*
1250	20–700 at 350°C h^{-1} 700–1250 at 100°C h^{-1}	92	0·6
1250	20–700 at 350°C h^{-1} 700–1000 at 50°C h^{-1} 1000–1250 at 10°C h^{-1}	95	1·4
1250	20–700 at 350°C h^{-1} 700–1000 at 50°C h^{-1} 1000–1250 at 5°C h^{-1}	95·5	1·8
1260	20–700 at 350°C h^{-1} 700–1000 at 50°C h^{-1} 1000–1260 at 5°C h^{-1}	96	3·2
1300	20–700 at 350°C h^{-1} 700–1000 at 50°C h^{-1} 1000–1300 at 4°C h^{-1}	96	4
1400	20–700 at 350°C h^{-1} 700–1000 at 50°C h^{-1} 1000–1400 at 4°C h^{-1}	95·5	~50 + 3
1230	20–700 at 350°C h^{-1} 700–1000 at 50°C h^{-1} 1000–1230 at 25°C h^{-1}	93	1
1230	**20–700 at 350°C h^{-1} 700–1000 at 50°C h^{-1} 1000–1230 at 4°C h^{-1}**	**96**	**1·6**
1230	20–700 at 350°C h^{-1} 700–1000 at 50°C h^{-1} 1000–1230 at 3°C h^{-1}	95	1·6
1230 (with a non-deagglomerated powder)	20–700 at 350°C h^{-1} 700–1000 at 50°C h^{-1} 1000–1250 at 4°C h^{-1}	61·5	~2 + 0·3

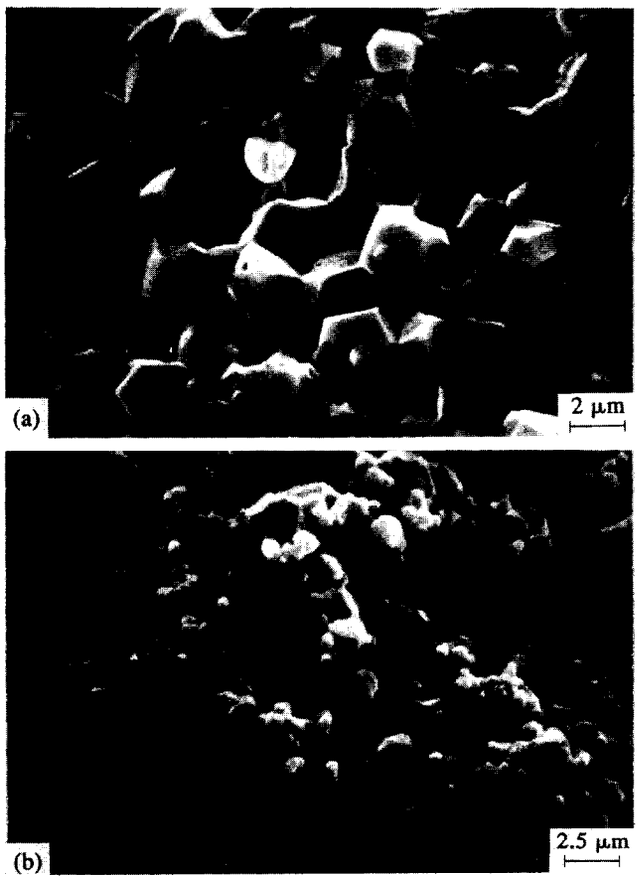


Fig. 3. Microstructure of $BaTiO_3$ ceramics sintered at 1230°C from (a) a deagglomerated powder and (b) a raw powder.

Our results are in good agreement with those of Hiesh and Fang,[12] who showed that:
(i) to obtain a high density and a uniform fine-grained microstructure, a uniform green compact with fine particles was needed;
(ii) it was possible to prepare dense ceramics from non-uniform green compacts but a higher sintering temperature should be used and the ceramics obtained exhibited a large grain size.

To minimize the sintering time it is possible to increase the final sintering temperature to 1300°C. We have followed the procedure previously described and investigated different heating rates. The results are reported in Table 2. It is important to note that an increase of the heating rate from 25 to 350°C h^{-1} between 700 and 1300°C induces a slight decrease of the density and a more sensible decrease of the grain size. This phenomenon was previously observed with the 1230°C sintering. Thus the thermal cycle chosen was the following: heating from 20 to 700°C at 350°C h^{-1} and from 700 to 1300°C at 200°C h^{-1}. The microstructure of the obtained ceramic exhibited an average fine grain size of 0·7 μm with 80% of the grains between 0·25 and 1 μm size (Fig. 4(a)). These sintering conditions will be called '1300°C sintering' in the text below.

Table 2. Sintering conditions with 1300°C final temperature. Density (in d_{th} %) and average grain size

Sintering rates	% d_{th}	*Grain size (μm)*
20–700°C at 350°C h^{-1} 700–1000°C at 50°C h^{-1} 1000–1300°C at 25°C h^{-1}	96	3·8
20–700°C at 350°C h^{-1} 700-1000°C at 50°C h^{-1} 1000–1300°C at 50°C h^{-1}	96·3	1·4
20–700°C at 350°C h^{-1} 700–1300°C at 100°C h^{-1}	94·4	0·8
20–700°C at 350°C h^{-1} 700–1300°C at 200°C h^{-1}	**94·5**	**0·7**
20–1300°C at 350°C h^{-1}	93	0·6

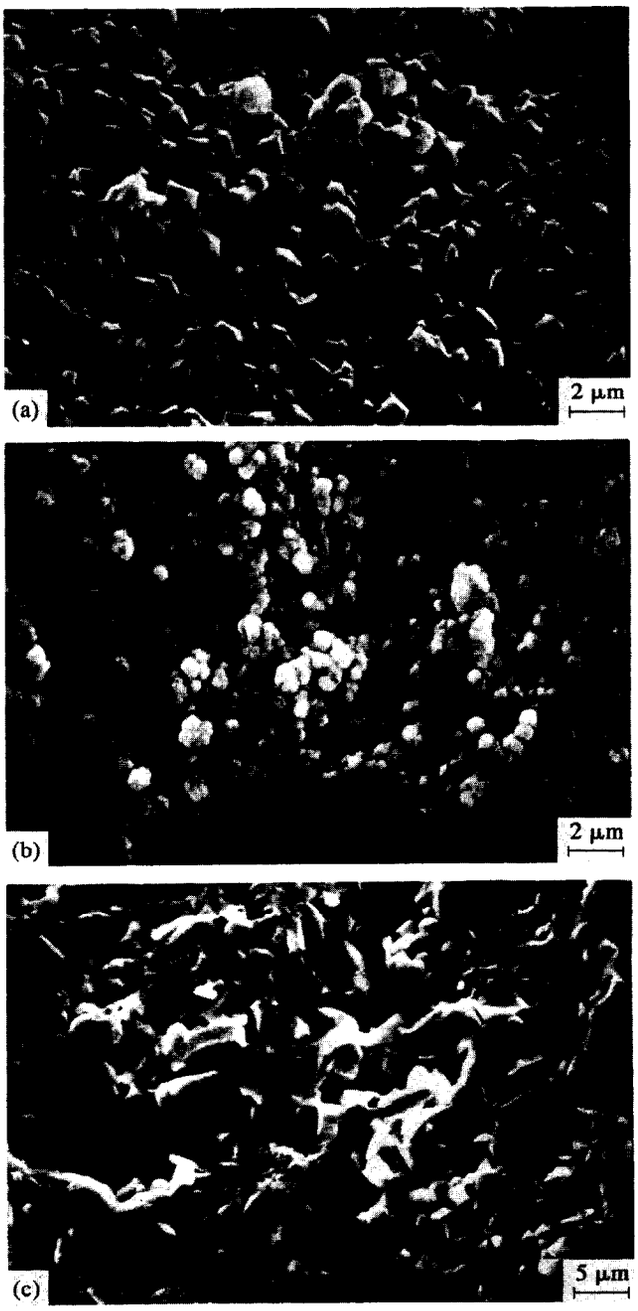


Fig. 4. Microstructure of $BaTiO_3$ ceramics sintered at 1300°C from (a) a deagglomerated powder, (b) a raw powder and (c) a raw powder after a dwelling time of 20 h.

Table 3. Characteristics of the ceramics obtained with deagglomerated powders and sintered at 1300°C versus the dwelling time at this temperature

Dwelling time	*% d_{th}*	*Grain size (μm)*
15 min	95·4	1·03
20 min	95·4	1·05
30 min	95·6	1·50
1 h	95·7	2·10
5 h	95·9	2·70
10 h	96·7	5·65
20 h	96·7	6·10

Table 4. Characteristics of the ceramics obtained with non-deagglomerated powders and sintered at 1300°C versus the dwelling time at this temperature

Dwelling time(h)	*% d_{th}*
0	72·7
1	85
4	85·2
10	85·6
20	86

On the other hand, the influence of the dwelling time was investigated and the results are reported in Table 3. It appears that an increase of the dwelling time has a weak effect on the final density but modifies the grain size and the grain size distribution. The longer the dwelling time, the larger the grain size and its distribution.

The sintering of green compacts made with a non-deagglomerated raw powder in the 1300°C sintering conditions yielded a final density of about 72% of d_{th} (Fig. 4(b)). After holds at 1300°C for different dwelling times, the final density increased up to 86% of d_{th}, after 20 h (Table 4). The ceramics showed anomalous grain growth, the amount of the biggest grains depending on the dwelling time (Fig. 4(c)).

Our results show the importance of a careful deagglomeration step in the elaboration of a sinterable powder. The homogeneity of the powder allows us to obtain both a good density and a well controlled grain size in the ceramics. The double optimized synthesis processes give ceramics with a narrow grain-size distribution centred on 1·6 μm (1230°C sintering) and 0·7 μm (1300°C sintering).

3.3 Characterization of optimized ceramics

Ceramics obtained with 1230 and 1300°C sintering conditions were analysed by different techniques. The IR reflectivity spectra recorded at room temperature did not reveal any trace of barium carbonate in both cases. TGA measurements did not allow us to detect any significant weight loss. Thus, another more sensitive technique was necessary to determine the residual carbon content in these two ceramics. The $^{12}C(d, p)^{13}C$ nuclear technique was used. For ceramics respectively sintered at 1230 and 1300°C, it gave carbon contents of 95 and 130 mg cm^{-2} in the surface layer (0·4 μm). The carbon content is higher in the ceramics obtained by the 1300°C sintering. This result can be explained as follows:

(i) if the residual carbon is assumed to be located at the grain boundaries, it is more important in the finer grain size ceramic;

(ii) during the 1230°C sintering thermal cycle, the treatment time in the furnace was much longer (about 83 h) than during the 1300°C sintering (8 h). Thus the diffusion of carbon from the bulk to the surface layer and then to the atmosphere is facilited, so the detected carbon content is weaker.

The sintering behaviour of the deagglomerated powder was studied by dilatometric measurements in the conditions of pressing (250 MPa) and heating rates of both the 1230 and 1300°C optimized sintering. The obtained shrinkage curves and their derivatives versus temperature are reported in Fig. 5. The derivative curve of the shrinkage versus temperature obtained at 1230°C with a very slow heating rate between 700 and 1230°C, exhibits two minima at about 1060 and 1200°C. Previous studies[2] carried out on the same powders sintered with a constant rate of 150°C h^{-1} showed only one minimum at 1060°C on the derivative curve. Only the difference in heating rate between the two experiments can explain the appearance of a second

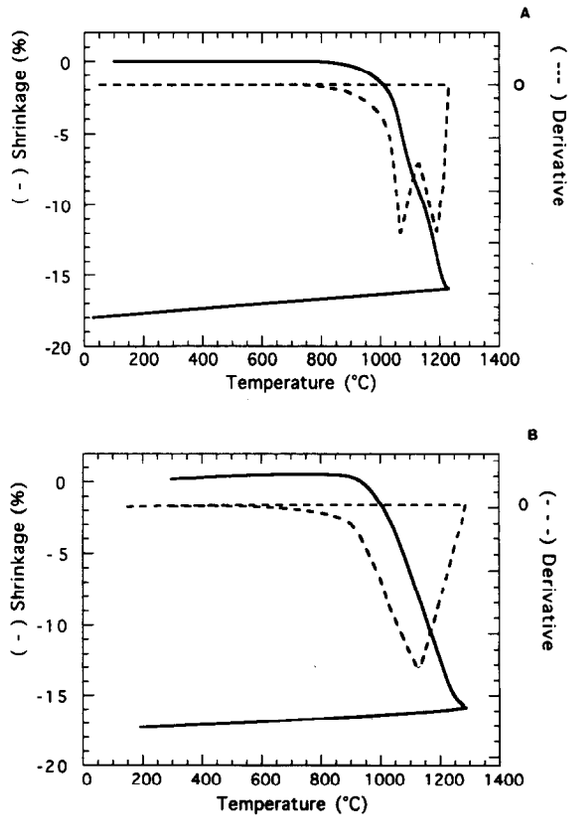


Fig. 5. Dilatometric curves obtained from $BaTiO_3$ ceramics sintered at (a) 1230°C and (b) 1300°C.

Table 5. Measurements of final densities (in %) of ceramics sintered at 1230 and 1300°C

Technique	*1230°C (%)*	*1300°C (%)*
Helium picnometry	98·3	97
Mercury intrusion	97·6	96·2
Shrinkage measurement	98·7	97·1
Geometrical measurement	96	94·5
Average value	97·7	96·2

minimum on the derivative curve in Fig. 5(a). This second minimum was observed only for very slow heating rates during the shrinkage. On the contrary, the shrinkage derivative curve obtained in the 1300°C sintering conditions exhibits only one minimum at 1130°C (Fig. 5(b)). The temperature of the minimum is shifted towards the high temperatures due to the faster heating rate (300 then 200°C h^{-1} instead of 150°C h^{-1} in Ref. 2). The shrinkage measurement reported at room temperature gives a value of the ceramic density. The final density of the two types of ceramic determined by different methods are given in Table 5. They are in very good agreement with the values deduced from shrinkage measurements. In both cases the final densities are satisfactory since they are greater than 96% of d_{th}.

X-ray diffraction patterns of the two ceramics are characteristic of a mixture of tetragonal and cubic phases. The 004–400 diffraction lines accu-

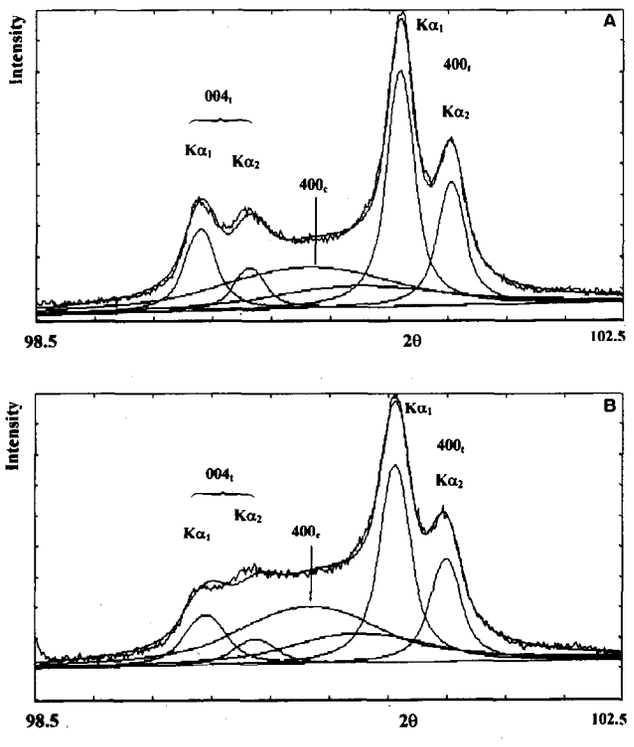


Fig. 6. X-ray diffraction patterns of the 400/004 lines and fits performed with pseudo-Voigt functions for (a) a 1230°C sintered ceramic and (b) a 1300°C sintered ceramic.

Table 6. Tetragonal (t) and cubic (c) phase ratio; average particle size (d) and thickness of the surface cubic phase (l) in the grains for the ceramics sintered at 1230 and 1300°C

	t/c	d(*μm*)	l(*μm*)	*% of cubic phase*
1230°C	1·08	1·6	0·24	52
1300°C	0·76	0·7	0·15	79

rately recorded were fitted with pseudo-Voigt functions. The integrated intensities of the fitted peaks (Fig. 6) allowed us to estimate roughly the relative amounts of the two phases. Three lines were observed: for the 1300°C sintered ceramic the lines at $2\theta = 99{\cdot}64°$ and $100{\cdot}95°$ correspond respectively to the 004 and 400 reflections in the tetragonal phase and the line at $2\theta = 100{\cdot}34°$ corresponds to the 400 reflection in the cubic phase; for the 1230°C sintered ceramic the cubic component is observed at the same diffraction angle whereas the 004 and 400 tetragonal reflections are observed at slightly different angles, $2\theta = 99{\cdot}61°$ and $2\theta = 100{\cdot}98°$, respectively. The results obtained from the integrated intensities giving the fraction of the tetragonal over the cubic phases (t/c) are listed in Table 6, as are the average particle diameters deduced from SEM photogaphs and TEM observations. From results published by Niepce[13] and Takeuchi *et al.*,[14] the thickness of the cubic phase located at the surface of a tetragonal $BaTiO_3$ grain can be estimated by a simple calculation from the t/c ratio[14] using the expression:

$$\frac{t}{c} = \frac{\frac{4}{3}\pi\left(\frac{d}{2} - l\right)^3}{\frac{4}{3}\pi\left(\frac{d}{2}\right)^3 - \frac{4}{3}\pi\left(\frac{d}{2} - l\right)^3}$$

where d is the ceramic grain size and l is the thickness of the cubic layer on the grain surface.

This expression is reduced to: $t/c \approx d/6l$ since $d >> 1$.

Results are in good agreement with those of Niepce[13,15] and Arlt:[16]

(i) at room temperature the presence of coexisting cubic and tetragonal phases in one particle is confirmed;

(ii) the amount of the cubic phase increases with the decrease of the ceramic grain size. Niepce and Arlt indicated that for a ceramic with grain size below 0·7μm, the cubic phase was obtained. In our case the cubic phase was mainly obtained in the ceramic exhibiting an average grain size of 0·7 μm. In the ceramic exhibiting an average grain size of 1·6 μm, the amount of the cubic phase is lower.

Figure 7 shows the temperature dependence of the relative dielectric constant versus temperature at several frequencies for the two optimized

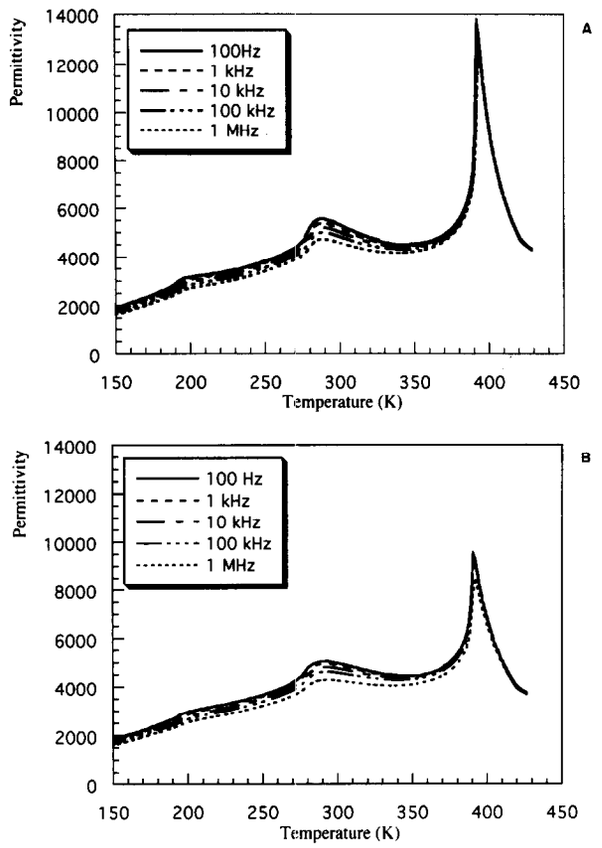


Fig. 7. Permittivity of $BaTiO_3$ ceramics sintered at (a) 1230°C and (b) 1300°C versus temperature at different measurement frequencies.

ceramics. The values of the relative dielectric constant ϵ' and loss factor tg δ at room temperature and at the ferroelectric transition, as well as the T_c temperatures, are reported in Table 7. We can observe that:

(i) the values of the permittivity obtained on the two ceramics depend on the grain size. These results confirm those of Niepce,[13] who showed that at room temperature the permittivity depends on the grain size and exhibits a maximum value for a grain size approximately equal to 0·8 μm;

(ii) the temperature of the phase transition increases with the grain size. This phenomenon was well known and described by several authors;[17–19]

(iii) the value of the permittivity at the ferroelectric transition is higher for a 1·6 μm grain size ceramic than for a 0·7 μm grain size one. This could be related to the amount of the cubic phase present in the latter ceramic which is not concerned by the ferroelectric transition.

Table 7. Dielectric characteristics of the ceramics

Grain size (μm)	*T_c(°C)*	*ϵ max*	*ϵ at 25°C*	*tg δ at 25°C*
1·6	120	13 000	5200	0·025
0·7	118	9 300	4900	0·03

4 Conclusions

The results obtained in this study may be summarized as follows.

(i) It is possible to obtain homogeneous fine-grained $BaTiO_3$ ceramics at quite low temperatures from powders elaborated by a resin citric process.

(ii) To avoid an anomalous grain growth and/or a bimodal grain-size distribution, a careful deagglomeration step of the raw powders is required.

(iii) Two sintering thermal cycles have been proposed to obtain ceramics with a density greater than 96% of d_{th} and a well-controlled grain size: a sintering cycle at 1230°C gave 1·6 μm grain size ceramics and a sintering cycle at 1300°C gave 0·7 μm grain size ceramics. In both cases a narrow grain size distribution was observed.

(iv) The ceramics obtained are free of barium carbonate, the residual carbon content has been estimated at about 400 ppm in the surface layer of the ceramics.

(v) The ceramics exhibit good dielectric characteristics in accordance with previous papers showing that, in $BaTiO_3$ ceramics, higher permittivity as well as low dielectric losses are obtained at room temperature for a grain size of about 0·8 μm.[13]

References

1. Proust, C., Miot, C. & Husson, E., Characterization of $BaTiO_3$ powder obtained by a chemical route. *J. Eur. Ceram. Soc.*, submitted.
2. Coutures, J. P., Odier, P. & Proust, C., Barium titanate formation by organic resins formed with mixed citrate. *J. Mater. Sci.*, **27** (1992) 1849–56.
3. Le Calvé-Proust, C., Husson, E., Odier, P. & Coutures, J. P., Sintering ability of $BaTiO_3$ powders elaborated by citric process. *J. Eur. Ceram. Soc.*, **12** (1993), 153–7.
4. Wengeler, H., Knobel, R., Kathrein, H., Freund, F., Demortier, G. & Wolf, G., Atomic carbon in magnesium oxide single crystals. Depth profiling, temperature- and time-dependent behavior. *J. Phys. Chem. Solids*, **43** (1982) 59–71.
5. Oberheuser, G., Kathrein, H., Demortier, G., Gouska, H. & Freund, F., Carbon in olivine single crystals analyzed by the $^{12}C(d,p)^{13}C$ method and by photoelectron spectroscopy. *Geochimica Cosmochimica Acta*, **47** (1983) 1117–29.
6. Mathez, E. A., Carbon abundances in mantle minerals determined by nuclear reaction analysis. *Geophys. Res. Lett.*, **11** (1984) 947–50.
7. Proust, C., Husson, E.,. Blondiaux, G. & Coutures, J. P., Residual carbon detection in barium titanate ceramics by nuclear reaction technique. *J. Eur. Ceram. Soc.*, in press.
8. Huez, M., Qualia, L. & Weber, G., Fonction d'excitation de la reaction $^{12}C(d,p)^{13}C$ entre 400 et 1350 keV. Distributions angulaires. *Nuclear Instr. Meth.*, **105** (1972) 197–203.

9. Lavielle, D., Poumarat, J., Montardi, Y., Bernard P. & Aguerre-Charriol, O., Microstructure/propriety relationship in chemically processed barium titanate for X7R characteristics. *Euroceramics II*, **3** (1991) 1903–7.
10. Demartin, M., Pethybridge, G. & Carry, C., Sintering, grain growth and de-sintering process in un-doped $BaTiO_3$. *Euroceramics III*, **1** (1993) 787–92.
11. Chen, J., Jin, W. & Yao, Y., Study of the anomalous grain growth of $BaTiO_3$ ceramics. *Ferroelectrics*, **142** (1993) 153–9.
12. Hiesh, H. L. & Fang, T. T., Effect of green states on sintering behavior and microstructural evolution of high-purity barium titanate. *J. Am Ceram. Soc.*, **73** (1990) 1566–73.
13. Niepce, J. C., Permittivity of fine grained $BaTiO_3$. *Electroceramics IV*, **1** (1994) 29–39.
14. Takeuchi, T., Ado, K., Asai, T., Kageyama, H., Saito, Y., Masquelier, C. & Nakamura O., Thickness of the cubic phase on barium titanate single-crystalline grains. *J. Am. Ceram. Soc.*, **77** (1994) 1665–8.
15. Caboche, G., Chaput, F., Boilot, J. P. & Niepce, J. C., Titanate de baryum à grains fins pour application diélectrique. *Silicates Industriels*, **5–6** (1993) 103–7.
16. Arlt, G., The influence of microstructure on the properties of the ferroelectric ceramics. *Ferroelectrics*, **104** (1990) 217–27.
17. Kinoshita, K. & Yamayi, A., Grain-size effects on dielectric properties in barium titanate ceramics. *J. Appl. Phys.*, **47** (1976) 371–3.
18. Fang, T. T., Hiesh, H. L. & Shiau, F. S., Effects of pore morphology and grain size on the dielectric properties and tetragonal-cubic phase transition of high-purity barium titanate. *J. Am. Ceram. Soc.*, **76** (1993) 205–11.
19. Wu, K. & Schulze, W. A., Aging of the weak-field dielectric response in fine- and coarse-grain ceramic $BaTiO_3$. *J. Am. Ceram. Soc.*, **75** (1992) 3390–5.

Journal of the European Ceramic Society 15 (1995) 1171–1176
© 1995 Elsevier Science Limited
Printed in Great Britain. All rights reserved
0955-2219(95)00101-8
0955-2219/95/$9.50

Preparation of $BaTiO_3$ by the Hydrothermal Method

Chang-Tai Xia, Er-Wei Shi, Wei-Zhuo Zhong & Jing-Kun Guo

Laboratory of Functional Inorganic Materials, Shanghai Institute of Ceramics, Chinese Academy of Sciences, Shanghai 200050, People's Republic of China.

(Received 23 March 1995; revised version received 11 May 1995; accepted 31 May 1995)

Abstract

The results of hydrothermal preparation of $BaTiO_3$ fine powders are reported. The effects of the reaction temperature, the molar ratio of Ba/Ti in the precursors, the chemical form of the precursors on the phase composition, the size and the morphology of the products are presented. The higher the temperature, the higher the basicity and the greater the molar ratio of Ba/Ti in the precursor, the easier the formation of the perovskite type $BaTiO_3$ crystallite will be. It was found that $BaTiO_3$ microcrystals(150–300 nm) could be synthesized through the hydrothermal reaction of commercial TiO_2 with $Ba(OH)_2$ aqueous solution, while the hydrothermal reaction of the newly prepared $Ti(OH)_4$ gel with the $Ba(OH)_2$ solution produced highly crystallized, well dispersed perovskite type $BaTiO_3$ crystallites with very fine (<100 nm) particles. The newly prepared $Ti(OH)_4$ gel proved to be suitable precursor for the hydrothermal preparation of $BaTiO_3$ fine powders. X-ray diffraction (XRD) of the hydrothermal $BaTiO_3$ powders reveals a simple cubic perovskite structure. Above that, the lattice constant decreased with the increase of the reaction temperature. These abnormal crystallographic features are assumed to result from lattice defects, due to OH^- incorporation in the perovskite lattice.

1 Introduction

$BaTiO_3$ is an ubiquitous electronic ceramic widely utilized in the manufacture of thermistors, multilayer capacitors (MLCs) and electro-optic devices.[1] $BaTiO_3$ powders are traditionally prepared via the calcination of $BaCO_3$ and TiO_2 or $BaTiO[C_2O_4]_2 \cdot 4H_2O$. As the temperature required is as high as 800–1100°C, the powders prepared are highly agglomerated and require extensive milling before they can be used in the various forming process. Low temperature, wet chemical routes offer an exciting possibility for the synthesis of high purity, homogeneous, ultrafine and multicomponent powders. Because of the possibility of producing highly crystallized, well dispersed and sintering active powders, the hydrothermal synthesis of ceramic powders is of great interest.

Christensen[2] and Kaneko[3] have shown that $BaTiO_3$ can be prepared from barium hydroxide solutions and oxide, esters or oxide gels of titanium, when temperatures from 380 to 500°C and pressures from 300 to 500 atm are applied. Recent work by Kutty and co-workers[4–6] demonstrates the synthesis of ultrafine $BaTiO_3$ powders at temperatures as low as 85°C and the pressures from 15 to 65 MPa. Hennings *et al.*[7] have reported the hydrothermal preparation of highly crystallized $BaTiO_3$ powders with a size of 200–300 nm from barium–titanium-acetate gel precursors.

We now report the results of the systematic study of the hydrothermal synthesis of $BaTiO_3$. The relation between the phase composition, size, morphology of the crystallites and the reaction temperature, the precursors, the molar ratio of Ba and Ti in the precursors have been found. The formation mechanism of $BaTiO_3$ under hydrothermal conditions has also been tentatively proposed.

2 Experimental Procedure

The precursors and the medium used in this study are shown in Table 1. The 160 ml reaction mixtures were charged into a Pt crucible of 200 ml capacity, which was then put into the autoclave and heated at 75–400°C for various durations. The pressure remained close to the vapour pressure curve of H_2O in this temperature range. The products were filtered and washed with dilute acetic acid to remove any excess $Ba(OH)_2$, and then washed with deionized water and alcohol and then air-dried at 120°C.

Identification of the phases was carried out by X-ray powder diffraction (XRD; Rigaku RAX-10). Transmission electron micrographs (TEM) were obtained from a JEOL JEM-2010 microscope. The extent of reaction was determined by analyzing the amount of OH^- in the residual solution.

Table 1. Precursors and solutions selected for hydrothermal synthesis of $BaTiO_3$ powders

No.	*Ba precursor*	*Ti precursor*	*Reaction medium*
1	$Ba(OH)_2 \cdot 8H_2O$	Commercial TiO_2	Aqueous solution
2	$Ba(CH_3COO)_2$ + NaOH	Commercial TiO_2	Aqueous solution
3	$Ba(OH)_2 \cdot 8H_2O$	Tetrabutyl titanate	Aqueous solution
4	$Ba(OH)_2 \cdot 8H_2O$	Tetrabutyl titanate	Ethanol 50 vol% aqueous solution

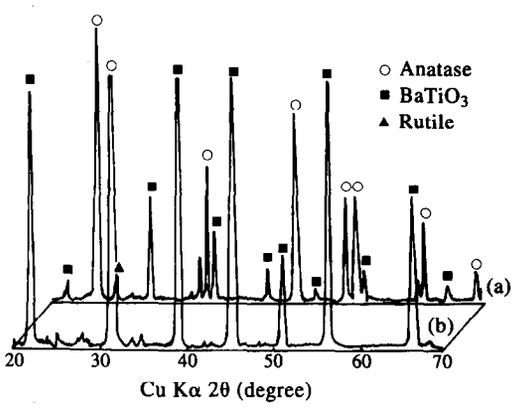


Fig. 1. XRD spectra of hydrothermal powders synthesized at (a) 75°C and (b) 400°C for 8 h using equimolar $Ba(OH)_2 \cdot 8H_2O$ and commercial TiO_2 powders.

3 Results and Discussion

3.1 The influence of temperature on the phase composition and morphology

Equimolar $Ba(OH)_2 \cdot 8H_2O$ and commercial TiO_2 powders (X-ray analysis showed that this titania consists principally of anatase with about 10–15% rutile) were hydrothermally processed at various temperatures for different durations. Figure 1(a) shows the XRD spectrum of the product of 75°C for 8 h. The $BaTiO_3$ peaks appeared besides the peaks of TiO_2, which means $BaTiO_3$ was formed. The products were nearly single phase $BaTiO_3$ when the precursors were treated at 400°C for 8 h (Fig. 1(b)). It was found by the analysis of the products synthesized at other temperatures (100, 150, 180, 200, 250 and 300°C) that the (101) peak of anatase was presented in all the products synthesized at the temperatures below 300°C.

Figure 2 illustrates the TEM morphologies of the powders prepared at different temperatures for 8 h. The morphologies of the powders were strongly dependent on the temperature. It can be easily seen from the photographs, that with an increase in temperature, the morphology of the powders changed from spheric cluster (Fig. 2(a)), to porous spheric cluster (Fig. 2(b, c)), and finally

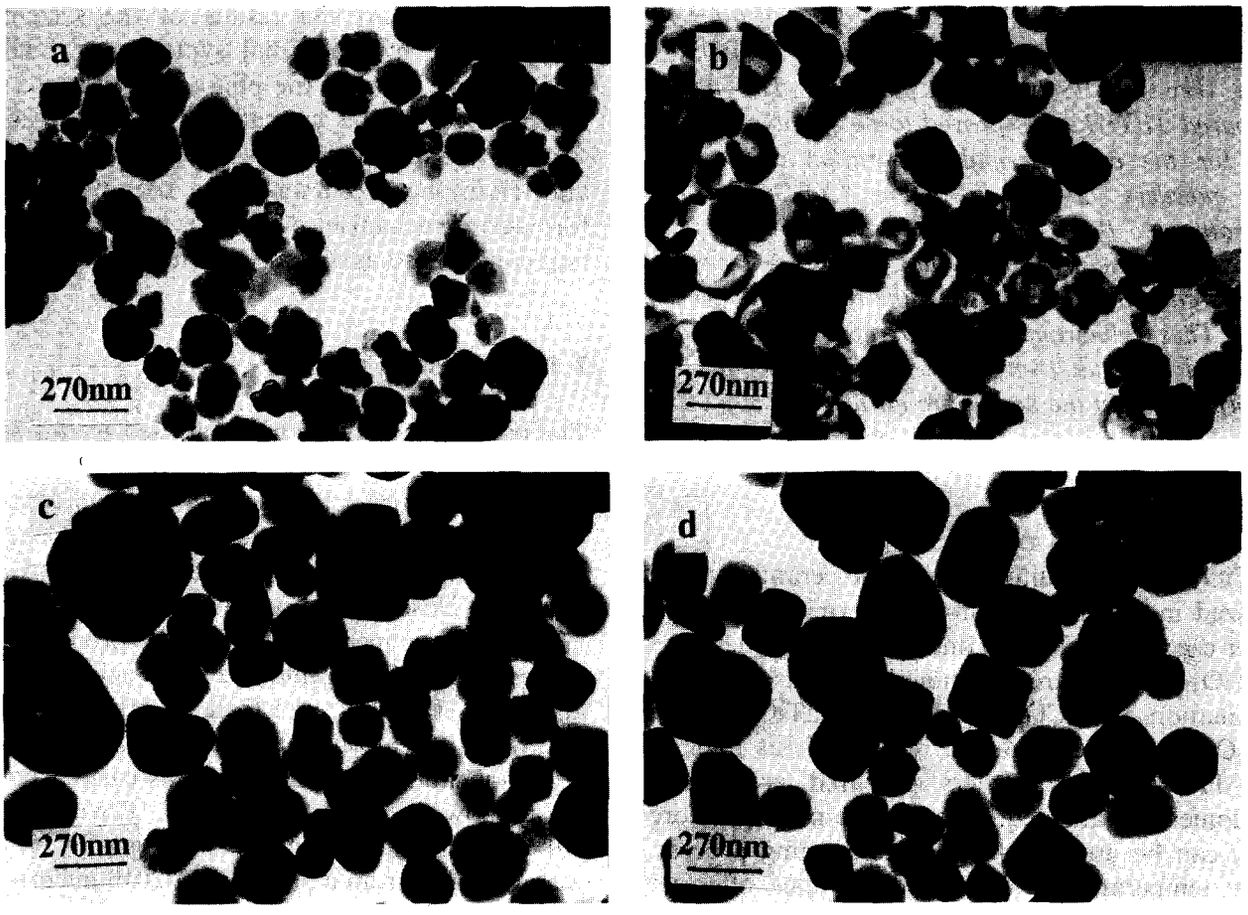


Fig. 2. TEM photographs of hydrothermal powders synthesized at (a) 75°C and (b) 400°C for 8 h using equimolar $Ba(OH)_2 \cdot 8H_2O$ and commercial TiO_2 powders.

Table 2. The relationship between reaction completeness and reaction temperature

Reaction temperature T(°C)	*Reaction completeness ρ(%)*
100	75·54
150	81·09
250	86·37
300	88·68
400	91·21

$Ba(OH)_2 \cdot 8H_2O + TiO_2$, m(Ba)/m(Ti)=1·0, 8 h.

formed well crystallized cubes or spheres (Fig. 2(d)). It can also be seen that the size of the crystallites increased slightly with the increase of reaction temperature.

The following reaction took place in the system:

$$TiO_2 + Ba(OH)_2 \rightarrow BaTiO_3(\text{crystallite}) + H_2O.$$

Since the $Ba(OH)_2 \cdot 8H_2O$ and TiO_2 used were of equal molar and there was no other OH^- source in the system, with the progress of the reaction, $BaTiO_3$ crystallites were formed and the amount of OH^- decreased. By defining

$$\rho = (1-\text{residual } OH^-/\text{initial } OH^-) \times 100\%,$$

the value of ρ can be approximately seen as the extent or the completeness of the reaction. Table 2 gives the ρ values for different temperatures. It can be clearly seen that the higher the reaction temperature, the greater the ρ value, which means the reaction took place more completely.

3.2 The relation between the lattice parameters and the reaction temperature

X-ray diffraction of hydrothermal $BaTiO_3$ revealed a simple cubic perovskite structure (Fig. 1) which is normally observed only at temperatures above the ferroelectric Curie point at 130°C or at very small crystallite size (d<0·15 μm). Above that, the lattice parameters changed with the change of reaction temperature as shown in Table 3. It can be seen from the table that the unit cell volume of the hydrothermal $BaTiO_3$ is larger than 'normal' coarse-grained $BaTiO_3$, moreover, with an increase in reaction temperature, the unit cell volume of

Table 3. The relationship between the lattice parameters of the hydrothermal $BaTiO_3$ microcrystals and the reaction temperature

Reaction temperature T(°C)	75	100	150	250	300	400
Lattice constant a (Å)	4·031	4·025	4·016	4·012	4·008	4·003
Unit cell volume Vc(Å^3)	65·50	65·21	64·77	64·58	64·38	64·14

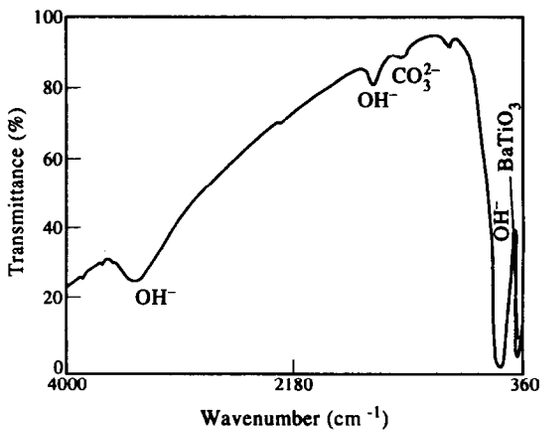


Fig. 3. IR spectrum of hydrothermal $BaTiO_3$ synthesized from $Ba(OH)_2 \cdot 8H_2O$ and TiO_2 powders.

the crystallites shrinks. When the temperature increased from 75 to 400°C, the unit cell volume shrank by about 2·08%. The unit cell volume of the crystallites prepared at 400°C for 8 h approached a value of 64 ≃ Å^3,[8] which is the typical value of 'normal' coarse-grained $BaTiO_3$ by classical calcination.

A typical IR spectrum (Fig. 3) of hydrothermal $BaTiO_3$ shows broad absorption in the region of 3200–3600 cm^{-1}, a shallow band around 1640 cm^{-1} and a strong band at 650 cm^{-1}. The 1640 cm^{-1} band (bending mode of H_2O) indicates that some H_2O is present. The strong band at 650 cm^{-1} is characteristic of the librational mode of OH^- groups and is more distinct than the OH^- stretching which is masked by the corresponding H_2O bands around 3600 cm^{-1}. A TG-DTA-MS study found that the samples gives out H and O when heated above 200°C. These phenomena suggest the OH^- is present in the lattice. Besides the $OH^\bullet$ defect, other defects may also form to meet the electroneutrality requisition. The presence of these defects suppressed the tetragonal distortion, so the crystallites can exist in cubic phase at room temperature. The defect concentration decreased when the reaction temperature increased, thus the unit cell volume of $BaTiO_3$ shrank.

3.3 The influence of Ba : Ti molar ratio in the precursors

With a fixed total amount of precursors (50 g), different Ba : Ti molar ratios of $Ba(OH)_2 \cdot 8H_2O$ and TiO_2 were hydrothermally treated at 300°C for 8 h. Figure 4 shows the XRD spectra of the products. From the figure, we can see the anatase (101) peak appeared for the lower molar ratio (1·0) (Fig. 4(a)). But the peak disappeared for the higher molar ratio (Fig. 4(b, c)). Another interesting phenomenon is that the (002) (200) and (102) (210) peaks are split for the molar ratio of

2·0, which suggests that tetragonal $BaTiO_3$ was formed in this case. Further investigations have proved this suggestion (Figs 5 and 6). The product was easily contaminated with $BaCO_3$ when a high Ba : Ti molar ratio precursor was used.

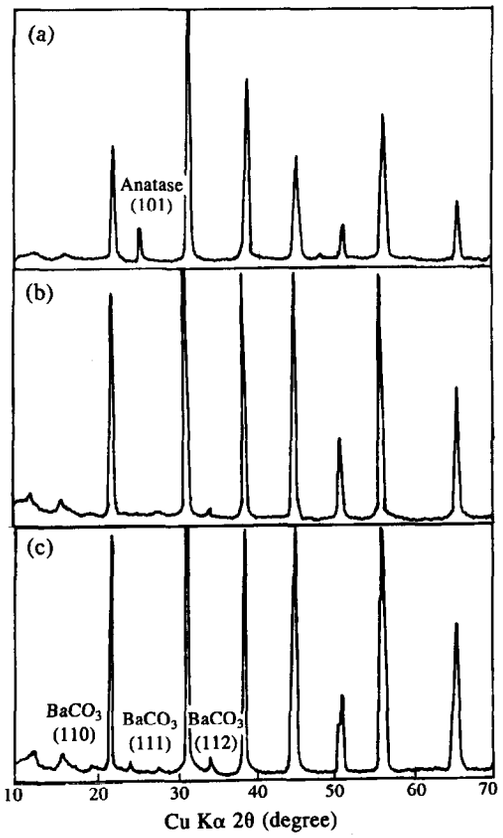


Fig. 4. XRD spectra of hydrothermal powders synthesized at 300°C for 8 h using different molar ratio of $Ba(OH)_2{\cdot}8H_2O$ and TiO_2 powders. (a) m(Ba)/m(Ti) = 1·0, (b) m(Ba)/m(Ti) = 1·5, (c) m(Ba)/m(Ti) = 2·0.

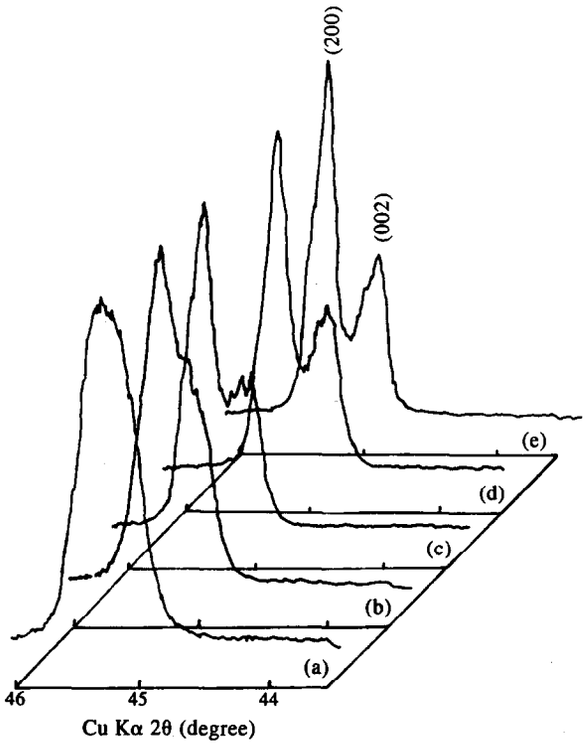


Fig. 5. X-ray diffraction traces of the (200) and (002) reflections for hydrothermal $BaTiO_3$ synthesized from different Ba/Ti molar ratio $Ba(OH)_2{\cdot}8H_2O$ and TiO_2 at room temperature. (a) 1 : 1, (b) 1·5 : 1, (c) 2·0 : 1, (d) 2·5 : 1, (e) 3·0 : 1.

3.4 The influence of the kind of precursors on the size and morphology of the crystallites

Figure 7 shows the TEM photographs of the powders prepared from different precursors. Well-crystallized $BaTiO_3$ with a size of 80–100 mn was formed (Fig. 7(a)) when precursors in $Ba(OH)_2$ aqueous solution were hydrothermally treated at 300°C for 8 h, however from the photograph some organic residual can be seen. It was found that the organic residual disappeared when some alcohol was added to the reaction solution. Figure 7(b) is the TEM photograph of the powders prepared from newly prepared $Ti(OH)_4$ gel(hydrolysis product of tetrabutyl titanate) and $Ba(OH)_2{\cdot}8H_2O$. The powders are highly crystallized, well dispersed cubic or spheric $BaTiO_3$ crystalites with a size less than 100 nm.

In summary, the kind of precursors have a strong influence on the size and the morphology of the $BaTiO_3$ synthesized.

3.5 The influences of medium

Experiments show that when $Ba(OH)_2{\cdot}8H_2O$ and TiO_2 were used as precursors, the formation of $BaTiO_3$ under hydrothermal conditions could be facilitated by using an alkaline mineralizer (e.g. NaOH). Figure 8 shows the XRD spectra of the powders synthesized at 300°C for 8 h in pure water and 1 mol/l NaOH aqueous solution. The amount of the residual TiO_2 in powders synthesized in the NaOH aqueous solution was distinctly less than in pure water, which means the reaction was more complete in the former case. The crystallinity of the $BaTiO_3$ synthesized in the NaOH aqueous solution was also higher (Fig. 9(b)).

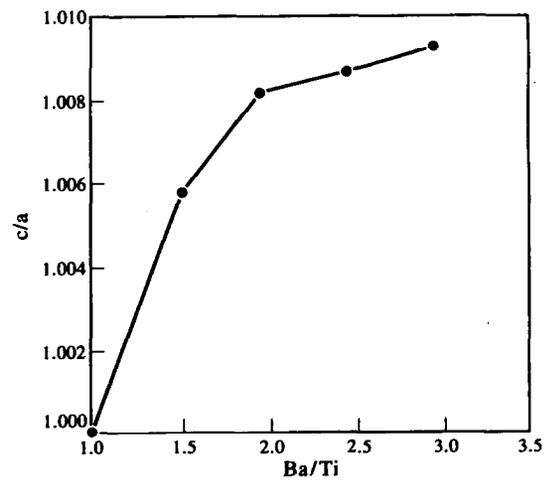


Fig. 6. The relationship between the *c/a* value of hydrothermal $BaTiO_3$ and the Ba:Ti molar ratio of $Ba(OH)_2{\cdot}8H_2O$ and TiO_2.

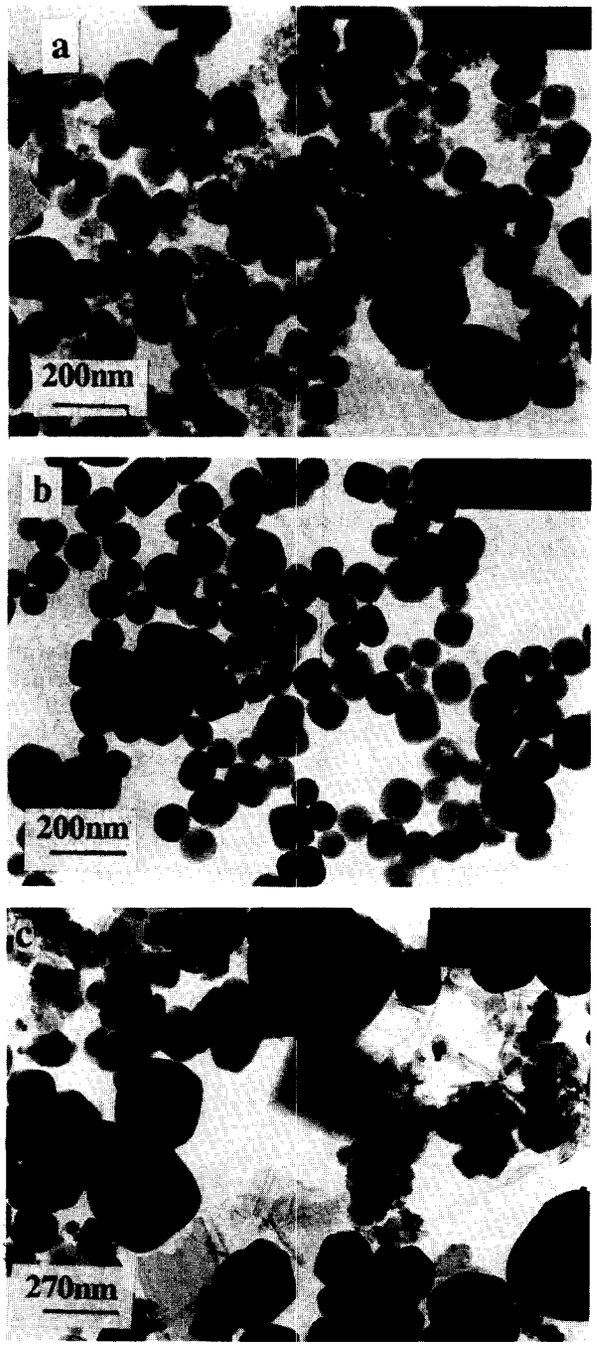


Fig. 7. TEM photographs of the powders prepared by (a) tetrabutyl titanate and $Ba(OH)_2$ aqueous solution; (b) newly prepared $Ti(OH)_4$ gel and $Ba(OH)_2$ aqueous solution; (c) commercial TiO_2 powder and $Ba(CH_3COO)_2$ in 1 mol/l NaOH aqueous solution.

The formation of ceramic powders under hydrothermal conditions is usually through a 'dissolution–crystallization' process.[9] The commercial TiO_2 powders are aggregates of particles with a primary size of 10–50 nm. When they are used as the Ti precursor, the interactions among these small particles are broken under the hydrothermal conditions. The powders are dissolved under the high temperature, high pressure and strong alkalinity of the system, and a variety of hydrated Ti–O ion groups are formed. These hydrated Ti–O ion groups are the growth units of $BaTiO_3$ crystallites. When the concentration of these growth

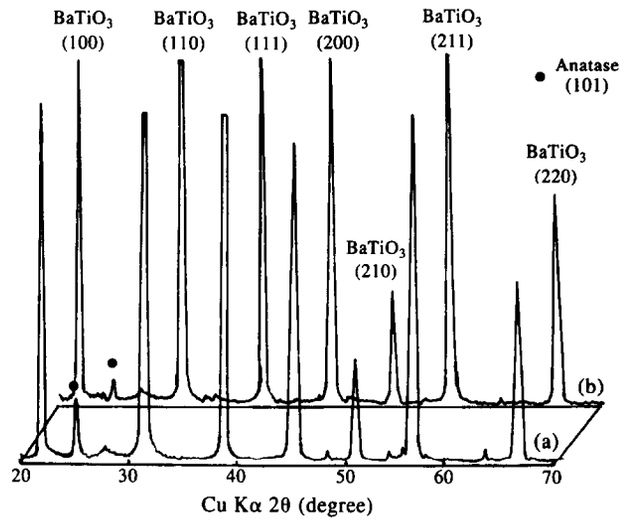


Fig. 8. XRD spectra of the powders synthesized at 300°C for 8 h in (a) pure water and (b) 1 mol/l NaOH aqueous solution.

units and Ba^{2+} reach or surpass the supersaturation for the formation of $BaTiO_3$ crystallites, the nucleation of $BaTiO_3$ begins and the crystallites grow. When freshly prepared $Ti(OH)_4$ gel is used as Ti precursor, the growth units are formed in a similar process, however, the growth units formed in these two systems are different in shape and size. Because the structure unit of TiO_2 is $Ti–O_6$ octahedron, so the growth units formed in this case are the linked $Ti(OH)_6$ octahedra units. The

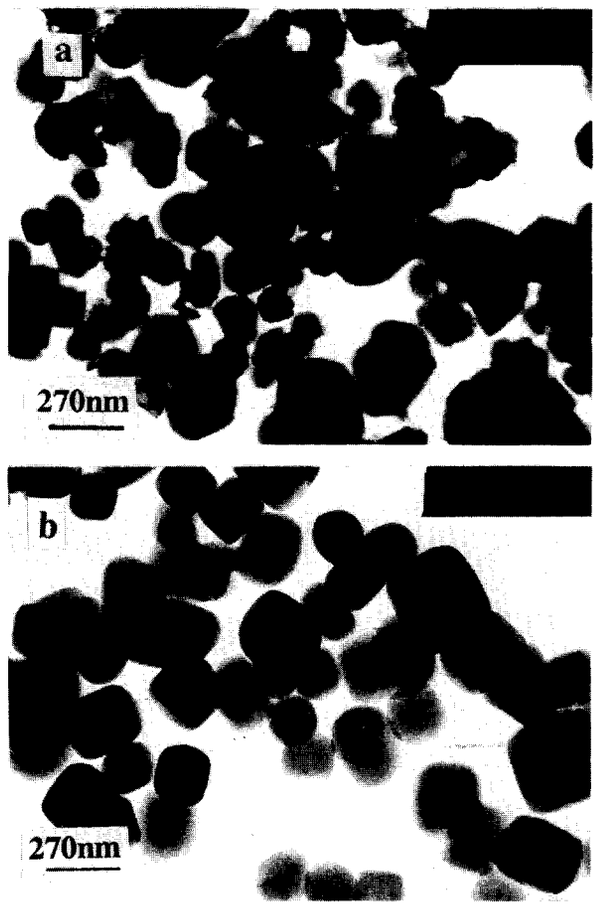


Fig. 9. TEM photographs of the powders synthesized at 300°C for 8 h in (a) pure water and (b) 1 mol/l NaOH aqueous solution.

structure similarity between these growth units and the $BaTiO_3$ crystal facilitate the nucleation and growth of the $BaTiO_3$ crystallites. On the contrary, the reticular structure of $Ti(OH)_4$ cause a slow nucleation and growth rate, so the $BaTiO_3$ produced from the reaction of the freshly prepared $Ti(OH)_4$ gel with the $Ba(OH)_2$ solution have a smaller size.

4 Conclusions

The main results of this study may be summarized as follows: (1) the higher the temperature, the higher the basicity and the greater the molar ratio of Ba/Ti in the precursor, the easier the formation of the perovskite type $BaTiO_3$ crystallite will be. (2) Hydrothermal reaction of the newly prepared $Ti(OH)_4$ gel with $Ba(OH)_2$ solution produced highly crystallized, well dispersed perovskite type $BaTiO_3$ crystallites with very fine (<100 nm) particles. The newly prepared $Ti(OH)_4$ gel turned out to be a suitable precursor for the hydrothermal preparation of $BaTiO_3$ fine powders. (3) X-ray diffraction of the hydrothermal $BaTiO_3$ powders reveals a simple cubic perovskite structure. The lattice constant (a) decreased with the increase of the reaction temperature. These abnormal crystallographic features are assumed to result from lattice defects, due to the OH^- incorporated in the perovskite lattice.

Acknowledgements

The authors acknowledge the financial support of the Chinese National Natural Sciences Foundation through grant 95332051.

References

1. Phule, P. P. & Risbud, S. H., Low-temperature synthesis and processing of electronic materials in the BaO–TiO_2 system. *J. Mater. Sci.*, **25** (1990) 1169–83.
2. Christensen, A. N., Hydrothermal preparation of barium titanate by transporting reactions. *Acta. Chem. Scand.*, **24** (1970) 2447.
3. Kaneko, S. & Imoto, F., Synthesis of fine-grained barium titanate by a hydrothermal reaction. *Nippon Kagaku Kaishi*, **6** (1975) 985.
4. Kutty, T. R. N. & Balachandran, R., Direct precipitation of lead zirconate titanate by the hydrothermal method. *Mater. Res. Bull.*, **19** (1984) 1479.
5. Vivekanadan, R. & Kutty, T. R. N., Hydrothermal synthesis of $Ba(Ti,Sn)O_3$ fine powders and dielectric properties of the corresponding ceramics. *Ceram. Int.*, **14** (1988) 207–16.
6. Vivekanadan, R., Philip, S. & Kutty, T. R. N., Hydrothermal preparation of $Ba(Ti,Zr)O_3$ fine powders. *Mater. Res. Bull.*, **22** (1987) 99.
7. Hennings, D., Rosenstein, G. & Schreinemacher, H., Hydrothermal preparation of barium titanate from barium–titanate acetate gel precursors. *J. Eur. Ceram. Soc.*, **8** (1991) 107–15.
8. Hennings, D. & Schreinemacher, S., Characterization of hydrothermal barium titanate, *J. Eur. Ceram. Soc.*, **9** (1992) 41–6.
9. Dawson, W. J., Hydrothermal synthesis of advanced ceramic powders. *Am. Ceram. Soc. Bull.*, **67** (1988) 1673–8.

Journal of the European Ceramic Society **15** (1995) 1177–1184
© 1995 Elsevier Science Limited
Printed in Great Britain. All rights reserved
0955-2219(95)00100-X
0955-2219/95/$9.50

Mechanical Behaviour of Partially Stabilized Zirconia Crystals with Terbia and Ceria Additives

George A. Gogotsi & Dmitry Yu. Ostrovoy

The Institute for Problems of Strength, National Academy of Sciences of Ukraine,
2 Timiryazevskaya St, 252014 Kiev, Ukraine

(Received 2 November 1994; revised version received 27 April 1995; accepted 31 May 1995)

Abstract

Mechanical behaviour of partially stabilized zirconia crystals (PSZC) with terbia and ceria additives was investigated under bending and indentation conditions. Test specimens were oriented along the [010] direction and along the axis of crystal growth. The PSZC bending strength (σ_b) was dependent on the crystallographic orientation of the specimens. The specimen volume subjected to stress influenced the PSZC strength. The highest mechanical characteristics were measured for ceria-doped crystals (σ_b = 1·9 GPa, K_{1c} = 11·4 MPa $m^{1/2}$, E_d = 366 GPa). The failure process was studied on the Vickers indentation, with special emphasis put on the development and propagation of lateral cracks. Anisotropy of lateral cracks in the (100) plane associated with that of the elastic moduli was revealed. At the same time anisotropy of radial cracks and hardness was not found. A new version of the equation to evaluate the fracture toughness (K_c^v) on the Vickers indentation was derived. The K_c^v values calculated by this equation correspond to those (K_{1c}) obtained by an SENB method.

1 Introduction

Considerable attention has recently been focused on partially stabilized zirconia crystals (PSZC),[1–3] some properties of which meet the requirements placed on structural materials. This rather high level of interest is probably also caused by technology[4] which allows the production of materials of high strength and fracture toughness. In published works e.g. Refs 3, 5 and 6, the authors mainly cited data on PSZC containing only yttria as a major additive (Y–PSZC). For testing, different, often contradictory procedures were used[3,7,8] with primary emphasis put on the physical nature of processes determining strength and deformation of these crystals[3,5]. It was shown[9,10] that other oxides of rare earth elements (ytterbium, cerium, etc.) present in Y–PSZC can also exert a positive influence not only on the process to make these crystals, but also on their physico mechanical characteristics. However, despite these data, certain problems associated, e.g. with the anisotropy of Y–PSZC properties still remain poorly investigated. Several results have been obtained[11,12] for the hardness of such crystals or for the development of cracks in them; however, detailed investigations of lateral cracks with the account of their crystallographic orientation have not been performed. As opposed to radial cracks, the latter can be of importance for such Y–PSZC applications as cutting elements of surgical instruments, bearing components, etc.[4,9] the production of which is accompanied with different machining, including abrasive.

The present work is therefore devoted to a complex investigation of mechanical properties of Y–PSZC containing terbia and ceria additives, with special emphasis on the development of lateral cracks in relation to other mechanical characteristics. This work continues our studies on zirconia crystals started in Refs 9 and 10.

2 Experimental Procedures

Partially stabilized zirconia single crystals with 3 mol% yttria and containing 0·3 mol% terbia (Y–Tb–PSZC) and 0·3 mol% ceria (Y–Ce–PSZC) were chosen for the investigations. These crystals, like those studied previously,[10] were prepared by direct high-frequency scull-melting technique at the Institute of General Physics, Russian Academy of Sciences.

Rectangular test specimens were cut from crystalline blocks with a diamond saw, their surfaces were ground and sharp edges rounded. The longitudinal axis of some specimens (Y–Tb–PSZC-A and Y–Ce–PSZC) was oriented by the Laue

back reflection method along the [010] direction, their mutually perpendicular surfaces corresponded to the {100} planes. The longitudinal axis of Y–Tb–PSZC-B specimens was approximately directed along the axis of crystal growth and was not strictly related to one of the characteristic directions in the cubic lattice,[13] i.e. the specimens were oriented in the same manner as for studying similar materials in Ref. 14.

Bending tests, as in Refs 4 and 9, were performed by our procedures.[15] All the specimens had the same cross-section (3·5 × 5·0 mm), the length of Y–Tb–PSZC-A specimens was about 25 mm, while the specimens of other crystals were about 45 mm long. The difference was determined by the dimensions of crystalline blocks. Therefore, the specimens were tested by three- and four-point bending. In the first case the span between supporting rollers was 20 (or 10) mm, in the second case it was 40 and 20 mm. Using different bending configurations, one could also evaluate a possible influence of the specimen volume subject to stress on the strength of the crystals under study.

In three-point bending tests the well known fact from applied mechanics was taken into account, viz. the plane stress state of the specimens occurring on such loading. Additional deflection of the specimens because of shear stresses can affect the magnitude of elastic moduli.[16] It is interesting that this fact is not usually taken into account during investigation of ceramics and single crystals. In this work we performed corrections of the experimental data obtained under three-point bending using the equation:[16]

$$E_{st} = \frac{L^3}{48J}\left[1+3\left(1+\nu\right)\left(\frac{h}{L}\right)^2\right]\frac{P}{\delta}, \qquad (1)$$

where E_{st} is the static elastic modulus on bending, P is the load, δ is the deflection, J is the moment of inertia of the cross-section, ν is Poisson's ratio, L is the span between supporting rollers and h is the height of a specimen.

Poisson's ratios (ν) were calculated from the data obtained on uniaxial compression of specimens. In this case lateral and longitudinal strain components were measured by resistance strain gauges glued to the specimen surfaces. These strain components were used to calculate known Poisson's ratio. Dynamic elastic moduli (E_d) were determined, as previously,[9,10] from longitudinal ultrasonic velocity data, v_l, measurements ($E_d=\rho v^2_l$, where ρ is the density of the material). It should be noted that here we used the concepts 'dynamic' and 'static' elastic moduli, though, as applied to crystals, one should speak rather about elastic constants for one or other crystallographic direction.[6,13] Thus, in our further discussions we confined ourselves to the above terminology which is widely used in engineering practice and can considerably simplify the analysis of the data.

The bending strength (σ_b) was calculated by applied mechanics known relations ($\sigma_b=2aP/bh^2$, where a is the length of a cantilever part of a specimen and b is the width of a specimen). As in Refs 9 and 10, a well known SENB method[17] was used to determine fracture toughness characteristics, e.g. the critical stress intensity factor (K_{1c}). The specimens were notched on their narrower surface (3·5 mm) over a half-height of their cross-section (2·5 mm) and placed with the same surface on the supporting rollers having a 20 mm span. The K_{1c} values were determined by the equation: $K_{1c} = \sigma_b c_n^{0.5} Y$, where c_n is the length of the notch and Y is the geometric factor determined from the tables.[17] The crack propagation in crystal specimens was studied by the traditional Vickers method. The data obtained were also used to evaluate the fracture toughness (K_c^V) of the crystals (see below).

3 Results

3.1 Bending strength, elasticity and fracture toughness

Major tests were performed on Y–Tb–PSZC-A specimens, the data on other crystals were used for comparison.

Strength characteristics were determined in the following way. The Y–TB–PSZC-A specimens were tested only by three-point bending, Y–Tb–PSZC-B and Y–Ce-PSZC were first tested by four-point bending, then by three-point (Table 1). The strength values (σ_b) of all studied specimens varied depending on the bending configuration. Thus, with a smaller span between supporting rollers, σ_b for the Y–Tb–PSZC-B and Y–Ce–PSZC specimens tends to increase (Table 1). The σ_b values of the Y–Tb–PSZC-A specimens were somewhat lower under such loading conditions. Maximum σ_b values (for several specimens, e.g. Y–Ce–PSZC they reached 1·9 GPa) corresponded to the highest values of elastic moduli (Table 2) for the [010] direction.

It is interesting to note that the differences were also observed in the nature of fracture surfaces for all specimens after bending tests. The Y–Tb–PSZC-A and Y–Ce–PSZC specimens exhibited traces of secondary cracking on their fracture surfaces visible even to the naked eye (Fig. 1(a)), while the fracture surface of Y–Tb–PSZC-B was smoother, displaying smaller flake-like cleavage. All the specimens (see also Ref. 9) are characterized by a step-wise propagation of the main crack

Table 1. Average bending strength of crystals

	Material						
	Y–Tb–PSZC-A		*Y–Tb–PSZC-B*			*Y–Ce–PSZC*	
Bending configuration[a]	↓ / ↑ 20 ↑	↓ / ↑ 10 ↑	↓ 40 ↓ / ↑ 20 ↑	↓ / ↑ 20 ↑	↓ / ↑ 10 ↑	↓ 40 ↓ / ↑ 20 ↑	↓ / ↑ 10 ↑
Bending strength(MPA)	1611	1197	416	630	853	1378	1698

[a]The figures give the span between supporting rollers (mm).

Table 2. Average physical characteristics of crystals

Material	*Density (g/cm³)*	*Ultrasonic velosity(m/s)*	*Elastic moduli (GPa)*	
			Dynamic	*Static*
Y–Tb–PSZC-A	6·06	7630	352	307[a] (334[b])
Y–Tb–PSZC-B	6·06	5399	177	166[c]
Y–CE–PSZC	6·07	7769	366	369[c]

[a]Three-point bending.
[b]Values corrected by eqn (1).
[c]Four-point bending.

front (Fig.1(b)). Fracture sources were concentrated in the surface layer on the side of a tensile zone, however we did not succeed in establishing their type because of the complex structure of fracture surfaces.

Bending tests of SENB specimens enabled K_{1c} values to be calculated, they were 9·96, 7·0 and 11·43 MPa $m^{1/2}$ on average for Y–TB–PSZC-A, Y–Tb–PSZC-B and Y–Ce–PSZC, respectively. In the first and third cases notch directions were coincident with [001].

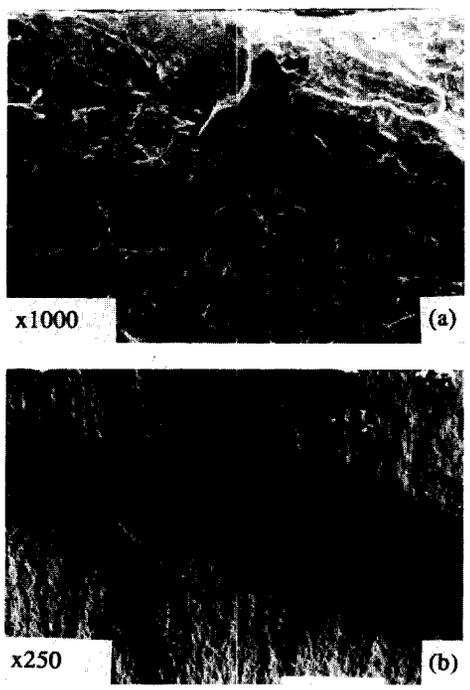


Fig. 1. (a) Fracture patterns of Y–Tb–PSZC-A specimens: flake-like surface cleavage, (b) step-wise propagation of the main crack front.

3.2 Vickers indentation tests

3.2.1 Indentation surfaces

Both groups of Y–TB–PSZC specimens were indented in the loading range of 0·1–200 N, since a further increase of loads resulted in less satisfactory impressions. The Y–Ce–PSZC specimens were also tested at higher loads (up to 300 N), since this problem arose to a less extent. The Vickers indenter was successively rotated through 360°C relative to the longitudinal axis of the specimen in a chosen plane only for Y–Tb–PSZC-A specimens, in the case of other crystals it was rotated only through 90°.

For all crystals, hardness values (H_v) determined from the impression half-diagonal[18] did not practically depend on the indentation direction in the planes under investigation (Fig. 2). In this case an increase in loading up to 70 N resulted in a certain decrease of H_v, e.g. for Y–Tb–PSZC-A from 14·3 GPa at 0·2 N to 12·5 GPa at 70 N. Starting from this load, H_v remained practically constant (this problem was detailed in Ref. 10).

In the process of indentation the cracks of different types were formed, viz. radial (Palmqvist)[10,19] and lateral,[10,20] or both. The presence of radial cracks is confirmed by the fact that partial grinding-off of the impressions resulted in the separation of such cracks from each corner of the impression (see also Refs 9 and 10). The extent of radial cracking was evaluated by an average length [$\bar{l} = \frac{1}{4}(l_1 + l_2 + l_3 + l_4$] of these cracks measured from each corner of the impression (Fig. 3). A relative size of lateral cracks was characterized by the parameter $L(\bar{R}) = \frac{\overline{ON} - \overline{OM}}{\overline{OM}} \approx \frac{\bar{R}}{0{\cdot}707a} - 1$ (Fig. 3), where $\overline{ON} = \bar{R}$ is the average distance from the impression center to the most distant part of the

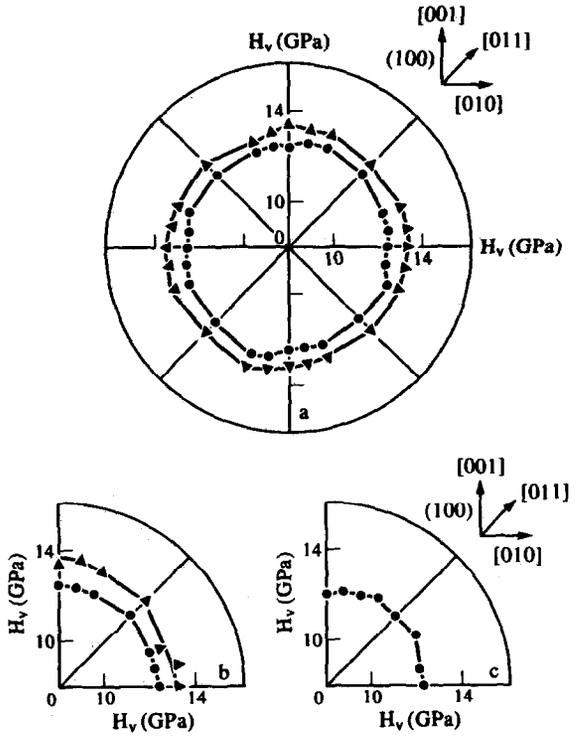


Fig. 2. Hardness (H_v) versus an angle of indenter rotation for: (a) Y–Tb–PSZC-A, (b) Y–Tb–PSZC-B, (c) Y–Ce–PSZC. Loads: 50 N (▲) and 100 N (●).

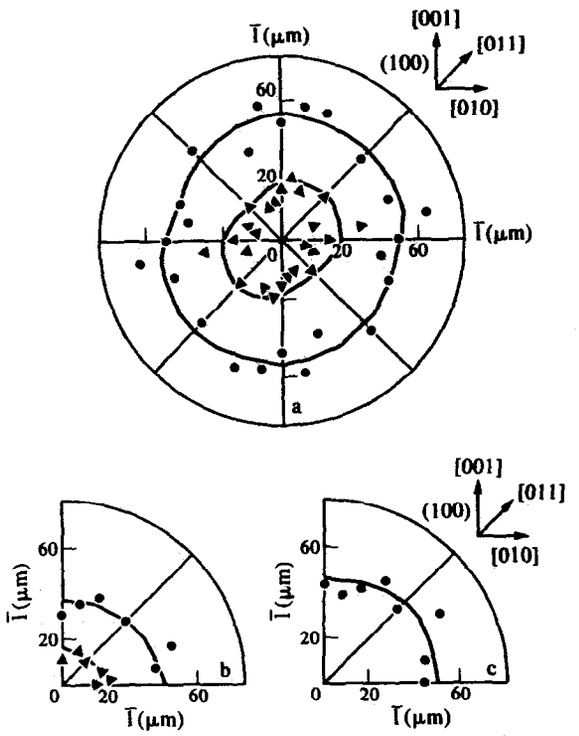


Fig. 4. Average length of radial cracks ($\bar{l}$) versus an angle of indenter rotation for (a) Y–Tb–PSZC-A, (b) Y–Tb–PSZC-B and (c) Y–Ce–PSZC. Loads: 50 N (▲) and 100 N (●).

front of the lateral crack calculated from each side of the impression, OM is the half-length of the impression side ($OM = a \sin 45°$) and a is the half-diagonal of the impression.

The experiments have demonstrated that the value of $\bar{l}$ for all crystals varies slightly depending on the indentation direction (Fig. 4). This may be investigated by drawing regression curves through a series of experimental points (Fig. 4). It was necessary to use this approach since experimental points had a relatively wide scatter in different directions. At the same time the extent of lateral cracking L ($\bar{R}$) differed considerably for the planes under consideration. Thus, when the indenter is turned in the (100) plane (Y–Tb–PSZC-A and Y–Ce–PSZC specimens), L ($\bar{R}$) varied from a certain maximum value ([010] direction) at a given load to a minimum one ([011] direction) and so on. If we average the data obtained (as in Fig. 4), they can graphically be represented as four-fold symmetry (Fig. 5(a),(c)). In this case $L(\bar{R})$ for Y–Ce–PSZC were lower (Fig. 5(c)) than those for Y–Tb–PSZC-A (Fig. 5(a)) at the same loads. For Y–Tb–PSZC-B

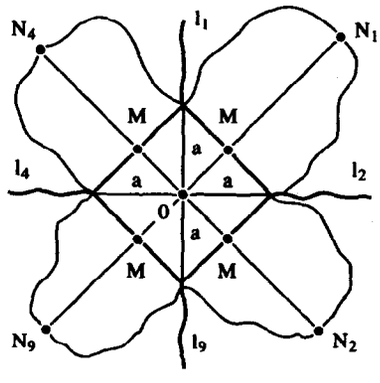


Fig. 3. Schematic representation of cracks formed around the Vickers impression (explanations in the text).

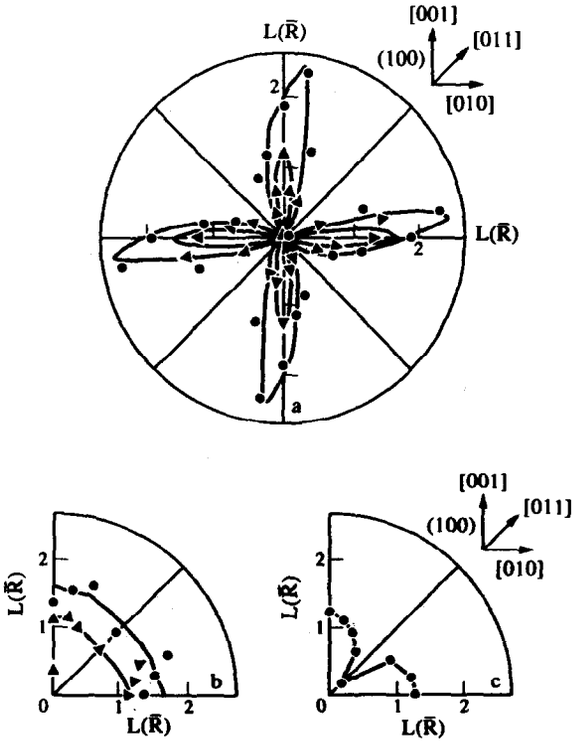


Fig. 5. Relative length of lateral cracks $L(\bar{R})$ versus an angle of indenter rotation for (a) Y–Tb–PSZC-A, (b) Y–Tb–PSZC-B and (c) Y–Ce–PSZC. Loads: 50 N (▲) and 100 N (●).

specimens $L(\bar{R})$ did not depend on the indentation direction, and its absolute values were somewhat different for different specimen surfaces (one of them is shown in Fig. 5(b)).

3.2.2 Fracture toughness

On the basis of earlier investigations,[9,21] we made the next step in terms of evaluating the fracture toughness of zirconia crystals from the length of radial cracks. For this purpose we used experimental values of a and $\bar{l}$ at various loads to plot calibration curves for each crystal[19] as a relation between normalized fracture toughness and normalized length of radial cracks. All these curves were approximated using an equation of the following type[22]

$$\frac{K_c^v \phi}{H_v a^{0.5}} \left(\frac{H_v}{E\phi}\right)^{0.4} = M \left(\frac{c}{a}\right)^{-N} . \quad (2)$$

In this equation the left side is the normalized fracture toughness, ϕ is the constraint factor ($\phi \approx 3$), H_v is the load-independent hardness and E is the static or dynamic elastic modulus. The right side contains the normalized length of radial cracks [$\frac{c}{a} = \frac{l+a}{a}$] and the coefficients ($M$ and N) are determined experimentally. In this case $c = l+a$ was taken as the length of radial cracks instead of ι (Fig. 4) which is often used in practice.[10,18,21] The value of K_c^v, as in Ref. 18, was set equal to K_{1c} and H_v = 12·5 GPa was chosen as its average value for all crystals in a load-independent regime. Major parameters of calibration curves in Fig. 6 being a log–log plot determined by the least-squares method are summarized in Table 3. The values of K_c^v calculated from these data, e.g. for Y–Tb–PSZC-A (Fig. 8), did not differ significantly from those obtained by the SENB method. Such calculations should also account for possible variations of elastic modulus (E) in different crystallographic directions.

We established that at least for Y–Tb–PSZC-A,

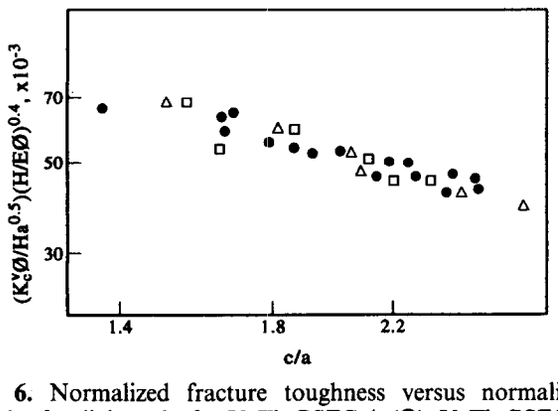


Fig. 6. Normalized fracture toughness versus normalized length of radial cracks for Y–Tb–PSZC-A (●), Y–Tb–PSZC–B (Δ) and Y–Ce–PSZC (□).

Table 3. M and N coefficients in eqn (2)

Material	*Coefficient*		*Correlation coefficient*
	M	*N*	
Y–Tb–PSZC-A	0·092	0·80	0·96
Y–Tb–PSZC-B	0·099	0·92	0·99
Y–Ce–PSZC	0·097	0·90	0·89

different E values, all other coefficients in the left side of eqn. (2) being constant, contributed only to M changes. At the same time the relations between a and c, e.g. in the [010] and [011] directions, were practically identical (equal values of N) despite a different extent of lateral cracking. The M and E values are inversely proportional, as a result we have practically coincident K_c^v values for a number of M and E values. Therefore, in our case the calculations were restricted to the M values (Table 3) corresponding to the E values obtained in the present work.

4 Discussion

The results obtained show that relatively high strength values correspond at least to the [010] direction in the (100) plane. This was already recognised.[9] By and large one may say that for such crystals, high strength values σ_b correspond to higher elastic moduli (Tables 1 and 2).

It should be noted that, for polished Y–PSZC specimens which contained only Y_2O_3, a σ_b of 2 GPa was found[2]. Among the crystals under investigation only some Y–Ce–PSZC specimens exhibited similar values of σ_b (~1.9 GPa), and the state of the specimen surface (ground or polished) for all crystals did not exert a noticeable influence on the magnitude of σ_b. This indicates that the strength of such crystals is probably determined

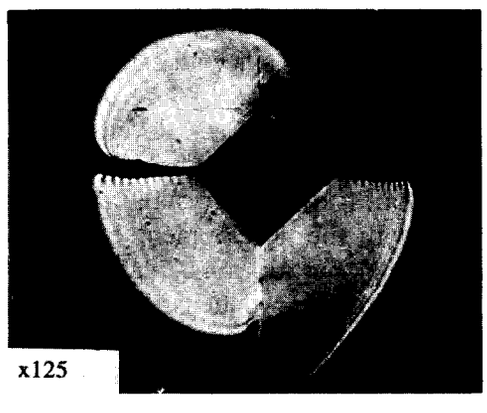


Fig. 7. Lateral and radial cracks around the impression on the Y–Ce–PSZC-A specimen surface corresponding (100) plane at a 150 N loading (the diagonals of the impression coincide with [010] and [001] directions).

rather by structural features in the bulk of the material rather than the surface effects. A reduction of σ_b for Y–Tb–PSZC-A specimens (Table 1) on three-point bending (10 mm span) could also be associated with the latter. Although for the specimens of other crystals a growth of σ_b was observed under the same loading conditions, which does not contradict Weibull's theory of strength.[23] Lower σ_b values for Y–Tb–PSZC-A specimens were not explained convincingly enough. However, such regularity is confirmed by testing of these specimens under different conditions.

Y–Tb–PSZC-A and Y–Ce–PSZC specimens exhibited the highest elastic moduli (Table 2). They are quite close to the literature data[6] for specimens of these crystals having similar orientation. The elastic moduli Y–Tb–PSZC-B specimens were much lower (Table 2). As was expected,[16] the static elastic moduli, E_{st}, determined for Y–Tb–PSZC-A specimens on their three-point bending, as in Ref. 9, were lower than the dynamic moduli E_d (Table 2). It is interesting that the uniaxial compression of these specimens in the [010] direction resulted in an elastic modulus of 370 GPa which slightly differed from E_d. The calculated Poisson's ratio (ν) was 0·17. It does not contradict[24] the values of ν for ceramics and related crystals which are usually in the range of 0·13–0·32. As a rule, materials with high elastic moduli exhibit lower ν. The value of E_{st} corrected by eqn. (1) was 334 GPa. For the specimens of other crystals this procedure was not necessary, since they were tested on four-point bending. A certain discrepancy between E_d and E_{st} for Y–Tb–PSZC-B obtained under the same loading conditions is probably associated with the fact that the specimen surfaces correspond to different crystallographic planes.

It should be noted that elastic moduli for Y–Tb–PSZC were measured on specimens cut from different crystalline blocks. However, they point to a considerable anisotropy of elastic properties of such crystals since all crystals were grown under similar conditions.

From the analysis of crack development around the impressions, it can be concluded that lateral cracks appearing in the crystals are not directly connected with the development of radial cracks. It is confirmed by additional data obtained, e.g. for Y–Tb–PSZC-A specimens. For them, depending on the indentation direction in the (100) plane, different sequence of crack types was observed. Thus, for the impressions where the diagonal is parallel to [010], a threshold value of the load (P_r) when first radial cracks appeared from the corners of the impression was 20 N. For the [011] direction P_r is equal to 15 N. Lateral cracks around the impressions when their diagonals were oriented along [010] were observed at a load (P_L) of 2 N, i.e. long before the radial ones appeared. The same was observed for Y–PSZC.[21] In the [011] direction the picture was quite opposite: radial cracks preceded the lateral ones. The latter were observed only at P_L=40–50 N. The Y–Ce–PSZC specimens in the [010] direction exhibited P_r=50 N and P_L=10 N. We could not establish certain specific P_r and P_L for Y–Tb–PSZC-B specimens since their surfaces displayed quite different fracture patterns. It should be noted that in Ref. 10 most equal values of P_L but higher values of P_r were observed for similar crystals in the same planes. This is probably caused by the fact that the tests in Ref. 10 were performed at loads of 50 N or higher as well as by the fact that, in the two cases, optical microscopes with different resolution levels were used.

For Y–Tb–PSZC-A and Y–Ce–PSZC the chipping around the impressions with the diagonals oriented along the [010] direction occurred starting from 70 and 200 N, respectively. This phenomenon is due to the uplift on the front of lateral cracks. These chips were observed in the [011] direction, e.g. for Y–Tb–PSZC-A already at 100 N or higher, whilst for Y–Tb–PSZC-B this value was not established because of a considerable scatter of experimental data for arbitrarily chosen directions.

Thus, the results show that in many cases radial cracks in these crystals play the role of a barrier for the propagation of the front of lateral cracks to an adjacent sector of the impression (Fig. 7), this was also observed for ceramics.[20] Radial cracks do not influence the distance of the front of lateral cracks from the center of an impression (ON in Fig. 3) for various loads and directions which also points to the absence of relationship between these types of cracks. For comparison, fully stabilized zirconia crystals (FSZC) exhibited[25] longer radial cracks in [110] as compared to [100] in the (100) plane. It was considered to be associated with the influence of lateral cracks. The latter were of minimum sizes in the [110] direction. Such influence is sometimes explained[20] by the redistribution of strain energy in favour of radial cracks due to a smaller extent of lateral cracking. As was shown above, we did not observe any noticeable anisotropy of radial cracking (Fig. 4) and, as a result, of the fracture toughness (see also [10]). Even when we increased the number of impressions up to 15, e.g. on the (100) surface of Y–Tb–PSZC-A specimens, 100 N loads give l values of 60 μm for [010] ($L(\bar{R})$=2) and of 72 μm for [011] ($L(\bar{R})$=0·19) which is within the scatter of

experimental data. It also applies to the hardness of such crystals (earlier noticed for Y–PSZC[12]), while FSZC displayed[26] its strong anisotropy in the (100) plane. The graphic representation of this anisotropy resembles the variation of elastic moduli[6] and $L(\bar{R})$ (in our case) (Fig. 5) in the same crystallographic planes. One may say that for Y–Tb–PSZC-A and Y–Ce–PSZC the anisotropy of lateral cracks is proportional to that of the elastic moduli: the higher $E_{st}(E_d)$, the higher $L(\bar{R})$. It is interesting that the same relationship was established[27] for several cubic ionic crystals but only between the anisotropy of elastic modulus and that of hardness.

We should also emphasize particular behaviour of crystals on indentation as the formation of 'irregular' radial cracks around some impressions (see also Refs 10,14), these cracks propagate from the sides of the impression or at an angle from its corners. Such cracks are the most characteristic of the impressions, the diagonals of which are oriented along [011]. We did not take them into account when the fracture toughness of crystals was evaluated.

To calculate fracture toughness (K_c^v) from the length of radial cracks, quite a number of semiempirical relations have been proposed,[18,19,22] based on the models of half-penny or Palmqvist cracks. The application of several well known and widely used equations[18]

$$K_c^v = 0{\cdot}028\, H_v a^{0.5} \left(\frac{E}{H_v}\right)^{0.5} \left(\frac{c}{a}\right)^{-1.5}, \tag{3}$$

$$K_c^v = 0{\cdot}142\, \frac{H_v a^{0.5}}{\phi} \left(\frac{E\phi}{H_v}\right)^{0.4} \left(\frac{c}{a}\right)^{-1.56} \tag{4}$$

and

$$K_c^v = 0{\cdot}035\, \frac{H_v a^{0.5}}{\phi} \left(\frac{E\phi}{H_v}\right)^{0.4} \left(\frac{c}{a} - 1\right)^{-0.5}. \tag{5}$$

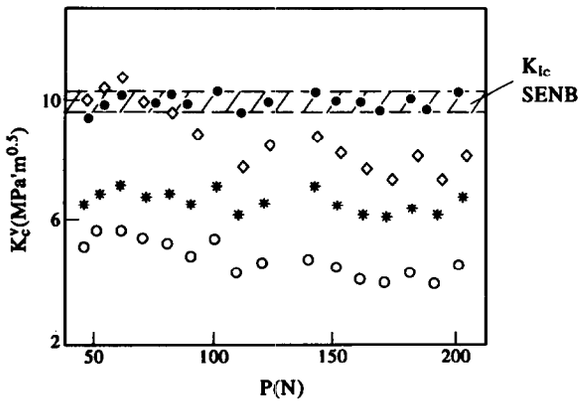


Fig. 8. Fracture toughness (K_c^v) versus the indentation load (P) for Y–Tb–PSZC-A determined by eqn (2) (●), eqn (3) (○), eqn (4) (◇) and eqn (5) (∗).

To evaluate fracture toughness, e.g. of Y–Tb–PSZC-A crystals, resulted (Fig. 8, see also Ref. 10) in K_c^v values which are lower than those obtained by a conventional (SENB) method. It can point to the differences in propagation of radial cracks in ceramics (eqns (3)–(5) were proposed for the latter) and in the crystals under study. Therefore, numerical coefficients from Table 3 substituted in eqn (2) which is similar to eqns (3)–(5) in its structure are more suitable for practical calculations of K_c^v. These coefficients characterize a real behaviour of such crystals on indentation. The equation derived in Ref. 21 which was used[10] to evaluate K_c^v of similar crystals contained coefficients somewhat different in their magnitude. Therefore, it should probably be considered as a foregoing approximation of the problem to be solved. The fact that calibration curves (Fig. 6, Table 3) are spaced so closely is most likely to be random in nature. A relative position of these curves can be different for the specimens of other crystals taking into account possible anisotropy of their mechanical characteristics.

5 Conclusions

The complex investigation of zirconia crystals stabilized with yttria and containing terbia and ceria additives gave additional information about the mechanical behaviour of these materials. It further elucidated the poorly studied field of lateral cracking of crystals on Vickers indentation. This information is also of great interest for the application of crystals as a material for surgical instruments,[9] since this lateral cracking resembles fracture features observed on the surface of scalpels during their sharpening. It gives the impression that the performance of these crystals at room temperature applications can be inferior to that of similar ceramics. It is associated with noticeable local failure when in contact with a sharp concentrator (some grains of abrasive powder, etc.). This behaviour of the crystals was not specially treated by earlier investigators.

In addition, the data obtained in the present work could be useful for the development of more perfect crystals possessing more uniform structure (data on fractographic investigations were published previously[9,10]). The results (including the equation for determining K_c^v) suggest that we should concentrate on the development of the most acceptable approaches for evaluating the fracture toughness of crystals. This problem should be given as much attention as that paid to advanced technical ceramics (see, e.g., Ref. 28).

Acknowledgements

The work was performed within the programme 'New Zirconia-Based Materials and Components' financed by the State Committee of Science and Technology of Ukraine. This research was made possible in part by Grant No. UBV000 from the International Science Foundation.

References

1. Ingel, R. P. & Rice, R. W., Room-temperature strength and fracture of ZrO_2–Y_2O_3 single crystals. *J. Am. Ceram. Soc.*, **65** (1982) C.108–9.
2. Ingel, R. P., Lewis, D., Bender, B. A. & Rice, R. W., Physical, microstructural and thermomechanical properties of ZrO_2 single crystals. In *Advances in Ceramics*, Vol. 12, *Science and Technology of Zirconia II*, eds N. Clausen, M. Ruhle & A. H. Heuer. American Ceramic Society, Columbus (1984) 408–14.
3. Heuer, A. H., Lanteri, V. & Dominguez-Rodriguez, A., High-temperature precipitation hardening of Y_2O_3 partially-stabilized ZrO_2 (Y–PSZ) single crystals. *Acta Metall.*, **37** (1989) 559–67.
4. Gogotsi, G. A., Lomonova, E. E. & Osiko, V. V., Studies of mechanical characteristics of zirconia single crystals for structural application. *Refractories*, **32** (1991) 14–7 (Transl. from Russian).
5. Lankford, J., Page, R. A. & Rabenberg, L., Deformation mechanism in yttria-stabilized zirconia. *J. Mater. Sci.*, **23** (1988) 4144–56.
6. Ingel, R. P. & Lewis, D., Elastic anisotropy in zirconia single crystals. *J. Am. Ceram. Soc.*, **71** (1980) 265–71.
7. Dominguez-Rodriguez, A., Lanteri, V. & Heuer, A. H., High-temperature precipitation hardening of two-phase Y_2O_3-partially-stabilized ZrO_2 single crystals: a first report. *J. Am. Ceram. Soc.*, **69** (1986) 285–7.
8. Lankford, J., Inverse strain rate effects and microplasticity in zirconia crystals. *J. Mater. Sci. Lett.*, **8** (1989) 947–9.
9. Gogotsi, G. A., Lomonova, E. E. & Pejchev, V. G., Strength and fracture toughness of zirconia crystals. *J. Eur. Ceram. Soc.*, **11** (1993) 123–32.
10. Gogotsi, G. A., Dub, S. N., Lomonova, E. E. & Ozersky, B. I., Vickers and Knoop indentation behaviour of cubic and partially stabilized zirconia crystals. *J. Eur. Ceram. Soc.*, **15** (1995) 405–13.
11. Martinez-Fernandez, J., Jimenez-Melendo, M., Dominguez-Rodriguez, A. & Heuer, A. H. Elevated temperature studies of microindentation of Y-PSZ. In *Proceedings of the 11th Risø International Symposium on Metallurgy and Materials Sciences: Structural Ceramics-Prossesing, Microstructure and Properties.* eds J. J. Bentzen *et al.* Risø National Laboratory, Roskilde, Denmark (1990) 413–8.
12. Saiki, A., Ishizawa, N., Mitsutani, N. & Kato, M., SEM observation of the stress-induced transformation by Vickers indentation in Y–PSZ crystals. *J. Ceram. Soc. Jpn. Int. Edn.*, **97** (1989) 41–6.
13. Ingel, R. P., Lewis, D., Errors in elastic constant measurements in single crystals. *J. Am. Ceram. Soc.*, **71** (1988) 261–4.
14. Gogotsi, G. A., Galenko, V. I., Ozersky, B. I., Lomonova, E. E., Myzina, V. A., Vishnyakova, M. A. & Kalabukchova, V. E., Strength and fracture toughness of yttria and terbia-doped zirconia crystals. *Refractories*, **34** (1993) 303–12 (Transl. from Russian).
15. Gogotsi, G. A., Test method of advanced ceramics, reasonable approaches for standardization of ceramics. *Key Engng. Mater.*, **56–57** (1991) 419–34.
16. Timoshenko, S. P., Strength and vibration of structural elements. *Nauka, Moscow*, (1975) 704 (in Russian).
17. Brown, W. F. & Srawley, J. E., Plane strain crack toughness testing of high strength metallic materials. ASTM STP 410. *Am. Soc. Test. Mater.*, (1967) 13–15.
18. Li, Z., Ghosh, A., Kobayashi, A. S. & Bradt, R. C., Indentation fracture toughness of sintered silicon carbide in the Palmqvist crack regime. *J. Am. Ceram. Soc.*, **72** (1989) 904–11.
19. Lankford, J., Indentation microstructure in the Palmqvist crack regime: implications for fracture toughness evaluation by the indentation method. *J. Mater. Sci. Lett.*, **1** (1982) 493–5.
20. Cook, R. F., Pascucci, M. R. & Phodes, W. H., Lateral cracks and microstructural effects in the indentation fracture of yttria. *J. Am. Ceram. Soc.*, **73** (1990) 1873–8.
21. Dub., S. N. & Gogotsi, G. A., Indentation fracture toughness of zirconia crystals. *J. Aust. Ceram. Soc.*, (in press).
22. Evans, A. G. & Charles, E. A., Fracture toughness determinations by indentation. *J. Am. Ceram. Soc.*, **59** (1976) 371–2.
23. Weibull, W., A statistical distribution function of wide applicatibility. *J. Appl. Mech.*, **18** (1951) 293–7.
24. French, S. S. J., Ceramics in reciprocating internal combustion engines. *SAE Techn. Pap. Ser.*, N841135 (1984) 14.
25. Pajares, A., Guiberteau, F., Dominguez-Rodriguez, A. & Heuer, A. H., Indentation-induced cracks and the toughness anisotropy of 9·4 mol%yttria-stabilized cubic zirconia single crystals. *J. Am. Ceram. Soc.*, **74** (1991) 859–91.
26. Pajares, A., Guiberteau, F., Dominguez-Rodriguez, A. & Heuer, A. H. Microhardness and fracture toughness anisotropy in cubic zirconium oxide single crystals. *J. Am. Ceram. Soc.*, **71** (1988) 332–3.
27. Sirdeshmukh, D. B. & Kishen Rao, K., Hardness anisotropy in cubic ionic crystals. *J. Mater. Sci. Lett.*, **7** (1988) 567–8.
28. Quinn, D. G., Salem, Y., Bar-en, Y., Cho, K., Foley, M. & Fang, H. Fracture toughness of advanced ceramics at room temperature. *J. Res. Natl Inst. Standards Technol.*, **97** (1992) 579–607.

Journal of the European Ceramic Society 15 (1995) 1185–1192
© 1995 Elsevier Science Limited
Printed in Great Britain. All rights reserved
0955-2219(95)00102-6
0955-2219/95/$9.50

Mechanical Property Characterization of a 9 mol% Ce–TZP Ceramic Material — I. Flexural Response

G. A. Gogotsi,[a] V. P. Zavada[a] & M. V. Swain[b]

[a]Institute for Problems of Strength, Ukranian Academy of Sciences, 252014 Kiev, Ukraine
[b]Department of Mechanical and Mechatronic Engineering, The University of Sydney, NSW 2006, Australia

(Received 5 August 1994; revised version received 13 March 1995; accepted 31 May 1995)

Abstract

Investigations were carried out on four tetragonal zirconia polycrystalline (TZP) ceramics of differing grain size containing 9 mol% CeO_2. Precision flexural tests on these materials were conducted to determine the elastic modulus, the non-linear deflection and the associated acoustic emission during such testing. The deformation was characterized in terms of the number and size of the transformation bands that developed during the non-linear response. The finest grained material initially exhibited permanent set without the presence of such bands, whereas all the coarser grained materials showed a linear relationship between the summation of the band widths and the residual deflection. The acoustic emission and plastic strain behaviour are discussed in terms of the number and size of the stress induced phase transformation bands.

1 Introduction

The development of tough ductile ceramics has been the long cherished dream of many materials engineers. Recently this situation has to some extent been realised with the development of Ce–tetragonal zirconia polycrystalline (TZP) materials which behave almost like mild-steel as shown initially by Tsukuma and Shimada[1] and subsequently verified by numerous authors.[2–6] The main emphasis of such papers has been to rationalize the basis of the non-linear response and the development of bands where the tetragonal grains had transformed to monoclinic zirconia without any associated cracking.

Ce–TZP materials are somewhat unique amongst the zirconia phase transformable materials in that the tetragonal (t) to monoclinic (m) transformation exhibits burst or autocatalytic behaviour. Previous studies by Reyes-Morel and Chen,[4] and Becher and Swain[7] have investigated this behaviour and shown that a strong grain size effect exists and influences the burst temperature M_B for the t → m transformation. The latter authors have also provided a simple thermodynamic explanation of this size effect, relating it to a critical nuclei size and degree of undercooling or applied stress to initiate the transformation.

In this paper a more critical appraisal is given of the force–displacement response of the Ce–TZP materials tested in four point flexure. In particular the non-linear response is characterised in terms of the acoustic emission that develops and the size and number of the transformation bands. In a previous paper the authors[8] also investigated acoustic emission activity during the flexure testing of Mg–PSZ ceramics. However, that study did not enable an unambiguous interpretation of the acoustic emission (AE) data, that is, whether it was generated by stress induced phase-transformation or microcracking of the coarse grained microstructure of that material.

2 Materials

The investigations were carried out on Ce–TZP ceramics containing 9 mol% CeO_2. These materials were sintered at temperatures from 1400 to 1550°C in air for 1 h and their fabrication has been described by Grathwohl and Liu.[2] The designation, sintering temperature, mean grain size and relative density are listed in Table 1.

Specimens in the form of rectangular bars 2 × 2·8 × 48 mm were cut from a large sintered plate and polished on two adjacent sides prior to flexure testing. Four point bending tests were conducted on a precision rig described elsewhere[9] with inner and outer supports of 20 and 40 mm at a crosshead speed of 0·5 mm/min. The specimen deflection and accumulated acoustic emission counts were measured during the test using the same procedure as described in Ref. 8.

Table 1. Designation and properties of investigated ceramics

Designation	*Temperature of sintering (°C)*	*Mean grain size (μm)*	*Relative density (%)*
Ce–TZP-I	1400	1·14	94
Ce–TZP-II	1450	1·62	97
Ce–TZP-III	1500	2·22	98
Ce–TZP-IV	1550	3·00	97

3 Results and Discussion

3.1 Force–displacement curves

3.1.1 Monotonic loading

Typical force–displacement (P–δ) curves and associated acoustic emission counts (P–N_Σ) of the four ceramics are shown in Fig. 1(a–d), and the results are summarized in Table 2. The brittleness measure has been discussed in detail elsewhere by Gogotsi[9] and is the ratio of the elastic to the total energy under the force–displacement curve at the onset of fracture. It is clear from the data in Table 2 that the materials differ insignificantly in terms of their density, elastic modulus and ultrasonic velocity. The force–displacement curves are similar to those reported by Grathwohl and Liu[2] in that there is initially a linear response from which the 'static' estimate of the elastic modulus was calculated.

Beyond the linear response region of the P–δ curves the materials exhibit inelastic behaviour that may be approximated by a straight line whose slope decreases with increasing grain size of the Ce–TZP material as shown schematically in Fig. 2(a). The critical load at the onset of inelastic behaviour P_{el} and for failure P_m for each of the ceramics is shown in Fig. 2(b). The maximum deflection δ_m and residual deflection δ_r (maximum deflection less elastic recovery) are shown in Fig. 2(c). The residual or plastic deflection, δ_r, is almost independent of the grain size of the material.

The materials exhibit significant differences in the form of the inelastic portion of the P–δ deformation. The Ce–TZP-1 material exhibits a very smooth curve with the onset of nonlinear behaviour only being determined by the almost imperceptible change in slope. This behaviour is similar to that observed with Mg–PSZ (TS grade) material. Whereas the materials CE–TZP-II to Ce–TZP-IV are characterized by very jerky behaviour with the magnitudes of the intermittent

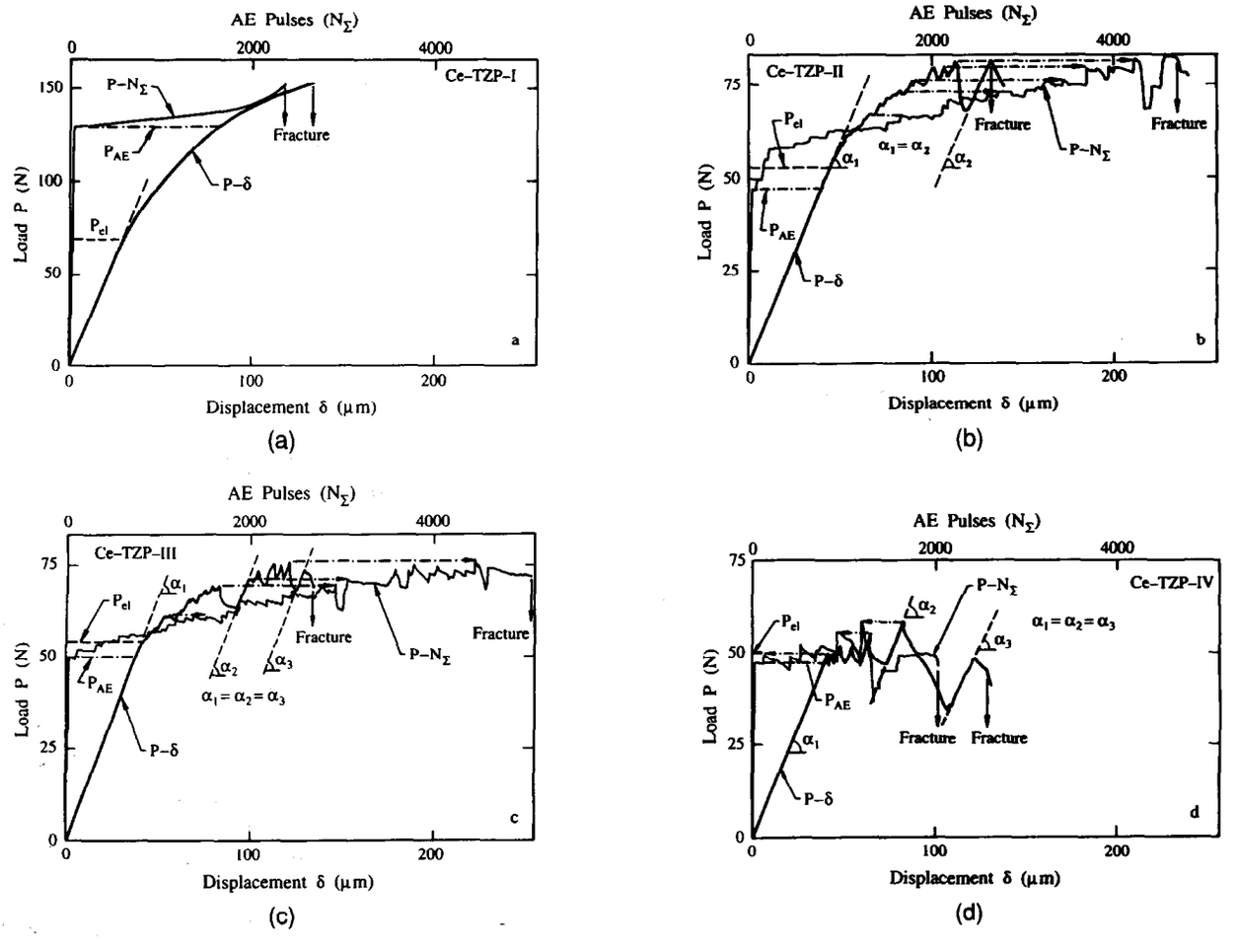


Fig. 1. Load–displacement (P–δ) and load–accumulated acoustic emission events (P–$N\epsilon$) for the four Ce–TZP materials. (a) Ce–TZP-I; (b) Ce–TZP-II; (c) Ce–TZP-III; and (d) Ce–TZP-IV.

Table 2. Physical and mechanical characteristics of Ce–TZP ceramics[a]

Ceramics	*Density* (g/cm^3)	*Ultrasound velocity* (*m/s*)	*MOR* (*MPa*)	*Ultimate strain* (10^{-4}*m/m*)	*Elasticity modulus* (*GPa*)		χ
					Dynamic	*Static*	
Ce–TZP-I	5·68	5459	451	47·3	175	169	0·34
Ce–TZP-II	6·00	5466	239	23·9	179	180	0·31
Ce–TZP-III	6·07	5465	223	23·5	181	175	0·15
Ce–TZP-IV	6·01	5411	177	28·7	176	175	0·15

[a]The crosshead speed is 0·5 mm/min.

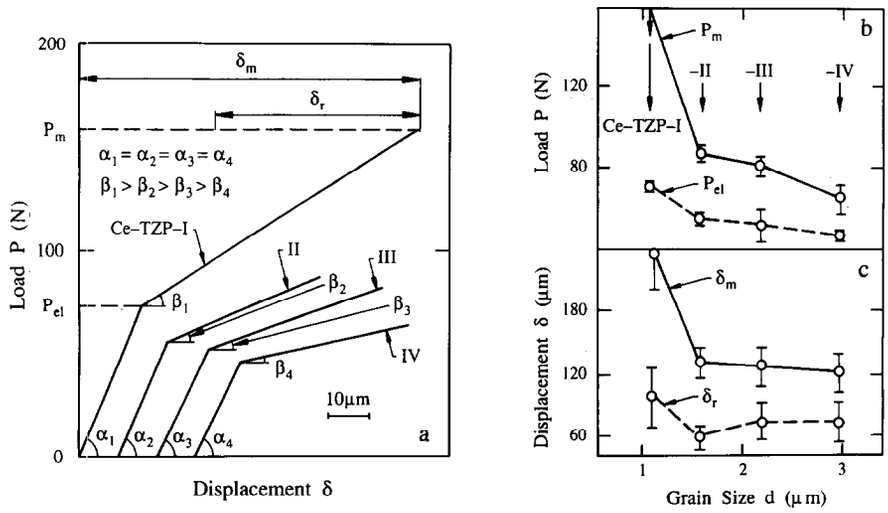


Fig. 2. (a) Schematic bi-linear approximation of the load–displacement diagrams for the various Ce–TZP materials; (b) comparison of the elastic limit load and maximum load; (c) the maximum and residual strain as a function of grain size.

load drops increasing with material grain size. These peculiarities of the P–δ response during monotonic loading appeared as part of the continuous load–deflection curves, and alternated with sharp load drops accompanied by an increase in deflection. It should also be noted that similar drops in load (but developing more slowly) were also occasionally observed for periods of up to a few minutes after the testing machine-crosshead had been stopped at maximum load. Thus although a time factor of loading can not be ruled out, nevertheless the shape of the P–δ curves did not essentially differ at crosshead speeds of 0·5 and 0·005 mm/min. Unfortunately, the limited number of samples did not enable this time dependent effect to be investigated in detail.

The nature of the load drops during continuous load–deformation curves should not be associated with the nucleation and growth of cracks in the specimen. Crack initiation or growth would lead to a change of the specimen compliance, $c = \tan^{-1}\alpha_1$ (Fig. 1(b, c or d)), by the value $\Delta c = \tan^{-1}\alpha_1 - \tan^{-1}\alpha_2$. Such a change in compliance should be related to a decrease in load ΔP_i by the relationship

$$\frac{\Delta c_i}{c_o} \simeq \frac{\Delta P_i}{P}.$$

This expression is also valid for the total change of specimen compliance Δc_i, which should be related to the sum of the successive load drops by the total value $\Sigma \Delta P_i$, i.e.

$$\frac{\Delta c_i}{c} \simeq \frac{\Sigma \Delta P_i}{P}.$$

The right-hand part of the above expression for samples Ce–TZP-III and -IV reaches 10–20%, such a change of compliance would have been readily measured on the reloading portion of the monotonic load–deflection curve after a few such load drops. However, the slope of these curves within the limit of experimental error (2–3%) showed undetectable change throughout the course of loading. In addition, the anticipated crack depth associated with such a load drop would have been readily visible, and in the range 0·6–1·0 mm.

Analysis of the acoustic emission data is of particular interest. This data which must be considered as only comparative because of the difficulty of attachment of the AE detector to such a small bar. It is for this reason that the total AE count to fracture was characterized by considerable scatter from specimen to specimen, which did not allow for example one to relate N_Σ values to

the grain size of the ceramics. However, the results consistently showed that for sample II, III and IV the onset of AE counts corresponds to the onset of nonlinearity of the P–δ curve, whereas for the Ce–TZP-I material the AE began only after considerable non-linearity. Also, one can clearly observe a correlation between AE outbursts and load drops (in Fig. 1(b–d) such correlations are connected by means of dashed horizontal lines). In contrast to this, very few AE events were detected during the continuous portions of the load–deflection curve.

3.1.2 Cyclic loading tests

To provide a more detailed understanding of the above deformation, sequential load–unloading cycles were performed on samples with polished tensile and adjacent side face. These materials were loaded to increasing maximum force and between each cycle the tensile and side surfaces were visually inspected. Such a testing procedure enabled us to quantify the surface deformation bands on the tensile surface that formed perpendicular to the longitudinal axis and their extension on the side surface. Typical P–δ curves and associated AE, P–N_Σ curves are shown in Figs 3–6 (a and b) for all the Ce–TZP materials. The location

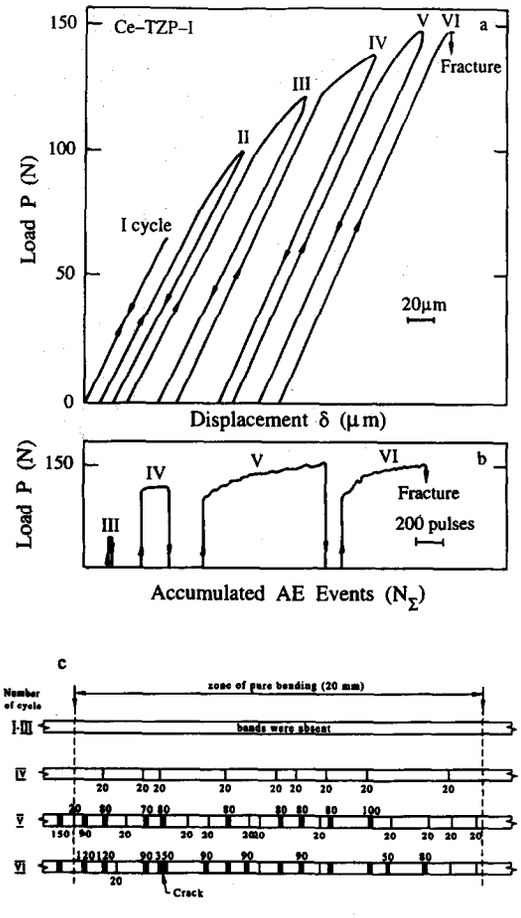


Fig. 3. (a) Cyclic load–displacement data; (b) accumulated AE events; and (c) location and width (in μm) of transformation bands in Ce–TZP-I.

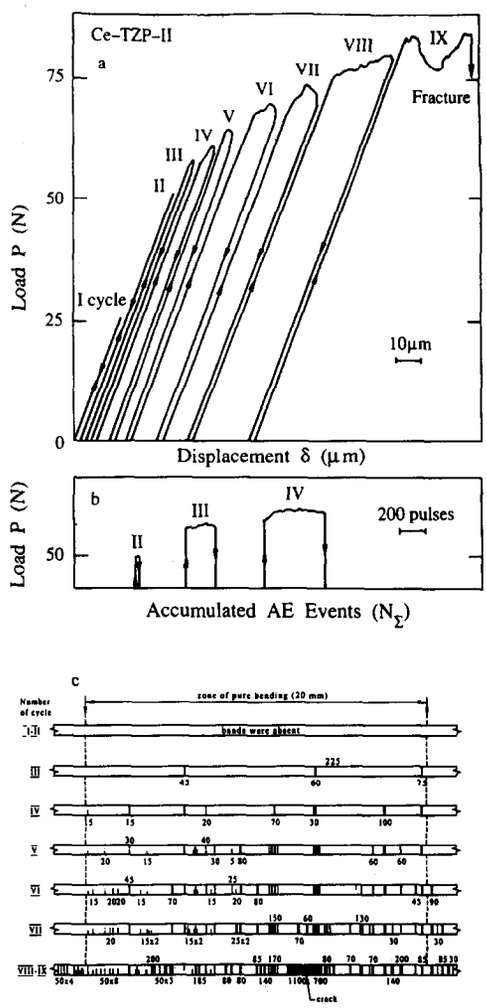


Fig. 4. (a) Cyclic load–displacement data; (b) accumulated AE events; and (c) location and width of transformation bands in Ce–TZP-II.

and size of the transformation bands on the tensile surface are shown in Figs 3–6(c) again for all the Ce–TZP materials. Representative micrographs of the transformation bands on the tensile and side surfaces for samples Ce–TZP-I to -III are shown in Fig. 7. In some instances the transformation band associated with the fracture surface is also visible in the micrograph. Previous examples of this type of deformation for Ce–TZP materials was first shown by Hannink and Swain[3] and reproduced by other authors.[2,4,6]

The present observations enable the following critical aspects of these transformation bands to be made:

(i) Deformation bands appear to initiate randomly and increase in number with increasing strain. They appear to be uniformly distributed within the region of constant stress of the four point flexure specimen. The bands are present only above a critical load (or stress) that for specimens Ce–TZP-II to -IV corresponds to the onset of permanent set or 'plastic' deformation, whereas for material Ce–TZP-I the initial stages of permanent set are not associated with band formation.

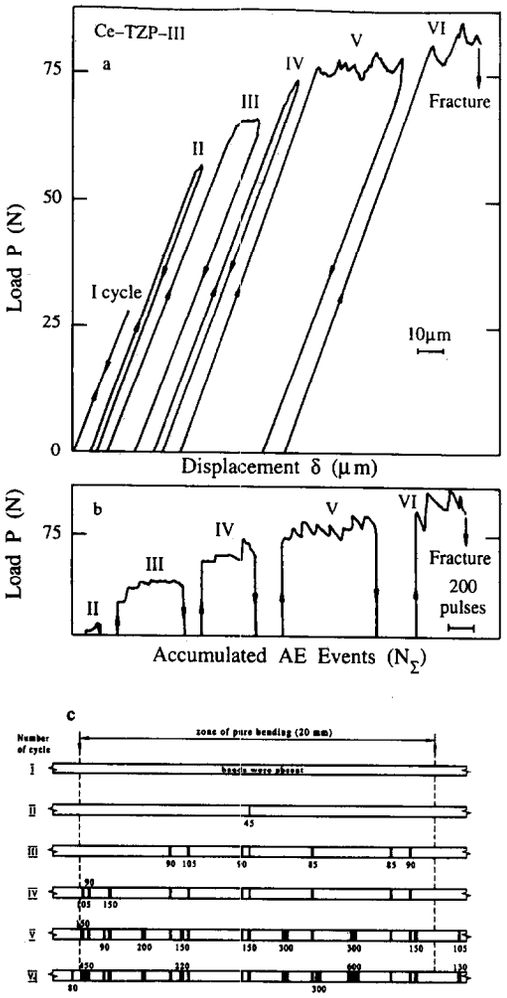


Fig. 5. (a) Cyclic load–displacement data; (b) accumulated AE events; and (c) location and width of transformation bands in Ce–TZP-III.

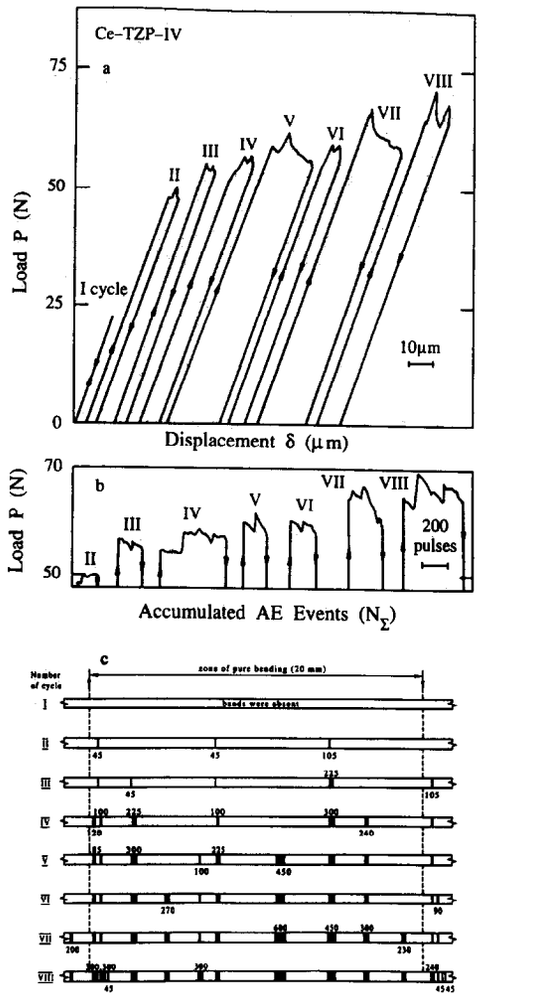


Fig. 6. (a) Cyclic load–displacement data; (b) accumulated AE events; and (c) location and width of transformation bands in Ce–TZP-IV.

(ii) With increasing loading cycles beyond the elastic limit new bands appear and those which were initiated during a previous cycle either increase in width discretely or remain unchanged up to fracture.

(iii) For each cycle the slope of the P–δ curve remains constant upon loading and unloading although the proportionality limit increases with each subsequent cycle. Upon loading to the proportional limit for each cycle no change in the number and size of the transformation bands or AE events is observed.

(iv) The observation of the first AE event coincided with the formation of the first transformation band for all of the Ce–TZP specimens. However, for sample Ce–TZP-I the first detectable AE event occurred after the onset of considerable 'plastic' strain.

(v) For specimens Ce–TZP-III and -IV, that exhibited more pronounced load drops during either monotonic or cyclic loading, a direct relationship between the number of load drops, AE event bursts and number of transformation bands was observed.

(vi) Fracture of the various specimens occurred almost in the centre of one of the widest pre-existing bands and never occurred at a new location.

A more detailed analysis of the deformation bands and their width at the moment of specimen fracture and a histogram plot of the transformation band widths is shown in Fig. 8. This figure reveals major distinctions between the various samples. In particular, the width of the transformation bands increases with specimen grain size. Thus, for example, whilst for the Ce–TZP-I specimen only narrow bands of width $\Delta_i \sim 20$ μm are formed, they are often grouped together in packets of three or four bands, or more at the fracture location. In contrast for specimens Ce–TZP-II to -IV the bands become increasingly thicker and fewer in number. The total number of transformation bands $n_{tr} = \epsilon n_{\Delta}$, observed on the tensile surface of the fractured specimen is also given on the histogram plots.

Analysis of the total width of the bands versus the number of bands formed during the loading

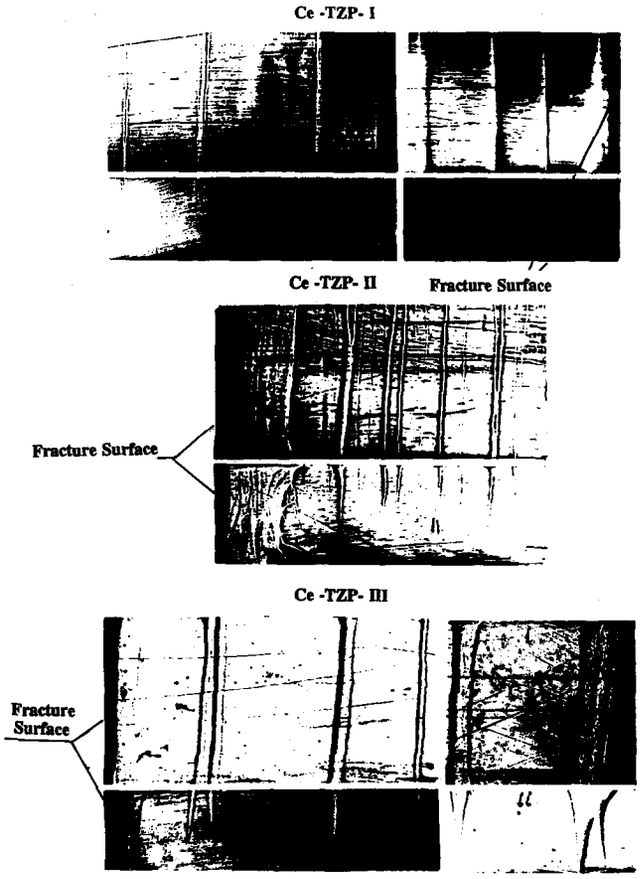


Fig. 7. Typical optical micrographs of the tensile and side faces of various Ce–TZP materials, illustrating the transformation banding.

cycles shows a nonlinear trend and increasing slope with increasing grain size as shown in Fig. 9. This behaviour is most pronounced for samples Ce–TZP-III and -IV, and appears to be related to the magnitude of the load drops with increasing strain during flexure. It is as though the easier initiation sites for transformation band nucleation become exhausted leading to overload conditions

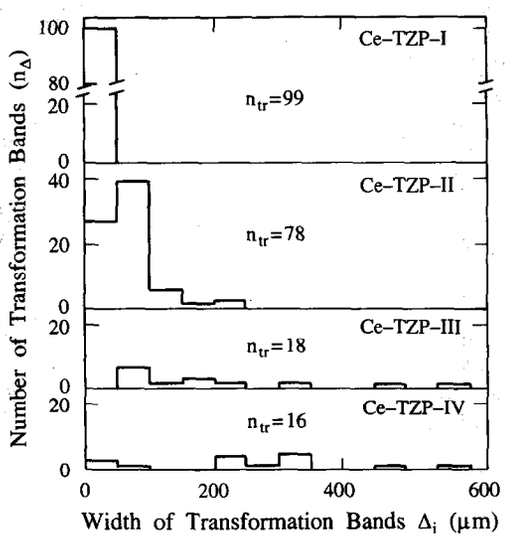


Fig. 8. Histograms of the number (n_Δ) and width (Δ_i) of the transformation bands developed on the tensile surface of the Ce–TZP materials.

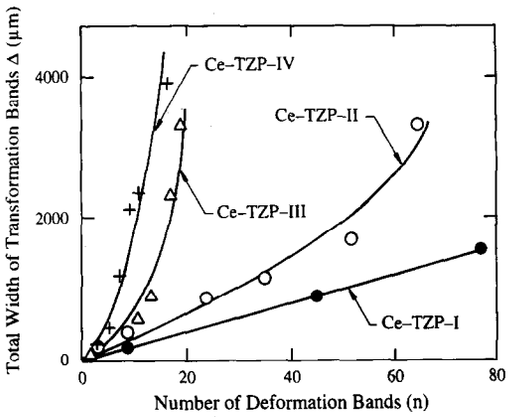


Fig. 9. Relationship between the total transformation band widths Δ versus the number of bands.

for the more difficult sites. This overload instability initiation condition leads to the formation of wider bands.

A more linear relationship may be established between the residual 'plastic' displacement δ_r and the sum of the widths of the transformation bands during each cycle as shown in Fig. 10. The obvious exception to the near universal curve is Ce–TZP-I, which in contrast to that shown in Fig. 9 is very nonlinear. For samples Ce–TZP-II to -IV a linear relationship of the form ($\delta_r = k_i \Delta$) fits the data very well, with the constant k_i tabulated for these materials in Table 3. It is not clear why sample Ce–TZP-I does not show such a linear dependence although it may be due to the presence of some fine scale microcracking as well as transformation that accounts for the significant plastic strain measured. However, one might have expected such microcracking to be associated with a reduction of specimen compliance with each loading cycle. Alternatively, some transformation reversibility upon unloading may occur, but this would be anticipated to have produced some non-linearity during the unloading phase. Perhaps with this sample some ferro-elastic tetragonal grain reorientation

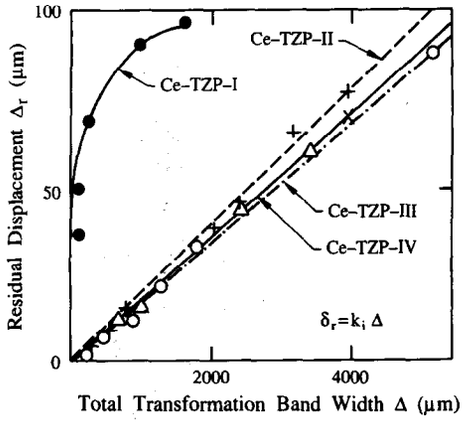


Fig. 10. Relationship between the residual displacement δ_r and the sum of the transformation band widths Δ.

Table 3.

Ceramics	k_1	k_2
Ce–TZP-I	—	25
Ce–TZP-II	0·0193	71
Ce–TZP-III	0·0177	117
Ce–TZP-IV	0·0169	126

as proposed by Virkar and Matsumoto[11] may be occurring during loading which is irreversible upon unloading. If this is the case then it suggests that the fine grained Ce–TZP material initially responds above a critical tensile stress to re-orientation of some tetragonal grains. Upon further loading these or perhaps other sites undergo transformation to monoclinic zirconia. Both of these processes (re-orientation and phase transformation) are associated with residual deformation. The absence of AE events during the initial phase of non-linear response of the Ce–TZP-I material (Fig. 1(a)) is also supportive of this interpretation.

It would be anticipated that because of the observed relationship between δ_r and the sum of the deformation bands Δ, a similar correlation should exist with the inelastic strain ϵ_r of the flexure specimen. For this purpose consider the point Δ = 4000 μm and δ_r = 70 μm (marked as a cross in Fig. 10), which may be thought of as the averaged value for specimens -II to -IV. Then using the simple relationship between strain, ϵ, to the flexure of a beam of height h and inner span length L (20 mm) namely

$$\epsilon = \frac{4h}{L^2}\,\delta\,,$$

this simple hypothesis may be confirmed. Upon substituting for h and δ_r(2·8 mm and 70 μm, respectively), $\epsilon_r = 1{\cdot}7 \times 10^{-3}$. Whereas taking into account that during the phase transformation of tetragonal to monoclinic zirconium oxide there is a volume dilation, ΔV ~4%, which is a linear strain of only ~1/3 (ΔV), that is 1·3%. Therefore, the anticipated 'plastic' strain associated with the total transformation band width is ~4000 μm × $1{\cdot}3 \times 10^{-2} \simeq 52$ μm and, therefore, its value is

$$\epsilon_i^{\Delta} \simeq \frac{\Delta l}{l} = \frac{52 \times 10^{-6}}{20 \times 10^{-3}} = 2{\cdot}6 \times 10^{-3}.$$

The difference between the predicted ϵ_i^{Δ} and measured strain ϵ_r may be accounted for if not all the tetragonal grains within the band are transformed to monoclinic. The present calculation suggests that less than 65% is transformed which is in reasonable agreement with micro-Raman measurements of the phase content of similar transformation bands in a 12 mol% Ce–TZP material by Becher and Swain.[7]

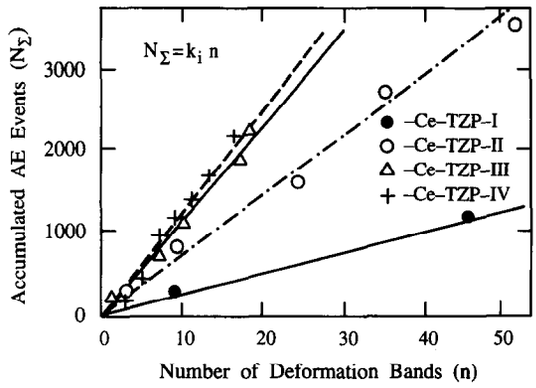


Fig. 11. Correlation between the total AE event count and the number of transformation bands.

Another interesting aspect of the present observations is the comparison of the number of AE pulses N_Σ obtained for a given number of loading cycles with the number of transformation bands, n (Fig. 11). This figure shows an excellent linear relationship for all the Ce–TZP materials with the slope increasing from sample I to IV. That is, this data may be represented by the simple expression $N_\Sigma = k_2 n$ where k_2 is given in Table 3 for all samples. Considering that AE events are associated with the appearance of deformation bands, one may assume that individual AE events are the result of burst like nucleation of such a band.

It is tempting to try to interrelate the observed strain hardening, increasing width of the bands, and the increasing magnitude of the load drops and AE events during the present experiments. Unlike metallic materials the strain hardening does not appear to be related to dislocation (or band) interaction or pile-up processes. Rather it is as though there is a distribution of defects within the materials that provide stress concentration sites from which the transformation bands are nucleated. Thus within the uniform tensile stress zone the initiation load or stress generates a critical tensile strain energy density at the largest defect site (flaw, pore or inclusion). When this local energy density exceeds a critical value it is released as a transformation band which lowers the total strain energy of the beam. As there is likely to be a distribution of such defect sizes within the beam the load must be increased to initiate a transformation band from the next most potent defect site upon the exhaustion of the previous largest defect. However, the increased total strain energy of the beam has the potential to form a wider band of transformation in the otherwise near homogeneous material. This process will continue until a pre-existing or newly initiated band results in the specimen fracture. A more detailed discussion of the fracture of this material is given in the accompanying paper.[12]

4 Conclusions

The present observations have shown the influence of grain size on the deformation behaviour of these 9 mol% Ce–TZP materials. It has been established, as previously shown by Becher and Swain,[7] that the onset of plastic deformation or ease of stress induced phase transformation is grain size dependent.

This study has established a relationship between the grain size and the width of the transformed bands generated on the tensile surface. It has also been shown that for the coarser grained Ce–TZP-II to -IV materials there is a linear relationship between the sum of the width of the transformation bands and the residual plastic strain ϵ_t. A simple analysis of this situation indicated that the accumulated strain was less than anticipated assuming all the tetragonal grains within the band transformed to monoclinic zirconia. The results could be rationalized if only 65% of the grains transformed which is in good agreement with Raman microprobe measurements of such bands by Becher and Swain.[7] It is suggested that a ferro-elastic grain re-orientation may be responsible for the observance of non-linear behaviour of the fine grained Ce–TZP-I material in the absence of transformation bands. Acoustic emission data showed a linear relationship between the number of bands and total AE events.

Acknowledgements

The authors wish to thank Dr T. S. Liu and Dr Grathwohl for the provision of the samples used in these tests. Collaboration was made possible by a grant from the Australian Department of Industry, Technology and Regional Development under the Bilateral Science Program.

References

1. Tsukuma, K. & Shimada, M., Strength, Fracture Toughness and Vickers hardness of CeO_2-stabilised ZrO_2, polycrystals (Ce–TZP). *J. Mater. Sci.*, **20** (1985) 1178.
2. Grathwohl, G. & Liu, T. S., Crack Resistance and Fatigue of Transforming Ceramics: II. CeO_2-stabilised Tetragonal ZrO_2. *J. Am. Ceram. Soc.*, **74** (1991) 3028.
3. Hannink, R. H. J. & Swain, M. V., Metastability of the Martensitic Transformation in a 12 mol% Ceria–Zirconia Alloy: I. Deformation and Fracture Observation. *J. Am. Ceram. Soc.*, **72** (1989) 90–8.
4. Reyes-Morel, P. E. & Chen, I.-W., Deformation Plasticity of CeO_2 Stabilised Tetragonal Zirconia Polycrystals: I. Stress Assistance and Autocatalysis. *J. Am. Ceram. Soc.*, **71** (1988) 343.
5. Swain, M. V. & Hannink, R. H. J., Metastability of the Martensitic Transformation in a 12mol% Ce–TZP Alloy: II. Grinding Studies. *J. Am. Ceram. Soc.*, **72** (1989).
6. Yu, C.-S. & Shetty, D. K., Transformation Zone Shape, Size and Crack Growth Resistance (*R*-Curve) Behaviour of Ceria Partially Stabilised Zirconia Polycrystals. *J. Am. Ceram. Soc.*, **72** (1989) 921.
7. Becher, P. F. & Swain, M. V., Grain Size Dependent Transformation Behaviour in Polyerystalline Tetragonal Zirconia. *J. Am. Ceram Soc.*, **75** (1992) 493.
8. Drozdov, A. V., Galenko, V. O., Gogotsi, G. A., Fasenko, F. A. & Swain, M. V., Acoustic Emission During Micro and Macrocrack growth in Mg–PSZ. *J. Am. Ceram. Soc.*, **74** (1991) 1922–7.
9. Gogotsi, G. A., Drozdov, A. V., Zavada, V. P. & Swain, M. V., Comparison of the Mechanical Behaviour of Zirconia Partically Stabilised with Yttria and Magnesia. *J. Aust. Ceram. Soc.*, **27** (1991) 37.
10. Gogotsi, G. A., In *Advanced Ceramics.* eds C. Ganguly, S. K. Roy & P. R. Roy. Trans. Tech. Publ., USA (1991) p. 411.
11. Gogotsi, G. A., Deformational Behaviour of Ceramics. *J. Eur. Ceram. Soc.*, **7** (1991) 87.
12. Virkar, A. V. & Matsumoto, R. L. K., Ferroelastic Domain Switching as a Toughening Mechanism in Tetragonal Zirconia. *J. Am. Ceram. Soc.*, **69** (1986) C224.
13. Gogotsi, G. A., Zavada, V. P. & Swain, M. V., Mechanical Property Characterisation of a 9% Ce–TZP Ceramic Material: II. Fracture Toughness. *J. Eur. Ceram. Soc.*, in press.

Journal of the European Ceramic Society 15 (1995) 1193–1199
© 1995 Elsevier Science Limited
Printed in Great Britain. All rights reserved
0955-2219(95)00103-4
0955-2219/95/$9.50

Wear Resistance of Stabilized Zirconias

A. Medevielle,[a] F. Thévenot[a] & D. Tréheux[b]

[a]Ecole des Mines de Saint Etienne, 42023 Saint Etienne Cedex, France
[b]Ecole Centrale de Lyon, 69131 Ecully Cedex, France

(Received 27 January 1995; revised version received 31 May 1995; accepted 31 May 1995)

Abstract

The wear resistance of stabilized zirconias was investigated on both a pin-on-disk machine and a Dangoumeau apparatus under dry and lubricated (water) conditions. Under the experimental conditions (80 N load and 12 mm/s speed) the wear mechanism can be described as initial plastic deformation and then grain pull-out. The role of the third-body in the interface of friction has been demonstrated with asymmetric couples where one of the antagonists is made of alumina. If for pure friction it is not easy to differentiate the magnesia partially stabilized zirconias (MgPSZ) from the yttria tetragonal zirconia polycrystal (YTZP), after shock tests we can conclude that the YTZP have a better wear behaviour than the MgPSZ, especially in the case of attrition applications.

1 Introduction

Recently, considerable attention has been applied to stabilized zirconia ceramics, because of their special mechanical, chemical and thermal properties. For the application of high capacity attrition mills for fine grinding and homogeneization millings, beads with a large surface and high energy input are required. High density, good sinterability and improved fracture toughness make stabilized zirconias very attractive as wear-resistant materials. However, their potential applications are still limited by the lack of reliable data concerning the wear behaviour and mechanism. Although a number of studies have been carried out to investigate the wear characteristics in a variety of conditions, most of them deal with metal/ceramic contacts and ceramic/ceramic friction is not well known as yet.

Scott[1] studied the wear behaviour of MgPSZ and suggested that their particular wear resistance depended on the amount of transformable phase in the sample. Aronov[2] also observed a range of temperature where the wear of MgPSZ decreased by three orders of magnitude. He proposed a phenomenological model to explain this wear by phase transformation due to frictional heating. Fisher *et al.*[3] examined the wear behaviour of tough and brittle zirconias in different environments. They concluded that water has a deleterious effect on wear resistance. Stachowiak *et al.*[4] found similar wear for both MgPSZ and YTZP in a pin-on-flat test despite their significant difference in grain size. The delamination and plastic deformation were considered as the main wear mechanisms. For Chen *et al.*[5] rapid wear of MgPSZ and YTZP was found in a special range of sliding speed, wear resistance of MgPSZ, however, remained better than that of YTZP. Lee *et al.*[6] carried out an extensive study on YTZP zirconias by setting wear maps. They identified wear transitions depending on the environment. In mild-wear regimes plastic deformation and microcutting are dominant. Thermal-shock-induced brittle fracture is the predominant mechanism causing severe wear in the high-speed regimes. Probable moisture-induced destabilization of YTZP is evident specifically under water-lubricated conditions.

Considering the results above, the wear behaviour of zirconia ceramics seems to be very sensitive to the structure of the material, and to the test parameters, such as temperature, environment and sliding speed as underlined by Liang *et al.*[7]

2 Experimental

2.1 Wear apparatus

The first wear tests were conducted on a pin-on-disk tribometer described in Fig. 1. The linear speed was 12 mm/s and the load applied by a dead-weight system of 8 kg, i.e. about 80 N. Wear is measured with a rugosimeter which gives the profile of the track on the disk. With width W, depth D and length L of the track it is possible to calculate the removed volume V:

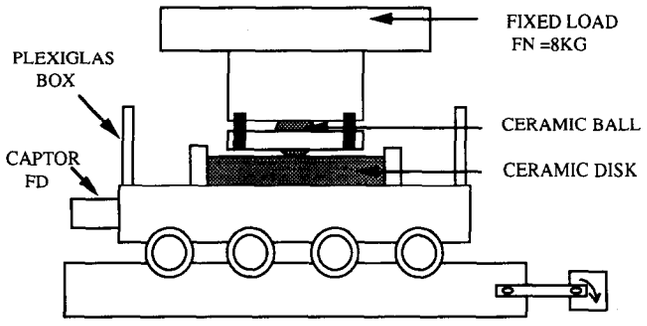


Fig. 1. Schematic representation of the pin-on-disk tribometer.

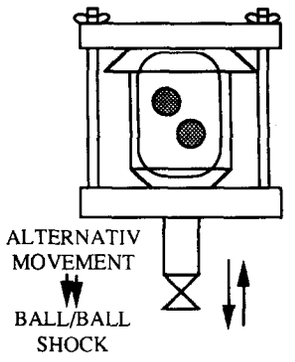


Fig. 2. Schematic representation of the Dangoumeau machine.

$$V = L\,(R^2 \arccos(\frac{R-D}{R}) - W\frac{R-D}{2}),$$

$$\text{where } R = \frac{D^2 + \frac{W^2}{4}}{2D}. \qquad (1)$$

For balls the wear volume is obtained from the scar diameter, knowing the radius of the ball:

$$V = \Pi\frac{R^3}{3}(2 - 2\cos\beta - \sin^2\beta\cos\beta),$$

$$\text{where } \beta = \arcsin(\frac{D}{2R}). \qquad (2)$$

A captor can measure the longitudinal force F_D, this leads to the coefficient of friction μ which is the ratio between the normal force F_N and the longitudinal force F_D.

Bearing in mind the attrition application we have chosen the Dangoumeau test which allows, by an oscillating movement, shock between two balls closed in a closed jar. This can be made both in air or in water, see Fig. 2.

2.2 Materials

The zirconias used for the investigations were of two kinds: either partially stabilized with magnesia (MgPSZ) or totally stabilized with yttria (YTZP) or a mixture of yttria and ceria (YCeTZP, YC). We have also studied alumina as a reference and a composite structure containing 80 wt% of YTZP and 20 wt% of Al_2O_3 (ATZ).

PSZ samples were sintered at 1700°C for 2 h then heat-treated at 1425°C to make the tetragonal phase precipitate in the cubic matrix. The average cubic grain size was about 30–50 μm, the tetragonal precipitates being submicronic. With long soaking times at 1425°C, these grew above the critical size[8] of ≈ 0·3 μm and become monoclinic on cooling. TZP ceramics were sintered between 1350 and 1500°C for 2 h and were constituted by grains of less than 1 μm. Phase contents were determined by X-ray diffraction analysis (XRDA).[9]

The surface roughness, R_a, of the disks was about 0·002 μm after polishing, the balls were as-sintered. Other properties of the materials are listed in Table 1.

3 Results

3.1 Wear results

Wear results of symmetric couples (ball and disk of the same ceramic) are given in Figs 3 and 4. In order to be clear we have only plotted data

Table 1. Properties of materials

Material	*Sintering route*	*Density (g/cm^{-3})*	*% Density*	*Ave. grain size (μm)*[a]	*Hardness GPa*	*Toughness ($GPa\sqrt{m}$)*	*% T*	*Symbol*
MgPSZ1	1700°C 2h 1425°C 4h	5·57	96	50/2 C/T	6·44	6·2	60[b]	○
MgPSZ2	1700°C 2h	5·65	98	50/0·3	10·22	6·13	97[b]	□
MgPSZ3	1700°C 2h	5·71	98	50/0·3	10·74	—	85[b]	×
YTZP1	1350°C 3h	5·83	99	0·766	10·68	5·2	100	◇
YTZP2	1475°C 2h	5·99	99	0·368	10·94	5·02	100	+
YTZP3	1450°C 2h	6·01	99	0·356	12·93	—	100	△
YTZP4	1450°C 2h	5·92	97	0·351	13·03	—	100	▽
YTZP5	1450°C 2h	6·05	100	0·367	13·55	5·46	100	⧅
YTZP6	1400°C 2h	6·08	100	0·333	13·60	—	100	⊞
YC	1450°C 2h	6·00	99	0·771	11·85	—	100	■
ATZ	1400°C 2h	5·45	97	0·454	16·10	—	100	⊡
Al_2O_3	1380°C 3h	3·95	99	≈ 1	18·23	—	—	⊙

[a] Interpolate method.
[b] Sum of cubic and tetragonal content.

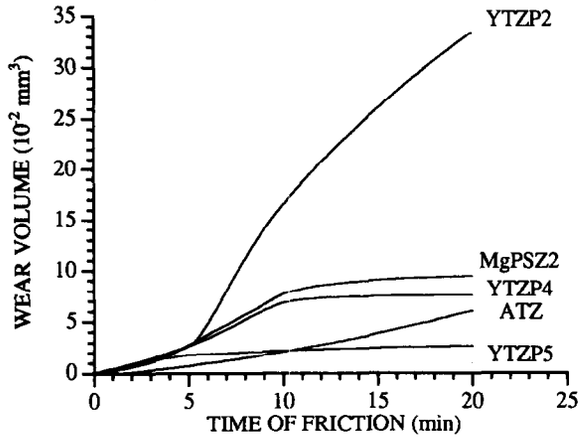


Fig. 3. Wear of disks in air (symmetric couples). (Schematic behaviour similar in air and in water).

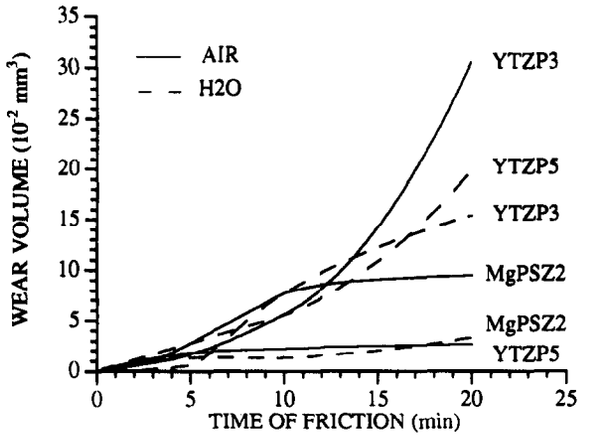


Fig. 5. Influence of water on disk wear. (Identical for balls and disks).

concerning some of the materials. No typical behaviour can be determined for MgPSZ or YTZP. The wear volume (for disks), or the scar volume (for balls), can remain quasi-constant, reach a steady-state value or increase with the friction time. A PSZ disk may react like a TZP one, whilst the wear of two TZP disks may be totally different. In fact we can only classify the ceramics according to the severity of wear, depending on the antagonist (ball or disk) and on the environment; no absolute classification is feasible. Concerning balls, however, the PSZ ceramics are less resistant than the TZP ones. We also note that the YTZP5 was the least worn TZP ceramic, both for disks and for balls and that the ATZ composite has one of the best wear behaviours.

The presence of water reduces the wear of PSZ ceramics, whereas in most cases it increases the wear of TZP ceramics as predicted by the literature[3,6] because of the destabilization of the tetragonal phase which transforms into the monoclinic one. When the tetragonal phase is very stable (YTZP3 and YTZP6) no transformation is possible and water has again a favourable effect on wear resistance (Fig. 5).

The addition of alumina in the ATZ composite leads to a better resistance (Figs 3 and 4), because of the increase in hardness. In all configurations the wear of this composite is one of the lowest. Alumina disks are just polished during friction, whereas alumina balls reacts like TZP balls.

To really compare our materials, we studied asymmetric couples where either the disk or the ball is in alumina. The wear volumes are given in Figs 6 and 7. The wear of balls rubbed against an

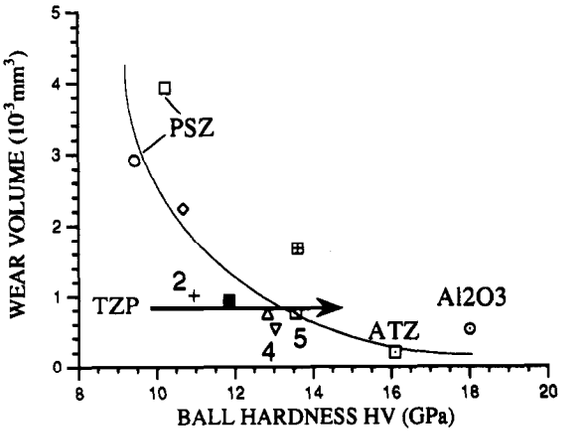


Fig. 6. Wear of balls on Al_2O_3 disk (water).

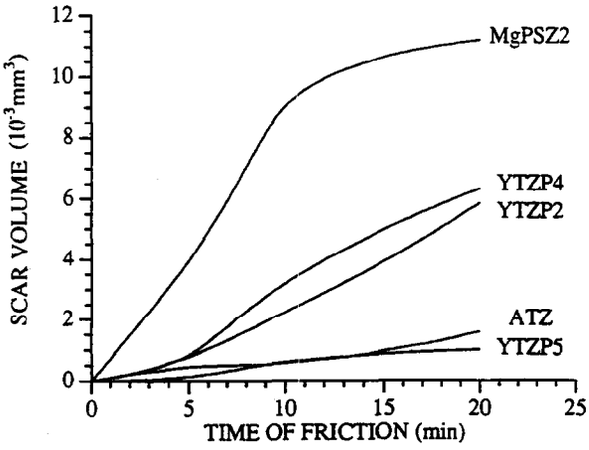


Fig. 4. Wear of balls in air (symmetric couples). (Schematic behaviour similar in air and in water)

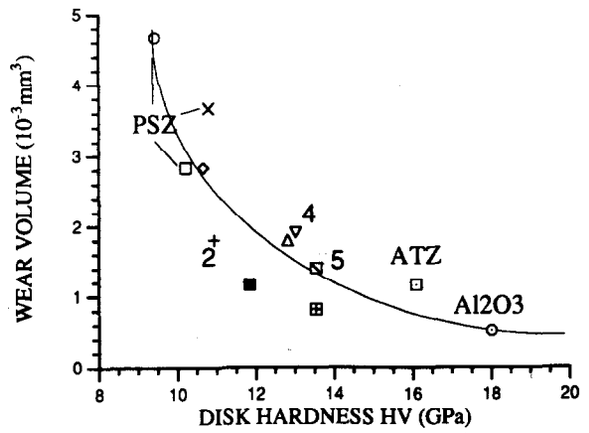


Fig. 7. Wear of Al_2O_3 ball on disk (water).

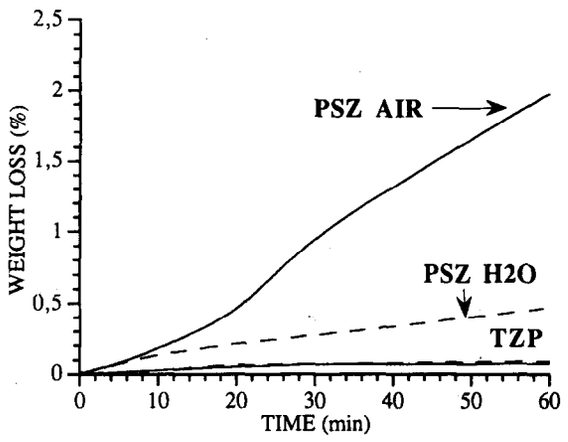


Fig. 8. Weight losses after Dangoumeau shock tests.

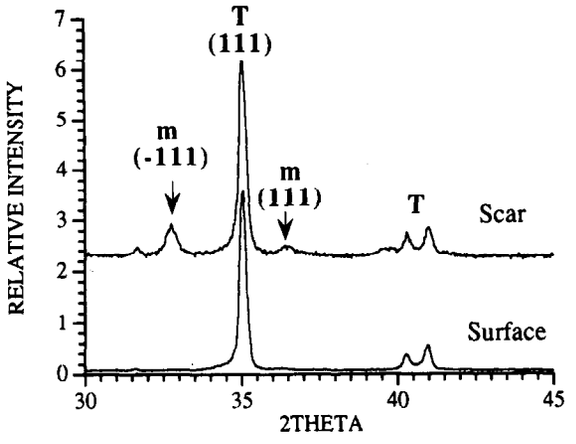


Fig. 9. Wear-induced surface transformation on a YTZP2 disk.

alumina plate had a tendency to decrease with increasing hardness, even when the wear of TZP seems to be independent of the material (except for YTZP1 and YTZP6 — see horizontal line in Fig. 6). The same tendency was observed for the wear of disks by an alumina ball: the harder the plate, the less worn. This was still true for the alumina ball which was worn more on smooth disks than on hard ones (Fig. 7). These results were valid both in air and in water.

After tests in the Dangoumeau[10] jar, the PSZ balls were strongly worn, especially in air where TZP are less sensitive. Water significantly reduces the wear of PSZ ceramics, whereas it has only a slight influence on TZP (Fig. 8). The ATZ balls were extremely spoilt and the alumina one totally destroyed (under the same experimental conditions).

3.2 Worn surface analysis

In order to understand the wear mechanisms of pins and disks, the worn surfaces were analysed both by a secondary electron microscope (SEM) with an EDAX attachment and by XRDA. A phase transformation can occur on the surface of the more transformable disks which reduces the wear rate (Fig. 9); wear debris are transformed into the monoclinic phase. When the surface of disks is too stable (no possible transformation) the disks are more worn because they are less able to absorb energy.

On the PSZ plate no real variation in the monoclinic content was observed. This can be explained by the reversal monoclinic → tetragonal transformation which takes place at the frictional interface. The tetragonal → monoclinic martensitic transformation occurs on cooling on the transformed monoclinic grains which results in a macroscopic steady-state.[11]

Wear of pins leads to the formation on the surface of a dense third body layer (Fig. 10) which consists of a mixture of the two antagonists (Fig. 11). After sliding on an alumina plate the presence of alumina on the surface of the TZP ball is obvious.

Different wear profiles are obtained after shock tests depending on the nature of the materials (Fig. 12). Grain pull-out is observed on TZP balls, transgranular fracture on PSZ balls (Fig. 12(a, b)) and macrochipping on ATZ balls with shearing of the alumina grains (Fig 12(c, d)).

4 Discussion

No significant difference between MgPSZ and YTZP can be observed after symmetric tests without shock, either in air or in water. The wear mechanism depends on the geometrical shape and not on the material. Wear of disks begins with

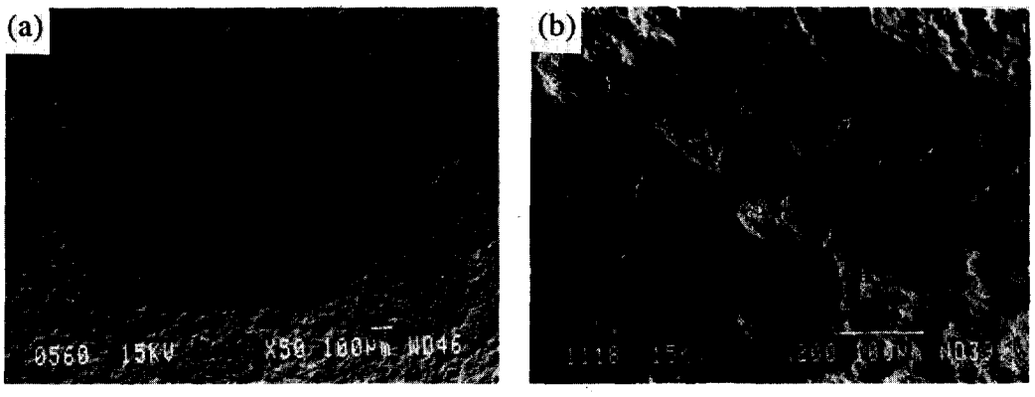


Fig. 10. Wear scar on a zirconia ball: (a) erosion of a YTZP2 ball; (b) dense layer on a YTZP4 ball.

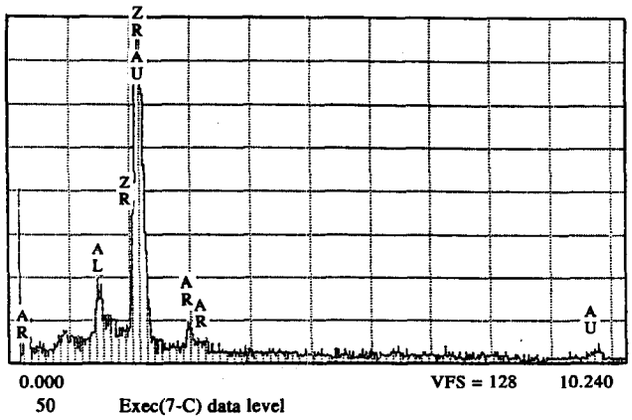


Fig. 11. Surface analysis of a YTZP2 ball rubbed on Al_2O_3. Presence of alumina on the ball.

plastic deformation or polishing of the surface, then above a typical critical strain value intergranular fracture occurs first along circular paths resulting from mechanical stresses (Fig. 13).

The properties of the materials (i.e. hardness, toughness, grain size, porosity, etc.) may influence the first steps in the wear process but then the adherence of the third body becomes the predominant factor. The constant load of 8 kg also has an influence, depending on the materials it can induce too high stress and cause severe wear.

Wear of balls starts with filing of the surface spheres and then wear is inversely proportional to the ability of debris to adhere to the surface and to form a dense protective layer. If debris cannot stick to the surface, extensive wear takes place. So the more easily the layer is formed, the less worn the pin. When these tests are conducted in water the PSZ properties are improved, those of the TZP are generally reduced (Fig. 5).

However, at this stage no real distinction can be seen between the different classes, even though the alumina–zirconia composite is in general less damaged. Friction tests with asymmetric couples clearly show the influence of material properties on wear: the soft PSZ ceramics are more worn and harder TZP ceramics are less worn against alumina, except the YTZP1 and YTZP6 balls which are less resistant.

Wear of an alumina ball on a disk confirms the important role of wear debris defined before as the third body in the interface. When sliding, the alumina ball creates abrasive debris which in turn can wear the alumina ball.

With shock tests (Dangoumeau) the TZP ceramics shows a better wear resistance than the PSZ, despite equivalent toughnesses. These tests also reveal the inadequacy of the ATZ ceramic because of the presence of brittle alumina. The analysis of the worn ball confirms that fracture occurs on alumina grains by pull-out or shearing.

Nevertheless, we can note that, for identical hardnesses and toughnesses, tribological properties can be very different. So we have to find other explanations: one may be the third body part because its adhesion to the surface is essential,

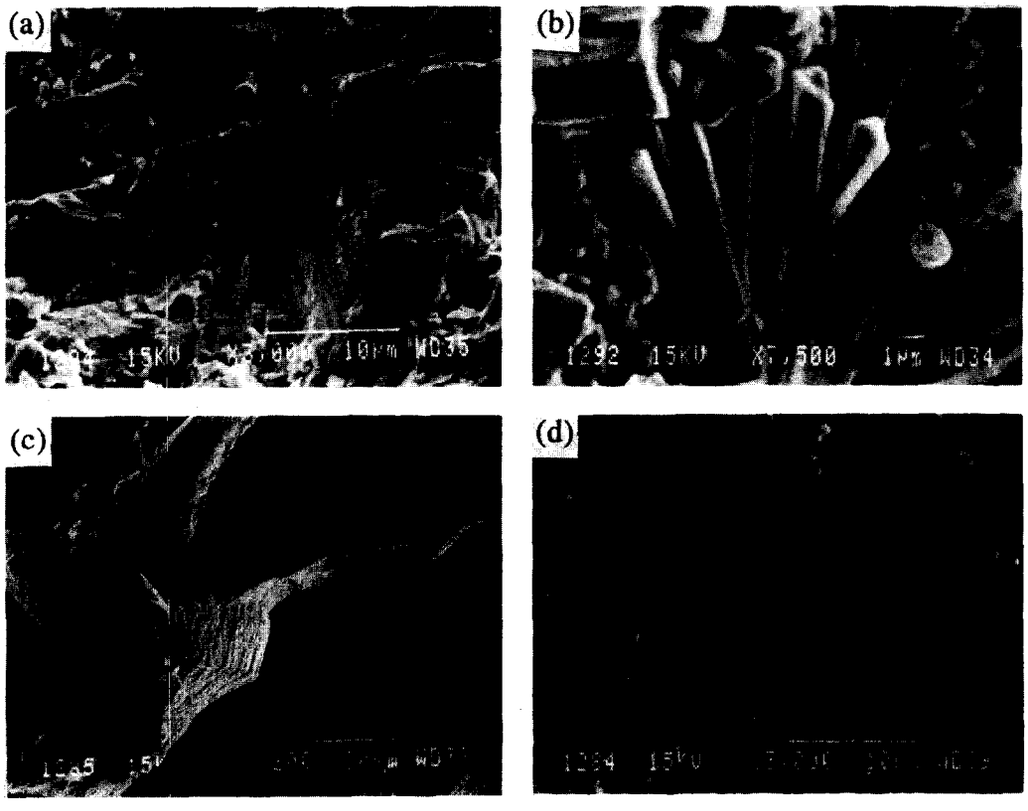


Fig. 12. Surface of worn balls after shock tests: (a, b) transgranular fracture for MgPSZ; (c, d) extensive macrochipping, shearing of Al_2O_3 grains for ATZ.

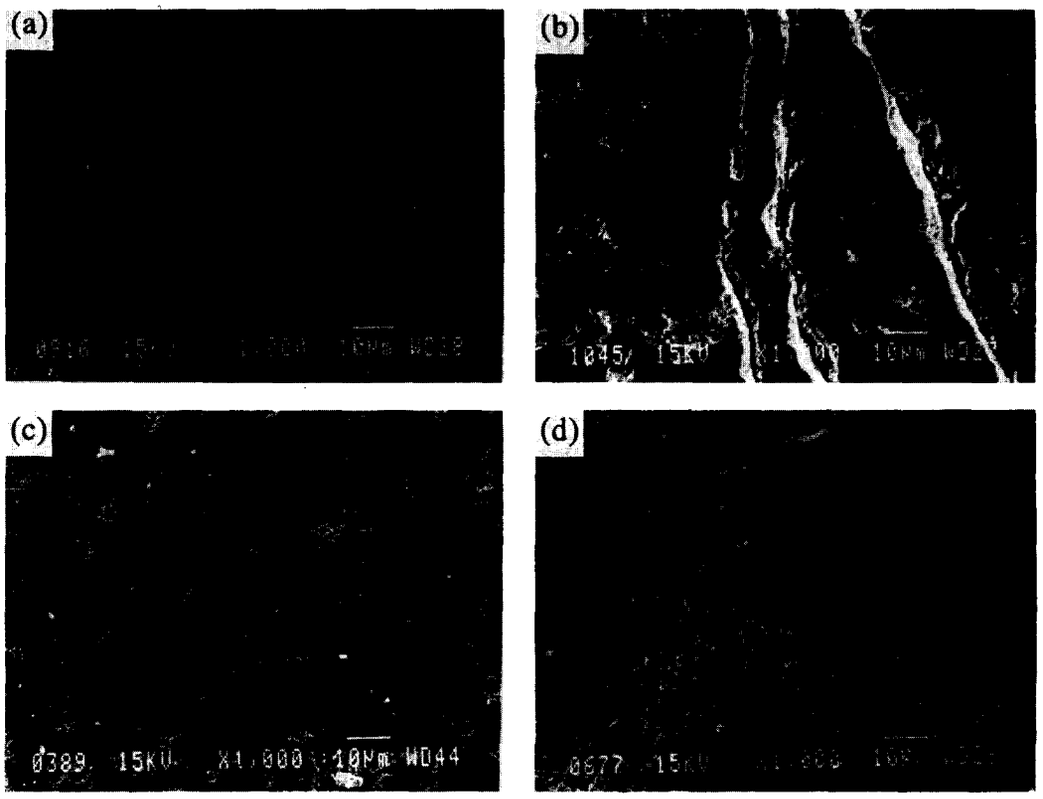


Fig. 13. Surface of worn disks after pin-on-disk tests (symmetric YTZP couple) Wear mechanism: (a) plastic deformation with micro-fracture and polishing; (b) circular fracture; (c) intergranular fracture with grain pullout; (d) failure.

however results may differ for equivalent compositions (TZP) so other properties interfere: the study of the influence of materials dielectrical properties (susceptibility) on wear is in hand. Thus electrostatic phenomena can affect:[12–14]

- — the first steps of wear (stored polarization energy relaxation which induces cracks)
- — the energetic balance of the martensitic transformation T → M
- — the charge effects (triboelectrification) in the contact area which depend on the presence of water and modify the electrostatical adherence of the third body.

5 Conclusions

With continuous friction without shock (pin-on-disk) wear of disks occurs first by plastic deformation then by microfracture, the third body debris control the final wear steps. Wear of balls depends on the ability of the dense protective third body surface layer to form. The more stable the layer, the less worn the ball. Generally speaking MgPSZ and YTZP are equivalent when tested symmetrically on a pin-on-disk tribometer. Although water has an effect on their wear behaviour, it reduces the wear of PSZ, whereas it has only a slight influence on the TZP tested. When rubbed against alumina the TZP are less worn than the PSZ. Introduction of alumina in zirconia ceramics leads to a strengthening and reduces sliding wear. TZP have a better wear resistance to shock tests than the PSZ. The addition of alumina results in the failure of the material. These results cannot be explained by the intrinsic mechanical properties of the materials. So we have to consider other parameters such as dielectrical phenomena like polarization energy, contact charges which can modify fracture of ceramics or third body adhesion.

Acknowledgement

This work was partly sponsored by the EEC (Feasibility Award BRE2-CT93-0692).

References

1. Scott, H. G., Friction and wear of zirconia at very low sliding speeds. *Wear Mater.*, (1985) 8–12.
2. Aronov, V., Friction induced strengthening mechanisms of magnesia partially stabilized zirconia. *J. Tribol.*, **109** (1987) 531–6.
3. Fischer, T. E., Anderson, M. P., Jahanmir, S. J. & Sahler, R., Friction and wear of tough and brittle zirconia in nitrogen, air, water, hexadecane and hexadecane containing stearic acid. *Wear*, **124** (1988) 133–48.
4. Stachowiak, G. W. & Stachowiak, G. B., Unlubricated friction and wear behaviour of toughened zirconia ceramics. *Wear*, **132** (1989) 151–71.
5. Chen, Y. M., Rigaut, B. & Armanet, F., Wear behaviour

of partially stabilized zirconia at high sliding speed. *J. Eur. Ceram. Soc.*, **6** (1990) 383–90.
6. Lee, S. W., Hsu, S. M., & Shen, M. C., Ceramic wear maps: zirconia. *J. Am. Ceram. Soc.*, **76** (1993) 1937–47
7. Liang, H., Fischer, T. E., Nauer, M., & Carry, C., Effect of grain boundary impurities on the mechanical and tribological properties of zirconia surfaces. *J. Am. Ceram. Soc.*, **76** (2) (1993) 325–9.
8. Lange, F. F., Transformation toughening. *J. Mater. Sci.*, **17** (1982) 240–6.
9. Fillit, R., Homerin, P., Schafer, J., Bruyas, H. & Thevenot, F., Quantitative XRD analysis of zirconia-toughened alumina ceramics. *J. Mater. Sci.*, **22** (1987) 3566–70.
10. Medevielle, A., Thevenot, F., Treheux, D., Wear resistance of partially stabilized zirconias. In *Bull. du Cercle d'Etude des Metaux*, **XVI**(9) (1994) 19.1–9.
11. Ishigaki, J. & Nagata, R., Friction and wear of partially stabilized zirconia. In *Int. Conf. Tribo. Frict. Lubr. Wear., Lond.*, (1987) 609–14.
12. Blaise, G. & Le Gressus, C., Flashover in insulators related to destabilization of a localized space charge. *C. R. Acad. Sci. Paris*, **314** (1992) 1017–24.
13. Fayeulle, S., Berroug, A., Hamzaoui, B. & Treheux, D., Influence of electrostatical phenomena on the friction properties of oxide ceramics. *Le Vide, les Couches Minces*, sup. n°260, (1992) 427–32.
14. Fayeulle, S., Berroug, A., Hamzaoui, B. & Treheux, D., Role of dielectric properties in the tribological behaviour of insulators. *Wear*, **162/164** (1993) 906–12.

Journal of the European Ceramic Society 15 (1995) 1201–1205
© 1995 Elsevier Science Limited
Printed in Great Britain. All rights reserved
0955-2219(95)00105-0
0955-2219/95/$9.50

Constitution of Mullite Glasses Produced by Ultra-rapid Quenching of Plasma-sprayed Melts

M. Schmücker,[a] H. Schneider,[a] M. Poorteman,[b] F. Cambier[b] & R. Meinhold[c]

[a]Institute for Materials Research, German Aerospace Research Establishment, D-51147 Köln, Germany
[b]Research Center of the Belgian Ceramic Industry, B-7000 Mons, Belgium
[c]New Zealand Institute for Industrial Research and Development, Lower Hutt, New Zealand

(Received 15 November 1994; revised version received 24 May 1995; accepted 31 May 1995)

Abstract

Spherical shaped spray-dried admixtures of chemical pure and very fine α-Al_2O_3 and quartz powders with mullite composition (72 wt% Al_2O_3, 28 wt% SiO_2) were used as starting materials. The spray-dried powders (10–100 μm) were melted in a nitrogen plasma flame and subsequently quenched in water thus producing spherical, hollow, and porous particles (≤100 μm). The as-quenched spherules consist of mullite glass, some residual α-Al_2O_3 and quartz, and a very low amount of newly formed mullite. Double quenching of the material increases the glass content to >90 wt.%. ^{27}Al and ^{29}Si MAS NMR studies show that the rapidly quenched mullite glass is composed of a network of (SiO)-tetrahedra and (AlO)-octahedra, -pentahedra, and -tetrahedra. The frequency distribution of (AlO)-structural units is similar to those in metakaolinite, type I (polymer) mullite precursors, and in other melt-quenched aluminium-silicate glasses suggesting strong structural similarities of these phases. This has been supported by the exothermic mullite crystallization process taking place at ≈ 980°C in all cases.

Introduction

Due to its excellent thermal shock and creep resistance, its high temperature strength and chemical stability mullite has become increasingly important as a structural high temperature material.[1,2] Various preparation methods have been investigated for mullite synthesis. The most important techniques are:

- mullite formation by reaction sintering of oxides or silicates,
- crystallization of mullite from melts,
- mullite formation from chemical precursors.

Conventional fabrication methods using powders or reaction sintering routes require high sintering temperatures (1600–1800°C) in order to produce dense ceramics. Ceramics with suitable densities can be achieved at much lower temperatures if chemical produced precursors are used as starting materials. An alternative method to process mullite ceramics at relatively low temperatures is densification of viscous glass particles with mullite composition and subsequent mullite crystallization.[3] However, preparation of glasses with mullite composition is difficult, since its glass forming ability is low, and extreme cooling rates are required to suppress crystallization during the quenching of the melt. This paper presents a possible glass formation route using ultra-rapid quenching of aluminium silicate liquids produced by melting the starting powder materials in a plasma flame. It also provides data on the structural constitution of Al_2O_3-rich aluminium silicate glasses.

Experimental

Starting material

An aqueous slip, corresponding to stoichiometric 3/2-mullite ($3Al_2O_3{\cdot}2SiO_2$) was prepared from chemically very pure α-Al_2O_3 (A16SG, ALCOA, USA) and quartz powders (SIPUR A1, Bremthaler Quarzitwerk, Germany). Mean grain size of the starting material as determined by laser diffraction was 0·68 μm for the alumina powder and 1·92 μm for the silica powder. The raw materials were admixed in water under conditions assuring high stability of the suspensions which was verified by zeta potential measurements (pH 10, dry matter content of 30%). Mixing took place in a vibration mill (Sweco) for 16 h using alumina balls. After milling the chemical composition of the raw materials was checked again. If there was enrichment in Al_2O_3 due to wear of α-Al_2O_3 milling balls the composition was adjusted to 3/2-mullite composition.

The slurry was spray-dried with a centrifugal rotating disc atomiser in an Anhydro Lab 1 spray dryer. By spray drying spherical agglomerates ranging from ≈ 10 to 100 μm in diameter were formed.

Plasma quenching experiments

The dried agglomerates were sprayed into a 24 kW DC plasma torch using nitrogen both as plasma and powder carrier gas (Fig. 1). The powder was introduced into the nozzle under a 70° angle. When leaving the plasma, the particles were quenched in water. Care was taken that the water surface was as close as possible to the plasma flame. A second batch of powders was prepared by sieving the already once quenched powder and quenching the fraction below 40 μm a second time. This double quenched material was used for subsequent structural investigations.

Characterization of plasma-quenched mullite glasses

The chemical composition of the starting material and of the quenched powders were determined by X-ray fluorescence analysis (ARL 8410). Differential thermal analyses (DTA) were performed with a computer-controlled Netzsch STA 409 apparatus (sensitivity: DTA: 50 mV) in air. About 80 mg of the samples and of the reference material (fired kaolinite), respectively, were heated up in Pt crucibles, with a constant heating rate of 10 K/min.

The contents of crystalline phases were determined by X-ray diffraction (Siemens D 5000 XRD equipment) comparing the diffraction line intensities of the quenched samples with those of a α-Al_2O_3 reference material.[4] Quenched powders were analyzed by optical microscopy, scanning-electron microscopy (SEM, Model 525 M, Philips) and transmission electron microscopy (Model 430 TEM, Philips, with LaB_6-filament, 300 kV accelerating voltage and a TRACOR system for energy dispersive X-ray spectroscopy (EDX)). Sample preparation for transmission electron microscopy was difficult, due to the small sizes and spherical, porous shapes of the quenched powder particles. However, by embedding the powders in epoxy and subsequent grinding and ion beam thinning electron transparent areas of a few microns were achieved.

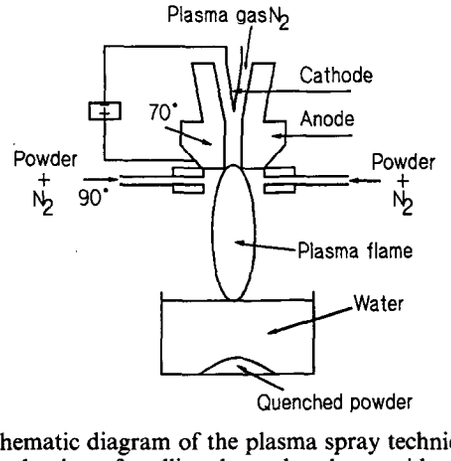


Fig. 1. Schematic diagram of the plasma spray technique used for the production of mullite glasses by ultra rapid quenching the melt droplets.

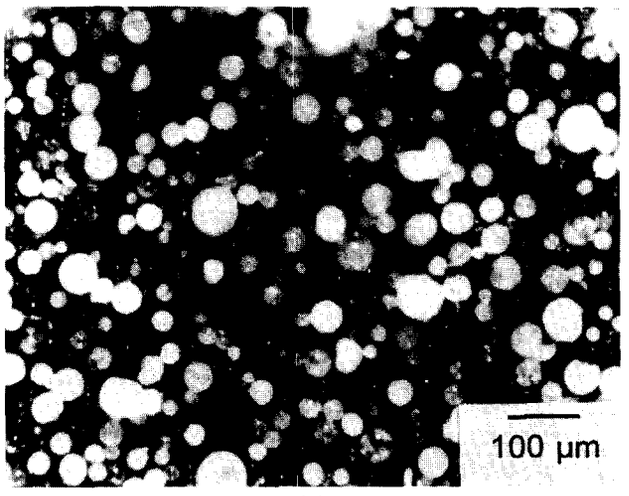
Nuclear magnetic resonance spectroscopy was performed in a Unity 500 spectrometer at 11.7T, using a Doty Scientific Magic Angle Spinning probe at a spinning speed of 10 kHz. For ^{29}Si 798 transients were accumulated with a delay of 100 s between 90° pulses. T_1 was found to be 52 + 9 s. Chemical shifts are referenced with respect to external tetramethylsilane. For ^{27}Al a 1 s delay between $\pi/12$ pulses was used and shifts referenced relative to a 0·1M aqueous aluminium sulfate solution.

Results and Discussion

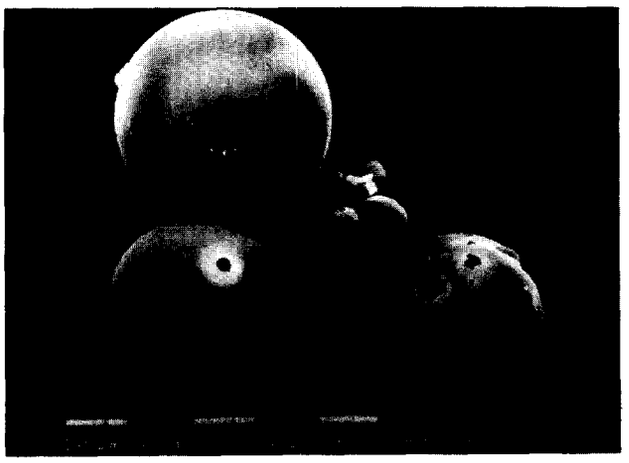
The spray-dried powders used for the plasma quenching experiments consisted of spherules composed of an admixture of very small quartz and α-Al_2O_3-crystallites. The powder particles exhibit spherical shapes ranging between about 10 and 100 μm. After plasma melting and subsequent rapid quenching the batch consists of hollow and porous spherules (Fig. 2(a) and (b)) with a similar size distribution as the starting spray-dried powder. The formation of hollow and porous spherules is attributed to the fact that gas molecules incorporated in the starting spray-dried spherules rapidly expand in the plasma flame.

The smaller grain fraction (≤20 μm) of the plasma sprayed and subsequently ultra-rapidly quenched materials consists of an optically transparent glass, whereas the coarser particles (≥20 μm) frequently are non-transparent due to light scattering on crystalline phases. By means of TEM and XRD α-Al_2O_3, quartz (Figs 3 and 4), and mullite were detected. Obviously the former are relictic starting compounds, whereas mullite crystallized from the melt in regions of relative low quenching rates. The correlation between size and crystalline phase content of the quenched powders has been proved unambiguously by quantitative XRD.

In order to achieve a high degree of glass formation ultra-rapidly plasma-quenched materials with a particle size below 40 μm was plasma-sprayed again under the same experimental conditions as in the first quenching run. After double plasma quenching the amount of residual quartz



(a)



(b)

Fig. 2. Ultra-rapidly quenched mullite glasses. (a) Optical micrograph showing mullite glass spherules (transparent), and partially crystallized glass spherules (white). (b) Scanning electron micrograph showing hollow and porous glass spherules.

and α-Al_2O_3 is reduced considerably with respect to the powder quenched only once (crystalline phase content $\approx$10 wt%). On the other hand the amount of newly formed mullite slightly increases

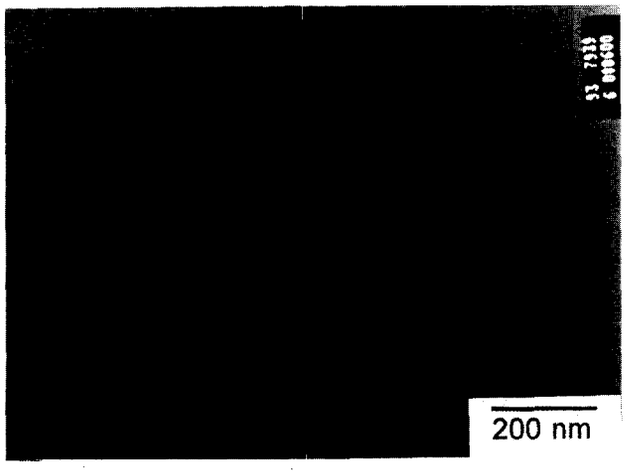


Fig. 3. Transmission electron (TEM) micrograph of ultra-rapidly quenched mullite glasses, showing a residual α-Al_2O_3 crystal embedded in a glassy matrix.

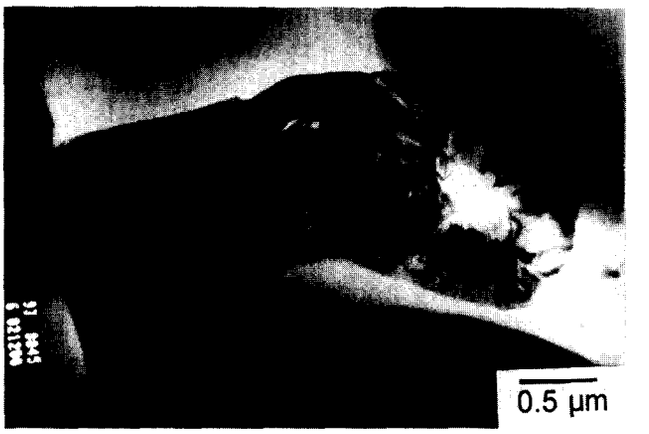


Fig. 4. Transmission electron micrograph of ultra-rapidly quenched mullite glass showing a large residual quartz crystal embedded in a glassy matrix.

in double quenched materials probably due to the crystallization of liquid phase on already existing mullite nuclei produced by the first quenching procedure.

The composition of the glass phase produced by plasma quenching as determined by EDX-analyses generally lies near 63 mol % Al_2O_3 and 37 mol % SiO_2 corresponding to a composition in between that of 3/2-mullite (60 mol % Al_2O_3) and of 2/1-mullite (66 mol % Al_2O_3). However, glass areas richer in SiO_2 are also detected. They are interpreted as to be due to unsufficient homogenization of the melt droplets during the short dwell time in the plasma flame. The fact that the bulk Al_2O_3 content of the plasma quenched powder is slightly higher than that of the starting material (74·5 wt% Al_2O_3 instead of 72 wt%) is attributed to a minor silica vaporization in the hot plasma flame.[5]

^{27}Al NMR spectra display broad signals near 2, 33, and 60 ppm and a sharp peak of higher intensity near 14 ppm (Fig. 5(a)). The broad 2, 33, and 60 ppm peaks are very similar to these described in some mullite precursors and in Al_2O_3-rich glasses in the system SiO_2–Al_2O_3.[6] They are assigned to octahedrally, pentahedrally, and tetra-

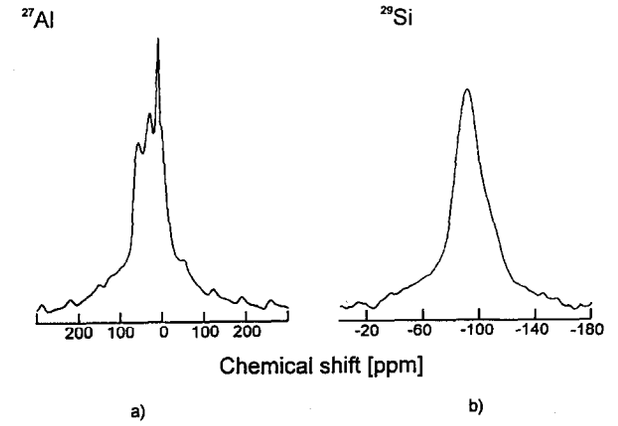


Fig. 5. Nuclear magnetic resonance (NMR) spectra of ultra-rapidly quenched mullite glass. (a) ^{27}Al; (b) ^{29}Si.

hedrally aluminium sites in the Al_2O_3-rich plasma-quenched glass, while the sharp and intense 14 ppm peak is due to the presence of α-Al_2O_3 (e.g. ref. 6). The broadness of ^{27}Al NMR-peaks associated with the glass phase show that the (Al O)-polyhedra may be distorted giving broadening by electric fields gradients or they may have a number of different environments. Though it is difficult to give quantitative approach of the relative abundance of the (Al O)-polyhedra in the glass, a predominance of (Al O)-pentahedra with respect to (Al O) octahedra and tetrahedra can be taken into account.

The ^{29}Si spectrum (Fig. 5(b)) shows a peak at –89·8 ppm and an upfield shoulder. The spectrum can be deconvoluted to show a peak at –89·3 ppm with 70% of the intensity and one at –104·8 with 23% of the intensity; the remaining 7% is a peak at –47·9 ppm. A slightly improved fit is found by fitting to four broad peaks with positions and intensities: –52·6 ppm (11%); –85·2 ppm (19%); –91·6 ppm (48%); –106·0 (22%). Thus about 22% of the Si occurs in a peak near –106 ppm with a width of 2300 Hz. This position is consistent with amorphous SiO_2 and the width indicates a variety of environments as often found in glasses, perhaps with contributions at more positive shifts from incorporation of Al. The main peak near –89 ppm is close to that in mullite itself. According to the studies of Engelhardt and Michel[7] and Mägi *et al.*[8] this is likely to arise from Si with a fully condensed oxygen network and perhaps surrounded by four Al cations; which fits well with the Al_2O_3-rich composition of the glassy phase. Again, the width of this peak (1900 Hz) indicates a variety of environments as often found in glassy materials. The peak near ≈50 ppm interestingly appears in the chemical shift region expected for silicon nitride or sialon which might form by high temperature reactions in the nitrogen plasma flame.

According to the ^{29}Si and ^{27}Al NMR studies the structural short-range-order of the (Si O)-tetrahedra, and of (Al O)-octahedra, -pentahedra and tetrahedra is very similar to these of metakaolinite, type I (polymer) mullite precursors and of melt quenched Al_2O_3-rich glasses of the system Al_2O_3–SiO_2 (see e.g. Schneider *et al.*[9]). The structural similarity of these materials also becomes evident by their crystallization behaviour. Differential thermal analysis (DTA) measurements carried out on corresponding powders all exhibit sharp and strong exotherms near 980°C which is associated with mullite crystallization in each case (Fig. 6). In a previous study on the constitution on non-crystalline mullite precursors it was suggested that the driving force of the 980°C reaction process is the dissappearence of (Al O)-pentahedra

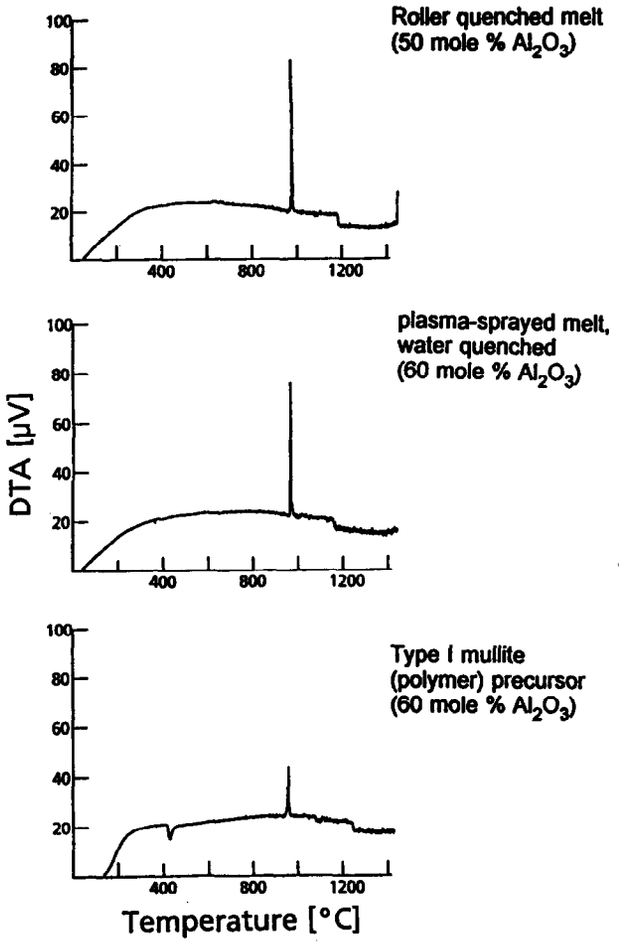


Fig. 6. Differential thermal analysis (DTA) curver of ultra-rapidly quenched mullite glass in comparison to type I (polymer) mullite precursor and roller-quenched aluminium silicate glasses.

due to its sudden instability in this temperature range and subsequent crystallization either of mullite or γ-Al_2O_3.[9]

It is an important result of the present study that mullite-type melt glasses can be produced under the extreme conditions of plasma spraying and subsequent water quenching, in spite of the extremely low viscosity of the melts.[10] However, glass formation is strongly influenced by particle size, which limits melting rate as well as quenching rate. Since the particles are melted in the plasma flame by propagation of a melting front from the outside to the inside of the particles[11] coarser grains cannot be completely melted in the plasma due to the low thermal conductivity (a few W/mK) of the material and the short dwell time in the plasma flame (about 1 ms[12]). On the other hand it is known from experiments of Gani and McPherson[3] that mullite formation by quenching melt droplets into water can be suppressed only if particle size remains below 19 μm. The size limit of glassy particles of ≈20 μm determined in our study agrees well with the observation of Gani and McPherson.

References

1. Aksay, I. A., Dabbs, D. M. & Sarikaya, M., Mullite for structural, electronic, and optical applications. *J. Am. Ceram. Soc.*, **74** (1991) 2343–58.
2. Schneider, H., Okada, K. & Pask, J. A., *Mullite and Mullite Ceramics*. John Wiley, Chichester (1994).
3. Gani, M. S. J. & McPherson, R., Crystallization of mullite from Al_2O_3–SiO_2 -glasses. *J. Austr. Ceram. Soc.*, **13** (1977) 21–4.
4. Deletter, M., Leriche, A. & Cambier, F., A linear model for both qualitative and quantitative X-ray analysis. *F. Sil. Ind.*, **57** (1992) 3–8.
5. Amouroux, J., Codron, J. L. & Morvan, D., Etude des propriétés réductrices d'un système C–H–O á haute température. Application á la réduction directe de SiO_2. *Ann. Chim. Fr.*, **3** (1978) 59–79.
6. Risbud, S. H., Kirkpatrick, R. J., Taglialavore, A. P. & Montez, B., Solid state NMR evidence of 4-, 5-, and 6-fold aluminium sites in roller quenched SiO_2–Al_2O_3 glasses. *J. Am. Ceram. Soc.*, **70** C10–2.
7. Engelhardt, G. & Michel, D., High Resolution Solid State NMR of Silicates and Zeolites. Wiley, New York (1987) 143–57.
8. Mägi, M., Lipmaa, E., Samoson, A., Engelhardt, G. & Grimmer, A. R., Solid state high resolution silicon-29 chemical shifts in silicates. *J. Phys. Chem.*, **88** (1984) 1518.
9. Schneider, H., Voll, D., Saruhan, B., Sanz, J., Schrader, G., Rüscher, C. & Mosset, A., Synthesis and structural characterization of non-crystalline mullite precursors. *J. Non-Cryst. Solids*, in press.
10. Rossin, R., Bersan, J. & Urbain, G., Etude de la viscosité de la laitiers liquides appartenant au sytème ternaire SiO_2–Al_2O_3–CaO. *Rev Hautes Tempér. Refract.*, **1** (1964) 159–70.
11. Vardelle, M., Vardelle, A., Fauchais, P. & Boulos, M. J., Plasma particle momentum and heat transfer in modelling and measurements. *A. J. Ch. E. J.* **29** (1983) 236–43.
12. Poorteman, M., Barbary, M., Pilate, P., Cambier, F., Geibel, A., Verstreken, P., Froyen, L., Vanderbiest, O. & Delaey, L., Plasma processing of ceramic and metallic raw materials. *Sil. Ind.*, **57** (1992) 49–57.

Journal of the European Ceramic Society 15 (1995) 1207–1212
© 1995 Elsevier Science Limited
Printed in Great Britain. All rights reserved
0955-2219(95)00096-8
0955-2219/95/$9.50

Mechanical–Thermal Synthesis of Al_2O_3–Cr Composite Powders

D. Osso,[a] O. Tillement,[a] A. Mocellin,[a]* G. Le Caer,[a] O. Babushkin[b] & T. Lindbäck[b]

[a]LSG2M-URA 159, Ecole des Mines, F-54042 Nancy Cedex, France
[b]Division of Engineering Materials, Luleå University of Technology, S-951 87 Luleå, Sweden

(Received 10 March 1995; revised version received 24 May 1995; accepted 25 May 1995)

Abstract

Three different approaches have been investigated to synthesize alumina–chromium composites by displacement reactions between aluminium and chromia. The reactions have been performed either by pure mechanosynthesis or pure thermal ignition or also by a combined mechanical and thermal activation process. Differential thermal analysis, dilatometry and high temperature X-ray diffraction have been used to show the various reaction mechanisms and chemical transformations. High-energy milling of the powder modifies the reactivity of the system. A partial pre-milling treatment not only reduces the reaction temperature but can also induce a different reaction path. It has been shown that an appropriate mechanical–thermal treatment leads to the synthesis of an alumina–chromia composite by a pure solid-state process: intermediate reaction stages exhibit little if any liquid phases.

1 Introduction

Solid-state displacement reactions proceed generally by diffusional transformations whereby two or more reactants form new product phases.[1] Such reactions are of considerable interest for producing ceramic/ceramic or metal/ceramic composites *in situ* with novel microstructures and possibly improved properties.[1–6] Depending upon the thermodynamic and kinetic parameters of the reacting system, several types of product morphology can be obtained: from interwoven to more or less connected and dispersed microstructures.[7] The control of such morphologies during synthesis is a critical aspect of these processes. Their detailed mechanisms and kinetics have been investigated in several typical cases and found to be strongly related to the diffusion paths and rates of individual species within the corresponding multicomponent system.[8–9]

In a conventional, thermally activated system, the diffusion processes are strongly related to temperature and the microstructure then depends on the thermal schedule. Nevertheless, for the case of some thermite reactions or self-propagating high temperature synthesis reactions (SHS), the prediction and control of the product morphology are less straightforward. In this type of reaction, involving for example the reduction of metallic oxides with aluminium to yield alumina and metals, a large quantity of heat is released,[10] which may be sufficient to heat some of the phases present above their melting points, thus making the control of microstructure difficult. Fine interwoven or dispersed homogeneous microstructures, favourable *a priori* for reaching high composite strength and toughness for example, require that displacement reactions be effected in carefully optimized conditions.

To this aim, a mechanical initiation of the reaction, referred to as 'mechanosynthesis', has been proposed as an alternative to the more classical thermal initiation. This mechanical process consists of repeated welding, fracturing and rewelding of powder particles in a high-energy ball charge. Reactive powder surfaces are brought into intimate contact and chemical reactions may take place gradually by short-range interdiffusion across welded interfaces. Then, after an appropriate milling time, the powders consist of finely divided, nanometre-sized crystallites with a high defect density and interface content. The exchange reaction occurs during this room temperature process. Sometimes the heat released during the reaction may initiate an unstable combustion effect which leads to a partial melting of the product and/or a phase separation as previously described, but in such a case a chemically inert substance[11] or a less reactive milling[10] can be used to keep the process under control. Although mechanosynthesis appears a simple and promising technique to

*To whom correspondence should be addressed.

yield homogeneous composite powders with nano-type characteristics, the benefits due to the displacement reaction approach may not be fully achieved as subsequent firing, necessary for consolidation into solid pieces, usually brings about coarsening and perhaps side reactions. Moreover, contamination from the milling environment is difficult to avoid.

To gain better understanding of the specific features, mechanisms and kinetics of reaction as influenced by thermal and mechanical activations respectively, the present experimental programme was devised so that sound comparisons could be made between either approach. It is conceivable that the results of such an investigation may subsequently find practical applications in composites processing via an optimized sequence of partial milling in order to bring the degree of reaction advancement to some appropriate level, followed by more conventional thermal activation up to completion. Three sets of experiments were consequently performed with a simple model system. The first one, consisting of pure thermal activation, was carried out with a blend of chromia and aluminium powders. The second, consisting of pure mechanical activation, was conducted by high-energy milling up to completion of the reaction. Finally, a combined mechanical and thermal activation was performed by short milling times followed by thermal treatment. These short milling times do not exceed the incubation time for the reaction when performed by grinding at room temperature.

2 Experimental Procedures

The starting high purity (>99·9%) powder materials were metallic aluminium and chromium oxide (Cr_2O_3). Average particle sizes of both these powders were in the micrometre range: 1·3 and 0·5 μm, respectively. The as-received atomized aluminium powders were oxidized on their surface and their typical alumina content was 0·5–1 wt%.[12]

Powder blends of aluminium and chromia were prepared in proportions corresponding to the reaction scheme:

$$Cr_2O_3 + 2Al \rightarrow Al_2O_3 + 2Cr \qquad (1)$$

Milling was carried out in a planetary ball-mill (Fritsch Pulverisette 7) under argon atmosphere. Grinding utensils (seven balls of 15 mm diameter and vials) were either hardened chromium steel or tungsten carbide.

Thermal differential analyses were performed with a Setaram HTC-1800K equipment under argon flux. Heating rate was 10 K min^{-1} and alumina was used as reference. Dilatometry experiments used an Adamel-Lhomargy DI 24 dilatometer under argon flux from 20 to 1500°C at a rate of 10 K min^{-1}. Samples (5 × 5 × 15 mm) were obtained by cold pressing the powders.

The resulting products were characterized at room temperature by X-ray diffraction (XRD) using CoK_α radiation. The mean crystallite size was estimated from the full-width at half-maximum of X-ray peaks.[13]

In addition, high temperature X-ray diffraction (HT-XRD) was used to follow directly the progress of reaction in samples pre-milled for different times with hardened steel tools. The XRD unit was a Philips powder diffractometer with a vertical goniometer PW 1050/25, graphite monochromator PW 1752/00, proportional counter for reflected beam PW 1711/10 and PW 1730/10 generator. The XRD was controlled by a PW 1710 diffractometer control system. The raw data were collected, processed and analysed with APD 1700 software supplied by Philips. The high temperature unit is based on an Anton-PAAR HTK-10 high temperature chamber. This standard equipment was re-engineered to increase the maximum working temperature to 2300 K. In designing the high temperature attachment, much attention was paid to the heating element. The platinum strip which is used as heater in the standard HTK-10 equipment was replaced by a graphite furnace.[14] The generator settings were 50 kV and 30 mA with a Cu-target tube. The temperature of the samples was measured with a Pt–13% Rh/Pt thermocouple. The runs were conducted with a quasi-constant heating rate of 7°C min^{-1} in a static helium atmosphere of 0·11 MPa. All scans were performed over a 2Θ range of 20–60°.

3 Results and Discussion

3.1 Thermal displacement reaction

Uncompacted $2Al/Cr_2O_3$ powder mixtures were heated to 1500°C in argon. These mixtures reacted, the chromium oxide being reduced by aluminium. The corresponding DTA is shown in Fig. 1. The endothermic melting of aluminium is quite apparent at 660°C, and the aluminothermic reaction is seen to initiate at 800°C and be completed at about 1200°C. The XRD analyses confirmed that the reaction products consisted of α-Al_2O_3 and chromium metal. HT-XRD revealed an amorphous liquid phase around 650°C, corresponding to the melting of aluminium (Fig. 2). No other intermediate transient phases were detected. Chromia is reduced in the simple direct but progressive way according to the following reaction as expected:

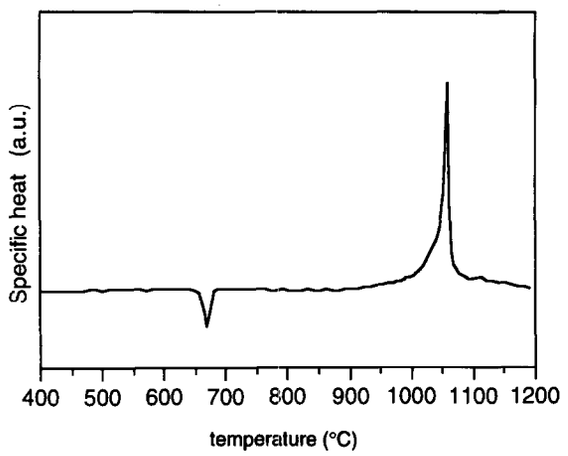


Fig. 1. DTA of 2Al + Cr_2O_3 powders (dT/dt = 10 K min^{-1}).

$$Cr_2O_3 + 2Al_{(liq)} \rightarrow \alpha\text{-}Al_2O_3 + 2Cr \quad (1)$$

Dilatometry experiments confirmed the melting of aluminium and showed a sudden expansion of the sample (Fig. 3). The slight shrinkage observed just before aluminium melting can be explained by particle rearrangements favoured by the increasing ductility of the Al phase. The slope discontinuity at 850°C has not yet been unambiguously rationalized. It does not result from the overall molar volume change which is negative for reaction (1). Neither can it be ascribed to an effective thermal expansion coefficient which would be higher after

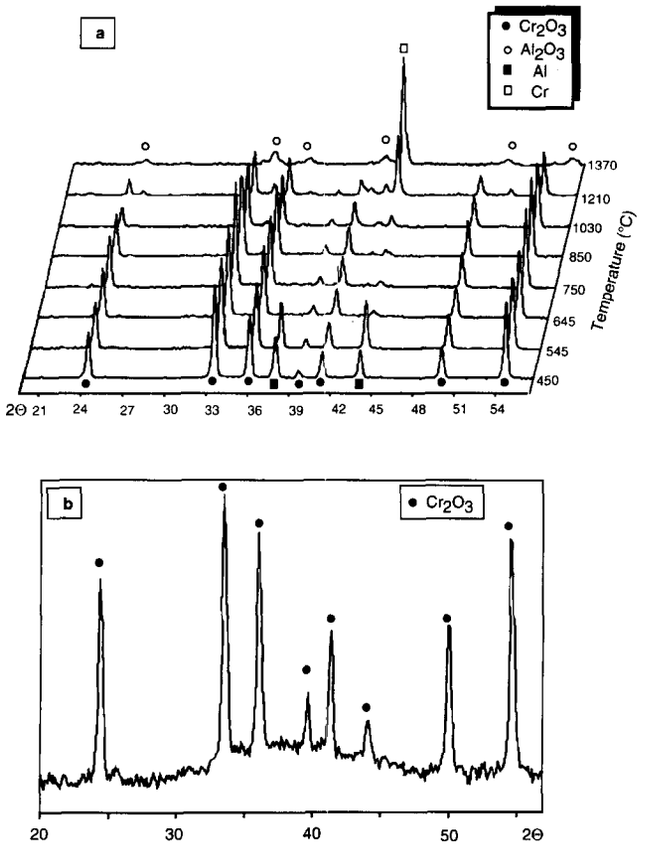


Fig. 2. HT-XRD patterns of 2Al + Cr_2O_3 powders: (a) as a function of temperature; (b) T = 650°C.

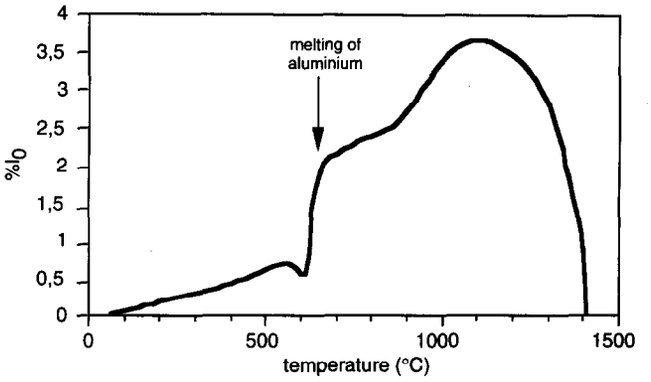


Fig. 3. Dilatometry of 2Al + Cr_2O_3 powders (dT/dt = 10 K min^{-1}).

the system has reacted than before, because re-heating the same sample after cool-down yields a different and smaller slope than upon this first heat-up. Bloating due to some gas evolution can also be ruled out since thermogravimetric experiments showed that, if anything, the sample mass tended to increase very slightly (presumably due to oxidation by residual oxygen present in the system). It may nonetheless be worth pointing out that 850°C coincides with the temperature at which Al_2O_3 characteristic lines are first detected on the HT-XRD patterns.

3.2 Mechanosynthesis

The synthesis of nanocomposite powders of alumina–Cr has been investigated by reactive milling with either hardened steel or tungsten carbide tools. In the former case, only a partial reaction was obtained. Even milling for 48 h was not enough to reach a complete transformation of the initial mixtures. In the latter case, the reaction starts suddenly after ~15 min incubation milling time (Fig. 4), then the reaction needs 1 h to be completed. Beyond that time, the XRD patterns show peaks of α-alumina and chromium, neither chromia nor aluminium could be detected by XRD.

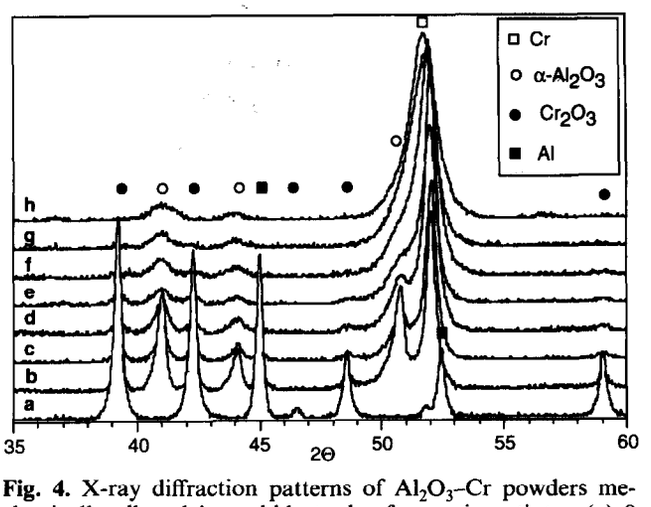


Fig. 4. X-ray diffraction patterns of Al_2O_3–Cr powders mechanically alloyed in carbide tools after various times: (a) 8 min; (b) 15 min; (c) 23 min; (d) 30 min; (e) 45 min; (f) 60 min, (g) 90 min; (h) 180 min.

After 1 h, nanometre-sized crystallites are produced from micrometre-sized powders (Fig. 5). And after a milling time of 3 h, for example, the mean crystallite size lies around 10 nm for both Al_2O_3 and Cr. The corresponding particles show homogeneous sub-micrometre microstructure of α-Al_2O_3 and chromium (Fig. 5).

No major changes were detected by differential thermal analysis on the powders milled for 3 h except for a large variation of the baseline up to 800°C. The diffraction patterns of samples before thermal treatment are identical to those of the original milled powders, except for the line width. Such variation of the DTA baseline and X-ray peak profiles with decreasing width reflect crystallite growth. Significant crystallite growth occurred only after reaching 900°C.[15]

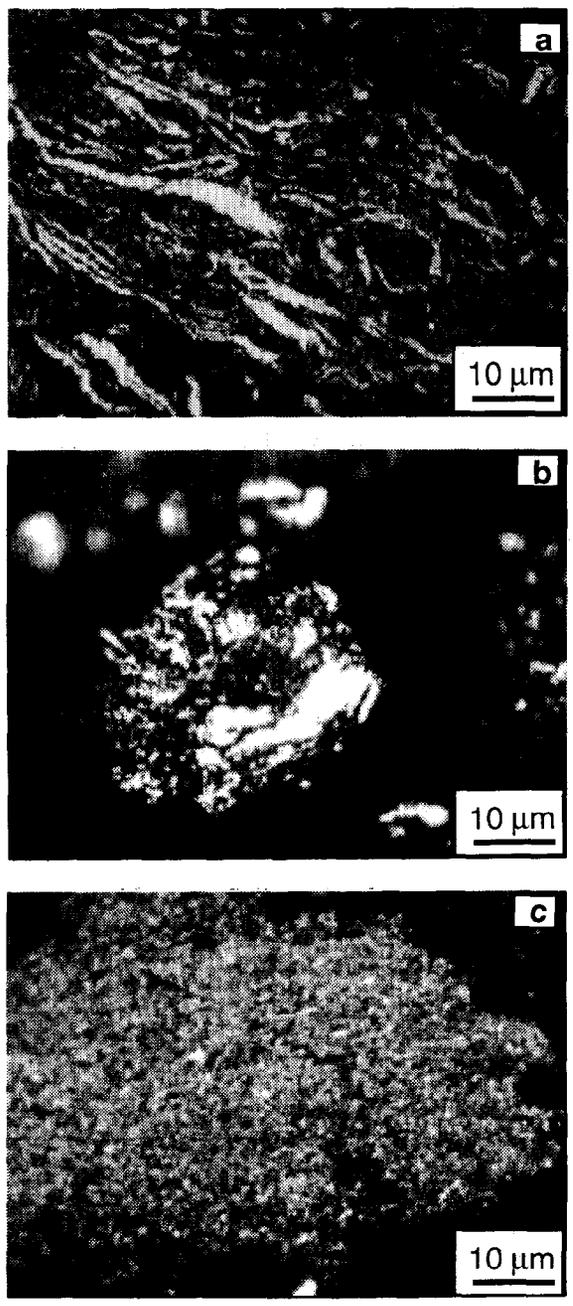


Fig. 5. Optical micrographs of Al_2O_3–Cr powders prepared by mechanosynthesis 2Al + Cr_2O_3 powders after various milling times: (a) 20 min; (b) 60 min; (c) 180 min. Light phase: chromium, dark phase: alumina.

3.3 Combined mechanical–thermal synthesis

The above experiments have shown the existence of an 'incubation time' during mechanosynthesis. A certain level of mixing, particle refinement and accumulation of lattice defects are thought to be needed for ignition, and then the combustion reaction may be completed rather quickly. The pre-ignition time depends on the experimental conditions and the start of the reaction is a direct consequence of the so enhanced chemical reactivity.[16]

To gain a better understanding of the effect of short milling on the subsequent course of events, two-stage experiments were carried out. The powders were mechanically alloyed with steel utensils using different grinding times within the incubation period, and the resulting powders then were thermally treated. The choice of steel grinding tools was made so that the kinetics of mechanosynthesis be slower and the incubation time longer than with the carbide utensils.[10] The reduction was studied by DTA (Fig. 6), dilatometry (Fig. 7) and high temperature X-ray diffraction (Fig. 8).

For the powders milled for 5 min, these different experiments revealed no large differences compared with the unmilled powders, i.e. the melting of aluminium and the occurrence of the displacement reaction were still observed in the range 650–750°C and 800–1200°C, respectively. Thus the first 5 min can be viewed as a time of mixing and of homogeneization at the particle size scale. No significant energy due to grinding is present in the

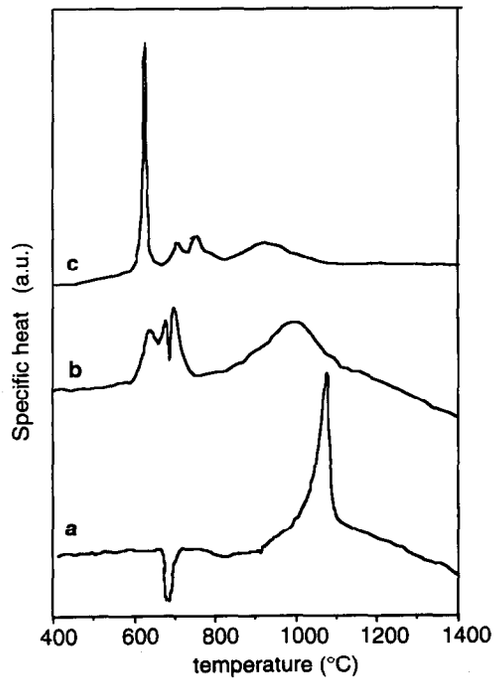


Fig. 6. DTA of milled 2Al + Cr_2O_3 powders (dT/dt = 10 K min^{-1}) after (a) 5 min, (b) 15 min and (c) 30 min.

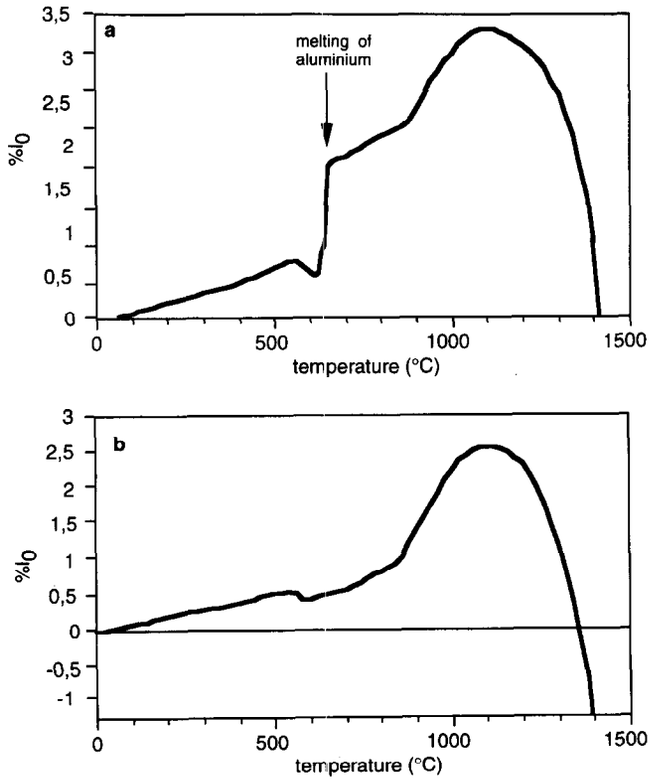


Fig. 7. Dilatometry of 2Al + Cr_2O_3 powders mechanically alloyed for (a) 15 min and (b) 30 min (dT/dt=10 K min $^{-1}$).

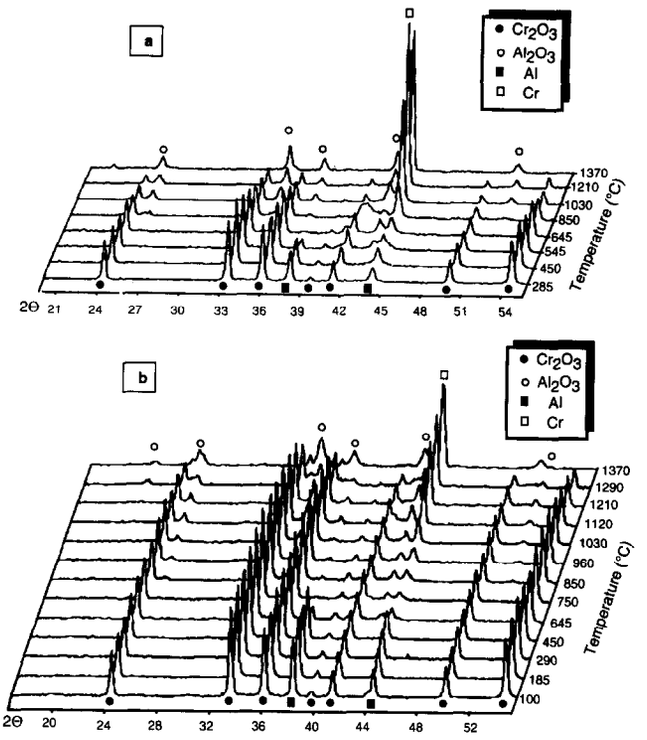


Fig. 8. HT-XRD patterns of 2Al + Cr_2O_3 powders mechanically alloyed for (a) 15 min and (b) 30 min.

crystallite, except possibly for a small amount of extra surface energy arising from a small reduction of average particle sizes.

For longer milling times (15 and 30 min), the experiments showed drastic differences. Concerning the melting of aluminium, we observed near 660°C a progressive decrease both of the endotherm in the DTA curves and of the expansion effect in the dilatometry curves. With the 30 min milled powders it was not possible to detect any aluminium melting. Parallel to this phenomenon, the large exotherms in the DTA curves due to the displacement reaction were modified. New exotherms appeared in the range 550–700°C, while the large exotherm centred near 1100°C progressively decreased in intensity with milling time and was shifted to lower temperatures. For the 30 min milled powders, only a weak thermal effect was observed between 800 and 1000°C, but a large exotherm was observed at 620°C. On the other hand, except for the modification of the aluminium melting, the dilatometry recordings were similar to those obtained with the unmilled thermally reacting system (Fig. 3).

The HT-XRD patterns help clarify the reaction path. First of all an amorphous liquid phase is observed around 650°C with the powders milled for short times. But this phase could not be observed for the 30 min powders. For this milling time, a solid-state reaction was obtained without any intermediate liquid phase.

For the 5 min milled powders, the (110)Cr peak was observed above 850°C and the converted fraction of chromia strongly increased above 1000°C. For the 30 min milled powders, however, a small amount of metallic chromium was detected at room temperature and the converted fraction of chromia was seen to increase above 600°C. The 15 min sample appeared to exhibit an intermediate behaviour and two steps may be identified. A first formation of chromium is observed in the range 650–800°C and a second formation appears above 1000°C. The temperature intervals of both chromium formation steps appear to correspond to exotherms observed on the DTA curves. Each exotherm, either between 600 and 650°C or 850 and 1200°C, thus corresponds to the heat released by the reduction of chromia by aluminium. It is interesting to note the presence of an intermediate second low temperature exotherm (650–750°C). This one is thought to be related to the transient formation of Al_7Cr and/or Al_6Cr compounds[17] observed by HT-XRD on the 15 and 30 min samples. The X-ray peaks were too few and too weak to allow for their compositions to be more precisely established but it is thought that formation of these phases is due to the reaction between the already formed chromium and the not yet reacted aluminium.

In summary, the present experiments revealed two different chemical reaction paths: a classical 'non-milled reaction' path (near 1000°C) between Cr_2O_3 and liquid aluminium, and a modified 'milled reaction' path (near 600°C) which is a pure solid-state reaction.

4 Conclusions

The present experiments show that, depending on activation mode and milling time, a displacement reaction path can be modified by an appropriate choice of experimental conditions. The onset of a reaction is essentially determined by its activation energy, i.e. the difference in energy between the activated and the initial states. Repeated milling enhances the reactivity of powder particles via the development of large amounts of interfaces and defects. During an 'incubation period', chemical characteristics are modified and energy is being stored in the powders, thereby reducing the activation barrier compared with that of the classical reaction route. If the thermal treatment provides an energy to overcome the activation barrier, due to the modification of the reaction path, the reaction may initiate at lower temperature and could result in different final microstructures.

Some monitoring of this residual activation barrier is then possible by the way of choosing the grinding conditions. Then, by appropriate choices of the chemical status of the reactants and the operating conditions (grinding and heating), the systems are allowed a greater freedom in selecting reaction paths than with temperature as the only activation parameter. The ability to control the size and morphology of the composite particles, while not demonstrated here, gives thermal–mechanical displacement reaction processing important advantages over other routes of synthesis. By avoiding the formation of liquid phase, such oriented reaction paths could bring novel solutions to the development of a whole range of composite microstructures.

Acknowledgements

J. L. Guichard and A. Scherhans are gratefully acknowledged for help with some of the experiments and the translation, respectively.

References

1. Henager, C. H., Brimhalland, J. L. & Hirth, J. P., Synthesis of a $MoSi_2$/SiC composite *in situ* using a solid state displacement reaction between Mo_2C and Si. *Scripta Met.*, **26** (1992) 585–604.
2. Grobety, G., Sperisen, T. & Mocellin, A., Influence of powder processing on mechanical properties of TiN/Al_2O_3 particulate composite prepared by reaction hot-pressing of AlN/TiO_2. *Sci. of Ceram.*, **14** (1987) 315–20.
3. Nishimura, C. & Liu, C. T., Reactive sintering of Ni_3Al under compression. *Acta Met.*, **41** (1993) 113–20.
4. Cutler, R. A., Rigtrup, K. M. & Virkar, A. V., Synthesis, sintering microstructure and mechanical properties of ceramics made by exothermic reactions. *J. Am. Ceram. Soc.*, **75** (1992) 36–43.
5. Cutler, R. A., Virkar, A. V. & Holt, J. B., Synthesis and densification of oxide–carbide composites. *Ceram. Eng. Sci. Proc.*, **6** (1985) 715–28.
6. Chaung, S. C., Kuo, C. T., Lee, C. S., Ho, C. T. & Li, A. K., Alumina–chromium carbide composite through an internal synthesis method. *J. Mater. Sci.*, **27** (1992) 5844–8.
7. Rapp, R. A., Ezis, A. & Yurek, G. J., Displacement reactions in the solid state. *Metall. Trans.*, **4** (1973) 1283–92.
8. Shatynski, S. R., Hirth, J. P. & Rapp, R. A., Solid-state displacement reactions between selected metals and sulfides. *Metall. Trans.*, **10A** (1979) 591–8.
9. Wang, L. L., Munir, Z. A. & Maximov, Y. M., Review thermite reactions: their utilization in the synthesis and processing of materials. *J. Mater. Sci.*, **28** (1993) 3693–708.
10. Osso, D., Tillement, O., Le Caer, G., Mocellin, A. and Matteazzi, P., Alumina–metal nanocermets by mechanosynthesis. In *8th CIMTECH, Proceedings of World Ceramics Congress and Forum on New Materials.* Techna srl, Faenza, Italy, 1994.
11. Schaffer, G. B. & McCormick, P. G., Displacement reactions during mechanical alloying. *Metall Trans.*, **21A** (1990) 2789–94.
12. Eckart-Werke, Technische information, F 385 (1992)1.
13. Matteazi, P. & Le Caer G., Synthesis of nanocrystalline alumina–metal composites by room temperature ball milling of metal oxide and aluminium. *J. Am. Ceram. Soc.*, **75** (1992) 2749–53.
14. Babushkin, O., Harrysson, R., Lindbäck, T. & Tegman, R., A high temperature graphite furnace for X-ray powder diffraction, *J. Meas. Sci. Technol.*, **4** (1993) 816–19.15.
Osso, D., Elaboration de nanocomposites alumine-métal par mécanosynthése. Thesis, Institut National Polytechnique de Lorraine, Nancy, France, 1995.
16. Boldyrev, V. V., Mechanochemistry and mechanical activation of solids. *Solid State Ionics*, **63–65** (1993) 537–43.
17. Reference patterns 39-1276, Powder diffraction file. JCPDS, USA.

Journal of the European Ceramic Society 15 (1995) 1213–1220
© 1995 Elsevier Science Limited
Printed in Great Britain. All rights reserved
0955-2219(95)00099-2
0955-2219/95/$9.50

The Solubility of Aluminium in Rare Earth Nitrogen Melilite Phases

K. S. Chee,[a] Y.-B. Cheng[a] & M. E. Smith[b]

[a]Department of Materials Engineering, Monash University, Melbourne, VIC 3168, Australia
[b]CSIRO Division of Materials Science and Technology, Melbourne, VIC 3168, Australia and Department of Physics, University of Kent, Canterbury CT2 7NR, UK

(Received 10 March 1995; revised version received 12 May 1995; accepted 31 May 1995)

Abstract

The incorporation of Al into nitrogen (N-)melilite phases has recently been reported [Cheng and Thompson, J. Am. Ceram. Soc., *77, 143–48 (1994)]. This occurrence allows simultaneous substitution of Al and O through replacement of Al–O for Si–N bonds and therefore, may offer potential improvement to the oxidation resistance properties of original N-melilite, which in the past was a problem that deterred the utilization of N-melilite as a grain boundary phase for Si_3N_4-based ceramics. In this work, the techniques of X-ray diffraction, scanning electron microscopy with quantitative energy dispersive X-ray spectroscopy and solid state ^{27}Al and ^{29}Si nuclear magnetic resonance spectroscopy with magic angle spinning have been used to study the solubility of Al in the structure of neodymium and samarium N-melilite phases.*

1 Introduction

N-melilites have the general formula $R_2Si_3O_3N_4$ (where R = yttrium or rare earth metals) and occur as an intermediate phase during the sintering of some Si_3N_4-based ceramics.[1] N-melilite has a tetragonal structure that is built up of an infinite linkage of corner-sharing $Si(O,N)_4$ units in tetrahedral sheets perpendicular to the [001] direction. Sandwiched between these sheets are Y^{3+} or rare earth Ln^{3+} ions which hold the silicon oxynitride layers together.[2] With a high nitrogen content of 67 eq%, N-melilite is very refractory; a melting point of ~1900°C has been quoted for yttrium N-melilite.[3] This feature alone makes N-melilite attractive as a grain boundary phase in Si_3N_4-based ceramics since the grain boundary phases control the high temperature performance of the materials, and grain boundary phases with superior thermal and chemical stability at elevated temperatures are highly sought after in Si_3N_4 materials research. Moreover, N-melilite is located in the phase compatibility regions of α and α–β SiAlONs, which in theory, can produce a good microstructure of SiAlONs with melilite as the only other secondary phase. These two characteristics of N-melilite combine to make it a potentially suitable grain boundary phase for Si_3N_4-based engineering ceramics. However, research in N-melilite has been slow coming primarily due to the poor reputation it has acquired during the early years of Si_3N_4 development. When yttria (Y_2O_3) was used in the 1970's as a sintering additive for Si_3N_4, a large number of silicon oxynitride phases emerged and N-melilite was one of them.[2] However, it was soon discovered that Si_3N_4 materials containing N-melilite had poor oxidation resistance with N-melilite oxidising rapidly at ~1000°C to form cristobalite and β-$Y_2Si_2O_7$.[3] The associated volume expansion of ~30% from the oxidation products caused extensive cracking of the ceramic component and presence of N-melilite has since been deemed undesirable.

Recent studies[4,5] have observed a significant solubility of Al in N-melilite phases resulting in a solid solution of the general formula, $R_2Si_{3-x}Al_xO_{3+x}N_{4-x}$ designated as M'_{ss}. In M'_{ss} phases, Si–N bonds are progressively being replaced by Al–O bonds as the Al solubility in the structure increases and this increase in oxygen content may provide a possible solution to the oxidation problem described above. M'_{ss} is gaining interest as a refractory grain boundary phase for SiAlON ceramics[6] with particular interest in the extent of Al solubility in M'_{ss} phases which will lead to a better understanding of their structure and properties and hence, the usefulness of these materials.

2 Experimental

Eight neodymium samples with the designed composition of $Nd_2Si_{3-x}Al_xO_{3+x}N_{4-x}$ (x = 0·0, 0·2, 0·6, 0·8, 1·0, 1·2, 1·4 and 2·0) along with two samarium

samples of composition $Sm_2Si_{3-x}Al_xO_{3+x}N_{4-x}$ (x = 0·2 and 1·0) were prepared from the starting powders of Si_3N_4 (Starck Berlin LC10), AlN (Starck Berlin Grade C), Al_2O_3 (Unilab) and Nd_2O_3 (CERAC), or Sm_2O_3 (Fluka) as appropriate. The surface oxide in both 'Si_3N_4' and 'AlN' was compensated using the calculated formulae of $Si_{2.823}N_{3.645}O_{0.177}$ for 'Si_3N_4' and $Al_{1.014}N_{0.985}O_{0.043}$ for 'AlN', which allow 4·0 wt% of SiO_2 for the Si_3N_4 powders and 3·5 wt% Al_2O_3 for the AlN powders. The pelletised powder mixes weighing approximately 3 g were placed into a BN-coated graphite crucible and sintered in an induction heating furnace with flowing nitrogen gas at 1700°C for 1 h. Weight loss of the samples after firing was less than 3 wt%.

The density of the sintered samples was determined by water immersion technique based on Archimedes Principle and all samples were boiled in water for 1 h prior to measurement. The crystalline phases were determined from powder X-ray diffraction (XRD) using a Rigaku Geigerflex diffractometer. Unit cell dimensions of the phases were calculated from the measured XRD peaks using a least square method[7] after calibration with Si as an internal standard. The actual Al content in the M'_{ss} phases was determined from quantitative EDXS using a ZAF correction method[8] with Y_2O_3 and elemental Al and Si as standards. The data was collected using a Jeol JSM-840 microscope operating at 10 kV and probe current of 1 nA with the final result being the mean of 10 experimental points. Micrographs of the phases were also taken with the Jeol JSM-840 operating in backscattered mode. MAS-NMR analysis was performed on a Varian VXR-600 spectrometer operating at 156·32 MHz for ^{27}Al and Bruker MSL-400 spectrometer operating at 79·47 MHz for ^{29}Si. The powdered samples were packed into conventional zirconia spinners and were spun at 12 and 4·5 kHz for ^{27}Al and ^{29}Si, respectively. ^{29}Si spectra were accumulated using 1·5 μs (tip angle ~30°) pulses with 15 s recycle delays while the corresponding conditions for ^{27}Al were 0·65 μs (15°) pulses and a 1–2 s recycle delay. ^{27}Al spectra were referenced against an external secondary standard of $Y_3Al_5O_{12}$ (AlO_6 = 0·7 ppm with respect to $[Al(H_2O)_6]^{3+}$). ^{29}Si MAS-NMR spectra were referenced to tetramethylsilane (TMS) at 0 ppm.

3 Results and Discussion

3.1 Weight loss and density

Compositions, weight loss and density of the neodymium samples after sintering at 1700°C for 1 h are shown in Table 1. There appears to be a trend whereby reduction in weight loss is accompanied by Al addition. The Al-free sample, N0 has a weight loss (ΔW) of 2·7% and this is reduced to 0·6% in the highest Al-containing sample, N20. All samples have a weight loss of < 3·0% which may in part be responsible for the relatively single-phase melilite samples obtained here since low weight loss is indicative of minimal changes to the starting composition during sintering. Density increases substantially with increasing Al addition, from 3·267 g/cm^3 in sample N0 to 4·618 g/cm^3 in sample N20. With increasing Al addition, the formation of a liquid phase which may possess a lower viscosity than the Al-free melilite composition is promoted, facilitating densification. The relatively high density of samples N14 and N20 may in part be due to the large amount of $NdAlO_3$ found in those samples since $NdAlO_3$ has a higher density than N-melilite.

3.2 Crystalline phases

The crystalline phases of the sintered samples as detected by X-ray diffraction (XRD) are shown in Table 1. Most of the samples except those with a high Al content produce almost single phase melilite with only trace amounts of apatite ($Nd_{10}(SiO_4)_6N_2$) and wollastonite ($NdSiO_2N$).

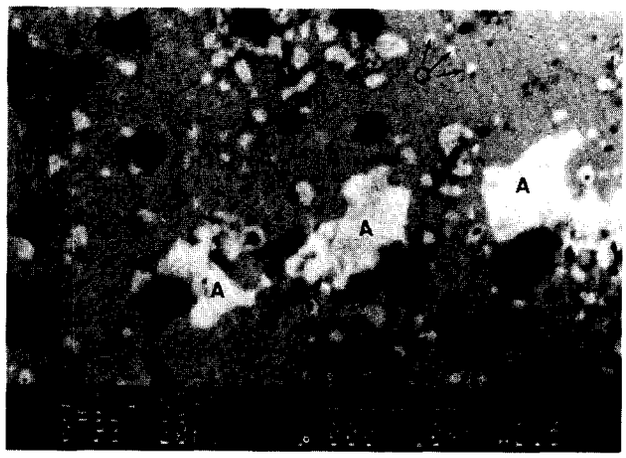
Table 1. Weight loss, density and crystalline phases of the sintered $Nd_2Si_{3-x}Al_xO_{3+x}N_{4-x}$ samples

Sample	*Designed Formula*	*X-value*	*ΔW(%)*	*D(g/cm³)*	*Crystalline phases as determined by XRD*				
					M	*M'ss*	*A*	*W*	*NdAlO₃*
N0	$Nd_2Si_3O_3N_4$	0·0	2·7	3·267	vs	—	w	mw	—
N2	$Nd_2Si_{2.8}Al_{0.2}O_{3.2}N_{3.8}$	0·2	2·0	3·696	—	vs	vw	mw	—
N6	$Nd_2Si_{2.4}Al_{0.6}O_{3.6}N_{3.4}$	0·6	1·4	3·611	—	vs	w	—	vw
N8	$Nd_2Si_{2.2}Al_{0.8}N_{3.8}N_{3.2}$	0·8	2·2	4·026	—	vs	vw	—	w
N10	$Nd_2Si_{2.0}Al_{1.0}O_{4.0}N_{3.0}$	1·0	1·1	4·335	—	vs	w	vw	m
N12	$Nd_2Si_{1.8}Al_{1.2}O_{4.2}N_{2.8}$	1·2	2·9	4·246	—	vs	vw	—	s
N14	$Nd_2Si_{1.6}Al_{1.4}O_{4.4}N_{2.6}$	1·4	1·6	4·451	—	s	ms	w	vs
N20	$Nd_2Si_{1.0}Al_{2.0}O_{5.0}N_{2.0}$	2·0	0·6	4·618	—	m	vw	—	vs

M = N-melilite ($Nd_2Si_3O_3N_4$); M'_{ss} = Al-containing N-melilite ($Nd_2Si_{3-x}Al_xO_{3+x}N_{4-x}$); A = apatite ($Nd_{10}(SiO_4)_6N_2$); W = wollastonite ($NdSiO_2N$).
X-Ray intensities: s = strong, m = medium, w = weak, v = very.

Neodymium N-melilite is detected in the Al-free sample N0, but from sample N2 onwards, the d-spacings for melilite phases continuously increase with Al addition indicating the formation of neodymium M'_{ss}. Similar to samarium and yttrium M'_{ss} phases,[4,5] the neodymium analogues do not display a different XRD pattern from that of Al-free N-melilite, implying a random solid solution with Al which does not alter the original melilite crystal structure. Apatite is observed in small amounts in all the sintered products and since there has been very little change in its lattice spacing, very limited Al, if any, is incorporated into the apatite structure.[9] Wollastonite is also detected in some of the samples. Neodymium wollastonite forms at a relatively low temperature and is unstable at high temperatures, melting at approximately 1700°C.[9] Slasor *et al.*[9] reported that wollastonite formation was dependent on firing schedule and with fast cooling, wollastonite did not appear. The wollastonite present here could have been retained during firing at 1700°C or it may have precipitated during the cooling process. Similar to apatite, neodymium wollastonite also exhibits limited Al solubility.[9] $NdAlO_3$, which is detected from sample N6 onwards forms readily and its concentration increases systematically with increasing Al content. In the Al-rich samples, N14 and N20, $NdAlO_3$ becomes the principal phase although M'_{ss} is still clearly present. A further increase in Al_2O_3 could only make $NdAlO_3$ so dominant that a reliable analysis for M'_{ss} phase become impossible. J-phase or the solid solution, J'_{ss} which was reported in the yttrium[5] and samarium[4] melilite-containing systems is not detected in any of the neodymium compositions produced in this work although neodymium J-phase is known to exist.[9]

Figure 1 shows the backscattered scanning electron microscopy (SEM), micrograph of sample N14 and quantitative energy dispersive X-ray spectroscopy (EDXS) spectra of the phases detected. SEM microstructural observation is in good agreement with phases identified by XRD. The EDXS spectrum of M'_{ss} clearly shows a substantial concentration of Al in this phase while for apatite, the Al peak is almost absent, indicative of negligible Al solubility. While atomic number contrast could not be distinguished between apatite and $NdAlO_3$ (both phases have a high neodymium concentration), EDXS is able to reveal that the smaller and relatively well-dispersed white regions are $NdAlO_3$ while apatite is significantly larger (Fig. 1).



matrix = M'_{ss} A = apatite O = $NdAlO_3$

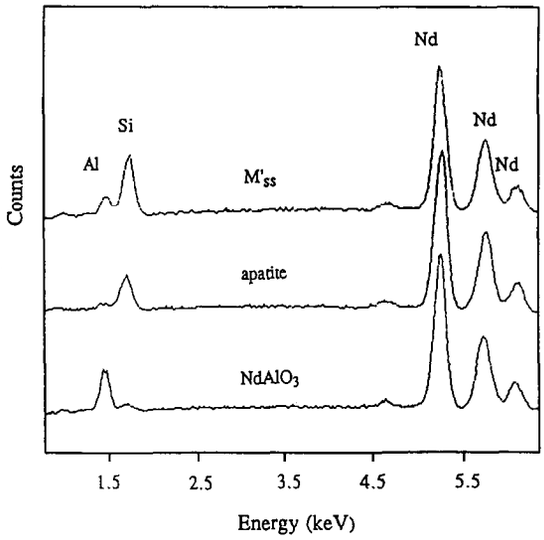


Fig. 1. Back-scattered SEM micrograph and EDXS spectra of sample N14.

3.3 Solubility of Al in neodymium M'_{ss}

Figure 2 shows the variation in the unit cell dimensions of neodymium M'_s as a function of starting x value in the designed composition, $Nd_2Si_{3-x}Al_xO_{3+x}N_{4-x}$. The starting x value ranging from 0·0 to 2·0 exhibits a relatively large expansion in both a and c lattices of the tetragonal M'_{ss} structure from x = 0·0 to about 1·0. Further increase in Al content beyond x = 1·0 produces a relatively smaller expansion rate indicating that the Al solubility of neodymium M'_{ss} is approaching saturation. A plot of cell dimension changes as a function of the measured amount of Al in the M'_{ss} phases as determined from quantitative EDXS is shown in Fig. 3 where, within the solubility limit the a and c lattices increase linearly with increasing Al according to the following equations:

$$a(\text{Å}) = 7{\cdot}719 + 0{\cdot}054x \quad (1)$$

$$c(\text{Å}) = 5{\cdot}032 + 0{\cdot}036x. \quad (2)$$

The above equations show a very similar lattice expansion to that exhibited by samarium M'_{ss}

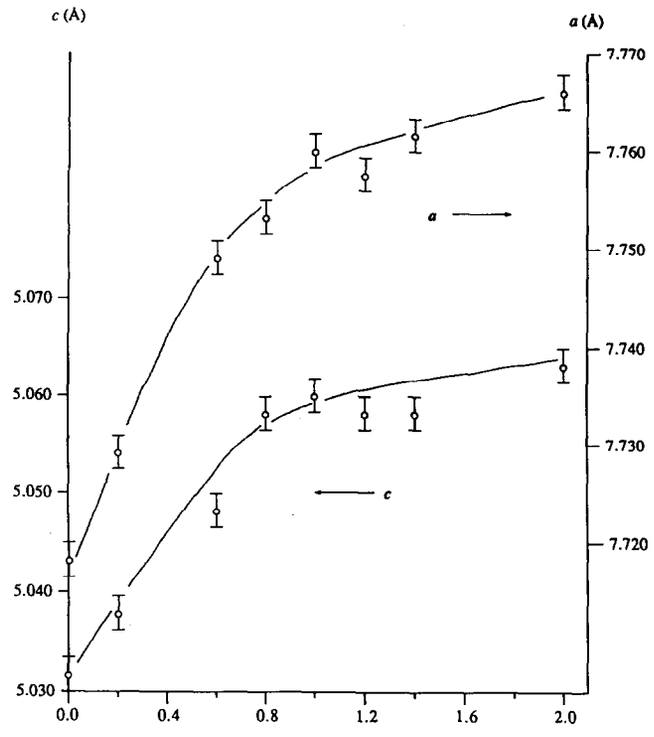


Fig. 2. Variation in the cell dimensions of neodymium M'_{ss} with starting x value.

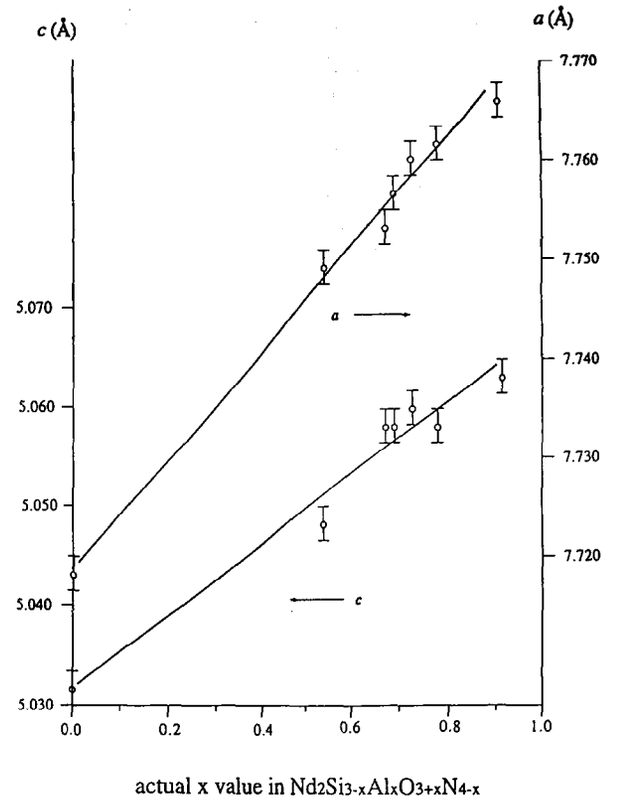


Fig. 3. Variation in the cell dimensions of neodymium M'_{ss} with actual x value determined from EDXS.

phases[4]. While both a and c lattices increase with Al addition, the calculated c/a ratio remains almost constant at 0·652 as shown in Table 2 indicating a random, uniform distribution of Al atoms within the M'_{ss} tetrahedral layers. Table 2 also provides a comparison between the designed x value and the actual Al concentration in M'_{ss} as determined by EDXS. Initially, most of the Al from the powder mixture is incorporated into M'_{ss} but as the composition further increased, discrepancy between the starting x and the actual x becomes larger. The maximum Al content obtained in neodymium M'_{ss} is $x = 0{\cdot}91$, implying that approximately one Si atom is replaced by an Al, therefore, giving a terminal composition of $Nd_2Si_{2\cdot0}Al_{1\cdot0}O_{4\cdot0}N_{3\cdot0}$.

The cell dimension measurements and EDXS analysis have clearly shown that neodymium M'_{ss} has a maximum Al solubility limit which is similar to that of samarium M'_{ss} phases[4] but higher than that of yttrium M'_{ss}.[5] It appears that the varying levels of Al substitution of different M'_{ss} phases may be related to the size of the interlayer cations. Table 3 is a compilation of experimental data on the formation of melilite phases in different systems with respect to the ionic radius of the cations. It is seen from Table 3 that there is a certain size criterion for N-melilite formation and in systems where the cation size is between ~0·9 and ~1·0 Å, N-melilite forms readily. If the cation radius is too big such as La^{3+} (1·016 Å) or too small as for Yb^{3+} (0·858 Å), N-melilite is not observed in those systems.

While the results shown in Table 3 are not conclusive, there seems to be a correlation between cation size and the maximum Al solubility limit where systems of relatively smaller cation sizes exhibit a significantly lower Al accommodation ability. Previous studies[4,5] have suggested that $x = 1{\cdot}0$ is the maximum Al solubility that can be accommodated by M'_{ss} phases without structural changes and it is seen from Table 3 that this limit has been achieved in the neodymium and samarium systems. Dy^{3+} and Y^{3+} which have ionic radii of 0·908 and 0·893 Å, respectively, have correspondingly lower Al solubility limits of $x = 0{\cdot}7$ and 0·6.

Table 2. Cell dimension calculations and EDXS measurements of the neodymium M'_{ss} samples

Sample	*Starting x-value*	*Actual x-value*	*Cell dimensions (Å) a (± 0·002) c (± 0·002)*		*c/a ratio*
N0	0·0	—	7·718	5·032	0·652
N2	0·2	[a]	7·729	5·037	0·652
N6	0·6	0·54	7·749	5·048	0·651
N8	0·8	0·67	7·753	5·058	0·652
N10	1·0	0·73	7·760	5·060	0·652
N12	1·2	0·69	7·757	5·058	0·652
N14	1·4	0·78	7·762	5·058	0·652
N20	2·0	0·91	7·766	5·063	0·652

[a]The actual Al content in this sample is too low to be reliably determined.

Table 3. Compilation of experimental data on the formation of N-melilite in different systems

Cation	*Ionic radius* r_R^{3+} (Å)[a]	$r_R^{+3}:r_O^{2-}$	*Al-free N-melilite formation*	*Formation of* M'_{ss}	*Maximum Al solubility in* M'_{ss}
La^{3+}	1·016	0·77	does not form [10]	no study	[b]
Nd^{3+}	0·995	0·75	observed[11]	observed	$x = \sim 1{\cdot}0$
Sm^{3+}	0·964	0·73	observed[11]	observed[4]	$x = \sim 1{\cdot}0$
Dy^{3+}	0·908	0·69	observed[11]	observed[12]	$x = \sim 0{\cdot}7$
Y^{3+}	0·893	0·68	observed (not at 1500°C)[11]	observed[5]	$x = \sim 0{\cdot}6$
Yb^{3+}	0·858	0·65	does not form [11,13]	no study	[b]

[a]Data from CRC Handbook of Chemistry and Physics, 72nd Edition, 1992.
[b]Experimental data currently unavailable.

Figure 4 is a schematic representation of the structure of yttrium melilite projection on (100). With non-bridging anions taking up position on the apex of the tetrahedra, each silicon oxynitride layer of the N-melilite structure possesses an overall negative charge that has to be balanced by the cations (e.g. Y^{3+}). These cations separate the silicon oxynitride layers by a finite distance. In systems with small cation sizes such as yttrium or dysprosium, the negatively charged layers are allowed to come relatively closer together and possibly create a repulsive force which may destabilise the melilite structure. A structurally unstable M'_{ss} phase may result in a low Al accommodation capability. The exact mechanism involved in this process is currently unknown but the size of the interlayer cations appears to play an important role in determining the level of Al substitution in M'_{ss} phases.

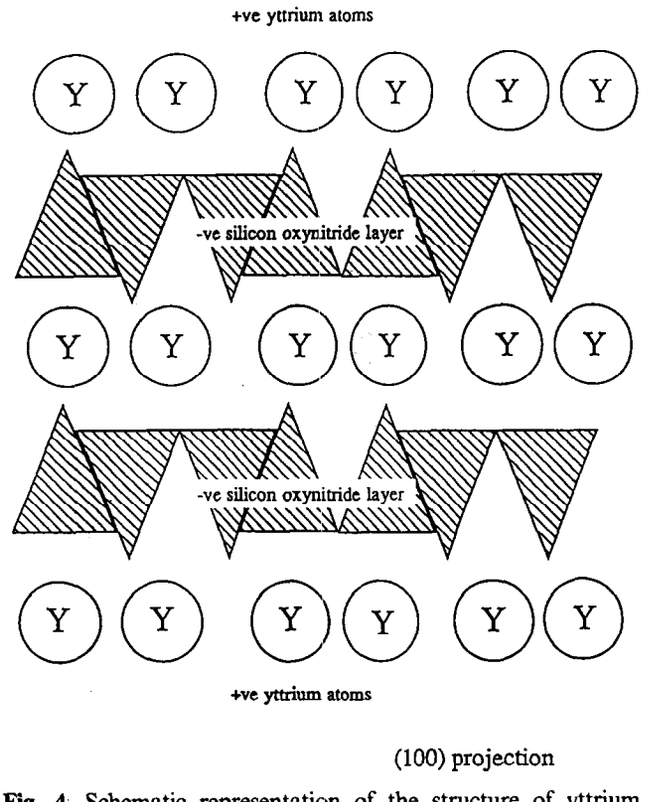


Fig. 4. Schematic representation of the structure of yttrium N-melilite showing the separation of the negatively charged silicon oxynitride layers by Y^{3+} cations.

3.4 ^{27}Al and ^{29}Si MAS-NMR data

Solid state ^{27}Al and ^{29}Si magic angle spinning NMR (MAS-NMR) were used to probe the Al and Si structural coordination in M'_{ss}. Paramagnetic ions possess unpaired electrons which produce large fluctuating magnetic field in the neighbourhood of the ions. The NMR signals from nearby nuclei can experience severe broadening, that for lanthanide stannates was found to be proportional to the square of the magnetic moment.[16] The unpaired electron can also produce a significant shift through the electron spin density being transferred onto the nucleus and is termed the Fermi contact shift. The magnitude of these effects depends on the relative orientation of the nuclei in the structure. This means that compared to diamagnetic analogues the NMR spectra may be much broader and show unconventional shift. Neodymium has a moderately large magnetic moment and contact shift[14] and it proved difficult to obtain NMR spectra from neodymium N-melilites. These effects are much smaller for samarium and NMR spectra could be obtained for samarium analogues. The two samarium samples prepared under identical conditions as those of the neodymium samples contain crystalline phases as shown in Table 4.

^{27}Al MAS-NMR spectra of the samarium samples, S2 ($x = 0{\cdot}2$) and S10 ($x = 1{\cdot}0$) are shown in Fig. 5(a) and (b), respectively. In Fig. 5(a) two resonances are observed, a sharp peak at 110 ppm and a much broader one centred at 55 ppm. From the literature, the 110 ppm resonance is attributed to AlN_4 coordination units.[15] However, it is unlikely that the substitution of Al–O for Si–N bonds in the melilite phase could lead to all Al in the AlN_4 coordination because this will cause charge imbalance in the solid solution. In addition, if some of the Al atoms are coordinated as AlN_4, there would have to be two distinct $Si_2(O,N)_7$ coordination in the M'_{ss} structure[15] but the present ^{29}Si NMR results could not strongly support this postulation (Fig. 6). The small area under the 110 ppm resonance is indicative of a very minor phase

Table 4. Weight loss, density and crystalline phases of the sintered $Sm_2Si_{3-x}Al_xO_{3+x}N_{4-x}$ samples

Sample	*Formula*	*x-value*	*ΔW(%)*	*D(g/cm³)*	*Crystalline phases as determined by XRD*		
					M'ss	*A*	*$SmAlO_3$*
S2	$Sm_2Si_{2.8}Al_{0.2}O_{3.2}N_{3.8}$	0·2	0·8	3·788	vs	w	—
S10	$Sm_2Si_{2.0}Al_{1.0}O_{4.0}N_{3.0}$	1·0	0·7	4·669	vs	w	m

M'_{ss} = Al-containing N-melilite ($Sm_2Si_{3-x}Al_xO_{3+x}N_{4-x}$); A = apatite ($Sm_{10}(SiO_4)_6N_2$).
X-Ray intensities: s = strong, m = medium, w = weak, v = very.

and previous studies[17] have attributed this peak to unreacted AlN which was beyond XRD detection. The other Al site in this sample is AlO_4 as represented by the resonance at 55 ppm. The much larger area under this peak suggests that it represents a structural unit of significant proportion. Since there are no Al-containing phases in sample S2 other than M'_{ss} according to XRD, this resonance must arise from the Al environment in the M'_{ss} structure. There are few signs of any paramagnetic broadening or shifting of these resonances which must be a result, at least for the N-melilite, of the orientation of the samarium and aluminium in the structure. The spectrum of S10 in Fig. 5(b) shows a principal resonance at 10 ppm which is attributed to AlO_6 units in $SmAlO_3$.[5] The strong intensity of this resonance corresponds to the XRD results which shows a significant amount of $SmAlO_3$ present in the sample. The ^{27}Al resonance from $SmAlO_3$ shows no noticeable shift from the position expected for AlO_6 units in such a structure, but there is an extensive envelope of broad sidebands which demonstrate the influence of the samarium ion. This indicates that the contact shift is small but the broadening effect marked. The peak at approximately 100 ppm is mainly the result of a spinning sideband which probably overlaps with a small amount of AlN_4 contribution. Similar to the low Al containing sample S2, sample S10 shows a clear peak at 55 ppm corresponding to AlO_4 coordination from M'_{ss}. A major difference between samarium and yttrium ^{27}Al spectra[16] is the absence of a well-defined 30 ppm resonance in the samarium samples. This confirms the correct assignment of the 30 ppm peak in the yttrium samples to the Al-containing J-phase (J'_{ss}) since samarium J'_{ss} does not form in the samples produced here hence, no corresponding 30 ppm or equivalent peaks are observed.

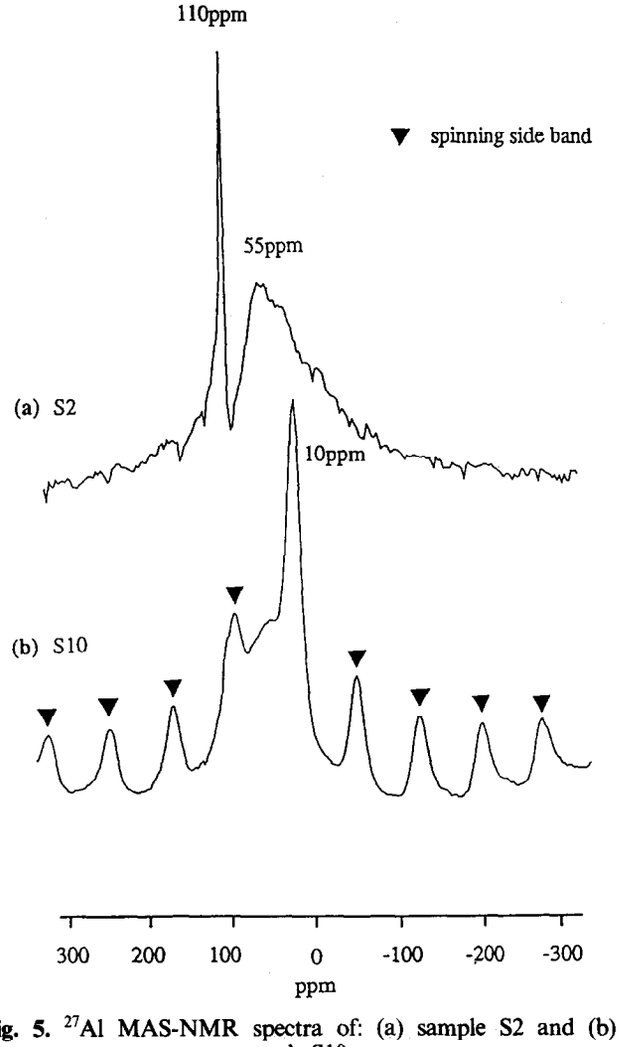


Fig. 5. ^{27}Al MAS-NMR spectra of: (a) sample S2 and (b) sample S10.

The ^{29}Si spectra of S2 and S10, shown in Figures 6(a) and (b) are very similar with both spectra producing a single resonance at approximately –35 ppm. The rest of the peaks in the two spectra are attributed to spinning sidebands and it appears that the Si environments in both low and high Al-containing samples are identical. Unlike yttrium silicon oxynitride compounds which have been extensively studied and a catalogue of ^{29}Si resonance positions defined,[18] phases in the samarium silicon oxynitride system have not been investigated by NMR and there is no reference to associate the ^{29}Si chemical shift values to particular Si environments. Apart from the 'normal' isotropic chemical shift, the resonance at –35 ppm also has an additional contact shift, further complicating peak assignment.[19] Obviously the fields produced by the Sm ion at the Al and Si sites in the M'_{ss} structure are slightly different. While the type of Si coordination which gives rise to the –35 ppm resonance is uncertain since this is not simply the chemical shift, the spectra provides unequivo-

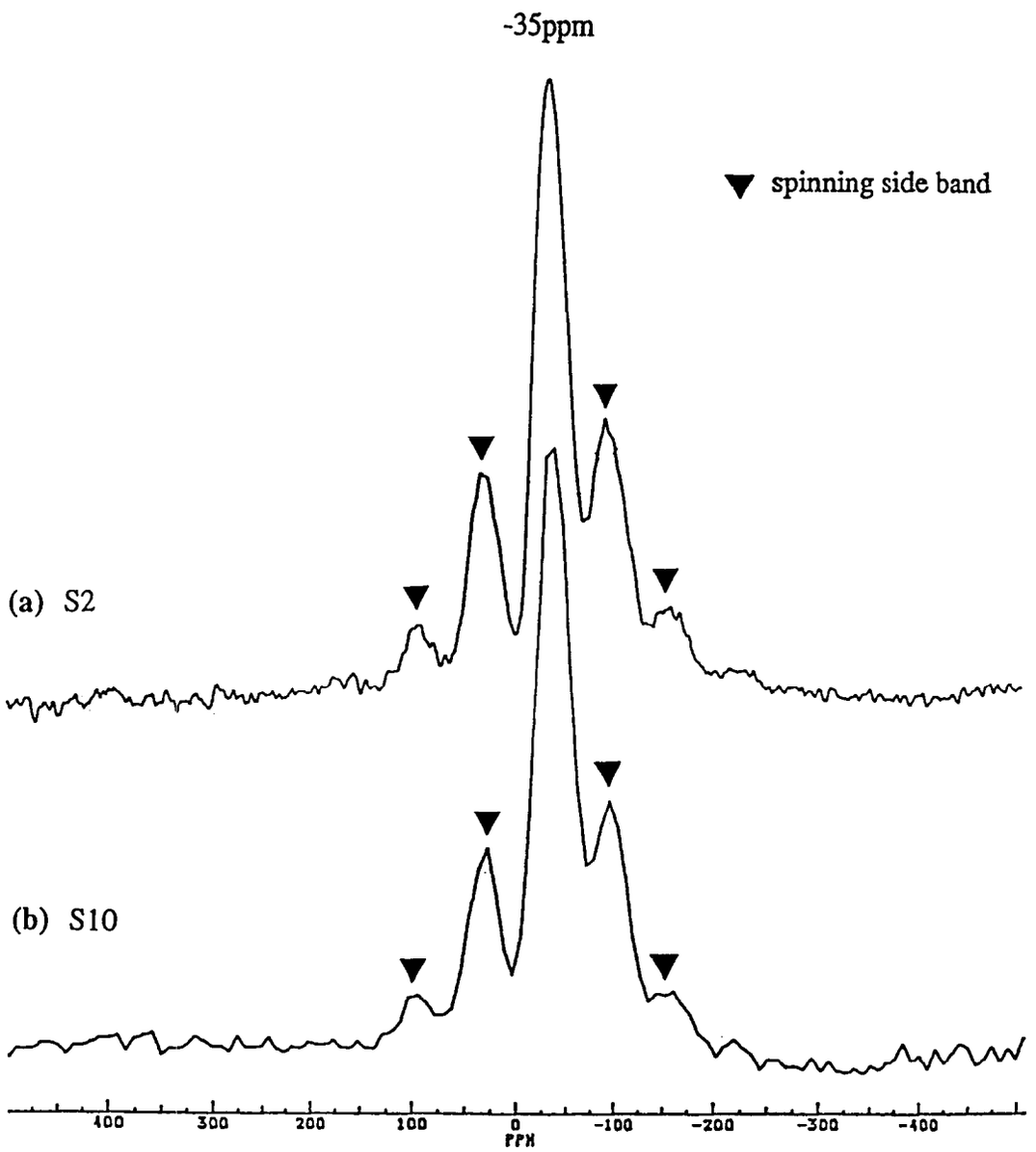


Fig. 6. ^{29}Si MAS-NMR spectra of: (a) sample S2 and (b) sample S10.

cal evidence that there is only one Si site in samarium M'_{ss} phases and by comparison with results from the yttrium system[16,18] the Si coordination in samarium M'_{ss} is more than likely to be SiO_2N_2.

From the ^{27}Al and ^{29}Si MAS-NMR data obtained, the predominant coordination's of Al and Si in samarium M'_{ss} are interpreted as AlO_4 and SiO_2N_2, respectively, and there is no evidence of transformation from one type of coordination to another with increasing Al solubility. The atomic arrangement of rare earth M'_{ss} is, therefore, similar to that proposed for yttrium M'_{ss}[16] where Al occupies the corner and centre positions of the M'_{ss} unit cell as shown in Fig. 7. From this model of atomic arrangement, the maximum number of Al atoms per unit cell will have to be two. This translates to an x value of 1·0 since two M'_{ss} chemical formulae of $R_2Si_{3-x}Al_xO_{3+x}N_{4-x}$ make up one unit cell, suggesting a terminal composition of $R_2Si_2AlO_4N_3$. This is in good agreement with the EDXS results described above where the maximum Al solubility for neodymium M'_{ss} approaches $x = 1{\cdot}0$.

4 Conclusions

There is a significant solubility of Al in neodymium M'_{ss} phases. A maximum of one Si can be replaced by Al giving the terminal composition of $Nd_2Si_2AlO_4N_3$. Cell dimension measurements and EDXS analysis have shown that neodymium M'_{ss} has a maximum Al solubility limit $x = 1$ in the formulae $Nd_2Si_{3-x}Al_xO_{3+x}N_{4-x}$, which is similar to that of samarium M'_{ss} phases but higher than that of yttrium M'_{ss}. This discrepancy is thought to be related to the size of the interlayer cations in the M'_{ss} structure. Structural investigation by MAS-NMR has suggested that samarium M'_{ss} phases consist predominantly of AlO_4 and SiO_2N_2 coordination units, regardless of the extent of Al solubility.

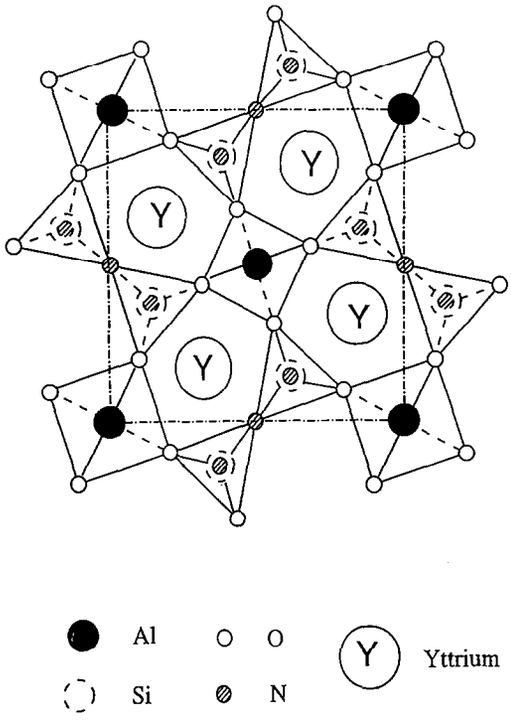


Fig. 7. Proposed atomic arrangement of yttrium M'_{ss} at the possible maximum Al solubility based on NMR results, after Ref. 18.

Acknowledgements

The authors wish to thank Dr T. J. Bastow from CSIRO Division of Materials Science and Technology for performing some of the NMR experiments. CSIRO is thanked for partial support and M. E. Smith thanks the SERC for access to the ultrahigh field facility at Edinburgh. K. S. Chee is a recipient of the Monash University Postgraduate Writing-Up Award.

References

1. Jack, K. H., Fabrication of dense nitrogen ceramics. In *Processing of Crystalline Ceramics*, eds H. Palmour III, R. F. Davis & T. M. Hane. Plenum Press, New York, (1978) pp. 561–78.
2. Jack, K. H., Review: sialons and related nitrogen ceramics. *J. Mater. Sci.*, **11** (1976) 1135–58.
3. Jack, K. H., Silicon nitride, sialons and related ceramics. In *Ceramics and Civilisation*, Vol III, *High-Technology Ceramics*. The American Ceramic Society, Columbus, OH, (1986) pp. 259–88.
4. Cheng, Y.-B. & Thompson, D. P., Aluminium-containing nitrogen melilite phases. *J. Am. Ceram. Soc.*, **77** (1994) 143–8.
5. Chee, K. S., Cheng, Y.-B., Smith, M. E. & Bastow, T. J., The solubility of aluminium in yttrium nitrogen melilite phases. In *Proceedings of the International Ceramic Conference Austceram 94*, eds C. C. Sorrell & A. J. Ruys. The Australian Ceramic Society, Sydney (1994). pp. 1031–6.
6. Cheng, Y.-B. & Thompson, D. P., Preparation and grain boundary devitrification of samarium α-sialon ceramics. *J. Eur. Ceram. Soc.*, **14**(7) (1994) 13–21.
7. Carr, A. J., *WEMAG* and *LATPAR* computer programs, University of Strathclyde, Glasgow (1989).
8. Ware, N. G., *S.P.E.E.D.* computer program, Australian National University, Canberra (1989).
9. Slasor, S., Liddell, K., and Thompson, D. P., The role of Nd_2O_3 as an additive in the formation of α' and β' sialons. In *Special Ceramics 8*, eds S. P. Howlett & D. Taylor. The Institute of Ceramics, Shelton, Staffordshire, UK, (1986) pp. 51–64.
10. Harris, R. K., Leach, M. J. & Thompson, D. P., Nitrogen-15 and oxygen-17 NMR spectroscopy of silicates and nitrogen ceramics. *Chem. Mater.*, **4** (1992) 260–7.
11. Wang, P. L., Sun, W. Y. & Yen, T. S., Formation and densification of *R*-α'-SiAlONs (R = Nd, Sm, Gd, Dy, Er and Yb). In *Silicon Nitride Ceramics: Scientific and Technological Advances*, Vol. 287. eds I.-W. Chen, P. F. Becher, M. Mitomo, G. Petzow & T.-S. Yen. Materials Research Society, (1993) pp. 387–92.
12. Yan, D.-S., Personal communication (1994).
13. Hoffman, M. J. & Petzow, G., Microstructural design of Si_3N_4 based ceramics. In *Silicon Nitride Ceramics: Scientific and Technological Advances*, Vol. 287. eds I.-W. Chen, P. F. Becher, M. Mitomo, G. Petzow & T.-S. Yen, Materials Research Society (1993) pp. 3–14.
14. Grey, C. P., Dobson, C. M., Cheetham, A. K. & Jakeman, R. J. B., Studies of rare-earth stannates by ^{119}Sn MAS NMR. The use of paramagnetic shift probes in the solid state. *J. Am. Chem. Soc.*, **111** (1989) 505–11.
15. Smith, M. E., Observation of mixed $Al(O,N)_4$ structural units by ^{27}Al magic angle spinning NMR. *J. Phys. Chem.*, **96** (1992) 1444–8.
16. Chee, K. S., Cheng, Y.-B. & Smith, M. E., NMR investigation on the structure of aluminium-containing yttrium nitrogen melilite (M'_{ss}). *Chem. Mater.*, in press.
17. Dupree, R., Lewis, M. H. & Smith, M. E., Structural characterisation of ceramic phases with high-resolution ^{27}Al NMR. *J. Appl. Cryst.*, **21** (1988) 109–16.
18. Dupree, R., Lewis, M. H. & Smith, M. E., High-resolution silicon-29 nuclear magnetic resonance in the Y–Si–O–N system. *J. Am. Chem. Soc.*, **110** (1988) 1083–7.
19. Grey, C. P., Smith, M. E., Cheetham, A. K., Dobson, C. M. & Dupree, R., ^{89}Y MAS NMR study of rare-earth pyrochores: paramagnetic shifts in the solid state. *J. Am. Chem. Soc.*, **112** (1990) 4670–5.

Journal of the European Ceramic Society **15** (1995) 1221–1228
© 1995 Elsevier Science Limited
Printed in Great Britain. All rights reserved
0955-2219(95)00085-2
0955-2219/95/$9.50

Phase Transformations in Sm (α+β)-SiAlON Ceramics during Post-sintering Heat Treatments

Rupeng Zhao & Yi-Bing Cheng*

Department of Materials Engineering, Monash University, Melbourne 3168, Australia

(Received 14 February 1995; revised version received 19 May 1995; accepted 22 May 1995)

Abstract

Phase transformations in Sm (α + β)-SiAlON ceramics during post-sintering heat treatments at 1300 and 1450°C were investigated using XRD, SEM, TEM and EDS techniques. The transformation from α to β SiAlON, (i.e. α' to β') phases was observed at both temperatures. However, other phase transformations occur simultaneously at grain boundaries of the materials and also involve the β' phase, namely, Glass $\rightarrow$ $SmAlO_3$ + β' and $SmAlO_3$ + $\beta' \rightarrow M'$. Their effects on the amount of β' in the materials must therefore be considered in the study of the α' to β' transformation. It is thought that the increase in the β':(α' + β') ratio during a heat treatment process depends not only on the rate of the α' to β' transformation, but also on the amount and composition of the intergranular phases.

1 Introduction

Post-sintering heat treatment is a technique commonly used in manufacturing SiAlON ceramics. The main objective of the post-sintering heat treatment includes the crystallisation of the glassy grain boundary phase in the materials to improve the materials' performance at elevated temperatures. This is usually achieved via a conventional glass-ceramic process during which the glass devitrifies at a temperature above its T_g point but without being 'melted'.[1,2] There has been much work in understanding of the grain boundary crystallisation, but very little attention has been paid to the effects of the post-sintering heat treatment on the stability of SiAlON phases until very recently. Mandal *et al.*[3] found that some α-SiAlON (α') phases could transform to β-SiAlON (β') during the process. It was observed that the transformation from α' to β' readily occurred in some rare earth α' + β' composite materials when heat-treated between 1000 and 1600°C and the extent of the transformation was more pronounced with increasing temperatures.[3] α' and β' have different mechanical properties,[4] therefore, these findings have opened a new possibility of tailoring the microstructures and properties of SiAlON ceramics in a way that was previously not expected.

α' and β' are two different crystallographic modifications of SiAlON structures.[5] Although both phases are basically built up of corner-sharing (Si,Al)(O, N)$_4$ tetrahedra, there is a distinct difference in the atomic arrangement between the two phases.[6] The bonds in SiAlON structures are strongly covalent and the atoms have a very low self-diffusivity even at 1800°C; these features bear the virtual responsibility of a relatively poor densification behaviour of Si_3N_4-based materials. The transformation between the α' and β' phases has a reconstructive nature which involves the breaking of chemical bonds and substantial atomic diffusion, and hence requires significant amounts of thermal energy. The transformation from α-Si_3N_4 to β-Si_3N_4 did not occur without the presence of a liquid phase in which α-Si_3N_4 grains could dissolve above ~ 1400°C.[7] All these facts naturally raise some questions on the mechanism of α' to β' phase transformations, particularly those taking place at temperatures below the eutectic of the system. The present paper provides some evidence of the α' to β' phase transformation in a Sm α' + β' ceramic composite at both below and above the eutectic temperatures, and further reveals additional phase transformations that could involve the β' phase during post-sintering heat treatments.

2 Experimental Details

Samples were prepared from Si_3N_4 (Starck, Berlin, LC10), AlN (Starck, Berlin, Grade B), Al_2O_3 (Alcoa, A17) and Sm_2O_3 (RE Acton, Rare Earth Products, 99.9%) powders with a starting composition

*To whom correspondence should be addressed.

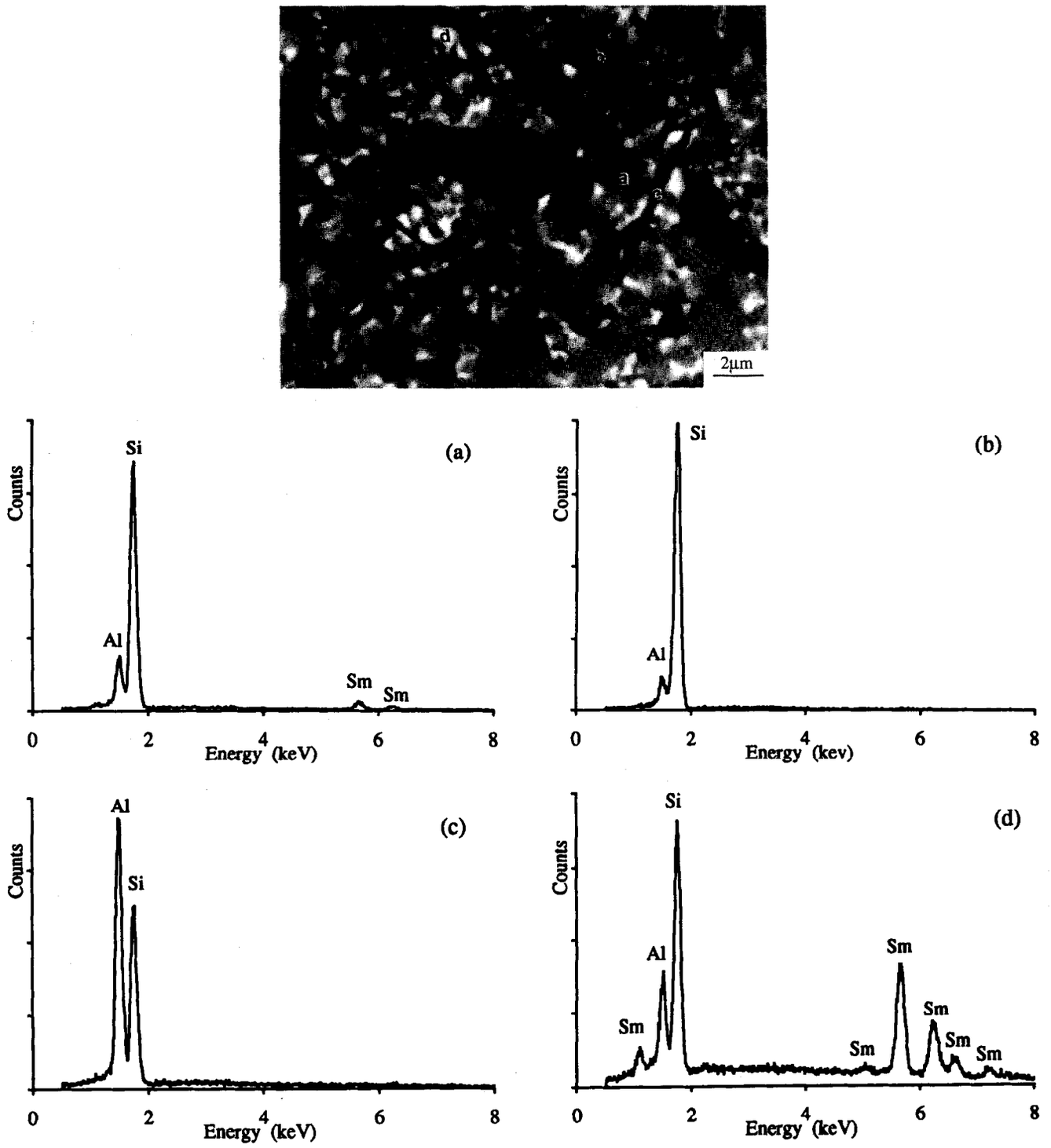


Fig. 1. SEM backscattered image of the as-sintered sample and EDS spectra from different phases. The white regions are intergranular glass, the grey grains are α' and the dark grains either β' or 21R. The EDS spectra of: (a) α'; (b) β'; (c) 21R and (d) grain boundary glass correspond to the regions marked on the micrograph.

of $Sm_{0.379}Si_{9.548}Al_{2.381}O_{1.668}N_{14.403}$. The pelleted green body of the designed composition was initially sintered at 1820°C for 4 h in an industrial furnace. The slow cooling rate of the furnace produced a SiAlON material with wollastonite as the grain boundary phase. Further sintering was carried out in a laboratory carbon resistance furnace at 1800°C for 30 min and the specimen was then cooled in the furnace. Due to a much faster cooling rate, the final material contains mainly α', a small amount of β' and 21R phases with an amorphous phase at grain boundaries.

The samples that contained glassy grain boundaries were subsequently heat-treated at 1300 and 1450°C respectively for various periods. The heat treatments were carried out in flowing nitrogen in an alumina tube furnace with heating and cooling rates of 3°C/min. After heat treatments, the surfaces of the samples were removed by grinding on SiC paper and the bulk of the material was exposed for

crystalline phase and microstructural examinations.

Scanning electron microscopy (SEM) observations and energy-dispersive X-ray spectroscopy analysis (EDS) were carried out using a JEOL 840A instrument. A JAVA image analyser was used to analyse the backscattered SEM electron images. A Philip CM20 TEM instrument fitted with an ultrathin-window EDS detector was used for microstructural observations and compositional analyses. Specimens for TEM were mechanically ground, dimpled to thickness of ~20 μm, and then ion-milled to electron transparency. All specimens were carbon coated before SEM and TEM observations to avoid surface charging.

Phase characterisation was performed with X-ray diffraction (XRD) using a Rigaku X-ray diffractometer. The relative amounts of α' and β' phases, i.e. the β':(α' + β') weight ratio, were calculated using the calibration curves developed by Liddell[8] with the intensities of the (210) peaks of both the α' and β' phases.

$$\beta'(\text{wt}\%) = K/[I_\alpha(210)/I_\beta(210) + K] \times 100\% \quad (1)$$

where K is a constant, equal to 0·702.

The amounts of crystalline grain boundary phases (namely, $SmAlO_3$ and the Al-containing N–melilite, M'[9]) after heat treatments were estimated by comparing appropriate XRD peak intensities of these phases with that of the 21R phase which remained unchanged throughout the heat treatment process. The specific result calculated from this way may possess a certain error, but the trends, i.e. the relative changes in the amount of $SmAlO_3$ and M' phases versus the heat treatment time and temperature, should be indicative. This is true for the β':(α' + β') ratio as well.

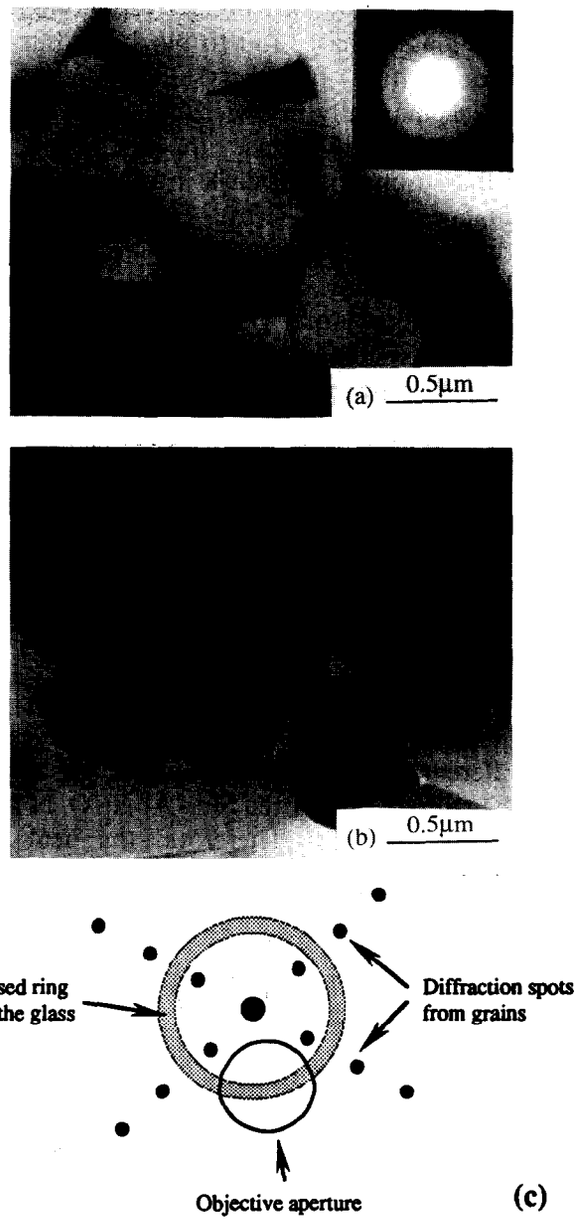


Fig. 2. TEM: (a) bright field and (b) diffused dark field images from the as-sintered specimen. (c) Schematic illustration of the objective aperture position for diffused dark field imaging. The glassy nature of the grain boundary phase is indicated by the electron diffraction rings (inset in (a)).

3 Results

3.1 The as-sintered materials

XRD analyses showed that the crystalline phases in the as-sintered sample consisted of mainly α' and β' phases, with a small amount of 21R polytypoid phase. The β':(α' + β') ratio was about 11%. Figure 1 shows a typical SEM backscattered image of the as-sintered material. Since the backscattered electron intensity depends mainly on the mean atomic number, the differences in the amounts of samarium presented in the α', β' and grain boundary phases make them easily identified. The white grain boundary regions are the intergranular glassy phase containing large amounts of samarium. The equiaxed grey regions are α' grains with a small amount of samarium, and the dark regions are β' or 21R phases with no samarium. This has been supported by the EDS analytical results (Fig. 1). The β' and 21R phases can be differentiated by EDS analyses or by their morphology. The needle-like grains with high aspect ratios are usually the 21R phase while the slightly elongated ones with low aspect ratios are β'. Image analyses indicate that the as-sintered sample contained around 75% α' and 10% intergranular glassy phase, with the rest being β' and 21R.

Figure 2 shows typical bright field and diffused dark field TEM images of the as-sintered sample. In the bright field image, the intergranular phase is darker because of its high samarium content. Diffused dark field images are obtained by using the objective aperture of the microscope to select

a part of the diffraction ring corresponding to the expected glassy phase, and to block all diffraction spots originating from crystalline grains,[10] as shown schematically in Fig. 2(c). As a result, the intergranular glassy phase appears bright while crystalline grains are all dark in the diffused dark field image (see Fig. 2(b)). Electron diffraction confirmed that the intergranular phase was amorphous, as indicated by the ring pattern (Fig. 2(a)). The intergranular glass comprises all five elements in the system, although its composition may vary slightly from pockets to pockets (Fig. 3). To a first order approximation (using calculated parameters and neglecting absorption effect), the estimated composition of the glass is around Sm:Si:Al = 0·7:1·0:0·8 and N:O = 1:2·3 (in atomic ratio). Therefore, the Si, O and N contents in the glass are significant.

3.2 Heat treatment at 1300°C

Post-sintering heat treatment was conducted at both 1300 and 1450°C respectively to investigate the different phase transformation behaviour. The eutectic temperature of the Sm– Al–Si–O–N system is about 1350°C.[11,12] Therefore, the heat treatments at 1300 and 1450°C represents the thermal processes below and above the eutectic temperature of the system respectively.

Samarium aluminate ($SmAlO_3$) was observed as the only devitrification product of the intergranular glass in the sample heat-treated at 1300°C. XRD results of the samples after heat treatments at this temperature for various periods are presented in Fig. 4. Both the β':(α' + β') ratio and the amount of $SmAlO_3$ increased with the duration of the heat treatment. The increases in $SmAlO_3$ and the β':(α' + β') ratio can be divided into two distinct stages according to the rate of the phase transformations. There is a rapid increase in both

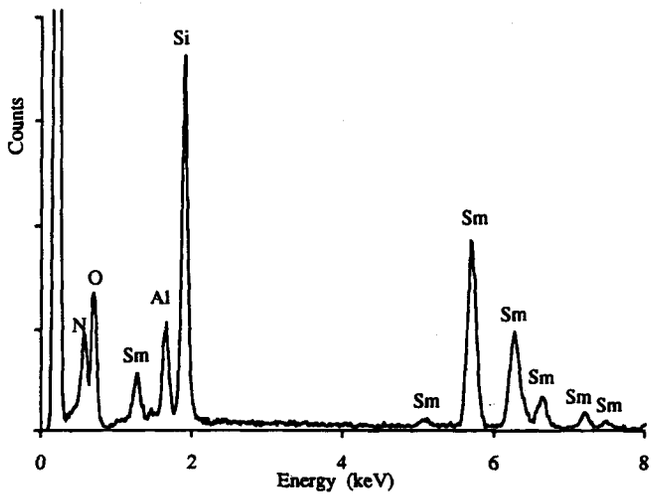


Fig. 3. EDS spectrum from the intergranular glassy phase in the material showing that it contains significant amounts of Si and N.

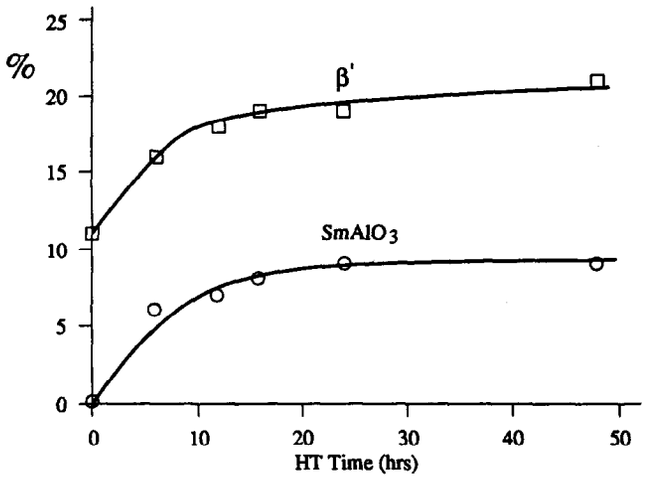


Fig. 4. The β':(α' + β') ratio and the relative $SmAlO_3$ fraction of the samples heat-treated at 1300°C as a function of heat treatment time.

$SmAlO_3$ and β' phases in the initial heat treatment stage ($0 < t < 6$ h). Further heat treatment up to 48 h resulted in only a slight increase in these two phases. The initial rapid increase in $SmAlO_3$ indicates that the intergranular glassy phase devitrifies very rapidly at the temperature, and grain boundary

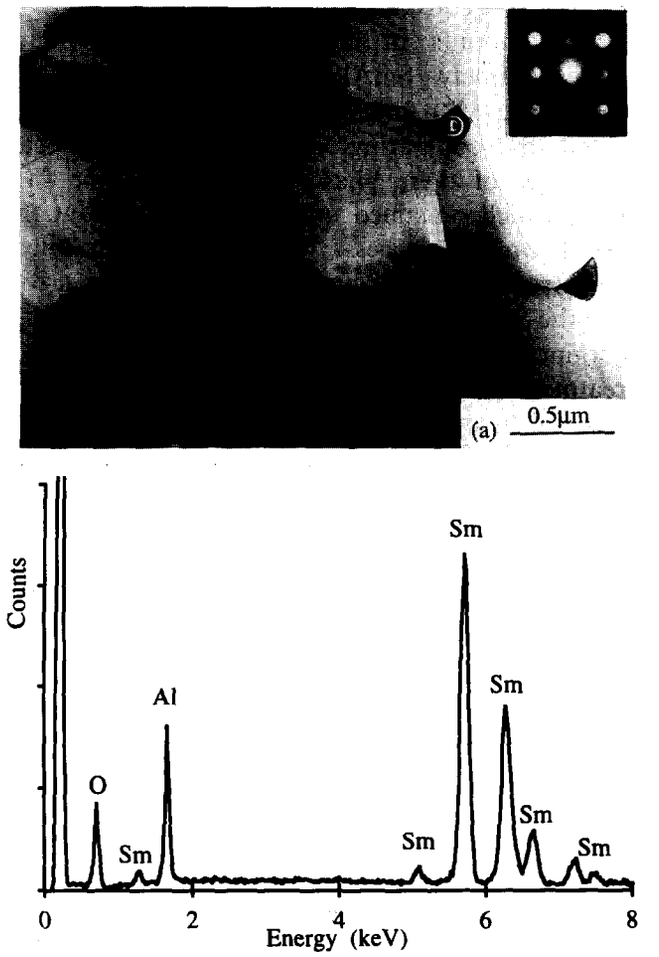


Fig. 5. (a) Typical TEM bright field image of the sample heat-treated at 1300°C for 24 h. The dark crystals at the grain boundaries are $SmAlO_3$ with an orthorhombic structure, as confirmed by electron diffraction from the crystal marked 'D' (inset) and by EDS analysis (b). The diffraction pattern is [001] zone for $SmAlO_3$.

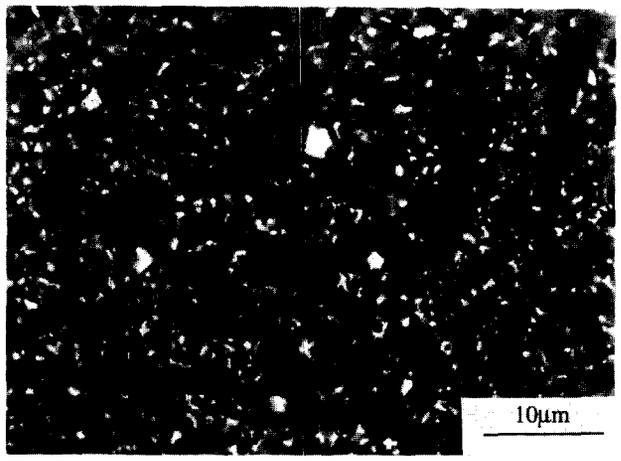


Fig. 6. SEM backscattered image of the sample after heat treatment at 1300°C for 24 h showing homogeneous distribution of $SmAlO_3$ crystals (the white phase).

devitrification may have been completed in a few hours. It is interesting to notice that the increase in the β':(α' + β') ratio follows a similar pattern as that of $SmAlO_3$.

TEM observations revealed that the glass phase in all multiple junctions of the as-received samples was fully crystallised after the heat treatment at 1300°C for 24 h. A typical bright field image is shown in Fig. 5(a). EDS analysis (Fig. 5(b)) and electron diffraction (Fig. 5(a)) confirmed $SmAlO_3$ as the intergranular crystalline phase. SEM observations on all samples heat-treated at 1300°C showed that apart from a few agglomerates of about 2 μm in size, the $SmAlO_3$ grains in general were homogeneously distributed, as shown in Fig. 6, indicating that there was no significant grain boundary migration during the heat treatment at this temperature.

3.3 Heat treatment at 1450°C

Figure 7 summarises the XRD results of the samples after heat treatments at 1450°C for various times. It can be seen from the figure that the β':(α' + β') ratio increases with the duration of the heat treatment. Such an increase in the β' phase can be partially explained in terms of the α' to β' transformation.[3] However, it has been noted that the rate of the increase in β' contents varies significantly with the heat treatment time; as a result, three distinct stages are recognised. In the first few hours, the β':(α' + β') ratio increases rapidly, more than 10% in 4 h. In the second stage (4 h < t < 16 h), the amount of β' remains almost unchanged. With further time, however, the β' phase increases again in the third stage (t > 16 h), but at a lower rate than that in the initial stage. Such a discrete nature of the change in the β':(α' + β') ratio during an isothermal process cannot be simply explained by the α' to β' transformation alone, and other mechanism(s) may also be involved.

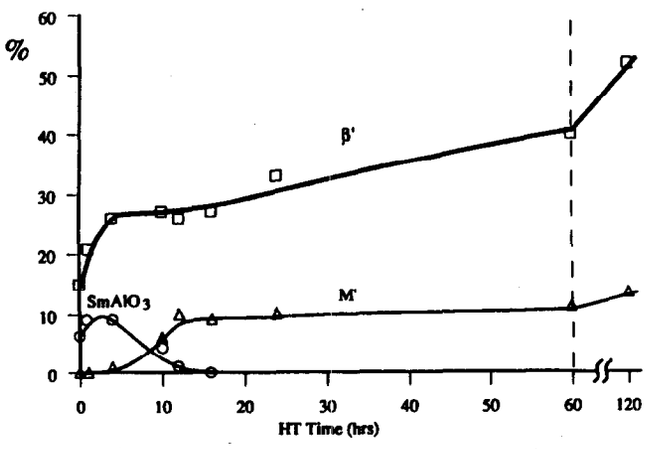


Fig. 7. The β':(α' + β') ratio, $SmAlO_3$ and M' fractions in the samples heat-treated at 1450°C as a function of heat treatment time. The result marked at zero hour in the figure was obtained by heating up the sample to 1450°C and then immediately cooling down to room temperature.

Both $SmAlO_3$ and M' were observed after heat treatment at 1450°C, but their relative contents varied with time. Figure 7 shows the weight fractions of the $SmAlO_3$ and M' phases in the samples. $SmAlO_3$ was observed in the initial stage of the heat treatment at 1450°C prior to the appearance of M'. The amount of $SmAlO_3$ reached a maximum after about 4 h then started to decrease, and completely disappeared after 12 h. The initial heat treatment at 1450°C did not produce any M' phase, but it appeared simultaneously with $SmAlO_3$ after 4 h, and then became the only grain boundary phase at the expense of $SmAlO_3$ in the samples heat-treated for longer than 12 h. There are two interesting correlations among the different phase changes at 1450°C: (i) the initial rapid increase in the β':(α' + β') ratio is associated with the rapid formation of $SmAlO_3$, similar to that observed at 1300°C, suggesting the formation of β' is associated with the devitrification of the intergranular glassy phase; and (ii) the plateau in the curve of the β':(α' + β') ratio is correlated with the decomposition of $SmAlO_3$ and the formation of M'.

Microstructures of the samples heat-treated at 1450°C were studied by SEM. Figures 8(a–c) show three typical SEM backscattered images of the samples heat-treated for 4, 12 and 24 h, respectively. EDS confirmed that the white grain boundary phase in Fig. 8(a) was $SmAlO_3$, while those in Figs 8(b) and (c) were M'. It can be seen from Fig. 8(a) that, as for heat treatment at 1300°C (Fig. 6), most $SmAlO_3$ grains are fine in morphology and are homogeneously distributed at grain boundaries despite a few large agglomerates of around 2 μm. There is virtually little difference in the microstructures of the grain boundary phase between samples heat-treated at 1300°C for 24 h and that at

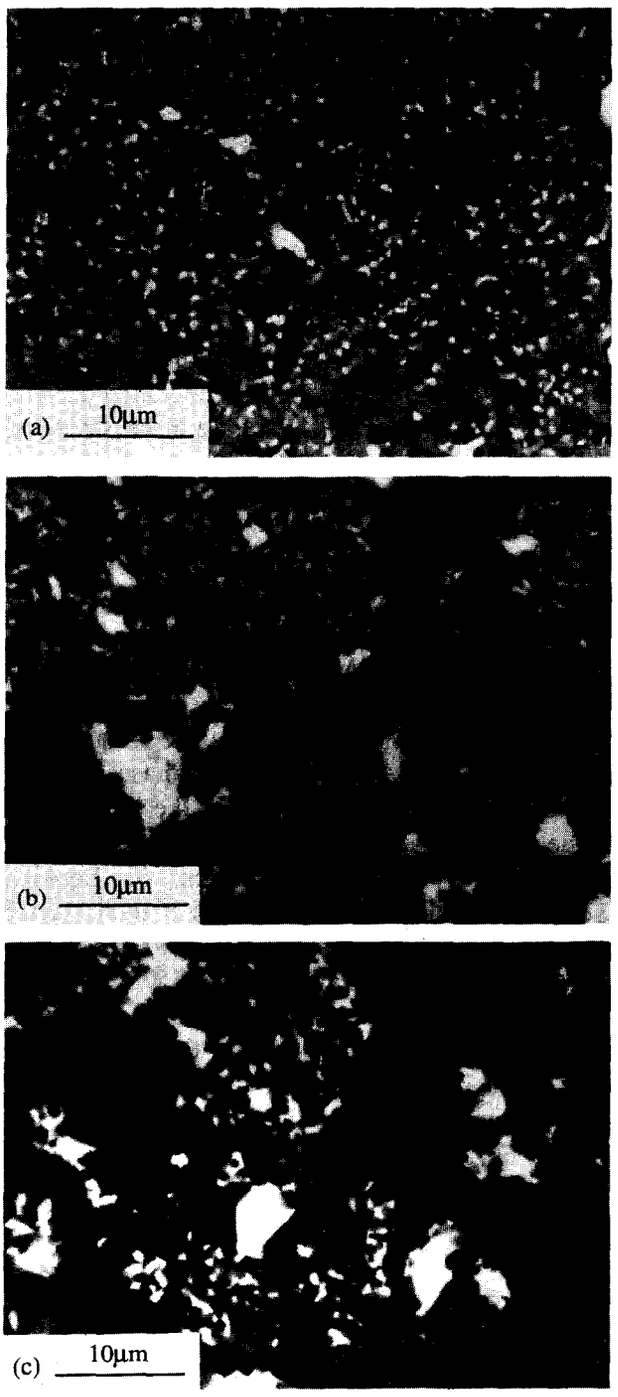


Fig. 8. SEM backscattered images of samples heat-treated at 1450°C for (a) 4 h, (b) 12 h and (c) 24 h. The grain boundary phase (white regions) was $SmAlO_3$ in (a), and the M' phase in both (b) and (c).

1450°C for 4 h, indicating that no significant grain boundary migration occurred when $SmAlO_3$ was formed. As a contrast, the distribution of M' grains is agglomerative and inhomogeneous (Figs 8(b) and (c)), suggesting that considerable intergranular migration has taken place. The grain boundary M' phase forms only above the eutectic temperature,[9] involving a liquid phase which promotes the grain boundary migration. TEM observations on samples heat-treated at 1450°C for 24 h failed to identify any residual amorphous phase (Figs 9 and 10), therefore the liquid phase that

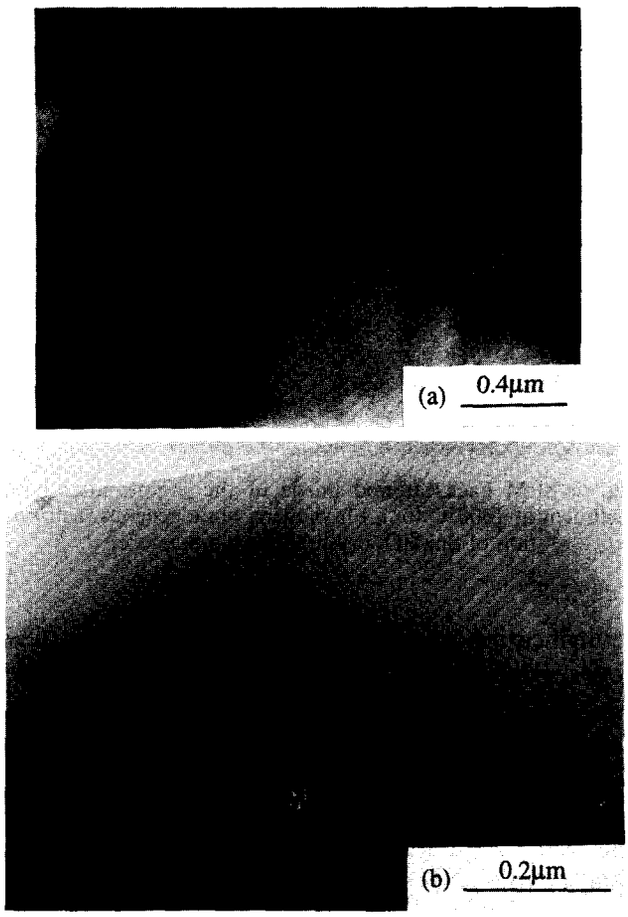


Fig. 9. Typical TEM bright field images of the sample heat-treated at 1450°C for 24 h. Note that little residual glass can be found at grain boundaries. The dark grain in (b) is the M' phase and other grains are either α' or β'.

exists at grain boundaries during the heat treatment must be of a transient nature.

4 Discussion

4.1 β-SiAlON formation during post-sintering heat treatments

The present results have shown that different

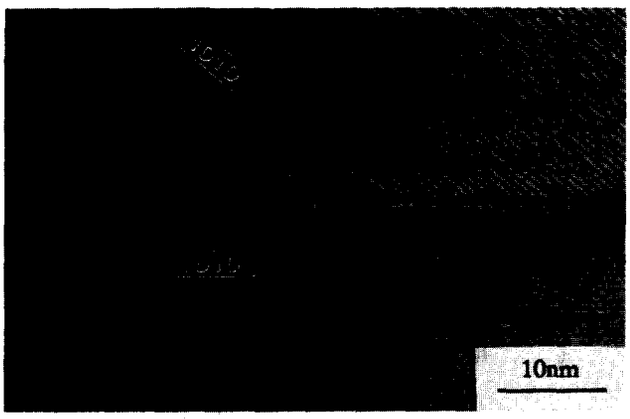


Fig. 10. High resolution lattice fringe image of the boundary between two α' grains in the sample heat-treated at 1450°C for 24 h. Fringes can be followed up to the boundary from either side, indicating the lack of a glass thin film.

phase transformations can take place during post-sintering heat treatments. The increase in the β' concentration after the heat treatments is significant and this provides some evidence for a phase transformation from α' to β' at the heat treatment temperatures. However, due to the simultaneous devitrification of the grain boundary glass and the formation of $SmAlO_3$ and M', other mechanisms may also contribute to the increase in β'.

Although the exact composition of the grain boundary glass is yet to be determined, preliminary EDS analyses indicate that the glassy phase contains all the five elements (Sm–Si–Al–O–N) with significant contents of both Si and N. When $SmAlO_3$ is formed by devitrification, it has consumed most samarium, aluminium and oxygen in the glass, leaving a phase rich in Si and N. However, extensive TEM analyses cannot detect any glassy phase in the samples after devitrification and this leads to a postulation that the residual Si and N in the glass have also formed a crystalline phase in an amount comparable with that of $SmAlO_3$. Considering there is no new unidentified phase from XRD analyses, the anticipated Si and N rich phase formed from the glass must be either α' and/or β'. It is known that Si and N in a glassy phase can partition in the existing SiAlON grains during grain boundary crystallisation.[1] Moreover, the observation of α' to β' transformations in the rare earth SiAlON systems between 1000 and 1500°C[3] indicates a lower free energy for the β' phase than that for the α' phase. Therefore it is thought that the precipitation of β' from the glassy phase is thermodynamically preferred at the present heat-treatment temperatures.

On account of the simultaneous rapid increase in both the β' and $SmAlO_3$ phases in the initial stage of the heat treatment at both 1300 and 1450°C, it is plausible to propose the following phase transformation:

$$\text{Glass} \rightarrow SmAlO_3 + \beta' \qquad (2)$$

Therefore the initial rapid increase in the β':($\alpha' + \beta'$) ratio during the heat treatments is attributed to a combined effect of two different mechanisms, namely, the α' to β' transformation and glass devitrification. The activation energy for the glass devitrification should be much lower than that for the α' to β' transformation at these temperatures, and hence the glass devitrification may make the major contribution to the increase in the β' content at the initial stage of heat treatment processes. The increase in the β':($\alpha' + \beta'$) ratio will therefore depend not only on the heat treatment conditions, but also on the amount and composition of the grain boundary glassy phase in the materials. Significant differences in the extent of the α' to β' phase transformation could occur in samples of the same SiAlON system if the amount and composition of the glassy phase are different.

Table 1. The β': ($\alpha' + \beta'$) ratio of two groups of samples after heat treatment at 1450°C

HT time (h) at 1450°C	*Group I (no glass) (%)*	*Group II (with glass) (%)*
Before HT	19	11
4	27	26
24	34	33

Note: The Group I samples were heat-treated at 1300°C for 24 h and contained $SmAlO_3$ as a grain boundary phase prior to the heat treatment at 1450°C, whereas the Group II samples were as-sintered with a glassy grain boundary phase before the heat treatment.

The proposed mechanism of the transformation, eqn (2), is further supported by another set of experiments in which two groups of samples are compared. Both groups were originally from the same bulk specimen and heat-treated at 1450°C for 4 and 24 h respectively. Prior to this heat treatment, the Group I samples were preheat-treated at 1300°C for 24 h, hence containing $SmAlO_3$ and very little glass, while the Group II samples had no pre-heat treatment and contained a glassy phase at grain boundaries. Table 1 shows the results after the heat treatment at 1450°C. Although the same amount of β' was found in both groups after heat treatments for 4 and 24 h, there appeared a significant difference in the rate of β' increase during the initial 4 h; the sample with a glassy phase (Group II) had a much higher yield of β' compared to the one that contained $SmAlO_3$ prior to the heat treatment (Group I). It is apparent that crystallisation of the intergranular glassy phase has made a significant contribution to the higher increase in the β':($\alpha' + \beta'$) ratio in Group II samples and so this is in agreement with the proposed transformation of eqn (3).

4.2 β-SiAlON consumption during phase transformations

Cheng and Thompson[13] found that the M' phase was the only stable intergranular crystalline phase above 1400°C in the Sm ($\alpha + \beta$)-SiAlON system. Although $SmAlO_3$ was observed in the initial stage of the heat treatment at 1450°C, possibly formed during the slow heating and cooling, it became unstable and formed a eutectic liquid through a reaction with other phases in the system upon further 1450°C heat-treatment. The experimental results indicate that the decomposition of $SmAlO_3$ results in the precipitation of the M'($Sm_3Si_2AlO_4N_3$) phase at the SiAlON grain-boundaries. However, the significant compositional

difference between these two phases implies that the phase transformation must involve an additional Si and N rich phase to complement the Sm–Al–O composition of the grain boundaries. The coincidence between the M' formation and the plateau in the curve of the β':(α' + β') ratio of Fig. 7 suggests that $SmAlO_3$ may have reacted with the β' phase to form a transient liquid necessary for the M' phase precipitation:

$$SmAlO_3 + \beta' \rightarrow \text{liquid} \rightarrow M' \qquad (3)$$

The existence of this transient liquid is supported by the observation that considerable grain boundary migration occurs when the M' phase forms (Fig. 8). The consumption of β' in the above reaction may be compensated by the simultaneous α' to β' transformation. As a result, a balance is maintained and the overall β' content in the sample remains unchanged as shown in Fig. 7. Once reaction (3) is complete, a further steady increase in β' is anticipated.

At 1450°C for 120 h, the relative β' content in the sample was 54%, a significant increase compared to the sample heat-treated for 24 h. This result strongly suggests the transformation from α' to β' during the extended heat treatment. The slight increase in the amount of the M' phase may accommodate the Sm released from the transformed α' structure.

5 Conclusions

Three different phase transformations may occur simultaneously during the post-sintering heat treatment of (α + β)-SiAlON ceramics: (i) grain boundary glass devitrification; (ii) phase transformations among different crystalline grain boundary phases; and (iii) the α' to β' phase transformation. Significant differences in the β':(α' + β') ratio of Sm (α + β)-SiAlON ceramics are observed when the samples are heat-treated at below and above the eutectic temperature of the system. Although there is a transformation between the α' and β' phases during the heat treatments at both the temperatures, other phase transformation mechanisms may also occur and affect the amount of β'.

Devitrification of the intergranular glassy phase can lead to the formation of β' via the transformation

$$\text{Glass} \rightarrow SmAlO_3 + \beta'$$

The amount and composition of the grain boundary glass could have significant effects on the change of the β' phase during the heat treatment. The stabilities of different crystalline intergranular phases may change with temperature, resulting in phase transformations that involve β' phases. In Sm (α + β)-SiAlON materials, the following transformation will take place if the heat treatment is above the eutectic temperature:

$$SmAlO_3 + \beta' \rightarrow \text{liquid} \rightarrow M'$$

These phase transformations may also occur in other rare earth (Ln) (α + β)-SiAlON composites during post-sintering heat-treatments, where the aluminate could be either $LnAlO_3$ or a YAG-type phase. The effects of these transformations on the β':(α' + β') ratio can be significant and have to be taken into account in any studies of the α' to β' phase transformation.

References

1. Lewis, M. H., Crystallisation of grain boundary phases in silicon nitride and SiAlON ceramics. In *Silicon Nitride 93, Key Engineering Materials*, Vol. 89–91, eds M. J. Hoffmann, P. F. Becher & G. Petzow, Trans Tech Publ., 1993 pp. 333–8.
2. Thompson, D. P., New grain boundary phases for nitrogen ceramics. In *MRS Symposium Proceedings: Silicon Nitride Ceramics — Science and Technological Advances*, eds I-Wei Chen *et al.*, MRS, Vol 287, 1993, pp. 79–92.
3. Mandal, H., Thompson, D. P. & Ekström, T., Reversible $\alpha \leftrightarrow \beta$ SiAlON transformation in heat-treated SiAlON ceramics. *J. Eur. Ceram. Soc.*, **12** (1993) 421–9.
4. Ekström, T. & Nygren, M. SiAlON ceramics. *J. Am. Ceram. Soc.*, **75** (1992) 259–76.
5. Jack, K. H., Review: SiAlONS and related nitrogen ceramics. *J. Mater. Sci.*, **11** (1976) 1135–58.
6. Hampshire, S. Nitride ceramics. In *Materials Science and Technology, Vol. 11, Structure and Properties of Ceramics.* ed. M. Swain, VCH, Weinheim, 1994, pp. 121–71.
7. Hampshire, S. & Jack, K. H., The kinetics of densification and phase transformation of nitrogen ceramics. In *Special Ceramics 7, Proc. Brit. Ceram. Soc.*, eds D. W. Taylor and P. Popper, **31** 1981, pp. 37–49.
8. Liddell, K., X-ray analysis of nitrogen ceramic phases, M.Sc Thesis, University of Newcastle upon Tyne, (1979).
9. Cheng, Y.-B. & Thompson, D. P. Aluminium-containing nitrogen melilite phases. *J. Am. Ceram. Soc.*, **77** (1994) 143–8.
10. Clark, D. R., On the detection of thin intergranular films by electron microscopy. *Ultramicroscopy*, **4** (1979) 33–44.
11. Cao, G. Z., Preparation and characterisation of α'-SiAlON ceramics. PhD Thesis, Eindhoven University of Technology (1991).
12. Wang, H. & Yen, T. S., Gas pressure sintering of Re–SiAlON, to be published in J. Eur. Ceram Soc. 1995.
13. Cheng, Y.-B. & Thompson, D. P., Preparation and grain boundary devitrification of samarium α-SiAlON ceramics. *J. Eur. Ceram. Soc.*, **14** (1994) 13–21.

Journal of the European Ceramic Society 15 (1995) 1229–1234
© 1995 Elsevier Science Limited
Printed in Great Britain. All rights reserved
0955-2219(95)00097-6
0955-2219/95/$9.50

Effect of Acid Treatment on the Formation of SiC Whiskers from Raw Rice Husks

Raghavarapu Venkata Krishnarao & Yashwanta Ramachandra Mahajan

Defence Metallurgical Research Laboratory, Kanchanbagh, Hyderabad–500258, India

(Received 30 January 1995; revised version received 19 May 1995; accepted 22 May 1995)

Abstract

Raw rice husks have been treated by boiling for 1 h in 5 N hydrochloric acid. The washed and dried acid-treated raw rice husks (TRRH) and untreated raw rice husks (RRH) were directly pyrolysed (without precoking) in argon atmosphere at different temperatures between 1050 and 1600°C. Silica obtained from TRRH has a lower level of impurities than that obtained from RRH. Acid treatment has been found to decrease the degree of crystallization of silica and carbon in rice husks. The whisker formation has been decreased in TRRH. As the carbon loss due to the formation of CO was high, the SiC content in the pyrolysed TRRH was higher than that in pyrolysed RRH.

1 Introduction

Silicon carbide (SiC) whiskers, useful in reinforcing light metal alloys and ceramics, are produced by thermal decomposition of rice husks (RHs). Lee and Cutler[1] performed the pioneering work on the formation of SiC from RHs. Later several reports appeared in the literature.[2–16]

A rice husk can be regarded as consisting of SiO_2 embedded in a matrix whose approximate average composition is 51 wt% carbon, 7 wt% hydrogen and 42 wt% oxygen.[6] Rice husks produce a high ash content, varying from 13 to 29 wt% depending on the variety, climate and geographical location. The ash is largely composed of silica (87–97%) with small amounts of alkalis and trace elements.[17] When RHs are converted, these impurities will enter into SiC. In this investigation the raw RHs were treated with hydrochloric acid to decrease the level of impurities. The acid-treated RHs (TRRH) and untreated raw RHs (RRH) were directly pyrolysed without precoking and the formation of SiC was studied.

2 Experimental Procedure

Dry raw RHs, which had been sieved to eliminate residual rice and clay particles, were used in this work. They contain 81·52 wt% of organic material and 18·48 wt% of ash (silica). The RRH were fed into 5 N hydrochloric acid and boiled for 1 h. The treated RHs were thoroughly washed with water and dried in an oven at 90°C. The acid-treated RHs (TRRH) were found to contain 74·64 wt% organic material and 25·36 wt% silica. The silica obtained by burning of organic material from RRH and TRRH was analysed by a Varian model AA-5 atomic absorption spectroscope (AAS).

A 15g sample of RHs was taken in a 2·5 mm thick walled cylindrical graphite container closed with a graphite lid. An ASTRO high temperature furnace, model 1000-3060-FP20 equipped with a Honeywell small target radiation pyrometer, model 939A3 was used for pyrolysis experiments. The RRH and TRRH were subjected to pyrolysis at different temperatures from 1050 to 1600°C for 1 h in an inert atmosphere of Ar at atmospheric pressure. Heating rate employed was $\approx$ 40°C min^{-1}. Argon flow was maintained at 0·1 1 min^{-1}.

The product of pyrolysis was analysed by X-ray diffraction (XRD), scanning electron microscopy (SEM) and chemical analysis. A Philips X-ray diffractometer, model PW1840 with Cu *K* radiation through Ni filter, was used. A scanning electron microscope from International Scientific Instruments, model ISI-100A, was used to study the morphology of SiC. The excess carbon content in the pyrolysed RH was determined by burning at 700°C for 3 h. The unreacted SiO_2 content was estimated by treating the carbon-eliminated sample with HF.

3 Results

SEM micrographs of the outer epidermis of RRH and TRRH are shown in Fig. 1. The part of the

RHs leached out due to acid treatment can be seen in Fig. 1(b). The XRD pattern of TRRH was not much different from that of RRH (Fig. 2(a)).

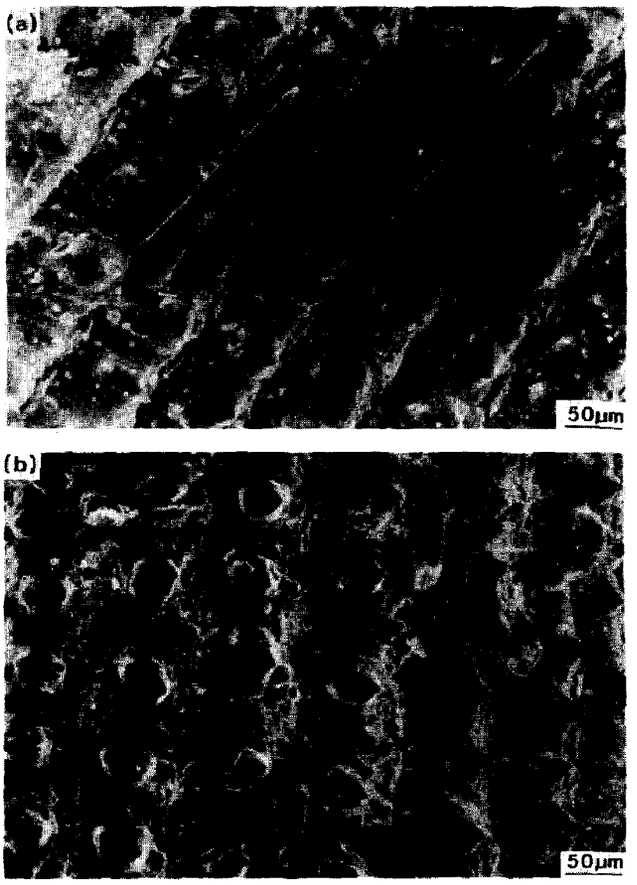


Fig. 1. SEM micrographs of outer epidermis of (a) RRH and (b) TRRH.

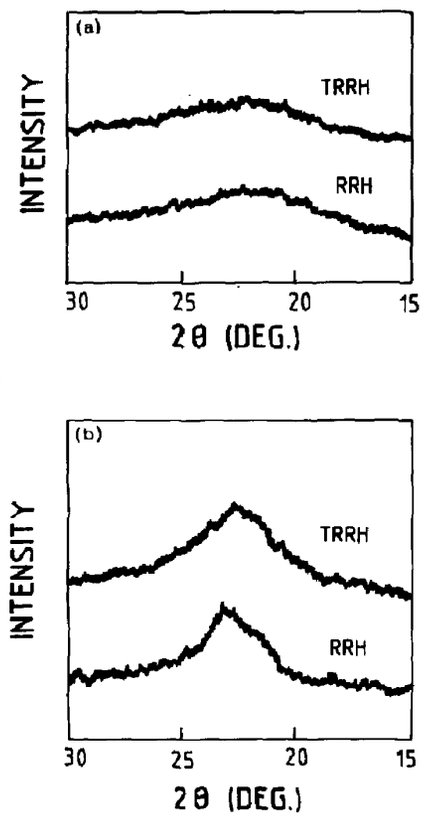


Fig. 2. XRD patterns of (a) RRH and TRRH, (b) silica from RHs.

Similarly, the XRD pattern of silica obtained from TRRH did not show any difference from

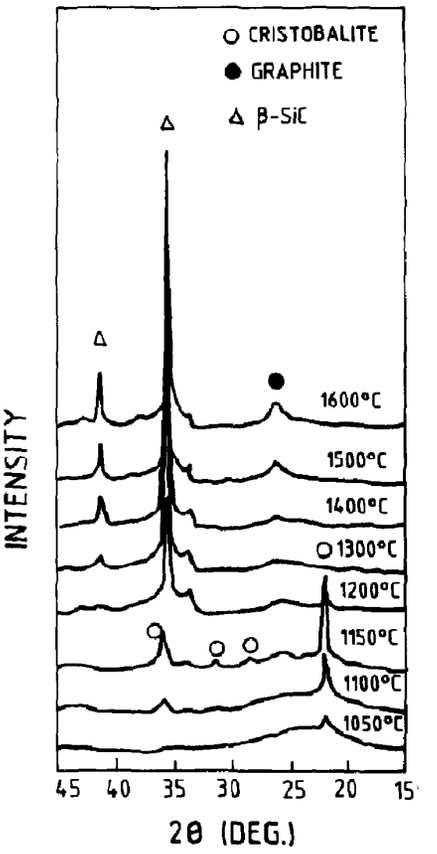


Fig. 3. XRD patterns of pyrolysed RRH samples.

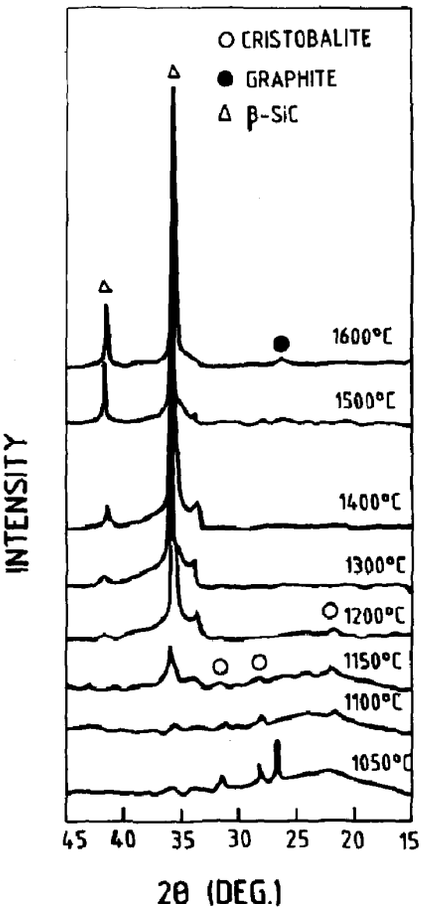


Fig. 4. XRD patterns of pyrolysed TRRH samples.

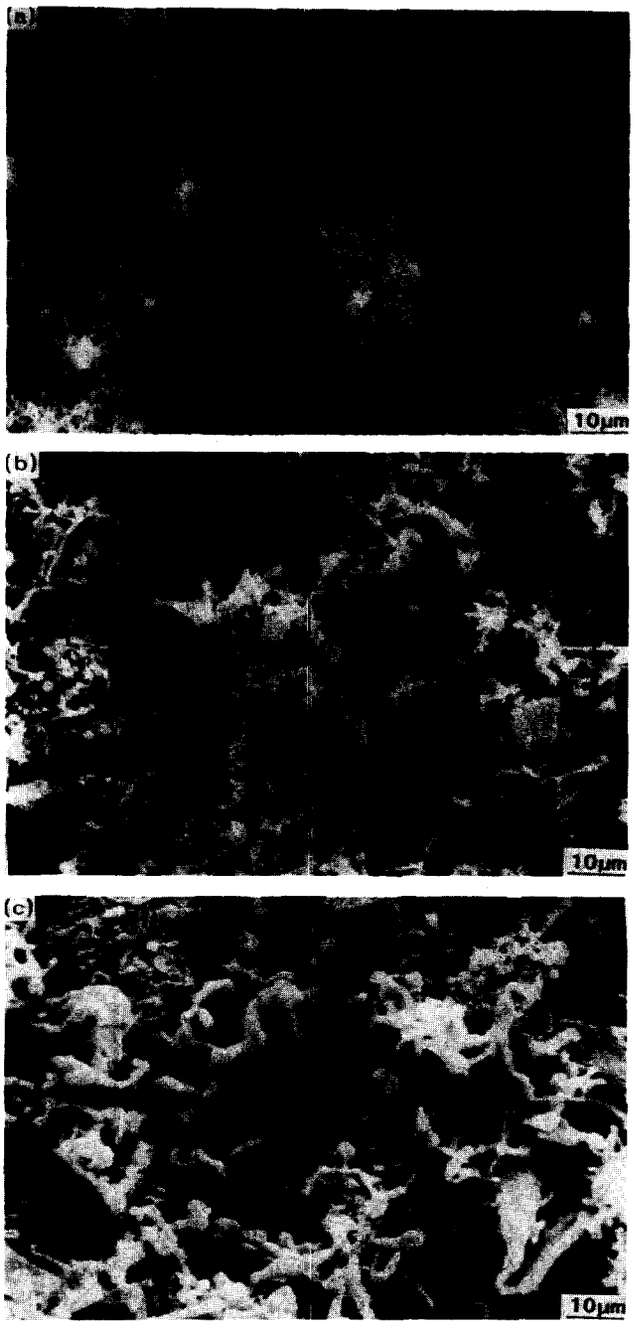


Fig. 5. SEM micrographs of RRH after pyrolysis at (a) 1200°C, (b) 1300°C and (c) 1600°C.

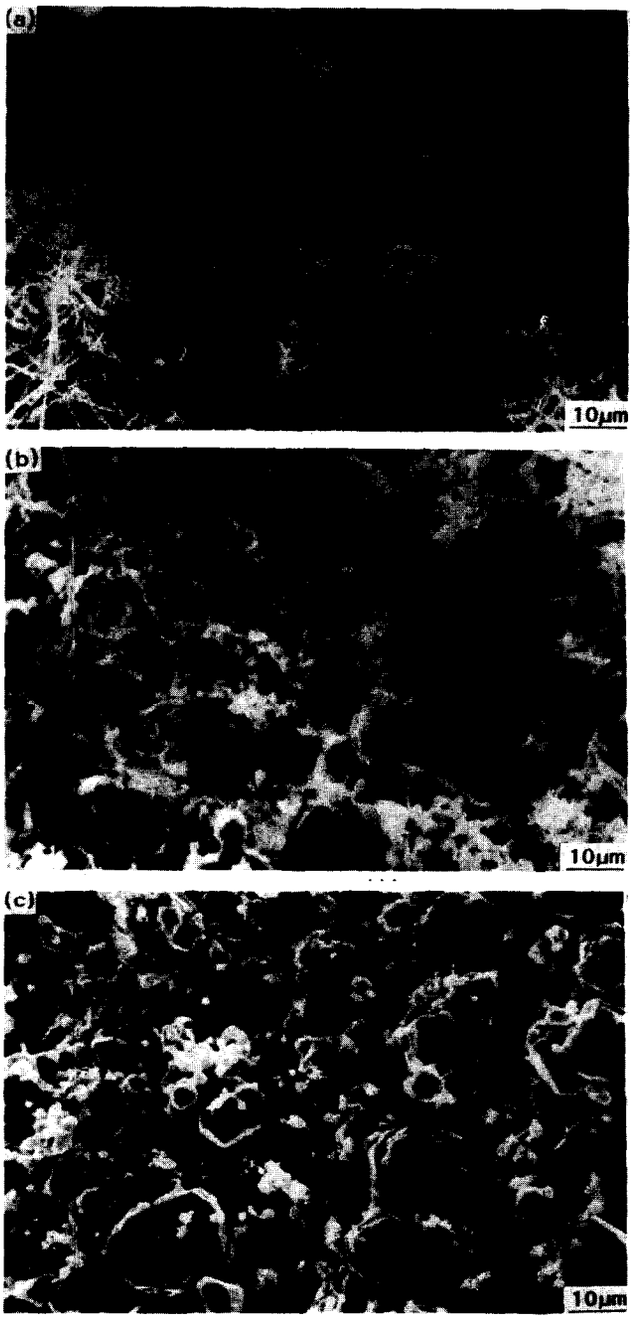


Fig. 6. SEM micrographs of TRRH after pyrolysis at (a) 1200°C, (b) 1500°C and (c) 1600°C.

that of silica obtained from RRH (Fig. 2(b)). The silica from TRRH appeared bright white. An AAS analysis revealed that the level of impurities in RH silica decreased considerably after acid treatment (Table 1).

Table 1. Impurity analysis (in wt%) of RH silica

Element	*Silica from*	
	RRH	*TRRH*
Al	0·50	0·25
Fe	0·60	0·30
Ca	0·44	0·33
Mg	0·41	0·13
Mn	0·069	0·0054
K	1·51	0·054
Na	0·064	0·063

The XRD patterns of pyrolysed RRH samples are shown in Fig. 3. The crystallization of amorphous silica to form cristobalite was the dominant process up to 1150°C. All the peaks of SiC appeared at and above 1300°C. At higher temperatures (1500 and 1600°C), the degree of graphitization of amorphous carbon was rapid. From Fig. 4 it is clear that the degree of crystallization of silica and carbon is negligible in TRRH samples.

Through SEM, the formation of considerable quantities of SiC whiskers has been observed in RRH samples pyrolysed up to 1400°C (Fig. 5). As the temperature of pyrolysis increased, thick and short whiskers formed (Fig. 5(b)). At higher temperatures, the whiskers formed at lower temperatures were converted into particulates

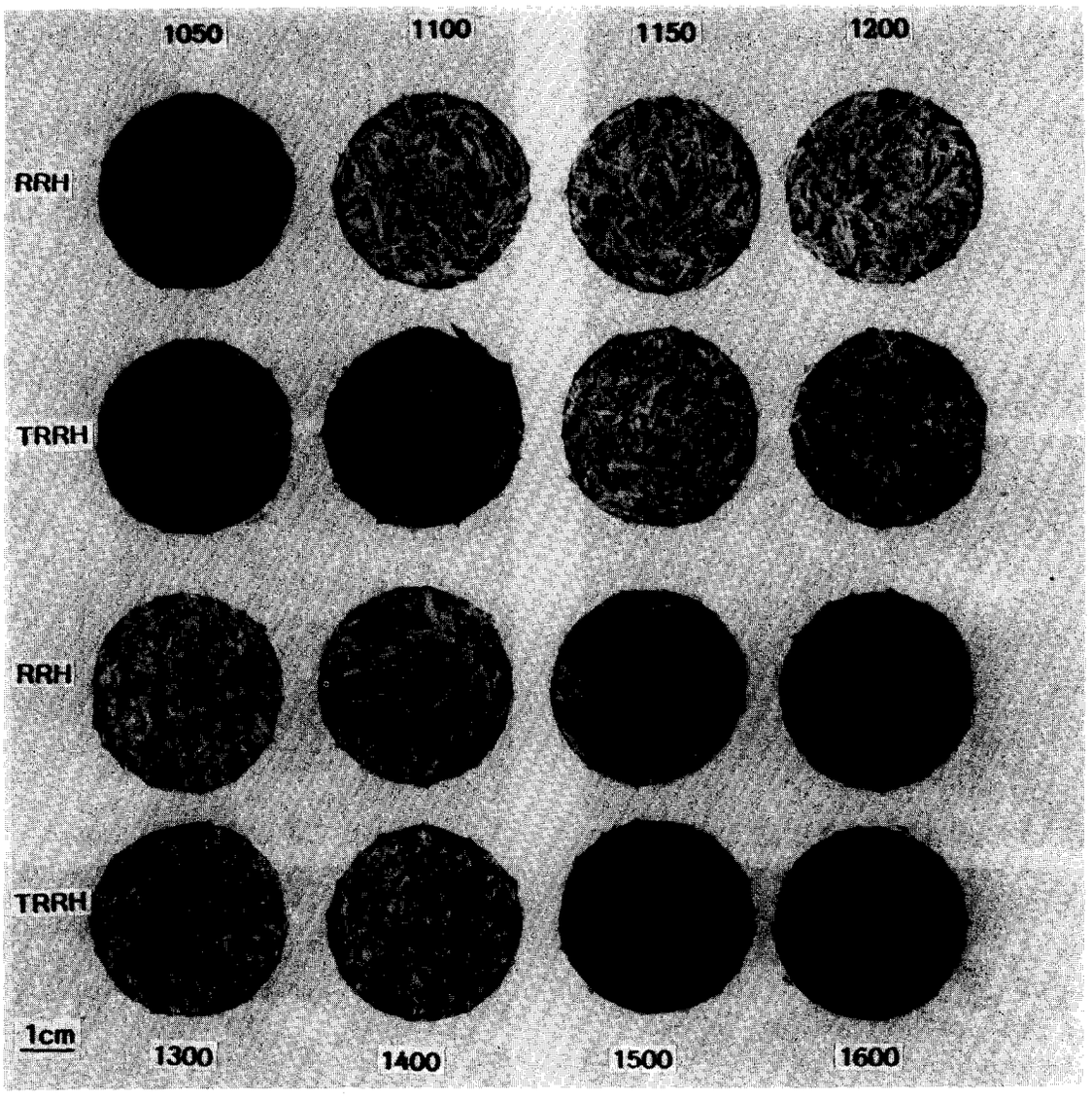


Fig. 7. Optical photograph of rice husks pyrolysed at different temperatures.

(Fig. 5(c)). Similarly in TRRH samples with increase in pyrolysis temperatures, formation of particulates has been observed (Fig. 6). However, the formation of SiC whiskers in TRRH samples was found to be lower than that in RRH samples. After identifying whiskers through SEM, the relative whitish appearance of pyrolysed RHs can be compared for a rough estimation of the percentage of SiC whiskers formed.[11] The appearance of RHs after pyrolysis is shown in Fig. 7. From this optical micrograph one can observe that the whitish deposition on TRRH at any pyrolysis temperature is lower than that on RRH.

The weight % of excess carbon, unreacted SiO_2, and the total SiC in the pyrolysed RHs is shown plotted in Fig. 8. The excess carbon content is very low in TRRH. The unreacted silica was slightly higher in TRRH up to 1150°C. The SiC content in TRRH is slightly low up to 1150°C and much higher above 1200°C. After acid treatment of RHs, as the part of organic matter was leached out, the silica content in TRRH has increased from 18·48 to 25·36%. Assuming that all the SiO_2 in the RHs becomes converted to SiC according to reaction $SiO_2 + 3C + C_{(excess)} \rightarrow SiC + 2CO + C_{(excess)}$, the theoretical values of SiC content and excess carbon in the product of pyrolysis can be calculated.[13] The theoretical values of SiC content in the converted RRH and TRRH are 14·88 and 22·14 wt%, respectively.

Similarly, the theoretical values of excess carbon are 81·52 wt% for RRH, and 77·86 wt% for TRRH. During the carbothermal reduction of silica to form SiC, the carbon loss as CO is generally higher than the theoretical value.[13] From Fig. 8 it is clear that the carbon loss as CO in TRRH is much higher than that in RRH.

4 Discussion

During pyrolysis of RHs at higher temperatures, four processes, i.e. graphitization of carbon, crystallization of amorphous silica, formation of SiC

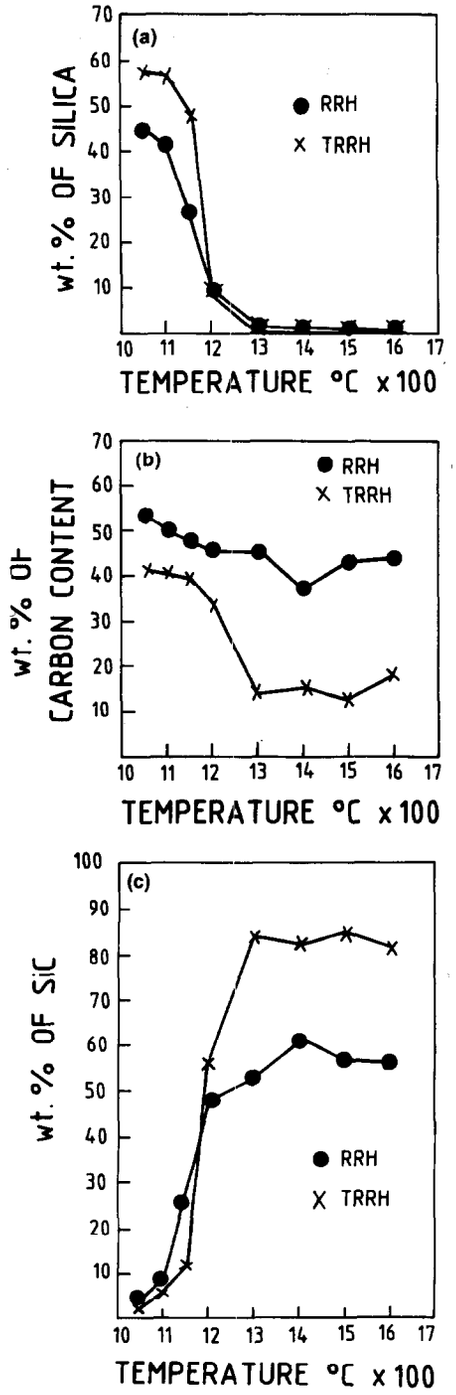


Fig. 8. Plots of (a) residual carbon, (b) unreacted silica and (c) SiC content, all versus pyrolysis temperature.

particles and formation of whiskers, are simultaneously advancing.[11] When RRHs are treated with acid, the cellulose which forms the main body of raw RHs is reduced and the carbohydrate is blackened due to the removal of oxygen. The proteins in the RHs are decomposed into amino acids, and the cellulose of large molecular weight is leached out as smaller molecular weight compounds.[18] The impurities in the RH are substantially removed (Table 1). This results in higher purity of RHs with a porous structure. Potassium (K) in the RH causes surface melting and accelerates the crystallization of amorphous silica to form cristobalite.[19] Due to the porous structure and low level of impurities like K, the crystallization of silica and carbon in TRRH was negligible (Fig. 4).

It is well known that SiC forms at relatively low temperature because of the intimate contact available for carbon and silica in RHs. The reaction between silica and carbon to form SiC can be represented as

$$SiO_2 + C \rightarrow SiO + CO \quad (1)$$

$$SiO + 2C \rightarrow SiC + CO \quad (2)$$

$$SiO_2 + 3C \rightarrow SiC + 2CO \quad (3)$$

Since the TRRH is porous, the intimacy between silica and carbon is disturbed. The quantity of SiC formed in TRRH up to 1150°C was slightly low (Fig. 8). When SiO_2 and carbon are gradually consumed by reaction (1), they no longer remain in contact. Then CO produced by reaction (1) reacts with SiO_2 to form SiO and CO_2 (reaction (4)). The CO_2 then reacts with carbon to form CO (reaction (5)).

$$CO + SiO_2 \rightarrow SiO + CO_2 \quad (4)$$

$$CO_2 + C \rightarrow 2CO \quad (5)$$

Because of porous structure and low degree of crystallization, carbon in TRRH can form a larger quantity of CO. This is evident from the very low quantity of residual carbon in TRRH (Fig. 8). The SiO formed by reaction (1) or (4) can be adsorbed by carbon and form isometric SiC particles. The carbon in TRRH could adsorb a larger quantity of SiO than the carbon in RRH. As the quantity of SiO that could be evolved from TRRH is low, the possibility of whisker formation is low (Fig. 7).

At higher temperatures, due to the rapid deposition of SiO and the high rate of formation of SiC, the whiskers formed at lower temperatures are converted into particulates through a process of coagulative recrystallization. Formation of particulates through coagulative recrystallization of SiC whiskers is observed in both RRH and TRRH (Figs 5 and 6).

The results from this investigation clearly show that under similar conditions of pyrolysis the formation of SiC whiskers is low in TRRH.

5 Conclusions

(i) Relatively pure and bright white silica is formed from acid-treated raw rice husks.
(ii) The degree of crystallization of silica and carbon in pyrolysed TRRH is decreased.
(iii) The formation of SiC whiskers in TRRH is lower than in RRH.

(iv) At pyrolysis temperatures higher than 1300°C the formation of SiC particulates is the dominant process.
(v) Residual carbon content in TRRH is lower than that in RRH.

Acknowledgements

One of the authors wishes to thank Professor M. M. Godkhindi, and Mr Mirdha of the Indian Institute of Technology, Kharagpur, for their help in obtaining XRD patterns. Authors are thankful to the Director, DMRL, Hyderabad, for giving permission to publish this paper.

References

1. Lee, J. G. & Cutler, I. B., Formation of silicon carbide from rice hulls. *Am. Ceram. Soc. Bull.*, **54** (1975) 195–8.
2. Milewski, J. W., Sandstrom, J. & Brown, W. S., Production of silicon carbide from rice hulls. In *Silicon Carbide–1973*. University of South Carolina Press, Columbia, SC, 1974, pp. 634–9.
3. Mansour, N. A. L. & Hanna, S. B., Silicon carbide and nitride from rice hulls. II. Effect of iron on the formation of silicon carbide. *Brit. Ceram. Trans. J.*, **68** (1979) 132–6.
4. Bechtold, B. C., Beatty, R. I. & Cook, J. L., Silicon carbide whiskers from rice hulls — a unique reinforcement. In *Progress in Science and Engineering Composites*, ed. T. Hayashi, K. Kawata & S. Umekawa. ICCM–IV, Tokyo, 1982, pp. 113–20.
5. Lakiza, S. N. & Dyban, Yu. P., Preparation of silicon carbide from rice husks. *Sov. Powder Metall. Metal. Ceram.*, **21** (1982) 117–21.
6. Sharma, N. K., Williams, W. S. & Zangvil, A., Formation and structure of silicon carbide whiskers from rice hulls. *J. Am. Ceram. Soc.*, **67** (1984) 715–20.
7. Martinell, J. R. & Helena, A. B., Influence of processing variables during rice hull pyrolysis on the formation of SiC whiskers. *Ceramicia (Sao Paulo)*, **35** (1989) 162–4.
8. Patel, M. & Kareera, A., SiC whiskers from rice husk: role of catalysts. *J. Mater. Sci. Lett.*, **8** (1989) 955–6.
9. Krishnarao, R. V. & Godkhindi, M. M., Distribution of silica in rice husk and its effect on the formation of silicon carbide. *Ceram. Int.*, **18** (1992) 243–9.
10. Ray, A. K, Mahanty, G. & Ghose, A., Effect of catalysts and temperature on silicon carbide whiskers formation from rice husk. *J. Mater. Sci. Lett.*, **10** (1991) 227–9.
11. Krishnarao, R. V., Godkhindi, M. M., Chakraborty, M. & Mukunda, P. G., Direct pyrolysis of raw rice husks for maximization of SiC whisker formation. *J. Am. Ceram. Soc.*, **74** (1991) 2869–75.
12. Krishnarao, R. V. & Godkhindi, M. M., Maximization of SiC whisker yield during the pyrolysis of burnt rice husks. *J. Mater Sci.*, **27** (1992) 1227–35.
13. Krishnarao, R. V. & Godkhindi, M.M., Studies on the formation of SiC whiskers from pulverized rice husk ashes. *Ceram. Int.*, **18** (1992) 35–42.
14. Krishnarao, R. V., Formation of SiC whiskers from rice husk silica–carbon black mixture: effect of preheat treatment. *J. Mater. Sci. Lett.*, **12** (1993) 1268–71.
15. Krishnarao, R. V., Effect of cobalt chloride treatment on the formation of SiC from burnt rice husks. *J. Eur. Ceram. Soc.*, **12** (1993) 395–401.
16. Krishnarao, R. V., Godkhindi, M. M., Chakraborty, M. & Mukunda, P.G., Formation of SiC whiskers from compacts of raw rice husks. *J. Mater. Sci.*, **29** (1994) 2741–4.
17. Houstan, D. F., Rice hulls. In *Rice Chemistry and Technology*. Am. Assoc. Cereal. Chemists., St. Paul, MN, 1972, pp. 301–52.
18. Tanaka, M., Niwano, K. & Kitano, Y., Production of Si_3N_4 and SiC whiskers. UK Patent GB 2 168 333 A, 18 June 1986.
19. Nakata, Y., Suzuki, M. & Okutami, T., Preparation and properties of SiO_2 from rice hulls. *Nippon Seramikkusu Kyokai Gakujutsu Ronbunshi*, **97** (1989) 842–9 (in Japanese).

Journal of the European Ceramic Society 15 (1995) 1235–1247
Elsevier Science Limited
Printed in Great Britain.
0955-2219/95/$9.50
0955-2219(95)00098-2

The Complexity of the Matrix Microstructure in SiC-Fiber-reinforced Glass Ceramic Composites

Franck Doreau, Hélène Maupas, Dominique Kervadec, Pierre Ruterana, Jean Vicens & Jean-Louis Chermant

LERMAT, URA CNRS n°. 1317, ISMRA, 6 Bd du Maréchal Juin, 14050 Caen Cedex, France

(Received 1 December 1994; accepted 25 May 1995)

Abstract

In this paper a critical examination of the diagrams of different silicate systems is presented: LAS, MAS YAS, MLAS and YMAS (A: alumina; L: lithia; M: magnesia; S: silica; Y: yttria). These systems have been developed to fabricate ceramic matrix composites based on a glass ceramic matrix, because of their low thermal expansion coefficient and good mechanical properties up to 1000°C. The observations and microanalyses, by transmission electron microscopy, of different batches of MLAS and YMAS confirm the complexity of the systems investigated.

Introduction

The new class of materials known as ceramic matrix composites (CMCs) is concerned with a ceramic matrix reinforced either by ceramic fibers, whiskers or particles. But the matrix could be (i) a monolithic ceramic — such as SiC, Al_2O_3, Si_3N_4... — or (ii) a glass ceramic. The first ones are prepared for CMC materials from the ceramic routes, that is to say sintering or chemical vapour infiltration (CVI) processes, and the second ones result from the glass route which is easier and needs a lower process temperature. Nevertheless the domain of applications of glass ceramic matrices is lower than for ceramic matrices — the 1000°C domain —, but is of interest for specific applications in parts for motor aerospace and aircraft engines due to their strength and low densities (~2·5).

The scope of this paper is to present and to comment upon the complexity of several glass ceramic matrices which occur due to the crystallographic characteristics of many silicate phases which can arise in a very narrow domain of temperatures and, moreover, which can also lead to allotropic transformations and/or ionic substitutions in the same temperature domain.

Due to the fact that the lithium aluminum silicate (LAS) system has crystalline phases with a very low thermal expansion coefficient, and because these phases can appear in a very controlled way, this system is one that is investigated most to fabricate CMCs. But we shall see that such a system is in fact extremely complex. To fabricate CMCs with SiC Nicalon fibers and a glass ceramic matrix, several requirements are necessary: the glass ceramic must be chemically compatible with the SiC fibers (or alumina fibers) in order to avoid a resultant fibers degradation. Moreover the matrix and fibers must have an elastic modulus different enough and a thermal expansion coefficient low enough to have a reinforced material which is not damaged during the process. Finally such materials have to involve a correct pull-out process to exhibit a good mechanical strength. The LAS system is the most suitable but there are other systems which also seem promising, but with some advantages and disadvantages:[1] CAS, MAS, YAS,... for ternary systems, or BMAS, MLAS, YMAS,... for quartenary systems. Among these different systems, we shall discuss the LAS, MAS, YAS, MLAS and YMAS systems.

The LAS, MAS and MLAS Systems

The Li_2O–Al_2O_3–SiO_2 system gives a wide range of compositions with the thermal expansion coefficient ranging from 0 to about 120 $10^{-7}°C^{-1}$.[2] These materials have a very good thermal shock resistance and consequently they are used either for cooker panels, saucepans, or for specific optical devices for space applications such as blanks for laser gyroscopes or for X-ray telescopes.[3] But this thermal expansion coefficient is considerably affected by the existence of some crystalline phases: for example, if the alumina content is low, the materials present a higher thermal expansion coefficient, while if its content is high, the result is a material with a zero thermal expansion value.

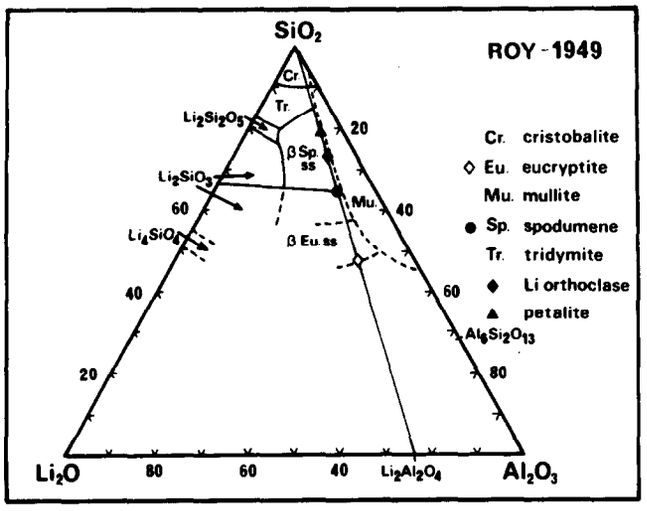


Fig. 1. Ternary diagram of phase equilibria of the Li_2O–Al_2O_3–SiO_2 system (LAS)[4]

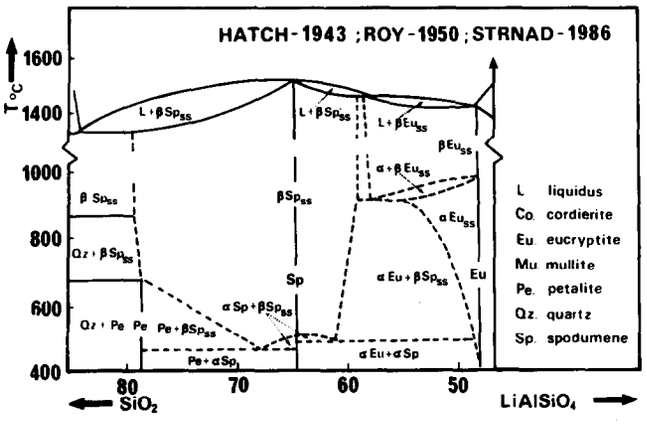


Fig. 2. Pseudo binary diagram of phase equilibria of the eucryptite–silica (Li_2O–Al_2O_3–$2SiO_2$–SiO_2) system.[4,5,7]

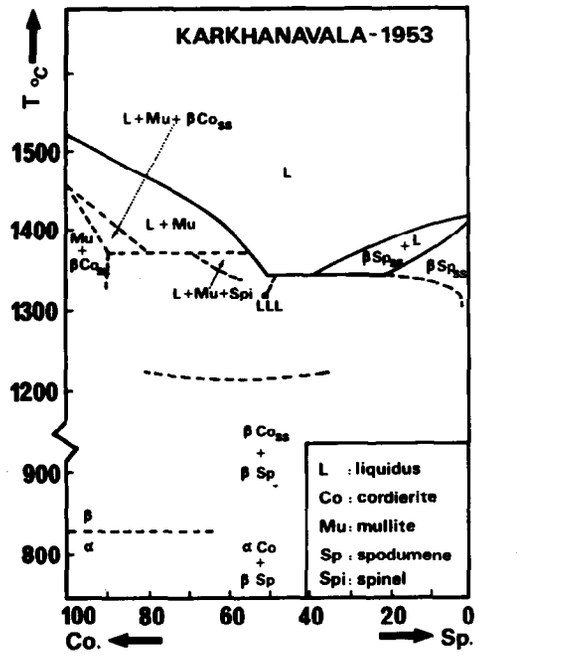


Fig. 3. Pseudo binary diagram of phase equilibria of the cordierite–spodumene (Co–Sp) ($2MgO$–$2Al_2O_3$–$5SiO_2$–Li_2O–Al_2O_3–$4SiO_2$) system (LLL: low limit of liquidus) after using the new nomenclature for α and β cordierite.[8]

There are no recent phase diagrams concerning the Li_2O–Al_2O_3–SiO_2 ternary system. The diagram proposed by Roy and Osborn in 1949[4] and by Roy *et al.* in 1950[5] is still used (Fig. 1). In this diagram we can see the presence of many different silicate phases such as β eucryptite, lithium orthoclase, mullite, petalite, β spodumene and tridymite.

Also useful are the pseudo binary diagrams eucryptite–silica which has also been reported by Hatch,[6] Roy *et. al.*[5] and slightly modified by Strnad in 1986 [7] (Fig. 2), and the pseudo binary diagram, cordierite–spodumene, proposed by Karkhanavala and Hummel,[8] (Fig. 3). For the latter diagram, we have used the new nomenclature for α cordierite (pseudo-hexagonal orthorhombic or low cordierite) and β cordierite (hexagonal or high cordierite).[9] Table 1 shows the crystallographic characteristics of some silicate phases which could appear in different M–M'–Si–O systems.[10]

From these three diagrams, the information from the works of Roy *et. al.*[4,5] and Karkhanavala and Hummel[8] concerning the eucryptite, spodumene, petalite and cordierite phases, and the eucryptite–silica and cordierite–spodumene pseudo binary systems, one can say:

Eucryptite: Li_2O–Al_2O_3–$2SiO_2$

— α eucryptite inverts into the high temperature form, β eucryptite, at 972 ±10°C during an incongruent melting;
— α eucryptite is rhombohedric, with the aluminum atoms in 6 coordination;
— it has been shown by Winkler[11] and also by Roy *et. al.*[5] that the structure of the β eucryptite is the same as that of the high temperature quartz, where the aluminum atoms are in the $A10_4$-tetrahedra.

Spodumene: Li_2O–Al_2O_3–$4SiO_2$

— the spodumene corresponds to the one found in the nature and to the high temperature form called β spodumene;
— the α form inverts in the β high temperature form at a maximum temperature of 500°C;
— it is a monoclinic pyroxene, with a tetragonal type structure.

Petalite: Li_2O–Al_2O_3–$8SiO_2$

— petalite is decomposed congruently to a β spodumene solid solution at 680± 10°C.

Cordierite: $2MgO$–$2Al_2O_3$–$5SiO_2$

— cordierite can appear in three crystallographic forms:[9]

(i) two low temperature forms, the stable low temperature α cordierite, which inverts reversibly to the high temperature β form at

Table 1. Crystallographic characteristics of different silicate phases which can appear in M–M'–Si–O systems

Name	*Formula*	*Crystallographic structure*	*Lattice parameters*					
			a Å	*b* Å	*c* Å	α	β	γ
Kyanite	Al_2SiO_5 Al_2O_3,SiO_2	Triclinic	7·112	7·844	5·574	90·09	101·11	105·99
Sillimanite	Al_2SiO_5 Al_2O_3,SiO_2	Orthorhombic	7·49	7·67	5·77	—	—	—
Mullite	$Al_6Si_2O_{13}$ $3Al_2O_3,2SiO_2$	Orthorhombic	7·546	7·690	2·884	—	—	—
Enstatite	$MgSiO_3$ MgO,SiO_2	Orthorhombic	18·23	8·84	5·19—	—	—	—
Protoenstatite	$MgSiO_3$ MgO,SiO_2	Orthorhombic	9·25	8·74	5·32—	—	—	—
Clinoenstatite	$MgSiO_3$ MgO,SiO_2	Triclinic	10·00	8·934	5·17	88 27	70 03	91 09'
Forsterite or Olivine	Mg_2SiO_4 $2MgO,SiO_2$	Orthorhombic	4·756	10·195	5·981	—	—	—
α Yttrium silicate	$Y_2Si_2O_7$ $Y_2O_3,2SiO_2$	Triclinic	6·59	6·64	12·25	94°00	89°20	93°10'
β Yttrium silicate or Keivite	$Y_2Si_2O_7$ $Y_2O_3,2SiO_2$	Monoclinic	6·875	8·970	4·721	—	101°74	—
Spinel	$MgAl_2O_4$ MgO,Al_2O_3	Cubic	8·0831	8·0831	8·0831	—	—	—
α Cordierite	$Mg_2Al_4Si_5O_{18}$ $2MgO,2Al_2O_3,5SiO_2$	Orthorhombic	9·721	17·062	9·339	—	—	—
β Cordierite or Indialite	$Mg_2Al_4Si_5O_{18}$ $2MgO,2Al_2O_3,5SiO_2$	Hexagonal	9·770	—	9·352	—	—	—
Sapphirine	$Mg_2Al_4SiO_{10}$ $2MgO,2Al_2O_3,SiO_2$	Monoclinic	9·94	14·40	9·79	—	110°50	—
α Eucryptite	$LiAlSiO_4$ $Li_2O,Al_2O_3,2SiO_2$	Hexagonal	13·48	—	9·001—	—	—	—
β Eucryptite	$LiAlSiO_4$ $Li_2O,Al_2O_3,2SiO_2$	Monoclinic	5·251	5·259	11·162	—	—	119°83
α Spodumene	$LiAlSi_2O_6$ $Li_2O,Al_2O_3,4SiO_2$	Monoclinic	9·52	8·32	5·25	—	111°20	—
β Spodumene	$LiAlSi_2O_6$ $Li_2O,Al_2O_3,4SiO_2$	Tetragonal	7·538	—	9·156	—	—	—
Lithium orthoclase	$LiAlSi_3O_8$ $Li_2O,Al_2O_3,6SiO_2$	Orthorhombic	18·24	10·54	10·57	—	—	—
Petalite	$LiAlSi_4O_{10}$ $Li_2O,Al_2O_3,8SiO_2$	Monoclinic	15·18	5·139	11·75	—	112°38	—
Lithium magnesium silicate	Li_2MgSiO_4 Li_2O,MgO,SiO_2	Orthorhombic	6·32	10·66	4·99	—	—	—

830°C under hydrothermal conditions, and the metastable μ cordierite which is produced by the glass crystallization in air at about 850°C;

(ii) one high temperature form which can be produced by heating the material or by crystallizing the glass at temperatures between 1000 and 1400°C; at 1460°C the material is decomposed into mullite and liquid, with a complete melting at 1530°C.

Eucryptite–silica

— from these diagrams and the authors' comments,[5] there exists the possibility that a complete series of solid solutions occur between β eucryptite and β spodumene at high temperature;

— crystals of α spodumene are formed in the 375–500°C range;

— spodumene is stable only until 500± 15°C;

— petalite is found to invert completely to β spodumene at about 700°C.

Cordierite–spodumene

— the pseudo binary system cordierite–spodumene[8] is also of interest;

— it shows that α cordierite, α cordierite solid solution, β cordierite, β spodumene, β spodumene solid solution (which is partially metastable) are identified phases, but with also the presence of corundum, mullite and spinel;

— the spinel phase could probably be a solid solution of Li and Mg spinels.

The MAS ($MgO–Al_2O_3–SiO_2$) system was originally investigated by several authors, Rankin and Merwin in 1918, modified by Bowen and Greig in 1924 and Greig in 1927 and was reported by Prokopowicz and Hummel in 1956.[12] Some details have been more recently reported by Osborn and Muan,[13] Jouenne[14] and Partridge *et. al.*[2] (Fig. 4). There is little information regarding the MLAS

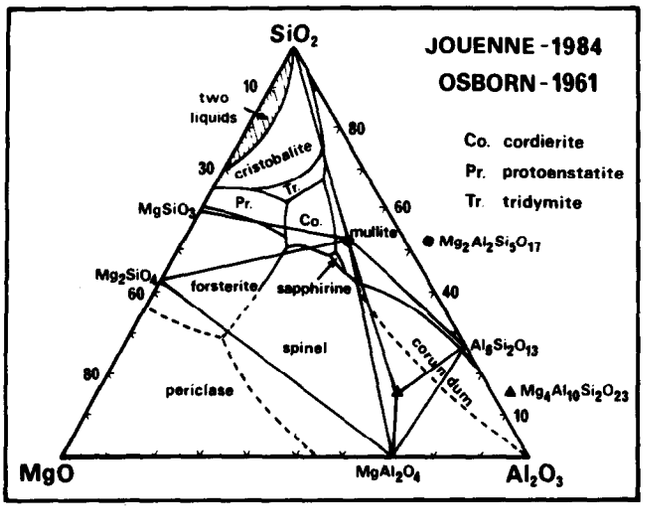


Fig. 4. Ternary diagram of phase equilibria of the $MgO–Al_2O_3–SiO_2$ system (MAS).[13]

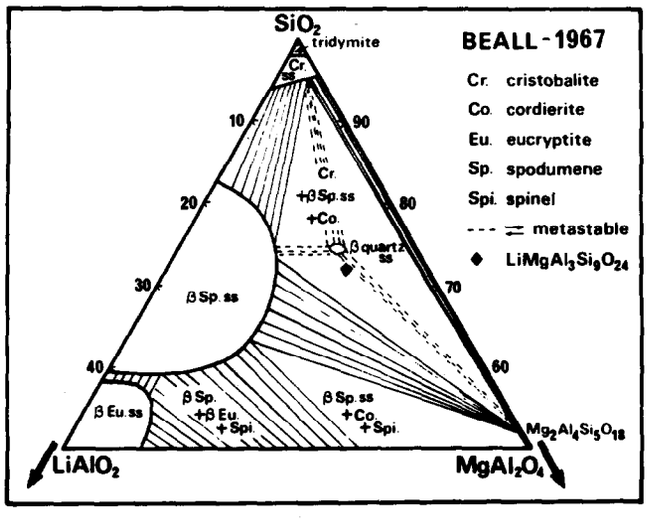


Fig. 5. Isothermal section at 1230°C for the pseudo ternary diagram of the $SiO_2–LiAlO_2–MgAl_2O_4$ system (MLAS).[15]

($MgO–Li_2O–Al_2O_3–SiO_2$) system,[12,15,16] (Fig. 5). It is based on cordierite ($2MgO–2Al_2O_3–5SiO_2$) and protoenstatite (or clinoenstatite (another allotropic form) according to different authors) ($MgO–SiO_2$), with other crystal phases: cristobalite (SiO_2), forsterite ($2MgO–SiO_2$), mullite ($3Al_2O_3–2SiO_2$) and spinel ($MgO–Al_2O_3$), and with the nucleating agents for cordierite based materials: TiO_2 or a combination of $TiO_2–ZrO_2$. As for LAS, it was found by Barry *et. al.*[17] that following the formation of the nucleating phase (a magnesium aluminosilicate structurally similar to the petalite), a number of intermediate phases appears prior to the development of the cordierite at about 1150–1250°C.

At high temperatures the relationships between spodumene and cordierite are very complex and involve also corundum, mullite and spinel, while at low temperatures, there exists a complete series of metastable solid solutions between μ cordierite and β spodumene.

In Ref. 18 details on the preparation of MLAS glass ceramic materials from a glass powder are given either by a traditional route (melting, nucleation and crystallization) or by simultaneous sintering and crystallization. The last method is largely cost-saving as it reduces the time at the fabrication temperature due to the difference in the viscosity. The interest of such a system (MLAS) is the ability to adjust the properties such as the thermal expansion coefficient, softening temperature, viscosity or the dielectric constant according to the chemical composition. Moreover it has been proved that the addition of MgO to $Li_2O–Al_2O_3–SiO_2$ glasses modifies the nonbridging oxygen, and consequently affects the bond strength, with a direct consequence on the glass transition temperature (T_g) of the MLAS.[19]

In the two pseudo ternary systems LAS and MAS, there exists equivalent crystallographic phases where cations can be located in a position of insertion. So it could be possible to combine the low values of the thermal expansion coefficient of LAS with the excellent mechanical properties of MAS. From the pseudo binary diagram,[8] there is effectively a large domain where there are both β spodumene solid solution and β cordierite. Moreover due to the similar sizes of Li^+ (0·68 Å) and Mg^{2+} (0·78 Å) there is a possible substitution which reinforces the glass ceramic phase.[15,20] Recently it has been shown that, in the presence of boron, there is also a substitution of boron for aluminum in the β eucryptite structure.[21]

The YAS and YMAS Systems

Systems based on Y_2O_3 are interesting because of

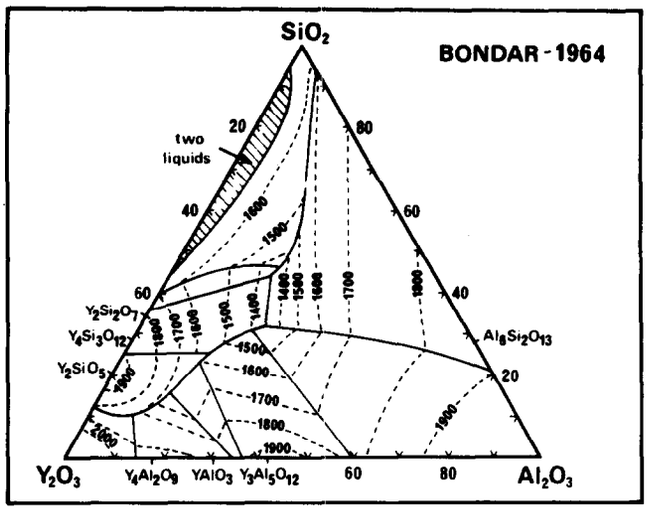


Fig. 6. Isothermal sections for the ternary diagram of the Y_2O_3–Al_2O_3–SiO_2 system (YAS).[24]

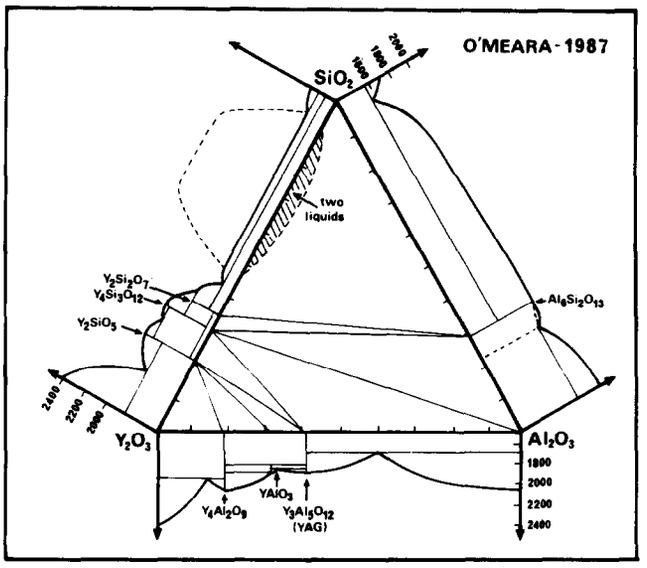


Fig. 7. Ternary and binary diagrams of phase equilibria of the Y_2O_3–Al_2O_3–SiO_2 system (YAS).[22]

its refractory nature and its oxidation resistance. Although the Y_2O_3–Al_2O_3–SiO_2 (YAS) system is extremely important for the understanding of sialons and β Si_3N_4 based ceramics containing Al_2O_3 and Y_2O_3 as sintering additives,[22] there is little information on this phase diagram. One can also note that this system was also investigated to develop YAS glass microspheres for radiotherapeutic applications (the ^{90}Y isotope being activated *in situ* by neutron bombardement, while Al, Si and O are not affected).[23]

Bondar and Galakov proposed a ternary diagram in 1964,[24] (Fig. 6), which was reinvestigated more recently by O'Meara *et al.* in 1987,[22] (Fig. 7). The crystalline identified phases are mainly yttrium disilicate (Y_2O_3–$2SiO_2$) under the two forms α and β (α being the main crystalline product), YAG ($3Y_2O_3$,$5Al_2O_3$) and mullite ($3Al_2O_3$,$2SiO_2$). However, Y_2O_3, Al_2O_3, and some other phases are unidentifiable using classical X-ray tables.

The YAS system has been investigated, more recently.[23] Ten glasses were fabricated at $T<1800$°C, each one corresponding to a specific composition. Among them only one gave a partially crystallized material. These authors were able to give some information and comments on the ternary diagram. As for the LAS system, the thermal expansion coefficient varies significantly with increasing the Y_2O_3 content, while it decreases as SiO_2 is added.[1] One of these compositions was also investigated later by other authors.[1] Their attention was focused on the fact that for the four polymorphic transformations of the $Y_2Si_2O_7$ phase, three different temperatures are reported for each transformation according to three different authors, (Table 2).[25–27] Moreover they found that the triclinic α form inverts in the β monoclinic form at 1285°C. In order to obtain good mechanical behaviour they proposed to sinter these materials above 1300°C to induce β $Y_2Si_2O_7$, otherwise brittle fracture behaviour will occur, which is an undesirable effect for CMC applications[1] as there is a change in the atomic volume associated with the allotropic transformations.[28]

Due to the fact that the distribution of the

Table 2. Yttrium pyrosilicate polymorphic characteristics[1,28]

Transition (volume change)	*Temperature of transition °C*	*Reversibility*	*References*
$\alpha \rightarrow \beta$			
triclinic monoclinic	1190 ± 50	No	Felsche, 1970[26]
(+6·233%)	1225 ± 10	No	Ito & Johnson, 1968[25]
	1225	Yes	Liddell & Thompson, 1986[27]
$\beta \rightarrow \gamma$	1350 ± 30	No	Felsche, 1970[26]
monoclinic monoclinic	1445 ± 10	No	Ito & Johnson, 1968[25]
(–0·198%)	1445	Yes	Liddell & Thompson, 1986[27]
$\gamma \rightarrow \delta$	1580 ± 30	Yes	Felsche, 1970[26]
monoclinic orthorhombic	1535 ± 10	Yes	Ito & Johnson, 1968[25]
(–1·733%)	1535	Yes	Liddell, Thompson, 1986[27]
($\beta \rightarrow \delta$:–1·984%)			

$Y_2Si_2O_7$ particles in these glasses is sufficiently uniform and dilute, Arita *et al.*[29] have recently investigated the nucleation and crystallization of different glass compositions in the system Y_2O_3–Al_2O_3–SiO_2. They found that it is very sensitive to the initial composition of the glass, that Al_2O_3 enhances the sinterability of such a system, and that some specific heat treatment allows us to crystallize all or part of the amorphous phase: that may result in improving their mechanical behaviour and particularly their creep resistance, and will be useful to know for further investigations.

There is no published quaternary diagram on the YMAS system. To our knowledge the only information on the two ternary MAS and YAS systems comes from Refs 30 and 31. Regarding the process and the relationships between the process and crystallographic phases appearing, one can make the following points.

In these materials there are mainly α $Y_2Si_2O_7$, cordierite ($2MgO$–$2Al_2O_3$–$5SiO_2$), and some spinel crystals. Up to 1200°C, the cordierite and α yttrium silicate ratios evolve very slightly, while for a temperature greater than 1230°C, the ratio of α $Y_2Si_2O_7$ decreases significantly while the β $Y_2Si_2O_7$ phase appears; this also corresponds to a decrease in the density (4·30 → 4·03).[25] If there is the presence of yttria, then the low temperature cordierite crystallizes. If the sintering temperature is well chosen (> 1200°C) and the heating rate fast enough to have a short treatment period at $T > 1200$°C to avoid the crystallization of the β $Y_2Si_2O_7$ phase, then the densification is complete within few minutes. So such materials must be fabricated in compromised conditions: at a temperature not too high, but high enough to have a good microstructure and a density not too far from the theorical one. As it has been shown in Ref. 1, in the case of the SiC–YAS composites, the rupture of SiC_f–YMAS also becomes less catastrophic with some pull-out if the temperature process is higher than 1250°C.

Materials and Techniques

Materials investigated in this paper were experimental CMCs with glass ceramic matrices reinforced with Nicalon NLM 202 SiC fibers (Nippon Carbon, Japan). Two types were studied.

SiC_f–MLAS composites were CMCs developed by Aérospatiale (Etablissement de Bordeaux France). The matrix was produced by a chemical sol–gel route. After drying the slurry of a $0{\cdot}5MgO$–$0{\cdot}5Li_2O_3$–$Al_2O_3 4SiO_2$ initial composition which impregnated SiC bundles, tapes are formed, stacked and then densified in a hot press under pressure, in the 1200–1300°C domain.[16,32] Two temperatures were used, T_1) and T_2 ($T_2 > T_1$). The phase crystallization is in fact obtained in controlling the pressing temperature (T_1 or T_2) as well as the cooling rates. The stability of the matrix depends upon the crystalline nature of the matrix phases. In the presence of the β eucryptite solid solution, the stability is limited to 1050°C in the MLAS system (and only to 950°C in the LAS system), (see for example Figs 1 and 5). Above this temperature there is the β eucryptite → β spodumene transformation which modifies the thermomechanical equilibria as the thermal expansion coefficients α are different. Then the new composite possesses new properties (α, σ_r, ...)[32] As-received materials were plates 120 × 100 × 3 mm^3 with either a 1D texture or a $(0–90°)_{ns}$ cross–ply texture, with n = 2 or 3 and *s* meaning for symmetry (Fig. 8(a)).

SiC_r–YMAS composites were fabricated by ONERA (Etablissement de Palaiseau, France) either by a chemical route from organometallic salts and a colloidal sol, or by a glassy route from oxide melting. The initial chemical compositions were always a mixture of oxides: Y_2O_3–MgO–Al_2O_3–SiO_2. Two composites were particularly investigated: Composite A for which the binder burnout is realized in a specific furnace at 700°C under air, while for Composite B it occurs during the hot pressing cycle at 500°C under vacuum.

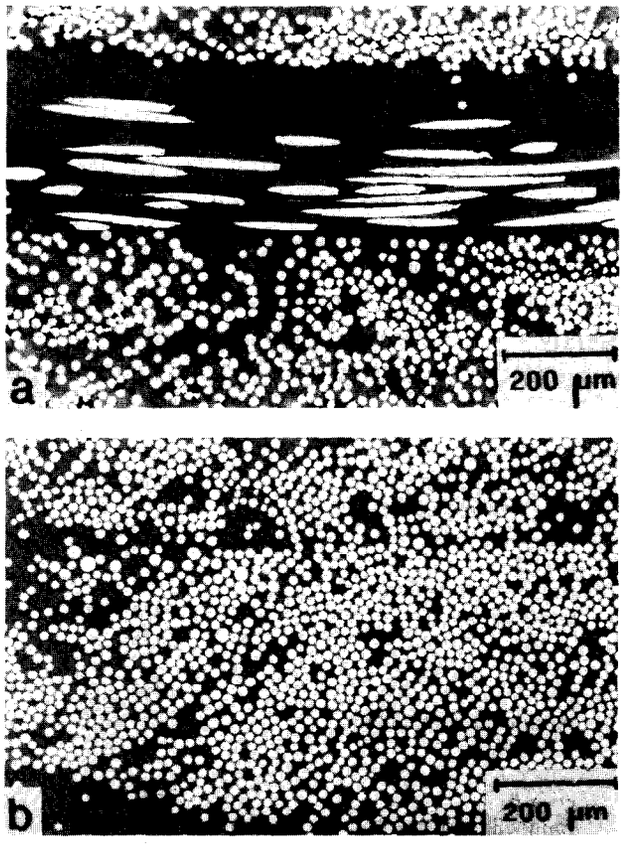


Fig. 8. Optical micrographs of the 2D SiC_f–MLAS (a) and of the 1D SiC_f–YLAS (b) composites.

Composite A is pressed under 10 MPa from 1000°C until 1300°C for 1 hr and then ceramised at 1200°C. Composite B, preloaded under 2 MPa from 500°C, is heated under vacuum until 500°C and pressed under 10 MPa when the maximum temperature, is reached (about 1300°C), and then ceramised at about 1200°C as for Composite A, the vacuum being maintained only until 700°C. Composites A are densified to 98% of the theoretical density and composites B up to the theoretical density. As-received materials were plates 100 × 100 × 3·5 mm^3 with a 1D texture (Fig. 8(b)).

All the specimens were cut with great care and very slowly using diamond wheels: either plates for rupture and creep experiments, or small samples inserted into cylinders of 3 or 2·7 mm in diameter and then cut. These last specimens were mechanically ground up to 50–100 μm, a dimpler was used to thin them up to about 10 μm and finally ion milled under argon (6 kV) at liquid nitrogen temperature (Gatan Duo Mill, Pleasanton, USA).

Microstructural investigations were performed: (i) by X-ray analysis; (ii) by transmission electron microscopy with a Jeol 200 CX and with a Topcon EM 002B: these two TEM operating at 200 kV, were equipped with a Kevex EDS microanalyser and were used to perform TEM, HREM and microanalysis studies; (iii) by scanning electron microsocopy with a Jeol 840 GLS with a Tracor 5200 EDS system, and a Zeiss DSM 60 with a Kevex system and (iv) by an electronprobe analyzer Jeol 6300 F.

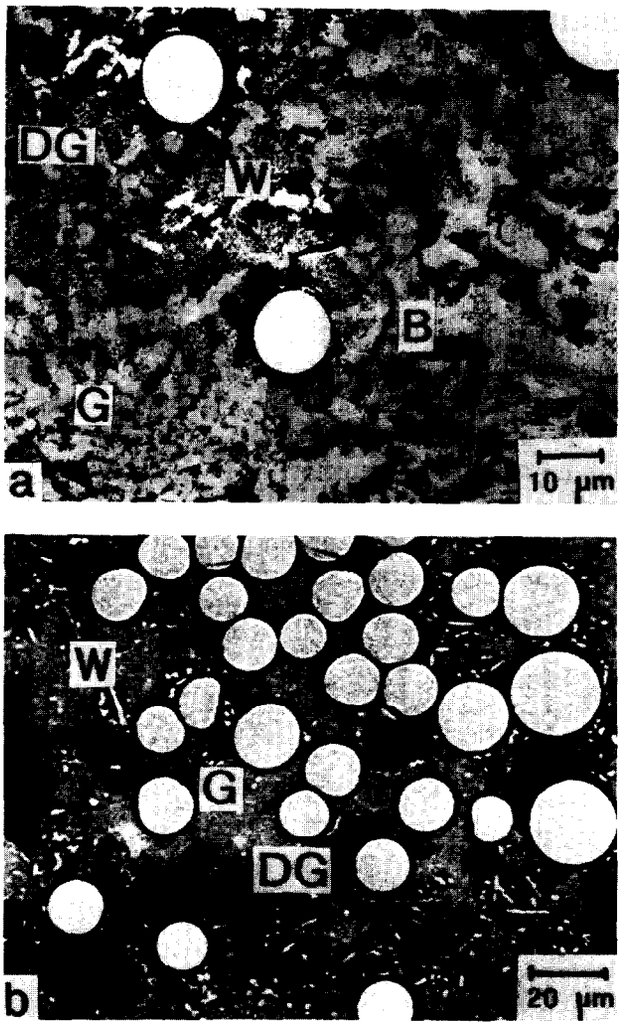


Fig. 9. Scanning electron micrographs of the MLAS matrices of the 1D (a) and 2D (b) composites (W = white: mullite, G = grey: cordierite, DG = dark grey: spodumene, B = black: carbon).

Results

Because of their very fine microstructure the composites have been investigated by scanning and transmission electron microscopies with microanalysis. The identification of the different present phases was confirmed regularly by X-ray analysis, EDS spectra and from the diffraction patterns.

SiC_f–MLAS

Although the 1D and 2D SiC_f–MLAS composites were elaborated in similar conditions, the as-received materials themselves differ, by several points. From observations and images of the MLAS matrix by scanning electron microscopy, it appears for the 2D materials white (W), grey (G) and dark grey (DG) areas, while for the 1D materials in addition there are black zones (B), (Figs 9(a) and (b)). All these phases seem to be not uniformally distributed inside the matrix.

The white phase was analyzed as mullite ($Al_6Si_2O_{13}$) as it coincides to crystals, generally elongated (Fig.10) and richer in aluminum than in silicon, with the correct ratio. The mullite crystals appear square section like. They are spread throughout the matrix with no particular orientation. The mullite needle shape is not so clearly observed in the 1D composite compared to the 2D ones. Moreover, the amount of mullite crystals is greater in the 2D than in the 1D materials. TEM

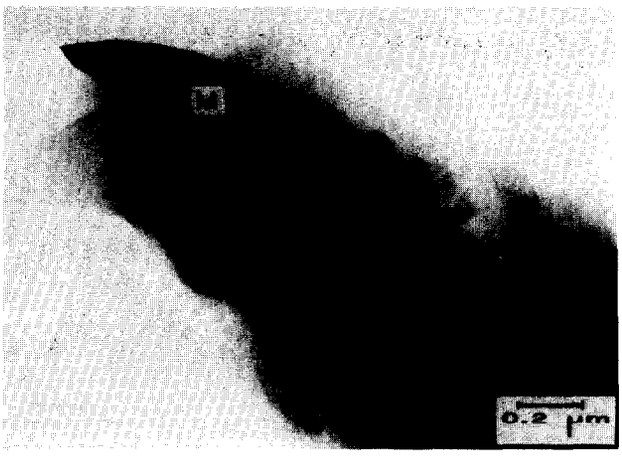


Fig. 10. TEM micrograph showing a mullite (M) needle in Bragg's conditions.

observations realised on the 1D composites show that these needles are sometimes surrounded by large crystals identified as β spodumene.

The dark-grey phase corresponds to the main phase only in the 1D materials: these areas are richer in silicon than in aluminum. Inside this phase the presence of magnesium is also detected. The presence of Mg is always detected whatever the phase is analyzed: mullite was even containing very few percent of Mg. By considering the Si/Al ratio and the diffraction patterns, the dark-grey phase was identified as β spodumene ($LiAlSi_2O_6$) or to a solid solution of β spodumene whose lithium cannot be detected, and where the magnesium ratio is not always the same in the whole specimen. The 1D composite investigated in TEM confirms that the main phase is β spodumene with quite large grains (Fig. 11). In the 2D materials, β spodumene zones appear only as inclusions dispersed in the grey phase.

These inclusions, recognised as β spodumene, have also been observed in 2D as-received SiC_f–MLAS composites, having a size greater than 100 nm.[33] The grey phase corresponding to the main phase in the 2D materials is the one richest in magnesium. Although the amount of magnesium is always lower than the theoretical value predicted from β cordierite formula ($Mg_2Al_4Si_5O_{18}$) this phase has been recognised as β cordierite or as a solid solution of β cordierite. These results of cordierite in the 2D material need further complementary investigations. In the 1D material β cordierite crystals have never been observed alone but always near to β spodumene crystals (Fig. 12).

Finally in the 1D materials one also observes black zones corresponding to areas with a very high concentration of carbon. This probably comes from the decomposition of organic compounds used during the fabrication of these composites as no carbon is used to coat the silicon fibers during the process route. Observations in TEM agree with this presence of carbon. Figure 13 shows carbon patches inside a β spodumene grain.

With regard to the fiber/matrix interface one observes several phases and turbostratic carbon layers. Close to the fiber side, EDS analysis gives

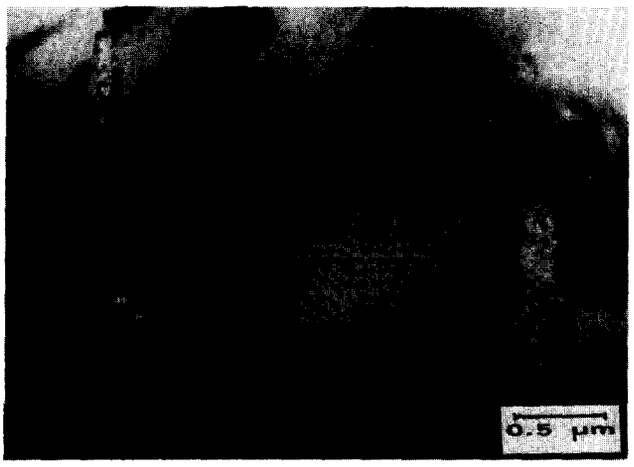


Fig. 11. Large grain of β spodumene observed in the 1D SiC_f–MLAS composite.

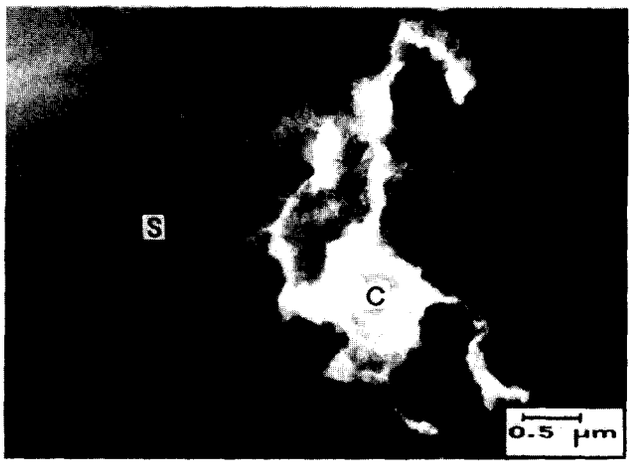


Fig. 13. Presence in the 1D composite of large carbon patches (C) inside spodumene grain (S).

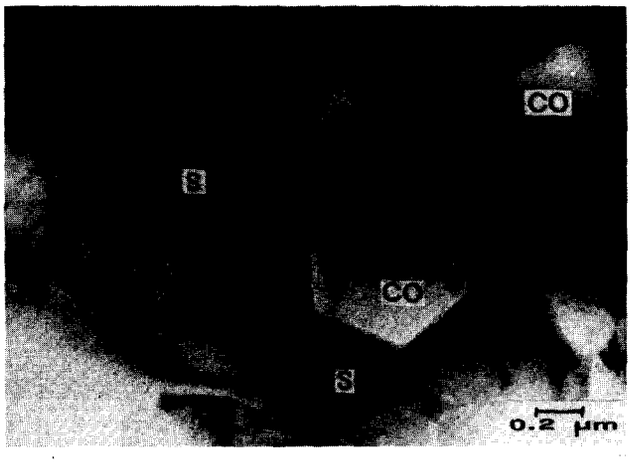


Fig. 12. Close mixture of β cordierite (CO) and β spodumene (S) grains in the 1D composite.

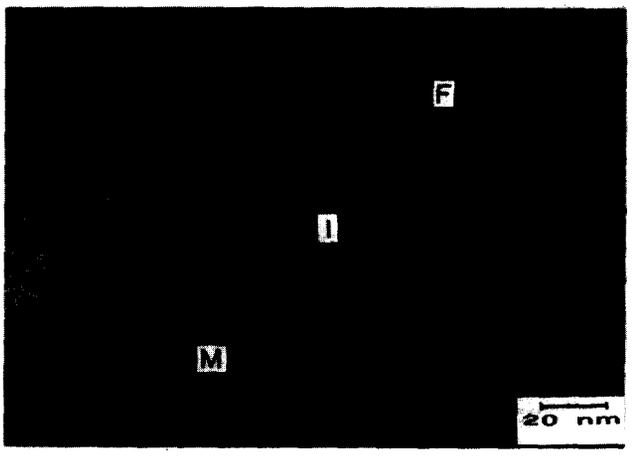
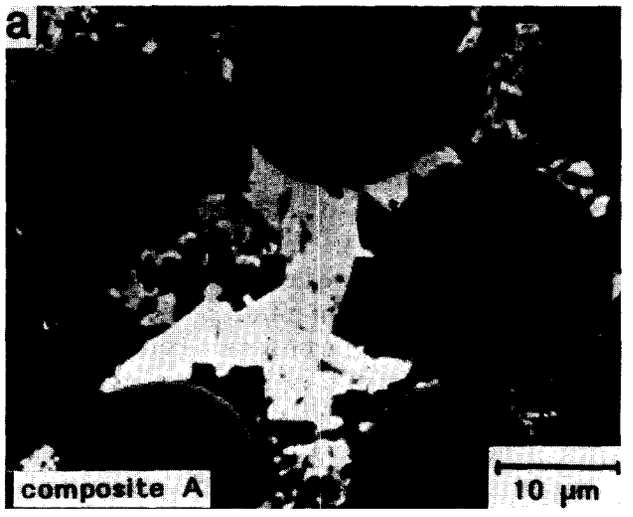


Fig. 14. Interface (I) between SiC fiber (F) and MLAS matrix (M) exhibiting mainly turbostratic carbon.

more silicon and oxygen and at the matrix side there is also a quite extended area along which the matrix appears to have reacted,[34] (Fig. 14). In these materials the interphase areas have a thickness which can vary from 10 to 100 nm.

SiC_f–YMAS

Figures 15(a) and (b) present the scanning electron micrographs of each composite. The phase containing yttrium appears in white. Large grains of that phase are present in Composite A. After microanalysis they have been identified as an yttrium silicate compound.[35] Due to the probe size (2 μm^3) it has not been possible to identify the small white grains as yttrium silicate. The black areas (Fig. 15(b)) show a phase rich in aluminum, magnesium and silicon elements, without the presence of yttrium. Composite B presents a more homogeneous microstructure without the presence of large grains. Globally the microstructure of these two types of composite is too fine to be analyzed at that scale because of the classical probe size used. Observations of Composite A reveals the existence of two main phases appearing in black and white. The dark crystals are distributed in a complex network and are elongated with a dendritic shape. Most of the yttrium phase is located in these zones (Fig. 16). The yttrium silicate has been identified as the high temperature form. The white areas generally correspond to more homogeneous zones. They are formed with cordierite crystals (the high cordierite) with a hexagonal symmetry (Fig 16).



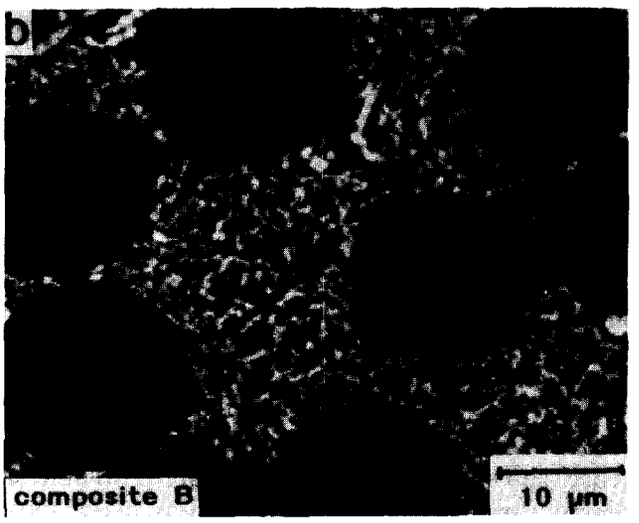


Fig. 15. SEM micrographs of the SiC_f–YMAS composite prepared by the sol–gel route (a) and by the glassy route (b).

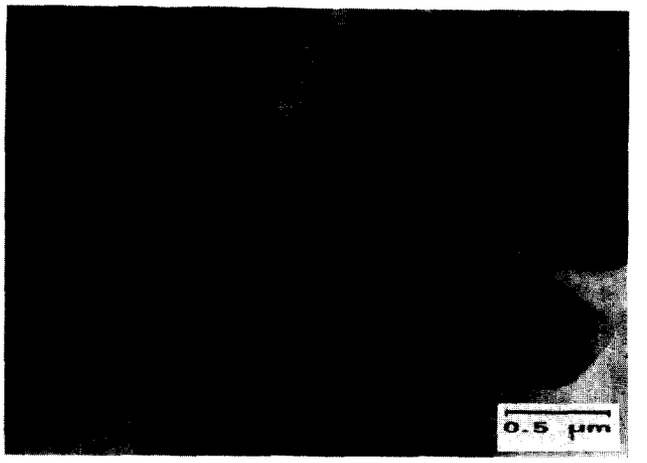


Fig. 16. Matrix formed by a network of yttrium silicate crystals with dendritic shape (dark) inside cordierite phase (clear), in Composite A.

For Composite A, some areas with a totally different microstructure also appear. An example is shown in Fig. 17. In that case, elongated and square shaped crystals are present in a phase which corresponds to a mixture of cordierite and yttrium silicate. These crystals were identified as mullite ($Al_6Si_2O_{13}$). Moreover some spinel crystals ($MgAl_2O_4$) are often observed within the cordierite or in the grain boundaries (Fig. 18)

Composite B exhibits the main microstructural features as Composite A. However, mullite crystals are rarely observed and the matrix appears finer and more homogeneous. In addition it has been observed that the cordierite crystals contain

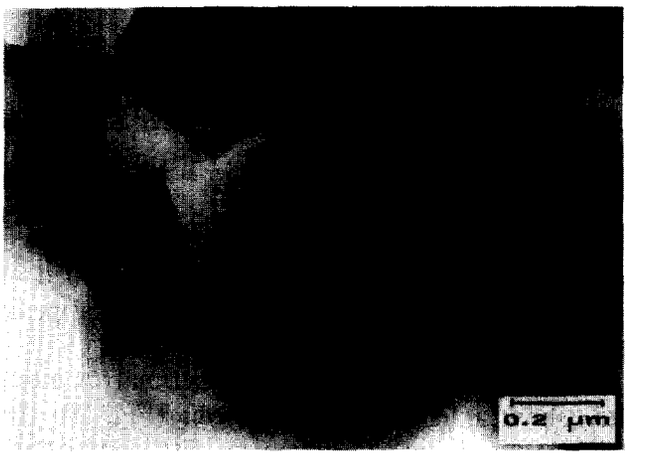


Fig. 17. Example of mullite crystal inside a mixture of yttrium silicate and cordierite in Composite A.

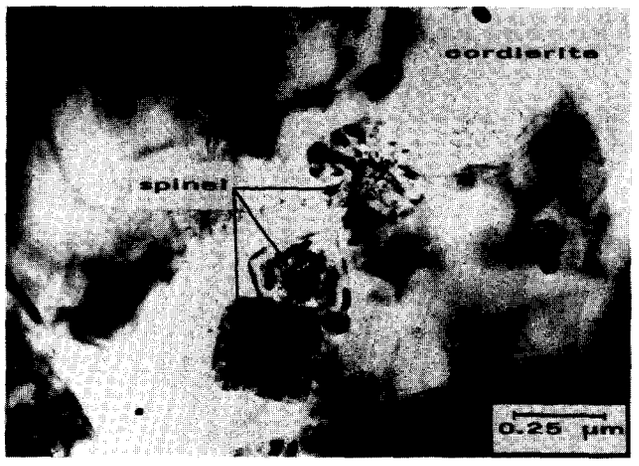


Fig. 18. Spinel crystals inside cordierite grain in Composite A.

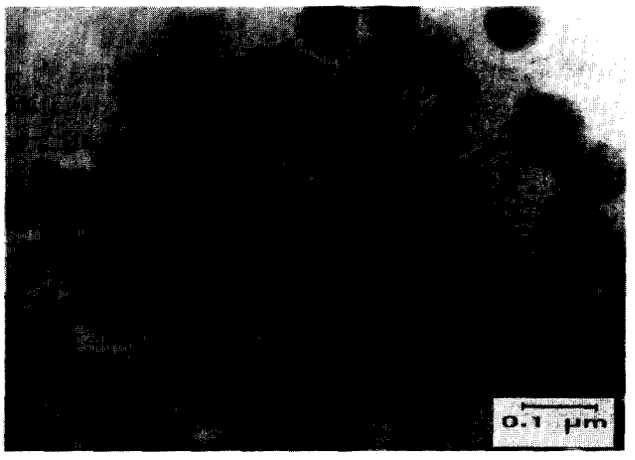


Fig. 19. Zirconia crystals inside cordierite phase in Composite B.

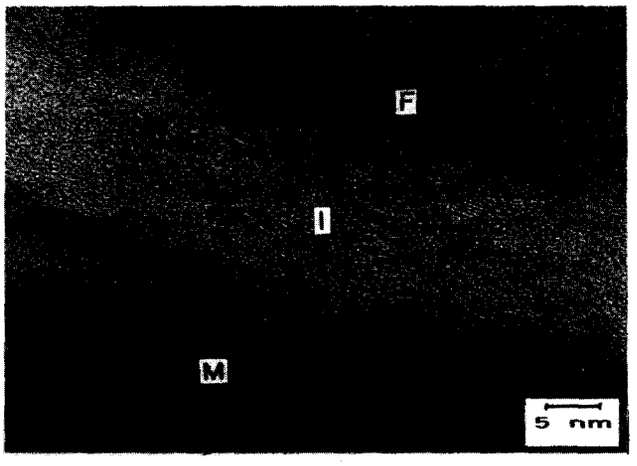


Fig. 20. HREM micrograph of the fiber/matrix interface, in Composite B.

some small inclusions (~20–100 nm) identified as zirconia (Fig. 19). At this scale, the matrix appears totally crystallized.

HREM observations at the fiber/matrix interface show a light contrasted layer (Fig. 20). Its thickness is about 20–30 nm in both composites. The nanostructure of the interface is similar to that one observed by Monthioux[36] in another type of glass ceramic composite (SiC_f–MLAS), with a layer of turbostratic carbon The sharp interface observed in the matrix side of the carbon layer and the diffuse interface observed on the Nicalon SiC fiber. support the concept of a carbon layer growing in the fiber.

Discussion

SiC_f–MLAS

The glass composite we had for the MLAS matrix — $0{\cdot}5MgO–0{\cdot}5Li_2O–1Al_2O_3–4SiO_2$ — is supposed to give as the first major phase, β eucryptite solid solution. As an immiscibility dome between SiO_2 and $Li_2O–Al_2O_3$ exists, one can have either a glass with the expected composition or a glass which can be richer or poorer in SiO_2 than expected. This leads to a β eucryptite solid solution in the LAS system whose composition can be quite far from the theoretical formula $Li_2O–Al_2O_3–2SiO_2$.[37]

The β eucryptite phase is subjected to microcracking and therefore has poor mechanical properties.[16] It is why one seeks to invert β eucryptite into β spodumene in this system. This transformation is possible whenever a glass composition has at least $3{\cdot}5SiO_2$ for $1MgO$ and $1Li_2O$[38] By heating the previous solid solution at 1050°C the transformation takes place and a β spodumene solid solution appears. This phase is suitable for thermomechanical applications generally because no microcracking appears. Moreover, it has recently been shown that this phase can be corroded easily by boiling sulfuric acid or by molten sodium nitrate.[39]

The precursor phase can have a composition in quite a large range, so it is not surprising that for the β spodumene a solid solution with different ratios of elements can crystallize.

At higher temperatures the MAS system (Fig. 4) considers the formation of β cordierite which also has no stable composition, particularly in magnesium. But substitution between Li^+ and Mg^{2+} are quite easy as they have a close ionic radii (Li^+:0·68 Å; Mg^{2+}:0·78 Å).

The presence of mullite crystals is evident in both the LAS and MAS systems (Figs 1 and 4) as they contain its existence domain.

The noticeable differences between the 1D and 2D materials in terms of majority phases is perhaps shown in the pseudo binary diagram cordierite–spodumene (Fig. 3).[8] To our knowledge this is the only one which makes a junction between the LAS and the MAS systems. Its existence shows that liquid phases are available at temperatures in the ternary diagrams taken separately. According to this diagram and depending upon the predominant phase in a cordierite–

spodumene mixture two different situations can arise. On one hand if we have more cordierite than spodu- mene a heat treatment will lead to even more cordierite and then to mullite. On the other hand a mixture richer in spodumene will give even more spodumene and less cordierite.

The association of cordierite and mullite was also predicted in Refs 13 and 14. It was noticed that in the MAS diagram the cordierite is able to melt incongruently by giving mullite at a temperature between 1355 and 1465°C.

In conclusion, the 1D SiC_f–MLAS matrix seems to belong to a system which has at the beginning more β spodumene than β cordierite, whilst for the 2D matrix it is the opposite. The materials evolution during creep tests confirm this assumption, as the 1D was evolving towards the β cordierite disparition to the benefit of β spodumene.[10] Concerning the 2D materials, no evolution between spodumene and cordierite has been reported as yet, but great enhancement of mullite crystals has been evident.

SiC_f–YMAS

Whatever the YMAS composites (A or B) one considers that the matrix contains two major and two minor phases, that is to say cordierite and yttrium silicate for the major and spinel and mullite for the minor. Besides this, zircone inclusions have been found in composite B. This can be easily explained by the oxide used in order to enhance the crystallization in the glassy route.

Microstructural observations and analyses on these materials have shown that yttrium silicate is the only compound which contains yttrium. This is in good agreement with previous investigations.[30,40] So it can be supposed that all the Y_2O_3 reacts with SiO_2 to form the $Y_2Si_2O_7$ phase.

Diffraction patterns allows us to identify the β form of that oxide. Because of the temperature of fabrication, it is in good agreement with the literature despite the fact that many temperatures are given for the same allotropic transformation according to different authors (cf. Table 2).

As yttrine is only in the $Y_2Si_2O_7$ silicate form, one can consider that alumina and magnesia react together to give binary or ternary compounds by reaction with silica as well. This leads us to consider the MAS system.

Moreover if one considers the amount of remaining silica, alumina and magnesia, it corresponds to a composition close to the sapphirine, which is present in the MAS ternary diagram. Unfortunately this phase has not been detected, but its existence domain is very small (Fig. 4). On that diagram one also notes that this phase is surrounded by three large domains corresponding to the three other phases identified in our composites, i.e. cordierite, mullite and spinel.

The cordierite is the second major phase with the yttrium silicate. It has been previously shown[13,14] that its formation by sintering begins at 1200°C. From the MAS diagram (Fig. 4) it appears as the phase existing at the lowest temperature domain. That is the reason why that phase appears as the most important at that fabrication temperature.

Very few mullite crystals appear in the YMAS matrix as silica reacts first to form cordierite rather than mullite because of its lower temperature of sintering (1200°C): that is in good agreement with the process temperature. As for the excess in magnesia, it reacts with alumina to form spinel above 1000°C.

Conclusion

The development of glass ceramic matrices is important in the field of ceramic matrix composites (CMCs) due to their very low thermal expansion coefficient and their good mechanical strength. So it requires a good knowledge of the corresponding pseudo–binary, ternary and quaternary diagrams. From their accurate analysis one can note many important difficulties: (i) different silicate phases can appear in very close domains; (ii) many allotropic transformations exist; (iii) different atom substitutions can arise and (iv) several crystallographic parameters of different silicate phases have the same value. These different points emphasize the complexity of knowing with accuracy which phases are present in the materials. Anyway, during long term applications, these silicate phases can evolve.

The management (control) of the stability of the glass ceramic matrices in these multicomponent systems is an essential step to consider applications for long durations, such as for motors, hypersonic structures, etc.... Moreover, for glass ceramic systems with aluminum or lithium reinforced by silicon carbide fibers, such as LAS, MAS, YAS, MLAS or YMAS systems, the diffusion of aluminum or lithium in the SiC fibers is an important factor to consider: it can act on the crystalline phases of the matrix due to change in composition and can make the fibers even more brittle. Moreover a matrix with lithium or lithium components can evaporate during the process.[41]

These different points have been illustrated by investigations in scanning and transmission electron microscopies with microanalysis, of the MLAS ($MgO–Li_2O–Al_2O_3–SiO_2$) and YMAS ($Y_2O_3–MgO–Al_2O_3–SiO_2$) systems.

It appears that the matrices in the 1D and 2D SiC_f–MLAS composites are slightly different, although the composition of the started gel and the process were the same. This simple fact shows the difficulty in obtaining any point reproductible matrices with exactly the same phases and distributions.

This is due to the multitude of possibilities deduced from the thermodynamic diagrams. In fact the detectable phases in the two composites are identical but their size distribution is not. The 1D matrix shows the following phase distribution: β spodumene > β cordierite >> ϵ mullite, while in the 2D it is β cordierite >> β spodumene > mullite. Consequently when the SiC_f–MLAS composites are submitted to creep test, the matrix which is not totally crystallized, will be subjected to chemical and morphological evolution. As the as-received matrices are not exactly equivalent, different ways of phase evolution will have to be considered. But depending on which scale we are working, these phenomena will be considered as crucial or as minor: for example, if one has to compare the damage due to a crack running from one ply to another with regard to a phase transformation.

The main phases in YMAS matrices were β $Y_2Si_2O_7$ and β cordierite, the secondary ones being mullite and spinel. It is maintained by a very complex network acting like a spider's web where minor and major phases are sometimes overlapping. One other advantage of this system is that no substitution can occur between magnesium and yttrium.

In the two YMAS and MLAS matrices one expects a more stable YMAS type matrix because this one is totally crystallized.

Acknowledgements

This work has been performed: (i) in the frame of the Groupement Scientifique GS 4C 'Comportements thermomécaniques des composites céramique–céramique à fibre' supported by CNES, CNRS, DRET, MRE and Aerospatiale, SEP and SNECMA companies, and (ii) under DRET contract no. 92/1221 A.

The authors want to warmly thank their colleagues Dr T. Chartier and Pr. B. T. Frit (URA CNRS n°320, Limoges, France), Mrs M. H. Ritti, Mr T. Grenier and Dr M. Parlier (ONERA, Châtillon sous Bagneux, France), Dr G. Larnac (Aérospatiale Company, Etablissement de Bordeaux, France) and Dr R. Pompe (Swedish Institute for Silicate Research, Göteborg, Sweden), for fruitful discussions.

References

1. Long, M. & Moore, R. E., Development of glass ceramic matrix composites for aircraft applications, *Sil. Ind.*, **7–8** (1990) 223–9.
2. Partridge, G., Elyard, C. A., Budd, M. I., Glass ceramics in substrate applications. In *Glasses and Glass-Ceramics*, ed. M. H. Lewis, Chapman and Hall, 1988 pp. 226–71.
3. Scheidler, H., Rodek, E., Li_2O–Al_2O_3–SiO_2 glass ceramics *Amer. Ceram. Bull.*, **68**(11) (1989) 1926–30.
4. Roy, R., & Osborn, E. F., The system lithium metasilicate spodumene silica, *J. Amer. Chem. Soc.*, **71** (1949) 2086–95.
5. Roy R., Roy, D. M. & Osborn, E. F., Compositional and stability relationships among the lithium aluminosilicates: eucryptite, spodumene, and petalite, *J. Amer. Ceram. Soc.*, **33**(5) (1950) 152–9.
6. Hatch, R. A., Phase equilibrium in the system: Li_2O–Al_2O_3–SiO_2, *Amer. Mineral.*, **28** (1943) 471–96.
7. Strnad, Z., Glass-ceramic materials, liquid phase separation, nucleation and crystallization. In *Glass Science and Technology 8*, Elsevier, 1986 pp. 76–89.
8. Karkhanavala, M. D. & Hummel, F. A., Reactions in the system Li_2O–MgO–Al_2O_3–SiO_2: I The cordierite–spodumene join, *J. Amer. Ceram. Soc.*, **36**(12) (1953) 393–7.
9. Gouby, I., Les cordiérites dopées aux alcalins. Influences du traitement thermique sur la structure cristalline et sur quelques propriétés physiques, Thèse de l'Université de Limoges, Feb. 1994.
10. Kervadec, D., Comportement en fluage sous flexion et microstructure d'un SiC_f–MLAS 1D, Thèse de Doctorat de l'Université de Caen, Dec. 1992.
11. Winkler, H. G. F., Synthese und Kristallstruktur des Eukryptits, $LiAlSiO_4$, *Acta. Cryst.* **1**(1) (1948) 27–34.
12. Prokopowicz, T. I., & Hummel, F. A., Reactions in the system Li_2O–MgO–Al_2O_3–SiO_2: II Phase equilibria in the high-silica region, *J. Amer. Ceram. Soc.*, **39**(8) (1956) 266–78.
13. Osborn, E. F. & Muan, A., (1961) cited by Jouenne, C. A., (1984).
14. Jouenne, C. A., *Traité de Céramiques et Matériaux Minéraux*, Editions Septima, 1984, pp. 185–7.
15. Beall, G. H., Karstetter, B. R. & Rittler, H. L., Crystallization and chemical strengthening of stuffed β-quartz glass ceramics, *J. Amer. Ceram. Soc.*, **50**(4) (1967) 181–90.
16. Larnac, G., Elaboration d'une matrice pour composites céramique–céramique par la voie sol–gel, Thèse de l'Université des Sciences et Techniques du Languedoc, Université de Montpellier II, April 1990.
17. Barry, T. I., Cox, J. M. & Morrell, R., Cordierite glass-ceramics-effect of TiO_2 and ZrO_2 content on phase sequence during heat treatment, *J. Mat. Sci.*, **13**(3) (1978) 594–610.
18. Coon, D. N., Simultaneous sintering and crystallization of a M_9O–Li_2O–Al_2O_3–SiO_2 glass powder, *J. Mat. Sci. Let.*, **7**(11) (1983) 1181–3.
19. Coon, D. N. & Neilson, R. M., Effect of M_9O additions on the glass transition temperature of LiO_2–Al_2O_3–SiO_2 glasses, *J. Mat. Sci. Let.*, **7**(1) (1988) 33–5.
20. Ray, S. & Muchow, G. M., High-quartz solid solution phases from thermally crystallized glasses of compositions, *J. Amer. Ceram. Soc.*, **51**(12) (1968) 678–82.
21. Mazza, D. & Lucco-Borlera, M., Effect of the substitution of boron for aluminum in the β-eucryptite $LiAlSiO_4$ structure, *J. Eur. Ceram. Soc.*, **13**(1) (1994) 61–5.
22. O'Meara, C. O., Dunlop, G. L. & Pompe, R., Phase relationships in the system SiO_2–Y_2O_3–Al_2O_3, In *6th CIMTEC*, ed. P. Vincenzini, Elsevier, 1987. pp. 265–70.
23. Hyatt, M. J. & Day, D. E., Glass properties in the yttria–alumina–silica system, *J. Amer. Ceram. Soc.*, **70**(10) (1987) C283–7.
24. Bondar, A. & Galakhov, F. Ya, Phase equilibria in the system Y_2O_3–Al_2O_3–SiO_2, *Izv. Akad. Nauk. SSSR, Ser. Khim*, **7** (1964) 1325–6.

25. Ito, J. & Johnson, H., Synthesis and study of yttrialite, *Amer. Mineral.*, **53** (Nov.–Dec.) (1968) 1940–52.
26. Felsche, J., Crystal data on the polymorphism of disilicate $Y_2Si_2O_7$, *Die Naturwissenschaften*, **57**(3) (1970) 127–8.
27. Liddell, K. & Thompson, D. P., X-ray diffraction data for yttrium silicates, *Brit Ceram. Trans. J.*, **85** (1986) 17–22.
28. Lee, W. E. & Hilmas, G. E., Microstructural changes in β–Si_3N_4 grains upon crystallizing the grain-boundary glass, *J. Amer. Ceram. Soc.*, **72**(10) (1989) 1931–7.
29. Arita, I. H., Wilkinson, D. S. & Purdy, G. R., Crystallization of yttria–aluminina–silica glasses, *J. Amer. Ceram. Soc.*, **75**(12) (1992) 3315–20.
30. Séraudie, C., Elaboration et propriétés thermomécaniques de composites à fibres de carbure de silicium et matrices vitrocéramiques, Thése de Doctorat de l'Université de Limoges, July 1990.
31. Grenier, T., Parent, P. & Parlier, M., Elaboration de composites SiC_f–MASY à l'échelle quart de grand, Technical Report ONERA-DRET 2–3762 MY, Aug. 1994.
32. Larnac, G., Pérès, P. & Donzac., J. M., Elaboration et caractérisation du composite à matrice vitrocéramique SiC–MASL., *Rev. Comp. Mat. Avancés*, **3 HS**, (1993) 27–41.
33. Backhaus–Ricoult, M., Mozdzierz, N., Imhoff, D., Eveno, P., Deschamps, J., Pelissier, B., Miloche, M. & Bahezre, C., Final Report on GS 4C, Comportments thermomécaniques des composites céramique–céramique à fibres, Jan. (1994).
34. Ruterana, P., Kervadec, D., Maupas, H. & Chermant, J. L., Microstructure and evolution of a *MLAS* matrix composite. In *Microscopy of Composite Materials II*, Oxford, UK, 11–13 April 1994. To appear in *J. Microscopy*, **177**(3) (1995) 272–8.
35. Vicens, J., Doreau, F. & Chermant, J. L., Microstructure of experimental SiC_f–YMAS type CMC materials, In *Microscopy of Composite Materials II*, Oxford, UK, 11–13, April 1994. *J. Microscopy* (1995), **177**(3) (1995) 242–50.
36. Monthioux, R., Nano et microstructure de composites SiC/MASL, *Rev. Comp. Mat. Avancés*, **3 HS**, (1993) 69–90.
37. Gillery, F. H & Buch, E. A., Thermal contraction of β-eucryptite (Li_2O–Al_2O_3–$2SiO_2$) by X-ray and dilatometry methods, *J. Amer. Ceram. Soc.*, **42**(4) (1949) 175–7.
38. Eppler, R. A., Glass formation and recrystallization in the lithium metasilicate region of the system Li_2O–Al_2O_3–SiO_2, *J. Amer. Ceram. Soc.*, **46**(4) (1963) 97–101.
39. Colomban, P., Ion exchange, fiber/silicates matrix reactions and hot corrosion in glass ceramic and ceramic matrix composites, 3rd Int. Conference on Ceramic–Ceramic Composites CCC–III. Mons, Belg., Oct. 18–20 1994 *Sil. Ind.* (1995), in press.
40. Nussbaum, H. & Montardi, Y., Elaboration et caractérisation de céramiques. Composites à matrice verre, Report Rhône–Poulenc, n°. 86/016, BC 26 (1988)
41. Chartier, T., Private communication (1994).

Journal of the European Ceramic Society **15** (1995) 1249–1251
© 1995 Elsevier Science Limited
Printed in Great Britain. All rights reserved
0955-2219(95)00080-8
0955-2219/95/$9.50

Contributor Index

Abello, L. 1149
Abreal, A. 841
Akbas, M. A. 57
Allemann, J. A. 951
Anderson, H. U. 867
Arwin, H. 313
Ashkin, A. 1101
Ashkin, D. 1101
Azough, F. 255

Babushkin, O. 921, 1101, 1111, 1207
Baddi, R. 989
Banerjee, S. 191
Baptista, J. L. 605
Battault, T. 1141
Baumard, J.-F. 899
Baykara, T. 165
Berger, A. 65, 95
Bernard, C. 551
Besson, J. L. 101
Binner, J. G. P. 1037
Blondiaux, G. 127
Bodet, R. 997
Bowman, K. J. 1119
Branda, F. 1025
Brandon, D. G. 1, 283
Bu-Kon Yu 155
Buri, A. 1025

Calderón-Moreno, J. M. 983
Cambier, F. 1201
Carisey, T. 1, 283
Carlson, W. B. 479
Carry, C. 9, 71
Ceccone, G. 563
Celotti, G. 735
Chartier, T. 101, 899
Chaudhuri, S. P. 1031
Chee, K. S. 1213
Chen, J. 313
Chen, M. 1079
Cheng, Y.-B. 415, 787, 1213, 1221
Chermant, J.-L. 1235
Chermant, L. 71
Chou, W. B. 291
Chu, H. 1007
Claussen, N. 395, 935
Collins, D. E. 1119
Cooke, R. G. 455
Costantini, A. 1025
Coster, M. 71
Cotterell, B. 1061
Coutures, J. P. 127
Crampon, J. 989
Cretin, M. 1149

Das, S. K. 191
Datta, P. K. 1007
Davis, P. A. 1037
Dayi Niaki, M. H. 343
De Arellano-López, A. R. 983
De Croon, M. H. J. M. 875, 887
De With, G. 1157
Demirci, M. 165
Deng, S. 513
Descamps, M. 357
Després, J.-F. 209
Disson, J. P. 185, 591, 683
Doh-Yeon Kim 371
Domínguez-Rodríguez, A. 983
Dong-Heon Lee 371
Doreau, F. 1235
Du, Y. 503
Duan, K. 1061
Dub, S. N. 405
Dubovetskü, I. D. 1037
Duclos, R. 989
Ducos, M. 637
Dumitrescu, L. F. S. 89
Dumitrescu, L. 239
Dupel, P. 801
Durand, B. 759
Dusza, J. 45
Duval-Riviere, M. L. 71

Edirisinghe, M. J. 109, 581
Edwards, D. P. 415
Ekström, T. 689, 1101
El-Korchi, T. 425
Erkalfa, H. 165
Evans, J. R. G. 117, 729

Fabry, P. 1149
Faivre, A. 135, 145
Fantozzi, G. 185, 591, 651, 683, 759, 833
Fernie, J. A. 1037
Ferrato, M. 899
Festa, D. 337
Fett, T. 307, 377, 643
Finch, D. S. 581
Fletcher, P. R. 859
Flynn, R. 1015
Fok, S. L. 905, 909
Fordham, R. J. 573
Forslund, B. 1087
Fraser, J. W. 851
Freer, R. 255
Friel, D. 425
Fujitani, H. 1043

Gabbay, E. 233
Gao, L. 349
Gao, J. H. 967
Garcia, D. E. 935
Gauckler, L. J. 811, 951
Gerteisen, G. 307
Godwod, K. 17
Goeuriot, D. 841
Goeuriot, P. 249
Gogotsi, G. A. 271, 405, 1177, 1185
Gonon, M. F. 185, 591, 683
Gontermann-Gehl, U. 741
Goretzki, H. 667
Gorter, H. 1079
Gorzawski, G. 95
Gotman, I. 527
Goujard, S. 551
Goursat, P. 1015
Graham, M. J. 851
Granon, A. 249
Graule, T. 811
Green, D. J. 655, 769, 777
Gritzner, G. 45
Gu, X. 823
Gueroult, B. 841
Guglielmi, M. 337
Guiban, M. Ä. 537
Guo, I.-K. 1171
Guo, J. 929
Guo, X. 25
Gutmanas, E. Y. 527

Hahnenberger, S. 307
Halitim, F. 833
Hammond, P. D. 117
Hampshire, S. 683, 1015
Hand, R. J. 823
Hannink, R. H. J. 415
Hardy, D. 769
Harris, B. 455
Hayashi, S. 521
Heim, M. 313, 319
Hendry, A. 801
Hennings, D. F. K. 795
Hérard, C. 135, 145
Hintzen, H. T. 599, 1079
Hirai, T. 329
Hoffmann, M. J. 225

Howell, F. S. 661
Hübner, H. 913
Hughes, A. E. 1125
Huisman, W. 811
Husson, E. 127, 631, 1163

Inagaki, M. 265
Innocenzi, P. 337
Ishizu, K.-I. 521
Itatani, K. 661

Jäger, C. 675
Janssen, R. 935
Jebrouni, M. 759
Jia, N. 997
Joo-Hwan Han 371
Jorand, Y. 469, 759

Kakihana, M. 503
Kanzaki, S. 173
Kasori, M. 435
Katz, R. N. 425
Kauermann, R. 913
Kavecký, S. 1071
Kervadec, D. 1235
Kikuchi, S. 521
Kinoshita, M. 661
Kishioka, A. 661
Kivilahti, J. K. 563
Kleitz, M. 51
Koc, R. 867
Kodentsov, A. A. 563
Kotte, J. F. A. K. 875
Kountouros, P. 1125
Koura, T. 503
Krafczyk, E. 741
Krishnarao, R. V. 1229
Kubo, K. 661

Lagace, M. 841
Langlais, F. 81
Laoui, T. 297
Laugier-Werth, A. 1
Lawson, S. 485
Le Caer, G. 1207
Leach, C. 33, 617, 859
Lee, W. E. 57
Lefort, P. 233
Leger, D. 357
Legros, R. 463, 1141
Lemaître, J. 135, 145
Lespiaux, D. 81
Levin, I. 283
Li, B. S. 959, 967
Li, H. X. 697
Liddell, K. 349
Lindbäck, T. 1207
Lomonova, E. E. 405
Lu, G. 225
Lucchini, E. 975
Luyten, J. 573

Maalal, B. 1135
Mahajan, Y. R. 1229
Mai, Y.-W. 1061
Malé, G. 537
Maliavski, N. 337
Mancinelli Degli Esposti, L. 337
Mandal, H. 349
Manier, M. 1135
Mantas, P. Q. 605
Marghussian, V. K. 343
Marino, F. 1065
Märki, H.-B. 951
Martin, G. 307, 643
Maupas, H. 1235
Mayer, J. 703, 717
Medevielle A. 1193
Meinhold, R. 1201
Mercurio, J. P. 1135
Merle D. 101
Metsclaar, R. 225, 599, 887, 1079, 1157
Metz, R. 463
Michel, B. 951
Mignard, F. 651
Miot, C. 127, 631, 1163
Misirli, Z. 165
Missiaen, J. M. 469
Mocellin, A. 1207
Mogilevsky, P. 527
Monceau, D. 851
Montanaro, L. 469
Monthioux, M. 209, 445
Moser, E. M. 951
Mosset, A. 675
Muccillo, E. N. S. 51
Muddle, B. C. 415, 787
Müller, G. 65, 95
Müller, W. F. 95
Munz, D. 307, 377, 643
Murat, M. 185, 591

Nabert, G. 667
Nanjangud, S. C. 655
Naslain, R. 81
Nestor, E. 1015
Nicholas, M. G. 563
Niepce, J. C. 623
Nordmann, A. 787
Nygren, M. 689

O'Meara, C. 319
Okada, K. 521
Olagnon, C. 651
Osso, D. 1207
Ostrovoy, D. Yu. 271
Ostrovoy, D. Y. 1177
Otsuka, N. 521
Ozersky, B. I. 405

Paletto, J. 759
Paletto, S. 833
Pandolfelli, V. C. 913
Pannhorst, W. 65
Parrick, J. 581
Peteves, S. D. 563
Petot, C. 637, 851
Petot-Ervas, G. 637, 851
Pomeroy, M. J. 1007
Pompe, R. 313, 319
Poorteman, M. 1201
Proust, C. 127, 631, 1163
Puchner, C. 45

Rafaniello, W. 425
Rahaman, M. N. 939
Ralph, B. 581
Ramesh, R. 1007, 1015
Rawlings, R. D. 33
Ray, A. K. 191
Reed, J. S. 479
Reenis, R. 1079
Riedel, R. 703, 717
Rigaud, M. 841
Riley, F. L. 573
Ringuet, G. 357
Rödel, J. 395
Rodrigues, J. A. 913
Rogers, K. A. 1119
Roman, Y. G. 875, 887
Rousset, A. 463, 1141
Routbort, J. L. 983
Roy, P. K. 191
Ruan, M. L. 959
Rühle, M. 717
Russell, J. D. 617
Russell-Floyd, R. S. 455
Ruterana, P. 1235

Sahu, S. 1071
Samdi, A. 759
Sarkar, P. 1031
Sarrazin, P. 623
Sasaki, M. 329
Sato, E. 9
Sbaizero, O. 975
Schamm, S. 81
Schmidt, H. 667
Schmücker, M. 675, 1201
Schneider, H. 675, 1201
Schreinemacher, H. 795
Schubert, H. 1125
Sebai, M. 1015
Seher, M. 703, 717
Seidel, J. 395, 935
Selçuk, A. 33
Sevely, J. 81
Sglavo, V. M. 777
Shaw, H. M. 109
Shi, E.-W. 1171
Shi, J. L. 363, 959, 967
Shimada, S. 265
Sjöberg, J. 1015
Smart, J. 905, 909
Smith, M. E. 1213
Sørensen, B. F. 1047
Sproule, G. I. 851
St John, H. 1125
Stalios, A. D. 573

Sternitzke, M. 95
Su Jen Lu 155
Sugihara, S. 1043
Sun, W. Y. 689, 697, 3349
Sundman, B. 89, 239
Swain, M. V. 1185
Szépvölgyi, J. 1071

Taha, M. 469, 759
Talreja, R. 1047
Tampieri, A. 735
Tanaka, H. 675
Tang, C.-Q. 25
Tchekounova, E. 337
Telle, R. 527
Terpstra, R. A. 599
Thévenot, F. 249, 841, 1193
Thierry, B. 357, 623
Thompson, D. P. 349
Tillement, O. 1207
Tomaszewski, H. 17
Toutanji, H. A. 425
Toy, Ç. 165
Tréheux, D. 833, 1193
Tressler, R. E. 997
Tu, H. Y. 689
Tuan, W. H. 291
Twitty, A. 455

Ueda, M. 265
Ueno, F. 435

Vahlas, C. 445
Valecillos, M. C. 173
Van Der Beek, G. P. 741
Van Der Biest, O. 297
Van Der Heijde, J. C. T. 599
Van Hal, P. F. 1157
Van Loo, F. J. J. 563
Van Rutten, J. W. T. 599
Vandenbulcke, L. 551
Vicens, J. 71, 1235
Vinga Szabó, D. 703, 717
Vleugels, J. 297
Vomacka, P. 921, 1111

Wang, P. L. 689
Warren, P. D. 201, 385
Warren, R. 513, 1111
Watari, K. 173
Wechsler, G. 425
Wei, Wen-Cheng J. 155
Willems, H. X. 1157
Winter, W. 65
Wolf, C. 913
Woodthorpe, J. 729

Xia, C.-T. 1171

Yan, D. S. 349, 689, 697
Yashima, M. 503
Yasuoka, M. 173
Yen, T. S. 363, 959, 967
Yoshimura, M. 503
Yu, G. 581
Yuan, R.-Z. 25

Zanchetta, A. 233
Zavada, V. P. 1185
Zhang, B. 929
Zhang, B. R. 1065
Zhang, T. 729
Zhang, X. 225
Zhao, R. 1221
Zheng, J. 479, 1087
Zhong, W.-Z. 1171
Zhong, Y. J. 255
Zhou, Y. 297
Zhou, Y. C. 939
Ziegler, G. 667

Journal of the European Ceramic Society **15** (1995) 1253–1262
© 1995 Elsevier Science Limited
Printed in Great Britain. All rights reserved
0955-2219(95)00091-6
0955-2219/95/$9.50

Contents of Volume 15

Number 1

1 Control of Texture in Al_2O_3 by Gel-casting
T. CARISEY, A. LAUGIER-WERTH & D. G. BRANDON (Israel)

9 Effect of Powder Granulometry and Pre-treatment on Sintering Behavior of Submicron-grained α-Alumina
E. SATO & C. CARRY (Switzerland)

17 Influence of Oxygen Partial Pressure on the Metastability of Undoped Zirconia Dispersed in Alumina Matrix
H. TOMASZEWSKI & K. GODWOD (Poland)

25 Grain Boundary Ionic Conduction in Zirconia-based Solid Electrolyte with Alumina Addition
X. GUO, C.-Q. TANG & R.-Z. YUAN (China)

33 Processing, Microstructure and Mechanical Properties of SiC Platelet-reinforced 3Y-TZP Composites
A. SELÇUK, C. LEACH & R. D. RAWLINGS (UK)

45 Nb_2O_5 and Ta_2O_5 Codoped Zirconia
G. GRITZNER, C. PUCHNER (Austria) & J. DUSZA (Slovakia)

51 Ionic Conductivity of Fully Stabilized ZrO_2:MgO and Blocking Effects
E. N. S. MUCCILLO (Brazil) & M. KLEITZ (France)

57 Synthesis and Sintering of PLZT Powder Made by Freeze/Alcohol Drying or Gelation of Citrate Solutions
M. A. AKBAS & W. E. LEE (UK)

65 TEM Investigation of Cordierite Crystallization from a Glass Powder with Composition $Mg_2Al_4Si_{11}O_{30}$
W. WINTER, A. BERGER, G. MÜLLER & W. PANNHORST (Germany)

71 Morphological Characterization of Hot-pressed α-SiC with Al-based Additives Deformed by Compression at High Temperature
M. L. DUVAL-RIVIERE, M. COSTER, L. CHERMANT, J. VICENS & C. CARRY (France)

81 Chlorine and Oxygen Inhibition Effects in the Deposition of SiC-based Ceramics from the Si–C–H–Cl System
D. LESPIAUX, F. LANGLAIS, R. NASLAIN, S. SCHAMM & J. SEVELY (France)

89 Computer Simulation of β'-Sialon Synthesis
L. F. S. DUMITRESCU & B. SUNDMAN (Sweden)

95 Oxygen Enrichment at Inversion Domain Boundaries in Aluminium Nitride—Influence on Thermal Conductivity
G. GORZAWSKI, M. STERNITZKE, W. F. MÜLLER, A. BERGER & G. MÜLLER (Germany)

Number 2

101 Laminar Ceramic Composites
T. CHARTIER, D. MERLE & J. L. BESSON (France)

109 Shrinkage and Particle Packing during Removal of Organic Vehicle from Ceramic Injection Mouldings
HEIDI M. SHAW & MOHAN J. EDIRISINGHE (UK)

117 The Use of Overpressure in Thermolytic Debinding of Moulded Ceramic Bodies
P. D. HAMMOND & J. R. G. EVANS (UK)

127 Laser Ablation of Barium Titanate Ceramics Prepared by the Citric Route: The Evolution of Residual Carbon Content
C. MIOT, C. PROUST, E. HUSSON, G. BLONDIAUX & J. P. COUTURES (France)

135 Surface Decontamination Treatments of Undoped $BaTiO_3$—Part I: Powder and Green Body Properties
CLAUDE HÉRARD, ANNELISE FAIVRE & JACQUES LEMAÎTRE (Switzerland)

145 Surface Decontamination Treatments of Undoped $BaTiO_3$—Part II: Influence on Sintering
CLAUDE HÉRARD, ANNELISE FAIVRE & JACQUES LEMAÎTRE (Switzerland)

155 Characterization of Submicron Alumina Dispersions with Poly(methacrylic acid) Polyelectrolyte
WEN-CHENG J. WEI, SU JEN LU & BU-KON YU (Taiwan)

165 The Densification and Microstructural Development of Al_2O_3 with Manganese Oxide Addition
H. ERKALFA, Z. MISIRLI, M. DEMIRCI, Ç. TOY & T. BAYKARA (Turkey)

173 Reaction Process and Densification Process of Mixed α'/β'-Sialon Ceramics
KOJI WATARI, MASAKI YASUOKA, MARIA CECILIA VALECILLOS & SHUZO KANZAKI (Japan)

185 Association of the CVI Process and of the Use of Polysilazane Precursor for the Elaboration of Ceramic Matrix Composites Reinforced by Continuous Fibres
M. F. GONON (Ireland), G. FANTOZZI, M. MURAT & J. P. DISSON (France)

Number 3

191 Fractography of Fatigued and Fractured Regions in a Silicon Carbide Whisker Reinforced Alumina Composite
A. K. RAY, S. K. DAS, P. K. ROY & S. BANERJEE (India)

201 Determining the Fracture Toughness of Brittle Materials by Hertzian Indentation
P. D. WARREN (UK)

209 Mechanical Properties of C/SiC Composites as Explained from their Interfacial Features
J.-F. DESPRÉS & M. MONTHIOUX (France)

225 Properties and Interface Structures of Ni and Ni–Ti Alloy Toughened Al_2O_3 Ceramic Composites
X. ZHANG, (The Netherlands), G. LU, M. J. HOFFMANN (Germany) &
R. METSELAAR (The Netherlands)

233 Thermal Expansion and Adhesion of Ceramic to Metal Sealings: Case of Porcelain–Kovar Junctions
A. ZANCHETTA, P. LEFORT & E. GABBAY (France)

239 A Thermodynamic Reassessment of the Si–Al–O–N System
L. DUMITRESCU & B. SUNDMAN (Sweden)

249 Aluminum Magnesium Oxynitride: A New Transparent Spinel Ceramic
A. GRANON, P. GOEURIOT & F. THEVENOT (France)

255 The Effect of $La_2Ti_3O_9$ Second Phase on the Microstructure and Dielectric Properties of $La_2Ti_2O_7$ Ceramics
Y. J. ZHONG, F. AZOUGH & R. FREER (UK)

265 Low Temperature Synthesis of Zinc Ferrite using Hydrazine Monohydrate
M. UEDA, S. SHIMADA & M. INAGAKI (Japan)

Number 4

271 Deformation and Strength of Engineering Ceramics and Single Crystals
G. A. GOGOTSI & D. YU. OSTROVOY (Ukraine)

283 Microstructure and Mechanical Properties of Textured Al_2O_3
T. CARISEY, I. LEVIN & D. G. BRANDON (Israel)

291 Toughening and Strengthening of Alumina with Silver Inclusions
W. B. CHOU & W. H. TUAN (Taiwan)

297 Toughening of X-Sialon with Al_2O_3 Platelets
Y. ZHOU, J. VLEUGELS, T. LAOUI & O. VAN DER BIEST (Belgium)

307 Fracture Tests for Ceramics under Mode-I, Mode-II and Mixed-Mode Loading
T. FETT, G. GERTEISEN, S. HAHNENBERGER, G. MARTIN & D. MUNZ (Germany)

313 Determination of Oxide Thickness on an Si_2N_2O–ZrO_2 Composite by Spectroscopic Ellipsometry
M. HEIM, H. ARWIN, J. CHEN & R. POMPE (Sweden)

319 The Oxidation Behaviour of a Porous Si_2N_2O–ZrO_2 Composite Material
COLETTE O'MEARA, MAIKEN HEIM & ROBERT POMPE (Sweden)

329 Corrosion Resistance of Ceramic-coated Stainless Steel in a Br_2–O_2–Ar Atmosphere
MAKOTO SASAKI & TOSHIO HIRAI (Japan)

337 Borosilicate Coatings on Mild Steel Prepared from Aqueous Amine Solutions: A Comparison with the Alkoxide Routes
N. MALIAVSKI, E. TCHEKOUNOVA (Russia), P. INNOCENZI, D. FESTA, M. GUGLIELMI & L. MANCINELLI DEGLI ESPOSTI (Italy)

343 Effects of Composition Changes on the Crystallization Behaviour and Properties of SiO_2–Al_2O_3–CaO–MgO (Fe_2O_3–Na_2O–K_2O) Glass-Ceramics
V. K. MARGHUSSIAN & M. H. DAYI NIAKI (Iran)

349 Subsolidus Phase Relationships in the Systems Ln_2O_3–Si_3N_4–AlN–Al_2O_3 (Ln = Nd, Sm)
W. Y. SUN, D. S. YAN, L. GAO (China), H. MANDAL, K. LIDDELL & D. P. THOMPSON (UK)

357 Tape-casting: Relationship Between Organic Constituents and the Physical and Mechanical Properties of Tapes
M. DESCAMPS, G. RINGUET, D. LEGER & B. THIERRY (France)

363 Densification and Microstructure Development of Alumina/Y-TZP Composite Powder (Y-TZP-rich) Compacts
J. L. SHI & T. S. YEN (China)

371 Fabrication of Low-Voltage ZnO Varistors by a Two-Step Process
JOO-HWAN HAN, DONG-HEON LEE & DOH-YEON KIM (South Korea)

Number 5

377 Bridging Stress Relations for Ceramic Materials
T. FETT & D. MUNZ (Germany)

385 Statistical Determination of Surface Flaw Distributions in Brittle Materials
P. D. WARREN (UK)

395 Reliability of Alumina Ceramics: Effect of Grain Size
J. SEIDEL, N. CLAUSSEN & J. RÖDEL (Germany)

405 Vickers and Knoop Indentation Behaviour of Cubic and Partially Stabilized Zirconia Crystals
G. A. GOGOTSI, S. N. DUB, E. E. LOMONOVA & B. I. OZERSKY (Ukraine)

415 The Development of Microstructure in Silicon Nitride-Bonded Silicon Carbide
D. P. EDWARDS, B. C. MUDDLE, Y.-B. CHENG & R. H. J. HANNINK (Australia)

425 Room Temperature Tensile and Flexural Strength of Ceramics in AlN–SiC System
H. A. TOUTANJI (Puerto Rico), D. FRIEL, T. EL-KORCHI, R. N. KATZ, G. WECHSLER & W. RAFANIELLO (USA)

435 Thermal Conductivity Improvement of YAG Added AlN Ceramics in the Grain Boundary Elimination Process
M. KASORI & F. UENO (Japan)

445 On the Thermal Degradation of Lox-M Tyranno® Fibres
C. VAHLAS & M. MONTHIOUX (France)

455 Thermal Shock Resistance on Nextel/Silica–Zirconia Ceramic-Matrix Composites Manufactured by Freeze-Gelation
A. TWITTY, R. S. RUSSELL-FLOYD, R. G. COOKE & B. HARRIS (UK)

463 The Preparation, Characterization and Electrical Properties of Electroceramics made of Copper–Cobalt Manganite Spinel: $Mn_{2\cdot6-x}Co_{0\cdot4}Cu_xO_4 0 \leq x \leq 1$
R. LEGROS, R. METZ & A. ROUSSET (France)

469 Compaction and Sintering Behaviour of Sol–Gel Powders
Y. JORAND, M. TAHA, J. M. MISSIAEN (France) & L. MONTANARO (Italy)

479 The Packing Density of Binary Powder Mixtures
J. ZHENG, W. B. CARLSON & J. S. REED (USA)

Number 6

Review

485 Environmental Degradation of Zirconia Ceramics
S. LAWSON (UK)

503 Thermodynamic Assessment of the ZrO_2–$LaO_{1\cdot5}$ System
Y. DU, M. YASHIMA, T. KOURA, M. KAKIHANA & M. YOSHIMURA (Japan)

513 Creep Properties of Single Crystal Oxides Evaluated by a Larson–Miller Procedure
S. DENG & R. WARREN (Sweden)

521 Effect of Vapor Atmosphere on the Formation Reaction of $MSiO_3$ (M = Mg, Ca, Sr and Ba)
S. HAYASHI, K.-I. ISHIZU, S. KIKUCHI, K. OKADA & N. OTSUKA (Japan)

527 Reactive Formation of Coatings at Boron Carbide Interface with Ti and Cr Powders
P. MOGILEVSKY, E. Y. GUTMANAS (Israel), I. GOTMAN (USA) & R. TELLE (Germany)

537 Experimental Study of the Ti–B–C System Using LPCVD
M. Ä. GUIBAN & G. MALÉ (France)

551 On the Chemical Vapor Deposition of Si/B/C-Based Coatings in Various Conditions of Supersaturation
S. GOUJARD, L. VANDENBULCKE & C. BERNARD (France)

563 The Brazing of Si_3N_4 with Ni–Cr–Si Alloys
G. CECCONE, M. G. NICHOLAS, S. D. PETEVES, A. A. KODENTSOV, J. K. KIVILAHTI & F. J. J. VAN LOO (The Netherlands)

573 Transmission Electron Microscopy of Intergranular Regions of Corroded Silicon Nitride
A. D. STALIOS, J. LUYTEN (Belgium), F. L. RILEY (UK) & R. J. FORDHAM (The Netherlands)

581 Synthesis of α-Silicon Nitride Powder from a Polymeric Precursor
G. YU, M. J. EDIRISINGHE, D. S. FINCH, B. RALPH & J. PARRICK (UK)

591 Manufacture of Monolithic Ceramic Bodies from a Polysilazane Precursor
M. F. GONON (Ireland), G. FANTOZZI, M. MURAT & J. P. DISSON (France)

599 Carbothermal Preparation and Characterisation of Ca-α-sialon
J. W. T. VAN RUTTEN, R. A. TERPSTRA, J. C. T. VAN DER HEIJDE, H. T. HINTZEN & R. METSELAAR (The Netherlands)

Number 7

605 The Barrier Height Formation in ZnO Varistors
P. Q. MANTAS & J. L. BAPTISTA (Portugal)

617 Problems Associated with Imaging Resistive Barriers in $BaTiO_3$ PTC Ceramics Using the SEM Conductive Mode
J. D. RUSSELL & C. LEACH (UK)

623 Forming Pressure Dependence of the Ferroelectric Domain Structure in Green Barium Titanate Pellets
P. SARRAZIN, B. THIERRY & J. C. NIEPCE (France)

631 Characterization of $BaTiO_3$ Powder Obtained by a Chemical Route
C. PROUST, C. MIOT & E. HUSSON (France)

637 Thermal Spray Spinel Coatings on Steel Substrates: Influence of the Substrate Composition and Temperature
C. PETOT, M. DUCOS & G. PETOT-ERVAS (France)

643 Creep Crack Growth in Alumina with a Glassy Phase
G. MARTIN, T. FETT & D. MUNZ (Germany)

651 Acoustic Emission Monitoring of Damage Evaluation in Ceramics Submitted to Thermal Shock
F. MIGNARD, C. OLAGNON & G. FANTOZZI (France)

655 Mechanical Behavior of Porous Glasses Produced by Sintering of Spherical Particles
S. C. NANJANGUD & D. J. GREEN (USA)

661 Some Properties of Aluminium-Nitride Powder Prepared by Metal–Organic Chemical Vapour Deposition
K. KUBO, K. ITATANI, F. S. HOWELL, A. KISHIOKA & M. KINOSHITA (Japan)

667 Characterization and Surface Chemistry of Uncoated and Coated Silicon Nitride Powders
H. SCHMIDT, G. NABERT, G. ZIEGLER & H. GORETZKI (Germany)

675 Structural Evolution of Non-Crystalline SiC Precursors Prepared from Tetra-Methoxysilane (TMOS) and Phenol Resin
H. SCHNEIDER (Germany), C. JÄGER (Germany), A. MOSSET (France), H. TANAKA (Japan) & M. SCHMÜCKER (Germany)

683 A Polysilazane Precursor for Si–C–N–O Matrix Composites
M. F. GONON, S. HAMPSHIRE (Ireland), J. P. DISSON & G. FANTOZZI (France)

689 Study on the Solid Solubility of Al in the Melilite Systems $R_2Si_{3-x}Al_xO_{3+x}N_{4-x}$ with R = Nd, Sm, Gd, Dy and Y
P. L. WANG, H. Y. TU, W. Y. SUN, D. S. YAN (China), M. NYGREN & T. EKSTRÖM (Sweden)

697 Mechanical Properties of Hot-Pressed 12H Ceramics
H. X. LI, W. Y. SUN & D. S. YAN (China)

Number 8

703 Polymer-Derived Si-Based Bulk Ceramics, Part I: Preparation, Processing and Properties
RALF RIEDEL, MARTIN SEHER, JOACHIM MAYER & D. VINGA SZABÓ (Germany)

717 Polymer-Derived Si-Based Ceramics, Part II: Microstructural Characterisation by Electron Spectroscopic Imaging
JOACHIM MAYER, D. VINGA SZABÓ, MANFRED RÜHLE, MARTIN SEHER & RALF RIEDEL (Germany)

729 Injection Moulding of Silicon Carbide Using an Organic Vehicle Based on a Preceramic Polymer
T. ZHANG, J. R. G. EVANS & J. WOODTHORPE (UK)

735 Synthesis and Densification Behaviour of Bi-Based Superconducting Powder by Organic Precursor
A. TAMPIERI & G. CELOTTI (Italy)

741 Binder Distribution in Green Ceramic Foils
G. P. VAN DER BEEK, U. GONTERMANN-GEHL & E. KRAFCZYK (Germany)

759 Compaction and Sintering Behaviour of Zirconia Powders
M. TAHA, J. PALETTO, Y. JORAND, G. FANTOZZI, A. SAMDI, M. JEBROUNI & B. DURAND (France)

769 Mechanical Properties of a Partially Sintered Alumina
DALE HARDY & DAVID J. GREEN (USA)

777 The Interrupted Static Fatigue Test for Evaluating Threshold Stress Intensity Factor in Ceramic Materials: A Numerical Analysis
VINCENZO M. SGLAVO & DAVID J. GREEN (USA)

787 Preparation of Dispersed Zirconia Barium Aluminosilicate Composites
A. NORDMANN, Y.-B. CHENG & B. C. MUDDLE (Australia)

795 Ca-acceptors in Dielectric Ceramics Sintered in Reducive Atmospheres
D. F. K. HENNINGS & H. SCHREINEMACHER (Germany)

801 Interfacial Reaction in Carbon Fibre-Sialon Ceramic Composites
P. DUPEL & A. HENDRY (UK)

Number 9

811 Alumina of High Reliability by Centrifugal Casting
W. HUISMAN, T. GRAULE & L. J. GAUCKLER (Switzerland)

823 The Production of Reinforced Aluminium/Alumina Bodies by Directed Metal Oxidation
X. GU & R. J. HAND (UK)

833 Study of Mechanical and Physicochemical Properties of Polycrystalline Alumina Implanted with Titanium
F. HALITIM, S. PALETTO, G. FANTOZZI & D. TREHEUX (France)

841 Effect of Y_2O_3 Addition on Alumina-Hex Boron Nitride Composites
A. ABREAL, D. GOEURIOT, F. THEVENOT (France), M. LAGACE, B. GUEROULT & M. RIGAUD (Canada)

851 Surface Segregation and Morphology of Mg-Doped α-Alumina Powders
D. MONCEAU, C. PETOT, G. PETOT-ERVAS (France), J. W. FRASER, M. J. GRAHAM & G. I. SPROULE (Canada)

859 Quality Assessment of MgO Substrate Materials for High T_c Superconductor Thin Films Using Cathodoluminescence Microscopy
P. R. FLETCHER & C. LEACH (UK)

867 Electrical and Thermal Transport Properties of (La,Ca) $(Cr,Co)O_3$
R. KOC & H. U. ANDERSON (USA)

875 Analysis of the Isothermal Forced Flow Chemical Vapour Infiltration Process. Part I: Theoretical Aspects
Y. G. ROMAN, J. F. A. K. KOTTE & M. H. J. M. DE CROON (The Netherlands)

887 Analysis of the Isothermal Forced Flow Chemical Vapour Infiltration Process. Part II: Experimental Study
Y. G. ROMAN, M. H. J. M. DE CROON & R. METSELAAR (The Netherlands)

899 Influence of the Debinding Method on the Mechanical Properties of Plastic Formed Ceramics
T. CHARTIER, M. FERRATO & J.-F. BAUMARD (France)

905 The Accuracy of Failure Predictions Based on Weibull Statistics
S. L. FOK & J. SMART (UK)

909 The Efficient Integration of the Orientation Integral in Weakest Link Finite Element Postprocessors
S. L. FOK & J. SMART (UK)

913 Effect of Mullite–Zirconia Additions on the Creep Behaviour of High-Alumina Refractories
C. WOLF, R. KAUERMANN, H. HÜBNER (Germany), J. A. RODRIGUES & V. C. PANDOLFELLI (Brazil)

921 Yttria–Alumina–Silica Glasses with Addition of Zirconia
P. VOMACKA & O. BABUSHKIN (Sweden)

929 Thermal Shock Resistance of $KZr_2P_3O_{12}$–$SrZr_4P_6O_{24}$ Ceramics
B. ZHANG & J. GUO (China)

Number 10

935 Fast Firing of Alumina
D. E. GARCIA, J. SEIDEL, R. JANSSEN & N. CLAUSSEN (Germany)

939 Effect of Solid Solution Additives on the Sintering of Ultra-fine CeO_2 Powders
M. N. RAHAMAN (USA) & Y. C. ZHOU (China)

951 Grain Growth of Differently Doped Zirconia
J. A. ALLEMANN, B. MICHEL, H.-B. MÄRKI, L. J. GAUCKLER & E. M. MOSER (Switzerland)

959 Processing of Nano-Y–TZP/Al_2O_3 Composites. I: Preparation and Characterization of Nano-Y–TZP/Al_2O_3 Composite Powders
J. L. SHI, B. S. LI, M. L. RUAN & T. S. YEN (China)

967 Processing of Nano-Y–TZP/Al_2O_3 Composites. II: Compaction and Sintering Behaviour of Nano-Y–TZP/Al_2O_3 Composite Powders
J. L. SHI, J. H. GAO, B. S. LI & T. S. YEN (China)

975 Alumina/Zirconia Multilayer Composites Obtained by Centrifugal Consolidation
E. LUCCHINI & O. SBAIZERO (Italy)

983 Microstructure and Creep Properties of Alumina/Zirconia Ceramics
J. M. CALDERÓN-MORENO, A. R. DE ARELLANO-LÓPEZ, A. DOMÍNGUEZ-RODRÍGUEZ (Spain) & J. L. ROUTBORT (USA)

989 Influence of Whisker Reinforcement on the Creep Behaviour of Zirconia Matrices
R. BADDI, J. CRAMPON & R. DUCLOS (France)

997 Thermomechanical Stability of Nicalon Fibres in a Carbon Monoxide Environment
R. BODET (France), N. JIA & R. E. TRESSLER (USA)

1007 Effect of Gaseous Environment on the Corrosion of β-Sialon Materials
R. RAMESH, M. J. POMEROY (Ireland), H. CHU & P. K. DATTA (UK)

1015 Oxidation Behaviour of Yttrium and Neodymium Oxynitride Glasses
M. SEBAI, J. SJÖBERG, P. GOURSAT (France), E. NESTOR, R. FLYNN, R. RAMESH & S. HAMPSHIRE (Ireland)

1025 Thermal Properties and Devitrification Behaviour of $(2-x)CaO{\cdot}x/3Y_2O_3{\cdot}2SiO_2$ Glasses
A. COSTANTINI, F. BRANDA & A. BURI (Italy)

1031 Constitution of Porcelain Before and After Heat-Treatment. I: Mineralogical Composition
S. P. CHAUDHURI & P. SARKAR (India)

1037 Characterisation of the Join of Electric Discharge Pulse Welded Ceramics
J. G. P. BINNER, P. A. DAVIS, J. A. FERNIE (UK) & I. D. DUBOVETSKÜ (Ukraine)

1043 Joining of $Y_1Ba_2Cu_3O_{7-x}$ and $Pb(Zr, Ti)O_3$, and their Interfaces
S. SUGIHARA & H. FUJITANI (Japan)

Number 11

1047 Toughness of Damage Tolerant Continuous Fibre Reinforced Ceramic Matrix Composites
B. F. SØRENSEN (Denmark) & R. TALREJA (USA)

1061 On the Paradox Between Crack Bridging and Crack Interaction in Quasi-Brittle Materials
K. DUAN, Y.-W. MAI (Australia) & B. COTTERELL (Singapore)

1065 Influence of 1 vol% Ni_3Al Addition on Sintering and Mechanical Properties of Reaction-Bonded Si_3N_4
B. R. ZHANG (China) & F. MARINO (Italy)

1071 Preparation of Fine Amorphous Silicon Nitride Powder in the System SiH_4–Ar–NH_3
S. SAHU, Š. KAVECKÝ (Slovakia) & J. SZÉPVÖLGYI (Hungary)

1079 Surface Characterization of Chemically Treated Aluminium Nitride Powders
R. METSELAAR, R. REENIS, M. CHEN, H. GORTER & H. T. HINTZEN (The Netherlands)

1087 Carbothermal Synthesis of Aluminium Oxynitride (ALON) Powder: Influence of Starting Materials and Synthesis Parameters
J. ZHENG & B. FORSLUND (Sweden)

1101 At-Temperature Observation of Phase Development in Yttrium α-Sialon
A. ASHKIN, D. ASHKIN, O. BABUSHKIN & T. EKSTRÖM (Sweden)

1111 Zirconia as a Nucleating Agent in a Yttria–Alumina–Silica Glass
P. VOMACKA, O. BABUSHKIN & R. WARREN (Sweden)

1119 Crystallization of Metastable Tetragonal Zirconia from the Decomposition of a Zirconium Alkoxide Derivative
D. E. COLLINS, K. A. ROGERS & K. J. BOWMAN (USA)

1125 Moisture Sensitive Degradation in TiO_2–Y_2O_3–ZrO_2
A. E. HUGHES, H. ST JOHN (Australia), P. KOUNTOUROS & H. SCHUBERT (Germany)

1135 Dielectric Properties of the Mixed Aurivillius Phases $M^{II}Bi_8Ti_7O_{27}$ (M^{II} = Ca, Sr, Ba and Pb)
B. MAALAL, M. MANIER & J. P. MERCURIO (France)

1141 Structural and Electrical Properties of Iron Manganite Spinels in Relation with Cationic Distribution
T. BATTAULT, R. LEGROS & A. ROUSSET (France)

1149 Study of $Li_{1+x}Al_xTi_{2-x}(PO_4)_3$ for Li^+ Potentiometric Sensors
M. CRETIN, P. FABRY & L. ABELLO (France)

1157 AC-Conductivity Measurements on γ-Aluminium Oxynitride
H. X. WILLEMS, P. F. VAN HAL, R. METSELAAR & G. DE WITH (The Netherlands)

Number 12

1163 Dense Ceramics of $BaTiO_3$ Produced from Powders Prepared by a Chemical Process
C. MIOT, C. PROUST & E. HUSSON (France)

1171 Preparation of $BaTiO_3$ by the Hydrothermal Method
C.-T. XIA, E.-W. SHI, W.-Z. ZHONG & J.-K. GUO (People's Republic of China)

1177 Mechanical Behaviour of Partially Stabilized Zirconia Crystals with Terbia and Ceria Additives
G. A. GOGOTSI & D. Yu. OSTROVOY (Ukraine)

1185 Mechanial Property Characterization of a 9 mol% Ce–TZP Ceramic Material — I. Flexural Response
G. A. GOGOTSI, V. P. ZAVADA (Ukraine) & M. V. SWAIN (Australia)

1193 Wear Resistance of Stabilized Zirconias
A. MEDEVIELLE, F. THÉVENOT & D. TRÉHEUX (France)

1201 Constitution of Mullite Glasses Produced by Ultra-rapid Quenching of Plasma-sprayed Melts
M. SCHMÜCKER, H. SCHNEIDER (Germany), M. POORTEMAN, F. CAMBIER (Belguim) & R. MEINHOLD (New Zealand)

1207 Mechanical–Thermal Synthesis of Al_2O_3–Cr Composite Powders
D. OSSO, O. TILLEMENT, A. MOCELLIN, G. LE CAER (France), O. BABUSHKIN & T. LINDBÄCK (Sweden)

1213 The Solubility of Aluminium in Rare Earth Nitrogen Melilite Phases
K. S. CHEE, Y.-B. CHENG (Australia) & M. E. SMITH (Australia & UK)

1221 Phase Transformations in Sm ($\alpha + \beta$)-SIAION Ceramics during Post-sintering Heat Treatments
R. ZHAO & Y.-B. CHENG (Australia)

1229 Effect of Acid Treatment on the Formation of SiC Whiskers from Raw Rice Husks
R. V. KRISHNARAO & Y. R. MAHAJAN (India)

1235 The Complexity of the Matrix Microstructure in SiC-fiber-reinforced Glass Ceramic Composites
F. DOREAU, H. MAUPAS, D. KERVADEC, P. RUTERANA, J. VICENS & J.-L. CHERMANT (France)

1249 Contributor Index
1253 Contents of Volume 15

Journal of the European Ceramic Society

Papers Published in Volumes 13 and 14

Contents of Volume 13

Number 1

1 Editorial

3 Particulate Composites in the Al_2O_3–SiO_2–TiO_2 System by Infiltration Processing
S. J. LI, F. QUEYROUX & P. BOCH (France)

11 Deformation of Ceria-Stabilised Tetragonal Zirconia Ceramics in Scratch Experiments with a Sharp Indenter
A. K. MUKHOPADHYAY, T. LIU, M. V. SWAIN & Y.-W. MAI (Australia)

25 Gel Densification and Ceramic Sintering of ZrO_2–Al_2O_3 Composites
W. ZHANG & F. P. GLASSER (UK)

33 Centrifugal Slip Casting of Zirconia (TZP)
W. HUISMAN, T. GRAULE & L. J. GAUCKLER (Switzerland)

41 A Model for the Formation of Nanosized SiC Powders by Laser-Induced Gas-Phase Reaction
J.-M. LIHRMANN & M. CAUCHETIER (France)

47 Theoretical and Experimental Studies of Fiber Pull-Out of SiC Fiber-Reinforced Glasses
C. H. HSUEH (USA), H. TSUDA, M. ENOKI & T. KISHI (Japan)

53 Thermal Stability of Electroconductive TiN-Reinforced Silicon Oxynitride Composites
W. LIN & J.-M. YANG (USA)

61 Effect of the Substitution of Boron for Aluminium in the β-Eucryptite $LiAlSiO_4$ Structure
D. MAZZA & M. LUCCO-BORLERA (Italy)

67 Enhanced Densification of Yttria by Addition of Titanium Oxide
G. GASGNIER, J. F. BAUMARD, M. BONCOEUR & M. BOUGOIN (France)

73 Study of the Behaviour of Al_2TiO_5 Materials in Reducing Atmosphere by Spectroscopic Techniques
A. DURÁN, H. WOHLFROMM & P. PENA (Spain)

81 High-Permittivity Dielectric Ceramics with High Endurance
D. F. K. HENNINGS, B. SCHREINEMACHER & H. SCHREINEMACHER (Germany)

Number 2

89 Yttria–Ceria Stabilized Tetragonal Zirconia Polycrystals: Sintering, Grain Growth and Grain Boundary Segregation
M. M. R. BOUTZ, A. J. A. WINNUBST & A. J. BURGGRAAF (The Netherlands)

103 Low Temperature Superplastic Flow of Yttria Stabilized Tetragonal Zirconia Polycrystals
M. M. R. BOUTZ, A. J. A. WINNUBST, A. J. BURGGRAAF (The Netherlands), M. NAUER & C. CARRY (Switzerland)

113 Preparation and Characterization of Highly Pure Fine Zircon Powder
Y. SHI, X. X. HUANG & D. S. YAN (China)

121 The Dependence of the 'Relaxor' Type of Dielectric Response on Chemical Composition: A Study of Zirconium-Substituted Lead Magnesium Niobate
A. W. TAVERNOR & N. W. THOMAS (UK)

129 Deterioration of Cordierite Honeycomb Structure for Diesel Emissions Control
L. MONTANARO, A. BACHIORRINI & A. NEGRO (Italy)

135 Porosity Development during Removal of Organic Vehicle from Ceramic Injection Mouldings
H. M. SHAW & M. J. EDIRISINGHE (UK)

143 Glass-Ceramics from Fly Ash with Added Li_2O
R. CIOFFI, P. PERNICE, A. ARONNE, M. CATAURO & G. QUATTRONI (Italy)

149 Flaw Tolerance and Toughness Curves in Two-Phase Particulate Composites: SiC/Glass System
H. CAI, N. P. PADTURE, B. M. HOOKS & B. R. LAWN (USA)

159 Surface Toughening of Liquid Phase Sintered Silicon Carbide by Surface Nitridation
P. GREIL, H. G. BOSSEMEYER, A. KLÜNER (Germany), JIANG DONGLIANG & SHE JIHONG (China)

167 High-Temperature Oxidation of CVD β-SiC Part I. Experimental Study
J. RODRÍGUEZ-VIEJO (Spain), F. SIBIEUDE (France) & M. T. CLAVAGUERA-MORA (Spain)

177 High-Temperature Oxidation of CVD β-SiC Part II. Relation between Oxygen Diffusion Coefficients and Parabolic Rate Constants
J. RODRÍGUEZ-VIEJO (Spain), F. SIBIEUDE (France) & M. T. CLAVAGUERA-MORA (Spain)

Number 3

185 Recent Progress in the Fabrication of Ceramic Negative Temperature Coefficient Thermistors
A. ROUSSET, R. LEGROS & A. LAGRANGE (France)

197 Failure Behaviour of Al_2O_3 with Glassy Phase at High Temperatures
T. FETT, M. MIßBACH & D. MUNZ (Germany)

211 Sintering of Wet-Milled Centrifugal Cast Alumina
P. HIDBER, F. BAADER, T. GRAULE & L. J. GAUCKLER (Switzerland)

221 Processing of Aluminium Nitride Powder by the Tape-Casting Process
M. DESCAMPS, G. MOREAU, M. MASCART & B. THIERRY (France)

229 Aluminium Nitride Ceramics with High Thermal Conductivity from Gas-Phase Synthesized Powders
P. GREIL, M. KULIG, D. HOTZA, H. LANGE & R. TISCHTAU (Germany)

239 Improvement of Oxidation Behaviour of Dense Silicon Nitride by Surface Modification
C. TAUT, M. HERRMANN, G. GROßE, P. THIELE (Germany) & Y. GOGOTSI (Japan)

247 Sintering, Hardness and Indentation Fracture Toughness (K_{IC}) of Mullite and its Composite with 15 wt% X-Phase Sialon
C. C. ANYA & A. HENDRY (UK)

257 Surface Scaling in SiC-Whisker–Alumina under Flowing Hydrogen at 1300–1500°C
WANG DEQING & H. F. LOPEZ (USA)

265 Characterization of Agglomerate Strength of Coprecipitated Superfine Zirconia Powders
J. L. SHI, Z. X. LIN, W. J. QIAN & T. S. YEN (China)

275 Thermal Stability of Cordierite Catalyst Supports Contaminated by Fe_2O_3, ZnO and V_2O_5
P. SCARDI, N. SARTORI, A. GIACHELLO, P. P. DEMAESTRI & F. BRANDA (Italy)

Number 4

283 Editorial

285 Synthesis and Characterization of Nanocomposite Si/C/N Powders by Laser Spray Pyrolysis of Hexamethyldisilazane
N. HERLIN, M. LUCE, E. MUSSET & M. CAUCHETIER (France)

293 Neutron Diffraction Study of the Amorphous Phase Structure in Silicon Carbonitride Ceramics Obtained by Pyrolysis of a Polyvinylsilazane
J. DIXMIER, R. BELLISSENT, D. BAHLOUL & P. GOURSAT (France)

299 Microstructure and Mechanical Behaviour of Self-Reinforced Si_3N_4 and Si_3N_4–SiC Whisker Composites
F. ROSSIGNOL, P. GOURSAT, J. L. BESSON & P. LESPADE (France)

313 Influence of Oxidation in SO_2–Air Mixtures on the Room-Temperature Strength of Silicon Nitride
J.-B. VEYRET, R. J. FORDHAM (The Netherlands) & M. BILLY (France)

323 Study of the Interaction between Liquid Aluminum and Silicon Nitride
L. MOURADOFF, A. LACHAU-DURAND, J. DESMAISON, J. C. LABBE, O. GRISOT & R. REZAKHANLOU (France)

329 Compatibility between Molybdenum and Aluminium Nitride
P. LEFORT & R. QUERIAUD (France)

335 Effect of Oxygen Content on the Corrosion of AlN Powder in Diluted Acid Solution
F. BARBA, P. ORTEGA, J. BERMUDO, M. I. OSENDI & J. S. MOYA (Spain)

339 An In-situ Study of the Oxidation of AlN Layers Elaborated by LPCVD Using X-Ray Diffraction
C. LABATUT, D. KHARCHI, B. ASPAR, F. SIBIEUDE & B. ARMAS (France)

345 Transmission Electron Microscopy Studies of AlN Deposits
D. DORIGNAC, A. MAZEL, Y. KIHN, J. SEVELY, B. ASPAR, B. ARMAS, C. COMBESCURE (France)

355 High Temperature Compressive Tests of Aluminium Nitride: Mechanical Properties and Microstructure
I. MASSON, J. P. FEIEREISEN, J. P. MICHEL, A. GEORGE, A. MOCELLIN & P. BLUMENFELD (France)

365 Reactivity in the Al_2O_3–AlN–MgO System. The MgAlON Spinel Phase
A. GRANON, P. GOEURIOT, F. THEVENOT, J. GUYADER, P. L'HARIDON & Y. LAURENT (France)

371 Nanometric Boron Nitride Powders: Laser Synthesis, Characterization and FT-IR Surface Study
M. I. BARATON, L. BOULANGER, M. CAUCHETIER (France), V. LORENZELLI (Italy), M. LUCE, T. MERLE, P. QUINTARD & Y. H. ZHOU (France)

379 Mechanical Properties and Oxidation Behaviour of HIPed Hafnium Nitride Ceramics
M. DESMAISON-BRUT, J. MONTINTIN, F. VALIN & M. BONCOEUR (France)

Number 5

387 V_2O_5, Nb_2O_5 and Ta_2O_5 Doped Zirconia Ceramics
G. GRITZNER & C. PUCHNER (Austria)

395 Subeutectoid Precipitate Growth Activation Energies in Mg-PSZ
C. S. MONTROSS (Australia)

403 Preparations and Characterisations of Ceramics Based on Cesium Titanate
V. PERES, P. FABRY, F. GENET & P. DEHAUDT (France)

411 Reaction Sintering of Aluminium Titanate: I — Effect of MgO Addition
V. BUSCAGLIA, P. NANNI, G. BATTILANA, G. ALIPRANDI (Italy) & C. CARRY (Switzerland)

419 Reaction Sintering of Aluminium Titanate: II — Effect of Different Alumina Powders
V. BUSCAGLIA, P. NANNI, G. BATTILANA, G. ALIPRANDI (Italy) & C. CARRY (Switzerland)

427 High Temperature Fracture of a SiC Whisker-Reinforced Alumina in Air and Vacuum
T. HANSON, A. H. SWAN & R. WARREN (Sweden)

437 Sintering Behaviour of Tape-Cast CMAS Glass–Ceramic Reinforced with Alumina Chopped Fibers
C. LEONELLI, T. MANFREDINI, G. C. PELLACANI & D. S. BLUNDO (Italy)

441 Constitution of the γ-Alumina Phase in Chemically Produced Mullite Precursors
H. SCHNEIDER, D. VOLL, B. SARUHAN, M. SCHMÜCKER, T. SCHALLER & A. SEBALD (Germany)

449 The Determination of the Crystallite Size in Alumina with Submicron-sized Crystallites
F. K. VAN DIJEN (Germany), K. KAMPFER & H. HOFMANN (Switzerland)

453 Stresses Near the Free Edge of the Interface in Ceramic-to-Metal Joints
D. MUNZ & Y. Y. YANG (Germany)

461 Preparation of R–α′–β′-Sialons (R = Sm, Gd, Dy, Y and Yb) by Pressureless Sintering
H. WANG, W.-Y. SUN, H.-R. ZHUANG & T.-S. YEN (China)

467 The Oxidation Kinetics of β-Sialon Ceramics
J. PERSSON & M. NYGREN (Sweden)

Number 6

485 Tape Casting of Zirconia for Ion Conducting Membranes: A Study of Dispersants
H. RAEDER, C. SIMON (Norway), T. CHARTIER (France) & H. L. TOFTEGAARD (Denmark)

493 Single-Target Sputter Deposition and Post-Processing of Perovskite Lead Titanate Thin Films
D. REMIENS, J. F. TIRLET, B. JABER, H. JOIRE, B. THIERRY & C. MORIAMEZ (France)

501 Significance of Specimen Size for the K_R-Curve Behavior of Quasi-Brittle Materials
E. H. LUTZ (Germany), M. V. SWAIN & P. S. COOK (Australia)

509 Comparison of Evaluation Procedures for the Subcritical Crack Growth Parameter n
H. PETERLIK (Austria)

521 Characterization of Glass–Ceramic Corrosion and Durability
S. N. SALAMA & S. M. SALMAN (Egypt)

529 Development, Characterization and Oxidation Behaviour of Si_3N_4–Al_2O_3 Ceramics
J. VLEUGELS & O. VAN DER BIEST (Belgium)

545 Sintering of Magnesium Oxide Obtained from Sea Water
N. PETRIC, B. PETRIC, V. MARTINAC, N. BOGDANIĆ, M. MIROŠEVIĆ-ANZULOVIĆ & M. LABOR (Croatia)

551 β-Sialon Ceramics with TiN Particle Inclusions
T. EKSTRÖM & P.-O. OLSSON (Sweden)

561 Influence of Matrix and Interface on the Mechanical Properties of Unidirectional Carbon/Carbon Composites
P. W. M. PETERS, G. LÜDENBACH, R. PLEGER & R. WEIß (Germany)

571 Contributor Index

573 Contents of Volume 13

Contents of Volume 14

Number 1

1 HREM and AEM Studies of Yb_2O_3-Fluxed Silicon Nitride Ceramics with and without CaO Addition
H.-J. KLEEBE, J. BRULEY & M. RÜHLE (Germany)

13 Preparation and Grain Boundary Devitrification of Samarium α-Sialon Ceramics
Y.-B. CHENG (Australia) & D. P. THOMPSON (UK)

23 Low-Shrinkage Refractories by an Infiltration Technique
N. LEQUEUX, P. LAROSE, P. BOCH & N. BURKARTH (France)

29 Fabrication of Yttria/Niobium Laminar Composites by Plasma Spraying
M. BONCOEUR & G. SCHNEDECKER (France)

37 The Interactions between Silver and Zirconia Inclusions and their Effects on the Toughening Behaviour of $Al_2O_3/(Ag + ZrO_2)$ Composites
W. H. TUAN & W. R. CHEN (China)

45 Effect of SrO on Densification and Mechanical Properties of Reaction-Sintered Mullite–Zirconia
S. KINIKOĞLU & M. MARSOĞLU (Turkey)

53 System Si–Al–Mg–O: Thermodynamic Aspects of its Influence on the Oxidation Resistance of Silicon Carbide at High Temperature
A. DERRE, M. DUCARROIR & M. ALLIBERT (France)

61 Characterization of $MgSiO_3$, $CaMgSi_2O_6$ and $CaSiO_3$ Precursor Powders by ^{29}Si MAS NMR
S. HAYASHI, K. OKADA & N. OTSUKA (Japan)

67 X-Ray Absorption Spectroscopy Study of the Local Structure and the Chemical State of Yttrium in Polycrystalline α-Alumina
M. K. LOUDJANI & R. CORTÈS (France)

77 Phase Transformations and Control of Habit in Lyothermal Synthesis of α-Al_2O_3
A. KAISER, D. SPORN & H. BERTAGNOLLI (Germany)

85 Low-Temperature Aqueous Preparation of Barium Metatitanate Powders
P. NANNI, M. LEONI, V. BUSCAGLIA & G. ALIPRANDI (Italy)

91 Damage Investigations in Unidirectional SiC-MAS.L Composite Materials under Quasi-Static Tensile Loading
M. DRISSI-HABTI, T. DESPIERRES, J. FOUBERT & M. GOMINA (France)

Number 2

97 Reaction Bonding of Aluminum Oxide (RBAO) Composites: Processing, Reaction Mechanisms and Properties
N. CLAUSSEN, S. WU & D. HOLZ (Germany)

111 In-situ Scanning Acoustic Microscopy of Crack Bridging in Alumina
T. J. MARROW, G. A. D. BRIGGS & S. G. ROBERTS (UK)

117 Preparation of an Alumina Aerogel with SiC Whisker Inclusion
Y. MIZUSHIMA & M. HORI (Japan)

123 Synthesis of Yttrium Aluminum Garnet Precursor Powders by Homogeneous Precipitation
D. J. SORDELET, M. AKINC, M. L. PANCHULA, Y. HAN (USA) & M. H. HAN (Korea)

131 Influence of Formation pH and Grinding of Precursors on Compaction and Sintering Behaviours of 3 mol% Y_2O_3–ZrO_2
A. SAMDI, B. DURAND (France), A. DAOUDI (Morocco), F. CHASSAGNEUX, J. P. DELOUME, M. TAHA, J. PALETTO & G. FANTOZZI (France)

143 Prediction of Overall Shape of Sintered Alumina Compacts
N. ÖZKAN & B. J. BRISCOE (UK)

153 R-Curve Behaviour in Ceramic Composites Produced by Directed Metal Oxidation
J. RÖDEL, M. SINDEL, M. DRANSMANN, R. W. STEINBRECH & N. CLAUSSEN (Germany)

163 Liquid Phase Sintering, Electrical Conductivity, and Chemical Stability of Lanthanum Chromite Doped with Calcium and Nickel
G. M. CHRISTIE, P. H. MIDDLETON & B. C. H. STEELE (UK)

177 Oxidation Effects on the Mechanical Properties of 2D Woven C/SiC Composites
F. LAMOUROUX & G. CAMUS (France)

Number 3

189 Synthesis of Monodispersed Silica Powders I. Particle Properties and Reaction Kinetics
H. GIESCHE (USA)

205 Synthesis of Monodispersed Silica Powders II. Controlled Growth Reaction and Continuous Production Process
H. GIESCHE (USA)

215 Residual Carbon Detection in Barium Titanate Ceramics by Nuclear Reaction Technique
C. PROUST, E. HUSSON, G. BLONDIAUX & J. P. COUTURES (France)

221 Influence of High Pressures and Temperatures on the Behaviour of Bismuth-Based Superconductors
T. A. PRIKHNA, V. S. MELNIKOV, V. V. KOVYLYAEV, V. E. MOSHCHIL, S. N. DUB, A. P. SHAPOVALOV, P. A. NAGORNY, P. P. GORBIK & V. F. SOLOVYOV (Ukraine)

227 Grain Boundary Modifications of Manganese Ferrites
J. H. BOY & G. P. WIRTZ (USA)

237 Interactions in the Sol–Gel Processing of Alumina–Zirconia Composites
V. SRDIĆ & L. RADONJIĆ (Yugoslavia)

245 Chemical Vapour Infiltration of TiB_2 and TiN in Porous Al_2O_3
J. P. DEKKER, P. J. VAN DER PUT, H. J. VERINGA & J. SCHOONMAN (The Netherlands)

257 Thermal Fatigue Resistance of CVD SiC/C Functionally Gradient Material
M. SASAKI & T. HIRAI (Japan)

261 Yttrium Oxynitride Glasses: Properties and Potential for Crystallisation to Glass-Ceramics
S. HAMPSHIRE, E. NESTOR, R. FLYNN (Ireland), J.-L. BESSON, T. ROUXEL, H. LEMERCIER, P. GOURSAT, M. SEBAI (France), D. P. THOMPSON & K. LIDDELL (UK)

275 Release of Foreign Matter During Sintering of Aluminium Nitride and Silicon Nitride
T. REETZ (Germany), H. W. GÄGGELER & D. T. JOST (Switzerland)

Number 4

281 Editorial

283 Texture Formation in Al_2O_3 Substrates
A. BÖCKER, H. J. BUNGE, J. HUBER & W. KRAHN (Germany)

295 Preparation and Characterization of Mullite–Zirconia Composites from Various Starting Materials
T. KOYAMA, S. HAYASHI, A. YASUMORI & K. OKADA (Japan)

303 Processing and Mechanical Properties of a Silicon Carbide Platelet/Alumina Matrix Composite
Y.-S. CHOU & D. J. GREEN (USA)

313 Thermal Behavior of Polymer-Derived Ceramics. IV. Si–C–N–O Fibers from an Oxygen-Cured Polycarbosilazane
O. DELVERDIER, M. MONTHIOUX, D. MOCAER & R. PAILLER (France)

327 A New Approach for Slow Crack Growth Measurement
C. OLAGNON, J. CHEVALIER, F. SUDREAU & G. FANTOZZI (France)

337 Solute Effect on Grain Growth in Ceria Ceramics
D. D. UPADHYAYA, R. BHAT, S. RAMANATHAN, S. K. ROY (India), H. SCHUBERT & G. PETZOW (Germany)

343 Pressureless Sintering and Phase Relationship of Samarium α-Sialons
Y.-B. CHENG (Australia) & D. P. THOMPSON (UK)

351 The Effect of B_2O_3 Addition on the Direct Sintering of Barium Hexaferrite
O. T. ÖZKAN, H. ERKALFA & A. YILDIRIM (Turkey)

359 Factors Affecting the Sintering and the Electrical Properties of Sr-Doped $LaCrO_3$
P. H. DUVIGNEAUD, P. PILATE & F. CAMBIER (Belgium)

369 Thermopower and Electrical Conductivity of Single Crystal and Polycrystalline CoO
G. BORCHARDT (Germany), K. KOWALSKI (France), J. NOWOTNY (Australia), M. REKAS & W. WEPPNER (Germany)

377 Glass Formation in the System Y_2O_3–Al_2O_3–SiO_2 Under Conditions of Laser Melting
R. HARRYSSON & P. VOMACKA (Sweden)

Number 5

383 Progress in the Fabrication of Si_3N_4 Turbine Rotors by Pressure Slip Casting
O. LYCKFELDT, E. LIDÉN, M. PERSSON, R. CARLSSON & P. APELL (Sweden)

397 The Design of a Circulating Fluid Bed Reactor for the Carbothermal Synthesis of Silicon Nitride
F. K. VAN DIJEN (Germany)

403 A Surface Study on Adsorption of Lignosulphonate on Mixed Si_3N_4–Y_2O_3 Powder Dispersions
H. FAGERHOLM, L.-S. JOHANSSON & J. B. ROSENHOLM (Finland)

411 Nitridation of SiC for the Production of SiC–Si_3N_4 Nanocomposites
E. GOMEZ, T. GÓMEZ-ACEBO, J. ECHEBERRÍA, I. ITURRIZA & F. CASTRO (Spain)

419 Fine SiC Inclusions and Grain Boundary Phases in Pressureless Sintered SiAlON
W.-C. J. WEI (Taiwan) & J. W. HALLORAN (USA)

427 Structure and Properties of Interlayers in Polymer-Derived C/SiC Composites
R. OSTERTAG, T. HAUG, J. WOLTERSDORF, E. PIPPEL, A. HÄHNEL & R. SCHNEIDER (Germany)

441 Thermal and Elastic Properties of Alumina–Silicon Carbide Whisker Composites
L. FABBRI, E. SCAFÈ & G. DINELLI (Italy)

447 The Brittle/Ductile Transition in Cubic Stabilised Zirconia
T. J. MARROW, S. G. ROBERTS & A. K. PEARCE-HIGGINS (UK)

455 The Effect of Boria and Titania Addition on the Crystallization and Sintering Behavior of Li_2O–Al_2O_3–$4SiO_2$ Glass
Y.-M. SUNG, S. A. DUNN & J. A. KOUTSKY (USA)

463 Temperature-Stable Dielectric Materials in the System $BaTiO_3$–Nb_2O_5–Co_3O_4
D. F. K. HENNINGS & B. S. SCHREINEMACHER (Germany)

473 An Initial Stage Model for the Sintering of Constrained Polycrystalline Thin Films
D. R. CARROLL & M. N. RAHAMAN (USA)

Number 6

481 On the Mechanism of Delamination Fracture of $BaTiO_3$-based PTC Thermistors
C. DEWITTE, R. ELST & F. DELANNAY (Belgium)

493 An Evaluation of Ce–Pr Oxides and Ce–Pr–Nb Oxides Mixed Conductors for Cathodes of Solid Oxide Fuel Cells: Structure, Thermal Expansion and Electrical Conductivity
M. NAUER (UK), CH. FTIKOS (Greece) & B. C. H. STEELE (UK)

501 Electrical Conductivity and Thermal Expansion of Bi_2O_3 Doped with Pr
CH. FTIKOS (Greece) & B. C. H. STEELE (UK)

505 Crystallite Growth Characteristics in Superfine Zirconia Powders and Compacts
J. L. SHI & T. S. YEN (China)

511 Mullite Formation by Reaction Sintering of Quartz and α-Al_2O_3—A TEM Study
M. SCHMÜCKER, W. ALBERS & H. SCHNEIDER (Germany)

517 Glass–Ceramic from Fly Ash with Added MgO and TiO_2
R. CIOFFI, P. PERNICE, A. ARONNE, M. CATAURO & G. QUATTRONI (Italy)

523 Mechanical Behaviour and Reliability of Sintered Clinker Portland
J. M. TORRALBA, L. E. G. CAMBRONERO & J. M. RUIZ-PRIETO (Spain)

529 Uniaxial Tensile and Creep Behaviour of an Alumina Fibre-Reinforced Ceramic Matrix Composite: I. Experimental Study
F. LAMOUROUX, M. STEEN & J. L. VALLÉS (The Netherlands)

539 Uniaxial Tensile and Creep Behaviour of an Alumina Fibre-Reinforced Ceramic Matrix Composite: II. Modelling of Tertiary Creep
F. LAMOUROUX, J. L. VALLÉS & M. STEEN (The Netherlands)

549 Liquid-Phase Hot-Pressing and WC-Particle Reinforcement of SiC–Si Composites
B. R. ZHANG (China), F. MARINO & M. FERRARIS (Italy)

557 Calculations of Chemical Equilibria in the Mo–B–N System
E. BENKO & A. WYCZESANY (Poland)

563 Contributor Index

565 Contents of Volume 14